ACTA METALLURGICA

Board of Governors

Dr. W. Boas

Professor D. S. Clark
Professor Ulrich Dehlinger
Dr. C. H. Lorig
Professor R. Maddin
Professor G. W. Rathenau
Professor R. L. Sproull

Mr. G. Macdonald Young

Dr. J. H. Hollomon, *Secretary-Treasurer*

Editor

Professor Bruce Chalmers, Division of Engineering and Applied Physics,
Harvard University, Cambridge, Massachusetts, U.S.A.

Assistant to the Editor

Mrs. K. K. Shanahan

Associate Editors

Professor N. Petch (*Great Britain*)
Professor P. Laurent (*France*)
Professor P. Coheur (*Belgium*)
Professor W. G. Burgers (*Holland*)
Professor Väinö Hovi (*Finland*)
Professor G. H. H. Wasserman (*Germany*)
Professor E. Rudberg (*Sweden*)
Dr. W. Boas (*Australia*)
Professor Antonio Scortecci (*Italy*)
Professor Seiji Kaya (*Japan*)
Professor F. R. N. Nabarro (*South Africa*)

Business Manager: Mr. D. J. Raymond

Business Office: Pergamon Press Inc., *Acta Metallurgica*, 122 East 55th Street, New York 22, N.Y.

VOL.
8
1960

The cost of subscription is $10.00 (U.S.) to members of the Sponsoring Societies, $15.00 to members of Co-operating Societies and $25.00 to individuals who are not members of either. Payment, which must be made in advance, may be made through a sponsoring or co-operating society, or direct to the business office of ACTA METALLURGICA. Changes of address should be sent to the Business Office. Back numbers are available from the Business Manager at the following rates:

All volumes (Vols. 1 through 8, 1953–1960): $28.00 Agency discount 10%

Single issues: Vols. 1–4 (bi-monthly) $6.00 per issue

Vols. 5–8 (monthly) $3.00 per issue

VOLUME 8
1960

CONTENTS OF VOLUME EIGHT

VOL.
8
1960

NUMBER 1

Dislocation etch pits and plastic deformation in calcite — R. E. Keith and J. J. Gilman — 1
Twinning and fracture of single crystals of 3% silicon iron — D. Hull — 11
Croissance des barbes de sulfure d'argent — J. Drott — 19
The heats of formation of solid nickel–copper and nickel–gold alloys — R. A. Oriani and W. K. Murphy — 23
Grain-boundary energies in gold–copper alloys — J. E. Hilliard, M. Cohen and B. L. Averbach — 26
Solution hardening by interaction of impurity gradients and dislocations — R. L. Fleischer — 32
The contribution of atmosphere locking to the strain-ageing of low carbon steels — D. V. Wilson and B. Russell — 36

Letters to the Editor

Heterogeneites structurales des couches superficielles de l'alliage magnetique Mumétal chauffé dans l'air — P. A. Jacquet — 47
Effect of vacancy condensation on the corrosion susceptibility of subgrain boundaries in aluminium — O. P. Arora and M. Metzger — 49
On the kinetics of irreversible hydrogen embrittlement — L. C. Weiner — 52
Entropy of long range order in Cu_3Au and Ni_3Fe — V. Hovi and K. Mansikka — 53
A discussion of "self-diffusion and inter-diffusion in gold–nickel alloys": A correlation with absolute rate theory — R. W. Armstrong, J. P. Hirth, and G. M. Pound — 55
Interstitial atoms in cold worked aluminum — M. E. Straumanis and T. Ejima — 56
On the growth of germanium dendrites — R. S. Wagner — 57
Discussion of "experimental evidence of boundary migration" — C. G. Dunn and J. L. Walter — 60
Erratum — A. C. Damask and G. J. Dienes — 64

NUMBER 2

The application of the Rowland mechanism to the problem of the nucleation of secondary crystals in cube-texture copper — C. A. Verbraak — 65
Isothermal reversion of the b.c.c. → h.c.p. transformation induced in β' AgCd by mechanical deformation — D. B. Masson — 71
The cobalt transformation — C. R. Houska, B. L. Averbach and M. Cohen — 81
The life history of individual slip lines during the plastic deformation of α-brass single crystals — J. T. Fourie — 88
Subcrystals in large vapour-grown crystals of tungsten — G. D. Rieck and H. A. C. M. Bruning — 97
Polygonization of 31% alpha-brass — V. Y. Doo — 106
Diffusion of antimony in copper single crystals — M. C. Inman and L. W. Barr — 112
Oxide nuclei and dislocations — F. W. Young, Jr — 117

Lettres au Rédacteur

The formation of (110) [001] recrystallization texture in a cold-rolled and annealed (110) [001] crystal of silicon-iron — Hsun Hu — 124
Discussion of paper entitled: "The formation of (110) [001] recrystallization texture in a cold-rolled and annealed (110) [001] crystal of silicon-iron" by Hsun Hu — J. L. Walter, W. R. Hibbard and C. G. Dunn — 126
Contribution of interface couples to the energy of a dislocation — F. A. McClintock — 127
Activation energy for deformation of metals at low temperatures — H. Conrad and H. Wiedersich — 128
Blue-brittle Armco ingot iron — A. W. Sleeswyk — 130
The effect of segregation on the solute diffusion enhancement due to the presence of dislocations — A. J. Mortlock — 132
Nucleation in recrystallization phenomena — R. A. Oriani — 134
Shear in zinc bicrystals — J. M. Galligan, S. Feuerstein and W. Luhman — 135

NUMBER 3

Effect of pressure on intermetallic layer growth — L. S. Castleman — 137
Dispersed particle hardening of aluminum–copper alloy single crystals — D. Dew-Hughes and W. D. Robertson — 147
The mechanism of hardening in aged aluminum–copper alloys — D. Dew-Hughes and W. D. Robertson — 156
The effect of solute precipitation on the resistivity of alloys — W. A. Harrison — 168
The interaction of dislocations and precipitates — R. B. Nicholson, G. Thomas and J. Nutting — 172
An X-ray structure investigation of the liquids of sodium, potassium and sodium–potassium alloys — B. R. Orton, B. A. Shaw and G. I. Williams — 177
Tensile deformation of aluminum single crystals at low temperatures — W. F. Hosford, Jr., R. L. Fleischer and W. A. Backofen — 187
Sur l'interaction d'une dislocation fixe et d'une dislocation mobile dans son plan de glissement — G. Saada — 200
Segregation in homogeneous alloys during sintering — G. C. Kuczynski, G. Matsumura and B. D. Cullity — 209

Briefe an den Herausgeber

Anisotropy in ultrasonic attenuation in single crystal aluminum — N. G. Einspruch — 216

NUMBER 4

A resistometric study of pre-precipitation in Al–10% Zn — C. Panseri and T. Federighi — 217
The analysis of the crystallography of martensitic transformations by the method of prism matching — B. A. Bilby and F. C. Frank — 239
Thermodynamics of formation of copper–magnesium and nickel–magnesium compounds from vapour pressure measurements — J. F. Smith and J. L. Christian — 249
Intermetallic phases in the aluminium–manganese binary system — M. A. Taylor — 256

Letters to the Editor

Reply to Discussion "Absolute grain boundary energies in copper" — M. A. Gjostein — 263
A new interpretation of the substructure of electropolished aluminium surfaces — M. Gy. Holló — 265
The breakdown of the protective oxide film on transition metal alloys — W. W. Smeltzer — 268
The effect of hydrostatic pressure on the potency of martensitic embryos — L. Kaufman, A. Leyenaar and J. S. Harvey — 270
Sur l'origine du processus de germination dans les reactions d'oxydation superficielle des metaux — J. Bénard — 272
Stability of retained austenite on ageing — E. G. Ramachandran and C. Dasarathy — 274
Reply to Discussion "Shear along grain boundaries of an aluminium–10 per cent zinc alloy deformed at room temperature" — N. J. Grant — 275

NUMBER 5

Kinetics of clustering in some aluminum alloys — D. Turnbull, H. S. Rosenbaum and H. N. Treaftis — 277
The interaction of parallel edge dislocation with a simple tilt dislocation wall — James C. M. Li — 296
Geometry and kinetics of the polygonization of sodium chloride — S. Amelinckx and R. Strumane — 312
Long-range order in Fe rich Fe–Al alloys—I. A zeroth approximation calculation of order with application to the phase diagram — P. S. Rudman — 321
Yield and fracture in polycrystalline niobium — M. A. Adams, A. C. Roberts and R. E. Smallman — 328
The stored energy of cold work and its relation to work softening — A. L. Titchener and M. B. Bever — 338

Lettres au Rédacteur

Application of Stroh's theory to intercrystalline creep cracking — C. W. Weaver — 343

NUMBER 6

Polyslip in single crystals — U. F. Kocks — 345
Some observations of slip lines on deformed copper whiskers — P. Charsley — 353
Oxidation of evaporated magnesium films — M. S. Cohen — 356
Crystallization from dilute metal solutions — L. Benjamin and R. F. Strickland-Constable — 362
Transformations in the β and ζ phases of the silver–zinc alloys — W. J. Kitchingman and J. I. Buckley — 373
The kinetics of wustite scale formation on iron — W. W. Smeltzer — 377
Sur la trempe des lacunes dans un polycristal à grains fins — A. Blandin et J. Friedel — 384
A study of solute diffusion in liquid tin — C. H. Ma and R. A. Swalin — 388
Elastic constants of copper–nickel alloys — R. E. Schmunk and Charles S. Smith — 396

Briefen den Herausgeber

Electron metallographic observations on the formation of fatigue cracks — H. A. Bendler and W. A. Wood — 402
Regular pile-up of dislocations in α-iron — E. Smith — 403

NUMBER 7

The crystallography of the cubic to orthorhombic transformation in the alloy AuCu — R. Smith and J. S. Bowles — 405
The thermodynamics of the chromium–iron system — O. Kubaschewski and G. Heymer — 416
The initiation of slip in silicon–iron — J. Holden — 424
Energy of the order–disorder transformation in AuCu — R. L. Orr, J. Luciat-Labry and R. Hultgren — 431
Thermodynamic analysis of binary liquid alloys of group IIB metals—III. The solutions of zinc, cadmium, indium, tin, thallium, lead and bismuth in mercury — O. J. Kleppa — 435
An X-ray diffraction study of irradiated molybdenum — D. L. Gray and W. V. Cummings, Jr. — 446
The influence of strain amplitude on the work hardening of copper crystals in alternating tension and compression — D. S. Kemsley and M. S. Paterson — 453
The contribution of precipitation to strain ageing in low carbon steels — D. V. Wilson and B. Russell — 468
Interactions between glide dislocations in a double pile-up in α-iron — Y. T. Chou, F. Garofalo and R. W. Whitmore — 480
Heats of formation of solid Au–Cu alloys — R. L. Orr — 489

Letter to the Editor

Cold work and subsequent electrical resistivity increases in pure aluminum — H. R. Peiffer and F. Stevenson — 494
Erratum — 496

NUMBER 8

An effect of impurity atoms on the energy relationship of (100) and (110) surfaces in high purity silicon iron — J. L. Walter and C. G. Dunn — 497
Effect of hydrogen on stability of micro cracks in iron and steel — F. Garofalo, Y. T. Chou and V. Ambegaokar — 504
Untersuchung des Gleitlinienbildes kubisch-flächenzentrierter Einkristalle — S. Mader und A. Seeger — 513

Sulfur segregation at α-iron grain boundaries—I. N. G. Ainslie, R. E. Hoffman and A. U. Seybolt 523
Sulfur segregation at α-iron grain boundaries—II. N. G. Ainslie, V. A. Phillips and D. Turnbull 528
Low temperature calorimetric measurements on isothermal aging of Al–Ag W. DeSorbo 539
Yielding and work-hardening in alpha-brasses P. Feltham and G. J. Copley 542
Annealing of X-ray induced surface hardening in NaCl R. Cuypers and S. Amelinckx 551
Theory of crystal growth and interface motion in crystalline materials John W. Cahn 554
Some elastic properties of an edge dislocation wall James. C. M. Li 563
The ω-phase in zirconium base alloys B. A. Hatt and J. A. Roberts 575

Lettre au Redacteur

Low-temperature stress-relaxation peaks in plastically deformed polycrystalline niobium R. H. Chambers and J. Schultz 585

NUMBER 9

A study of elongation and ageing in Al–4% Cu and Al–4% Cu 0.05% In crystals J. M. Silcock 589
Effects of non-uniformities on the hardening of crystals R. L. Fleischer 598
The thermal diffusion of carbon in α and γ iron P. Shewmon 605
Criteria for yielding of dispersion-strengthened alloys G. S. Ansell and F. V. Lenel 612
The mechanism of oxidation of iron in carbon monoxide–carbon dioxide mixtures F. Pettit, R. Yinger and J. B. Wagner, Jr. 617
Initial stages of plastic deformation in copper and aluminum A. R. Rosenfield and B. L. Averbach 624
Self-diffusion of alpha-iron in a large temperature gradient W. G. Brammer 630
Phase transformations in cerium C. J. McHargue and H. L. Yakel, Jr. 637
Evaporation and thermal etching E. D. Hondros and A. J. W. Moore 647
Dislocations and brittle fracture in elemental and compound semiconductors M. S. Abrahams and L. Ekstrom 654

Briefen den Herausgeber

Knight shifts in potassium, indium and yttrium metals W. H. Jones, Jr., T. P. Graham and R. G. Barnes 663
Residual resistance of copper annealed in an O_2 atmosphere R. L. Dolecek and D. J. Schultz 664
Effect of grain size on crack propagation J. J. Gilman 665
Athermal stabilization of austenite E. G. Ramachandran and C. Dasarathy 666

VOL.
8
1960

NUMBER 10

Discontinuous mode of dissolution of a β phase precipitate into α Cu–Cd solid solutions M. S. Sulonen 669
The lattice spacing relationships in close-packed α and ζ phases based on gold T. B. Massalski and H. W. King 677
Lattice spacing relationships and the electronic band structure of close-packed α and ζ phases of gold-based alloys T. B. Massalski and H. W. King 684
Irradiation hardening in copper and nickel M. J. Makin and F. J. Minter 691
Diffusion dans le système uranium–titane Y. Adda et J. Philibert 700
Precipitation in gold–platinum alloys—I. Thermodynamics L. J. van der Toorn and T. J. Tiedema 711
Precipitation in gold–platinum alloys—II. Influence of the spinodal curve on the rate and the mechanism of the precipitation process L. J. van der Toorn 715

Letters to the Editor

Note on the interaction of interstitially dissolved carbon atoms in α-iron A. J. Bosman, P. E. Brommer, L. C. H. Eykelenboom, C. J. Schinkel and G. W. Rathenau 728
Hydrogen and austenite stabilization E. G. Ramachandran and C. Dasarathy 729
On the temperature dependence of flow stress in quenched aluminum crystals L. E. Tanner 730
Method for measuring the free energy of a solid surface M. J. Fraser 732
Mechanical twinning in thin evaporated gold films A. Catlin, W. P. Walker and K. R. Lawless 734
Discussion of Williams' comments on "The influence of grain size on the stored energy and mechanical properties of copper" (Part 1) L. M. Clarebrough, M. E. Hargreaves and M. H. Loretto 736
(Part 2) J. F. Nicholas 737
The low temperature tensile properties of niobium A. A. Johnson 737
Observations on the work-hardening of zinc crystals in alternating tension and compression D. S. Kemsley 740
Identification of the diffusion of iron ions in magnetite employing markers D. Fuller 743
Erratum 745

NUMBER 11

Kinetics of later stages of clustering in Al–Cu alloy D. Turnbull and R. L. Cormia 747
The influence of an electric potential gradient on the thermal etching of silver E. D. Hondros and A. J. W. Moore 751
The Oxidation of titanium in oxygen at high temperatures J. Stringer 758
Contribution of dislocation line tension and the density of the solute atmosphere to the yield point in strain aged ingot iron T. Mura and J. O. Brittain 767
Dispersion hardening W. H. Meiklejohn and R. E. Skoda 773
A theory of diffusion of impurities in pure silver J. M. Tobin 781
On the effective surface energy involved in the brittle fracture of 70/30 brass H. Nichols and W. Rostoker 788
Cottrell locking and the flow stress in iron H. Conrad and G. Schoeck 791

The influence of impurities on the annealing of nickel after cold work
L. M. Clarebrough, M. E. Hargreaves, M. H. Loretto and G. W. West 797
Note on the thermodynamics of the liquidus and solidus curves in systems with complete solid solubility; the system silver–gold O. J. Kleppa 804

Lettres au Rédacteur

Porosity in plastically deformed single crystals F. D. Rosi and M. S. Abrahams 807
Twinning in iron E. Bull Simonsen 809
The effect of pressure on the second stage parabolic rate in the oxidation of titanium J. Stringer 810
The structure of slip band extrusion by transmission electron microscopy
P. J. E. Forsyth and C. A. Stubbington 811
Migration energies in quenched and deformed gold M. Meshii and J. W. Kauffman 815
On Meiklejohn and Skoda's letter "Dispersion Hardening" D. Dew-Hughes 816
Thermal cycling creep of α-uranium A. C. Roberts 817
Use of the marker method in studying the mechanism of oxidation of metals
S. Mrowec and T. Werber 819

NUMBER 12

Magnetic analysis of the precipitation of iron from beta brass A. E. Berkowitz and P. J. Flanders 823
Thermodynamics of the solid solutions of mercury in silver and gold
H. W. Rayson and W. A. Alexander 833
Sur le durcissement du a la recombinaison des dislocations G. Saada 841
Ductile–brittle transition in alpha brass H. Nichols and W. Rostoker 848
The growth of twins in tin single crystals as observed by transmission electron microscopy
J. T. Fourie, F. Weinberg and F. W. C. Boswell 851
Gaseous decarburization of white cast irons J. Burke, J. Bell and D. R. Bourne 864
On the determination of diffusion coefficients in chemical diffusion R. W. Balluffi 871
Electron-microscopic study of recrystallization twins in copper E. Votava and H. Hatwell 874
Influence of plastic deformation on the annealing of quenched gold S. Yoshida and J. S. Koehler 878
Dilute solutions in alloys C. B. Alcock and F. D. Richardson 882
Activities of manganese in solid platinum
K. P. Abraham, M. W. Davies, J. L. Barton and F. D. Richardson 888

Briefen den Herausgeber

Stress induced ordering in gold–silver alloys T. J. Turner and G. P. Williams Jr. 891
The orientation of martensite in austenite H. M. Otte 892
Effect of zone-refining and orientation on the hardness of high purity rhenium
A. Lawley and R. Maddin 896
Entstehung und Orientierung von Wolfram-Whiskern H. Ahlborn and G. Wassermann 897
Growth substructures in weld metal F. A. C. Calvo, K. P. Bentley and R. G. Baker 898
Twinning in vanadium C. J. McHargue 900
The use of lattice spacings data to evaluate the effective valency of transition metals in Ag-based h.c.p. phases T. B. Massalski and H. W. King 900
Electron microscopic investigation of the phase transformation of thin cobalt samples E. Votava 901

AUTHOR INDEX

Abraham, K. P. 888
Abrahams, M. S. 654, 807
Adams, M. A. 328
Adda, Y. 700
Ahlborn, H. 897
Ainslie, N. G. 523, 528
Alcock, C. B. 882
Alexander, W. A. 833
Ambegaokar, V. 504
Amelinckx, S. 312, 551
Ansell, G. S. 612
Armstrong, R. W. 55
Arora, O. P. 49
Averbach, B. L. 26, 81, 624
Backofen, W. A. 187
Baker, R. G. 898
Balluffi, R. W. 871
Barnes, R. G. 663
Barr, L. W. 112
Barton, J. L. 888
Bell, J. 864
Bénard, J. 272
Bendler, A. H. 402
Benjamin, L. 362
Bentley, K. P. 898
Berkowitz, A. E. 823
Bever, M. B. 338
Bilby, B. A. 239
Blandin, A. 384
Bosman, A. J. 728
Boswell, F. W. C. 851
Bourne, D. R. 864
Bowles, J. S. 405
Brammer, W. G. 630
Brittain, J. O. 767
Brommer, P. E. 728
Bruning, H. A. C. M. 97
Buckley, J. I. 373
Burke, J. 864
Cahn, J. W. 554
Calvo, F. A. C. 898
Castleman, L. S. 137
Catlin, A. 734
Chambers, R. H. 585
Charsley, P. 353
Chou, Y. T. 480, 504
Christian, J. L. 249
Clarebrough, L. M. 736, 797
Cohen, M. 26, 81
Cohen, M. S. 356
Conrad, H. 128, 791
Copley, G. J. 542
Cormia, R. L. 747
Cullity, B. D. 209
Cummings, W. V., Jr. 446
Cuypers, R. 551
Damask, A. C. 64
Dasarathy, C. 274, 666, 729
Davies, M. W. 888
Desorbo, W. 539
Dew-Hughes, D. 147, 156, 816
Dienes, G. J. 64
Dolecek, R. L. 664
Doo, V. Y. 106
Drott, J. 19
Dunn, C. G. 60, 126, 497
Einspruch, N. G. 216
Ejima, T. 56
Ekstrom, L. 654
Eykelenboom, L. C. H. 728
Federighi, T. 217
Feltham, P. 542
Feuerstein, S. 135
Flanders, P. J. 823
Fleischer, R. L. 32, 187, 598
Forsyth, P. J. E. 811
Fourie, J. T. 88, 851
Frank, F. C. 239
Fraser, M. J. 732
Friedel, J. 384
Fuller, D. 743
Galligan, J. M. 135
Garofalo, F. 480, 504
Gilman, J. J. 1, 665
Gjostein, M. A. 263
Graham, T. P. 663
Grant, N. J. 275
Gray, D. L. 446
Hargreaves, M. E. 736, 797
Harrison, W. A. 168
Harvey, J. S. 270
Hatt, B. A. 575
Hatwell, H. 874
Heymer, G. 416
Hibbard, W. R. 126
Hilliard, J. E. 26
Hirth, J. P. 55
Hoffman, R. E. 523
Holden, J. 424
Holló, M. Gy. 265
Hondros, E. D. 647, 751
Hosford, W. F., Jr. 187
Houska, C. R. 81
Hovi, V. 53
Hsun Hu, 124
Hull, D. 11
Hultgren, R. 431
Inman, M. C. 112
Jacquet, P. A. 47
Johnson, A. A. 737
Jones, W. H., Jr. 663
Kauffman, J. W. 815
Kaufman, L. 270
Keith, R. E. 1
Kemsley, D. S. 453, 740
King, H. W. 677, 684, 900
Kitchingman, W. J. 373
Kleppa, O. J. 435, 804
Kocks, U. F. 345
Koehler, J. S. 878
Kubaschewski, O. 416
Kuczynski, G. C. 209
Lawless, K. R. 734
Lawley, A. 896
Lenel, F. V. 612
Leyenaar, A. 270
Li, J. C. M. 296, 563
Loretto, M. H. 736, 797
Luciat-Labry, J. 431
Luhman, W. 135
Ma, C. H. 388
McClintock, F. A. 127
McHargue, C. J. 637, 900
Maddin, R. 896
Mader, S. 513
Makin, M. J. 691
Mansikka, K. 53
Massalski, T. B. 677, 684, 900
Masson, D. B. 71
Matsumura, G. 209
Meiklejohn, W. H. 773
Meshii, M. 815
Metzger, M. 49
Minter, F. J. 691
Moore, A. J. W. 647, 751
Mortlock, A. J. 132
Mrowec, S. 819
Mura, T. 767
Murphy, W. K. 23
Nicholas, J. F. 737
Nichols, H. 788, 848
Nicholson, R. B. 172
Nutting, J. 172
Oriani, R. A. 23, 134
Orr, R. L. 431, 489
Orton, B. R. 177
Otte, H. M. 892
Panseri, C. 217
Paterson, M. S. 453
Peiffer, H. R. 494
Pettit, F. 617
Philibert, J. 700
Phillips, V. A. 528
Pound, G. M. 55
Ramachandran, E. G. 274, 666, 729
Rathenau, G. W. 728
Rayson, H. W. 833
Richardson, F. D. 882, 888
Rieck, G. D. 97
Roberts, A. C. 328, 817
Roberts, J. A. 575
Robertson, W. D. 147, 156
Rosenbaum, H. S. 277
Rosenfield, A. R. 624
Rosi, F. D. 807
Rostoker, W. 788, 848
Rudman, P. S. 321
Russell, B. 36, 468
Saada, G. 200, 841
Schinkel, C. J. 728
Schmunk, R. E. 396
Schoeck, G. 791
Schultz, D. J. 664
Schultz, J. 585
Seeger, A. 513
Seybolt, A. U. 523
Shaw, B. A. 177
Shewmon, P. 605
Silcock, J. M. 589
Simonsen, Bull, E. 809
Skoda, R. E. 773
Sleeswyk, A. W. 130
Smallman, R. E. 328
Smeltzer, W. W. 268, 377
Smith, C. S. 396
Smith, E. 403
Smith, J. F. 249
Smith, R. 405
Stevenson, F. 494
Straumanis, M. E. 56
Strickland-Constable, R. F. 362
Stringer, J. 758, 810
Strumane, R. 312
Stubbington, C. A. 811
Sulonen, M. S. 669
Swalin, R. A. 388
Tanner, L. E. 730
Taylor, M. A. 256
Thomas, G. 172
Tiedema, T. J. 711
Titchener, A. L. 338
Tobin, J. M. 781
Toorn, van der, L. J. 711, 715
Treaftis, H. N. 277
Turnbull, D. 277, 528, 747
Turner, T. J. 891
Verbraak, C. A. 65
Votava, E. 874, 901
Wagner, J. B., Jr. 617
Wagner, R. S. 57
Walker, W. P. 734
Walter, J. L. 60, 126, 497
Wassermann, G. 897
Weaver, C. W. 343
Weinberg, F. 851
Weiner, L. C. 52
Werber, T. 819
West, G. W. 797
Whitmore, R. W. 480
Wiedersich, H. 128
Williams, G. I. 177
Williams, G. P., Jr. 891
Wilson, D. V. 36, 468
Wood, W. A. 402
Yakel, H. L., Jr. 637
Yinger, R. 617
Yoshida, S. 878
Young, F. W., Jr. 117

VOL. 8 1960

DISLOCATION ETCH PITS AND PLASTIC DEFORMATION IN CALCITE*

R. E. KEITH and J. J. GILMAN†

This investigation was concerned with the development of an etch-pitting procedure for calcite crystals ($CaCO_3$). Calcite is of interest because of its plastic properties, especially its capacity for mechanical twinning. Etch-pits were produced on calcite using a number of different reagents. The pits were found to have unique shapes characteristic of each chemical, its concentration, and the nature of any diluent used with it. Concentrated formic acid produced the most satisfactory pits, and it was verified that these pits resulted from dislocations. The known glide elements of calcite were confirmed by observing arrays of etch-pits on the glide planes. Dislocation structures were observed in twins.

PIQURES DE CORROSION ET DEFORMATION PLASTIQUE DE LA CALCITE

Cette étude est relative au développement d'une méthode de production de piqûres de corrosion sur les cristaux de calcite ($CaCO_3$). Ce minéral est intéressant à cause de ses propriétés plastiques et particulièrement de son aptitude au maclage mécanique.

Les auteurs ont pu produire des piqûres de corrosion sur la calcite en utilisant différents réactifs. Ils ont trouvé que celles-ci avaient une forme unique pour chaque réactif utilisé en fonction de sa concentration et de la nature du solvant utilisé. C'est l'acide formique concentré qui produit les piqûres les les plus intéressantes et on a pu prouver que leur formation était en relation avec la présence de dislocations. Les éléments de glissement connus pour la calcite ont pu être confirmés en observant la distribution des piqûres de corrosion sur les plans de glissement. Enfin, dans les macles, les auteurs ont également observé des distributions de dislocations.

ÄTZGRUBEN AN VERSETZUNGEN UND PLASTISCHE VERFORMUNG VON KALKSPAT

Ziel der Untersuchung war die Entwicklung eines Verfahrens zur Erzeugung von Ätzgruben an Kalkspatkristallen ($CaCO_3$). Kalkspat ist interessant wegen seiner plastischen Eigenschaften, insbesondere seiner Fähigkeit zur Bildung mechanischer Zwillinge. Die Ätzgruben wurden mit Hilfe einer Anzahl verschiedener Reagenzien erzeugt. Die Form der Gruben hing eindeutig ab vom Reagens, seiner Konzentration und dem benutzten Lösungsmittel. Konzentrierte Ameisensäure ergab die besten Gruben, und es liess sich beweisen, dass diese Gruben von Versetzungen herrührten. Die Anordnung der Ätzgruben auf den Gleitebenen bestätigte die bekannten Gleitelemente von Kalkspat. Bei Zwillingen wurden die Versetzungsstrukturen beobachtet.

VOL. 8 1960

INTRODUCTION

Calcite, the rhombohedral form of calcium carbonate, is one of the most perfect naturally-occurring crystals.[1] Specimens used in this investigation, for example, contained around 1×10^4 dislocation lines/cm^2. It cleaves well on rhombohedral planes, is transparent, and has a Moh hardness of 3. These properties make it an easy material to handle.

Mineralogists for many years have made use of etch attack figures to determine the symmetry of crystals, although the technique has now been largely supplanted by X-ray diffraction. The etching of calcite has been studied by a number of investigators (for example, references 2–4), and the fact that the etch-pits sometimes occur in orderly arrays has been reported,[4] but it was not appreciated that these pits can often be correlated with the defect (dislocation) structures of the crystals. Investigators have reported etch-pit patterns on a variety of other metallic and non-metallic crystals, and the technique has been widely used to study crystal growth and plastic deformation.[5,6]

The ability of calcite to form large, straight-sided mechanical twins is well known.[7] In fact, mechanical twins were first discovered in it.[8] Calcite also undergoes translation gliding or slip.[9]

The objects of the present research were: first, to develop an etch-pitting procedure to reveal dislocations in calcite; and, second, to use this procedure for studying its deformation.

MATERIAL

Clear, colorless calcite crystals were purchased‡ in the form of cleavage rhombohedra. These crystals were converted into right prisms by sawing off and mechanically polishing two opposite ends. Individual specimens of any desired size were then cleaved out of the prisms perpendicular to the polished ends. All

* Received March 2, 1959.

† General Electric Research Laboratory, Schenectady, New York.

‡ From Ward's Natural Science Establishment.

of the observations of etch-pits were made on as-cleaved surfaces.

ETCHING TECHNIQUE

Calcite requires somewhat different etchants than other materials on which etch-pits have been produced. Alkaline solutions do not attack calcite at reasonable rates at room temperature, and mineral acids cause excessively rapid attack with CO_2 evolution. However, weak acids or acids moderated by an inert vehicle can be used successfully. In selecting specific etchants, the work of Honess and Jones[2] provided a starting point.

The etching treatments that were used in the present investigation are listed in Table 1. Crystals were immersed in the reagents at room temperature and gently agitated for the appropriate time. They were then rinsed successively in running tap water, 95% ethanol, and ether.

TABLE 1.

Etchant	Maximum concentration	Other concentrations, parts by volume	Typical etching times, (sec)	Optical rotation (deg)	Figure
Formic acid HCOOH	90%	—	15	—	1a
		1 : 1 H_2O	5		1b
		1 : 10 H_2O	1 1/2		1c
		1 : 1 Ethanol	45		4
		1 : 1 Glycerol	90		5
Acetic acid CH_3COOH	99.9%	—	360	—	2a
		1 : 1 H_2O	75		2b
		1 : 10 H_2O	30		2c
Propionic acid CH_3CH_2COOH	95%	—	*	—	—
		1 : 1 H_2O	120		3a
			30		
Lactic acid $CH_3CH(OH)COOH$	85%	—	15	0.28	6
Maleic acid HOOCCH:CHCOOH	Sat'd. H_2O soln.	—	15	0.05	7
Tartaric acid $HOOC(CHOH)_2COOH$	Fresh sat'd. H_2O soln.	—	10	10.70	8
	2-month old soln.	—	—	7.31	—
Citric acid HOOC $CH_2C(OH)$ (COOH) CH_2COOH	Sat'd. H_2O soln.	—	90	0.07	9
Ethylene diamine Tetra-acetic acid $(HOOC\ CH_2)_2N\ CH_2CH_2\ N(CH_2COOH)_2$	Sat'd. H_2O soln.	—	90	—	10
Nitric acid	70%	1 : 100 Ethanol	90	—	11

* No attack after 6 min.

RESULTS

The shapes of the etch-pits were specific to the chemicals that were used, their concentrations, and the nature of any diluents used with them. They are probably also a function of temperature, but this was not studied.

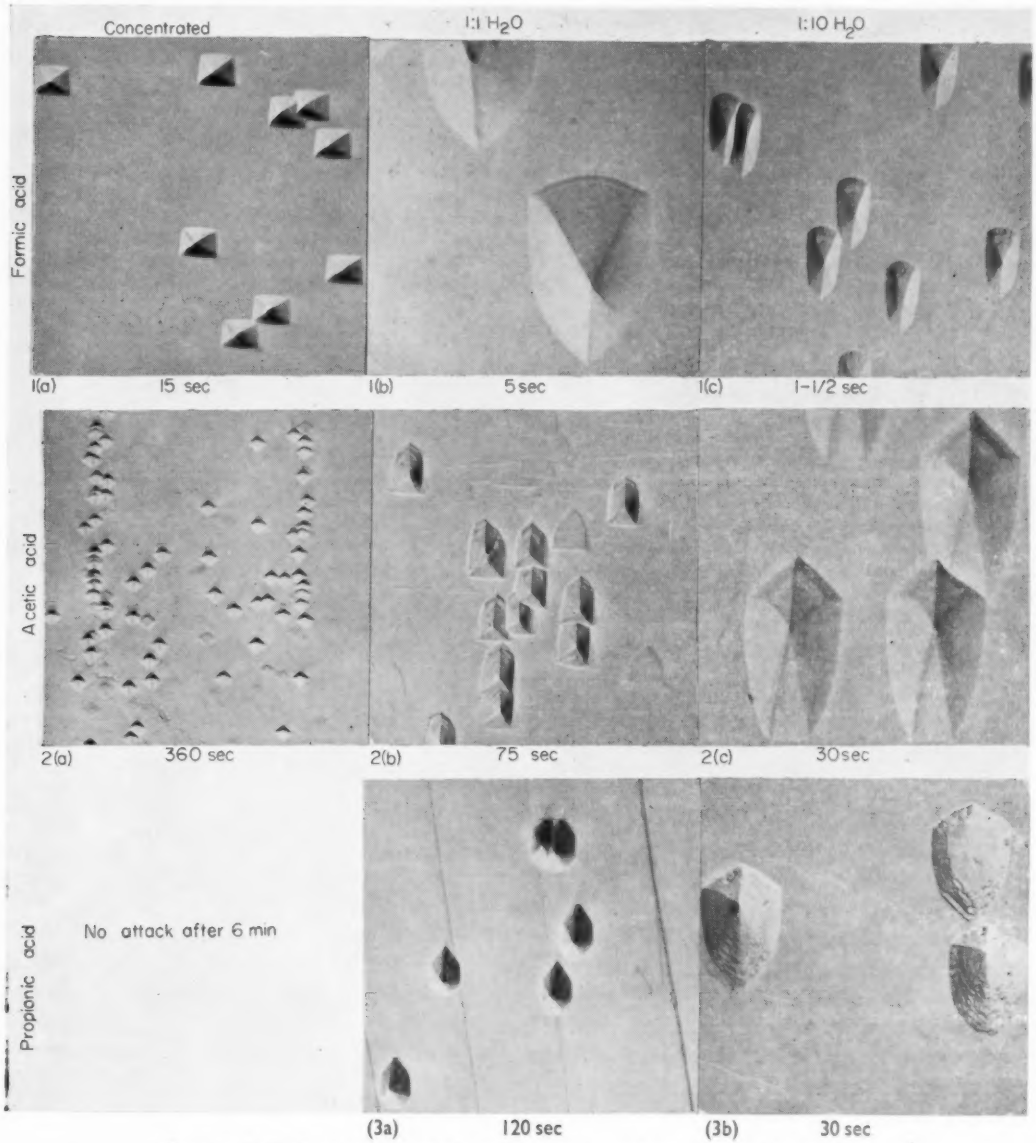
Monocarboxylic acids

Crystals were etched with various concentrations of three homologous acids: formic, acetic, and propionic. Examples of the resulting etch-pits appear in Figs. 1–3. The observation plane (Figs. 1 through 11) is the (010) cleavage plane. The [101] direction is toward the top of the page, and the [010]-axis extends into the page.*

The rate of attack varied inversely with both the length of the carbon chain of the acid, and with its concentration. The latter effect may be due to the more complete ionization that occurs in dilute solutions of weak acids. For each acid, a dilution was reached beyond which the attack began to become general and the quality of pits deteriorated. This effect appears in Fig. 3b for propionic acid. Very dilute acid solutions cause terracing and large, irregular flat pits which apparently are not related to the defect structure of the crystal.

One interesting observation was that the orientations of the pits differed for concentrated formic and acetic acids (Figs. 1a and 2a). The pits produced by formic

* The rhombohedral, or Miller, system of indexing is used in preference to the hexagonal, or Bravais, system.



FIGS. 1–3. Etch-pits produced by formic, acetic, and propionic acids. ×500.

acid have their edges roughly parallel and perpendicular to [101], while the edges of those produced by acetic acid are parallel and perpendicular to [100]. Gilman and Johnston[10] have noticed a similar orientation difference between pits produced on lithium fluoride by their Etch *W* and Etch *A*.

If a diluent other than water is used, the shapes of the pits may be changed. Figs 4 and 5 show pits resulting from attack by ethanol and glycerol solutions of formic acid and should be compared with Fig 1b.

Substituted monocarboxylic acid

Lactic acid was the only etchant in this class. It differs from acetic acid by having a chemically inactive hydroxyl group attached to the carbon next to the carboxyl group instead of hydrogen. For dilutions less than 1 H_2O : 5 acid, the pits do not differ a great deal from those of acetic acid, but at greater dilution the shapes of the pits change to ovals (Fig. 6) and then to lenses.

Dicarboxylic acids

Oxalic acid, the simplest dicarboxylic acid, did not give pits, but resulted only in overall staining of the crystal. Maleic acid made the striking pits shown in Fig. 7. Tartaric acid resulted in the asymmetric pits shown in Fig. 8. These were the only asymmetric pits



FIG. 4. 1 : 1 Formic acid-ethanol. 45 sec. ×500.

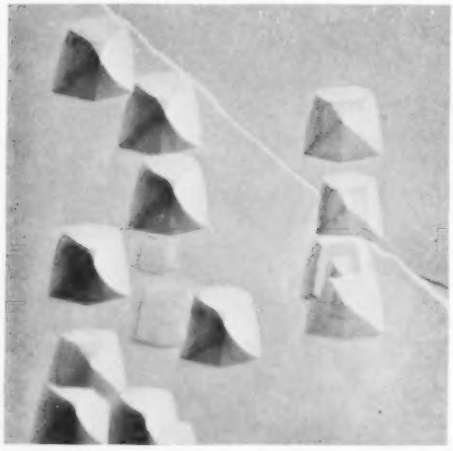


FIG. 5. 1 : 1 Formic acid-glycerol. 90 sec. ×500.



FIG. 6. 1 : 1 Lactic acid-H_2O. 15 sec. ×500.

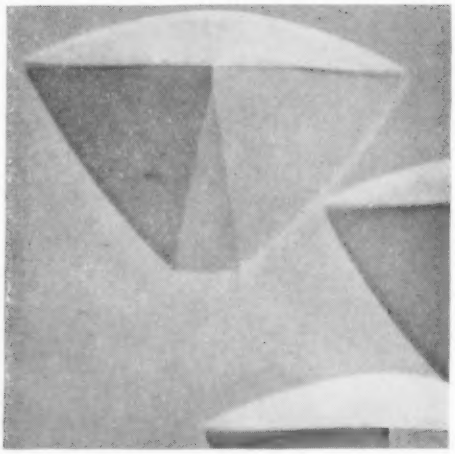


FIG. 7. Saturated maleic acid. 15 sec. ×500.

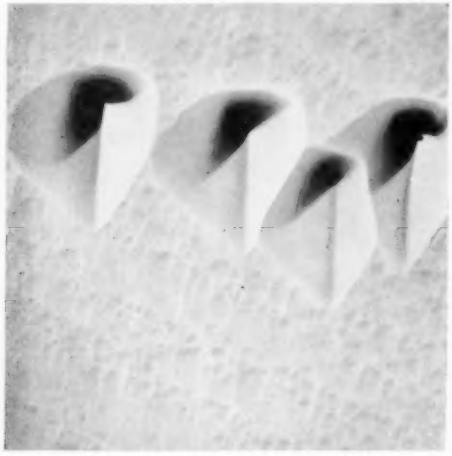


FIG. 8. Saturated tartaric acid. 10 sec. ×500.

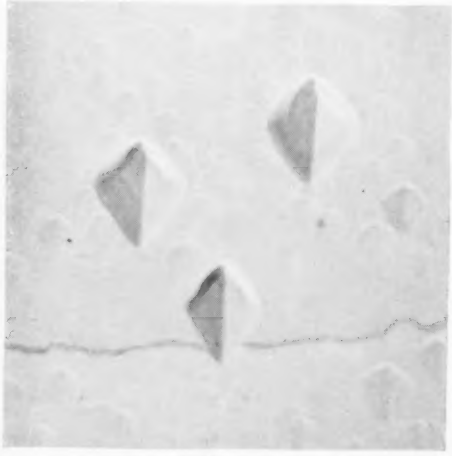


FIG. 9. Saturated citric acid. 90 sec. ×500.

observed in this investigation. Since asymmetry of etch-pits has been correlated with optical activity of the etchant,[2] the acids that are capable of stereoisomerism were checked for optical activity. The results are listed in Table 1. They show that the tartaric acid was the only optically active etchant. The optical activity probably resulted from the method of manufacture, and the other acids were racemic mixtures.

Tricarboxylic acids

Citric acid was the only tricarboxylic acid that was studied (Fig. 9).

Tetracarboxylic acids

Ethylene diamine tetra-acetic acid resulted in the pits shown in Fig. 10.

At this stage of the investigation, it had become apparent that etch-pits can be produced on calcite with no difficulty. Next a search was undertaken for a polishing reagent which could be used to smooth rough surfaces that resulted from cleavage or deep etching. Dilute aqueous solutions of HCl, HNO_3, H_2SO_4, and acetic acid were tried, with the same results as those of Boos[3] and Pfefferkorn[4]. Large, flat, rhomic etch figures and preferential attack at cleavage steps resulted. A powerful chelating agent for calcium, the tetra-sodium salt of ethylene diamine tetra-acetic acid, also failed. Ammonium chloride solutions resulted in rhombic pits. Alcoholic and glyceryl solutions of mineral acids resulted in etch-pits (Fig. 11). To date, no satisfactory chemical polishing agent for calcite has been discovered.

VOL. 8 1960



FIG. 10. Saturated ethylene diamine tetra-acetic acid. 90 sec. ×500.

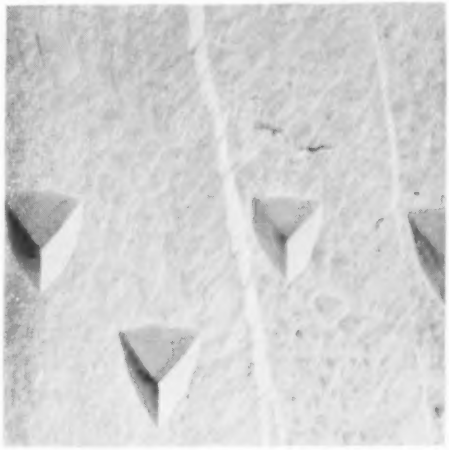


FIG. 11. 1 : 100 Nitric acid-H_2O. 90 sec. ×500.

CORRELATION OF ETCH-PITS WITH DISLOCATIONS

Two methods were used to find out whether the etch-pits that have been described above are located at dislocations. Because it produces sharp pyramidal pits, concentrated formic acid was chosen as the most suitable reagent for routine use, and the dislocation correlation tests were made with it.

(1) *Matching cleavage faces*

Since dislocations are line defects, if a cleavage fracture is passed through the network of dislocations in a crystal, the dislocation etch-pit patterns on the two fracture faces should correspond to each other. As Fig. 12 shows, this correspondence for calcite–formic acid is very close except in the region where a cleavage step crosses the field.

(2) *Dislocation movement*

In an etched crystal, if a dislocation is moved away from its etch-pit by the action of a stress, the etch-pit should become flat-bottomed during further etching. At the same time, a sharp-bottomed pit should appear at the new location of the dislocation. Fig. 13 shows such a case for calcite bent at 500°C.

Although the pits produced by all the reagents that were investigated are probably associated with dislocations, only concentrated formic acid was tested.

DISCUSSION OF ETCH-PITTING RESULTS

The shape of an etch-pit is determined by relative rates of chemical attack in different crystallographic directions. These rates in turn depend upon interactions between the ions in the etchants and the geometric arrangements of the ions on the crystal surfaces. Thus the present observations of etch-pit

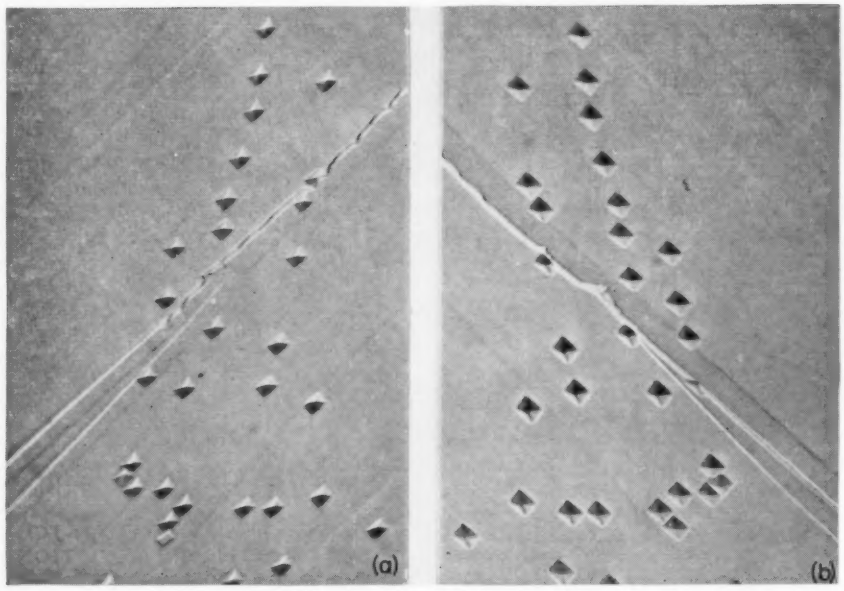


FIG. 12. Matching cleavage faces. Etched. ×500.



FIG. 13. Dislocation motion. Flat-bottomed pit at former site. Smaller pointed pit at new site. Specimen was stressed between etchings. ×500.

shapes that are specific to each reagent confirm the views of previous investigators (particularly Honess and Jones, and Boos) that the anions of the etchants are involved in the dissolution process, and not just the hydrogen ions. The fact that the right- or left-handedness of the asymmetric pits that are produced by optically active etchants can be reversed by interchanging the *d*- or *l*-forms of the etchant[2] cannot be easily explained in any other way.

APPLICATION OF ETCH-PITTING TO PLASTIC DEFORMATION

Turner *et al.*[9] have made a careful and thorough study of the deformation of calcite using petrography, essentially a macroscopic technique. A summary of their findings concerning the glide systems, converted to Miller indices, is as follows:

(1) Twin gliding occurs on the {110} planes in the [001] directions;

(2) {100}[011] translation gliding (slip) occurs in the temperature range 20°–300°C;

(3) $\{11\bar{1}\}[011]$ translation gliding occurs at or near room temperature.

They found no evidence of either translation gliding on {110} planes in the reverse sense to twinning, or of translation gliding on the (111) plane. Both of these glide systems had previously been suggested as possibilities in calcite.

Translation gliding

The etch-pit technique, as developed in this investigation, tells nothing about glide directions, but in most other respects it gave results in agreement with those of Turner *et al.*

The mobilities of dislocations in calcite are very low at room temperature, but become appreciable at higher temperatures. Fig. 14 shows three sides of a prismatic beam of calcite that was loaded as a three-point beam at a maximum fiber stress of 2200 g/mm² at the center of the span for 2 hr at 500°C. The stereographic analysis of Fig. 15 identified the bands of Fig. 14 as resulting from glide on $(\bar{1}11)$—a plane equivalent to $(11\bar{1})$—and (100).

Fig. 16 shows a deformation figure made by pressing a crystal at 500°C with a rounded glass rod. In

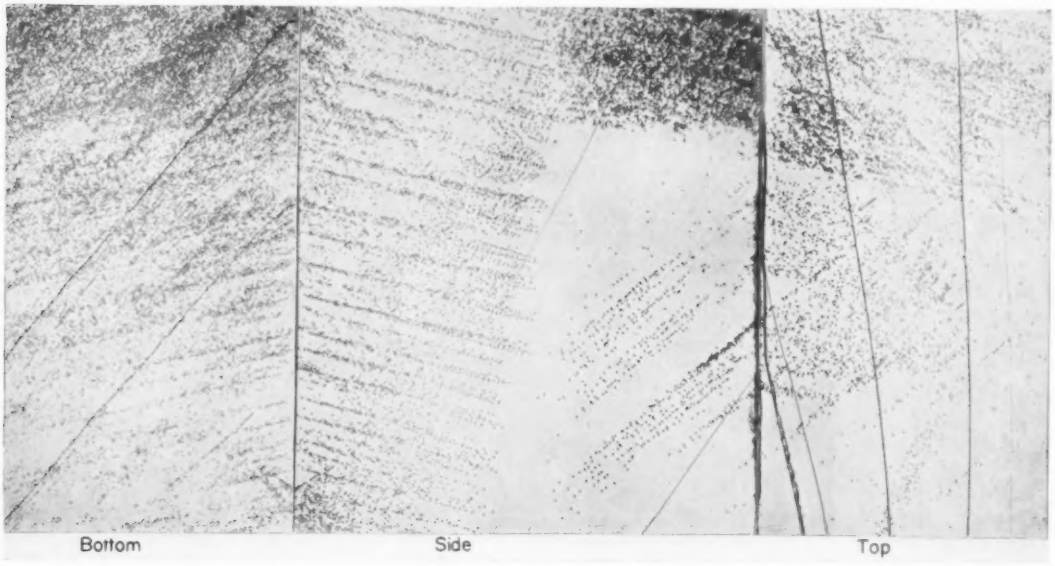


FIG. 14a. Three surfaces of a specimen loaded in three-point bending for 2 hours at 500°C, then etched. ×50.

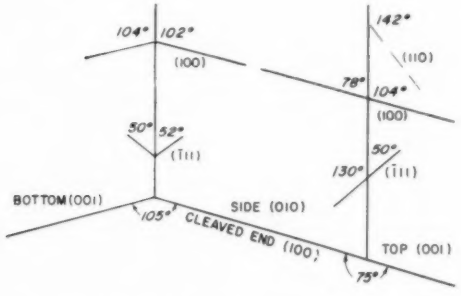


FIG. 14b. Key to Fig. 14a. Angles were measured microscopically on specimen.

addition to translation gliding, this region contains (110) twinning and (100) and (001) cleavage. The semi-circular interference fringes result from parting on the (110) twin interface.

The only respect in which the results of these experiments differed from those of Turner *et al.* was that $\{11\bar{1}\}$ translation gliding appeared to be much more extensive than {100} gliding over the temperature range from room temperature to 600°C. Above 600°C, appreciable decomposition of the crystal occurred during the time necessary to make experiments. The total deformations in the present work were much smaller than those attained by Turner *et al.*, however, and this may account for this difference in the results.

There was no conclusive evidence of translation gliding on either (110) or (111), in agreement with those workers.

Twinning

Twinning was produced either by longitudinal compression of cleaved prisms, or by shear of cleavage rhombs. Both methods tended to result in a series of narrow twins rather than in the enlargement of a single twinned region.

When twinned crystals were etched, a striking structure was sometimes developed (Fig. 17). The intense black markings occurred only on the

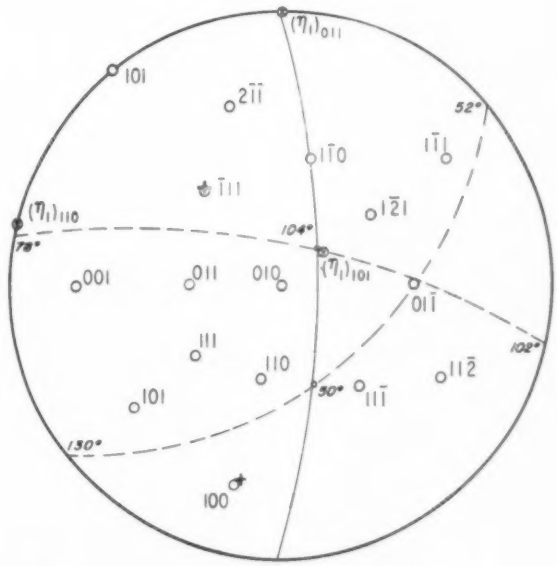


FIG. 15. Stereographic analysis of deformation appearing in Fig. 14a.

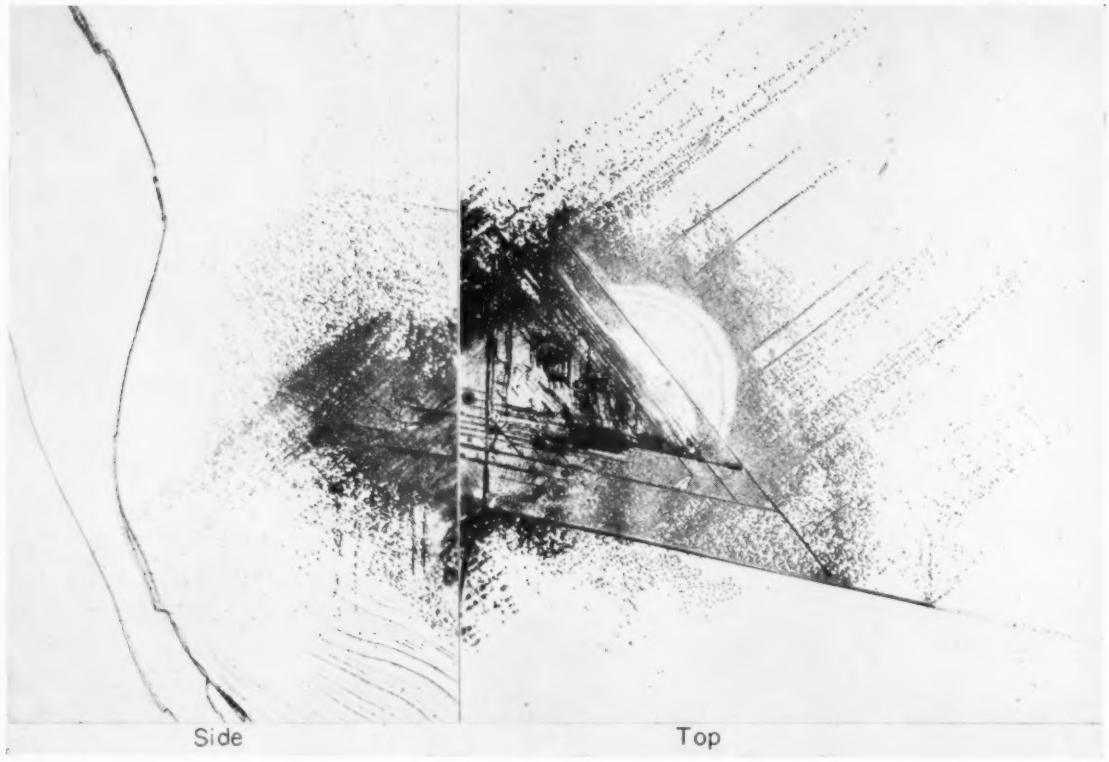


FIG. 16. Deformation figure at edge of crystal. Made by pressing with a glass rod. Crystal was at 500°C. Orientation matches Fig. 14. ×50.



FIG. 17. Surface markings on twins. Cleaved before twinning. ×150.

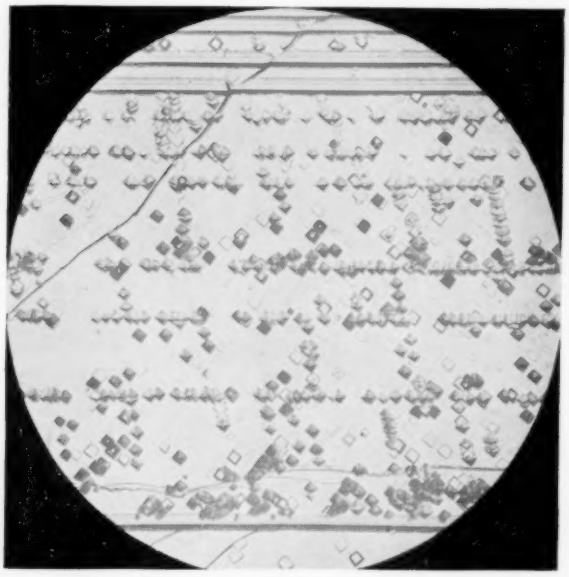


FIG. 18. Etch pits in twin. Cleaved after twinning. Etched 60 sec. ×95.

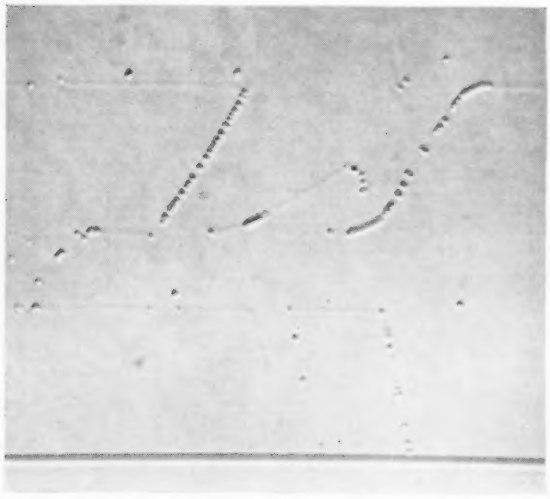


FIG. 19. Etch pits and grooves in twin of Fig. 18. Etched 5 sec. ×500.

side of the twin that made an obtuse angle with the observation plane. The proportion of the twin that was covered by the markings differed from one twin to another. Prolonged etching showed that these markings, some of which were barely visible before etching, and which were presumably fine cracks, existed only in a shallow region near the surface. Furthermore, they were never observed on specimens cleaved after twinning. The line on which the markings begin may be a useful indication of the initial position of one twin interface, but the markings are not an essential part of the twinning mechanism.

To avoid extraneous surface effects, crystals were first twinned, and then layers were cleaved off their surfaces. This is readily done for the faces parallel to the plane of shear. An interesting effect was observed with respect to the surfaces of cleaved twins. The twinned regions were always relatively smooth, whereas the untwinned portions of the crystals contained large numbers of cleavage steps in the neighborhood of the twins. Low[11] has observed a similar effect in iron–silicon crystals that were cleaved after twinning.

Fig. 18 shows a twin after it was cleaved and etched. The larger number of etch pits ($3 \times 10^4/cm^2$) shows that the twin is less perfect than the parent crystals. Many of the pits are flat-bottomed and

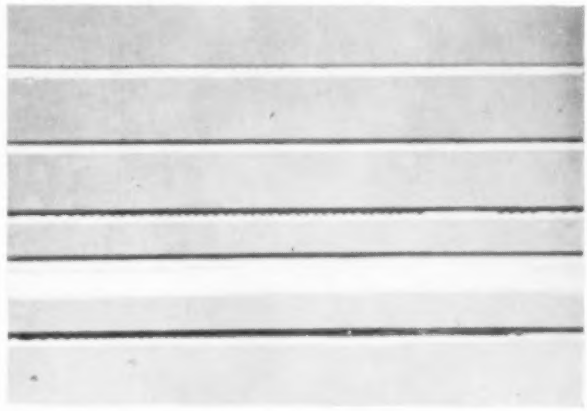


FIG. 21. Etch figure in twin interfaces. ×250.

presumably result from point-defect clusters.[12] In addition to the pits, shallow grooves are often visible after a light etch (Fig. 19). The grooves usually lie in crystallographic directions, possibly along the traces of {100} planes. They are associated with etch pits and terminate either at etch pits or at the twin interface. The segments of the grooves that are parallel to the twin interface define a series of straight lines which may indicate rest positions of twin interface which moved intermittently. The grooves apparently arise from imperfections lying on or very near the surface and parallel to the observation plane. Heavy etching seems to show that the grooves disappear, but the surface detail becomes very difficult to follow. If the surface is renewed by cleaving off a thin layer, structure that is similar to the previous one reappears (Fig. 20). The positions of the grooves and etch-pits differ from those on the previous surface, but the segments parallel to the twin interfaces again define the same set of parallel lines.

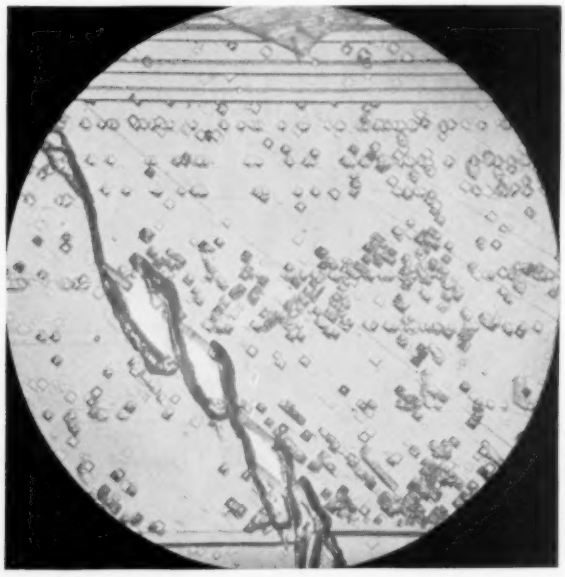


FIG. 20. Field of Fig. 18. Layer 1/16 in. thick removed by cleavage. Etched 60 sec. ×95.

VOL. 8 1960

There are at least two explanations that could account for the grooves. They might represent dislocation segments lying just beneath the observation plane. (Some grooves resemble dislocation loops.) Alternatively, the grooves might be debris tracks (point-defect clusters) left by moving dislocations. The segments parallel to the twin interfaces would then represent migration of dislocation segments in the interface during the brief interval when the interface was at rest.

It was reasoned that if the grooves were dislocation segments, similar grooves might be observed in a bent beam cleaved on an active glide plane. The beam of Figs. 12–14 was cleaved transversely. Although the resulting surface was well populated with etch pits, there were no grooves.

A final observation was the existence of etch-pit arrays in some twin interfaces (Fig. 21). In some cases, further etching caused the pits to disappear, and their origin remains uncertain.

ACKNOWLEDGMENTS

The authors wish to acknowledge valuable discussions with Dr. W. G. Johnston during the investigation. Mr. V. J. DeCarlo prepared the photographic prints.

REFERENCES

1. N. W. H. Addink, *Rec. trav. chim.* **70,** 202 (1951).
2. A. P. Honess and J. R. Jones, *Tech. Pap. Pa. Miner. Exp. Sta.* No. 35 (1937).
3. A. Boos, *Neues Jb. Miner., Mh.* A**78,** 89 (1943).
4. G. Pfefferkorn, *Optik* **7,** Sonderheft 2, 208 (1950).
5. W. G. Pfann in *Solid State Physics,* (Edited by F. Seitz and D. Turnbull) Vol. 4., p. 423. Academic Press, New York (1957).
6. W. G. Johnston and J. J. Gilman, *J. Appl. Phys.* **30** (1959).
7. R. W. Cahn, *Advances in Physics* **3,** 363 (1954).
8. D. Brewster, *Edinb. J. Sci.* **9,** 311 (1826).
9. F. J. Turner, D. T. Griggs and H. Heard, *Bull. Geol. Soc. Amer.* **65,** 883 (1954).
10. J. J. Gilman and W. G. Johnston, in *Dislocations and Mechanical Properties of Crystals,* (Edited by J. C. Fisher, W. G. Johnston, R. Thompson and T. Vreeland, jr.) p. 116. John Wiley, New York (1957).
11. J. R. Low, jr. Private communication.
12. J. J. Gilman and W. G. Johnston, *J. Appl. Phys.* **29,** 877 (1958).

TWINNING AND FRACTURE OF SINGLE CRYSTALS OF 3% SILICON IRON*

D. HULL†

Thin sheet single crystal (001) specimens of a 3% silicon iron have been strained in tension at −196°C in the [010] direction. Twins formed, in preference to slip, on four prominent planes (12̄1), (1̄21), (1̄2̄1), and (121), which are all equivalent with respect to the applied stress. The morphology of the twins has been studied. They are in general parallel sided, but at the free surface one side of the twin is smooth and the other has a characteristic zig-zag marking. The markings are steps on the surface which are probably produced by a slip process. The crystals fractured without measurable deformation as a result of (010) cleavage cracks nucleated at the intersection of twins. Only intersections in which the twins meet on a plane normal to the applied stress produced cracks. The (010) cracks were often deflected along twin interfaces; on the zig-zag edge of the twin the crack followed the twin interface and on the smooth edge a stepped crack of (010) and (100) cleavage facets was produced.

MACLAGE ET RUPTURE DE MONOCRISTAUX DE FER-SILICIUM (3%)

Des feuilles minces monocristallines (001) de fer-silicium (3%) ont été déformées par traction à −196°C dans la direction [010]. Des macles se produisent de préférence au glissement sur 4 plans déterminés (12̄1), (1̄21), (1̄2̄1), et (121), qui sont équivalents par rapport à la direction de la tension appliquée. L'auteur a étudié la morphologie de ces macles. Elles sont en général à bords parallèles, mais à la surface libre du cristal, l'un des côtés de la macle possède une allure caractéristique en zig-zag. Ces marques sont des crans sur la surface: ils sont probablement dûs à un mécanisme de glissement. Les cristaux se sont rompus sans déformation mesurable par suite de fissures de clivage (010) produites à l'intersection des macles. Seules les intersections où les macles se rencontrent dans un plan normal à la tension appliquée produisent ces fissures. Les fissures (010) sont souvent déviées le long des interfaces de macles; sur le côté irrégulier de la macle, la fissure suit l'interface tandis que sur le côté rectiligne une fissure échelonnée, formée de facettes de clivage (010) et (100) a été observée.

ZWILLINGSBILDUNG UND BRUCH VON EINKRISTALLEN AUS EISEN MIT 3% SILIZIUM

Einkristalline Proben in der Form dünner Streifen mit (001)-Orientierung aus Eisen mit 3% Silizium wurden bei −196°C in der [010]-Richtung gedehnt. Es bildeten sich vorzugsweise Zwillinge auf den vier spannungsmässig gleichbegünstigten Ebenen (12̄1), (1̄21), (1̄2̄1) und (121). Die Morphologie der Zwillinge wurde untersucht. Sie sind im allgemeinen parallel begrenzt, doch ist auf der freien Oberfläche die eine Seite des Zwillings glatt, während die andere Seite charakteristisch gezackt erscheint. Es handelt sich dabei um Oberflächenstufen, die vermutlich von Gleitvorgängen herrühren. Der Bruch trat ohne messbare Verformung ein als Folge von Spaltrissen auf (010)-Ebenen. Die Risse entstanden längs der Schnittlinie zweier Zwillinge, und zwar nur längs solcher Schnittlinien, die in einer Ebene senkrecht zur angelegten Spannung lagen. Die (010)-Risse verliefen oft zu den Zwillingsgrenzen hin; auf der gezackten Seite des Zwillings folgte der Riss der Zwilingsgrenze und auf der glatten Seite des Zwillings entstand ein stufenartiger Riss mit (010)- und-(100) Spaltflächen.

VOL. 8 1960

1. INTRODUCTION

Recent work has emphasised the importance of explaining the brittle fracture of single crystals. This cannot result from a crack initiated by the pile-up of dislocations at a grain boundary as proposed by Petch[1], Mott[2], Stroh[3] and others for polycrystalline materials. To overcome this difficulty Biggs and Pratt[4] suggested that a strong barrier to slip, similar to a grain boundary, is produced by a twin and that the crack can be initiated by the pile-up of slip dislocations at a twin boundary. A somewhat similar mechanism to this has been observed by Stokes *et al.*[5] in magnesium oxide, in which small cracks were produced at the intersection of a slip band with a kink band.

An alternative approach to the pile-up mechanism has been made by Cottrell[6]. It is proposed that the cleavage crack is formed at the intersection of slip on two (110) planes when dislocations with Burgers vectors $\frac{1}{2}\mathbf{a}[\bar{1}11]$ and $\frac{1}{2}\mathbf{a}[111]$ combine to form a new dislocation with a Burgers vector $\mathbf{a}[001]$. Further slip dislocations running into the intersection open the new dislocation into a cleavage crack. In experiments to determine the mechanism of crack formation in single crystals of silicon iron Hull[7] found that at −196°C cleavage resulted from the intersection of twins before any slip was observed. A similar effect has been reported by Cahn[8] in molybdenum and Bell and Cahn[9] in zinc.

Appreciable plastic deformation can occur by twinning and it is clear that twinning is closely associated with the formation and growth of cracks. It is important, therefore, that both the properties

* Received March 18, 1959.

† Metallurgy Division, Atomic Energy Research Establishment, Harwell, England.

of twins and their effect on fracture is known so that the wider problem of brittle fracture can be understood. In this paper the twinning and fracture of single crystals of a 3% silicon iron are described in detail.

2. EXPERIMENTAL DETAILS

Single crystals of high purity 3% silicon iron were cut from a large-grained polycrystalline sheet 0.002 in. thick. The plane of the sheet was parallel to the (001) cube face and the sides of the specimen corresponded to cube edges. The specimens, which were approximately 0.8 in. long and 0.15 in. wide, were electropolished before testing in a solution of chromium trioxide in glacial acetic acid using the method developed by Morris[10]. It was possible to polish both sides of the specimen without appreciable staining. The tests were made at −196°C in a hard beam tensile machine with a strain rate of 0.013 min^{-1}. The stress was applied in the [010] direction. After fracture the polished surfaces of the specimen and the cleavage faces were examined metallographically.

3. RESULTS

3.1. *Morphology of twins*

At −196°C fracture occurred in these crystals without any measurable deformation; fracture and the onset of twinning appeared to be coincident. The twins were readily visible on the polished surface because of the relief effects produced. The twins can be classed into three sections depending on the conditions under which they formed; (1) large twins, often crossing the whole of the specimen, which formed under the direct effect of the applied stress, (2) smaller twins which formed in local regions of high stress, e.g. close to large twins and cracks, and (3) fine short twins which were present only along the edges of cleavage cracks and which were probably nucleated by the high stresses associated with the propagation of these cracks. Fig. 1 shows a cleavage crack with fine twins along the edge, and also some of the large twins. The morphology of all the twins appeared to be identical and this investigation is concerned only with the large prominent twins.

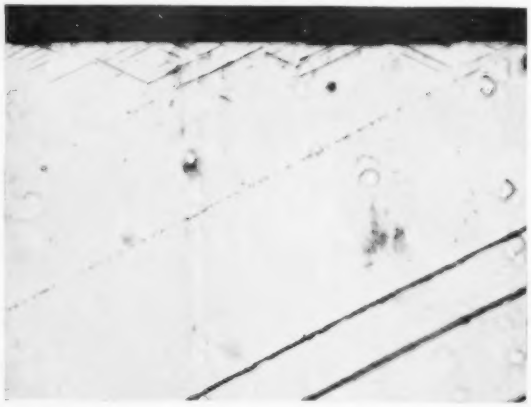


FIG. 1. An (010) cleavage edge with fine twins and prominent twins. ×600.

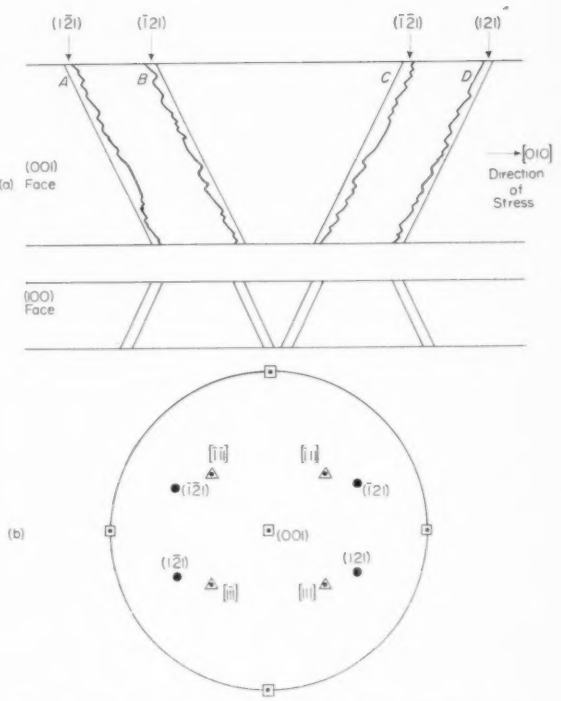


FIG. 2. Position of main twins and their orientations, (*a*) two faces of the specimen at right angles, showing the twins and the position of the zig-zag markings, and (*b*) a standard (001) stereographic projection with the directions of twinning and poles of the twinning planes.

Measurements of the twin traces on the polished surface and the edge normal to this surface showed that the large twins were confined to four twinning systems, namely,

$$(1\bar{2}1)\,[111].....A$$
$$(\bar{1}21)\,[\bar{1}\bar{1}1].....B$$
$$(\bar{1}\bar{2}1)\,[\bar{1}11].....C$$
$$(121)\,[1\bar{1}1].....D$$

The positions of these twins on the specimen and on a (001) standard projection are illustrated in Figs. 2a and 2b respectively. On the (001) face they appear as two parallel sets of twins with opposite tilts. The four twinning systems are equivalent to each other with respect to the applied tensile stress, since the twinning plane and direction make the same angles, 35°16′ and 54°44′ respectively, with the (010) axis. The resolved shear stress on the twinning plane in the twinning direction is therefore the same for

the four systems, and this accounts for the appearance of approximately equal numbers of all four types of twin.

The angle of tilt produced by the large twins was measured on the (001) face by determining the width of the twin and the difference in height across this width using line profile microscopy. The method gave an accuracy of $\pm 1°$. It was not possible to measure the tilt produced on the edges of the specimen, to determine the direction and magnitude of the twinning shear. The measured tilt on the (001) face, however, agreed closely with the value of $17°42'$ calculated from the theoretical twinning shear $\sqrt{2}/2$.

Whilst the twins were in general of uniform thickness, close examination revealed that one side of the twin was smooth and the other showed a characteristic zig-zag marking (Fig. 3). On some twins the markings extended along the whole length, and on others only a few markings were produced. When two parallel twins occurred on the (001) face with opposite tilts, e.g. $(1\bar{2}1)$ and $(\bar{1}21)$, the zig-zag markings appeared on opposite sides. When the same two twins were observed on the other side of the thin sheet specimen, the markings were reversed as seen in Fig. 4. Thus the zig-zag markings do not pass through the specimen on one side of a twin and therefore, either they are reversed through the thickness of the specimen or they are produced by an effect peculiar to the surface.

Examination of the specimens using high magnifications and line profile microscopy showed that the markings were steps on the surface. Figs. 5 and 6 show multiple line profiles across a twin: for the twinned region the lines have been deflected but remain straight, indicating that the twins result from a microscopically homogeneous shear; at the zig-zag the profiles are displaced, indicating a step on the surface at these points. The appearance of the step is illustrated in Fig. 7. In all cases the zig-zag occurred at the top of the tilted region. The heights of the steps on the edges of twins were equivalent to the overall shear in the twin, cf. Fig. 8 (a and b), and the step height xy was equal to $yz \tan \alpha$, where α is the angle of tilt produced by the twin. A number of examples have been observed in which the step

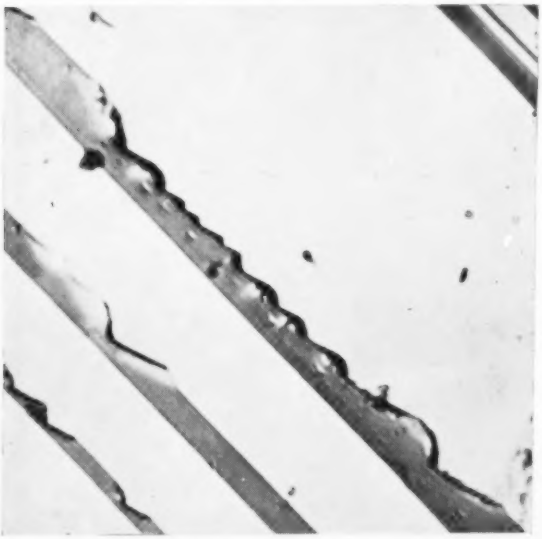


FIG. 3. General field showing twins with zig-zag markings. ×700.

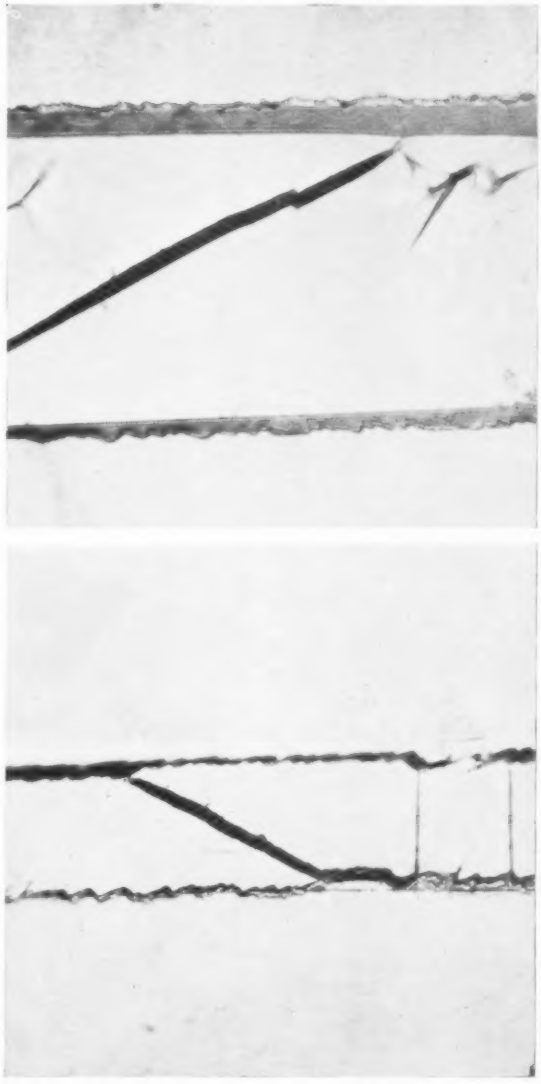


FIG. 4. Opposite sides of a specimen containing two twins $(1\bar{2}1)$ and $(\bar{1}21)$. The zig-zag markings have been reversed. A (010) cleavage crack has also formed. ×750.

VOL. 8 1960

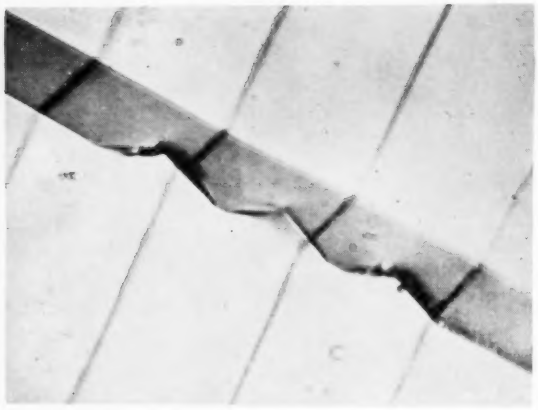


FIG. 5. Multiple profiles across a twin; note the centre notch does not show a step. ×750.

has not formed completely, but the zig-zag still occurs, e.g. the centre zig-zag in Fig. 5; here the pointed region appears to bend over.

The traces of the markings on the twins were measured. The long sections were 45° to the [010] direction and the short sections were between 90° and 120° to the long sections. The positions of the long sections could be measured accurately, but those of the short sections depended on the focus position (Fig. 8). The arrangement of the markings for the four prominent twin systems has been given in Fig. 2.

It is possible to explain these effects without assuming a specific model for the nucleation and growth of twins. If a simple shear model is considered (Fig. 9) the reversal of the zig-zag markings is explained since the points p and p' are equivalent with respect to the free surface as also are q and q'. The probable way in which the markings are formed is illustrated in Fig. 7. The twinning shear has tilted the regions $ABB'A'$ about AA'. However, the thickness of the twin inside the specimen is larger than AB, part

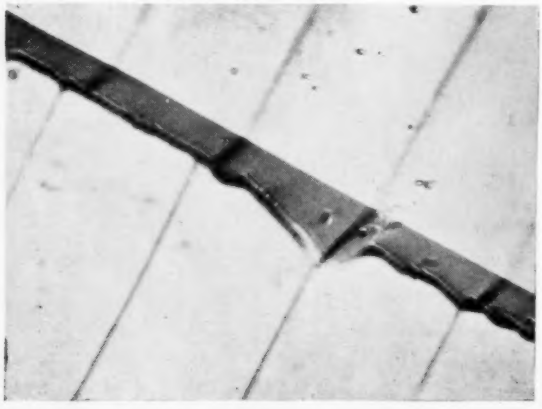


FIG. 6. Multiple profiles across a twin. ×750.

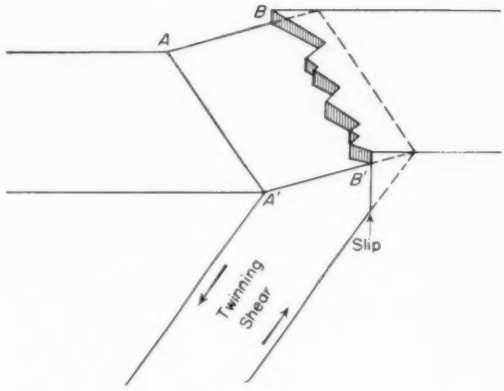
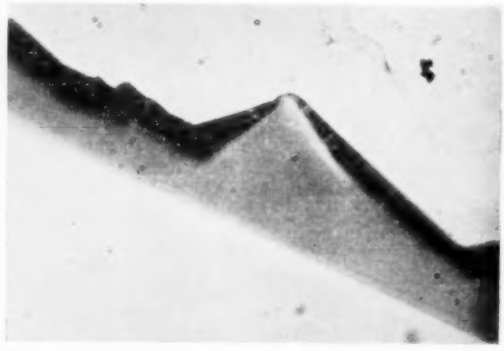


FIG. 7. Diagrammatic illustration of a twin containing a zig-zag marking on one side.



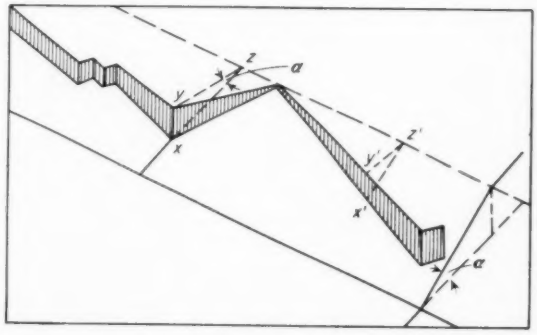


FIG. 8. A twin with a prominent zig-zag; the step height $x'y'$ is equal to $y'z'$ tan α. ×2000.

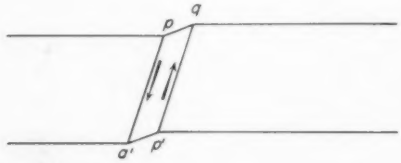


FIG. 9. Simple shear model for twinning.

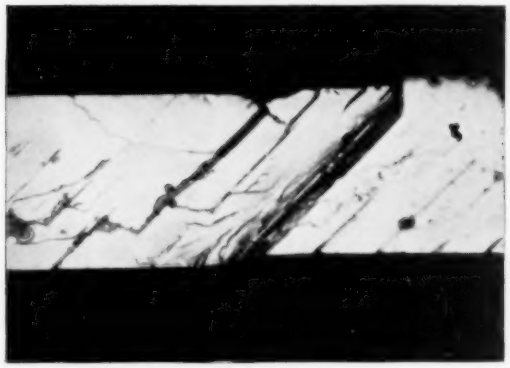


FIG. 10. A (010) cleavage face with a $(1\bar{2}1)$ twin at 45°; note the intersection of the twin with the two free surfaces. ×1000.

of the twin is held up below the surface, and slip occurs in preference to twinning. Fig. 10, which is a photograph of a (010) cleavage face with a $(1\bar{2}1)$ twin across it at 45°, supports the model. The intersections of the twin with the two (001) surfaces give the two extremes of the effect illustrated in Fig. 7, namely a uniform tilt across the whole width of the twin and a single step without any tilted region. The hold up of the twin below the surface is shown clearly.

3.2. *Nucleation of cracks by twins*

Six crystals were examined in detail and they contained over twenty individual cracks. Four of the crystals contained only one crack which crossed the whole of the specimen, and the other two had broken into three pieces. All but two of the cracks originated at the intersection of twins. On the surface illustrated in Fig. 2 there are four possible twin intersections i.e. *A–C*, *A–D*, *B–C* and *B–D*, but *A–C* is equivalent to *B–D* and *A–D* is equivalent to *B–C*. In all cases the cracks were initiated at an *A–D* type intersection and none could be attributed to *A–C* type intersections. Fig. 11 shows a typical crack formed at an *A–D* intersection and Fig. 12 the same field

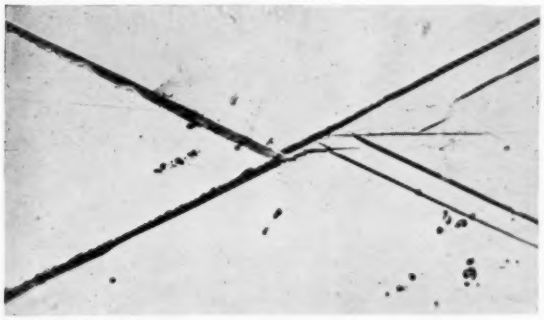


FIG. 11. An *A–D* type twin intersection producing a crack. ×140.

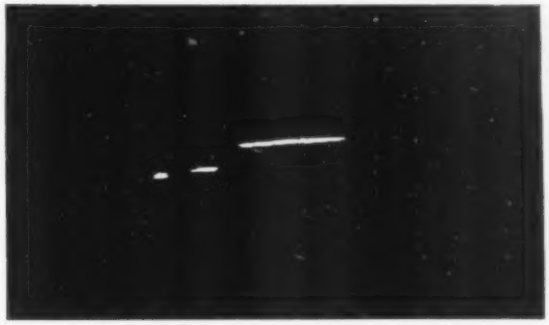


FIG. 12. Same field as Fig. 11 viewed with transmitted light. ×140.

viewed with transmitted light showing the position of the crack. Not all the *A–D* intersections resulted in a crack, as seen in Fig. 13. Severe distortion has occurred which is symmetrical about the [100] direction. An *A–C* intersection is shown in Fig. 14. The two cracks which were initiated without any apparent twin intersections occurred between two parallel twins with opposite tilts on the surface; this is illustrated in Fig. 15. Between the twins large numbers of cleavage cracks have formed which were readily detected by viewing with transmitted light.

3.3. *Propagation of cleavage cracks*

In the absence of large twins the cleavage crack is extremely straight and the only markings on the surface are a few fine twins that are localised close to the cleavage edge (Fig. 1), and which produce fine markings on the cleavage face (Fig. 10). However, when the (010) cleavage crack meets a twin it is often deflected along the twin face (Fig. 16). The appearance of the crack depends on the particular edge of the twin it has followed. On the edge of the twin having the fine zig-zag markings the crack follows these markings (Fig. 17), but on the smooth edge of the twin the

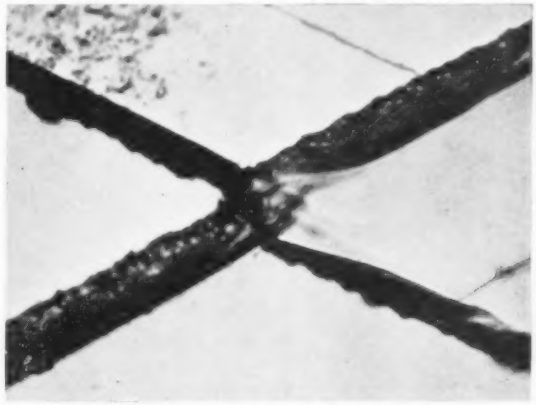


FIG. 13. An *A–D* type intersection that has not formed a crack. ×1000.

VOL. 8 1960

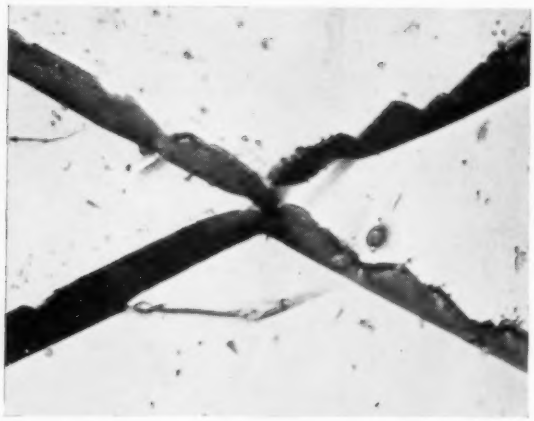


FIG. 14. An A–C type intersection. ×1000.

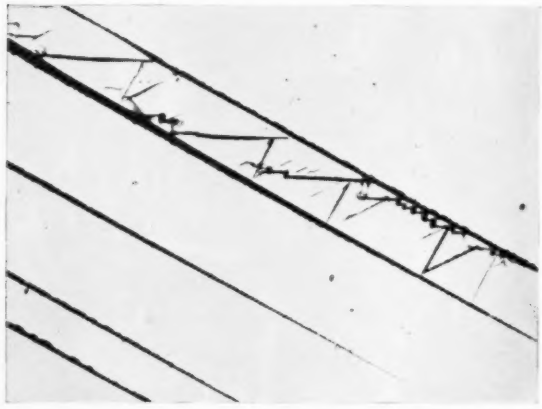


FIG. 15. Two twins, $(1\bar{2}1)$ and $(\bar{1}21)$, with multiple (010) cleavage cracks between them. ×140.

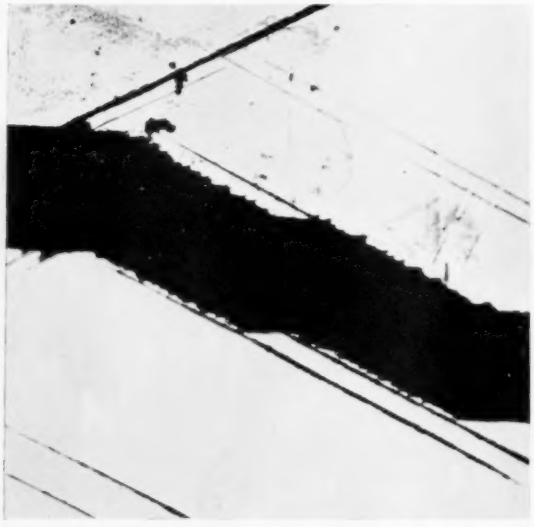


FIG. 16. Two pieces of a single crystal showing (010) cleavage cracks deflected along twin boundaries. ×140.

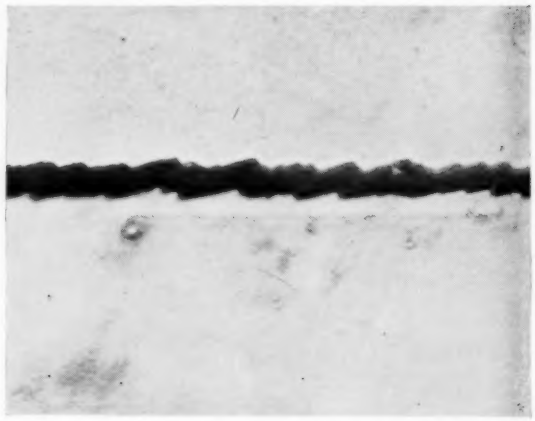


FIG. 17. Cleavage crack along zig-zag edge of a twin. ×1500.

crack has a step like structure made up of short sections of (100) and (010) cleavage facets (Fig. 18). The face of such a crack is shown in Fig. 19. The cleavage facets are at the top of the photograph and the lower region is a cleavage face which has followed the face of a {112} twin. Fig. 20 is a particularly good example of a smooth edge of a twin with a stepped cleavage crack.

Cleavage cracks which have not crossed the whole of the specimen usually stop at the boundaries of large twins. Some cracks terminate in an untwinned region and fine slip lines or small twins are produced at the tip.

4. DISCUSSION

The observations have shown that when a twin meets the surface a characteristic zig-zag marking is formed on one edge of the twin, whilst the other edge remains smooth. The markings consist of stepped regions which are probably produced by slip. Barrett



FIG. 18. Stepped cleavage crack along smooth edge of a twin made up of (010) and (100) cleavage facets. Opposite side of crystal from field shown in Fig. 17. ×1500.

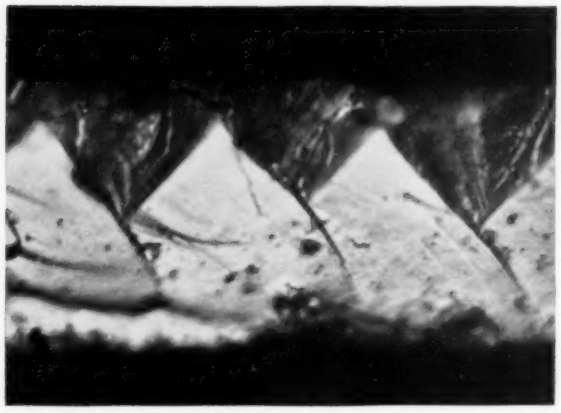


FIG. 19. Cleavage along a twin face. The top part is the stepped cleavage along the smooth edge of the twin, and the lower part the twin interface. ×1000.

and Bakish[11] have observed similar serrations on twins formed in tantalum. In this case the notches are definitely associated with slip lines between the twins, and these workers suggest that the stress concentration at the end of a slip line is responsible for them. This cannot be true for the twins examined in the present work since no slip lines were formed away from the twin.

It is difficult to understand the occurrence of slip, rather than further twinning, near the surface although it is well established that twin bands can be held up at obstacles, including a free surface. The area of new surface produced by slip, e.g. on a $(0\bar{1}1)$ plane, at the edge of a twin is many times larger than the increase that would be produced by twinning; so unless the surface energy of the twin face is far greater than that of the slip face, surface energy effects cannot be a dominant factor.

A possible explanation is that a simple dislocation reaction occurs which allows the stress in the twin to be relieved by a slip process resulting from dislocation sources close to the surface. If the twinning dislocation has the same vector as the slip dislocations involved, the steps will be produced with very little distortion of the lattice. This cannot explain the effect completely since it would result in the zig-zag markings coming right through the specimen on the same side of the twin. However, there would be a large reduction in distortion if the long sections of the zig-zags were produced by slip dislocations with the same vectors as the twinning dislocations. Considering a $(1\bar{2}1)$ twin, the long sections of the markings agree exactly with the $(1\bar{1}0)$ plane which has a [111] slip direction. The vector of the twinning dislocation also lies in the [111] direction. The formation of the short sections, which are less regular than the long sections and often appear broad and distorted, must be accompanied by much greater deformation.

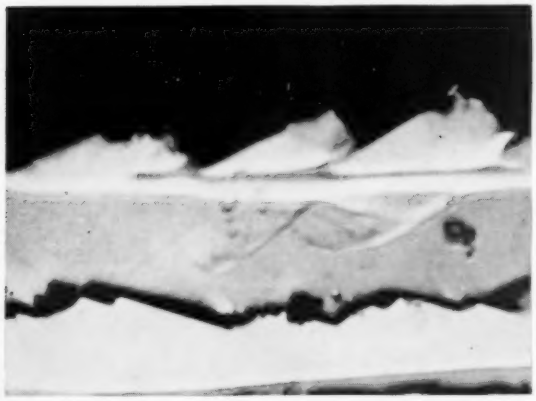


FIG. 20. Stepped cleavage along the smooth edge of a twin. ×1650.

It has been pointed out previously[7] that cracks produced by twin intersections may result from an effect similar to that producing Rose's channels in calcite.[12] If a parallel sided twin is held up inside a crystal, a hole will be formed at the end if the stresses produced are not relieved by plastic deformation. Larger effects are possible when one twin meets another.[13] In practice, twins in silicon iron taper at their ends and the stress concentration produces plastic deformation. However, it is known that twins form at very high speed and it is possible, particularly at low temperatures, that one may interact with another to produce a crack before plastic deformation by slip occurs.

In the present experiments it was found that only *A–D* type twin intersections produced cracks. In the *A–D* intersection of $(1\bar{2}1)$ and (121) twins the two planes intersect along the $[\bar{1}01]$ direction, and when the twins have a finite thickness, in the (010) plane, which is normal to the tensile stress. Combination of twinning dislocations $\frac{1}{6}\mathbf{a}[1\bar{1}1]$ and $\frac{1}{6}\mathbf{a}[111]$, producing the $(1\bar{2}1)$ and (121) twins, gives a dislocation with a Burgers vector $\frac{1}{3}\mathbf{a}[101]$. If this occurs the plane of intersection of the twins will consist of a sheet of $\frac{1}{3}\mathbf{a}[101]$ dislocations, or in effect a sheet of small holes. This approach is equivalent to considering the formation of Rose's channels on each atomic plane. For an *A–C* type intersection of $(1\bar{2}1)$ and $(\bar{1}21)$ twins, the planes intersect along the [012] direction and the twins meet in the (100) plane which contains the direction of stress. The essential difference, therefore, between an *A–D* and an *A–C* intersection is the plane on which they meet. In the former the applied stress is normal to the plane and will tend to open it into a cleavage crack, and in the

VOL. 8 1960

latter the stress has no component across the plane.

Nucleation of cracks by intersecting twins is similar in some respects to the intersecting slip mechanism proposed by Cottrell[6]. In particular, there are two factors affecting the formation and propagation of a crack, the shear stress operating in the twins to produce the crack and the direct tensile stress acting across the crack embryo. The controlling factor governing brittle fracture will depend on whether the resolved shear stress to produce a crack-forming twin intersection is greater than the tensile stress to propagate the newly formed crack.

Whilst cleavage, or parting, along a twin interface has been observed in uranium by Cahn[14], and in magnesium by Reed-Hill and Robertson[15], cleavage in body-centred cubic metals is normally confined to {001} cleavage faces. In the present experiments there is evidence for cleavage along the twin interface. This is probably associated with the slip step produced at the zig-zag markings on the edge of the twin. Such a step will produce a line of weakness resulting in a stress concentration and in cleavage at the twin interface at this point. On the smooth edge of the twin no such weakness is present, and the cleavage crack forms a stepped series of {001} cleavage facets in preference to following the twin interface.

ACKNOWLEDGMENTS

The author is grateful to Professor A. H. Cottrell, Dr. J. W. Christian, Mr. R. S. Barnes and many colleagues for useful discussions.

REFERENCES

1. N. J. Petch, *J. Iron St. Inst.* **173,** 25 (1953).
2. N. F. Mott, *J. Iron St. Inst.* **183,** 233 (1956).
3. A. N. Stroh, *Proc. Roy. Soc.* **223**A, 404 (1954).
4. W. D. Biggs and P. L. Pratt, *Acta Met.* **6,** 694 (1958).
5. R. J. Stokes, T. L. Johnston and C. H. Li, *Phil. Mag.* **3,** 718 (1958).
6. A. H. Cottrell, *Trans. Amer. Inst. Min. (Metall.) Engrs.* **212,** 192 (1958).
7. D. Hull, *Phil. Mag.* **3,** 1468 (1958).
8. R. W. Cahn, *J. Inst. Met.* **83,** 493 (1955).
9. R. L. Bell and R. W. Cahn, *J. Inst. Met.* **86,** 433 (1958).
10. C. E. Morris, *Metal Prog.* **56,** 696 (1949).
11. C. S. Barrett and R. Bakish, *Trans. Amer. Inst. Min. (Metall.) Engrs.* **212,** 122 (1958).
12. G. Rose, *Abh. preuss. Akad. Wiss.* 57 (1868).
13. O. Mugge, *Z. anorg. Chem.* **121,** 68 (1922).
14. R. W. Cahn, *Acta Met.* **1,** 49 (1953).
15. R. E. Reed-Hill and W. D. Robertson, *Acta Met.* **5,** 728 (1957).

GROWTH OF SILVER SULPHIDE WHISKERS*

J. DROTT†

The filament growth on silver after reaction with hydrogen sulphide at room temperature has been studied by electron microscopy and electron diffraction.

The filaments are β-silver sulphide and grow from the tip. The growth direction of a long whisker was [414]. The elastic strain on a curved whisker was found to be about 1.3 per cent. Many of the whiskers display offset portions and branches. Kinks often sprout small irregular whiskers. Interruption of the sulphidation reaction seems to influence the morphology of the whiskers on further sulphidation.

It is suggested that the whiskers grow on mounds having a much less perfect structure than the whiskers themselves.

CROISSANCE DES BARBES DE SULFURE D'ARGENT

L'auteur étudie par microscopie et diffraction électroniques la croissance de filaments sur l'argent après réaction avec l'hydrogène sulfurique à la température ambiante.

Les filaments sont constitués par le sulfure et ils croissent à partir de la pointe. La direction de croissance d'une longue barbe a été trouvée [414]. La déformation élastique d'une barbe courbée a été trouvée égale à 1,3 pour cent. Beaucoup de ces barbes présentent des ramifications. Des pliages se manifestent également sur des barbes irrégulières.

Une interruption de la réaction de sulfuration semble avoir une influence sur la morphologie des barbes obtenues après sulfuration ultérieure.

L'auteur suggère que les barbes pousseraient sur de petites excroissances ayant une structure beaucoup moins parfaite que les barbes elles-mêmes.

WACHSTUM VON SILBER-SULFID-FADENKRISTALLEN

Mit Hilfe von Elektronenmikroskopie und Elektronenbeugung wurde das Wachstum von Fadenkristallen (Whiskers) auf Silber nach Reaktion mit Schwefelwasserstoff bei Raumtemperatur untersucht.

Die Fadenkristalle sind β-Silbersulfid und wachsen von der Spitze aus. Die Wachstumsrichtung eines langen Fadenkristalls war [414]. Die elastische Verzerrung eines gekrümmten Fadenkristalls betrug etwa 1,3 prozent. Viele der Fadenkristalle zeigen versetzte Abschnitte und Verzweigungen. Von Knicken gehen oft kleine unregelmässige Whiskers aus. Vorübergehende Unterbrechung der Schwefelwasserstoffbehandlung scheint die Morphologie des weiteren Wachstums in Schwefelwasserstoff zu beeinflussen. Cyanidlösung griff die Kristalle nicht beobachtbar an.

Vermutlich wachsen die Fadenkristalle auf Wällen, deren Struktur erheblich weniger vollkommen ist als die der Whiskers selbst.

VOL. 8 1960

Filament growth on silver in the presence of sulphur has been observed by Arnold[1], Margottet[2,3], and Ringström[4]. Terem[5] obtained needles of a few millimeters length by the reaction of hydrogen sulphide and silver at elevated temperatures. In an investigation into the relation between growth morphology and kinetics for the reaction between silver and hydrogen sulphide at room temperature, Fischmeister and Drott[6] encountered needles of varying sizes and shapes. As much work is now being done on whisker growth it was considered of interest to investigate these needles further.

EXPERIMENTAL

Silver sheet 0.2 mm thick was used. According to spectroscopic analysis by the supplier,‡ the impurity level of the material was below 8 p.p.m., the most important impurities being 2 p.p.m. Fe, 1 p.p.m. Ca, 1 p.p.m. Pb, 1 p.p.m. Na. Four cornered holes with a side about 40 μ were punched with a needle in the end of a 4 cm long strip of silver sheet. The strips were degreased in ethyl alcohol in a Soxhlet-type apparatus, electrolytically polished in an alkaline cyanide bath[7] and slightly etched in 0.1N nitric acid, after which they were washed in distilled water and again in ethyl alcohol. They were then placed in a polythene holder inside a glass vessel that was filled with an atmosphere of air, nearly saturated with water, containing 2% hydrogen sulphide by volume. The tank hydrogen sulphide used was passed through glasswool containing iodine, a solution of potassium iodide, a solution of barium hydroxide and finally washed in water. The edges surrounding the holes in the strips were examined in silhouette with an electron microscope permitting selected area diffraction. Figs. 1 (a–c) show the same area on one of the

* Received March 14, 1959.

† Institute of Chemistry, University of Uppsala, Uppsala, Sweden.

‡ Messrs. Johnson, Matthey & Co., London.

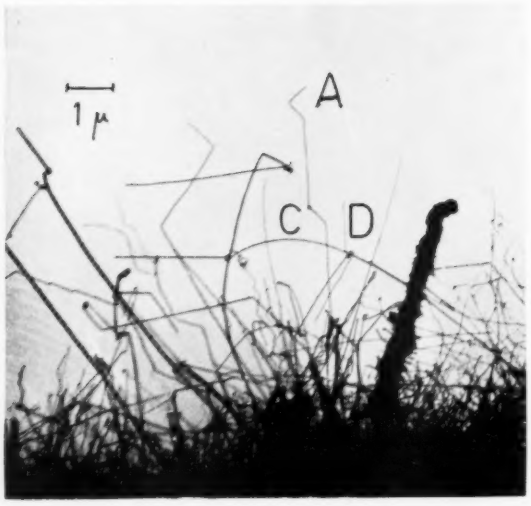


FIG. 1a. Growth after 304 hr sulphidation.



FIG. 1c. Growth after 448 hr sulphidation.

edges after 304, 376 and 448 hr sulphidation respectively. There is some difficulty in getting the sample into the exact position every time, due to the construction of the object holder, but this does not seriously affect the observations made. Fig. 2 shows a strip tarnished for the same length of time as 1c but allowed to remain in its hydrogen sulphide atmosphere for the duration of the reaction.

RESULTS

To determine the nature and growth direction of the needles electron diffraction was used. Diffraction pictures taken showed that the filaments were β-silver sulphide. The discovery of a solitary very long needle (see Fig. 3) made possible the determination of its growth direction. Unfortunately, attempts to reproduce a satisfactory print failed because of the small size of the diffraction spots. These spots were elongated in the growth direction of the crystal. Several spots not parallel to the majority were assumed to arise from another crystal in the vicinity and were not used in the indexing. The growth direction of the observed needle was $[\bar{4}14]$. The lattice parameters used[8] were $a = 9.531$ Å, $b = 6.925$ Å, $c = 8.278$ Å, $\beta = 123.85°$.

A comparison between Figs. 1a and 1b reveals that the needles grow from the tip (A). The sticking together of sulphide needles and growth around the place of contact[9] may be observed in Fig. 1b (B) as well as the breaking up of the junction in Fig. 1c (B). We have many examples of filaments with an offset



FIG. 1b. Growth after 376 hr sulphidation.

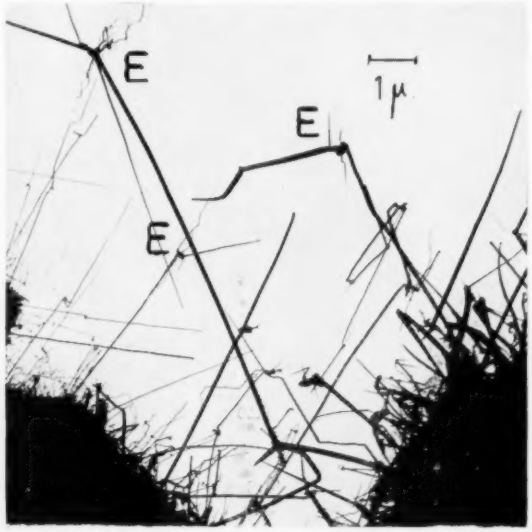


FIG. 2. Growth after 448 hr uninterrupted sulphidation.

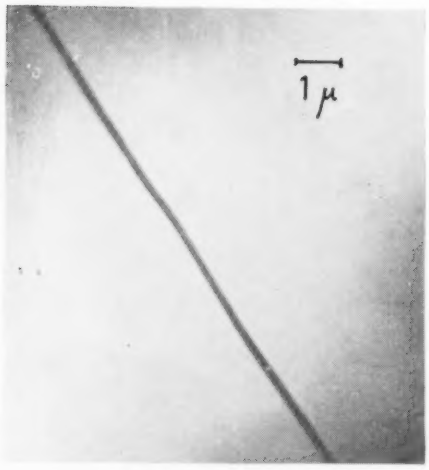


FIG. 3. Silver sulphide whisker.

portion as described by Arnold,[1] the most prominent one being (*A*). Perhaps the most interesting feature of the photographs is the curved whisker Fig. 1a–b (*C*) which is shown kinked in Fig. 1c (*C*). From the radius of curvature and the diameter of the whisker the elastic strain can be calculated. In this case it is found to be 1.3 per cent. This value is somewhat uncertain as we do not know the radius of curvature the moment before kinking, nor do we know if the whisker is in the same plane as the paper. This value of the elastic strain in a silver sulphide whisker is nevertheless of the same order as those found for other whiskers.[10,11] Many of the whiskers grow branches and even the curved whisker (*C*) displays a branch (*D*). The kinks often sprout small, irregular whiskers Fig. 2 (*E*). It seems that the exposure to air and/or the heating in the electron microscope influence the whisker growth, because after a picture is taken the filaments often change growth direction. Thus the control strip shown in Fig. 2 with its straight whiskers contrasts with the comparable Fig. 1c with its many irregular whisker tips.

It has been found that silver whiskers dissolve more slowly in nitric acid than does bulk silver and that the attack is at the tip.[12] During an attempt to dissolve silver sulphide whiskers in potassium cyanide solution, no attack at the tips or the kinks could be detected. Fig. 4a shows needle growth before submersion in 0.5N potassium cyanide solution and Fig. 4b after 12 min submersion. As a control measure, to ascertain if any change was due to the breaking of needles by water resistance or surface tension, the strip had been moved about in distilled water before taking picture 4a. Comparison of plates taken before and after the water treatment showed that very little change had occurred. After 12 min in the cyanide bath the formerly dull black silver plate had acquired a metallic lustre. Though the kinks and the tips suffered no visible attack many whiskers, especially the longest ones, are missing or found lying in a position more nearly parallel to the silver surface than before attack. A possible explanation is that solution takes place at the root. The whiskers seem to grow on "mounds".[6] These mounds are probably made up of many very small crystals and are thus more susceptible to attack than the highly perfect whiskers. The dissolving of the mounds would account for the "chopping down" of the whiskers and the metallic lustre acquired by the surface of the strip.



FIG. 4a. Needle growth before cyanide treatment.



FIG. 4b. Needle growth after cyanide treatment.

CONCLUSION

The silver sulphide whiskers investigated are single crystals of high perfection growing from their tips.

VOL. 8 1960

The whiskers seem to be situated on mounds that have a much less perfect structure. Kinks and branches are displayed by the whiskers.

ACKNOWLEDGMENTS

I wish to thank Prof. G. Hägg for the facilities placed at my disposal. Thanks are also due to Dr. H. Fischmeister and Mr. R. Rosenstein for valuable discussions. The work has been supported financially by a grant to Dr. H. Fischmeister from The Swedish Natural Science and Technical Research Councils.

REFERENCES

1. S. M. Arnold, *Tech. Proc. 43rd Ann. Convention Amer. Electroplaters Soc.* Bell Telephone System Monograph 2635 (1956).
2. J. Margottet, *C.R. Acad. Sci., Paris* **85,** 1142 (1877).
3. J. Margottet, *Annales de l'Ecole Normale superieure* **8**(2nd), 247 (1879).
4. C. Ringström, Communicated in discussion at the Scandinavian Corrosion Meeting, Stockholm (1958).
5. H. N. Terem, *Rev fac. sci. Univ. Istanbul* **18** A, 81 (1953).
6. H. Fischmeister and J. Drott, Presented at the Scandinavian Corrosion Meeting (1958). *Acta Met.* **7,** 777 (1959).
7. D. Gray, *Metal Finishing* **47,** 35 (1949).
8. S. Djurle, *Acta Chem. Scand.* **12,** 1427 (1958).
9. G. Pfefferkorn, *Tech. Mitt.* **47,** 452 (1954).
10. C. Herring and J. K. Galt, *Phys. Rev.* **85,** 1060 (1952).
11. W. W. Piper and W. L. Roth, *Phys. Rev.* **92,** 503 (1953).
12. J. F. Green and A. A. Woolf, *Research* **11,** 38 (1958).

THE HEATS OF FORMATION OF SOLID NICKEL-COPPER AND NICKEL-GOLD ALLOYS*

R. A. ORIANI† and W. K. MURPHY†

The enthalpies of formation at 640°C of solid Ni–Cu and Ni–Au alloys have been measured as a function of composition by means of a differential solution calorimeter. Both systems are characterized by positive heats of formation. The concentration variations of the partial molar heats of solution of Cu and of Ni in liquid Sn at 640°C have been explored. It is shown that Cu in Sn does not satisfy the requirements of the quasi chemical theory, whereas Ni in Sn does so within experimental uncertainty.

LES CHALEURS DE FORMATION DES ALLIAGES CUIVRE-NICKEL ET OR-NICKEL

Les enthalpies de formation à 640°C des alliages solides de cuivre-nickel et d'or-nickel ont été mesurées en fonction de la composition à l'aide d'un calorimètre différentiel.

Les deux systèmes sont caractérisés par des chaleurs de formations positives.

Les auteurs ont également examiné les variations, des chaleurs partielles molaires de solution du cuivre et du nickel dans l'étain liquide à 640°C en fonction de la concentration.

Ils ont montré que pour le cuivre ces variations ne satisfont pas aux exigences de la théorie quasi chimique tandis que celles du nickel dans l'étain y répondent bien, compte tenu des erreurs expérimentales.

WÄRMETÖNUNGEN VON NICKEL-KUPFER UND NICKEL-GOLD MISCHKRISTALLEN

Die Bildungsenthalpien von Ni–Cu und Ni–Au Mischkristallen wurden bei 640°C als Funktion der Zusammensetzung mit Hilfe eines differentiellen Lösungskalorimeters gemessen. Beide Systeme weisen eine positive Bildungswärme auf. Die Ändernugen der partiellen molaren Lösungswärmen von Cu und Ni in flüssigem Sn bei 640°C wurden in Abhängigkeit von der Konzentration untersucht. Es zeigt sich, dass Cu in Sn die Forderungen der quasichemischen Theorie nicht erfüllt, während diese bei Ni in Sn innerhalb der experimentellen Unsicherheiten erfüllt sind.

VOL.
8
1960

The solid solutions of nickel and copper are of interest because of the desirability of attempting to observe the energetic effect of the filling of the *d*-shell vacancies in nickel that occurs as copper is dissolved in the nickel. The nickel–gold alloy system is of interest because of the apparent anomaly represented by the finding[1] of positive short-range order in a miscibility gap system. The thermodynamics of this system has already been investigated[2] by a galvanic cell technique, but, because of the well known difficulties associated with the evaluation of properties that depend upon the temperature derivative of the cell e.m.f., it has been deemed worthwhile to carry out calorimetric measurements of the enthalpy of formation of the terminal solid solutions.

EXPERIMENTAL

The calorimeter employed in this work has been described in detail elsewhere.[3] It is a differential solution calorimeter employing liquid tin as solvent, one cell of which receives the alloy and the other cell the corresponding amount of the pure metals. The alloy and the metals are held in separate discharge chambers until they have attained the same temperature as the solvent tin, whereupon the metals are dropped into the respective solvent containers. The difference between the heats of solution in the two solvent containers is observed through an amplified differential thermocouple signal which is recorded before, during, and after the dissolution of the metals. Each cell was calibrated electrically at various solute concentrations during the course of the experiments; when the metal concentration in the tin reached about 5 at. % that charge of tin was replaced by a fresh charge. If the individual calibration factors of the two cells differed by more than the sum of the uncertainties in the knowledge of those calibration factors, then the apparent heats of formation were corrected for the deviation from twinness of the two cells.

Because of the slow rate of dissolution of pure nickel and of the nickel alloys into liquid tin, the calorimeter was operated at 640°C at the fastest available stirring rate. This high temperature, however, causes an appreciable deviation from Newtonian cooling, leading to greater difficulty in accounting for the heat lost during the long dissolution process. These difficulties, coupled with the smallness of the heats of formation, account for the magnitude of scatter in the final results.

* Received March 6, 1959.

† General Electric Research Laboratory, Schenectady, New York. Now at U.S. Steel Corporation, Edgar C. Bain Laboratory for Fundamental Research, Monroeville, Pennsylvania.

TABLE 1. Partial molar heats of solution in liquid tin

Solute 2	Temperature (°C)	$\overline{\Delta H}_2$ (s) (cal/g atom)	Deviation from least-squares line (cal/g atom)
Cu (s)	425	$2808 - 5238x_{Cu}$	±14
	640	$3312 - 7894x_{Cu}$	±20
Ag (s)	306	$3579 - 4322x_{Ag}$	±23
	450	$3729 - 6925x_{Ag}$	±12
	640	3785	
Ni (s)	640	$-9464 + 23770x_{Ni}$	±80

RESULTS

The variation with concentration of the partial molar enthalpy of solution of solid copper and of solid nickel into liquid tin at 640°C has been obtained incidentally to the main investigation. This information is of interest in connection with the adequacy of statistical models for describing very dilute solutions.[4] The present results, to which have been added relevant data from prior work,[4] are collected in Table 1. The equations for $\overline{\Delta H}_2(s)$ for solid Cu and Ni at 640°C represent the present experimental work up to a solute concentration in tin of 0.013 mole fraction, whereas the equations based on prior work[4] at the lower temperatures represent data up to a solute concentration of 0.02 mole fraction.

Fig. 1 presents the enthalpy of formation of solid Ni–Cu solutions from the solid components at 640°C. The vertical bars represent the mean deviation of the data, based on at least three totally independent determinations at any one composition. The accuracy of the data may be partially evaluated from the estimated inaccuracies of about ±0.5 per cent in the knowledge of the calibration factors, and about ±0.2 per cent for the chemical composition of the alloys. The enthalpy of formation of solid Ni–Au solutions is shown in Fig. 2; a dotted line represents the course of the curve in the two-phase field.

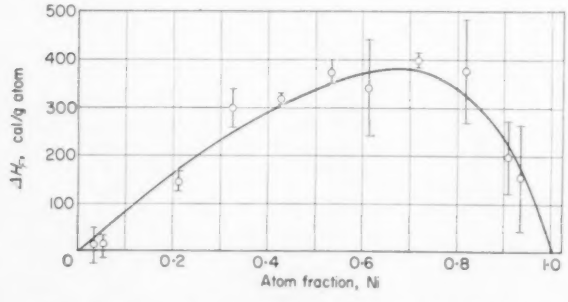


FIG. 1. The enthalpy of formation of nickel–copper solid solutions at 640°C; the reference state is the pure components at 640°C.

DISCUSSION

It has previously been pointed out[4] that the variation with concentration of the partial molar heats of solution of the liquid noble metals in liquid tin at low concentrations cannot be described by any variant of the quasi-chemical model that assumes the constancy of the pairwise interaction energies. The same statement can be made for the present data for Cu in liquid Sn at 640°C. However, it is interesting, though fortuitous, that the concentration variation for liquid nickel dissolved in liquid tin does agree, within experimental uncertainty, with the Bragg–Williams approximation.

$$\overline{\Delta H}_{Ni(l)} = \overline{\Delta H}_{Ni(l)}\,(1 - x_{Ni})^2$$

The results in Table 1 show that $(\partial \Delta H_2/\partial x_2)_T$ for both Cu and Ag varies markedly with temperature, but the physical reason for this variation is not at all understood.

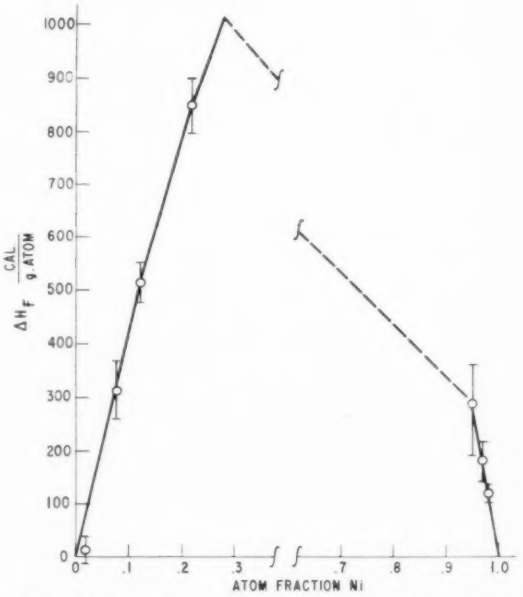


FIG. 2. The enthalpy of formation of nickel–gold solid solutions at 640°C; the reference state is the pure components at 640°C.

Kubaschewski *et al.*[5] have obtained a value of about 540 cal/g atom for the enthalpy of formation of equiatomic Ni–Cu solution at 722°C by means of a reaction calorimeter. Since the ΔH_F of these alloys may have some temperature variation because of the ferromagnetic character of nickel, it cannot be stated whether or not there is agreement between these authors' work and the present data at 640°C. The same comment applies more strongly to the preliminary results of Leach[6] for the ΔH_F of solutions in the composition range 20–40 at % nickel in copper

at 0°C. The present results confirm calculated values of ΔH_F for Cu–Ni by Meijering[7] but disagree markedly with the calculations of Rastogi and Verma[8], who propose a ΔH_F curve rising to 2000 cal/g atom at $x_{Ni} = 0.3$, and dropping to −7500 cal/g atom at $x_{Ni} = 0.8$. The positive character of ΔH_F for Ni–Cu found in the present work is in qualitative agreement with the positive excess free energy of solution found by Nanis[9] and by Pratt[10], both by electrochemical cells, and that calculated by Alcock[11] from the measurements of Fukusima and Mitui[12] on the solubility of hydrogen in Ni–Cu alloys. The positive nature of the ΔH_F leads one, according to the quasi-chemical model, to expect clustering (negative short-range order) in the Ni–Cu solid solutions. It is interesting that Köster and Schüle[13] have concluded that clustering exists, from the behavior during ageing of the electrical resistivity and of the Hall coefficient of Ni–Cu alloys, although such a conclusion can only be a tentative one. The same conclusion has been reached by Ryan *et al.*[14] from the variation of magnetic susceptibility upon neutron irradiation.

The scatter in the present results for Ni–Cu prevents us from seeing the effect, if any, upon the energetics due to the completion of the filling of the *d*-shell vacancies in nickel at $x_{Cu} = 0.6$. An interesting feature of the ΔH_F curve is the marked assymmetry, such that the addition of Cu to pure Ni leads to a much larger endothermic effect than does the addition of Ni to pure Cu.

The present results for the Ni–Au solid solutions at 640°C show positive values for ΔH_F, as is to be expected for a miscibility gap system. The magnitudes are smaller, by a factor of about two, than those obtained by Seigle *et al.*[2] using a galvanic cell technique at 900°C. The disparity between the two sets of data probably cannot be reconciled through the temperature variation of the ΔH_F, as evidenced[15] by the smallness of the ΔC_P of formation of an almost equitomic alloy. The present results confirm the surmise of Kubaschewski and Catterall[16] that the enthalpy of formation is probably smaller than that given by Seigle *et al.* and agree qualitatively with the preliminary calorimetric results of Genta.[17]

If one assumes that the excess free energy of formation as measured by Seigle *et al.* is correct, though the quantities depending on the temperature dependence of the galvanic cell e.m.f. are not, and if one adopts a value, extrapolated from the present work, of about 1500 cal/g atom for the heat of formation at 900°C for $Ni_{0.5}$ $Au_{0.5}$, one obtains $\Delta S^e \approx 0.4$ cal/g atom-deg instead of the 1.47 cal/g atom-deg of reference 2. The excess entropy of formation of 0.4 must be compared with the value of 1.07 ± 0.2 cal/g atom-deg measured by DeSorbo[18] and Oriani[15] for the vibrational contribution to the excess entropy of formation. This means that the equitomic Ni–Au alloy has a magnetic contribution to the entropy of formation of about −0.7 cal/g atom-deg.

The question of whether or not the Ni–Au system exhibits positive short-range order is at present an open one, since recent work of Münster and Sagel[19] disagrees with that of Flinn *et al.*[1] in finding negative, not positive, short-range order. The present work cannot help decide between these two investigations because, even though quasi-chemical theory unambiguously associates a positive heat of formation with negative short-range order, physically and more realistically there need not be a correlation between the two.[4] This is basically because the kind and extent of short-range order in the solution depend upon the relative values of the pairwise bonding energies among the various kinds of pairs as these exist in the solution, and not on the energies in the pure components; on the other hand, the sign and magnitude of the ΔH_F values depend markedly upon the properties of the pure components.

VOL. 8 1960

REFERENCES

1. P. A. Flinn, B. L. Averbach and M. Cohen, *Acta Met.* **1,** 664 (1953).
2. L. L. Seigle, M. Cohen and B. L. Averbach, *J. Metals, N.Y.* **4,** 1320 (1952).
3. R. A. Oriani and W. K. Murphy, *J. Phys. Chem.* **62,** 327 (1958).
4. R. A. Oriani and W. K. Murphy, *Proceedings of the Symposium on Physical Chemistry of Metallic Solutions*, National Physical Laboratory, Teddington (1958).
5. O. Kubaschewski, W. A. Dench and V. Genta, *Proceedings of the Symposium on Physical Chemistry of Metallic Solutions*, National Physical Laboratory, Teddington (1958).
6. J. S. Ll. Leach. Private communication; J. S. Ll. Leach and M. B. Bever, *Trans. Amer. Inst. Min. (Metall.) Engrs.* **215,** 708 (1959).
7. J. L. Meijering. Private communication.
8. R. P. Rastogi and K. T. R. Verma, *Current Science, India* **24,** 336 (1955).
9. L. S. Nanis. Master's Thesis, Massachusetts Institute of Technology (1954).
10. J. Pratt. Private communication.
11. C. B. Alcock, *Proceedings of the Symposium on Physical Chemistry of Metallic Solutions*, National Physical Laboratory, Teddington (1958).
12. M. Fukusima and S. Mitui, *Sci. Rep. Tohoku Univ., Honda Anniv. Vol.* 940 (1936).
13. W. Köster and W. Schüle, *Z. Metall.* **48,** 592 (1957).
14. F. M. Ryan, E. W. Pugh and R. Smoluchowski. Private communication; *Bull. Amer. Phys. Soc.* (March 1959).
15. R. A. Oriani, *Acta Met.* **3,** 232 (1955).
16. O. Kubaschewski and J. A. Catterall, *Thermochemical Data of Alloys*. Pergamon Press, London (1956).
17. V. Genta, ref. 16, p. 50.
18. W. DeSorbo, *Acta Met.* **3,** 227 (1955).
19. A. Münster and K. Sagel, *Proceedings of the Symposium on Physical Chemistry of Metallic Solutions*, National Physical Laboratory, Teddington (1958).

GRAIN-BOUNDARY ENERGIES IN GOLD–COPPER ALLOYS*

J. E. HILLIARD,† M. COHEN‡ and B. L. AVERBACH‡

The ratio of grain-boundary to surface energy has been determined as a function of composition in the gold–copper system. From interferometric measurements of the boundary groove angles in specimens thermally etched at 850°C, the following average grain-boundary to surface-energy ratios were obtained: 0.25, 0.28, 0.34, 0.42, 0.37, and 0.36 at 0, 20, 40, 60, 80, and 100 at. % copper, respectively. Existing data for the surface energies yield 370, 320, 310, 390, 430 and 590 erg cm^{-2}, respectively, for the absolute grain-boundary energies. A calculation is included of the boundary adsorption corresponding to this energy variation, and an estimate is made of the minimum number of atoms required at the grain boundary to accommodate the calculated absorption.

ENERGIES DES JOINTS DE GRAINS DANS LES ALLIAGES OR-CUIVRE

Les auteurs ont déterminé le rapport entre l'énergie de joint de grains et énergie de surface dans le système or-cuivre en fonction de la composition des alliages.

Par des mesures interférométriques des angles de frontière d'échantillon attaqués thermiquement à 850°C, les rapports suivants ont été obtenus: 0,25, 0,28, 0,34, 0,42, 0,37 et 0,36 à 0,20, 0,40, 0,60, 0,80 et 100%.

Les données existantes pour les énergies de surface sont respectivement de: 370, 320, 310, 390, 430 et 590 erg cm^{-2}.

Pour les énergies absolues de frontière les auteurs donnent également une méthode de calcul de l'adsorption de frontière correspondant à cette variation d'énergie et une estimation du nombre minimum d'atomes requis au joint en fonction de l'adsorption calculée.

KORNGRENZENENERGIEN VON GOLD-KUPFER LEGIERUNGEN

Im Kupfer–Gold System wurde das Verhältnis der Korngrenzenenergie zur Oberflächenenergie als Fumktion der Zusammensetzung bestimmt. Nach einer thermischen Ätzung der Proben bei 850°C wurden die Furchenwinkel der Korngrenzen interferometrisch gemessen. Es ergaben sich folgende durchschnittliche Verhältnisse der Korngrenzenenergie zur Oberflächenenergie: 0,25, 0,28, 0,34, 0,42, 0,37 und 0,36 bei 0, 20, 40, 60, 80, beziehungsweise 100 Atom% Cu. Vorhandene Daten der Oberflächenenergien liefern für die absoluten Korngrenzenenergien 370, 320, 310, 390, 430, beziehungsweise 590 erg cm^{-2}. Die Absorption an der Korngrenze wird entsprechend diesem Energieverlauf berechnet und es wird eine Abschätzung mitgeteilt über die Mindestzahl von Atomen, die in der Korngrenze notwendig sind, um mit der berechneten Absorption übereinzustimmen.

1. INTRODUCTION

Although the orientation dependence of grain-boundary energies has been extensively studied, surprisingly little attention has been given to their variation with composition. In fact, the present investigation on Au–Cu alloys seems to be the first to permit an evaluation of boundary energies over the complete compositional range of an alloy system. The measurements to be reported are those for the ratio of grain-boundary to surface energy. The results of a complementary study on the surface energies by White *et al.*[1] were used to derive the absolute boundary energies.

The technique employed was that of measuring the grain-boundary groove angle at the surface of a thermally etched specimen. This groove results from the local equilibrium between the boundary and surface energies (Fig. 1). The equilibrium configuration of the three boundaries depends not only on their relative energies but also, as was shown by Herring[2], on the derivatives of the energies with respect to orientation. Unfortunately, some of the latter quantities are neither known nor readily measureable. It is, therefore, customary to assume that the energies are isotropic. With this condition, it is easily shown that at equilibrium,

$$\sigma_{GB}/\sigma_S = 2\cos(\theta/2), \tag{1}$$

in which σ_{GB} is the grain-boundary energy, σ_S the surface energy, and θ the boundary groove angle. A measurement of θ thus yields the ratio (σ_{GB}/σ_S).

2. PREPARATION OF SPECIMENS

Five alloys with nominal compositions of 20, 40, 50, 60, and 80 at. % Cu were prepared from 99.99+% Au and 99.999% Cu. The charges were induction

* This work was performed in the Department of Metallurgy at the Massachusetts Institute of Technology under the sponsorship of the United States Atomic Energy Commission. Received March 9, 1959.

† Present address: General Electric Research Laboratory, Schenectady, New York.

‡ Department of Metallurgy, Massachusetts Institute of Technology, Cambridge 39, Massachusetts.

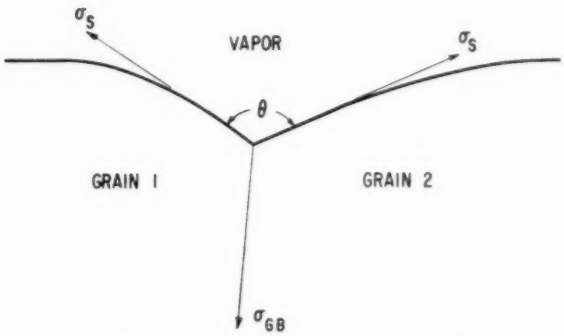


FIG. 1. Equilibrium between the grain-boundary energy, σ_{GB}, and the surface energy, σ_s, at a thermally etched grain-boundary groove.

melted in recrystallized alumina crucibles and bottom-poured into a chill mold. Both the melting and casting were carried out under vacuum. Samples of the pure components were cut from the as-received materials which were in the form of $\frac{1}{4}$ in. rod. All specimens were homogenized at 850°C for 1 week under purified argon.

Since attempts at electropolishing were unsuccessful, the specimens had to be mechanically polished. This was done as carefully as possible on diamond grit wheels with alternate etching to minimize surface distortion. The specimens were then placed in individual Vycor tubes, and heated for a few minutes in purified hydrogen to reduce possible surface oxides. Immediately afterwards, the tubes were evacuated and sealed off.

In any given run, the specimens were first heated at a few degrees below their melting points for about 30 min to minimize subsequent grain-boundary migration. The furnace temperature was then lowered, and the specimens held at 850 $\pm$ 2°C for 3–6 days for the thermal etching of the grain boundaries.

3. MEASUREMENT OF THE BOUNDARY GROOVE ANGLE

The groove profile, and hence the angle, was determined interferometrically—a technique which has also been used by Mykura[3]. About half of the measurements were made with a conventional Bausch and Lomb metallograph and the remainder with a Zeiss interference microscope.

The only modification required with the metallograph was the replacement of the illuminator by a monochromatic source. This consisted of a high intensity mercury arc lamp and a filter to isolate the 5461 Å mercury line. A cover glass silvered to give about 50 per cent reflectivity was used as an optical flat. The silvered side of the cover glass was held in close contact with the specimen surface by a thin film of immersion oil which also served to improve the fringe contrast. With the set-up just described, the optical flat was essentially parallel to the specimen surface so that a grain-boundary groove produced a set of approximately parallel fringes, as shown in Fig. 2.



FIG. 2. Interferogram of grain-boundary grooves taken on a standard metallograph with ×41 objective Hg light source (λ = 5461 Å) magnification ×1000

The interference microscope was of the Linnik type in which the specimen and optical flat were viewed by separate objectives. With this arrangement, the inclination of the optical flat to the specimen surface was readily adjustable. However, this microscope gave strictly two-beam interference, whereas the partially reflecting cover glass provided some degree of multibeam interferometry. The latter resulted in a sharper fringe pattern, as will be seen from a comparison of Figs. 2 and 3a. The type of interferogram shown in Fig. 3b was obtained when the optical flat was inclined to the surface. This gave a direct representation of the groove profile and was particularly useful in detecting abnormalities such as an abrupt change of slope in the groove wall. (Such a discontinuity would be expected at certain critical orientations if the surface energy were sufficiently anisotropic.)

The parallel-fringe pattern (Figs. 2 and 3a) proved the more suitable for estimating the groove angles encountered in the present work. The interference

VOL. 8 1960

patterns were photographed and the distance between fringes measured on the negative. These observations together with a determination of the magnification permitted the groove profile to be plotted as shown in Fig. 4a. For a straight groove wall making an angle ϕ with the optical flat, the spacing between fringes would be expected[4] to correspond to a change in depth of $\lambda/2\mu \cos \phi$, where λ is the wavelength of the light and μ the refractive index of the immersion oil. Since in the present work $\phi < 14°$, the factor of $\cos \phi$ was sufficiently close to unity to be neglected.

A more serious source of error has been discovered by Tolmon and Wood[5]. These authors found experimentally that, with objectives of high numerical aperture (such as were used in the present work), the vertical interval between fringes was about 10 per cent greater than $\lambda/2\mu$. They attributed the increase to the convergence of the illumination from the objective. To correct for this effect in the present work, a vertical interval of 1.1 $\lambda/2\mu$ was adopted in plotting the groove profiles. This yielded a relative grain-boundary energy approximately 10 per cent greater than if an interval of $\lambda/2\mu$ had been used.

In nearly every instance, the cross-section of the groove walls obeyed a relationship of the form

$$Y = aX - bX^2 + c,$$

where Y and X are coordinates normal and parallel, respectively, to the specimen surface, and a, b, and c are constants. Although this relationship was discovered empirically, its use was later justified theoretically by Mullins.[6] Instead of attempting to determine graphically the groove angle at the root, a method was adopted to take advantage of the parabolic profile. The fringe spacings on each side of the groove were plotted (Fig. 4b) as Y/X vs. X, with Y and X measured from an origin located at the fringe nearest to the root of the groove. Hence, $c = 0$. If δ_1 is the lateral distance between the origin and the root of the groove, and θ_1 the angle at the root made by the groove wall with the Y-axis, then

$$\begin{aligned} \cot \theta_1 &= [dY/dX]_{X=-\delta_1}, \\ &= a + 2b\delta_1, \\ &= [Y/X]_{X=-2\delta_1}. \end{aligned}$$

Thus cot θ_1, and similarly cot θ_2, are given by the construction shown in Fig. 4b.

The reproducibility of the interferometric technique was checked by making a sequence of observations at short intervals along a boundary. For a groove angle of 160°, the measurements agreed within 0.1°.

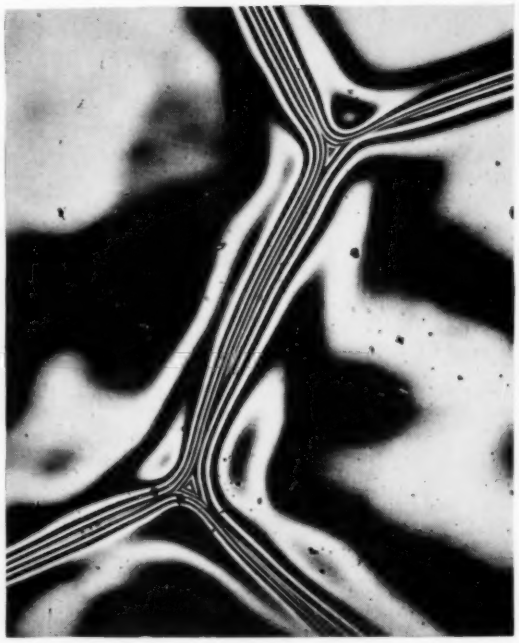


FIG. 3a. Interferograms of grain boundary grooves, taken on interference microscope with thallium light source. ($\lambda = 5350$ Å) Magnification ×900. Optical flat parallel to specimen surface.

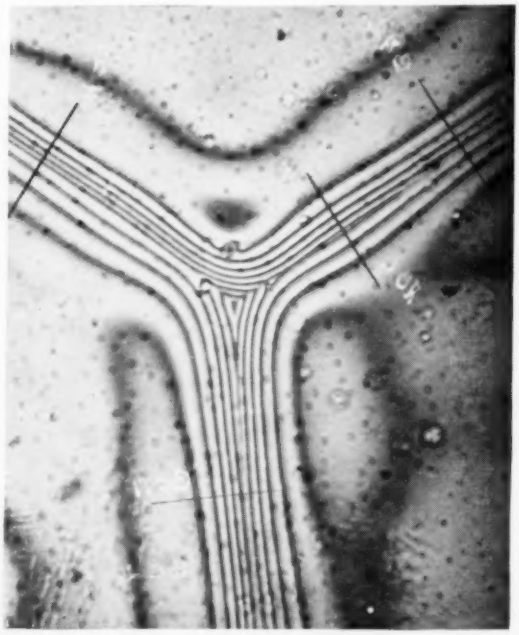


FIG. 3b. Interferograms of grain boundary. Grooves, taken on interference microscope with thallium light source. ($\lambda = 5350$ Å) Magnification ×900. Optical flat inclined to specimen surface.

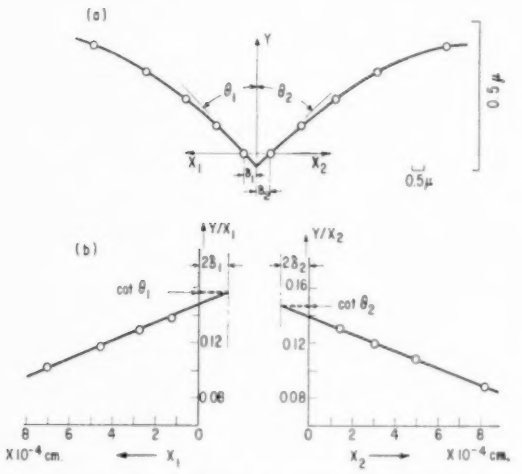


FIG. 4. (a) Profile of grain boundary groove from measurements on parallel-fringe pattern. (b) Derived plot of y/x versus x.

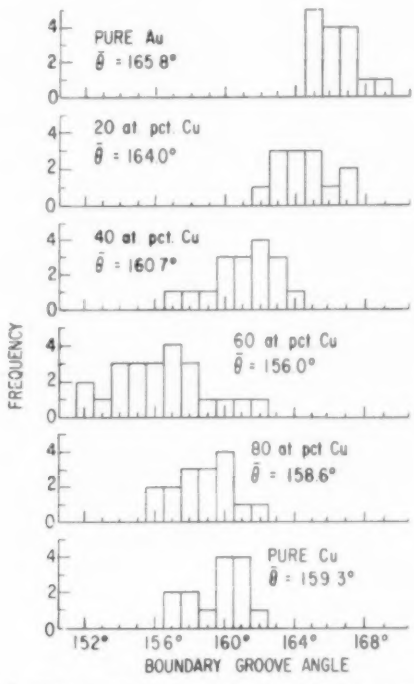


FIG. 5. Plots of frequency of grain boundary groove angle, θ, versus θ for six Au–Cu alloys thermally etched at 850°C.

An additional advantage of this technique is that the percentage error in estimating the relative boundary energy should be approximately independent of the absolute value of the energy, whereas any method which utilizes a direct measurement of the groove angle will have a percentage error that becomes infinite as the absolute energy approaches zero.

EXPERIMENTAL RESULTS

For the alloy containing 50 at. % Cu, measurement of the groove angles was precluded by severe distortion of the surface. This distortion was presumably caused by the ordering transformation and occurred even when the specimens were quenched from the thermal-etching temperature. No trouble was encountered with the other compositions.

Only well developed grooves were selected for analysis; low-energy boundaries were excluded. Care was also exercised to ensure that the measured groove was actually attached to a grain boundary and was not merely a scar left behind by a moving boundary.

From the frequency plots in Fig. 5, it will be seen that the groove angles for a particular alloy ranged over several degrees. Such a spread has been observed in all previous measurements and presumably arises from some anisotropy in the boundary and surface energies.

Satisfactory agreement was found with the previous work of Bailey and Watkins[7] on pure copper; they have reported groove angles of 158° and 160° for specimens thermally etched in hydrogen at 800° and 900°C, respectively. However, the groove angle of 165.8° for pure gold was somewhat larger than the 164.5° measured by Buttner *et al.*[8] on fine gold wires thermally etched at 1027°C. The former angle gives a ratio for σ_{GB}/σ_S about 9 per cent less than the latter. It is unlikely that this discrepancy can be accounted for by the difference in temperature of the two sets of measurements, because for copper it is known[9] that the ratio σ_{GB}/σ_S is essentially constant over the range 825° to 1070°C. However, the discrepancy could be explained by the fact that the boundaries observed by Buttner *et al.* were mainly between (100) and/or (111) faces, and might therefore have an average energy different from that characteristic of the specimens studied here.

The relative boundary energies, σ_{GB}/σ_S, calculated from the average groove angles by use of equation (1) are plotted as a function of composition in Fig. 6a. Though two separate curves meeting in a peak could have been drawn through the experimental points, it was considered preferable to smooth the data in plotting the absolute grain-boundary energies (Fig. 6c). The latter were derived from the surface-energy data (Fig. 6b) of White *et al.*[1] These values were obtained at temperatures ranging from 880° to 1050°C. (approximately 99 per cent of the solidus temperature for each alloy). In the pure components, the surface energies decrease[10] with increasing temperature at 4–10 per cent per 100°C. However, because the

VOL. 8 1960

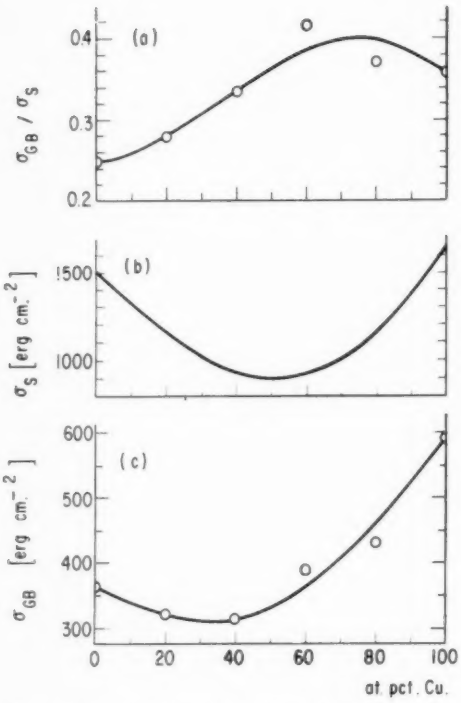


FIG. 6. Compositional variation in the Au–Cu system of
(a) The ratio σ_{GB}/σ_S.
(b) The surface energy, σ_S, (from data of White, Adams and Wulff[1]), and,
(c) The grain boundary energy, σ_{GB}.

temperature dependence in the alloys is unknown, no attempt was made to correct the surface energies to the 850°C isotherm employed for the grain-boundary measurements. As a result, the absolute values plotted in Fig. 6c may be several per cent lower than the true energies.

4. DISCUSSION

In the absence of a specific model for a high-angle boundary, no quantitative explanation can be offered for the compositional dependence of σ_{GB}. However, because of the appreciable difference in atomic sizes of the components in this system, the observed decrease in σ_{GB} on alloying is not unexpected. With atoms of different sizes available, it is reasonable to suppose that a better fit, and thus a lower energy, can be attained at alloy boundaries than at pure-metal boundaries.

We will now consider the application of the present results to the calculation of the adsorption at the grain boundaries. At constant temperature, the Gibbs adsorption equation gives

$$-(d\sigma_{GB}/dx) = \Gamma_{Cu}(d\mu_{Cu}/dx) + \Gamma_{Au}(d\mu_{Au}/dx) \quad (2)$$

in which x is the atomic fraction of copper in the bulk alloy, μ the chemical potential, and Γ the excess amount of component at the boundary. Following Gibbs[11], we will define the excess as the difference per unit area of boundary between the actual number of atoms of a component in the alloy and the number that would have been present in the same volume if the material on each side of the boundary had remained unchanged up to an imaginary dividing surface. Since we are considering a grain boundary between two identical phases, the excess quantities are independent of the location of this dividing surface.

Because there is only a single equation relating Γ_{Cu} and Γ_{Au} to the observed thermodynamic properties, it is not possible to estimate the individual values of the two excesses. However, as was pointed out by Cahn and Hilliard[12], we can obtain a parameter $\Gamma_{Cu(Au)}$ defined by

$$\Gamma_{Cu(Au)} = \Gamma_{Cu} - x\Gamma_{Au}/(1-x);$$

since, by application of the Gibbs–Duhem relation

$$x(d\mu_{Cu}/dx) + (1-x)(d\mu_{Au}/dx) = 0,$$

equation (2) can be rewritten

$$\begin{aligned} -(d\sigma_{GB}/dx) &= (d\mu_{Cu}/dx)[\Gamma_{Cu} - x\Gamma_{Au}/(1-x)], \\ &= (d\mu_{Cu}/dx)\Gamma_{Cu(Au)}. \end{aligned} \quad (3)$$

The parameter $\Gamma_{Cu(Au)}$ can be regarded as the excess number of copper atoms over the quantity that would be required just to maintain the bulk composition at the boundary with the quantity of gold actually present.

Similarly, for $\Gamma_{Au(Cu)}$ we have

$$\begin{aligned} \Gamma_{Au(Cu)} &= \Gamma_{Au} - (1-x)\Gamma_{Cu}/x, \\ &= -[(1-x)/x]\Gamma_{Cu(Au)}. \end{aligned} \quad (4)$$

The values of $\Gamma_{Cu(Au)}$ and $\Gamma_{Au(Cu)}$ given in Table 1 were computed by substituting in (3) the values of $d\sigma_{GB}/dx$ and $d\mu_{Cu}/dx$ listed in columns 2 and 3. The derivative $d\sigma_{GB}/dx$ was determined from the slope of the σ_{GB} vs. x curve in Fig. 6c. For the evaluation of $d\mu_{Cu}/dx$ the thermodynamic data selected by Kubaschewski and Catterall[13] were used in conjunction with the relation:

$$\begin{aligned} d\mu_{Cu}/dx = (kT/x) + (1-x)^2 \times \\ (d/dx)[F_{Cu}{}^E/(1-x)^2] - 2F_{Cu}{}^E/(1-x), \end{aligned}$$

in which $F_{Cu}{}^E$ is the excess partial free energy of copper. This procedure is less susceptible to error than direct measurement of the slope of a μ_{Cu} vs. x plot.

The calculated values of $\Gamma_{Cu(Au)}$ and $\Gamma_{Au(Cu)}$

TABLE 1. Adsorption at the grain boundaries of Au–Cu alloys at 850°C

1	2	3	4	5
At. fract. of Cu(x)	$d\mu_{Cu}/dx$ (erg. atom^{-1} $\times$ 10^{+13})	$d\sigma_{GB}/dx$ (erg. Å^{-2} $\times$ 10^{+13})	$\Gamma_{Cu(Au)}$ (atom. Å^{-2})	$\Gamma_{Au(Cu)}$ (atom. Å^{-2})
0.1	15.5	−0.25	0.016	−0.15
0.2	9.1	−0.14	0.015	−0.062
0.4	7.0	0.09	−0.012	0.019
0.6	6.3	0.34	−0.054	0.036
0.8	3.8	0.58	−0.15	0.038
0.9	2.3	0.69	−0.30	0.033

provide an indication of the minimum number of atoms that must be associated with the grain boundary. This can be demonstrated as follows.

Let us suppose that the alloy composition and density remain unchanged up to within a certain number of atomic layers on each side of the grain boundary. The change in composition and other effects of the boundary are thus confined to a region bounded by two imaginary dividing surfaces. Let N be the actual number of atoms in this region per unit area of grain boundary, and α the number which would have been present in the absence of the grain boundary. Then, if x^B is the average atomic fraction of copper in the boundary region, we have by definition of the excess quantities

$$\Gamma_{Cu} = Nx^B - \alpha x,$$

and

$$\Gamma_{Au} = N(1 - x^B) - \alpha(1 - x).$$

Eliminating α, we obtain

$$\begin{aligned} N(x^B - x)/(1 - x) &= \Gamma_{Cu} - [x/(1 - x)]\Gamma_{Au} \\ &= \Gamma_{Cu(Au)}, \end{aligned}$$

which, on rearrangement, yields

$$N = [(1 - x)/(x^B - x)]\Gamma_{Cu(Au)}. \qquad (5)$$

Now the atomic fraction, x^B, must lie in the range $0 \leq x^B \leq 1$. This requirement in conjunction with (5) leads to the following inequalities:

$$N \geq \Gamma_{Cu(Au)}, \quad \text{if} \quad \Gamma_{Cu(Au)} > 0;$$

and

$$N \geq -[(1 - x)/x]\Gamma_{Cu(Au)} = \Gamma_{Au(Cu)}, \quad \text{if } \Gamma_{Cu(Au)} < 0. \qquad (6)$$

In other words, a certain minimum number of atoms is required in the boundary region to accommodate the excess or deficiency of copper atoms.

Applying (6) to the data given in columns 4 and 5 of Table 1, it will be seen that the greatest minimum value required for N is 0.038 atom Å^{-2} at $x = 0.8$. The average lattice parameter is approximately 3.8 Å, so that a single (100) plane in the *bulk* alloy will contain 0.14 atom Å^{-2}. Thus, providing the density of the grain-boundary region is not less than 0.038/0.14 ($\sim$1/4) that of the bulk alloy, the excess gold at $x = 0.8$ *could* be accommodated in a monolayer.

It must be emphasized that the preceding computation only provides an estimate of the *minimum* number of atoms associated with a unit area of the grain boundary. Unfortunately, there is no method of calculating thermodynamically from the available data the actual thickness, composition and density of the boundary.

REFERENCES

1. S. S. WHITE, C. M. ADAMS and J. WULFF, *Trans. Amer. Inst. Min. (Metall.) Engrs.* To be published.
2. C. HERRING, *The Physics of Powder Metallurgy*, (Edited by W. E. KINGSTON), p. 143. McGraw-Hill, New York (1951).
3. H. MYKURA, *Acta Met.* **3**, 436 (1955).
4. H. MYKURA, *Proc. Phys. Soc.* **67**B, 281 (1954).
5. F. R. TOLMON and J. G. WOOD, *J. Sci. Instr.* **33**, 236 (1956).
6. W. MULLINS, *J. Appl. Phys.* **28**, 333 (1957).
7. G. L. C. BAILEY and H. C. WATKINS, *Proc. Phys. Soc. Lond.* **63**B, 350 (1950).
8. F. H. BUTTNER, H. UDIN and J. WULFF, *Trans. Amer. Inst. Min. (Metall.) Engrs.* **197**, 313 (1953).
9. N. GJOSTEIN, Private Communication.
10. H. UDIN, *Metal Interfaces*, p. 122. American Society for Metals, Cleveland (1952).
11. J. W. GIBBS, *Collected Works*, Vol. 1, p. 224. Yale University Press, New Haven (1948).
12. J. W. CAHN and J. E. HILLIARD, *Acta Met.* **7**, 219 (1959).
13. O. KUBASHEWSKI and J. A. CATTERALL, *Thermochemical Data of Alloys*, p. 61. Pergamon Press, London (1956).

VOL. 8 1960

SOLUTION HARDENING BY INTERACTION OF IMPURITY GRADIENTS AND DISLOCATIONS*

R. L. FLEISCHER†

The Cottrell interaction[3] between dislocations and impurity atoms may give rise to significant interaction stresses when the impurity concentration is not uniform.

DURCISSEMENT DE SOLUTION PAR INTERACTION DE GRADIENTS D'IMPURETES ET DE DISLOCATIONS

L'interaction de Cottrell entre les dislocations et les atomes d'impuretés peut donner lieu à des tensions importantes lorsque la concentration en impuretés n'est pas uniforme.

HÄRTESTEIGERUNG INFOLGE WECHSELWIRKUNG VON VERSETZUNGEN MIT DEM KONZENTRATIONSGRADIENTEN GELÖSTER VERUNREINIGUNGEN

Die Cottrellsche Wechselwirkung zwischen Versetzungen und Verunreinigungsatomen kann beträchtliche Wechselwirkungsspannungen verursachen, wenn die Konzentration der Verunreinigung nicht konstant ist.

It has been realized, since it was pointed out qualitatively by Parker and Hazlett[1], that nonuniform distributions of impurity atoms should contribute to solution hardening. It is the purpose of this discussion to describe possible mechanisms of such hardening and to indicate in some detail how one of these should affect the motion of dislocations. The results will then be compared to some existing experimental data.

Three types of interaction will be mentioned here: (i) lattice parameter interactions, (ii) elastic constant interactions, and (iii) Cottrell interactions. Lattice parameter interaction may be considered as follows: If solute concentration varies over many atomic distances, a variation in lattice parameter will result. If an edge dislocation then moves along a direction in which this variation occurs (or a screw dislocation moves perpendicular to such a direction), either a dislocation-like displacement or a misfit across the slip plane will be created by the dislocation. Since either implies an increase in energy, the dislocation will be retarded by a force given by the rate of increase of the appropriate energy.

Elastic constant interactions arise because the elastic "constants" are not constant when there are variations in composition. Head[2] has indicated how abrupt changes may give rise to forces on dislocations. His approach may be applied to continuous changes also. Hardening due to lattice parameter or elastic constant changes is relevant to other cases in addition to solution hardening. A separate discussion is planned.

Cottrell interaction is the elastic interaction of a dislocation with impurity atoms,[3] summed for all the atoms in the stress field. A calculation will be made for the Cottrell interaction in a two-dimensional case with a simple one-dimensional variation of impurity concentration. Throughout the following it will be assumed that only low temperatures are involved, low in the sense that migration of atoms or vacancies is negligible. Hence the solute distribution remains constant and dislocation climb is absent.

CALCULATION OF COTTRELL INTERACTION

Let us suppose that the impurity distribution varies in the x-direction only and that the dislocation remains essentially straight; then, if an edge dislocation glides in the x-direction, equal numbers of impurity atoms enter the compression and the tension regions on either side of the slip plane. There is then no net difference in total energy. But if the dislocation glides toward the impurities at an angle to the x-direction, this is no longer true, since the stress field encounters more impurity atoms on one side of the slip plane than the other. Now an estimate of the interaction energy and the resultant force on a dislocation is made for a simple impurity distribution.

Given an edge dislocation (Fig. 1) whose stress field extends over an effective radius r_∞, in a region where at a distance x_0 the concentration of impurities changes from $c = 0$ to $c = c_0$, it is desired to find the energy of interaction of the dislocation with the impurities.

The energy of interaction of one such atom a distance r from the dislocation is, according to Bilby's refinement[4] of Cottrell's result,

$$E_0 = A \sin (\theta - \phi)/r,$$

* Received April 9, 1959.

† Metals Processing Laboratory, Department of Metallurgy, Massachusetts Institute of Technology, Cambridge, Massachusetts.

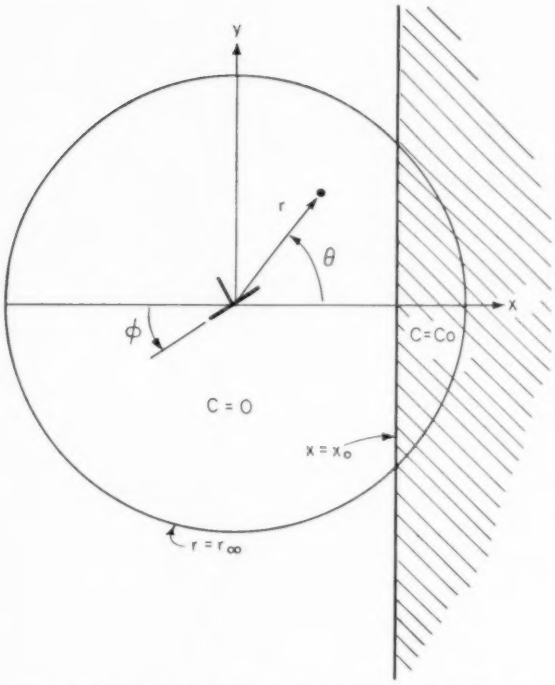


FIG. 1. Edge dislocation in a medium containing a discontinuity in solute concentration.

where the edge dislocation is tilted by an angle ϕ relative to the X-axis. $A = 4Gr_0^3\, b\varepsilon$, where G = shear modulus, r_0^3 = atomic volume, b = slip distance, and $\varepsilon = (R - r_0)/r_0$, where R^3 = volume of impurity atom.

In a unit volume the energy change would be E_0 times the number of impurity atoms per unit volume (c_0/r_0^3), so that the total energy change due to the interaction of the dislocation and the impurity atoms is

$$E_{\text{total}} = \int_{\text{volume}} (E_0 c_0/r_0^3)\, dV$$

or an energy/length

$$E = \int_{\text{area}} (4Gc_0\varepsilon b \sin(\theta - \phi)/r)\, dS$$

For the case given,

$$E = 4Gc_0\varepsilon b \int_{\cos^{-1}(x_0/r_\infty)}^{\cos^{-1}(x_0/r_\infty)} \int_{x_0/\cos\theta}^{r_\infty} \sin(\theta - \phi)\, dr\, d\theta \qquad x_0 \geq 0$$

$$= 8Gc_0\varepsilon b \sin\phi \left\{ x_0 \cos^{-1}\left(\frac{x_0}{r_\infty}\right) - (r_\infty^2 - x_0^2)^{1/2} \right\} \quad (1)$$

The force on the dislocation is dE/dx_0, and the effective stress on the dislocation is $(1/b)(dE/dx_0) = 8c_0G\varepsilon \sin\phi \cos^{-1}(x_0/r_\infty)$. This stress is along the x-direction rather than the slip plane of the dislocation, which is at an angle ϕ. Hence the stress along the slip plane is given by inserting a factor $\cos\phi$ into the above expression, giving

$$\tau = 4Gc_0\varepsilon \sin(2\phi) \cos^{-1}(x_0/r_\infty) \quad (2)$$

By symmetry this stress is central about $x_0 = 0$, so that a dislocation would either be attracted to the position $x_0 = 0$, requiring energy to move it away, or will be repelled, so that a stress would be necessary to drive it over the $x_0 = 0$ position.

The maximum value of τ is then at $x_0 = 0$ and is

$$\tau = 2\pi Gc_0\varepsilon \sin 2\phi. \quad (3)$$

The expression in equation (2) may be generalized to more complicated impurity distributions by replacing c_0 by $(dc/dx)\, dx$ where dc/dx is the gradient of impurity. Then

$$\tau = 4G\varepsilon \sin(2\phi) \left\{ \int_0^{r_\infty} (dc/dx) \cos^{-1}(x/r_\infty)\, dx - \int_{r_\infty}^{0} (dc/dx) \cos^{-1}(-x/r_\infty)\, dx. \right\} \quad (4)$$

$$= 4G\varepsilon \sin(2\phi) \left\{ \int_0^{\pi} c\, d\theta - \pi c_{x=0} \right\}$$

where $\cos\theta = x/r_\infty$

For a linear variation of impurity from zero to r_∞

$$\tau = 4G\varepsilon(dc/dx)r_\infty \sin 2\phi, \quad (5)$$

so that the effect of a slow variation is comparable with that of a discrete jump in concentration, where the jump is equal to the total variation $r_\infty (dc/dx)$ through the region containing the stress field of the dislocation.

For the dislocation at the extremum of a parabolic distribution of impurities with $dc/dx = (dc/dx)_{r_\infty}$ at r_∞,

$$\tau = \pi G\varepsilon(dc/dx)_{r_\infty} r_\infty \sin 2\phi. \quad (6)$$

APPLICATIONS TO EXISTING EXPERIMENTAL RESULTS

It is interesting to compare the magnitude of the effect considered here with the effect of hardening from a uniform solid solution. Mott and Nabarro[5] calculated an increase in the flow stress of the order of $G\varepsilon c$, which means that the effect of variations in concentration would be comparable if the variations are as large as the total average concentration. Here, as in the theory of uniform concentration solution hardening, there is a characteristic length which is of importance: i.e. it is the total change in concentration across the region (of radius r_∞) containing the stress field of the dislocation that determines the appropriate value of c.

There exist a number of cases where it is possible to give qualitative descriptions of the distribution of

VOL. 8 1960

point irregularities and hence, wherever mechanical properties have been measured, approximate comparisons with experiment should be possible.

1. *Irradiation produced defects*

Aerts *et al.*[6] observed extra hardening in irradiated NaCl crystals in regions where there would be a concentration gradient. In particular their Fig. 18 shows hardness over the boundary between irradiated and non-irradiated regions. An extra hardening at the boundary was of the order of 2–4 kg/mm², as compared to a total hardening in the uniformly irradiated region of 6–8 kg/mm². Hence, as was just suggested to be possible, the extra hardening was of the order of the total hardening.*

2. *Impurity segregation to boundaries*

Ball[8] has shown that the flow stress of polycrystalline aluminum is a function of the subgrain size but not of the disorientation across the boundaries. If only the dislocation structure were important in determining the strength of the boundary, the strength would be expected to depend on this disorientation. Since this is not the situation, it may be that the impurity content of the boundaries determines the flow stress and is constant, as theoretical calculations by Webb[9] have shown it should be under suitable conditions. This hypothesis would be consistent both with Fleischer and Chalmers'[10] view and Wiseman's[11] conclusion that interactions of solute atoms with substructure are important.

3. *Angular dependence*

The factor sin (2ϕ) of equations (2–6) provides in principle a means of testing the theory. Fortunately the presence of the other two effects (due to changes in lattice parameter and elastic constant) can be shown to be unimportant and hence do not complicate the issue. The sin (2ϕ) factor indicates that, as far as the Cottrell interaction is concerned, the maximum obstruction of dislocation flow should occur when the slip direction is at 45° to the impurity gradients, and the minimum at 0° or 90°. For a tensile sample with gradients along the axis and with the primary slip system at 45° to the axis, primary slip should be difficult and secondary slip relatively easier, so that the observed work hardening rate should be greater when the gradients are present. This effect appears to have been observed by Fleischer and Chalmers[10] in some tests of effects of growth rate. Their Fig. 12 shows stress–strain curves for two crystals grown at 75 cm/hr by hand motion of the furnace. This type of furnace motion inherently involves fluctuations in the real growth rate and hence in the impurity concentration. In both of these samples the initial work hardening rate was greater than that observed for samples grown at more constant growth rates. In one of the two crystals secondary slip occurred immediately, so that no easy glide was present.

It should be clear that other explanations of the various effects just described are possible. It is desired here merely to point out that the effects are consistent with what is to be expected from changes in impurity concentration.

DISCUSSION

The considerations discussed here should be relevant to coring, which is perhaps the most universal process that results in non-uniform impurity distributions. Once the distribution is known in sufficient detail, it should be possible to calculate the contribution to the flow stress. Under the usual conditions where several elements are present as impurities, their effects should superimpose. It is necessary to know both the distribution of impurities and the sign of the strain they impose, before this superposition can be made. In order to be useful, the impurity distribution must be known over distances of the order of the spacing between dislocations. Unfortunately in most practical cases this is not yet experimentally possible, although for low dislocation densities the electron probe is capable of satisfactory resolving power.

CONCLUSION

An estimate of elastic interactions of dislocations with non-uniform solute distributions indicates that mechanical properties may be strongly affected.

ACKNOWLEDGMENTS

The author is pleased to express his thanks to his associates of the Department of Metallurgy, Massachusetts Institute of Technology, and the Division of Engineering and Applied Physics, Harvard, for helpful discussions, and particularly to B. Chalmers for pointing out the importance of changes in elastic constants. The financial support of the Atomic Energy Commission is gratefully acknowledged.

* Aerts *et al.* attributed the hardness increase to elastic strains. If the linear strain is $1/3 \cdot 10^{-4}$, the stress ($\approx \varepsilon E$) is less than 200 g/mm², which is appreciably less than the increase observed. Here it has been assumed that the density change, estimated to be 0.01 per cent for alkali halides,[7] contributed an elastic strain at the boundary.

REFERENCES

1. E. R. Parker and T. H. Hazlett, *Relation of Properties to Microstructure*, p. 30. American Society for Metals, Cleveland (1954).
2. A. K. Head, *Phil. Mag.* **44**, 92 (1953).
3. A. H. Cottrell, *Dislocations and Plastic Flow in Crystals*. Oxford (1953).
4. B. A. Bilby, *Proc. Phys. Soc.* A**63**, 191 (1950).
5. N. F. Mott and F. R. N. Nabarro, *Proc. Phys. Soc.* **52**, 86 (1940).
6. E. Aerts, S. Amelinckx and W. Dekeyser, *Acta Met.* **7**, 29 (1959).
7. I. Estermann, W. J. Leivo and O. Stern, *Phys. Rev.* **75**, 627 (1949).
8. C. J. Ball, *Phil. Mag.* **2**, 1011 (1957).
9. W. W. Webb, *Acta Met.* **5**, 89 (1957).
10. R. L. Fleischer and B. Chalmers, *Trans. Amer. Soc. Min. (Metall.) Engrs.* **212**, 265 (1958).
11. C. D. Wiseman, *Trans. Amer. Soc. Min. (Metall.) Engrs.* **212**, 847 (1958).

VOL.
8
1960

THE CONTRIBUTION OF ATMOSPHERE LOCKING TO THE STRAIN-AGEING OF LOW CARBON STEELS*

D. V. WILSON† and B. RUSSELL

Cottrell locking of dislocations and precipitation hardening can both contribute to the increase in the lower yield stress which develops during the strain-ageing of low carbon steels. An analysis of stress–strain relationships based on the Petch equation, $\sigma_y = \sigma_i + k_y d^{-1/2}$,[8,11] allows a separation of the contributions of these two sources of hardening. Observations of the development of changes in the tensile stress–strain relationship during ageing have shown that atmosphere locking develops first, causing an increase in $k_y d^{-1/2}$ with little change in σ_i. An estimation based on the Cottrell–Bilby equation[1] suggests that this first stage is completed when the dislocation atmosphere density reaches a value between one and two atoms per atom plane. After completion of the first stage, further segregation of solute has little or no effect on dislocation pinning: the increases in yield stress are then due to increases in σ_i and must be caused by solute cluster formation or precipitation. In a strain-aged steel, the contribution of atmosphere locking to the lower yield stress is rather small compared with that in an annealed steel of the same grain size. This may be a consequence of the finer scale of the dislocation network in the cold worked material.

CONTRIBUTION DU BLOCAGE DES ATMOSPHERES AU VIEILLISSEMENT DE DEFORMATION DES ACIERS A BAS CARBONE

Le blocage des dislocations et le durcissement de précipitation peuvent contribuer à l'accroissement de la limité élastique inférieure au cour du vieillissement de déformation des aciers à bas carbone.

L'analyse des relations tension-déformation basée sur l'équation de Petch $\sigma_y = \sigma_i + k_y d^{-1/2}$[8,11] permet les contributions de ces deux sources de durcissement.

L'examen des modifications intervenant dans la relation tension-déformation au cours du vieillissement a montré que le blocage des atmosphères se produit d'abord et qu'il provoque un accroissement en $k_y d^{-1/2}$ et une faible modification en σ_i.

Une estimation qui s'appuie sur l'équation de Cottrell–Bilby permet de penser que ce premier stade est terminé lorsque la densité des atmosphères atteint une valeur comprise entre 1 et 2 atomes par plan atomique.

Aprés ce premier stade une ségrégation ultérieure des atomes solutés n'a pratiquement plus d'effet sur le blocage des dislocations: l'augmentation de la limite élastique sont alors dûs à des accroissements de σ_i et peuvent être provoqués par la formation d'amas ou par une précipitation. Dans l'acier déformé et molli la contribution du blocage des atmosphères à la limité élastique inférieure est plutôt petite en comparaison avec un acier recuit de même grosseur de grain.

Ceci peut-être une conséquence de l'existence d'un réseau plus serré de dislocations dans l'acier déformé.

BEITRAG DER COTTRELL-ATMOSPHÄRE ZUR VERFORMUNGS-ALTERUNG KOHLENSTOFFARMER STÄHLE

Sowohl das Festhalten von Versetzungen an Cottrell-Atmosphären wie Ausscheidungs-Härtung können an der Erhöhung der unteren Streckgrenze beteiligt sein, die sich bei der Verformungsalterung kohlenstoffarmer Stähle zeigt. Analysiert man die Spannungs-Dehnungs-Beziehung mit Hilfe der Gleichung von Petch, $\sigma_y = \sigma_i + k_y d^{-1/2}$,[8,11] so lassen sich die Beiträge dieser zwei Ursachen der Härtesteigerung trennen. Beobachtung der Veränderungen in der Spannungs-Dehnungs-Beziehung während des Alterns zeigt, dass die Festlegung der Versetzungen an den Atmosphären zuerst eintritt; sie erhöht $k_y d^{-1/2}$, während σ_i sich wenig ändert. Nach einer Abschätzung auf Grund der Cottrell-Bilby-Gleichung dürfte diese erste Stufe beendet sein, wenn die Dichte der Atmosphäre ein bis zwei Atome pro Atomebene beträgt. Ist die erste Stufe beendet, so hat die weitere Abscheidung gelöster Atome wenig oder keinen Einfluss auf das Festhalten von Versetzungen: Die weitere Zunahme der Streckgrenze beruht auf der Zunahme von σ_i und muss durch Zusammenlagerung gelöster Atome oder durch Ausscheidung verursacht sein. Bei einem verformungsgealterten Stahl ist der Beitrag der Atmosphären zur unteren Streckgrenze ziemlich klein verglichen mit dem bei getempertem Stahl gleicher Korngrösse. Dies mag daran liegen, dass das Versetzungs-Netzwerk beim kaltverformten Material feiner ist.

1. INTRODUCTION

It is well established that strain-ageing in low-carbon steels is due to the diffusion of interstitial solute atoms to free dislocations generated during plastic deformation; in this way the dislocations are re-anchored and the sharp yield point returns.[1–4] It is also evident that segregation need not stop when all the dislocation sites allowing strong interactions with solute atoms are occupied.[3,5] This absence of a saturation effect must be due to some form of precipitation of the solute atoms collected by the dislocations. Commercial steels commonly contain more available interstitial solute than is needed to complete

* Received March 13, 1959.

† Department of Industrial Metallurgy, University of Birmingham.

Cottrell locking after moderate cold working. Thus, in general, atmosphere formation and precipitation hardening will both contribute to the increase in yield stress observed during strain ageing,[6] and our understanding of the mechanical behaviour of strain-aged steels requires a separation of the effects of these two sources of hardening.

Interpretations based on the relationship

$$\sigma_y = \sigma_i + k_y d^{-1/2} \tag{1}$$

which describes the dependence of the lower yield stress σ_y on the grain diameter $2d$,[7] have been developed, notably by Petch,[8,9,10] to provide a method which separates the factors contributing to the lower yield strength of annealed polycrystalline iron. During Lüders band propagation, it is believed that unpinned sources release many dislocations which pile up at the grain boundaries. These provide stress concentrations which are limited by the grain size, and which act with the applied stress to unpin nearby dislocations in the next grain. Movement of the free dislocations is opposed by internal stresses, the effects of which are represented by the 'friction' stress term σ_i. The detailed mechanism of yield propagation is represented in Cottrell's equation[11]

$$\sigma_y = \frac{\sigma_i + \sigma_d (l/d)^{1/2}}{1 + (l/d)^{1/2}} \tag{2}$$

where l is the distance from the pile-ups to the nearest sources and σ_d is the unpinning stress. When $d \gg l$ equation (2) simplifies to (1). Thus $k_y = \sigma_d l^{1/2}$ and is a measure of the pinning of the dislocations. Heslop and Petch[10] have shown that σ_i may be resolved into two parts. The first of these, which varies little with temperature, represents the stress needed to move free dislocations against the resistance due to structural irregularities provided by dissolved solutes, fine precipitates, dislocations and sub-structures. The second term, on the other hand, is sensitive to temperature and is thought to be due mainly to the Peierls–Nabarro force.

Yield propagation in a strain-aged steel is believed to be essentially similar to that in the annealed condition. Thus strain-ageing should provide an opportunity for observing the effects of the growth of σ_d, due to dislocation locking, and changes in σ_i, due to segregation and precipitation, while d and l remain constant. However, cold working increases σ_i and greatly reduces the variation of σ_y with grain size. Even in fine grained strain-aged steels, it appears, σ_y is not very sensitive to σ_d (Fig. 4 of this paper). Also it is rather difficult to test if d, the effective length of the dislocation pile-ups, retains its direct relationship with grain diameter after moderate deformations.

However, $k_y d^{-1/2}$ may also be estimated from Lüders strain, independently of the grain size dependence of σ_y. This latter approach is based on the argument that the specimen undergoes Lüders strain to recover, by work-hardening, the yield strength it loses through the disappearance of $k_y d^{-1/2}$ on becoming plastic.[11] This method is appropriate in the case of strain-ageing because the value of the flow stress before ageing can be measured precisely and because the analysis is concerned more particularly with changes in k_y and σ_i.

This paper describes a study of strain-ageing based on such an analysis of the tensile stress-strain relationships observed at different stages of the ageing process.

2. EXPERIMENTAL METHOD

The material used, all from the bottom section of a single ingot of good quality commercial rimming steel, was of the following composition in wt. %:—

C 0.038; N 0.0042; Mn 0.40; Si 0.008; S 0.017;
P 0.008; Ni 0.06; Cu 0.07; Sn 0.01; Al 0.001

Sheets of five different grain sizes were prepared by the strain-anneal method. In the final annealing treatment they were heated at 700°C for 2 hr in purified nitrogen, followed by cooling to 200°C in 18 hr. This had no appreciable effect on the nitrogen content. Numerous tests showed that the ranges of grain size obtained in each group of sheets were:—

Grain Size No.	1	2	3	4	5
Mean (Grains/mm²)	51	195	730	1380	1850
Range (Grains/mm²)	43–62	180–215	673–798	1250–1500	1650–2100

Tensile specimens of 0.5 × 0.07 in. cross section were machined from the sheets, those for a given experiment being taken from adjacent positions. Excepting the test pieces used for the experiment described in Section 7, all the specimens were heated at 200°C for 2000 min and then cooled rapidly before prestraining. After this heat treatment the strain-ageing behaviour was very similar to that shown after commercial "box" annealing; a negligible amount of carbon would be left in solution and strain-ageing would be due to dissolved nitrogen (i.e. $\leqslant$0.004 wt. %. Thus the possible contribution of stress-induced ordering to strain-ageing would be small.[12])

Excepting specimens used in the experiment described in Section 6, all the test pieces were pre-strained to 4 per cent elongation before ageing. This

VOL. 8 1960

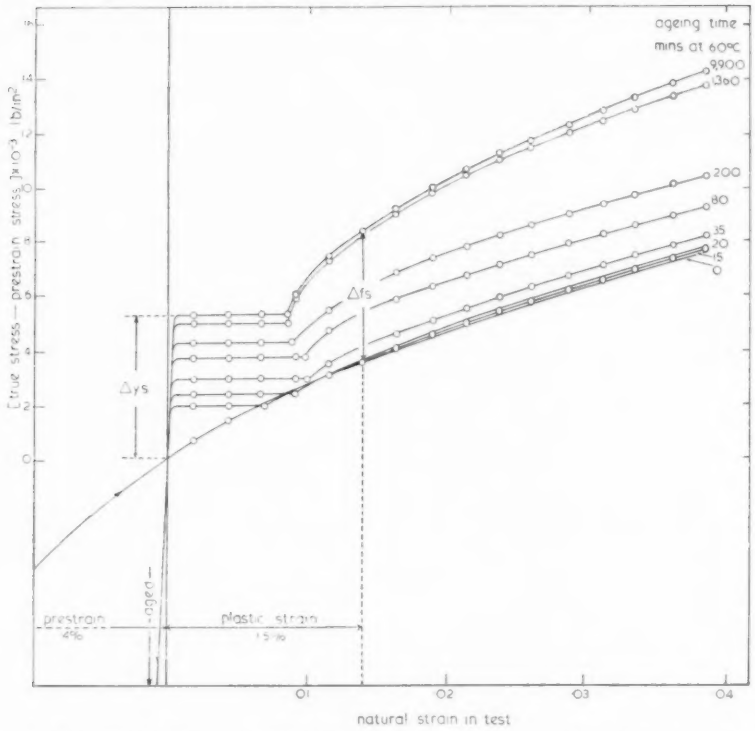


FIG. 1. Progressive changes in the tensile stress-strain relationship of grain size I steel due to strain-ageing at 60°C after 4 per cent prestrain.

was sufficient to exceed Lüders strain in annealed material of the finest grain size. The machined edges of the specimens were lightly polished before testing. A simple Lüders band system was established during yield at room temperatures, giving unambiguous values of the lower yield stress.

Both prestraining and test straining were carried out at a strain rate of 10^{-4} sec^{-1}, using a hard beam testing machine and a Lindley extensometer. Except in one experiment, the prestrained specimens were aged for appropriate periods at 60° ± 1°C in an oil bath.

3. CHANGES IN THE TENSILE STRESS–STRAIN RELATIONSHIP DUE TO STRAIN-AGEING

The representative stress–strain curves in Fig. 1 illustrate the main features of a sequence of changes which was observed with each of the grain sizes tested. By reference to these changes the ageing process may be divided into four stages:—

(1) During the first ½ hr of ageing at 60°C the lower yield stress and Lüders strain increased rapidly and almost in step, while at strains beyond the yield, in the regime of homogeneous deformation, the stress-strain relationship was little affected by the ageing treatment.

(2) Beyond an ageing time which varied slightly with different sets of specimens, but which was typically about 35 min at 60°C, the Lüders strain changed very slowly, or not at all, with further ageing.* The yield stress continued to increase, however, and this was now accompanied by a rise in the level of the stress–strain curve beyond the yield point. Up to a stage of ageing reached in about 150 min at 60°C no appreciable change in the rate of work hardening was detected.

(3) On ageing for more than about 150 min at 60°C the yield stress and flow stress beyond the yield point continued to increase slowly, but from this point further ageing was accompanied by an increase in the steel's ability to work harden. At this stage also, the first significant changes in ultimate tensile strength and elongation at fracture were observed. Maximum values of the yield strength, the ultimate tensile strength and the coefficient of work hardening were reached only after about 10^4 min at 60°C.

(4) After ageing for appreciably longer times than 10^4 min at 60°C some evidence of "overageing" was observed; i.e. there was a very slow decrease in yield strength, ultimate tensile strength and the coefficient of work hardening, an increase in the elongation at

* This observation was made previously by Tardif and Ball[4].

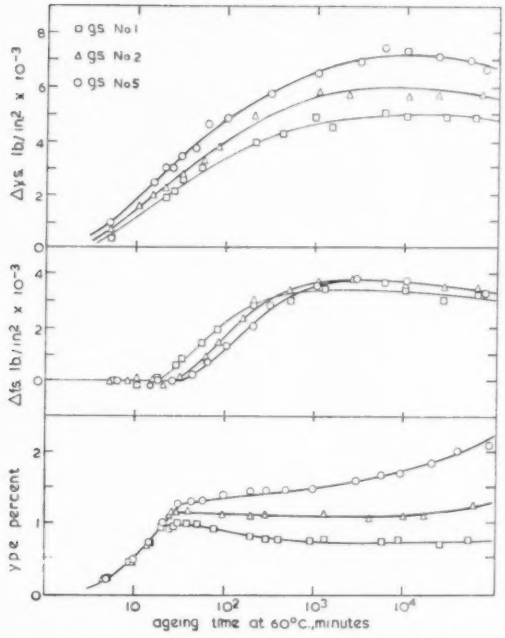


FIG. 2. Changes in lower yield stress (Δ *y.s.*), in flow stress beyond the yield ($\Delta f.s.$) and in Lüders strain (*y.p.e.*) with ageing time at 60°C after 4 per cent prestrain. g.s. No. 1, 51; g.s. No. 2, 195; g.s. No. 5, 1850, grains per mm².

fracture and, with the finer grain sizes, some increase in Lüders strain.

For present purposes the most important of these observations are concerned with the changes in the lower yield stress, $\Delta y.s.$; in the flow stress beyond yield, $\Delta f.s.$; and in Lüders strain, *y.p.e.* These quantities were measured in each of the complete series tested (Grain sizes 1, 2 and 5) and are plotted in Fig. 2 as a function of ageing time.

The test strains at which $\Delta f.s.$ was measured were 1.5 per cent elongation in the case of grain sizes 1 and 2, and 2.5 per cent in the case of grain size 5. These values were chosen to be not greatly in excess of Lüders strain, but beyond the short, rapid rise in stress which usually occurs at the end of yielding. (In tests at room temperature using low strain rates, it is likely that, immediately after the completion of yielding, straining is not at first uniform along the gauge length, owing to the effects of strain ageing behind the Lüders band front.)

Fig. 2 shows that the main features of the changes due to strain ageing were not very sensitive to grain size.

4. THE RELATIONSHIP OF CHANGES IN LOWER YIELD STRESS, FLOW STRESS AND LÜDERS STRAIN

Perhaps the most interesting observation illustrated in Fig. 2 is the approximate constancy of Lüders strain beyond the first stage of ageing. In terms of equation (1) this suggests that the rise in yield stress after the first stage is due almost entirely to increases in σ_i. Therefore, insofar as the changes in σ_i are represented by the changes in the flow stress beyond the yield, the function $\Delta y.s. - \Delta f.s.$ should mirror the observed changes in Lüders strain. Fig. 3a shows that this is approximately so.

The tendency for $\Delta y.s. - \Delta f.s.$ to decrease beyond ageing times of about 100–150 min is to be expected, since values of $\Delta f.s.$ observed at a finite test strain are then influenced by the increased work hardening due to ageing. Essentially, in Fig. 3a, we are using the change in flow stress beyond the yield to estimate $\Delta f.s._0$, the change in yield stress which would be observed if no dislocation locking occurred. Clearly this will be accurate only if the rates of work hardening in the aged and unaged conditions are identical up to the strain at which $\Delta f.s.$ is measured. It appears that this difficulty can be at least partly overcome if $f.s._0$ is estimated directly, by extrapolation back to zero plastic strain of the rising part of the stress–strain curve observed beyond the yield. This part of the curve is represented fairly well by a simple power law.[13] Thus linear extrapolations can be made using a plot of log true stress against log natural strain. Values of $\Delta f.s._0$ obtained in this way were used to plot $\Delta y.s. - \Delta f.s._0$ in Fig. 3b.

These results strongly support the idea that $k_y d^{-1/2}$ remained almost constant between the end of the

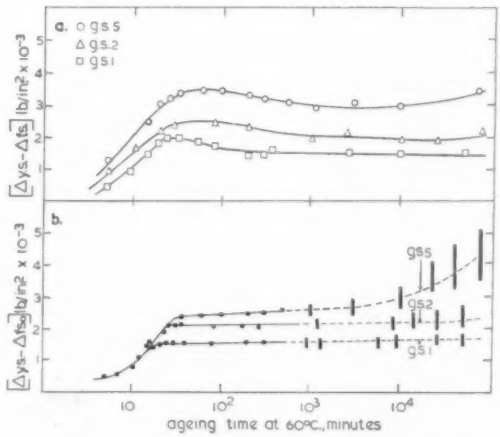


FIG. 3. (a) The difference between the increase in Δ *y.s.* and the increases in flow stress measured beyond the yield, ($\Delta f.s.$),
and (b) The differences between the increases in Δ *y.s.* and $\Delta f.s._0$ obtained by extrapolation of the stress-strain curve. Aged at 60°C after 4 per cent prestrain.
In 3b the points are elongated to represent the uncertainty of the extrapolations of results for the longer ageing time.

VOL. 8 1960

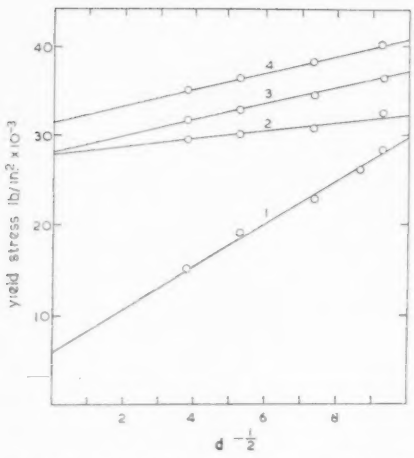


FIG. 4. The variation of the lower yield (tensile) stress with $d^{-1/2}$ where d is half the grain diameter in mms. Curve 1, annealed specimens. Curves 2 to 4, testpieces all prestrained 4 per cent and, Curve 2, unaged; Curve 3, aged to the end of the first stage; Curve 4, 'fully' aged (10^4 min. at 60°C).

first stage of ageing and the stage at which maximum yield strength was reached. However, the two methods represented in Figs. 3a and 3b give rather different results for the magnitude of the contribution of atmosphere locking to the yield stress, particularly with the fine grained steel. For specimens in the first stage of ageing, and particularly with grain size 5, there was some evidence that work hardening during Lüders strain was slightly less than that of unaged specimens deformed homogeneously through the same strain interval. Since the values of $\Delta f.s.$ used in Fig. 3a are all based on the flow stress of unaged specimens, this method may tend to underestimate the value of $\Delta f.s._0$. On the other hand, it is likely that the extrapolation method tends to underestimate $\Delta y.s.-\Delta f.s._0$ in Fig. 3b. In this case the results are sensitive to the work hardening coefficient used. The extrapolations were based on the slopes of the stress–strain curves beyond the sudden rise in stress immediately after yield. Possibly this gives too low a value of work hardening.

This uncertainty does not affect the main conclusions suggested by the analysis. These are, in terms of equation (1):—

(1) The first stage of ageing is concerned with the growth of $k_y d^{-1/2}$ (and, therefore, with the growth of dislocation atmospheres). Up to the end of the first stage no change in σ_i was detected in tests at room temperatures.

(2) The end of the first stage of ageing is defined rather clearly because further ageing has little or no effect on the value of Lüders strain.

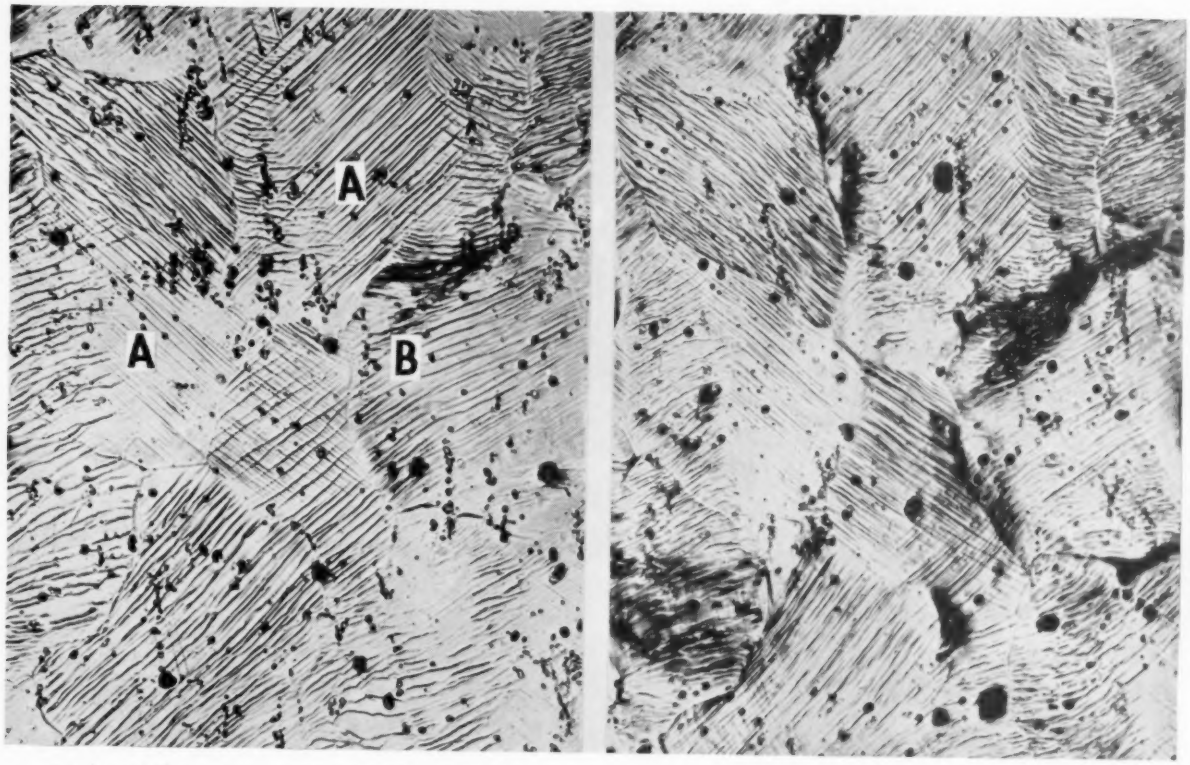
(3) Beyond the first stage, further increases in σ_y are due almost entirely to increases in σ_i (and, therefore, are probably caused by some form of clustering or precipitation of the solute atoms, which increases the "friction" stress without affecting the "unpinning" stress σ_d)

5. THE EFFECTS OF GRAIN SIZE

It is obvious that the observed flow stress values considered in the previous two sections cannot be precisely equivalent to the σ_i term in equation (1), since the former vary slightly with grain size. In Fig. 4 values of the lower yield stress observed at three different stages of the ageing process are plotted as a function of $d^{-1/2}$ (where d is half the grain diameter). The (tensile) stress equivalent to σ_i may then be obtained by extrapolation to $d^{-1/2} = 0$. For comparison, values of the lower yield stress for the same materials in the annealed condition are also plotted (Curve 1.)

The main features of the results shown in Fig. 4 are those to be expected from the analysis made in the previous section. Thus most of the increase in $k_y d^{-1/2}$ occurs during the first stage of ageing and, beyond this, further increases in σ_y are due almost entirely to increases in σ_i. It is also evident that cold working increases σ_i and greatly reduces the variation of σ_y with grain size. Even in an aged, fine grained material, it appears, the main contribution to σ_y is made by the σ_i term and $k_y d^{-1/2}$ is comparatively small at room temperature. However, estimates of σ_i based on extrapolation to $d^{-1/2} = 0$ will be valid only if a direct relationship with grain size is retained by the lengths of the dislocation pile-ups which are responsible for triggering off slip from one grain to the next. In Fig. 4 it is shown that lines 2 and 3 (representing, respectively, the flow stress values at the end of prestraining and yield stress values at the end of the first stage of ageing) can be drawn to give about the same value of σ_i. Thus the results are consistent with the possibility that the simple relationship of the stress concentration factor with the grain size is preserved after 4 per cent deformation. However, the range of grain sizes examined is hardly sufficient to establish this.

Metallographic observations were made on electropolished specimens of grain size 1, which were strained 4 per cent, aged 1 hr at 60°C, polished smooth again, then strained a further 4 per cent and re-examined in the same area. Slip in the annealed material gave characteristically heavy, fairly widely spaced bands, while those in the aged material were often rather finer and more closely spaced (Fig. 5), suggesting that more dislocation sources were operating in the latter case.



(a) Annealed specimen electropolished and then strained 4 per cent.

(b) Same area after strain-ageing for 1 hr. at 60°C, repolishing and then straining a further 4 per cent.

FIG. 5. Slip bands in grain size 1 material ×150.

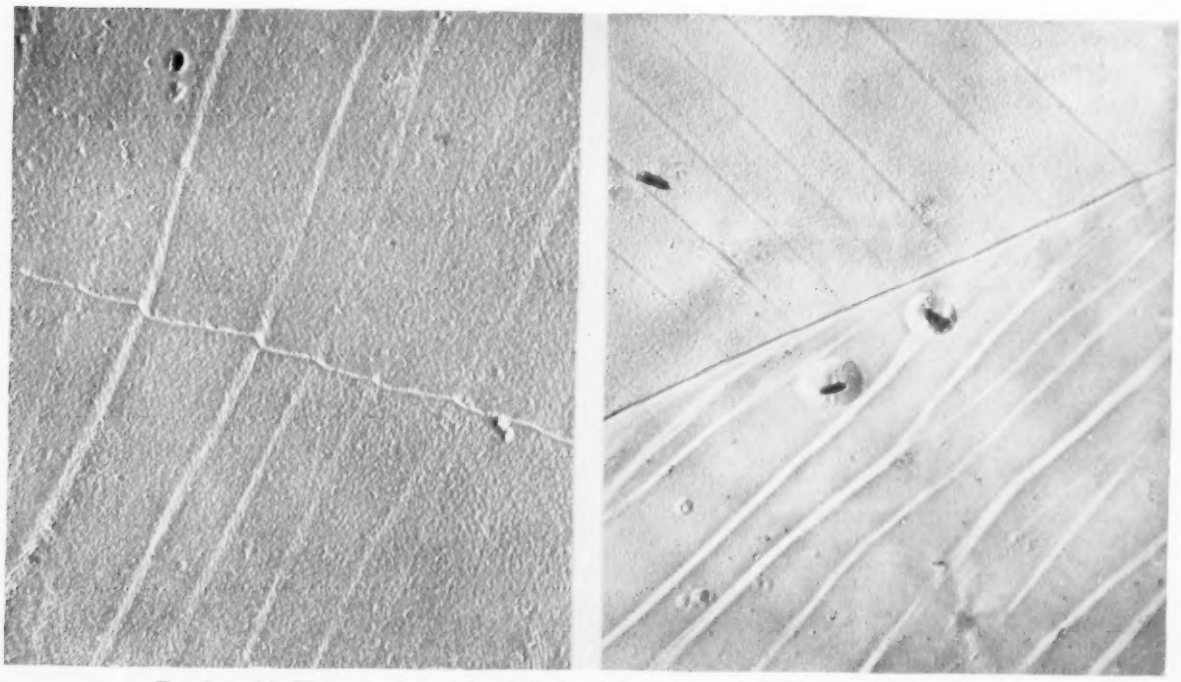


FIG. 6a and b. Electron micrographs of slip bands in grain size I material after 4 per cent strain. Carbon replicas shadowed at 1 : 1. ×5000.

VOL. 8 1960

In the neighbourhood of grain boundaries the slip bands showed a variety of behaviour. In some cases slip appeared to run through a boundary into a neighbouring grain (Fig. 6a). This occurred even when slip in the second grain was predominantly on some other system (Grains A in Fig. 5a). But quite commonly the heavy slip bands stopped short a little way from the boundaries (Grain B in Fig. 5a), giving way to diffuse wavy slip which could be detected in electron micrographs (Fig. 6b). The frequently observed deflection of slip bands, and slip on secondary systems in their neighbourhood, suggested that such boundaries presented major obstacles to slip propagation. These grain boundary features were also seen after deforming in the strain-aged condition. Almost always slip in the strain-aged material occurred on systems parallel to those active in the annealed material, so that the general appearance throughout a given area was strikingly similar. Although, in some grains, clearly defined slip traces tended to be shorter in the strain-aged than in the annealed material, slip bands occupying an appreciable proportion of a grain diameter were not uncommon. Quite probably in the strain-aged material, as in the annealed steel, large angle boundaries remained the dominant barriers to dislocation movement.

If we can assume that the relationship of the stress concentration factor to grain size was preserved after deformation, then, in the strain-aged specimen, the value of k_y,($= \sigma_d l^{1/2}$ where l is the distance from the pile-ups to the nearest sources in the next grain,) was only about one third of that in the annealed condition. Once atmosphere formation is complete the 'unpinning' stress σ_d is expected to be the same as that in the annealed materials. Hence this suggests that cold working reduced the value of l to roughly one tenth of that in the annealed specimens. This is in reasonable agreement with the expected change in the scale of the dislocation network.

6. THE EFFECT OF STRAIN-AGEING ON THE TEMPERATURE DEPENDENCE OF THE YIELD STRESS

The results described in earlier sections appear to provide a clear separation of the contributions to the increase in yield stress made by atmosphere formation on the one hand and by precipitation (or cluster formation) on the other. It is interesting that the latter processes, which must occur on the dislocations, do not appear to have any appreciable effect on the 'unpinning' stress σ_d. This suggests that the spacing of the precipitates (or clusters) must be such as not to affect the critical event in the unpinning process which, as Cottrell and Bilby have shown,[1] probably involves the throwing forward of a small loop, only a few atomic spacings wide, from the dislocation line. Once such a local break-away has occurred the applied stress can separate the rest of the dislocation from its anchorage.

This observation suggests an independent method for testing the main conclusions we have reached. When dislocations are locked by atmospheres the effect of temperature on the yield point is strong, because the internal stress barrier which opposes escape of a dislocation from its atmosphere is very narrow.[14] We expect the stress barriers associated with precipitates to be much wider and their contribution to the temperature dependence of the yield stress to be comparatively small. Thus the temperature dependence of the yield stress should increase during the first stage of ageing, while Cottrell atmospheres are forming, but subsequent solute segregation, to form clusters or precipitates, should cause little further increase.

Such an experiment demands rather precise measurements because, in strain aged materials, the contribution of atmosphere locking to the yield stress is relatively small. The principal obstacle to a direct approach proved to be that complex Lüders bands invariably formed at temperatures usefully below room temperature. In consequence comparable values of the lower yield stress could not be identified. This complication, and errors arising from specimen to specimen variations, were avoided by making a comparison of yield stress values at two temperatures using a single specimen. The experimental method is illustrated in Fig. 7. The specimens, all of grain

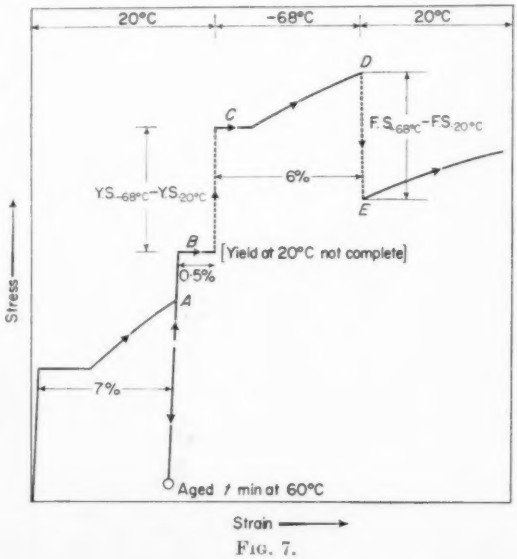


FIG. 7.

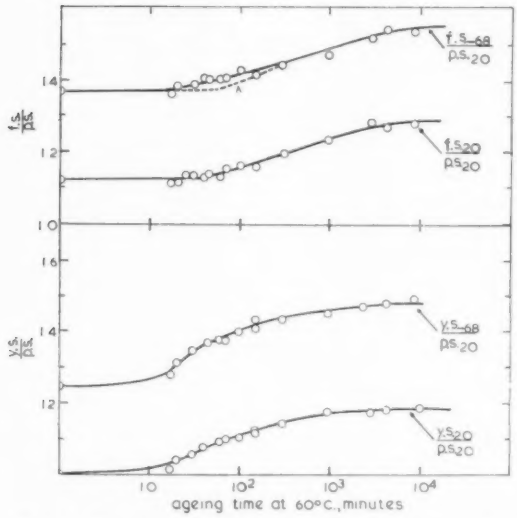


FIG. 8. Increases in the flow stress ($f.s.$) measured at 6.5 per cent test strain, and in lower yield stress ($y.s.$) during strain-ageing of grain size 2 specimens, prestrained 7 per cent and aged at 60°C.

Top. The ratios of the values of $f.s.$, measured at 20°C and −68°C, to the stress at the end of prestraining ($p.s.$) measured at 20°C.

Bottom. The ratios of $y.s.$ values, measured at 20°C and −68°C, to the prestrain stress measured at 20°C.

size 2, were prestrained 7 per cent at room temperature and then aged for differing periods at 60°C without removing the specimens from the grips. The test straining was started at room temperature and in this way a simple Lüders band system was initiated at yield. Once the value of the lower yield stress at room temperature had been established the specimen was cooled rapidly to −68°C and, within a few minutes, the test was resumed at the lower temperature. The simple Lüders bands already established continued to propagate, and an unambiguous value of the lower yield stress at −68°C was obtained. Straining was continued at the lower temperature to a test strain of 6½ per cent, which was beyond the end of yield for all specimens. At this point the cold acetone surrounding the specimen was removed rapidly and replaced by water at 20°C, so that testing could be resumed at the higher temperature within a few minutes.

The effects of strain ageing on the lower yield stress, measured at 20°C and −68°C, and on the corresponding flow stress values at a test strain of 6½ per cent, are represented in Fig. 8. The results are presented as the ratios of these four stress measurements to the stress observed at the end of prestraining the same specimen (at 20°C).

Fig. 8 shows that ageing had little effect on the difference in the two flow stress values, measured at 20°C and −68°C, $(f.s._{-68} - f.s._{20})$. The difference in the lower yield stress at the two temperatures, $(y.s._{-68} - y.s._{20})$, on the other hand, increased appreciably during the first stage of ageing. However, the main source of the temperature dependence of the yield stress in the strain aged condition appears to be the temperature sensitive component of the "friction" stress σ_i.[10] In the experiment, $(f.s._{-68} - f.s._{20})$ and $(y.s._{-68} - y.s._{20})$ were measured directly in a single specimen. Once it was established that the flow stress difference was only slightly affected by strain ageing, these quantities could be used to provide a separation of the contribution made by strain ageing alone to the temperature dependence of the lower yield stress.

In Fig 9 $(y.s._{-68} - y.s._{20}) - (f.s._{-68} - f.s._{20})$ is plotted as a function of ageing time. This shows that the amount by which the temperature dependence of the yield stress exceeded that of the flow stress increased during the first stage of ageing and thereafter remained roughly constant.

Our main conclusions about the character of the components of the increase in yield stress due to strain-ageing are thus supported by the experimental results summarized in Figs. 8 and 9. Strain ageing evidently increases the temperature dependence of the lower yield stress appreciably during the period of atmosphere formation, but subsequent segregation has little effect. It is interesting, however, that the flow stress curves shown in Fig. 8 are not precisely parallel. The broken line A, drawn parallel to the flow stress curve for 20°C, shows there was probably a small difference in the value of $(f.s._{-68} - f.s._{20})$ for specimens aged within the interval of about 50–100 min. This earlier evidence of a small rise in flow stress due to strain ageing, when the tests were made at −68°C, might indicate that thermal agitation can make a significant contribution to surmounting the stress barriers due to the first-formed clusters or subprecipitates. However, this apparent change in the temperature dependence of the flow stress disappeared with further development of the precipitation process.

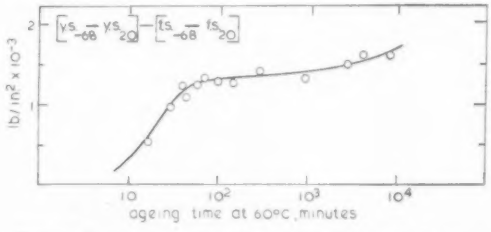


FIG. 9. Development of the contribution of atmosphere locking to the temperature dependence of the lower yield stress in grain size 2 specimens prestrained 7 per cent and aged at 60°C.

VOL. 8 1960

Perhaps a more likely explanation is that the first-formed solute segregates have only a limited lifetime at room temperature once plastic flow separates them from their host dislocations. At a strain rate of 10^{-4} sec^{-1} the Lüders bands would take up to a few minutes to traverse the gauge length. In tests at −68°C dispersion of segregates by diffusion would be comparatively slow and mechanical evidence of 'stable' segregates is to be expected earlier in the ageing process.

7. THE EFFECTS OF THE DISSOLVED SOLUTE CONTENT

The conclusion that solute segregation occurring after the completion of atmosphere formation has little or no effect on σ_d suggests that, in fully aged low-carbon steels, Lüders strain will be independent of the dissolved interstitial solute content provided this exceeds the small amount required to complete atmosphere formation.

To test this prediction, specimens of reduced solute contents were prepared, all from the same steel, by annealing for differing periods in wet hydrogen at 800°C. After this treatment the sheets were reduced 50 per cent in thickness by rolling and then recrystallized and homogenized, generally by annealing in purified argon. (Specimens which were almost carbon-free provided an exception: in this case recrystallization was also carried out in wet hydrogen.) The recrystallization annealing treatments, which varied from 20 hr at 700°C in the case of specimens decarburised for less than 2 hr, down to 1 hr at 600°C for fully decarburised specimens, were designed to provide test pieces of comparable grain size throughout the range of compositions. In this way all the specimens treated in wet hydrogen for up to 20 hr, which covered practically the whole range of compositions of interest for present purposes, were obtained with a final annealed grain size of 700 ± 100 grains/mm^2. After the appropriate annealing treatments the specimens were cooled to 500°C, held at this temperature for 15 min, and then quenched in water. Specimens of identical history were tested in pairs, one, to be used for strain-ageing, being prestrained to give 4 per cent elongation immediately after quenching, while the other was tested at once, to measure the properties in the unaged condition. The prestrained testpieces were all 'fully' aged by holding at 80°C for 2000 min (equivalent to a little over 10^4 min at 60°C) before testing.

The observed values of Lüders strain and the changes in the lower yield stress, in the flow stress beyond the yield, and in the ultimate tensile strength, due to "full" ageing are given in Fig. 10 as a function

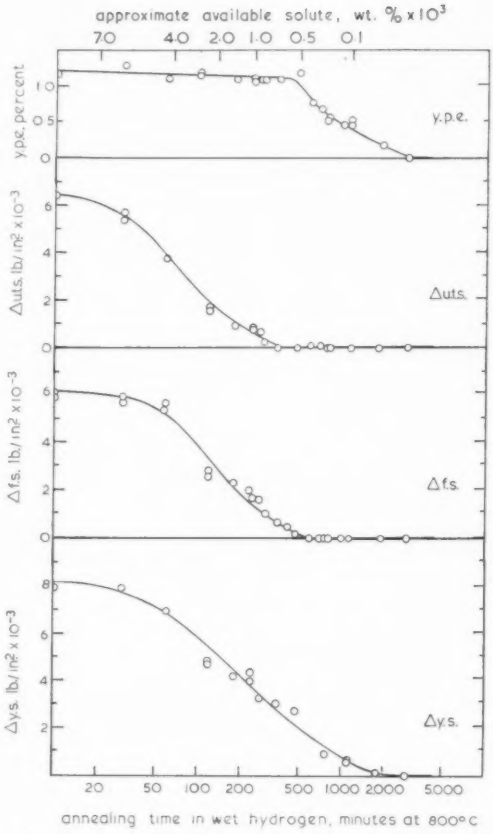


FIG. 10. The effect of dissolved solute content on the increases in lower yield stress (Δ *y.s.*), in flow stress at 1.5 per cent test strain (Δ *f.s.*) in the ultimate tensile strength (Δ *u.t.s.*) and on Lüders strain (*y.p.e.*) due to 'full' ageing by heating at 80°C for 2000 min after 4% prestrain.

of time of treatment in wet hydrogen. The approximate dissolved solute contents given along the top of this figure are based on equilibrium solubility data and on electrical resistivity measurements, made on untreated specimens and at two intermediate compositions. In the case of the resistivity measurements it was assumed that the change in resistivity is proportional to the amount of solute segregating throughout the ageing process.

As expected, the sequence of changes illustrated in Fig. 10 is essentially the reverse of that observed during the development of strain-ageing in an ordinary low-carbon steel. Considering properties in the 'fully aged' condition, a reduction of the amount of solute available for the process results in an immediate reduction in the extent of the increases in yield stress, in flow stress beyond the yield and in ultimate tensile strength. At first, however, Lüders strain is insensitive to solute content. After a substantial reduction in the solute content a composition

is reached at which strain ageing has no effect on the ultimate tensile strength,* and a further reduction leads to the elimination of any rise in flow stress due to ageing. The composition at this latter point is a critical one, for any further reduction in solute content leads to a decrease in the Lüders strain shown by fully aged specimens.

Evidently, at this point, the dissolved solute is just sufficient to complete atmosphere locking. (Electrical resistivity measurements gave the critical composition as approximately 0.0005 wt. % carbon for the particular experimental conditions. Calculations based on the Cottrell–Bilby equation,[1] using a value of 1.5×10^{-20} dyne cm^2 for the interaction parameter A, gave a dislocation atmosphere density of a little over one atom per atom plane at the completion of atmosphere locking.)

Below the critical composition Lüders strain becomes sensitive to solute content and decreases in step with the change in yield stress on further decarburisation until, finally, strain-ageing is eliminated.

8. SUMMARY AND CONCLUSIONS

The picture of strain-ageing in low carbon steels suggested by this investigation has the following features:—

(1) In the early stages of ageing, nitrogen or carbon atoms diffuse to free dislocations and are able to occupy sites where interaction is strong. Thus atmosphere pinning of the dislocations becomes progressively more effective during the first stage of ageing, causing the yield stress and Lüders strain to increase together fairly rapidly. Probably, at this stage, there is very little increase in the resistance to movement of the dislocations once they have been freed from their atmospheres. In moderately deformed, slowly cooled steels the segregation of about 0.0005–0.001 wt. % solute is sufficient to complete atmosphere locking. Calculations based on the Cottrell–Bilby equation suggest that the atmosphere density is only 1 or 2 atoms per atom plane at the end of this first stage of ageing.

(2) The lower yield stress of low carbon steels is less sensitive to grain size in the strain-aged condition than it is in annealed materials. Also the temperature dependence of the yield stress in deformed specimens shows only a small increase as a result of strain ageing. This behaviour results from the proportionately rather small contribution made by atmosphere locking to the lower yield stress in strain-aged steels. Its underlying cause is possibly the fine scale of the dislocation network, which reduces the stress concentration which must be exerted, by dislocation 'pile-ups' at the grain boundaries, in order to unpin potential sources in neighbouring grains.

(3) Segregation of solute to dislocations does not stop when atmosphere formation is complete, but subsequent segregation has little or no effect on the stress required to unpin the dislocations. Thus Lüders strain is little affected by ageing beyond the end of the first stage. Further rises in yield stress are due almost entirely to changes in microstructure which increase resistance to the movement of free dislocations. Almost certainly these changes are solute cluster formation or actual precipitation. Evidently such local groupings of the segregating solute atoms occur only when all dislocation sites allowing strong interactions are occupied. In the later stages of ageing, continuing segregation causes an increase in the steel's ability to work harden and a decrease in its ductility. This is consistent with the idea that stable precipitates are formed in the later stages of ageing.

* A similar result has been reported by Hundy[6].

VOL. 8 1960

ACKNOWLEDGMENTS

The authors wish to thank Professor E. C. Rollason for the provision of facilities for the research, and the Steel Company of Wales for giving the materials.

REFERENCES

1. A. H. Cottrell and B. A. Bilby, *Proc. Phys. Soc.* A **62,** 49 (1949).
2. S. Harper, *Phys. Rev.* **83,** 709 (1951).
3. W. R. Thomas and G. M. Leak, *J. Iron Steel Inst.* **180,** 155 (1955).
4. H. P. Tardif and C. S. Ball, *J. Iron Steel Inst.* **182,** 9 (1956).
5. A. H. Cottrell, *Seminar on Relation of Properties to Microstructure*, p. 131. American Society for Metals, Cleveland, Ohio (1953).
6. B. B. Hundy, *Metallurgia* **53,** 203 (1956).
7. E. O. Hall, *Proc. Phys. Soc.* B **64,** 747 (1951).
8. N. J. Petch, *J. Iron. Steel Inst.* **174,** 25 (1953).
9. A. Cracknell and N. J. Petch, *Acta Met.* **3,** 186 (1955).
10. J. Heslop and N. J. Petch, *Phil. Mag.* **1,** 866 (1956).
11. A. H. Cottrell, *Trans. Amer. Inst. Min. (Metall.) Engrs.* **212,** 192 (1958).
12. D. V. Wilson, B. Russell and J. D. Eshelby, *Acta Met.* **7,** 628 (1959).
13. J. H. Hollomon, *Trans. Amer. Inst. Min. (Metall.) Engrs.* **162,** 268 (1945).
14. A. H. Cottrell, *Conference on Properties of Materials at High Rates of Strain*. Institution of Mechanical Engineers, London (1957).

Hétérogénéités structurales des couches superficielles de l'alliage magnétique Mumétal chauffé dans l'air*

Dans une récente publication consacrée à l'alliage magnétique Fer–Cobalt–Nickel (Permivar) monocristallin, Heidenreich *et al.*[1] ont mis en évidence une relation entre l'efficacité du traitement de recuit magnétique, d'une part, la teneur en oxygène et la structure du cristal, d'autre part. Il apparait qu'une teneur minimale en oxygène est nécessaire pour que l'alliage réponde favorablement au traitement. Dans ces conditions la structure est caractérisée par un aspect macroscopique particulier de la surface attaquée et par la présence de traînées (111) sur le diagramme de diffraction d'électrons. Les auteurs sont conduits à attribuer cette structure à des défauts du réseau créés par l'accumulation d'atomes d'oxygène dans les plans (111), étape intermédiaire entre la solution solide idéale pour des concentrations très minimes d'oxygène, et la séparation d'oxydes de composition définie pour les concentrations plus fortes.

Lors d'une étude métallographique encore en cours nous avons eu l'occasion d'observer avec l'alliage Mumétal (composition Ni : 67%—Fe : 17%—Cr : 2%—Cu : 5%) des aspects structuraux que nous interprétons comme la conséquence de la diffusion de l'oxygène dans les couches sous-jacentes à la surface.

Les échantillons sont des languettes mesurant 25 × 3 mm prélevées dans du ruban d'épaisseur 0, 23 mm qui avait été traité dans l'atmosphére ordinaire à 1000°C pendant 1 heure, refroidi, puis recuit, également à l'air, 6 heures à 400°C. La surface brute de traitement, qui posséde d'ailleurs l'éclat métallique, est polie avec la technique du tampon électrolytique[2] par périodes successives de 30 secondes. Connaissant la vitesse de dissolution, de l'ordre de 4 microns/minute, on peut ainsi suivre l'évolution de la microstructure à divers niveaux de l'épaisseur du ruban. Quelques uns des résultats obtenus sont reproduits Figs. 1–8.

Jusqu'à la profondeur de 6 microns environ les frontières intergranulaires sont marquées par des constituants de deux sortes. Les uns de couler noire et de forme arrondie, ressemblant à des piqûres, se raréfient à mesure que la distance sous la surface augmente. Les autres de teinte gris clair sont des plaquettes plus ou moins irrégulières qui débordent

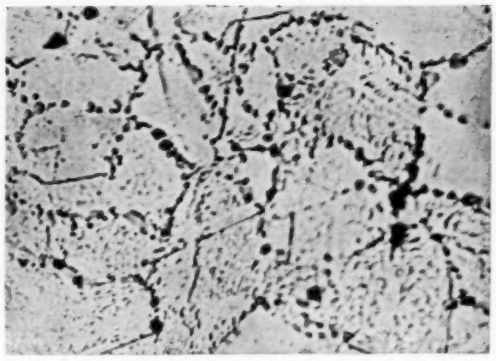


FIG. 1. Micrographie en fond clair normal; Dissolution 6 microns. × 1 000

le joint fictif sur des distances relativement considérables. A l'intérieur des grains et à ces mêmes niveaux, les éléments du premier type sont totalement absents. En revanche, on y trouve des plaquettes dispersées, leur taille et conséquemment la netteté de leurs contours s'affaiblissant en fonction de la profondeur. Il est important de souligner que le nombre et la taille des plaquettes intragranulaires varient d'un grain à un autre et que dans chacun d'eux elles sont à peu près alignées selon une seule orientation spécifique. Ainsi qu'on peut le voir à mi hauteur de la figure 2 le passage d'un joint de macle se traduit par le changement de direction prévu pour les traces d'une famille de plans cristallographiques interceptant la surface examinée.

Fig. 2 montre aussi vers sa partie inférieure des éléments orientés émanant d'un volumineux constituant intergranulaire.

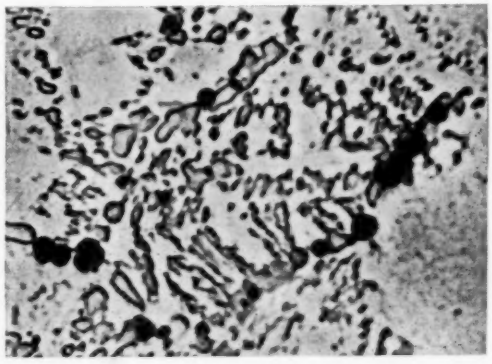


FIG. 2. Micrographie en fond clair normal; Dissolution 6 microns. × 2 000.

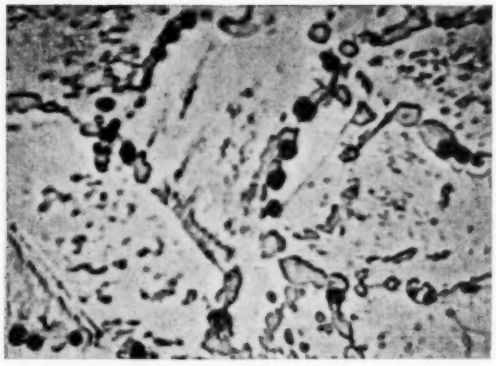


FIG. 3. Micrographie en fond clair normal;
Dissolution 6 microns. ×2 000.

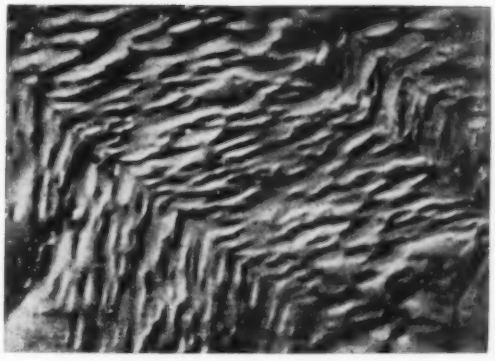


FIG. 5. Micrographie en contraste interférentiel
à deux ondes polarisées;
Dissolution 8 microns. ×2 000

Dès que l'épaisseur de matière dissoute atteint 8 microns environ les frontières des grains contiennent encore quelques inclusions noires, mais les hétérogénéités transgranulaires ont pratiquement disparu (Fig. 4). Cependant, si la surface est observée avec le dispositif du contraste interférentiel à deux ondes polarisées qui met en évidence des accidents du profil pouvant descendre jusqu'à quelques dizaines d'Angströms[3], la matrice de certains grains présente les curieux aspects visibles sous fort grossissement Fig. 5–8. Il s'agit de bandes, plus ou moins continues ou fragmentées mais conservant toujours une orientation définie spécifique du grain considéré, et à cet égard les cristaux maclés des Figs. 5 et 6 sont tout à fait caractéristiques. On observe aussi des bandes très étroites, ou stries, parsemées de quelques points. Quelquefois, même, l'effet de bandes disparait pour laisser place à un réseau de très fines ponctuations, qui n'est pas sans suggérer un arrangement de dislocations, et semble correspondre au stade visible ultime du phénomène (Fig. 8).

Lorsque le niveau atteint la cote 12–15 microns sous la surface initiale l'état poli parfait est obtenu, c'est à dire qu'il n'est plus possible de révéler de signes d'hétérogénéités, à l'exception de très rares et très discrètes ponctuations strictement intergranulaires.

Les caractéristiques bien connues de la dissolution anodique dans les conditions du polissage électrolytique, d'une part, l'aspect, la répartition et l'évolution en fonction de la profondeur des trois principaux types d'hétérogénéites, d'autre part, conduisent aux interprétation suivantes.

(1°) Les éléments noirs arrondis sont des oxydes normaux plus ou moins corrodés pendant le polissage.

(2°) Lorsque leurs contours sont bien délimités, c'est à dire dans les régions assez proches de la surface, les plaquettes inter- et transgranulaires traduisent manifestement une phase toute diffèrente de la matrice et qui pourrait être un oxyde de l'un des composants de l'alliage. Ce caractére de phase s'estompe dans les couches plus profondes, et, en tout cas, il devient problématique pour les plus petits éléments à la limite du pouvoir de résolution.

(3°) Il n'est plus possible d'attribuer le caractère de phase, pris dans son sens habituel, aux bandes, stries

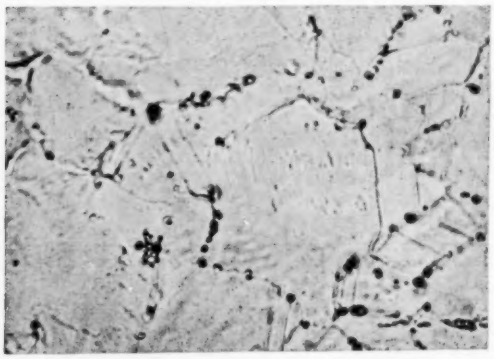


FIG. 4. Micrographie en fond clair normal;
Dissolution 8 microns. ×1 000.

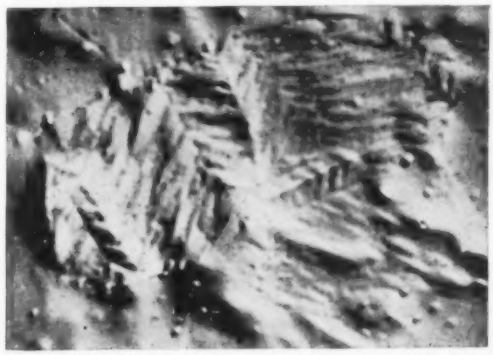


FIG. 6. Micrographie en contraste interférentiel
à deux ondes polarisées;
Dissolution 8 microns. ×2 000.

VOL. 8 1960



FIG. 7. Micrographie en contraste interférentiel à deux ondes polarisées;
Dissolution 8 microns. ×2 000.

et micro ponctuations qui remplacent, loin sous la surface, les constituants précédents tout en conservant le critère d'orientation.

Les différences de niveau extrêment minimes, conséquences de vitesses de dissolution anodique variables d'une région à une autre d'un même grain, et que seule révèle le contraste interférentiel, sont assez comparables à celles montrées par la surface polie électrolytiquement d'une solution solide de deux métaux présentant de notables fluctuations de concentration en atomes du soluté. Toutefois, à notre connaissance, on n'a jamais observé encore à l'échelle du microscope optique des hétérogénéités de concentration de solution métallique en relation aussi flagrante avec le réseau cristallographique du grain. C'est pourquoi l'hypothèse qui ferait intervenir un appauvrissement par diffusion centrifuge des atomes de l'élément le plus oxydable ne parait pas devoir être retenue. Un autre argument contre cette hypothèse est le fait qui ressort de la comparaison des Figs. 2 et 3 avec les Figs. 5–8, à savoir que les plaquettes bien formées ne couvrent qu'une fraction

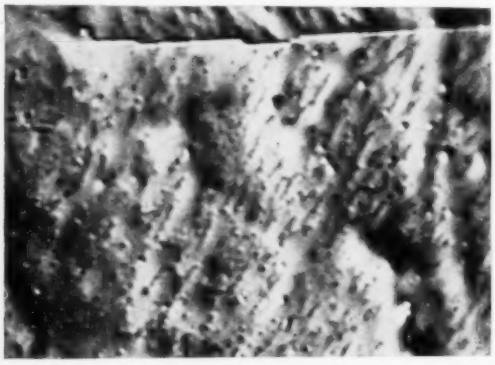


FIG. 8. Micrographie en contraste interférentiel à deux ondes polarisées;
Dissolution 8 microns. ×2 000.

de la surface du grain, alors qu'au contraire les stries et les bandes s'étendent, lorsqu'elles existent, sur la superficie entière. Bien que la preuve formelle n'en soit pas encore apportée, nous pensons que les grains dans lesquels se développe cette sous-structure spéciale sont ceux qui au stade de dissolution antérieur ne contenaient pas de plaquettes volumineuses et bien formées, mais une précipitation dispersée (par exemple la portion du grain en bas et à droite sur la Fig. 2). De telles différences traduisent des vitesses de diffusion de l'oxygène dans le cristal très variables selon l'orientation de celui-ci et il est à présumer que la sous structure en question se manifestera quand la concentration en oxygène est insuffisante pour former une quantité appréciable d'oxydes.

Finalement, pour expliquer cette structure nouvelle nous sommes conduit à admettre que l'état sous lequel se trouve l'oxygène est intermédiaire entre la solution solide vraie et la séparation d'une phase oxyde de composition stoechiométrique. Cette interprétation rejoint donc celle de Heidenreich et de ses collaborateurs qui considérent des défauts du réseau provoqués par l'accumulation d'atomes d'oxygène dans les plans (111). Or, précisément, les micrographies Figs. 5–8 nous paraissent typiques de défauts ou imperfections de ce genre, reconnues par les auteurs mentionnés d'une manière peut être moins directe mais néamoins fort convaincante. Bien entendu, il est possible, sinon très probable, que la technique métallographique employée ici ne détecte que les défauts les plus accentués. Toutefois nos micrographies optiques Figs. 7 et 8 ne sont pas tellement différentes de l'image électronique Fig. 4 du mémoire référence (1).

Pour terminer nous voudrions faire un rapprochement qui nous parait s'imposer entre les résultats décrits ci-dessus et les observations de Moreau et Bénard relatives aux aspects morphologiques de l'oxydation superficielle des alliages fer–chrome et nickel–chrome dans des milieux entrêmement dilués en oxygène (atmosphères H_2O–H_2).[4,5] Sans entrer dans les détails on ne peut s'empêcher de remarquer l'analogie, pour ne pas dire la similitude, de la Fig. 2 ci-contre avec la Fig. 5 du mémoire référence (4) montrant les germes d'oxydes orientées sur la surface d'un alliage Ni–Cr : 4,6%. Il existe également une ressemblance entre nos Figs. 5–8 et les stries transgranulaires parallèles à une famille de plans (111), caractérisant le profil d'équilibre décrites par les auteurs précités, et dont la genèse ferait intervenir un processus de chemisorption, d'ailleurs réversible, des atomes d'oxygène.

Ainsi, au moins d'un point de vue strictement

morphologique, et dans la mesure qu'autorise le rapprochement de résultats tirés d'alliages de compositions non identiques, les phénomènes qui se déroulent sous la surface exposée à un milieu riche en oxygène ne seraient pas essentiellement différents de ceux qui se localisent sur cette surface lorsque le milieu est, au contraire, très pauvre en oxygène.

La relation éventuelle entre les deux cas particuliers du profil d'équilibre de la surface et de la sous-structure interne en bandes et en stries mériterait de faire l'objet d'expériences systématiques, car l'hypothèse de la chemisorption pour le premier n'exclue pas les défauts dans le réseau qui expliquent le second.

Notons, enfin, l'intérêt du tampon électrolytique dans des recherches de ce genre impliquant la dissolution lente et progressive des couches superficielles. Ce moyen est d'ailleurs déjà utilisé pour la détermination spectrographique de l'appauvrissement en composants mineurs au cours de l'oxydation prolongée et à haute température d'alliages complexes.[6]

P. A. Jacquet

75, Rue Jeanne-D'Arc
Saint-Mande (Seine) Dau

VOL. 8 1960

Bibliographie

1. R. H. Heidenreich, E. A. Nesbitt et R. D. Burbank, *J. Appl. Phys.* **30,** 995 (1959).
2. P. A. Jacquet, *C.R. Acad. Sci., Paris* **243,** 2068 (1956); Note Technique ONERA No. 40 (1957).
3. A. R. Weill, *J. Phys. Radium, Phys. Appliq.* **19,** 181A (1958).
4. J. Moreau et J. Benard, *J. Inst. Met.* **83,** 87 (1954–55).
5. J. Moreau et J. Benard, *J. Chim. Phys.* **53,** 787 (1956).
6. Melle. H. Malamand. Communication privée.

* Received September 16, 1959.

Effect of vacancy condensation on the corrosion susceptibility of subgrain boundaries in aluminum*

Rapid and selective corrosion along subgrain boundaries in high-purity aluminum cooled at an intermediate rate from elevated temperatures can be produced by exposure to hydrochloric acid of appropriate composition.[1,2] Explanation of the unusual corrosion susceptibility in terms of atmospheres of impurities seems unsatisfactory. The possibility that the susceptibility is a result of the condensation of lattice vacancies on the sub-boundaries during cooling has been investigated by comparing an etch pattern with the pattern, described recently by Doherty and Davis,[3] of surface pits formed under the oxide film by the condensation of vacancies.

It may first be noted that the sub-boundary etch pattern in aluminum produced by Lacombe's aqua regia plus hydrofluoric acid reagent has been shown to be strongly dependent on the distribution of impurities.[4,5] The rapid corrosion of high-angle grain boundaries in hydrochloric acid also depends on impurities.[2] There are several reasons why high sub-boundary susceptibility in hydrochloric acid is not ascribed to impurity Cottrell atmospheres. For one thing, the susceptibility is low after slow cooling and greatest after cooling at a fairly high rate[2] (present practice involves cooling a $1\frac{1}{2}$ mm sheet in a stream of air from a temperature in the range 550°–645°C). For another, this cooling rate seems too high to permit formation of the relatively concentrated atmosphere presumed to be necessary.[1] For the purpose of estimating this, it is supposed that an atomic concentration of roughly 0.05 extending for the three atom layers on each side of the boundary is required. The total atomic solute concentration in these studies is 10^{-4} or less so that, even if most of the solutes present participate and have interaction energies with the boundary of 0.3 eV, the atmosphere will be much too dilute, even at equilibrium, except below, say, 350°C. The boundary must drain more than 10^3 atom layers so that the product of diffusion coefficient and time must be greater than 10^{-9} for the postulated atmosphere to form. The volume chemical diffusion coefficient, for the solute given in Nowick's estimates[6] which has the highest diffusion rate in aluminum, is 10^{-11} cm^2/sec at 350°C and 10^{-12} at 300°C (these figures agree with recent data for 0.0% Zn[7]). Since the sub-boundary corrosion can be produced in specimens which cool through the range 350°–300°C in less than 15 sec, it can be produced in specimens which would have, on a generous estimate, sub-boundary Cottrell atmospheres substantially more dilute than supposed necessary. The excess vacancies present during cooling cannot enhance solute atom diffusion to boundaries, since Doherty and Davis' observations show that the excess vacancies themselves migrate to the boundaries. The third objection to the impurity atmosphere hypothesis is that sub-boundary corrosion at about the same rate has been observed in five lots of aluminum from 99.97 to 99.996%, and has been observed in both ends of crystals grown from the melt, where solute content would differ because of its redistribution during solidification.

The vacancy condensation hypothesis was tested on a $1\frac{1}{2} \times 10 \times 100$ mm crystal of approximately (122) [$\bar{2}12$] orientation of 99.99 + % aluminum (0.004% Fe, 0.002% Cu, 0.0007% Si, 0.0001% Na, <0.0002% for

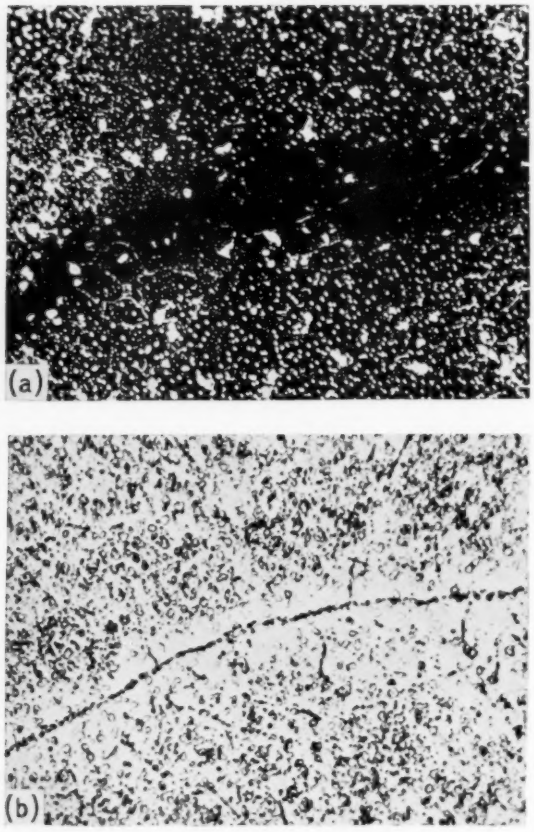


FIG. 1. Region including a lineage boundary in unbent portion of crystal. ×500.

(a) As air-cooled from 645°C showing vacancy condensation pits. Fine lines are believed to be cracks in the oxide film. Dark field illumination.

(b) Structure of the same field after subsequently electropolishing and etching anodically. Vertical illumination.

Mg, Mn, Ca). It was electropolished, bent over part of its length to a 5 cm radius, and studies made of the flat portion and the first part of the bent portion after annealing in air at 645°C for 48 hr and cooling in a stream of air. Figs. 1 and 2 show the condensation pits observed on the previously electropolished surface after cooling from the anneal, together with the structure obtained after again electropolishing and then etching anodically in 12% hydrochloric acid for 8 hr at 0.05 mA/cm². Anodic etching was desirable in the present case since it gives essentially the same behavior and is capable of much closer control than the straight chemical methods involving hydrochloric acid. The condensation pit pattern in Fig. 1a near a wandering lineage boundary (about 5′ tilt) shows the distributed pits formed by vacancies piped to the surface along dislocations which have gathered more than they can absorb,† and the depleted zone from which the boundary has drained vacancies and absorbed them. The etched surface (Fig. 1b) also shows distributed pits (flat-bottomed and not deeper than $\frac{1}{2}\mu$) and a depleted zone; however the boundary itself is now visible as an etched groove (about 3μ deep). It is to be noted that the etching was conducted under continuous microscopic examination and the pit density is known to have been changing slowly, if at all, with time when the etching was terminated to avoid excessive impingement of the pits on one another. In both Figs. 1a and 1b, the pit density is about 1×10^7 cm^{-2} and the total width of the depleted zone about 20μ. This comparison suggests that dislocations and dislocation boundaries on which vacancies have condensed have enhanced corrosion susceptibility under the conditions employed and provide sites at which attack is initiated. In the case of the boundary, where the dislocation density is high, attack penetrates faster than it spreads out from the narrow zone in which it starts.

Fig. 2 shows the similarity of condensation and etch pit patterns for a variety of boundaries (the orientation differences determined from Schulz X-ray photographs are 5′–6′ for the lineage boundaries on the left and 2′–5′ for the long polygonization boundaries on the right). There is as expected some variation in the character of the depleted zone and the depth of the etched groove (not visible at this magnification) from one boundary to another. The polygonization boundaries appear as more or less continuous grooves on the side surface as well as on the face.

Where the boundaries are near one another, they would be expected to compete for vacancies and have lower susceptibility. This was noted in some of the areas in Fig. 2b; studies on other specimens indicate that it depends somewhat on the character or orientation difference of the boundary, but boundaries much closer than the 20μ width of the depleted zone observed here always have distinctly lower susceptibility. A behavior comparable to that of the matrix would be expected in boundaries of sufficiently low orientation difference—a simple 1′ tilt boundary has a dislocation concentration only a few times more than the value for the distributed dislocations deduced from the pit density in Fig. 1. A number of segments of what are believed to be such low orientation difference boundaries are visible in Fig. 1b.

The most likely explanation for the higher corrosion rate at dislocations in these studies is believed to be

† This view of the mechanism of pit formation differs from the one given in reference 3.

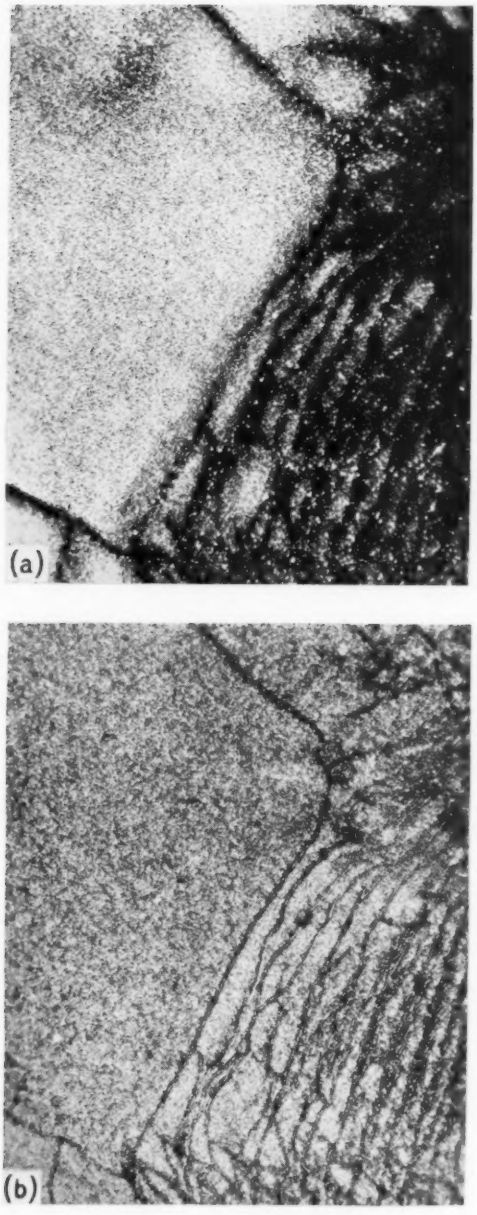


FIG. 2. Transition region from the unbent to the polygonized zone. Oblique illumination. ×30.
(a) As air cooled from 645°C.
(b) After electropolishing and etching anodically.

broadly as follows, along lines suggested by the work of Pryor[8]. The aluminum exposed to the acid is soon protected by a very thin film of low ionic and electronic conductivity, so that the corrosion rate is quite low except where dislocations or impurities in the metal make it easier to form lattice defects in the film and there is thus some slow attack. Edge dislocation lines on which vacancies have condensed have high jog densities; when the slowly corroding surface arrives at a jog, a defect is injected into the film, e.g. when the jog is at the layer just below the surface of the metal it will be destroyed by the movement of one atom from one surface site to an adjacent one. Continued rapid attack will occur if the enhanced local corrosion due to increased local film conductivity progresses to the next jog before the effect of the additional conductivity is lost. Vacancies or vacancy pairs associated with screw dislocations would have the same effect. The vacancy concentration at sufficiently elevated temperatures is more than enough to produce high jog densities even if some are piped to the surface; a vacancy concentration of 10^{-6}, for example, is equivalent to several vacancies per site along the dislocation lines at a dislocation density of 10^{8} cm^{-2}.

The sub-boundary corrosion susceptibility in 99.98% aluminum water-quenched from 600°C is low[1,2] and has been observed to remain so after aging 4 years at room temperature. This is not inconsistent with the fact that relaxation times of days or less are associated with effects on the plastic properties of aluminum quenched and aged at room temperature[9,10]—the plastic properties will be responsive to the formation of only a small number of jogs. The vacancies in quenched specimens would be expected to be largely tied up at impurity traps[11] or as sheets which have collapsed to form small dislocation loops.[12] It is noteworthy that the sub-boundary susceptibility in specimens water-quenched from 600°C and reheated for 4 hr periods was restored by reheating to 300°C but not below this temperature[2]—this is in accord with the view that most of the vacancies in the as-quenched state were strongly bound at locations other than pre-existing dislocations and dislocation boundaries. Sub-boundary etching after aging at room temperature has been observed in aluminum–zinc alloys air cooled from elevated temperatures.[13,14] Since the change in etching behavior occurs in as low as 15 min for the 12% zinc alloy and since the room-temperature interdiffusion coefficient estimated from recent data[7] is only 10^{-19} cm^2/sec for this alloy, the change in etching behavior cannot represent the formation of zinc atmospheres unless atomic diffusion is enhanced by excess vacancies. A large excess of vacancies can apparently be trapped in the lattice at room temperature in these alloys.[15] In this case it appears possible that vacancies freed from their traps may significantly enhance atomic diffusion before they are annihilated at dislocations, so that it is not clear whether the change in sub-boundary etching behavior

VOL. 8 1960

is associated with zinc atmospheres or vacancy–dislocation interactions.

This work was supported by the Office of Naval Research.

O. P. Arora
M. Metzger

Department of Mining and Metallurgical Engineering
University of Illinois
Urbana, Illinois

References

1. M. Metzger and J. Intrater, *Nature, Lond.* **174,** 547 (1954).
2. M. Metzger and J. Intrater, *NACA Technical Note* 3281 (1955).
3. P. E. Doherty and R. S. Davis, *Acta Met.* **7,** 118 (1959).
4. G. Wyon and P. Lacombe, *Conference on Defects in Crystalline Solids*, p. 187. Physical Society, London (1955).
5. G. Wyon, J.-M. Marchin and P. Lacombe, *Rev. Métall.* **53,** 945 (1956).
6. A. S. Nowick, *J. Appl. Phys.* **22,** 1182 (1951).
7. J. E. Hilliard, B. L. Averbach and M. Cohen, *Acta Met.* **7,** 86 (1959).
8. M. J. Pryor, *Z. Electrochem.* **61,** 782 (1958).
9. R. Maddin and A. H. Cottrell, *Phil. Mag.* **46,** 735 (1955).
10. M. Levy and M. Metzger, *Phil. Mag.* **46,** 1021 (1955).
11. W. M. Lomer and A. H. Cottrell, *Phil. Mag.* **46,** 711 (1955).
12. P. B. Hirsch, J. Silcox, R. E. Smallman and K. H. Westmacott, *Phil. Mag.* **3,** 897 (1958).
13. P. Lacombe and A. Berghezan, *C. R. Acad. Sci., Paris* **226,** 2152 (1948).
14. A. Berghezan, *Rev. Métall.* **49,** 99 (1952).
15. E. C. Ellwood, *J. Inst. Met.* **80,** 217 (1952).

* Received April 8, 1959; revised version June 23, 1959.

On the kinetics of irreversible hydrogen embrittlement*

Irons and steels subjected to a pressurized hydrogen environment at elevated temperatures for sufficient periods of time are susceptible to a permanent embrittlement manifested as intergranular fractures accompanied by reduced ductility and strength properties.[1–4] This phenomenon has been termed "hydrogen attack". It is differentiated from the usual hydrogen embrittlement by the fact that the latter is a *reversible* type of phenomenon while hydrogen attack is *irreversible* in that original ductility cannot be restored by a low temperature anneal. Hydrogen attack has generally been thought to be due to the chemical reaction of hydrogen and carbides (internal decarburization) at the grain boundaries, resulting in methane whose pressure builds up causing localized grain boundary fissuring and thus giving rise to deterioration of the material. Since this model fails satisfactorily to explain many observations of this phenomenon, a fundamental investigation on irreversible hydrogen embrittlement has been undertaken to obtain sufficient accurate knowledge of the effect in order to derive a suitable mechanism. Although this study is still in progress, the experimental results describing the kinetics of hydrogen attack appear sufficiently significant to be presented immediately, since no quantitative data of this kind have previously been reported.

The data which are to be presented were obtained on a low-carbon, killed steel subjected to a hydrogen pressure of 700 lb/in². Subsequent to exposure at the desired temperature and for the desired length of time, the specimens were baked at about 400°F (205°C) in a nitrogen atmosphere to remove residual hydrogen, and thus eliminate any cause of reversible hydrogen embrittlement. Hydrogen attack is defined here as the per cent loss in reduction of area, and was measured on miniature round tensile specimens (0.090 in. diameter, 0.5 in. gauge length) tested at room temperature in an Instron testing machine at a cross head speed of 0.5 in./min.

Fig. 1 presents per cent hydrogen attack vs. exposure time curves at 800°, 900°, 1000°, and 1100°F (427°, 482°, 538°, and 593°C) respectively; each point represents a mean value obtained from three or four specimens. The curves all have the same shape and each can be considered to be made up of four segments, namely: (1) an incubation time, t_0, before which no permanent embrittlement occurs, as detected by the criterion selected; (2) an "instantaneous" steep rate of attack over a short time interval, of 2–4 hr, in which the material rapidly proceeds to an advanced stage of embrittlement; (3) a decreasing transient rate; and finally (4) a low steady-state rate of attack. Whether or not this same kinetic pattern occurs for all materials and all types of exposure conditions has still to be determined.

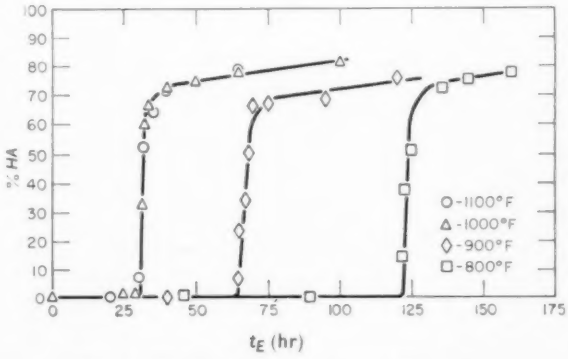


Fig. 1. Hydrogen attack vs. exposure time at 700 lb/in² H_2 pressure.

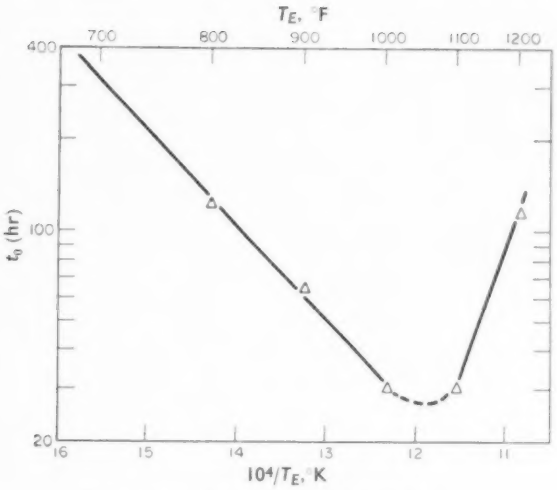


FIG. 2. t_0 vs. $1/T_E$ at 700 lb/in² H_2 pressure.

From Fig. 1, it is clearly seen that up to 1000°F the effect of exposure temperature, T_E, on the kinetics of hydrogen attack is primarily manifested as a pronounced effect on t_0. The data observed at 1100°F suggest that above about 1000°F another process is coming into play and acting in a direction opposite to that of the rate controlling process operating below this temperature. While no definite effects of T_E were observed on the attack rates, there are insufficient data definitely to establish this as a conclusion. In any event, if T_E does have some effect on these rates, it must be small over the temperature range studied and much less than its effect on t_0.

In addition to the deterioration of ductility, strength properties are also affected. Both tensile and yield strengths decrease concomitantly with ductility as exposure time is increased at any of the temperatures investigated. The percentage decrease of both is approximately 33 per cent. Since internal decarburization is accompanying hydrogen attack, a portion of this decrease is probably due directly to the loss of carbon content from the steel.

A plot of $\ln t_0$ vs. $1/T_E$, (T_E in °K), results in a "C" type curve as seen in Fig. 2; however, up to 1000°F a straight line relationship holds which can be written mathematically as:

$$t_0 = A \exp(Q/RT_E) = 3.78 \times 10^{-3} \times \exp(14{,}600/RT_E) \qquad (P_{H_2} = 700 \text{ lb/in}^2)$$

where T_E is exposure temperature in degrees Kelvin and A, Q and R are constants, the latter being the gas constant. Although it may be premature to interpret Q as an activation energy, the value of 14,600 cal/mole rules out the simple diffusion of carbon[5] or hydrogen[6] in iron acting as the rate controlling process at temperatures up to 1000°F. The influence of changes in hydrogen pressure on this value is still to be determined.

L. C. WEINER

Design Engineering Division
Esso Research & Engineering Co.
Linden, New Jersey

References

1. G. A. NELSON, *Proc. Amer. Petroleum Inst.* **7**, 29M163-74 (1949).
2. G. A. NELSON and R. T. EFFINGER, *Welding J.* **34**, 128 (1955).
3. J. K. STANLEY, *Trans. Amer. Soc. Metals* **44**, 1097 (1952).
4. C. DE BLEAULIEU, *Rev. Métall.* **55**, 495 (1958).
5. C. A. WERT, *Phys. Rev.* **79**, 601 (1950).
6. T. M. STROSS and F. C. TOMKINS, *J. Chem. Soc.* p. 230 (1956).

* Received July 15, 1959.

VOL. 8 1960

Entropy of long range order in Cu_3Au and Ni_3Fe *

It is known from statistical mechanics[1] that the entropy is given by equation

$$S = k \log g(s) \qquad (1)$$

Here k is Boltzmann's constant, s the long range order parameter, and $g(s)$ the number of ways of arranging N atoms over the lattice in a way consistent with a given value of s. In this formula the short range order parameter of atoms, σ, has been neglected.

In a previous paper[2] the authors investigated the entropy of long range order in the case of β-brass by using certain combinatory number and experimental specific heats.

In the work now to be reported an analogous investigation has been carried out for the binary metallic alloys Cu_3Au and Ni_3Fe. For that purpose the combinatory number (*cf* e.g. Fowler and Guggenheim[3]) was used, giving

$$g(s) = \left(\frac{r_a^{r_a} r_b^{r_b}}{[r_a(r_a + r_b s)]^{r_a(r_a + r_b s)} [r_a r_b (1 - s)]^{2 r_a r_b (1-s)} \times [r_b(r_b + r_a s)]^{r_b(r_b + r_a s)}} \right)^N \qquad (2)$$

Here N is the total number of atoms of the system (Avogadro's number in the case of one mole), and r_a

and r_b are the atomic fractions of the components ($r_a < r_b$).

We find from equations (1) and (2) that the change of entropy corresponding to the values of s_1 and s_2 at temperatures T_1 and T_2 ($T_1 > T_2$), respectively, can be obtained from equation

$$\Delta S = R \log \left\{ \frac{[r_a(r_a + r_b s_2)]^{r_a(r_a + r_b s_2)} [r_a r_b (1 - s_2)]^{2 r_a r_b (1 - s_2)} \times [r_b(r_b + r_a s_2)]^{r_b(r_b + r_a s_2)}}{[r_a(r_a + r_b s_1)]^{r_a(r_a + r_b s_1)} [r_a r_b (1 - s_1)]^{2 r_a r_b (1 - s_1)} \times [r_b(r_b + r_a s_1)]^{r_b(r_b + r_a s_1)}} \right\}, \tag{3}$$

where R stands for the gas constant.

On the other hand, the change of entropy corresponding to the same temperature difference can be determined by carrying out the following integration:

$$\Delta S = \int_{T_2}^{T_1} \frac{c[s(T)]}{T} dT \tag{4}$$

Here $c[s(T)]$ denotes the configurational contribution to the specific heat of the system, and T the absolute temperature. If the quantities s and $c[s(T)]$ are known as functions of temperature, the entropy of long range order, ΔS, can be calculated from (3) and (4). The influence of the short range order of atoms on the entropy has of course been neglected.

In the cases of Cu_3Au and Ni_3Fe we calculated numerical values for the entropy of long range order which corresponded to the temperature ranges 250°–380°C and 115°–525°C, respectively. Both experimental and theoretical values of s were used for the determination of ΔS in the case of Cu_3Au. For Ni_3Fe the quantity ΔS was determined only by means of the theoretical values of s because of the lack of suitable experimental data.

TABLE 1

	ΔS values (cal/g degree)	
	Cu_3Au	Ni_3Fe
ΔS_{exp}	0.0039	0.0036
$\Delta S^{(1)}{}_{theor}$	0.0013	0.0014
$\Delta S^{(2)}{}_{theor}$	0.0021	0.0030
$\Delta S^{(3)}{}_{theor}$	0.0016	—
$\Delta S^{(4)}{}_{theor}$	0.0011	—

The results are given in Table 1. By using the experimental specific heat curve determined by Sykes and Jones[4] for Cu_3Au, the changes in the total and the vibrational entropies, ΔS_{tot} and ΔS_{vibr} respectively, were integrated separately. In this way, we obtained the difference

$$\Delta S_{exp} = \Delta S_{tot} - \Delta S_{vibr},$$

which represents the entropy of long range order. On the other hand, the quantity $\Delta S^{(1)}{}_{theor}$ was calculated from equation (3) by substituting for s the experimental values of Wilchinsky[5]. The quantities $\Delta S^{(2)}{}_{theor}$, $\Delta S^{(3)}{}_{theor}$, and $\Delta S^{(4)}{}_{theor}$ were determined from the same equation by using theoretical values of s which were calculated by Cowley[6] by different approximate methods. In the case of Ni_3Fe we used the experimental specific heat curve determined by Kaya and Nakayama[7]. However, the values of s had to be computed by means of the two approximations appearing in Cowley's paper.[6]

It can be seen from Table 1 that in both cases the values of entropy based on the combinatory number (2) are somewhat smaller than those obtained from the experimental specific heat curves. However, the agreement can be regarded as quite good. The theoretical values of entropy are in good agreement with each other. Thus, it may be concluded that the combinatory number (2) gives a rather good approximation for the entropy of long range order in the cases of Cu_3Au and Ni_3Fe.

In explanation of the difference between ΔS_{exp} and ΔS_{theor}, the approximate nature of $g(s)$ and the possible errors in the experimental specific heats may be mentioned.

The authors wish to thank Mr. M. Muhonen for his help in the numerical calculations.

V. HOVI
K. MANSIKKA
Wihuri Physical Laboratory
University of Turku
Turku, Finland

References

1. D. TER HAAR, *Elements of Statistical Mechanics* (1st Ed.), p. 258, Rinehart, New York (1954).
2. V. HOVI and K. MANSIKKA, *Ann. Univ. Turkuensis* AI, No. 35 (1959).
3. R. H. FOWLER and E. A. GUGGENHEIM, *Statistical Thermodynamics* (3rd Ed), p. 598, Cambridge University Press (1952).
4. C. SYKES and F. W. JONES, *Proc. Roy. Soc.* **A157,** 213 (1936).
5. Z. W. WILCHINSKY, *J. App. Phys.* **15,** 806 (1944).
6. J. M. COWLEY, *Phys. Rev.* **77,** 669 (1950).
7. S. KAYA and M. NAKAYAMA, *Z. Phys.* **112,** 420 (1939).

* Received September 8, 1959.

A discussion of "self-diffusion and interdiffusion in gold–nickel alloys":[1] A correlation with absolute rate theory*

Fisher *et al.*[2] derived from absolute rate theory the following expression for the self-diffusion coefficient of a component in a homogeneous alloy:

$$D_i = \alpha\, \nu_i^* \lambda_i^2 \{(\gamma_i/\gamma_i^*)[1 + (d \ln \gamma_i/d \ln c_i)]\} \times \exp(-\Delta F_i^\circ/RT), \quad (1)$$

where α is the number of paths of jump distance ν_i in either the forward or reverse direction, ν_i^* is the frequency of passage of an activated complex across the free energy barrier, γ_i and γ_i^* are the activity coefficients of the normal and activated species, c_i is the concentration of the ith species, R is gas constant, T is absolute temperature, and ΔF_i° is the free energy difference between normal and activated species i in the standard state of infinite dilution of activated species in *pure* species i. At the time Fisher *et al.*[2] developed equation (1), radioactive tracer techniques for determining self-diffusion coefficients in alloys were not available, so they made special assumptions about γ_i^* in order to compare equation (1) with experiment. Making such assumptions about γ_i^* is now unnecessary as will be shown in the following.

Combining equation (1) with the Darken[3] equation for chemical diffusion in a binary system,

$$\bar{D} = N_2 D_1 + N_1 D_2, \quad (2)$$

one obtains

$$\bar{D} = [1 + (d \ln \gamma_1/d \ln c_1)]\,(N_2 D_1^\circ \gamma_1/\gamma_1^* + N_1 D_2^\circ \gamma_2/\gamma_2^*), \quad (3)$$

where D_1° and D_2° are the diffusion coefficients relating to standard state conditions and have the form

$$D_i^\circ = \alpha \lambda_i^2 \nu_i^* \exp(-\Delta F_i^\circ/RT). \quad (4)$$

In order to retain a general form, one may accept equations (1) and (3). However, to facilitate comparison with experimental data, it is necessary to evaluate γ_i^* and ΔF_i° by independent means. Since this is not possible at the present time, it is expedient to include both factors together. i.e., place γ_i^* in the exponential. γ_i^* formally expresses the effect of composition on the environment of the activated solute (including concentration and distribution of vacancies in diffusion by the vacancy mechanism). γ_i^* is not unity, even though the concentration of activated complexes is very low, because the standard state of activated species refers to infinite dilution in pure normal species. Inclusion of γ_i^* in the exponential provides the means by which variation of the free energy of activation ΔF_i^* with solute concentration may be expressed.

Thus,

$$D_i = \alpha \nu_i^* \lambda_i^2 \gamma_i [1 + (d \ln \gamma_i/d \ln c_i)] \times \exp(-\Delta F_i^*/RT). \quad (5)$$

TABLE 1. Compilation of activity coefficients of activated species,‡ nickel–gold, 900°C.

N_{Au} ($\times$ 100)	D^R_{Au} (cm²/sec $\times$ 10^9)	γ_{Au}	γ_{Au}^*	D^R_{Ni}(cm²/sec $\times$ 10^{11})	γ_{Ni}	γ_{Ni}^*
0	0.010	~11.0	990	0.06	1.00	1.00
5	0.017	9.2	486	0.4	1.0_1	0.15
10	0.030	5.9	177	1.2	1.0_3	0.05
15	0.048	4.2	79	2.5	1.0_8	0.02_6
20	0.080	3.2	36	4.8	1.1_4	0.01_4
25	0.12	2.6	19	8.2	1.2_1	0.008_9
30	0.19	2.2	10	13	1.2_9	0.006_0
35	0.28	1.9_5	6.2	19	1.3_7	0.004_3
40	0.42	1.7_5	3.7	28	1.4_7	0.0031_5
45	0.58	1.6_0	2.5	36	1.5_8	0.0026_3
50	0.75	1.4_8	1.8	50	1.6_6	0.0019_8
55	0.90	1.3_8	1.4	62	1.8	0.0017_7
60	1.06	1.3_0	1.1_0	78	2.0	0.0015_2
65	1.18	1.2_5	0.95	92	2.1	0.0013_8
70	1.30	1.1_9	0.82	105	2.4	0.0013_3
75	1.32	1.1_5	0.79	114	2.7	0.0014_2
80	1.35	1.0_9	0.73	120	3.2	0.0015
85	1.32	1.0_6	0.72	120	3.9	0.0019
90	1.25	1.0_3	0.74	115	4.8	0.0025
95	1.10	1.0_1	0.83	105	7.2	0.0041
100	0.90	1.00	1.00	90	~8.0	0.0053

‡ Pure solvent is taken as the standard state for normal species: infinite dilution of activated Au *in pure Au* and of activated N_i *in pure* N_i are taken as standard states for activated species. Also $D^\circ_{Au} = 9 \times 10^{-10}$ cm²/sec, and $D^\circ_{Ni} = 6 \times 10^{-13}$ cm²/sec. Diffusion data were taken from reference (1); activity data from reference (4).

VOL. 8 1960

Considering equation (3) it is apparent that the self (radioactive) diffusion coefficient in a homogeneous alloy,

$$D_i^R = (\gamma_i/\gamma_i^*)D_i^0, \qquad (6)$$

includes the activity coefficient terms. Thus, since $B_i = D_i^R/RT$, the mobility terms in the Darken equations are functions of the activity coefficients. It is evident that, accepting equation (6), the phenomenological treatment[3] of diffusion is consistent with the absolute rate theory.

Equation (6) may be used to determine γ_i^* from experimental data on D_i^R and γ_i as a function of N_i. The results of such a computation are presented in Table 1. The diffusion data for the system nickel–gold were taken from Reynolds *et al.*[1], and the activity coefficients were taken from the work of Seigle *et al.*[4]. It is felt that the resulting values for γ_i^* are reasonable in view of the following qualitative arguments. As the concentration of nickel is increased, the activated gold atom "sees" a more compact lattice, and also the equilibrium concentration of vacancies should decrease. Accordingly, it is reasonable to expect γ_{Au}^* to become large in the nickel-rich regions as is observed in Table 1. By similar reasoning one would expect γ_{Ni}^* to become small in the gold-rich solutions.†

Hence in this case, absolute rate theory gives a plausible rationalization of the results of diffusion measurements in the system gold–nickel.

Metals Research Laboratory R. W. Armstrong
Carnegie Institute of Technology J. P. Hirth
Pittsburgh 13, *Pennsylvania* G. M. Pound

References

1. J. E. Reynolds, B. L. Averbach and M. Cohen, *Acta, Met.*, **5,** 29 (1957).
2. J. C. Fisher, J. H. Hollomon, and D. Turnball, *Trans. Amer. Inst. Min. (Metall.) Engrs.* **175,** 202 (1948).
3. L. S. Darken, *Trans. Amer. Inst. Min. (Metall.) Engrs.* **175,** 184 (1948).
4. L. L. Seigle, M. Cohen and B. L. Averbach, *Trans. Amer. Inst. Min. (Metall.) Engrs.* **194,** 1320 (1952).

* This work was supported by the U.S. Office of Naval Research. Received July 31, 1959; revised version October 22, 1959.

† In this qualitative argument non-ideal interactions between solute atoms and vacancies are ignored.

Interstitial atoms in cold worked aluminum*

This question arose when it was found here that cold drawn Al wires (0.3 mm in diameter, above 90 per cent cold reduction) have a slightly *higher* density than the same wires recrystallized at 250°C for 15 min in vacuum (Al from the Aluminum Company of America, +99.99% pure). Although there is some evidence that the density of cold worked metals is lower than that of recrystallized ones,[1,2] there are also measurements showing no effect or the opposite behaviour. Such metals are, according to Tammann[1], Sn, Cu, Cd, Ag, Au, and there is confirmation by others (Cu,[3] Ag[4] and other metals[5,6]). Microcrack formation may be responsible for the lower density of cold worked metals.[7–11]

As density measurements[12] alone do not reveal the actual conditions in a crystalline lattice, precision lattice constant determinations[13] of cold drawn and recrystallized Al wires were also made. In such a case, n', the actual number of atoms per unit cell can be calculated from

$$n' = vdN_0/A$$

where v is the volume of the unit cell, d the density, N_0 Avogadro's number[14] and A the atomic weight of Al. If $n' > n$, n being the ideal number of atoms per unit cell, excess atoms are present in the metal; if $n' = n$, the lattice is sound, and if $n' < n$, vacant sites are predominant. For comparison, n' of recrystallized zone-refined Al (AIAG, Switzerland) was also determined. The results are summarized in Table 1.

The first line of the table shows that the lattice of the zone-refined Al is sound because the deviation $n' - n = 0.00041$ is within the limits of error (± 0.00044, calculated from error propagation). On the other hand the 99.99% Al contains excess atoms, as $n' - n$ is completely outside the error span. However, the increased density can be explained by higher density segregations, observed e.g. by Cuff and Grant in such a metal.[15] There is no such explanation for the cold worked metal (3rd line of the table) and, at present, we have to assume, there are interstitial atoms at a concentration of at least 4 atoms per 1000 unit cells. These atoms are forced into interstitial positions during cold work and may be called arresting or blocking dislocations, because they resist the process of slipping, causing the strain hardening of the metal. At low temperatures these interstitial atoms do not move but leave their positions for the regular ones upon reception of some energy, e.g. in the form of heat (recovery of Al), decreasing the density of the metal.

Thus, according to this concept the cold worked metal consists of fibers or tractions of higher density strain-hardened metal (due to presence of interstitial atoms) and of micro cracks or fissures, which may or may not, depending on various obstacles, outbalance the density increase induced by cold work. The fissures close at higher temperatures causing a density

TABLE 1. n' of recrystallized and of hard Al wires
$N_0 = 6.02368 \times 10^{23}$; $A = 26.98$; for the 99.99% Al—26.98015; $v = a^3$. d and a at 25°C.

Al	d_{25} (g cm^{-3})	a_{25} (Å)	n' (atoms/unit cell)
99.9998 recryst.	2.69808 $\pm$0.00009†	4.04958 $\pm$0.00003	4.00041
+99.99 recryst.	2.6993 $\pm$0.0005‡	4.04947 $\pm$0.00004	4.0019
+99.99 cold dr.	2.7004 $\pm$0.0002**	4.04944 ∥ 4.04963 ⊥ $\pm$0.00004	4.0040

† Standard deviation s from 12 determin.
‡ s from 8 determ.
** s from 6 determ.
∥ a in the direction of wire axis
⊥ a perpendicular to the axis

increase of the metal. This concept of strain hardening is in agreement with the views of Schmid[16] and Boas[17].

The present investigation was sponsored by the National Science Foundation under the contract G-2585.

University of Missouri M. E. STRAUMANIS
School of Mines and Metallurgy T. EJIMA
Rolla, Missouri

VOL. 8 1960

References

1. See e.g. in G. TAMMANN, *Metallkunde* (4th Ed.), p. 169. Ver. Leopold Voss, Leipzig (1932).
2. W. G. BURGERS in G. MASING's *Handbuch der Metallphysik.*, Vol. III, 2, p. 201. Akad. Verlagsges, Leipzig (1940).
3. J. S. SMART, A. A. SMITH and J. A. PHILIPS, *Trans. Amer. Inst. Min. (Metall.) Engrs.* **143,** 272 (1941).
4. P. H. MILLER and J. W. M. DU MOND, *Phys. Rev.* **57,** 198 (1940).
5. T. M. LOWRY and R. G. PARKER, *J. Chem. Soc.* Tr. **107,** 1005, 1013, 1018 (1915).
6. C. G. MAIER, *Trans. Amer. Inst. Min. (Metall.) Engrs.* **122,** 121 (1936).
7. N. F. MOTT, *Proc. Roy. Soc.* A. **220,** 1 (1953).
8. A. N. STROH, *Phil. Mag.* **2,** 1 (1957).
9. W. BOAS in *Dislocations and Mechanical properties of crystals* (by J. C. FISHER *et al.*), pp. 342, 346. Wiley, New York (1957).
10. J. L. SNOEK, *Phil. Mag.* **41,** 1188 (1950).
11. L. M. CLAREBROUGH, M. E. HARGREAVES and G. W. WEST, *Phil. Mag.* **1,** 528 (1956); *Proc. Roy. Soc.* A **232,** 252 (1953).
12. M. E. STRAUMANIS, *Amer. Mineralog.* **38,** 662 (1953).
13. M. E. STRAUMANIS and A. IEVIŅŠ, *The precision determination of lattice constants by the asymmetric method* (partial translation by K. E. BEU). Goodyear Atomic Corp., Portsmouth, Ohio (1959).
14. A. SMAKULA, J. KALNAJS and V. SILS, *Phys. Rev.* **99,** 1747 (1955).
15. F. B. CUFF and N. J. GRANT, *J. Inst. Met.* **87,** 248 (1958/59).
16. E. SCHMID and W. BOAS, *Kristallplastizitat.* Springer, Berlin (1935); Engl. ed. Hughes, London (1950).
17. W. BOAS, *Physics of metals and alloys.* p. 131. Wiley, New York (1949).

* Received January 27, 1958; revised version November 2, 1959.

On the growth of germanium dendrites*

Billig[1] reported on the growth of plate-like dendrites of germanium by pulling from a seeded supercooled melt. The faces were parallel to {111}, and the pulling direction was [$\bar{1}\bar{1}2$]. Later, Billig and Holmes[2] reported that every such dendrite contained a thin lamella bounded by twin planes parallel to the main faces of the dendrite. To date, neither the presence of the lamella nor its connection with the growth of the dendrite has been satisfactorily explained.

We show here that growth of germanium crystals in contact with a supercooled melt can be either slow (polyhedral) or very rapid (dendritic) depending on the crystallographic nature of the seed. We propose a mechanism for the dendritic† growth process and present experimental evidence for it. The essence of the mechanism is that the two twin planes which bound the lamella produce in the sides of the growing dendrite a self-perpetuating system of grooves in which nucleation and growth occur readily. If only one, or no, twin plane is present, growth will be slow and polyhedral.

We assume the following:

(1) The rate of growth of a germanium single crystal in a supercooled melt is limited by the rate of surface nucleation on the {111} faces. Thus, a growing germanium crystal will be completely bounded by its slowly growing {111} faces (polyhedral growth). If such a crystal contains a coherent twin plane, there will be either a *groove* or a *ridge*, bounded by {111}

† We use the term "dendritic" for convenience, although the growth mechanism described here differs from that of conventional dendrites.

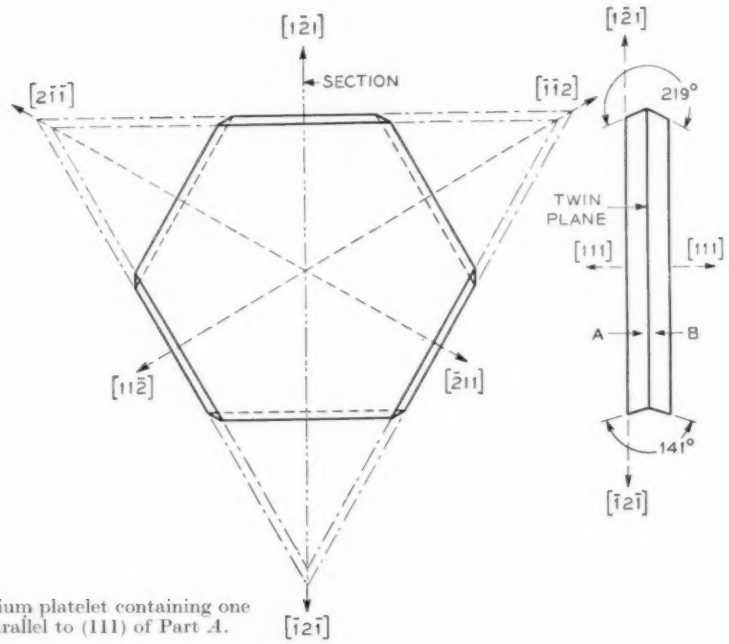


FIG. 1. Germanium platelet containing one twin plane parallel to (111) of Part A.

faces, where the twin plane intersects the growing surface of the crystal.

(2) Growth is rapid at a groove, because nucleation occurs readily in the step at the center line of the groove, and atom layers rapidly spread over the entire faces of the groove. Growth is slow on the planes that form a ridge because it is limited by the rate of surface nucleation.

We first show that a germanium platelet bounded by {111} faces and containing only one twin plane does not continue to grow rapidly. As shown in Fig. 1 the twin plane is parallel to the (111) plane of upper part A of the platelet. At the intersection of the twin plane with the external surface, grooves of angle 141° and ridges of angle 219° are formed by the {111} planes of parts A and B.

During crystal growth, atom layers nucleated at the center line of a groove rapidly cover the groove faces only, causing a rapid net growth normal to the groove. On the other hand, growth outside the grooves is slow because it is controlled by surface nucleation on the {111} planes. As growth proceeds, the ridges of the hexagonal platelet become longer at the expense of the grooves, until finally the platelet assumes a triangular shape, bounded on its sides entirely by ridges. Further growth will be polyhedral.

To confirm this experimentally, seed crystals of germanium, containing one twin plane parallel to (111), were prepared having external faces parallel to (111) and (101). A seed crystal was brought in contact with a 60g melt with either a [$\bar{1}$2$\bar{1}$] or [1$\bar{2}$1] direction vertically downward. The melt temperature was adjusted to give a stationary solid–liquid interface and then reduced about 20°C, as measured by a thermocouple 0.5 cm below the surface. The crystal

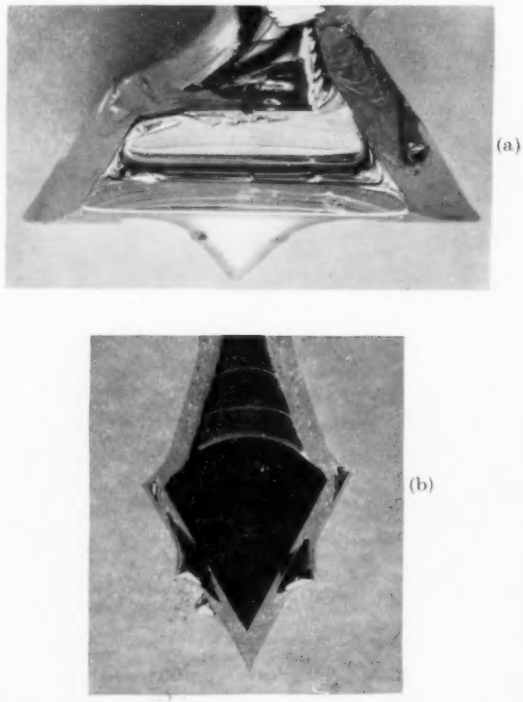


FIG. 2. Germanium crystal containing one twin plane; (a) grown in the [1$\bar{2}$1] direction, (b) grown in the [12$\bar{1}$] direction.

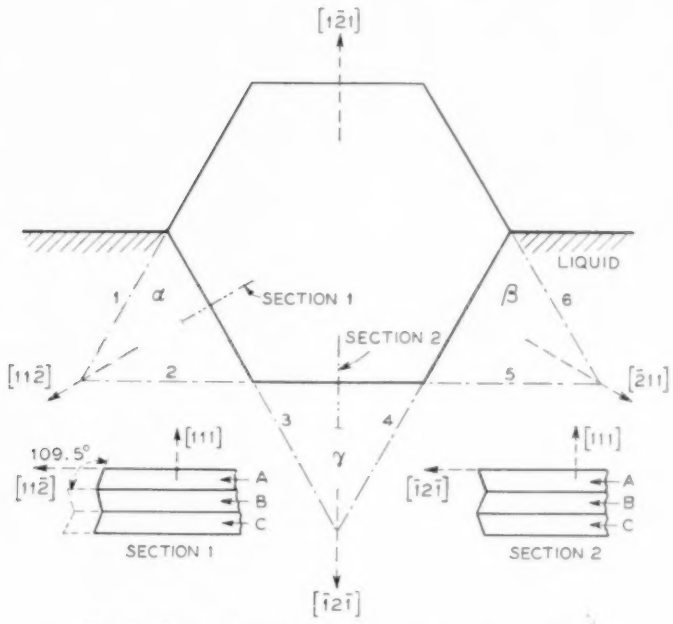


FIG. 3. Germanium platelet containing two twin planes parallel to (111) of Part A.

was then withdrawn at a rate of about 0.05 cm/sec until it became separated from the melt.

Fig. 2a shows such a crystal grown in the [1$\bar{2}$1] direction. The crystal grew, as predicted, in the shape of a triangular platelet with one corner pointing upward and with its side faces bounded by ridges. Similarly, a crystal grown in the [$\bar{1}$2$\bar{1}$] direction grew into a triangular platelet bounded by ridges and pointing downward as shown in Fig. 2b. (The conical protrusions are frozen droplets of liquid that clung to the crystal.) Experiments of this kind were repeated many times with supercoolings ranging from 5° to 45°C. Dendritic growth was never observed.

On the other hand, dendritic growth in germanium occurs readily, even at small supercooling, if the melt is nucleated with: (1) a germanium dendrite which contains at least two parallel twin planes, or (2) a seed crystal cut out of a large germanium crystal which contains two parallel twin planes.

Many germanium dendrites, grown at different supercoolings and nucleated by different methods, including heterogeneous nucleation, were examined microscopically. No dendrite contained one twin plane only. All dendrites contained two or more twin planes.

It appears, therefore, that besides supercooling, a necessary condition for dendritic growth in germanium is a seed crystal that contains at least two parallel twin planes. A simplified explanation of the dendritic growth of such a seed crystal will now be given with reference to Fig. 3. The platelet, which contains two twin planes, consists of three parts, A, B and C. We assume, again, that the platelet is bounded by {111} faces. At the periphery of the platelet, there are alternating ridges and grooves, formed by intersecting {111} faces of the two outer parts A and C and the center part B. Parts A and B form grooves normal to [$\bar{1}$2$\bar{1}$], [$\bar{1}\bar{1}$2] and [2$\bar{1}\bar{1}$]; parts B and C form grooves normal to [1$\bar{2}$1], [11$\bar{2}$] and [$\bar{2}$11].‡ Assume the platelet to be submerged in a supercooled liquid up to the indicated level. Parts B and C can grow by the "groove mechanism" in the [11$\bar{2}$] and [$\bar{2}$11] directions forming triangles α and β until bounded by ridges, 1, 2, 5 and 6. Similarly, parts A and B will grow downward forming the triangular platelet γ bounded by ridges 3 and 4.

Each part which is "left behind" now has formed a groove, of angle 109.5° with its neighboring part, indicated in section (1) of Fig. 3. Part A, therefore, can advance in the [11$\bar{2}$] and [$\bar{2}$11] directions, part C in the [$\bar{1}$2$\bar{1}$] direction. As soon as part A reaches the ridges 1, 2 and 5, 6 of the triangular platelets α and β, it forms a 141° groove with part B. Similarly, part C forms a groove with part B as soon as it advances to ridges 3, 4. Growth can then continue in the described manner.

Because of the peculiar orientation relationship between the three parts (A, B and C) grooves will be

‡ Crystallographic directions refer to part A.

VOL. 8 1960

continuously generated as growth proceeds. In accordance with the discussed mechanism of growth, a germanium dendrite containing two twin planes should exhibit a six-fold growth symmetry.

Fig. 4 shows a photograph of such a dendrite, whose

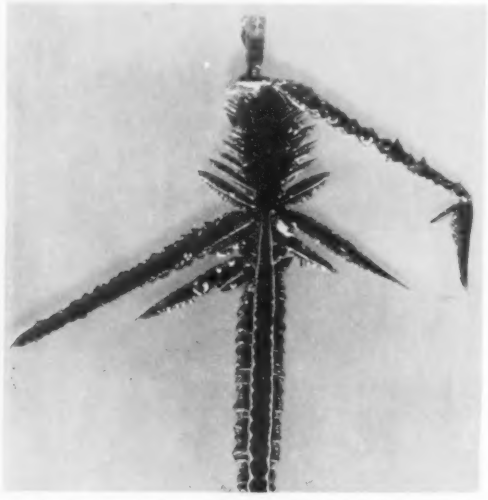


FIG. 4. Germanium dendrite containing two twin planes exhibiting six-fold growth symmetry.

rate of withdrawal from the supercooled melt was momentarily stopped. "Branching" occurred in the four ⟨211⟩ directions which are inclined to the [12̄1] direction of withdrawal.

The observed external shapes of germanium dendrites[1] can be explained by imagining the following sequence of events. At time t_0, the dendrite whose geometry is shown in Fig. 5 starts to grow into a supercooled melt. After completing three growth cycles, (the contours are marked 1, 2 and 3), at time t_1 the dendrite is pulled upward until the bottom of the dendrite is at the surface of the melt. Repetitions of this process give a saw-tooth appearance to the sides of the dendrite. Triangles 3 may not develop fully since they require backward growth; and this would give a 120° tooth angle instead of the 60° angle shown in Fig. 5. Both shapes are actually observed, as can be seen in Fig. 4.

This mechanism accounts for growth in width and length; however, these dendrites also grow in thickness, presumably by surface nucleation. The proposed mechanism is by no means a complete description of the morphology of these dendrites. However, it accounts for some of the main features of the growth of dendritic platelets in germanium. It is likely, however, that this mechanism may be effective in platelike growth of other materials either from the liquid or from the vapor.

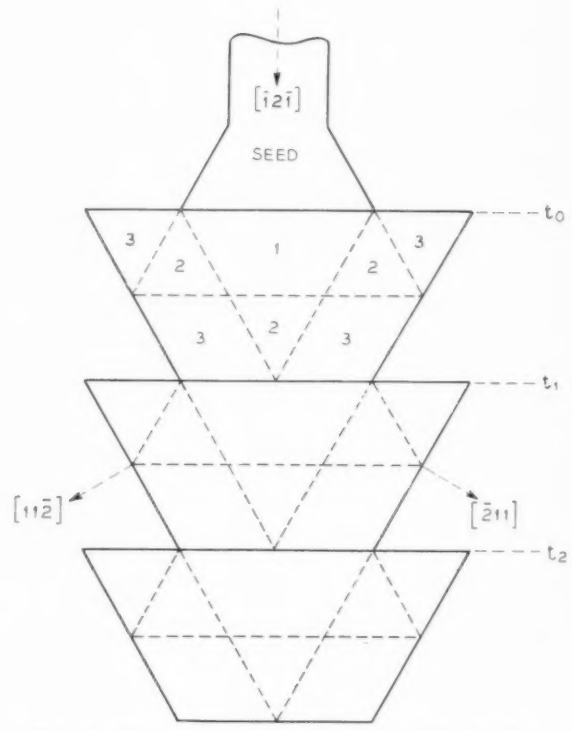


FIG. 5. Growth sequence of a germanium platelet containing two parallel twin planes.

The author wishes to thank W. G. Pfann for many helpful discussions and K. E. Benson for timely experimental assistance.

R. S. WAGNER

Bell Telephone Laboratories, Inc.
Murray Hill, N. J.

References

1. E. BILLIG, *Proc. Roy. Soc.* **229** A, 346 (1955).
2. E. BILLIG and P. J. HOLMES, *Acta Met.* **5**, 53 (1957).

* Received November 5, 1959.

Discussion of "experimental evidence of boundary migration"

In a recent letter to this journal,[1] Ferro *et al.* correlated oxide patterns on the surface of silicon iron with grain boundary migration. They suggested that recrystallized regions (areas swept by grain boundaries) were less susceptible to oxidation than unrecrystallized regions (areas not swept by grain boundaries). We have also observed a correlation between oxide patterns and grain boundary migration in high-purity silicon iron but have interpreted the origins of the patterns differently. The following examples of oxide patterns provide the basis for our interpretation and conclusions.

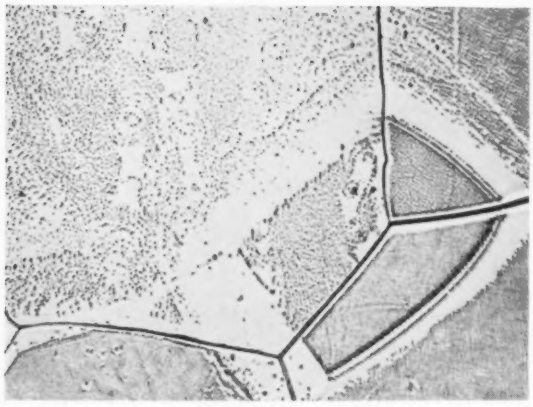


FIG. 1. Sample 0.0055 in. (0.14 mm) thick, annealed for 30 min at 1100°C after a 20 min heating-up period. ×500.

The material, containing 3% silicon and less than 0.006 wt. % impurities, was cold-rolled either to 0.006 in. or to 0.012 in. thick and electropolished prior to the anneal. The annealing atmosphere was purified argon at a pressure of 1 atm. A dew point of less than −70°C was obtained by passing tank argon through a tower containing titanium chips heated to 1000°C. The samples were suspended by a silicon-iron wire in a sealed container.

The formation of oxide particles depended on several factors: the oxygen or water vapor content of the argon, the oxygen content of the silicon iron, the temperature of annealing, the time of purging allowed to remove occluded water vapor from the container, and the rate of heating to the anneal temperature. Most of the oxygen required to form the oxide patterns came from the sample; a small amount possibly came from occluded water vapor. These two sources of oxygen were not constant; they depended on time and annealing conditions.

Since the samples were in the cold-rolled condition prior to the anneal, recrystallization and normal grain growth occurred quickly, until a relatively stable two-dimensional grain structure resulted.[2]

Fig. 1 shows some oxide (particle) patterns after an anneal of 30 min at 1100°C. The oxide patterns show that the four-sided grain was removed during the anneal and that further grain boundary migration occurred. The uneven and sometimes circular pattern of oxides in the large grain, away from the grain boundary region, however, is a result of thermal etching of the grain and not a result of boundary migration. This grain has a (111) plane within 1° of the plane of the sample. The thermal etch striations can be seen in the region nearly free of oxides.[3] The last-forming part of the (111) grain, which resulted from the disappearance of the four-sided grain, has a higher oxide density. We interpret these observations to mean that: (a) the oxides had largely formed prior to the start of disappearance of the four-sided grain; (b) the interaction of the boundary and oxides created broken lines of oxides during spasmodic migration; however, slow and steady boundary migration resulted in broad bands free, or nearly free, of oxides; (c) no additional oxides were being formed during this period of boundary migration; (d) only negligible boundary–oxide interaction occurred when the rate of boundary migration increased sufficiently as a result of increased boundary curvatures of the shrinking grain; and (e) further changes in the oxide patterns occurred because of a change of lattice orientation or because of thermal etching.

A different pattern of oxides is shown in Fig. 2. This three-sided grain, oriented about 8° from (111), was also thermally etched. The rows of oxides are roughly parallel to the line of intersection of the (111) plane with the surface of the sample. Many of the large oxides in Fig. 2 coincide with the boundaries of the shrinking, three-sided grain. Other large oxides lie in rows slightly ahead of two of the advancing boundaries. The largest oxide is at the junction of two such advance lines of oxides, i.e. opposite a junction of three boundaries. There is an approximate two-fold symmetry to the pattern of oxides shown in the upper grain. This grain has a (110) plane 15° from the plane of the sample. Similar symmetrical patterns have been observed on other grains near (110). Such grains form a thermal etch pattern (observable in electron micrographs) during long anneals at 1200°C in impure argon that is similar to the present pattern formed by the oxides.

The number of oxide particles on the (111) grain is 3.3×10^7 cm^{-2}; for (110) type grains the number density is near 10^8 cm^{-2}. In general, such densities are dependent on the orientation of the underlying grain in agreement with results obtained by Moreau and Benard for Ni–Cr alloys.[4]

Both the transitory nature of surface conditions and the oxide–boundary interaction effects are shown in Fig. 3. The oxide patterns in Fig. 3a show that grains *A* and *B* had been growing into grain *C* during the 30 min anneal at 1200°C in purified argon. The same area, shown in Fig. 3b, after a 15 min reanneal, confirms the growth of grains *A* and *B*. As a result of the second anneal many new but smaller oxide particles were added to the areas originally free of oxides. All of the original oxides on grain *A* retained their positions during the second anneal. However,

VOL. 8 1960

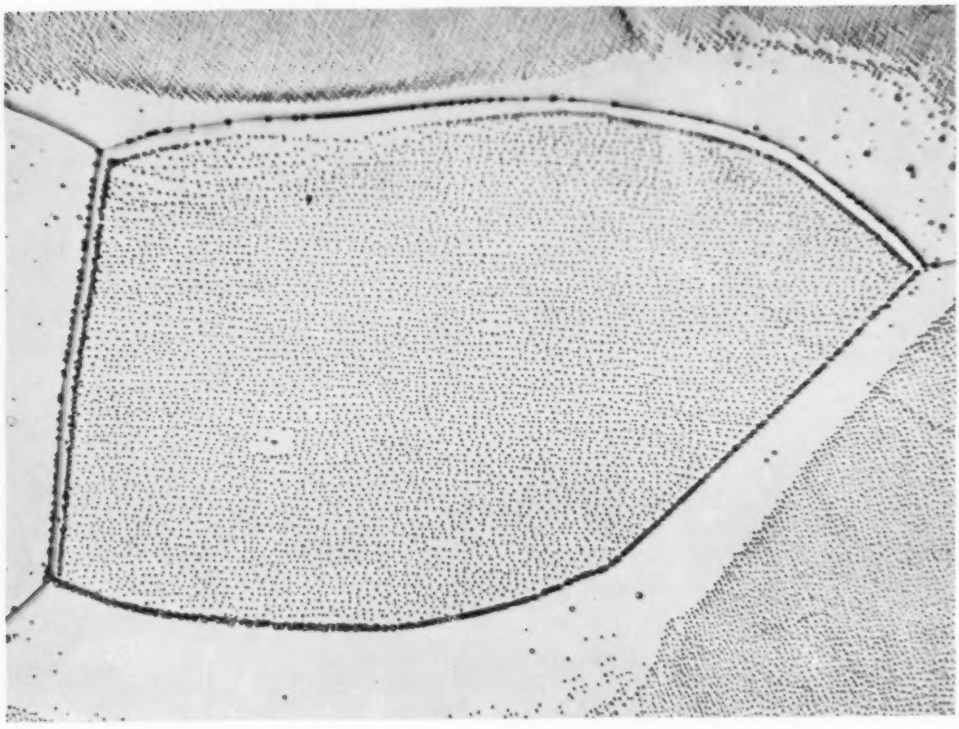
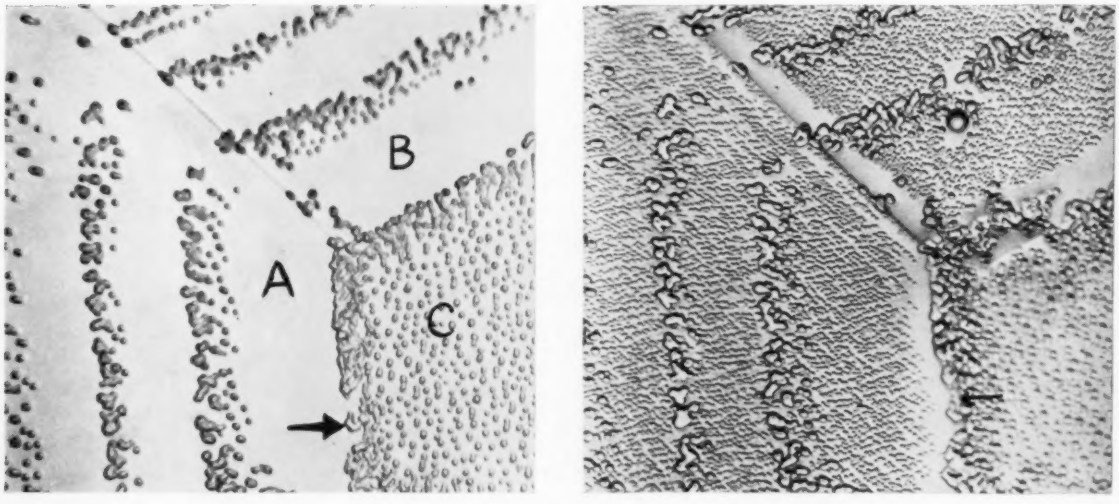


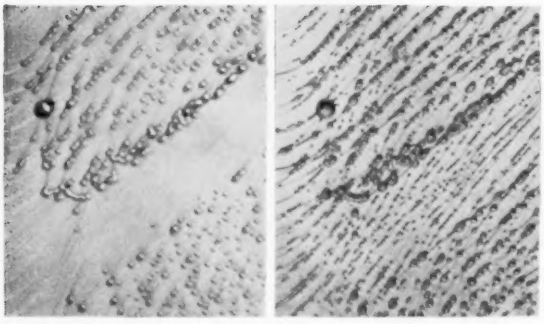
FIG. 2. Same as Fig. 1, but different area. ×500.



(a) (b)

FIG. 3. Sample 0.0115 in. (0.28 mm) thick, annealed at 1200°C. Heating-up period 15 min.
(a) After a 30 min anneal at temperature. (b) After a 15 min reanneal. ×1000.

the positions of other oxides were not always maintained. For example, the oxide particle at the boundary (see arrow in Fig. 3a) is 4μ to the right of its original position and slightly behind the boundary after the second anneal (see arrow in Fig. 3b). Such movement of large oxide particles is not understood. It appears that along the stationary A–B boundary some of the large oxide particles in grain B moved away from the boundary. This may indicate that the shape (or a changing condition) of the surface of grain B in the vicinity of the boundary is unfavorable to either the retention or the formation of oxides. In



(a) (b)

FIG. 4. Same as Fig. 3 but different area. ×1000.

this connection no new oxides formed in grain B close to the A–B boundary, but they did form on the grain A side of the boundary. The lack of new small oxides in the area swept by the B–C boundary may have resulted from migration of the boundary after all such new oxides had formed. A large, coalescing, mass of original oxides near the junction point, however, was left behind by the moving B–C boundary. Other original oxides have moved forward on both the B–C and A–C boundaries.

In another area of the sample new (small) oxides were observed along the thermally etched striations that had formed during the first anneal. This is shown in Figs. 4a and 4b for a grain with its (100) plane within 3° of the surface. The correspondence between the position of new oxides and thermal striations indicates that surface shape is important in the determination of nucleating sites of oxides.

From the above information the conclusion is drawn that both thermal faceting and thermal grooving are important factors in the formation of oxide patterns.

General Electric Research Laboratory C. G. DUNN
Schenectady, New York J. L. WALTER

References

1. A. FERRO, C. SARI and G. VENTURELLO, *Acta Met.* **7**, 430 (1959).
2. C. G. DUNN and J. L. WALTER, Submitted to *Amer. Inst. Min. (Metall.) Engrs.* for publication.
3. C. G. DUNN and J. L. WALTER, *Acta Met.* **7**, 648 (1959).
4. J. MOREAU and J. BENARD, *J. Inst. Met.* **83**, 87 (1954).

* Received October 19, 1959; revised version November 13, 1959.

VOL. 8 1960

ERRATUM

A recent letter by the writers (*Acta Met.* **7,** 818 (1959)) discusses the manner of dissociation of a chain of vacancies. A result of the kinetic argument is that the number of vacancy pairs is greater than single vacancies. This fact was mentioned in a note by R. R. Hasiguti, *J. Phys. Soc. Japan* **8,** 798 (1953). The writers regret that this reference was omitted.

A. C. Damask and G. J. Dienes

Brookhaven National Laboratory, Upton, N.Y.

THE APPLICATION OF THE ROWLAND MECHANISM TO THE PROBLEM OF THE NUCLEATION OF SECONDARY CRYSTALS IN CUBE-TEXTURE COPPER*

C. A. VERBRAAK†

Experimental evidence is provided that the growth of large secondary crystals with the Kronberg and Wilson orientations is preceded by the formation of crystals with the orientation {111}⟨112⟩ during the secondary recrystallization of heavily twinned cube-texture copper. The nucleation of the {111}⟨112⟩-crystals is explained with the aid of the Rowland lattice model. The crystals with the Kronberg and Wilson orientations are first and second order twins of the initially formed {111}⟨112⟩-crystals.

APPLICATION DU MECANISME DE ROWLAND AU PROBLEME DE LA GERMINATION DE CRISTAUX SECONDAIRES DANS LE CUIVRE A TEXTURE CUBIQUE

L'auteur démontre expérimentalement que la croissance de grands cristaux secondaires possédant les orientations de Kronberg et Wilson, est précédée par la formation de cristaux d'orientation {111} ⟨112⟩ au cours de la recrystallisation secondaire de cuivre à texture cubique fortement maclée. La germination de cristaux {111} ⟨112⟩ est expliquée à l'aide du modèle réticulaire de Rowland. Les cristaux possédant les orientations de Kronberg et Wilson sont des macles du premier et du second ordre des cristaux initiaux possédant l'orientation {111} ⟨112⟩.

ANWENDUNGEN DES ROWLAND MECHANISMUS AUF KEIMBILDUNGSFRAGEN BEI DER SEKUNDÄREN REKRISTALLISATION VON KUPFER MIT WÜRFELTEXTUR

Es wird von Versuchen über die sekundäre Rekristallisation von stark verzwillingtem Kupfer mit Würfeltextur berichtet. Die Ergebnisse zeigen, dass vor dem Wachstum grosser sekundärer Kristalle mit Kronberg und Wilson Orientierungen sich Kristalle mit {111}⟨112⟩ Orientierung bilden. Die Keimbildung dieser {111}⟨112⟩ Kristalle wird mit Hilfe des Rowlandschen Gittermodells erklärt. Die Kristalle mit Kronberg und Wilson Orientierungen sind die Zwillinge erster und zweiter Ordnung der ursprünglich entstandenen {111}⟨112⟩ Kristalle.

VOL. 8 1960

1. INTRODUCTION

The growth of large crystals during the secondary recrystallization of cube-texture material has been the subject of many investigations. The principle orientations of these secondary crystals as reported in the literature can be classified as follows:

(a) Crystals with an orientation that can be described as a rotation of the cube-orientation about the rolling direction: Dahl and Pawlek[1] (rotation over an angle of 30°), Kronberg and Wilson[2] (rotation over an angle of 19°), Rathenau and Custers[3] (described as a {210}-texture), and Burgers *et al.*[4].

(b) Crystals with an orientation that can be obtained by rotating the cube-orientation about one of its four octahedral poles: Bowles and Boas[5] (approximately 30°), Kronberg and Wilson[2] (asymmetrical rotations over angles of 22° in one direction and 38° in the other direction), Rathenau and Custers[3] (described as a {112}-texture), Burgers *et al.*[4] (rotations of approximately 15° and 30°), and Beck *et al.*[6].

(c) Crystals with a (111)-plane parallel to the rolling plane: Burgers *et al.*,[4] and Sharp and Dunn[7].

The twinning frequency of the various secondary crystals depends on the orientation relationship between the growing secondary crystal and the matrix (see, e.g. Burgers *et al.*[4]).

Another important experimental fact is the observation made by Kronberg and Wilson that no secondary crystals are formed in twin-free cube-texture copper. From this observation these authors concluded that the stacking-fault energy is the driving force for the nucleation of the secondary crystals. This suggestion is confirmed by our previous experiments on copper single crystals.[8] We observed that a copper single crystal with an initial orientation $(\bar{1}10)$ [110] after a rolling reduction of 98.5 per cent and 15 min anneal at 400°C recrystallizes into a sharp cube-texture, which is more heavily twinned than the

* This work is part of the research programme of the Research group "Metals F.O.M.-T.N.O." of the "Stichting voor Fundamenteel Onderzoek der Materie" (Foundation for Fundamental Research of Matter-F.O.M.) and was also made possible by financial support from the "Nederlandse Organisatie voor Zuiver-Wetenschappelijk Onderzoek" (Netherlands Organization for Pure Research-Z.W.O.). Received March 13, 1959.

† Laboratory of Physical Chemistry, Technical University, Delft, Holland.

cube-texture formed on annealing cold-rolled polycrystalline copper. In accordance with the conception of Kronberg and Wilson we observed that in this more heavily twinned cube-texture a greater number of secondary crystals of a smaller size is formed during the secondary recrystallization.

We have now chosen these cold-rolled ($\bar{1}10$) [110]-copper single crystals for our present study of the secondary recrystallization, because the smaller size of the secondary crystals formed in these specimens (the average size of the secondary crystals varied between 0.1 and 1 mm) makes it possible to determine pole-figures with the aid of an integrating X-ray technique. In this way a statistically more correct picture of the secondary recrystallization can be obtained than by determining the orientations of large secondary crystals separately by ordinary Laue methods.

2. EXPERIMENTAL PROCEDURE

Recrystallization at different temperatures in the range 300°–1040°C was carried out in a vacuum furnace. For temperatures in the range 300°– 800°C an annealing period of 15 min was chosen, and for temperatures of 900°– 1040°C a period of 1 hr. The time to reach the final recrystallization temperature varied from 2 to 5 min. The recrystallization at all temperatures was carried out directly on the cold-rolled specimens, i.e. without pre-anneal at a lower temperature.

For the construction of the pole-figures, X-ray photographs were taken with the various positions of the specimen 5° apart, using an integrating X-ray camera (the construction of the camera did not permit measurements of the centre of the pole-figure).

For a more quantitative comparison of the texture components, the intensities of the X-ray reflections from crystallographic planes parallel to the rolling plane were measured using a stabilized X-ray diffraction apparatus with precision goniometer and Geiger counter.*

3. EXPERIMENTAL RESULTS

The octahedral pole-figure of a specimen annealed for 15 min at 700°C is shown in Fig. 1. In this specimen there is still an appreciable amount of the cube-texture left. There are, however, three other types of orientation formed (compare also Fig. 5):

(1) A $\{111\}\langle 112\rangle$-twin texture.

(2) Four twins of the $\{111\}\langle 112\rangle$-texture, which are identical with the orientations described by Kronberg and Wilson as a rotation about the octahedral poles of the cube-texture over an angle of 22°, and will be later referred to as type (A) crystals (approximate orientation: $\{511\}\langle 172\rangle$).

(3) Four twins of the type (A) crystals, which are identical with the orientations described by Kronberg and Wilson as rotations of 38° about the octahedral poles of the cube-texture, and will be later referred to as type (B) crystals (approximate orientation: $\{235\}\langle 412\rangle$).

The octahedral pole-figure of a specimen annealed for 1 hr at 1040°C is shown in Fig. 2. In this specimen

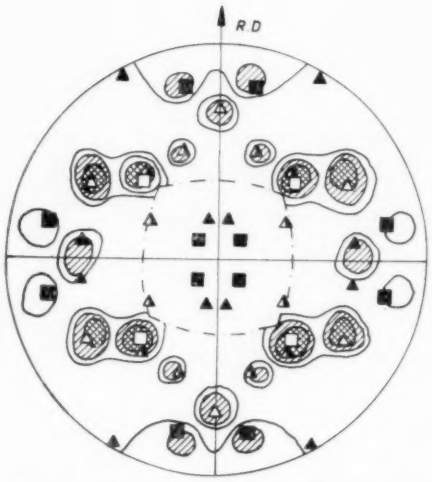


FIG. 1. Octahedral pole-figure of a ($\bar{1}10$)[110] copper single crystal cold-rolled to 98.5 per cent reduction and annealed for 15 min at 700°C
□ cube-texture
■ twins of the cube-texture
△ $\{111\}\langle 112\rangle$-texture
▲ type (A) texture
▲ type (B) texture

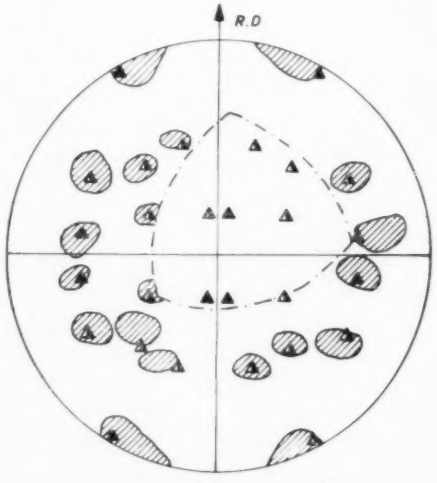


FIG. 2. Octahedral pole-figure of a ($\bar{1}10$)[110] copper single crystal cold-rolled to 98.5 per cent reduction and annealed for 1 hr at 1040°C
▲ type (A) texture
▲ type (B) texture

* Philips, Type PW 1010.

the secondary recrystallization is completed, resulting in a sharp texture containing the type (A) and type (B) orientations.

The relative intensities of the cube, $\{111\}\langle 112\rangle$ and type (A) textures for different annealing temperatures can be determined by measuring the intensities of the X-ray reflections of the planes (200), (111) and (115) parallel to the rolling plane.

As shown in Fig. 3,* the intensity of the cube-texture in specimens containing oxygen rises steadily with higher annealing temperatures, while no secondary recrystallization occurs. This has already been reported by Wood.[9] In pure copper, however, the intensity of the cube-texture in these specimens (cold-rolled $(\bar{1}10)[110]$-crystals) reaches a maximum at annealing temperatures of 400°–500°C and decreases at higher annealing temperatures, at the cost of secondary crystals.

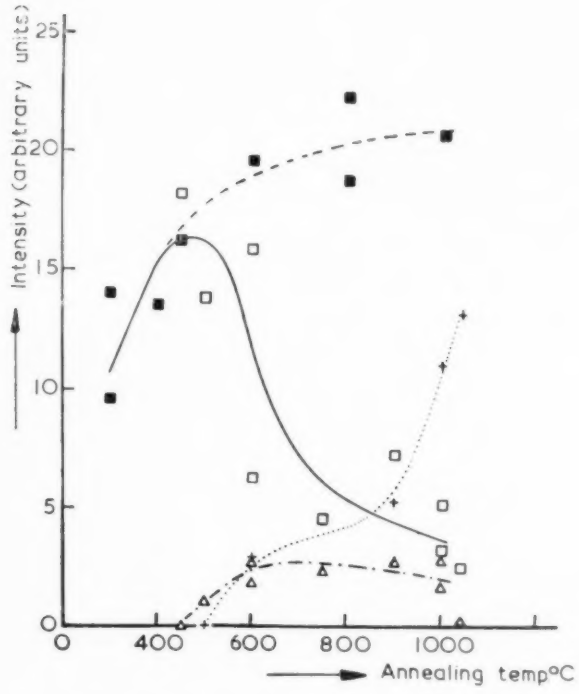


FIG. 3. Relative intensities of X-ray reflections of crystallographic planes parallel to the rolling plane

■ – – – – ■ (200)-reflection in specimens containing oxygen
□ ——— □ (200)-reflection in specimens of pure copper
△ — · — △ (111)-reflection in specimens of pure copper
+ · · · · · · + (115)-reflection in specimens of pure copper

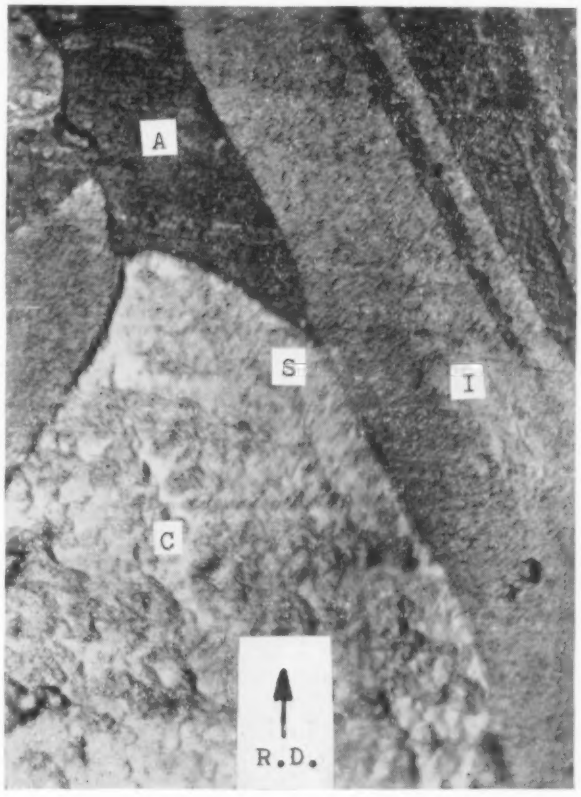


FIG. 4. Photomicrograph of partially secondary recrystallized specimen. ×800

(C) cube-texture matrix
(I) $\{111\}\langle 112\rangle$-crystal
(A) type (A) crystal
(S) nucleation site of type (A) crystal

The $\{111\}\langle 112\rangle$-texture is formed in the narrow temperature range 450°–600°C while at higher temperatures the growth of these crystals ceases, in spite of the fact that the secondary recrystallization after 15 min anneal at 600°C is far from complete.

The formation of the type (A) texture starts in the same temperature range as the $\{111\}\langle 112\rangle$-texture, but unlike the latter, the type (A) crystals are able to grow at higher annealing temperatures.

Metallographic examination reveals also three types of secondary crystals in these specimens:

(1) Crystals with one set of twin-boundaries making an angle of 30° with the rolling direction (crystal marked (I) in Fig. 4).

(2) Crystals with two sets of twin-boundaries making angles of 30° and 45° respectively with the rolling direction (crystal marked (A) in Fig. 4). A typical example of this type can also be seen in the paper by Burgers *et al.*[4] (crystal marked A in Fig. 3 of their paper).

* The measurements shown in this figure were made on specimens cut from the same strip of a cold-rolled $(\bar{1}10)[110]$-crystal. Several other strips were investigated and in each case the same phenomena were observed. Due to minor differences in the rolling process, however, the maximum intensity of the cube-texture and the start of the secondary recrystallization occur at different annealing temperatures in various strips. The clearest picture of the successive intensity ratios can therefore be obtained by plotting in a single figure only the measurements on specimens of the same strip.

VOL. 8 1960

(3) Crystals with one set of twin-boundaries making an angle of 45° with the rolling direction.

Although it was not possible to determine the orientations of these crystals separately (because of their small size), it is most likely from the evidence of the twin-boundaries, and from the orientations of similar but larger crystals in the specimens of Burgers *et al.*, that these crystals belong to the {111}⟨112⟩, type (*A*), and type (*B*) textures respectively. Boundaries making an angle of 30° with the rolling direction are thus twin-boundaries between a {111}⟨112⟩ and a type (*A*) crystal, whereas those at 45° to the rolling direction are either twin-boundaries between type (*A*) and type (*B*) crystals, or octahedral twist-boundaries between type (*A*) or type (*B*) crystals and the cube-texture matrix.

Metallographic examination of partially secondary recrystallized specimens also provides evidence of twinning by stimulation (see also e.g. Burgers and May[10]), as shown in Fig. 4. In this figure the area marked (*C*) is the cube-texture matrix, the crystal marked (*I*) has from the evidence of the twin-boundaries a {111}⟨112⟩-orientation, whereas the crystal marked (*A*) is apparently, from the appearance of the boundaries, nucleated by stimulation at point (*S*) by the growing crystal (*I*). In completely secondary recrystallized specimens, crystals with the shade of crystal (*A*) in Fig. 4 show two sets of twin-boundaries making angles of 30° and 45° with the rolling direction, which is an indication that this stimulated crystal belongs to the type (*A*) texture.

4. DISCUSSION OF RESULTS

From the X-ray evidence that the growth of the {111}⟨112⟩-components terminates long before the secondary recrystallization is completed (Fig. 3), and from metallographic examination (Fig. 4), we conclude that the type (*A*) crystals are stimulation twins of the {111}⟨112⟩-crystals. As shown in the stereographic projection of Fig. 5, a twinning operation on the octahedral plane (1) of a (111)[11$\bar{2}$]-crystal results in a type (*A*) orientation, which has an octahedral plane (2) nearly in common with the cube-orientation, and has an orientation that can be described as a rotation of the cube-orientation about this octahedral pole through an angle of 22°. A stimulation of this type (*A*) crystal by a (111)[11$\bar{2}$]-crystal is very likely, because the cube-orientation of the matrix is nearer to this type (*A*) orientation than to (111)[11$\bar{2}$]. Furthermore, this type (*A*) orientation has an octahedral plane in common with the cube-orientation, and is therefore more favourably orientated for growth into the cube-texture than a (111)[11$\bar{2}$]-crystal. At this point we would like to draw the attention to the fact that a (111)[11$\bar{2}$]-crystal has a greater twinning frequency than a type (*A*) crystal, as already reported by Burgers *et al.*[5].

If now the growing crystal (*A*) encounters a twin of the cube-texture (see Fig. 5), a second twinning operation might occur on the octahedral plane (2) resulting in a type (*B*) orientation, because this type (*B*) orientation is nearer to this twin of the cube-texture than the type (*A*) orientation.

The type (*B*) orientation is also favourably oriented for growth into the cube-texture because it has the same octahedral plane (2) in common with the cube-texture.

The same cycle can be performed by twinning on octahedral plane (3) of the (111)[11$\bar{2}$]-orientation, and by twinning on the two corresponding octahedral planes of the (111)[$\bar{1}$12]-orientation. In this way four type (*A*) and four type (*B*) orientations can be formed.*

A twinning operation on octahedral plane (4) of the (111)[11$\bar{2}$]-orientation is not likely, because this twinning does not result in an orientation which has an octahedral plane in common with the cube-texture.

From the point of view set out above, it is now understandable why the secondary crystals have orientations that can be described by asymmetrical rotations about the octahedral poles of the cube-texture through angles of 22° in one direction and 38° in the opposite direction, whereas, if growth-selectivity was the only governing principle, equal rotations in both directions would be expected.

---

* Although Sharp and Dunn[7] do not mention the exact orientations of the secondary crystals, the directions of the twin-boundaries in Figs. 1 and 2 of their paper, and the statement that a {115}-plane of crystal *C* in Fig. 2 coincides with a {111}-plane of crystal *A*, provide sufficient evidence that the dark crystals in Fig. 1 and the crystals *B* and *C* in Fig. 2 belong to the {111}⟨112⟩-texture, whereas the large grain in Fig. 1 and crystal *A* in Fig. 2 are type (*A*) crystals. The {111}⟨112⟩-crystals in the specimens of Sharp and Dunn are then stimulated by a type (*A*) crystal. At first sight this seems to be contrary to our conception that it is the type (*A*) crystal that is stimulated by the {111}⟨112⟩-crystals. Their results cannot, however, be compared with our experiments, because in their case the specimens were moved into a furnace with a temperature gradient, whereas our specimens were annealed at a uniform temperature. The fact that the {111}⟨112⟩-crystals observed by Sharp and Dunn always contained both twin components of the {111}⟨112⟩-orientation at the nucleation site (crystals *B* and *C* in Fig. 2), shows that even in this case a normal twinning operation of the type (*A*) crystal can hardly be the origin of the {111}⟨112⟩ twinned crystals.

In our opinion the {111}⟨112⟩-crystals in the specimens of Sharp and Dunn are formed as follows. When the boundary of a type (*A*) crystal (moving with the temperature gradient and also marked *A* in Fig. 2 of their paper) encounters a heavily twinned area of the cube-texture matrix (a potential nucleation site of a {111}⟨112⟩-crystal), a Rowland mechanism occurs, which then necessarily results in the nucleation of both twins of the {111}⟨112⟩-texture, as will be discussed later in this paper.

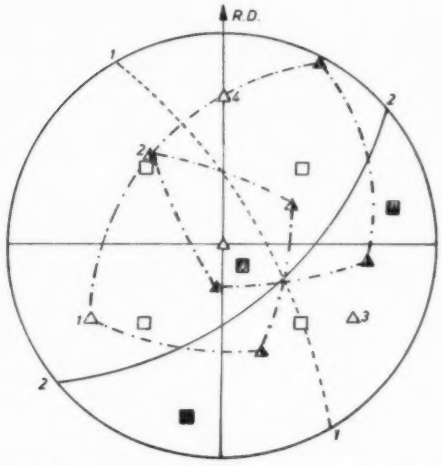


FIG. 5. Stereographic projection of the twinning operations of the {111}⟨112⟩-texture resulting in the type (*A*) and type (*B*) orientations

□ octahedral poles of the cube-orientation
■ octahedral poles of a twin of the cube-orientation
△ (111)[11$\bar{2}$]-orientation
▲ type (*A*) orientation
▲ type (*B*) orientation

The problem of the nucleation of the secondary crystals is now reduced to that of the nucleation of the {111}⟨112⟩-texture. The only experimental guidance as yet available for the solution of this problem is the proportionality between the number of secondary crystals and the number of twins in the cube-texture, indicating that the elimination of the twin stacking-faults of the cube-texture is the driving force for the nucleation of the {111}{112}-texture (Kronberg and Wilson considered the elimination of those stacking-faults to be the driving force of the nucleation of the type (*A*) and type (*B*) crystals directly).

In our paper concerning the nucleation of the cube-texture[8] we have shown that a cube-recrystallization-texture can be formed on annealing quite different rolling-textures, if only these rolling-textures contain a heavily twinned {112}⟨111⟩-texture component. From this observation we concluded that the cube-texture is nucleated by the untwinning of this {112}⟨111⟩ twin-texture by means of an inverse Rowland mechanism. We will now apply a similar ⟨112⟩ slip-mechanism to the problem of the nucleation of the {111}⟨112⟩-texture.

First of all we have to bear in mind, however, that in the case of the nucleation of the cube-texture only one set of stacking-faults, namely those on the twin-plane of the {112}⟨111⟩-texture, had to be eliminated, which can be achieved by an inverse Rowland mechanism, whereas in our present problem four sets of stacking-faults of equal frequency on the four octahedral poles of the cube-texture matrix must be eliminated co-operatively.

A possible mechanism is shown in Figs. 6, a and b. The white balls in Fig. 6a compose a half-octahedron with a cube-orientation (the rolling direction is C_2C_4 and the rolling plane $C_2C_3C_4$) on which two darker balls T_1 and T_2 are placed in twin-position. If now the original cube-plane $C_2C_3C_4$ is transformed into an octahedral plane by means of a normal Rowland mechanism (see Fig. 6b), the original cube-orientation is transformed into a (111)[11$\bar{2}$]-orientation, while the atoms T_1 and T_2 automatically shift into this same orientation by retaining their positions on the two operating octahedral slip-planes (only one of these planes, $C_1C_3C_4$ is visible in Fig. 6). The two other octahedral planes (only one, $C_1C_2C_3$, is visible in Fig. 6) are transformed into cube-planes and any stacking-faults on these planes will therefore be eliminated in the same way as the untwinning by an inverse Rowland mechanism.* The complementary orientation (111)[$\bar{1}$12] is not shown in Fig. 6, but will be formed simultaneously during the transformation of the cube-plane $C_2C_3C_4$ of Fig. 6a into the octahedral (twin-)plane $C_2C_3C_4$ of Fig. 6b.

Although the elimination of the four sets of stacking-faults of the cube-texture in this way leads to a {111}⟨112⟩-texture, we have to bear in mind that this elimination of stacking-faults can be achieved by six different Rowland transformations of the cube-texture, leading to the following orientations:

	direction of compression	*direction of extension*
{111}⟨112⟩	transverse direction	rolling direction
{111}⟨110⟩	rolling direction	transverse direction
{112}⟨111⟩	transverse direction	normal direction
{110}⟨111⟩	normal direction	transverse direction
{112}⟨110⟩	rolling direction	normal direction
{110}⟨112⟩	normal direction	rolling direction

An explanation has now to be sought as to why, of those six possible orientations, only one is formed in an observable quantity.

By assuming that the surface energy favours a plane of high density at the surface of the strip, all

* In a previous paper[11] we have demonstrated that a *normal* Rowland transformation and an *inverse* Rowland transformation are both the results of the same type of co-operative ⟨112⟩ slip-operations on two octahedral planes. In both cases stacking-faults can be formed and eliminated. To avoid confusing the two transformations, we always refer to the transformation of the main texture-components. Thus the untwinning of the {112}⟨111⟩ twin-texture resulting in a cube-texture[8] is an *inverse* Rowland mechanism although it is accompanied by twinning on the octahedral planes of the cube-texture. For the same reason the transformation of the cube-texture into the {111}⟨112⟩-texture is a *normal* Rowland mechanism although it is accompanied by the elimination of the twins of the cube-texture. For a description of the difference between a normal and an inverse Rowland mechanism we refer to Burgers and Verbraak[12].

VOL. 8 1960

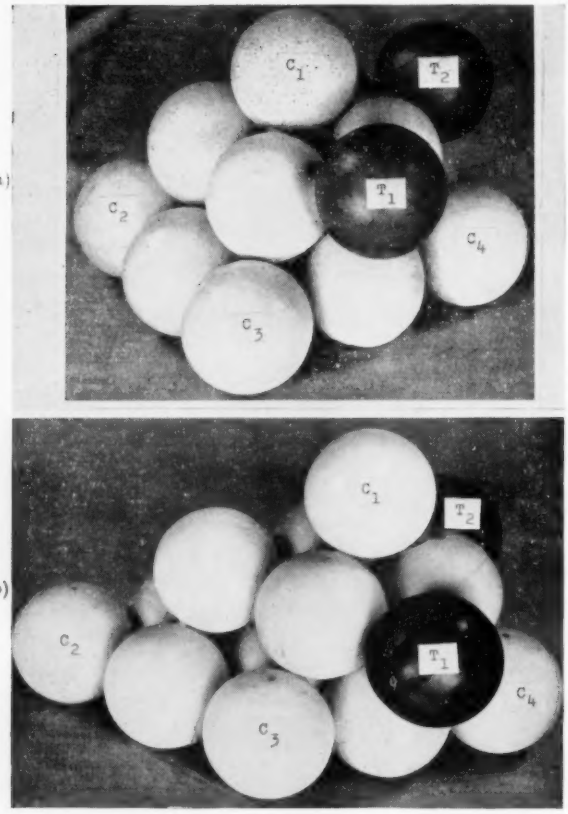


FIG. 6. Lattice model showing the Rowland transformation of the cube-texture and twins into the {111}⟨112⟩-orientation.

orientations but {111}⟨112⟩ and {111}⟨110⟩ are unfavourable. Of these two only the {111}⟨112⟩-orientation preserves the two most favourable ⟨110⟩-gliding directions of the original rolling process and is able to eliminate a possible remnant of the ⟨110⟩ stacking-faults discussed in our previous paper.[8] If the above suppositions are correct, the greatest decrease of free energy will be obtained by the Rowland transformation leading to a {111}⟨112⟩-texture.

If in a single-texture matrix the six possible Rowland transformations are equally frequent, the twinning cycle described in this paper would result in an annealing texture, containing orientations which can be related to the original single-texture matrix by symmetrical rotations around octahedral poles through angles of both 22° and 38° in each direction. The general impression will then be an average rotation of about 30°, if we assume a normal spread of the original single-texture matrix of 10°.

It might be a trick of nature that two annealing twins of a Rowland transformation (type (*A*) and type (*B*) orientations) are also favourably oriented for growth-selectivity, and it would therefore be interesting to know whether intermediate texture components (such as the {111}⟨112⟩-components during the secondary recrystallization of cube-texture copper) can also be detected in other cases, where rotations around octahedral poles are observed during the recrystallization of a single-texture matrix.

Secondary crystals with an orientation that can be described by a rotation of the cube-texture about the rolling direction were not observed in our specimens. These orientations, found by some authors starting with polycrystalline copper, might be caused by the growth of {210}-texture components sometimes accompanying the cube-texture as discussed in a previous paper.[8]

ACKNOWLEDGMENTS

The author is indebted to Professor W. G. Burgers and Dr. T. J. Tiedema for continued encouragement and advice.

REFERENCES

1. O. DAHL and F. PAWLEK, *Z. Metallk.* **28**, 266 (1936).
2. M. L. KRONBERG and F. W. WILSON, *Trans. Amer. Inst. Min. (Metall.) Engrs.* **185**, 501 (1949).
3. G. W. RATHENAU and J. F. H. CUSTERS, *Philips Res. Rep.* **4**, 241 (1949).
4. W. G. BURGERS, J. C. MEYS and T. J. TIEDEMA, *Acta Met.* **1**, 75, (1953).
5. J. S. BOWLES and W. BOAS, *J. Inst. Met.* **74**, 501 (1948).
6. P. A. BECK, J. TOWER and P. R. SPERRY, *Trans. Amer. Inst. Min. (Metall.) Engrs.* **185**, 203 (1949).
7. M. SHARP and C. G. DUNN, *J. Metals* **4**, 1344 (1952).
8. C. A. VERBRAAK, *Acta Met.* **6**, 580 (1958).
9. D. L. WOOD, *J. Metals* **9**, 406 (1957).
10. W. G. BURGERS and W. MAY, *Rec. Trav. Chim. Pays-Bas* **64**, 5 (1945).
11. C. A. VERBRAAK, *Proc. Koninkl. Ned. Akad. Wetensch.* B **60**, 393 (1957).
12. W. G. BURGERS and C. A. VERBRAAK, *Acta Met.* **5**, 765 (1957).

ISOTHERMAL REVERSION OF THE B.C.C. → H.C.P. TRANSFORMATION INDUCED IN β' AgCd BY MECHANICAL DEFORMATION*

D. B. MASSON†

The hexagonal close-packed structure induced in β' AgCd by mechanical deformation was found to revert gradually to the original body-centered cubic structure at room temperature. The rate of reversion was measured for several alloys of composition around 50 at. %. The reversion rate was found to be dependent on composition and temperature; the process appeared to be thermally activated with an activation energy of about 23 kcal/mole. The rate data were found to agree with equations that have been derived by other authors for nucleation and growth processes.

REVERSION ISOTHERME DE LA TRANSFORMATION CUBIQUE CENTREE → HEXAGONALE COMPACTE INDUITE DANS LE β' AgCd PAR UNE DEFORMATION MECANIQUE

La structure hexagonale compacte induite dans le β' AgCd par une déformation mécanique, peut subir, à la température ambiante, une réversion graduelle vers la structure originale cubique centrée. L'auteur a mesuré la vitesse de réversion de nombreux alliages de composition atomique voisine de 50%. Cette vitesse dépend de la composition et de la température; le mécanisme semble activé thermiquement et correspond à une énergie d'activation voisine de 23 kcal/mole. Les vitesses déterminées expérimentalement sont en accord avec les équations établies par d'autres auteurs pour les mécanismes de germination et croissance.

ISOTHERME RÜCKBILDUNG DER IN β' AgCd DURCH MECHANISCHE VERFORMUNG INDUZIERTEN UMWANDLUNG KUBISCH RAUMZENTRIERT → HEXAGONAL

Durch mechanische Verformung lässt sich in β' AgCd eine hexagonal dichteste Struktur erzeugen. Diese bildet sich bei Raum-temperatur allmählich in die ursprüngliche kubisch raumzentrierte Struktur zurück. Die Rückbildungsgeschwindigkeit von verschiedenen Legierungen der Zusammensetzung um etwa 50 Atom% wurde gemessen. Sie hängt nach den vorliegenden Untersuchungen von der Zusammensetzung und der Temperatur ab; der Vorgang scheint thermisch aktiviert zu sein mit einer Aktivierungsenergie von etwa 23 kcal/Mol. Die Geschwindigkeitswerte stimmen mit Gleichungen überein, die andere Autoren für Keimbildungs- und Wachstumsvorgänge abgeleitet haben.

VOL. 8 1960

INTRODUCTION

The promotion of martensitic transformations by mechanical deformation is a well documented phenomenon. Hess and Barrett[1], for example, found that plastic deformation induced the f.c.c. → h.c.p. transformations of cobalt and cobalt–nickel alloys at temperatures appreciably above those observed for spontaneous transformation on cooling; a similar effect, opposite in sign, was noted for the h.c.p. → f.c.c. reversion on heating. In this case plastic deformation was thought to have supplanted thermal agitation in overcoming the activation energy of the transformations. The same behavior was noted by Barrett[2] with the alkali metals lithium and sodium, by Barrett and Trautz[3] in several lithium–magnesium alloys, by Massalski and Barrett[4] in β' CuZn, and by Masson and Barrett[5,6] in β' AgCd. However, in all the examples cited, except those in β' CuZn and β' AgCd, the low-temperature structure induced by mechanical deformation proved to be stable when heated to temperatures considerably above M_d, the temperature of their cold work-induced formation. In sodium, for example, lines from the X-ray powder pattern of the hexagonal structure induced by mechanical deformation at 5°K persisted when the metal was heated at 60°K with only a slight decrease in intensity. Similar situations were also found in cobalt and lithium.

Somewhat different behavior was observed in β' CuZn and β' AgCd. In these alloys mechanical deformation was found to change the structure from its original body-centered cubic to either hexagonal close-packed (AgCd) or to both hexagonal close-packed and face-centered cubic (CuZn) structures. In contrast to the behavior observed in sodium these deformation-induced structures gradually reverted to the original b.c.c. without heating above M_d. The reversion rate depended on both temperature and composition. The present investigation was undertaken to study the kinetics of the reversion of the cold work-induced h.c.p. structure to b.c.c. in β' AgCd and explain, if possible, the instability of this cold work-induced transformation product.

Both β' CuZn and β' AgCd possess an ordered body-centered cubic structure. Although superlattice lines cannot generally be detected by X-ray diffraction because of the adjacent positions of the elements of the

* This work was supported in part by the sponsors of the Institute for the Study of Metals at the University of Chicago, by ONR Contract N6ori-02004, and by a fellowship given to the author by the Monsanto Chemical Company. Received April 6, 1959.

† Department of Mechanical Engineering, the Rice Institute, Houston, Texas.

respective alloys in the periodic chart, measurements of the temperature dependence of the elastic modulus by Köster[7] have shown them to be ordered. It is quite possible, however, that the mechanical deformation producing the observed structural transformation might have reduced the degree of long-range order—in fact, such disorder induced by cold work has been suggested as the cause for the transformation in β' CuZn[4,8] and β' AgCd.[6] Whether or not it may cause a structural transformation, the disordering of superlattices by cold work is well recognized. Dehlinger and Graf[9] and Dahl[10] observed that cold work caused superlattice lines in ordered AuCu and $AuCu_3$ to disappear; furthermore, as a result of cold work the resistivity of ordered $AuCu_3$ increased to that of the disordered alloy. Similar effects were observed by Linde[11] in ordered CuPt; by Schafer[12] in FeAl; and by Honeycombe and Boas[13] in β' CuZn. These considerations led Massalski and Barrett[4] to attribute the b.c.c.→(f.c.c., h.c.p.) transformation of β' CuZn to an increase of the free energy of the b.c.c. phase caused by cold work-induced disordering; Kaufman[8] concurred with this opinion in his thermodynamic interpretation of their results.

Therefore, in the following treatment of the cold work-induced transformation of ordered b.c.c. AgCd to a h.c.p. structure and the subsequent spontaneous h.c.p.→b.c.c. reversion at room temperature, it will be assumed that mechanical deformation can have two effects—(1) it may aid in overcoming the activation energy of the transformation and (2) it may reduce the long-range order of the initial structure.

EXPERIMENTAL PROCEDURE AND RESULTS

All samples studied were prepared by fusing predetermined amounts of the constituent metals under an inert atmosphere in transparent Vycor tubes. A detailed description of the preparation, analysis and heat treatment of the samples has been published previously.[5] The compositions in weight and atomic percentage are given in Columns 1 and 2 of Table 1. As can be seen, all are very near 50 at.% and therefore have a composition only slightly removed from that of the 1 : 1 atomic ratio of perfect order. The form in which the samples were ultimately obtained, prior to the treatment described in the following paragraphs, was that of large grained pellets, quenched from 823°K, having an ordered body-centered cubic structure. The beta structure which was obtained was slightly metastable for many of these alloys; at equilibrium they would fall within the two phase ($\alpha + \beta'$) and ($\beta' + \gamma$) fields at room temperature. No phase separation occurred, however, presumably because of the low diffusion rates expected at this temperature.

The kinetic study of the h.c.p. → b.c.c. reversion after mechanical deformation was divided into two parts. The first part involved measuring the reversion rate of alloys of several different compositions, holding the temperature constant at 300°K; the second involved measuring the reversion rate at several temperatures for each different alloy. The mechanical deformation to which the samples were subjected was that achieved by filing the pellets; this was found to be sufficient to induce the initial b.c.c. → h.c.p. transformation. Reversion rates were determined by measuring the intensity of one of the b.c.c. X-ray peaks diffracted from the cold-worked filings, as a function of time.

For the kinetic studies at 300°K, filings were made from the pellets, screened through 200 mesh and mounted immediately on a G.E. XRD-3 X-ray diffraction unit. The detector was set to receive the b.c.c. 110 peak, and intensity was counted as a function of time. Since it was desired that data collected from one run should be capable of comparison with data from alloys of other compositions, all b.c.c. 110 peak intensities were normalized to background. This was done by taking the quotient of the 110 peak intensity divided by the measured background intensity. This corrected for the factors affecting absolute intensities of both peak and background (such as X-ray tube current and detector voltage) which might not remain constant from one run to the next; actually the correction was very small because of the uniformity of the runs. Care was taken that the layer of powder was thick enough to appear infinitely thick to the X-ray beam, so that all radiation was absorbed in each case.

Isothermal reversion curves plotted from data collected in this manner at 300°K are shown in Figs. 1 and 2, with the normalized intensity ratios plotted as the ordinate and the time elapsed since filing as the abscissa. It should be noted that all curves had approximately the same initial intensity ratio, indicating that equal amounts of this cubic structure (assumed to be zero; see reference (5)) were initially present. The curves in Fig. 1 show the time dependence of the reversion of compositions of less than 50 at. % silver; those of Fig. 2 for compositions in excess of this value. The composition dependence is obvious.

Two features of the isothermals of Figs. 1 and 2 are of special interest. The first of these is the induction time (i.e. initial periods where $dI/dt = 0$) before the reversion starts; the second is the slope of

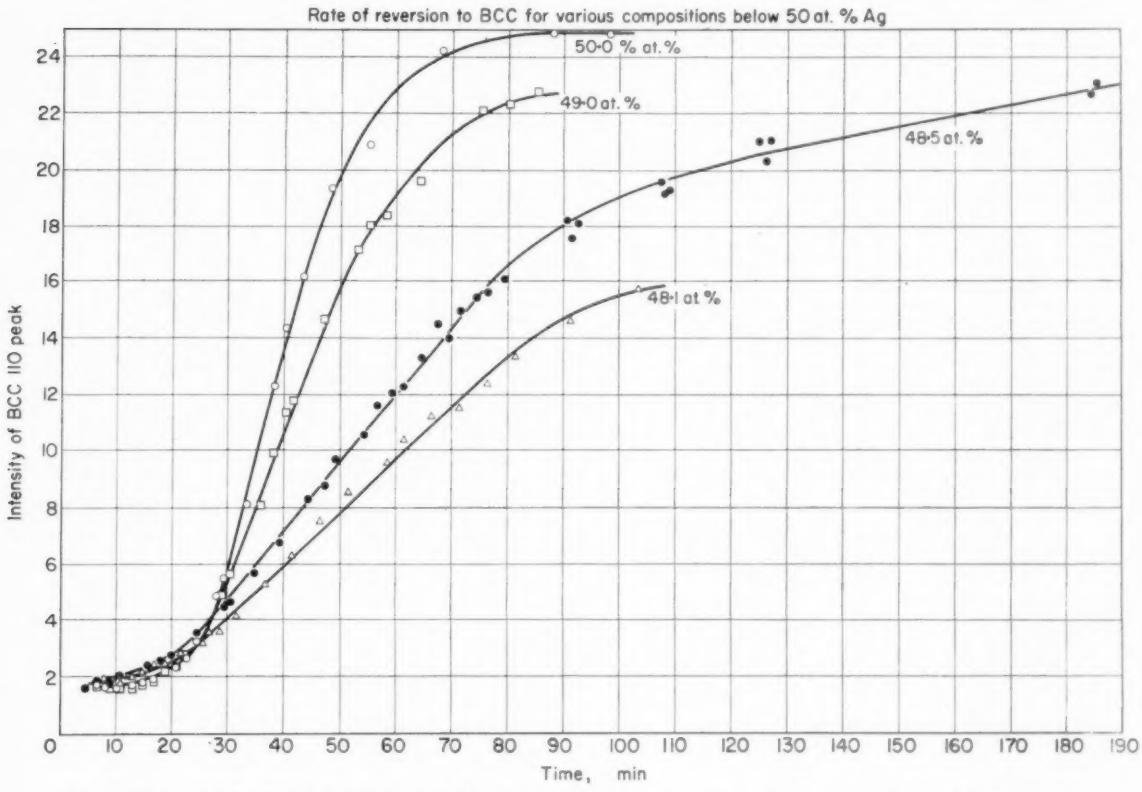


FIG. 1. Normalized intensity of the b.c.c. 110 peak as a function of time elapsed since mechanical deformation during the reversion at room temperature of alloys containing less than 50 at. % Ag. The initial intensity is only slightly greater than background (i.e., normalized intensity greater than one) which indicates very little of the b.c.c. structure was present immediately after deformation.

the curves over the range where the reversion is occurring rapidly. It can be seen that the induction time is quite long for some compositions, but is shortened markedly by small decreases in silver content. In the isothermals of Fig. 1 on the low silver side, the induction time is so short that the reversion appears to begin immediately after filing (i.e. dI/dt is never zero). The slope of the curves, on the other hand, shows a composition dependence that is symmetrical about 50 at. %. As the 1 : 1 atomic ratio is approached from the high silver side these slopes become increasingly steeper—they reach a maximum at 50 at. % and then decrease with further decrease in silver. Both features will prove to be of interest in the analysis of the rate curves given below.

The determination of reversion rates as a function of temperature over the range 300°–360°K was accomplished by a similar technique. However, a different sample mount was needed to maintain the temperature at the desired level throughout the reversion. The mount used has been described previously[6] in connection with applications around 78°K; however, it was found to be equally useful around room temperature. The sample was held in the X-ray beam on a copper holder heated by a heater consisting of a small coil of nichrome wire. Any temperature over the range 300°–360°K could be maintained as long as needed (2–3 hr) within ±0.1° by manual control of the heater current. Sample temperatures were measured by a copper-constantan thermocouple varnished to the mount in a position immediately adjacent to the area exposed to the X-ray beam. The holder was heated to the desired temperature prior to filing the sample—filings were then made, screened through 200 mesh immediately and pressed into a coating of grease on the copper mount. The high heat capacity of the mount kept temperature fluctuations low during this operation, since transfer times were short and temperatures were not far removed from ambient. The temperature of the mount, as measured immediately after the sample transfer, was maintained throughout the reversion. Samples could be filed, screened, mounted and aligned in the beam for intensity measurement at temperature within 3 min

VOL. 8 1960

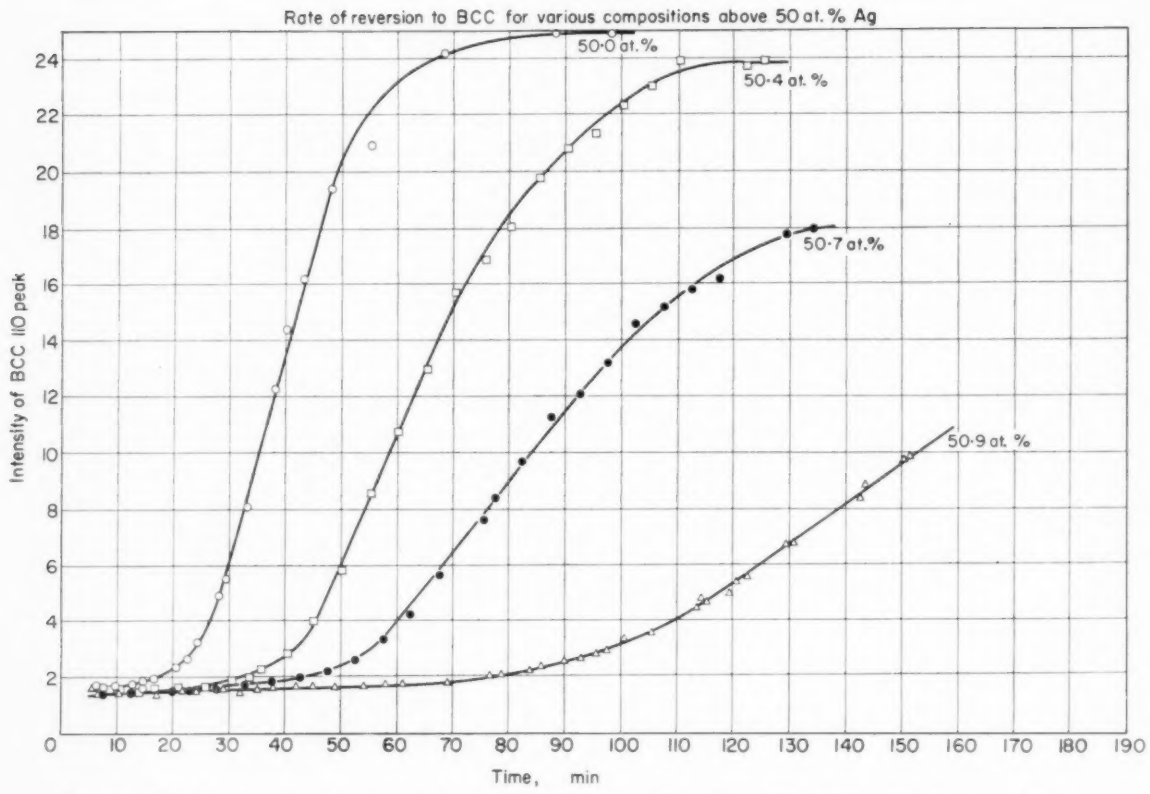


FIG. 2. Data for the reversion at room temperature in compositions above 50 at.% Ag plotted on coordinates the same as those of Fig. 1. Above 50 at % an induction time occurs prior to the reversion, but is absent in compositions below 50 at. %. Note that the slopes of the curves have their maximum value at 50 at. % and diminish on either side of this composition.

of the time filing. Diffracted intensity of the b.c.c. 110 peak was measured as a function of time at 1/2, 1, or 2 min intervals, depending on the temperature and reversion rate.

A typical series of isothermals for the reversion of one alloy is shown in Fig. 3. The percentage of sample reverted is plotted on the ordinate vs. ln time on the abscissa. The temperature of reversion is shown beside each curve. It can be seen that the curves are parallel but displaced along the ln time axis—this is especially true in the early stages of the transformation (below 75 per cent reversion). The reversion rate is obviously temperature dependent, since an increase of only 19° caused a 10-fold decrease in the half time.

In the experiments described above, the alloys always possessed the b.c.c. structure prior to filing; however, the following experiment was performed to show that a b.c.c. structure was not needed initially for the cold worked alloy to change gradually to b.c.c. following deformation. Reference to the Ag–Cd phase diagram[14] shows that an alloy containing 48.5 at. % silver lies entirely within the hexagonal ζ field at 623°K. It was found that this ζ phase could be retained at room temperature by quenching. Quenched filings retained their h.c.p. ζ structure for weeks: however, cold worked filings made from a quenched pellet "reverted" from the cold worked h.c.p. structure to b.c.c. in a few hours. Apparently the cold work, and not necessarily the structure present prior to deformation, is the factor necessary to initiate the change. It should be emphasized that cold working the quenched h.c.p. ζ phase did not result immediately in "reversion" to a b.c.c. structure—this "reversion" occurred over the time of a few hours at room temperature, similar to the behavior shown in Fig. 1 where the structure was b.c.c. prior to deformation.

Quite striking color changes were observed during the structural transformations. The metal was generally pink when it possessed the b.c.c. structure—this pink coloration of β phases has been noted by many investigators. When the orthorhombic structure was obtained as the result of cooling[5] or the h.c.p. structure as a result of cold working, however, the color turned to metallic silver. After the b.c.c. structure

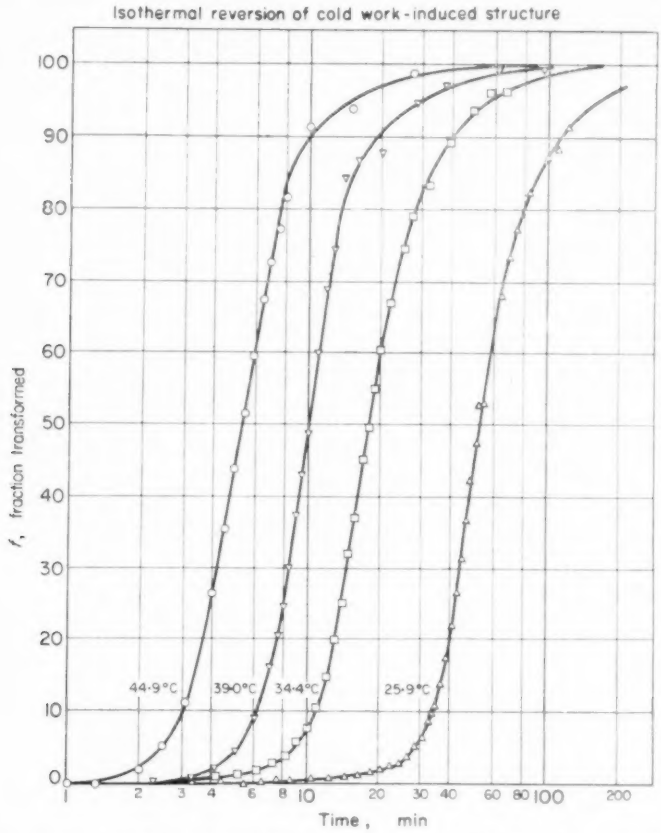


FIG. 3. Per cent reversion-product in the 50 at. % alloy vs. time elapsed since deformation at several temperatures. Curves are parallel but displaced along the ln time axis, as would be expected if the reversion obeys the Arrhenius Equation.

had been regained by heating the orthorhombic phase or by allowing the h.c.p. phase to revert spontaneously, the pink coloration was also regained.

ACTIVATION ENERGY OF REVERSION

The activation energy for the reversion from the cold work-induced h.c.p. structure could be obtained from the data plotted in Fig. 3. If the reversion was a thermally activated process the temperature dependence of the reaction rate constant, b, should obey the well known Arrhenius Equation.

$$b = A \exp(-Q/RT) \tag{1}$$

b = reaction rate constant

A = frequency factor, assumed to be a constant

Q = activation energy

T = absolute temperature, °K

R = gas constant

Equation (1) cannot be used directly since the experimental data appear as fraction transformed, f, as a function of time, t, at several temperatures (Fig. 3). However, for any given value of f the rate constant is proportional to the reciprocal of the time needed to attain f at that temperature.

Thus,

$$b(T) \propto (1/t)F(f) \tag{2}$$

where

$F(f)$ = some function of f

f = fraction transformed at time t

t = time elapsed since deformation

Equation (1) can be rewritten in terms of t for any constant value of f, and we get

$$t = A' \exp(Q/RT) \tag{3}$$

A' = constant containing A and F

Thus a plot of the logarithm of the time needed to attain a given value of f vs. $1/T$ will have a slope of Q/R if equation (1) is applicable to the data.

This is shown plotted for the reversion of AgCd 50.0 at. % silver in Fig. 4—data from the reversion of other compositions give similar curves. In Fig. 4

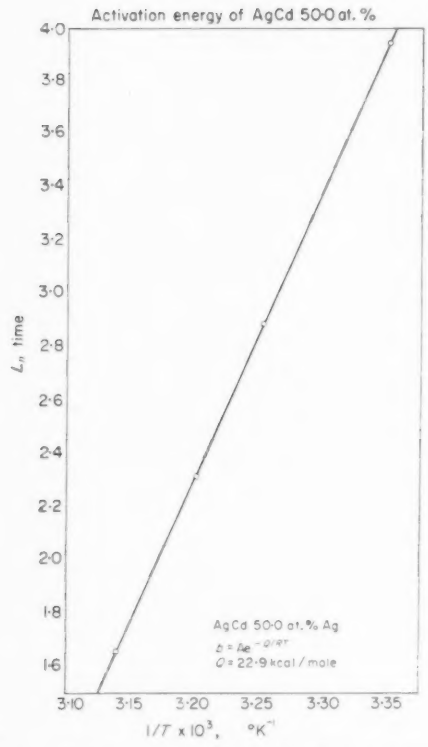


FIG. 4. Ln time required to attain 50 per cent reversion vs. reciprocal of the absolute temperature. Slope yields an activation energy of 22.9 kcal/mole.

the points fall on a straight line whose slope yields a value of 22.9 kcal/mole for the activation energy. These points are for $f = 0.5$, but the curves of Fig. 3 are so nearly parallel that values of f from 0.2 to 0.7 give the same slope and activations energy within ± 0.2 kcal/mole. Below $f = 0.2$ and above $f = 0.7$ the slopes of f vs. ln time are changing so rapidly that small errors in curve fitting cause large errors in ln time. Nevertheless the data indicate that, over the temperature range covered, the reversion is a thermally activated process with a temperature-independent activation energy. Curves similar to those of Figs. 3 and 4 were determined for the reversion of several alloys around 50 at. %; the activation energies from these data are given in Column 3 of Table 1. It is note-worthy that these activation energies are very nearly the same for compositions near the 1 : 1 atomic ratio, but increase when the amount of silver is either increased or decreased from this equiatomic composition.

TABLE 1. Activation energies for the hexagonal to cubic reversion.

Composition, at. % Ag	Composition, wt. % Ag	Activation energy, (kcal/mole)
52.0	51.0	27.9 ± 0.2
50.7	49.7	23.3 ± 0.2
50.4	49.4	23.1 ± 0.2
50.0	49.0	22.9 ± 0.2
48.1	47.1	23.4 ± 0.2
47.0	46.0	34.2 ± 0.2

RATE THEORY OF REVERSION

The sigmoid shaped curves shown in Fig. 3 resemble those found by investigators who have measured recrystallization rates of cold-worked metals. This leads one to apply the equations that have been developed for such nucleation and growth processes—as will be seen, the agreement is good. Equations have been derived by Johnson and Mehl[15] and by Avrami[16] giving the fraction transformed, f, as a function of time, t, for such a process. The general form of these equations is shown below in equation (4).

$$f = 1 - \exp(-Bt^k) \tag{4}$$

B = constant containing rates of growth and nucleation

k = constant whose magnitude depends upon particle shape

Equation (4) was derived for the situation in which the following three conditions are obeyed: (1) the reaction proceeds within a homogeneous matrix which undergoes no concentration change, (2) nucleation is random throughout the matrix, and (3) rate of radial growth is constant. In the special case where the shape of the growing precipitate is spherical and constant rates of nucleation and growth are maintained throughout the transformation, the value of the constant, k, should be 4. If the rates of nucleation and radial growth do not remain constant or if the particle does not grow in a spherical shape, the value of k may fall as low as 1.

The assumption made in the derivation of equation (4) should be applicable to the present structural reversion of cold-worked AgCd. The alloys consisted of a homogeneous solid solution prior to mechanical deformation; because of the low temperature maintained during reversion no long-range diffusion and the accompanying concentration changes should have occurred. Nucleation sites should have been distributed randomly throughout the sample, since it consisted of finely divided (−200 mesh) particles having identical thermal and mechanical histories. Constant rate of growth of the precipitate is perhaps the most tenuous assumption; however, as will be seen later, departure from constant growth rates might explain the variation of the constant k from the ideal value of 4.

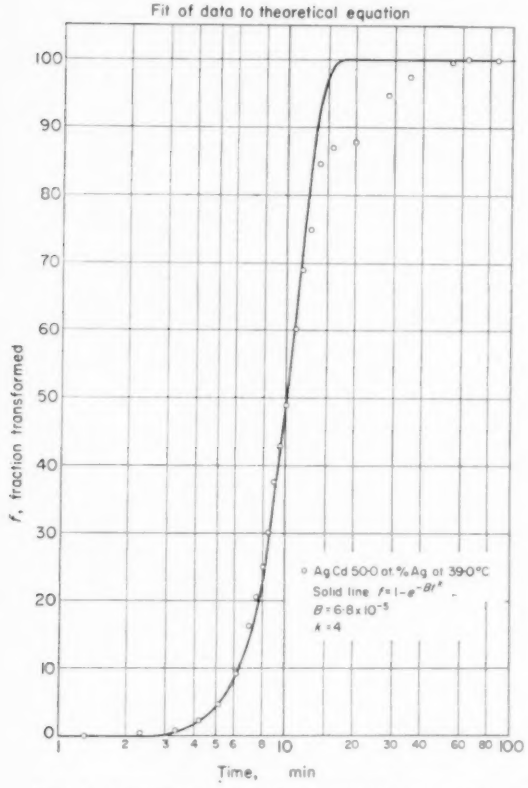


FIG. 5. Agreement of the data (points) for reversion of the 50 at. % alloy at 312.0°K with the curve (solid line predicted by equation (4). Note that a value of $k = 4$, predicted by the theory for spherical growth, is the value which also gives best agreement between these data and equation (4).

Attempts to fit the present data to equation (4) were quite successful. The agreement between some of the data and the rate curve predicted by equation (4) is shown in Fig. 5. The parameters k and B were obtained from plots of $\ln \ln [1/(1-f)]$ vs. $\ln t$; according to equation (4) these should be a straight line of slope k and intercept $\ln B$ on the $\ln \ln[1/(1-f)]$ axis. Agreement shown in Fig. 5 is good until the final stages of the transformation, at which point the equation predicts a greater reversion rate than was actually observed.

Notice that the value $k = 4$ was used in calculating the theoretical curve of Fig. 5. This is the value predicted by both the Johnson and Mehl, and Avrami theories for constant rates of growth and nucleation. Although temperature appears to have no systematic effect on k for any given alloy, on both sides of the 1 : 1 atomic ratio k becomes smaller than 4 as the composition departs from 50 at. %. This is shown in Table 2 where k values are listed for the isothermal reversion of each composition. The values calculated for B from equation (4) are also shown in Table 2.

TABLE 2. Composition and temperature dependence of the constants k and B from the rate equation

Composition At. % Ag	Temperature °K	k	Average k	B
52.0	332.2	3.0		2.3×10^{-4}
52.0	328.8	2.8		1.3×10^{-4}
52.0	324.2	2.6	2.7	4.0×10^{-5}
52.0	315.2	2.5		4.5×10^{-6}
50.7	317.5	3.7		1.0×10^{-4}
50.7	312.8	4.1		6.3×10^{-6}
50.7	307.8	4.0	4.0	6.6×10^{-7}
50.7	300.5	4.2		5.6×10^{-9}
50.4	317.4	4.4		6.9×10^{-5}
50.4	312.0	3.6		4.0×10^{-5}
50.4	305.9	4.0	4.1	5.5×10^{-7}
50.4	299.9	4.4		3.6×10^{-9}
50.0	317.9	3.9		1.4×10^{-3}
50.0	312.0	4.1		6.6×10^{-5}
50.0	307.4	3.9	4.1	2.6×10^{-5}
50.0	298.9	4.5		1.1×10^{-6}
48.1	313.4	1.9		2.3×10^{-2}
48.1	308.1	1.7		1.2×10^{-2}
48.1	303.9	2.1	2.0	1.7×10^{-3}
48.1	298.1	2.2		1.9×10^{-4}
47.0	311.0	1.3		5.5×10^{-2}
47.0	306.8	1.4	1.6	1.4×10^{-2}
47.0	298.6	2.0		3.5×10^{-4}

Several representative plots of $\ln \ln [1/(1-f)]$ vs. $\ln t$ are shown in Fig. 6. These were plotted for several different compositions since the purpose was to emphasize the composition dependence of the slopes—for any given composition the curves at different temperatures are toughly parallel (see k in Table 2). The importance of the curves is not that they approximate straight lines, since the ln ln plot tends to minimize curvature of any function, but that they have slopes in the range predicted by the mathematical analysis and that the maximum slope observed, 4, is also the maximum value predicted by the analysis. The curves of Fig. 6 all depart from linearity during the final stages of the transformation; this is the same disagreement between theory and experiment as observed in Fig. 5. This behavior has been observed previously[16] in cases where the analysis has been applied, and Avrami attributed it to the depletion of nucleation sites during the transformation. Possibly by this stage the reversion had progressed so far that the correction for impingement of growing spheres made by Avrami and by Johnson and Mehl was not sufficient to account for the deceleration; growth rate might also no longer be constant.

Equation (4) has also been applied previously to recrystallization rate studies with about the same

VOL. 8 1960

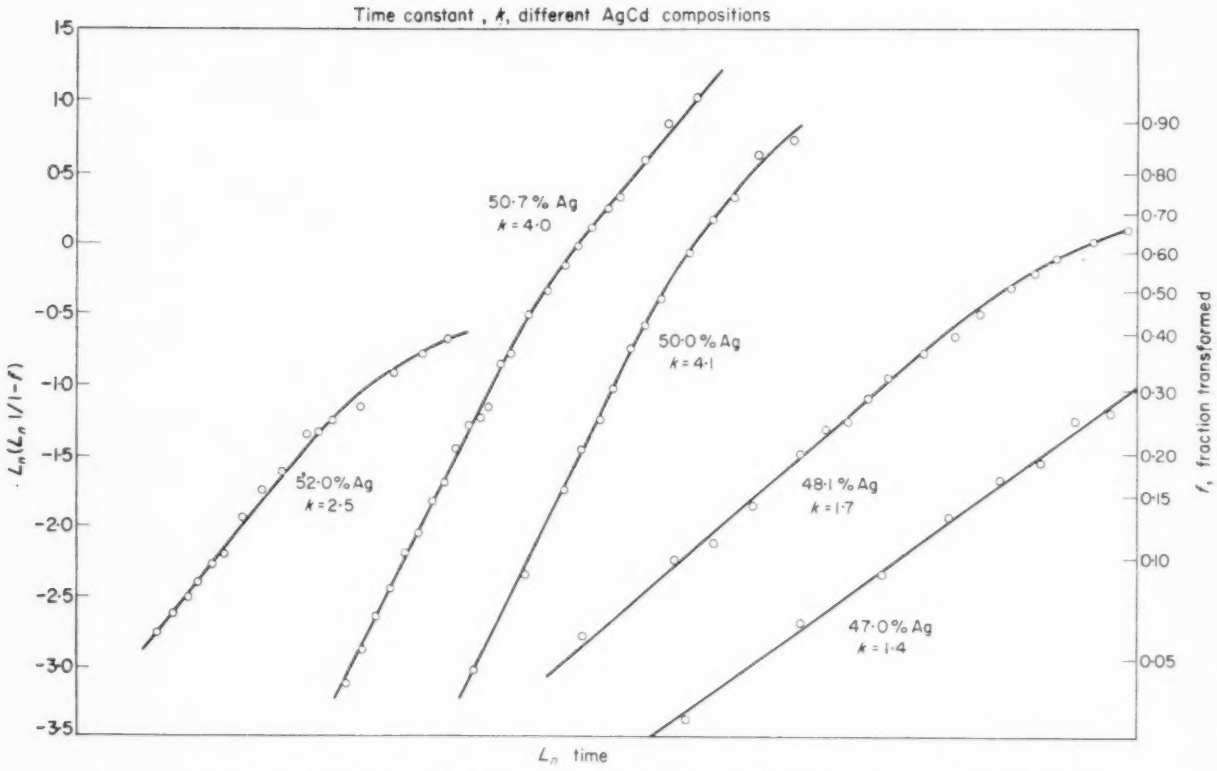


FIG. 6. Ln ln $[1/(1-f)]$ vs. ln time elapsed since deformation. The slope of these curves is equal to k; their intercept on the ln ln $[1/(1-f)]$ axis gives the value of B in equation (4). These show the composition dependence of k at constant temperature; curves for the same composition but different temperatures are parallel (see Table 2). If the data agreed perfectly with equation (4) these would be straight lines.

success as was found here. Recrystallization also occurs without long range diffusion, although it does not occur with a structural change as was observed here. In particular, Gordon,[17] Decker and Harker[18] and Michalak and Hibbard[19] have found equation (4) applicable to the recrystallization of copper; Stanley and Mehl[20] to the recrystallization of silicon ferrite; and Anderson and Mehl[21] to the recrystallization of aluminum. In all cases where growth rates were studied they were found to be constant,[20,21] which is consistent with the assumptions made in the analysis. However, it has been observed by these workers that the rate of nucleation is time dependent throughout the recrystallization—this has proved difficult to handle quantitatively.

DISCUSSION

The atomic mechanism that is postulated to explain the observed phenomena is the following. The mechanical deformation accompanying the filing of the quenched pellets was thought to be sufficient to decrease the long-range order of the body-centered cubic β' structure. Because of the high free energy of the disordered b.c.c. structure at low temperatures, the resulting configuration was unstable and transformed to an energetically more favorable close-packed hexagonal structure. This transformation was aided by mechanical deformation, in addition to the disordering, and was probably of the martensitic type.

However, the tendency toward ordering of the Ag and Cd atoms was apparently so great at 300°K that small ordered regions nucleated within the disordered h.c.p. matrix. Since the ordered b.c.c. structure was the equilibrium configuration at room temperature, the nuclei possessed that structure. The nuclei were thought to grow by means of short-range jumps of atoms across an incoherent interface separating matrix from "precipitate". This was believed to be more probable than a shear mechanism for the reversion because the process was isothermal and apparently was thermally activated. Isothermal martensitic reactions are quite rare—furthermore, martensitic transformations proceed with such rapid growth rates once they are nucleated that the gradual growth observed here seems more consistent with a diffusion-controlled mechanism.

The activation energies in Table 1 are nearly constant over a narrow range around the 1 : 1 atomic

ratio, but increase markedly on either side of this composition. A possible cause for this increase in the energy barrier impeding the passage of atoms from the h.c.p. matrix to the b.c.c. precipitate is suggested by the narrow composition range of the β' field at room temperature. Since some of the compositions having a high activation energy fall in the $(\alpha + \beta')$ or $(\beta' + \gamma)$ phase fields, possibly traces of α or γ were depositing at the interface and impeding the growth of the precipitate. The width of the β' region at room temperature is about as great as the composition range where the activation energy remains constant at its lowest value; compositions where Q becomes larger are those which might be in a two phase field. If traces of such a phase did form, however, diffraction of X-rays from them could not be detected by the Geiger counter used.

An alternative explanation of the behavior of the reversion kinetics is suggested by the symmetrical decrease of k in alloys having compositions on either side of 50 at. %. In Avrami's analysis the dependence of f on the fourth power of time arose from the product of the t^1 dependence of constant nucleation rate multiplied by the t^3 dependence of constant radial growth of a three dimensional particle. If depletion of the available nuclei occurred early in the process, however, only the t^3 relationship required by spherical growth would be observed. However, if the product grew in two dimensional plates or one dimensional needles, the time dependence could have dropped as low as the first power of t. In all cases k should fall between 1 and 4.

Nabarro[22] has calculated from strain considerations in a crystal of cubic symmetry that a spherically shaped precipitate causes maximum strain in the surrounding matrix while a two dimensional disk is the shape causing least strain. At the 1 : 1 atomic ratio where the maximum number of A–B bonds (energetically favored in an ordered lattice) might occur, the reversion would be expected to be driven most strongly and k could be expected to have its highest value—in this case approaching the value of 4 predicted for a spherical precipitate. On departing from the 1 : 1 composition, however, fewer A–B bonds would be formed and therefore a smaller energy difference would be available to "drive" the reversion. Shapes more favored by strain considerations might form—these would cause the composition effect on k shown by the data in Table 2 and by the curves of Fig. 1 and 2. Michalak and Hibbard[19] and Avrami[16] claim similar relationships between the parameter k and precipitate shape, and offer some experimental evidence in support of this relationship.

It was noted above that the isothermal reversion curves, Figs. 1 and 2, showed composition-dependent induction times. These can be interpreted with the aid of equation (4), in which they are related to the constant B of the exponential term. This constant contains a geometry factor for impingement and the variables N and G (N = rate of nucleation, G = rate of linear growth) in the combination NG^3. Values of B calculated from the intercepts of the curves in Fig. 6 on the $\ln \ln [1/(1-f)]$ axis are given in Table 2. It can be seen that B is temperature dependent, as would be expected, but is also affected markedly by composition. A temperature increase of 19° is seen to increase B by a factor of 10^5; variation of cadmium content by only 3 at. % also increases B by a factor of about 10^5. The reason for this large composition dependence is not understood; however, this is the origin of the induction effect shown in Fig. 2.

SUMMARY

Cold worked β' AgCd which has undergone a b.c.c. → h.c.p. structural transformation as the result of mechanical deformation was found to revert spontaneously to the original b.c.c. structure at room temperature. A kinetic study of this reversion was made by measuring the intensity of X-rays diffracted by powder samples as a function of time elapsed since mechanical deformation. The reversion rate was determined for several alloys of compositions around 50 at. % over the temperature range 298°–332°K. This rate was found to be dependent on the composition and temperature; the process was apparently thermally activated with an activation energy of about 23 kcal/mole, depending on the composition. The isothermal reversion curves obeyed theoretical rate equations derived by Johnson and Mehl[15] and Avrami[16] for nucleation and growth processes. It was suggested that the original b.c.c. → h.c.p. transformation was caused by a reduction in the long-range order accompanying the cold work, and that the reversion occurred as ordered b.c.c. domains nucleated within the disordered h.c.p. matrix. The h.c.p. → b.c.c. reversion was believed to be analogous to the recrystallization of a cold worked metal, with the exception that a crystal structure change was involved and the transformed b.c.c. domains were much smaller (since the work was done on −200 mesh filings) than conventional recrystallized grains in macro samples. The color of the powder samples was also found to depend on the crystal structure of the alloy.

ACKNOWLEDGMENT

Special acknowledgment is given for the advice of Professor C. S. Barrett in connection with the work;

VOL. 8 1960

the author is also grateful for the comments offered by Professors O. J. Kleppa, N. H. Nachtrieb, and C. S. Smith.

REFERENCES

1. J. B. Hess and C. S. Barrett, *Trans. Amer. Inst. Min. (Metall.) Engrs.* **194,** 645 (1952).
2. C. S. Barrett, *Acta Cryst., Camb.* **9,** 671 (1956).
3. C. S. Barrett and O. R. Trautz, *Trans. Amer. Inst. Min. (Metall.) Engrs.* **175,** 579 (1948).
4. T. B. Massalski and C. S. Barrett, *Trans. Amer. Inst. Min. (Metall.) Engrs.* **209,** 455 (1957).
5. D. B. Masson and C. S. Barrett, *Trans. Amer. Min. (Metall.) Engrs.* **212,** 260 (1958).
6. D. B. Masson. Paper submitted to *Trans. Amer. Inst. Min. (Metall.) Engrs.*
7. W. Köster, *Z. Metallk.* **32,** 145 (1940).
8. L. Kaufman. Private Communication.
9. U. Dehlinger and L. Graf, *Z. Phys.* **64,** 359 (1930).
10. O. Dahl, *Z. Metallk.* **28,** 133 (1936).
11. J. O. Linde, *Ann. d. Physik.* **30,** 151 (1937).
12. K. Schafer, *Naturwiss* **21,** 207 (1933).
13. R. W. K. Honeycombe and W. Boas, *Australian. J. Sci. Res.* **1,** 190 (1948).
14. M. Hansen, *Constitution of Binary Alloys* (2nd Ed.) p. 14. McGraw-Hill, New York (1958).
15. W. A. Johnson and R. F. Mehl, *Trans. Amer. Inst. Min. (Metall.) Engrs.* **135,** 416 (1939).
16. M. Avrami, *J. Chem. Phys.* **8,** 212 (1940).
17. P. Gordon, *Trans. Amer. Inst. Min. (Metall.) Engrs.* **203,** 1043 (1955).
18. B. F. Decker and D. Harker, *Trans. Amer. Inst. Min. (Metall.) Engrs.* **188,** 887 (1950).
19. J. T. Michalak and W. R. Hibbard, *Trans. Amer. Inst. Min. (Metall.) Engrs.* **209,** 101 (1957).
20. J. K. Stanely and R. F. Mehl, *Trans. Amer. Inst. Min. (Metall.) Engrs.* **150,** 260 (1942).
21. W. A. Anderson and R. F. Mehl, *Trans. Amer. Inst. Min. (Metall.) Engrs.* **161,** 140 (1945).
22. F. R. N. Nabarro, *Proc. Phys. Soc.* **52,** 90 (1940).

THE COBALT TRANSFORMATION*

C. R. HOUSKA,† B. L. AVERBACH‡ and M. COHEN‡

The f.c.c. ⇌ h.c.p. transformation in cobalt powder (equilibrium temperature = 417°C) has been studied by X-ray methods and correlated with the density of stacking faults in both phases. Only the h.c.p. phase is present in the cold-worked powder. The line broadening due to local strains and small particle sizes can be essentially removed by annealing at 300°C, leaving a residual broadening that permits a quantitative determination of the density of random growth and deformation faults. The latter are present in smaller numbers than the growth faults, and are more readily removed by recovery treatments.

When the h.c.p. phase is generated from the f.c.c. phase by cooling through the allotropic transformation range, two types of faulted regions become evident: region 1 contains only deformation faults, and region 2 contains both deformation and growth faults. It is suggested that region 1 constitutes the first part of the h.c.p. phase to form on cooling, while region 2 represents the latter part of the transformation. Approximately 25–30 per cent of the parent f.c.c. phase is retained at room temperature under these conditions.

Faulting in the f.c.c. phase can be detected with some assurance only after the cooling transformation is underway, but the extent of such faulting is small compared to that in the h.c.p. phase. The observed faulting in both phases is produced mainly by the allotropic transformation, and is not inherited from the parent phase. The faulting generated in the parent phase by the cooling transformation can be partly removed by holding at subcritical temperatures; it is thought that this relaxation process removes barriers to the f.c.c. → h.c.p. transformation and is responsible for the small increments of the h.c.p. phase which form isothermally in the same temperature range.

An analysis of the broadening effects in the various diffraction lines suggests that the stacking faults do not terminate within the crystallites or subgrains, but extend to the boundaries. No evidence is found to signify any reversible extension or contraction of the faulting with changing temperature; that is, the faults observed are not in thermodynamic balance.

LA TRANSFORMATION DU COBALT

Les auteurs ont étudié, par des méthodes de rayons X, la transformation c.f.c. ⇌ h.c. de cobalt en poudre (température d'équilibre = 417°C). Ils ont également étudié la densité des fautes d'empilement dans les deux phases de la transformation. Seule la phase h.c. existe dans la poudre déformée à froid. L'élargissement des raies dû à des déformations locales et aux dimensions faibles des particules, disparaît par un traitement à 300°C. L'élargissement résiduel permet une détermination quantitative de la densité des fautes de croissance et de déformation. Ces dernières sont moins nombreuses que les fautes de croissance et son plus facilement éliminées par des traitements de revenu. Lorsque la phase h.c. se forme au départ de phase c.f.c. par refroidissement au travers de la transformation allotropique, deux types de régions imparfaites apparaissent: la région 1 contient uniquement des fautes de déformation et la région 2 contient à la fois des fautes de déformation et de croissance. Les auteurs pensent que la région 1 correspond à la première zone où la phase h.c. s'est formée au refroidissement tandis que la région 2 représente la fin de la transformation. Dans ces conditions, 25 à 30% de la phase mère c.f.c. sont retenus à la température ambiante. Dans la phase c.f.c., les défauts peuvent être aperçus avec quelque certitude, uniquement lorsque leur transformation au refroidissement est en cours. L'importance de ces défauts est faible vis-à-vis de celle de la phase h.c. Les fautes observées dans les deux phases proviennent principalement de la transformation allotropique et non de la phase mère.

Les fautes apparues dans la phase en cours du refroidissement peuvent être partiellement éliminées par un maintien à des températures sub-critiques; on croit que ce mécanisme de relaxation élimine les obstacles à la transformation c.f.c. → h.c. et est responsable des petits incréments de la phase h.c. qui se forme de manière isotherme dans la même gamme de temperature.

Une analyse des effets d'elargissement des différentes raies de diffraction permet aux auteurs de suggérer que les fautes d'empilement ne se terminent pas à l'intérieur des cristallites ou sous-grains mais s'étendent jusqu'aux joints.

On n'a pas obtenu de résultat qui permette de croire à une extension ou une contraction réversible de ces défauts avec une modification de température; ceux-ci ne correspondent donc pas à un état d'équilibre thermodynamique.

DIE KOBALT–UMWANDLUNG

An Kobaltpulver wurde die Umwandlung kubisch-flächenzentriert ⇌ hexagonal dichtest gepackt (Gleichgewichtstemperatur 417°C) mit Röntgenmethoden untersucht und mit der Dichte der Stapelfehler in beiden Phasen in Beziehung gesetzt. Im kalt bearbeiteten Pulver findet sich nur die hexagonale Phase. Die Linienverbreiterung infolge lokaler Verzerrungen und geringer Teilchengrösse lässt sich durch Anlassen bei 300°C weitgehend beseitigen; die verbleibende Verbreiterung gestattet eine quantitative Bestimmung der Dichte von Wachstums- und Deformations-Stapelfehlern. Die letzteren sind in

* This paper is based on a doctorate thesis presented in January 1957 by C. R. Houska to the Department of Metallurgy at the Massachusetts Institute of Technology, Cambridge, Massachusetts. The research was sponsored by the United States Atomic Energy Commission. Received April 27, 1959.

† Department of Metallurgy, Massachusetts Institute of Technology.

‡ Now at Union Carbide Research Institute

VOL. 8 1960

geringerer Anzahl vorhanden als die Wachstums-Stapelfehler und lassen sich durch Erholungsbehandlungen leichter beseitigen.

Erzeugt man die hexagonale Phase mittels Abkühlung der kubischen durch das Temperaturintervall der allotropen Umwandlung hindurch, so zeigen sich zwei Arten fehlerhafter Bereiche: Bereich 1 enthält nur Deformations-Stapelfehler, Bereich 2 enthält sowohl Deformations- wie Wachstumsfehler. Es wird vorgeschlagen, dass Bereich 1 den bei Abkühlung zuerst entstehenden Teil der hexagonalen Phase darstellt, während Bereich 2 zuletzt entsteht. Unter den hier vorliegenden Bedingungen bleiben bei Raumtemperatur etwa 25–30% der kubischen Matrix erhalten.

In der kubischen Phase können Stapelfehler mit einiger Sicherheit erst entdeckt werden, wenn die mit der Abkühlung verbundene Umwandlung schon im Gang ist. Das Ausmass der Stapelfehler ist jedoch gering verglichen mit dem der hexagonalen Phase. In beiden Phasen entstehen die Stapelfehler hauptsächlich durch die allotrope Umwandlung und stammen nicht aus der Matrix. Die bei der Abkühlung und Umwandlung in der Matrix entstehenden Stapelfehler lassen sich teilweise beseitigen, wenn man die Probe bei subkritischen Temperaturen hält. Vermutlich beseitigt dieser Relaxationsprozess Hindernisse der Umwandlung kubisch → hexagonal und ist verantwortlich für den geringen Zuwachs der hexagonalen Phase, der sich in demselben Temperaturgebiet isotherm bildet.

Eine Untersuchung der Verbreiterungseffekte verschiedener Beugungslinien deutet darauf hin, dass die Stapelfehler nicht in den Kristalliten oder Subkörnern endigen, sondern sich bis an die Korngrenzen erstrecken. Für eine reversible Ausdehnung oder Zusammenziehung der Stapelfehler bei Temperaturänderungen findet sich keinerlei Anzeichen; die beobachteten Stapelfehler befinden sich also nicht im thermodynamischen Gleichgewicht.

1. INTRODUCTION

There has been much interest in the allotropic transformation of cobalt because of the apparent simplicity of the phase change

$$\text{f.c.c.} \underset{\text{heating}}{\overset{\text{cooling}}{\rightleftharpoons}} \text{h.c.p.}$$

The thermodynamic equilibrium occurs at 417°C,[1] but appreciable hysteresis is observed between the heating (430°C) and cooling (390°C) transformations.[2] The kinetics of these reactions are predominantly athermal, although (as will be shown) isothermal components are operative to some degree. These characteristics, together with the diffusionless nature of the phase change, permit one to designate it as martensitic.[3] The displacive features of the cooling transformation have been analyzed recently by Takeuchi and Honma[4] who concluded that the macroscopic surface tilts normally encountered in martensitic reactions (and also in cobalt–nickel alloys) are so small in pure cobalt that they escape detection. The "homogeneous" shears are only 100–300 Å thick, and because they can take place readily in three 120° directions on the close-packed plane, few (if any) gross upheavals on the surface are developed.

As in other martensitic reactions, the same crystals of the parent phase can be regenerated by reversing the transformations,[5] and this can be repeated through a number of cycles.[6] Thermodynamic considerations indicate that the driving force required to start the reaction in either direction is quite small being only a few cal/mole[2] compared to a few hundred for iron-base alloys.[7]

Stacking faults have been found in h.c.p. cobalt after the cooling transformation,[8–10] and in the f.c.c. phase of cobalt–nickel alloys after plastic deformation.[11] However, the nature and distribution of the faulting in the cobalt phases have not been studied in relation to the transformation. This is the main purpose of the present work. It was thought that the details of faulting and the transformation characteristics might shed light on each other.

2. EXPERIMENTAL METHODS

The fractional amount of each phase present was determined by *at temperature* X-ray measurements of the integrated line intensities $(101)_{\text{h.c.p.}}$ and $(200)_{\text{f.c.c.}}$, with occasional checks on $(002)_{\text{h.c.p.}}$, $(111)_{\text{f.c.c.}}$ and $(004)_{\text{h.c.p.}}$, $(222)_{\text{f.c.c.}}$. A Geiger-counter spectrometer with filtered Fe$K\alpha$ radiation was used for this purpose. The measurements were conducted on powder briquettes prepared by grinding cobalt of 99.99+ % purity* with an alundum wheel, and collecting the cobalt powder magnetically. The −325 mesh powder was cold pressed into $1 \times \frac{1}{2} \times \frac{1}{8}$ in. slabs.† Heating of the specimen on the spectrometer was carried out in a purified helium atmosphere.

The diffraction-line profiles were analyzed by Fourier methods, as described elsewhere,[10] and interpreted in terms of the stacking faults present. Information was obtained on the density of stacking faults, their type (growth or deformation faults) and distribution. However, this could be done quantitatively only with the h.c.p. phase; the diffraction lines of the f.c.c. phase were always comparatively sharp and only semi-quantitative conclusions could be drawn.

* Obtained from Johnson, Matthey and Company, Ltd., London, England.

† Although these specimens could be handled without crumbling, they should be regarded essentially as powders from the X-ray and transformation standpoints.

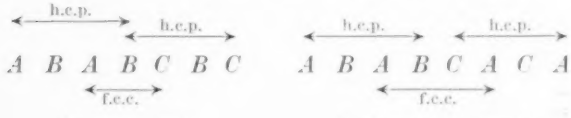
The annealing twins observed metallographically by Bibring *et al.*[12] would not be expected to affect these line-broadening considerations.

3. DISCUSSION OF RESULTS

The as-pressed powders were completely h.c.p. and exhibited a weak texture, the basal plane of the particles tending to lie parallel to the compression surface. The diffraction lines were extremely broad due to the presence of local strains and/or small particle sizes, thus obscuring the stacking-fault contributions. However, a series of recovery experiments showed that, at temperatures up to about 300°C, the broadening due to local strains and small particle sizes could be essentially removed, leaving a fairly constant residual broadening that was attributable to stacking faults. After 2 hr at 300°C, a local-strain and particle-size analysis[13] was carried out on the (002) and (004) reflections* of the h.c.p. phase; the local strains were very small (less than 5×10^{-4} based on a distance of 100 interplanar spacings) and the average particle size was large (over 1000 Å).

During the recovery process, the stacking fault density was not correspondingly changed. This could be inferred from the following experiment. Diffraction lines of the type $h - k = 3t \pm 1$, $l \neq 0$ are broadened when stacking faults exist in the h.c.p. phase (t is an integer).[10] Thus, the (101) line should be broadened by stacking faults while the (002) should not. Yet both of these lines displayed the same rate of sharpening as a function of temperature when the as-pressed briquettes were annealed up to 300°C. The activation energy for the recovery process was about 20,000 cal/mole.

Growth faults and deformation faults were found after the local-strain and particle-size broadening was removed by annealing for 2 hr at 300°C. These stacking faults may be depicted as:



Growth fault Deformation fault

The letters A, B, and C represent the conventional stacking of close-packed planes. Either type of fault can be produced by the growing-together of two out-of-phase h.c.p. lattices, while the deformation fault can also be formed by partial slip which converts A planes into C planes and (automatically) B planes into A planes. The growth fault contains three planes of f.c.c. stacking, whereas the deformation fault contains four such planes.

The density of both types of faulting is represented in Table 1 by means of the notation $1 : p$, where p is the average number of reference planes to be sampled before one faulty sequence is found. Growth faults were found to be more prevalent than deformation faults. Further sharpening of the (101), (102) and (103) lines occurred when the annealing treatment was increased to 7 days at 300°C and 2 days at 390°C. This sharpening was caused by a decrease in the probability of finding deformation faults, but there was no equivalent change in the occurrence of growth faults. Both types of faulting appeared to be distributed at random in contrast (as will be discussed later) to the faulting in the h.c.p. phase when generated from the f.c.c. phase on cooling. Evidently, deformation faults can be removed more readily than growth faults; this may come about because a deformation fault contains a larger volume of the unstable f.c.c. configuration than does a growth fault, or because a deformation fault can be "unslipped" merely by the passage of a partial dislocation along a single close-packed plane.

It could be inferred that, for the most part, the faults did not terminate within the crystallites or subgrains but extended across to the boundaries. This was manifested by the fact that after the local-strain and particle-size effects had been removed, the broadening due to the stacking faults was confined to reflections of the types $h - k = 3t \pm 1$, $l \neq 0$, while reflections of the type $(hk0)$ and $(00l)$ were quite sharp.[10] If the faults terminated within the subgrains and were therefore bounded by dislocation loops or extended dislocations, the $(hk0)$ and $(00l)$ lines would be subject to strain broadening. This situation was not found.

Sebilleau and Bibring[2] have reported the surprising result that when cold-worked h.c.p. cobalt is heated quickly to 350°C, some f.c.c. phase is produced even though it is normally unstable relative to the h.c.p. phase at this temperature. This finding was confirmed in the present work. The f.c.c. phase thus formed was of the order of 5 per cent and increased at 400°C, but at each such temperature the reaction took place in less than 10 min (the time required for the X-ray measurement) and ceased despite continued holding for 6 hr. Although this phenomenon was probably related to the stacking faults present in the h.c.p. phase, it should be recognized that the increased intensity of the f.c.c. phase must have come from very much larger regions than the stacking-fault layers. Conceivably, the equilibrium temperature can be lowered by the energy of cold working (the enthalpy of the allotropic

* These lines are not effected by stacking faults.

VOL. 8 1960

TABLE 1. Stacking faults in cold-worked h.c.p. cobalt

Annealing temp., °C	Annealing time	Integral breadth* (101) degrees in 2θ	Stacking-fault probability		
			Growth	Deformation	Total
300	2 hr	0.62	1 : 31	1 : 53	1 : 20
300	7 days	0.49	1 : 26	1 : 125	1 : 21
300 + 390	7 days + 2 days	0.46	1 : 28	1 : 250	1 : 25

* Integral line breadth = area of diffraction peak divided by height of peak.

transformation is only 60 cal/mole, which is about the same magnitude as the energy stored by cold working), and hence the f.c.c. phase may be generated below 417°C, at least in localized regions, if much recovery is not allowed to occur in advance. Once the f.c.c. phase has been formed in this way, it may persist even if recovery then ensues because the driving force tending to restore the h.c.p. increment is very small at these temperatures.

On heating pressed powders above 417°C, both athermal and isothermal components of the h.c.p.→f.c.c. reaction were observed. At 430°C, 12 per cent of the f.c.c. phase formed rapidly (within 10 min) and 5 per cent more in 6 hr. At 450°C, the corresponding values were 15 and 12 per cent and at 470°C, they were 45 and 34 per cent.

The h.c.p. →f.c.c. transformation during heating did not go to completion until above 500°C. Grain growth became quite noticeable in the diffraction patterns at about 600°C. On cooling from temperatures of 600°–1000°C, the amount of the f.c.c. phase retained at room temperature was 25–30 per cent, and tended to be larger for air cooling than for furnace cooling. The relative insensitivity to the heating temperature in this range may have resulted from the fact that grain growth and enhanced perfection of the parent phase can work in opposite directions in influencing martensitic transformations. Bibring *et al.*[12] have found that the f.c.c. phase is not retained at room temperature in massive, coarse-grained specimens, which is in contrast with the behavior of the powder specimens used in the present work.

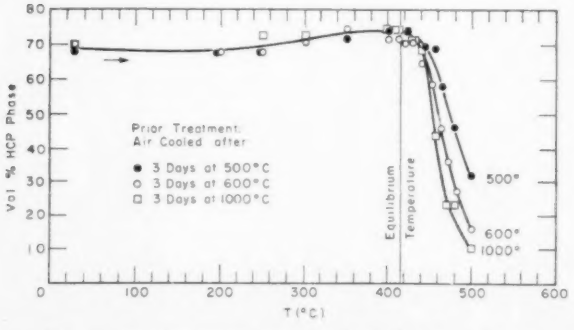


FIG. 1. Heating transformation in Co h.c.p. →f.c.c.

Starting now with specimens that had been annealed at 500°, 600°, and 1000°C and air cooled to room temperature, the heating transformation was traced again, this time dealing with the 70–75 per cent of h.c.p. phase that had been produced by the prior cooling transformation. Each of the specimens

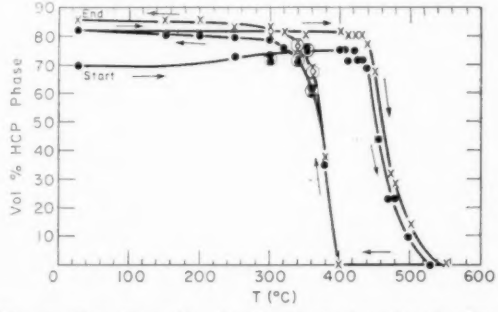


FIG. 2. Transformation hysteresis during slow heating and cooling of cobalt previously annealed at 1000°C for 3 days and air cooled to room temperature. Circled points indicate isothermal transformation.

(Fig. 1) showed a small increase in the amount of h.c.p. phase on heating in the range of 300°–400°C. Above 420°C, the reverse h.c.p. ← f.c.c. transformation was found to set in more rapidly the higher the previous annealing temperature. This effect of prior history may be connected with the grain size and perfection of the f.c.c. phase generated by the annealing treatment.

Fig. 2 traces two complete cycles of transformation, commencing with a specimen that had been air cooled from 1000°C. Each plotted point represents a 40 min hold. Again the formation of additional h.c.p. phase was noted during the heating before the h.c.p. ← f.c.c. reaction occurred. During the second heating, however, this formation of h.c.p. did not take place; the subcritical increment of transformation was found more

TABLE 2. Stacking faults in h.c.p. cobalt produced by the cooling transformation

Treatment	Integral breadth* (101) degrees in 2θ	Per cent region 1	Per cent region 2	Stacking-fault probability			
				Region 1		Region 2	
				Growth	Deformation	Growth	Deformation
600°C, 3 days, air cooled	0.90	35	65	Nil	1 : 33	1 : 12	1 : 33
900°C, 3 days, air cooled	0.45	40	60	Nil	1 : 290	1 : 17	1 : 300

* Integral line breadth = area of diffraction peak divided by height of peak.

frequently in specimens that had been previously air-cooled, and less so in specimens that had been slowly cooled from above the critical temperature. The cooling transformation f.c.c. ← h.c.p. set in just below 400°C (after the conversion to the f.c.c. phase was complete at 550°C) and was mainly athermal, although a few per cent of isothermal transformation could invariably be detected if the holding time were doubled at any given temperature in the transformation range. This was also the case for the aforementioned increment of f.c.c. → h.c.p. transformation noted on subcritical heating. The encircled points in Fig. 2 indicate these isothermal effects.

The stacking-fault probabilities in the h.c.p. phase after air cooling from 600° and 900°C are shown in Table 2. In these instances, the faulting appeared to be distributed into two regions. Region 1, comprising about 35 per cent of the 75 per cent h.c.p. phase present, contained only (random) deformation faults; region 2, constituting the remainder of the h.c.p. phase, contained both deformation and growth faults, with the latter predominating. The density of deformation faulting was about the same in the two regions and decreased markedly when the annealing temperature was raised from 600° to 900°C. Yet the density of growth faults was not greatly changed by this difference in annealing temperature. Considerable grain growth had occurred in the f.c.c. phase when the annealing temperature was increased from 600° to 900°C. The local-strain and particle-size broadening in the as-transformed h.c.p. phase was insignificant compared to the stacking-fault broadening, i.e., the ($hk0$) and ($00l$) lines remained sharp.

In every instance, the f.c.c. diffraction lines were sharper than those of the coexisting h.c.p. phase. The $(200)_{f.c.c.}$ line can be broadened by local strain, small particle size, and stacking faults. However, since the local-strain and particle-size effects were small in the h.c.p. phase as produced by the allotropic transformation, it was assumed that a similar situation prevailed in the f.c.c. phase, and the entire broadening was ascribed to stacking faults. The integral breadth of the $(200)_{f.c.c.}$ line after air cooling to room temperature from 500°, 600° and 1000°C was found to decrease in that order. This trend corresponded to a decrease in the stacking-fault probability of roughly 1:60, 1:80, and 1:160, respectively.

On reheating (see Fig. 3), sharpening of the $(200)_{f.c.c.}$ line started at about 200°C and continued smoothly through the critical temperature. The decrease in

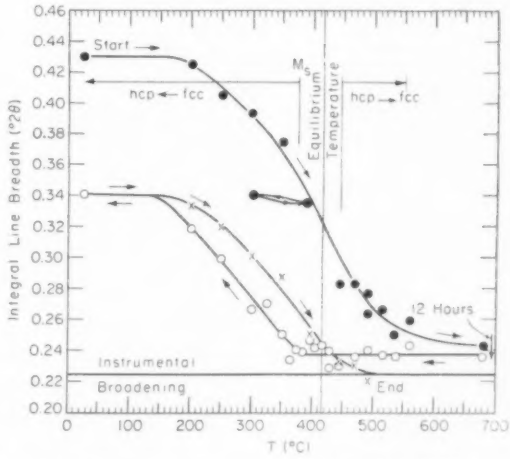


FIG. 3. At temperature breadth of the cobalt (200) f.c.c. line. Specimen annealed at 500°C for 3 days and air cooled prior to the cycles shown.

stacking-fault probability in the f.c.c. phase, suggested by this progressive line sharpening, was not reversible; as shown in Fig. 3, broadening did not occur when the heating was interrupted at 400°C and the specimen cooled to 300°C. In addition, there was no return of the broadening when the f.c.c. phase was cooled from 690°C to the equilibrium temperature. However, when the f.c.c. → h.c.p. reaction set in on cooling, concomitant line broadening took place (which was also the case for the aforementioned broadening of the

VOL. 8 1960

h.c.p. lines). A second heating resulted in line sharpening again. In all instances, some subcritical isothermal f.c.c. → h.c.p. transformation attended the line sharpening on heating.

It is evident that the faulting in both phases must have been produced largely by the cooling transformation, and was not inherited from the parent phase. Furthermore, no indication of an equilibrium adjustment between partials or extended dislocations was found on heating or cooling. For example, when the f.c.c. phase was cooled from above the critical temperature, the increasing relative stability of the h.c.p. phase should have caused an increase in the stacking-fault broadening if the partial dislocations were present in thermodynamic balance. This was not observed. Correspondingly, the reduction of stacking faults in the f.c.c. phase on heating could not be attributed to the decreasing relative stability of the h.c.p. phase because the recovery process was not critically affected by heating through the equilibrium temperature. The line sharpening was rather due to a relaxation process involving the removal of entire stacking-fault planes in the f.c.c. phase whenever the annealing kinetics were favorable.

4. RELATIONSHIP BETWEEN THE OBSERVED STACKING FAULTS AND THE COBALT TRANSFORMATION

According to Table 2, the stacking faults in the h.c.p. cobalt produced by the allotropic transformation are not uniformly distributed. Region 1 contains only deformation faults, while region 2 contains both deformation and growth faults, and is much less perfect than region 1. This difference in perfection is due primarily to the concentration of growth faults in region 2. It is likely that region 1 represents the first part of the h.c.p. phase to form on cooling, where partitioning of the matrix is negligible and the transformation strains can be readily accommodated by slip and deformation faulting in both phases. In addition, the faulting of the parent phase during transformation may provide extra out-of-phase embryos for subsequent nucleation, or this induced faulting may be inherited by the h.c.p. phase in the growth process. In any case, the density of deformation faults in such transformed regions might be expected to be very sensitive to the grain size and state of perfection of the parent phase, which is in line with the large decrease in the deformation-fault probability in region 1 when the annealing temperature is raised from 600° to 900°C (Table 2).

During the latter part of the transformation on cooling, partitioning becomes more pronounced and parallel layers of the h.c.p. phase come together, resulting in growth faults where the two h.c.p. lattices happen to be out-of-phase. This, then, would correspond to the situation in region 2. The deformation faults in region 2 may originate partly in the same way (by growth) and partly through inheritance of the f.c.c. faulting generated during the earlier stages of the reaction.

Seeger[14] has proposed a propagation mechanism for the diffusionless f.c.c. → h.c.p. transformation in cobalt, consisting of a pair of like partial dislocations that rotate around a perpendicular screw dislocation and thereby convert the *ABCABC* stacking to *ABABAB* along an advancing helix. The present findings require three modifications in this mechanism: (a) Inasmuch as virtually no macroscopic displacements are observed, at least three sets of dislocation mills are necessary to enable the shear to take place with almost equal ease in any of the three 120° directions in the close-packed plane. (b) In view of the numerous stacking faults found in the h.c.p. phase, the rotating partials must be capable of making "mistakes" and accepting faults in the f.c.c. phase without becoming jammed. (c) The dislocation mills must lie preferentially at crystallite or subgrain boundaries to account for the fact that the stacking faults do not appear to terminate within the h.c.p. lattice or assume an equilibrium spacing.

The isothermal component of the f.c.c. → h.c.p. reaction, observed on interrupted cooling in the transformation range or on reheating air-cooled specimens to 300°–400°C, appears to be associated with the increased perfection of the f.c.c. phase that occurs in this range. This suggests that the removal of stacking faults (probably deformation faults) in the f.c.c. phase may facilitate the dislocation motions which convert the f.c.c. configuration to h.c.p. All of these phenomena are consistent with a diffusionless type of transformation. On the other hand, the isothermal part of the h.c.p. → f.c.c. reaction at temperatures of 430°–470°C in the initially cold worked powder may well involve diffusion.

5. CONCLUSIONS

1. Random growth and deformation faults can be measured quantitatively in cold-worked h.c.p. cobalt powder, after a low-temperature recovery treatment to remove the local-strain and particle-size broadening The f.c.c. phase is not present in this condition.

2. When the h.c.p. phase is generated on cooling from the f.c.c. region, stacking faults are introduced, but they are not random. Region 1 contains only deformation faults, and region 2 contains both deformation and growth faults. It is postulated that region 1

constitutes the first part of the h.c.p. phase to form on cooling, while region 2 represents the latter part of the transformation. Approximately 25–30 per cent of the parent f.c.c. phase is retained at room temperature under these conditions.

3. The diffraction lines of the f.c.c. phase are relatively sharp at temperatures above the critical, indicating a very low probability of stacking faults in the parent phase. No broadening is detected on cooling to, and through, the equilibrium temperature. However, broadening does ensue on further cooling when the allotropic change sets in. Thus, the observed faulting in both phases is produced mainly by the transformation, and is not inherited from the parent phase.

4. The faulting in both phases can be partly removed by heating at subcritical temperatures. This is not a reversible process. Isothermal transformation of f.c.c. → h.c.p. takes place concomitantly; it is thought that this transformation results from the removal of stacking-fault barriers.

5. The broadening effects in the various diffraction lines indicate that the stacking faults do not terminate within the crystallites or subgrains, but extend to the boundaries. No evidence is found to signify any reversible extension or contraction of the faulting in either phase with changing temperature.

6. It should be emphasized that the above findings were obtained on powder specimens and do not necessarily apply to massive specimens.

VOL. 8 1960

6. ACKNOWLEDGMENTS

The authors express their appreciation to the U.S. Atomic Energy Commission for the sponsorship of this research, and to Messrs. E. Keplin and R. Goss for their technical assistance.

7. REFERENCES

1. J. B. Hess and C. S. Barrett, *J. Met.* **4,** 645 (1952).
2. F. Sebilleau and H. Bibring, *The Mechanism of Phase Transformations in Metals*, p. 209 Institute of Metals, London (1955).
3. A. R. Troiano and J. L. Tokich, *Trans. Amer. Inst. Min. (Metall.) Engrs.* **175,** 728 (1948).
4. S. Takeuchi and T. Honma, *Sci. Rep. Res. Inst., Tohoku University* Ser. A **9,** 492 and 508 (1957).
5. Z. Nishiyama *Sci. Rep. Tohoku Univ.* **26,** 77 (1936).
6. V. J. Kehrer and H. J. Leideiser, *J. Chem. Phys.* **21,** 570 (1953).
7. L. Kaufman and M. Cohen, *Trans. Amer. Inst. Min. (Metall.) Engrs.* **206,** 1393 (1956).
8. O. S. Edwards and H. Lipson, *Proc. Roy. Soc.* **180,** A, 268 (1942).
9. T. R. Anantharaman and J. W. Christian, *Acta Cryst., Camb.* **9,** 479 (1956).
10. C. R. Houska and B. L. Averbach, *Acta Cryst. Camb.* **11,** 139 (1958).
11. T. Broom and C. S. Barrett, *Acta Met.* **1,** 305 (1953).
12. H. Bibring F. Sebilleau, and C. Buckle, *J. Inst. Met.* **87,** 71 (1958).
13. B. E. Warren and B. L. Averbach, *J. Appl. Phys.* **23,** 497 (1952).
14. A. Seeger, *Z. Metallk.* **47,** 653 (1956).

THE LIFE HISTORY OF INDIVIDUAL SLIP LINES DURING THE PLASTIC DEFORMATION OF α-BRASS SINGLE CRYSTALS*

J. T. FOURIE†

The development of slip line structures in two α-brass single crystals of different orientation is investigated experimentally with the electron microscope. By using a selected area replica technique, definite areas are photographed repeatedly at intervals of approximately 2 per cent extension in thirty-six stages for one crystal and twenty-six stages for another. The results of average glide and density measurements of slip lines confirm an orientation effect observed in an earlier investigation. This is explained in terms of the formation of Lomer–Cottrell sessile dislocations. Measurements on individual lines indicate that these grow in depth, not continuously, but in definite steps as the extension is increased. These growth steps often occur simultaneously and can be attributed to the production of dislocation bursts by sources activated by strong local fluctuations in the internal stress field around them. As an alternative, a mechanism involving cross-slip between a number of lines is proposed. The formation of cross-slip itself is discussed with reference to successive micrographs of selected areas. These are explained by assuming that a dislocation source is activated on the cross-slip plane as a result of high internal stresses.

L'EVOLUTION DE LIGNES DE GLISSEMENT INDIVIDUELLES AU COURS DE LA DEFORMATION PLASTIQUE DE MONOCRISTAUX DE LAITON α

L'auteur a examiné au microscope électronique le déplacement de lignes de glissement dans deux monocristaux de laiton α d'orientations différentes. Il utilise une technique d'empreinte permettant de repérer exactement la région examinée. Les régions ont pu alors être photographiées, dans trente-six états de déformation pour le premier cristal et dans vingt-six états de déformation pour le second cristal. Chacun de ces examens correspond alors à une modification d'environ 2% de l'allongement au cours de la déformation. Les résultats du glissement moyen et de la densité des lignes de glissement confirment l'effet d'orientation observé au cours d'un travail antérieur.

L'auteur explique cet effet en faisant intervenir la formation de dislocations sessiles de Lomer-Cottrell. Des mesures effectuées sur des lignes individuelles de glissement indiquent que celles-ci croissent en profondeur de manière discontinue mais de quantités déterminées lorsque la déformation s'accroît. Ces seuils de croissance apparaissent souvent simultanément et peuvent être attribués à la production de groupes de dislocation par des sources activées par de fortes fluctuations locales du champ de tensions internes qui les entoure. L'auteur propose d'expliquer cet effet par un mécanisme qui fait intervenir le glissement croisé entre un certain nombre de lignes. L'apparition de ce glissement croisé est discutée en se référant aux micrographies successives d'une région bien déterminée. L'auteur explique les micrographies obtenues en admettant qu'une source de glissement est active sur le plan de glissement croisé par suite de fortes tensions internes.

DIE LEBENSGESCHICHTE EINZELNER GLEITLINIEN WÄHREND DER PLASTISCHEN VERFORMUNG VON EINKRISTALLEN AUS α-MESSING

Die Entwicklung der Gleitinien auf zwei α-Messing Einkristallen verschiedener Orientierung wird elektronenmikroskopisch untersucht. Durch eine gezielte Abdruckmethode werden bestimmte Gebiete nach Dehnungsintervallen von etwa 2% wiederholt aufgenommen, bei einem Kristall in 36 Stufen und bei dem anderen in 26 Stufen. Die Ergebnisse der durchschnittlichen Gleitung und die Messungen der Gleitliniendichte bestätigen einen Orientierungseffekt, der in früheren Untersuchungen beobachtet wurde. Er wird durch die Bildung von unbeweglichen Lomer–Cottrell Versetzungen erklart. Messungen an individuellen Gleitlinien zeigen, dass ihre Tiefe mit wachsender Verformung nicht kontinuierlich sondern in bestimmten Stufen zunimmt. Diese Wachstumsstufen treten oft gleichzeitig auf und können dem Auftreten von Versetzungsausbrüchen zugeordnet werden aus Quellen, die durch starke lokale Schwankungen des inneren Spannungsfeldes aktiviert werden. Als Alternative wird ein Quergleitungsmechanismus zwischen einer Reihe von Gleitlinien vorgeschlagen. Die Bildung der Quergleitung selbst wird anhand einiger aufeinanderfolgender Bilder von ausgewählten Gebieten besprochen. Sie wird erklärt durch die Annahme, dass als Folge hoher innerer Spannungen eine Versetzungsquelle auf der Quergleitebene aktiviert wird.

1. INTRODUCTION

Previous electron microscope investigations of slip lines on metal surfaces have all been carried out by what can be termed random replica techniques. This means that there is no control over which part of the surface is ultimately seen in the microscope, nor is it possible to photograph the same area more than once. One exception is a paper by Mader[1] where the same area is photographed a second time after further extension of the crystal.

The aim of the present work was chiefly that of

* Received March 9, 1959.

† National Physical Research Laboratory, South African Council for Scientific and Industrial Research, Pretoria, South Africa.

employing a recently developed selected area replica technique[2] to repeat and refine the measurements obtained by Fourie and Wilsdorf[3] on plastically deformed α-brass single crystals. The random replica technique used in the latter investigation necessitated the analysis of a large number of photographs before any conclusions could be drawn. The new technique, however, has made it possible to single out individual slip lines and examine their behaviour as plastic deformation is increased, thus greatly simplifying the measurements and improving their reliability. The results described in this paper include measurements on the variation of the average glide per slip line and the change in density of slip lines in specific areas during plastic deformation. In addition, measurements on the growth of individual lines are discussed as well as the formation of cross-slip and its association with other slip systems. Dislocation models are suggested which account for the development of the surface structures.

2. EXPERIMENTAL

(i) *Preparation of single crystals*

The single crystals used in this investigation were grown from the melt in a graphite crucible of internal rectangular cross-section 1.2 × 2.4 mm according to a modified Bridgman method. The final composition of the crystals was 20% zinc and 80% copper, with traces of Fe, Pb and Ni as impurities. The orientations of the crystals were determined from Laue photographs and the two crystals chosen (57 and 61) had orientations as shown in Fig. 1. The crystals used in the previous investigation[3] are also shown in this diagram.

Polishing of the crystals was done electrolytically in a bath of 35% phosphoric acid at 2.6 V.

(ii) *Deformation of single crystals*

A simple tensile machine was used for extending the crystals. Crystal 57 had earlier been cut into two lengths, the one being used in the previous investigation[3] and the other in the present investigation, where it was extended in thirty-six steps of about 2 per cent elongation from 1/2 to 79 per cent. Crystal 61 was extended in twenty-six steps from 1 to 62 per cent. The crystals were *unloaded* after every step of deformation for the purpose of replicating the surface. To eliminate the effect of widely differing strain values along the length of α-brass crystals at small deformations (Piercy *et al.*[4]), the increase in the distance between two micro indentation marks, initially 0.04 mm apart, was measured at ×500 magnification. In this manner the strain in that portion of the crystal was determined relatively accurately. The replica technique which is described below permitted any area in this narrow selected portion of the crystal to be photographed. The measured strain could thus be associated with the amount of slip shown in the actual micrograph to an even greater accuracy than in the previous investigation.[3]

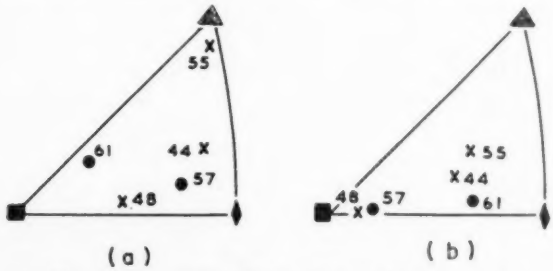


FIG. 1. The orientations of crystals. (a) Axes. (b) Surfaces.

(iii) *Selected area replication*

The technique used in this investigation is the same in principle as the selected area replica technique described by Fourie[2]. However, a few important changes have been introduced, and the final technique may briefly be summarized as follows:

(a) A primary Formvar replica backed with bedacryl is made according to Bradley[5].

(b) The primary replica is shadow cast with Pt from a line source as described by Hall[6]. The amount of Pt is calculated to give a layer 25 Å thick and the sample is placed 10 cm from the source, the shadowing angle being about 30°. Without breaking the vacuum in the evaporation plant, the platinum layer is then backed with a carbon layer about 100 Å thick.

(c) The bedacryl layer is dissolved and the replica transferred to a newly cleaved mica surface as described in detail elsewhere.[2]

(d) The carbon film, now facing upwards on the mica plate, is covered with a thin collodion film by flooding with a 1/4 per cent solution in amyl acetate and allowing this to drain vertically on filter paper.

(e) The specimen carrier is positioned with respect to reference marks replicated from the original sample, and is fixed in position by allowing a 1 per cent bedacryl in benzene solution to penetrate between replica and specimen carrier. After allowing the bedacryl to harden for 5 min the carrier is securely fixed in position along its edges with 20 per cent collodion in amyl acetate.

(f) The replica is detached from the mica plate by placing in distilled water for 5 min.

(g) The specimen carrier is placed in chloroform for 30 min during which time the Formvar and bedacryl layers are completely dissolved.

VOL. 8 1960

The replica thus obtained is essentially a shadow-cast primary replica, backed with carbon and collodion. As the photographs in the present work indicate, there is a considerable improvement in resolution. A further advantage is that practically no replicas are lost through breakages, thus saving a large amount of preparation time.

3. MEASUREMENTS AND RESULTS

For the purpose of slip line measurement, three zones were selected on the replica of each crystal surface with the aid of the electron microscope. These zones were contained in an area 1×0.15 mm, the area of the slit in the specimen carrier. Selection of the zones was at random. Every selected zone was photographed at each step of its deformation so that for crystal 57 three series of thirty-six photographs, and for crystal 61 three series of twenty-six photographs, were taken. The magnification used was $\times 9{,}000$. The glide in the slip lines and their densities were calculated from measured widths and densities according to the well known formulae given in reference (3).

(i) *The average glide per slip line*

In order to obtain a reliable value for the average glide, two fixed reference slip lines were chosen near the extremities of each zone at its highest deformation (e.g. lines A and E in Fig. 4h). On all photographs of lower deformations only those slip lines appearing between these two references slip lines were measured. Normally the distance between the reference slip lines was about $8\,\mu$. Four photographs representing suitably spaced strain values were measured for all three zones of each crystal. The results for each crystal were then combined. The average glide was obtained by dividing the total glide in the measured lines by the total number of lines. The results for the two crystals are given in Fig. 2.

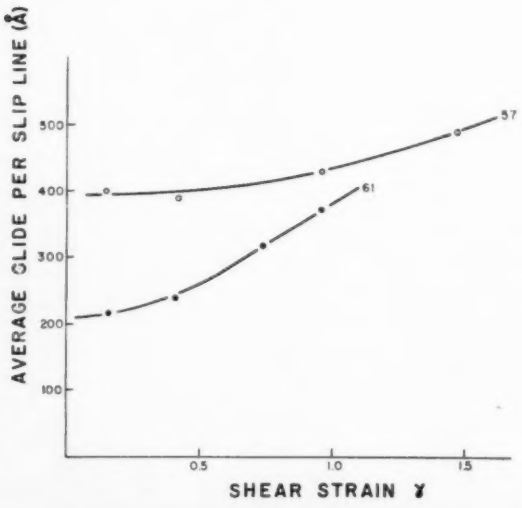


FIG. 2. The average glide per slip line vs. the shear strain γ.

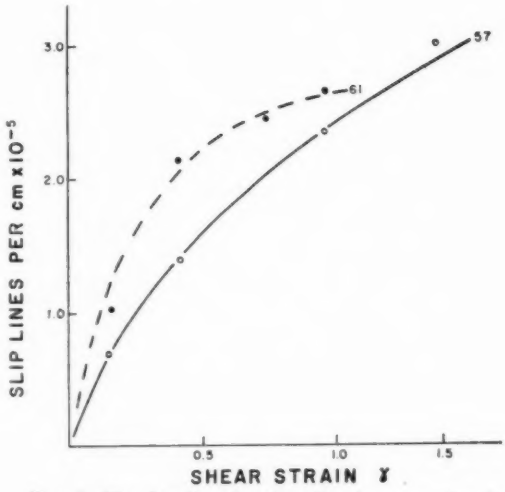


FIG. 3. The density of active slip planes vs. the shear strain γ.

For crystal 57 the average glide at the beginning of deformation is about 400 Å per slip line, while for crystal 61 it is about 200 Å. This indicates that dislocations causing slip in 57 encounter fewer obstacles than those in 61 during the initial stages of deformation. However, the rate of increase in average glide with increased deformation is much greater in the case of 61. This can be explained if many more of the active slip planes for 61 than for 57 are initiated in the early stages of deformation. Thus the later stages of deformation of 61 would proceed to a large extent by the growth of already existent lines, while for 57 many new lines would be activated with less growth on the initial lines.

If this result is compared with similar measurements on crystals which were investigated by a random replica technique[3] a definite correlation is found. In the latter investigation four crystals were used, namely crystals 44, 48, 55 and 57 (the other length of the crystal used in the present investigation). The orientations are shown in Fig. 1. The measured averaged glide values for 44 and 57 are about 280 Å at the beginning of deformation while for 48 and 55 the values are about 220 Å and 180 Å respectively. Furthermore the rate of increase in average glide is greatest for 55, while that for 48 is greater than for either 44 or 57.

The results obtained with the more sensitive experimental technique in the present investigation

thus confirm the orientation effect observed previously.[3] The significance of these results will be discussed later in terms of dislocations.

(ii) *The density of slip lines*

The density of slip lines is defined as the number of slip lines per cm measured perpendicularly to the active slip planes. In the present investigation this was determined in the same way as the average glide, namely by counting the number of lines between two definite slip lines in each selected area and dividing by the perpendicular distance between the slip planes of the two reference slip lines.

The results of measurements are presented in Fig. 3. The manner in which the density of lines increases in each crystal supports the deductions made from average glide curves. For crystal 61 there is a rapid increase at the beginning but the rate falls off considerably later on. Crystal 57 shows a smaller rate of increase at the beginning which, however, does not fall off as much during the later stages of deformation.

These curves cannot be compared with those from the previous investigation[3] as those measurements were made with reference to the width of slip line clusters and not to an area between two definite slip planes. It may be mentioned here that the distribution of slip line depths was found to be similar to those reported by Fourie and Wilsdorf[3].

VOL. 8 1960

(iii) *Growth of individual lines*

To determine the way in which single slip lines develop during plastic deformation, several lines were selected in every zone. Their selection was at random except for the fact that they appeared as prominent lines at large extensions. This distinction is essential for obtaining a high relative accuracy of measurement. The widths of the slip lines were measured at a constant position along their lengths for every extension. For this purpose a line was drawn perpendicularly across the slip lines in exactly the same position for all photographs of a particular zone (e.g. dotted line XY in Fig. 9). The glide in the slip lines was then determined from their widths at the points of intersection with the reference line. A typical series of photographs of the development of surface structures on crystal 57 is shown in Fig. 4. Here eight from a series of thirty-six photographs are arranged in order of increasing deformation from 1/2 to 72 per cent extension. The lines which were measured in this particular case are marked at the edge of the photographs.

Examples of the curves obtained from these measurements are given in Figs. 5 and 6 for crystals 57 and 61 respectively. Here the glide values in individual lines are plotted against the macroscopic shear strain. It is immediately evident that the growth of slip lines does not take place continuously but rather in definite steps. The height and number of these steps vary from line to line. However, what is more remarkable is that the majority of these growth steps occur simultaneously with growth steps in other lines. The arrows on the abscissae mark positions at which cessation of growth occurs simultaneously in different lines. For example in zone III of crystal 57 (see Fig. 5), there is simultaneous cessation in growth by lines A and F at $\gamma = 0.2$, by lines B, C, D, F and G at $\gamma = 0.55$, and by lines A, E and G at $\gamma = 0.8$. In the case of crystal 61 zone I (Fig. 6) we find lines A, B, C, D, F and G experiencing simultaneous cessation in growth at the point $\gamma = 0.7$. The growth steps in line E are evidently in no way associated with the others.

This type of curve was obtained for all of the six zones investigated. Fig. 5 is more typical of the general form of the curves obtained for individual lines. That is, they normally exhibited two or more steps in their glide–shear curves.

A further interesting phenomenon displayed by these curves is that the unloading of the crystal after each extension does not appear to affect the growth of the slip lines appreciably. This is particularly well demonstrated by the curves of lines C, D and F in Fig. 6 where all points on the steep portion of the curves lie on a smooth curve with every point representing an unloading of the crystal.

(iv) *Development of cross-slip*

The development of cross-slip with increasing deformation, and its association with the primary slip system, are problems which have stimulated much discussion since this type of slip was first recognized in an investigation of α-brass single crystals (Maddin *et al.*)[7]. At present it is generally accepted that cross-slip is intimately associated with the development of slip lines in face-centred cubic metals.[1,3,8,9] The following discussion is based on common phenomena which are specially evident in the examples given in Figs. 4, 7 and 8.

In Fig. 4c a cross-slip line has branched off line D. This cross-slip line has caused all portions of intersected lines to the left of it to be displaced towards the *bottom* end of the photograph and in Fig. 4e this displacement is at a maximum. In Fig. 4f, however, a new cross-slip line has developed above line D, and has

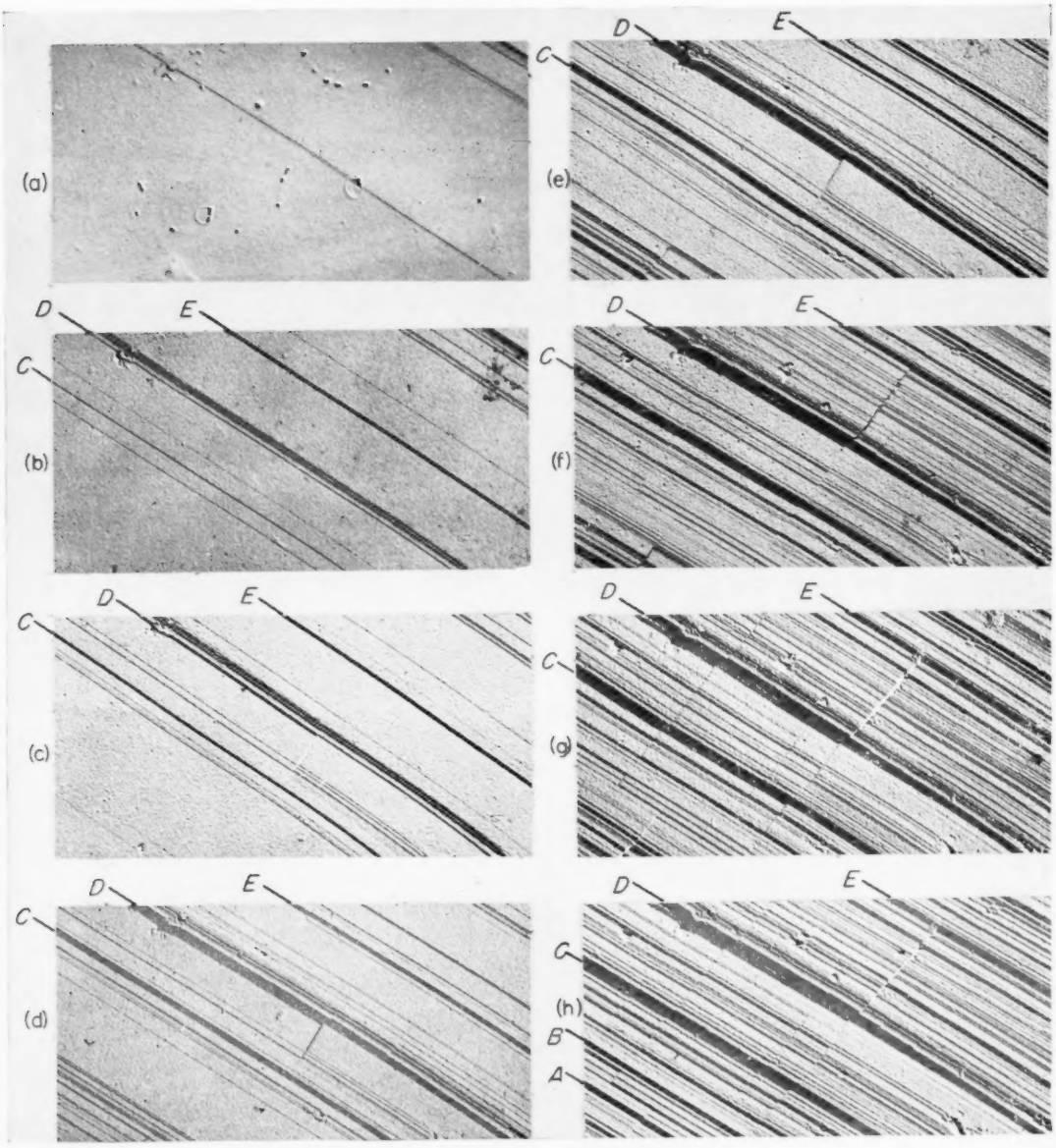


FIG. 4. The development of slip lines on crystal 57 zone I. ×9,000.
(a) $\varepsilon = 0.005$, $\gamma = 0.01$; (b) $\varepsilon = 0.04$, $\gamma = 0.08$; (c) $\varepsilon = 0.06$, $\gamma = 0.12$; (d) $\varepsilon = 0.16$, $\gamma = 0.32$;
(e) $\varepsilon = 0.23$, $\gamma = 0.46$; (f) $\varepsilon = 0.45$, $\gamma = 0.90$; (g) $\varepsilon = 0.57$, $\gamma = 1.14$; (h) $\varepsilon = 0.72$, $\gamma = 1.44$.

displaced portions of intersected lines to the left of it towards the *top* end of the photograph. The slip direction in this line must therefore differ by 180° to that in the first cross-slip line, since only the forward and reverse slip directions are possible for the same slip system. Further, its slip has taken place on the identical slip plane on which the first cross-slip line developed. This is obvious because the slip in the first cross-slip line has to a large extent been annulled by the dislocations of the second cross-slip line extending downwards beyond line *D*. To assess this it is necessary to look along the slip lines of the primary system and compare respective displacements in successive photographs, e.g. by looking along the lower edge of line *D* it can be seen that the downward displacement of the left hand portion has decreased considerably from Fig. 4e to Fig. 4f.

A striking example of the growth of slip lines by cross-slip is found in Fig. 7. In Fig. 7a a slip line *P* has grown considerably in depth at the point where a cross-slip line joins it to line *Q*, which has also experienced an increase in depth. In Fig. 7b, it is

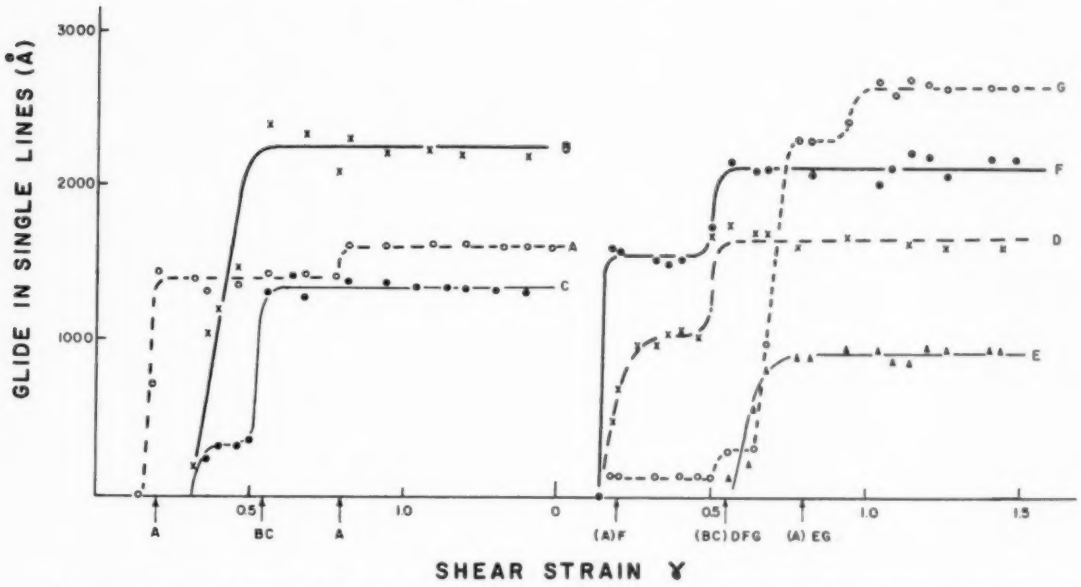


FIG. 5. The glide in single slip lines in crystal 57 zone III plotted against the shear strain in the crystal γ.

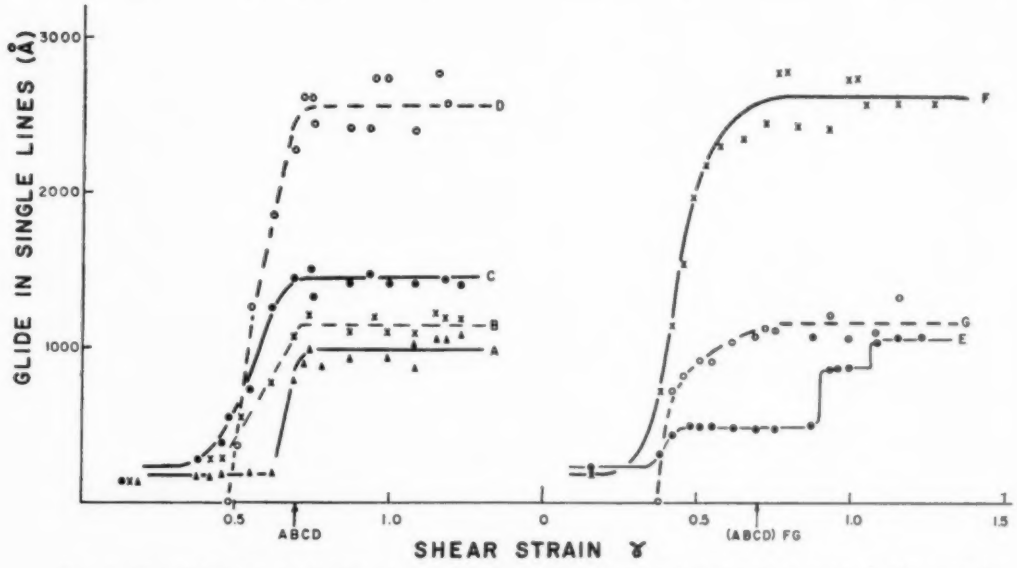


FIG. 6. The glide in single slip lines in crystal 61 zone I plotted against the shear strain in the crystal γ.

evident that the latter process has repeated itself and the resulting increases in depth of the lines P and Q are tremendous. It is also interesting to note that the cross-slip line has extended beyond Q and caused a considerable increase in R by joining to that line. In other words the lines Q and R have experienced simultaneous growth due to cross-slip. The cross-slip line has also extended upwards from line P and caused slip in the reverse direction. Fig. 7c shows a further increase in the depth of lines P, Q and R due to the passage of more dislocations along the same cross-slip line.

The phenomenon of the slip direction being reversed on the same cross-slip plane, as described in both of the above examples, is often encountered in α-brass. It can best be explained by assuming that a dislocation source of the cross-slip system is activated by local internal stress fluctuations due to pile-ups. These fluctuations are apparently so great that a previously activated source can be made to operate in the reverse direction. In some cases the observed phenomena are more easily explained by assuming that more than one source is located on the same slip plane, and that these are activated in turn. The

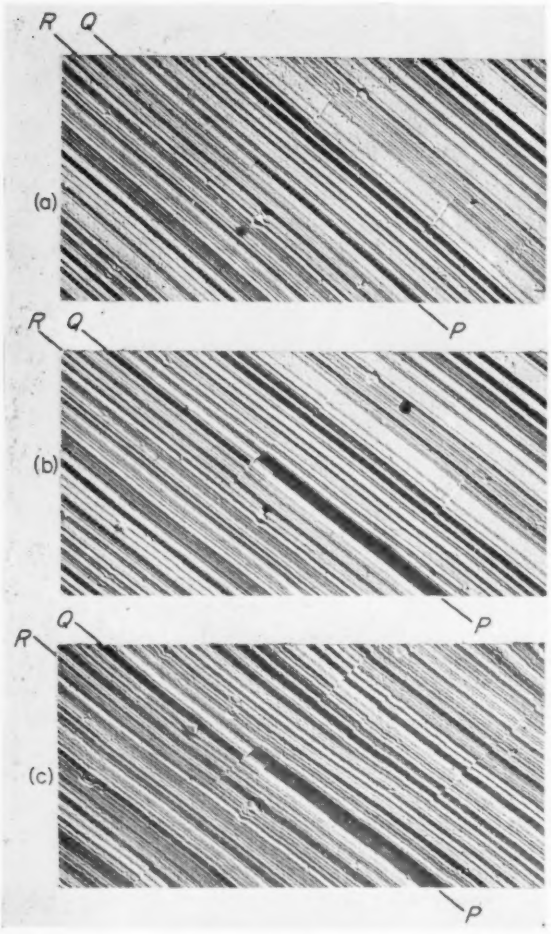


FIG. 7. The growth of slip lines by cross-slip. ×9,000. (a) $\varepsilon = 0.34$, $\gamma = 0.68$; (b) $\varepsilon = 0.39$, $\gamma = 0.78$; (c) $\varepsilon = 0.70$, $\gamma = 1.40$.

dislocations produced by these sources in the cross-slip plane are supposedly annihilated when they meet screw dislocations of opposite sign piled up in slip lines of the primary slip system, with a resultant increase in the depth of these slip lines.

From the phenomena observed in Figs. 4 and 7 it appears further that once a slip source has been activated on a cross-slip plane, it is highly probable that further cross-slip will be repeated along the same slip plane. This means that whatever mechanism is responsible for the so-called coarse slip in the primary system (characteristic of α-brass and not found in pure metals[10]), is, in the case of α-brass also responsible for the "softening" of a cross-slip plane during its initial activation, with a resultant preferential slip on this plane.

Fig. 8 is an extract of the last few photographs taken of zone II crystal 61. Here the conjugate system (white lines) has become active and the same type of slip line growth by preferential cross-slip on a single plane is shown to operate in the conjugate system.

(v) *Measurements at cross-slip intersections*

If there is a change in the amount of glide in a primary slip line at the point where it is intersected by a cross-slip line, it can be shown by actual measurement that the same change in glide takes place in the intersecting cross-slip line. For this type of measurement, the crystal surface should be so oriented that the glide in slip lines of both the primary and cross-slip systems can be measured with comparable accuracy. This condition is best obtained when the glide direction is inclined about 40°–60° to the respective slip line traces on the crystal surface. In Fig. 10a micrograph of a crystal surface suitably oriented for observing this phenomenon is shown.

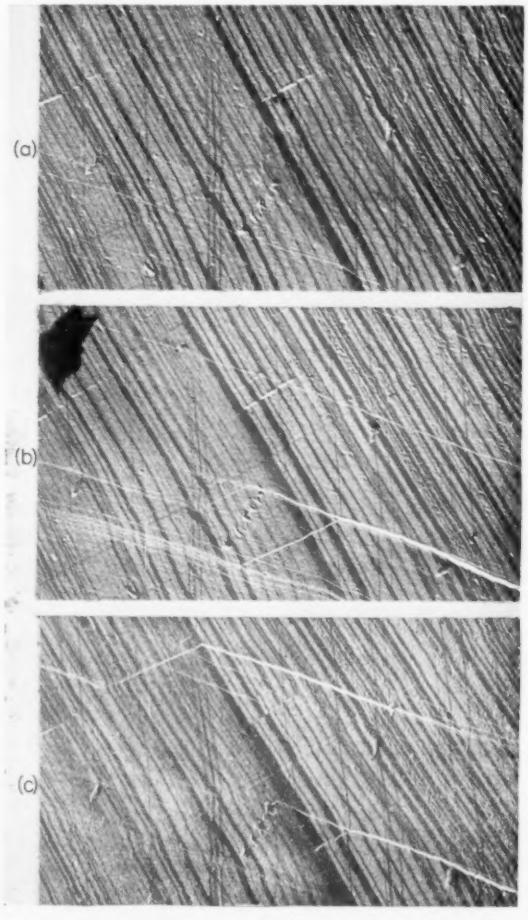


FIG. 8. The growth of slip lines of the conjugate system (white lines) by cross-slip. ×9,000. (a) $\varepsilon = 0.61$; (b) $\varepsilon = 0.63$; (c) $\varepsilon = 0.65$.

TABLE I.

Change in glide of primary system slip line (Å)	Change in glide of associated cross-slip line (Å)
1350	1310
310	330
1250	1060
1140	1150
1420	1390

A number of measurements were carried out on intersection points of slip lines and the results are contained in Table 1.

Taking into account the experimental error involved in making absolute measurements on replicas (see reference 11), all these results indicate that the change in glide in a slip line of the primary system is equivalent to the corresponding change in glide of a cross-slip line at the point of intersection of the two lines.

4. DISCUSSION AND CONCLUSIONS

It will now be shown that the results obtained in this investigation are in agreement with the theory which attributes work-hardening to the formation of Lomer–Cottrell sessile dislocations. It will also be shown that the step-wise manner in which slip lines grow can be accounted for by the theory of dislocation bursts proposed by Mott[12], or alternatively by a theory based on certain cross-slip phenomena.

As the results in Figs. 2 and 3 indicate, and also the results of the previous investigation,[3] crystals with orientations such as 55 and 61 accommodate much less glide on single planes at the start of deformation, than do crystals oriented as 44 and 57 (see Fig. 1). Since the crystals were all grown from the same material and according to the same method, the number of inherent obstacles to slip should be the same. In other words the differences in surface structure must be due to a difference in the rate of production of obstacles formed as a result of plastic deformation. It has been shown by Seeger *et al.*[8] that crystals such as 55 and 61, whose axial orientations lie close to the great circle joining the [100] and [111] directions, are inclined to form Lomer–Cottrell dislocations from the beginning of deformation, since the Lomer–Cottrell reaction is stimulated by the increasingly high resolved shear stress on the conjugate system. In crystals with orientations such as 44 and 57, on the other hand, the tendency to form sessile dislocations rapidly diminishes as the tensile axis moves towards the interior of the stereographic triangle. On the basis of these predictions it is possible to explain the orientation dependence observed in the development of slip lines in α-brass. Consequently, it appears that the formation in Lomer–Cottrell barriers plays an important part of limiting the amount of slip in slip lines during plastic flow.

A further interesting result that has emerged from this investigation is that the growth of slip lines in α-brass single crystals takes place in definite steps, and that these steps often occur simultaneously. This phenomenon, evident in Figs. 5 and 6, cannot be regarded as coincidental, since it was found to be present in all of six randomly selected areas. These sudden increases in slip line depths are similar to the effect which would be produced by the dislocation bursts proposed by Mott[12]. The term "dislocation bursts" refers to the case where a limited number of sources produce a large number of dislocations during a small increase in the overall strain. These bursts are supposed to occur as a result of strong local fluctuations during plastic flow in the internal stress field near the dislocation sources. The bursts would therefore occur simultaneously in a number of closely situated lines (i.e. within a distance of about 5 μ) provided that their respective sources were situated so close together that they could all be similarly affected by fluctuations in the local stress field. If σ_i is the local stress required to activate the dislocation sources, then the simultaneous dislocation bursts of a number of sources can be expected when the component of σ_i in the direction of the applied stress is below a certain value for all the sources participating.

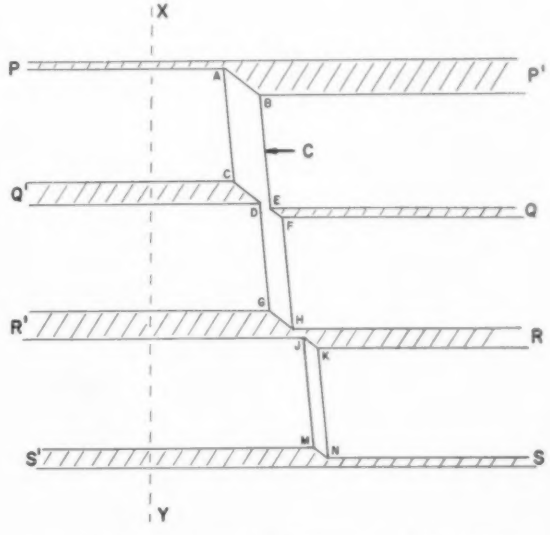


FIG. 9. A diagrammatic representation of the manner in which cross-slip could account for simultaneous growth in slip lines.

VOL. 8 1960

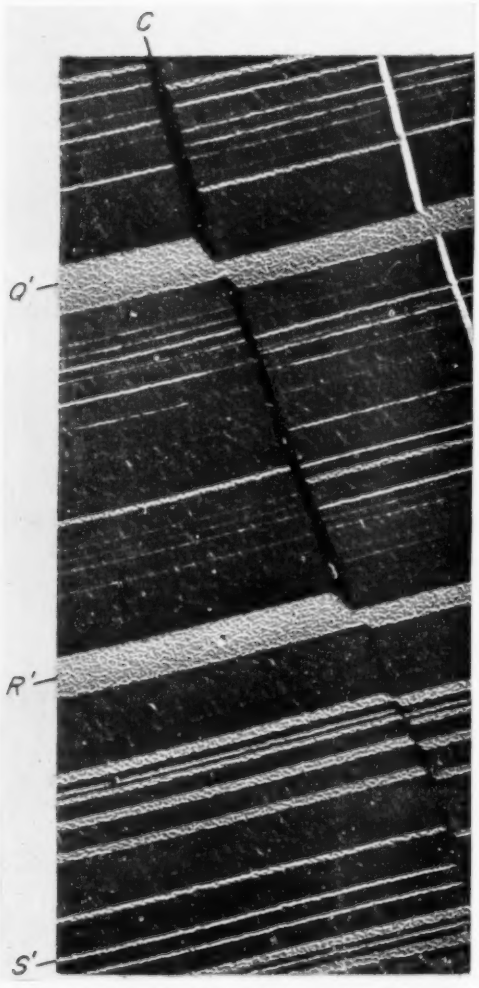


FIG. 10. An example of a possible model which could account for the simultaneous growth of slip lines. ×20,000. $\varepsilon = 0.30$, $\gamma = 0.57$.

There will also be a simultaneous cessation of the bursts when a rise in the local internal stress inactivates the sources concerned.

As an alternative to the mechanism of dislocation bursts, a certain cross-slip phenomenon in α-brass can be used to explain the simultaneous development of slip lines. Fig. 9 represents a type of surface structure often observed in α-brass. A cross-slip line C has connected a line P of the primary system with lines Q, R and S, causing these lines to grow by different amounts to lines P', Q', R' and S'. Now, if the widths of these lines were measured along the dotted line XY, then the lines Q, R and S would be observed to have grown simultaneously to form lines Q', R' and S'. This could occur according to the model for cross-slip mentioned earlier. A good practical example is given in Fig. 10 where lines Q', R' and S' have resulted from dislocations moving in cross-slip line C.

5. ACKNOWLEDGMENTS

The author would like to thank Dr. H. G. F. Wilsdorf of the Franklin Institute Laboratories for Research and Development, Philadelphia, for reading the manuscript and making valuable suggestions. Similarly the author is indebted to Prof. F. R. N. Nabarro of the University of the Witwatersrand for a most helpful discussion in connection with this investigation.

The paper is published with the permission of the South African Council for Scientific and Industrial Research.

REFERENCES

1. S. MADER, *Z. Phys.* **149**, 73 (1957).
2. J. T. FOURIE, *J. Appl. Phys.* **29**, 608 (1958).
3. J. T. FOURIE and H. G. F. WILSDORF, *Acta Met.* **7**, 339 (1959)
4. G. R. PIERCY, R. W. CAHN, and A. H. COTTRELL, *Acta Met.* **3**, 331 (1955).
5. D. E. BRADELY, *J. Inst. Met.* **83**, 35 (1954).
6. C. E. HALL, *Introduction to Electron Microscopy*, p. 311. McGraw-Hill, New York (1953).
7. R. MADDIN, C. H. MATHEWSON and W. R. HIBBARD, *Trans. Amer. Inst. Min. (Metall.) Engrs.* **175**, 86 (1948).
8. A. SEEGER, J. DIEHL, S. MADER and H. REBSTOCK, *Phil. Mag.* **2**, 323 (1957).
9. P. HAASEN, *Phil. Mag.* **3**, 384 (1958).
10. D. KUHLMANN-WILSDORF and H. WILSDORF, *Acta Met.* **1**, 394 (1953).
11. H. WILSDORF and J. T. FOURIE, *Acta Met.* **4**, 271 (1956).
12. N. F. MOTT, *Proceedings of Lake Placid Conference*, p. 462 (1957).

SUBCRYSTALS IN LARGE VAPOUR-GROWN CRYSTALS OF TUNGSTEN*

G. D. RIECK and H. A. C. M. BRUNING†

Single crystals of tungsten, grown by decomposition of the chloride in the vapour phase, were investigated. A substructure has been found both with X-ray and microscopic techniques. The disorientation between the subcrystals is at random and is therefore different from that found in single crystals in recrystallized doped tungsten wires. The occurrence of a substructure or even dendritic branches depends upon the circumstances during the growth. The rows of etch pits on the photomicrographs of etched surfaces are of the same nature as those found by other authors on tungsten prepared in a different manner. Electron-microscope pictures of etched surfaces sometimes reveal pyramid shaped etch hills and whisker-like needles, which are supposed to be subcrystals grown with the highest perfection, during temporarily favourable conditions.

SOUS-STRUCTURES DANS DE LARGES CRISTAUX DE TUNGSTENE FORMES A PARTIR DE LA PHASE VAPEUR

Les auteurs ont examiné des monocristaux de tungstène formés par décomposition du chlorure dans la phase vapeur. Ils ont observé la présence d'une sous-structure, à la fois par les techniques de rayons X et de microscopie. La désorientation entre les sous-grains est quelconque et diffère ainsi de celle trouvée dans des monocristaux de fils de tungstène dopés et recristallisés. La formation d'une sous-structure ou même de branches dendritiques dépend des conditions de croissance. Les rangées de piqûres de corrosion sur les micrographies sont de même nature que celles trouvées par d'autres auteurs sur du tungstène préparé de façon différente. Les micrographies électroniques de surfaces attaquées révèlent parfois des piqûres pyramidales et des aiguilles semblables aux barbes. Ces dernières pourraient être des sous-grains de haute perfection formés par suite de l'existence temporaire de conditions favorables.

SUBKRISTALLE VON GROSSEN, AUS DEM DAMPF GEWACHSENEN WOLFRAMKRISTALLEN

Durch Chloridzersetzung wurden aus der Dampfphase Wolframeinkristalle hergestellt. Röntgenographische und mikroskopische Untersuchungen zeigten das Vorhandensein einer Substruktur an. Die Orientierungsunterschiede zwischen den Subkristallen sind regellos und somit verschieden von denen bei Einkristallen aus dotierten rekristallisierten Wolframdrähten. Das Auftreten einer Substruktur oder von dentritischen Ästen hängt von den Verhältnissen während des Wachstums ab. Auf mikroskopischen Bildern von geätzten Oberflächen finden sich Reihen von Ätzgrübchen derselben Art, wie sie andere Autoren bei verschiedenartig präpariertem Wolfram gefunden haben. Elektronenmikroskopische Bilder von geätzten Oberflächen weisen zuweilen pyramidenförmige Ätzhügel und whiskerähnliche Nadeln auf, die vermutlich Subkristalle darstellen, die während zeitweilig günstigen Bedingungen mit höchster Vollkommenheit gewachsen sind.

VOL. 8 1960

1. INTRODUCTION

Some years ago a substructure with systematic disorientations was found in large crystals in recrystallized wires of tungsten to which a so called dope was added.[1] This fragmentation was enhanced when the crystals were plastically bent. We wished to compare the perfection and behaviour in bending of those crystals with that of single crystals of pure tungsten. In drawn wires of "pure" tungsten, crystals of sufficiently large dimensions (e.g. about 1 cm in length) cannot easily be obtained. For this reason we used crystals of "pure" tungsten which were prepared by decomposing the vapour of tungsten chloride (according to the van Arkel process[2]) on a heated single-crystal wire of small diameter. This single-crystal core itself contained a ThO_2 dope and therefore had to be removed afterwards from the final crystal. The resulting small rods of "pure" tungsten were investigated by means of X-rays and also metallographically, and showed a different type of substructure compared with that in the crystals in drawn and recrystallized doped wires. Sometimes this substructure can develop into a dendritic growth. It seemed therefore worthwhile to consider the perfection of the vapour-grown crystals in relation to the circumstances of growth. We extended the investigation with electron-microscopical examination of original and etched surfaces. For comparison we also investigated crystals of zone-melted tungsten.

2. THE CRYSTALS

For the preparation of single crystals according to the van Arkel method[2] a single-crystal tungsten wire is resistance-heated to about 2000°–2300°C in an atmosphere of tungsten hexachloride vapour. The

* Received March 17, 1959.

† Philips Research Laboratories, N.V. Philips' Gloeilampenfabrieken, Eindhoven, Netherlands.

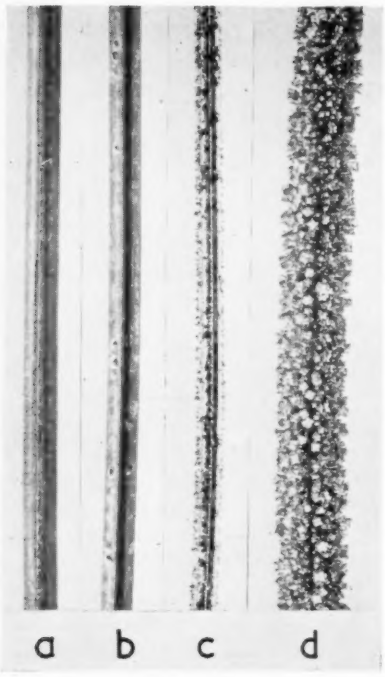


FIG. 1. Vapour-grown tungsten crystals. ×3.
(a) with small number of irregularities
(b) with some protruding pyramids
(c) with many small pips
(d) with many dendritic branches.

wires on which the tungsten deposits were in our case so called Pintch single crystal[3] wires of 100μ diameter. They consist of tungsten with an additive of 1% ThO_2, which favours exaggerated grain growth. After suitable deformation such a wire can be passed through a furnace at a velocity at which it recrystallizes into one long single crystal. The wires used were old stock from a commercial source. The WCl_6 was purified by sublimation just before use. The vessel containing the wire and the WCl_6, in which the decomposition takes place, is thoroughly degassed and heated to about 120°–140°C in order to obtain sufficient vapour pressure of WCl_6. The chlorine which is formed according to the reaction $WCl_6 \rightarrow W + 3Cl_2$ is bound by another tungsten wire heated to about 1200°C, resulting in regeneration of the hexachloride. The vapour pressure of the WCl_6 and the temperature of the single-crystal wire determine the rate of decomposition of the WCl_6 and hence of the growth of the single crystal.

Depending on this rate of growth and on the absence or presence of small amounts of contaminating gases, e.g. oxygen, one may obtain either "real" single crystals which show, macroscopically, virtually no irregularities; or else crystals with a more or less uneven surface. The irregularities can be restricted to small pyramids protruding from the crystal, but in an extreme case they comprise a covering of protruding branched crystals along the whole length of the wire. Fig. 1a–d shows (a) an example of a good single crystal, (b) one with a few small pyramids, (c) one with many small pips on the surface, and (d) one which is covered with "branches". The crystals with many branches were obtained when trying to grow an additional layer on "good" crystals (of about 1 mm diameter) under unfavourable purity conditions and very rapidly.

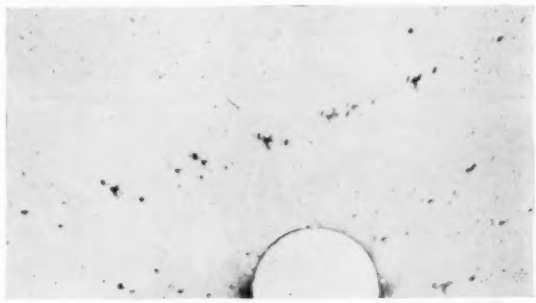


FIG. 3. Laue back-reflection diagrams obtained with a microbeam. The spots are split in a non-systematic way.

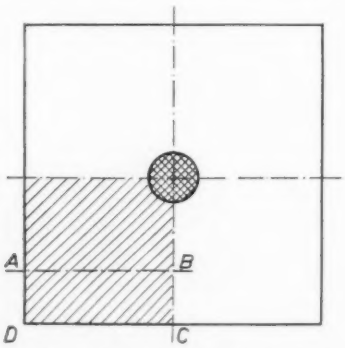
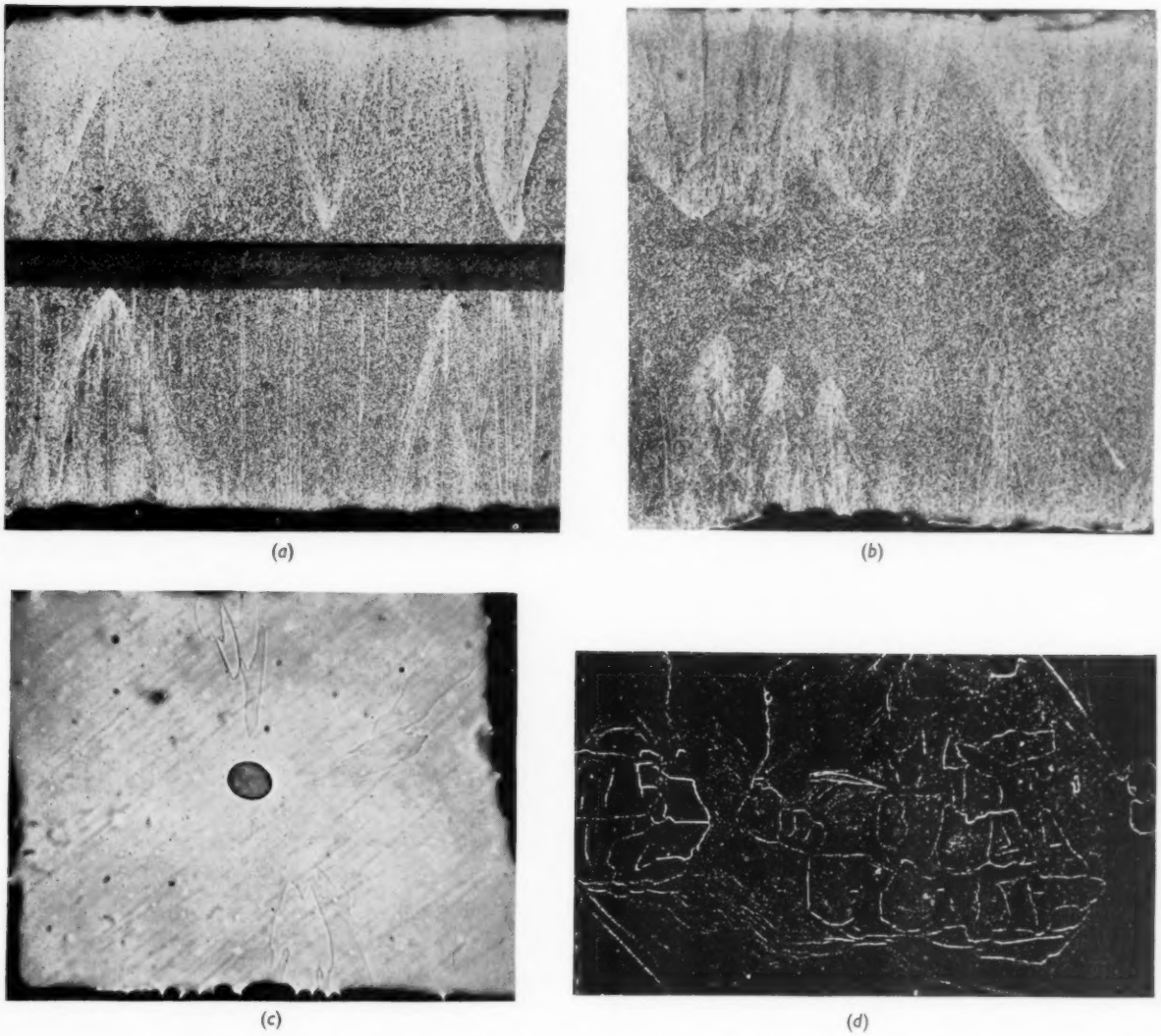


FIG. 2. The abrasion procedure of a vapour-grown tungsten crystal (cross section). Hatched area: the resulting pure single crystal. Surface AB of part $ABCD$ was investigated.

Three of the "good" crystals were chosen for investigation, by X-ray methods, on fragmentation.[1] In order to eliminate the influence of the core of the ThO_2-doped wire, we abraded a crystal of about 4 cm length until the plane of abrasion reached the core wire. Another quarter of the crystal was then removed by abrasion along a direction perpendicular to the first and again parallel to the wire axis. The remaining part of the core, forming now an edge of the prism, loosened during the subsequent etching away of the deformed outer layer, and a "pure" tungsten rod of about 4 cm length remained. Fig. 2



(a) (b) (c) (d)

FIG. 4. Sections of vapour-grown tungsten crystals (etched 20 sec in 10% H_2O_2). ×67.
(a) longitudinal through central wire (b) the same but just outside the central wire.
(c) etched cross section perpendicular to the central wire (d) longitudinal, just below the outer surface of the crystal.

illustrates this procedure. In this figure some surfaces are indicated by letters, to which we will refer in the section on the electron microscopical investigation. Spectrochemical analysis of the "pure" crystals gave:

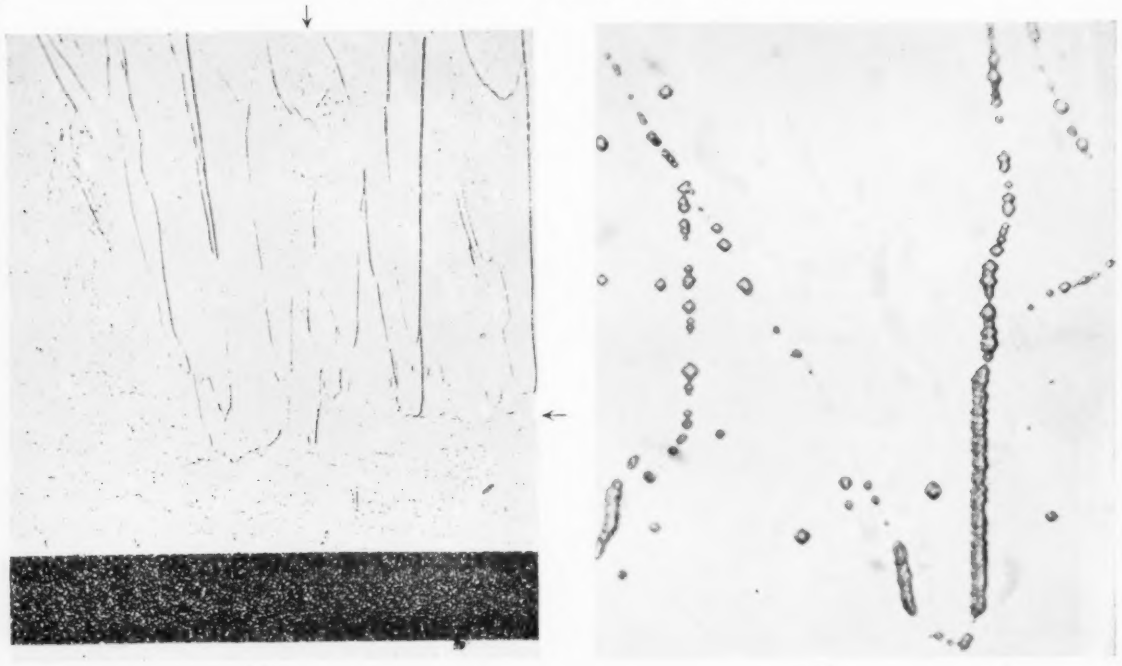
Al	Cu	Fe	Mo	Si	Th
<0.0002%	0.0002%	0.0002%	0.01%	<0.001%	—

For comparison tungsten crystals were made by zone-melting a sintered and swaged rod of the metal with less than 0.001% of any impurities (except Mo), applying the "floating-zone" technique. The floating molten zone crystallizes at a rate of 3.5 cm/hr to a few parallel single crystals or, after repetition of the melting, even to one single crystal. As purification was not the main purpose of this melting, no final chemical analysis was made of the crystal.*

3. X-RAY INVESTIGATION

In order to compare the structure of the vapour-grown crystals with those in recrystallized doped tungsten wires, we took microbeam Laue back-reflection photographs. This method was as described for the crystals in drawn wires.[1] In some cases we obtained patterns from the vapour-grown crystals from which the presence of subcrystals with orientation differences ranging from some minutes to several degrees could be deduced. The splitting up of the

* We are indebted to Mr. H. T. Schaap for preparing these crystals.



(a) (b)

FIG. 5a. Sub-boundary in vapour-grown crystal. 5b. Idem: area around point of intersection of arrows in Fig 5a, enlarged. ×1300.

spots was found to be especially pronounced when the crystals showed also some macroscopic irregularities (as in Fig. 1b). Fig. 3 represents such a Laue back-reflection diagram. We could not, however, detect any systematic type of splitting up of the spots common to the majority of the diagrams, as was found for the crystals in recrystallized drawn wires. Neither did bending and rebending of the crystals induce this. Bending proved to be possible in all three cases, but is not always possible with the unabraded vapour-grown crystals. Splitting up of the spots did sometimes occur but was not confined to the direction corresponding with a rotation of the subcrystals around the rod axis. The same was found on diagrams from unabraded crystals which had been bent and rebent.

The difference in substructure between the vapour-grown crystals and those grown by recrystallization in a drawn wire of doped tungsten, confirms the assumption that the peculiar behaviour of the latter crystals must be a result of the presence of the dope, namely in the form of strings or planes parallel to the wire direction. Such strings are of course absent in the vapour grown crystals.

4. MICROSCOPICAL INVESTIGATION

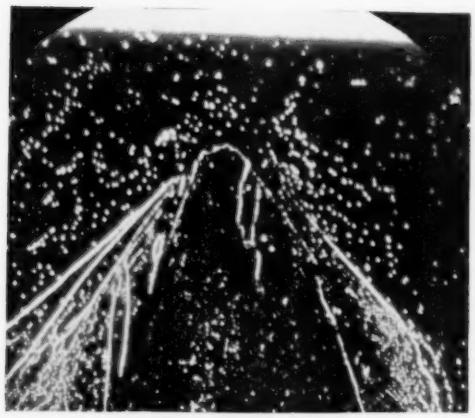
After abrasion, sections of the vapour-grown crystals were electrolytically polished in a solution of 0.1% NaOH by applying a voltage of 10 V for about 1 hr. The current density was about 50 mA/cm². After polishing, the crystals were etched in different ways, namely:

(a) chemically: for 1 min in equal parts of a 10% potassium ferricyanide and a 3% NaOH solution in water,

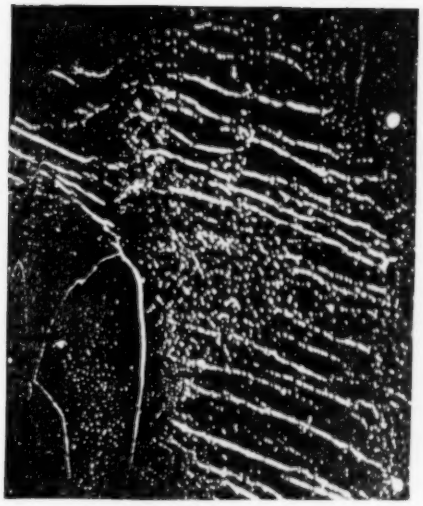
(b) chemically: for 20 sec in a boiling solution of 10% H_2O_2 in water,

(c) electrolytically: for 10–20 sec in a solution of 1% NaOH in water and with an applied potential of 1 V.

When we could see macroscopically some irregularities on the crystal faces, then the optical micrograph showed sub-boundaries as illustrated in Fig. 4. Fig. 4a is a longitudinal cross section through the central wire and Fig. 4b shows a section in a plane just outside this wire. They indicate more or less cone shaped subcrystals with the top of the cone pointing to the central wire. The same applies to Fig. 4c, a cross section perpendicular to the central wire. The closed loops seen in a plane parallel to the wire, but just under the outer surface of the single crystal, are in accordance with this idea (Fig. 4d). Moreover we traced several of these cones by a stepwise abrading away of the metal, taking photomicrographs at each step. One can then see a widening of the loops, from the central wire to the outside of the crystal. Fig. 5a shows a boundary like that in Fig. 4a at a higher magnification, and Fig. 5b a detail enlarged

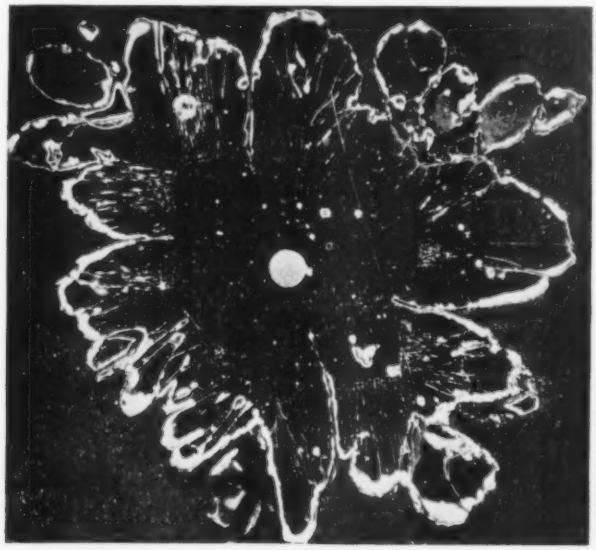


(a)

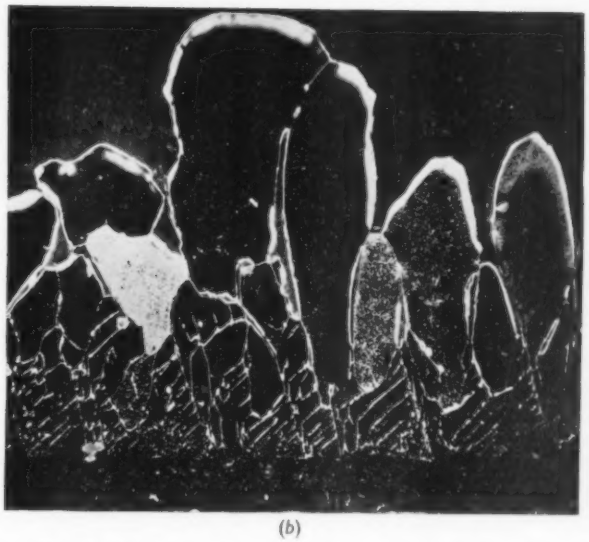


(b)

FIG. 6a and b. Sub-boundaries in crystal with irregularities.



(a)



(b)

FIG. 7. Good crystal on which a very imperfect crystal has been grown. ×50.
(a) perpendicular to wire axis
(b) parallel to wire axis

1300 times. We can see that the sub-boundary lines are built up as rows of etch pits. The density of etch pits on those lines can be estimated as at least 15,000 cm^{-1}. These pits may well, therefore, represent dislocations, for this density would then correspond to a disorientation of one to a few minutes as was indeed observed with the X-ray micro-beam technique. The inside of the cones often shows fewer etch pits than the surroundings. If we investigate crystals with many protruding pyramids we find on the photomicrograph the same type of pattern but with many more etch pits. The pits are often aligned along parallel lines (Fig. 6).

The occurrence of the substructures is closely related to the circumstances under which the crystal grows. This can be illustrated by taking a vapour-grown crystal, without faults and with a diameter of about 1 mm, and subjecting it to a renewed growth process but now in a less pure atmosphere (the initial vacuum being rather poor) and also at a faster rate. We then obtain crystals like those depicted in Figs. 1c and d. A cross section of such crystals shows an inner part practically without sub-grain boundaries and an outer part containing many boundaries starting where the imperfect growth has begun (Fig. 7). Many of these

VOL. 8 1960

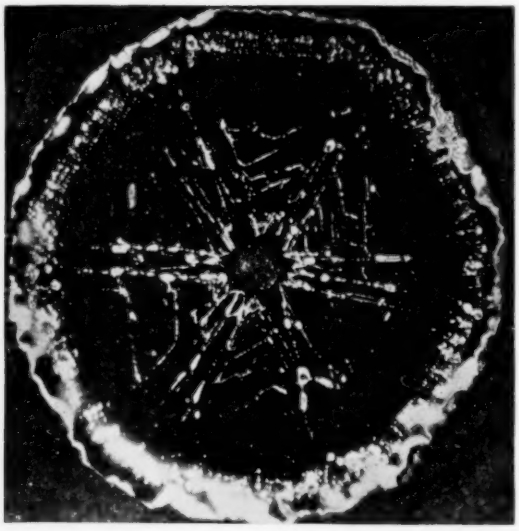


FIG. 8. Cross section perpendicular to wire direction which is [111] axis. ×60.

boundaries start as rows of separate pits, then form real lines and develop into crystal boundaries of the more or less separate dendritic crystals. This corresponds with a gradually increasing difference in orientation between the parts of the crystal.

The relation of rows of etch pits to growth and crystallographic orientation is illustrated by Fig. 8 representing a cross section perpendicular to [111], the wire direction.

For a few of the dendritic branches which were shaped more or less like pyramids, we determined the orientation of their "axis". It proved to be [100].

The zone-melted tungsten crystals investigated with the above mentioned etchants showed only etch pits at random and no substructures.

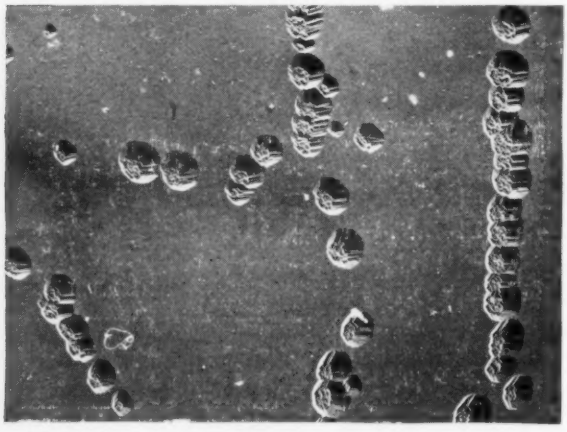


FIG. 9. Etch pits in tungsten crystal (etched: 20 sec in 10% H_2O_2). ×8000.

5. ELECTRON-MICROSCOPICAL INVESTIGATION

The outer surface of the vapour-grown crystals, and their sections, were studied with a Philips EM 100-B electron microscope. The first pictures were obtained by the indirect methacrylate–SiO_2 replica technique. For the remainder, however, a direct carbon replica was made, the surface being first shadowed with platinum, then the carbon layer applied (whilst the sample was rotated) and finally the replica separated from the surface of the metal by dissolving the latter. The same electrolytic polishing and etching techniques were used as described above.

In addition to the rows of etch pits as shown in Fig. 9, some remarkable details are seen, namely etch hills and whisker-like needles. On the unetched outer surface of the crystals we sometimes see pyramids like those of Fig. 10. But on the surface of etched crystals too we have seen hills or pips like

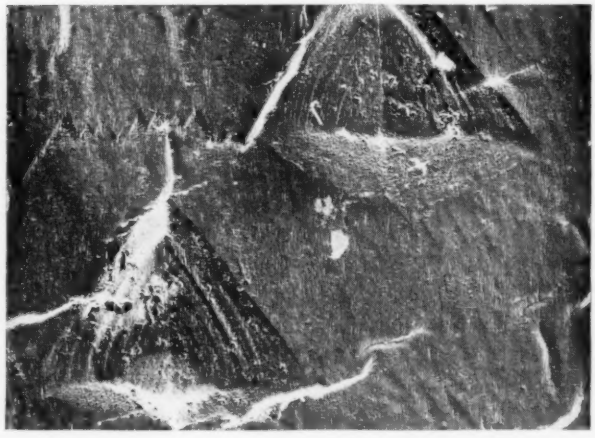
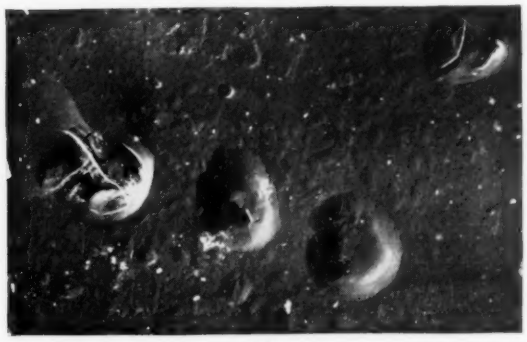


FIG. 10. Pyramid on surface of vapour-grown W-crystal, unetched. ×5000.

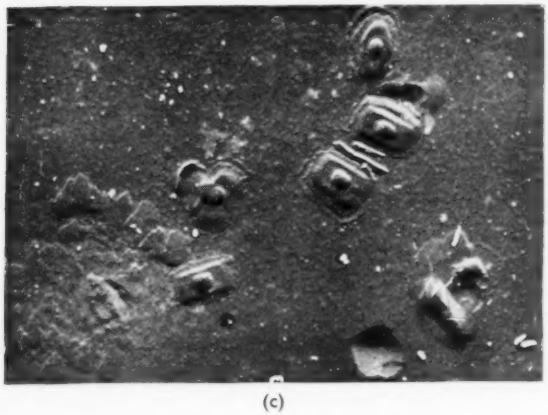
those shown in Figs. 11a, b and c. They are generally rounded like those of Fig. 11a, but a few are found with steps as in Figs. 11b and 11c. Judging from the deviations from parallelism and in the 45° angles between the contour lines of the pyramids in Fig. 11c, small orientation differences seem to be present (up to 5°). The pyramids are seen here on the plane of abrasion, which corresponds roughly to a (510) face, and in Fig. 11c the boundaries could represent intersections with (100) and (110) faces; in Fig. 11b apart from three (100) and (110) faces a (210) face can also be present. The latter etch hills are found on an "inner" surface like AB in Fig. 2 and one must therefore keep in mind that these pyramids have their tops pointing towards the interior of the crystal (although not exactly to the central wire), whereas the



(a)



(b)



(c)

FIG. 11a. Etch hill on "inner" surface of vapour-grown W-crystal. ×9000.
b and c Etch hills of pyramid shape. ×50,000 and ×9000.

pyramids of Fig. 9 stand on the outer surface of the crystal.

Very remarkable too are the small needle-like crystals which protrude from the etched surface, Fig. 12a. Fig. 12b shows one of these enlarged 35,000 times. The black central line on the right of the white rod in Fig. 12b represents the hollow core in the carbon replica, where the "whisker" has been. The core can only be seen easily where the whisker starts to protrude from the surface, because only there has no platinum or carbon come between the needle and the surface (on the original photographic negative this core is seen to be present over almost the whole length of the white rod). The cross section of this core is about 50 mμ; the length of the needles are 1–3 μ. These needles are found on different crystals after etching either with boiling H_2O_2 solution or with $K_3Fe(CN)_6 + NaOH$, and also on the unetched outer surface of a crystal with irregularities (like Fig. 1b). As the nonmetallic compounds of tungsten, e.g. chlorides or oxychlorides, would dissolve in both etching agents more quickly than the metal itself, we must assume that those whisker-like needles consist of tungsten metal which has withstood the etching agent somewhat better than the surrounding material. It was not possible to determine the crystallographic direction of the needles (e.g. in Fig. 12a), and thus we

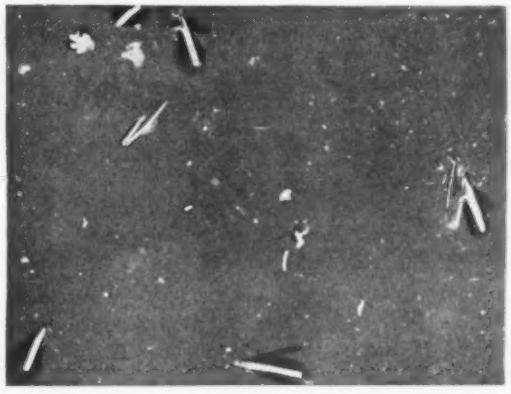


FIG. 12a Whisker-like needles on "inner" surface of etched vapour-grown W-crystal (etched 10 min in 3% H_2O_2. ×6000.

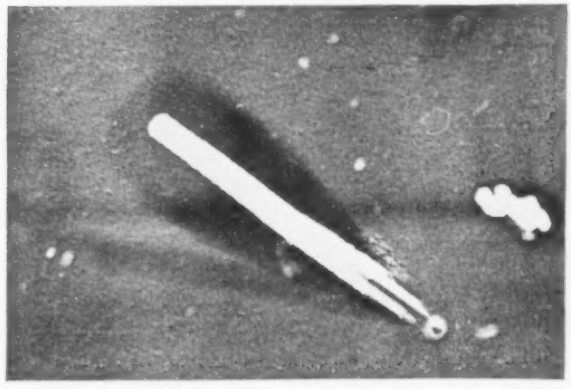


FIG. 12b One whisker enlarged. (linear shadow from Pt, rounded shadow from C). ×35,000.

VOL. 8 1960

do not know whether those directions are crystallographically related to each other, or not.

6. DISCUSSION OF RESULTS

It is known that most crystals grow with faults and that only very seldom are ideal crystals formed. Rapid growth and the presence of contaminations will favour the generation of imperfections. Substructures in crystals of tungsten have been reported when the crystals were grown in drawn doped wires[1] and also when they had grown in arc melted metal.[3,4] The substructure in crystals grown in doped wires is, however, as we showed above, of a different nature from that in crystals grown from the vapour phase or from molten metal. Strings of contaminations in the wires are thought to be responsible for this difference.[1] The direction of growth is radial in the case of the vapour-grown crystals, and thus a disorientation, as in wire-grown or other crystals grown axially,[5] is not to be expected. It is remarkable that the pictures of the substructures found here in vapour-grown crystals closely resemble those found by Geach and Jones[4] in crystals from arc-melted tungsten. That we did not find the same kind of subcrystals in the single crystal made by zone melting the metal can be explained by the much lower rate of growth used (3.5 cm/hr) compared with that mentioned by Geach and Jones (13 mm/min). This then is in accordance with the observation of Chalmers *et al.* who found less subgrains at slower crystal growth. Dendritic growth occurs when the rate of growth is too high. We have seen that by varying the circumstances a gradual change occurs from crystals with a small amount of substructure to the formation of dendritic branches on the crystal. The orientation differences between the subcrystals can thus be considered as a first step towards dendritic growth. The same correlation is found by Weinberg and Chalmers[8] in lead crystals grown from the melt. The relation between the number of etch pits and the degree of disorientation occurring indicates that the etch pits we observed could correspond with dislocations just as could those found by Geach and Jones, and by Wolff[5], by different etching techniques.

Etch hills have also been found on α-iron by van Wijk and van Dijck[9], and on Tantalum by Bakish[10], both again being body-centred cubic metals. The etch hills indicate that the material of the hill is less attacked by the etchant than is the surrounding metal. This might be explained by assuming that the hills consist of more perfectly grown crystals, and one is inclined to think of growth spirals. It could be that during a short period in which the transport of new material to the growing crystal was temporarily decreased, resulting in a low concentration, the spiral was formed on top of a screw dislocation emerging from the metal, and that afterwards this spiral was embedded in metal deposited at higher concentration. The pyramids are found on the surface AB of the part $ABCD$ in Fig. 2. If we assume a direction of growth from AB towards CD, then the pyramids must have grown from the top to the bottom. A growth direction from CD towards AB, corresponding to a growth from the bottom towards the top of the pyramids, cannot however be excluded, in view of the irregularities observed in the less perfect crystals. The difference in rate of solution in the etchant between the spiral and its surroundings seems to be very small, for we have observed the etch hills in only very few cases. The hills with rounded summits may represent pyramids which have been partly dissolved by the etchant. The view that the cone-shaped subcrystals are often more perfect than their surroundings is in accordance with the fact that, in the micrographs, the latter regions have more etch pits than the former, though this also might have been brought about by a difference in orientation.

The "etch whiskers" are more common, and could be explained in the same way as follows: During the deposition of the metal on the hot wire the vacuum pump is used from time to time in order to maintain an adequate vacuum. This results in a change in the vapour pressure, which gives only a short period favourable for the growth of whiskers. Those whiskers actually form at several points but when the pressure increases again the normal growth can continue, and the protruding whisker is embedded in newly formed material. Afterwards the whisker, by reason of its perfection, dissolves less readily in the etchant than does the surrounding material. We have found whiskers on all kinds of etched surfaces, but also on a fresh unetched outer surface of a crystal. In the latter case the stopping of the growth process will, for a short period, provide a lower concentration of the decomposing halide. Webb and Riebling[11] studied the formation of metal whiskers by reduction of the halides with hydrogen, and found that the transport of the metal is performed by the halide vapour. This confirms the view that in our case too, of decomposition without hydrogen, small changes in vapour pressure have a large influence on the local concentration of metal vapour and hence on the growth of the metal single crystal or whisker.

Even the pyramid shaped dendritic branches can be a result of the difficulty of transport of metal atoms to places near the central wire. They are grown

too rapidly, however, for us to expect them to show growth spirals or whiskers.

ACKNOWLEDGMENTS

We thank Mr. H. B. Haanstra for help and advice on the electronmicroscopical work, Mr. P. C. van der Linden who prepared some of the crystals and Mr. J. Israel for making the first micrographs 4 and 5.

REFERENCES

1. G. D. RIECK, *Acta Met.* **4,** 47 (1956).
2. A. E. v. ARKEL, *Physica, Eindhoven* **3,** 76 (1923); *Metallwirtschaft* **13,** 405 (1934).
3. e.g. C. J. SMITHELLS, *Tungsten*, p. 143. London (1952).
4. G. A. GEACH and F. O. JONES, 3e *Plansee Seminar*, Reutte (1958).
5. E. TEGHTSOONIAN and B. CHALMERS, *Canad. J. Phys.* **29,** 370 (1951); *Ibid.* **30,** 358 (1952).
6. U. E. WOLFF, *Acta Met.* **6,** 559 (1958).
7. J. W. RUTTER and B. CHALMERS, *Canad. J. Phys.* **31,** 15 (1953).
8. F. WEINBERG and B. CHALMERS, *Canad. J. Phys.* **29,** 382 (1951).
9. F. VAN WIJK and J. A. B. VAN DIJCK, *Acta Met.* **4,** 657 (1956).
10. R. BAKISH, *Acta Met.* **6,** 120 (1958).
11. W. W. WEBB and E. F. RIEBLING, *J. Chem. Phys.* **28,** 1242 (1958).

VOL.
8
1960

POLYGONIZATION OF 31% ALPHA-BRASS*

V. Y. DOO†

31% alpha-brass crystals grown by melting high purity copper and zinc together were used in this investigation. Single crystals bent within, as well as slightly beyond, the single slip region were polygonized to form dislocation walls perpendicular to the major set of slip planes after a final anneal of 1–2 hr at 700°C or 750°C. Bent polycrystalline specimens having very high dislocation densities in all sets of active slip planes were polygonized to form subgrain boundaries after a similar anneal.

Even though the stacking fault energy of alpha-brass is likely to be lower than that of the copper, the former polygonized at a relatively lower temperature. It is believed that the high self-diffusivity of alpha-brass is one of the important factors which facilitated the climbing of its dislocations. The present results substantiated Barnes[1] prediction that the dissociated dislocations can climb.

POLYGONISATION DU LAITON α à 31 POUR CENT

Dans ce travail, l'auteur utilise des cristaux de laiton α (à 31 pour cent) préparés par fusion de cuivre et de zinc de hautes puretés. Des monocristaux courbés aussi bien en-dehors que dans le domaine de glissement unique ont été polygonisés (avec formation de parois de sislocations perpendiculaires aux plans de glissement principaux) après un recuit final de 1 à 2 heures, à 700°C ou 750°C.

Des échantillons polycristallins contenant une densité élevée de dislocations sur tous les groupes de plans de glissement actif ont également été polygonisés (formation de sous-joints) après un traitement similaire.

Bien que l'énergie correspondant aux défauts d'empilement dans le laiton α soit vraisemblablement plus faible que celle correspondant au cuivre pur, le premier polygonise à une température relativement plus basse. L'auteur pense que l'auto-diffusion élevée du laiton α est l'un des facilitent la "montée" des dislocations. Les résultats décrits appuient la prédiction de Barnes[1], d'après qui les dislocations dissociées peuvent subir la "montée".

POLYGONISATION VON ALPHA-MESSING MIT 31% ZINK

In dieser Untersuchung wurden Kristalle von Alpha-Messing mit 31% Zink aus hochreinem Kupfer und Zink erschmolzen. Einkristalle, die innerhalb des Gebiets der Einfachgleitung gebogen worden waren und solche, die etwas stärker gebogen worden waren, wurden polygonisiert und enthielten nach einer Glühung von ein bis zwei Stunden bei 700° oder 750°C Versetzungswände senkrecht zur Schar der Hauptgleitebenen. Gebogene vielkristalline Proben mit hoher Versetzungsdichte in allen aktiven Gleitebenen wurden polygonisiert; nach einer ähnlichen Wärmebehandlung bildeten sich Subkorngrenzen.

Obwohl die Stapelfehlerenergie von Alpha-Messing wahrscheinlich geringer ist, als die von Kupfer, polygonisierte Messing bei verhältnismassig tieferen Temperaturen. Es wird angenommen, dass die hohe Selbstdiffusion von Alpha-Messing einer der wichtigen Faktoren ist, der das Klettern der Versetzungen erleichtert. Die Ergebnisse unterstützen die Voraussage von Barnes[1], dass aufgespaltene Vertsetzungen klettern können.

1. INTRODUCTION

It is well known that dislocation lines in close-packed metals can be dissociated into two partial dislocations with a stacking fault between. The width of the stacking fault depends upon the magnitude of its energy, i.e., the lower the energy the wider the stacking fault. It is also known that the rate of dislocation climb depends mainly upon the width of the stacking faults separating two partial dislocations. Aluminum has a high stacking fault energy, so its dislocations climb rapidly at a temperature considerably below its melting point. On the other hand copper has a low stacking fault energy, so its dislocations are reluctant to climb even at a temperature near its melting point.

Because the frequency of annealing twins increases as zinc is added to copper,[2] the stacking fault energy of alpha-brass should be even lower than that of copper. Hence one may expect the dislocations in alpha-brass to climb at a rate even slower than copper if the width of the stacking fault is the only controlling factor.

Since dislocation climb is a self-diffusion process the self-diffusivity should have some effect on the rate of climb. The reported self-diffusivities of copper and zinc in alpha-brass[3] are considerably higher than that of copper in pure copper.[4] Therefore, the self-diffusivity is more favorable for dislocation climb in alpha-brass than in copper, while its stacking fault energy is *less* favorable. This work was designed to investigate the polygonization behavior of alpha-brass.

2. EXPERIMENTAL

2.1. *Specimen preparation*

Large grain alpha-brass (31% Zn) was grown by melting high purity copper and zinc together in a

* Received February 18, 1959.

† Mining and Metallurgy Department, University of Illinois. Present address: The Product Development Laboratory, International Business Machines Corporation, Poughkeepsie, New York.

spectrographically pure graphite crucible enclosed in an evacuated Vycor capsule. The large grains were cut into slabs about $3 \times 6 \times 16$ mm in size by using a jewel saw. All faces except the ends of each slab were ground through a series of metallographic abrasive papers to a final grinding on 4-0 grade paper. A deep etching in 1 : 1 HNO_3 was then given to all slabs until sharp Laue spots appeared on the Laue back-reflection X-ray film. Finally, each slab was electro-polished in an orthophosphoric acid solution. The final size was about $1 \times 3 \times 14$ mm for single crystal specimens and about 30 per cent thicker for polycrystal specimens.

The orientation of the single crystal slabs deviated slightly from the ideal orientation which has its [112] pole parallel to the bending axis, and its $(11\bar{1})$ and $(1\bar{1}0)$ planes making a 45° angle to the large face. The orientation deviation ranged from a 3° to a 12° rotation around the longitudinal axis. The polycrystalline slabs contained two to three grains with the largest ones more than two-thirds of the slab size. The orientations of these large grains were as follows: Group (1) had a (111)[$1\bar{1}0$] orientation while group (2) had its [110] pole and [111] pole making about a 15° angle with the largest face pole and bending axis, respectively. These orientations were very susceptible to multislip in the very early stages of bending.

The specimens were bent as shown in Fig. 1. The mandrel was 25.4 mm in diameter and the radius of curvature of the supporting piece was 14 mm. Fig. 1a shows the earliest stage of bending which was three-point loading. In later stages it gradually changed into four-point and then to five-point loading as shown in Fig. 1b. The single crystal specimens, bent to a position just before that in which the center contacting point lost contact with the mandrel, showed only the most favorable slip system to be operating. Beyond that point other slip systems became active. However, the most favorable slip system showed the highest slip line density as expected.

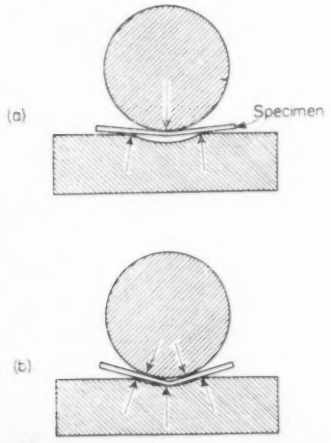


FIG. 1. Showing the ways in which the alpha-brass specimens were bent. (a) Early stage of bending. (b) Later stage of bending.

For annealing, all specimens were put in graphite boats and then sealed in Vycor capsules under a pressure of 5×10^{-6} mm Hg. Temperature variation in the furnace was controlled to within ± 3°C.

2.2. *Microscopic and X-ray examinations*

Jacquet's electro-etch method[5] was used to reveal the substructures. Because the conditions for the success of this etch method were quite critical, several trials had sometimes to be made before a satisfactory result could be obtained. After repeated electro-polishing and etching, not only the specimen thickness was reduced considerably but also the originally sharp edges were rounded off rapidly. Hence the region that could be focused under a microscope was gradually reduced into a narrow strip.

The Laue back-reflection X-ray method was used to investigate structural changes in the specimen after each treatment. A 0.13 mm collimator and a specimen–film distance setting of 30 mm were found to give sufficient resolution.

3. RESULTS

In each case described below, experiments were repeated on two or more specimens under the same conditions. The results were found to be reproducible. The single crystal specimens which had their orientations close to the ideal orientation, for one active slip system in bending, polygonized in approximately the same manner regardless of whether single slip or multislip occurred during bending. On the other hand, the unfavorably oriented polycrystal specimens polygonized in an entirely different manner.

3.1. *Favorably oriented specimens, single slip*

Fig. 2 (a) shows the slip lines immediately after bending. That they extend well into the neutral axis is apparent. Dislocations were clearly revealed after electro-etching (Fig. 2b). The dislocation density along the slip line was more or less uniform. Only a small number of dislocations had climbed out of their slip planes after the specimen was annealed for 2 hr at 400°C (Fig. 2c). Also the average dislocation density showed little change. The strain distribution was maximum on the surface and gradually decreased to zero at the neutral axis. The approximate average dislocation density was calculated by assuming the

VOL. 8 1960

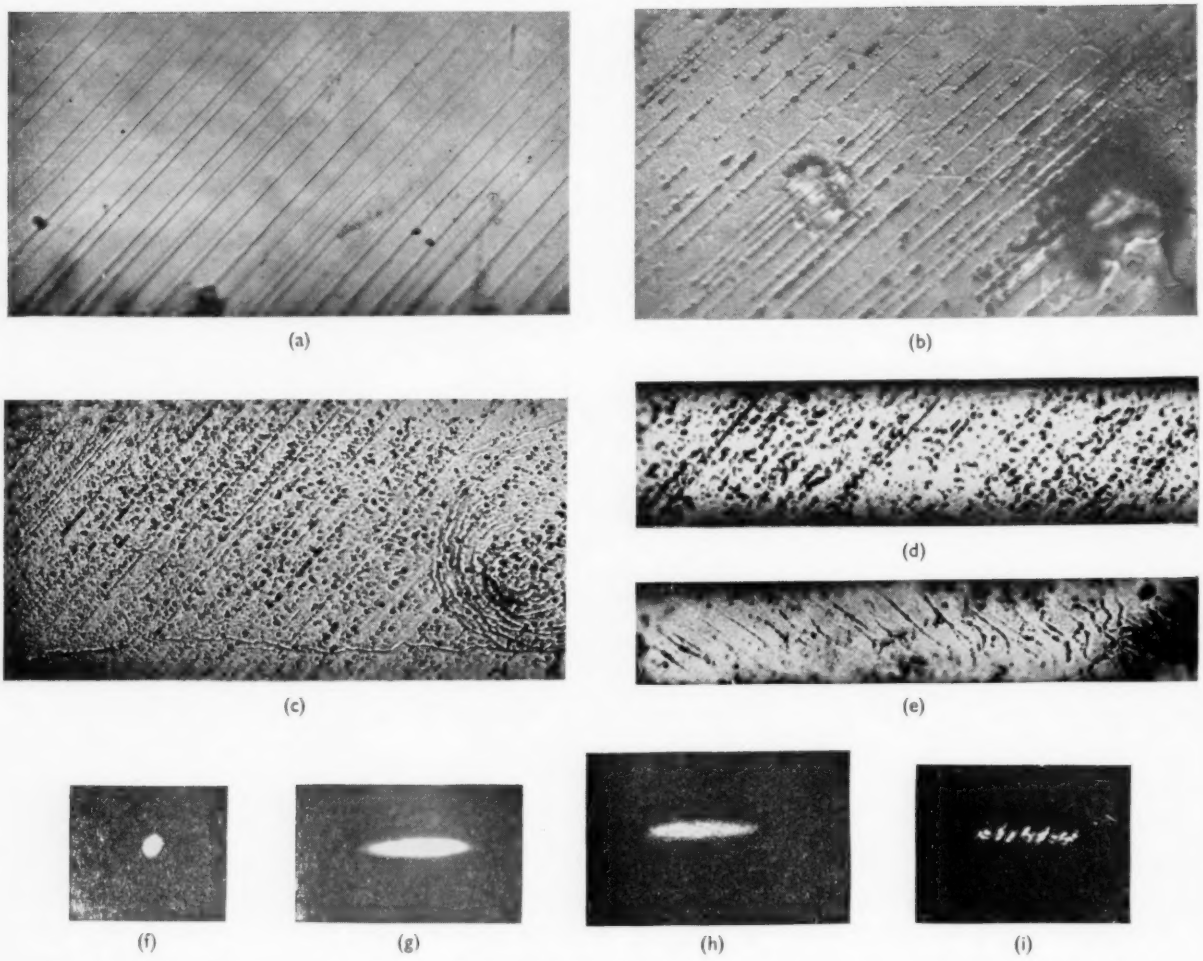


FIG. 2. Bent single crystal, single slip. Annealed successively at different temperatures. (a) Immediately after bending. ×250. (b) Same as (a) + electro-polish and then electro-etch. ×250. (c) Annealed 2 hr at 400°C, electro-polished and then electro-etched. ×250. (d) Same as (c) + 1hr at 650°C, electro-polished and then electro-etched. ×250. (e) Same as (d) + 1 hr at 750°C, electro-polished and then electro-etched. ×250. (f) (112) X-ray reflection, before bending. ×6. (g) (112) X-ray reflection of (a). ×6. (h) (112) X-ray reflection of (d). ×6. (i) (112) X-ray reflection of (e). ×6.

strain change through the specimen to be directly proportional to distance from the neutral axis. The average dislocation density thus calculated was found to be approximately one-third of that actually counted. When the specimen was annealed for 1 hr at 650°C, more dislocations climbed out of their slip planes (Fig. 2d). The average dislocation density was reduced to about half of its original value. Further anneal at 750°C for 1 hr practically completed the polygonization (Fig. 2e). The X-ray results were in good agreement with the microscopic observations (Figs. 2f–2i).

3.2. *Favorably oriented specimens, multislip*

These specimens were bent until the five-point loading stage was reached (Fig. 1b). Three active slip systems were found after bending (Fig. 3a). However, the slip line density of the most favorable slip system was much higher than in the other two systems. Annealing for 2 hr at 550°C resulted in the appearance of only traces of slip lines of the most favorable slip system (Fig. 3b). Most dislocations of the other two sets of slip planes had climbed out of their slip planes and may have annihilated part of the opposite sign dislocations. Additional annealing at 700°C for 2 hr completed the polygonization (Fig. 3c). Again the X-ray evidence showed good agreement with microscopic observation (Figs. 3d and 3e).

3.3. *Unfavorably oriented specimens, multislip*

These specimens were bent to about the same extent as the specimen shown in Fig. 3a. The very high slip

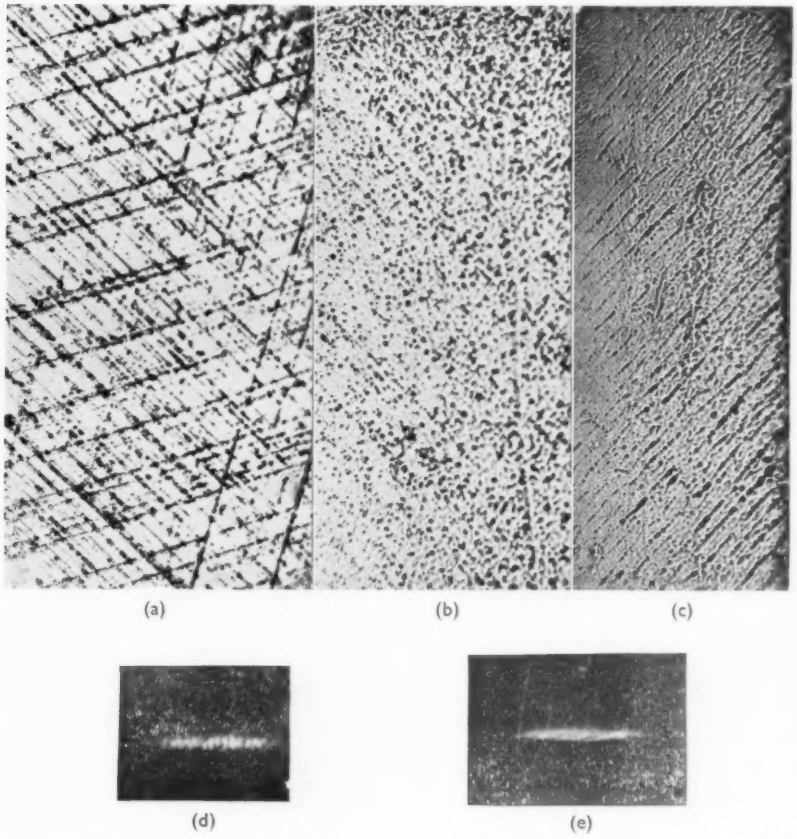


FIG. 3. Bent single crystal, multislip. Annealed successively at different temperatures. (a) As bent. Electro-polished and then electro-etched. ×250. (b) Annealed 2 hr at 550°C, electro-polished and then electro-etched. ×250. (c) Same as (b) + 2 hr at 700°C, electro-polished and then electro-etched. ×250. (d) (112) X-ray reflection of (b). ×6. (e) (112) X-ray reflection of (c). ×6.

VOL. 8 1960

line density resulted from their large initial thicknesses, and hence large surface strain (Fig. 4a). Even annealing 2 hr at 650°C clearly showed traces of slip lines of all three slip systems (Fig. 4b). However, the average dislocation density was reduced considerably. Further annealing at 750°C for 2 hr produced well defined subgrain boundaries (Figs. 4c and 4d). The X-ray results again confirmed the microscopic observations.

4. DISCUSSION

The reluctant polygonization of high purity copper has been reported by earlier workers.[6,7] This was interpreted as a result of the wide stacking fault between two dissociated partial dislocations in the copper, as first suggested by Seeger[8]. Some earlier workers[6] believed that in order that the extended dislocations may be able to climb, they must first combine. Later Young[9] found that a very small amount of tellurium in copper facilitated polygonization to a great extent. He suggested that the added tellurium in copper might have either mechanically hindered the two partials from dissociating, or actually increased the stacking fault energy.

The fact that the frequency of annealing twins increases as zinc is added to copper[2] indicates that the stacking fault energy of alpha-brass must be lower than that of copper. Hence the width of the stacking faults between two partials in alpha-brass should be larger than that in copper. If stacking fault width is the sole factor controlling rate of climb, the dislocations would be even more reluctant to climb in alpha-brass than in copper. However, the present results showed that the alpha-brass has practically completed its polygonization at about $T/T_{\text{m.p.}}=0{\cdot}77$, compared to $T/T_{\text{m.p.}}=0{\cdot}97$ in copper.[6]

In analyzing the climb of edge dislocations in f.c.c. crystals in terms of atomic movements, Barnes[1] concluded that a dislocation will climb even when it is dissociated, although then it will climb less readily. Since the climb of a dislocation is a process of self-diffusion, the magnitudes of the self-diffusivities of

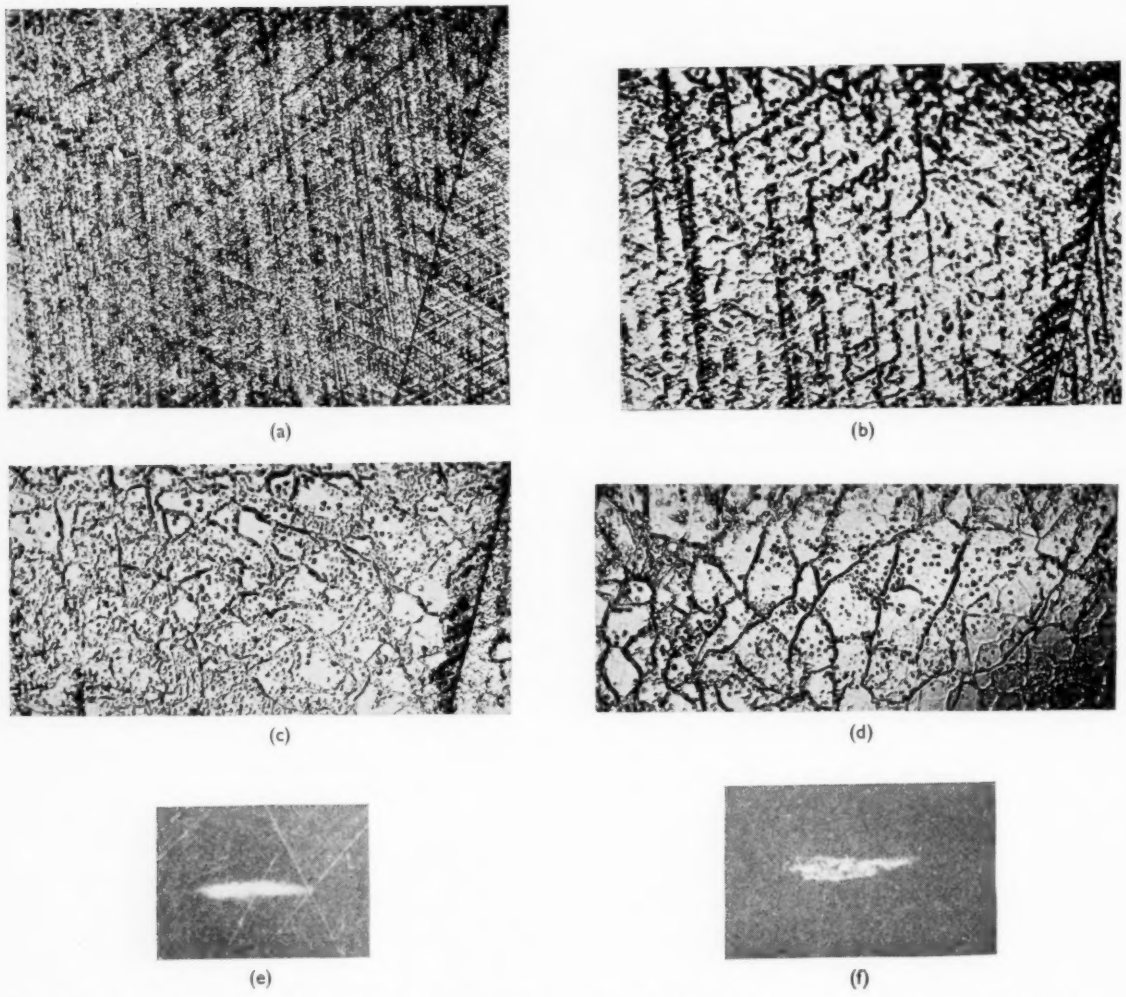


FIG. 4. Bent polycrystalline plate, multislip. Annealed successively at different temperatures. (a) As bent. Electro-polished and then electro-etched. ×250. (b) Same as (a) + 2 hr at 650°C, electro-polished and then electro-etched. ×250. (c) Same as (b) + 2 hr at 750°C, electro-polished and then electro-etched. ×250. (d) Same as (c) except about 3 mm away from the grain boundary. Electro-polished and then electro-etched. ×250. (e) (110) X-ray reflection of (b). ×6.

the elements in a particular crystal must not be overlooked. For two different metals of the same stacking fault energy, that which has the larger self-diffusivity obviously would climb faster. By using the latest available self-diffusion results,[3,4] the ratio of the self-diffusivities of copper (D^*_{Cu}) and of zinc (D^*_{Zn}) in alpha-brass to that of copper (D_{Cu}) in high purity copper at 700°C were calculated. These were $D^*_{Cu}/D_{Cu} = 25$ and $D^*_{Zn}/D_{Cu} = 100$. This large self-diffusivity of alpha-brass is believed to have facilitated the climbing of its dislocations, and hence enabled alpha-brass to polygonize at a relatively low temperature even though it had wide stacking faults between two partials. (Since the twins were formed during the annealing of the cold-worked brass, there is little evidence that its stacking fault energy has been reduced at the annealing temperature.) Thus the dissociated dislocations can climb as predicted by Barnes[1]. However, when $D^*_{Zn}\ (T_1) = D_{Cu}\ (T_2)$, where $T_2 > T_1$, it was found that alpha-brass still polygonized faster than pure copper. This indicates that factors other than the self-diffusion coefficient affect the rate of polygonization.

The favorably oriented single crystals, which were bent beyond the single slip region, polygonized in a manner similar to those bent within the single slip region, i.e. a single set of dislocation walls was formed perpendicular to the major set of slip planes. In fact, those dislocation walls were better defined than those in the single slip crystals. According to

Barnes[1], jogs are required for dissociated dislocations to climb. Dislocations in two minor sets of slip planes supplied many jogs to the dislocations in the major set of slip planes. However, if the dislocation density in all slip planes were about equal and very high, those dislocations would be more or less tangled up. On annealing, rather complicated dislocation networks or subgrain boundaries would be formed. Incidently, these substructures greatly resemble those found in the copper–alpha-brass diffusion zone by Doo and Balluffi[10]. This strongly indicates that multislip occurred in the diffusion zone.

ACKNOWLEDGMENT

The author wishes to thank Drs. R. W. Balluffi and T. A. Read of the Mining and Metallurgy Department, University of Illinois, for their support of this investigation. Appreciation is also expressed to Drs. A. S. Nowick and R. W. Vook for helpful discussion.

REFERENCES

1. R. S. Barnes, *Acta Met.* **2,** 380 (1954).
2. W. R. Hibbard, Jr., J. C. Lise and S. F. Reiter, *Trans. Amer. Inst. Min. (Metall.) Engrs.* **188,** 1020 (1950).
3. J. Hino, C. T. Tomizuka and C. Wert, *Acta Met.* **5,** 41 (1957).
4. D. Lazarus, private communication.
5. P. A. Jacquet, *Acta Met.* **2,** 752 (1954).
6. C. T. Wei, M. Parathasarathi and P. A. Beck, *J. Appl. Phys.* **28,** 874 (1957).
7. F. W. Young and N. Cabrera, *J. Appl. Phys.* **28,** 777 (1957).
8. A. Seeger, *Rept. of the Conf. on Defects in Crystalline Solids, Univ. of Bristol, England*, p. 328. Physical Society, London (1954).
9. F. W. Young, *J. Appl. Phys.* **29,** 60 (1958).
10. V. Y. Doo and R. W. Balluffi, *Acta Met.* **6,** 428 (1958).

VOL.
8
1960

DIFFUSION OF ANTIMONY IN COPPER SINGLE CRYSTALS*

M. C. INMAN† and L. W. BARR†‡

The rate of diffusion of antimony in copper single crystals has been measured over the temperature range 600°–1000°C by means of a sectioning technique employing the Sb^{124} radio-isotope as tracer. The diffusion activation energy and frequency factor were found to be 42000 ± 700 cal $mole^{-1}$ and 0.34 ± 0.12 cm^2 sec^{-1}. This result is compared with existing data on the diffusion of impurity atoms in copper.

DIFFUSION DE L'ANTIMOINE DANS DES MONOCRISTAUX DE CUIVRE

Les auteurs ont mesuré la vitesse de diffusion de l'antimoine dans des monocristaux de cuivre pour une gamme de temperatures comprises entre 600 et 1000°C, en utilisant une technique de coupe qui fait intervenir le radio-isotope Sb^{124} comme traceur. L'énergie d'activation de diffusion et le facteur de fréquence sont de 42000 ± 700 cal môle^{-1} et 0.34 ± 0,12 cm2 sec^{-1}. Ce résultat est comparé avec les données existantes sur la diffusion d'atomes d'impuretés dans le cuivre.

DIE DIFFUSION VON ANTIMON IN KUPFEREINKRISTALLEN

Die Diffusionsgeschwindigkeit von Antimon in Kupfereinkristallen wurde im Temperaturbereich von 600° bis 1000°C mit Hilfe einer Trenntechnik bestimmt, wobei das Isotop Sb^{124} als radioaktives Spurenelement benützt wurde. Die Aktivierungsenergie der Diffusion und der Frequenzfaktor ergaben sich zu 42000 ± 700 cal/Mol und 0,34 ± 0,12 cm^2 sec^{-1}. Dieses Ergebnis wird verglichen mit vorhandenen Daten über die Diffusion von Verunreinigungsatomen in Kupfer.

INTRODUCTION

The diffusion behaviour of impurity elements in a given solvent has been interpreted from two points of view. Lazarus[1] has proposed that the amount by which the diffusion activation energy of an impurity differs from that of the solvent is proportional to the excess valence of the impurity with respect to the solvent. On the other hand, recent systematic investigations by Mercer and Shuttleworth[2] on the diffusion rates of impurity elements in copper have led these authors to believe that atomic size is the most important factor.

The present work on the diffusion of antimony in copper single crystals was undertaken partly in connection with studies of the segregation behaviour of this element in copper, and partly to provide a further test of the relative importance of valence and size in respect to impurity diffusion rates.

EXPERIMENTAL

Single crystals of copper were grown by the Bridgman method from electrolytic stock of 99.99% purity. Cylindrical specimens 1.9 cm diameter and 1.25 cm thick were cut from the ingots with a jeweller's saw. The faces of each specimen were lapped flat on a fine carborundum wheel, and the lapped surfaces then electropolished in an orthophosphoric acid solution to ensure removal of the worked layer. X-ray back reflection photographs of the electropolished surfaces indicated that all worked material had been removed. These surfaces were then carefully cleaned and one surface of each specimen was coated with a layer of radioactive antimony about 200 Å thick by vacuum evaporation of irradiated antimony metal. Spectrographic purity antimony was used, which after irradiation had been aged to allow the induced 2.8 day Sb^{122} activity to decay to negligible proportions with respect to the 60 day Sb^{124} activity.

Diffusion anneals were carried out with pairs of specimens placed, with their active faces in contact, inside copper cylinders, the ends of which were closed with tightly fitting copper plugs. A preliminary trial diffusion anneal at 859°C showed that some antimony activity evaporated from the specimen surfaces to deposit upon the internal surfaces of the copper cylinder during the anneal. Further evidence of this loss of surface activity appeared in the diffusion penetration curves, one of which is shown in Fig. 1. To prevent antimony evaporation, all subsequent diffusion specimens were first coated with a 200 Å layer of radioactive antimony which was then covered with a thinner (100 Å) evaporated layer of inactive spectrographic quality copper. The specimens were then annealed as before, in pairs, with the copper coated active faces in contact. With this procedure no detectable evaporation of the antimony occurred, and the diffusion penetration curves (one of which is reproduced in Fig. 2) were linear to the origin. This

* Received April 21, 1959.
† Metallurgy Division, National Physical Laboratory, Teddington, Middlesex.
‡ Now at National Research Council, Ottawa, Canada.

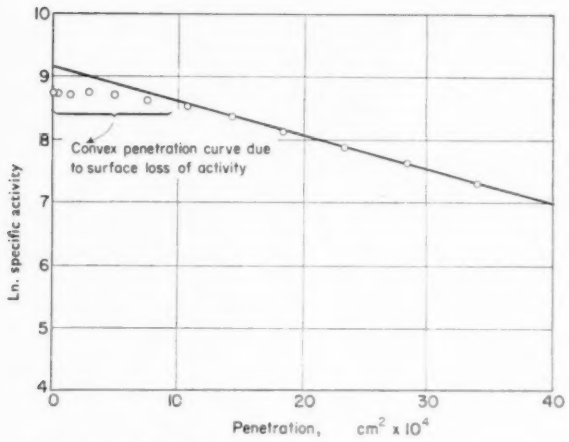


FIG. 1. Diffusion penetration curve at 859°C—convex at the origin owing to surface loss of activity during diffusion anneal.

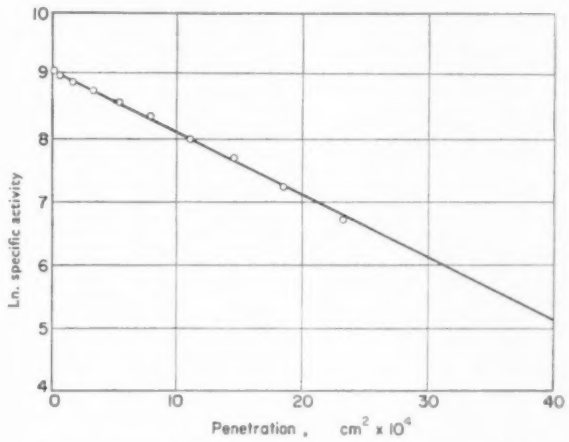


FIG. 2. Typical diffusion penetration curve (806°C) obtained from specimen with evaporated copper layer (see text).

double layer technique should also overcome the difficulty which is sometimes encountered of anomalously high activity at the surface of the diffusion specimens due to oxide formation.

A furnace with a temperature gradient of less than 0.2°C/cm over a central length of 7 cm was used for the diffusion anneals. The furnace temperature was regulated with a precision of better than ± 0.5°C by an electronic control unit operating from a voltage stabilised mains supply. The controlling element was a platinum resistance thermometer which was wound longitudinally inside alumina quills so that it lay symmetrically around the central 30 cm length of the furnace tube. The specimen temperature was measured with a platinum 13% rhodium-platinum thermocouple located in the copper container, at a distance of 2 cm from the active specimen faces.

After annealing, diffusion penetration curves were determined by a sectioning technique. Each specimen was first examined to check mono-crystallinity, and the end remote from the active face was then machined to a diameter of 1.25 cm so that the specimen could be held in a precision collet chuck in the lathe for sectioning. The active face was aligned normal to the lathe axis within limits of ± 0.0005 cm by means of a dial gauge in contact at the periphery of this face. The active end of the specimen was then machined to a diameter of 1.25 cm before sectioning, to eliminate surface effects. Great care was necessary to avoid burring at the periphery of the specimen when making facing cuts, since the copper crystals were very soft. This difficulty was encountered by Makin *et al.*[3] in their measurements of self diffusion in gold, and they describe a special cutting procedure which eliminates the effect. However, in the present case it was possible to avoid burring by the use of very sharp cutting tools of suitable shape which had been previously tested on a dummy copper specimen. The thickness of each section (excepting the first) was determined by advancing the lathe saddle the required distance, the advance being measured with a band transmission dial gauge mounted on the lathe bed with its stylus in contact with an adjustable metal reference surface solidly bolted to the saddle. Earlier calibration tests showed that the dial gauge was not in error by more than ± 0.0005 cm at selected points of its range.

A serious difficulty in the sectioning procedure arose from the fact that the first section (which determines the origin of measurement of penetration distance) had a very variable weight; this being the case however carefully the cutting tool was positioned just to make contact with the specimen surface before the dial gauge was set to its zero reading. Since the weights of all succeeding sections were almost always constant to within 5 per cent, the procedure finally adopted was to compute the thickness of the first section from its weight, taking the mean of the weights of all succeeding sections as the true weight of a section of nominal thickness, usually 0.005 cm. The metal turnings from each section were collected and weighed in individual glass collecting bottles which were attached in turn to a perspex box enclosing specimen and cutting tool.

The contents of each collecting bottle were dissolved in a fixed volume of a nitric/hydrochloric acid mixture, and the activities measured on a scintillation counter fitted with a sodium iodide well crystal. To minimise the effect of small variations in counting geometry, only gamma radiation from the 60 day Sb^{124} activity

VOL. 8 1960

was counted and, since the collecting bottles were of precision manufacture, highly reproducible counts were obtained. All section activities were determined to a statistical accuracy of ± 1 per cent.

RESULTS

For impurity diffusion from a thin plane surface layer into a semi-infinite solid, the concentration c of the impurity at a distance x cm from this surface, after annealing for t sec at a temperature T is given by:

$$c = s(\pi Dt)^{-1/2} \exp(-x^2/4Dt) \quad (1)$$

where s is the initial concentration of impurity atoms at the plane surface and D is the impurity diffusion coefficient in $cm^2\ sec^{-1}$. In the present work, impurity concentration was expressed in terms of activity/unit mass (specific activity). From equation (1), a plot of ln (specific activity) vs. x^2, at each annealing temperature, yields a straight line of slope $-1/4Dt$ from which D can be determined.

The diffusion coefficient of antimony was measured at nine temperatures in the range 600°–1002°C. A typical diffusion penetration curve is shown in Fig. 2. In each case a least squares determination of the line of best fit was made, and a summary of the results is given in Table 1.

The individual values of D in this table were corrected for the time taken by the diffusion specimens to reach the annealing temperature. The true anneal time $t(T_A)$ is given by the expression:

$$t(T_A) = t'(T_A) + \int_0^t \exp(-Q/RT)\,dt / \exp(-Q/RT_A) \quad (2)$$

where $t'(T_A)$ is the time spent at the annealing temperature T_A, and the second term is a correction factor to convert the time t, taken by the specimen to reach this temperature, into an equivalent period at temperature T_A. This integral was graphically evaluated from specimen temperature measurements taken during the heating up period using an approximate value for Q, and the correction factor amounted to $2\frac{1}{2}$ per cent of $t'(T_A)$ at the highest annealing temperature. No correction was necessary for the cooling period after each anneal, since the specimens were rapidly quenched to a temperature at which diffusion was negligible.

The temperature dependence of the diffusion coefficient closely followed the usual Arrhenius relation:

$$D = D_0 \exp(-Q/RT) \quad (3)$$

as shown by Fig. 3, where the logarithm of the mean of each pair of values for D at a given temperature is plotted against the reciprocal temperature. The frequency factor D_0 and the activation energy Q were found from the intercept and slope of the least squares line of best fit, yielding the final result:

$$D_0 = 0.34 \pm 0.12\ cm^2\ sec^{-1}$$
$$Q = 42{,}000 \pm 700\ cal\ mole^{-1}$$

where the quoted errors correspond to the 95 per cent reliability limits. An estimate of possible systematic errors in specimen temperature and penetration depth measurements was made from the known thermocouple and dial gauge calibrations, but the resultant shift in the values of D_0 and Q was well within the given limits of error which are therefore believed to be realistic.

Table 1. Diffusion of antimony in copper

Temp. (°C)	Diffusion Coefficient ($cm^2\ sec^{-1}$)
600	0.975×10^{-11} 0.929×10^{-11}
653	4.45×10^{-11} 4.39×10^{-11}
706	1.43×10^{-10} 1.35×10^{-10}
758	**5.10×10^{-10} 4.33×10^{-10}
806	0.944×10^{-9} **1.19×10^{-9}
859	2.58×10^{-9} 2.63×10^{-9}
898	4.66×10^{-9} 4.63×10^{-9}
955	1.12×10^{-8} 1.08×10^{-8}
1002	2.12×10^{-8} 2.24×10^{-8}

** These results are believed to be in error owing to the occurrence of excessively thick first sections during the activity-penetration curve determinations.

DISCUSSION

The rates of diffusion of a number of impurity elements in copper have now been measured at low levels of concentration using the radio-tracer method,

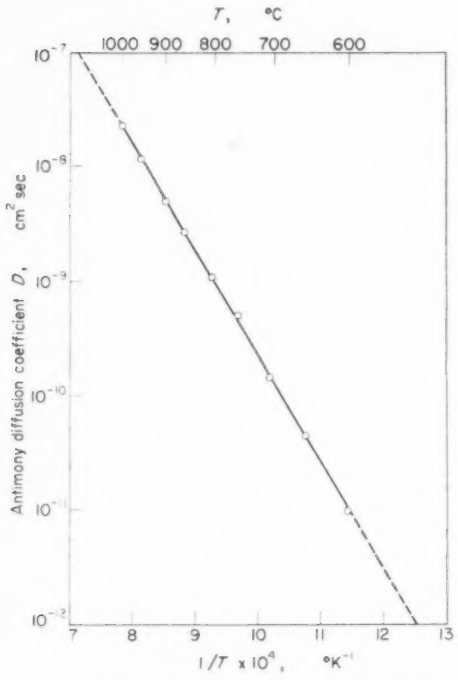


FIG. 3. Diffusion of antimony in copper.

and a summary of the available data for diffusion in copper is presented in Table 2. Since all these measurements were made with copper single crystals, interference by grain boundary diffusion processes would not be expected. However, in the case of iron and cobalt, Makliet[4] found a definite upward curvature in the plot of ln D vs. $1/T$, the measured low temperature values of D being consistently above the extrapolation of the high temperature results by as much as 30 per cent. After a thorough consideration of possible reasons for this effect, Makliet tentatively concluded that it was a consequence of the randomly distributed dislocations ordinarily present in a metal which may enhance the volume diffusion process without any change in the Gaussian nature of the experimental penetration curves, in the manner proposed by Hart[5]. Grain boundary diffusion was discounted because of the excellent linearity of the plot of ln (specific activity) vs. square of penetration depth. A similar linearity was observed in the present work on antimony diffusion, and in addition, ln D was also a linear function of the reciprocal temperature down to the lowest temperature of observation (600°C).

For a copper solvent, the theory of Lazarus[1] predicts that for a fixed screening radius of 0.55 Å, the activation energy difference between impurity diffusion and solvent self diffusion will be given by:

$$Q_{\text{solvent}} - Q_{\text{impurity}} = 3.36\,Z \qquad (4)$$

where Z is the valence difference between impurity and solvent atoms. A refinement of Lazarus' treatment was made by Alfred and March[6] and in Table 2 the experimental ($Q_{\text{solvent}} - Q_{\text{impurity}}$) is compared with the predictions of Lazarus, and Alfred and March, using values of Z based upon the nominal "periodic table" valencies of the impurity elements concerned. It is apparent that neither the Lazarus nor the Alfred and March treatments give a quantitative prediction of ($Q_{\text{solvent}} - Q_{\text{impurity}}$), although there is qualitative agreement between experiment and theory on the point that impurity elements with positive Z will diffuse faster, and those with negative Z slower, than the solvent copper. It will be noted that for the transition elements iron, cobalt and

TABLE 2. Impurity atom diffusion in copper

Impurity Element	Reference	D_0 (cm² sec⁻¹)	Q (kcal mole⁻¹)	Assigned Excess Valence Z	($Q_{\text{solvent}} - Q_{\text{impurity}}$) kcal mole⁻¹			Goldschmidt Diameter (Å)
					Experimental	Lazarus	Alfred and March	
Nickel	Makliet[4]	2.7	56.5	−1	−9.4	−3.4	−4.7	2.49
Cobalt	Sakamoto[7]	5.7	55.2	−2	−8.1	−6.7	−12.4	2.50
Cobalt	Makliet[4]	1.9	54.1		−7.0			
Iron	Makliet[4]	1.4	51.8	−3	−4.7	−10.1	−23.6	2.52
Copper	Kuper *et al.*[8]	0.47	47.1	0	—	—	—	2.55
Zinc	Hino *et al.*[9]	0.34	45.6	+1	+1.5	+3.4	+2.6	2.75
Cadmium	Hirone *et al.*[10]	0.93	45.7	+1	+1.4	+3.4	+2.6	3.04
Antimony	Present work	0.34	42.0	+4	+5.1	+13.4	+7.4	3.23

VOL. 8 1960

nickel, the trend of activation energies is in the reverse order to that predicted by theory, which may be due to the very uncertain value of Z assigned to these elements.

With regard to the suggestion of Mercer and Shuttleworth[2] that atomic size is the most important factor, it will be seen from Table 2 that the Goldschmidt diameters correlate qualitatively with the observed diffusion activation energies, in so far as the activation energy for diffusion decreases with increase of atomic diameter. The more rapid diffusion of the larger impurity atoms would appear to imply a lower vacancy formation energy next to these atoms, as a consequence of the relief of lattice strain around a large foreign atom.

However, it is clear that attempts to disentangle the relative importance of size and valence, in cases where both are variable, meet with only partial success, and the most profitable next step would appear to lie in a more careful choice of impurity elements. In this connection, the rare earth series of metals offers interesting possibilities, for here one might hope that only size effects will be significant, the valence factor being relatively constant.

ACKNOWLEDGMENTS

The work described above has been carried out as part of the General Research Programme of the National Physical Laboratory, and this paper is published by permission of the Director of the Laboratory. One of the authors (L. W. B.) is indebted to the Department of Scientific and Industrial Research for a maintenance grant.

The authors' thanks are also due to Dr. L. M. T. Hopkin for a supply of copper single crystals.

REFERENCES

1. D. Lazarus, *Phys. Rev.* **93,** 973 (1954).
2. L. Mercer and R. Shuttlewoth. To be published.
3. S. M. Makin, A. H. Rowe, and A. D. LeClaire, *Proc. Phys. Soc.* **70,** 545 (1957).
4. C. A. Makliet, *Phys. Rev.* **109,** 1964 (1958).
5. E. W. Hart, *Acta Met.* **5,** 597 (1957).
6. L. C. R. Alfred and N. H. March, *Phys. Rev.* **103,** 877 (1956).
7. M. Sakamoto, *J. Phys. Soc. Japan* **13,** 845 (1958).
8. A. Kuper, H. Letaw, L. Slifkin, E. Sonder, and C. T. Tomizuka, *Phys. Rev.* **96,** 1224 (1954).
9. J. Hino, C. T. Tomizuka, and C. Wert, *Acta Met.* **5,** 41 (1954).
10. T. Hirone, N. Kunitoni, M. Sakamoto, and H. Yamaki, *J. Phys. Soc. Japan* **13,** 838 (1958).

OXIDE NUCLEI AND DISLOCATIONS*

F. W. YOUNG, Jr.†

Crystals of 99.999 per cent copper and of copper doped with various impurities were bent so as to introduce regular arrays of dislocations and were oxidized by three techniques in order to determine if there was a correspondence between dislocations and oxide nuclei. For crystals doped with Te or with Sn, and for crystals of OFHC copper it was found that nuclei were formed at dislocations. For 99.999 per cent copper and for copper doped with Si there was no correlation between oxide nuclei and dislocations. Also, oxide nuclei were formed on crystals of all purities which were not related to dislocations.

GERMES D'OXYDES ET DISLOCATIONS

L'auteur utilise des cristaux de cuivre à 99,999% dopés avec différentes impuretés. Ces cristaux ont été courbés de façon à introduire des réseaux réguliers de dislocations et oxydés par trois techniques différentes de manière à déterminer s'il existait une correspondance entre les dislocations et les germes d'oxydes.

Pour les cristaux dopés avec Te ou Sn et pour des cristaux de cuivre OFHC, l'auteur trouve que les germes se forment sur les dislocations. Pour le cuivre à 99,999% et pour le cuivre dopé avec Si, il n'existe pas de corrélation entre les germes d'oxydes et les dislocations.

En outre, des germes d'oxydes se sont formés sur des cristaux de toutes puretés sans être en relation avec des dislocations.

OXYDKERNE UND VERSETZUNGEN

Kristalle aus 99,999% Kupfer und aus Kupfer mit verschiedenen Verunreinigungen wurden gebogen, üm regelmassige Versetzungsanordnungen zu erzeugen. Sie wurden mittels dreier verschiedener Techniken oxydiert, und es wurde untersucht, ob eine Beziehung zwischen den Versetzungen und den Oxydkernen bestand. Bei Kristallen, die mit Te oder Sn dotiert waren, und bei Kristallen aus OFHC-Kupfer bildeten sich Kerne an Versetzungen. Bei Kristallen aus 99,999% Kupfer und bei Si-dotierten liess sich kein Zusammenhang zwischen Oxydkernen und Versetzungen feststellen. Bei Kristallen aller Reinheitsgrade wurden darüber hinaus Oxydkerne ohne Zusammenhang mit Versetzungen gebildet.

VOL. 8 1960

Since the discovery that in thin oxide films on metals there are numerous very small areas in which the oxide is thicker than the base film,[1] there has been speculation as to the cause of this phenomenon. A correspondence between these areas, called oxide nuclei, and dislocations, has been suggested by Cabrera[2], who has presented a theoretical treatment of the effect of the strain energy at dislocations on the growth of oxide nuclei. Also, it is well known that the impurities in crystals tend to collect about the dislocations "Cottrell atmosphere". These impurities might change the chemical potential of the dislocations and thus affect the ease of evaporating a metal atom into the oxide at points where the dislocation meets the surface. Or, the impurity atoms may increase the rate of oxidation with the dislocations acting as a line source of impurity atoms. No theoretical discussion of the effect of dislocations with a "Cottrell atmosphere" on the oxidation of metals has been published.

The author has shown that regular arrays of dislocations can be introduced into copper crystals by appropriate bending and annealing.[3] This paper reports the oxidation of such crystals and demonstrates a correspondence between oxide nuclei and dislocations.

* Received May 15, 1959.

† Solid State Division, Oak Ridge National Laboratory, Oak Ridge, Tennessee.

EXPERIMENTAL

Copper

One group of copper crystals with the orientation shown in Fig. 1 was grown in vacuum from the melt by seeding. These crystals were either $1 \times 0.2 \times 8$ or $1 \times 0.4 \times 8$ cm as grown; using a jeweler's saw, two samples 3.5 cm long were carefully sawed from each crystal for experimentation. Some crystals were grown from 99.999 per cent copper; others were doped with 0.05 to 0.01 atomic per cent tin or silicon during growth. Some of the 99.999 per cent crystals were doped with Te (~0.01) at. %) by heating the crystal at 1000°C in approximately half an atmosphere of Te

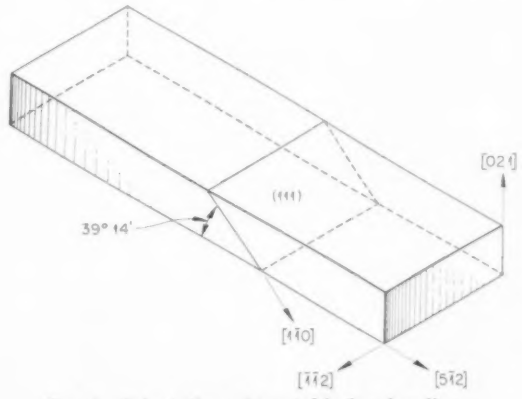


FIG. 1. Orientation of crystal before bending.

for 24 hr. Another group of crystals were grown as cylinders, 1 cm in diameter with a hemisphere on one end, from OFHC and 99.999 per cent copper. A few of these crystals had a [$\bar{1}\bar{1}2$] normal to the cylinder axis.

In crystals of copper doped with Te and in OFHC crystals the dislocations can be revealed as electrolytic etch pits. Well-defined arrays of dislocations were produced in these crystals by bending around [$\bar{1}\bar{1}2$] and annealing, as previously described.[3,4] The dislocations which were produced by this bending and which ended in the ($\bar{1}\bar{1}2$) face were edge in character; the ones ending in (021) were principally screw in character. The distance between dislocations could be controlled by the radius of the bend and by the temperature of annealing. After a 500°C anneal of a crystal bent to a 3-cm radius the dislocations which ended in the ($\bar{1}\bar{1}2$) face could be detected as electrolytic etch pits which were in rows along [$1\bar{1}0$] and approximately 1 μ apart in the rows; after annealing at 1000°C, where polygonization occurred, the etch pits were in rows normal to [$1\bar{1}0$] and approximately 0.1 μ apart in the rows.[3,4] In copper doped with Sn or Si it was not possible to detect the dislocations as etch pits, and in 99.999 per cent copper, the dislocations could be detected as chemical etch pits only on (111) faces.[5] However, it was shown by X-ray diffraction that such crystals can polygonize.[4] A polygonized crystal of pure copper or one containing tin or silicon should have dislocation arrays similar to those exhibited by copper doped with Te.

In most experiments a crystal was bent, annealed at the desired temperature in vacuum and then annealed for 12 hr at 500°C in hydrogen. In cases where it was desired to investigate the effect of hydrogen dissolved in the crystal on the subsequent oxidation, the crystal was not given the final anneal in hydrogen. For the doped crystals it was always necessary to anneal at least 12 hr at 500°C to move the impurity atoms to the new dislocations formed by bending.

The crystals were oxidized using three different techniques.

I. The crystal was electropolished, washed, dried and annealed in hydrogen for one hr at 500°C.[6] The crystal was then cooled to the temperature of oxidation, the hydrogen evacuated with a mechanical pump, and one atmosphere of purified oxygen admitted.

II. The crystal was washed, polished and dried as above, and suspended on a quartz hook in a Pyrex bulb attached to a high vacuum system. The crystal was annealed in hydrogen at 500°C for one hr and the system evacuated and baked out. Then the specimen was heated by induction to 1000°C in a vacuum of 5×10^{-9} mm of Hg, cooled in this vacuum to the temperature of oxidation and oxidized in one atmosphere of purified oxygen. Since copper was evaporated by this treatment and since the crystal was cooled in high vacuum, the surface should be free of contaminants other than those in the crystal itself. However, the surface was faceted after this treatment, the facets being more pronounced on the less pure copper than on the 99.999 per cent copper.

III. This method was similar to that described by Gronlund[7]. The crystal was electropolished, washed and dried, and suspended in a Pyrex vessel attached to a high vacuum system. After annealing in hydrogen at 500°C the crystal was cooled to the temperature of oxidation, the hydrogen evacuated to a pressure of 1×10^{-7} mm of Hg and the crystal oxidized in 1 to 10 microns of pure oxygen.

Nickel

A few experiments were performed on nickel. A crystal, grown from "Nivac" nickel (99.95 per cent), was machined into a cylinder with cylinder axis parallel to [021]. This crystal was bent about the [$\bar{1}\bar{1}2$] and heated to 1300°C in a vacuum of 5×10^{-8} mm of Hg for 2 hr. The crystal was oxidized after a high temperature–high vacuum anneal according to the method described previously.[8] No study was made of the etching of dislocations in nickel. It was assumed for the purpose of this paper that the bent nickel crystal would have dislocations arranged in rows in a manner similar to that determined for copper.

RESULTS

Oxide nuclei at dislocations

A copper crystal doped with Te was bent (approximately 3 cm radius) and annealed first at 1000°C in vacuum for 1 hr, and then at 500°C in hydrogen for 12 hr. The crystal was oxidized at 300°C according to method (I) until the first order purple color appeared on the ($\bar{1}\bar{1}2$) face. A photomicrograph of the ($\bar{1}\bar{1}2$) is shown in Fig. 2. The oxide nuclei are visible as blue dots in a red background and lie along the dislocation boundaries.

Another crystal doped with Te was bent (approximately 3 cm radius) and annealed at 1000°C in vacuum, followed by a 12 hr anneal in hydrogen at 500°C. This crystal was about 1 mm thick after this treatment. It was then oxidized at 325°C according to method (I) to the first order purple color on ($\bar{1}\bar{1}2$). The blue oxide-nuclei along the polygon boundaries are shown in Fig. 3. The crystal was then electropolished and electroetched. A photomicrograph of the

VOL.
8
1960

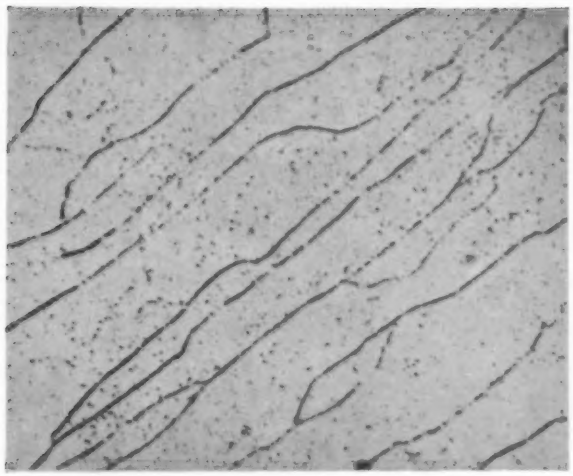


FIG. 2. Oxide nuclei at polygon boundaries. ×500.

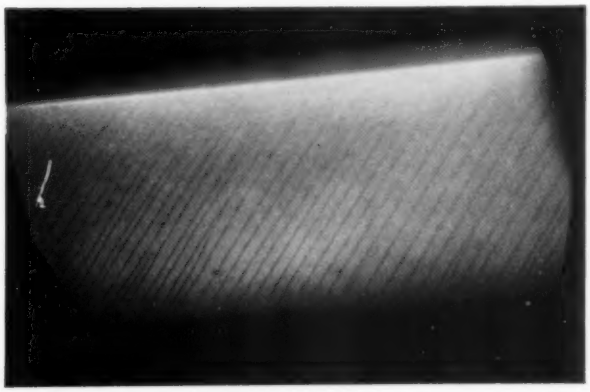
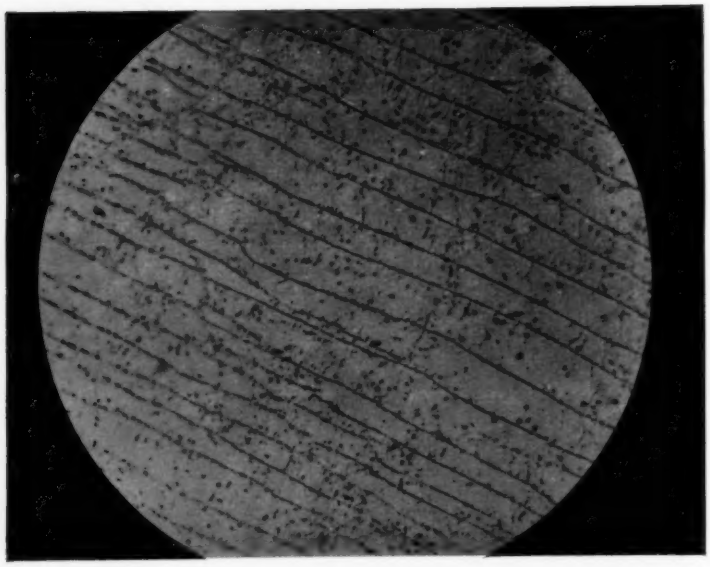
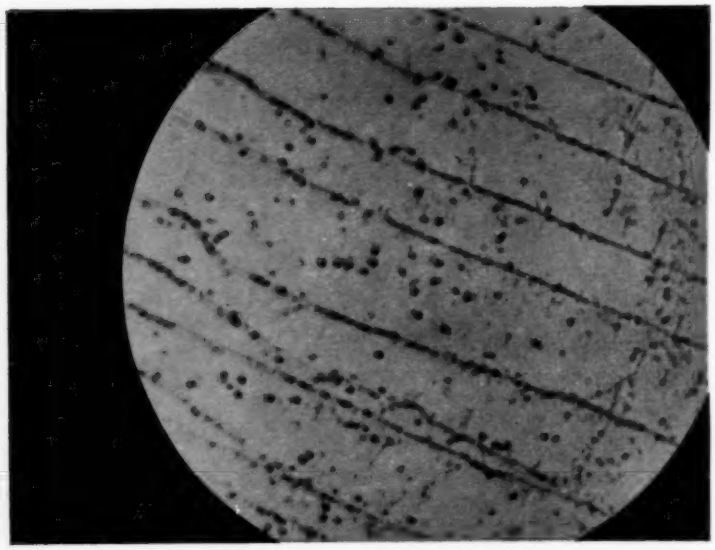


FIG. 3. Oxide nuclei at polygon boundaries ×100.



(a) $\times 250$.



(b) $\times 500$.

FIG. 5. Oxide nuclei at polygon boundaries.

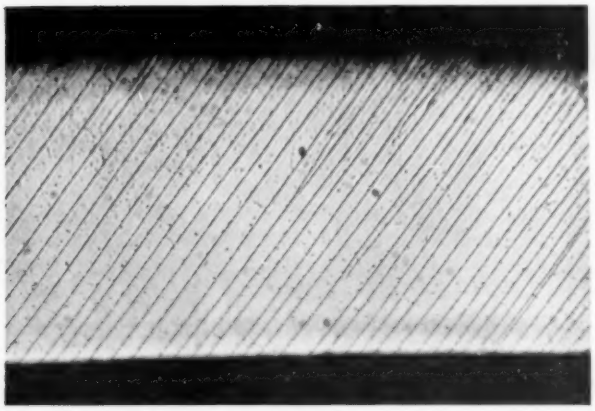


FIG. 4. Electrolytic etch pits—same area as Fig. 3. ×100.

etch pits on the same area as Fig. 3 is shown in Fig. 4. When allowance is made for the fact that $\sim 10\mu$ of copper was removed by the polishing, the photomicrographs exhibit an exact correspondence between oxide nuclei and electrolytic pits.

A third crystal doped with Te was given the same treatment as the first two, and then oxidized according to method (I) at 275°C to the first order purple on $(\bar{1}\bar{1}2)$. Photomicrographs of the $(\bar{1}\bar{1}2)$ are shown in Fig. 5. After electropolishing and electroetching, the the same area was photographed and is shown in Fig. 6.

A crystal doped with Te was bent and annealed at 500°C for 12 hr in hydrogen, then oxidized by method (I) at 300°C until the first order purple appeared on the $(\bar{1}\bar{1}2)$. On examination of the $(\bar{1}\bar{1}2)$ with the optical microscope, oxide nuclei corresponding to dislocations were seen as blue spots on the red background. In this case, the dislocations lay principally in rows along $[1\bar{1}0]$ and were approximately 1μ apart (see Fig. 3 of ref. 3). Thus, the oxide nuclei were separate entities. The fact that the oxide nuclei were blue and the background film was red implies that the nuclei were approximately 200 Å thicker than the background film.

An electron micrograph of a pre-shadowed carbon replica of this oxide film is shown in Fig. 7. Here the oxide nuclei were clearly resolved as projections above the background film, and the height of the projections was measured from the shadow length as approximately 300 Å. This was in good agreement with the height of the nuclei as estimated from the interference colors.

The temperature or time of oxidation was not critical in obtaining oxide nuclei at dislocations, since nuclei were observed on crystals oxidized at temperatures from 200 to 325°C. Maximum visual contrast between nuclei and background film was obtained with the film thickness described above. However, for both thinner (<150 Å) and thicker (>1000 Å) films the nuclei could be seen as dots of a different color from the background film on the $(\bar{1}\bar{1}2)$.

Oxide nuclei corresponding to screw dislocations were observed on the (021). The rate of oxidation of (021) is much greater than $(\bar{1}\bar{1}2)$.[6] Thus, in the time that a first order purple film formed on $(\bar{1}\bar{1}2)$, a film about 4000 Å thick formed on (021). This thicker film exhibited interference colors, and the nuclei on (021) also appeared under the optical microscope as colored dots. It was not possible to determine the relative thickness of the oxide nuclei and the background film.

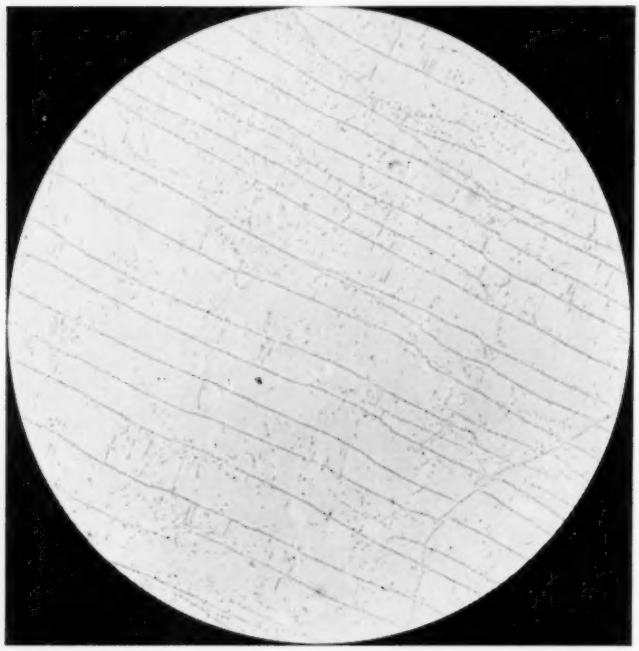
It was a necessary condition for the formation of oxide nuclei at dislocations in copper doped with Te that the crystal be annealed in hydrogen prior to oxidation. When crystals were oxidized which had not been annealed in hydrogen, no nuclei were observed at the dislocations. Also, it was found that the size of the nuclei increased monotonically with the time of annealing in hydrogen for times from one to eight hours.

In addition to the clearly resolved oxide nuclei described above, there was observed both with the optical and electron microscope another "set of nuclei" (henceforth called nuclei *B*) in the background film. They were smaller and more numerous than the nuclei related to dislocations (henceforth called nuclei *A*). As seen with the optical microscope the nuclei *B* were barely resolvable purple spots in the red background film, implying that nuclei *B* were approximately 100 Å thicker than the base film and that the spacing was $\sim 0.1\mu$. From the electron micrograph, Fig. 7, the height was measured as approximately 100 Å and the spacing was 0.2μ. Again, the optical and electron microscope observations were in good agreement.

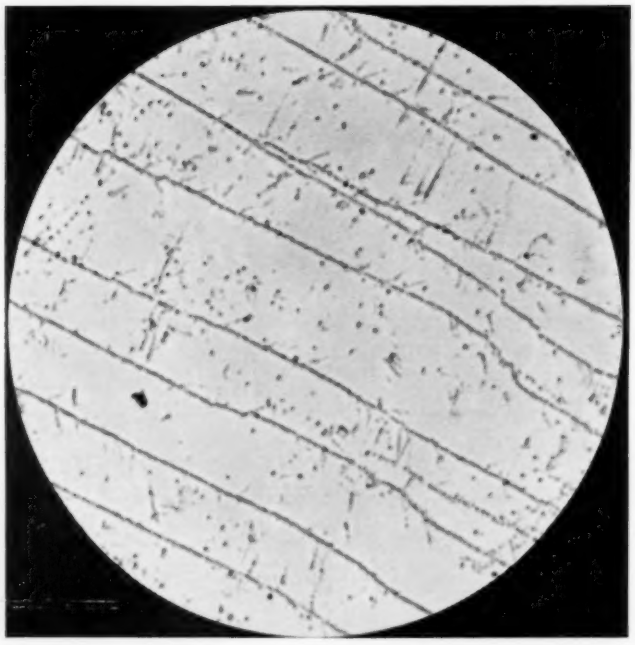
A polygonized crystal of copper doped with Te was oxidized according to method (II) at 200°C for 30 min. Oxide nuclei were seen along polygon boundaries on both $(\bar{1}\bar{1}2)$ and (021). Since the crystal was faceted by the preoxidation treatment, the oxide nuclei were not as distinct as those shown in Figs. 3–6. Small nuclei, which were not related to the dislocations, were also seen with the aid of the optical microscope. These small nuclei were somewhat larger than the ones denoted above as nuclei *B*, but for simplicity they will also be called nuclei *B*.

The 99.999 per cent copper crystals and the crystals with the various impurities were tested for nuclei formation in a similar way to that described

VOL. 8 1960



(a)



(b)

FIG. 6. Electrolytic etch pits in same area as Fig. 5 (a) ×250; (b) ×500.

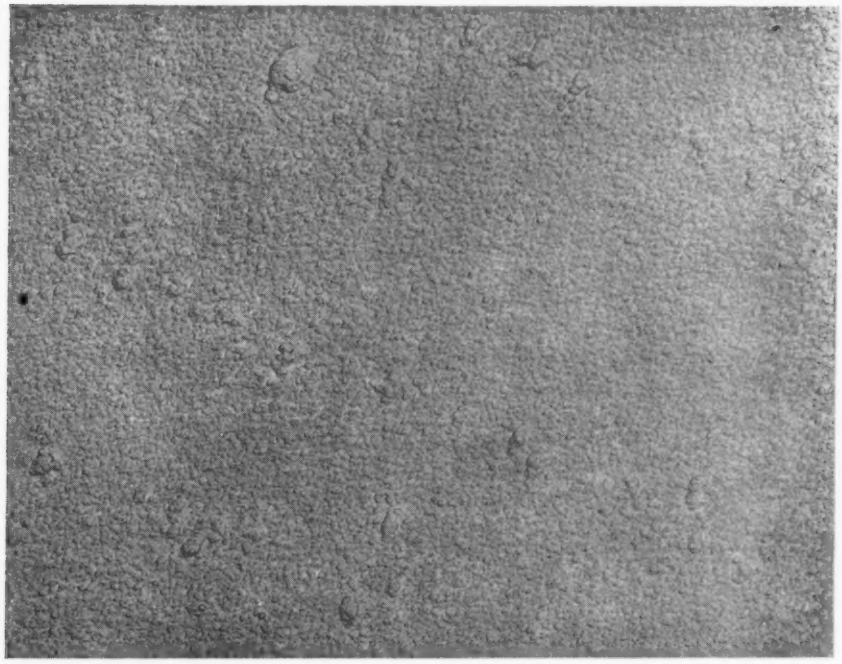


FIG. 7. Electron micrograph of pre-shadowed carbon replica of oxide film ×5500.

VOL. 8 1960

for copper doped with Te. The results are summarized in Table 1. The notation in that table that an anneal in hydrogen was necessary applies to annealing in hydrogen prior to oxidation as described for copper doped with Te.

Oxides nuclei not related to dislocations

Clearly, the nuclei *B* described above were not related to dislocations. Also, oxide nuclei not related to dislocations were formed on copper oxidized according to method (III). Benard and co-workers reported that the number and size of the nuclei formed during oxidation according to method (III) were a function of the temperature and the oxygen pressure. Both Gronlund[7] and Menzel[9] showed that the number and the arrangement of the nuclei were related to the orientation of the copper crystal, and that under certain conditions of oxidation the nuclei were oxide crystals which lay in rings around the (311) pole (see Fig. 7 of ref. 7 and Figs. 1–5 of ref. 9).

Crystals of OFHC and 99.999 per cent copper which had been bent and polygonized were oxidized in the present study according to method (III). The results of these experiments were in agreement with the findings of Gronlund and Menzel, and there was no evidence that these oxide nuclei were related to the dislocations in the copper crystals. When OFHC

TABLE 1.

	Copper +0.01% Te	Copper +0.05% Sn	Copper +0.1% Si	99.999 per cent Copper	OFHC Copper
Oxidized by Method (I)	Nuclei at dislocations anneal in H_2 necessary Nuclei *B*	Nuclei *B*	Nuclei *B*	Nuclei *B*	Nuclei at dislocations anneal in H_2 necessary Nuclei *B*
Oxidized by Method (II)	Nuclei at dislocations Nuclei *B*	Nuclei at dislocations Nuclei *B*	Nuclei *B*	Nuclei *B*	Nuclei at dislocations Nuclei *B*

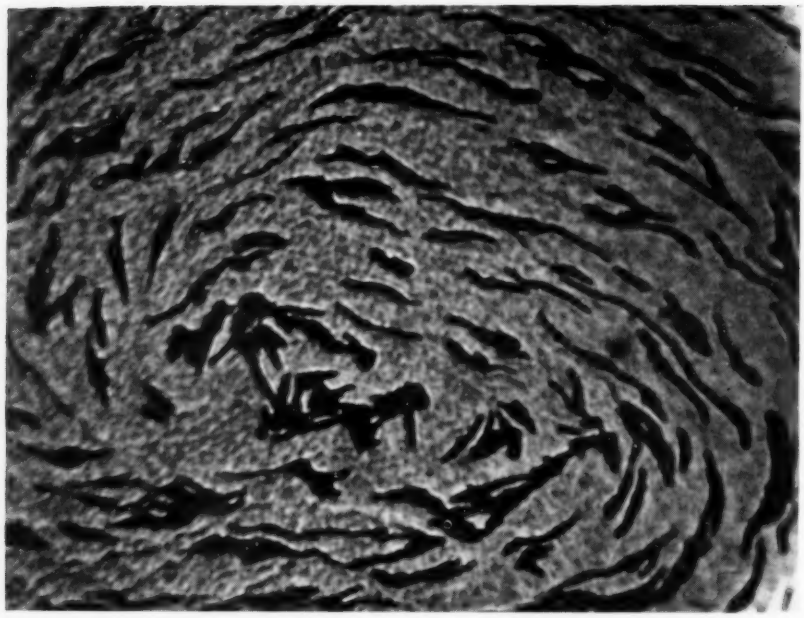


FIG. 8. Oxide nuclei around (111) pole of nickel crystal ×500.

crystal spheres were oxidized at 475°C in 10μ of oxygen for 1 hr, oxide nuclei were formed which lay in rings around the (311) pole.

Experiments with nickel

The formation of oxide nuclei on nickel was reported earlier by Lawless *et al.*[8], who showed that the number of nuclei was related to the orientation of the nickel. The nickel crystal described above was oxidized 30 min at 500°C in one atm of oxygen. On examination with the optical microscope, lines of oxide were seen which probably corresponded to polygon boundaries. These lines of oxide corresponded to lines of etch pits which were formed on etching the nickel in $FeCl_3$–HCl–EtOH. However, it has not been demonstrated that such etch pits correspond to dislocations.

A nickel crystal sphere was oxidized in 10μ of oxygen for 30 min at 500°C. Oxide nuclei were formed and the number of nuclei was a function of the crystal orientation. These nuclei lay in circles around the (111) and (311) poles, as shown in Fig. 8.

DISCUSSION

Oxide nuclei *A* were formed at dislocations only by certain methods of oxidation and only if certain impurities were in the copper. There was a one-to-one correlation of oxide nuclei to dislocations in copper doped with Te. In OFHC copper and in copper doped with Sn, there was clearly a correlation between oxide nuclei and dislocations. For 99.999 per cent copper and for copper doped with Si there was no evidence that oxide nuclei were formed at dislocations. It was concluded that it was necessary to have certain impurities collected about the dislocations in order for oxide nuclei to be formed there. Probably the dislocations were acting as line sources of impurity atoms, and these impurity atoms were increasing the rate of oxidation in the immediate vicinity of the dislocation. Since nuclei were not observed at dislocations in copper doped with Si, it was concluded that not all impurities in copper promote the formation of oxide nuclei at dislocations.

The mechanism by which Te increases the rate of oxidation of copper is not known. Further, there is no explanation, at present, of the role which hydrogen, dissolved in the crystal, plays in this enhancement of the oxidation. It is known that a trace of hydrogen sulfide in the oxidizing atmosphere greatly increases the rate of oxidation of copper. It has been suggested that the sulfur ions are incorporated into the oxide lattice and make it more pervious to diffusing ions.[10] Te may act in a similar way. Sulfur and Te are normally found as impurities in OFHC copper. This may account for the formation of oxide nuclei at dislocations in this material. No explanation can be given at present for the enhancement of oxidation at dislocations in copper doped with tin.

Oxide nuclei which were not related to dislocations were found on copper by the three methods of oxidation employed. The appearance and number of these nuclei varied with the method of oxidation so that it is probable that different factors influenced

their nucleation and growth. The occurrence of nuclei B in all the copper crystals when oxidized by method (I), even the copper-doped-with-Te crystals which simultaneously had nuclei at the dislocations, clearly demonstrated that dislocations in the metal were not necessary for the formation of oxide nuclei. These facts imply that for such nuclei the nucleation phenomenon occurred in the oxide film during the growth process. Cathcart[11], by examination with the electron microscope of oxide films stripped from 99.999 per cent copper which was oxidized according to method (I), has obtained evidence that oxide nuclei are nucleated in the oxide film and then grow in size. Therefore, it was concluded that for pure copper the dislocations in the metal did not play a role in the formation of the oxide nuclei and probably did not play a significant role in the oxidation process.

Cabrera[2] suggested the possibility that the points where dislocations meet the surface would have a chemical potential sufficiently different from the remainder of the surface to cause enhanced oxidation at these points. From the results presented here, it appears that the difference in potential at clean dislocations is not sufficient to promote the formation of oxide nuclei. If the chemical potential at dislocations with "Cottrell atmospheres" is considerably different from that at clean dislocations and/or the remainder of the surface, the formation of nuclei at such dislocations might be explained in a manner similar to that of Cabrera. Another explanation is that the impurity atoms, incorporated into the oxide, alter the rate of oxidation, and the dislocations simply act as a line source of the impurity atoms. It is not clear from these experiments which of these explanations would be more satisfactory.

It should be emphasized that the impurity content of the crystals used in this study was very low. Oxygen free-high conductivity copper has often been used in investigations of the oxidation rate of copper, it being among the purest copper available until recently. The crystals of copper doped with Te were 99.99 per cent copper, which has generally been considered high purity by investigators of the rate of oxidation of metals. Thus, the fact that the rate of oxidation can be greatly increased at points where dislocations meet the surface in slightly impure copper obviously has practical significance.

Although the experimental results on nickel were less complete, they were consistent with those on copper, and therefore it seems reasonable to draw the same conclusions. It was possible to obtain oxide nuclei which apparently corresponded to dislocations, and nuclei were also obtained, under other conditions of oxidation, which clearly did not correspond to dislocations. All these experiments were on nickel of intermediate purity. Since high purity nickel is not at present available, it has not been possible to determine if oxide nuclei would be formed at dislocations on such material.

SUMMARY

(1) There was a correlation between oxide nuclei and dislocations in copper doped with Te or Sn and in OFHC copper. Oxide nuclei were not formed at dislocations in 99.999 per cent copper or in copper doped with Si.

(2) In order that nuclei be formed at dislocations in the impure copper it was necessary that hydrogen be dissolved in the copper. No explanation of this result is known.

(3) Dislocations in the metal were not necessary for the formation of oxide nuclei.

(4) Dislocations apparently played no role in the oxidation of pure copper.

ACKNOWLEDGMENT

It is a pleasure to acknowledge the help of R. M. Wallace who made the color photomicrographs and of L. H. Jenkins in the preparation of this paper.

REFERENCES

1. J. Bardolle and J. Benard, *Rev. Metall.* **49,** 613 (1952). E. A. Gulbransen and W. R. McMillan, *J. Appl. Phys.* **24,** 1416 (1953). W. W. Harris, F. L. Ball and A. T. Gwathmey, *Acta Met.* **5,** 574 (1957).
2. N. Cabrera, *Semiconductor Surface Physics*, p. 327. University of Pennsylvania Press, Pennsylvania (1956); *J. Chim. Phys.* **53,** 675 (1956).
3. F. W. Young, Jr., *J. Appl. Phys.* **29,** 760 (1958).
4. F. W. Young, Jr., and N. Cabrera, *J. Appl. Phys.* **28,** 777 (1957).
5. L. C. Lovell and J. H. Wernick, to be published.
6. F. W. Young, Jr., J. V. Cathcart and A. T. Gwathmey, *Acta Met.* **4,** 145 (1956).
7. F. Gronlund, *J. Chim. Phys.* **53,** 660 (1956).
8. K. R. Lawless, F. W. Young, Jr., and A. T. Gwathmey, *J. Chim. Phys.* **53,** 667 (1956).
9. E. Menzel and W. Stossel, *Naturwissenschaften* **41,** 302 (1954). E. Menzel, W. Stossel, and C. Menzel-Kopp, *Z. Naturf.* **12a,** 404 (1957).
10. U. R. Evans, *Metallic Corrosion Passivity and Protections*, p. 151. Edward, London (1948).
11. J. V. Cathcart, private communication.

VOL. 8 1960

The formation of (110)[001] recrystallization texture in a cold-rolled and annealed (110) [001] crystal of silicon-iron*

It has been reported[1,2] that the deformation texture of a 70 per cent cold-rolled Si–Fe crystal with an initial orientation of (110)[001] consists of mainly (111)[$\bar{1}$12] and (111)[11$\bar{2}$], plus a weak component of (100)[011]. In the pole figure there are also regions of very low intensity which can be described as a very weak component of the (110)[001] orientation. This cold-rolled crystal recrystallizes into a single (110)[001] texture upon annealing at temperatures around 1000°C. Thus, the orientation of the recrystallization texture is the same as that of the original crystal. Walter and Hibbard[2] have interpreted this and similar situations in other crystals in the following manner: The very weak component in the deformation texture, which has the orientation of the original crystal, may have served to nucleate the recrystallization texture.

During a study of the development of the rolling and annealing textures in a series of 3% Si–Fe single crystals, evidence was obtained to indicate that Walter and Hibbard's interpretation is unlikely. The deformation texture of a 70 per cent cold-rolled crystal of initial orientation near (110)[001] is shown in Fig. 1. This specimen was completely recrystallized upon annealing at 800°C for 15 min, and the resulting texture consisted of a single (110)[001] orientation, as shown in Fig. 2. The change in orientation can thus be described as a [110] rotation of 35° from both of the (111)[112] type main deformation texture components, as indicated by the arrows. These results are in good agreement with those reported in the literature.[1,2] In another experiment, an identical specimen was annealed at lower temperatures in order to study the initial stages of recrystallization. After a 24 hr anneal at 450°C no recrystallization could be observed microscopically. The specimen was then reannealed for 2 hr at 550°C. At this stage a slight reorientation was noted in the pole figure (Fig. 3), and partial recrystallization was observed microscopically (Fig. 4). The reorientation may be described as a shift in the orientation spread, in such a way that it no longer includes the (110)[001] orientation. Presumably then regions of the deformed crystal with the (110)[001] orientation must have recrystallized during the earliest stage of the annealing process, giving way to some other orientations, possibly near (210)[001].

The same specimen was completely recrystallized by subsequent annealing at 800°C for 15 min. The

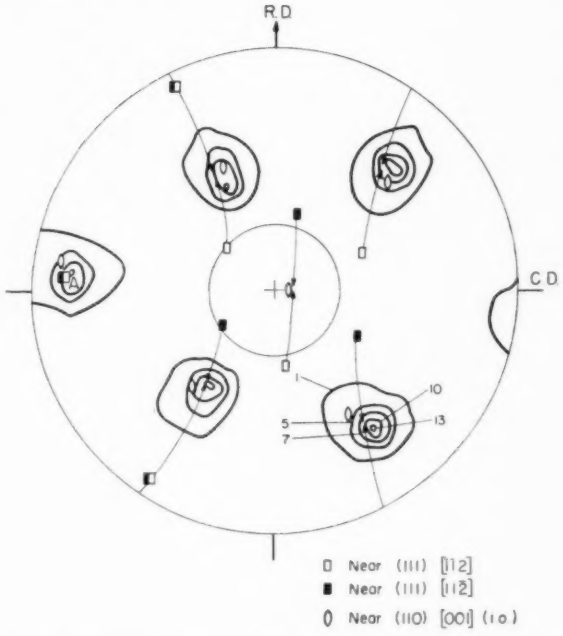


FIG. 2. (110) pole figure of the crystal as in Fig. 1 after annealing at 800°C–15 min. ◊ initial orientation of the crystal, close to the mean orientation of the recrystallization texture. □ and ■, mean orientations of the main deformation texture components. Arrows indicate rotations of 35° around the (110) pole *A* of the deformation texture.

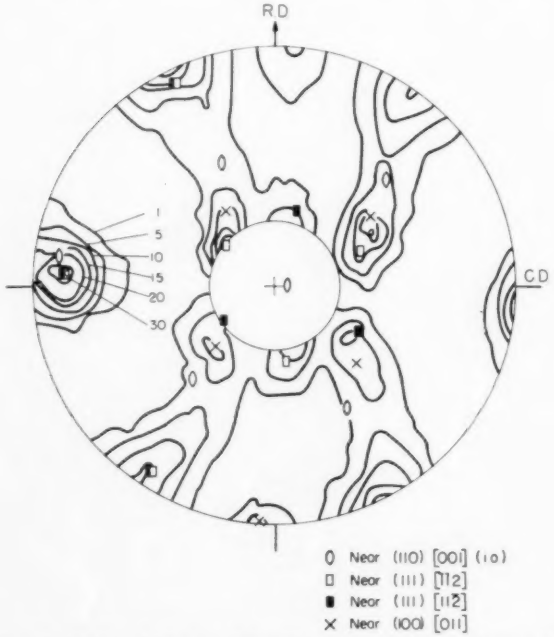


FIG. 1. (110) pole figure of the 70 per cent cold-rolled crystal. ◊ initial orientation. Intensity contours are expressed as multiples of random intensity determined with a carbonyl iron powder specimen.

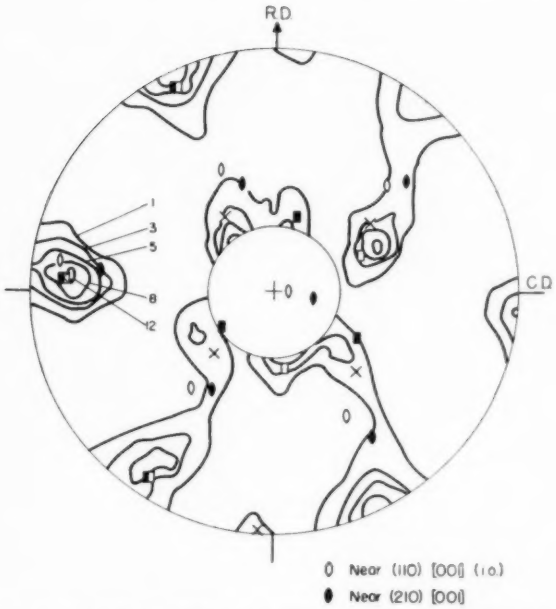


FIG. 3. (110) pole figure of the annealed crystal after 450°C–24 hr then 550°C–2 hr, showing that a shift in the orientation spread has taken place so that the (110)[001] orientation ◊ is no longer included in the texture, while the rest of the deformation texture remains unchanged in orientation.

resulting texture, instead of being the usual (110)[001] type as shown in Fig. 2, was the (210)[001] type (Fig. 5). (The same texture was also obtained from another specimen, which was annealed at 550°C for 24 hr.†) Another specimen was first annealed at

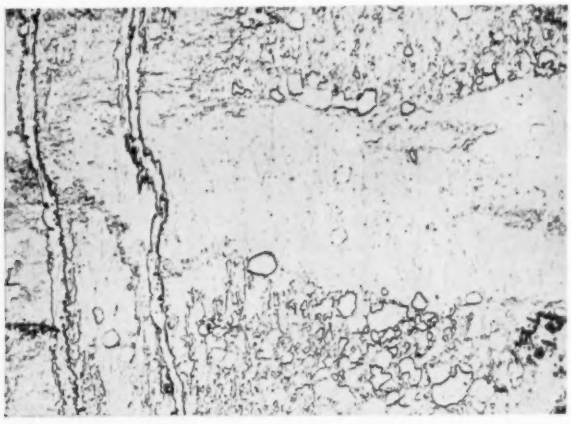


FIG. 4. Microstructure of the specimen used in Fig. 3, showing recrystallized grains formed in regions between deformation bands, and at strain markings within the bands, while the other structural elements remain unchanged. ×290.

† In view of this result, the doubly annealed (64 hr at 550°C, then 1 min at 980°C) specimen of Dunn[1] should have been completely recrystallized with a resulting texture of the (210)[001] orientation in much less than 64 hr at 550°C. Also, his final texture of the (110)[001] plus the (210)[001] type orientations after 1 min at 980°C would be a result of growth during both the prolonged annealing at 550°C and the final anneal.

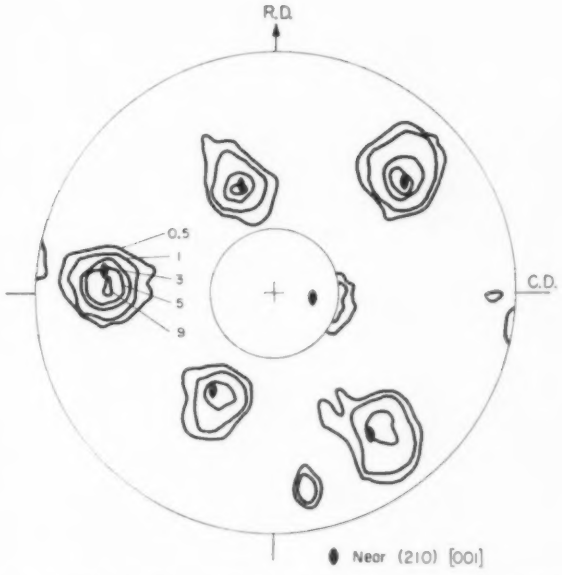


FIG. 5. (110) pole figure of the specimen used in Figs. 3 and 4 after being completely recrystallized by further annealing 800°C–15 min. ◖ mean orientation of the recrystallization texture.

550°C for 2 hr, and then annealed at 950°C for 1 min in a lead bath. The specimen was completely recrystallized and the resulting texture was of the (110)[001] type (Fig. 6).

The results indicate that annealing at 550°C for 2 hr eliminates the orientation scatter around

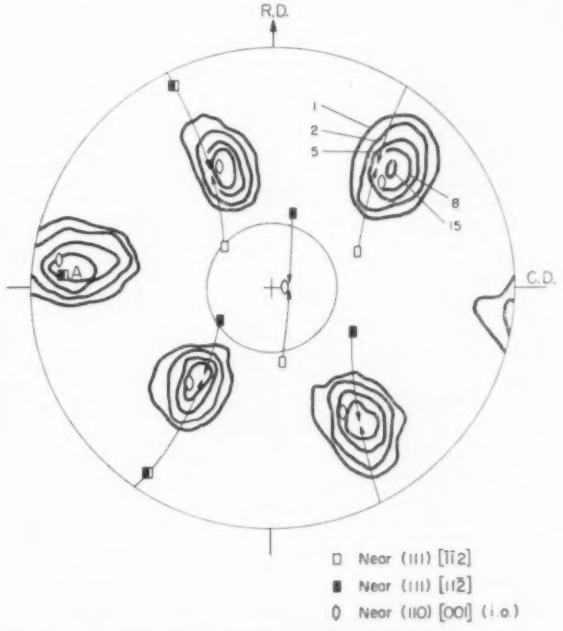


FIG. 6. (110) pole figure of the annealed crystal after 550°C–2 hr, then 950°C–1 min in a lead bath. The notation is that used in Fig. 2.

(110)[001], and that, nevertheless, subsequent annealing at 950°C for 1 min produced a sharp (110)[001] recrystallization texture identical with that obtained on annealing at 800°C for 15 min without a preceding 550°C anneal. Consequently, it appears that the presence of a measurable minor (110)[001] component before the final recrystallization anneal is not a necessary condition for the formation of the (110)[001] recrystallization texture. If any trace of this orientation is still left in the texture after the 550°C anneal, its volume fraction is not larger than that of almost any other orientation, as far as this could be determined from the present data.

HSUN HU

Edgar C. Bain Laboratory
for Fundamental Research
United States Steel Corporation, Monroeville, Pa.

References

1. C. G. DUNN, *Acta Met.* **2**, 173 (1954).
2. J. L. WALTER and W. R. HIBBARD, JR., *Trans. Amer. Inst. Min. (Metall.) Engrs.* **212**, 731 (1958).

* Received April 3, 1959.

Discussion of paper entitled: "The formation of (110)[001] recrystallization texture in a cold-rolled and annealed (110)[001] crystal of silicon-iron" by Hsun Hu*

The author considers as "unlikely" the interpretation of Walter and Hibbard[1] that minor components of the deformation texture (preformed nuclei) having the same orientation as the initial single crystal may serve as the origin of the recrystallization texture. His conclusion is based on the fact that different recrystallization textures are obtained if a cold rolled (110)[001] single crystal is annealed at different temperatures. The author's data, however, do not warrant such a conclusion since the pole figures are not sufficiently accurate to show pole densities below 1 random: it will be shown that orientations representing pole densities as low as 1/100 random may convert the sample to a strong texture of the same orientation.

From Fig. 1 (author's data) it can be seen that the cold rolled crystal contains a (110)[001] "minor component." This crystal, when annealed at temperatures of 800°C or higher without a prior low temperature anneal, recrystallized to a (110)[001] texture as would be expected according to Walter and Hibbard. Thus the primary recrystallization texture is related to a minor component of the deformation texture, which in turn has the same orientation as the virgin crystal.

If the rolled crystal is annealed at 450° and 550°C, the author claims the presence of a new component, (210)[001], which, he says, derives from the (110)[001] minor component of the deformation texture. However, there is a (210)[001] minor component in the deformation texture (from author's Fig. 1) that is just as strong as the (110)[001] minor component although the author did not mention its presence. This minor component could have served as the source of nuclei for the low temperature recrystallization texture even though it did not have the orientation of the virgin crystal.† In addition, the author states that the (210)[001] component grew at the expense of the (110)[001] component of the deformation texture; the latter component had "largely" disappeared after the anneal at 550°C. However, the (210)[001] component, according to the intensity levels of the pole figures, appears to remain unchanged after the anneal at 550°C. For some reason (perhaps a difference in specimen thickness or X-ray beam intensity) the deformation texture shown in the pole figure of Fig. 3 appears to be reduced one level of intensity without the appearance of compensating primary recrystallization components. This change in intensity levels could account for the apparent disappearance of the (110)[001] component. If the change in intensity levels is real and the (210)[001] component is strengthened by the anneal, the pole figure indicates that it could just as well have been growing into and consuming the (111)[112] components of the deformed matrix.

Because the (110)[001] component of the deformation texture appears to be reduced during the low temperature anneal, the author suggests that the formation of the strong (110)[001] texture after a subsequent higher temperature anneal results from "spontaneous recrystallization" of the (111)[112] matrix. However, as long as even a small amount of material remains in this orientation, it could act as nuclei for primary recrystallization. For instance, let us consider that there is an average pole density of 1/2 random (not shown by author) for all directions within 5° of (110)[001]. This could supply nuclei representing a fraction of 2×10^{-3} of the sample. It is not unreasonable to assume that nuclei could grow from a diameter of 1–30μ, for a volume increase of 2.7×10^4 to 1. Consequently, only 2 per cent of the available orientations is needed to convert the sample to a very strong (110)[001] texture. This

† For additional examples see references 2 and 3.

nuclei part of the cold rolled texture represents a pole density contribution as small as 1/100 random, much too small to be detected. Thus the fact remains, based on the data presented by the author, that either recrystallization texture could have derived from minor components of the deformation texture although these may not be seen as part of the deformation texture.

The author's data on the effect of different kinds of anneals on the relative amounts of (110)[001] and (210)[001] textures agree with those obtained by Dunn, particularly since there is a significant difference in the initial orientations of single crystals and a possible large effect of widening of the sample during rolling.[2] Considering the importance of the conditions of the sample (thickness) and the rolling (amount of widening) to the final result, these details should have been noted by the author.

J. L. Walter
W. R. Hibbard
C. G. Dunn
General Electric
Research Laboratory
Schenectady, N.Y.

References

1. J. L. Walter and W. R. Hibbard, Jr., *Trans. Amer. Inst. Min. (Metall.) Engrs.* **212,** 731 (1958).
2. C. G. Dunn and P. K. Koh, *Trans. Amer. Inst. Min. (Metall.) Engrs.* **206,** 1017 (1956).
3. C. G. Dunn, *Acta Met.* **2,** 173 (1954).

* Received June 18, 1959.

VOL. 8 1960

Contribution of interface couples to the energy of a dislocation*

As noted by Bishop and Hill[1] and developed by McClintock *et al.*[2] the usual concepts of stress and strain may be inadequate if there exist periodic variations in stress on an atomic scale, or distributed couples as well as distributed forces (stress) on an interface or section through the material. It was shown by McClintock *et al.*[2] that these effects would only be important in the presence of very high strain gradients such as might be found around a dislocation.

An estimate of the magnitude of the effects of interface couples on dislocations may be obtained from the energy contributed by them if the displacements are those usually found around a screw dislocation. Taking the x_1 and x_2 axes normal to, and the x_3 axis parallel to, the screw dislocation having a Burgers vector b, the only displacement is that in the x_3 direction, u_3:

$$u_3 = (b/2\pi) \tan^{-1} (x_1/x_2) \tag{1}$$

From this assumed displacement the components of lattice rotation and then lattice curvature can be found as follows:

$$\omega_1 = -\frac{1}{2}\left(\frac{\partial u_3}{\partial x_2}\right), \qquad \omega_2 = \frac{1}{2}\frac{\partial u_3}{\partial x_1};$$
$$\kappa_{12} = \frac{\partial \omega_1}{\partial x_2}, \qquad \kappa_{11} = \frac{\partial \omega_1}{\partial x_1}, \text{ etc.} \tag{2}$$

To get the energy some assumption must be made about a stress–strain relation. In the absence of volume couples the rotations themselves are not important, and thus there are 15 measures of deformation: 6 components of strain and 9 components of curvature. There are in general 9 components of stress and 9 interface couples, but only the average shear stress components of the type $(\sigma_{xy} + \sigma_{yx})/2$ are likely to affect the strains leaving 6 components of stress and 9 interface couples. A general stress–strain relation would thus involve $15(15 + 1)/2$, or 120 elastic constants rather than the figure mentioned previously by McClintock *et al.*[2] More simply for an isotropic crystal, a given component of curvature is produced solely by the corresponding component of interface couple. An upper limit to the interface couple χ_{ij} due to the curvature κ_{ij} with a lattice spacing b is

$$\chi_{ij} = Gb^2\kappa_{ij}. \tag{3}$$

Combination of equations (1, 2 and 3) yields a strain energy density in terms of the radius from the center of the dislocation, r, of

$$\sum_{ij} \frac{\chi_{ij}^2}{2Gb^2} = \frac{Gb^4}{16\pi^2 r^4} \tag{4}$$

When this energy density is integrated from b to infinity, the total energy is $Gb^2/16\pi$ as compared to the value of $(Gb^2/4\pi) \log (R_0/b)$ commonly considered for a screw dislocation. Thus as long as the major contribution to the energy of a dislocation comes from the elastic region separated from it by a distance b or more, the effect of interface couples may fortunately be neglected.

F. A. McClintock
Mechanical Engineering Department
Massachusetts Institute of Technology
Cambridge 39, Massachusetts

References

1. J. F. W. Bishop and R. Hill, *Phil. Mag.* Ser. 7, **42,** 414 (1951).
2. F. A. McClintock, P. A. André, K. R. Scherdt, and R. E. Stoeckly, *Nature, Lond.* **182,** 652–653 (1958).

* This research was supported by the United States Air Force through the Air Force Office of Scientific Research and Development Command, under Contract No. AF 18(600)-957. Received July 16, 1959.

Activation energy for deformation of metals at low temperatures*

It is now generally accepted that in many cases deformation of metals is governed by thermal activated processes. If a single activation process is the controlling mechanism for the deformation, the strain rate ($\dot{\epsilon}$) can be expressed by

$$\dot{\epsilon} = A \exp(-G/RT) = A \exp(S/R) \exp(-H/RT) \quad (1)$$

where A is effectively the product of the rate at which attempts to overcome the barrier are made and the strain produced by a successful fluctuation. $G = H - TS$ is the Gibbs' free energy of activation, H the enthalpy of activation (commonly termed "activation energy"), and S the entropy of activation. A, G, H and S will generally depend upon stress, temperature and structure. Only if certain simplifying assumptions are made can values for H be derived from experimental data.

Basinski[1] recently proposed an equation for obtaining H from low temperature creep data taking into account the change in shear modulus with temperature. In the derivation of this equation he assumed that:

(1) A and S are independent of stress and temperature, and

(2) to a first approximation H is a constant for a constant ratio of applied stress σ to the shear modulus μ at any strain, i.e., $H = H(\sigma/\mu)$

Recent experimental evidence,[2–4] however, indicates that if equation (1) describes low temperature deformation, the activation energy is not a function of σ/μ but rather a function of the effective stress, $\bar{\sigma} = \sigma - \sigma_\mu$, where σ_μ is the long range internal stress field at any given structure and is proportional to the shear modulus μ. Moreover, the results of Dorn and co-workers,[5] and Thornton and Hirsch[6] indicate that H may also be a direct function of the temperature. This then suggests an activation energy of the form

$$H = H(T,\bar{\sigma}) \quad (3)$$

A consequence of a temperature dependence of H is a temperature dependence of S in accord with the general thermodynamic relationship:

$$\left(\frac{\partial H}{\partial T}\right)_{\bar{\sigma}} = T\left(\frac{\partial S}{\partial T}\right)_{\bar{\sigma}} \quad (4)$$

The purpose of the present note is to deduce expressions for the activation energy when equations (1) and (3) define the deformation behavior.

Differentiating equation (1) with respect to temperature gives

$$\left(\frac{\partial G}{\partial T}\right)_{\dot{\epsilon}} = \left(\frac{\partial G}{\partial T}\right)_{\bar{\sigma}} + \left(\frac{\partial G}{\partial \bar{\sigma}}\right)_T \left(\frac{\partial \bar{\sigma}}{\partial T}\right)_{\dot{\epsilon}} = -R \ln \dot{\epsilon}/A \quad (5)$$

Combining equations (1) and (5) we have

$$G(T,\bar{\sigma}) = T\left(\frac{\partial G}{\partial \bar{\sigma}}\right)_T \left(\frac{\partial \bar{\sigma}}{\partial T}\right)_{\dot{\epsilon}} + T\left(\frac{\partial G}{\partial T}\right)_{\bar{\sigma}} \quad (6)$$

Further, differentiating equation (1) with respect to $\ln \epsilon/A$ gives

$$\left(\frac{\partial G}{\partial \ln \dot{\epsilon}/A}\right)_T = \left(\frac{\partial G}{\partial \bar{\sigma}}\right)_T \left(\frac{\partial \bar{\sigma}}{\partial \ln \dot{\epsilon}/A}\right)_T = -RT \quad (7)$$

Substituting $(\partial G/\partial \bar{\sigma})_T$ obtained from equation (7) into equation (6), we obtain

$$G(T,\bar{\sigma}) = H - TS = -RT^2 \left[\frac{\left(\frac{\partial \sigma}{\partial T}\right)_{\dot{\epsilon}} - \frac{\sigma_\mu}{\mu}\frac{d\mu}{dT}}{\left(\frac{\partial \sigma}{\partial \ln \dot{\epsilon}/A}\right)_T}\right] + T\left(\frac{\partial G}{\partial T}\right)_{\bar{\sigma}} \quad (8)$$

which applies to constant strain rate (tensile) tests. Further, since

$$\left(\frac{\partial \ln \dot{\epsilon}/A}{\partial T}\right)_\sigma = \left(\frac{\partial \ln \dot{\epsilon}/A}{\partial T}\right)_{\bar{\sigma}} - \left(\frac{\partial \ln \dot{\epsilon}/A}{\partial \bar{\sigma}}\right)_T \left(\frac{d\,\sigma_\mu}{dT}\right) \quad (9)$$

and from equation (1)

$$\left(\frac{\partial \ln \dot{\epsilon}/A}{\partial T}\right)_{\bar{\sigma}} = \left(\frac{G}{RT^2}\right) - \left(\frac{1}{RT}\right)\left(\frac{\partial G}{\partial T}\right)_{\bar{\sigma}} \quad (10)$$

we obtain by substituting equation (10) into equation (9)

$$G(T,\bar{\sigma}) = H - TS = RT^2\left[\left(\frac{\partial \ln \dot{\epsilon}/A}{\partial T}\right)_\sigma + \left(\frac{\partial \ln \dot{\epsilon}/A}{\partial \sigma}\right)_T \left(\frac{\sigma_\mu}{\mu}\frac{d\mu}{dT}\right)\right] + T\left(\frac{\partial G}{\partial T}\right)_\sigma \quad (11)$$

which applies to constant stress (creep) tests.

Since in general

$$(\partial G/\partial T)_{\bar{\sigma}} = -S$$

it follows from equations (8) and (11):

$$H(T,\bar{\sigma}) = -RT^2 \left[\frac{\left(\frac{\partial \sigma}{\partial T}\right)_{\dot{\epsilon}} - \frac{\sigma_\mu}{\mu}\frac{d\mu}{dT}}{\left(\frac{\partial \sigma}{\partial \ln \dot{\epsilon}/A}\right)_T}\right] \quad (8a)$$

and

$$H(T,\bar{\sigma}) = RT^2\left[\left(\frac{\partial \ln \dot{\epsilon}/A}{\partial T}\right)_\sigma + \left(\frac{\partial \ln \dot{\epsilon}/A}{\partial \sigma}\right)_T \frac{\sigma_\mu}{\mu}\frac{d\mu}{dT}\right] \quad (11a)$$

The right hand side of equation (11a) is essentially the same as Basinski's equation for the activation energy $H(\sigma/\mu)$ with the exception that the total stress σ is replaced by the internal stress σ_μ.

To determine H experimentally one must obtain the parameters of equations (8a) or (11a) at a constant structure. The term structure here refers to the nature of the obstacle and the number of places where thermal activation can occur. If we assume A of equation (1) is independent of T and $\bar{\sigma}$,† the parameters of equations (8a) and (11a) can be obtained as follows: $(\partial \ln \dot{\epsilon}/\partial T)_\sigma$ is obtained by incremental changes in temperature during a creep test;[5,7–9] $(\partial \ln \dot{\epsilon}/\partial \sigma)_T$ is obtained either from incremental loading creep tests[2–4,6,7] or from a change in strain rate during a tensile test;[4] $(\partial \sigma/\partial T)_{\dot{\epsilon}}$ is obtained from the change in flow stress caused by a change in temperature for a constant strain rate.

σ_μ can only be obtained indirectly. For undeformed specimens the value of σ_μ is frequently given by the constant flow stress (when corrected for the variation of shear modulus with temperature) at high temperature.[10,11] Similarly, for deformed specimens, the value of σ_μ can sometimes be obtained from flow stress measurements at temperatures which are still below the temperature at which static recovery occurs but high enough for the activation process not to be the controlling process. In other cases, if the thermal component of the flow stress is relatively independent of the amount of deformation, σ_μ is given by[2,4,10,11]

$$\sigma_\mu = \sigma_\mu{}^0 + \int_0^\epsilon h \, d\epsilon \tag{12}$$

where $\sigma_\mu{}^0$ is the value of the internal stress for the undeformed specimen and $\int_0^\epsilon h \, d\epsilon$ represents the increase due to strain hardening. Here $h = d\sigma/d\epsilon$ is the strain-hardening coefficient given by the slope of the experimentally determined stress–strain curve.

If none of the above methods for obtaining σ_μ applies, an approximation for H can be obtained by assuming that σ_μ in equations (8a) and (11a) is equal to the applied stress, similar to the assumption made by Basinski[1]. The error associated with this approximation will depend on the relative values of the thermal component of the flow stress and σ_μ. The approximation is probably not too bad for large strains, i.e. at large values of σ_μ.

Even though H can be determined from the available experimental data on a number of metals, it is impossible to decide from these data whether H is a function of both $\bar{\sigma}$ and T or just $\bar{\sigma}$ alone or T alone. For instance, the assumption that $H = H(\bar{\sigma})$ (i.e. H depends only on the stress) with A and S constant gives from equation (1)

$$H = T(S - R \ln \dot{\epsilon}/A), \tag{14}$$

which indicates that the activation energy measured over a wide temperature range at essentially the same strain rate has to be proportional to the temperature, which is approximately what Dorn and his co-workers[5] have found for Al and Cu at low temperatures. This apparent temperature variation of the activation energy could then be due entirely to the fact that tests at low temperatures are made at high effective stress and vice versa rather than the effect of temperature *per se*. Similarly, the dependence of H on temperature suggested by Thornton and Hirsch[6] may be due entirely to effects associated with changes in $\bar{\sigma}$ which occur when tests are conducted at different temperatures. To separate the effects of temperature and stress on the activation energy, tests would have to be conducted over a very wide range of $\bar{\sigma}$ (or $\dot{\epsilon}$) at constant temperature. In practice the range of strain rates covered is usually only two or three orders of magnitude. According to equation (14) this yields a change in activation energy which is within the experimental error in the measurements of H. Thus, somewhat larger ranges of strain rate will have to be investigated to establish the effect of $\bar{\sigma}$ on H. The significance of this is shown in Fig. 1. Here the shaded area represents the small

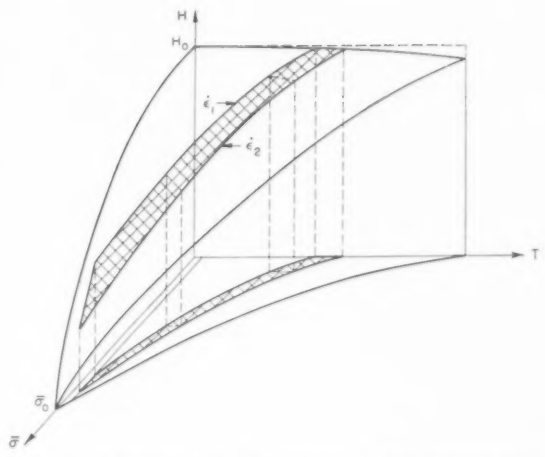


FIG. 1. Schematic of the surface of the activation energy for plastic flow as a function of the effective stress $\bar{\sigma}$ and temperature T. Shaded area represents narrow region generally investigated experimentally.

† This assumption has not been substantiated experimentally.

VOL. 8 1960

region of the $H(\bar{\sigma},T)$ surface which is generally investigated experimentally.

H. CONRAD
H. WIEDERSICH

Metallurgy Department
Westinghouse Research Laboratories
Pittsburgh 35, Pennsylvania

References

1. Z. S. BASINSKI, *Acta Met.* **5,** 684 (1957).
2. H. CONRAD and W. D. ROBERTSON, *Trans. Amer. Inst. Min. (Metall.) Engrs.* **209,** 503 (1957).
3. H. CONRAD and W. D. ROBERTSON, *Trans. Amer. Inst. Min. (Metall.) Engrs.* **212,** 536 (1958).
4. H. CONRAD, *Acta Met.* **6,** 339 (1958).
5. J. E. DORN, *Creep and Recovery*, p. 255. American Society for Metals, Cleveland (1957).
6. P. R. THORNTON and P. P. HIRSCH, *Phil. Mag.* **3,** 738 (1958).
7. R. BECKER, *Z. Phys.* **26,** 919 (1926).
8. R. BECKER and W. BOAS, *Metall. Wirtsch.* **8,** 317 (1929).
9. G. LUCAS and G. MASING, *Z. Metallk.* **43,** 341 (1952).
10. A. SEEGER, *Z. Naturf.* **9a,** 758, 819, 856 (1954).
11. A. SEEGER, *Phil. Mag.* **45,** 771 (1954).

* Received January 16, 1959; revised version September 22, 1959.

Blue-brittle Armco ingot iron*

During a previous investigation[1] of the mechanical properties of an Armco iron showing the characteristics of "blue-brittleness" at temperatures as low as 0°C, it was found that this material exhibits several anomalous features. In connection with the irregular stress–strain curves obtained it was pointed out that in general such curves could be the result of an anomalous dependence of the stress σ on the strain rate $\dot{\varepsilon}$. This dependence may be defined as:

$$\left.\begin{aligned} &\sigma_1(\varepsilon_1, \dot{\varepsilon}_1) < \sigma_2(\varepsilon_2, \dot{\varepsilon}_2), \\ \text{in which} \quad &\varepsilon_1 = \varepsilon_2 \\ \text{and} \quad &\dot{\varepsilon}_1 > \varepsilon_2 \end{aligned}\right\} \qquad (1)$$

The deformation should then take place in an irregular and localized fashion. In the case of blue-brittle material this anomalous behaviour is thought to be due to the diffusion of interstitial atoms towards moving dislocations.[2]

In the series of experiments presented here, the character of the irregular stress–strain curves and the connection between diffusion of interstitials and this type of deformation were investigated in somewhat more detail. The following details of the experimental conditions may be of interest: specimens of the material were strained at very accurately maintained rates of strain in a 5-ton Instron tensile testing machine. During each test the specimen and the jaws around the heads of the specimen were submerged in an oil-filled thermostat in which the temperature was maintained with an accuracy of ± 0.05°C. The jaws were made self-centering by means of Hookean keys. In some tests simultaneously with the load–elongation curve, which was autographically recorded, point-to-point diameter readings on the gauge section of the specimen were obtained (Fig. 1). A scissors-type diameter gauge in which the sensitive element operates outside the thermostat was constructed for this purpose.

The Armco iron of which the specimens were made had been annealed for 1 hr at 870°C; the grain size was approximately 550 grains/mm^2. After this heat treatment, specimens with a ground surface on the gauge section were machined from the stock. The

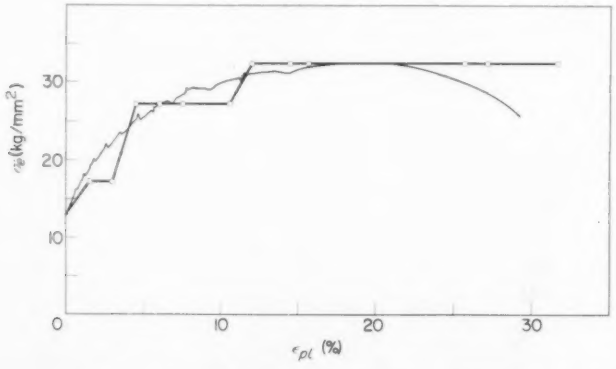


FIG. 1. Local and overall stress–strain curves of blue-brittle Armco iron at 90°C and a strain rate of 12.5 $\times 10^{-4}$ sec^{-1}.

diameter of the specimens was 4 mm, the gauge length 15 mm. The composition of the material was the following:

	C	N	P	S	Cu
weight %	0.014	0.018	0.004	0.021	0.10

Fig. 1 is a diagram of engineering stress vs. plastic strain in which both the curve obtained for the total gauge length and the curve deduced from diameter readings at one point in the middle of the specimen are represented. It appears that the local plastic deformation does indeed take place by sudden spurts at a relatively high local rate of strain. The overall rate of strain was $\sim 10^{-3}$ sec^{-1}, whereas the local rate of strain was estimated at $\sim 2 \times 10^{-2}$ sec^{-1}.

In the blue-brittle temperature region the unstable plastic deformation which manifests itself by the irregular stress–strain curves takes place at low rates of strain. At a sufficiently high strain rate the deformation is stable and smooth curves are obtained. Apparently a critical strain rate exists which represents the transition between the two types of behaviour. It was noticed that at strain rates just below the critical value the character of the irregular curves changed in a narrow region of strain rate from "spiky" to more or less garland-like, as illustrated in Fig. 2. This phenomenon made it comparatively easy to recognize the critical rate of strain. A series of tests was carried out at different temperatures, in which the critical rate of strain was determined as a value in between a rate at which the curve was regular and one at which the curve was serrated.

If we assume that the critical rate of strain $\dot{\varepsilon}_{CR}$ is proportional to the mean velocity with which interstitial atoms diffuse through the iron lattice towards

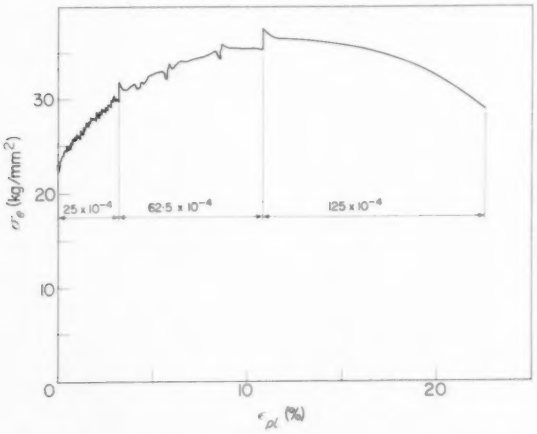


FIG. 2. Stress–strain curve at 140° C and three rates of strain.

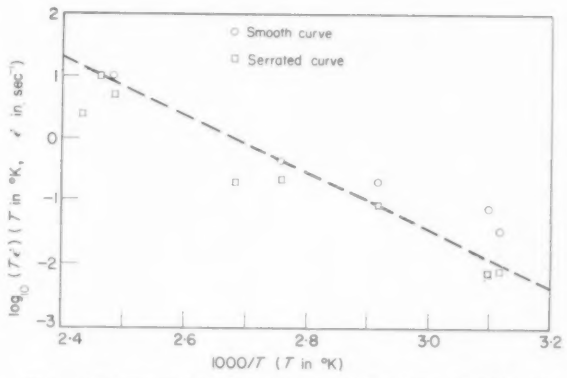


FIG. 3. Diagram showing the transition from smooth to serrated stress–strain curves as a function of temperature and rate of strain.

a dislocation, we obtain: (Cottrell and Bilby[3]):

$$\dot{\varepsilon}_{CR} = C \cdot (D/RT) \tag{2}$$

where C is a constant dependent on dislocation density and the physical properties of the iron lattice and where the other symbols have their usual connotation.

The diffusion coefficient D of interstitials in a b.c.c lattice was shown by Wert and Zener[4] to be adequately represented by:

$$D = D_0 \exp(-A/RT) \tag{3}$$

The values of D_0 and A were determined both for the diffusion of C and N in the Fe lattice by Wert[5,6]. His results were:

N in Fe: $D_0 = 0.003$ cm^2/sec $A = 18{,}200$ cal
C in Fe: $D_0 = 0.02$ cm^2/sec $A = 20{,}100$ cal

In the temperature region in which our experiments were carried out the value of the diffusion coefficient for carbon is about 4 orders of magnitude higher than for nitrogen. It would therefore appear justified to neglect the influence of nitrogen diffusion.

In Fig. 3 the results of the critical-rate experiments are given in a $\log(T \cdot \dot{\varepsilon})$ vs. $1000/T$ diagram. According to the above theory the critical rate of strain should be a straight line in this diagram: here it is plotted as the boundary line between points representing regular and serrated curves. The activation energy as determined from this diagram is 20,400 cal, which is in good agreement with the activation energy for the diffusion of carbon of 20,100 cal.[6] Considering the inherent lack of accuracy of the method this seems to confirm the correctness of the postulated relation between diffusion of interstitial atoms and the irregularity of the plastic deformation of this type of material.

VOL. 8 1960

Thanks are due to Mr. J. Raadsen for his able assistance during the experiments.

Koninklijke/Shell-Laboratorium A. W. SLEESWYK
Amsterdam

References

1. A. W. SLEESWYK, *Acta Met.* **6,** 598 (1958).
2. F. R. N. NABARRO, *Report of Conference on Strength of Solids*, p. 38. Physical Society, London (1948).
3. A. H. COTTRELL and B. A. BILBY, *Proc. Phys. Soc.* A**62,** 49 (1949).
4. C. WERT and C. ZENER, *Phys. Rev.* **76,** 1169 (1949).
5. C. WERT, *Phys. Rev.* **79,** 601 (1950).
6. C. WERT, *J. Appl. Phys.* **21,** 1196 (1950).

* Received August 4, 1959.

The effect of segregation on the solute diffusion enhancement due to the presence of dislocations*

Turnbull and Hoffman[1] first showed that isolated dislocation "pipes" can exhibit diffusivities greatly in excess of the surrounding lattice, and can therefore act as short-circuiting paths relative to lattice diffusion. They further noted that the presence of such defects in single crystal material would be expected to produce anomalously high diffusion coefficients at relatively low temperatures. Later, Hart[2] was able to obtain order of magnitude agreement between the calculated dislocation pipe contribution and the observed self-diffusion coefficient enhancement in silver at 600°C, the enhancement being identified with the difference between the observed diffusion coefficient and that obtained by extrapolation from high temperatures.

Tomizuka[3] subsequently emphasised the fact that, if the presence of dislocations does in fact enhance the overall diffusion, an accurate set of data obtained using single crystals should exhibit a gradual fall in activation energy as the temperature decreases. It was further claimed that available data on the diffusion of antimony in silver at tracer concentrations did exhibit an overall change of 2.4 kcal/mole in the apparent activation energy over a 400°C range of measurement. A smaller change of 0.5 kcal/mole over a 300 centigrade degree range was also noted for self-diffusion in silver. Both of these results appeared to correlate satisfactorily with Hart's theory of the effect.

It is the purpose of this note, however, to draw attention to the fact that Hart's theory should be modified when discussing the diffusion of impurities in a given solvent as opposed to the self-diffusion of the solvent atoms themselves, because of the possible natural segregation of the impurity atoms towards these dislocation pipes. The way in which information concerning this segregation might be obtained from diffusion coefficient measurements will also be discussed.

If D_d and D_l are the diffusion coefficients in the dislocation pipe and in the undisturbed lattice respectively, then Hart's expression for the observed diffusion coefficient D can be written

$$D = D_d f + D_l(1 - f) \tag{1}$$

where f is the fraction of all atoms "in dislocations". Here it is assumed that encounters with dislocations are sufficiently frequent for the overall *concentration* vs. *penetration distance* profile to remain defined by a single diffusion coefficient.

At relatively high temperatures D and D_l are very nearly equal, the overall diffusion being little affected by the presence of dislocation pipes. If ΔD is the discrepancy between the observed diffusion coefficient at low temperatures and that obtained by extrapolation from high temperatures, then

$$\begin{aligned}\Delta D &= D - D_l \\ &= fD_d\end{aligned}$$

from (1), since D_d is very much greater than D_l.

In terms of ratios this becomes

$$\Delta D/D_l = f(D_d/D_l) \tag{1a}$$

For self-diffusion f measures the fraction of the total migration time that a given atom spends in dislocation pipes, assuming equal probability of occupation of all sites. However, if we are considering an impurity the sites within a dislocation pipe can be more probable of occupation due to the operation of a tendency towards segregation. Suppose C_d/C_l is the equilibrium ratio of the average fractional concentration in the pipe to that in the lattice, and n the number of sites that go to make up a typical cross-sectional area of the pipe. Then, provided the overall concentration is close to C_l, the fraction of the total migration time that the impurity atom spends in dislocation pipes is given approximately by nf_0C_d/C_l, f_0 being the fraction of all atoms in sites along the lines of maximum binding in the dislocations. As defined f is equal to nf_0, the inclusion of the factor n providing for more explicit reference in the calculation to the effective cross-sectional area of the dislocation.

Thus, equation (1a) may be generalized to

$$\Delta D/D_l = nf_0C_dD_d/C_lD_l \tag{2}$$

Segregation towards dislocations has been discussed by Cottrell[4] who points out that it can be due to

elastic or electrical interactions between the strain field of the dislocation and the solute atom, although of the two the elastic interaction predominates. It is also pointed out that segregation (and therefore C_d/C_l) can be expected to decrease as the temperature increases, as will also the ratio D_d/D_l, so that $\Delta D/D_l$ can be expected to decrease more sharply still under these conditions.

The diffusion of iron, cobalt and nickel in copper, studied by Mackliet[5], may be cases to which the effects of segregation apply in varying degrees. The results exhibit a 22 per cent enhancement for iron at 719°C, 23 per cent for cobalt at 701°C, and no significant deviation from strictly lattice diffusion for nickel. Also, there is a marked solubility difference between these elements in copper, being only a few per cent for iron and cobalt but 100 per cent for nickel. The direction of this correlation between diffusion coefficient enhancement and solubility is consistent with Perryman's[6] generalization that a given concentration of solute is accommodated by the lattice more readily as the solubility increases, producing a smaller tendency to segregate to boundaries than otherwise.

Sufficient information is available to enable some rough calculations to be made of the segregation actually taking place in these systems. In the first place, interpolation from the measurements of the grain boundary diffusion of nickel in copper due to Yukawa and Sinnott[7] indicates that D_d/D_l is about 1.5×10^5 at 710°C for this solute. Although the calculations would obviously be improved by having a precise knowledge of this ratio in each case, it is reasonable to assume that it is not greatly different for iron and cobalt. (For example, calculations by Turnbull and Hoffman[1] indicate that the ratio of grain boundary to lattice diffusion in copper is about the same for the three solutes zinc, silver and nickel.) Secondly, Hirsch[8] has given the range 4×10^6 to 2×10^7 lines/cm^2 for the dislocation density in annealed copper. Finally, following Hendrickson and Machlin[9], who make use of an estimate of the dislocation pipe diameter in silver of 10^{-7} cm, n can be calculated to be of order 10. Using these values C_d/C_l turns out to be within the range 10–10^2 for iron and cobalt in copper at 710°C.

By equating these values of C_d/C_l to exp (V/kT), kT having its usual meaning, the solute atom–dislocation binding energy V turns out to be about a few tenths of an electron volt, which is not unreasonable. An alternative method of finding V when more low temperature data are available would be to plot log $(\Delta D/D_l)$ against $1/T$; provided the activation energies for D_d and D_l are known, V could then be calculated from the slope of the resultant straight line.

Of course, calculations of this sort cannot be regarded as good evidence for the presence of segregation of this type; a more direct experimental demonstration is required. Apart from varying the operative dislocation density, one way of doing this would be to measure the diffusion of the solute as a function of temperature in an alloy in which the concentration of solute has been so increased that the concentration difference between the dislocations and the matrix is appreciably reduced. This is possible because the dislocations will saturate before the matrix. If segregation is suspected to be taking place at low concentrations, then the diffusion coefficient enhancement at low temperatures can be expected to be less for the alloy. When f is much less than C_l the minimum overall concentration for which the dislocations are saturated is given by the reciprocal of the segregation ratio C_d/C_l; for example, if this ratio is 10^2 then $C_{\min}$ is equal to 1 per cent.

The case of antimony diffusing in silver mentioned earlier is worthwhile re-examining in the light of what has been said, since the relatively low solubility (less than 10 per cent) of antimony in silver also points to a possible tendency towards segregation. If the observed enhancement of the self-diffusion of silver at low temperatures (4 per cent at 630°C) is used to calculate the effective dislocation density via equation (1a), a figure of about 3×10^7 lines/cm^2 is obtained: applied to antimony in silver this would appear to indicate that no significant segregation is taking place. However, such an interpretation is not really warranted since the operative dislocation density could easily be quite different from this. For example, direct measurements by Hendrickson and Machlin[10] give a dislocation density in annealed silver crystals of about 2×10^6 lines/cm^2. Determination of the average dislocation density of the specimens employed in future experiments before and after their diffusion annealing should help to remove uncertainties of this type.

The author is indebted to Mr. A. D. Le Claire of this Division for some helpful discussions.

A. J. Mortlock

Metallurgy Division
Atomic Energy Research Establishment
Harwell, Berks

References

1. D. Turnbull and R. E. Hoffman, *Acta Met.* **2**, 419 (1954).
2. E. W. Hart, *Acta Met.* **5**, 597 (1957).
3. C. T. Tomizuka, *Acta Met.* **6**, 660 (1958).

VOL. 8 1960

4. A. H. COTTRELL, *Seminar on Relation of Properties to Microstructure*, p. 131. American Society for Metals, Cleveland (1953).
5. C. A. MACKLIET, *Phys. Rev.* **109**, 1964 (1958).
6. E. C. W. PERRYMAN, *Trans. Amer. Inst. Min. (Metall.) Engrs.* **197**, 911 (1953).
7. S. YUKAWA and M. J. SINNOTT, *Trans. Amer. Inst. Min (Metall.) Engrs.* **203**, 996 (1955).
8. P. B. HIRSCH, *Progress in Metal Physics* Vol. 6, p. 284. Pergamon Press, London (1956).
9. A. A. HENDRICKSON and E. S. MACHLIN, *Trans. Amer. Inst. Min. (Metall.) Engrs.* **200**, 1035 (1954).
10. A. A. HENDRICKSON and E. S. MACHLIN, *Acta Met.* **3**, 64 (1955).

* Received August 21, 1959.

Nucleation in recrystallization phenomena*

Orowan[1] has argued that thermal nucleation cannot play a role in the recrystallization process because the activation free energy required for the nucleation, given by $(16\pi/3)\sigma^3/(\delta F)^2$, is much too large to be supplied thermally at the recrystallization/temperatures. In this expression, σ is the interfacial free energy between cold-worked and annealed material, and δF is the decrement in volume free energy upon the annealing of a unit volume of material. Orowan's argument depends upon utilizing for δF the experimental magnitudes of the energy put in by cold work. Burke and Turnbull[2] recognize, however, that there may be regions where the effects of cold work are concentrated and where thermal nucleation is possible because δF is sufficiently large. Furthermore, Beck[3] has stated that all theories for primary recrystallization recognize the condition, first formulated by Becker[4], that a strain-free nucleus is stable and capable of growth in a strained matrix if it is not smaller than a certain critical size. The purpose of this note is to point out that there is a general consideration concerning nucleation that sheds some light on the understanding of the recrystallization phenomena.

If state α of a substance is metastable with respect to state β of that substance, then nucleation is a step for the transformation $\alpha \rightarrow \beta$. This necessity follows essentially from the definition of metastability, namely that, although α has a higher free energy than does β, any small variation of any internal parameter, ξ, will increase the free energy of α. Therefore, the system must transform cooperatively over a large region so that the inhibition due to the variation of ξ is relegated to the interface and appears in the term σ, and statistical fluctuations can push the system past the barrier represented by $(16\pi/3)\sigma^3/(\delta F)^2$. On the other hand, if α is not metastable with respect to β, that is, if there exists some variation of the relevant ξ that decreases $F(\alpha)$, and if the path along the ξ-variation is not too resistive then nucleation need not be depended upon for $\alpha \rightarrow \beta$. If such a path is very resistive, due to some kinetic inhibition, then nucleation along some other path may be preferred. [It would seem that one can assert that if there exists no parameter ξ the magnitudes of which distinguish α from β and that can vary continuously from α to β, then that transformation must be nucleated. However, the existence in principle of such a continuous variation of ξ does not guarantee the absence of nucleation, since $F(\alpha)$ may thereby be increased. An example of the latter would be the rotation of a ferromagnetic domain under the action of an external field, where ξ would be the fraction of properly oriented atomic spins.]

For the transformation of a cold-worked crystal, α, to the annealed condition, β, the relevant parameter would be the dislocation density, ρ_d. A crystal of high ρ_d is not metastable with respect to the dislocation-free crystal since a decrease in ρ_d necessarily decreases $F(\alpha)$. Hence, the transformation $\alpha \rightarrow \beta$ need not proceed through a nucleation step and the question of the critical size of a strain-free region need not arise. The transformation simply proceeds by the progressive annihilation of dislocations as a consequence of vacancy migration etc., and indeed this is what is thought to occur in the initial recovery stage. It is to be noted that the reason for the absence of nucleation is fundamentally different from that adduced by Orowan[1]. Within any one cold-worked grain one ought to see a gradual and continuous decrease of ρ_d. The grain shape and size, and hence the texture, will change in the process due (1) to absorption of α in one grain by β in an adjacent grain with consequent grain-boundary motion, and (2) to accompanying (though unrelated) grain boundary motion driven by the interfacial free energy.

However, should the disappearance of the dislocations become kinetically inhibited, as by some locking mechanism, then nucleation of a strain-free region within the disturbed region may become an alternative mechanism, but only if the dislocation density is so high that the δF is locally large enough that the nucleation can be thermally activated. We see that a small region of high dislocation density, while necessary for nucleation as Burke and Turnbull suggested,[2] is not a sufficient condition: it must also be characterized by a mutual locking among the dislocations. The magnitude of the nucleation barrier will depend sensitively through δF and σ upon the details of the dislocation configuration at any one region. However, since the unpinning of the dislocations is a thermally activated process, holding at temperature will decrease the number of regions for which a nucleation

mechanism is a possible alternative. One concludes that if any nucleation occurs in the recrystallization process, it must be a rare event and its contribution to the process must be very slight. It also follows that the origin of recrystallization textures must be sought in the growth phenomena and not in oriented nucleation.

The writer has profited from a discussion of these ideas with Dr. J. C. M. Li and Professor P. A. Beck.

Edgar C. Bain Laboratory R. A. ORIANI
For Fundamental Research
United States Steel Corporation
Research Center
Monroeville, Pennsylvania

References

1. E. OROWAN, in *Dislocations in Metals* (Edited by M. COHEN). *Amer. Inst. Min. (Metall.) Engrs.*, New York. (1954).
2. J. E. BURKE and D. TURNBULL, *Progress in Metal Physics*, Vol. 3, p. 220. Pergamon Press, London (1952).
3. P. A. BECK, *Advanc. Phys.* **3**, 245 (1954).
4. R. BECKER, *Z. Tech. Phys.* **7**, 547 (1926).

* Received October 19, 1959.

VOL. 8 1960

Shear in zinc bicrystals*

The purpose of this communication is to report the difference in mechanical behavior of bicrystals and single crystals in simple shear. Bicrystals of 99.99% zinc were deformed in simple shear at room temperature with the shearing apparatus shown schematically in Fig. 1a.

The shearing of the crystal is allowed to take place in such a manner that only vertical motion can occur. In Fig. 1b is shown the relative orientations of the component crystals in the bicrystal. Fig. 2 shows behavior of bicrystals as compared to single crystals. These results are typical of five separate tests on five different bicrystals and five single crystals.

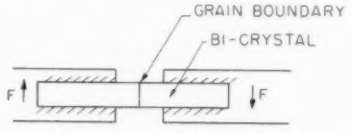


FIG. 1a. Schematic of shearing apparatus.

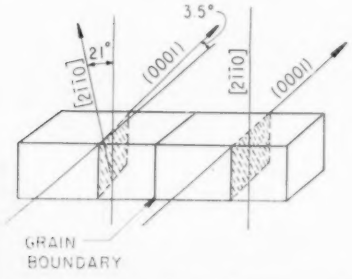


FIG. 1b. Relative orientation of component crystals in bicrystal.

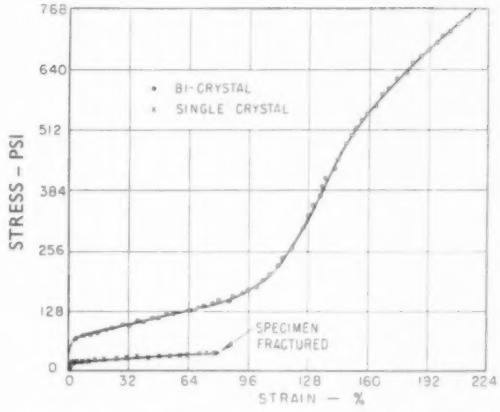


FIG. 2. Shear stress vs. shear strain for Zn crystals.

The most noticeable difference in behavior between the bicrystals and the single crystal (acid-sawed from the bicrystal specimen) is the low stress to cause fracture of the single crystal of a similar orientation to one of the components of the bicrystal. This

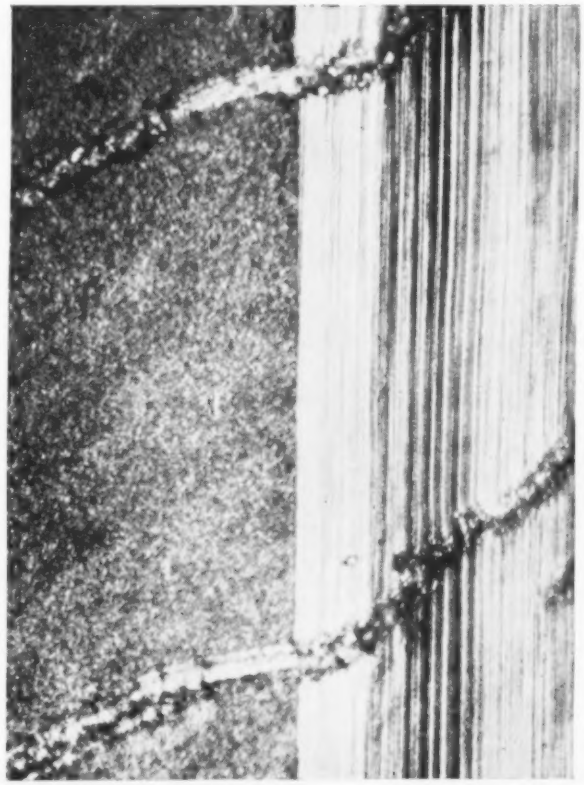


FIG. 3. Region of shear at grain boundary. ×200.

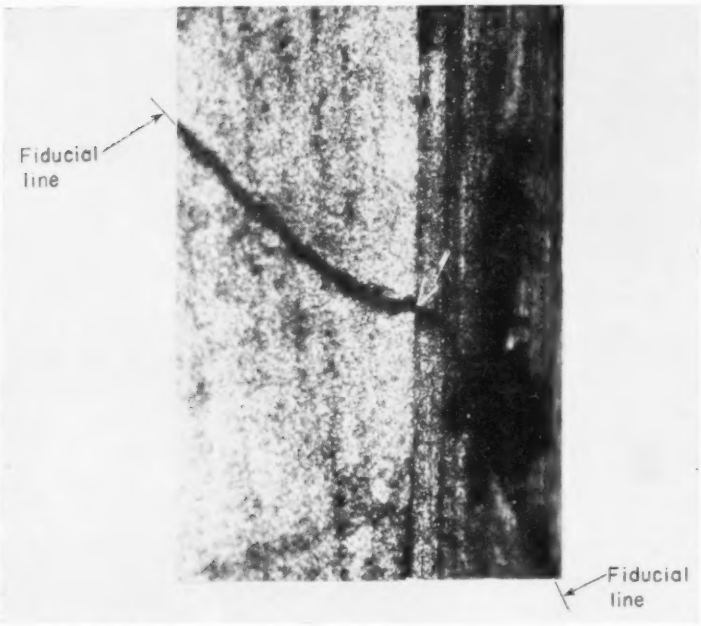


FIG. 4. Grain boundary shear. ×200. (Arrow indicates displaced fiducial line.)

fracture did not occur at the grips, but in the center of the gauge section. A possible interpretation is that the grain boundary in the bicrystal is able to absorb any crack nucleus which is initiated during the deformation. Fig. 3 is a micrograph of the grain boundary. After approximately 150 per cent extension, the deformation in this region is noticeably inhomogeneous, there being a region where the inscribed fiducial marks do not follow the same bending of the specimen which has taken place over the rest of the gauge section. Twinning did not occur in the gauge section. Indeed, as shown in Fig. 4, grain boundary shear has occurred but the region immediately adjacent to the grain boundary has not rotated under the bending moment inherent in this shearing process. Thus it can be concluded that a grain boundary shows a greater resistance to the bending moment but does deform by movement of the one grain with respect to another. This movement could possibly be the adsorption mechanism of the crack nuclei, since the bicrystal does not crack at the same extension as the single crystal. In fact, no cracks could be detected microscopically in the bicrystal specimens at deformations of 150 per cent.

This research was supported by the Office of Naval Research.

J. M. GALLIGAN
S. FEUERSTEIN
W. LUHMAN

Minerals Research Laboratory
University of California
Berkeley

* Received July 15, 1959; revised version November 16, 1959.

EFFECT OF PRESSURE ON INTERMETALLIC LAYER GROWTH*

L. S. CASTLEMAN†

The effect of hydrostatic pressure on the kinetics of intermetallic layer growth in interdiffusing three-phase two component systems has been examined theoretically. A system has been selected for detailed analysis, in which the kinetics of layer growth are controlled by equilibrium interface concentrations and by the diffusion coefficient in the growing intermetallic phase. An equation has been derived which enables one to estimate the relative importance to intermetallic layer growth of pressure-induced changes in the diffusion coefficient and pressure-induced shifts in the interface boundary concentrations. Also, an estimate has been made of the importance of pressure-induced shifts in equilibrium concentrations in affecting the kinetics of growth of the ε (UAl_3) phase layer in the aluminum–uranium system and of the γ (Ni_2Al_3) phase layer in the aluminum–nickel system. It is concluded that the pressure-induced increase in ε growth rate cannot be rationalized on the basis of shifts in the equilibrium concentrations. The pressure-induced decrease in growth rate of the γ phase is attributed primarily to a decrease in diffusion coefficient; equilibrium concentration shifts play a minor role.

EFFET DE LA PRESSION SUR LA CROISSANCE DES COUCHES INTERMETALLIQUES

L'auteur a étudié théoriquement l'effet de la pression hydrostatique sur la cinétique de la croissance de couches intermétalliques dans des systèmes binaires possédant trois phases interdiffusantes. Il a soumis à une analyse détaillée un système dans lequel la cinétique de croissance de la couche est contrôlée par les concentrations d'équilibre à l'interface et par le coefficient de diffusion de la phase intermétallique croissante. Il établit une relation qui permet d'estimer l'importance relative, sur la croissance de la phase intermétallique, de variations du coefficient de diffusion et de fluctuations des concentrations à l'interface induite par la pression.

L'auteur a également estimé l'importance de fluctuations dues à la pression dans les concentrations d'équilibre sur la cinétique de croissance de la couche ε (UAl_3) dans le système aluminium-uranium et de la phase γ (Ni_2Al_3) dans le système aluminium-nickel. On arrive ainsi à la conclusion que l'augmentation de la vitesse de croissance dans la phase ε, induite par une variation de pression, ni peut pas etre estimée sur la base de fluctuations dans les concentrations d'équilibre uniquement. La diminution de la vitesse de croissance de la phase γ induite par la pression, est attribuée essentiellement à une diminution du coefficient de diffusion; les fluctuations de la concentration d'équilibre jouent un rôle secondaire.

DIE WIRKUNG DES DRUCKS AUF DAS WACHSTUM INTERMETALLISCHER SCHICHTEN

Die Wirkung des hydrostatischen Drucks auf die Wachstumskinetik intermetallischer Schichten in dreiphasigen Systemen aus zwei ineinander diffundierten Komponenten wurde theoretisch untersucht. Für die genaue Analyse wurde ein System ausgewählt, in dem die Wachstumskinetik solcher Schichten durch die Gleichgewichtskonzentrationen an der Grenzfläche und durch den Diffusionskoeffizienten in der wachsenden intermetallischen Phase bestimmt ist. Eine Gleichung wurde abgeleitet, aus der man den relativen Einfluß von druckinduzierten Änderungen des Diffusionskoeffizienten und von druckinduzierten Verschiebungen der Grenzflächenkonzentrationen auf das Wachstum einer intermetallischen Schicht abschätzen kann. Weiterhin wurde der Einfluß der druckinduzierten Konzentrationsverschiebungen auf die Wachstumskinetik von Schichten aus ε-(UAl_3)-Phase im Uran-Aluminiumsystem und aus γ-(Ni_2Al_3)-Phase im Aluminium-Nickelsystem abgeschätzt. Es folgt daraus, daß sich die druckinduzierte Zunahme der ε-Wachstumsgeschwindigkeit als Folge der Verschiebungen der Gleichgewichtskonzentrationen nicht ergibt. Wird die druckinduzierte Abnahme der γ-Phase wird hauptsächlich einer Abnahme des Diffusionskoeffizienten zugeschrieben. Verschiebungen der Gleichgewichtskonzentrationen spielen hier eine untergeordnete Rolle.

INTRODUCTION

The effect of hydrostatic pressure on diffusion phenomena has been the subject of increasing attention during the past decade. It is now well-established that the self-diffusion coefficients of elements are reduced by hydrostatic pressure[1,2] and that the anisotropy of self-diffusion coefficients is reduced in non-cubic metals such as zinc.[3] The decrease in diffusion coefficients is traced to an increase in the heat of activation for self-diffusion, which is a measure of the increased difficulty that an ion experiences in jumping from one lattice site to another in the compressed lattice. However, in multiphase multicomponent systems undergoing interdiffusion, such as occurs in diffusion bonding applications, the situation is much more complicated. Not only must one consider the effects of pressure on diffusion coefficients, but also the effects of pressure on phase equilibria; appreciable changes in phase equilibria

* Received March 2, 1959; revised August 11, 1959.

† Sylvania Research Laboratories, a division of Sylvania Electric Products Inc. Bayside, N.Y.

VOL. 8 1960

would change interface concentrations, which in turn would influence the course of interdiffusion. The effect of pressure on the kinetics of growth of intermetallic layers in two-component systems can be quite marked; for example, the growth of the Ni_2Al_3 phase during interdiffusion in the aluminum–nickel system is appreciably diminished by applied pressure,[4] whereas the opposite is true in the case of UAl_3, which grows more rapidly during interdiffusion in the aluminum-uranium system as the applied pressure is increased.[5] Although it is possible to explain pressure-induced reductions in growth rates as resulting solely from decreases in diffusion coefficients,[6] it is not possible, except in special cases,[7] to rationalize pressure-induced increases in growth rates without taking into account phase equilibria. Accordingly, it is the purpose of this paper to estimate the magnitude of shifts in phase equilibria as a function of pressure, and to compare the relative importance of such changes with that of pressure-induced changes in diffusion coefficients in controlling the course of multiphase diffusion.

RELATIVE IMPORTANCE OF CHANGES IN DIFFUSION COEFFICIENTS AND IN INTERFACE CONCENTRATIONS

We first attempt to estimate the relative importance to intermetallic layer growth of pressure-induced changes in diffusion coefficients as compared with pressure-induced shifts in the interface boundary concentrations. To do so for the general case of multiphase diffusion in multicomponent systems is quite difficult, since the equations describing interdiffusion are complicated.[8] We therefore restrict our attention to a three-phase two-component system in which one intermediate phase nucleates, quickly forms a uniform, thin layer and then proceeds to grow into the adjacent phases at equal rates. The equilibrium phase diagram and the concentration vs. distance curve obtained for this case are shown schematically in Fig. 1; for simplicity, we assume negligible solubility in the terminal phases. It is evident that in a couple made up of components A and B and diffused for a time at temperature T_d, the β phase causes two discontinuities to appear in the concentration vs. distance curve; as is shown in Fig. 1, the concentrations at the discontinuities or interface boundaries are usually assumed (with experimental justification) to correspond to the equilibrium concentrations $C_{A\beta}$ and $C_{\beta B}$ of the equilibrium phase diagram.[9,10] The solution of the diffusion equation for this case acquires a relatively simple form if the following additional assumptions are made[9]: (i) the A and B atoms interdiffuse at the same rate independently of composition; (ii) no volume changes occur during interdiffusion; and (iii), the interfaces are displaced equally and parabolically according to the relation $\lambda_i = (-1)^i b t^{1/2}$, where λ_i is the position of the ith interface, $(i = 1,2)$, t is the interdiffusion time, and b is a temperature-dependent time-independent constant. A consequence of assumption (i), for our particular case, is that $(C_A - C_{A\beta}) = C_{\beta B}$ (see Fig. 1). Under these circumstances, we obtain the following relationship:

$$\frac{\sqrt{\pi}}{2} C_{\beta B} b = \frac{(C_{A\beta} - C_{\beta B}) D^{1/2} \exp(-b^2/4D)}{2 \operatorname{erf}(b/2D^{1/2})} \quad (1)$$

where D is the chemical diffusivity in the β phase, and $\operatorname{erf}(b/2D^{1/2}) \equiv \frac{2}{\sqrt{\pi}} \int_0^{(b/2D^{1/2})} \exp(-u^2)\, du$ the well-known Gaussian error integral. If we define $z^2 \equiv b^2/4D$, equation (1) simplifies to the following form:

$$z e^{z^2} \operatorname{erf}(z) = \frac{C_{A\beta} - C_{\beta B}}{2\sqrt{\pi}\, C_{\beta B}}. \quad (2)$$

By differentiating equation (2) with respect to pressure P and manipulating the resulting terms, we eventually derive the following expression:

$$\frac{1}{z}\frac{dz}{dP} = \frac{C_{A\beta}}{C_{A\beta}(1 + 2z^2) - C_{\beta B}(1 - 2z^2)} \times \left(\frac{1}{C_{A\beta}}\frac{dC_{A\beta}}{dP} - \frac{1}{C_{\beta B}}\frac{dC_{\beta B}}{dP}\right) \quad (3)$$

which is equivalent to

$$\left(\frac{1}{b}\frac{db}{dP}\right) = \frac{1}{2}\left(\frac{1}{D}\frac{dD}{dP}\right) + \mu\left(\frac{1}{C_{A\beta}}\frac{dC_{A\beta}}{dP} - \frac{1}{C_{\beta B}}\frac{dC_{\beta B}}{dP}\right) \quad (4)$$

where

$$\mu \equiv \frac{C_{A\beta}}{C_{A\beta}(1 + b^2/2D) - C_{\beta B}(1 - b^2/2D)}. \quad (5)$$

It is clear that the relative importance of pressure-induced concentration changes as contrasted with pressure-induced diffusivity changes depends upon the value of μ. If it is assumed that the fractional change in the diffusivity is equal to the bracketed term in equation (4) involving fractional changes in the concentrations, it is clear that a value $\mu \gg \frac{1}{2}$ will cause pressure-induced concentration changes to outweigh any effects resulting from pressure-induced diffusivity changes; if $\mu \ll \frac{1}{2}$, the situation is reversed. If $\mu \sim \frac{1}{2}$, both effects must be considered in evaluating changes in the kinetics of layer growth. In any case, the effect on layer growth is simply calculated from the relationship $\tau = 2bt^{1/2}$ where τ is the layer thickness

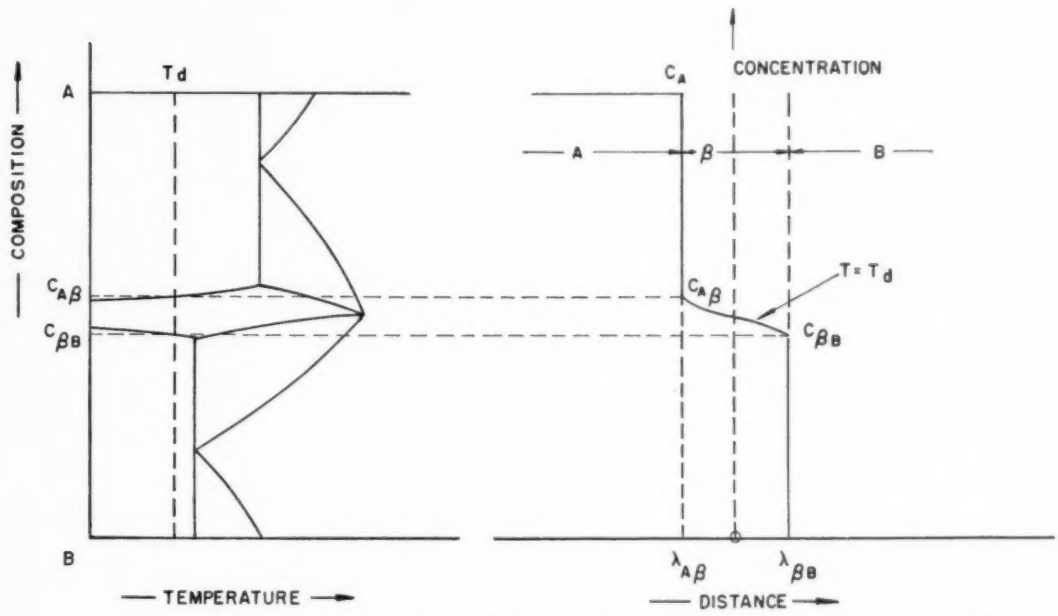


FIG. 1. Equilibrium phase diagram and concentration–penetration curve for a hypothetical three-phase two-component metallic system.

of the β phase; it is obvious that $\frac{1}{\tau}\left(\frac{\partial \tau}{\partial P}\right)_t = \frac{1}{b}\left(\frac{\partial b}{\partial P}\right)_t$.

The function μ is plotted vs. the dimensionless parameter $z \equiv b/2D^{1/2}$ in Fig. 2. It is evident that $\mu > \frac{1}{2}$ if $z < \frac{1}{2}\sqrt{2}$ and that $\mu < \frac{1}{2}$ if $z > \frac{1}{2}\sqrt{2}$; $\mu = \frac{1}{2}$ when $z = \frac{1}{2}\sqrt{2}$. The width of the solubility range $(C_{A\beta} - C_{\beta B})$ does not play an important role, unless $z < 0.5$; below this value μ increases rapidly, such that $\mu \gg \frac{1}{2}$, if $z < 0.1$ and if $(C_{A\beta} - C_{\beta B}) \leqslant 4$ per cent.

It is interesting to calculate the values of z for interface motion in systems such as aluminum–nickel[6] and aluminum–uranium[7], where data are available. Calculations show that in the aluminum–nickel system z is about 0.5 for atmospheric pressure runs at 500°C; by contrast, in the aluminum–uranium system z is about 0.03 for runs at 1.25 tons/in^2 (170 atm) and at 520°C. On the basis of these results, one would predict that pressure-induced changes in the interface concentrations in the aluminum–uranium system would be far more important than in the aluminum–nickel system; this will be discussed more fully later.

MAGNITUDE OF PRESSURE-INDUCED CHANGES IN DIFFUSION COEFFICIENTS AND IN EQUILIBRIUM CONCENTRATIONS

In the discussion above, we have determined for a relatively simple case of interdiffusion the comparative importance to layer growth of equivalent pressure-induced changes in diffusion coefficients and in interface concentrations. It is now necessary to evaluate the magnitude of the changes in the diffusion coefficients and the equilibrium concentrations which can reasonably be expected to occur.

From the data of Ref. (1) and (3), we find that the diffusion coefficient of sodium is decreased 75 per cent if the hydrostatic pressure is increased to 3900 atm; in zinc, the diffusion coefficient along a direction perpendicular to the basal plane is decreased 42 per cent by a hydrostatic pressure of 2000 atm, whereas the decrease is 11 per cent parallel to the basal plane. On the basis of these data, it seems reasonable to expect decreases in diffusion coefficients in solid solutions of the order of 10–20 per cent for pressures of 2000 atm.

Unfortunately, there are no reported data on the effect of hydrostatic pressure on equilibrium concentrations in multiphase metallic systems. It therefore becomes necessary to obtain a reasonable estimate of the magnitude of the effect. We shall do so by considering the effect of hydrostatic pressure on the free energies of the phases in equilibria. It was shown by Gibbs[11] that if curves of the free energies per gram atom of all possible phases in a two-component system are plotted as a function of composition, the concentrations at the ends of the common tangents are the equilibrium concentrations (if the free energies on the tangent lines lie below the curves); furthermore, he pointed out that the application of hydrostatic pressure must raise the free energies of the phases and thus shift the positions of the common tangents. It

VOL. 8 1960

is not difficult to show, using well-known thermodynamic relationships, that the Gibbs free energy of a phase $F_p(\beta)$ varies with pressure approximately as follows:

$$F_p(\beta) = F_0(\beta) + \int_{p_0}^{p} V(\beta)\, dP$$
$$\cong F_0(\beta) + V_0(\beta)\Delta P + \frac{1}{2!} V_0(\beta)\beta_\beta(\Delta P)^2 + \ldots \quad (6)$$

where $F_0(\beta)$ is the free energy per gram atom of the β phase, β_β is the isothermal compressibility of the β phase, and ΔP is the increase in hydrostatic pressure. If we consider pressures such that $\Delta P < 10^4$ atm

$$\frac{1}{2!} V_0(\beta)\beta_\beta(\Delta P)^2 < 0.01\ V_0(\beta)\Delta P.$$

Since $\beta_\beta \sim 10^{-6}$ atm^{-1}[12] so, to a first approximation, we can neglect the higher order terms in ΔP and consider $[F_p(\beta) - F_0(\beta)] \sim V_0(\beta)\Delta P$. Thus, if we know how the gram atomic volume of a phase varies with composition, we can readily estimate the extent to which its free energy curve is raised by hydrostatic pressure. In certain cases, Vegard's law applies,[13] and the lattice spacings and thus the gram atomic volume are simply a linear function of atomic composition; in other cases, the gram atomic volumes would have to be determined experimentally. Once the free energy curves are available for all the phases at the elevated pressures, it is a simple matter to determine graphically the shifts in equilibrium concentration with pressure.

Using the $V\Delta P$ relationship to estimate the magnitudes of the free energy increases we find it reasonable to expect the maximum free energy increase to be less than 1500 cal/g atom for applied hydrostatic pressures of 5000 atm or less. The gram atomic volumes of most metals range from 6–20 cm^3/g atom[14] (except for the alkali metals and the alkaline earths, which go up to as high as 70 cm^3/g atom). It is likely that the intermetallic phases will not have values much greater; for example, this is the case for the aluminum–nickel and the aluminum–uranium systems, as is shown in the table:

Phase	Volume per g atom	Phase	Volume per g atom
Al	10.0[14]	Al	10.0[14]
$NiAl_3$ (β)	8.8*	UAl_4 (ζ)	12.1[16]
Ni_2Al_3 (γ)	8.3*	UAl_3 (ε)	11.7[17]
NiAl (δ)	7.2*	UAl_2 (δ)	12.0[18]
Ni_3Al (ε)	6.8*	U	12.7[14]
Ni	6.6[14]		

* Calculated from X-ray diffraction data in Ref. (15)

A further point to be considered is that it is the difference in volumes of the phases in a system which will determine the shift in the common tangent on the free energy diagram and thus the shift in equilibrium compositions. Thus, if we assume that a difference in volume of 10 cm^3/g atom exists between two phases, at a pressure of 5000 atm, the relative increase in free energy of one phase over the other is 50,000 cm^3 atm or 1210 cal. In most cases, the free energy differences will probably be much less.

We turn next to an examination of the extent to which equilibrium concentrations can be expected to shift in a two-phase two-component system as the free energy curves of the two phases α and β are raised by pressure. As has been pointed out previously, one can determine this graphically for any specific cases where the necessary thermodynamic data are available. Alternatively, one can calculate the shifts analytically by means of the following expression:[19]

$$\left(\frac{\partial C_B^{\alpha}}{\partial P}\right)_T = -\frac{(1 - C_B^{\beta})(\bar{V}_A^{\alpha} - \bar{V}_A^{\beta}) + C_B^{\beta}(\bar{V}_B^{\alpha} - \bar{V}_B^{\beta})}{(C_B^{\beta} - C_B^{\alpha})} \times \frac{(1 - C_B^{\alpha})}{(\partial \mu_B^{\alpha}/\partial C_B^{\alpha})_{T,P}} \quad (7)$$

where $C_B^{\alpha}, C_B^{\beta}$ = equilibrium concentrations of component B in the α and β phases at atmospheric pressure

$\bar{V}_A^{\alpha}, \bar{V}_A^{\beta}$ = partial molal volumes of component A in the α and β phases at the concentrations C_B^{α} and C_B^{β}, respectively

$\bar{V}_B^{\alpha}, \bar{V}_B^{\beta}$ = partial molal volumes of component B in the α and β phases at the concentrations C_B^{α} and C_B^{β}, respectively

$\mu_B^{\alpha}, \mu_B^{\beta}$ = chemical potentials of component B in the α and β phases at the concentrations C_B^{α} and C_B^{β}, respectively.

Equation (7) indicates the extent to which the equilibrium concentration of the α phase is shifted by pressure; a similar expression is obtained for the shift in the β phase equilibrium concentration, if the superscripts involving α and β are interchanged. For many systems, however, including aluminum–nickel and aluminum–uranium, the thermodynamic data needed to evaluate the pressure-induced equilibrium concentration shifts are not available; nevertheless,

useful qualitative and semi-quantitative information can be obtained by the use of suitable approximations which provide one with additional insight of a geometrical nature. We shall therefore examine the consequences of several approximations and the extent to which they can be trusted.

As was mentioned earlier, the equilibrium concentrations of the α and β phases are those corresponding to the end points of the common tangent. The first assumption we make is that the free energy curves may be suitably approximated by circular arcs in the vicinity of the extremities of their common tangents. If R^α and R^β are the radii of curvature, it is not difficult to show that equation (7) is transformed to the following relationship:

$$\left(\frac{\partial C_B{}^\alpha}{\partial P}\right)_T = -[(1 - C_B{}^\beta)(\bar{V}_A{}^\alpha - \bar{V}_A{}^\beta) + C_B{}^\beta(\bar{V}_B{}^\alpha - \bar{V}_B{}^\beta)] \times \frac{R^\alpha}{M^\alpha} \qquad (8)$$

where

$$M^\alpha \equiv (C_B{}^\beta - C_B{}^\alpha)\,[1 + (\partial F^\alpha/\partial C_B{}^\alpha)^2{}_{T,P}]^{3/2}$$

F^α is the free energy per gram atom at the concentration $C_B{}^\alpha$.

A similar expression holds for $\left(\frac{\partial C_B{}^\beta}{\partial P}\right)_T$ if the superscripts involving α and β are interchanged. Since $\left(\frac{\partial F^\alpha}{\partial C_B{}^\alpha}\right) = \left(\frac{\partial F^\beta}{\partial C_B{}^\beta}\right)$ at the equilibrium concentrations, $M^\alpha = M^\beta$. Equation (8) is thus more useful than equation (7) in determining relative changes in equilibrium concentrations if one has an idea as to the values of R^α and R^β for a particular case. We can obtain some appreciation for the curvatures of free energy curves corresponding to terminal solid solutions and intermediate alloy phases by arbitrarily standardizing co-ordinate scales for plots of free energy per gram atom vs. composition curves and examining available data. For convenience, we select scales such that the interval used for one atom per cent on the abscissa is equal to the interval used to denote 10 cal/g atom on the ordinate. Using these scales, we find by replotting Seigle's data for the gold–nickel system[20] that the curvatures of the α phase free energy curves in which a wide solubility range exists have radii of the order $R^\alpha = 60$; on the other hand, the curvature of the α' phase curve, where the solubility is about 10 atom per cent, is such that $R^\alpha = 8$. Free energy curves calculated from Lawson's theoretically derived equation of state for binary metallic systems[21] also show similar ranges for radii of curvature.* Thus, in the absence of data for any specific case, it seems reasonable to assume that values of radii of curvature for intermediate alloy phases having highly restricted solubility ranges (up to 10 atom per cent) will be of the order of 1–10.

The approximation involving the radius of curvature is not particularly restrictive since we can in principle fit a circular arc to a portion of the free energy per gram atom vs. composition curve so as to make the error introduced by the use of equation (8) instead of equation (7) as small as we wish. Equation (8) can be still further simplified if we can assume safely that $V_\alpha \cong \bar{V}_A{}^\alpha \cong \bar{V}_B{}^\alpha$ and that $V_\beta \cong \bar{V}_A{}^\beta \cong \bar{V}_B{}^\beta$, where V_α and V_β are the mean volumes per gram atom of the α and β phases respectively. It is easy to show that equation (8) then simplifies to the following relationship:

$$\left(\frac{\partial C_B{}^\alpha}{\partial P}\right)_T = -\frac{(V_\alpha - V_\beta)R^\alpha}{M^\alpha} \qquad (9)$$

where, as before, the expression for $\left(\frac{\partial C_B{}^\beta}{\partial P}\right)_T$ is obtained by the interchange of the superscripts α and β. The assumption expressed analytically above can be shown to have the geometrical consequence that the effect of pressure will be merely one of displacing the free energy per gram atom vs. composition curves upward without changing their shapes in the vicinity of the common tangent extremities.[22] In practical situations, equation (9) proves useful for systems where (i) it is suspected that the variation in volume per gram atom over the composition range of each of the phases is monotonic and small or (ii) where the solubility ranges of the phases are so small that it is difficult to obtain an accurate measure of the variation in volume per gram atom with composition.

It must be emphasized, however, that the assumptions embodied in equation (9) are highly restrictive[22] and that it must therefore be used with caution.

We next set out to determine the percent change in the atmospheric pressure value of $C_{A\beta}$ of the hypothetical β intermetallic phase in whose growth we are interested (Fig. 1). We assume the situation to be that indicated in Fig. 3, where the free energy of formation of the β phase is several hundred cal/g atom below the free energy of formation of an ideal solid solution of the same composition. We also assume that the curve of free energy per gram atom varies sharply with composition so that $R_\beta = 1$ (corresponding to a solubility range of 2 atom per cent or less) and the

* A numerical error found in Lawson's paper has been corrected.

VOL. 8 1960

TABLE 1. Pressure-induced shift in equilibrium interface concentration $C_{A\beta}$*

$(F_\beta - F_A)$ (cal/g atom)	$V_B - V_A$ (cm³/g atom)	P (atm)	$(F_\beta' - F_A')$ cal/g atom)	$\Delta C_{A\beta}$ (atom per cent)	$[\Delta C_{A\beta}/C_{A\beta}]\,100$ (per cent)
1500	5	1000	1379	0.01	0.02
		5000	895	0.08	0.16
	1	1000	1476	<0.01	<0.01
		5000	1379	0.01	0.02
2000	5	1000	1879	0.01	0.02
		5000	1395	0.03	0.06
	1	1000	1976	<0.01	<0.01
		5000	1879	0.01	0.02
3000	5	1000	2879	<0.01	<0.01
		5000	2395	0.015	0.03
	1	1000	2976	<0.01	<0.01
		5000	2879	<0.01	<0.01

* R_β assumed to be 1 so that $C_{A\beta} = 49$

pressure-induced change in shape can be neglected. We convert equation (9) to the following form:

$$\Delta C_{A\beta} \cong -\frac{[(V_A - V_\beta)\Delta P]R^\beta}{C_{A\beta}\sec^3\phi_0}$$

$$\cong -\frac{R^\beta[(F_\beta' - F_\alpha') - (F_\beta - F_\alpha)]}{C_{A\beta}\sec^3\phi_0} \qquad (10)$$

where $(F_\beta - F_\alpha)$ is the free energy of formation per gram atom of the β phase at the stoichiometric composition AB and at atmospheric pressure, $(F_\beta' - F_\alpha')$ is the corresponding quantity at elevated pressure, and ϕ_0 is the angle between the abscissa and the common tangent at atmospheric pressure. Equation (10) can then be used to evaluate the value of $\Delta C_{A\beta}$. An even simpler and more accurate way to evaluate $\Delta C_{A\beta}$ is to use the relation

$$\Delta C_{A\beta} = R^\beta(\sin\phi' - \sin\phi_0), \qquad (11)$$

where ϕ' is the angle between the abscissa and the common tangent at elevated pressure, and ϕ_0 is as defined above. Equation (11) is easily derived geometrically and embodies the same assumptions as those used in deriving equation (9). Using equation (11), we obtain the results listed in Table 1. We see that the shifts in composition of $C_{A\beta}$ are very small indeed and do not exceed 0.1 per cent of the original composition unless a pressure-induced free energy increase of over 600 cal per gram atom (25,000 cm³ atm) is postulated.

It is now possible to evaluate the relative importance of pressure-induced shifts in the equilibrium concentrations at the interfaces as compared with pressure induced changes in the diffusion coefficient for the β phase. As we have found, it is unlikely to expect per cent changes in the original concentrations greater than a few tenths of a percent for an intermediate alloy phase having restricted solubility unless very high pressures (greater than 5000 atm) are used and the phase has an unusually high mean gram atomic volume in comparison to adjacent phases. On the other hand, it is reasonable to expect the diffusion coefficient of the intermediate alloy phase to be diminished by at least one order of magnitude (and perhaps two orders) greater than the equilibrium concentration changes. Consequently, by referring to equation (4), we conclude that a pressure-induced change in interface concentration is not important unless the function μ is at least greater than five and perhaps greater than fifty. For the β phase, we see by looking at Fig. 2 that $5 \leqslant \mu \leqslant 25$ if $0 \leqslant z \leqslant 0.25$; thus, if the pressure-induced decrease in diffusion coefficient is 10 per cent or greater, the pressure-induced concentration changes can probably be neglected.

INTERDIFFUSION IN THE ALUMINUM–NICKEL AND ALUMINUM–URANIUM SYSTEMS

We shall now attempt to rationalize the experimental results obtained in investigations of intermetallic layer growth in the aluminum–nickel and in the aluminum–uranium systems. We shall use the analysis developed above for a three-phase two-component system, even though we recognize that both systems exhibit far more complicated equilibrium relationships involving many more phases. Also, we shall be forced to make additional approximations for want of experimental data.

In the aluminum–nickel system and in the aluminum–uranium system, the kinetics of growth of the $\gamma(Ni_2Al_3)$ phase and the $\varepsilon(UAl_3)$ phase have been

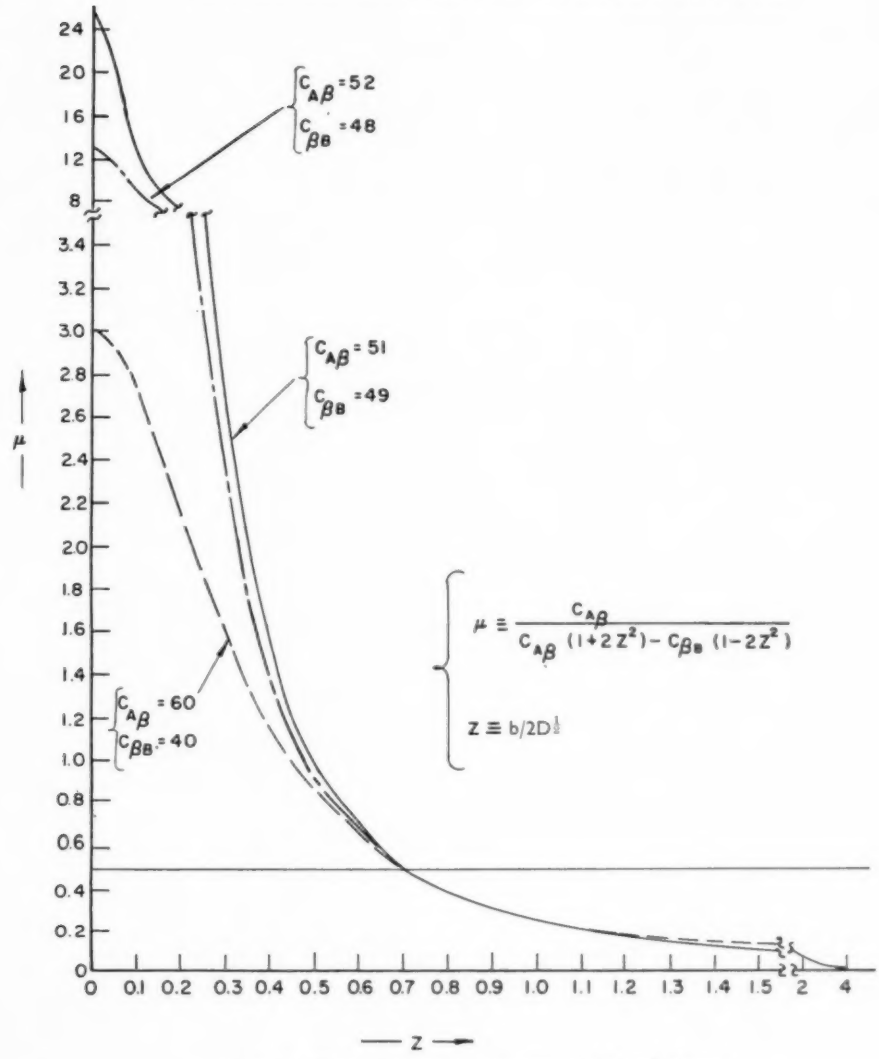


FIG. 2. Plot of μ vs. z (parameters defined above).

shown to be particularly susceptible to applied pressure;[5,6,7] the thickness of the $\gamma(Ni_2Al_3)$ phase is diminished, whereas the thickness of the $\varepsilon(UAl_3)$ phase is considerably enhanced. In Table 2 are listed typical values for the layer thicknesses obtained as a function of pressure.

Thus, at the times and temperatures employed, a pressure of 1360 atm reduces the $\gamma(Ni_2Al_3)$ layer thickness by 20 per cent, whereas the $\varepsilon(UAl_3)$ layer thickness is increased 200–450 per cent.

We now set out to evaluate on a first order approximation basis the relative effects of concentration

TABLE 2

Pressure		$\gamma(Ni_2Al_3)$			$\varepsilon(UAl_3)$		
t.s.i.	atm	Temp. (°C)	Time (hr)	Thickness (mm)	Temp. (°C)	Time (hr)	Thickness (mm)
0.007	1	500	96	0.083	520	3	(0.32)*
1.25	170	—	—	—	520	3	0.62
5	680	500	96	0.071	520	3	1.45
10	1360	500	96	0.066	520	3	1.75

* Estimated by extrapolation

VOL. 8 1960

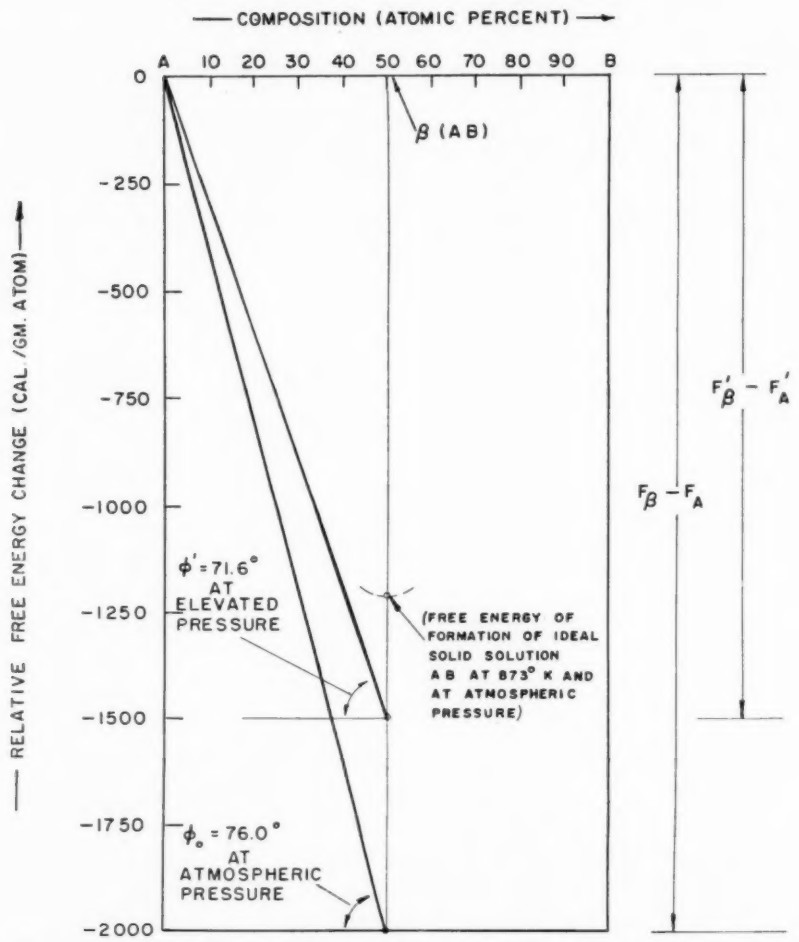


FIG. 3. Hypothetical change in free energy relationships as a function of pressure between intermediate alloy phase β (AB) and a terminal solid solution—both having highly restricted solubility ranges.

changes as compared with changes in the diffusion coefficients on layer growth in the two systems. To do so, we use equation (4), treating the differentials as increments and recognizing the fact that the solution represented by the equation does not rigorously fit the systems analysed. We obtain estimates of the pressure-induced changes in interface motion from the growth data in the table above; we evaluate μ_γ and μ_ε by calculating values of z_γ and z_ε from layer growth data available in Ref. (6) and (7) and then using Fig. 2; finally, we estimate the upper and lower bounds of the fractional changes in concentrations from hypothetical free energy curve approximations and from mean atomic volume data. Once all this is done, the fractional change in interface motion due to pressure-induced reductions in the diffusion coefficients can be calculated from equation (4). The details of the calculations for the aluminum–uranium system can be found in the Appendix; the results for the aluminum–nickel system have been obtained similarly. The calculated values are listed in Table 3.

TABLE 3

Intermetallic phase	Temp. (°C)	Pressure change (atm)	$\frac{\Delta\tau}{\tau}$	Solubility range (at. % U or Ni)	Solubility range Increase at. % U or Ni) min.	max.	$\frac{\Delta D}{D}$
$\varepsilon(UAl_3)$	520	170–680	1.34	24–28	—	+0.5	+2.24
	520	170–680	1.34	24–28	+0.3	—	+2.40
	520	170–680	1.34	24–26	—	+0.2	+2.33
	520	170–680	1.34	24–26	+0.2	—	+2.33
	500	1–680	−0.144	37–41	—	+0.3	−0.30
$\gamma(Ni_2Al_3)$	500	1–680	−0.144	37–41	−2.6	—	−0.22

τ = thickness of layer

We first consider the results obtained for the aluminum–uranium system. For reasons indicated earlier, it is reasonable to expect that pressure will decrease the diffusion coefficient of the ε phase (or at least not increase it). If the calculation is to predict this result, it follows that the second term on the right-hand side of equation (4), which includes the effect on layer growth of the pressure-induced change in equilibrium concentration, must be at least as large as the fractional increase in ε-layer thickness. However, it is clear from the calculated large positive values of $(\Delta D/D)$ in Table 3 that such is not the case. It thus appears unlikely that pressure-induced changes in equilibrium concentrations can be used to explain the observed increases in ε-layer growth. An alternative explanation has been advanced by Castleman and Seigle[7] that pressure could increase layer growth by repressing the tendency for the formation of macroscopic voids and thus effectively increasing the cross-sectional area available for interdiffusion. This explanation requires additional experimental verification.

In the aluminum–nickel system a similar calculation shows (see Table 4) that the concentration changes affect γ layer growth much less than do the decreases in the diffusion coefficient. It proves possible to rationalize the layer growth data regardless of the manner in which pressure affects the equilibrium concentrations. It seems plausible, however, to expect that pressure will not decrease the diffusion coefficient by as much as 30 per cent. On this basis, the diminution in layer growth may be due in part to a decrease in the solubility range of a few tenths of a per cent.

VOL. 8 1960

SUMMARY

In the preceding discussion, we have examined the problem of determining the effect of hydrostatic pressure on the course of multiphase diffusion in systems in which an intermetallic phase nucleates and grows uniformly at the original interface of a diffusion couple. In order to obtain some quantitative insight, we have considered a highly idealized case of interdiffusion in a three-phase two-component system, in which the kinetics of layer growth are controlled by equilibrium interface concentrations and by the diffusion coefficient in the intermetallic phase. An equation has been derived which enables us to estimate the relative importance to intermetallic layer growth of pressure-induced changes in the diffusion coefficients and pressure-induced shifts in the interface boundary concentrations. The equation shows that the importance of equilibrium concentration changes depends upon the magnitude of the dimensionless parameter, $z = \lambda/2(Dt)^{1/2}$, where λ is the mean interface displacement, D is the diffusion coefficient of the intermetallic phase, and t is the interdiffusion time. A given change in concentration becomes relatively quite important when z is very small. We have estimated the magnitude of such changes by evaluating the extent to which hydrostatic pressure influences the phase equilibria. We have next considered the pressure-induced increase in the growth rate of the $\varepsilon(UAl_3)$ phase of the aluminum–uranium system and the pressure-induced decrease in growth rate of the $\gamma(Ni_2Al_3)$ phase of the aluminum–nickel system. We have decided that it is not possible to rationalize the growth kinetics of the ε phase on the basis of the extent to which pressure increases the equilibrium solubility range. Finally, we have concluded that the pressure-induced decrease in the γ phase diffusion co-efficient is more important to the growth kinetics of the γ phase than equilibrium solubility range changes.

ACKNOWLEDGMENTS

The author is pleased to acknowledge the helpful discussions that he held with Dr. L. Seigle during the course of this work. He also wishes to thank Dr. J. Brett, who critically read the manuscript and suggested several improvements. This work was performed as part of AEC Contract No. AT(30-1)2102.

REFERENCES

1. N. H. Nachtrieb, J. H. Weil, E. Catalano and A. W. Lawson, *J. Chem. Phys.* **22,** 1189 (1952).
2. N. H. Nachtrieb and A. W. Lawson, *J. Chem. Phys.* **23,** 1193 (1955).
3. T. Liu and H. G. Drickamer, *J. Chem. Phys.* **22,** 312 (1954).
4. S. Storcheim, J. L. Zambrow and H. H. Hausner, *Trans. Amer. Inst. Min. (Metall.) Engrs.*, **200,** 269 (1954).
5. A. D. LeClaire and I. J. Bear, *J. Nucl. Energy* **2,** 229 (1956).
6. L. S. Castleman and L. Seigle, *Trans. Amer. Inst. Min. (Metall.) Engrs.* **212,** 589 (1958).
7. L. S. Castleman and L. Seigle, *Fundamentals of Diffusional Bonding*—III, Sylvania Electric Products Report SEP-251 (1958).
8. J. S. Kirkaldy, *Canad. J. Phys.* **36,** 899 (1958).
9. L. S. Castleman, *Nucl. Sci. Engng.* **4,** 209 (1958).
10. V. Macres, J. T. Norton and R. E. Ogilvie, *J. Met., N.Y.* **11,** 72 (1959).
11. J. W. Gibbs, *On the Equilibrium of Heterogeneous Substances*, p. 120. Collected Works, Yale University Press, New Haven (1948).
12. W. Hume-Rothery and G. V. Raynor, *The Structure of Metals and Alloys*, p. 74. Institute of Metals, London (1954).
13. C. S. Barrett, *Structure of Metals*, p. 202. McGraw-Hill, New York (1943).
14. *Metals Handbook*, p. 20. American Society for Metals, Cleveland, Ohio (1948).
15. A. J. Bradley and A. Taylor, *Proc. Roy. Soc.* A**159,** 56 (1937).
16. B. S. Borie, Jr., *Trans. Amer. Inst. Min. (Metall.) Engrs.* **191,** 800 (1951).
17. P. Gordon and A. R. Kaufmann, *Trans. Amer. Inst. Min. (Metall.) Engrs.* **188,** 182 (1950).

18. R. E. Rundle and A. S. Wilson, *Acta Cryst.* **2,** 148 (1949).
19. J. E. Hilliard and J. W. Cahn, to be published.
20. L. L. Seigle, M. Cohen and B. L. Averbach, *Trans. Amer. Inst. Min. (Metall.) Engrs.* **194,** 1320 (1952).
21. A. W. Lawson, *J. Chem. Phys.* **15,** 831 (1947).
22. Unpublished work.

APPENDIX

We wish to estimate the relative effects of concentration changes and diffusion coefficient changes on ε phase layer growth in the aluminum–uranium system for a pressure change from 170 atm (1½ tons/in²) to 680 atm (5 tons/in²). We begin by rewriting equation (4), using a more suitable notation:

$$\left(\frac{1}{b}\frac{\Delta b}{\Delta P}\right) = \frac{1}{2}\left(\frac{1}{D}\frac{\Delta D}{\Delta P}\right) + \mu\left[\left(\frac{\Delta C_+}{C_+}\right) - \left(\frac{\Delta C_-}{C}\right)\right] \qquad (A.1)$$

Here, we assume that we can use the differentials as increments; also, the value b is considered to be the mean value for both UAl_3 interfaces $\left(\text{this implies that } \frac{1}{\tau}\frac{\Delta\tau}{\Delta P} = \frac{1}{b}\frac{\Delta b}{\Delta P}\right)$. The concentration C_+ is the equilibrium value on the high uranium side of the intermetallic phase and C_- is the lower equilibrium value; a positive value of ΔC_+ or ΔC_- implies that the uranium concentration has increased. A further assumption is made that the ε phase has a solubility range of several at. %; this assumption is based on unpublished data showing that a solubility range does exist, contrary to the information in the published phase diagram (Ref. 17), that it is 2–6 atom per cent wide and extends more to the U-rich side than to the Al-rich side.

From the thickness data given in the table, we determine that

$$b \cong \frac{\tau}{2}t^{-1/2} = \frac{0.062}{2}(3 \times 3600)^{-1/2} = 2.98 \times 10^{-4}\ \text{cm sec}^{-1/2}.$$

Also, from thickness data tabulated elsewhere (Ref. 7), we estimate that $D \cong 0.05 \exp(-12{,}000/RT)$ and that $D_{500°C} = 2 \times 10^{-5}$ cm² sec^{-1}; thus

$$z \equiv b/2D^{1/2} \cong \frac{2.98 \times 10^{-4}}{2(2 \times 10^{-5})^{1/2}} \cong 0.03.$$

Using Fig. 2, we note that $\mu \cong 12$ for $z = 0.03$.

We now estimate the equilibrium concentration shift due to the pressure increase. From the gram atomic volume data we note that

$$\Delta V_{UAl_4 \to \varepsilon} \equiv V_{UAl_3} - V_{UAl_4} = -0.4\ \text{cm}^3/\text{g atom},$$

and that

$$\Delta V_{UAl_4 \to UAl_2} \equiv V_{UAl_2} - V_{UAl_4} = -0.1\ \text{cm}^3/\text{g atom}.$$

Thus, we calculate that

$$\Delta F_{UAl_4 \to UAl_2} = \Delta P(\Delta V_{UAl_4 \to UAl_2}) = (680\text{–}170)(0.0242)(-0.1)$$
$$= -1.23\ \text{cal/g atom}$$

$$\Delta F_{UAl_4 \to \varepsilon} = \Delta P(\Delta V_{UAl_4 \to \varepsilon}) = (680\text{–}170)(0.0242)(-0.4)$$
$$= -4.92\ \text{cal/g atom}.$$

Using these data, we construct plots of Gibbs free energy vs. composition curves to obtain upper and lower bounds for the changes in equilibrium concentrations produced by pressure; as previously indicated, we approximate the shapes of the curves by circular arcs whose radii are unaffected by pressure. For the first calculation, we assume that $R = 4$ for the ε phase and a solubility range of 4 atom per cent; for the UAl_2 and UAl_4 phases, we assume that $R \ll 4$ and that the solubility ranges are negligible. With a little graphical experimentation, we determine the maximum and minimum changes in the equilibrium concentrations of the ε phase produced by the displacements in the curves corresponding to the free energy changes calculated above. A similar procedure is used to obtain the other values listed in Table 4.

We encounter a problem in calculating the fractional changes in concentration. It must be remembered that equation (A.1) applies to a situation in which $(C_A - C_{A\beta}) = C_{\beta B}$ (see Fig. 1); thus, no ambiguity is introduced if the concentration is expressed either in terms of A or of B atoms. However, in the present instance, the values $\left(\frac{\Delta C_+}{C_+}\right)$ and $\left(\frac{\Delta C_-}{C_-}\right)$ definitely do depend upon whether we express the concentrations in terms of uranium or of aluminum. We arbitrarily choose uranium concentrations, since this choice will maximize the values of the fractional changes and will be consistent with our intention of obtaining estimates of maximum pressure–induced concentration effects.

The values obtained above are inserted in equation (A.1), and the results are tabulated below. Similar calculations are made for $R_\varepsilon = 2$, and for the $\gamma(Ni_2Al_3)$ phase in the aluminum–nickel system, and these results are also included:

TABLE 4

Phase	Solubility range (at. % U)	ΔP	R	$\left(\frac{\Delta C_+}{C_+}\right)$	$\left(\frac{\Delta C_-}{C_-}\right)$	μ	$\mu\left[\left(\frac{\Delta C_+}{C_+}\right) - \left(\frac{\Delta C_-}{C_-}\right)\right]$	$\frac{\Delta b}{b}$	$\frac{\Delta D}{D}$
ε (UAl_3)	24–28	510	4	+0.018	0	12.0	+0.22	1.34	+2.24
				+0.007	−0.004	12.0	+0.14	1.34	+2.40
	23–27	510	4	+0.018	0	12.0	+0.22	1.34	+2.24
				+0.007	−0.004	12.0	+0.14	1.34	+2.40
	24–28	510	2	0	0	12.0	0	1.34	+2.68
				0	0	12.0	0	1.34	+2.68
	24–26	510	2	+0.008	0	22.5	+0.17	1.34	+2.33
				+0.004	−0.004	22.5	+0.17	1.34	+2.33
γ (Ni_2Al_3)	37–41	680	4	−0.034	0	0.98	−0.033	−0.144	−0.22
				0	−0.008	0.98	+0.008	−0.144	−0.30

DISPERSED PARTICLE HARDENING OF ALUMINUM–COPPER ALLOY SINGLE CRYSTALS*

D. DEW-HUGHES† and W. D. ROBERTSON‡

Single crystals were grown in aluminum–copper alloys containing from 3 to 5 per cent copper. These crystals were strained in tension after receiving heat treatments designed to develop $CuAl_2$ particles of varying sizes and distributions. Values of the critical resolved shear stress were found to be inversely proportional to the mean spacing between particles, in accordance with Orowan's theory. Fisher, Hart and Pry's theory that dislocation rings formed around the particles during deformation make a large contribution to work hardening, has received confirmation from the experimental results on these crystals. While a crystallographically defined critical resolved shear stress was observed, deformation took place mostly by multiple slip, the external characteristics of the deformation being similar to those of polycrystalline material.

DURCISSEMENT PAR PRECIPITES DISPERSES DE MONOCRISTAUX D'ALLIAGES ALUMINIUM-CUIVRE

Les auteurs ont préparé des monocristaux d'alliages aluminium-cuivre contenant de 3 à 5 pour cent de cuivre. Ces cristaux ont été déformés par traction après des traitements thermiques favorables à la formation de particules de $CuAl_2$ de tailles et de distribution différentes. En accord avec la théorie d'Orowan, les valeurs de la tension de cisaillement critique sont inversément proportionnelles à l'écartement moyen des particules. Sur la base des résultats expérimentaux obtenus sur ces cristaux, les auteurs peuvent confirmer la validité de la théorie de Fisher, Hart et Pry, selon laquelle les anneaux de dislocation formés autour des particules pendant la déformation apportent une contribution importante au durcissement. Bien que l'on ait observé une tension de cisaillement critique définie cristallographiquement, la déformation se produit principalement par glissement multiple, les caractéristiques extérieures de la déformation étant semblables à celles des polycristaux.

AUSHÄRTUNG VON EINKRISTALLEN AUS ALUMINIUM-KUPFER LEGIERUNGEN DURCH AUSGESCHIEDENE TEILCHEN

Aus Aluminium-Kupfer Legierungen mit 3–5 Prozent Kupfergehalt wurden Einkristalle hergestellt. Nach Wärmebehandlungen, die zur Bildung von $CuAl_2$-Teilchen verschiedener Größe und Verteilung führten, wurden die Kristalle im Zugversuch untersucht. Die Werte der kritischen Schubspannung ergaben sich in Übereinstimmung mit der Theorie von Orowan als umgekehrt proportional zum mittleren Abstand zwischen den ausgeschiedenen Teilchen. Die experimentellen Ergebnisse bestätigen die Theorie von Fisher, Hart und Pry, daß Versetzungsringe, die sich während der Verformung um die Teilchen herum bilden, zur Verfestigung stark beitragen. Es wurde zwar eine kristallographisch definierte kritische Schubspannung beobachtet, doch die Verformung erfolgte meist durch Vielfachgleitung. Dabei waren die äußeren Züge der Verformung ähnlich wie bei vielkristallinem Material.

VOL. 8 1960

INTRODUCTION

The effectiveness of a dispersed second phase for increasing the strength of a metallic matrix is now well established. Despite its technological importance, however, few investigations have been carried out to elucidate the mechanism of dispersed particle hardening. The first of these investigations was that of Gensamer *et al.*[1] who studied the effects of carbide dispersions in ferritic steels. They showed that, for a wide range of dispersions produced either by the pearlite reaction or by tempering martensite, the flow stress increased as the logarithm of the mean ferrite path decreased and was independent of carbon content or type of dispersion. The later results of Roberts *et al.*[2] agree well with Gensamer's findings.

Gregory and Grant[3] found that, in S.A.P. type materials, the strength was a linear function of the reciprocal of the spacing between the Al_2O_2 particles in the aluminum matrix. Gregory[4] found the same relationship in internally oxidized silver–aluminum alloys. This agrees with the predicted mechanism of Orowan[5,6], provided that the particles are uniformly dispersed in the grains and not concentrated at the grain boundaries. On the other hand, the data of Lenel *et al.*[7] on Al–Al_2O_3 alloys, in which the Al_2O_3 particles appear as flakes rather than spheroids, favor the Gensamer relation. Shaw *et al.*[8] using aluminum containing 3, 4 and 5 per cent copper and given differing heat treatments in the overaged region, obtained samples with a wide range of $CuAl_2$ particle dispersion. They found that at room temperature the initial flow stress varied as the matrix mean free path

* Received May 4, 1959. This paper is abstracted from a thesis by D. Dew-Hughes submitted to the Graduate Division of the Yale School of Engineering in partial fulfillment of the requirements for the degree of Doctor of Engineering.

† International Business Machines Corporation, Research Center, Poughkeepsie, N.Y.

‡ Hammond Metallurgical Laboratory, Yale University, New Haven, Conn.

to the power 0.15. Thomas and Nutting[9] using the electron microscope, studied the formation and appearance of slip lines on the surface of individual crystals in polycrystalline Al–4% Cu and Al–7% Mg alloys deformed to fracture after different ageing treatments. In the overaged alloys, the slip lines appeared to avoid the $CuAl_2$ and Mg_2Al_3 particles completely, by climbing over them.

Several theories have been advanced to explain the mechanism of dispersed particle strengthening.

Gensamer *et al.*[1], in order to account for the observed semi-logarithmic relationship, offered the following explanation. The particles divide the material into blocks, whose dimensions are equal to the interparticle spacing, and limit the mean dislocation path to the dimensions of these blocks. The number of dislocations moving over this mean dislocation path to produce a given macroscopic strain will be inversely proportional to the mean path. To produce strain at a certain time rate, dislocations must be generated at a rate which is also inversely proportional to this path length. If the relation between the rate of formation of dislocations and the applied stress is known, then the effect of the mean dislocation path on the resistance to deformation at constant strain and constant strain rate is also known. The relation between speed of deformation and stress is thought to be semi-logarithmic, at least for copper and steel at low temperatures.[10,11] If the speed of deformation is proportional to the rate of generation of dislocations, then the stress should be proportional to the negative logarithm of the mean interparticle spacing. As noted previously, this relation has been confirmed in ferritic steels and for Al–Al_2O_3 alloys in which the oxide particles are in the form of flakes.

Orowan[5,6] has proposed that the critical shear stress of a crystal should be proportional to the reciprocal of the mean spacing between particles. He suggested that as a dislocation approaches two non-deforming particles it will bow out between them, finally connecting with itself beyond them and leaving a dislocation ring around each particle. The stress necessary to bow out the dislocation is inversely proportional to the radius of curvature assumed, and the maximum stress corresponds to the minimum radius of curvature through which the dislocation passes. This minimum radius of curvature is taken to be equal to half the distance between the particles. If the mean distance between particles is d, then the critical shear stress $\tau_c = \dfrac{2\alpha\mu b}{d}$, where μ is the shear modulus of the matrix, b the Burgers vector, and α is a constant obtainable from dislocation theory. This relation is in agreement with the previously mentioned results of Gregory[4] and Gregory and Grant[3].

No mechanistic theory has yet been offered to explain the results of Shaw *et al.*[8]

One other theory will be mentioned here; namely, that of Fisher *et al.*[12] in which the contribution of precipitate particles to work-hardening is considered. It does not attempt to account for the critical shear stress of the material, but assumes that the accumulation of dislocation rings left around precipitate particles lying in the active slip planes, due to the operation of the Orowan mechanism, give rise to a back stress which must be overcome by dislocations moving on the plane. This back stress is assumed to be a significant contribution to work-hardening. The results of Fisher, Hart and Pry's[12] computations show that, after a given amount of deformation, the shear stress for further deformation, τ_h, should be given by $\tau_h = (3N\mu bf^{3/2}/r) + \tau'_h$ where N is the number of dislocation rings around each particle, f is the volume fraction of precipitate, r is the mean planar particle radius and τ'_h is the increment in flow stress due to all other sources of work-hardening. τ'_h may or may not be negligible. The shear stress on a particle due to the N loops around it is approximately $N\mu b/r$ and cannot exceed the theoretical critical shear stress for the particle. As the particles are usually small, they may be considered to be nearly perfect and their critical shear strength should be approximately 0.1μ.[13] If r is of the order 10^3b, N will have a maximum value of the order of 100. Fisher *et al.* applied their theory to the results of Shaw *et al.*[8] and found reasonable agreement between theory and observation.

The present investigation was undertaken to evaluate quantitatively the various existing theories and to supply necessary data for their extension. The work was performed with single crystals, to eliminate grain boundary effects and to define the shearing stresses with respect to the structure. The aluminum–copper system was chosen because single crystals of dilute aluminum–copper alloys could be grown and particles of the $CuAl_2$ phase could be precipitated without causing recrystallization.* Furthermore, particle size and dispersion could conveniently be varied by the use of suitable heat treatments.

EXPERIMENTAL

High purity aluminum–copper alloys were supplied by the Aluminum Company of America's Research Laboratories in the form of 0.25 in. thick rolled sheet.

* B. S. Berry, private communication.

TABLE 1.

Nominal composition	Mark	Composition (wt. %)			
wt. % of copper		Cu	Fe	Si	Mg
3	*C*	3.00	0.002	0.002	0.001
4	*D*	3.97	0.002	0.003	0.001
5	*E*	5.05	0.002	0.001	0.001

Their composition, from the analysis supplied by the manufacturer, is given in Table 1.

Single crystals, 1/8 in. × 1/4 in. and 10 to 15 in. long, were grown with all these alloys. The 3 and 5 per cent Cu alloys crystals were grown from the liquid in a graphite mold under an argon atmosphere. The mold was supported in a horizontal position while a travelling furnace was drawn away from the growing crystal. The furnace temperature was 750°C, and the rate of travel was 8 cm/hr. The 4 per cent Cu single crystals were grown by the strain–anneal technique. Strips, 1/8 in. × 1/4 in. × 15 in. were machined from the alloy, and annealed for 5 min at 550°C. They were then strained 1.5 per cent in tension, and a travelling furnace, maintained at 550°C, was passed over them at a rate of 0.65 cm/hr. This technique produced a yield of more than 50 per cent single crystals. Attempts to grow crystals in 3 and 5 per cent Cu alloys by the same method were unsuccessful, and therefore crystals of these two alloys were grown from the liquid.

Since the directional growth of crystals from the melt might produce an end-to-end segregation of copper, specimens cut from each end of several crystals were overaged for 2 days at 300°C and the number of precipitated θ particles at each end was compared. It was found that the number of particles at each end did not differ significantly, and it was concluded that the compositional variation along the length of crystals grown from the melt was negligible. This examination did, however, indicate that considerable coring was present. This was completely removed (as indicated by microscopic examination) by annealing the crystals for 5 days at 550°C prior to subsequent heat treatments.

Tensile specimens were obtained by cutting the crystals into 5 in. lengths and carefully milling a gauge length of 2 in., with a reduced cross section of 1/8 in. × 1/8 in., from the center of each specimen. The specimen shoulders were left at the original 1/8 in. × 1/4 in. cross-section. The specimens were then etched for 30 min in a 10 per cent NaOH solution, to remove the worked surface layers. Each specimen then received a number, the number being preceded by a letter, *C*, *D* or *E*, to indicate its nominal composition of 3, 4 or 5 per cent copper, respectively.

All solution treatments were carried out for 2 days in an electric furnace maintained at 540°C. As quenching strains, introduced by a too-rapid quench, might cause subsequent precipitation to occur preferentially on activated slip planes, some crystals were quenched in acetone, aged for 30 min at 400°C, sectioned and polished. The precipitated θ particles did not lie on a pattern of slip planes and, therefore, it was assumed that an acetone quench did not cause appreciable quenching strain. An acetone quench was therefore used prior to all ageing treatments.

Ageing treatments, to produce the stable θ precipitate, were carried out for various times in electric muffle furnaces at 350°, 400° and 450°C, followed by a 48 hr anneal at 300°C to establish the equilibrium matrix composition of 0.45 per cent copper, irrespective of prior ageing temperature.

Stress–strain curves for the crystals were obtained with an Instron tensile machine. The load could be read to better than one per cent, and the strain to one quarter of one per cent. A constant strain rate of 0.1/min was employed.

In order to determine the size of precipitated particles, a small section was removed from the middle of each overaged crystal after testing. This was mounted, polished and photographed at a magnification of 1350×, using an oil-immersion objective. The number of particles in a known area were then counted, to give a value η, the number of particles per unit area intersected by the plane of polish. The coarser particles were photographed at a magnification of 540×, to avoid the statistical variations in counting the much smaller number of particles found on one photograph at 1350×. Many of the crystals were sectioned and polished in three mutally perpendicular planes, and the particle counts on all sections were repeated several times. In some cases, the counts were repeated by a second person. The variation in η from all of these different counts on any one crystal were no greater than plus or minus 5 per cent.

To calculate mean particle radius and mean interparticle spacing, it was assumed that all particles were spherical, and that they were uniformly distributed throughout the matrix. Neither of these assumptions are, in fact, perfectly valid and they break down completely for coarse particles. It was also assumed that each particle on the plane of polish had associated with it a "circle of influence." If the radius of this

VOL. 8 1960

TABLE 2. Overaged crystals

Crystal	Heat	Treatment	τ_c(kg/mm²)	τ_h(kg/mm²)	$\eta \times 10^{-5}$	$1/d \times 10^{-3}$ cm	$f/r \times 10^{-3}$ cm^{-1}
*C1b	1 min	400°C	1.04	4.83	138	3.29	1.16
C2	10 min	400°C	1.06	4.10	146	3.38	1.19
C3b	1 hr	400°C	1.33	5.43	132	3.22	1.13
C5	10 hr	400°C	0.83	3.61	73	2.39	0.84
C6	24 hr	400°C	0.62	3.52	60	2.17	0.76
D11a	48 hr	300°C	1.43	5.81	320	5.01	2.17
D13a	48 hr	300°C	1.43				
D15	48 hr	300°C	1.43				
D26	48 hr	300°C	1.65				
D42a	48 hr	300°C	1.44	4.38	315	4.97	2.05
D47	48 hr	300°C	1.44				
D50	48 hr	300°C	1.49				
D54	48 hr	300°C	1.39				
E2b	1 min	450°C	1.35	5.25	230	4.42	2.03
E3b	10 min	450°C	1.34	5.15	192	3.88	1.85
E7	1 hr	450°C	1.27	4.89	140	3.31	1.58
E8	10 hr	450°C	1.51	5.42	180	3.75	1.79
E9	24 hr	450°C	1.76	6.10	162	3.56	1.70
D20a	10 min	450°C	1.39	5.33	270	4.60	1.90
D20b	1 hr	450°C	1.02	4.28	150	3.43	1.42
D21	6 hr	450°C	0.94	4.00	120	3.07	1.27
D29	24 hr	450°C	0.98	4.29	90	2.65	1.10
D38b	1 min	400°C	1.48		330	5.08	
D38c	10 min	400°C	1.38		260	4.51	
D43a	1 hr	400°C	1.05	4.94	200	3.96	1.64
D43b	6 hr	400°C	0.91	4.64	160	3.54	1.46
D43c	1 min	350°C	1.08		210	4.06	
D57a	10 min	350°C	1.18		230	4.24	
D57b	1 hr	350°C	1.26	5.35	250	2.44	1.83
D57c	6 hr	350°C	1.52		340	5.16	
D69a	24 hr	350°C	1.35	5.38	280	4.68	1.94
D69b	48 hr	350°C	1.16	4.94	200	3.96	1.64
D71a	1 min	450°C	1.72	6.24	440	5.87	2.43
D71b	48 hr	450°C	0.98	3.71	32	1.58	0.65
D75	92 hr	450°C	0.78	3.81	22	1.31	0.54
D76	230 hr	450°C	0.82	3.71	26	1.43	0.59
D22b	96 hr	450°C	1.06	3.67	31	1.56	0.64
D30b	96 hr	450°C	1.08	4.00	28	1.48	0.61

* Marks C, D, E correspond to 3, 4, 5 per cent Cu, respectively.

circle of influence is R, and the planar particle radius is r, then $r^2/R^2 = f$, where f is the volume fraction of the particles in the matrix. The number of particles per unit area $\eta = \dfrac{1}{\pi R^2}$, and the mean planar interparticle distance d will be approximately equal to $2R$. Thus, knowing the number of particles intercepted per unit plane area, the mean planar interparticle distance d and the mean planar particle radius r can be calculated.

The volume fraction of precipitate can be obtained from the aluminum–copper phase diagram together with the values of the density of the α solid solution and the θ phase. From the phase diagram, at 300°C, an alloy in the two phase region consists of a mixture of the α phase, with 0.45 per cent Cu, and the θ phase, containing 53.2 per cent Cu. The densities of these phases, calculated from lattice constants,[14,15] are 2.73 and 4.35 respectively. For the 3, 4 and 5 per cent alloys, we then get values of f equal to 0.031, 0.043 and 0.057.

RESULTS

The results of tensile tests on crystals containing various sizes and dispersions of $CuAl_2$ particles are summarized in Table 2. A very steep initial rate of work-hardening is characteristic of the stress–strain curves for these crystals. This may be seen in the typical curves shown in Fig. 1. Since the orientations

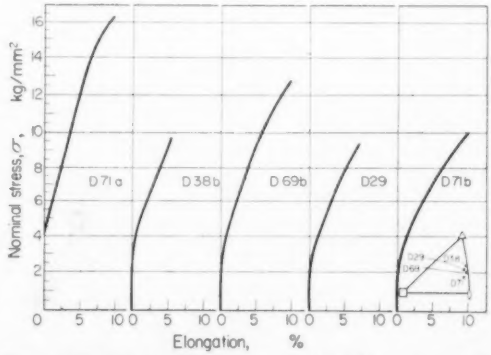


FIG. 1. Nominal stress versus elongation curves for 4 per cent Cu crystals tested after ageing to give differing $CuAl_2$ particle sizes.

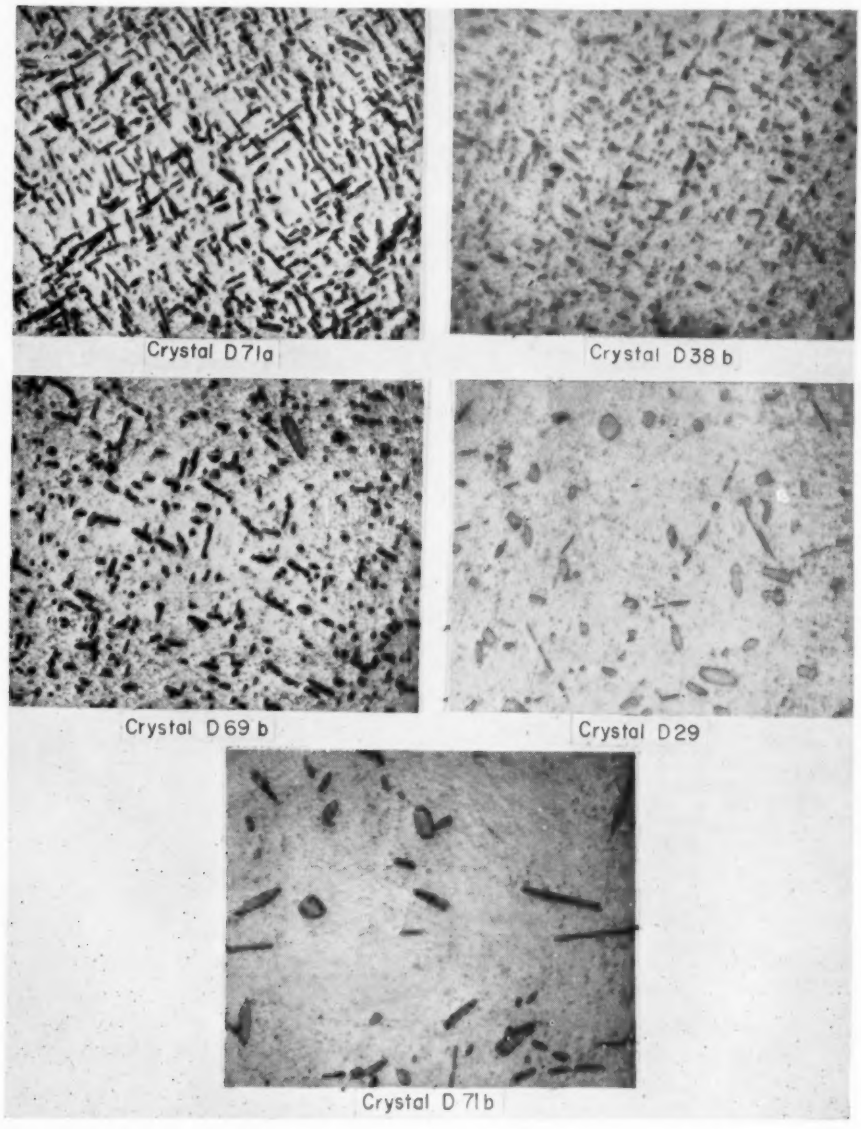


FIG. 2. Photomicrographs of overaged 4 per cent Cu crystals showing the $CuAl_2$ θ phase. Etched with Keller's reagent. ×1350

of the crystals are nearly the same, the shape of the curves is dependent only upon the number and size of the precipitate particles, which is to be expected from the theories of Orowan[5,6] and of Fisher *et al.*[12] Both the critical resolved shear stress and the rate of work hardening increase as the number of particles increases and their size decreases. Fig. 2 shows the structures corresponding to the curves shown in Fig. 1.

A group of crystals of differing orientation were given the same ageing treatment, 48 hr at 300°C, prior to testing. The small variation of the values of critical resolved shear stress (Table 2) shows that, in the overaged condition, these crystals obey the critical resolved shear stress law. Stress-strain curves for these crystals are shown in Fig. 3. However, back reflection Laue X-ray photographs of these and other overaged crystals after deformation indicate no change in orientation. Moreover, slip lines were not visible on the surfaces of any of the overaged crystals. It would seem, that while the initial deformation takes place on the system most favorably oriented for slip, the rate of work-hardening on that plane is so high that after only a small amount of deformation the flow stress on the active plane is such that the applied stress, now resolved onto another slip system, is greater than the critical stress for that system.

VOL. 8 1960

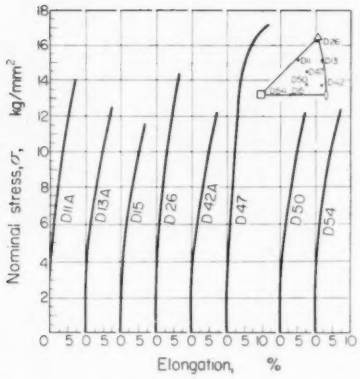


FIG. 3. Nominal stress versus elongation curves for 4 per cent Cu crystals of differing orientations tested after ageing for 48 hr at 300°C.

Thus a second slip system is brought into operation, as are, similarly, all other systems capable of operating. Several slip systems are then operating simultaneously after only a small amount of deformation and, accordingly, the stress–strain curves are necessarily plotted in terms of nominal stress and strain instead of resolved shear stress and true glide strain.

Further evidence of multiple slip is provided by the appearance of the fracture of overaged crystals. This, as can be seen from Fig. 4a, is similar to the fracture of a polycrystalline specimen, and is characteristic of fracture where several slip systems are in operation. A micrograph of a fractured specimen, Fig. 4b, shows that the particles have not deformed by a detectable amount even in the region of fracture. This observation supports the contention, which is the basis



FIG. 4a. Fracture, crystal *D*50, aged 48 hr 300°C. ×8

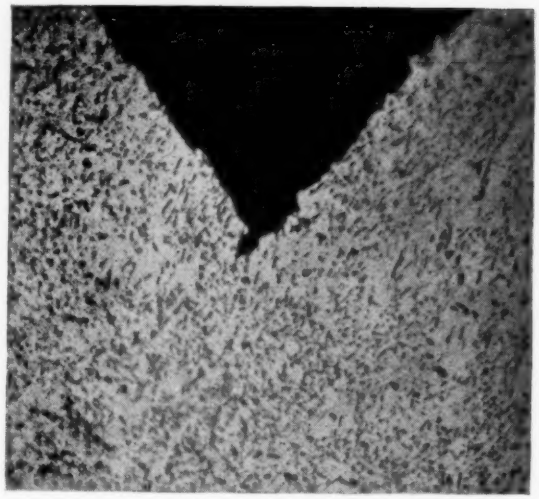


FIG. 4b. Micrograph of fracture, crystal *D*26, aged 48 hr 300°C. Etched with Keller's reagent. ×540

of both the theories of Orowan and of Fisher *et al.* that these particles are not sheared during plastic deformation of the matrix.

In order to test the theory of Orowan, which indicates that the critical resolved shear stress should vary as the reciprocal mean interplanar distance between centers of particles, a plot of τ_c versus $1/d$ was made, Fig. 5. Except for a group of crystals containing very coarse, plate shaped particles, a good correlation can be obtained for the 4 per cent Cu crystals. However, the points for the 3 per cent Cu and particularly the 5 per cent Cu crystals (grown from the liquid alloy) show considerable scatter from the straight line relationship. The scatter is not systematic, and no method of replotting the data has been found which brings these points into line with those of the 4 per cent Cu crystals. The slope of the best straight line through the points for the 4 per

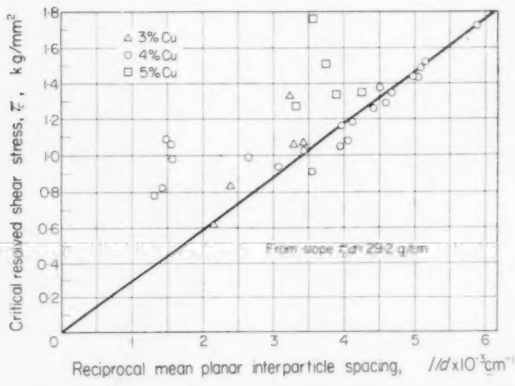


FIG. 5. Plot of critical resolved shear stress versus reciprocal mean planar interparticle spacing.

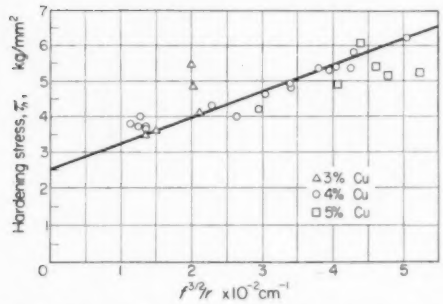


FIG. 6. Plot of hardening stress, the stress at 0.07 strain resolved onto the initial slip plane, versus the volume fraction of precipitate to the three halves power divided by the mean planar particle radius.

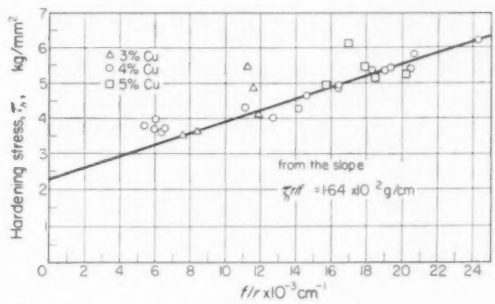


FIG. 7. Plot of hardening stress, the stress at 0.07 strain resolved onto the initial slip plane, versus the volume fraction of precipitate divided by the mean planar particle radius.

cent crystals is 29.2 g/cm. Despite the scatter, this plot showed a better correlation than either the Gensamer logarithmic relation or that of Shaw *et al.*, $\tau_c \propto d^{-0.15}$.

Fisher, Hart and Pry's theory of work-hardening suggests that a hardening stress τ_h should be proportional to the three halves power of the volume fraction of precipitate divided by the mean planar particle radius. Due to the fact that slip in the overaged crystals is not confined to one plane, it was rather difficult to decide what to use as a measure of τ_h. The best correlation was obtained with the flow stress, at an elongation of 7 per cent, resolved onto the initial glide plane.

The plot of τ_h versus $f^{3/2}/r$ is shown in Fig. 6. Again, the correlation is poor for the crystals containing 3 and 5 per cent copper, though in this case the deviations are systematic; the points for 3 per cent Cu crystals lie to one side, and those for 5 per cent Cu crystals to the other side, of the best straight line drawn through the points for the 4 per cent Cu crystals. This suggested that a change in the exponent of f might give a better correlation. In Fig. 7, τ_h is plotted as a function of f/r, and shows a better correlation. Plotted in this manner, the slope of the best straight line is 1.64×10^2 g/cm, and the intercept, τ_h', is 2.3 kg/mm^2.

DISCUSSION

The experimental results indicating that the critical resolved shear stress is a linear function of the reciprocal mean planar particle spacing are generally in conformity with Orowan's theory.[5,6] Furthermore, the slope of the best line through the points is also in accord with the theory. However, the disappointingly large scatter requires some explanation and the most obvious cause may be in the method of calculating the spacing.

The mean planar interparticle spacing, d, is calculated upon two assumptions; that the particles are spherical and that they are uniformly distributed. The group of 4 per cent Cu crystals which deviates widely from the linear relationship consists of crystals containing very coarse particles, for which neither of these assumptions is correct. The particles are precipitated as discs, and their size and distribution is not uniform. Whilst the particles in all crystals tend to be disc-like in shape, this shape is not so exaggerated and the distribution is much more uniform in the crystals containing finer precipitates. The 3 per cent Cu crystals, whose deviation from the straight line is fairly small, also show this tendency toward unsymmetrical precipitates. The disc-shaped precipitates occur in a much more exaggerated form in the 5 per cent Cu crystals, the extreme case being that for crystal *E*9, which shows the largest deviation from the line. As the 3 and 5 per cent Cu crystals both show a greater tendency to form disc-shaped precipitates than the 4 per cent Cu crystals, it may be assumed that this tendency is in some way connected with the less perfect structure of crystals grown from the liquid. There is a direct correlation between the observed deviation of the particles from an ideal shape and distribution and the deviation from the straight line relationship required by the Orowan theory. It seems probable, therefore, that the calculated values of particle spacing in these crystals are in error.

The value of d in the Orowan theory is actually the mean distance of closest approach between particles. In the case of small spherical particles, this is approximated closely by the mean distance between centers of particles. However, for discs, d will be very much smaller than the mean distance between centers. Whilst the mean distance between centers can easily be calculated from a count of the number of particles per unit area of plane of polish, the distance of closest approach of non-spherical particles is not readily susceptible to calculation in the present case. Thus it was not found possible to correct the values of d

VOL. 8 1960

for a more exact verification of the Orowan theory.

Only under the, not unreasonable, assumption that the deviations in shear stress are due to incorrect values for d, can verification of the Orowan theory be claimed. Under this assumption, a straight line was drawn through the points for the 4 per cent Cu crystals excluding points for crystals containing the largest plate-shaped particles. This line has a slope of 29.2 g/cm. According to Orowan's theory,

$$\tau_c = \frac{2\alpha\mu b}{d} .$$

For aluminum, $\mu = 2.5 \times 10^{11}$ dynes/cm^2, $b = 2.8 \times 10^{-8}$ cm. The constant α is shown by Cottrell[16] to be given by:

$$\alpha = \frac{1}{2\pi(1-\nu)} \ln\left(\frac{\lambda}{r_0}\right) ,$$

where ν is Poisson's ratio, r_0 is the distance from the center of a dislocation, within which Hooke's Law is no longer obeyed, and λ is a measure of the deviation of the dislocation from a straight line. In this case, λ is of the order of $10^3 \times r_0$ (order of the spacing between particles), giving α an approximate value of 2. According to theory, the slope of the line should then be

$$2\alpha\mu b = 28 \text{ g/cm}.$$

Agreement of theory and experiment is excellent and, provided that the above qualification is accepted, it may be said that the theory is completely substantiated.

In testing the Fisher, Hart and Pry[12] theory, a plot of the hardening stress τ_h versus f/r was found to give a somewhat better correlation than the τ_h versus $f^{3/2}/r$ plot required by the theory. The former relationship may be obtained from the original analysis in the following manner.

By the use of a magnetic analog, Fisher *et al.* showed that the back stress τ_h on a dislocation source, due to the formation of dislocation loops about non-deforming particles as a result of the operation of the Orowan mechanism, is given by:

$$\tau_h = 1.3\mu b\left[1 - \frac{1/2\nu}{(1-\nu)}\right]\frac{r^2 N}{R^2 R_M} ,$$

where μ, b and ν have their usual meaning, N is equal to the number of dislocation loops about a particle, r is the mean planar particle radius, R the radius of the area of influence associated with each particle, R_M is the distance of closest approach of a source to a precipitate particle, averaged over the extent of the source. Fisher *et al.* then suggest that R_M is some fraction of R, namely 1/3; with ν also equal to 1/3 they obtain:

$$\tau_h = 3\mu b N \frac{f^{3/2}}{r} ,$$

where f, the volume fraction of precipitate, is equal to r^2/R^2.

It has been shown, however, that the experimental relationship is more nearly of the form:

$$\tau_h = K\frac{f}{r} ,$$

where K is some constant. If we go back to the original (Fisher *et al.*[12]) equation for τ_h, it may be rewritten, taking $\nu = 1/3$:

$$\tau_h = \mu b N \frac{f}{R_M} .$$

Comparison of this equation with experiment indicates that R_M must be taken as being proportional to r, and not R as assumed by Fisher *et al.* If R_M is set equal to pr, the equation then becomes:

$$\tau_h = \frac{\mu b N f}{pr}$$

and a plot of τ_h versus f/r will have a slope equal to $\mu bN/p$. With N equal to its maximum value of the order of 100, the theoretical line slope should then be $700/p$ g/cm. From Fig. 7 the experimental line slope is found to be 164 g/cm. Thus p has a value of approximately 4. This means that the distance of closest approach of a source to a precipitate particle is about 4 times the particle radius.

The fact that the intercept of the plot of τ_h as a function of f/r is equal to 2.3 kg/mm^2 indicates that other sources of work-hardening are not negligible. The most probable cause of work-hardening, after that of the Fisher, Hart and Pry mechanism, is the interaction of dislocations on intersecting slip planes, particularly as in these crystals multiple slip begins after very little deformation. Tensile experiments on solid solution aluminum alloy single crystals containing from 1 to 5 per cent copper, the results of which will be presented in another paper,[17] give average values of resolved shear stress at 7 per cent elongation which extrapolate to 0.8 kg/mm^2 at the composition, 0.45 per cent Cu, equivalent to the matrix composition of the present overaged alloys. Crystals which have deformed in double slip give values 25 per cent to 50 per cent higher than the average values. It is to be expected that crystals deformed in multiple slip will show values of resolved shear stress which are higher than the average by an even greater

factor. The contribution of the matrix solid solution to the resolved shear stress at 7 per cent elongation in the overaged crystals is expected to be from 1.5 to 2 kg/mm², which is of the order of the observed value of τ_h', 2.3 kg/mm².

Whilst the theories of Orowan and of Fisher *et al.* have been verified for dispersions of $CuAl_2$ particles in aluminum–copper single crystals, the results of Shaw *et al.* are still unexplained. It may be that their results are due to some grain-boundary effect, as the presence of particles in grain boundaries may limit the nucleation, by slip that has already occurred in one grain, of slip in an adjacent grain.

When the configuration of dispersed particles is such as to enclose essentially independent blocks of the matrix, the Gensamer relation between flow stress and interparticle spacing is to be expected. It is possible that other types of dispersion may give rise to other relations.

CONCLUSIONS

From the foregoing discussion, the following conclusions may be reached.

(1) From the results of the majority of aluminum 4 per cent copper single crystals aged to give the equilibrium, incoherent θ precipitate it has been shown that deformation takes place by the "bowing-out" of dislocations between precipitate particles. The critical resolved shear stress of these crystals is determined by the minimum radius of curvature assumed by the dislocations during this process and is given, to a first approximation, by the Orowan formula:

$$\tau_c = 2\alpha\mu b/d.$$

Deviations of the experimental data from this relationship can be explained by the fact that d, the interparticle spacing for the crystals concerned, is less than the calculated value when the precipitate particles do not approximate to the ideal spherical shape. Whilst the deviations can be explained, there is no guarantee that correct values of d would place the points for these crystals on the theoretical equation, and the present confirmation of Orowan's theory should be regarded as tentative.

(2) A large contribution to work-hardening in the overaged crystals has been shown to be due to the back-stress resulting from dislocation rings left around precipitate particles after the operation of the Orowan mechanism, as suggested by Fisher *et al.* The experimental data fits a modification of their theory, in which the hardening stress is given by:

$$\tau_h = \frac{\mu b N f}{pr},$$

where the constant p has a value of approximately 4, indicating that the distance of closest approach of a dislocation source to a non deforming particle is about four times the particle radius.

(3) While a crystallographically defined critical shear stress was observed, the rapid rate of work-hardening causes slip-systems, other than those most favorably oriented for slip, to become operative. This "non-deforming particle" behavior is characterized by a lack of orientation rotation during plastic deformation, the absence of slip lines on the surface of the crystal, and a fracture similar in appearance to that of fine-grained polycrystalline material.

ACKNOWLEDGMENT

This work was conducted under contract for the Office of Naval Research. Reproduction, in whole or in part, is permitted for any purpose of the United States Government. The authors are indebted to the Aluminum Company of America for preparing the alloys, and to the Forestry Department of Yale University and, in particular, Mr. R. Kellogg for the use of an Instron Testing Machine.

REFERENCES

1. M. Gensamer, E. B. Pearsall, W. S. Pellini and J. R. Low, *Trans. Amer. Soc. Metals* **30,** 983 (1942).
2. C. S. Roberts, R. C. Carruthers and B. L. Averbach, *Trans. Amer. Soc. Metals* **44,** 1150 (1952).
3. E. Gregory and N. J. Grant, *Trans. Amer. Inst. Min. (Metall.) Engrs.* **200,** 247 (1954).
4. E. Gregory, Ph.D. Thesis, Cambridge University (1951).
5. E. Orowan, *Symp. on Internal Stresses*, p. 451. Institute of Metals, London (1948).
6. E. Orowan, *Dislocations in Metals*, p. 131. Amer. Inst. Min. Metall. Engrs., New York (1954).
7. F. V. Lenel, A. B. Backenstro and M. V. Rose, *Trans. Amer. Inst. Min. (Metall.) Engrs.* **209,** 124 (1957).
8. R. B. Shaw, L. A. Shepard, C. D. Starr and J. E. Dorn, *Trans. Amer. Soc. Metals*, **45,** 249 (1953).
9. G. Thomas and J. Nutting, *J. Inst. Met.* **86,** 7 (1957-58).
10. H. Deulter, *Phys. Z.* **33,** 247 (1932).
11. M. Manjoine and A. Nadai, *Proc. Amer. Soc. Test. Mater.* **40,** 822 (1940).
12. J. C. Fisher, E. W. Hart and R. H. Pry, *Acta Met.* **1,** 336 (1953).
13. A. H. Cottrell, *Dislocations and Plastic Flow in Crystals*, p. 8. Clarendon Press, Oxford (1953).
14. E. C. Ellwood and J. M. Silcock, *J. Inst. Met.* **74,** 457 (1947-48).
15. A. J. Bradley and P. Jones, *J. Inst. Met.* **51,** 131 (1933).
16. A. H. Cottrell, *Dislocations and Plastic Flow in Crystals*, p. 51. Clarendon Press, Oxford (1953).
17. D. Dew-Hughes and W. D. Robertson, *Acta Met.* **8,** (1960).

VOL. 8 1960

THE MECHANISM OF HARDENING IN AGED ALUMINUM–COPPER ALLOYS*

D. DEW-HUGHES† and W. D. ROBERTSON‡

Single crystals were grown in aluminum–copper alloys containing from 1 to 5 per cent copper. Crystals were tested in tension after an air-quench from the solution-treating temperatures. The aging behaviour of crystals containing 4 per cent copper was studied by X-rays and by hardness tests.

Four per cent copper crystals were tested in tension after aging for various times at 130°C and 190°C. Crystals in all stages of aging obeyed the critical resolved shear stress law, though crystals containing θ' particles deformed by multiple slip in the same manner as that previously found for overaged crystals.

Strengthening due to the presence of Guinier–Preston zones was calculated by summing the contributions from Mott and Nabarro's coherency strain strengthening, Kelly's chemical strengthening and the strength of the residual solid solution. The calculated values of critical resolved shear stress are in agreement with measured values on crystals aged for 2 (GP-I) and 10 (GP-II) days at 130°C and for 5 (GP-I) days at 110°C.

LE MECANISME DE DURCISSEMENT D'ALLIAGES Al-Cu VIEILLIS

Les auteurs ont préparé des monocristaux d'alliages Cu-Al contenant de 1 à 5 pour cent de cuivre. Ces cristaux ont été soumis à des essais de traction après avoir subi un traitement de trempe à l'air au départ de températures correspondant à la solubilité complète des deux éléments constituants. Les auteurs ont étudié par des essais aux rayons X et en dureté, le comportement au vieillissement de cristaux contenant 4 pour cent cuivre. Ces cristaux ont été soumis à des essais de traction après des vieillissements à temps variable aux températures de 130 et 190°C. Quel que soit leur degré de vieillissement, ces cristaux obéissent à la loi de la tension de cisaillement critique, tandis que d'autres cristaux contenant les particules de la phase θ' se déforment par glissement multiple de manière identique à celle observée précédemment pour des cristaux survieillis. Le durcissement dû à la présence de zones de Guinier-Preston, a été calculé en additionnant les contributions dues au durcissement de Mott et Nabarro pour une déformation cohérente, au durcissement chimique de Kelly et au durcissement de la solution solide résiduelle. Les valeurs calculées pour la tension de cisaillement critique sont en accord avec les valeurs mesurées pour des cristaux vieillis pendant 2(GP-I) et 10(GP-II) jours à 130°C et pendant 5 jours (GP-I) à 110°C.

MECHANISMUS DER KALTAUSHÄRTUNG BEI GEALTERTEN ALUMINIUM-KUPFER-KRISTALLEN

Von Aluminium-Kupfer-Legierungen mit 1–5% Kupfer wurden Einkristalle gezüchtet. Die Kristalle wurden nach dem Lösungsglühen in Luft abgeschreckt und im Zugversuch geprüft. Das Alterungsverhalten von Kristallen mit 4% Kupfer wurde mit Röntgenstrahlen und Härteprüfungen untersucht.

Kristalle mit 4% Kupfer wurden nach verschieden langer Auslagerung bei 130°C bzw. 190°C im Zugversuch geprüft. Kristalle aller Alterungsstadien gehorchten dem Gesetz konstanter kritischer Schubspannung, obwohl Kristalle, die θ'-Teilchen enthielten, bei Verformung in gleicher Weise Mehrfachgleitung zeigten, wie es früher für überalterte Kristalle gefunden worden war.

Die Härtesteigerung infolge der Guinier-Preston-Zonen wurde berechnet durch Addition der Härtesteigerung infolge kohärenter Verzerrungen nach Mott und Nabarro, der chemischen Härtesteigerung nach Kelly und der Härte der übrigen festen Lösung. Die berechneten Werte der kritischen Schubspannung stimmen für Kristalle, die zwei und zehn Tage bei 130°C bzw. funf Tage bei 110°C ausgelagert waren, mit den gemessenen Werten überein.

INTRODUCTION

The mechanism of aging in terms of structural changes taking place in a supersaturated solid solution is well understood and has been ably discussed by Hardy and Heal[1]. The aluminum–copper system, in particular, has been thoroughly investigated.[2] The manner in which these structural changes increase the strength of age-hardenable alloys is not so well understood. Only two quantitative theories of the strength of age-hardened alloys have been presented. Mott and Nabarro[3] consider the interaction between dislocations and internal stresses caused by the presence of solute atom clusters (Guinier-Preston zones) in the matrix prior to coherent precipitation. Kelly and Fine[4], using heats of reversion as a measure of the energy of copper or silver atoms in Guinier-Preston zones, estimated the stress necessary to force a dislocation through these zones. The results of their calculations were consistent with measured flow stresses in polycrystalline Al–Cu and Al–Ag alloys.

The strength parameter computed from any dislocation theory of age-hardening will be the critical resolved shear-stress for plastic deformation of single

* Received May 4, 1959. This paper is abstracted from a thesis by D. Dew-Hughes submitted to the Graduate Division of the Yale School of Engineering in partial fulfillment of the requirements for the degree of Doctor of Engineering.

† International Business Machines Corporation, Research Center, Poughkeepsie, New York.

‡ Hammond Metallurgical Laboratory, Yale University, New Haven, Conn.

crystals. Few studies of plastic deformation of single crystals of an age-hardened material have been reported. Karnop and Sachs[5] studied changes in cross-section during deformation of Al–5% Cu single crystals in two conditions; after aging for 30 min at 100°C, and after furnace cooling to 300°C. Carlsen and Honeycombe[6] obtained stress–strain curves on Al–3.5% Cu crystals in the unaged condition (quenched), after aging to peak hardness and in the overaged condition. Tensile tests were carried out at both room temperature and at the boiling point of liquid nitrogen, on crystals of varying orientation. Their results indicated that the unaged and overaged crystals obeyed Schmid's[7] critical resolved shear stress law, but that crystals aged to peak hardness did not obey this law.

Kelly and Chiou[8] measured the critical resolved shear stress of Al–4% Cu single crystals, aged for 24 hr at 125°C to give Guinier-Preston zones of the first kind (GP-I), at temperatures between 77°K and 373°K. By changing the temperature during deformation, they also measured the change of flow stress with temperature. Both of these quantities increase gradually with decreasing temperature down to about 160°K; below this temperature the rise is very marked. Subsequent investigation of Al–3.85% Cu crystals aged at 190°C by Kelly[9] and his associates J. G. Byrne, C. Chiou, A. Lassila and S. Sato showed that the temperature dependence of flow stress for crystals containing GP-II zones was much less than for GP-I and approximately the same as the elastic modulus; furthermore, the strength of crystals containing GP-I zones is considerably greater than for GP-II zones at low temperatures, due to the increase in critical resolved shear stress with temperature in the former case. Kelly[9], to whom we are indebted for a copy of his paper in advance of publication, interprets these results in the following way.

In the case of GP-I zones in Al–Cu, the zones are only one atom plane thick and the dislocation shears only one Cu–Cu bond at a time. As the bond energy is of the order of 0.1eV[10,11], at ordinary temperatures this shearing process is thermally activated and only makes a contribution to the strength at low temperatures. For Al–Cu alloys containing Guinier-Preston zones of the second kind (GP-II), which are a few unit cells thick, and for Al–Ag alloys in which the zones are spherical, dislocations shear several Cu–Cu or Ag–Ag bonds in moving through one burgers vector and thermal activation of this process is negligible up to temperatures above which the zones are unstable. In the latter cases the chemical strengthening may be an important contribution to the overall strength of the crystals, and in fact Kelly's calculated values for critical resolved shear stresses of aged Al–Cu and Al–Ag crystals which agree well with experimental results.

The work described in this paper, which was proceeding simultaneously but independently of that of Kelly and his associates, was performed in an attempt to evaluate further the theories of hardening in aged alloys. Tensile experiments were performed on single crystals of aluminum–copper alloys, in the unaged condition and after aging for various times at 130°C or 190°C, which produces GP-zones of types I and II and the coherent transition precipitate, θ'.

EXPERIMENTAL

In addition to the 3, 4 and 5 per cent Cu single crystals, produced from materials and by methods described in a previous paper,[12] single crystals were also grown, from the liquid, in 1 and 2 per cent Cu alloys of the following compositions: 1.01 per cent Cu, 0.002 per cent Fe, 0.001 per cent Si; and 1.95 per cent Cu, 0.001 per cent Fe, and other elements were not detected. All of this material and the analysis were supplied by the Aluminum Company of America's Research Laboratories. The method of preparation of tensile specimens with a 2 in. gauge length and a reduced cross section of 1/8 in. × 1/8 in. was identical to that used previously. Crystals were prefixed with a letter *A*, *B*, *C*, *D* or *E* indicating nominal compositions of 1, 2, 3, 4 or 5 per cent copper, respectively.

All solution treatments were carried out for 2 days in an electric furnace maintained at 540°C. The crystals were quenched to room temperature in acetone, prior to aging. As it was later found that the severity of the quench had a considerable effect on the critical resolved shear stress of unaged crystals, though not on the kinetics of the subsequent hardening process, all crystals to be tested in the unaged condition, with two exceptions, were air-cooled after the solution treatment. Aging at 130°C and 190°C was carried out in a silicone oil bath controlled to ±1/2°C.

Chemical macro-polishing of the crystals, for slip line observations, was performed in a boiling solution of 80 per cent phosphoric acid, 15 per cent acetic acid and 5 per cent nitric acid.

In order to confirm that the aging treatments produced the same structures as described by Silcock[2], a series of 4 per cent Cu crystals were aged at 130°C and 190°C and hardness readings taken as a function of time. The hardness measurements were made on a Tukon microhardness machine, using a

VOL. 8 1960

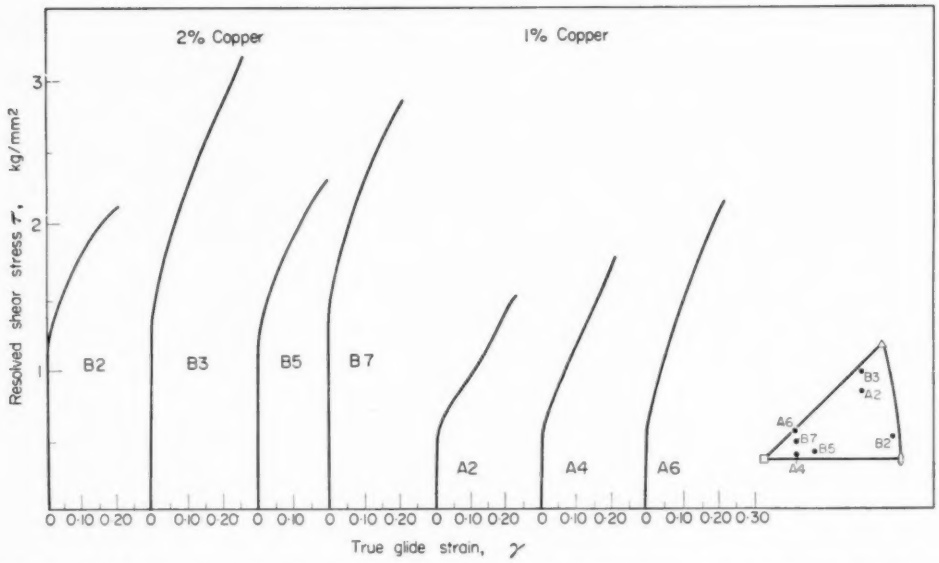


FIG. 1. Resolved shear stress versus true glide strain curves for 1 per cent and 2 per cent Cu crystals tested in the unaged condition after an air quench.

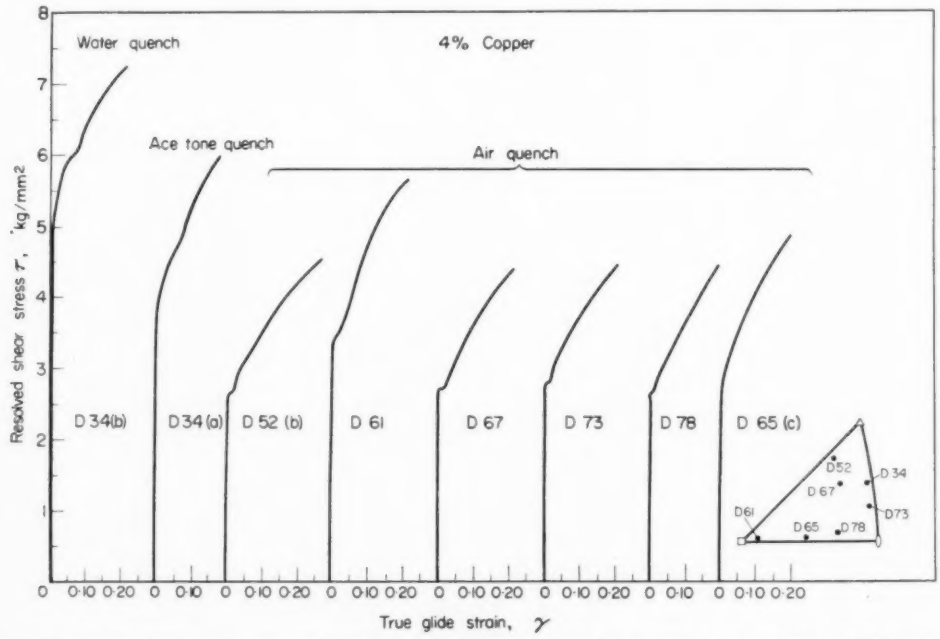


FIG. 2. Resolved shear stress versus true glide strain curves for 4 per cent Cu crystals tested in the unaged condition after quenching in water, acetone, and air.

Vickers diamond and a 3 kg load. A thin slice, parallel to a {100} plane, was cut from a crystal and aged along with the hardness specimens. Transmission Laue X-ray photographs were taken at various stages during aging. The hardness curves and the streaks and spots developed on the X-ray photographs were essentially identical with those obtained by Silcock for the same aging treatments. It is therefore reasonable to use Silcocks' measurements of zone diameter in the analysis of the present results.

Crystals were also allowed to age at room temperature and their progress was followed by hardness readings. It was found that room temperature aging occurred much more rapidly than had been suspected, and care was exercised to ensure that all tensile tests were carried out immediately after the completion

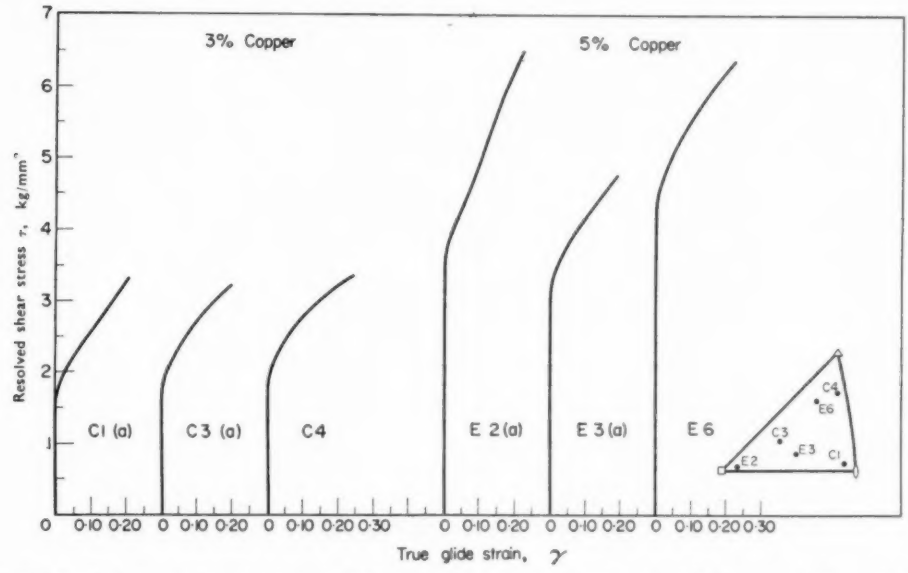


FIG. 3. Resolved shear stress versus true glide strain curves for 3 per cent and 5 per cent Cu crystals tested in the unaged condition after an air quench.

of the heat treatment and before a significant change in properties occurred.

Stress–strain curves for the crystals were obtained with an Instron tensile machine. The load could be read to better than one per cent, and the strain to one quarter of one per cent. A constant strain rate of 0.2 in/min (1.7×10^{-3} sec^{-1}) was employed. All tensile tests were performed at room temperature.

RESULTS

Stress–strain curves for 1, 2, 3, 4 and 5 per cent Cu crystals tested in the unaged condition immediately after quenching are shown in Figs. 1–3. The values of critical resolved shear stress for these and all other crystals are given in Tables 1–4. Some of the air-quenched 4 per cent Cu crystals show what appears to be a small yield point. This was not observed in any other of the crystals.

It is interesting to compare the curves for the 4 per cent Cu crystals tested after quenching in different media. The strength increases rapidly with the severity of the quench. Values of critical resolved shear stress for these crystals after quenching in air, acetone and water are 2.7, 3.7 and 4.6 kg/mm², respectively.

These results indicate that an air quench is rapid enough to prevent precipitation, or at least, there is less precipitation than in water or acetone quenches, since the air-quenched crystals have the *lowest* critical resolved shear stress. Furthermore, the lack of preferential precipitation along slip planes on aging after quenching[12] indicates that quenching strains are not large in these crystals. Eliminating aging and quenching strains, the cause of the increase in critical resolved shear stress with a more rapid quench is

TABLE 1. Unaged crystals

Crystal	λ_0	χ_0	Heat treatment	τ_c(kg/mm²)
*A*2	35	59	Air quenched	0.48
*A*4	44	49	,, ,,	0.54
*A*6	36	56	,, ,,	0.59
*B*2	52	44	,, ,,	1.08
*B*3	34	63	,, ,,	1.39
*B*5	45	46	,, ,,	1.11
*B*7	39	53	,, ,,	1.37
*C*1a	57	37	,, ,,	1.66
*C*3a	39	51	,, ,,	1.84
*C*4	39	59	,, ,,	1.87
*D*34b	45	53	Water quenched	4.60
*D*34a	45	53	Acetone quenched	3.69
*D*52b	31	65	Air quenched	2.61
*D*61	44	52	,, ,,	3.32
*D*65c	48	42	,, ,,	2.77
*D*67	41	53	,, ,,	2.68
*D*73	57	45	,, ,,	2.76
*D*78	52	39	,, ,,	2.66
*E*2a	44	53	,, ,,	3.57
*E*3a	47	43	,, ,,	3.15
*E*6	36	58	,, ,,	4.36

λ_0 = Initial angle between slip direction and tensile axis.
χ_0 = Initial angle between normal to slip plane and tensile axis.

TABLE 2. Aging at 110°C

Crystal	λ_0	χ_0	Aging time (hr)	τ_c(kg/mm²)
*D*82	42	48	120	7.98
*D*84	49	42	120	7.42

TABLE 3. Aging at 130°C

Crystal	λ_0	χ_0	Aging time (hr)	τ_c(kg/mm²)
*D*18	41	51	48	7.31
*D*41b	44	46	48	7.53
*D*42c	52	44	48	7.19
*D*52a	31	65	48	7.07
*D*55b	39	60	48	7.99
*D*40	45	51	2	5.46
*D*60	42	55	5	6.68
*D*62a	40	56	10	7.16
*D*62b	40	56	20	7.45
*D*28	41	57	50	7.43
*D*64a	40	58	100	8.95
*D*64b	40	58	200	10.01
*D*64c	40	58	500	10.51

TABLE 4. Aging at 190°C

Crystal	λ_0	χ_0	Aging time (hr)	τ_c(kg/mm²)
*D*87	41	61	5	6.06
*D*88	34	62	5	7.52
*D*91	31	63	5	7.76
*D*89	45	55	196	5.88
*D*92	32	63	196	5.97
*D*93	40	56	196	5.85
*D*94	31	62	196	5.72
*D*95	38	61	196	5.27
*D*44b	44	46	2	5.88
*D*83	41	51	5	6.88
*D*80	42	48	10	7.90
*D*81	41	50	20	8.36
*D*79	38	56	50	8.23
*D*74	45	46	50	8.19
*D*85	42	58	100	7.54
*D*86	45	49	200	6.36

probably associated with quenched-in vacancies. These results may be compared to those of Maddin and Cottrell[13], who found that high purity aluminum single crystals, when quenched from 600°C into iced brine, had a critical resolved shear stress 5–10 times greater than that for a furnace cooled crystal. In their case, the increase in strength was assumed to be due to an excess of quenched-in vacancies interacting with dislocations. This same explanation would be acceptable in the present case, but Silcock* claims that the excess of vacancies present immediately after a rapid quench allows of such rapid diffusion that some GP–I zones are formed almost instantaneously; thus the increase in strength upon rapid quenching is only indirectly due to a non-equilibrium excess of quenched-in vacancies.

The critical resolved shear stress as a function of composition for the unaged crystals is shown in Fig. 4. The slope of the line is 1.53 kg/mm²/at.% Cu. Crystals of all compositions but the 5 per cent Cu show very

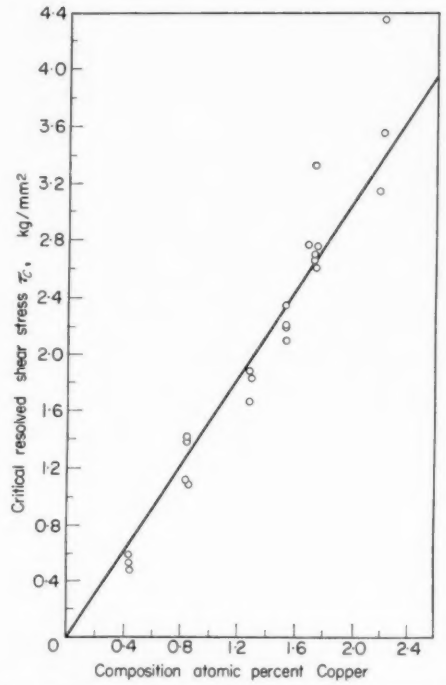


FIG. 4. Plot of critical resolved shear stress versus composition for crystals tested in the unaged condition after an air quench. Values for the 1.54 at. % Cu crystals were taken from Carlsen and Honeycombe[6].

little scatter, indicating that Schmid's critical resolved shear stress law is obeyed and the surfaces of the deformed, unaged 4 per cent Cu crystals show coarse slip clusters, typical of solid solution alloys. The reason for the large scatter in the results for the 5 per cent Cu crystals is not apparent. The remarkably consistent values for 3.5 per cent Cu crystals were taken from the work of Carlsen and Honeycombe[6].

As the results of Carlsen and Honeycombe had indicated that the critical resolved shear stress law was not obeyed by crystals aged to produce the pre-precipitation structures, 4 per cent Cu crystals of varying orientations, aged to give these structures, were tested. These crystals were given one of three aging treatments: 48 hr at 130°C to develop GP-I zones (Table 3), 5 hr at 190°C to develop GP-II zones (Table 4) and 196 hr at 190°C to develop θ' particles (Table 4). The results of these tests showed little variation in critical resolved shear stress values in each of the three groups of crystals, indicating that the critical resolved shear stress law *is* obeyed for all of these structures. X-ray photographs taken after a few per cent elongation of the crystals aged to contain GP-I or GP-II zones showed orientation changes consistent with deformation taking place on only one slip system and in accord with the maximum resolved shear stress.

* Private communication.

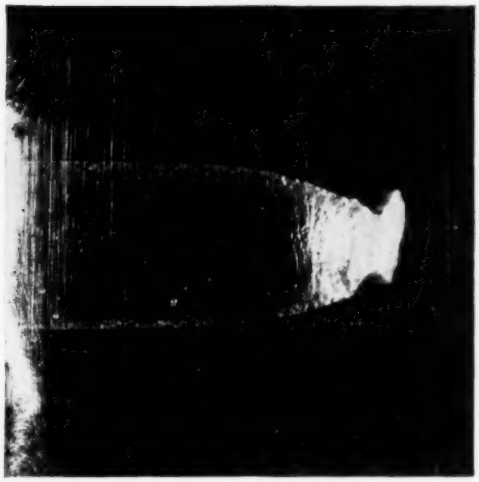


FIG. 5. Fracture, crystal *D*65b, aged 200 hr 190°C. ×8

Crystals aged at 190°C for 196 hr, however, exhibited a behavior similar to that previously reported for the overaged crystals.[12] The stress–strain curves show a rapid initial rate of work-hardening, and the fracture, shown in Fig. 5, is similar to that of polycrystalline material; furthermore, X-ray photographs show that the orientation of the crystal remains essentially unchanged during deformation. These results indicate that the θ' particles interact with dislocations in the same manner as the θ particles.[12]

Tensile tests were conducted on two series of 4 per cent Cu crystals aged for varying times at 130°C and 190°C. The stress–strain curves for these crystals are shown in Figs. 6 and 7. From Fig. 7 will be noted the fact that the crystals aged for 100 hr and 200 hr at 190°C show the curve characteristic of the overaged crystals.[12] This behavior, similar to that of overaged crystals, is apparent as soon as the structure becomes predominantly θ'; that is, immediately after the peak at 190°C, and it continues right through the overaged region.

The values of critical resolved shear stress as a function of aging time are shown in Fig. 8. These curves are similar to the hardness curves, though the tensile test is a more sensitive measure of the degree of aging than is the hardness test.

For specimens deformed after aging at both 130°C and 190°C, the coarse slip bands observed on unaged specimens become progressively finer and more numerous as the aging time is increased. In the case of aging at 190°C, slip lines completely disappear after aging for more than 50 hr. There is also a tendency to increased wavyness of the slip lines as the aging time increases. Photographs of the surfaces of deformed crystals showing slip lines are given in Figs. 9 and 10. The coarse slip clusters seen in the unaged crystals are those typical of a solid solution alloy. As aging progresses, the depletion of the matrix in copper gives rise to the finer slip lines which are characteristic of pure metals. The wavyness of the lines presumably results from dislocations attempting to avoid, wherever possible, Guinier–Preston zones.

An interesting feature of the deformation of these crystals is the mode of fracture. Crystals containing predominantly non-deforming particles, such as θ or θ', as has already been stated, fracture in a manner

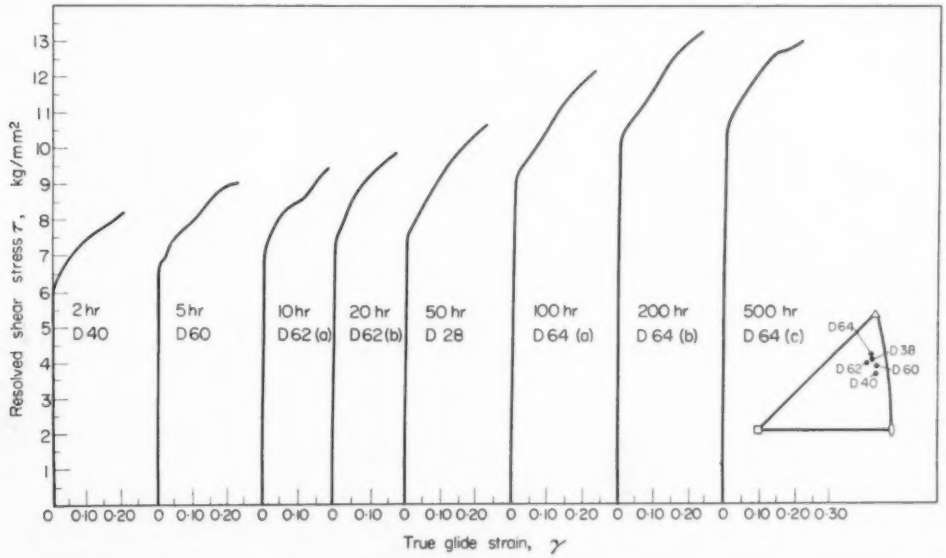


FIG. 6. Resolved shear stress versus true glide strain curves for 4 per cent Cu crystals tested after aging for various times at 130°C.

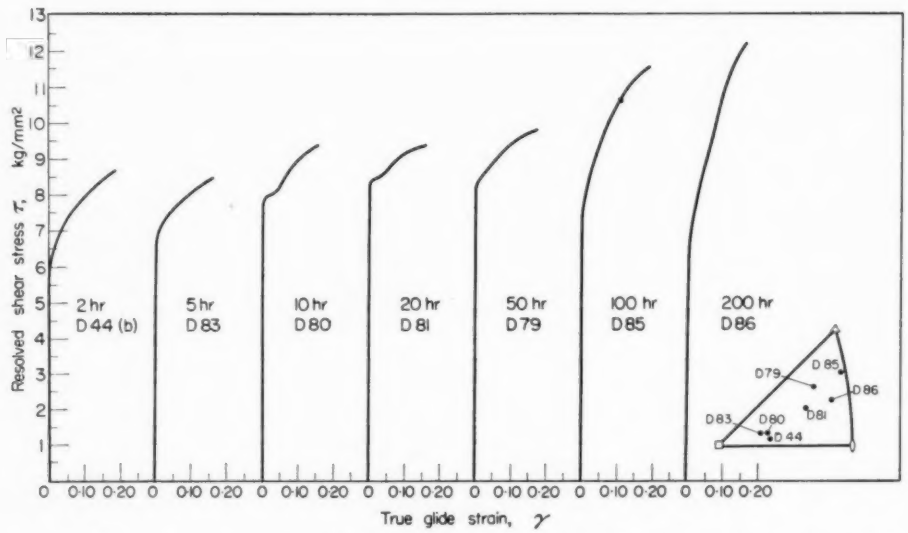


FIG. 7. Resolved shear stress versus true glide strain curves for 4 per cent Cu crystals tested after aging for various times at 190°C.

characteristic of polycrystalline materials. This is the type of fracture to be expected if several slip systems are in simultaneous operation. In crystals containing predominantly Guinier–Preston zones of either type, fracture takes place in an unusual way. Deformation continues on a narrow band of slip planes—either on one or two slip systems, depending upon the orientation of the crystal—and fracture occurs by shearing of the material completely across the band. These fractures are shown in Fig. 11. The plane of fracture is the primary {111} slip plane. The width of the band of deformed material, from both X-ray and microscopic measurements, is 0.1–0.2 mm. As will be shown later, deformation of crystals containing Guinier–Preston zones occurs by dislocations shearing through the zones. As a result of this shearing, a weak plane is developed in the crystal permitting considerable deformation in a narrow band, and hence of fracture along the slip plane. Shearing takes place on two planes, if sufficient rotation has occurred during deformation that a second slip system has become operative, or if the crystal is oriented for conjugate slip. Fig. 11b shows a fracture produced under conditions where extensive slip has taken place simultaneously on groups of planes in two intersecting slip systems.

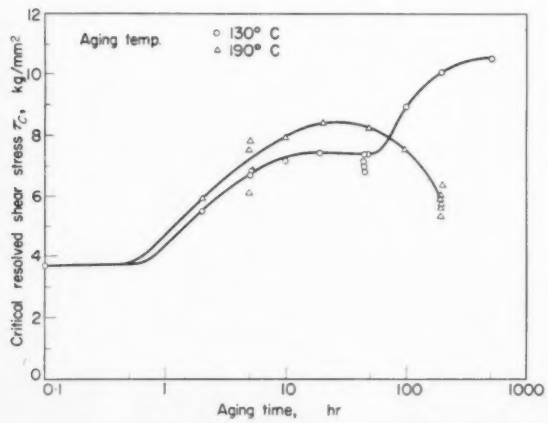


FIG. 8. Critical resolved shear stress versus aging time for 4 per cent Cu crystals tested after aging at 130°C and 190°C.

DISCUSSION

It is interesting to compare the experimental results with quantities calculated from the Mott and Nabarro theory.[3] Applied to solid solution hardening, the theory indicates that the critical resolved shear stress τ is given by:

$$\tau \simeq 2.5\ \mu\epsilon^{4/3}c$$

where c is the atomic concentration of solute, ϵ is the fractional difference in size between the solute and solvent atoms ($\epsilon = 0.1$ for copper in aluminum) and μ is the shear modulus ($\mu = 2.5 \times 10^{11}$ dynes/cm^2 for aluminum). Then

$$\tau/c \simeq 2.5\ \mu\epsilon^{4/3} \simeq 290\ \text{kg/mm}^2.$$

The plot of τ versus concentration for the unaged crystals, Fig. 4, gives the expected linear dependence of critical resolved shear stress on concentration, but the slope of this line, equal to 1.53 kg/mm^2/at.% Cu, is about half that required by the theory.

An alternative theory of the strength of Al–Cu solid solutions is the suggestion by Schoeck[14] that groups of solute atoms near a dislocation relax according to

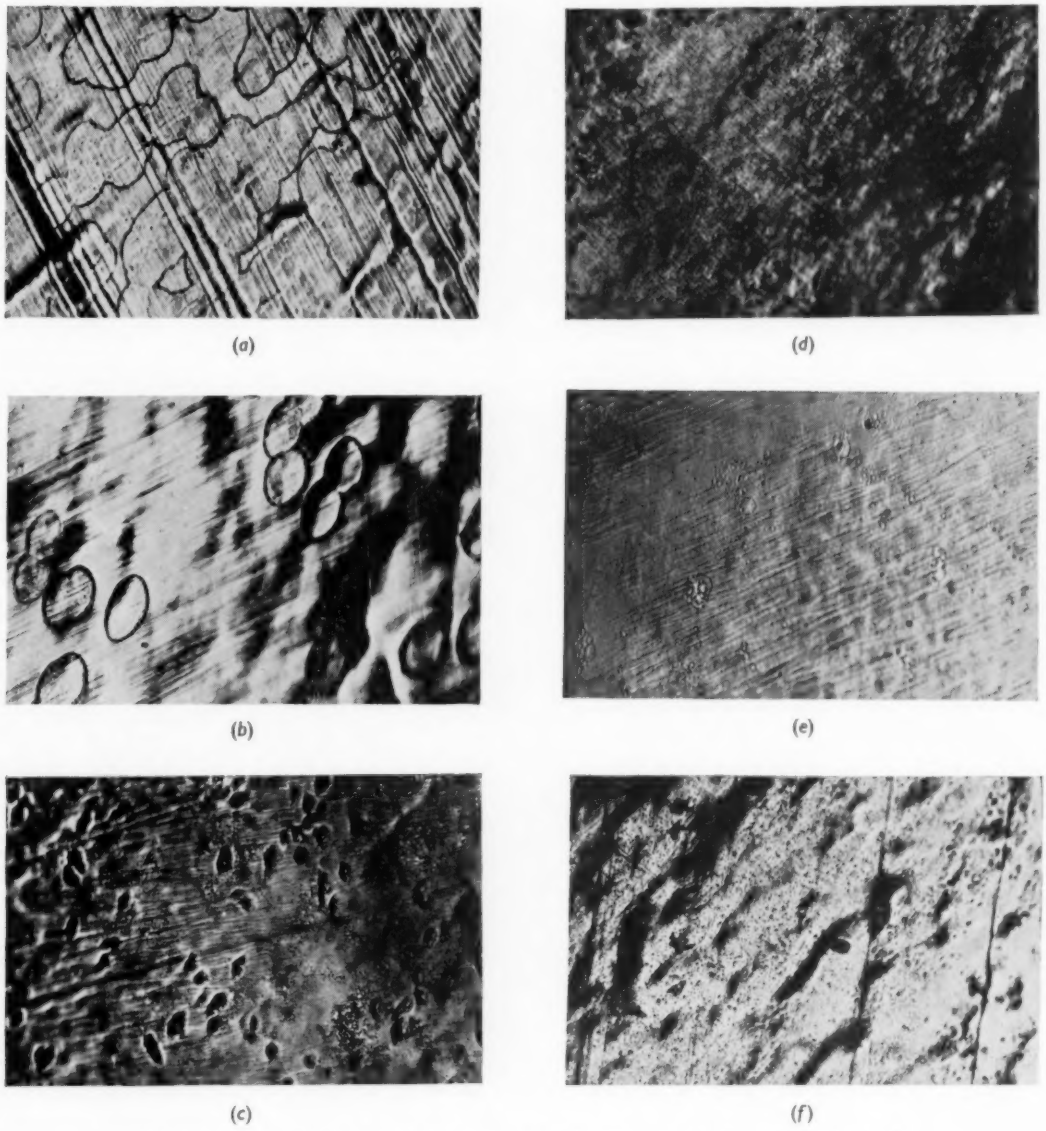


FIG. 9. Slip lines on the surface of crystals deformed after aging at 130°C. ×100

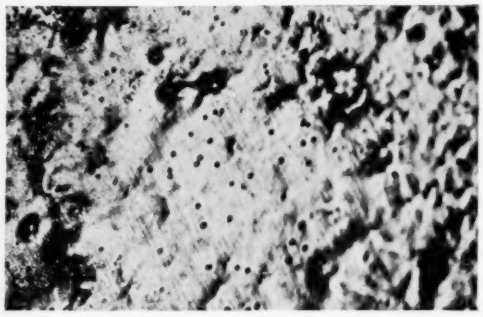
VOL. 8 1960

the Zener model under the influence of the stress field of the dislocation. It is conceivable that in these alloys such an "ordered Zener atmosphere" exists, as a very large Zener peak has been found in Al–Cu solid solutions.[15] The atmosphere, acting as a frictional drag to the motion of the dislocation, may provide the principal contribution to the strength.

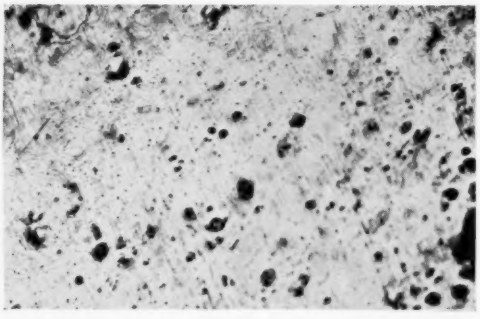
Before applying the various theories of strengthening produced by Guinier–Preston zones, it is advantageous to make an estimate of the amount of copper which goes into the zones. Kelly assumes that all the copper is present in the zones. Guinier[16] states "it is very probable that when the aging, even at room temperature, is practically finished (2 days), more than half of the copper atoms are concentrated in the zones." A better estimate of the amount of copper atoms in the zones can be obtained from the construction of a modified equilibrium diagram. The solvus line between a primary solid solution and a two phase mixture in an equilibrium diagram is a plot of the temperature dependence of the composition of the solid solution whose chemical free energy is equal to the chemical free energy of the second phase. Such a plot ignores the contributions of surface energy and strain energy to the total free energy change on precipitating the second phase. These contributions



(a)



(b)

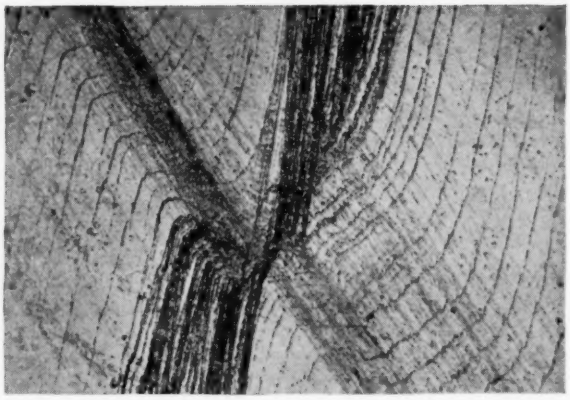


(c)

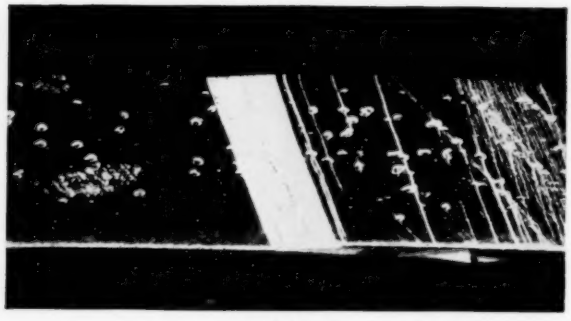
FIG. 10. Slip lines on the surface of crystals deformed after aging at 190°C. ×100



(a)



(b)



(c)

FIG. 11. Aspects of extensive glide prior to fracture in aged 4 per cent Cu crystals.

are negligible for incoherent precipitates of large size. In the case of coherent precipitates, such as Guinier–Preston zones, the surface energy term is negligible, but the energy contribution due to the large coherency strains cannot be neglected. This extra strain energy term has the effect of lowering the solvus line, as the strain energy will always be positive. The aluminum-copper phase diagram must therefore be modified to show the solvus lines for the various pre-precipitation structures. Beton and Rollason[11] have constructed, from reversion data in aluminum–copper alloys, a phase diagram showing the solvus lines for GP-I and GP-II zones. The atom fraction of copper in the zones can be calculated from this diagram.

The strength of crystals containing GP zones may then arise from three sources: (1) strain due to the

presence of the zones, (2) the chemical effect of disordering the metastable array of copper atoms as dislocations shear through a zone and (3) a contribution from the solid solution, since not all the copper atoms are necessarily present in the zones.

Mott and Nabarro, assuming spherical zones and calculating the shear strain at the average distance of any point in the matrix from the nearest zone, give the maximum critical resolved shear stress τ_{st} of crystals containing zones by:

$$\tau_{st} = 2\,\mu\epsilon c \qquad (1)$$

where μ is the shear modulus of the matrix, ϵ is the fractional difference in size between solvent and solute atoms, and c is the atomic concentration of copper atoms in the zones. For the disc-shaped zones actually found in Al–Cu alloys, the shear strain will be less than that due to spherical zones, but the average distance of any point to the nearest zone will also be less, and to a first approximation we may apply their formula to the disc-shaped zones.

The chemical strengthening effect τ_c, calculated by Kelly[9] is:

$$\tau_c\, b^2 d = K\ \Delta E/2 \qquad (2)$$

where b is the Burger's vector of the dislocation, d is the mean planar distance between zones, ΔE is the difference in energy between a copper atom in a zone and in the matrix and K is the number of copper–copper bonds broken per zone as a dislocation moves one burger's vector. For GP-I zones, $K = 1$ as the zones consist of one plane of copper atoms. At room temperature ($kT = 0.025$ eV) thermal energy will allow the dislocations to shear through the zones with little or no increase in stress, and thus the chemical effect will be negligible. Kelly and Chou[8] found that crystals containing GP-I zones showed a significant increase in critical resolved shear stress only at temperatures below 160°K at a strain rate of 10^{-4} sec^{-1}. In the present investigation, values of critical resolved shear stress were obtained on similar crystals, tested at room temperature, which were identical with those obtained by Kelly and Chiou at a strain rate 17 times slower. This indicates that at the higher strain rate any significant increase in critical resolved shear stress must occur at a temperature below 300°K. Therefore the activation energy of the process causing the increased critical resolved shear stress at low temperatures cannot be greater than 0.1 eV, which is the right order of magnitude of $\Delta E/2$.

GP-II zones, when first formed from GP-I zones, are $\sim$ 100 AU in diameter and one unit cell thick; they may grow to 1500 AU in diameter, at which point they are 100 AU or twelve unit cells thick.[2] After aging for 5 days at 130°C the GP-II zone diameter is 350°AU, and by interpolation their thickness may be assumed to be $\sim$ 30 AU or approximately four unit cells; thus for crystals in this condition $K = 4$. ΔE is estimated from the heat of reversion given by Suzuki[10], or the heat of solution of GP-I zones measured by Beton and Rollason[11]. These results gave ΔE a value of between 0.08 and 0.24 eV. In the subsequent calculations the mean value of 0.16 eV will be used.

Table 5 gives the calculated contributions to the critical resolved shear stress due to the three effects and compares them with the experimental results on crystals aged for 2 days and for 10 days at 130°C. As a further check, two crystals were aged for 5 days at 110°C, and values for these crystals are included in Table 5. τ_s is the solid solution effect and is obtained from Fig. 4. τ_{st} is the contribution due to internal strain and is calculated from equation (1). The chemical effect, τ_c, is calculated from equation (2). Zone diameters (h) are taken from the work of Silcock *et al.*[2]; c and c', the atomic concentration of copper in zones and in solid solution, respectively, are obtained from Beton and Rollason's data.[11] The mean planar distance between zones, d, is calculated in the following manner. From the known size of the zones, the mean planar area of the zones is calculated. The number of copper atoms, x, in the mean planar area of a zone is arrived at from a knowledge of the zone structure. The number of copper atoms per unit

TABLE 5

Aging treatment	Structure	h(A.U.)	d(A.U.)	c	c'	τ_s (kg/mm²)	τ_{st} (kg/mm²)	τ_c (kg/mm²)	τ total (kg/mm²)*	τ measured (kg/mm²)
2 days at 130°C	GP-I	100	155	0.0095	0.0079	1.2	4.8	1.0	6.0	7.4
10 days at 130°C	GP-II	350	530	0.0148	0.0026	0.4	7.4	1.2	9.0	10.1
5 days at 110°C	GP-I	80	125	0.0118	0.0056	0.9	6.0	1.3	6.9	7.7

* In this column, τ_c for GP-I zones has not been included, as strengthening from this source will be negligible at room temperature.

VOL. 8 1960

plane area, y, is obtained from the atom fraction of copper atoms which are in the zones. Then the number of zones intersected per unit plane area, N, is equal to y/x. If associated in the plane with each zone is a "region of influence" of diameter d, then d is the required mean planar distance between zones, and is given by:

$$d = \left[\frac{4}{\pi N}\right]^{1/2}.$$

In Table 5, τ total is obtained by adding the values of τ_s, τ_{st} and, in the case of GP-II zones, τ_c. In accord with Kelly's results,[9] τ_c for GP-I zones is believed to be unimportant at room temperature and is therefore not included in τ total. While there is no guarantee that the true critical resolved shear stress is obtained by a simple addition of the various contributions, this method of combining these contributions has been chosen in this instance as being the simplest method. Justification for this is given by the agreement between calculated and experimentally observed values of critical resolved shear stress, which is remarkably good, though consistently low in all cases, for crystals aged for 2 days and 10 days at 130°C, and 5 days at 110°C. The chemical effect for crystals containing GP-I zones is too small, by a factor of 4, to account for the increase in critical resolved shear stress observed by Kelly and Chiou[8] at low temperatures. Using the largest value for ΔE and estimating the expected increase in the solid solution contribution at low temperatures gives a value which is still several kilograms per square millimeter below Kelly and Chiou's value for the critical resolved shear stress at 77°K. The possibility of a fourth effect being operative at low temperatures cannot be overlooked. Excess vacancies are very easily quenched into Al–Cu alloys,* and these may interact directly with dislocations, condense to form sessiles, or promote further precipitation of Guinier–Preston zones from the remaining solid solution.[17] Further experiments should be performed at low temperatures to clear up this point.

When the crystals are aged such that the precipitated structure becomes predominantly θ', their critical resolved shear stress drops. The behavior of these crystals, from the shape of the stress–strain curve, the lack of visible slip lines, lack of rotation during deformation and the mode of fracture, is identical with that reported for crystals containing the θ phase.[12] This suggests that the θ' particles are large enough to interact with dislocations in exactly the same manner as do the incoherent θ particles. Unfortunately, the θ' particles are of such a size that they are too small to be measured under the optical microscope and too large to be measured by X-ray methods; therefore an analysis of the critical resolved shear stress with respect to interparticle distance, similar to the analysis of the results on crystals containing θ particles,[12] was not possible.

* B. S Berry, private communication.

CONCLUSIONS

(1) The strength of aged crystals containing Guinier–Preston zones is due to three effects; the internal strains caused by the presence of these zones, the chemical effect from the energy required to break bonds between solute atoms as a dislocation shears through a zone and the strengthening effect from the residual solid solution. Good agreement between results calculated for these effects and experimental data on 4 per cent Cu crystals aged at 110°C and 130°C is obtained.

(2) A consequence of shearing dislocations through zones is that fracture takes place by extensive shear on a narrow band of planes parallel to the primary slip plane.

(3) Tensile experiments on 4 per cent Cu crystals aged at 190°C have shown that crystals, aged beyond the peak of the aging curve and containing the θ' structure, exhibit the same non-deforming particle behavior as do overaged crystals containing the θ precipitate.

(4) Crystals in all stages of aging obey Schmid's critical resolved shear stress law.

ACKNOWLEDGMENT

This work was conducted under Contract with the Office of Naval Research. Reproduction, in whole or in part, is permitted for any purpose of the United States Government. The authors are indebted to the Aluminum Company of America for preparing the alloys, and to the Forestry Department of Yale University and, in particular, Mr. R. Kellog for the use of an Instron Testing Machine.

REFERENCES

1. H. K. Hardy and T. J. Heal, *Progr. Met. Phys.* **5,** 143 (1954).
2. J. M. Silcock, T. J. Heal and H. K. Hardy, *J. Inst. Met.* **82,** 239 (1953–54).
3. N. F. Mott and F. R. N. Nabarro, *Proc. Phys. Soc. Lond.* **52,** 86 (1940). *Physical Society Conference on Strength of Solids, Bristol,* p. 1 Phys. Soc., London (1948).
4. A. Kelly and M. E. Fine, *Acta. Met.* **5,** 365 (1957).
5. R. Karnop and G. Sachs, *Z. Phys.* **49,** 480 (1928).
6. K. M. Carlsen and R. W. K. Honeycombe, *J. Inst. Met.* **83,** 449 (1954–55).
7. E. Schmid and W. Boas, *Plasticity of Crystals,* p. 105 F. A. Hughes, London (1950).
8. A. Kelly and C. Chiou, *Acta. Met.* **6,** 565 (1958).
9. A. Kelly, *AFOSR TN*-58-1083 *AD* 207530 (1958).

10. T. SUZUKI, *Sci. Rep. Res. Insts. Tohoku Univ.* **A1,** 183 (1949).
11. R. H. BETON and E. C. ROLLASON, *J. Inst. Met.* **86,** 85 (1957–58).
12. D. DEW-HUGHES and W. D. ROBERTSON, *Acta Met.* **8,** 147 (1960).
13. R. MADDIN and A. H. COTTRELL, *Phil. Mag.* **46,** 735 (1955).
14. G. C. SCHOECK, *Phys. Rev.* **102,** 1458 (1956).
15. B. S. BERRY, and A. S. NOWICK, *NACA, TN* 4225 (August 1958).
16. A. GUINIER, *Trans. Amer. Inst. Min. (Metall.) Engrs.* **206,** 673 (1956).
17. W. DESORBO, H. N. TREAFTIS and D. TURNBULL, *Acta Met.* **6,** 401 (1958).

VOL.
8
1960

THE EFFECT OF SOLUTE PRECIPITATION ON THE RESISTIVITY OF ALLOYS*

W. A. HARRISON†

The effect of clustering upon the residual resistivity of alloys is treated using a free-electron model. The effects of lattice strain are taken into account as a change in the effective valence of the solute.

INFLUENCE DE LA PRECIPITATION SUR LA RESISTIVITÉ DES ALLIAGES

L'auteur étudie l'influence de la ségrégation sur la résistivité résiduelle des alliages en se basant sur un modèle d'électrons libres. Il tient compte des effets de la déformation du réseau comme une variation de la valence effective de l'élément en solution.

DER EINFLUSS VON AUSSCHEIDUNGEN AUF DEN ELEKTRISCHEN WIDERSTAND VON LEGIERUNGEN

Der Einfluß einer Entmischung auf den Restwiderstand von Legierungen wird im Rahmen eines Modells freier Elektronen behandelt. Die Wirkung von Gitterverzerrungen wird durch eine Änderung der effektiven Valenz des gelösten Elements in die Rechnung einbezogen.

1. INTRODUCTION

Electrical resistivity is frequently used as an indicator of the progress of precipitation phenomena in an alloy; that is, the decomposition of a supersaturated metallic solution. It is found experimentally that the resistivity generally drops as the precipitation proceeds. This seems intuitively reasonable in terms of the segregation of scattering centers (solute atoms) during clustering. In some cases, however, an initial rise in resistivity is observed, followed by the same general decrease. (For a review of this phenomenon, see Geisler[1].) This behavior is particularly prominent in certain aluminum alloys as shown, for example, by the recent studies of Turnbull *et al.*[2] on Al(Cu), Al(Ag), and Al(Zn) and of Frederighi[3] on Al(Ag). Mott[4] has suggested that the maximum may be associated with a matching of cluster size and electron wavelength; it has also been suggested that maxima may be associated in some way with any difference in the solvent and solute atom size.

In view of the current interest in this problem, it seems appropriate to make a semi-quantitative analysis of these suggestions in order to determine which are, in fact, plausible explanations for the observed phenomena.

2. GENERAL APPROACH

There are, in principle, three aspects of the clustering process which we would like to understand in order to treat the problem: the average cluster size, as a function of time, during the precipitation; the distribution of cluster sizes at each time; and the cluster shapes at each time.

The average cluster size can be determined experimentally by X-ray techniques. Hence, we will give our results as resistivity as a function of average cluster size.

We might attempt to calculate the distribution of cluster sizes during precipitation, but this calculation would depend rather sensitively upon the details of the binding energy of the solute atoms to each other; furthermore, this energy presumably depends upon cluster size in an important way. We will consider the cluster-size distribution phenomenologically, with a very crude estimate of the distribution, to see how this affects our results. Let X_n be the fraction of the solute atoms which are in clusters of exactly n atoms. Then the resistivity due to the solute will be proportional to the average resistivity per atom $\bar{\rho}$, given by

$$\bar{\rho} = \sum X_n(n)\,\rho(n), \tag{1}$$

where $\rho(n)$ is the resistivity *per atom* for a cluster of n atoms. Now X_n will be peaked around an average cluster size $\bar{n} = \Sigma\, nX_n$. The width of this peak will presumably be of the order of $\sqrt{\bar{n}}$. If $\rho(n)$ does not vary greatly over the range $\bar{n} - \sqrt{\bar{n}} < n < \bar{n} + \sqrt{\bar{n}}$, we may replace $\rho(n)$ by $\rho(\bar{n})$, and take it out of the sum in (1). Then $\bar{\rho}$ becomes equal to $\rho(\bar{n})$, and the cluster size distribution may be considered infinitely narrow. From our curves for $\rho(n)$ given in the next section, we see that this approximation is quite good when n becomes much greater than four, but that for very small clusters it is not a good approximation. The effect of the distribution of sizes is to partially

* Received May 12, 1959.
† General Electric Research Laboratory, Schenectady, New York.

smear out any variations in $\rho(\bar{n})$ which we may obtain when the clusters are small. We will neglect the spread in sizes throughout, but keep it in mind in interpreting the results.

Precipitating atoms may tend to form spherical clusters, needle-like clusters or platelets. In any of these cases, different clusters may have different shapes, and, in principle, we should average over these shapes. However, there is some reason to hope that the cluster shape will not be important, since in making a resistance measurement we will see a large number of clusters with all possible orientations. Furthermore, the fact that the resistivity per atom is about the same for atoms lying along a line as it is for dispersed atoms[5] suggests that the shapes are not extremely important. It therefore seems justified to consider only spherical clusters, which is a very major mathematical simplification of the problem.

Our model for the clustering of atoms, therefore, is spherical scattering centers, each containing $\bar{n}$ atomic volumes.

In order to calculate the resistivity arising from each cluster, we will assume a square-well scattering potential associated with the cluster; the diameter of the potential being determined by the diameter of the cluster, and the depth of the potential being determined by the valence difference between the solute and solvent atoms. Effects of the lattice distortion will be taken into account by introducing an effective valence, which depends upon the strain. These approximations may be justified theoretically by a careful treatment of the problem, using the cellular method for calculating the wave-functions in perturbed lattices.[6] They are justified experimentally by the success of such approximations in explaining the trends in resistivity of dispersed alloys as a function of valence and of atomic size.[7] In addition, we will make the Born approximation in performing the calculations. This should certainly be precise enough for our purposes, but the modifications which would arise from a more accurate calculation will be pointed out. Finally, in making the free-electron approximation, we set the number of free electrons per atom equal to the valence of the solvent.

3. SIMPLE CLUSTERING

We consider first clustering when the effects of strain are negligible. In this case we wish simply to calculate the contribution to the resistivity of a spherical square well as a function of volume. The depth of the well is to be determined by the valence difference (that is, by screening considerations). It will be convenient to make the calculation in terms of the phase shifts of electron states at the Fermi surface, since both resistivity and screening may be written simply in terms of them. The phase shift for an electron of angular-momentum quantum number l due to a square well of depth V and radius r_0 is given by*

$$\delta_l = -\frac{2mk_0V}{\hbar^2}\int_0^{r_0} r^2 j_l^2(k_0 r)\,dr. \tag{2}$$

Here k_0 is the Fermi wave number.

The total number of screening electrons associated with such a potential is given by†

$$n_e = (2/\pi)\sum_l (2l+1)\delta_l = -(2V/3\pi E_F) r_0^3 k_0^3, \tag{3}$$

where use has been made of equation (2) and the relation $\sum_l (2l+1) j_l^2 = 1$. Equation (3) may be simplified by using the free electron density of states for an electron gas with Z_0 electrons per atom, and noting that a sphere of radius r_0 has a volume equal to that of $\bar{n}$ atomic cells in our model;

$$\frac{2}{(2\pi)^3}\left(\frac{4}{3}\pi k_0^3\right)\left(\frac{4}{3}\pi r_0^3\right) = \bar{n}Z_0. \tag{4}$$

From (3) and (4) we may evaluate n_e, which we set equal to the net ionic charge to be screened, $\bar{n}(Z - Z_0)$, where Z is the valence of the solute. We solve for V and obtain

$$V = -\frac{2E_F}{3}\frac{Z - Z_0}{Z_0},$$

which may be inserted in equation (2) to give

$$\delta_l = \frac{2}{3}\frac{(Z - Z_0)}{Z_0}\int_0^{k_0 r_0} x^2 j_l^2(x)\,dx.$$

The resistivity per cluster may be written in terms of these phase shifts‡ and divided by $\bar{n}$ to give the resistivity per atomic percent of solute

$$\Delta\rho = \frac{4\pi h}{100e^2 k_0 \bar{n}}\sum_l (l+1)(\delta_l - \delta_{l+1})^2 \equiv$$

$$\equiv \frac{4\pi^2 h}{100e^2 k_0}\left(\frac{Z - Z_0}{Z_0}\right)^2 P(k_0 r_0), \tag{5}$$

where P is a function of $k_0 r_0$ only, and is readily evaluated using properties of the spherical Bessel functions[8] and their tabulated values. The $P(k_0 r_0)$ defined by (5) is shown in Fig. 1. The abscissa is linear in the cluster radius r_0, though calibrated in terms of $\bar{n}$, assuming *one* free electron per atom in the

* See Ref. 6, equation (34) with surface terms dropped.
† The Friedel sum rule, verified for crystals in Ref. 6.
‡ See Ref. 6, $\sin(\delta_l - \delta_{l+1})$ is replaced by $(\delta_l - \delta_{l+1})$ in the Born approximation.

VOL. 8 1960

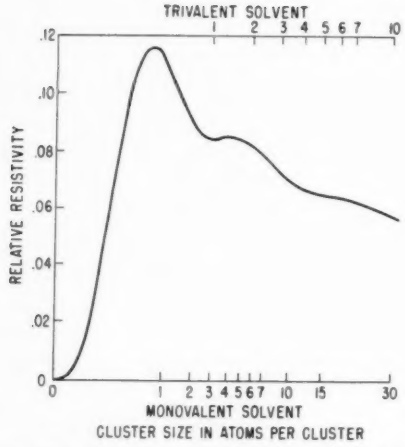


FIG. 1. The variation of the resistivity per atomic per cent of solute in an alloy during clustering of the solute. The abscissa is linear in the cluster radius; the scale at the bottom being for a monovalent solvent; that at the top, for a trivalent solvent.

solvent ($Z_0 = 1$) for the lower scale. If we make the assumption of three free-electrons per atom for a trivalent solvent, the scale at the top of the figure is appropriate. The ordinate gives the resistivity per atomic per cent in units of

$$\frac{4\pi^2 h}{100e^2 k_0}\left(\frac{Z - Z_0}{Z_0}\right)^2.$$

We see that a peak in the resistivity per atom does occur as suggested by Mott, but that this peak is located at cluster sizes of about one atom per cluster or less and does not, therefore, explain the resistance maximum on clustering. If an exact calculation of the phase shifts is made, rather than the Born approximation given in equation (2), the peak is shifted to the right for solutes of net positive valence and to the left for net negative valence. However, the shifts are not large and are toward smaller sizes for the alloys of aluminum mentioned earlier. The second maximum is certainly too small to be important. Thus it seems unlikely that these peaks are the cause of the observed resistance maximum.

We do notice that there is a rather steady decline in the resistivity upon clustering as expected, this drop being of the order of 30 or 40 per cent when $\bar{n}$ becomes of the order of ten. We expect such a trend to continue until the cluster diameter becomes of the order of the mean free path of the electrons and the current is deflected by the particles. Then a macroscopic treatment becomes appropriate, and the resistance should be independent of further clustering.

4. STRAIN EFFECTS

It has been shown[6] that to a good approximation the strains around an imperfection can be taken into account by introducing a correction to the valence of an impurity which is proportional to the strain. This is, of course, in contradiction to the point of view that a distortion of the lattice always gives an enhanced resistivity. It is true that one could calculate the scattering due to strain alone and that this would be positive. It is the interference terms between the effect of the strain and of the imperfection which may be of either sign. A relaxation of the lattice outward corresponds to a removal of ionic charge from the region of the imperfection and therefore a lowering of its effective valence. This turns out to be the major effect of such strains.

Blatt[7] has shown that in a monovalent solvent the magnitude of this correction is given by $\delta Z = -(3/\gamma)(\delta a/a)$, where

$$\gamma = \frac{3(1 - \sigma)}{1 + \sigma},$$

σ being Poisson's ratio. For $\sigma = 0.3$ we have $3/\gamma = 1.9$. $\delta a/a$ is the relative change in X-ray lattice parameter in per cent per atomic per cent of impurity. For the case of a polyvalent solvent, it is appropriate to multiply this by Z_0:

$$\delta Z = -(3/\gamma)Z_0(\delta a/a). \tag{6}$$

Thus we must replace Z by $Z + \delta Z$ in the coefficient of the resistance in equation (5). It would also be appropriate to make suitable adjustments in the radius of the square-well potential, but such corrections would be minor, and we do not make them. Now $\delta a/a$ will change as clustering proceeds, and hence there will be a change in the resistance due to this effect, this correction being given by the factor

$$\left(\frac{Z - Z_0 + \delta Z}{Z - Z_0}\right)^2,$$

with δZ given by equation (6). Thus this contribution can be calculated explicitly once measurements of $\delta a/a$ are made during clustering. If $\delta a/a$ is negative for the alloys studied by Turnbull *et al.*[2], and if it approaches zero during clustering, this would tend to give a rising resistivity (followed, of course, by the drop indicated in Fig. 1) and the possibility of a maximum. This would also be the case if $\delta a/a$ were positive and became larger during clustering. The limited data on the change in lattice parameter reported by Geisler[1] do not appear to support such an explanation, but a more careful study would be desirable.

5. CONCLUSION

We have seen that a rather slow drop in resistivity upon clustering is understandable in terms of a decrease in scattering cross-section per solute atom for large clusters. We see also that a peak in the scattering cross-section per atom occurs, but that it lies at about one atom per cluster and therefore would not give rise to a maximum in the resistivity.*

A crude treatment of the effects of strain indicates that it could give rise to a maximum and that the magnitude of this effect can be estimated directly in terms of X-ray lattice-parameter measurements made during clustering.

ACKNOWLEDGMENTS

The author is indebted to D. Turnbull for bringing this problem to his attention and for helpful comments. The author has benefitted also from discussions of the problem with M. B. Webb.

REFERENCES

1. A. H. Geisler, *Phase Transformations in Solids* (R. Smoluchowski, ed.) pp. 387–545. John Wiley, New York (1951).
2. D. Turnbull, H. S. Rosenbaum and H. N. Treaftis, *Acta Met.*, in press.
3. T. Frederighi, *Acta Met.*, in press.
4. N. F. Mott, Discussion of M. L. V. Gayler, *J. Inst. Metals* **60,** 267 (1937).
5. W. A. Harrison, *J. Phys. Chem. Solids* **5,** 44 (1958).
6. W. A. Harrison, *Phys. Rev.* **110,** 14 (1958).
7. F. J. Blatt, *Phys. Rev.* **108,** 285 (1957); *Phys. Rev.* **108,** 1204 (1957).
8. L. I. Schiff, *Quantum Mechanics,* p. 78. McGraw-Hill, New York (1949).

* Note added in proof. Recent studies of the electronic structure of aluminum by the author (*Phys. Rev.* **116,** (1959)) indicate that the Fermi surface consists of several relatively small sheets rather than a three-electron sphere. Thus the $\rho(n)$ curve should correspond to a suitable superposition of several curves, some corresponding to valence considerably less than one and having their maxima shifted to the right. Such an effect may easily be the source of the observed resistance maximum.

VOL. 8 1960

THE INTERACTION OF DISLOCATIONS AND PRECIPITATES*

R. B. NICHOLSON, G. THOMAS and J. NUTTING†

Thin foils of various aged aluminium alloys have been examined by transmission in the electron microscope. Dislocations, introduced by rolling before thinning, have been observed to move under the action of thermally induced stresses. The interactions of these dislocations and precipitates has been studied and the results show that dislocations pass through zones, coherent and partially coherent precipitates, but not through incoherent precipitates.

INTER-ACTIONS ENTRE DISLOCATIONS ET PRECIPITES

Les auteurs ont examiné au microscope électronique des feuilles minces de différents alliages d'aluminium vieilli. Les dislocations introduites par laminage avant amincissement, se déplacent sous l'action de tensions induites thermiquement. Les auteurs ont étudié les interactions entre ces dislocations et les précipités. Les résultats montrent que les dislocations traversent des zones contenant des précipités parfaitement ou partiellement cohérents mais ne traversent pas les zones où existent des précipités incohérents.

DIE WECHSELWIRKUNG VON VERSETZUNGEN MIT AUSSCHEIDUNGEN

Dünne Folien aus verschieden ausgehärteten Aluminium-Legierungen wurden im Elektronenmikroskop durchstrahlt. Vor der Präparation der dünnen Folien waren Versetzungen durch Walzen eingeführt worden; diese bewegten sich unter der Wirkung thermisch induzierter Spannungen. Die Wechselwirkung dieser Versetzungen mit den Ausscheidungen wurde untersucht. Die Ergebnisse zeigen, dass die Versetzungen Zonen, kohärente und teilweise kohärente Ausscheidungen durchdringen, jedoch inkohärente Ausscheidungen nicht durchdringen.

INTRODUCTION

With the advent of techniques for thinning pure metals and alloys for transmission electron microscopy it became apparent that it should be possible for the interaction of dislocations and precipitated phases to be observed directly in the electron microscope. There are numerous difficulties in such an investigation the chief of which is obtaining dislocation movement in the thin foils. The simplest method of making dislocations move is to heat the foils locally by increasing the intensity of the focussed electron beam when the thermal gradients induce shear stresses.[1] However this method is only suitable for plastically deforming soft alloys because of the relatively low stresses obtained. Experiments using a deformation stage in the electron microscope have so far not proved as successful as had been anticipated but work is continuing on this problem. The purpose of the present paper is to describe the results already obtained using the thermal method of stressing the foils.

The alloys examined (Al–4%Cu, Al–10%Zn and Al–7½%Zn–2½%Mg) were heat treated to give suitable structures at various stages of ageing and over-ageing and then deformed a few per cent by rolling. Thin foils of these alloys were prepared by a technique previously described.[2] The foils were examined in a Siemens Elmiskop I electron microscope operating at 80 or 100 kV.

It has been shown that the dislocations remaining in Al–Cu alloys after solution treatment become immobile as a result of climb of the screw components into helices due to the condensation of excess vacancies retained by quenching.[3] It is probable that copper atoms aggregate preferentially at the edge components of the dislocations and in this alloy[4] and in Al–Mg–Zn[5] it has been shown that dislocations are sites for preferential precipitation. Consequently, dislocations in the matrix are locked, and free dislocations can only come from grain boundary sources. Fig. 3, which is a micrograph of an aged Al–Mg–Zn alloy, shows such a source in operation. The dislocation A has been emitted by the boundary and moves easily in the precipitate free region.

Dislocations locked by precipitates could act as Frank–Read sources[5] but the initial free length is so small that a very high stress would be required to make them active. As a result dislocations from such sources have not been observed in thin foils. There is no experimental evidence for other sources of dislocations and consequently it is probable that most of the dislocations causing slip are emitted from grain boundaries or the foil edges. The estimated stress obtained by heating foils in the electron beam[1] is about $G/1000$ which is not sufficient to operate these

* Received May 11, 1959.

† Department of Metallurgy, Cambridge University, England.

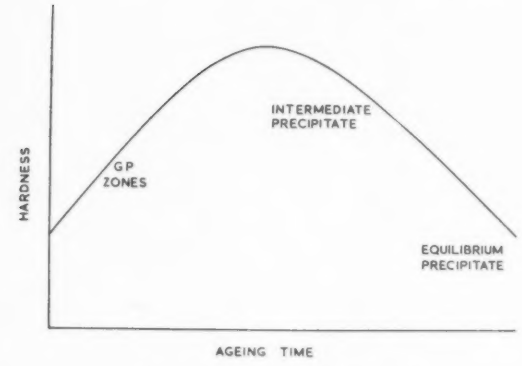


FIG. 1. Schematic ageing curve.

sources in most of the heat treated alloys which have been investigated and so no dislocation movement is observed in thin foils of undeformed specimens. Consequently the bulk specimens were lightly rolled, introducing glissile dislocations in the grains, some of which were in a position where they could undergo further glide under thermally induced stresses in the electron microscope. Observations which have been made on the movement of these dislocations through foils containing zones and precipitates are described and discussed in relation to our present state of knowledge concerning the deformation of two-phase alloys.

VOL. 8 1960

AGEING CHARACTERISTICS

The changes occurring during ageing of the various alloys are shown schematically in Fig. 1.

In aluminium copper alloys the GP-zones consist of copper rich platelets parallel to {100} and fully coherent with the matrix. They are 1–10 atoms thick and up to 500 Å long. In the other alloys examined the zones are spherical and up to 100 Å diameter. The intermediate precipitate in Al–Cu is the θ' phase, also parallel to {100}, and partially coherent with the matrix whilst those in the other alloys (zinc in Al–Zn and M′–$MgZn_2$ in Al–Mg–Zn) are partially coherent and parallel to {111}. Over-ageing produces the non-coherent phases $CuAl_2$ in Al–Cu, zinc in Al–Zn and $MgZn_2$ in Al–Zn–Mg.

THE GENERAL CASES OF ZONES AND COHERENT OR PARTIALLY COHERENT PRECIPITATES

When precipitates are coherent or partially coherent with the matrix then, under a suitable stress, the precipitates should deform with the matrix. When this occurs it is possible to observe the displacement of the precipitates. Some examples of this have already been published by Thomas and Nutting[6] and Koda and Takeyama[7] but in many of the micrographs not all the precipitates intersected by slip lines showed any change in shape. It can easily be shown by considering the passage of dislocations of various Burgers vectors through the precipitates in a f.c.c. matrix that a change in shape of the precipitate is only detected at surfaces of certain crystallographic orientations notably near (100); e.g. Fig. 2, where the surface which is almost (100) shows θ' precipitates in two orientations which have been displaced as a result of slip. This micrograph is typical of the surface effects of plastic deformation in alloys containing partially coherent precipitates. The same result should be obtained in alloys where the precipitates are fully coherent or where zones are present but replica methods have not been able to confirm this.

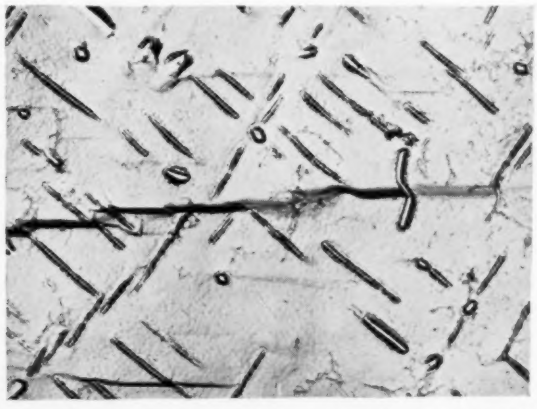


FIG. 2. Oxide replica Al–4%Cu, θ' precipitates. ×15,000



FIG. 3. Thin foil Al–7½%Zn–2½% Mg, M′ precipitates. ×80,000

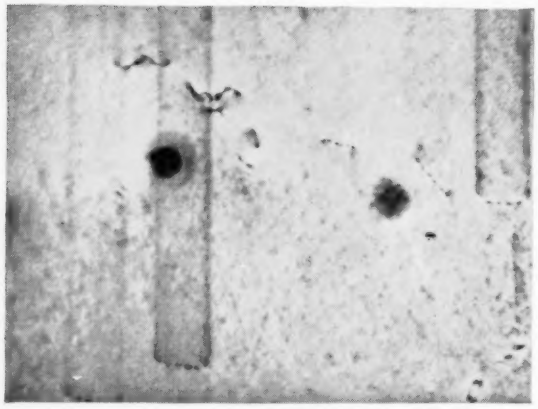


FIG. 4. Thin foil Al–10%Zn zones. ×70,000

ZONES AND FULLY COHERENT PRECIPITATES

Dislocations in foils containing zones have been made to move under the action of thermally induced stresses, but subsequently the specimen is no longer in a condition suitable for high resolution electron microscopy because of deposition of a carbon layer on the foil surface. Consequently it has not yet been possible to detect the displacement of a zone after a dislocation has been observed to move through the foil. However dislocation motion has been studied in some detail, and in all cases it appears that the dislocations pass through the zones and are not in general held up at each zone. Fig. 4 is an example of moving dislocations in an Al–Zn alloy where the zones are about 30 Å in diameter. This is typical of dislocation movement in all the alloys aged to produce only zones. The thermal stresses in the foil fluctuate continuously and consequently a dislocation may rest in a certain position for several minutes before the stress is large enough to move it again. This position, where the shape of the dislocation is dictated by the stress field in the foil and the line tension of the dislocation, is of some interest and an example is shown in Fig. 5. This is a micrograph of the Al–4%Cu alloy aged to produce GP-II zones and the dislocations, e.g. at *A*, are partially curved out between the zones although they are only about 250 Å apart. If the radius of curvature of the dislocation is measured just before it passes through the precipitate, the stress required for this process can be calculated. This is difficult in the case of Fig. 5, but an approximate measurement on the original plate indicates a radius of curvature of ~200 Å. This leads to a calculated flow stress of ~17 kg/mm², which is rather higher than the measured flow stress of this alloy when determined on more massive test pieces. However it seems



FIG. 5. Thin foil Al–4%Cu, G.P.-II zones. ×80,000

probable that, even when the dislocations are moving rapidly through the specimen, they curve out momentarily between the zones before passing through them. This picture is consistent with the results of Jan[8] on the Al–Ag system.

PARTIALLY COHERENT PRECIPITATES

The formation of partially coherent precipitates leads to a general softening of the alloy. This is thought to be due to the disappearance of long range elastic strain fields in the matrix (in cases where they had previously existed), solute depletion of the solid solution and increasing coarseness of the precipitate with a corresponding increase in precipitate spacing.

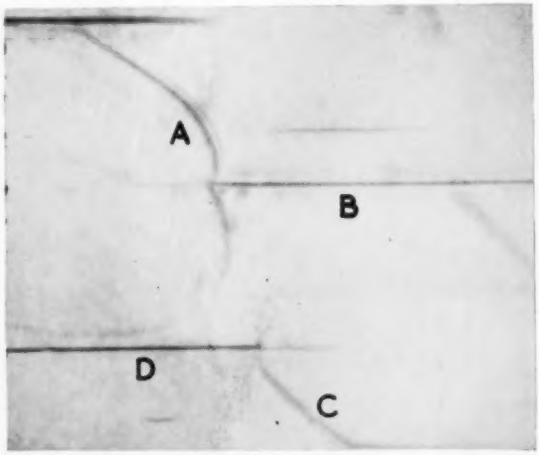


FIG. 6. Thin foil Al–4%Cu, θ′ precipitates. ×60,000

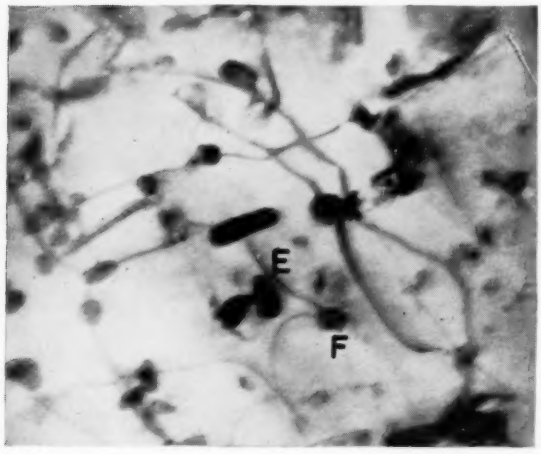


FIG. 7. Thin foil Al–7½%Zn–2½% Mg M′ precipitates. ×80,000

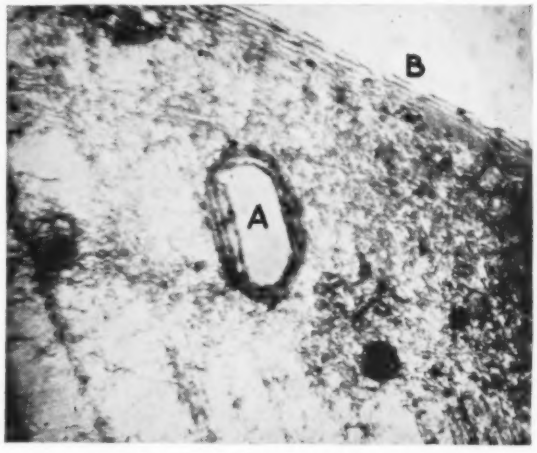


FIG. 9. Thin foil Al–7½Zn–2½% Mg, complex precipitate. ×25,000

Oxide replica methods have been particularly satisfactory for revealing the displacement of partially coherent precipitates as a result of slip (Fig. 2). The present observations have confirmed that the dislocations do in fact pass through the precipitates although they are initially held up at the interface. In Fig. 6, a micrograph taken from an Al–4%Cu alloy showing θ' precipitates, the dislocation at A is beginning to bow out around the precipitate B, while at C another dislocation has passed through part of the precipitate D. Similarly in Fig. 7, from an Al–Mg–Zn alloy aged to produce the partially coherent M′ precipitate on {111} planes, a dislocation E has been held out of shape by the precipitate F while Fig. 8 shows a series of dislocations which probably all lie in the same slip plane and are moving through a number of parallel precipitates. A close study of the dislocation lines in this micrograph reveals a number of irregularities and it is thought that these are jogs introduced by the passage of the dislocations through the precipitates.



FIG. 8. Thin foil Al–7½%Zn–2½% Mg M′ precipitates. ×50,000

The interface between a partially coherent precipitate and the matrix is thought to consist of a simple network of structural dislocations which would be a local barrier to dislocation movement. The results obtained in the present investigation have qualitatively confirmed this but it is shown that the barrier can be overcome. The measured flow stresses for bulk specimens are lower when the partially coherent phases are present (Fig. 1), and it must be presumed therefore that the stresses required to force dislocations through the structural dislocation network are considerably less than those required to overcome the long range elastic strain fields associated with some zones and fully coherent precipitates.

NON-COHERENT PRECIPITATES

The oxide replica work reported by Thomas and Nutting[6] showed that in specimens aged to precipitate non-coherent phases, deformation at room temperature produced slip lines which did not cut through the precipitates. It was not possible to decide from these surface studies whether loops of dislocation were left around the precipitates either as a result of cross-slip (Hirsch[9]) or without cross-slip (Orowan[10] and Fisher *et al.*[11]). However it seems more reasonable to expect dislocations to avoid precipitates by a process of cross-slip and this has been discussed in detail previously.[6]

In Fig. 9 the particle A is a non-coherent intermetallic compound (probably $FeMnAl_6$) in a commercial Al–Mg–Zn alloy. The dislocations were introduced before the specimen was thinned and it is clear that although there are many dislocations in

VOL. 8 1960

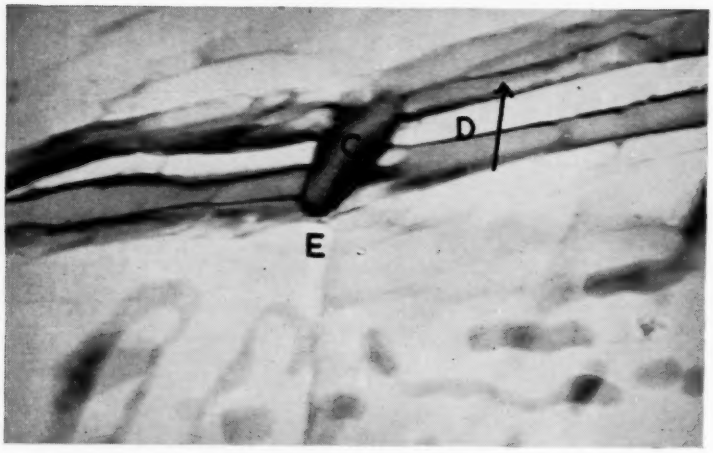


FIG. 10. Thin foil Al–4% Cu, θ precipitate. ×30,000

the matrix, there are none inside the particle. The fringes round the particle A were found to be sensitive to orientation, i.e. by tilting the specimen they could be made to disappear. This suggests that they are not a structural feature but simply an interference effect similar to the fringes at the grain boundary B. This micrograph shows that dislocations avoid non-coherent phases but it is not possible to decide how this is accomplished.

In Fig. 10 the particle C extends throughout the thickness of the foil and the dislocations D were observed to move in the direction indicated. Consequently, the interaction is not typical of bulk material as the Hirsch mechanism[9] cannot operate. We would expect dislocation loops to form round the particle C as predicted by Orowan[10] and a few segments of loops are visible at E in Fig. 10.

CONCLUSIONS

The present paper has shown that it is possible to see dislocation precipitate interactions in the interior of metal crystals. It is probable that dislocations pass through zones, coherent and partially coherent precipitates, but avoid non-coherent phases by a cross-slip mechanism.

New experiments are in progress involving the use of a deformation stage in the electron microscope.

ACKNOWLEDGMENTS

The authors would like to thank Professor A. H. Cottrell, F.R.S., for his interest and encouragement. We are grateful to the Department of Scientific and Industrial Research for the award of a Maintenance Grant (R. B. N.) and to Imperial Chemical Industries for the award of a Fellowship (G. T.).

REFERENCES

1. P. B. HIRSCH, R. W. HORNE and M. J. WHELAN, *Phil. Mag.* (ser. 8) **1,** 677 (1956).
2. R. B. NICHOLSON, G. THOMAS and J. NUTTING, *Brit. J. Appl. Phys.* **9,** 23 (1958).
3. G. THOMAS and M. J. WHELAN, *Phil. Mag.* (ser. 8) **4,** 511 (1959).
4. G. THOMAS and J. NUTTING, *Acta Met.* **7,** 515 (1959).
5. G. THOMAS, *Phil. Mag.* (ser. 8) **4,** 606 (1959).
6. G. THOMAS and J. NUTTING, *J. Inst. Met.* **86,** 7 (1957–58).
7. S. KODA and T. TAKEYAMA, *J. Inst. Met.* **86,** 277 (1957–58).
8. J–P. JAN, *J. Appl. Phys.* **26,** 1291 (1955).
9. P. B. HIRSCH, *J. Inst. Met.* **86,** 13 (1957–58).
10. E. OROWAN, *Symposium on Internal Stresses in Metals and Alloys*, p. 447. Institute of Metals, London (1948).
11. J. C. FISHER, E. W. HART and R. H. PRY, *Acta Met.* **1,** 336 (1953).

AN X-RAY STRUCTURE INVESTIGATION OF THE LIQUIDS OF SODIUM, POTASSIUM AND SODIUM–POTASSIUM ALLOYS*

B. R. ORTON,† B. A. SHAW‡ and G. I. WILLIAMS†

The X-ray structures of liquid sodium, potassium and sodium–potassium alloys have been investigated by an improved method. By using a reservoir technique a plane horizontal surface of liquid metal has been examined by a monochromatic X-ray beam in a focusing Geiger diffractometer. Thus the absorption correction, which is one of the greatest sources of error in previous work, is constant and omitted from the analysis.

The radial distribution method of analysis has been used to interpret the results. None of the liquids examined shows evidence of structure other than that associated with a statistical mixture of atoms. In particular the position of the intensity peak is found to depend in a fairly simple way on alloy composition and does not show the marked deviation at compound composition Na_2K as reported by other workers.

The use of the radial distribution method has been examined critically. It is felt that the method is adequate for interpreting simple liquid structures provided suitable modification functions are used to expose spurious detail.

EXAMEN PAR RAYONS X DES STRUCTURES DU SODIUM, DU POTASSIUM ET DES ALLIAGES SODIUM-POTASSIUM A L'ETAT LIQUIDE

Les auteurs ont examiné les structures du sodium, du potassium et des alliages sodium-potassium liquides, à l'aide d'une technique améliorée de rayons X. Par l'emploi d'un réservoir, il a été possible d'examiner une surface plane horizontale de métal liquide, à l'aide d'un faisceau monochromatique de rayons X. L'enregistrement du faisceau diffracté se fait sur un diffractomêtre à compteur de Geiger. Dans ces conditions, la correction d'absorption qui est une des plus grandes sources d'erreur des travaux antérieurs devient constante et n'intervient plus dans l'analyse des résultats. Pour interpréter les résultats, les auteurs ont utilisé la méthode d'analyse par distribution radiale. Aucun des liquides examinés n'a montré une structure autre que celle associée à un mélange statistique d'atomes. En particulier, la position du pic d'intensité est liée par une relation simple à la composition stoechiométrique correspondant à Na_2K, comme l'avaient indiqué d'autres chercheurs.

Les auteurs discutent de l'opportunité de l'emploi de la méthode de dislocation radiale. Ils pensent que cette méthode est adaptée à l'interprétation de structures liquides simples à condition que des fonctions appropriées soient utilisées pour éliminer certains éléments aberrants.

RÖNTGENOGRAPHISCHE UNTERSUCHUNG VON FLÜSSIGEM NATRIUM, KALIUM UND NATRIUM-KALIUM-LEGIERUNGEN

Die Struktur von flüssigem Natrium, Kalium sowie Natrium-Kalium-Legierungen wurde mit einer verbesserten Röntgenmethodik untersucht. Durch Benutzung eines Reservoirs wurde eine horizontale ebene Oberfläche des flüssigen Metalls erzeugt. Diese wurde mit einem monochromatischen Röntgensstrahl in einem fokussierenden Geiger-Diffraktometer untersucht. Die Absorptionskorrektur, die in früheren Arbeiten eine der größten Fehlerquellen darstellt, ist daher konstant und fällt bei der Analyse der Ergebnisse weg.

Zur Deutung der Ergebnisse wurde die Darstellung durch eine radiale Verteilungsfunktion gewählt. Bei keiner der untersuchten Flüssigkeiten finden sich Anzeichen für eine andere Struktur als sie einer statistischen Mischung der Atome entspricht. Insbesondere hängt die Lage des Intensitätsmaximums in ziemlich einfacher Weise von der Legierungszusammensetzung ab. Die ausgeprägten Abweichungen, wie sie von anderen Autoren für die Zusammensetzung Na_2K berichtet wurden, zeigten sich nicht.

Die Möglichkeit der Darstellung durch eine radiale Verteilungsfunktion wurde kritisch geprüft. Die Methode dürfte zur Deutung einfacher Flüssigkeitsstrukturen geeignet sein; dabei sind jedoch passende Modifikations-Funktionen anzubringen, um vorgetäuschte Besonderheiten als solche zu erkennen.

VOL. 8 1960

1. INTRODUCTION

There have been many investigations into the atomic structures of liquid metals.[1] In some of the recent work the use of a strictly monochromatic source of X-rays together with Geiger counter recording has increased the reliability of the results.[2] In the case of sodium, potassium and sodium–potassium alloys, one of the main sources of error, the absorption correction, still remains. The experimental difficulties with these metals are such that the liquid specimens examined have always been contained in thin glass quills. The glass contributes but little to the diffraction pattern but the absorption correction error of the specimen as a whole can be significant, particularly for potassium-rich alloys. Furthermore with such a specimen it is difficult to determine the composition accurately and to establish that the sample is homogeneous.

* Received May 5, 1959.

† Fulmer Research Institute Ltd., Stoke Poges, Buckinghamshire.

‡ Late Fulmer Research Institute, now Transitron Electronic Corporation, Wakefield, Massachusetts, U.S.A.

It was decided therefore to develop a technique for examining specimens having a plane unrestricted surface. With a suitably designed camera diffractions from the window material can be isolated from those arising at the specimen, and by rotating both the X-ray source and diffraction counter about the horizontal axis of the diffractometer, the absorption correction is kept constant and therefore can be omitted from the interpretation. Large specimens are used to overcome problems of homogeneity and chemical analysis.

The sodium–potassium constitutional diagram is shown in Fig. 1. The liquids examined include the compound composition Na_2K, which is a Cl4 hexagonal Laves phase in the solid, and the eutectic at 65 at.% K. Previous workers had reported a discontinuity in the intensity peak/composition curve at Na_2K composition.[3]

In order to investigate the effect on the structures of both actual temperature and excess temperature above the liquidus, it was proposed to examine liquid sodium at temperatures up to 200°C and the other liquids at a constant temperature just above 100°C and then at a small temperature increment above the liquidus.

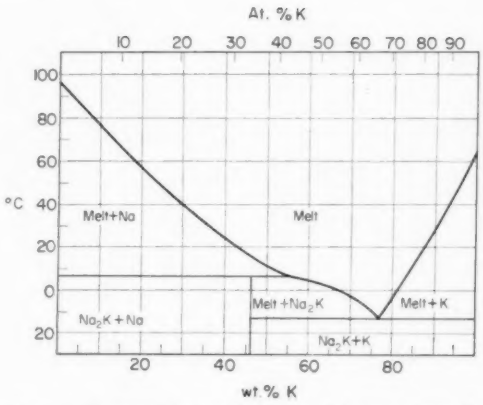


FIG. 1. The equilibrium diagram of the system sodium–potassium.

2. EXPERIMENTAL

(a) *X-ray diffractometer*

The experimental installation is shown in Fig. 2, with the liquid metals camera in position at the centre of the diffractometer. In order to maintain the Bragg–Brentano focusing condition both the X-ray tube, together with monochromator and monitor counter, and the diffractions counter are pivoted about the horizontal axis of the diffractometer.

The X-ray tube and quartz focusing monochromator are carried on a platform which is rotated about the axis by means of a capstan wheel and screw. Fine adjustment is provided for initial alignment of tube and monochromator.

The diffractions counter with its probe unit is pivoted about the axis by means of a large bracket which is counterbalanced. A movable clamp operating on the disc D holds the arm in position. Fine adjustment of the counter relative to the clamp is obtained by operating a knurled screw. The counter can be adjusted about the diffractometer axis and moved laterally.

It was not practicable to link the movements of X-ray source with the diffraction counter in order to maintain automatic focusing. These are carried out independently. The positions are given by Vernier scales moving over the disc D which is graduated in degrees. Diffractions can be recorded at angles up to $\theta = 70°$.

A cathetometer with graduated eyepiece is sighted through a hole drilled along the length of the diffractometer axis enabling the specimen to be positioned on this axis. The position of the specimen is observed with respect to an illuminated slit in a stationary part of the diffractometer so that any misalignment of cathetometer does not affect the specimen setting.

The specimen level can be set to within 0.1 mm. A change in level of 0.5 mm produces a shift in peak position of 0.003 in $\sin\theta/\lambda$ at $\theta = 12°$, which is the approximate position of the potassium peak. The angular calibration of the diffractometer was checked with aluminium sheet and powder and found to be correct within 5 min of arc. In the region of the potassium peak recorded values of $\sin\theta/\lambda$ are probably correct to within 0.002, the errors being correspondingly less at higher angles.

(b) *Camera and reservoir system*

The camera and reservoir feed system shown in Fig. 3 provide and maintain a plane clean surface of liquid metal, suitable for diffraction studies, at the centre of the diffractometer. The camera consists of a cylinder fitted with a circular crucible having two concentric sections. The central section is connected to the feed pipe of the reservoir while an outlet pipe is used to drain away any liquid metal forced over into the outer section. It is provided with glass end-plates affording good visual observation of the liquid metal surface and an X-ray window of Al/Si foil 0.0015 in. thick around half its circumference.[4] A small scraper, operated from outside the camera, facilitates the flow of metal from inner to outer section of the specimen holder and also enables traces of oxide to be removed from the specimen surface. During X-ray exposure it

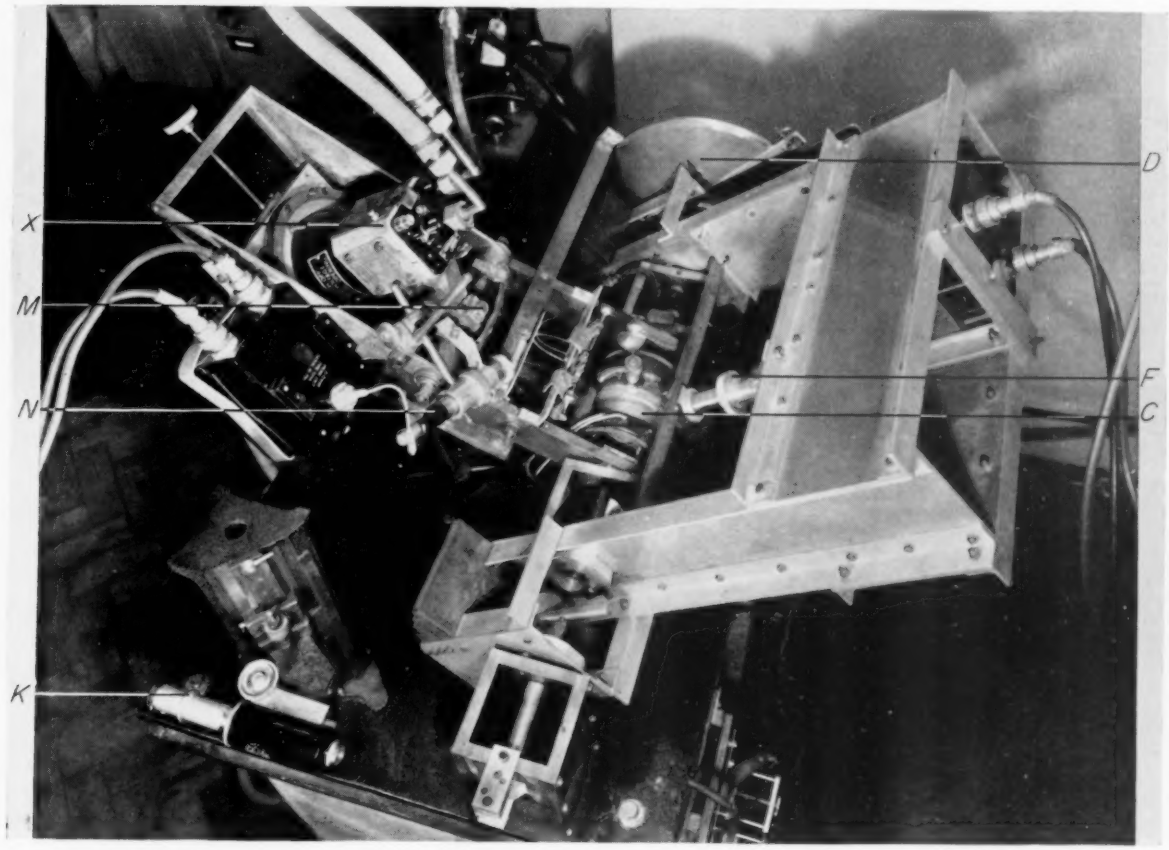


FIG. 2. Diffractometer. *D* Graduated disc. *C* Aluminium-silicon X-Ray window. *F* Diffraction counter. *X* X-Ray tube. *M* Monochromator. *N* Monitor. *K* Cathetometer.

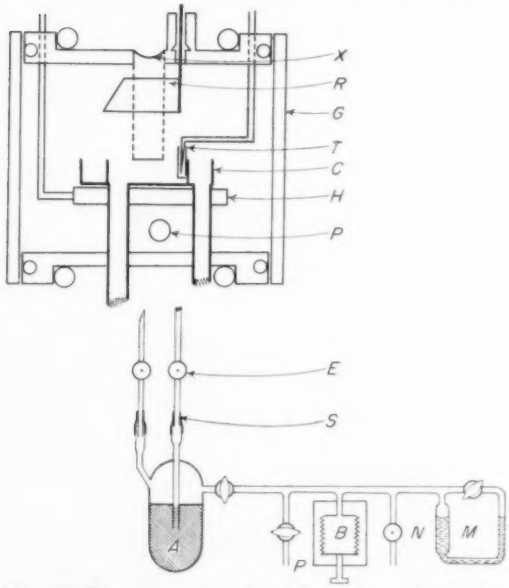


FIG. 3. The Camera and feed system. *X* X-Ray window. *R* Scraper. *G* Glass end plates. *T* Thermocouple. *C* Crucible. *H* Heater. *P* Pumps. *E* Nimonic valve. *S* Silicone rubber joints. *A* Ampoule. *B* Bellows. *N* Needle valve. *M* Manometer.

is retracted to the top of the camera where it screens off those diffractions arising from the incident X-ray beam striking the camera window, which might otherwise scatter into the counter. The camera body, crucible, feed pipes and scraper are made of 18/8/1 stainless steel, this being a suitable material for containing sodium and potassium.[5] Demountable joints are fitted with "O" ring seals, and the whole is water cooled. The crucible is fitted with a small furnace fed by a Variac operating from a stabilised source of a.c. A sheathed thermocouple of chromel-alumel is immersed in the liquid metal contained in the outer section of the specimen holder.

The feed system consists of a reservoir in the form of a glass ampoule of capacity 200–300 cm^3 fitted with magnetically breakable vacuum seals. The delivery and return tubes overlap closely the corresponding tubes of the camera enabling silicone rubber to aomplete the vacuum seals without exposure to liquid metal. The system is wound with heater tapes for melting the metal under investigation. Nimonic valves for controlling the flow of liquid metal are included in the delivery pipes to the camera.

VOL. 8 1960

A pressure of argon is used to force the liquid metal up into the camera. The level is indicated by the mercury manometer M and controlled by the needle valve N and adjustable metal bellows B. A layer of silicone oil prevents evaporation of the mercury into the vacuum system.

(c) *Preparation of specimens*

The specimens were prepared by a filtration process to remove oxides and insolubles. In the case of the alloys these were prepared in a separate container, then introduced into the filtering apparatus and adjustments to composition made before filtering. The filtering tower delivered the liquid metal to an ampoule fitted with magnetically breakable seals where it was then sealed under vacuum until required.

(d) *Operating procedure*

(i) *Specimen*. The ampoule containing the specimen was introduced into the apparatus as shown in Fig. 3. After heating the system, liquid metal was raised into the camera by increasing the argon pressure. Fine adjustment of meniscus height was carried out by operating the bellows B. If the liquid surface obtained by this first pass appeared contaminated it was caused to overflow into the outer crucible and thence returned to the ampoule. A further supply of liquid metal was then raised into the camera. By suitable manipulation it was possible to obtain a clean mirror-like surface in the camera. With a vacuum better than 10^{-5} mm Hg this could be maintained for about 5 hr. After this period a small degree of contamination may be detected, causing interference colours to be seen on the surface. A new surface may then be obtained as above.

By causing the metal to solidify near the inlet valve an effective seal is obtained thus preventing small bubbles of argon from passing through the system and disturbing the liquid metal surface with possible splashing on to the X-ray window.

The level of the liquid metal surface was observed with the cathetometer throughout the run. Usually no measurable change in specimen position could be detected by the graduated eyepiece which was capable of indicating a difference of less than 0.1 mm. When small variations were observed these were measured and the apparent angle of diffraction corrected accordingly.

The specimen temperature was recorded throughout on a fast moving chart recorder.

(ii) *Counting procedure*. Copper $K\alpha$ radiation generated at 50 kVp 25 mA, from a set having full wave rectification and operating on stabilized a.c., was used throughout. The slit width of the diffraction counter was 0.9 mm subtending an angle of 30 min of arc at the centre of the diffractometer radius 9 cm. Counts were recorded on a scaling unit for a standard X-ray monochromatic output as measured by the monitor. Measurements were taken at specific angular positions of the diffractometer, the intervals being 15 min of arc in the region of the main diffraction peak, 30 min over the subsidary peak and one degree at higher values of $\sin\theta/\lambda$ where the intensity varies but slowly.

The observed intensity was plotted as a function of $\sin\theta/\lambda$ during the run so that points of interest or ambiguity could be re-examined immediately.

After completing the available range of diffraction angles the intensity of the main peak was re-examined critically for variation in counts arising from growth of surface oxide during the exposure.

The X-ray intensities were corrected for losses in both counters, background count and polarisation.[6] It was not possible to measure intensities below $\sin\theta/\lambda = 0.07$ and so it was assumed that the X-ray intensity could be extrapolated smoothly to zero at the origin.

3. RADIAL DISTRIBUTION ANALYSIS

The radial distribution method of analysis of intensity scattered by a non-crystalline array of atoms is well established.[1,6,7] Provided experimental intensities very near the main beam are excluded, application of the Fourier integral theorem leads to the following expression for atomic density as a function of distance from a reference atom:

$$4\pi r^2\rho(r) = 4\pi r^2\rho_0 + 2r/\pi \int_0^\infty si(s)\sin rs\,ds, \qquad (1)$$

where $\rho(r)$ = number of atoms/unit volume at a distance r from the reference atom, i.e. $4\pi r^2\rho(r)\,dr$ = number of atoms contained in a spherical shell of radius r, thickness dr.

ρ_0 = average atomic density
$s = 4\pi \sin\theta/\lambda$ and
$i(s) = I/Nf^2 - 1$ where
N = number of atoms in the irradiated specimen,
f = scattering factor of each atom, and
I = the coherent component of the experimentally determined scattered radiation expressed in electron units.

(a) *Curve fitting*

At sufficiently high values of $\sin\theta/\lambda$ for interference effects to be absent from the diffraction pattern, the total scattered intensity is the sum of the coherent scatter produced by the same number of atoms

scattering independently with no evidence of structure, i.e. Nf^2, together with the appropriate incoherent or Compton scatter. These values are tabulated in electron units.[8] By matching the corrected experimental intensity curve to this total independent scatter at high angles, the experimental curve is expressed in electron units. Hence I, the coherent component, may be obtained in these units and used to derive values of $i(s)$.

An alternative method of deriving the factor of proportionality for expressing intensities in electron units was used in some cases.[9] This factor is obtained from a consideration of the complete diffraction curve and is given by

$$\int_0^{s_a} I.s\, ds \Big/ \int_0^{s_a} f^2 s\, ds,$$

where s_a is the upper limit of the experimental diffraction data.

(b) *Evaluation of integral*

In order to evaluate the integral of equation (1) the experimental amplitude function $si(s)$ was plotted against s and values of sin rs taken from tables.[10] For each value of r the summation $\Sigma\, si(s) \sin rs\, \Delta s$ was carried out over 60 equidistant values of s. Between 1 and 4 Å values of r at intervals of 0.2 Å were adopted; at higher values the interval was 0.5 Å. Using 120 equidistant values of s the summations differed by less than 1 per cent from the corresponding ones obtained with 60 values, implying that the increment adopted was sufficiently small.

The mean atomic density ρ_0 is calculated from published data.[5]

(c) *Sources of error in radial distribution analysis*

The greatest source of error is usually the absorption correction. The effective absorption is difficult to determine for specimens contained in glass quills which may have even slight variations in cross section. In the present work the correction is constant for all values of θ and thus can be omitted from the analysis.

Other sources of error are those due to termination of series, discrete errors in the $si(s)$ function, and errors in curve fitting. It is possible to reduce the errors arising from termination of series by extending the range of experimental intensity data. This may be extended to larger values of s by using Mo$K\alpha$ radiation in addition to the Cu$K\alpha$ radiation which is essential for accurate determination of position of the first diffraction peak. The intensity curve obtained with Cu$K\alpha$ must first be matched to that with Mo$K\alpha$ before matching to electron units. It is felt that the difficulties incurred in this preliminary matching outweigh the potential advantages of the method. Moreover in the liquids examined there was little evidence of structure beyond s values of $7A^{-1}$ and so there is but small advantage in extending this limit.

Spurious ripples in the radial distribution curve can be suppressed by applying an artificial temperature factor of the form $\exp(-A \sin^2\theta)$ to the $si(s)$ amplitude.[6,11] This has been adopted in the present work. The factor A is chosen so that the $si(s)$ value at $s_{\max}$ is reduced to about one tenth.

By applying such modification functions and inspecting the radial distribution curves for periodic spurious ripples it is usually possible to identify the sources of error. Ripples persisting at very small values of r, are invalid from atomic size considerations and usually arise from bad curve matching.

(d) *Extension to liquids having more than one type of atom*

It can be shown[12] that the general version of equation (1) is

$$\Sigma K_m 4\pi r^2 \rho_m = \Sigma K_m 4\pi r^2 \rho_0 + 2r/\pi \int_0^{\infty} si(s) \sin rs\, ds \quad (2)$$

where the summation is over the molecular composition.

K_m = effective number of electrons in atom and given by $K_m{}^* = f_m/f_e$

ρ_0 = average number of electrons/unit volume in absence of structure.

ρ_m = number of electrons/volume, with structure.

$4\pi r^2 \rho_m\, dr$ = number of electrons in shell between r and $r + dr$, i.e. number of atoms x effective electrons/atom in shell between r and $r + dr$,

$\Sigma K_m 4\pi r^2 \rho_m$ = total (effective number of electrons)^2 in unit shell volume.

$$i(s) = \frac{I_{eu} - \Sigma f_m{}^2}{f_e^2}.$$

If $\Sigma K_m 4\pi r^2 \rho_m$ is evaluated and plotted as a function of r, the area under the curve between r_1 and r_2 is $\int_{r_1}^{r_2} (\Sigma K_m 4\pi r^2 \rho_m)\, dr$ and represents the total (effective number of electrons)^2 in a shell, r_1–r_2. This type of approach has been adopted in analysing the experimental intensity data of the alloys. In this case the molecular structure cannot be assumed and the average values of f_e, $\Sigma f_m{}^2$ and incoherent scatter are

* K_m is not strictly constant but the shapes of f/θ curves for all atoms are similar and so an average value can be taken.

VOL. 8 1960

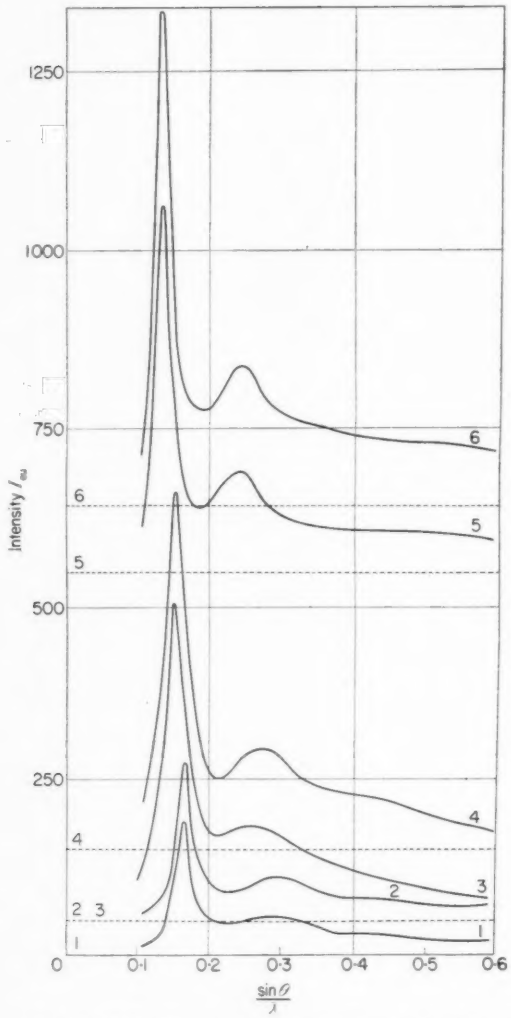


FIG. 4. Diffraction patterns for sodium, potassium and sodium 35.4 at.% potassium. (1) Sodium at 205°C. (2) Sodium at 114°C. (3) Sodium 35.4 at.% potassium at 114°C. (4) Sodium at 35.4 at.% potassium at 23°C. (5) Potassium at 114°C. (6) Potassium at 80°C.

calculated for the appropriate atomic fractions of sodium, a, and potassium, b, in the alloy:

$$f_e = \frac{af_{Na} + bf_K}{aZ_{Na} + bZ_K}$$

$$\Sigma f_m^2 = af_{Na}^2\, bf_K^2.$$

4. RESULTS

(a) *Intensity function*

Figure 4 shows the corrected intensities, expressed in electron units, as a function of $\sin\theta/\lambda$ for the liquids Na, K and Na 35.4 at.% K. At both temperatures of experiment all the curves are similar in shape, consisting of two well defined peaks with traces of a further shallow ripple at high angles. The intensity

TABLE 1. Intensity functions

Liquid	Temp. (°C)	Peak Position $\sin\theta/\lambda$		Reference
		This work	Other workers	
Na	114	0.166		
	150	0.166		
	203	0.164		
	103		0.160	Tarasov and Warren[16]
	100		0.160	Trimble and Gingrich[17]
Na 14.2 at.% K	114	0.157		Interpolated from Henderson and Gingrich[3]
	115		0.151	
Na 35.4 at.% K	23	0.144		
	114	0.150		As above
	115		0.136	
Na 57.2 at.% K	114	0.140		As above
	115		0.134	
Na 78.12 at.% K	23	0.137		As above
	115		0.134	
K	80	0.131		Thomas and Gingrich[18]
	114	0.131		
	70		0.130	

curves for the liquids of compositions Na 14.2 at.% K, Na 57.2 at.% K and Na 78.1 at.% K are not shown. These are similar in form to those of Fig. 4.

The results are summarized in Table 1 and compared with those of other workers.

In Fig. 5 the positions of the first peaks are plotted against alloy composition. It is seen that the peak positions depend almost linearly on composition, with

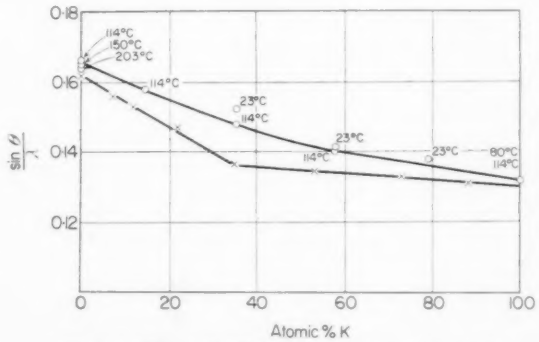


FIG. 5. Change in diffraction peak position with composition.

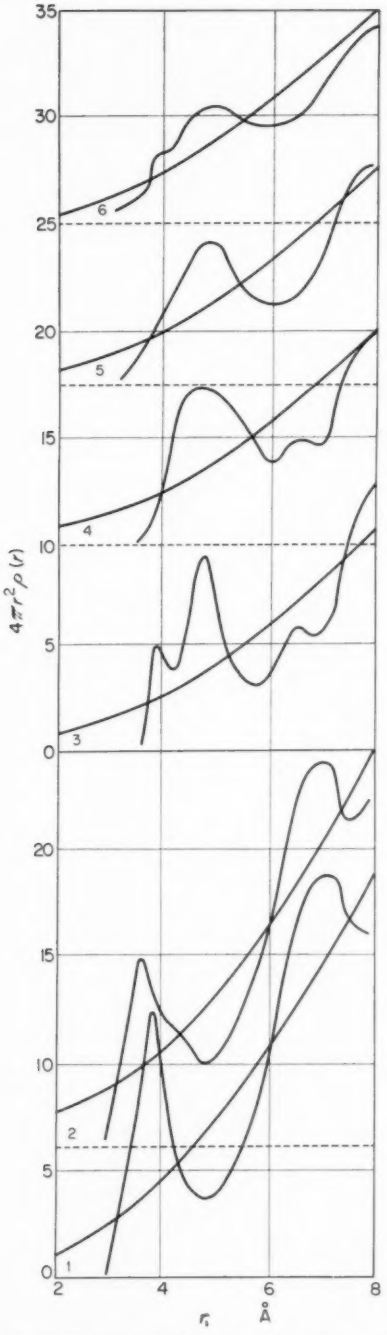


FIG. 6. Radial distribution functions for sodium and potassium. (1) Sodium at 114°C. (2) Sodium at 205°C. (3) Potassium at 80°C. (4) Potassium at 80°C with artificial temperature factor applied. (5) Potassium at 80°C data cut off at $\frac{\sin\theta}{\lambda} = 0.47$. (6) Potassium at 114°C with artificial temperature factor applied.

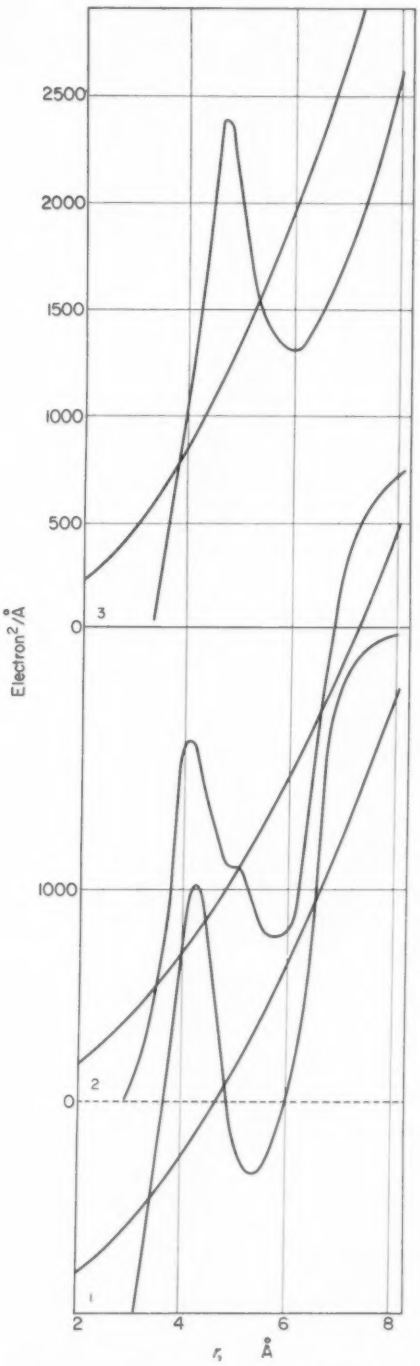


FIG. 7. Distribution curves showing $\Sigma 4\pi r^2 K_m \rho_m(r)$ in electrons²/Å for the alloys, sodium 35.4 at.% potassium and sodium 78.12 at.% potassium. (1) Sodium 35.4 at.% potassium at 23°C with artificial temperature factor applied. (2) Sodium 35.4 at.% potassium at 114°C with artificial temperature factor applied. (3) Sodium 78.12 at.% potassium at 23°C with artificial temperature factor applied.

VOL. 8 1960

but small deviation for this line. These results differ from those of Gingrich and Henderson[3] where a systematic negative deviation was observed being greatest at the compound composition Na_2K.

(b) *Radial distribution function*

Typical radial distribution curves calculated from the appropriate intensity functions are shown in Figs. 6 and 7. Each curve oscillates about a smooth continuous curve which represents the average atomic distribution within the liquid, $4\pi r^2\rho_0$, where ρ_0 is the average atomic density. The curves obtained for sodium at different temperatures do not show many spurious ripples. Those for potassium do contain certain ripples. The effect of applying a modification function as discussed in Section 3c is shown.

The positions of the first peak of the radial distribution curves give the distance of closest approach while the area under the curve between r_1 and r_2 $\int_{r_1}^{r_2} 4\pi r^2\rho(r)\,dr$, represents the total number of atoms within this range of distances from the reference atom. In the liquids examined the appropriate area to the right of this peak is not always well defined and therefore this area has also been evaluated by the method of Morgan and Warren[13] where the distribution on this side of the peak is made symmetrical with that on the left. It is claimed that in this method the contribution due to atoms interpreted as belonging to the second shell is omitted.

Assuming an average scattering factor per atom the average number of neighbours in the Na–K alloys are evaluated as for the pure metals.

The results are given in Table 2 together with those of previous workers. Near the melting point the values for sodium (ten atoms at 3.8 Å) and potassium (nine atoms at 4.8 Å) agree with those of other workers. For sodium at higher temperatures the position of the first peak, and to a greater extent the area under this peak, are not well defined depending on the method of evaluating the area so that the co-ordination number derived in these cases is of doubtful significance.

5. DISCUSSION

The results of earlier workers in determining melting points, heats of formation and viscosities of liquid sodium–potassium alloys (summarised by Venkateswarlu and Sriraman[14]) indicate that the structure of the Na_2K compound is still evident in the liquid state. Further the interpretation made by Bannerjee of X-ray work in this system supported this view.[15] More recently Gingrich and Henderson[3] in another X-ray investigation did observe a marked discontinuity in the sin θ/λ/composition curve at Na_2K. This was not, however, regarded as conclusive evidence for the existence of the compound in the liquid.

Recent magnetic susceptibility measurements on liquid alloys of this system by Venkateswarlu and Sriraman show that this property changes in a simple linear fashion with alloy composition, with no evidence of compound formation,[14] which is more consistent with the present results.

In the present work neither the intensity function nor the radial distribution function provides evidence for the existence of structure in liquids of the sodium–potassium alloys other than that existing in the liquids of the pure elements themselves. The intensity curves of the alloys are simple, showing two or three smooth ripples as do those of the elements. Thus on this evidence there is no reason for regarding the alloy liquids as anything but a statistical mixture of Na and K atoms.

The graph of sin θ/λ/alloy composition does deviate from a linear Vegard's law type of relationship as already reported by Gringrich and Henderson[3]. However, the extent of the deviation is smaller in the present work and there is no real evidence of the discontinuity at the Cl4 Laves compound Na_2K as reported by these authors.

It should be mentioned that the previous work was carried out with Mo$K\alpha$ radiation, and specimens contained in thin glass capillaries. The present work with Cu$K\alpha$ should be capable of higher accuracy. Furthermore with a capillary the composition of the actual specimen might be difficult to determine particularly since it is probable that the glass is attacked by the potassium component. In the present work large specimens are used, affording ample material for chemical analysis, while the materials and design of the camera make it unlikely that attack by the liquid metal will be significant.

The method of radial distribution analysis can be applied to simple liquids provided that the limitations of the method are appreciated and that the data is scrutinised for sources of error giving rise to spurious detail in the radial distribution curves. In particular, the application of a modification function such as the arbitrary temperature factor is to be recommended.

The evaluation of an effective co-ordination number from the atomic distribution curve is somewhat ambiguous. In the first instance application of a modification function does change the shape of this curve. This effect, however, is relatively small and can be calculated. Secondly, and more important, the way in which the effective area under the first peak should be determined is not well defined. Some

TABLE 2. Radial distribution function

Liquid	Temp (°C)	First peak position (Å)		Reference	Area under 1st peak (number of atoms)					
					Peak made symmetrical		R.H.S. of peak extrapolated to zero	$\int_{r_1}^{r_2} 4\pi r^2 \rho(r)\, dr$		
		This work	Other workers		This work	Other workers		no.	r_1	r_2
Na	114	3.8			10		9	13	3	5
	150	3.6			6		9	9	3	4.4
	203	3.6			5		8	11	3	5
	103		3.86	Tarasov and Warren[16]		10				
	100		3.8	Trimble and Gingrich[17]		9				
Na 35.4 at.% K	23	4.2[a,b,e]			8,9[b],9[a],9[e]		9,10[b],11[a],9[e]	10	3.6	4.8
								9[b]	3.6	4.8
								13[a]	3.2	5.5
								9[e]	3.1	5.0
	114	4.0, 4.1[a], 4.1[e]			6, 9[a], 9[e]		5, 11[a], 9[e]	7	3.4	4.4
								15[a]	3.2	6.0
								9[e]	3.1	5.0
	115		4.4	Interpolated from Gingrich and Henderson[3]						
Na 78.12 at.% K	23	4.6[a,c]			9[a], 10[c]		13[a], 10[c]	10[a]	3.4	5.0
								11[c]	3.4	5.0
	115		4.55	Interpolated from Gingrich and Henderson[3]						
K	80	4.8[f], 4.8[g] 4.7[d]			9, 10[a], 9[d]		7, 10[a], 12[d]	12	3.6	6.0
								12[a]	3.6	6.0
								12[d]	3.4	6.0
	114	4.8[f], 4.5[d] 4.8[g]			9, 8[a], 7[d]			13	3.6	6.0
								13[a]	3.6	6.0
	70		4.6	Thomas and Gingrich[18]		8		8[d]	3.6	6.2
	100		4.7	Lashko[19]		10				

(a) = Artificial temperature factor applied $A = 2.6974$.
(b) = Artificial temperature factor applied $A = 0.8117$.
(c) = Using $si(s)$ cut off at $\sin\theta/\lambda = 0.35$
(d) = Using $si(s)$ cut off at $\sin\theta/\lambda = 0.46$
(e) = Curve matching over the range $\sin\theta/\lambda = 0.4$ to 0.5.
(f) = Distorted, due to artificial temperature factor.
(g) = Distorted, due to spurious peak.

workers have preferred to make the right hand side of this peak symmetrical with the left for this purpose. In many cases, however, the precise method used to determine the areas are not reported. Table 2 shows the co-ordination numbers derived from a symmetrical peak, and also from an evaluation of the total area under the curve. The discrepancy between apparent co-ordination numbers determined by the two methods is very large for those curves obtained at higher temperatures and it is concluded that the symmetrical peak approach is not valid in these cases.

Those limitations are important in any application of radial distribution analysis. However, the lack of definite structure deduced for the Na–K liquids is not due to these limitations but rather it is concluded that wherever the solid has high symmetry the liquid will have simple statistical packing which, by its very nature, cannot be further illuminated by radical distribution analysis. (In this context the availability of information on the solid structure for comparison is clearly desirable.) On the other hand, where the solid has low symmetry or tendency to molecular grouping then may evidence of similar structure in the liquid be expected. The extent to which the radial distribution analysis and other approaches are useful in revealing this structure is being currently investigated, but in any case it is felt that further contributions to an understanding of liquid metal structures must arise from the study of these low symmetry metals and alloys.

VOL. 8 1960

ACKNOWLEDGMENTS

This work was part of a programme carried out for Metallurgy Division, A.E.R.E., Harwell, and thanks are due to the Director for permission to publish.

The authors wish to thank Dr. R. E. Smallman and Mr. G. W. Horsley of A.E.R.E. for helpful discussions, and Dr. B. T. R. Frost (A.E.R.E.) and Dr. E. A. Calnan (Fulmer Research Institute) for advice and encouragement throughout the course of the work.

REFERENCES

1. N. S. Gingrich, *Rev. Mod. Phys.* **15,** 90 (1943).
2. R. E. Smallman and B. R. T. Frost, *Acta Met.* **4,** 611 (1956).
3. N. S. Gingrich and R. E. Henderson, *J. Chem. Phys.* **20,** 1117 (1952).
4. A. G. Provan, B. A. Shaw and G. I. Williams, *J. Sci. Instrum.* **33,** 445 (1956).
5. *Liquid Metals Handbook, Sodium-Nak Supplement*, A.E.C., Department of the Navy, Washington, D.C. (1955).
6. H. P. Klug and L. E. Alexander, *X-Ray Diffraction Procedures.* Wiley, New York (1954).
7. B. E. Warren, *Phys. Rev.* **46,** 368, (1934).
8. A. H. Compton and S. K. Allison, *X-Rays in Theory and Experiment.* Wiley, New York (1934).
9. R. Hultgren, B. E. Warren and N. S. Gingrich, *J. Chem. Phys.* **3,** 351 (1935).
10. *Tables of Sines and Cosines for Radian Arguments.* National Bureau of Standards, Washington, (1955).
11. W. L. Bragg and J. West, *Phil. Mag.* **10,** 823 (1930).
12. B. E. Warren, H. Krutter and O. Morningstar, *J. Amer. Ceram. Soc.* **29,** 202 (1936).
13. J. Morgan and B. E. Warren, *J. Chem. Phys.* **6,** 666 (1938).
14. K. Venkateswarlu and S. Sriraman, *Z. Naturf.* **13a,** 455 (1958).
15. K. Bannerjee, *Indian J. Phys.* **3,** 399 (1928).
16. L. Tarasov and B. E. Warren, *J. Chem. Phys.* **4,** 236 (1936).
17. F. H. Trimble and N. S. Gingrich, *Phys. Rev.* **53,** 278 (1938).
18. C. D. Thomas and N. S. Gingrich, *J. Chem. Phys.* **53,** 278 (1938).
19. Lashko, *Fiz. Zhur. Ukrain.* **1,** 403 (1956).

TENSILE DEFORMATION OF ALUMINUM SINGLE CRYSTALS AT LOW TEMPERATURES*

W. F. HOSFORD, Jr.,† R. L. FLEISCHER† and W. A. BACKOFEN†

Tension tests on aluminum single crystals of approximately [001], [111], [112] and [123] axial orientations were made at 4.2, 77, 200 and 273°K. It was a general observation that the hardening rate passed through a maximum and then decreased continuously with increasing stress, the decrease being less rapid at the lower temperatures. There were no findings, under any circumstance, of a constant stage II slope in the stress-strain curves.

At 273°K, after initially rapid hardening, [001] crystals deformed primarily by operation of two slip systems with conjugate relationship; multiple necks were formed but the accompanying lattice rotation prevented failure by necking until large strains. At lower temperatures all four stressed slip directions were active in the [001] crystals and hardening continued to higher stresses. With the four directions, two perpendicular sets of Lomer–Cottrell barriers could form, as contrasted to one set at 273°K, thus producing greater hardening. Slip markings at the lower temperatures tended to follow {110} traces, but this may be explained by a fine mixture of cross slip on two {111} planes, necessary to avoid the barriers.

In [111] crystals, approximately equal operation of the three favored directions at all temperatures prevented lattice rotation and maintained a high hardening rate.

DEFORMATION PAR TRACTION A BASSE TEMPERATURE DE MONOCRISTAUX D'ALUMINIUM

Des essais de traction sur des monocristaux d'aluminium dont l'orientation axiale était environ [001], [111], [112] et [123] ont été effectués à 4,2, 77, 200 et 273°K. Les auteurs ont observé que d'une manière générale, la vitesse de durcissement passe par un maximum, puis diminue continuellement lorsque la tension augmente, la diminution étant moins rapide aux basses températures. En aucune circonstance, ils n'ont pu mettre en évidence un deuxième stade à coefficient angulaire constant dans les courbes tension-déformation.

A 273°K, après un durcissement initial rapide, les cristaux [001] se sont déformés en premier lieu par l'intervention de deux systèmes de glissement avec une relation conjuguée; plusieurs constrictions se sont formées, mais la rotation du réseau qui s'accompagne le phénomène a empêché la rupture jusqu'aux grandes déformations. Aux plus basses températures, les quatre directions de glissement sous tension étaient actives dans les cristaux [001] et le durcissement a continué vers des tensions plus élevées. Avec les quatre directions, deux groupes perpendiculaires de barrières de Lomer-Cottrell pourraient se former, en opposition à un groupe à 273°K, produisant ainsi un durcissement plus élevé. Les lignes de glissement aux basses températures avaient tendance à suivre les traces des plans (110), mais ceci peut s'expliquer par un mélange fin de glissement croisé sur deux plans (111) nécessaires pour éviter les barrières.

Dans les cristaux [111] le glissement approximativement égal sur les trois directions favorisées, ont empêché pour toutes les températures la rotation du réseau et ont maintenu une vitesse de durcissement élevée.

ZUGVERFORMUNG VON ALUMINIUMEINKRISTALLEN BEI TIEFEN TEMPERATUREN

An Aluminiumeinkristallen mit Stabachsen nahezu parallel zu [001]-, [111]-, [112]- und [123]-Richtungen wurden bei 4,2°, 77°, 200° und 273°K Zugversuche durchgeführt. Allgemein wurde beobachtet, daß der Verfestigungsanstieg ein Maximum durchlief und danach mit zunehmender Spannung kontinuierlich abfiel; der Abfall war bei tiefen Temperaturen geringer. Unter keinen Umständen ergaben sich bei den Verfestigungskurven Anzeichen eines Bereichs II mit konstantem Anstieg.

Bei 273°K verformten sich [001]-Kristalle nach anfänglicher starker Verfestigung hauptsächlich durch die Tätigkeit zweier zueinander konjugierter Gleitsysteme. Dabei bildeten sich zahlreiche Einschnürungen, aber die mit ihnen zusammen auftretenden Gitterdrehungen bewirkten, daß diese erst nach großen Verformungen zum Bruch führten. Bei tiefen Temperaturen waren in einem [001]-Kristall alle vier beanspruchten Gleitrichtungen in Tätigkeit und die Verfestigung stieg bis zu höheren Spannungen an. Mit den vier Gleitrichtungen können sich zwei zueinander senkrechte Scharen von Lomer-Cottrell-Versetzungen bilden im Gegensatz zu der einen Schar bei 273°K; dadurch entsteht eine größere Verfestigung. Die Gleitlinien zeigten bei tieferen Temperaturen eine Tendenz, den Spuren von {110}-Ebenen zu folgen, doch läßt sich dies als eine feine Mischung von Quergleitung auf zwei {111}-Ebenen erklären, welche notwendig ist, um die Hindernisse zu umgehen.

In den [111]-Kristallen wurden durch eine nahezu gleichstarke Tätigkeit der drei begünstigten Gleitrichtungen bei allen Temperaturen Gitterdrehungen verhindert und ein starker Verfestigungsanstieg erreicht.

* Received July 15, 1959. This paper is based on a thesis by W. F. Hosford, Jr. submitted to the Massachusetts Institute of Technology in partial fulfillment of the requirements for the degree of Doctor of Science.

† Department of Metallurgy, Metals Processing Laboratory, Massachusetts Institute of Technology, Cambridge, Mass.

VOL. 8 1960

1. INTRODUCTION

The stress-strain curves for single crystals of face-centered cubic metals have been described in terms of three distinct stages;[1–4] stage I or easy glide, stage II with a high and constant strain hardening rate and stage III with a diminishing rate of hardening. The small extent of stage II hardening reported for metals with high stacking-fault energy has been explained in terms of the narrow separation of partial dislocations and the low energy for recombination.[3,4] For aluminum there is thought to be no well developed stage II at room temperature because low stresses and thermal activation are able to drive the partials together and cause stage III to start before stage II is fully developed. Few low-temperature measurements have been made on aluminum, but data of Staubwasser[5] at 78°K and Sosin and Koehler[6] at 4.2°K and 78°K have been cited as evidence for a well developed stage II at such temperatures.[4]

Stage III hardening is quite orientation sensitive as shown by Lücke and Lange[7,8], and Staubwasser[5] for aluminum. At room temperature the difference between the [111] and [001] orientations is striking. Both show initially rapid hardening, but crystals with the [111] orientation continue to harden rapidly to such high stresses that they may be even stronger than polycrystalline specimens. In contrast, the initially high hardening rate of [001] crystals decreases so rapidly that after about 5 per cent elongation the engineering stress-strain curves become very flat until failure. Kocks[9] has reported that over 60 per cent elongation may occur during this very flat region at room temperature. The flatness of these curves extending over such large strains is remarkable considering that necking would be expected to start when the load reaches a maximum value. Staubwasser's[5] data indicate that the difference between these two orientations at liquid air temperature is less marked.

A recent paper[10] has pointed out a similarity between the hardening characteristics of single crystals with [111] and [001] orientations and polycrystalline specimens. In view of the importance of polycrystalline behavior these orientations become of particular interest for a strain hardening study. To develop information on this problem, especially the contrast between [111] and [001], aluminum single crystals have been tested in tension over a temperature range extending down to liquid helium temperature (4.2°K).

2. EXPERIMENTAL PROCEDURES

Single crystals of approximately [111], [001], [112] and [123] axial orientation were grown by seeding from the melt according to an established method.[11] Starting material was 99.99 + per cent pure aluminum and growth was at an average rate of about 0.8 in/hr (furnace motion at 0.4 in/hr). Cross sections were rectangular, $1/4 \times 3/16$ in. as grown, and lengths were 4–5 in. The crystals were annealed for 24 hr at 610°C and furnace cooled for 8 hr. Orientations were then checked by the Laue back-reflection technique. The actual orientations which differed by $1\frac{1}{2}$–2° from the ideal are shown in Fig. 1. The rotational orientations were such that the wider face was approximately a {110} plane for the [001], [111] and [112] axial orientations, and a {541} plane for the [123] orientation.

Reduced gage sections were produced in either of two ways. For the harder orientations, [001] and [111], gage sections of about 3 in. were prepared by masking the ends of the crystals with rubber cement and chemically dissolving material in an aqueous solution of 5 per cent NaOH and 10 per cent $NaNO_2$.[12] Finally the reduced length was electropolished in a solution of 5 parts methanol and 1 part perchloric acid cooled to between −40°C and −10°C. Grips for loading the specimens were split steel collars which fitted over the enlarged ends. Woods' metal was cast into the grips to fill the space around the crystal thus insuring good seating of the specimen. A cast polycrystalline sample with about 20 grains to the cross section, prepared and gripped in the same manner as the [001] and [111] crystals, was included for testing at 4.2°K. For the softer orientations, [112] and [123], a less heavily reduced section about 4 in. long was produced by electropolishing alone. These specimens were gripped simply by clamping the heads between serrated jaws.

The testing was done in a hard type machine described elsewhere,[13] consisting essentially of one tube suspended vertically within a larger tube. The upper end of the inner tube was attached by a universal joint to a load cell and was driven upward at a constant rate. The upper grip on the crystal was

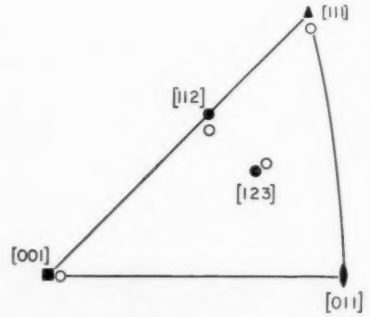


FIG. 1. Axial orientations of crystals tested (open circles).

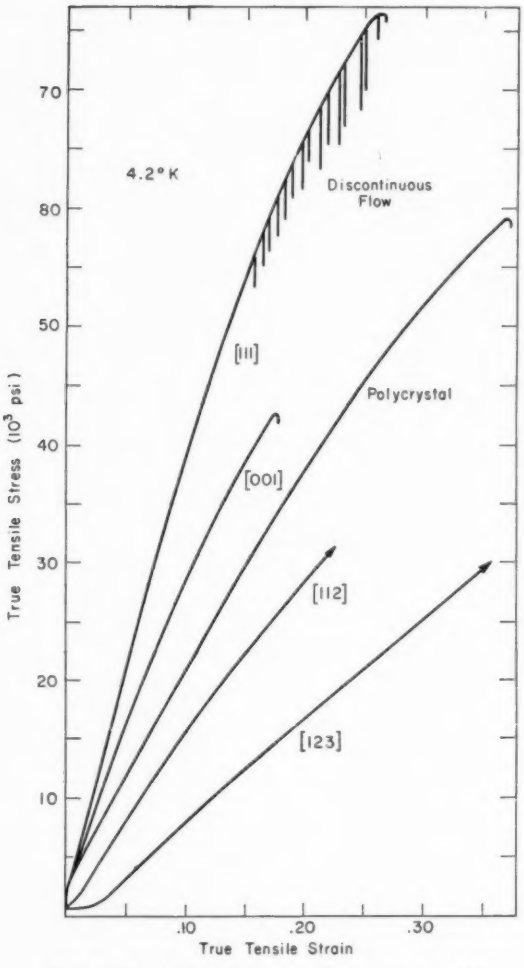


FIG. 2. True tensile stress-strain curves at 4.2°K.

rigidly fixed to the lower end of the inner tube, while the lower grip was attached to the lower end of the outer tube. For the [001] and [111] crystals the lower grip was pinned so that it was free to rotate, while for the [112] and [123] crystals it was not. Tests were made at various temperatures by immersing the crystal in baths of ice water at 273°K, trichloroethylene and dry ice at 200°K, liquid nitrogen at 77°K or liquid helium at 4.2°K. A record of load was obtained from the output of a resistance strain-gage bridge mounted on the load cell and extension was measured by recording crosshead movement. Maximum stress and strain sensitivities were ± 5 p.s.i. and $\pm 10^{-4}$. The accuracy of the stress measurements was estimated at ± 4 per cent. A constant strain rate of about 4.5×10^{-3}/min was employed throughout.

Shear stress and shear strain were calculated assuming octahedral slip on the most favored systems with no lattice rotation for the [001], [111] and [112] orientations. The calculations were made for these crystals by applying the initial Schmid resolving factor, $m = \cos\lambda \cos\phi$, to the true tensile stress-strain curves; the angles are those included between the tensile axis and slip direction, λ, and tensile axis and slip-plane normal, ϕ. For the [123] orientation, single slip was assumed at the beginning and the analysis of Schmid and Boas[14] was used until the calculated rotation brought the axis to [112]; then data were treated as for the other crystals.

3. RESULTS

Strain hardening characteristics are presented in terms of true tensile stress–strain curves, σ vs. ε (Figs. 2–5) as well as shear stress–strain curves, τ vs. γ (Figs. 6–9). Both types of curves are shown because the first is free of uncertainty about stress and strain resolution while the second is the more usual and, in some respects, more fundamental. For comparable temperatures and orientations, the latter agree quite

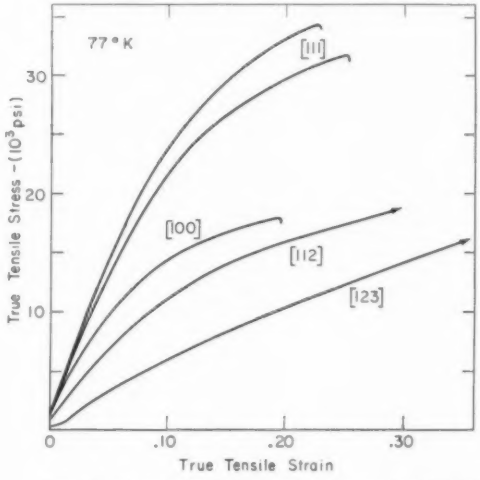


FIG. 3. True tensile stress-strain curves at 77°K.

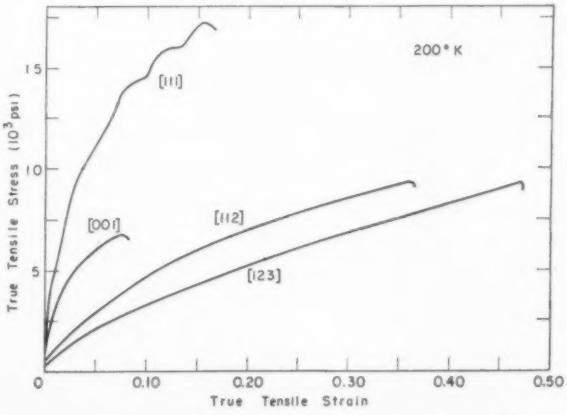


FIG. 4. True tensile stress-strain curves at 200°K.

VOL. 8 1960

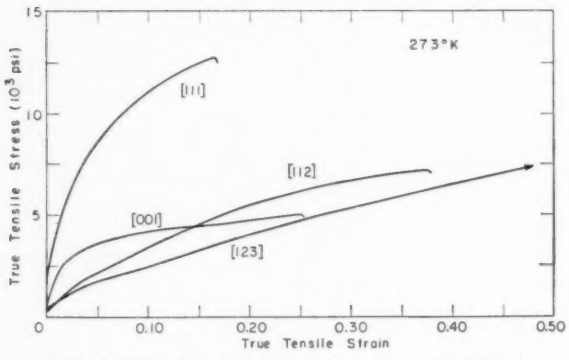


FIG. 5. True tensile stress-strain curves at 273°K.

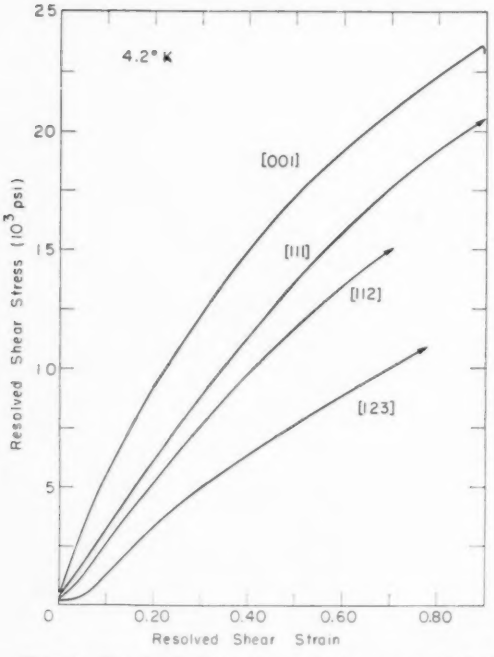


FIG. 6. Resolved shear stress-strain curves at 4.2°K.

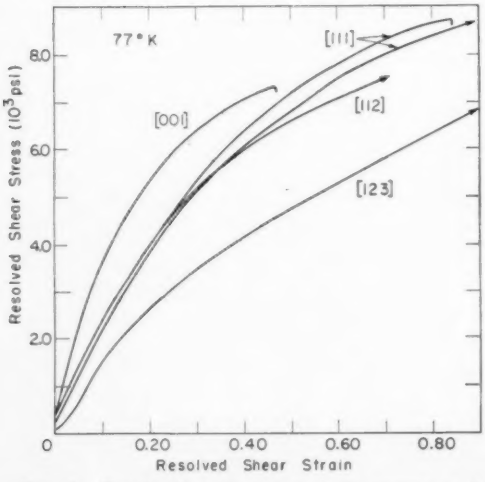


FIG. 7. Resolved shear stress-strain curves at 77°K.

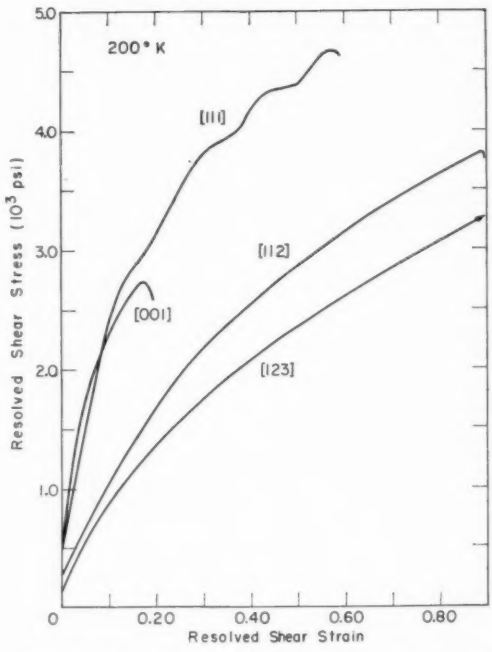


FIG. 8. Resolved shear stress-strain curves at 200°K.

well with data of Staubwasser.[5] Note that on a tensile stress basis the [111] crystal is the strongest, even stronger than a polycrystalline sample at 4.2°K, while [001] shows highest strength in terms of resolved shear at the lower temperatures.

The onset of stage III is usually defined by the stress at which departure from linear hardening begins. Inspection of the curves indicates a gradual bending over. Accordingly, for determination of τ_3 at transition to stage III the slopes $\theta = d\sigma/d\varepsilon$ were calculated from

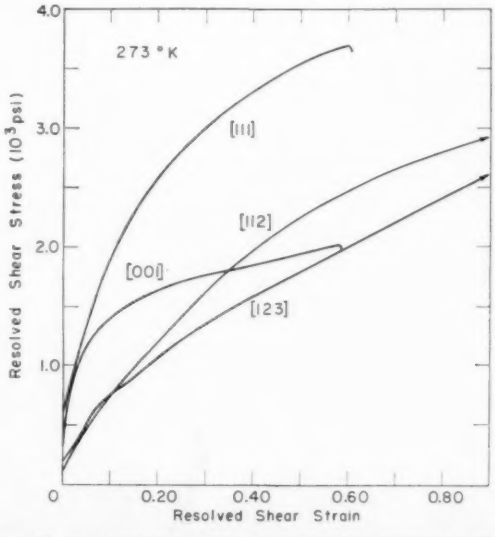


FIG. 9. Resolved shear stress-strain curves at 273°K.

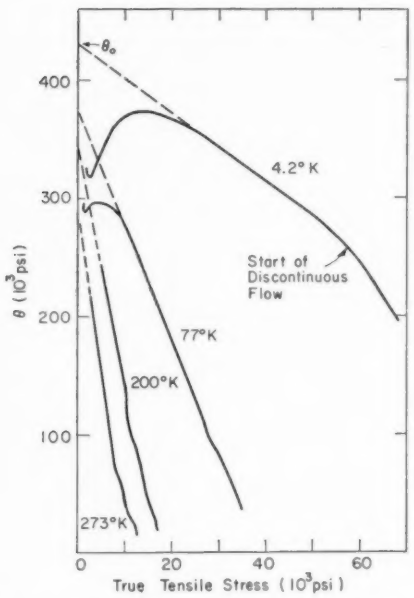


FIG. 10. Slope of the true stress-strain curves, θ against true stress, σ, for [111] crystals. The value of θ extrapolated to $\sigma = 0$ is θ_0, the slope of the straight line portion is $-B$.

the original recorded data and plotted as a function of stress. On such a plot, a break from linear stage II should be apparent as a drop in slope from the constant stage II value. There were no constant (maximum) slope regions for any of the tests, however, although the initial steepness of the curves might have given an illusion of straightness; examples are presented in Fig. 10. Instead, the slopes for [111], [112] and [123] increased rapidly to a maximum and then dropped continuously with increasing stress, often falling almost linearly with the stress. For the [001] orientation the decrease was continuous from the beginning. Thus there appears to be no unique stress τ_3 at which stage III starts.

A summary of the hardening behavior has been made with parameters of two kinds: the slope extrapolated to zero stress, $(d\sigma/d\varepsilon)_{\sigma=0} = \theta_0$ or $(d\tau/d\gamma)_{\tau=0} = m^2\,\theta_0$, and the rate of decay of the slope with stress, $-d\theta/d\sigma = B$ or $-d(d\tau/d\gamma)/d\tau = mB$. All are listed in Table 1. Two temperature effects are seen; θ_0 increases somewhat and B falls almost linearly with decreasing temperature. A large orientation effect is evident, with θ_0 values for the multiple-slip orientations [111] and [001] being much higher than for [112] and [123]. In a [111] vs. [001] comparison, θ_0 is greater for [111], while on the resolved-shear basis, $m^2\theta_0$ is higher for the [001]. The rates of decay of hardening, B and mB, are both consistently higher for [001], especially at the higher temperatures.

TABLE 1. Hardening parameters

	T°K	[111]	[100]	[112]	[123]
θ_0 (10^3 p.s.i.)	4.2	455	300	180	110
	77	380	290	155	90
	200	345	230	65	~50
	273	300	~240	~55	~40
B	4.2	3.3	3.5	2.2	~4
	77	9.7	14.5	7.4	~10
	200	20.5	33	10	~12
	273	28	~90	~15	~15
$m^2\theta_0$(10^3 p.s.i.)	4.2	34	50	30	24
	77	28	48	26	19
	200	25.5	38	11	~11
	273	22	~40	~9	~8.5
mB	4.2	0.9	1.2	0.9	~2.2
	77	2.6	5.9	3.0	~4.6
	200	5.5	13	4	~6
	273	7.6	37	~6	~7

[001] *Orientation*

273°K. Results from three tests are plotted in Fig. 11 in terms of engineering stress (σ_E = load/original cross section) and strain (ε_E = length change/initial gage length). Multiple necking was found in all crystals and in the one giving the cyclic curve the numbers of necks and stress cycles were comparable. Correlation could not be exact, however, as both necking and cycling varied in intensity so that counting each was hardly possible.

Strain along the crystals developed in such a manner as to preserve a rectangular cross section. Reductions in the two thickness directions were not generally equal at the necks and the direction of greater reduction sometimes changed from one region

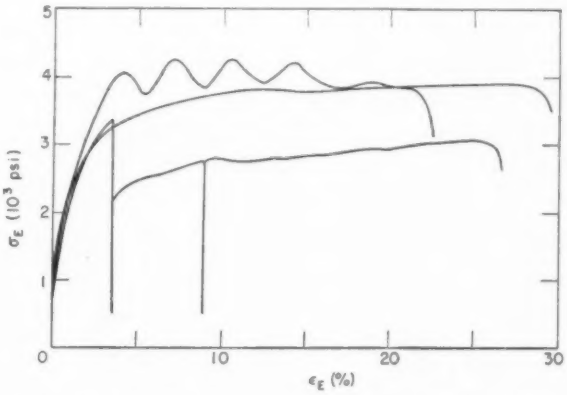


FIG. 11. Engineering stress-strain curves for three [001] crystals at 273°K. One test (lowest curve) was interrupted twice for surface observations. The lower value σ_E after the first unloading is due to reduction of the cross section by electropolishing.

VOL. 8 1960

to another. A crystal pulled to separation developed a chisel fracture from necking being continued by reduction in one dimension; thickness strains, lattice rotations and slip markings along the length of this particular crystal are given in Fig. 12. The stressed slip systems in the [001] crystals may be represented by an octahedron with ⟨110⟩ edges and {111} faces. Fig. 13 shows a top view of such an octahedron, together with the thickness reductions and lattice rotations produced by simultaneous operation of various combinations of slip directions.

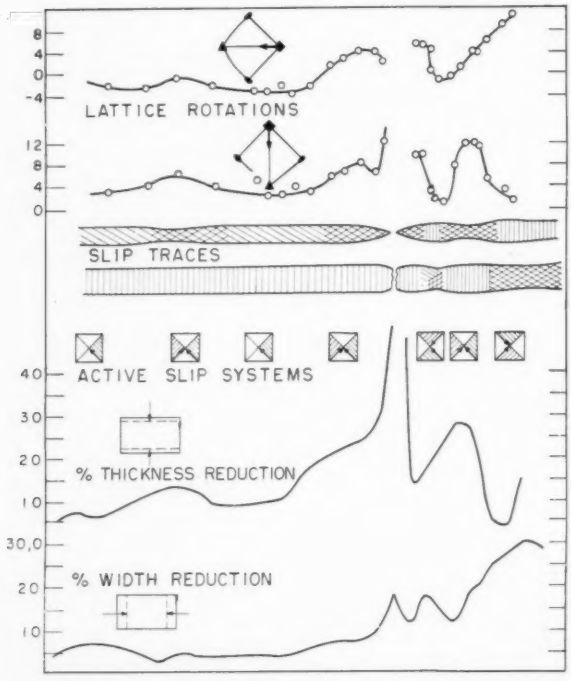


FIG. 12. Variation along the length of a [001] crystal extended at 273°K of: Reductions in the two thickness dimensions, prominent slip traces, components of lattice rotation (in degrees). The active slip systems are indicated by top views (along tensile axis) of octahedra with ⟨110⟩ edges and {111} faces.

Slip lines were long and clear on all of these crystals tested at 273°K. Traces of the four octahedral planes could be found although they seldom appeared intermixed. On a crystal examined after 3–1/2 per cent elongation, there were several areas where parallel traces of one plane changed abruptly to traces of a cross slip plane* (Fig. 14). After necks were

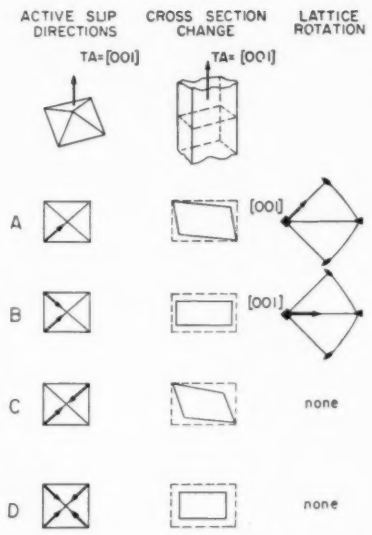


FIG. 13. Cross sectional changes and lattice rotations produced by operation of various combinations of slip directions in [001] crystals with (110) and (1$\bar{1}$0) faces. (TA = tensile axis).

formed, predominate lines within these regions corresponded to traces of two slip planes with conjugate relationship (Fig. 15). Some wavy and less sharply defined lines following traces of {110} planes were also found, most often at the ends of the necked regions (Fig. 16); occasionally these could be resolved into traces along two {111} planes.

Laue photographs were taken at intervals along the length of a broken crystal (Fig. 12). Because of

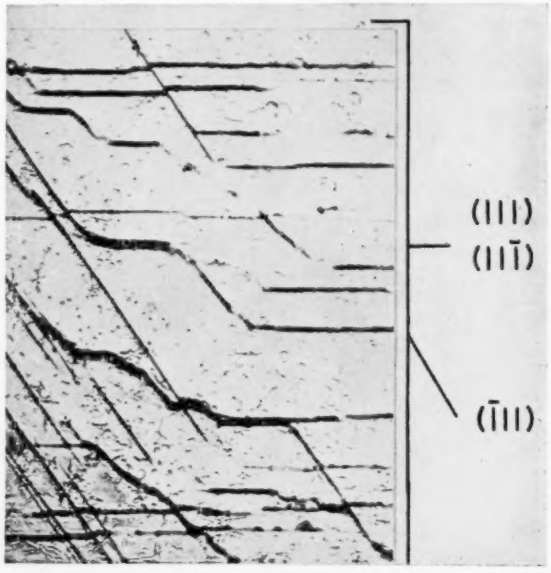


FIG. 14. Cross slip in [001] crystal after 3½ per cent elongation at 273°K. Tensile axis vertical, (110) surface. ×500

* The terms primary, conjugate, cross-slip and critical (unexpected) slip are used as defined elsewhere[15, 8]. Because more than one slip system is equally favored for the [001], [111] and [112] orientations, the distinction between primary and conjugate is arbitrary. Likewise, for the [001] and [111] orientations the distinction between primary and cross-slip planes is arbitrary. Nevertheless the concepts of conjugate and of cross-slip relationships between two slip systems are still useful.

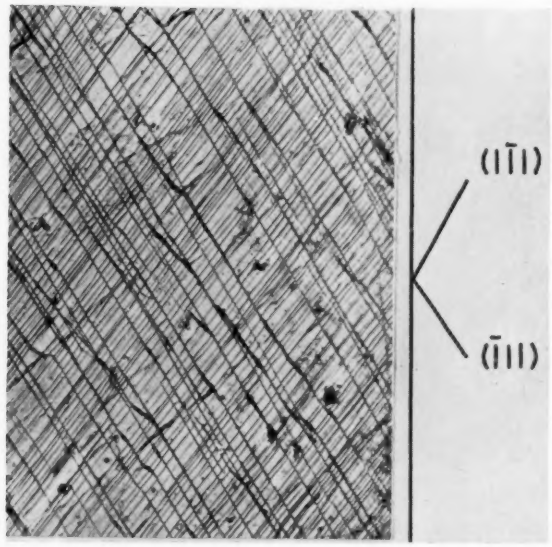


FIG. 15. Conjugate slip in necked region of [001] crystal tested at 273°K, tensile axis vertical, (110) surface. ×200

difficulty in aligning the deformed parts of the crystal with the X-ray apparatus the error in the absolute magnitude of the rotations may be as much as 2° to 3°, but the relative rotation along the deformed part is probably accurate to ½° to 1°. Since the direction as well as the magnitude of the rotation varied with position on the crystal, rotations are shown in terms of the component rotations from [001] in two mutually perpendicular directions toward ⟨112⟩ poles. Although

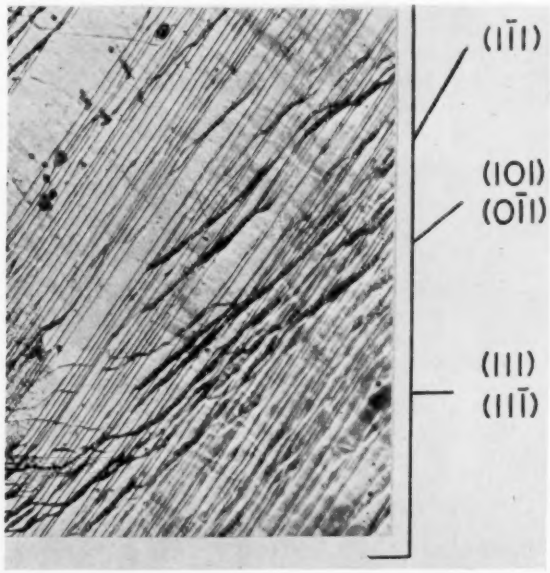


FIG. 16. Wavy slip following {110} traces at end of necked region of [001] crystal tested at 273°K, tensile axis vertical, (110) surface. ×200

rotations of up to 12° were measured, the Laue spots normally remained sharp indicating that local distortion was not severe.

The lattice rotations were generally consistent with the measurements of thickness strains, which indicate that slip in the necked regions must have been predominately along ⟨110⟩ directions at 60° to one another (Fig. 13b), and with the further observations of slip lines which show that the planes were {111} in conjugate relationship.

200°K. Strong slip markings were limited to a small region about a single neck (Figs. 17 and 18). The bands were wavy, followed the traces of {110} planes on all surfaces and seemed to correspond only



FIG. 17. Slip lines following two {110} traces in neck of [001] crystal tested at 200°K. ca. ×1½

to traces of two mutually perpendicular sets of planes. There were very few lines corresponding to {111} traces. In the necked region the cross section became diamond-shaped, indicating in agreement with surface observations that two mutually perpendicular directions operated (Fig. 13c). The strong markings were absent away from the neck, although surface appearance still suggested {110} slip (Fig. 19); as reduction here was equal in both dimensions and the cross-section remained rectangular, slip along all four stressed directions must have made approximately equal contributions to the total strain (Fig. 13d).

77°K *and 4.2*°K. There were none of the obvious surface markings, only an appearance similar to Fig. 19 but with a finer pattern. At both temperatures reductions were equal in the two thickness directions,

VOL. 8 1960

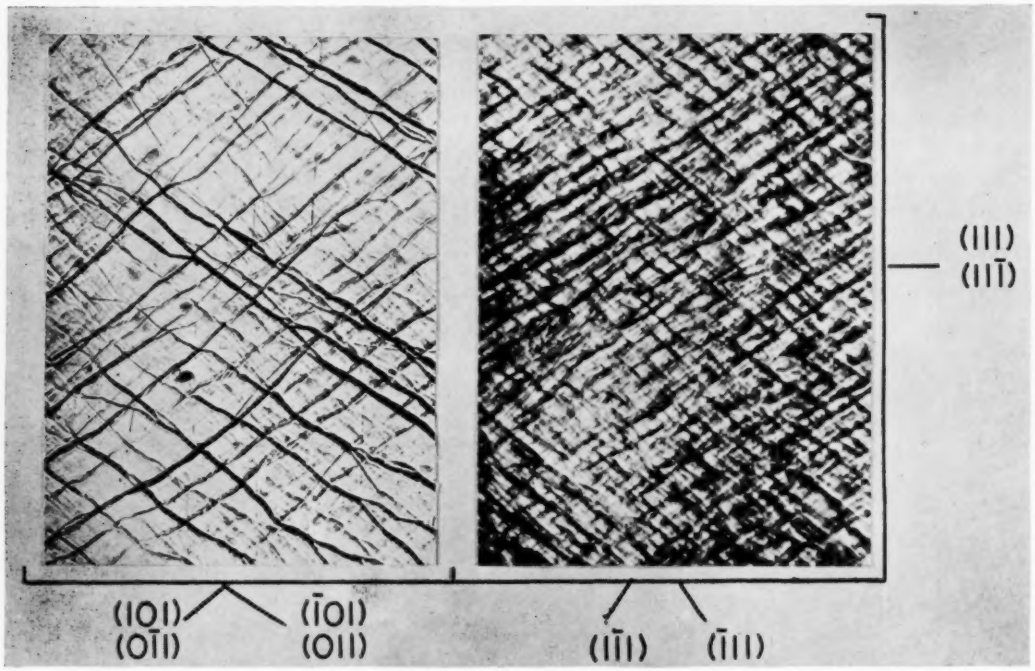


FIG. 18. Slip lines following {110} traces near neck of [001] crystal tested at 200°K. Tensile axis vertical, (110) surface. ×250

FIG. 19. Surface pattern suggesting {110} slip on same crystal away from neck. ×110

and the neck in a crystal that had been fractured at 4.2°K was still rectangular in cross section. No rotations appeared in Laue photographs, which showed little asterism. A necessary conclusion again seems to be slip on all four stressed ⟨110⟩ directions (Fig. 13d).

Elongations. For all crystals the percent elongation measured over the entire gage section at failure tended to decrease at higher temperatures, as the lower hardening rates led to necking at lower strains. The trend for [001] crystals was reversed, however, between 200 and 273°K as shown in Fig. 20.

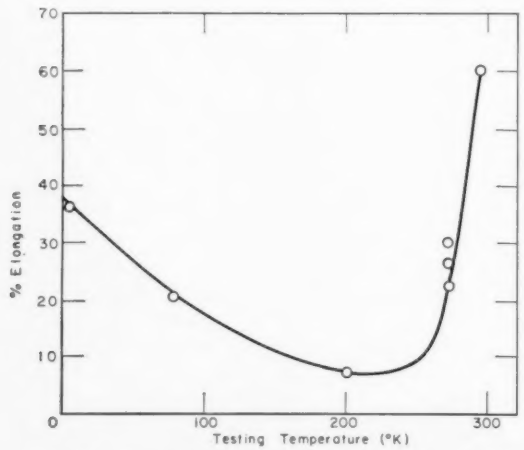


FIG. 20. Elongation over gage section at failure for [001] crystals as a function of temperature. Terminal value for room temperature is from Kocks[9].

The large elongation with little or no increase in load at 273°K is particularly unusual. The general criterion for unstable flow is that $dP/dl = 0$, where P is the tensile load and l the specimen length. Once necking begins, localized deformation usually continues to failure. An increased rate of hardening in the neck would be needed to cause deformation to cease there and continue elsewhere. One factor which would seem to give such an effect is additional stress set up by the lattice rotation in the neck. As the slip becomes confined, a gradient of orientation into adjacent regions is established. Such a gradient may be expected to result in stresses tending to oppose additional flow and rotation so that very gradual necks are formed and an appreciable overall elongation occurs.

[111] *Orientation*

The most striking surface features on the [111] crystals after large strains were ridges extending diagonally across the wider faces (1$\bar{1}$0) (Fig. 21). Corresponding steps were formed on the other faces (11$\bar{2}$). Ridges were found on all specimens but were more numerous at the lower temperatures. From



FIG. 21. Ridges developed on [111] crystals pulled to failure. Left to right 273°K,7 7°K, and 4.2°K, ca. ×1

surface observations at low strains during a 77°K test the origin was found to be bands of finely clustered slip on the most highly stressed plane. The slip clusters in turn possibly developed because of an original 2° deviation from [111] (Fig. 22). Slip on this primary plane resulted in the markings and brought the orientation to [111] where it was stable. Then slip along all three possible directions maintained the orientation and preserved a rectangular cross section. With continued extension, slip appeared confined between the inactive ridges (Fig. 23). Markings near one of the ridges at 4.2°K suggested {100} slip. Laue pictures showed severe asterism, individual spots becoming spread over as much as 5°.

Discontinuous flow as described by Basinski[13] was observed only for this orientation and only at 4.2°K when the tensile stress reached 56,000 p.s.i., a level higher than any encountered in all other tests. Failure occurred by an abrupt shearing across the entire specimen before an appreciable neck had developed. While the fracture surface was not perfectly planar it approximated a {100} plane; its appearance was similar to that observed by Blewitt *et al.*[16] on a copper crystal at 4.2°K and by Beevers and Honeycombe[17] on an age hardened crystal of an aluminum alloy at room temperature. A similar fracture was also found in the polycrystalline bar at 4.2°K. Other [111] crystals necked but were not pulled to separation.

[112] *and* [123] *Orientations*

Slip lines corresponded to traces of the two most favored {111} planes, primary and conjugate, with the exception of the [123] orientation tested at 200°K. One end of this crystal slipped on the primary and conjugate planes, while the other end slipped only on the critical plane so that a sharp boundary developed between the two regions of different slip. Similar previous observations[18–20] of critical slip have been attributed to grip-induced stresses arising during single slip.[20]

Necks could be formed eventually with sufficient

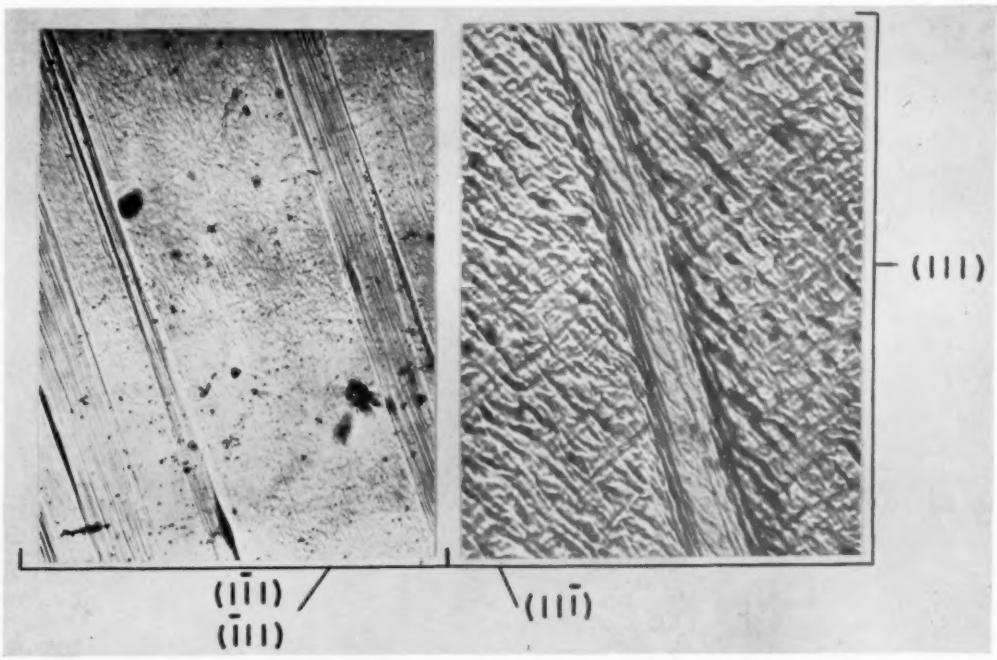


FIG. 22. Clustered slip in [111] crystal after 1/2 per cent elongation at 77°K. Tensile axis vertical, (1$\bar{1}$0) surface. ×50

FIG. 23. Surface of [111] crystal pulled to failure at 77°K showing ridge developed from clustered slip and surface between ridges. (110) surface. ×300

VOL. 8 1960

stretching, by operation of the primary and conjugate systems. The [123] crystal tested in ice water developed two necks, although the test was not continued far enough for any load drop.

4. DISCUSSION

Absence of Linear Hardening

The finding of a continuously changing slope (Fig. 10) raises the question of whether separate stages II and III do in fact exist in aluminum. The absence of a well defined transition stress, τ_3, means at least that the stages must overlap, some dislocations passing through or over barriers at all stresses.

In comparing metals of different stacking-fault energy, the rate at which barriers are overcome at low stresses might be expected to be less in one of lower energy, like copper, than in another of higher energy, such as aluminum. A more slowly changing hardening rate would follow, and this may explain in part why a linear stage II has been reported, particularly for the former kind of material.

The theories of Seeger[3,4] and Friedel[21] both predict linear hardening, although by different models. With reference to either theory, the continuous decrease of slope might then be rationalized by the operation of a process of barrier surmounting or breakdown that proceeds at an increasing rate as stress builds up. A more specific theoretical trouble is the absence of a unique stress, τ_3, for the beginning of stage III, which has been used in the past to estimate the relative stacking-fault energies of different metals.[22]

Orientation Dependence of Strain Hardening

An explanation of the various hardening behaviors must be based on how the nature and distribution of slip barriers depend upon crystal orientation.

[001] *Orientation*

In these crystals there are four equally stressed {111} slip planes with two equally favored ⟨110⟩ slip directions in each. The reactions between active dislocations[23] produce two sets of Lomer–Cottrell (L–C) barriers along the unstressed ⟨110⟩ directions as illustrated schematically in Fig. 24; each set of barriers may be produced by two possible reactions. Since these barriers are not parallel to active slip directions, screw dislocations cannot be expected to pile up behind them. Dislocations in the pile-ups must be more strongly edge than screw. Cross slip under such conditions has been discussed and it has been shown to require either non-conservative dislocation movement or the creation of new dislocation loops.[24] The situation pictured, therefore, is not as favorable for cross slip as Seeger's model in which screws are piled up parallel to the barriers.[3,4]

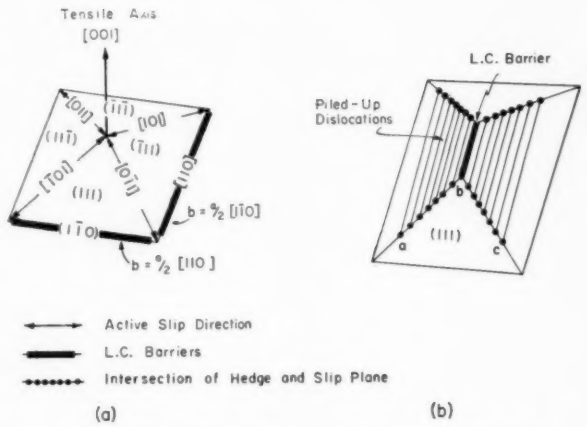


FIG. 24. (a) Octahedron representing slip systems for [001] orientation, with the two perpendicular sets of Lomer–Cottrell barriers lying along unstressed ⟨110⟩ directions. (b) Lomer–Cottrell barrier along [110] with piled-up dislocations on (111) and (11$\bar{1}$) planes forming a hedge along stressed ⟨110⟩ directions in (111) plane.

With this geometry, L–C barriers on any slip plane are parallel and serve as obstacles to dislocation motion in only the one direction on that plane. Another type of obstacle is necessary to prevent dislocation loops from expanding parallel to barriers. Kocks[9] has advanced the idea that piled-up dislocations in one plane form an effective obstacle to slip on intersecting planes because they are closely and systematically spaced and therefore pierce the other slip planes as a "hedge"; such a compact array is a much more effective obstacle to slip than a random forest of the same number of dislocations. A result is that barriers, in the form of hedges, will be parallel to active slip directions, such as *ab* and *bc* in Fig. 24b. Now pure screw dislocations may pile up here and cross slip readily, which would explain the early cross-slip observations in the 273°K test (Fig. 14).

With a L–C barrier that is long relative to the width of pile up (or length of hedge), there will be obstacles to slip on more of the intersecting or pierced planes; such a composite barrier, therefore, may interfere more with slip on those planes not involved in the initial L–C formation.[9] This argument has some use in explaining the areas of extensive slip on conjugate systems (Fig. 15). Slip on a pair of these systems will produce one of the two possible sets of L–C barriers. Should one set develop to a somewhat greater degree, slip on planes involved in producing the other will be suppressed to the larger extent; or, hardening on the latent systems will be the higher. To account for the

low hardening rate at 273°K, it seems essential that barrier break-down occur; under sufficient stress this may in fact happen. The breakdown interval would be short, however, as L–C barriers should quickly be reformed by other dislocations in the pile ups. Such a sequence may also contribute to the change in hardening rate that first promotes and then acts to suppress necking. A further need in a rationale of [001] hardening is a reason for the sharp temperature dependence of barrier strength; apparently starting at about 273°K the effect of thermal fluctuations added to the pile-up pressure is enough to give extensive barrier penetration or breakdown.

The fact that slip markings at low temperatures follow {110} traces may be explained in either of two ways: there may be {110} slip, or the traces may result from a fine intermixture of primary and cross slip on {111} planes. For aluminum there are many reports in the literature of non-octahedral slip on planes containing ⟨110⟩ directions. These observations have been made near grain boundaries,[18,20,25–27] in single crystals at high temperatures[28,29] and recently[17] in age hardened Al–4%Cu crystals under high stress at room temperature. Certainly the possibility of such slip has been shown to be reasonable.[30,31] Further, on a purely geometric basis, the {110} planes in [001] crystals sustain the highest resolved shear stress; for this orientation the ratio of Schmid resolving factors $m_{\{110\}\langle 110\rangle}$ to $m_{\{111\}\langle 110\rangle}$ is 1.22. With {110} slip, however, effective slip barriers cannot be obtained from L–C type reactions, so that the high rate of low-temperature hardening would not be explained by current models.

By means of the electron microscope wavy and apparently non-octahedral slip traces on aluminum crystals oriented near [111] have been resolved to fine multiple slip.[32] The wavy character of the apparent {110} traces suggests that they could have resulted from slip on {111} planes with operation in nearly equal amounts of planes having a primary and cross slip relationship. The fact that four directions must have been active to preserve the original proportions of the cross section implies the presence of similar obstacles on all planes. With such an arrangement, comparable amounts of slip and cross slip are more reasonably expected.

An explanation of why four active systems operate at low temperature while only two predominate at 273°K may lie in the relative dimensions of the L–C barrier and its hedge. At the lower temperatures, more dislocations can be expected to pile up behind a L–C barrier to give a wider hedge. At the same time, the L–C barriers may be shorter if their formation

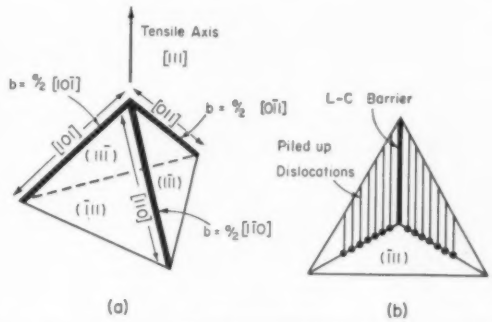


FIG. 25. (a) Tetrahedron representing slip systems for [111] crystals, with three sets of Lomer–Cottrell barriers lying along stressed ⟨110⟩ directions. (b) Lomer–Cottrell barrier along [011] with piled-up dislocations on (11$\bar{1}$) and (1$\bar{1}$1) planes forming a hedge along ⟨110⟩ directions in ($\bar{1}$11) plane.

requires jog-free sections of dislocation lines, since jogs will be less mobile at the lower temperatures. Thus shorter and wider L–C barrier-hedges may result, which do not have the effect of blocking latent systems more strongly than active ones.

[111] *Orientation*

The disposition of slip systems and L–C barriers in the [111] crystals may be represented by a tetrahedron, with ⟨110⟩ edges and {111} planes. Fig. 25 shows that there are three equally stressed {111} slip planes each containing two equally favored ⟨110⟩ directions, giving six systems identically stressed with all others being unstressed. Possible L–C reactions can produce three sets of barriers (one set for each reaction), which lie parallel to the slip directions. Now active screws can pile up in the manner envisioned by Seeger, and cross slip over barriers is possible.

Although two barriers could form on a given slip plane and thus confine the dislocation loops on that plane, the likelihood of two separate interactions occurring on a specific atomic plane should be small. Again, following Kocks' argument,[9] each slip plane may be penetrated by hedges of dislocations piled up behind L–C barriers formed on the other planes. The geometry of the [111] orientation is such that the hedges penetrating a plane would form an array parallel to the L–C barriers on that plane (Fig. 25b). Therefore L–C barriers would be reinforced by parallel hedges and be less likely to break down than the L–C barriers in the [001] crystals where the hedge array cannot be parallel to, and hence does not reinforce, the barriers. The initially similar hardening rates in [001] and [111] crystals (Figs. 7–9) may be due to rapid formation of L–C barriers. Because [111] barriers are the stronger, however, hardening persists even at the highest temperature of 273°K.

VOL. 8 1960

[112] *and* [123] *Orientations*

In the [112] orientation the two equally favored slip systems are the suitable ones for L–C barrier formation. Barriers should be formed also by less favored systems as the stress is raised; the hedges produced by these barriers would then tend to confine dislocation loops on the primary and conjugate planes from expanding parallel to the first-formed barriers. Accordingly, while the original hardening rates are not high, the hardening persists to large strains with a low rate of decay.

The condition in the [123] orientation is somewhat similar. Slip on one system is initially favored but as the tensile axis rotates toward [112], slip on the conjugate system is encouraged and the argument follows that for the [112] case.

Polycrystalline Strain Hardening

In works by Kocks[10], strain hardening was regarded as identical in polycrystals and single crystals of [001] and [111] orientations. The underlying assumptions were the same rate of shear hardening, $d\tau/d\gamma$, in all cases and five equally active slip systems in the polycrystal. For aluminum at room temperature good agreement was found between the stress-strain curves of polycrystals, [111] single crystals and [001] single crystals in the initial rapidly hardening part.

Data of the present work do not show such agreement at 4.2°K. A preferred orientation is assumed for the cast polycrystal in which [001] is perpendicular to the tensile axis. For the two most favored slip systems the average Schmid orientation factor in the polycrystal is then about 0.47;[20] for three and four systems the average factor drops to 0.39 and 0.35, respectively. If the same rate of shear-hardening on active slip systems is assumed for the polycrystal and the [001] single crystal an average factor of 0.48 for the polycrystal is necessary to produce agreement between the experimental curves. Such a value would imply that most of the slip in the polycrystal occurs on no more than two systems. To bring the [111] and polycrystal curves together requires an average Schmid factor of 0.37 for the polycrystal, implying that most of the slip occurs on three or four active systems.

Thus if all specimens actually harden at the same rate, the implication is that less than five slip systems are active in the polycrystal. An alternative explanation is that the hardening rate is lower in the polycrystal than in the single crystals.

5. SUMMARY

Tension tests were made on differently oriented aluminum single crystals at various low temperatures down to 4.2°K. The principal findings were:

(1) No linear stage II was observed in any of the tests. The slopes of the stress–strain curves increase to a maximum value and immediately begin to decrease with stress continuing to rise. Strong temperature dependence is found in the initial rate of decay of the slope with stress, which is almost proportional to the temperature.

(2) After small strains in [001] crystals at 273°K, deformation occurs primarily by the operation of two slip systems with conjugate relationship. The accompanying lattice rotation accounts for large elongations despite a low work hardening rate. The low work hardening rate is explained, in turn, by the effects of having but a single set of Lomer–Cottrell barriers formed in one of the planes by operation of these slip systems. At lower temperatures all four stressed slip directions are active; much higher work hardening rates are now explained by the effects of two perpendicular sets of Lomer–Cottrell barriers. It is suggested that slip lines along {110} traces at low temperatures may reflect a fine mixture of cross-slip on two {111} planes necessary to avoid such barriers.

(3) Crystals of [111] orientation deform by approximately equal slip in the three favored directions at all test temperatures. Thus deformation modes of [111] and [001] crystals become increasingly alike at lower temperatures, when differences in hardening behavior diminish.

ACKNOWLEDGMENTS

The authors wish to thank the U.S. Atomic Energy Commission for support of this work under Contract No. AT (30–1)–1310. The aluminum was supplied by the Aluminum Company of America. The authors are pleased to acknowledge helpful discussions with U. F. Kocks.

REFERENCES

1. J. Diehl, S. Mader, and A. Seeger, *Z. Metallk.* **46,** 650 (1955).
2. J. Diehl, *Z. Metallk.* **47,** 331 (1956).
3. A. Seeger, J. Diehl, S. Mader and H. Rebstock, *Phil. Mag.* **2,** 323 (1957).
4. A. Seeger, *Dislocations and Mechanical Properties of Crystals*, p. 243 (Eds. J. C. Fisher, W. G. Johnston, R. Thomson and T. Vreeland) Wiley, New York (1957).
5. W. Staubwasser, *Acta Met.* **7,** 43 (1959). Thesis, Univ. Göttingen, (1954).
6. A. Sosin and J. S. Koehler, *Phys. Rev.* **101,** 972 (1956).
7. K. Lücke and H. Lange, *Z. Metallk.* **43,** 55 (1952).
8. H. Lange and K. Lücke, *Z. Metallk.* **44,** 183 (1953).
9. U. F. Kocks, Ph.D. Thesis, Harvard Univ. (1959).
10. U. F. Kocks, *Acta Met.* **6,** 85 (1958).
11. B. Chalmers, *Canad. J. Phys.* **31,** 132 (1953).
12. R. S. Davis, private communication.
13. Z. S. Basinski, *Proc. Roy. Soc.* A **240,** 229 (1957).

14. E. SCHMID and W. BOAS, *Kristallplastizitat*. Springer, Berlin (1935).
15. F. D. ROSI and C. H. MATHEWSON, *Trans. Amer. Inst. Min. (Metall.) Engrs.* **188,** 1159 (1950).
16. T. H. BLEWITT, R. R. COLTMAN and J. K. REDMAN, *Dislocations and Mechanical Properties of Crystalline Solids*, p. 179. Wiley, New York (1957).
17. C. J. BEEVERS and R. W. K. HONEYCOMBE in *Conference on Fracture, Swampscott, Mass., (1959)*.
18. J. D. LIVINGSTON, Ph.D. Thesis, Harvard Univ. (1956).
19. C. ELBAUM, private communication.
20. R. L. FLEISCHER and W. A. BACKOFEN, to be published, AIME (1960).
21. J. FRIEDEL, *Phil. Mag.* (ser. 7) **46,** 1169 (1955).
22. P. HAASEN, *Phil. Mag.* (ser. 8) **3,** 384 (1958).
23. A. H. COTTRELL, *Dislocations and Plastic Flow in Crystals*, p. 170. Clarendon Press, Oxford (1953).
24. R. L. FLEISCHER, *Acta Met.* **6,** 553 (1958).
25. W. BOAS and G. OGILVIE, *Acta Met.* **2,** 655 (1954).
26. T. OJALA, C. ELBAUM and W. C. WINEGARD, *Trans. Amer. Inst. Min. (Metall.) Engrs.* **206,** 1344 (1956).
27. J. D. LIVINGSTON and B. CHALMERS, *Acta Met.* **5,** 322 (1957).
28. W. BOAS and E. SCHMID, *Z. Phys.* **71,** 703 (1931).
29. R. D. JOHNSON, A. P. YOUNG and A. D. SCHWOPE, *Nat. Advis. Comm. for Aeronautics, Tech. Note* 3351 (1955).
30. A. J. E. FOREMAN and W. LOMER, *Phil. Mag.* (ser. 7) **46,** 73 (1955).
31. A. J. E. FOREMAN, *Acta Met.* **3,** 73 (1955).
32. H. WILSDORF and D. KUHLMAN-WILSDORF, *Trans. Amer. Inst. Min. (Metall.) Engrs.* **194,** 527 (1952).

VOL.
8
1960

SUR L'INTERACTION D'UNE DISLOCATION FIXE ET D'UNE DISLOCATION MOBILE DANS SON PLAN DE GLISSEMENT*

G. SAADA†

Dans cet article, nous proposons un modèle pour l'étude détaillée du passage d'une forêt de dislocations par une dislocation mobile dans son plan de glissement. Nous montrons sur un exemple qu'en l'absence de contraintes extérieures, il n'existe pas, dans un plan de glissement, de boucle fermée, stable entourant un arbre de la forêt. Ce résultat semble devoir être général. Nous montrons également que le passage d'un arbre répulsif se fait sans grande modification de la forme de la ligne. S'il glisse facilement, le cran créé au passage d'un arbre ne produira un nombre appréciable de lacunes, que si l'arbre est attractif. Nous concluons par quelques applications à l'étude du durcissement, en montrant notamment que les dislocations situées dans des plans de glissement voisins de celui de la dislocation mobile exercent des contraintes du même ordre que celles qui sont dues aux arbres percant le plan de glissement.

ON THE INTERACTION BETWEEN A FIXED DISLOCATION AND A MOBILE DISLOCATION IN ITS SLIP PLANE

The author proposes a model for the detailed study of the passage of a dislocation moving in its slip plane through a dislocation "forest". In the absence of exterior constraints, there does not exist, in the slip plane, a stable loop enclosing one of the "trees" of this "forest". This result seems to be general, the author also shows that the passage of a repulsive "tree" is made without a significant modification of the shape of the line. If slip is not too difficult, the jog created by the passage of a "tree" will produce an appreciable number of vacancies only if the "tree" is attractive. The author concludes by citing several applications in the study of hardening. It is shown, in particular, that the dislocations situated in slip planes near those of the moving dislocations exert constraints of the same order as those due to "trees" cutting the slip plane.

DIE WECHSELWIRKUNG EINER FESTEN VERSETZUNG MIT EINER IN IHRER GLEITEBENE BEWEGLICHEN VERSETZUNG

Im folgenden wird ein Modell vorgeschlagen, an welchem ausführlich untersucht werden kann, wie sich eine in ihrer Gleitebene bewegliche Versetzung durch einen Versetzungswald bewegt. Ohne äußere Spannungen existiert, wie an einem Beispiel gezeigt wird, auf einer Gleitebene kein geschlossener Versetzungsring, der einen Baum des Waldes umschließt. Dieses Ergebnis scheint allgemein zu sein. Es wird weiterhin gezeigt, daß eine Versetzung einen abstoßenden Baum ohne große Modifikation der Form der Versetzungslinie durchdringt. Ein beim Durchschneiden eines Baumes entstandener Sprung erzeugt, wenn er leicht gleitet, nur dann eine beträchtliche Anzahl von Leerstellen, wenn der Baum anziehend wirkt. Abschließend werden einige Anwendungen auf das Problem der Verfestigung gegeben. Dabei wird insbesondere gezeigt, daß die in den zur Gleitebene der beweglichen Versetzung benachbarten Gleitebenen liegenden Versetzungen auf diese Versetzung Spannungen ausüben, die in der gleichen Größenordnung sind wie diejenigen, welche von den Bäumen herrühren, die die Gleitebene durchdringen.

1. INTRODUCTION

Nous nous proposons d'étudier le champ de contraintes d'une dislocation quelconque L dans un plan P' d'orientation quelconque vis-à-vis de celle-ci. Nous allons montrer que l'on peut, sans modifier qualitativement les résultats, supposer que L est une dislocation coin dont le vecteur de Burgers est situé dans P'. Dans ce cas simple, nous étudierons l'équilibre d'une boucle L' de dislocation glissant dans P', en équilibre avec les contraintes créées par L. Nous montrerons qu'il ne peut exister de telles boucles. Nous appliquerons les résultats précédents à l'étude de la traversée d'une forêt de dislocations par une dislocation mobile dans son plan de glissement et conclurons sur des applications à l'étude du durcissement. Nous négligeons les effets dûs à une montée des dislocations et supposons que les dislocations ne sont pas dissociées.

2. INTERACTION DE 2 DISLOCATIONS RECTILIGNES DONT L'UNE EST MOBILE DANS SON PLAN DE GLISSEMENT

2.1. *Généralités*

La dislocation fixe L est définie par:

(i) sa position, axe Ox_3 du trièdre trirectangle $Ox_1\,x_2\,x_3$ (Fig. 1),

(ii) son vecteur de Burgers $\mathbf{b}$ de coordonnées respectivement b_{c_1}, b_{c_2}, b_v sur Ox_1, Ox_2, Ox_3.

Le sens de L est le sens positif sur Ox_3.

La dislocation L' est définie par:

(i) son plan de glissement P', plan $x_1\,O_y$, repéré par l'angle $\alpha = (\mathbf{Ox_2}, \mathbf{Oy})$ où Oy est perpendiculaire à Ox_1.

* Reçu le 24 Mars, 1959.

† Physique des Solides, 60, boulevard Saint-Michel, Paris 6e.

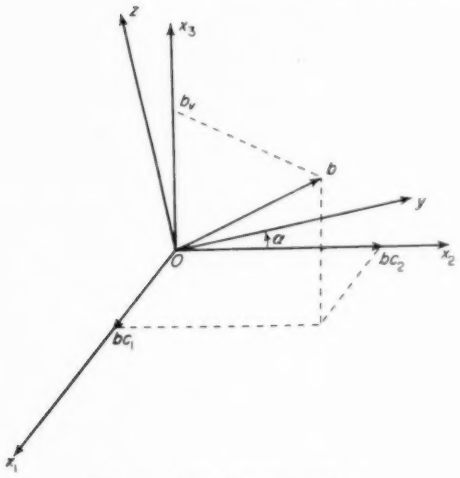


FIG. 1. Géométrie du problème.

(ii) son vecteur de Burgers $\mathbf{b}'$, de coordonnées $(b_1'\ b_y'\ 0)$ dans le trièdre trirectangle $(Ox_1\ yz)$ soit $(b_1', b_2' = b_y' \cos\alpha,\ b_3' = b_y' \sin\alpha)$ dans le trièdre $(Ox_1x_2x_3)$.

Le vecteur unitaire $(\mathbf{L}')$ porté par la dislocation, repéré par $(\mathbf{Ox_1}, \mathbf{L}') = \varphi$.

Étant données 3 dislocations L_1, L_2, L_3 portées par Ox_3 de vecteur de Burgers respectivement $\mathbf{b}_{c_1}$, $\mathbf{b}_{c_2}$, $\mathbf{b}_v$, le champ de contraintes de la dislocation L précédemment définie est obtenu en superposant les champs de contraintes dûs à L_1, L_2, L_3.

2.2. Contraintes exercées par L sur un petit élément rectiligne de L'

2.2.1. *Contraintes exercées par* L_1. Le tenseur des contraintes exercées par la dislocation coin L_1 en un point M de coordonnées polaires (r,θ) (voir Fig. 2) est:[1]

$$\sigma_{11} = -\frac{D_{c_1} \sin\theta\,(2+\cos 2\theta)}{r}$$

$$\sigma_{22} = \frac{D_{c_1} \sin\theta \cos 2\theta}{r}$$

$$\sigma_{33} = \nu(\sigma_{11} + \sigma_{22})$$

$$\sigma_{12} = \sigma_{21} = \frac{D_{c_1} \cos 2\theta \cos\theta}{r}$$

$$D_{c_1} = \frac{\mu b_{c_1}}{2\pi(1-\nu)}$$

μ et ν sont respectivement le module de cisaillement et le coefficient de Poisson du cristal. Les autres composantes du tenseur sont nulles.

La force par unité de longueur exercée par L_1 sur un élément rectiligne de L' est, si nous nous limitons aux forces s'exerçant dans le plan de glissement:[2]

$$F = \sum_{ij} b_i' \sigma_{ij} n_j$$

$\mathbf{F}$ est normale à L' et ses composantes sur Ox_1 et Oy sont:

$$F_{1_1} = U_{c_1} \sin\varphi$$

$$F_{y_1} = U_{c_1} \cos\varphi$$

avec:

$$U_{c_1} = \frac{A_{c_1}}{r} G_{c_1}(\theta)$$

$$A_{c_1} = D_{c_1} b_y' \sin\alpha\cos\alpha$$

$$G_{c_1}(\theta) = -2\nu \sin\theta + e\cos\theta\cos 2\theta - \sin\theta\cos 2\theta$$

et $$e = \frac{b'_1}{b_y' \cos\alpha}$$

2.2.2. *Contraintes exercées par la dislocation coin* L_2. Un calcul analogue donne alors:

$$F_{1_2} = -U_{c_2} \sin\varphi$$

$$F_{y_2} = U_{c_2} \cos\varphi$$

$$U_{c_2} = \frac{A_{c_2}}{r} G_{c_2}(\theta)$$

$$G_{c_2}(\theta) = 2(1-\nu)\sin\theta + \sin\theta\cos 2\theta + 2\cos\theta\cos 2\theta$$

A_{c_2} se déduit de A_{c_1} par substitution de b_{c_2} à b_{c_1}; les définitions de F_{1_2} F_{y_2} U_{c_2} sont évidentes.

2.2.3. *Contraintes exercées par la dislocation vis* L_3. On a alors:

$$F_{1_v} = -U_0 \sin\varphi$$

$$F_y = U_0 \cos\varphi$$

$$U_0 = -\frac{A_0}{r} G_0(\theta)$$

$$A_0 = \frac{\mu b_0 b_y' \cos\alpha}{2\pi}$$

$$G_0(\theta) = -\frac{\sin\alpha}{\cos\varphi} \cos(\theta - \varphi)$$

$$\operatorname{tg}\varphi' = \frac{e}{\operatorname{tg}\alpha}$$

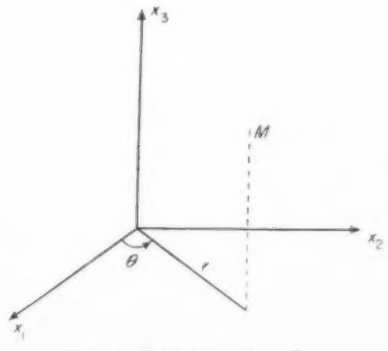


FIG. 2. Définition de r, θ.

VOL. 8 1960

2.2.4. *Contraintes exercées par L.* La force exercée par L sur l'unité de longueur de longueur de L' est alors:

$$F_{1L} = F_{11} + F_{12} + F_{10} = -U \sin \varphi$$

$$F_{y_L} = F_{y_1} + F_{y_2} + F_{y_L} = U \cos \varphi$$

$$U = \frac{A_{c_1} G_{c_1}(\theta) + A_{c_2} G_{c_2}(\theta) + A_0 G_0(\theta)}{r}$$

Les fonctions $G_{c_1}(\theta)$ et $G_{c_2}(\theta)$ ont à peu près la même allure; $G_0(\theta)$ est une fonction plus simple. Nous étudierons donc essentiellement dans ce qui suit, le cas de la dislocation coin L_1. Pour simplifier l'exposé, nous supprimerons l'indice 1 dans la suite.

2.3. *Forme d'équilibre d'une boucle de dislocation L' dans son plan de glissement, placée dans le champ de contraintes de L*

2.3.1. *Généralités.* Nous supposons ici qu'un élément de L' est soumis à deux contraintes:

les contraintes créées par L

la tension de ligne τ de L'

Si ρ' est le rayon de courbure de L' au point de coordonnées (r,θ), l'équation d'équilibre de L' s'écrit:

$$\frac{AG(\theta)}{r} - \frac{\tau}{\rho'} = 0 \qquad (1a)$$

Cette équation lie les coordonnées du point courant de la *projection* L_0' de L' dans $x_1 Ox_2$ (voir Fig. 3) au rayon de courbure ρ' de L'. Si ρ est le rayon de courbure de L_0', le théorème de Meusnier[3] nous apprend que $\rho' = \rho \cos \alpha$, si $\alpha \neq \pi/2$. L'équation précédente peut alors d'écrire:

$$\frac{A \cos \alpha}{\tau} \frac{G(\theta)}{r} - \frac{1}{\rho} = 0 \qquad (1b)$$

Cette équation différentielle nous permet de déterminer la *projection* L_0' de la boucle L' sur le plan $x_1 Ox_2$.

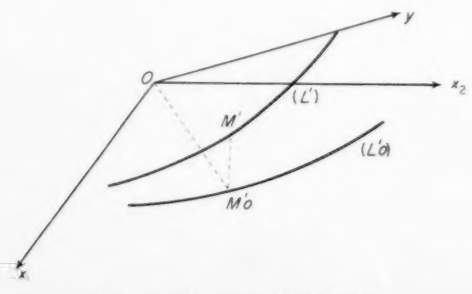


FIG. 3. Théorème de Meusnier.

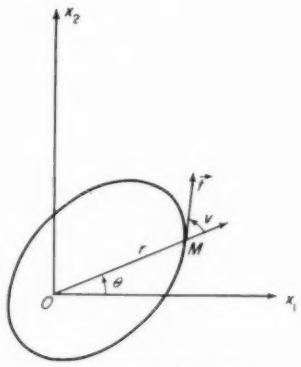


FIG. 4. Définition de v.

2.3.2. *Hypothèses faites sur la tension de ligne.* La tension de ligne en un point est en principe donnée par l'expression:

$$\tau = \frac{\mu b'^2}{4\pi(1-\nu)} \ln \frac{2\rho'}{b_0}$$

b_0 étant un paramètre de l'ordre de grandeur des dimensions atomiques.

Nous supposerons ici que ρ' varie suffisamment lentement pour que nous puissions considérer que $\ln(\rho'/b_0) = \lambda$, λ étant un paramètre que nous définirons dans les applications. D'où

$$\tau = \frac{\lambda \mu b'^2}{4\pi(1-\nu)}$$

2.3.3. *Résolution de l'équation* (1) *dans un cas particulier du système* C.F.C. On montre en annexe que l'équation (1) est équivalente au système:

$$\frac{A \cos \alpha}{\tau} G(\theta) - \left(1 + \frac{dv}{d\theta}\right) \sin v = 0 \qquad (2)$$

$$\frac{rd\theta}{dr} = \operatorname{tg} v \qquad (3)$$

Dans ces équations, v est l'angle du rayon vecteur et du vecteur tangent à L_0' au point courant (voir Fig. 4).

Le système (2.3) a été résolu numériquement (cf. annexe) dans le cas du système C.F.C. pour $\nu = 0{,}34$ valeur qui correspond à l'Aluminium.

En fait les résultats obtenus dépendent essentiellement de $G(\theta)$ qui, elle-même, dépend très peu de ν dans la mesure où, pour les métaux C.F.C., $0{,}25 < \nu < 0{,}4$. Les résultats trouvés sont donc qualitativement valables pour tous les métaux C.F.C.

Nous avons supposé que L et L' étaient dans les plans denses (111) et (11$\bar{1}$) avec $\mathbf{b} = \frac{a\sqrt{2}}{2}[1\bar{1}0]$ et $\mathbf{b}' = \frac{a\sqrt{2}}{2}[101]$. On en déduit

$$\cos\alpha = \frac{2\sqrt{2}}{3} \qquad \sin\alpha = \frac{1}{3}$$

$$b = \frac{a\sqrt{2}}{2} \qquad b_1' = \frac{a\sqrt{2}}{4}$$

$$b_2' = \frac{a\sqrt{3}}{3} \qquad b_3' = \frac{a}{2\sqrt{6}}$$

$$b_y' = \frac{a\sqrt{3}}{2\sqrt{2}} \qquad D = 0{,}167a\mu$$

$$\frac{A}{\tau\cos\alpha} = \frac{0{,}58}{\lambda} \qquad A = 0{,}52\,a^2\cos\alpha$$

a est le côté du cube élémentaire, $e = 0{,}6$.

La résolution donne les résultats suivants:

(i) Il ne peut y avoir de boucle fermée en équilibre avec L.

(ii) Il y a une double infinité de courbes plus ou moins ondulées correspondant à des positions d'équilibre instable. On montre en annexe que pour une valeur donnée de λ ces courbes se classent en une infinité de courbes homothétiques.

Ces résultats dépendent uniquement de l'allure générale de $G(\theta)$. Une dislocation de type L_2 ou L_3 ou une superposition quelconque de dislocation L_1 L_2 L_3 donneraient donc des résultats analogues.

3. EQUILIBRE D'UN ARC DE DISLOCATION SOUMIS A UNE CISSION σ ET PLACE DANS LE CHAMP DE CONTRAINTES D'UNE RANGÉE DE DISLOCATIONS FIXES ÉQUIDISTANTES

3.1. *Remarque préliminaire*

Nous avons étudié l'équilibre d'une boucle de dislocation (L') (Fig. 5) en présence de L. Nous avons

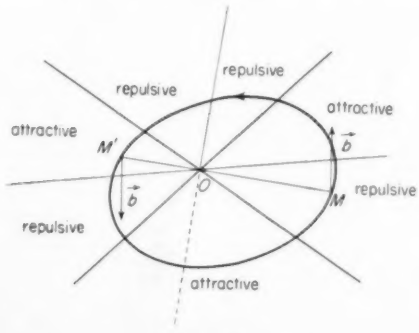


FIG. 5.

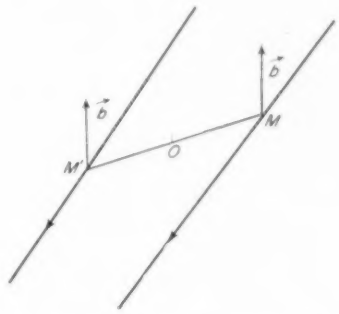


FIG. 6. Signe des contraintes autour d'une dislocation.

trouvé que lorsque la force qui s'exerce en un point $M(r,\theta)$ est attractive, la force s'exerçant au point $M'(r', \theta + \pi)$ est répulsive et vice versa. De plus, si $r = r'$ les forces s'exerçant en M et M' ont même intensité. Ces faits s'expriment analytiquement par l'ensemble de relations:

$$U = \frac{A}{r}G(\theta)$$

$$G(\theta + \pi) = -G(\theta)$$

D'un point de vue plus intuitif, on peut remarquer que, pour écrire l'équation d'équilibre de la boucle, on oriente cette boucle et que si les petits segments plaçés en M et M' ont même orientation relativement à cette convention, ils sont en fait dirigés en sens contraire si on les considère comme des segments indépendants.

Ceci montre (Fig. 6) que si l'on considère arc de dislocation L' *non fermé* la force appliquée au point $M(r, \theta)$ de l'arc avant passage et au point $M'(r', \theta + \pi)$ après passage est soit toujours attractive, soit toujours répulsive. Ainsi, lorsqu'un arc de dislocation arrive dans une zone répulsive et parvient à passer l'arbre L, il se retrouve dans une zone répulsive et est repoussé par L.

3.2. *Généralités*

Soit une rangée de n dislocations identiques du type L_1 que nous appellerons $L_1, L_2 \ldots L_i \ldots L_n$ disposées comme l'indique la Fig. 7.

Avec les notations de la figure, l'équation d'équilibre s'écrit:

$$\sum_{i=1}^{i=n} \frac{A\,G(\theta_i)}{r_i} - \frac{\tau}{\rho\cos\alpha} + \sigma b' = 0 \qquad (4)$$

Cette équation n'est pas résoluble rigoureusement et nous ferons les approximations suivantes:

VOL. 8 1960

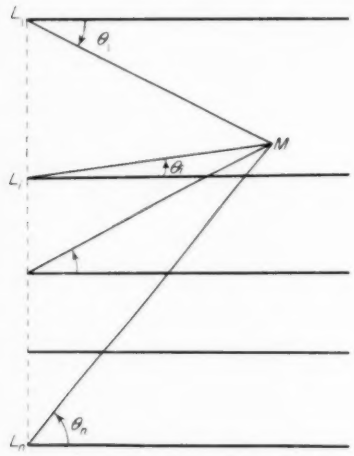


FIG. 7. Définition des r_i et θ_i.

Dans les domaines définis par

$$\left|\frac{A\ G(\theta_i)}{r_i}\right| > |\sigma b'| \tag{5}$$

nous considérerons que L' n'est soumise qu'aux contraintes dues à L_i.

L'équation d'équilibre est alors l'équation (1).

Dans les domaines définis par

$$\left|\frac{A\ G(\theta_i)}{r_i}\right| < |\sigma b'| \text{ quel que soit } i \tag{6}$$

nous considérerons que L' est uniquement soumise à la contrainte $\sigma b'$. La courbe d'équilibre est alors un cercle de rayon R. L'équation d'équilibre est alors:

$$\sigma b' - \frac{\tau}{R} = 0 \tag{7}$$

Nous supposerons que les L_i sont suffisamment éloignées pour que, au voisinage d'une L_i, les contraintes dues aux autres dislocations soient négligeables.

Nous avons représenté Fig. 8 la courbe

$$r = \frac{A\ G(\theta)}{\sigma b}$$

pour une valeur donnée de σ.

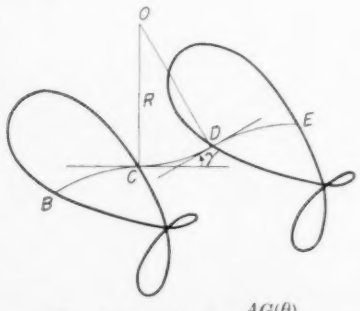


FIG. 8. Courbe $r = \frac{AG(\theta)}{\sigma b}$.

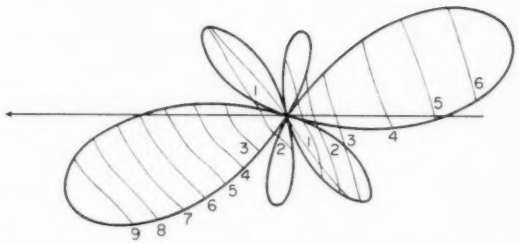


FIG. 9. Construction des solutions de l'équation (4).

3.3. *Forme d'équilibre de L'*

Nous déterminons la forme d'équilibre de L' de la manière suivante (voir Fig. 9):

Nous traçons l'antiprojection dans P', des 2 courbes définies par $\frac{AG(\theta)}{r} = \pm\sigma b$ et un arc BC de dislocation limité à son intersection avec les courbes ci-dessus. Nous avons alors une solution approchée de l'équation (4) dans le domaine défini par l'inégalité (5). Nous raccordons cette solution à une solution de l'équation (7) qui est une solution approchée de (4) dans le domaine défini par l'inéquation (6). Nous obtenons un arc de cercle CD tangent en C à BC. Nous arrêtons cette solution au point D tel que la tangente en D à CD soit parallèle à la tangente en B à BC.

En D nous recommençons la même construction qu'en B. Nous obtenons ainsi la disposition que doivent avoir les dislocations L_i pour que L' soit en équilibre sous l'action conjuguée de la cission σ et des contraintes créées par la rangée de dislocations.

Nous pouvons écrire en effet que:

$$CD = 2\ R \sin\frac{\gamma}{2}$$

La distance $L_i\ L_{i+1}$ est alors:

$$L_i\ L_{i+1} \simeq BD \simeq BC + CD$$

Nous avons évalué graphiquement cette distance.

3.4. *Application à un cas particulier du système* C.F.C.

3.4.1. *Généralités.* Dans le cas particulier étudié au paragraphe 2.3.3 nous pouvons préciser la forme d'équilibre de L' en fonction de son orientation générale et de sa distance aux dislocations fixes. Nous avons choisi dans cet exemple $\frac{\sigma}{\mu} \simeq 10^{-3}$.

Les résultats peuvent aisément être étendus à toutes les valeurs de σ. On montre en effet en annexe que pour une valeur donnée de la tension de ligne les courbes se classent en familles homothétiques. Les tracés obtenus sont donc valables quel que soit σ/μ à condition de supposer que l'on a modifié l'échelle.

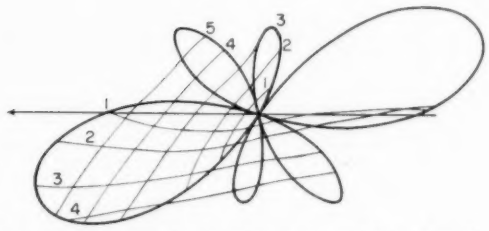


FIG. 10. Forme des dislocations mobiles dans les cas 1 et 4.

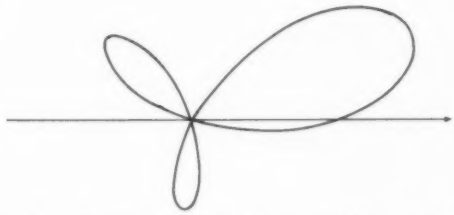


FIG. 11. Forme des dislocations mobiles dans les cas 2 et 3.

Le traçé des courbes L' nous a conduit dans chaque cas à prendre des valeurs $\lambda = 2$ pour les 2 courbes les plus proches de L et $\lambda = 4$ pour les courbes plus éloignées.

3.4.2. *Étude de quatre orientations de L'.* Nous avons fait cette étude dans trois cas où L repousse L' et dans le cas où L attire L'. Nous dressons pour chaque cas un tableau dans lequel nous indiquons le numéro de la courbe, la valeur du coefficient $\beta = \dfrac{\mu b}{\sigma l}$, la distance minima entre la courbe et le point où L perce le plan de glissement de L', l'unité de mesure étant l.

Cas 1, Fig. 10 partie gauche

Courbes n°	1	2	3	4	5	6	7	8	9
β	32	18	16,8	15,2	16	15,2	14,8	15,2	22
d/b	32	28	24	20	16	12	8	2	4

Cas 2, Fig. 11 haut

Courbes n°	1	2	3	4	5
β	9,6	9,6	18	14	13,2
d/b	16	12	8	2	4

Cas 3, Fig. 11 bas

Courbes n°	1	2	3	4
β	10,8	29,2	18	40
d/b	12	8	4	2

Cas 4, Fig. 10 partie droite

Courbes n°	1	2	3	4	5
$-\beta$	24	52	24	72	36
d/b	24	16	8	4	2

Remarquons tout d'abord que le 4^e cas correspond à des valeurs de β négatives, c'est-à-dire au cas où L attire L'. Les valeurs de β trouvées indiquent que, après passage d'une dislocation attractive, celle-ci continue à exercer une action non négligeable qui n'est pas fonction monotone de la distance.

Remarquons toutefois que les valeurs de l trouvées ici sont de l'ordre de $60a$, c'est-à-dire correspondent à un écrouissage considérable rarement réalisé.

Dans les trois premiers cas, la dislocation L est répulsive; les valeurs de l sont comprises entre 50 et $150a$ environ; les forces de répulsion sont du même ordre de grandeur dans les trois cas. Il faut cependant remarquer que dans le premier cas, la force répulsive s'exerce jusqu'à une assez grande distance ($35a$) sur une faible portion de L' tandis que dans les cas 2 et 3 la force répulsive s'exerce à des distances deux fois plus faible environ mais sur une portion de L' sensiblement plus importante. Dans le cas 1, d'autre part, le passage proprement dit de la dislocation est plus facile que l'approche. On peut remarquer aussi que le secteur répulsif est un peu supérieur à 180°.

4. CONCLUSIONS—APPLICATION AU DURCISSEMENT

En conclusion, l'étude précédente permet de préciser certains points concernant la forme d'équilibre d'une dislocation dans un cristal écroui; la peine qu'elle a à se déplacer et finalement sa possibilité de créer des lacunes.

4.1. *Forme d'équilibre d'une dislocation dans un cristal écroui*

Seeger[4], Hirsch[5] et Friedel[6] ont insisté sur le fait qu'en l'absence de contraintes appliquées, une dislocation est soumise à des contraintes dues à la forêt de dislocations perçant son plan de glissement. Elle est attirée par certains "arbres" et se recombine avec eux, ce qui lui donne une allure en zigzags (cf. Fig. 12); entre deux recombinaisons, elle oscille un peu de part et d'autre d'une course rectiligne, du fait de l'interaction à grande distance avec les autres arbres.

Notre étude conduit aux conclusions suivantes:

(a) A grandes distances, aucun arbre n'est purement attractif. Les recombinaisons sont donc un peu moins

VOL. 8 1960

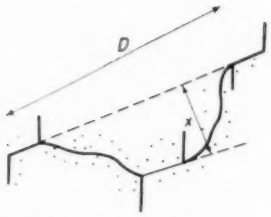


FIG. 12. Déviation des dislocations mobiles.

probables que ne le calculent les auteurs précédents. *Les zigzags sont donc très peu marqués.*

(b) Les ondulations entre recombinaisons sont dues autant aux arcs de dislocations *qui ne percent pas le plan de glissement* qu'à ceux qui le percent. L'étude du paragraphe 3 montre en effet que les ondulations produites par des arbres "répulsifs" sont peu marquées.

Les arcs du réseau plus ou moins parallèles au plan de glissement et voisins de celui-ci produisent des contraintes de l'ordre de $\sigma_i = \dfrac{\mu b}{2\pi l}$. Les ondulations de courbure $\dfrac{1}{\rho} \simeq \dfrac{\sigma_i}{\tau}$ qui en résultent sont au moins du même ordre que celles dues aux arbres qui percent le plan de glissement.

(c) Enfin nos calculs indiquent qu'*une boucle L' fermée entourant un arbre L n'est pas en équilibre dans son plan de glissement.* Si donc on observe des boucles, elles ne sont pas dans un plan de glissement.

4.2. *Durcissement*

Hirsch[5] suggère que la partie du durcissement qui varie peu avec la température[7] est dûe aux interactions à grandes distances des boucles L mobiles avec les arbres qui percent leurs plans de glissement.

Notre étude montre que *ce durcissement est probablement dû plutôt aux interactions à grandes distances avec les arcs du réseau de dislocations qui sont voisins du plan de glissement mais ne le percent pas.* En effet:

(a) Notre étude calcule la contrainte $\sigma_M = \dfrac{\mu b}{\beta l}$ nécéssaire pour faire passer quasistatiquement un arbre répulsif (s'il n'y avait pas formation de cran). Nous trouvons des valeurs inférieures à que celles qui sont nécessaires pour détruire une combinaison attractive (Friedel, non publié).

(b) Pour faire passer un arbre, il faut exercer cette contrainte sur une distance à l'arbre de plusieurs dizaines de distances interatomiques. L'agitation thermique ne peut pas faciliter notablement ce passage. Le durcissement qui en résulte varie donc peu avec la température.

(c) La contrainte σ_M calculée est évidemment un peu plus forte que celle nécessaire à un passage dynamique où la dislocation utiliserait son énergie cinétique emmagasinée pour passer la barrière de potentiel.[5]

(d) Mais, avec $\beta \geqslant 15$ à 20, la contrainte σ_M calculée dans notre étude est inférieure à celle dûe aux arcs du réseau de dislocations qui ne percent pas le plan de glissement. Ces contraintes sont en effet de l'ordre de

$$\sigma_i \simeq \frac{\mu b}{2\pi l}$$

Cette formule devrait donc donner, dans tous les cas, l'ordre de grandeur de la partie du durcissement qui varie peu avec la température.

4.3. *Création de lacunes par écrouissage*

Finalement le passage des arbres d'une "forêt" de dislocations vis a été invoqué pour la formation de lacunes.[8,9] Notre étude permet de préciser un peu l'importance de ce mécanisme:

(a) Au passage d'un "arbre" répulsif, la figure 10 montre que la dislocation mobile est très peu déviée. Ainsi la répulsion due à l'arbre n'est *pas* suffisante pour courber les deux portions de L' et les amener à se recombiner en avant de l'arbre, suivant le schéma de la Fig. 13(a). Une telle recombinaison aurait créée une rangée AB de lacunes ou d'atomes interstitiels.[8] De plus, l'angle φ que fait la dislocation L' à son passage de L (Fig. 13b) est tellement obtus qu'il y a assez peu de chances pour que la direction du vecteur de Burgers b' de L' ne soit pas comprise dans cet angle. On sait que c'est la seule disposition qui puisse amener le cran à monter hors de son plan de glissement, tout au moins dans les structures où les crans glissent facilement.[9]

(b) Au passage d'un "arbre" attractif au contraire, la dislocation L' doit se courber fortement pour que la recombinaison soit détruite (forts angles φ_1 et φ_2, Fig. 13c). Il y a alors une forte chance pour que le vecteur de Burgers $\mathbf{b}'$ soit situé hors de l'angle fait par L, à son contact avec L. Un assez grand nombre de

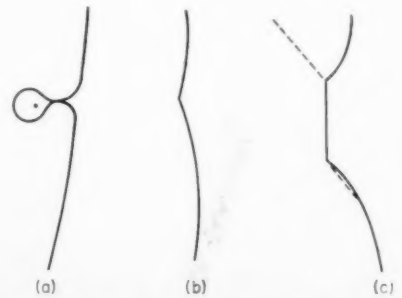


FIG. 13. Formation de cran par passage d'arbres.

lacunes peut alors être créé par montée du cran après le passage de l'arbre.

En conclusion, *les passages d'arbres attractifs avec recombinaison peuvent seuls créer un nombre appréciable de lacunes pour les portions de dislocations L' à caractére vis assez marqué.*

REMERCIEMENTS

Je tiens à remercier ici Monsieur Jacques Friedel qui m'a proposé cette étude, pour les nombreux conseils qu'il m'a prodigués tout au long de mon travail.

Je remercie également Monsieur Michel Henon de l'Institut d'Astrophysique qui a bien voulu résoudre l'équation (1) à l'aide d'une machine analogique de sa conception.

ANNEXE

Étude de l'Équation

$$\frac{A\cos\alpha}{\tau}\frac{G(\theta)}{r}-\frac{1}{\rho}=0 \qquad (1')$$

A.1. *Système équivalent à l'équation* (1')

Soit v l'angle du rayon vecteur PM et du vecteur tangent t à OM (Fig. 5), nous pouvons écrire:

$$\frac{1}{\rho}=\frac{d\theta+dv}{ds} \qquad (8)$$

$$r\frac{d\theta}{dr}=\mathrm{tg}\,v \qquad (3)$$

$$ds=rd\theta/\sin v \qquad (9)$$

En portant l'équation (8) dans (1'), il vient

$$\frac{A\cos\alpha}{\tau}\frac{G(\theta)}{r}-\frac{d\theta+dv}{ds}=0$$

ce qui avec l'équation (9) donne:

$$\frac{A\cos\alpha}{\tau}G(\theta)-\left(1+\frac{dv}{d\theta}\right)\sin v=0 \qquad (2)$$

Sauf à l'origine, l'équation (1') est équivalente au système (2.3).

A.2. *Résolution du système* (2.3)

Nous avons traçé la courbe $y=G(\theta)$, Fig. 14. Le système (2.3) a été résolu à l'aide d'une machine analogique pour $\lambda=1{,}2{,}4$.

Posons $v=\frac{\pi}{2}+u$

l'équation (2) s'écrit alors:

$$\frac{A\cos\alpha}{\tau}G(\theta)-\left(1+\frac{du}{d\theta}\right)\cos u=0$$

ou encore

$$\frac{d\theta}{\cos u}=\frac{du}{\frac{A\cos\alpha}{\tau}G(\theta)-\cos u}$$

Soit dt la valeur commune des deux rapports ci-dessus, (2.3) devient alors:

$$\frac{d\theta}{dt}=\cos u \qquad (10)$$

$$\frac{du}{dt}=\frac{G(\theta)}{\delta}-\cos u \qquad (11)$$

$$\frac{d\log r}{dt}=-\sin u \qquad (12)$$

avec

$$\delta=\frac{\tau}{A\cos\alpha}$$

On a exploré le domaine $-180^\circ\leqslant\theta\leqslant+180^\circ$

$$-90^\circ\leqslant u\leqslant 90^\circ$$

$$0\leqslant\log\frac{r}{r_0}\leqslant 3$$

On a parfois dépassé ces limites pour suivre les solutions. r_0 est une constante d'intégration sur laquelle nous revenons plus loin.

A.3. *Résultats*

A.3.1. *Forme d'équilibre des courbes.* Il n'y a pas de boucles fermées. Toutes les courbes présentent des branches infinies aux points où:

$$G(\theta)=0$$
$$G'(\theta)<0$$

Ceci semble être une propriété générale des solutions de l'équation (1'). Les fonctions $G(\theta)$ définies au paragraphe 2 de notre étude présentent toutes cette propriété pour une valeur de θ au moins dans l'intervalle $\left(-\frac{\pi}{2},+\frac{\pi}{2}\right)$. C'est sur cette propriété que nous fondons l'affirmation qu'il n'y a pas de

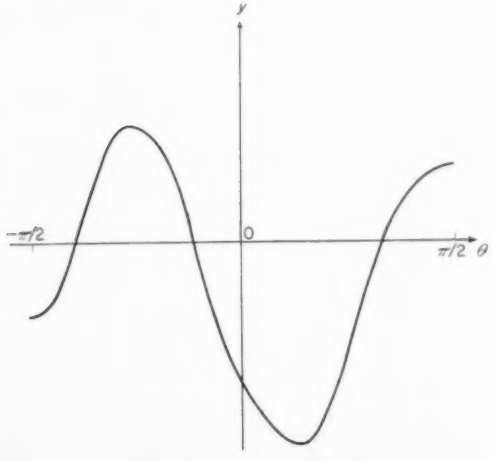


FIG. 14. Courbe $G_{c_1}(\theta)$.

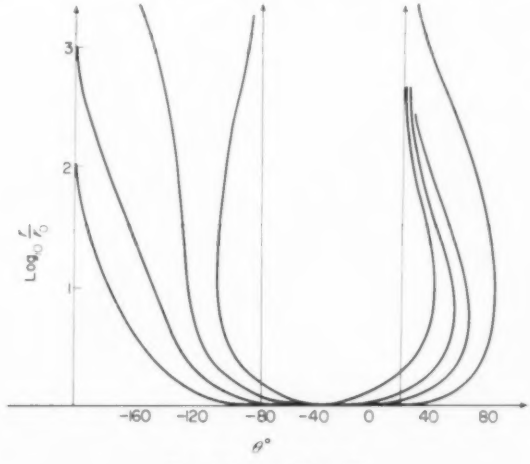


FIG. 15. Courbes $r(\theta)$.

VOL. 8 1960

boucles fermées dans un plan de glissement, en équilibre avec le champ de contraintes donné.

A.3.2. *Signification de* r_0. Pour une valeur de λ donnée, les solutions peuvent se classer *en familles de courbes homothétiques*.

Si nous revenons au système (2.3), nous constatons que lorsque l'équation (3) a des solutions, elles sont de la forme:

$$\log \frac{r}{r_0} = \int f(\theta)\, d\theta \quad \text{avec} \quad f(\theta) = \frac{1}{\operatorname{tg} v(\theta)}$$

$v(\theta)$ étant une intégrale de l'équation (2).

Ce qui implique que les solutions $r(\theta)$ correspondant à une $f(\theta)$ donc à une $v(\theta)$ se déduisent les unes des autres par homothétie, le rapport d'homothétie étant égal à r_0.

On a traçé Fig. 15 quelques courbes $\log r(\theta)$.

BIBLIOGRAPHIE

1. F. R. Nabarro, *Advanc. Phys.* **1,** 271 (1952).
2. M. O. Peack and J. S. Koehler, *Phys. Rev.* **80,** 436 (1950).
3. J. Bass, *Cours de Mathématiques* p. 439. Masson, Paris.
4. A. Seeger, *Phi. Mag.* (ser. 7) **45,** 771 (1954).
5. P. B. Hirsch.
6. J. Friedel, *Detroit Conference on Fatigue* (1958).
7. A. H. Cottrell and R. J. Stokes, *Proc. Roy. Soc.* A**233,** 17 (1955).
8. F. Seitz, *Advanc. Phys.* **1,** 43 (1952).
9. N. F. Mott in *Dislocations and Mechanical Properties of Crystals* (Eds.: J. C. Fisher, W. A. Johnston, R. Thomson and T. Vreeland, Jr.) p. 469. Wiley, New York (1957).

SEGREGATION IN HOMOGENEOUS ALLOYS DURING SINTERING*

G. C. KUCZYNSKI,† G. MATSUMURA† and B. D. CULLITY†

The vacancy gradient set up by the sharp curvature of the neck between two sintered particles can under favorable conditions produce a considerable segregation in a completely homogenized solid solution. This effect was demonstrated by the precipitate in Cu–In and Cu–Ag alloys occurring in the neck cavity at a higher temperature than indicated by the solvus line and at a lower one than the solidus temperature. These results are supported by the appearance of side peaks and a shift of the peaks of X-ray lines.

SEGREGATION DANS DES ALLIAGES HOMOGENES PENDANT LE FRITTAGE

Le gradient de lacunes établi par la courbure de la zone de contact de deux particules frittées peut, dans des conditions favorables, être la cause d'une ségrégation importante dans une solution solide completement homogénisée. Cet effet a été mis en évidence par les précipités dans les alliages Cu-In et Cu-Ag qui apparaissent dans la cavité de cette zone à une température supérieure à celle indiquée par la ligne de solubilité et inférieure à celle du solidus. Ces résultats sont confirmés par l'apparition de raies supplémentaires et un déplacement des pics des rayons X.

AUSSCHEIDUNGEN IN HOMOGENEN LEGIERUNGEN WÄHREND DES SINTERNS

Die starke Oberflächenkrümmung des Berührungsgebietes, in welchem zwei Teilchen zusammen gesintert sind, erzeugt dort einen Leerstellengradienten und dieser kann unter günstigen Umständen eine beträchtliche Ausscheidung in einer vollkommen homogenen festen Lösung zur Folge haben. Dieser Effekt wurde durch Ausscheidungen in Cu-In und Cu-Ag Legierungen aufgezeigt, die in dem genannten Berührungsgebiet bei Temperaturen oberhalb der Löslichkeitslinie und unterhalb der Soliduslinie auftreten. Die Ergebnisse werden unterstützt durch Beobachtungen von Seitenmaxima und Linienverschiebungen auf Röntgenaufnahmen.

VOL. 8 1960

INTRODUCTION

An analysis of the sintering phenomenon[1] has indicated that, in the case of metals of not too high vapor pressure, the experimental results can be interpreted in terms of volume diffusion of atoms towards the contact area between two sintered particles. This diffusion flow is caused by the excess vacancy concentration gradient beneath the concave surface of the neck joining the two particles. The excess concentration of vacancies ΔC can be expressed as a function of the radius of curvature of the neck[1] ρ:

$$\Delta C = \frac{\gamma V_0}{RT\rho} C_0 \qquad (1)$$

where C_0 is the equilibrium vacancy concentration beneath a flat surface, γ the surface tension of the material, V_0 its molar volume, R the gas constant, and T the Kelvin temperature. The solution of the flow equation yields a relationship between the radius of the neck x and the time t at constant temperature:

$$\frac{x^5}{a^2} = \frac{K\gamma V_0}{RT} D_t \qquad (2)$$

where a is the radius of the sintered particle or wire, D the self-diffusion coefficient, and K a constant of the order of 100, depending on the details of the geometry of the system. This relation has been frequently verified by direct measurements. The geometrical details referred to in the above discussion are illustrated in the schematic sketch of two sintered particles shown in Fig. 1.

However, if two particles or wires are made of homogenized alloy and if the diffusion coefficients of the components are not necessarily the same, one may expect greater concentration of the faster diffusing atoms in the neck area, at least at the early stage of sintering when the vacancy gradient due to the smallness of the radius of curvature ρ is large. Under suitable conditions this excess concentration may

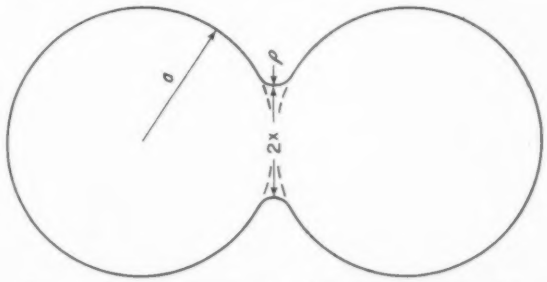


FIG. 1. Schematic representation of a cross section through two spherical particles or wires partially sintered.

* Received March 25, 1959. This paper represents part of a thesis by G. Matsumura, submitted in partial fulfillment of requirements for the degree of Master of Science to the Graduate School of the University of Notre Dame.

† Department of Metallurgy, University of Notre Dame, Notre Dame, Indiana.

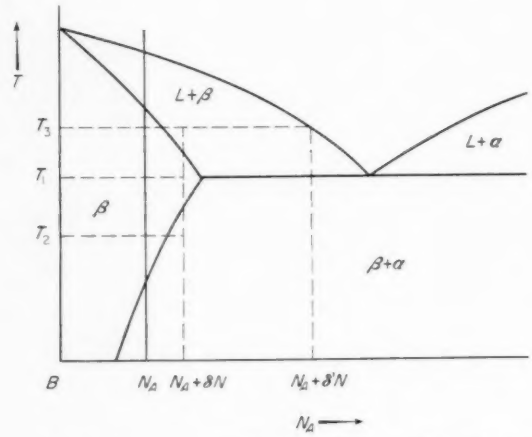


FIG. 2. Schematic equilibrium diagram of a system of limited solubility.

result in segregation of a homogeneous alloy in the neck area. The exploration of this effect is the subject of the present paper.

EXPERIMENTAL

Several experiments were designed to detect the above mentioned effect. One of them consisted in heating a compact composed of a bundle of wires of a well homogenized binary alloy of concentration N_A of atoms A at a temperature T_1 (Fig. 2) well within the region of solubility β. If the reasoning sketched above is correct, and if D_A, the self-diffusion coefficient of atoms A, is greater than D_B, the self-diffusion coefficient of component B, then during the sintering of the wires the concentration of A in the necks formed between the wires should shift from N_A to $N_A + \delta N_A$. If after a certain time of sintering the temperature is lowered to T_2, at which the solid solution β in the neck region is unstable, the A-rich phase α should precipitate out in that region and become visible under the microscope. Another variant of this method is to heat the compact just below the solidus temperature, for instance at T_3 of Fig. 2. If a sufficient number of A atoms accumulate in the neck, the alloy should melt and the composition of the molten phase should correspond to concentration $N_A + \delta' N_A$. After rapid cooling, to prevent homogenization, the molten part of the neck should be converted into an α-rich solid.

The first alloy so treated contained 8 at. % of indium in copper. The alloy was well homogenized by heating it at 700°C for a week and then drawn into wire of 0.010 in. diameter; the wires were homogenized again at about 700°C for several days and then twisted together to facilitate sintering. They were heated at 690°C for 16 hr followed by ageing at 485°C, about 5° higher than the temperature at which the indium-rich phase precipitates out. The photomicrograph of a neck between two wires after this heat treatment is shown in Fig. 3. The precipitation of β phase in the neck is clearly visible.

Sintering near the solidus temperature was also tried on these wires. The solidus temperature for the Cu + 8 at. % In alloy was carefully determined as 765°C. The wire compacts were heated at 760°C for 2 hr in vacuum, quenched and examined metallographically. Fig. 4 represents the neck area after this heat treatment and shows the indium-rich inclusions.

Copper–silver alloys form a simple eutectic system with limited solubilities on both sides and they are therefore well suited for this type of experiment.

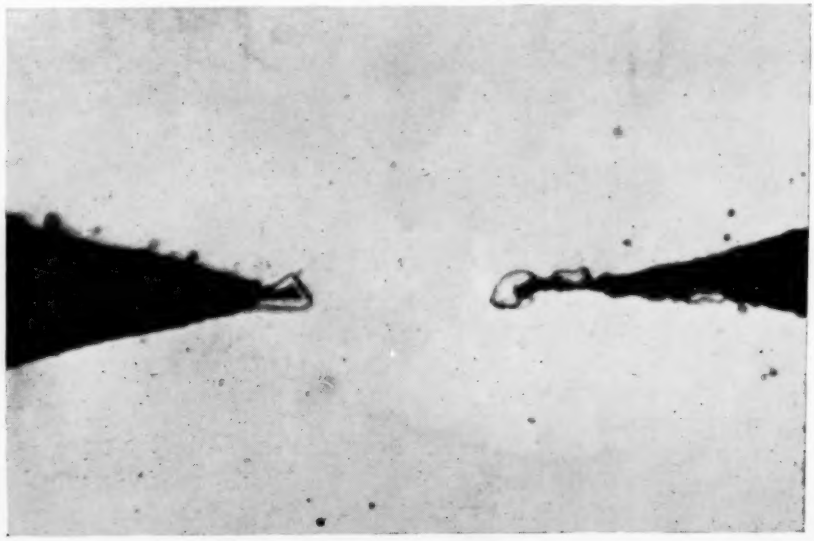


FIG. 3. The neck between two wires prepared from homogenized Cu + 8 at. % In alloy, after sintering at 690°C for 16 hr followed by ageing at 485°C for 12 hr. Etched with $NH_4OH + H_2O_2$. ×1500

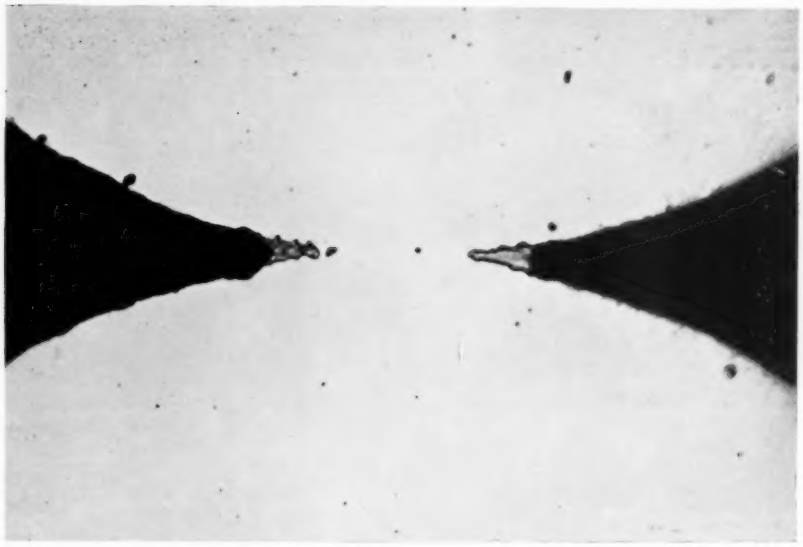


FIG. 4. The neck between two wires prepared from homogenized Cu + 8 at. % In alloy, after sintering at 760°C for 2 hr. Etched with $NH_4OH + H_2O_2$. ×500

Alloys of copper containing 4.5 at.% silver and silver containing 10 at. % copper were homogenized and drawn into wires 0.016 in. in diameter. Two compacts composed of twisted copper-rich alloy wires were sintered at 920°C for 10 min and 2 hr respectively. That temperature is some 5–10° lower than the solidus temperature for this alloy. Fig. 5(a) shows silver-rich alloy solidified in the neck after 10 min of sintering followed by quenching. The photomicrograph of the neck in the compact allowed to sinter for 2 hr is given in Fig. 5(b). It should be noted that the neck in this case is free of high-silver alloy, because enough time was allowed for rediffusion to take place. The silver-rich wire compacts were heated at 830°C, about 5° below their solidus temperature, for 10 min and quenched; Fig. 6 shows the neck area after this treatment. The copper-rich alloy which gathered in the neck cavities was removed by the etchant, leaving behind black, zigzag-like pores. This would indicate that, in dilute solutions of copper and silver, the diffusion coefficient of the solute is greater than that of the solvent.

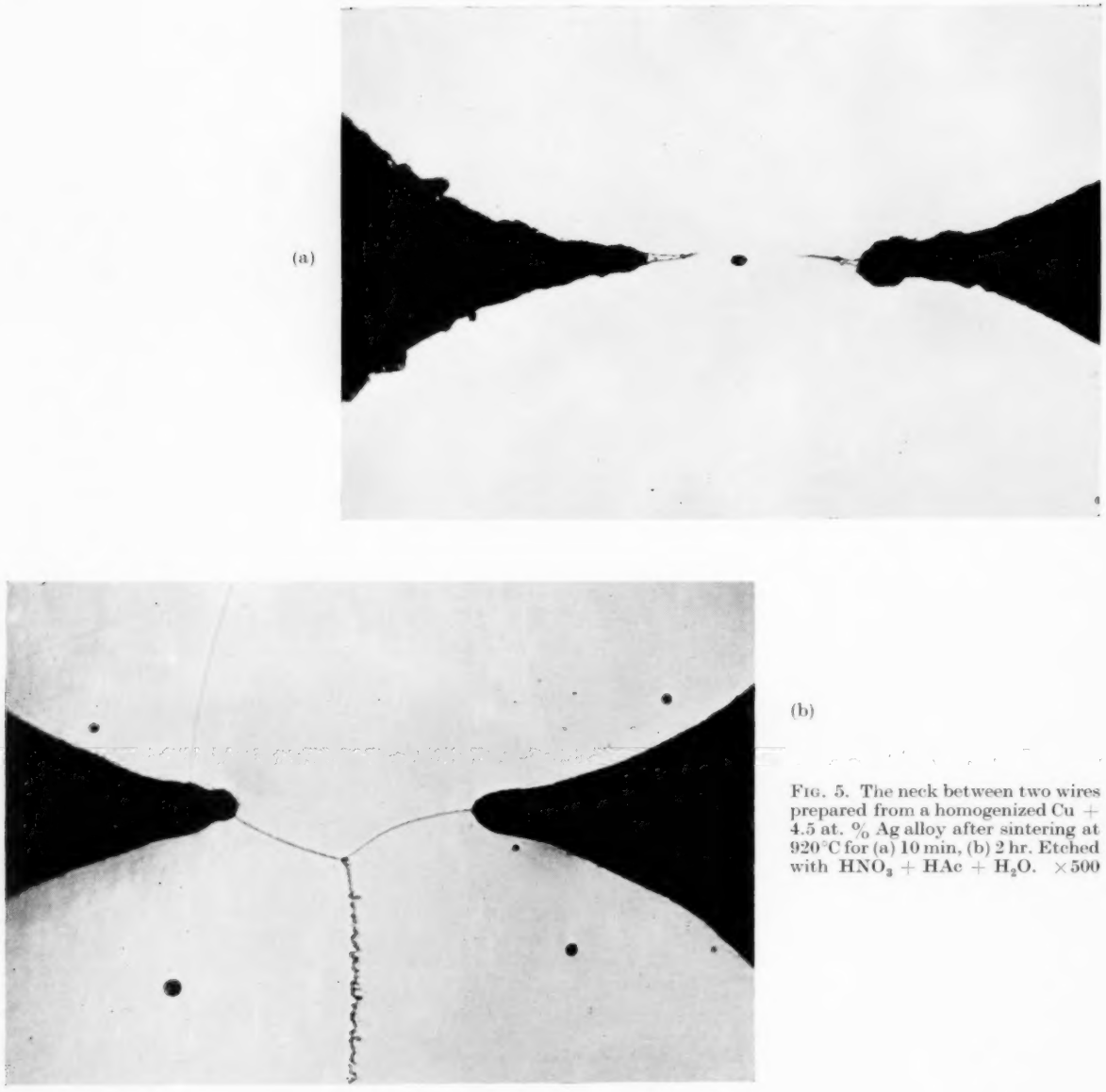
Attempts were made to obtain a quantitative estimate of the degree of segregation at a sintered interface by X-ray diffraction. Any change in composition which occurs in a solid solution is accompanied by a change in lattice parameter and consequently by a small shift in the position of a back-reflection line. The experiments were made on an alloy of copper containing 3.5 at. % gold. Minus 200 mesh filings from a well-homogenized ingot were annealed and lightly pressed at 10 t/in² into flat compacts; these were given sintering treatments at two temperatures, 800° and 750°C, for times ranging from 5 min to 62 hr and X-rayed at intervals. The position of the 420 $K\alpha_1$ peak was measured with filtered copper radiation on a General Electric XRD-3 diffractometer. Line intensities were measured with a scaler at 2θ intervals of 0.02° in the neighbourhood of a peak, and the position of the peak was obtained from a plotted profile of each line. The error in estimating peak position is estimated to be $\pm$ 0.02° of 2θ.

The results for a sintering temperature of 750°C are shown by the upper curve of Fig. 7, where the value of the peak position given on the left-hand ordinate is that measured on a sample of loose, unpressed filings annealed for 20 min at 600°C. The other points, obtained from the sintered compact, show that the diffraction line shifts rather quickly to lower angles and then moves more slowly back toward its original position. The maximum shift is −0.34° of 2θ. Translated into composition change, this corresponds to a change in gold content from 3.5 to about 4.4 at. %.

It was expected that this line shift would occur even more quickly at higher sintering temperatures. But at 800°C no significant change in line position in either direction was found, as shown by the results in the lower part of Fig. 7. Instead of line shifting, a new satellite peak appeared beside the main one on the low-angle side. The 420 line profile from this compact, sintered for 15 min at 800°C, is given by the upper curve of Fig. 8. It shows a definite side peak at a 2θ position 0.64° less than the main peak, corresponding to a gold content of about 5.1 at. %; this side peak disappeared after a further 15 min of sintering.

The side peak could not be reproduced in the second

VOL. 8 1960



(a)

(b)

FIG. 5. The neck between two wires prepared from a homogenized Cu + 4.5 at. % Ag alloy after sintering at 920°C for (a) 10 min, (b) 2 hr. Etched with HNO_3 + HAc + H_2O. ×500

series of 800°C sintering, the ones summarized in the lower part of Fig. 7. Instead a small "shelf" in the background appeared, beginning at about the same distance from the main peak as the previously observed side peak, as shown by the lower curve in Fig. 8, which also applies to a sintering time of 15 min. (The two main peaks in Fig. 8 did not occur at the same 2θ position because of a small difference between the actual compositions of the two compacts. They have been shifted in Fig. 8 to make the main peak positions agree.) This "shelf" was less prominent, or entirely absent, for sintering times longer or shorter than 15 min.

DISCUSSION

Let us consider two spherical particles of the same radius a, made of a well-homogenized binary alloy containing N_A and N_B atom fractions of atoms A and B respectively. If these two particles are brought in contact and heated, a neck of radius x will grow in accordance with equation (2). Let us further assume that $D_A > D_B$, where D_A and D_B are the coefficients of self diffusion of atoms A and B, respectively. Because of the unequal diffusion flow an excess concentration δN_A of atoms A will build up in the neck area. Then the difference of the flux of A atoms over that of B atoms, ΔJ, in the neck will change at a

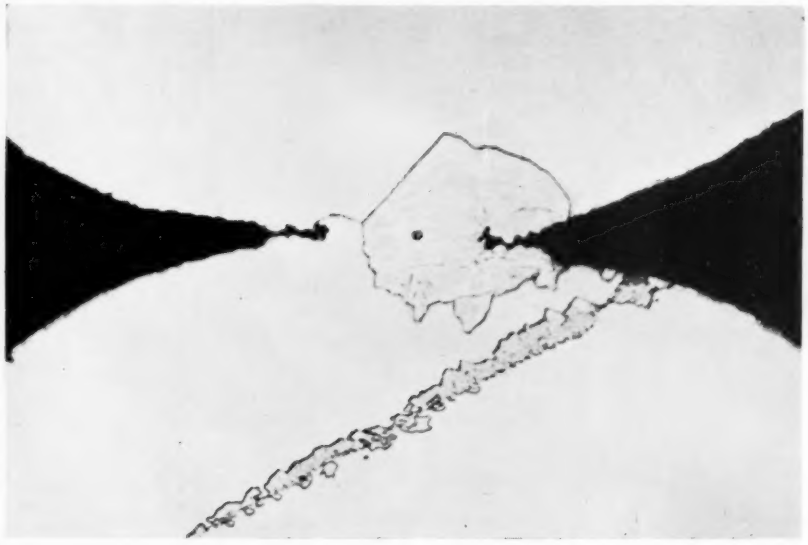


FIG. 6. The neck between two wires prepared from a homogenized Ag + 10 at. % Cu alloy, after sintering at 830°C for 10 min. Etched with $NH_4OH + H_2O_2$. 500×.

rate given approximately by the following equation:

$$\Delta J = \frac{D_A - D_B}{kT} \nabla \mu + \frac{\left(D_A \frac{\partial \mu_A}{\partial N_A} - D_B \frac{\partial \mu_B}{\nabla N_A} \right)}{kT} \nabla N_A \quad (3)$$

where k is Boltzmann's constant, T the absolute temperature, $\nabla \mu$ the gradient of the chemical potential of vacancies in the volume of the neck, and μ_A and μ_B the chemical potentials of components A and B, respectively. The second term of the right side of Equation (3) represents the flux of atoms A diffusing back into the alloy due to the concentration gradient ∇N_A produced by the greater flux of A atoms, as discussed above. Thus, according to this equation, δN_A will increase originally, reach a maximum corresponding to a certain critical radius of curvature ρ_c of the neck, and then decrease, because of the outflow of atoms A caused by the gradient ∇N_A. The value of ρ_c can be calculated from equation (3) by putting $\Delta J = 0$.

After applying the Gibbs–Duhem relation and taking as a first approximation

$$\nabla \mu = \frac{2\gamma\Omega_0}{\rho^2}$$

and

$$\nabla N_A = -\frac{\delta N_A}{\rho}$$

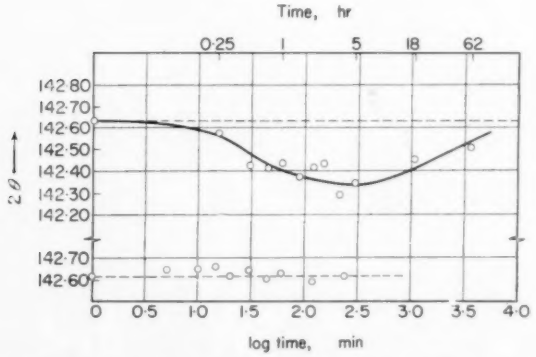


FIG. 7. Position of 420 $K\alpha_1$ peak from a copper–gold alloy as a function of sintering time at 750° and 800°C.

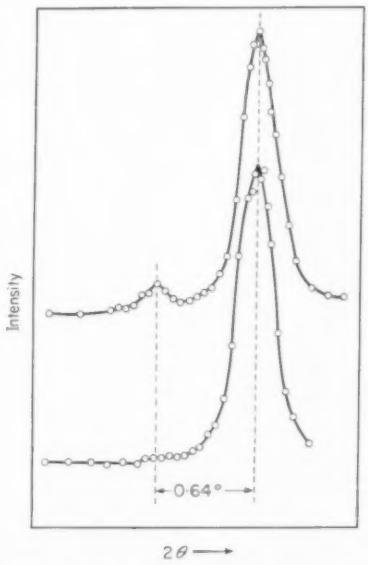


FIG. 8. Profiles of 420 $K\alpha_1$ lines from two different copper–gold compacts, both containing 3.5 at. % gold, after sintering for 15 min at 800°C.

VOL. 8 1960

where Ω_0 is the mean atomic volume of the alloy, we obtain

$$\rho_c = \frac{2(D_A - D_B)\gamma\Omega_0}{\left(D_A + \frac{N_A}{N_B} D_B\right) \frac{\partial \mu_A}{\partial N_A} \delta N_A} . \qquad (4)$$

If we limit ourselves only to an estimate of the order of magnitude of ρ_c, we may assume that the terms containing diffusion coefficients in the numerator and denominator of equation (4) are equal. Therefore

$$\rho_c \cong \frac{2\gamma\Omega_0}{\frac{\partial \mu_A}{\partial N_A} \delta N_A} . \qquad (5)$$

Furthermore, since $\frac{\partial \mu_A}{\partial N_A}$ can be expressed as well known function of N_A and the activity coefficient f_A, we obtain

$$\rho_c \cong \frac{2\gamma\Omega_0}{kT\delta N_A} \frac{N_A}{1 + \frac{\mathrm{d} \ln f_A}{\mathrm{d} \ln N_A}} . \qquad (6)$$

If further we assume that the solution is regular and its enthalpy per mol ΔH is

$$\Delta H = -N_A N_B \varepsilon$$

where $\varepsilon = \varepsilon_{AB} - \frac{\varepsilon_{AA} + \varepsilon_{BB}}{2}$ (ε_{AB}, ε_{AA}, ε_{BB} being the energies of AB, AA, BB bonds, respectively), then

$$\mu_A = kT \ln N_A - N_B{}^2 \varepsilon$$

and

$$\frac{\partial \mu_A}{\partial N_A} = \frac{kT}{N_A} + 2N_B \varepsilon .$$

Equation (5) for the critical radius can be written

$$\rho_c = \frac{2\gamma\Omega_0 N_A}{\delta N_A (kT + 2N_A N_B \varepsilon)} \qquad (7)$$

This equation lends itself conveniently to qualitative discussion of the segregation effect. ρ_c will be the greater, the smaller is the denominator, or when ε is negative. This condition prevails when the alloy has a tendency for clustering, which sometimes results in separation into two phases as is the case in the systems Cu–Ag or Cu–In discussed above. The order of magnitude of the neck radius x can be estimated from the relation $\rho_c = \frac{x^2}{4a}$ and equation (7). Assuming the limiting case of an ideal solution $\varepsilon = 0$, which definitely tends to underestimate ρ_c, and taking $\gamma \cong 10^3$ dyne/cm, $\Omega_0 \cong 10^{-23}$ cm^3, $kT = 1.4 \times 10^{-13}$ erg, $N_a \cong 10^{-1}$, $\delta N_A \cong 10^{-3}$, and $a = 2 \times 10^{-2}$ cm, we obtain $\rho_c \sim 10^{-5}$ cm and $x \sim 9 \times 10^{-4}$ cm. This value, in view of the crudity of our assumptions, is in fair agreement with the observed neck radius of 2.5×10^{-3} cm for sintered copper–silver alloy wires.

The diffraction results are less clear cut. The existence of a low-angle side peak in Fig. 8 is evidence that a portion of the compact is richer in gold than the remainder. This portion can be identified with the neck region. The ratio of the areas under the peaks, or the area of the "shelf" and the main peak in Fig. 8, is about 0.04, which should correspond to $\frac{x}{a} \cong 0.6$, if the mean radius of a particle is assumed to be 20 μ. In order to obtain a similar value for this ratio from equation (2), the diffusion coefficient of gold in the alloy at 800°C should be of the order of magnitude of 10^{-8} cm^2/sec, a not unreasonable value. The magnitude of $\frac{x}{a}$ corresponding to ρ_c can also be calculated from the extrapolated data on free energies of Cu–Au alloys determined experimentally by R. L. Orr and R. Hultgren[2]. This calculation yields $\frac{x}{a} \cong 0.2$ which, in view of our assumptions, can be regarded as in fair agreement with the figure given above.

The shifting of the whole line at 750°C, as shown in Fig. 7, seems to indicate that the whole surface layer of the alloy becomes poorer in copper. This effect cannot be due to the preferential evaporation of copper from the specimen because, in the first place, the position of the line eventually returns to its original value, and secondly, the effect should be more pronounced at 800°C, but instead, as we have seen above, it is totally absent. Therefore it seems that the shift is due to the predominance of surface diffusion at 750°C. This would mean that, although at 800°C the volume self-diffusion coefficient of gold is higher than that of copper at 750°C, the surface migration of copper would have to be faster than that of gold. Such an inversion has been shown to occur in alloy systems during sintering.[3] For instance, in the Fe–Ni system, volume diffusion of iron is faster than that of nickel but at lower temperatures, where surface diffusion is predominant, the opposite is true. Moreover, the temperature at which surface diffusion predominates over volume diffusion seems to be quite high in alloy systems. This problem is now the subject of further investigation.

ACKNOWLEDGMENTS

The authors are grateful to Dr. C. Herring of Bell Telephone Laboratory for very illuminating discussions, to Dr. E. W. Wise of the International Nickel Company, Inc., for encouragement and helpful suggestions and to the International Nickel Company, Inc., for sponsoring this research.

REFERENCES

1. G. C. KUCZYNSKI, *Trans. Amer. Inst. Min. (Metall.) Engrs.* **185,** 169 (1949).
2. R. L. ORR and R. HULTGREN, *The Heats of Formation of Solid Gold–Copper Alloys.* Rep. no. 76, Issue no. 2, Minerals Research Laboratory, University of California, Berkeley, California (1956).
3. P. F. STABLEIN, Jr., *Sintering in Two or More Component Systems.* Doctoral Thesis, Department of Metallurgy, University of Notre Dame, Notre Dame, Indiana (1958).

VOL.
8
1960

Anisotropy in ultrasonic attenuation in single crystal aluminum*

Granato and Lücke[1], using a vibrating dislocation model studied earlier by Koehler[2], have constructed a successful theory for explanation of mechanical damping in crystalline solids. They[3] have also indicated that internal friction should be sensitive to the crystal orientation and to the distribution of the dislocations over the various slip systems. Granato and Lücke[4] have performed the detailed calculation of the resolved shear stress factors for f.c.c. materials. It is the purpose of this note to compare recent measurements in single crystal aluminum with the predictions of the anisotropy calculation.

The resolved shear stress factor is defined as $\tau^2/2U$ where $\tau^2 = \frac{1}{12}\sum\tau_i^2$, where τ_i is the resolved shear stress on the ith slip system, (there are 12 slip systems in f.c.c. materials) and U is the elastic energy density. The resolved shear stress factors appropriate in the megacycle frequency range for a f.c.c. material, assuming a uniform distribution of dislocations, and the numerical values for aluminum are given in Table 1 as well as results of measurements in two samples of high purity aluminum.

Sample A is an approximately 1-in. cube prepared from a single crystal ingot grown from a melt of 99.999 per cent pure aluminum. Sample B was taken from an ingot containing several large grains prepared by the strain anneal technique from a rod of 99.999 per cent pure aluminum; the surfaces of Sample B are about 25 per cent smaller in area than those of Sample A. Each sample has a pair of accurately parallel (001) and (110) surfaces oriented by the Laue back-reflection technique. The ultrasonic measurements were made using the electronic equipment described by Chick *et al.*[5]. The measurements reported were made at 105 Mc/s and at room temperature. 15 Mc/s quartz transducers (X-cut for compressional waves, AC-cut for shear waves) were bonded to the samples by Nonaq stopcock grease.

Examination of Table 1 shows that the theory predicts the sequence of magnitudes of the five measured attenuations. A striking feature of the measurements is the excellent agreement of the two measurements (shear wave in [001] and fast shear wave in [110]) that should be identical for a given sample. Deviations from the predicted values of attenuation are surprisingly small and may be ascribed to a non-uniform distribution of dislocations, or to the presence of other loss mechanisms such as the thermoelastic effect.

The author thanks Professor A. V. Granato and Professor K. Lücke for communicating the results of their calculations prior to publication; he also acknowledges with thanks the interest and stimulation of Professor Rohn Truell; he thanks Mr. W. Oates and Mr. N. Pitula for their valuable assistance in preparation of the samples.

N. G. Einspruch

Texas Instruments Inc.
Central Research Laboratories
Dallas 21, *Texas*

References

1. A. V. Granato and K. Lücke, *J. Appl. Phys.* **27**, 583 (1956).
2. J. S. Koehler, *Imperfections in Nearly Perfect Crystals* p. 197. Wiley, New York (1952).
3. A. V. Granato and K. Lücke, *J. Appl. Phys.* **28**, 635 (1957).
4. A. V. Granato and K. Lücke, to be published.
5. Chick, Anderson and Truell, *J. Acoust. Soc. Amer.* **32**, 186 (1960).

* Supported in part by Office of Ordnance Research, U.S. Army, under Contract DA-19-020-ORD-4830. Received November 17, 1959.

Table 1. Resolved shear stress factors and results of measurements

Propagation direction	Polarization direction	$\tau^2/2U$		Measured attenuation	
		General f.c.c.	Al	A	B
[001]	Compressional wave	$\frac{1}{9}\left(1-\frac{c_{12}}{c_{11}}\right)^2\rho v^2$	1.00*	1.00*	1.00*
[001]	Shear wave (isotropic)	$\frac{1}{9}\rho v^2$	1.47	1.80	2.15
[110]	Compressional wave	$\frac{1}{9}\frac{4c_{44}^2+(c_{11}-c_{12})^2}{(c_{11}+c_{12}+2c_{44})^2}\rho v^2$	0.52	0.91	0.69
[110]	[001]	$\frac{1}{9}\rho v^2$	1.47	1.73	2.20
[110]	$[1\bar{1}0]$	$\frac{1}{3}\rho v^2$	3.56	2.94	2.95

* Normalized c_{ij} = elastic constant ρ = density v = appropriate elastic wave velocity

A RESISTOMETRIC STUDY OF PRE-PRECIPITATION IN Al–10% Zn*

C. PANSERI† and T. FEDERIGHI†

An extensive investigation of the influence of quenching and aging temperatures upon the pre-precipitation phenomenon in Al–10% Zn has been carried out by means of resistivity measurements at liquid nitrogen temperature.

It has been found that an appreciable clustering of solute atoms takes place during the quenching itself and that the rate of pre-precipitation during isochronal or isothermal aging increases greatly with quenching temperature; the energy of formation of vacancies in the alloy, evaluated by the dependence of the rate of clustering on the quenching temperature, is 0.70 ± 0.02 eV, as compared with the value 0.76 ± 0.04 eV previously reported for pure aluminum. The final size of zones during isothermal aging at 40°C is larger after quenching from 350°C and decreases both for lower and for higher quenching temperatures. The presence of a "slow reaction" after quenching from 600°C has also been detected.

Concerning the influence of aging temperature it has been found that the amount of increase in resistivity decreases greatly by increasing the aging temperature and that the activation energies of the phenomenon (derived from the times to reach the maximum in resistivity) are 0.43 ± 0.02 eV after quenching from 300°C, and 0.38 ± 0.02 eV after quenching from 450°C. Other miscellaneous results on the effect of varying the aging temperature and on the reversion phenomenon are reported.

The results are interpreted in terms of a simple picture of the pre-precipitation phenomenon; the role of vacancies appears to be a fundamental one in determining the rate of pre-precipitation which is stopped only when all the excess of quenched-in vacancies is eliminated; the mechanism of elimination of vacancies appear to be, roughly, the same as in pure aluminum. The variation of the maximum increase in resistivity against the various aging temperatures has been explained in terms of a variation of the number of zones which form; in this way it appears that the number of zones is higher the lower the aging temperature, and that if the aging temperature is changed also the number of zones tends to change so as to establish the new equilibrium number; however this can be accomplished only if an excess of quenched-in vacancies is still present.

Finally other related questions such as the reversion phenomenon, the "slow reaction" and the meaning of the activation energies are discussed.

ETUDE DE LA RESISTIVITE ELECTRIQUE AU COURS DE LA PRE-PRECIPITATION DANS Al–10% Zn

Les auteurs ont poursuivi une étude systématique de l'influence de la trempe et des températures de vieillissement sur le phénomène de pré-précipitation dans l'alliage Al–10% Zn à partir de mesures de résistivité à la température de l'azote liquide.

Ils ont trouvé qu'une ségrégation appréciable d'atomes dissous prend place au cours de la trempe elle-même. La vitesse de pré-précipitation au course du vieillissement isochrone ou isotherme augmente rapidement avec la température de trempe. L'énergie de formation de lacunes dans l'alliage, évaluée à partir de la vitesse de ségrégation en fonction de cette température, est égale à 0,70 ± 0,02 eV (la valeur rapportée antérieurement pour l'aluminium pur est 0,76 ± 0,04 eV). La taille finale des zones formées au cours du vieillissement isotherme à 40°C est plus grande après une trempe de 350°C; elle décroît pour des températures plus élevées ou plus basses. L'existence d'une "réaction lente" a également été observée après une trempe de 600°C.

Quant à l'influence de la température de vieillissement, on constate que l'accroissement de résistivité diminue considérablement lorsque cette température s'élève. Les énergies d'activation du processus, déduites du temps nécessaire pour atteindre le maximum de résistivité sont 0,43 ± 0,02 eV après trempe de 300°C et 0,38 ± 0,02 eV après trempe de 450°C. D'autres résultats ont été obtenus sur les variations de température de vieillissement et sur le phénomène de réversion. Ces observations peuvent être interprétées à l'aide d'un modèle simple: le rôle des lacunes paraît fondamental pour la vitesse de pré-précipitation. Celle-ci s'arrête seulement lorsque toutes les lacunes trempées en excès ont été éliminées; ce mécanisme paraît grossièrement identique à celui trouvé dans l'aluminium pur. La variation de l'accroissement maximum de résistivité en fonction des diverses températures de vieillissement peut s'expliquer à partir du nombre de zones formées. Ce dernier est d'autant plus élevé que la température de vieilllissement est plus basse. Toute variation de la température de vieillissement entraîne une variation du nombre de zones en vue d'un nouvel équilibre. Toutefois, cela ne peut s'accomplir que s'il reste un excès de lacunes trempées. Les auteurs discutent enfin la réversion, la "réaction lente" et la signification des énergies d'activation.

UNTERSUCHUNG DER VOR-AUSSCHEIDUNG IN Al–10% Zn DURCH WIDERSTANDSMESSUNGEN

Der Einfluß der Abschreck- und Anlaßtemperaturen auf die Vor-Ausscheidung in Al–10% Zn wurde ausführlich untersucht durch Widerstandsmessungen bei der Temperatur des flüssigen Stickstoffs.

Während des Abschreckens findet beträchtliche Zusammenlagerung gelöster Atome statt; die Geschwindigkeit der Vor-Ausscheidung bei isochronem oder isothermem Anlassen nimmt mit der Abschrecktemperatur stark zu. Aus der Abhängigkeit der Geschwindigkeit des Zusammenlagerns von der Abschrecktemperatur wurde die Bildungsenergie für Leerstellen zu 0,70 ± 0,02 eV bestimmt,

* Received April 21, 1959.

† Istituto Sperimentale Metalli Leggeri, C.P.129, Novara (Italy).

VOL. 8 1960

während für reines Aluminium früher der Wert 0,76 ± 0,04 eV angegeben wurde. Lagert man bei 40°C aus, so werden die Zonen am größten nach Abschrecken von 350°C, für höhere oder niedrigere Abschrecktemperatur bleiben sie kleiner. Nach Abschrecken von 600°C wurde das Vorhandensein einer "langsamen Reaktion" entdeckt.

Die gesamte Widerstandserhöhung nimmt mit steigender Auslagerungstemperatur stark ab. Die Aktivierungsenergien des Vorgangs (bestimmt aus der Zeit, in der das Widerstandsmaximum erreicht wird) sind 0,43 ± 0,02 eV nach Abschrecken von 300°C und 0,38 ± 0,02 eV nach Abschrecken von 450°C. Weitere vermischte Resultate über den Einfluß wechselnder Anlaßtemperatur und über die Erscheinung der Umkehrung werden berichtet.

Die Ergebnisse werden mit Hilfe eines einfachen Bildes der Vor-Ausscheidung gedeutet; die Leerstellen bestimmen grundlegend die Geschwindigkeit der Vor-Ausscheidung; diese hört erst auf, wenn der gesamte Überschuß an eingefrorenen Leerstellen verschwunden ist; der Mechanismus des Verschwindens der Leerstellen scheint etwa derselbe zu sein wie bei reinem Aluminium. Die Änderung der maximalen Widerstandszunahme mit der Auslagerungstemperatur läßt sich erklären durch eine Änderung der Anzahl der gebildeten Zonen; die Anzahl der Zonen scheint also umso höher zu sein, je niedriger die Auslagerungstemperatur ist; bei Änderung der Auslagerungstemperatur scheint sich die Zahl der Zonen der neuen Gleichgewichtszahl zu nähern, sofern noch ein Überschuß an eingefrorenen Leerstellen vorhanden ist.

Zum Schluß werden verwandte Fragen wie die Erscheinung der Umkehrung, die "langsame Reaktion" und die Bedeutung der Aktivierungsenergien diskutiert.

INTRODUCTION

The electrical resistivity, hardness and other properties of many supersaturated aluminum rich alloys (for example Al–Cu, Al–Zn and Al–Ag alloys) change markedly at about room temperature; these property changes are attributed to the segregation of solute atoms into initially small coherent clusters which, when they have grown enough in size, are identified with the solute-rich and matrix-coherent zones which produce certain X-ray diffraction effects (the Guinier–Preston zones in the Al–Cu alloys are the best known example). Since evidence has been reported (see, for example, Guinier[1,2]) that solute clusters or zones are by no means a necessary step for true precipitation (if precipitation is the formation of a new metastable or stable phase with a distinct crystallographic structure), the process of clustering or zone formation is frequently called pre-precipitation.

An interesting characteristic of zones is their relatively very high rate of formation which is several order of magnitude higher than would be expected; several considerations reviewed elsewhere [3,4] support the view that this high rate of pre-precipitation can be explained on the basis of a non-equilibrium high concentration of vacancies, corresponding to about that in equilibrium at the homogenization temperature and retained in the specimen by the rapid quench.

Additional experimental evidence of the correctness of the hypothesis of quenched-in vacancies was reported by Graf[5] who investigated in the Al–Zn 10% alloy the effect of quenching temperature on the rate of pre-precipitation at room temperature (in the Al–Zn alloys the formation of solute rich spherical zones takes place during pre-precipitation, below about 100°C).[6–8] The fundamental result of Graf was that the rate of pre-precipitation, as evaluated by means of hardness measurements, was greatly increased with quenching temperature in the range 200–460°C, which is inside the solid solution range (it is extending from 180 to 615°C). This effect can be immediately correlated with a higher concentration of quenched-in vacancies with quenching temperature. The decrease in the rate of hardening observed with quenching from above 460°C was attributed by Graf to a smaller concentration of quenched-in vacancies.

Although Graf tried also to test quantitatively the hypothesis of quenched-in vacancies, obtaining results in good agreement with the expected values (see hereafter), hardness measurements do not allow usually a high accuracy, expecially in this alloy which hardens very quickly at room temperature.[9,10] Therefore it was decided to carry out a new investigation on the Al–Zn 10% alloy by means of electrical resistivity measurements, including in the research the study of the effects of quenching and aging temperatures. In this way it was hoped to gain a better understanding of the role of vacancies in pre-precipitation and, at the same time, to clarify some characteristics of the phenomenon.

Resistivity was selected as it was known that it is strongly influenced by pre-precipitation in the Al–Zn 10% alloy;[11] variations of resistivity of the order of 20 per cent can be observed. This fact and the large solid solubility range make this alloy very interesting for investigations on the pre-precipitation phenomenon.

It is necessary to point out however, that the variation of resistivity during pre-precipitation does not follow a simple law; in this alloy, as in other aluminum base alloys,[11] the clustering of solute atoms is accompanied at the beginning by an "anomalous" increase in resistivity, followed after some time by a

decrease; it seems therefore that the contribution of clusters to resistivity is larger when they reach a "critical size" which must be small since the maximum in resistivity is usually observed in the initial stage of aging. This peculiar behaviour of resistivity is by no means a complication; on the contrary, as it will be shown below, one can employ this phenomenon to deduce some interesting characteristics of pre-precipitation.

The question of the origin of this anomalous increase is yet unsolved; it may be possibly assumed that when clusters have reached a size of the order of magnitude of the wave length of the conduction electrons they might contribute an extra scattering;[12] on the other hand Fine[13] has tried to explain the resistivity increase in the Al–Cu alloys in terms of dislocations in the zone–matrix boundary. The question needs therefore more theoretical and experimental investigations. It is necessary to point out however, that for the purposes of this paper the understanding of the physical reason of the anomalous increase is not essential.

Just when this paper was written in its first version, Turnbull *et al.*[14] submitted for publication their paper concerning the kinetics of clustering in some aluminum alloys (Al–Cu, Al–Ag and Al–Zn alloys), in which they have reached many conclusions similar to those arrived at in this paper; the analysis of some similar or dissimilar points between the two papers will be deferred until the discussion.

VOL. 8 1960

EXPERIMENTAL PART

The alloy was prepared from high purity aluminum (99.995 per cent) and high purity zinc (99.99 per cent); the true weight composition resulted Zn = 10.2 per cent (4.47 at.%).

Wire samples 1 mm in diameter and about 40 cm in length, were employed in the research; to simplify operations they were wound like a lamp coil filament and supported by an insulating rod. To carry out measurements with the usual potentiometric system, four wire contacts (two for each end) were soldered to each sample; these wires had the same composition as the samples. After soldering and mounting, each sample was annealed several hours at 440°C and then water quenched and aged at room temperature for some days; this was to assure a quick resolution of zinc in the subsequent operations.

Quenching operations were carried out by manual extraction of samples from the furnace and by rapid immersion in the cooling medium (brine at 2°C); then samples were immediately transferred to a liquid nitrogen bath. This procedure was quite similar to that employed recently for a study of annealing of quenched-in vacancies in aluminum.[15] For the interpretation of what follows it is useful to remember, that in these conditions the quenched-in concentration of vacancies is increased with quenching temperature up to 600°C, although a large fraction of the high temperature vacancies is lost during quenching. Aging of the sample was carried out at temperatures in the range −100°C–220°C employing suitable liquid stirred baths; after each treatment samples were again transferred to a liquid nitrogen bath for measurement.

Resistance measurements were carried out at liquid nitrogen temperature with a potentiometric system, employing a Wenner type potentiometer. A dummy sample (quenched some time before, to assure the constancy in resistivity) was employed to correct the variations of temperature of the bath; however it seems that some difference in the temperature coefficient of resistivity for the dummy sample and for other samples should exist; in effect the reproducibility of resistance measurements was found to be one part in 10^4, instead of one part in 10^5 as it was found for the pure aluminum work. Nevertheless this precision was largely adequate for our work.

The resistivity variations were computed by the relation: $\Delta\rho = \rho_0 \cdot \Delta R/R_0$; in this formula R_0 is the resistance of the sample (at −195°C) obtained after quenching from low temperature (200–215°C) and without aging; $\Delta R = R - R_0$ is the variation of resistance of the sample, with reference to R_0, when it has reached—by quenching or by aging—the value R; finally, ρ_0 is the resistivity of the alloy at −195°C after quenching from low temperatures (200°C–215°C); this was previously evaluated in 1.24 ± 0.02 $\mu\Omega$ cm. In the following R_0 (or ρ_0) will be referred to as the "reference value" since it should refer to a homogenized solid solution of zinc in aluminum without any appreciable (or very small) clustering of the solute atoms; also, the concentration of quenched-in vacancies, after quenching from 200°C, is so small to be undetectable.

The variation of restivity $\Delta\rho$ have been always reported in m$\mu\Omega$ cm $= 10^{-9}$ Ω cm.

RESULTS

Influence of quenching temperature on resistivity

In preliminary experiments it was recognized that the initial value of resistivity of a sample, namely the value after quenching and without aging, *greatly* increases with quenching temperature; this was a rather surprising result since all quenching temperatures were selected in the range of existence of the

TABLE 1. Influence of cooling medium from 400°C, on the "initial" increase of resistivity. Results are given for two samples

Cooling medium	$\Delta\rho$ m$\mu\Omega$ cm
Oil at 20°C	122–115
Water at 17°C	113–103
Brine at 2°C	76–78
Alcohol–water mixture at −48°C	50–45

solid solution. Therefore it was decided to investigate this point first.

Typical results obtained for three different samples and expressed as $\Delta\rho$, are plotted on logarithmic scale in Fig. 1 versus the reciprocal of the absolute quenching temperature. At low quenching temperatures, $\Delta\rho$ apparently satisfies an Arrhenius type relation with an activation energy of about 0.66 eV; above 500°C however, something like a saturation effect seems to exist.

About the origin of this "quenched-in resistivity" or "initial" increase, one can advance at least two hypotheses: (a) it can be due to some kind of quenched-in defects, like vacancies; (b) it can be due to the presence of small clusters of zinc atoms; these clusters could form during the quenching action itself or could exist originally at the quenching temperature.

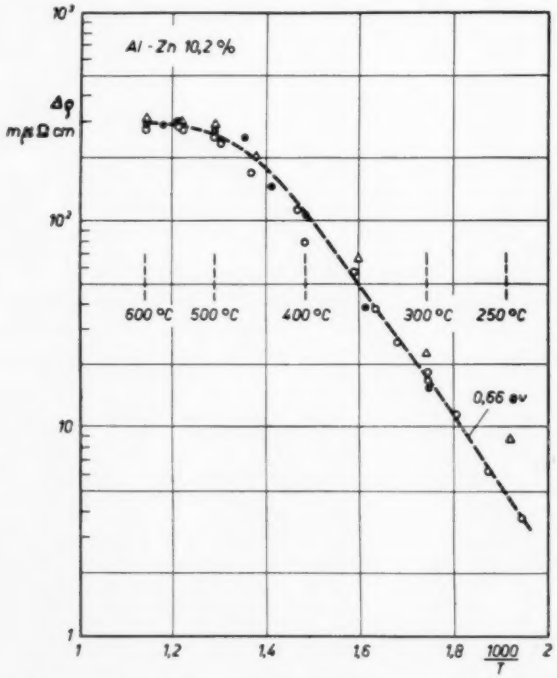


FIG. 1. Log of the "initial" increase in resistivity, namely the increase which takes place with quenching (without aging), plotted versus the reciprocal of the absolute quenching temperature. Results are given for three different samples.

Now there is no doubt that quenched-in vacancies contribute to the increase in resistivity; however in pure aluminum, samples quenched in similar experimental conditions[15] show an increase of resistivity with quenching, say from 500°C, of about 8 m$\mu\Omega$ cm, compared with the 250 m$\mu\Omega$ cm reported in Fig. 1. Since too large a concentration of vacancies should be present to explain the actual results, it appears more reasonable to attribute the largest part of the observed $\Delta\rho$ to the clustering of solute atoms. This view is confirmed by the following facts: (i) during isothermal or isochronal aging (as reported afterwards) of samples quenched from low temperature, namely of samples without appreciable initial increase of resistivity, an increase in resistivity about 200–300m$\mu\Omega$ cm can be observed; this shows that the increase of resistivity due to the formation of clusters is sufficiently large to justify the results in Fig. 1; (ii) an additional investigation on the effects of quenching rate has shown, as reported in Table 1, that the increase in resistivity by quenching from 400°C is *reduced* by increasing the quenching rate, while one should observe the contrary in the case of quenched-in vacancies.

This last investigation shows that a large amount of clustering takes place during the quenching itself. An indirect confirmation of this deduction is given also by the analysis of the dependence of the increase in resistivity with quenching temperature shown in Fig. 1; effectively one should expect that the amount of clustering during quenching should be controlled by the equilibrium concentration of vacancies; now, it will be shown afterwards that the energy of formation of vacancies in this alloy is about 0.70 eV, which is in good agreement with the value reported in Fig. 1.

In conclusion one is forced to deduce that the tendency to clustering in the Al–Zn 10% alloy is so strong that it can take place to a large extent during quenching; obviously, the amount of clustering will be largely influenced by the experimental quenching conditions such as quenching temperature, size of sample, quenching bath and so on. It is pointed out however, that the presence of very small clusters in equilibrium at the homogenization temperature is not excluded by the actual results; these clusters were experimentally observed by X-ray analysis[16] in more concentrated Al–Zn alloys.

Isochronal aging

To plan the isothermal experiments reported in the following, it was necessary to know the range of aging temperatures for which the variation of resistivity takes place in a reasonable time. For this purpose it was thought useful to investigate first the influence of

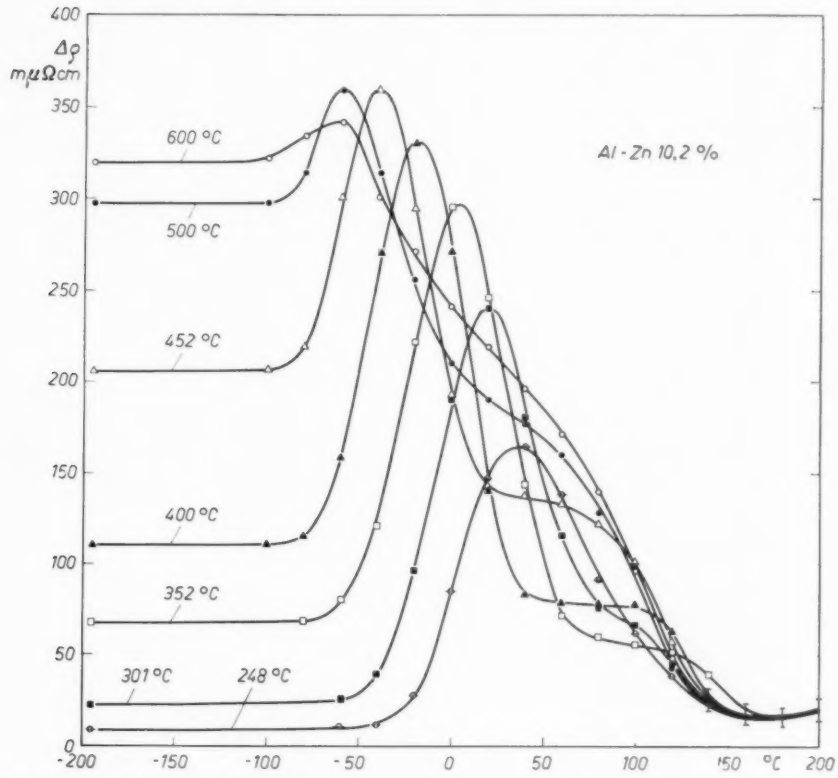


FIG. 2. Isochronal aging curves (2 min at temperatures increasing at steps of 20°C) after quenching from several temperatures. Another curve, not given here, was obtained after quenching from 550°C and was quite in intermediate position between the 500 and 600°C curves.

quenching temperatures by means of an isochronal aging procedure. In this way it was hoped also to gain a general picture of the pre-precipitation phenomenon.

The set of isochronal aging curves is reported in Fig. 2; for each isochronal curve the sample was aged 2 min at increasing temperatures at steps of 20°C in the range between —100–220°C; after each treatment the variation of resistance in liquid nitrogen was determined.

Isochronal aging curves appear to be rather complex and the effect of quenching temperatures appears to be noticeable. To simplify the interpretation of the results it is useful to examine first the results obtained after quenching from 400°C; the analysis can be summarized as follows:

(1) an "initial" increase of resistivity after quenching is present; this is agreement with the data of Fig. 1 and can be attributed to a large extent, as said above, to clustering of solute atoms during the quenching itself;

(2) a subsequent appreciable increase in resistivity takes place during aging, reaching a maximum at about —20°C; a decrease follows till about +40°C; these effects can be roughly attributed to the formation and growth of zones which should reach their critical dimension at about —20°C (under these experimental conditions);

(3) finally, after a *plateau* from +40 to 100°C, resistivity shows a new decrease reaching a value slightly larger than the reference value ρ_0; this decrease is probably to be connected with the "reversion" phenomenon, namely with the dissolution of zones. This point will be discussed more extensively later.

Extending now the analysis to the other results, the effect of quenching temperature can be summarized as follows:

(4) the initial increase of resistivity increases with quenching temperature, in agreement with the data of Fig. 1;

(5) the temperature at which the maximum value of resistivity is observed in aging, is lowered by increasing the quenching temperature (except for the temperature of 600°C); this fact is qualitatively in agreement with the hypothesis of quenched-in vacancies, whose concentration increases with quenching temperature;

(6) the maximum value in resistivity reached during ageing increases with quenching temperature (again

VOL. 8 1960

with the exception of 600°C); since the formation of zones takes place at lower temperatures by increasing the quenching temperature (point 5), this increase can be connected—as shown below—with the fact that the number of zones which form is higher the lower the aging temperature;

(7) the *plateau* is less detectable for lower quenching temperatures; since the formation of zones takes place at higher temperatures (point 5), the effects due to their growth and to reversion cannot be easily separated;

(8) the *plateau* is less detectable also for higher quenching temperatures; since many clusters are originated during quenching, it may be that a very scattered distribution in dimension of zones is now present so that it is again impossible to separate clearly the effects due to zone growth and to reversion; a quite different explanation however could be advanced in terms of the "slow reaction" discussed below.

For clarity, another isochronal curve obtained after quenching from 550°C is not shown in Fig. 2; it was in intermediate position between the 500 and 600°C isochronal curves.

Isothermal aging at 20°C

The principal object of this section was the quantitative testing of the hypothesis of quenched-in vacancies. For this purpose a set of isothermal aging curves was planned at 20°C after quenching from several temperatures selected in the range 220–340°C; higher quenching temperatures were not reputed suitable for the actual purpose, since the large initial increase of resistivity which takes place with quenching temperature could have had some unknown influence on the result.

The experimental aging curves are reported in Fig. 3; again it is significant that the effect of the quenching temperature is qualitatively in agreement with expectation: the higher the quenching temperature, the quicker the formation and growth of zones, the shorter the time to reach the maximum in resistivity (namely the critical size of clusters).

As the aging curves appear to be quite similar in shape, the quantitative test also is straightforward: in effect one should expect, in terms of quenched-in vacancies, that the rate of formation of zones, namely the rate of variation of resistivity, should be proportional to the factor $\exp(-E_f'/kT_Q)$ where T_Q is the quenching temperature and E_f' the energy of formation of vacancies in the alloy. Obviously this expectation is valid only if no appreciable clustering of vacancies takes place, as is reasonable to expect because of the low quenching temperatures (see also below).

In Fig. 4, the logarithm of times to reach the maximum $\Delta\rho_M$ and the values $\Delta\rho = 200\ \text{m}\mu\Omega\,\text{cm}$ before and after the maximum are plotted with the reciprocal of the absolute quenching temperatures. As expected, experimental points lie on straight lines and the value $E_f' = 0.70 \pm 0.02$ eV can be deduced for the energy of formation. This value, which was

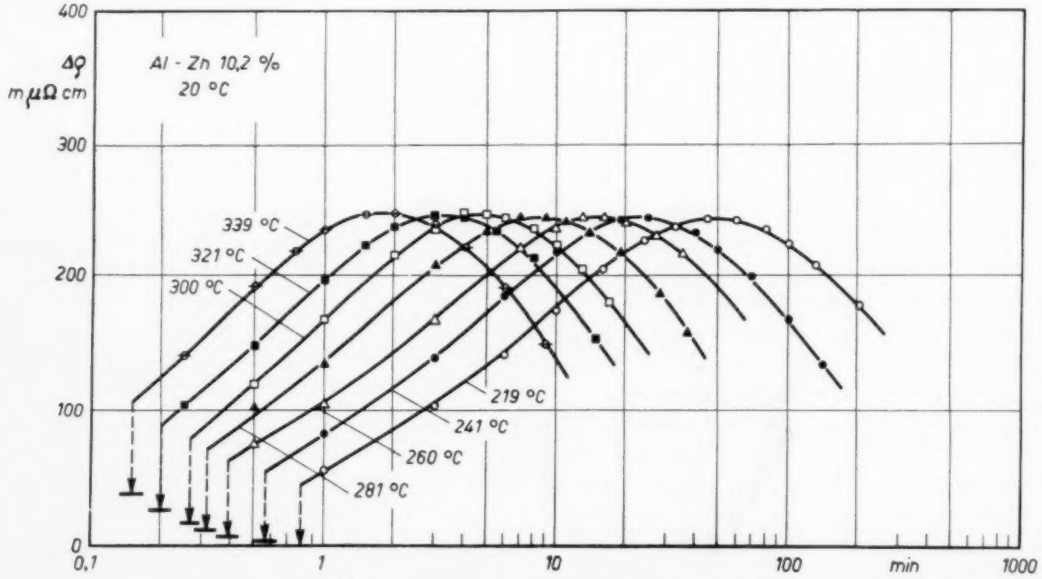


FIG. 3. Influence of quenching temperature on isothermal aging curves at 20°C. The segment shows the initial increase in resistivity which takes place with quenching. Note that the maximum increase is independent from the initial increase.

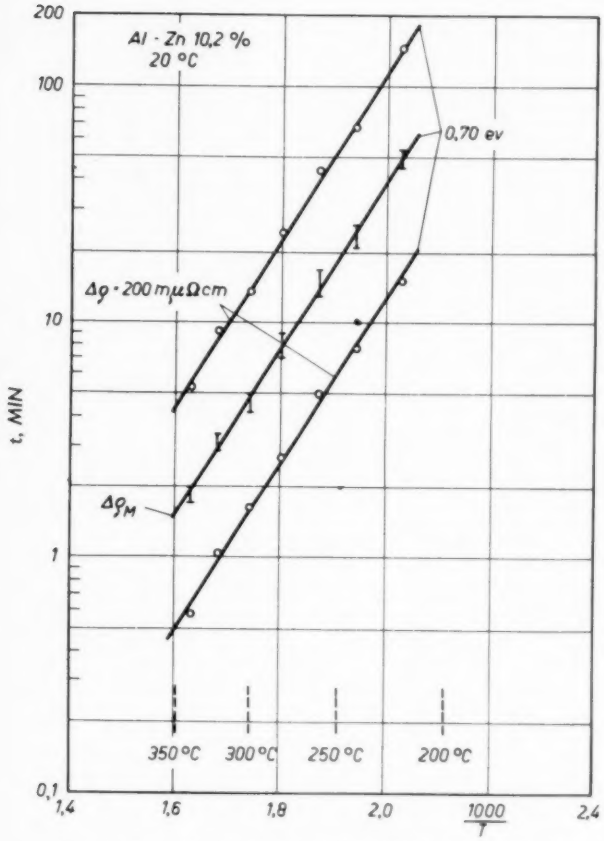


FIG. 4. Log of the times to reach the maximum in resistivity and the values $\Delta\rho = 200\ m\mu\ \Omega$ cm before and after the maximum, for the data in Fig. 3, plotted versus the reciprocal of the absolute quenching temperature.

obtained also for another sample (results are not given here), is in good agreement with the value $E_f = 0.76 \pm 0.04$ eV reported for pure aluminum quenched under similar experimental conditions*[15] and with the results of Graf[5] who deduced, by hardness measurements, the value $E_f' \sim 0.60$–0.66 eV.

It is significant that this result is also in agreement with the idea that the energy of formation of vacancies in alloys should be in general smaller than in pure metals.[18] In this alloy many vacancies should be near a zinc atom at high temperature; therefore the difference $E_e = E_f - E_f' \sim 0.06$ eV should be about the binding energy of vacancies with zinc atoms. Since this binding energy seems to be relatively small, one should expect that the motion of vacancies, with reference to pure aluminum, should not be much influenced by the presence of zinc atoms; in other words, the annealing of quenched-in vacancies should occur in this alloy in about the same way as in pure aluminum; this view will be confirmed below.

Thus the preceding results give good evidence that at least in the Al–Zn alloys the rate of pre-precipitation is mainly controlled by the concentration of quenched-in vacancies; additional evidence is also provided by the analysis of auxiliary results described in a following section.

Influence of aging temperature

The object of this set of tests was the investigation of the dependence of the rate of pre-precipitation upon the aging temperature, namely the determination of the activation energy of the phenomenon, which, in terms of the hypothesis of quenched-in vacancies, one should expect to be of the same order of magnitude of the migration energy of vacancies.

For this purpose a set of isothermal curves was planned at several aging temperatures, after quenching from a selected temperature.

In Fig. 5 a first set of isothermal curves obtained after quenching from 300°C is reported; this quenching temperature was selected low enough to assure no appreciable clustering of vacancies.[15]

From Fig. 5 it is immediately evident that (i) the time to reach the maximum increases, as expected, by decreasing the aging temperature; (ii) the value of $\Delta\rho_M$, namely the maximum increase of resistivity, is largely dependent upon the aging temperature.

This last property was a rather unexpected one, and its obvious meaning is that "something" is changing with aging temperature in the pre-precipitation phenomenon.†

An immediate important consequence of this is that in general it would be incorrect to deduce the activation energy of the phenomenon from the time the sample needs to reach a given variation of resistivity, since equal amount of variation of resistivity at different aging temperatures do not refer to the same physical state of the sample.

This difficulty can be removed if one introduced the assumption that *in isothermal aging* all zones have reached, at any time, about the same radius r or, in other words, that zones all begin to grow at the same time after quenching and at the same rate. Although this assumption is probably too over simplified, it will be accepted in the following as working hypothesis (for some justification of this hypothesis, see discussion).

* The true energy of formation of vacancies in pure aluminum is probably slightly higher;[17] however we have referred here to the value obtained in the same experimental conditions adopted in this work.

† This feature appears to be a general property of the pre-precipitation phenomenon, since it was recently observed also in Al–Ag alloys[11] and in Al–Cu alloys (not yet published results).

VOL. 8 1960

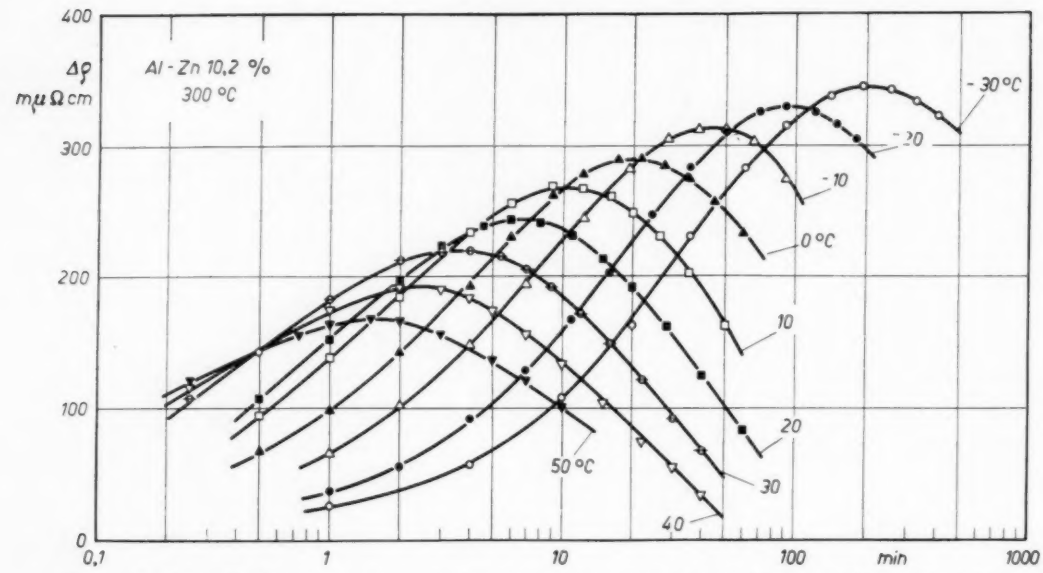


FIG. 5. Isothermal aging curves at several temperatures for a sample quenched from 300°C. The initial increase in resistivity which takes place with quenching, is in the range 15–20 mμ Ω cm.

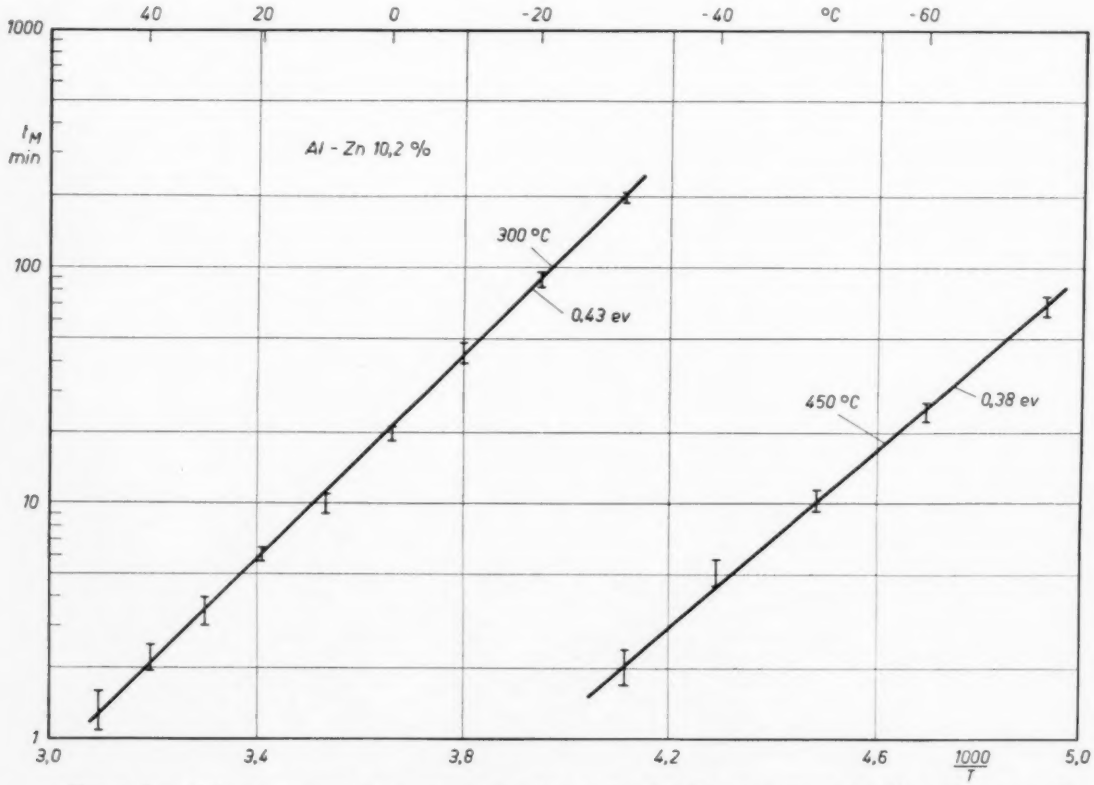


FIG. 6. Log of time t_M to reach the maximum, for data in Fig. 5 (left) and in Fig. 7 (right), plotted versus the reciprocal of the absolute aging temperature.

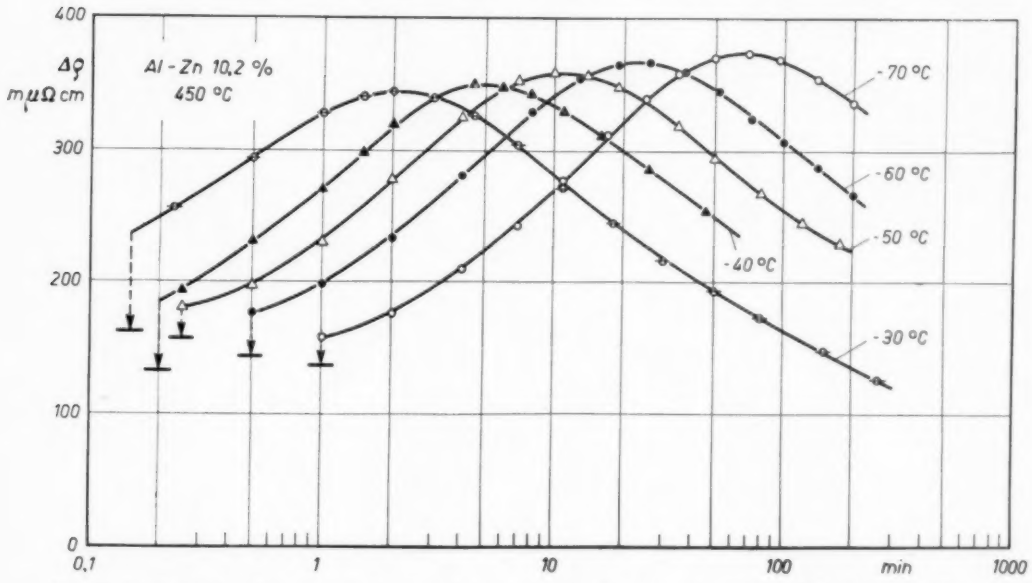


FIG. 7. Isothermal aging curves at several temperatures for a sample quenched from 450°C. The segment shows the initial increase in resistivity which takes place with quenching.

With this assumption it should be then correct to deduce the activation energy of the phenomenon by the time necessary to reach the maximum in resistivity since, at that time, all zones have reached, at each aging temperature, the same critical size.* In Fig. 6, left, it is shown that the logarithmic plotting of the times to reach the maximum, with the reciprocal of the absolute aging temperature gives, as expected, a straight line; the value of the activation energy results $E_m' = 0.43 \pm 0.02$ eV; just the same value was obtained for another sample (results not given here).

Another set of isothermal curves obtained after quenching from 450°C is reported in Fig. 7; in this case the activation energy, computed in the same way as above, gives (see Fig. 6, right) $E_m' = 0.38 \pm 0.02$ eV.

The correct interpretation of the actual results will be discussed later. Here it is now interesting to pay some attention to the dependence of $\Delta\rho_M$ upon the aging temperature; this is shown in Fig. 8, whose experimental points are deduced from the data in Fig. 5, Fig. 7 and other isothermal results (not given here) obtained after quenching from 260°C.

The experimental points can be formally represented by the law:

$$\Delta\rho_M = \Delta\rho_{0M}[1 - S \cdot \exp(-E/kT_A)] \quad (1)$$

where $\Delta\rho_{0M} = 388$ m$\mu\Omega$ cm, $S = 61.2$, $E = 0.13$ eV and T_A the absolute aging temperature; the fit of experimental points to this expression is shown by the continuous curve in Fig. 8.

Now if one takes in account again the above introduced hypothesis that all zones have reached about the same size at any time, then the value $\Delta\rho_M$ is proportional to the number of zones z_A which have formed per unit volume at each aging temperature T_A.

Therefore, from the preceding results one can deduce that *the number of zones is determined by the aging temperature (it is higher at lower aging temperatures), while it is not dependent upon the quenching temperature, at least in the range* 220–340°C (see Fig. 3).

Some possible meaning of equation (1) will not be discussed here; however it appears that $\Delta\rho_{0M}$, *which is independent of quenching temperature*, should be proportional to the maximum number of zones which could form.

Some other properties of zones

A set of results obtained by aging at several temperatures is reported in Fig. 9. Curve *A* is an extended isothermal aging curve obtained at +40°C after quenching from 300°C, and carried out in an attempt to find the time for complete reaction. As judged by resistivity variation, pre-precipitation stops after a relatively short time (about 300 min). This time is of the order of magnitude of that necessary for the elimination of vacancies in pure aluminum

* It is implicitly assumed also that the number of jumps for zinc atoms to form zones is independent of the number of zones which form; this should be correct especially at the beginning of aging, since the atoms gather into zones from their close surroundings.

VOL. 8 1960

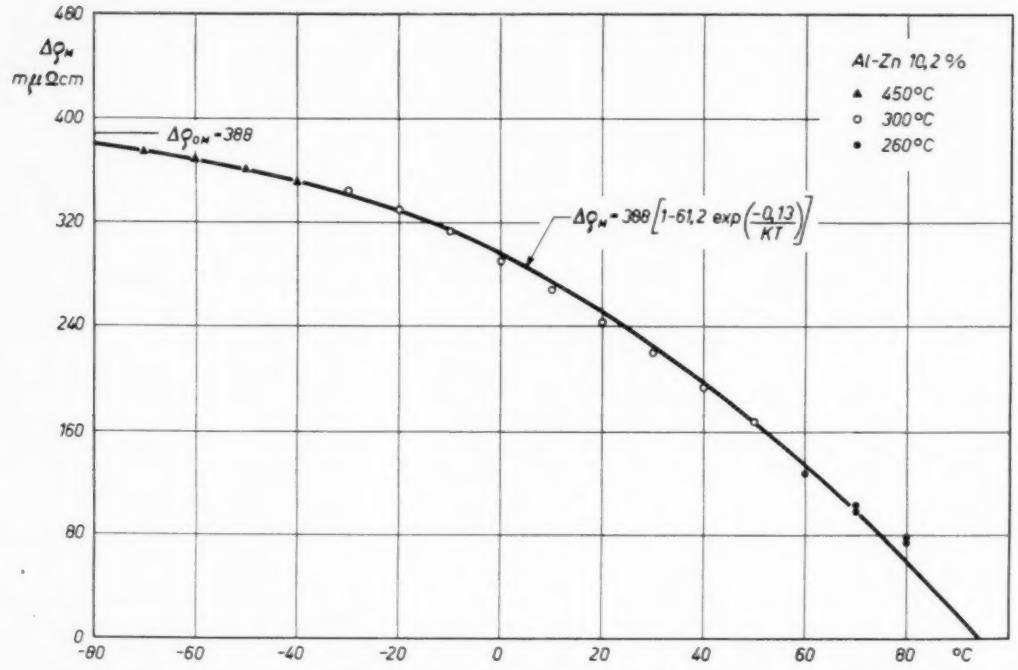


FIG. 8. Maximum increase in resistivity $\Delta\rho_M$, observed in isothermal aging, plotted versus aging temperature The data are deduced from the curves in Figs. 5 and 7 and from other isothermal curves (not given here) obtained after quenching from 260°C. The interpolating curve is calculated by the law given.

quenched from lower temperatures*[15,17,19]; one can deduce therefore that the reaction is probably stopped in consequence of the elimination of the excess of quenched-in vacancies and not because a metastable thermodynamic equilibrium has been reached. This conclusion will be better confirmed in the following section. Furthermore, it is significant that a negative value of $\Delta\rho(\infty)$ is observed at the end, namely a value of ρ lower than the reference value ρ_0: this means that when zones can grow enough, as they do apparently in this case, their contribution to resistivity is less than that due to the corresponding number of zinc atoms in the homogenized solution.

After these results, the aging of the sample was continued without interruption at 0°C; however, as shown by curve B, no additional variation of resistivity was detected (in curve B time is again taken as zero at the beginning of aging at 0°C); one can deduce therefore that a complete isothermally aged sample is stable at lower temperatures.

This deduction is not true if sample is not fully aged; to show this the sample was again quenched from 300°C and partially aged at 40°C until zones had reached their critical dimension (namely the maximum in resistivity); then aging was continued without interruption at 0°C. The results are shown by curve C; it is significant that an additional increase in resistivity is observed, instead of a decrease. This increase can be interpreted as due to the formation of new zones, which while being small, should produce an increase in resistivity larger than the decrease due to the growth of those zones which had previously reached their critical size at 40°C. The initial part of curve C is also reported in Fig. 10, curve C' (time is taken as zero at the beginning of aging at 0°C); furthermore in the same Fig. 10, the decrease in resistivity as expected for the increase in size of those zones which had previously reached their critical size at 40°C is shown by curve D'. This curve was computed from some data in Fig. 9: the variation of resistivity after the maximum of the isothermal curve D at 0°C, described hereafter, was multiplied by the ratio of maximum values of curve A and D, which should give the ratio of the number of zones at each temperature. The difference $C'-D'$ in Fig. 10 is therefore the increase due to the formation of new zones; the value of the maximum in resistivity ($\sim 80\ m\mu\ \Omega$ cm) is only slightly smaller than the difference between $\Delta\rho_M$ at 0°C and 40°C (about $100\ m\mu\ \Omega$ cm); this confirms the preceding deduction that aging temperature (with the exception of solute concentration not investigated here) is the fundamental factor

* The time for annealing vacancies in pure aluminum, in consequence of clustering effects, is largely dependent upon quenching temperature; it is of the order of a few minutes at room temperature after quenching from 600°C and goes up to some hours after quenching from lower temperatures.[19]

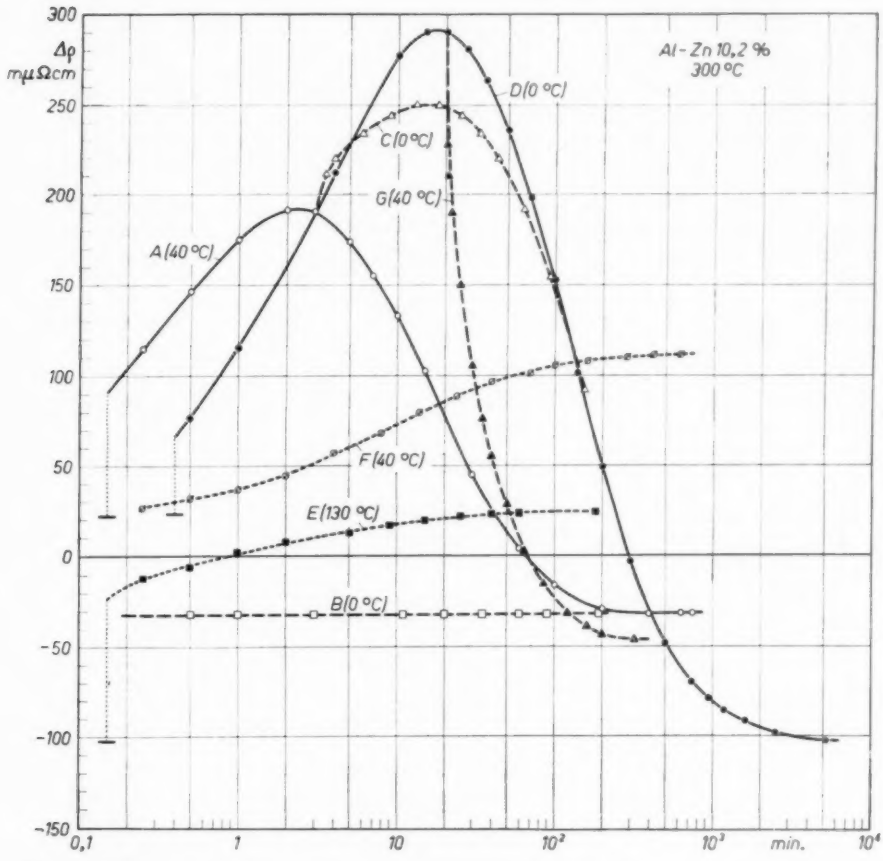


FIG. 9. Miscellaneous data about the properties of zones. Curve *A* shows an extended isothermal curve at 40°C for a sample quenched from 300°C; the aging was then continued without interruption at 0°C (curve *B*). After new quenching from 300°C, sample was again aged at 40°C, till the maximum was reached, and then aging was continued at 0°C (curve *C*). Curve *D* is another extended isothermal curve at 0°C after a new quench from 300°C; the aging was then continued at 130°C (Curve *E*) at which temperature one should observe reversion; finally the sample was again aged at 40°C, (curve *F*). After a new quench from 300°C, sample was partially aged at 0°C till the maximum was reached and then aging was continued at +40°C (curve *G*). For curves *B*, *E* and *F*, time is taken as zero in beginning the aging at the proper temperatures. Note that the crossing of curve *D* with the origin of curve *C* is casual.

affecting the number of zones; *however only if vacancies are present to allow the pre-precipitation phenomenon to take place*. It is also significant that the time that the new growing zones require to reach their critical size at 0°C (about 28 min) is slightly longer than time required for direct aging at 0°C (about 20 min); this can be attributed to a reduction of the concentration of quenched-in vacancies during the initial aging at 40°C.

Coming back to Fig. 9, another extended isothermal aging curve after quenching from 300°C, was obtained at 0°C (curve *D*); this is quite similar in shape to curve *A*; since a greater number of zones is now present, the observed maximum in resistivity is higher than at 40°C and the negative final value $\Delta\rho(\infty)$ is lower, in qualitatively agreement with expectation; the agreement however is not quantitative since the ratio of maximum values is about 1.5 and the ratio of final values is 3.2; the reason of this is not clear: it may be that a number of zones is destroyed in aging at 40°C or that the mean number of jumps for annihilation of vacancies is higher at 0°C than at 40°C so that the final size of zones is different. However to look for quantitative agreement it should be first necessary to investigate the reproducibility of the final value $\Delta\rho(\infty)$ for each aging curve.

After the results of curve *D*, the sample was subsequently aged without interruption at 130°C: at this temperature one should observe the reversion phenomenon. The result is shown by curve *E* (time is taken as zero at the beginning of aging at 130°C); as expected, resistivity quickly reaches about the reference value; however the final value obtained is slightly, but significantly, higher than the reference

VOL. 8 1960

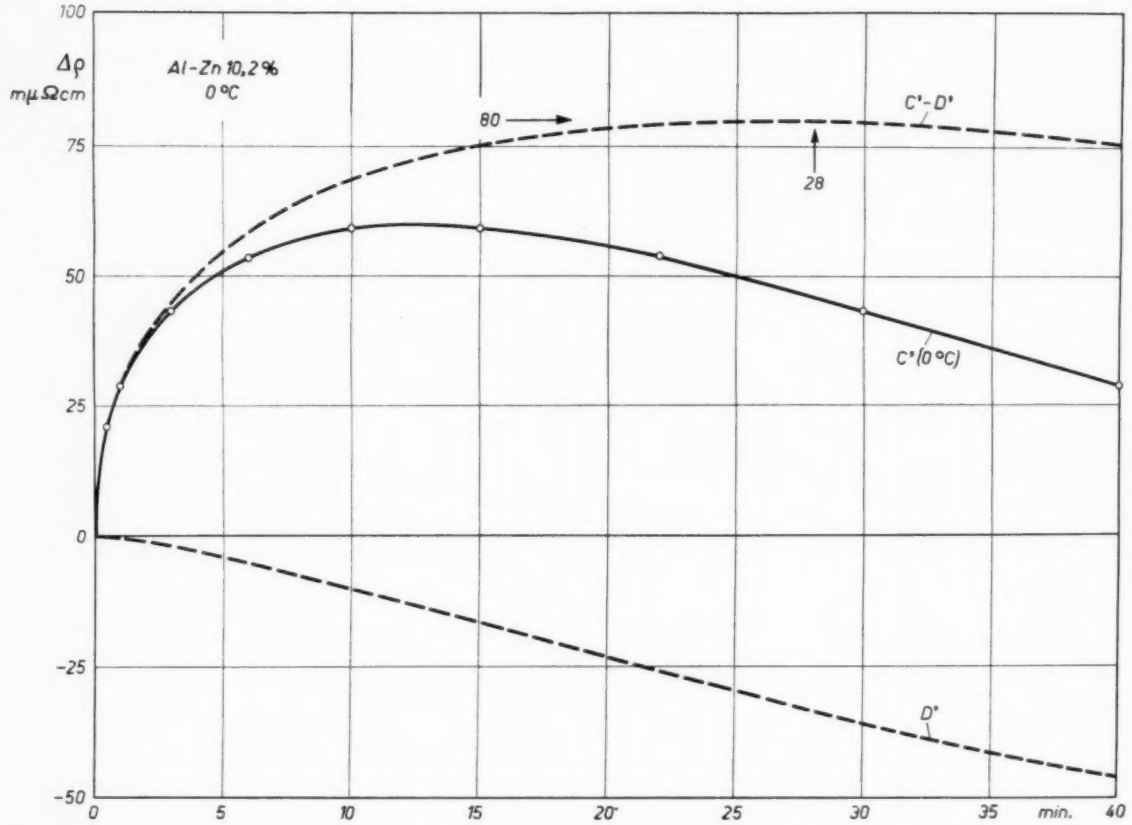


FIG. 10. Curve C' is the same as curve C in Fig. 9, but time is taken as zero in beginning aging at 0°C; curve D' shows the decrease of resistivity due to the growth beyond the critical size of those zones which had previously formed at 40°C (see text). The difference of the two curves gives the variation of resistivity due to the formation of a new number of zones.

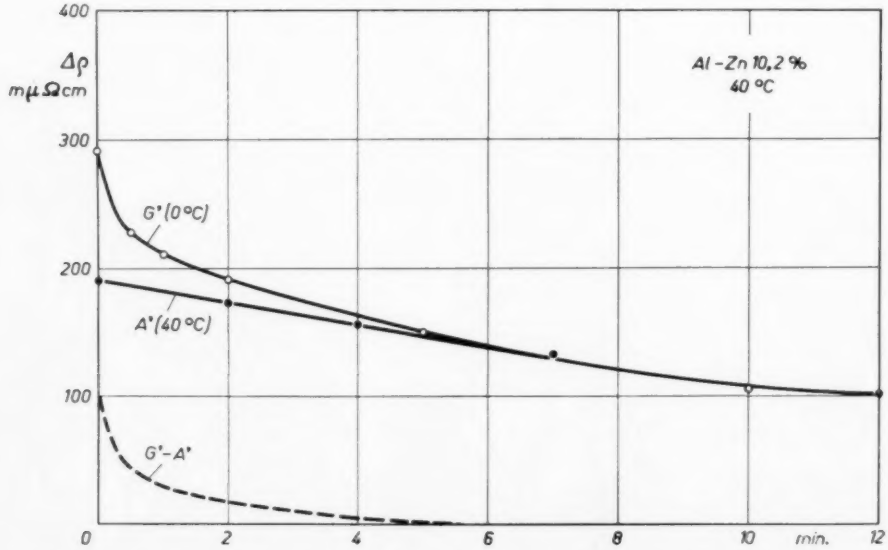


FIG. 11. Curve G' is the same as curve G in Fig. 9, but time is taken as zero in beginning aging at 40°C; curve A' shows the decrease observed after the maximum in curve A, Fig. 9. The difference of the two curves should be proportional to the difference in the number of zones.

value; the reason of this will be explained in a following section. After reversion a new aging at 40°C takes place very slowly; this is shown by curve F (time is again taken as zero at the beginning of aging at 40°C); it appears that the concentration of vacancies is now much lower than after a direct quench, so that zones cannot reach even their critical size.

Some attention was finally paid to the instability of zones while they are still small; for this purpose a sample was again quenched from 300°C and aged at 0°C until zones had reached their critical dimension (namely the maximum in resistivity); then aging was continued without interruption at 40°C (curve G); since the equilibrium number of zones at 40°C is smaller than the equilibrium number at 0°C, one should expect that the excess number of zones at 40°C should be eliminated. The correctness of this view is shown in Fig. 11 where curve G' reproduces the initial part of curve G of Fig. 9 (time is again taken as zero at the beginning of aging at 40°C); yet in Fig. 11 curve A, reproduces the decrease in resistivity observed after the maximum in direct aging at 40°C (from curve A, Fig. 9); the difference in the initial values of the two curves can be related to the difference in the number of zones of critical size which have formed at 0°C and at 40°C. As shown by the difference of the two curves, it appears that during aging at 40°C the excess of zones previously formed at 0°C is eliminated in a few minutes. This result is again in agreement with the preceding deduction that aging temperature is the only fundamental factor effecting the number of zones. It is to be noted however, as shown in Fig. 9, that there is a slight difference in the final value of resistivity of the two curves (A and G).

Extended isothermal aging at 40°C

After obtaining the preceding results it was finally decided to carry out some investigation also on the possible influence of the annealing mechanism of vacancies on the final size of zones.

To understand clearly the reason of this set of tests, it is useful to remember that in pure aluminum the concentration of initial quenched-in vacancies influences greatly the mechanism of their annealing out. In particular it was recently recognized[15] that if the quenching temperature is increased, an increasing number of agglomerates or, generally speaking, clusters of vacancies is formed; these clusters are annealed out at relatively higher temperatures (~150°C) with an activation energy comparable with that of self-diffusion in aluminum;[20] it is suggested (but not yet proved) that these clusters may be identified with the dislocation loops observed recently by Hirsh *et al.*[21] by transmission electron microscopy.

In consequence of the formation of these clusters or dislocation loops, the mean number of jumps for annihilation of vacancies is largely decreased with quenching temperature, above that temperature at which clustering becomes appreciable. If the process of annealing takes place in about the same way also in the actual alloy (and the low value of the binding energy between vacancies and zinc atoms suggests this), then the extent of diffusion of zinc atoms, namely the final size of zones in isothermal aging, should be largely influenced by the quenching temperature; in particular one should expect an increasing size with quenching temperature, in the low temperature range (where concentration of vacancies grows without appreciable clustering), and a decreasing size in the temperature range, where clustering effects are predominant. Graf[5] had found that the largest size of zones is obtained by quenching from 350°C; however he attributed the decrease in size for the higher quenching temperatures to a reduction of the concentration of quenched-in defects.

To prove experimentally the correctness of these ideas, the set of isothermal aging curves reported in Fig. 12 was carried out at 40°C, after quenching from several temperatures selected in the range from 200 to 600°C.

The influence of quenching temperature, as expected, is very strong. A first obvious point to be noted is that, in agreement with the data in Fig. 3, the time to reach the maximum in resistivity is smaller the higher the quenching temperature. For the highest quenching temperatures the maximum is no longer detectable; this is because the time to reach it is very short (see for example the curve after quenching from 450°C) and because the large increase of resistivity which takes place during quenching masks the phenomenon. The height of the maximum, when detectable, is practically independent by quenching temperature; however if the quenching temperature is 500°C or higher, the initial increase of resistivity is higher than the maximum observed in aging after quenching from lower temperatures; this means, obviously, that immediately after quenching the number of clusters is larger than that which would form at 40°C. Probably the excess of clusters is eliminated by aging at 40°C; however the question cannot be solved clearly by the data Fig. 12.

Concerning the final value $\Delta\rho(\infty)$ of resistivity it is pointed out that since the number of zones originating in isothermal aging should be appreciably independent of quenching temperature, at least for the

VOL. 8 1960

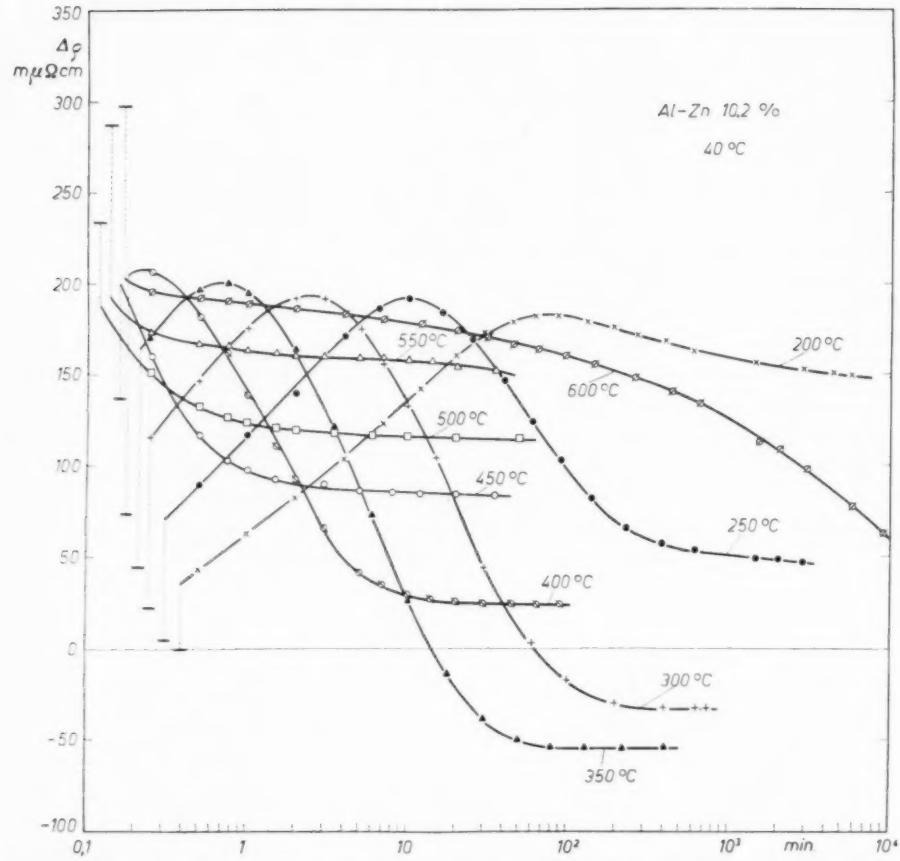


FIG. 12. Isothermal aging curves at 40°C after quenching from several temperatures. The segment shows the initial increase of resistivity which takes place with quenching.

lower quenching temperatures, the differences in the final value of resistivity in Fig. 12 should be due to differences in the final size of zones. Now, keeping in mind that the previous isothermal results have shown that the contribution of zones to resistivity (when they are larger than critical size) is lower the larger is their size, it is deduced from Fig. 12, that the largest size of zones is obtained after quenching from about 350°C. As expected, if the sample is quenched from lower temperatures the concentration of quenched-in vacancies is reduced and zones can grow only to a smaller size; if the sample is quenched from higher temperatures the concentration of quenched-in vacancies is higher but now the clustering effect becomes preponderant and again zones cannot grow to a larger size.

It is also significant that the time to reach a constant value of resistivity decreases with increasing quenching temperature (apart from the result for 600°C, examined hereafter); this is just what one should expect from the data of annealing of vacancies in pure aluminum [15,19] in which case it was recognized that the time to anneal out vacancies (the first stage) is appreciably decreased by increasing quenching temperature. Unfortunately the data do not permit exact quantitative testing; however there is no doubt that the times to anneal vacancies in pure aluminum and to stop the growth of zones in the Al–Zn10% alloy are just of the same order of magnitude.

Since in pure aluminum appreciable clustering was observed above 400°C,[15]—while we observed it above 350°C,—it may be that the presence of zinc slightly improves the formation of clusters of vacancies.

Finally, it is to point out that in the development of the isothermal curve after quenching from 600°C in Fig. 12, it was recognized that a slow variation in resistivity was present; after 10^4 min this variation was still appreciable. This phenomenon will be referred to as "slow reaction" in the Al–Zn alloys, and will be discussed later. A similar slow reaction seems to be present also for the 550°C quench, but more additional experimental investigations would be necessary to establish this point.

In conclusion, the actual results are in very good

agreement with expectation and with Graf's results. Besides they give new evidence that the rate of pre-precipitation is controlled by the concentration of quenched-in vacancies and suggest that *the growth of zones is stopped when no excess of vacancies is no more available*; finally, they give evidence that *the process of annealing of vacancies takes place in about the same way as in pure aluminum*; therefore it should be possible to observe, in the actual alloy, the presence of clusters of vacancies (or dislocation loops) in the same way as in pure aluminum.

Isochronal reversion

To investigate better the reversion phenomenon, a sample was isothermally aged for 900 min at about 18°C, after quenching from 300°C, and then aged 2 min at increasing temperatures at steps of 20°C, till 220°C.

The results are shown in Fig. 13 by the white-circle points; the first point is negative since during the isothermal aging zones had grown enough so that sample had reached a value of resistivity lower than the reference value. It is significant that resistivity is not constant at increasing aging temperatures; qualitatively the results can be explained by a progressive reduction in the number of zones, in agreement with what one should expect, keeping in mind the data in Fig. 8. The reduction in the number of zones is apparently complete at temperatures higher than 140°C; above this temperature a value of resistivity slightly higher than the reference value is obtained: this apparently strange increase seems to be due to the experimental procedure: if the sample, after 220°C aging, instead of being dipped directly in liquid nitrogen, as usual, is first quenched in brine at 2°C and then dipped in liquid nitrogen, the lower point is obtained which is nearly equal to the reference value.

This last result shows both the correctness of interpretation of the reversion phenomenon and the fact that some clustering takes place during the direct liquid nitrogen quenching. Also the slightly higher values (than reference value) obtained in isochronal aging above 140°C (Fig. 2) and in isothermal reversion at 130°C (curve *E*, Fig. 9) can be probably explained in the same way.

A quite similar isochronal reversion was carried out also for the sample quenched from 600°C and aged for $1.2 \cdot 10^4$ min at 40°C, in Fig. 12. In this case zones had grown little beyond critical size so that the resistivity had stopped at a value higher than the reference value. The results are shown again in Fig. 13, by the black points; now the reversion is obviously accompanied by a decrease in the resistivity, in the same way as was found in isochronal aging.

DISCUSSION

A picture of the pre-precipitation phenomenon in the Al–Zn *alloys*

The interpretation of many results obtained in the actual research has been advanced with each set of results; before adding some other general considerations, it is useful to summarize a general picture of

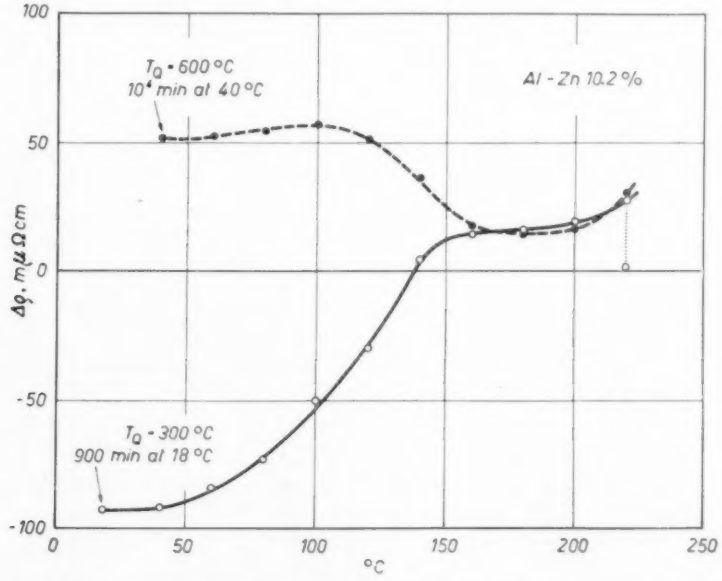


FIG. 13. Isochronal study of reversion (2 min at each temperature) for two samples previously isothermally aged as shown. The last empty circle point was obtained after a second aging at 220°C, then by quenching in brine and hence dipping into liquid nitrogen.

VOL. 8 1960

the Al–Zn alloys which can be deduced from the experimental results.

The fundamental aims of the present work were (i) to gain a better understanding of the role of vacancies in pre-precipitation and (ii) if possible, to clarify some characteristics of the phenomenon.

Concerning the first point, the data show clearly that the role of vacancies in pre-precipitation in the Al–Zn alloys is a very fundamental one: while there is no doubt that a noticeable driving force exists for zinc atoms in compelling them to move to form zones in the supersaturated solid solution, it appears to be well established that the kinetics of the phenomenon are controlled by the concentration of vacancies. This is shown clearly by the results of Fig. 3 and in a less direct way by the results of Fig. 12.

The picture one can trace, especially from the data of Fig. 12, about the mechanism of pre-precipitation in the Al–Zn alloys is a very simple one, and it is in agreement with what one should expect in terms of no appreciable interaction between vacancies and zinc atoms. Effectively, by this assumption one should expect that the large excess of vacancies introduced by quenching should be eliminated in the same way as in pure aluminum, namely principally by the formation of an increasing number of clusters of vacancies or dislocation loops with increasing quenching temperature; since during this process an appreciable amount of diffusion takes place, zinc atoms can move to form zones; when no more appreciable excess of free vacancies is present, the growth of zones practically stops. Since the excess of vacancies is progressively eliminated, the rate of pre-precipitation, which is very large at the beginning, decreases continuously with time. As in the case of pure aluminum for the elimination of vacancies, the reaction takes place in a few hours if the quenching temperature is low, or in a few minutes if the quenching temperature is high, in consequence of the clustering of vacancies (the slow reaction will be considered hereafter). This is in agreement also with the experimental fact that the Al–Zn alloys harden in a few minutes after quenching from high temperature,[9–10] and only if the quenching is carried out from relatively low temperature the phenomenon can be easily observed.[5]

Concerning the second point, some interesting properties of the pre-precipitation phenomenon have also been established.* Again the picture one can draw of the pre-precipitation phenomenon is a very simple one:

(i) the number of zones which form during isothermal ageing is controlled principally by the aging temperature and not by the quenching temperature, at least in the range 200–350°C; this means that *the number of zones which form is also independent of the number of clusters which form during quenching* (as judged by the increase in resistivity which takes place by quenching, see Fig. 3); furthermore it is independent of the concentration of vacancies and hence of the diffusion coefficient of zinc; these properties are shown by the independence of the maximum in resistivity on quenching temperature in Figs. 3 and 12.

(ii) The number of zones decreases largely by increasing the aging temperatures; this is shown by the data reported in Fig. 8.

(iii) If, after partial aging, the sample is aged at a different temperature, there is a tendency for zones to establish their new equilibrium number; however this can happen only if vacancies are still present to allow an appreciable rate of diffusion; these properties are shown by some data in Fig. 9.

Another interesting question to be considered is whether any direct correlation can exist between zones and dislocation loops (or clusters of vacancies). The answer is certainly negative since the number of zones, as said above, is controlled principally by the aging temperature while the number of loops is strongly influenced by the quenching temperature. Another argument favouring the independence between zones and loops is furnished by the consideration that loops are quickly annealed out at about 150°C[20] while zones are subjected to reversion also at lower temperatures. It is useful to emphasize however, that the number of loops which form will influence largely the final size of zones which is controlled by the total amount of diffusion.

Obviously the preceding considerations do not exclude the possibility that a fraction of vacancies can be trapped inside zones or that solute atoms can favour the nucleation of dislocation loops or clusters accelerate the formation of dislocation loops or clusters of vacancies or, finally, that a fraction of the solute atoms can segregate directly on loops (or on other dislocations) instead of moving to form zones. Incidentally, it is also to be remembered that the segregation of the solute atoms on small dislocation loops (which probably form also in other aluminum alloys) could greatly accelerate the nucleation of some precipitating phases.[22]

The slow reaction

It has been found that a "slow reaction" takes place in the Al–Zn 10% alloy at 40°C after quenching

* It is to be remembered that the considerations concerning pre-precipitation have been derived by the assumption that zones begin to grow all together after quenching; some justifications of this hypothesis will be reported in a following section.

from 600°C (Fig. 12), namely, the variation of resistivity occurs over a period of many days (and probably of weeks) which is too long to be accounted by the time that vacancies need for clustering. This slow reaction however is probably still too fast to be explained in terms of equilibrium diffusion coefficient.

It is well known that an apparently similar slow reaction occurs usually for the Al–Cu alloys; effectively in these alloys the property changes occur over a period of weeks at room temperature.

Several mechanisms have been recently advanced by Turnbull *et al.*[14] to explain the slow reaction and will not be reviewed here. However it is pointed out that the interpretation of the results in Fig. 12 gives good evidence that the slow reaction in the Al–Zn alloy should be connected with the presence of many small dislocation loops or clusters of vacancies. The concentration of these defects, in effect, increases greatly with quenching temperature while their size probably decreases.

Concerning the mechanism by which the presence of dislocation loops can speed up the rate of diffusion, it can be related to the enhancement of the local vacancy concentration near the dislocation loops or to a short circuiting solute diffusion along gliding dislocation loops.[14]

If the slow reaction in the Al–Cu alloys can be related to the same cause it may be that copper is much more effective than zinc in promoting the formation of small dislocation loops so that the slow reaction can be observed in the Al–Cu alloys also for lower quenching temperatures.

The presence of a slow reaction can justify also the fact that the *plateau* is not detectable in isochronal aging curve after quenching from 600°C in Fig. 2; in effect in this case the growth of zones should take place so slowly that the effect due to the growth of zones cannot be distinguished from the reversion. If this interpretation is correct then one should deduce from Fig. 2 that a slow reaction is probably present after the 500 and 550°C quenching also.

The reversion phenomenon

The fact, that aging temperature is the fundamental factor (besides concentration) affecting the number of zones, can throw new light on the nature of the reversion phenomenon. If a sample is first aged at relatively low temperature and then aged at a higher temperature, then, as stated above, it will transform so as to establish the new number of zones; now, by extrapolating the law (1) it is found that at about 94°C the number of zones in equilibrium is zero; therefore if a sample, previously aged at low temperatures, is annealed above 94°C all zones will be eliminated. This is exactly what we call the reversion phenomenon.

The concept of "partial reversion" can be also introduced; the partial reversion takes place when a sample aged at low temperature is transferred at a higher temperature but lower than 94°C. Thus a partial reversion should take place during each step (up to 80°C) in isochronal aging in Fig. 2; in this case there should be both a tendency for a reduction in the number of zones previously formed at lower temperature, and for the growth of that number of zones which are in thermodynamic equilibrium.

It is to point out that following the above interpretation of reversion, the size reached by zones should be of no particular importance in determining the amount of reversion; however it is probable that the size that zones had previously reached will largely influence the time necessary for reversion (or partial reversion); other factors controlling the time for reversion should be the reversion temperature and the concentration of vacancies (in excess, or in thermodynamic equilibrium).

From the preceding results it appears that the temperature of 94°C can be considered as the higher limit for pre-precipitation, in the actual alloy. This view is in agreement with the observation that during extended aging at 100°C the formation of hexagonal Zn platelets, namely a true precipitate, can be observed in more concentrated alloys.[6,23]

Incidentally, it is to note that in the actual case the true precipitate should never be found, even in isochronal aging or in isochronal reversion: this is because the times of aging were always short and because the selected alloy was dilute enough so that supersaturation is rapidly decreasing with increasing temperature (complete solubility is reached at 180°C).

The migration energy

It is useful to pay some attention to the values obtained for the activation energies of the phenomenon.

First let us discuss the value obtained after quenching from 300°C; this is a sufficiently low temperature that practically only single vacancies should be present. The experimental value $E_m' = 0.43 \pm 0.02$ eV appear to be slightly, but significantly, smaller than the value of the migration energy of single vacancies which should be near 0.60 eV.[15,17] One could think therefore that this result is not in agreement with what one should expect in terms of the hypothesis of quenched-in vacancies. However it is emphasized that it would be incorrect to expect the

VOL. 8 1960

rate of pre-precipitation to be controlled by just the same activation energy as for the motion of vacancies. In effect it is to be remembered that the experimental value E_m' was derived from resistivity variations due to the redistribution of zinc atoms; therefore E_m' should signify the "effective" activation energy for the movement of zinc atoms, namely the effective migration energy of zinc atoms and not that of vacancies.

To show that the two would not in general coincide, let us remember that the diffusion coefficient of zinc D_{Zn}, can be written[18,24]

$$D_{Zn} = \frac{1}{6} \cdot a^2 \cdot \nu_{Zn} \cdot f \cdot p \tag{2}$$

where a is the jump distance, p is the proportion of zinc atoms which are associated with a vacancy, ν_{Zn} is the number of jumps/sec which a zinc atom makes into an *associated* vacancy and f is the so called correlation factor. Now p is proportional to the factor $\exp(-0.70/kT_Q)$, therefore it is a constant for any quenching temperature T_Q; ν_{Zn} has the value:

$$\nu_{Zn} = \nu_0' \exp(-E_{Zn}/kT_A) \tag{3}$$

where T_A is the aging temperature and E_{Zn} is the "true" activation energy for the movement of a zinc atom into an associated vacancy.

The correlation factor can be written:[18,24]

$$f = \frac{2\nu_{Al} + 7K_1}{2\nu_{Al} + 7K_1 + 2\nu_{Zn}}. \tag{4}$$

In this expression

$$\nu_{Al} = \nu_0 \exp(-E_m^v/kT_A) \tag{5}$$

is the number of jumps/sec which a solvent atom makes into an associated vacancy; this number is governed by the migration energy of the vacancy E_m^v; finally

$$K_1 = \nu_0'' \exp[-(E_m^v + E_l)/kT_A] \tag{6}$$

is the frequency of dissociation of couples solute-vacancy which is governed by the sum of E_m^v with binding energy E_l of a vacancy with a solute atom. In the above expressions, ν_0, ν_0' and ν_0'', which contain appropriate entropy factors, are of the order of 10^{13}–10^{14} sec^{-1}.

Now, by combination of the preceeding equations (2–4) it is seen that, for any selected quenching temperature (p = const.) the experimental activation energy E_m' derived from the dependence of the clustering phenomenon on the aging temperature is given by:

$$E_m' = E_{Zn} - k[d(\ln f)/d(1/T_A)] \tag{7}$$

which would be in general different from the migration energy of single vacancies in pure aluminum. In the above expression the second term in the right-hand member is the contribution of the correlation factor which, in consequence of equations (3–6), will not be independent of aging temperature. Quite recently Manning[25] has shown that this contribution might be quite important. Therefore we have to distinguish E_m' as the "effective" or experimental migration energy and E_{Zn} as the "true" activation energy of zinc atoms to occupy an associate vacancy.

The sum of the experimental value E_m' and the formation energy E_f', which control the factor p, should give the activation energy Q_{Zn} for the diffusion coefficient of zinc in aluminum. One obtains therefore from the preceding results $Q_{Zn} = 1.13 \pm 0.04$ eV, which is just of the order of magnitude usually reported in literature for the chemical diffusion of zinc in aluminum (see for example Clare)[26]. A direct determination of Q_{Zn} by the employment of the radioactive isotope Zn^{65} has been carried out quite recently on several Al–Zn alloys;[27] in particular for the Al–Zn 4.33 at.% Zn, which is very near the present alloy, the value $Q_{Zn} = 1.23 \pm 0.03$ eV was found. The agreement is good enough, and this confirms again the correctness of the general interpretation of the results; however it appears that a small, but significant, difference exists between the two determinations of Q_{Zn}. The origin of this discrepancy is not known.

Let us consider now the value $E_m' = 0.38 \pm 0.02$ eV obtained after quenching from 450°C. In pure aluminum the activation energy obtained after quenching from about the same temperature[15,19] is much lower (~0.3 eV) than the migration energy expected for single vacancies; this was interpreted as due to the presence of a relatively large concentration of divacancies. If these defects are present in the Al–Zn 10% also, then one can deduce that they influence slightly the effective migration energy of zinc atoms.

The contribution of zones to resistivity

With reference to the unit volume (a cube of 1 cm side) let $\Delta\rho_z(r)$ be the contribution to resistivity of one zone of radius r, $\Delta\rho_s$ the contribution of an isolated solute atom to resistivity, n_s the total number of solute and z the number of zones (all having radius r). Then the total contribution $\bar{\Delta}\rho$ to resistivity, of isolated atoms and of zones is:

$$\bar{\Delta}\rho = n_s\Delta\rho_s + z\left[\Delta\rho_z(r) - \frac{16\pi c}{3}(r/a)^3\,\Delta\rho_s\right] \tag{8}$$

where a is the lattice parameter and c the fraction of solute inside zones (supposed constant).

Since $n_s \Delta\rho_s$ is constant, the experimental variation $\Delta\rho$ of resistivity is simply given by:

$$\Delta\rho = z\left[\Delta\rho_z(r) - \frac{16\pi c}{3}(r/a)^3\,\Delta\rho_s\right] \equiv z\phi(r) \quad (9)$$

where the function $\phi(r)$ is the contribution to resistivity of a zone of radius r corrected for the depletion of the matrix.

From the present results it appears that $\phi(r)$ increases largely with r, when r is small, until a critical radius r_1 is reached for which $\phi(r_1)$ obtains its maximum value; then for values of r higher than r_1, $\phi(r)$ decreases continuously until a second critical size r_2, is reached for which $\phi(r_2) = 0$; for values of r higher than r_2 the value of $\phi(r)$ is negative; in fact, values of resistivity lower than the reference value were experimentally observed in isothermal aging (Fig. 9, A and D).

Equation (9) relates the radius of zones r, which is functions of time, with their contribution to resistivity. Since the left hand member $\Delta\rho(t)$ is experimentally known—it is the variation observed in an isothermal aging curve—the above expression is an implicit relation between the functions $\phi(r)$ and $r(t)$. If one could know the law of variation of size of zones $r = r(t)$, then one could determine experimentally the function $\phi = \phi(r)$; *vice versa* if one would know this function, one could determine the law of variation of radius $r = r(t)$, namely the kinetics of the phenomenon.

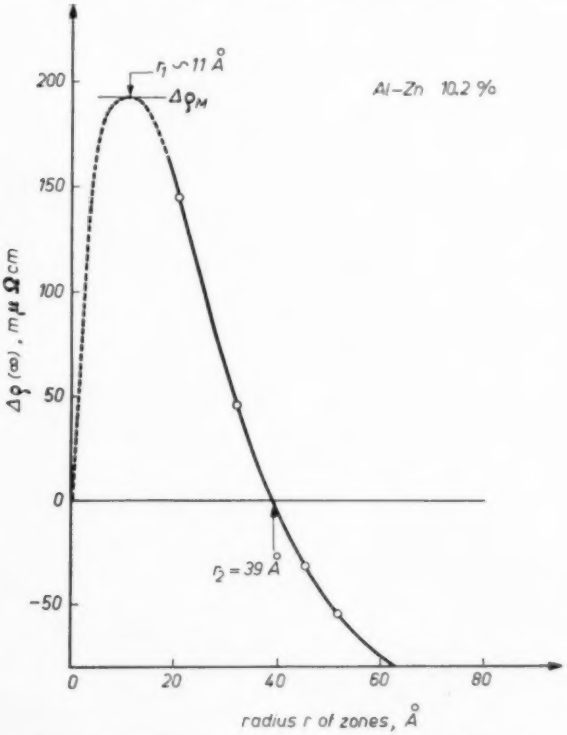


FIG. 14. The final values of resistivity $\Delta\rho(\infty)$ observed in aging at 40°C after quenching from 200, 250, 300 and 350°C (from the data in Fig. 12) plotted against the radius of zones obtained after quenching from the same temperatures, as determined by Graf[5]. The curve should represent the function $z\phi(r)$ (see text).

From the experimental point of view it should be possible to determine the shape of the function $\phi(r)$ by carrying out at the same time, during isothermal aging, the measurement of the variation of resistivity and of the radius of zones by X-ray analysis, on the same sample. Obviously to carry out such measurements easily, the sample should be quenched from relatively low temperatures so that the pre-precipitation phenomenon should take place very slowly. Another way to determine the shape of $\phi(r)$ is given by the determination of the final radius of zones and the final value $\Delta\rho(\infty)$ of resistivity on the same sample isothermally aged, after quenching from several temperatures; this is possible since the number of zones z which form is not appreciably changed by quenching from relatively low temperatures. For instance Graf[5] has reported that the radius of a zone after quenching from 200, 250, 300 and 350°C is given by 21, 32, 43.5 and 52.5 Å respectively; these values are plotted in Fig. 14 with the final values of resistivity obtained in isothermal aging (see Fig. 12) after quenching from the same temperatures; the curve obtained should be just proportional, by the factor z, to the function $\phi(r)$. Since the observed maximum in resistivity in Fig. 12, was about 192mμΩ cm the critical radius r_1 is estimated to be about 11 Å, while the critical radius r_2 should be 39 Å. However these values should be considered with great caution, since quenching conditions, sizes of sample and aging temperatures and times were not the same in the two investigations.

On the dependence of $\Delta\rho_M$ upon aging temperature

Many important features about the pre-precipitation phenomenon have been derived from the assumption (referred here as hypothesis 1) that the number of zones which form in isothermal aging varies with aging temperature. This is the more straightforward and simple interpretation of the experimental fact that $\Delta\rho_M$ varies with aging temperature.

Since the above assumption could be questionable, it is necessary to pay some attention to other possible interpretations of the dependence of $\Delta\rho_M$ upon aging temperature.

For this purpose it is to be remembered that until

VOL. 8 1960

now it has been assumed that all zones had reached, at any time, a same radius r, during isothermal aging; obviously, this is too crude a simplification. To picture the pre-precipitation phenomenon in a more realistic way, it is necessary to consider the distribution function $g(r,t)$ which gives the probability for a zone, at any time t, to have a radius in the range r to $r + dr$; at any time this function will satisfy the condition

$$\int_0^\infty g(r,t)\, dr = 1\,. \tag{10}$$

In particular let $g(r,t_M) = g_{MA}(r)$ be the distribution function at the aging temperature T_A and at time t_M, when resistivity has reached the maximum; this function can be imagined approximately as a bell-shaped function centred about the critical radius r_1. If z_{MA} is the number of zones which are present at time t_M, the total contribution of zones to resistivity, (at time t_M) is:

$$\Delta\rho_{MA} = z_{MA} \int_0^\infty \phi(r)\, g_{MA}(r)\, dr \tag{11}$$

where the $\phi(r)$ is the contribution to resistivity of a zone of radius r (corrected for the depletion of the matrix); this function should be shaped like the curve drawn in Fig. 14.

Now it appears from equation (11) that to change $\Delta\rho_{MA}$ with aging temperature T_A, there are two limiting ways: to change z_{MA} or to change g_{MA}. Since the first way, as shown hereafter, can be connected with two different possibilities, we can make three different hypothesis to explain the change of $\Delta\rho_{MA}$ with aging temperature:

(1) Following the first hypothesis, a number z_A of zones is formed *ab initio* in aging, and is constant with time; however it is *dependent* upon aging temperatures; substantially this is the working hypothesis (or hypothesis 1) accepted until now.

(2) In the second hypothesis it is supposed that a number z_0 of zones is formed at the beginning; however this number decreases continuously in time as zones grow in size, but *with a different law at each aging temperature*, so that a different value z_{MA} is obtained for any aging temperature.

(3) To clarify the third hypothesis, it is to be noted that if g_{MA} is flattened for values of r near r_1, then $\Delta\rho_{MA}$ is lower, since for the condition of equation (10) there would be more zones with a radius different from r_1, giving a lower contribution to resistivity. Therefore to explain the experimental results, it is sufficient to flatten $g_{MA}(r)$ at increasing aging temperatures.

Although it is impossible, from the experimental data, to establish without any doubt the quantitative contribution of each mechanism to the variation of $\Delta\rho_{MA}$, it is possible to give some evidence that the largest part of the variation should be explained in terms of the first hypothesis. To show this the isothermal curves of Fig. 3 are again plotted in Fig. 15 in normalized form, both versus the time to reach the maximum and to the maximum increase in resistivity. It is significant that all curves superpose quite well; this means that, at any normalized time t/t_M all experimental curves are similar in shape and differ only by a proportionality factor. A quite similar result was obtained also for the isothermal set of curves in Fig. 6. Now the general expression of the contribution of zones to resistivity $\Delta\rho_A(t/t_M)$, at the aging temperature T_A and at normalized time t/t_M, can be written:

$$\Delta\rho_A(t/t_M) = z_A\,(t/t_M) \int_0^\infty \phi(r) \cdot g_A(r,t/t_M)\, dr \tag{12}$$

and, obviously, the only simple way to obtain, at any time t/t_M, the isothermal curves differing only by a proportionality factor at the different aging temperatures, is to change z_A and to let the function $g(r,t/t_M)$ be independent of the aging temperature. It is to be noted, however, that there are two possibilities concerning z_A; it may be constant in time, at each aging temperature (and this is just a working hypothesis, or hypothesis 1, accepted until now) or it can change with normalized time t/t_M *but with the same law at any temperature* so that the ratio of the number of zones at any two aging temperatures, is constant at any normalized time t/t_M. Obviously this second possibility which is different from hypothesis 2, is only a variation of hypothesis 1, from which it cannot at present be distinguished; for the actual purposes however the question is not very important since in this case the only thing to change in the preceding survey of pre-precipitation is that the law (1) (or the data in Fig. 8) would give the number of zones which are present at each aging temperature, at time t/t_M.

For this reason, and for its great simplicity, we have interpreted the experimental results by the mechanism 1 (or its variant), although it cannot yet be considered quite proved. Unfortunately from the theoretical point of view no calculation exists, to our knowledge, concerning the number of zones which should form at each aging temperature. Dehlinger and Knapp[28] (D. K.) have calculated, for Al–Ag alloys, the fraction of solute which would be in clusters at each aging temperature, but this function is substantially the product of the number z of clusters for the number i of solute atoms in each cluster; no

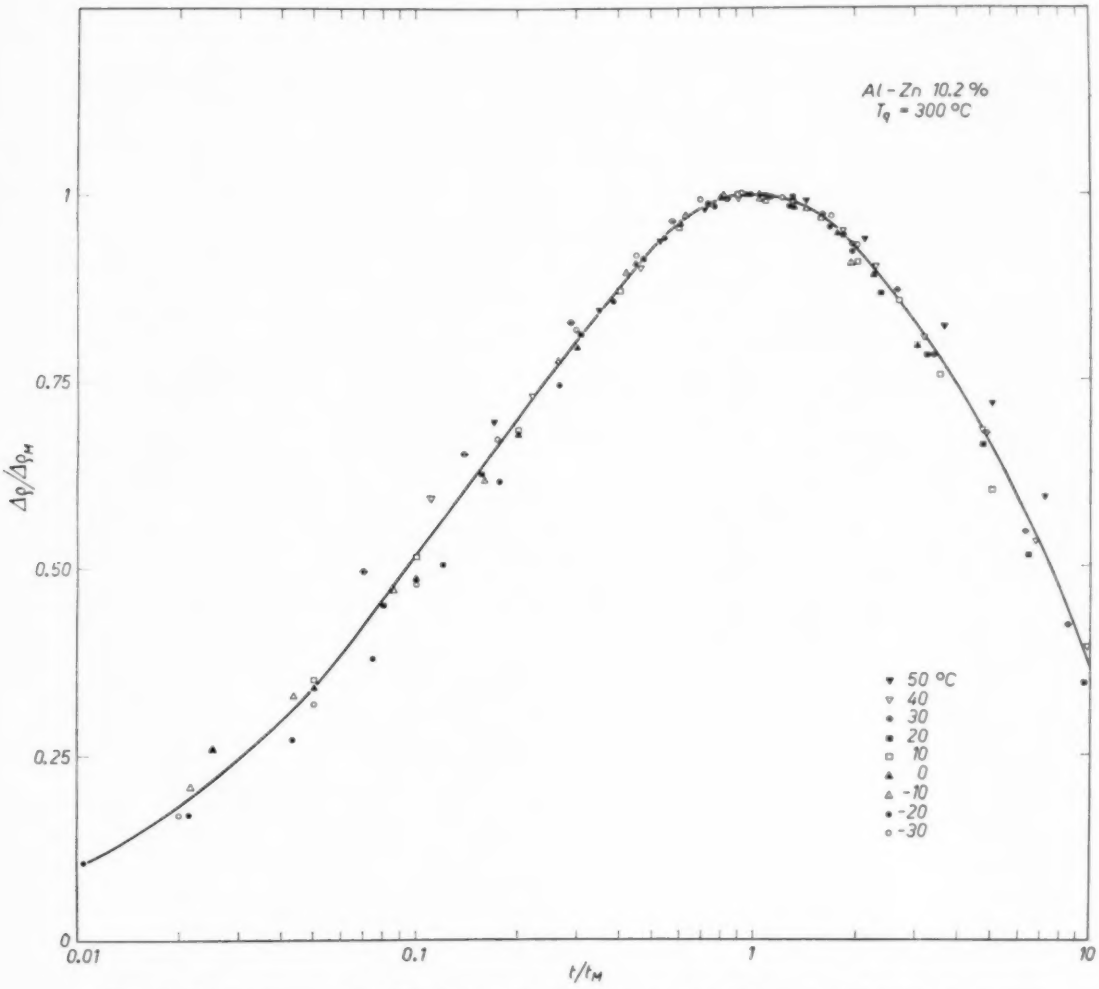


FIG. 15. The same curves as in Fig. 5 plotted in normalized form with respect both to the time to reach the maximum t_M and the maximum increase in resistivity $\Delta\rho_M$.

sure indication therefore can be deduced about the variation of z with aging temperature. It may be significant however, that the dependence of zi upon aging temperature (see Fig. 3 of D. K's paper), is qualitatively in good agreement with the data in Fig. 8; this means that if the final size of zones (namely the number i) is not too largely dependent upon aging temperature, then the data in Fig. 8, interpreted as the variation in the number of zones (following hypothesis 1) are qualitatively in good agreement with the theoretical data of D. K.

Finally, it is useful to call attention to a theoretical consequence of hypothesis 1; following this hypothesis (namely the dependence of the number of zones on aging temperature and its independence from the clusters which form during quenching) one can deduce that the largest reduction in the free energy of the supersaturated solid solution is due to the number of zones which forms, while their internal structure and size are only of minor importance.

Some recent results concerning the Al–Zn *alloys*

As said at the beginning, similar conclusions to that reported in this work about the role of vacancies in pre-precipitation, have been reached independently by Turnbull *et al.*[14].

Here it appears useful to note some points of similarity or dissimilarity between the two investigations, with reference to their results on the Al–Zn 3.4 at.% alloy.

The shape of the isothermal aging curves they observed was quite similar to that reported in this paper. The activation energy for clustering, deduced from the time scale factor necessary for the superposition of the resistivity variations before reaching the maximum, after quenching from 300°C, was found

VOL. 8 1960

to be 0.39 ± 0.04 eV, which is in good agreement with the value previously reported.

However it is to be pointed out that they did not observe explicitly the dependence of the maximum increase in resistivity (or following our interpretation, of the number of zones) upon the aging temperature. Since they were carrying out measurements directly at the aging temperature, it may be that it was not easy in this way, to recognize the contribution to resistivity due to zones and the contribution due to the changing of the aging (and measuring) temperature.

Neverthless, it is significant to point out that they were implicitly observing the phenomenon when they were reporting (Fig. 18 of their paper) the apparent strange property that it is possible for the resistivity to rise with time at a low temperature but to fall down with time at a higher aging temperature. Obviously in this case the experimental conditions were so favourably selected that they were observing the formation of new zones at the lower temperature and the elimination of the excess of zones at the higher temperature (in a similar way reported in Fig. 9, curves C and G, of this paper).

CONCLUSIONS

The preceding results have shown that for its peculiar feature the Al–Zn 10% alloy is very suitable for the investigation of the role of vacancies in pre-precipitation and of many characteristics of the phenomenon. It is significant, however, that for these investigations the employment of low temperature measurements is of *fundamental importance*, since many changes take place very quickly in the alloy, not only at room temperature but also during quenching itself.

The experimental work on the Al–Zn 10% alloy, although apparently extensive, is to be considered only of preliminary nature; many features of the phenomenon have been explored, but only very few have been thoroughly investigated. The only sure conclusions which can be drawn are that the role of vacancies is a very fundamental one, that their mechanism of elimination is not much dissimilar from that which takes place in pure aluminum and that the rate of pre-precipitation is practically stopped when all the excess of quenched-in vacancies is eliminated, unless a slow reaction is occurring when many dislocations loops are present.

Many other deductions, concerning the characteristics of the pre-precipitation phenomenon, although very suggestive, are still to be considered carefully, since they have been based upon a particular interpretation of the experimental fact that the maximum in resistivity changes with aging temperature. Although some evidence has been reported for the correctness of the interpretation given, the question will probably be solved definitively by other means.

Other items, which would yet deserve extensive investigations by resistivity measurements, are the influence of zinc concentration, the determination of the activation energy of reversion and of the slow-reaction phenomenon, and the influence of the addition of a third solute (for example Mg) on the pre-precipitation phenomenon. Furthermore, it would be interesting to investigate by means of resistivity measurements and X-rays analysis the contribution of zones to resistivity in function of their size (this would lead to the determination of the kinetics of the phenomenon); by means of electron transmission microscopy, the existence of dislocation loops and finally, from a theoretical point of view, the law of variation of number of zones with aging temperature.

ACKNOWLEDGMENTS

The authors wish to thank Dr. D. Turnbull for letting them know his results before publication, and Professor E. Germagnoli of CISE for some criticism and comment.

REFERENCES

1. A. Guinier, *J. Met., N.Y.* **8**, 673 (1956).
2. A. Guinier, *Suppl. Nuovo Cimento* **7**, 466 (1958).
3. W. DeSorbo, H. N. Treaftis and D. Turnbull, *Acta Met.* **6**, 401 (1958).
4. T. Federighi, *Acta Met.* **6**, 379 (1958).
5. R. Graf, *C.R. Acad. Sci. Paris* **246**, 1544 (1958).
6. A. Guinier, *Métaux et Corros.* **18**, 209 (1943).
7. A. Guinier, *Mesures* **11**, 382 (1946).
8. A. Guinier, *Int. Conf. Phys. Metals, Amsterdam 1948*, p. 148.
9. J. Herenguel and G. Chaudron, *Rev. Mét.* **41**, 33 (1944).
10. E. C. W. Perryman and J. C. Blade, *J. Inst. Met.* **77**, 282 (1950).
11. T. Federighi and L. Passari, *Acta Met.* **7**, 422 (1959).
12. N. F. Mott, *J. Inst. Met.* **60**, 267 (1937).
13. N. E. Fine, *Acta Met.* **7**, 228 (1959).
14. D. Turnbull, H. S. Rosenbaum and H. N. Treaftis, *Acta Met.* in press (1960).
15. C. Panseri and T. Federighi, *Phil. Mag.* **3**, 1223 (1958).
16. P. S. Rudman, P. A. Flinn and B. L. Averbach, *J. Appl. Phys.* **24**, 365 (1953).
17. W. DeSorbo and D. Turnbull, *Acta Met.* **7**, 83 (1959).
18. W. M. Lomer, *Monogr. Ser. Inst. Metals* no. 23, p. 79 (1957).
19. C. Panseri and T. Federighi, to be published.
20. T. Federighi, *Phil. Mag.* **4**, 502 (1959).
21. P. B. Hirsch, J. Silcox, R. E. Smallman and K. H. Westmacott, *Phil. Mag.* **3**, 897 (1958).
22. H. S. Rosenbaum and D. Turnbull, *Acta Met.* **6**, 653 (1958).
23. A. H. Geisler, C. S. Barrett and R. F. Mehl, *Trans. Amer. Inst. Min. (Metall.) Engrs.* **152**, 201 (1943).
24. A. D. LeClaire and A. B. Lidiard, *Phil. Mag.* **1**, 518 (1956).
25. J. R. Manning, *Phys. Rev. Letters* **1**, 365 (1958).
26. J. W. H. Clare, *Metallurgia, Manchr.* **57**, 273 (1958).
27. J. E. Hilliard, B. L. Averbach and Morris Cohen, *Acta Met.* **7**, 86 (1959).
28. U. Dehlinger and H. Knapp, *Z. Metallk.* **43**, 223 (1952).

THE ANALYSIS OF THE CRYSTALLOGRAPHY OF MARTENSITIC TRANSFORMATIONS BY THE METHOD OF PRISM MATCHING*

B. A. BILBY† and F. C. FRANK‡

A method of analysing the crystallographic features of martensitic transformations by considering the matching of triangular prisms formed by lattice lines in the two structures is described. The theory is illustrated by a detailed application to the martensitic transformation observed in an iron nickel alloy by Greninger and Troiano. The method is compared with other equivalent treatments and its advantages and disadvantages discussed.

ANALYSE CRISTALLOGRAPHIQUE DES TRANSFORMATIONS MARTENSITIQUE PAR LA METHODE D'ASSEMBLAGE DE PRISMES

Les auteurs décrivent une méthode d'analyse des caractéristiques cristallographique des transformations martensitiques qui considère l'assemblage des prismes triangulaires formés par les lignes réticulaires des deux phases.

La théorie est illustrée par une application détaillée à la transformation martensitique des alliages Fe-Ni observée par Greninger et Troiano. Les auteurs comparent leur méthode à d'autres techniques équivalentes et discutent de ses possibilités.

ANALYSE DER KRISTALLOGRAPHIE MARTENSITISCHER UMWANDLUNGEN DURCH ANPASSUNG VON PRISMEN

Es wird eine Methode zur Analyse der kristallographischen Eigenschaften martensitischer Umwandlungen beschrieben. Dabei geht man aus vom Aneinanderpassen dreieckiger Prismen, die von Gitterlinien in den beiden Sturkturen gebildet werden. Zur Erläuterung wird die Theorie auf die von Greninger und Troiano an einer Eisen-Nickel-Legierung beobachtete martensitische Umwandlung angewandt. Sie wird mit äquivalenten Behandlungsmethoden verglichen, und ihre Vor- und Nachteile werden diskutiert.

VOL. 8 1960

1. INTRODUCTION

There have been a number of analyses of the crystallography of martensitic transformations in the last few years; except for the most recent ones,[1,2] they have been discussed and compared fully elsewhere.[3,4] All share the common fundamental assumption that the shape deformation accompanying the transformation must be at least approximately an invariant plane strain, but differ in the (small) distortions of the interface which are allowed and in the types of associated slip or twinning processes which are postulated. For most treatments the essential input data are the correspondence, the crystallographic details of the slip or twinning process and the lattice parameters of the two phases; the habit plane, shape deformation, orientation relationship and the amount of the slip or twinning [5–7] or the dislocation structure of the interface[1] are then calculated.

The discussion of the $\{225\}_\gamma$ habit in iron-carbon alloys by a matching method[8] differs a little from the above treatments, in that the first emphasis is placed on the nature of the lattice continuity at the transformation interface. It is assumed that the $[01\bar{1}]_\gamma$ and $[111]_\alpha$ directions are common in the interface, the difference in lattice spacing being accommodated by elastic distortion. The invariance of a line in the interface perpendicular to this direction is then assured by a simple matching treatment, and finally the additional atom movements needed to complete the lattice transformation are inferred, and compensated by the introduction of an array of screw dislocations in the interface.

The two-dimensional matching appropriate to this special case, where one lattice row is assumed to be common to the two structures has been extended by using a three-dimensional "prism-matching" technique. A first account of this was given by one of us (B. A. B.) to the Martensite Symposium at the International Union of Crystallography in Paris, 1954, whose proceedings were not published, and a brief description also appeared in a recent review.[3] Because the sequence of assumptions differs from those in other methods, and because the treatment is simple and intuitive, yet related closely to the discussion in terms of surface dislocations,[1] it seems desirable to present a fuller account of this technique. Accordingly, in the present paper, the method is illustrated in some detail by applying it to the discussion of the $\{225\}_\gamma$ and $\{15\ 3\ 10\}_\gamma$ habits in iron–carbon alloys, where it permits some study of possible

* Received February 27, 1959.
† Metallurgy Department, University of Sheffield.
‡ Physics Department, University of Bristol.

criteria for distinguishing the different habits observed.[1]

2. THE HABIT PLANE

As before,[8] we refer the body-centred martensite structure (αI) to a face-centred tetragonal cell (αF) whose axes correspond to the face-centred cubic cell of the austenite (γ). The face-centred cell $\mathbf{A}_i$ is given in terms of the conventional body-centred cell $\mathbf{a}_i$ ($|\mathbf{a}_1| = a_\alpha$, $|\mathbf{a}_2| = a_\alpha$, $|\mathbf{a}_3| = c_\alpha$) by the relation

$$\mathbf{A}_i = (A\,|\,a)_i{}^k\,\mathbf{a}_k,\ (A\,|\,a)_i{}^k = \begin{bmatrix} 1 & \bar{1} & 0 \\ 1 & 1 & 0 \\ 0 & 0 & 1 \end{bmatrix}. \quad (1)$$

The Greninger–Troiano orientation relationship[9] becomes:

$$(111)_\gamma \| (111)_{\alpha F} \text{ (within } 1^\circ)$$
$$[01\bar{1}]_\gamma \wedge [01\bar{1}]_{\alpha F} = 2.5^\circ$$

and the habit plane is $(15\ 10\ 3)_\gamma$. The plane with large indices is presumably irrational.

Our general approach is to postulate a certain minimum conformity of the two mutually transforming lattices across the interface between them. Except in very special circumstances, we expect this interface to contain dislocations, and if these are to move in unison, they should be parallel and have the same Burgers vector. Accordingly, prominent lattice rows, associated with the modes of deformation of the two structures, will be continuous across the interface, since the Burgers vectors of the dislocations will be along these rows. In the present case, we take these rows to be the usual slip directions in the two structures, namely the $\langle 110\rangle_\gamma$ and $\langle 111\rangle_{\alpha I}$ directions. Further, since the $(111)_F$ planes are nearly parallel in the observed orientation relationship, it is assumed that these planes meet edge on in the interface, and that the matching rows lie in these planes. Possible matching rows are thus $[01\bar{1}]_F$ or the physically equivalent $[10\bar{1}]_F$; the $[1\bar{1}0]_F$ direction is excluded since in the α-structure this is $[1\bar{1}0]_{\alpha F} = [0\bar{1}0]_{\alpha I}$, and is not a normal slip direction. The γ-structure viewed along $[01\bar{1}]_\gamma$ is shown in Fig. 1. For the α-structure viewed along $[01\bar{1}]_{\alpha F}$ the lattice rows appear similarly, except that the dimensions of the triangle ABC are slightly different. Our fundamental conformity postulate is then that $[01\bar{1}]_F$ rows and $(111)_F$ planes meet in the interface. Since this meeting must occur everywhere in the interface, the matching is a three dimensional one and may be achieved by ensuring the continuity of the similarly situated triangular prisms with generators along the $ABC\,[01\bar{1}]_F$ lines in the two structures.

The matching problem is readily solved by elementary trigonometry. Two triangular prisms, whose generators are $[01\bar{1}]_F$ lines in the α and γ lattices and whose heights are equal to the spacings d_α and d_γ of the $(111)_{\alpha F}$ and $(111)_\gamma$ planes, must be truncated in such a way that the truncated ends match. In this problem, there are four unknowns–for each prism two parameters to define the obliquity of the truncating plane–and there are three equations, since a triangle has three sides. We are left with one degree of freedom. A convenient solution of this problem for general prisms of given right section is derived in the appendix. All the quantities are expressed in terms

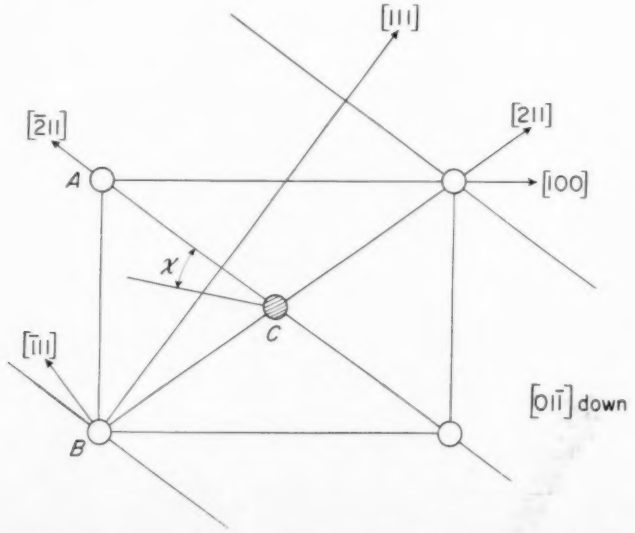


FIG. 1. The γ structure viewed along $[01\bar{1}]_\gamma$. The full circle is at height $\frac{1}{2}$.

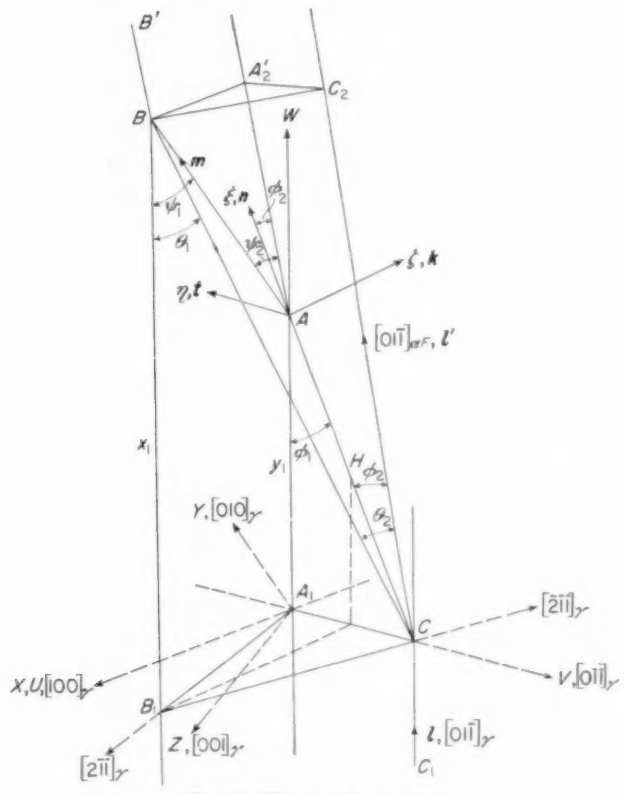


FIG. 2. The α and γ prisms.

of a parameter x; corresponding to the one degree of freedom, an infinity of solutions is obtained as x varies.

The application of this general solution to our example is shown in Fig. 2, where the notation is that of the appendix. Prism 1 in the γ-lattice is bounded by the vertical generators $B_1B = x_1$, $A_1A = y_1$ and C_1C, all parallel to $[01\bar{1}]_\gamma$, and A_1B_1C is a right section of it. ABC is the plane of contact, and BB', AA_2', CC_2 are the generators parallel to $[01\bar{1}]_{\alpha I}$ of the prism 2 in the α-lattice, of which $A_2'BC_2$ is a right section. In Fig. 2, the right section of the prism 2 through C intersects only the generators $B'B$ and $A_2'A$ produced, so that $x_2 = CC_2$ and $y_2 = x_2 - AA_2'$. The relevant crystallographic directions are indicated in Fig. 2, and it is easily shown that $a_1 = c_1 = a_\gamma\sqrt{6}/4$, $b_1 = a_\gamma\sqrt{2}/2$, $a_2 = c_2 = a_{\alpha I}[(1 + r^2)/(2 + r^2)]^{\frac{1}{2}}$, and $b_2 = a_{\alpha I} r\sqrt{2}/(2 + r^2)^{\frac{1}{2}}$, where $r = (c/a)_{\alpha I}$. The standard austenite axes are denoted by X, Y, Z; the axes U, V, W are derived from these by a 135° rotation about X. The axes ξ, η, ζ are such that ξ is parallel to $\mathbf{n}$, a unit vector along CA; ζ is parallel to $\mathbf{k}$, a unit vector parallel to the normal to the habit plane ABC; and η is parallel to $\mathbf{t} = \mathbf{k} \times \mathbf{n}$. $\mathbf{m}$, $\mathbf{l}$ and $\mathbf{l}'$ are unit vectors parallel to AB, $[01\bar{1}]_\gamma$ and $[01\bar{1}]_{\alpha I}$, respectively.

In terms of the quantities derived in the appendix, the habit plane normal $\boldsymbol{\nu} = -\mathbf{k}$, may be written down at once in the U, V, W system, and a simple transformation gives for its components in the standard X, Y, Z system:

$$\left.\begin{aligned} \nu_1 &= +M(2x_1 - y_1) \\ &= +M[2x - A/x - (Bx - AC/2x)] \\ \nu_2 &= +M(y_1 - b_1) \\ &= +M[Bx - (AC/2x) - b_1] \\ \nu_3 &= +M(y_1 + b_1) \\ &= +M[Bx - (AC/2x) + b_1] \end{aligned}\right\} \quad (2)$$

Here, M is a normalising factor > 0. We use $\boldsymbol{\nu} = -\mathbf{k}$ so that all components are positive for small positive x values. The variation of the habit plane normal for $-\infty \leqslant x \leqslant +\infty$ is shown in the stereogram of Fig. 3, where $(100)_\gamma$ is the plane of projection. The values of lattice parameters used are those given by Greninger and Troiano[8], namely, in Angstrom Units:

$$\left.\begin{aligned} a_\gamma &= 3.592 \pm 0.005 \\ a_{\alpha I} &= 2.845 \pm 0.005 \\ (c/a)_{\alpha I} &= 1.045 \pm 0.005 \end{aligned}\right\} \quad (3)$$

VOL. 8 1960

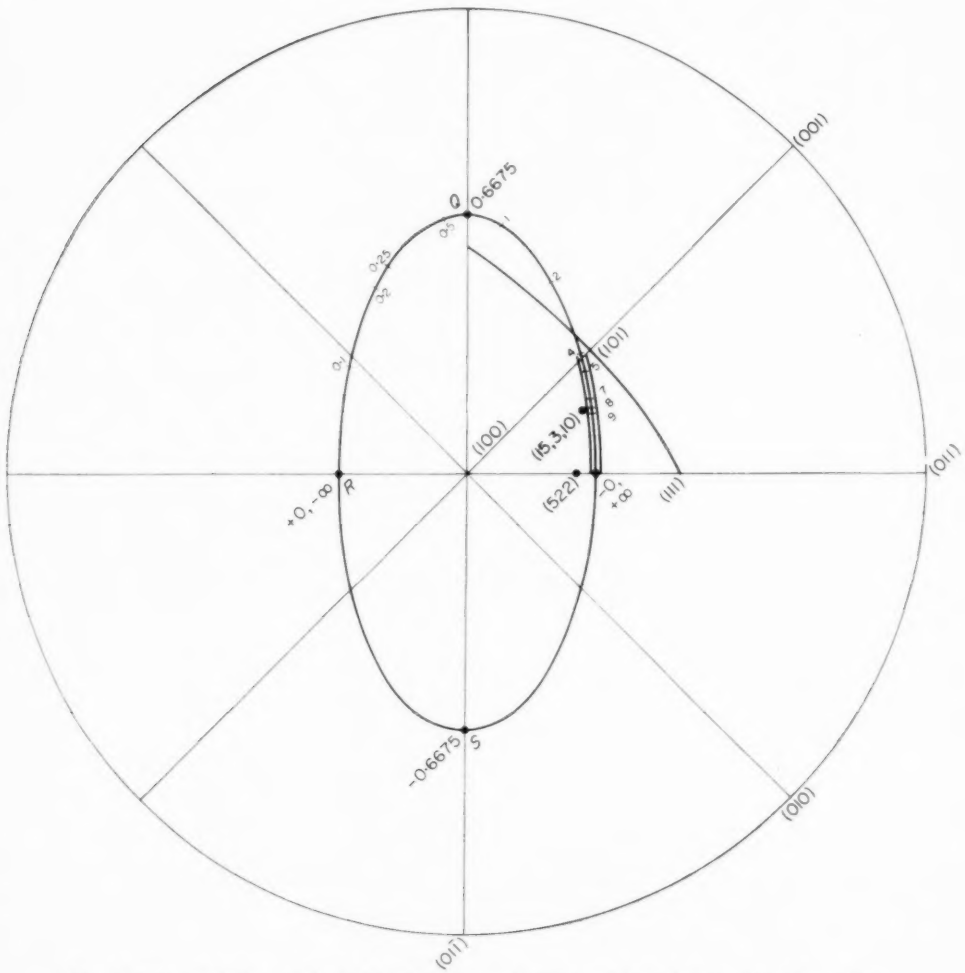


FIG. 3. The variation of the habit plane normal. The numbers denote the values of x.

The satellite lines in the inner triangle represent an estimate of the variation in the predicted habit plane due to the uncertainties in the lattice parameters. Since the two original errors are essentially one in $a_\gamma/a_{\alpha I}$ of 0.224 per cent and one in $(c/a)_{\alpha I}$ of 0.478 per cent, the two lines were obtained by increasing a_1, b_1, and c_1 by 0.224 per cent, and a_2, b_2 and c_2 by 0.478 per cent, respectively.

In the stereogram all the predicted $\boldsymbol{\nu}$ values are represented with positive ν_1 component, by changing the sign of all three components where necessary. It is evident that the variation in habit plane normal for $-\infty \leqslant x \leqslant +\infty$ is obtained from the variation taking it from $P(x = +\infty)$ to $Q(x = +\sqrt{AC/2B} = 0.66748)$. This symmetry arises for the following reasons. Firstly, for any matching plane another match exists on this plane reflected in the plane normal to the γ prism generators $[01\bar{1}]$. This alternative corresponds in Fig. 3 to a change in the sign of x, which in general changes the predicted habit plane from (pqr) to $(\bar{p}, \bar{r}, \bar{q}) \equiv (prq)$. As the γ-prism is in this case isosceles, matching is also possible on (pqr) and (prq) reflected in $(011)_\gamma$, that is on $(p\bar{q}\bar{r})$ and $(p\bar{r}\bar{q})$, respectively. The relation between x values x' and x'' giving habit planes reflected in $(011)_\gamma$ is $x'x'' = AC/2B$. This follows because B and C have the form

$$B = \tau(1 + \sqrt{1 - 2/\tau}),\ C = \tau(1 - \sqrt{1 - 2/\tau}) \quad (4)$$

where $\tau = (b\delta b)/(2a\delta a)$, in the notation of the appendix. The numerical agreement between the $\boldsymbol{\nu}$ values for $x = \pm 0$ $\{\boldsymbol{\nu} = \pm M_1(2 - C, C, C)\}$ and $x = \pm\infty\{\boldsymbol{\nu} = \pm M_2(2 - B, B, B)\}$ also arises from this relation. For these values of x, the matching degenerates to the two-dimensional one,[8] with the $[01\bar{1}]$ directions lying in the matching plane. Finally, the alternative solution mentioned in the appendix, and arising from the possibility of interchanging B and C, gives the same habit plane for a value x' related to x by $x'x = -A/2$.

For any x value therefore, there are two distinct habit planes, and as x varies from $-\infty \leqslant x \leqslant +\infty$, a double infinity of habit planes all lying on the locus of Fig. 3.

For $x = -8$, the predicted habit plane has $\boldsymbol{\nu} = (0.8052, 0.5622, 0.1884)$ which is only 1° 49′ from the observed value (15 10 3). For $x = \pm\infty$, the predicted habit plane approaches that observed in the Kurdjumow–Sachs[10] type martensite—$(522)_\gamma$—, although, of course, in Fig. 3 lattice parameters for the Greninger–Troiano alloy[9] are used. The use of the matching treatment for the $(522)_\gamma$ habit[8] has already been discussed.[3,11]

So far, in our analysis, the parameter x has been used simply to define the one degree of freedom in the matching problem. We have now to consider the physical significance of its variation, and to see whether criteria for selecting the value $x = -8$ in the Greninger–Troiano alloy can be determined. To this end, we now consider the shape deformation during the transformation and the atom movements additional to those given by the prism deformation which are needed to complete it.

VOL. 8 1960

3. THE SHAPE DEFORMATION

This is the deformation which carries one prism into the other, and which, at the same time, contracts the γ prism along its generators, so that the $[01\bar{1}]_\gamma$ spacing becomes the $[01\bar{1}]_{\alpha F}$ spacing. This contraction is by the factor $f = \sqrt{2 + r^2}/(s\sqrt{2}) = 0.9848$ for the Greninger–Troiano alloy, where $s = a_\gamma/a_{\alpha I}$ and $r = (c/a)_{\alpha I}$. Since the shape deformation leaves the habit plane invariant, it may be specified completely by its effect on a unit vector $\mathbf{k}$ scribed initially normal to the habit plane. If $\mathbf{k}$ becomes $\mathbf{k}'$ under the shape deformation, then the latter carries any vector $\mathbf{R}$ to $\mathbf{R}'$ where

$$\mathbf{R}' = \mathbf{R} + (\mathbf{R} \cdot \mathbf{k})\mathbf{u} \tag{5}$$

and $\mathbf{u} = \mathbf{k}' - \mathbf{k}$.

Fig. 4 shows a portion of the matched prisms at the corner C of the habit plane triangle ABC: the notation of Fig. 2 is employed. The unit vector $\mathbf{l}$ along $[01\bar{1}]_\gamma$ becomes $f\mathbf{l}'$, where $\mathbf{l}'$ is a unit vector along $[01\bar{1}]_{\alpha F}$, and $LM = f\mathbf{l}' - \mathbf{l}$. The components of $\mathbf{l}'$ and $\mathbf{l}$ in the ξ, η, ζ axes are then, in the notation of the appendix:

$$\mathbf{l}_\xi = \cos\phi_1 = y_1/b_0 \tag{6}$$

$$\mathbf{l}_\xi' = \cos\phi_2 = y_2/b_0 \tag{7}$$

$$\mathbf{l}_\eta = (\cos\theta_1 - \cos\phi_1 \cos C)/\sin C \tag{8}$$

$$\mathbf{l}_\eta' = (\cos\theta_2 - \cos\phi_2 \cos C)/\sin C \tag{9}$$

and $\mathbf{l}_\zeta = \sqrt{1 - \mathbf{l}_\xi^2 - \mathbf{l}_\eta^2}$, $\mathbf{l}_\zeta' = \sqrt{1 - \mathbf{l}_\zeta'^2 - \mathbf{l}_\eta'^2}$.

Here $\cos\theta_1 = x_1/a_0$, $\cos\theta_2 = x_2/a_0$, and

$$\cos C = (b_1^2/2 + (x_1 y_1))/a_0 b_0. \tag{10}$$

The shape deformation is conveniently measured by the angle γ_1 between $\mathbf{k}$ and $\mathbf{k}'$, given by

$$\cos\gamma_1 = (\mathbf{k}' \cdot \mathbf{k})/|\mathbf{k}'|. \tag{11}$$

Now, from Fig. 4,

$$\mathbf{k}' = \mathbf{k} + (f\mathbf{l}' - \mathbf{l})/l_\zeta \tag{12}$$

so

$$\mathbf{k}' \cdot \mathbf{k} = f l_\zeta'/l_\zeta = |\mathbf{k}'| \cos\gamma_1 = V \tag{13}$$

where V is the ratio of the volume before and after the transformation. Equation (13) shows that l_ζ and l_ζ' must be taken with the same sign.
Hence,

$$\cos\gamma_1 = Fl_\zeta'/[(Fl_\xi' - l_\xi)^2 + (Fl_\eta' - l_\eta)^2 + f^2 l_\zeta'^2]^{\frac{1}{2}}. \tag{14}$$

Finally, the unit vector in the direction of motion (which is the same for all points) is given by

$$\mathbf{p} = \mathbf{u}/|\mathbf{u}| = (\mathbf{k}' - \mathbf{k})/|\mathbf{k}' - \mathbf{k}| \tag{15}$$

Fig. 5 shows the angle γ_1 plotted as a function of the parameter x, for $1 \leqslant x \leqslant 100$*. The expression (14) for $\cos\gamma_1$ is even in x because l_ξ, l_ξ', l_η, l_η' are all odd in x, while $l_\zeta = \cos([01\bar{1}]_\gamma \wedge \mathbf{k}) = (k_2 - k_3)/\sqrt{2} = Mb_1\sqrt{2}$ which is even in x and > 0. l_ζ' is thus also positive and even in x. As $x \to +\infty$, $\gamma_1 \to \pi/2$. As has been discussed in Section 2 above, variations of x outside the range $0.6675 \leqslant x \leqslant +\infty$ correspond to reflection of the habit plane for some x in this range either in the prism generators or in the $(011)_\gamma$ plane. Clearly, therefore the curve in Fig. 5 will rise to $\gamma_1 = \pi/2$ as $x \to +0$ and will, of course, be repeated for negative values of x. From the figure it is evident that the criterion of small shape deformation favours $|x|$ values between about 4 and 10, and that as the (522) habit is approached the shape deformation must increase very rapidly if the postulated match is maintained. The x values may be restricted further by considering the additional atom movements needed to produce the final martensite structure.

4. THE DISLOCATION ARRAY AND THE ORIENTATION RELATIONSHIP

We have postulated that the shape change associated with the transformation carries the γ prism into

* For given x, the alternative solution obtained by interchanging B and C gives in general, another value of $\cos\gamma_1$. The study of these alternative solutions is, however, more conveniently carried out by using the analysis based on surface dislocation theory,[1] which has now been programmed for the Ferranti Pegasus computer.[12] One of us (B. A. B.) is indebted to Dr. A. G. Crocker for drawing his attention to this point, and for valuable discussion of it.

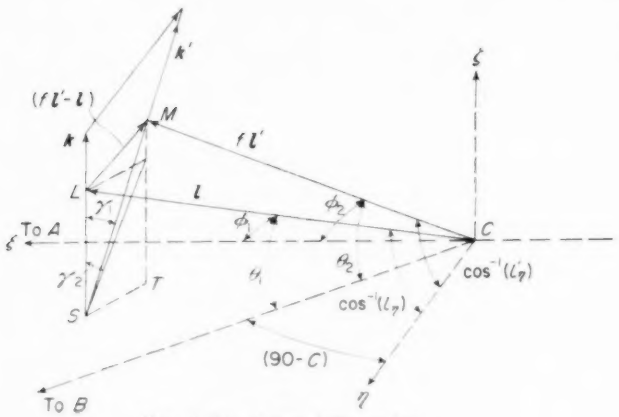


FIG. 4. The shape deformation.

the α, and at the same time adjusts the spacing of the atoms along the $[01\bar{1}]_F$ rows (which are close packed directions in both phases). Any additional deformation of the α-prism which is needed to make martensite must therefore be compensated by dislocations in the moving interface, so that there is no other shape change. We have argued that the Burgers vectors of the dislocations will lie along the $[01\bar{1}]_F$ rows, and that the array will consist of like, parallel dislocations, so that it may move in unison. Accordingly, it must produce a simple shear in the direction of the prism generators, on *some* plane containing these generators. Thus, the additional atom movements must also consist of a simple shear in this direction, and, moreover, the plane on which the shear occurs will be unchanged by them. Therefore this plane must already have the martensite structure as a result of the prism (shape) deformation only. Now, for an arbitrary choice of the parameter x, it is not clear that there will be any plane containing the $[01\bar{1}]_\gamma$ direction satisfying this requirement. In a full discussion, therefore, we must first find the deformation produced in a selected plane containing $[01\bar{1}]_\gamma$ by the shape deformation for different values of x, and compare this deformation with that required to produce the martensite structure within the plane. On this basis, x-values and corresponding planes may be selected, on any of which the transformation may be completed by a simple shear. These possibilities will be distinguished by their x-values (habit plane and shape deformation) and the magnitude of the additional simple shear required.

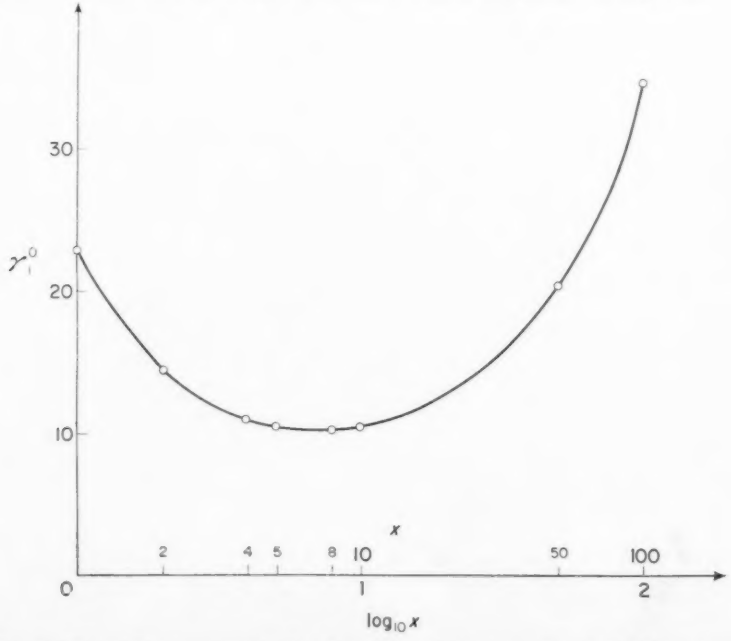


FIG. 5. The angle γ_1, measuring the shape deformation, as a function of the parameter x.

However, we shall not give such a discussion here, but examine only the simplest possibility. This is that the plane on which the simple shear occurs is carried to its final state merely by the contraction of the $[01\bar{1}]_\gamma$ spacing along the prism generators; that is, the plane receives, during the shape deformation, only a uniaxial deformation along $[01\bar{1}]_F$ and is otherwise undeformed.

This hypothesis immediately restricts the plane to be $(011)_F$; for this is the only plane which can attain its final structure in this way, if we suppose, as is the usual assumption,[1,7,11] that the lattice pure strain during the transformation is that originally suggested by Bain[13], namely one which compresses the f.c.c. γ cell by the factor $\lambda = c_{\alpha I}/a_\gamma$ along one of its sides and expands it uniformly by the factor $\mu = a_{\alpha F}/a_\gamma = a_{\alpha I}\sqrt{2}/a_\gamma$ in all directions at right angles to this side. This is because, for any of the three possible pure strains, $[01\bar{1}]_\gamma$ lies in a plane containing two of the principal axes of strain, namely $(100)_\gamma$. Hence $[100]_\gamma$ is the only line which remains normal to $[01\bar{1}]_\gamma$, and so $(011)_\gamma$ is the only plane through $[01\bar{1}]_\gamma$ which undergoes a uniaxial deformation.

We have now to find the value of x at which the shape deformation produces only a uniaxial deformation of the $(011)_\gamma$ plane. Fig. 6 shows the shape deformation of the b-face of the prism; as the $[01\bar{1}]_\gamma$ generators become $[01\bar{1}]_{\alpha F}$ generators, $AT \rightarrow AT''$, and $CT'/CT = f$, the ratio of the spacings along these directions. The shear s_b in this face is given by

$$s_b = \tan \gamma_b = \cot \rho = (\cos \phi_2 - f \cos \phi_1)/\sin \phi_2 \quad (16)$$

where the ϕ's are given by equations (6) and (7). A similar expression—with ϕ_1 replaced by θ_1 and ϕ_2 by θ_2, with θ's defined above—gives the shear s_a in the a-face of the prism. From $s_a(x)$ and $s_b(x)$ the shear in any plane making, say, χ, with the b-face of the γ-prism (Fig. 1), is readily calculated to be

$$s(\chi) = (a_1 s_a - b_1 s_b) \sin \chi/(c_1 \sin A_1) + b_1 s_b \sin (A_1 + \chi)/(a_1 \sin B_1) \quad (17)$$

where $\sin A_1 = \sqrt{2/3}$, $\sin B_1 = 2\sqrt{2}/3$. With this definition, a decrease in the angle between the $[01\bar{1}]_\gamma$ and the TA direction corresponds to a positive value of $s(\chi)$. For $(011)_\gamma$, $\chi = \pi/2$, and we thus find that $s(\pi/2) = 0$ when $|x| \sim 8$. It will be seen from Fig. 5 that this value of x makes the shape deformation, as measured by the angle γ_2, very nearly a minimum. This provides additional justification for our simplifying hypothesis.

To determine the density of dislocations in the interface, the additional shear on the $(011)_F$ plane needed to produce the martensite structure must be found. The shear in the plane perpendicular to $(011)_\gamma$ produced by the shape deformation is given by equation (17) with $\chi = 0$. This gives $s(0) = s_b = -0.062$ for $x = -8$.

Fig. 7 shows a projection of the modified γ-lattice on the $(100)_\gamma$ plane. After applying the shape deformation, the $[01\bar{1}]_F$ spacing will be correct, and also the spacing of the $(011)_F$ planes, but the atoms will not be in the correct positions along the $[01\bar{1}]_F$ rows. Two possible ways in which the martensite structure may be generated are shown in the figure, where the αF cells P and Q are outlined by dotted lines. In the shear on $(011)_F$ leading to P, $[011]_\gamma \rightarrow [0\bar{1}\bar{1}]_{\alpha F}$, and in that leading to Q, $[011]_\gamma \rightarrow [011]_{\alpha F}$. Clearly the two possibilities give twin-related martensites, twinned by reflection in the usual $(011)_{\alpha F} = (112)_{\alpha I}$ twinning plane of the body centred αI lattice.

The angle σ between the directions $[010]_{\alpha F}$ and $[01\bar{1}]_{\alpha F}$ of the α-phase is readily calculated from the αF lattice parameters to be 36° 28′. Thus the two possible shears are s_P in the $[0\bar{1}1]_{\alpha F}$ direction or s_Q in the $[01\bar{1}]_{\alpha F}$ direction, where

$$s_P = \cot 2\sigma + s(0) = 0.245$$
$$s_Q = \cot 2\sigma - s(0) = 0.369.$$

These additional shears can take place without affecting the shape change if they are just compensated by a suitable array of dislocations in the interface. These dislocations must lie in the $(011)_F$ plane and in the contact surface, and so along the line BH in Fig. 2. If their Burgers vectors are along $[01\bar{1}]_F$ and

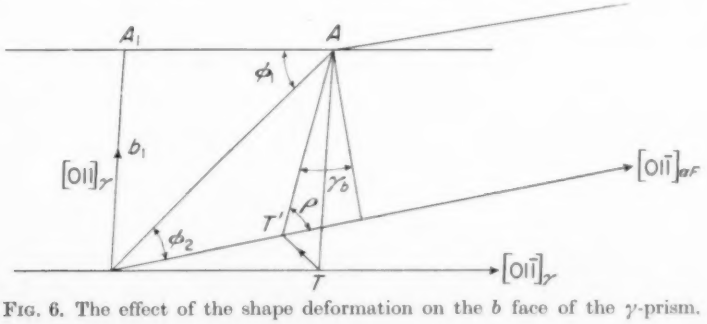


FIG. 6. The effect of the shape deformation on the b face of the γ-prism.

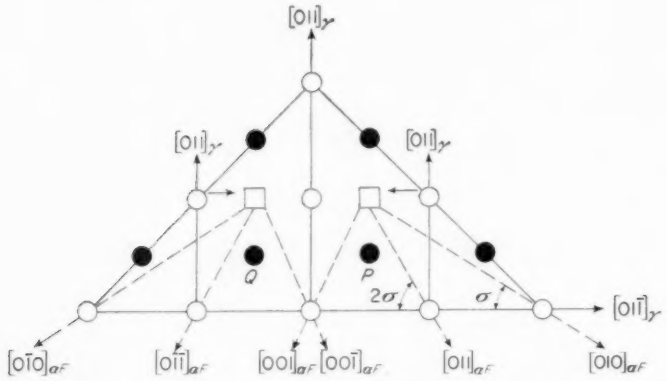


FIG. 7. The modified γ-lattice projected on the $(100)_\gamma$ plane. The full circles are at height $\frac{1}{2}$.

equal in magnitude to t_α, the $[01\bar{1}]_{\alpha F}$ spacing, and there is one dislocation for every n $(011)_{\alpha F}$ planes, they produce a shear $s_d = 2t_\alpha/b_2 n$. This gives $n = 5.7$ and $n = 8.5$ for the two possible shears s_Q and s_P considered above. The larger value of n, corresponding to the smaller value of s_P will give the smaller value for the energy of the dislocations in the interface. It may readily be verified that, as has already been noted,[11] the orientation observed by Greninger and Troiano[9] is apparently that corresponding to the smaller value s_P.

The orientation relationship predicted by this treatment may be examined by considering the angles between the $(111)_F$ planes, and between the $[01\bar{1}]_F$ directions. The angle between $(111)_\gamma$ and $(111)_{\alpha F}$ may be found exactly by finding the components of $\mathbf{v} = \mathbf{m} \times \mathbf{l}'$ (Fig. 2) in the X-system, and so the angle between $\mathbf{v}$ and $[111]_\gamma$. To a sufficient approximation, however, we may use the expression (A.27) in the appendix for $-\delta\omega$. The angle between $[01\bar{1}]_\gamma$ and $[01\bar{1}]_{\alpha F}$ is simply that between $\mathbf{l}$ and $\mathbf{l}'$. Thus, we find

$$-\delta\omega \sim (111)_\gamma \wedge (111)_{\alpha F} = 14'$$

$$\cos^{-1}(\mathbf{l}\cdot\mathbf{l}') = [01\bar{1}]_\gamma \wedge [01\bar{1}]_{\alpha F} = 3.1^\circ.$$

The martensite axes are fixed in relation to those of the γ-phase by the fact that the α-structure is one of the two possible twins on the $(011)_F = (112)_{\alpha I}$ plane.

Clearly, instead of compensating the shear s_P by the slip due to a suitable dislocation array as considered above, we may instead combine a stack of fine twins with shears $\pm \cot 2\sigma$ and appropriate thickness ratio to give resultant shears s_P or s_Q, as considered by Wechsler, Lieberman and Read (WLR)[7]*. Our numerical values for s_P and s_Q agree very closely with the g-values, $g_1 = 0.2457$ and $g_2 = 0.3687$, calculated from equation (53) of their paper. However, s_P and s_Q are of opposite sign and refer to twin-related martensites with the same habit plane, while g_1 and g_2 have the same sign and refer to martensites from one correspondence but with different habit planes. A detailed study of the algebraic expressions for the g's shows at once how the numerical agreement arises.

There is a slight numerical discrepancy with the shears 0.2505 and 0.3639 given for this alloy by Bowles and MacKenzie[11], presumably because they use for their dilatation parameter θ^2 a value of $\theta^2 = 0.630$, rather than the value 0.627 which corresponds to an undistorted habit plane. Of course, in this matching method, as in the analysis of WLR, the habit plane is undistorted, and the shape deformation is exactly an invariant plane strain.

Finally, for further comparison with the observations, we calculate the direction of movement in the shape deformation. Following WLR, we calculate a unit vector $\mathbf{q}$ along the projection of $\mathbf{u}$ on to the habit plane; this may then be compared with the estimates of the observed "shear" direction.[9] The vector $\mathbf{q}$ is parallel to ST in Fig. 4 and in the (ξ, η, ζ) axes has the components $N(Fl_\xi' - l_\xi, Fl_\eta' - l_\eta, 0)$ where N is a normalising factor. For $x = -8$ we find

$$\mathbf{q} = (q_x, q_y, q_z) = (\overline{0.5929}, 0.7690, \overline{0.2389}).$$

When the "shear" is expressed on the plane $\mathbf{v} = -\mathbf{k}$, the appropriate "shear" vector is $-\mathbf{q}$.

The angle γ_2 in Fig. 4 is given by

$$\tan\gamma_2 = 1/Nl_\zeta. \tag{18}$$

5. DISCUSSION

Our results may be summarised in Table 1, in which the theoretical values are for $x = -8$, and the experimental ones from the paper of Greninger

* This treatment using the slip due to a dislocation array in the prism matching method was first reported by one of us (F. C. F.) in a letter to Professor Read in May 1953, in reply to a communication from him enclosing an account of the treatment by alternating twinning.

TABLE 1

		Experimental	Theoretical	WLR
			$x = -8$	
Habit Plane	p_x	0.8208	0.8052	0.8027
	p_y	0.5472	0.5622	0.5691
	p_z	0.1642	0.1884	0.1783
		(15, 10, 3)		
Orientation relationship	$(111)_\gamma \wedge (111)_{\alpha' F}$	$< 1°$	14′	15′
	$[01\bar{1}]_\gamma \wedge [01\bar{1}]_{\alpha' F}$	2.5°	3.1°	3°
Shape deformation	"Shear" angle	$\gamma = 10.66°$	γ_2 10.28° γ_1 10.55°	γ_2 10.33° γ_1 10.71°
	Direction of shear $— q_x$	0.5642*	0.5929	0.5964
	$— q_y$	0.7315	0.7690	0.7660
	$— q_z$	0.3828	0.2389	0.2400

* A mean estimated by WLR[7] from the experimental results.[9]

and Troiano[9]. In addition we give also the theoretical values of WLR[7] for this alloy, which has also been treated with similar results by Bowles and MacKenzie[11].

In this table, we have made the appropriate permutation of habit plane indices in the WLR results to make them agree with our situation. (We have $[01\bar{1}]_\gamma$ nearly parallel to a $\langle 111 \rangle_{\alpha' I}$ direction and habit plane (15 10 3), while they have $[1\bar{1}0]_\gamma$ nearly parallel to $\langle 111 \rangle_{\alpha' I}$ and habit plane (10 3 15)).

It is clear that we have, by this elementary matching analysis arrived at the same solution to the problem as the other treatments using matrix algebra.[1,5–7] Perhaps the most instructive feature of the present method is that, by focusing attention on the continuity across the interface, it enables the actual atom movements accompanying the transformation to be readily visualised. Indeed, in some of the other treatments,[5,6] it is emphasised that the analysis connects only the initial and final states, and that no picture of the atom movements is provided.

Also, Fig. 5 shows that the dislocation structure postulated in the interface (or the shear plane on which the heterogeneous atom movements occur) is such as to make the shape deformation nearly a minimum; in particular, if the postulated match is maintained, the shape deformation rises rapidly as the habit plane moves towards (522). We might then anticipate that this match is confined to habit planes near the centre of the stereographic triangle, and that there is a distinct change in the nature of the conformity as we move away from this region.

On the other hand although the matching method permits a rapid assessment of whether an observed habit plane is consistent with a given match, more powerful, if less intuitive, methods are now available for the systematic investigation of the other features of a given transformation. In particular, the analysis using surface dislocations,[1] which has now been programmed for the Pegasus digital computer,[12] provides a more convenient alternative for extensive calculations.

ACKNOWLEDGMENTS

We are indebted to Dr. A. G. Crocker for valuable discussions.

One of us (B. A. B.) wishes to thank the University of Sheffield for the award of the J. H. Andrew Research Fellowship.

REFERENCES

1. R. BULLOUGH and B. A. BILBY, *Proc. Phys. Soc., Lond.* B **69**, 1276 (1956).
2. D. S. LIEBERMAN, *Acta Met.* **6**, 680 (1958).
3. B. A. BILBY and J. W. CHRISTIAN, *Monogr. Ser. Inst. Metals* no. 18, p. 121 (1955).
4. J. W. CHRISTIAN, *J. Inst. Met.* **84**, 386, 394 (1956).
5. J. S. BOWLES and J. K. MACKENZIE, *Acta Met.* **2**, 129 (1954).
6. J. K. MACKENZIE and J. S. BOWLES, *Acta Met.* **2**, 138 (1954).
7. M. S. WECHSLER, D. S. LIEBERMAN and T. A. READ, *Trans. Amer. Inst. Min. (Metall.) Engrs.* **197**, 1503 (1953).
8. F. C. FRANK, *Acta Met.* **1**, 15 (1953).
9. A. B. GRENINGER and A. R. TROIANO, *Trans. Amer. Inst. Min. (Metall.) Engrs.* **185**, 591 (1949).
10. G. KURDJUMOW and G. SACHS, *Z. Phys.* **64**, 325 (1930).
11. J. S. BOWLES and J. K. MACKENZIE, *Acta. Met.* **2**, 224 (1954).
12. B. A. BILBY, *Yearb. Roy. Soc., Rep. Res.*, p. 37 (1958).
13. E. C. BAIN, *Trans. Amer. Inst. Min. (Metall.) Engrs.* **70**, 25 (1924).

APPENDIX

The matching of prisms

The problem of matching together two given lattices so that all rows of one family in the first meet all rows of one family in the second on a particular plane, without regard for atomic positions along those rows, reduces to that of matching the ends of two triangular prisms.

Let two triangular prisms whose right sections have sides, a_1, b_1, c_1 and a_2, b_2, c_2, respectively, be so oriented that they match on the triangle ABC. Through the point C describe planes CA_1B_1 and CA_2B_2 perpendicular to the generators of the first and second, respectively. Let the lengths along edges of the first prism, B_1B and A_1A, be x_1 and y_1; and the lengths along edges of the second prism, B_2B and A_2A be x_2 and y_2. Then we have three equations:

$$x_1^2 + a_1^2 = x_2^2 + a_2^2 = a_0^2 \qquad \text{(A.1)}$$

$$y_1^2 + b_1^2 = y_2^2 + b_2^2 = b_0^2 \qquad \text{(A.2)}$$

$$(x_1 - y_1)^2 + c_1^2 = (x_2 - y_2)^2 + c_2^2 = c_0^2 \qquad \text{(A.3)}$$

where a_0, b_0 and c_0 denote the sides of the triangle ABC. Now let us re-express the variables and the constants in terms of means and differences, thus

$$x = \tfrac{1}{2}(x_1 + x_2) \qquad \delta x = x_2 - x_1$$

$$a = \tfrac{1}{2}(a_1 + a_2) \qquad \delta a = a_2 - a_1 \text{ etc.} \qquad \text{(A.4)}$$

Equations (A1—3) now become

$$x\delta x = -a\delta a \qquad \text{(A.5)}$$

$$y\delta y = -b\delta b \qquad \text{(A.6)}$$

$$(x - y)(\delta x - \delta y) = -c\delta c. \qquad \text{(A.7)}$$

VOL. 8 1960

By combination of these we can derive two equations

$$y/x + \delta y/\delta x = (a\delta a + b\delta b - c\delta c)/a\delta a \quad \text{(A.8)}$$

$$x/y + \delta x/\delta y = (a\delta a + b\delta b - c\delta c)/b\delta b \quad \text{(A.9)}$$

whence it follows that y/x and $\delta y/\delta x$ are conjugate roots of the same quadratic equation. Solving this, and employing equation (5) once more we obtain equations giving δx, y and δy as simple functions of x:

$$\delta x = A/x \quad \text{(A.10)}$$

$$y = Bx \quad \text{(A.11)}$$

$$\delta y = AC/x \quad \text{(A.12)}$$

where A, B and C depend only on the dimensions of the prisms:

$$A = -a\delta a \quad \text{(A.13)}$$

$$B = \{a\delta a + b\delta b - c\delta c + [(a\delta a + b\delta b - c\delta c)^2 - 4a\delta a b\delta b]^{1/2}\}/2a\delta a \quad \text{(A.14)}$$

$$C = \{a\delta a + b\delta b - c\delta c - [(a\delta a + b\delta b - c\delta c)^2 - 4a\delta a b\delta b]^{1/2}\}/2a\delta a \quad \text{(A.15)}$$

and B and C may be interchanged to give an alternative solution.

The angles θ_1, ϕ_1, ψ_1, θ_2, ϕ_2, ψ_2 between the generators of the prisms and the traces of their a, b and c faces in the matching plane are calculable from the equations:

$$\tan\theta_1 = a_1/x_1; \quad \tan\phi_1 = b_1/y_1; \quad \tan\psi_1 = c_1/(x_1 - y_1) \quad \text{(A.16)}$$

$$\tan\theta_2 = a_2/x_2; \quad \tan\phi_2 = b_2/y_2; \quad \tan\psi_2 = c_2/(x_2 - y_2) \quad \text{(A.17)}$$

The differences $\theta_2 - \theta_1 = \delta\theta$ etc., are given by

$$\sin\delta\theta = \tan\theta_1 \cdot (a_2/a_1 - \cos\delta\theta) \quad \text{(A.18)}$$

$$\sin\delta\phi = \tan\phi_1 \cdot (b_2/b_1 - \cos\delta\phi) \quad \text{(A.19)}$$

$$\sin\delta\psi = \tan\psi_1 \cdot (c_2/c_1 - \cos\delta\psi) \quad \text{(A.20)}$$

which are suitable for iterative approximation; or if they are small by

$$\delta\theta = \delta a/x = -\delta x/a \quad \text{(A.21)}$$

$$\delta\phi = \delta b/y = -\delta y/b \quad \text{(A.22)}$$

$$\delta\psi = \delta c/(x - y) = (\delta y - \delta x)/c. \quad \text{(A.23)}$$

The dihedral angle ω_1 between the matching plane and the c_1 face of the first prism is given by the formula

$$\tan^2\omega_1 = \frac{{c_1}^2 + (x_1 - y_1)^2}{[x_1c_1/(a_1\sin\beta_1) - (x_1 - y_1)\cot\beta_1]^2} \quad \text{(A.24)}$$

where β_1 is the angle between the a_1 and c_1 faces given by

$$\cos\beta_1 = ({a_1}^2 - {b_1}^2 + {c_1}^2)/2a_1c_1. \quad \text{(A.25)}$$

The difference $\omega_2 - \omega_1 = \delta\omega$ is given by

$$\sin\delta\omega = \tan\omega_1 \cdot [a_2\sin\beta_2/(a_1\sin\beta_1) - \cos\delta\omega] \quad \text{(A.26)}$$

in a form suitable for iterative approximation: or, if $\delta\omega$ is small by

$$\delta\omega = \tan\omega_1 \cdot [a_2\sin\beta_2/(a_1\sin\beta_1) - 1]. \quad \text{(A.27)}$$

When the calculation refers to a lattice, $a_1\sin\beta_1$ is the spacing between planes of the family c_1.

THERMODYNAMICS OF FORMATION OF COPPER–MAGNESIUM AND NICKEL–MAGNESIUM COMPOUNDS FROM VAPOR PRESSURE MEASUREMENTS*†

J. F. SMITH and J. L. CHRISTIAN‡

The magnesium vapor pressures over copper–magnesium and nickel–magnesium alloys have been measured by the Knudsen effusion method in the temperature range, 400–1100°K. The free energies, enthalpies and entropies of formation of Mg_2Cu, $MgCu_2$, Mg_2Ni and $MgNi_2$ were computed from the vapor pressure data. The results indicate that the bond strengths in the nickel–magnesium compounds are appreciably greater than in the corresponding copper–magnesium compounds.

THERMODYNAMIQUE DE LA FORMATION DES COMPOSES CUIVRE–MAGNESIUM ET NICKEL–MAGNESIUM A PARTIR DE MESURES DES TENSIONS DE VAPEUR

Les tensions de vapeur des alliages cuivre–magnésium et nickel–magnesium ont été mesurées par la méthode d'effusion de Knudsen dans le domaine de températures allant de 400 à 1100°K. De ces valeurs ont été déduites les énergies libres, les enthalpies et les entropies de formation de Mg_2Cu, $MgCu_2$, Mg_2Ni et $MgNi_2$.

Les résultats indiquent que les liaisons dans les composés de nickel–magnésium sont sérieusement plus fortes que les correspondantes dans les composés cuivre–magnésium.

THERMODYNAMISCHE DATEN ZUR BILDUNG VON KUPFER–MAGNESIUM UND NICKEL–MAGNESIUM VERBINDUNGEN AUS DAMPFDRUCKMESSUNGEN

Der Magnesiumdampfdruck über Kupfer–Magnesium und Nickel–Magnesium Legierungen wurde nach der Knudsenschen Effusionsmethode im Temperaturbereich von 400° bis 1100° K gemessen. Die freien Energien, Enthalpien und Entropien für die Bildung von Mg_2Cu, $MgCu_2$, Mg_2Ni und $MgNi_2$ wurden aus den Dampfdruckdaten berechnet. Die Ergebnisse zeigen, daß die Bindungskräfte der Nickel–Magnesium Verbindungen beträchtlich größer sind als die der entsprechenden Kupfer–Magnesium Verbindungen.

VOL. 8 1960

INTRODUCTION

Measurement of the vapor pressure of magnesium over a series of copper–magnesium and nickel–magnesium alloys was undertaken in order to determine the thermodynamics of formation of the compounds, Mg_2Cu, $MgCu_2$, Mg_2Ni and $MgNi_2$. No thermodynamic data relating to the formation of any of these compounds was found in standard compilations. Accumulation of such data for a large number of intermetallic compounds is desirable in order to correlate energies and entropies of formation with crystal structure and, hence, with intermetallic bonding. In the present case, elemental copper and nickel have closely comparable crystal structures, cohesive energies, atomic sizes and electronegativities which indicates a close similarity in the elemental bonding. The four compounds in question are structurally related and all exhibit high coordination numbers with the average in each structure being $13\frac{1}{3}$ neighbors per atom.

$MgCu_2$ and $MgNi_2$, together with $MgZn_2$, are the prototypes of the respective Laves structures: C15, C36 and C14. The crystallography of these structures has been discussed in detail by Berry and Raynor[1]. The atomic coordination in the structures is the same, but the structures differ in layering arrangement. If the formulae are represented as AB_2, each A atom is coordinated to four A atoms and to twelve B atoms while each B atom is coordinated to six A atoms and to six B atoms. Both atomic species occur in the structures as interpenetrating three-dimensional networks.

The structures[2,3] of Mg_2Cu and Mg_2Ni have been determined, and while Mg_2Cu is orthorhombic and Mg_2Ni is hexagonal, the atomic coordination is in both cases very nearly the same as in the tetragonal C16 structure. Again, if the formulae are represented as A_2B, each A atom is coordinated to eleven A atoms and to four B atoms and each B atom is coordinated to eight A atoms and to two B atoms. The A species forms a three-dimensional network, but, in contrast to the Laves structures, the B species run through the structure as one-dimensional threads or chains. In the C16 structure all of these threads run parallel while in the Mg_2Cu and Mg_2Ni structures the threads

* Received April 6, 1959.

† Contribution no. 740, Institute for Atomic Research and Department of Chemistry; Iowa State College, Ames, Iowa. Work was performed in the Ames Laboratory of the U.S. Atomic Energy Commission.

‡ Present address: Convair Astronautics, San Diego, Calif.

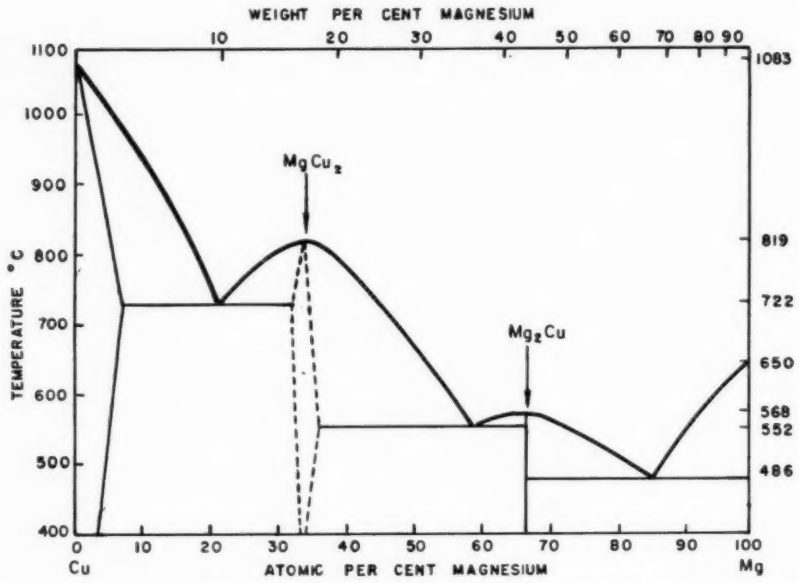


FIG. 1. Temperature–composition diagram for the copper–magnesium system (after Hansen and Anderko).

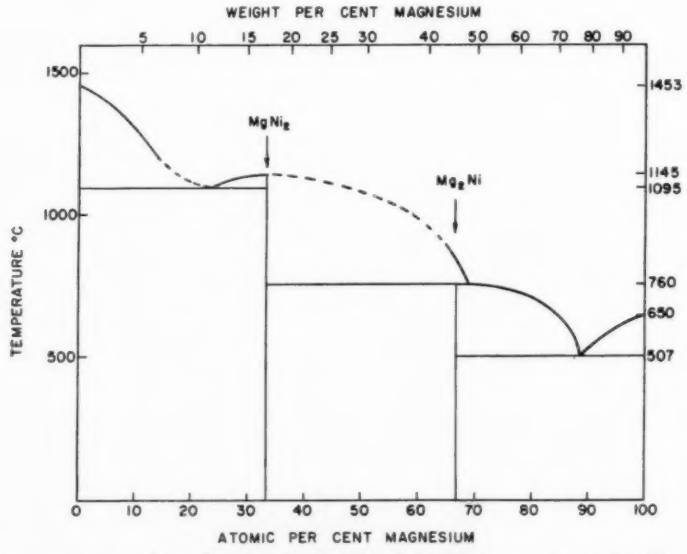


FIG. 2. Temperature–composition diagram for the nickel–magnesium system (after Hansen and Anderko).

run parallel within a given layer, but the direction varies from layer to layer.

The phase diagrams[4] of the copper–magnesium and nickel–magnesium systems are shown in Fig. 1 and Fig. 2, respectively. The diagrams are quite similar. No composition variation is indicated for the compounds Mg_2Cu, Mg_2Ni and $MgNi_2$ while a homogeneity range extending from about 32.8–35.5 at. % is shown for $MgCu_2$. The activity variation accompanying this narrow homogeneity range is expected to be small and, in view of the precision of the vapor pressure measurements, has been neglected in the treatment of the data.

EXPERIMENTAL RESULTS

Magnesium vapor pressures were measured by the Knudsen effusion method.[5] The apparatus has been described in a previous paper.[6] With this apparatus the amount of effused vapor was determined by weight loss. No solid angle calculations, consideration of condensing efficiency or additional analytical techniques were necessary. The magnesium vapor

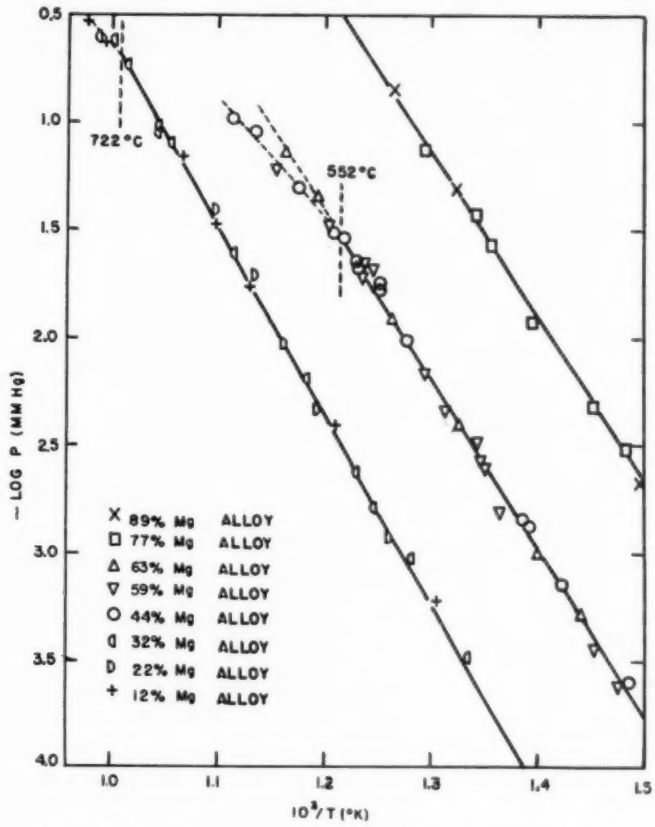


FIG. 3. Vapor pressures measured over copper–magnesium alloys.

was assumed to behave as an ideal monatomic gas; evidence supporting this assumption is the good agreement between magnesium vapor pressures measured by Schneider and Stoll[7] using a gas transport method and magnesium vapor pressures determined by the effusion method using the monatomic gas assumption. Chemical and spectrographic analyses of some of the condensate from the walls of the effusion apparatus were made after separate series of vapor pressure measurements above copper–magnesium and above nickel–magnesium alloys. The analytical results showed that neither copper nor nickel contributed significantly to the measured vapor pressures and that in both systems the measured vapor pressures could be treated as being due solely to magnesium.

Vapor pressures were measured over copper–magnesium alloys containing 12, 22, 32, 44, 59, 63, 77 and 89 at. % magnesium and over nickel–magnesium alloys containing 16, 30, 32, 49, 65, 77 and 87 at. % magnesium. The phase relationships in the alloys were checked both metallographically and by X-ray analysis. A plot of the copper–magnesium data is shown in Fig. 3 and a plot of the nickel–magnesium data is shown in Fig. 4. In both cases it can be seen that the measured vapor pressures are consistent with the phase diagrams. A summary of the data is shown in Table 1 where the parameters for the best linear fits to the experimental points are tabulated.

The measured vapor pressures over copper–magnesium alloys containing 77 and 89 at. % magnesium and over nickel–magnesium alloys containing 77 and 87 at. % magnesium were found to be in excellent agreement with the previously derived equation,[6]

$$\log P^{\circ}\,(\text{atm}) = 7.919 - 7796T^{-1} - 0.589 \log T - (0.16 \times 10^{-3})T + (0.85 \times 10^{4})T^{-2}, \quad (1)$$

for the vapor pressure over pure magnesium. Such agreement is expected if the terminal solubilities of copper in magnesium and nickel in magnesium are as small as indicated by the phase diagrams.

THERMODYNAMICS OF FORMATION OF $MgCu_2$ AND $MgNi_2$

Vapor pressures measured over copper–magnesium alloys containing 12, 22 and 32 at. % magnesium

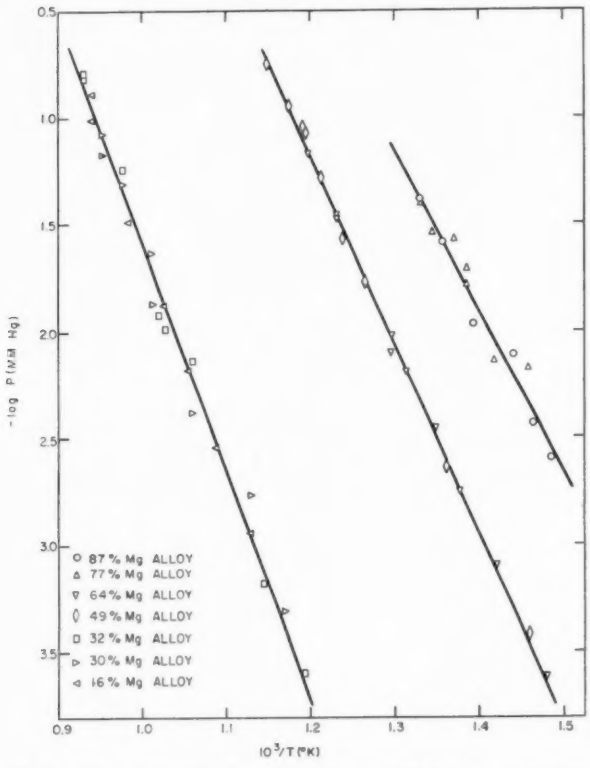


FIG. 4. Vapor pressures measured over nickel–magnesium alloys.

TABLE 1. Linear representation of measured vapor pressures $\log P$ (mm Hg) $= AT^{-1} + B$

Pressure	Over phase region	$-A$	B
P^{I}	$MgCu_2 + Mg_2Cu$	7830 ± 110	8.00 ± 0.20
P^{II}	$Cu + MgCu_2$	8540 ± 130	7.90 ± 0.20
P^{III}	$MgNi_2 + Mg_2Ni$	8840 ± 90	9.42 ± 0.11
P^{IV}	$Ni + MgNi_2$	10700 ± 200	9.12 ± 0.20
P^{o}	pure Mg	7550 ± 130	8.69 ± 0.19

represent the equilibrium vapor pressures for the reaction,

$$MgCu_2\,(s) \rightleftharpoons Mg\,(g) + 2\,Cu\,(soln),$$
$$\Delta F^{\circ} = -RT \ln P^{II} a_{Cu}^2, \qquad (2)$$

where P^{II} is the magnesium vapor pressure, a_{Cu} is the activity of copper in the terminal solid solution and ΔF° is the free energy associated with the dissociation of the compound into pure solid copper and magnesium gas at one atmosphere pressure. The available data on the terminal solubility of magnesium in copper is not highly accurate,[4] but the experimental points indicate a variation from about 97–93 at. % copper in the temperature range of the vapor pressure measurements. The temperature dependence of the mole fraction of copper, N_{Cu}, in the terminal solutions was found to be quite adequately represented by the simple formula,

$$-RT \ln N_{Cu}^2 = -310 + 0.595T. \qquad (3)$$

If the Raoult's law approximation, $a_{Cu} = N_{Cu}$, is made, this expression is simply the free energy contribution in equation (2) arising from the dissolution of pure solid copper to form solid solution. Any error introduced into the evaluation of the enthalpy and entropy of formation of $MgCu_2$ through use of the Raoult's law approximation or because of inexact knowledge of the composition of the terminal solutions is apt to be much less than the uncertainties arising from the precision limits of the vapor pressure measurements.

Since the heat capacity of $MgCu_2$ has been measured, the temperature dependence of the free energy of the reaction in equation (2) may be obtained through use of a defined sigma function,[8] $\Sigma = \Delta H_0\, T^{-1} + I$. The constants, ΔH_0 and I, are the integration constants arising, respectively, from the integrals, $\int \Delta C_p\, dT$ and $\int d\,(\Delta F^{\circ}/T)$. The experimental values for the heat capacities of the compound[9] $MgCu_2$ and for pure copper[10] were combined with the ideal value for magnesium vapor to obtain for the reaction,

$$\Delta C_p = 1.12 - (5.50 \times 10^{-3})T. \qquad (4)$$

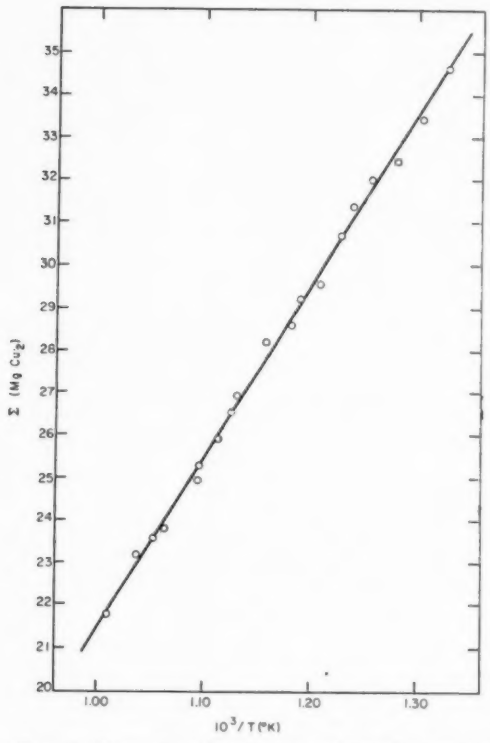


FIG. 5. Sigma function versus reciprocal temperature for the dissociation of $MgCu_2$.

The relationship between ΔF° in equation (2) was combined with the relationships obtained from the integrals to obtain

$$\Sigma\,(MgCu_2) = -R \ln P^{II} N_{Cu}^2 + 1.12 \ln T - (2.75 \times 10^{-3})T. \quad (5)$$

Numerical values for the sigma function were computed from the measured vapor pressures and the temperature dependence of N_{Cu}. A plot of the sigma function versus reciprocal temperature is shown in Fig. 5. The degree of linearity of this plot is a check of the consistency of the data. The constants, ΔH_0 and I, were evaluated through use of the method of least squares: $\Delta H_0 = 40.27 \pm 0.54$ kcal/mol and $I = -18.80 \pm 0.63$ cal/mol deg.

The numerical constants for the sigma function can be substituted into equation (5), and the equation can then be rearranged to obtain ΔF° for equation (2). This ΔF° may be combined with the ΔF° computed from equation (1) for the process of sublimation of pure magnesium. This combination gives the free energy of formation of the compound $MgCu_2$ from the elements in their standard states and may be expressed as

$$Mg\ (s) + 2\ Cu\ (s) \rightleftharpoons MgCu_2\ (s), \qquad \Delta F^\circ = RT \ln P^{II} N_{Cu}^2 / P^\circ, \quad (6)$$

with

$$\Delta F^\circ = -4600 + 5.27\ T \log T - (2.00 \times 10^{-3})T^2 - (0.39 \times 10^5)T^{-1} - 17.44T, \quad (7a)$$

$$\Delta H^\circ = -4600 - 2.29\ T + (2.00 \times 10^{-3})T^2 - (0.78 \times 10^5)T^{-1}, \quad (7b)$$

$$\Delta S^\circ = 15.15 - 5.27 \log T + (4.00 \times 10^{-3})T - (0.39 \times 10^5)T^{-2}. \quad (7c)$$

These relationships were used to compute values for the enthalpy and entropy of formation: $\Delta H^\circ_{298} = -5.4 \pm 1.1$ kcal/mol and $\Delta S^\circ_{298} = 2.8 \pm 1.5$ cal/mol deg.

Vapor pressures measured above nickel–magnesium alloys containing 16, 30 and 32 at. % magnesium represent the equilibrium vapor pressures over the region of solid nickel plus the compound $MgNi_2$. These vapor pressure data may be treated in a manner analogous to the treatment of the copper–magnesium data. In the case of the nickel–magnesium alloys, the terminal solubility of magnesium in nickel is negligible[4] and the activity of nickel may be set equal to unity at all temperatures. Heat capacity data for the compound[9] $MgNi_2$ and for pure nickel[10] were combined with the ideal value for magnesium vapor to obtain

$$\Delta C_p = 1.10 - (3.32 \times 10^{-3})T \quad (8)$$

for the process of sublimation of magnesium from $MgNi_2$. Measured values for the vapor pressure, P^{IV}, were used to evaluate a sigma function for this sublimation process. A plot of the sigma function versus reciprocal temperature is shown in Fig. 6. The integration constants were evaluated by the method of least squares: $\Delta H_0 = 48.1 \pm 1.1$ kcal/mol and $I = -21.7 \pm 1.1$ cal/mol deg. These numerical constants were utilized to obtain for the reaction,

$$Mg\ (s) + 2\ Ni\ (s) \rightleftharpoons MgNi_2\ (s), \qquad \Delta F^\circ = RT \ln P^{IV}/P^\circ, \quad (9)$$

the following relationships for the thermodynamic functions representing the formation of the compound from the pure elements:

$$\Delta F^\circ = -12400 + 5.23\ T \log T - (0.91 \times 10^{-3})T^2 - (0.39 \times 10^5)T^{-1} - 14.5T; \quad (10a)$$

$$\Delta H^\circ = -12400 - 2.27\ T + (0.91 \times 10^{-3})T^2 - (0.78 \times 10^5)T^{-1}; \quad (10b)$$

$$\Delta S^\circ = 12.26 - 5.23 \log T + (1.82 \times 10^{-3})T - (0.39 \times 10^5)T^{-2}. \quad (10c)$$

It should be noted that these formulae are based upon heat capacity and vapor pressure values taken above the Curie temperature of nickel. In principle, a correction for the magnetization of nickel should be

VOL. 8 1960

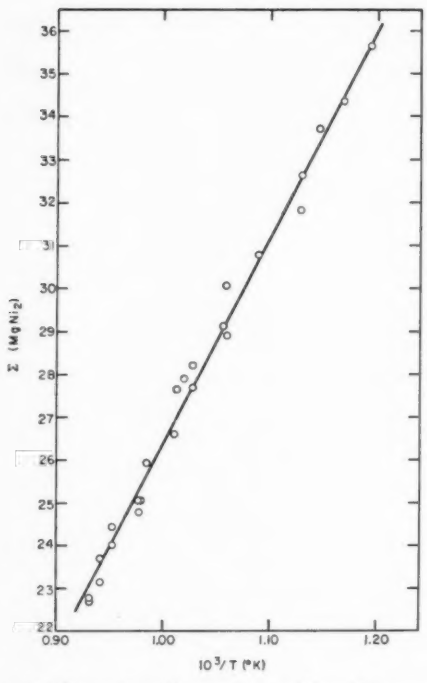


FIG. 6. Sigma function versus reciprocal temperature for the dissociation of $MgNi_2$.

made when extrapolating these formulae to calculate entropies and energies of formation below the Curie temperature. However, calculation of this correction on the basis of the heat capacity data tabulated by Kelley[10] shows that in the range between room temperature and the Curie point the correction is less than the experimental uncertainty and may be neglected. Values for the enthalpy and entropy of formation were computed as: $\Delta H^\circ_{298} = -13.3 \pm 1.5$ kcal/mol and $\Delta S^\circ_{298} = -0.6 \pm 1.4$ cal/mol deg.

THERMODYNAMICS OF FORMATION OF Mg_2Cu AND Mg_2Ni

The equilibrium vapor pressures for the reaction,

$$Mg_2Cu\ (s) \rightleftharpoons \tfrac{3}{2}Mg\ (g) + \tfrac{1}{2}MgCu_2\ (s), \qquad (11)$$
$$\Delta F^\circ = -(3/2)\ RT \ln P^{\mathrm{I}},$$

were obtained from measurements above copper–magnesium alloys containing 44, 59 and 63 at. % magnesium. Equation (11) may be combined with equation (6) and with the description of the sublimation process for pure magnesium to obtain

$$2\ Mg\ (s) + Cu\ (s) \rightleftharpoons Mg_2Cu\ (s),$$
$$\Delta F^\circ = RT\ [\tfrac{1}{2} \ln (P^{\mathrm{II}} N^2_{Cu}/P^\circ) + (\tfrac{3}{2}) \ln (P^{\mathrm{I}}/P^\circ)]. \qquad (12)$$

Since no heat capacity data were available for the compound Mg_2Cu, it was assumed that ΔC_p for the reaction was zero. The appropriate vapor pressure relationships shown in Table 1 and the mole fraction relationship in equation (3) were substituted into equation (12) to obtain as a mean for the temperature range of measurement,

$$\Delta F^\circ = -(4.0 \pm 1.8) \times 10^3 - (6.8 \pm 3.6)T. \qquad (13)$$

The relatively large uncertainties result because of the cumulative errors from three separate sets of measurements; the use of the enthalpy and entropy values as 298°K values is likely to be valid within the precision of measurement.

Since no heat capacity data were available for the compound Mg_2Ni, the nickel–magnesium data were treated in a manner completely analogous to that for the copper–magnesium data. Vapor pressures measured above the nickel–magnesium alloys containing 49 and 64 at. % magnesium represent the equilibrium vapor pressures over the two phase region of $MgNi_2$ plus Mg_2Ni. Appropriate combination of the thermodynamic processes describing the equilibrium between the compounds, the sublimation of pure magnesium and the formation of $MgNi_2$ were made to obtain

$$2\ Mg\ (s) + Ni\ (s) \rightleftharpoons Mg_2Ni\ (s),$$
$$\Delta F^\circ = RT\ [\tfrac{1}{2} \ln (P^{\mathrm{IV}}/P^\circ) + (\tfrac{3}{2}) \ln (P^{\mathrm{III}}/P^\circ)] \qquad (14)$$
$$= -(16.0 \pm 2.2) \times 10^3 + (6.0 \pm 2.9)T.$$

DISCUSSION

Pertinent data relative to the formation of $MgCu_2$, $MgNi_2$, Mg_2Cu, Mg_2Ni and related compounds are summarized in Table 2, and some general observations may be noted. The compounds are listed in order of decreasing magnitude of the enthalpy of formation. There is indication from the tabulation that compounds of higher melting point tend to have larger heats of formation. But, contrary to the results correlated by Kubaschewski[11], there is little apparent correlation between the enthalpies of formation and either the absolute or relative volume contraction accompanying compound formation. Improved precision in lattice parameter determinations might alter somewhat the values for the volume contractions, but it is most unlikely that this would improve a correlation between enthalpy and volume contraction. Possibly the lack of correlation in the present instance is attributable to the fact that the compounds here under consideration are normally considered to result because of atomic size effects while the volume–enthalpy correlation achieved by Kubaschewski was for structures normally considered to form because of electron/atom ratios. In Table 2 a trend toward increased cohesion with an increase in the number of valence electrons is indicated if the nominal number of valence electrons is based on the ordinary chemical

TABLE 2. Data on the formation of $MgCu_2$, $MgNi_2$, Mg_2Cu, Mg_2Ni, and related compounds

Compound	Structure	$-\Delta H_{298}$ (kcal/mol)	$+\Delta S_{298}$ (cal/mol deg)	$-\Delta V$ (cm³/mol)	(%)	Nominal no. bonding electrons	Melting point (°C)
			(a) Laves structures				
$CeAl_2$	C15	39.0 ± 3.0	—	0.8	2.1	9	1465
$LaAl_2$	C15	36.1	—	1.6	3.7	9	1424
$ZrZn_2$	C15	35.3 ± 0.7	−16.2 ± 0.7	1.7	5.4	8	1180
$MgNi_2$	C36	13.3 ± 1.5	−0.6 ± 1.4	3.2	11.8	6	1145
$MgZn_2$	C14	12.8 ± 0.5	—	2.2	6.8	6	590
$CaMg_2$	C14	8.3 ± 2.9	−1.1 ± 4.3	3.0	5.6	6	714
$MgCu_2$	C15	5.4 ± 1.1	2.8 ± 1.5	1.7	6.2	4	819
KNa_2	C14	—	0.9	1.1	1.2	3	dec. 6.6
			(b) C16 and related structures				
Mg_2Ni	~C16	16.0 ± 2.2	−6.0 ± 2.9	3.7	10.8	6	dec. 760
Al_2Cu	C16	9.5 ± 1.0	—	0.1	0.5	7	591
Mg_2Cu	~C16	4.0 ± 1.8	6.8 ± 3.6	2.2	6.2	5	568

Structure and lattice parameter data for ΔV calculation were taken from W. B. PEARSON, *Handbook of Lattice Spacings and Structures of Metals*, Pergamon Press, New York (1958); melting point data (except $ZrZn_2$) from M. HANSEN and K. ANDERKO, *Constitution of Binary Alloys*, 2nd Ed., McGraw-Hill, New York (1958); and the thermodynamic values as follows:
(a) $CeAl_2$, $LaAl_2$, $MgZn_2$, Al_2Cu: O. KUBASCHEWSKI and E. EVANS, *Metallurgical Thermochemistry*, Academic Press, New York (1951);
(b) $ZrZn_2$: P. CHIOTTI and G. R. KILP, *Trans. Amer. Inst. Min (Metall.) Engrs.*, to be published.
(c) $CaMg_2$: J. F. SMITH and R. L. SMYTHE, *Acta Met.* **7**, 261 (1959).
(d) Na_2K: entropy calculated from heat capacity data of KRIER, CRAIG and WALLACE, *J. Phys. Chem.* **61**, 522 (1957);
(e) $MgNi_2$, $MgCu_2$, Mg_2Ni, Mg_2Cu: this investigation.

VOL. 8 1960

valence: Zr: 4; Al, Ce, La: 3; Ca, Mg, Ni, Zn: 2; Cu, K, Na: 1. No such trend is found if Pauling valences[12] are subsituted for the ordinary chemical valences. Lastly, four out of five of the Laves phases show quite small values for the entropies of formation. More data must be acquired before it can be ascertained whether or not such low values for the entropies of formation are typical of Laves stuctures in general.

The enthalpy of formation of $MgCu_2$ is larger than the enthalpy of formation of Mg_2Cu. This is in accord with the general rule[9] that, within a given system, the heats of formation per gram atom of the compounds occur in the same order as the melting points. This order of the enthalpies of formation is inverted in the nickel–magnesium system with the peritectic decomposition of Mg_2Ni occurring below the melting point of $MgNi_2$. This exception to the general rule must be attributable to the fact that the relatively large negative entropy of formation of Mg_2Ni opposes high temperature stability.

Since the close crystallographic relationships between the respective compounds in the two alloy systems necessitates equal numbers of ligands, the larger enthalpies of formation of the nickel–magnesium compounds compared to the respective copper–magnesium compounds indicate appreciably greater bond strengths in the nickel–magnesium compounds than in the copper–magnesium compounds. The relatively greater volume contraction of the nickel–magnesium compounds is also consistent with stronger bonding. In addition, the negative entropies of formation of the nickel–magnesium compounds indicate reduced vibrational freedom and greater localization of the atoms in the compounds compared to the elemental structures and is indicative of stronger and more rigid bonds in the compounds. In contrast, the entropies of formation of the copper–magnesium compounds are positive. Hence, comparison of the entropies of formation also indicates that the bonding in the nickel-magnesium compounds is stronger than in the copper–magnesium compounds.

REFERENCES

1. R. L. BERRY and G. V. RAYNOR, *Acta Cryst., Camb.* **6**, 178 (1953).
2. K. SCHUBERT and K. ANDERKO, *Naturwiss.* **38**, 46 and 259 (1951); *Z. Metallk.* **42**, 321 (1951).
3. G. EKWALL and A. WESTGREN, *Ark. Kemi. Min. Geol.* **14B**, No. 7 (1940).
4. M. HANSEN and K. ANDERKO, *Constitution of Binary Alloys*, (2nd Ed.), pp. 594 and 909. McGraw-Hill, New York (1958).
5. M. KNUDSEN, *Ann. Phys. Lpz.* **28**, 999 (1909).
6. J. F. SMITH and R. L. SMYTHE, *Acta Met.* **7**, 261 (1959).
7. A. SCHNEIDER and E. K. STOLL, *Z. Elektrochem.* **47**, 519 (1941).
8. L. S. DARKEN and R. W. GURRY, *Physical Chemistry of Metals*, pp. 225–231. McGraw-Hill, New York (1953).
9. O. KUBASCHEWSKI and E. EVANS, *Metallurgical Thermochemistry*, pp. 288, 290 and 185. Academic Press, New York (1951).
10. K. K. KELLEY, *Bull. U.S. Bur. Mins.* no. 476 (1949).
11. O. KUBASCHEWSKI, *Z. Elektrochem.* **47**, 623 (1941).
12. L. PAULING, *Theory of Alloy Phases*, p. 220. Am. Soc. for Metals, Cleveland, Ohio (1956).

INTERMETALLIC PHASES IN THE ALUMINIUM-MANGANESE BINARY SYSTEM*

M. A. TAYLOR†

The region of the aluminium-manganese phase diagram from 33 to 45 wt.% manganese has been investigated by means of X-ray analysis, density measurements, and microsections. Two previously unknown intermetallic compounds have been isolated, and a third known phase shown to be stable only at high temperatures. Crystallographic and chemical studies of the various phases are described, and corrections to the published phase diagram are suggested.

PHASES INTERMETALLIQUES DANS LE SYSTEME BINAIRE ALUMINIUM–MANGANESE

Le diagramme de phase aluminium–manganèse a été étudié dans la région de 33 à 45% (en poids) de manganèse par une analyse aux rayons X, par des mesures de densité et par l'observation de microsections. Deux composés intermétalliques inconnus ont été isolés. L'auteur a observé également qu'une troisième phase déjà identifiée n'est stable qu'aux températures élevées.

L'étude cristallographique et chimique des diverses phases est décrite et des corrections sont suggérées à propos des diagrammes de phase antérieurement publiés.

INTERMETALLISCHE VERBINDUNGEN IM SYSTEM ALUMINIUM–MANGAN

Im Phasendiagramm Aluminium–Mangan wurde das Gebiet von 33 bis 45 Gewichts–Prozent Mangan röntgenographisch, densitometrisch und metallographisch untersucht. Zwei bisher unbekannte intermetallische Verbindungen wurden isoliert, von einer dritten wurde gezeigt, daß sie nur bei hohen Temperaturen stabil ist. Es werden kristallographische und chemische Untersuchungen der verschiedenen Phasen beschrieben und Korrekturen an den veröffentlichten Phasendiagrammen vorgeschlagen.

INTRODUCTION

Attempts to produce the '$MnAl_3$' phase referred to by Hofmann[1] revealed several errors in the published Al–Mn phase diagram (Hansen[2]). A melt at 34.6 per cent Mn‡ quenched from 850°C contained hexagonal crystals with unit cell dimensions:

$$a = 19.95 \pm 0.01 \text{ Å}$$
$$c = 24.52 \pm 0.01 \text{ Å}.$$

This phase is hereafter referred to as μ(AlMn). A second melt at 40.0 per cent Mn, also quenched from 850°C, contained hexagonal crystals with unit cell dimensions:

$$a = 7.54 \pm 0.01 \text{ Å}$$
$$c = 7.90 \pm 0.01 \text{ Å}.$$

This phase is referred to as ϕ(AlMn). Each of these ingots contained more than one phase. Neither of the two hexagonal phases had previously been found in the Al–Mn binary system, and furthermore the '$MnAl_3$' phase could not be found in either ingot.

These observations led to an investigation of the aluminium-rich region of the phase diagram, and suggestions for its correction have been made. It must be stressed here that the prime purpose of the investigation was not the exact determination of the form of the phase diagram (and hence no thermal analysis has been done), but rather to establish the chemical compositions and crystallographic characteristics of the various intermetallic compounds found in the system, and to examine their stability at a limited number of temperatures.

A survey of the literature showed that knowledge of the region from 35–45 per cent Mn is very uncertain, but that the region 0–35 per cent Mn appears to be reasonably well established. Eleven melts were therefore made up at 1 per cent composition intervals in the range 35–45 per cent Mn and annealed at 780°C; these were examined by X-ray powder photographs, density measurements and microsections. Selected single crystals were examined by X-ray oscillation photographs. Subsequently sixteen further melts, in a wider composition range, were made up, annealed at various temperatures, and examined by the above methods.

PREVIOUS WORK

Many investigations of the Al–Mn system have been reported, and the reader is referred to Hansen[2] (from which Fig. 1 has been adapted) for a detailed discussion and relevant references. Only points of particular interest in relation to the present work are mentioned here.

The nature of the phases X and '$MnAl_3$' is still uncertain. The exact composition and homogeneity range of the phase '$MnAl_3$' is not satisfactorily

* Received March 16, 1959.

† Crystallographic Laboratory, Cavendish Laboratory, Cambridge. Now at Metallurgy Division, A.E.R.E., Harwell.

‡ Weight percentages are used throughout this paper.

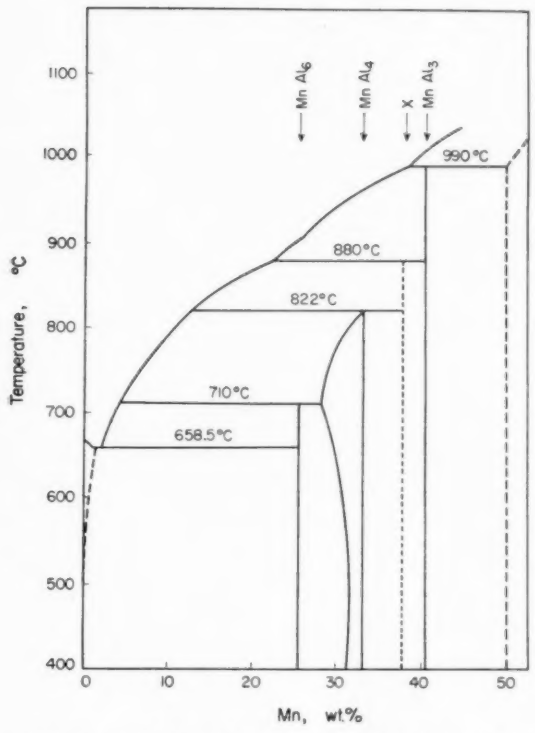


FIG. 1. Aluminium-rich region of published aluminium–manganese phase diagram Hansen[2].
Adapted by permission from *Constitution of Binary Alloys* by M. Hansen. Copyright McGraw-Hill Book Co. (1958).

established, although Hofmann[1] isolated crystals of the phase, measured its unit cell dimensions, and gave its chemical composition (from chemical analyses of the single crystals) as 41 per cent Mn. Phillips[3] established the phase X as having a composition between 33.7 and 41.4 per cent Mn and suggested it may be the phase found with monoclinic or triclinic habit in ingots of 20–40 per cent Mn. Hofmann[1] and Bland[4] determined the unit cell dimensions of this triclinic crystal—i.e. δ(AlMn)—and the latter gave its composition, from crystallographic considerations, as 42.5 per cent Mn (i.e. Mn_4Al_{11}), in agreement with the previous statement of Hanemann & Schrader[5] that it is richer in manganese content than $MnAl_3$. It seems possible, in view of the disagreement of the various compositions assigned, that the phase described by Phillips is not δ(AlMn) but a different phase, probably μ(AlMn) or ϕ(AlMn).

In addition to the peritectic temperatures associated with the formation of $MnAl_6$ and $MnAl_4$, thermal arrests have also been observed at 880°C,[3,6] at 920°C[6] and at 990°C.[7–9] The effect at 920°C was not observed by Phillips, and has therefore not been given in the published phase diagram; furthermore, correlation between the formation of the phases X and '$MnAl_3$' and the thermal arrests has not been satisfactorily established.

It must be added here that Phillips, on whose work the phase diagram in the region 30–45 per cent Mn is to a large extent based, was unable to anneal his specimens to equilibrium in the range 34–37 per cent Mn.

To summarise, one can say that knowledge of the composition and homogeneity ranges of the phases with composition between 35–45 per cent Mn appears reasonably well established.

IDENTIFICATION OF INTERMETALLIC PHASES

Possible methods of identification include recognition of crystal habit, chemical analysis, etching characteristics and X-ray analysis. In the present work it was decided that identification could best be carried out in terms of crystallographic characteristics, but that supporting evidence from as many other sources as possible is also necessary. The chemical composition is, of course, essential in the description of any phase.

PREPARATION OF SPECIMENS

The methods used to produce pure homogeneous ingots are now described. The manganese and aluminium were each of 99.99 per cent purity. The alloys were melted in recrystallized alumina crucibles, under a protective atmosphere of argon.

For a given specimen the aluminium and the manganese were melted together in an induction furnace. The resulting ingot was then cracked up and remelted in the induction furnace, this being done to ensure that all the manganese melted and to attempt to homogenise the ingot. The specimen was then annealed in a resistance furnace and finally quenched. The average weight of a specimen was twelve grams.

Previous work indicated that long anneals are necessary even at high temperatures in order to attain equilibrium conditions in these alloys. Some evaporation from the ingots, however, occurs during this prolonged annealing. To determine its extent, and also to check the long-range homogeneity in an ingot, a specimen of initial composition 35 per cent Mn was made and a piece of it analysed. The analysis yielded 34.7 per cent Mn, thus verifying that the evaporation was small and the long-range homogeneity satisfactory.

Details of the various annealing treatments are given below:

Melts A were made at 1 per cent composition intervals in the range 35–45 per cent Mn and

VOL. 8 1960

annealed for 10 days at 780°C. It was found that the '$MnAl_3$' phase (taking Hofmann's crystallographic data as a means of identification) was not stable in this region, and that melts at 35 and 36 per cent Mn had not reached equilibrium.

Melts B were quenched from 950°C, after being annealed at this temperature for half an hour. This was done to test for the existence of '$MnAl_3$' at temperatures above 780°C.

Melts C were annealed at 850°C for 14 days. This was done in a successful attempt to produce equilibrium in alloys of the same compositions as those that had not reached equilibrium in Melts *A*. Melts *C* showed the existence of a phase with composition apparently between $MnAl_4$ (i.e. 33.5 per cent Mn) and 35 per cent Mn.

Melts D were therefore made at 33–35 per cent Mn and annealed for 2 weeks at 810°C. Equilibrium was attained in these ingots.

METHODS OF EXAMINATION OF INGOTS

(a) *Density measurements*

The density of the ingot was measured by the displacement method, using distilled water. The ingots were cracked open and several solid pieces from each were used. Measurements made on three different specimens from each ingot gave a mean value of the density reproducible to within ± 1 per cent.

The specimens were slightly porous, and therefore slightly less dense than crystallographically ideal crystals. The degree of porosity should, however, be similar in ingots that have undergone identical heat treatments, and it may be assumed that the actual density is in some approximately fixed ratio to the ideally perfect density. The validity of this approximation is shown by the results below.

In a plot of density versus composition for ingots after similar heat treatments, peaks of maximum density may be expected at the stoichiometric compositions of the various intermetallic phases, and minima in the intermediate two-phase regions.

(b) *Metallography*

Microsections of samples from each ingot were prepared. Etching by total immersion for about 30 sec in ½ per cent HF was found to outline the various phases satisfactorily.

(c) *X-ray examination*

Powder photographs of representative samples from each ingot were taken using FeKα* radiation.

* FeKα, although not the most suitable for use with these alloys, was the only available radiation.

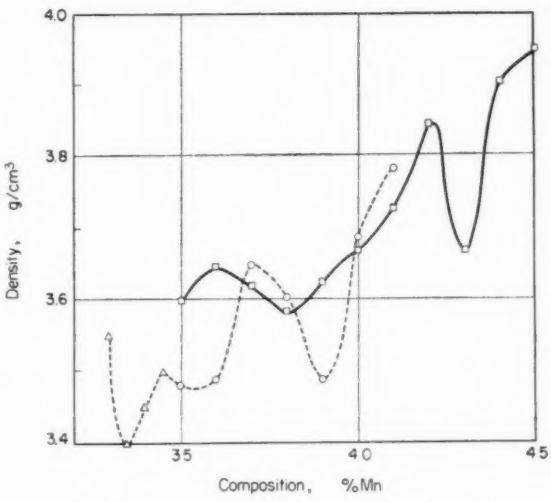


FIG. 2. Density measurements of aluminium–manganese alloys.
□ Specimens annealed at 780°C for 10 days (*A*)
○ Specimens annealed at 850°C for 14 days (*C*)
△ Specimens annealed at 810°C for 14 days (*D*).

Large single crystals of each phase were identified by means of rotation photographs, and powdered so as to produce "standard" powder photographs of each phase. From comparison of the former photographs with the "standards", the phases present in a given alloy could be identified. The unit cell of a phase can, in principle, be determined from its powder photograph, but unambiguous results cannot be guaranteed, and single-crystal rotation photographs were used to determine the unit cells of the various phases.

EXPERIMENTAL RESULTS

(a) *Density measurements*

The results of the density determinations are given in Figs. 2 and 3.

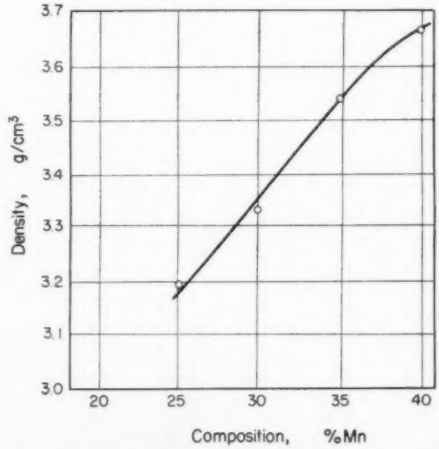


FIG. 3. Density measurements of aluminium–manganese alloys. Specimens quenched from 950°C (B).

TABLE 1. Aluminium–manganese intermetallic phases identified by X-ray powder photographs

Melts *A*: annealed for 10 days at 750°C

Composition (%Mn)	35	36	37	38	39	40	41	42	43	44	45
Phases observed	$\phi\mu\delta$	$\phi\delta\mu$	$\phi\delta$	$\phi\delta$	$\delta\phi$	$\delta\phi$	$\delta\phi$	Aδ	Aδ	Aδ	Aδ

Melts *C*: annealed for 14 days at 850°C

Composition (%Mn)	35	36	37	38	39	40	41
Phases observed	$\phi\mu$	$\phi\delta$	$\phi\delta$	$\phi\delta$	$\delta\phi$	$\delta\phi$	$\delta\phi$

Melts *D*: annealed for 14 days at 810°C

Composition (%Mn)	33	33½	34	34½
Phases observed	$MnAl_4$	$MnAl_4$,μ	μ,$MnAl_4$	μ

Melts *B*: quenched from 950°C

Composition (%Mn)	25	30	35	40
Phases observed	'$MnAl_3$', ϕ,μ,$MnAl_4$	'$MnAl_3$', ϕ,μ	'$MnAl_3$', ϕ,μ	*A*, '$MnAl_3$'

The phase present in the greater amount is listed first in each case.

The plots of density against composition in Fig. 2 suggest that intermetallic phases may occur in the alloys *A* at compositions close to 36 and 42 per cent Mn, in alloys *C* close to 37 per cent Mn and in alloys *D* close to 34½ per cent Mn; intermetallic compounds were in fact found very close to these compositions. Fig. 3 shows the variation of density with composition for a series of alloys quenched from 950°C. It is not, of course, claimed that this is an infallible method of determining the existence of intermetallic compounds: it is, however, expected to give indications which, in this case, proved very useful.

(b) *X-ray examination*

The results obtained from the X-ray powder photographs are given in Table 1. Phase *A* is the intermetallic compound richer in manganese than δ(AlMn): it was not studied here, as it was not of immediate interest. The unit cells of the various phases are given in Table 2. The phases ϕ(AlMn) and μ(AlMn) were previously unknown in the binary Al–Mn system: the unit cell dimensions obtained for $MnAl_6$, $MnAl_4$, '$MnAl_3$' and δ(AlMn) agreed with those given in the listed references.

(c) *Microsections*

The X-ray examination had shown certain of the melts *A* to contain three phases: this implies that the material had not reached an equilibrium state, and microsections of these specimens were therefore particularly valuable. Microsections of other specimens were taken, with the intention both of confirming the results of the X-ray work and of identifying the etching characteristics of the various phases prior to an examination of the ingots containing three phases.

Photographs of certain microsections are reproduced:

Fig. 4 shows a specimen of 39 per cent Mn after annealing for 10 days at 780°C. The two phases δ and ϕ are indicated. δ and ϕ were distinguished as follows: an ingot of 41 per cent Mn was known (from the X-ray data) to contain only a small amount of ϕ and hence the etching colour of each phase was deduced. This procedure was also applied to determine the etching characteristics of other phases.

Fig. 5 shows the specimen of 35 per cent Mn after annealing for 10 days at 780°C. The three phases δ, ϕ and μ are indicated. The μ phase etches in a rather similar colour to δ, but since X-ray analysis has shown that three phases are present, a distinction can be made. The appearance of the μ phase as a relatively fine deposit suggests that it may possibly grow at the expense of the δ phase after a sufficiently long anneal. These considerations showed the need for Melts *C* and *D*. X-ray examination showed these further melts each to consist of two phases: this was confirmed by microsection examination, which also showed the μ phase to occur as a coarser deposit (as anticipated) than in the three-phase ingot.

Fig. 6 shows a specimen of 35 per cent Mn annealed for 14 days at 850°C, phases μ and ϕ being indicated.

Fig. 7 shows a specimen of 34 per cent Mn annealed

TABLE 2. Unit cell dimensions of aluminium–manganese intermetallic compounds

Phase	Crystal system	Unit cell dimensions	Previous measurements
$MnAl_6$	Orthorhombic	$a = 6.50$ Å $b = 7.55$ Å $c = 8.87$ Å	Hofmann[1] Nicol[11]
$MnAl_4$	Hexagonal	$a = 28.4$ Å $c = 12.4$ Å	Hofmann [1] Bland[12]
μ(AlMn)	Hexagonal	$a = 19.95$ Å $c = 24.52$ Å	—
ϕ(AlMn)	Hexagonal	$a = 7.54$ Å $c = 7.90$ Å	—
'$MnAl_3$'	Orthorhombic	$a = 12.59$ Å $b = 14.80$ Å $c = 12.42$ Å	Hofmann[1]
δ(AlMn)	Triclinic	$a = 5.1$ Å $b = 17.1$ Å $c = 5.0$ Å; $\alpha = 93°$ $\beta = 100°$ $\gamma = 89°$	Bland[12] Hofmann[1]

VOL. 8 1960

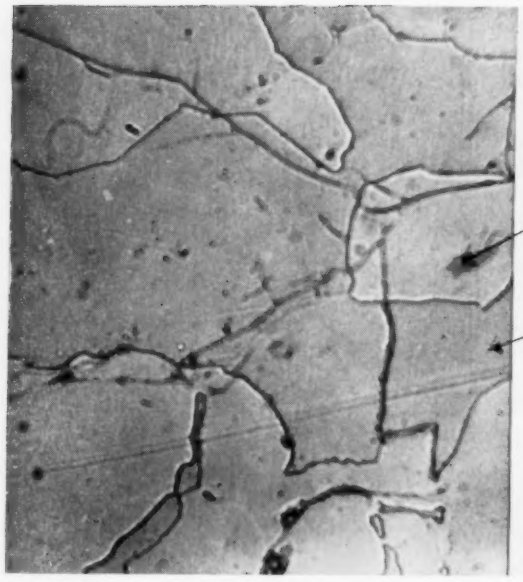


FIG. 4. Microsection of Al–39 per cent Mn annealed for 10 days at 780°C. ×400



FIG. 5. Microsection of Al–35 per cent Mn annealed for 10 days at 780°C. ×400

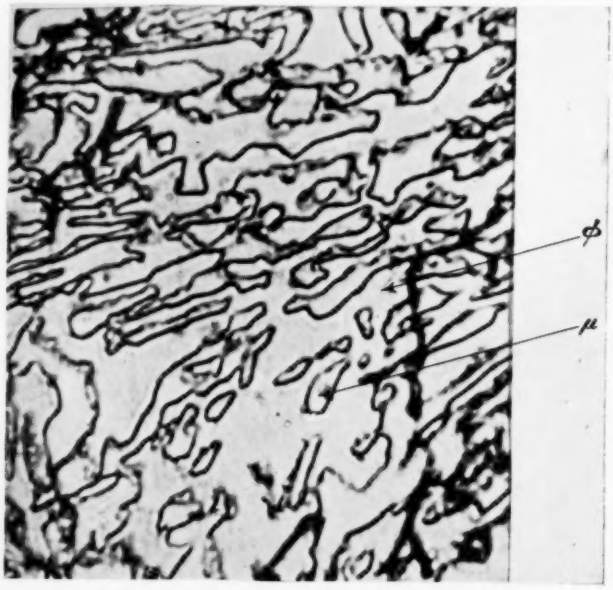


FIG. 6. Microsection of Al–35 per cent Mn annealed for 2 weeks at 850°C. ×800

for two weeks at 810°C; the crystals of $MnAl_4$ in a background of μ(AlMn) are clearly visible.

Micrographic examination of the ingots *B* (quenched from 950°C) showed them to contain several phases (as many as four in some cases) distributed in a cored fashion. The quench had not been very rapid, and the constituents present could not all be identified with absolute certainty; the investigation was not continued. The two points of interest were (i) that the ingots at 25, 30 and 35 per cent Mn contained a primary deposit ('$MnAl_3$') different from that in the 40 per cent Mn ingot (presumably *A*) and (ii) that no crystals of the δ phase were observed in these ingots.

Fig. 8 shows a specimen of 35 per cent Mn quenched from 950°C.

DISCUSSION

A complete description of a series of intermetallic compounds requires not only unit cell measurements,

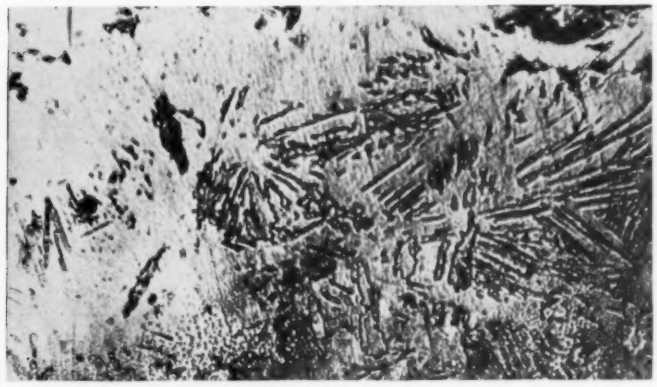


FIG. 7. Microsection of Al–34 per cent Mn annealed for 2 weeks at 810°C. ×400

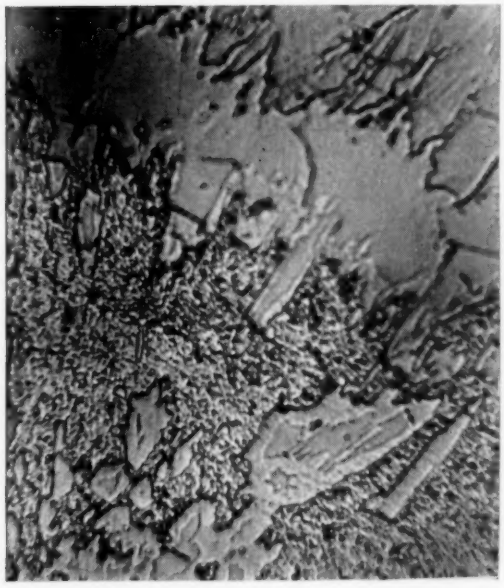


FIG. 8. Microsection of Al–35 per cent Mn quenched from 950°C.

but also the specification of their homogeneity ranges. From the X-ray and microsection work it is possible to fix the compositions, given in Table 3, at which each phase is stable. This method of assigning a composition to a phase is more satisfactory than chemical analysis of the single crystals, as these may be deficient in one element and thus not yield the exact composition. Only two of the intermetallic compounds reported above—i.e. $MnAl_4$ and μ(AlMn)—have been grown as single-phase ingots, probably because many have very narrow composition ranges.

In Table 3 the 'crystallographic' compositions of the phases for which they are known are also listed. (The 'crystallographic' composition is that of a crystal in which every atomic site is filled by the atom of the correct type.) It is, of course, quite possible that a phase is not stable at its true 'crystallographic' composition.[10] The agreement between the observed compositions and the 'crystallographic' compositions is good.

The published phase diagram (Fig. 1) has been shown to be incorrect, and though this work was not primarily designed to correct it, some tentative suggestions for improvement may be made.

It seems possible that the thermal arrest at 920°C observed by Dix *et al.*[6] does represent a peritectic reaction associated with the formation of some intermetallic phase. The present work has shown '$MnAl_3$' to be stable at 950°C but not below 850°C; also δ(AlMn) was not observed as a constituent of any melts quenched from 950°C. These facts and the other results reported above are all explained by the proposed phase diagram given in Fig. 9. The existence of the horizontal dotted line is not established, but is suggested in an attempt to produce a phase diagram in accordance with the facts; the temperature of the dotted line lies above 850°C. The intermetallic compounds richer in manganese than $MnAl_4$ are shown as line compounds, as their composition ranges, being small, have not been established.

TABLE 3. Chemical compositions of aluminium–manganese intermetallic phases

Phase	Composition from present work (%Mn)	'Crystallographic' composition (%Mn)	Composition suggested by density measurements (%Mn)
$MnAl_4$	33*	unknown	—
μ(AlMn)	34.5	unknown	34.5–35
ϕ(AlMn)	36–37	38 (Taylor[13])	36–38
'$MnAl_3$'	—	unknown	—
δ(AlMn)	41.5	42.5 (Bland[4])	42

* $MnAl_4$ is generally assumed to exist over a finite composition range: the composition 33 per cent Mn represents the manganese-rich limit of such a range.

VOL. 8 1960

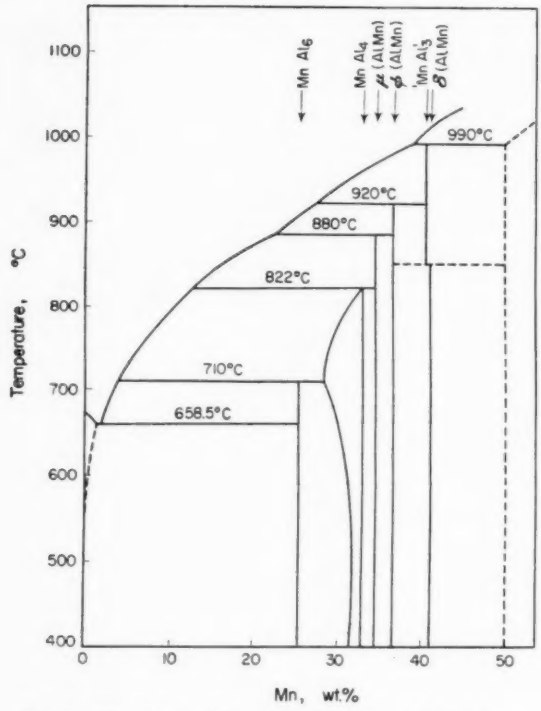


FIG. 9. Aluminium-rich region of suggested aluminium–manganese phase diagram.

ACKNOWLEDGMENTS

I wish to thank the Department of Scientific and Industrial Research for the award of a Research Studentship. This research forms part of a project supported by the Air Force Office of Scientific Research of the Air Research and Development Command, United States Air Force, through its European Office, under Contract No. AF. 61(052)-50. Some of the equipment used was purchased with the help of a generous award from the Government Grants Committee of the Royal Society.

I am greatly indebted to Professor N. F. Mott and Dr. W. H. Taylor for the provision of facilities and for their interest in the work. I should also like to thank Dr. P. Jane Brown and Mr. J. B. Forsyth for their help and encouragement. Aluminium Laboratories Ltd., Banbury, kindly gave the super-purity aluminium used in this work.

REFERENCES

1. W. HOFMANN, *Aluminium* Berlin **20,** 865 (1938).
2. M. HANSEN, *Constitution of Binary Alloys.* McGraw-Hill, New York (1958).
3. H. W. L. PHILLIPS, *J. Inst. Met.* **69,** 275 (1943).
4. J. A. BLAND, *Acta Cryst.* **11,** 236 (1958).
5. H. HANEMANN and A. SCHRADER *Atlas Metallographicus,* Bd. 3, Teil 1, S. 58. Borntraeger, Berlin (1941).
6. E. H. DIX, W. L. FINK and L. A. WILLEY, *Trans. Amer. Inst. Min. (Metall.) Engrs.* **104,** 335 (1933).
7. G. HINDRICHS, *Z. Anorg. Chem.* **59,** 444 (1908).
8. T. ISHIWARA, *Sci. Rep. Tohoku Univ.* (d) **19,** (1930).
9. W. KÖSTER and W. BECHTHOLD, *Z. Metallk.* **30,** 294 (1938).
10. H. LIPSON and A. J. C. WILSON, *J. Iron St. Inst.* **142,** 107 (1940).
11. A. D. I. NICOL, *Acta Cryst.* **6,** 285 (1953).
12. J. A. BLAND, Thesis, University of Cambridge (1956).
13. M. A. TAYLOR, *Acta Cryst.* **12,** 393 (1959).

Reply to Discussion "Absolute grain boundary energies in copper"*

In his note, *Absolute grain boundary energies in copper*, Fleischer[1] contends that, in computing the theoretical value of E_0 for [001] tilt boundaries in copper, sufficient allowance was not made by Gjostein and Rhines[2] for the decrease in elastic moduli that occurs over the temperature range from room temperature to 1065°C. Fleischer claims that the Young's Modulus data of Koster[3] indicate that the reduction in moduli should be 59 per cent, as opposed to the 15 per cent correction that was originally applied. From this he concludes that the theoretical E_0 agrees with the slope of the large angle portion of a plot of E/θ vs. ln θ. To explain the change in slope that such a plot shows when $\theta < 5°$, he attempts to demonstrate that the presence of a small twist component in the boundary may as much as double the slope as θ decreases. This interpretation is opposed to the one originally given by Gjostein and Rhines[2]. They found that the Read–Shockley equation agreed with the experimental values only when $\theta < 5°$, and suggested that the deviations observed at larger angles resulted from the fact that as θ increases the strain energy becomes confined to regions in which Hookes Law no longer is obeyed.

It is the purpose of this note to show that, (i) the reduction in elastic constants used by Fleischer is unrealistically large and results in erroneous conclusions, and (ii) that while it is true that the presence of a small twist component will affect the magnitude of E_0, his analysis is based on a fallacious assumption, which leads to a magnification of this effect.

Elastic moduli

For an [001] tilt boundary, E_0 is a function of C_{11}, C_{12} and C_{44} (equation (5) of Ref. (2)) and, ideally, values for these constants at 1065°C should be used to calculate E_0 at this temperature. Unfortunately, these data were not available and in lieu of this method, the room temperature values were reduced 15 per cent, as was suggested by Read[4]. To use as a substitute for this latter procedure, an extrapolation of Young's Modulus data of Koster[3], which were taken on polycrystalline specimens, may be criticized on two points: modulus measurements made on polycrystalline specimens may give erroneously low values at high temperature and, less importantly, the magnitude of the temperature variation of Young's modulus need not be the same as that for the particular function of C_{11}, C_{12} and C_{44}, that occurs in the equation for E_0. Concerning the first point, Zener[5] has discussed Koster's work, pointing out that the marked deviations from a linear decrease in modulus with temperature result from the relaxation of shear stress by viscous grain boundaries. Moreover, Alers[6] has pointed out that, in the case of zinc, his measurements on single crystals decrease in a linear manner with temperature, whereas Koster's measurements on polycrystalline zinc show large deviations from linearity at high temperatures.

Other work also supports this point of view. Kamentsky[7] has determined Young's Modulus for copper single crystals over the temperature range 25°C–750°C. Up to about 450°C the modulus decreases linearly. Above this temperature, deviations from linearity occur and vary exponentially with temperature, while the ratio of Q^{-1} to $\Delta E/E$ remains constant. From this Kamentsky concludes that the true moduli are linear functions of temperature, and the high temperature drop is caused by dislocation effects—possibly thermal unpinning. He also points out that the theoretical work of Bradburn[8] and Ludloff[9] predicts a linear variation of modulus with temperature.

It would seem, therefore, in view of the present state of knowledge bearing on this subject, that a linear relationship between modulus and temperature is a good approximation. If the data of Alers[6] for C_{11}, C_{12} and C_{44} are extrapolated from room temperature to 1065°C, the following values are obtained:

$$C_{11} = 13.7 \times 10^{11} \text{ dynes/cm}^2$$
$$C_{12} = 11.0 \times 10^{11} \text{ dynes/cm}^2$$
$$C_{44} = 4.98 \times 10^{11} \text{ dynes/cm}^2.$$

These constants give a value of 1200 ergs/cm² for E_0 at 1065°C. This value differs significantly from the large angle experimental value of 820 ± 15 ergs/cm² and provides no support for Fleischer's claim that experiment and theory agree at large angles.

Effect of a twist component

In this section it will be shown that the discrepancy between the experimental small-angle-E_0, 1520 ± 100 ergs/cm², and theoretical value of 1200 ergs/cm² may be accounted for by the presence of a small twist component in the boundaries having $\theta < 5°$. The

VOL. 8 1960

treatment given here is a development of theory of Frank[10] and Read and Shockley[11] for a complex grain boundary, and it differs in concept from that put forth by Fleischer.

The basic difference seems to lie in Fleischer's assumption that the total energy of the grain boundary E may be broken into the sum of two components: a tilt energy E_e, which varies with the tilt angle θ_e according to Read–Shockley relationship, and a twist energy E_s, which is taken to be independent of θ_e. Using this assumption, he finds that the slope of the E/θ_e vs. $\ln \theta_e$ plot is given by $-E_0 - E_s/\theta_e$, so that as θ_e decreases the slope becomes increasingly more negative. However, it should be noted that when $\theta_e = 0$, there remains only a pure twist boundary and the slope should approach a value corresponding to E_0 for a twist boundary. But according to relation given above, the slope should become infinite. A singularity of this type does not appear in the treatment given below.

Frank's method[10] for determining the dislocation densities in a general grain boundary shows that they are proportional to θ, where θ is defined now as the magnitude of the relative rotation, about a common axis $\bar{u}$, that brings the two grains into coincidence. Read[4] has shown that the total energy per unit area of the complex grain boundary is given by

$$E = \theta \sum_i N_i \varepsilon_i \tag{1}$$

where N_i is the density per unit θ of the ith set of dislocations, and ε_i is the energy of the ith set. This equation may be written in the form

$$E = E_0 \theta (A - \ln \theta) \tag{2a}$$

$$E_0 = \tfrac{1}{2} \sum_i \tau_{0i} N_i b_i^2. \tag{2b}$$

In equation (2b), τ_{0i} is dependent upon the elastic constants of the material and the direction of the dislocation line.

Noting that $\theta \simeq \theta_e$, for the boundaries under discussion (the twist component is $\leqslant 0.2°$), an examination of equations (2) shows that it *cannot* be placed in the form $E/\theta_e = E_0(A - \ln \theta) + E_s/\theta_e$, as Fleischer assumes. The effect of small twist component on E_0 can be evaluated, however, from equation (2b), which shows that E_0 is composed of a sum of energy terms, $\tau_{0i} b_i^2$, each contributing to the total E_0 in proportion to the density per unit θ of the ith set dislocations, N_i. In an f.c.c. lattice a general grain boundary may be composed of only three sets of dislocations, and in the special case where $\bar{u}$ lies in the plane of the grain boundary, i.e. it is a pure tilt boundary, only two sets are needed. Read and Shockley[11] have derived an expression for E_0 from equation (2b), for this latter case, taking $\bar{u} = [001]$; their result was used by Gjostein and Rhines[2] to evaluate the theoretical E_0 at small angles.

The effect of a small twist component may be studied by relaxing the requirement that $\bar{u}$ be in the plane of the grain boundary. In this case, a twist component will be present in the boundary, necessitating the introduction of a third set of dislocations. For such a grain boundary, the densities N_1, N_2 and N_3 may be found from a relationship given by Read[4]

$$\bar{N}_i = \bar{b}_i^* \times \bar{u} - \bar{n}(\bar{n} \cdot \bar{b}_i^* \times \bar{u}) \tag{3}$$

where $\bar{N}_i$ is vector which lies in the plane of the boundary, having a magnitude N_i and a direction normal to the ith set of dislocations, $\bar{n}$ is the normal to the grain boundary and $\bar{b}_i^*$ may be found from the following equation by rotation of the subscripts

$$\bar{b}_1^* = \frac{\bar{b}_2 \times \bar{b}_3}{\bar{b}_1 \cdot \bar{b}_2 \times \bar{b}_3}, \text{ and so forth.} \tag{4}$$

When the X, Y and Z axes are taken along the $\langle 100 \rangle$ directions of one the crystals, and the definitions of the various vectors are taken to be

$$\bar{b}_1 = a/2[011], \quad \bar{b}_2 = a/2[0\bar{1}1], \quad \bar{b}_3 = a/2[101],$$
$$\bar{u} = [\cos \psi, \sin \psi, 0] \quad \text{and} \quad \bar{n} = [0, \cos \phi, \sin \phi],$$

the following results are obtained:

$$N_1^2 = 1/a^2\{\sin^2 \psi + [\sin \phi \cos \psi + \cos \phi (\cos \psi + \sin \psi)]^2\} \tag{5}$$

$$N_2^2 = 1/a^2\{\sin^2 \psi + [\sin \phi \cos \psi - \cos \phi (\cos \psi - \sin \psi)]^2\} \tag{6}$$

$$N_3^2 = 4/a^2(\sin^2 \psi)(\cos^2 \phi)(1 + \sin^2 \phi). \tag{7}$$

When $\psi = 0$, the boundary is pure tilt, and $N_1 = \frac{1}{a}(\sin \phi + \cos \phi)$, $N_2 = \frac{1}{a}(\sin \phi - \cos \phi)$ and $N_3 = 0$, which are the results obtained by Read and Shockley[11]. To evaluate the effect for a symmetrical tilt boundary that is of interest, let $\phi = \theta/2$. Then, provided $\theta/2 \ll 1$, equations (5), (6) and (7) become

$$N_1 = 1/a \sqrt{(1 + 2 \sin \psi \cos \psi + \sin^2 \psi)} \tag{8}$$

$$N_2 = 1/a \sqrt{(1 - 2 \sin \psi \cos \psi + \sin^2 \psi)} \tag{9}$$

$$N_3 = 2/a(\sin \psi). \tag{10}$$

On substituting the relationships given above into equation (2b) and assuming that the τ_{0i} are all equal to the value used by Read and Shockley[11] for dislocations lying along $\langle 100 \rangle$ directions, the result is

$$E_0 = \frac{\tau_0 a}{4} \{(1 + 2 \sin \psi \cos \psi + \sin^2 \psi)^{\frac{1}{2}} + (1 - 2 \sin \psi \cos \psi + \sin^2 \psi)^{\frac{1}{2}} + 2 \sin \psi\}. \tag{11}$$

Table 1

E_0 ergs/cm²	θ_s	θ_e	sin ψ	ψ
1200	0	—	0	0
1250	0.2	5	0.04	2.3°
1320	0.2	2	0.1	5.7°
1560	0.2	0.6	0.3	18°

Since in this work $\psi < 20°$, the sum of the first two terms enclosed in the bracket may be replaced by a constant, having a value of about two, thus allowing E_0 to be written as

$$E_0 \cong \frac{\tau_0 a}{2}(1 + \sin\psi), \quad \text{for} \quad \psi < 20°. \quad (12)$$

For small values of the tilt and twist components of θ, the magnitude of ψ may be found from the relation

$$\tan\psi \cong \frac{\theta_s}{\theta_e}. \quad (13)$$

It is clear then from equations (12) and (13) that if θ_s has an average value of the order 0.2°, ψ will have its largest value when θ_e is small. Table 1 illustrates that for $\theta_e = 0.6°$, the smallest tilt angle studied, E_0 may be as large as 1560† ergs/cm², and that presence of a small twist component only affects E_0 significantly when $\theta_e < 5°$.

The variation of E_0 from 1560 to 1320 ergs/cm², as θ_e increases from 0.6° to 2°, agrees well with the experimental value in this range, namely, 1520 ± 100 ergs/cm². In the neighbourhood of $\theta = 3$–7°, the experimental slope changes from 1520 to 820 ergs/cm². This result is compatible with the corresponding theoretical value of 1200 ergs/cm² for $\theta = 5°$. It should be noted that theory and experiment do not agree when $\theta > 5°$. This is true also in the case of [001] twist boundaries, where the theoretical value of 1100 ergs/cm² differs significantly from the large angle slope of 770 ergs/cm².

It is believed that the arguments presented above show that the Read–Shockley equation agrees with experiment only when θ is small as is to be expected in view of the fact that its derivation is subject to the limitation that spacing of the dislocations in the boundary should be much larger than diameter of the region, surrounding the dislocation line, which encloses material experiencing non-Hookean strains.

Metallurgy Dept. N. A. GJOSTEIN
Scientific Laboratories
Ford Motor Company
Dearborn, Michigan

† This value may be even larger, since θ_s is difficult to evaluate when θ_e is small.

VOL. 8 1960

References

1. R. L. FLEISCHER, *Acta Met.* **7**, 817 (1959).
2. N. A. GJOSTEIN and F. N. RHINES, *Acta Met.* **7**, 319 (1959).
3. W. KOSTER, *Z. Metallk.* **39**, 1 (1948).
4. W. T. READ, *Dislocations in crystals*, p. 195. McGraw-Hill, New York (1953).
5. C. ZENER, in *Imperfections in Nearly Perfect Crystals*, p. 289. Wiley, New York (1952).
6. G. A. Alers. Submitted to *J. Appl. Phys.*
7. L. A. KAMENTSKY, Thesis, Cornell University, Dept. of Engrg. Phys.; available in *Air Force Off. Sci. Res. Rept.* No. 1, Contr. No. A.F. 18(600)1000, Sept. 1, 1956.
8. M. BRADBURN, *Proc. Camb. Phil. Soc.* **39**, 113 (1943).
9. H. F. LUDLOFF, *J. Accoust. Soc. Amer.* **12**, 193 (1940).
10. F. C. FRANK, *Carnegie Institute of Technology Symposium on the Plastic Deformation of Crystalline Solids* p. 150. U.S. Dept. of Commerce, Office of Technical Services Washington 25, D.C.
11. W. T. READ and W. SHOCKLEY in *Imperfections in Nearly Perfect Crystals*, p. 352. Wiley, New York (1952).

* Received November 16, 1959.

A new interpretation of the substructure of electropolished aluminium surfaces*

No satisfactory interpretation has yet been established for the forming mechanism of the fine substructure revealed by means of electron microscope on the surface of electropolished aluminium.

The "selfstructure" of brightened aluminium surfaces discovered with replica methods first by Bucknell and Geach[1], and Brown[2], studied later by Nutting and Cosslett[3], examined in detail by Welsh[4] in different electrolytes, has been interpreted last by Bussy[5] in connection with the preferential dissolution ability depending on the orientation of crystal faces.

Successful studies of the cell structure and the formation mechanism of the porous anodic oxide coatings on aluminium were made by Keller *et al.*[6], Booker *et al.*[7], Paganelli[8] and others.

In spite of all these investigations no satisfactory explanation is yet given for the repeatedly stated great similarity of size and arrangement between the hexagonal cell structure of anodic oxide coatings and the so-called "selfstructure" for electropolished surface layers. The reason for these uncertainties can be attributed to the fact that electropolished surfaces were examined hitherto merely by different replica methods.

Systematic investigation of electrobrightening baths led to a suitable electrolyte to develop a solid, porous oxide layer, thin enough to be employed for transmission electron microscopy, without the aid of replication.

Rolled, annealed and cold worked samples of high-purity (99.99 per cent) *A*- and commercial (99.5 per cent) *B*-aluminium and an Al–Mg alloy called NAUTAL, *N*, were polished anodically using an

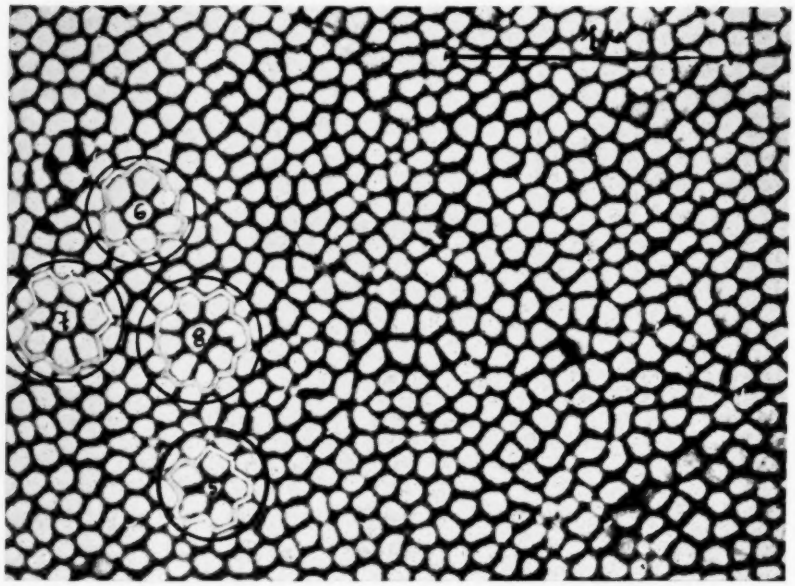


FIG. 1. Electromicrograph of an oxide film formed by electropolishing 99.5 per cent aluminium in the phosphoric acid–butyl alcohol bath at 36 V. The normal cell arrangement (6) and the faults of hexagonal packing (5, 7 and 8) are marked. × 41,000

electrolyte of 80 vol.% phosphoric acid (sp. gr. 1.75) and vol.% *n*-butyl alcohol. The potential was varied from 10 to 40 V rectified a.c., the current density was 3 to 5 A/dm². The process was continued for 10–15 min at 60–65 C°.†

After polishing, the samples were rinsed in distilled water, the surface scribed into squares and stripped immediately with the mercury chloride method. The oxide films were examined in a Trüb, Täuber and Co. electron microscope at 40 kV.

Figure 1 shows the electron micrograph of the thin oxide layer stripped off the surface of electropolished commercial aluminium. The hexagonal packing of the cells is the same as the structure observed as pore-base patterns of thick porous aluminium oxide coatings.[6–8] But in the present case the image is not given by the replication of the pore-base pattern, but by the direct transmission of the oxide film. The dark network is formed by the cellwalls. The white fields between them are the pores. The barrier layer at the pore base is—under the given forming conditions—thin enough to be easily transmitted by the electron beam.

The most frequent irregularity of the network is the deviation of the hexagonal packing, when one cell is surrounded by 5, 7 or 8—instead of 6—cells. The number of such faults per unit area was counted. The density of imperfections is $10^9/cm^2$. This distortion of the network led sometimes to form irregulated rows of cells or even spirals. But furrow structures and globular markings—as Welsh[4] found using replica method at the examination of surfaces polished in a phosphoric acid–alcohol bath—were never observed.

The cell-structure formed was the same at the surfaces of all the three materials (*A*, *B* and *N*). The shape and arrangement of cells did not change with increasing voltage. A striking difference in cell-size and pore-size, depending on voltage could, however, be stated.

Measurements were made on electron micrographs taken of films got at different voltages. Cell-diameter, *C*, pore-diameter, *p*, and wall thickness, *D*, and the density of cells per unit area were determined.

Figure 2 gives a graphical illustration of the main-measured data. The spacing–voltage relations give parabolic curves. The straight line marked in the graph refers to the size–voltage curve given by Keller and co-workers[6] for the case of anodic oxidation in phosphoric acid bath.

Based on the above measurements and the interpretation of experimental results, a new scheme for the cell-structure of the oxide layer formed by anodical polishing was supposed. The scheme given in Fig. 3 differs from the well-known scheme, given by Keller *et al.*[6] for porous anodic oxide layers, in pore-shape, in relative pore-size and in the thickness of the barrier layer.

† Details concerning the characteristics of the electropolishing bath with all its experimental and theoretical aspects as well as practical application are published elsewhere[9,10] by Mrs. E. Lichtenberger–Bajza.

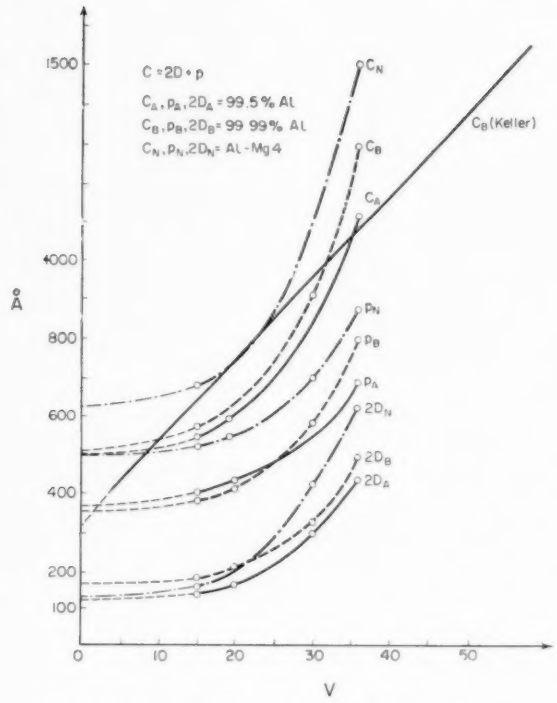


FIG. 2. Size–voltage curves. C_A, C_B, C_N = cell diameter –voltage function; p_A, p_B, p_N = pore diameter–voltage function; $2D_A$, $2D_B$, $2D_N$ = voltage function of the measured double cell wall thickness; C_B(Keller) = the linear function got by Keller *et al.*[6] on anodic oxide films.

Investigations were made to determine the orientation dependence of the observed structure. Further experimental details, analysis of the curves, interpretation of the result and discussion of concerning work of the abovementioned authors will be published elsewhere.[11]

Experiments are still going on. From the results obtained hitherto, and considering the mutual dissolving and oxidating effect of electrolytes used for anodic treatment and the orientated anisotropy of both dissolution and oxidation processes, the following interpretation can be drawn:

The formation of hexagonal cell structure of the anodic coatings and the granulated, dotted, furrowed or hexagonal patterns of electropolished surface are equally consequences of the anisotropy of mutual dissolution and oxidation rate evolved on aluminium surfaces both determined by grain orientation.

The scale and character of voltage dependence of the substructure depends on the relative dissolving and oxidating power of the bath.

Under conditions of *anodic oxidation* the size–voltage *function is linear* and the formed film corresponds to the scheme of cell structure given by Keller and co-workers.[6]

Under conditions of *electropolishing*, the size–voltage functions of cell and pore diameters give *parabolic type curves* and the structure of the formed film corresponds to the scheme in Fig. 3.

In both cases there can be stated a p_0 *value*, extrapolated to *zero voltage*. That value is reciprocally *determined by the metal and the electrolyte*.

The arrangement and distribution of the pore centers is governed by the *active spots* of the surface and is therefore in certain electrolytes orientation dependent as well.

Summary

Electron micrographs, made with direct transmission of thin oxide film formed by electropolishing in a phosphoric acid–butyl alcohol bath, showed characteristic patterns of hexagonal network. Size–voltage relations of cell size and pore diameter gave parabolic type curves. A new scheme is proposed for the hexagonal structure of oxide films formed by electropolishing.

A general interpretation is offered for the formation of the cell structure of anodic oxide films and for the pattern developing during electropolishing by extending the theory of Bussy[5], supposing mutual interaction of the anisotropy of dissolution and oxidation rate depending on grain orientation.

The author acknowledges Mrs. E. Lichtenberger-Bajza for valuable suggestions and co-operation,

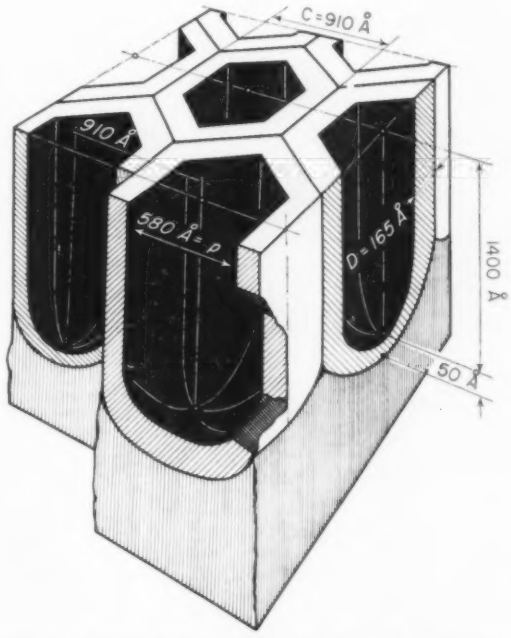


FIG. 3. Scheme of the idealized cell structure of porous oxide films formed by electropolishing.

VOL. 8 1960

Ing. P. Bussy for sending his thesis which made possible the interpretation based on his theory, Mrs. A. Fülöp for assistance in the experimental work and Ing. Gy. Stark for helpful advice and criticism.

M. Gy. Holló

Research Institute for Technical Physics
of the Hungarian Academy of Sciences
Department of Micromorphology
Budapest

References

1. G. L. Bucknell and G. A. Geach, *Nature, Lond.* **164**, 231 (1949).
2. A. F. Brown, *Nature, Lond.* **163**, 961 (1949); *Metallurgical Applications of the Electron Microscope* p. 103. Institute of Metals, London (1950).
3. J. Nutting and V. E. Cosslett, *ibid.* p. 57.
4. N. C. Welsh, *J. Inst. Met.* **85**, 129 (1956–57).
5. P. Bussy, *Application de la micrographie électronique a l'étude de certains aspects de la surface de cristaux et de la nature des joints intergranulaires dans le cas de l'aluminium, Publ. sci. Minist. Air* No. 325 (1957).
6. F. Keller, M. S. Hunter and D. I. Robinson, *Trans. Electrochem. Soc.* **100**, 411 (1953).
7. C. J. L. Booker, J. L. Wood and A. Walsh, *Brit. J. Appl. Phys.* **8**, 347 (1957).
8. M. Paganelli, *Aluminio* **27**, (1958).
9. E. Lichtenberger-Bajza, *Metalloberfläche* **13**, 65 (1959).
10. E. Lichtenberger-Bajza, Paper read at the *XVIIth International Congress of Pure and Applied Chemistry, München*, 30. *Aug.*–6. *Sept.* 1959.
11. M. Gy. Holló, *Rev. Met.* **57**, 23 (1960).

* Received November 23, 1959.

The breakdown of the protective oxide film on transition metal alloys*

In oxidation studies, investigators have given little significance to the factor that the activities rather than the concentrations of metals in alloys determine the inner boundary condition for the metal gradient in the superficial oxide layer. Panish *et al.*[1] have determined the activities of nickel and chromium in the binary alloys over the temperature range 750°–965°C. Because the activity coefficients were much less than unity and smaller at lower temperatures for the alloys containing up to 30 per cent chromium, they have suggested that the decreased partial molar free energy contents of nickel and chromium account partially for the corrosion resistance of these alloys. In agreement with this hypothesis, Smeltzer[2] has accounted for a continuous change in slope of an Arrhenius coefficient of parabolic oxidation constants for a nickel–cobalt alloy over the temperature range of its magnetic transformation by variations of the partial molar free energy contents of nickel and cobalt.

It is reasonable, therefore, to assume that the oxidation characteristics of transition metal alloys are determined partially by the non-ideal thermodynamic behaviour of the alloying constituents. However, available results for the oxidation resistant nickel–chromium and iron–chromium steels cannot be analyzed in accordance to this consideration because the oxidation curves are discontinuous. Caplan and Cohen[3] have shown that these alloys oxidize more rapidly after breakdown of the extraordinary protective oxide film rich in chromium.

This communication demonstrates that initial breaks in oxidation curves of iron–chromium alloys are associated with the ferritic–austenitic phase transformation in the alloy. This transformation is caused by preferential oxidation of chromium at a rate much larger than its replenishment by diffusion to the metal–oxide interface. The stress resulting from this transformation causes breakdown of the protective film.

To demonstrate this type of film breakdown, oxidation tests were carried out on a binary iron–12 wt.% chromium alloy in oxygen at atmospheric pressure. The kinetics of film and scale growth were determined with a microbalance and a torsion spring enclosed in glass vacuum assemblies. The specimens were polished to 4/0 emery and vacuum annealed *in situ* for 2 hr at 825°C before oxidation. This alloy maintains the ferritic structure at 825°C irrespective of the amount of chromium preferential oxidation. On the other hand, ferrite changes to austenite during oxidation at 855°C by depletion of the surface concentration of chromium to 9.5 per cent.

The results of scaling experiments at 825°C and 855°C, Fig. 1, demonstrated the breakdown of the

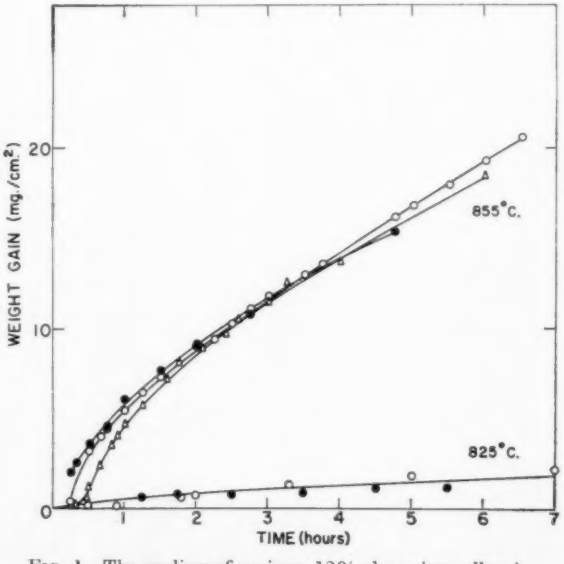


Fig. 1. The scaling of an iron–12% chromium alloy in oxygen at 825° and 855°C.

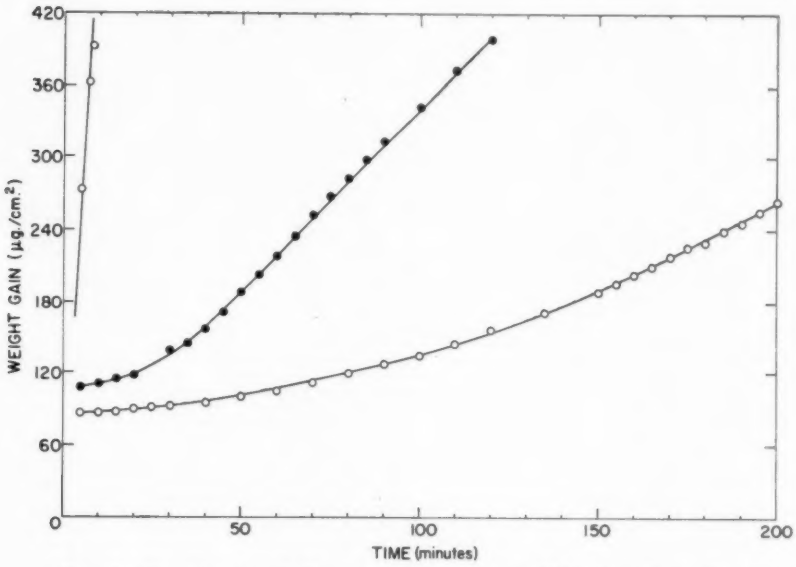


FIG. 2. The kinetics of film growth on an iron–12% chromium alloy in oxygen at 855°C.

protective film by the phase transformation in the alloy. The oxidation curve at 825°C was continuous. Upon elevation of the temperature to 855°C, the initial oxidation rate was similar to that at 825°C. However, this initial rate transformed within exposures of 30 min to a much larger rate. This latter rate was characteristic of austenite of small chromium content.[4]

The breakdown of the protective film was markedly illustrated by microbalance measurements. As illustrated by the curves in Fig. 2, the film attempted to maintain its protective property at 855°C after an initial rapid uptake of oxygen to approximately 100 $\mu g/cm^2$. This property was destroyed after 10 min by oxidation at localized areas. The different distribution of these areas on the three test specimens caused large variations of the oxidation rates. These areas, Figs. 3 and 4, have arisen presumably where

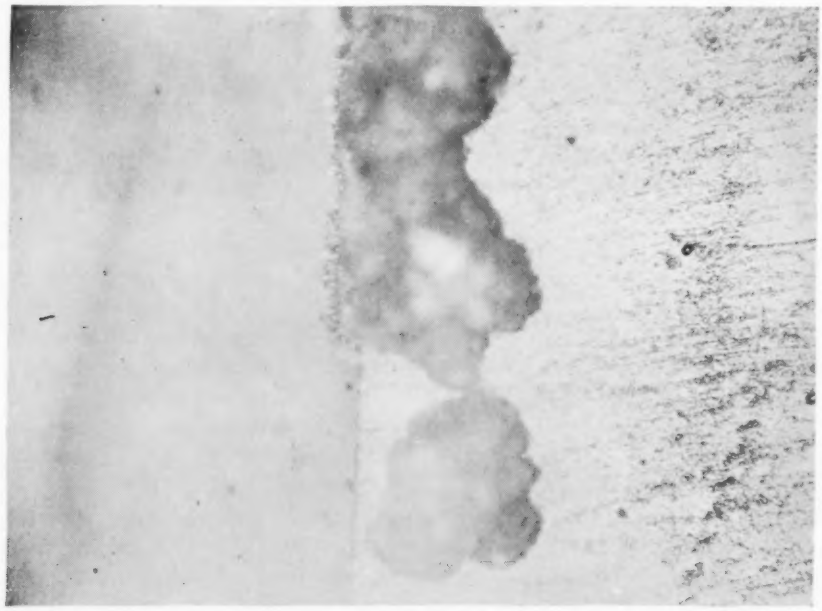


FIG. 3. Localized areas of oxidation on iron–12% chromium alloy exposed in oxygen for 2 hr at 855°C. ×100

VOL. 8 1960



FIG. 4. Oxide whisker growths at boundaries of localized areas of oxidation on iron–12% chromium alloy. ×900

chromium was sufficiently depleted for formation of the austenitic phase. The relief of stress resulting from this transformation was shown by the protuberance of the oxidation product from the specimen edge, Fig. 3, and the large density of oxide whiskers at the boundaries of the localized areas of oxidation, Fig. 4.

One may conclude from these results that continuous oxidation curves for iron–chromium alloys may be obtained under experimental conditions where preferential oxidation of an alloy constituent does not cause the ferritic–austenitic phase transformation. These continuous curves, which would be amenable to analysis by oxidation diffusion theory, may then be analyzed to test the hypothesis that the oxidation resistance of iron–chromium steels is determined partially by negative deviations of the alloy constituents from ideal thermodynamic behaviour.

This research was completed at Metals Research Laboratory, Carnegie Institute of Technology, Pittsburgh 13, Pa., U.S.A., under auspices of the Office of Scientific Research, Air Research and Development Command.

W. W. SMELTZER

Department of Metallurgy and
Metallurgical Engineering
Hamilton College, McMaster University
Hamilton, Ontario, Canada

References

1. M. B. PANISH, R. F. NEWTON, W. R. GRIMES and F. F. BLANKENSHIP, *J. Phys. Chem.* **62,** 980 (1958).
2. W. W. SMELTZER, *Acta Met.* **7,** 191 (1959).
3. D. CAPLAN and M. COHEN, *Corrosion* **15,** 141 *t* (1959).
4. H. J. YEARIAN, E. C. RANDELL and T. A. LONGO, *Corrosion* **12,** 515 *t* (1956).

* Received December 1, 1959.

The effect of hydrostatic pressure on the potency of martensitic embryos*

Recent theories[1,2] concerning the athermal and isothermal kinetics of martensitic transformations require the presence of pre-existing embryos of appreciable size, as "frozen-in" during cooling from the austenitizing treatment. These embryos are b.c.c. structures which are thought to be stabilized by dislocations associated with the embroyos.

Direct observation of the embroyos has been recently reported by Richman *et al.*[3] who performed electron transmission microscopy on thin foils of austenitic iron–nickel alloys having M_s temperatures below room temperatures.

It is well known that hydrostatic pressure depresses the M_s temperature of iron base alloys by changing the bulk thermodynamics in such a manner as to stabilize the f.c.c. austenite relative to the b.c.c. martensite.

Patel and Cohen[4] observed a decrease in M_s of about 8.5°C per kiloatmosphere (katm) in a 70:30 Fe–Ni alloy at pressures up to 6 katm. Normann and Scheil[5] observed a similar depression of M_s, about 5°C per katm, in a 75:25 Fe–Ni alloy at pressures up to 4 katm. In this laboratory we have recently

investigated the effect of hydrostatic pressure on the f.c.c. ⇋ b.c.c. reaction in a 90:10 Fe–Ni alloy at pressures up to 60 katm.[6] It was found that M_s is depressed by about 5°C per katm and that A_s is also depressed, by about 2°C per katm. In addition, we have observed that the lower branch of the γ-loop in the iron–chromium system is depressed by about 250°C at 50 katm.[6]

The aforementioned experiments are carried out by placing a specimen of the alloy in question in a high-pressure cell and measuring the electrical resistance as a function of temperature while the pressure is maintained. The resulting hysteresis loop defines M_s and A_s *at the applied high-pressure*. Repeating this experiment at various pressures yields the experimental values for $(\Delta M_s/\Delta P)$ and $(\Delta A_s/\Delta P)$.

The effects of hydrostatic pressure can be predicted by utilizing the known 1-atm thermodynamics of the f.c.c. ⇌ b.c.c. reactions in the iron–nickel[7] and iron–chromium[8] systems together with the difference in specific volume between the austenite and martensite.[1,4] Satisfactory agreement is obtained between the calculated and observed depression of M_s and A_s despite the approximations necessitated by lack of available data concerning the compressibilities of the b.c.c. and f.c.c. phases as a function of temperature and composition.

In view of the effect of hydrostatic pressure on the thermodynamics of iron–nickel alloys, it was possible to predict that the application of hydrostatic pressure during the austenitization should produce a profound change in the potency or size of martensitic embryos, over and above the influence of pressure acting *during* the transformation. Crude calculations concerning the energetics of the formation of chemically unstable embroyos have been described in the literature.[1,2] The results of these calculations are depicted graphically in Fig. 14 of Ref. (2). It is shown that the radius of chemically-unstable embryos increases as the temperature decreases until a freezing-in temperature, T_f, is reached. At T_f, the embryo radius attains some effective size r_e and is "frozen-in". Subsequent cooling into the temperature range where martensite formation occurs results in the cataclysmic growth of the embryo at a temperature defined by[1,2]

$$r_e = 9\,\frac{\sigma A}{\Delta f^2_{M_s}} \qquad (1)$$

where σ is the interfacial energy, A is the strain energy constant, $\Delta f^{\alpha'\to\gamma}_{M_s}$ is the driving force per unit volume for the martensitic transformation at M_s, and r_e is the disk radius of the frozen-in embryo.

From equation (1) it is evident that if r_e can be decreased, i.e. by decreasing the effective embryo radius frozen in during cooling, then cataclysmic growth should require a larger value of $\Delta f^{\alpha'\to\gamma}_{M_s}$, and the M_s temperature would be decreased.

The increase in embryo radius with decreasing temperature shown in Fig. 14 Ref. (2) arises primarily from the fact that, for $T_2 > T_1 > T_0$ (i.e. $\Delta f = 0$ at T_0), $\Delta f^{\gamma\to\alpha'}(T_2) > \Delta f^{\gamma\to\alpha'}(T_1)$. Hence, the embryo radius characteristic of T_2, $r_e(T_2)$, is smaller than the radius characteristic of T_1, $r_e(T_1)$. However, the application of hydrostatic pressure at T_1 increases $\Delta f^{\gamma\to\alpha'}(T_1)$ so that

$$\Delta f^{\gamma\to\alpha'}(T_1, P) > \Delta f^{\gamma\to\alpha'}(T_1, P = 1\text{ atm}) \qquad (2)$$

or that

$$r_e(T_1, P) < r_e(T_1, P = 1\text{ atm}) \qquad (3)$$

we are thus led to the conclusion that the application of hydrostatic pressure at austenitizing temperatures above T_f followed by quenching under pressure should result in the "freezing-in" of smaller embryos. These in turn would lower M_s even at 1 atm, provided that the high-pressure is removed *below* T_f.

In order to test this prediction, the following experiments were carried out. An alloy containing 32.4 at.% nickel in the form of a 0.062 in. diam. × 3 in. long rod was austenitized at 1000°C for 2 hr in an evacuated capsule. This particular alloy had been used in an earlier experiment by one of the authors[9] and was observed to have an $M_s = 127$°K and $T_0 = 370$°K at atmospheric pressure. The rod was cut into 0.10 in. lengths and five control specimens taken from the rod were quenched into liquid nitrogen (78°K). Metallographic examination showed that all of the specimens then contained large quantities of martensite, i.e. more than 50 per cent.

Several of these specimens were heat treated for 10 min under a hydrostatic pressure of 50 katm at temperatures ranging from 400°C to 1000°C. Following the high-pressure heat treatment, the specimens were quenched under pressure to 100°C in the high-pressure cell and then cooled to room temperature. The pressure was then released to 1 atm. No deformation of the specimens was observed. Subsequently, the specimens were quenched into liquid nitrogen for 10 min and returned to room temperature for metallographic examination.

It was found in the foregoing series that specimens heat treated under a pressure of 50 katm at or below 500°C contained more than 50 per cent martensite while those specimens treated at or above 550°C were completely austenitic.

Several other specimens were similarly treated

VOL. 8 1960

except that a hydrostatic pressure of 25 katm were used. It was found that specimens treated at or below 600°C contained more than 50 per cent martensite, while those treated at or above 650°C were completely austenitic.

Since dislocation motion is restricted below T_f, it seemed desirable to determine T_f by locating the temperature at which the embryo contraction caused by quenching under pressure could be removed. In order to investigate the annealing or growth of embryos suppressed by the high-pressure treatment a specimen was heated at 700°C under a pressure of 25 katm for 10 min. Subsequent quenching under pressure to 100°C and refrigeration in liquid nitrogen at 1 atm would have yielded a completely austenitic structure. However, following the 10-min treatment at 700°C and 25 katm, the pressure in the cell was released and the temperature maintained for 30 min at 700°C and 1 atm. The specimen was then quenched to 100°C, removed from the cell and refrigerated in liquid nitrogen. The resulting structure contained more than 50 per cent martensite. In addition to demonstrating the reversibility of the pressure effect, this experiment eliminates the possibility of attributing these observations to contamination during high-pressure treatment. This experiment was repeated at 650°C, and the resulting structure also contained more than 50 per cent martensite. Similar results were obtained at 650 and 700°C using a hydrostatic pressure of 50 katm.

A third series of specimens was heat treated for 10 min at 550°C and 50 katm in the high-pressure cell. These specimens were quenched under pressure to 100°C, removed from the cell and refrigerated in liquid nitrogen. The resulting structure was 100 per cent austenite. Specimens of this series were then annealed for 30 min at various temperatures at 1 atm and quenched into liquid nitrogen. Specimens annealed at or below 600°C were completely austenitic, indicating that the annealing temperature was too low to restore the original embryo sizes, while those annealed at or above 650°C contained more than 50 per cent martensite.

Both the annealing studies and the pressure-quenching experiments carried out at 25 katm indicate a freezing-in temperature of 625°C $\pm$ 25°C for embryos in this alloy. However, the pressure-quenching experiments carried out at 50 katm indicate that the M_s can be lowered by applying hydrostatic pressure at temperatures above 525°C $\pm$ 25°C. The reason for this difference in the freezing-in temperature, T_f, is not altogether clear. It should be pointed out that the pressure transmitting medium used in our experiments is pyrophillite, a solid compound possessing nearly isotropically-ideal properties. Consequently, although the applied pressure was nearly hydrostatic, there may be some non-hydrostatic components which could have introduced a limited amount of plastic strain that was undetected in our experiments. Since the non-hydrostatic component undoubtedly increased as the applied pressure increased, it might have contributed significantly at 50 katm but not at 25 katm. On the other hand, the observed difference in the freezing-in temperature may be associated with more subtle factors and will be more exaustively studied in future work.

Nevertheless, these experiments demonstrate the possibility of producing irreversible effects in metals by high-pressure treatment. In addition, they lend considerable support to the thesis that martensitic nucleation is controlled by the potency of embryos having the martensitic structure and existing at temperatures where the austenite has the lower bulk chemical free energy.

It is apparent that hydrostatic pressure can decrease the embryo size and lead to a lowering of M_s, even though the pressure during the transformation itself is one of atmosphere.

Manufacturing Laboratories Inc., Cambridge, Massachusetts

L. KAUFMAN
A. LEYENAAR
J. S. HARVEY

References

1. L. KAUFMAN and M. COHEN, *Progress in Metal Physics* Vol. 7, p. 165. Pergamon Press, London (1958).
2. M. COHEN, *Trans. Amer. Inst. Min. (Metall.)Engrs.* **212**, 171 (1958).
3. M. RICHMAN, M. COHEN and H. G. F. WILSDORF, *Acta Met.* **7**, 879 (1959).
4. J. R. PATEL and M. COHEN, *Acta Met.* **1**, 531 (1953).
5. W. NORMANN and E. SCHEIL. Private Communication (to be published in *Arch. Eisenhütten*).
6. L. KAUFMAN, H. UDIN and S. A. KULIN, Fall Meeting *Amer. Inst. Min. (Metall.) Engrs.* 1959 (to be published).
7. L. KAUFMAN and M. COHEN, *Trans. Amer. Inst. Min. (Metall.) Engrs.* **206**, 1393 (1956).
8. L. KAUFMAN, *Trans. Amer. Inst. Min. (Metall.) Engrs.* **215**, 218 (1959).
9. L. KAUFMAN and M. COHEN, *The Mechanism of Phase Transformations in Metals* p. 187. Institute of Metals, London (1955).

* This work has been sponsored by the Materials Laboratory, Wright Air Development Center, Dayton, Ohio, under Contract No. AF33(616)-6837. Received December 10, 1959.

Sur l'origine du processus de germination dans les reactions d'oxydation superficielle des metaux*

L'existence d'un processus de germination dans les réactions d'oxydation des métaux a été signalée dès

1951 par Bardolle et Bénard dans le cas du fer.[1] Confirmées peu après par Gulbransen[2] ces premières observations furent étendues ultérieurement à d'autres métaux,[3–7] à des alliages[8–10] et tout récemment à une réaction de sulfuration.[11] Cet ensemble de résultats expérimentaux a permis d'établir le caractère général du phénomène, mais l'origine de celui-ci donne lieu depuis quelques années à des interprétations contradictoires au sujet desquelles nous désirons nous prononcer.

Dès que l'existence de la germination des oxydes à la surface des métaux fut signalée, plusieurs auteurs attribuèrent celle-ci à une oxydation préférentielle du métal à l'affleurement des dislocations.[10,12] Cabrerna[13] montra en particulier que la théorie permettait de justifier cette hypothèse, déjà utilisée avec succès pour expliquer les attaques ponctuelles des surfaces métalliques dans les solutions.[14,15]

Il nous semblait cependant qu'une telle interprétation était difficilement compatible avec l'ensemble de nos observations et en particulier avec le fait, bien établi dans le cas du cuivre, que le nombre des germes formés sur une surface était fonction de la pression. Nous fûmes pour cette raison amenés avec Grønlund à tenter d'assimiler le processus de germination de l'oxyde à une coalescence à la surface d'un film extrèmement mince d'oxyde primaire.[16] Dans cette conception il n'était plus nécessaire d'admettre que la localisation des germes était liée à celle des défauts du métal et l'influence des facteurs d'ambiance se justifiait aisément.

Des observations récentes de Young[17], de Bénard *et al.*[18] et de Bouillon et Stevens[19] semblent pouvoir résoudre les difficultés issues de cette dualité d'interprétation. Young a montré en effet que s'il existe effectivement une relation topographique entre les dislocations et les germes d'oxydation dans du *cuivre de pureté moyenne*, cette relation disparait lorsqu'on soumet à l'oxydation ménagée du *cuivre de haute pureté*. Dans les conditions expérimentales adoptées par cet auteur les dislocations n'exercent donc une influence sur l'amorçage de la réaction d'oxydation à chaud, que dans le mesure où des impuretés de haute affinité s'y trouvent associées. Il s'agit donc dans ce cas d'une réaction d'oxydation sélective classique, réaction qu'il est parfaitement licite d'utiliser, comme l'ont fait certains auteurs,[10] pour déceler les dislocations à la surface du métal.

En contrepartie, le processus fondamental de germination indépendant des imperfections chimiques ou structurales du métal, dont nous avions postulé l'existence, se trouve confirmé par ces travaux et peut être décrit de la façon suivante.[18,19] Au début de la réaction le métal se recouvre d'un film d'oxyde dont l'épaisseur s'accroit jusqu'à une valeur critique de l'ordre de quelques dizaines d'Angströms qui correspond à la limite d'influence du substrat. Au-delà, l'oxyde qui continue à se former sur l'ensemble de la surface tend à se rassembler autour de certains centres de cristallisation. Le nombre moyen de ces centres sur une surface d'orientation cristallographique donnée, dans des conditions de température et de pression données, correspond à un équilibre compétitif fixé par la valeur des constantes de diffusion superficielle du métal et de l'oxygène à la surface du film de base. Il n'est pas exclu que sur certains métaux ce dernier soit un simple film d'oxygène chimisorbé.

La redistribution superficielle du produit de la réaction, qui est à l'origine du phénomène de germination, ne peut s'observer commodément qu'à des températures telles que la diffusion superficielle soit suffisamment active, et sous des pressions partielles de l'agent oxydant assez basses pour que la vitesse globale de la réaction soit relativement lente. Le processus subsiste, sous une forme plus difficilement perceptible il est vrai, à des températures plus basses et sous des pressions partielles plus élevées.[7] L'aspect granuleux que les films d'oxydes ou de sulfures d'épaisseur interférentielle offrent fréquemment à l'examen à fort grossissement peut être considéré comme un témoignage de cette étape de leur croissance. Cette interprétation présente des analogies étroites avec celle qui est donnée de la condensation des liquides polaires à la surface des solides au cours de laquelle on observe dans certaines conditions la coexistence d'un film stable d'épaisseur invariable, en équilibre avec des lentilles liquides de volume croissant.[20]

Le fait que le processus fondamental de germination qui vient d'être décrit puisse se superposer à la germination induite par les impuretés, lorsque les expériences sont faites sur des métaux de pureté moyenne ou sur des alliages, explique les difficultés éprouvées au cours de ces dernières années pour distinguer les deux phénomènes.

J. Bénard

Ecole Nationale Supérieure de Chimie
Paris

Bibliographie

1. J. Bardolle et J. Bénard, *C. R. Acad. Sci., Paris* **232**, 231 (1951).
2. E. Gulbransen, McMillan et K. Andrew, *Trans. Amer. Inst. Min. (Metall.) Engrs.* **6**, 1027 (1954).
3. F. Grønlund et J. Bénard, *C. R. Acad. Sci., Paris* **240**, 624 (1955); *J. Chim. Phys.* **53**, 660 (1956).
4. E. Menzel et W. Stossel, *Naturwissenschaften* **41**, 302 (1954).

VOL. 8 1960

5. E. Menzel et C. Menzel-Kopp, *Z. Naturf.* **13a**, 985 (1958).
6. U. Martius, *Canad. J. Phys.* **33**, 466 (1955).
7. W. Harris, F. Ball et A. Gwathmey, *Acta. Met.* **5**, 574 (1957).
8. J. Moreau et J. Bénard, *J. Inst. Met.* **83**, 87 (1954).
9. J. Moreau et J. Bénard, *J. Chim. Phys.* **53**, 787 (1956).
10. W. Hibbart et C. Dunn, *Acta Met.* **4**, 306 (1956).
11. J. Oudar et J. Bénard, *Acta Met.* **7**, 295 (1959).
12. A. Hendrickson et E. Machlin, *Acta Met.* **3**, 64 (1955).
13. N. Cabrerna, *J. Chim. Phys.* **53**, 675 (1956).
14. P. Lacombe et L. Beaujard, *J. Inst. Met.* **74**, 1 (1947).
15. P. Jacquet, *Acta Met.* **2**, 752 (1954).
16. F. Grønlund, Thèse, Paris (1957).
17. F. Young, *Acta Met.* **8**, 117 (1960).
18. J. Bénard, F. Grønlund, J. Oudar et M. Duret, Z. *Elektrochem.* **63**, 799 (1959).
19. Y. Bouillon, F. Bouillon et Stevens, *C. R. Acad. Sci., Paris*, **249**, 2571 (1959).
20. B. Derjaguin et Z. Zorin in *Solid Gas Interface* p. 145. Butterworths, Londres (1957).

* Reçu le 27 Novembre, 1959.

Stability of retained austenite on ageing*

The stability of retained austenite is generally indicated by the parameter θ—the extent to which austenite, retained at a given temperature, has to be further cooled if it should just commence to transform to martensite. The effect on θ, of factors like time and temperature of ageing and the amount of the contiguous athermal martensite has been studied amongst others by Edmondson[1], Morgan and Ko[2], Glover and Smith[3], Das Gupta and Lement[4] and Crussard and Philibert[5].

Edmondson as well as Glover and Smith have observed that θ reaches a maximum value in periods ranging from a few minutes at ageing temperatures of the order of 100°C–150°C to a few hours at lower temperatures of the order of 35°C. From the data of Harris[6] on the speeds of penetration of carbon in the face-centred iron lattice in low carbon steels (with a core carbon content about 0.20 per cent and a surface carbon content about 1 per cent greater), the speed of interstitial diffusion of carbon at about 125°C is seen to be of the order of 10^{-8} cms/hr and about a thousand times less, i.e. 10^{-11} cms/hr, at room temperatures. If deactivation of the austenitic strain embryos takes place, as envisaged by Cohen *et al.*[7], by carbon atoms interstitially diffusing towards and being captured by them, as the average distance between two carbon atoms in the austenitic condition in a 1 per cent C steel is of the order of 6×10^{-8} cm, the same order of the times, experimentally observed for θ to reach a maximum value at 100°C to 150°C and estimated for carbon atoms to interstitially migrate a few Å units, lends strong support to Cohen's original concept for the mechanism of stabilization of austenite.

As the average distance between two carbon atoms in a 1 per cent "homogenized" austenite is only about 6×10^{-8} cm, a strain embryo, supposed to be associated with dislocations in the austenite lattice, may itself include one or more carbon atoms and will, in any case, not probably have a concentration of carbon within it, so much lower than in the surrounding austenite as to encourage or allow carbon atoms to diffuse by themselves into it. It is therefore essential that an appreciable concentration gradient for carbon must exist in austenite, if carbon atoms are to diffuse at sufficiently high rates, and further essential to indicate the source for providing such a concentration gradient.

The required concentration gradient can be provided either by a microsegregation of the originally homogeneously interstitially distributed carbon atoms of the austenite or by the provision of a carbon-rich region, as for instance from the associated martensite phase, in which carbon has a higher activity.

Segregation of the interstitial carbon atoms, especially in homogenised high-carbon austenite, to the extent necessary for providing high concentration gradients, can be taken as virtually impossible, as can also be inferred from the views of Fisher *et al.*[8] and of Kumar and Quarrell[9]. The probability of such microsegregation taking place can be calculated from purely statistical considerations and has been found to be vanishingly small. The required gradient has thus to be attributed to the martensite phase itself.

The role of internal stress on the speed of diffusion of carbon atoms is not clear at present. Cohen has indicated that diffusion is accelerated in the presence of internal stress, although Bhat and Lloyd[10] observe the opposite. If the speed of diffusion of carbon atoms is governed by the magnitude of the internal stresses in the retained austenite,—increasing with greater internal stress, since at higher ageing temperatures internal stress relief would be greater,—the residual internal stress would be smaller. The speeds of carbon diffusion must therefore be reduced and the time required for θ to attain a maximum value must increase, a conclusion opposite to the experimental observations of both Edmondson, and Glover and Smith. It is felt that these difficulties will not arise if temperature is regarded as the controlling factor.

The above concepts, based on the associated martensite phase, and the random thermal agitation of carbon atoms, which increasingly tends at higher temperatures to divert them from proceeding directly to the strain embryos, would together satisfactorily explain the effect on θ of both the proportion of adjacent athermal martensite as well as of ageing temperature.

In alloy steels the stability is further affected by the relative affinity for carbon of the alloying elements which tend to group round strain centres. One may therefore expect the stability to increase with the carbide-forming tendency of the alloying element. Grain size control by small additions of aluminium may not however affect the stability particularly.

We thank Dr. B. R. Nijhawan, Director, National Metallurgical Laboratory for kind discussion and permission to publish this note.

E. G. Ramachandran
C. Dasarathy

National Metallurgical Laboratory
Jamshedpur-7, India

References

1. B. Edmondson, *Acta. Met.* **5,** 208 (1957).
2. E. R. Morgan and T. Ko, *Acta. Met.* **1,** 36 (1953).
3. S. G. Glover and T. B. Smith, *Mechanism of Phase Transformations in Metals* p. 265. Institute of Metals, London (1956).
4. S. C. Das Gupta and B. S. Lement, *Trans. Amer. Inst. Min. (Metall.) Engrs.* **197,** 530 (1953).
5. C. Crussard and J. Philibert, Discussion on Ref. (3).
6. W. J. Harris, *Metal Progr.* **2,** 44 (1943).
7. M. Cohen, E. S. Machlin and V. G. Paranjpe, *Thermodynamics in Physical Metallurgy* p. 162. American Society for Metals, Cleveland, Ohio (1949).
8. J. C. Fisher, J. H. Hollomon and D. Turnbull, *Trans. Amer. Inst. Min. (Metall.) Engrs.* **185,** 691 (1949).
9. R. Kumar and A. G. Quarrell, *J. Iron St. Inst.* **187,** 195 (1957).
10. U. V. Bhat and H. K. Lloyd, *J. Iron St. Inst.* **165,** 382 (1950).

* Received December 16, 1959.

VOL. 8 1960

Reply to Discussion "Shear along grain boundaries of an aluminum–10 per cent zinc alloy deformed at room temperature"

Contrary to the discussion by Dr. Perryman[1], our experience has been that the precipitation of a phase at the grain boundary tends to promote intercrystalline cracking rather than to diminish it. In previous work[2] it was reported that aluminum alloys containing 10 and 20 per cent zinc were subject to intercrystalline cracking at high temperatures (solid solution condition), the degree of intercrystalline cracking becoming worse with increasing zinc content. It was also reported that tensile tests at room temperature, after ageing at room temperature, also resulted in brittle intercrystalline cracking in the 10 and 12 per cent zinc alloys.[3]

Under the circumstances, it would appear that intercrystalline cracking would have been expected whether the alloy was single-phase or contained a precipitate. The truly important thing is that grain boundary shear took place at 0.33 of the absolute solidus temperature. This is certainly not an expected phenomenon, and was worth noting. If a precipitate was present, which is likely, it would make grain boundary shearing much more difficult since the precipitate particles would tend to lock the grain boundary, forcing intercrystalline shear to take place in smaller increments, and to a much smaller extent. Thus the obvious evidence of grain boundary shear at room temperature is indeed of interest.

N. J. Grant

Dept. of Metallurgy
Massachusetts Institute of Technology
Cambridge, Mass.

References

1. E. C. W. Perryman, *Acta Met.* **7,** 648 (1959).
2. G. D. Gemmell and N. J. Grant, *J. Metals, N.Y.* **9,** 417 (1957).
3. H. C. Chang and N. J. Grant, *J. Metals, N.Y.* **8,** 1241 (1956).

* Received December 11, 1959.

KINETICS OF CLUSTERING IN SOME ALUMINUM ALLOYS*

D. TURNBULL, H. S. ROSENBAUM and H. N. TREAFTIS†

The kinetics of clustering of solute in the aluminum rich alloys Al(Cu), Al(Ag) and Al(Zn) was investigated by means of resistivity measurements. In each of the alloys there is, after a rapid quench from the homogenization temperature, a fast initial clustering at temperatures 200°–300°K. This reaction proceeds with an activation energy 0.5–0.6 eV in Al(Cu) and Al(Ag) alloys, and 0.4 eV in Al(Zn) alloys. In Al(Cu) and Al(Ag) alloys the isothermal progress of the reaction is, to a first approximation, independent of solute concentration.

The forms of the isotherms are interpreted on the hypothesis that from the atomically dispersed state the reaction corresponds to the surface energy driven growth of large clusters at the expense of smaller ones. The growth rate, the total progress of the reaction, and their marked variation with thermal history, are satisfactorily interpreted with the quenched-in vacancy hypothesis if it is supposed, in addition, that sensible nucleation of dislocation loops occurs at very high vacancy supersaturations. We present evidence that the limiting cluster size is dictated by *kinetic* rather than by *thermodynamic* factors.

We have found that in very dilute Al(Ag) alloys the isothermal resistivity [as in the case of Al(Zn) and Al(Cu)] rises with time in the earliest stages of clustering.

After the rapid initial clustering there is a further slow reaction in Al(Cu) alloys which occurs over a period of several weeks. This rate is still much greater than that calculated from the extrapolated values of the high temperature diffusion constant of Cu in Al. Some possible interpretations of this slow reaction are outlined.

CINETIQUE DE SEGREGATION DANS QUELQUES ALLIAGES D'ALUMINIUM

La cinétique de ségrégation du soluté dans les alliages Al-Cu, Al-Ag et Al-Zn riches en aluminium a été étudiée au moyen de mesures de résistivité électrique. Dans chacun de ces alliages et après trempe rapide à partir de la température d'homogénéisation, une ségrégation rapide se manifeste d'abord à des températures comprises entre 200 et 300°K. Cette réaction met en jeu une énergie d'activation de 0.5 à 0.6 eV pour Al-Cu et Al-Ag et de 0.4 eV pour Al-Zn.

Dans les alliages Al-Cu et Al-Ag, l'évolution isotherme de la réaction est en première approximation indépendante de la concentration du soluté. La forme des isothermes est interprétée avec l'hypothèse d'après laquelle la réaction correspond à la croissance (due à l'énergie de surface) de gros amas au détriment d'autres plus petits. La vitesse de croissance le progrès total de la réaction et leur variation avec l'histoire thermique sont interprétées de façon satisfaisante à partir de l'hypothèse de trempe des lacunes et si on suppose en plus qu'une nucléation importante d'anneaux de dislocations apparaît pour de hautes concentrations en lacunes.

Les auteurs montrent que la taille limite des amas est déterminée par les facteurs cinétiques plutôt que thermodynamiques.

Les auteurs ont trouvé que dans les alliages très dilués Al-Ag, la résistivité isotherme (comme dans le cas de Al-Zn et Al-Cu) augmente au cours du temps dans les stades initiaux de la ségrégation.

Après la ségrégation initiale rapide, il y a ensuite une réaction lente dans les alliages Al-Cu qui se déroule sur une période de plusieurs semaines.

Cette itesse est encore beaucoup plus élevée que celle calculée à partir des valeurs extrapolées à haute température des constantes de diffusion de Cu dans Al. Quelques interprétations possibles de cette réaction lente sont envisagées.

KINETIK DER ENTMISCHUNG BEI EINIGEN ALUMINIUM-LEGIERUNGEN

Mit Hilfe von Widerstandsmessungen wurde die Kinetik der Entmischung des Zusatzes bei den Aluminium-reichen Legierungen Al(Cu), Al(Ag) und Al(Zn) untersucht. Nach schnellem Abschrecken von der Homogenisierungstemperatur tritt bei jeder dieser Legierungen eine anfängliche schnelle Entmischung bei Temperaturen von 200°–300°K auf. Diese Reaktion läuft ab mit einer Aktivierungsenergie von 0.5–0.6 eV bei Al(Cu)- und Al(Ag)-Legierungen und 0.4 eV bei Al(Zn)-Legierungen. Bei Al(Cu)- und Al(Ag)-Legierungen hängt der isotherme Ablauf der Reaktion in erster Näherung nicht von der Konzentration des Zusatzes ab.

Die Isothermen werden auf Grund der Hypothese interpretiert, daß die Reaktion dem durch die Oberflächenenergie verursachten Wachstum großer Agglomerate auf Kosten kleiner entspricht, und zwar beginnend vom Zustand atomarer Dispersion. Die Wachstumsgeschwindigkeit, der allgemeine Fortgang der Reaktion und die ausgesprochene Abhängigkeit von der vorhergegangenen Warmebehandlung lassen sich durch die Hypothese eingefrorener Leerstellen zufriedenstellend erklären, wenn man zusätzlich annimmt, daß bei sehr hohen Überschußkonzentrationen von Leerstellen merkliche Bildung von Versetzungsschleifen eintritt. Wir bringen Beweise dafür, daß die Größe der Agglomerate durch kinetische und nicht durch thermodynamische Faktoren begrenzt wird.

* Received February 5, 1959; revised version April 8, 1959.

† General Electric Research Laboratory Schenectady, New York.

VOL. 8 1960

In sehr verdünnten Al(Ag)-Legierungen steigt [wie bei Al(Zn) und Al(Cu)] der isotherme Widerstand in den ersten Stadien der Entmischung.

Nach der anfänglichen schnellen Zusammenlagerung tritt bei Al(Cu)-Legierungen eine weitere langsame Reaktion auf, die sich über einige Wochen erstreckt. Diese Reaktionsgeschwindigkeit ist immer noch viel größer, als man sie mit extrapolierten Werten der Diffusionskonstanten von Cu in Al bei hohen Temperaturen berechnet. Einige Erklärungsmöglichkeiten dieser langsamen Reaktion werden angegeben.

INTRODUCTION

In some supersaturated aluminum alloys [for example Al(Cu), Al(Ag) and Al(Zn)] the solute segregates at comparatively low temperature into very small solute-rich clusters which are structurally continuous (coherent) with the parent solid solution. These clusters can be very numerous (e.g. more than 10^{18} cm^{-3}) and may contain of the order of 100 or fewer atoms. The somewhat larger clusters which give the diffraction effects discovered by Guinier[1] and Preston[2] are known as Guinier–Preston zones. In earlier papers[3,4] it was suggested that the mean cluster size enlarges continuously at low temperatures by a process of competitive growth. The rate of enlargement finally becomes so small that the zone size becomes effectively constant. However, we believe that in infinite time the zones would reach a macroscopic size; therefore we classify clustering and zone formation as precipitation processes.

Clustering seems to occur in those systems in which the energy difference between solvent and solute in the solvent structure is quite small. It appears[5,6] that there is no appreciable coherent clustering of silicon in aluminum alloys. Pure silicon has a diamond cubic structure and there is no evidence that a low energy face-centered cubic modification exists.

It is now well known that G.P. zone formation in Al(Cu) occurs near room temperature at rates many orders of magnitude greater than that inferred from the extrapolated values of the diffusion coefficients of copper in aluminum measured at high temperature. DeSorbo *et al.*[4] have shown that the earliest stages of clustering in Al(Cu) are even much faster than had been heretofore supposed and are governed by an activation energy of 0.52 eV. Turnbull and Treaftis[7] showed that, contrary to what had been supposed earlier, the initial stages of clustering in Al(Ag) alloys are also extraordinarily rapid at low temperatures and are controlled by an activation energy very near that for Al(Cu) alloys.

Various theories for the rapid clustering in aluminum alloys have been reviewed elsewhere. It now appears[4,8,9] that the initial rapid clustering in Al(Cu) and Al(Ag) alloys can be explained most simply on the basis of the "quenched-in vacancy" hypothesis. That is, the rapid rate of clustering is effected by a high vacancy concentration, corresponding to equilibrium at the homogenization temperature, retained in the specimen by the rapid quench.

This paper describes a more extensive investigation of the kinetics of clustering in Al(Ag), Al(Cu), and Al(Zn) alloys.

EXPERIMENTAL

Material and preparation of alloys

The Al used in preparation of the alloys was of 99.996 per cent purity. Qualitative emission spectrographic methods showed the impurities to be slight traces of Ag, Cu and Mg. The following elements were looked for but not detected: Fe, Si, Zn, Sn, Pb, Bi, Pt, Ni, Co, Mn, Ir, Cd, Sb, Te, Ti and Li. The Ag used was 99.994 per cent pure, and the Cu and Zn were of 99.999 per cent purity.

Preparation of the 1.9 at.% Cu alloy has been reported elsewhere.[4] The Al(Ag), Al(Zn) and additional compositions of Al(Cu) alloys were vacuum cast in graphite crucibles. The final composition was determined by analyzing the specimens used for the measurements, with an accuracy of ± 0.05 wt.%, after the measurements were completed.

The various alloys were formed into a 0.076 cm diameter wire by cold swaging and drawing; then they were rolled to form ribbons 0.010 cm thick and about 0.2 cm wide. A 120 cm length of ribbon was split from each end to provide voltage and current leads for the central section (3 cm in length) which served as the specimen. The specimen of the 0.4 at.% copper alloy was a 0.025 cm diameter wire 25 cm long, in the form of a coil 0.32 cm in diameter and ~ 3.8 cm long. In this case the longer specimen was required to obtain the desired accuracy in the resistance measurements.

Homogenization and quenching

The homogenization atmosphere was usually hydrogen, but the results were not altered appreciably when helium or air was used instead. The rectangular furnace used was described earlier.[10] The specimens were mounted on a small "transite" plate that was free to rotate below the opening in the bottom of the furnace (Fig. 1). After homogenization, the specimens were swung out of the furnace and into the quenching medium directly beneath the furnace.

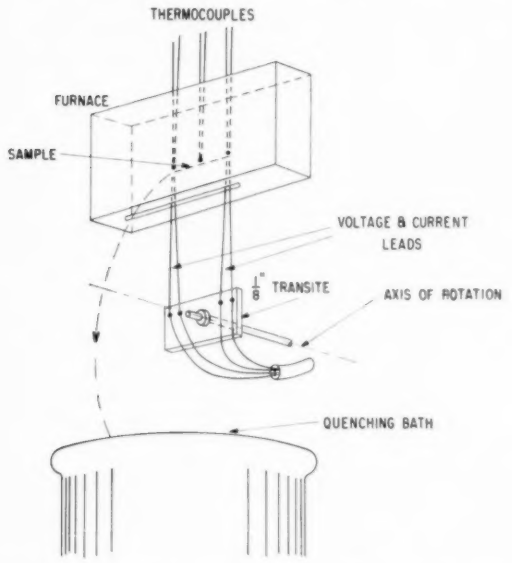


FIG. 1. Quenching arrangement. The sample was supported by the voltage and current leads in the furnace. The quench was effected by rotating the sample into the quenching bath by hand as shown.

The cooling rate during quenching was determined by applying the voltage drop from across the specimen to the vertical deflection plates of an oscilloscope. The resulting curve was then photographed by a Polaroid camera attachment. Since the current in the circuit was kept constant, the curve is a representation of the variation of temperature with time. When the specimens were quenched in water, the total time elapsed in cooling from homogenization temperature* to bath temperature was 25 msec, corresponding to an average cooling rate of 25,000°C sec^{-1}. About the same rate of quenching was obtained when the bath was a eutectic mixture of $CaCl_2$ and water at −50°C. A small amount of potassium dichromate was added to this bath to minimize corrosion of the specimens. In some experiments a a small elliptic furnace was used; this consisted of an aluminum shell wrapped around elliptical transite ends, with a General Electric infrared tube at one focus providing a line source of heat, and a gold sheet cylinder at the other focus. The gold cylinder was coated with Al_2O_3 powder in order to increase its infrared absorption, and a "lavite" cylinder was placed inside to improve the emissivity to the specimen. The specimen came into the lavite cylinder through aligned slots in the bottom of the furnace and the gold heating cylinder. The opening of the furnace was placed within 3 cm of the quenching bath. With this apparatus quenching rates of 40,000°–50,000°C sec^{-1} were obtained.

The Al(3.6 at.% Zn) alloy was homogenized at 300°C. The Al(Cu) alloys, 0.85–2.25 at.% Cu, were homogenized at 550°C, and the 0.4 at.% Cu alloy at temperatures ranging between 350° and 550°C. The Al(Ag) alloys, 0.6–6.1 at.% Ag, were usually homogenized at 550°C, but in some experiments with *dilute* alloys temperatures between 350° and 600°C were used.

Measurement of resistance

The current in the resistance measuring circuit, which was described earlier,[4] was kept constant at 1.0 ± 10^{-5} A by continuously monitoring the voltage drop across a standard resistor. Recording the voltage drop across the specimen gave the resistance in ohms directly. Accurate recording of the resistance was begun within 5–15 sec after the quench. Using the most sensitive recorder scale, 0.2 mV for full scale deflection, the resistance was determined to $\pm 2 \times 10^{-6}\ \Omega$, and with the least sensitive scale (1.0 mV max) to $\pm 1 \times 10^{-5}\ \Omega$. The uncertainty in the measured resistance change varied between 0.5 and 3 per cent depending on the magnitude of the change.

RESULTS

Resistance–temperature behavior of quenched alloys on continuous heating

The occurrence of low temperature reactions can be displayed by continuously heating the specimen after quenching to a low temperature. In these experiments the specimens are homogenized, quenched in brine at −50°C, and immediately transferred to a liquid nitrogen bath. The resistance is then measured continuously as the temperature is increased (using a suitable inert bath fluid for each temperature range) at a rate of about 20°C hr^{-1}.

The results for an Al(Cu), an Al(Ag) and an Al(Zn) alloy are displayed in Fig. 2. In all three cases the resistivity at the lowest temperatures is very near the value obtained by linear extrapolation from temperatures above the thermodynamic temperature of complete solution. In agreement with earlier results the behaviour of resistivity upon continuous heating gives evidence for low temperature reactions in all three systems.

In the Al(Ag) alloys the resistivity begins to fall away from the ρ vs. T straight line relation at 225°K (−48°C) and finally reaches a plateau which at 0°C is about 8 per cent below the solid solution value as

* For a homogenizing temperature of 550°C the temperature drop in the specimen from the time it left the furnace to the time it contacted the quenching bath was between 10° and 15°C.

VOL. 8 1960

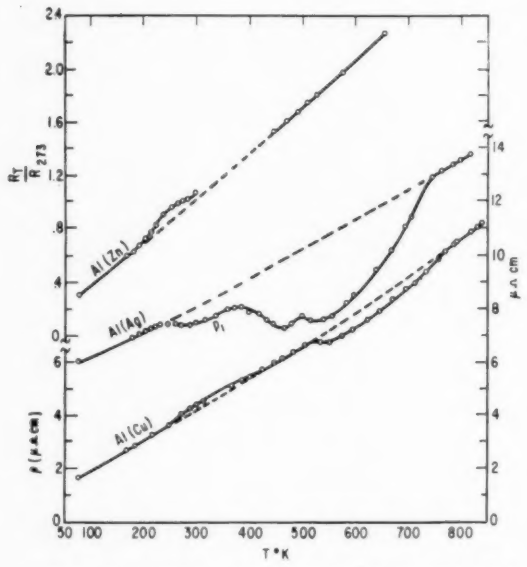


FIG. 2. Resistivity as a function of the temperature for an Al(3.6 at.% Zn), an Al(5.5 at.% Ag) and an Al (1.7 at.% Cu) alloy. The specimens were quenched to 223°K (−50°C) from the homogenization temperature and then immediately put into liquid N_2. They were then slowly heated (~20°C/hr) while the measurements were made. The lower scale (resistivity) is for the Al(Ag) and Al(Cu). The upper scale (in fractional resistance) is for Al(Zn).

the temperature is increased further. The difference between the resistivity of the solid solution and the "plateau" value, corresponding to completion of the low temperature reaction, increases linearly with silver concentration. This is shown in Fig. 3.

There is evidence for further reactions leading to resistance lowering beginning at 375°K (102°C) and 500°K (227°C). It is significant that after the low temperature reaction has occurred in the initially homogeneous alloy, the alloy is stable up to 100°C at a resistance level far higher than that of the ε' state (see Borelius[11]) which forms in slower quenches.

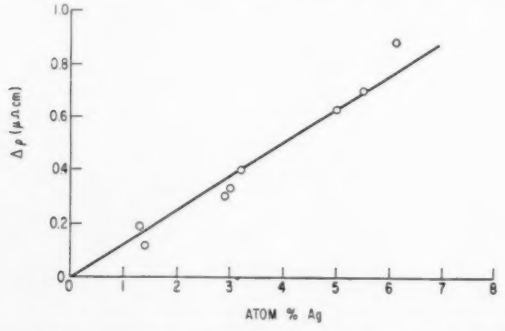


FIG. 3. Extent of low temperature reaction in Al(Ag) alloys. The specimens were homogenized at 550°C, quenched into ice water, and the "low temperature reaction" allowed to go to completion (to state p_1 in Fig. 2) isothermally at 0°C. The total resistivity change for this reaction is plotted as a function of Ag content.

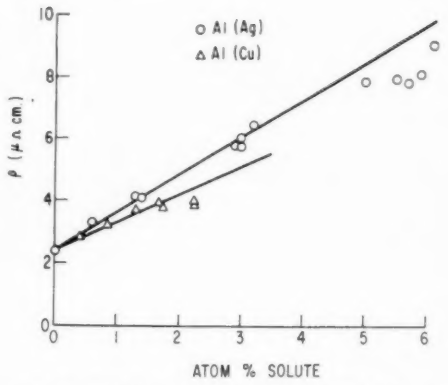


FIG. 4. Resistivity of Al(Ag) and Al(Cu) alloys as a function of their compositions. These values represent the state immediately after a quench to 0°C.

The beginning of the low temperature reaction in the Al(Zn) and Al(Cu) alloys is indicated by an increase in resistivity above that of the straight line ρ vs. T relation for the homogeneous solution. In Al(Zn) the reaction becomes perceptible at 200°K (−73°C) and leads to a resistivity increase, relative to the homogeneous solid solution, which reaches 10 per cent at 250°K and then falls away.*

In the Al(Cu) alloy the reaction becomes perceptible at 250°K (−23°C) and leads to a resistivity increase, relative to the homogeneous solution, which is at most 4 per cent.

Resistivity–concentration relations for Al(Ag) *and* Al(Cu) *at* 0°C

Figure 4 shows the variation of resistivity with concentration for the quenched Al(Ag) and Al(Cu) alloys in their initial state at 0°C. These data were obtained by measuring the resistivity–time curves of ribbon-shaped (0.01 × 0.2 × 3 cm) specimens quenched into an ice bath (0°C) after homogenization. (The ice was kept from the specimen by a wire mesh basket.) The resistivities plotted are the extrapolated values at $t = 0$. Identical results were obtained when the specimens were first quenched in a brine bath at −50°C and then transferred to the 0°C bath. It is seen that at the lowest concentrations the resistivity increases *linearly* with concentration in both alloys. For Al(Cu) the resistivity increase is 1.0 $\mu\Omega$ cm/at.% and for Al(Ag) 1.2 $\mu\Omega$ cm/at.%.

The falling of the resistivity of Al(Cu) from the linear relation at high concentration is not understood since clustering, under these conditions, would lead to a resistivity increase.

* An extensive investigation of the kinetics of clustering in Al(Zn) alloys has been made independently by Prof. Guinier[12].

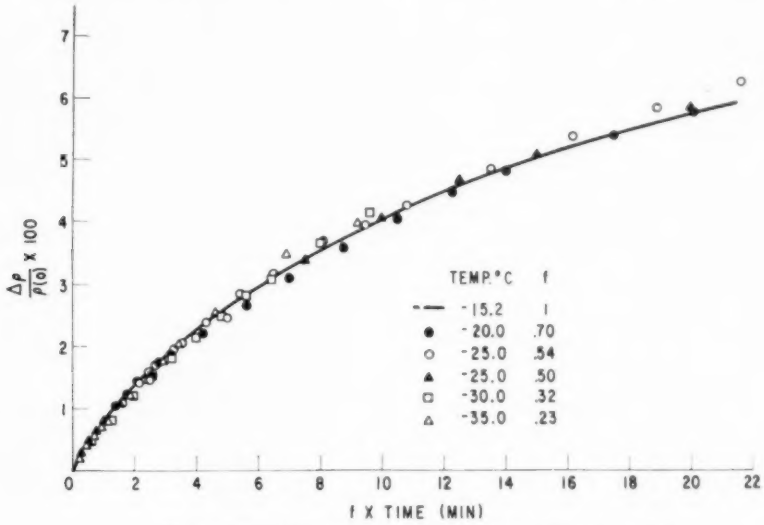


FIG. 5. Fractional change of resistivity [i.e. ratio of $\Delta\rho(t)$ to the extrapolated value of $\rho(t=0)$] vs. a normalized time scale for an Al(3.6 at.% Zn) alloy. The alloy was homogenized at 300°C, quenched into brine at −45°C and then aged isothermally in alcohol at the indicated temperatures. The curves were made to superpose by multiplying the time by the indicated scaling factor f.

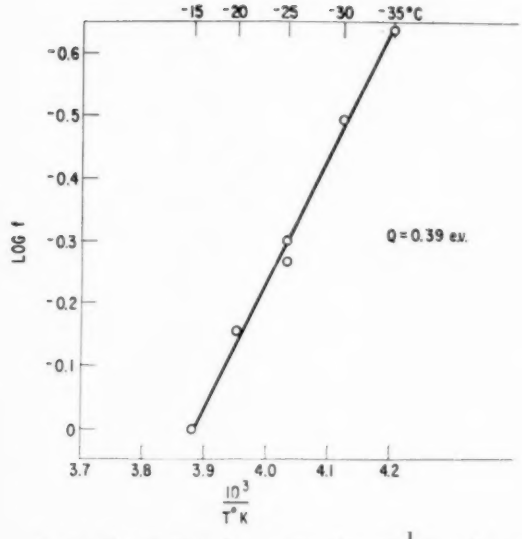


FIG. 6. Log f plotted as a function of $\frac{1}{T}$ for data of Fig. 5.

Rate of clustering at low temperatures and its temperature dependence

Resistance–time relations at different low temperatures were obtained for Al(3.6 at.% Zn) alloys using procedures similar to those already described for the Al(Ag) and Al(Cu) alloys. The specimens were quenched from the homogenization temperature into brine at −50°C and immediately up-quenched to the aging temperature.

As noted earlier,[4,7] the isotherms of resistivity–time for the low temperature clustering in Al(Cu) and Al(Ag) can be superposed by multiplying the time at a given temperature by a suitable factor f. The low temperature isotherms for Al(Zn) alloys can be superposed similarly as shown in Fig. 5. It was found (see Fig. 6), as with Al(Cu) and Al(Ag), that the dependence of f on temperature is satisfactorily described by an Arrhenius type of relation. The activation energies for the low temperature reaction calculated from this relation are summarized for all three systems in Table 1.

The activation energy governing zinc clustering is seen to be somewhat less than that for copper and silver clustering. The apparent increase of activation energy for silver clustering with decreasing concentration is hardly significant. It had already been pointed out[4,8,13] that the activation energies for

TABLE 1. Activation energy, Q, governing rate of low temperature clustering in aluminum alloys. Calculated from relation: $f = A \exp[-Q/RT]$

Solute	Solute concentration (at. %)	Activation energy (eV)
Copper	2.0	0.51 ± 0.05
Silver	1.3	0.565 ± 0.05
Silver	2.5	0.52 ± 0.05
Silver	8.5	0.49 ± 0.05
Zinc	3.6	0.39 ± 0.04

All the data fall within the specified limits

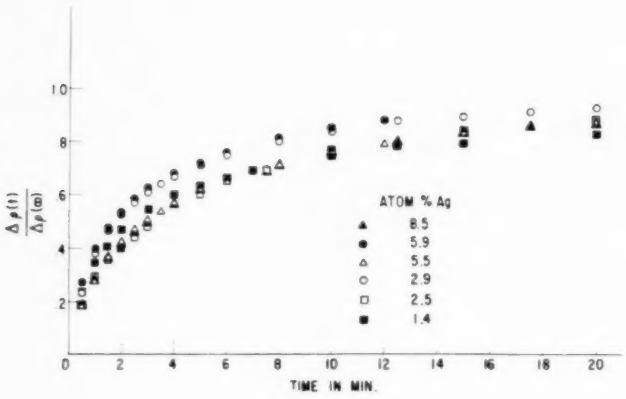


FIG. 7. Isothermal aging curves for various Al(Ag) alloys. The specimens were homogenized at 550°C, quenched into brine at −45°C, and then aged isothermally in water at 0°C. The fractional resistivity change (i.e. the change of resistivity at time t divided by the total change) is plotted as a function of time.

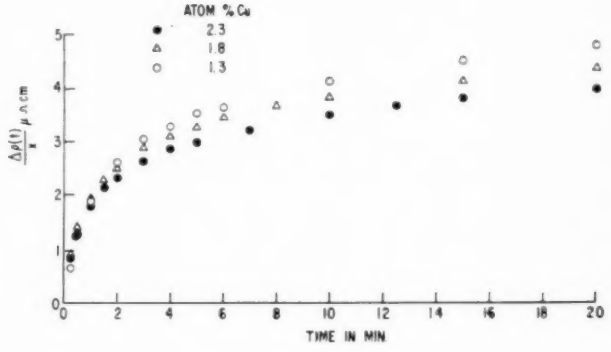


Fig. 8. Ratio of the resistivity change $\Delta\rho(t)$ to the Cu concentration, X, vs. time for various Al(Cu) alloys. The specimens were homogenized at 550°C, quenched into ice water and then aged isothermally in water at 0°C.

clustering of copper and silver are near that governing the annealing-out of point defects in pure aluminum.

Dependence of rate of clustering on solute concentration

Turnbull and Treaftis[7] pointed out that, to a first approximation, the rate of initial clustering in Al(Ag) alloys is independent of the solute concentration, X. That is dy/dt, where y is defined by

$$y = [\Delta\rho(t)]/\Delta\rho_\infty \qquad (1)$$

where $\Delta\rho(t)$ and $\Delta\rho_\infty$ are the total changes in resistivity due to clustering after times t and infinity, respectively, is approximately independent of X. Since $\Delta\rho_\infty$ is proportional to X (see Fig. 3) we can also define y by

$$y = [\Delta\rho(t)]/kX. \qquad (2)$$

The more complete results on the Al(Ag) alloys we have now are displayed in Fig. 7 and confirm this conclusion. It is seen that in the earliest stages of clustering $y = f(t)$ is nearly independent of X over quite a wide concentration range. However, in the later stages the rate, dy/dt, tends to be somewhat higher in the more concentrated alloys.

Because of the maximum in the isothermal resistance with time, $\Delta\rho_\infty$ cannot be defined for Al(Cu) alloys. However, it is reasonable to suppose that equation (2) is valid in this case. Indeed, we find (see Fig. 8) that $\Delta\rho(t)/X = f(t)$ for Al(Cu) is nearly independent of X between $X = 0.013$ and $X = 0.024$.

We have no such measurements on Al(Zn) alloys.

Effect of thermal history on the kinetics of clustering

We have found that if the quenching rate of Al(Ag) alloys is lowered, either by making the specimen thicker or quenching into fluids with lower quenching efficiency, the initial resistivities are significantly lower than the homogeneous solution values. Using the same experimental procedure as that used by Borelius[11], we confirmed the existence of the ε' state that he reported.[11] ε' is manifested by a resistivity about 50 per cent below the homogeneous solution value. We also found that the initial rate of clustering in Al(Ag), as well as the initial resistivity, was less with lower rates of quenching.

If, instead of being quenched from the homogenization temperature to a sub-zero temperature and then warmed up, the Al(Ag) alloy is quenched directly into water near room temperature or higher, the resistivity ultimately falls to a limiting value considerably below the plateau of the p_1 state (which at 0°C is 7–8 per cent below the homogeneous solution value). The higher the temperature of the water quench the greater is the total decrease in resistivity; this is shown in Fig. 9.

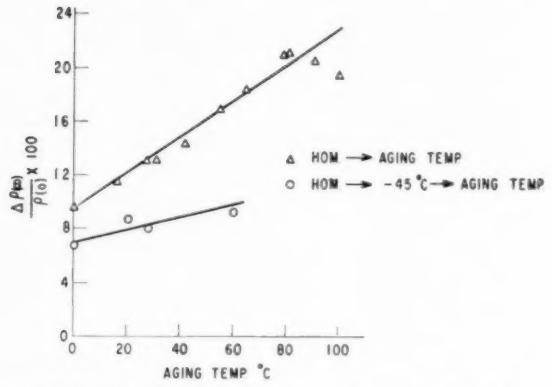


Fig. 9. Ratio of the total decrease in resistivity $\Delta\rho(\infty)$, to the initial resistivity, $\rho(0)$, plotted as a function of the aging temperature in an Al(3.0 at.% Ag) alloy. The alloy was homogenized at 550°C and quenched into water at the indicated temperature. The reactions were allowed to continue until the rate of resistivity decrease became imperceptible.

DeSorbo *et al.*[4] showed that the rate of clustering in Al(Cu) alloys at low temperature is decreased if the quench from the homogenization temperature is interrupted for an appreciable time t_i at 200°C. (We shall call this the "quench-interruption effect".) More specifically, it was found that the rate of resistivity increase, $\dot{\rho}$, for some constant $\Delta\rho(t)$, at 0°C in a 2.0 at.% copper alloy decreases as $1/(t_i +$ constant). Thus $\dot{\rho}(t_i)$, in units of $\dot{\rho}$ (0) at $t_i = 0$, was 1/10 at $t_i = 10$ sec and 1/300 at $t_i = 120$ sec.

We have now studied the effect of varying the temperature at which the quench of Al(2 at.% Cu) is interrupted. In these experiments the quench from 550°C is interrupted for a period of 10 sec at temperatures between 160°C and 225°C and then quenched to 0°C and held. The *initial* rate of change of resistivity $\dot{\rho}_0$ at 0°C is plotted against the intermediate temperature T_i in Fig. 10. For the T_i range 185–225° C, $\dot{\rho}_0$ increases with decreasing T_i. Below $T_i = 180$°C the results were very inconsistent, but it appeared that below $T_i = 170$°C $\dot{\rho}_0$ tends to fall with decreasing T_i.

If, after being quenched from 550°C to 0°C, the Al(2 at.% Cu) specimen is given a 2 min reversion treatment at 200°C (i.e. up-quenched from 0°C to 200°C and held there) *the rate of clustering after again quenching to* 0°C *is* 2400 *times slower than after a direct quench from* 550°C *to* 0°C. The corresponding isotherms are shown in Fig. 11.

It is significant that the reversion treatment had much less effect on the rate of clustering in specimens whose quench from 550°C had been interrupted at 200°C. The 0°C isotherm for this treatment is also shown in Fig. 11. The rate is about 10 times the rate in the directly quenched specimen that had had a reversion treatment, and nearly the same as that after

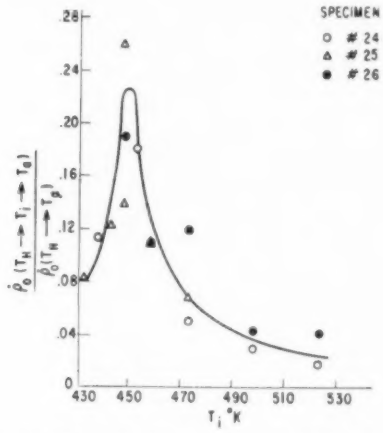


Fig. 10. Normalized rate of resistivity change as a function of the temperature at which the quench was interrupted. The normalized rate is the ratio of the initial rate of resistivity change, $\dot{\rho}$, after an interrupted quench, to the initial rate after a direct quench. The alloy, Al(2 at.% Cu), was homogenized at 823°K (550°C), quenched into a silicone oil bath at the indicated temperature for 10 sec, and then quenched to 273°K (0°C) where the isothermal rates were measured.

a quench interruption (2 min at 200°C) without subsequent reversion.

Clustering in Al(Ag) *alloys after the low temperature reaction*

We have investigated the rate of clustering in an Al(2.8 at.% Ag) alloy after the completion of the low temperature reaction. That is, the initial state, p_1, in these experiments corresponds to the resistivity

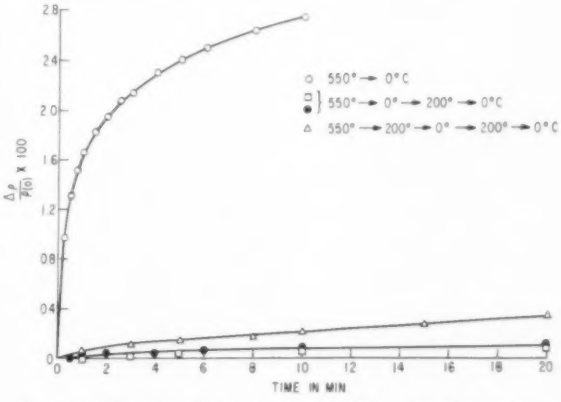


Fig. 11. Fractional change in resistivity (i.e. the ratio of the change in resistivity, $\Delta\rho$, to the initial resistivity) vs. aging time at 273°K (0°C) for an Al(2 at.% Cu) alloy after the indicated quenching and aging sequences. For the upper curve the specimen was quenched directly to 273°K (0°C). For the middle curve it was quenched to 273°K (0°C) for 1 hr, up-quenched to 473°K (200°C) for 2 min and then again quenched to 273°K (0°C). For the lower curve it was quenched from 823°K (550°C) to 473°K (200°C) for 2 min, then quenched to 273°K (0°C) for 1 hr, up-quenched to 473°K (200°C) for 2 min and finally quenched to 273°K (0°C).

VOL. 8 1960

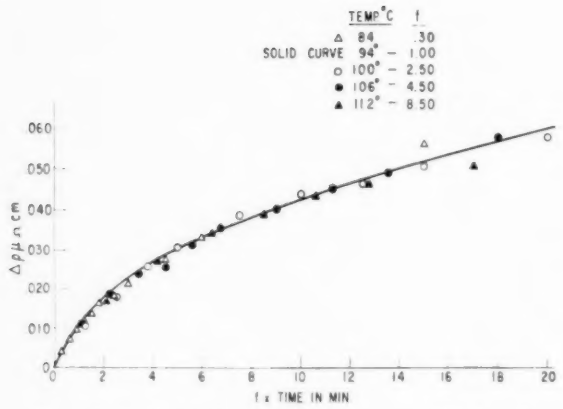


FIG. 12. Isothermal aging curves for an Al(2.8 at.% Ag) alloy that was homogenized at 550°C, quenched into ice water for 1 hr (0°C) and then up-quenched into an oil bath at the indicated aging temperature. The change in resistivity is plotted against the time (as normalized by the appropriate factor, f) at the aging temperature.

plateau, p_1, which, at 0°C, is about 8 per cent below the homogeneous solution value. The final state corresponds roughly to a resistivity about 20–25 per cent below the homogeneous solution value at 0°C. This state was stable to a temperature of 500°K (227°C) in the continuous heating experiments for the alloy composition 5.5 at.% Ag (Fig. 2). The transition to this state occurs at an appreciable rate at temperatures exceeding 353°K (80°C).

The procedure was to quench the alloy from 550°C to 0°C and hold for 1 hr at 0°C. This brought the alloy to the p_1 state. It was then immediately up-quenched to a temperature within the range 80°–170°C and held. Two sets of isotherms were obtained, the isotherms of each set differing only by time scale factors, f. One set (see Fig. 12) was in the temperature range 80°–120°C and could be described approximately by the relation $\Delta\rho = \gamma t^{1/2}$ where γ is a function of T. The other set was in the temperature range 120°–170°C.

The temperature dependence of the time scale factors, f, is described by an Arrhenius equation for each set of isotherms. The apparent activation energy for the low temperature isotherms (see Fig. 13 for the Arrhenius plot) is 1.5 ± 0.15 eV; that for the high temperature isotherms is 1.0 ± 0.1 eV. The initial resistivities in these experiments were higher than the values extrapolated linearly along the p_1 plateau. The difference increased with increasing temperature being 1 per cent at 100°C and 3 per cent at 170°C. This may reflect some re-solution of the clusters from the p_1 state.

The resistivity maximum in clustering

It was well known that when Al(Cu) or Al(Zn)

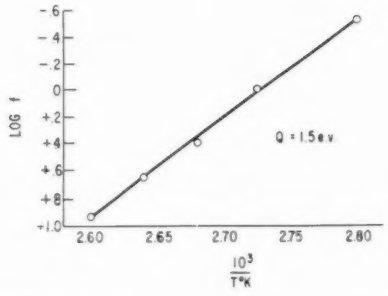


FIG. 13. Log of the time scale factor f as a function of $\frac{1}{T}$. The data are those of Fig. 12.

alloys are quenched from the homogenization temperature to comparatively low temperatures, the isothermal resistivity rises at first. With longer times or at higher temperatures it reaches a maximum value and then falls off.

This resistivity increase with initial clustering is contrary to expectations based on simple theory for the effect of solute segregation. Mott[14] suggested that particles with diameters of the order of magnitude of the wave length of the conduction electrons might contribute an extra scattering. Also it has been supposed that the effect is associated with the difference between the solvent and solute atom sizes. However, a very pronounced resistivity maximum occurs in Al(Zn) alloys even though the sizes of Al and Zn atoms in the face-centered cubic modification are not very different.

It had been supposed that Al(Ag) alloys, in which the atom size of solute and solvent differ by less than 1 per cent, do not exhibit the resistivity maximum. However, Federighi[15] and we, independently, have found that the isothermal resistivity of *dilute* Al(Ag) alloys does exhibit a maximum with time when the specimens are quenched from a comparatively low homogenization temperature. Our results for an Al(1.4 at.% Ag) alloy held at 0°C, after homogenization at various temperatures in the range 350°–550°C, are shown in Fig. 14. The maximum becomes apparent in specimens quenched from homogenization temperatures 450°C and below. At 353°C the maximum increase over the initial resistivity is 1½ per cent. Fig. 15 shows a similar set of isotherms at 20°C for a 2.8 at.% Ag alloy. Similar effects were obtained for a 0.6 at.% alloy. We have established that the appearance of the maximum is independent of the homogenization furnace atmosphere.

The initial resistivity, $\rho(0)$, at the aging temperature in these experiments varies somewhat with homogenization temperature. In the more concentrated alloys $\rho(0)$ decreases with increasing

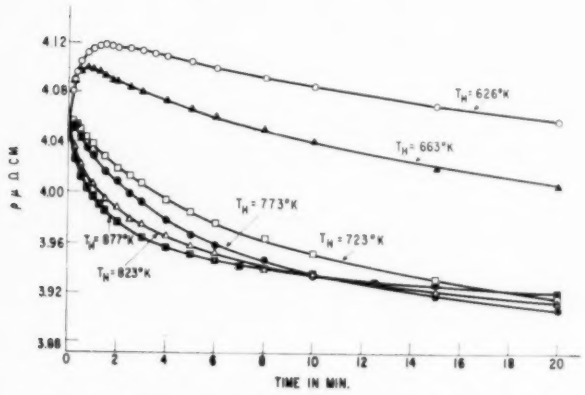


FIG. 14. Isothermal aging curves for an Al(1.4 at.% Ag) alloy at 273°K (0°C). The alloy was homogenized at the various indicated temperatures. Resistivity is plotted against time at 0°C.

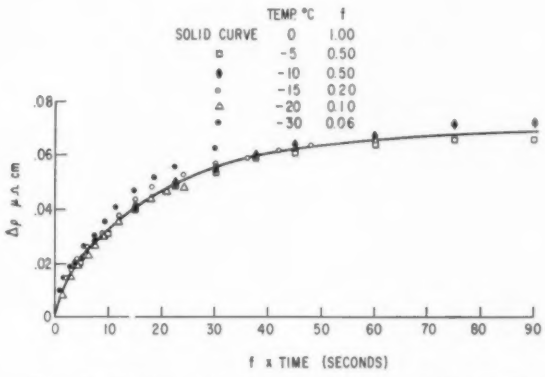


FIG. 16. Isothermal aging curves for an Al(1.4 at.% Ag) alloy that was homogenzied at 353°C, quenched into ice water and then aged at the indicated temperatures. The change in resistivity is plotted as a function of a normalized time scale.

homogenization temperature T_H (see Fig. 15); in the 0.6 at.% alloy $\rho(0)$ increases with T_H. However this latter effect may be due to added resistivity of the lattice defects which would increase with increasing temperature and which would make a relatively large contribution to $\rho(0)$ in the most dilute alloys.

It is significant that the initial ascending parts of a particular set of isotherms for a given T_H and silver content differ only by time scale factors, f. This is shown in Fig. 16 for an Al(14. at.% Ag) alloy and with $T_H = 626$°K (353°C). These scale factors are related to temperature by the Arrhenius equation with an activation energy 0.57 eV.

The resistivity maximum for Al(Zn) alloys can be quite large even at relatively high zinc contents. Fig. 17 shows an isotherm at −45°C for an Al(11.9 at.% Zn) alloy. The resistivity increased 15 per cent before falling.

In Al(Zn) alloys it is possible for the resistivity to rise with time at a low temperature but in the *same state* to fall with time at a higher aging temperature. This effect was discovered by Meyer[16]. We observed it in the thermal cycling of an Al(3.6 at.% Zn) alloy

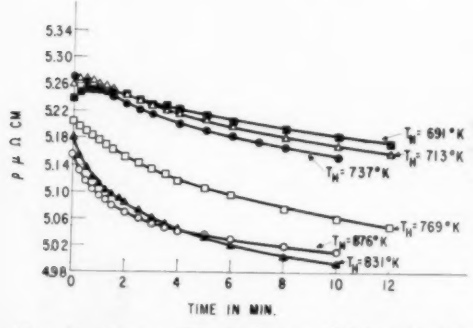


FIG. 15. Same as Fig. 14 for an Al(2.8 at.% Ag) alloy aged at 20°C.

between 0°C and 23°C. Our results are shown in Fig. 18. In these experiments the aging was carried out for a time at 0°C. The specimen was then up-quenched to 23°C, held there awhile, and then down-quenched to zero. This process was repeated several times. The isotherms obtained by uninterrupted aging are also shown. It is seen that after a time the resistivity is falling at 23°C but it continues to rise at 0°C after down-quenching from a falling state at 23°C. It is significant that the rise or fall of resistivity that occurs at one temperature is transmitted to the initial resistivity (for that cycle) at the other temperature. (For some unknown reason the fourth cycle in the data of Fig. 18 is an exception to this.)

Clustering in dilute alloys

In relatively dilute alloys the quenched-in vacancies can make a contribution to the resistivity comparable in magnitude to the change in resistivity due to low temperature clustering. For example, the data of DeSorbo and Turnbull[13,17] indicate that the lattice defects in equilibrium in *pure* aluminum at 550°C contribute 0.05 $\mu\Omega$ cm to the resistivity. This is significant compared with the 0.13 $\mu\Omega$ cm resistivity decrease accompanying the formation of the p_1 state in an Al(1 at.% Ag) alloy. One possible effect of this vacancy resistivity contribution was noted in the preceding section.

We have observed some very marked effects of the vacancy resistivity contribution on the resistivity isotherms of very dilute Al(Cu) alloys. In these experiments an Al(0.43 at.% Cu) alloy was made into a thin wire 0.025 cm in diameter. A 25-cm length of this wire was put into the form of a helix 0.32 cm in diameter and 3.8 cm long for the resistivity measurements. The specimen was homogenized in the elliptic

VOL. 8 1960

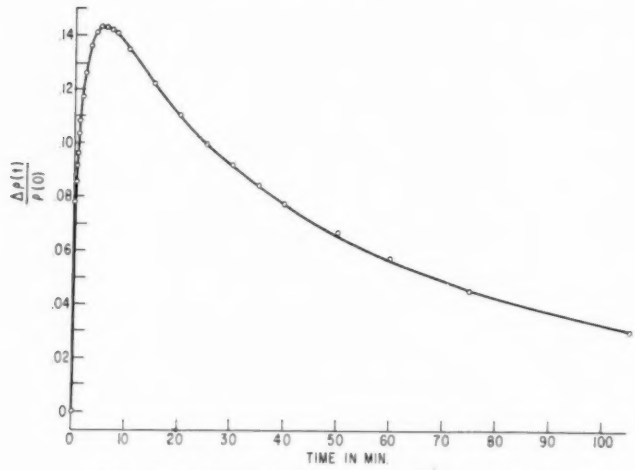


FIG. 17. Isothermal aging curve for an Al(11.9 at.% Zn) alloy at −45°C. The specimen was homogenized at 380°C and quenched directly to −45°C. The fractional change in resistivity, i.e. the ratio of the resistivity at time t, $\Delta\rho(t)$ to the extrapolated value at $t = 0$, is plotted as a function of the time at −45°C.

radiation furnace described earlier and quenched into a water bath at 0°C.

The isotherms so obtained for different homogenization temperatures are shown in Fig. 19. It is seen that, just as in the case of dilute Al(Ag) alloys, the resistivity initially rises with time when the homogenization temperature is low, but it falls at first when T_H is 550°C.

These isotherms can be interpreted, in part, if it is supposed that the total resistivity change, $\Delta\rho$, at any time is made up of two parts. One part, $\Delta\rho_c$, is a quantity that is due to clustering and is positive under these experimental conditions; the other part, $\Delta\rho_v$, is a negative quantity resulting from the leaking out of lattice vacancies. That is:

$$\Delta\rho = \Delta\rho_c + \Delta\rho_v. \tag{3}$$

In this alloy the clusters apparently dissolve (retrogress) at 100°C. Therefore $\Delta\rho_c$ can be estimated by heating the alloy at 100°C and then measuring the resistivity immediately after quenching to the aging temperature. This was done after each isothermal run, and the resulting resistivity change, $\Delta\rho_c$ due to

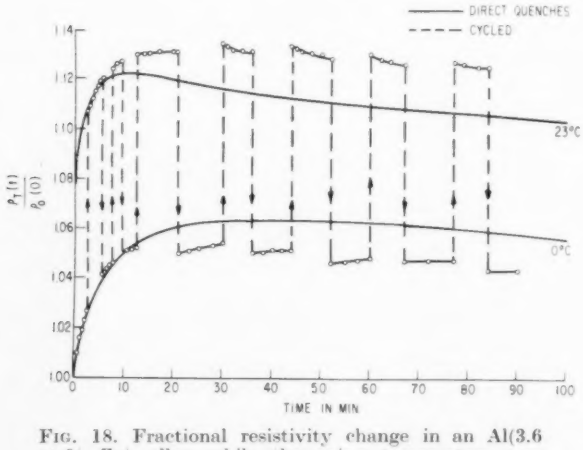


FIG. 18. Fractional resistivity change in an Al(3.6 at.% Zn) alloy while the aging temperature was alternated between 0°C and 23°C. The specimen was homogenized at 300°C and quenched into an ice water bath. The ordinate is the ratio of the resistivity, $\rho_T(t)$ to the initial resistivity at 0°C, $\rho_0(0)$.

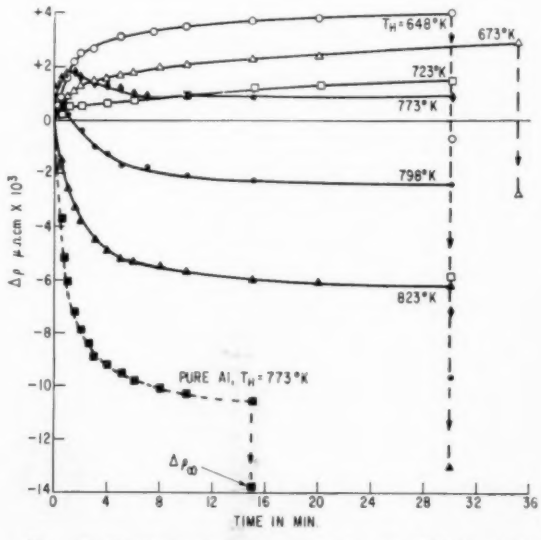


FIG. 19. Isothermal aging curves for an Al(0.43 at.% Cu) alloy that was homogenized at the indicated temperatures and quenched directly to 273°K (0°C). The change in resistivity is shown as a function of the time at 0°C.

TABLE 2. Resistivity changes in an Al(0.43 at.% Cu) alloy aged at 0°C after homogenization at various temperatures, T_H

T_H (°K)	t (min)	$\Delta\rho$ ($\mu\Omega$ cm)	$\Delta\rho_c$	$\Delta\rho_v$	$\Delta\rho_v^\circ$ for pure aluminum*
673	45	+0.0032	+0.0059	−0.0027	−0.0036
698	30	+0.0030	+0.0067	−0.0037	−0.0060
723	30	+0.0015	+0.0075	−0.0060	−0.0095
748	30	+0.0011	+0.0083	−0.0072	−0.0148
773	30	+0.0003	+0.0064	−0.0061	−0.021
798	30	−0.0024	+0.0075	−0.0099	−0.031
823	30	−0.0062	+0.0069	−0.0131	−0.043

* Resistivity due to lattice defects in equilibrium at T_H in pure aluminum calculated from data of DeSorbo and Turnbull[17].

cluster re-solution, is shown in Fig. 19 for each case. The contribution of the vacancies, $\Delta\rho_v$, at the end of the experiment is then found by subtracting $\Delta\rho_c$ from $\Delta\rho$ as indicated by equation (3).

The values of $\Delta\rho_c$ and $\Delta\rho_v$ so calculated are summarized in Table 2.

We show in the sixth column of Table 2 the resistivity $\Delta\rho_v^\circ$ due to vacancies *in equilibrium* in *pure* aluminum. At the corresponding homogenization temperature $\Delta\rho_v$ for the dilute alloy is near $\Delta\rho_v^\circ$, but it increases less rapidly with T_H than does $\Delta\rho_v^\circ$ with T. Of course the resistivities due to vacancies are not necessarily the same in pure aluminum and in dilute alloys. However, we would expect the vacancy resistivity found in our experiments to be substantially lower than the total of that due to vacancies in equilibrium at T_H. There are two reasons for this expectation: (1) In quenching from relatively high temperatures usually it is not possible to cool fast enough to retain all the defects in the specimen in equilibrium at that temperature. (2) It may be that 30 min at 0°C is insufficient time, under the conditions, for all the vacancies to leak out of the alloy.

Also shown in Fig. 19 is an isotherm at 0°C for pure aluminum homogenized at 500°C and quenched in the same way as the alloys. The total change in resistivity, 0.014 $\mu\Omega$ cm, is to be compared with the $\Delta\rho_v^\circ$ value of 0.021 $\mu\Omega$ cm.

Effect of cold-working on the rate of clustering

In an earlier paper[4] it was shown that light cold working has but little effect upon the kinetics of clustering in Al(Cu) alloys quenched directly from the homogenization to the aging temperature. If, however, the quench had been interrupted by holding at 200°C so that the clustering rate at 25°C and below was substantially reduced, light cold working (done by bending the specimen plastically in liquid nitrogen prior to aging) had the effect of restoring the clustering rate nearly to its value in specimens quenched directly from T_H to the aging temperature.

We have done similar experiments with Al(Ag) alloys. In one set of experiments an Al(1.4 at.% Ag) alloy was homogenized at 600°C, quenched into brine at −50°C, then transferred to a liquid-nitrogen bath and finally cold worked by plastic bending. It was aged at 0°C. The resulting isotherm and the corresponding isotherm for the undeformed specimen are shown in Fig. 20. A similar pair of isotherms is shown in the figure for this alloy homogenized at 350°C.

These results indicate that light cold working has little effect on the rate of clustering in Al(Ag) alloys excepting to lower it condiserably in the later stages for the alloy quenched from $T_H = 873$°K (600°C).

In another experiment an Al(6 at.% Ag) alloy was homogenized at 550°C, quenched into brine at −50°C and then aged at −10°C. Then at various stages during aging the specimen was cold-worked slightly either at −10°C or −196°C. In all cases the rate of clustering after the cold-working was slightly, but perceptibly, increased.

Thus, as in the case of Al(Cu) alloys, light cold-working has no pronounced effect upon the initial rate of clustering in Al(Ag) alloys quenched *directly* from the homogenization to the aging temperature.

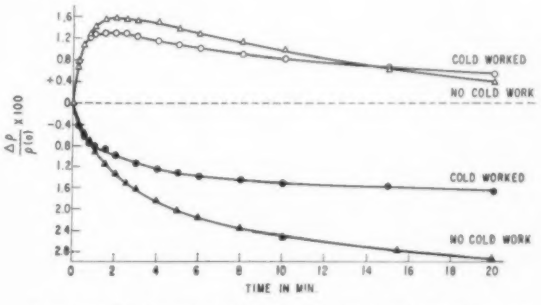


FIG. 20. Effect of cold-work on the isothermal aging curves of an Al(1.4 at.%Ag) alloy. Cold-work was done in liquid N_2 after the quench from the homogenization temperature, but before the subsequent aging. The upper pair of curves are for a homogenization temperature, T_H, of 350°C, while in the lower pair of curves $T_H = 600$°C. The ratio of the resistivity change $\Delta\rho$, to the initial resistivity, ρ_0, is plotted as a function of the time at the aging temperature, 0°C.

VOL. 8 1960

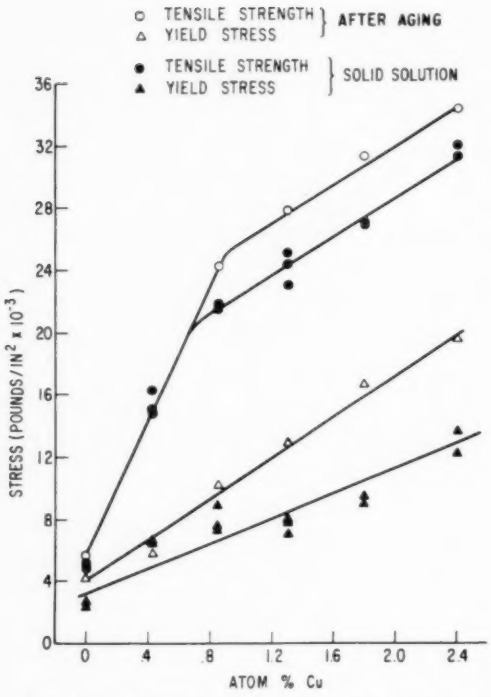


FIG. 21. Fracture and yield stress as a function of Cu content in Al(Cu) alloys is shown for both the "aged" condition (containing clusters) and the "retrogressed" condition (little or no clustering present). The stress values shown here are the ratio of the load to the unstrained cross-sectional area. The yield stress values are the stress at $\Delta l/l_0 = 0.002$, where Δl is the change in length and l_0 is the unstrained length. The alloys containing clusters had been homogenized at 550°C, quenched into water at room temperature and immediately transferred to a liquid N_2 bath. They were then aged at room temperature for 20 min before testing. The "retrogressed" or "solid solution," condition was attained by homogenizing as above, quenching into water at 0°C, aging at 0°C for various times (30 min for the 0.42, 0.85 and 1.3 at.% alloys; 15 min for the 1.8 and 2.4 at.% alloys), and finally putting the specimens into silicone oil at an appropriate retrogression temperature (150°C for the 0.42%, 175°C for the 0.85 at.%, and 200°C for the more concentrated alloys) for 2 min. All tests were made at room temperature.

Effect of clustering on stress–strain relations

Some observations were made on the flow stress and tensile strength of Al(Cu) alloys as a function of copper concentration and clustering. The tests were made at 27°C using the Instron tensile testing apparatus. The alloy specimens were 0.01 cm × 0.24 cm × 3.0 cm.

All were homogenized at 550°C, quenched to room temperature, then immediately transferred to a liquid nitrogen bath and stored there. (The pure aluminum specimens were treated in exactly the same way as the alloy specimens.)

The specimens were then aged for various periods (up to 20 min) at room temperature and the stress–strain relations determined immediately afterward. The resulting tensile strengths and flow stresses at 0.2 per cent strain for the alloys aged 20 min are plotted against copper composition in Fig. 21.

Also shown in the figure are the corresponding data for alloys in which the clusters formed after aging at 0°C were dissolved by a short reversion treatment at 200°C. The resulting state should approximate closely that of the homogeneous solid solution during the test since reversion decreases the clustering rate by a factor of more than 2000. It is apparent that the strength increases markedly with increasing copper content and that clustering results in somewhat additional strengthening.

It is also of interest that the stress–strain curves for the alloys, but not for the pure Al control sample, are serrated in the plastic region. This was true for both those specimens that contained clusters and for those that were given the reversion treatments. The amplitude of serration was a maximum for the 1.3 at.% Cu alloy and was lesser for both the more dilute and the more concentrated alloys. This serration phenomenon, attributable to the presence of the solute, is called the "Portevin–LeChatelier effect"[18] and has been noticed in Al(Si) alloys[5] as well as those reported here.

INTERPRETATION

Association of resistivity change and clustering

In the foregoing it was assumed tacitly that the resistivity changes do reflect the clustering of a large proportion of the solute in solution. Evidence that this is so for the Al(Cu) system is that relatively large amounts of energy[4,19] are released concurrently with the resistivity changes. Also the X-ray data[1,2] indicate that a large fraction of copper is associated in zones by the time the G.P. zone stage is reached.

There is now similar evidence that the low temperature resistivity changes in Al(Ag) alloys are to be attributed to extensive clustering of silver. Thus DeSorbo[20] has found that, during the low temperature reaction, the amount of energy released in Al(Ag) alloys is of the order of that released in Al(Cu) under similar conditions.

Also Webb[21] has concluded from his small-angle X-ray scattering measurements, that in the p_1 state, which results from the low temperature reaction, most of the silver exists as very small clusters.

Therefore we shall assume that the resistivity changes we have measured are due to solute clustering.

Mechanism of initial clustering at low temperatures

The results in this paper have to do with the early

stages of clustering in aluminum alloys. After the early stage there is, in Al(Cu) at least, a further process, indicated by resistivity and mechanical property changes, that occurs over a period of months at room temperature. This will be discussed later.

It has already been shown[4,8,9,13] that the earlier results[4,9,10] on the kinetics of initial clustering are in good qualitative agreement with the quenched-in vacancy hypothesis (see Introduction). We will show now that our new results are also in very good agreement with this hypothesis. Similar conclusions about the mechanism of clustering in Al(Zn) have been reached by Guinier[12].

The rate of resistivity change due to clustering may be written

$$\dot{\rho} = D_s F(t, X) \tag{4}$$

where D_s is the diffusion coefficient of the solute and $F(t, X)$ is an additional factor dependent on the time t at the aging temperature and the initial solute concentration X; D_s also may depend on t and X. We shall defer the question of the form of $F(t, X)$ to the next section and in this consider D_s and its variation with thermal history and time.

We assume for simplicity that all the diffusion is effected by single vacancies (thus we ignore contributions from associated vacancies); then

$$D_s = D_v P_v \tag{5}$$

where D_v, a function of T (and possibly X), is the diffusivity of the vacancies and P_v is the probability that a lattice site is occupied by a vacancy and is a function of thermal history and time.

If a specimen is quenched rapidly from the homogenization temperature T_H to a low temperature T_a the concentration of vacancies present initially at T_a may be near the equilibrium value $P_v(T_H)$ at T_H. With time at T_a the concentration will decay from $P_v(T_H)$ to $P_v(T_a)$, the equilibrium value at T_a. During the decay period τ, D_s and $\dot{\rho}$ will of course fall as P_v. We have then to find how much clustering can occur in a supersaturated alloy during this period.

This problem is quite complicated, but with some simplifying approximations we can estimate roughly the maximum extent of the clustering. For this estimate we assume that D_s is constant at its initial value during the decay period. In this period the solute can collect from a region of linear dimension L_a given by

$$L_a \approx [8 D_v P_v(T_H)\tau]^{1/2}. \tag{6}$$

The vacancies are annihilated at sinks (dislocations, grain boundaries, etc.) having a mean spacing, L_v. Therefore τ also should satisfy the relation

$$L_v \approx (8 D_v \tau)^{1/2}. \tag{7}$$

Where τ is defined as the period during which P_v and therefore D_s fall to $1/e$ of their original values. L_a can be related to L_v as follows:

$$L_a \approx [P_v(T_H)]^{1/2} L_v. \tag{8}$$

The number of atoms n in the largest cluster that could form in the decay period is then

$$n \approx X\left(\frac{L_a}{a_0}\right)^3 \tag{9a}$$

or

$$n \approx X[P_v(T_H)]^{3/2}\left(\frac{L_v}{a_0}\right) \tag{9b}$$

where a_0 is the atom diameter.

In the simplest case L_v is just the mean spacing of dislocations existing in the specimen during homogenization; we expect that this will be of the order of 10^4–10^5 atom spacings. However at very high vacancy supersaturation, such as would exist following a rapid quench from a comparatively high to a low temperature, an appreciable number of vacancy clusters would nucleate homogeneously. These clusters could annihilate vacancies and thus reduce L_v. We have discussed some possible effects of these clusters on precipitation in earlier publications.[4,5,6] The possibility that such vacancy clusters might take the form of dislocation rings (such as would result from the collapse of a disc-shaped void) has long been considered.[22,23] Recently Hirsch *et al.*[24] actually observed such rings in aluminum specimens quenched from 600°C.

From nucleation theory it is expected that the concentration of vacancy clusters or dislocation rings depends strongly on the quenching rate, $\dot{T}$, and on the difference ΔT between the initial and final temperatures in the quench. In particular the vacancy supersaturation and the resulting dislocation ring concentration at the terminal temperature should increase with both $\dot{T}$ and ΔT. Actually $\dot{T}$ and ΔT probably must exceed some nearly critical values before the nucleation of dislocation rings becomes detectable. In consequence of this *it is possible that the rate of vacancy annihilation at a given vacancy concentration, which normally decreases with decreasing temperature, actually will rise with falling temperature for ΔT near that required for sensible nucleation of dislocation rings.*

At constant $P_v(T_H)$ the only factor in the relative rate of clustering, $\dot{\rho}/\Delta\rho_\infty$, which is temperature dependent is the diffusion coefficient D_v of the vacancies. Therefore the activation energy Q_c for solute clustering should be the same as the activation energy, Q_v, for the annealing of vacancies out of the

VOL. 8 1960

alloy. Neither D_v nor $P_v(T)$ have been measured for the solutions that we have investigated. In our calculations we shall assume that $P_v(T)$ and D_v for Al(Cu) and Al(Ag) are the same as for pure aluminum. The correspondence between the activation energies for volume diffusion in the three cases (1.4 ± 0.1 eV for Al- (self-diffusion),[25] 1.4 ± 0.1 eV for Al(Cu),[26] 1.5 ± 0.1 eV for Al(Ag)[27] supports but does not prove this assumption. According to the recent results of DeSorbo and Turnbull[17,28] (see also Panseri and Federighi[29])

$$D_v \approx 10^{-1\pm1} \exp(-0.6 \text{ eV}/kT) \text{ cm}^2\text{sec}^{-1} \quad (10a)$$

and

$$P_v(T) \approx 10^{1.3\pm0.5} \exp(-0.8 \text{ eV}/kT) \quad (10b)$$

for pure aluminum. These values were obtained by assuming a resistivity contribution of 1.5 $\mu\Omega$ cm per at.% of vacancies.

In support of the quenched-in vacancy hypothesis Q_c for Al(Ag) and Al(Cu) alloys (0.5–0.55 eV, see Table 1) is quite close to Q_v for pure aluminum.* This confirms our earlier results.[4,7] Q_c for the clustering of zinc in aluminum (0.4 eV) is considerably below Q_v for aluminum, but the activation energy for high temperature diffusion of Zn in Al is also lower[27] (1.2 eV compared with 1.4 eV).

Now we consider some qualitative features of the kinetics of clustering in Al(Ag) or Al(Cu) alloys quenched directly from a high homogenization temperature, e.g. 550°C, to a low temperature, e.g. 0°C. As a result of the high vacancy supersaturation, many dislocation loops probably nucleate and from the results of Hirsch *et al.*[24] we may expect that their spacing, and therefore L_v, would be of the order of 10^3 atom spacings. It follows from equation (9b) that, under these conditions with $P_v(T_H) \approx 10^{-4}$, the clusters formed in a 1 at.% alloy could contain about ten solute atoms. Consistent with this Webb[21] concludes from his low angle scattering data that the average number of silver atoms per cluster in an Al(1.3 at.% Ag) alloy in the p_1 state is about ten.

From equations (5) and (10) the solute diffusion constant D_s immediately after quenching would be $10^{-15.5\pm1.5}$ cm^{2}sec^{-1} at 0°C. It would decay with time to the value $10^{-25.4\pm1.5}$ cm^{2}sec^{-1} corresponding to defect equilibrium at 0°C. Under the conditions assumed, the observed clustering could occur in a minimum period of 1 min (equation (6) with $D_s = 10^{-15.5}$ cm^{2}sec^{-1}). This result is compatible with the observations.

When the quench is interrupted at an intermediate temperature T_i above the solution temperature of the clusters the defect concentration will start to fall from $P_v(T_H)$ toward the equilibrium value $P_v(T_i)$ at T_i. Detectable nucleation of dislocation rings should not occur if T_i is comparatively high. Quench interruption can have two effects on the subsequent aging rate at low temperature T_a. First, since the initial value of P_v will be lower than after a direct quench from $T_H \rightarrow T_a$, the clustering rate will be correspondingly low; secondly, the probability of nucleation of dislocation loops at T_a will be lessened because of the lower defect supersaturation.

Actually the low temperature clustering rate in Al(Cu) decreases with time of interruption t_i at 200°C at least to a value, after $t_i = 120$ sec, about 1/300 of the rate for $t_i = 0$. This factor is about 10 times greater than the theoretical maximum which is $\frac{P_v(473°\text{K})}{P_v(823°\text{K})} \approx \frac{1}{4000}$. The rate of annihilation of vacancies at 473°K (200°C) inferred from the variation of clustering rate with t_i implies that the spacing, L_v, of vacancy sinks at 473°K (200°C) must be much greater than after a quench 823°K → 273°K (550°C → 0°C). Thus it appears, as was suggested by DeSorbo *et al.*[4] that the undercooling from 823 to 473°K (550 to 200°C) may be insufficient for appreciable nucleation of vacancy clusters in Al(Cu).

At constant L_v and for constant t_i, too small for the approach of defect equilibrium at T_i, the low temperature clustering rate should increase with decreasing T_i. This does indeed occur in Al(Cu) (see Fig. 10) for T_i between 458°K (185°C) and 498°K (225°C). The opposite and more erratic behaviour for $T_i < 453$°K (180°C) may have one of the following causes: (i) Appreciable nucleation of dislocation loops occurs below but not above 450–460°K after quenches from 823°K. Thus, although D_v falls with T_i, the vacancy annihilation rate below 450°K increases because of decreasing L_v. (ii) Some different type of copper clustering occurs at 433 to 453°K. Such association would retard the subsequent clustering at low temperatures.

The clustering rate in Al(Cu) following a reversion treatment (273°K → 473°K (1 min) → 273°K after 823°K → 273°K) was 2400 times smaller (see Fig. 11) than the rate after the direct quench 823°K → 273°K. This factor of 2400 is near the theoretical value

* Actually the apparent activation energy Q_v for the motion of defects in pure aluminum ranges from 0.5 to 0.7 eV depending on the specimen purity and defect concentration (Q_v is highest for the lowest P_v and highest purity). At the P_v levels existing in most of our experiments Q_v would fall between 0.5 and 0.6 eV. This variation in Q_v is probably due to the motion of different kinds or defects resulting from the association of vacancies with other vacancies and impurity atoms.

$\frac{P_v(823°K)}{P_v(473°K)} = 4000$. The comparatively rapid attainment of vacancy equilibrium at 473°K, implied by this result, may be due to the operation of dislocation loops formed after the quench 823°K → 273°K. It is significant that, if the initial quench is interrupted for 60 sec at 473°K, the treatment being otherwise the same (i.e. 823°K → 473°K (1 min) → 273°K → 473°K (1 min) → 273°K), the clustering rate is only a factor of 400 less than immediately after a direct quench from 823°K. It appears that in this treatment the vacancy concentration never fell to its equilibrium value at 473°K. This may indicate that dislocation rings, because of the relatively small ΔT values, were not nucleated at any stage of the treatment. Thus the results are consistent with the notion that appreciable nucleation of dislocation rings occurred after the quenches $823 \rightarrow T < 450$°K but not after the quenches $823 \rightarrow T > 450$°K or 473 → 273°K.

Rough calculations based on nucleation theory, taking the free surface tension as 1140 ergs/cm², indicate that nucleation of *spherical* voids would become appreciable at supersaturations $\frac{P_v(T_H)}{P_v(T)} > 10^{9.5}$. This corresponds to $T \sim 300$°K for $T_H = 823$°K. Presumably a lesser supersaturation would be required for the nucleation of disc-shaped voids since there would be some attraction between aluminum surfaces separated by only one atom diameter.

Our measurements on dilute Al(Cu) alloys (see Fig. 19 and Table 2) appear to demonstrate quite clearly that clustering and vacancy annihilation in these alloys occur simultaneously, the total resistivity changes in the processes being of the same order of magnitude in dilute alloys. Our present results are not sufficiently complete to determine the rates of resistivity changes, $\Delta\dot{\rho}_c$ for clustering and $\Delta\dot{\rho}_v$ for vacancy annihilation, individually. This could be done by determining $\Delta\rho_c$ and $\Delta\rho_v$ (by means of the 100°C solution treatment) at various times for a constant homogenization temperature.

Dependence of clustering rate on time and composition

We now take up the problem, deferred from the preceding section, of the form of the kinetic law, $F(X, t)$ in equation (4), for clustering. In contrast to normal precipitation processes, the isothermal rate of property change during clustering decreases continuously with time from the beginning. This has been interpreted on the hypothesis[3] that there is no nucleation barrier to clustering at the existing solute supersaturations. On the basis of ordinary nucleation theory the nucleation barrier will not exist (the critical radius would be less than the atomic radius) for relatively large supersaturations, and if the surface energy σ between the clusters and matrix is small. For the systems we investigated, the supersaturation at low temperatures must be very large. With no nucleation barrier it was proposed that clustering is simply a process of competitive growth, driven by surface energy, whereby single atoms are on the average lost by smaller clusters and collected by larger ones. The mean cluster radius, $\bar{r}$, thus increases continuously beginning at the atomic radius. It was shown[4] that the energy and resistance isotherms for the Al(Cu) system appear to be in accord with this interpretation. We now give a highly simplified and crude formulation of this interpretation which leads to a relation between the rate of property change and solute concentration.

It is assumed first that the rate of energy release in clustering is proportional to the rate of decrease of the total surface area of clusters per unit volume. Therefore we may write for the energy $U(t)$ of the clusters at time t,

$$U(t) = \frac{\alpha X}{\bar{r}(t)} \tag{11a}$$

where α is a constant and $\bar{r}(t)$ is the mean cluster radius at time, t. Also the energy at $t = 0$ and t_∞ is, respectively,

$$U_0 = \frac{\alpha X}{r_0} \tag{11b}$$

and

$$U_\infty = \frac{\alpha X}{\bar{r}_f} \tag{11c}$$

where r_0 is the atomic radius; and $\bar{r}_f$, the radius after "infinite" time, is supposed to be finite rather than infinite because the clustering will be imperceptible after the vacancy supersaturation has decayed completely.

It follows that

$$\Delta U_\infty = U_0 - U_\infty = \alpha X\left(\frac{1}{r_0} - \frac{1}{\bar{r}_f}\right) \tag{12a}$$

$$\Delta U(t) = U_0 - U(t) = \alpha X\left(\frac{1}{r_0} - \frac{1}{\bar{r}(t)}\right) \tag{12b}$$

and

$$\frac{\Delta U(t)}{\Delta U_\infty} = \frac{\bar{r}_f}{\bar{r}(t)}\left(\frac{(\bar{r}(t) - r_0}{\bar{r}_f - r_0}\right). \tag{12c}$$

If r_0 is neglected in comparison with $\bar{r}_f$ then $\Delta U_\infty = \alpha X/r_0$ and the equation simplifies to

$$\frac{\Delta U(t)}{\Delta U_\infty} = 1 - \frac{r_0}{\bar{r}(t)}. \tag{13}$$

VOL. 8 1960

We have now to find $\bar{r}(t)$. This has not been done rigorously, but we shall adapt the probably oversimplified analysis of Greenwood[31]. He treats the kinetics of competitive growth of precipitate particles and obtains an expression having the form

$$\bar{r}^3 - r_0^3 = \beta \frac{C_e D_S t}{T} \tag{14}$$

where β is a constant for the material and C_e is the equilibrium concentration of solute. This result is based on the following assumptions: (a) The particles are widely separated in comparison with their diameters. Greenwood advances qualitative arguments to show that the result would not be altered seriously if this assumption were relaxed. (b) The form of the cluster size distribution function remains constant. (c) The "phase" inside the clusters has the properties of the bulk material as altered by the presence of an interface, and the interfacial energy is independent of the particle size. (d) The equilibrium concentration (of single atoms) is not far different from the actual concentration. These last two assumptions are almost certainly not valid in the growth of very small clusters, such as we are concerned with. However, we can compensate somewhat for the errors introduced by these assumptions if in Greenwood's derivation we replace C_e by λC_e, where λ is a multiplier which makes λC_e of the order of magnitude of the existing concentration. Equation (14) then becomes

$$\bar{r}(t)^3 - r_0^3 = \frac{\beta D_S \lambda C_e t}{T} = K D_S t. \tag{15}$$

By substituting equation (15) into (13) we obtain

$$\frac{\Delta U(t)}{\Delta U_\infty} = 1 - \frac{r_0}{(K D_S t + r_0^3)^{1/3}}. \tag{16}$$

DeSorbo *et al.*[4] found that the forms of the resistivity and energy release isotherms in their early stages are the same for an Al(2 at.% Cu) alloy. If this is generally true, then

$$\frac{\Delta\rho(t)}{\Delta\rho_\infty} = 1 - \frac{r_0}{(K D_S t + r_0^3)^{1/3}}. \tag{17}$$

An equation of similar form is obtained if the clusters are assumed platelike rather than spherical. The derivation also is based on the assumption, almost certainly not fulfilled in our experiments, that D_S is independent of time.

Equation (17) requires, in agreement with experiment (see Figs. 7 and 8), that the extent of clustering, $\Delta\rho(t)/\Delta\rho_\infty$, at a given time be independent of the solute concentration. Also it has a form that can describe satisfactorily the resistivity and energy release isotherms in the Al(Cu) clustering.[4] However, in view of the serious approximations necessary for the derivation, the significance of the agreement must be considered to be, at best, very qualitative.

Cluster-size in Al(Ag) *alloys*

We now take up the problem of the different states in Al(Ag) alloys produced by different thermal histories.

On the basis of the quenched-in vacancy hypothesis we expect that at low temperatures there will be a limiting cluster size imposed by both the spacing, L_v, of the vacancy annihilation centers and the initial vacancy concentration P_v^0. The number, n_m, of atoms in the largest cluster should be given approximately by equation (9b) with $P_v(T_H)$ replaced by P_v^0 for generality. Thus there will be apparently different end states of the clustering reaction dictated by the thermal history, which determines L_v and P_v^0.

Evidence for the existence of such different end states comes from investigations on Al(Ag). In their p_1 state (see Fig. 2) these alloys probably contain dislocation loops with a nearly constant spacing. As already noted, if we take the spacing $\sim 10^3$ atoms found by Hirsch *et al.*[24] for pure aluminum, we calculate for the 1 at.% alloy a maximum cluster size ($n_m \sim 10$ atoms) in good agreement with Webb's[21] estimate from X-ray data. Also, in good agreement with Webb's results, equation (9b) predicts that n_m should increase *linearly* with solute concentration.

It has already been noted that the dislocation loop density should decrease with increasing terminal temperature T_f of the quench from a constant high temperature (provided that time is allowed for appreciable movement of the vacancies at T_f). Therefore L_v and n_m should increase with increasing T_f. There are no X-ray estimates of the variation of n_m with T_f but the total resistivity change (see Fig. 9) $\Delta\rho_\infty$ does increase with T_f. This implies an increase of n_m with T_f, in qualitative agreement with our interpretation.

All other factors being the same, the dislocation loop density should decrease as the quenching rate $\dot{T}$ decreases. Of course P_v^0 also will decrease with decreasing $\dot{T}$. However it is probable that there is an intermediate range of $\dot{T}$ for which $(P_v^0)^{3/2}\left(\frac{L_v}{a_0}\right)^3$ and hence n_m (see equation 9b) is a maximum. In fact the resistivity end state[11] for relatively slow quenches is far below our p_1 state.

These results on Al(Ag) alloys are consistent with the following hypothesis:

The variation in resistivity end-state in Al(Ag) *alloys with thermal treatment is caused by differences that are imposed on the limiting cluster size by the resultant dislocation spacing and defect concentration rather than by variation in cluster structure or composition. Therefore, that low temperature clustering does not continue to macroscopic precipitation is due to kinetic rather than thermodynamic limitations.*

The mechanism of clustering in Al(Ag) alloys, initially in the p_1 state, at higher temperatures 80–170°C is not yet understood. The rate of the process is considerably larger than that deduced from the high temperature diffusion of Ag in Al (activation energy 1.4 eV) and would correspond (for a reasonable D_0 value) to an activation energy 1.0 to 1.2 eV. This is near the apparent activation energy (1.0 eV) for the higher temperature (120-170°C) isotherms but considerably less than that (1.5 eV) for the 80-120°C isotherms (see Fig. 13). It appears that the problem of accounting for this reaction is very similar to the problem of the mechanism of the slow reaction in Al(Cu) alloys which is discussed in the last section of this paper.

The resistivity maximum

In view of the results on Al(Ag) (see Figs. 14–16 and also Federighi[15]) and Al(Zn) (Fig. 17) it appears that the cause for the "anomalous" isothermal resistivity increase with time must be other than size disparity between solute and solvent atoms. There remains Mott's[14] suggestion that the phenomenon is due to extra scattering by clusters with diameter of order of magnitude of the wavelength of the electrons scattered.

The effect appears in Al(Ag) alloys only at relatively low silver concentration. Federighi[15] suggests that the effect is missed in the concentrated alloys because of clustering during the quench. However, as we have seen (Fig. 7), there appears to be little or no effect of solute concentration on the relative rate of clustering. An alternative explanation for the concentration effect in Al(Ag) is that the clusters responsible for critical scattering contain very few atoms (e.g. 2 or 3). Then in a concentrated alloy with random positioning of the atoms, there would already be a large concentration of such clusters.

The anomalous resistivity effect is certainly much more prominent in Al(Zn) alloys, in which it also persists to relatively higher concentrations, than in Al(Ag). It appears that the clusters which would give rise to the critical scattering are considerably larger in Al(Zn) than in Al(Ag).

It is not obvious from Mott's explanation why the resistivity of an alloy in a given state sometimes falls at one temperature but rises with time at a lower temperature as shown for Al(Zn) in Fig. 18.

Effect of cold-working

Since light cold-working has very little effect on the rate of clustering in alloys quenched from high temperatures, we conclude that it did not produce as many vacancies as were already present, i.e. a concentration $\sim 10^{-4}$. Light cold-working does enhance the rate of clustering[4] in alloys in which the vacancy concentration should be initially small (ca. 10^{-6}).

The slow reaction in Al(Cu)

The results of this investigation appear to leave little doubt about the qualitative features of the mechanism of initial clustering in aluminum alloys at low temperatures. However the additional slow property changes in Al(Cu) alloys that occur over a period of many days and weeks at room temperature still have to be accounted for.

These results imply an effective solute diffusion constant for the long time reaction of the order of $D_S \sim 10^{-18}$ cm^{2}sec^{-1} which is $10^{5.5}$ (equation 10) times the value ($D_S = 10^{-23.5 \pm 1.5}$ cm^{2}sec^{-1}) expected at vacancy *equilibrium* at room temperature. As already noted, a similar problem is encountered in connection with the 80-170°C reaction in Al(Ag) alloys.

Four possible alternative explanations for the slow reaction occur to us. These are:

(1) At vacancy concentrations 10^{-7} or less the approach of the vacancy concentration to equilibrium [$P_v(300°\text{K}) = 10^{-12}$] at room temperature requires periods of the order of the duration of the slow reaction. Such a slow equilibration seems unlikely since it is expected that closely spaced dislocation rings exist in the alloys and in view of the observed rapid rate of vacancy annihilation (Fig. 19) at higher vacancy concentrations. However the information on the rates of vacancy annihilation all comes from measurements at vacancy concentration levels exceeding 2×10^{-7}. There is a possibility that the annihilation efficiency of dislocation rings becomes very small with decreasing supersaturation at a supersaturation level which is still relatively high.

(2) It may be that the mean radius $\bar{s}$ of the dislocation loops is so small that the vacancy concentration $P_v(\bar{s})$, in equilibrium with them, is several orders of magnitude larger than the equilibrium

VOL. 8 1960

concentration $P_v(T)$ in a well annealed crystal. $P_v(\bar{s})$ should be related to $P_v(T)$ by

$$P_v(\bar{s}) = P_v(T) \exp\left(\frac{\sigma v}{\bar{s}kT}\right) \tag{18}$$

where σ is the dislocation line tension and v the atomic volume of the alloy. With such dislocation rings present the apparent activation energy for diffusion would be reduced by $\frac{\sigma v}{\bar{s}}$. Taking the dislocation line tension to be, Gb, the products of the shear modulus of aluminum and the atom diameter, we find that the observed rate enhancement can be accounted for with $\bar{s} \leqslant 2 \times 10^{-7}$ cm. This radius is much smaller than that, 10^{-6} cm, of the rings observed for pure aluminum by Hirsch *et al.* However in this case it is possible that the rings may have enlarged somewhat before observation due to heating of the specimen in the electron beam. Also the solute might promote more profuse nucleation of loops in the alloys.

(3) Hart[32] has suggested that vacancies may associate with solute clusters to form relatively stable complexes with appreciable mobility. The slow reaction might be due to the movement of such complexes. Detailed calculations on the rate of this process have not yet been made.

(4) The reaction may be brought about by the short circuiting of solute diffusion by the dislocation rings. With the rings present the total dislocation content ($\sim 10^9$–10^{10} cm/cm^3) would be high enough to bring about the observed reaction if the dislocations glide during the process; this would serve to expose, after a considerable time, a large fraction of the solute to the diffusion short circuit.[33] However it is still not clear just how this glide would be motivated. Fisher and Hollomon[34] suggested that the decrease in chemical potential accompanying clustering might set up a suitable stress, but no microscopic mechanism was proposed. Probably considerable distortion exists around the copper clusters formed initially. This distortion may promote some glide of small rings. Jones and Mitchell[35] showed that dislocation rings in silver chloride are generated and caused to glide by internal strains due to differential thermal expansion of inclusions or to actual precipitate particles.

If the slow reaction is caused either by the glide of dislocation rings or by the enhancement of the vacancy concentration by the high curvature of the rings, which would increase the solute diffusion rate correspondingly, it follows that *the rate of the slow reaction should be many orders of magnitude lower in specimens quenched so slowly that the rings do not nucleate*. Experiments to check this are now in progress.

SUMMARY

After a rapid quench from a suitable homogenizing temperature a fast initial clustering reaction occurs in the Al(Cu), Al(Ag) and Al(Zn) alloys at 200–300°K. The reaction has an energy of activation of 0.5–0.6 eV in Al(Cu) and Al(Ag), and is 0.4 eV in Al(Zn).

If the quench of an Al(Cu) alloy is interrupted for a short time at 333–498°K, the rate of clustering is markedly reduced (by as much as a factor of 400). The rate after an interrupted quench is significantly higher than that after a reversion treatment. It is believed that this difference may be due to the presence of dislocation loops in the specimens having the reversion treatment. These loops may facilitate the equilibration of vacancies.

In Al(Ag) and Al(Cu) alloys the initial rate of clustering after a rapid quench from the homogenization temperature is nearly independent of the solute concentration.

The behavior of the resistivity during isothermal aging was found to be similar in all three alloy systems. Under suitable conditions the isothermal resistivity initially increases, reaches a maximum value and then decreases. The temperature dependence of the rate of the initial increase of resistivity in Al(Ag) alloys was found to be 0.57 eV which is close to the values previously found for the initial decrease in resistivity under conditions where the initial increase does not appear. The amplitude of the maximum in the Al(Zn) alloy is substantially greater than those observed for Al(Cu) or Al(Ag).

In a dilute Al(Cu) alloy the vacancy contribution to the change in resistivity was measured and found to be within a factor of 2 or 3 of the values calculated or observed for pure aluminum. The clustering of solute and the annealing of vacancies occur simultaneously.

There are slower reactions in the Al(Cu) and Al(Ag) alloys that occur after the initial rapid "low temperature clustering"; the rate of this slower reaction is still greater and more rapid than can be expected from the extrapolated high temperature diffusion data.

Many of these phenomena can be explained by: (1) the enhanced solute mobility during the annealing out of quenched-in vacancies and (2) the formation of dislocation loops which form by (probably homogeneous) nucleation of vacancy aggregates at very high vacancy supersaturations. Other workers have observed such dislocation loops in pure aluminum,[24]

but the loops have not yet been directly observed in these alloys.

REFERENCES

1. A. GUINIER, *Nature, Lond.* **142,** 569 (1938); *C.R. Acad. Sci., Paris* **206,** 1641 (1938).
2. G. D. PRESTON, *Proc. Roy. Soc.* A **167,** 526 (1938); *Phil. Mag.* **26,** 855 (1938).
3. D. TURNBULL, *Solid State Physics* Vol. 3, pp. 225–306. Academic Press, New York (1956).
4. W. DESORBO, H. N. TREAFTIS and D. TURNBULL, *Acta Met.* **6,** 401 (1958).
5. H. S. ROSENBAUM and D. TURNBULL, *Acta Met.* **6,** 653 (1958).
6. H. S. ROSENBAUM and D. TURNBULL, *Acta Met.* **7,** 644 (1959).
7. D. TURNBULL and H. N. TREAFTIS, *Acta Met.* **5,** 534 (1957).
8. T. FEDERIGHI, *Acta Met.* **6,** 379 (1958).
9. C. W. TUCKER and M. B. WEBB, *Acta Met.* **7,** 187 (1959).
10. D. TURNBULL and H. N. TREAFTIS, *Acta Met.* **3,** 43 (1955).
11. G. BORELIUS, *Rep. Bristol Conf. on Defects in Crystalline Solids,* pp. 169–174. Physical Society, London (1955).
12. A. GUINIER, *Solid State Physics,* Vol. 9, pp. 294–400. Academic Press, New York (1959).
13. W. DESORBO and D. TURNBULL, *Bull. Amer. Phys. Soc.* **2,** 263 (1957).
14. N. F. MOTT, Discussion of M. L. V. GAYLER, *J. Inst. Met.* **60,** 267 (1937).
15. T. FEDERIGHI and L. PASSARI *Acta Met.* **7,** 422 (1959).
16. H. MEYER, *Z. Phys.* **76,** 268 (1932).
17. W. DESORBO and D. TURNBULL, *Acta Met.* **7,** 83 (1959).
18. A. H. COTTRELL, *Relation of Properties to Microstructure,* pp. 154–158. American Society for Metals, Cleveland, Ohio (1954).
19. G. BORELIUS, J. ANDERSON and K. GULLBERG, *Ingen-VetenskAkad. Handl.* No. 169 (1943).
20. W. DESORBO, to be published.
21. M. B. WEBB, *Acta Met.* **7,** 748 (1959).
22. F. C. FRANK, *Carnegie Institute of Technology (Pittsburgh) Symposium on the Plastic Deformation of Crystalline Solids,* p. 150 (1950).
23. F. SEITZ, *Phys. Rev.* **79,** 890 (1950).
24. P. B. HIRSCH, J. SILCOX, R. E. SMALLMAN and K. H. WESTMACOTT, *Phil. Mag.* **3,** 897 (1958).
25. J. SPOKAS, Thesis, Department of Physics, University of Illinois, Urbana (1957).
26. R. M. BRICK and A. PHILLIPS, *Trans. Amer. Inst. Min. (Metall.) Engrs.* **124,** 331 (1937).
27. A. BEERWALD, *Z. Elektrochem.* **45,** 789 (1939).
28. W. DESORBO and D. TURNBULL, *Phys. Rev.* **115,** 560 (1959).
29. C. PANSIERI and T. FEDERIGHI, *Phil. Mag.* **3,** 1223 (1958).
30. J. S. KOEHLER, F. SEITZ and J. E. BAUERLE, *Phys. Rev.* **107,** 1499 (1957).
31. C. W. GREENWOOD, *Acta Met.* **4,** 243 (1956).
32. E. W. HART, *Acta Met.* **6,** 553 (1958).
33. D. TURNBULL, *Rep. Bristol Conf. on Defects in Crystalline Solids,* pp. 203–211. Physical Society, London (1955).
34. J. C. FISHER and J. H. HOLLOMON, *Acta Met.* **3,** 608 (1955).
35. D. A. JONES and J. W. MITCHELL, *Phil. Mag.* **3,** 1 (1958).

VOL.
8
1960

THE INTERACTION OF PARALLEL EDGE DISLOCATIONS WITH A SIMPLE TILT DISLOCATION WALL*

JAMES C. M. LI†

An elastic theory analysis of the interaction of a dislocation wall (tilt substructure boundary) with parallel approaching dislocations whose slip vectors are the same as those of the dislocations in the wall is reported. It is found that such a wall fully or partially pinned is a less effective barrier for the penetration of dislocations than a single pinned dislocation on the same slip plane as the approaching dislocation. Quantitative results for the equilibrium positions of the free dislocations in the wall and the forces exerted on the approaching dislocation in various cases are presented. Free dislocations in the wall usually reduce the resistance of the wall to the penetration of approaching dislocations. The interaction between a wall and a solute atom is found to be less than that between the single nearest dislocation with the same solute atom. It is suggested that the experimental evidence which leads to the concept of hardening by substructures of this kind needs further interpretation. The segregation of vacancies and solute atoms to the dislocations probably plays a more important role in the hardening effect than the appearance of substructure.

INTERACTION DES DISLOCATIONS DES-COINS PARALLÈLES UNE PAROI DE DISLOCATIONS DE ROTATION PURE

L'auteur expose une analyse de la théorie élastique de l'interaction d'une paroi de dislocations (frontière de sous-structure de rotation pure) avec des dislocations parallèles dont les vecteurs de glissement sont similaires à ceux des dislocations de la paroi. Il trouve qu'une telle paroi entièrementou partiellement bloquée est un obstacle moins hermétique à la pénétration de dislocations qu'une simple dislocation ancrée sur le même plan de glissement. Les résultats quantitatifs pour la détermination des positions d'équilibre des dislocations libres de la paroi et des forces exercées sur une dislocation qui s'en approche, sont présentés pour de nombreux cas. Les dislocations libres de la paroi réduisent également la résistance opposée par celles-ci à la pénétration de dislocations extérieures. L'interaction entre une paroi et un atome dissous est inférieure à celle qui existe entre cet atome et la dislocation simple la plus proche.

L'auteur pense qu'il est nécessaire de revoir l'interprétation des résultats expérimentaux qui a conduit au concept de durcissement par des sous-structures de cette espèce. La ségrégation des lacunes et des atomes dissous joue probablement un rôle beaucoup plus important dans le durcissement, que la formation de sous-structures.

DIE WECHSELWIRKUNG EINER PARALLELE STUFENVERSETZUNGEN MIT EINER EINFACHEN STUFENVERSETZUNGSWAND

Es wird über eine elastizitätstheoretische Analyse der Wechselwirkung einer Versetzungswand (Neigungs-Kleinwinkelkorngrenze) mit parallelen Versetzungen berichtet; dabei nähern sich diese Versetzungen der Wand und haben den gleichen Gleitvektor, wie diejenigen in der Wand. Man findet, dass eine solche ganz oder teilweise festgehaltene Wand für die durchdringenden Versetzungen ein weniger wirksames Hindernis ist als eine einzelne verankerte Versetzung, die sich auf derselben Gleitebene befindet wie die sich nähernde Versetzung. Quantitative Ergebnisse werden für die Gleichgewichtslagen der freien Versetzungen in der Wand mitgeteilt, sowie für die Kräfte, die auf die sich nähernde Versetzung in verschiedenen Fällen ausgeübt werden. Freie Versetzungen in der Wand erniedrigen im allgeminen den Widerstand gegen Durchdringung der Wand für die sich nähernden Versetzungen. Die Wechselwirkung zwischen einer Wand und einem gelösten Atom ist kleiner als diejenige zwischen der nächstgelegenen Einzelversetzung und demselben gelösten Atom. Est ist anzunehmen, dass die experimentellen Befunde, die zu der Vorstellung einer Härtesteigerung durch Substrukturen dieser Art führen, einer ewiteren Deutung bedürfen. Die Ausscheidung von Leerstellen und gelösten Atomen an den Versetzungen spielt vermutlich bei der Härtesteigerung eine wichtigere Rolle als das Auftreten einer Substruktur.

INTRODUCTION

One stage in the process of work hardening[1] in most metals is the formation of subgrain boundaries which are regarded as barriers to moving dislocations.[2–6] The fact that the increase in yield strength is accompanied by the appearance of subboundaries leads one to think that the dislocation walls play an important role in the plastic behavior of crystals. However, as pointed out by Washburn[7], most of the classical test conditions were too complex

* Received March 5, 1959; revised June 15, 1959; presented in part at the Washington Meeting of the American Physical Society, *Bull. Amer. Phys. Soc.* **4**, 264 (1959).

† Fundamental Research Laboratory, U.S. Steel Corporation, Monroeville, Pa.

to establish any definite mechanism of the interaction of approaching dislocations with dislocation walls. In studying such a mechanism for the case of a simple tilt substructure boundary in zinc single crystals, Washburn[7] concluded that, "a pair of edge dislocation boundaries had an almost negligible strengthening effect unless the crystal containing the boundaries had been heated to a temperature close to the melting point prior to testing." In a similar study, Li *et al.*[6] observed also such annealing effect. The fact that rapid cooling increases the effectiveness of the barrier led them to suspect that the interaction of vacancies with dislocations in the boundary may increase the strength of the material. Washburn[7], with the concept that a wall is more effective than the randomly distributed dislocations, explained that high temperature annealing causes better polygonization. Actually, as pointed out by Mott[8], a grid of dislocations of this type has no long range stress field. Whether a polygonized wall is a more effective barrier to the penetration of dislocations than a set of randomly distributed dislocations is not really known. More recently, Washburn *et al.*[9] declared that, "grown-in substructure boundaries were apparently not effective barriers and played no role in the plastic properties." In view of the difficulties involved in finding a clear-cut experiment, it seems advisable to continue a theoretical discussion which Taylor[10] started 25 years ago. For the simplicity of calculation, we shall restrict our discussion in this report to simple tilt boundaries with the hope that more complicated boundaries will be studied later.

Before the dislocation model was completed, Taylor[10] indicated even then that a misfit boundary has regions which are opaque to dislocations as well as regions which are transparent to dislocations. It is evident, therefore, that a dislocation wall cannot be a complete barrier to the penetration of dislocations A dislocation model of the tilt boundary was first suggested by Burgers[11] and a complete discussion was given by Read and Shockley[12]. The force exerted by a dislocation wall on an approaching dislocation has been discussed by Nabarro[13] and by Cottrell[2]. Seeger[14] investigated the potential energy of a dislocation with respect to a dislocation wall by integrating the force from infinity. A more complete and quantitative discussion about the force and energy required for a dislocation to penetrate a pinned or a partially free wall does not seem to be available. It is the purpose of this report to supply this information and to discuss the consequences to the concept of work hardening.

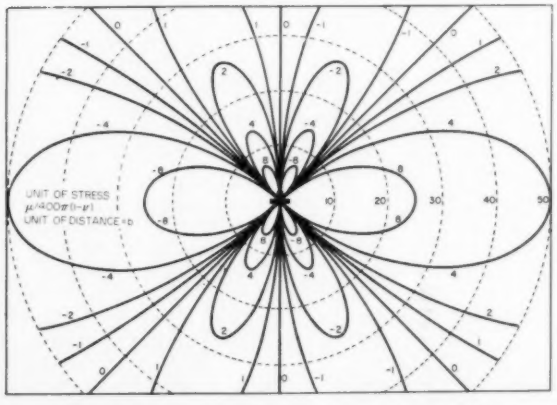


FIG. 1. Constant stress curves for a single edge dislocation.

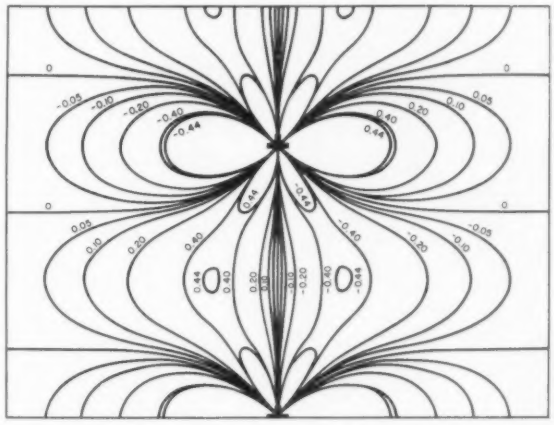


FIG. 2. Shear stress distribution at a dislocation wall. unit of stress $\mu b/2(1-\nu)h$.

THE SHEAR STRESS FIELD OF A DISLOCATION WALL

The shear stress σ_{xy} at any point (x, y) with respect to a single edge dislocation is[15]

$$\sigma_{xy} = \frac{\mu b}{2\pi(1-\nu)} \cdot \frac{x(x^2-y^2)}{(x^2+y^2)^2} \tag{1}$$

or, if expressed in polar co-ordinates,

$$\sigma_{xy} = \frac{\mu b \cos\theta \cos 2\theta}{2\pi r(1-\nu)} \tag{2}$$

where μ is the shear modulus, b the magnitude of the Burgers' vector whose direction is the same as the x-axis and ν is the Poisson's ratio. Fig. 1 shows the constant shear stress curves around an edge dislocation. These curves distort when several dislocations form a dislocation wall as shown in Fig. 2. The shear stress at a dislocation wall formed by a

VOL. 8 1960

vertical array of evenly spaced edge dislocations of the same Burgers' vector is given by[16]

$$\sigma_{xy} = \frac{\mu b}{2\pi(1-\nu)} \frac{\pi^2 x}{h^2} \frac{\cosh \frac{2\pi x}{h} \cos \frac{2\pi y}{h} - 1}{2\left(\sinh^2 \frac{\pi x}{h} + \sin^2 \frac{\pi y}{h}\right)^2} \quad (3)$$

where (x, y) are the co-ordinates of a point relative to one of the dislocations in the wall and h is the spacing between the dislocations. The curve for zero shear stress at a dislocation wall is given by the following equations:

$$\cosh \frac{2\pi x}{h} \cos \frac{2\pi y}{h} = 1 \quad (4)$$

and

$$x = 0. \quad (5)$$

Therefore, a dislocation wall divides the crystal into regions where a single edge dislocation will be either attracted or repelled by the wall as shown in Fig. 3. Equation (3) is plotted in Fig. 4. It is seen that due to the mutual cancellation of the stresses of individual dislocations, the stress field is concentrated within

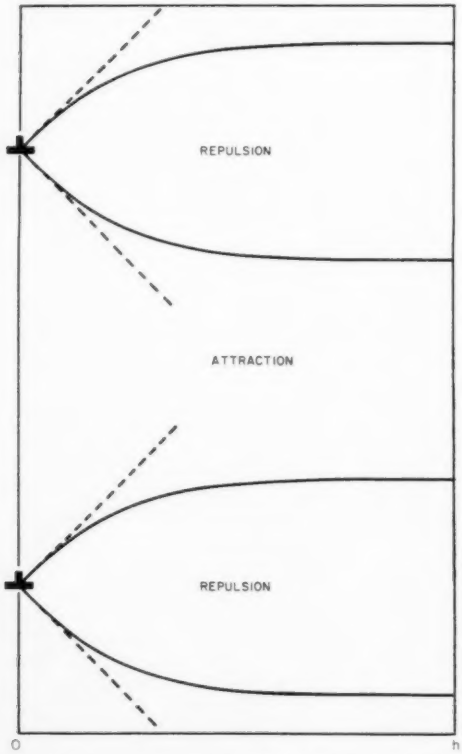


FIG. 3. Nature of force due to a dislocation wall on a single dislocation of the same slip vector; dotted line shows the situation when the wall is replaced by a single dislocation.

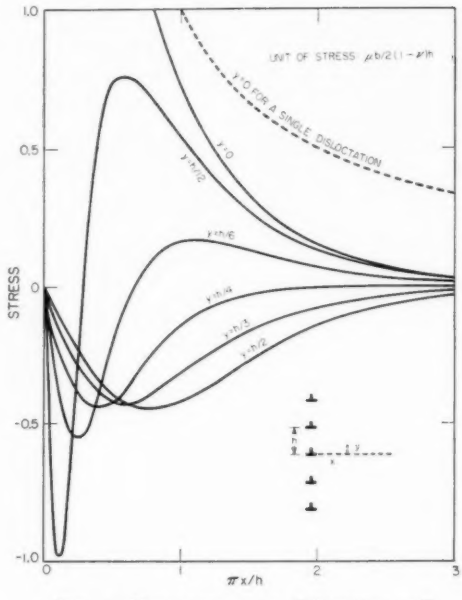


FIG. 4. Shear stress at a dislocation wall.

$x = \pm h$ at a dislocation wall. Outside this region, the crystal is almost perfect and free of internal stresses. This is consistent with the fact that polygonization is involved in recovery.

THE INTERACTION OF A DISLOCATION WITH A PINNED DISLOCATION WALL

In view of the nature of the stress field of a dislocation wall, a wall cannot seem to interact with another dislocation much more than a single dislocation. To simplify the discussion, let us first assume that the wall is pinned by point defects such that it lies in a stress field[17] of the form of the derivatives of Dirac's δ-function. In other words, the point defects are not to alter the stress field of the dislocations. Then from equation (3), the force per unit length exerted on another dislocation at (x, y) by the wall is[18]

$$\frac{\mu b^2}{2\pi(1-\nu)} \cdot \frac{2\pi\alpha}{h} \cdot \frac{\cosh 2\alpha \cos 2\lambda - 1}{(\cosh 2\alpha - \cos 2\lambda)^2} \quad (6)$$

where

$$\alpha = \pi x/h \quad (7)$$

and

$$\lambda = \pi y/h. \quad (8)$$

The force exerted on the same dislocation but by a single dislocation situated on the same slip plane at the wall is, from equation (1),

$$\frac{\mu b^2}{2\pi(1-\nu)} \cdot \frac{\pi}{h} \cdot \frac{1}{\alpha}. \quad (9)$$

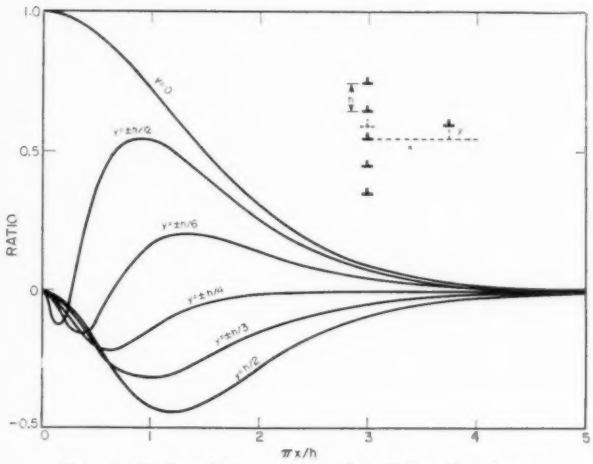


FIG. 5. Ratio of force on an edge dislocation due to a dislocation wall to that on the same dislocation due to another edge dislocation on the same slip plane situated at the same distance as the wall.

The ratio of the forces given by expressions (6) and (9) is

$$2\alpha^2 \cdot \frac{\cosh 2\alpha \cos 2\lambda - 1}{(\cosh 2\alpha - \cos 2\lambda)^2}. \tag{10}$$

This is plotted in Fig. 5.

It is seen that this ratio is always less than unity. In other words, a dislocation wall can never attract or repel another dislocation more than a single dislocation located at the distance of the wall. The wall becomes even weaker when the dislocation spacings become smaller. A large angle dislocation wall exerts less force on a dislocation than a small angle one does on the same dislocation. This is shown in Fig. 6. However, the maximum force exerted by the wall on an approaching dislocation moving along the slip plane, $y = h/2$, is proportional to the angle of the wall. Therefore, if the wall is the only barrier

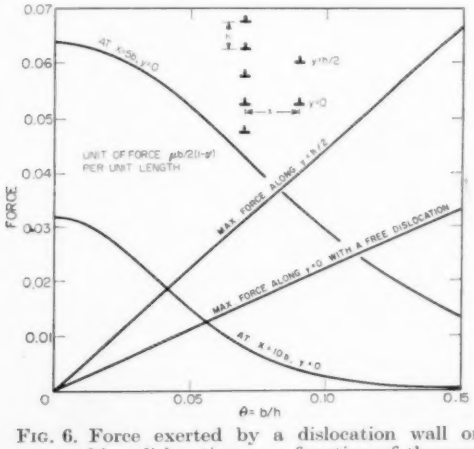


FIG. 6. Force exerted by a dislocation wall on an approaching dislocation as a function of the angle of the wall.

preventing yielding, the yield stress should vary linearly with the dislocation density or the angle of the wall. The case with a free dislocation in the wall will be discussed later.

The maximum repulsive or attractive force exerted by a pinned dislocation wall to an approaching dislocation can be seen from Fig. 4. The maximum repulsive or attractive force exerted by the nearest single dislocation in the wall can be calculated from equation (1) to be

$$\frac{\mu b}{2\pi(1-\nu)} \cdot \frac{1}{4y} = \frac{\mu b}{2h(1-\nu)} \frac{1}{4\lambda}. \tag{11}$$

The maximum forces and the ratio of the two extremes are plotted in Fig. 7. It is seen that the maximum

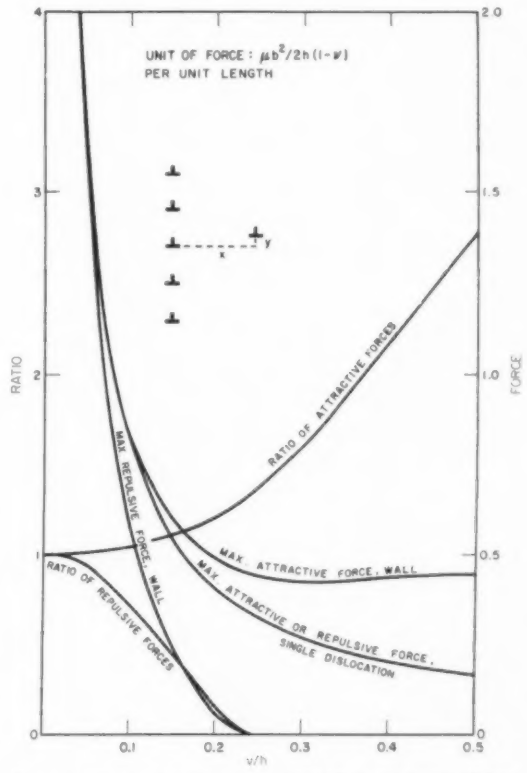


FIG. 7. The maximum forces exerted on an approaching dislocation by a dislocation wall and that exerted on the same dislocation by a single nearest dislocation in the wall and their ratio.

ratio is 2.8 although it may be less than 1. In other words, the stress which is needed to push a dislocation through a wall is at most three times the stress which is needed to push the same dislocation through the dislocation forest before polygonization. It follows also, from the calculation of Eshelby *et al.*[18] that at the stress which can push a dislocation through the forest, no more than three dislocations can pile up

VOL. 8 1960

against a wall at $y = h/2$. If yielding happens when 60 per cent of the dislocations are moving through the wall, the stress required should be about 20 per cent more than that before polygonization. However, since the repulsive force of a wall is always less than that of the dislocation forest and the resistance of the wall due to attractive forces can be important only when the approaching dislocation loses its kinetic energy before it hits the wall, it is likely that polygonization will not significantly increase the strength of the material.

The work that is required to move a dislocation from infinity to a dislocation wall can be obtained by integration of the expression (6),[14]

$$\frac{\mu b^2}{2\pi(1-\nu)} \int_{\alpha}^{\infty} \frac{\cosh 2\alpha \cos 2\lambda - 1}{(\cosh 2\alpha - \cos 2\lambda)^2} d\alpha^2$$

$$= \frac{\mu b^2}{2\pi(1-\nu)} \left[\frac{\alpha \sinh 2\alpha}{\cosh 2\alpha - \cos 2\lambda} - \tfrac{1}{2} \ln 2(\cosh 2\alpha - \cos 2\lambda) \right]. \qquad (12)$$

This represents the energy of interaction of a dislocation with a wall. It is plotted in Fig. 8. It is seen that a dislocation wall can trap approaching dislocations as observed by Bainbridge *et al.*[19]. However, the energy of interaction is weak compared to that between two dislocations separated by the same distance. The work that is required to bring two dislocations together from a distance x_0 to x is seen from equation (9):

$$\frac{\mu b^2}{2\pi(1-\nu)} \ln \frac{x_0}{x}. \qquad (13)$$

For the sake of comparison, the interaction energy between two dislocations relative to that at $x_0 = 5h/\pi$ is plotted also in Fig. 8. It is seen that much more work is needed to bring two dislocations together than that to bring a dislocation close to the wall. Following the same argument, the trapping power of a dislocation wall is much less than that of a dislocation with a negative Burgers' vector.

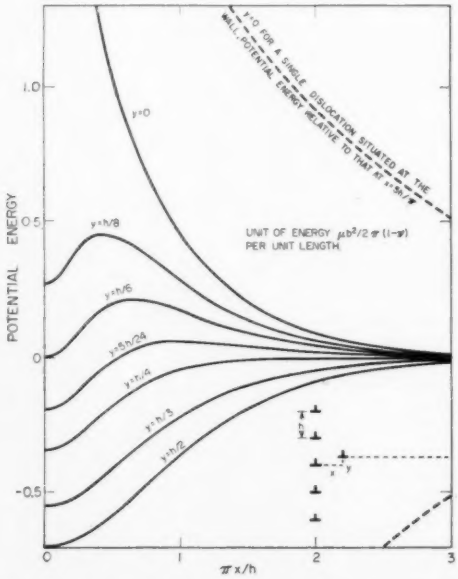


FIG. 8. The potential energy per unit length of a dislocation near a dislocation wall relative to that at infinity.

THE DISPLACEMENT OF A FREE DISLOCATION IN A DISLOCATION WALL BY AN APPROACHING DISLOCATION

It is seen from the foregoing discussion that the repulsive force of a pinned dislocation wall on an approaching dislocation becomes very large (although less than that of a single dislocation) when the approaching dislocation is on the same slip plane as that of one of the dislocations in the wall. If that dislocation is not pinned by point defects, it can be displaced by the approaching one if the latter has enough kinetic energy. For the simplicity of the treatment, we shall assume, as before, that the wall is otherwise pinned by point defects and lies in a stress field of the derivative of Dirac's δ-function, except that one of the dislocations is free and is on the same slip plane as the approaching one. Since the free dislocation will assume equilibrium positions in accordance with the distance of the approaching one, the interaction of the wall with the approaching dislocation will be different from the case where the whole wall is pinned.

At equilibrium, let the free dislocation assume a distance x from the wall while the approaching dislocation is at x_0 from the wall. The force exerted by the wall on the free dislocation is

$$\frac{\mu b^2}{2\pi(1-\nu)} \left(\frac{\pi^2 x}{h^2} \frac{1}{\sinh^2 \pi x/h} - \frac{1}{x} \right) \text{ per unit length.} \qquad (14)$$

The force exerted on the free dislocation by the approaching dislocation is

$$\frac{\mu b^2}{2\pi(1-\nu)} \frac{1}{x - x_0} \text{ per unit length.} \qquad (15)$$

Since the free dislocation is at equilibrium, we have

$$\frac{\pi^2 x}{h^2} \frac{1}{\sinh^2 \pi x/h} - \frac{1}{x} + \frac{1}{x - x_0} = 0 \qquad (16)$$

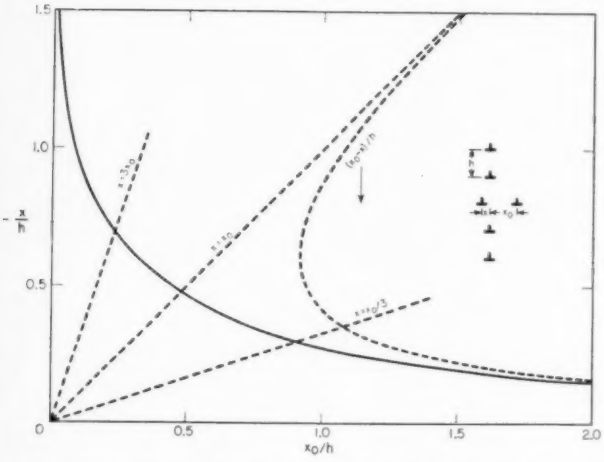


FIG. 9. Equilibrium distances of a free dislocation in a dislocation wall, x, as a function of the distance x_0, of an approaching dislocation on the same slip plane.

or

$$\frac{x_0}{x_0 - x} = \left(\frac{\alpha}{\sinh \alpha}\right)^2. \tag{17}$$

This is plotted in Fig. 9. It is seen that when a dislocation is approaching a wall, a free dislocation on the same slip plane originally in the wall will leave the wall and move to the other side of the wall in the same direction as that of the approaching dislocation.

The work that is required for an approaching dislocation to displace a free dislocation in a dislocation wall can be calculated from the force exerted on the approaching dislocation which is given by the sum of equations (14) and (15) after interchanging x and x_0:

$$\frac{\mu b^2}{2h(1-\nu)}\left(\frac{\alpha_0}{\sinh^2 \alpha_0} - \frac{1}{\alpha_0} + \frac{1}{\alpha_0 - \alpha}\right) \text{ per unit length} \tag{18}$$

or after substituting equation (17)

$$\frac{\mu b^2}{2h(1-\nu)\alpha_0}\left[\left(\frac{\alpha_0}{\sinh \alpha_0}\right)^2 + \left(\frac{\alpha}{\sinh \alpha}\right)^2 - 1\right]$$

per unit length. (19)

This is plotted in Fig. 10. It is seen that when there is a free dislocation in the wall, the approaching dislocation feels a slight attractive force at large distances and a repulsive force at small distances. This is entirely different from the case where the whole wall is pinned. In that case the approaching dislocation feels very strong repulsive forces especially at small distances. For example, comparing Figs. 4 and 10, one can see that at $x = h/\pi$, the repulsive force of the pinned wall is ten times as great as that of an otherwise pinned wall except that there is a free dislocation. The maximum repulsive force varies linearly with the angle of the wall as shown in Fig. 6. Now the work that is needed to replace a free dislocation in the wall can be obtained by integration of equation (18) first at $\alpha = 0$ for the approaching dislocation to move to the pinned wall then at constant α_0 after interchanging α and α_0 for

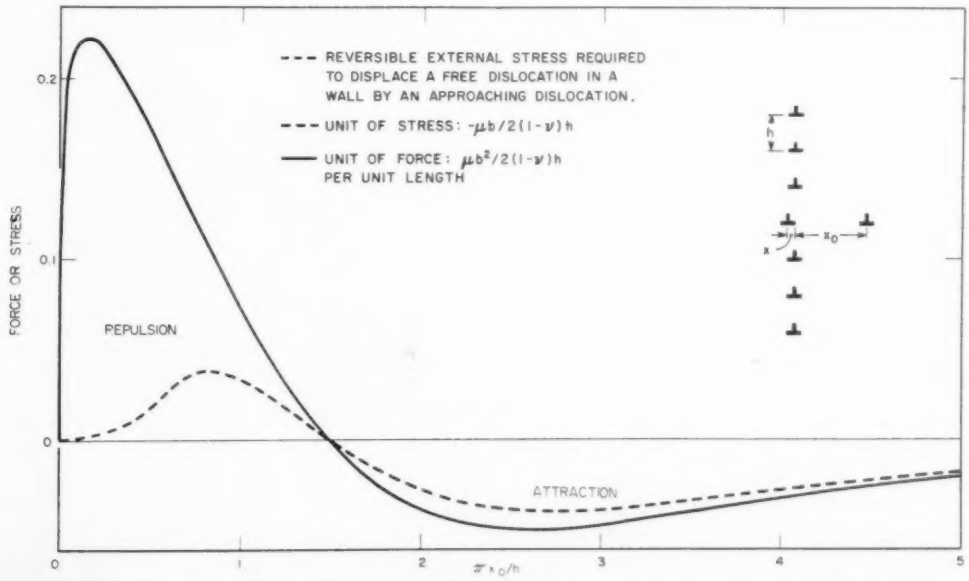


FIG. 10. Force exerted on an approaching dislocation by a dislocation wall in which there is a free dislocation on the same slip plane as that of the approaching one.

VOL. 8 1960

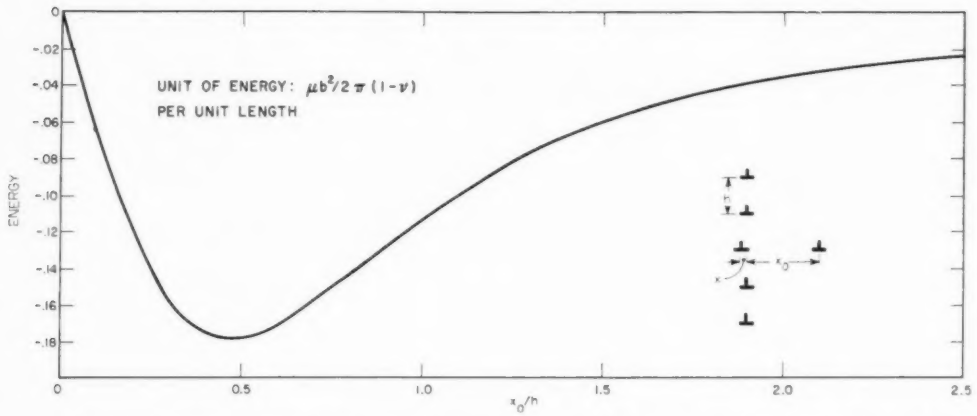


FIG. 11. The interaction of a dislocation with a dislocation wall when the former is on the slip plane of a free dislocation originally in the wall.

the free dislocation to move to the equilibrium position. The result is

$$\frac{\mu b^2}{2\pi(1-\nu)}\left[\alpha_0 \coth \alpha_0 + \alpha \coth \alpha + \ln \frac{\alpha\alpha_0}{2e(\alpha_0-\alpha)\sinh \alpha_0 \sinh \alpha}\right] \text{ per unit length.} \quad (20)$$

This is plotted in Fig. 11. It is seen that theoretically no work is needed to replace a free dislocation in a wall by another dislocation. The wall with the free dislocation attracts a dislocation to an equilibrium position at about $x_0 = 0.47\,h$. At this point, if the approaching dislocation has enough kinetic energy, it can jump into the wall. However, complete displacement depends also on the amount of resistance that the free dislocation encounters on its way to infinity.

Therefore, the stable structure with two dislocations symmetrically located at two sides of the wall may exist in actual crystals. That this is the case has been demonstrated by Gilman[20] and by Oberly[21] where two dislocations appear at two sides of the wall situated at a distance from the wall which is only 15 per cent greater than that predicted by theory.

The displacement is even easier if an external stress, σ, is applied in the common slip plane of the free dislocation in the wall and the approaching dislocation. The equilibrium positions of the two dislocations are thus,

$$\frac{\alpha}{\sinh^2 \alpha} + \frac{\alpha_0}{\alpha(\alpha-\alpha_0)} + \frac{2\sigma h(1-\nu)}{\mu b} = 0 \quad (21)$$

$$\frac{\alpha_0}{\sinh^2 \alpha_0} + \frac{\alpha}{\alpha_0(\alpha_0-\alpha)} + \frac{2\sigma h(1-\nu)}{\mu b} = 0. \quad (22)$$

A plot of α versus α_0 can be made by eliminating σ from the above two equations. It is shown in Fig. 12. The general behavior is similar to the case where there is no external stress applied except that here the two dislocations are equivalent. The external stress calculated from either of the above two equations is plotted in Fig. 10. It is seen that even lower stress is required to displace a free dislocation in a dislocation wall by an approaching dislocation.

Since the structure of two free dislocations located at two sides of the wall is a stable one, it seems advisable to see how this structure behaves toward another approaching dislocation on the same slip plane. Let the two free dislocations assume equilibrium positions x_1 and x_2 from the wall while the approaching one is at x_0. We have the following two equations instead of equation (16) for the conditions of equilibrium:

$$\frac{\alpha_1}{\sinh^2 \alpha_1} - \frac{1}{\alpha_0-\alpha_1} + \frac{1}{\alpha_1-\alpha_2} - \frac{1}{\alpha_1} = 0 \quad (23)$$

$$\frac{\alpha_2}{\sinh^2 \alpha_2} - \frac{1}{\alpha_0-\alpha_2} + \frac{1}{\alpha_2-\alpha_1} - \frac{1}{\alpha_2} = 0. \quad (24)$$

Numerical solution of the above simultaneous equations is very laborious. A graphical method is designed to simplify the procedure. A function f is defined as follows:

$$f_i = \left(\frac{\alpha_i}{\sinh \alpha_i}\right)^2 - \frac{\alpha_i}{\alpha_0-\alpha_i} \quad (25)$$

where i is 1 or 2. Then it can be easily shown that equations (23) and (24) are equivalent to

$$f_1 + f_2 = 1 \quad (26)$$

$$\alpha_1 f_1 + \alpha_2 f_2 = 0. \quad (27)$$

For each α_0, f_1 can be plotted against α_1 using equation

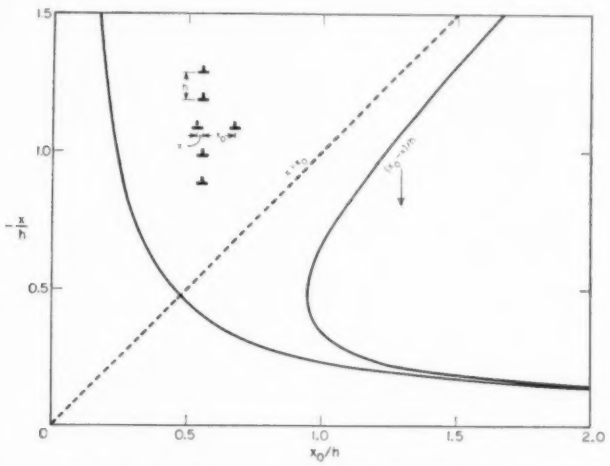


FIG. 12. Equilibrium distance of a free dislocation in a dislocation wall and an approaching dislocation on the same slip plane under the influence of an externally applied stress.

(25). Another plot can be made between the same variables by taking any α_2 reading off f_2 from the previous plot, and then calculating f_1 and then α_1 from equations (26) and (27). The intersection of the two plots gives the solution.

The result is shown in Fig. 13. It is seen that when a dislocation is approaching the previously-mentioned stable structure with one free dislocation on each side of the wall, the two free dislocations will move in the direction of that of the approaching dislocation until the distance of the approaching dislocation is about eight dislocation spacings ($\alpha_0 = 24$) from the wall. At this critical distance, the system becomes unstable. If the approaching dislocation comes closer to the wall, the middle free dislocation will go across the wall and assume a position shown by the dotted line in Fig. 13 and the other free dislocation will go to minus infinity. To insure the continuity of curves, nature provides two metastable positions for the free dislocations in case that the approaching dislocation

VOL. 8 1960

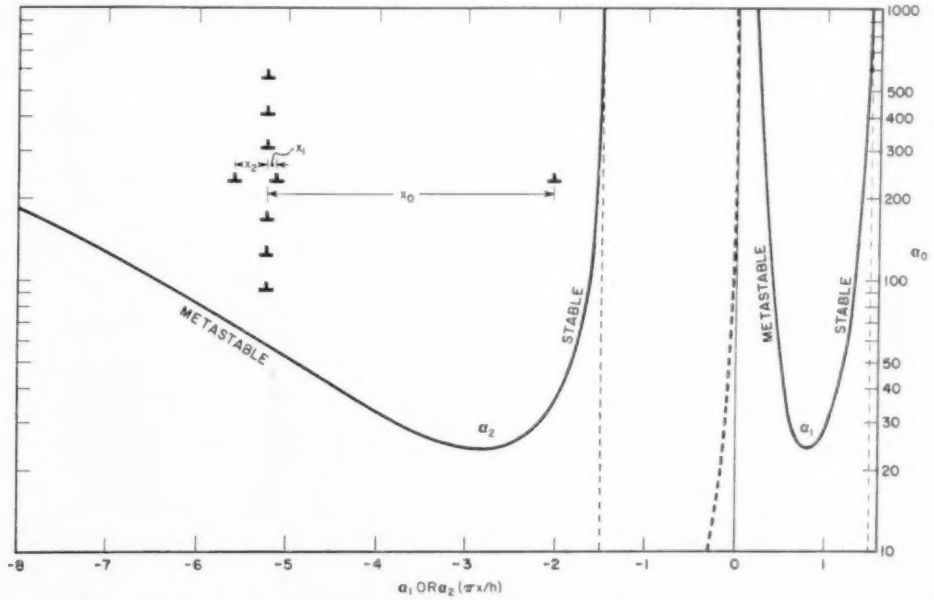


FIG. 13. Equilibrium distances of two free dislocations, one of which is originally in a dislocation wall, when a third dislocation is approaching the wall. All three dislocations are on the same slip plane. Dotted line gives the distance of one free dislocation when the other is at infinity. Refer also to Fig. 9.

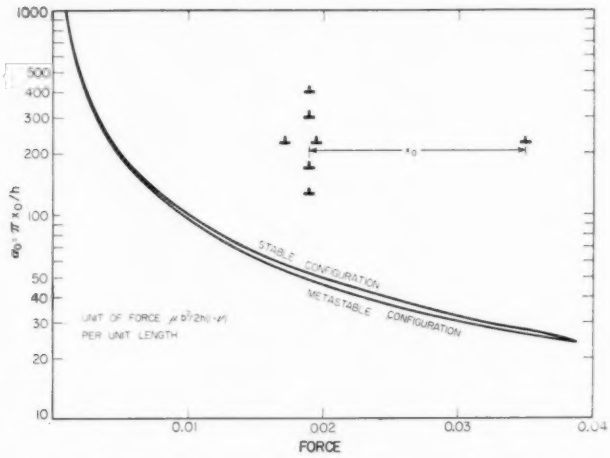


FIG. 14. Force exerted on an approaching dislocation toward a dislocation wall where there are two free dislocations on the same slip plane as the approaching one and one of the free dislocations is originally in the wall.

departs away from the wall. The free dislocations may have enough kinetic energy to assume the metastable positions.

The force that the approaching dislocation feels can be calculated as before with the result:

$$\frac{\mu b^2}{2h(1-\nu)}\left(\frac{\alpha_0}{\sinh^2\alpha_0}-\frac{1}{\alpha_0}+\frac{1}{\alpha_0-\alpha_1}+\frac{1}{\alpha_0-\alpha_2}\right) \quad \text{per unit length,} \quad (28)$$

or when equations (23) and (24) are introduced:

$$\frac{\mu b^2}{2h(1-\nu)}\frac{1}{\alpha_0}\left[\left(\frac{\alpha_0}{\sinh\alpha_0}\right)^2+\left(\frac{\alpha_1}{\sinh\alpha_1}\right)^2+\left(\frac{\alpha_2}{\sinh\alpha_2}\right)^2\right] \text{ per unit length.} \quad (29)$$

This is plotted in Fig. 14. It is seen that at large distances, the force becomes simply

$$\frac{\mu b^2}{2\pi(1-\nu)}\cdot\frac{1}{x_0}. \quad (30)$$

In other words, at large distances, the approaching dislocation feels a force the same as that exerted by a single dislocation situated at the wall. However, since the approaching dislocation cannot go closer than $\alpha_0 = 24$ before the system becomes unstable, the force can never exceed 0.04 with the unit given in Fig. 14. Therefore, no more than two dislocations can go near a wall on the same slip plane and a piling up of dislocations against a free dislocation in the wall is not likely to happen. Even if a few dislocations can pile up at low applied stresses, it is not likely that a crack of the type discussed by Stroh[22] can be formed at the wall.

THE PENETRATION OF AN APPROACHING DISLOCATION BETWEEN TWO DISLOCATIONS IN A WALL

The foregoing seems to indicate that when there is a free dislocation in the wall, the resistance of the wall to the penetration of approaching dislocations along the slip plane of the free dislocation becomes weak. To replace the free dislocation, the first dislocation requires an internal stress of about $0.22\ \mu b/2(1-\nu)h$ or an external stress of about $0.04\ \mu b/2(1-\nu)h$. At a smaller stress, a stable structure is formed instead. This structure becomes unstable when a second dislocation is approaching at an internal stress of about $0.04\ \mu b/2(1-\nu)h$ or a smaller external stress. This dislocation cannot approach nearer than about eight dislocation spacings in the wall. The free dislocation originally in the wall can be displaced by the effect of a third dislocation at even a smaller stress.

It seems interesting to investigate the case where the slip plane of the approaching dislocation is in the middle of two dislocations in the wall. When the wall is pinned, the approaching dislocation feels only attractive forces as shown in Fig. 4. It will be caught by the wall and requires a stress of about $0.45\ \mu b/2(1-\nu)h$ in order to penetrate. However, a second approaching dislocation can push the first one through at a lower stress. This is similar to the case where there is a free dislocation in the wall. The first dislocation will assume a distance x from the wall at

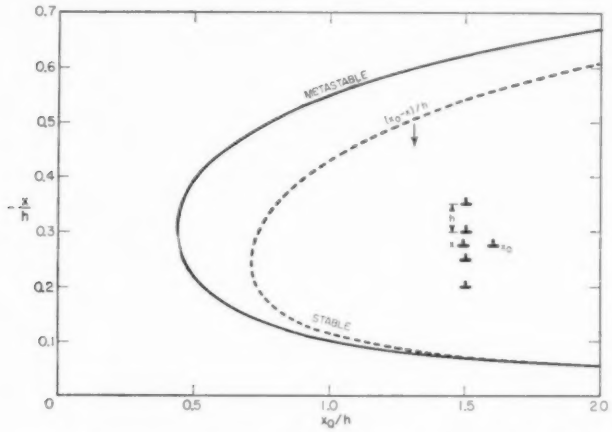


FIG. 15. Equilibrium distances of a dislocation caught between two dislocations in a wall while another dislocation is approaching the wall.

equilibrium in accordance with the distance x_0 of the second dislocation:

$$\frac{x}{x - x_0} = \left(\frac{\alpha}{\cosh \alpha}\right)^2. \tag{31}$$

This is plotted in Fig. 15. It is seen that there is a critical distance of the second dislocation beyond which the first dislocation has no equilibrium position. The minimum separation between the two dislocations is about 0.7 h. Here again for a small angle boundary, no Stroh crack can be produced because the separation between the two leading dislocations is too big. The force exerted on the second dislocation is simply

$$\frac{\mu b^2}{2h(1-\nu)} \left(\frac{1}{\alpha_0 - \alpha} - \frac{\alpha_0}{\cosh^2 \alpha_0}\right) \text{ per unit length} \tag{32}$$

which is plotted in Fig. 16. It is seen that at an internal stress of about 0.28 $\mu b/2h(1-\nu)$, the second dislocation can push the first one through the wall. The stress required at the critical distance is only about 0.12 $\mu b/2h(1-\nu)$. The case of metastable configurations is similar to the one discussed previously.

The displacement in this case will be also easier if an external stress is applied. The equilibrium positions of the two dislocations are

$$-\frac{\alpha}{\cosh^2 \alpha} - \frac{1}{\alpha_0 - \alpha} + \frac{2\sigma h(1-\nu)}{\mu b} = 0 \tag{33}$$

$$-\frac{\alpha_0}{\cosh^2 \alpha_0} - \frac{1}{\alpha - \alpha_0} + \frac{2\sigma h(1-\nu)}{\mu b} = 0. \tag{34}$$

A plot of α versus α_0 is shown in Fig. 17. The general

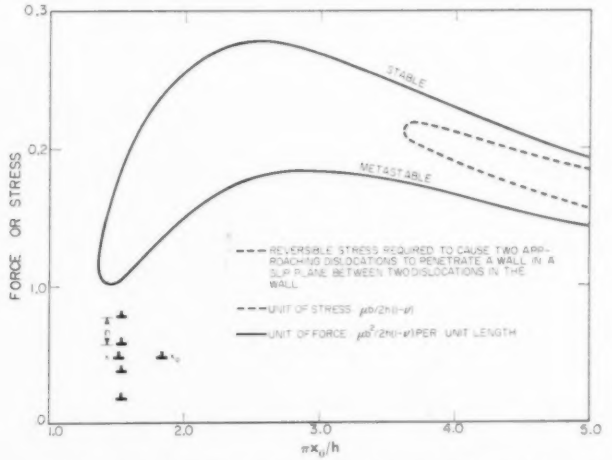


FIG. 16. Force exerted on a second approaching dislocation when the first one is caught between two dislocations in a wall.

VOL. 8 1960

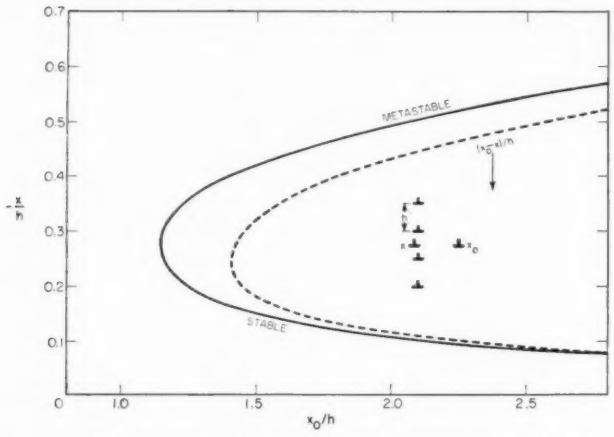


FIG. 17. Equilibrium distances for two approaching dislocations to penetrate a dislocation wall between two dislocations in the wall under a reversible external stress.

behavior is quite similar except that the minimum separation between the two dislocations is now about 1.4 h which is larger than before. No close pile-up of dislocations seems to be possible against a free dislocation in a wall. The reversible external stress required to maintain equilibrium at each distance is plotted in Fig. 16. It is seen that the stress required to push the first dislocation through the wall is smaller than the case without external stress.

The situation is slightly different if the approaching dislocation glides between two free dislocations in a wall. The free dislocations will assume equilibrium positions, x, according to the following equation:

$$A(\beta) + 2B[2(\beta_0 - \beta)] + B(\beta) = 0 \qquad (35)$$

where

$$\beta = x/h$$

$$\beta_0 = x_0/h$$

and A and B are functions defined by

$$A(\beta) = \frac{1}{\beta}\left[\left(\frac{\pi\beta}{\sinh \pi\beta}\right)^2 - 1\right] \qquad (36)$$

$$B(\beta) = \beta\,\frac{(1-\beta^2)}{(1+\beta^2)^2}. \qquad (37)$$

Equation (35) is plotted in Fig. 18. It is seen that the free dislocations will oscillate when the approaching dislocation glides through the wall. But the distance never exceeds 0.22 h. The force exerted on the approaching dislocation is

$$\frac{\mu b^2}{2h(1-\nu)}\left\{\frac{4}{\pi}\,B(2\beta_0) - \frac{4}{\pi}\,B[2(\beta_0-\beta)] - \frac{\alpha_0}{\cosh^2 \alpha_0}\right\}$$

per unit length, (38)

which is plotted in Fig. 19. Although the general shape remains similar to the case of a pinned wall, the maximum attractive force is increased to 0.55 $\mu b/2h(1-\nu)$.

THE INTERACTION OF A DISLOCATION WITH A PARTIALLY-FREE DISLOCATION WALL

The foregoing discussion indicates that the repulsive

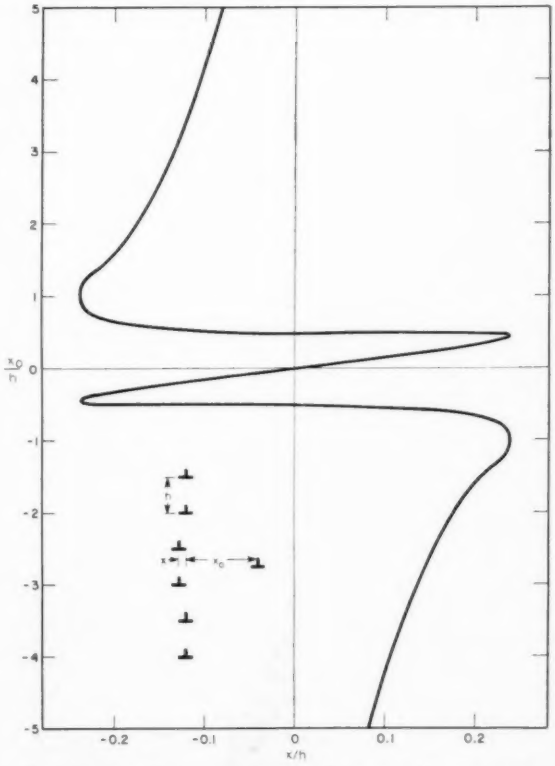


FIG. 18. Equilibrium distances of two adjacent free dislocations in a dislocation wall when an approaching dislocation glides through the wall between them.

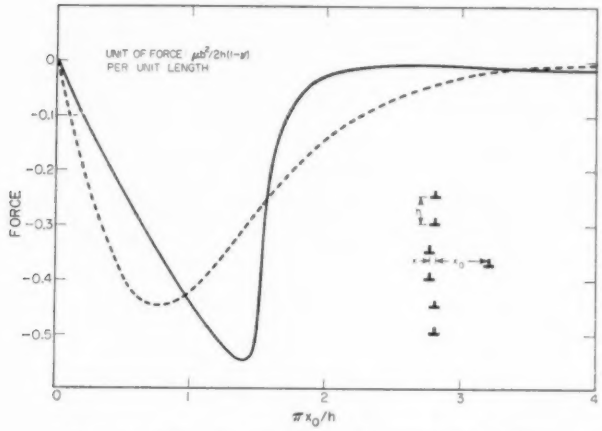


FIG. 19. Force acting on an approaching dislocation on a slip plane between two free dislocations in a wall.

force of a pinned dislocation wall toward an approaching dislocation is always less than that of a single pinned dislocation located at the distance of the wall and that a wall with a free dislocation does not offer much resistance to the approaching dislocations in displacing the free dislocation. This is also true for two free dislocations in the wall when the approaching dislocation glides between them. It remains to show also how these conclusions can still hold when there are more free dislocations in the wall.

Theoretically when the whole wall is free, the wall will move toward the approaching dislocation to form a stable structure and then move with it. Practically this is not likely to happen unless the external stress is also applied to the wall. The dislocations at large distances have so little interaction that they will probably not be affected by the approaching dislocation. That this must be the case is shown by the following example.

Suppose that there are two free dislocations in the wall, one above and one below a pinned dislocation on whose slip plane a foreign dislocation is approaching. Due to the symmetry of the stresses, the two free dislocations will assume the same equilibrium position x' from the wall when the approaching dislocation is at a distance x_0. This can be easily calculated with the result

$$A(\beta') + \tfrac{1}{2}B\left(\frac{\beta'}{2}\right) + B(\beta_0 - \beta') = 0 \qquad (39)$$

where

$$\beta' = x'/h$$

$$\beta_0 = x_0/h$$

and A and B are functions defined by equations (36) and (37). Equation (39) is plotted in Fig. 20. It is seen that the free dislocations first move in the same direction as that of the approaching dislocation, then in the opposite direction, and then in the same direction again. However, the distances that the free dislocations move never exceed 0.1 h from the wall. Because of their proximity, these dislocations should show the largest effect. The effect will be negligible if there are free dislocations at other locations. This can be further demonstrated by analyzing the force

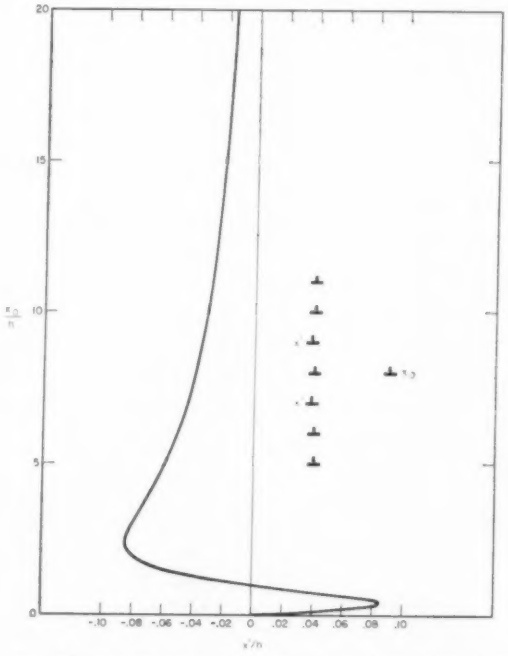


FIG. 20. Equilibrium distances of two free dislocations in a dislocation wall, one above and one below a pinned dislocation, when a foreign dislocation on the same slip plane as the pinned one is approaching the wall.

VOL. 8 1960

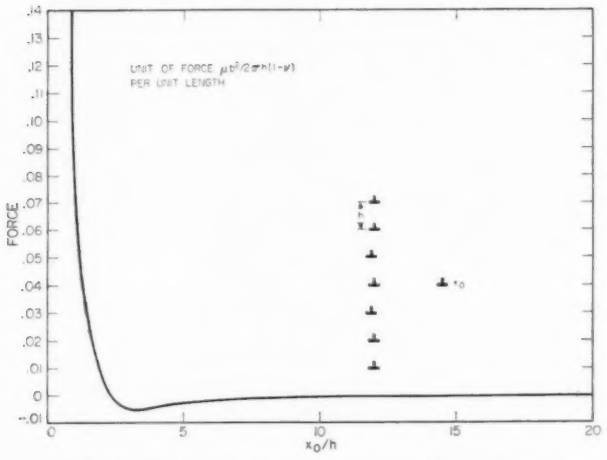


FIG. 21. Force acting on an approaching dislocation by a dislocation wall where there is a pinned dislocation on the same slip plane as the approaching one and there are two free dislocations, one above and one below the pinned one.

which acts on the approaching dislocation. The force is

$$\frac{\mu b^2}{2\pi h 1(-\nu)}\left[A(\beta_0)+\frac{1}{\beta_0}+2B(\beta'-\beta_0)+2B(\beta_0)\right]$$

per unit length. (40)

This is plotted in Fig. 21. The force is attractive at large distances but replusive at small distances. The force being zero at $x_0 = 2.3\,h$ indicates a stable configuration for the system with three free dislocations. When $x_0 < h$ where the force becomes large, it approaches the same force which is exerted by a pinned wall. In other words, the existence of some free dislocations in the wall reduces further the resistance of the wall toward approaching dislocations.

We shall conclude this section by examining another example where instead of the pinned dislocation in the above case, let us have three consecutive free dislocations in a wall. At equilibrium, let the middle free dislocation assume a position x. We have

$$A(\beta)-\frac{1}{\beta_0-\beta}+2B(\beta'-\beta)+2B(\beta)=0 \quad (41)$$

$$A(\beta')+B(\beta')+\tfrac{1}{2}B\left(\frac{\beta'}{2}\right)+B(\beta-\beta')+B(\beta_0-\beta')=0. \quad (42)$$

The result is shown in Fig. 22. It is seen that when the foreign dislocation is approaching the wall, all three free dislocations move in the same direction as that of the approaching one until about $x_0 = 1.7\,h$ after which the upper and the lower free dislocations begin to change direction and move toward the wall. At $x_0 = 0.47\,h$, the upper and lower dislocations get back into the wall and the middle free dislocation is at $x = -0.47\,h$. This is the stable structure mentioned before. Before this event, the approaching dislocation feels a force more attractive than that in the case when only the middle dislocation is free, as it can easily be seen from the graph. At this event, the force acting on the approaching dislocation is obviously zero. After this event, the approaching dislocation feels a repulsive force. Since now the upper and the lower dislocation move out of the wall and toward the approaching dislocation, the repulsive force will first be smaller and then somewhat larger than that in the case when only the middle dislocation is free. When the approaching dislocation gets into the wall, it still feels some repulsive force. At the critical moment when $x_0 = 0.05\,h$, the system becomes unstable with the final result that the middle free dislocation goes to minus infinity and the rest form a dislocation wall. This apparent discontinuity is again removed by nature with a series of metastable states in case that the approaching dislocation reverses the direction. The approaching dislocation now feels less repulsive force and finally the force reduces to zero. The final state is also a dislocation wall with a free dislocation at minus infinity. The story can then repeat itself with another approaching dislocation. It is now clear that a greater number of free dislocations in the wall cannot offer much more resistance to an approaching dislocation. They usually contribute to the weakness of the wall as also shown by Vreeland[23].

THE EFFECT OF SOLUTE ATOMS

It seems desirable to include in this report a discussion of whether the interaction of a dislocation

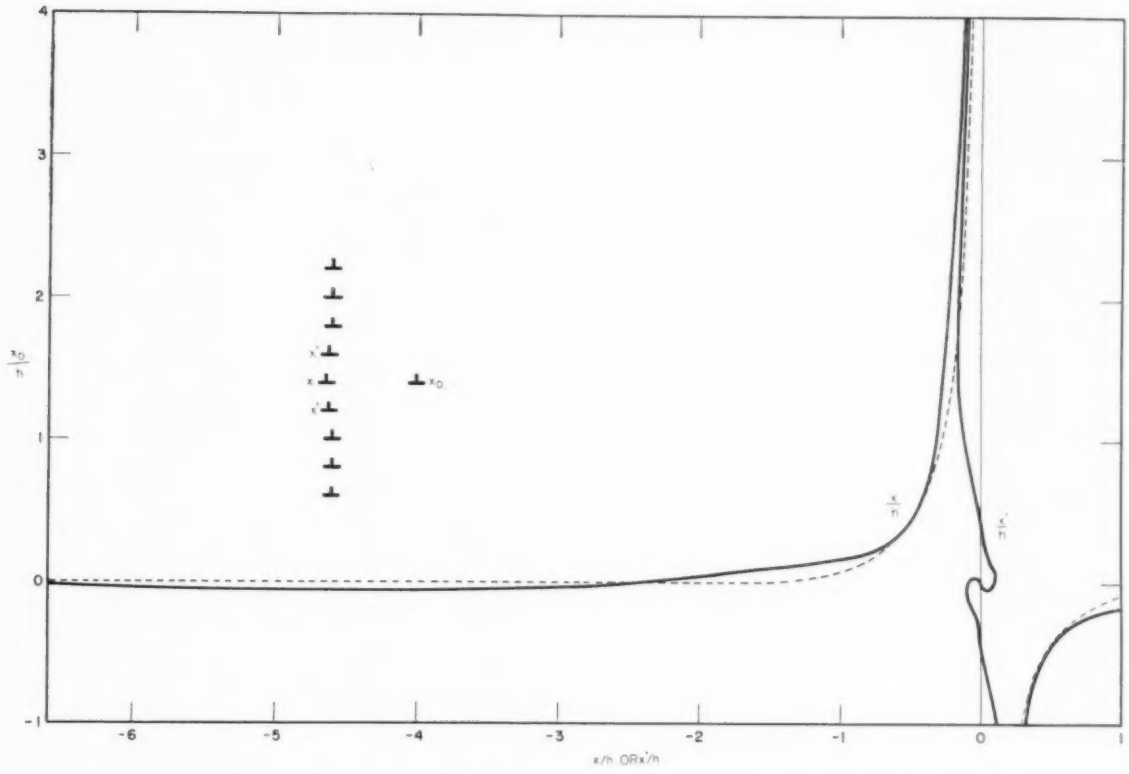


FIG. 22. Equilibrium positions for three free dislocations in a dislocation wall, one on the slip plane of an approaching dislocation, one above and one below it. The curves include sections for metastable equilibrium. Dotted line indicates the case where only the middle dislocation is free.

wall with solute atoms will affect the foregoing conclusions. The interaction of the type involving a Cottrell atmosphere has been discussed by Webb[24]. It can be seen that the ratio of the interaction energy (potential energy relative to a widely separated state) of a solute atom with a dislocation wall to that of the same solute atom with a single dislocation situated at the origin is

$$\frac{\alpha^2 + \lambda^2}{\lambda} \cdot \frac{\sin \lambda \cos \lambda}{\sin^2 \lambda + \sinh^2 \alpha} \tag{43}$$

where the symbols are defined by equations (7) and (8). Equation (43) is plotted in Fig. 23. It is seen that the ratio is always less than unity. The amount of solute atoms per unit length of dislocation which will segregate around a dislocation wall can never be more than that which will segregate around a single dislocation at equilibrium. This is true whether Boltzmann or Fermi–Dirac[25] statistics are used. Therefore it seems that it should be easier for an approaching dislocation to displace a pinned dislocation in a wall than to displace a single pinned dislocation.

CONCLUSIONS

(1) A dislocation wall of evenly spaced dislocations separates the crystal at large distances from the wall into evenly spaced bands (Fig. 3) by planes parallel to the slip planes of the dislocations in the wall. The thickness of each band is one half of the dislocation spacings in the wall. Any single dislocation located in the band containing the slip plane of one of the dislocations in the wall will be repelled by the wall. Dislocations located in other bands will be attracted by the wall.

(2) A pinned dislocation wall attracts or repels an approaching dislocation less than a single dislocation situated at the distance of the wall.

(3) A dislocation wall with a free dislocation attracts an approaching dislocation to form a stable structure with two dislocations symmetrically placed on two sides of the wall.

(4) The above stable structure becomes unstable when another dislocation on the same slip plane as the two dislocations approaches the wall closer than eight dislocation spacings in the wall.

(5) A pinned dislocation wall attracts the first

VOL. 8 1960

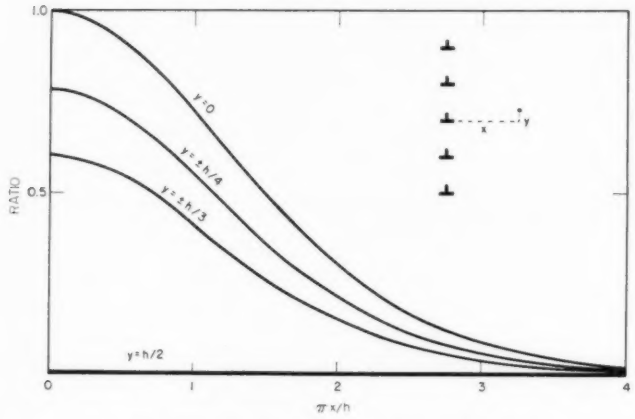


FIG. 23. Ratio of interaction energy of a solute atom with a dislocation wall to that of the same solute atom with a single dislocation situated at the origin.

approaching dislocation on a slip plane between two dislocations in the wall but repels the second approaching dislocation. The second dislocation can push the first one through the wall by approaching the wall closer than about half the dislocation spacings in the wall.

(6) The force exerted by a dislocation wall on an approaching dislocation located at a certain distance from the wall decreases when the angle of the wall increases. However, the minimum stress necessary to push an approaching dislocation through the wall or to displace a free dislocation by an approaching dislocation increases linearly with the angle of the wall.

(7) Two consecutive free dislocations in a wall will oscillate back and forth with a maximum amplitude of about 0.22 of the dislocation spacings in the wall when an approaching dislocation glides through the wall on a slip plane between them.

(8) A dislocation wall with two free dislocations, one above and one below a pinned one, attracts an approaching dislocation on the same slip plane as the pinned one to form a stable structure with the two free dislocations at −0.085 and the approaching one at 2.35 of the dislocation spacings in the wall.

(9) A dislocation wall with three consecutive free dislocations attracts an approaching dislocation on the same slip plane as the middle free dislocation more than the case described in conclusion (3) to form the same stable structure.

(10) The energy of interaction of a solute atom with a wall is less than that of the same solute atom with the single nearest dislocation in the wall.

The above results indicate that a simple tilt dislocation wall is not a very effective barrier to the penetration of parallel dislocations of the same slip vector. The fact that the yield stress increases when a deformed crystal is heated to a high temperature is probably due to the increased concentration of vacancies or the increased rate of diffusion of solute atoms, both of which can segregate into dislocations and jog or pin them. The appearance of substructure is also a result of heating and is probably not the cause of hardening. This seems to explain the results of Washburn[7], Li *et al.*[6] and Washburn *et al.*[9]. This point of view is also supported by some recent observations of Stokes[26] that no fatigue crack can be produced in Zn crystals by pile-up of dislocations against a subboundary.

It should be pointed out here that in order to discuss the actual motion of a dislocation, some estimate of the Peirls–Nabarro forces near a subboundary is necessary. This is found, however, not a very simple matter. An approximate calculation will be tried out and reported at a later date.

ACKNOWLEDGMENTS

The author wishes to thank Drs. L. S. Darken, F. Garofalo and Y. T. Chou, all of this Laboratory, and Professors E. R. Parker and Charles Johnson of the University of California, for valuable discussions. He also wishes to thank Mr. R. W. Whitmore, also of this Laboratory, for some of the numerical calculations.

REFERENCES

1. P. A. BECK, *Acta Met.* **1**, 422 (1953), *Advanc. Phys.* **3**, 245 (1954).
2. A. H. COTTRELL, in *Symposium on Plastic Deformation of Crystalline Solids*, p. 60, Mellon Institute, Pittsburgh, May 1950.
3. E. R. PARKER and T. HAZLETT, *Seminar on Relation of Properties to Microstructure*, 35*th National Metal Congress*, p. 30. Cleveland, Ohio, Oct. 1953.
4. C. J. BALL, in *Dislocation and Mechanical Properties of Crystals* (Eds.: J. C. FISHER, W. G. JOHNSTON, R. THOMSON and T. VREELAND, Jr.) p. 353, Wiley, New York (1957).

5. D. McLean and A. E. L. Tate, *Rev. Métall.* **48**, 765 (1951).
6. C. H. Li, J. Washburn and E. R. Parker, *Trans. Amer. Inst. Min. (Metall.) Engrs.* **197**; *J. Metals* **5**, 1223 (1953).
7. J. Washburn, *Trans. Amer. Inst. Min. (Metall.) Engrs.* **203**; *J. Metals* **7**, 675 (1955); see also *ibid.* 1262, discussion by P. L. Pratt.
8. N. F. Mott, *Phil. Mag.* **43**, 1151 (1952).
9. J. Washburn, A. E. Gorum and E. R. Parker, *Trans. Amer. Inst. Min. (Metall.) Engrs.* **215**, 230 (1959).
10. G. I. Taylor, *Proc. Roy. Soc.* A**145**, 362 388 (1934).
11. J. M. Burgers, *Proc. Acad. Sci. Inst.* **42**, 293 (1939); see also W. L. Bragg, *Proc. Phys. Soc.* **52**, 54 (1940).
12. W. T. Read and W. Shockley, *Phys. Rev.* **78**, 275 (1950).
13. F. R. N. Nabarro, *Advanc. Phys.* **1**, 269 (1952).
14. A. Seeger, *Naturwissenschaften* **38**, 526 (1951).
15. A. H. Cottrell, *Dislocations and Plastic Flow in Crystals* p. 34. Clarendon Press, Oxford (1953).
16. Ref. 15, p. 94.
17. J. D. Eshelby, F. C. Frank and F. R. N. Nabarro, *Phil. Mag.* **42**, 351 (1951).
18. Ref. 15, p. 19.
19. D. W. Bainbridge, C. H. Li and E. H. Edwards, *Acta Met.* **2**, 322 (1954).
20. J. J. Gilman, *Trans. Amer. Inst. Min. (Metall.) Engrs.* **206**, *J. Metals* **8**, 998 (1956).
21. J. J. Oberly, *Trans. Amer. Inst. Min. (Metall.) Engrs.* **200**, 1025 (1954).
22. A. N. Stroh, *Proc. Roy. Soc.* A**223**, 404 (1954). A**232**, 548 (1955).
23. T. Vreeland, Jr., *Acta Met.* **7**, 240 (1959).
24. W. W. Webb, *Acta Met.* **5**, 89 (1957).
25. D. N. Beshers, *Acta Met.* **6**, 521 (1958).
26. R. J. Stokes, *The Behavior of Zinc Single Crystals Fatigued in Simple Shear*, Office of Naval Research report, University of California (1957).

VOL.
8
1960

GEOMETRY AND KINETICS OF THE POLYGONIZATION OF SODIUM CHLORIDE*

S. AMELINCKX† and R. STRUMANE‡

The geometry and kinetics of the domain growth during polygonization of sodium chloride is studied. It is found that the breaking up of ending walls is the dominating process in the initial stages, whilst the Y-shaped junctions dominate the growth process in the final stages.

The interaction between growth in subboundaries and the newly formed polygon walls is also considered. In an appendix the interaction of isolated edge dislocations with a wall of edge dislocations is discussed in some detail.

The kinetics of the polygonization process was studied by means of isothermal annealing curves. Two different activation energies are found: one for the low temperature range (49 kcal/mol) and one for temperatures above 375°C (30 kcal/mol). The difference between these two activation energies is interpreted as the activation energy for jog formation; its value is 0.6–0.8 eV.

GEOMETRIE ET CINETIQUE DE LA POLYGONISATION DU CHLORURE DE SODIUM

Les auteurs ont étudié la géométrie et la cinétique de croissance des domaines de polygonisation du chlorure de sodium. Ils ont trouvé que le processus essentiel dans les stades initiaux fait apparaître des parois semi-infinies.

Par contre, des jonctions en forme d'*Y* caractérisent les stades finaux.

Ils ont aussi considéré l'interaction entre les dous-joints existants et les parois polygonales nouvellement formées. En appendice, ils discutent en détail l'interaction de dislocations-coin isolées avec une paroi de telles dislocations.

La cinétiqe de pyolgonisation a été étudiée à l'aide de courbes isothermes de restauration. Deux énergies d'activation ont été trou ées: l'une à basse température (49 kcal/mole) et l'autre pour des températures supérieures à 375°C (30 kcal/mole).

La différence entre ces deux énergies d'activation est interpretée comme l'énergie d'activation nécessaire à la formation de crans; sa valeur est de 0.6 à 0.8 eV.

GEOMETRIE UND KINETIK DER POLYGONISATION VON NATRIUMCHLORID

Die Geometrie und die Kinetik des Wachstums von Subkörnern während der Polygonisation von Natriumchlorid wird untersucht. Wie sich zeigt, lösen sich in den ersten Stadien vorzugsweise die Enden von Versetzungswänden auf, während sich in den letzten Stadien des Wachstumsvorgangs überwiegend *Y*-förmige Verzweigungen bilden.

Die Wechselwirkung zwischen ursprünglichen Kleinwinkelkorngrenzen und neugebildeten Versetzungswänden wird ebenfalls betrachtet. In einem Anhang wird die Wechselwirkung einer einzelnen Stufenversetzung mit einer Stufenversetzungswand ausführlich diskutiert.

Die Kinetik des Polygonisationsvorgangs wurde durch isotherme Erholungskurven untersucht. Es ergaben sich zwei Aktivierungsenergien: Eine für den Bereich tiefer Temperaturen (49 kcal/Mol) und eine für Temperaturen oberhalb 375°C (30 kcal/Mol). Die Differenz dieser beiden Aktivierungsenergien wird als Aktivierungsenergie für die Bildung von Versetzungssprüngen gedeutet; sie beträgt 0,6–0,8 eV.

INTRODUCTION

Polygonization has been observed in a large number of crystals. The majority of these studies are mainly concerned with the geometrical aspects. Observations concerning the kinetics are due to Dunn and Hibbard[1,2] for silicon iron and to Gilman[3] for zinc.

The methods used in these studies were mainly etching and X-ray diffraction. A method suitable for the study of crystals presenting a pronounced cleavage plane has been described for NaCl by one of the present authors[4] and has been used successfully by Gilman[3] for his study of zinc. The same method is used here for the observations concerning the kinetics of the phenomenon.

Polygonization of NaCl has been observed previously by means of X-rays[5] and by means of etchpits.[6] No systematic study of the geometry of polygonization has so far been made by the use of decoration methods, although occasionally polygonized structures have been observed.[7] The purpose of this paper is to present the results of such observations in NaCl, KCl and KBr as well as the results of a study of the kinetics of polygonization in NaCl.

GEOMETRICAL ASPECTS

(a) *Methods of observation*

The methods of decoration have been described previously.[7,8] They essentially consist in doping the crystal during growth from the melt with 0.75 wt.% of AgCl or AgBr according to the type of alkali halide.

* Received March 15, 1959; revised July 15, 1959.

† Laboratorium voor Kristalkunde, Rozier 6, Gent, Belgium. Now at S.C.K., Mol-Donk, Belgium.

‡ S.C.K., Mol-Donk, Belgium.

The decoration of the dislocations is then achieved by an anneal in hydrogen.

The method is well suited for the study of annealing structures as it is already inevitably accompanied by an annealing treatment. If the total annealing time is larger than the anneal required for decoration, a heat treatment in air precedes the decoration heat treatment. The decoration consists of small silver particles which can be observed in ultramicroscopic illumination.

For the study of the first stages of polygonization use has been made of a method described more recently.[9] The crystal is now doped with 0.4 per cent of $AgNO_3$ by weight addition to the melt, and decoration is achieved by X-irradiation during 3–4 hr by means of a copper target X-ray tube operated at 40 kV, 20 mA, the specimen being placed on the window, followed by an anneal in air of 1 hr at 500°C. This method leaves the dislocation pattern undisturbed as could be proved by showing that small dislocation half loops are maintained in the crystal. In this case the decoration is due to small cavities containing the gaseous decomposition products of the NO_3^- group.[10]

VOL. 8 1960

(b) *Preparation of specimens*

The specimens are cleaved parallelopipeds from a large crystal of KCl, KBr or NaCl, grown by the Czochralski method. The specimens are bent under a water film to a radius of curvature of 30 mm, and they are then annealed for various times. For the short annealing periods the annealing time is at the same time used for decoration.

(c) *Results*

(i) *Specimens deformed on a single glide system.* The glide systems in the NaCl structure are of the type $(a/2)[110], (1\bar{1}0)$. Usually two systems with glide planes parallel to the axis of bending are active at the same time. The outer regions of the crystal are however very often deformed on one system only. It very often happens that the regions on both sides of the neutral plane are deformed on a different glide system; this then gives rise, after annealing, to the "chevron" structure, as shown e.g. in Fig. 1.

The very first stage of polygonization consists of course in a rearrangement of the dislocations in their glide plane. To illustrate this we refer to Fig. 2. In this particular case the crystal was not bent, but indented somewhere in the left bottom corner. The traces of the glide planes are parallel to the largest dimensions of the photograph. Focussing deeper into the crystal tells us that the dislocations are inclined at an angle of about 45° with respect to the observation plane. They are further found to be still in their glide planes. We assume therefore that the dislocations were in the observed configuration immediately after deformation. The photograph shows that the dislocations have a definite tendency to adopt positions "one on top of the other" which is their equilibrium position. The first stage in polygonization in KCl therefore takes place already at room temperature; this was also confirmed by means of etching.

We will now illustrate successive stages in the formation of domain walls during increasing annealing periods. The annealing temperature is always 700°C ± 10°C; the annealing periods were 2 hr, 4 hr, 8 hr and 12 hr.

Typical regions of these crystals are represented in the series of photographs, Figs. 3–6; the plane of the photograph is perpendicular to the bending axis, dots represent dislocation lines intersecting the plane of observation. After annealing at higher temperatures the dislocations are very nearly perpendicular to the plane of observation: they have nearly pure edge



FIG. 1. Polygonized structure of NaCl (doped with AgCl), bent about an axis normal to the plane of the photograph. ×150

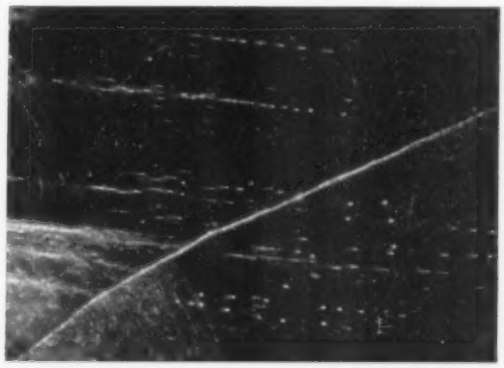


FIG. 2. Crystal of KCl (doped with $AgNO_3$) deformed by indentation in the left bottom corner. ×400

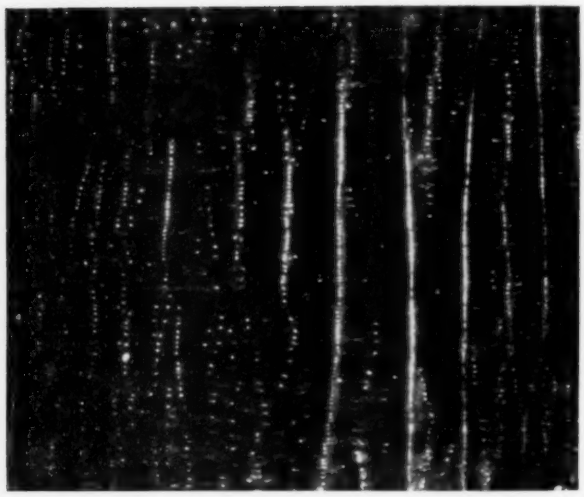


Fig. 3.

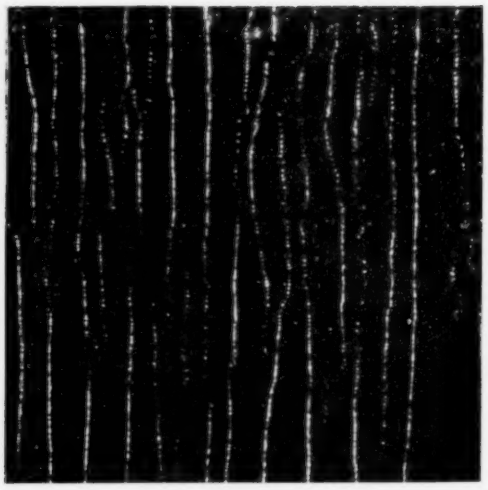


Fig. 4.

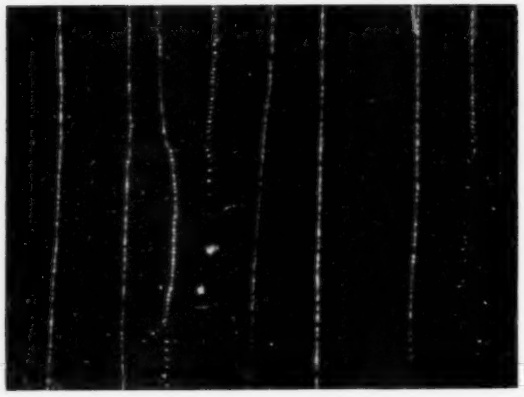


Fig. 5.

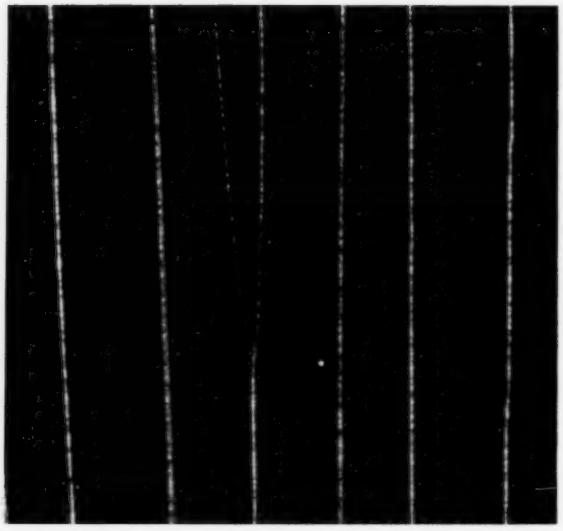


Fig. 6.

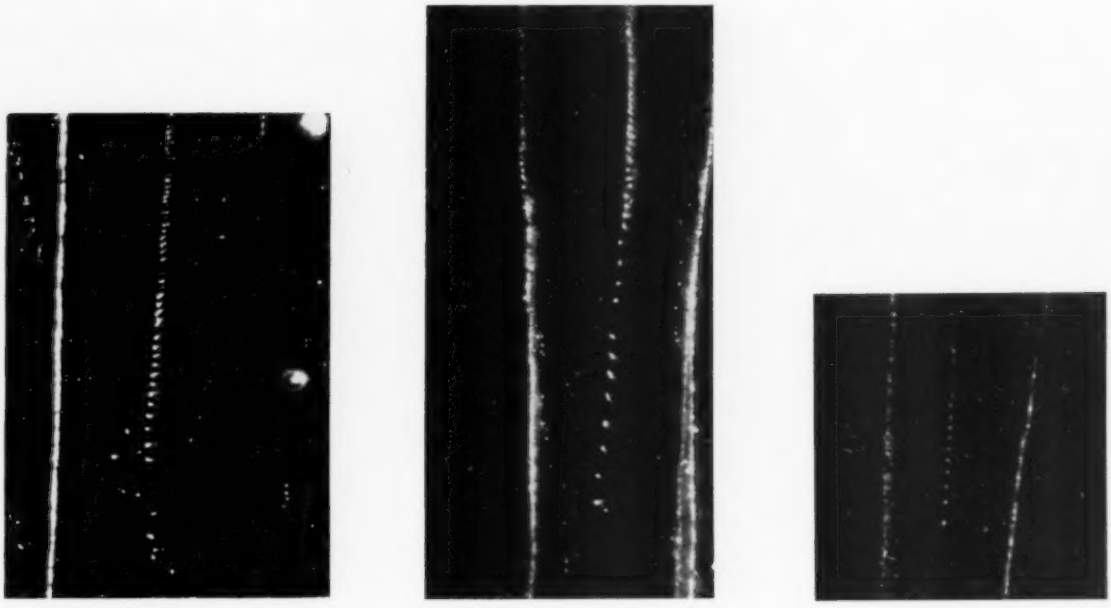
FIGS. 3–6. Crystals of KCl (doped with AgCl), bent to a radius of 3 cm and annealed for respectively 2, 4, 8 and 12 hr. ×600

character. The photographs represent at the same time the typical configurations which illustrate the way in which domains coarsen.

These characteristic features are those already described earlier for silicon iron[1,2] and zinc[3]: the *Y*-junctions and the semi-infinite walls. We find that in the polygonization of alkali halides the initial stage is characterized by the frequent occurrence of semi-infinite walls (see Fig. 7a,b,c); in the latter stages the *Y*-junctions become more important.

It is easy to visualize how the semi-infinite walls are generated in the crystal. If the number of dislocations in parallel glide planes, immediately after deformation, differs, one gets a situation as shown in Fig. 8. The first effect of the annealing will now be a rearrangement in the glide planes, and in the given situation this will give rise to a configuration as shown in Fig. 8(b); it is clear that a semi-infinite wall results.

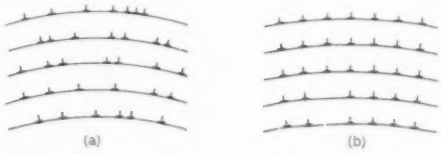
The behaviour of the semi-infinite walls under an annealing treatment has been considered by Friedel[11]. Due to the mutual repulsion of dislocations in the wall the dislocations will be induced to climb. As the top dislocation is subject to a stress field due to all other dislocations, it will climb the greatest distance; the following dislocation will climb less as it is subject



(a) (b) (c)

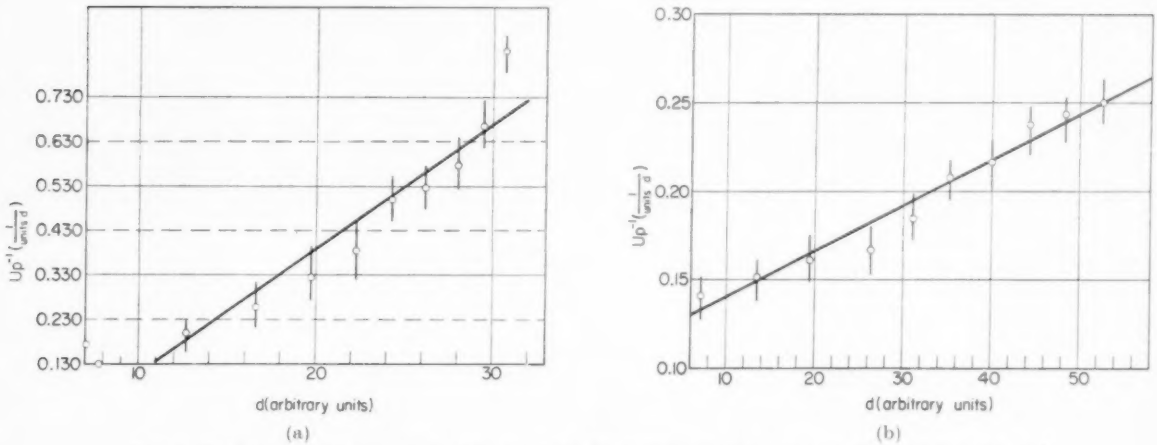
FIG. 7. Semi-infinite dislocation walls. Note the regular variation in spacing. ×600

VOL. 8 1960



(a) (b)

FIG. 8. The generation of semi-infinite walls (a) immediately after bending (b) after rearrangement.

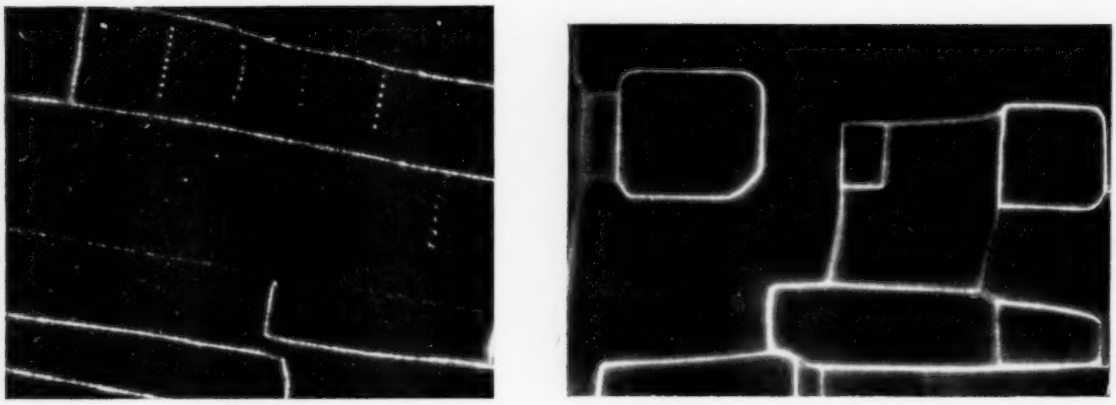


(a) (b)

FIG. 9. Relationship between u_p and d_p (u_p = distance between dislocations with index p and $p+1$; d_p = distance of dislocations with index p from leading dislocation).

to the back stress of the first and to the stress field of all following dislocations. The resulting rearrangement will produce a configuration where distances between dislocations gradually increase towards the end of the wall. The distances between successive dislocations u_p have been measured on enlarged photographs. Friedel's interpretation leads to a linear relationship between $1/u_p$ (u_p-distance between dislocations with index p and $p+1$) and d_p (distance of dislocation with index p from the leading dislocation). This is approximately verified by our observation, as shown by Fig. 9(a,b).

(ii) *Specimens deformed on two glide systems.* We



(a) (b)

FIG. 10. (a) Intersecting dislocation walls. Note the depletion in the region adjacent to the wall with large orientation difference. (b) Intersecting high angle walls. ×600

will now consider the geometrical configurations characteristic for specimens deformed on two glide systems with mutually perpendicular Burgers vectors. Mutually perpendicular dislocation walls then usually form. At some intersection points a small section of asymmetrical tilt boundary is formed: this is usually the case when the two intersecting tilt boundaries have comparable angles of misorientation. Examples of this are shown in Ref. (7): one example is also visible in Fig. 10(b).

The behaviour is somewhat different if the two intersecting tilt boundaries have very different misorientation angles. The boundary which has the smallest tilt angle then usually ends some distance from the intersection point (Fig. 10a). In a few cases



FIG. 11. The interaction of a single edge dislocation with a wall of edge dislocations. ×600

this may be due to a lack of decoration: the boundary acting as a sink of impurities and vacancies may drain its neighbourhood and prevent decoration. In the cases shown (Fig. 10a), this is however not the case.

To explain this behaviour, we consider the interaction of a single edge dislocation with a wall of edge dislocations of the kind shown in Fig. 11. This calculation is given in the appendix. From this calculation it is clear that the dislocation A will be induced to climb towards the wall XY, and as moreover the end dislocation of the finite wall UV is repelled by all the others of that wall, this dislocation will be taken up into the wall XY, which then becomes slightly asymmetrical. This mechanism is shown schematically in Fig. 12. The width of the region which is in this way depleted of dislocations will depend upon the angle of misorientation of the boundary XY. The larger this angle the smaller the region of influence: this explains the difference in behaviour between the two ends of a finite wall as visible e.g. in Fig. 10(a).

(d) *Interaction of walls with pre-existing subboundaries*

Whereas certain pre-existing subboundaries are crossed without any visible interaction by newly formed walls, this is not always the case and very often zig-zag shaped subboundaries result as visible in Figs. 13 and 14. As a consequence of "double decoration"[12] both the original position of the subboundary and the final position can easily be recognized.

The straight lines correspond to the original position of the subboundary, the zig-zag lines indicate the final position. The interaction may be pictured as in Figs. 15 and 16.

We now discuss these two cases separately. In

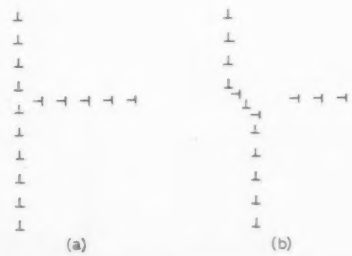


FIG. 12. The formation of a slightly asymmetrical part in a wall.

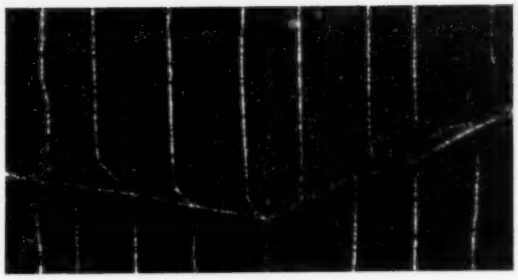


Fig. 13.

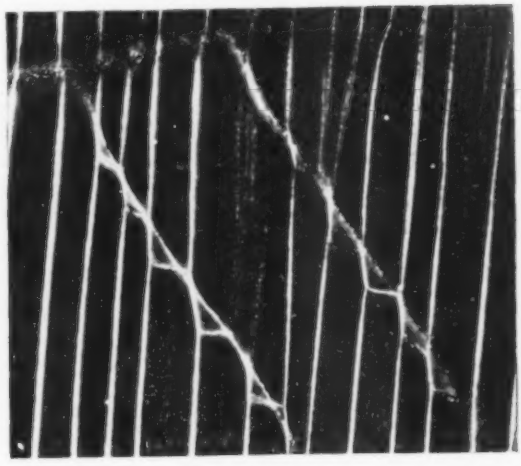


Fig. 14.

FIG. 13 and 14: Interaction of polygonization wall with pre-existing subboundary. ×400

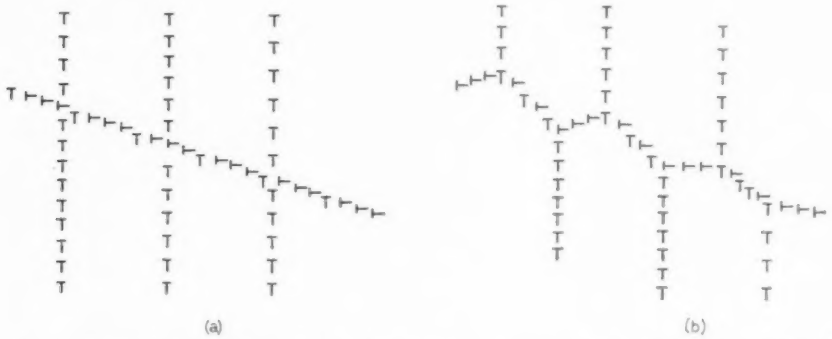


FIG. 15. Formation of zig-zag shaped boundary as a consequence of the interaction of polygonization walls and a pre-existing boundary. The original boundary contains a number of dislocations of the same sign with respect to dislocations in the wall.

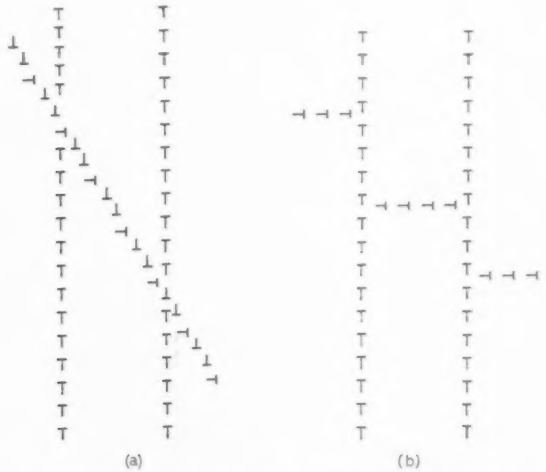


FIG. 16. Formation of zig-zag shaped boundary as a consequence of the interaction of polygonization walls and a pre-existing boundary. The original boundary contains a number of dislocations of opposite sign with respect to the dislocations in the wall.

VOL. 8 1960

the first example, shown in Fig. 14, the original boundary contains a number of dislocations of a sign opposite to the sign of the dislocations forming the polygon wall. Anneal now results in a mutual annihilation of dislocations of opposite sign. The resulting situation is pictured in Fig. 16(b), while the original configuration was as shown in Fig. 16(a).

The second possibility is pictured in Fig. 15: here the original subboundary contains dislocations of the same sign as those of the intersecting walls. Mixed sections of subboundary now result and the configuration of 15(b) is formed. An observed example is shown in Fig. 13. Double decoration has again revealed the original position of the subboundary (the straight lines) and the final shape (zig-zag lines).

KINETICS

(a) *Experimental methods*

To derive the activation energies of the process we measured the growth rate of the polygon domains at different temperatures, for the same radius of curvature of specimens. The specimens were prepared in the following way: Small cleavage parallelopipeds of $25 \times 10 \times 4$ mm were all bent to the same radius of curvature (30 mm) by pressing them against a cylindrical metal piece of this radius. The specimens were wet during the deformation and the metal piece was covered with wet filter paper as well, in order to minimize damage to the crystal. It should be noted that all specimens were cleaved from the same crystal, grown in this laboratory by the Czochralski method. Batches of ten specimens were then annealed in air for various time intervals and at different temperatures. After cooling they are cleaved following a plane parallel to the axis of bending: the cleavage plane has then polygonal character and the domains can be observed in reflected light. The method of observation is the Françon method of phase contrast in polarized light.[13] This method "translates" orientation differences into colour differences. The cleavage plane is thus seen as a set of parallel strips of different colour. Photographs are taken and the mean width of the domains is deduced for every batch of specimens.

The isothermal growth rate curves are plotted in Fig. 17. Vertically is plotted the mean orientation difference between walls which is deduced from the mean width of domains. Horizontally we plot the logarithm of time. It is readily visible that the curves level off for long annealing times, the more rapidly the higher the temperature. The slope of the initial rectilinear part is used to derive the growth rate.

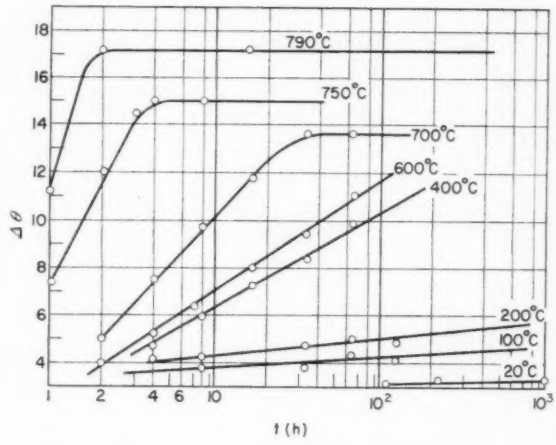


FIG. 17. Isothermal domain growth curves for NaCl.

The log of the growth rate $d\theta/dt$ versus the reciprocal of temperature is plotted in Fig. 18. It is clear that the curve consists of two rectilinear parts with a break corresponding to a temperature of 375°C. The corresponding activation energies for the two parts of the curve are respectively 49 kcal/mol at low temperatures and 30 kcal/mol at high temperatures. Gilman[3] found similarly two different activation energies at high and low temperatures for zinc.

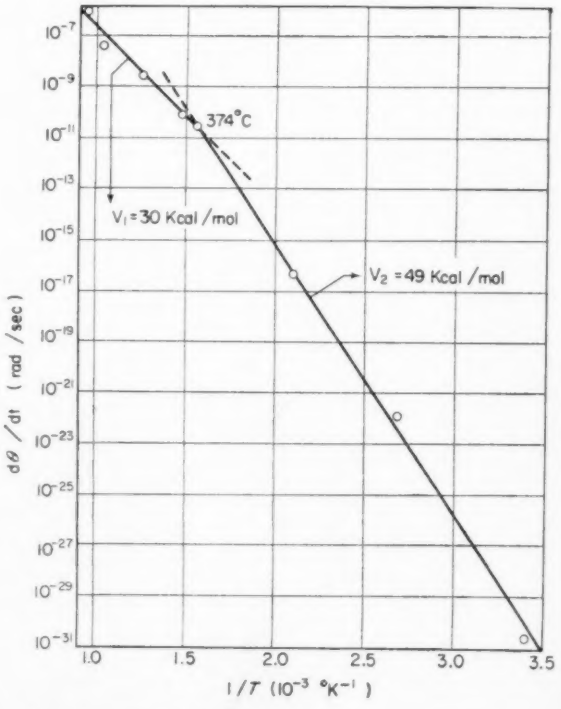


FIG. 18. Plot of the log of growth rate versus the inverse of temperature.

(b) *Discussion of the kinetics*

According to Mott[14] and Friedel[11] we can use the polygonization data to obtain the energy of jog formation U_{fj} by the use of two procedures:

(i) the difference in activation energy at temperatures above and below the break gives directly the quantity U_{fj}; $U_{fj} = 19$ kcal/mol $= 0.8$ eV.

(ii) the quantity U_{fj} is given by the formula

$$U_{fj} = kT_c \ln (l/b)$$

where T_c is the temperature at the break in the curve and l is the size of the domains at that temperature. Substituting for T_c 647°K and $l = 2 \cdot 10^{-3}$ cm, gives $U_{fj} = 13.4$ kcal/mol $= 0.6$ eV.

It is clear that in our case the correspondence of the two values is not too unsatisfactory. This was not the case for zinc, using Gilman's data, and Friedel[11] showed that the jog energy differs by a factor of 2 according to the method used to derive it.

For the activation energy in the high temperature range we find 30 kcal/mol which is to be compared with the activation energy deduced from conductivity measurements.

It is clear that a direct comparison is difficult as this activation energy depends on the impurity contents of the specimens; values of 20.600 cal/mol and 47.200 cal/mol, respectively, for low and high temperature range are given in the literature. Measurements made in this laboratory of the ionic conductivity of NaCl specimens, prepared in the same circumstances, indicated that almost for the entire range of temperatures used in the polygonization experiments, impurity conductivity prevails. The value of 30 kcal/mol found here from the polygonization data is therefore not unreasonable.

Taking into account line energy only and considering the jog as a small segment of dislocation line, its energy can be estimated as $0.1\ \mu\ b_1{}^2 b_2$,[11] where b_1 is the Burgers vector and b_2 the "length" of the jog. One can now consider two kinds of jogs; neutral ones with $b_2 = a\sqrt{2}$ or charged ones with $b_2 = a/2$ or $a/2\sqrt{2}$. The value computed on the assumption of a neutral jog and taking $\mu = 1500$ kg/mm^2 fits best the observed value. The measurements therefore suggest that the majority of jogs is probably neutral. This may be due to the fact that dissociating a neutral jog into two oppositely charged jogs requires an extra amount of energy, due to coulomb interaction.

ACKNOWLEDGMENTS

We wish to thank Professor W. Dekeyser for his continuous interest and useful discussions. This work is part of a research programme supported by I.R.S.I.A. (Institute pour l'encouragement de la Recherche Scientifique dans l'Industrie et l'Agriculture; Comité d'etude de l'Etat Solide) and by S.C.K. (Studiecentrum voor Kernenergie). We are also indebted to Dr. J. Goens, Director of S.C.K., for permission to publish these results.

REFERENCES

1. G. G. Dunn and W. R. Hibbard, *Acta Met.* **3**, 409 (1955).
2. W. R. Hibbard and G. G. Dunn, *Acta Met.* **4**, 306 (1956).
3. J. J. Gilman, *Acta Met.* **3**, 277 (1955).
4. S. Amelinckx, *Nature, Lond.* **173**, 993 (1954).
5. S. Konobejevsky and I. Mirer, *Z. Kristallogr.* **81**, 69 (1932).
6. S. Amelinckx, *Acta Met.* **2**, 848 (1954).
7. S. Amelinckx, in *Dislocations and Mechanical Properties of Crystals* (Eds. J. C. Fisher, W. G. Johnston, R. Thomson and T. Vreeland, Jr.). Wiley, New York (1957).
8. W. van der Vorst and W. Dekeyser, *Phil. Mag.* **1**, 882 (1956).
9. S. Amelinckx, *Phil. Mag.* **3**, 653 (1958).
10. S. Amelinckx, W. Maenhout-van der Vorst and W. Dekeyser, *Acta Met.* **7**, 8 (1959).
11. J. Friedel, *Les dislocations*. Gauthiers-Villars, Paris (1956).
12. S. Amelinckx, *Acta Met.* **6**, 34 (1958).
13. M. Françon, *Rev. Opt. (théor. instrum.)* **31**, 65, 170 (1952).
14. N. F. Mott, *Proc. Roy. Soc.* A **220**, 1 (1954).
15. J. M. Burgers, *Proc. Akad. Sci. Amst.* **42**, 293 (1939).
16. A. H. Cottrell, *Dislocations and Plastic Flow in Crystals* p. 98. Clarendon Press, Oxford (1953).
17. F. R. N. Nabarro, *Adv. Phys.* **1**, 271 (1952).

APPENDIX

In this appendix we describe, in some more detail than has been done previously, the interaction of isolated dislocations with a wall of edge dislocations.

The stress component $\sigma_{xy}{}^b$ due to an infinite wall of edge dislocations has been calculated by Burgers[15]; the other components can be found in the same way by summation over all dislocations in the wall.[16] The results are given by the equations:

$$\sigma_{xy}{}^b = \frac{D\pi^2 x \cosh 2\pi q \cos 2\pi p - 1}{2h^2 \quad (\sinh^2 q\pi + \sin^2 p\pi)^2} \tag{1}$$

$$\sigma_{xx}{}^b = -\frac{\pi D}{2h} \frac{q\pi \sinh^2 q\pi + \sin^2 p\pi + \sinh^2 q\pi}{(\sinh^2 q\pi + \sin^2 p\pi)^2} \sin 2\pi p \tag{2}$$

$$\sigma_{yy}{}^b = -\frac{\pi D}{2h} \frac{\sin^2 p\pi + \sinh^2 q\pi - q\pi \sinh^2 q\pi}{(\sinh^2 q\pi + \sin^2 p\pi)^2} \sin 2\pi p \tag{3}$$

where $D = b\mu/2\pi(1 - \nu)$
$h =$ distance between dislocations in the wall
$p = y/h$
$q = x/h$.

The signs of these stresses in the neighbourhood of the wall are represented in Figs. 19 and 20, which shows also the lines along which the stresses vanish. From these diagrams it is easy to deduce the sign of the force to which an isolated edge dislocation is subject.

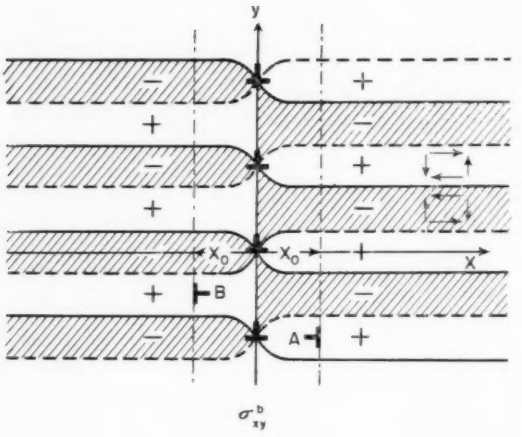
(a) *Edge dislocations of the same Burgers vector as those of the wall*

(i) *Same sign.* From Fig. 19(a) it is clear that dislocations will tend to glide towards the wall in the cross hatched region, whilst they will be repelled in the other regions. This was already discussed in a quantitative way by Nabarro[17]. The component of force in the glide plane is given by $F_x = b\,\sigma_{xy}{}^b$.[4]

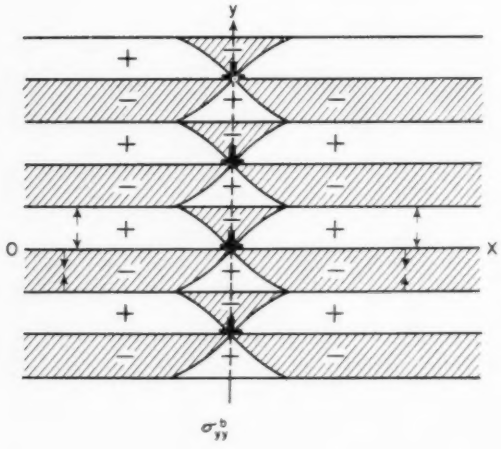
If climb is an allowed procedure one has however also to take into account that the dislocation is subject to a force perpendicular to the glide plane given by $F_y = -b\,\sigma_{xx}{}^b$[5] and which induces climb.

From Fig. 20 it is clear that the sign of this force is such

VOL. 8 1960



(a)



(b)

FIG. 19. (a) The stresses $\sigma_{xy}{}^b$ due to the boundary.
(b) The stresses $\sigma_{yy}{}^b$ due to the boundary.

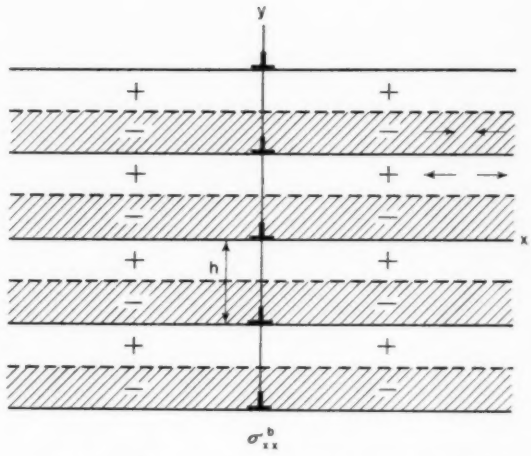


FIG. 20. The stress $\sigma_{xx}{}^b$ due to the wall of edge dislocations.

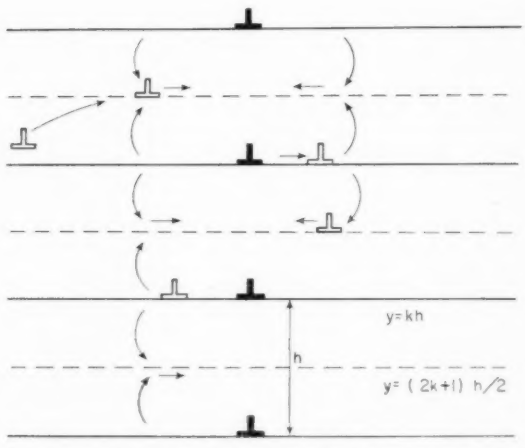


FIG. 21. Paths followed by isolated edges, during their migration towards the wall.

that it tends to bring the edge dislocation into the planes $y = (2k + 1)\, h/2$ in which they can glide off towards the wall. Consequently, all edge dislocations in the region adjacent to the boundary will finally be taken up into the boundary. The paths the dislocations will follow during anneal are schematized in Fig. 21.

(ii) *Opposite sign*. The dislocations will now be repelled in the cross hatched regions of Fig. 19(a) and attracted in the others. From Fig. 19(b) it is clear, on the other hand, that they will be induced to climb towards the planes $y = hk$ in which they are attracted towards the wall. They will finally be annihilated by a dislocation of the wall.

(b) *Edge dislocations having a Burgers vector perpendicular to the one of the dislocations in the wall*

(i) *Positive dislocations* (Fig. 19(a), dislocation *A*). The equilibrium positions with respect to glide are given by the intersection points of the curve represented by a solid line and the glide plane; the magnitude of the force causing glide is $F_y = b\, \sigma_{xy}{}^b$. In these positions the dislocations are however subject to a force in the x-direction $F_x = b\sigma_{yy}{}^b$ and which induces them to climb towards the wall Fig. 19(b). Both force components vanish, near to the dislocation in the wall, on a line forming an angle of 45° with the glide plane, which is such that regions of compression and dilatation overlap. The result is again that dislocations in the neighbourhood of the wall will be pulled into the wall, which now however acquires asymmetrical character.

(ii) *Negative dislocations* (Fig. 19(a), dislocation *B*). The same considerations as above apply apart from a change in the sign of the forces; the dotted lines now represent equilibrium positions for glide in Fig. 19(a).

LONG-RANGE ORDER IN Fe RICH Fe–Al ALLOYS—I

A ZEROTH APPROXIMATION CALCULATION OF ORDER WITH APPLICATION TO THE PHASE DIAGRAM*

P. S. RUDMAN†

It is shown that a quasi-chemical description of long-range order in Fe rich Fe–Al alloys requires two independent order parameters and at least second neighbour bonding. Using the zeroth approximation, the defining equations for order are obtained. The transformation temperature consequences of the calculation are employed in evaluating experimental data and a revised version of the Fe–Al phase diagram is arrived at. It is shown that for compositions greater than 25 at.% Al the onset of Fe_3Al type order is well approximated by the independent ordering of a simple cubic lattice to a NaCl structure but at an effective composition depending on the perfection of the FeAl type order. From the experimental values of the transition temperatures at the composition Fe_3Al it is calculated that the ratio of the second to the first neighbour interchange energies is about one half.

ORDRE A GRANDE DISTANCE DANS LES ALLIAGES Fe–Al RICHES EN FER—I
CALCUL DE L'ORDRE PAR APPROXIMATION DE ZERO EN VUE DE L'APPLICATION AU DIAGRAMME DE PHASE

L'auteur montre que la description quasi-chimique de l'ordre à grande distance dans les alliages Fe-Al riches en fer exige deux paramètres d'ordre indépendants et à tout le moins des liaisons avec le deuxième voisin. En utilisant une approximation de zéro, il établit les équations relatives à un tel ordre. Les conséquences sur la température de transformation d'un tel calcul, sont comparées aux données expérimentales. L'auteur établit ainsi une version modifiée du diagramme de phases Fe-Al. Pour les alliages contenant plus de 25% at. d'aluminium, l'apparition d'un ordre du type Fe_3Al peut être interprétée, sur la base d'une structure du type NaCl, par la formation d'un ordre indépendant dans un réseau cubique simple. Il faut cependant considérer dans ce cas que la composition effective de l'alliage où se produit un tel ordre dépend de la perfection de l'ordre du type FeAl. Sur la base des valeurs expérimentales des températures de transition pour le composé Fe_3Al, onpeut calculer le rapport des énergies d'échange entre le premier et le deuxième voisin; ce rapport est voisin de $\frac{1}{2}$.

FERNORDNUNG IN FE-REICHEN FE-AL-LEGIERUNGEN—I
BERECHNUNG DER ORDNUNGSEINSTELLUNG IN NULLTER NÄHERUNG MIT ANWENDUNG AUF DAS PHASEN-DIAGRAMM

Eine quasi-chemische Beschreibung der Fernordnung in Fe-reichen Fe-Al-Legierungen erfordert zwei unabhängige Ordnungsparameter und Bindungen bis mindestens zu Nachbarn zweiter Ordnung. Die bestimmenden Gleichungen für die Ordnung werden in nullter Näherung angegeben. Die Schlüsse, die die Rechnung auf die Umwandlungstemperatur ziehen läßt, werden bei der Verwertung experimentellen Materials benutzt, es ergibt sich ein geändertes Fe-Al-Phasendiagramm. Für Zusammensetzungen mit mehr als 25 % Al läßt sich das Einsetzen der Ordnung vom Fe_3-Al-Typ durch folgendes Modell gut annähern: Ein einfach kubisches Gitter ordnet sich unabhängig zur NaCl-Struktur, doch hängt die effektive Zusammensetzung vom Grad der Ordnung des Typs FeAl ab. Aus den experimentellen Werten der Übergangstemperaturen bei der Zusammensetzung Fe_3Al läßt sich berechnen, däß das Verhältnis der Wechselwirkungsenergien von Nachbarn zweiter und erster Ordnung etwa einhalb beträgt.

VOL. 8 1960

1. INTRODUCTION

The Fe rich Fe–Al alloys exhibit two types of ordering, the FeAl type and the Fe_3Al type. To describe both types of order with common parameters we divide the structure into four interpenetrating face-centered cubic lattices related to the origin by translations: [000], $[\frac{1}{4}\,\frac{1}{4}\,\frac{1}{4}]$, $[\frac{1}{2}\,\frac{1}{2}\,\frac{1}{2}]$ and $[\frac{3}{4}\,\frac{3}{4}\,\frac{3}{4}]$. However, we will assume that the compositions of the 000 and the $\frac{1}{2}\,\frac{1}{2}\,\frac{1}{2}$ lattices are always identical (such is the indication of the available experimental evidence). Let us call the 000 plus the $\frac{1}{2}\,\frac{1}{2}\,\frac{1}{2}$ lattice sites α sites, the $\frac{1}{4}\,\frac{1}{4}\,\frac{1}{4}$ lattice sites β sites and the $\frac{3}{4}\,\frac{3}{4}\,\frac{3}{4}$ lattice sites γ sites. These definitions are illustrated in Fig. 1. For FeAl type order the β and γ lattices are identically occupied. For Fe_3Al type order, Fe atoms preferentially occupy the α and β sites and Al atoms the γ sites. For disorder the α, β and γ lattices are identically occupied.

To sum up in more general terms, the definitions for describing the ordering found in the Fe rich Fe–Al alloys, we consider a binary system of A and of B species of atoms in the composition range 0–50 per cent of B. We define the overall alloy composition

* Received May 12 1959. Part of this work has been sponsored by the Wright Air Development Center of the Air Research and Development Command, USAF through its European Office under Contract No. AF 61(052)-122.

† Department of Physics, Israel Institute of Technology, Haifa, Israel.

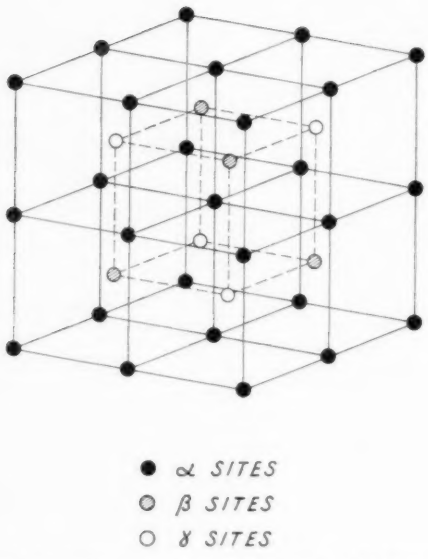


FIG. 1. Lattice sites for ordering in Fe–Al alloys.

as the number of B atoms divided by the total number of atoms and represent this by x. We define the composition of a particular lattice as the number of B atoms on the particular lattice divided by the total number of lattice sites of the particular lattice and let $[\alpha]$, $[\beta]$ and $[\gamma]$ represent the composition of the α, β and γ lattices respectively. For disorder we have:

$$[\alpha] = [\beta] = [\gamma] = x$$

For FeAl type order we have:

$$[\alpha] \neq [\beta] = [\gamma]$$

but as $x \to 0.5$ and T (temperature) $\to 0$

$$[\alpha] \to 0, \text{ and } [\beta] = [\gamma] \to 1$$

For Fe_3Al type order we have:

$$[\alpha] \neq [\beta] \neq [\gamma]$$

but as $x \to 0.25$ and as $T \to 0$

$$[\alpha] \to [\beta] \to 0; \quad [\gamma] \to 1.$$

It is of interest to notice that the β and γ lattices form a NaCl structure. The transformation Fe_3Al order to FeAl order is thus represented as

$$[\alpha] \neq [\beta] \neq [\gamma] \to [\alpha] \neq [\beta] = [\gamma].$$

To the extent that $[\alpha]$ is constant during the transformation, this change of order is equivalent to the disordering of a NaCl structure and is thus apparently the only known example of disordering of a simple cubic lattice and is thus of unique theoretical interest. We shall see later that for $x > 0.25$ the constancy of $[\alpha]$ during this transformation is to be expected.

2. DEFINITIONS OF ORDER PARAMETERS

We will consider here, in general terms, the number of independent parameters necessary to describe order in a multicomponent system. This treatment follows closely that of Wojciechowski[1]. We assume that the structure may be divided into l interpenetrating lattices and that there are n species of atoms.

Each lattice we denote by $i : i := 1, 2, \ldots l$

Each specie we denote by $j : j := 1, 2, \ldots n$.

Consider a_{ij} = number of species j on lattice i. Assuming all the lattice sites to be occupied, we then must have:

l equations of the type $\sum_j a_{ij} = N_i$ = number of lattice sites of type i, and n equations of the type $\sum_i a_{ij} = N_j$ = number of atoms of species j; but these $n + l$ equations are interdependent by the relation:

$$\sum_i N_i = \sum_j N_j = N$$

= total number of atoms = total number of lattice sites. We thus have nl unknowns (the a_{ij}'s), $n + l - 1$ independent equations and hence the number of independent order-parameters is:

$$F = nl - (n + l - 1) = (n - 1)(l - 1).$$

The description of order in Fe rich Fe–Al alloys thus requires two independent order parameters ($n = 2$, $l = 3$). Of the three order parameters, $[\alpha]$, $[\beta]$ and $[\gamma]$, only two are independent. The interelation we can simply obtain.

Assuming

N_α = number of α lattice sites,

N_β = number of β lattice sites,

N_γ = number of γ lattice sites, then

$[\alpha] N_\alpha + [\beta] N_\beta + [\gamma] N_\gamma = xN$ = number of B atoms

$N_\alpha + N_\beta + N_\gamma = N$ = number of lattice sites

but since $N_\alpha = 2N_\beta = 2N_\gamma = \frac{1}{2}N$, thus

$$2([\alpha] - x) + ([\beta] - x) + ([\gamma] - x) = 0.$$

This last equation gives the interdependence of the order parameters. Long-range order is generally described by the Bragg–Williams parameter S. For most of the structures for which the long-range order has been measured, stoichiometric compositions and with only one independent order parameter, the definition of this parameter may be made in either of two equivalent ways:

(1) $S = 1$ for perfect order, $S = 0$ for disorder and S = linear function of the lattice population numbers.

(2) In X-ray or neutron or electron diffraction from an ordered lattice: $S^2 = K\frac{I_{ss}}{I_f}$

where I_{ss} = integrated intensity from a superstructure line

I_f = integrated intensity from a fundamental line

K = constant independent of the degree of order.

For non-stoichiometric composition there is no standard method of definition and one may refer to Fowler and Guggenheim[2], Cowley[3] or Jaumot and Sutcliffe[4] for alternative choices. It will be necessary here to define two parameters and convenient choices are:

$$S_{11} = 2(x - [\alpha])$$

$$S_{31} = ([\gamma] - x) - ([\beta] - x) = 2([\alpha] + [\gamma] - 2x).$$

These definitions have the properties that

for perfect FeAl order:

$S_{11} = 1$ (i.e. at 0.5 Fe–0.5 Al);

for perfect Fe_3Al order:

$S_{31} = 1$ (i.e. at 0.75 Fe–0.25 Al);

for FeAl type order:

$S_{31} = 0$;

for perfect disorder:

$S_{11} = S_{31} = 0$;

for superstructures reflections common to both FeAl and Fe_3Al:

$$S_{11}^2 = K\frac{I_{ss}}{I_f};$$

for superstructure reflections common to Fe_3Al only:

$$S_{31}^2 = K\frac{I_{ss}}{I_f}.$$

At arbitrary composition, maximum FeAl type order is no B's on the α lattice; and maximum Fe_3Al type order is no B's on the α lattice and the maximum number of B's on the γ lattice. Under these conditions the S's take the following values: for FeAl type order, S_{11} max $= 2x$, $S_{31} = 0$; and for Fe_3Al type order, S_{11} max $= 2x$, S_{31} max $= 4x$ (for $x < 0.25$) and S_{31} max $= (1 - 4x)$ (for $x > 0.25$).

3. THE ENERGY OF Fe–Al ALLOYS ACCORDING TO QUASI-CHEMICAL BOND THEORY

A simple approach to the calculation of the internal energy of a solid solution is to attribute the energy to pair type chemical bonds. In a binary system these will be A–A, B–B and A–B where the bond energies E_{AA}, E_{BB} and E_{AB} are generally assumed to be independent of composition, temperature and order but to be a function of the distance between the sites of the interacting pair. The energy is generally assumed to be such a rapidly decreasing function of intersite distance that interactions between second and farther distant neighbours can be neglected.

We note that in Fe–Al alloys, the first neighbour interactions are either of the form α–β or α–γ. Thus when only first neighbour interactions are considered, the surroundings of a β site is identical to that of a γ site and hence there is no reason for $[\beta] \neq [\gamma]$. But $[\beta] = [\gamma]$ implies FeAl type order and hence we conclude that for Fe_3Al order to exist we must introduce at least second nearest neighbours. Although third nearest neighbour interactions are not required for stability, since second neighbour interactions cannot be neglected with respect to the first, similarly we can expect third neighbour interactions not to be negligible with respect to the second, and hence we shall include first, second and third neighbour interaction energies.

We shall employ the zeroth approximation which assumes that the occupation probability of any lattice site depends only on the composition of the lattice. Letting E_{AA}, E_{AA}', E_{AA}'', etc., be the first, second and third neighbour bond energies, and

$$v_1 = E_{AB} - \frac{E_{AA} + E_{BB}}{2}, \; v_2 = E_{AB'} - \frac{E_{AA}' + E_{BB}'}{2}$$

and

$$v_3 = E_{AB}'' - \frac{E_{AA}'' + E_{BB}''}{2}$$

be the respective interchange energies, we obtain for the bonding energy due to first, second and third neighbour interactions, respectively:

$$E_1 = 4N\{(1-x)E_{AA} + xE_{BB} + [2x(1-x) + \tfrac{1}{2}S_{11}^2]v_1\}$$

$$E_2 = 3N\{(1-x)E_{AA}' + xE_{BB}' + [2x(1-x) + \tfrac{1}{4}(S_{31}^2 - 2S_{11}^2)]v_2\}$$

$$E_3 = 6N\{(1-x)E_{AA}'' + xE_{BB}'' + [2x(1-x) - \tfrac{1}{4}(S_{31}^2 + 2S_{11}^2)]v_3\}.$$

We note that E_1 is independent of S_{31} in agreement with our previous qualitative argument that first neighbour interactions only are incapable of causing Fe_3Al type order.

4. ENTROPY OF Fe–Al ALLOYS

The calculation of entropy involves solving the combinatorial problem of the number of ways the $(1 - x)$ A and x B atoms can be arranged on $\frac{N}{2}$ α

VOL. 8 1960

sites, $\frac{N}{4}$ β sites and $\frac{N}{4}$ γ sites for a given state of order. The exact solution of this problem has not as yet been given. We shall employ what has been called the Zeroth approximation.[2] According to this approximation we obtain for the entropy:

$$S = -\frac{R}{4}\{4\ln 2 + 2[\alpha]\ln[\alpha] + [\beta]\ln[\beta] + [\gamma]\ln[\gamma] + 2(1-[\alpha])\ln(1-[\alpha]) + (1-[\beta])\ln(1-[\beta]) + (1-[\gamma])\ln(1-[\gamma])\}$$

where: R = gas constant.

5. DERIVATION OF THE DEFINING FOR LONG-RANGE ORDER IN Fe–Al ALLOYS

The defining equations governing order are determined by minimizing the free energy, $F = E - TS$, with respect to the independent order parameters. It is convenient to obtain the definitive equations in the forms:

$$\frac{\partial F}{\partial S_{11}} - \frac{\partial F}{\partial S_{31}} = 0, \quad \text{and} \quad \frac{\partial F}{\partial S_{31}} = 0$$

which yield respectively:

$$(4v_1 - 3v_2 - 6v_3)\frac{4S_{11}}{kT} - (3v_2 - 6v_3)\frac{2S_{31}}{kT} + \ln\frac{2(1-x)+S_{11}}{2x-S_{11}}\cdot\frac{2x+(S_{11}-S_{31})}{2(1-x)-(S_{11}-S_{31})} = 0$$

$$(3v_2 - 6v_3)\frac{4S_{31}}{kT} + \ln\frac{2x+(S_{11}+S_{31})}{2(1-x)-(S_{11}+S_{31})} \times \frac{2(1-x)-(S_{11}-S_{31})}{2x+(S_{11}-S_{31})} = 0.$$

These equations must be solved either numerically or graphically to obtain S_{11} and S_{31}.

6. APPLICATION TO THE Fe–Al PHASE DIAGRAM

Even without explicit solution, several consequences concerning the phase diagram may be obtained from these equations. $S_{31} = 0$ is always a root and in this case we obtain

$$(4v_1 - 3v_2 - 6v_3)\frac{4S_{11}}{kT} + \ln\frac{2(1-x)+S_{11}}{2(1-x)-S_{11}} \times \frac{2x+S_{11}}{2x-S_{11}} = 0$$

This is the well known solution for the CsCl structure but taking into account next nearest neighbour interactions. It is also known that for this case the order–disorder transition is second order for all compositions and hence the criterion for the transition temperature is that the solution $S_{11} = 0$ goes from a minimum to a maximum at $T = T_c$. Thus $(\partial^2 F/\partial {S_{11}}^2) = 0$, $S_{11} = 0$ defines $T = T_c$ and we obtain

$$T_c = -4x(1-x)\frac{(4v_1 - 3v_2 - 6v_3)}{k}.$$

For the transition $\mathrm{Fe_3Al} \rightarrow \begin{cases}\text{FeAl or}\\ \text{disorder}\end{cases}$, if we *assume* that this is also a second order phase change, $(\partial^2 F/\partial {S_{31}}^2) = 0$, $S_{31} = 0$, defines $T = T_c'$ and we obtain

$$T_c' = -4(x + S_{11}/2)\left[(1-x) - \frac{S_{11}'}{2}\right]\frac{(3v_2 - 6v_3)}{k}$$

S_{11}' is simply obtained by solving for S_{11} at $T = T_c'$ in the previously given defining equation for the CsCl structure. We note that the effect of FeAl order on $\mathrm{Fe_3Al}$ order, provided that a second order transformation obtains, is simply to shift the composition of the $\beta + \gamma$ lattice from x to $x + S_{11}/2$.

The phase diagram shows that in the region $x < 0.25$ the transformation $\mathrm{Fe_3Al} \rightarrow$ disorder occurs. We can show that a second order $\mathrm{Fe_3Al} \rightarrow$ disorder transition is unlikely. For this to occur we must have $T_c = T_c'$ and $S_{11} = S_{31} = 0$. Using our equation for the critical temperatures we obtain $T_c = T_c'$ only when $v_1/v_2 = 3/2$.

We can generalize this result and conclude that a second order transformation in a multi-independent order parameter system that requires $(\partial^2 F/\partial S^2) = 0$ simultaneously for more than one independent order parameter is unlikely to occur. It is to be noted that Guttman[5] had concluded that the $\mathrm{Fe_3Al} \rightarrow$ disorder transformation was second order because of the rule that first order transformations occur only in close packed structures. We see that this rule must be restricted to systems where there is only one independent order parameter.

For $x > 0.25$, the phase diagram shows $T_c' \ll T_c$. In this case $S_{11} \rightarrow S_{11}\,\max = 2x$ for $T \leq T_c'$ and the defining equation for S_{31} approaches the form:

$$(3v_2 - 6v_3)\frac{4S_{31}}{kT} + \ln\frac{4x+S_{31}}{4x-S_{31}}\cdot\frac{2(1-2x)+S_{31}}{2(1-2x)-S_{31}} = 0$$

This obviously describes the disordering of a NaCl structure, a second order phase change, with a critical temperature

$$T_c' = -2x(1-2x)4(3v_2 - 6v_3)/k.$$

The existing experimental determinations of the Fe rich region of the Fe–Al phase diagram are not in

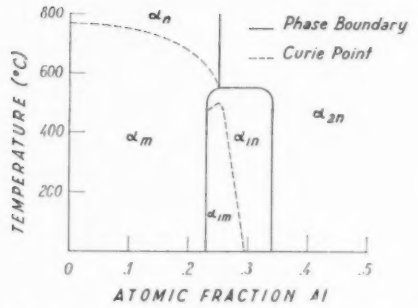


FIG. 2. Fe–Al phase diagram according to metals handbook.

agreement. However, on the basis of the previous results we can synthesize the available data and obtain a more reasonable and consistent phase diagram than presently exists.

Figure 2 presents the generally accepted phase diagram[6] and Fig. 3 a recent determination by the X-ray lattice parameter method due to Taylor and Jones[7].

The designation of phases is according to the Metals Handbook scheme[6]:

α = disorder b.c.c. n = non-ferromagnetic
α_1 = Fe_3Al type order m = ferromagnetic
α_2 = FeAl type order
(e.g. α_{1n} = non-ferromagnetic Fe_3Al type order).

The Metals Handbook version is admittedly only indicative of the phases present and their general relative position and is not to be taken at face value. The Taylor–Jones version[7] is the result of a meticulous X-ray lattice parameter study. However, the diagram as presented is inconsistent. There is no meaning to the existence of a Curie point boundary within a two phase field as they are present in the $\alpha_1 + \alpha_2$ field and in the $\alpha + \alpha_1$ field. The difficulty with their phase diagram interpretation of their data appears to be that for second order phase changes*

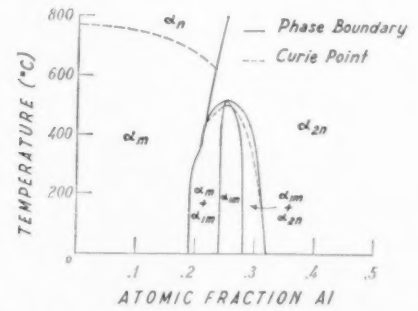


FIG. 3. Fe–Al phase diagram according to Taylor and Jones.

* As we have discussed previously we would expect the α_1/α_2 boundary to be for $x > 0.25$ and for Curie points.

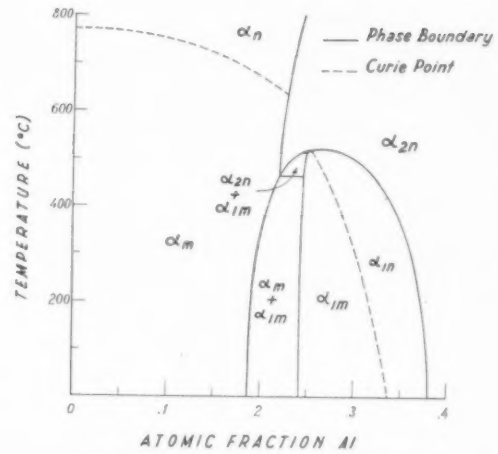


FIG. 4. Revised Fe–Al phase diagram.

the lattice parameter method does not give a sufficiently sharp presentation of a phase boundary. Accordingly, in Fig. 4 is presented a revised version of the Fe–Al phase diagram obtained by using the theory previously derived to weight the various experimental determinations.

Taylor and Jones' phase boundary is accepted for the boundary α/α_1, this being probably a classical phase change and hence amenable to the X-ray lattice parameter method. The α/α_2 boundary, though apparently a second order phase change as indicated both by theory and experiment, is also taken from Taylor and Jones. The α_1/α_2 boundary and the Curie points in the α_1 phase are taken from the thermal, electrical resistivity and magnetic measurements of Sykes and Evans[8]. The Curie points in the α phase are due to Parsons *et al.*[9] and their magnetic data is also consistent with the Taylor-Jones $\alpha/\alpha + \alpha_1$, boundary. The extent of the α_1 field (from the boundary $\alpha/\alpha + \alpha_1$ to α_1/α_2) at room temperature is also consistent with the X-ray measurements of Bradley and Jay[10].

The unappreciated existence of the two phase field, $\alpha + \alpha_1$, and the non-recognition of the formation of the Fe_3Al type order as being possibly of the normal "A prefers B" type but between second neighbours has had a very profound effect on order–disorder theory. Hume-Rothery and Raynor[11] and co-workers interpreting the Bradley and Jay[10] X-ray data in the $\alpha + \alpha_1$ region on the assumption of a single phase were led to view the ordering process as Al atoms (or solute atoms in general) maintaining the maximum distances from each other and this suggested the minimizing of strain energy as the driving force.

The assumption of homogeneity in the $\alpha + \alpha_1$

VOL. 8 1960

region led Bradley and Jay[10] to interpret their results as if the α and β sites were equivalent and Takagi[12] accepting this equivalence in his statistical theory of ordering obtained the result that Fe_3Al and Cu_3Au are governed by identical definitive equations.

Although the specification of the phase boundaries in the Fe–Al system still leaves much to be desired, they are in principle capable of very accurate determination. Referring to the analytical expressions obtained for the order–disorder transition temperature T_c and T_c', we note that the interchange energy combinations $(4v_1 - 3v_2 - 6v_3)$ and $(v_2 - 2v_3)$ are capable of determination from the experimental values of T_c and T_c'. Thus the combination of FeAl and Fe_3Al order appears to offer the further unique possibility of a measure of the range of bond energies from the positions of the phase boundaries. Since there are three unknowns v_1, v_2 and v_3 and only two independent experimental determinations, T_c and T_c', are available; some assumption must be made to estimate the v's:

Considering $v_2/v_1 = m$ and $v_3/v_1 = n$, we obtain for the ratio of the transition temperatures the relation:

$$\frac{T_c'}{T_c} = \frac{(x + S_{11}/2)(1 - x - S_{11}/2)}{x \qquad (1 - x)} \qquad \frac{3m - 6n}{4 - 3m - 6n}.$$

Using the experimental values of $x = 0.25$, $T_c = 1100°K$, $T_c' = 800°K$ and the calculated value $S_{11}' = 0.43$ we obtain:

$$\frac{3m - 6n}{4 - 3m - 6n} = 0.55\,.$$

Since this ratio is not far from unity, we can as a first approximation neglect n and we obtain that $m = \frac{1}{2}$. A second method of estimating the range of the bonding energies is to assume a bonding energy law of the form $v \sim r^{-p}$. We then have that

$$m = (\tfrac{3}{4})^{p/2}, \quad n = (\tfrac{3}{8})^{p/2}$$

and by trial and error we obtain that $p = 4$ in which case $m = 0.56$ and $n = 0.14$. Thus we obtain that $0.50 < (v_2/v_1) < 0.56$.

It is of interest to note that Fournet[11] has obtained, by an analysis of short range and long-range order, values of $v_2/v_1 = -\frac{1}{2}$ for Cu_3Au and $v_2/v_1 = \frac{1}{3}$ for CuZn.

Assuming that ratios of the v's do not vary with composition, requiring $T_c = 1100°K$ and $T_c' = 800°K$ at $x = 0.25$, the phase boundaries as given by the Zeroth approximation are fixed and the resulting diagram is presented in Fig. 5.

The asymmetry of the Fe_3Al phase is due to the composition shift of the $\beta + \gamma$ lattice by $S_{11}/2$ and this asymmetry is to be noted in the experimental

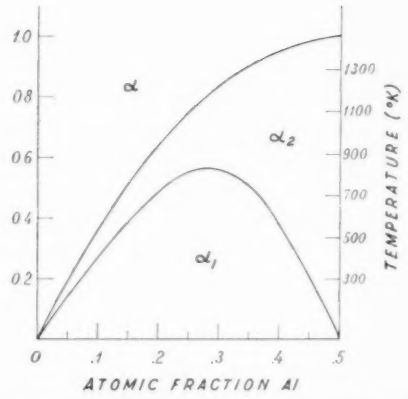


FIG. 5. Fe–Al phase diagram according to Zeroth approximation.

diagram. Detailed agreement with observation is not obtained. Whether this is due to the non-constancy of the v's or due to the effect of the ferromagnetic transformation that has been completely neglected here, or due to the insufficiency of the Zeroth approximation cannot be unambiguously determined. The major inadequacy, the too extensive order existence fields, is however a chronic deficiency of the Zeroth approximation and is probably the source of error.

The phase diagram in an ordering system is not simply the specification of the critical temperatures but also requires the specification of the variation of order with temperature and composition within the phase fields. In the present case this determination requires the simultaneous solution of the two transcendental defining equations. This calculation has been carried out graphically for the composition Fe_3Al and the results are presented in Fig. 6. It was found that to within the accuracy of the calculation (approximately $\Delta S = \pm 0.005$) the onset of Fe_3Al type order, $S_{31} \neq 0$, did not influence the value of S_{11}. It was also found that for $T/T_c < 0.7$ (Fe_3Al

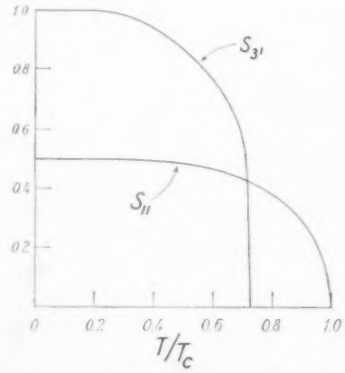


FIG. 6. Temperature dependence of long-range order at the composition Fe–Al.

type ordering begins at $T/T_c = 0.727$) the calculated value for S_{31} was not changed by assuming $S_{11} = S_{11}$ max $= 2x$.

7. SUMMARY OF RESULTS

A Zeroth approximation calculation with two independent long range order parameters describing FeAl and Fe_3Al type order has been given. The transition temperature consequences show that: the transition Fe_3Al order → FeAl order for x (atomic fraction Al) > 0.25 is probably of the second order; and that for $x < 0.25$ the transition Fe_3Al order → disorder is probably of the first order. Combining these conclusions with a new evaluation of experimental data a revised version of the Fe-rich solid solution region of the Fe–Al phase diagram is arrived at.

The complete phase diagram prediction of the Zeroth approximation is given and detailed agreement with experiment is not obtained. This is attributed mainly to the inadequacy of the Zeroth approximation.

It has been shown that for $x > 0.25$ the ordering can be treated to a good approximation as two effectively independent transformations: disorder → FeAl order as ordering of a body-centered cubic lattice at the given composition to a CsCl structure; and FeAl order → Fe_3Al order as ordering of a simple cubic lattice to a NaCl structure but at an effective composition equal to the given composition plus half the value of the FeAl type order. This is a very fortunate set of circumstances because it permits to treat these transformations by the higher approximation methods that have been developed and applied for these cases.[5] Formally one could of course treat the unseparated problem by the higher approximations but practically the computation necessary for solution would be prohibitive.

It is shown that Fe_3Al owes its existence to second neighbour interactions while FeAl order is due to nearest neighbour interactions. From the experimental value of the ratio of the respective transition temperatures for the computation Fe_3Al the ratio of the second to first interchange energy, v_2/v_1, is calculated to be about one half whether or not third neighbour bonds are considered.

ACKNOWLEDGMENT

The graphical calculation of the long-range order parameters was performed by Mrs. O. Baraquet.

REFERENCES

1. K. F. Wojciechowski, *Acta Met.* **6,** 396 (1958).
2. R. Fowler and E. A. Guggenheim, *Statistical Thermodynamics.* Cambridge University Press (1952).
3. J. M. Cowley, *Phys. Rev.* **77,** 669 (1950).
4. F. E. Jaumot and C. H. Sutcliffe, *Acta Met.* **2,** 63 (1954).
5. L. Guttman, *Order-Disorder Phenomena in Metal in Solid State Physics* (Eds. F. Seitz and D. Turnbull) Vol. 3, Academic Press, New York (1956).
6. *Metals Handbook* p. 1161. American Society for Metals, Cleveland, Ohio (1948); H. W. L. Phillips, *The Equilibrium Diagram of the System Aluminium–Iron, Annotated Equilibrium Diagram,* No. 13. Institute of Metals, London (1955).
7. A. Taylor and R. N. Jones, *Phys. Chem. Solids,* **6,** 16 (1958).
8. C. Sykes and H. Evans, *J. Iron St. Inst.* **131,** 225 (1935).
9. D. Parson, W. Sucksmith and H. E. Thompson, *Phil. Mag.* **3,** 1174 (1958).
10. A. J. Bradley and A. H. Jay, *Proc. Roy. Soc.* A**136,** 210 (1932).
11. W. Hume-Rothery and G. V. Raynor, *The Structure of Metals and Alloys.* Institute of Metals, London (1954).
12. Y. Takagi, *Proc. Phys.-Math. Soc. Japan* **23,** 44 (1941).

VOL. 8 1960

YIELD AND FRACTURE IN POLYCRYSTALLINE NIOBIUM*

M. A. ADAMS†, A. C. ROBERTS‡ and R. E. SMALLMAN§

Tensile tests on specimens prepared from an ingot of electron-bombardment melted niobium have shown that the material undergoes a ductile–brittle transition and can be made to twin. The variation of yield stress σ_y with grain-size $2d$ has been used to determine the effect of temperature (293°K–20°K at a strain-rate of 2.02×10^{-4} sec^{-1}) and strain-rate (2.02×10^{-4} sec^{-1}–6.18×10^{-2} sec^{-1} at 77°K) on the values of σ_i and k_y in a Petch type equation $\sigma_y = \sigma_i + k_y d^{-1/2}$, the results indicating that the ductile–brittle transition characteristics are in accordance with Cottrell's transition equation $(\sigma_i d^{1/2} + k_y)k_y = \beta\mu\gamma$. Niobium shows a greater resistance to brittleness than carburized α-iron because it has a smaller k_y value, and the reluctance of the material to twin except under extreme conditions of low temperature or high strain-rate is also attributed to a low value of k_y. The mechanical behaviour of niobium relative to that of other body-centred cubic transition metals is discussed.

DEFORMATION ET RUPTURE DU NIOBIUM POLYCRISTALLIN

Les auteurs ont soumis à des essais de traction des échantillons de niobium préparés au four de fusion à bombardement d'électrons. Il résulte de ces essais que ce métal possède une courbe de transition du type ductile–fragile et qu'il peut subir un maclage. La variation de la tension de déformation σ_y avec le grain-size $2d$ permet de déterminer l'effet de la température (293°K–20°K pour une vitesse de déformation de 2.02×10^{-4} sec^{-1}) et de la vitesse de déformation (2.02×10^{-4} sec^{-1}–6.18×10^{-2} sec^{-1} à 77°K) sur les valeurs de σ_i et k_y dans l'équation de Petch $\sigma_y = \sigma_i + k_y d^{-1/2}$. Les résultats indiquent que les caractéristiques de la transition rupture fragile-rupture ductile sont en accord avec l'équation de Cottrell $(\sigma_i d^{1/2} + k_y)k_y = \beta\mu\gamma$. Le niobium montre une plus grande résistance à la fragilité que le fer α carburé parce qu'il possède une valeur de k_y plus faible. Exception faite de son comportement dans des conditions particulières à basse température ou sous une vitesse de déformation élevée, la résistance de ce métal au maclage peut être attribuée à la faible valeur de k_y. Les auteurs discutent enfin du comportement mécanique du niobium comparé à celui des métaux de transition cristallisant également dans le système cubique centré.

FLIEBEN UND BRUCH VON VIELKRISTALLINEM Niob

Zerreißproben wurden aus Niob hergestellt, das durch Elektronenbombardement erschmolzen worden war. Die Zugversuche zeigten, daß bei diesem Material ein Übergang duktil-spröde auftritt und daß es sich verzwillingen läßt. Die Abhängigkeit der Fließgrenze σ_y von der Korngröße $2d$ wurde benützt, um den Einfluß der Temperatur (293°K – 20°K bei einer Dehnungsgeschwindigkeit von $2{,}02 \times 10^{-4}$ sec^{-1}) und der Dehnungsgeschwindigkeit ($2{,}02 \times 10^{-4}$ sec^{-1} – $6{,}18 \times 10^{-2}$ sec^{-1} bei 77°K) auf die Parameter σ_i und k_y in der Gleichung nach Petch $\sigma_y = \sigma_i + k_y d^{-1/2}$ zu bestimmen. Die Ergebnisse zeigen, daß die Gesetzmäßigkeiten des Übergangs duktil-spröde mit Cottrells Übergangsgleichung ($(\sigma_i d^{1/2} + k_y)k_y = \beta\mu\gamma$) übereinstimmen. Niob zeigt einen größeren Widerstand gegen Sprödigkeit als aufgekohltes α-Eisen wegen seines kleineren k_y-Wertes. Die geringe Neigung des Materials zur Zwillingsbildung außer bei extremen Bedingungen tiefer Temperatur oder hoher Dehnungsgeschwindigkeit wird ebenfalls dem kleinen k_y-Wert zugeschrieben. Das mechanische Verhalten von Niob wird mit dem anderer kubisch-raumzentrierter Übergangsmetalle verglichen und diskutiert.

1. INTRODUCTION

Although in recent years the plastic deformation and brittle fracture behaviour of mild steel has received considerable attention[1–4] other body-centred cubic metals have been relatively neglected. This has been due partly to the expected similarity in behaviour with α-iron, and partly to the small usage of the high melting point refractory metals vanadium, tantalum, niobium and molybdenum in industry. However, the increased importance of these metals, particularly in the gas turbine and nuclear energy fields, indicates the need for a more detailed investigation of their mechanical properties. Work is described in this paper on the tensile behaviour of niobium purified by electron-bombardment melting. Tensile tests on commercially pure niobium have been described by Wessel and Lawthers[5].

For mild steel it has been shown, both theoretically and experimentally,[3,6–8] that the shear stress σ_y for yield propagation varies with the grain diameter $2d$ according to the equation:

$$\left.\begin{aligned} &\sigma_y = \sigma_i + \sigma_D\, l^{1/2}\, d^{-1/2} \\ \text{or}\quad &\\ &\sigma_y = \sigma_i + k_y\, d^{-1/2} \qquad (k_y = \sigma_D\, l^{1/2}) \end{aligned}\right\} \qquad (1)$$

where, following Cottrell's notation,[8] σ_D is the shear stress to unpin a dislocation from its atmosphere,

* Received May 12, 1959.

† Materials Research Corporation, Yonkers, New York, U.S.A.; formerly Metallurgy Division, Atomic Energy Research Establishment, Harwell.

‡ Metallurgy Division, Atomic Energy Research Establishment, Harwell.

§ Department of Physical Metallurgy, University of Birmingham; formerly Metallurgy Division, Atomic Energy Research Establishment, Harwell.

TABLE 1. Typical analysis for niobium melted by electron bombardment

Impurity elements	Si	Fe	O_2	H_2	N_2	Ta	C	others
per cent present	0.150	0.300	0.01	0.02	0.05	0.30	0.07	0.03

σ_i the shear stress resisting the movement of dislocations across the slip plane after they have been unpinned, and l the distance from piled-up dislocations at the head of the plastic front to the nearest Frank-Read sources. In the present experiments the effect on σ_i and k_y of varying temperature (293°K–20°K at a strain-rate of 2.02×10^{-4} sec^{-1}) and strain-rate (2.02×10^{-4} sec^{-1}–6.18×10^{-2} sec^{-1} at 77°K) has been determined from measurements of yield stress on niobium specimens covering a range of grain sizes, and conditions for the occurrence of (a) twinning and (b) a ductile–brittle transition have been established.

2. EXPERIMENTAL PROCEDURE

Specimens were made from an ingot of commercially pure niobium which had been melted by electron bombardment. This treatment reduces markedly the gaseous impurities oxygen and nitrogen without radically affecting the metallic impurities. A typical analysis after melting is shown in Table 1.

Texture free wire of 1.25 mm diameter was prepared from the ingot by alternate cold swaging (50 per cent reduction in area) and annealing (1075°C for 1 hr in tantalum foil) treatments. After a final swage to 1 mm diameter, batches of 7.5-cm long wires were annealed (in tantalum foil) at temperatures from 1075°C to 1415°C to give the range of grain sizes shown in Table 2. 1075°C was established as the minimum recrystallization temperature, giving grains of about 0.005 cm diameter, whilst the 1415°C anneal resulted in wires with some grains across the complete section. For these wires the grain diameter was taken as the major axis of a plane at 45° to the wire axis, this corresponding to the plane of maximum shear stress. All anneals were made in a dynamic vacuum of between 10^{-5} and 10^{-6} mm Hg.

Wires were mounted for straining by soldering their ends with Wood's metal into close-fitting brass bosses fitted with loops to engage hooks in the tensile machine. Each end of the wire was shotblasted and then electro-plated with a 0.025 mm copper layer to allow tinning. The Wood's metal was held in a constant temperature water bath, so that the specimens never exceeded a temperature of 80°C.

TABLE 2. Grain-sizes of the specimens

Heat treatment	Grain size $2d$(cm)	$d^{-1/2}$ cm$^{-1/2}$
1 hr at 1075°C	0.00476	20.5
1 hr at 1190°C	0.00951	14.5
1 hr at 1260°C	0.0312	8.2
2 hr at 1415°C	0.1414	3.76

Tensile tests were made in the autographically recording "hard" tensile machine described by Adams[9]. The gauge length of the specimens was 2.8 cm and for most of the tests the machine was driven at a constant cross-head speed of 0.00057 cm sec^{-1} (strain rate 2.02×10^{-4} sec^{-1}); in a series of fast strain-rate tests this speed was increased to 0.173 cm sec^{-1} (strain rate 6.18×10^{-2} sec^{-1}).

3. RESULTS

3.1 *Slow strain-rate tests at* 293°K, 195°K, *and* 77°K

Figure 1 shows characteristic stress–strain curves for specimens of the finest grain-size tested at 293°K, 195°K and 77°K, with a strain rate of 2.02×10^{-4} sec^{-1}. At the two highest temperatures the curves are typical of a strain-ageing material, and lowering the temperature from 293°K to 195°K changes the shape of the curve only slightly by increasing the size of the yield point and decreasing the amount of uniform elongation. A further lowering of the testing temperature to 77°K, however, causes a marked change in behaviour; the upper yield stress is not very sharp and after a very small uniform elongation, necking occurs, the load then dropping steadily until fracture. At this temperature the high stress required to move the first dislocations must be sufficient to overcome any internal stresses created in the lattice during deformation. All fractures were of the fibrous type and the ductility of the material, measured from the percentage reduction in area at the fracture, was decreased slightly with decreasing temperature from about 99 per cent at 293°K to about 80 per cent at 77°K.

Typical curves for the coarest grained samples are shown in Fig. 2. The only marked difference from the fine-grained material is the reduced uniform elongation at 293°K and 195°K. Necking in the coarse-grained specimens occurred across single grains at all three temperatures, resulting in knife-edge fractures.

In Fig. 3 the lower yield tensile stress values of a series of niobium specimens are shown as a function of $d^{-1/2}$ at the three testing temperatures. For the

VOL. 8 1960

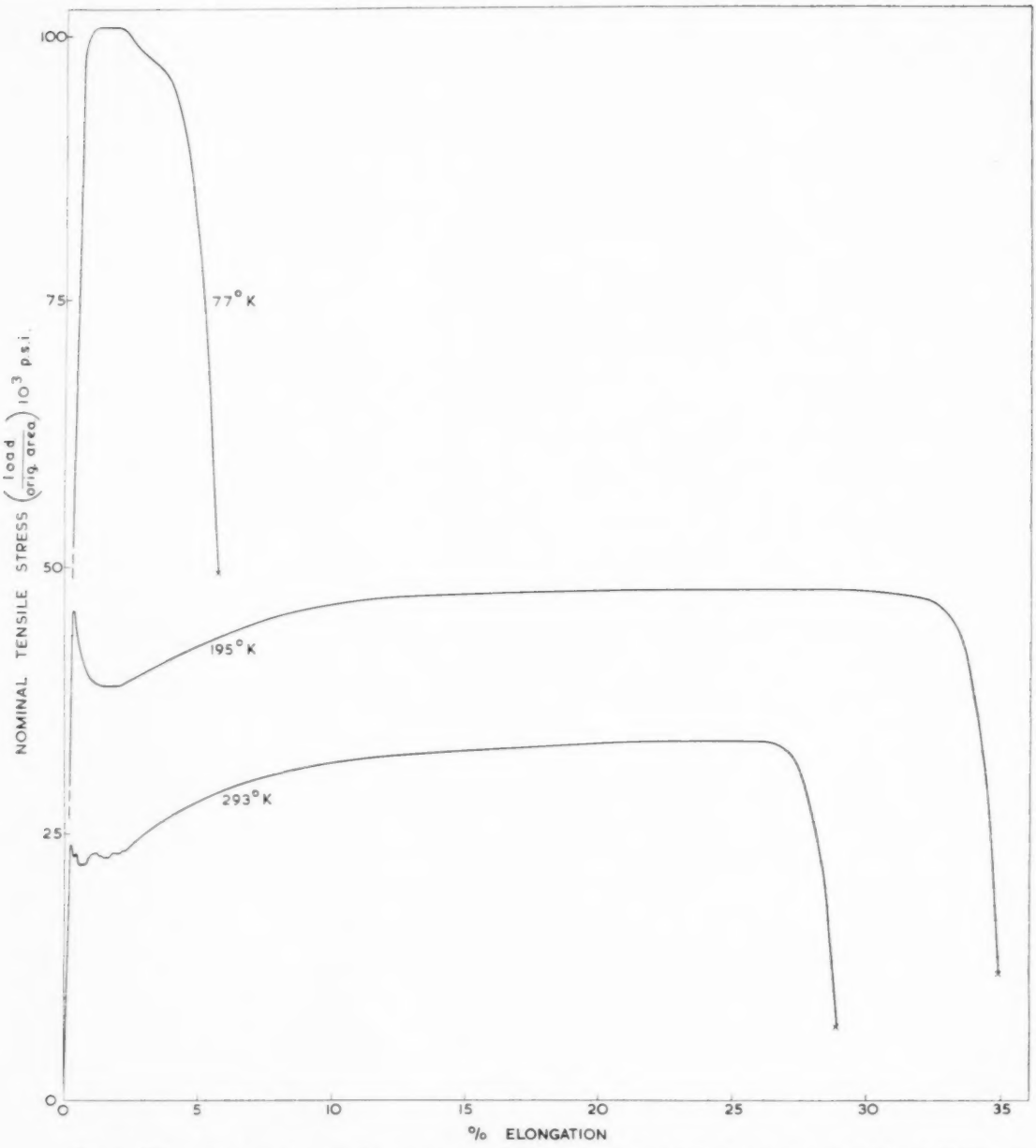


FIG. 1. Effect of temperature on the stress–strain curve of specimens of the finest grain-size ($2d = 0.00476$ cm) extended at a rate of 2.02×10^{-4} sec^{-1}.

195°K tests, specimens of four different grain-sizes were used whilst at the other two temperatures only the finest and coarsest grained samples were tested. Since in the tests at 77°K no clearly defined lower yield elongation was evident, it was necessary to estimate the position of the lower yield point. This was taken as the first inflexion in the stress–strain curve after the initial drop in load. Each point on the graph is the average for several tests at that temperature and grain size; the maximum scatter on individual tests amounted to about ± 5 per cent of the mean value.

From the curves of Fig. 3, σ_i and k_y for the three temperatures have been estimated (see Table 3). Here, shear stresses rather than tensile stresses (to a first approximation the shear stress is half the tensile stress) are used in accordance with equation (1). The σ_i values carry a possible error of about the same amount as the lower yield stresses, whilst the errors in k_y may be larger, possibly ± 50 per cent.

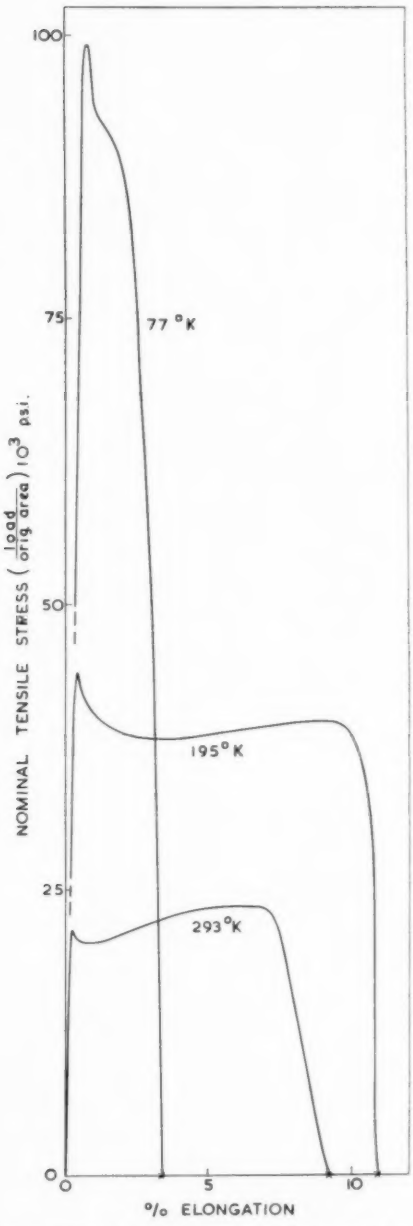


FIG. 2. Effect of temperature on the stress–strain curve of specimens of the coarsest grain-size ($2d = 0.1414$ cm) extended at a rate of 2.02×10^{-4} sec^{-1}.

k_y is very small, about an order of magnitude less than that for En2 steel at 195°K,[10] and increases slowly with decreasing temperature; σ_i increases more rapidly with decreasing temperature, particularly between 195°K and 77°K, and is somewhat larger (about 25–50 per cent) than that for En2 steel[10] at all three temperatures.

3.2 *Slow strain-rate tests at* 20°K

In the experiments of Section 3.1 all specimens showed completely ductile fractures, even at a temperature as low as that of liquid nitrogen. This behaviour is unusual in a transition metal of body-centred cubic structure, and to see if brittleness could be induced at lower temperatures a series of slow strain-rate (2.02×10^{-4} sec^{-1}) tests was made at 20°K on specimens covering the complete grain-size range. The results are summarized by the representative stress–strain curves of Fig. 4. Specimens of the coarsest grain-size failed by total cleavage with no macroscopic plastic elongation. Those of the two intermediate grain-sizes also cleaved, but only after they had elongated plastically for a few per cent, and work-hardened considerably. The finest grained material deformed plastically with rapid work-hardening, necked and finally failed by a mixed shear and cleavage fracture at the neck.

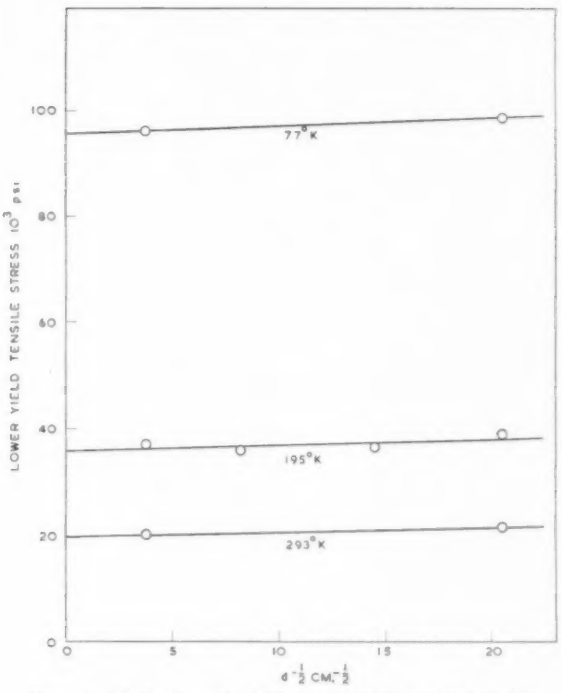


FIG. 3. Variation of yield stress with grain-size for specimens extended at a rate of 2.02×10^{-4} sec^{-1} at 293°K, 195°K and 77°K.

The stress–strain curves of all the specimens which extended plastically showed very distinct jerks, particularly in the early stages of plastic flow. Each

TABLE 3. Values of σ_i and k_y at three temperatures. Strain rate = 2.02×10^{-4} sec^{-1}

Temperature	77°K	195°K	293°K
σ_i (lb/in^2)	48,000	18,000	10,000
k_y (c.g.s.)	5.18×10^6	3.8×10^6	2.76×10^6

VOL. 8 1960

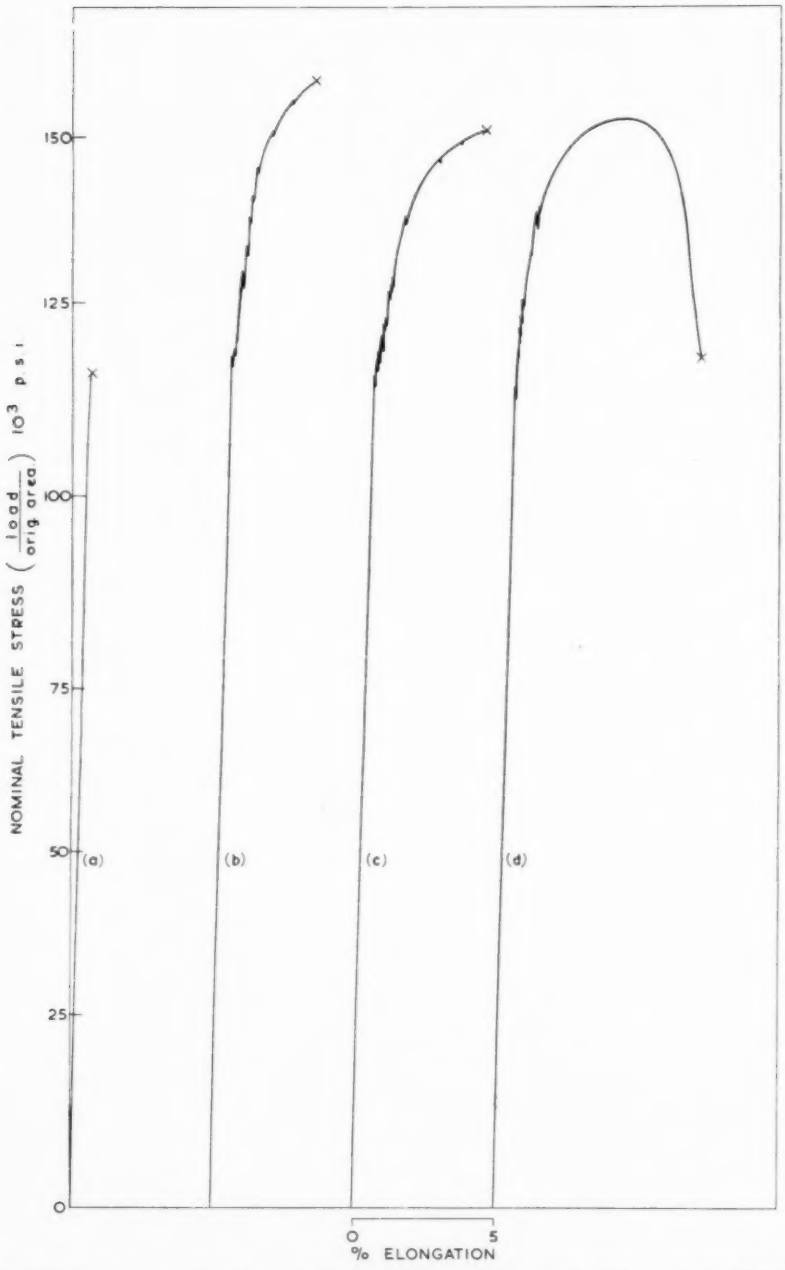


FIG. 4. Effect of grain-size on the stress–strain curves of specimens extended at a rate of 2.02×10^{-4} sec^{-1} at 20°K; (a) grain-size $2d = 0.1414$ cm, (b) grain-size $2d = 0.0312$ cm, (c) grain-size $2d = 0.00951$ cm, (d) grain-size $2d = 0.00476$ cm.

jerk was accompanied by an audible click, suggestive of deformation twinning. A metallographic examination confirmed that twins are formed. The specimen surfaces showed slip lines and other markings resembling the Neumann bands observed in iron. These markings were removed by polishing but re-appeared after etching (Fig. 5) and they persisted after an anneal of 1 hr at 850°C, a heat treatment that would have removed a low temperature martensite phase.

The coarse-grained cleaved specimens also showed twin bands after polishing and etching (Fig. 6), but it is open to contention whether these twins were formed immediately prior to fracture (one of the stress–strain curves did show a twinning burst before the specimen broke) or were nucleated by shock waves accompanying the fracture. Double surface

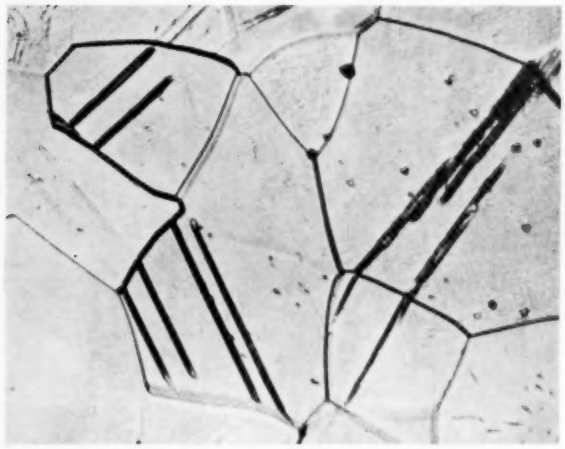


FIG. 5. Deformation twins in a specimen of the second finest grain-size ($2d = 0.00951$ cm) extended to fracture at 20°K. Polished and etched (95 per cent HNO_3, 5 per cent HF) after tensile-testing. ×340

analysis of several sets of prominent bands on large grains, using X-ray back-reflection Laue data, gave the twinning plane as {112} in agreement with observations on other body-centred cubic metals.

After finding twins in the specimens deformed at 20°K a careful metallographic examination was made of all the specimens tested at the higher temperatures. In no case was a twin band observed, either on the surface or after polishing and etching.

For the specimens of the three finer grain sizes the stress–strain curves indicate that the first macroscopic plastic deformation occurred by twinning, and the tensile stress at yield was within a few per cent of 116,000 lb/in² in all cases. Because twinning interferes it is impossible to obtain a direct k_y measurement from these tests, and the reliability of a σ_i measurement is somewhat uncertain. However, the stress–strain curves indicate some slip interspersed with the initial twins, which suggests that a value $\sigma_i = 58{,}000$ lb/in² is reasonable. Cleavage stress values, except for the coarsest grained specimens, all of which failed at around 116,000 lb/in² tensile, were very scattered. They varied from 150,000 to 200,000 lb/in² tensile in specimens of 0.0095 cm grain size, and from 150,000 to 180,000 lb/in² tensile for those of 0.031 cm grain-size. Fracture stresses for the finest grained material, subject to considerable errors because of the difficulty of estimating the area of the neck, ranged from about 250,000 to 280,000 lb/in² tensile.

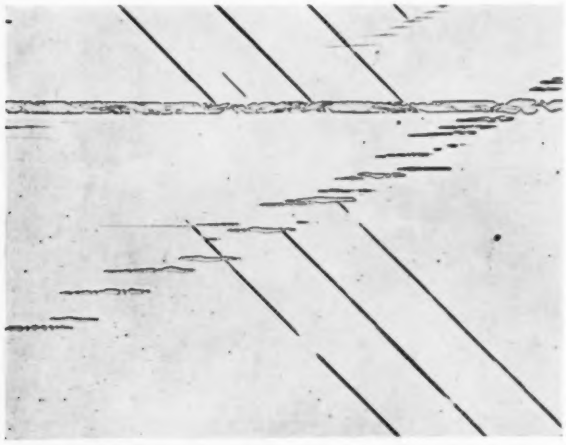


FIG. 6. Deformation twins in a specimen of the coarsest grain-size ($2d = 0.1414$ cm) extended to fracture at 20°K. Polished and etched (95 per cent HNO_3, 5 per cent HF) after tensile testing. ×140

A portion of a fractured specimen of the coarsest grain-size was mounted in a Laue back-reflection camera with the normal to the cleavage surface aligned at first parallel and then at 30° to the X-ray beam. Analysis of the two films gave the cleavage plane as {100}.

3.3 *Fast strain-rate tests at* 77°K

Many mechanical property changes which arise from lowering the testing temperature can be simulated by increasing the strain-rate at constant temperature. Consequently, tests were made at 77°K to see if an increased strain-rate at this temperature would induce the transition to brittleness observed in the experiments of Section 3.2.

In preliminary tests the strain-rate was increased by a factor of about 20. This raised the yield stress of all specimens by about 10 per cent but otherwise did not appreciably alter the form of the stress–strain curve, or change the mode of deformation or fracture. Increasing the strain-rate a further 15 times (to 6.18×10^{-2} sec^{-1}) resulted in stress–strain curves of the form shown in Fig. 7. At this very fast rate of testing specimens of the coarsest grain-size cleaved without macroscopic plastic deformation; those of the three finer grain-sizes deformed plastically at constant stress for a few per cent elongation and finally failed by a shear fracture after necking.

No jerks were seen in any of the stress–strain curves, but all test pieces were polished and etched, and carefully examined for twins over the complete gauge-length. Some of the specimens of each grain-size showed small twins on two or three of their grains, whilst in other samples no twinning was observed at all. By comparison all specimens deformed at 20°K showed well marked twins on at least half of their grains.

Cleavage and yield stress figures obtained from the fast strain-rate tests are plotted as a function of $d^{-1/2}$

VOL. 8 1960

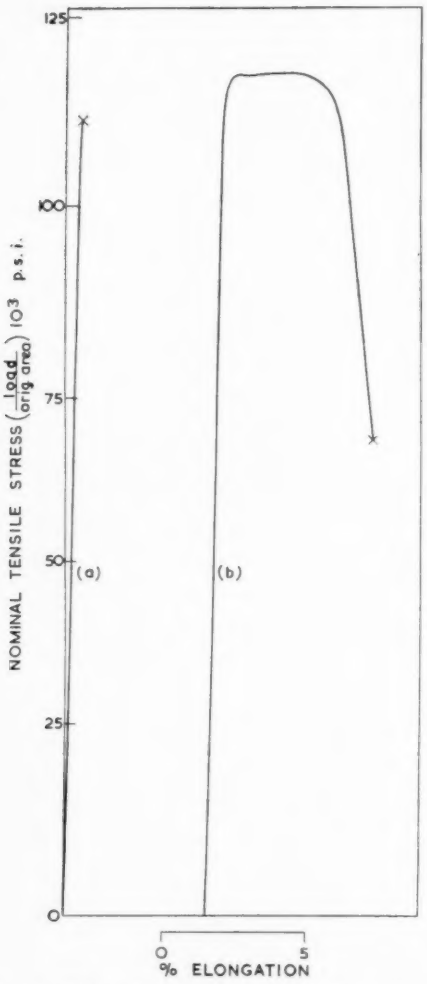


FIG. 7. Effect of grain-size on the stress–strain curve of specimens extended at a rate of 6.18×10^{-2} sec^{-1} at 77°K; (a) grain-size $2d = 0.1414$ cm, (b) grain-size $2d = 0.00476$ cm. Specimens of the two intermediate grain-sizes give curves of the same form as (b).

in Fig. 8 which also shows, for comparison, the slow strain-rate results. Average values from several specimens are used, the scatter on individual tests lying within the limits quoted in Section 3.1. The graph gives a value of $\sigma_i = 56{,}500$ lb/in^2 and $k_y = 7.25 \times 10^6$ c.g.s. at the fast strain-rate.

4. DISCUSSION

The present experiments have shown that niobium follows the same general pattern of mechanical behaviour as other body-centred cubic transition metals. Thus, one can obtain by a suitable choice of temperature or strain-rate a change from complete ductility to complete brittleness, and from slip to twinning as a possible mode of deformation. It remains now to examine those factors which may

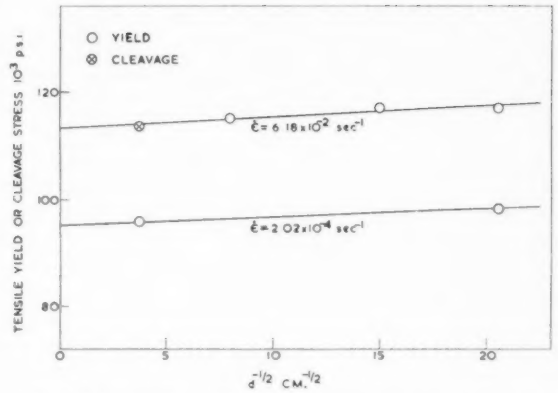


FIG. 8. Variation of yield (or cleavage) stress with grain-size for specimens extended at 77°K at rates of 2.02×10^{-4} sec^{-1} and 6.18×10^{-2} sec^{-1}.

account for the detailed differences between niobium and other metals of like structure whose mechanical properties have been investigated.

Deformation by slip

A notable feature of the experiments at 77°K and above, in which plastic deformation occurred solely or predominantly by slip, is that the yield propagation stress increases only slightly with decreasing grain-size; k_y for niobium is almost an order of magnitude smaller than that for En2 steel[10] at 77°K, and over 20 times smaller than that for molybdenum[11] at 293°K. On the basis of equation (1) this means that in niobium purified by electron-bombardment melting the atmosphere locking of dislocations is rather slight. This result may seem surprising since the stress–strain curves at 293°K and 195°K show a well-marked upper and lower yield point. It must be remembered, however, that the size of the yield drop is an unreliable quantitative measure of the amount of dislocation locking because the experimental value of the upper yield stress depends sensitively on specimen preparation and on tensile machine characteristics.[12–14] One way in which the form of the curves does indicate a small k_y value is from the amount of the lower yield elongation. If for the tests at 293°K and 195°K the portion of the curve immediately following the yield elongation is extrapolated to zero strain, the stress value obtained is a rough measure of σ_i. Then, from equation (1), the difference in stress $\Delta\sigma$ between the lower yield stress and the extrapolated value is equal to $k_y d^{-1/2}$. With small lower yield elongations and low rates of work hardening immediately afterwards, as observed in the present tests, the values of $\Delta\sigma$ and consequently of k_y, are small.

The yield strength of niobium deformed by slip can be attributed chiefly to the friction stress σ_i

resisting the movement of dislocations that have been unpinned from their atmospheres, and the dependence of the yield strength on temperature and strain-rate arises primarily from variations of σ_i. Frictional resistance to dislocation movement could be caused by (a) randomly dispersed impurity atoms in solid solution, (b) precipitated impurities, (c) other dislocations in the lattice, (d) the Peierls–Nabarro force. It is not immediately obvious which of these is most likely to give the required sensitivity of σ_i to temperature and strain-rate, but the work of Heslop and Petch[15] on steel suggests that the Peierls–Nabarro force probably makes the most significant contribution.

Deformation by twinning

Twinning was observed in the present experiments only under conditions of extreme low temperature or high strain-rate. Thus, although niobium can be made to twin it does so with reluctance, compared for example with carburized α-iron. A general explanation for this behaviour can be found in the ideas that Biggs and Pratt[16] have recently developed from the theories of Cottrell and Bilby[17] and Bilby and Entwisle[18] to explain their results on the twinning of iron crystals. The theory shows that twin nucleation is more difficult than twin propagation, and Biggs and Pratt suggest that nucleation is brought about by the stress concentration at the head of a rapidly piled-up array of dislocations produced by a burst of slip as a Frank–Read source is released from its atmosphere. With other things equal it should be easier to produce a slip burst suitable for twin nucleation in a material such as carburized α-iron with strongly locked dislocations (large k_y value) than in one such as niobium in which the dislocation locking is relatively slight (small value of k_y). It is of interest in this context to note that tantalum apparently has a small k_y value[8] and exhibits, like niobium, a reluctance to twin.[19]

All the specimens which deformed plastically at 20°K showed the same pattern of behaviour; (a) small amounts of slip interspersed between extensive bursts of twinning in the early stages of deformation, (b) a preponderence of slip with only occasional twinning as deformation was continued, (c) an ability (in contrast to the behaviour of specimens tested at 77°K) to work-harden whilst deforming by slip. These observations are again in accord with the model of twinning discussed above. Twins, once formed, may themselves act as barriers, allowing further dislocation pile-up and further twin nucleation. After a time, however, most of the Frank–Read sources will have been released from their atmospheres, and the generation of slip dislocations will then no longer occur in sharp bursts so that twin nucleation is suppressed. Presumably the action of twins as barriers to slip dislocations results in the rapid work-hardening observed at 20°K.

Cleavage

When considering the ductile–brittle transition characteristics of niobium it is again instructive to make comparisons with carburized α-iron. In the present slow strain-rate tests all the specimens were completely ductile at 77°K, and only the coarsest grained samples became completely brittle at 20°K; with En2 steel tested at the same strain-rate, specimens of a grain size only slightly greater than that of the finest grained niobium are almost completely brittle at 77°K.[10] To find possible reasons why, of the two materials, niobium should show the greater resistance to brittleness in tensile tests we turn to the recent brittle fracture theory of Cottrell[8].*

Developing the idea that the difficult stage in the fracture process is crack propagation rather than crack nucleation, Cottrell proposes a mechanism for forming crack nuclei from dislocations on intersecting slip planes. It is shown that two ⟨111⟩ dislocations gliding in {110} planes can react with a lowering of energy to form a pure edge dislocation in the {100} cleavage plane.

$$\tfrac{1}{2}a[\bar{1}11] + \tfrac{1}{2}a[111] \rightarrow a[001].$$

The new dislocation, equivalent geometrically to a "cleavage wedge" of material between adjacent {100} faces, is thought to be the crack nucleus. The nucleus will grow easily as successive dislocations run into it until it reaches a size of the same order of length as the slip bands forming it. The applied stress then becomes directly responsible for crack growth and if the crack size is greater than the Griffith value fracture will result; otherwise the material will be ductile. A calculation of the critical crack size shows that the ductile–brittle transition will occur when the relationship

$$(\sigma_i d^{1/2} + k_y)k_y = \beta\mu\gamma \qquad (2)$$

is satisfied, where μ is the shear modulus, γ the effective surface energy for the propagation of cracks and β a constant equal to 1 for uniaxial tension (ordinary tensile test) and $\frac{1}{3}$ for triaxial tension (tests

* See also Petch's[20] recent theory of the ductile–brittle transition in impact tests on notched specimens. This theory can be extended to tensile tests, and gives a transition equation of the same form as that developed by Cottrell with the constants slightly altered.

VOL. 8 1960

TABLE 4. Critical values of $(\sigma_i\, d^{1/2} + k_y)k_y$ on either side of the ductile–brittle transition point

Temp. of testing (°K)	Strain rate (sec^{-1})	σ_i (lb/in^2)	k_y (c.g.s. $\times 10^6$)	Grain size $2d$ (cm)	Behaviour	$(\sigma_i d^{1/2} + k_y)k_y$ (c.g.s. $\times 10^{15}$)
77	6.18×10^{-2}	56,500	7.25	0.1414	brittle	7.57
20	2.02×10^{-4}	58,000	5.87*	0.1414	brittle	6.28
77	2.02×10^{-4}	48,000	5.18	0.1414	ductile	4.59
77	6.18×10^{-2}	56,500	7.25	0.0312	ductile	3.47
20	2.02×10^{-4}	58,000	5.87	0.0312	ductile	2.88

* Estimated by extrapolating the k_y values measured at the higher temperatures.

on notched specimens). σ_i, k_y and d retain the same significance as in equation (1). Cottrell also points out that equation (2), although obtained originally from a detailed analysis of the above process, should be valid quite generally for the growth of cracks created by the conversion of glide dislocations into cavity dislocations.

Under conditions where the value of the left hand side of equation (2) is less than the value of the right hand side, ductile behaviour should be observed; when the left hand side exceeds the right hand side the behaviour should be brittle. In a given material brittleness should be favoured by low temperature and high strain-rate (large values of σ_i and k_y) and by large grain size, which is in qualitative agreement with the present results. To test the theory quantitatively we note that in our experiments the transition from ductile to completely brittle behaviour has been approached in four different ways: (i) by changing the strain-rate from 2.02×10^{-4} sec^{-1} to 6.18×10^{-2} sec^{-1} in tests at 77°K on specimens with a grain diameter $2d = 0.1414$ cm; (ii) by changing the grain diameter from $2d = 0.0312$ cm to $2d = 0.1414$ cm in the fast strain-rate tests at 77°K; (iii) by changing the testing temperature from 77°K to 20°K in the slow strain-rate tests on specimens with a grain diameter of $2d = 0.1414$ cm; (iv) by changing the grain diameter from $2d = 0.0312$ cm to $2d = 0.1414$ cm in the tests at 20°K. $\beta \cdot \mu \cdot \gamma$ may be reasonably assumed to remain insensitive to the various experimental changes so that if the theory is correct the value of $(\sigma_i\, d^{1/2} + k_y)k_y$ in every case where the behaviour is brittle should exceed any value of $(\sigma_i\, d^{1/2} + k_y)k_y$ for an experiment in which ductility is observed. The values listed in Table 4 show that the results are in fact in accord with the theory.

The closest limits we have from the experiments show that a transition from ductile to completely brittle behaviour occurs when $(\sigma_i\, d^{1/2} + k_y)k_y$ changes from 4.59×10^{15} c.g.s. to 6.28×10^{15} c.g.s. Thus with $\beta = 1$ and $\mu = 4 \times 10^{11}$ dyne cm^{-2} we find that the effective surface energy γ is given by 1.57×10^4 ergs $cm^{-2} > \gamma > 1.15 \times 10^4$ ergs cm^{-2}; or $\gamma = 1.36 \times 10^4$ ergs $cm^{-2} \pm 15$ per cent. This value is close to the experimentally determined value of γ for En2 steel,[10] and about 5 times larger than the true surface energy of niobium, 2.7×10^3 ergs cm^{-2}, estimated from the data of Taylor[21]. An effective surface energy greater than the true one appears to be a general feature of brittle fracture results, and is thought to be mainly due to the irreversible work of tearing at river lines and grain boundaries.[22]

Whilst showing some ductility, the specimens of the three finer grain sizes tested at 20°K did finally fail by cleavage (or by a mixed shear and cleavage fracture in the finest grain-size case). For such specimens, in which σ_i is raised by work-hardening during the test, the theory predicts a linear increase in fracture stress σ_f with $d^{-1/2}$ along a line which extrapolates to $\sigma_f = 0$ at $d^{-1/2} = 0$. From the few rather scattered results obtained in the present experiments it appears that specimens of the second coarsest grain-size give approximately the correct fracture stress values, whilst those of the two finer grain sizes have fracture stresses that are too low: further results covering the grain-size range more fully would, however, be required to test this part of the theory properly.

The increased tendency towards brittleness in En2 steel compared with niobium is to be expected from equation (2). At comparable temperatures and strain-rates σ_i and γ are similar for the two materials; but k_y for En2 steel is about 10 times as large as that of niobium and μ is about twice as large. Therefore, at a given temperature the transition value of $d^{-1/2}$ for En2 steel should be about 5 times larger than that for niobium. The measured transition $d^{-1/2}$ for En2 steel at 77°K is about 17 $cm^{-1/2}$, and the estimated transition $d^{-1/2}$ from the niobium experiments at the same temperature and strain-rate is 3.2 $cm^{-1/2}$; the ratio of the two values is in fair agreement with the theoretical predictions.

Cottrell's transition formula gives a good explanation of the present results, which suggests that the growth of the crack is the critical stage in the fracture process. The mechanism whereby glide dislocations

change to cavity dislocations to nucleate a crack is still in some doubt.[23]

Other processes in which cracks grow out of slip or deformation twin bands cannot be ruled out, since a similar formula is to be expected for these also. The possible importance of twins in the nucleation of cracks has been stressed by Bell and Cahn[24], and by Biggs and Pratt[16]. The present experiments demonstrate, however, that twinning is not always essential to brittle fracture, since examples were obtained in the fast strain-rate tests at 77°K of cleaved specimens which contained no twins. The fact that so often in body-centred cubic transition metals the onset of twinning and cleavage occurs under similar conditions is probably explained by the close dependence of both phenomena on the strength of the dislocation locking.

5. CONCLUSIONS

(1) The general mechanical behaviour of niobium is similar to that of the other body-centred cubic transition metals in that the material undergoes a ductile–brittle transition and can be made to twin.

(2) The ductile–brittle transition characteristics of niobium are adequately described by Cottrell's transition equation. The purified niobium used in the present tests shows a greater resistance to brittleness than carburized α-iron because of the smaller value of its dislocation locking term k_y.

(3) The small value of the dislocation locking strength is the reason why purified niobium is reluctant to twin.

(4) Twinning is not essential to cleavage in niobium. Twinning and cleavage are generally found under similar conditions of temperature and strain-rate in the body-centred cubic transition metals because both phenomena depend on the dislocation locking strength.

VOL. 8 1960

ACKNOWLEDGMENTS

The authors are indebted to Professor A. H. Cottrell F.R.S. for many useful discussions, and to Dr. D. Hull for assistance with the experiments at 20°K.

REFERENCES

1. W. P. Rees, B. E. Hopkins and H. R. Tipler, *J. Iron St. Inst.* **69,** 157 (1951).
2. *Behaviour of Metals at Low Temperatures.* American Society for Metals, Cleveland (1953).
3. N. J. Petch, *J. Iron St. Inst.* **173,** 25 (1953).
4. J. R. Low, in *International Union of Theoretical and Applied Mechanics. Madrid Colloquium on Deformation and Flow of Solids*, p. 60. Springer, Berlin (1956).
5. E. T. Wessel and D. D. Lawthers, *Westinghouse Res. Lab. Sci. Paper* 6-94701-5-Pl, (1957).
6. E. O. Hall, *Proc. Phys. Soc., Lond.* **64**B, 747 (1951).
7. J. R. Low, *Symposium on Relation of Properties to Microstructure*, p. 163. American Society for Metals, Cleveland (1953).
8. A. H. Cottrell, *Trans. Amer. Inst. Min. (Metall.) Engrs.* **212,** 192 (1958).
9. M. A. Adams, *Rep. U.K. Atom. Energy Res. Estab.* No. M/R2604 (1958).
10. D. Hull and I. Mogford, *Phil. Mag.* **3,** 1213 (1958).
11. A. A. Johnson, *Phil. Mag.* **4,** 194 (1959).
12. J. G. Docherty and F. W. Thorne, *Engng. Lond.* **132,** 295 (1931).
13. W. Sylvestrowicz and E. O. Hall, *Proc. Phys. Soc. Lond.* **64**B, 495 (1951).
14. H. W. Paxton, *J. Appl. Phys.* **24,** 104 (1953).
15. J. Heslop and N. J. Petch, *Phil. Mag.* **1,** 866 (1956).
16. W. D. Biggs and P. L. Pratt, *Acta Met.* **6,** 694 (1958).
17. A. H. Cottrell and B. A. Bilby, *Phil. Mag.* **42,** 573 (1951).
18. B. A. Bilby and A. R. Entwisle, *Acta Met.* **2,** 15 (1954).
19. C. S. Barrett and R. Bakish, *Trans. Amer. Inst. Min. (Metall.) Engrs.* **212,** 122 (1958).
20. N. J. Petch, *Phil. Mag.* **3,** 1089 (1958).
21. J. W. Taylor, *J. Inst. Met.* **86,** 456, (1958).
22. J. J. Gilman and W. G. Johnston, *Dislocations and Mechanical Properties of Crystals* (Ed. by J. C. Fisher, W. A. Johnston, R. Thomson and T. Vreeland, Jr.) p. 116. Wiley, New York (1957).
23. A. N. Stroh, *Crack Nucleation in Body-centred Cubic Metals*, Paper given at Fracture Conference, April 12–14 (1959), Swampscott, Mass., U.S.A.
24. R. L. Bell and R. W. Cahn, *Proc. Roy. Soc.* **A239,** 494 (1957).

THE STORED ENERGY OF COLD WORK AND ITS RELATION TO WORK SOFTENING*

A. L. TITCHENER† and M. B. BEVER‡

One set of wires of an 82.6 Au–17.4 Ag (wt.%) alloy was drawn at −195°C to a true strain of 0.62. A second set, after drawing at −195°C to a strain of 0.62, was annealed at room temperature. Two further sets were drawn at −195°C to a strain of 0.62, brought to room temperature and drawn to total strains of 0.85 and 1.08.

The energy stored by these wires was measured by tin-solution calorimetry. Annealing at room temperature reduced the stored energy from 90 to 51 cal/g-atom. Working at room temperature caused a further reduction to approximately 30 cal/g-atom. This release of stored energy induced by cold work is closely related to the phenomenon of work softening. Hardness measurements confirmed that the gold–silver wires underwent work softening.

The results are discussed in relation to the imperfections likely to account for the changes in stored energy and hardness.

EFFET DE L'ENERGIE RETENUE AU COURS DE LA DEFORMATION A FROID SUR L'ADOUCISSEMENT

Les auteurs ont préparé par tréfilage à −195°C, une série de fils d'un alliage à 82,6% Au–17,4% Ag. La déformation de ces fils est de 0,62. Certains d'entre eux ont été recuits à température ambiante. D'autres, après avoir été tréfilés dans les mêmes conditions ont été réchauffés jusqu'à la température ambiante et tréfilés à nouveau de façon à obtenir une déformation totale de 0,85 et de 1,08. L'énergie retenue par ce fil a été mesurée par calorimétrie. Les auteurs ont constaté que le recuit à la température ambiante réduit l'énergie retenue de 90 à 51 cal/atome gr. Le tréfilage à la température ambiante provoque une diminution supplémentaire de l'ordre de 30 cal/atome gr. Cette diminution de l'énergie, induite par déformation à froid, est en relation étroite avec le phénomène d'adoucissement par déformation. Des mesures de dureté ont confirmé que les fils d'alliages Au–Ag subissaient un tel adoucissement.

Les auteurs discutent ces résultats en faisant intervenir les imperfections susceptibles d'expliquer de telles modifications de l'énergie retenue et de la dureté.

BEI KALTVERFORMUNG GESPEICHERTE ENERGIE UND IHRE BEZIEHUNG ZUR ENTFESTIGUNG

Eine Gruppe von Drähten aus einer 82,6 Au–17,4 Ag-Legierung (Gewichtsprozent) wurde bei −195°C bis zu einer wahren Dehnung von 0,62 zugverformt. Eine zweite Gruppe wurde nach Zugverformung bei −195°C bis zu einer Dehnung von 0,62 bei Raumtemperatur ausgelagert. Zwei weitere Gruppen wurden bei −195°C bis zu einer Dehnung 0,62 zugverformt und dann bei Raumtemperatur weiter verformt bis zu einer Gesamtdehnung von 0,85 bzw. 1,08.

Die in diesen Drähten gespeicherte Energie wurde in einem Zinn-Lösungs-Kalorimeter gemessen. Auslagern bei Raumtemperatur verringerte die gespeicherte Energie von 90 auf 51 cal/g-Atom, Verformung bei Raumtemperatur verringerte sie weiter auf etwa 30 cal/g-Atom. Diese durch die Kaltverformung freigewordene gespeicherte Energie steht in enger Beziehung zur Erscheinung der Entfestigung. Die Entfestigung wurde durch Härtemessungen bestätigt.

Die Ergebnisse werden im Hinblick auf die Gitterfehler diskutiert, die vermutlich für die Änderungen von gespeicherter Energie und Härte verantwortlich sind.

1. INTRODUCTION

Cottrell and Stokes[1,2] observed that aluminum single crystals in tension tests involving an increase of temperature at some stage of the test, exhibited a sharp drop in the flow stress on further straining at the higher temperature. This "irreversible" decrease in the flow stress was additional to the usual "reversible" decrease occurring purely as a result of raising the temperature of testing. Cottrell and Stokes designated the sharp drop in yield as "work softening". They observed it with several combinations of temperatures including that of −183°C and 20°C. Work softening has also been reported by Kelly[3] for single crystals of aluminum, and by Adams and Cottrell[4] and Seeger *et al.*[5] for single crystals of copper. The phenomenon has been observed in polycrystalline aluminum of commercial purity.[6]

The changes in mechanical properties of a metal resulting from cold work are related to the changes in internal energy. As early as 1934, Taylor and

* Received April 24, 1958; revised June 19, 1959. This paper is based on part of a thesis by A. L. Titchener submitted, January 1958, to the Massachusetts Institute of Technology in partial fulfillment of the requirements for the Degree of Doctor of Science.

† Department of Metallurgy, Massachusetts Institute of Technology, Cambridge, Massachusetts; now University of Auckland, Auckland, New Zealand.

‡ Department of Metallurgy, Massachusetts Institute of Technology, Cambridge, Massachusetts.

Quinney[7] showed that with copper in torsion the stored energy of cold work and the amount of strain hardening followed parallel courses when plotted against expended energy, and that both reached saturation levels after about the same degree of deformation. The tendency of a metal towards saturation with stored energy has since been reported in a number of investigations[8–10] and may be inferred from others.[11–13] It is now known that energy may be stored in a metal by a variety of mechanisms,[11,14] so that there is not a strict correlation between strain hardening and the storing of energy. Nevertheless, the main contribution to the stored energy of cold work, except in special cases, arises from the generation of dislocations, which is also the chief cause of strain hardening.

The effect of the temperature of deformation on the energy stored in gold–silver alloys has been investigated by Leach *et al.*[15] and Greenfield and Bever[16]. With an 82.6 Au–17.4 Ag (wt. %) alloy Greenfield and Bever measured the energy stored in chips formed by drilling at −195°C and at room temperature. They also investigated the evolution of this energy. In chips formed at room temperature the stored energy amounted to 88 cal/g-atom; in chips formed at −195°C the corresponding value was 206 cal/g-atom. When chips formed at −195°C were annealed at room temperature, the stored energy decreased to 154 cal/g-atom, which was still 66 cal/g-atom higher than the energy stored in chips formed at room temperature.

In the present investigation attention was directed primarily at the surplus of stored energy remaining after room-temperature annealing of specimens deformed at −195°C, and at the effects of further deformation on this surplus. Corresponding changes of the mechanical properties were followed by measuring the hardness. An 82.6 Au–17.4 Ag alloy was used.

2. EXPERIMENTAL PROCEDURES

The stored energy was measured by tin-solution calorimetry. As the equipment and its operation have been described in earlier papers,[16,17] only an outline is given here.

The method consists in measuring the heat effect associated with the dissolution of a known weight of gold–silver alloy in molten tin. If annealed and cold-worked samples are added in succession from the same standard temperature, and suitable corrections are made for the change in the heat of solution with changing composition of the tin bath, the difference between the two heat effects represents the difference in enthalpy, and, with negligible error, the difference in internal energy of the two samples, i.e. the stored energy of cold work.

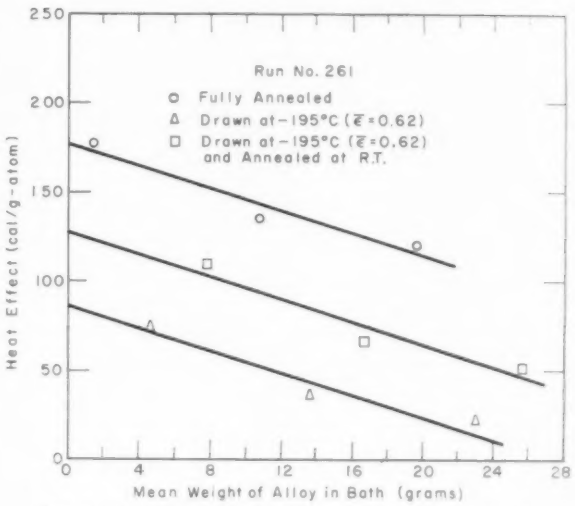


FIG. 1. Example of heat effects measured in a calorimetric run.

In this investigation, unknowns were run against fully annealed standards. In most runs two different unknowns were compared with the standards, and additions made in rotation. This is shown in Fig. 1, which also illustrates the dependence of the heat of solution on composition of the tin bath and the principle underlying the difference method by which the stored energy was measured. The calorimeter was operated at temperatures close to 250°C; all samples were added from −195°C. The calorimeter was calibrated by adding, at the end of each run, a known weight of tin from 0°C. The measured values of the stored energy are estimated to be accurate within 5 cal/g-atom.

The preparation of wires of suitable "starting size" and the technique of drawing samples under liquid nitrogen and preparing them at that temperature for addition to the calorimeter are described in detail elsewhere.[10] In the present investigation the drawing speed was 2.4 in/min. Room temperature was held at 22 ± 1°C.

It was necessary to measure the following:

(1) the energy stored after straining an amount, $\bar{\epsilon}_1$, at −195°C;

(2) the energy stored after straining an amount, $\bar{\epsilon}_1$, at −195°C and annealing at room temperature;

(3) the energy stored after straining an amount, $\bar{\epsilon}_1$, at −195°C, annealing at room temperature and straining an additional amount, $\bar{\epsilon}_2$, at room temperature.

The changes in stored energy with increasing

VOL. 8 1960

TABLE 1. Effect of strain and temperature history on the stored energy of cold work. Stored energy, cal/g-atom

Run no.	Drawn at −195°C to $\bar{\varepsilon}_1 = 0.62$	Drawn at −195°C to $\bar{\varepsilon}_1 = 0.62$; annealed at R.T.	Drawn at −195°C to $\bar{\varepsilon}_1 = 0.62$; annealed at R.T.; drawn at R.T. to $\bar{\varepsilon}_2 = 0.23$; $(\bar{\varepsilon}_1 + \bar{\varepsilon}_2 = 0.85)$	Drawn at −195°C to $\bar{\varepsilon}_1 = 0.62$; annealed at R.T.; drawn at R.T. to $\bar{\varepsilon}_2 = 0.46$; $(\bar{\varepsilon}_1 + \bar{\varepsilon}_2 = 1.08)$
260	87	52		
261	92	50		
262			31	
263			26	
267				42
268			31	31
269			32	26
Average	90	51	30	33

strain at −195°C and at room temperature were known from a related investigation.[10]

A standard sequence of dies was used and samples were drawn from a common starting size. As added to the calorimeter, therefore, they had diameters that depended on the total strain they had been given. The starting size, namely 0.055 in. diameter, was chosen so that these diameters were close to 0.035 in., which gave the highest accuracy in the calorimetry. The reduction under liquid nitrogen was in every case to 0.0403 in. diameter, representing a true strain, $\bar{\varepsilon}_1$, of 0.62. The additional reduction at room temperature, after room-temperature annealing, was to a diameter of either 0.0359 in. ($\bar{\varepsilon}_2 = 0.23$) or 0.032 in. ($\bar{\varepsilon}_2 = 0.46$). The sequence of dies used was 0.048, 0.043, 0.0403, 0.0359 and 0.032 in. diameter.

Strains were calculated from the nominal diameters of the dies. It was assumed that all dies shrank in the same ratio when cooled to −195°C; no allowance was made for any difference between the coefficients of linear expansion of the dies and the wire.

Since two different sets of unknowns were added to the calorimeter in each run, annealed and cold-worked samples of the same diameter could not always be used. Within the range of diameters from 0.0226 to 0.0403 in., however, no systematic difference could be detected in the heat effects. The annealed samples for each run were prepared in the manner described elsewhere.[10] Their finished diameters ranged from 0.032 to 0.0403 in.

For the samples cold worked at −195°C and annealed at room temperature, or both annealed and drawn at room temperature, the time at room temperature was 2 hr in Runs 260 and 262. Otherwise it was 13 hr.

In the experiments involving straining at two temperatures, the time at room temperature after completion of room-temperature drawing varied from 3 to 30 min. The time of storage at −195°C after completion of the room-temperature stage of drawing varied from 2 to 9 hr. These variations produced no systematic differences in the measured values of the stored energy.

Measurements of hardness were confined to specimens cold worked at −195°C and annealed at room temperature, or cold worked at −195°C and annealed and worked at room temperature. A Wilson "Tukon" testing machine with a Knoop indenter carrying a load of 100 gr was used. Ten indentations were made on a diametral section of each wire, with the long diagonal of the indenter parallel to the axis of the wires. These indentations were spaced at approximately equal intervals along the center of each specimen.

3. RESULTS AND DISCUSSION

The energy released by annealing at room temperature

The measured values of the stored energy are listed in Table 1. They are shown as a function of strain in Fig. 2; the paths in this figure are schematic only. The figure includes a curve of the energy stored in wires of the same composition drawn at room

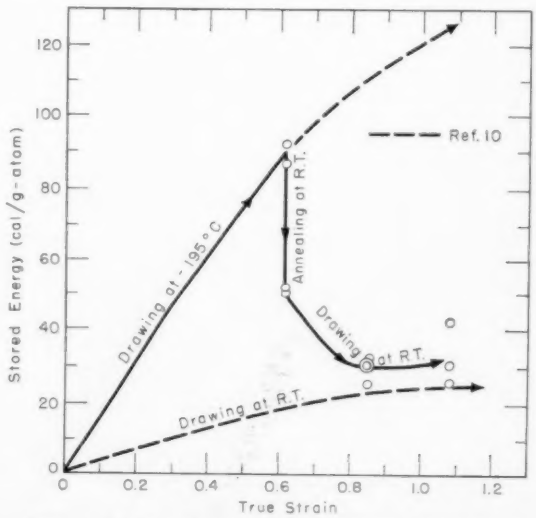


FIG. 2. Effect of strain and temperature history on the stored energy of cold work.

temperature, and also indicates the change in the stored energy with continuing strain at −195°C.[10]

When wires drawn at −195°C to a true strain of 0.62 were annealed at room temperature, the stored energy decreased from 90 to 51 cal/g-atom. Within experimental error, this decrease was not affected by changing the annealing time from 2 to 13 hr. This decrease corresponds to that observed by Greenfield and Bever[16], and cited in Section 1 above. It represents the disappearance or re-arrangement of defects mobile at room temperature. Greenfield and Bever discussed possible causes of the decrease, emphasizing the importance of vacancies, and also the possibility of re-arrangement of dislocations. In the light of recently published investigations into the twinning and faulting of gold and silver and the twinning of their alloys,[18–20] it is now possible to extend the analysis of Greenfield and Bever, and to estimate the approximate contributions of the various defects responsible for the energy that is stored at −195°C and released at room temperature. This partition of the energy will be discussed elsewhere.[21]

The energy released by straining at room temperature

The energy stored in wires annealed at room temperature after being drawn at −195°C was appreciably higher than that stored in wires drawn to the same strain at room temperature (Fig. 2). Similar behavior was observed by Greenfield and Bever[16], as noted in Section 1. When wires drawn at −195°C and annealed at room temperature were subjected to a secondary drawing at room temperature, the stored energy decreased. Figure 2 summarizes the results. It should be noted that the slight increase in the stored energy (from 30 to 33 cal/g-atom), indicated as occurring between the total strains of 0.85 and 1.08, was not definitely established. There was appreciable scatter in the values obtained for the energy stored at the latter strain. If the value of 42 cal/g-atom (Table 1) is rejected, the average value of the stored energy at a strain of 1.08 becomes 29 cal/g-atom, and the effect of increasing the room-temperature strain from 0.85 to 1.08 appears to be very slight.

Wires drawn at −195°C and then given the annealing and straining treatments described in the preceding paragraph showed changes in hardness. The Knoop hardness of wire strained to 0.62 at −195°C and annealed at room temperature was 124.3 with a standard deviation of ±3.0. Drawing at room temperature reduced the hardness to 113.6 ± 3.1 at a strain of 0.85 and 112.4 ± 2.6 at a strain of 1.08. This last value differed only slightly from that obtained on wire drawn wholly at room temperature. The changes in hardness are shown in Fig. 3. As with the stored energy, the details of the path by which the hardness decreases with strain at room temperature were not established. In particular it is possible that the initial drop in hardness (and in stored energy) can be induced by a much smaller strain than that associated with the reduction ($\bar{\epsilon}_2 = 0.23$) used in the wire drawing.

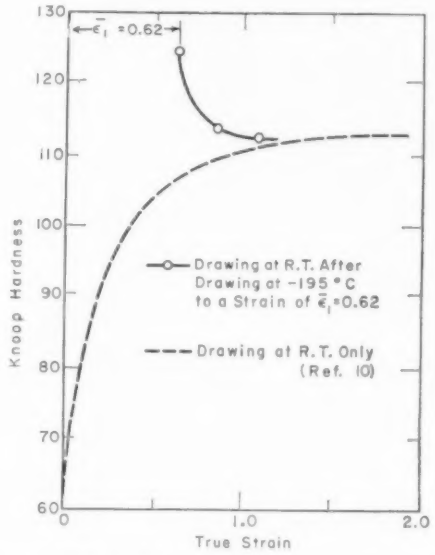


FIG. 3. Effect of drawing at room temperature on the hardness of wires previously drawn at −195°C and annealed at room temperature.

Of the possible mechanisms operating to reduce the stored energy during secondary deformation at room temperature, several can be dismissed. Vacancies are mobile even below room temperature and have little effect on the strength properties. Stacking faults also are probably mobile at room temperature.[20] Further, as will be shown elsewhere,[21] they are likely to contribute only about 5 cal/g-atom towards the stored energy. Twins on a metallographically observable scale do not increase the stored energy by amounts that can be measured by present methods. Twin faults on a fine scale, however, can do so. Twin faults are less mobile than stacking faults;[20,22] like stacking faults, they may cause some work hardening. However, the amount of stored energy due to twin faults is probably only about 5 cal/g-atom.[21] It seems unlikely, therefore, that the decrease in the stored energy occurring during the secondary room-temperature deformation can be explained by the disappearance of twin faults.

There remains the possibility that the decrease in the stored energy is due to the annihilation of dislocations. This explanation would account for the

VOL. 8 1960

observed softening, and moreover, the amount of energy released (21 cal/g-atom) would correspond to the annihilation of about 10^{12} dislocations per cm^2—a not improbable figure. On this explanation, the phenomenon is one of work softening of the kind reported by Stokes and Cottrell[1,2] and others.[3–6] According to Cottrell and Stokes[2], work softening is the result of the catastrophic release of glide dislocations piled up behind sessile dislocations. Friedel[23] advanced a similar explanation. Kelly[3] and Seeger *et al.*[5] concluded that cross slip was responsible. Although it cannot be decided at present which of the two theories applies, it is possible that the concurrent decreases in the stored energy and the hardness observed in the polycrystalline gold–silver alloy represent predominantly the same mechanism as that operating in aluminum and copper single crystals of high purity. This does not preclude the possibility that some small fraction of the decrease may have been due to the disappearance, under the activation of stress, of twin faults.

ACKNOWLEDGMENTS

The authors take pleasure in acknowledging the suggestion of Dr. H. C. Rogers of the General Electric Research Laboratory which led them to undertake the present investigation. They are indebted to Mr. Benjamin Howell for capable assistance in the experimental work and to Mr. Barton Roessler for helpful discussions. Thanks are due to Nuclear Metals, Inc. for the generous loan of wire drawing dies. The work was supported by the U.S. Atomic Energy Commission under Contract No. At(30-1)-1002.

REFERENCES

1. R. J. Stokes and A. H. Cottrell, *Acta Met.* **2,** 341 (1954).
2. A. H. Cottrell and R. J. Stokes, *Proc. Roy. Soc.* A**233,** 17 (1955).
3. A. Kelly, *Phil. Mag.* **1,** 835 (1956).
4. M. A. Adams and A. H. Cottrell, *Phil. Mag.* **46,** 1187 (1955).
5. A. Seeger, J. Diehl, S. Mader and H. Rebstock, *Phil. Mag.* **2,** 323 (1957).
6. W. F. Hosford, Jr., personal communication.
7. G. I. Taylor and H. Quinney, *Proc. Roy. Soc.* A**143,** 307 (1934).
8. M. B. Bever and L. B. Ticknor, *Acta Met.* **1,** 116 (1953).
9. M. B. Bever, E. R. Marshall and L. B. Ticknor, *J. Appl. Phys.* **24,** 1176 (1953).
10. A. L. Titchener and M. B. Bever, *Trans. Amer. Inst. Min. (Metall.) Engrs.* **215,** 326 (1959).
11. L. M. Clarebrough, M. E. Hargreaves and G. W. West, *Proc. Roy. Soc.* A**232,** 252 (1955).
12. P. Gordon, *Trans. Amer. Inst. Min. (Metall.) Engrs.* **203,** 1043 (1955).
13. V. I. Khotkevich, E. G. Chaikovskii and V. V. Zashkvara, *Dokl. Akad. Nauk. SSSR.* **96,** 483 (1954).
14. B. L. Averbach, M. F. Comerford, M. B. Bever and J. S. Ll. Leach, *Acta Met.* **4,** 477 (1956).
15. J. S. Ll. Leach, E. G. Loewen and M. B. Bever, *J. Appl. Phys.* **26,** 728 (1955).
16. P. Greenfield and M. B. Bever, *Acta Met.* **4,** 433 (1956).
17. L. B. Ticknor and M. B. Bever, *Trans. Amer. Inst. Min. (Metall.) Engrs.* **194,** 941 (1952).
18. H. Suzuki and C. S. Barrett, *Acta Met.* **6,** 156 (1958).
19. R. J. Block, J. B. Cohen and M. B. Bever, *Trans. Amer. Inst. Min. (Metall.) Engrs.* **212,** 300 (1958).
20. C. N. J. Wagner, *Acta Met.* **5,** 477 (1957).
21. A. L. Titchener and M. B. Bever, to be published.
22. C. N. J. Wagner, *Acta Met.* **5,** 427 (1957).
23. J. Friedel, *Phil. Mag.* **46,** 1169 (1955).

Application of Stroh's theory to intercrystalline creep cracking*

In considering the conditions for intercrystalline cracking during creep of some commercial alloys, McLean[1] has made use of the Stroh formula for brittle fracture,[2] in which the critical stress to form a cleavage crack is

$$\sigma_s^2 \geqslant \frac{12\gamma G}{\pi L} \qquad (1)$$

where σ_s is the maximum applied shear stress, γ is the surface energy per unit area of the surface of the crack formed, G is the shear modulus and L the length of the slipping plane. Substitution of the length of the sliding grain boundary for that of the slip plane in the formula permits an estimate of the critical stress for triple point cracking to be made, and McLean found that, except in the case of Nimonic 80A, the observed maximum shear stress for triple point cracking (2.5 tons/in^2) was in good agreement with that estimated from Stroh's theory. The Stroh formula assumes slip on a uniform plane, as in a pure metal or simple solid solution, where values of the surface (or interface) energy are reasonably constant; the same is assumed, of course, of the sliding boundaries in McLean's creep tests. When the sliding interface or boundary is not homogeneous, however, as when precipitate particles or twins are present,[3] the areas of maximum surface energy become less than that of the total sliding surface, with the result that L in the formula becomes smaller; the critical stress for triple point cracking will therefore increase for a given value of the surface energy.

Work at these Laboratories has shown how, in Nimonic 80A-type alloys, the formation of microcracks may be controlled by microstructure to the extent that triple point cracking may be suppressed even under a maximum applied shear stress of 8.5 tons/in^2. With duplex intergranular precipitates, consisting mainly of carbides as shown in Fig. 1, only dispersed intergranular cavitation occurred. The cavities were confined to the spaces between the precipitate particles, which thus also determined their maximum stable size. Direct correlation was also found between the amount of cracking, duration of test and elongation at fracture,[4] suggesting that the cracks were able to spread more easily along the grain–grain interface than along the grain–carbide interface, across which the relative shear would average only one half.

These effects have an important bearing on the rate of propagation of the cavities into microcracks leading to fracture and also require a modified application of Stroh's formula, on the lines indicated above, to determine the true relation between the applied shear stress and triple point cracking. In the microstructures shown, the length of the sliding interface should be taken as the average distance between precipitate particles (i.e. representing the areas of maximum surface energy) rather than the length of the whole grain boundary or the average grain diameter,[1] since only conditions of maximum shear are considered. In Fig. 1 the precipitates are closely spaced, with cavities roughly spherical in shape, whilst in Fig. 2, with more widely spaced precipitates, the cavities are longer and more crack-like. Specimens having the first structure fractured in 637 hr with 3.9 per cent elongation; those having the second, failed in 216 hr with only 0.54 per cent elongation, under a tensile stress of 17 tons/in^2 at 750°C.

Substituting values of L taken from the micrographs into equation (1): from Fig. 1, the average width of cavity, L, is approximately 1 μ; taking $\sigma_s = 17/2$ tons/in^2 and $G = 8 \times 10^{11}$ dyn/cm^2, the energy of the surface of the new crack becomes approximately 500 ergs/cm^2 which is in good agreement with McLean's estimates and confirms the validity of the assumptions. The action of the precipitate particles in reducing the width of the areas of maximum surface energy thus explains the absence of triple point cracking at these high stresses. The earlier fracture of the structure of Fig. 2 may be explained in the same manner. Thus, with $L = 5 \times 10^{-3}$ cm and $\gamma = 500$ ergs/cm^2 as above, the critical applied shear stress for crack formation becomes only 3.6 tons/in^2. In this structure therefore, cracks would be expected to propagate at a faster rate than in that of Fig. 1.

A similar result emerges from Inglis' treatment (reported by Zener[5]) in which the stress concentration factor at the tip of a crack is expressed as a function of the crack length and the radius of the tip of the crack:

$$\sigma_c = \left(\sqrt{\frac{t}{\frac{1}{2}L}} + \sqrt{\frac{\frac{1}{2}L}{t}}\right)\sigma_s \qquad (2)$$

where σ_c is the stress at the tip of the crack, t is the radius of the crack, L its length and σ_s is again the maximum applied shear stress. Taking t as about the same in both structures and L much larger than t,

VOL. 8 1960

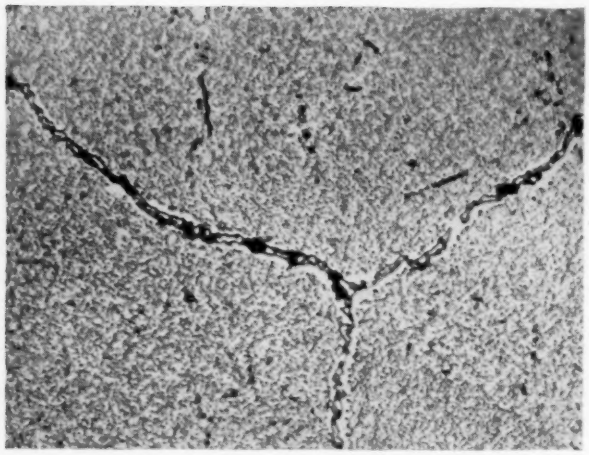


FIG. 1. Small spherical cavities in grain boundary containing closely spaced carbide precipitates. ×1000

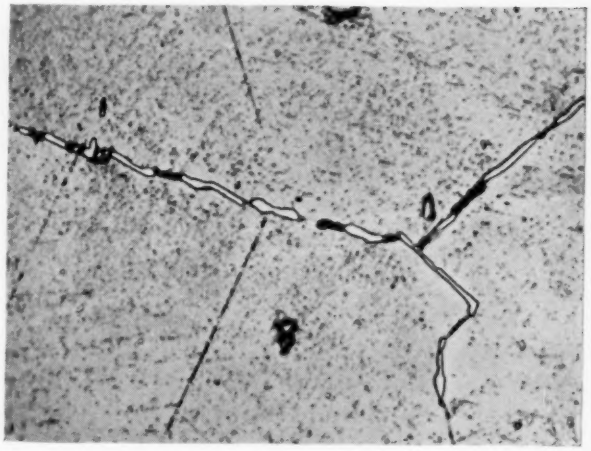


FIG. 2. Long crack-like cavities in grain boundary containing widely spaced carbide precipitates. ×1000

the ratio of the two stresses at the tips of the cracks is

$$\sqrt{\frac{10^{-3}/t}{5 \times 10^{-3}/t}}$$

or $\sim\frac{1}{2}$, i.e. the stress at the tip of the longer cavity is about double that in the shorter, and a faster rate of growth would again be expected.

This paper is published by permission of the Chief Scientist, Australian Defence Scientific Service, Department of Supply, Melbourne, Australia.

C. W. WEAVER

Australian Defence Scientific Service
Defence Standards Laboratories
Maribyrnong, Victoria, Australia

References

1. D. MCLEAN, *J. Inst. Met.* **85,** 468 (1956-57).
2. A. N. STROH, *Proc. Roy. Soc.* A **223,** 404 (1954).
3. C. W. WEAVER, *J. Inst. Met.* **87,** 126 (1958-59).
4. C. W. WEAVER, submitted to *J. Inst. Met.*
5. C. ZENER, *Elasticity and Anelasticity of Metals* p.129. University of Chicago Press (1948).

* Received August 26, 1959.

POLYSLIP IN SINGLE CRYSTALS*

U. F. KOCKS†

Simultaneous slip on six or eight glide systems in f.c.c. single crystals was studied by work-hardening, surface, and X-ray observations, and theoretically. Experiments were done on aluminum at room temperature, on four of the five crystallographic types of polyslip. They show that there are two extremely different kinds of behavior, typified by ⟨100⟩ and ⟨111⟩ tension.

These differences cannot be explained by any of the known mechanisms. Two additional mechanisms are proposed, one for the suppression of "critical" glide systems by the formation of large sessile jogs; the other concerning the action of pile-ups as "hedges" for intersecting glide systems.

GLISSEMENT MULTIPLE DES MONOCRISTAUX

L'auteur a étudié le glissement simultané suivant six ou huit systèmes de glissement de monocristaux cubiques à faces centrées. Cette étude a été réalisée simultanément sur des bases théoriques et sur des bases pratiques par des observations de durcissement structural, de rayons X et de surface de ces monocristaux. Des essais ont été effectués à la température ambiante sur des monocristaux d'aluminium et pour quatre des cinq types cristallographiques de glissement multiple. Ils montrent qu'il existe deux comportements extrêmement différents, selon ⟨100⟩ et ⟨111⟩.

Ces différences ne peuvent pas être expliquées par un mécanisme connu. L'auteur propose deux mécanismes additionnels dont l'un envisage des systèmes de glissement critique par la formation de larges crans sessiles et l'autre concernant l'action des empilements sur les systèmes de glissement qui se recoupent.

VIELFACHGLEITUNG IN EINKRISTALLEN

Die simultane Gleitung kubisch-flächenzentrierter Kristalle auf sechs oder acht Gleitsystemen wurde durch Verfestigungsmessungen, Oberflächenbeobachtungen, röntgenographische Methoden und theoretisch untersucht. An Aluminium wurden bei Raumtemperatur Experimente über vier der fünf kristallographischen Typen von Vielfachgleitung angestellt. Sie zeigen, daß es zwei extrem verschiedene Arten von Vielfachgleitung gibt, die zu charakterisieren sind durch Zug in ⟨100⟩- und ⟨111⟩-Richtung.

Diese Unterschiede lassen sich durch keinen der bekannten Mechanismen erklären. Es werden zwei zusätzliche Mechanismen vorgeschlagen, einer zur Unterdrückung "kritischer" Gleitsysteme durch die Bildung großer unbeweglicher Versetzungssprünge; und der andere betrachtet Versetzungsgruppen, die als "Hecken" für durchschneidende Gleitsysteme wirken.

VOL. 8 1960

INTRODUCTION

The mechanisms and theories of the plastic deformation of high-purity f.c.c. single crystals have until now been based on ideas and experiments in which the strain is provided by slip on *one* glide system, and the hardening, in some instances, by interaction of the gliding dislocations with dislocations of other glide systems which were either present in the elementary structure or generated in small amounts during the deformation. It has also been realized[1] that this dislocation interaction is very dependent upon the specific crystallographic relationship of the interacting dislocations. Very rarely has the extreme case been considered in detail, where two or more glide systems are equally favored by the external conditions, and where thus certain dislocation interactions are more likely to occur than others, viz. those between active systems. Two kinds of multiple slip conditions seem to be particularly illustrative: slip on two systems (where large differences are found depending on which two systems are involved), and extreme multiple slip or "polyslip", of which tension in the ⟨100⟩ and ⟨111⟩ directions are examples, the other cases being obtained by stress states other than tension. A glance at Fig. 1 shows that not only are these cases different from single slip orientations, but also there is a marked difference between ⟨100⟩ and ⟨111⟩. The two curves are not only distinguished quantitatively (in that one reaches twice as high a shear stress as the other), but they are quite different in character. The different *number* of glide systems in the two cases (8 and 6) can certainly not explain this, so the specific combination of glide systems must play an important role.

These orientations are generally regarded as special, there being only two in the whole stereographic triangle for tensile tests. On the other hand, they are special only with respect to the standard test where a uni-axial strain is prescribed. In the more general

* Received July 1, 1959.

† Gordon McKay Laboratory, Harvard University, Cambridge, Mass.

This work represents part of a Ph.D. thesis accepted by the Division of Engineering and Applied Physics, Harvard University, April 1959.

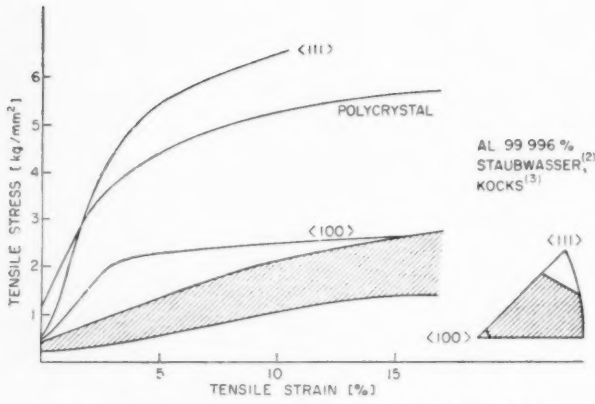


FIG. 1. Work-hardening in tension, for single crystals of various orientations and a polycrystal.

case of a strain that is completely prescribed in all components, five independent* glide systems have to operate to satisfy the boundary conditions. There are good reasons to believe that this situation is somewhat akin to the actual situation in a grain in a polycrystal. For this reason, it was previously proposed[3] that the strain-hardening behavior of polycrystals should be compared to single crystals in polyslip. It was found[3] (upon application of Taylor's method for averaging the orientations of the grains), that this procedure yields good experimental agreement with the ⟨111⟩ single crystal, but not with one of ⟨100⟩ orientation, in aluminum.

* "Dependent" glide systems are, for example, the three systems in one glide plane.

In connection with his interest in polycrystals, Bishop[4] established that there are only five crystallographically different stress states that can activate polyslip†. These five states we call A to E (Table 1). Types A and B have been discussed above, type C is a pure shear in a cubic plane and cubic direction, type D is a combined stress of shear and either tension or compression, whereas type E can be obtained by shear in a non-crystallographic plane and direction.

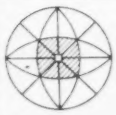
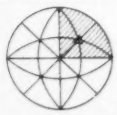
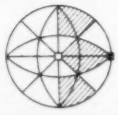
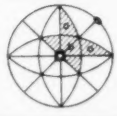
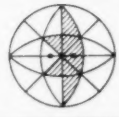
In this investigation, we have studied the behavior of high-purity aluminum single crystals in polyslip, firstly by work-hardening, surface, and X-ray observations on the crystals in ⟨100⟩ and ⟨111⟩ tension, and secondly by realizing two of the other three polyslip states (types C and D).

For this purpose, a technique was established which allows the realization of relatively pure shear states in certain crystallographic directions. It is based upon the torsion of hollow thin-walled prisms with cross-sections of regular polygons. For the above cases the cross-sections are square and in a (100) plane; the direction of the webs is [010] and [001] for type C, [011] and [01$\bar{1}$] for type D. The crystals were grown with a solid cross-section, carefully machined, and the work-hardened surface layer

† "Polyslip" we strictly define by a stress state that produces the same resolved shear stress on five independent glide systems. It is a consequence of the f.c.c. symmetry that the stress is actually the same on six or eight systems, *and is zero on all others*. This latter fact makes the analysis of dislocation interactions especially simple.

Table 1.

THE FIVE TYPES OF POLYSLIP

Type	A	B	C	D	E
Realization	[100] Tension	[111] Tension	(100)[010] Shear	[100] Compression +(100)[011] Shear	(100)[010] Shear +(110)[110] Shear
Stereographic Projection					
Crystallographic Model (Arrows: Slip Directions, Heavy Lines: Direction of Lomer-Cottrell Locks)					
No. of Slip Systems	8	6	8	6	8
No. of Lomer-Cottrell Locks, In Parenthesis: Per Plane	2 (1)	3 (2)	2 (1)	3(2)	4 (2)
Slip Directions Parallel to Lomer-Cottrell Locks?	no	yes	no	yes (2) / yes (2) / no (2)	yes (4) / no (4)
"Elastic Latent Hardening" On Some Systems Softening?	no	yes	yes	yes / no / yes	yes / no
"Critical" Pairs (Producing Sessile Jogs)	yes	no	yes	no / yes	yes

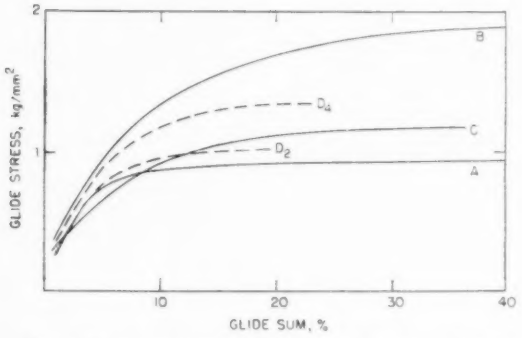


FIG. 2. Work-hardening of four polyslip types (Type D: averages).

removed chemically. The technique is not suitable for observations at small strains, but does give good work-hardening information within about ± 10 per cent at higher strains. It will be described in detail elsewhere.[5]

OBSERVATIONS

Work-hardening

The work-hardening behavior of the different polyslip types is quite different (Fig. 2). None shows any easy glide region. Types A and B ($\langle 100 \rangle$ and $\langle 111 \rangle$ tension) show a very similar, steep and approximately linear stage with a slope of about $G/150$. They both depart from this stage at about the same stress level, but subsequently the $\langle 111 \rangle$ curve behaves qualitatively similar to a classical "stage III", whereas the $\langle 100 \rangle$ curve shows a rather pronounced bend and a virtually flat work-hardening curve from there on to failure at about 60 per cent tensile strain.*

The experiments in torsion and combined torsion and compression showed that type C behaves in a way very similar to type A. The combined test D gives two curves, one for two participating glide systems, the other for the remaining four. The former of these again behaves in a way similar to type A, the latter is somewhat ambiguous. In addition, a rather large scatter was observed in type D which may be partly due to the limitations of the experimental technique.

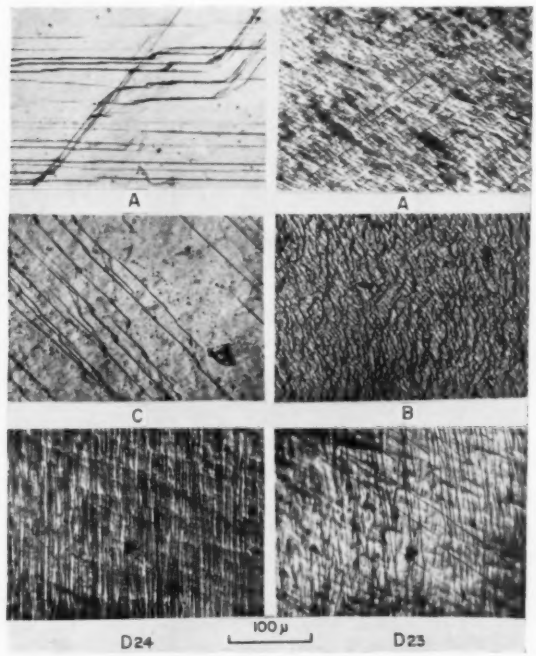


FIG. 3. Slip traces of four polyslip types (Type D on two different crystals). B and D_{23} showed high work-hardening.

Surface and X-ray observations

Again there are marked differences in this respect between the two categories established by $\langle 100 \rangle$ and $\langle 111 \rangle$ tension (Fig. 3). Whereas $\langle 111 \rangle$ exhibits the expected slip line pattern of short and wavy slip lines of many systems, $\langle 100 \rangle$ shows long, strong, straight slip lines, almost similar to those observed in brass, and usually of only few slip systems. The cumulative pattern shows most often two, rather than four sets of slip traces (with their respective cross-slips). The slip lines produced during an increment of 1 per cent strain, after 15 per cent pre-strain and re-polishing, often consist of only one set of traces. Also in this respect, type C was similar to type A, and type D was again somewhat ambiguous although closer to type A. The variation in surface patterns corresponded to that in work-hardening.

The X-ray observations are consistent with the other results (Fig. 4). $\langle 111 \rangle$ crystals show an extremely pronounced "spherical asterism" which indicates that all or many of the equally favored slip systems were actually operative, and that many dislocations must have remained in the crystal. In the case of $\langle 100 \rangle$, there is very little asterism, and this of the standard, elongated variety. Orientation change was not observed in the case of $\langle 111 \rangle$ tension, whereas in $\langle 100 \rangle$ it followed the path expected under an instability for one instantaneous glide system (Fig. 4).

Latent hardening

Some unexpected observations were made on the effect of a change of stress state from one polyslip type to another. An example of this is a type C

* Engineering not true stresses are plotted, because it was felt that the preference for a zero slope in this diagram, together with the absence of necking, must be of special significance.

VOL. 8 1960

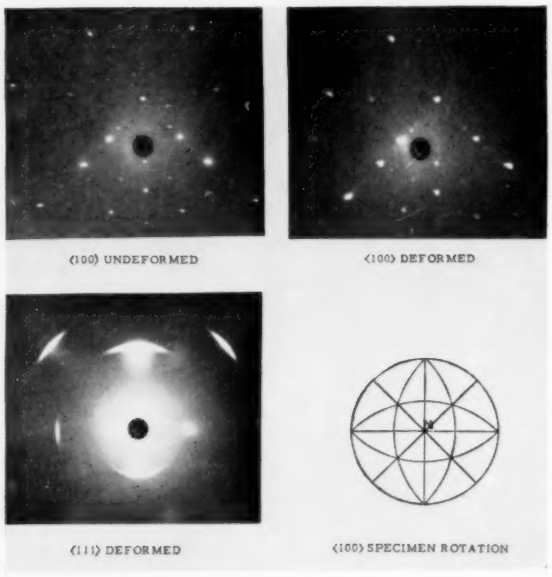


FIG. 4. X-ray observations.

shear followed by a type A compression ($\bar{A}$), or vice versa (Fig. 5). In the former case, the new flow stress was the same as the old flow stress, but a considerable subsequent hardening reminiscent of stage II ensued, up to a level similar to that reached by ⟨111⟩ tension. In the reverse case, however, type C was not at all affected by a previous operation of type A. More detailed observations of this type of test will be reported later.

DISCUSSION

A number of hypotheses were considered for explaining the observed differences between the various polyslip types. Each one of these hypotheses applies in different ways to the different polyslip types. These were therefore classified as in Table 1. It is one consequence of the experiments that any explanation will have to fit types A and C in the same manner, and allow for some strong differences in type B. We shall outline all arguments on the cases of ⟨100⟩ tension (type A) and ⟨111⟩ tension (type B).

It is difficult to visualize how any mechanism based on a random forest would give a sufficiently strong dependence on the exact combination of glide systems.

Elastic latent hardening

The only previous attempt to explain the orientation dependence of the work-hardening behavior of single crystals specifically including the symmetric orientations,[6] involved the elastic interaction between hardened glide planes. The back stress of dislocations on one glide system must have, in an individual glide plane, a component equal and opposite to the external resolved shear stress on this system. If this back stress is resolved on all other glide systems by the "tensor formula" (neglecting all other stress components) the effect is not only different in magnitude but sometimes different in sign, for different secondary glide systems. This is shown in Fig. 6. If it is now assumed in any polyslip state, that one of the systems is accidentally preferred, and the effect of this on the other "active" systems investigated, it may be seen that the resolved back stress works in the *same* direction as the external stress on some of the secondary systems in ⟨111⟩ tension (minus sign); in ⟨100⟩ tension, on the other hand, all these back stresses work against the external stress. This idea could thus very well explain the difference in stability between the two cases.

The experiments show clearly that this argument cannot be of importance, because then types B and C would have to behave in a similar way, and different from type A (Table 1). This result is not particularly disturbing, since the theoretical assumptions made are subject to severe criticisms.

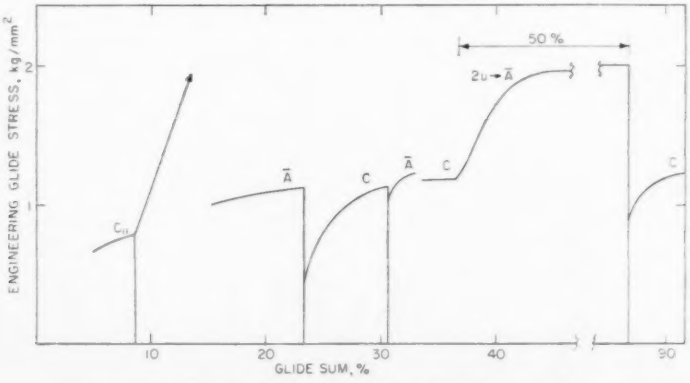


FIG. 5. Latent hardening in polyslip.

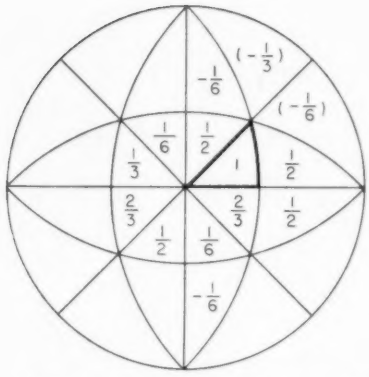


FIG. 6. Relative resolved shear stresses under direct shear on one glide system.

Suppression of glide systems

One of the most surprising results is that in some types of polyslip there is an instability for the operation of only a few of the systems that are equally stressed (and an ensuing instability in orientation), whereas in others this is not so. This is reminiscent of the difference between, say, a ⟨211⟩ and a ⟨210⟩ single crystal, where the primary and conjugate systems are equally stressed in the former while the primary and critical systems are equally stressed in the latter.[7] In the former case both systems actually operate at all times and at any point in the crystal. In the latter case, however, the actual strain always occurs on only one system, in any one place, and the crystal exhibits a particularly large amount of easy glide. This cannot be attributed to the change in orientation away from the symmetry position of a crystal for which one system is preferred. This in fact would develop only very slowly with strain, and can thus not explain the initial instability and the easy glide.*

These differences between ⟨100⟩ and ⟨111⟩ on the one hand, and between ⟨210⟩ and ⟨211⟩ on the other, may be linked. It may easily be seen that in the case of ⟨100⟩, there are many pairs of systems in the "critical" relationship, whereas in the case of ⟨111⟩ there are none. If one consistently eliminates critical relationships in the case of ⟨100⟩, one ends up with a most likely active combination of glide systems that include the primary and conjugate types, both with their respective cross-slips. This is consistent with the surface observations.

A mechanism for the suppression of one of two glide systems in critical relationship, follows from a consideration of dislocation intersections. An intersection of dislocations of the two systems considered, as some other intersections, produces jogs in both dislocations. If now one of these two systems happens to operate first, it will produce large jogs in the intersecting system, whereas each dislocation of the temporarily active system will only contain a unit jog. Thus the effect on the temporarily inactive system is larger, and the instability will thus be propagated. This is particularly serious if the large jogs produced are sessile.† An analysis shows that they are sessile (glide plane {100})‡ in just this, and only this, case of a "critical" relationship.

It is believed that this mechanism is the initial cause for the suppression of glide systems in some orientations, and the difference in orientation stability is only a consequence. The behavior of the polyslip type *C* is consistent with this explanation.

Lomer–Cottrell dislocations

There are only six sets of Lomer–Cottrell dislocations. An analysis was made of which of these six locks would form in the various polyslip states, under the working assumption that interactions involving dislocations of latent systems (zero resolved shear stress) can be neglected with respect to interactions between dislocations produced in the active systems.

The interesting result is that in both type *A* and type *C*, only two sets of Lomer–Cottrell dislocations are formed, one lying in each glide plane. The situation is illustrated in the crystallographic models in Table 1. In these cases, each active glide plane contains only one set of parallel Lomer–Cottrell dislocations. In the case of types *B* and *D*, however, three sets of Lomer–Cottrell dislocations are formed, and two are contained in each glide plane.

Qualitatively, this would seem to be consistent with the fact that the former group work-hardens less than the latter. Quantitatively, however, it is surprising that both groups should show such a similar stage II hardening, if the process involved is the piling up of dislocations against Lomer–Cottrell locks (Friedel[9], Seeger[1]). In the case of types *A* and *C*, the Lomer–Cottrell locks do not even form a closed "box", or at least the box is very long compared to that in the other cases. According to the theories of Friedel and Seeger, this arrangement should not give any second stage at all. In fact, Seeger[1] quotes it as a possible mechanism for stage I.

This difficulty, as well as similar difficulties in

* ⟨210⟩ is a stable orientation in a compression test, yet its slip line pattern was observed to be the same as in tension. This experiment was suggested by R. L. Fleischer.

† The glide plane is, of course, well defined for large jogs (dislocations), whereas it is not, according to Seeger and Blank[8], for unit jogs.

‡ i.e. Lomer–Cottrell type (W. F. Hosford and R. L. Fleischer, *Acta Met.* **7**, 816 (1959).)

VOL. 8 1960

quantitatively explaining the different stress levels at the later stages, and furthermore the experimental fact that type *D* does not classify with type *B* as much as this argument would suggest, seem to eliminate the possibility of explaining all the effects by Lomer–Cottrell dislocations alone. An extension of the known mechanisms of hardening by obstacles is proposed in the next section.

INTERPRETATION

Hedges

If Lomer–Cottrell dislocations are formed, and some further slip spreads from the two participating sources, dislocations pile up on both systems. Such a pile-up, in addition to obstructing further glide in its own system, as has often been considered, should also provide a strong obstacle to dislocations on other systems. Fig. 7 is an attempt to illustrate this. Pile-ups form two-dimensional walls which have long-range stress fields, as opposed to polygonization walls and kink bands. If they are strong enough, they can thus provide an effective obstacle to slip even in other glide planes, by temperature-independent elastic interaction. This would be consistent with observations in stage II.

Since the pile-ups considered as obstacles should be contained in an individual glide plane (or a "package" of a very few) they should be rather straight walls at the intersection with other glide planes. They thus provide the possibility of cross-slip in this other glide plane. In addition, the pile-ups may be cut through by dislocations on a different glide plane, which should be particularly important for dislocations whose Burgers vectors do not lie parallel to the wall. This process is akin to "forest cutting". The extremely non-random arrangement discussed in our case should require much higher stresses at the same temperature than cutting of a random forest. In analogy and contradistinction to the random "forest", the name "hedges" has been proposed for the pile-up walls if they act in the manner discussed.

Pile-ups in aluminum at room temperature are generally expected to be very small. Still, a group of, say, 5 dislocations does present an obstacle different from a single dislocation. The fact that the hedge structure has two parameters, the number of dislocations in the hedge and the distance between hedges, makes it most useful for the following and possibly other applications.

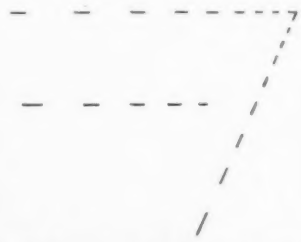


FIG. 7. Pile-ups form "hedges" for dislocations on other glide planes. (The glide directions in the two parallel glide planes may not be the same; the effect is also exerted on the third and fourth glide planes.)

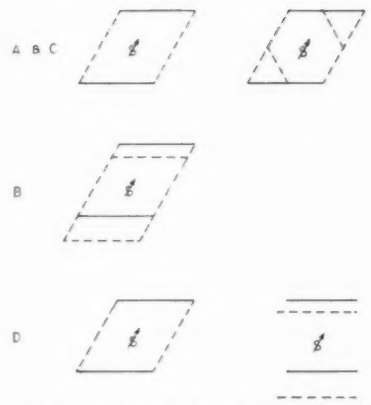


FIG. 8. Configuration of obstacles in glide plane for various polyslip types, after suppression of critical glide systems
(——— Lomer–Cottrell locks, – – – – – hedges).

A major advantage of these hedges is that they are two-dimensional and thus more likely to form obstacles to slip in an individual plane than the linear Lomer–Cottrell dislocations.

For an analysis of the hedges present in a crystal of any particular polyslip type, we now no longer need as stringent a working assumption as was introduced in the discussion of Lomer–Cottrell dislocations. In fact, *all* Lomer–Cottrell dislocations may be formed, but we assume that the *strain* in the latent systems and in suppressed "critical" systems is so much less than in the actually operative glide systems that their hedges can be neglected.

Association of work-hardening stages and mechanisms

Figure 8 shows sketches, for the various polyslip types, of the structure of obstacles in an individual arbitrary glide plane, according to the previous considerations: hedges of actually operating systems, which pierce the glide plane, and only *those* Lomer–Cottrell locks that are formed with a dislocation of the source under consideration. (No emphasis is placed on the relative position of the various obstacles, only on the relative directions.)

It is clear that in all cases are the glide planes sufficiently "boxed-in" (except one component of type *D*) to give a second stage according to either of the mechanisms of Friedel[9] or Seeger[1].

On the other hand, we now have three different

relief mechanisms. Firstly, there is cross-slip of the screw dislocations lying parallel to hedges, secondly, dislocations may break through Lomer–Cottrell barriers, and thirdly they may cut through hedges that are not parallel to the Burgers vector. We deduce from our experiments that this sequence is the correct one for increasing stress.

Firstly, it should be noted that at least two different relief mechanisms may be expected from the experiments. The departure from stage II (onset of stage III) was noted to occur at about the same stress in all cases. The flat region in types *A* and *C* may then be rated as an extra stage (say stage IV). It has its own dependence on impurities and temperature.* This is what should be expected for a separate relief mechanism.

Seeger[1] has shown that cross-slip should always be expected before break-through of Lomer–Cottrell barriers, and has associated it, following Diehl[11], with the first essential departure from the straight part II of the stress–strain curve. This seems to hold also in the polyslip cases. We observed cross-slip microscopically at this stage. All polyslip curves have roughly equal stress at the initiation of this stage III, and all (except one component of type *D*) have hedges parallel to their slip directions. The "box" sizes should then be about the same at this point; this is reasonable if all sources have by now been active.

That the onset of cross-slip occurs at a stress about 3 times as high in polyslip as in single slip orientations, must mean that the slip length, i.e. the distance between hedges, is smaller, at this point, by about a factor 9[12] in polyslip as in single slip, which is not unreasonable.

The work-hardening slope following this first relief cannot be zero (or practically so) as long as only the screw dislocations can escape from the glide plane. The extremely low work-hardening slope of types *A* and *C* soon after part III has set in, can only mean that the one remaining obstacle in some of the glide planes has become ineffective: that the dislocations have broken through the Lomer–Cottrell locks. A stationary pile-up should then be found behind the locks which permits continuous break-through at a constant stress. This shear stress was observed to be 1 kg/mm^2. For this value, Stroh[13] has estimated the number of dislocations in the pile-up that would effect break-through, to be between about 10 (for recombination) and about 100 (for dissociation of the two reacting dislocations). Tentatively applying the formula of Eshelby *et al.*[12] with a unit proportionality factor, we find for the average distance between locks 10–100 μ.

There is one type of obstacle left which distinguishes type *B* and one component of type *D* from all the other cases: this is the hedge not parallel to the Burgers vector. From the experimental results it must then be inferred that an intersection of these hedges is harder, by about a factor 2, than the two previously discussed processes, or even that it never occurs.

Since it is hard to imagine how an individual hedge should be stronger than an individual Lomer–Cottrell lock, the average distance of hedges of the type occurring in ⟨111⟩ tension must be smaller by at least a factor 4[12] than the average distance between two Lomer–Cottrell dislocations formed from the same source. This result is not unreasonable in view of the fact that hedges increase the volume of influence of any one Lomer–Cottrell dislocation many times. The number of Lomer–Cottrell locks whose hedges extend into an individual glide plane region, limited itself by two Lomer–Cottrell dislocations, must be at least four.

Latent hardening

The proposed mechanisms are also consistent with the observations on latent hardening. The initially surprising result that the latent hardening in type *C* due to a previous operation of type *A* is zero, whereas in the reverse case it is quite high and is followed by a high rate of work-hardening to a level similar to that reached by ⟨111⟩ tension, can now be explained. Slip in type *A* produces hedges which are parallel to active slip directions in type *C* and can thus be by-passed by cross-slip, whereas the hedges of type *C* are not parallel to the slip directions of type *A*. This distinction is not completely unambiguous but possible and likely.

CONCLUSION

Some observations on extreme multiple slip cases could not be explained by any of the previously proposed work-hardening mechanisms. The extension suggested, an action of pile-ups as "hedges" for

* Hosford[10] has observed that ⟨100⟩ and ⟨111⟩ tensile curves and surface patterns become increasingly similar as the temperature is decreased. Our own observations show that the level of the ⟨100⟩ plateau is higher the higher the amount of impurities although the basic character of the ⟨100⟩ curve is preserved. S. Howe and C. Elbaum (priv. comm.) have observed on Al at high temperature that the orientation dependence of work-hardening disappears although the differences in slip line pattern and change of shape persist. In terms of our mechanism, their observations indicate that the ledges in a ⟨111⟩ Al crystal become transparent between 400 and 600°C.

VOL. 8 1960

intersecting glide systems, fits all experimental observations.

This may be partly due to the fact that hedges are two-parameter obstacles, as distinct from both Lomer–Cottrell dislocations and a random forest. On the other hand, the additional parameter may be actually needed in view of the great number of phenomena to be explained. A discussion of the possible importance of hedges for the general theory of work-hardening, including single slip orientations, is left for a later paper.

ACKNOWLEDGMENTS

I have derived great benefit from discussions with all members of the Metallurgy Group in the Division of Engineering and Applied Physics at Harvard University. In particular, I sincerely appreciate the constant help and encouragement by Professors B. Chalmers and R. S. Davis. Also, the frequent discussions with Professor R. L. Fleischer and Mr. W. F. Hosford are gratefully acknowledged. This work was supported by an ONR research contract.

REFERENCES

1. A. Seeger, J. Diehl, S. Mader and H. Rebstock, *Phil. Mag.* **2,** 323 (1957); A. Seeger in *Dislocations and Mechanical Properties of Crystals* (Ed. by J. C. Fisher, W. A. Johnston, R. Thomson and T. Vreeland, Jr.) p. 243. Wiley, New York (1957).
2. W. Staubwasser, *Acta Met.* **7,** 43 (1959).
3. U. F. Kocks, *Acta Met.* **6,** 85 (1958).
4. J. F. W. Bishop, *Phil. Mag.* **44,** 51 (1953).
5. U. F. Kocks, R. S. Davis and B. Chalmers, to be published.
6. P. Haasen and G. Leibfried, *Z. Phys.* **131,** 538 (1952); P. Haasen, *Z. Phys.* **136,** 26 (1953).
7. R. S. Davis and U. F. Kocks, to be published.
8. A. Seeger and H. Blank, *Z. Naturf.* **9a,** 262 (1954).
9. J. Friedel, *Phil. Mag.* **46,** 1169 (1955).
10. W. F. Hosford, Sc.D. thesis, Massachusetts Institute of Technology (1959).
11. J. Diehl, *Z. Metallk.* **47,** 331, 411 (1956).
12. J. Eshelby, F. C. Frank and F. R. N. Nabarro, *Phil. Mag.* **42,** 351 (1951).
13. A. N. Stroh, *Phil. Mag.* **1,** 489 (1956).

SOME OBSERVATIONS OF SLIP LINES ON DEFORMED COPPER WHISKERS*

P. CHARSLEY†

Observations on slip markings which are produced during the tensile deformation of copper whiskers indicate that visible cross-slip does not necessarily occur during the propagation of a Lüders band. A mechanism is proposed whereby such a band propagates as a result of the stress concentration between the slipped and unslipped regions of the whisker.

QUELQUES OBSERVATIONS DE LIGNES DE GLISSEMENT SUR DES BARBES DE CUIVRE DEFORMEES

Les lignes de glissement qui apparaissent au cours de la déformation par traction sur des barbes de cuivre indiquent que le glissement croisé ne se produit pas nécessairement pendant la propagation d'une bande de Lüders. L'auteur propose un mécanisme au cours duquel une telle bande a la possibilité de se propager par suite d'une concentration de tensions à l'interface des régions de la barbe qui sont respectivement déformées et non déformées.

EINIGE GLEITLINIENBEOBACHTUNGEN AN VERFORMTEN FADENKRISTALLEN AUS KUPFER

Untersuchungen von Gleitspuren, die bei Zugversuchen auf Kupferwhiskern entstehen, zeigen, daß sichtbare Quergleitung nicht notwendig bei der Ausbreitung eines Lüdersbandes auftritt. Es wird ein Mechanismus vorgeschlagen, wodurch sich solch ein Band ausbreitet als Folge der Spannungskonzentration zwischen dem geglittenen und nicht geglittenen Gebiet des Whiskers.

VOL. 8 1960

The plastic deformation of copper and silver whiskers has been reported in some detail by Brenner[1]. He found that after an initial yield point (usually at a very high stress) the whiskers deformed plastically by the propagation of one or more Lüders bands at stresses of the order of one twentieth of the initial yield stress. It was proposed by Brenner that the Lüders band is propagated through an essentially perfect whisker by a double cross-slip mechanism; this proposal was based on the observation of multiple slip on copper whiskers in some cases. Observations which indicate that neither double cross-slip nor any other multiple slip mechanism is essential for the propagation of the Lüders band are reported in this paper.

The stress–strain curves of a number of copper whiskers (grown by the reduction of cuprous iodide) with ⟨100⟩, ⟨110⟩ and ⟨111⟩ orientations have been measured and observations made of the slip lines formed. By measuring the angles of the various slip traces it was found that for all three orientations the best developed faces were {110}; it was assumed that the traces all resulted from slip on {111} planes. In some cases goniometric measurements of the angles between the faces were also made and these were consistent with the indices of the faces deduced from the slip trace angles.

Observations were made with a low powered (×50) microscope during plastic deformation and under a high powered (up to ×800) microscope when the whisker had been removed from the tensile machine. In several cases whiskers were removed from the machine after some Lüders band propagation but before any work-hardening. The general conclusion from these observations was that, although slip on several systems did occur in some cases, when the Lüders band had propagated at a constant stress and no work-hardening had occurred, slip was confined to only one system. When the Lüders band propagated at a varying stress, slip on several systems was observed but the slip was much more intense on one system than on any other.

In Fig. 1 can be seen the slip which resulted in the case of a ⟨110⟩ orientation whisker after a Lüders band had propagated at a stress constant to within 2 per cent. Fig. 2 shows slip on two systems in the case of a ⟨100⟩ orientation whisker after the Lüders band had propagated at stresses which varied between 2 and 4 kg/mm². In Fig. 2 it can be seen that the "primary" slip extends along the whole length of the whisker and is intense in localized regions whilst slip also occurs on a secondary system in isolated patches. Some of the secondary slip is open to the interpretation that it is single cross-slip.

Carbon replicas shadowed at $\tan^{-1}\frac{1}{2}$ with gold–palladium were made of several deformed copper whiskers. These whiskers were deformed in tension in a simple jig so that the Lüders band had propagated

* Received June 25, 1959.

† Research Laboratory, Associated Electrical Industries Limited, Aldermaston Court, Aldermaston, Berkshire. Present address: Battersea College of Technology, Physics Department, Battersea Park Road, London, S.W.11.

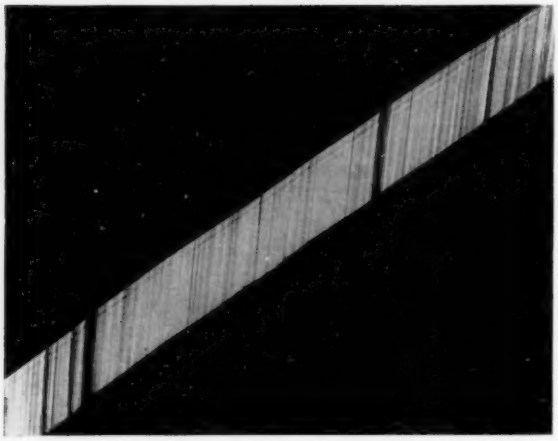


FIG. 1. Slip lines on a ⟨110⟩ orientation whisker. ×350

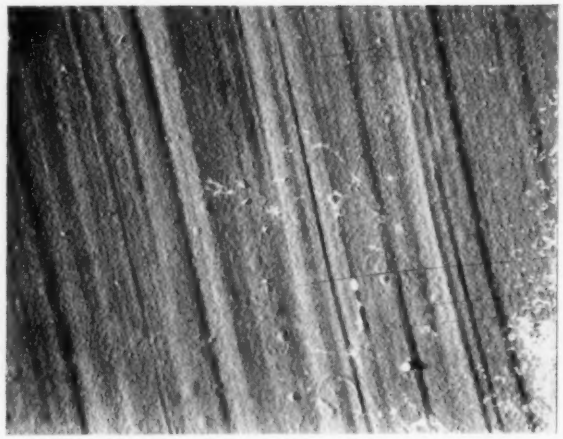


FIG. 3. Carbon replica of slip in strained copper whisker. ×8400

along the whisker. In Fig. 3 is shown a whisker of about 30 μ mean diameter from which satisfactory micrographs were obtained from two adjacent faces over a length of about 0.1 mm. Slip was visible on only one system for the whole area of both whisker surfaces investigated. It was difficult to determine the step heights accurately on these replicas but they were never more than about 300 Å; in some cases slip lines were seen to end. Replicas were obtained from two other whiskers with mean diameters between 10 and 20 μ; these showed slip on only one system. The mean spacings between the lines for these three whiskers were 0.03, 0.1 and 0.3 μ in order of decreasing whisker diameter.

Some replicas were obtained of a deformed whisker 11 μ wide and 2 μ thick and these present a strikingly different appearance from the three whiskers of larger mean diameter as is shown in Fig. 4. Although, like the other whiskers, slip has given rise to only one slip trace some of the slip lines are of great depth. Several slip lines, which appeared to be individual slip steps, were about 0.8 μ deep; this is an appreciable fraction of the whisker thickness. The mean spacing between the lines was about 0.4 μ.

DISCUSSION

Brenner has proposed that the Lüders band propagates along the whisker by a double cross-slip mechanism. However, cross-slip is a process which can occur in copper, at room-temperature, only at high stresses such as can exist at the head of a piled up group of dislocations (see Schoeck and Seeger[2]). For double cross-slip to occur, a further pile up of dislocations is necessary on the cross-slip system. In the case of whiskers of ⟨100⟩ orientation, in particular, the resolved shear stress factor is the same for the "cross-slip

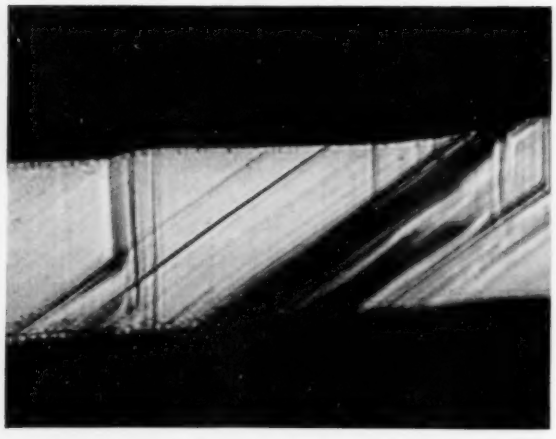


FIG. 2. Slip lines on a ⟨100⟩ orientation whisker. ×1050

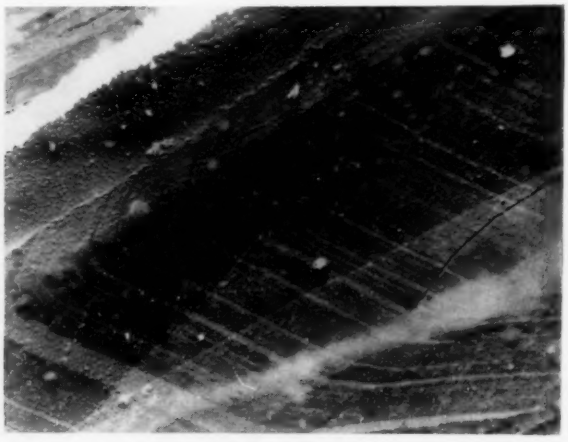


FIG. 4. Carbon replica of a deformed whisker of small diameter. ×8000

system" as for the "primary slip system." Thus if the double cross-slip mechanism were operative comparable amounts of slip would be expected on both slip systems. In contrast to this the experimental results indicate that visible cross-slip does not necessarily occur during the Lüders band propagation.

An alternative mechanism, more in agreement with the experimental results, is that the Lüders band propagates as a result of the stress concentration between the slipped and unslipped regions of the whisker. The observation of Lüders band propagation in zinc and cadmium whiskers by Coleman *et al.*[3] supports this idea in so far as slip on any planes other than the basal planes is extremely unlikely.

ACKNOWLEDGMENTS

The author wishes to thank Dr. T. E. Allibone, F.R.S., Director of this Laboratory, for permission to publish this Paper.

REFERENCES

1. S. S. Brenner, *J. Appl. Phys.* **28,** 1023 (1957).
2. G. Schoeck and A. Seeger in *Rep. Bristol Conf. on Defects in Crystalline Solids.* p. 340. Physical Society, London (1955).
3. R. V. Coleman, B. Price and N. Cabrera, *J. Appl. Phys.* **28,** 1361 (1957).

VOL.
8
1960

OXIDATION OF EVAPORATED MAGNESIUM FILMS*†

M. S. COHEN‡

The oxidation at low pressures and temperatures of evaporated magnesium films was studied by the Wagener flow method. In the initial period of the oxidation the sticking probability usually increased with the uptake of oxygen, suggesting a nucleation effect. In the second period of the oxidation the sticking probability fell rapidly; an average total oxide thickness of 27 Å was reached. A remarkable independence of the sticking probability to temperature and pressure changes was observed in this second period. The oxidized magnesium surfaces were studied by electron diffraction and electron microscopy.

OXYDATION DE FILMS DE MAGNESIUM OBTENUS PAR EVAPORATION

L'oxydation aux basses pressions et températures de films de magnésium obtenus par évaporation, a été étudiée par la méthode d'écoulement de Wagener. Dans la première période de l'oxydation, la probabilité de "stincking" augmente habituellement avec le captage d'oxygène, ce qui suggère un effet de germination. Dans la seconde partie de l'oxydation, la probabilité de "stincking" diminue rapidement; une épaisseur totale moyenne de 27 Å a été atteinte. Dans cette seconde période, l'indépendance de la probabilité de "stincking" par rapport aux variations de pression et de température est remarquable. La surface du magnésium oxydé a été étudiée par diffraction d'électrons et par microscopie électronique.

OXYDATION AUFGEDAMPFTER MAGNESIUM-FILME

Die Oxydation aufgedampfter Magnesium-Filme bei niedrigen Drücken und Temperaturen wurde mit Hilfe der Flußmethode von Wagener untersucht. In der Anfangsperiode der Oxydation wuchs die Haftwahrscheinlichkeit in der Regel mit der Menge des aufgenommenen Sauerstoffs. In der zweiten Periode fiel die Haftwahrscheinlichkeit schnell; im Mittel wurde eine Gesamtdicke des Oxydfilms von 27 Å erreicht. Die Haftwahrscheinlichkeit war in dieser zweiten Periode von Temperatur- und Druckänderungen bemerkenswert unabhängig. Die oxydierten Magnesium-Oberflächen wurden mittels Elektronenbeugung und Elektronenmikroskopie untersucht.

INTRODUCTION

The reaction rate of a clean metal surface with oxygen is initially very high, but at low temperatures the reaction rate soon decreases rapidly so that an oxide film is formed whose total thickness is extremely small. Very delicate techniques must therefore be used to study this phenomenon. The flow method developed by Wagener[1] for the study of gettering seems very promising for the study of the thin oxide region; Bloomer[2] has used it to study the oxidation mechanism of barium. The following is an account of the application of this method to the oxidation of evaporated magnesium films.§

APPARATUS AND PROCEDURE

The apparatus shown in Fig. 1 was constructed according to modern high vacuum techniques:[3]

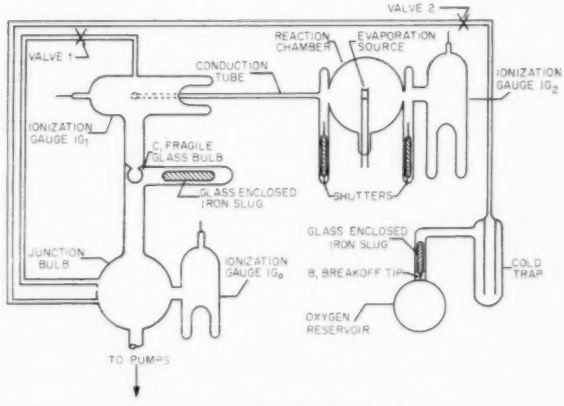


FIG. 1. Schematic diagram of the oxidation apparatus.

Pyrex glass was the main constructional material, the ionization gauges were of the Bayard–Alpert type, and the entire system could be baked out.

Care in the preparation of the magnesium evaporation source was necessary to prevent excessive evolution of gas during the evaporation of the magnesium. Magnesium‖ was first deposited on the evaporation source, a tab of thin tantalum sheet, in an auxiliary vacuum system. The source was then quickly sealed into the oxidation apparatus. At the

* Received July 9, 1959.

† This paper is based on a thesis presented to Cornell University in partial fulfillment of the requirements for the Ph.D. The work was supported by the Metallurgy Branch of the Office of Naval Research under Contract No. Nonr-401 (31).

‡ Department of Engineering Physics, Cornell University, Ithaca, New York. Now at Lincoln Laboratory, Massachusetts Institute of Technology.

§ More details of this work can be found in the Cornell Thesis or in *Tech. Rep. Off. Naval Res.* No. 2, Contract No. Nonr-401 (31), Project No. NR 036-035.

A discussion based partly on the present work has been presented by T. N. RHODIN in *Structure and Properties of Thin Films* edited by C. A. NEUGEBAUER, J. B. NEWKIRK, D. A. VERMILYEA, Wiley, New York (1959). See also H. SACK, *Z. Elektrochem.* **63**, 806 (1959).

‖ The author thanks the Dow Chemical Co. for providing triply sublimed magnesium (approximately 99.999 per cent pure).

proper time the magnesium was re-evaporated from the source by passing a current through the tantalum tab.

After the installation of the magnesium source the system, with both valves open, was evacuated and baked, and the ionization gauges were degassed. After the system had cooled valves 1 and 2 were closed, and the pressure was allowed to decrease by ion pumping. When the pressure had attained a value below about 5×10^{-9} mm Hg the magnesium was slowly evaporated on the Pyrex walls of the reaction chamber, the shutters being closed to confine the magnesium to this chamber. The breakoff tip B on the reservoir of reagent grade oxygen was then broken, and a flow of oxygen started. The oxygen flowed through a liquid nitrogen cold trap to the pumps, the flow rate being adjusted by valve 2 until a desired value of pressure was read by IG_0.

To start the experiment the large thin-glass bulb C was broken. Oxygen then flowed from IG_1 through the conduction tube into the reaction chamber. The flow rate could be found from the conductance of the conduction tube (130 cm^3/sec at 25°C) and the readings of IG_1 and IG_2, which were continuously monitored during the experiment. A constant temperature bath permitted the performance of experiments at temperatures ranging from −76°C to 136°C.

VOL. 8 1960

COMPUTATIONS

Let P_1 and P_2 be the pressures read by IG_1 and IG_2 respectively, F the conductance of the conduction tube, R the oxygen uptake rate, W the cumulative uptake, A the apparent geometric surface area of the magnesium, and S the sticking probability. The latter is defined as the ratio of the number of molecules taken up by the surface per second to the number impinging on the surface per second. Since the pressures are low enough for Knudsen flow[4] to occur,

$$R = F(P_1 - P_2). \tag{1}$$

Integrating (1) from time zero to time t yields $W(t)$. Since the number of oxygen molecules impinging on the magnesium surface per second per cm^2 is proportional to the pressure P_2,

$$S = R/kP_2A, \tag{2}$$

where k is a known constant.[4] R, W, and S as functions of time were computed for each experiment.

Not only the magnesium, however, but also gauge IG_2 acts as a sink for oxygen because of the pumping action of an ionization gauge. In the results presented below the flow rate due to the pumping action of IG_2 has been subtracted from the measured flow rate, where the former was taken as the flow rate at the end of an experiment when the magnesium is saturated and only IG_2 is consuming oxygen. Thermomolecular flow[4] was also taken into account in the computations for experiments in which the reaction chamber was not at the same temperature as the ionization gauges.

The errors associated with the experimental determination of S were analyzed by the method presented by Wagener[5]. The accuracy of S decreases as S decreases; for values of S of 10^{-2} and above the error is about 10 per cent, while for S of the order of 10^{-4} it is 25 per cent. Thus the accuracy decreases rapidly toward the end of an experiment.

Other sources of error may be associated with the ionization gauges. Activated oxygen may be produced and may influence the results of later parts of the experiments, as pointed out by Bloomer[2]. Schlier[6] has found that an ionization gauge may also produce carbon monoxide and carbon dioxide when operated in oxygen, but apparently there are circumstances in which the gauge is inactive.[7] This phenomenon could have been of importance probably only in the very last part of one of the present experiments: Wagener[5] has shown that carbon monoxide does not react with magnesium. Thus if carbon monoxide had been present in an appreciable quantity P_2 would have been large and this would have given an apparent low value of S. It is, of course, conceivable that traces of carbon monoxide or other gases were present and that these traces had some catalytic influence on the nucleation and growth of the oxide.

In summary, errors caused by chemical activity or by oxygen pumping of the ionization gauges should be of importance only near the ends of the present experiments, where the experimental error is large anyway.

RESULTS

Magnesium proved to be a difficult metal to study. The high reactivity with oxygen and glass, combined with a high vapor pressure and the refractory character of the oxide made the production of a clean and reproducible surface difficult. In the following discussion only those results are reported where there was reasonable assurance that a clean surface was present.

Since the structure of the surface influences the oxidation kinetics it was also desirable to examine the surface of the magnesium by electron diffraction and electron microscopy.

Surface structure investigations

A small slab of glass was put into the reaction chamber before every experiment, and the magnesium film evaporated on it was examined by electron

diffraction and electron microscopy* after the oxidation experiment was completed. Reflection electron diffraction revealed a strong tendency for the magnesium to be deposited with the basal plane parallel to the glass substrate; weak magnesium oxide rings were also present in each diffraction pattern.

To produce replicas for electron microscopy the magnesium surface was first shadowed with platinum at an angle of about 15°, and a carbon film was evaporated over the platinum. The replica was then separated from the magnesium by immersing the sample in nitric acid. Fig. 2 is a representative electron micrograph of such a replica.

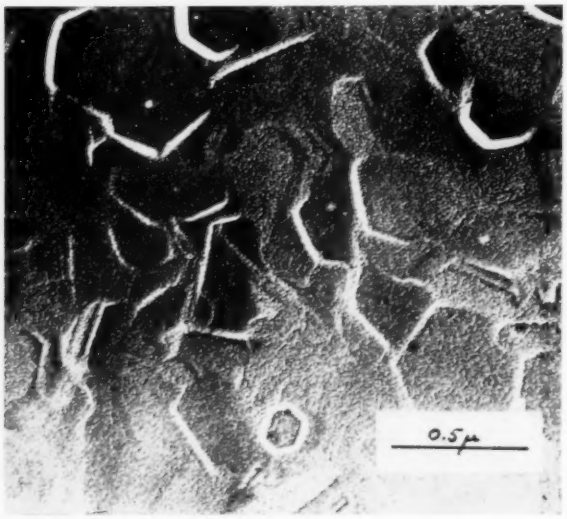


FIG. 2. Electron micrograph of a replica of a magnesium surface; Exp. 15.

Electron microscopy showed magnesium crystal platelets which were parallel or slightly inclined to the glass surface, with diameters ranging from 1,000 Å to 5,000 Å. The orientational tendency revealed by electron diffraction was thus confirmed. Examination of electron micrographs also showed that the true surface area should not be more than about 20 per cent or 30 per cent greater than the geometric area.

Unfortunately little can be concluded about the structure of the oxide not only because of the uncertain resolution of the replication technique, but also because the samples had to be transferred through air from the reaction chamber to the replicating apparatus. They were thus subjected to further oxidation, which gave an additional unknown treatment to the surface. Experiments using high-vacuum replication techniques, which should reduce the ambiguity, are now in progress.

* The author thanks Professor B. M. Siegel and Mr. J. Strozier for their assistance in the electron microscopy work.

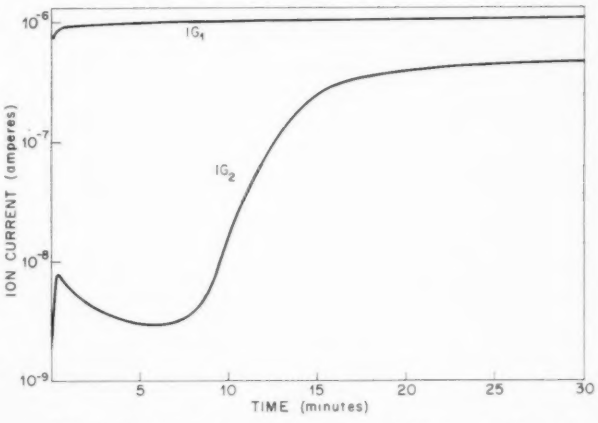


FIG. 3. Ion currents of gauges IG_1 and IG_2 versus time; Exp. 15.

Kinetics

In Fig. 3, the ion currents in gauges IG_1 and IG_2 are shown as functions of time for a typical experiment. The low values of the currents occurring during the first minute are caused by the large initial pumping speed of the ionization gauges and the glass walls. This large speed rapidly decays to a value of about 100 cm³/sec. The ionization gauge pumping is not again important until the period near the end of the experiment, where it is responsible for the fact that P_2 does not rise to meet P_1. This behavior of the ionization gauges was confirmed in auxiliary experiments performed without magnesium; results similar to those of Bills and Carleton[8] were obtained.

The results of the experiments are most conveniently expressed by curves of sticking probability S versus cumulative uptake W, as shown in Fig. 4 for a typical

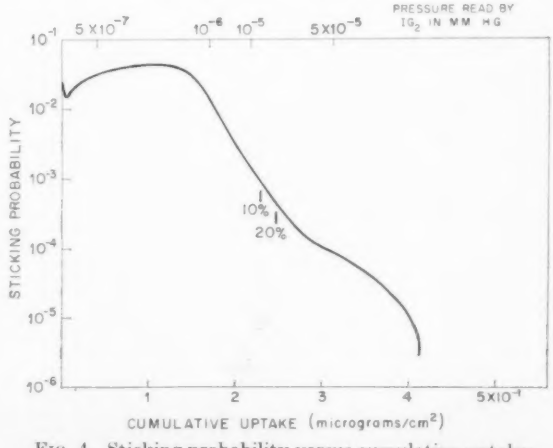


FIG. 4. Sticking probability versus cumulative uptake; Exp. 15.

TABLE 1. Summary of data from several experiments

Exp. no.	Temperature of exp. (°C)	Max. R (μg/cm^2 min)	W at knee in S vs. W curve (μg/cm^2)	Total W (μg/cm^2)	Max. S
5	27	0.30×10^{-2}	0.47×10^{-1}	2.35×10^{-1}	3.5×10^{-2}
8	72	1.46	0.96	3.83	6.02
9	136	0.80	1.43	4.00	5.23
10	−75	0.90	1.20	3.60	10.5
15	27	1.89	1.48	4.10	4.40
17*	27	—	1.48	3.16	—
18†	24 and −76	—	1.76	3.75	—

* Pressure jumps made.
† Temperature jump made.

experiment. Here W is expressed as the weight of oxide per unit area. In this figure, the points marked "10 per cent" and "20 per cent" show when the ionization-gauge pumping-speed correction, discussed above, amounted to 10 per cent and 20 per cent of the sticking probability, respectively. The pressure P_2 in the reaction chamber is indicated at the top of the figure. As is seen from Fig. 4, a first period of high sticking probability S is followed by a second period of rapidly decreasing S; this was observed in all the oxidation experiments. Results from several of the experiments are summarized in Table 1.

The pressure dependence of S was investigated in one experiment. At specific times during the period of decreasing S, valve 2 was abruptly either slightly opened or slightly closed. This changed the pressure P_1 and hence P_2 in a very short time; the time was so short that the surface condition, i.e. the cumulative uptake W, was essentially the same before and after the pressure jump. Thus information could be obtained about the change of S with pressure for a given state of oxidation. The ratios of pressures P_2 before and after the jump ranged from 2 to 15.

The data showed that S was proportional to P_2 to the −0.2 power. Because of the experimental errors, however, these results would also be consistent with a pressure-independent sticking probability.

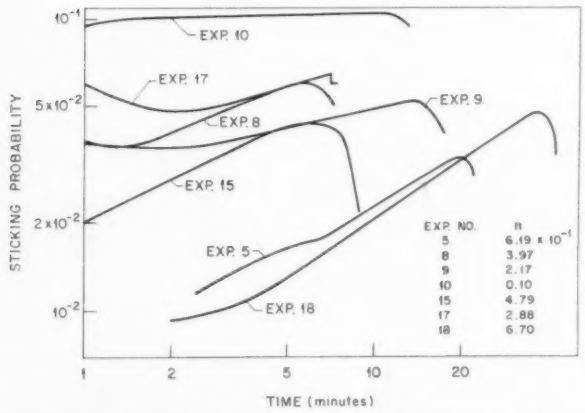


FIG. 5. Sticking probability versus time (log–log plot); the first period of several experiments. The value of n giving a fit to Equation (3) is given for each curve.

In another experiment the temperature was lowered from 24°C to −76°C during the period of decreasing S; this change was again abrupt in order to preserve the surface condition before and after the temperature change. The very small apparent change in S that did occur was probably caused by transients which arose when the temperature bath was installed. The fact that the oxidation characteristics are similar for experiments at different temperatures (Table 1) also indicates a small temperature dependence of the oxidation rate.

DISCUSSION

Region of high sticking probability

During the very first period of the oxidation of a metal, when oxygen reacts with the clean metal surface, it is to be expected that the sticking probability S will be much greater than during the later period, when a thicker oxide is present. An increase of S with cumulative uptake in the first period, however, as indicated in Fig. 5, has not generally been observed and is not expected on the basis of the usual concepts of oxide film formation. This effect has also been reported by Della Porta[9] for various gases on barium, and by Bloomer[2] for oxygen on barium; results by Eisinger and Law[10] for oxygen on silicon may also be an example of this phenomenon. The observations of Addiss[11] for oxygen on magnesium made with a vacuum microbalance are consistent with such an effect.

To explain this phenomenon, Bloomer[2] postulates the existence of nucleation sites on the clean metal surface; oxidation would preferentially start at these sites and the oxide would grow outward from them. With this model Bloomer obtains for a Wagener-type experiment (constant oxygen flow and therefore constant oxidation rate) the growth law

$$S \propto t^n, \qquad (3)$$

VOL. 8 1960

where the value of n is dependent on the mode of growth of the nuclei; for flat, circular "islands" n is 1/2, while for hemispherical islands n is 2/3.

It is seen from Table 1 and Fig. 5 that the quantities relating to the first (high S) period of an experiment vary considerably from experiment to experiment: The values of n, the cumulative uptake at the knee in the S versus W curve, and the maximum value of S attained are often quite different. In spite of these variations, however, it may be concluded from the present work and that of Addiss[11] that a nucleation phenomenon can indeed explain the experimental results, that the effect in question lasts for a period beyond that of the formation of the first monolayer, and that the phenomenon is very sensitive to the surface condition of the magnesium.

One possible cause of differences in results from experiment to experiment may be variations in the concentration and nature of the surface defects in the magnesium, which may serve as nucleation centers. These variations could easily be caused by differences in the conditions prevailing during the magnesium evaporation. Variations in the concentrations and possible types of nucleation centers may cause differences in the modes of growth of the oxide islands, thus leading to differences in the values of the exponent n in equation (3). If the concentration of nucleation centers were very high, for instance, the nucleation rate would be more important than the growth rate and a value of n close to zero would be expected. Very low values of n consistent with a high nucleation-center density were observed in some experiments not presented in Table 1. In these experiments the magnesium had reacted with the glass walls; this reaction may be associated with a high density of surface defects.

It should be noted, however, that the Bloomer mechanism is a simplified one, and does not explicitly consider the influence of such processes as chemisorption on the oxide and the metal, dissociation of the oxygen molecule, and surface diffusion.

Region of rapidly decreasing sticking probability

The following statements can be made for the region of decreasing S: The average total uptake, based on the bulk density of magnesium oxide, was 27 Å; this value agrees well with the data of Reimann[12], and Ehrke and Slack[13]. The sticking probability was remarkably independent of temperature and pressure in the low temperature and pressure range studied. The scatter in the experimental results (Table 1) serves to emphasize again the strong dependence of the oxidation process on the state of the magnesium surface.

Many oxidation theories for the thin oxide region have been presented by various authors. Of the rate equations predicted by these theories, two have been particularly useful: the direct logarithmic equation

$$R = dx/dt = Be^{-bx}, \tag{4}$$

and the inverse logarithmic equation

$$R = dx/dt = Ae^{a/x}, \tag{5}$$

where R is the uptake rate, x the oxide thickness, t the time and A, a, B and b are constants.

The data for the region of decreasing S can be fitted satisfactorily by the direct logarithmic equation (4) by choosing different values of b for the first and second parts of the experimental curves. A single value of a, on the other hand, allows a good fit of the data by the inverse logarithmic equation (5).

Among the many theories developed for the thin oxide region, the one suggested by Mott[14] has received considerable attention. Although the numerical values of the constant a calculated from the experiments are of the order of magnitude predicted by the theory, the lack of temperature and pressure dependence of the sticking probability are incompatible with this theory (and with many other theories) in its present form.

A theory proposed by Landsberg[15], on the other hand, which leads to the direct logarithmic equation, is in agreement with the experimentally-found pressure dependence; since the theory does not make specific statements about the temperature dependence it is not in contradiction with the present results. The strong influence of the surface condition is also compatible with Landsberg's mechanism, which emphasizes the presence of active centers on the surface. The change of the constant b to a lower value during the period of decreasing sticking probability may also be interpreted within the framework of the Landsberg theory: The existence of two (or more) varieties of active centers, which are deactivated by oxygen molecules at different rates, is postulated; this immediately leads to the experimentally observed result.

The Landsberg theory does not, however, contain specific statements concerning the nature of the active centers or the processes of their deactivation and the creation of new centers. It therefore cannot predict the values of the constants b and B.

It is quite likely that the oxidation of magnesium involves a complex heterogeneous, multistage process. It is thus not surprising that the existing theories of oxidation, which are based on highly simplified mechanisms, cannot accurately describe the present results in detail.

ACKNOWLEDGMENTS

The author expresses his gratitude to Professors H. S. Sack and T. N. Rhodin for helpful discussions on the experimental work and the preparation of the manuscript.

REFERENCES

1. S. Wagener, *Proc. Inst. Elec. Engrs.* Part 3, **99,** 135 (1952).
2. R. N. Bloomer, *Brit. J. Appl. Phys.* **8,** 40, 321 (1957).
3. D. Alpert, *J. Appl. Phys.* **24,** 860 (1953); D. Alpert and R. S. Buritz, *J. Appl. Phys.* **25,** 202 (1954).
4. S. Dushman, *Scientific Foundations of Vacuum Technique.* Wiley, New York (1949).
5. S. Wagener, *J. Phys. Chem.* **60,** 567 (1956).
6. R. E. Schlier, *J. Appl. Phys.* **29,** 1162 (1958).
7. J. Eisinger, *J. Chem. Phys.* **30,** 412 (1959).
8. D. G. Bills and N. P. Carleton, *J. Appl. Phys.* **29,** 692 (1958).
9. P. Della Porta, *Vacuum* **4,** 284, 464 (1954).
10. J. Eisinger and J. T. Law, *J. Chem. Phys.* **30,** 410 (1959).
11. R. Addiss, Thesis, Cornell University (1958).
12. A. L. Reimann, *Phil. Mag.* **18,** 1117 (1934).
13. L. F. Ehrke and C. M. Slack, *J. Appl. Phys.* **11,** 129 (1940).
14. N. F. Mott, *Rep. Progr. Phys.* **12,** 163 (1948–49).
15. P. T. Landsberg, *J. Chem. Phys.* **23,** 1079 (1955).

VOL.
8
1960

CRYSTALLIZATION FROM DILUTE METAL SOLUTIONS*

L. BENJAMIN† and R. F. STRICKLAND-CONSTABLE‡

The nucleation and crystal growth from solutions of zinc in mercury have been studied; the test amalgam formed one pole of a concentration cell whose e.m.f. was used as a continuous measure of the concentration. The metastable region in which spontaneous nucleation could not occur extended to 2°C below the saturation temperature. Nucleation at temperatures below the metastable region normally produced a crop of fine crystals mainly suspended in the liquid phase, which sometimes subsequently aggregated into a solid cap at the surface or walls. The rate of nucleation varied approximately as exp $(-\text{const}/\Delta T^2)$. Stirring increased the nucleation rate by only a factor of about 5. The rates observed were immensely greater than those reported by Hollomon and Turnbull for pure metals subdivided into small drops: this would suggest heterogeneous nucleation on foreign particles. But if a first crop of crystals was allowed to form and removed from the system the subsequent rate of nucleation was not significantly reduced by this treatment, and this would suggest that the rate cannot depend on the presence of foreign particles. One possible explanation is that nucleation may all occur only at the glass wall, and the growing crystallites are subsequently floated into the solution. Another depends on the further observation that if a small number of crystals is added to a solution cooled at such a rate as to keep it within the metastable region (where spontaneous nucleation cannot otherwise occur) an immense crop of nuclei is produced equal in number to that obtained with spontaneous nucleation at temperatures below the metastable region: in other words it would appear that nuclei breed nuclei with a high multiplication factor. The high rates of nucleation of a bulk liquid phase may therefore be due to this breeding of nuclei, and not to heterogeneous nucleation. If massive zinc is added to an amalgam which is in equilibrium with a solid phase which has been obtained by cooling a solution from higher temperatures, the massive zinc dissolves and is reprecipitated as very fine crystals; this is attributed to the metastability of the α-phase at the temperatures in question. From e.m.f. data on 2-phase amalgams heats of solution were calculated. The solid phase in these experiments could be largely freed from mercury by centrifugation, and was found to consist of hexagonal plates and prisms rounded by stirring.

CRISTALLISATION DANS LES SOLUTIONS METALLIQUES DILUEES

Les auteurs étudient la germination et la croissance des cristaux dans des solutions de zinc dans le mecure; l'amalgame d'essais constitue un pôle d'une cellule de concentration dont le f.c.m. sert de mesure continue de la concentration. La région métastable dans laquelle la germination spontanée n'a pas lieu s'étend jusque 2°C en-dessous de la température de saturation. La germination aux températures inférieures à la région métastable produit normalement un amas de cristaux en suspension dans la phase liquide qui, parfois, donnent un aggrégat à la surface ou sur les parois. La vitesse de germination varie approximativement comme exp $(-\text{const}/\Delta T^2)$. L'agitation augmente la vitesse de germination d'un facteur de 5 seulement. Les vitesses observées sont inversément plus grandes que celles signalées par Hollomon et Turnbull pour des métaux purs subdivisés en gouttelettes: ceci pourrait suggérer une germination hétérogène sur des particules étrangères. Mais si on forme un premier amas de cristaux et puis le retire du système, la vitesse de nucléation subséquante n'est pas réduite sensiblement par ce traitement, et cela montrerait que la vitesse ne peut dépendre de la présence de particules étrangères. Une explication possible est que la germination peut avoir lieu seulement sur les parois en verre et les cristallites en croissance sont ensuite entraînées de la solution. On observe ainsi que si on ajoute un petit nombre de cristaux dans la solution refroidie à une vitesse telle qu'elle reste dans la région métastable (où la nucléation spontanée ne peut avoir lieu autrement), un amas considérable de cristaux sont produits égaux en nombre à ceux obtenus lors de la nucléation spontanée à des températures inférieures à la région métastable: en d'autres mots, il apparaîtrait que les germes nourissent les germes avec un facteur de multiplication élevé. Les grandes vitesses de germination dans la masse du liquide peuvent par conséquent être dues à cette formation de germes et non à une germination hétérogène. Si on ajoute du zinc massif dans l'amalgame qui est en équilibre avec une phase solide obtenue par refroidissement de la solution à partir de températures plus élevées, le zinc massif se dissout et reprécipite en particules très fines; ce phénomène est attribué à la méta-stabilité de la phase α aux températures envisagées. Des données sur les f.e.m. d'amalgames biphasés, les chaleurs de solution sont calculées. La phase solide dans ces expériences a pu être séparée du mercure par centrifugation et il a été montré qu'elle est constituée de plaquettes et prismes hexagonaux, arrondis par l'agitation.

DIE KRISTALLISATION AUS VERDÜNNTEN METALLÖSUNGEN

Die Keimbildung und das Kristallwachstum von Lösungen des Zinks in Quecksilber wurden untersucht. Dabei bildete das untersuchte Amalgam den einen Pol einer Konzentrationszelle, deren EMK als kontinuierliches Maß für die Konzentration benützt wurde. Das metastabile Gebiet, in dem keine spontane Keimbildung stattfinden konnte, erstreckte sich bis 2°C unterhalb der Sättigungstemperatur.

* Received July 11, 1959. † Imperial College, London. Present address: National Research Council, Ottawa, Canada.
‡ Imperial College, London.

Die Keimbildung bei Temperaturen unterhalb des metastabilen Gebiets erzeugte normalerweise eine Menge von feinen Kristallen, die hauptsächlich in der flüssigen Phase suspendiert waren und die sich manchmal zu einer festen Schicht an der Oberfläche oder an den Gefäßwänden zusammenballten. Die Keimbildungsgeschwindigkeit variierte etwa wie $\exp(-\text{const}/\Delta T^2)$. Rühren erhöhte die Keimbildungsgeschwindigkeit nur etwa um einen Faktor 5. Die beobachteten Geschwindigkeiten waren ungeheuer viel größer als diejenigen, welche Hollomon und Turnbull in kleinen Tropfen reiner Metalle gefunden hatten; deshalb würde man eine heterogene Keimbildung an Fremdstoffteilchen vermuten. Aber wenn nach der ersten Bildung einer Menge von Kristallen diese aus dem System entfernt wurden, so wurde dadurch die nachfolgende Keimbildungsgeschwindigkeit nicht wesentlich erniedrigt und dies laßt vermuten, vermuten, daß die Geschwindigkeit nicht von der Anwesenheit fremder Teilchen herrühren kann. Zur Erklärung dieses Verhaltens kann man annehmen, daß sich Keime überhaupt nur an der Glaswand bilden können, und daß die wachsenden Kristalle anschließend in die Lösung geschwemmt werden. Eine andere Erklärung stützt sich auf die weitere Beobachtung, daß eine ungeheure Menge von Keimen erzeugt wird, wenn eine kleine Anzahl von Kristallen einer Lösung zugesetzt wird, die so abgekühlt wird, daß sie im metastabilen Bereich bleibt (wo sonst eine spontane Keimbildung nicht möglich ist). Diese Menge ist gleichgroß wie die, welche durch spontane Keimbildung unterhalb des metastabilen Bereichs entsteht: Es scheint kurz gesagt so, als ob Keime mit großem Vermehrungsfaktor Keime erzeugen. Stellt man durch Abkühlen von höheren Temperaturen ein Amalgam her, das mit einer festen Phase im Gleichgewicht steht und setzt festes Zink zu, so löst sich dieses und scheidet sich in der Form sehr feiner Kristalle wieder aus; dies wird dem metastabilen Zustand der α-Phase bei den in Frage kommenden Temperaturen zugeschrieben. Aus EMK-Daten von zweiphasigen Amalgamen wurden Lösungswärmen berechnet. Die feste Phase konnte bei diesen Versuchen weitgehend durch Zentrifugieren vom Quecksilber abgetrennt werden. Sie besteht aus hexagonalen Blättchen und Prismen, die durch das Rühren abgerundet sind.

INTRODUCTION

If liquid metals are to be used as heat transfer media in nuclear reactors difficulties may arise owing to the deposition at the cold end of material dissolved out of the container wall at the hot end. This practical problem provided the starting point to an investigation into the general subject of the deposition of crystals from dilute metal solutions. Zinc amalgams have been chosen because of their convenient solubility range (2–4 per cent w/w at 20–60°C) and because of their good electrochemical behaviour. Three solid solution phases are believed to exist[1-8] over the range studied, namely α (pure zinc), $T >$ 42.9°C; β (43–53 per cent w/w), T 20–42.9°C; γ (30–40 per cent w/w Zn) $T < 20$°C.

CONCENTRATION CELL

A concentration cell was set up in order to provide a means for the continuous estimation of the concentration of zinc in a test solution:

$$\text{Hg, Zn(1)} \mid \text{Zn SO}_4\text{ (aq.)} \mid \text{Hg, Zn(2)}.$$

If the concentration of the amalgam in one of the electrodes is maintained constant to serve as a standard, the e.m.f. of the cell serves as a measure of the instantaneous concentration in the other. Three (or more) static electrodes were often combined in one piece of apparatus—type (i). Later experiments were carried out in a type (ii) cell in which the test electrode was provided with a stirrer, and also with a cone and socket joint for easy removal of the amalgam, as shown in Fig. 1. The zinc used was supplied as a sample of special purity by U.K.A.E.A., Harwell.

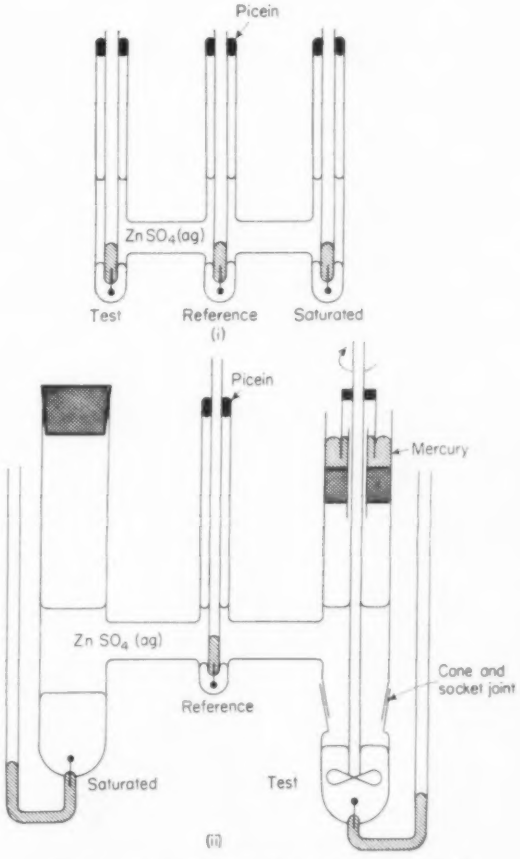


FIG. 1. Concentration cell, type (ii), (stirred).

VOL. 8 1960

NUCLEATION IN UNSTIRRED AMALGAMS

The first nucleation experiments were carried out in a type (i) 3 electrode cell. The reference electrode was a dilute amalgam (0.1–1 per cent w/w) of fixed composition, prepared by direct dissolution of zinc, this being first treated with dilute HCl and washed. A two-phase amalgam, containing excess solid zinc, constituted the 'saturated' electrode. Under equilibrium conditions the e.m.f. of this electrode should reflect the activity of zinc in the liquid phase in equilibrium with the solid phase. The test electrode contained sufficient zinc to be saturated at some convenient temperature T_0.

Platinum contacts, sealed into glass, were used as shown, the length making contact with the amalgam being kept as short as possible. The 2 M $ZnSO_4$ (aq.) was prepared from recrystallized salt. Removal of oxygen in amalgam cells is always difficult: most of the oxygen was removed in the present experiments by boiling the $ZnSO_4$ solution and placing in position in a stream of nitrogen. Before taking measurements the cell was always left a day or two during which any small amounts of oxygen left would react with zinc in the electrodes. The cell was placed in a thermostat controlled to ± 0.02°C.

The electrodes having been filled and set up, the thermostat was usually held at >10°C above the saturation temperature, T_0, of the test electrode, for >20 hr. It was then cooled at a rate of about 3°C/hr during which the e.m.f. of the test and saturated electrodes—both with respect to the standard electrode—were recorded. The results of a typical experiment are shown in Fig. 2. At T_0, the saturation temperature of the test amalgam, E(test) = E(sat.). Supersaturation occurs on cooling below T_0, until at the point C, approximately 3°C below T_0, crystallization takes place in the test electrode; on further cooling, E(test) approaches E(sat.). This experiment gave similar results when repeated with values of T_0 varying from 24 to 79°C.

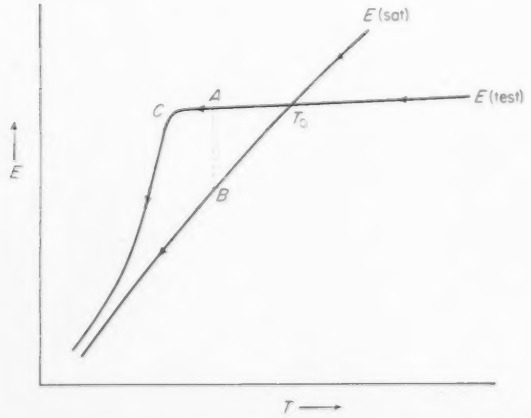


FIG. 2. e.m.f. (E) plotted against temperature (T) for a saturated and a test electrode. (Cooling).

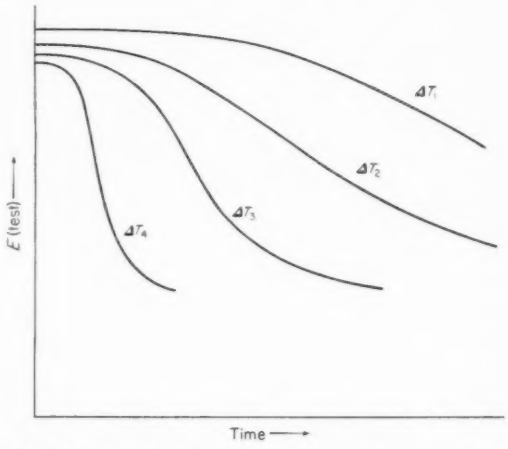


FIG. 3. e.m.f. against time at constant temperature for four different ΔT.

In a further type of experiment the rate of nucleation was measured at a *fixed* temperature, T_A, ($T_A < T_0$); the system was cooled rapidly from T_0 to T_A (see Fig. 2), and then was held at temperature T_A, during which the supersaturation was slowly removed along $A \ldots B$, and during which e.m.f. measurements were made. Results of a set of four runs with a given amalgam are shown in Fig. 3 where E(test) is plotted against time; the four runs correspond to four different values of $\Delta T = T_0 - T_A$.

The curves were always of the same sigmoid form, approaching E(sat.) at infinite time. ΔT values varied from about 2°C, when no crystallization occurred in 24 hr, to around 5°C. Corresponding changes in E(test) during crystallization were 200–800 μV. Because the system requires some time (15 min) to attain complete temperature equilibrium, inaccuracies are introduced into initial E(test) values: in cases of rapid crystallization, it was consequently necessary to estimate the initial values of E(test) by extrapolation of values from Fig. 2.

The shape of the curves may be accounted for by means of the following simplified theory. Over the small ranges in question E(test)–E(sat.) will be taken as proportional to C(test)–C(sat.), where C is the concentration of zinc. It is then assumed that a certain number of nuclei are first formed at about the same time and that no further nuclei are formed thereafter. If the subsequent rate of growth is assumed diffusion controlled, this rate can be considered proportional to the area of the crystal surface multiplied

by the concentration gradient. If the diffusion boundary layer is assumed of constant thickness, the concentration gradient will be proportional to $(C-C_{sat})$, where C is the concentration in the bulk phase (assumed uniform) and C_{sat} that at the crystal face, assumed saturated.* The area of crystal will be approximately proportional to $(C_0 - C)^{2/3}$ where C_0 is the initial bulk concentration. The rate of change of the bulk concentration will then be

$$\frac{dC}{dt} = -k(C - C_{sat})(C_0 - C)^{2/3} \qquad (1)$$

where k is a constant.

The shapes of the crystallization curves (Fig. 3) agree well with those predicted by equation (1), and in particular, the point of inflection is seen to occur at 40 per cent crystallization.

In order to use this equation it will be assumed that the reciprocal of the time, $t_{0.4}$, to reach the point of inflexion at 40 per cent crystallization can be considered to be a measure of the rate of nucleation, and the rates so calculated will be compared with theory in what follows. The results obtained with 3 unstirred electrodes are given in Table 1.

An equation representing the rate of nucleation of pure metals has been proposed by Hollomon and Turnbull[3] namely

$$I = \underset{A}{\left[\frac{nkT}{h}\right]}\left[\exp\left\{\frac{-16\pi T_0^2\sigma^3}{3(\Delta H)^2\,(\Delta T)^2 kT}\right\}\right]\underset{B}{}\underset{C}{\left[\frac{\Delta F_A}{kT}\right]} \qquad (2)$$

where n is the number of molecules of liquid metal per cm^3; k, the gas constant per molecule; h, Planck's constant; σ, the surface Gibbs function per unit area; ΔH, the latent heat of fusion per unit volume of solid; ΔF_A, the Gibbs function of activation for self-diffusion; and T, the abs. temp °K.

For solutions n will be the number of molecules of solute per cm^3, ΔF_A will refer to the diffusion of the solute. For the case of heterogeneous nucleation equation (2) is modified by Hollomon and Turnbull as follows: n is replaced by n', the number of molecules of solute in contact with the heterogeneous nucleating surfaces, and σ^3 is replaced by $\sigma^3 f(\theta)$, where θ is said to be the angle of wetting of solid nucleus on the solid nucleating surface. Alternatively $\sigma^3 f(\theta)$ may be regarded simply as a quantity which in some way measures the surface Gibbs function for the heterogeneous case.

* This treatment neglects the observation of Lewis and Bennett[2] who report that the chemical rate is partially controlling in the case of dissolution of zinc crystals in mercury.

TABLE 1. Comparative nucleation rates in unstirred amalgams

T(°C)	$1/(\Delta T)^2$	$t_{0.4}$(min)	log $(1000/t_{0.4})$
(a) 4.66 g	2.90 per cent w/w amalgam.		$T_0 = 40.90$°C
2.30	0.189	26	1.585
2.10	0.227	35	1.456
1.90	0.277	65	1.187
1.80	0.309	135	0.870
1.70	0.346	168	0.775
1.60	0.391	385	0.415
1.35	0.550	1000	0.00
(b) 6.454 g	2.65 per cent amalgam.		$T_0 = 36.87$°C
2.05	0.238	22.5	1.648
1.53	0.427	71	1.149
1.07	0.873	320	0.495
1.73	0.334	55	1.260
1.31	0.581	185	0.733
1.41	0.503	131	0.883
(c) 4.841 g	2.08 per cent amalgam.		$T_0 = 23.21$°C
4.01	0.062	12	1.921
2.41	0.172	119	0.925
3.01	0.110	39	1.409
1.99	0.253	350	0.456

Taking logarithms of both sides of equation (2) there is obtained the approximate relation

$$\log_{10} I \sim \text{const.} - \left\{\frac{16\pi T s^3}{2.3 \times 3(\Delta H)^2 k}\right\}(\Delta T)^{-2} \qquad (3)$$

where s^3 is written for either σ^3 or $\sigma^3 f(\theta)$ and where we have taken $\Delta F_A/kT$ as substantially constant with respect to temperature. The slope of $\log_{10} I$ plotted against $(\Delta T)^{-2}$ will be equal to the quantity in curly brackets, and from this the value of s can be calculated. The experimental results of Table 1 are plotted as $\log_{10}(100/t_{0.4})$ against $(\Delta T)^{-2}$ in Fig. 4, where it will be seen that the experimental points fall reasonably well on straight lines. The values of s calculated from the slopes are given in Table 2, where the molar volume of

TABLE 2. Unstirred electrode

Run	T_0(°C)	Slope	s
1	41	−6.0	3.30
2	37	−2.78	2.56
3	23	−7.78	3.67

zinc has been taken as 9.5 cm^3/g-atom and the latent heat of solution in mercury as 9.5×10^{10} ergs/g-atom.

If these values of $s = \sigma$ are used in equation (2) the rate to be expected for homogeneous nucleation may be calculated. For instance for $\sigma = 3.3$ and $\Delta T =$ (say) 2°C, bracket B is found equal to 3×10^{-2}. Taking the concentration as 0.029 w/w of solution at 41°C, the rate is found to be $I = 7 \times 10^{32}$. This is immensely greater than the value of 10^3–10^5 nuclei/sec

VOL. 8 1960

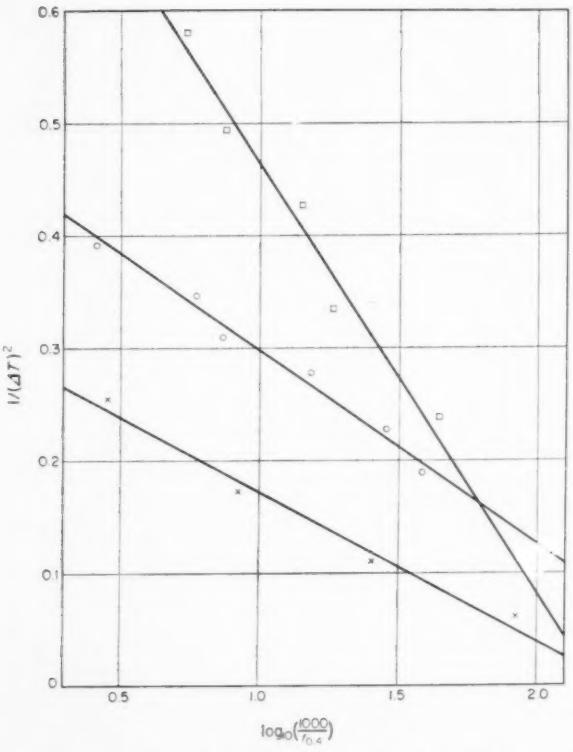


FIG. 4. $1/\Delta T^2$ against $\log_{10}(1000/t_{0.4})$ for three different amalgams (unstirred). T in °C, $t_{0.4}$ in min.
T_0 23.2°C × × × ; 36.9°C □ □ □ ; 40.9°C ○ ○ ○ .

which may be obtained by estimating roughly the number of small crystals formed in a given experiment by direct observation.

The low observed rate must therefore correspond to a very low value of bracket A. The low value of bracket A, the low values of s, and the fact that nucleation is being observed in a bulk phase would suggest, according to the expressed views of Hollomon and Turnbull[3], that nucleation is taking place on heterogeneous particles as nucleating centres.

If this is so it should be possible to observe a reduction in rate if means be found to reduce the number of nucleating particles. Accordingly experiments were carried out in which the test electrode without stirrer was slowly cooled until sufficient zinc had crystallized to form a solid cap at the amalgam surface; the liquid amalgam was then drawn away from the cap by sucking out a small portion of the liquid through a side arm, the cap being at the same time supported by a glass rod. In this way it was hoped to remove a considerable number of heterogeneous nuclei with the crystallized phase, when the remaining liquid amalgam should show slower nucleation rates.

In a typical experiment the test amalgam had a saturation temperature of 62°C, and after the cell had been kept at 80°C overnight the temperature was lowered to approximately 40°C for at least 12 hr. After separating the liquid amalgam from the solid cap the cell was heated overnight at some degrees above the new T_0 value, and the rate of nucleation was then determined as usual, by cooling to a fixed temperature below this T_0. The results of three experiments were as follows:

(a) Slow pre-crystallization from 43°C to 31°C: separated amalgam heated 5°C above new T_0 value overnight: then it was found that $t_{0.4} = 20$ min for $\Delta T = 3.00$°C. (Compare $t_{0.4} \sim 350$ min from unstirred results shown in Fig. 5.)

(b) Rapid pre-crystallization from 62°C to 41°C: separated amalgam held at 2.5°C above the new T_0 overnight: then $t_{0.4} = 8$ min for $\Delta T = 4.9$°C (Compare $t_{0.4} \sim 4$ min extrapolated from Table 1(a).)

(c) Slow pre-crystallization from 62°C to 43°C: separated amalgam heated 5°C above new T_0 overnight: then $t_{0.4} = 33$ min for $\Delta T = 4.87$°C. (Compare $t_{0.4} \sim 4$ min extrapolated from Table 1(a).)

Estimates have been given above in brackets of the values of $t_{0.4}$ for a corresponding run at the same T_0 and ΔT but without pre-crystallization, based on the values from the runs of Figs. 4 and 5. In case (a) the run with pre-crystallization is seen to be about 17 times faster and in case (c) about 8 times slower than in the original runs: in case (b) the rates are about the same. Since the complete removal of foreign nuclei might be expected to increase the possible supercooling to a figure measured in some tens of degrees, the relatively small effect on the rates just quoted is hardly considered significant and is not much greater than the chance variation between successive batches of amalgam. These observations appear therefore to throw some doubt on the idea that nucleation is on heterogeneous particles suspended in the liquid. Other explanations are taken up in the Discussion.

NUCLEATION IN STIRRED AMALGAMS

It was observed that when using stirring rates of 1000 r.p.m. in type (ii) cells, E(test) was lowered by 100–150 μV in concentrated amalgams, and by much larger values in dilute. However, when stirring was stopped, E(test) rapidly returned to its static value over approximately 30 sec. In crystallization rate studies, therefore, stirring was stopped one minute prior to measuring e.m.f. values. This gave much more consistent results than trying to measure e.m.f. with

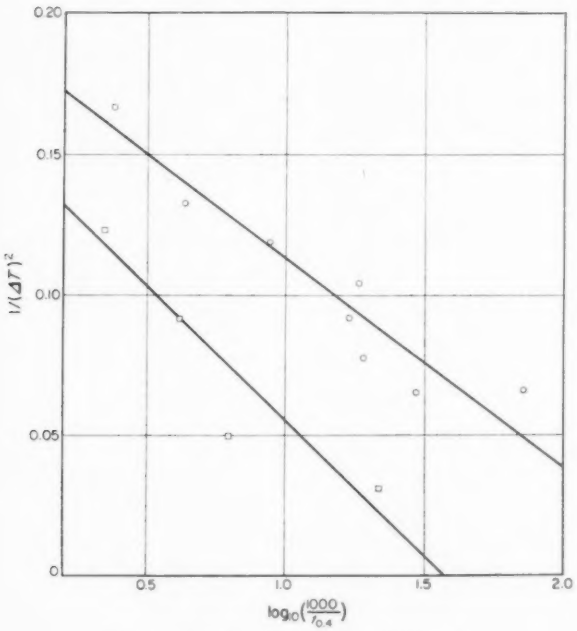


FIG. 5. $1/\Delta T^2$ against $\log_{10}(1000/t_{0.4})$. Unstirred □ □ □; stirred ○ ○ ○.

VOL. 8 1960

continuous stirring. Values for nucleation rates in the amalgam stirred at 700 r.p.m. were compared with static values in the same amalgam and electrode, results being shown in Fig. 5. The results were considerably more erratic than in unstirred systems: they show that the stirred rate is only about 5 times greater than the unstirred.

SOLUBILITY AND ACTIVITY COEFFICIENTS

Experiments, not reported in detail were undertaken, which substantially confirmed the solubility measurements of Cohen and Inouye[6]. Activity coefficients were also measured and found to be largely temperature independent, this point being of significance in the calculations of heats of solution given later.

CRYSTALLIZATION

Experiments were carried out in a glass vessel to study qualitatively the effect of cooling, stirring, etc., on the nature and quantity of the crystals produced. Both α and β phases are known to form hexagonal crystals. On cooling a solution below T_0, two extreme cases were observed. In the first a very large number (about 250,000 in 4 g amalgam) of minute crystals about 0.1–0.2 mm diameter, were found suspended in the liquid phase, as illustrated in Fig. 6, the glass wall of the crystallization cell being free from attached crystals. In the other extreme case the whole of the crystallized solid formed a cap on the surface, together with a narrow collar round the wall just below the cap and attached to it, and with a few isolated crystals attached to the clear glass below the collar. Rapid stirring, rapid cooling and smooth glass walls tended to produce the first result. Slow cooling of an unstirred amalgam in a cell with roughened walls produced the maximum adhesion as in the second case. Intermediate results in which the crystals were partly suspended in the liquid and partly attached to the walls or forming a solid cap on the surface could be produced by various combinations of the external conditions.

The collar of crystals referred to above was only loosely attached to the wall, and could easily be separated from it: but in certain experiments, especially at slow rates of cooling, a certain small number (up to ~1000 in certain cases) of crystals appeared to be growing firmly attached to the wall: it is possible that these were directly nucleated on the wall. As a



FIG. 6. Examples of crystals suspended in the liquid phase: rounded hexagonal prisms 0.1–0.2 mm diameter. Rapid cooling, stirred.



FIG. 7. Crystallites produced by seeding with massive zinc with stirring and slow cooling. Same magnification as Fig. 6.

result of a considerable number and variety of experiments it was clear that the bulk of the solid formed is usually grown in the solution as minute crystals: if it is finally found as a solid cap, or attached as a solid band to the glass wall, this was normally because of the aggregation and subsequent growing together of crystallites coming from the liquid phase, rather than to initial growth on the wall: and this applied both to smooth and roughened walls.

The individual crystallites formed in solution varied from perfect hexagonal plates to somewhat rounded and hollowed out forms, usually of very uniform size.

Separation of the mercury from the precipitated crystallites presented at first some difficulty, but it was ultimately found that a relatively complete separation could be effected by centrifugation with a no. 3 sintered filter as a support, using an acceleration in excess of 1000 g.

SEEDING EXPERIMENTS

Attempts were made to cause growth to take place on small numbers of nuclei added from an external source by holding the solution inside the metastable region, i.e. using a ΔT of 0.5–1.0°C which is less than that required to produce nucleation. Once crystallization had occurred as shown by removal of the supersaturation, the solution was allowed to cool very slowly, with stirring, as in the experiments just described, and again keeping ΔT at values not above 1°C: in this it was hoped that the added nuclei would grow and no others form.

Three types of added solid phase were used, consisting of (a) a drop of amalgam which had been recently nucleated by strong cooling and therefore contained a large number of small crystals, (b) numbers of small crystallites (0.1 mm diameter) obtained by centrifugation from previous crystallization experiments, and (c) massive zinc.

(a) With a small drop of nucleated amalgam, the resulting number of crystallites was approximately the same as if the whole amalgam had been allowed to nucleate and crystallize by strong cooling without the addition of external nuclei. This experiment, performed twice, appeared therefore to show that, although the added nuclei removed the supersaturation, they gave rise to an immense crop of new nuclei.

(b) When a known number (~200) of visible crystallites were used, a very similar result was obtained, namely the formation of a large number of small rounded crystals (aggregated at the walls) as found earlier when the whole amalgam was allowed to nucleate. Once again, therefore, these experiments show that large numbers of nuclei are produced under supersaturation conditions which normally exclude their formation.

(c) Similar numbers and size of crystals were obtained when seeding was effected by massive (polycrystalline) zinc. In this case all the crystals, about 500,000 in number, were present in the bulk of the amalgam as shown in Fig. 7, (which may be compared with Fig. 6 at the same magnification). Even more remarkable, however, was the reduction in size of the added zinc (0.66–0.060 g) which, therefore, instead of growing due to crystallization, had actually dissolved.

SOLUTION OF ZINC IN SATURATED AMALGAMS

In view of the result obtained when massive zinc was added to a supersaturated solution, a series of experiments were now carried out in which massive, amalgamated zinc was added to saturated amalgams,

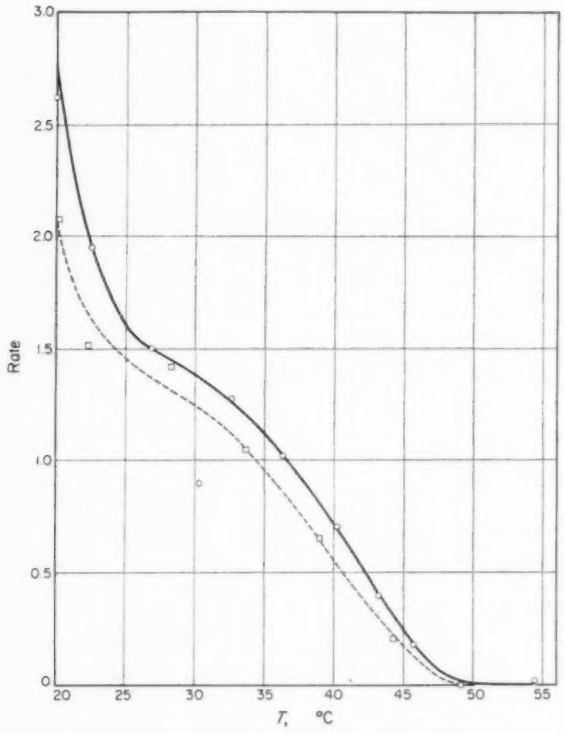


FIG. 8. Comparative rate of solution against temperature (°C).
Polycrystalline ○ ○ ○; single crystal □ □ □.

i.e. amalgams which were in equilibrium with a solid phase precipitated by cooling from a higher saturation temperature. The massive zinc was added for a given time, at a constant temperature, and then removed, centrifuged to free from liquid amalgam and reweighed. Any crystals loosely attached to the zinc, similar to those in the liquid, were scraped off before weighing. Cells of type (ii) were used with vigorous stirring (500–700 r.p.m.).

It was at one time suggested that this solubility of massive zinc in "saturated" solutions might be due to the presence in polycrystalline zinc of intergranular disordered zinc: accordingly runs were also carried out using single crystals of zinc. The runs in both series were performed in a random order, each run lasting 18 hr. The rates of both series are given in Table 3 and are plotted in Fig. 8 against temperature in °C. Since rate will presumably be proportional to surface area, the rates used in the figure were taken as proportional to $(m_0^{1/3}-m^{1/3})$, where m_0, m are the initial and final masses of added zinc. As can be seen, dissolution rates increase with lowering of temperature, being virtually zero above 50°C. Rates increase more rapidly about the two transition points, α–β at 42.9°C, β–γ at 20°C. These results may perhaps be explained on the grounds that the added α zinc is the less stable phase below 42.9°C and will therefore dissolve, the driving force for this dissolution increasing with lowering of temperature. Similarly, below 20°C the α zinc is even less stable and a further increase in dissolution should take place. Since the two types of added zinc show similar behaviour, dissolution cannot only be due to differences in solubility of granular and inter-granular zinc.

TABLE 3. Comparative dissolution rates for zinc in saturated amalgams (stirred at 500–700 r.p.m.)

T(°C)	m_0 (g)	m 18 hr (g)	per cent loss	comparative rate
(a) Polycrystalline zinc				
19.98	0.561	0.048	91.8	2.63
20.48	0.571	0.0	100	4.64
22.52	0.644	0.126	80.3	1.95
26.94	0.765	0.238	68.8	1.50
30.28	0.488	0.257	47.5	0.90
32.70	0.565	0.215	62.0	1.28
36.28	0.710	0.340	52.1	1.02
40.24	0.608	0.375	38.3	0.70
43.20	0.709	0.543	23.0	0.40
45.70	0.770	0.690	10.0	0.18
49.15	0.712	0.726	0.0	0.00
54.36	0.692	0.686	0.9	0.02
(b) Single-crystal zinc				
20.16	0.668	0.112	83.2	2.08
20.80	0.596	0.0	100	4.64
22.30	0.608	0.184	69.7	1.52
28.20	0.607	0.204	66.5	1.42
33.70	0.594	0.275	53.8	1.05
39.00	0.623	0.396	36.5	0.65
44.26	0.534	0.464	13.1	0.21

In order to confirm this explanation of the dissolution, an experiment was carried out with the β phase instead of zinc, this being obtained by removing from the walls of the cell, following the experiments with polycrystalline zinc, the solid layer of crystallized zinc. This had formed in the course of the experiments and was centrifuged to remove excess amalgam. A small portion was analysed and found to contain 58.7 wt. % Hg—very near that expected for the β phase at room temperature.[6] This specimen was fairly compact and its dissolution rate found to be 0.10 at 28.77°C—very low compared to that found with zinc, thus confirming that dissolution may occur due to α zinc being metastable below 42.9°C.

The fact that dissolution of α zinc also appears to occur at temperatures *above* 42.9°C is however difficult to explain on any grounds.

ANOMALOUS E.M.F. VALUES

While carrying out all types of experiment it was ocasionally observed that the e.m.f. of the test electrode (i.e. one which had recently been crystallized

VOL. 8 1960

by cooling and which contained only a little solid phase) remained indefinitely higher than that of the saturated electrode containing considerable excess of solid phase: the differences, δE, observed falling usually within the range 200–300 μV.

The effect does not appear consistently, even on repeat runs with the same electrode system. In experiments with cells of type (i) the effect was very rarely observed; also, the presence of δE was usually, although not always, more apparent in a cell which had been in use some days or weeks when the temperature was continually being raised and lowered during runs. Leads and contacts were not responsible for the effect since their interchange or renewal did not alter the e.m.f. The effect was usually absent when both electrodes were stirred and only occasionally present when neither electrode was stirred.

Changes in e.m.f. of two-phase zinc amalgams with time have been observed by Cohen and van Ginneken[9]. The effects were attributed by these authors to the non-equilibrium of the α and β phases and it is reasonable to suppose that the present δE effect is also connected with this phenomenon, although it has not so far proved possible to lay down the precise form of this connexion. A reconsideration of the experimental work given earlier will show that none of the principal conclusions need be invalidated by the possible existence of this effect. In any case in most of the experiments the data obtained showed that no δE effect was in fact present. In the seeding experiments the existence of a δE effect would in any case mean that the true supersaturation was even less than that apparently observed.

SOLUBILITY AND HEAT OF SOLUTION

Two cases are to be considered, namely the heat of solution of zinc (α phase) at temperatures above 42.9°C, and that of the β phase below this temperature. The heats of solution considered here will be the heats absorbed when 1 mole of the solid phase dissolves at constant temperature into an infinite liquid phase which will be just saturated at the end of the process. (The significance of the different kinds of latent heat of phase change has been discussed by Strickland-Constable[4].) The heat of solution of pure zinc will be

$$\bar{H}_L - H_S = RT^2\left(\frac{\partial \ln (x_L \gamma_L)}{\partial x_L}\right)_T \left(\frac{dx_L}{dT}\right)_{sat} \qquad (4)$$

where $\bar{H}_L$ is the partial molar enthalpy of zinc in the liquid phase, H_S the enthalpy of solid α zinc, x_L the mole fraction of zinc in the liquid phase on the saturation line, γ_L the activity coefficient of zinc in the liquid phase based on $\gamma_L \to 1$ for $x_L \to 0$; sat refers to saturated liquid phase.

Since, as already stated, γ_L is virtually temperature independent in the composition ranges in question, equation (4) may be written

$$\bar{H}_L - H_S = RT^2\left(\frac{d \ln (x_L \gamma_L)}{dT}\right)_{sat}.$$

The e.m.f., E, of a cell having an electrode consisting of liquid amalgam saturated with solid α zinc, and a standard dilute amalgam electrode will vary with temperature according to the equation

$$\frac{d \ln (x_L \gamma_L)}{dT} = \frac{nF}{R}\frac{d(E/T)}{dT}$$

where x_L, γ_L refer to the saturated electrode. Consequently

$$\bar{H}_L - H_S = nF\left(\frac{d(E/T)}{d(1/T)}\right)_{sat}. \qquad (5)$$

If E/T is plotted against $1/T$ the slope will be equal to $(\bar{H}_L - H_S)nF$.

The corresponding heat of solution of the β phase, $\Delta H(\text{L})$, is given by the equation

$$\Delta H(\text{L}) = T(x_S - x_L)\left(\frac{\partial^2 G_L}{\partial {x_L}^2}\right)_T \left(\frac{dx_L}{dT}\right)_{sat} = 0.$$

This is obtained at once from the general equations for phase equilibrium: it is for instance derived from equation (25) of Strickland-Constable[4] by putting $dP = 0$, by equating $\Delta S(\text{G})$ of that equation to $\Delta H(\text{L})/T$, and by changing G to L and L to S in the other sub- and super-scripts labelling the phases. G_L is the molar Gibbs function of the liquid phase; x_S the mole fraction of zinc in the solid phase.

Now

$$\left(\frac{\partial^2 G_L}{\partial {x_L}^2}\right)_T = \frac{1}{1 - x_L}\left(\frac{\partial \mu_L}{\partial x_L}\right)_T = \frac{RT}{1 - x_L}\left(\frac{\partial \ln (x_L \gamma_L)}{\partial x_L}\right)_T$$

where μ_L is the chemical potential of zinc in the liquid phase, and therefore

$$\Delta H(\text{L}) = \frac{x_S - x_L}{1 - x_L} RT^2\left(\frac{d \ln (x_L \gamma_L)}{dT}\right)_{sat}$$

$$= \frac{x_S - x_L}{1 - x_L} nF\left(\frac{d(E/T)}{d(1/T)}\right)_{sat}. \qquad (6)$$

The right-hand side of this equation is the same as that of equation (5) multiplied by the factor $(x_S - x_L)/(1 - x_L)$.

A cell having one saturated two-phase electrode (saturated at about 80°C) and one dilute standard electrode was allowed to cool very slowly with stirring

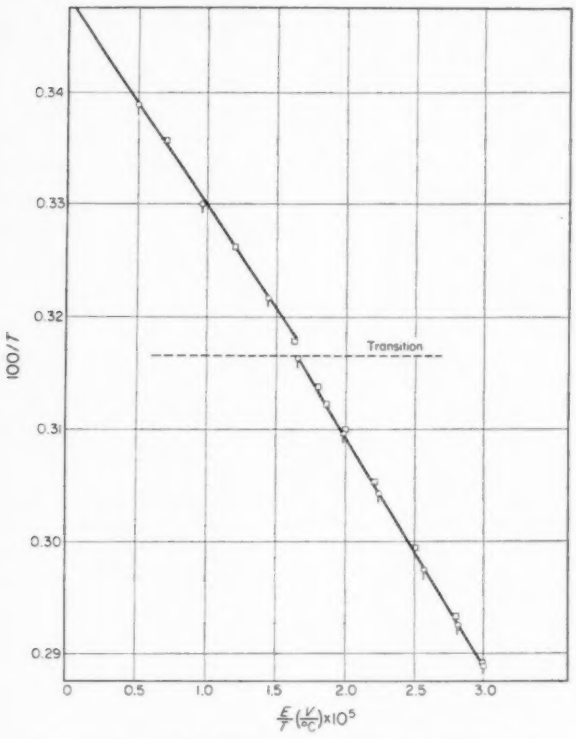


FIG. 9. Heat of solution experiments. $100/T$ against $\frac{E(\text{volts})}{T(^\circ\text{C})} \times 10^5$.

of the saturated electrode: from time to time readings were taken after the temperature had been held constant for half an hour. The results are plotted in Fig. 9 as E/T against $1/T$. The points appear to fall on two straight lines of nearly equal slope. That above the transition point of 42.9°C has a slope corresponding, according to equation (5), to a heat of solution of α zinc of 2,220 cal/g-atom. This is in good agreement with a figure of ~2,250 cal/g-atom which has been quoted in I.C.T.[5] for the heat of solution of pure zinc in mercury.

The curve below 42.9°C has a slope which is not very different from the one above: if it is assumed that the solid phase with which the liquid is in equilibrium is again α zinc the heat of solution according to equation (5) would be 2,520 cal/g-atom, a figure not very different from that obtained above 42.9°C. If on the other hand the solution is considered to be in equilibrium with the solid β phase, then the heat of solution will be given according to equation (6) as

$$\Delta H(\text{L}) = \frac{0.75-0.086}{0.914} \times 2{,}520 = 1830 \text{ cal/g-atom},$$

where $x_S = 0.75$, $x_L = 0{\cdot}086$ have been taken for the compositions.[1,6]

The latent heat of fusion of mercury is 556, so that a reasonable estimate for the heat of solution of the β phase would be

$$0.70 \times 2{,}220 + 0.30 \times 556 = 1722,$$

which is not very different from the figure of 1830 calculated from the experimental figures assuming that the solid is the β phase. The results below the transition point would therefore appear to be consistent with a solid phase which may either be stable β or metastable α.

DISCUSSION

In assessing the results of the rate of nucleation experiments, the low values of bracket A and of σ, and the fact that the experiments were on a bulk phase rather than on small drops would suggest that nucleation is occurring on heterogeneous particles suspended in the liquid. But the fact that the removal of a first crop of crystals did not reduce the subsequent rate of nucleation appears inconsistent with this view. Two possible explanations, which are not mutually exclusive, are offered.

By the first it would appear possible that nuclei are formed at certain points on the glass wall, and as they grow bigger are floated off into the liquid phase: such nucleating centres would not be affected by the removal of a preliminary crop of crystals, and the subsequent nucleation rate would remain unchanged.

The second explanation takes into account the observation that nuclei appear to breed nuclei—a small number of nuclei added to a slightly supersaturated solution apparently give rise to a crop of crystals immensely more numerous than the added nuclei. If this is the case it is no longer necessary to assume that nucleation of a bulk phase is mainly heterogeneous. The nucleation of small drops could still be due to an essentially homogeneous process governed by equation (2), but the nucleation of a bulk phase would occur by a two stage process: First a small number of nuclei are formed by a process that may be either homogeneous or heterogeneous according to circumstances, and whose rate might therefore depend on the presence or absence of foreign particles; in the second stage a much greater number of nuclei are produced by some process of reproduction.* According to this view therefore the high rate of nucleation of a bulk phase as compared with a small drop could in many cases be due to the high rate of the reproduction process, rather than to the presence of heterogeneous nucleating centres.

* This breeding process must however be considered to occur only if the supersaturation exceeds a certain limit, and there must still exist a region of very low supersaturation where crystals will grow without breeding.

VOL. 8 1960

If the existence of the reproduction process is accepted it will in general be necessary to take account of it in calculations of the rate of nucleation of bulk phases; more however would need to be known about the details of the process before an attempt could be made to account for the log $I/\Delta T^{-2}$ relation observed in the present case.

In conclusion, reference will be made to the fact that breeding of nuclei has already been postulated by other workers. For instance it is mentioned as an accepted fact by McCabe[7,10] when discussing industrial crystallization processes.

ACKNOWLEDGMENT

The authors gratefully acknowledge the provision of an apparatus grant, and of a maintenance grant for L. Benjamin by U.K.A.E.A., Harwell, who also kindly supplied specially pure specimens of polycrystalline zinc and other metals, and a single crystal of zinc.

REFERENCES

1. M. Hansen, *Der Aufbau der Zweistofflegierungen*. Springer, Berlin (1936).
2. J. B. Lewis and J. A. R. Bennett, *Transport and chemical control in the dissolution of metals in mercury*. (unclass.) Rep. Atom. Energy Res. Estab., Harwell, CE/R (1958).
3. J. H. Hollomon and D. Turnbull, *The Solidification of Metals and Alloys*: Symp. Amer. Inst. Min. (Metall.) Engrs., 12th Feb. 1950, p. 1. Wiley, New York (1951).
4. R. F. Strickland-Constable, *Proc. Roy. Soc.* **A209,** 14 (1951).
5. *International Critical Tables*, Vol. V, p. 187. McGraw-Hill, New York (1929).
6. E. Cohen and K. Inouye, *Z. Phys. Chem.* **71,** 625, (1910).
7. *Chemical Engineers Handbook*, p. 1056, 3rd Ed. (Ed. J. H. Perry). McGraw-Hill, New York (1950).
8. *Metals Handbook*, p. 1222. (Ed. Taylor Lyman.) American Society for Metals, Cleveland (1948).
9. E. Cohen and P. J. H. van Ginneken, *Z. Phys. Chem.* **75,** 437 (1911).
10. H. H. Ting and W. L. McCabe, *Industr. Engng. Chem.* **26,** 1201 (1934).

TRANSFORMATIONS IN THE β AND ζ PHASES OF THE SILVER–ZINC ALLOYS*†

W. J. KITCHINGMAN‡ and J. I. BUCKLEY§

The mechanisms of the transformations $\zeta \rightleftharpoons \beta$ in a silver–zinc alloy of 49.97 at.% silver have been investigated by means of electrical resistivity measurements. Values obtained at various rates of heating and cooling in the temperature range 210°C–340°C are given. The transformation $\zeta \rightarrow \beta$ takes place by breakdown of the ζ structure to give a partially ordered β structure which subsequently disorders. The transformation $\beta \rightarrow \zeta$ is accompanied by the formation of anti-phase domains.

TRANSFORMATION DANS LES PHASES β ET ζ D'ALLIAGES ARGENT–ZINC

Les auteurs étudient les mécanismes des transformations $\zeta \rightleftharpoons \beta$ dans un alliage argent–zinc à 49,97 at. % argent au moyen de mesures de résistivité électrique. Ils donnent les valeurs obtenues pour diverses vitesses de chauffage et de refroidissement entre 210° et 340°C. La transformation $\zeta \rightarrow \beta$ a lieu pour donner une structure β partiellement ordonnée qui se désordonne par la suite. La transformation $\beta \rightarrow \zeta$ est accompagnée par la formation de domaines antiphase.

UMWANDLUNG DER β- UND ζ-PHASE VON SILBER–ZINK-LEGIERUNGEN

Mit Hilfe von Messungen des elektrischen Widerstandes wurden die Umwandlungsmechanismen $\zeta \rightleftharpoons \beta$ an einer Silber-Zink-Legierung mit 49,97 Atom % Silber untersucht. Meßwerte für verschiedene Heizungs- und Abkühlungsgeschwindigkeiten im Temperaturgebiet 210°C bis 340°C werden angegeben. Bei der Umwandlung $\zeta \rightarrow \beta$ bricht die ζ-Struktur zusammen und ergibt eine teilweise geordnete β-Struktur, deren Ordnung dann verschwidnet. Bei der Umwandlung $\beta \rightarrow \zeta$ bilden sich Antiphasenbereiche.

VOL. 8 1960

INTRODUCTION

The β phase of the silver–zinc alloys occurs around the composition 50 at. % silver. It exists only above temperatures around 265°C and has a disordered body centred cubic structure. Below this temperature it transforms to a complex hexagonal structure, the ζ phase. The β phase may be retained on quenching from above 265°C but orders during the quench to give a body centred cubic structure of the cesium chloride type.

The structure of the ζ phase has been investigated by Edmunds and Qrashi[1,2]. They showed that the β and ζ structures are closely related. The b.c.c. β structure may also be considered as a hexagonal structure with its c axis along the cube diagonal. The ζ structure is obtained from the β structure by movement of atoms mainly in the direction of the cube diagonal. Both structures have a unit cell containing nine atoms. The ζ structure is partially ordered.

EXPERIMENTAL METHOD

An alloy of composition 49.97 at. % silver was prepared by melting high purity silver and zinc in an argon atmosphere. The ingot was homogenized for 48 hr at 550°C, hot forged and machined to give a cylindrical specimen approximately 1 cm in diameter and 10 cm long. It was then annealed in evacuated Pyrex tube at 250°C for several days to give the ζ structure.

The specimen was enclosed in a specially designed furnace as described by Buckley[3]. This could be evacuated to better than 10^{-4} mm of mercury. The temperature of the specimen was varied by differing heating and cooling rates applied to the furnace using a pulse controlled variac. Heating and cooling rates of 0.2°C/min and 2.5°C/min were used in the temperature range 210°C–340°C. Measurements of the resistance were made by comparing the potential fall across the specimen, with that across a standard resistance connected in series. Values of the resistance were also obtained under conditions of temperature equilibrium at various temperatures within the range 210°C–340°C. To obtain these the specimen was maintained at the measuring temperature until no further change in resistance occurred. The time for this was 3–5 hr depending upon the measuring temperature. The specimen temperature could be controlled during these measurements to ∓ 0.1°C.

RESULTS

The results obtained are shown in Figs. 1–4. Only the equilibrium curve is shown in full. The other curves are similar except for the regions around the transition temperature and the temperatures at which departures from linearity in the curve occur. These temperatures are noted below and the region of the

* Received July 6, 1959.

† This paper contains some results presented at a conference on metals of the X-ray group of the Institute of Physics, London, November 1958.

‡ Metallurgy Department, College of Science and Technology, Manchester.

§ Now at Brunel College of Technology, Acton, London.

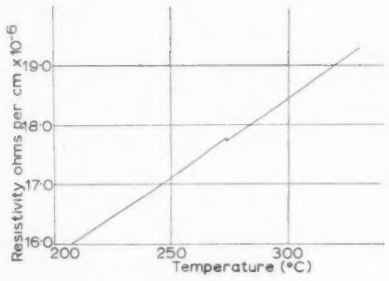


FIG. 1. Resistivity–temperature curve under conditions of temperature equilibrium in the range 210°C–340°C.

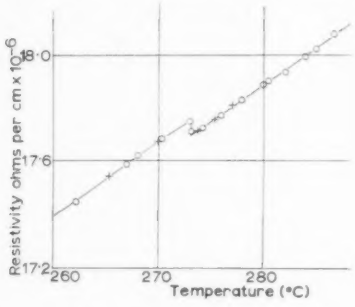


FIG. 2. Detail of the region around the transformation temperature of the resistivity–temperature curve under conditions of temperature equilibrium.
○ cooling. + heating.

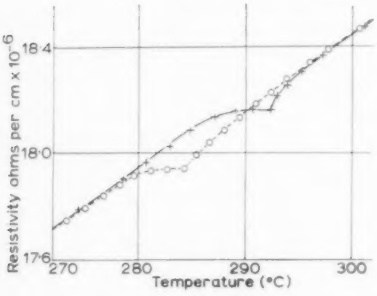


FIG. 3. Resistivity–temperature curves at fixed heating rates.
○ heating at 0.2°C/min.
+ heating at 2.5°C/min.

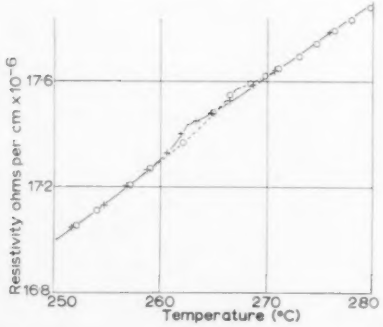


FIG. 4. Resistivity–temperature curves at fixed cooling rates.
○ cooling at 0.2°C/min.
+ cooling at 2.5°C/min.

transition temperature is shown in detail for each curve. Figs. 1 and 2 show the values under conditions of temperature equilibrium both on heating and cooling, the curves are coincident. Fig. 1 shows the complete curve, Fig. 2 detail around the transition temperature, Figs. 3 and 4 show the curves obtained at the heating and cooling rates of 0.2°C/min and 2.5°C/min. The heating curves at the two rates are similar, the higher rate of heating however displaces the transformation temperature from 284°C to 292°C. The equilibrium transformation temperature from Fig. 1 is 273°C. The full curves show that as the ζ phase approaches the transition temperature a departure from linearity occurs—at ~240°C for 0.2°C/min heating and at ~232°C for 2.5°C/min heating—both curves show an increase in resistivity above the linear extrapolated value. The equilibrium curve shows a similar feature occurring at ~241°C.

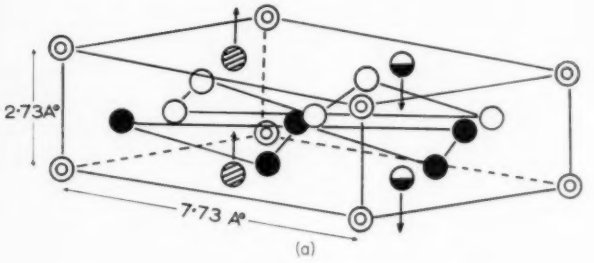
At the transition point the resistivity falls sharply as the β phase is formed. It then increases until a temperature of 298°C for the 0.2°C/min curve and 301°C for the 2.5°C/min curve after which both curves become linear. These features are absent in the equilibrium curve.

The curves on cooling at the two rates differ from the heating curves around the transition temperature. The cooling curve for the β phase departs from linearity at 278°C for the rate 0.2°C/min and 272°C for the rate 2.5°C/min. At the transition point both show a sharp peak, the major point of difference from the heating curves. The transition temperatures are 267°C for the 0.2°C/min cooling note and 262°C at 2.5°C/min. The ζ phase curves are not linear until ~241°C for the 0.2°C/min rate and ~232°C for the 2.5°C/min rate, the same as the heating curve values.

DISCUSSION

Examination of the results of Edmunds and Qrashi[1] show that the unit cell of the ζ structure and the β structure from which it is derived are similar. One third of this cell is shown in Fig. 5. The ζ structure is obtained from the β structure mainly by movements of the atoms labelled (b) and (b^1) in the directions shown. Their movement relative to the basal plane of the ζ phase structure is ~0.68 Å, their distance apart being 2.82 Å. The atoms in the positions (a), (b) and (b^1) are almost 100 per cent zinc whilst those in the positions (c) and (c^1) are 75 per cent silver.

Consideration of nearest neighbour distances shows that in the β phase structure each atom has eight nearest neighbours at distances of 2.73 Å. In the ζ phase structure each (a) atom which is zinc has six (c) or (c^1) atoms around it, which are 75 per cent silver,



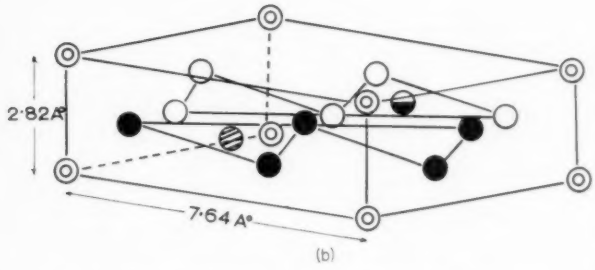


FIG. 5. Clinographic view of (*a*) β phase structure and (*b*) the corresponding ζ phase structure showing the changes in the unit cell dimensions and the movement of (*b*) and (b^1) atoms.
◎ (*a*) type atom. ○ (*c*) type atom.
● (c^1) type atom. ◍ (*b*) type atom.
◒ (b^1) type atom (after Edmunds and Qrashi).

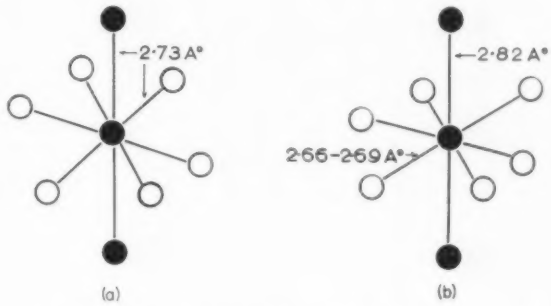


FIG. 6. Nearest neighbour groups in the corresponding (*a*) β phase structure, and (*b*) ζ phase structure.
● 100 per cent zinc. ○ 75 per cent silver.

at a distance of 2.66 Å, and two (*a*) atoms at a distance 2.82 Å. Each (*b*) atom, which is zinc, has six (*c*) atoms, 75 per cent silver at 2.69 Å, and two (*b*) atoms at a distance of 2.82 Å. A similar arrangement to this latter exists between the (b^1) and (c^1) atoms. These groups of eight which are found in the ζ structure are different from nearest neighbour groups in the β structure in that they are arranged parallel to the hexagonal *c* axis. Both arrangements are shown in Fig. 6.

The atoms in positions (*a*) were found to have a preferred thermal vibration of ~0·2 Å in the direction of the *c* axis. Some variation in the scattering due to (*b*) and (b^1) atoms also occurs, but the variation showed no definite direction of preferred vibration. The authors conclude that the groups of atoms (*c*) and (c^1) are in the position of close packing of spheres with (*a*) and (*b*) atoms occupying the cavities between them. These atoms have a freedom of movement of about 0.2 Å.

These facts, especially the favoured position of the zinc atoms, suggest that ordering of the β phase may be important in the transformations $\beta \rightleftharpoons \zeta$ and examination of the resistivity curves support this conclusion. The curve obtained by heating the specimen from the ζ state may be explained as follows: as the temperature rises the vibration of the atoms in the ζ structure becomes abnormal, the curve is no longer linear, at the transition temperature the ζ structure bonds break down and the atoms assume the structure of the β phase which is similar but with different bond distances. This β phase structure still retains the order present in the ζ phase structure. We therefore have the β phase structure with partial long range order since each ζ crystal transforms into a β crystal. This accounts for the dip in the resistivity curve as the temperature increases. Further increase in the temperature causes the long range order to break up and the structure becomes that of the disordered β phase. The resistivity curve shows a gradual increase in resistance followed by linearity in accordance with this.

The curve obtained on cooling is explained as follows. At some temperatures the β phase begins to order; Warren and Suoninen[4] have shown that short range order exists at temperatures above 265°C in this phase. During the ordering process areas form within a single β crystal with the degree of order associated with that of the ζ phase and β' phase. There is competition between these two structural forms which is dependent upon the rate of cooling. The crystal may be considered to be divided into domains which are out of phase with each other. The boundaries between these domains lead to reflection of the electrons after the manner of Lipson's[5] antiphase domains. The increase in resistivity due to this reflection causes the curve to peak. If the rate of cooling is low enough the domains will all form the ζ phase structure. This phase has the lesser free energy at low temperatures. The ordered β' phase, when obtained by quenching, transforms on heating at about 130°C to give the ζ phase.

A single β crystal on slow cooling will give rise to many ζ crystals. A somewhat greater rate of cooling

VOL. 8 1960

will produce a mixture of ζ and β' crystals, fast cooling gives only β' crystals. This can be shown by X-ray measurements and has been described by Owen and Edmunds[6].

The equilibrium heating and cooling curves show that the alloy of composition 49.98 at. % silver transforms at 273°C and that the width of the two phase region is ~1°C. This agrees with the equilibrium diagram of Hume-Rothery *et al.*[7].

SUMMARY

The transformations may be summarized as follows. As the temperature of the β phase falls, partial ordering occurs. When the zinc atoms are in certain preferred positions due to this ordering an adjustment of nearest neighbour distances takes place. Its effect on the crystal structure is to cause an expansion across the {11.1} faces and a contraction across the {30.0} faces. This leads to interaction between the Fermi surface and the Brillouin zone boundary which results in the stabilization of the ζ structure as described by Kitchingman[8]. Anti-phase domains occur in the transformation and it is characterized by a single β crystal forming many ζ crystals, probably in the manner described by Bergmann and Jarros[9].

On heating the ζ structure, an abnormal thermal vibration of the atoms occurs in the region 230°C–240°C depending upon the heating rate. At the transition temperature the ζ structure bonding breaks down and the structure takes up the excess energy by forming the β phase structure. This latter is partially ordered in the manner of the ζ phase. Since each ζ crystal will form a similar β crystal no anti-phase domains are formed, but a β phase structure with partial long range order is obtained. On further heating this disorders.

ACKNOWLEDGMENTS

The authors wish to thank Dr. H. T. Hall, College of Science and Technology, Manchester, and Dr. G. Bullock, Department of Physical Metallurgy, University of Birmingham, for many helpful discussions.

REFERENCES

1. I. G. Edmunds and M. Qrashi, *Acta. Cryst., Camb.* **4,** 417 (1951).
2. M. Qrashi, Thesis, Univ. Manchester (1949).
3. J. I. Buckley, Thesis, Univ. Manchester (1958).
4. B. E. Warren and E. Suoninen, *Acta. Met.* **6,** 172 (1958).
5. H. S. Lipson, *Progr. Met. Phys.* **2,** 1 (1950).
6. E. A. Owen and I. G. Edmunds, *J. Inst. Met.*, **57,** 297 (1938).
7. W. Hume-Rothery, K. W. Andrews, H. E. Davies and C. R. Oswin *Proc. Roy. Soc.* A**177,** 149 (1941).
8. W. J. Kitchingman, Conference on metals of X-ray group of the Institute of Physics, London, November 1958, to be reported in *Brit. J. Appl. Phys.*
9. G. Bergmann and W. Jaross, *Acta. Cryst., Camb.* **8,** 232 (1955).

THE KINETICS OF WUSTITE SCALE FORMATION ON IRON*

W. W. SMELTZER†

The kinetics of scale formation on iron in carbon dioxide atmospheres have been determined in the temperature range 600°–1100°C by a thermogravimetric technique. The scale constituents were identified by means of X-ray and microscopic examinations. The oxidation rates obeyed linear and parabolic time laws for short and long exposures respectively. Linear scaling was determined by the rate of incorporation of chemisorbed oxygen into the wustite lattice at temperatures lower than 910°C, and by dissociation of carbon dioxide and incorporation of oxygen into wustite at higher temperatures. The theoretical temperature coefficient of the parabolic rational rate constant for wustite formation was evaluated over the temperature range of its stability. Results from the literature on parabolic oxidation of iron in oxygen were in good agreement with the theoretical evaluation, whereas the results obtained for oxidation in carbon dioxide were of smaller magnitude above the Curie temperature of iron. This behavior was explained by the consideration that the chemical activity of oxygen in wustite at the oxide–gas interface was insufficient for equilibration of wustite with magnetite.

LA CINETIQUE DE FORMATION DE WUSTITE SUR LE FER

L'auteur étudie par une technique thermogravimétrique, la cinétique de formation de couches d'oxyde sur le fer dans une atmosphère de dioxide de carbone, dans le domaine de température de 600° à 1100°C. Il identifie les constituants de la couche d'oxyde par des examens microscopiques et aux rayons X. Les vitesses d'oxydation obéissent à des lois linéaires et paraboliques pour des expositions de courte et longue durées respectivement. L'oxydation linéaire est déterminée par la vitesse d'incorporation dans le réseau de wustite d'oxygène chemi-sorbé pour des températures inférieures à 910°C, et par la dissociation du dioxyde de carbure et l'incorporation d'oxygène dans le wustite aux températures plus élevées. Le coefficient de température théorique de la constante de la vitesse parabolique de formation de wustite est calculé pour le domaine des températures où elle est stable. Les résultats publiés dans la littérature sur l'oxydation parabolique du fer dans l'oxygène sont en bas accord avec les calculs théoriques, tandis que les résultats obtenus pour l'oxydation dans le dioxyde de carbone sont plus faibles au-dessus de la température de Curie du fer. L'auteur explique ce comportement en considérant que l'activité chimique de l'oxygène dans le wustite à l'interface oxyde-gaz est insuffisante pour équilibrer le wustite avec le magnétite.

KINETIK DER BILDUNG VON WÜSTIT-SCHICHTEN AUF EISEN

Mittels einer thermo-gravimetrischen Technik wurde die Kinetik der Bildung von Oxydschichten auf Eisen in einer Kohlendioxyd-Atmosphäre im Temperaturbereich 600°–1100°C bestimmt; die Bestandteile der Schicht wurden durch röntgenographische und mikroskopische Prüfmethoden identifiziert. Für die Oxydationsgeschwindigkeit gilt ein lineares bzw. parabolisches Zeitgesetz für kurze bzw. lange Einwirkungszeiten. Die lineare Schichtbildung wurde bei Temperaturen bis 910°C durch die Einbaurate des chemisorbierten Sauerstoffs in das Wüstit-Gitter bestimmt, durch die Dissoziation des Kohlendioxyds und den Einbau des Sauerstoffs in den Wüstit bei höherer Temperatur. Der theoretische Temperatur-Koeffizient der Geschwindigkeitskonstanten im parabolischen Zeitgesetz der Wüstit-Bildung wurde für den Temperaturbereich von dessen Gültigkeit bestimmt. Literaturangaben über das parabolische Oxydationsgesetz bei Eisen in Sauerstoff stimmen mit der theoretischen Bestimmung gut überein; die Ergebnisse für Oxydation in Kohlendioxyd sind jedoch oberhalb der Curietemperatur von Eisen von geringerer Größe. Das ließ sich durch die Überlegung erklären, daß die chemische Aktivität des Sauerstoffs im Wüstit an der Grenzfläche Oxyd-Gas für die Einstellung des Gleichgewichts Wüstit-Magnetit nicht ausreicht.

INTRODUCTION

Studies on the scaling of iron have provided results suitable for the understanding of many oxidation processes at elevated temperatures. The growth of multilayer scales of wustite, magnetite and hematite were determined to be controlled by the diffusion of the reactants across the oxide layers by Davies *et al.*[1] and Himmel *et al.*[2] in substantial agreement with the Wagner theory of parabolic scaling.[3] Recently, Engell[4] has evaluated the diffusion coefficient of iron vacancies in wustite. Since this evaluation was independent of vacancy concentration, substantion was obtained for the postulates of the Wagner theory. The oxidation of iron may be controlled to a constant rate by a chemisorption reaction for low values of the oxygen chemical potential at the oxide–gas interface. Hauffe and Pfeiffer[5], and Pfeiffer and Laubmeyer[6] have determined the influence of carbon dioxide and

* Received June 25, 1959. This work forms part of a research project sponsored by the Air Force Office of Scientific Research, Air Research and Development Command.

† Metals Research Laboratory, Carnegie Institute of Technology, Pittsburgh, Pennsylvania. Present address: Department of Metallurgy and Metallurgical Engineering, Hamilton College, McMaster University, Hamilton, Ontario, Canada.

VOL. 8 1960

oxygen pressures on these rates. By means of X-ray examination of the oxide scales, Arkharov[7] has shown that oxidation in carbon dioxide was limited initially by the rate of oxygen supply to the wustite surface, and finally by a decreasing supply of iron to the reaction surface leading to formation of an outer magnetite layer.

The kinetics of scale formation in carbon dioxide have not been determined over a broad temperature range. Moreover, Fischbeck *et al.*[8], Bénard and Talbot[9], and Seigneurin and Forrestier[10] have reported anomalous scaling kinetics in the temperature range of the magnetic transformation of iron and at the transformation temperature of alpha to gamma iron. In a further attempt to elucidate the reaction kinetics, the linear and parabolic scaling rates in carbon dioxide have been determined over the temperature range 600°–1100°C in this investigation. The scale constituents have been identified microscopically and by X-rays. To a first approximation, the dependence of the oxidation kinetics on temperature and pressure of the gaseous reactant may be explained by adsorption and oxidation theories.

EXPERIMENTAL

A glass vacuum assembly containing a metal spring balance similar to that described by Davies *et al.*[1] was used in the investigation of the oxidation kinetics. To allow carbon dioxide to flow around the suspended iron specimen, a gauge containing Octoil *S* high vacuum liquid was connected by a vacuum stopcock and Pyrex glass tubing to an outlet in the bottom of the mullite reaction tube. Carbon dioxide flowed downwards through this tube and escaped through the gauge to the laboratory environment. The temperature of the furnace in the region for suspension of a specimen was controlled to ± 2°C. Cathetometer measurements of the spiral metal spring were reproducible to 0.01 cm; this displacement corresponded to 0.5 mg weight changes of the 0.8 g specimens. Upon the assumption of a uniform thick oxide scale of bulk density on the geometric area of the specimen, 1 mg O/cm^2 was equivalent to 7 microns of wustite.

Scale formation was studied as a function of time and temperature in carbon dioxide at 765 mm pressure. Before oxidation, a specimen was annealed in a vacuum of 10^{-5} mm during the heating period of approximately 3 hr to 890°C and for 30 min at this temperature. The furnace was then adjusted to the test temperature and the specimen was annealed further for 1 hr. Carbon dioxide was then admitted to the reaction tube and controlled to a flow of 12 cm/min.

A series of specimens was quenched from the test temperatures to 0°C. For this purpose, one reaction tube was equipped with a mercury trap below the carbon-dioxide outlet. An oxidized specimen was allowed to fall freely into mercury held at 0°C by removal of the suspension wire from the pin on the revolving glass winch. After the furnace had cooled, the specimen was removed from the reaction tube by means of a magnet.

Cross-sections of the quenched specimens were examined microscopically. Ortho-bond *A* room setting resin supplied by the Vernon–Benshoff Company proved to be a satisfactory mounting plastic. The oxide phases in the scales were distinguishable after etching with a 5 per cent Nital solution. These phases were identified from X-ray patterns using the powder technique and intensity graphs obtained on a General Electric diffractometer by X-ray bombardment of the external scale surfaces.

The high purity iron has been described by Himmel *et al.*[2]. A conductometric analysis showed an impurity content of 0.004 per cent carbon. Slabs 3/8 in. thick were cut from the vacuum melted and cast 6×2 in. diameter ingot and cold rolled by multiple passes to 0.03 in. sheet. Specimens 0.02 in. thick were prepared from sections of these sheets by abrasion with metallographic papers to a 4/0 fineness. Carbon dioxide supplied by the Airco Corporation was purified of water vapor by passage through magnesium perchlorate desiccant.

RESULTS

The results of oxidation tests in the temperature range 600°–1100°C for exposures to 100 hr are illustrated in Figs. 1 and 2. In Fig. 1, the results are represented by rectilinear plots of weight gains, mg O/cm^2, versus time for exposures to 40 hr. The results for long exposures are represented in Fig. 2 by parabolic plots, weight gains versus (time)$^{1/2}$. The tests were completed in duplicate at each temperature; the reproducibility is illustrated by the rate constant evaluations in Figs. 4 and 5.

The constituents in the scales at different temperatures and exposure times are reported in Table 1. Microscopic examinations were used to identify phases which occurred as outermost layers or precipitates in wustite.

A photomicrograph of a scale formed on iron during a long exposure of 100 hr at 700°C is illustrated in Fig. 3. The duplex scale consisted of an outer magnetite layer on wustite. Also, the external magnetite surface exhibited projecting crystallites due to whisker type growth. Even at this relatively low

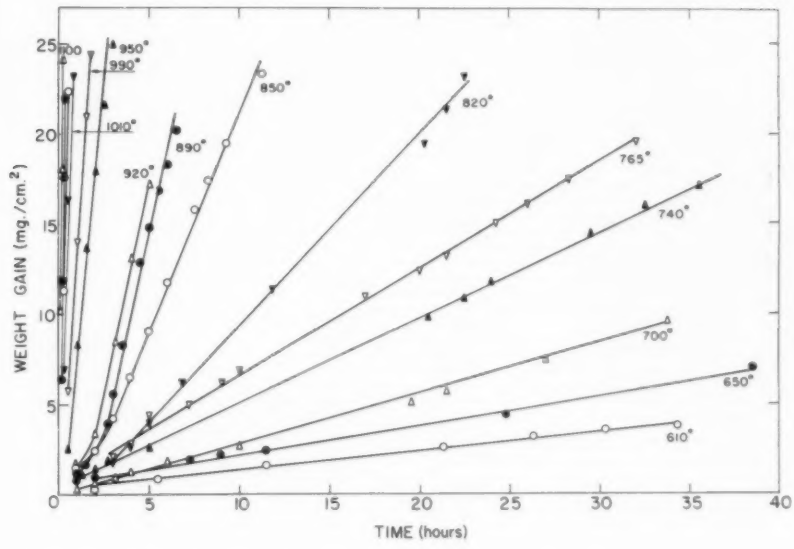


FIG. 1. Scaling of iron in carbon dioxide at 765 mm pressure over the temperature range 600°–1100°C.

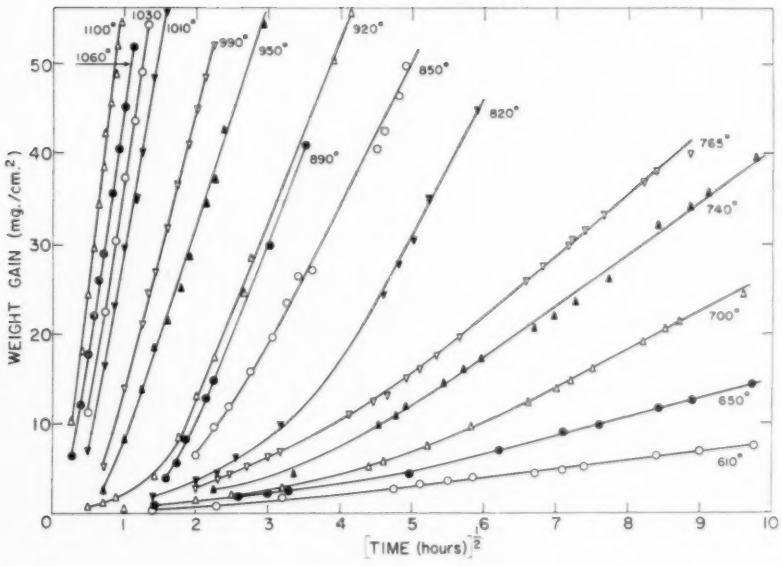


FIG. 2. Scaling of iron in carbon dioxide at 765 mm pressure over the temperature range 600°–1100°C.

temperature, wustite was the main consituent of the scale.

DISCUSSION

The plots in Figs. 1 and 2 demonstrate that the oxidation rates may be represented initially by a linear relationship which transforms to a parabolic relationship at long exposures. Consequently, the kinetics are interpreted by two time laws of metal oxidation:

$$\left(\frac{\Delta m}{A}\right) = K_L t \tag{1}$$

$$\left(\frac{\Delta m}{A}\right)^2 = K_P t. \tag{2}$$

The weight gain of a specimen for unit surface area, $\Delta m/A$, is equivalent to the thickness of the oxide layer, and K_L and K_P are the linear and parabolic rate constants of oxidation respectively.

The following reaction mechanism represents the processes for linear and parabolic oxidation of iron to wustite:

$$CO_2 \rightarrow O^{=}_{(ads)} + 2\oplus_{(o)} + CO_{(g)} \tag{3}$$

$$O^{=}_{(ads)} \rightarrow FeO + Fe^{++}_{\square\,(o)} \tag{4}$$

$$Fe^{++}_{\square\,(o)} + 2\oplus_{(o)} \rightleftharpoons Fe^{++}_{\square\,(i)} + 2\oplus_{(i)} \tag{5}$$

$$Fe + Fe^{++}_{\square\,(i)} + 2\oplus_{(i)} \rightleftharpoons \text{Null} \tag{6}$$

$$O^{=}_{(ads)} + 2\oplus_{(o)} \rightarrow \tfrac{1}{2}O_2. \tag{7}$$

VOL. 8 1960

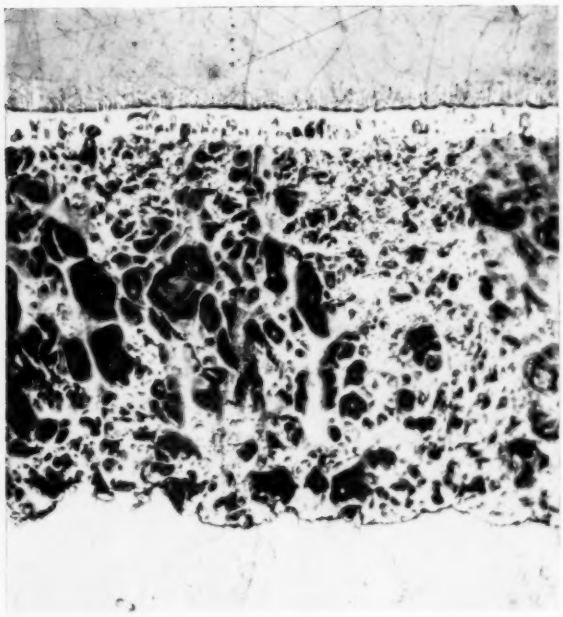


FIG. 3. Photomicrograph of duplex scale on iron after exposure for 100 hr at 700°C in carbon dioxide: ×160 (40 sec etch in 5% Nital solution).

The subscripts (g), (o) and (i) refer to gas, the lattice defect structure at the oxide–gas and metal–oxide interfaces repectively. For electrical neutrality in the oxide layer, an iron vacancy is equivalent to two ferric ions. These ions are designated positive holes in the reaction mechanism.

Oxidation would obey a parabolic law if the concentrations of vacancies and positive holes in equations (3), (4) and (7) were of sufficient magnitude to cause vacancy diffusion via its gradient across the oxide scale, equation (5), to determine the reaction rate. Since a linear law is observed, the processes represented in equations (3), (4) and (7) determine the initial reaction rate.

According to the viewpoint of Hauffe and Pfeiffer[5], the constant oxidation rates are determined by a

TABLE 1. Oxide constituents in scales on iron specimens quenched from test temperature

Temperature (°C)	Exposure (hr)	X-ray identification (P, powder d, diffractometer)	Microscopic examination (×500)
610	16	FeO, Fe_3O_4 (d)	
610	100	Fe_3O_4 (d)	
700	16	FeO, Fe_3O_4 (P)	
700	36.5	FeO, Fe_3O_4 (P)	precipitate of Fe_3O_4 from quench
700	100	Fe_3O_4 (d)	duplex scale
700	141	Fe_3O_4 (d)	duplex scale
850	8	FeO (P)	
850	10	FeO (P)	
920	4	FeO (P)	
920	10	FeO, Fe_3O_4 (P)	precipitate of Fe_3O_4 from quench
950	1	FeO (P)	
990	1	FeO (P)	
1010	4	FeO (d)	
1010	4	FeO, Fe_3O_4 (P)	precipitate of Fe_3O_4 from quench
1100	1	FeO (P)	

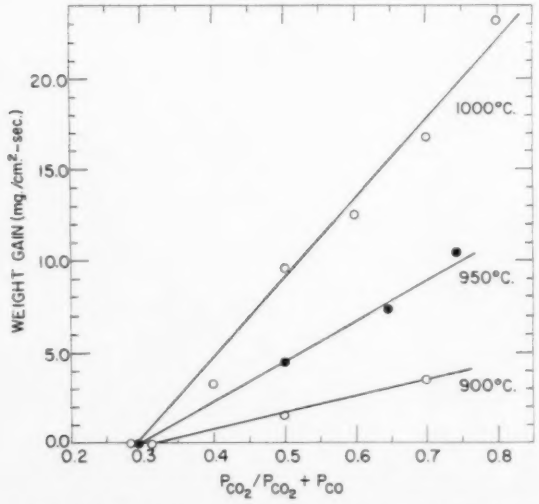


FIG. 4. The dependency of the linear rate constants for wustite scale formation on partial pressures of carbon dioxide at 900°, 950° and 1000°C (Hauffe and Pfeiffer[5]).

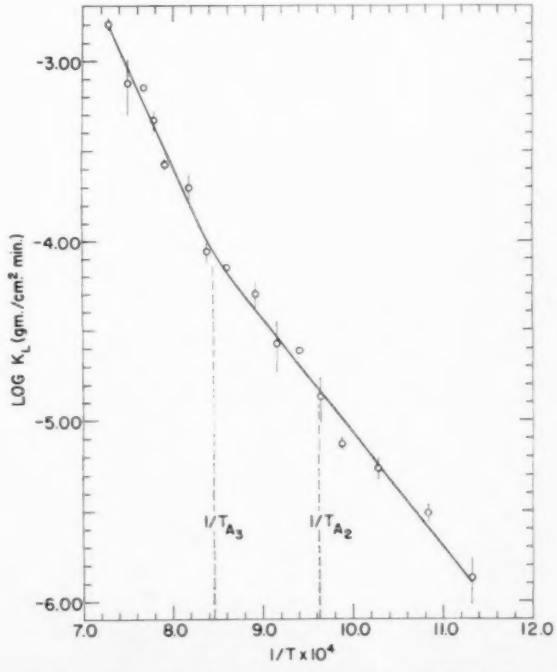


FIG. 5. The Arrhenius plot of linear rate constants for wustite scale formation.

chemisorption reaction. This reaction may be controlled by dissociation of carbon dioxide and/or incorporation of chemisorbed oxygen into the wustite lattice. If the surface coverage, θ, of absorbed oxygen is constant,

$$\frac{d\theta}{dt} = 0$$

$$= k_3(P_{CO_2} - P^*_{CO_2})(1 - \theta) - k_4\theta - k_7\left[\oplus_{(o)}\right]^2\theta \quad (8)$$

and,

$$\theta = \frac{k_3}{k_4 + k_7K}\,(P_{CO^2} - P^*_{CO^2}) \Big/ 1 + \frac{k_3}{k_4 + k_7K} \times (P_{CO_2} - P^*_{CO_2}). \quad (9)$$

Here, k_3, k_4 and k_7 are the rate constants for oxygen chemisorption, wustite formation and oxygen desorption respectively, $P^*_{CO_2}$ is the partial pressure of carbon dioxide over wustite equilibrated with iron, and K is a constant related to the equilibrium constant of reaction (6). If the assumption is made that linear oxidation is determined by incorporation of chemisorbed oxygen into wustite:

$$K_L = k_4\theta = \frac{k_3\,k_4}{k_4 + k_7\,K}\left(P_{CO_2} - P^*_{CO_2}\right) \Big/ 1 + \frac{k_3}{k_4 + k_7\,K}\left(P_{CO_2} - P^*_{OC_2}\right) \quad (10)$$

If $k_3 \ll k_4 + k_7K$,

$$K_L = k_4\theta = \frac{k_3k_4}{k_4 + k_7\,K}\left(P_{CO_2} - P^*_{CO_2}\right). \quad (11)$$

It is assumed that parabolic oxidation is determined by diffusion of reactants in the oxide scale according to the Wagner theory. Engell[4] has shown that the current of iron vacancies in wustite is

$$J_\square = 3D_\square \text{ grad } C_\square = 3D_\square\,(C_\square{}^{(o)} - C_\square{}^{(i)})/x. \quad (12)$$

Upon substitution of the following parameters in equation (12),

$$x = \frac{1}{\delta\bar{f}_2}\left(\frac{\Delta m}{A}\right) \quad (13)$$

$$y = \frac{C_\square}{C_{Fe} + C_\square} \quad (14)$$

$$J_\square = \frac{1}{16}\frac{d}{dt}\left(\frac{\Delta m}{A}\right) \quad (15)$$

the parabolic equation may be derived where,

$$K_P = 6\bar{f}_2\bar{\delta}D_\square\,\{(y\delta f_2)^{(o)} - (y\delta f_2)^{(i)}\}. \quad (16)$$

In these expressions $\bar{f}_2$ is the weight fraction of oxygen in wustite of average density $\bar{\delta}$. The superscripts (o) and (i) have the usual significance for properties at the oxide interfaces. Therefore, the parabolic rate constant may be evaluated from the diffusivity of vacancies, wustite densities and parameters of the iron–oxygen phase diagram if the activity of oxygen at the oxide–gas interface is equivalent to its equilibrium value.

Tests of the theoretical expression, equation (11), for the linear rate constant are illustrated in Figs. 4 and 5. The kinetics may be dependent to the first order on the partial pressure of carbon dioxide. Plots are illustrated in Fig. 4 of the scaling constants determined by Hauffe and Pfeiffer[5] in the temperature range 900°–1000°C versus the partial pressure of carbon dioxide. These plots show that the linear rate constants for wustite scale formation are directly dependent on the partial pressures of carbon dioxide greater than the values for equilibration of wustite with iron.

The activation energies of oxidation and vacancy diffusion may be equivalent since incorporation of oxygen into wustite, equation (4), is equivalent to vacancy formation in the vicinity of an adsorbed oxygen ion. Engell[4] has given two evaluations of the diffusivity coefficient from chemical-tracer and electrochemical measurements. These are,

$$D_\square(\text{cm}^2/\text{min}) = 1.22 \times 10^{-1} \exp -29{,}700/RT \quad (17)$$

$$D_\square(\text{cm}^2/\text{min}) = 2.35 \times 10^{-1} \exp -30{,}500/RT. \quad (18)$$

The Arrhenius temperature coefficient of the linear scaling constants is illustrated in Fig. 5. The constants may be represented by a linear plot below 910°C, the transformation temperature, T_3, of alpha to gamma iron. The activation energy of 28.8 ± 3 kcal/mole is equivalent to that for vacancy diffusion. Thus, equation (11) accounts for the pressure and temperature dependency of the scaling kinetics, and leads one to conclude that the scaling of alpha iron is determined by incorporation of chemisorbed oxygen into wustite.

The linear constants at temperatures greater than 920°C cannot be represented by the Arrhenius coefficient of the lower temperature range. The constants are larger than evaluations from this coefficient and, also, the activation energy of 50.5 ± 5 kcal/mole is much larger than the value of 30 kcal/mole for vacancy diffusion. The dissociation energy of carbon dioxide is 67.6 kcal/mole. Apparently, the dissociation of carbon dioxide and incorporation of chemisorbed oxygen into wustite are both rate determining processes of oxidation at high temperatures.

VOL. 8 1960

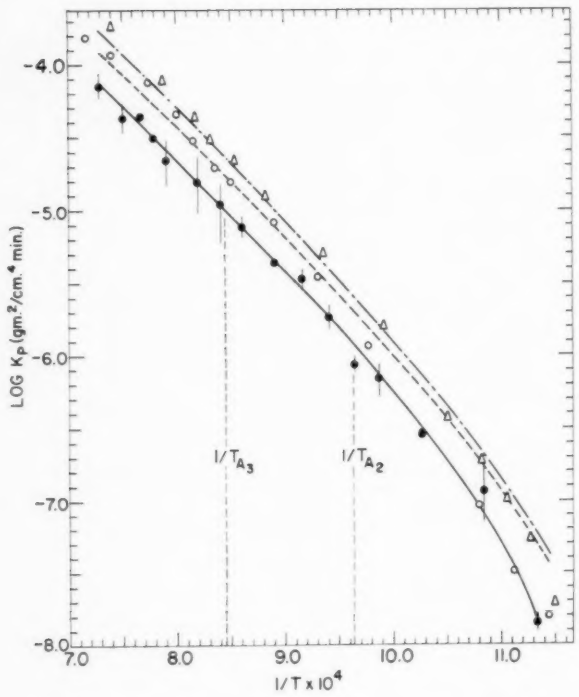


FIG. 6. Arrhenius temperature coefficients of parabolic oxidation constants:
—.— theoretical coefficient with $D_{\square}$ determined from electrochemical measurements (Engell[4]).
– – – theoretical coefficient with $D_{\square}$ determined from iron self-diffusion measurements (Engell[4]).
——— experimental coefficient of parabolic constants for oxidation in carbon dioxide.
△ experimental determinations of parabolic constants for oxidation in oxygen (Schmahl *et al.*[12]).
○ experimental determinations of parabolic constants for oxidation in oxygen (Davies *et al.*[1]).

This viewpoint is borne out by the finding that linear rapidly transforms to parabolic oxidation at temperatures greater than 920°C (Fig. 2). During the brief period of linear oxidation, the gradient of iron vacancies is rapidly established to a value for parabolic oxidation by an increase in the oxygen content of wustite at the oxide–gas interface.

To this time, the temperature coefficient of the parabolic rational rate constant for a metal has not been published. This coefficient for wustite scale formation is illustrated in Fig. 6. Two evaluations were carried out by means of equation (16). The parabolic constants were evaluated for 100° increments in the temperature range 600°–1100°C by using the two determinations for the diffusivity of iron vacancies, and data from the iron–oxygen phase diagram[4] and the density determinations of wustite.[11] The theoretical coefficients represent adequately the extensive determinations of Schmahl *et al.*[12] and Davies *et al.*[1] for the oxidation of iron in oxygen at 1 atm pressure. The occurrence of magnetite and hematite as outer layers on wustite has not been taken into account in the calculations because Paidassi[13] has shown that the relative thickness of these layers is only 5 per cent of the total scale thickness at temperatures from 700° to 1250°C.

The good agreement between the theoretical and experimental temperature coefficients for iron oxidation in oxygen contributes further substantiation for the validity of the Wagner theory[3] over the temperature range in which wustite is stable. It is to be noted that the temperature coefficient of the parabolic constants in carbon dioxide is smaller than the theoretical curve. Moreover, these constants at temperatures above the Curie point of iron are smaller than those for oxidation in oxygen at 1 atm pressure. This behavior may be explained by the following consideration: the chemical activity of oxygen in wustite at the oxide–gas interface in carbon dioxide is insufficient for equilibration of wustite with magnetite. Consequently, the gradient of iron vacancies in wustite is smaller during oxidation in carbon dioxide than in oxygen. The results of X-ray and microscopic examination in Table 1 substantiate this viewpoint. The scale consisted of wustite at temperatures greater than 700°C for the experimental exposures because the chemical potential of oxygen was insufficient for magnetite formation.

Evaluations of the parabolic constants in carbon dioxide and those by Davies *et al.*[1] in oxygen are equal but of smaller magnitude than the theoretical values below the Curie temperature of iron. Perhaps this phenomenon is associated with the effect of the metal substrate on the physical parameters of wustite. The oxide in the relatively thin scales may be under considerable stress since the molar volume ratio of bulk crystalline wustite to iron is approximately 1.7. This suggests that the parameters required to define the diffusion of vacancies through these thin scales are smaller than those used from the iron–oxygen phase diagram in the theoretical calculations.

Both theoretical and experimental Arrhenius coefficients of parabolic constants are curvilinear over the temperature range in which wustite is stable. Since the Arrhenius coefficient for the diffusivity of vacancies is linear, the curvature in the coefficient of oxidation constants is determined by the variation of wustite composition with temperature. Within the experimental accuracy, these coefficients are continuous at temperatures about the transformation point (910°C) of alpha to gamma iron. The curvatures in the plots are largest below the Curie point of iron (765°C) to the wustite eutectoid point (570°C)

wherein the composition of wustite and, therefore, the concentration gradient of iron vacancies undergo the largest variation.

SUMMARY

The kinetics of scale formation on iron in carbon dioxide atmospheres have been determined in the temperature range 600°–1100°C. Identification of the scale constituents by X-ray and microscopic techniques has shown that wustite was the only constituent at high temperatures for the experimental exposures, whereas wustite and magnetite formed a duplex scale at temperatures below the Curie point of iron. Linear scaling was determined by incorporation of oxygen into wustite at temperatures lower than 910°, and by dissociation of carbon dioxide and incorporation of oxygen into wustite at higher temperatures. The theoretical temperature coefficient of the parabolic rational rate constant was evaluated for wustite scale formation. Results from the literature on parabolic oxidation of iron in oxygen at 1 atm pressure were in good agreement with this evaluation. The temperature coefficient of the parabolic constants for oxidation of iron in carbon dioxide was smaller than the theoretical coefficient because the activity of oxygen in wustite was insufficient for formation of magnetite. Finally, the large curvature of the Arrhenius coefficient of parabolic oxidation constants from the Curie point of iron to the wustite eutectoid point was caused by the change of wustite composition with temperature.

ACKNOWLEDGMENTS

The author wishes to express his thanks to Mr. R. E. Miller for his assistance throughout this investigation, and to Mr. R. T. Keelan for structure determinations by X-rays.

REFERENCES

1. M. H. Davies, M. T. Simnad and C. E. Birchenall, *Trans. Amer. Inst. Min. (Metall.) Engrs.* **191,** 889 (1951).
2. L. Himmel, R. F. Mehl and C. E. Birchenall, *Trans. Amer. Inst. Min. (Metall.) Engrs.* **197,** 827 (1953).
3. C. Wagner, *Diffusion and High Temperature Oxidation of Metals: Atom Movements* p. 153. American Society for Metals, Cleveland, Ohio (1951).
4. H. J. Engell, *Acta Met.* **6,** 439 (1958).
5. K. Hauffe and H. Pfeiffer, *Z. Metallk.* **44,** 27 (1953).
6. H. Pfeiffer and C. Laubmeyer, *Z. Elektrochem* **59,** 579 (1955).
7. V. I. Arkharov, *Fiz. Met. Metalloved. Akad. Nauk.SSSR* **5,** 251 (1957).
8. K. Fischbeck, L. Neundeubel and F. Salzer, *Z. Elektrochem.* **40,** 517 (1934).
9. J. Bénard and J. Talbot, *C.R. Acad. Sci., Paris* **226,** 912 (1948).
10. L. Seigneurin and H. Forestier, *C.R. Acad. Sci., Paris* **243,** 2052 (1956).
11. E. R. Jette and F. Foote, *J. Chem. Phys.* **1,** 29 (1933).
12. N. G. Schmahl, H. Baumann and H. Schenck, *Arch. Eisenhüttenw.* **29,** 41, 83 (1958).
13. J. Paidassi, *Acta Met.* **6,** 69 (1958).

VOL. 8 1960

SUR LA TREMPE DES LACUNES DANS UN POLYCRISTAL À GRAINS FINS*

A. BLANDIN et J. FRIEDEL†

Quand les lacunes de trempe s'annihilent de préférence à la surface de l'éprouvette ou aux joints des grains, la résistance mesurée doit décroître exponentiellement avec le temps pour des temps supérieurs à quelques minutes. La constante de temps varie avec les dimensions des grains, et donne une mesure absolue du coefficient de diffusion $D = D_0 \exp(-U/kT)$ des lacunes. Les conditions d'application de ces formules—grains fins et trempes de températures modérées—semblent remplies dans des expériences récentes par Germagnoli *et al.*, qui donnent $D_0 \simeq 5$ c.g.s. et $U = 1{,}3$ eV pour le cuivre et $D_0 \simeq 15$ c.g.s. et $U = 1{,}5$ eV pour le platine.

ON THE QUENCHING OF VACANCIES IN A FINE GRAINED POLYCRYSTAL

When quenched vacancies disappear preferentially at the outside surface or at grain boundaries, the measured resistance should decrease exponentially with time, after a few minutes. The time constant varies with the dimensions of the grains and gives an absolute value of the diffusion constant $D = D_0 \exp(-U/kT)$ of the vacancies. This analysis should be valid for fine grains and quenches from moderate temperatures. These conditions seem to be fulfilled in recent experiments by Germagnoli *et al.* leading to $D_0 \simeq 5$ c.g.s. with $U = 1.3$ eV for copper and $D_0 \simeq 15$ c.g.s. with $U = 1.5$ eV for platinum.

ABSCHRECKEN VON LEERSTELLEN IN EINEM FEINKÖRNIGEN POLYKRISTALL

Wenn die eingefrorenen Leerstellen vorzugsweise an der Probenoberfläche oder an Korngrenzen verschwinden, muß der gemessene Widerstand nach Verlauf einiger Minuten exponentiell mit der Zeit abnehmen. Die Zeitkonstante hängt von der Korngröße ab und gibt ein absolutes Maß für die Diffusionskonstante $D = D_0 \exp(-U/kT)$ der Leerstellen. Die Anwendungsbedingungen der gegebenen Formeln—feine Körner und mäßige Abschrecktemperaturen—scheinen bei den Experimenten von Germagnoli *et al.* aus neuerer Zeit erfüllt zu sein. Diese ergeben $D_0 \simeq 5$ c.g.s. und $U = 1{,}3$ eV für Kupfer und $D_0 \simeq 15$ c.g.s. und $U = 1{,}5$ eV für Platin.

1. INTRODUCTION

De récentes mesures[1] de la résistance électrique de fils metalliques trempés donnent un accroissement de résistance $\Delta\rho$ qui disparaît au cours du temps t suivant une loi de type exponentiel

$$\Delta\rho(t) = A \exp(-Bt). \tag{1}$$

où A et B sont deux constantes, pour des temps supérieurs à quelques minutes.

Une loi de ce type est prévue quand les lacunes s'annihilent sur un nombre fixe de dislocations.[2,3] Mais pour des cristaux assez *petits*, les lacunes doivent s'annihiler de préférence à la surface ou aux joints des grains. Le but de cet article est de montrer qu'une relation du type (1) est aussi prévue dans ce cas. La valeur du coefficient B dépend alors de la taille et de la forme des grains. Il fournit une mesure *absolue* du coefficient D de diffusion des lacunes. Des revenus à des températures T différentes permettent donc de déterminer l'énergie d'activation U du déplacement des lacunes, mais aussi la constante D_0 dans l'expression

$$D = D_0 \exp(-U/kT). \tag{2}$$

On traite le problème de la diffusion des lacunes dans une plaque, un cylindre ou une sphère, quand elles ne peuvent s'annihiler que sur la surface extérieure. Le cas de la plaque doit s'appliquer à des lames minces et aux structures perlitiques; celui du cylindre aux fils fins utilisés dans les expériences citées ci-dessus,[1] qui sont sans doute constituées d'une suite de grains nettement plus longs que le diamètre des fils. Le cas de la sphère doit être approximativement valable pour des polycristaux à grains fins et équiaxes. On déduit ensuite de cette étude la résistance pour chacun de ces trois cas, et on compare les résultats avec les mesures expérimentales.

On suppose dans tout ce qui suit *une température de trempe assez basse* pour que les lacunes se déplacent et s'annihilent individuellement, sans former de bilacunes ou d'amas plus gros.

2. DIFFUSION DES LACUNES

Soient T la température de revenu, c_0 la concentration de lacunes en équilibre à la température T, $f(\mathbf{r})$ la concentration en excès des lacunes au point $\mathbf{r}$ au temps 0 (juste après la trempe), $c(\mathbf{r}, t)$ la concentration en lacunes au temps t au point $\mathbf{r}$. c vérifie l'équation de diffusion $D\Delta c = \dfrac{\partial c}{\partial t}$ où D est le coefficient de diffusion à la température T.

* Reçule 30 Juin, 1959.

† Physique des Solides, B.P. no. 11 Orsay (S. et O.) France.

On étudie trois cas: (1) la plaque infinie d'épaisseur $2R$;
(2) le cylindre infini de rayon R;
(3) la sphère de rayon R.

Avec les conditions initiales ainsi données $c(\mathbf{r}, 0) = c_0 + f(\mathbf{r})$ et les conditions aux limites $c(R, t) = c_0$, les solutions de l'équation de diffusion sont respectivement, dans les trois cas envisagés,[4]

$$c = c_0 + \frac{4}{\pi} \sum_{n \text{ impair}}^{\infty} \exp\left(-n^2 \frac{D\pi^2}{4R^2} t\right) \cos\frac{n\pi x}{2R} \alpha n \quad (3)$$

avec $\alpha_n = \frac{\pi}{2R}\int_0^R f(x') \cos\frac{n\pi x'}{2R}\, dx$

$$c = c_0 + 2\sum_{n=1}^{\infty} \exp\left(-x_n{}^2 \frac{D}{R^2} t\right) \frac{J_0\left(x_n \frac{r}{R}\right)}{x_n J_0'(x_n)} \beta_n \quad (4)$$

avec $\beta_n = \frac{x_n}{R^2 J_0'(x_n)} \int_0^R r' f(r') J_0\left(x_n \frac{r'}{R}\right) dr'$

$$c = c_0 + \frac{2R}{\pi r} \sum_{n=1}^{\infty} (-1)^{n-1} \exp\left(-n^2 \frac{D\pi^2}{R^2} t\right) \times \sin\frac{n\pi r}{R} \gamma_n \quad (5)$$

avec $\gamma_n = (-1)^{n-1} \frac{\pi}{R^2} \int_0^R r' f(r') \sin\frac{n\pi r'}{R}\, dr'$.

Les x_n sont les racines positives de $J_0(x_n) = 0$ où $J_0(x)$ est la fonction de Bessel d'ordre 0.

On remarque que la diffusion peut être étudiée dans deux intervalles de temps:

(a) Pour t petit tel que $(D\pi^2/R^2)t \ll 1$, tous les termes des séries (3), (4), (5) participent à la valeur de c; c est voisin de sa valeur initiale $f(r)$ sauf au voisinage de sa surface, et dépend fortement de la répartition initiale $f(r)$. C'est la période de temps pendant laquelle s'établit le régime (b).

(b) Quand $(D\pi^2/R^2)t \geqslant 1$, dans les séries donnant c, seuls comptent les deux premiers termes. On a alors un régime "quasi stationnaire" où la répartition initiale des lacunes en sursaturation n'intervient que par les valeurs de α_1, β_1 ou γ_1. On peut remarquer que pour toute répartition initiale raisonnable des lacunes, ces trois coefficients sont du même ordre de grandeur que la sursaturation moyenne en lacunes. Si cette sursaturation était uniforme et égale à c_1, on aurait exactement $\alpha_1 = \beta_1 = \gamma_1 = c_1$. Dans la seconde phase de la diffusion, la répartition des lacunes et leur diffusion est donc la même que si la sursaturation initiale était uniforme.

3. RÉSISTANCE DÛE AUX LACUNES

Dans le calcul de la résistivité, il faut tenir compte de ce que la concentration en lacunes est loin d'être uniforme pendant le revenu. Mais il faut également tenir compte de la présence d'impuretés et éventuellement des phonons. On peut en général supposer que la concentration de tous ces défauts à la température de mesure est suffisante pour fixer aux électrons un libre parcours moyen l_0 très inférieur à la taille R des grains. Dans ces conditions, la diffusion des électrons par la surface est négligeable et on peut étudier la conductibilité d'une plaque (ou d'un fil) en ajoutant les conductivités dues à de petites sections d'aire ds dont les dimensions sont grandes par rapport à l_0, mais petites par rapport à R.

Dans les expériences citées[1] la concentration en impuretés est de l'ordre de 10^{-4}. La concentration initiale en lacunes est en moyenne de 10^{-5}. On traite d'abord le cas où *la concentration en impuretés est très supérieure à la concentration en lacunes*. C'est le cas le plus simple à analyser.

Cas de la lacune

Le courant est perpendiculaire à la direction $0x$. Pour des temps suffisamment longs, $(\pi^2 Dt/R^2 \geqslant 1)$, on a

$$c \simeq c_0 + \frac{4\alpha_1}{\pi} \exp\left(-\frac{D\pi^2}{4R^2} t\right) \cos\frac{\pi x}{2R}.$$

Si ρ_0 est la résistance totale à l'équilibre à la température de revenu (due aux impuretés, lacunes et phonons) et ρ_l la portion de cette résistance qui est due aux lacunes, la résistance $\rho(t)$ au temps t est donnée par:

$$\frac{1}{\rho(t)} = \frac{1}{R}\int_0^R \frac{dx}{\rho_0 + \rho_l \frac{4\alpha_1}{\pi c_0} \exp\left(-\frac{D\pi^2}{4R^2} t\right) \cos\frac{\pi x}{2R}}.$$

Comme on suppose $\frac{\alpha_1}{c_0} \rho_l \ll \rho_0$, on peut écrire:

$$\rho(t) = \rho_0 + \frac{8}{\pi^2} \frac{\alpha_1}{c_0} \rho_l \exp\left(-\frac{D\pi^2}{4R^2} t\right). \quad (6)$$

c'est-à-dire un excès de résistance $\Delta\rho(t) = \rho(t) - \rho_0$ de la forme de l'équation (1). Le coefficient B ne dépend que des conditions géométriques et de la température de revenu. Le coefficient A, lui, dépend des conditions de trempe; il est de l'ordre de $(8/\pi^2)\Delta\rho(0)$ (valeur exacte pour le cas où la concentration en lacunes après la trempe serait uniforme).

Il est à remarquer que dans ce cas, la répartition des lacunes a peu d'importance car elles jouent un rôle secondaire dans la diffusion des électrons. On peut à peu de choses près ajouter simplement les résistances dues aux impuretés et aux lacunes.

VOL. 8 1960

Cas du cylindre et de la sphère

Le cas du cylindre et de la sphère* se traitent de même. On trouve les résultats au Tableau 1.
Le coefficient A est donné pour une concentration initiale de lacunes uniformes. x_1 est le premier zéro de J_0 et a pour valeur 2,405.

On peut envisager le cas d'un *métal très pur*, où la concentration en impuretés est de l'ordre de la concentration en lacunes c_0 à l'équilibre à la température de revenu. Si l'on mesure les résistances à tres basse température, la résistance ρ_0 mesurée dans lès conditions d'équilibre est peu supérieure à la portion ρ_l dûe aux lacunes. Elles sont toutes deux bien inférieures à la résistance $\Delta\rho(0)$ dûe à l'excès de lacunes après trempe. Le comportement de la résistance en fonction du temps est alors plus complexe. On ne peut plus du tout ajouter les résistances dues

Tableau 1

	Lame	Cylindre	Sphère
B	$\frac{D\pi^2}{4R^2}$	$D\frac{x_1^2}{R^2}$	$D\frac{\pi^2}{R^2}$
A	$\frac{8}{\pi^2}\Delta\rho(0)$	$\frac{4}{x_1^2}\Delta\rho(0)$	$\frac{6}{\pi^2}\Delta\rho(0)$

aux différents diffuseurs. La phase de temps $D\frac{\pi^2}{R^2} \geqslant 1$ est alors à décomposer en deux intervalles: pour t suffisamment grand pour que la concentration des lacunes en sursaturation soit petite par rapport à la concentration d'équilibre $\left[\frac{\alpha_1}{c_0}\exp\left(-\frac{D\pi^2}{R^2}t\right) < 1\right]$, on retrouve les mêmes résultats que ci-dessus. Par contre, pour la période de temps $1 < \exp\left(+\frac{D\pi^2}{R^2}t\right) < \frac{\alpha^1}{c_0}$, la résistance $\rho(t)$ est donnée encore par une loi du type (1) avec le *même coefficient B que ci-dessus*, mais des coefficients A qui valent

$$\frac{\Delta\rho(0)}{\log\frac{\Delta\rho(0)}{\rho_0}} \quad \text{et} \quad \frac{2\Delta\rho(0)}{\log\frac{\Delta\rho(0)}{\rho_0}}$$

à une ou deux dimensions.

En conclusion, quelle que soit la pureté du cristal, on a, pour $(D\pi^2/R^2)t > 1$, une loi exponentielle (1) avec le même coefficient B, mais des valeurs de A différentes. En fait, dans le cas des expériences usuelles où les impuretés sont plus nombreuses que les lacunes trempées les formules du Tableau 1 s'appliquent.

* La cas de la sphère s'applique à un polycristal à grains équiaxes où chaque cristal est assimilé à une sphère. Les dimensions des cristaux étant très supérieures au libre parcours moyen l_0, on peut négliger la résistance due aux joints de grains.

Tableau 2. Coefficient de diffusion pour un fil de cuivre de 20 μ de rayon trempé de 930°K

T°K	619	633	666	700	736
t_0 (min)	200	150	25	8	3
D c.g.s. $\times 10^{10}$	(0,6)	(0,8)	4,65	15	40

4. COMPARAISON AVEC LES RÉSULTATS EXPÉRIMENTAUX

L'étude ci-dessus montre que, quelle que soit al répartiton initiale des lacunes, c'est-à-dire quelle que soit la température et la cinétique de la trempe, $\Delta\rho(t)$ doit avoir dans un large domaine de temps une variation exponentielle, avec les valeurs du coefficient B données dans le Tableau 1. Il serait donc intéressant de vérifier cette constance de la valeur de B quand la température ou la cinétique de trempe varient.

Les conditions physiques où la formule (1) est valable sont les suivantes:

(i) Annihilation des lacunes à la surface extérieure ou sur les joints de grain, donc:

grains fins:

faibles contraintes thermiques pendant la trempe, de manière à ne pas former *trop de dislocations*;[5] température de trempe pas trop élevée, de manière à éviter la *formation de bilacunes*[3] ou de boucles de dislocations.[6]

(ii) Temps de recuit suffisamment long. La condition $Bt \geqslant 1$ exige comme on le voit ci-dessous des *températures de recuit pas trop basses*.

Ces conditions doivent être remplies dans les expériences de Germagnoli *et al.* mesurant la résistivité de fils fins de cuivre[1] et de platine[8] (quand la température de trempe est assez basse).

La limite inférieure de temps t_0 définie par $Bt_0 = 1$ est donnée dans les Tableaux 2 et 3. On en déduit les valeurs de D. Les valeurs pour les plus basses températures sont assez incertaines du fait que la condition $Bt > 1$ est assez mal satisfaite.

On déduit de ces mesures les énergies d'activation

Tableau 3. Coefficient de diffusion pour un fil de platine de 20 μ de rayon trempé de 1413°K

T°K	651	667	687	714	725	743	762
t_0 (min)	500	140	5	30	20	10	5
D c.g.s. $\times 10^{10}$	(0,3)	0,86	2,1	3,9	5,7	12	25

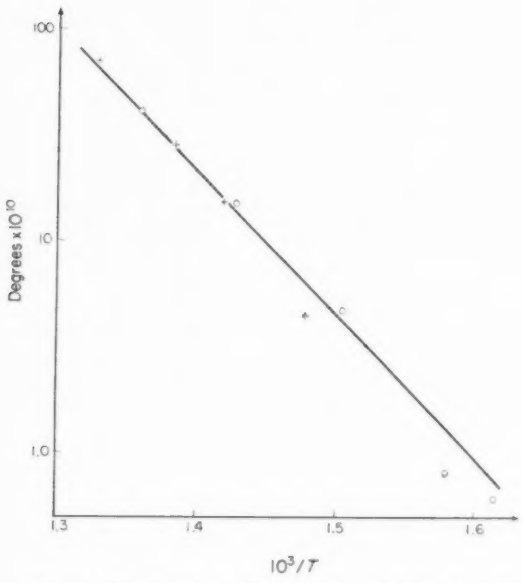


FIG. 1. Coefficient de diffusion D. ○ fil Cu $R = 20\ \mu$, + fil Cu $R = 35\ \mu$.

de déplacement des lacunes $U_{Cu} = 1{,}3$ eV et $U_{Pt} = 1{,}5$ eV déjà données[1,7] et les valeurs de la constante $D_0 \simeq 5$ c.g.s. pour le cuivre et $D_0 \simeq 15$ c.g.s. pour le platine, valeurs très raisonnables.

La constante B doit varier en R^{-2}. Ceci semble le cas pour les fils de cuivre de 20 μ et 35 μ étudiés par Germagnoli[8] (Fig. 1) quand on leur a fait subir une série de trempes qui doivent stabiliser la cinétique de revenu en éliminant la plupart des dislocations. La constante observée dans les gros fils au cours des premières trempes est plus forte; elle varie moins lentement que R^{-2} parce que les dislocations jouent un rôle d'autant plus important que le rayon est plus gros.

Il serait intéressant d'avoir des résultats expérimentaux plus nombreux, de manière à vérifier:

(1) la non influence de la trempe;

(2) la loi de proportionnalité de B en R^{-2};

(3) la loi (1) dans le cas d'échantillons polycristallins.

REMERCIEMENT

Les auteurs tiennent à remercier le Dr. E. Germagnoli pour leur avoir aimablement communiqué des résultats avant publication.

BIBLIOGRAPHIE

(1) G. AIROLDI, G. L. BACCHELLA et E. GERMAGNOLI, *Phys. Rev. Letters*, **2,** 145 (1959).

(2) J. S. KOEHLER, F. SEITZ et J. E. BAUERLE, *Phys. Rev.* **107,** 1499 (1957).

(3) J. F. BAUERLE et J. S. KOEHLER, *Phys. Rev.* **107,** 1493 (1957).

(4) Voir par exemple H. S. CARLSLAW et J. C. JAEGER, *Conduction of Heat in Solids.* Oxford University Press (1947).

(5) M. WINTENBERGER, *C. R. Acad. Sci., Paris* **244,** 2800 (1957).

(6) P. B. HIRSCH, J. SILCOX, R. E. SMALLMAN and K. H. WESTMACOTT, *Phil. Mag.* **3,** 897 (1958); **4,** 7 (1959).

(7) G. L. BACCHELLA, E. GERMAGNOLI et S. GRANATA, *J. Appl. Phys.* **30,** 748 (1959).

(8) E. GERMAGNOLI, communication privée.

VOL. 8 1960

A STUDY OF SOLUTE DIFFUSION IN LIQUID TIN*

C. H. MA† and R. A. SWALIN†

The diffusion of aluminum, zinc, silver, copper and nickel in liquid tin has been investigated by the capillary-reservoir technique in a temperature range from about 240°C to 480°C. All of the solutes investigated were present in dilute solutions ranging from 0.2 to 0.7 wt. %. The solutes were chosen so as to cover a range of relative partial molal enthalpies from large positive values to large negative values. On the basis of the self-diffusion of tin, it is found that the ratios of D_{solute} to D_{self} are 4.70, 1.90, 1.57, 1.15 and 1.10, respectively for aluminum, zinc, silver, copper and nickel within ± 15 or 20 per cent error. Diffusion coefficients of copper and nickel can be considered to be identical with that of tin within experimental error. The Stokes–Einstein and Eyring equations which consider only the factor of atom size, do not predict accurately the relative order of diffusion coefficients amongst the solutes. They do, however, predict the order of magnitude of the diffusion constant. On the basis of fluctuation theory, it is expected that those solutes which have a large positive relative partial molal enthalpy diffuse considerably faster than those solutes which have a large negative relative partial molal enthalpy since there is a much higher probability of significant density fluctuations occurring in the vicinity of the solute atoms in the former case. The data appear to be in agreement with this conclusion. Unfortunately no quantitative comparison is feasible at the present time because of the lack of potential energy versus distance data for solute-solvent neighbors in solution. It is further proposed that in dilute solutions, the diffusion coefficient of a solute approaches that of the solvent if the solute has a zero or large negative relative partial molal enthalpy in the solvent.

ETUDE DE LA DIFFUSION DE DIFFERENTS METAUX DANS L'ETAIN LIQUIDE

Les auteurs ont étudié par une technique de capilarité, la diffusion de l'aluminium, du zinc, de l'argent, du cuivre et du nickel dans l'étain liquide pour une gamme de températures comprises entre 240 et 480°C. Cette étude s'intéresse à des solutions diluées contenant de 0,2 à 0,7 % en poids de métal dissous. Le choix de ces derniers a été effectué de telle manière que l'on couvre une gamme d'enthalpie molaire relative partielle, s'étendant des plus grandes valeurs positives ju squ'aux plus grandes valeurs négatives. La connaissance de l'auto-diffusion de l'étain permet de trouver que les rapports D_{dissous} à $D_{\text{auto-diffusion}}$ sont respectivement 4,70, 1,90, 1,57, 1,15 et 1,10 pour l'aluminium, le zinc, l'argent, le cuivre et le nickel; l'erreur sur la valeur de ces rapports est comprise entre 15 et 20%; dans les limites de la précision de la méthode, les coefficients de diffusion du cuivre et du nickel doivent être considérés comme étant identiques à celui de l'étain. Les équations de Stokes–Einstein et Eyring qui considèrent uniquement le facteur de taille atomique, ne permettent pas de prévoir avec précision l'ordre relatif des coefficients de diffusion des différents métaux étudiés. Par contre, ces équations permettent d'estimer l'ordre de grandeur de la constante de diffusion. Sur la base de la théorie des fluctuations, on peut s'attendre à ce que les éléments dissous qui possèdent une enthalpie partielle molaire relative fortement positive, diffusent beaucoup plus rapidement que ceux dont l'enthalpie partielle molaire relative est fortement négative. En effet, il existe une beaucoup plus grande probabilité d'obtenir des fluctuations de densité importantes au voisinage des atomes dissous de la première espèce. Les résultats de l'étude semblent être en accord avec cette conclusion. Malheureusement, une comparaison quantitative ne peut être effectuée à l'heure présente, par suite du manque de données relatives aux valeurs de l'énergie potentielle en fonction de la distance avec les groupements atome solvant-atome dissous. Les auteurs suggèrent en outre que dans les solutions diluées, le coefficient de diffusion de l'élement dissous s'approche de celui de l'élément solvant lorsque cet élément dissous possède une enthalpie partielle molaire relative fortement négative dans le solvant considéré.

UNTERSUCHUNG DER DIFFUSION GELÖSTER ATOME IN FLÜSSIGEM ZINN

Mit Hilfe der Kapillar-Reservoir-Technik wurde die Diffusion von Aluminium, Zink, Silber, Kupfer und Nickel in flüssigem Zinn im Temperaturgebiet 240°C bis 480°C untersucht. Alle gelösten Substanzen befanden sich in verdünnter Lösung mit 0,2 bis 0,7 Gewichtsprozent. Die gelösten Metalle wurden so gewählt, daß die relativen partiellen molaren Enthalpien von großen positiven bis zu großen negativen Werten reichten. Geht man von der Selbstdiffusion von Zinn aus, ergeben sich für das Verhältnis D_{Zusatz} zu D_{selbst}die Werte 4.70, 1.90, 1.57, 1.15 und 1.10 für Aluminium, Zink, Silber, Kupfer bzw. Nickel mit ± 15 oder 20% Fehler. Die Diffusionskonstanten von Kupfer und Nickel können im Rahmen der Versuchsfehler gleich der von Zinn gesetzt werden. Die Gleichungen von Stokes-Einstein und von Eyring, die nor den Einfluß der Atomgröße in Betracht ziehen, geben keine zutreffende Aussage über die Reihenfolge der Diffusionskonstanten der gelösten Substanzen. Sie geben jedoch die richtige Größenordnung der Diffusionskonstanten. Auf der Grundlage der Fluktuationstheorie erwartet man, daß die gelösten Metalle, die eine große positive relative partielle molare Enthalpie haben, beträchtlich schneller diffundieren als die mit großer negativer relativer partieller molarer Enthalpie, da im ersten Fall die Wahrscheinlichkeit für beträchtliche Dichteschwankungen in der Umgebung der gelösten Atome viel größer ist. Die Meßergebnisse scheinen mit diesem Schluß in Einklang zu sein. Ein quantitativer Vergleich ist zur Zeit leider nicht möglich, da die Abstandsabhängigkeit der Wechselwirkungsenergie von gelöstem und Lösungsmittelatom in der Lösung nicht bekannt ist. Weiter wird vorgeschlagen, daß die Diffusionskonstante einer gelösten Substanz praktisch gleich der des Lösungsmittels ist, wenn die relative partielle molare Enthalpie der gelösten Substanz null ist oder großen negativen Wert hat.

* Received October 5, 1959.

† Department of Metallurgy, University of Minnesota, Minneapolis, Minnesota.

VOL. 8 1960

1. INTRODUCTION

The phenomenon of diffusion in the liquid state is in an embryonic state insofar as an understanding of the diffusion mechanism is concerned. This lack of understanding is due both to a relative paucity of experimental work particularly with very dilute solutions and to the difficulty of elucidating, quantitatively, the structure of even simple monatomic liquid metals. There are two prominent equations used to relate diffusion coefficients of liquid metal to the properties of the solvent and the diffusing particle, namely, the Stokes–Einstein and Eyring equations. Both equations relate the diffusion coefficient of the species in question to the viscosity of the solvent and the radius of the diffusing particle. The general applicability of the Stokes–Einstein and Eyring equations has been verified since upon substitution of experimental self-diffusion coefficients for liquid metals and viscosity data into the equations, a value of the radius about equal to the ionic radius is obtained. Some investigators have gone so far as to attempt to deduce the effective charge on the diffusing ion from the size of the radius obtained. This practice is highly questionable, however, since in spite of the contribution of the Stokes–Einstein and Eyring equations to our understanding of the diffusion process, they are probably over-simplifications since local interactions between the diffusing species of interest and the solvent atoms are neglected. For solute diffusion in particular this attractive or repulsive interaction between solute and solvent might be expected to play an important role in the diffusion process.

The purpose of the present study is to make a comparative study of solute diffusion in a given solvent in order to test the general applicability of the Stokes–Einstein and Eyring equations and the importance of solute-solvent interactions. To the writers' knowledge no suitable data are currently available in the literature since most of the data have been obtained for fairly concentrated alloys which complicates interpretation since the measured value of diffusion coefficient will be a function of the intrinsic diffusion constants of solvent and solute as well as the activity coefficient.[1] For this reason, the data to be presented here were obtained for solutions as dilute as our analytical procedures would allow. The solutes themselves were chosen so as to cover a wide range of solute-solvent interaction ranging from large attractive interactions to large repulsive interactions, that is to say covering a range of relative partial molal enthalpies from large negative quantities to large positive quantities. Tin was chosen for the solvent in the present study because of its low melting point, the availability of X-ray data for the liquid state, and the rather wide availability of thermodynamic data. The solutes chosen were aluminum, zinc, silver, copper and nickel.

2. EXPERIMENTAL WORK

A. *General diffusion method*

There are a number of methods available in the literature for studying liquid diffusion, but most of them are applicable only to diffusion of non-metallic solutions for which relatively low temperature techniques can be used. In the field of diffusion of liquid metals, the methods available in the literature are relatively few. In recent years, the most widely used technique in the study of liquid metal diffusion is the so-called capillary-reservoir method.[2–7] This method was first used by Anderson and Saddington in 1949.[2]

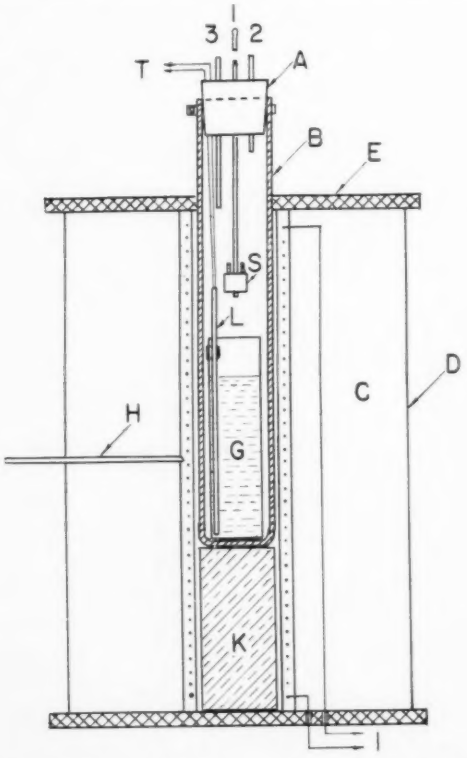
In the capillary-reservoir method, the metallic sample containing the solute to be investigated is contained in a small capillary with one end sealed. This capillary is then dipped vertically into a large reservoir of pure molten solvent metal at a chosen temperature. After a given period of time, the capillary is taken out of the reservoir and a determination of the solute diffusion coefficient is made according to a method discussed in a later section. In liquid diffusion studies, convection currents are generally a problem and thus have to be eliminated in order for reliable results to be obtained. In the capillary-reservoir method, convection currents are largely avoided because of the small diameter of capillary tubing. Besides this method is relatively insensitive to slight vibrations or disturbances in the vicinity of the diffusion apparatus. Because of these advantages, the capillary-reservoir method has been chosen for the present investigation.

B. *Preparation of diffusion sample*

1. *Alloy preparation.* The solute percentages of diffusion alloys were chosen approximately in the range between 0.2 to 0.7 wt.%. Since the average weight of a sample is about 200 mg the lower limit of concentration of a particular solute element is mainly dictated by the sensitivity of the chemical analytical method for the particular element. In this study all solute elements are analysed by the spectrophotometric method. After the concentration of a particular alloy has been determined, known proportions of the solute element and the solvent tin are mixed so as to obtain the desired concentration. The alloy mixture is then placed in a high purity graphite crucible 2 in. high and 1 in. in diameter. This crucible is placed into a long silica tube of $2\frac{1}{2}$ in. inside diameter with one

end sealed. The top of the silica tube is fitted with a rubber stopper. The silica tube is placed vertically in a cylindrical resistance furnace, having a 5 in. zone of uniform temperature. Connections are made through holes in the stopper to a mechanical vacuum pump and McLeod gauge. There is also a Pyrex rod passing through the center of the stopper in the silica tube for stirring purposes. The system is pumped out and when the pressure in the silica tube becomes less than 20 μ Hg, the power to the furnace is turned on. The alloy mixture is heated continuously at about 750°C for 70 hr *in vacuo*, after which the power to the furnace is turned off. When the furnace has cooled below 480°C the Pyrex stirring rod is lowered into the molten alloy and the liquid bath is agitated several minutes to insure uniformity of alloy composition.

2. *Capillary filling process.* Two different sizes of Pyrex capillary tubing are used in the present study. One size has an OD of 5–6 mm and an ID of 3/4 mm.



A. HARD RUBBER PLUG
B. SILICA TUBE
C. INSULATION
D. METAL SHELL
E. TRANSITE BOARD
G. TIN RESERVOIR
H. CONTROLLING THERMOCOUPLE PROTECTION TUBE
I. HEATING WIRE LEADS
K. SUPPORTING BRICK
L. ALUMINA THERMOCOUPLE PROTECTION TUBE
S. SAMPLE HOLDER READY TO DIP INTO TIN RESERVOIR FOR DIFFUSION
T. MEASURING Pt.-10 %Rh. COUPLE
1. SAMPLE HOLDER ROD
2. HELIUM OUTLET
3. HELIUM INLET

FIG. 1. Diffusion anneal furnace.

The other has an OD of 7 mm and an ID of $1\frac{1}{4}$ mm. The apparatus used for the capillary filling process is basically the same as that used in preparing the alloy. In the capillary filling process, however, a helium gas facility is provided in the system in addition to the vacuum equipment. After the system is pumped out, the empty capillaries are dipped into the molten alloy bath. Helium gas is then admitted into the system. After a few minutes the capillaries, now filled with alloys, are slowly pulled out of the molten alloy bath and the system is allowed to cool.

C. *Diffusion annealing*

The diffusion anneal furnace and accessories are similar to the apparatus described above; however, the temperature control and measuring devices are more elaborate in the diffusion annealing apparatus. This apparatus is shown schematically in Fig. 1.

The solvent tin is contained in a large graphite crucible with an OD of $2\frac{1}{2}$ in. and an ID of 2 in. with a length of 12 in. The reason for using the large crucible for the diffusion anneal is discussed later. About 4 lb of tin are used for each alloy system. This tin reservoir is placed in a long silica tube. Samples for the diffusion study are held in a sample holder which is similar to the capillary holder in the filling technique. Two samples are used in each diffusion anneal treatment. The temperature of the diffusion bath is measured with calibrated platinum–platinum, 10% rhodium thermocouple. The temperature range used in the present diffusion study is from about 240°C to 480°C.

The bath was not stirred during the diffusion anneal. Preliminary investigations indicated that excessive vibration resulted from stirring and so it was decided to eliminate this possible cause of error. It was felt that convection currents existing in the tin bath would be sufficient to remove the solute as it diffused from the capillary into the reservoir.

The diffusion anneal time was varied between 1.5 hr and 6.5 hr. There appeared to be no influence of the duration of the diffusion anneal time on the diffusion coefficient obtained thus indicating that D is independent of time as it should be if our boundary conditions used in the solution of Fick's second law are appropriate. This fact also indicates that the diffusion constant is independent of solute concentration, at least in the vicinity of the concentration used in this investigation. This is what one would expect for dilute systems, such as those investigated here.

D. *Chemical analysis*

As mentioned previously, the chemical analyses are performed using the spectrophotometric method.

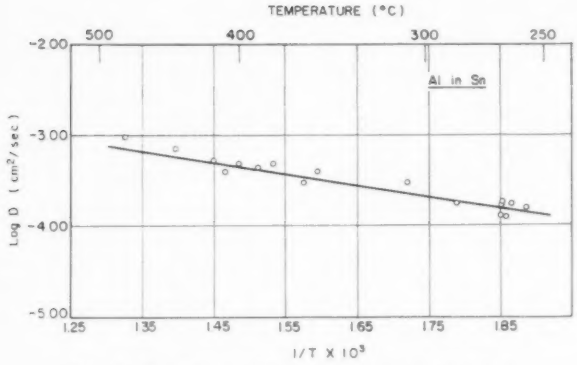


FIG. 2. Log D vs. $1/T$ plot for aluminum in tin.

Since tin is generally found to interfere with this type of analysis if present in appreciable quantity, it has to be separated first from the solute element in a sample. This is done by first dissolving the alloy in 40 per cent hydrobromic acid and then by evaporating the tin as $SnBr_4$ in a mixed solution of hydrobromic acid and bromine over a hot water bath.[8] The methods of analysis used for the solutes are generally standard methods. The aurintricarboxylate method[9] is used for analyzing the aluminum alloy. The mixed color dithizone method is used for zinc,[9] the modified copper dithizone method is used for silver,[8] a modified dithizone method is used for copper,[8] and the dimethylgloxime method is used for the determination of nickel.[9]

3. CALCULATION OF DIFFUSION COEFFICIENTS

The choice of the method of calculation for the diffusion coefficient depends, of course, on experimental boundary conditions. Most of the methods used for calculating diffusion coefficients require a penetration versus distance curve for the diffusion sample, thus involving sectioning and analyzing of the diffusion sample. In the present study, a method for calculation without involving sectioning was selected. The main reason for choosing this method is that in liquid diffusion, the concentration gradient of the diffusion sample may be distorted during solidification after the diffusion process, thus affecting the accuracy of the calculated diffusion coefficient. It is felt that the method used whereby sectioning is avoided after solidification would improve the accuracy of the calculated diffusion coefficients provided that sufficient number of samples are studied.

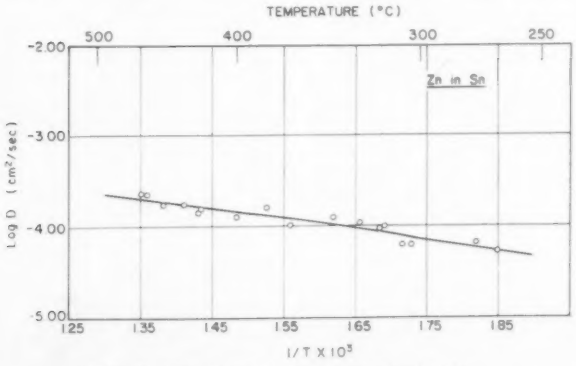


FIG. 3. Log D vs. $1/T$ plot for zinc in tin.

A large volume of tin was used as a reservoir in the diffusion anneal process. The purpose of this was that the diffusion would occur into essentially an infinite sink, thus simplifying the solution of Fick's second law. Under these boundary conditions, solution of Fick's second law becomes

$$\frac{C}{C_0} = \frac{4}{\pi}\sum_{n=0}^{n=\infty}\frac{(-1)^n}{2n+1}\exp\left[-(2n+1)^2\pi^2 Dt/4L^2\right] \times \cos\frac{(2n+1)\pi x}{2L} \quad (1)$$

where C is the concentration of solute, t is time, x is the distance along the cylinder axis in the capillary. C_0 is the initial concentration of solute and L is the length of the diffusion capillary. Integrating equation (1) so as to obtain the average concentration in the capillary after time t yields the following equation,

$$\frac{C_{av}}{C_0} = \frac{8}{\pi^2}\sum_{n=0}^{n=\infty}\frac{1}{(2n+1)^2}\exp\left[-(2n+1)^2\pi^2 Dt/4L^2\right]. \quad (2)$$

For sufficiently long times all terms with n higher than 0 can be neglected in the above equation, thereby simplifying it to

$$\frac{C_{av}}{C_0} = \frac{8}{\pi^2}\exp\left[\frac{-\pi^2 Dt}{4L^2}\right]. \quad (3)$$

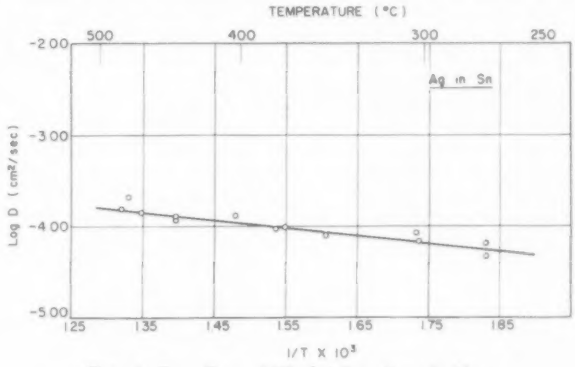


FIG. 4. Log D vs. $1/T$ plot for silver in tin.

4. EXPERIMENTAL RESULTS

A. *Presentation of diffusion data*

The data are presented in graphical form in Figs. 2–6 in which log D is plotted versus the reciprocal of the

VOL. 8 1960

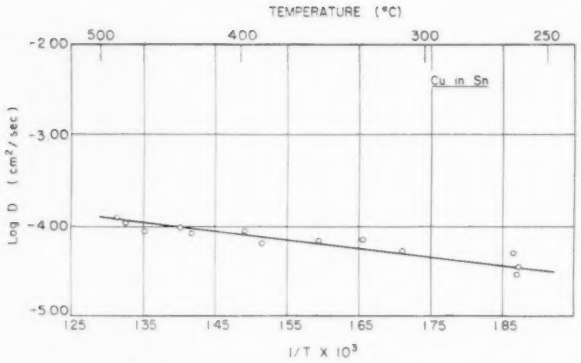


FIG. 5. Log D vs. $1/T$ plot for copper in tin.

absolute temperature. In these figures a single point in some cases represents an average of two diffusion coefficients. Assuming the temperature dependence of the diffusion coefficient is given by

$$D = D_0 \exp\left[\frac{-Q}{RT}\right] \tag{4}$$

values of D_0 and Q obtained from the experimental data are listed in Table 1. Also included in Table 1 are the values of D_0 and Q for self-diffusion of tin in tin as determined by Careri and Paoletti[5].

B. *Discussion of errors*

The calculation of errors in the diffusion coefficients is, of course, a difficult task. Some idea of the errors inherent in the study, however, can be obtained from a study of the scatter in the values of D about the best straight line on a log D versus the reciprocal of the absolute temperature plot. Using standard methods of analysis[10] mean square errors in D, D_0 and Q can be estimated. It is found that the probable errors in D values are ± 18 per cent, ± 18 per cent, ± 16 per cent, ± 17 per cent and ± 12 per cent respectively for aluminum, zinc, silver, copper and nickel. This spread of error values reflects uncertainties of ± 750 cal, ± 750 cal, ± 650 cal, ± 700 cal and

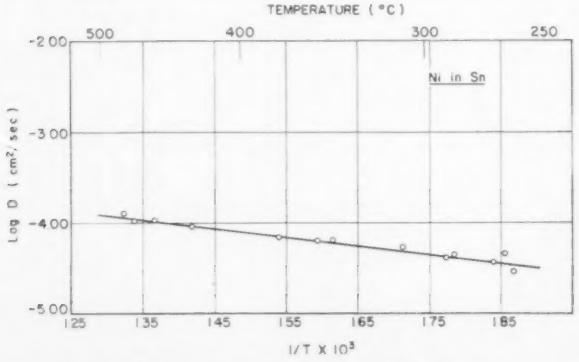


FIG. 6. Log D vs. $1/T$ plot for nickel in tin.

TABLE 1. Values of D_0 and Q for the diffusion of aluminum, zinc, silver, copper, nickel and tin in tin

Element	D_0(cm²/sec)	Q(cal/mole)
Al	1.9×10^{-3}	5200
Zn	6.2×10^{-4}	4880
Ag	2.6×10^{-4}	4200
Cu	1.8×10^{-4}	4200
Ni	2.3×10^{-4}	4530
Sn[5]	2.2×10^{-4}	4570

± 550 cal in Q for aluminum, zinc, silver, copper and nickel respectively. The errors in log D_0 are ± 0.27, ± 0.27, ± 0.23, ± 0.24 and ± 0.15 respectively for aluminum, zinc, silver, copper and nickel. It thus appears that the error in individual diffusion coefficients is about 15–20 per cent.

Because the errors in D_0 and Q are about the same magnitude as the differences between the D_0 and Q values themselves, it seems fruitless to speculate on the significance of the differences between the diffusion properties of the solutes by comparing these quantities. As a result, another approach is used in the next section, namely, a comparison is made between the relative values of the diffusion coefficients themselves at a constant temperature.

5. DISCUSSION OF THE RESULTS

A. *General remarks concerning the experimental results*

For convenience of discussion concerning the nature of the experimental results, a log D versus reciprocal of the absolute temperature plot for all five solutes studied in this investigation and also tin is shown in Fig. 7. A glance at this plot will show the magnitude of the diffusion coefficients of the solutes studied, and also the relative order among the solutes. From this plot, it can be seen clearly that aluminum has the highest diffusion coefficient followed by zinc, silver, copper and nickel at a given temperature. Copper

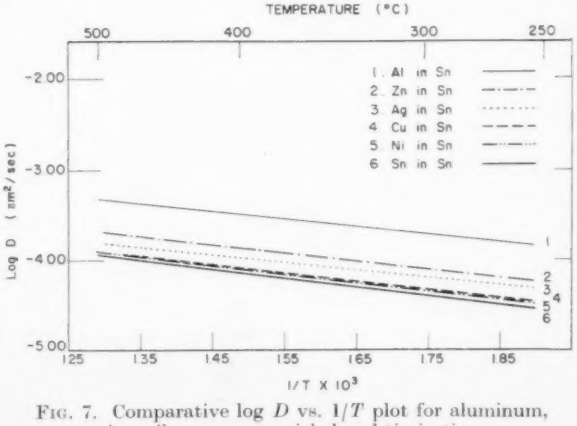


FIG. 7. Comparative log D vs. $1/T$ plot for aluminum, zinc, silver, copper, nickel and tin in tin.

and nickel have almost identical diffusion coefficients. It is interesting to note that the slopes seem to be about all the same within experimental error. There very possibly are differences but these are too small to be detected.

B. *Discussion of the Stokes–Einstein equation and Eyring equation in connection with the experimental results*

The most generalized Stokes–Einstein equation takes the following form[11]

$$\frac{D\eta}{kT} = \frac{1}{6\pi r} \cdot \frac{1 + 3\eta/\beta r}{1 + 2\eta/\beta r}. \tag{5}$$

Here β is the coefficient of sliding friction and D, T, k, r and η are the diffusion coefficient, absolute temperature, Boltzmann's constant, radius of the diffusing particle and coefficient of viscosity, respectively. When the diffusing particle is small, β equals 0 and equation (5) becomes

$$D = \frac{kT}{4\pi\eta r}. \tag{6}$$

When the diffusing particle is large, β equals infinity and the following equation results

$$D = \frac{kT}{6\pi\eta r}. \tag{7}$$

Equation (7) is known generally as the Stokes–Einstein equation. Since solute diffusion of liquid metals probably deals with particles of atomic dimensions, equation (6) is likely to be more applicable. This equation differs by a factor of 2π from Eyring's equation. An analysis performed by Li[12] indicates that a correction should be made to Eyring's equation in order to give proper meaning to the velocity of the diffusing atom relative to its neighbors. The two equations are thus found to be identical when the diffusing particle is small.

The ability of the Stokes–Einstein and Eyring equations in predicting the absolute value of the diffusion coefficient for the individual solutes can be analysed if the atomic radius of each solute is calculated from the experimental diffusion coefficients on the basis of the equations and then compared with the known radii of the solutes such as the Goldschmidt radii or ionic radii. This comparison is made in Table 2.

Table 2 shows that the Stokes–Einstein or Eyring equation predicts the diffusion coefficients better than within an order of magnitude. However, they do not predict the relative diffusion coefficients of the solutes. It is interesting to note also in agreement with the work of others on self diffusion that the ionic radii seem to give better fit with the diffusion data than the Goldschmidt atomic radii.

TABLE 2. Comparison of atomic radii calculated on the basis of experimental results using the Stokes–Einstein or modified Eyring equation (12) with the Goldschmidt atomic radii and ionic radii

Element	Radius calculated from equation (6) (Å)	Goldschmidt atomic radius (Å)	Ionic radius (Å)
Al	0.13	1.43	0.57
Zn	0.40	1.37	0.83
Ag	0.52	1.44	1.13
Cu	0.71	1.28	0.96
Ni	0.71	1.25	0.87

C. *Discussion of the experimental results with regard to fluctuation theory*

Recently Swalin[13] advanced a theory of self-diffusion of liquid metals. In this theory it is postulated that diffusion results from the movement of atoms small and variable distances as the result of local density fluctuations. An equation was derived relating the self-diffusion constant to the interaction energy between a diffusing ion and its neighbors. A very important term in the theory is the energy of interaction between a diffusing ion and its nearest neighbors. In the case of solute diffusion, we are interested in the probability and the magnitude of local density fluctuations in the vicinity of the solute atom. It would be expected, using quasi-chemical reasoning, that the probability of a local density fluctuation is related to the relative partial molal enthalpy of the solute. Quantitative calculations with regard to the theory are difficult to make because of the lack of potential energy versus distance curve for pairs of unlike atoms in solution. Nevertheless, qualitative predictions are possible on the basis of the binding energy between the solute and solvent atoms. It is expected that solutes with positive relative partial molal enthalpies will have large and numerous density fluctuations in the vicinity of the solute atoms, hence leading to large solute diffusion coefficients. On the other hand, solutes with negative relative partial molal enthalpies, would tend to have smaller fluctuation, resulting in a smaller diffusion coefficient. In order to check this, qualitatively, it is interesting to compare the diffusion coefficients of the solutes studied in this investigation with the respective relative partial molal enthalpies in tin using thermodynamic data compiled by Kubaschewski and Catterall[14]. A plot of the ratio $D_{\text{solute}}/D_{\text{self}}$ versus the relative partial molal enthalpy of the solutes is shown in Fig. 8. On this figure, the probable error is

VOL. 8 1960

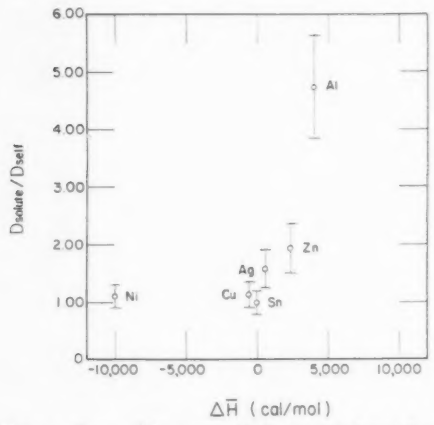


FIG. 8. D_{solute}/D_{self} vs. relative partial molal enthalpy of solutes in liquid tin.

shown for each point. A definite trend is to be noted from this figure. Aluminum which has a large positive relative partial molal enthalpy diffuses 5 times faster than does tin in tin at 620°K. Zinc, which has a somewhat smaller relative partial molal enthalpy, diffuses about twice as fast as tin and silver, which has a relatively small relative partial molal enthalpy, diffuses about 50 per cent faster than tin, whereas copper, which has a very slightly negative relative partial molal enthalpy, diffuses at about the same rate as tin, and nickel, which has an extremely large negative relative partial molal enthalpy, also diffuses at the same rate as does tin.

The results of this investigation indicate that those solutes which have a large repulsive interaction with the solvent tend to diffuse faster than the solvent itself, and further the greater the repulsion the larger the solute diffusion coefficient. On the other hand, however, it appears that the solutes which have large attractive interactions with the solvent tend to diffuse at the same rate as the solvent, thus indicating that the properties of the solvent itself govern the diffusion rate. This latter result is perhaps not too difficult to understand. For purposes of illustration let us consider an extreme case, one in which the relative partial molal enthalpy of the solute approaches minus infinity. For a dilute solution, this would result in a stable cluster consisting of the solute atom surrounded by numerous solvent atoms tightly bound together. At first glance, it might be expected that the diffusion coefficient of this cluster would be much less than that of the self-diffusion coefficient of tin because the radius of this cluster is about three times as large as the radius of the tin atom and hence according to the Stokes–Einstein or Eyring equation, its diffusion coefficient would be expected to be 3 times less. This, however, is not the case. According to Li[12] the Stokes–Einstein equation can be expressed as follows

$$\frac{D\eta}{kT} = \frac{\sigma - \tau}{2\sigma}\left(\frac{N}{V}\right)^{1/3} \tag{8}$$

where σ is the number of the nearest neighbors surrounding the diffusing particle, τ is the number of nearest neighbors in one layer and N/V is the reciprocal volume of the diffusing particle. In the case of the cluster, its radius is about $3r_0$, where r_0 is the radius of the tin atom. Hence $(N/V)^{1/3}$ is equal to $1/3\sqrt[3]{4}r_0$, σ equals sixty-four and τ equals twelve as calculated from geometrical considerations alone. Substituting these values to equation (8) we get

$$D = \frac{kT}{12\eta\pi_0} \sim \frac{kT}{4\pi\eta r_0}. \tag{9}$$

It can be seen that equation (9) is identical to the Stokes–Einstein equation. This indicates therefore that, for those solutes which have large negative relative partial molal enthalpies, the diffusion properties of the solvent governs their diffusion rates. On the other hand, it seems reasonable that those solutes which have positive relative partial molal enthalpies will have a higher probability of having significant fluctuations in their vicinity so that diffusion of these solutes will be enhanced.

For the case where the solute has an intermediate negative relative partial molal enthalpy (a region for which experimental data is lacking) the situation is more complex. Fluctuation theory suggests that there will be a smaller probability of density fluctuations in the vicinity of the solute compared with solvent, thus yielding a lower diffusion coefficient for the solute than the solvent. On the other hand, the cluster concept discussed above would tend to make the diffusion coefficients equal. It is difficult to assess the relative importance of each of these factors. At this point, it should be said that more data in similar systems would be welcome in order to test the general validity of these concepts.

6. SUMMARY

The diffusion of aluminum, zinc, silver, copper and nickel in liquid tin has been investigated by the capillary-reservoir technique in a temperature range from about 240°C to 480°C. All of the solutes investigated were present in dilute solutions ranging from 0.2 to 0.7 wt. %. The solutes were chosen so as to cover a range of relative partial molal enthalpies from large positive values to large negative values. On the basis of the self-diffusion of tin, it is found that the ratios of D_{solute} to D_{self} are 4.70, 1.90, 1.57, 1.15 and

1.10, respectively for aluminum, zinc, silver, copper and nickel within ± 15 or 20 per cent error. Diffusion coefficients of copper and nickel can be considered to be identical with that of tin within experimental error. The Stokes–Einstein and Eyring equations which consider only the factor of atom size, do not predict accurately the relative order of diffusion coefficients amongst the solutes. They do, however, predict the order of magnitude of the diffusion coefficients themselves. It appears, therefore, that factors other than size must be taken into account in evaluating the diffusion constant. On the basis of fluctuation theory, it is expected that those solutes which have a large positive relative partial molal enthalpy diffuse considerably faster than those solutes which have a large negative relative partial molal enthalpy since there is a much higher probability of significant density fluctuations occurring in the vicinity of the solute atoms in the former case. The data appear to be in agreement with this conclusion. Unfortunately, no quantitative comparison is feasible at the present time because of the lack of potential energy versus distance data for solute-solvent neighbors in solution. It is further proposed that in dilute solutions, the diffusion coefficient of a solute approaches that of the solvent if the solute has a zero or large negative relative partial molal enthalpy in the solvent.

VOL.
8
1960

ACKNOWLEDGMENT

The authors wish to thank the Research Corporation for financial support of this investigation.

REFERENCES

1. L. S. Darken, *Trans. Amer. Inst. Min. (Metall.) Engrs.* **175,** 184 (1948).
2. J. S. Anderson and K. Saddington, *J. Chem. Soc.* **5,** 381 (1949).
3. R. E. Grace and G. Derge, *Trans. Amer. Inst. Min. (Metall.) Engrs.* **203,** 839 (1955).
4. S. J. Rothman and L. D. Hall, *Trans. Amer. Inst. Min. (Metall.) Engrs.* **206,** 199 (1956).
5. G. Careri and A. Paoletti, *Nuovo Cimento* **2,** 575 (1955).
6. R. E. Hoffman, *J. Chem. Phys.* **20,** 1567 (1952).
7. R. E. Meyer and N. H. Nachtrieb, *J. Chem. Phys.* **23,** 405 (1955).
8. M. Farnsworth and J. Pekola, in *Symposium on Tin.* Amer. Soc. Test. Mat., Philadelphia (1952).
9. E. B. Sandell, *Colorimetric Determination of Traces of Metals* (2nd Ed.). Interscience, New York (1950).
10. H. Margenau and G. M. Murphy, *The Mathematics of Physics and Chemistry* (2nd Ed.). Van Nostrand, Princeton, N.J. (1957).
11. W. Sutherland, *Phil. Mag.* **9,** 781 (1905).
12. J. C. M. Li and P. Chang, *J. Chem. Phys.* **23,** 518 (1955).
13. R. A. Swalin, *Acta Met.*, **7,** 736 (1959).
14. O. Kubaschewski and J. A. Catterall, *Thermochemical Data of Alloys.* Pergamon Press, London (1956).

ELASTIC CONSTANTS OF COPPER–NICKEL ALLOYS*

R. E. SCHMUNK† and CHARLES S. SMITH‡

The elastic constants of single crystals of copper and of dilute alloys of copper with nickel have been measured using the ultrasonic pulse-echo technique. All fundamental elastic constants increase with composition in contrast to results previously obtained for solutes to the right of copper in the periodic table. In terms of $C_0^{-1}\,(dC/dx)$ the values are: C_{44}, (0.57); $(C_{11}-C_{12})/2$, (0.70); $(C_{11}+2C_{12})/3$, (0.17) per atom fraction. These values have been corrected for lattice parameter change upon alloying by using experimental data on the pressure derivatives of the elastic constants of pure copper. The remaining effect is owing to alloying alone and is still positive for both shear constants. This result may be interpreted as indicating a stiffening of the short-range crystal forces because the neutral nickel ion-core is larger than the iso-electronic copper ion-core, and a decrease in the long-range electrostatic forces because of the decrease in the average ion-core charge.

CONSTANTES ELASTIQUES DES ALLIAGES CUIVRE–NICKEL

Les auteurs ont mesuré les constantes élastiques de monocristaux de cuivre et d'alliages dilués de cuivre dans le nickel en utilisant une méthode d'ultra-sons. Toutes les constantes elastiques fondamentales croissent parallèlement à la composition. Ce résultat s'oppose à ceux précédemment obtenus pour des éléments dissous situés à la droite du cuivre dans le tableau périodique. En fonction de $C_0^{-1}\,(dC/dx)$, les valeurs sont: C_{44}, (0,57); $(C_{11}-C_{12})/2$, (0,70); $(C_{11}+2C_{12})/3$, (0,17) par fraction atomique. Pour le calcul de ces valeurs, on a tenu compte de la modification du paramètre réticulaire dans l'alliage en utilisant les données expérimentales sur les dérivées par rapport à la pression des constantes élastiques du cuivre pur. Un effet supplémentaire est du à l'alliage. Il est positif pour les deux constantes de cisaillement. Ce résultat peut etre interprété comme indiquant un durcissement des forces du cristal à petite distance parce que le noyau de l'ion neutre de nickel est plus grand que le noyau de l'ion de cuivre iso-électronique. Enfin, ce résultat indique aussi une diminution des forces électrostatiques à grande distance, par suite d'une diminution de la charge moyenne du noyau ionique.

ELASTISCHE KONSTANTEN VON KUPFER-NICKEL-LEGIERUNGEN

Mit Hilfe der Ultraschall-Puls-Echo-Technik wurden die elastischen Konstanten von Kupfer und von Legierungen von Kupfer mit Nickel in verdünnter Lösung gemessen. Alle grundlegenden elastischen Konstanten wachsen mit der Zulegierung, im Gegensatz zu früheren Ergebnissen für Zusätze, die im periodischen System rechts von Kupfer stehen. Ausgedrückt in $C_0^{-1}(dC/dx)$ ergeben sich folgende Werte: C_{44}, (0.57); $(C_{11}-C_{12})/2$, (0.70); $(C_{11}+2C_{12})/3$, (0.17), auf den Atom-bruchteil bezogen. Bei diesen Werten ist der Einfluß der Änderung der Gitterkonstanten infolge der Zulegierung bereits abgezogen; dabei wurden experimentelle Werte für die Ableitungen der elastischen Konstanten von reinem Kupfer nach dem Druck benutzt. Der übrigbleibende Effekt rührt nur von der Zulegierung her und ist für beide Scherkonstanten noch positiv. Das Ergebnis läßt sich wie folgt interpretieren: Die kurzreichenden Kristallkräfte werden versteift, da der neutrale Nickel-Atomrumpf größer ist als der isoelektronische Kupfer-Atomrumpf, die weitreichenden elektrostatischen Kräfte dagegen nehmen ab, da die mittlere Ionenladung abnimmt.

INTRODUCTION

In previous publications from this laboratory the single crystal elastic constants of dilute copper alloys[1,2] and dilute silver alloys[3] have been reported and interpreted in terms of conventionally recognized long-range and short-range interactions in the solvent metals. All solutes studied were on the right of the two solvents in the periodic table with the exception of palladium in silver. The Ag–Pd result was also qualitatively different from those for other solutes. For this reason a study of the homologous Cu–Ni alloys was started to test further the physical picture already put forward. At the same time a very careful study of pure copper was undertaken because this pure solvent had not previously been measured in this laboratory and it seemed desirable to have all work on as comparable a basis as possible.

A difficult point in the interpretation of alloy data arises in the correction which must be made for the effect of the change of lattice constant with alloying. While the lattice constant change is not large, the elastic constant change arising from it is often a substantial fraction of the whole change. This correction had previously been made on theoretical grounds.[1–3] It is now possible to make this correction on a completely *experimental* basis since data on the variation of the elastic constants with pressure (and hence volume) are now available.[4] The use of

* Received August 3, 1959.

† Formerly at Case Institute of Technology. Now at Phillips Petroleum Company, Atomic Energy Division, Idaho Falls, Idaho.

‡ Case Institute of Technology, Cleveland, Ohio.

the experimental correction does not make a qualitative change in the interpretation of the present and previous data; it does simplify the correction and remove all ambiguity from it.

EXPERIMENTAL PROCEDURE

The single crystals used in this experiment were prepared with only minor modifications of the procedures already described.[2,3] A larger temperature gradient of 40 C°/in. was obtained by the use of a heat-sink. Graphite crucibles and a hydrogen atmosphere were used with cooling rates of 50 C°/hr.

An approximate orientation of the crystals was obtained with an optical goniometer. Characteristic light reflections were obtained from the [100], [110] and [111] type poles developed by the nitric acid etch. The latter of these was rather sensitive to etching and was not observed in all cases. The crystals were then cut with a water-cooled abrasive wheel to give specimens with acoustic surfaces as nearly perpendicular to the [110] direction as possible.

The acoustic surfaces were prepared by etching off the cold worked layer produced by the cut-off saw, waxing the specimen into a 2 in. diameter steel lapping ring, and lapping flat and parallel through metallographic papers to 3/0.

The three acoustic waves were measured using the ultrasonic pulse-echo method. The 10 Mc/sec quartz transducers were cemented to the single crystal specimens with phenyl salicylate. Half in. diameter transducers were used in the experiment, X-cut quartz producing longitudinal waves propagated in the [110] direction. The shear waves were produced by orienting a Y-cut quartz to give particle motion in either [001] or [110] direction with a [110] propagation direction. Transit times, T, observed were approximately 5.7 μsec for the longitudinal wave and 9.7 and 17.3 μsec for the two shear waves, the lengths of the different specimens being about the same. Measurements of the transit times for the waves were reproducible to within 0.1 per cent.

Transit time corrections, arising from an end effect at the quartz transducer, were applied to these measurements. These corrections were determined by observing the change in transit times when a second quartz transducer was cemented to the far end of the crystal. The corrections that were applied in this experiment were based on this procedure and on previous work on copper alloys done in the laboratory.[1,2] These corrections are $\Delta T = 0.026$ μsec for the longitudinal wave and $\Delta T = 0.028, 0.030$ μsec for the fast and slow shear waves, respectively, the quantities being subtracted from T.

Table 1. Chemical analyses and average compositions

Average composition at. % Ni	Analysis, wt. %		
	top Ni	bottom Ni	C
00			0.01
2.34	2.14	2.19	
3.02	2.83	2.79	
4.49	4.15	4.17	
6.02	5.55	5.67	0.006
9.73	9.20	8.95	0.03

After the acoustic measurements were completed on a crystal, one of the polished faces was etched to remove the polish layer and a back reflection Laue pattern taken to determine accurately the orientation of the crystal, which in all cases was within 3° of the desired [110] direction. The advantages of the [110] orientation are twofold: first, the reduction of the data to obtain the elastic constants is greatly simplified,[3] and secondly, the quantities of most interest, C_{44} and $(C_{11} - C_{12})/2$ are determined directly.

Chemical analyses by the J. H. Herron Company on two samples cut from the single crystal ingot at each end of the section used for the ultrasonic measurements were in excellent agreement as shown in Table 1. In order to guard against the remote possibility of the formation of Ni_3C the carbon analyses shown in the table were also carried out with results no larger than would be expected from gross pick-up of carbon from the graphite crucibles which were used.

Results of the chemical analyses were used in determining the average composition of the crystals used for the ultrasonic measurements. The densities of the crystals were then calculated from the composition and lattice parameter data.[5]

All of the alloy crystals grown exhibited the familiar woodgrain appearance as noted previously by other authors.[1] The specimens used for the ultrasonic measurements were cut from the lower ends of the crystals where this effect was less noticeable. The presence of the short-range segregation in the crystals did not have any noticeable effect on the production of good echo patterns in the ultrasonic measurements.

One pure copper crystal was grown and three specimens of different lengths were cut from it. Each specimen was measured separately and the elastic constants calculated independently.

RESULTS

The elastic stiffness, C_{ij}, are connected with the acoustic wave velocities in the [110] direction by the

VOL. 8 1960

TABLE 2. Elastic constants of copper in units of 10^{12} dyne cm^{-2}

Investigator	C	C'	B_s
LAZARUS[7], 298°K	0.756	0.235	1.396
GOENS[8], room temperature	0.753	0.236	1.383
OVERTON and GAFFNEY[9], 300°K	0.7539	0.2348	1.371
This paper, length 1.1 cm	0.7521	0.2328	1.367
This paper, length 1.4 cm	0.7500	0.2340	1.371
This paper, length 1.9 cm	0.7513	0.2328	1.371
This paper, average 300°K	0.7511	0.2332	1.370

following equations, which also serve to define a shorthand notation.

$$\begin{aligned} C &= C_{44} &&= \rho V_5^2 \\ C' &= (C_{11} - C_{12})/2 &&= \rho V_4^2 \\ C_{11}' &= (C_{11} + C_{12} + 2C_{44})/2 = \rho V_2^2. \end{aligned} \quad (1)$$

In these relations, ρ is the density, V_2 is the longitudinal wave velocity and V_5 and V_4 are the velocities of shear waves with particle motion in the [001] and [1$\bar{1}$0] directions respectively. We are interested in the shear stiffness C and C' which are given directly from the measurements, and in the adiabatic bulk modulus, which may be obtained only by combining the measurements as follows:

$$B_s = (C_{11} + 2C_{12})/3 = \rho V_2^2 - \rho V_5^2 - \rho V_4^2/3. \quad (2)$$

The fundamental elastic stiffness C, C' and B_s have been computed using essentially equations (1) and (2) but making slight corrections arising in small misorientations from [110].[6] Since the transit times, and hence velocities, are reproducible to 0.1 per cent, the relative precision of these results may be placed at 0.2 per cent. Taking into account experimental uncertainties common to all these crystals, the absolute accuracy is felt to be 0.5 per cent.

The results for pure copper are displayed in Table 2 and compared with those of other investigators.[6–8] Our three crystals were of the different lengths shown; there appears to be no systematic trend on that account. Our results are consistently just slightly lower than those of the other investigators who used a different method,[8] or a significantly different version of the pulse-echo method.[7,9] The *isothermal* bulk modulus computed from our work, 1.332×10^{12} dyne-cm^{-2}, is 3 per cent low compared with the most recent value of Bridgman[10], 1.377×10^{12} dyne cm^{-2}, determined by the measurement of linear compression. The present measurements for pure copper are, however, made with exactly the same technique and apparatus as for the Cu–Ni alloys, and as for the copper alloys reported previously.[1] All determinations which are to be used to study the effect of alloying are, therefore, on a strictly comparable basis.

TABLE 3. Elastic constants of Cu–Ni alloys in units of 10^{12} dyne cm^{-2}

At. % Ni	C	C'	B_s
00	0.7511	0.2332	1.370
2.34	0.7631	0.2372	1.377
3.02	0.7674	0.2375	1.377
4.49	0.7731	0.2409	1.380
6.04	0.7812	0.2434	1.386
9.73	0.7909	0.2489	1.392

The fundamental constants of the Cu–Ni alloys are given in Table 3. These constants, normalized to those of pure copper, are shown plotted against nickel concentration in Fig. 1. The lines shown in the figure are a least squares fit of the data, in which equal weight was given to each experimental point

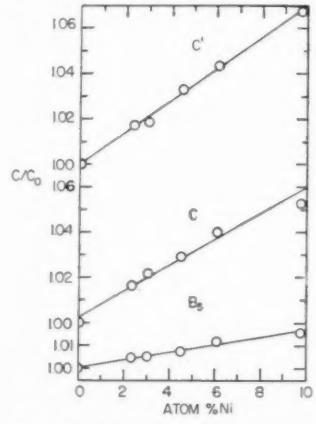


FIG. 1. The fundamental elastic constants of Cu–Ni alloys normalized to those of pure copper.

with the exception of 9.7% Ni. This crystal was given half the weight of the others because of the poorer reproducibility of the acoustic measurements for it. The excellent internal consistency of the data is exhibited by the fact that all points, with the exception of three, lie within 0.2 per cent of the least squares line. One of the exceptions is C for pure copper, but this is really a result of having included the 9.7% Ni alloy in the least squares procedure. The slopes of the least squares lines expressed as $C_0^{-1}(dC/dx)$, are: C, 0.57; C', 0.70; and B_s, 0.17 per atom fraction.

It is observed that all fundamental constants *increase* upon adding Ni solute. This result is just opposite to that found previously for the solutes Zn, Ga, Ge, Al and Si, which have higher valence than Cu and caused a *decrease* in all fundamental constants. The significant feature common to all solutes is that the *absolute magnitude* of the *fractional* change in C'

TABLE 4. Lattice parameter correction for Cu–Ni alloys using equation (3). Composition is expressed as atom fraction of nickel

		C	C'
Total change	$\frac{1}{C_0}\left(\frac{dC}{dx}\right)$	0.57	0.70
Ref. (4)	$\frac{1}{C_0}\left(\frac{dC}{d\ln a}\right)_{x=0}$	−12.77	−10.20
Ref. (5)	$\frac{1}{a}\frac{da}{dx}$	-2.89×10^{-2}	-2.89×10^{-2}
Correction for lattice parameter change	$\left(\frac{1}{C_0}\frac{dC}{d\ln a}\right)_{x=0}\left(\frac{1}{a}\frac{da}{dx}\right)$	0.369	0.295
Change owing to alloying	$\frac{1}{C_0}\left(\frac{dC}{dx}\right)_a$	0.20	0.40

is greater than the absolute magnitude of the fractional change in C.

For most solutes a significant fraction of the total change in the elastic stiffness arises in the change in lattice parameter, a, upon alloying. For the purpose of interpretation in microscopic terms one would like to know the change which a solute would produce *at constant lattice parameter*. A correction may be made on theoretical grounds,[1,3] but this procedure necessarily invokes the very microscopic model which it is desired to test. Fortunately, there is now available an entirely experimental, and hence unambiguous, method of making the correction which makes use of the recently determined pressure derivatives of the elastic constants.[4]

The pressure derivative of an elastic constant, dC/dP, permits one to compute immediately the quantity $dC/d\ln a$ at constant composition. The total fractional derivative of C with respect to composition is given by

$$\frac{1}{C_0}\frac{dC}{dx} = \frac{1}{C_0}\left(\frac{dC}{dx}\right)_a + \frac{1}{C_0}\left(\frac{dC}{d\ln a}\right)_{x=0}\left(\frac{1}{a}\frac{da}{dX}\right). \quad (3)$$

The quantity on the left side of equation (3) is the one which is directly observed, the second term on the right side is the lattice parameter correction term, while the first term on the right represents the quantity which is desired. The numerical details of this correction are given in Table 4 for the shear constants C and C'. It is seen that the *decrease* of lattice parameter causes a pronounced *stiffening* of the crystal, amounting to about half of the total change.

The basic result of this work which we should like to interpret is given in the last line of Table 4. It is observed that this quantity, $C_0^{-1}(dC/dx)_a$, is still positive for both C and C', and that the change at constant lattice parameter for C' is still larger than that for C. The correction for lattice constant change makes a quantitative difference but not a qualitative one.

A comment on the numerical validity of this correction is in order. Lattice parameter-composition data is well established for this system. The precision of the pressure measurements is surprisingly high at 2 per cent reproducibility and our experience suggests that the accuracy is nearly that good also. Thus, the correction is known as well as the observed data for Cu–Ni alloys (and considerably better than the data for the previous copper alloys). The effect owing to alloying alone may then be regarded as known to within ± 0.02 per atom fraction.

INTERPRETATION

The interpretation of the Cu–Ni results proceeds in a manner similar to that previously employed for other solutes in copper. It is assumed that there are only two important contributions to the shear constants C and C', one arising from long-range electrostatic forces, the other from short-range repulsive forces between *ion-cores*. The elastic constants are obtained from the crystal binding energy by taking the second derivative with respect to the appropriate strain. Any contributions to this energy other than the two mentioned are presumed to depend only on the volume, and hence do not contribute to the shear constants.

The long-range electrostatic contribution for both shear constants of f.c.c. metals has been calculated by Fuchs[11]. The theoretical results which may be termed the electrostatic stiffnesses, C_E and C_E', are:

$$C_E = 0.9479(2e^2/a^4); \quad C_E' = 0.1058(2e^2/a^4).$$

The ion-core stiffnesses, C_I and C_I', are then obtained by taking the difference between the measured stiffnesses and Fuchs' electrostatic stiffnesses. The

VOL. 8 1960

resulting values for pure copper, in units of 10^{12} dyne cm^{-2} are:

$$C_E = 0.257; \quad C_E' = 0.0286;$$
$$C_I = 0.496; \quad C_I' = 0.2047.$$

This simple procedure for getting C_I and C_I' is the same as that employed for silver alloys;[3] it is somewhat different from that originally used for copper alloys.[1]

The change in shear constant upon alloying is presumed to be the result of changes in both the long-range and the short-range stiffnesses. The former depends on the square of the net ion charge, and it is hence assumed that the electrostatic stiffness for the alloy is equal to that for pure copper multiplied by an empirical parameter Z^2 *which, however, is expected to be close to unity*. The ion-core stiffness is proportional to the average short-range bond energy between pairs of ion-cores, and the change in this stiffness is hence expected to be proportional to the concentration of solute, x, so long as we are in the dilute range. The constant of proportionality has been designated by α, which should be a constant characteristic of a particular solute element.

The shear constants for the alloy will thus be given by

$$C = C_E Z^2 + C_I(1 + \alpha x)$$
$$C' = C_E' Z^2 + C_I'(1 + \alpha x) \qquad (4)$$

where the coefficients of Z^2 and $(1 + \alpha x)$ are the values for pure copper quoted above. If we subtract from C and C' the constants for pure copper, and then divide by the latter and by the composition, we obtain the fractional change in C and C' per atom fraction solute,

$$C_0^{-1}\Delta C/x = 0.341(Z^2 - 1)\,x + 0.659\alpha$$
$$C_0'^{-1}\Delta C'/x = 0.123(Z^2 - 1)\,x + 0.877\alpha. \qquad (5)$$

In equations (5) the numerical coefficients are the quantities C_E/C_0, C_I/C_0, etc. Their determinant is not zero as C' depends more heavily on the ion-core contribution than does C. This fact enables us to separate the long-range and short-range effects of alloying by solving equations (5) for α and $(Z^2 - 1)/x$.

Since equations (5) take no account of lattice constant change we must use data corrected for it. The derivative form $C_0^{-1}(dC/dx)_a$ is so corrected and may be used in place of the difference form $C_0^{-1}\Delta C/x$ since for Cu–Ni alloys the stiffnesses vary linearly with composition. Upon substitution of the last line of Table 4 in equations (5), we have the results,

$$\alpha = +0.52, \qquad Z^2 = 1 - 0.40x,$$

describing the behavior of the elastic shear constants of Cu–Ni alloys.

The result, $\alpha > 0$, is in physical agreement with the expected change in short-range *ion-core* interaction upon alloying Cu with Ni. The closed-shell ion-cores in question all have twenty-eight electrons, with a nuclear charge of twenty-eight for Ni, twenty-nine for Cu, etc. One expects the ion-core size to decrease monotonically in the iso-electronic sequence Ni–Cu–Zn–Ga–Ge as the nuclear charge increases. Since the short-range interaction is sharply dependent on the amount of nearest-neighbor ion-core overlap, the Ni–Cu repulsive interaction is expected to be greater than the Cu–Cu interaction leading to a value of $\alpha > 0$ in these dilute alloys. Similarly for the solutes to the right of Cu in the iso-electronic sequence we should expect $\alpha < 0$ as is already known.[1] There is in fact a monotonic decrease in α from a positive value for Ni through increasingly negative values for Zn, Ga and Ge solutes just as expected.

The other example of a transition metal solute in this series of studies was that of a Ag–Pd alloy reported by Bacon and Smith[3]. At that time the lattice parameter correction had to be made on a theoretical basis and the value of α turned out to be slightly negative. The Ag–Pd data can now also be corrected for lattice parameter change by the use of Ag pressure data with the result that $\alpha = +0.10$. Thus Pd in Ag behaves like Ni in Cu, both giving $\alpha > 0$. The iso-electronic ion-core sequence, Pd–Ag–Cd–In–Sn, is thus completely analogous with the corresponding copper sequence with respect to the parameter α, and both agree with simple physical expectation.

We turn now to the parameter Z which describes the change in long-range stiffness contribution upon alloying, under the assumption of the first paragraph of this section. The result for Cu–Ni alloys, $Z^2 = 1\text{–}0.40\,x$, may be expressed as $Z = 1 - 0.20\,x$ for the small compositions to which the analysis applies. For the purpose of comparison we introduce the average ion-core charge (or electron/atom ratio), $q = 1 - x$, with the expectation that $1 > Z > q$. We see that Z does fall within the physically reasonable limits and, significantly, much nearer to unity than to q. This result is expected on elementary considerations of valence charge distribution and is in contrast to the situation for the solutes Zn, Ga and Ge for which the *experimental result* is that $Z \simeq q$.

The elastic constant measurements for the Ag–Pd alloy yield $Z = 1 - 0.30\,x$ when corrected for lattice parameter change in the manner described here. Thus the long-range parameter for this system also agrees

with that for Cu–Ni in that $1 > Z > q$ for both. Since the *experimental result* for Cd, In and Sn solutes in Ag is $Z \simeq q$, the whole silver iso-electronic sequence is completely analogous to the copper iso-electronic sequence with respect to Z also.

The situation for Cu and Ag alloys which has just been described has been reviewed recently by Huntington[12] who displays in graphical form the composite results for all these alloys. These values for Z and α have been reduced from the data exactly as described in this paper. It is clear from these plots that in this series of experiments the major feature which is not clearly understood is the *experimental result* that $Z \simeq q$, rather than a value just greater than unity, for solutes to the right of the noble metal in the periodic table. A value of Z near to unity is expected for these solutes also, on the simple and physically necessary picture of excess solute charge screened by a pile-up of valence electron charge.[1,3] We emphasize, however, that Z is an empirical parameter which, with α, does describe the experimental position *within the framework of the analysis outlined here.*

The salient assumption of this analysis is that the shear stiffnesses of the noble metals and their alloys arise in just the two terms stated in equations (4). Since the behavior of Z for the transition metal solutes is quite plausible, one is led to examine the assumption specifically for alloys of $q > 1$. It may be that a third physical contribution to the shear stiffness begins to enter only upon increasing q from unity. In this case it is clear that the new contribution is greater for C than for C' and that its presence is measured by, approximately, $Z - 1$. Such a contribution could arise from the Fermi energy of the valence electrons in the situation where the Fermi surface is not spherical. Several recent experiments have suggested that the Fermi surface in copper may be warped, but no quantitative estimates of possible Fermi contributions to C and C' appear to have been made.

ACKNOWLEDGMENTS

This research was supported by the Office of Naval Research and by the National Carbon Company.

REFERENCES

1. J. R. Neighbours and C. S. Smith, *Acta Met.* **2,** 591 (1954).
2. C. S. Smith and J. W. Burns, *J. Appl. Phys.* **24,** 15 (1953).
3. R. Bacon and C. S. Smith, *Acta Met.* **4,** 337 (1956).
4. W. B. Daniels and C. S. Smith, *Phys. Rev.* **111,** 713 (1958).
5. Abstracted in K. Polmanteer's Master's Thesis, Case Institute of Technology, TM 65 (1950).
6. J. R. Neighbours and C. S. Smith, *J. Appl. Phys.* **21,** 1338 (1950).
7. D. Lazarus, *Phys. Rev.* **74,** 1726 (1948).
8. E. Goens, *Ann. Physik.* **17,** 233 (1933).
9. W. C. Overton, Jr. and J. Gaffney, *Phys. Rev.* **98,** 969 (1955).
10. P. W. Bridgman, *Proc. Amer. Acad. Arts Sci.* **74,** 189 (1948).
11. K. Fuchs, *Proc. Roy. Soc.* A**153,** 622 (1936).
12. H. B. Huntington, *Solid State Physics* **7,** 335 (1958).

VOL. 8 1960

Electron metallographic observations on the formation of fatigue cracks*

Wood[1] has developed a method for following the formation and growth of fatigue cracks using the optical microscope for observation. Since optical techniques are necessarily limited in resolution, a study is being conducted to test the applicability of electron microscopy for obtaining greater detail in the observations. The fatigue specimens were prepared in the manner described by Wood and then replicated for electron microscopy.

Cylindrical rods approximately 0.2 inches in diameter of OFHC polycrystalline copper were fatigued by alternating torsion. The amplitude was such as to produce a shear strain at the surface of ± 0.002. After the rods had been exercised for a certain number of cycles, 2.2×10^6 cycles in the present case, they were silver plated to protect the surface. A flat about 0.01 inches wide was then ground parallel to the longitudinal axis on the surface which was then mechanically polished and etched. Preshadowed carbon positive replicas were made by first stripping a relatively thick parlodion negative replica from the specimen. The negative is then shadowed with tungsten oxide followed by a supporting film of carbon deposited at normal incidence. The parlodion is dissolved in amyl acetate before viewing the replica in the electron microscope. Since the micrographs presented here were enlarged directly from electron micrographs of these replicas, shadows cast by steps or projections facing the shadowing source are in light contrast to the background, while the steps or projections themselves appear in dark contrast.

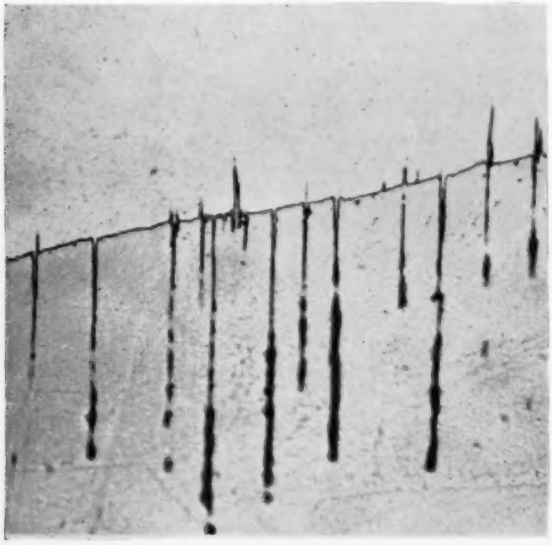


FIG. 1a. Optical micrograph of fatigue specimen. ×500

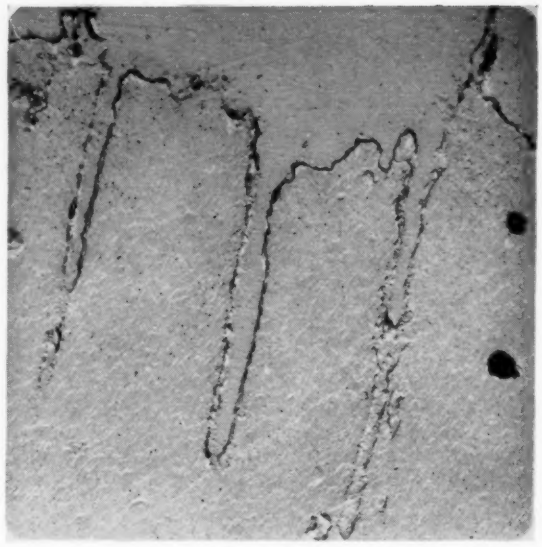


FIG. 1b. Electron micrograph of fatigue specimen. ×4800

Figure 1a is a typical optical micrograph showing the fissures produced at or near the surface of fatigue specimens. An electron micrograph of a similar region is shown in Fig. 1b. Although the ammonium persulphate etch used on the specimens shown in Figs. 1a and 1b does not reveal any crystallographic detail, the gain in clarity of the electron micrograph is apparent. If a dilute solution of nitric acid is used as an etchant, the additional information that is displayed by electron microscopy is shown in Figs. 2 and 3. In Fig. 2 the evident disruption of the lattice that is produced at the root of a fissure is shown. Fig. 3 shows a grain containing etched-up slip bands. The accumulation of crystalline damage along these slip planes is believed to be a forerunner of the fissures that develop later.

In view of these observations it seems apparent that electron microscope work can extend the original work done with the optical microscope. This earlier work suggested that fatigue early in the life of a metal produced zones which etched up on the special sections as traces of abnormally distorted slip planes. These zones then opened into fissures. However, it was not



FIG. 2. Electron micrograph of a fissure. ×4800

certain that these zones were not fissures in the first place. The electron microscope work now shows that the zones do in fact etch up while they are still distorted slip planes, as illustrated by Fig. 3; further work should therefore throw more light on the transition to fissures. Furthermore, the electron microscope shows that what appear under the optical microscope as continuous fissures are, in general, better described as links of smaller discontinuous fissures. This suggests that the fissures leading to fatigue cracking start in even more localized areas of abnormal distortion than the optical microscope would indicate.

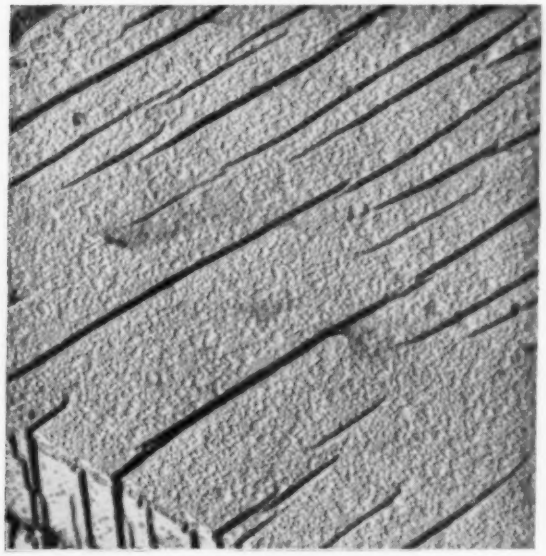


FIG. 3. Electron micrograph of etched up slip planes. ×20,000

Many electron micrographs demonstrating this feature have been obtained.

Research Laboratories, H. A. BENDLER
General Motors Corporation
Warren, Michigan

Baillieu Laboratory, W. A. WOOD
University of Melbourne
Victoria, Australia

Reference

1. W. A. WOOD, *Phil. Mag.* **3**, 692 (1958).

* Received January 20, 1960.

Regular pile-up of dislocations in α-iron*

In the course of a research program involving the study of thin foils of iron in the electron microscope a regular pile-up of dislocations against a particle was observed (Fig. 1). Although regular pile-ups of this type are common in slightly deformed α-brass and austenitic stainless steel, pile-ups in α-iron are usually very irregular, often appearing as a tangled mass of dislocations. A regular pile-up in α-iron has been observed only once and does not appear to have been reported previously.

No source of the dislocations was observed but there was a grain boundary about 2 μ from the pile-up. The bowing and spacing of the dislocations indicates

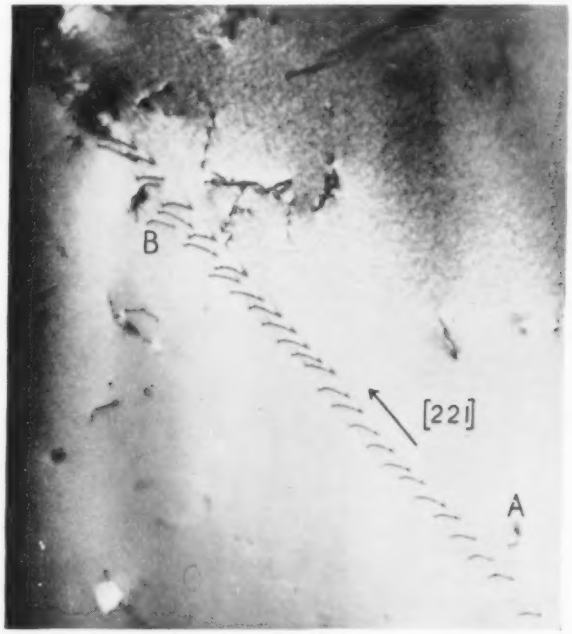


FIG. 1. Regular pile-up of dislocations in α-iron. Micrograph of thin foil. ×40,000

VOL. 8 1960

that they are piled up against the particle which is in the top left-hand corner of the picture. During observation the single dislocation A, which is bowed in the opposite direction to those in the pile-up, was seen to move away from the particle leaving slip traces behind it. The dislocation B, which is bowed in the same way as those in the pile-up, also has slip traces behind it, indicating that it has moved in a direction opposite to A. None of the dislocations in the pile-up nor any of the random dislocations was seen to move.

From the morphology of carbide particles in the same grain as the pile-up and from electron diffraction data the dislocations were found to be lying in a (110) plane. A [221] direction in the plane of the foil is shown on the figure.

The difference in contrast of the ferrite and the random dislocations on each side of the pile-up is due to a slight change in orientation of the foil and may be caused by slight tilting of the iron lattice by the pile-up.

The Burgers vector of the dislocations could not be found but since in iron, dislocations with an appreciable screw component can cross-slip relatively easily, it may be that the dislocations forming the pile-up have only a small screw component and are unable to cross-slip. The Burgers vector could then be along a [111] direction which makes an angle of 15°48′ with the [221] direction in the (110) slip plane of the dislocations.

The specimen was of polycrystalline iron containing about 0.015 per cent carbon. The original strip, 0.004 in. thick, was cooled from 700°C to room temperature in about 30 min. The foils were produced by a method similar to that of Bollmann[1], using an electrolyte of about 15 per cent perchloric acid in acetic acid. The foil was examined in a Siemens Elmiskop I electron microscope.

Dendritic carbide particles similar to those observed by Leslie *et al.*[2] were found in the iron. They were found to grow on the (110) and (111) planes along [111], [112] and [110] directions. The foil contained many dislocations and there were dislocations around the particles suggesting that the foil had been deformed. This had not been done deliberately but may have resulted from handling during preparation.

Department of Mines and Technical Surveys
Ottawa, Canada

E. Smith

References

1. W. Bollmann, *Phys. Rev.* **103,** 1588 (1956).
2. W. C. Leslie, R. M. Fisher and N. Sen, *Acta Met.* **7,** 632 (1959).

* Received January 15, 1960.

THE CRYSTALLOGRAPHY OF THE CUBIC TO ORTHORHOMBIC TRANSFORMATION IN THE ALLOY AuCu*

R. SMITH† and J. S. BOWLES‡

The habit plane, orientation relationships and shape change associated with the transformation to the ordered orthorhombic phase in the alloy CuAu have been measured and are shown to conform with the phenomenological theory of martensitic transformations.[2–4] The agreement with the theory is systematically better when some dilation of the habit plane is permitted. It has been found that groups of four plates having an irrational habit close to $\{110\}_C$ develop into compound plates parallel to $\{110\}_C$.

L'ASPECT CRISTALLOGRAPHIQUE DE LA TRANSFORMATION DU SYSTEME CUBIQUE EN SYSTEME ORTHORHOMBIQUE DANS L'ALLIAGE Au–Cu

Les auteurs ont déterminé le plan d'habitat, les relations d'orientation et la modification de forme, qui sont associés à la formation de la phase orthorhombique ordonnée dans l'alliage Cu–Au.

Ils montrent que ces relations sont conformes à la théorie phénoménologique des transformations martensitiques.[2–4] Ils constatent que l'accord avec la théorie est systématiquement meilleur lorsque l'on autorise une certaine dilatation du plan d'habitat. Ils montrent que des groupes de quatre plaques ayant un habitat irrationnel proche de $\{110\}_C$ se développent en plaques composées parallèles à $\{110\}_C$.

KRISTALLOGRAPHIE DER KUBISCH-ORTHORHOMBISCHEN UMWANDLUNG DER LEGIERUNG AuCu

Habitusebene, Orientierungsbeziehungen und Gestaltänderung, die mit der Umwandlung der Legierung CuAu in die geordnete orthorhombische Phase verbunden sind, wurden gemessen; sie stimmen mit der phänomenologischen Theorie martensitischer Umwandlungen[2–4] überein. Die Übereinstimmung mit der Theorie wird systematisch verbessert, wenn man eine gewisse Dilation der Habitusebene zuläßt. Gruppen von vier platten, die einen irrationalen Habitus nahe an $\{110\}_C$ haben, werden zu zusammengesetzten Platten parallel zu $\{110\}_C$.

VOL. 8 1960

1. INTRODUCTION

Investigation of the precipitation of the phase CuBe during ageing of copper–beryllium alloys[1] has shown that the crystallography of this transformation is consistent with the phenomenological theory of martensitic transformations.[2–4] This result provides some support for the idea that a common (dislocation) mechanism may be involved both in martensitic transformations and in the early stages of diffusion controlled transformations. The present investigation of the transformation in the alloy AuCu was undertaken to test further the validity of this idea.

The ordering in AuCu and the accompanying changes in lattice symmetry have been the subject of numerous investigations.[5–9] These investigations have shown that two closely related superlattices with different symmetries can form from the disordered face-centred cubic structure. When ordering occurs below approximately 380°C, the ordered phase has a face-centred tetragonal structure in which the copper and gold atoms occupy alternate planes normal to the c axis. Between approximately 410°C and 380°C a complex ordered structure forms which has a pseudo-cell which is face-centred orthorhombic. This pseudo-cell has a b/a ratio in the range 0.9982–0.997, but apart from this it is similar in dimensions to the unit cell of the ordered tetragonal structure. According to Johansson and Linde[6], the complex ordered structure has an orthorhombic unit cell comprising ten of the pseudo-cells side by side in the direction of the a axis; the atomic planes perpendicular to the c axis are again occupied alternately by copper and gold atoms but the stacking order of the atoms changes over after five pseudo-cells. The axial ratio c/b of both structures decreases with decreasing temperature from about 0.939 at 410°C to about 0.926 at 300°C.

Isothermal transformation studies of each transformation[9,10] have established beyond doubt that the rates are diffusion-controlled; typical C-shaped curves are obtained if the times for different degrees of transformation are plotted against the transformation temperature. On the other hand, the microstructures produced by these transformations[11] are similar in appearance to those produced by martensitic transformations. Because of this similarity it seemed probable that the transformations would produce relief effects on polished surfaces. Preliminary experiments showed that this was indeed the case, so that it became of interest to discover whether the geometrical features of these transformations conformed with the phenomenological theory of martensitic

* Received April 15, 1959.

† Formerly, School of Metallurgy, University of Melbourne, Carlton N.3, Victoria, now Australian Atomic Energy Research Establishment, Sutherland, N.S.W., Australia.

‡ School of Metallurgy, University of New South Wales, Kensington, N.S.W., Australia.

transformations. It was found that the cubic to tetragonal transformation does not proceed by the production of tetragonal crystals within the cubic matrix so that it was not appropriate to attempt to apply the theory to this transformation. The cubic to orthorhombic transformation, on the other hand, was found to proceed by the growth of orthorhombic crystals at the expense of the cubic matrix and so should conform with the theory. Accordingly, measurements of lattice parameters, orientation relationships, habit planes, and surface relief, were made for the cubic or orthorhombic transformation.

The general characteristics of each of the transformations are described in Section 2 and the detailed analyses of the crystallography of the cubic to orthorhombic transformation in Section 3. In Section 4 the results of this investigation are compared with the predictions of the theory.

2. GENERAL CHARACTERISTICS

(a) *Experimental methods*

The materials used were oxygen-free high conductivity copper and "double-refined" gold, both of 99.99 wt.% purity; the copper contained 0.002 wt.% of silver, oxygen and sulphur, and the main impurities in the gold were silver and copper. Cylindrical specimens (6 mm diameter by 6 cm long), of equiatomic composition were prepared by induction melting in evacuated silica capsules, and these specimens were then converted to single crystals by the Bridgman technique. Some of the single crystals were allowed to cool to room temperature in the temperature gradient to yield the tetragonal structure; others were water-quenched from above 450°C to retain the disordered cubic structure at room temperature.

To produce the orthorhombic structure, specimens cut from the single crystals were heated for 1 hr at 800°C and transformed isothermally at temperatures in the range 380–405°C. The tetragonal structure was studied mainly on specimens cut from the single crystals which had been cooled in the temperature gradient, but some observations were also made on specimens heated for 1 hr at 800°C, quenched to room temperature and then transformed isothermally at temperatures in the range 250–350°C. These heat treatments were usually carried out in a salt bath, the specimens being contained in evacuated silica capsules, but in a few cases specimens were heat treated in the evacuated chamber of a hot stage microscope[12] and the progress of the transformation followed visually.

For the study of relief effects, the specimens were obtained initially in the disordered cubic condition, and metallographically polished before heat-treatment. A mechanical polish sufficed for this purpose, but for the general examination of microstructures, specimens were polished either electrolytically or by "polish-attack". The electrolyte consisted of hydrochloric acid, nitric acid and water in the proportions 1:3:4 by volume, and polishing was carried out at 0.8 V. A mixture of hydrochloric and chromic acids was used in the polish-attack method.

(b) *Experimental observations*

Transformation in the temperature range 380–410°C produced microstructures of the type illustrated in Fig. 1. The plates in these microstructures were observable either as relief effects or after polishing and etching. When etched specimens were examined in polarized light, a single system of fine parallel sub-bands became visible in each plate (Figs. 2 and 3).

It was established by X-ray examination of partly transformed specimens that the plates had the orthorhombic structure and the surrounding matrix, the

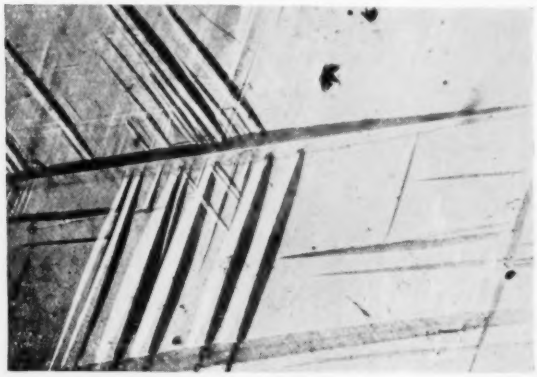


FIG. 1. Relief effects produced after 18 hr at 400°C. ×50

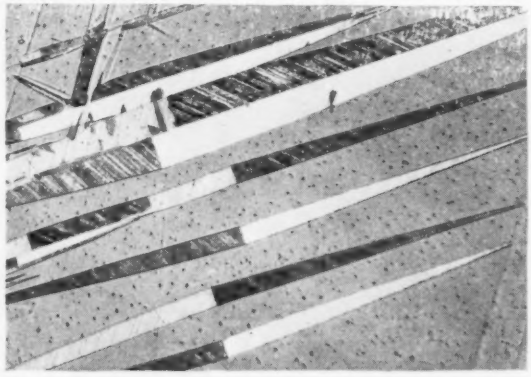


FIG. 2. Microstructure showing sub-bands, "diamond" figures and pseudo habit plane, in specimen transformed 18 hr at 400°C. Polarized light. ×150

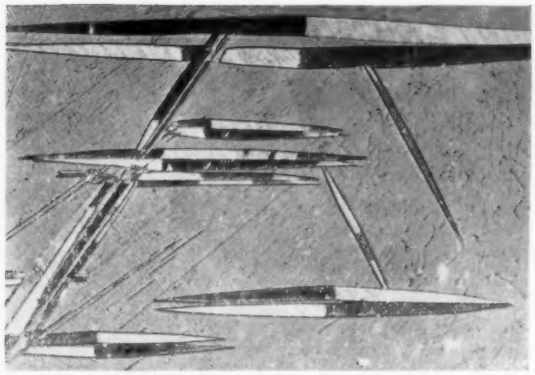


FIG. 3. "Diamond" figures in specimen transformed 2 hr at 390°C. Polarized light. ×300

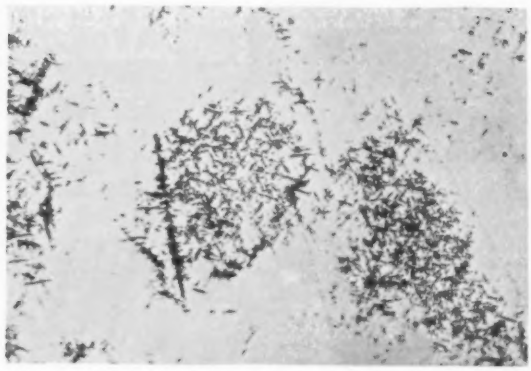


FIG. 5. Large numbers of small plates formed in 5 min at 380°C. ×200

disordered face-centred cubic structure. This is consistent with the results of Kallbach *et al.*[9] who showed that the orthorhombic phase develops at the expense of the cubic phase.

The plates produced during the early stages of the transformation were almost invariably arranged in groups of four and appeared on the surface being examined as roughly diamond shaped figures. From the form of these figures and the fact that habit plane determinations showed that the group consisted of four non-parallel variants of the same crystallographic plane, it seems likely that the groups of plates had the form of a pyramid. This suggests strongly that all four plates were nucleated at a common point, the apex of the pyramid.

Observation with the hot stage microscope showed that, in all cases, transformation commenced by the formation of isolated groups of small plates which then grew slowly by lengthwise growth and, to a lesser extent, by thickening of the plates. Occasionally, a fully grown group of plates appeared suddenly, but this can be attributed to the arrival at the surface of a group of plates nucleated in the interior. In some cases, when the plates had grown to a certain stage, other plates grew uniformly along the four sides of the diamond, and occasionally lengthwise extension occurred by the formation of another set of plates. This, together with the growth of the plates towards the interior of the pyramid, led to the development of long bands parallel to a pseudo habit plane (Fig. 4).

In agreement with the results of other workers,[9,10] the kinetics were found to be typical of a diffusion-controlled transformation, with the overall rate of transformation being strongly temperature-dependent. At 400°C there was an incubation period of approximately 15 hr, and the transformation was usually completed in 25 hr. At 390°C transformation started after about 1.5 hr and was complete in 4 hr. At 380°C transformation was complete in 20 min. At higher temperatures the rate of nucleation was small and a relatively small number of well-developed plates was produced (Fig. 2), but at lower temperatures nucleation was rapid and a large number of small plates was produced (Fig. 5).

Isothermal transformation to the tetragonal phase at temperatures in the range 250–350°C yielded

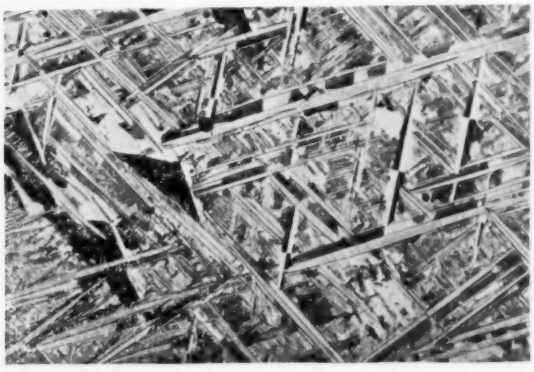


FIG. 4. Specimen completely transformed after 4 hr at 390°C. Polarized light. ×100

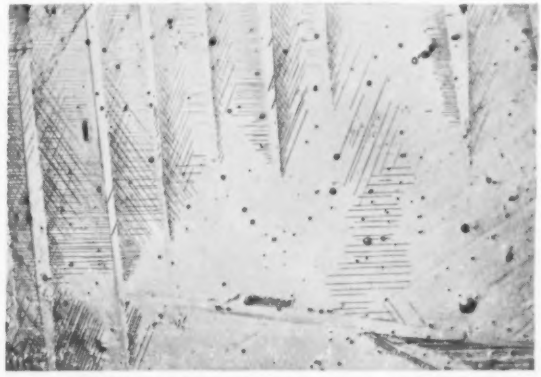


FIG. 6. Single crystal cooled in temperature gradient, showing tetragonal phase with {101} twins and slip markings. ×40

VOL. 8 1960

microstructures of the type shown in Fig. 6, the structure being observable either in relief or after polishing and etching. Similar structures were obtained when the single crystals were slowly cooled in the temperature gradient, and in this case, the formation of the structure was accompanied by audible clicks and produced a macroscopic distortion of the crystal. The microstructures consisted of one or more families of wide bands within which were numerous slip-markings. At first it was thought that the bands could be identified as plates of the ordered tetragonal phase growing at the expense of a disordered cubic matrix. However, X-ray examination of the specimen illustrated in Fig. 6 showed that both the bands and the continuous matrix in which they appeared were ordered and tetragonal ($a = 3.95$ Å, $c = 3.68$ Å). The bands were found to be $\{101\}$ twins of the tetragonal matrix, and an analysis of the relief effects showed that the tilts produced on two surfaces by the formation of the bands were those that would be expected if the bands were formed by mechanical twinning of the tetragonal matrix.

The tetragonal transformation was followed both on the hot-stage microscope during cooling from 800°C and also while heating specimens that had previously been quenched; the rate of change of temperature in each case was of the order of 50°C/min. These experiments showed that during heating, the banded structure formed at about 250°C and during cooling at about 360°C, and that in each case it formed in a matter of seconds. The full-sized bands seemed to appear instantaneously over the surface of the specimen, but the relief effects were not well defined at first, and some time elapsed before they became fully developed. At no stage was there any indication of a heterogeneous process in which plates of the tetragonal phase were growing at the expense of a cubic matrix.

Attempts were made to produce specimens containing both the cubic and tetragonal phases, by cooling single crystals, 6 cm long, in a temperature gradient, and quenching after transformation had begun at the cooler end. Five specimens were produced in this way, and each had a disordered cubic structure at one end and an ordered tetragonal structure at the other (Fig. 7). There was, however, no definite interface between these two structures; instead there seemed to be a zone where one structure changed gradually into the other. A series of Laue and Weissenberg patterns taken across the transition zone shown in Fig. 7 showed that a single orientation of the disordered cubic structure existed from the untransformed end of the crystal up to a point 2.5 mm from the end of the tetragonal bands. Beyond this point and up to point B (approximately 2 mm) two orientations existed which had a maximum orientation difference of 1°. Close to point B these two orientations were found to be slightly tetragonal ($c/a = 0.99$) with a small degree of order. Beyond point B and up to point C there was a marked increase in the degree of order and a decrease in the axial ratio c/a, such that at point C within the banded region the axial ratio was approximately 0.939. Beyond point C the only observable change was a slight decrease in the axial ratio, which reached a constant value of approximately 0.935 at point D.

From these results it is clear that, for the conditions studied, the tetragonal phase does not form at the expense of the cubic phase by the advancement of a well-defined interface. The results are consistent with the view that the bands are mechanical twins which form after some degree of order and tetragonality has developed.

3. CRYSTALLOGRAPHIC FEATURES OF THE CUBIC TO ORTHORHOMBIC TRANSFORMATION

(a) *Experimental methods*

The detailed analysis of the crystallographic features of the cubic to orthorhombic transformation was carried out on a group of four well-developed plates of the orthorhombic phase (Fig. 8). This group of plates was produced in a specimen containing 50.2 at.% gold by heating to 800°C for 1 hr, transforming isothermally at 400°C ± 2°C for 42 hr and then quenching to room temperature. Before this heat-treatment the specimen had been obtained in the disordered condition and one surface had been polished.

The analysis of the homogeneous strain accompanying the transformation was limited to the measurement of the tilts produced by the four plates on the original polished surface of the specimen. These measurements were made by multiple-beam interferometry.

The habit planes of the plates and the plane of the sub-bands were determined from trace measurements on two surfaces. For this purpose, the specimen was prepared as shown in Fig. 9 so that traces of each plate were exposed on two surfaces. To minimize errors due to the presence of a lineage structure in the specimen, the trace measurements and the orientation determinations were made on two small regions, one for each pair of plates A, B and C, D at the positions shown in Fig. 9. Since the sides of the plates were not parallel, measurements were made of the traces on both sides of each plate, and the mean values were

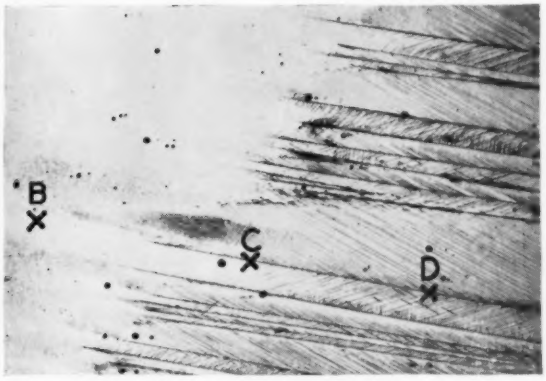


FIG. 7. Transition zone between the cubic structure and the twinned tetragonal structure in a single crystal quenched after partial transformation in a temperature gradient. ×50

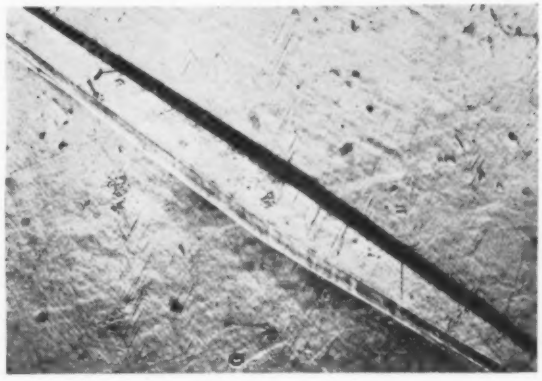


FIG. 8. Relief effects produced by the group of orthorhombic plates used in the crystallographic study. ×40

used for the habit plane determination. The crystal orientations were determined by a rotating crystal X-ray method in which two rotation patterns were taken about known axes at right angles. The orientation of particular planes could then be determined from the angles between the normals to the planes and each of the rotation axes. The error in this method was estimated to be less than 0.5°. The measurements of the traces of the habit planes were considered to be accurate to within ±0.25° and those of the sub-bands to within ±2°.

The orientation relationships between the cubic and orthorhombic phases were determined from oscillating crystal X-ray photographs containing reflections from both phases. The plates were examined two at a time by masking off with a paste of litharge and glycerine, all of the specimen surface except strips, 0.005 in. wide, across the pairs of plates *A*,*B* and *C*,*D*. For each pair of plates two oscillation photographs, about axes at right angles, were taken on each of three surfaces of the specimen. A typical pair of photographs showing a $(200)_C$ reflection on the zero layer line with the $\{200\}_O$ reflections clustered about it, is reproduced in Fig. 10. In determining from such patterns the relative positions of the $\{100\}_C$ and $\{100\}_O$ axes, a correction had to be made in some cases because of the combined effect of the divergence of the beam and the separation of the plates, on the spacing of the orthorhombic reflections.

The lattice parameter of the disordered face-centred cubic phase was determined from the reflections on the zero layer line of a single crystal rotation pattern. The parameters of the orthorhombic phase were determined relative to this cubic parameter. For this purpose several oscillating crystal patterns were recorded on the same film so that reflections from $(400)_C$, $(400)_O$, $(040)_O$ and $(004)_O$ were all obtained on the zero layer line. The orthorhombic parameters were calculated from the distances between the cobalt Kα- reflections on such a film, and the known cubic parameter.

A detailed account of these techniques is given in Ref. (13).

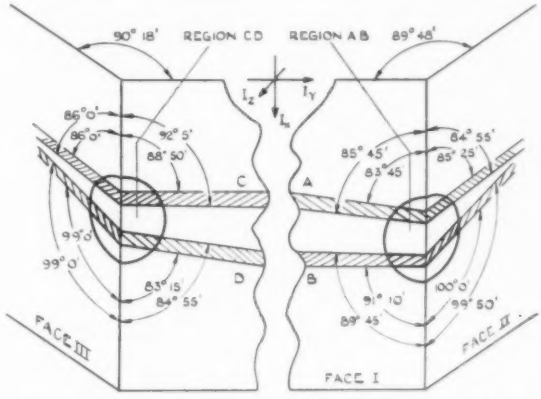


FIG. 9. Sketch of specimen showing the traces of the four plates *A*, *B*, *C* and *D* on three surfaces.

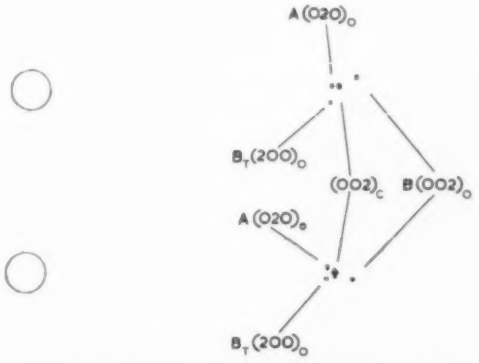


FIG. 10. Oscillation patterns showing $(200)_C$ reflections and associated group of $(200)_O$ reflections. CoKα radiation. ×2.5

VOL. 8 1960

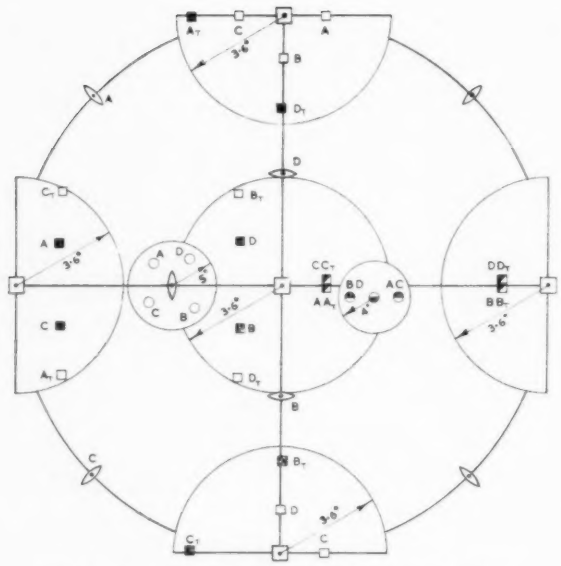


FIG. 11. Stereographic projection showing the orientation relative to the cubic axes, of (i) the normal to the original polished surface and the tilted surfaces of plates *A*, *B*, *C* and *D* (half filled circles); (ii) the normals to the habit planes of the four plates, (unfilled circles); (iii) the $\{110\}_C$ planes associated with the sub-bands in each plate; (iv) the orthorhombic axes of the two orientations in each of the four plates *A*, *B*, *C* and *D*. The unfilled, half filled and filled squares represent *a*′, *b* and *c* axes, respectively.

(b) *Experimental results*

The results of the habit-plane determinations on the four plates are shown in Figs. 11 and 12. Figure 11 shows the orientation of the plates relative to the axes of the original cubic crystal and in Fig. 12 the normals to the four planes have all been plotted in the same stereographic triangle. The main source of uncertainty in the habit plane determination arises from the non-parallelism of the sides of the plates. Calculations of the extreme positions, using first the outside edges and then the inside edges, showed that this could cause an error of between ± 0.75 and $\pm 1.5°$ in the direction at right angles to the $[001]_C$–$[011]_C$ boundary, but in the direction parallel to this boundary the error would be negligible except in the case of plate *C* where it could amount to $\pm 0.25°$. Other sources of error are the errors in measurement of the traces, $\pm 0.25°$, and the error in the orientation determination less than 0.5°. It can be seen from Fig. 12 that the four habit planes are variants of a single plane to within these limits of accuracy.

It was found that the plane of the sub-bands within each plate was within 3° of a $\{110\}$ plane of the original cubic crystal. The relevant $\{110\}_C$ planes are indicated in Fig. 11: for each plate the normal to the relevant $\{110\}_C$ plane lies in that stereographic

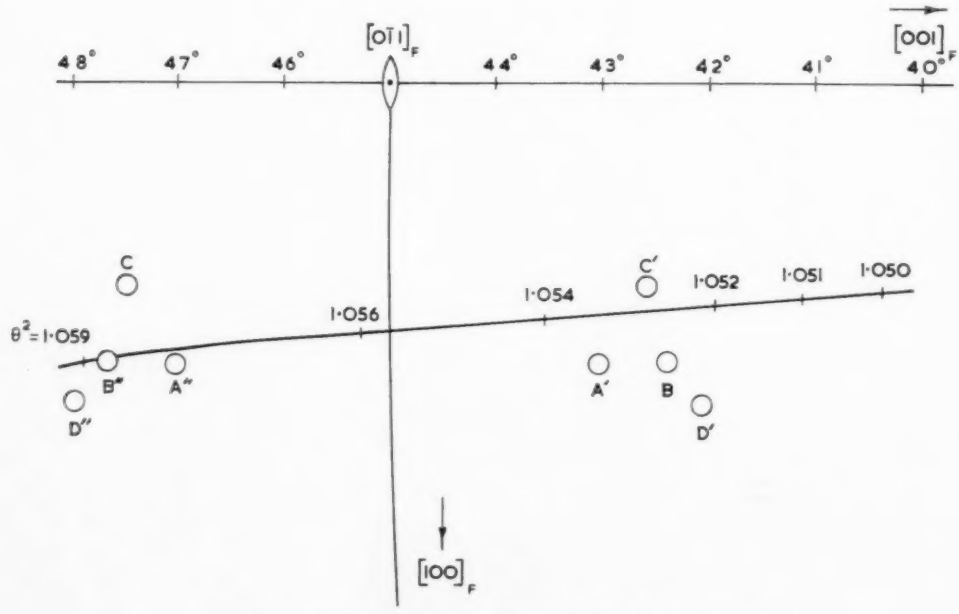


FIG. 12. Stereographic projection showing the variations of habit plane with θ^2 for the $(\alpha+, \omega-)$ solution, and the measured habit planes (circles). Only the circles marked *B* and *C* are in their measured positions; the other poles have been transferred by symmetry operations to the stereographic triangles shown.

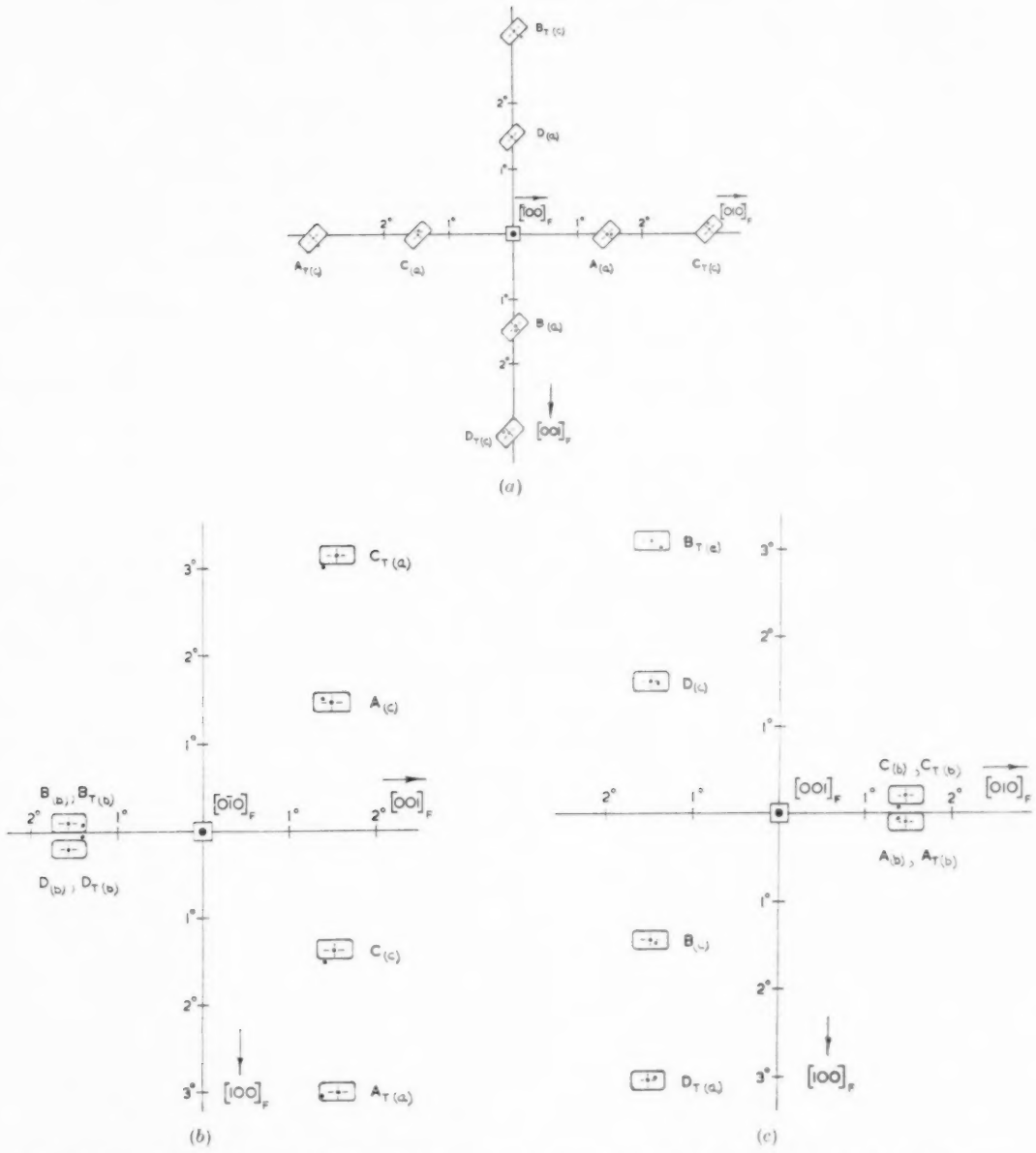


FIG. 13. Stereographic projections showing the measured orientations of the twenty-four $\langle 100 \rangle_O$ axes (crosses) relative to the $\langle 100 \rangle_C$ axes. The rectangles indicate the estimated error of these determinations. The orientations predicted by the theory are also shown (dots).

triangle which has a $\langle 100 \rangle_C$–$\langle 111 \rangle_C$ boundary, common with the stereographic triangle containing the normal to the habit plane of the plate.

The results of the orientation determinations are shown in Figs. 11 and 13. Each of the four plates was found to contain two twin orthorhombic orientations making a total of eight orientations in all. Fig. 13 shows the orientations of the 24 $\langle 100 \rangle_O$ axes relative to the $\langle 100 \rangle_C$ axes and indicates the accuracy of the measurement. Fig. 11 shows the relative orientations of the orthorhombic axes and the four habit planes, and also shows which orientations were found in each plate. Inspection of this diagram shows that the twinning plane relating the two orientations in each plate is a $\{101\}_O$ plane and that in each case this plane coincides with the plane of the sub-bands in that plate.

The angles through which the original polished surface was tilted by the production of the four plates were found to be equal within the accuracy of the

TABLE 1. Analysis of surface tilts produced by plates A, B, C and D on an orignal surface taken as $(0.07846, 0.61566, 0.78409)_C$

Plate	Orientation of tilted surfaces	
	Measured	Predicted
A	$(0.08083, 0.65252, 0.75345)_C$	$(0.08045, 0.65261, 0.75341)_C$
B	$(0.07992, 0.57716, 0.81271)_C$	$(0.07955, 0.57735, 0.81261)_C$
C	$(0.07707, 0.65274, 0.75365)_C$	$(0.07690, 0.65258, 0.75381)_C$
D	$(0.07518, 0.57745, 0.81295)_C$	$(0.07599, 0.57774, 0.81267)_C$

The predicted angle of tilt is in all cases $2^\circ\ 45' \pm 1'$ in agreement with the measured value $2^\circ\ 45'$.

method used. The measured angle was $2^\circ\ 45'$. Plates A and C were tilted in (approximately) opposite senses to plates B and D. The normals to the original and tilted surfaces are shown in Fig. 11 and unit vectors in the directions of these normals are given in Table 1.

The lattice parameter, a, of the face-centred cubic phase was found to be 3.872 Å ± 0.002. Using this value to calibrate the composite film (Section 3), the values obtained for the axial ratios–b/a' and c/a' of the orthorhombic pseudo-cell—were 0.9960 ± 0.0003 and 0.9244 ± 0.0003, respectively. The value obtained for the ratio a'/a of the orthorhombic to the cubic lattice parameter, was 1.0276 ± 0.0003. The parameters of the orthorhombic pseudo cell were thus $a' = 3.976$ Å, $b = 3.963$ Å and $c = 3.678$ Å.

4. COMPARISON OF THEORY AND EXPERIMENT

The phenomenological theory of martensitic transformations was developed from an analysis of the geometrical features associated with the formation of martensite plates within a parent crystal. The present investigation has shown that the low temperature transformation to the tetragonal structure in Au–Cu does not occur by the formation of plates of the new phase within the old. Hence, it does not conform with the characteristics on which the phenomenological theory is based and it is not appropriate to attempt to apply the theory to this transformation. The transformation to the orthorhombic phase, on the other hand, exhibits the same kind of geometrical features as martensitic transformations and it is therefore appropriate to see whether this transformation conforms with the theory.

The data required for substitution into the equations of the theory are the correspondence between the original and final lattices, the operative twinning plane and the axial ratios of the orthorhombic lattice. Considering the variant B in Fig. 11 it is evident that the correspondence for this variant is given by the relation*

$$[\mathrm{o}\ ;\ \mathbf{y}] = \mathbf{I}[\mathrm{c}\ ;\ \mathbf{x}]$$

where $\mathbf{I}$ is the identity matrix.

The operative twinning planes associated with the various orthorhombic orientations were identified by the sub-band analysis and this identification was confirmed by the observation that the twinning plane of the twin orientations found in each plate was the same as the plane of the sub-bands in that plate. Thus, from Fig. 11, the plane from which the twinning plane in variant B was generated may be identified as the plane $(101)_C$. The axial ratios of the orthorhombic lattice have been given in the preceding section.

The predictions of the theory may now be calculated by substituting these data into the equations derived in Ref. (3). The theory involves a variable parameter, $\theta = \delta a'/a$, where a and a' are the lattice parameters of the cubic and orthorhombic phases respectively, and δ defines a small unknown dilation. For any given value of θ the theory yields four solutions for the habit plane, these being simply variants of the same plane. The variation of the habit plane with θ^2 predicted by using the $(\alpha+,\ \omega-)$ solution,[3] is shown in Fig. 12. The variable parameter θ^2 is evaluated by finding that value which gives the best agreement with the observed habit plane. It can be seen from Fig. 12 that the predicted habit plane is in good agreement with the observed habit plane, B, when $\theta^2 = 1.053$, and this value has been used in deriving the predictions described below. Since the measured value of a'/a is 1.076, it follows that $\delta = 0.9986$. It should be noted that although the predicted habit plane versus θ^2 curve also passes close to the experimental habit plane, C, it is not permissible to evaluate θ^2 to give agreement with this habit plane, since the generation of the orientations in plate C involves a correspondence and twinning plane different from those used in deriving the habit plane versus θ^2 curve. It should also be noted that if δ is assumed to be exactly unity,[3,4] in which case $\theta^2 = (a'/a)^2 = 1.056$, the predicted habit plane is then about three degrees from the observed plane and in the neighbouring stereographic triangle.

Of the four strain matrices that are obtained on substitution in the equations of Ref. (3), only one defines directly any of the eight orientations in the four plates studied. This solution, the $(\alpha+,\ \omega-)$

* The notation used in this paper is the same as that used in (2) and (3). The basis symbols o and c refer to the orthorhombic and cubic bases respectively, the metric (o**G**o) of the orthorhombic basis being (diag. $(a')^2$, b^2, c^2).

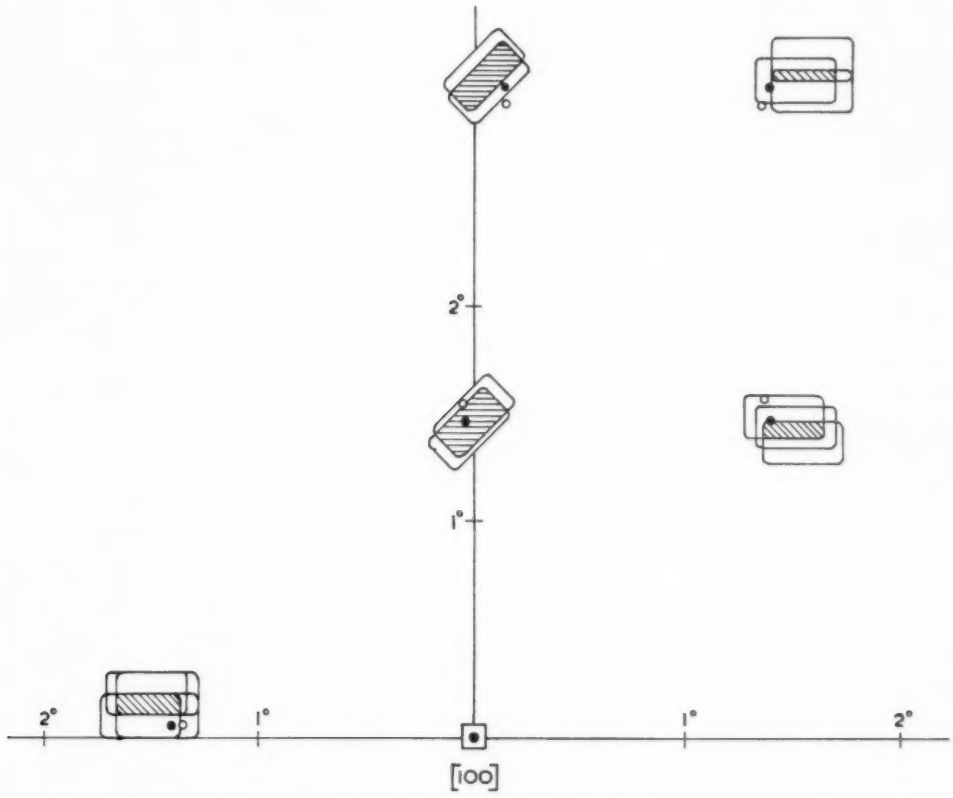


FIG. 14. Stereographic projection showing the data of Fig. 13 reduced by symmetry operations to a group of five poles around one $\langle 100 \rangle_C$ axis. The shaded areas are the areas common to the separate determinations of each pole. The orientations predicted for $\theta^2 = 1.053$, $\delta = 0.9986$ and $\theta^2 = 1.056$, $\delta = 1$ are shown as filled circles and open circles, respectively.

VOL. 8 1960

solution, describes the B orientation directly. This result is expected because the B orientation is the only one of the eight orientations present for which the above choice of correspondence and twinning plane is appropriate. Of the other three solutions, one describes an orientation that is a twin of a variant of the B orientation, and the other two describe variants of these two orientations.

The invariant line strain for the $(\alpha+, \omega-)$ solution is

$$(\mathrm{c}\mathbf{S}\mathrm{c}) = \begin{pmatrix} 1.025815, & 0.001258, & 0.024519 \\ -0.000620, & 1.021767, & -0.023012 \\ -0.026548, & 0.024773, & 0.947970 \end{pmatrix}.$$

Since the correspondence is described by the identity matrix, it follows that the successive columns of this strain matrix are vectors describing the orientation relative to the basis c of the axes $[100]_O$, $[010]_O$ and $[001]_O$ respectively. These predicted directions are plotted in Fig. 13 for comparison with the measured orientation relationship. The predictions for the other seven orientations are also shown in Fig. 13. The predicted orientations A, C and D are simply variants of the predicted orientation B and have been derived therefrom by performing the symmetry operations that produce the required changes of habit plane. The twin orientations A_t, B_t, C_t and D_t, have been derived from the $(\alpha-, \omega-)$ solution in a similar manner. It can be seen from Fig. 13 that in all cases the agreement between the predicted and measured orientation is very good. In Fig. 14 the orientations predicted for $\theta^2 = 1.053$ and for $\theta^2 = 1.056$ have been plotted for comparison with the experimental data. For this purpose, the experimental observations have been reduced by means of the appropriate symmetry operations to a group of five poles around one $\langle 100 \rangle_C$ axis. It can be seen from this presentation of the results that the predictions for $\theta^2 = 1.053$ are systematically in better agreement than those for $\theta^2 = 1.056$.

The invariant plane strain, describing the shape change accompanying the transformation, was found by substitution into the equations of Ref. (3) to be

$$(\mathrm{c}\mathbf{P}_1\mathrm{c}) = \mathsf{I} + m\,\mathsf{dp}'$$

where

$\mathsf{d} = [0.038122, \quad 0.659595; \quad 0.750654]_C$,

$\mathsf{p}' = (-0.037122, \quad 0.677769, \quad -0.734336)_C$ and

$m = \quad 0.048692$.

The surface tilts produced by each of the four plates A, B, C and D were calculated using the above strain and the appropriate variants of the original surface. The calculated angles of tilt for plates A, B, C and D were 2° 45′, 2° 44′, 2° 44′ and 2° 44′, respectively, in excellent agreement with the measured angle of 2° 45′ ±5′. In each case the predicted tilt was in the observed sense, Table 1.

5. DISCUSSION

The results of the present investigation not only establish that the diffusion controlled cubic to orthorhombic transformation in AuCu conforms with the phenomenological theory of martensitic transformations, but they also provide a more critical test of the theory than has previously been made. The agreement between the predicted and observed habit planes is of particular interest in this respect. Hitherto, the habit planes in AuCu and in the various other systems such as indium–thallium, in which cubic to tetragonal transformations occur, were thought to be exactly parallel to $\{110\}_C$ planes. This caused some difficulty, for the theory never predicted a $\{110\}_C$ habit but always an irrational plane close to $\{110\}_C$. The present work removes this difficulty for not only has the existence of the irrational habit plane been demonstrated, but it has also been shown that the lateral growth of such plates can produce compound plates having a pseudo habit plane, $\{110\}_C$. It now seems certain that the $\{110\}_C$ habits that have been observed in indium–thallium and other similar systems are also pseudo habit planes. In these cases the axial ratios are much nearer to unity than in AuCu and consequently the true habit planes are much closer to $\{110\}_C$ so that it would be difficult to distinguish experimentally between the two. It should be noted that it is not permissible to regard the $\{110\}_C$ junction plane as the habit plane for to do so would not be consistent with one of the original postulates from which the theory was developed, viz. that no line in the habit plane is rotated by the transformation. The midrib of the compound plate is not an unrotated line but is composed of lengths rotated in opposite senses to give a saw tooth effect.

With regard to the proposed dilation, the predictions of the habit plane and orientation relationship have been shown to be systematically in better agreement with the experimental results when θ^2 is chosen to have the value 1.053 ($\delta = 0.9986$), than for the case $\theta^2 = (a'/a)^2 = 1.056$, which corresponds to $\delta = 1$. In the case of the orientation relationship, the predictions for both values of θ^2 are probably within the experimental error but the habit plane results indicate a more definite decision in favour of $\theta^2 = 1.053$. Even the most unfavourable combination of errors does not eliminate the discrepancy between the habit plane predicted for $\delta = 1$ and the experimental result. The habit plane predicted for $(a'/a)^2 = 1.0273$, $b/a' = 0.9957$, $c/a' = 0.9241$, i.e. the worst combination of parametric errors, lies on the curve in Fig. 12 exactly one degree to the right of the point, $\theta^2 = 1.056$. This is still outside the experimental error, ±0.75°, of even the most favourably situated plate, A.

From one point of view it is not particularly surprising to find that the crystallographic features of this transformation conform with the phenomenological theory of martensitic transformations. As Bilby[14] has pointed out, the kind of analysis which has been applied to martensite crystallography should be applicable to any transformation that produces relief effects corresponding to a homogeneous strain; this is because the shape change must then be approximately an invariant plane strain. However, if as is widely believed, the crystallographic features of martensitic transformations are a consequence of a special kind of transformation mechanism, then it is very interesting to find the same crystallography, and hence presumably the same kind of mechanism, in AuCu where the transformation is accompanied by place exchanges between neighbouring atoms.

The view is widely held that a transformation gives rise to relief effects when the interface between the phases is such that it can maintain its structural identity during migration. The kind of interface that is envisaged is an array of dislocations which, as it moves, produces both the growth of the new structure and the displacements of the parent phase that generate the relief. Whilst there can be little doubt that the growth of the orthorhombic plates in AuCu proceeds in such a fashion it is not clear at what stage of growth the martensitic type of interface is established. A number of workers in the field of martensitic nucleation favour the idea that martensite plates develop from faulted regions produced in the metastable parent phase by dissociation of dislocations. These faulted regions could grow by displacement of the imperfect dislocations surrounding them but, in general, their structure cannot be exactly that of the new phase; as Bilby[15] has shown, the most general lattice strain that can be achieved by dislocation

dissociation is an invariant plane strain. Thus to create a martensite nucleus with the required interface, further deformation of the faulted region is needed.

This kind of mechanism is at variance with that proposed by Newkirk *et al.*[16–18]. From an analysis of the diffuse diffraction effects in the alloy CoPt these workers proposed that the ordered phase forms as platelets coherent with the {110} planes of the matrix. They proposed that these platelets develop into plates of microscopic dimensions, the lattice strain produced by the coherence being relieved by self deformation. The orientation relationship implied by this proposal, $(110)_C \| (101)_T$; $(010)_C \| (001)_T$ and the habit plane $\{110\}_C$ are clearly incompatible with the present results. Thus although Newkirk *et al.* believed that their mechanism would also apply to the ordering of AuCu it is now clear that this cannot be true, at least for the transformation to the orthorhombic phase. With regard to diffuse diffraction effects the position is that these studies have never been carried out on AuCu specimens quenched directly to an ageing temperature at which the orthorhombic phase forms so that it is not known whether the early stages of the formation of orthorhombic plates give rise to such effects. However, diffuse diffraction might be expected from thin plates produced by dissociation of dislocations.

The present results for the low temperature cubic to tetragonal transformation are consistent, however, with the mechanism of Newkirk *et al.* and in particular are consistent with the view that the relief effect in this transformation are attributable to self deformation by {101} mechanical twinning of the tetragonal product. This is a little surprising for such twinning, if it occurred in the ordered structure, would change the orientation of the *c* axis relative to the layers of copper and gold atoms, unless it was accompanied by a re-arrangement of the atoms. From the observation that these relief effects are faint at first but become progressively sharper, it seems that twinning occurs first at a very early stage of ordering and that additional shearing takes place as the degree of order in the twinned portions increases.

Published work on the alloys CoPt and FePt, both of which possess superlattices, does not exclude the possibility that in these cases a tetragonal product could be produced by a mechanism similar to that operating in the case of orthorhombic AuCu. It should also be noted that the present work has not established that the high temperature mode of transformation in AuCu always yields an orthorhombic product. The possibility remains that a tetragonal phase may be produced in this manner at some temperatures.

ACKNOWLEDGMENTS

The authors wish to thank Dr. J. K. Mackenzie for many helpful discussions in the course of this work and Dr. W. Boas and Dr. L. M. Clarebrough for their helpful criticisms of the manuscript.

REFERENCES

1. J. S. Bowles and W. J. McG. Tegart, *Acta Met.* **3**, 590 (1955).
2. J. S. Bowles and J. K. Mackenzie, *Acta Met.* **2**, 129 (1954).
3. J. K. Mackenzie and J. S. Bowles, *Acta Met.* **2**, 138 (1954).
4. M. S. Wechsler, D. S. Lieberman and T. A. Read, *Trans. Amer. Inst. Min. (Metall.) Engrs.* **197**, 1503 (1953).
5. C. H. Johansson and J. O. Linde, *Ann. Phys., Paris* **78**, 439 (1925).
6. C. H. Johansson and J. O. Linde, *Ann. Phys., Paris* **25**, 1 (1936).
7. W. Gorsky, *Z. Phys.* **50**, 64 (1928).
8. R. Hultgren and L. Tarnopol, *Trans. Amer. Inst. Min. (Metall.) Engrs.* **133**, 228 (1939).
9. O. Kallbach, J. Nystrom and G. Borelius, *Ingen Vetensk-Akad. Handl.* no. 157, 21 (1941).
10. G. C. Kucsynski, R. F. Hochman and M. Doyamo, *J. Appl. Phys.* **26**, 871 (1955).
11. J. L. Haughton and R. J. Payne, *J. Inst. Met.* **46**, 457 (1931).
12. G. J. Ogilvie and G. Brinson, *J. Sci. Instrum.* **32**, no. 5 (1955).
13. R. Smith, Ph.D. Thesis, University of Melbourne (1957).
14. B. A. Bilby, *The Mechanism of Phase Transformations in Metals*, p. 335. Institute of Metals, London (1956).
15. B. A. Bilby, *Phil. Mag.* **44**, 782 (1953).
16. J. B. Newkirk, R. Smoluchowski, A. H. Geisler and D. L. Martin, *J. Appl. Phys.* **22**, 290 (1951).
17. J. B. Newkirk, A. H. Geisler, D. L. Martin and R. Smoluchowski, *Trans. Amer. Inst. Min. (Metall.) Engrs.* **188**, 1249 (1950).
18. J. B. Newkirk, R. Smoluchowski, A. H. Geisler and D. L. Martin, *Acta Cryst., Camb.* **4**, 507 (1951).

VOL. 8 1960

THE THERMODYNAMICS OF THE CHROMIUM–IRON SYSTEM*

O. KUBASCHEWSKI† and G. HEYMER†‡

A method for the determination of the vapour pressure of chromium has been devised by combining Knudsen's effusion method with tracer analysis using Cr-51 of half-life 27.8 days. The vapour pressures determined in the temperature range 1170°–1400°C agree with previous work and may be represented by the equation

$$\log p_{\text{atm}} = -19{,}700/T + 6.92.$$

The heat of sublimation at 298°K is 94.0 kcal/g-atom, the boiling point is estimated to be 2680°C.

The chromium pressures in the system chromium–iron have been measured at 1340°–1370°C for various compositions. The activity curve shows some positive deviation from Raoult's line.

Assuming the solid and liquid solutions to be regular, and using thermal data for the minimum in the liquidus curve and the maximum of the σ-α transformation together with Backhurst's atomic heat data for this transformation, the phase boundaries, α-liquid and α-σ, have been calculated and found to agree essentially with the experimental phase diagram. The solidus–liquidus gap was, however, found to be narrower than hitherto assumed, and the α-σ boundary has been extended to lower temperatures.

LA THERMODYNAMIQUE DU SYSTEME FER–CHROME

Les auteurs ont imaginé une méthode pour la détermination de la pression de vapeur du chrome en combinant la méthode Knudsen avec une analyse par traceur où l'on utilise le Cr-51 dont la demi-vie est de 27,8. Les pressions de vapeur déterminées dans la gamme de températures comprises entre 1170 et 1400°C sont en accord avec les travaux antérieurs. Elles peuvent être représentées par l'équation

$$\log p_{\text{atm}} = 19{,}700/T + 6{,}92.$$

La chaleur de sublimation à 298°K est de 94,0 kcal/atome gr. et le point d'ébullition est estimé à 2680°C. Les pressions du chrome dans le système fer–chrome ont été mesurées à 1340–1370°C pour différentes compositions. La courbe d'activité montre un écart positif par rapport à la droite de Raoult.

Les auteurs font l'hypothèse que les solutions solides et liquides sont régulières et utilisent les données thermiques pour le minimum du liquidus et le maximum de la transformation $\sigma - \alpha$ ainsi que les résultats de chaleur atomique obtenus par Backhurst pour cette transformation. Dans ces conditions, les limites de phase liquide-α et α-σ ont été calculées. Elles correspondent bien à celles que l'on obtient en traçant expérimentalement le diagramme de phase.

Cependant, la lacune solidus-liquidus apparaît plus étroite qu'on ne l'admettait jusqu'à présent et la limite de phase α-σ peut être prolongée jusqu'à des températures plus basses.

DIE THERMODYNAMIK DES SYSTEMS CHROM–EISEN

Durch Kombination des Ausströmungs-Verfahrens nach Knudsen und der Nachweismethoden durch radioaktive Isotope (benutzt wurde Cr-51, Halbwertszeit 27.8 Tage) wurde eine Methode zur Bestimmung des Dampfdrucks entwickelt. Die im Bereich 1170°–1400°C bestimmten Dampfdrücke stimmen mit früheren Arbeiten überein und lassen sich darstellen durch

$$\log p_{\text{atm}} = -19{,}700/T + 6.92.$$

Die Sublimationswärme bei 298°K beträgt 94.0 kcal/g-Atom, der Siedepunkt wird auf 2680°C geschätzt.

Der Dampfdruck des Chrom im System Eisen–Chrom wurde für verschiedene Zusammensetzungen bei 1340°–1370°C gemessen. Die Aktivitätskurve zeigt positive Abweichungen von der Raoult-Geraden.

Nimmt man die feste und flüssige Lösung als regulär an und benutzt thermische Daten für das Minimum in der Liquiduskurve und das Maximum der σ-α-Transformation in Verbindung mit den Werten von Backhurst für die Umwandlungswärme dieser Transformation, so stimmen die berechneten Phasengrenzen (α-flüssig und α-σ) im wesentlichen mit dem experimentellen Phasendiagramm überein. Der Abstand zwischen Solidus- und Liquiduslinie erwies sich jedoch als kleiner als bisher angenommen wurde; ferner ergab sich der Verlauf der α-σ-Grenze bei tieferen Temperaturen.

Thermochemical data of metallic systems with melting points below 1100°C are being obtained in various laboratories at a satisfactory rate. In view of the potential practical application of such data it is desirable to study in particular high melting-point alloys, and this requires further experimental developments in high-temperature calorimetry and equilibrium measurements. The present paper describes an application of Knudsen's effusion method, combined with a tracer method in order to increase its sensitivity, to chromium–iron alloys. Such a method was devised by Birchenall and Schadel[1] who applied it to silver alloys; in this case it was possible to restrict the temperature range to below 1000°C, to place the cell unscreened into an evacuated vessel, to use induction heating and to collect only a proportion of less than 10 per cent of the evaporating atoms for analysis. The vapour pressure of chromium is

* Received May 16, 1959.

† National Physical Laboratory, Metallurgy Division, Teddington, England.

‡ Present address: Göttingen University.

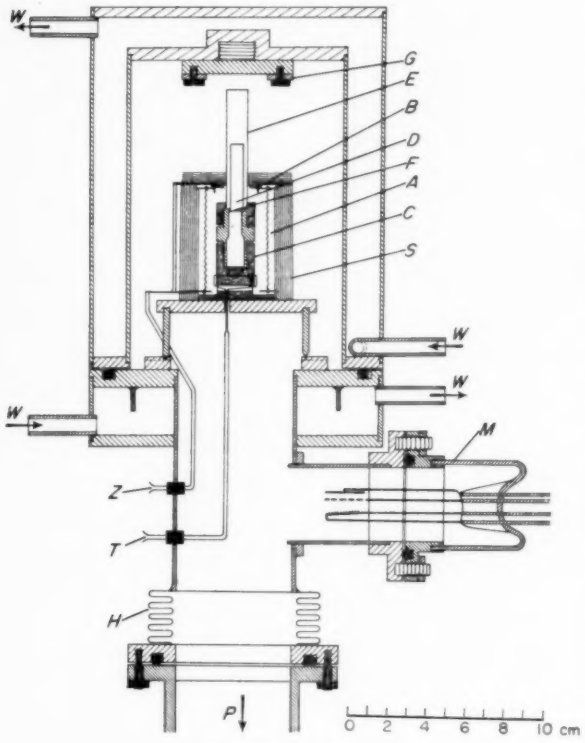


FIG. 1. Effusion apparatus.

considerably lower than that of silver, and higher temperatures of measurement are therefore required for chromium and its alloys.

EXPERIMENTAL

The apparatus shown in Fig. 1 was constructed with due regard to the conditions governing the evaluation of effusion measurements. These conditions were enumerated by Birchenall and Schadel[1], for instance, and need not be repeated here. In order to increase the sensitivity of the method, the chromium was irradiated in the pile at Harwell, prior to alloying.

In order to secure an even temperature distribution in the cell at 1200°–1500°C it must be surrounded by metal foils, reflecting the heat radiation, with an opening at the top for the vapour beam. Preliminary experiments showed that such an arrangement of the shields caused a reflection of the evaporating atoms, making the evaluation uncertain. This difficulty was overcome by placing a tantalum tube (*E*) on top of the cell. (A similar device had already been used by Gross *et al.*[2] for the study of equilibria involving subhalides of aluminium.) The substance was partly condensed within the tantalum funnel, the remainder being collected on the water cooled tantalum disc at *G*. Some of the chromium, however, condensed within the hot zone of the funnel and formed an alloy with the tantalum which could not be dissolved quantitatively for analysis. A thin-walled (0.03 mm) molybdenum tube *D* was therefore placed in the tantalum funnel, and was later dissolved completely together with the chromium condensate in aqua regia.

The furnace (*A*) consisted of two cylinders of 0.1 mm tantalum sheet held by two rings made of 0.4 mm molybdenum sheet with holes for the molybdenum heating wire, which was insulated from the molybdenum rings by small pieces of alumina tubing. The diameter of the furnace was 4.8 cm, its height 6.4 cm. The radiation shields were made of tantalum and nickel foils. The heat loss upwards was compensated by an additional heating coil at *B*, held by a tantalum frame bearing small insulating alumina tubes.

In order to attain a temperature of 1450°C, the furnace required 320 W, the additional furnace 150 W. The voltage was kept constant by a stabilizer, but additional regulation by hand was necessary in order to keep the temperature constant to within ±0.5°C. The apparatus was heated within 5–6 min from 1000° to 1400°C and attained equilibrium within 3 more min. When the current was switched off, it cooled to 1000°C within 2 min.

The cell (*C*) was turned from a molybdenum cylinder. The upper part formed a ring screwed on to the lower part holding down a 0.1 mm tantalum foil. This bears the effusion hole, the area of which was measured by means of a microscope. The foil with hole was replaced after every third to fifth experiment.

The position of the Pt–13% Rh–Pt thermocouple is shown in Fig. 1. For calibration, a standard thermocouple was introduced into the cell in such a way that its hot junction was at the bottom of the cell. In addition, wires of high-purity copper and nickel respectively carrying a current of 0.002 A were fixed within the cell in such a way that the current was interrupted when the wire melted. The melting temperatures agreed within ±2°C with the ones obtained by the calibration with the standard thermocouple.

The vacuum produced by the combined action of an oil diffusion pump and a mechanical oil pump was 2×10^{-5} mm Hg at 1400°C. The vacuum was measured by an ionisation gauge.

The chromium powder used contained 0.46 per cent O, 0.005 per cent S, 0.026 per cent Fe and traces of Si, Bi and Cu. The residual oxide was not likely to affect the vapour pressure results since the vapour pressure of Cr_2O_3 is lower than that of Cr by several logarithmic units. The iron powder contained 0.07 per cent O, 0.005 per cent S, 0.015 per cent C,

VOL. 8 1960

0.05 per cent Mn, traces of Si, Cu, Ni, Cr and Al, and was treated in hydrogen in order to reduce the oxygen content. The active metal was chromium-51 formed in the pile from chromium-50, no other isotopes being formed. Only 3 per cent of the disintegrations of ^{51}Cr produce γ radiation, the remainder being so soft that the disintegrations had no effect on the counter used in the present work. The half-life of chromium-51 is 27.8 days, and the maximum activity after one week of irradiation with a pile factor of ten was 21 mc/g.

The weighed metal powders were mixed mechanically for 24 hr, compacted at a pressure of 2000 kg cm^{-2}, sintered at 1430°C for several hours in a high vacuum and cooled rapidly. From the particle size of the powders and diffusion data for Cr–Fe it was estimated that this treatment ensured complete alloying. Turnings of these alloys were made and 1–2 g filled into the cell.

The effusing substance was collected on the surfaces of the two funnels (D and E) and the tantalum disc at G. It was dissolved by conc. hydrochloric acid, the molybdenum being dissolved entirely by the addition of conc. nitric acid. After concentration, the activity (of an aliquot portion) was determined in a Geiger counter and compared with the activity of a standard solution containing a known amount (m_{st}) of Cr of the same batch, the concentrations of the two solutions being kept approximately equal. The screening effects of the molybdenum and the alloy metal in the test solution were negligibly small.

For evaluation, the usual effusion equation cannot be applied directly, since the vapour flowed first through a small hole and then through a narrow tube. In such a case the following equation is obtained for the equilibrium pressure of chromium in the cell, p_{Cr}, from Knudsen's considerations.[3]

$$p_{Cr} = \frac{m}{t\sqrt{\rho}}\left[\frac{\sqrt{(2\pi)}}{a} + \frac{3}{8}\sqrt{\frac{2}{\pi}}\frac{L}{r^3}\right] \qquad (1)$$

where $\rho = 1.2 \times 10^{-8}\, M/T$, M the molecular weight of the vapour, t = time in seconds, m the mass of chromium passing through the hole, a its area in cm^2, L the distance from hole to condensation zone in the molybdenum tube (in cm), and r the radius (in cm) of this tube.

The validity of equation (1) depends on the following conditions: (i) The ratio of the mean free path of the atoms in the gas to the diameter of the hole must be larger than, say, ten. (ii) The mean free path must be greater than the diameter of the tube. (iii) The effective surface area of the volatile metal must be large in relation to the area of the hole. This was studied experimentally by measuring the vapour pressure with various hole diameters. Up to a hole diameter of 1 mm no deviations of p from the average was observed. (iv) The wall thickness of the hole should be as small as possible. In the present case the wall thickness was 0.1 mm. A small correction[4] has been used:

$$K = 1/(1 + 0.5\, b/c) \text{ for } 0 < b/c < 1.5 \text{ mm} \qquad (2)$$

where b is the wall thickness and c the radius of the hole. The expression $\sqrt{(2\pi)}/a$ in equation (1) must be divided by K. (v) The temperature at the hole must be at least as high as the temperature in the cell. This was achieved by the use of the additional heating coil B in Fig. 1. (vi) The vacuum must be so good that the mean free path of the chromium is not noticeably reduced by other gas particles.

All these conditions have been observed in the present study. In addition, the fact that the active and inactive chromium have different atomic weights must be taken into account. Using the subscripts A and I for the active and inactive substances respectively of the original compositions, and a and i for the same after effusion, we have

$$m_a/m_i = p_A\sqrt{M_A}/p_I\sqrt{M_I} = x\sqrt{(M_A/M_I)} \qquad (3)$$

where $x = p_A/p_I = n_A/n_I$ that is the ratio of the isotopes in the starting material.

The total amount of effusing substance is $m_E = m_a + m_i = m_a[1 + (1/x)\sqrt{(M_I/M_A)}]$. For the standard solution $n_A/n_I = m_A M_I/m_I M_A$, and its total $m_{st} = m_A + m_I = m_A(1 + M_I/xM_A)$. Hence

$$\frac{m_E}{m_{st}} = \frac{m_a}{m_A}\frac{[1 + (1/x)\sqrt{(M_I/M_A)}]}{(1 + M_I/xM_A)} = \frac{m_a}{m_A}\frac{(x\sqrt{M_A} + \sqrt{M_I})\sqrt{M_A}}{(xM_A + M_I)}. \qquad (4)$$

The ratio m_a/m_A is measured by the ratio of the radioactivities of the effusing substance and the standard solution, C_E/C_{st}, and we obtain:

$$m_E = \frac{C_E}{C_{st}}\, m_{st}\frac{xM_A + \sqrt{(M_I M_A)}}{xM_A + M_I}. \qquad (5)$$

In the present case $x = n_A/n_I \approx 10^{-17}$, that is so small that xM_A can be neglected, and equation (5) reduces to

$$m_E = (C_E/C_{st})m_{st}\sqrt{(M_A/M_I)} \qquad (6)$$

where $M_A = 51.0$ and $M_I = M$ (in equation 1a) = 52.01.

If the mass of the effusion chromium is therefore to be determined from the ratio of the radioactivities of the effused dissolved chromium and the standard

solution, equation (1) must be combined with equations (2) and (6). Using the known constant quantities, the following equation is finally obtained:

$$p_{Cr} = \frac{0.2808\, C_E m_{st} \sqrt{T}}{C_{st} \cdot t} \left(\frac{8.378}{aK} + \frac{L}{r^3} \right) \text{[mm Hg]}. \tag{7}$$

The second term on the RHS of the equation constituted less than 2.5 per cent of the total. The error made by disregarding the temperature gradient along the molybdenum tube was therefore much less than 1 per cent of the total pressure. Similarly, the error due to the finite extension of the condensation zone (± 0.5 cm) was very small.

The time t was measured on a stop-watch, and the error involved was less than ± 0.1 per cent but the correction for effusion taking place during heating and cooling introduced an error of ± 0.4 per cent. The weight of the solute in the standard solution, m_{st}, was determined with an accuracy of ± 0.1 per cent. The statistical error of the Geiger counter was $100/\sqrt{\text{counts}}$, corresponding to about 1–1.5 per cent in the present work, for the standard solution as well as the test solution (C_{st} and C_E). The area of the hole, a, was determined with an accuracy of ± 2 per cent. The absolute temperature, T, was known within ± 4°C corresponding to an error of ± 0.1 per cent in $\sqrt{T}$. The error in L/r^3 was ± 15 per cent, but, since L/r^3 never exceeded 2.5 per cent of the term $8.378/aK$, the vapour pressure results were affected only by ± 0.4 per cent.

The maximum error in p_{Cr} thus amounts to ± 5.5 per cent. Since the absolute temperature was known to ± 4°C, corresponding to an error of about ± 7 per cent in p_{Cr}, the total maximum error for the measurements on pure chromium becomes ± 13 per cent, which is quite satisfactory for vapour pressure measurements at high temperatures. The probable error is, of course, smaller.

The activity measurements must be treated somewhat differently. The error due to the inaccuracy of temperature measurement becomes smaller because the relative error must be used, and this was less than ± 1 per cent: measurements on pure chromium and the alloys were carried out alternately. Consequently, other errors partly cancel each other out, and it is estimated that the maximum error in the activity values at, say, $N_{Cr} = 0.2$ is ± 22 per cent which is also satisfactory.

RESULTS

Ten measurements of the vapour pressure of pure chromium were carried out in the temperature range 1170°–1397°C. The results are plotted in Fig. 2. It is seen that the results of Speiser *et al.*[5] who used the Langmuir effusion method, and those of McCabe *et al.*[6] who used the Knudsen effusion method, determining losses in weight, are in excellent agreement with the present results. The maximum deviation from the straight line, represented by

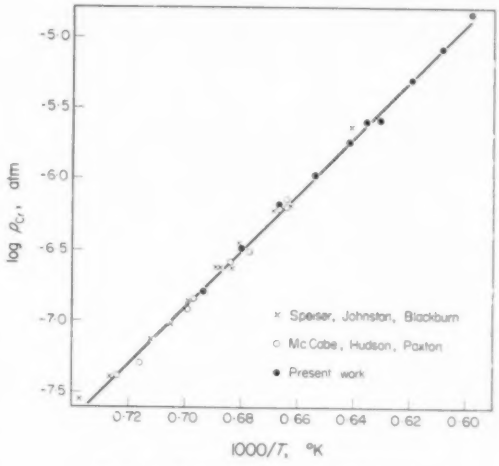


FIG. 2. Vapour pressure of chromium.

$$\log p_{\text{atm}} = -19{,}700\, T^{-1} + 6.92, \tag{8}$$

do not exceed ± 20 per cent. The results of Baur and Brunner[7] who used a not very reliable boiling-point method are certainly too high by at least two logarithmic units in this temperature range, although their extrapolated boiling point at 1 atm is approximately correct.

Measurements of the dissociation pressures of chromium–iron alloys were carried out at 1341°, 1355° and 1370°C. The chromium content of every alloy was determined before and after each series of runs. A known amount of alloy was dissolved and filtered to remove all traces of chromic oxide, and the radioactivity of an aliquot portion of this solution compared with that of the standard solution. It was found that this percentage decreased slightly after long effusion times, obviously because of the loss of chromium by evaporation. Calculations showed that these amounts corresponded to the theoretical ones. Since the experimental conditions were adjusted in such a way as to give approximately the same effusion mass in every experiment, the mole fraction of chromium was obtained for every experiment by interpolating linearly between the initial and final chromium contents within every series of runs.

The results are listed in Table 1. The activities are plotted in Fig. 3. The effect of temperature is disregarded because of the small temperature interval studied. The activities obtained by McCabe *et al.*[6],

VOL. 8 1960

TABLE 1. Activities in the iron–chromium system

No.	Analysis, at. % Cr		N_{Cr}	T°K	p_{Cr} (mm Hg)	a_{Cr}
	before	after				
33	5.13		0.0513	1643	7.72×10^{-4}	0.115
34			0.0474	1628	5.60×10^{-4}	0.112
35			0.0436	1614	4.225×10^{-4}	0.107
36		3.98	0.0398	1643	6.705×10^{-4}	0.100
25	8.28		0.0828	1628	7.69×10^{-4}	0.153
26			0.0813	1614	5.94×10^{-4}	0.151
27		7.98	0.0798	1643	9.79×10^{-4}	0.146
28	29.83		0.2983	1643	2.61×10^{-3}	0.391
29			0.2973	1614	1.57×10^{-3}	0.398
30			0.2965	1643	2.62×10^{-3}	0.391
31			0.2955	1628	2.01×10^{-3}	0.402
32		29.45	0.2945	1628	2.00×10^{-3}	
22			0.501	1643	3.54×10^{-3}	0.528
23			0.501	1628	2.72×10^{-3}	0.543
24		50.05	0.5005	1614	2.11×10^{-3}	0.534
37	69.9		0.699	1643	4.76×10^{-3}	0.712
38		69.9	0.699	1628	3.63×10^{-3}	0.727

obtained at 1205–1249°C, are also plotted in Fig. 3. Since McCabe *et al.* determined total vapour pressures and estimated from these the chromium pressures, the present ones, measured directly, should be somewhat more accurate. In view of the errors involved, the agreement between the two sets of data may be regarded as very reasonable. The difference has, however, some effect on the assessment of the phase boundaries.

The activity data published by Vintaikin[8] appear to be too high, but, according to a private communication from F. D. Richardson and C. Mannerskantz, they have confirmed the present activity curve at two compositions ($N_{Cr} = 0.1$ and 0.3) using the somewhat cumbersome method of equilibration of the alloys with H_2O–H_2 mixtures (e.g.[9]).

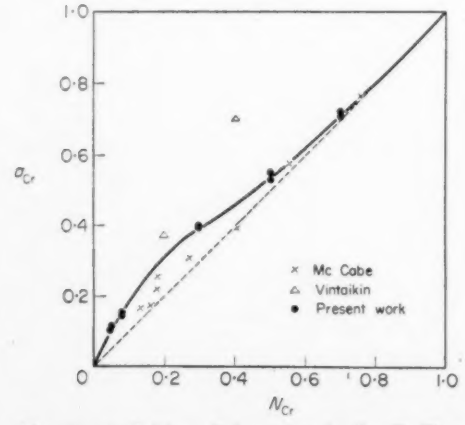


FIG. 3. Activities of chromium in the Cr–Fe system.

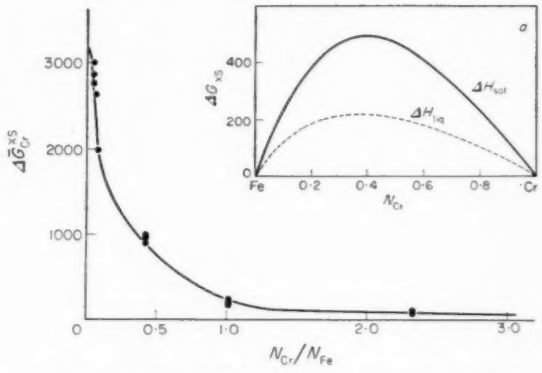


FIG. 4. Partial and (Fig. 4a) integral excess free energies in the Cr–Fe system.

EVALUATION

Chromium

Equation (8) may be expressed in terms of free energies of evaporation:

$$\Delta G_{Cr} = 90{,}120 - 31.66\ T. \qquad (9)$$

The atomic heat of solid chromium is known,[10] that of a monatomic vapour is 5 cal/degree. Using an average value, $\Delta Cp = -3.1$, for the range from room temperatue to the melting point of chromium (1850°C) equation (9) may be extended for this temperature range, and the following equation is obtained:

$$\Delta G_{(Cr)} = 94{,}900 + 7.15\ T \log T - 57.55\ T \text{ (cal)}. \qquad (10)$$

The atomic heat of liquid chromium just above the melting point is 9.4 cal/degree,[10] but generally atomic heats of liquids decrease with increasing temperature, and a value of 8.6 appears to be a fair estimate for the range from the melting point to the boiling point. With this and an estimated entropy of fusion of 2.2 cal[10] at the melting point, the free energy of fusion becomes

$$\Delta G_{fusion} = 3650 - 1.15\ T \log T + 2.13\ T \text{ (cal)} \qquad (11)$$

and the free energy of evaporation up to the boiling point, thus,

$$\Delta G_{\{Cr\}} = 91{,}250 + 8.3\ T \log T - 59.68\ T \text{ (cal)}. \qquad (12)$$

With this equation the boiling point of chromium at $p_{Cr} = 1$ atm is found to be 2680°C which agrees, coincidentally, well with the one given by Baur and Brunner[7] (2660°C). Heats and entropies of evaporation and sublimation are listed in Table 2. The entropy of evaporation is a few units higher than would

be expected from Trouton's rule, but is lower than the value obtained from the measurements of Speiser *et al.*[5] alone.

TABLE 2. Evaporation data of chromium

	at 298°K	m.p. 2123°K	b.p. 2953°K
Heat of sublimation, (kcal/g-atom)	94.0	88.4	—
Heat of evaporation, (kcal/g-atom)	90.2	83.6	80.6
Entropy of sublimation, (e.u./g-atom)	36.8	30.7	—
Entropy of evaporation, (e.u./g-atom)	35.55	28.45	27.3

Chromium–iron

From the activities in Table 1 the partial excess free energies of chromium in solid chromium–iron alloys have been calculated by means of the equation $\Delta\bar{G}_{Cr}^{xs} = 4.575\ T \log \gamma_{Cr}$ where $\gamma_{Cr} = a_{Cr}/N_{Cr}$ is the activity coefficient. The values are plotted in Fig. 4 against x in $FeCr_x$: and the integrated curve, ΔG^{xs}, is shown in the side diagram (Fig. 4a). The corresponding curve of McCabe *et al.*[6] is symmetrical and about 200 cal/g-atom lower at $N = 0.5$.

In view of the low excess free energies the assumption is certainly justified that the solid Cr–Fe system is regular, as has also been pointed out by McCabe. Thus, the curves in Fig. 4 are identical with the partial and integral heats of solution respectively.

The chromium–iron equilibrium diagram. The thermochemical data above together with the calorimetric results of Backhurst[11] may be used to assess approximately the phase boundaries solid–liquid and σ–α of the Cr–Fe equilibrium diagram.

The heats of mixing of the α alloys is given by the curve in Fig. 4a, the entropies of mixing in a regular binary solution by $\Delta S = -R(N_{Cr} \ln N_{Cr} + N_{Fe} \ln N_{Fe})$. Adcock[12] determined the phase boundaries solidus–liquidus and found a minimum at 1517°C* and $N_{Cr} = 0.23$. At this temperature and composition the free energy of formation of the α solid solution is obtained as -1490 cal/g-atom. Since this is equally the free energy of formation of the liquid solution from the solid metals its heat of solution from the liquid metals can be obtained using the heats and entropies of fusion of pure chromium and iron, assuming that the liquid solutions are also regular, and $\Delta G_{liq} = 200$ cal/g-atom is found. In order to calculate the solidus and liquid lines the heat of formation of the liquid solutions must be known over the whole range of composition. For this a somewhat arbitrary assumption is made, namely that the ratio $\Delta H/_{sol}\Delta H_{liq}$ is the same at all compositions as at $N_{Cr} = 0.23$. The corresponding ΔH_{liq} curve has been drawn as a dotted line in Fig. 4a.

When free energy curves are calculated at various temperatures between 1500°C and 1850°C from $\Delta G_{liq} = \Delta H_{liq} + RT(N_{Cr} \ln N_{Cr} + N_{Fe} \ln N_{Fe})$ and $\Delta G_{sol} = \Delta H_{sol} + RT(N_{Cr} \ln N_{Cr} + N_{Fe} \ln N_{Fe})$ and the heats and entropies of fusion of chromium and iron, the tangents touching both these curves give the solidus and liquidus compositions at each temperature. The resulting curve is drawn in Fig. 5 and compared with Adcock's[12] experimental points and McCabe's[6] calculated curves. It is seen that the calculated liquidus curve agrees fairly well with the experimental one, being about 10 degrees higher in the range $N_{Cr} = 0.5$–0.75. The accuracy of the calculated curve is certainly not better than ± 10°C, particularly in view of the assumption made with respect to the heat of mixing of the liquid solutions. The main point to be noted from these calculations is that the heterogenous solidus–liquidus gap is much narrower than has hitherto been accepted on the basis of Adcock's experimental points. This result can be confirmed directly, that is, without the use of any assumptions for high chromium concentrations.

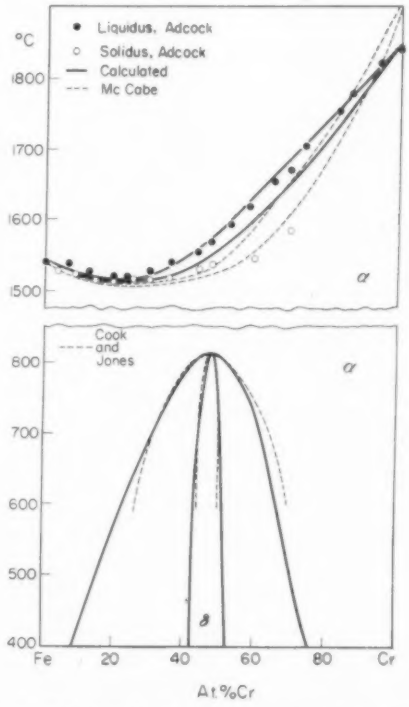


FIG. 5. Calculated and experimental phase boundaries in the Cr–Fe equilibrium diagram.

* Adcock's temperatures have been corrected so as to agree with the accepted melting point of iron of 1539°C.

VOL. 8 1960

According to Fig. 3 Raoult's law holds very nearly for $N_{Cr} > 0.6$, and the width of the solidus + liquid range is thus given by the entropy of fusion of chromium (σ_f) according to

$$\sigma_f (T_{Cr} - T) = -4.574\ T \log (N_{Cr}/N_{Cr}')$$

where N_{Cr} and N_{Cr}' are the atomic fractions of chromium at the liquidus and solidus points at temperature T; T_{Cr} is the melting point of chromium −2123°K.

McCabe's procedure to accept the experimental data for the minimum composition and temperature, and to reject the remainder of the experimental liquidus curve on the strength of the calculated one is not permissible and is bound to discredit the thermodynamic approach to phase-boundary determinations which is likely to be applied to an ever increasing extent, but only in connexion with the thermal results wherever the thermochemical data are not complete. McCabe's curves are correct in that the heterogenous gap is narrower than observed experimentally, and this result seems to have some general significance. Wagner[13], for instance, showed by means of the available thermochemical information that the liquidus–solidus gap in the system silver–gold is 1.3°C at $N = 0.5$ in contrast to an experimental value of 10°C.

Such a simple assumption as for the liquid phase cannot be made for the σ phase, but for this, additional thermochemical information is available. Backhurst[11] devised an adiabatic high-temperature calorimeter and measured the specific heats of an Fe–Cr alloy containing 45.8 at.% Cr in the α and σ states as well as the heat of transformation of $\sigma \rightarrow \alpha$. The atomic heats of σ and α are very nearly equal, and are also equal to those calculated additively from the atomic heats of the pure metals. Thus ΔCp can be disregarded. On the specimen used the heat of transformation was found to be 356 cal/g-atom. The σ content of the specimen, which was made in the authors' Division, was estimated to be 90–95 per cent. Martens and Duwez[14] estimated the transition heat of an alloy containing 46.5 at.% Cr from the duration of a thermal arrest as well as from a comparison of heating-temperature/time curves for the alloy and pure iron. Their results, 342 and 365 cal/g-atom respectively, agree very well with Backhurst's value. Here again, a correction must be made for incomplete conversion to σ, and a value of $L_{\sigma-\alpha} = 400$ cal/g-atom has been accepted.

With this value and the heat of formation of α Cr–Fe at $N_{Cr} = 0.46$, the heat of formation of σ becomes 85 cal/g-atom, and it will be assumed that this applies to the range $N_{Cr} = 0.43$–0.54. The σ phase has its maximum at $N_{Cr} = 0.47$ and 815°C according to Cook and Jones[15]. Using this information, the heat of transformation and the entropy of mixing of α, the entropy of formation of σ at $N_{Cr} = 0.47$ is obtained −1.01 cal/g-atom. The entropy of formation of σ is likely to have its maximum at $N = 0.5$, and the entropies estimated from the experimental curve near the maximum have been taken to apply equally near $N_{Cr} = 0.53$. Thus the construction of the entropy curve of σ at $N_{Cr} = 0.44$–0.56 involves some arbitrariness, but this should not seriously affect the following evaluation.

Having the heats and entropies of formation of both the α and σ phases, the free energy curves have been drawn for various temperatures between 400°C and 750°C and the positions of the phase boundaries obtained from the common tangents. The resulting phase boundaries are compared with the experimental ones of Cook and Jones[15] in Fig. 5. The agreement is quite good; the calculated curves lie somewhat to the left of the experimental ones, but there is some experimental evidence[14] that very long annealing at 600°C would shift the $\alpha/(\alpha + \sigma)$ boundary below 26 at.% Cr. This argument cannot apply to the chromium-rich $(\alpha + \sigma)/\alpha$ boundary for which the experimental curve appears to be the more reliable.

Probably the lack of agreement of the $(\sigma + \alpha)/\alpha$ boundary is due to the heats of transformation $\sigma \rightarrow \alpha$ being somewhat too low, since the methods used tend to give low rather than high results. The choice of the ΔS curve for σ cannot have affected the evaluation to that extent. It follows that the $\sigma + \alpha$ miscibility gaps should be wider at low temperatures, rather than narrower, on both the chromium-poor and chromium-rich sides.

One interesting point to note is that the asymmetric shape of the $\Delta H\alpha$ curve (Fig. 4a) accounts for the fact that the position of σ is shifted to below $N_{Cr} = 0.5$. The symmetrical $\Delta H\alpha$ curve used by McCabe would require a symmetrical position of σ.

It is thus seen that the phase boundaries of the iron–chromium system can be obtained in fairly good agreement with the thermal results from the available thermochemical information, if the positions for the minimum liquid–solid and the maximum $\sigma - \alpha$ are used. The new results of these calculations are the extension of the $\alpha/\sigma + \alpha/\sigma/\sigma + \alpha/\alpha$ boundaries to lower temperatures (not accessible to the thermal methods), and that the solidus–liquidus gap is narrower than assumed hitherto.

ACKNOWLEDGMENT

The work described above has been carried out as

part of the General Research Programme of the National Physical Laboratory, and this paper is published by permission of the Director of the Laboratory.

REFERENCES

1. H. M. SCHADEL and C. E. BIRCHENALL, *J. Metals, N.Y.* **2,** 1134 (1950).
2. P. GROSS, C. S. CAMPBELL, P. J. C. KENT and D. L. LEVI, *Disc. Faraday Soc.* **4,** 206 (1948).
3. M. KNUDSEN, *Ann. Phys*, p. 40 (4) **28,** 75, 999 (1909); **29,** 179 (1909).
4. R. SPEISER and H. L. JOHNSTON, *Trans. Amer. Soc. Metals* **42,** 283 (1950).
5. R. SPEISER, H. L. JOHNSTON and P. BLACKBURN, *J. Amer. Chem. Soc.* **72,** 4142 (1950).
6. C. L. MCCABE, R. G. HUDSON and H. W. PAXTON, *Trans. Amer. Inst. Min. (Metall.) Engrs.* **212,** 102 (1958).
7. E. BAUR and R. BRUNNER, *Helv. Chim. Acta* **17,** 958 (1934).
8. E. Z. VINTAIKIN, *Dokl. Akad. Nauk SSSR* **118,** 977 (1958).
9. O. KUBASCHEWSKI and O. VON GOLDBECK, *Trans. Faraday Soc.* **45,** 948 (1949).
10. O. KUBASCHEWSKI and E. L. EVANS, *Metallurgical Thermochemistry* (3rd Ed.). Pergamon, London (1958).
11. I. BACKHURST, *J. Iron St. Inst.* **189,** 124 (1958).
12. F. ADCOCK, *J. Iron St. Inst.* **124,** 99 (1931).
13. C. WAGNER, *Acta Met.* **2,** 242 (1954).
14. H. MARTENS and P. DUWEZ, *J. Metals, N.Y.* **8,** 614 (1956).
15. A. F. COOK and F. W. JONES, *J. Iron St. Inst.* **148,** 217 (1943).
16. F. J. SHORTSLEEVE and M. E. NICHOLSON, *Trans. Amer. Soc. Metals* **43,** 142 (1951).

VOL.
8
1960

THE INITIATION OF SLIP IN SILICON–IRON*

J. HOLDEN†

Observations have been made on the deformation of silicon–iron crystals containing small precipitates surrounded by clusters of dislocations. Slip bands are observed to develop from the clusters, and two mechanisms are distinguished.

APPARITION DU GLISSEMENT DANS LE FER–SILICIUM

L'auteur a observé la déformation de cristaux de fer–silicium contenant des petits précipités entourés par des amas de dislocations.

Des bandes de glissement se forment à partir de ces amas. Leur formation répond à deux mécanismes distincts.

DER GLEITBEGINN BEI SILIZIUM–EISEN

Über die Verformung von Silizium–Eisen–Kristallen mit kleinen Ausscheidungen, die von Versetzungsanhäufungen umgeben sind, wurden Beobachtungen angestellt. Es zeigte sich, daß sich aus diesen Ansammlungen Gleitbänder entwickeln und zwei Mechanismen unterschieden werden können.

INTRODUCTION

The use of etch pits in silicon–iron crystals to determine dislocation sites has been established by Dunn and Hibbard[1,2] in the course of polygonization studies. Further investigation of the conditions, under which dislocations will cause these etch pits to develop, has been carried out by Suits and Low[3] who have found that, in regions of heavy deformation, etch pitting may not be observed if the carbon content of the material is too low. This impurity must be present in sufficient quantity to form an atmosphere around the dislocations to enable the etching to take place. Suits and Low employed low-temperature carburization and ageing processes to increase the carbon content of their heavily deformed specimens and to cause etching at dislocation sites in regions of high dislocation density.

The present observations relate to silicon–iron specimens carburized at a relatively high temperature; a treatment resulting in a sparse distribution of participates. These precipitates are observed to have associated with them a distribution of etch pits marking the sites of the dislocations formed around the precipitates during either their growth or the cooling of the specimens to room temperature. Observations have been made of the way the associated dislocations multiply during subsequent cyclic and tensile deformation.

SPECIMEN PREPARATION

Tensile and fatigue specimens were cut from 3 per cent silicon–iron strip, 0.013 in. thick, and the surfaces electro-polished in the chrome–acetic acid solution described by Morris[4]. The specimens were carburized at 800°C for 30 min in an atmosphere of hydrogen which had been bubbled through heptane. The grains were several millimetres in diameter, and metallographic observations were confined to those grains in which the surface of polish was within a few degrees of a (110) plane, as determined from Laue photographs. Electro-etching revealed that platelet precipitates were oriented so that the long axis appearing in the surface of polish was parallel to traces of (100) planes. The precipitates were surrounded by clusters of etch pits of characteristic distribution. Fig. 1(a) shows typical precipitates, their long axis being up to 20 μ in length. It is seen that the precipitates with this axis in

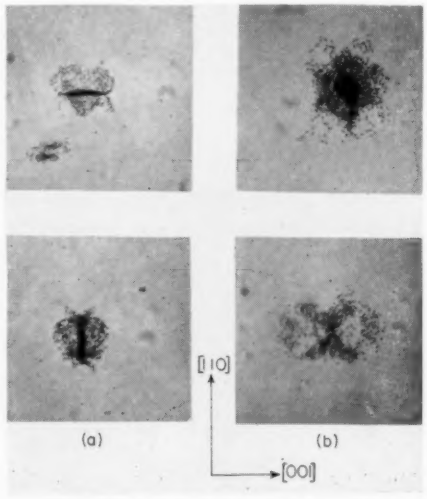


FIG. 1. (a) Platelet precipitates and etch pit clusters; (b) pattern of etch pits for the cases when the plane of polish passes either through or above spherical precipitates. ×1000

* Received July 20, 1959.

† National Engineering Laboratory, East Kilbride, Glasgow.

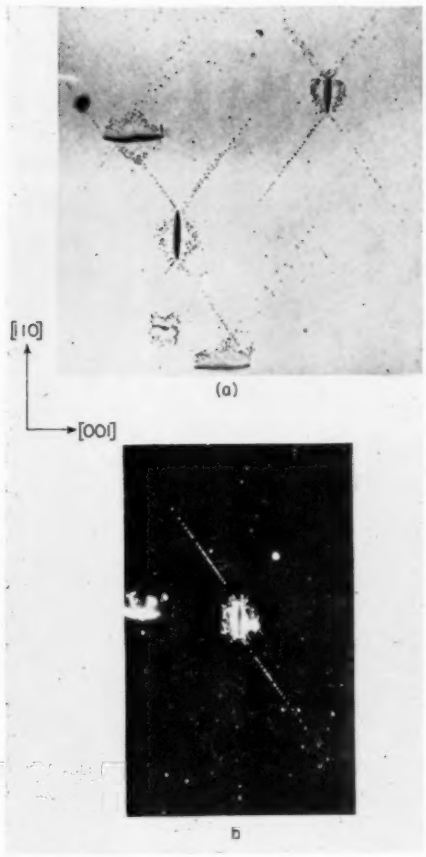


FIG. 2. (a) Etch-pit sites radiating from clusters around [110] and [001] platelets; (b) co-linear etch-pit sites. ×1000

a [110] direction and which therefore lie in a plane normal to the polished surface have a symmetrical distribution of etch pits around them, while those with the axis in a [001] direction have an asymmetrical cluster. Removal of surface layers in thicknesses of 5 μ by repeated electro-polishing showed that the precipitates were of platelet shape and that they were confined to the surfaces of the specimens to a depth $\simeq$30 μ. In addition to the platelets, spherical precipitates were also produced in the carburization treatments. Fig. 1(b) shows such precipitates and their associated etch pits for the case of the plane of polish passing through the precipitate and for the case when the precipitate was some 15 μ below the plane of polish. The characteristic figure-of-eight distribution of the etch pits, lying in the [001] direction, in the latter case is repeated when polishing has continued through the precipitate level to reach planes several microns further in the specimen. At the grain boundaries, precipitates and associated etch-pit clusters of more irregular shape were formed, the immediate region of the grain boundary being free from precipitates within the grains.

DEFORMATION OF SPECIMENS

Three different ways of deforming the specimens were used, namely, tensile tests in a hard beam machine at a strain rate of 10^{-4}/sec; pulsating tension in a small fatigue machine at 2000 c/min, and cutting the specimens with a guillotine.

The additional etch pits produced at platelet precipitates, after the specimen had been cut with a guillotine and electro-etched, are illustrated in Fig. 2(a). The new etch pits form along the traces of (110) planes and radiate from the dislocation sites within the clusters around the platelets. The new etch pits are found to form a co-linear array only when they are limited in number. Fig. 2(b) shows a typical example of such an array in which some 20 to 30 pits extend over $\simeq$20 μ. When a greater number of pits are produced from a precipitate cluster during cutting of the specimen, the characteristic sideways displacement of individual pits from the initial line is apparent. This displacement may be quite marked resulting in a wide dispersal of the row of pits as in the case of the pits arising from the precipitates lying in the [001] direction in Fig. 2(a). When the deformation is such as to cause larger numbers of pits to form around precipitates, the sideways displacement of individual pits has an opposite sense for slip traces developed in opposite directions, an effect illustrated in Fig. 3.

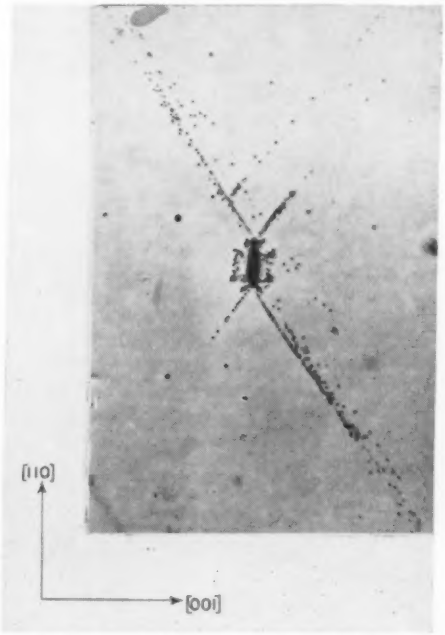


FIG. 3. Displacement of etch pits in opposite senses for slip traces developed in opposite directions. ×1000

VOL. 8 1960

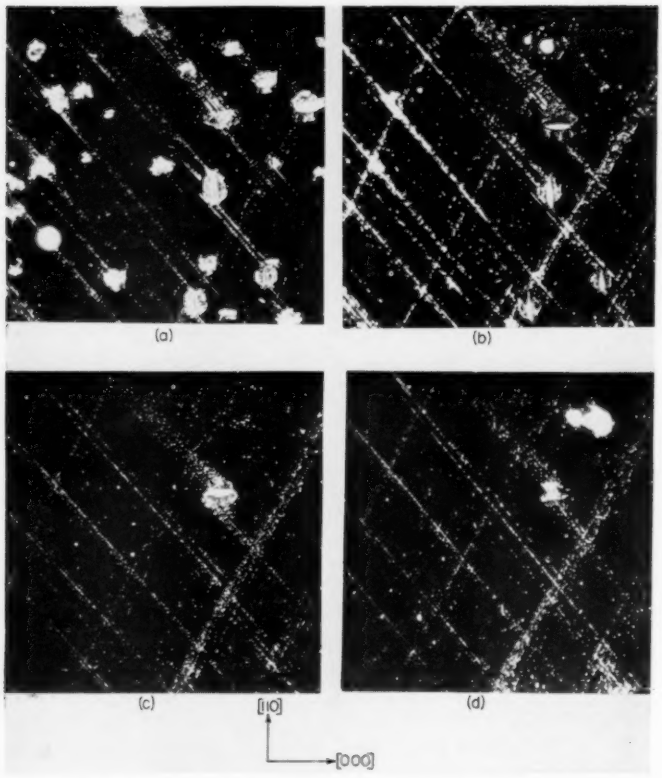


FIG. 4. Field of view of platelets, associated etch-pit clusters and (110) slip traces as successive surface layers 5 μ thick, are removed. $\times 500$

When very dense, the etch pits form bands extending entirely across the grain but still recognizably based on the precipitate clusters.

The bands of etch pits delineating slip traces could again be predominantly related to pre-existing etch pit clusters around precipitates for the case of tensile specimens slightly deformed to plastic strains $\simeq 0.1$ per cent and then electro-etched. In addition to crystallographic traces the clusters around grain-boundary precipitates were observed to be prolific sources of non-crystallographic wavy slip traces, characteristic of deformed b.c.c. metals.[5] The changing appearance of precipitates, their associated etch pits and the etch pits generated by a small tensile strain as successive surface layers, 5 μ thick, are electro-polished from the specimen, is illustrated in Fig. 4. After deformation, the etched surface shows slip traces associated with platelet precipitates; removing a 5 μ-thick surface layer removes most of the smaller platelets and reveals some precipitates just below the original surface. A further 5 μ removal leaves only one precipitate in the original field of view, and when this is removed in the next stage of polishing a cluster of etch pits marks its site. The individual slip traces can be recognized and persist into the body of the crystal when polishing-off of further layers is continued.

Tensile specimens could only be used for observations at small strains, since the effect of carburizing the silicon iron was to cause twinning to occur after a small initial strain at room temperature. The stress–strain curves of carburized specimens are shown in Fig. 5. Curve 1 shows the sudden drop of load that occurs in a hard beam machine after a small plastic strain, and this drop of load is caused by the development of a band of twins across the tensile specimen. Upon reloading immediately, the specimen flows plastically with no further twinning, c.f. curve 2. Ageing the specimen at 150°C for 30 min causes the twinning yield to again occur upon reloading. Once this has occurred the specimens flow plastically with no further twinning, as shown in curves 3 and 4 of Fig. 5.

As is well known, the formation of twins in polycrystalline specimens gives rise to further local deformation at intersections of the twins with grain boundaries, with each other and when they terminate within a grain, due to the necessity of accommodating

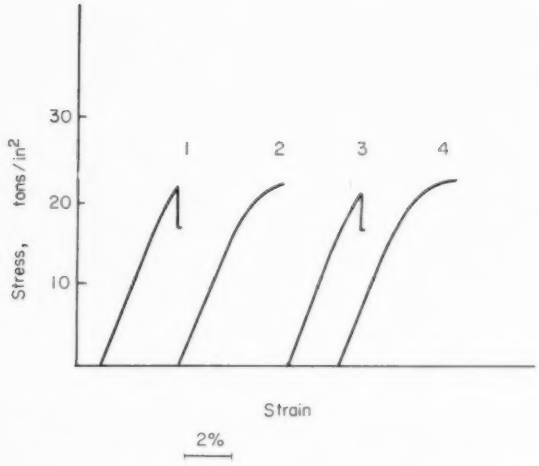


FIG. 5. Stress–strain curves of carburized silicon iron specimens: (1) First loading, (2) immediate reloading, (3) loaded after aging, (4) immediate reloading.

the twinning shear. A more regular form of deformation is, however, observed to accompany the room-temperature twinning in the carburized silicon iron. Rows of etch pits are observed to develop from one of the interfaces between twin and matrix. Fig. 6(a) illustrates the position of the incipient rows of pits, in relation to the twin band AB. The grouping of the rows along the entire trace of a twin interface is shown in Fig. 6(b) for the case of a small twin which extends from the grain boundary GB, where a twin intersection has occurred, and terminates within the grain. In addition to forming slip traces at the tip of the twin, the etch pits form rows at right angles to the twin, the traces being restricted to one side and grouped together. The further tensile deformation of specimens containing such twins causes the side tracks to extend and to develop into dense arrays of etch-pit sites.

FATIGUE SPECIMENS

Specimens deformed in pulsating tension at a relatively low range of cyclic stress and examined at intervals, facilitated the observation of the development of etch-pit sites around precipitates, since the twinning yield, which occurred at an early stage of the tensile tests, was absent. In plain fatigue specimens, the developing slip traces were observed to include many of the wavy non-crystallographic type. These traces were associated with the precipitates within the grains in a different manner from the crystallographic traces already described. The wavy slip traces appeared to develop by a process which involved the dissolution of one side of the figure-of-eight etch-pit pattern found above and below the plane of spherical precipitates. A stage in this process



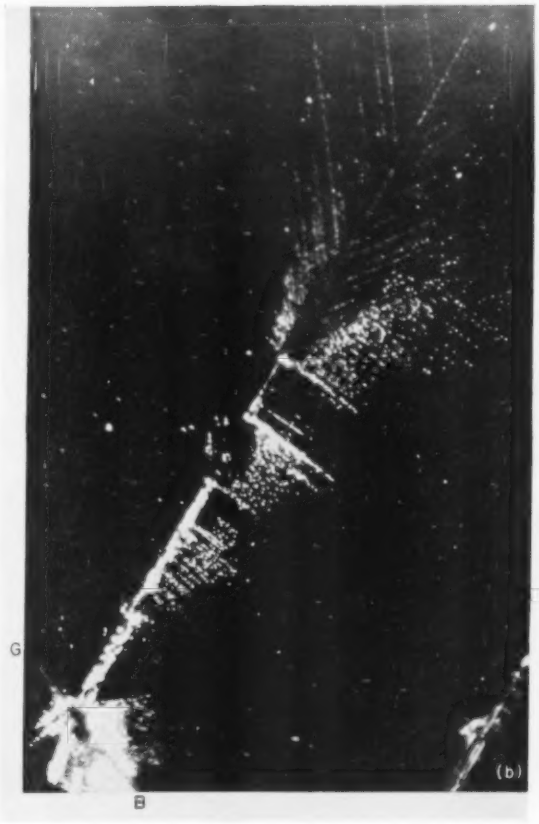


FIG. 6. (a) Rows of etch pits on one side of (112) twin interface. ×1000 (b) Etch pits along a (112) twin which terminates within the grain and at the grain boundary GB. ×570

VOL. 8 1960

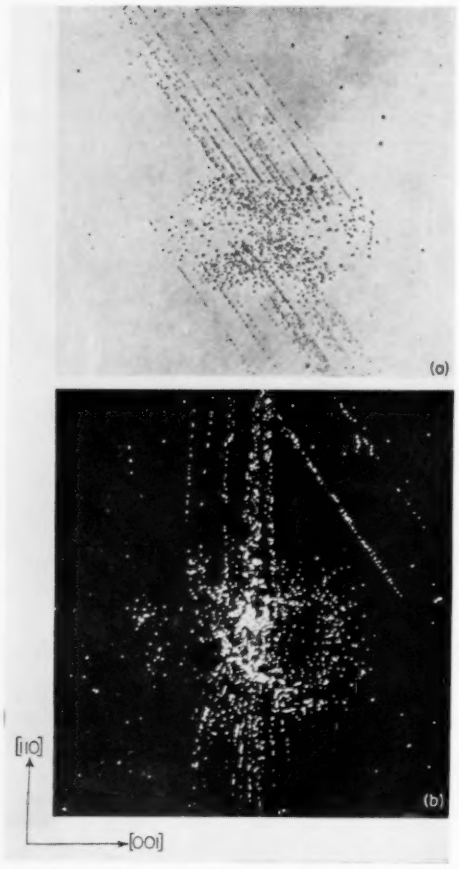


FIG. 7. (a) Formation of (110) slip trace without dissolution of original etch pit pattern; (b) formation of wavy slip trace and dissolution of original etch pit pattern. ×1000

is illustrated in Fig. 7(b), the developing wavy slip trace being vertical. Under further cycles of stress the wavy slip traces spanned the grain, thickened and increased in etch-pit density. The sites of precipitates and original etch-pit clusters were then distinguished by deviations in the slip traces.

When the figure-of-eight patterns were associated with crystallographic (110) slip traces, they remained intact as in Fig. 7(a). Repeated electro-polishing-off of layers shows that such (110) traces were associated with the dislocations in the cluster close to the precipitate surfaces as in the cases described for tensile and guillotine deformation.

Fatigue specimens containing notches electro-etched to indicate the region of stress concentration at the notch as a region of dense etch pits. When the region of stress concentration fell entirely within a grain the non-crystallographic nature of the slip traces was illustrated by their curvature in conformity with the region of stress concentration. In



FIG. 8. Formation of short slip traces in region affected by a prominent slip zone in an adjoining grain, (pulsating tension). ×2250

plain fatigue specimens, stress concentration effects arose in parts of grains where broad slip zones in neighbouring grains met the common-grain boundary. In many cases, the resulting local regions of stress concentration did not then include any precipitate clusters. In these conditions, continued pulsating tension led to the production of numbers of extremely short slip traces. The short slip traces were then observed to develop by the process of sideways displacement, already noted for traces radiating from precipitate clusters. Fig. 8 illustrates such typical short traces at two stages of development. The specimen was subject to a period of pulsating tension and heavily etched, then given a further period of stressing and lightly etched. The etch-pit sites arising in the second period are therefore more lightly developed than the sites present after the first stressing period.

DISCUSSION

The background density of etch pits in the silicon iron specimens was $\simeq 10^6/\text{cm}^2$, increasing in the region of the precipitate clusters to $\simeq 100.10^6/\text{cm}^2$. The shear stress necessary to form the clusters could arise during the growth of the precipitate[6] or during the cooling of the specimen to room temperature when differences in thermal expansion between matrix and precipitate would be operative. The complete shape of individual dislocation loops around precipitates could not be determined from the present observations but the symmetry of the clusters around spherical

precipitates suggests that the loops are related to the eight [111] directions.

Since the etch-pit sites in the clusters etch in a similar manner to the general background sites, the dislocations at the clusters are probably pinned by solute atoms in the same way as in the rest of the crystal. The generation of new etch-pit sites that occurs at the clusters around platelet precipitates when the specimen is deformed is probaly caused, therefore, by the stress concentration effect due to the precipitate operating upon a dislocation source close to its periphery. For the case of the precipitates illustrated in Fig. 2(a), the position of the new etch pits can be understood if, after a limited number of dislocation loops have been generated by the initial source, the further development of sites involves the displacement of dislocations from the active plane. A source model with this characteristic has been used by Koehler[7] in considering the relation of work-hardening to the lamellar spacing in slip bands. The hypothesis was then made that—after a given Frank–Read source has produced a number of loops and the process of generation has failed to carry through—thermal fluctuations and local obstacles may produce stresses which, when acting upon portions of dislocations of screw type, carry a sufficient length of dislocation into a new glide plane far enough from the original plane to enable further slip to occur. The geometry of this process is reproduced in Fig. 9.

For the present material, deformed during cutting by guillotine, the number of loops generated by the initial source was of the order of thirty. In the case of [110] precipitates, they extended some 20 μ along the slip plane trace before sideways displacement of a particular dislocation loop occurred to lead to further generation of loops. As observed in the (110) plane of polish, the sideways displacement of the first etch pit to fall out of the line of the twenty or thirty pits forming the initial slip trace was quite marked, being $\simeq 0.2\ \mu$. This suggests that glide of the dislocation was involved. This is supported by the observed wide dispersion of initial etch pits which could occur under the influence of a suitably directed principle stress, cf. Fig. 2(a). In the case of tensile and guillotine deformation, the observed relation between developed slip zones and the precipitate clusters from which they arose, indicates that the multiplication process arising from the displacement of dislocations from the operative slip plane was capable of producing sufficient dislocations as the specimen was strained without the need for further primary source activation. The increasing strain in the specimens developed by an increase in the strain in the bands located upon an initial source in a precipitate cluster.

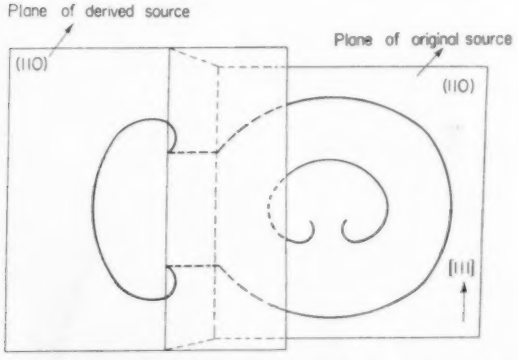


FIG. 9. Illustrating the slip produced when a length of screw dislocation is carried over into a nearby (110) plane.

Under the different strain condition of pulsating tension at low stress levels non-crystallographic slip traces could also be observed to form from precipitate clusters. They originated by the dissolution of the figure-of-eight patterns as illustrated in Fig. 7(b). This process may be accounted for if it is assumed that the original etch-pit pattern is formed by the intersection of the plane of polish with large dislocation loops $\simeq 10\ \mu$ in diameter. The loops being stabilized in potential troughs caused by the stress field of the precipitate and associated dislocations. Under pulsating tension these loops expand and, upon meeting local obstacles, portions of screw dislocations glide out of the plane of the loop and become capable of source action as before. The observation that the resultant slip traces curve smoothly around obstacles such as precipitates or follow a region of stress concentration due to a notch suggests that few loops are generated before screw dislocations again glide into new planes. Under conditions of pulsating tension at low stress levels the loop multiplication process favours the displacement of screw dislocations from slip planes as against the generation of co-planar loops which is observed in tension at strain rates of the order of 10^{-4}/sec. The contribution to the strain in a specimen by the movement of screw dislocations is therefore favoured by conditions of small cyclic strain.

Only in the case of fatigue specimens in which the development of a prominent slip zone affected a part of a neighbouring grain free from precipitate clusters were closely spaced primary sources initiated. These sources, first observed after a few loops had been generated, were spaced several microns apart in the region of stress concentration and developed at an early stage by the displacement process. In the other

VOL. 8 1960

deformation conditions investigated the source multiplication process based upon precipitate clusters was prolific enough to account for all the broad bands of slip which were developed.

On the displacement model the development of slip bands would lead to dislocation loops containing many jogs and to arrays in which dislocations from later sources overlapped the regions of earlier ones. This situation would be a contributory cause to the limitation of the number of loops from any particular source. However, the observed limitation of the number of co-planar etch pits around [110] precipitates at the beginning of deformation would indicate that the limitation of the number of loops was an inherent feature of the source action.

The action of twinning at room temperature was also observed to lead to new etch pit sites along slip traces at one of the twin interfaces. If we suppose twinning to take place by the process suggested by Cottrell and Bilby[8], then the limitation of the etch pits to one interface would be expected. The state of locking of the original dislocations which enabled the twinning mode of deformation to operate in the specimen would no longer be effective in the next stage of flow when the newly created dislocations multiplied and caused slip.

CONCLUSIONS

In silicon–iron specimens containing precipitates and associated dislocation clusters, slip bands develop either by the initiation of a source at the precipitate or by the expansion of an existing dislocation loop in the associated cluster. In each case, the growth of the slip band involves the production of further sources by the carrying over of parts of screw dislocations from active loops into new planes, after the active sources have produced relatively few loops. Twinning at room temperature also produces slip sources along one interface of the twin and matrix.

ACKNOWLEDGMENTS

The work has been carried out as part of the research programme of the National Engineering Laboratory of the Department of Scientific and Industrial Research and the paper is published by permission of the Director of the Laboratory.

REFERENCES

1. C. G. Dunn and W. R. Hibbard, *Acta Met.* **3,** 409 (1955).
2. C. G. Dunn and W. R. Hibbard, *Acta. Met.*, **4,** 306 (1956).
3. J. C. Suits and J. R. Low, *Acta Met.* **5,** 285 (1957).
4. C. E. Morris, *Metal Progr.* (5), **56,** 696 (1949).
5. F. L. Vogel and R. M. Brick, *J. Metals, N.Y.* **5,** 700 (1953).
6. F. R. N. Nabarro, *Proc. Roy. Soc.* A**175,** 519 (1940).
7. J. S. Koehler, *Phys. Rev.* **86,** 52 (1952).
8. A. H. Cottrell and B. A. Bilby, *Phil. Mag.* **42,** 573 (1951).

ENERGY OF THE ORDER–DISORDER TRANSFORMATION IN AuCu*

R. L. ORR†, J. LUCIAT-LABRY‡ and R. HULTGREN†

The heat of formation of AuCu has been determined at various temperatures up to 900°K. From these and other data it has been possible to establish the energy of disordering as a function of temperature, assuming that, except for the disordering reaction, the heat of formation should be invariant with temperature (Kopp's law). This result has been discussed in terms of existing X-ray diffraction measurements of long-range and short-range order parameters for the alloy. Nearly 40 per cent of the energy effect occurs below 658°K, where the X-ray results indicate the long-range order is 97 per cent complete. Before this surprising result is accepted, X-ray measurements of order should be made at temperature, rather than on quenched alloys. Above the critical temperature indications of the destruction of short-range order are found.

ENERGIE DE TRANSFORMATION ORDRE–DESORDRE DANS LES ALLIAGES Au–Cu

La chaleur de formation de Au–Cu a été déterminée pour des températures différentes jusqu'à 900°K. Avec ces résultats et d'autres, il a été possible de déterminer l'énergie de désordre comme fonction de température, supposant que, excepté pour la réaction de désordre, la chaleur de formation serait invariable avec la température (loi de Kopp).

Ce résultat a été discuté en considérant des mesures antérieures par diffraction de rayons X des paramètres de l'ordre à grande et à petite distance. A peu près 40 pour cent de l'effet d'énergie se trouvent en dessous de 658°K où les résultats des rayons X indiquent que l'ordre à grande distance est de 97 pour cent. Avant que ce résultats surprenant soit accepté, l'étude du phénomène d'ordre par diffraction de rayons X devrait être faite à haute température plutôt que sur les alliages trempés. Au-dessus de la température critique, on a trouvé des indications d'une destruction de l'ordre à petite distance.

DIE ENERGIE DER ENTORDNUNGSUMWANDLUNG VON AuCu

Die Bildungswärme von AuCu wurde bei verschiedenen Temperaturen bis 900°K bestimmt. Aus diesen und aus anderen Daten war es möglich, die Energie der Entordnung als Funktion der Temperatur zu bestimmen unter der Annahme, daß die Bildungswärme mit Ausnahme der Entordnungsreaktion unabhängig von der Temperatur ist (Koppsches Gesetz). Das Ergebnis wird an Hand von veröffentlichten röntgenographischen Messungen der Fernordnungs- und Nahordnungsparameter dieser Legierung diskutiert. Nahezu 40 prozent des Energieeffekts tritt unterhalb 658°K auf, wo sich nach den röntgenographischen Befunden die Fernordnung zu 97 prozent eingestellt hat. Bevor dieses überraschende Ergebnis angenommen wird, sollten röntgenographische Ordnungsuntersuchungen bei hoher Temperatur durchgeführt werden und nicht an abgeschreckten Legierungen. Oberhalb der kritischen Temperatur wurden Anzeichen für den Abbau der Nahordnung gefunden.

VOL. 8 1960

INTRODUCTION

Order-disorder changes which are known to occur in many alloy systems are accompanied by considerable heat and entropy effects. However, no extensive correlations seem to have been made between these effects, determined experimentally, and the degree of long-range or short-range order as determined by X-ray diffraction. The development of models for the mechanisms of the various types of ordering processes has been hampered by the lack of adequate data for the variation of the configurational energy and the degree of order with temperature, both in the long-range and short-range order regions.

Most studies of the degree of order present in an alloy as a function of temperature have been performed on quenched samples, making the assumption that the degree of order found at room temperature is the equilibrium degree of order at the temperature from which the alloy was quenched. Unfortunately, this may not be true. Recent evidence has shown that there occurs a considerable increase in the degree of short-range ordering during even the fastest quench from the region above the critical temperature for superlattice formation.[1–3] Thus the only measurements in these regions which can be considered reliable are those made at the temperature where equilibrium has been established This same effect may or may not occur within the long-range order region; this has not yet been determined.

Of all the alloy systems showing superlattice formation, the gold–copper system is perhaps the best known and has been the most extensively studied. Gold and copper are completely miscible in the solid state, forming a complete series of face-centered–cubic solid solutions at elevated temperatures. At lower temperatures ordered superlattice structures are found[4] at three compositions, Au_3Cu, AuCu and $AuCu_3$. When an ordered alloy is heated above its critical temperature, T_c, long-range order completely

* Received July 28, 1959.

† Department of Mineral Technology, University of California, Berkeley 4, California.

‡ Formerly, University of California. Much of this article was abstracted from the M.S. Thesis of Jean Luciat-Labry, University of California, 1958.

disappears, but a considerable degree of short-range order persists which decreases as the temperature is raised.[1,5]

The AuCu ordered phase at low temperatures, $AuCu_I$, has a tetragonal structure ($c/a \sim 0.93$) formed by alternate layers of Au and Cu atoms on the (002) planes. Between about 658°K and the critical temperature, 683°K, the equilibrium structure is an orthorhombic modification of the tetragonal structure, $AuCu_{II}$, in which the Au and Cu atoms change layers along one axis after every fifth cell. The degree of order for AuCu as a function of temperature has been determined by Roberts[1]. Between 480 and 653°K Roberts measured the degree of long-range order, S, present in alloys quenched from temperatures in that range by determining relative intensities of superlattice and fundamental X-ray diffraction peaks. Short-range order parameters were determined by Fourier analysis of X-ray patterns for alloys held at two temperatures above the critical temperature, 698 and 798°K, and for one alloy quenched from 773°K.

A number of measurements have been made from which it is possible to obtain the variation of heat of formation of AuCu with temperature from room temperature to slightly above the critical temperature. Heats of formation measured by liquid tin solution calorimetry have been determined by Oriani and Murphy[6] at 653, 673 and 723°K. Hirabayashi[7] measured the heat capacity of AuCu from room temperature to approximately 740°K, finding a first-order latent heat of transformation at 695°K, taken by him as the critical temperature. From these data the change of heat of formation with temperature may be calculated. Borelius *et al.*[8] made direct measurements of the heat evolved when AuCu was quenched from a temperature above the critical one, 703°K, to several temperatures near 650°K.

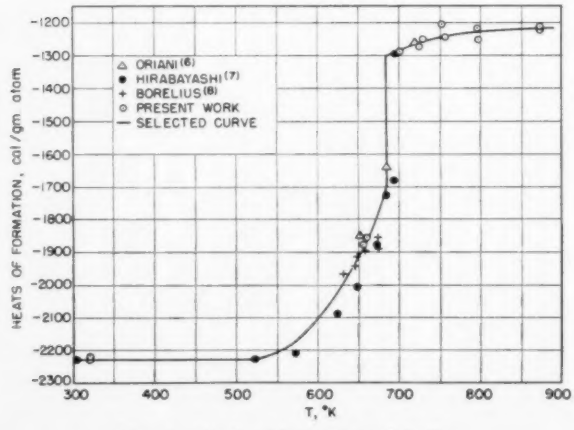


FIG. 1. Heats of formation of AuCu.

All the results are shown plotted in Fig. 1, using the selected value of −1290 cal/g-atom for the heat of formation at 700°K in plotting the results of Hirabayashi and of Borelius *et al.* The variation of heat of formation of AuCu with temperature below the critical temperature appears to have been fairly well established. No measurements have been made, however, of the variation of heat of formation within the short-range order region above T_c. In this paper work is described in which the heat of formation was measured at several temperatures in a range extending almost 200°K above the critical temperature. Measurements were also made at two temperatures within the long-range order region.

EXPERIMENTAL

Approximately 13 g of AuCu was prepared from appropriate amounts of 99.95 per cent pure Au and 99.98 per cent pure Cu, melted together in an evacuated and sealed quartz tube followed by a rapid quench in water. The loss in weight was a negligible 0.05 per cent. After cold-working, the ingot was sealed in an evacuated vycor tube and homogenized for two weeks at 1123°K. Filings taken from both ends of the ingot were mixed, strain annealed at 873°K for 1 hr, then rapidly quenched in water. The sharp well-resolved high-angle diffraction peaks observed in X-ray examination using CuKα radiation showed the alloys to be homogeneous and to have the correct lattice constant for 50 at.% composition.[9] Superlattice lines were absent in the quenched filings.

The ingot was then broken into small pieces, of suitable size for the measurements, which were then strain annealed and rapidly quenched as were the filings. In order to develop a fully ordered sample, half of the alloy was annealed for 12 days at 653°K followed by a cooling period of 10° per day until a temperature of 473°K was reached. X-ray diffraction examination of filings given the same ordering treatment revealed strong, well-resolved superlattice lines.

Specimens containing about 600 mg of the alloy were prepared for liquid tin solution calorimetry by enclosing pieces of the alloy in gold foil capsules. Heats of solution of the alloy and the pure metals in liquid tin at 700°K were determined using apparatus and procedures described in detail in a previous publication.[10] Each specimen was heated for at least 12 hr in the dispenser at some predetermined temperature, T, before dropping it into the tin bath. The heat of formation at each temperature, T, was obtained by subtracting the heat of solution of the

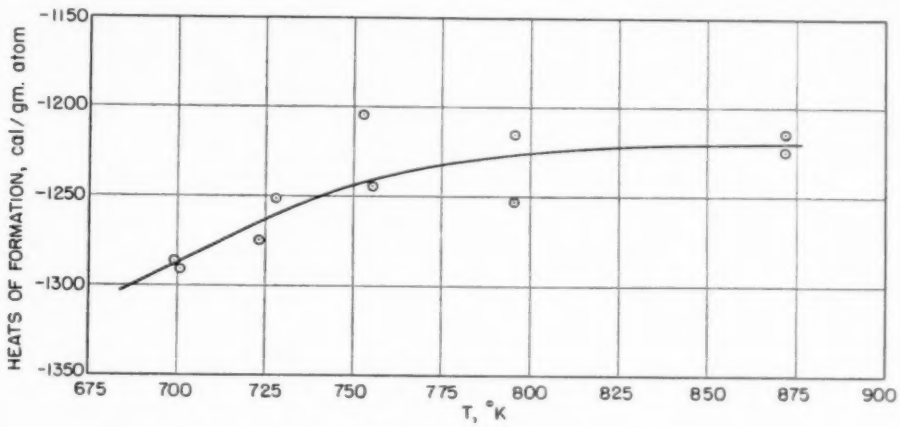


FIG. 2. Heats of formation of AuCu above the critical temperature.

alloy from the heats of solution of corresponding amounts of the pure metals, all starting from the same initial temperature, T. Samples used for measurements below the critical temperature were initially ordered; at higher temperatures the initially disordered samples were used. The results are plotted in Fig. 1, and the results obtained in the short-range order region above T_c are also shown in Fig. 2.

DISCUSSION

Where comparisons are possible, the results are found to agree well with previous data, especially those of Oriani and Borelius and co-workers.[6,8] Apparently the data of Hirabayashi[7] show some hysteresis toward higher temperatures, probably resulting from the rather fast rate of temperature rise (2°/min) used in those heat capacity measurements. This is indicated by the fact that the latent heat was found by Hirabayashi at a temperature 12° above the accepted critical temperature.

Above the critical temperature, as seen in Fig. 2, the heat of formation slowly becomes less exothermic as the temperature is raised. The initial portion of the curve given in Fig. 2 suggests an average value of $\Delta Cp \sim 1.1$ cal/deg g-atom in the temperature interval immediately above T_c, in excellent agreement with the measurement of Hirabayashi[7] near 700°K. At the higher temperatures of measurement the heat of formation appears to change much more slowly, indicating a decreasing value of ΔCp with increasing temperature.

From the presently obtained data, the data already referred to, and the e.m.f. measurements of Oriani[11] and Weibke and Quadt[12], the thermodynamic properties of AuCu as a function of temperature have been evaluated and are presented in Table 1. Assuming that the changes in the heat and entropy of formation are due only to the change in configuration with temperature, the tabulated quantities, $\Delta H_T - \Delta H_{298}$ and $\Delta S_T - \Delta S_{298}$, give, respectively, the configurational energy and entropy above those of the perfectly ordered solid phase. The total long-range ordering energy is about 930 cal/g-atom, of which approximately 540 cal is absorbed by the

TABLE 1. The thermodynamic functions of AuCu as a function of temperature

T, (°K)	Phase	Cp	ΔCp	ΔF_T	ΔH_T	ΔS_T	$\Delta H_T - \Delta H_{298}$	$\Delta S_T - \Delta S_{298}$
298	$AuCu^{I}$	6.0	0.0	−2190	−2230	−0.13	0	0.00
400		6.1	0.0	−2180	−2230	−0.13	0	0.00
500		6.2	0.0	−2170	−2230	−0.12	0	0.01
523		6.3	0.0	−2170	−2230	−0.11	0	0.02
550		7.1	0.8	−2170	−2210	−0.07	20	0.06
600		8.6	2.2	−2160	−2110	0.08	120	0.21
650		13.0	6.6	−2180	−1910	0.42	320	0.55
658	$AuCu^{II}$	13.1	6.6	−2180	−1875	0.46	355	0.59
683		13.1	6.6	−2200	−1690	0.75	540	0.88
683	AuCu(D)	7.6	1.1	−2200	−1300	1.32	930	1.45
700		7.6	1.1	−2220	−1290	1.33	940	1.46
750		7.1	0.6	−2280	−1240	1.39	990	1.52
800		6.8	0.2	−2360	−1225	1.42	1005	1.55
850		6.7	0.0	−2430	−1220	1.42	1010	1.55
900		6.8	0.0	−2500	−1220	1.42	1010	1.55

ΔF_T, ΔH_T, $\Delta H_T - \Delta H_{298}$: cal/g atom
Cp, ΔCp, ΔS_T, $\Delta S_T - \Delta S_{298}$: cal/deg-g. atom

VOL. 8 1960

ordered alloy on being heated through a 160° range below the critical temperature in a second order reaction; the remaining 390 cal appearing as a latent heat at T_c. There is apparently no discontinuous change in energy between $AuCu^{I}$ and $AuCu^{II}$.

The X-ray measurements of Roberts[1] on alloys quenched from several temperatures below T_c show that the degree of long-range order is essentially perfect at low temperatures, decreasing to about 0.97 at 653°K. According to Roberts the data indicated a somewhat lower degree of long-range order in the $AuCu^{II}$ range, although the structural relations were not comparable to those in $AuCu^{I}$. At the critical temperature the degree of long-range order drops discontinuously to zero.

The decrease of only 3 per cent in the degree of long-range order found by Roberts prior to the disappearance of $AuCu^{I}$ would appear to be surprising in view of the accompanying absorption of almost 40 per cent of the long-range ordering energy, indicating the apparent futility of attempting to analyse the relation between the two in terms of nearest neighbor bonds. Unfortunately these X-ray measurements were made on quenched alloys; the equilibrium degree of order at higher temperatures might be considerably less than Roberts found. This serves to emphasize the need for X-ray measurements of the degree of order made at the temperatures of interest and thus eliminating the doubt which must be cast on data obtained from quenched alloys. If Roberts' results were to be confirmed by such measurements, the X-ray and energy measurements would give differing indications of the relative amount of disordering which has occurred up to a given temperature. This would appear to be a significant observation with regard to the development of a model for the order-disorder reaction in AuCu.

Roberts states that since the variation of order in $AuCu^{I}$ is terminated at 658°K by the appearance of $AuCu^{II}$, it is not obvious whether the critical temperature for the variation in $AuCu^{I}$ might not be higher than T_c for $AuCu^{II}$, 683°K. This could not be the case, however, for the free energy of $AuCu^{I}$ is higher than that of $AuCu^{II}$ at temperatures above 658°K. Thus $AuCu^{I}$ would become unstable with respect to the disordered phase at a lower temperature than does $AuCu^{II}$.

The changing value of the heat of formation in the range above the critical temperature indicates the destruction of short-range order with increasing temperature. In terms of unlike nearest neighbor bonds, Roberts' measurements of short-range order parameters for AuCu held at two temperatures above T_c show that the alloy is about 36.9 per cent of the way toward perfect order at 698°K and about 35.4 per cent at 798°K. While the uncertainties in these data are too large to permit any extensive calculations, this observed decrease in the amount of short-range order is certainly in qualitative accord with the results of the present measurements. More, and possibly even sharp, changes in the values of Cp and the degree of short-range order may occur at higher temperatures, as have been found for the alloy $AuCu_3$.[13]

The present work has served to tie together previously existing measurements of the energy relations in AuCu and to extend them into the short-range order region above the critical temperature. The use of heat of formation measurements as a function of temperature as a method of detecting and estimating the extent of configurational changes in alloys with increasing temperature is thought to possess some advantages over X-ray and heat capacity measuring techniques. High temperature X-ray measurements are more difficult to interpret and appear to be less precise than heat of formation studies. Also, in the procedure described here, the alloy may be held at the temperature at which its heat of formation is to be determined for more than sufficient time to insure its being in its equilibrium state at that temperature. In heat capacity determinations involving the addition of energy at a fixed rate, the rate of temperature rise may be too fast to allow equilibrium to be maintained.

ACKNOWLEDGMENTS

The authors would like to express their appreciation to the Office of Ordnance Research for their continued interest and support. They also wish to thank Mrs. K. Herring for help in the experimentation and Mrs. L. Warner Diller for aiding in the evaluation of the previously reported data.

REFERENCES

1. B. W. Roberts, *Acta Met.* **2,** 597 (1954).
2. B. Borie and B. E. Warren, *J. Appl. Phys.* **27,** 1562 (1956).
3. R. L. Orr, data to be published.
4. M. Hansen, *Constitution of Binary Alloys.* McGraw-Hill, New York (1958).
5. J. M. Cowley, *J. Appl. Phys.* **21,** 24 (1950).
6. R. A. Oriani and W. K. Murphy, *J. Phys. Chem. Solids* **6,** 277 (1958).
7. M. Hirabayashi, *J. Japan Inst. Met.* **15,** 565 (1951).
8. G. Borelius, L. E. Larsson and H. Selberg, *Ark. Fys.* **2,** 161 (1950).
9. W. B. Pearson, *A Handbook of Lattice Spacings and Structures of Metals and Alloys.* Pergamon Press, New York (1958).
10. R. L. Orr, A. Goldberg and R. Hultgren, *Rev. Sci. Instrum.* **28,** 767 (1957).
11. R. A. Oriani, *Acta Met.* **2,** 608 (1954).
12. F. Weibke and U. F. Quadt, *Z. Elektrochem.* **45,** 715 (1939).
13. G. C. Kuczynski and M. Doyama, *J. Appl. Phys.* **27,** 651 (1956).

THERMODYNAMIC ANALYSIS OF BINARY LIQUID ALLOYS OF GROUP IIB METALS—III

THE SOLUTIONS OF ZINC, CADMIUM, INDIUM, TIN, THALLIUM, LEAD AND BISMUTH IN MERCURY*

O. J. KLEPPA†

The heats of solution of seven other group B metals in mercury were determined calorimetrically at 150° over a fairly wide range in composition. The relative partial enthalpies of mercury were derived, and were compared with excess free energies obtained from the literature.

Unlike the corresponding alloys of zinc and cadmium, the considered mercury systems show no correlation between the excess enthalpy, the excess entropy and the valence difference between solvent and solute. However, the observed heats of formation seem to reflect the competition between an "electro-negativity" factor, which gives rise to negative terms in the enthalpy, and a "misfit" factor, which gives rise to positive terms.

ANALYSES THERMODYNAMIQUES DES MELANGES LIQUIDES BINAIRES DU GROUPE DE METAUX IIB—III

LES SOLUTIONS DE ZINC, CADMIUM, INDIUM, ÉTAIN, THALLIUM, PLOMB ET BISMUTH DANS LE MERCURE

Pour un grand nombre de compositions, les chaleurs de solution de sept autres métaux du groupe B dans le mercure ont été déterminées par voie calorimétrique à 150°. Les enthalpies partielles relatives de mercure ont été dérivées et comparées avec l'excès des énergies libres renseignées dans la littérature.

Contrairement aux alliages correspondants de zinc et de cadmium, il n'existe pas de corrélation entre l'excès de l'énergie libre, l'excès d'enthalpies et la différence de valence entre le solvant et le soluté pour les systèmes de mercure en considération.

Cependant les chaleurs de formation observées semblent indiquer une compétition entre un facteur d'électro-négativité, dont déri-vent des termes négatifs dans l'enthalpie et un facteur d'anomalie dont dérivent des termes positifs.

THERMODYNAMISCHE ANALYSE BINÄRER FLÜSSIGER LEGIERUNGEN VON METALLEN DER GRUPPE IIB—III

DIE LÖSUNGEN VON ZINK, CADMIUM, INDIUM, ZINN, THALLIUM, BLEI UND WISMUT IN QUECKSILBER

Die Lösungswärmen von sieben anderen Metallen der Gruppe B in Quecksilber wurden über einen ziemlich weiten Zusammensetzungsbereich bei 150° kalorimetrisch bestimmt. Die relativen partiellen Enthalpien von Quecksilber wurden daraus abgeleitet und mit den freien Überschuß-Energien aus der Literatur verglichen.

Im Gegensatz zu den entsprechenden Legierungen von Zink und Cadmium zeigen die betrachteten Quecksilbersysteme keine Beziehung zwischen Überschuß-Enthalpie, Überschuß-Entropie und der Wertigkeitsdifferenz zwischen Lösungsmittel und gelöster Substanz. Die beobachteten Bildungswärmen scheinen jedoch den Widerstreit zwischen der "Elektro-Negativität", die einen negativen Beitrag zur Enthalpie liefert, und den Störungen im "Aneinanderpassen" der Atome, die zu positiven Beiträgen führen, wiederzuspiegeln.

VOL. 8 1960

INTRODUCTION

During the past 50–60 years physical chemists have devoted considerable attention to the equilibrium properties of mercury solutions. Consequently these systems have been studied by many of the methods of solution chemistry, such as the e.m.f. and vapor pressure methods, calorimetry, etc. However, a survey of the literature shows that most of the reported thermodynamic information on these liquid alloys was obtained at room temperature, where most metals dissolve only to a very limited extent in mercury. The information on more concentrated solutions consists in the main of vapor pressure data. Here the measurements of Hildebrand and co-workers[1–4] are most comprehensive and also appear to be most reliable. Unfortunately Hildebrand *et al.* did not explore the temperature dependence of the excess free energy of mixing. Therefore these earlier investigations throw little light on the relative importance of heat and entropy in the mercury solution systems.

In recent communications the author has surveyed

* Received August 14, 1959.

† Institute for the Study of Metals, University of Chicago.

the thermodynamic properties of solutions in liquid zinc and cadmium.[5–7] In this work it is demonstrated that for solutions in these metals semi-quantitative correlations exist between the relative partial enthalpy of the solvent, the partial excess entropy of the solvent and the difference in valence between solvent and solute: the larger the valence difference, the larger the partial enthalpy and also the larger the excess entropy. However, these correlations do not carry over to the partial excess free energies or to the phase diagrams.

In the present communication we extend this survey to solutions in liquid mercury. First we present some new calorimetric information on the heat of formation of liquid mercury alloys at 150°. At this temperature the solubilities of most of the considered solutes are of the order of 50 at.%, while the vapor pressure of mercury still is so low that the measurements can be carried out in an open calorimeter. Relative partial heat contents for mercury derived from the new results will then be compared with corresponding free energies obtained from equilibrium work.

EXPERIMENTAL

The calorimetric measurements reported in the present work were all carried out in the high temperature reaction calorimeter previously described by the author.[8] Because of the known health hazards associated with the handling of hot mercury, this metal was always contained under a blanket of mineral oil when heated above room temperature. While most experiments were performed at 150 (±1)°, a few runs on each system were also carried out at 100°, and in the case of indium–mercury, at 40° and at 160°.

While this investigation was in progress the author became aware of a possible source of systematic errors, not previously fully appreciated, in past measurements carried out in the mentioned calorimeter. This led us to restudy the electrical calibration procedure in some detail, and we arrived at the following conclusions: In most of our earlier work we studied *endothermic* reactions, and we attempted to compensate for the heat effect of the reaction by generating an equivalent amount of electrical energy in a separate calibration experiment. This experiment usually was carried out immediately after the endothermic reaction. As a result of this compensation between reaction and calibration heats, there was little change in the total heat content of our calorimetric system (calorimeter block plus surrounding quasithermostated jacket), and there was no significant systematic error. For these experiments we find good agreement between the results obtained in our own work and in later work on the same systems.[9]

However, equally close agreement has not always been found for *exothermic* reactions.[9] In such experiments there is heat generation both in the reaction proper and in the electrical calibration. Thus the heat content of the calorimetric system increases in the course of a run. This will in turn give rise to systematic errors, which under unfavorable circumstances may amount to several per cent. Fortunately, it was possible to reduce this systematic error to acceptable proportions (i.e. to about 1 per cent or less) by using the mean of two calibrations, one carried out immediately before and one immediately after the exothermic reaction proper. Such a procedure was adopted for the exothermic experiments reported in the present work.

For calorimetric experiments which led to the formation of relatively dilute liquid alloys (below 10–15 per cent solute), the rates of dissolution of the various solid metals in mercury were quite rapid,

TABLE 1. Molar integral heats of formation of liquid solutions of zinc and cadmium in mercury

	Composition, x_{solute}	No. of g atoms	ΔH^M, J/g atom
(a) Hg–Zn, 100°C	0.0343	0.8284	341
	0.0375	0.7484	357
	0.0469	0.5753	449
	0.0670	0.8577	637
	0.0910	0.6033	850
Hg–Zn, 150°C	0.0314	0.6216	309
	0.0332	0.758	325
	0.0372	0.772	372
	0.0374	0.609	376
	0.0529	0.553	518
	0.0735	0.803	738
	0.0848	0.3185	820
	0.1142	0.591	1094
	0.1143	0.827	1105
	0.1485	0.1545	1424
	0.2027	0.1737	1864
	0.2604	0.1779	2305
	0.2773	Dil.	2457
	0.2870	Dil.	2512
(b) Hg–Cd, 100°C	0.0345	1.054	−68
	0.0541	0.598	−105
	0.0820	1.091	−160
	0.1068	0.633	−198
Hg–Cd, 150°C	0.0249	1.032	−45.5
	0.0458	0.503	−84
	0.0482	0.554	−85
	0.0521	0.579	−96
	0.0543	1.064	−97
	0.1021	1.120	−177
	0.1063	0.300	−191
	0.1652	0.632	−251
	0.2299	0.315	−294
	0.3965	0.214	−148
	0.446	Dil.	+22

TABLE 2. Molar integral heats of formation of liquid solutions of indium and thallium in mercury

	Composition, x_{solute}	No. of g atoms	ΔH^M, J/g atom	$\frac{\Delta H^M(\text{In(l)})}{x_{In}\, x_{Hg}}$, kJ
(a) Hg–In, 40°C	0.0696	0.7332	−360	−9.06
	0.0774	0.3458	−403	−9.17
	0.0790	0.5409	−393	−8.94
	0.0843	0.5436	−421	−9.01
	0.0889	0.5473	−444	−9.06
Hg–In, 100°C	0.0563	0.508	−311	−9.31
	0.0794	0.250	−422	−9.31
	0.0881	0.520	−459	−9.29
	0.1505	0.565	−673	−9.10
	0.1660	0.276	−747	−9.31
Hg–In, 150°C	0.0312	0.821	−176	−9.19
	0.0528	0.575	−293	−9.30
	0.1067	0.890	−520	−9.10
	0.1099	0.314	−527	−9.05
	0.1373	0.632	−628	−9.08
	0.2557	0.376	−890	−9.06
Hg–In (l), 160°C	0.0767	0.5947	−652	−9.21
	0.1443	0.6418	−1133	−9.17
	0.2048	0.2774	−1488	−9.14
	0.4133	0.1701	−2235	−9.22
	0.4834	0.2908	−2262	−9.06
	0.6008	0.3191	−2137	−8.91
	0.6512	0.2158	−1974	−8.69
	0.7775	0.2466	−1435	−8.29
	0.7895	0.6158	−1400	−8.42
	0.9194	0.5154	−587	−7.92
	0.9387	0.5180	−444	−7.71
(b) Hg–Tl, 100°C	0.0299	0.734	−50	
	0.0571	0.495	−67	
	0.0635	0.761	−68	
	0.1060	0.811	−34	
	0.1560	0.553	+43.5	
Hg–Tl, 150°C	0.0229	0.765	−27	
	0.0539	0.428	−42	
	0.0778	0.811	−29	
	0.1030	0.834	+0	
	0.1241	0.252	+33	
	0.1770	Dil.	+175	
	0.1920	0.181	+207	
	0.2838	0.110	+508	
	0.3382	0.220	+826	
	0.3382	Dil.	+813	
	0.4524	Dil.	+1240	
	0.471	Dil.	+1510	
	0.5024	Dil.	+1538	
	0.5280	Dil.	+1710	
	0.552	0.177	+1770	

and the experiments usually were concluded in 25–30 min. (Most of this time arises from lags in the solid calorimeter block.) On the other hand, in experiments which led to the formation of liquid alloys of composition approaching that of the liquidus, solution rates were much slower, and some experiments lasted as much as 60 min. In these long time runs the experimental errors are larger than for the more dilute alloys. As a check of our results in the higher concentration range we performed also a few dilution experiments. In these experiments a concentrated liquid alloy of known composition was dissolved in about 1 mole of pure mercury. The heat of formation of the concentrated alloy was then obtained from the observed heat effect combined with the (known) heat of formation of the more dilute alloy. It will be seen from the results recorded below that there is good agreement between the results obtained by these two methods.

The mercury used in the present work was of triply distilled commercial quality. The other metals were all of better than 99.9 per cent purity, as determined by semi-quantitative spectrographic analysis.

RESULTS. COMPARISON WITH EARLIER DATA

In the course of the present investigation approximately twenty calorimetric experiments were carried

VOL. 8 1960

TABLE 3. Molar integral heats of formation of liquid solutions of tin, lead and bismuth in mercury

	Composition, x_{solute}	No. of g atoms	ΔH^M, J/g atom
(a) Hg–Sn, 100°C	0.0207	0.804	269
	0.0219	0.522	282
	0.0411	0.564	518
	0.0447	0.535	565
	0.0568	0.835	712
	0.0758	0.585	926
Hg–Sn, 150°C	0.01904	0.964	249
	0.0273	0.718	355
	0.0311	0.653	400
	0.03115	0.565	410
	0.0351	0.563	450
	0.0552	1.001	689
	0.0611	0.674	756
	0.0826	0.597	1008
	0.0846	0.762	1036
	0.1179	0.274	1351
	0.1828	0.181	2012
	0.2626	0.131	2716
	0.403	0.161	3774
	0.546	Dil.	4790
(b) Hg–Pb, 100°C	0.01344	0.854	126
	0.02486	0.864	231
	0.0292	0.595	272
	0.0720	0.623	632
Hg–Pb, 150C	0.01885	0.996	184
	0.02135	0.805	207
	0.02913	0.557	273
	0.0305	0.548	284
	0.0548	0.833	490
	0.0566	0.551	496
	0.0807	0.588	686
	0.1126	0.295	884
	0.1538	0.200	1131
	0.2507	0.139	1587
	0.294	Dil.	1725
	0.3767	0.124	2020
(c) Hg–Bi, 100°C	0.0258	0.584	406
	0.0351	0.589	541
	0.0604	0.605	901
	0.0706	0.612	1034
Hg–Bi, 150°C	0.0295	0.554	471
	0.0317	0.546	495
	0.0370	0.559	584
	0.0667	0.566	998
	0.0673	0.275	1017
	0.0819	0.586	1218
	0.1177	0.289	1651
	0.1462	0.178	2044
	0.212	Dil.	2813
	0.2485	0.136	3280
	0.2618	0.206	3379
	0.2975	Dil.	3820
	0.3980	0.170	4900
	0.419	Dil.	5125

out on each of the seven systems studied. The amount of metal used, the composition of the liquid alloy formed, and the measured molar heats of formation (ΔH^M) are recorded in Tables 1–3. From these experimental data we have calculated the quantities $\Delta H^M/x_{solute}$. These are plotted versus composition in Figs. 1–3 along with a few results reported in earlier calorimetric work.

Mercury–zinc

From our results on this system, which are recorded in Table 1 and plotted in Fig. 1, we obtain a limiting heat of solution of zinc in mercury at 150° of +10.1 kJ/g atom. The corresponding figure at 100° is 9.8 kJ, which gives a ΔC_p for zinc in mercury of the order of +6 J/deg in this temperature range. A much lower heat of solution, 7.7 kJ at 97°, was previously reported by Tammann and Ohler[10]. On the other hand, from e.m.f. work at room temperatures Richards and Lewis[11] obtained a relative partial heat content for zinc in a 3 at.% amalgam of 9.4 kJ/g atom, in good agreement with the present work. Our results also agree well with very recent unpublished e.m.f. results by Wilson and Ward[12].

Figure 1 shows that for the whole concentration range explored in the present work, i.e. from about 3 to 30 at.% zinc, $\Delta H^M/x_{Zn}$ appears to change linearly with x_{Zn}. A least squares treatment of the data gives a slope of this line of −4.4 kJ/g atom. Thus we get (see below)

$$\Delta \bar{H}_{Hg} = 4.4x_{Zn}^2 \text{ kJ } (x_{Zn} < 0.3).$$

It is of interest to compare this slope with corresponding values which can be calculated from the room temperature work on quite dilute alloys of

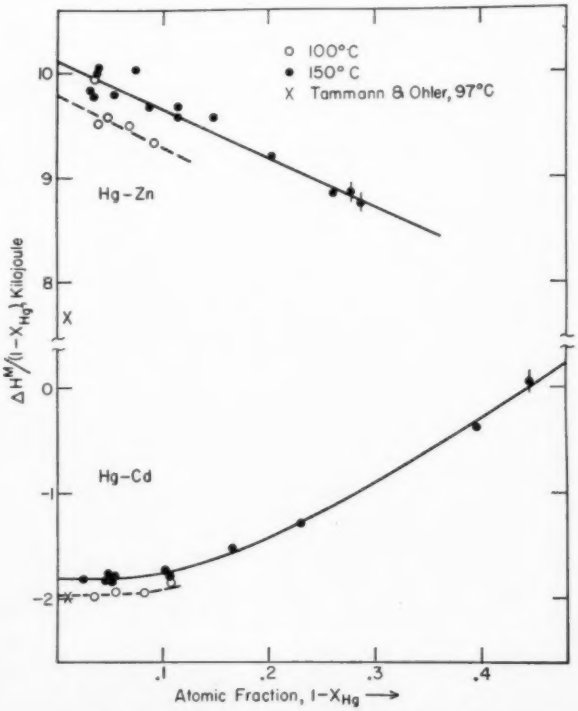


FIG. 1. Heats of formation of liquid alloys of mercury with zinc and cadmium.

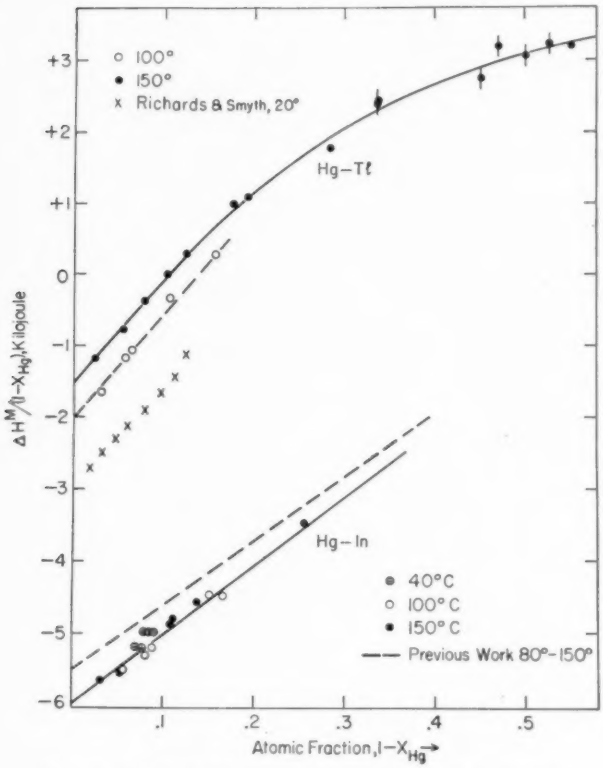


FIG. 2. Heats of formation of liquid alloys of mercury with indium and thallium.

Richards *et al.* From the calorimetric dilution experiments of Richards and Forbes[13] we derive a slope of −3.7 kJ/g atom, and from the e.m.f. data of Richards and Garrod-Thomas[14] −5.1 kJ. The agreement must be considered satisfactory and indicates that our slope applies also below 3 at.% zinc.

Mercury–cadmium

While the solution of zinc in mercury at 150° is an endothermic process, the solution of cadmium is exothermic at low cadmium concentration. From our results at 150° we obtain a limiting heat of solution of −1.81 kJ/g atom; at 100° a value near −1.96 kJ is indicated. The latter figure agrees very well with the result of Tammann and Ohler[10], −1.98 kJ at 97°. If we assume a $\Delta\bar{C}_p$ for cadmium in mercury of +2 to +3 J/deg, our results are also in good agreement with the room temperature e.m.f. value of −2.11 kJ reported by Richards and Lewis[11].

It will be noted from Fig. 1 that $\Delta H^M/x_{Cd}$ has a zero slope at low x_{Cd}. This interesting result confirms e.m.f. and calorimetric dilution experiments at room temperature by Richards *et al.*[13,14], and also more recent calorimetric results of Teeter[15].

Mercury–indium

Heat of formation data for this system were reported recently by Kleppa and Kaplan[16]. However, the author suspected that these data might be associated with a small systematic error (see "Experimental" above). Therefore the heats of formation were re-determined at 40°, 100°, 150° —In(s)— and at 160°—In(l)—. The results will be found in Table 2 and are plotted in Fig. 2. It will be noted that the new data confirm our earlier conclusion that the heats of formation in this system vary relatively little with temperature. On the other hand, we also find that the new values numerically are some 5 per cent larger than those reported previously. Thus the limiting heat of solution of solid indium in mercury is found to be −5.9 kJ/g atom, compared to the earlier value of −5.6 kJ. If we correct this new result for the heat of fusion of indium (3.26 kg/g atom[17]), we obtain a limiting heat of solution of liquid indium in

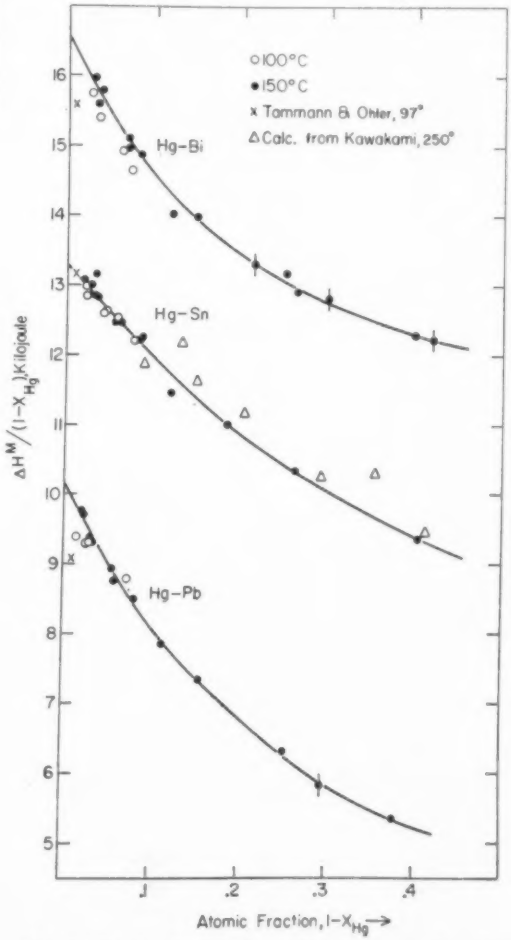


FIG. 3. Heats of formation of liquid alloys of mercury with tin, lead and bismuth.

VOL. 8 1960

mercury of -9.1_6 kJ. This is in excellent agreement with the new heat of mixing data at 160°.

For this system we have included in Table 2 a column which gives $\Delta H^M[\text{In(l)}]/x_{\text{In}}x_{\text{Hg}}$. For the experiments with solid indium this quantity was calculated under the assumption that the heat of fusion of indium is 3.26 kJ, independent of temperature. It will be noted that with only one exception the experiments with less than 50 per cent indium give values of this quotient in the range from −9.0 to −9.3 kJ with a mean of −9.15. Thus we find that in this concentration range the heat of mixing of liquid indium and mercury can be represented by a simple one constant expression. As a consequence the relative partial heat content of mercury may be derived from the expression $\Delta\bar{H}_{\text{Hg}} = -9.1_5 x_{\text{In}}^2$ kJ/g atom ($x_{\text{In}} < 0.5$).

Our new heat data, particularly for the low indium range, are in agreement with heats derived from room temperature e.m.f. work by Janjic-Tatic[18]. However, the old e.m.f. work on very dilute alloys by Richards and Garrod-Thomas[14] yield a somewhat higher slope of $\Delta H^M/x_{\text{In}}$ versus x_{In} than our new data.

Mercury–thallium

Due to the high solubility of thallium in mercury at room temperature (about 45 per cent), the liquid alloys of this system have been studied extensively in the past. The now classical investigations by Richards and co-workers are particularly noteworthy, the most important single study being that of Richards and Daniels[19]. Much of the earlier work on this system is discussed in some detail by Lewis and Randall[20] and more recently by Teeter[21]. Where a comparison is possible the heat data obtained in the present study are in good agreement with the results of earlier work. Thus we find that the heat of solution of thallium in mercury depends strongly on temperature between 100 and 150°, with limiting heats of solution of −2.0 and −1.5 kJ/g atom respectively. This gives a $\Delta\bar{C}_p$ for thallium in mercury of about +10 J/deg. From the work of Richards *et al.* the corresponding value near room temperature is about +12 J/deg. If we extrapolate our own results for the limiting heats of solution to room temperatures we get a value of the order of −2.8 to −3.0 kJ. Calorimetrically Richards and Smyth[22] obtained −2.97 kJ at 20°, while the e.m.f. work of Richards and Daniels yields a numerically slightly higher figure.

From the graph in Fig. 2 we obtain a limiting slope of $\Delta H^M/x_{\text{Tl}}$ versus x_{Tl} of +15 kJ/g atom. Within the precision of our measurements and of those of Richards and Smyth, we are not able to detect any change in this slope between 20° and 150°. However, there are available for these alloys also partial molar heat data for mercury at 30°, derived from the e.m.f. work of Richards and Daniels. We have plotted these data in Fig. 5, along with corresponding results for 150° derived from the present work. In principle these two sets of data should permit an evaluation of the average relative partial molar heat capacities for mercury between 30° and 150°. For example, at $x_{\text{Tl}} = 0.1$, we get in this way a value of $\Delta\bar{C}_p$ (Hg) of about +0.16 J/deg. The corresponding figure obtained directly from the room temperature heat capacity work of Richards and Daniels is +0.2 J/deg. Similar comparisons can be carried out at other concentrations. On the whole these comparisons tend to yield somewhat lower values for $\Delta\bar{C}_p$ (Hg) than those derived from Richards and Daniels.

Mercury–tin

The experimental values of $\Delta H^M/x_{\text{Sn}}$ are plotted in Fig. 3, along with corresponding data for the mercury–lead and mercury–bismuth systems. For mercury–tin our results show little or no dependence of the heat of formation on temperature, with a limiting heat of solution both at 100° and at 150° close to +13.3 kJ/g atom. Here our figure is in excellent agreement with that of Tammann and Ohler[10]. The limiting slope of $\Delta H^M/x_{\text{Sn}}$ versus x_{Sn} derived from our new measurements is −14 kJ/g atom. This is in complete agreement with the room temperature e.m.f. work on very dilute alloys by Richards and Garrod-Thomas[14].

For mercury–tin there are available heat of mixing data for the liquid metals at 250° reported by Kawakami[23]. Setting the heat of fusion of tin equal to 7.06 kJ/g atom,[17] we have calculated $\Delta H^M/x_{\text{Sn}}$ for solid tin from Kawakami's data, and included these values in Fig. 3. It will be noted that our own results agree fairly well with Kawakami's. The small systematic difference between the two sets of data may indicate a slight temperature dependence of ΔH^M, or possibly an error in the adopted heat of fusion.

Mercury–lead

For this system we derive a limiting heat of solution of +10.1 kJ/g atom at 150°. The value at 100° probably is smaller by 0.1–0.2 kJ. In this case our result is higher than that reported by Tammann and Ohler[10]. From the e.m.f. measurements by Hoyt and Stegeman[24] and by Richards and Garrod-Thomas[14] it also is possible to calculate the limiting heat of solution of lead in mercury at room temperature.

The e.m.f. value is about 11 kJ/g atom, i.e. somewhat higher than our own calorimetric result.

From Fig. 3 we derive a limiting slope of $\Delta H^M/x_{Pb}$ versus x_{Pb} of about -22 kJ/g atom at low lead concentrations. Here the work of Richards and Garrod-Thomas on alloys with less than 1 at.% lead yields a numerically somewhat larger value, namely -28 kJ. It is possible that the difference between these two values is significant, i.e. that the curvature in $\Delta H^M/x_{Pb}$ persists even below 2 at.% lead, which was the lowest concentration covered in the present study.

Mercury–bismuth

The limiting heat of solution of bismuth in mercury is 16.5 kJ/g atom at 150°; at 100° a value about 0.2 to 0.3 kJ smaller is indicated. Tammann and Ohler's value[10] at 97° was 15.6 kJ (at $x_{Bi} = 0.006$).

From Fig. 3 we obtain a limiting slope of $\Delta H^M/x_{Bi}$ versus x_{Bi} of about -22 kJ/g atom, i.e. the same value as for lead. However, our data do not cover the concentration range below 2.5 per cent bismuth. No e.m.f. data for this system were found in the literature.

SUMMARY OF THERMODYNAMIC DATA

From the smoothed curves drawn in Figs. 1–3 it is convenient to derive relative partial molar heat contents for the mercury-rich solutions by the following procedure: Consider

$$\Delta H^M = xf(x). \tag{1}$$

Here x is the mole fraction of solute, while $f(x)$ represents the experimentally determined curve. From equation (1) we readily obtain the following expressions for the relative partial molar heat contents of solvent and solute:

$$\Delta \bar{H}_{\text{solvent}} = -x^2\, df/dx \tag{2a}$$

$$\Delta \bar{H}_{\text{solute}} = f(x) + x(1-x)\, df/dx. \tag{2b}$$

In Table 4 we give a summary of the limiting values of $f(x)$ and df/dx at 150°.

Due to the relatively low curvature of the $f(x)$ curve in the low solute region the outlined procedure is more convenient than the usual method of intercepts based on ΔH^M proper. Even so it is immediately obvious that the calculated partial molar data are more uncertain than the integral quantities from which they are derived. We estimate the uncertainty in the relative partial enthalpies for mercury plotted in Figs. 4–6 to be of the order of 5 per cent for most of the concentration range up to 30 at.% of solute.

In Figs. 4–6 we give also the excess partial molar free energies for mercury in the considered systems. Most of these data were calculated from the already mentioned vapor pressure work of Hildebrand and co-workers.[1–4] Only for mercury–thallium, mercury–indium and for fairly dilute solutions of zinc in mercury

TABLE 4. Characteristic heat constants for dilute solutions in mercury at 150°. Data in kJ/g atom

Solute	Limiting heat of solution, $f(x=0)$		Limiting slope $(df/dx)_{x=0}$
	Solute (s)	Solute (l)*	
Zn	10.1	2.8	−4.4
Cd	-1.8_2	−8.2	0
In	−5.9	-9.1_5	9.1_5
Sn	13.3	6.2	−14
Tl	−1.5	−6.2†	15
Pb	10.1	5.1	−22
Bi	16.5	5.6	−22

* These values were obtained from those in the previous column by subtracting the heats of fusion of the solutes, taken from Kubaschewski and Evans[17].

† This value is corrected both for the heat of fusion of Tl and for the heat of transformation from α-Tl to β-Tl.

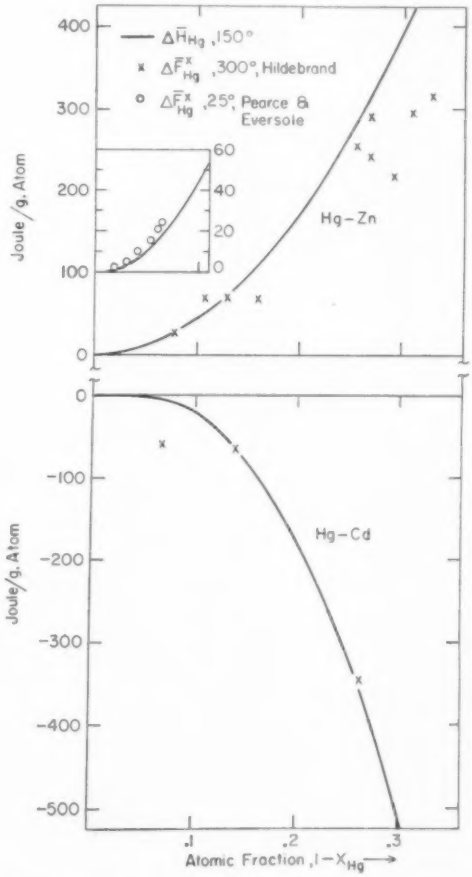


FIG. 4. Relative partial heat contents and excess free energies of mercury in liquid alloys with zinc and cadmium.

VOL. 8 1960

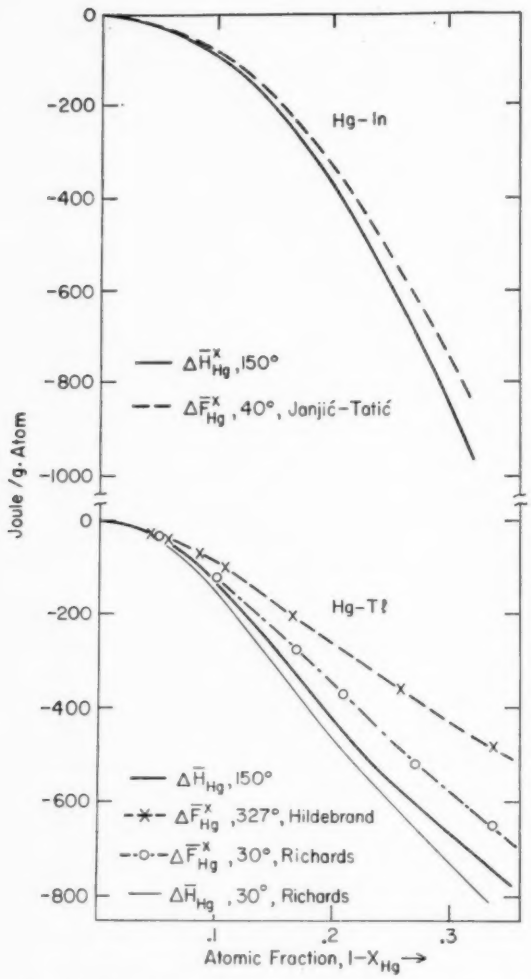


FIG. 5. Relative partial heat contents and free energies of mercury in liquid alloys with indium and thallium.

have we adopted excess free energies derived from room temperature e.m.f. work. As we are in the present survey concerned in particular with the partial properties of the common solvent (mercury), these free energies were calculated from Gibbs–Duhem integrations of the experimental (excess) partial free energies for the more electro-positive component (Tl, In, Zn).

In our past work on the binary liquid alloys involving zinc and cadmium we found that excess partial free energies for these metals, of accuracy comparable to data obtained from good e.m.f. work, frequently could be obtained from the appropriate binary phase diagram. Unfortunately this approach is less useful for the mercury systems. This is due to a number of factors, the most important of which are related to the low melting point of mercury. For example, in mercury systems liquidus analysis as carried out in Ref. (5) will provide partial free energy information for the higher melting component only. To get the corresponding information for mercury we must carry out also a Gibbs–Duhem integration. Because the free energies derived from the liquidus apply over a range in temperatures, this integration is likely to be associated with some uncertainty. Other complications arise from the relatively high solid solubility of mercury in other metals, and from the existence of intermetallic phases in several of the considered systems. For these reasons we have not included thermodynamic data derived from the liquidus in the present survey.

DISCUSSION

Our theoretical understanding of the factors which govern the solution properties of alloy systems is not yet in a very satisfactory state. Although some attempts have been made in recent years to explain and to derive thermodynamic properties of metallic solutions from reasonably realistic physical models (see e.g. Friedel[25]), theoretical work of this type has on the whole met with only limited success.

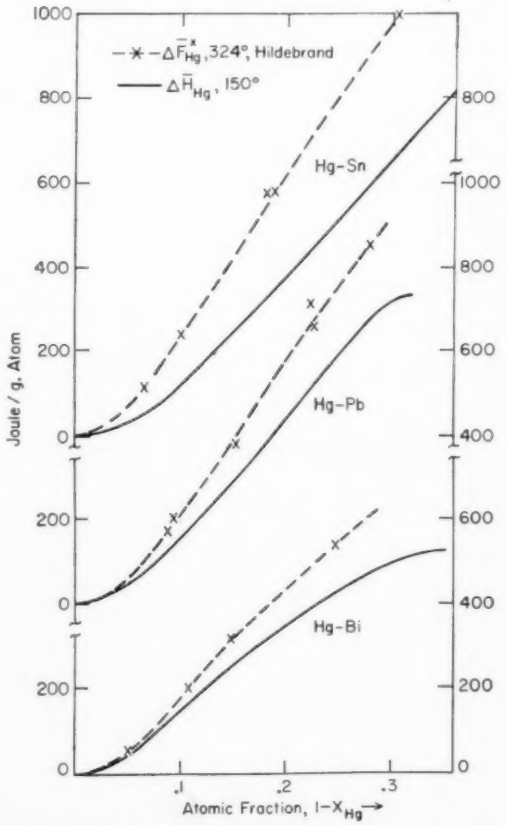


FIG. 6. Relative partial heat contents and free energies of mercury in liquid alloys with tin, lead and bismuth.

In the present discussion we shall not attempt to delve deep into the very complex problems of metal–metal interaction. Instead we shall be satisfied with adopting a systematic and phenomenological approach.

The Hume–Rothery school has demonstrated that three factors are of principal importance in determining the equilibrium properties of metallic solid solutions:

(1) The "electrochemical factor" or better the "electronegativity factor", i.e. the difference in electronegativity of the two components.

(2) The difference in the atomic size of the components, i.e. the "size factor".

(3) The difference in the characteristic valence of the components, or the "valence factor".

Of course, these factors are not mutually independent. However, their effect on the solution properties may to a first approximation be summarized in the following way: If there is a significant difference in electronegativity between two elements (metals) there usually will be a tendency toward chemical bonding between them. Alloys of two such metals often form ordered intermetallic phases, and will have some negative contribution to the overall heat (energy) of formation. On the other hand, a difference in atomic size similarly tends to contribute a positive term (a "misfit" energy) to the heat of formation. For size factors larger than about 15 per cent this term usually is so large that solid solubility is quite restricted. Finally, it is found that difference in the characteristic valence of the two components usually gives rise to some energetic asymmetry, i.e. to deviations of the thermodynamic excess functions from the simple symmetrical form predicted by the naive solution theories.[6]

These statements refer to the situation in solid solutions. However, they should apply equally well for liquid alloys, although the "size" or "misfit" factor is less critical in the liquid than in the solid state. In fact the tendency toward positive values of the heat of mixing in the liquid state seems to correlate better with the separation of the two partners in the periodic system, or with the difference in Hildebrand "solubility parameter", than with the size difference alone.[6]

In the present communication we are particularly interested in possible valence effects which may arise from a difference in the number of quasi-free electrons of the two partners. Therefore it seems appropriate to consider first under which conditions such effects may be anticipated: If we exclude specific compound formation according to conventional chemical valence rules, it may be predicted that pronounced valence effects are most likely to be observed when the electronegativity factor and the size factor are both relatively small. Such is, for example, the case for many of the Hume–Rothery type systems formed by copper and silver with metals of higher valence: According to Gordy[26] the electronegativity of copper and silver is 1.8, which is not much larger than for zinc, cadmium, gallium and indium, for all of which he lists the same value, 1.5. However, on the same scale the electronegativity of gold is 2.3, which is higher than for any other metal. This accounts for the tendency of gold to form quite strongly bonded compounds with the mentioned metals. It also explains why the Hume–Rothery valence rules apply less well for the corresponding alloys of gold.

For the alloys of zinc and cadmium with gallium, indium, tin, etc., the size and electronegativity factors are also of modest magnitude. Thus it is not surprising that valence correlated solution properties are observed in these systems.

As we go on to consider the liquid alloys of mercury it should be noted that according to Gordy's tabulation the electronegativity of mercury is comparable to that of copper and silver (1.8), while its atomic size is only slightly larger than that of cadmium. Accordingly, one might expect to find valence correlated properties also in mercury solutions.

Group IIB *solutes: zinc and cadmium*

It is recalled that the liquid system zinc–cadmium is remarkably simple, with thermodynamic properties approaching those of a "regular" solution. Thus the enthalpy of mixing is positive and very nearly symmetrical, while the excess entropy is quite small. However, when dissolved in mercury these two metals show very different behavior: While the mercury–cadmium system is exothermic, mixtures of mercury and liquid zinc are endothermic and somewhat unsymmetrical, i.e. the value of df/dx at $x = 0$ differs numerically from $f(x = 0)$. The zero slope for $\Delta H^M/x_{Cd}$ versus x_{Cd} for low concentrations of cadmium in mercury is of particular interest. From quasi-chemical theory a behavior of this type is predicted for strongly exothermic systems.[27]* However, ΔH^M for cadmium–mercury is not very strongly negative and is of the same order of magnitude as for indium–mercury and thallium–mercury. From Fig. 2 it will be noted that these two systems show no evidence of a leveling off of $\Delta H^M/x$ in the dilute range.

It is of some interest to compare the behavior of liquid solutions formed among the group II metals

* In this reference it is incorrectly predicted that one might expect the ratio $(df/dx)_{x=0}/f(0)$ to become *negative* for sufficiently large negative values of $f(0)$.

VOL. 8 1960

with those formed among their neighbors in group III. Unpublished measurements by the author show that the liquid system gallium–indium is quite similar to zinc–cadmium. Thus it has a symmetrical heat of mixing curve with a nearly constant "interaction parameter", $\Delta H^M/x(1-x)$, of about 4.5 kJ. The corresponding value for zinc–cadmium is 9 kJ. On the other hand, indium–thallium, unlike cadmium–mercury, is weakly endothermic, with limiting heats of solution near 2 kJ for indium in thallium and near 3 kJ for thallium in indium. The gallium–thallium system exhibits a liquid miscibility gap, i.e. it has a much larger positive heat of mixing than zinc–mercury. We have measured the limiting heat of solution of gallium in thallium at 450° and found a value of about +16 kJ. This compares with about 2.8 kJ for liquid zinc in mercury.

These differences may be accounted for in terms of the competition between the "misfit" factor and the "electronegativity" factor: According to Gordy[26] the elements zinc, cadmium, gallium, indium and thallium all have essentially the same electronegativity (1.5), while that of mercury is higher (1.8). Thus the heats of mixing for zinc–cadmium and for the alloys formed among the group III metals may be attributed to the "misfit" factor alone. On the other hand, in zinc–mercury and in zinc–cadmium there are significant differences in electronegativity between the two components. For cadmium–mercury the resultant ΔH^M is negative, while for zinc–mercury the electronegativity difference is not large enough to change the size of ΔH^M from positive to negative.

In Fig. 4 the relative heat contents for mercury in mercury–zinc and mercury–cadmium are compared with the corresponding excess free energies. This graph indicates that in these systems the excess entropies for mercury probably are small, at least as long as the solute concentration is below 30 at.%. However, the scatter in the experimental free energy data makes this conclusion somewhat tentative. Note, for example, that the e.m.f. data of Pearce and Eversole[28] point toward small negative partial excess entropies at low zinc contents, while Hildebrand's vapor pressures at higher zinc concentrations suggest positive excess entropies.

Group IIIB *solutes: indium and thallium*

For indium–mercury and thallium–mercury the heats of mixing of the liquid metals are negative; i.e. the electronegativity factor predominates. However, there are important differences between the heat data for the two systems. Thus the indium–mercury system has a nearly symmetrical heat of mixing curve, while the data for low concentrations of thallium in mercury point toward a significant energetic asymmetry.

From Table 4 it will be noted that the limiting values of (df/dx) for these systems are about 9 and 15 kJ/g atom, respectively. The positive signs of these slopes agree with Friedel's theory for solutes of valence larger than the solvent.[25]

Due to the low solubility of gallium in mercury we were unable to study the gallium–mercury system in the present investigation: From phase diagram information (see Hansen and Anderko[29]), it is known that this system has an extensive miscibility gap at 100°C. Thus it must have also a positive enthalpy of mixing, probably comparable to that of gallium–thallium. Here the "misfit" energy clearly outweighs the electronegativity factor.

Figure 5 shows that for these two systems the excess partial molar entropies of mercury in the high mercury range are *negative* (−0.2 to −0.3 J/deg mole at 25 per cent solute). They appear to be somewhat more negative for thallium than for indium. It is recalled that for indium and thallium in cadmium the excess entropies of cadmium are *positive*, and that they are of comparable magnitude as long as the solute concentration is not too large (+0.4 to 0.5 J/deg mole at 25 per cent solute). At higher solute concentrations the excess entropies of cadmium are larger for cadmium–thallium than for cadmium–indium.

Group IVB *and group* VB *solutes: tin, lead and bismuth*

The electronegativities of these three elements are 1.7–1.8, 1.6–1.8 and 1.8, respectively.[26] As the corresponding value for mercury is 1.8, it may be expected that the negative contributions to the overall enthalpy of mixing for these solutes should be quite small. This is confirmed by the fact that the considered binary alloys are all endothermic. In fact Table 4 shows that the limiting heats of solution of (liquid) tin, lead and bismuth in mercury are of comparable magnitude, +5 to +6 kJ/g atom at 150°. On the other hand, from Fig. 3 we note that these systems differ somewhat with respect to energetic asymmetry: Although the slopes of $\Delta H^M/x$ versus x start out with similar values for lead and bismuth, our results suggest that ΔH^M for liquid lead–mercury should become negative at high lead contents. This would explain the "anomalous" vapor pressures noted in this system by Hildebrand.[4] It correlates also with the existence of the solid intermetallic phase "Pb_2Hg".[29] For tin in mercury the initial slope is numerically smaller than for the other two systems. As a consequence the energetic asymmetry

also is less pronounced. Nevertheless, numerically the limiting slope is still more than twice as large as the limiting heat of solution of liquid tin in mercury.

From the partial heat curves plotted in Fig. 6 it will be noted that the mentioned differences between these three solutes are not strongly reflected in the relative partial heat contents for mercury, $\Delta\bar{H}_{Hg}$, as long as the solute concentrations are below 25–30 per cent. However, the graphs for lead and bismuth suggest that $\Delta\bar{H}_{Hg}$ for these two solutes approaches maxima at solute concentrations above 30 per cent.

The heat data for these three systems are not in harmony with the predictions of the Friedel theory.[25] Instead they show similarities with the solutions of tin, lead and bismuth in cadmium and zinc. It will be recalled that the latter systems are all endothermic. They also exhibit a very significant degree of energetic asymmetry, correlated with the difference in valence between the two components.

From Fig. 6 we see finally that for tin, lead and bismuth as solutes the partial excess entropies of mercury are *negative*. Again the mercury solutions differ from the solutions in cadmium and zinc. Note that for lead and bismuth in mercury the negative excess entropies are quite small (about -0.2 J/deg at 25 at.%). The negative excess entropies for tin appear to be somewhat larger.

VOL. 8 1960

SUMMARY AND CONCLUSIONS

The thermodynamic properties of solutions of seven group B elements in mercury have been surveyed, with a view toward the possible correlation between the excess partial thermodynamic functions for the solvent (mercury), and the valence of the solute. The picture which emerges is one of considerable complexity, and no correlations with valence were found. Clearly the mercury solutions differ both from solutions in liquid zinc and cadmium, and from solutions in Hume–Rothery type alloys.

On the whole the properties of the mercury systems considered in the present work seem to reflect the competition between an "electronegativity factor", which gives rise to negative terms in ΔH^M, and a "misfit" factor, which gives rise to positive terms. In the alloys with cadmium, indium and thallium, the first term predominates, while in the alloys with zinc, tin, lead and bismuth the second term is larger.

ACKNOWLEDGMENTS

This research was supported in part by the Office of Naval Research under contract No. Nori-2121 with the University of Chicago.

REFERENCES

1. J. H. Hildebrand, *Trans. Electrochem. Soc.* **22**, 319 (1912).
2. J. H. Hildebrand and E. D. Eastman, *J. Amer. Chem. Soc.* **36**, 2020 (1914).
3. J. H. Hildebrand and E. D. Eastman, *J. Amer. Chem. Soc.* **37**, 2452 (1915).
4. J. H. Hildebrand, A. H. Foster and C. W. Beebe, *J. Amer. Chem. Soc.* **42**, 545 (1920).
5. O. J. Kleppa, *Acta Met.* **6**, 223, 233 (1958).
6. O. J. Kleppa, *Liquid Metals and Solidification*, American Society for Metals, Cleveland (1958).
7. O. J. Kleppa and C. E. Thalmayer, *J. Phys. Chem.* **63**, 1953 (1959).
8. O. J. Kleppa, *J. Phys. Chem.* **59**, 175 (1955).
9. R. A. Oriani and W. K. Murphy, *Proceedings N.P.L. Symposium on Metallic Solutions and Intermetallic Compounds*, H.M.S.O. London (1959).
10. G. Tammann and E. Ohler, *Z. Anorg. Chem.* **135**, 118 (1924).
11. T. W. Richards and G. N. Lewis, *Z. Phys. Chem.* **28**, 1 (1898).
12. J. R. Wilson and R. G. Ward, private communication.
13. T. W. Richards and G. S. Forbes, *Z. Phys. Chem.* **58**, 683 (1907).
14. T. W. Richards and R. N. Garrod-Thomas, *Z. Phys. Chem.* **72**, 165 (1910).
15. C. E. Teeter, Jr., *J. Amer. Chem. Soc.* **53**, 3927 (1931).
16. O. J. Kleppa and M. Kaplan, *J. Phys. Chem.* **61**, 1120 (1957).
17. O. Kubaschewski and E. Ll. Evans, *Metallurgical Thermochemistry*, Butterworth–Springer, London (1951).
18. O. Janjic-Tatic, private communication.
19. T. W. Richards and F. Daniels, *J. Amer. Chem. Soc.* **41**, 1732 (1919).
20. G. N. Lewis and M. Randall, *Thermodynamics*, McGraw-Hill, New York (1923).
21. C. E. Teeter, Jr., *J. Amer. Chem. Soc.* **53**, 3917 (1931).
22. T. W. Richards and C. P. Smyth, *J. Amer. Chem. Soc.* **45**, 1455 (1923).
23. M. Kawakami, *Sci. Rep. Tohoku Univ.* (I) **16**, 915 (1927).
24. C. S. Hoyt and G. Stegeman, *J. Phys. Chem.* **38**, 753 (1934).
25. J. Friedel, *Advanc. Phys.* **3**, 446 (1954).
26. W. Gordy and W. J. O. Thomas, *J. Chem. Phys.* **24**, 439 (1956).
27. O. J. Kleppa, *K. Norske Vidensk. Selsk. Skr.*, no. 6, p. 18 (1956).
28. J. N. Pearce and J. F. Eversole, *J. Phys. Chem.* **32**, 209 (1928).
29. M. Hansen and K. Anderko, *Constitution of Binary Alloys* (2n Ed.), McGraw-Hill, New York (1958).

AN X-RAY DIFFRACTION STUDY OF IRRADIATED MOLYBDENUM*†

D. L. GRAY‡ and W. V. CUMMINGS, Jr.‡

Changes in the lattice parameter, X-ray line width and micro-hardness of commercial molybdenum were observed after irradiation at 35 ± 5°C to various total fast neutron exposures from 6.5×10^{16} to 1.2×10^{20} nvt (neutrons per cm²). The lattice parameter vs. neutron exposure curve maximizes near 5.0×10^{19} nvt, and at 1.2×10^{20} nvt a net decrease from the pre-irradiation value occurs. Both line width and micro-hardness increase with neutron exposure and although the micro-hardness approaches a limiting value with increasing irradiation, the values of line width do not. These effects in irradiated molybdenum are discussed from the standpoint of some recovery reactions which may occur in reactor during irradiation and it is concluded that (1) interstitial atoms produced by neutron bombardment are mobile at the irradiation temperature, 35°C, (2) during the initial stages of irradiation a substantial number of interstitials become trapped at small substitutional impurity atoms and (3) interstitial cluster formation and growth predominates during the remainder of the irradiation. Some mechanisms of interstitial cluster formation and growth are discussed.

ETUDE DE DIFFRACTION PAR RAYONS X SUR LE MOLYBDENE IRRADIE

Après l'exposition à des flux de neutrons rapides variants de $6{,}5 \cdot 10^{16}$ à $1{,}2 \cdot 10^{20}$ nvt (neutrons par cm²) des changements du paramètre du réseau, de la longueur des rayons X et de la microdureté du molybdène commercial ont été observés après une irradiation à 35 ± 5°C. Si l'on fait un diagramme paramètre du réseau en fonction des valeurs maximales des courbes d'exposition aux neutrons à $5{,}0 \cdot 10^{19}$ nvt et à $1{,}2 \cdot 10^{20}$ nvt, une diminution nette du paramètre réseau irradié est observée. La largeur des raies et la microdureté augmentent avec le temps d'exposition aux neutrons, et quoique la microdureté s'approche d'une valeur limite, en augmentant l'irradiation, les largeurs des raies ne changent pas de cette façon. Ces effets dans le molybdène irradié ont été discutés du point de vue de quelques réactions de restauration qui pourraient avoir lieu dans un réacteur pendant l'irradiation et l'on a conclu que des lacunes d'atomes, produites par le bombardement de neutrons, sont mobiles à la température d'irradiation de 35°C. Pendant la première période de l'irridiation un nombre considérable de lacunes se rassemblent au voisinage des petits atomes d'impureté en solution de substitution. La formation et le grossissement des nuages de lacunes prédominent pendant que l'irridation continue. Quelques mécanismes de formation et de grossissement des nuages des lacunes sont discutés.

RÖNTGEN-UNTERSUCHUNG VON BESTRAHLTEM MOLYBDÄN

Änderungen des Gitterparameters, der Breite der Röntgen-Linien und der Mikrohärte wurden bei kommerziellem Molybdän beobachtet, das bei 35° ± 5°C neutronenbestrahlt worden war, wobei der gesamte Fluß schneller Neutronen von 6.5×10^{16} bis 1.2×10^{20} nvt (Neutronen pro cm²) reichte. Der Gitterparameter zeigt in Abhängigkeit von der Bestrahlungsdosis ein Maximum bei 5.0×10^{19} nvt, und bei 1.2×10^{20} nvt ist er geringer als vor der Bestrahlung. Linienbreite und Mikrohärte nehmen mit der Neutronendosis zu; die Mikrohärte erreicht im Gegensatz zur Linienbreite einen Sättigungswert. Diese Effekte bei bestrahltem Molybdän werden diskutiert vom Standpunkt einiger Erholungsreaktionen, die im Reaktor während der Bestrahlung ablaufen können. Es wird geschlossen: (1) Zwischengitteratome, die durch die einfallenden Neutronen erzeugt werden, sind bei der Bestrahlungstemperatur von 35°C beweglich. (2) Während des ersten Stadiums der Bestrahlung wird eine beträchtliche Zahl von Zwischengitteratomen von kleinen substitutionellen Verunreinigungsatomen eingefangen. (3) Während der übrigen Bestrahlungszeit herrschen Bildung und Wachstum von Zusammenballungen der Zwischengitteratome vor. Einige Mechanismen, die zur Bildung und zum Wachstum von Zwischengitteratom-Zusammenballungen führen, werden diskutiert.

INTRODUCTION

Recent work[1,2] has shown that the lattice parameter of molybdenum increases with neutron irradiation for integrated exposures up to 10^{19} nvt. Physical length changes[1] have also been observed and are in accordance with the lattice parameter increases. These effects lend credence to the idea that interstitial atoms are present at room temperature in irradiated molybdenum. Nevertheless, questions still remain concerning the nature of the residual damage. It is not clear whether the interstitials are present as single isolated defects, pairs, clusters, or are trapped at small substitutional impurity atoms. A comparison of existing data indicates that the molybdenum examined by Adam and Martin[1] contained less residual expansion than that examined here.[2] These differences are not necessarily contradictory.

The object of this investigation is (1) to learn more about the defects resulting from neutron irradiation of molybdenum, and (2) to explain differences in existing data. With these objects in mind, the results of

* Received August 19, 1959.
† This investigation was performed under Contract No. W-31-109-Eng-52 between the Atomic Energy Commission and General Electric Company.
‡ Hanford Atomic Products Operation, Richland, Washington.

additional neutron exposures as great as 1.2×10^{20} nvt (neutrons per cm^2) are presented. The effect of such exposures upon lattice parameter, X-ray line width and micro-hardness is quite marked and some conclusions regarding the nature of the residual damage in molybdenum can be drawn from the nature of these property changes.

EXPERIMENTAL PROCEDURE

The specimens used for this investigation were made from wrought commercial molybdenum of the following composition (weight per cent): Fe, 0.03; Mn, 0.01; Al, 0.01; Ni, 0.01; Si, 0.01; Mg, 0.01; Cu, 0.01. Prior to irradiation samples $0.5 \times 0.5 \times 0.1$ in. were given a stress relieving anneal in vacuum at 900°C for 1 hr. After this heat treatment the X-ray lines were sharpened sufficiently so that no serious interference of the $K\alpha_1$ and $K\alpha_2$ reflections occurred at high diffraction angles.

The molybdenum specimens were irradiated in two groups in the Materials Testing Reactor to various integrated fast neutron exposures from 6.5×10^{16} to 1.2×10^{20} nvt (neutrons per cm^2). During the irradiation the specimens were in contact with the cooling water at a temperature of 30° to 40°C. The series of exposures from 6.5×10^{16} to 6.0×10^{19} nvt were obtained in an estimated fast neutron flux (greater than 1 MeV) of 1.8×10^{13} neutrons/cm^2/sec. The power level of the reactor was increased during the remainder of the experiment with the result that one group of samples was exposed to a fast flux of 1.8×10^{13} neutrons/cm^2/sec for 1004 hr and then was exposed to a fast flux of 2.4×10^{13} neutrons/cm^2/sec for the remaining 636 hr of irradiation; a total integrated exposure of 1.2×10^{20} nvt was obtained for this set of samples.

A Norelco diffractometer with a copper tube operating at 50 KV and 15 ma was used to determine the profile of the molybdenum (400)Kα reflections. A scintillation counter was used with a single channel pulse height analyser in order to discriminate against the background radio-activity. The diffraction profiles were determined by the method of fixed counts taken every 0.05° 2 θ over the background and every 0.02° 2 θ over the peaks. A line drawn through the center of gravity of the (400)Kα_1 reflection was used to find the value of 2 θ, from which the lattice parameter was calculated. The lattice parameter of the irradiated material was compared to that of the unirradiated material and the resulting difference expressed as a per cent. When little irradiation-induced line broadening was present the accuracy of the measurements was at least one part in 60,000. When line broadening caused serious interference between the $K\alpha_1$ and $K\alpha_2$ reflections, the lines were separated by assuming that the intensity of the experimentally determined profile could be represented by a function

$$g(x) = f(x) + \tfrac{1}{2} f(x - \delta)$$

where $f(x)$ is the intensity contribution of the (400)Kα_1 reflection, $\frac{1}{2} f(x - \delta)$ is the intensity contribution of the (400)Kα_2 reflection and δ is the normal separation of the $K\alpha_1$ from $K\alpha_2$. Starting at the low angle side of the peak at zero background and laying off distances δ, one can then reconstruct the two (400)Kα reflections. The 2 θ value obtained from the center of gravity of the separated $K\alpha_1$ reflection was selected for lattice parameter calculations. After the X-ray measurements were complete, micro-hardness of some of the samples was measured as a supplement to the X-ray data.

RESULTS

The lattice parameter, X-ray diffraction line width and micro-hardness of molybdenum are changed by neutron irradiation and the nature of the changes depend upon the total exposure. The per cent lattice parameter changes are tabulated in Table 1 for the various exposures, together with values of the line width of the (400)Kα_1 reflection. These values and some hardness data are plotted in Fig. 1 as a function of integrated fast neutron flux. Referring to Fig. 1, it can be seen that the increase in irradiation-induced line broadening is only slight at exposures from 10^{16} to 10^{19} nvt, and then increases markedly with increasing irradiation. In the range of exposures studied there is no tendency of the line width changes to approach a limiting value with increasing exposure. On the contrary, the line broadening increases almost linearly with exposure. Micro-hardness increases from the unirradiated value of 233 DPH (10 k load) to 306 DPH after an exposure of 5.0×10^{19} nvt, after which a sharp bend in the exposure curve results. Little additional hardness increase was caused by exposures above 5.0×10^{19} nvt. It was noted that for the first few exposures only a slight hardness change was detectable. Since the changes were small it is not really certain whether the slope of the hardness curve is initially low and then increasing, or whether it is increasing almost linearly with exposure.

The lowest exposure was effective in increasing the lattice parameter and in the low exposure range from 10^{16} to 10^{19} nvt the lattice parameter increased rapidly and almost linearly. Near 5.0×10^{19} nvt the curve passed through a maximum and at the highest

VOL. 8 1960

TABLE 1. X-ray data; irradiated molybdenum

Time in reactor (sec)	Integrated fast neutron exposure (nvt)	Sample number	Per cent lattice parameter change	Width of (400)Kα_1 reflection at half height‡
3.6×10^3	6.5×10^{16}	5	0.011	0.47
		6	0.009	0.47
		7	0.011	0.47
3.6×10^4	6.5×10^{17}	8	0.014	0.45
		9	0.016	0.47
		10	0.016	0.47
		11	0.014	0.47
1.5×10^5	2.8×10^{18}	15	0.025	0.50
		16	0.022	0.50
		18	0.024	0.50
2.2×10^5	3.9×10^{18}	22	0.024	0.50
		24	0.025	0.50
		25	0.025	0.49
3.6×10^5	6.5×10^{18}	12	0.031	0.50
		13	0.033	0.52
		14	0.032	0.51
3.7×10^5	6.7×10^{18}	19	0.031	0.51
		20	0.028	0.47
1.3×10^6	2.3×10^{19}	26	0.041	0.54
		28	0.043	0.55
2.8×10^6	5.0×10^{19}	29	0.048	0.64
		30	0.049	0.64
3.3×10^6	6.0×10^{19}	4	0.042	0.75
3.6×10^6* and 2.3×10^6†	1.2×10^{20}	33	−0.004	1.10
		34	−0.004	1.10
		35	−0.004	1.10

* At fast flux of 1.8×10^{13} nv.
† At fast flux of 2.4×10^{13} nv.
‡ Unirradiated value was 0.44° 2 θ.

exposure, 1.2×10^{20} nvt, a net decrease of 0.004 per cent below the pre-irradiation value resulted. The diffraction line profiles obtained from the three samples irradiated to 1.2×10^{20} nvt were identical. The method of peak separation outlined above was used in order to find the value of 2 θ. The accuracy of the lattice parameter determination was somewhat less than for the other samples and has been indicated by bracketing the data point in Fig. 1. In view of the high exposure lattice parameter change, other X-ray reflections were examined in order to determine if anisotropic dimension changes had occurred, especially in the most heavily irradiated specimens. No such evidence was found. Nor was there evidence of preferential line broadening. A calculation of the rate of increase of foreign atoms with irradiation time was carried out in order to evaluate possible effects due to the build-up of foreign atoms by transmutations. The average thermal flux was 10^{14} neutrons/cm^2/sec and the effects of n–α, n–p, n–γ, and n–$2n$ reactions were considered. The concentration c, of foreign atoms (primarily Nb, Tc, Ru, and Zr) was found to be related to the time in reactor t, by the following expression:

$$c = 6 \times 10^{-10} t$$

where c is atomic per cent and t is in seconds. Thus, at exposures of 2×10^{18}, 2.3×10^{19} and 1.2×10^{20}

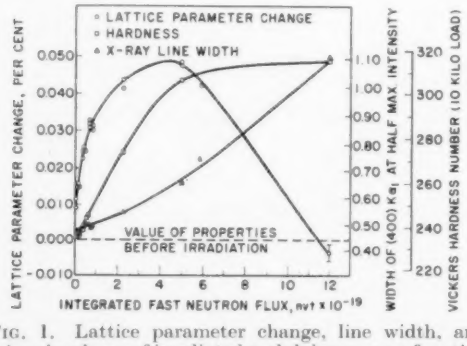


FIG. 1. Lattice parameter change, line width, and micro-hardness of irradiated molybdenum as a function of neutron exposure.

nvt the estimated concentration of foreign atoms from transmutations is 0.0001 per cent, 0.0008 per cent and 0.0035 per cent, respectively. These concentrations were negligible compared to the original impurity content of the molybdenum and therefore effects due to these additional impurities may be omitted in the discussion to follow.

DISCUSSION

Several irradiation effects are of note: (1) The rapid initial increase of lattice expansion, accompanied by very little line broadening or hardness change, (2) the maximum in the lattice parameter exposure curve, (3) the increase of line broadening with irradiation, (4) the breakover in the hardness-exposure curve and (5) the net lattice parameter contraction at the highest exposure. In considering these effects it seems apparent that the character of the damage is changing with continuing neutron exposure. During the bombardment, recombination or annihilation of existing damage must be occurring due to defect diffusion. There might also be changes in the defect distributions caused by the bombardment. The magnitude of measured properties, such as lattice parameter, line width and hardness, will depend upon the amount and kind of damage resulting during irradiation, and the shape of the property versus exposure curves will depend upon the atomic reactions which occur during irradiation since they are in essence a measure of the rate of build-up of various reaction products. The large increase of line width in molybdenum at high exposures, together with the increased hardness indicates that considerable damage has been retained as a result of the irradiations. The three exposure curves when compared point to the fact that the processes occurring during irradiation result in a complex type of damage.

Before presenting a model to explain the irradiation results in molybdenum, some recovery reactions which could take place during irradiation will be discussed from the standpoint of the manner in which the resulting defects will influence the net lattice parameter change with neutron exposure. Only two cases of thermal recovery during irradiation will be discussed: (1) Mutual interstitial–vacancy recovery, and (2) formation and growth of interstitial clusters. For the purpose of illustration it will be assumed that only single defects are produced by irradiation and that the defects are uniformly distributed throughout the material. The per cent lattice parameter change at any neutron exposure E will be represented by

$$A = A(I) + A(V)$$

where $A(I)$ = the per cent dimension change resulting from interstitial defects

and $A(V)$ = the per cent dimension change resulting from vacancies.

Case 1: *Annihilation of interstitials and vacancies.* Consider the situation where single interstitials and vacancies are produced in equal numbers and where mutual interstitial–vacancy annihilation is the only recovery reaction occurring during irradiation. The net lattice parameter change at a given exposure will be

$$A = a_i n_i - a_v n_v$$

where n_i and n_v are the instantaneous concentrations of interstitials and vacancies, respectively, and a_i and $-a_v$ are constants proportional to the dimension change caused by a single interstitial or vacancy, respectively. The constants a_i and $-a_v$ are assumed to be related by $a_i = ca_v$ where $|c| > 1$. If there is a fixed relationship between n_i and n_v during irradiation, then the net lattice expansion will always be linearly proportional to the defect concentration. The appearance of the lattice parameter exposure curve will be similar to that shown in Fig. 2. The two components $A(I) = a_i n_i$ and $A(V) = -a_v n_v$ are shown as dotted lines which both approach a limiting value as the rate of defect recovery approaches the rate of defect production in the reactor. The resultant lattice parameter curve A is shown as a solid line and also approaches a limiting value. At any given exposure $A = kn_i = kn_v$, where $k = [1 - (1/c)]a_i$. It is seen that under the conditions outlined above A will always be positive, but that A vs. E will not pass through a maximum.

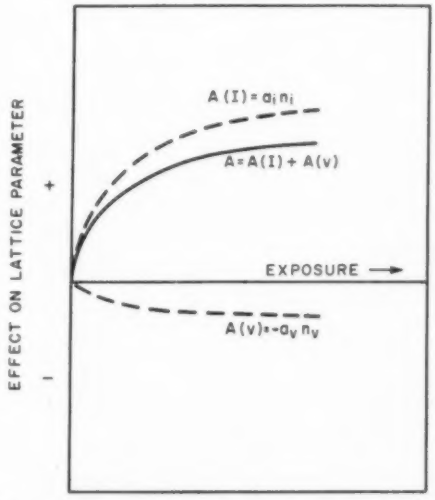


FIG. 2. Appearance of a lattice parameter neutron exposure curve when mutual interstitial–vacancy annihilation occurs during irradiation (schematic).

VOL. 8 1960

Case 2: Formation of interstitial clusters. Consider the situation where (1) the interstitials are mobile, (2) interstitial vacancy annihilation is negligible, (3) interstitial cluster formation begins shortly after the initial exposure and (4) the average cluster size increases during irradiation. At any exposure E, there will be a number of cluster sizes present in various concentrations. Suppose that x is the effective cluster size and n_{ix} the effective cluster concentration, then

$$xn_{ix} = n_v.$$

For a single interstitial $x = 1$. The lattice parameter expansion at any exposure E, is given by

$$A = a_{ix}n_{ix} - a_v n_v \quad \text{and} \quad \frac{A(I)}{A(V)} = -\frac{a_{ix}}{xa_v},$$

where a_{ix} is proportional to the dimension change of a cluster of size x. It is reasonable to suppose that initially a_{ix} increases slowly with regard to x, and that a point may be reached where a_{ix} is essentially constant over several values of x. With large x, depending upon the geometry of the cluster, the term a_{ix} may in fact begin to decrease with increasing x. All of these effects tend to reduce the ratio $A(I)/A(V)$ of interstitial contributions to vacancy contributions, with the result that $A(V)$ would be changing faster than $A(I)$ with increasing effective cluster size x. Thus, when cluster size is increasing, the net lattice parameter change A should pass through a maximum with increasing exposure and even become negative at high exposures. A schematic illustration of how the growth of interstitial clusters during irradiation might affect the lattice parameter exposure curve is shown in Fig. 3. The vacancy term $A(V)$ is shown to decrease almost linearly while the interstitial term $A(I)$ is shown as approaching a limiting value as x increases. When the two curves are summed, the curve A of Fig. 3 results and it can be seen that it bears a resemblance to the lattice parameter data of Fig. 1. A point of interest regarding clustering is that the effective cluster size must increase with exposure in order for A to maximize with increasing exposure.

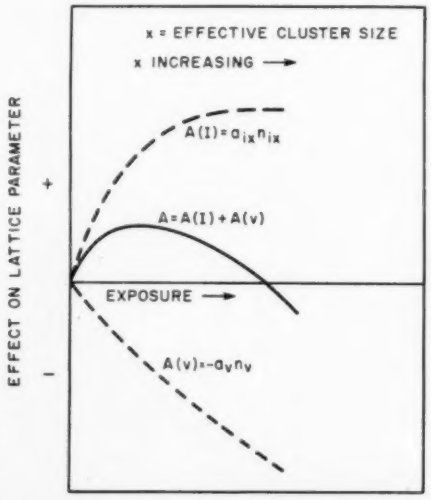


FIG. 3. Appearance of a lattice parameter neutron exposure curve when interstitial cluster growth occurs during irradiation (schematic).

Two cases of residual damage build-up have been discussed in order to illustrate the effects of certain recovery reactions upon the shape of the lattice parameter exposure curve. Although a simple type of damage was assumed, in order to isolate effects, it was possible to show that the growth of interstitial clusters can cause a maximum in the lattice parameter exposure curve. Now inspection of the data in Fig. 1 shows that in the low exposure region below 10^{19} nvt interstitial clustering cannot be the predominant reaction since the lattice parameter increases rapidly with little accompanying change in hardness or line broadening. Above 10^{19} nvt where line broadening increases, hardness increases, and where lattice parameter passes through a maximum, interstitial clustering becomes important. Since the concept of interstitial cluster growth is valid for molybdenum, it can be inferred that the interstitial atoms produced by neutron bombardment are mobile at the irradiation temperature. All these effects will be dealt with below.

It might be mentioned here that recovery of neutron damage below 35°C has been investigated by Kinchin and Thompson[3] who observed changes in the electrical resistance of molybdenum irradiated with neutrons at −196°C. After irradiation to $\sim 10^{18}$ nvt, a recovery process was noted at −170°C and was followed by gradual recovery up to and above 35°C. The inference that interstitials are mobile during irradiation at 35°C is in accordance with their findings.

Returning to the damage effects which occur below 10^{19} nvt or so, it is necessary to determine in what manner the interstitials can be retained after irradiation at 35°C. Neutron damage may produce a variety of defects such as interstitials, vacancies, interstitial clusters, vacancy clusters, etc. Thus in the early stages of irradiation there are several possible recovery reactions which the mobile interstitials can undergo. In addition to reacting with defects produced by irradiation the interstitials may also react with defects present before neutron irradiation such as small substitutional impurity atoms. The molybdenum used in this experiment contained a large

number of impurity atoms and these, too, must be considered as sinks for mobile interstitials.

Calling an interstitial I, a vacancy V, an interstitial cluster I_x, a vacancy cluster V_x (where x is the cluster size), a small substitutional impurity atom T, a trapped interstitial TI, etc., the primary possibilities for recombination are:

(1) $I + V =$ annihilation
(2) $I + I = I_2$
(3) $I + T = TI$
(4) $I + I_x = I_{x+1}$
(5) $I + V_x = V_{x-1}$.

If the five reactions were to proceed simultaneously, the rate of disappearance of interstitials would depend upon their instantaneous concentration, the instantaneous concentration of reactants and the reaction probabilities or cross-sections for interstitial capture of the various reactants. The relative rate at which any one of the reactions will go will also depend upon these factors. On the basis of concentration alone reactions (4) and (5) can probably be eliminated as major recovery steps below 10^{19} nvt. This leaves reactions (1) to (3). We know $n_t \gg n_i$ and $n_t \gg n_v$ in the initial stages of irradiation. We also know that there are several types of small substitutional impurities in the molybdenum used for this experiment, and that some of these impurities may be more effective in trapping interstitials than others. If the average interstitial capture cross-section of these small impurities is less than that of vacancies and greater than that of interstitials then reaction (3) should occur simultaneously with reaction (1), and it is expected that both of these reactions will proceed much faster than reaction (2).

Previous annealing studies[2] on the low exposure molybdenum have shown that in the temperature range from 100° to 200°C there is a reaction characterized by first order kinetics and accounting for recovery of 20–30 per cent of the residual expansion. This reaction was due to the trapping of interstitials at small impurity atoms. The reaction though fairly sluggish at 100°C could be supposed to have proceeded rapidly during irradiation at 35°C. An alternate possibility is that the reaction was due to release and re-trapping of defects trapped at the irradiation temperature. In either case defect trapping is known to occur in molybdenum above 35°C, and from the exposure data and annealing data is expected to occur during irradiation.

It was mentioned earlier that the molybdenum irradiated by Adam and Martin[1] showed less residual expansion than that irradiated here. If trapping does occur during the initial stages of irradiation one could expect the initial portion of the lattice parameter curve to depend in part upon impurity content. A comparison of that data with the present data indicated that the differences in residual expansion could be correlated with impurity content. Some typical order of magnitude values taken from expansion vs. exposure curves are itemized in Table 2. From Table 2 it may be seen that residual expansion increases with increasing impurity content. This type of behavior is just what can be expected if interstitials are trapped during low exposure irradiations, since as the number of trapping sites is increased the fraction of interstitials trapped will also increase. As the number of traps is decreased, the number of interstitials being annihilated at vacancies will increase. This is conclusive evidence that interstitial trapping occurs in the initial stages of irradiation at 35°C.

In the low exposure region from 6.5×10^{16} to 10^{19} nvt it is concluded that while neutron irradiation is taking place, the single interstitials produced by the bombardment are migrating primarily to vacancies and to small impurity atoms. The lattice expansion is due principally to the difference between the expansion caused by trapped interstitials and the contraction resulting from lattice vacancies. The small amount of line broadening is attributed to the presence of a few clusters produced either at the

TABLE 2. Effect of impurity content upon residual expansion of irradiated molybdenum

Reference	Molybdenum impurity content	Expansion at 6×10^{18} nvt	Expansion at 1.5×10^{19} nvt
(1)	None detected spectroscopically	0.003%*	0.008%*
(1)	0.01% Fe	0.010%†	0.020%†
(2) and present work	0.09%	0.030%*	0.038%*

* From lattice parameter measurements.
† From macroscopic linear dimension measurements.

VOL. 8 1960

trapping sites by diffusion or by neutron bombardment. The hardening may be principally due to these multiple defects.

Cluster growth becomes important at exposures above 10^{19} nvt. It is here that lattice parameter approaches a maximum while hardness increases rapidly and it is here that line width begins to increase significantly. There are at least two sites for cluster nucleation and growth: (1) the trapped interstitials or (2) immobile interstitial clusters produced by the neutron bombardment. There is a strong possibility that cluster growth begins at the sites of trapped interstitials. There are several reasons for thinking so. First, the hardness curve in relation to the lattice parameter curve indicates that cluster formation is rapid after 10^{19} nvt. For rapid cluster formation there should be a large number of available sites. There are a large number of trapped interstitial sites. The build-up of immobile clusters produced by irradiation appears to be small initially, as seen from the line broadening. Therefore, much of the initial cluster formation may occur at trapped interstitials forming defects of the TI_x type. As the TI_x formation progresses there will be a simultaneous build-up of immobile defects produced by the irradiation itself. As the single interstitials become annihilated at vacancies or form clusters, these immobile defects will account for an increasing proportion of the total damage. Among these immobile defects there will be some of the I_x type, which will supply new sources for cluster growth. As irradiation progresses it is expected that cluster growth will occur at either type of site. In this manner a considerable amount of damage can be retained with extended exposures.

The continued increase in line width over the entire range of exposures may be interpreted as evidence that both the cluster size and number is increasing with neutron exposure. This would support the idea that the clustering effect is due to the constant production of highly immobile defects in addition to those being formed by interstitial diffusion. The hardness curve is apparently dependent upon cluster size and concentration since it is in the region where clustering becomes important that the largest hardness increases are sustained. The breakover in the hardness exposure curve indicates that a point has been reached where further cluster formation has no effect in hardening the molybdenum.

The fact that interstitial cluster growth occurs during irradiation implies that the cross-section for interstitial capture of the trapped interstitials and of the interstitial clusters themselves is large. For if the number of single vacancies produced by neutron irradiation is comparable to the number of single interstitials, the growth of interstitial clusters is going to result in an excess of single vacancies. In that case if interstitial clustering is going to proceed preferentially, the interstitial capture cross-section of the new defects must be large, in fact it may increase with increasing cluster size. This circumstance poses some interesting questions regarding such things as the cluster geometry and effective size.

To summarize, the following conclusions are drawn from this investigation:

(1) Interstitials are mobile at the irradiation temperature.

(2) In the initial stages of irradiation ($<10^{19}$ nvt) the predominant interstitial recovery reactions are annihilation at vacancies and trapping at small substitutional impurity atoms.

(3) At moderate and high exposures ($>10^{19}$ nvt) formation and growth of interstitial clusters predominates.

The interstitial clustering is postulated to result from: (1) Diffusion of interstitials to the sites of trapped interstitials, i.e. to TI sites which then become TI_x sites, and (2) by diffusion of interstitials to clusters formed by the neutron bombardment itself. In a material which contains a large number of trapping sites the first mode of formation should govern the early stages of clustering, but in a material with only a few trapping sites, the cluster formation will be due to the second process. Thus, for comparable exposures, it could be expected that the number of clusters would decrease with increasing purity.

These postulates may be checked by varying impurity content, irradiation temperature and neutron flux in order to evaluate the role of (1) impurity atoms as trapping and cluster sites, (2) interstitial diffusion in determining cluster growth rate and (3) immobile irradiation produced defects in determining cluster growth rate and property changes.

ACKNOWLEDGMENT

The authors wish to thank M. L. Sorick for assistance in the X-ray work.

REFERENCES

1. J. Adam and D. G. Martin, *Phil. Mag.* **3**, 1329 (1958).
2. D. L. Gray, *Acta Met.* **7**, 431 (1959).
3. G. H. Kinchin and M. W. Thompson, *J. Nucl. Energy* **6**, 275 (1958)

THE INFLUENCE OF STRAIN AMPLITUDE ON THE WORK HARDENING OF COPPER CRYSTALS IN ALTERNATING TENSION AND COMPRESSION*

D. S. KEMSLEY† and M. S. PATERSON‡

For a given cumulative strain, the work hardening of copper crystals in alternating straining is always less than in a tensile test. At a plastic-strain amplitude of 0.0001, the hardening is very low and nearly the same for all orientations. For larger amplitudes the behaviour varies widely with orientation; in general, the rate of work hardening increases steadily with strain amplitude, but for orientations away from [110] there is a sharp increase in hardening rate above a certain amplitude. In this rapid hardening stage, prominent secondary slip is observed, which is otherwise absent.

It is suggested that there are two principal mechanisms of hardening: (1) a basic hardening similar to that in stage I of tensile tests, during which slip is mainly confined to the primary plane; (2) a rapid hardening, resulting from extensive obstruction of the primary slip by slip on secondary planes. The mutual interference of slip in two directions in the primary plane may also be important for some orientations.

L'INFLUENCE DE L'AMPLITUDE DE LA DEFORMATION SUR LE DURCISSEMENT DE CRISTAUX DE CUIVRE EN TENSION ET COMPRESSION ALTERNEES

Pour une déformation cumulative donnée, le durcissement de cristaux de cuivre en déformation alternée est toujours inférieur à celui obtenu au cours d'un essai de traction. Pour une amplitude de déformation plastique de 0,0001, le durcissement est très faible et pratiquement identique pour toutes les orientations. Pour des amplitudes plus grandes, le comportement varie grandement avec l'orientation. En général, la vitesse dedurcissement s'accroît régulièrement avec l'amplitude de la déformation mais pour des orientations autres que [110] on observe une augmentation importante de la vitesse de durcissement au-delà d'une certaine valeur de l'amplitude.

Au cours de ce durcissement rapide, on observe l'apparition de glissements secondaires inexistants dans les autres cas. Les auteurs suggèrent qu'il existe deux mécanismes principaux de durcissement:

1°—un durcissement principal identique à celui qui apparaît au cours du premier stade des essais de traction. Dans ce cas, le glissement intervient principalement sur le plan primaire.

2°—un durcissement rapide qui résulte de ce que la propagation du glissement primaire est contrariée par des glissement sur des plans secondaires.

Pour certaines orientations, l'interaction mutuelle de glissement dans deux directions du plan principal peut également présenter une certaine importance.

EINFLUß DER VERZERRUNGSAMPLITUDE AUF DIE VERFESTIGUNG VON KUPFERKRISTALLEN BEI WECHSEL VON ZUG UND DRUCK

Für eine gegebene Gesamtverzerrung ist die Verfestigung von Kupferkristallen bei Wechselbeanspruchung immer geringer als im Zugversuch. Bei einer Amplitude der plastischen Verzerrung von 0.0001 ist die Verfestigung sehr gering und fast dieselbe für alle Orientierungen. Für größere Amplituden hängt das Verhalten stark von der Orientierung ab; im allgemeinen nimmt die Verfestigung mit der Verzerrungsamplitude gleichmäßig zu, aber für Orientierungen, die von [110] entfernt sind, ergibt sich oberhalb einer gewissen Amplitude ein scharfer Anstieg. Bei diesem schnellen Verfestigungsanstieg beobachtet man sekundäre Gleitung, die sonst fehlt.

Zwei hauptsächliche Verfestigungsmechanismen werden vorgeschlagen: (1) eine Grundverfestigung ähnlich der im Teil I bei Zugversuch, während der sich die Gleitung hauptsächlich auf die primäre Gleitebene beschränkt; (2) eine schnelle Verfestigung, bei der Gleitung in sekundären Ebenen die Gleitung in der primären Ebene sehr stark behindert. Für einige Orientierungen mag auch die Wechselwirkung von zwei Gleitrichtungen in der primären Gleitebene von Bedeutung sein.

VOL. 8 1960

INTRODUCTION

The plastic deformation of single crystals of metals in unidirectional straining has been extensively investigated under various conditions of orientation, temperature, impurity content, etc., and the experimental results form the main basis for current theories of work hardening. From experiments with a single reversal of the direction of straining, it is also well-known that the work hardening that raises the yield stress for further straining in the same sense is less effective in raising the yield stress for subsequent straining in the opposite sense (Bauschinger effect). However, the effects of *repeatedly* reversing the direction of straining (alternating straining) have received much less attention.

Experiments on the work hardening of single crystals of metals during slow alternating straining have been done by Held[1] and Scholl[2] (shear tests on tin and aluminum respectively) and by Thompson *et al.*[3], Charsley and Thompson[4] and Paterson[5] (tension-compression experiments on aluminum, aluminum and copper respectively). The experiments of

* Received August 20, 1959.

† Formerly Department of Geophysics, The Australian National University, Canberra, Australia; seconded from Aeronautical Research Laboratories, Department of Supply, Melbourne, Australia. Now at The Queen's College, Oxford, England.

‡ Department of Geophysics, The Australian National University, Canberra, Australia.

Thompson *et al.* were done at constant stress amplitude, while in those of Held, Scholl and Paterson the plastic strain amplitude was constant. In most cases, the occurrence of progressive hardening during alternating straining was demonstrated. Similarly, work hardening during alternating straining has also been observed in polycrystalline metals by Wood and Segall[6], and Dugdale[7]. For a given strain, there is, in general, less hardening in alternating straining than in unidirectional straining. Similarly, alternating straining gives rise to less X-ray line broadening.[8]

In the previous work on copper crystals by one of the authors,[5] the influence of orientation on the behaviour in alternating tension and compression was studied at one plastic strain amplitude and effects akin to the "easy glide" in tensile tests were observed. In the present experiments, the influence of the amplitude of the plastic strain has been studied for various orientations.

PREPARATION OF SPECIMENS

The specimen material was copper of 99.999 per cent purity, prepared by Messrs. Johnson, Matthey and Co. and drawn to wire of 1.5 mm diameter by them. After etching, single crystals were grown from the melt at a rate of 3.75 cm/hr, using a travelling furnace inclined at about 60° to the horizontal. A very slight taper (about 1 in 3000) in the spectrographically pure graphite moulds ensured that crystals could be removed without sticking.

The orientations selected for study are shown in Fig. 1; one seed crystal of each orientation was used in growing the specimens. The orientation of each specimen was determined by the back-reflection Laue X-ray method to within about $\pm 1°$ and departures from the seed orientation did not obviously exceed this. There was no metallographic evidence for mosaic structure in the specimens, although mosaic boundaries had been observed, after electropolishing, in two crystals grown at a rate of 12 cm/hr. A 4-cm length of crystal, sufficient for two specimens, was grown from the seed each time. The specimens were cut off with nitric acid on a reciprocating thread and were then electropolished in a solution of orthophosphoric acid for 30 min.

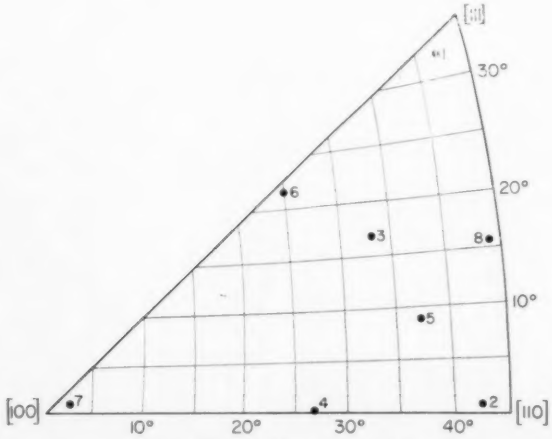


FIG. 1. Orientations of crystals.

The specimens were about 1.5 mm in diameter and the free length after mounting in the testing machine was about 7 mm. The length and diameter measurements were made optically.

EXPERIMENTAL METHODS

The same testing machine was used as in the earlier work.[5] It has been described in detail elsewhere.[9] Strictly axial tensile and compressive loads could be applied at rates similar to those used in normal tensile testing. Discontinuities in the measured load and extension when passing from tension to compression or vice versa were eliminated in the design of the gauges. The previous method of gripping the specimens was again used; firstly a steel shoulder, cemented to one end of the specimen, was clamped in the machine and then the other end of the specimen was set in solder.

During the cyclic straining, allowance was made for elastic strains to ensure that the plastic strain amplitude remained constant throughout a given test. By noting the peak tensile and compressive loads, it was possible to derive a strain-hardening curve in which the peak resolved shear stress was plotted against the total absolute (cumulative) glide strain.

The time taken to reach a cumulative glide strain of 0.6 varied from about 20 min for the largest strain amplitude to about 3 hr for the smallest. These variations in length of test are considered to be unimportant, since measurements made at the larger amplitudes after rest periods of up to 8 days gave no evidence of recovery.

Duplicate tests were made for all orientations. Additional tests were made when marked variability in results was obtained.

EXPERIMENTAL RESULTS

(a) *Work-hardening curves*

In Fig. 2(a)–(h), the peak resolved shear stress is plotted against the cumulative glide strain (that is, the number of half-cycles times the plastic glide strain amplitude) for tests on copper crystals of the orientations shown in Fig. 1. For each orientation, curves are given for strain amplitudes of 0.02,

VOL. 8 1960

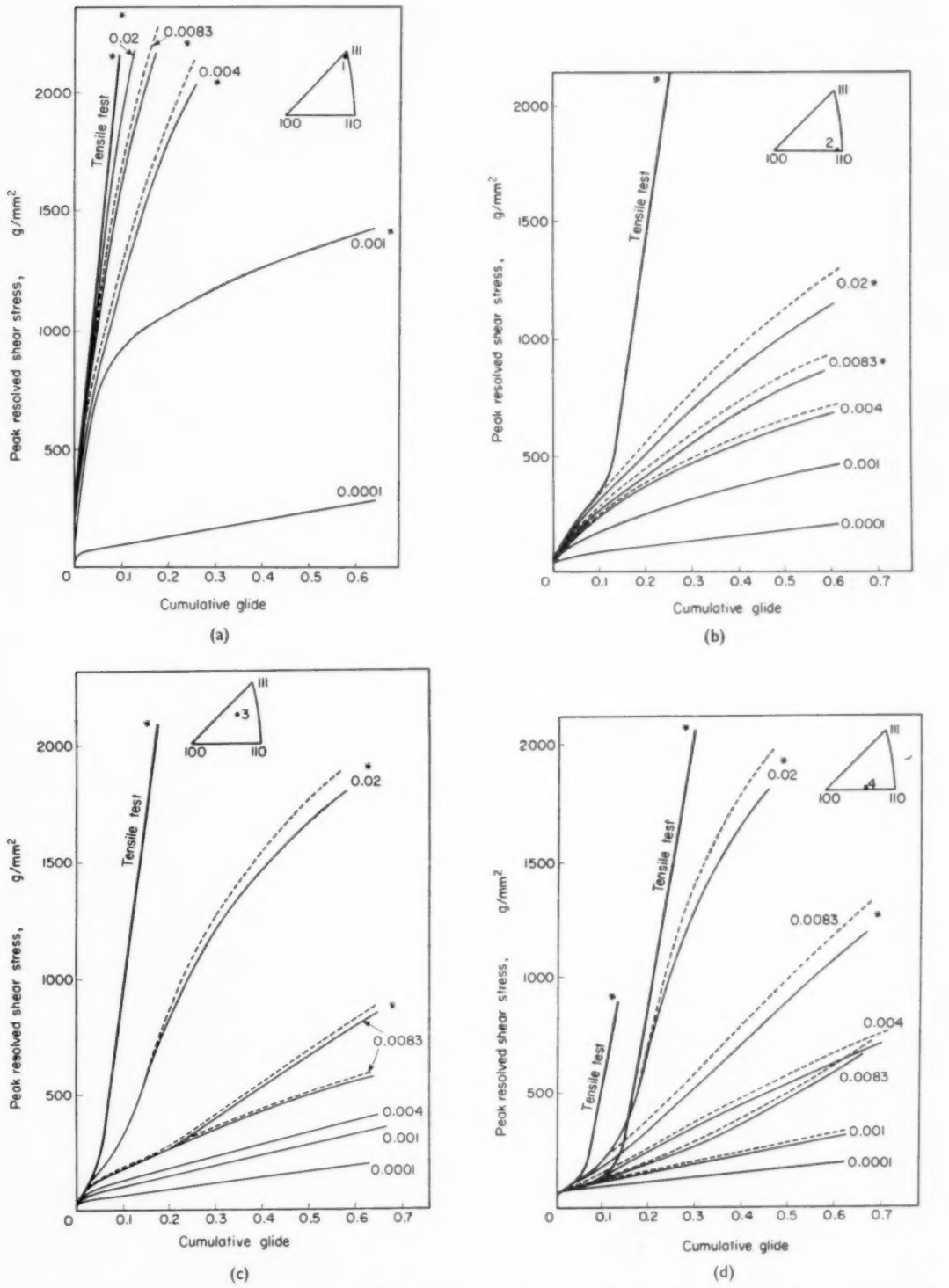


FIG. 2. Work hardening curves for different orientations; the numbers indicate the plastic-strain amplitude. * indicates Kossel lines in Laue photographs. – – – compressive half-cycles. ——— tensile half-cycles.

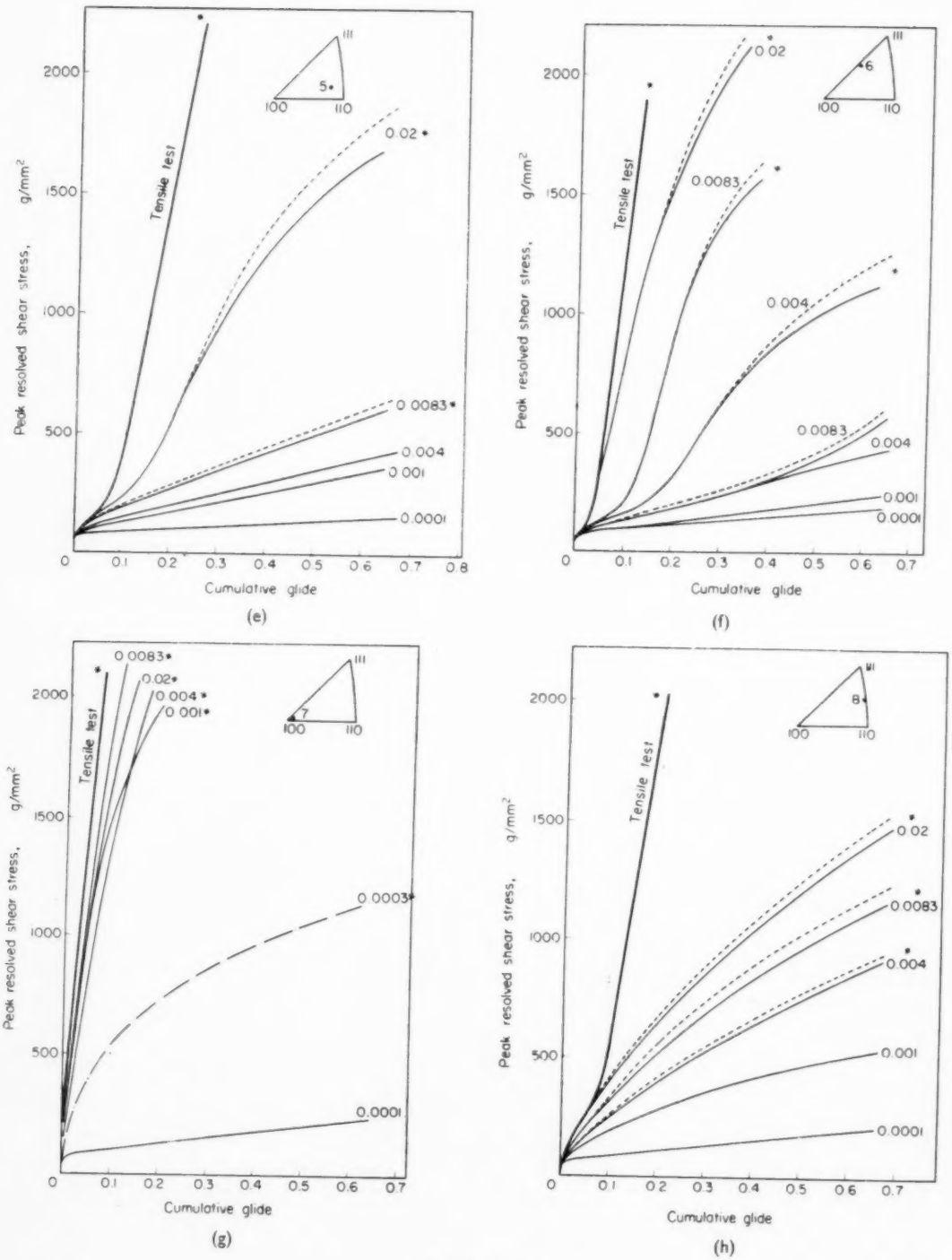

Peak resolved shear stress, g/mm²
Cumulative glide
Tensile test
0.02
0.0083
0.004
0.001
0.0001
0.0003
(e)
(f)
(g)
(h)

FIG. 2 (*contd.*)

0.0083, 0.004, 0.001 and 0.0001, expressed as plastic shear strain resolved on the primary glide system. The results of tensile tests are also shown in the same figures.

In most cases, the results of repeat tests under the same conditions agreed within about 10 per cent and only the lower curves have been given in the figures. In the cases in which the reproductibility was poor, the highest and lowest curves are given; there was some irregular behaviour in orientation 3 at amplitude 0.0083 (Fig. 2c), but excessive variability was only encountered in orientation 4 at amplitude 0.0083 (Fig. 2d) and in orientation 6 at amplitudes 0.0083 and 0.004 (Fig. 2f). Such variability in behaviour was noticed for similar orientations in the previous work[5] on copper at amplitude 0.0083 and also in tensile tests on aluminum by Davis *et al.*[10]. The maximum variability found in the present tests is illustrated in Fig. 3, which gives the work-hardening curves for four crystals of orientation 6 at amplitude 0.0083. This behaviour suggests an inherent instability in the work-hardening process under these conditions, rather than a greater sensitivity to handling, since the early parts of the work-hardening curves, and especially the critical shear stress values, are closely reproducible; moreover, the reproducibility of results for the same orientations at small amplitudes was good.

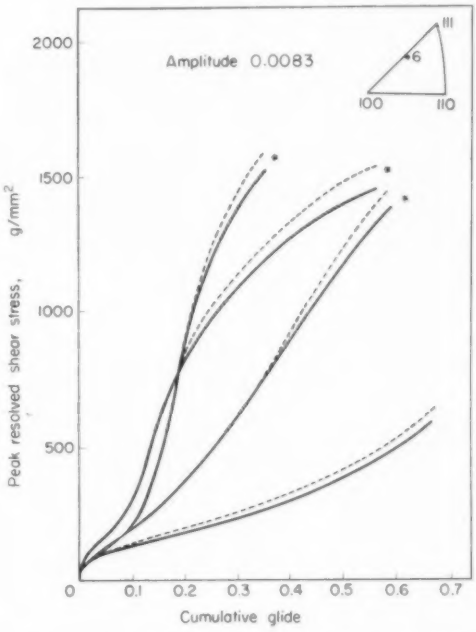


FIG. 3. Variability of work hardening for orientation 6 at amplitude 0.0083. * indicates Kossel lines in Laue photographs.
– – – compressive half-cycles.
——— tensile half-cycles.

As in the previous work,[5] it was generally observed that the yield stress in compression increased slightly more rapidly than that in tension, regardless of whether the first half-cycle was compressive or tensile. Therefore, the curves for the tensile and compressive half-cycles have been plotted separately in Fig. 2(a)–(h). The difference is usually negligible at small amplitudes, but it tends to increase with cumulative strain at the larger amplitudes. The results of tests on polycrystalline copper showed a similar trend but the effect was smaller. No instrumental factor has been found which could produce such an effect; in alternating-straining tests on a steel specimen in the elastic range, no significant zero-shift was observed.

Comparison of Fig. 2(a)–(h) shows the very strong influence of orientation on the work hardening of copper crystals in alternating straining. The results at strain amplitude 0.0083 are in excellent accord with those of the previous work,[5] which showed that crystals with orientations near the [111] and [100] corners of the stereographic triangle work harden much more rapidly than those near the [110] corner, while there is intermediate behaviour for other orientations; a double inflexion in the work-hardening curves occurs for some orientations, especially those near the centres of the [100]–[111] and [100]–[110] boundaries. The new results for other amplitudes show a similar influence of orientation, which is seen to be very important at all amplitudes except the lowest.

The strain amplitude has a very striking influence on the work hardening. For a given orientation, the trend is always for the work-hardening curve to be lower for smaller amplitudes. However, the details depend on the orientation. For the orientations near [100] and [111], the work-hardening curves for alternating straining do not depart markedly from the tensile curves until the strain amplitude is less than about 0.001; however, decreasing the amplitude below 0.001 results in a radical lowering of the work-hardening curve (Fig. 2a and Fig. 2g). This abrupt change in work-hardening behaviour occurs at a slightly lower amplitude for orientation 7, near [100], than for orientation 1, near [111]; thus, extra experiments at strain amplitude 0.0003 for orientation 7 (Fig. 2g) reveal a behaviour similar to that at strain amplitude 0.001 for orientation 1.

For orientation 2, near [110] (Fig. 2b), the course of work-hardening at amplitude 0.02 is already well below the tensile curve (except for the easy glide region). With decreasing strain amplitude, there is a regular lowering of the work-hardening curve. Similar

VOL. 8 1960

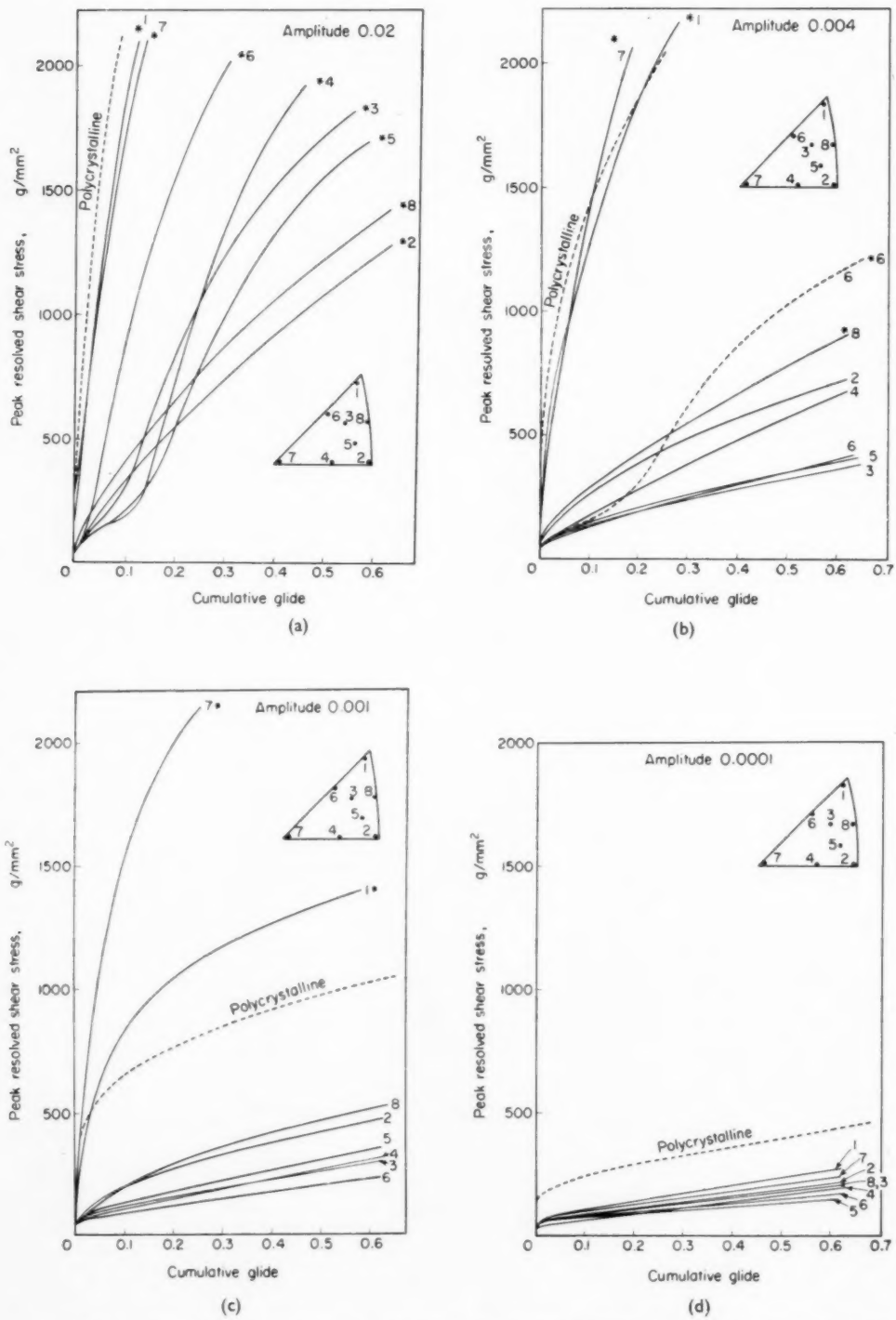


FIG. 4. Work hardening curves for different plastic-strain amplitudes; the numbers indicate the orientations. * indicates Kossel lines in Laue photographs.

behaviour is observed for orientation 8 (Fig. 2h), near the middle of the [110]–[111] boundary.

For the other orientations (Fig. 2e–f), the work-hardening curve obtained at amplitude 0.02 has a double inflexion, like the tensile curve but with very little intermediate "linear" part; its course is only slightly below the tensile curve for the orientations near the boundaries (4 and 6) but departs more for the others (3 and 5). The tendency for the work-hardening curve to be double-inflected persists to lower amplitudes for the orientations near the boundaries and is associated with the marked variability of behaviour mentioned previously. At low amplitudes, the behaviour for all these orientations is regular, like that of orientation 2.

The influence of orientation on the work hardening at a given amplitude is shown more clearly in Fig. 4(a)–(d) in which curves from Figs. 2(a)–(h) have been replotted, averaging the results for tensile and compressive half-cycles. Thus it is seen that, at amplitude 0.02, the inflected curves for orientations 3, 4, 5 and 6 lie wholly below the curves for the orientations near [111] and [100]; however, while they also fall initially below the curve for the orientation near [110], the upward inflexion takes them above it. At amplitudes below about 0.004, the upward inflexion is absent and the course of work-hardening for the orientations 3, 4, 5 and 6 is now wholly below that for the orientation near [110] and

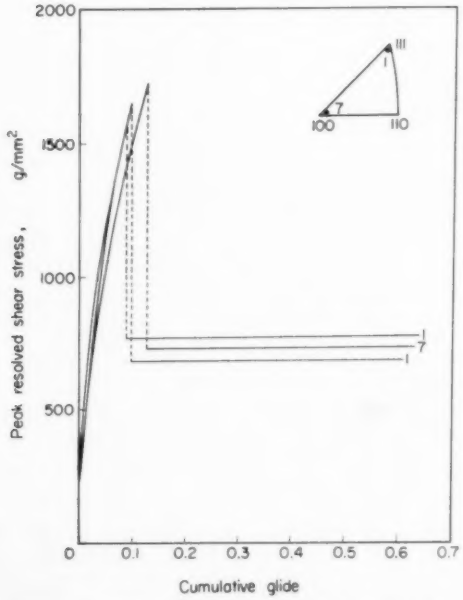


FIG. 5. Effect of change of amplitude on work hardening for orientations 1 and 7; initial amplitude 0.0083 and 0.004 respectively, subsequent amplitude 0.0001 in each case.

depends only slightly on amplitude. The work-hardening curve for the orientation near [110] always falls below the curves for the orientations near [111] and [100]. However, for all orientations at amplitude 0.0001 the work-hardening rates are very low and probably the same, within experimental error.

(b) *Change of amplitude*

In three experiments on crystals oriented near [111] and [100], alternating straining at an amplitude giving rapid hardening up to a peak resolved shear stress of about 1500 g mm^{-2} was followed by straining at amplitude 0.0001 (Fig. 5). Two specimens of orientation 1 were strained initially at amplitude 0.0083; the third specimen, of orientation 7, was strained initially at amplitude 0.004. In each case, there was no work hardening (or softening) during the subsequent straining at amplitude 0.0001; however, the stresses were higher than those shown in Fig. 4(d) because of the increased yield stress resulting from the prior straining at larger amplitude.

TABLE 1. Critical shear stresses

Orientation no.	Critical shear stress (g mm^{-2})	Standard deviation	Number of tests
1	42	7	16
2	25	4	13
3	28	5	14
4	25	3	16
5	27	4	12
6	30	4	15
7	38	7	14
8	26	4	12

(c) *Critical shear stress*

In each experiment the critical shear stress was determined by plotting the initial part of the stress–strain curve in the first half cycle and noting the point at which it departed clearly from the elastic line. The results are given in Table 1. There appears to be a significant departure from the Schmid law only for orientations 1 and 7, near [111] and [100] respectively. Excluding these, the average value is 27 g mm^{-2}, which is lower than previously published figures. The reason for this figure being lower than the values obtained by Paterson[5] with the same apparatus is not clear but is presumed to be connected with minor improvements in the technique of preparing the crystals, although this is not reflected in the work-hardening behaviour.

(d) *Microscopic observations*

After testing, each specimen was examined under simple vertical illumination and photographed at 200 magnification. The curvature of the surface made

VOL. 8 1960

phase-contrast microscopy unsatisfactory but was of advantage in providing conditions of oblique illumination at the edge, thereby helping in the observation of fine slip. It was also found that fine slip was more readily recognized in photographs than visually.

In general, the features observed on tensile specimens were similar to those described by previous workers.[11,12] Alternating straining at larger amplitudes produced some of the same features but no kink bands.

For the orientations near [111] and [100], tensile specimens showed strong clustering of the slip on one or more systems, with fine slip also evident between the clusters, giving a mottled appearance (Fig. 6a). After alternating straining at amplitude 0.02, specimens of these orientations showed the same features but the slip lines were more sharply defined and the mottling was greatly reduced (Fig. 6b). At smaller strain amplitudes, the clustering of the slip and the presence of more than one slip system persisted until the amplitude was reduced below 0.004 for orientation 1 and below 0.001 for orientation 7; the slip lines became progressively less prominent as the strain amplitude was reduced but their spacing did not obviously change. For both these orientations, only one set of very faint slip lines could be seen at amplitude 0.0001 (Fig. 6c). The disappearance of secondary slip below a certain strain amplitude is correlated with the striking lowering of the work-hardening curve mentioned previously.

For orientations 2, 3, 5 and 8, the clustering of the primary slip in tensile specimens was slight (orientation 2, Fig. 7a) or absent (orientations 3, 5 and 8); the secondary slip was uniformly distributed for orientation 2 but occurred in bands for orientations 3, 5 and 8. In the alternating straining tests no secondary slip was observed at any amplitude for these orientations, and the primary slip was always uniformly distributed (Fig. 7b and Fig. 7c). With decreasing amplitude, the slip lines became less prominent until they were scarcely discernible at the lowest amplitude, but their spacing did not obviously change.

For orientation 4, tensile specimens showed bands of secondary slip but the primary slip was not markedly clustered (Fig. 8a). In alternating straining tests, secondary slip was observed at amplitude 0.02 (Fig. 8b); there was also another set of secondary slip lines in one part of the specimen that gave the highest hardening curve at amplitude 0.0083. The other specimens tested at amplitude 0.0083 and all specimens tested at lower amplitudes showed only uniform primary slip, the prominence of which diminished as the amplitude decreased (Fig. 8c).

For orientation 6, tensile specimens showed duplex slip, with some clustering of the main set of slip lines. Duplex slip also occurred in specimens subjected to alternating straining at amplitude 0.02. At amplitudes 0.0083 and 0.004, duplex slip was observed in the specimens giving high hardening rates; the other specimens tested at these amplitudes and all specimens tested at lower amplitudes showed only primary slip, which was fainter for smaller amplitudes.

Thus for orientations 4 and 6, the variable behaviour at the intermediate amplitudes can be correlated with a variation in slip pattern, a high work-hardening curve being associated with the appearance of marked secondary slip.

(e) *X-ray observations*

A Laue X-ray photograph was taken for each specimen after testing, using a simple back-reflection technique with a film-to-specimen distance of 3 cm. The usual asterism of Laue spots was present after tensile testing, but no asterism was observed after alternating straining, even at amplitude 0.02.

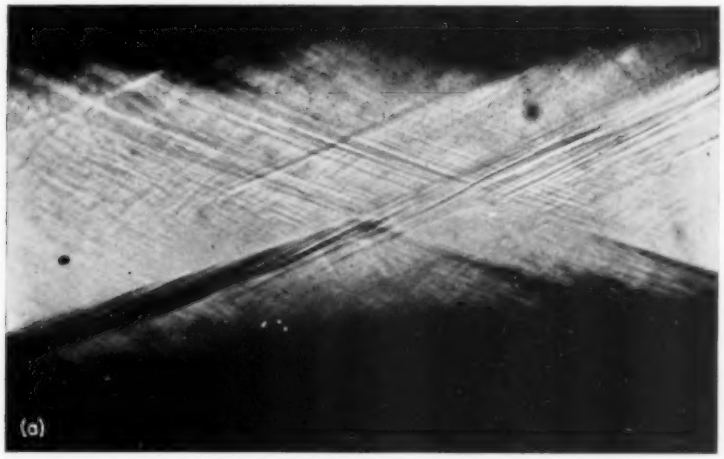
The appearance of well-defined Kossel lines in Laue photographs in certain cases after alternating straining has been discussed in the previous paper.[5] In the present work, Kossel lines have been observed for specimens tested in tension and in alternating straining at the larger amplitudes (see curves marked with asterisks in Figs. 2–4).

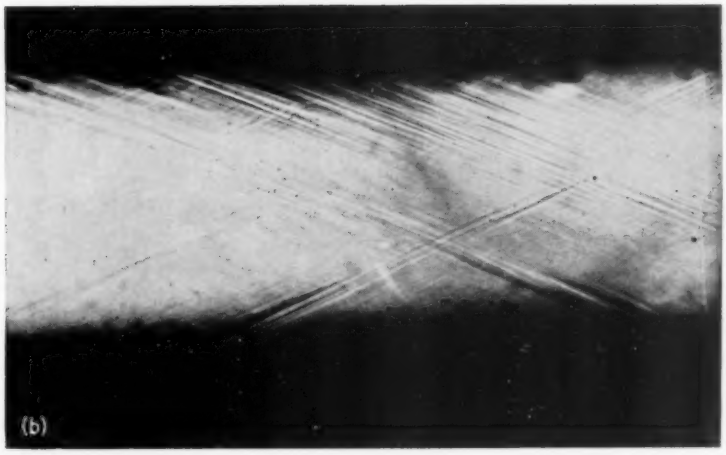
The Kossel lines were clearest after alternating straining of specimens of orientations 1 and 7 (near [111] and [100] respectively) at amplitudes for which the hardening rate was very high; they were not observed at amplitude 0.0001 for these orientations. Similarly for other orientations, Kossel lines were observed in both tensile and alternating straining when the hardening rate was fairly high (such that the stress was raised above about 1500 g mm^{-2} in the course of the test) but they were otherwise absent.

(f) *Tests on polycrystalline copper*

For comparison, tensile and alternating-straining tests were also made on polycrystalline copper. The specimen dimensions and material were the same as for the single crystals. The specimens were prepared by annealing the drawn wire in a vacuum at 900°C and had a grain size of about 0.2 mm. X-ray photographs showed no appreciable preferred orientation in the specimens. The testing procedure was the same as for the single crystals.

The axial normal strain amplitudes were chosen to be equal to 0.435 times the resolved shear strain amplitudes used in the single crystal tests; this is





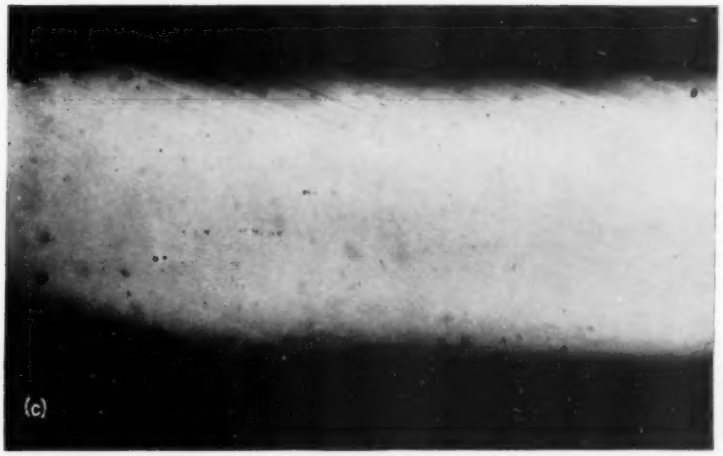


FIG. 6. Photomicrographs of specimens of orientation 1 after straining. ×200. (a) Tensile; (b) alternating straining, amplitude 0.02; (c) alternating straining, amplitude 0.0001.

VOL. 8 1960

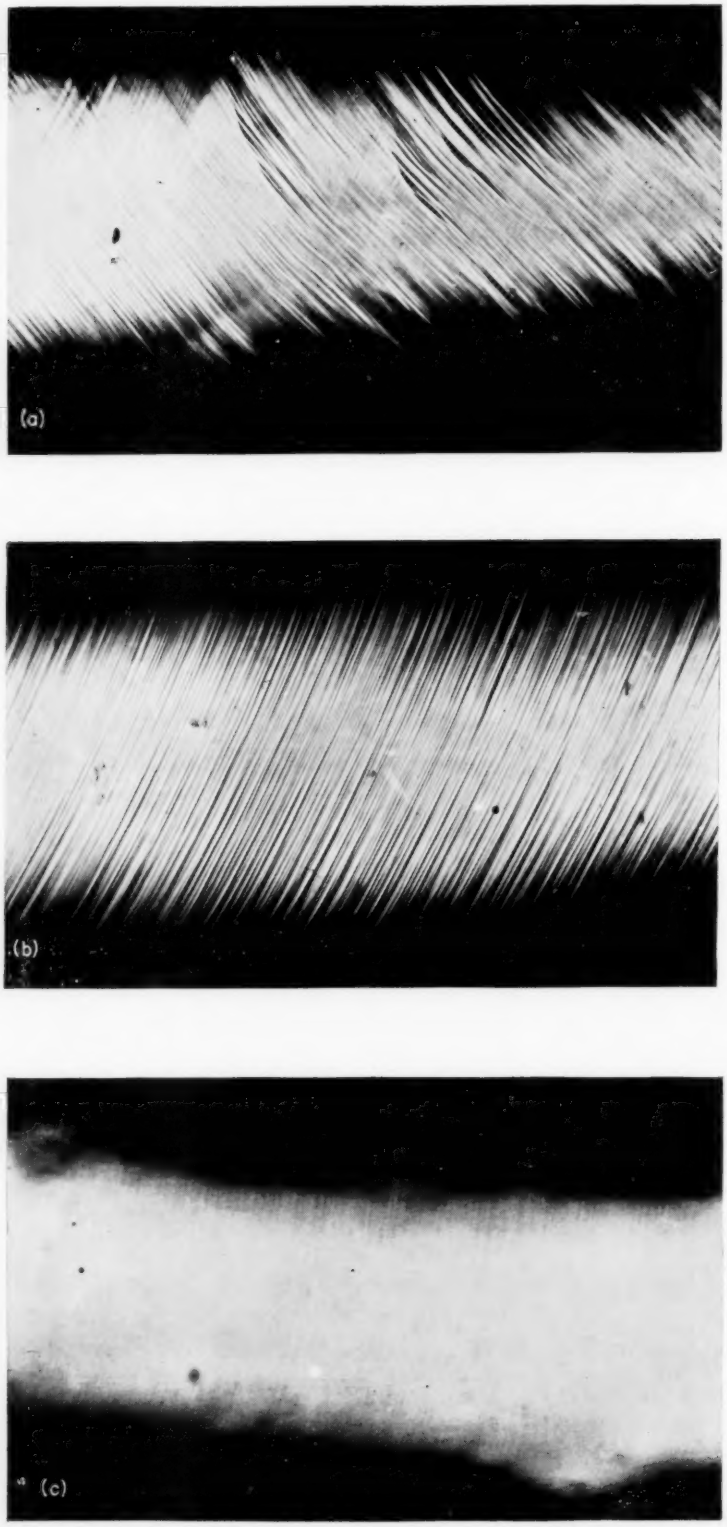
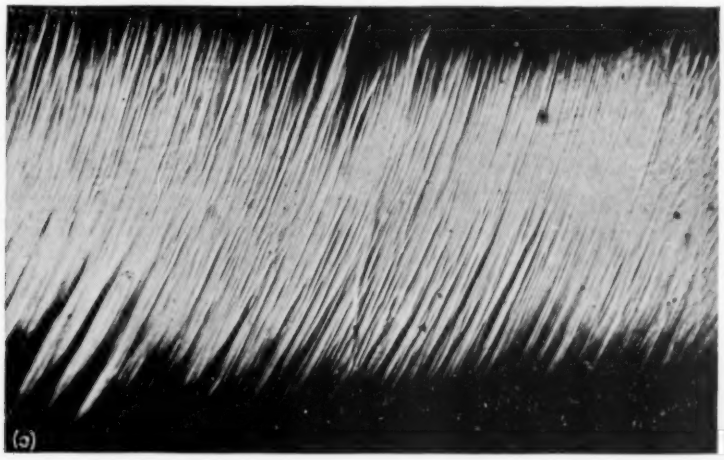
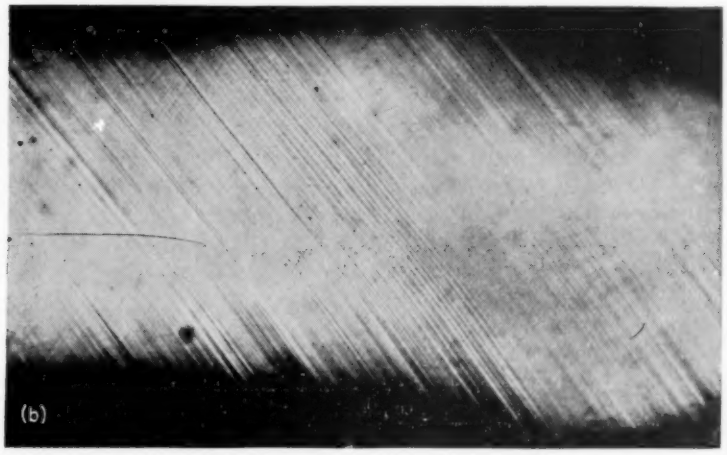


FIG. 7. Photomicrographs of specimens of orientation 2 after straining. ×200. (a) Tensile; (b) alternating straining, amplitude 0.02; (c) alternating straining, amplitude 0.0001.





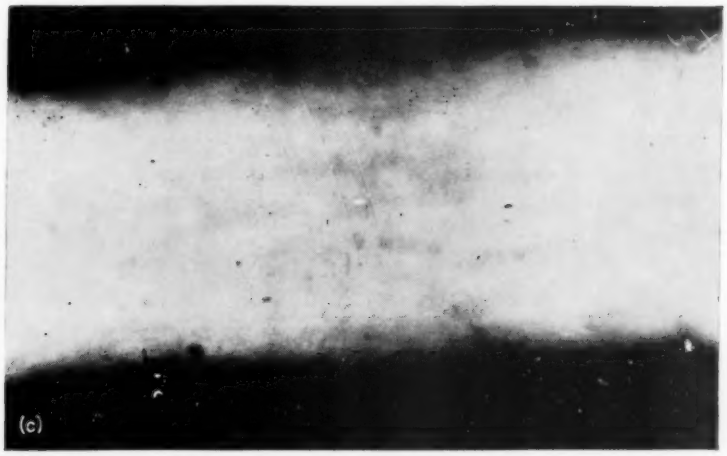


FIG. 8. Photomicrographs of specimens of orientation 4 after straining, ×200. (a) Tensile; (b) alternating straining, amplitude 0.02; (c) alternating straining, amplitude 0.0001.

VOL. 8 1960

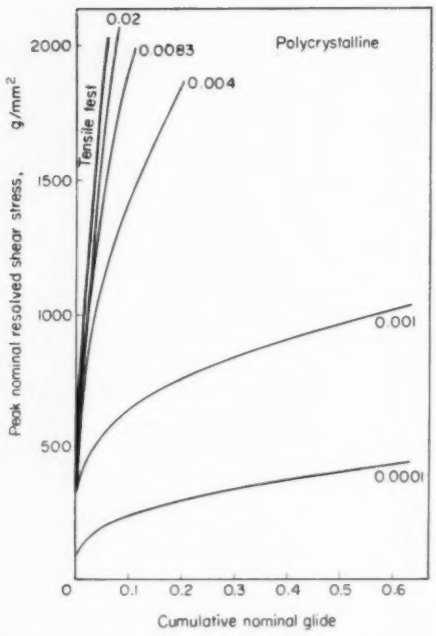


FIG. 9. Work-hardening curves for polycrystalline copper; the numbers indicate the plastic-strain amplitude, expressed as "equivalent" glide strain.

equivalent to using the average of the ratios of axial normal strain to resolved shear strain for all orientations in the stereographic triangle. In addition, an "equivalent resolved shear stress", equal to 0.435 times the axial normal stress, has been plotted.

The results of the tests are given in Fig. 9, and the same curves have also been included in Fig. 4(a)–(d). A departure from elastic behaviour is already discernible at an "equivalent resolved shear stress" of about 30 g mm^{-2}, which corresponds approximately to the average critical shear stress for the single crystals.

The work-hardening rate in alternating straining does not depart markedly from that in tension until the amplitude is decreased below about 0.004. Further decrease of amplitude is accompanied by a marked lowering of the hardening curve. This behaviour is closely similar to that shown by single crystals of orientations near [100] and [111]. The hardening curve at the smallest amplitude is about twice as high as that for single crystals. However, it is not clear whether this difference can be wholly ascribed to the influence of grain boundaries because of the uncertainty associated with the use of an "equivalent orientation".

Secondary slip was only observed in some grains in the specimens deformed at amplitudes greater than 0.004. At the smaller amplitudes, slip became very faint and was only seen in a few grains at amplitudes 0.001 and 0.0001.

The present results agree approximately with those of Wood and Segall[6] and Dugdale[7] at comparable amplitudes but extend to lower amplitudes at which the work hardening is much less. On the other hand these workers have shown that for the larger amplitudes the rate of work hardening also becomes very small at cumulative strains several times greater than those studied here.

(g) *Summary of results*

For copper crystals subjected to alternating tension and compression, the curve of peak stress vs. cumulative strain always falls below the tensile curve and is lower the smaller the plastic strain amplitude. The details of this trend vary with orientation as follows:

(1) For the orientations near [111] and [100], the hardening curve remains steep down to an amplitude of about 0.001, at which there is a sudden transition to a very low hardening rate.

(2) For the orientations near [110] and the midpoint of the [110]-[111] boundary, the hardening curve at amplitude 0.02 is already appreciably below the tensile curve, and there is a regular lowering with amplitude.

(3) For the orientations near the midpoints of the [100]–[111] and [100]–[110] boundaries and in the middle of the stereographic triangle, there is an upward inflection in the hardening curves obtained at large amplitudes; at lower amplitudes the inflexion is absent.

(4) At the lowest amplitude (0.0001), all orientations give a similar low hardening rate, about an order of magnitude less than that in the easy glide stage in tensile tests.

Appreciable amounts of secondary slip are generally observed on specimens tested at amplitudes for which high hardening rates occur. Otherwise, only primary slip is observed after alternating straining; this decreases in prominence but does not appear to change markedly in spacing as the amplitude is decreased.

Polycrystalline specimens behave similarly in alternating straining to single crystals oriented near [100] or [111].

No work softening was observed in three experiments in which the strain amplitude was changed from a large to a small value during testing.

DISCUSSION

1. *Reversibility of plastic deformation*

Taking the plot of peak stress versus total absolute

strain as a measure of the work hardening in alternating straining, we find that this hardening is always less than for unidirectional straining. Thus, during alternating straining, an appreciable fraction of the normal hardening either does not develop or is reversible (cf. Bauschinger effect). This fraction increases with decreasing plastic-strain amplitude, in a way that depends strongly on orientation. Thus it may be concluded that there is an appreciable reversibility of the deformation process, which becomes more important at smaller strain amplitudes.

The fact that slip lines develop during alternating straining indicates that the slip occurring during reverse half-cycles is not entirely a reversal of that occurring in forward half-cycles. This is already well-known from fatigue studies and suggests that slip has a ratchet-like property. Thus, since the resultant macroscopic strain is zero, the resultant slip will be of one sense in some places and of the opposite sense in others, giving rise to an oscillation in the resultant plastic strain on the microscopic scale. As the strain amplitude is decreased, the diminishing prominence of the slip lines suggests that these oscillations of local strain become smaller, probably due to a greater reversibility of slip at smaller amplitudes (the ratchet-mechanism being less effective); however, definite conclusions cannot be drawn from surface observations alone, since the amount of slip may vary within a slip plane in a way that depends on amplitude.

For single strain reversals, Buckley and Entwistle[13] have shown that the ratio of Bauschinger strain to prestrain increases as the prestrain decreases, which suggests that there is an increased reversibility of deformation at smaller prestrains. This is probably closely related to the present observations. However, Buckley and Entwistle have not published data from which conclusions about the influence of orientation can be drawn.

VOL. 8 1960

2. *Hardening processes*

The variation in behaviour with orientation of the copper crystals suggests that more than one hardening process is involved in alternating straining. In the following discussion we shall attempt to show that the main features of the results can be accounted for in terms of two hardening processes, which we shall call the "basic hardening process" (cf. Seeger[14]) and the "rapid hardening process".

The *basic hardening process* is distinguished by a very low rate of work hardening. It is assumed to be alone effective at low amplitudes for all orientations, and in the stage preceding the upward inflexion in the hardening curves at larger amplitudes for orientations 3, 4, 5 and 6. Slip on only one set of planes is visible in all these cases.

For orientations 2 and 8 near the [110]–[111] boundary, the basic hardening process also probably predominates at larger amplitudes, since the hardening curves are of similar, simple shape (although no longer linear) to those at the lower amplitudes and still only single slip is visible. However, the increase of hardening rate with amplitude is accentuated for these orientations. This suggests that slip in different directions on the primary plane is mutually hindering in some degree. However, it is not clear whether this is an essential part of the basic hardening mechanism or an additional factor.

The *rapid hardening process* predominates for orientations 1 and 7 at amplitudes above about 0.001 and for orientations 3, 4, 5 and 6 at large amplitudes after the upward inflexion has appeared in the hardening curve. Since secondary slip is visible in these cases (except for orientations 3 and 5) it seems that, in the rapid hardening process, slip on secondary planes has a marked obstructing effect on slip on the primary plane (cf. stages II and III of the tensile curve). Also in the rapid hardening process, the ratchet-mechanism in the slip seems to be especially effective since the slip lines are always fairly prominent.

There is evidence, therefore, that an important distinction between the rapid and basic hardening processes is whether or not there is yielding on secondary slip planes, evidenced by microscopically-visible secondary slip. This yielding will involve the movement (partly ratchet-like) of considerable numbers of dislocations, as contrasted to limited activity at stresses below the yield stress. In other words, during the basic hardening process the latent hardening on secondary planes maintains the yield stress in these above the actual resolved shear stress; when this condition no longer holds, rapid hardening begins.

An attempt to represent some possible situations for different orientations is made in Fig. 10(a) and (b). The curve A represents the basic hardening on the primary plane while curve B represents the latent hardening on the most-favoured secondary plane. The stress on the secondary plane (curve C) will be a constant fraction of the stress on the primary plane (curve A), since the orientation is unchanged during alternating straining. Yielding on the secondary plane will occur when curve C intersects curve B.

Figure 10(a) depicts situations in which the yielding on the secondary plane will not occur and in which therefore only the basic hardening process will be observed. This may arise due to the orientation being

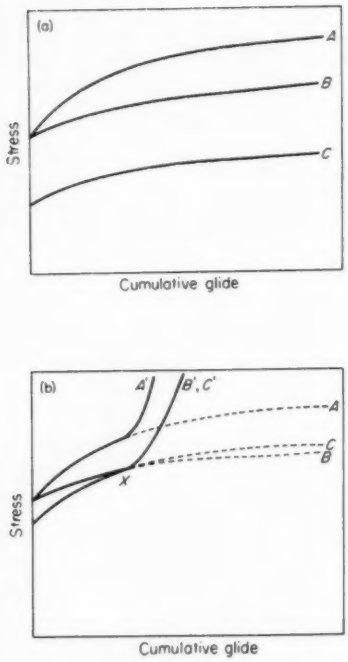


FIG. 10. Schematic representation of conditions in (a) basic hardening, (b) the incidence of rapid hardening.

such that the ratio of the resolved shear stresses in secondary and primary planes is considerably less than unity (as illustrated), or that the curves are all nearly horizontal. The former situation could be expected for orientations far from the [100]–[111] and [100]–[110] boundaries, and the latter for all orientations at the minimum amplitude.

Figure 10(b) shows how an upward inflexion can arise due to yielding on the secondary plane at point X. This is most likely to occur when the ratio of curves C and A is near unity, as for orientations near the [100]–[111] and [100]–[110] boundaries. Moreover, in these cases, the sensitivity of the position of the point of intersection X to slight changes in slope of the curves might explain the variability that is observed at the larger amplitudes for some of these orientations. For orientations 1 and 7, the point X is presumably passed in the first half-cycle (except at very small amplitudes); these orientations therefore show rapid hardening from the beginning.

The absence of a doubly-inflected hardening curve at intermediate amplitudes for orientations 1 and 7, and the dissimilar behaviour of orientations 2 and 4 (which should have about the same ratio of curves C to A) are not readily explained. However, in these cases, slip in the second direction in the primary plane may be appreciably influencing the slope of curve B.

3. *Relation to current dislocation theories*

The partial reversibility of slip and the diminution of work hardening with strain amplitude are the chief aspects of alternating deformation to be explained by dislocation theory. In this section we will point out where our experiments may bear on current theories.

The development of microscopically-visible slip is generally believed to involve the generation of dislocations, e.g. by the Frank–Read mechanism. Without restrictive conditions, however, the Frank–Read mechanism is completely reversible, the dislocation loops either collapsing or being annihilated by loops produced in the opposite half-cycles. In order to explain the "ratchet-mechanism" in slip, one must assume some additional factor that can cause operation of a Frank–Read source in a preferred direction. Mott[15] has discussed several possibilities for this.

In the basic hardening process, the mechanism is probably similar to that in stage I (easy glide) of tensile tests; its nature is equally obscure except for the suggestion that slip in two directions in the primary slip plane may be important, at least in an auxiliary role. We shall therefore only discuss here the rapid hardening process, considering the relevance of the two main theories of the hardening in stage II of tensile tests, viz. the theories of interaction and intersection hardening.

Interaction hardening[16–18] involves the long-range hindering of the motion of dislocations by elastic strain fields around immobile distortion centres, usually considered to be Lomer–Cottrell locks. Interaction hardening might therefore plausibly explain the rapid hardening process since yielding in a suitable secondary system could greatly increase the possibility of Lomer–Cottrell reactions, and the dependence on orientation could be explained in the way discussed by Clarebrough and Hargreaves[19]. However, whatever the nature of the immobile distortion centres, the requirement here is that most of them should not be dispersed when the direction of straining is reversed. In this respect, the effectiveness of Lomer–Cottrell locks is doubtful, for it may not be difficult to reverse the reaction, especially if dislocations of opposite sign to the original reacting dislocations are moved in when the direction of straining is reversed.

In *intersection hardening*,[20,21] the resistance to further strain arises from the short-range forces hindering the dislocations from cutting through the "forest" of dislocations in intersecting planes. This hypothesis has been preferred recently by some writers[22,23] for explaining stage II of the tensile

curve. It is also more attractive in some respects for explaining the rapid hardening stage in alternating deformation. Thus, when yielding occurs on secondary planes, rapid hardening will result from the rapid increase in the forest density. Moreover, the hardening could be expected to persist to a large extent when the direction of straining is reversed, since the complicated sequence of intersection, jog movement, etc., is unlikely to be preserved in reverse.

ACKNOWLEDGMENT

The authors are grateful to the Chief Scientist, Department of Supply, Melbourne, for the secondment of one of us (D. S. K.) to Canberra, which made this work possible, and for permission to publish this paper.

REFERENCES

1. H. HELD, *Z. Metallk.* **32,** 201 (1940).
2. H. SCHOLL, *Z. Metallk.* **48,** 258 (1957).
3. N. THOMPSON, C. K. COOGAN and J. G. RIDER, *J. Inst. Met.* **84,** 73 (1955).
4. P. CHARSLEY and N. THOMPSON, *Phil. Mag.* **3,** 1098 (1958).
5. M. S. PATERSON, *Acta Met.* **3,** 491 (1955).
6. W. A. WOOD and R. SEGALL, *Proc. Roy. Soc.* A**242,** 180 (1957).
7. D. S. DUGDALE, *J. Mech. Phys. Solid* **7,** 135 (1959).
8. M. S. PATERSON, *Acta Met.* **2,** 823 (1954).
9. M. S. PATERSON, *J. Sci. Instrum.* **32,** 356 (1955).
10. R. S. DAVIS, R. L. FLEISHER, J. D. LIVINGSTON and B. CHALMERS, *Trans. Amer. Inst. Min. (Metall.) Engrs.* **209,** 136 (1957).
11. F. D. ROSI, *Trans. Amer. Inst. Min. (Metall.) Engrs.* **200,** 1009 (1954).
12. J. J. BECKER and J. N. HOBSTETTER, *Trans. Amer. Inst. Min. (Metall.) Engrs.* **197,** 1231 (1953).
13. S. N. BUCKLEY and K. M. ENTWISTLE, *Acta Met.* **4,** 352 (1956).
14. A. SEEGER, *Z. Naturf.* **9**a, 758 (1954). Also in *Dislocations and Mechanical Properties of Crystals*, p. 284 (Ed. J. C. FISHER *et al.*) Wiley, New York (1956).
15. N. F. MOTT in *Dislocations and Mechanical Properties of Crystals*, p. 458 (Ed. J. C. FISHER *et al.*) Wiley, New York (1956).
16. N. F. MOTT, *Phil. Mag.* **43,** 1151 (1952).
17. J. FRIEDEL, *Phil. Mag.* **46,** 1169 (1955).
18. A. SEEGER in *Dislocations and Mechanical Properties of Crystals*, p. 243 (Ed. J. C. FISHER *et al.*) Wiley, New York (1956).
19. L. M. CLAREBROUGH and M. E. HARGREAVES, *Progr. Metal Phys.* **8,** 1, (1959).
20. A. H. COTTRELL, *Dislocations and Plastic Flow in Crystals*, p. 172. Clarendon Press, Oxford (1953).
21. A. SEEGER in *Defects in Crystalline Solids*, p. 391. Physical Society, London (1955).
22. Z. S. BASINSKI, *Phil. Mag.* **4,** 393 (1959).
23. P. B. HIRSCH, private communication.

VOL.
8
1960

THE CONTRIBUTION OF PRECIPITATION TO STRAIN AGEING IN LOW CARBON STEELS*

D. V. WILSON† and B. RUSSELL‡

At first strain ageing in a low carbon steel is concerned with atmosphere locking of dislocations, but mechanical tests have shown that solute segregation beyond this first stage increases strength by a form of precipitation hardening. A comparison of the change in lower yield stress ΔY and in electrical resistivity during strain ageing shows that there is a sudden decrease in the effectiveness of solute segregation, in further increasing ΔY, at the end of the first stage. Estimates based on the Cottrell–Bilby equation[8] suggest that this occurs at dislocation atmosphere densities not greatly in excess of one atom per atom plane.

Segregates formed just beyond the completion of atmosphere locking disperse rapidly on re-straining and ageing, and are probably solute clusters. Continued ageing gives more stable precipitates, probably along the dislocations, but an electron microscopical examination has shown that, at ageing temperatures of 60°C or less, these remain extremely small.

The increase in ΔY during the early stages of precipitation is approximately proportional to the number of solute atoms segregating to unit length of dislocation, and is insensitive to the dislocation density L. But at higher segregate concentrations (~3–10 times that required for atmosphere locking) continued segregation is less effective in increasing ΔY, also ΔY tends to increase with L. The increment in strain hardening capacity due to precipitation is sensitive to the amount of prestrain, and appears to be approximately proportional to $L^{3/2}$. Assuming precipitation is on dislocations, this agrees with the relationship suggested by Fisher *et al.*[16].

EFFET DE LA PRECIPITATION SUR LE VIEILLISSEMENT DE DEFORMATION DES ACIERS A BAS CARBONE

En première approximation, le vieillissement de déformation d'un acier à bas carbone s'explique par la formation d'atmosphères autour des dislocations. Cependant, les essais mécaniques ont montré qu'une ségrégation d'atomes dissous au-delà de ce premier stade accroitra la résistance par une sorte de durcissement de précipitation. Une comparison entre la variation de la limite élastique inférieure ΔY et résistivité électrique au cours du vieillissement de déformation, montre qu'il apparaît une diminution soudaine de l'action de la ségregation des atomes dissous à la fin du premier stade. Des estimations qui s'appuient sur l'équation de Cottrell–Bilby permettent de suggérer que cet effet apparaît our des densités de dislocations d'atmosphères qui ne dépassent pas un atome par plan atomique.

Les ségrégats qui se forment lorsque l'atmosphère est complète, se dispersent rapidement au cours de la déformation et du vieillissement. Ils forment probablement des amas d'atomes dissous. Lorsque le vieillissement se poursuit, ils produisent des précipités plus stables, vraisemblablement le long des dislocations. Des examens au microscope électronique ont montré que pour des températures de vieillissement de 60°C ou moins, ces précipités demeurent extrêmement petits. L'accroissement de ΔY au cours des premiers stades de précipitation est à peu près proportionnel au nombre d'atomes dissous qui ségrègent par unité de longueur de la dislocation. Il est indépendant de la densité de dislocation L. Par contre, pour des concentrations en atomes ségrégés plus élevées (3 à 10 fois les concentrations nécessaires pour la formation des atmosphères"), l'accroissement de ΔY lorsque la ségrégation se poursuit, est moins accentué. Dans ce cas, ΔY montre une tendance à croître également avec L. L'augmentation de la capacité de durcissement de déformation, par suite de cette précipitation, dépend de l'importance de la déformation initiale. Elle est sensiblement proportionnelle à $L^{3/2}$. En admettant que la précipitation se produit sur les dislocations, ce résultat est en accord avec la relation proposée par Fisher et ses collaborateurs[16].

DER BEITRAG DER AUSSCHEIDUNG ZUR VERFORMUNGSALTERUNG KOHLENSTOFFARMER STÄHLE

Die Verformungsalterung eines kohlenstoffarmen Stahles hängt zunächst mit der Festlegung von Versetzungen durch Cottrell-Atmosphären zusammen. Verformungsversuche haben jedoch ergeben, daß die Ausscheidung von gelösten Stoffen über dies erste Stadium hinaus die Härte durch eine Art Ausscheidungshärtung vergrößert. Ein Vergleich der Änderung der unteren Streckgrenze ΔY und des Widerstandes während der Verformungsalterung zeigt, daß der Einfluß der Ausscheidung der Zusätze auf ΔY, der zu einer Erhöhung führt, am Ende dieses ersten Stadiums plötzlich abnimmt. Abschätzungen auf Grund der Cottrell–Bilby–Gleichung[8] zeigen, daß dies bei einer Dichte der Atmosphäre geschieht, die wenig größer ist als ein Atom pro Netzebene.

Ausscheidungen, die unmittelbar nach Vervollständigung der Blockierung durch die Atmosphären entstehen, lösen sich bei Neu-Verformung und Alterung rasch auf und sind wahrscheinlich Zusammenballungen der gelösten Atome. Setzt man die Alterung fort, so entstehen stabilere Ausscheidungen,

* Received September 5, 1959.

† Department of Industrial Metallurgy, University of Birmingham, England.

‡ University of Queensland, Australia, formerly at the Department of Industrial Metallurgy, University of Birmingham, England.

wahrscheinlich entlang den Versetzungen, aber elektronenmikroskopische Untersuchung zeigt, daß sie bei Alterungstemperaturen unterhalb 60°C äußerst klein bleiben.

Die Zunahme von ΔY ist in den frühen Stadien der Ausscheidung genähert proportional der Zahl der Zusatzatome, die sich pro Längeneinheit der Versetzung ausscheiden, und hängt nicht von der Versetzungsdichte L ab. Wenn mehr ausgeschieden ist (3–10 mal so viel wie zur Blockierung durch Atmosphärenbildung nötig ist), wird durch weitere Ausscheidung ΔY nicht mehr so stark erhönt; ΔY beginnt auch mit L zuzunehmen. Die Härtezunahme, die infolge der Ausscheidung bei Verformung erreicht werden kann, hängt von der Vorverformung ab und scheint genähert proportional zu $L^{3/2}$ zu sein. Dies stimmt mit der von Fisher *et al.*[16] vorgeschlagenen Beziehung überein, wenn man annimmt, daß die Ausscheidung an den Versetzungen stattfindet.

1. INTRODUCTION

There have been numerous experimental investigations of strain ageing in α-iron, based either on the measurement of changes in a physical property such as internal friction or on the changes in mechanical properties, although attempts to combine the two approaches in a single investigation are rare. Both types of experiment give evidence that segregation of carbon and nitrogen to dislocations can continue beyond atmosphere formation to a form of precipitation.[1–4]

Some features of the kinetics of the precipitation stage of strain ageing are still in dispute. Several investigators have observed time–transformation relationships for the later stages of ageing in good agreement with Harper's modification of the Cottrell–Bilby equation, which considers segregation to be induced by the stress fields of dislocations.[2,5,6] More recently, however, Doremus[7] has shown that diffusion to carbide precipitates in deformed iron, at least for ageing temperatures above about 60°C, is probably controlled by solute concentration gradients set up round the precipitates.

Interpretation of results for initial rates of ageing is not complicated by the necessity of allowing for the effects of impingement of diffusion fields or concentration differences, and there is rather general agreement[1,2,5,6] that segregation at first follows a (time) $t^{2/3}$ law, as predicted by Cottrell and Bilby[8]. Thomas and Leak, using internal friction measurements, found that a $t^{2/3}$ law was followed quite closely up to about half-completion of ageing in specimens containing up to 0.015 wt.% carbon or nitrogen, which were prestrained 7 per cent and aged at temperatures up to about 60°C.

Surprisingly, the changes in yield strength and hardness due to strain ageing follow a similar pattern.[2,8,9] Typically the first third or half of the increase in strength follows a $t^{2/3}$ law quite closely and beyond this the rate diminishes rapidly. This observation has led some investigators to assume that the change in strength is approximately proportional to the amount of solute segregating throughout the ageing process.

The Cottrell–Bilby equation may be written:

$$n(t) = 3\left(\frac{\pi}{2}\right)^{1/3} n_0 L \left(\frac{A D t}{kT}\right)^{2/3}. \qquad (1)$$

Where $\frac{n(t)}{n_0}$ is the fraction of the total dissolved solute migrating to dislocations in time t at a temperature T, D is the diffusion coefficient and A the interaction parameter, which has been estimated in the range 1.4 to 3.0×10^{-20} dyn cm^2 for carbon and nitrogen in iron. A useful property of this equation is that it provides a simple means for estimating the dislocation density L from experimental observations of the initial rate of strain ageing; hence atmosphere densities at different stages of ageing may also be derived. Using internal friction measurements on specimens containing more than 0.01 wt.% solute which have been prestrained less than about 10 per cent, typical estimates[2] suggest that between ten and fifty solute atoms have segregated to each atomic plane along the dislocations at the completion of ageing. If these results are accepted, it must be concluded that a $t^{2/3}$ law is followed beyond the completion of atmosphere locking. Mechanical tests, which give evidence of precipitation in the later stages of ageing with similar specimens, provide support for the idea that high "atmosphere" densities develop, but any assumption that the increase in strength is approximately proportional to the amount of solute segregating throughout ageing raises a serious difficulty. It is unlikely that segregating solute can continue to be so effective in raising the yield strength once the sites of strong interaction are all occupied.

Mechanical tests provide a means of separating the contributions of atmosphere locking and of precipitation to the rise in yield stress in strain ageing.[4]

Factors contributing to the lower yield stress σ_y can be represented in an expression of the form:

$$\sigma_y = \sigma_i + k_y d^{-1/2}. \qquad (2)$$

Here σ_i represents resistance to the movement of free dislocations. d depends on grain size, and is expected to remain constant in a given specimen during strain ageing. k_y provides a measure of the

VOL. 8 1960

strength of dislocation pinning; thus atmosphere formation affects σ_y by increasing k_y. Segregation beyond the completion of atmosphere locking is observed to have little effect on k_y, but continues to raise σ_y by increasing σ_i.

This paper is concerned with an exploration of the precipitation stages of strain ageing, based principally on mechanical properties, but some electrical resistivity measurements have also been used to estimate the amounts of solute involved at various stages of ageing.

In an earlier paper[4] it was shown that properties related to atmosphere locking, such as yield stress and Luders strain, depend on grain size. Typical results, for a slowly cooled steel prestrained 4 per cent, are reproduced in Fig. 1, to allow comparison with results for the corresponding changes in ultimate tensile strength, work hardening coefficient and elongation to fracture. These last three properties provide mechanical evidence of precipitation in strain ageing. Evidently grain size has no important influence on the contributions of precipitation to the changes in properties. The most interesting variables affecting precipitation behaviour are the dissolved solute content and the dislocation density. Particular attention has been given to these in the present investigation.

2. EXPERIMENTAL METHODS

A high quality commercial steel of the following composition in wt. % was used throughout:

C 0.038; N 0.0042; Mn 0.40; Si 0.008; S 0.017; P 0.008; Ni 0.06; Cu 0.07; Sn 0.01; Al 0.001.

This steel was the same as that used in the earlier investigations,[4] as was the material of reduced solute content, prepared by decarburizing in wet hydrogen. Methods of preparing the test pieces and of tensile testing, (using a strain rate of 10^{-4} sec^{-1}), were also the same as those described previously. Generally accelerated ageing was carried out at 60°C $\pm$ 1°C in an oil bath.

Steel of three different grain sizes was used in the first experiment (Fig. 1), but subsequently material of a single grain size (200 $\pm$ 20 grains per mm^2) was used for most of the mechanical tests.

The apparatus and method used for electrical resistivity measurements was similar in principle to that described by Cottrell and Churchman[10]. The standard and test-specimen wires, both of 0.035 in. diameter and approximately 10 ft long, were wound side by side on a flexible former which was immersed in a thermostatically controlled oil bath. Using a potentiometer reading to 0.1 μV, the dimensions of the wires permitted sufficient sensitivity with a current of 20 mA flowing. The standard wire was prestrained 4 per cent and then aged for 5×10^4 min at 60°C and a further week at room temperature before the experiments. The test specimens were stretched and assembled sufficiently rapidly to allow readings to start within 15 min of stretching.

3. RESULTS

Effects of grain size

Figure 1 summarizes mechanical test results obtained with material of three different grain sizes. All the test pieces used in this experiment were furnace cooled to 200°C, maintained at this temperature for 2000 min, and then water quenched, after which they were prestrained 4 per cent and aged at 60°C for times indicated in the figure. With this preliminary heat treatment strain ageing would be due almost entirely to dissolved nitrogen ($\leqslant$0.004 wt.%).

With this low solute content the contributions of atmosphere locking and of precipitation, to the rise in

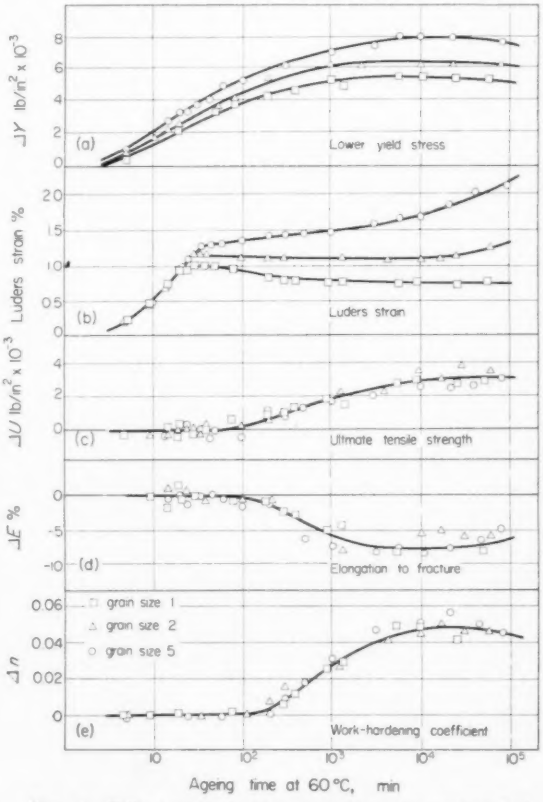


FIG. 1. Effect of grain size on changes in mechanical properties due to strain ageing. Specimens quenched from 200°C and prestrained 4 per cent. Grain size in grains/mm^2: (1), 50; (2), 195; (5), 1850.

yield stress in fully aged specimens, were of comparable magnitudes, (a behaviour similar to that shown by commercially annealed steels). It is noteworthy that changes in ultimate tensile strength, work hardening and ductility developed only after about 100 min ageing at 60°C, while the development of Luders strain suggested that atmosphere locking was completed after about 35 min ageing.

Effects of variations in dissolved solute

Figure 2 illustrates the development of the changes in mechanical properties with ageing time in four groups of specimens having rather widely different dissolved solute contents, all of which were prestrained 4 per cent before ageing. Specimens of group 1 were water quenched from 600°C before prestraining, those of group 2 were furnace cooled to 200°C, held at this temperature for 2000 min and then water quenched. Groups 3 and 4 were treated in wet hydrogen at 800°C for 8 and 13 hr respectively and quenched from 500°C. Equilibrium solubility data shows that group 1 specimens would start with about 0.014 wt.% dissolved solute (approximately 0.01 carbon and 0.004 nitrogen). The available solute contents of the other groups were estimated from the changes in electrical resistivity due to full ageing (2×10^4 min at 60°C). Assuming that the resistivity change due to the segregation of nitrogen is about 1.3 times that due to carbon, these results suggested that 0.0022 wt.% (nitrogen) segregated in group 2 specimens, while in groups 3 and 4 the values were approximately 0.0005 and less than 0.0002 wt.% (carbon) respectively.

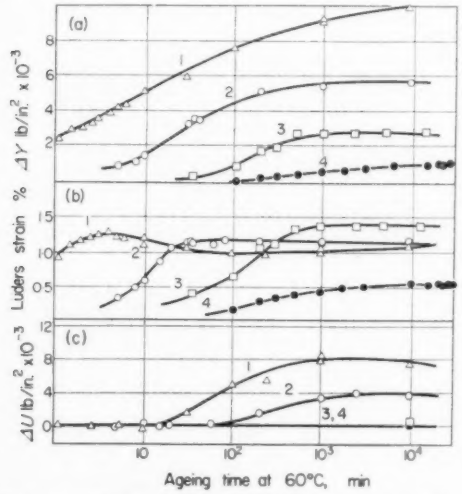


FIG. 2. Effect of dissolved solute content on changes in lower yield stress ΔY, ultimate tensile strength ΔU and Luders strain, due to strain ageing after 4 per cent prestrain. Estimated available solute in wt.%: Group (1) curves, 0.014; group (2), 0.0022; group (3), approximately 0.0005; group (4), <0.0002.

It has been suggested that Luders strain increases appreciably only during atmosphere formation, and that the value of Luders strain in fully aged specimens is therefore insensitive to the solute content, provided it exceeds the small amount required to complete atmosphere locking.[4] The results in Fig. 2(b) illustrate this clearly. Evidently specimens in groups 1 to 3 contained enough solute to complete locking while group 4 specimens did not. (However, the very close agreement between the maximum values of Luders strain in groups 1 to 3 is probably partly fortuitous, since the rate of work hardening is influenced by the dissolved solute content.)

Identification of the times taken to complete atmosphere locking in groups 1 to 3 from the results for Luders strain shows that the increase in yield stress ΔY was at this stage rather similar with each group of specimens (Fig. 2a). Beyond this first stage of ageing further rises in ΔY are ascribed to the effects of solute cluster formation or precipitation. This further rise was negligible in group 3 specimens, but it became the dominant contribution to ΔY in the later stages of ageing in the case of specimens quenched from 600°C. Only specimens of groups 1 and 2 showed a rise in ultimate tensile strength due to ageing: evidently specimens of group 3 were of a critical composition, sufficient to complete atmosphere locking but insufficient to allow the formation of stable precipitates.

Relation of changes in yield strength to solute segregation

Considered together, the results in Fig. 2 show that solute segregating to form atmospheres is a good deal more effective in raising the yield stress than is that which forms precipitates, also, in the precipitation stage, the solute becomes less effective as precipitation develops. To gain a more quantitative picture of the relation between ΔY and the amounts of solute segregating, tensile and resistivity test pieces were prepared in the form of wires of 0.035 in. diameter. These allowed a comparison of the changes in electrical resistivity and mechanical properties to be made in specimens of identical history. Three different batches of wire were made having the same thermal pretreatments as the specimens of groups 1 to 3 used in the previous experiment (Fig. 2). The wires were stretched 4 per cent and were aged at 20°C for 3 weeks, so that the early stages of ageing could be followed in detail. Finally, however, ageing was completed by heating at 60°C for a total of 2×10^4 min.

Results obtained with specimens furnace cooled from 700 to 200°C, held at this temperature for 2000 min, water quenched and finally stretched 4.2 per

VOL. 8 1960

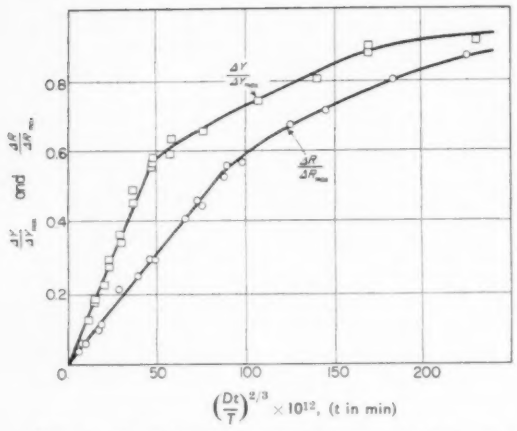


FIG. 3. Fractional changes in lower yield stress and resistivity as a function of $(Dt/T)^{2/3}$ for specimens quenched from 200°C and prestrained 4 per cent.

cent are plotted in Fig. 3. Values of ΔY obtained with the wire specimens proved to be insufficiently accurate, but averaged values did not appear to differ significantly from those obtained with large test pieces and results with the latter have been used in Fig. 3. It is immediately apparent that the formal resemblance between the variations of strength and of resistivity with ageing time is partly fortuitous. Although both followed a $t^{2/3}$ law quite closely up to about half completion of the measured change, in fact the rise in yield stress ceased to follow this law when less than a third of the total solute had segregated. The ageing time at which ΔY departed from its linear relationship with $t^{2/3}$ was apparently identical with the time required to achieve an approximately constant value of Luders strain. Thus the resistivity results support the view that segregation of solute continues to follow the $t^{2/3}$ law beyond the completion of atmosphere locking. The rather sudden change in the effectiveness of the solute in raising the yield stress at this critical point, (Fig. 4), provides a method of estimating the time required to complete atmosphere locking which is independent of measurements of Luders strain.

Results with specimens quenched from 600°C showed similar features. The resistivity change again followed a $t^{2/3}$ law beyond the completion of atmosphere locking and almost up to the ageing times at which the first rise in ultimate tensile strength was detected. In this case ΔY reached about 0.45 of its maximum value at its point of departure from a linear relationship with $t^{2/3}$, but the resistivity results suggested that only about one tenth of the total solute had segregated at this stage.

If equation (1) accurately describes the process of solute segretation during periods in which the $t^{2/3}$ law is obeyed, then the amounts of solute segregating to a unit length of dislocation in a given time within these periods can be derived at once. It follows, once it has been established that the $t^{2/3}$ law holds beyond the completion of atmosphere locking, that the atmosphere densities required to complete locking can be derived directly from tensile test results, without reference to estimates of the dislocation densities. Atmosphere densities for locking derived in this way, using the ageing times required to reach an approximately constant value of Luders strain (Fig. 2) and the quoted estimates of initial solute concentrations, are given in Table 1.

Estimates of dislocation densities and of atmosphere densities at different stages of ageing, made using the resistivity measurements to evaluate $n(t)/n_0$ in equation (1) in the usual way,[2] are also given in Table 1. Values of 1.5×10^{-20} dyn cm^2 for the interaction parameter A and of 2.4 Å for the mean atomic spacing along the dislocations were assumed in these calculations. Values for the diffusion coefficients were taken from Fast and Verrijp's results.[11]

It is a disadvantage of the electrical resistivity method that the measured change does not remain strictly proportional to the numbers of solute atoms segregating throughout ageing. In the precipitation stage segregation becomes rather more effective in reducing resistivity, presumably because the residual effects of compact precipitates are less than those of atmospheres and early precipitates. The changes in internal friction and electrical resistivity have been compared in detail by Pitsch[6]. His results, for specimens with 0.01 per cent carbon, prestrained 4.8 per cent and aged at 90°C, suggest that the necessary corrections are negligible for present purposes for the segregation of up to about 0.005 wt.% solute. Thus, for the decarburized specimens and those quenched from 200°C, it has been assumed that the numbers of atoms segregating were directly proportional to the resistivity change. Results for specimens quenched from 600°C (containing about 0.014 wt.% solute) have been corrected using the results in Pitsch's Figs. 5 and 6, (although these may not be precisely applicable due to the difference in ageing temperatures). In the case of specimens quenched from 600°C it was also necessary to make allowance for the differing diffusion coefficients of the two solutes taking part in ageing. The method used was the same as that adopted by Cottrell and Leak[9].

As expected, present results (Table 1) for dislocation densities and for atmosphere densities at the completion of ageing are in reasonable agreement with those of earlier investigators. It is interesting, however,

TABLE 1

Heat treatment		Quenched from 600°C	Quenched from 200°C	Wet hydrogen treated for 8 hr, quenched from 500°C
	Available solute (wt.%)	0.014 (0.01C + 0.004N)	0.0022N	~0.0005C
Resistivity measurements	Dislocation density (lines/cm²) (4 per cent strain)	1.0×10^{11}	5.1×10^{10}	$\sim 4 \times 10^{10}$
	"Atmosphere" density at completion of ageing (atoms/atom plane)	12.0	3.5	~1
	Fraction of solute segregated at completion of locking (*from Fig. 4.)	0.10*	0.30*	~1
	Atmosphere density at completion of locking (atoms/atom plane)	1.2	1.1	~1
	Atmosphere density at first rise in tensile strength (atoms/atom plane)	1.9	2.2	
Tensile tests	Time in min to complete locking at 60°C (from Luders strain)	4.	33	550
	Atmosphere density at completion of locking (atoms/atom plane)	1.2	1.1	~0.9

that simple theory also gives reasonable values for atmosphere densities at the completion of locking. This suggests the calculations of dislocation densities based on equation (1) are not greatly in error.

The form of the relationship between ΔY and the amount of solute segregating suggested by Fig. 3 is plotted directly in Fig. 4, using solute concentrations derived from the resistivity measurements on specimens quenched from 200°C. Results obtained with specimens quenched from 600°C are also plotted, although these are less certain due to the additional assumptions required. We have interpreted the sudden change in slope of the yield stress relationships in Fig. 4

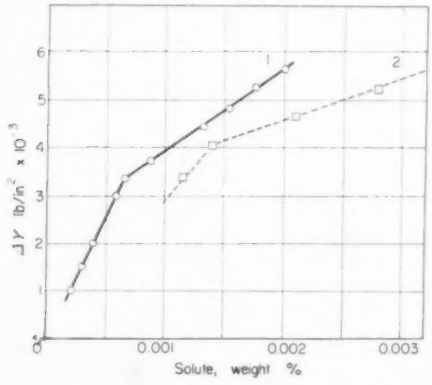


FIG. 4. Relation between solute segregation and rise in yield stress in the early stages of strain ageing. Specimen quenching temperatures and estimated dislocation densities (in lines/cm²), respectively: Curve (1), 200°C and 5.1×10^{10}; curve (2), 600°C and 1.0×10^{11}.

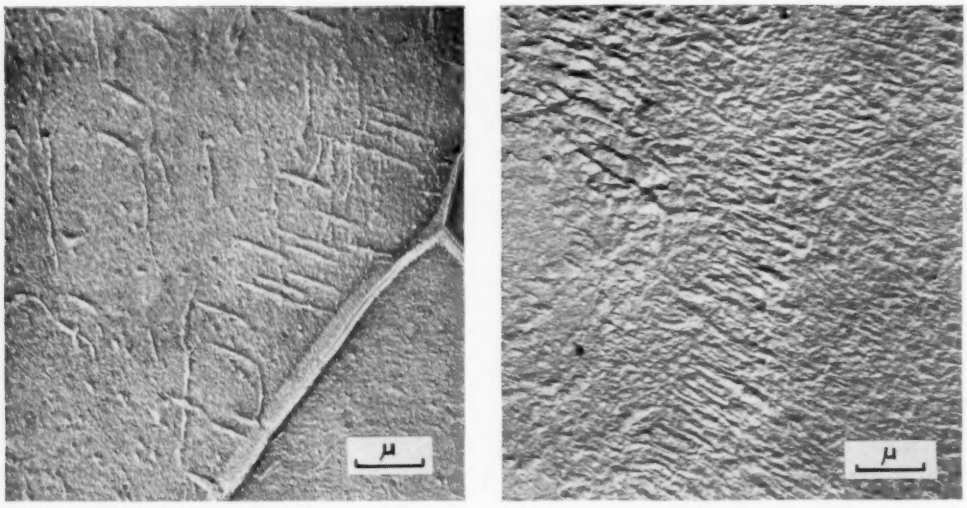
as being due to the completion of atmosphere locking. Just beyond this stage, the solute is only about one third as effective in raising the yield stress as it is in the earlier stages of segregation.

During atmosphere formation the rise in ΔY in a given specimen was proportional to the numbers of solute atoms segregating, within the accuracy of the measurements. However, specimens of differing dislocation densities gave rather similar values for ΔY at the completion of locking. This result suggests that the increase in ΔY during atmosphere formation depends on the proportion of the sites allowing strong interaction which are occupied (i.e. the atmosphere density) rather than on the volumetric concentration of the solute involved.

Results in Fig. 4 suggest that increases in ΔY beyond the completion of locking are at first also almost proportional to the amount of solute segregating to unit length of dislocation. In more advanced stages of segregation however, the effectiveness of the solute in raising ΔY decreases appreciably (Fig. 2) and, if a comparison is made of specimens having differing prestrains aged to equivalent stages of precipitation (Table 2), it is clear that ΔY tends to increase with dislocation density in the later stages of ageing.

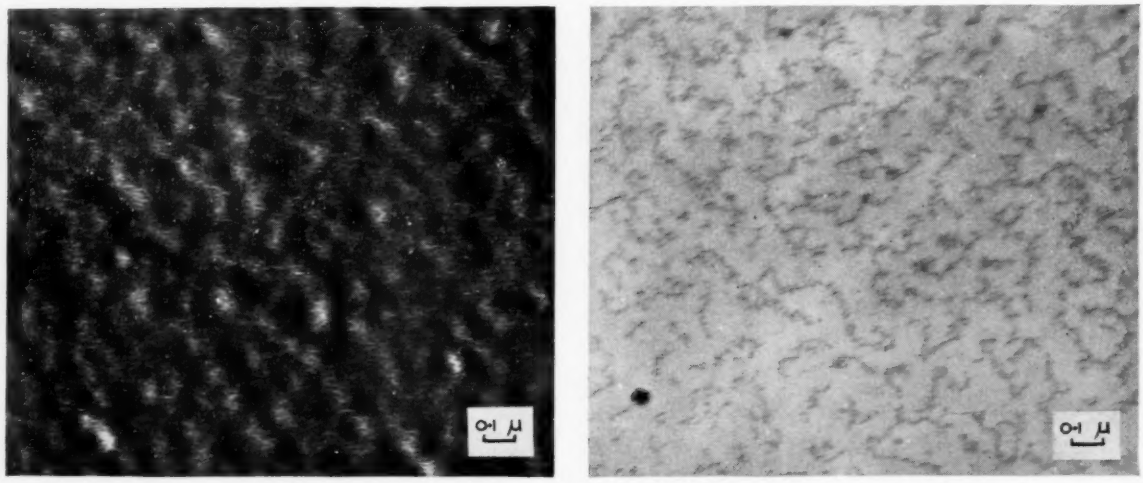
Evidence of precipitate characteristics

Direct carbon replicas were prepared from specimens electropolished in a perchloric–acetic acid solution. Deformed specimens, aged at 60°C and etched in dilute nital or picral solutions, generally showed very



(a) (b)

FIG. 5. Specimens quenched from 600°C, (a) undeformed and (b) stretched 4 per cent. Aged for 10^4 min at 60°C. (Etched in 1 per cent nital. Direct carbon replicas shadowed 2/1.)



(a) (b)

FIG. 6. Specimens quenched from 400°C, stretched 4 per cent and aged for 10^4 min at 150°C. (a) shadowed 1/1, (b) extraction replica.

numerous rounded or pyramidal mounds. In some grains these occurred in short linear arrays or took the form of ridges. In undeformed specimens, quenched from 600°C and aged at 60°C for 10^4 min, similar but clearer and less numerous etching features occurred. In a small proportion of the grains these took the form of clearly defined lines (Fig. 5a). Their appearance is similar to the "continuously decorated" dislocations observed by Low and Guard in silicon iron,[12] and it is likely that they represent single dislocations which happened to be close to the plane of polishing for a part of their lengths. In strained and aged specimens the pattern of etching features was more confused, but occasionally arrays of closely spaced and roughly parallel ridges were seen (Fig. 5b). These could also be due to dislocations decorated by solute segregation.

No clear evidence of discrete particles of a new precipitate was seen in specimens prestrained 4 per cent and aged at 60°C for up to 4×10^4 min, although possible evidence of fine structure associated with the mounds and ridges was seen towards the end of this ageing period. Specimens strained 4 per cent and "over-aged" by heating at 150°C for 10^4 min gave

much clearer evidence of what appeared to be very fine particles of precipitate, apparently predominantly associated with the etching mounds and ridges (Fig. 6a). An attempt to obtain an extraction replica from such a specimen proved successful (Fig. 6b). This shows fine precipitates, possibly less than 50 Å thick (~ the effective resolving power of the microscope), arranged in compact groups or lines which have a spacing approaching 1000 Å. These could be derived from fine, closely spaced precipitates lying along a tangled network of dislocations in the deformed grains.

The observation that metallographic evidence of discrete precipitates is confined to "over-aged" conditions implies that precipitation in strain-ageing below about 100°C is probably on a very fine scale, but it remains necessary to rely on mechanical tests for useful evidence of the early stages of the transformation. The segregation of quite small concentrations of solute beyond that required for atmosphere locking is sufficient to cause an appreciable increase in strength (Figs. 2 and 4): thus the initial development of "precipitation" strengthening may be associated with the formation of clusters of solute atoms, probably at close intervals along the dislocations. Solute clusters and the earliest precipitates may depend on their association with dislocations to reduce strain energy, and they may tend to redissolve if the dislocations are moved away (and new dislocations are generated) in subsequent straining. Certainly the repeated straining and ageing experiments by Hundy[13] suggest that some re-solution of precipitates can occur in the presence of free dislocations. This approach provides a method for exploring the stability of the precipitates present at different stages in the ageing process.

The initial rate of rise in the yield strength of a freshly strained specimen gives a sensitive indication of the concentration of solute available for strain ageing and is rather insensitive to variations in dislocation density, (Figs. 2 and 9). Thus, in principle, the initial rate of increase in ΔY shown by re-strained specimens can be used to explore the amount of solute removed from solution to form stable precipitates in an earlier ageing treatment. Figure 7 summarizes the results of such an experiment in which six test pieces of a single grain size were prepared by quenching from 200°C and stretching 4 per cent before ageing at 60°C for 0, 30, 100, 400, 1000 and 10,000 min respectively. After these first ageing treatments all the test pieces were re-strained 2 per cent and finally aged for 60 min at 60°C. The values of ΔY, due to the final ageing treatment only, are plotted in Fig. 7 as a function of the time of the first ageing treatment.

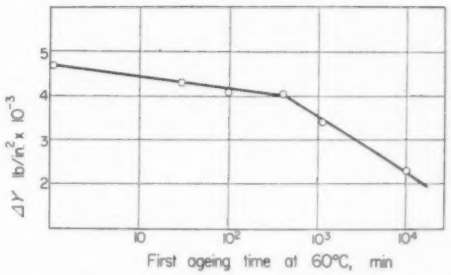


FIG. 7. Rise in yield stress due to a second ageing of 1 hr at 60°C in specimens previously prestrained 4 per cent, aged for the times indicated and then re-strained 2 per cent.

These results suggest that the segregates present after strain ageing for times up to 400 min at 60°C in the first ageing treatment, redissolve rather easily at 60°C to supply solute to new dislocations. Thus Fig. 3 suggests that more than 80 per cent of the available solute (~ 0.002 wt.%) would have segregated to form atmospheres and precipitates after 400 min at 60°C, yet up to this stage the rate of ageing after the second straining was not greatly affected by the earlier ageing treatment. However, quantitative conclusions cannot be drawn from this result because distribution of the solute would be inhomogeneous after the first ageing. On the other hand there is clear evidence that after first ageing treatments of more than about 10^3 min at 60°C a proportion of the solute had formed precipitates which did not redissolve rapidly at 60°C. Thus specimens aged for 10^4 min before re-straining showed an initial rate of increase of ΔY on re-ageing which was about half of that occurring in a first ageing treatment after the same total deformation.

Even after a first ageing of 10^4 min at 60°C some re-solution of precipitates may have occurred on re-straining and ageing. Changes in resistivity are expected to be insensitive to the segregation of solute which is derived from precipitates during the course of ageing. The total change in resistivity in the second ageing of a wire, which had previously been stretched 4 per cent, aged for 10^4 min at 60°C and then re-strained 2 per cent, was found to be a little less than 0.3 of the change in resistivity observed in the first ageing of a similar wire which was prestrained 6 per cent. (The wires used in these measurements were drawn from the untreated steel, as described earlier, and were quenched from 200°C before the first prestraining. In both cases the change in resistivity due to ageing for 10^4 min at 60°C was measured.)

When specimens which have previously been strain aged sufficiently to precipitate nearly all the dissolved solute are re-strained, it is likely that the second ageing is concerned almost exclusively with reforming

VOL. 8 1960

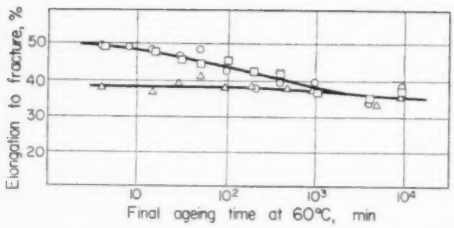


FIG. 8. Changes in ductility during a second ageing after re-straining. Before re-straining and final ageing, the specimens were quenched from 200°C, prestrained $3\frac{1}{2}$ per cent and then aged at 60°C for the following times: ○ 0 min; □ 150 min; △ 10^4 min.

atmospheres. Re-solution of precipitates can be involved because the dislocation density is higher after the second straining. Fig. 8 shows that ductility measurements, made during the course of a second ageing, gave little or no evidence of further precipitation in specimens which had previously been strained $3\frac{1}{2}$ per cent, aged for 10^4 min at 60°C and then strained a further 2 per cent before re-ageing. On the other hand the fall in ductility in the second ageing of specimens which had previously been aged for only 150 min at 60°C before re-straining was indistinguishable from that observed in a first ageing after the same total deformation.

Effects of variations in prestraining

Figure 9 gives results showing that a variation of prestrain in the range 2–7 per cent extension has only small effects on the changes in ΔY in subsequent ageing. These tests were all made on test pieces of 200 ± 20 grains/mm^2, quenched from 200°C before prestraining. Observations of the ageing times required for the growth of Luders strain to an approximately constant value, (35 ± 5 min at 60°C with each of the three conditions), suggested that the time to complete atmosphere locking was also little affected by varying the prestrain in this range.

The dislocation density would probably be almost doubled by increasing the prestrain from 2 to 7 per cent. These results therefore support an earlier

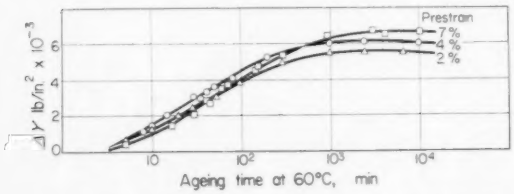


FIG. 9. Effect of prestrains in the range 2–7 per cent on the change in lower yield stress due to ageing. Specimens of 200 grains/mm^2, quenched from 200°C before prestraining.

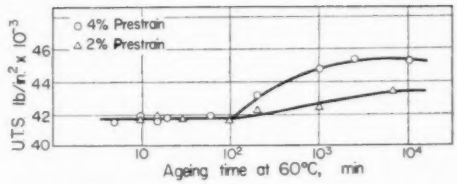


FIG. 10. Effect of prestrain on the change in ultimate tensile strength due to ageing in specimens quenched from 200°C before prestraining.

conclusion, that the rate of increase in ΔY during atmosphere formation is rather insensitive to dislocation density and is principally dependent on the amount of solute segregating per dislocation (i.e. the atmosphere density). This might be expected if yield propagation is concerned with a successive unlocking of individual dislocations.

Luders strain itself is sensitive to the prestrain because the initial rate of work hardening in test straining is reduced by increasing the amount of prestrain. (In the present tests the "limiting value" of Luders strain increased from about 0.8 per cent, in the case of specimens prestrained 2 per cent, up to about 2.0 per cent for specimens prestrained 7 per cent.)

Even in the "precipitation" stages of ageing the increases in ΔY are not very sensitive to variations in prestrain, but the results in Fig. 9 suggest that increasing the prestrain can give slightly larger values of ΔY in the later stages of ageing. In contrast to its small effect on ΔY, the amount of prestrain has a strong effect on the rate of work hardening shown by fully aged specimens. In the present tests, for example, doubling the amount of prestrain in the range 2–7 per cent extension approximately doubled the final values of ΔU (Fig. 10). This contrast in the effects of prestrain on ΔY and ΔU has been noted previously by Hundy[3].

It is possible that existing theories of alloy hardening can adequately explain the main features of the changes in mechanical properties on strain-ageing, and the effects of varying prestrain, if we consider a model in which the distribution of the segregates is controlled by the dislocation network. Writing equation (2) in the form;

$$\sigma_y = \sigma_i + \sigma_d l^{1/2} d^{-1/2}, \qquad (3)$$

where σ_d represents the unpinning stress and l the distance from grain boundary barriers to the nearest sources,[14] it may be noted that, during atmosphere formation, ΔY increases with σ_d, while σ_i remains practically unaffected until atmosphere formation is

completed.[4] It follows, if d is independent of the prestrain, that in specimens of constant grain size which have been aged up to the completion of atmosphere locking, the amount of prestrain should influence ΔY only through its effect on l, which is expected to vary with the spacing of the dislocation network. This suggests that $l^{1/2}$, hence ΔY due to atmospheres, should vary only slowly with changes in prestrain.

After the completion of atmosphere locking the segregation of a further 0.002 wt.% solute is sufficient to raise the flow stress by about 3000 lb/in^2. Although appreciably less effective in raising the yield stress than is atmosphere formation, judged as a precipitation hardening process the second stage of ageing is an efficient means of strengthening. In this respect early precipitation behaviour resembles hardening by groups of solute atoms or coherent precipitates of near critical dispersion. If most of this precipitation is on dislocations, the precipitates must form lines of very small, closely spaced particles through which free dislocations can be forced only with difficulty. The mean spacing between such line barriers, however, will be several hundred Ångstrom units and, with respect to the effects of changing the spacing of the dislocation network on which precipitation occurs, the behaviour of the strain aged material appears more closely analogous to that of "overaged" dispersion hardened alloys. A moderate change in dispersion of such an alloy has a relatively minor effect on the yield stress but can alter the strain hardening rate appreciably.[15]

The theory of Hart[15] and Fisher *et al.*[16] shows that, if the separation of the precipitates is sufficient to allow dislocations to be forced forward between individual particles, and if dislocation loops are left behind encircling the particles, then an appreciable hardening increment is to be expected on plastic straining, due to the back-stresses from the trapped loops. In terms of this model, mechanical effects in the precipitation stages of ageing can be interpreted as consequences of a progressive increase in the strength of the precipitates. Segregation just beyond the completion of atmosphere locking raises the flow stress without increasing the strain hardening, suggesting that free dislocations can be forced through the line barriers at a lower applied stress than that required for loop formation. After the segregation of an amount of solute which is roughly twice that required to complete atmosphere locking, however, an additional source of work hardening develops and this increases progressively, but at a diminishing rate, with further segregation.

Fisher *et al.*[16] suggested that the additional hardening increment τ_h, due to trapped loops, is given by

$$\tau_h = GK\left(\frac{r}{\Lambda}\right)^3\left(\frac{N\mathbf{b}}{r}\right). \qquad (4)$$

Where G is the rigidity modulus, $\mathbf{b}$ the Burgers vector, N the mean number of loops encircling a barrier, and K a constant ≈ 3. In the present case r is the diameter of the line barriers and Λ their mean spacing ($= L^{-1/2}$, where L is the number of dislocations in unit area). The stress in the precipitates ($\approx (N\mathbf{b}G)/r$) will increase with N during straining until a limiting value is reached, depending on the shear strength of the barriers. In dispersion hardened alloys τ_h appears to reach its limiting value after between 5 and 15 per cent extension.

Equation (4) predicts that τ_h will be inversely proportional to Λ^3 for precipitates of equal strengths. Thus, in strain aged materials, the additional strain hardening due to precipitation might be expected to be proportional to $L^{3/2}$ at equivalent stages of ageing.

Table 2 gives tensile test results, on specimens of similar composition and grain size, which were prestrained 2, 4 and 15 per cent respectively. The test pieces were quenched from 600°C before prestraining to give about 0.014 wt.% dissolved solute so that, in each case, only a small proportion of the available solute was consumed in atmosphere formation. Comparison of a number of estimates of dislocation densities based on strain ageing in iron suggests that L is closely proportional to $\varepsilon^{0.41}$, where ε is the extension in per cent.[17] This gives the estimated ratios of dislocation densities in Table 2. Values of ΔY due to ageing, and of the increase in flow stress ΔF measured at 10 per cent test strain, were measured at the completion of atmosphere locking and towards the end of ageing, at equivalent stages of precipitation in each group of specimens. (The values of ΔF at the completion of locking were negligible.) To compare ΔY and ΔF values at equal precipitate strengths, it was assumed that this would occur when equal numbers of solute atoms had segregated to unit length of dislocation. Times to reach stages of precipitation, in the specimens prestrained 2 and 4 per cent, equivalent to that in specimens strained 15 per cent, and aged for 10^4 min at 60°C, were estimated from the earlier resistivity measurements.

Although the range of dislocation densities is insufficient to provide a critical test, the results show that ΔY is insensitive to L (although the increment due to precipitation hardening could be inversely proportional to the dislocation spacing). On the other

VOL. 8 1960

TABLE 2

Prestrain (per cent)	15	4	2
Ratios of dislocation densities, $L/L_{15\%}$, assuming $L \propto \epsilon^{0.41}$	1	0.58	0.44
ΔY at completion of atmosphere locking, lb/in$^2 \times 10^{-3}$ (Values at full return of Luders strain).	4.0	4.3	4.1
Estimated times to reach equivalent stages of precipitation (min at 60°C).	10^4	10^3	9×10^2
ΔY at equal precipitate strengths, lb/in$^2 \times 10^{-3}$ (ageing times given above).	10.5	9.4	8.2
ΔF at equal precipitate strengths, lb/in$^2 \times 10^{-3}$ (measured at 10% test strain).	15.9	7.2	3.7
Ratios of changes in flow stress, $\Delta F/\Delta F_{15\%}$.	1	0.45	0.23
$(L/L_{15\%})^{3/2}$	1	0.44	0.29

hand, ΔF, measured at a test strain of 10 per cent, appears to be approximately proportional to $L^{3/2}$ at equivalent stages of the precipitation process.

The low ductility of aged specimens which have been more heavily prestrained limits the range of dislocation densities which can be explored. When aged to the completion of atmosphere locking, specimens prestrained more than about 15 per cent fracture at the lower yield stress with little or no general elongation. It is interesting that, if further strain ageing causes precipitation in such specimens, it can greatly improve the general elongation by increasing strain hardening.

4. SUMMARY AND CONCLUSIONS

(a) Present results confirm an earlier conclusion[4] that, on the evidence of the return of the sharp yield point, the segregation of about 0.001 wt.% carbon or nitrogen is sufficient to complete atmosphere locking in a moderately deformed low carbon steel. Estimates based on the Cottrell–Bilby equation suggest that this first stage of strain ageing is complete when the atmosphere density reaches a value not greatly in excess of one atom per atom plane.

(b) It is evident that the sites allowing strong interaction of the solute with dislocations are all occupied at the end of the first stage of ageing; nevertheless further segregation, of an amount of solute equal to that required for the first stage, is sufficient to cause an additional rise in the lower yield stress which is roughly one third of that due to the primary atmosphere locking. A $t^{2/3}$ law of segregation continues to be followed in this second stage (at least for ageing temperatures below, perhaps, 60°C); also, as in the first stage, the change in the lower yield stress, ΔY, is approximately proportional to the numbers of solute atoms segregating to unit length of dislocation.

Up to the end of this second stage, tensile tests (10^{-4} sec^{-1} strain rate) give no evidence of changes in strength or ductility at large test strains, suggesting that the segregates which increase ΔY may "evaporate" quite rapidly during continued straining at room temperature. Thus the second stage of ageing might be considered to involve the formation of an "outer atmosphere."[8] However, segregation beyond the end of the first stage causes little change in dislocation pinning (σ_d in equation 3). ΔY is raised because resistance to the motion of free dislocations is increased. It is concluded that solute clusters must be formed at favourable sites along the dislocations: thus the second stage of ageing can be regarded as a first step towards precipitation.

(c) When the amount of segregation reaches appreciably more than double that required to complete atmosphere locking, the segregates become stable enough to cause changes in strength, ductility and strain hardening capacity at large test strains in tensile tests at room temperature. As this third stage of ageing develops, continued segregation of solute becomes appreciably less effective in further increasing ΔY. Nevertheless, precipitation at 60°C or less evidently remains on an extremely fine scale. Even after the segregation of about 0.014 wt.% solute at 60°C in specimens prestrained 4 per cent, no clear evidence of discrete particles of precipitate was seen using direct carbon replicas in an electron microscopical examination. (Fine particles, possibly ~50 Å thick, apparently associated with dislocation sites, were detected after ageing at 150°C for several days.)

Mechanical tests suggest that precipitates formed in the third stage of ageing are at first small enough to redissolve rapidly in a second ageing treatment at 60°C, if the specimens are re-strained, to form free dislocations, after the first ageing.

(d) The increase in yield stress due to strain ageing is insensitive to moderate variations in prestrain, particularly in the early stages of ageing. However, tests with specimens in which the segregate concentration was more than 5 times that required for atmosphere locking suggest that the contribution of precipitation hardening to ΔY, (measured at equivalent stages of precipitation), tends to increase with dislocation density.

In contrast to its rather small effect on ΔY, increasing prestrain causes a marked increase in

strain hardening capacity in the third stage of ageing. It is suggested that, while the lines of fine precipitates formed along dislocations can develop to provide effective local barriers to dislocation movement, the spacing of these line barriers is sufficient to allow a build-up of dislocation loops, encircling the barriers, in subsequent straining. With prestrains in the range 2–15 per cent, the observed additional strain hardening due to precipitation appears roughly proportional to $L^{3/2}$, (where L is the original number of dislocations in unit area). Assuming an analogy with strain hardening in "overaged" dispersion hardened alloys, this is in agreement with a prediction made by Fisher *et al.*[16].

Such an additional mechanism of dislocation multiplication, introduced by strain ageing beyond the second stage, may play an essential role in the development of high strengths in low carbon steels by simultaneous straining and ageing (e.g. 140×10^3 lb/in^3 tensile strength in a 0.04 per cent carbon steel quenched from 700°C and "warm-worked" to about 70 per cent reduction).

ACKNOWLEDGMENTS

We wish to thank Professor E. C. Rollason for the provision of facilities, the Steel Company of Wales for giving the steel and Messrs. B. N. Das and D. J. Latham, who carried out the repeated straining and ageing experiments.

REFERENCES

1. W. Dahl and K. Lücke, *Arch. Eisenhüttenw.* **25,** 241 (1954).
2. W. R. Thomas and G. M. Leak, *J. Iron St. Inst.* **180,** 155 (1955).
3. B. B. Hundy, *Metallurgia, Manchr.* **53,** 203 (1956).
4. D. V. Wilson and B. Russell, *Acta. Met.* **8,** 36 (1960).
5. S. Harper, *Phys. Rev.* **83,** 709 (1951).
6. W. Pitsch and K. Lücke, *Arch. Eisenhüttenw.* **27,** 45 (1956).
7. R. H. Doremus, *Acta. Met.* **6,** 647 (1958).
8. A. H. Cottrell and B. A. Bilby, *Proc. Phys. Soc. Lond.* A**62,** 49 (1949).
9. A. H. Cottrell and G. M. Leak, *J. Iron St. Inst.* **172,** 301 (1952).
10. A. H. Cottrell and A. T. Churchman, *J. Iron St. Inst.* **162,** 271 (1949).
11. J. D. Fast and M. B. Verrijp, *J. Iron St. Inst.* **176,** 24 (1954).
12. J. R. Low and R. W. Guard, *Acta. Met.* **7,** 171 (1959).
13. B. B. Hundy and T. D. Boxall, *Metallurgia, Manchr.* **55,** 27 (1957).
14. A. H. Cottrell, *Trans. Amer. Inst. Min. (Metall.) Engrs.* **212,** 192 (1958).
15. E. W. Hart, *Relation of Properties to Microstructure*, p. 95. American Society for Metals, Cleveland (1954).
16. J. C. Fisher, E. W. Hart and R. H. Pry, *Acta Met.* **1,** 336 (1953).
17. W. Wepner, *Acta Met.* **5,** 703 (1957).

VOL. 8 1960

INTERACTIONS BETWEEN GLIDE DISLOCATIONS IN A DOUBLE PILE-UP IN α-IRON *

Y. T. CHOU,† F. GAROFALO† and R. W. WHITMORE†

The equilibrium distribution of arrested glide dislocations on two intersecting slip planes in α-iron is computed taking into account the elastic anisotropy. From the equilibrium distribution of dislocations calculation is made of the stresses near the tip of the double pile-up (that is, a pile-up on each of two intersecting slip planes). For fifty dislocations the shear stress at the tip of a double pile-up is calculated to be 1360 σ_0, where σ_0 is the applied stress in the slip plane. This stress is greater by a factor of 27 than the tip stress of a single pile-up of the same size. The high stress concentration at the tip of a double pile-up indicates, as suggested by Cottrell, that such a dislocation arrangement could lead to initiation of cleavage cracks in α-iron.

DETERMINATION DANS LE CAS DU FER α DES INTERACTIONS ENTRE DISLOCATIONS DE GLISSEMENT FORMANT UN EMPILEMENT DOUBLE

Les auteurs évaluent la distribution à l'équilibre de dislocations de glissement bloquées sur deux plans de glissement sécants du fer α en faisant intervenir les effets de l'anisotropie élastique. A partir de cette distribution à l'équilibre, ils calculent les tensions au voisinage de l'extrêmité du double empilement (c'est-à-dire un empilement sur chacun des deux plans de glissement sécants). Dans le cas où cet empilement intéresse une cinquantaine de dislocations, la tension de cisaillement à l'extrêmité du double empilement est égale à 1360 σ_0 si σ_0 est la tension appliquée au plan de glissement.

Cette tension est 27 fois plus grande que la tension existant à l'extrêmité d'un empilement simple de même taille. Cette concentration de tensions à l'extrèmité d'un empilement double indique, comme Cottrell l'a suggéré, qu'un tel assemblage de dislocations peut provoquer l'apparition de fissures de clivage dans le fer α.

WECHSELWIRKUNGEN ZWISCHEN GLEITFÄHIGEN VERSETZUNGEN IN EINER DOPPELTEN AUFSTAUUNG IN α-EISEN

Die Gleichgewichtsverteilung festgehaltener Gleitversetzungen auf zwei sich schneidenden Gleitebenen in α-Eisen wird berechnet unter Berücksichtigung der elastischen Anisotropie. Aus der Gleichgewichtsverteilung der Versetzungen ergeben sich die Spannungen an der Spitze der doppelten Aufstauung (d.h. einer Aufstauung auf jeder der beiden sich schneidenden Gleitebenen). Für fünfzig Versetzungen berechnet sich die Spannung an der Spitze der doppelten Aufstauung zu 1360σ_0, wo σ_0 die angelegte Spannung in der Gleitebene ist. Diese Spannung ist um den Faktor 27 größer als die Spannung an der Spitze einer einzelnen Aufstauung gleicher Größe. Wie schon von Cottrell vorgeschlagen, zeigt die hohe Spannungskonzentration an der Spitze einer doppelten Aufstauung, daß solch eine Versetzungsanordnung einen Spaltbruch in α-Eisen einleiten könnte.

INTRODUCTION

The role of dislocation pile-up groups in the fracture of metals is well established.[1] Early in 1948, Zener[2] proposed that a pile-up of dislocations against a barrier can produce a sufficient stress concentration to initiate a crack. This concept was further developed by Stroh[3] into a quantitative theory of fracture. One of his conclusions is that a crack in general should form when, in a plastically deformed metal, about 1000 dislocations are piled up against a barrier of sufficient strength. More recently, Cottrell[4], in considering fracture in b.c.c. metals, has suggested that a crack can be initiated by a double dislocation pile-up on two intersecting slip planes. This concept applies in particular to metal crystals such as α-iron, which exhibit appropriate slip and cleavage planes. However, no detailed quantitative analysis was given in his work, especially of the interaction between dislocations in the two pile-up groups or the stress distribution in the vicinity of the tip. It is the purpose of this paper to examine these factors in detail.

A double pile-up of dislocations consists of a system of two intersecting rows of similar dislocations arrested by a common barrier. The common barrier may be an immovable dislocation, a precipitated particle, or a phase boundary. In the present paper a quantitative analysis is presented of the equilibrium position of glide dislocations in a symmetrical double pile-up in α-iron. The analysis is based on the anisotropic elasticity theory developed by Eshelby *et al.*[5]. The stresses in the vicinity of the tip of the arrested dislocation rows are calculated and compared to those at the tip of a single dislocation pile-up. A brief discussion of Cottrell's theory on the initiation of cleavage cracks at the tip of a double pile-up of glide dislocations is included.

* Received July 15, 1959.

† Edgar C. Bain Laboratory for Fundamental Research, United States Steel Corporation Research Center, Monroeville, Pennsylvania.

VOL. 8 1960

EQUILIBRIUM POSITION OF DISLOCATIONS IN A DOUBLE PILE-UP

In a double pile-up group of dislocations, as shown in Fig. 1, the shear stresses σ_{02} and σ_{01}, the attraction as well as repulsion between the dislocations on different planes and repulsion between those on the same plane lead to a certain equilibrium distribution of dislocations along each of the two planes. Suppose for two orthogonal slip planes (110) and (1$\bar{1}$0) in α-iron as shown in Fig. 2(a) and (b), the dislocations lie parallel to the [001] direction. To determine the equilibrium distribution of dislocations along the two slip planes by anisotropic elasticity theory it is convenient to employ two sets of Cartesian coordinate systems:

(1) x^0-, y^0- and z^0-axis along the cube axes [100], [010] and [001], respectively, and

(2) x-, y- and z-axis along [110], [1$\bar{1}$0] and [001], respectively.

The second system is obtained by a 45° rotation of the first system about the z^0-axis. As shown in Fig. 2(b), it is assumed that n similar, straight dislocation lines with Burgers vector $a/2$ [111] are gliding in the (1$\bar{1}$0) plane. In a similar manner n dislocations with Burgers vector $a/2$ [1$\bar{1}\bar{1}$] are gliding along the (110) plane. All dislocation lines are parallel to the z-axis. The shear stress σ_0 is acting in both planes, (110) and (1$\bar{1}$0), and is normal in each case to the z-axis.

According to Cottrell[4] the lead dislocations in Fig. 2(b) can coalesce to form a single dislocation:*

$$a/2\,[111] + a/2\,[1\bar{1}\bar{1}] \rightarrow a\,[100]. \qquad (1)$$

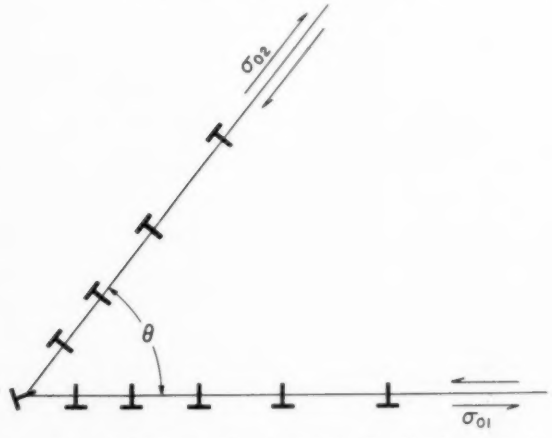


FIG. 1. Schematic representation of a simple type of double pile-up of dislocations.

* The slip planes in the present work follow the choice of coordinate systems and differ from those chosen by Cottrell[4]. The reaction shown here, however, is the same as that shown by Cottrell.

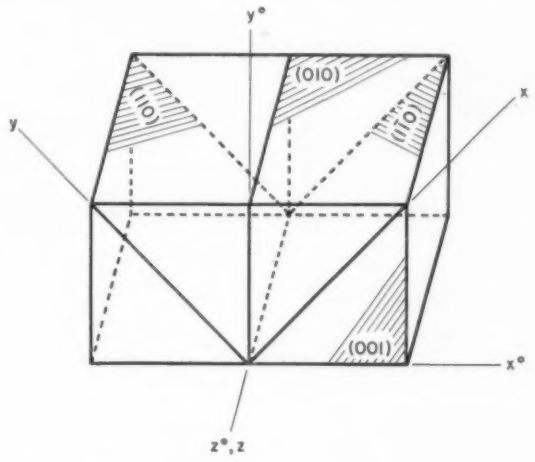


FIG. 2a. Crystallographic planes and the coordination systems used in anisotropic analysis of a dislocation double pile-up in alpha iron.

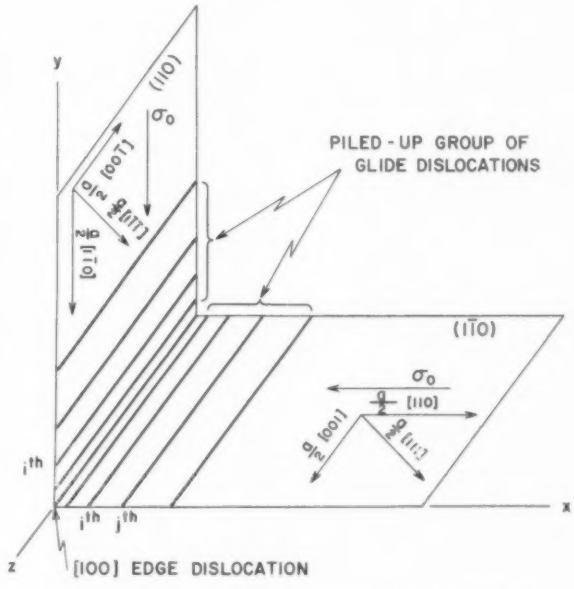


FIG. 2b. A symmetrical double pile-up of dislocations in alpha iron.

The new edge dislocation, which has a lower elastic energy, is stable and may act as a barrier. Thus, in this case a symmetrical double pile-up is formed.

The Burgers vector of each glide dislocation can be resolved into screw and edge components as follows:

$$\text{in } (1\bar{1}0) \quad a/2\,[111] \rightarrow a/2\,[001] + a/2\,[110]$$

$$\text{in } (110) \quad a/2\,[1\bar{1}\bar{1}] \rightarrow a/2\,[00\bar{1}] + a/2\,[1\bar{1}0]. \qquad (2)$$

For a straight dislocation in (110) plane (x–z or y–z plane) and along [001] (z-axis) the stress components

due to the screw components are for an anisotropic cubic crystal:

$$\sigma_{zx} = -\frac{C_{44}b_s}{2\pi}\frac{y}{x^2+y^2}$$

$$\sigma_{zy} = \frac{C_{44}b_s}{2\pi}\frac{x}{x^2+y^2} \tag{3}$$

where b_s is Burgers vector of the screw component and C_{44} is an elastic coefficient referred to the coordinate system chosen.

The stresses due to the edge components are

$$\sigma_{xx} = -A\frac{y(Bx^2+y^2)}{(x^2+y^2)^2+Cx^2y^2}$$

$$\sigma_{yy} = A\frac{y(x^2-y^2)}{(x^2+y^2)^2+Cx^2y^2}$$

$$\sigma_{xy} = A\frac{x(x^2-y^2)}{(x^2+y^2)^2+Cx^2y^2} \tag{4}$$

where

$$A = \frac{b_e}{2\pi}(C_{11}+C_{12})\left\{\frac{C_{66}(C_{11}-C_{12})}{C_{11}(C_{11}+C_{12}+2C_{66})}\right\}^{1/2}$$

$$B = \frac{(C_{11}-C_{12})(C_{11}+C_{12}+2C_{66})}{C_{11}C_{66}} - 1 \tag{5}$$

and

$$C = 2\left(\frac{C_{11}+C_{12}}{C_{11}}\right)\left(\frac{C_{11}-C_{12}}{2C_{66}} - 1\right)$$

and where b_e is the Burgers vector of the edge component; and C_{ij}'s are the elastic coefficients referring to the x–y–z coordinate system. Since only the values of $C^0{}_{ij}$'s (referring to the x^0–y^0–z^0 system) are found in the literature for cubic crystals, one has to transform the C_{ij}'s into $C^0{}_{ij}$'s according to the following equations:

$$C_{11} = C_{22} = 1/2\,(C^0{}_{11} + C^0{}_{12} + 2C_{44}{}^0)$$

$$C_{12} = 1/2\,(C^0{}_{11} + C^0{}_{12} - 2C_{44}{}^0) \tag{6}$$

$$C_{44} = C_{44}{}^0$$

and

$$C_{66} = 1/2\,(C^0{}_{11} - C^0{}_{12}).$$

The x-component of shear force which is acting on the j_{th} dislocation in the x–z plane is determined as follows:

(1) For all glide dislocations in the same plane the shear force becomes

$$F_{j1} = \frac{C_{44}b_s{}^2}{2\pi}\sum_{\substack{i=1\\ i\neq j}}^{n-1}\frac{1}{x_j-x_i} + Ab_e\sum_{\substack{i=1\\ i\neq j}}^{n-1}\frac{1}{x_j-x_i}, \tag{7}$$

(2) For all glide dislocations in the y–z plane it is

$$F_{j2} = -\frac{C_{44}b_s{}^2}{2\pi}\sum_{i=1}^{n-1}\frac{x_i}{y_i{}^2+x_j{}^2} + Ab_e\sum_{i=1}^{n-1}\frac{y_i(x_j{}^2-y_i{}^2)}{(y_i{}^2+x_j{}^2)+Cy_i{}^2x_j{}^2}. \tag{8}$$

Because of the existing symmetry it is possible to substitute x_i for y_i in equation (8), hence

$$F_{j2} = -\frac{C_{44}b_s{}^2}{2\pi}\sum_{i=1}^{n-1}\frac{x_j}{x_i{}^2+x_j{}^2} + Ab_e\sum_{i=1}^{n-1}\frac{x_i(x_j{}^2-x_i{}^2)}{(x_i{}^2+x_j{}^2)^2Cx_i{}^2x_j{}^2} \tag{9}$$

and

(3) for the dislocation with Burgers vector $b_e{}^0 = a$ [100] in the cleavage plane (010) the shear force is

$$F_{j3} = b_e\sqrt{2}/2\,A^0\left(\frac{1+B^0}{4+C^0}\right)\frac{1}{x_j} \tag{10}$$

where A^0, B^0 and C^0 are the same constants as A, B and C, respectively, except that in the former $C^0{}_{ij}$'s and $b_e{}^0$ are used and in A, B and C, C_{ij}'s and b_e are used.

For a condition of equilibrium the summation of the shear forces must equal zero and it is found therefore that

$$b_e\sqrt{2}/2\,A^0\left(\frac{1+B^0}{4+C^0}\right)\frac{1}{x_j} + \left(\frac{C_{44}b_s{}^2}{2\pi} + A\,b_e\right)\times\sum_{\substack{i=1\\ i\neq 1}}^{n-1}\frac{1}{x_j-x_i} - \frac{C_{44}b_s{}^2}{2\pi}\sum_{i=1}^{n-1}\frac{x_j}{x_i{}^2+x_j{}^2} + Ab_e\sum_{i=1}^{n-1}\frac{x_i(x_j{}^2-x_i{}^2)}{(x_i{}^2+x_j{}^2)^2+Cx_i{}^2x_j{}^2}\,b_e\sigma_0 = 0 \tag{11}$$

$$j = 1,2,3,\ldots.(n-1).$$

Substituting $C^0{}_{ij}$'s for C_{ij}'s, taking $D/2\sigma_0$ as unit of length where

$$D = \frac{1}{2\pi b_e}\left\{b_s{}^2C_{44}{}^0 + b_e{}^2(C_{11}{}^0 + C_{12}{}^0)\times\left[\frac{C_{44}{}^0(C_{11}{}^0-C_{12}{}^0)}{C_{11}{}^0(C_{11}{}^0+C_{12}{}^0+2C_{44}{}^0)}\right]^{1/2}\right\} \tag{12}$$

and rearranging one obtains

$$\frac{\beta}{x_j} + \sum_{\substack{i=1\\ i\neq j}}^{n-1}\frac{1}{x_j-x_i} - (1-\beta)\sum_{i=1}^{n-1}\frac{x_i}{x_i{}^2+x_j{}^2} + \beta\sum_{i=1}^{n-1}x_i\frac{(x_j{}^2-x_i{}^2)}{(x_i{}^2+x_j{}^2)^2+Cx_i{}^2x_j{}^2} - \frac{1}{2} = 0 \tag{13}$$

$$j = 1,2,3,\ldots.(n-1)$$

where

$$\beta = \sqrt{2}/2b_e{}^0b_e\frac{(C_{11}{}^0+C^0{}_{12})\,(C_{11}{}^0-C_{12}{}^0)^{1/2}}{\{b_s{}^2[C_{11}{}^0C_{44}{}^0(C_{11}{}^0+C_{12}{}^0+2C_{44}{}^0)]^{1/2}+b_e{}^2(C_{11}{}^0+C_{12}{}^0)[C_{11}{}^0-C_{12}]^{1/2}\}} \tag{14}$$

$$C = 4\frac{(C_{11}^0 + C_{12}^0)(-C_{11}^0 + C_{12}^0 + 2C_{44}^0)}{(C_{11}^0 - C_{12}^0)(C_{11}^0 + C_{12}^0 + 2C_{44}^0)}. \quad (15)$$

For isotropic cubic crystals, i.e.

$$C_{44}^0 = 1/2(C_{11}^0 - C_{12}^0) = G$$
$$C_{11}^0/(C_{11}^0 + C_{12}^0) = 1 - \nu \quad (16)$$

where G is the shear modulus and ν is the Poisson's ratio

$$D \text{ reduces to } \bar{D} = \frac{G}{2\pi b_e}\left(b_s^2 + \frac{2}{(1-\nu)}b_e^2\right)$$
$$\beta \text{ reduces to } \bar{\beta} = \sqrt{2}/2\, b_e^0 b_e/[b_s^2(1-\nu) + b_e^2] \quad (17)$$
$$\text{and } C \text{ reduces to } \bar{C} = 0.$$

The force equilibrium equations therefore become

$$\frac{\bar{\beta}}{x_j} + \sum_{\substack{i=1\\ i\neq j}}^{n-1}\frac{1}{x_j - x_i} - (1-\bar{\beta})\sum_{i=1}^{n-1}\frac{x_j}{x_i^2 + x_j^2} + \bar{\beta}\sum_{i=1}^{n-1}\frac{x_i(x_j^2 - x_i^2)}{x_i^2 + x_j^2)^2} - 1/2 = 0 \quad (18)$$
$$j = 1,2,3, \ldots (n-1).$$

The equilibrium positions of $2(n-1)$ glide dislocations can be determined from equation (13) for anisotropic crystals and by equation (18) for isotropic crystals. No analytical solutions have been found for these relations but a suitable numerical solution is possible. By modifying the Newton–Raphson iteration method[6] numerical data have been obtained on the IBM-650 and 704 digital computers. The values of C_{ij}^0's for α-iron used in the numerical solution are given by Schmidt and Boas[7] as

$$C_{11}^0 = 2.37 \times 10^{12}\ \text{dyn/cm}^2$$
$$C_{12}^0 = 1.41 \times 10^{12}\ \text{dyn/cm}^2$$
$$C_{44}^0 = 1.16 \times 10^{12}\ \text{dyn/cm}^2$$

and $b_e = \sqrt{2}/2\, a$, $b_s = 1/2\, a$.

The computed values of x_i's for n = 2–10, 15, 20, 25, 30, 40 and 50 are given in Table 1. For purposes of comparison, the corresponding values for a single pile-up* arrested by a barrier along [001] axis are computed and given in Table 2.

* Similar work has been done by D. Kuhlmann-Wilsdorf at the University of Pennsylvania.[8]

TABLE 1. Equilibrium position of glide dislocations in symmetrical double pile-ups (for α-iron)

n	x_i (unit length $D/2\sigma_0$) $i = 1, 2, \ldots, (n-1)$										
2	0.932										
3	0.404,	2.75									
4	0.231,	1.54,	4.89								
5	0.151,	1.00,	3.09,	7.21							
6	0.108,	0.710,	2.18,	4.90,	9.64						
7	0.0809,	0.533,	1.63,	3.63,	6.89,	12.2					
8	0.0633,	0.417,	1.27,	2.82,	5.28,	8.99,	14.7				
9	0.0511,	0.336,	1.02,	2.27,	4.22,	7.09,	11.2,	17.3			
10	0.0422,	0.278,	0.845,	1.87,	3.47,	5.79,	9.01,	13.5,	20.0		
15	0.0203,	0.134,	0.406,	0.895,	1.66,	2.74,	4.20,	6.09,	8.49,	11.5,	15.2,
	19.8,	25.6,	33.6								
20	0.0122,	0.0800,	0.243,	0.535,	0.988,	1.63,	2.50,	3.61,	5.01,	6.71,	8.76,
	11.2,	14.1,	17.4,	21.4,	26.0,	31.6,	38.5,	47.6			
25	0.00817,	0.0537,	0.163,	0.360,	0.664,	1.10,	1.68,	2.42,	3.35,	4.48,	5.84,
	7.44,	9.30,	11.4,	13.9,	16.7,	19.9,	23.5,	27.6,	32.3,	37.7,	44.1,
	51.8,	61.9									
30	0.00591,	0.0389,	0.118,	0.260,	0.480,	0.793,	1.21,	1.75,	2.42,	0.324,	4.21,
	5.36,	6.69,	8.22,	9.96,	11.9,	14.1,	16.6,	19.4,	22.5,	25.9,	29.7,
	33.9,	38.6,	43.9,	50.0,	57.0,	65.4,	76.3				
40	0.00356,	0.0234,	0.0711,	0.157,	0.289,	0.477,	0.728,	1.05,	1.45,	1.94,	2.53,
	3.21,	4.00,	4.91,	5.94,	7.10,	8.40,	9.85,	11.4,	13.2,	15.1,	17.2,
	19.5,	22.0,	24.8,	27.7,	30.9,	34.3,	38.0,	42.1,	46.5,	51.2,	56.4,
	62.1,	68.4,	75.5,	83.6,	93.1,	105					
50	0.00240,	0.0158,	0.0479,	0.106,	0.195,	0.321,	0.491,	0.709,	0.980,	1.31,	1.70,
	2.16,	2.70,	3.31,	4.00,	4.78,	5.65,	6.61,	7.68,	8.85,	10.1,	11.5,
	13.0,	14.7,	16.5,	18.4,	20.4,	22.6	25.0,	27.5,	30.2,	33.0,	36.1,
	39.3,	42.8,	46.4,	50.4,	54.6,	59.0,	63.8,	68.9,	74.4,	80.4,	86.9,
	94.0,	102,	111,	121,	135						

VOL. 8 1960

TABLE 2. Equilibrium position of glide dislocations in single pile-ups (general)

n	x_j (unit length $D/2\sigma_0$) $i = 1, 2, \ldots, (n-1)$									
2	2.000									
3	1.268,	4.732								
4	0.9358,	3.305,	7.759							
5	0.7432,	2.571,	5.731,	10.95						
6	0.6170,	2.113,	4.611,	8.399,	14.26					
7	0.5275,	1.796,	3.876,	6.918,	11.23,	17.65				
8	0.4610,	1.564,	3.352,	5.916,	9.421,	14.19,	21.09			
9	0.4094,	1.385,	2.956,	5.182,	8.162,	12.07,	17.25,	24.59		
10	0.3680,	1.243,	2.645,	4.616,	7.220,	10.57,	14.83,	20.38,	28.12	
15	0.2445,	0.8228,	1.740,	3.007,	4.639,	6.660,	9.097,	11.99,	15.40,	19.42,
	24.15,	29.82,	36.82,	46.18						
20	0.1837,	0.6168,	1.301,	2.240,	3.441,	4.911,	6.661,	8.706,	11.06,	13.75,
	16.80,	20.24,	24.13,	28.53,	33.52,	39.26,	45.95,	54.05,	64.65	
25	0.1469,	0.4932,	1.039,	1.786,	2.739,	3.900,	5.275,	6.870,	8.693,	10.75,
	13.06,	15.63,	18.48,	21.62,	25.09,	28.90,	33.11,	37.76,	42.93,	48.70,
	55.23,	62.76,	71.74,	83.37						
30	0.1224,	0.4106,	0.8646,	1.485,	2.275,	3.236,	4.370,	5.682,	7.174,	8.854,
	10.72,	12.79,	15.07,	17.56,	20.28,	23.23,	26.44,	29.92,	33.69,	37.78,
	42.22,	47.06,	52.34,	58.13,	64.56,	71.76,	79.99,	89.73,	102.2	
40	0.09178,	0.3078,	0.6477,	1.112,	1.701,	2.417,	3.260,	4.231,	5.333,	6.566,
	7.934,	9.438,	11.08,	12.87,	14.80,	16.88,	19.12,	21.51,	24.07,	26.80,
	29.71,	32.81,	36.10,	39.60,	43.31,	47.26,	51.45,	55.92,	60.67,	65.75,
	71.18,	77.01,	83.31,	90.14,	97.63,	105.9,	115.3,	126.3,	140.4	
50	0.07342,	0.2462,	0.5179,	0.8889,	1.359,	1.930,	2.601,	3.374,	4.249,	5.226,
	6.308,	7.495,	8.789,	10.19,	11.70,	13.32,	15.06,	16.91,	18.88,	20.97,
	23.18,	25.52,	27.99,	30.59,	33.33,	36.21,	39.24,	42.42,	45.77,	49.27,
	52.95,	56.82,	60.87,	65.13,	69.61,	74.32,	79.28,	84.51,	90.04,	95.89,
	102.1,	108.7,	115.9,	123.5,	131.9,	141.1,	151.4,	163.5,	178.8	

In the single pile-up, the force equilibrium equations for isotropic and anisotropic cases are identical, namely:

$$\frac{1}{x_j} + \sum_{\substack{i=1 \\ i \neq j}}^{n-1} \frac{1}{x_j - x_i} - 1/2 = 0 \quad j = 1, 2, \ldots, (n-1) \tag{19}$$

where x_i's, as in the double pile-up case, are dimensionless numbers with the unit of $D/2\sigma_0$. The value of D, however, is different for isotropic and anisotropic crystals. Eshelby *et al.*[9] have shown that the x_i's are the zeros of $L_n'(x)$, the derivative of the n_{th} Laquerre polynomial.

Several formulas may be empirically formulated for symmetrical double pile-up systems. These relations showing the distribution of the first three dislocations (Fig. 3) are

$$\begin{aligned} x_1 &= 2.53\,(1/n)^{1.78} \\ x_2 &= 16.6\,(1/n)^{1.78} \quad 10 \leq n \leq 50 \\ x_3 &= 50.6\,(1/n)^{1.78} \end{aligned} \tag{20}$$

with an error of ± 1 per cent.

The range of the pile-up, L, that is the length of the slip plane occupied by one of the piled-up groups satisfies the relation

$$L = 2.87\,n - 8.9 \qquad 10 \leq n \leq 50 \tag{21}$$

with an error of ± 2 per cent (Fig. 4).

STRESS DISTRIBUTION NEAR THE TIP OF A DOUBLE PILE-UP

In a double pile-up group of glide dislocations certain interactions arise between individual dislocations. These interactions determine the distribution of dislocations and consequently the stress distribution. The stress function at an arbitrary point about the tip of a double pile-up can be calculated by a summation over all stresses associated with each dislocation. In the general case a three-dimensional problem arises. However, in other cases the stress function reduces to a simple type. One such case is for the stresses along the plane of symmetry.

The stress values which are of interest are: (1) the normal stress, σ_n, which is normal to the plane of symmetry and (2) the shear stress at the tip, $(\sigma_{xy})_0$.

The normal stress is expressed by the relation

$$\sigma_n = -2\beta\sigma_0\left[1/x + \sum_{i=1}^{n-1}\left\{\frac{x[(B-1)(X-x_i)^2 + 2x^2] + 2(x-x_i)[(x-x_i)^2 - x^2]}{[(x-x_i)^2 + x^2]^2 + Cx^2(x-x_i)^2}\right\}\right]. \tag{22}$$

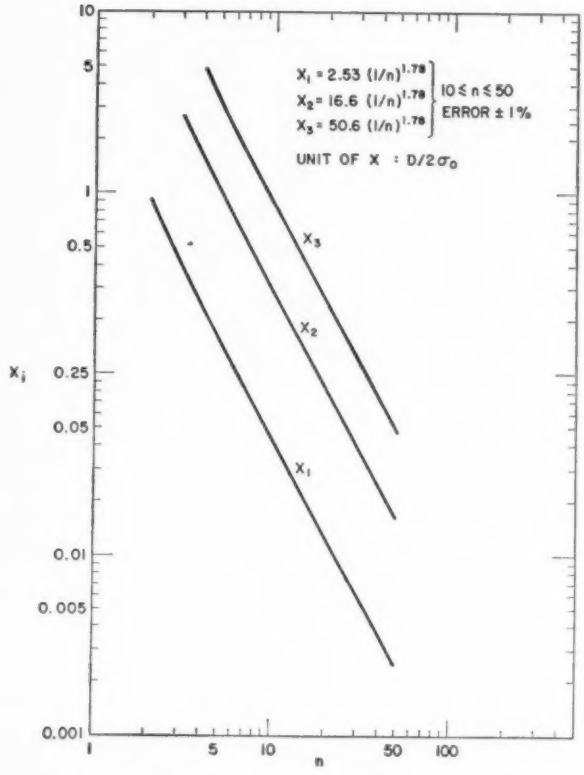


FIG. 3. Equilibrium position of the first three glide dislocations in a double pile-up in alpha iron.

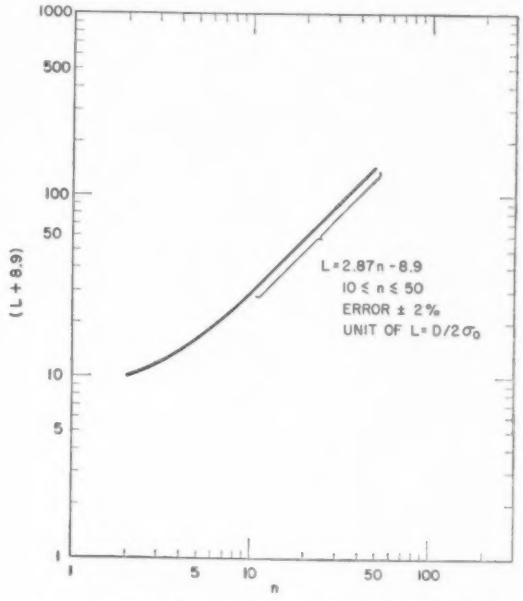


FIG. 4. The relationship between the range of a double pile-up, L, and the number of dislocations, n, within the range.

Results for the normal stress for $n = 25$, 40 and 50 are shown in Figs. 5 and 6. In the results shown in Fig. 5, the part contributed by the immobile dislocation has been omitted. This part has been included in computing the results shown in Fig. 6. One may note that near the tip the normal stresses increase rapidly as the number of dislocations increases. On the other hand, the width of the high stress region decreases with increase of n. These features can be seen more clearly in Fig. 5 than in Fig. 6. Another point of interest in these results is the fact that the maximum normal stress occurs on the tension side of the double pile-up, that is, to the left of the double pile-up shown in Fig. 2(b).

The shear stress at the tip of the double pile-up, by excluding the immobile dislocation, is given by

$$(\sigma_{xy})_0 = \sigma_0\left\{1 + 4\beta\sum_{i=1}^{n-1}\frac{1}{x_i}\right\}. \tag{23}$$

The results obtained from relation (23) for different numbers of dislocations in each of the two rows of the pile-up are given in Table 3. A plot of the results in Table 3 is shown in Fig. 7. The linear relation in the plot of Fig. 7 leads to the expression

$$(\sigma_{xy})_0 = 1.29\, n^{1.78}\sigma_0 \quad 10 \leq n \leq 50 \tag{24}$$

with an error of ± 1 per cent.

An upper and a lower limit of $(\sigma_{xy})_0$ can be found to substantiate relation (24) by the following argument: Because of the double pile-up it should be obvious that $(\sigma_{xy})_0$ is greater than $(2n-1)\sigma_0$ which is simply the sum of the tip stresses of two single pile-ups. The maximum effect of the second row of dislocations on the first dislocation in the first row cannot be greater than $(n-1)\sigma_0$. This is also true for all other dislocations in the first row. Thus, the maximum effect of the second row on the first is to raise the shear stress from σ_0 to $n\sigma_0$. It follows then that the maximum shear stress at the tip cannot exceed $[2n(n-1)+1]\sigma_0$ leading to the condition

$$(2n-1)\sigma_0 < (\sigma_{xy})_0 < (2n^2 - 2n + 1)\sigma_0. \tag{25}$$

It is obvious therefore that relation (24) is reasonable.

VOL. 8 1960

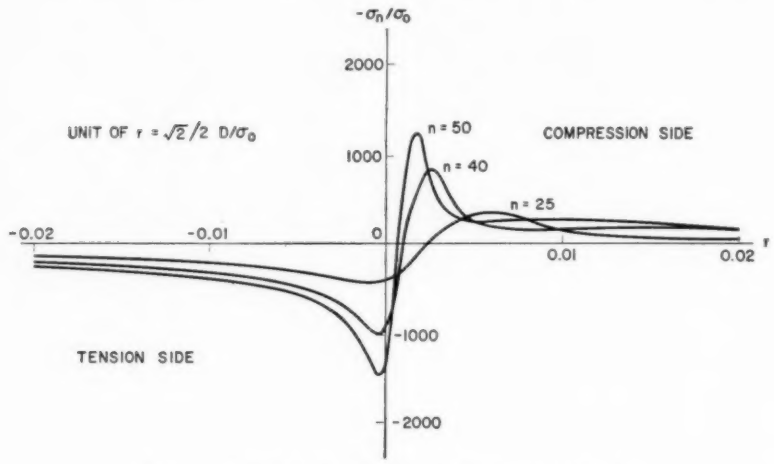


FIG. 5. Distribution of normal stress, σ_n, along the (100) plane of symmetry: [100] edge dislocations excluded.

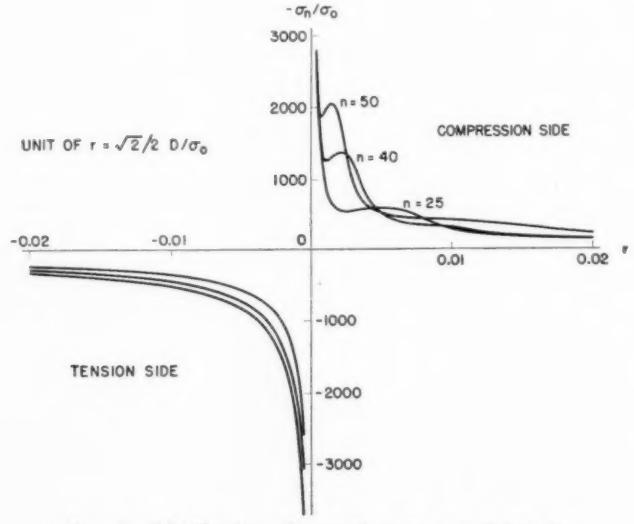


FIG. 6. Distribution of normal stress, σ_n, along the (100) plane of symmetry: [100] edge dislocation included.

TABLE 3. Tip stresses of symmetrical double pile-ups in α-iron (anisotropic)

n	$(\sigma_{xy})_0/\sigma_0$
2	3.76
3	8.31
4	14.4
5	21.8
6	30.6
7	40.5
8	51.7
9	64.1
10	77.5
15	161
20	269
25	400
30	552
40	917
50	1360

It should also be noted that the effect of anisotropy becomes significant for a double pile-up group in α-iron. Calculations indicate that for five dislocations in each row the tip stress for the anisotropic case is about 25 per cent greater than that for the isotropic case. For twenty dislocations this difference becomes 47 per cent and for fifty dislocations 62 per cent.

DISCUSSION

For a single pile-up of dislocations against a barrier the shear stress at the tip of the pile-up reaches a value which is equivalent to $n\sigma_0$.[9,10] Thus, for fifty dislocations a stress of 50 σ_0 should be attained. But for a double pile-up of fifty dislocations

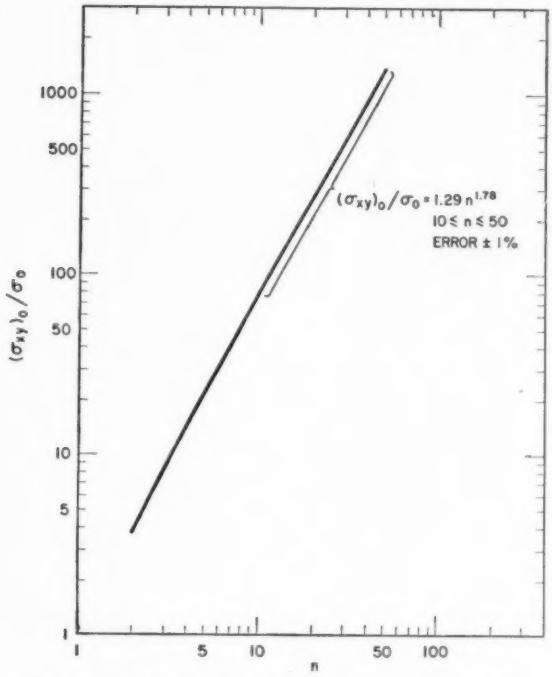


FIG. 7. The relationship between tip stress $(\sigma_{xy})_0$ and number of dislocations, n.

VOL. 8 1960

in α-iron, it is found from the present analysis that from relation (24) a stress of 1360 σ_0 is reached. Hence, a double pile-up shows a greater stress intensification which increases the stress by a factor of about 27.

For a shear stress of $\sigma_0 = 10^9$ dyn/cm², which is essentially the shear stress at rupture for iron at low temperatures, the distance x, between the two leading dislocations is about 7 a for a single pile-up of fifty dislocations. However, in a double pile-up of a similar size $x = 0.2\,a$ for the same applied shear stress. Thus, for the double pile-up the stage of dislocation coalescence has been reached. According to Stroh's analysis,[3] it seems that fifty dislocations are sufficient for the initiation of a micro-crack. This is not the case for the single pile-up which would require an appreciably greater number of dislocations to reach the coalescence stage and micro-crack formation. It is also of interest to note that a double pile-up of fifty dislocations on each glide plane corresponds to a local dislocation density of 10^{10} dislocation lines per cm². Such a dislocation density is observed in high-purity iron tested in tension at very low temperatures.[11]

It should be made clear, however, that the double pile-up arrangement can initiate a micro-crack only if the barrier has sufficient strength to allow the stress to increase until a micro-crack is formed. Stroh[12] has shown that a pure [100] dislocation may not be an effective barrier. However, if the [100] dislocation is pinned by foreign atoms or is blocked by precipitated particles, it may become a suitable barrier.

CONCLUSIONS

A detailed study of the equilibrium distribution of dislocations and the stress distribution at the tip of a double pile-up group in α-iron leads to the following conclusions:

1. A double dislocation pile-up generates a high stress concentration at the tip. In α-iron the stress concentration developed is much higher for a double pile-up than for a single pile-up having an equivalent number of dislocations.

2. The equilibrium positions of the first three dislocations in the two pile-up groups of n-dislocations each can be determined from the following empirical formulas:

$$x_1 = 2.53\,(1/n)^{1.78}$$

$$x_2 = 16.6\,(1/n)^{1.78}, \quad 10 \leq n \leq 50$$

$$x_3 = 50.6\,(1/n)^{1.78}$$

with an error of ±1 per cent.

3. The range L of the double pile-up can be expressed by

$$L = 2.87\,n - 8.9, \quad 10 \leq n \leq 50$$

with an error of ±2 per cent.

4. The shear stress at the tip is found to be

$$(\sigma_{xy})_0 = 1.29\,n^{1.78}, \quad 10 \leq n \leq 50$$

with an error of ±1 per cent.

5. When the barrier at the tip of the double pile-up is of sufficient strength, fifty dislocations in each of the two rows would be sufficient to initiate a micro-crack in α-iron.

ACKNOWLEDGMENT

The authors are indebted to Dr. J. C. M. Li for many enlightening discussions, to Drs. R. L. Rickett and L. S. Darken for their constant encouragement and support and to J. Malone of the Gary Works for programming the numerical solution for the IBM-704 digital computer.

REFERENCES

1. Conference on *The Atomic Mechanisms of Fracture*, preprint. Swampscott, Massachusetts (1959).
2. C. ZENER, *Fracturing of Metals* p. 3. American Society for Metals, Cleveland (1948).
3. A. N. STROH, *Proc. Roy. Soc.*, A**223**, 404 (1954), 548 (1955); *Advanc. Phys.* **6**, 418 (1957).

4. A. H. COTTRELL, *Trans. Amer. Inst. Min. (Metall.) Engrs.* **212,** 192 (1958).
5. J. D. ESHELBY, W. T. READ and W. SHOCKLEY, *Acta Met.* **1,** 251 (1953).
6. F. B. HILDEBRAND, *Introduction to Numerical Analysis* p. 447. McGraw-Hill, New York (1956).
7. E. SCHMIDT and W. BOAS, *Plasticity of Crystals.* Hughes, London (1950).
8. D. KUHLMANN-WILSDORF, Abstract in *Program of AIME Annual Meeting* (Feb. 1959).
9. J. D. ESHELBY, F. C. FRANK and F. R. N. NABARRO *Phil. Mag.* **42,** 351 (1951).
10. A. H. COTTRELL, *Progr. Met. Phys.* **1,** 77 (1949).
11. M. GENSAMER, private communication.
12. A. N. STROH, reported at Conference on *The Atomic Mechanisms of Fracture* (1959), cf. Ref. (1).

HEATS OF FORMATION OF SOLID Au-Cu ALLOYS*

R. L. ORR†

Heats of formation have been measured by liquid tin solution calorimetry for a complete series of Au–Cu alloys in equilibrium states at 720°K and for the same alloys at 320°K after rapid quenching from 873°K. The asymmetry in the heat of formation curve at 720°K is in accord with observations on the variation of short range order with composition. The considerably more exothermic heats of formation found for the quenched alloys are ascribed to an increase in the degree of short range order during quenching, which is consistent with the results of both X-ray and kinetic studies. Heats of formation of fully ordered AuCu and $AuCu_3$ alloys have also been measured from which their configurational energies with respect to the "disordered" alloys at 720°K have been obtained.

CHALEURS DE FORMATION DES ALLIAGES SOLIDES Au–Cu

Des chaleurs de formation ont été mesurées par voie calorimétrique dans l'étain liquide pour toute une série d'alliages Au–Cu à l'état d'équilibre à 720°K, et encore pour quelques alliages à 320°K après les avoir trempés à une température de 873°K. L'asymétrie dans la courbe de la chaleur de formation à 720°K correspond aux observations de la variation de l'ordre à proche distance avec la composition. Les chaleurs de formation considérablement plus exothermiques que l'on a trouvées pour les alliages trempés sont attribuées à un accroissement du degré d'ordre à petite distance pendant la trempe; cet accroissement est en accord avec les résultats obtenus lors de l'étude par rayons X et lors de l'étude cinétique. Des chaleurs de formation d'alliages Au–Cu et $Au–Cu_3$ complètement ordonnées ont été mesurées aussi; leurs énergies de configuration par rapport aux alliages désordonnés à 720°K ont été obtenues.

BILDUNGSWÄRMEN FESTER Au–Cu–LEGIERUNGEN

Die Bildungswärmen einer vollständigen Reihe von Au–Cu–Legierungen wurden durch Lösungskalorimetrie in flüssigem Zinn bei 720°K im Gleichgewichtszustand und bei 320°K nach raschem Abschrecken von 873°K gemessen. Bei 720°K zeigte die Kurve der Bildungswärme eine Asymmetrie, die mit den Beobachtungen über die Abhängigkeit der Nahordnung von der Zusammensetzung übereinstimmt. Bei den abgeschreckten Legierungen wurde eine beträchtlich größere exotherme Bildungswärme gefunden. Dies wird einer Zunahme des Nahordnungsgrades während des Abschreckens zugeschrieben, die mit röntgenographischen und kinetischen Untersuchungen im Einklang ist. Die Bildungswärmen von vollständig geordneten AuCu- und $AuCu_3$-Legierungen wurden ebenfalls gemessen. Daraus wurden ihre Konfigurationsenergien bezüglich der "entordneten" Legierungen bei 720°K bestimmt.

VOL. 8 1960

1. INTRODUCTION

The Au–Cu system has often served as the prototype of an alloy system showing order–disorder phenomena and thus involving the closely related concepts of strain energy, short range order and superlattice formation. Existing knowledge of the thermochemistry of the Au–Cu system, however, is far from complete, and the ordering processes involved are still not completely understood.

The $AuCu_3$ and AuCu superlattices have been well known for some time.[1] Below 633°K $AuCu_3$ forms a superlattice derived from the high temperature f.c.c. phase with Au atoms occupying the cube corners and Cu atoms occupying the cube faces. At low temperatures the AuCu ordered phase has a tetragonal structure resulting from alternate layers of Au and Cu atoms forming on the (002) planes of the high temperature f.c.c. phase. Between 658°K and the critical temperature, 683°K, the stable structure for that alloy is an orthorhombic modification of the tetragonal structure in which the Au and Cu atoms change layers along one axis after every fifth cell.

Recent X-ray diffraction studies of Batterman[2] and calorimetric studies of d'Heurle and Gordon[3] have confirmed the existence of a third ordered phase at and near the composition Au_3Cu, detected earlier by Johansson and Linde[4], Hirabayashi[5], and Ogawa and Watanabe[6]. Batterman found the critical temperature to be 472 ± 3°K at 75 at.% Au increasing to 504 ± 3°K at 68 at.% Au. The ordered phase was shown to consist of ordered antiphase domains about 50 Å in size; no annealing treatment was found which would cause the domains to coalesce. Alloys containing more than 75 at.% Au could not be ordered at any temperature.

Above the critical temperatures, the continuous f.c.c. solid solution phase has been shown to possess considerable amounts of short range order, the degree of order decreasing with increasing temperature.[7,8] Recent evidence has suggested that the equilibrium configuration present at high temperatures is not

* Received December 2, 1959; revised January 15, 1960.
† Department of Mineral Technology, University of California, Berkeley, California.

6A–(4 pp.)

maintained upon even very rapid quenching, contradicting an assumption which has often been made in the past. Roberts[7] found the degree of short range order in AuCu to increase markedly during a rapid quench from a temperature almost 100° above its critical temperature. The results of Borie and Warren[9] indicate similar behavior for $AuCu_3$.

Heat of formation data provide a direct measure of the difference between the total bonding energy of an alloy and that of its pure component metals. For an ordering alloy it may be assumed as a first approximation that differences between the bonding energies of ordered, partly ordered and disordered states with respect to the pure components are due primarily to differences in configuration.[10] This assumes that possible accompanying differences in the vibrational energy contribution may be neglected. Thus heat of formation measurements of such alloys as a function of temperature or of previous thermal history may present an advantageous method of detecting and estimating the extent of the accompanying configurational changes. Previously reported direct calorimetric measurements of the heats of formation of Au–Cu alloys within the disordered region are limited to only three compositions, and only one measurement has been reported for a quenched disordered alloy. The present paper describes the determination of the heats of formation of a series of nine alloys within the disordered region and of the same alloys after rapid quenching from the disordered region. The heats of formation of the ordered phases are also reported. An attempt is made to interpret the results in terms of the ordering processes involved.

2. EXPERIMENTAL

(a) *Preparation of alloys*

Nine Au–Cu alloys were prepared containing 10, 25, 40, 50, 60, 70, 75, 80 and 90 at.% Cu. The Au and Cu used in the preparation and also for measurements on the pure metals were shown by spectrographic analysis to be 99.99 per cent and 99.98 per cent pure, respectively.

Three to ten g ingots of the alloys were prepared by melting the metals in sealed evacuated quartz tubes at 1473°K for about 5 min with frequent shaking, after which the tubes were quenched in cold water. Weight losses on fusion were 0.1 per cent or less and were considered negligible. The resulting ingots were cold worked and homogenized under vacuum at temperatures about 50° below the respective solidus temperatures for 2 weeks.

Filings taken from both ends of each ingot were annealed in evacuated Pyrex tubes at 873°K for 1 hr after which they were given a rapid quench by crushing the tubes under cold water. Sharp well-resolved high-angle X-ray diffraction peaks obtained using $CuK\alpha$ radiation showed the alloys to be homogeneous, and the measured lattice constants were in excellent agreement with previous data,[11,12] confirming the accuracy of the compositions. No superlattice lines were present in the diffraction patterns, indicating no long range order to have originated in the quench.

The ingots were then rolled to a thickness of about 1 mm and cut into pieces about 1 or 2 mm square, a convenient size for use in the thermodynamic measurements. The cuttings were annealed *in vacuo* at 873°K for 2 hr followed by a rapid quench in water as for the filings.

Portions of the cuttings and filings of the $AuCu_3$ and AuCu compositions were heat treated at 653°K for 2 weeks, after which the temperature was gradually reduced to 523°K over a 20-day period. After a week at this temperature the specimens were furnace cooled to room temperature. X-ray diffraction patterns were taken of filings of the two ordered phases thus developed. The narrow widths and sharp peaks of the superlattice lines and calculations based on the relative intensities of the fundamental and superlattice reflections showed the degree of long range order in both phases to be virtually perfect.

Similarly, cuttings and filings of the Au_3Cu composition were annealed at 473°K for 6 weeks in an attempt to develop the ordered phase for that composition. Since the results of Batterman[2] were not available at the time this work was done, the annealing temperature chosen was probably too high. The X-ray diffraction pattern of the annealed filings did not reveal any superlattice lines.

(b) *Apparatus and methods*

Heats of solution of the alloys and the pure metals in liquid tin were measured using the calorimetric apparatus and methods described in detail in a previous publication.[13] For the measurements specimens weighing about 0.80 g were prepared by enclosing cuttings of the alloys or pure metals in tin or gold foil capsules. The liquid tin bath was maintained at about 700°K for all the runs, at which temperature the solution times varied from less than 1 min for pure Au to about 6 min for pure Cu.

Measurements were made of the total heat effect for the pure metals or alloys going from the solid states at a pre-drop temperature, T, to the dissolved states at the solution temperature, 700°K. Specimens dropped from a temperature within the disordered

region were held for several days in the dispenser at the elevated temperature before dropping them into the bath. The heats of formation at temperature T were obtained by subtracting the heats of sulution of the alloys from the heats of solution of corresponding amounts of the pure metals, all starting from the same initial temperature T.

3. RESULTS AND DISCUSSION

Six determinations of the heat of solution of each of the pure metals evaluated at the solution temperature, 700°K, yielded the average values of -5170 ± 21 cal/g-atom for Au and 2840 ± 15 cal/g-atom for Cu. Since the measurements were made in dilute solution, the values are approximately the relative partial molal heat contents of Au and Cu in infinitely dilute solution in liquid tin at 700°K with respect to the solid metals at that temperature, i e. $(\bar{H} - H^\circ)_{700^\circ K, x_{Sn}=1}$. The average values are in excellent agreement with other determinations conducted in this laboratory[13] and by Oriani and Murphy[14].

The heats of formation of the rapidly quenched and of the ordered alloys were determined at 320°K. For the alloys in equilibrium at high temperatures, the average pre-drop temperature, and thus the temperature at which the heats of formation were determined was 720°K. All the experimental results are listed in Table 1 and are shown plotted in Fig. 1. Results are included for the specimen of Au_3Cu which was given an attempted ordering heat treatment even though it showed no superlattice lines, for reasons which will be discussed later.

TABLE 1. Measured heats of formation for Au–Cu alloys

Alloy, x_{Cu}	Heat of formation (cal/g-atom)		
	720°K equilibrium	320°K quenched	320°K ordered
0.10	−331 −290	−368 −366	
0.25	−715 −698 −710	−958 −967	(−910)* (−914)
0.40	−1076	−1437 −1473 −1427	
0.50	−1226 −1234	−1634 −1661 −1601	−2149 −2166 −2142
0.60	−1275	−1559 −1569	
0.70	−1145 −1192	−1337 −1350	
0.75	−1083 −1051	−1145 −1213	−1736 −1681 −1700
0.80	−891	−941 −999 −964	
0.90	−437	−463 −437 −503	

*Not fully ordered; see text

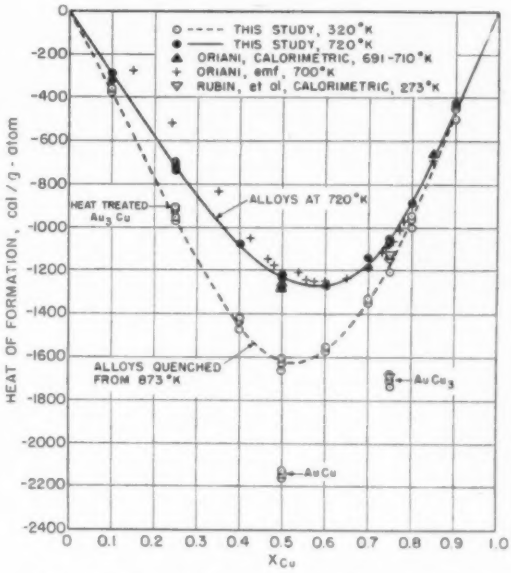


FIG. 1. Heats of formation of solid Au–Cu alloys.

Oriani and Murphy[14,15] measured the heats of formation of three disordered alloys in a differential liquid tin calorimeter, obtaining -1285 ± 31 cal/g-atom (708°K) and -1259 ± 8 cal/g-atom (710°K) for $Au_{0.50}Cu_{0.50}$, -1150 cal/g-atom (693°K) for $Au_{0.25}Cu_{0.75}$ and -658 ± 32 cal/g-atom (691°K) for $Au_{0.15}Cu_{0.85}$. The values are plotted in Fig. 1, showing quite good agreement, especially considering the somewhat lower temperatures of measurement which probably resulted in more short range order and thus more exothermic heats of formation for $Au_{0.50}Cu_{0.50}$ and $Au_{0.25}Cu_{0.75}$. Also shown are the values of the heats of formation obtained at 700°K by Oriani[16] from e.m.f. measurements. The agreement is excellent at Cu concentrations above $x_{Cu} = 0.50$, but going to lower Cu concentrations the e.m.f. values appear to become progressively more in error.

Also shown in Fig. 1 are the data of Rubin *et al.*[17], who studied the $Au_{0.25}Cu_{0.75}$ alloy by liquid tin calorimetry. They found -1124 ± 55 cal/g-atom for the heat of formation at 273°K of an alloy rapidly quenched from above the critical temperature and -1682 ± 30 cal/g-atom for the ordered alloy. Both values are in good agreement with the present work.

VOL. 8 1960

The present heat of formation measurements at 720°K lie on a smooth but asymmetric curve skewed toward the Cu-rich side of the composition range. The energetic asymmetry is shown by the relative partial molal heat contents for the solutes at infinite dilution, $(\bar{H} - H^\circ)_{Au} = -4650$ cal/g-atom at $x_{Cu} = 1$ and $(\bar{H} - H^\circ)_{Cu} = -3000$ cal/g-atom at $x_{Au} = 1$. The skewing toward more exothermic values is toward the side of the composition range where the tendency toward long range ordering is the greater. Also, theoretical calculations by Cowley[18] on the variation of short range order with composition predict larger degrees of local order for Cu rich than for Au rich alloys. The calculated curve for short range order vs. composition is skewed much like the heat of formation curve at 720°K, with a maximum at $x_{Cu} \approx 0.55$. As shown by the high temperature X-ray measurements of Roberts[7] on AuCu and Cowley[8] on $AuCu_3$ the alloys at 720°K possess considerable degrees of short range order. Interpolating between their temperatures of measurement one finds that in terms of nearest neighbor Au–Cu bonds, AuCu is still about 36.5 per cent and $AuCu_3$ about 44.5 per cent of the way toward perfect order at 720°K.

Averaging the presently measured values for the heat of formation of ordered AuCu with further measurements on the same alloy performed in this laboratory[19] yields an average value of −2180 cal/g-atom for the fully ordered alloy. The difference between that value and the heat of formation of AuCu at 720°K is then −950 cal/g-atom, which, assuming differences in vibrational contributions to be negligible is the difference in configurational energy between the two states. The corresponding difference in configurational energy for $AuCu_3$ between the ordered alloy and the equilibrium state at 720°K is found to be −640 cal/g-atom. Because of the large amounts of short range order present in the alloys at 720°K, the total ordering energies will be greater than the values obtained here.

In a Borelius type calorimeter, d'Heurle and Gordon[3] found −320 cal/g-atom to be the ordering energy evolved by an alloy of Au_3Cu (72.5 at.% Au) quenched from 773°K and reheated in the calorimeter to 351°K. From C_p measurements, Hirabayashi[5] found 270 cal/g-atom to be the transformational energy absorbed between 403°K and 543°K.

The present measurements indicate the configurational energy at 320°K of Au_3Cu previously heat treated for six weeks at 473°K to be −200 cal/g-atom with respect to the equilibrium state at 720°K. This suggests that a considerable amount of order was developed even though no superlattice lines were formed. Batterman[2], and d'Heurle and Gordon[3] report that even in the fully ordered alloy the domain size was very small resulting in relatively weak superlattice lines. Also, the latter investigators found no superlattice lines at all in an alloy ordered at 373°K, even after a heat evolution of 320 cal/g-atom. It would thus appear that most of the ordering energy involved may be of short range origin. The quenched alloy has a heat of formation 50 cal/g-atom more exothermic than the heat treated alloy, suggesting that even more short range order was developed in the quenched alloy. This might possibly be the case as it is in accord with the observations of Borie and Warren[9] on $AuCu_3$.

As can be seen in Fig. 1, the heats of formation at 320°K of the alloys quenched rapidly from 873°K are considerably more exothermic than the heats of formation at 720°K over most of the composition range. The difference reaches a maximum of 400 cal/g-atom at $x_{Cu} = 0.45$ and decreases linearly and symmetrically on both sides of this composition to 0 at $x_{Cu} = 0$ and $x_{Cu} \approx 0.90$. The difference can not be due to lattice strains or excess defects arising in the rapid quenching as these would have an endothermic effect on the heats of formation, decreasing the difference between the two sets of measurements. It is believed that the observed difference is due primarily to the increase in the degree of short range order which occurs for most of the alloys during even the most rapid quench. For AuCu the increase in exothermicity is over 40 per cent of the long range ordering energy.

Supporting evidence for the suspected increase in short range order during quenching is supplied by Roberts[7], who found a specimen of AuCu rapidly quenched from 773°K to be 47.4 per cent of the way from complete disorder to perfect order, an increase of almost 11 per cent from the value of 36.5 per cent at 720°K. Borie and Warren[9] found a higher degree of short range order in $AuCu_3$ quenched from above 873°K than when quenched from below that temperature. The only reasonable interpretation of this result is that more short range order arose during the quench from the higher temperatures.

Most presently accepted theories agree that the long range ordering processes in Au–Cu alloys are ones of nucleation and growth.[10] The results of the present investigation are in accord with kinetic studies[20,21] which indicate that changes in the degree of local order may occur quite rapidly, depending on the previous disordering temperature, whereas the rate of domain growth or coalescence is relatively slow. The variation with composition of the difference between the heats of formation of the quenched alloys and of

the equilibrium alloys at 720°K would seem to suggest that the increase in short range order with quenching was greater for Au-rich than for Cu-rich alloys. This in turn appears to contradict the X-ray and thermodynamic evidence that at 720°K the tendency toward short range order is greater for the Cu-rich alloys. This might be interpreted as indicating that the Au-rich alloys retain a larger degree of atomic mobility to lower temperatures than do the Cu-rich alloys, thus permitting the equilibrium degree of short range order characteristic of a lower temperature to be "frozen in" during the quench of the former.

ACKNOWLEDGMENTS

The author is indebted to Professor Ralph Hultgren for many valuable contributions extended throughout this work. He would also like to thank Mrs. Kate Herring for aiding in the experimental work. This work has been conducted with the support of the Office of Ordnance Research, U.S. Army.

REFERENCES

1. M. Hansen, *Constitution of Binary Alloys* (2nd Ed.). McGraw-Hill, New York (1958).
2. B. W. Batterman, *J. Appl. Phys.* **28,** 556 (1957).
3. F. d'Heurle and P. Gordon, Tech. Rep. No. 4, Naval Res. Con. Nonr 1406 (03), NR 031-50. Illinois Inst. Tech. (1959)
4. C. H. Johansson and J. O. Linde, *Ann. Phys. Lpz.* **25,** 1 (1936).
5. M. Hirabayashi, *J. Phys. Soc. Japan* **6,** 129 (1951).
6. S. Ogawa and D. Watanabe, *J. Appl. Phys.* **22,** 1502 (1951).
7. B. W. Roberts, *Acta Met.* **2,** 597 (1954).
8. J. M. Cowley, *J. Appl. Phys.* **21,** 24 (1950).
9. C. B. Borie and B. E. Warren, *J. Appl. Phys.* **27,** 1562 (1956).
10. L. Guttman, *Solid State Physics* **3,** 145 (1956).
11. W. B. Pearson, *A Handbook of Lattice Spacings and Structures of Metals and Alloys.* Pergamon Press, New York (1958).
12. R. Hultgren, private communication.
13. R. L. Orr, A. Goldberg and R. Hultgren, *Rev. Sci. Instrum.* **28,** 767 (1957).
14. R. A. Oriani and W. K. Murphy, *J. Phys. Chem.* **62,** 327 (1958).
15. R. A. Oriani and W. K. Murphy, *J. Phys. Chem. Solids* **6,** 277 (1958).
16. R. A. Oriani, *Acta Met.* **2,** 608 (1954).
17. L. R. Rubin, J. S. Ll. Leach and M. B. Bever, *Trans. Amer. Inst. Min. (Metall.) Engrs.* **203,** 281 (1955).
18. J. M. Cowley, *Phys. Rev.* **77,** 669 (1950).
19. R. L. Orr, J. Luciat-Labry and R. Hultgren, *Acta Met.* **8,** 432 (1960).
20. G. C. Kuczynski, R. Hochman and M. Doyama, *J. Appl. Phys.* **26,** 871 (1955).
21. G. C. Kuczynski and M. Doyama, *J. Appl. Phys.* **27,** 651 (1956).

VOL. 8 1960

LETTER TO THE EDITOR

Cold work and subsequent electrical resistivity increases in pure aluminum*

Recently Winterberger[1] published a paper, part of which was devoted to a study of the electrical resistivity increase, $\Delta\rho$, caused by cold-working aluminum. He noted that the resistivity increased with elongation, ε, according to the relation

$$\Delta\rho = c\varepsilon \tag{1}$$

where c is a constant which is in part dependent on the impurity content of the specimen. This constant c, it was shown, can be represented by

$$c = c_v + c_d. \tag{2}$$

The first constant, c_v, represents the contribution of point defects to the extra-resistivity and c_d is due to the contribution of line defects to the extra-resistivity. The former constant was found to be independent of and the latter constant dependent on impurity concentration. The dislocation contribution to the resistivity for a given elongation increased with increasing impurity content. Winterberger concluded that the impurities were acting as dislocation pinning points, and an increase in the number of pinning points would tend to yield a larger dislocation density and thus a higher resistivity increase for a given elongation.

Figure 1 is a plot of c_d against impurity concentration. The constant c_d was calculated from the data of Winterberger[1]. It is to be noted that c_d increases linearly with impurity concentration.† In the figure, an arrow marks the value of c_d at an impurity concentration of 140 p.p.m. This latter concentration is the impurity content of aluminum that was used in experiments at this laboratory.[2] The constants c_d and c_v as determined from Winterberger's data are shown in Table 1. The first row shows the values of the constants c_v and c_d for the vacancy and dislocation contributions respectively for aluminum deformed at room temperature and containing 140 p.p.m. impurities.

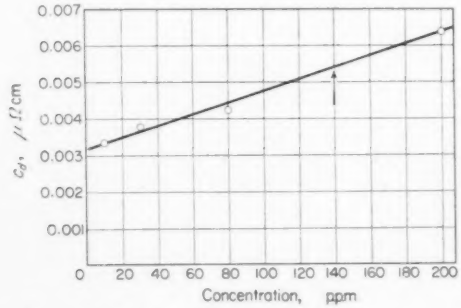


FIG. 1. The effect of impurity concentration on the contribution of dislocations to the resistivity of metals cold-worked at 25°C. (After Winterberger.)

† A similar result has been obtained in this laboratory for a dispersion hardened silver alloy. The dispersed phase was aluminum oxide and the constant, c, increased linearly with concentration of alumina.

TABLE 1

c_v ($\mu\Omega$ cm)	c_d ($\mu\Omega$ cm)	Temperature of deformation
4×10^{-3}	5.35×10^{-3}	Room temperature
12×10^{-3}	9.1×10^{-3}	Liquid N_2

According to Winterberger, the increase of resistivity at 78°K for a given elongation is three times as much as is obtained during room temperature deformation for the vacancy contribution and 1.7 times for the dislocation contribution. Applying these factors to Winterberger's data for aluminum with 140 p.p.m. impurities one obtains the values of the constants c_v and c_d for a 78°K deformation. These are shown in the second row of Table 1.

From these latter numbers it can be calculated that following deformation at 78°K approximately 58 per cent of the extra-resistivity is attributable to point defects (i.e. the portion recoverable at room temperature). Peiffer[2] has obtained a 62 per cent recovery with his material. The agreement is within the scatter of data noted by Peiffer. The agreement with Sosin[3], who performed some work on single crystals of aluminum, is also satisfactory.

A disagreement does exist, however, when one compares Winterberger's value for c, which includes both the vacancy and dislocation contribution, with the value obtained by Peiffer. From Winterberger's results, the constant c is 0.021 $\mu\Omega$ cm. Peiffer[2] has obtained, for a given specimen of his aluminum, $c = 0.166$ $\mu\Omega$ cm. The difference obtained is quite large.

The authors believe this discrepancy exists because of the differences in initial condition of the aluminum (i.e. the amount of internal strain present in material before deformation at 78°K). The constant c, obtained by Peiffer, was obtained from experiments

on aluminum in a cold-drawn condition and Winterberger's aluminum was very well annealed. It has been noted in this laboratory that the initial condition had little or no effect on the percentage of resistivity recovered at room temperature,[2] but did influence the amount of increase per unit elongation.[4]

The authors submit that the reason the values of the constants disagree is that the samples of aluminum were in different conditions of strain initially. The material in a higher state of strain showed the greater increase in resistivity for a given elongation.

RIAS H. R. Peiffer
7212 *Bellona Avenue* F. Stevenson
Baltimore 12, *Maryland*

References

1. Winterberger, *Acta Met.* **7,** 549 (1959).
2. H. R. Peiffer, *J. Appl. Phys.* **29,** 1581 (1958).
3. A. Sosin and J. S. Koehler, *Phys. Rev.* **94,** 1422 (1954).
4. H. R. Peiffer, unpublished.

* Received December 8, 1959.

VOL.
8
1960

ERRATUM

C. H. Ma and R. A. Swalin. *Acta Met.* **8**, 388–395 (1960)

Because of a computational error the D_0 values given in Table 1 are incorrect and should all be a factor of 10 larger than reported. The corrected values are as follows:

Table 1. Values of D_0 and Q for the diffusion of alumnium, zinc, silver, copper, nickel and tin in tin

Element	D_0(cm²/sec)	Q(cal/mole)
Al	1.9×10^{-2}	5200
Zn	6.2×10^{-3}	4880
Ag	2.6×10^{-3}	4200
Cu	1.8×10^{-3}	4200
Ni	2.3×10^{-3}	4530
Sn[5]	2.2×10^{-3}	4570

AN EFFECT OF IMPURITY ATOMS ON THE ENERGY RELATIONSHIP OF (100) AND (110) SURFACES IN HIGH PURITY SILICON IRON*

J. L. WALTER and C. G. DUNN†

The migration of grain boundaries between (110) grains and (100) grains in high purity 3% silicon iron sheet was investigated at 1200°C to determine whether or not impurity atoms could effect a reversal in the direction of boundary migration. Boundaries were found that advanced into the (100) grains in a vacuum anneal, then reversed their direction of migration and advanced into the (110) grains in a subsequent anneal in impure argon, and then reversed back to the initial direction of migration in a final vacuum anneal. Evidence was found for surface energy driving forces in both kinds of anneals. In the anneals in argon, but not in vacuum, the surfaces of the (100) grains were thermally etched. The results could be satisfactorily explained on the basis that the impure argon supplied oxygen atoms and that the vacuum anneals removed oxygen. The conclusions reached were (a) under proper conditions impurity atoms can effect a reversal in the direction of boundary migration, (b) $\gamma'_{110} < \gamma'_{100}$ in the vacuum anneals and $\gamma'_{100} < \gamma'_{110}$ in the anneals in impure argon, (c) the effect of the impurity is to reduce γ'_{100} more than γ'_{110} and (d) the high density plane, (110), is not always the low energy plane.

UN EFFET DES ATOMES D'IMPURETE SUR LES SURFACES DE GRAIN D'ORIENTATION (100) ET (110) DANS FERS AU SILICIUM DE HAUTE PURETE

La migration de joints de grains entre des grains (110) et (100) dans des feuillards de fer à 3 % Si a été étudiée à 1200°C afin de déterminer si des atomes d'impureté peuvent agir sur la direction de migration du joint. On a trouvé des frontières qui avancent dans les grains (100) après un recuit sous vide, puis qui renversent leur direction de migration et avancent dans les grains (110) après un recuit subséquent dans un argon impur, et enfin qui reprennent la direction initiale de migration dans un recuit final sous vide. Dans chaque type de recuit, les forces motrices nécessaires au mouvement de surface ont été établies. Dans les recuits sous argon, mais non sous vide, les surfaces des grains (100) sont attaquées thermiquement.

Les résultats ont pu être expliqués d'une manière satisfaisante sur la base des impuretés de l'argon et notamment les atomes d'oxygène; les recuits sous vide retirant l'oxygène.

Les conclusions que l'on a pu établir sont:

(a) sous des conditions adéquates, des atomes d'impureté peuvent agir sur un renversement de la direction de migration d'un joint de grain

(b) $\gamma'_{110} < \gamma'_{100}$ dans les recuits sous vide et $\gamma'_{100} < \gamma'_{110}$ dans les recuits sous argon impur.

(c) l'effet de l'impureté est de réduire γ'_{100} plus que γ'_{110} et (d) le plan de forte densité (110), n'est pas toujours le plan ayant l'énergie la plus basse.

EINFLUß VON VERUNREINIGUNGSATOMEN AUF DAS VERHÄLTNIS DER ENERGIEN VON (100)- UND (110)-FLÄCHEN IN SEHR REINEM SILIZIUM-EISEN

Bei 1200°C wurde die Wanderung von Korngrenzen zwischen (110)-Körnern und (100)-Körnern in Blech aus sehr reinem Eisen mit 3% Silizium untersucht, um zu entscheiden, ob Verunreinigungsatome die Richtung der Korngrenzenwanderung umkehren können oder nicht. Es wurden Korngrenzen gefunden, die bei Glühen in Vakuum sich in die (100)-Körner hinein bewegten, bei darauffolgendem Glühen in verunreinigtem Argon die Wanderungsrichtung umkehrten und sich in die (110)-Körner hinein bewegten und schließlich bei nochmaligem Glühen in Vakuum wieder die anfängliche Wanderungsrichtung einschlugen. Bei beiden Glühprozessen ergaben sich Anzeichen dafür, daß die Oberflächenenergie die treibende Kraft war. Bei Glühen in Argon, aber nicht in Vakuum, wurde die Oberfläche der (100)-Körner thermisch geätzt. Zur Erklärung reicht die Vorstellung aus, daß das verunreinigte Argon Sauerstoffatome liefert, während das Vakuumglühen Sauerstoff entfernt. Folgende Schlußfolgerungen wurden gezogen: (a) unter geeigneten Bedingungen können Verunreinigungsatome die Wanderungsrichtung umkehren, (b) bei Glühen in Vakuum ist $\gamma'_{110} < \gamma'_{100}$ bei Glühen in verunreinigtem Argon $\gamma'_{100} < \gamma'_{110}$, (c) die Verunreinigung verringert γ'_{100} stärker als γ'_{110} und (d) die dichtest besetzte Ebene (110) ist nicht immer die Ebene geringster Energie.

INTRODUCTION

The surface energy at the interface of a flat metal crystal and its atmosphere is known to depend on the kind of crystallographic plane exposed and the kind and amount of impurity atoms present. Theoretically, the crystallographic plane with highest density of atoms should have the lowest surface energy.[1–4] The presence of impurity atoms at the surface may change this relationship, however. Variations in surface energy with adsorbed impurity atoms have been reported from observations on surface steps or facets that form during thermal etching at high temperatures.[5–7] According to the results obtained by Moore[7] on silver annealed in air at 900°C, the high density (111) plane has the lowest surface energy.

* Received May 25, 1959.

† General Electric Research Laboratories, Schenectady, New York.

VOL. 8 1960

The interaction of the surfaces of two grains with the common grain boundary can also be used to obtain information on the relative surface energies. When the interaction leads to boundary migration and measurable grain boundary curvatures, it is possible to compare the surface energies of the two grains.[8] Using this method on high purity 3% silicon iron, Walter and Dunn found that the surface energy of the (110) plane, γ_{110}, was lower than the surface energy of the (100) plane, γ_{100}, by about 70 ergs/cm^2 at 1200°C in vacuum. Because the (110) plane is the high density plane for 3% silicon iron the result agrees with the theory that the high density plane should be the plane of lowest surface energy.

Since adsorbed oxygen is known to have a very large effect on the average surface energy of silver,[9] it is possible that the agreement between lowest surface energy and high density plane for silver in the presence of oxygen may be coincidental. The agreement for silicon iron may also be questioned since little is known about the effect of impurities on the surface energies. Because the effect might reasonably be large, additional information on this point would be valuable to the understanding of surface phenomena in general. Such information is also important to the understanding of recrystallization and grain growth textures since surface energy driving forces are known to be responsible for the phenomenon of tertiary recrystallization in high purity silicon iron.[8]

The present paper gives the results of an investigation on the effects of annealing atmospheres on the direction of migration of boundaries between (100) and (110) grains. The direction of motion and the curvatures of these boundaries supplies information concerning the effect of impurity atoms on relative values of γ_{100} and γ_{110} in high purity 3% silicon iron.

EXPERIMENTAL PROCEDURE

Previously a method was found for producing sheet material with large grains oriented with the (100) plane in the plane of the sheet and other grains with the (110) plane in the plane of the sheet.[8] This method, involving incomplete tertiary recrystallization, was used to obtain suitable starting samples for the present study. To obtain the samples, sheet material 0.3 mm thick was prepared by a combination of hot rolling and cold rolling operations starting with a vacuum melted ingot of iron containing approximately 3 per cent silicon. The total impurity content was less than 0.005 wt.%. The samples were electropolished to remove surface imperfections and then annealed in vacuum at pressures below 5×10^{-4} mm Hg at 1200°C for 1–3 hr. The times at temperature were long enough to produce large (100) grains by secondary recrystallization but short enough to prevent the samples from being converted entirely to the (110) [001] texture by tertiary recrystallization.

After preparation the samples were annealed in impure argon (welding grade, dew point of −70°F) at atmospheric pressure and a temperature of 1200°C. Certain samples were given a second anneal either in argon or in vacuum following the first anneal in argon.

X-ray data for orientation determinations and photomicrographs of selected surface areas were obtained before and after the anneals. The direction of migration of the boundaries was determined by observing either boundary groove records left in the surface[8] (method 1) or the change in extent of thermal etching[10] in the vicinity of the boundary (method 2). Previous observations[10] showed that thermal etching of crystal surfaces tends to remove and obscure shallow grooves that otherwise might be used to determine the direction of boundary migration by method 1. On the other hand the extent of thermal etching (which is dependent on the time at temperature) is negligible in the immediate area traversed by a fast moving boundary and increases with distance behind the moving boundary.

EXPERIMENTAL RESULTS

Initial vacuum anneal

After the first anneal in vacuum at 1200°C the samples consisted of large (110) and (100) grains. As the anneal ended boundaries between (110) and (100) grains (hereafter referred to as (110)/(100) boundaries) had been moving, according to boundary groove records left in the surface. In all cases (110) grains had been growing at the expense of (100) grains. A number of (110)/(100) grain boundaries were moving away from their centers of curvature in the surface; this agrees with the former results[8] and indicates that $\gamma_{110} < \gamma_{100}$ at this point.

The surfaces after the vacuum anneal were almost specular and relatively smooth except for a number of odd surface patterns (see Fig. 2b). These were similar to surface patterns found by Batdorf and Smits[11] on the surface of a silicon crystal disoriented 0.5° from (111) and annealed in vacuum at 1325°C. They attributed the patterns to the formation of flat (111) areas as silicon evaporated and suggested that these surfaces were more stable than others.

First argon anneal

In the preliminary experiments on the effect of annealing in impure argon after the vacuum anneal,



FIG. 1. Photomicrograph showing boundary region of (100) and (110) grains after a 3-hr anneal in vacuum at 1200°C and a 6-hr anneal in argon at 1200°C. ×500

VOL. 8 1960

no attempt was made to follow specific grain boundaries. The grains with (100) planes almost parallel to the surface were found to be thermally etched to form striations as shown in Fig. 1. Grains close to (110) had, in some cases, a mottled appearance caused by faceting on a small scale (see Fig. 1). On the basis of the change in extent of thermal etching of (100) grains with distance from a moving boundary (method 2 for determining the direction of boundary migration) many examples were found indicating growth of (100) grains into (110) grains. A number of (110)/(100) grain boundaries were found that had been migrating away from their centers of curvature in the surface of the sample. An example is shown in Fig. 1 (direction of migration is shown by the arrow).

Second argon anneal

One sample was given a 1-hr reanneal in argon after data had been obtained on a specific (110)/(100) boundary. Further migration of this boundary occurred as a result of growth of the (100) grain. A radial cross section was obtained at one portion of the boundary to determine the direction and radius of curvature in the cross-section. The center of curvature was within the (110) grain (the grain being consumed) and the radius was 1.8 mm. A difference in surface energy with $\gamma_{100} < \gamma_{110}$ would account for the growth of the (100) grain and for the radius of curvature. An approximate relation between the surface energy difference $\gamma_B - \gamma_A$ and the grain boundary energy γ_{AB} is[8]

$$\gamma_B - \gamma_A \simeq \gamma_{AB} \frac{t}{2r} \tag{1}$$

where t is the thickness of the sample and r is the radius of curvature in the radial cross-section. Equation (1) for the present example gives

$$\gamma_{110} - \gamma_{100} \simeq (0.08)\gamma_{AB}. \tag{2}$$

This result indicates that the difference in surface energy at 1200°C in tank argon is approximately 8 per cent of the grain boundary energy. No value will be assigned to the grain boundary energy, which is not necessarily constant throughout the vacuum and argon anneals.

Second vacuum anneal

A second set of samples had been given an initial anneal at 1200°C for 1.5 hr in vacuum to produce large (100) and (110) grains. At this point evidence for the relationship $\gamma_{110} < \gamma_{100}$ was found from a study of (110)/(100) grain boundary migrations. After recording the positions and directions of migration of specific boundaries the samples were given an additional anneal of 1 hr at 1200°C in argon. Migration of (110)/(100) grain boundaries occurred according to the relationship $\gamma_{100} < \gamma_{110}$. Photomicrographs were taken of the boundaries. The samples were then annealed for 10 min at 1200°C in vacuum at a pressure of 6×10^{-6} mm Hg. The thermal etching on the surfaces of (100) grains from the argon anneal was almost completely removed. The direction of migration of the (110)/(100) boundaries was found to be reversed by the vacuum anneal. Illustrations of the changes in direction as a function of annealing atmosphere are shown in Figs. 2–4. The arrows drawn on the figures indicate boundaries and directions of migration.

Figures 2 and 3 are photomicrographs of two areas before and after the 10-min anneal in vacuum. The (110) planes of the (110) grains were 2° and 3°, respectively, from the plane of the sheet. Except for the patterns left from the vacuum anneals (presumably caused by evaporation) these (110) grains appeared to be unetched. Figs. 2 and 3 apply to one (100) grain, which was 4° off orientation. This grain was thermally etched to striations during the argon anneal (Figs. 2a and 3a, the grain on the right) but returned to the unetched condition in the final vacuum anneal (Figs. 2b and 3b). The (110)/(100) grain boundary that lies near the center of Fig. 2(a) had been moving to the left during the anneal in argon.

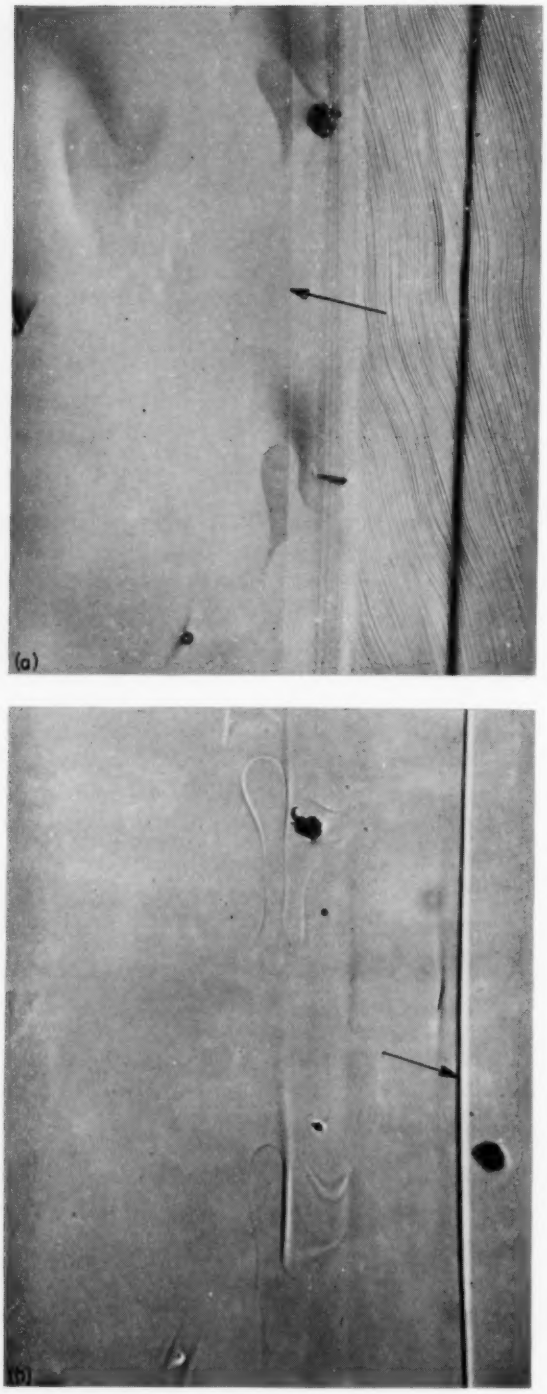


FIG. 2. Boundary region of (100) and (110) grains after various anneals at 1200°C. ×500
(a) 1.5-hr vacuum plus 1-hr argon
(b) same area as (a) after 10-min vacuum.

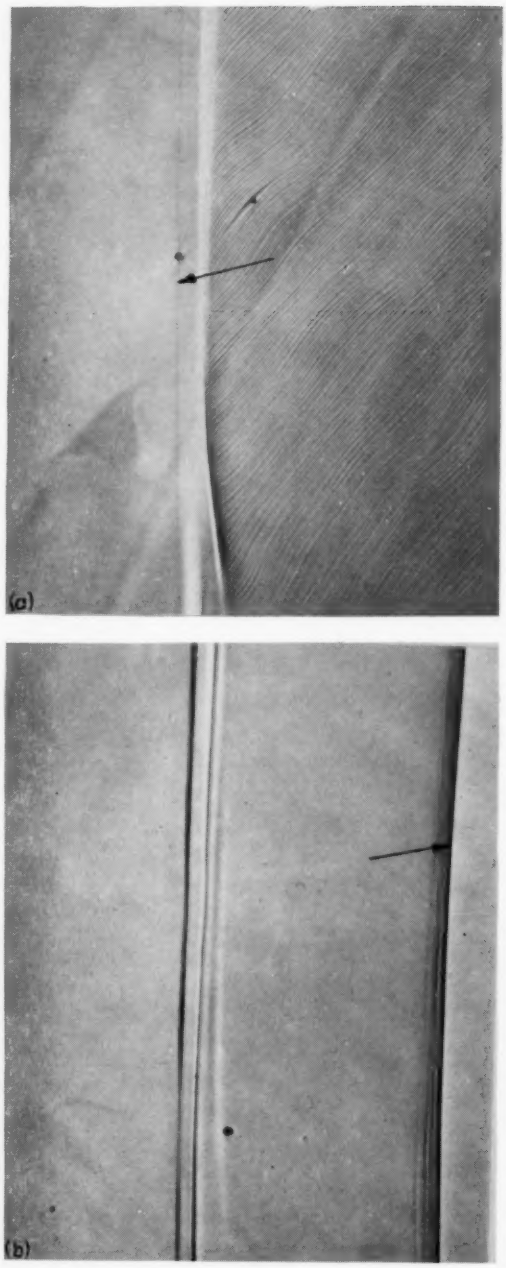


FIG. 3. Boundary region of (100) and (110) grains after various anneals at 1200°C. ×500
(a) 1.5-hr vacuum plus 1-hr argon
(b) same area as (a) after 10-min vacuum.

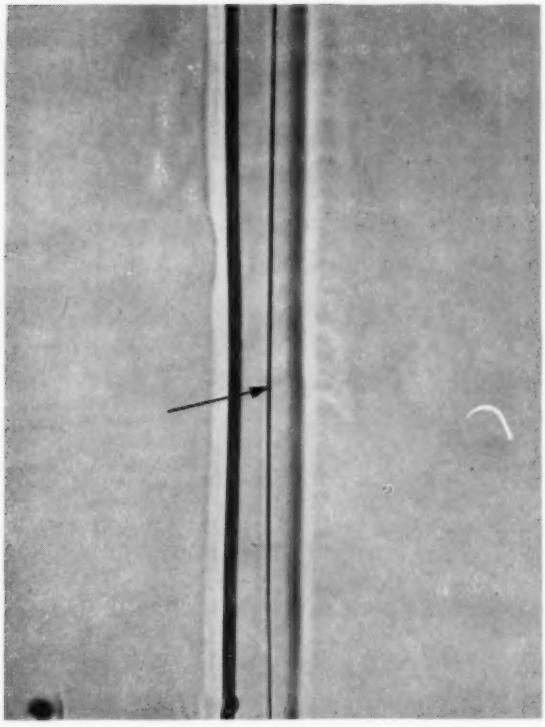


FIG. 4. Boundary region of (100) and (110) grains showing final boundary position between two former positions. After 1.5-hr vacuum, 1-hr argon, and 10-min vacuum anneal at 1200°C. ×500

After the anneal in vacuum this boundary was found to the right near a former position (Fig. 2b); hence the direction of migration was reversed during this anneal in vacuum. Fig. 3(a) and (b) shows the same result; the (110)/(100) boundary is to the left of center in Fig. 3(a) and migrating to the left, but is far to the right in Fig. 3(b), and is migrating to the right. Thus it is seen that (100) grains grow at the expense of (110) grains during the anneals in argon whereas the (110) grains grow at the expense of the (100) grains during anneals in vacuum.

When thermal grooving at the grain boundary retards boundary migration, only small movements result and the change in the direction of migration caused by reversible changes in surface energy shows up immediately in the thermal groove records. Fig. 4, for example, shows the final position of a (110)/(100) grain boundary lying between two former positions where deep grooves had developed. The tilt of the (100) plane is 1°, that of the (110) plane is 2°. The (100) grain, which is on the right in the figure, grew at the expense of the (110) grain during the anneal in argon according to the thermal groove records. The distance the boundary had moved to the left from its initial position was 20 μ. During the 10-min anneal in vacuum the boundary moved 12 μ in the opposite direction to a position between the two former positions.

DISCUSSION

Surface energy driving force

In a previous paper[8] it was shown that the driving force (free energy decrease per unit volume transferred) for growth of grain A into a grain B could be expressed as approximately $2(\gamma_B - \gamma_A)/t$, where γ_A and γ_B are the surface free energies of grains A and B, respectively, and t is the thickness of the sheet. This relationship may be used in the present paper since surface energy driving forces are also involved. As before, the value of $\gamma_{100} - \gamma_{110}$ must be positive for the vacuum anneals to account for the growth of the (110) grain into the (100) grain. In the impure argon, however, $\gamma_{100} - \gamma_{110}$ must be negative since the (100) grain grew into the (110) grain. The reversal can be explained in terms of an impurity effect on the absolute values of the surface energies, i.e., the γ's are a function of some impurity. An estimate of $\gamma_{100} - \gamma_{110}$ for the present two levels of the impurity would require the use of equation (1); this will be discussed later. The fact that $\gamma_{100} - \gamma_{110}$ is either positive or negative, depending on the impurities in the vacuum and the argon, indicates that the effect of the impurity is larger for the (100) plane than it is for the (110) plane.

Oxygen vs. *surface energies*

To understand the reason for the change in surface energies it is helpful to examine the thermal etching characteristics as a function of the anneal atmosphere. The high purity silicon iron used in this study does not thermally etch when annealed in vacuum. Thermal etching occurs when samples are reannealed in impure argon but does not occur if the oxygen gas and water vapor are removed from the argon. Thus thermal etching is caused by oxygen or water vapor in the argon and not by the argon itself. Furthermore, if the material contains sufficient oxygen, then thermal etching will occur during the first few minutes of the anneal in vacuum; but as the oxygen is removed from the material below about 10 p.p.m., the etching effect disappears.[10] Etching persists for a much longer time if the oxygen-containing material is annealed in purified argon. These effects have been compared with thermal etching of other metals,[10] including iron.[6]

The tendency for the silicon iron to thermally etch in the oxygen-bearing atmosphere is explained in terms of a lowering of surface energies resulting from

VOL. 8 1960

the adsorption of oxygen at the surface.[10] The reduction of surface energies in silicon iron may be similar to the changes in surface energy reported for silver. Buttner *et al.*[9] reported that the average surface energy of silver decreased in a linear manner with the logarithm of the partial pressure of oxygen in mixtures of oxygen and helium. At the partial pressure of oxygen in air the surface energy was only about one third of its value in pure helium.

The effect of adsorbed oxygen then is to lower γ_{100} more than γ_{110}. From equation (1) an approximate calculation of $\gamma_{110} - \gamma_{100}$ for anneals in argon gives a value of 8 per cent of the grain boundary energy γ_{AB}. A previous calculation[8] of $\gamma_{100} - \gamma_{110}$ for anneals in vacuum gave a value of 7 per cent of the grain boundary energy. The grain boundary energy should not be taken as a constant, however, since it is possible that the presence of oxygen changed the grain boundary energy as well as the surface energies. Buttner[12] reported, for instance, that the equilibrium angles at the intersections of grain boundaries and the surface of silver remained essentially unchanged as a function of partial pressure of oxygen, indicating that the oxygen changed the grain boundary energy as well as the surface energies. Therefore, since the grain boundary energy may not have been constant during the present experiments it is suggested that further data are needed for a quantitative evaluation of the effect of oxygen on surface energies. The effect of oxygen may be summarized qualitatively as follows:

$$\gamma_{100} < \gamma_{110} \quad \text{in impure argon}$$
$$\gamma_{110} < \gamma_{100} \quad \text{in vacuum.}$$

Surface conditions

The surfaces of samples annealed in argon and those annealed in vacuum were examined by electron diffraction techniques to determine whether oxide phases were present at the surface. There were small (1 μ diameter) oxide "beads" widely dispersed on the surface of the samples annealed in argon; no evidence was found however for the presence of a continuous oxide phase at the surface. Accordingly, the thermal etching found in the high purity silicon iron and the changes in surface energy may be associated with oxygen as a chemisorbed surface layer. It has been suggested that chemisorbed oxygen is responsible for thermal etching in iron[6] and silver.[7]

Energy vs. *high density plane*

The foregoing results suggest that chemisorbed oxygen on (100) and (110) surfaces results in a change in surface energies, such that the (100) plane becomes lower in energy than the high density plane. This result does not disagree with theory, because the high density plane is the plane of lowest energy when the oxygen content is lowered, as in the vacuum anneal. Thus, calculations based on a model that does not include impurity atoms at the surface may fail to define the low energy plane under all conditions of the surface. The agreement between low energy plane and high density plane found for silver may therefore be regarded as fortuitous.

Secondary and tertiary recrystallization

The results of this study provide an explanation of the new mechanism of secondary recrystallization in high purity silicon iron discussed by Detert[13] and experimentally confirmed by Walter[14]. Also explained is the phenomenon of tertiary recrystallization.[8]

In the presence of oxygen (or possibly an equivalent impurity) in the annealing atmosphere or in the material, (100) grains are favored to grow because γ_{100} is lower than γ_{110}, and presumably lower than the surface energies of other orientations present. The result is the cube texture if the [001] direction of the primary grains is restricted to the rolling direction by the prior processing. A few small (110)[001] grains may remain. However, since a reversal of surface energy can occur as the oxygen is removed from the material by the atmosphere, the remaining (110) grains that are above a critical size[8] finally grow because $\gamma_{100} - \gamma_{110}$ has become both positive and large enough to provide a net driving force.

From the above considerations it also follows that, if the silicon iron were pure enough, γ_{110} would always be lower than γ_{100}. The (100) grains then would not grow since they would lack the advantage of the lowest surface energy. The (110) grains would have the lowest surface energy and therefore would be favored to grow on the basis of the largest driving force. Some results in agreement with this expectation have been obtained and additional experiments are contemplated.

CONCLUSIONS

(1) Under proper conditions oxygen atoms may, via the atmosphere used during annealing, effect a change in the direction of migration of grain boundaries in high purity 3% silicon iron.

(2) In vacuum at pressures below 5×10^{-4} mm Hg the energy of the (110) surface is less than the energy of the (100) surface, but in impure argon (dew point of $-70°$F) the energy of the (100) surface is less than the energy of the (110) surface, at 1200°C.

(3) The effect of the oxygen is to lower the energy of the (100) surface more than the energy of the (110) surface.

(4) The high density plane, (110), is not always the plane of lowest surface energy.

ACKNOWLEDGMENTS

The authors wish to extend thanks to Miss E. Freeman and H. Brandhorst for their technical assistance and to J. M. Lommel and R. L. Fullman for their criticism of the manuscript.

REFERENCES

1. R. FRICKE, *Z. Phys. Chem.* B**52,** 284 (1942).
2. T. N. STRANSKI and R. SUHRMANN, *Z. Kristallogr.* **105,** 481 (1944).
3. T. N. STRANSKI and R. SUHRMANN, *Ann. Phys.* **1,** 153 (1947).
4. J. FRIEDEL, B. D. CULLITY and C. CRUSSARD, *Acta Met.* **1,** 79 (1953).
5. B. CHALMERS, R. KING and R. SHUTTLEWORTH, *Proc. Roy. Soc.* A**193,** 465 (1948).
6. J. BENARD, J. MOREAU and F. GRONLUND, *C.R. Acad. Sci., Paris* **246,** 756 (1958).
7. A. J. W. MOORE, *Acta Met.* **6,** 293 (1958).
8. J. L. WALTER and C. G. DUNN, *Trans. Amer. Inst. Min. (Metall.) Engrs.*, **215,** 465 (1959).
9. F. H. BUTTNER, E. R. FUNK and H. UDIN, *J. Phys. Chem.* **56,** 657 (1952).
10. C. G. DUNN and J. L. WALTER, *Acta Met.*, **7,** 648 (1959). Also Surface Effects on Grain Boundary Migration, reported at *Amer. Inst. Min. (Metall.) Engrs. Meeting, San Francisco*, 1959.
11. R. L. BATDORF and F. M. SMITS, *J. Appl. Phys.* **30,** 259 (1959).
12. F. H. BUTTNER, Sc. D. Thesis, Mass. Inst Tech. (May 1951). See also *Metal Interfaces*, p. 129, Amer. Soc. Metals, Cleveland (1951).
13. K. DETERT, *Acta Met.* **7,** 589 (1959).
14. J. L. WALTER, *Acta Met.* **7,** 424 (1959).

VOL.
8
1960

EFFECT OF HYDROGEN ON STABILITY OF MICRO CRACKS IN IRON AND STEEL*

F. GAROFALO†, Y. T. CHOU† and V. AMBEGAOKAR‡

Much evidence is available which indicates that hydrogen embrittlement and propagation of internal cracks in iron and steel are promoted by hydrogen gas in voids or micro cracks which may be formed by plastic deformation. It seems likely that these micro cracks originate from a dislocation pile-up as suggested by Stroh.

As shown by Stroh, a stable micro crack can exist in a metal until a critical external stress is reached when the micro crack becomes self propagating. For this condition, it is found that the Stroh relation is analogous to the Griffith and Cottrell relations and differs from these only by a constant factor. As shown in this paper, a Stroh crack also ceases to be stable when a critical internal pressure is reached in the absense of an external stress. It is shown that in iron and steel, the amount of hydrogen needed to reach the critical pressure is within the range found experimentally for extensive internal cracking.

The stability of a micro crack is also considered for the condition of an imposed external stress and internal pressure. It is predicted, as observed experimentally by others, that pronounced hydrogen embrittlement of iron or steel may be caused by as little as 2 cm^3 of hydrogen per 100 g of metal (approximately 2 p.p.m.).

INFLUENCE DE L'HYDROGENE SUR LA STABILITE DE MICROFISSURES DANS LE FER ET L'ACIER

Il existe plusieurs données qui indiquent que la fragilisation par l'hydrogène et la propagation de fissures internes dans le fer et l'acier sont dues à l'hydrogène gazeux dans les vides ou les micro-fissures qui peuvent se former par déformation plastique. Il semble probable, ainsi que l'a indiqué Stroh, que ces microfissures ont leur origine dans des dislocations d'empilement.

Comme Stroh l'a montré, une microfissure stable peut exister dans un métal jusqu'à ce qu'une tension critique extérieure soit atteinte: la microfissure se propage alors par elle-même. Pour cette condition, on trouve que la relation de Stroh est analogue aux relations de Griffith et Cottrell et diffère de celle-ci uniquement par un facteur constant. L'étude de cet article montre qu'une fissure de Stroh cesse ainsi d'être stable lorsque une pression critique interne est atteinte en absence d'une tension extérieure. On montre que dans le fer et l'acier, la quantité de l'hydrogène nécessaire pour atteindre la pression critique est dans les limites trouvées expérimentalement pour fissuration interne étendue.

On considère également la stabilité d'une microfissure pour la condition d'une tension externe imposée et d'une pression intérieure. On peut prévoir, et des travaux d'autres auteurs le confirment, qu'une fissuration interne par l'hydrogène dans le fer et l'acier peut être occasionnée par une quantité aussi faible que 2 cc d'hydrogène par 100 gr de métal (approximativement 2 p.p.m.).

DER EINFLUß DES WASSERSTOFFS AUF DIE STABILITÄT VON MIKRORISSEN IN EISEN UND STAHL

Es gibt viele Hinweise darauf, daß die Wasserstoffversprödung und die Ausbreitung innerer Risse in Eisen und Stahl durch gasförmigen Wasserstoff unterstützt wird, welcher sich in Poren oder in Mikrorissen befindet, die sich bei der plastischen Verformung bilden können. Es erscheint wahrscheinlich, daß diese Mikrorisse nach einem Vorschlag von Stroh als Folge von Versetzungsaufstauungen entstehen.

Wie Stroh gezeigt hat, kann in einem Metallsolange ein stabiler Mikroriss bestehen, bis eine kritische äußere Spannung erreicht ist, unter welcher der Riß anfängt, sich zu vergrößern. Es zeigt sich, daß die Strohsche Beziehung unter dieser Bedingung analog ist zu den Beziehungen von Griffith und Cottrell und sich von diesen nur um einen konstanten Faktor unterscheidet. Wie in der vorliegenden Arbeit gezeigt wird, hört ein Strohscher Riß ohne eine äußere Spannung ebenfalls auf stabil zu sein, wenn ein kritischer innerer Druck erreicht wird. Es wird gezeigt, daß bei Eisen und Stahl die für den kritischen Druck notwendige Menge an Wasserstoff innerhalb des Bereichs ist, der experimentell für eine ausgiebige innere Rißbildung gefunden wurde.

Die Stabilität eines Mikrorisses wird weiterhin betrachtet unter einer von außen angelegten Spannung und einem im Innern wirkenden Druck. Es wird vorhergesagt, daß 2 cm^3 Wasserstoff in 100 g Metall (näherungsweise 2 p.p.m.) ausreichen, um eine ausgesprochene Wasserstoffversprödung von Eisen oder Stahl zu verursachen, wie sie experimentell von anderen beobachtet worden ist.

INTRODUCTION

The effect of hydrogen on the physical and mechanical properties of iron and iron alloys has received much attention during the present century.[1-15] Although a large amount of experimental

* Received June 1, 1959; revised October 14, 1959.

† Edgar C. Bain Laboratory for Fundamental Research, U.S. Steel Corporation Research Center, Monroeville, Pa.

‡ Department of Physics, Carnegie Institute of Technology, Pittsburgh, Pa.

evidence has been obtained on the influence of hydrogen on the mechanical properties of iron and iron alloys, the basic aspects of the mechanism of hydrogen embrittlement, involving formation and propagation of internal cracks in the presence of hydrogen are not yet well understood. A number of pertinent facts, however, have been reported which may lead to a better understanding of this phenomenon.

The degree of hydrogen embrittlement is found to be dependent on the strain rate and test temperature.[6,15] At high rates of straining at normal temperatures, the degree of hydrogen embrittlement is essentially nil.[6] A similar behavior is found at temperatures below about −115°C when employing normal rates of straining.[6,15] It has also been observed, however, that hydrogen embrittlement is reduced at normal temperatures under low rates of straining[6] and embrittlement is predominant within only a certain range of strain rates.*

The experimental observations reported in the literature indicate that hydrogen embrittlement is diffusion dependent,[5] at least in part. Such embrittlement depends on diffusion of hydrogen to special sites which are originated by plastic deformation. It is believed that diffusion of hydrogen leads to a condition of local equilibrium between atomic hydrogen dissolved in the lattice and molecular hydrogen present in lattice defects. It is likely then that hydrogen embrittlement is related largely to accumulation of hydrogen gas under high pressure within lattice defects such as micro cracks.[7] The lack of embrittlement at high strain rates or low temperatures is undoubtedly related to the inability of hydrogen to diffuse rapidly enough to micro cracks during a test. However, the fact that essentially little embrittlement is found at very low rates of straining indicates that factors other than diffusivity may also be operative. The micro cracks which lead to hydrogen embrittlement may be formed by dislocation pile-ups at various obstacles as described by Stroh[16] and Cottrell[17].

In order to understand further the phenomenon of hydrogen embrittlement in iron and steel, an analysis is presented in this paper of the effect of occluded hydrogen on the stability and propagation of micro cracks, first in the absence and secondly in the presence of an external stress. An analysis of the stability of a micro crack in the absence of hydrogen but with an imposed external stress is also presented.

* Static fatigue or delayed rupture determined from a notched sample may indicate that hydrogen embrittlement is also found at low strain rates. However, the stress and strain distribution and strain rate cannot be easily determined in a static fatigue test since this phenomenon is related to stress concentration effects just beneath the specimen surface. In the present analysis, the phenomenon of static fatigue will not be discussed.

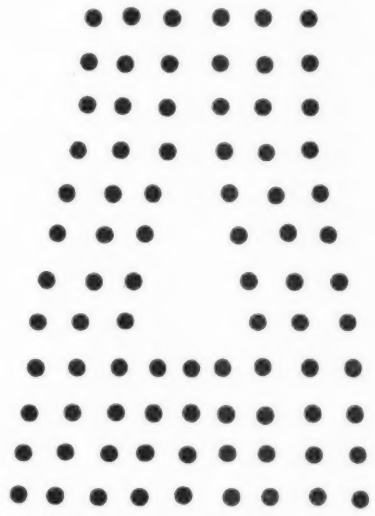


FIG. 1. Dislocation with a Burgers vector of three atomic spacings constituting an incipient Stroh crack (after Stroh, Ref. 16).

INITIATION OF MICRO CRACKS

A detailed analysis of the formation and growth of micro cracks through plastic flow has been presented in recent years by Stroh[16] and extended by Cottrell[17]. The initiation of a so-called "Stroh" crack results from the stress concentration developed at the tip of a pile-up of edge dislocations which is blocked by such obstacles as grain boundaries, precipitated particles,* arrays of sessile dislocations or, as suggested by Cottrell, at intersections of slip lines. As the shear stress forcing the dislocations against the obstacles is increased, the leading dislocations may be compelled to form a single dislocation or, as usually referred to, a "Stroh" crack.

Figure 1 shows schematically a dislocation with a Burgers vector of three atomic spacings, which in essence constitutes a very early stage in the formation of a micro crack by the coalescence of three edge dislocations. As suggested by Stroh, once a micro crack is found at the tip of a dislocation pile-up it will have a certain stability. The stability of such a micro crack, however, will depend on the imposed conditions of internal pressure within the crack and also on any imposed external stress. The effects of internal pressure, external stress and combined

* As discussed by Low[18], only hard precipitated particles may have sufficient shear strengths to permit a dislocation pile-up of the required number of dislocations for crack initiation.

VOL. 8 1960

internal pressure and external stress on the stability of a micro crack are discussed below.

EFFECT OF INTERNAL PRESSURE ON THE ENERGY OF A "STROH" CRACK

The strain energy necessary for the formation of a "Stroh" crack of Burgers vector $n'b$ and length C has been found to be:[16]

$$\frac{(n')^2b^2GL}{4\pi\,(1-\nu)}\ln\frac{4R}{C} \tag{1}$$

where n', the strength, is the total number of coalesced edge dislocations, b is Burgers vector (for a dislocation of unit strength), G is the shear modulus, L is the length perpendicular to the plane of Fig. 1, the distance R is an upper limit of integration corresponding to grain or sample size and ν is Poisson's ratio. In order to determine the increase in the strain energy of a Stroh crack by internal pressure, P, it may be imagined that the pressure is increased slowly within the crack causing elastic deformation at the crack surface. At this surface, the stresses developed by the pile-up of edge dislocations reduce to zero; therefore, the work performed by the pressure, P, is simply additive to the strain energy given in equation (1). Since $n'b$, the maximum width of the crack, is much smaller than the length, C, it will be assumed that the pressure, P, exerts a stress on the "Stroh" crack walls perpendicular to the axis of symmetry of the crack. As shown in the appendix, the effect of the internal pressure leads to the addition of a shallow ellipse of minor semi-axis $PC\,(1-\nu)/2G$ to the "Stroh" crack contour. The total volume of the added ellipse is $P(1-\nu)LC^2\pi/4G$ and the total work done by the pressure is

$$P^2\pi(1-\nu)LC^2/8G. \tag{2}$$

The factor of $\frac{1}{2}$ results from the increase in pressure from zero to P as the ellipse is formed. The total strain energy of the expanded "Stroh" crack is the sum of equations (1) and (2):

$$U=\frac{(n')^2b^2GL}{4\pi(1-\nu)}\ln\frac{4R}{C}+P^2\pi(1-\nu)LC^2/8G. \tag{3}$$

STABILITY OF A MICRO CRACK UNDER INTERNAL PRESSURE

As the length of the Stroh crack is increased, the total surface energy, $2\gamma CL$ may also increase depending on the effect of pressure on the surface tension, γ. The effect of this term on the crack length is introduced by a postulate initiated by Griffith[19]. The crack should have a tendency to grow or shrink depending on whether the work done by the pressure during a small change in crack length is greater or less than the increase in strain and surface energy of the crack. A stable crack length therefore should correspond to a minimum value (with respect to a change in length at fixed pressure) of the expression $U+2\gamma CL-PV$, where V is the volume of the crack. A similar approach has been employed by de Kacinczy[5] in discussing the growth of a disk-shaped crack under internal pressure in an external stress field. However, in this case, the effect of the pressure on the strain energy and crack volume at a fixed crack radius was neglected. An expression for the crack contour in the absence of internal pressure has been given by Stroh[16]. From this expression and the results of the appendix, the volume of the crack becomes

$$V=\tfrac{1}{2}\,n'bLC+\frac{P\pi(1-\nu)LC^2}{4G} \tag{4}$$

and the total energy of the micro crack becomes

$$E_T=\frac{(n')^2b^2GL}{4\pi(1-\nu)}\ln\frac{4R}{C}+2\gamma LC-\frac{P^2\pi(1-\nu)LC^2}{8G}-\frac{Pn'bLC}{2}. \tag{5}$$

The critical crack length, C_{cr}, which corresponds to an unstable crack can be determined as follows: differentiating relation (5) with respect to the crack length and equating to zero, one finds:

$$\frac{\pi(1-\nu)}{4G}P^2C^2+\left[\frac{Pn'b}{2}-2\gamma\right]C+\frac{(n')^2b^2G}{4\pi(1-\nu)}=0. \tag{6}$$

For a stable crack length $\dfrac{(\partial^2E_T)}{(\partial C^2)}>0$, which leads to

$$PC<\frac{n'bG}{\pi(1-\nu)}. \tag{7}$$

The critical condition for instability is given by the simultaneous solution of relation (6) and $PC=(n'bG)/[\pi(1-\nu)]$, giving for the critical crack length:

$$C_{cr}=\frac{(n')^2b^2G}{2\pi(1-\nu)\gamma}. \tag{8}$$

By substituting relation (8) in $PC=(n'bG)/[\pi(1-\nu)]$, the critical pressure becomes

$$P_{cr}=\frac{2\gamma}{n'b} \tag{9}$$

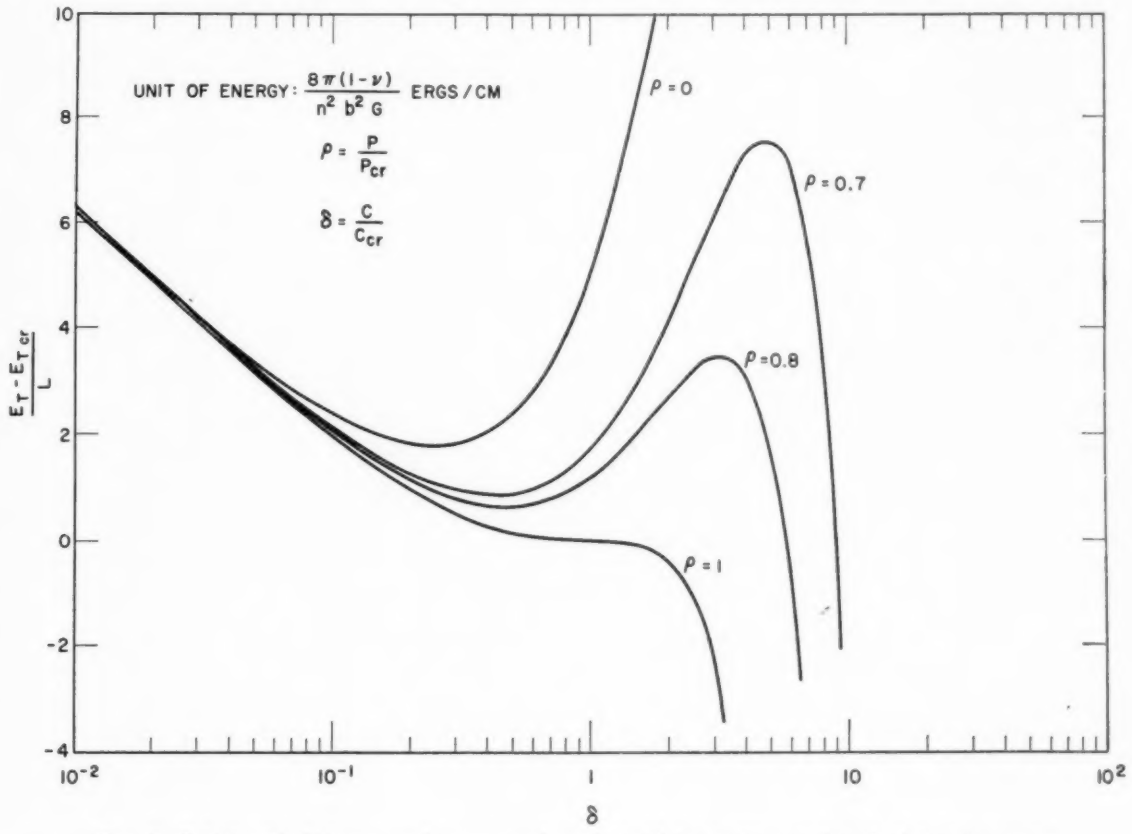


FIG. 2. Relationship between crack energy and crack length for a micro crack under internal pressure.

and by eliminating n' in (8) and (9) the relation between P_{cr} and C_{cr} becomes*

$$P_{cr} = \left\{\frac{2G\gamma}{\pi(1-\nu)C_{cr}}\right\}^{1/2}. \tag{10}$$

By substituting (8) and (9) in (5) the critical energy $(E_T)_{cr}/L$ becomes

$$\frac{(n')^2 b G}{4\pi(1-\nu)}\left(\ln\frac{4R}{C_{cr}} + 3/2\right).$$

A plot of the crack energy against the crack length as the pressure varies from $P = 0$ to $P = P_{cr}$ is shown in Fig. 2. The ordinate is $[E_T - (E_T)_{cr}]/L$ with units $[8\pi(1-\nu)]/(n^2b^2G)$ ergs/cm and the abscissa, δ, is the ratio C/C_{cr}. The pressure is indicated by, ρ, which is the ratio P/P_{cr}. The curve for $P = 0$, that is $\rho = 0$, shows the variation of the energy with crack length for a "Stroh" crack. The stable "Stroh" crack length, C_s, corresponds to the crack length at the energy minimum. Stroh[16] has shown this value to be: $C_s = (n')^2 b^2 G/8\pi(1-\nu)\gamma_0$, where γ_0 is the surface tension of the pure material. For a "Stroh" crack the energy increases continuously beyond the minimum as the crack length increases. For $P > 0$ or $\rho > 0$, the energy goes through a minimum and except for P_{cr} or $\rho = 1$, it goes also through a maximum. The crack becomes unstable when $P = P_{cr}$ or $\rho = 1$. For this pressure the energy continuously decreases with crack length and C_{cr}, which may be calculated from relation (8) is reached when $\delta = 1$. It is also possible to determine C_{cr} from C_s by substituting the relation for C_s into relation (8), giving $C_{cr} = 4(\gamma_0/\gamma)C_s$. Although no physical significance is associated with the crack length at the energy maximum, it may be observed that the crack becomes unstable when the values for crack length at the energy minimum and maximum approach one another.

The relationship between the equilibrium crack length and P up to P_{cr} can be determined from relation (6) which reduces to:

$$C = \frac{2G}{\pi(1-\nu)P^2}\left[\left(2\gamma - \frac{Pn'b}{2}\right) \pm 2\gamma\left(1 - \frac{Pn'b}{2\gamma}\right)^{1/2}\right]. \tag{11}$$

* If it is assumed, as suggested recently by Cottrell[17], that a micro crack forms at the intersection of two orthogonal slip lines, relation (10) remains unchanged.

VOL. 8 1960

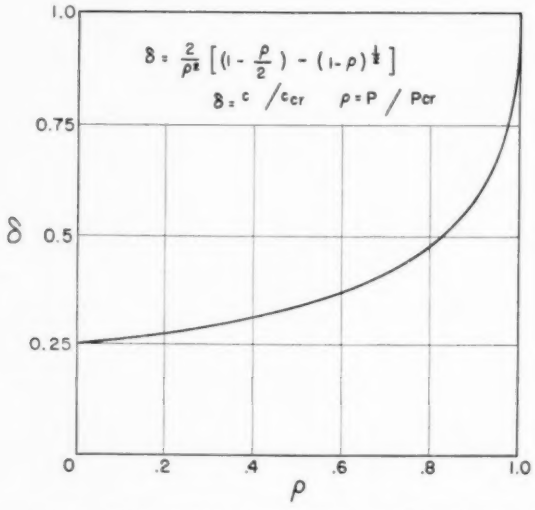


FIG. 3. Relationship between crack length and internal pressure.

The condition for real roots in relation (11) is

$$\frac{P_H' b}{2\gamma} \leq 1 \text{ or } P \leq P_{cr}.$$

The change in equilibrium crack length with pressure becomes from relation (11) by setting $\delta = C/C_{cr}$ and $\rho = P/P_{cr}$

$$\delta = 2\rho^{-2}[(1 - \rho/2) \pm (1 - \rho)^{1/2}]. \tag{12}$$

As indicated previously, only the minimum in the relationship between total energy change and crack length is of interest; therefore, only the negative sign need be examined in relation (12). The final relation thus becomes:

$$\delta = 2\rho^{-2}[(1 - \rho/2) - (1 - \rho)^{1/2}]. \tag{13}$$

A graph of this relation is shown in Fig. 3, which shows that the crack length increases very rapidly as P approaches P_{cr}.

The above analysis shows that once a "Stroh" crack is formed, a sufficiently high internal pressure will promote self propagation even in the absence of external stresses. Hydrogen in solid solution in α-iron can provide a source of high pressure within existing "Stroh" cracks.

As is generally known, hydrogen has been associated with the formation of internal cracks, normally referred to as flakes or hair-line cracks, in commercial steels and in samples purposely impregnated with hydrogen.[7,20] It is very likely that "Stroh" or "Cottrell" cracks in iron and steel can be initiated in several ways. Stresses developed during cooling from high temperatures or during phase transformations, particularly in segregated areas, may promote Stroh cracks by a dislocation pile-up. Similarly, prestraining can promote Stroh crack formation.

An estimate of the range of P_{cr} for self propagation of a "Stroh" crack in α-iron can be obtained for relation (10).* It is necessary, however, to determine first the dependence of the surface tension on hydrogen pressure. The change in surface tension can be calculated by combining the Gibbs adsorption equation, the Langmuir isotherm and Sieverts law as discussed by Petch[21]. For a diatomic molecule which disassociates the effective surface tension becomes

$$\gamma = \gamma_0 - 2\Gamma_s kT \ln [1 + (Af)^{1/2}] \tag{14}$$

where Γ_s is the number of hydrogen molecules per unit area adsorbed at saturation on the crack surface, A is a constant, k and T have the usual meaning and f is the fugacity which may be determined from Sieverts law for hydrogen in iron. From the results of Phragmen[22] and others,[23] Sieverts law becomes

$$f^{1/2} = 0.438\, X \exp\left(\frac{3453}{T}\right) \tag{15}$$

where X is the concentration of hydrogen (lattice dissolved) in iron in cm³/100 g. Phragmen[22] also gives the following relationship between hydrogen concentration, pressure and temperature:

$$X = 6.35 \times 10^{-2} P^{1/2} \exp\left(\frac{-3453 + 7.3 \times 10^{-8} P}{T}\right). \tag{16}$$

From relations (10), (14) and (15), the critical pressure for self propagation of a "Stroh" crack in iron and steel subjected to internal hydrogen pressure becomes

$$P_{cr} = \frac{2}{n'b}\gamma_0 - 2\Gamma_s kT \times \left[\ln [1 + 2.78 \times 10^{-2} A^{1/2} P_{cr}^{1/2} \exp\left(\frac{7.3 \times 10^{-8} P_{cr}}{T}\right)\right]. \tag{17}$$

In relation (17) n' refers to the strength of a stable "Stroh" crack in iron and steel, that is the number of coalesced dislocations forming the crack, and, as will be shown later, a stable crack can contain no more than six dislocations. Thus by assuming n' to be between five and three dislocations and inserting in relation (17) values of Γ_s and A suggested by Petch[21], an estimate of the range of P_{cr} can be calculated. Using a value of 1.6×10^3 ergs/cm² for γ_0 as suggested

* In polycrystalline iron such cracks may propagate only over limited distances because in traversing grain boundaries additional energy other than the surface energy may be required.

by Stroh[16], the range in P_{cr} at room temperature is found to be between 1.5×10^{10} dyn/cm^2 (1.53×10^4 atm) and 2.2×10^{10} dyn/cm^2 (2.2×10^4 atm). From relation (16), the amount of hydrogen dissolved in α-iron at room temperature necessary to develop such pressures should be between 2.5 cm^3/100 g and 13.5 cm^3/100 g (2 to 12 p.p.m.). Except in cases where careful heat treating practices are employed to minimize cooling stresses, hydrogen concentrations of this magnitude are found to produce profuse internal cracking in a variety of commercial steels.[7,20]

STABILITY OF A MICRO CRACK UNDER IMPOSED EXTERNAL TENSILE STRESS

As shown by Stroh[16], the total crack energy under an external tensile stress becomes:

$$E_T = \frac{(n')^2 b^2 G L}{4\pi(1-\nu)} \ln \frac{4R}{C} + 2\gamma LC - \frac{\pi(1-\nu)L}{8G}(\sigma_1^2 + \sigma_2^2)C^2 - \tfrac{1}{2}Ln'\sigma b_1 \sin\theta C \qquad (18)$$

where σ_1 is the component of the external stress normal to the major axis of the micro crack, σ_2 is the stress component parallel to the major axis and θ is the angle between the plane of resolved maximum shear stress and the major axis of the micro crack. All other quantities have been defined previously. By differentiating relation (18) and examining for extreme values, the relation for the crack length becomes:

$$C = \frac{G}{\pi(1-\nu)(\sigma_1^2 + \sigma_2^2)}\left\{(4\gamma - n'b\sigma_1 \sin\theta) \pm \left[4\gamma^2 - 2\gamma n'b\sigma_1 \sin\theta - \frac{(n')^2 b^2}{4}(\sigma_1^2 \cos^2\theta + \sigma_2^2)\right]^{1/2}\right\}. \qquad (19)$$

The crack will become self-propagating when

$$4\gamma = n'b[(\sigma_1^2 + \sigma_2^2)^{1/2} + \sigma_1 \sin\theta] \qquad (20)$$

and the critical crack length becomes:

$$C_{cr} = \frac{4\gamma G}{\pi(1-\nu)}[(\sigma_1^2 + \sigma_2^2) + (\sigma_1^2 + \sigma_2^2)^{1/2}\sigma_1 \sin\theta]^{-1}. \qquad (21)$$

According to Stroh, $\theta = \cos^{-1}\frac{1}{3}$, $\sigma_1 = 0.186\ \sigma$ and $\sigma_2 = 0.389\ \sigma$, where σ is the externally applied tensile stress. Thus relation (21) reduces to

$$C_{cr} = \frac{15\gamma G}{\pi(1-\nu)\sigma_{cr}^2}. \qquad (22)$$

The critical stress for rupture in tension therefore becomes:

$$\sigma_{cr} = \left[\frac{15\gamma G}{\pi(1-\nu)C_{cr}}\right]^{1/2}. \qquad (23)$$

It is quite obvious that relation (23) for an equivalent crack length is analogous to the Griffith relation:[19]

$$\sigma = \left[\frac{8\gamma G}{\pi(1-\nu)C}\right]^{1/2}$$

and differs from it only by a constant factor. A similar relation is also found if the crack is initiated at the intersection of two orthagonal slip lines as suggested by Cottrell[17]. This relation becomes:

$$\sigma_{cr} = \left[\frac{2\gamma G}{(1-\nu)C_{cr}}\right]^{1/2}$$

and differs by a constant factor from both the Stroh or Griffith relation.

It is possible by employing relation (23) to determine from experimental results the variation of the critical crack length with grain size by assuming that σ_{cr} is equivalent to the stress at rupture. A comparison of C_{cr} and grain diameter is made from the results of Petch[21] on mild steel specimens tested in simple tension at -115°C. The values of the critical stress for rupture, obtained from the results of Petch for various grain diameters, and the computed critical lengths are given in Table 1. For these calculations, γ is assumed as 1.6×10^3 ergs/cm^2 and G as 10^{12} dyn/cm^2. Only the results obtained on specimens free of hydrogen are discussed here. As may be observed from Table 1 the critical crack lengths computed are appreciably less than the grain diameter. It has been assumed at times in conjunction with the Griffith concept, that the critical crack length for self propagation may be of the order of one-half or one grain diameter.[16,21] It should be mentioned that in the present analysis, the energy of plastic flow during crack propagation[18,24] has been omitted.* Therefore, for cases where appreciable plastic deformation occurs during crack propagation relation (23) as well as the Griffith and Cottrell relations underestimate the critical crack length. However, if the surface energy term is merely adjusted by a constant amount[18,24] a direct proportionality between the critical crack length and grain diameter, is still not found.

STABILITY OF A MICRO CRACK UNDER INTERNAL PRESSURE AND EXTERNAL TENSILE STRESS

Further insight into the mechanism of hydrogen embrittlement can be obtained by determining the combined effect of internal pressure and external

* This assumption is reasonable if unstable cracks propagate only over one to two grain diameters and join other such cracks to complete total rupture.

VOL. 8 1960

TABLE 1. Critical crack lengths calculated from tensile test results at −115°C of Petch[21] on mild steel free of hydrogen and with 10 cm³ H in 100 g Fe

Grain dia. (cm)	Free of hydrogen		With hydrogen	
	σ_f (dyn/cm²)	C_{cr} (cm)	σ_f (dyn/cm²)	C_{cr} (cm)
∞ *	5.38×10^9	3.83×10^{-4}	4.56×10^9	5.99×10^{-7}
1.11×10^{-2}	7.17×10^9	2.16×10^{-4}	5.57×10^9	5.96×10^{-7}
4.0×10^{-3}	8.4×10^9	1.57×10^{-4}	5.80×10^9	5.95×10^{-7}
2.0×10^{-3}	9.62×10^9	1.20×10^{-4}	6.98×10^9	5.94×10^{-7}
1.0×10^{-3}	1.09×10^{10}	9.34×10^{-5}	7.70×10^9	5.93×10^{-7}
8.3×10^{-4}	1.20×10^{10}	7.71×10^{-5}	8.40×10^9	5.90×10^{-7}

* Computed from extrapolated values.

stress on the conditions for instability of a micro crack. The total energy of a micro crack initiated by a dislocation pile-up and subjected to internal pressure and external stress becomes:†

$$E_T = \frac{(n')^2 b^2 G L}{4\pi(1-\nu)} \ln \frac{4R}{C} + 2\gamma LC - \frac{\pi(1-\nu)}{8G} L(\sigma_1^2 + \sigma_2^2 + P^2)C^2 - \tfrac{1}{2} n' b L(\sigma_1 \sin\theta + P)C. \quad (24)$$

All quantities in relation (24) have been defined previously. By differentiating with respect to C and solving for extreme values, the critical crack length,‡ C_{cr}, becomes

$$C_{cr} = \frac{4\gamma G}{\pi(1-\nu)} \left[(0.186\,\sigma_f^2 + P^2) + (0.186\,\sigma_f^2 + P^2)^{1/2} \times (0.175\,\sigma_f + P) \right]^{-1} \quad (25)$$

where σ_f is the external stress at fracture and P is the internal pressure. Critical crack lengths have been computed from this relation by using values of σ_f reported by Petch[21] on hydrogen-impregnated mild steel samples of various grain diameters tested at −115°C. The computed results are shown in Table 1. As reported by Petch, the samples contained about 10 cm³ of hydrogen per 100 g of iron (8 p.p.m.). The effective surface tension and pressure were computed on the basis of this amount of hydrogen from relations (14) and (16), respectively. The extent of plastic deformation during crack propagation is not known and therefore this factor has been omitted in the present analysis.

† Relation (24) is obtained from relation (18) by introducing a pressure term.

‡ If a micro crack forms at the junction of two orthagonal slip lines,[17] relation (25) becomes,

$$C_{cr} = \frac{2\gamma G}{\pi(1-\nu)(P^2 + \sigma_f^2)}.$$

The difference between this relation and relation (25) is brought about by an orientation difference in the two cases between axial load and crack axis.

Two observations are of interest from the results of Table 1. The first is that for equivalent grain sizes, the computed critical crack lengths are appreciably smaller than those in the absence of hydrogen. The second observation is that with hydrogen present, the critical crack size remains constant as the grain size is changed. The fact that the critical crack length remains essentially constant with grain size indicates that the internal pressure is sufficiently high in the present case to propagate a newly formed Stroh crack without increasing the external stress greatly.§

From the results in Table 1, it is possible to estimate the number of dislocations (n') coalesced to form a stable Stroh crack. The length of the stable crack must be smaller than all critical lengths given in Table 1. Thus, a stable Stroh crack must have a length less than 5.90×10^{-7} cm. From the relation for the length of a stable Stroh crack, $C_s = (n')^2 b^2 G / 8\pi(1-\nu)\gamma_0$, it is found for iron that n' cannot be greater than six dislocations. This estimate is based, of course, on the assumption that the fracture strength values reported in Table 1 correspond to the critical stress values necessary for self propagation of micro cracks. A further assumption is that the degree of plastic deformation during crack propagation is nil. These assumptions are proper if complete rupture in a tensile specimen occurs by the joining of many cracks which propagated across one or at the most two grains. Under these conditions equation (25) may apply. In the event that appreciable plastic deformation occurs during crack propagation the number of dislocations coalesced in a stable crack should be appreciably greater than the number estimated here.

An independent estimate and substantiation of the sub-microscopic nature of stable micro cracks has

§ If the pressure decreases sharply as the crack becomes large, the external stress must be sufficient to completely rupture the sample.

been made by Straumanis[25]. In this work precise X-ray lattice measurements and density determinations on cold-worked, high-purity aluminum were employed and the size of stable micro cracks has been estimated to be of the order of 3–4 atom diameters.

The approximate amount of hydrogen in solid solution in α-iron* necessary to cause a measurable degree of hydrogen embrittlement may be calculated from relation (25). Setting $\beta = P/\sigma_f$, the following is obtained from relation (25):

$$\sigma_f^2 C_{cr} = \frac{4\gamma G}{\pi(1-\nu)[(\beta^2+0.186)+(\beta^2+0.186)^{1/2}(\beta+0.175)]} \quad (26)$$

In analysing the change in $\sigma_f^2 C_{cr}$ with β it should be pointed out that both σ_f and β cannot exceed certain limits. σ_f, as mentioned previously, cannot be less than the yield strength σ_y and β cannot exceed P_{max}/σ_y. From relation (16) it can be shown[22] that P_{max} cannot exceed 4.7×10^{10} dyn/cm². By assuming for mild steel that $\sigma_y = 3 \times 10^9$ dyn/cm², β has an upper limit of about sixteen. Up to $\beta = 3$, $\sigma_f^2 C_{cr}$ decreases rapidly, however, between $\beta = 3$ and $\beta = 16$ the drop is quite small. As indicated from Table 1, impregnation with hydrogen decreases both σ_f and C_{cr}. Therefore beyond $\beta = 3$ appreciable hydrogen embrittlement in iron and steel should be observed. Assuming a fracture stress of 5×10^9 dyn/cm² at 18°C for a medium grain-sized mild steel, it is found for $\beta = 3$, that the concentration of hydrogen in solid solution should be about 2 cm³/100 g (2 p.p.m.). For this concentration and beyond a measurable degree of hydrogen embrittlement should be observed. Such a prediction is in good agreement with experimental observations[7,20] which indicate that ductility is reduced by an appreciable amount with hydrogen concentrations in excess of 2 cm³/100 g.

In estimating the lower limit of hydrogen concentration to produce embrittlement it has been assumed that the equilibrium hydrogen pressure in the iron lattice and in the newly formed micro cracks remains constant and can be calculated from relation (16). This would imply that it must be also assumed that the initiation of micro cracks must occur before any large amount of plastic deformation occurs. Recent results indicate that relation (16) does not apply for steels which are plastically deformed prior to hydrogen impregnation.[26] For an equivalent amount of dissolved hydrogen the equilibrium pressure in cold-worked steels is found to be appreciably less than in annealed steels.[26] This observation agrees qualitatively with the results of recent limited tests showing that for hydrogen concentrations which would embrittle annealed steel samples severely, no embrittlement is found in samples cold-worked prior to hydrogen impregnation.

* Hydrogen segregated to dislocations is neglected in all computations in this paper.

SUMMARY

This paper presents the results of an analysis of the effect of internal pressure resulting from the presence of occluded hydrogen on stability and propagation of "Stroh" or "Cottrell" cracks, first in the absence and secondly in the presence of an external stress. An analysis of the stability of such a crack in the absence of hydrogen, but with an imposed external stress, is also presented.

In determining the stability of such a crack under a constant internal pressure, it is found that the crack becomes unstable when the pressure within the crack reaches a critical value. By use of the finding that the crack may be formed by the coalescence of five to three dislocations, it is computed that the critical pressure for self propagation is of the order of 1.5×10^{10}–2.2×10^{10} dyn/cm² (1.5×10^4–2.2×10^4 atm). The amount of lattice dissolved hydrogen in α-iron at room temperature necessary to develop pressures of this magnitude varies from 2.5 to 13.5 cm³/100 g of iron (2 to 12 p.p.m.). In a variety of commercial steels, hydrogen concentrations within this range have been found to produce profuse internal cracking.

The analysis presented in this paper, in conjunction with test results published by others, indicates that the critical crack length for self-propagation is decreased appreciably by the presence of hydrogen. If the hydrogen content and therefore the internal pressure is sufficiently great and remains constant, the critical crack length remains essentially constant as the grain diameter is decreased. It is shown in this case that the internal pressure is the controlling factor in determining rupture propagation. It is concluded that if the external stress is sufficient to initiate a "Stroh" crack, then the internal pressure developed by occluded hydrogen can cause rupture. For steel with a medium grain size, appreciable hydrogen embrittlement should be found with as little as 2 cm³ of hydrogen/100 g of iron (2 p.p.m.).

ACKNOWLEDGMENT

The authors thank J. C. M. Li, H. A. Puente and L. S. Darken for the many discussions and helpful suggestions offered. The help of W. F. Domis and R. R. Keck is also acknowledged.

VOL. 8 1960

REFERENCES

1. G. A. Moore and D. P. Smith, *Trans. Amer. Inst. Min. (Metall.) Engrs.* **135,** 225 (1939).
2. W. D. Robertson (Editor), *Stress Corrosion and Embrittlement* p. 163. Wiley, New York (1956).
3. C. E. Sims, *Gases in Metals* p. 144. Amer. Soc. Metals. Cleveland (1953).
4. L. S. Darken and R. P. Smith, *Corrosion* **5,** 1 (1949).
5. F. de Kacinczy, *Jernkontor. Ann.* **140,** 347 (1956); *J. Iron St. Inst.* **177,** 85 (1954).
6. P. Bastien and P. Azou, *C.R. Acad. Sci., Paris* **229,** 549 (1949); **231,** 147 (1950); **232,** 69 (1951); *Rev. Met.* **49,** 837 (1952).
7. J. H. Andrew, A. K. Bose, G. A. Geach and H. Lee, *J. Iron St. Inst.* **146,** 193 (1942); J. H. Andrew, A. K. Bose, H. Lee and A. G. Quarrell, *J. Iron St. Inst.* **146,** 203 (1942); J. H. Andrew, H. Lee, A. K. Mallik and A. G. Quarrell, *J. Iron St. Inst.* **153,** 67 (1946).
8. J. D. Hobson and C. Sykes, *J. Iron St. Inst.* **169,** 209 (1951); J. D. Hobson and J. Hewitt, *J. Iron St. Inst.* **173,** 131 (1953).
9. C. E. Sims, G. A. Moore and D. W. Williams, *Trans. Amer. Inst. Min. (Metall.) Engrs.* **176,** 283 (1948).
10. J. B. Seabrook, N. J. Grant and D. Carney *Trans. Amer. Inst. Min. (Metall.) Engrs.* **188,** 1317 (1950).
11. I. N. Sneddon, *Proc. Roy. Soc.* A**187,** 229 (1946). I. N. Sneddon and H. A. Elliot, *Quart. Appl. Math.* **4,** 262 (1947).
12. H. G. Vaughan and M. E. de Morton, *Welding J.* **4,** 40 (1957); *Acta Met.* **4,** 234 (1956).
13. H. C. Rogers, *Acta Met.* **2,** 167 (1954); *Acta Met.* **4,** 114 (1956); *Acta Met.* **5,** 112 (1957).
14. A. Cracknell and N. J. Petch, *Acta Met.* **3,** 200 (1955).
15. J. G. Morlet, H. H. Johnson and A. R. Troiano, *J. Iron St. Inst.* **188,** 37 (1958).
16. A. N. Stroh, *Proc. Roy. Soc.* A**223,** 404 (1954); *Proc. Roy. Soc.* A**232,** 548 (1955); *Advanc. Phys.* **6,** 418, (1957).
17. A. H. Cottrell, *Trans. Amer. Soc. Min. (Metall.) Engrs.* **212,** 192 (1958).
18. J. R. Low, Jr. in *Deformation and Flow of Solids* (Editor, R. Grammel). Springer, Berlin (1956).
19. A. A. Griffith, *Phil. Trans.* A**221,** 163 (1921).
20. C. Sykes, H. H. Burton and C. C. Gregg, *J. Iron St. Inst.* **156,** 155 (1947).
21. N. J. Petch, *Phil. Mag.* **1,** 331 (1956).
22. G. Phragmen, *Jernkont. Ann.* **128,** 537 (1944).
23. Smithsells and Ransley, *Proc. Roy. Soc.* A**150,** 172 (1935).
24. E. Orowan in *Fatigue and Fracture of Metals* (Editor, W. M. Murray). Wiley, New York (1952).
25. M. E. Straumanis, unpublished work on X-ray and density studies in cold-worked aluminium.
26. M. L. Hill and E. W. Johnsen, *Trans. Amer. Inst. Min. (Metall.) Engrs.* **215,** 717 (1959).
27. H. M. Westergaard, *J. Appl. Mech.* **6,** 49 (1939).

APPENDIX

The change in shape of a micro crack under an imposed internal pressure may be determined as follows:[11,27]

For simplicity a crack of length 2 is assumed. Because of the symmetry of the problem it is only necessary to consider a semi-infinite elastic continuum. With reference to Fig. 4, the appropriate boundary conditions are

(a) $\tau_{xx} = -P \qquad -1 < y < 1,\ x = 0;$

(b) $\tau_{xy} = 0 \qquad -1 < y < 1,\ x = 0;$

(c) $u = 0 \qquad |y| < 1,\ x = 0.$

Here τ_{xx} and τ_{yy} are components of stress, u is the x component of displacement and P is the pressure. The function

$$X(x, y) = -\int_0^\infty \Phi(t) \cos ty(1 + tx)e^{-tx}\, dt/t^2 \qquad \text{(A 1)}$$

satisfies $\nabla^4\chi = 0$ and is an Airy stress function. Here Φ is as yet an unknown function of the dummy variable of integration t. The expressions for τ_{xx} and u which follow from this assumption for χ are:

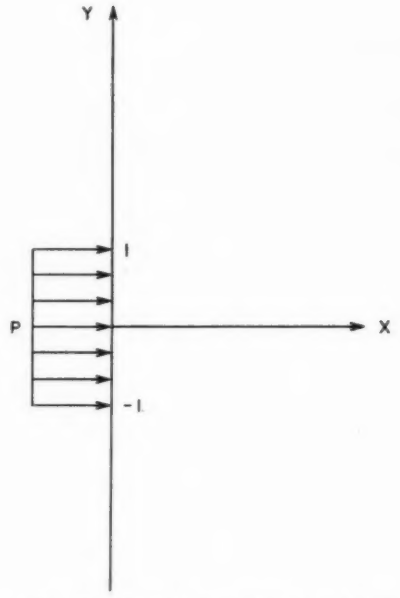


Fig. 4. Coordinate system employed in determining stability of micro crack subjected to internal pressure.

$$\tau_{xx} = \int_0^\infty \Phi(t) \cos ty(1 + tx)\, e^{-tx}\, dt, \qquad \text{(A 2)}$$

$$u = -\tfrac{1}{2}G\int_0^\infty \Phi(t) \cos ty(2 - 2\nu + tx)e^{-tx}\, dt/t. \qquad \text{(A 3)}$$

The choice of Φ satisfies the boundary condition b; moreover, it leads to stresses which approach zero as x becomes large. By applying the other two boundary conditions, the following pair of integral equations are found:

$$\begin{aligned} &\int_0^\infty \Phi(t) \cos ty\, dt = -P \qquad 0 < y < 1 \\ &\int_0^\infty \Phi(t) \cos ty\, dt/t = 0 \qquad 1 < y < \infty\,. \end{aligned} \qquad \text{(A 4)}$$

This pair of coupled equations implies[16]

$$\begin{aligned} \Phi(t) &= -t/\pi \int_0^1 \mu J_0(\mu t) d\mu \int_{-1}^1 P(1 - \xi^2)^{-1/2}\, d\xi \\ &= -PJ_1(t). \end{aligned}$$

(The relationship $zJ_0^1(z) = -[zJ_1(z)]$ has been used.) Here J_0 and J_1 are Bessel functions, and μ and ξ are variables of integration. By substituting the expression for Φ into (A 3), it is found that

$$\begin{aligned} Gu &= (1 - \nu)P \int_0^\infty J_1(t) \cos ty\, dt/t \\ &= [P(1 - \nu)[1 - y^2]^{1/2} \qquad y < 1 \\ &\qquad\qquad 0, \quad y < 1. \end{aligned}$$

For a crack of length c,

$$u = \frac{P(1 - \nu)}{G}\,[c^2/4 - y^2]^{1/2} \text{ for } |y| \leq c/2. \qquad \text{(A 6)}$$

Relation (A 6) corresponds to the elliptical shape mentioned in the text. Since a linear theory is assumed, this shape should be added to the original crack contour. The expressions for the increase in strain energy and volume follow directly from this result.

UNTERSUCHUNG DES GLEITLINIENBILDES KUBISCH-FLÄCHENZENTRIERTER EINKRISTALLE*

S. MADER und A. SEEGER†

Am Beispiel von Kupfer wird zunächst das sog. normale Gleitlinienbild kubisch-flächenzentrierter Metallkristalle besprochen. Als Störungen werden vor allem Striemen und Knickbänder beobachtet. Deren Auftreten wird als Funktion des Verformungsgrades, insbesondere in den Bereichen I, II und III der Verfestigungskurve, untersucht. Die Striemen erweisen sich als eine grobe Form der bei der sog. strukturierten Feingleitung des Bereichs II im Elektronenmikroskop zu beobachtenden Abgleitungsinhomogenitäten. Bei den Knickbändern hat man zwei Arten und auch zwei Entstehungsweisen zu unterscheiden. Von diesen tritt eine erst im Bereich III der Verfestigungskurve auf. Diese Knickbänder sind eine Folgeerscheinung der thermisch aktivierten Quergleitung. Es wird gezeigt, dass sich auch die Fragmentierung (Zellbildung) verformter Kristalle als ein damit eng zusammenhängendes Phänomen verstehen lässt.

ON THE SLIP LINE PATTERN OF FACE-CENTERED CUBIC METAL CRYSTALS

Using copper as an example, the so-called normal slip line pattern of face-centred cubic metal crystals is discussed. The normal pattern is perturbed by the appearance of striae and kink bands. Their variation with strain is examined, particularly in relation to stages I, II, III of the stress–strain curve. The striae turn out to be a coarse form of the strain inhomogeneities, which are observed by the electron microscope in the "structurized fine slip" of stage II. Two different types of kink bands, associated with two modes of formation, have to be distinguished. One of these types occurs in stage III of the stress–strain curve only. It is a consequence of the thermally activated cross slip occurring in stage III. It is shown that the fragmentation (cell formation) of deformed crystals is a closely related phenomenon.

SUR LE RESEAU DE LIGNES DE GLISSEMENT DANS LES MONOCRISTAUX CUBIQUES A FACES CENTREES

Les auteurs discutent, en prenant le cuivre comme exemple, le réseau de lignes de glissement normal des cristaux métalliques cubiques à faces centrées. Ils observent comme perturbation surtout des "stries" et des "kink-bands". Ils examinent leur apparition en fonction du degré de déformation, en particulier dans les domaines I, II, III de la courbe tension-déformation. Ils montrent que les "stries" sont une forme grossière des inhomogénéités de déformation que l'on observe au microscope électronique lors du glissement à structure fine du stade II. Ils ont pu distinguer deux types différents de "kink-bands" associées avec deux modes de formation. Un de ces types a lieu uniquement lors du troisiéme stade de la courbe tension-déformation. Ces "kink-bands" sont une conséquence du glissement de cisaillement par activation thermique. Ils montrent que la fragmentation de cristaux déformés est une phénoméne étroitement lié.

VOL. 8 1960

EINLEITUNG

In den letzten Jahren konnten viele Vorgänge, die bei der plastischen Verformung von Metallkristallen ablaufen, aufgeklärt und mit Hilfe der Versetzungstheorie gedeutet werden. (Eine umfassende Darstellung der experimentellen Ergebnisse und der theoretischen Deutung findet man an anderer Stelle.[1]) Dabei erwies es sich als aufschlussreich, gleichzeitig mit der Untersuchung der mechanischen Verfestigung lichtmikroskopische und elektronenmikroskopische Beobachtungen über die Gleitlinienbildung anzustellen. Bei der Untersuchung von Kupferkristallen konnten auf diese Weise den verschiedenen Bereichen der Verfestigungskurve bestimmte typische Gleitlinienbilder zugeordnet werden;[2] im folgenden Abschnitt über die normale Gleitlinienbildung wird darüber kurz berichtet. (Unter dem normalen Gleitlinienbild wollen wir dasjenige verstehen, welches im beschränkten Gesichtsfeld des Elektronenmikroskops am häufigsten zu sehen ist.) Die Ergebnisse von anderen elektronenmikroskopischen Gleitlinienuntersuchungen (z.B. Wilsdorf und Kuhlmann-Wilsdorf[3] und Noggle und Koehler[4]), die hauptsächlich an Aluminium durchgeführt wurden, lassen sich in die bei unseren Untersuchungen aufgefundenen Gesetzmässigkeiten der normalen Gleitung einordnen; diese sind also typisch für kubisch-flächenzentrierte Metalle.

Es lag deshalb nahe, auch die in der Literatur häufig besprochenen Störungen der normalen Gleitung in derselben Weise zu untersuchen und sie gegebenenfalls den verschiedenen Verfestigungsbereichen zuzuordnen. Nach Honeycombe[5] und Calnan[6] unterscheidet man zwei Arten von Störungen: die *Striemen* (striae) genannten Oberflächengebiete, in denen die Gleitlinien des primären Gleitsystems nur sehr schwach ausgebildet sind und in denen auch bei unsymmetrischen Orientierungen starke sekundäre Gleitspuren auftreten können, und die erstmals von Cahn[7] beobachteten *Knickbänder*. Dies sind Schichten im

* Received June 30, 1959.

† Institut für theoretische und angewandte Physik der Technischen Hochschule Stuttgart und Max-Planck-Institut für Metallforschung, Stuttgart, Deutschland.

verformten Kristall, die etwa senkrecht auf der Gleitrichtung stehen. Die durch die plastische Dehnung hervorgerufene Gitterdrehung ist in den Knickbändern geringer als in den umgebenden Kristallbereichen; sie geben daher Anlass zu einem Asterismus der Laue-Reflexe, der einer lokalen Drehung des Gitters um die zur Gleitrichtung senkrechte ⟨112⟩-Richtung entspricht. In den Knickbändern verlaufen Gleitlinien S-förmig gekrümmt; jene sind dadurch im mikroskopischen Bild leicht zu erkennen. Sie entstehen nicht nur als Folge von inhomogener Verformung etwa in der Nähe der Kristalleinspannung, sondern sind vielmehr, wie im folgenden gezeigt wird, eine natürliche Folge der bei der Verformung auftretenden Versetzungsbewegungen. Der Stand der experimentellen und theoretischen Untersuchungen über diese Fragen im Jahre 1958 wird von Seeger[1] zusammenfassend behandelt.

Eine in der vorliegenden Arbeit nicht experimentell untersuchte, aber von verformten Vielkristallen her wohl bekannte Erscheinung, die sog. Fragmentierung oder Zellbildung, wird in der Diskussion mitbehandelt werden. Es zeigt sich dabei, dass auch sie, ähnlich wie die Knickbandbildung, eine natürliche Konsequenz der Versetzungsbewegung während des Verformungsvorganges ist.

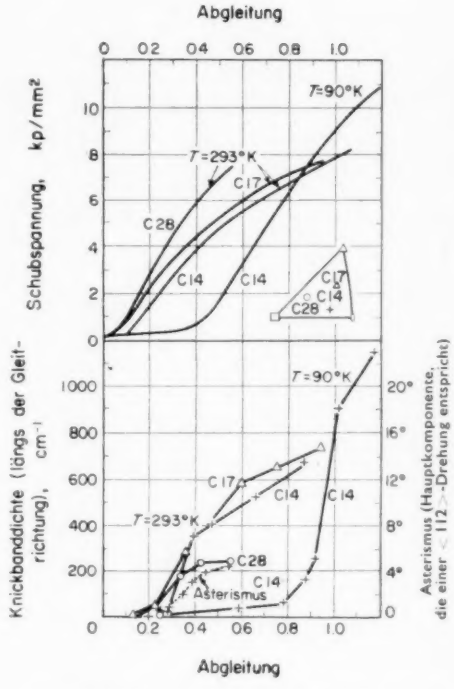


FIG. 1a(oben). Verfestigungskurven und Orientierungen der bei $T = 293$°K und $T = 90$°K (Kristall C 14) gedehnten Kupfereinkristalle.
FIG. 1b(unten). Knickbanddichten der untersuchten Kristalle und Asterismus des bei $T = 293$°K gedehnten Kristalls C 14.

EXPERIMENTELLE METHODE

Runde Einkristalle aus 99,98 Prozent Kupfer wurden nach dem Bridgman-Verfahren in Graphittiegeln hergestellt; durch Verwendung von Impflingen konnten mehrere Kristalle mit gleichen Orientierungen gezüchtet werden. Sie wurden mit einer Abgleitgeschwindigkeit von etwa 3×10^{-4} sek^{-1} gedehnt. Die Verfestigungskurven zeigt Fig. 1(a). Sie bestehen, wie Diehl *et al.*[8,9] bemerkten, aus drei Bereichen, die jeweils eine eigene Temperaturabhängigkeit zeigen. Auf den linearen Bereich I (easy glide) folgt der ebenfalls lineare Bereich II mit maximalem und temperaturunabhängigem Verfestigungsanstieg; an diesen schliesst sich der Bereich III mit geringerem Verfestigungsanstieg an. Die Einsatzspannung von Bereich III steigt mit sinkender Temperatur; sie ist die zu ausgiebiger thermisch aktivierter Quergleitung erforderliche Mindestspannung.[1]

Zur Untersuchung der Gleitlinienbildung in den einzelnen Verfestigungsbereichen erwies es sich als zweckmässig, die Verfestigungskurve in kurzen Intervallen zu durchlaufen, wobei die Kristalle vor jedem Intervall neu poliert wurden. Dadurch kann man einerseits die neu entstehenden Gleitlinien, die "aktiven Gleitlinien", sicher dem durchlaufenen Verfestigungsintervall zuordnen, andrerseits erhält man für die elektronenmikroskopische Untersuchung übersichtliche Bilder, da der Untergrund an Gleitlinien von der vorhergehenden Verformung fehlt. Teilweise wurde zwischen zwei Dehnungs-Intervallen nicht neu poliert; die Gleitlinien des gleichen Bereichs der Kristalloberfläche wurden dann am Ende der Intervalle miteinander verglichen. So konnten die Ergebnisse einzelner Intervalle zu einem Gesamtbild der aufgetretenen Gleitlinienerscheinungen zusammengefügt werden.

Die Kristalle wurden in phosphorsäurehaltigen Bädern elektrolytisch poliert. Für die elektronenmikroskopische Untersuchung wurden palladiumbeschattete Kohleabdrücke verwendet.[2,9]

Alle im folgenden wiedergegebenen Gleitlinienbilder stammen von Kristallen der Orientierung C 14 nach verschiedenen Verformungen bei Raumtemperatur (ausgenommen Fig. 7). Die elektronenmikroskopischen Bilder (Fig. 2, 3, 5 und 6) sind der Umgebung des Scheitels der Gleitellipse entnommen; bei den lichtmikroskopischen Aufnahmen (Fig. 7–10) ist die Stabachse parallel zur kurzen Seite des Bildes.

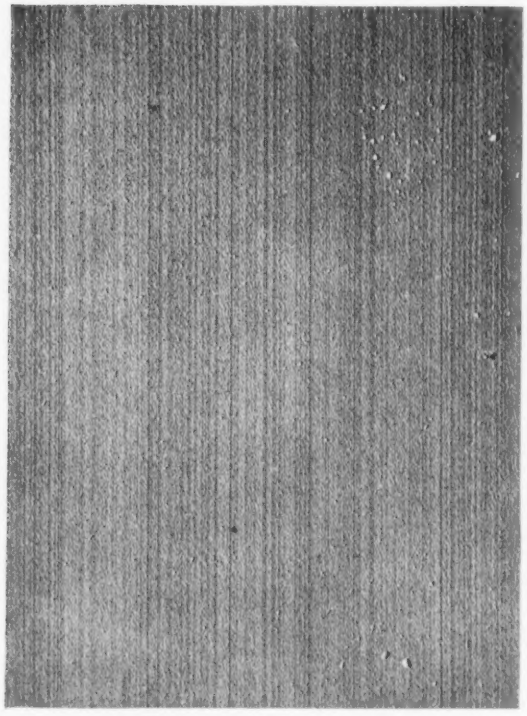


FIG. 2. Gleichmässige Feingleitung im Bereich I der Verfestigungskurve entsprechend 0 . . . 9,4 Prozent Abgleitung. ×15.000

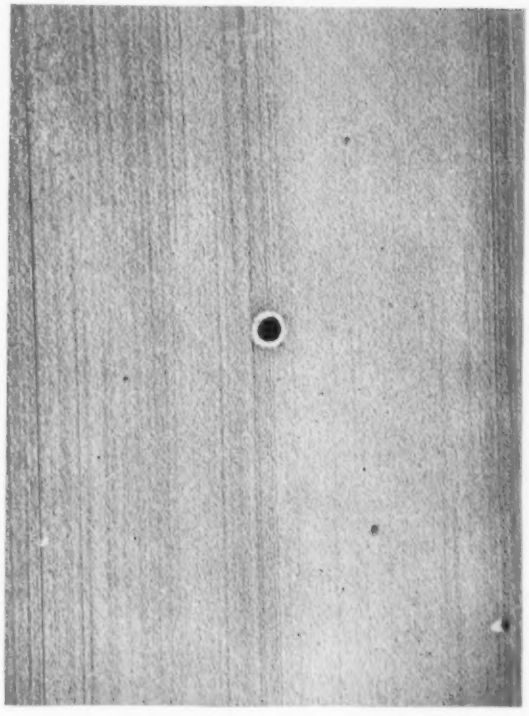


FIG. 3. Strukturierte Feingleitung im Bereich II, entsprechend 12,5 . . . 21,8 Prozent Abgleitung. ×12.000

VOL. 8 1960

ELEKTRONENMIKROSKOPISCHE UNTERSUCHUNG DER NORMALEN GLEITUNG[2]

Ein typisches Gleitlinienbild aus Bereich I zeigt Fig. 2; es ist zu charakterisieren als *gleichmässige Feingleitung*. Die Gleitlinien sind sehr lang, im Mittel etwa 0,6 mm; die Stufenhöhe ist sehr gering, sie entspricht im Mittel einem Gleitschritt von 12 Atomabständen. Die Gleitung breitet sich unbehindert über grosse Gebiete der Gleitebenen aus.

Im Bereich II entsteht dagegen eine *strukturierte Feingleitung*, Fig. 3. Die lokale Gleitliniendichte schwankt stark. Aus nacheinanderfolgenden Bildern des gleichen Oberflächenbereichs nach Abgleitungen von jeweils etwa 5 Prozent ist zu entnehmen, dass bei weiterer Verformung die Gleitung vornehmlich in den Gebieten stattfindet, die im vorhergehenden Intervall von Gleitlinien frei geblieben waren. Die Stufenhöhe der einzelnen Gleitlinien entspricht jetzt einem mittleren Gleitschritt von etwa zwanzig Atomabständen. Sie ist unabhängig von der Grösse der Verformungsintervalle; der Vergleich von nacheinanderfolgenden Bildern zeigt, dass die Stufenhöhe der einmal gebildeten Gleitlinien nur selten später weiter wächst. Die Länge der bei zusätzlicher Verformung neu entstehenden (aktiven) Gleitlinien nimmt mit wachsender Gesamtabgleitung ab. Fig. 4 zeigt am Beispiel von Kristallen der Orientierung C 14 den linearen Zusammenhang zwischen der reziproken Länge der aktiven Gleitlinien auf dem Scheitel des Kristalls und der Abgleitung. Bei gegebener Abgleitung wächst die Länge der Linien zur Seite des Kristalls hin auf etwa den doppelten Betrag an. Die aktiven Gleitlinien werden auch bei anderen kubisch-flächenzentrierten Kristallen mit wachsender Verformung kürzer. In Fig. 4 sind als weitere Beispiele Ergebnisse von Kronmüller[10] an Nickel- und Nickel + 20 Prozent Kobalt-Einkristallen eingetragen. Schon Blewitt *et al.*[11]

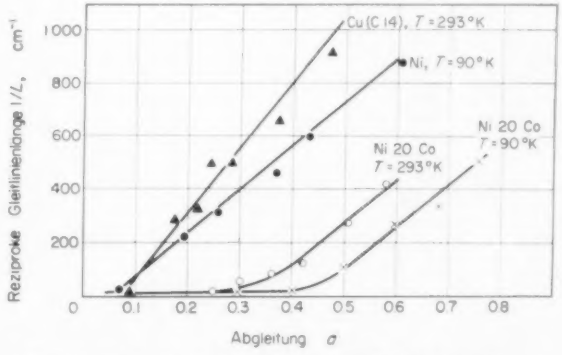


FIG. 4. Reziproke Länge der aktiven Gleitlinien aufgetragen über der Gesamtabgleitung am Ende der Dehnungsintervalle, in denen sie neu entstanden sind.

und Rebstock[12] hatten bei lichtmikroskopischen Dunkelfelduntersuchungen eine Gesetzmässigkeit dieser Art gefunden, allerdings mit etwas anderen Parametern.

Im Bereich III bündeln sich die neu entstehenden Gleitlinien zu *Gleitbändern*, wobei mit zunehmender Abgleitung immer häufiger und immer deutlicher Spuren von *Quergleitung* auftreten, Fig. 5. Bei hohen Abgleitungen sind die neu entstehenden Gleitbänder fragmentiert; die einzelnen *Gleitbandfragmente* sind häufig durch Quergleitung miteinander verbunden, Fig. 6. Die Stufenhöhe der einzelnen Gleitlinien wächst im Gegensatz zum Bereich II bis auf etwa 100 Atomabstände, während die Länge der neu entstehenden Gleitlinien und auch die Länge der neu entstehenden Gleitbandfragmente weiterhin abnimmt. Die Gleitbandfragmente sind stets ein wenig länger als die einzelnen Gleitlinien.

LICHTMIKROSKOPISCHE BEOBACHTUNGEN VON STÖRUNGEN DER NORMALEN GLEITUNG

Die gegenseitigen Abstände und die Ausdehnung der gestörten Bereiche sind von einer solchen Grössenordnung, dass sie am zweckmässigsten mit dem Lichtmikroskop untersucht werden. Dabei findet man schon vom Ende des Bereichs I an Schwankungen der örtlichen Gleitliniendichte; besonders deutlich werden diese im Bereich II. Die bei der normalen Gleitung des Bereichs II (strukturierte Feingleitung) beschriebenen Gebiete mit geringer Gleitliniendichte variieren sehr stark in ihren Ausmassen. Ihre Länge schwankt zwischen einigen 100 μ und dem ganzen Kristallumfang, ihre Breite zwischen 10 μ und 100 μ. Die mittleren Abstände dieser Gebiete wachsen bei Kristallen mittlerer Orientierung (C 14) von etwa 100 μ am Ende von Bereich I bis auf etwa 500 μ im Bereich III. Schliesslich bedecken die bei einer Zusatzdehnung neu entstehenden Gleitbänder den Kristall so gleichmässig, dass keine gleitlinienfreie Gebiete mehr zu erkennen sind. In den grösseren Gebieten mit geringer Gleitliniendichte findet man vor allem auf den Oberflächenbereichen ausserhalb des Scheitels Spuren von ausgiebiger sekundärer Gleitung. Es ergibt sich also ein stetiger Übergang von der *strukturierten Feingleitung* zu den eingangs erwähnten *Striemen*. Die sekundäre Gleitung wird umso stärker, je mehr sich die Orientierung der Stabachse der Symmetralen [100]–[111] nähert. Besonders auffällig ist die auch bei mittelorientierten Kristallen auftretende Gleitung des Quergleitsystems, die gelegentlich ein gleitlinienarmes Striemengebiet ausfüllt, Fig. 7. Bänder dieser Art sind jedoch selten, ihre gegenseitigen Abstände betragen etwa 5–10 mm. Wir vermuten,

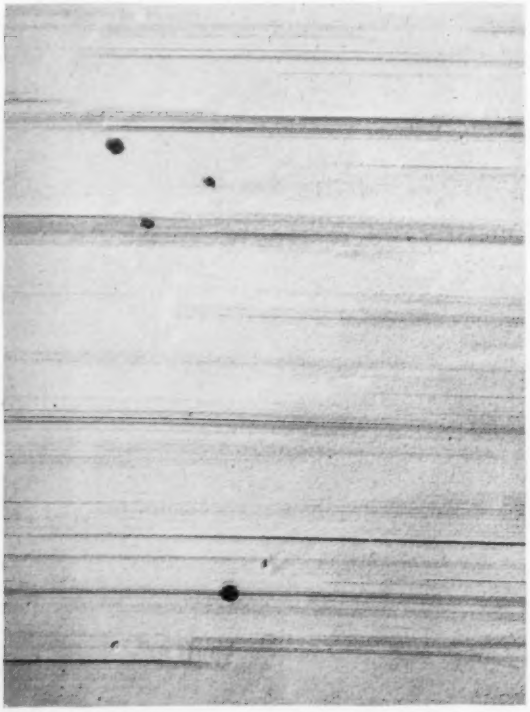


FIG. 5. Gleitbänder mit Quergleitung im Bereich III, entsprechend 38 . . . 47,5 Prozent Abgleitung. ×6000

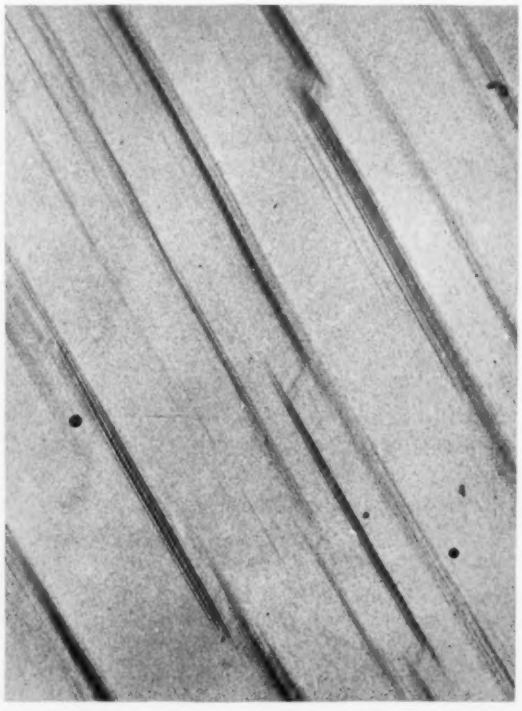


FIG. 6. Fragmentierte Gleitbänder im Bereich III, entsprechend 59 . . . 69 Prozent Abgleitung. ×8000



FIG. 7. Strukturierte Gleitung im Bereich II; Striemen mit Gleitung auf der Quergleitebene, entsprechend 43 . . . 59 Prozent Abgleitung bei $T = 90$ K. ×330

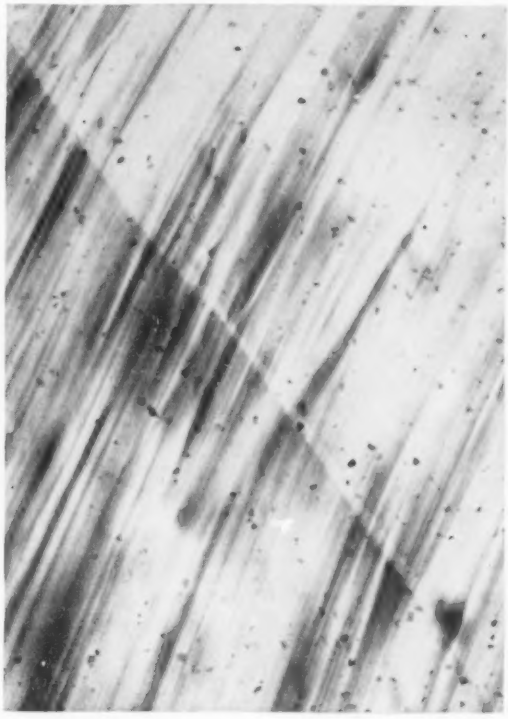


FIG. 8. Knickband und strukturierte Gleitung im Bereich II, entsprechend 12 . . . 19,5 Prozent Abgleitung. ×330

VOL. 8 1960

dass diese spezielle Art von sekundärer Gleitung auf der geringen latenten Verfestigung des Quergleitsystems beruht; die Versetzungen dieses Systems können diejenigen des primären Gleitsystems ohne Sprungbildung schneiden. Diese Gleitung ist also ähnlich wie die Quergleitung bei α-Messing[13] und in ihrem Wesen verschieden von der thermisch aktivierten Quergleitung im Verfestigungsbereich III, bei der die Schraubenanteile von Versetzungsringen des primären Gleitsystems ihre Gleitebene verlassen.

Die zweite Art von Störungen sind *Knickbänder*. Wie eingangs erwähnt, sind sie mikroskopisch an dem *S*-förmig gekrümmten Gleitlinienverlauf deutlich zu erkennen; eine schräge Auflichtbeleuchtung verstärkt ihren Kontrast, Fig. 8–10. Im Gegensatz zu den Gleitlinien treten nach Abpolieren und weiterem Verformen eines Kristalls die früher vorhandenen Knickbänder wieder in Erscheinung wegen der mit ihnen verbundenen Gitterdrehung. In Fig. 1(b) ist die Dichte der Knickbänder, gezählt längs der Gleitrichtung, als Funktion der Abgleitung aufgetragen. Zur Ermittlung dieser Kurven wurden die Knickbänder über mehrere cm des homogen verformten Mittelteils der Kristalle abgezählt; die inhomogen verformten Gebiete in der Nähe der Einspannungen wurden nicht mitbenützt. Die Knickbanddichte längs der Stabachse wurde dann mit Hilfe der bekannten Orientierung der Kristalle in die Dichte längs der Gleitrichtung umgerechnet.

Die Kurven zeigen für Kristallorientierungen, die der Symmetralen [100]–[111] des Orientierungsdreiecks nicht benachbart sind, eine bemerkenswerte Ähnlichkeit zu den zugehörigen Verfestigungskurven (Fig. 1); besonders deutlich ist diese Ähnlichkeit bei dem bei 90°K verformten Kristall der Orientierung C 14. Im Bereich I entstehen nahezu keine Knickbänder. Im Bereich II wächst die Knickbanddichte nur schwach. Nach Erreichen des Bereichs III steigt sie auf einen hohen Wert an. Der mittlere Abstand zwischen zwei Knickbändern ist nun etwa gleich der Länge der Gleitbandfragmente auf der Seite des Kristalls. Bei weiterer Verformung im Bereich III nimmt der mittlere Abstand der Knickbänder weiter ab im selben Mass, in dem die aktiven Gleitlinien auf der Seite des Kristalls kürzer werden. Er ist jedoch immer etwas grösser als die aktive Gleitlinienlänge bei derselben Abgleitung. Ein Vergleich von Fig. 4 mit Fig. 1(b) zeigt diese Verhältnisse für die bei Raumtemperatur verformten Kristalle der Orientierung C 14. In Fig. 4 sind die Längen der aktiven Gleitlinien auf dem Scheitel des Kristalls dargestellt. Da sie auf der Seite etwa die doppelte Länge haben, müssen zum

numerischen Vergleich von Fig. 4 mit Fig. 1(b) die Ordinatenwerte der Fig. 4 halbiert werden.

Die bisher geschilderten Versuche beziehen sich auf *Kupferkristalle*. An Aluminium liegen in der Literatur zahlreiche Beobachtungen vor, die zum grössten Teil nach Verformung bei Raumtemperatur angestellt wurden. Da in diesem Falle der Bereich III schon bei geringen Verformungsgraden einsetzt, bevor der Bereich II sich ausbilden kann, lassen sich diese Beobachtungen nicht in ähnlich eindeutiger Weise der Verfestigungskurve zuordnen. Deshalb untersuchten wir *Aluminiumkristalle* nach einer Verformung bei 90°K, bei der die Verfestigungskurve ähnlich verläuft wie bei Kupfer. Die beobachteten Knickbanddichten wiesen die gleiche Korrelation zur Verfestigungskurve auf wie im Falle von Kupfer.

Die im Bereich II entstehenden Knickbänder variieren in ihrer Länge zwischen 100 μ und dem halben Kristallumfang. Die längsten erstrecken sich vom einen Scheitel des Kristalls zu dem gegenüberliegenden Scheitel und verlaufen dort, wo sie die Seite des Kristalls überqueren, durch ein Gebiet mit ausgiebiger Gleitung auf sekundären Gleitsystemen. Sie sind zunächst schmal und bei etwa 500 fach vergrössernder Betrachtung geradlinig, d.h. sie erscheinen auf dem Kristall als Schnittlinie der Oberfläche mit einer bei dieser Vergrösserung gut definierten Ebene, Fig. 8. Ein Teil dieser Bänder wird bei der weiteren Verformung im Bereich III ausserordentlich breit und zeigt im Inneren deutliche Spuren von sekundärer Gleitung, Fig. 9. Im Gegensatz dazu sind die im Bereich III entstehenden Knickbänder sehr schmal, nur etwa 100 μ–200 μ lang, gewellt und oft durch Verzweigungen miteinander verbunden, Fig. 10. Man muss also hinsichtlich des mikroskopischen Bildes zwischen diesen beiden Arten von Knickbändern unterscheiden, die in verschiedenen Verfestigungsbereichen und, wie später gezeigt wird, aus verschiedenen Ursachen entstehen. Fig. 9 zeigt beide Knickband-Typen. Das (im Bild steiler verlaufende) starke Knickband hatte sich schon im Bereich II gebildet. Seine Ebene hat an der mit der weiteren Abgleitung verknüpften Gitterdrehung teilgenommen und ist geneigt gegen die Ebene der im Bereich III entstandenen schmäleren Knickbänder.

Bei Kristallorientierungen nahe der Symmetralen [100]–[111], die schon von Anfang an auf zwei gleichberechtigten Systemen gleiten oder nach geringer Dehnung Doppelgleitung zeigen, bilden sich oft striemenartige, d.h. von einer der beiden möglichen



FIG. 9. Knickbänder und Gleitbänder im Bereich III entsprechend 39 . . . 51,5 Prozent Abgleitung. Das breite Knickband war schon im Bereich II entstanden. ×330



FIG. 10. Knickbänder und Gleitbänder im Bereich III, entsprechend 51,5 . . . 66 Prozent Abgleitung. ×330

Gleitebenenscharen begrenzte Schichten aus. Im Inneren dieser Schichten erfolgt die Gleitung entweder auf dem System mit der zur Berandungsebene parallelen Gleitebene oder auf dem dazu konjugierten System (Bänder zweiter Gleichung). In dem erstgenannten Fall der Striemen mit primärer Gleitung sind in den Striemen ebenfalls Knickbänder sichtbar mit einer Dichte, die vergleichbar ist mit der bei unsymmetrisch orientierten Kristallen gefundenen Knickbanddichte.

Von den Kristallen der Orientierung C 14 wurden nach verschiedenen Dehnungen Laue-Aufnahmen gemacht. Die Reflexe vergrössern sich mit zunehmender Verformung vor allem in einer Richtung, die (im Rahmen der Genauigkeit, mit der die unfokussierten Rückstrahlaufnahmen ausgewertet werden konnten) einer Drehung einzelner Kristallbereiche um die zur Gleitrichtung senkrechte ⟨112⟩-Richtung zugeordnet werden kann. Der Betrag dieser Drehung ist ebenfalls in Fig. 1(b) eingetragen (gestrichelte Kurve); er verläuft in Abhängigkeit von der Abgleitung ähnlich wie die Knickbanddichte. Die Vergrösserung der Reflexe in anderen Richtungen als der des Hauptasterismus zeigt denselben Gang wie die in Fig. 1(b) eingetragene Drehung, sie erreicht aber nur etwa ein Viertel des Betrags derselben. Die Krümmung der Gleitlinien entspricht, soweit sie mikroskopisch aufgelöst werden konnte, einer Gitterdrehung in den Knickbändern nach Fig. 12(c).

DISKUSSION

Gleitlinien von kubisch–flächenzentrierten Metallen wurden bisher am ausführlichsten auf Aluminium-Kristallen untersucht.[3,4] Will man die Ergebnisse von Aluminium mit den vorliegenden von Kupfer vergleichen, so ist zu beachten, dass die Verfestigungskurven von Kupfer bei Raumtemperatur ähnlich sind denjenigen von Aluminium bei tiefen Temperaturen. Dementsprechend müssen die Gleitlinienbilder von Kupfer mit den Untersuchungen von Noggle und Koehler[4] verglichen werden, die bei 78°K auf Aluminiumkristallen in den Bereichen I und II nur Feingleitung und im Bereich III schmale Gleitbänder finden. Die Stufenhöhen sind in derselben Grössenordnung wie die hier für Kupfer angegebenen. Die ausführlichen Untersuchungen von Wilsdorf und Kuhlmann-Wilsdorf[3] über die bei Raumtemperatur auf Aluminium gebildeten Gleitlinien zeigen einige Züge der bei Kupfer im Bereich III beobachteten Gleitung, nämlich Bündelung der Gleitlinien zu Gleitbändern und Quergleitung. Dies ist nach dem Verfestigungsverhalten von Aluminium zu erwarten, denn bei Raumtemperatur ist bei den meisten Kristallorientierungen die Einsatzspannung von Bereich III so klein, dass sich dieser Bereich unmittelbar an das Ende von Bereich I anschliesst. Es gibt allerdings quantitative Unterschiede; die Gleitbänder sind bei Aluminium bei Raumtemperatur aus einer grösseren Zahl einzelner Gleitlinien aufgebaut; die Stufenhöhe der einzelnen Gleitlinien ist größer als bei Kupfer und die Gleitbänder sind länger, so dass die bei Kupfer stark auffallende Fragmentierung der Gleitbänder auf elektronenmikroskopischen Aufnahmen von Aluminium kaum in Erscheinung tritt. Quergleitungsspuren wurden auf Aluminium-Kristallen nicht in allen Fällen beobachtet.[3,4] Dies mag auf der Tatsache beruhen, dass diese Spuren sehr schwach sind und, wie unsere eigenen Erfahrungen bei Kupfer zeigten, oft nur bei günstiger Auswahl der Beschattungsrichtung einen nachweisbaren Bildkontrast ergeben.

Der Gleichartigkeit der normalen Gleitlinienbildung von Kupfer und Aluminium bei tiefen Temperaturen entsprechen analoge Beobachtungen der *Gleitstörungen*. Müller und Leibfried[14] beobachten auf Aluminium-Kristallen, die bei 80°K um 12 Prozent gedehnt worden waren, Knickbanddichten von 300–400/cm.

Über den *Asterismus*, der ein Indiz für das Vorhandensein von Knickbändern ist, liegen an verschieden stark gedehnten Aluminiumeinkristallen Untersuchungen von Lange und Lücke[15] (bei Raumtemperatur) und von Staubwasser[16] (bei Raumtemperatur und −195°C) vor. Es zeigt sich, dass bei beiden untersuchten Verformungstemperaturen der Asterismus nach Einsetzen des Bereichs III in ähnlicher Weise wie bei Kupfer anwächst—vergl. Fig. 11 in Zit.[16] und Fig. 90 in Zit[1] mit der in unserer Fig. 1b eingeteichneten gestrichelten, sich auf Kupfer (bei Raumzemperatur verformt) beziehenden Kurve.

Eine sehr ausführliche mikroskopische Untersuchung der bei Raumtemperatur auf verformten Aluminium-Kristallen auftretenden Gleitstörungen, der mit ihnen verbundenen Veränderungen der Laue-Reflexe sowie ihrer Abhängigkeit von der Kristallorientierung gaben Jaoul *et al.*[17] Vom Verformungsbeginn an bilden sich breite Knickbänder, die hinsichtlich ihres mikroskopischen Bildes denen ähnlich sind, die sich bei Kupfer vor Erreichen des Bereichs III bilden, Fig. 8 und 9. Nach Einsetzen des Bereichs III finden Jaoul *et al.* auf Aluminium-Kristallen mikroskopisch schwach sichtbare Knickbänder (micropliages), die den von uns dem Bereich III zugeordneten Knickbändern entsprechen und die bei Kupfer die überwiegende Mehrzahl aller vorhandenen Knickbänder ausmachen. Allerdings konnte die von Jaoul *et al.* beobachtete Gitterdrehung innerhalb der

VOL. 8 1960

"micropliages", die—im Gegensatz zur Drehung in den grösseren Knickbändern—*stärker* ist als in den umgebenden Kristallbereichen, in unserem Fall nicht aufgefunden werden; während wir aus der Laue-Aufnahme keine eindeutigen Schlüsse ziehen konnten, weist die Krümmung der Gleitlinien in den schwächeren Knickbändern darauf hin, dass die Orientierungsänderung auch in den schwachen Knickbändern hinter derjenigen der Matrix zurückbleibt.

Eine *versetzungstheoretische Deutung* der vorliegenden Befunde knüpft an die Theorie der Verfestigung kubisch-flächenzentrierter Kristalle an.[1] Danach entstehen im Verfestigungsbereich II durch Versetzungsbewegungen in sekundären Gleitsystemen auf den Hauptgleitebenen eine zunehmende Anzahl von Lomer–Cottrell-Versetzungen, die die Hauptgleitebenen längs ⟨110⟩-Richtungen durchziehen, und die die Laufwege der aus einer Quelle kommenden Versetzungen begrenzen. Es bilden sich Gleitzonen aus, die von Lomer–Cottrell-Versetzungen begrenzt sind und an deren Rand diejenigen Versetzungen aufgestaut sind, die die Gleitung innerhalb der Zone bewerkstelligt haben.

Gleitlinien sind, wie Fig. 11(a) zeigt, die Schnittlinien dieser Gleitzonen mit der Kristalloberfläche; die Stufenhöhe der Gleitlinien ist gleich der Anzahl der innerhalb der Gleitzonen aufgestauten Versetzungen, in unserem Fall also etwa zwanzig. Auf dem Scheitel des Kristalls sind die Stufenanteile der Versetzungsringe aus dem Kristall ausgetreten, vom Ende einer Gleitlinie aus erstrecken sich die Schraubenanteile in den Kristall hinein, auf der Seite des Kristalls entsprechend die Stufenanteile. Aus dem Verhältnis der Gleitlinienlängen auf dem Scheitel und auf der Seite (etwa 1 : 2) schliesst man auf die in Fig. 11(a) dargestellte Form der Zonen.

Die mit wachsender Verformung steigende Dichte der Lomer–Cottrell-Versetzungen bewirkt, dass die neu entstehenden Gleitzonen immer kleiner werden und die Länge der aktiven Gleitlinien abnimmt. Die damit verbundene Zunahme der Dichte von aufgestauten Versetzungsgruppen ist verantwortlich für den Anstieg der Verfestigung. Bisher liegen über Gleitlinienlängen nur wenige systematische elektronenmikroskopische Messungen vor, obwohl aus ihnen und aus Messungen der Stufenhöhen die Dichte der aufgestauten Gruppen und die Anzahl der sie aufbauenden Versetzungen bestimmt werden kann. Wie am vorliegenden Beispiel von Kupfer[2] und weiterhin an Nickel- und Nickel–Kobalt-Legierungen[10] gezeigt wurde, erhält man aus Gleitliniendaten eine gute Übereinstimmung mit dem mechanisch gemessenen Verfestigungsanstieg im Bereich II.

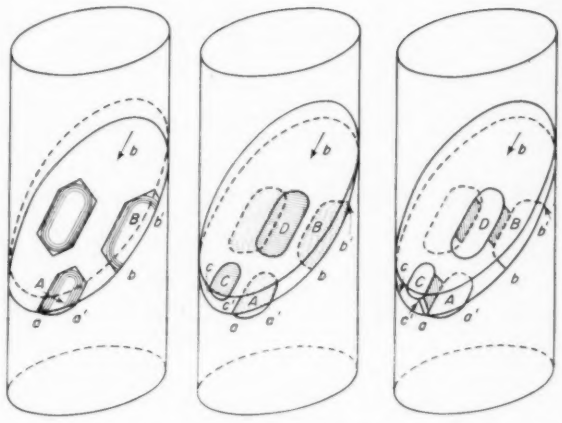


FIG. 11. Gleitzonen im verformten Kristall: (a) in einer einzelnen Gleitebene, (b) in zwei benachbarten Gleitebenen, (c) nach Annihilation der Schraubenversetzungen durch Quergleitung.

Im Bereich III reicht bei gegebener Temperatur die Spannung aus, um ausgiebige Quergleitung einzuleiten. Diese überträgt nach dem Modell der doppelten Quergleitung die Gleitung von einer Gleitzone zu der benachbarten in einem Gleitband.[1,9] Die Fig. 11 und 12 zeigen schematisch die Vorgänge, die sich weiterhin im Bereich III abspielen. In Fig. 12 ist die Aufsicht auf die Seitenfläche mit den Projektionen (nicht den Austrittspunkten) der Stufenanteile einiger Gleitzonen dargestellt. In Fig. 11(b) sind zunächst zwei benachbarte Gleitebenen mit ihren Gleitzonen wiedergegeben. Die Gleitzonen A, B und C ergeben auf der Oberfläche die Gleitlinien aa', bb' und cc'. Befinden sich nun A und C bzw. B und D in einer solchen gegenseitigen Lage, dass die Schraubenanteile verschiedenen Vorzeichens einander gegenüberliegen, so können diese sich nach Quergleitung (wenigstens teilweise) annihilieren, Fig. 11(c). Auf der Scheitelfläche entsteht eine Quergleitlinie ac'. Die Rückspannungen auf die Versetzungsquellen der Gleitzonen werden unter Umständen verringert, so dass sie

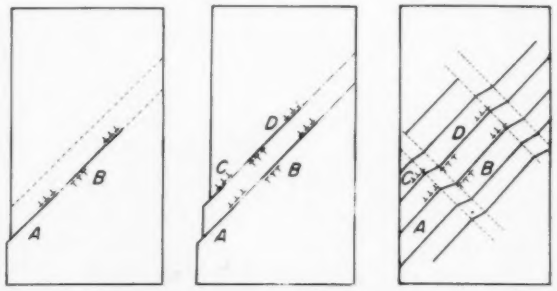


FIG. 12. Bildung von Knickbändern im Gefolge der Quergleitung. (a), (b) u. (c) zeigen die Stufenversetzungen der entsprechenden Gleitzonen von Fig. 11. Teilfigur (c): Keim eines Knickbandes.

neue Versetzungen liefern können. Dadurch wachsen einzelne Gleitstufen weiter.

Die Seitenansicht von Fig. 12(c) zeigt, dass jetzt auf der Hauptgleitebene ein Überschuss von Stufenversetzungen zurückgeblieben ist. Diese können in senkrechten Versetzungswänden angeordnet sein oder nach kurzen Gleitbewegungen eine solche energetisch günstige Anordnung erreichen. Wie aus Fig. 12(c) hervorgeht, entsteht dann gerade der Keim eines Knickbandes. Die Spannungsfelder dieser Knickbandkeime können nun wenigstens teilweise die Rolle der Lomer–Cottrell-Versetzungen übernehmen, die Laufwege der Stufenanteile von neu entstehenden Gleitzonen begrenzen und dadurch ihrerseits senkrecht zur Gleitebene wachsen. Die Verhältnisse sind ähnlich wie in dem Modell von Frank und Stroh[18] für das seitliche Wachsen eines Knickbandes. Da aber die Knickbandabstände stets etwas grösser sind als mittlere Länge der einzelnen aktiven Gleitlinien, spielen für die Begrenzung der Stufenlaufwege auch weiterhin Lomer–Cottrell-Versetzungen eine Rolle.

Bevor wir weitere Konsequenzen der im Vorstehenden behandelten Prozesse, insbesondere für die "Fragmentierung" der Kristalle, besprechen, wenden wir uns der Diskussion der im Bereich I und II der Verfestigungskurve entstehenden Knickbändern zu. Im Gegensatz zu Bereich III entstehen hier die Knickbänder wohl als Folge von Schwankungen der Versetzungsgrundstruktur. Wie Staubwasser[16] gezeigt hat, bilden sich zunächst einfache Versetzungswände von der Art der Kleinwinkelkorngrenzen. Aus ihnen entstehen später Knickbänder. Müller[19] untersuchte die dabei möglichen Entstehungsmechanismen und zeigte, dass zur Stabilisierung solcher Anordnungen Versetzungsbewegungen auf sekundären Gleitsystemen, sog. Ergänzungsgleitung, notwendig ist. Die sekundäre Gleitung, die in dem aus dem Bereich II stammenden Knickband der Fig. 9 sichtbar ist, dürfte wohl als Ergänzungsgleitung zu deuten sein.

Bei der Diskussion der Knickbandbildung in Bereich III als Folge der Quergleitung haben wir untersucht, was mit den Stufenversetzungen geschieht, die nach der Quergleitung der Schraubenversetzungen in der *primären Gleitebene* zurückbleiben, und dabei gefunden, dass sie wohl zu der beobachteten verstärkten Knickbandbildung Anlass geben. Wie Fig. 13 zeigt, hinterlässt die Quergleitung der Schraubenversetzungen jedoch auch in der *Quergleitebene* Stufenversetzungen, die den Zusammenhang der durch Quergleitung entwichenen Schraubenversetzungen mit den in der primären Gleitebene zurückgebliebenen Versetzungsteilen einer Gleitzone herstellen. Die Stufenversetzungen in den Quergleitebenen haben

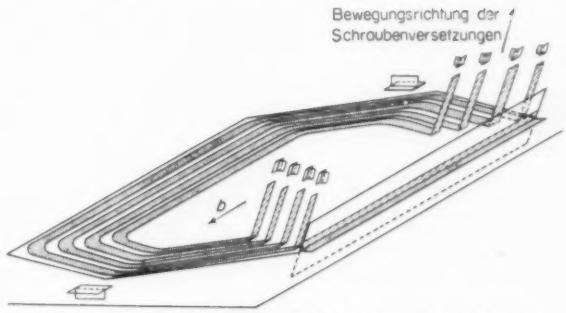


FIG. 13. Zellbildung im Gefolge der Quergleitung.

in grosser Näherung eine Anordnung, wie sie in sog. unsymmetrischen Kleinwinkelkorngrenzen auftritt. Es ist zu erwarten, dass das mit dieser Anordnung verknüpfte weitreichende Spannungsfeld durch "Ergänzungsgleitung" auf latenten Gleitsystemen, wie sie in etwas anderem Zusammenhang Müller[19] betrachtet hat, abgebaut wird. Auf diese Weise bilden sich unsymmetrische Kleinwinkelkorngrenzen. Der Durchmesser der von ihnen begrenzten "Subkörner" ist von der Grössenordnung der Gleitzonendurchmesser und damit der Gleitlinienlänge.

Die Bildung solcher Subkörner, auch Zellbildung oder Fragmentierung genannt, ist von einer grossen Zahl von Autoren an verformten Vielkristallen untersucht worden, und zwar vor allem mit röntgenographischen oder metallographischen Verfahren. Eine ausführliche Zusammenfassung hierüber gibt Hirsch[20], so dass wir auf detaillierte Literaturangaben verzichten können. In neuerer Zeit sind derartige von Versetzungswänden begrenzte Zellen vor allem in verformtem Aluminium im Elektronenmikroskop in direkter Durchstrahlung beobachtet worden.[21]

Wir sind der Auffassung, dass die Bildung dieser Wände durch den in Fig. 13 dargestellten, mit der Quergleitung zusammenhängenden Mechanismus erfolgt. Die empirischen Argumente für diese Auffassung sind schon früher diskutiert worden: (i) Das Auftreten der Zellbildung bei verschiedenen Metallen und Temperaturen geht parallel zur Häufigkeit der Quergleitung.[22] Sie lässt sich dagegen nicht mit dem Klettern der Stufenversetzungen korrelieren, das man möglicherweise als geschwindigkeitsbestimmend für die Zellbildung (ähnlich wie bei der Polygonisierung) ansehen könnte. (ii) Der vorgeschlagene Mechanismus erklärt zwanglos die von Kelly[23] sowie von Gay *et al.*[24] gefundene Variation der Zelldurchmesser mit dem Verformungsgrad.[25]

SCHLUSSBEMERKUNGEN

Die beiden Hauptergebnisse der vorliegenden Arbeit sind die folgenden:

VOL. 8 1960

(1) Die "sekundären" Erscheinungen des Gleitlinienbildes verformter kubisch–flächenzentrierter Einkristalle, die meist als Störungen des "normalen" Gleitlinienbildes beschrieben werden, hängen gesetzmässig mit dem normalen Gleitlinienbild und damit mit dem Verfestigungs- und Verformungsmechanismus in den drei Bereichen der Verfestigungskurve zusammen. Insbesondere wurde gezeigt, dass man zwei verschiedene Entstehungsweisen der Knickbänder zu betrachten hat. Während in den Bereichen I und II verhältnismässig starke, aber seltene Knickbänder wohl aus Kleinwinkelkorngrenzen entstehen, sind die schwächeren, aber sehr zahlreichen in Teil III zu beobachtenden Knickbänder eine direkte Folge der im Bereich III einsetzenden thermisch aktivierten Quergleitung. Auch das Auftreten des Asterismus ist mit dieser Deutung im Einklang.

(2) Mit der Quergleitung und der Knickbandbildung in Bereich III ist in direkter Weise auch die Bildung von Kleinwinkelkorngrenzen verknüpft. Diese Erscheinung ist wohl für die von Vielkristalluntersuchungen her wohlbekannte Fragmentierung der Kristallite ("Zellbildung", "Subkornbildung") verantwortlich. Damit ist auch diese Erscheinung als eine zwangsläufige Konsequenz des Verformungsvorgangs (speziell der thermisch aktivierten Quergleitung) erklärt.

ANNERKENNUNG

Die Verfasser danken Herrn Professor Dehlinger für sein Interesse und der Deutschen Forschungsgemeinschaft für die Unterstützung der Arbeit durch Sachbeihilfen.

LITERATUR

1. A. Seeger, *Handbuch der Physik*, Bd. 7/2, Seite 1, Springer, Berlin (1958).
2. S. Mader, *Z. Phys.* **149,** 73 (1957).
3. H. Wilsdorf und D. Kuhlmann-Wilsdorf, *Z. Angew. Phys.* **4,** 361, 409, 418 (1952).
4. T. S. Noggle und J. S. Koehler, *J. Appl. Phys.* **28,** 53 (1957).
5. R. W. K. Honeycombe, *J. Inst. Met.* **80,** 49 (1951).
6. E. A. Calnan, *Acta Cryst., Camb.* **5,** 557 (1952).
7. R. W. Cahn, *J. Inst. Met.* **79,** 129 (1956).
8. J. Diehl, Diss. Stuttgart (1955); *Z. Metallk.* **47,** 321 (1956).
9. J. Diehl, S. Mader und A. Seeger, *Z. Metallk.* **46,** 650 (1955).
10. H. Kronmüller, *Z. Phys.* **154,** 574 (1959), insbes. Fig. 15.
11. T. H. Blewitt, R. R. Coltman und J. K. Redman, *Rep. Bristol Conf. Defects in Crystalline Solids*, S. 369. Physical Society, London (1955).
12. H. Rebstock, *Z. Metallk.* **48,** 206 (1957).
13. A. Seeger, *Z. Naturf.* **11a,** 985 (1956).
14. H. Müller und G. Leibfried, *Z. Phys.* **142,** 87 (1955).
15. H. Lange und K. Lücke, *Z. Metallk.* **44,** 183 (1953).
16. W. Staubwasser, *Acta Met.* **7,** 43 (1959).
17. B. Jaoul, I. Bricot und P. Lacombe, *Rev. Métall.* **54,** 756 (1957).
18. F. C. Frank und A. N. Stroh, *Proc. Roy. Soc.* B**65,** 811 (1952).
19. H. Müller, Diss. Göttingen (1957); *Z. Metallk.* **50,** 165 (1959).
20. P. B. Hirsch, *Progr. Met. Phys.* **6,** 236 (1956).
21. P. B. Hirsch, R. W. Horne und M. J. Whelan, *Phil. Mag.* **1,** 677 (1956).
22. A. Seeger in *Madrid Colloquium on Deformation and Flow of Solids* (hrsg. von R. Grammel), S. 90. Springer, Berlin (1956).
23. A. Kelly, *Acta Cryst., Camb.* **7,** 554 (1954).
24. P. Gay, P. B. Hirsch und A. Kelly, *Acta Cryst., Camb.* **7,** 41 (1954).
25. A. Seeger in *Dislocations and Mechanical Properties of Crystals* (hrsg. von J. C. Fisher, W. G. Johnston, R. Thomson und T. Vreeland, Jr.), S. 243. Wiley, New York (1957).

SULFUR SEGREGATION AT α-IRON GRAIN BOUNDARIES—I*

N. G. AINSLIE, R. E. HOFFMAN and A. U. SEYBOLT†

Radioactive sulfur has been introduced simultaneously into single crystal and polycrystal specimens of high purity alpha iron by reaction with H_2S. After lengthy annealing and rapid quenching, the polycrystals are found to contain 50–100 per cent more sulfur than the single crystals, and the excess sulfur in the polycrystals is found to be concentrated at the grain boundaries. All available evidence indicates that the sulfur was in solid solution at the equilibration temperature, although the amount of sulfur segregated at the boundaries is much greater than can be accounted for on the basis of equilibrium adsorption.

SEGREGATION DU SOUFRE DANS LES JOINTS DE GRAINS DU FER α—I

Du soufre radioactif a été introduit par réaction avec H_2S, simultanément dans des échantillons mono et polycrystallins de fer α de haute pureté. Après recuit prolongé et trempe rapide, les échantillons polycristallins contiennent 50–100% plus de soufre que les monocristaux; l'excédent du soufre dans les polycristaux était concentré aux limites des grains. Toutes les données disponibles indiquent que le soufre était en solution solide à la température d'équilibre, malgré que la quantité de soufre ségrégée aux frontières est considérablement plus grande que celle à laquelle on pourrait s'attendre sur la base d'équilibre d'adsorption.

KORNGRENZENAUSSCHEIDUNG VON SCHWEFEL IN α-EISEN—I

Durch Reaktion mit H_2S wurde radioaktiver Schwefel in Einkristalle und in vielkristalline Proben aus α-Eisen hoher Reinheit eingeführt. Nach längerem Glühen und raschem Abschrecken fanden sich in den vielkristallinen Proben 50–100% mehr Schwefel als in den Einkristallen. Der überschüssige Schwefel war in den vielkristallinen Proben an den Korngrenzen angereichert. Alle Befunde weisen darauf hin, daß der Schwefel bei der Glühtemperatur in fester Lösung war, obwohl der Betrag des an den Korngrenzen ausgeschiedenen Schwefels viel größer ist, als man auf Grund der Gleichgewichtsadsorption annehem würde.

VOL. 8 1960

INTRODUCTION

The possibility of solute adsorption at grain boundaries in metals has been recognized for a long time, and numerous attempts have been made to demonstrate the existence of such segregation in a wide variety of systems. However, much of the evidence is rather indirect, largely because the excess amount of solute that can exist as an equilibrium segregate is usually so small that quantitative measurements, or even detection, are difficult.

Within the past several years direct quantitative measurements of boundary segregation, obtained using special techniques, have been reported and interpreted in terms of equilibrium adsorption. Thomas and Chalmers[1] showed autoradiographic evidence of the enrichment of radioactive polonium, present in very small concentration, at tilt boundaries in lead–bismuth bicrystals. However, Maroun *et al.*[2], attempting to duplicate these results were able to find segregation at the intersection of boundaries with the free surface, but not at internal boundaries. They suggested that the segregation observed by Thomas and Chalmers may have been the result of preferential diffusion of polonium along the boundaries to form an oxide on the surface. Ward[3] favors the interpretation of Maroun *et al.* on the basis that the extent of segregation measured by Thomas and Chalmers is too great to be due to an equilibrium adsorption.

Recently, Inman and Tipler[4] demonstrated the presence of excess radioactive phosphorus at grain boundary fracture surfaces of α-iron. Their conclusion that this excess was due to equilibrium adsorption has been criticized by Cahn and Hilliard[5] who showed that the observed amount of excess phosphorus was at least an order of magnitude greater than the maximum amount calculated from the Gibbs adsorption equation. As a result of subsequent identification of precipitate particles at the fracture surfaces, Inman and Tipler[6] modified their position and concluded that most of the previously observed excess phosphorus was probably present in the form of compounds with foreign elements.

In experiments on internal friction Lagerberg and Josefson[7] observed that the carbon damping peak of α-iron was smaller in fine grained than in coarse grained specimens having the same total carbon content. Since the height of the damping peak is presumed proportional only to the amount of carbon dissolved in the lattice, they concluded that the fine grained specimens, because of more total grain boundary area than in the coarse grained specimens, were adsorbing greater amounts of carbon at the grain boundaries. However, Stark *et al.*[8] have presented evidence which indicates that a significant

* Received August 3, 1959.

† General Electric Research Laboratory, Schenectady, New York. The work is being submitted to Rensselaer Polytechnic Institute by N. G. Ainslie in partial fulfillment of the requirements for the degree of Doctor of Philosophy.

amount of carbide precipitation may occur during even the most rapid quenches from the solution temperature, and they interpret the observations of Lagerberg and Josefson as indicating only that more extensive carbide precipitation occurred in the fine-grained than in the coarse-grained material.

Preliminary autoradiographic evidence for enrichment of radioactive sulfur in α-iron has been reported in a previous publication.[9] The object of the current investigation was to examine the nature of this segregation under carefully controlled conditions in order to establish its origin. During the course of this work, we also became aware of the results of a similar investigation by Leymonie *et al.*[10] who found grain boundary segregation of sulfur in slowly cooled specimens of α-iron, but not in quenched specimens. Their results suggested that the slow cooling permitted the sulfur to diffuse to the grain boundaries and precipitate there preferentially. As will be seen below our results cannot be interpreted in terms of grain boundary precipitation of sulfides.

EXPERIMENTAL

High purity iron, obtained from the National Research Corporation, was converted by a previously described gradient anneal technique[11] into strips containing regions of very large crystals separated by low angle boundaries only and other regions comprised entirely of small grains. An example is shown in Fig. 1. These strips were machine-ground from 0.095 in. to 0.006 in. and decarburized for several days at 900°C in pure dry hydrogen. Pairs of specimens were then cut from adjacent areas of the strips in such a manner that one of each pair consisted of a single grain, while the other contained many fine grains (average grain size 0.035 cm).

For each pair of specimens, a fused silica capsule was prepared, and a mixture of powdered Fe and FeS containing S^{35} was placed in the bottom thereof. The pair of specimens was supported side by side on a constriction near the center of the capsule. Prior to being sealed off the capsules were evacuated and filled with dry hydrogen to a pressure of 25 cm of Hg. The capsules were then suspended vertically in a furnace with a slight temperature gradient, so that the temperature of the specimens (890°C) was about 50° higher than the temperature of the Fe–FeS mixture. In this manner formation of FeS on the specimens was prevented. The specimens were held at constant temperature for 2 weeks to ensure equilibration. At the end of the annealing period, the capsules were rapidly ejected from the furnace and crushed under ice water. It is estimated that the quench time was less than 1 sec.

The sulfurized specimens were ground and polished, on either one or both faces, to a final thickness of about 0.003 in. Autoradiographs were prepared by placing a polished face in close contact with Kodak "no-screen" X-ray film for suitable exposure periods; the film was developed in the standard manner.

The relative amounts of radioactive sulfur in each specimen of a given pair were measured by counting fixed areas (~0.4 cm^2) of the polished faces, using care to ensure reproducible geometry. Counting was accomplished with a thin mica end-window G.M. counter in conjunction with conventional scaling circuits.

In addition, standard chemical analyses for total sulfur were made on some of the pairs of specimens that had been polished on both sides.

RESULTS AND DISCUSSION

Typical autoradiographs of a pair of specimens are shown in Fig. 2. It is clear that the grain boundary regions are considerably enriched in sulfur relative to the interiors of the grains. The grain boundaries shown are predominantly high angle. Considerably less sulfur was found to segregate at low angle boundaries. Fig. 3 shows a photomicrograph and the corresponding autoradiograph of a region containing entirely low angle boundaries. Although segregation is not observed at all boundaries, visible darkening on the

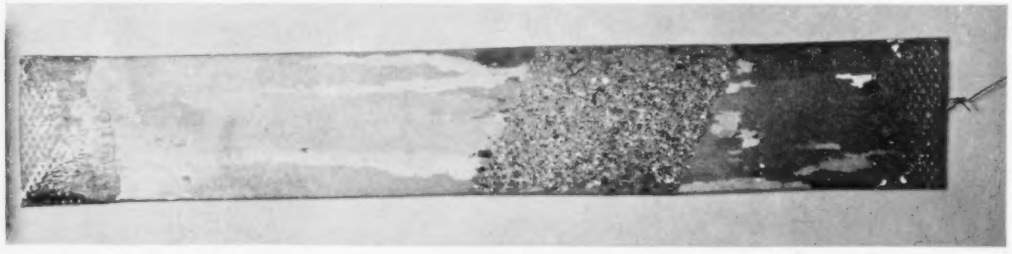
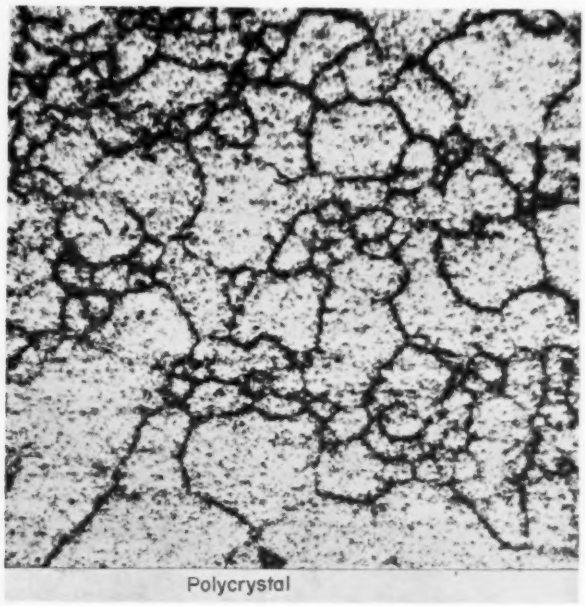


FIG. 1. Bar of pure iron containing regions of very large crystals as well as regions of relatively fine grains. The boundaries separating the regions demark what were, before a gradient anneal, Lüders fronts. Although only parts of the bar were critically strained, the entire bar underwent a gradient anneal. ×½





VOL.
8
1960

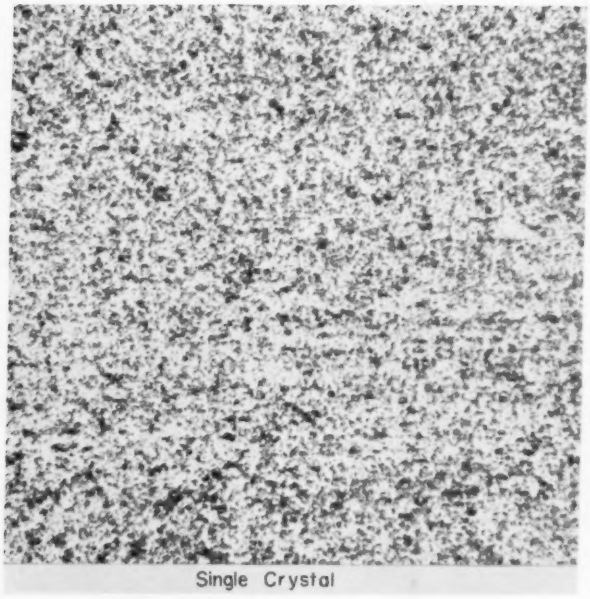


FIG. 2. Comparison between the autoradiographs of a pure iron single crystal and its polycrystal mate after equilibration. ×15

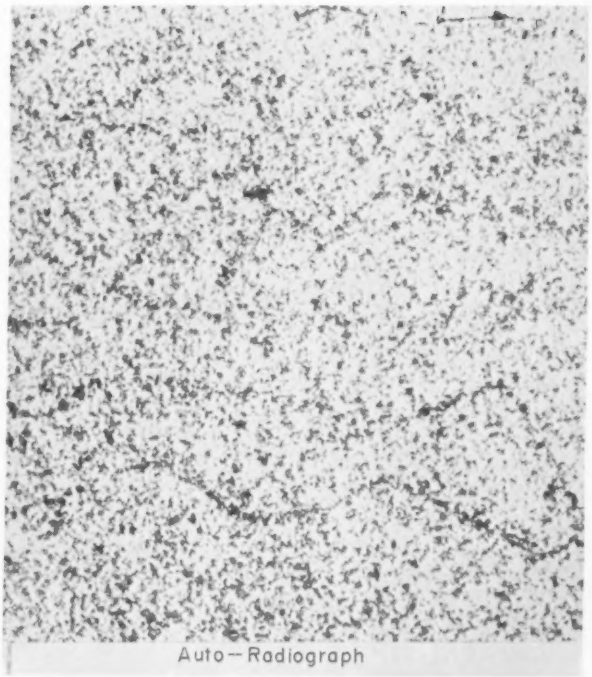


FIG. 3. Comparison between photomicrograph and autoradiograph of a pure iron specimen containing low angle boundaries after equilibration. The sulfur segregates to much lesser extents in these boundaries than in the ordinary high-angle boundaries. Notice the variation from boundary to boundary. These low angle boundaries were sometimes present in the iron bars after the gradient anneal (see Fig. 1). ×20

TABLE I

Specimen number	Ratio of polycrystal to single crystal radioactivity	Per cent sulfur (95% Confidence)	
		Polycrystal	Single crystal
117	1.86	—	—
119	1.57	—	—
166A	1.95	0.026 ± 0.005%	0.013 ± 0.005%
166B	1.57	0.021 ± 0.005%	0.015 ± 0.005%
166C	1.45	0.016 ± 0.005%	0.016 ± 0.005%

autoradiographs can be clearly distinguished at boundaries with misorientations as low as 5 degrees.

The results of the radiochemical and chemical analyses for sulfur are summarized in Table 1.

Only the ratio of polycrystal to single crystal radioactivity is tabulated since the specific activity of the S^{35} was not the same for all specimen pairs. Although the chemical analyses are of somewhat limited accuracy because of small sample weights, the correspondence with the radiochemical ratios is as good as could be expected. In view of the fact that the sulfur content of the single crystals was quite reproducible, the variations in concentration among the polycrystal samples is attributed to differences in grain size and misorientation. At any rate, it is clear that in all cases the polycrystalline samples contain 50–100 per cent more sulfur than the single crystals.*

The magnitude of the sulfur excess in the polycrystalline samples is abnormally large, corresponding to a grain-boundary layer of pure sulfur at least 100 atom layers in thickness. On the basis of a calculation similar to that of Cahn and Hilliard[5], it is estimated that this excess is at least 30 times larger than anticipated from the Gibbs adsorption equation. Thus it appears unlikely that the enrichment could be due solely to equilibrium segregation.

On the other hand, since the polycrystals contain more total sulfur than the single crystals, it seems highly probable that the non-uniform distribution of sulfur must have existed at the annealing temperature and was not merely the result of heterogeneous precipitation during cooling. A non-uniform distribution at temperature could conceivably arise from the formation of sulfides (either of iron or of impurity elements) at the boundaries. However, since the samples were undersaturated with respect to bulk FeS, a film of FeS formed at the boundaries as a result of favorable surface energies is thermodynamically indistinguishable from an equilibrium segregate, and the amount of sulfur thus bound could not exceed the small amount predicted from the Gibbs equation. It also seems highly improbable that the sulfur excess in the polycrystals could be due to impurity sulfides since the impurity contents of the specimens should be very nearly identical. This conclusion is further confirmed by direct analytical results. Qualitative emission spectrographic analyses failed to reveal the presence of Al, Ba, Ca, Ce, Co, Mg, Mo, Na, Ni, Si, Sr, Ti, V and Zn, however, trace amounts of Cu, Cr, and Mn, in both the single crystal and polycrystal specimens were observed. Subsequently quantitative analyses showed Cr and Mn to be present to the extent of 0.0002 and 0.0008 wt. %, respectively; an analysis for copper was not made since its sulfide is less stable than that of iron. Thus the total amount of known impurities capable of forming stable sulfides appears to be an order of magnitude smaller than would be required to account for the observed excess sulfur, and there is no evidence for a difference in impurity content between the polycrystal and single crystal specimens.

It is highly probable that, under the conditions of the experiment, sulfur would diffuse into the iron much more rapidly along the grain boundaries than through the bulks of the grains, and, in the early stages of reaction, the sulfur concentration in the vicinity of the boundaries would be higher than elsewhere. However, on the basis of known diffusion data,[9] the duration of the anneal was far in excess of the time required for homogenization by bulk diffusion. Consequently, the possibility that the observed non-uniform sulfur distribution could be the result of a diffusion transient seems to be ruled out.

Thus the observed distribution of sulfur appears to be qualitatively characteristic of an equilibrium segregation, yet the amount of segregated sulfur unquestionably exceeds that calculated on the basis of reasonable estimates of the grain boundary energy of α-iron. Also, there remains the discrepancy between our observations and those of Leymonie *et al.*[10], who could detect no sulfur segregation in quenched α-iron.

A possible reconciliation of this apparent dilemma

* It may be worth noting that in a set of samples accidentally contaminated with carbon, as evidenced by the appearance of small areas of austenite decomposition products in the microstructure, no segregation of sulfur in the ferrite grain boundaries was observed autoradiographically, and the radioactivities of the single crystals and polycrystals were the same. The significance of this observation is not clear.

has evolved from the results of a subsequent electron microscopic examination of grain boundary regions in samples similar to those used here. The results of that investigation and their consequences will be presented in the following paper.

CONCLUSIONS

(1) Sulfur can segregate in the neighborhood of α-iron grain boundaries, apparently as an equilibrium solute, in directly observable and measurable amounts.

(2) Although polycrystal specimens exhibiting this grain boundary segregation of sulfur contained 50–100 per cent more sulfur than did single crystal control specimens, the amount of apparent grain boundary adsorption exceeds, by a factor of at least 30, that permitted by the Gibbs adsorption equation. The extra sulfur contained in the polycrystals would, if concentrated at the grain boundaries, be sufficient to coat the boundaries with 100–150 atom thicknesses of pure sulfur.

(3) The grained boundary excess of sulfur cannot be explained by preferential grain boundary diffusion and concomitantly incomplete bulk diffusion, nor can it be explained in terms of preferential grain boundary precipitation of sulfides.

ACKNOWLEDGMENT

We gratefully acknowledge the help and critical interest of J. W. Cahn, J. E. Hilliard, E. W. Hart and L. Guttman.

REFERENCES

1. W. R. Thomas and B. Chalmers, *Acta Met.* **3,** 17 (1955).
2. A. T. Maroun, A. Rosenberg and S. S. Sheinin, *Acta Met.* **5,** 117 (1957).
3. R. G. Ward, *Acta Met.* **5,** 681 (1957).
4. M. C. Inman and H. R. Tipler, *Acta Met.* **6,** 73 (1958).
5. J. W. Cahn and J. E. Hilliard, *Acta Met.* **7,** 219 (1959).
6. M. C. Inman and H. R. Tipler, *Acta Met.* **7,** 221 (1959).
7. G. Lagerberg and Å. Josefson, *Acta Met.* **3,** 236 (1955).
8. P. Stark, B. L. Averbach and M. Cohen, *Acta Met.* **6,** 149 (1958).
9. N. G. Ainslie and A. U. Seybolt, *J. Iron St. Inst.* **194,** (1960).
10. C. Leymonie, P. Coulomb and P. Lacombe, *C.R. Acad. Sci., Paris* **245,** 931 (1957).
11. N. G. Ainslie and A. U. Seybolt, *On the Preparation of Large Crystals of Pure Iron*, Gen. Elect. Res. Lab., Met. Cer. Dept., Memo MC-60 (June 1958).

VOL.
8
1960

SULFUR SEGREGATION AT α-IRON GRAIN BOUNDARIES—II*

N. G. AINSLIE, V. A. PHILLIPS and D. TURNBULL†

Alpha iron grain boundaries containing large excesses of adsorbed sulfur were examined using transmission electron microscopy. The study revealed that the grain boundaries of the sulfurized iron were commonly associated with very high density dislocation networks that could extend several microns into the bodies of the grains. The dense networks were not observed in pure, sulfur-free iron. The networks are thought to form when the sulfur, having first entered the specimens by preferential diffusion along grain boundaries, diffuses from the grain boundaries laterally into the grains. The sulfur, which diffuses in iron as a substitutional element about 30 times faster than iron self-diffuses, establishes a diverging vacancy flux toward the boundaries. The result is a vacancy undersaturation in the neighborhood of the boundaries that accounts, it is believed, for the high dislocation density; the vacancy undersaturation causes dislocation multiplication by "down-climb".

The abnormal segregation of sulfur in the vicinity of α-iron grain boundaries is explained if it is assumed that sulfur is adsorbed by dislocations in the boundary networks. The possible effects of these grain boundary networks on certain other metallurgical phenomena are considered.

SEGREGATION DU SOUFRE DANS LES JOINTS DE GRAINS DE FER α—II

Par microscopie électronique de transmission, on examine des frontières de fer alpha contenant en excès considérable du soufre adsorbé. L'étude a révélé que les joints de grains du fer sulfuré étaient associés à des réseaux de dislocation de grande densité qui s'étendraient sur plusieurs microns à l'intérieur des grains. Les réseaux denses n'ont pas été observés dans du fer pur exempt de soufre. On suppose que les reseaux se forment lorsque le soufre, après s'être introduit par diffusion préférentielle le long des joints de grains, diffuse des frontières vers l'intérieur des grains. Le soufre qui diffuse dans le fer comme un élément de substitution 30 fois plus vite que ne diffuse le fer, établit un flux divergent de lacunes vers les frontières. Le résultat est une sous-saturation en lacunes dans le voisinage des joints qui explique, on le croit, la grande densité de dislocation; la sous-saturation en lacunes provoque la multiplication des dislocations par "diffusion".

La ségrégation anormale du soufre au voisinage des joints des grains du fer alpha est expliquée si l'on admet que le soufre est adsorbé par le réseau de dislocations aux frontiéres. Les effets possibles de ces réseaux aux frontières sur quelques autres phénomènes métallurgiques, sont considérés.

KORNGRENZENAUSSCHEIDUNG VON SCHWEFEL IN α-EISEN—II

Korngrenzen von α-Eisen, die viel überschüssig adsorbierten Schwefel enthalten, wurden elektronenmikroskopisch mit Durchstrahlung untersucht. Es zeigte sich, daß die Korngrenzen von aufgeschwefeltem Eisen üblicherweise mit einem sehr dichten Versetzungsnetzwerk verbunden sind, welches sich mehrere Mikron weit in das Korninnere erstrecken kann. Die dichten Netzwerke wurden in reinem schwefelfreiem Eisen nicht beobachtet. Es wird angenommen, daß sich die Netzwerke bilden, wenn der Schwefel von der Korngrenzen aus in das Korninnere diffundiert, nachdem er zuvor durch bevorzugte Diffusion entlang den Korngrenzen in die Probe eingedrungen war. Der Schwefel, der im Eisen als Substitutionselement eine 30mal höhere Diffusionsgeschwindigkeit besitzt als die Geschwindigkeit der Selbstdiffusion des Eisens, erzeugt einen zur Korngrenze hin abnehmenden Leerstellenfluß. Als Ergebnis stellt sich in der Nachbarschaft der Korngrenze eine Untersättigung an Leerstellen ein, die für die hohe Versetzungsdichte verantwortlich ist; die Leerstellenuntersättigung gibt Anlaß au Versetzungsvervielfachung durch "Herabklettern".

Die abnormale Ausscheidung von Schwefel in der Umgebung von Korngrenzen im α-Eisen wird erklärt, wenn man annimmt, daß der Schwefel an den Versetzungen des Korngrenzennetzwerks adsorbiert ist. Es werden weitere mögliche Einflüsse dieses Korngrenzennetzwerks auf andere metallurgische Phänomene in Betracht gezogen.

INTRODUCTION

In the preceding paper it was shown that comparatively large amounts of sulfur may segregate in the vicinity of grain boundaries even though the solubility of iron sulfide is not exceeded. The purpose of the present investigation was to find an explanation for the unusual segregation phenomenon. One likely possibility that was suggested is that the dislocation density might be unusually large in the immediate vicinity of the boundaries; the abnormal segregation

* Received August 3, 1959.

† General Electric Research Laboratory, Schenectady, New York. The work is being submitted to Rensselaer Polytechnic Institute by N. G. Ainslie in partial fulfillment of the requirements for the degree of Doctor of Philosophy.

might result from the adsorption of sulfur on these dislocations. Therefore the grain boundary regions in pure and sulfurized iron were examined by transmission electron microscopy.

EXPERIMENTAL

Annealed Ferrovac iron of 0.040 in. thickness was taken from the same lot as that used in the original sulfur segregation work and cold rolled to 0.006 in. As before, it was decarburized in wet hydrogen and then annealed for several hours at 890°C in flowing pure, dry hydrogen. Specimens approximately $\frac{1}{2} \times \frac{1}{2}$ in. were cut and encapsulated in fused silica tubes along with some FeS and hydrogen. The capsules were then annealed for various times at 890°C. The hydrogen reacted with the FeS to form H_2S in equilibrium proportions which then sulfurized the specimens. After annealing, the specimens were either quickly quenched by crushing the capsules on an anvil under water, or slowly brought to room temperature by allowing the capsules to air cool. Care was taken not to deform the specimens during the quenching operation. No attempt was made in these experiments to keep the sulfur potential of the H_2S below that necessary to saturate the iron as was done in the investigation described in the preceding paper; it was always at saturation value.

Control specimens of pure iron were given the same treatment but with FeS omitted. Some of the control specimens were quenched; others were slow cooled, in order to determine if changes occurred upon quenching.

After being sulfurized, the specimens were mounted flat with Apiezon wax on blocks of iron and metallographically ground on both surfaces to a final thickness of 0.003 in. They were removed from the iron blocks and then electropolished to very thin sections that could be examined by transmission electron microscopy. The electropolishing technique was essentially that employed by Tomlinson[1] and by Whelan *et al.*[2]. The electrolyte was 95 per cent glacial acetic acid plus 5 per cent perchloric acid; the cathode was stainless steel.

The specimens were coated at the edges with stop-off lacquer and then thinned down by electropolishing using 45–60 V. When two holes appeared in the unlacquered regions of a specimen and grew almost to impingement with only a thin bridge of iron separating them, the polishing operation was stopped. The specimens were quickly removed from the bath, rinsed in absolute alcohol and then placed in a vacuum dessicator since they always corroded if not kept under vacuum. The narrow bridge of iron was then carefully cut away with fine scissors and examined in the electron microscope.

It was very much easier to obtain usable pure iron specimens than sulfurized specimens since the pure iron thinned down fairly uniformly during polishing whereas the sulfurized iron tended to thin unevenly. In both the sulfurized and the unsulfurized iron, the grain boundaries were to very slight extents attacked preferentially during polishing. As a result the holes that ultimately appeared in the specimens tended to form at grain boundaries. Since the thin sections that were examined in the electron microscope usually appeared at the edges of these holes, the areas examined probably did not represent random samples of the specimens, but rather areas associated with grain boundaries that disappeared in the polishing operation.

A Siemens Elmiskop I electron microscope was used throughout this work, and operated on the 100 kV range. Specimens were sandwiched between two 100 mesh Athene copper grids and placed in the stereoscopic specimen holder which permits the specimen to be tilted through about $\pm 5°$ by means of an external control. The double condenser was employed throughout so as to illuminate a small spot only a little larger than the field diameter, thus minimizing heating of the specimen. Specimens were first examined at low power to find areas that were thin enough (below ~500 Å) to permit detailed examination at high magnification. Suitable regions were surveyed at commonly 8000 and 40,000 magnifications, tilting where necessary to reveal the dislocations present in a particular grain. Numerous plates were taken of many areas and on many samples in order to obtain representative results. The plates were all enlarged 4 × or more for detailed study.

RESULTS

There was a marked difference in structure between the sulfurized and the unsulfurized iron specimens. In the latter the dislocation density was relatively low and, although some areas contained complex, tangled dislocations, well formed, complete networks were absent. In the heavily sulfurized specimens, on the other hand, areas of high dislocation density were common in the form of well-developed networks. Lightly sulfurized specimens were intermediate in structure. The detailed results follow.

Pure iron

Figures 1 and 2 show the typical structure of regions adjoining grain boundaries in two pure iron control specimens. The particular samples depicted

VOL. 8 1960

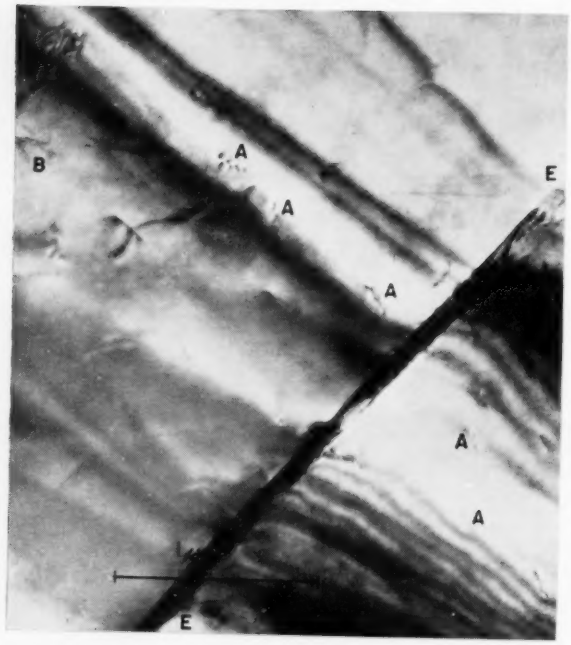


FIG. 1. Pure iron control specimen water-quenched from 890°C. Note the following: *EE* grain boundary, *A* simple dislocations showing typical contrast, *B* complex dislocations. ×30,000

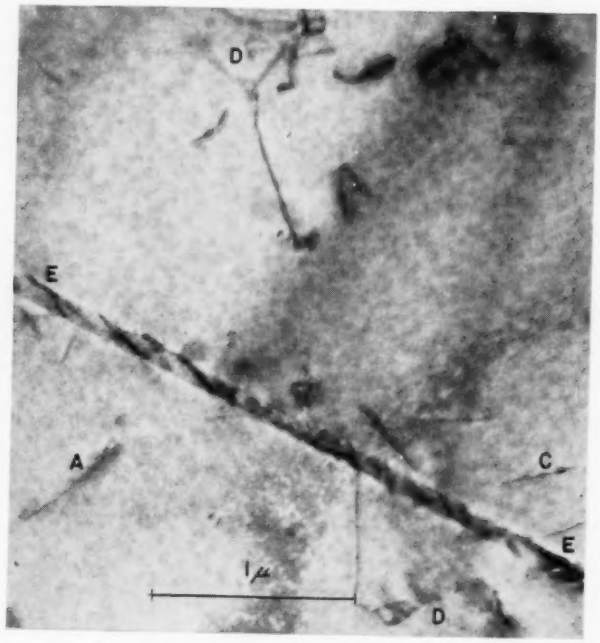


FIG. 2. As Fig. 1 but different piece of sample. In addition to *A* and *EE* (see Fig. 1) note *C* simple, and *D* complex dislocations showing unusual double line contrast. Note individual dislocations of different orientation lying apparently in the plane of the grain boundary. ×30,000

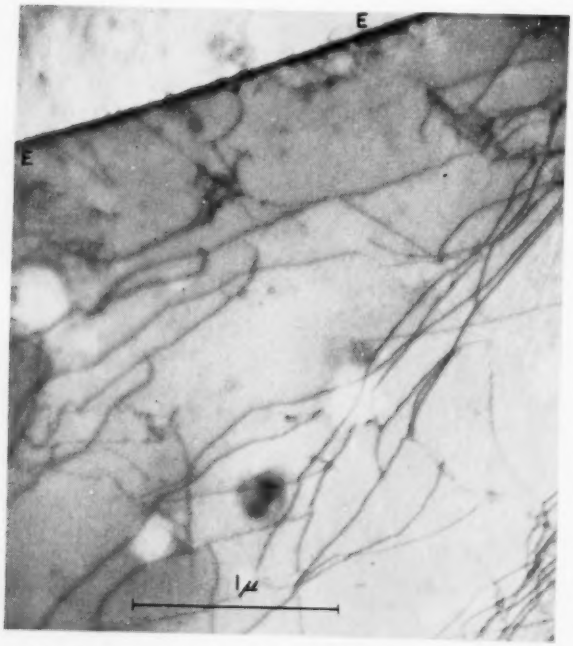


FIG. 3. Typical "high" dislocation density area in iron sulfurized for 4 hr and water-quenched. Note grain boundary *EE*. ×30,000

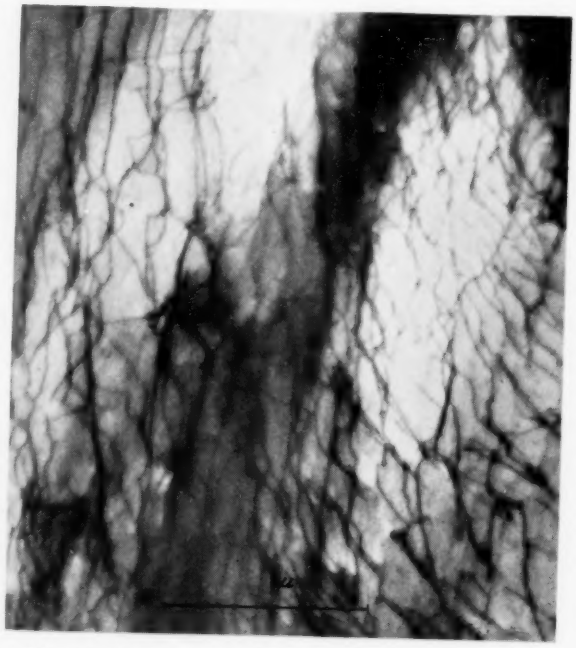


FIG. 4. Area in specimen sulfurized for 17 hr and water-quenched. ×30,000

were water-quenched. In Fig. 1 Bragg fringes are visible roughly perpendicular to the grain boundary; similar rather diffuse fringes are visible in Fig. 2. The mottled background in Fig. 2 should be disregarded. Since the depth of field is greater than the foil thickness, the traces of the grain boundary on the upper and lower surfaces of the foil are frequently seen in the photographs. In Figs. 1 and 2 the grain boundary traces are separated by ≈ 1000 Å, which, for an assumed foil thickness of 500 Å, would correspond to $\sim 25^\circ$ inclination of the boundary plane to the plane of the foil. Interference fringes running parallel to the boundary trace may be seen in Fig. 1 in the overlapping wedge regions of the two grains. Of incidental interest is the fact that individual dislocations lying apparently in the plane of the grain boundary can be seen in Fig. 2.

Region *A* (Fig. 1) shows the typical contrast of a dislocation running obliquely through the foil from surface to surface. The complex shape of dislocations such as *B* (Figs. 1 and 2) is believed to be due to the fact that quenching stresses activated dislocation sources and caused glide. The unusual double line contrast effects at *C* and *D* (Fig. 2) are not fully understood at present. The dislocation content of the specimens shown in Figs. 1 and 2 are both roughly estimated to be 2.5×10^7 cm^{-2}. (This figure and later estimates are obtained by squaring the reciprocal mean line spacing. In this case it corresponds to a mean spacing of 2×10^{-4} cm.) Higher densities than this were never observed in either the quenched or slow cooled pure iron.

Sulfurized iron

(a) *Effect of sulfurization time.* After sulfurization most regions of the foil adjoining grain boundaries showed line networks running into the boundaries. Occasionally networks were seen that had no apparent connection with grain boundaries. The extent and density of the networks increased with increasing sulfurization time. Figs. 3–5 show typical high network density regions observed in specimens sulfurized 4 hr, 17 hr and 10 days, respectively. The networks were clearly revealed only at a critical tilt. For example, in Fig. 5 more contrast is evident near the diffuse Bragg fringe than elsewhere. There were always some areas in the foil unfavorably oriented in which nothing could be seen. In view of these observations and in the light of experience in other ferritic materials, it became clear that these networks were composed of dislocations.

Rough estimates of the dislocation densities in the regions shown in Figs. 3–5 give 6×10^9 cm^{-2} after 4 hr, 1.5×10^{10} cm^{-2} after 17 hr and 4×10^{10} cm^{-2} after 10 days of sulfurization. This means that the specimens sulfurized for 10 days exhibited dislocation densities at least 1000 times as great as the pure iron. The 10-day specimens frequently had dislocation densities so great that estimates could not be made because of insufficient resolution.

In addition to high network density regions (Figs. 3–5) described above, other areas of much lower density could usually be found in the same specimen. For example, compare the area shown in Fig. 6 having a dislocation density of 8×10^8 cm^{-2} with that in Fig. 4, described above, having a dislocation density of 1.5×10^{10}. Whereas after 4 hr of sulfurization high density networks were fairly scarce, after 10 days of sulfurization low density regions were scarce.

Diffusion of sulfur into the specimen is calculated to be virtually complete after 4–5 days; however, because of the scatter in dislocation densities within a single specimen, the time variation in density indicated by the results just quoted can hardly be considered significant and it is still not established whether the density stops increasing after five days.

(b) *Extent of networks.* Many attempts were made to find transparent, correctly oriented regions larger than the grain size in the sulfurized specimens in order to see whether or not the networks changed in density towards the centre of the grains. Figs. 7 and 8 show one of several such regions observed in samples sulfurized for 17 hr in which a marked decrease in dislocation density occurred on moving away from the boundary. In this grain the dislocation density is roughly 2×10^{10} cm^{-2} in the region 0.1–1 μ in from the boundary, and 4×10^8 cm^{-2} at a distance $3\frac{1}{2}$–$4\frac{1}{2}$ μ from the boundary. The density within 0.1 μ of the boundary is considerably higher than 10^{10} but the resolution is not sufficient for a quantitative estimate. Hence the dislocation density does fall off with distance from the grain boundary so that in the center regions of the grains there are only isolated dislocations.

In samples sulfurized for 10 days the networks were much more extensive and in many cases it was not possible to determine whether or not they disappeared at distances far from the boundaries.

(c) *Other examples of networks.* Two additional examples of high density dislocation networks adjoining grain boundaries are shown in Figs. 9 and 10 in samples quenched after 10 days and 17 hr sulfurizing, respectively. A rough estimate gives dislocation densities here of 10^{11} cm^{-2} (Fig. 9) and 10^{10} cm^{-2} (Fig. 10). Fig. 10 may be compared with Figs. 7–8 and shows a grain in which the density of

VOL. 8 1960

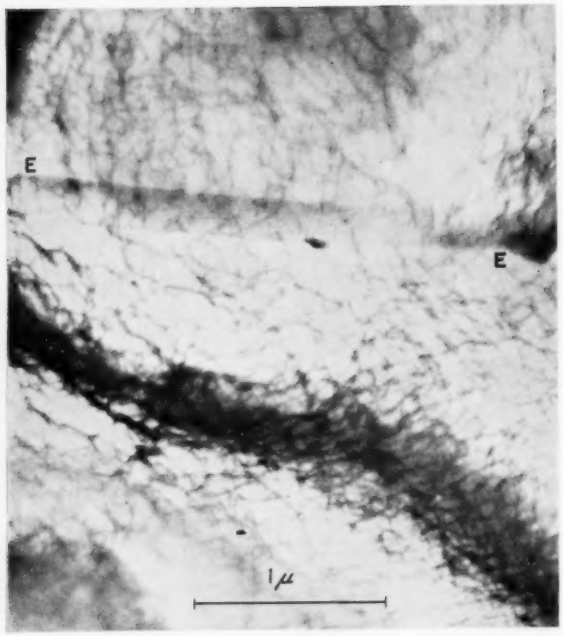


FIG. 5. Area in specimen sulfurized for 10 days and water-quenched. Note grain boundary *EE*. ×30,000

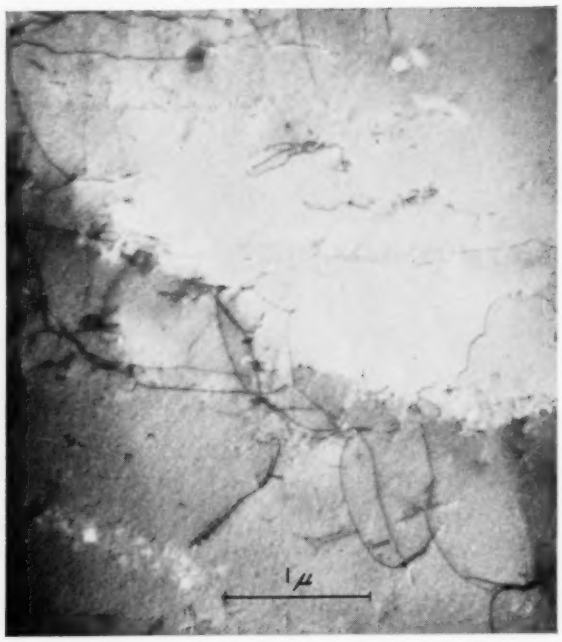


FIG. 6. As Fig. 4 but different area, in this case typical of a "low" dislocation density area. ×20,000

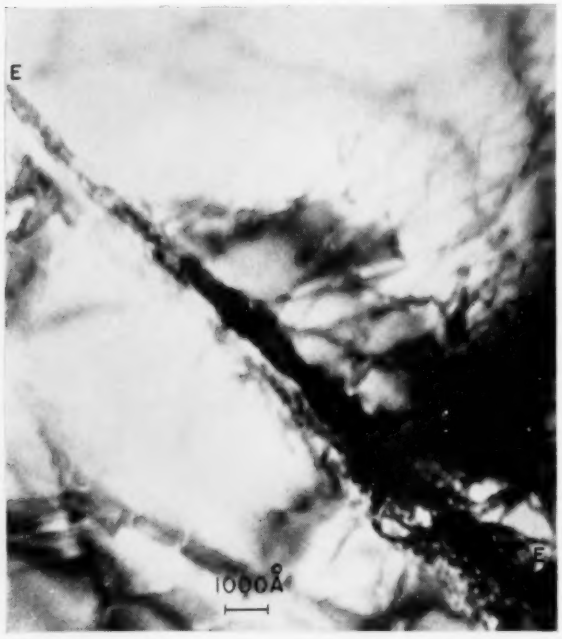


FIG. 7. Showing network near grain boundary *EE* in a sample sulfurized for 17 hr and water-quenched. ×60,000



FIG. 8. Area near centre of lower grain seen in Fig. 7; the hole is about 4 μ from the grain boundary. Occasional isolated dislocations may be seen. ×60,000



FIG. 9. Sulfurized for 10 days and water-quenched. Note: *EE* grain boundary, *EFG* "recovered area". ×40,000



FIG. 10. Sulfurized for 17 hr and water-quenched. Note grain boundary *EE* and network. ×15,000

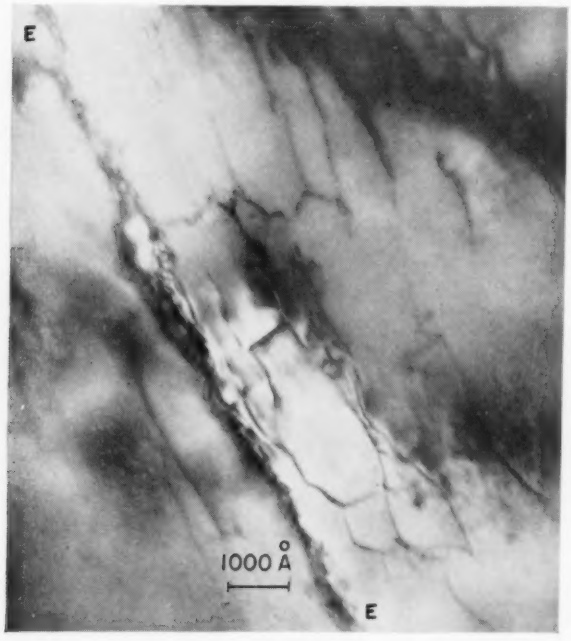


FIG. 11. Sulfurized for 10 days and water-quenched. Note grain boundary *EE* and rather regular network adjoining. ×80,000



FIG. 12. Sulfurized for 25 hr and air cooled. Note grain boundary *EE* and network. ×80,000

VOL. 8 1960

the dislocation network did not decrease with distance from the grain boundary at least up to the 10 μ limit of visibility. Immediately adjoining the grain boundary shown in Fig. 9 is a light area EFG. Selected area diffraction showed that this area had the same orientation as the surrounding grain. In view of its lower dislocation content, it might be interpreted as a partially recovered area.

Figure 11 shows an example of a very regular network.

(d) *Effect of cooling rate.* Experiments were carried out to determine if the dislocation network structure is affected by the quench following sulfurization. A quartz capsule containing iron specimens that had undergone sulfurization for 25 hr was air cooled instead of quenched. Fig. 12 shows a region of one such specimen. The dislocation density of the region shown is 2×10^{11} cm^{-2}. We conclude from this that the dislocation network structure is not modified significantly by the quenching operation.

DISCUSSION

We have seen that, somehow during sulfurization, the dislocation density in the neighborhood of the alpha iron grain boundaries increases to values comparable with the dislocation densities expected of fully work-hardened materials. We now show that the formation of the grain boundary dislocation networks in the iron–sulfur alloys and the abnormal segregation of sulfur in the neighborhood of the grain boundaries can be interpreted satisfactorily on the basis of the mechanism outlined as follows:

(1) Sulfur diffuses into the iron preferentially along grain boundaries.

(2) The sulfur then enters the iron lattice predominantly as a substitutional atom and diffuses laterally from the grain boundaries at a rate much greater than that of the counter-diffusing iron.

(3) This inequality between the sulfur and iron diffusion fluxes results in an undersaturation of lattice vacancies or, conversely, a supersaturation of occupied substitutional sites, near the grain boundaries. This vacancy undersaturation is relieved by dislocation "down-climb" (that is, the downward growth of the extra half plane of atoms in a positive edge dislocation). The continued down-climb process results ultimately in dislocation networks such as are seen in the photographs.

(4) The sulfur atoms are positively adsorbed at the dislocations, thus leading to the abnormally high grain boundary segregation reported in the previous paper.

In the following paragraphs we shall describe in more detail the good accord between the experimental results and the suggested mechanism:

Diffusion of sulfur in alpha-iron

It has been shown elsewhere[3] that sulfur diffuses preferentially along the grain boundaries at all temperatures in the alpha range of iron. The specimens used in the present investigation were $\approx$0.015 cm sheet having a grain size (mean linear intercept length, L/N) of 0.035 cm. It is very likely therefore that a significant fraction of the sulfur entered the specimens first by diffusing along grain boundaries and then diffusing laterally into the grains by volume diffusion.

Formation of dislocation networks

Diffusion measurements[3–5] show that the volume diffusion coefficient of sulfur in alpha iron is about 30 times the volume self-diffusion coefficient of iron at 890°C. It is therefore expected that the lateral diffusion flux of sulfur into the grains from the grain boundaries would be much greater than the counter-flux of iron. If most of the sulfur enters the iron lattice substitutionally, the difference between the sulfur flux and the countercurrent iron flux must be made up by a diverging flux of lattice vacancies toward the grain boundaries and thus to a vacancy undersaturation in the boundary region. Such a vacancy undersaturation will cause down-climb of existing dislocations and possibly nucleation of interstitial discs of atoms.

The sulfur concentration in the diffusion zone is considerably greater than the equilibrium vacancy concentration. Therefore, if there were no internal sources of vacancies, the vacancy undersaturation could reach extremely large values since

$$\frac{\partial C_s}{\partial t} \simeq -\frac{\partial C_v}{\partial t},$$

where C_s and C_v represent the substitutional sulfur and vacancy concentrations, respectively (the iron flux is neglected), and t represents time. It is conceivable, then, that the homogeneous nucleation of interstitial discs could occur were it not possible to relieve the vacancy undersaturation by other means.

It is probable, however, that the vacancy undersaturation is relieved primarily by the down-climb of existing dislocations. A regenerative climb mechanism such as that proposed by Bardeen and Herring[6] would be necessary for dislocation multiplication.

Doo and Baluffi[7] have already demonstrated that continued climb of dislocations, resulting from unequal diffusion fluxes can lead to a large increase in dislocation and substructure density and, ultimately, to recrystallization in the diffusion zone of alpha brass single crystals. It is possible that dislocation networks had formed but that their experimental resolution was not sufficient to reveal it. The substructure formed at and near the external surfaces of the brass crystals after inward diffusion of zinc from the vapor.* Doo and Baluffi found also that slip occurred in the diffusion zone, presumably to accommodate the volume change accompanying the diffusion process. However, it is unlikely that such slip occurred in the present experiments since the total flux was quite small.

We will now calculate the vacancy undersaturation necessary to cause the down-climb of dislocations to curvatures corresponding to the reciprocal dislocation spacings observed on the photographs.

Degree of vacancy undersaturation

First consider the homogeneous nucleation of interstitial discs of iron atoms driven by a vacancy undersaturation:

We assume that the total energy of a circular prismatic dislocation in the form of an interstitial disc is

$$E = \left\{ \frac{\mu b^2}{2\pi(1-\nu)} \left[\ln \frac{r}{r_0} + \frac{1}{2} \right] + 2k \right\} \pi r$$

where μ = the shear modulus, b = the burgers vector, ν = Poisson's ratio, r = radius of the disc, r_0 = half-radius of the dislocation core, k = core energy per unit length of dislocation comprising the disc.

The equivalent surface tension of the circular edge of the disc is then

$$\sigma = \frac{E}{2\pi r b} = \frac{\mu b}{4\pi(1-\nu)} \left[\ln \frac{r}{r_0} + \frac{1}{2} \right] + \frac{k}{b}.$$

Using $r_0 = 10^{-8}$ cm and $k = 1$ eV per atom plane, classical nucleation theory gives $\approx 5 \times 10^4$ as the vacancy undersaturation ratio necessary for sensible homogeneous nucleation of interstitial discs, and 5×10^{-8} cm as the critical disc radius. The formula for the prismatic loop energy is adapted from the more familiar one derived for the energy of a pair of parallel, straight edge dislocations of opposite sign.[8] The curvature of the interstitial disc would cause the energy to be higher than that given by the formula; on the other hand the formula does not take into account the lowering of the energy which would result from the adsorption of solute on dislocations. In view of this large barrier to nucleation, then, it is probable that the vacancy undersaturation is relieved by down-climb of existing dislocations rather than by homogeneous nucleation of interstitial discs.

Using the above formula for σ and the Gibbs–Thomson equation applied to the present case (i.e. $\sigma/r = [(kT)/V] \ln S$, where S is the undersaturation ratio and V is the atomic volume), one can calculate the undersaturation ratio necessary to prevent a dislocation line of given curvature from becoming straight. Choosing 10^{-5} and 10^{-6} as typical of the radii of curvature seen in the photographs, one calculates that undersaturation ratios of only 1.16 and 2.94, respectively, are required. At these radii the particular elastic model chosen is relatively unimportant; setting $\sigma = \mu b + k/b$, which is a gross over-estimate at small radii, roughly the same undersaturation ratios are obtained.

Interaction between sulfur and dislocations–dislocation stability

The minimum sulfur excess—0.005 wt.% of the entire specimen at grain size 0.035 cm (mean linear intercept length)—in the vicinity of the grain boundaries reported in the previous paper corresponds to about 10^{17} sulfur atoms/cm^2 of boundary. Since the average density of dislocations in the networks after the long sulfurizing times is 10^{11} lines/cm^2, the sulfur excess can be accommodated by adsorption at the boundary dislocation networks if ten sulfur atoms are adsorbed per dislocation core atom and the network extends for a distance of 15 μ on either side of the boundary. Our observations on the extent of the networks is consistent with this requirement and therefore support the hypothesis that the abnormal segregation is due to sulfur adsorption at the boundary networks.

The persistence of the networks at 890° for periods considerably longer than the calculated duration of the diffusion current is somewhat surprising. Of course the energy density of the networks and the driving free energy for their disappearance must have been lowered greatly by the adsorption of sulfur. It is even conceivable that the free energy of the system is lowered by the formation of sulfur-coated dislocations. Our observations neither confirm nor rule out this possibility. The dislocations in the networks were usually curved, but in some cases were quite straight (see Fig. 10), appearing as rubber bands

* Volume diffusion from the free surface occurred also in the present experiments with the probable result that dislocation networks formed there as well, possibly accounting for the observation of some networks apparently unassociated with grain boundaries.

VOL. 8 1960

stretched between pinning points, thus implying thermodynamic instability. Also, the occurrence of recovery, such as may have led to the clear area in Fig. 9, already alluded to, would require that the tension of the coated dislocations be positive. It seems probable that the remarkable persistence of the networks is due to their topological stability coupled with the greatly lowered driving free energy for their disappearance that results from the solute adsorption.

ADDITIONAL CONSEQUENCES OF MODEL

The mechanism that we have proposed for the formation of dislocation networks should be generally operative within a crystalline phase at constant temperature whenever the following conditions are fulfilled:

(1) Composition gradients exist, (2) the partially segregated components exist at least partially in the substitutional state and interdiffuse at different rates in such a manner as to create a vacancy undersaturation locally.

There are many ways in which chemical inhomogeneities in a solid solution can arise. For example, considerable segregation usually occurs in the solidification process. Also, local solute gradients must exist during formation or dissolution of precipitate particles.

It is evident that the mechanism which has been described is one of the ways whereby the dislocation content of crystals can increase. Since interstitial atoms usually diffuse much more rapidly than substitutional atoms, a situation particularly favorable for dislocation production by this mechanism is one in which the solute, at equilibrium, exists not only as a substitutional atom, but also to a significant extent as an interstitial. If the concentration of the atoms occupying interstitial sites is of the same order of magnitude, or larger, than the vacancy concentration, the interstitial atoms could diffuse ahead of the substitutional atoms and jump into vacancies, and thus create vacancy undersaturation.

We now consider the possible effects dislocation networks have upon certain grain boundary phenomena.

Abnormal segregation at interfaces

If, as apparently is the case in the iron–sulfur system, solute is strongly bound to dislocations, a large excess will be adsorbed and retained by dislocation networks in the vicinity of grain boundaries. Furthermore, since the mechanism would operate also at free surfaces, segregation should occur there as well.

It is evident, then, that experiments to test for positive adsorption of impurities at crystal interfaces must be designed very carefully in order to avoid conditions that will lead to the formation of dislocation networks at the interfaces. It is possible that some of the unusual interfacial segregations reported in the literature (see the preceding paper), which give the impression of anomalously broad grain boundaries, were actually caused by impurity adsorption at grain boundary dislocation networks. Also, it is understandable that the quantitative measurements of such segregation do not fit the Gibbs adsorption equation applied to the grain boundary alone.

The work of Leymonie *et al.*[9] deserves special attention here since they also investigated the iron–sulfur system. Using autoradiography they observed grain boundary segregation of sulfur in very slowly cooled specimens, but not in quenched specimens. The observations suggested that the sulfur, given sufficient time, preferred to diffuse to the grain boundaries and precipitate there as sulfides. The important point, however, is that the quenched specimens did not exhibit grain boundary segregation. The main difference between the experiments of those authors and the present experiments lies in the manner in which the sulfur was introduced; instead of allowing the sulfur to enter the specimens by solid state diffusion, they prepared a melt of iron and sulfur, and, by so doing, very likely minimized diffusion gradients. We feel that this difference in specimen preparation reconciles the differences in the results of the two investigations.

Diffusion along interfaces

It has been shown[10] that in some instances diffusion occurs as rapidly along dislocation channels as along high angle grain boundaries. Therefore, unless the adsorbed solute strongly interferes with diffusion along the dislocations, the formation of a dense dislocation network at the grain boundaries can greatly increase the capacity of the grain boundary region for preferential transport of solute.*

---

* Note added in proof: There is some evidence to support the suggestion that an enhanced grain boundary diffusion rate may result from grain boundary dislocation networks. Leymonie and Lacombe (unpublished work, private communication) find that the product, $D_{Fe}{}^{*}\delta$, where D^{Fe*} is the grain boundary self-diffusion coefficient of α-iron, and δ is the grain boundary "width", is five times greater in iron containing grain boundary-adsorbed sulfur than in pure iron. The observation suggests that perhaps the grain boundary width, is effectively larger in the sulfur-bearing iron than in the pure iron. Dislocation networks, such as are observed in the present experiments, may also exist in the alloys of Leymonie and Lacombe.

Grain boundary migration

It is known that certain impurities in amounts well within the solubility limit can markedly retard the motion of grain boundaries. One mechanism whereby this can occur has been treated in detail by Lücke and Detert[11]. An alternative mechanism that may sometimes operate is the pinning of grain boundaries by an impurity generated dislocation network. Grain boundaries can, in fact, be pinned by dislocation networks of whatever origin. Let ϵ be the excess free energy density arising from the dislocation network; we suppose that ϵ is directly proportional to the local density of dislocation lines. In the impurity generated grain boundary networks this density, and hence ϵ, falls off sharply with distance away from the boundary. If the boundary moves, it will very likely for topological reasons extend the network of the growing grain and consume the network of the shrinking grain. Therefore, since ϵ is a maximum at the initial position of the grain boundary, the dislocation energy must necessarily increase as a result of grain boundary displacement. The restraining pressure on the boundary would be given by

$$p = \Delta\epsilon$$

where $\Delta\epsilon$ is the change in energy density across the boundary. Let us suppose that interfacial curvature provides the driving force for boundary migration. Then, in order for the boundary to move further, the restraining pressure on the boundary due to the network would have to be exceeded by an opposing pressure arising from grain boundary curvature. Specifically, for a spherical grain, the following condition would have to hold in order that the grain boundary migrate: $(2\sigma/r) > \Delta\epsilon$, where r = radius of the spherical grain and σ = surface energy. Substituting $10^{11}\,\mu b^2$ for $\Delta\epsilon$ and 750 ergs/cm^2 for σ, we find that $r < 2.5 \times 10^{-5}$ cm in order that boundary motion occur. One does not ordinarily observe grain radii this small, hence networks of this density could pin grain boundaries in ordinary alloys. The calculation was made using values of σ and $\Delta\epsilon$ characteristic of clean boundaries and dislocations. The resulting error in r should not be too great, however, since one expects σ and $\Delta\epsilon$ to be decreased proportionally by the addition of solute.

Mechanical properties

Grain boundary dislocation networks produced in the suggested manner can be expected to affect mechanical properties. The presence of extensive grain boundary networks could promote intergranular brittle fracture at low temperatures since the propagation of slip through grain boundaries would be made more difficult by such networks. Also, such networks might lead to high temperature intercrystalline creep fracture, observed in alloys but not in super pure metals, by pinning grain boundaries so that they could not migrate rapidly enough to reduce local stress concentrations.

As already suggested, dislocation networks can be formed by the operation of the proposed mechanism during the formation, or dissolution, of precipitate particles. It is required only that precipitation be accompanied by a suitable vacancy flux.* For example, the volume of carbide particles precipitated from iron is greater than the volume of the solution transformed. Thus during carbide precipitation the particles will tend to be stressed, and the local vacancy concentration displaced relative to its equilibrium value. To relieve these local transformation stresses in the vicinity of the particles, a vacancy flux, and accompanying dislocation climb, would result.

Thus in certain precipitation processes the dislocation content around each particle would increase as the particle grows. It has already been suggested by Bartlett and Mitchell[12], and more recently by Huggins[13], that dislocations surrounding precipitate particles might be an important contributing factor to precipitation hardening. Bartlett and Mitchell[12] have demonstrated that dislocation loops can form, possibly by homogeneous nucleation, around precipitating particles to relieve transformation stresses. It is evident that such stresses might also be relieved by the climb of existing dislocations in the vicinity of growing precipitate particles.

SUMMARY AND CONCLUSIONS

(1) High purity alpha-iron polycrystals containing sulfur as a result of exposure to H_2S tend to exhibit a dense dislocation network structure associated in general with the grain boundaries. The networks are quite extensive, spanning in some cases up to 15 μ on either side of the boundaries. The dislocation densities of the networks are comparable with those expected of fully cold worked metals. In contrast, pure, unsulfurized iron does not exhibit such networks.

(2) The networks probably form by a regenerative climb process; sulfur rushes in along the grain boundaries and then diffuses laterally into the bodies

* A vacancy supersaturation, resulting from a converging vacancy flux, might also produce dislocations in the same manner as an undersaturation; instead of "down-climb" the process would be by "up-climb". In this case there can also be very large departures from equilibrium, however, beyond a certain critical supersaturation, vacancy cluster formation might be the predominant effect.

VOL. 8 1960

of the grains, establishing a Kirkendall diffusion zone and a concomitant vacancy undersaturation. The vacancy undersaturation provides the driving energy for the climb and multiplication of dislocations.

(3) The apparent greater solubility of sulfur in polycrystals than in single crystals of iron reported in the preceding paper, is now qualitatively explained in terms of sulfur adsorption at the dislocation networks.

ACKNOWLEDGMENT

This investigation was stimulated by the results of Whelan, Hirsch, Horne and Bollmann showing that high densities of dislocations may sometimes exist at grain boundaries. We are especially indebted to H. S. Rosenbaum for calling our attention to the observations of Whelan *et al.* and their possible connection with the grain boundary segregation of sulfur.

REFERENCES

1. H. M. Tomlinson, *Phil. Mag.* **3,** 867 (1958).
2. M. J. Whelan, P. B. Hirsch, R. W. Horne and W. Bollman, *Proc. Roy. Soc.* A**240,** 524 (1957).
3. N. G. Ainslie and A. U. Seybolt, *J. Iron St. Inst.*, **194,** 341 (1960).
4. F. S. Buffington, I. D. Bakalar and M. Cohen in *The Physics of Powder Metallurgy* (Editor W. E. Kingston). McGraw-Hill, New York (1951).
5. C. E. Birchenall and R. F. Mehl, *J. Appl. Phys.* **19,** 217L (1948).
6. J. Bardeen and C. Herring in *Imperfections in Nearly Perfect Crystals* p. 277. Wiley, New York (1952).
7. V. Y. Doo and R. W. Baluffi, *Acta Met.* **6,** 428 (1958).
8. A. H. Cottrell, *Dislocations and Plastic Flow in Crystals* p. 50, equation (2.55). Clarendon Press, Oxford (1953).
9. C. Leymonie, P. Coulomb and P. Lacombe, *C.R. Acad. Sci., Paris,* **245,** 931 (1957).
10. D. Turnbull and R. E. Hoffman, *Acta Met.* **2,** 419 (1953).
11. K. Lücke and K. Detert, *Acta Met.* **5,** 628 (1957).
12. J. T. Bartlett and J. W. Mitchell, *Phil. Mag.* **3,** 334 (1958).
13. R. G. Huggins, *Acta Met.* **7,** 357 (1959).

LOW TEMPERATURE CALORIMETRIC MEASUREMENTS ON ISOTHERMAL AGING OF Al–Ag*

W. DeSORBO†

On quenching aluminum containing 1.3 at.% silver, energy is released upon isothermal holds at low temperatures (~245°K). The amount of energy evolved, over a measured period of time (32–140 min) after the initiation of the reaction (clustering of silver atoms), amounts to 6–7 cal/g-atom of alloy for "slow" quenches and about 2–2.5 cal/g-atom of alloy for "fast" quenches. These results are consistent with the resistometric studies of Turnbull *et al.* who pointed out the existence of two states in quenched Al–Ag alloys.

MESURES CALORIMETRIQUES A BASSE TEMPERATURE SUR LE VIEILLISSEMENT ISOTHERME DE Al–Ag

Par trempe d'un alliage Al–1,3 at. % Ag, de l'énergie est libérée lors du maintien à basse température (~245°K). La quantité d'énergie qui se dégage sur une période de 32 à 140 minutes après l'initiation de la réaction (ségrégation des atomes d'argent), atteint 6–7 cal/at. gr pour des trempes lentes et 2–2,5 cal/at. gr pour des trempes rapides. Ces résultats sont en accord avec les études de résistivité de Turnbull et ses collaborateurs qui ont mis en évidence l'existence de deux états des alliages Al–Ag trempés.

KALORIMETRISCHE MESSUNGEN DES ISOTHERMEN AUSLAGERNS VON Al–Ag BEI TIEFEN TEMPERATUREN

Nach dem Abschrecken von Aluminium mit 1,3 Atom% Silber wird bei isothermem Auslagern bei tiefen Temperaturen (~245°K) Energie frei. Der Betrag, der während einer bestimmten Zeitdauer (32–140 Min.) nach Beginn der Reaktion (Zusammenlagerung der Silberatome) entwickelten Energie beträgt bei langsamem Abschrecken 6–7 cal/g-Atom der Legierung und nach schnellem Abschrecken etwa 2–2,5 cal/g-Atom der Legierung. Die Ergebnisse sind im Einklang mit Widerstandsmessungen von von Turnbull *et al.*, welche auf die Existenz von zwei Zuständen in abgeschreckten Al–Ag-Legierungen hingewiesen haben.

VOL. 8 1960

Turnbull and Treaftis[1] have recently pointed out the existence of a rapid isothermal resistivity decrease upon quenching Al–Ag alloys at temperatures 210–300°K. This decrease reached a maximum of 7–8 per cent below the extrapolated solid solution value. They suggested that this behavior could be due to a low temperature reaction such as the formation of silver rich clusters at anomalously high rates (p_1 state). Previously, Borelius[2] had reported, results later confirmed by Koster and Knödler[3], that upon quenching Al–Ag alloys at 300°K, the resistivity was as much as 40 per cent less (for an $X_{Ag} = 0.075$) than the extrapolated solid solution value. They attributed this low value of resistivity of the Al–Ag alloy to the formation, during quench, of an ε' state consisting of silver clusters in solution.

More recently Turnbull *et al.*[4], in extending their studies on kinetics of clustering in some aluminum alloys, indicated that in Al–Ag Borelius' ε' state could be obtained by using his experimental technique for quenching, i.e. by cooling the specimen at rates slower than those used by Turnbull and Treaftis (Ref. cited). Furthermore, they showed that with "fast" cooling rates (approximately 25,000°C/sec), the ε' state was suppressed in favor of the p_1 state verifying the earlier results.[1] The existence of these two states was further demonstrated by their detailed resistance behavior of the quenched alloys on continuous heating.

In these above studies it has been assumed that the resistivity changes observed reflect directly the clustering of the solute atoms in solution. Some corroborative evidence for this would be calorimetric measurements of the energy associated with clustering as already observed, for example, in the low temperature reaction of quenched Al–Cu alloys.[5,6] The purpose of this note is to present some such results on the low temperature reaction associated with quenched specimens of Al–Ag which are consistent with the resistometric studies of Turnbull *et al.*[1,4].

The calorimeter and the procedure have already been described.[6] The Al–Ag samples were made from the same stock as that used by Turnbull *et al.* (Ref.

* Received September 14, 1959.

† General Electric Research Laboratory, Schenectady, New York.

cited). The atom fraction of silver, $X_{Ag} = 0.013_3$. An ingot of the material was cold rolled to strips having a thickness of 0.010 in. Samples made from these strips measured $\frac{1}{2} \times \frac{3}{8}$ in. The homogenization temperature T_H in all cases amounted to approximately 540°C. For "fast" quenches the experimental technique of Turnbull *et al.*[1,4] was used i.e. a rectangular furnace with samples mounted on "transite" frame. The quenching medium was water–alcohol mixture maintained at approximately −40°C. After the quench the specimen was rapidly transferred to ethyl alcohol maintained at about −100°C; and while submerged, the thermocouple leads (spot welded to the specimen) were attached to the silver cone of the calorimeter.[6] In the transfer of the cone (with the sample attached to it) to the calorimeter, a cold stream of dry nitrogen gas, maintained at about −100°C, was kept on the specimen. Hence from the time of quench to the time of transfer of the specimen to the calorimeter, all efforts were made to suppress the reaction. In contrast to this, "slow" quenches refer to the procedure where the specimen was heated in a furnace, manually removed from it, quenched into alcohol–water mixture (−40°C) and then dried with blotting paper in a cold dry stream of nitrogen gas.

The energy evolved and measured in the early stages of the reaction after quench are shown in Fig. 1, both for the "fast" and "slow" quenches. The aging temperature (T_a) was approximately 245°K. (It is interesting to note here, since it is not shown in Fig. 1, that a small amount of energy was barely detectable at an aging temperature as low as 210°K.) Unlike the resistometric studies, the time of the first measurement of energy released (t_i) varied from 15 to 32 min from the start of the reaction (t_0).* For the time interval 32–140 min the energy released following "slow" quenches amounts to 6–7 cal/g-atom of alloy; whereas for "fast" quenches the energy released during the same time interval amounts to 2–2.5 cal/g-atom of alloy. If we compare these results with those of Turnbull *et al.*[1,4] and preclude the possibility of more energy being released prior to t_i for the "fast" quench than for the "slow" quench, then it could be stated that the larger evolution of energy is associated with the ε' state; whereas upon more rapidly cooling the specimen after homogenization a smaller release of energy is associated with the p_1 state. One possible explanation of these results has already been advanced by Turnbull *et al.*[4] based on a quenched-in vacancy hypothesis in addition to having the occurrence, at very high vacancy supersaturation, of sensible nucleation of dislocation loops. This model has been used by them in discussing observed reaction rates, rate dependence on thermal history, extent of reaction etc. occurring in quenched specimens of Al–Cu, Al–Zn and Al–Ag. According to this interpretation the cluster configuration in Al–Ag in the early phase of the reaction after quench would be the same in each state but limited by the distance between vacancy sinks, i.e. by dislocation spacings and quenched-in defect concentration. However, another possibility that cannot be ruled out at this time is that these two states may actually be two different configurations having an energy difference.

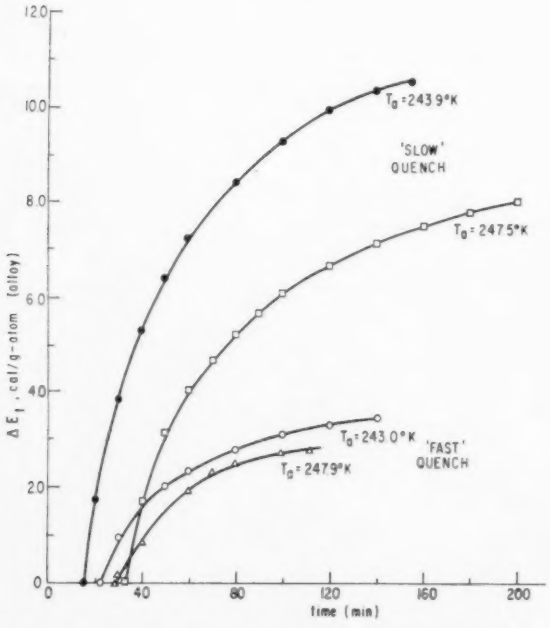


FIG. 1. Energy released on aging Al–Ag ($X_{Ag} = 0.013$) specimens after (a) "slow" and (b) "fast" quenches. Homogenization temperature, $T_H \simeq 540$°C.

It is also pertinent to point out that in attempting to measure energy released upon quenching Al–1% Si specimen at 0°C there was no detectable energy evolved. This result is also consistent with the resistometric data of Rosenbaum and Turnbull[7,8] and Federighi[9]. These authors observed no deviation in the resistivity curve from the extrapolated solid solution value for a quenched specimen of Al–Si on continuous heating until a temperature of about 180°C was attained.

The author has benefited from discussions with D. Turnbull.

* This work was done immediately after the calorimetric studies on Al–Cu.[6] These t_i values are comparable to those obtained in that investigation.

REFERENCES

1. D. Turnbull and H. N. Treaftis, *Acta. Met.* **5,** 534 (1957).
2. G. Borelius, *Rep. Bristol Conf. on Defects in Crystalline Solids*, p. 169. Physical Society, London (1955).
3. W. Koster and A. Knödler, *Z. Metallk.* **46,** 632 (1955).
4. D. Turnbull, H. S. Rosenbaum and H. N. Treaftis, *Acta Met.* In press.
5. G. Borelius, J. Anderson and K. Gullberg, *IngenVetensk Akad. Handl.* No. 169 (1943).
6. W. DeSorbo, H. N. Treaftis and D. Turnbull, *Acta Met.* **6,** 401 (1958).
7. H. S. Rosenbaum and D. Turnbull, *Acta Met.* **6,** 653 (1958).
8. H. S. Rosenbaum and D. Turnbull, *Acta Met.* In press.
9. T. Federighi, private communication to D. Turnbull.

VOL.
8
1960

YIELDING AND WORK-HARDENING IN ALPHA-BRASSES*

P. FELTHAM and G. J. COPLEY†

The tensile yield stress σ_y of polycrystalline α-brasses containing up to 35 per cent of zinc, recrystallized at 800°C and strained in the range 77–291°K, was found to vary with temperature and composition as the resolved shear stress τ_y of brass single crystals, with $\tau_y/\sigma_y \simeq \frac{1}{3}$. Linear hardening, at a rate of about $G/20$, terminates at a tensile stress $\sigma_c(T)$; parabolic hardening above σ_c is ascribed to the spreading of slip from glide zones in which small numbers of dislocations are confined by Cottrell–Lomer barriers. The pronounced increase of σ_y and σ_c with rising zinc content or decreasing temperature is interpreted in terms of changes in the Peierls–Nabarro force resulting from the diminution of the core widths of partial dislocations; a major part of the increase of σ_c appears however to be associated with the steady decline of the stacking-fault energy as the α–β phase boundary is approached.

RESISTANCE ELASTIQUE ET DURCISSEMENT DE DEFORMATION DANS LE LAITON α

On trouve que la limite élastique σ_y de laitons α polycristallins contenant jusque 35 % de zinc, recristallisés à 800°C et déformés entre 77 et 291°K, varie avec la température et la composition comme la tension de cisaillement τ_y de monocristaux de laiton, avec $\tau_y/\sigma_y \simeq \frac{1}{3}$. Le durcissement linéaire avec une vitesse approximative de $G/20$, se termine à une tension de traction de $\sigma_c(T)$; le durcissement parabolique au-dessus de σ_c est attribué à la divergence de la déformation des zones de glissement dans lesquelles un petit nombre de dislocations sont confinées par des barrières de Cottrell–Lomer. On interprète l'augmentation prononcée de σ_y et σ_c avec les teneurs croissantes de zinc ou par des températures decroissantes en fonction de changements de la force de Peierls–Nabarro qui résulte d'une diminution de la largeur d'une dislocation partielle; une grande partie de l'augmentation de σ_c apparaît cependant être associée à la diminution continue de l'énergie des fautes d'empilement au fur et à mesure que l'on s'approche de la frontière α–β.

FLIEßSPANNUNG UND VERFESTIGUNG VON ALPHA-MESSING

Die Fließspannung σ_y von vielkristallinem α-Messing mit Konzentrationen bis 35% Zink, welches bei 800°C rekristallisiert und im Bereich von 77° bis 291°K gedehnt worden war, änderte sich mit der Temperatur und der Zusammensetzung so, wie die kritische Schubspannung τ_y von Messingeinkristallen, sodaß $\tau_y/\sigma_y \simeq 1/3$ ist. Eine lineare Verfestigung mit einem Anstisg von etwa $G/20$ reicht bis zu einer Zugspannung $\sigma_c(T)$; die parabolische Verfestigung oberhalb σ_c wird der Ausbreitung der Gleitung aus Gleitzonen zugeschrieben, in welchen eine kleine Anzahl von Versetzungen durch Lomer–Cottrell-Hindernisse eingesperrt ist. Die ausgesprochene Zunahme von σ_y und σ_c mit wachsendem Zinkgehalt und abnehmender Temperatur wird gedeutet als Folge von Änderungen der Peierls–Nabarro-Spannung, welche herrühren von einer Verengung des Versetzungskerns der Halbversetzungen. Ein bedeutender Teil des Zuwachses von σ_c scheint jedoch mit der stetigen Abnahme der Stapelfehlerenergie bei Annäherung an die α–β-Phasengrenze verknüpft zu sein.

INTRODUCTION

In their paper on the work-hardening in face-centred cubic metals Feltham and Meakin[1] showed that in rods of polycrystalline copper of 99.991 per cent purity recrystallized above 500°C the mode of hardening on deformation at 77, 195 and 293°K was linear up to a temperature dependent tensile stress σ_c, and the mechanism of hardening was the same as that occurring in the linear stage observed in single crystals after the termination of easy-glide. With the assumption that at stresses above σ_c local "yielding" took place by the spreading of slip from small glide zones formed in the linear stage, and that this resulted in interaction hardening, they obtained for the coefficient of work-hardening in this, parabolic, stage the relation

$$\chi_p = d\sigma^2/d\varepsilon, \tag{1}$$

where

$$\chi_p \simeq (G/\pi)(L/L_F)\sigma_c. \tag{2}$$

In equation (1) and (2) σ is the applied tensile stress, ε the tensile strain, G the shear modulus, and $2L/2L_F$ the ratio of the average lengths of the glide zones before and after circumvention of the Cottrell–Lomer barriers by dislocations contained by them. Equation (2) correlated their measured values of χ_p and σ_c well, with $L/L_F \simeq 2$.

The main object of the present work was to study work-hardening in polycrystals of a simple copper-base substitutional alloy, more particularly, to examine the effect of alloying on the magnitude of σ_c, χ_p, and on the ratio $\chi_p/\sigma_c G$, and to obtain some indication of the influence of solid solution hardening on the tensile yield stress σ_y. Alpha-brasses were chosen because data on the work-hardening and yielding of single crystals were available[2,3] for comparison; low temperatures were employed because the variation with

* Received June 30, 1959; revised October 13, 1959.
† The University, Leeds, Yorkshire, England.

temperature of the parameters was then expected to be large, and complications arising from thermal recovery could be avoided.

EXPERIMENTAL

2.1 *Materials and method*

The nominal zinc contents of the brasses were 10, 20, 30 and 35 per cent by weight; detailed analyses have been given previously.[4] As the atomic weight of copper differs from that of zinc by less than 3%, weight percentages are almost equal to the corresponding atomic concentrations, and the former have been used for the representation of experimental results throughout this work.

Rod shaped specimens 13 cm long and of 0.2 cm diameters were wrapped in thin brass foil of the same composition in batches of ten, and each batch was then sealed into a separate evacuated silica tube and annealed at 600°C until the grain size had attained 3×10^{-3} cm. A second series of specimens was annealed at 800°C, in this case the grain size was 4.5×10^{-3} cm. In both cases the tubes cooled freely in air after withdrawal from the furnace. The annealing periods, given in Table 1, were determined from published data.[4] The grain sizes were checked by microscopy. No significant zinc loss was detected after annealing, either optically or gravimetrically.

TABLE 1

Brass	Annealing time (min)	
	600°C	800°C
90/10	40	15
80/20	20	14
70/30	15	13
65/35	12	12

All annealed specimens were deep etched, electropolished and slightly re-etched prior to deformation in tension in a motor-driven Hounsfield tensometer at a strain rate of approximately 10^{-4}/sec.

Liquid nitrogen, powdered carbon dioxide in alcohol, and methyl cyclohexane maintained just below its freezing point (149°K) were used as coolants. However, experimental difficulties precluded the extensive use of the organic liquid.

2.2 *Stress–strain curves*

Linear hardening was not discernible in the brasses annealed at 600°C, although this temperature had previously[1] been found high enough to reduce σ_y below σ_c, and thus lead to linear hardening in copper. The specimens exhibited a definite yield point, which was followed by a yield point elongation, i.e. a small virtually horizontal part of the stress–strain curve. (Curves b, c, d in Fig. 1.)

A similar yield point elongation was not found with rods annealed at 800°C; only a residual slight flattening of the stress–strain curve at the foot of the linear stage was then occasionally noticeable, for example in the 80/20 brass (Fig. 2). Upper and lower yield points could however be introduced also into these specimens by strain-ageing at constant strain for a few minutes at room temperature, i.e. considerably below the temperature (200°C) used by Ardley and Cottrell[3] to induce yielding in single crystals of alpha-brass.

Linear hardening was observed in specimens annealed at 800°C (Fig. 3). It terminates at a strain of 1–1.5 per cent, as in copper.[1]

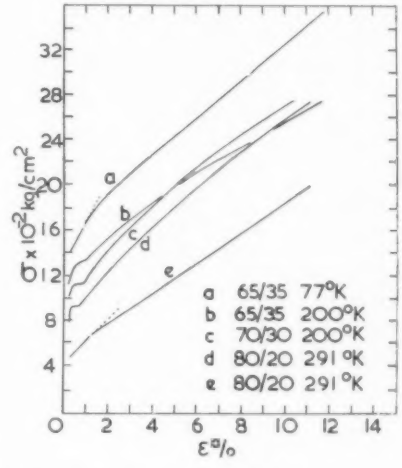


FIG. 1. Stress–strain curves of brasses annealed at 800°C (*a* and *e*) and 600°C (*b*, *c* and *d*).

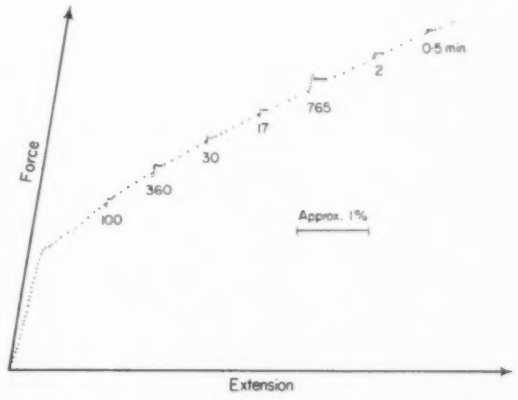


FIG. 2. Drum-chart of force–extension curve of 80/20 brass annealed at 800°C and periodically aged at constant strain during deformation at room temperature. Figures give ageing times in minutes.

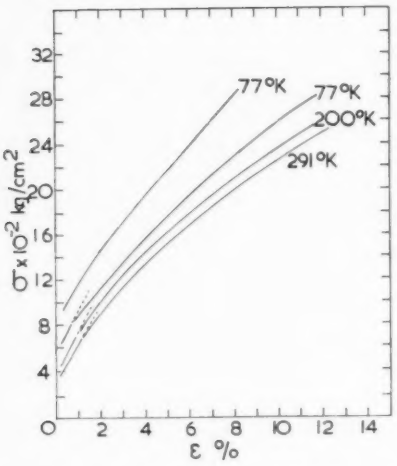


FIG. 3. Stress–strain curves of 70/30 brasses annealed at 800°C except for uppermost curve, for which the annealing temperature was 600°C.

2.3 *Yield points*

The yield points were taken to be the stresses at which deviations from the linearity of the stress–strain curve in the elastic range first became apparent, and lie in general slightly below the stress at which abrupt yielding set in, as may be seen from Fig. 1 in which only the strictly linear (Hookean) parts of the curves are omitted. The effect of temperature and composition on the yield point σ_y are shown in Figs. 4 and 5.

In order to be able to distinguish between the influence of the substructure and that due to grain size on the yield point, a few specimens of the 70/30 brass were annealed at 500°C for $\frac{1}{2}$, 1 and 2 hr, and subsequently strained at room temperature. As may be seen from Table 2, a significant grain size dependence is not in evidence; as in the case of copper,* the effect of grain size on σ_y is probably small. The differences between the magnitudes of corresponding yield points (Figs. 4 and 5) must therefore be ascribed mainly to differences in the intragranular substructures.

X-ray back reflection photographs showed fragmented spots of the type ascribed by Jacquet[6] to polygonization; by means of his etching technique substructures similar to those found by Young[7] in copper single crystals which had been allowed to polygonize at high temperatures, and by Hibbard and Dunn[8] in silicon iron, were disclosed (Fig. 6).

The development of the sub-boundaries was most readily observed in large grains, as these maintained their identity during recrystallization over comparatively long periods. Electron micrography showed the straight lines shown in the grains in Fig. 6 to form from fragmented wavy lines, which in turn had formed by the alignment of elementary segments about 0.5 μ long, each delineated by a row of etch pits. By deforming a specimen until all three sets of slip traces are visible in some of the grains having a well defined substructure, it is easily shown that the directions of the sub-boundaries do not coincide with

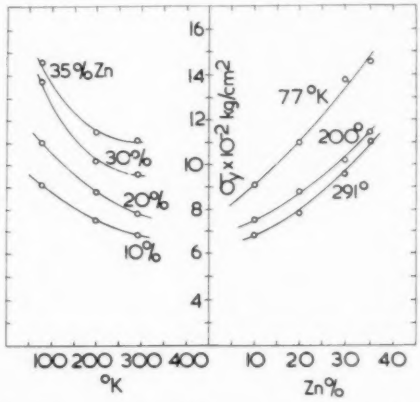


FIG. 4. Temperature and concentration dependence of the tensile yield stress of brasses annealed at 600°C to a constant grain size of 3.0×10^{-3} cm.

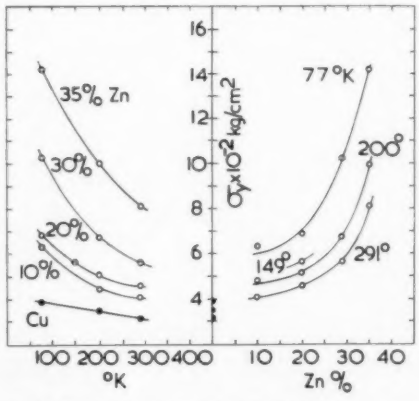


FIG. 5. As Fig. 4, but annealed at 800°C to a constant grain size of 4.5×10^{-3} cm.

TABLE 2

Annealing time (hr)	Grain size (cm $\times 10^{-3}$)	σ_y (kg/cm²)	$\chi_\rho \times 10^{-7}$ (kg²/cm⁴)
0.5	2.7	630	7.5
1.0	3.8	560	7.0
2.0	5.4	600	7.3

* Feltham and Meakin[5] found that in 99.99 per cent copper annealed *in vacuo* it was possible to increase the grain size by a factor of 8 without decreasing the yield stress by more than about 5 per cent. A high grain size dependence of the yield stress in face-centred cubic metals and solid solutions, if found, is probably attributable mainly to the solution treatment and to intragranular recovery after cold-work which accompany the grain-growth anneal.

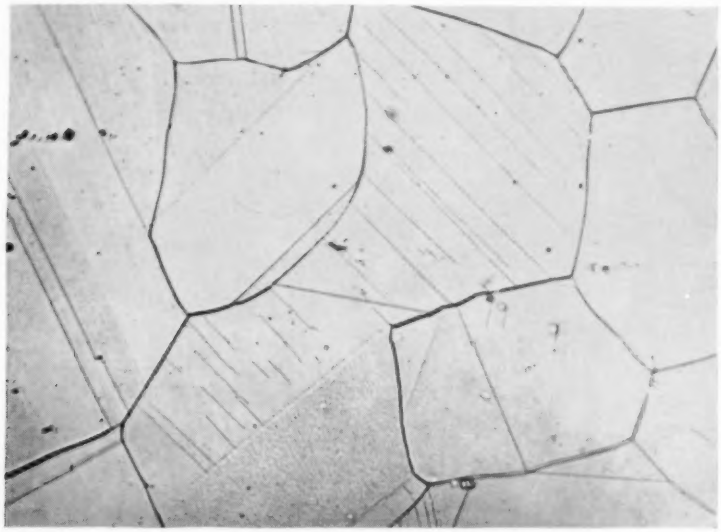


FIG. 6. Intragranular substructures in 70/30 brass annealed at 800°C for 13 min. Jacquet's etch.

any of the slip directions. In fact, as may be inferred from Fig. 6 in which lines are seen to be perpendicular to an annealing twin boundary, the sub-boundaries tend to be normal to slip planes.

2.4 *Linear and parabolic hardening*

The rate of work-hardening in the linear stage ($\chi_l \equiv d\sigma/d\varepsilon$) of specimens annealed at 800°C is shown in Table 3. Due to slight interference by the residual yield point elongation the slopes could not be determined with accuracy; they are however close to the corresponding values obtained with copper annealed at 600°C,[1] which are also included in the table.

Figure 7 shows the log–log representation of the parts of the stress–strain curves above σ_c of 90/10 specimens annealed at 800°C (full circles). The coefficient $m \equiv d(\log\ \varepsilon)/d(\log\ \sigma)$ derived from the slopes is close to 2.0, as was already noted by French and Hibbard[9] in their work on brasses.

By displacing the points horizontally to the left by a constant amount $\varepsilon_0 = -0.5$ per cent the points indicated by the empty circles are obtained. The lines drawn through the displaced points represent the relation

$$\sigma^2 = \chi_p(\varepsilon - \varepsilon_0) \qquad (3)$$

previously derived for copper.[1] With specimens annealed at 600°C a positive value of ε_0 of about 0.1 per cent was required to satisfy equation (3). χ_p of brasses annealed at 600°C is given in Fig. 8; σ_c (Fig. 9) was however determined by using rods annealed at 800°C.

While corresponding values of χ_p of 90/10 brass annealed at 600 or 800°C were equal within the limits of experimental error this equality did not extend to the other brasses. The stress–strain curves of the alloys with higher zinc contents, annealed at 800°C, were virtually linear, and no attempt was made to evaluate χ_p in these cases. The data relating to copper, given in Figs. 8 and 9 as well as in later diagrams, were taken from the work of Feltham and Meakin[1].

TABLE 3

Brass	°K	$\chi_l \times 10^{-4}$ (kg/cm²)	$G \times 10^{-5}$ (kg/cm²)	$(\chi_p/\sigma_c G) \times 10$
Cu	291	2.8	4.83	1.35
	200	3.2	5.00	1.40
	77	3.6	5.18	1.62
90/10	291	3.1	4.65	1.76
	200	3.6	4.82	1.76
	77	3.7	5.00	1.78
80/20	291	2.0	4.46	2.03
	200	1.6	4.65	1.94
	149	—	4.68	1.96
	77	2.1	4.80	1.96
70/30	291	1.7	4.30	1.62
	200	2.1	4.46	1.54
	77	2.1	4.60	1.70
65/35	291	2.1	4.20	1.24
	200	2.0	4.35	1.12
	77	1.9	4.50	1.26

DISCUSSION

3.1 *The tensile yield stress*

Table 4 shows the ratio σ_y/τ_y, where τ_y is the resolved yield stress in shear of nominally 90/10 and

VOL. 8 1960

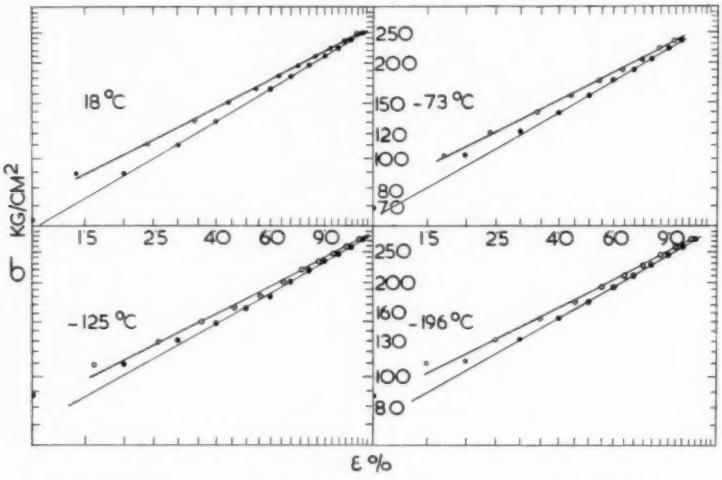


FIG. 7. Log–log representation of the stress–strain curves of 90/10 brasses above σ_c. Annealed at 800°C; grain size 4.5×10^{-3}cm. Empty circles represent equation (3) and are obtained by displacing the measured points by $\frac{1}{2}$ per cent of strain.

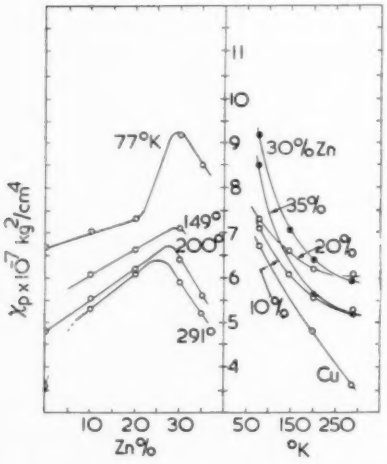


FIG. 8. Temperature and concentration dependence of the coefficient of parabolic work-hardening.

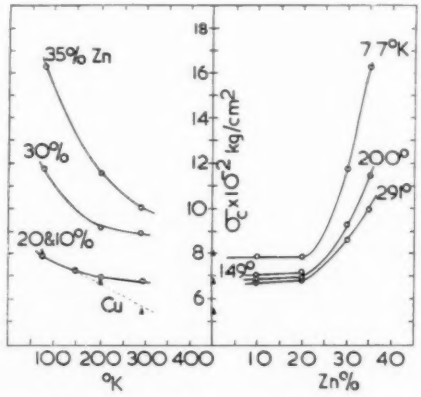


FIG. 9. Dependence of the tensile stress σ_c, at which linear hardening terminates, on temperature and solute concentration.

70/30 brass single crystals as plotted by Suzuki[2] from his own measurements and those of Jamison and Sherrill[10]. Allowing for experimental error and slight differences between the compositions of the single crystals and the corresponding polycrystals the ratio is seen to be temperature independent and fairly close to the value of 3.1 indicated by theory[11] if τ_y of an isolated grain of the polycrystal is assumed equal to that of a single crystal. We shall regard the constancy of this ratio as an adequate basis for assuming the functional forms of both, the temperature and composition dependence of the yield stress of polycrystalline brasses annealed at 800°C to be the same as for single crystals.

TABLE 4

Brass	Stress (kg/cm²)	219°K	200°K	77°K
90/10	σ_y	396	483	630
	τ_y	123	140	200
	σ_y/τ_y	3.2	3.4	3.2
70/30	σ_y	562	675	1028
	τ_y	144	187	280
	σ_y/τ_y	3.9	3.6	3.7

A theoretical treatment of yielding in alpha-brass crystals has been given by Ardley and Cottrell[3]; more recently general treatments of solid solution hardening have been developed by Suzuki[2] and

Flinn[12]. Suzuki concurs with Ardley and Cottrell in ascribing the increase of the yield point of brasses with zinc content at low temperatures primarily to Cottrell locking of dislocations by zinc atoms. According to him the locking force, and hence also the yield stress, should vary with temperature such that (his equation 8):

$$\sigma_y = A/(T + B), \tag{4}$$

where A and B depend upon the elastic constants and the solute concentration. The linear dependence of $1/\sigma_y$ on T, implied by equation (4), applies quite well to the data obtained with the brasses annealed at 800°C (Fig. 10). However Suzuki's treatment predicts only a very slight effect of concentration on σ_y at low temperatures with zinc contents of 10 per cent or more, and a steady decline of σ_y as the amount of zinc exceeds about 22 per cent. This is not born out either by the single crystal data (his Fig. 10) or by the present measurements (Figs. 5 and 10). Fig. 11 shows that $(1/\sigma_y)_0$, obtained by extrapolation to 0°K in Fig. 10, is approximately proportional to the square of the solute concentration; the value for copper falls however off the line in this representation.

Flinn[12] ascribes the effect of zinc content on σ_y in alpha-brasses to chemical interaction between the stacking-fault region of extended dislocations and solute atoms. The temperature dependence is again of the form given by equation (4) (Flinn's equation 17). His own data give for brasses $B = 2300$°K in equation (4), so that σ_y could not increase by more than about 1.5 per cent in the interval 300–0°K. Clearly therefore this form of hardening cannot account for the observed σ_y–T relation (Fig. 5), except possibly at temperatures exceeding about 400°K.

We shall now propose an interpretation of the

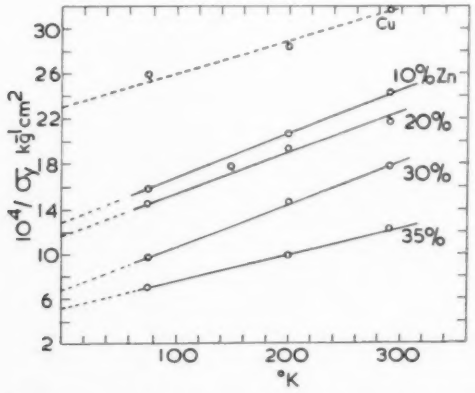


FIG. 10. The yield stress of brasses annealed at 800°C to a constant grain size of 4.5×10^{-3} cm as function of temperature. The copper was annealed for 2 hr at 600°C to a grain size of 2.5×10^{-3} cm.[1]

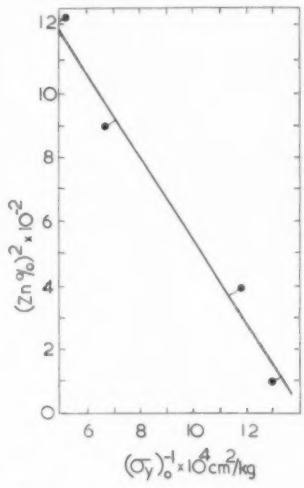


FIG. 11. The inverse of the tensile yield stress at 0°K, obtained by extrapolation in Fig. 10, as function of the square of the solute concentration.

strong concentration and temperature dependence of σ_y at low temperatures in terms of the variation of the Peierls–Nabarro force, and shall utilize the relation between the core width w of a partial $[2\bar{1}\bar{1}]$ dislocation and the width η of the stacking-fault ribbon separating it from its conjugate $[1\bar{2}1]$, as derived by Seeger and Schoeck[13].

It is evident from their Fig. 4 and Table IIb, on taking elastic constants appropriate to copper, that if the stacking-fault energy is assumed to decrease almost linearly with zinc content from 40 to 50 erg/cm^2 for copper to almost 0 at 50 per cent zinc,[12] and hence that w/η is 2–3 times smaller in a 65/35 brass than in copper, that w will decrease by about 10 per cent in that concentration range, i.e. 0–35 per cent Zn.

The Peierls–Nabarro shear stress for a partial dislocation in a close-packed lattice is given by[14]

$$\tau_{PN} = (2G/1 - \nu) \exp(-2\pi w/b), \tag{5}$$

with Poisson's ratio ν omitted if the associated pair is of the pure screw type. For a partial edge dislocation in copper Schoeck and Seeger give $w = 1.5b$, so that the exponent in equation (5) is then equal to -9.4. A reduction of w by 10 per cent would therefore increase τ_{PN} by a factor of exp (-0.94), i.e. approximately 2.6 times, neglecting changes in G. With $G = 5 \times 10^5$ kg/cm^2 and $\nu = 0.4$, τ_{PN} for such a partial dislocation in copper is then found to be 138 kg/cm^2. The corresponding tensile stress in the case of a polycrystal would be about 435 kg/cm^2, and for 65/35 alpha-brass about 1130 kg/cm^2. In view of the approximations inherent in the Peierls–Nabarro

VOL. 8 1960

model these values can be regarded as satisfactory on comparison with the data in Fig. 5, assuming $\tau_{PN} = \tau_y - \tau_{\text{chem}}$, where $\tau_{\text{chem}} = (\tau_y)_{400^\circ\text{K}}$.

Further, if it is assumed that over restricted ranges of T

$$w = w_0(1 + \alpha T), \tag{6}$$

as proposed by Petch[15], where α is a small positive constant, a linear relation between $\log(\sigma_y - \sigma_{\text{chem}})$ and T at constant composition is indicated by equation (5). Semi-log plots of $\sigma_y - \sigma_{\text{chem}}$ against T are in fact virtually straight over the whole temperature range investigated. The interpretation of the effect of alloying and temperature on the yield stress in terms of changes in the Peierls–Nabarro force thus appears to be promising.

3.2 *Linear hardening*

The rate and mechanism of hardening in the linear stage, and the strains up to which it extended, were found to be similar to those observed in copper, previously discussed by Feltham and Meakin[1]. They suggest that in face-centred cubic metals σ_c is the stress at which Cottrell–Lomer barriers cease to be effective obstacles to the propagation of slip. The temperature dependence of σ_c would then be expected to be of very nearly the same form[16] irrespective of whether the barriers are circumvented by cross-slip or broken by a mechanism of the type considered by Stroh[17]; in either case a stress-induced dislocation reaction must take place.

The variation of σ_c with temperature in the case of the break-down of the barrier in copper by Stroh's mechanism of recombination—his Fig. 4, curve (b)—is represented by Σ in Fig. 12, where

$$\Sigma \equiv (n\sigma_c/2G)^{1/2}. \tag{7}$$

In Stroh's treatment n is the number of dislocations piled up against the Cottrell–Lomer barrier, and is assumed to be proportional to σ_c/G. Σ is therefore a direct measure of σ_c/G.

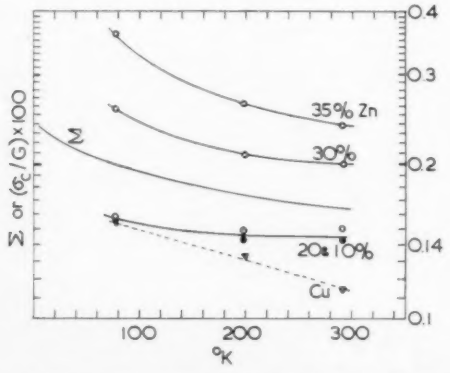


FIG. 12. Temperature dependence of σ_c/G. Σ from equation (7).

The shear modulus G, used in deriving σ_c/G, was obtained from the approximate relation

$$G = 5.25(1 - 3.7\times10^{-4}T)(1 - 0.365C_{\text{Zn}}) \times 10^5 \text{ kg/cm}^2 \tag{8}$$

constructed on the assumption that G decreased with increasing temperature linearly at a rate equal to that previously used for copper,[1] and that its composition dependence was equal to that found in brasses at room temperature. C_{Zn} is the weight fraction of zinc in the brass.

We shall attempt to explain the composition dependence of σ_c/G apparent from Fig. 9 by considering the stress required to recombine two straight partial dislocations of unit length at 0°K into a complete screw dislocation according to the reaction

$$\frac{1}{6}b\,[1\bar{2}1] + \frac{1}{6}b\,[2\bar{1}\bar{1}] = \frac{1}{2}b\,[1\bar{1}0], \tag{9}$$

assuming this to be the most important contribution to the stress in the process allowing the dislocation to escape over a barrier.

Now the force of repulsion per unit length is

$$F = (Gb_1b_2/2\pi r) - \gamma, \tag{10}$$

where b_1 and b_2 are the vectors on the left of equation (9), r the distance between the dislocations and γ the stacking-fault energy. If we write

$$F = n\tau_c(b/2) = nb\sigma_c/6 \tag{11}$$

when the dislocations recombine, with $r \simeq 2b$, i.e. about twice the width of a partial screw dislocation, and where n is the number of dislocations piled up against the mobile partial dislocation, then from equations (10) and (11)

$$n\sigma_c = (6/b)\left[\frac{Gb}{48\pi} - \gamma\right]. \tag{12}$$

On taking $G = 5 \times 10^{11}$ dyn/cm^2, $b = 2.5 \times 10^{-8}$ cm and $\gamma = 50$ erg/cm^2 at 0°K, it is apparent that a reduction of γ to zero will increase the bracketted term in equation (12) from 33 to 83 erg/cm^2, so that the change of σ_c with concentration due to the decrease of γ should not exceed $(83/33)^{1/2}$, i.e. about 1.6 times. (The square root of the ratio has been taken because, as in equation (7), n is assumed to be proportional to σ_c/G.) This factor is of the right order as may be seen from Fig. 12.* On taking account of

* The shape of the curve representing the composition dependence of σ_c (Fig. 9) suggests that the most rapid decline of γ (equation 12) takes place close to the α–β phase boundary.

the diminution of the core width, and hence of the critical value of r, with increasing solute concentrations, better agreement could be obtained. If τ_c for copper is taken to be 1100 kg/cm^2, slightly extrapolating from values obtained by Blewitt *et al.*[18] at 4.2°K, equations (11) and (12) yield $n \simeq 3$ for copper. We shall revert to the consideration of this result below.

3.3 *Parabolic hardening*

The ratio $\chi_p/\sigma_c G$, determined from values of χ_p and σ_c obtained with brasses annealed at 600 and 800°C respectively, appears to be temperature independent (Table 3). The arithmetic means, plotted in Fig. 13 against the zinc content, show a pronounced peak at about 25 per cent zinc, similar to the peaks of χ_p in the isotherms in Fig. 8.

Now, according to Feltham and Meakin[1]

$$\chi_p/\sigma_c G = (L/L_F)/\pi \qquad (13)$$

where $2L/2L_F$ is the ratio of the lengths of the slip zones above and below σ_c, respectively. An obvious interpretation of the peak shown in Fig. 13 is to relate it to a maximum of the L/L_F ratio arising from the pronounced tendency to Lueder's band formation in brasses[19] containing 20–30 per cent of zinc.*

If it is assumed that the stacking-fault energy increases uniformly with the zinc concentration,[12] the occurrence of the peaks at about 25 per cent of zinc cannot, in the main, be a consequence of the associated increase of σ_c, as is also apparent from the absence of a maximum of σ_c in Fig. 9. It may however be due to short range order localized in the immediate vicinity of the dislocation cores, i.e. a particular form of Cottrell locking, which may also account for the formation of Lueder's lines.

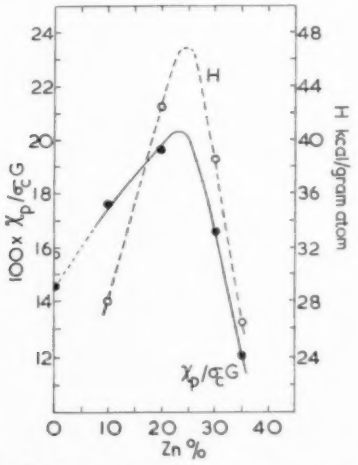


FIG. 13. Effect of zinc content on the ratio $\chi_p/\sigma_c G$ at low temperatures, and the activation energy of creep in the range 400–650°C.[20]

Evidence of short range order in alpha-brasses has been obtained by a number of workers,[22–24] and Masumoto[24] and co-workers believe that their specific-heat measurements indicate the existence of the Cu_3Zn superlattice in the ordered domains. Also, Pavlov and Pereturina[25] propose short range ordering as the cause of the occurrence of an upper yield point in the Cu–Ni system strain aged under stress in the same manner as the 80/20 brass in the present work.

While, as already mentioned, the work-hardening of the 90/10 brass above σ_c was found to be parabolic irrespective of whether the specimens had been annealed at 600 or 800°C, the hardening of brasses with higher zinc contents was virtually linear above σ_c (Fig. 1). This linearity appears to accompany the tendency to Lueder's band formation and the ability of the bands to propagate relatively unimpeded by substructure in the brasses annealed at 800°C.

The existence of dislocation pile-ups containing a large number of dislocations, which have been observed in 70/30 brass[6] and also in austenitic stainless steel,[26] is also seemingly a consequence of yielding resulting from dislocation locking due to local order. Large pile-ups have not so far been observed in pure metals. Mott[27] has in fact suggested that in pure face-centred metals Cottrell–Lomer locking would intervene, in the process of deformation, to prevent more than about six dislocations piling up against a barrier. The value $n \simeq 3$ derived in Section 3.2 for copper at low temperatures is also of this order of magnitude.

Although equations (1) and (2) were found to describe work-hardening of the brasses satisfactorily, with certain qualifications arising from the tendency to Lueder's band formation, the small values of n indicated above show that in the equation

$$L_F/n = Gb/\pi(\sigma_c - \sigma_f) \qquad (14)$$

given by Feltham and Meakin[1], in which $2L_F$ is the length of the slip zones containing n dislocations and σ_f a small stress equal to about twice the yield stress in shear of single crystals; both, L_F and n, must be regarded as being about an order of magnitude smaller than estimated by them.

If $d \equiv L_F/n$ is taken to be a measure of the distance between dislocations lying behind barriers as the applied stress reaches σ_c, then at low temperatures in

* A peak, again at about 25 per cent of zinc, has also been observed[20] in the concentration dependence of the activation energy H of high-temperature creep in the range 400–650°C, measured by the temperature cycling method.[21] (Fig. 13).

VOL. 8 1960

copper $d \simeq 5 \times 10^{-6}$ cm. As d is nearly proportional to $1/\sigma_c$ (equation 14), it would be expected to increase approximately exponentially with temperature, as may be inferred from Fig. 9.

ACKNOWLEDGMENTS

We are grateful to Dr. R. W. Armstrong for a number of valuable suggestions.

REFERENCES

1. P. Feltham and J. D. Meakin, *Phil. Mag.* **2,** 1237 (1957).
2. H. Suzuki in *Dislocations and Mechanical Properties of Crystals* (Edited by J. C. Fisher, W. A. Johnston, R. Thompson and T. Vreeland) p. 361, Wiley, New York (1957).
3. G. W. Ardley and A. H. Cottrell, *Proc. Roy. Soc.* A**219,** 328 (1953).
4. P. Feltham and G. G. Copley, *Acta Met.* **6,** 539 (1958).
5. P. Feltham and J. D. Meakin, *Phil. Mag.* **2,** 105 (1957).
6. P. A. Jacquet, *Acta Met.* **2,** 770 (1954).
7. F. W. Young, *J. Appl. Phys.* **29,** 760 (1958).
8. W. R. Hibbard and C. G. Dunn, *Creep and Recovery*, p. 52. Amer. Soc. Metals, Cleveland (1957).
9. R. S. French and W. R. Hibbard, *Trans. Amer. Inst. Min. (Metall.) Engrs.* **188,** 53 (1950).
10. R. E. Jamison and F. A. Sherrill, *Acta Met.* **4,** 197 (1956).
11. U. F. Kocks, *Acta Met.* **6,** 85 (1958).
12. P. A. Flinn, *Acta Met.* **6,** 631 (1958).
13. A. Seeger and G. Schoeck, *Acta Met.* **1,** 520 (1953).
14. F. R. N. Nabarro, *Advanc. Phys.* **1,** 371 (1952).
15. N. J. Petch, *Phil. Mag.* **3,** 1089 (1958).
16. P. Feltham, *Phil. Mag.* **3,** 806 (1958).
17. A. N. Stroh, *Phil. Mag.* **1,** 489 (1956).
18. T. H. Blewitt, R. R. Coltman and J. R. Redman in *Defects in Crystalline Solids* p. 369. Physical Society, London (1955).
19. G. R. Piercy, R. W. Cahn and A. H. Cottrell, *Acta Met.* **3,** 331 (1955).
20. P. Feltham and G. J. Copley, *Phil. Mag.* (In press).
21. P. Feltham and J. D. Meakin, *Acta Met.* **7,** 614 (1959).
22. B. G. Childs and A. D. Le Claire, *Acta Met.* **2,** 718 (1954).
23. A. D. Le Claire and W. M. Lomer, *Acta Met.* **2,** 732 (1954).
24. H. Masumoto, H. Saito and M. Sugihara, *Sci. Rep. Res. Inst. Tohoku Univ.* A**4,** 480 (1952).
25. V. A. Pavlov and I. A. Pereturina, *Fiz. Met. Metalloved., Akad. Nauk. S.S.S.R.* **6,** 717 (1958).
26. M. J. Whelan, P. B. Hirsch, R. W. Horne and W. Bollmann, *Proc. Roy. Soc.* A**240,** 524 (1957).
27. N. F. Mott, *Phil. Mag.* **43,** 1151 (1952).

ANNEALING OF X-RAY INDUCED SURFACE HARDENING IN NaCl*

R. CUYPERS and S. AMELINCKX†

Rocksalt crystals were irradiated with X-rays. The so produced surface hardening and the resoftening due to annealing at different temperatures were followed. The activation energy of the process associated with the annealing in the temperature range 150°–300°C was derived. In agreement with experimental results obtained by other workers, we find it likely to assume that clusters of point defects are the principal cause of the surface hardening. For annealing temperatures below 300°C the resoftening would mainly result from the growth in size of these aggregates, and their corresponding decrease in number.

RECUIT DU DURCISSEMENT DE SURFACE INDUIT PAR LES RAYONS X DANS DES CRISTAUX NaCl

Les cristaux de NaCl ont été irradiés à l'aide de rayons X. Le durcissement de surface ainsi obtenu et la restauration due au recuit à des températures différentes a été étudiée. L'énergie d'activation lors du recuit dans la gamme de températures entre 150 et 300°C a été déterminée. En accord avec les résultats expérimentaux obtenus par d'autres chercheurs, nous trouvons que les ségrégations de défauts ponctuels sont la cause principale du durcissement de surface.

Pour des températures de recuit sous 300°C, la restauration résulte principalement de la croissance des dimensions de ces agrégats et de la décroissance de leur nombre.

ERHOLUNG DER DURCH RÖNTGENBESTRAHLUNG VON NaCl INDUZIERTEN OBERFLÄCHENHÄRTUNG

Steinsalzkristalle wurden mit Röntgenstrahlen bestrahlt. Die entstehende Oberflächenhärtung und der Abbau derselben wurde durch Glühen bei verschieden Temperaturen verfolgt. Die Aktivierungsenergie für den mit dieser Erholung verbundenen Vorgang wurde im Temperaturbereich von 150° bis 300°C bestimmt. In Übereinstimmung mit experimentellen Ergebnissen anderer Autoren sind wahrscheinlich Ansammlungen von punktförmigen Gitterfehlern die Haupsursache der Oberflächenhärtung. Bei Glühtemperaturen unterhalb 300°C würde dann der Härteabbau haupt sächlich davon herrühren, daß die Größe dieser Aggregate wächst und ihre Anzahl entsprechend abnimmt.

VOL. 8 1960

In order to gain additional information on the mechanism of surface hardening in NaCl X-irradiated at room temperature (20°C), isothermal annealing experiments were performed by pulse annealing at a given temperature, in the range 150°–300°C. The surface microhardness of the crystals was determined at room temperature by means of a Vickers type indentor. The crystals were irradiated for 3 hr by means of unfiltered copper radiation (40 kV, 20 mA), the measured surface being at 5.5 cm of the copper target. Two methods of determining the hardness were used:

(i) measuring the diameter of the indentation,[1–3]

(ii) measuring the etched deformation pattern caused by the indentation.[3,4]

Although the second method is apparently more sensitive, the spread in the results turned out to be larger too. The two methods were applied in parallel; they lead however to essentially the same results.

Figure 1 represents the averaged isothermal annealing curves for a large number of measurements. The Vicker's hardness is plotted versus annealing time.

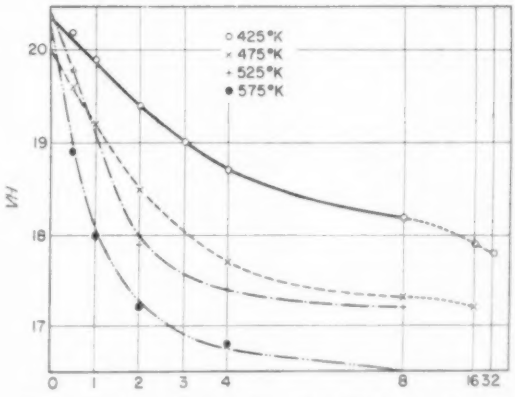


FIG. 1. Isothermal annealing of the Vickers hardness at the following temperatures: 425°K, 475°K, 525°K, 575°K.

Each point represents the average of at least fifty observations. This large number was necessary to make sure that the unavoidable scatter in this type of measurement did not mask the real value. It proved further necessary to make the indentations on the irradiated face in such a way that gradients in hardness, due to inhomogeneities in the crystal or to variations in radiation dose, were averaged out. This was achieved by placing the indentations

* Received July 13, 1959; revised November 13, 1959.

† Laboratorium voor Kristalkunde, Rozier 6, Gent, Belgium.

corresponding to a given datum point of Fig. 1 at the node points of a square grid over the whole of the irradiated area. Successive grids of indentations were shifted one with respect to the other over a sufficient distance to avoid interference of the patterns. Fig. 2 shows the fractional change in Vickers hardness during anneal.

At the beginning and at the end of each annealing experiment the hardness in the unirradiated part also was measured, to make sure that no quench hardening had occurred. It may be noted also that for annealing temperatures less than 300°C the hardness did not drop to its value in the unirradiated part of the crystal, even at annealing times of more than 1 hr (see Fig. 1).

If we assume that the effect, which causes the hardening decrease during annealing, satisfies first-order kinetics, we may write the equation

$$dy/dt = -Ky \tag{1}$$

where t is the annealing time, y represents $(\Delta H)_t/(\Delta H)_0$—where $(\Delta H)_t$ is the increase in Vickers hardness remaining after an anneal of t seconds—and where K is a rate constant dependent on the annealing temperature T by the equation

$$K = K_0 \exp(-E/kT). \tag{2}$$

In this last equation E is the activation energy and k the Boltzmann constant.

The differential equation (1) has the solution

$$y = y_0 \exp[-tK(T)]. \tag{3}$$

If then t_i and t_j are the annealing times needed to give y the value $\frac{1}{2}$ at the respective temperatures T_i and T_j, it is easy to see from equations (2) and (3) that t_i and t_j must be related to T_i and T_j by

$$\ln(t_i/t_j) = (E/k)(1/T_i - 1/T_j). \tag{4}$$

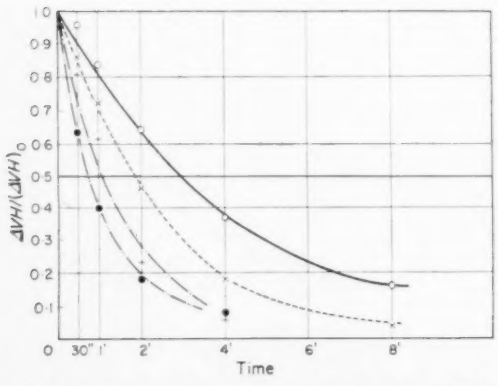


FIG. 2. Isothermal annealing of the fractional increase in Vickers hardness.

From this equation the value of the activation energy E was calculated from the graphically estimated values of t_i and t_j. The results are summarized in column 1 of Table 1.

Another method for the calculation of E comes immediately from equation (2). Indeed, if we write equation (2) for the annealing temperatures T_i and T_j, it follows that

$$E = k(1/T_i - 1/T_j)^{-1} \ln(K_j/K_i) \tag{5}$$

where K_i and K_j are the values of K corresponding to T_i and T_j. In equation (5), K_j/K_i can be calculated from equation (3) when the corresponding values of y are measured for the same annealing time t at the different annealing temperatures T_i and T_j. The values of E obtained in this manner are given in column 2 of Table 1, from which we conclude that $E = 0.19\,\text{eV} \pm 0.02\,\text{eV}$.

TABLE 1

T_i(°K)	T_j(°K)	1(eV)	2(eV)
425	475	0.200	0.202
425	525	0.208	0.199
425	575	0.193	0.192
475	525	0.200	0.198
475	575	0.186	0.186
525	575	0.175	0.171
Average value for E		0.194 eV	0.191 eV

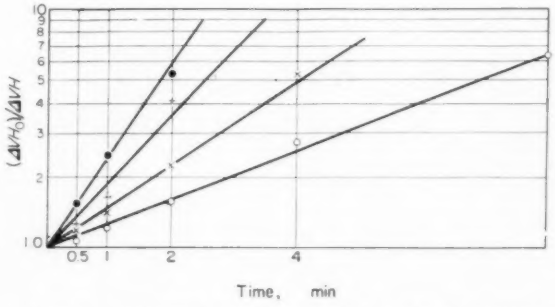


FIG. 3. Isothermal annealing of the fractional increase in Vickers hardness on a logarithmic plot.

The curves of Fig. 2 can be represented approximately by equation (3). The fit can be judged from the plots of Fig. 3, the curves should become straight lines there. The slope of these lines is a convenient measure for the rate of softening at each temperature. Another method to control the fit of the experimental data with the higher stated equations, can be given by noting that, since K must satisfy equation (2), $\ln K/K_0$ must be a linear function of $1/T$. In Fig. 4, we have plotted in logarithmic scale against $1/T$ an experimental value that is directly proportional to K/K_0.

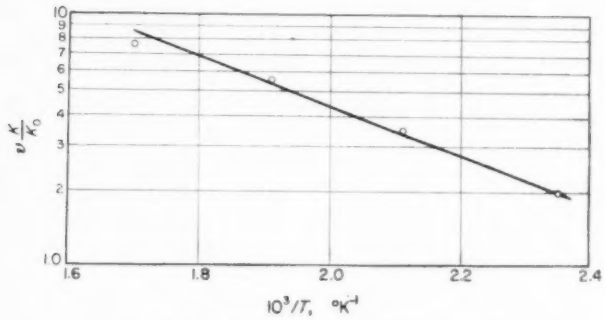


FIG. 4. Plot of rate constant versus $1/T$.

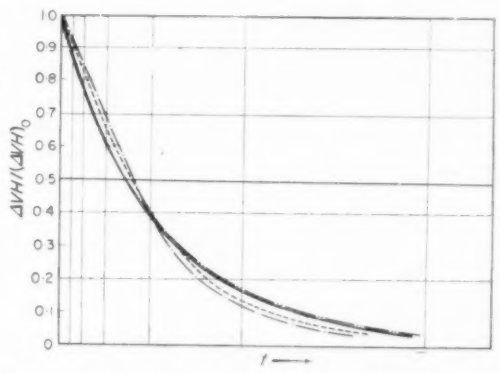


FIG. 5. Isothermal annealing of the fractional increase in Vickers hardness on a reduced time scale.

A sensitive verification of the value of this activation energy can be obtained by replotting the original annealing curves on a reduced time scale, using the activation energy as found in the indicated fashion. Such a plot is shown in Fig. 5; for $E = 0.19$ eV the best fit is found.

We also tried to interpret the results on the basis of second order kinetics, but this led to less good fit with the experimental results, although the difference was not clear cut.

Although the data simulate a simple first-order process, with a relatively good approximation, the magnitude of the apparent activation energy makes it improbable that we are measuring the true activation energy of such a process. The frequency factor derived on the basis of the found activation energy is several orders of magnitude smaller than any reasonable value. It is therefore suggested that we are dealing with a number of processes distributed in activation energy in such a way that approximately a simple process is simulated.

Isochronal annealing also pointed to a complicated process, since no well-defined annealing steps are found; instead a more continuous type of annealing takes place in the considered temperature interval. In view of previous results this can be understood if we consider that vacancy clusters of varying sizes are the hardening entities. If the softening is indeed connected with the migration and growth (eventually elimination) of these complexes, it is reasonable that since there are probably wide variations in size, there should also be a wide spread in the spectrum of activation energies.

The most reasonable assumption seems to be that the migrating defects are higher complexes of vacancies. Arguments to support this point of view are:

(a) Measurements[5,6] of the annealing of density changes and colour center concentrations in proton irradiated NaCl indicated that no appreciable loss of vacancies, but instead an agglomeration, occurs at temperatures below 200°C. Above 200°C the density increases and the R' band disappears,[6] which implies that at these temperatures, some vacancy clusters must dissociate and disappear. Some aggregates, however, seem to remain stable until temperatures above 300°C. This behaviour could explain our observation that an annealing temperature of at least 300°C is needed to reduce the hardness of the crystal to its original value.

(b) From correlated measurements of hardening and colour center absorption made in this laboratory[3] it was also concluded that aggregates of point defects were probably responsible for the hardening. This point of view was also adopted by Gilman and Johnston[7] in the case of LiF.

The present measurements are consistent with the picture postulated previously, in which the softening was associated with the growth of the aggregates and the resulting "over-aging".

ACKNOWLEDGMENTS

The authors are grateful to Professor Dr. W. Dekeyser for many helpful discussions. One of us (R. C.) is indebted to the "Centre National Belge de Chimie Physique Moléculaire" for a grant.

REFERENCES

1. YIN YUAN LI, *Acta Met.* **1,** 455 (1953).
2. D. R. WESTERVELT, *Acta Met.* **1,** 755 (1953).
3. E. AERTS, S. AMELINCKX and W. DEKEYSER, *Acta Met.* **7,** 29 (1959).
4. W. H. VAUGHAN and J. W. DAVISSON, *Acta Met.* **6,** 554 (1958).
5. K. KOBAYASHI, *Phys. Rev.* **102,** 348 (1956).
6. K. KOBAYASHI, *Phys. Rev.* **107,** 41 (1957).
7. J. J. GILMAN and W. G. JOHNSTON, *J. Appl. Phys.* **29,** 877 (1958).

VOL. 8 1960

THEORY OF CRYSTAL GROWTH AND INTERFACE MOTION IN CRYSTALLINE MATERIALS*

JOHN W. CAHN†

The theory of crystal growth for diffuse and for non-singular surfaces is re-examined. It is found that if a critical driving force is exceeded the surface will be able to advance normal to itself without needing steps; if this driving force is not exceeded lateral step motion is necessary. For extremely diffuse interfaces this critical driving force will be so small that any measurable driving force will exceed it. For sharp interfaces the critical driving force will be very large, and most growth will occur by lateral step motion. For most systems however the critical driving force should be accessible experimentally.

In addition the nature of a step in a diffuse interface is discussed and its energy calculated. The conditions for interface motion by classical nucleation or screw dislocation mechanisms are derived.

THEORIE DE LA CROISSANCE DE CRISTAUX ET MOUVEMENT D'INTERFACE DANS DES MATERIAUX CRISTALLINS

La théorie de la croissance cristalline par des surfaces diffuses et sans singularité, a été réexaminée.

On a montré que si une force motrice critique est dépassée, la surface est apte à se mouvoir normalement à elle-même sans discontinuité.

Si la force motrice n'est atteinte, un mouvement discontinu latéral est nécessaire.

Pour des interfaces très diffuses, la force de mouvement critique peut être si faible que toute force motrice mesurable la dépassera.

Pour des interfaces nettes, la force motrice critique sera très grande et une croissance importante aura lieu par mouvement latéral discontinu. Pour la plupart des systèmes cependant la force motrice critique sera accessible experimentalement.

Enfin, la nature de la discontinuité dans une interface diffuse a été discutée et son énergie calculée.

Les conditions pour un mouvement d'interface par nucléation classique ou des mécanismes de dislocation-vis en ont été déduites.

THEORIE DES KRISTALLWACHSTUMS UND DER BEWEGUNG VON GRENZFLÄCHEN VON KRISTALLINEM MATERIAL

Die Theorie des Kristallwachstums für diffuse und nicht-singuläre Grenzflächen wird überprüft. Überschreitet die treibende Kraft einen kritischen Wert, so kann sich die Fläche in der Normalen-Richtung verschieben, ohne daß Stufen nötig sind. Für extrem diffuse Grenzflächen ist der kritische Wert so klein, daß jede meßbare treibende Kraft ihn überschreitet. Für scharfe Grenzflächen wird der kritische Wert der treibenden Kraft sehr groß sein, das Wachstum wird meist durch seitliche Bewegung von Stufen erfolgen. Für die meisten Systeme sollte die kritische treibende Kraft jedoch experimentell erreichbar sein.

Zusätzlich wird die Gestalt einer Stufe in einer diffusen Grenzfläche diskutiert und ihre Energie berechnet. Die Bedingungen für eine Bewegung der Grenzfläche durch klassische Keimbildung und einen Schraubenversetzungs-Mechanismus werden hergeleitet.

In the theory of crystal growth one distinguishes[1] between two major mechanisms:

(1) The surface advances by the lateral motion of steps one interplanar distance (or some integral multiple thereof) in height. An element of surface undergoes no change and does not advance normal to itself except during the passage of a step, and then it advances by the step height. It has been customary to assume the surfaces are sharp and that the steps have steep risers. We will here consider the step more generally as the transition between two adjacent regions of a surface, parallel to each other and identical in configuration, displaced from one another by an integral number of lattice planes. It is thus possible to conceive of a step in a diffuse surface even though the step height is much smaller than the thickness of the surface.

(2) The surface advances normal to itself without needing steps. This means that in the presence of a driving force every element of surface is capable of continued change leading to advance of the surface. For a sharp surface this continued change may be considered crystal growth by the more or less uniform change over large areas of each successive new layer to fit into the crystal whereas the growth of a diffuse surface requires simultaneous changes in several successive layers.

The distinction between these mechanisms is two-fold; one is geometrical–lateral motion of steps vs. motion of the whole surface normal to itself; the other based on the time sequence of an element of surface—no motion or change except when a step passes vs. continual change. We shall term the first

* Received Movember 9, 1959.

† General Electric Research Laboratory, Schenectady, New York.

mechanism nonuniform or lateral growth, and the second uniform or normal growth.

The prediction of which mechanism will be operative in a particular system is basic to the understanding of crystal growth. Two criteria have been used to make this prediction:

(1) The first is whether or not the surface is diffuse.[1,2] A diffuse surface is one in which the change from one phase to the other is gradual, occurring over several atom planes, and is in contrast to a sharp surface for which the major property change is confined to within one interplanar distance. The diffuse interface is thought to be able to advance normal to itself. What constitutes sufficient diffuseness and whether there is an abrupt transition from one mechanism to the other with increasing diffuseness has never been fully discussed.

(2) The other criterion is based on whether or not a surface is singular.[3,4] A singular surface is one for which the surface tension as a function of orientation has a pointed minimum. Growth of singular surfaces is known to require steps, whereas it is usually believed that non-singular surfaces can continuously advance normal to themselves.

VOL. 8 1960

The two criteria for the classification of systems according to expected growth mechanism have often been used interchangeably although they do not give identical answers. Furthermore, for either of the criteria the details for borderline cases have not been explored. It is for instance quite conceivable that a surface which is non-singular in the absence of a driving force could become singular when a driving force is applied.

The purpose of the present paper is to develop another criterion for classification. Consider the necessary requirements for the appearance of lateral growth. It is evident that the lateral growth mechanism will be found when any area in the surface can reach a metastable equilibrium configuration in the presence of the driving force. It will then tend to remain in such an equilibrium configuration until the passage of a step. Afterwards the configuration will be identical except that each part of the surface has advanced by the step height. If the surface cannot reach equilibrium in the presence of the driving force, then it will continue to advance without waiting for the lateral motion of steps.

The distinguishing feature is thus the ability of the surface to reach equilibrium in the presence of the driving force. In this paper we will therefore explore the nature of this equilibrium. The conclusion that is found is that, for every surface or interface in a crystalline medium, there exists a critical driving force, which, if exceeded, will enable the surface or interface to move normal to itself, and, if not exceeded, will require the lateral growth mechanism. This criterion, based on driving force will be compared with the other two criteria already described. Much of what will be discussed will apply not only to surfaces between a solid and a fluid, but also to interfaces in a crystalline medium when the same lattice extends into both phases as in order antiphase domain boundaries and ferromagnetic and ferroelectric domain walls.

In the next section we will examine the origin and magnitude of the minima that occur in the free energies of surfaces, interfaces and domain walls when these are in a crystalline medium. We shall find a lateral growth mechanism in all cases at sufficiently low driving force, and the details of this mechanism for diffuse interfaces will be explored in subsequent sections.

1. THE LATTICE RESISTANCE TO INTERFACE MOTION

In the absence of a driving force, an interface held parallel to a low index crystallographic plane will assume an equilibrium configuration. Because the interface is in a crystalline medium the identical configuration, displaced by an integral number of lattice planes, will also be an equilibrium configuration. We can conceive of the interface being forced to advance normal to itself. It can reassume the lowest free energy configuration only when it has advanced by an integral number of interplanar distances. All stages of intermediate advancement must correspond to configurations of higher free energy. In this section we will be concerned with this increase in free energy, which gives rise to a lattice resistance to the motion of the interface and results in a critical driving force necessary for the interface to advance uniformly normal to itself.

For a sharp interface these concepts are obvious, and it is generally accepted that lateral growth will persist until extremely high driving forces. The intermediate states of uniform advance may here be thought of as the various fractional coverages of one layer of atoms. One can conceive of the chemical potential necessary to maintain a given degree of coverage.[2] This chemical potential will reach some maximum value at some intermediate coverage and this maximum value defines the critical driving force, which is expected to be quite large.

For a diffuse interface there are many conceivable paths of advance from one equilibrium position to the next. We are aided by the fact that the path of interest to us proceeds over the lowest free energy barrier. This barrier, because it also represents an

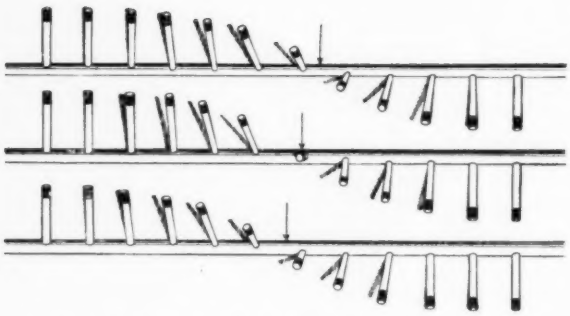


FIG. 1. Schematic drawing of a domain wall advancing. Each rod represents the direction of magnetization of a plane of atoms; each row of rods represents the domain wall at an instant of time. The arrow points to the center of the domain wall.

extremum in free energy (a saddlepoint), will also satisfy the same equilibrium equations which we use to obtain the equilibrium configuration. Fig. 1 illustrates schematically for a 180° magnetic domain wall two types of interface configurations each satisfying the conditions of equilibrium but differing in free energy. The domain wall with no spins in the hardest direction (i.e. symmetrical about an interstitial plane) is the lower in free energy.[5] Fig. 2 gives schematically the free energy as a function of position of the boundary.

We shall now concern ourselves with computing approximately the variation in free energy that an interface encounters as it is forced to advance uniformly through a crystalline medium in such a manner that the interface remains parallel to such a low index lattice plane.

We shall assume that the excess free energy F per unit area of interface in the absence of a driving force can be represented by a sum over the lattice plane of the form

$$F = a \sum_{n=-\infty}^{\infty} \{f(u_n) + Ka^{-2}(u_n - u_{n+1})^2\} \quad (1.1)$$
$$u_{-\infty} = u' \quad u_{\infty} = u'' \quad f(u') = f(u'') = 0$$

where u_n is some parameter which characterizes the nth lattice plane, u' and u'' the values of u in the two phases; a is the interplanar distance and K is a constant. For example u might represent the fraction of sites occupied, the composition, the angle which the magnetization makes with some specified direction or the degree of order. The function $f(u_n)$ represents the increase in free energy accompanying the creation of a unit volume of homogeneous material characterized by u_n from the materials reservoirs of the two bulk phases. The second term represents the additional work necessary to place such material in an environment of varying u_n and has been called the gradient energy.[6] In magnetic domain wall theory $f(u_n)$ is the crystal anisotropy energy and the second term is the exchange energy.[7] The extremals in F are obtained from the values of the u_n's given by a set of the difference equations

$$\frac{df}{du_n} + 2Ka^{-2}(2u_n - u_{n+1} - u_{n-1}) = 0. \quad (1.2)$$

Equation (1.2) may be substituted into equation (1.1) to give for the surface tension σ

$$\sigma = a \sum_n \left\{ f(u_n) - \tfrac{1}{2} u_n \frac{df}{du_n} \right\} \quad (1.3)$$

where the values of the u_n's must satisfy equation (1.2).

In general at least two sets of u_n's can be found, one corresponding to the surface tension of the equilibrium configuration, the other to the surface tension at the saddle. Because of the lattice structure, each set of u_n's is also a solution if each n is changed by an integer, corresponding to a translation of the surface by an integral number of lattice planes.

Sharp interfaces occur when the values of f for intermediate values of u are large compared to $Ka^{-2}(u' - u'')^2$. The solutions to equation (1.2) and hence σ are readily obtained. However for diffuse interfaces the solving of equation (1.2) represents considerable work, which can be reduced by an approximation which changes equation (1.2) into a differential equation.[6]

By changing the u's into a continuous variable of z, the distance normal to the boundary, we obtain for equation (1.2) the differential equation

$$\frac{\partial f}{\partial u} + 2K \frac{d^2u}{dz^2} = 0$$

which may be integrated to give

$$f = K\left(\frac{du}{dz}\right)^2$$

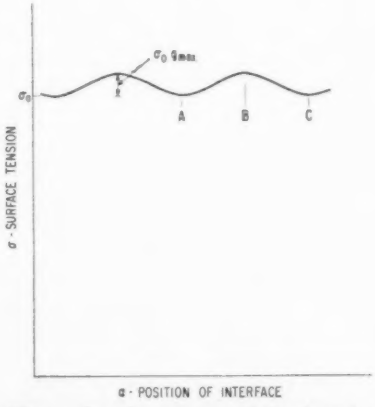


FIG. 2. The surface free energy of the domain wall of Fig. 1 as a function of its position. Minima correspond to configurations A and C, and maxima to B.

or

$$Z = \int_{u(0)}^{u(z)} \sqrt{(K/f)}\, du \tag{1.4}$$

in which u for $z = 0$ has been arbitrarily chosen.

In identifying the continuous variable $u(z)$ with the u_n's there is a certain arbitrariness in choosing the values of z corresponding to a lattice plane. Once the value of z for one lattice plane has been chosen the rest are determined. Let the value of z corresponding to the position of the 0th lattice plane be $-\alpha$. The quantity α thus gives the position of the interface relative to a fixed plane in the lattice.

Then

$$u_0 = u(-\alpha)$$

and

$$u_n = u(na - \alpha).$$

Using the method of Poisson sums* we are now in a position to evaluate the surface tension as a function of α from equation (1.3) and from the $u(z)$ obtained from a solution of equation (1.4).

$$\sigma = \int_{-\infty}^{+\infty} \left(f(u) - \tfrac{1}{2}u\frac{df}{du}\right) dz + 2\sum_{s=1}^{\infty}\left[A_s \cos\frac{2\pi s\alpha}{a} - B_s \sin\frac{2\pi s\alpha}{a}\right] \tag{1.5}$$

where

$$A_s = \int_{-\infty}^{+\infty} \left(f(u) - \tfrac{1}{2}u\frac{df}{du}\right) \cos\frac{2\pi sz}{a}\, dz$$

$$B_s = \int_{-\infty}^{+\infty} \left(f(u) - \tfrac{1}{2}u\frac{df}{du}\right) \sin\frac{2\pi sz}{a}\, dz.$$

The first term is the value of the surface tension if one assumes the interface to be in continuous medium. The second term describes the periodic variation of the surface tension as the interface is made to move uniformly through the lattice, and constitutes the lattice resistance to the motion of the interface. The main assumption in deriving this term is that the interface is described by the same function $u(z)$ regardless of the value of α. This is probably a good assumption for diffuse interfaces.[9]

In order to obtain some feeling for the magnitude of the quantities let us assume that

$$f(u) = f_0(1 - u^2)^2$$

$$u' = -1 \qquad u'' = 1.$$

Then the solution to equation (1.4) is

$$u = \tanh \sqrt{(f_0/K)}z \tag{1.6}$$

and equation (1.5) gives

$$\sigma = \frac{8}{3}\sqrt{(Kf_0)}\left\{1 + \frac{2\pi^2 K^{\frac{1}{2}}}{af_0^{\frac{1}{2}}}\sum_{s=1}^{\infty} s\left(1 - \frac{\pi^2 s^2 K}{2a^2 f_0}\right) \times \operatorname{cosech}\left(\frac{\pi^2 s}{a}\sqrt{\frac{K}{f_0}}\right)\cos\frac{2\pi s\alpha}{a}\right\}. \tag{1.7}$$

The quantity $n \equiv 2\sqrt{(K/f_0a^2)}$ may be thought of as the thickness of the interface in numbers of lattice planes. For n large equation (1.7) reduces to

$$\sigma = \frac{8}{3}\sqrt{(Kf_0)}\left\{1 - \frac{\pi^4 n^3}{2^4}\exp\left(-\frac{\pi^2 n}{2}\right)\cos\frac{2\pi\alpha}{a}\right\} \tag{1.8}$$

which shows that σ rapidly becomes insensitive to the position of the interface as n becomes large. It

---

* The Poisson sum formula[8] enables one to sum the values at periodic intervals of a function of a continuous variable

$$\sum_{n=-\infty}^{+\infty} y(na) = \frac{\sqrt{(2\pi)}}{a}\sum_{s=-\infty}^{+\infty} Y\left(\frac{2\pi s}{a}\right)$$

where $Y\left(\frac{2\pi s}{a}\right)$ is the Fourier cosine transform of y

$$Y\left(\frac{2\pi s}{a}\right) = \frac{1}{\sqrt{(2\pi)}}\int_{-\infty}^{+\infty} y(z)\cos\frac{2\pi z}{a}\, dz\,.$$

Since changing the sign of s does not affect the value of the Y's

$$\sum_{n=-\infty}^{n=\infty} y(na) = \frac{1}{a}\int_{-\infty}^{+\infty} y(z)\, dz + \frac{2\sqrt{(2\pi)}}{a}\sum_{s=1}^{\infty} Y\left(\frac{2\pi s}{a}\right).$$

The meaning of the Poisson sum formula is quite straightforward. Consider just the first two terms. We are trying to evaluate the sum of the values at periodic intervals of a function of a continuous variable. The integral of this function, the first term of the sum, is a first approximation, but it weighs all parts of the function equally heavily. The integral

$$\int_{-\infty}^{\infty} y(z)\cos\frac{2\pi z}{a}\, dz = \sqrt{(2\pi)}Y\left(\frac{2\pi}{a}\right)$$

tests whether the first term is a good approximation. It compares the value of y when z/a is close to being an integer with when it is not close to being an integer and makes a first approximation to the difference between the sum and the integral. The other terms represent higher correction terms.

The advantages of the Poisson sum method for this problem are the rapid convergence of the series for diffuse interfaces and also the ease with which the position α of the interface can be introduced. Consider the sum for various positions.

$$\sum_{n=-\infty}^{\infty} y(na - \alpha) = \frac{1}{a}\int_{-\infty}^{+\infty} y(z - \alpha)\, dz + \frac{2}{a}\sum_{s=1}^{\infty}\int_{-\infty}^{+\infty} y(z - \alpha)\cos\frac{2\pi sz}{a}\, dz$$

$$= \frac{1}{a}\int_{-\infty}^{\infty} y(z)\, dz + \frac{2\sqrt{(2\pi)}}{a}\sum_{s=1}^{\infty}\left\{Y_{\cos}\left(\frac{2\pi s}{a}\right)\cos\frac{2\pi s\alpha}{a} - Y_{\sin}\left(\frac{2\pi s}{a}\right)\sin\frac{2\pi s\alpha}{a}\right\}$$

where

$$Y_{\cos}\left(\frac{2\pi s}{a}\right) = \frac{1}{\sqrt{(2\pi)}}\int_{-\infty}^{+\infty} y(z)\cos\frac{2\pi sz}{a}\, dz$$

$$Y_{\sin}\left(\frac{2\pi s}{a}\right) = \frac{1}{\sqrt{(2\pi)}}\int_{-\infty}^{+\infty} y(z)\sin\frac{2\pi sz}{a}\, dz\,.$$

The periodic variation of the sum with α is thus conveniently expressed in terms of a Fourier series.

VOL. 8 1960

will be useful to introduce $g(\alpha) \geq 0$, a dimensionless periodic function of α defined by

$$\sigma(\alpha) = [1 + g(\alpha)]\sigma_0 \tag{1.9}$$

where σ_0 is the minimum value of σ as a function of α. The periodic part of σ is thus given by $\sigma_0 g(\alpha)$, and $g(\alpha)$ is the fractional change in surface tension from the equilibrium value for the position given by α. For that value of α, $g = 0$. The approximate equation (1.8) gives

$$g = \frac{\pi^4 n^3}{2^4} \exp\left(\frac{-\pi^2 n}{2}\right)\left(1 - \cos\frac{2\pi\alpha}{a}\right).$$

In the presence of a driving force the variation per unit area of surface in total free energy of a system due to uniform motion of the interface $\delta\alpha$ is approximately given by

$$\delta F = \left(\Delta F_v + \sigma_0 \frac{dg}{d\alpha}\right)\delta\alpha \tag{1.10}$$

where ΔF_v is the driving force, the change in free energy when the surface sweeps through a unit volume. The lateral growth mechanism is required only when there exists a value of α for which $\Delta F_v + \sigma_0(dg/d\alpha) = 0$. The maximum value of $\sigma_0(dg)/(d\alpha)$ for large n is given by $\pi\sigma_0 g_{\max}/a$. Hence

$$-\Delta F_v = \frac{\pi\sigma_0 g_{\max}}{a} \tag{1.11}$$

represents a driving force necessary to permit uniform advance of a diffuse interface. Such an advance does not need steps, and if in addition there are no diffusional barriers to motion, as in the case of a magnetic domain wall, the interface will be glissile, that is, it will be able to move without thermal activation. The free energy of the system as a function of interface position when the critical driving force is applied is shown in Fig. 3.

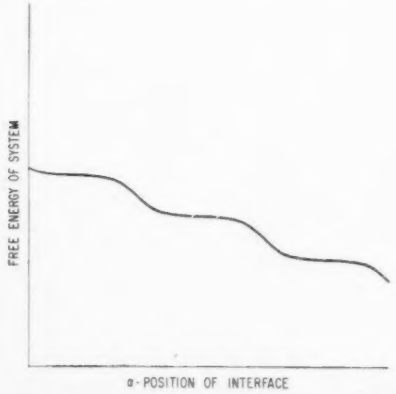


FIG. 3. The free energy of the system as a function of interface position when the critical driving force (equation 1.11) is applied.

Since the actual thickness of the diffuse interface is relatively insensitive to orientation[6] the thickness in terms of the number of lattice planes is inversely proportional to the interplanar distance a and hence directly proportional to the density of lattice sites. Thus the resistance to motion is greatest for close packed planes and zero for irrational index planes.

Although we derived $g(\alpha)$ as a function of interface thickness n for large n, the concept of $g(\alpha)$ is perfectly valid for sharp interfaces. It is possible to find a continuous function $u(z)$ in which the change from u' to u'' is confined to a distance of the order of one interplanar spacing which will adequately describe the surface at intermediate stages of uniform advance. For sharp interfaces the maximum value of $g(\alpha)$ can then be obtained directly from equation (1.1) and usually will be of the order of unity. This corresponds to a very high driving force.

At the other extreme we have the situation of a magnetic domain wall where n is of the order of one hundred. Here $g(\alpha)$ is so small that the critical driving force corresponds to undetectably small magnetic fields and any measurable driving force will exceed it. We thus find that for these extreme cases the criterion being developed in this paper agrees with the criterion based on diffuseness. But for systems having interfaces with intermediate degrees of diffuseness the critical driving force will be of measurable magnitude and both lateral and uniform growth should be observed.

It might be reasoned that when $g(\alpha)$ is sufficiently small the interface should be able to advance uniformly by thermal fluctuation. This is true if one considers a small enough area of the interface, but it is obvious that it cannot occur simultaneously over a large area. We thus are led naturally to a lateral mechanism, the mechanism of growth by two dimensional nucleation. We will next consider this mechanism and the other main mechanism of lateral growth, the screw dislocation mechanism. For both of these mechanisms we will first have to consider the nature of the step, the transition between two portions of the surface differing in degree of advancement.

2. THE FREE ENERGY OF A STEP IN A DIFFUSE INTERFACE

In the previous section it was shown that the interfacial free energy is a periodic function of the position of the interface relative to the lattice. The periodic part of the free energy becomes small compared to the surface tension as one considers more diffuse boundaries. This periodic energy represents a force tending to keep the interface

parallel to the low index crystallographic planes. It is well established that when a sharp interface is slightly inclined to a crystallographic direction, that the interface consists of large areas which follow the crystallographic direction and which are bounded by steps of height corresponding to an integral number of interplanar distances. In this section we will examine the nature and energy of the steps as we consider progressively more diffuse interfaces.

Consider an interface not quite parallel to a low index crystallographic plane. We may describe its position by giving α as a function of the x and y, the coordinates in the crystallographic plane. Then we can define the function L such that the excess free energy due the inclination of the surface is given by

$$\int \left\{ g(\alpha)\sigma_0 + L\left[\left(\frac{\partial \alpha}{\partial x}\right)^2 + \left(\frac{\partial \alpha}{\partial y}\right)^2 \right] \right\} dx\, dy\,. \qquad (2.1)$$

The first term represents the work (equation 1.9) to move the surface parallel to the low-index crystallographic plane to the position α, and the second term represents the work of inclining the surface from the low-index direction to the direction given by the x and y derivatives of α. The quantity L may be identified if we assume that $u(z)$ is independent of α and its derivatives. This gives

$$\left(\frac{\partial u}{\partial x}\right)^2 = \left(\frac{\partial u}{\partial z}\right)^2 \left(\frac{\partial \alpha}{\partial x}\right)^2 \qquad (2.2)$$

$$\left(\frac{\partial u}{\partial y}\right)^2 = \left(\frac{\partial u}{\partial z}\right)^2 \left(\frac{\partial \alpha}{\partial y}\right)^2 .$$

For a cubic lattice and a scalar u

$$L\left[\left(\frac{\partial \alpha}{\partial x}\right)^2 + \left(\frac{\partial \alpha}{\partial y}\right)^2\right] dx\, dy = dx\, dy \int_{-\infty}^{+\infty} K\left[\left(\frac{\partial u}{\partial x}\right)^2 + \left(\frac{\partial u}{\partial y}\right)^2\right] dz$$

where K has the same meaning as in equation (1).

Combining equation (2.2) with the above, we obtain

$$L = \int K\left(\frac{\partial u}{\partial z}\right)^2 dz = \tfrac{1}{2}\sigma_0 \qquad (2.3)$$

which is the result one would have obtained if one noted that the surface energy per unit area in the continuum or cubic symmetry and scalar u is independent of orientation. If we now seek a minimum for equation (2.1) for the situation that $g = 0$ for $x = \pm\infty$ and $\alpha(+\infty) - \alpha(-\infty) = a$ we obtain that

$$\frac{1}{2}\left(\frac{d\alpha}{dx}\right)^2 = g(\alpha)$$

and that the excess energy ε per unit length of step is

$$\varepsilon = \sqrt{2}\sigma_0 \int_0^a \sqrt{g}\, d\alpha \qquad (2.4)$$

or approximately

$$\frac{\varepsilon}{a\sigma_0} = \sqrt{g_{\max}}\,. \qquad (2.5)$$

One also may define a width of the step by

$$w = \frac{a}{\left(\frac{d\alpha}{dx}\right)_{\max}} = \frac{a}{\sqrt{g_{\max}}}\,. \qquad (2.6)$$

The value of w is expected to be very much larger than the thickness of the interface. This is not unreasonable even for a relatively sharp interface. For instance on a solid vapor surface it is calculated[1] that the equilibrium steps are quite ragged with jogs and holes extending over a number of atom distances, the width being greater, the greater is the equilibrium adsorption. It has usually been assumed that $\varepsilon/a\sigma_0 = 1$, but it is certainly always less than one and will be quite small for diffuse interfaces.

Since for small deviations from the crystallographic direction a surface can be represented by a series of steps, a knowledge of the step energy will enable one to derive the shape of the minima of the polar plot of the surface tension near the low angle crystallographic directions and from this shape it can be determined whether the surface can be considered singular or not.

If θ is the angle between the surface and a low index crystallographic direction and σ_0 the surface tension for a surface having the crystallographic direction then in a cubic material for θ large enough that the number of steps exceeds the intrinsic number due to thermal fluctuations.

$$\frac{\sigma}{\sigma_0} = 1 + \left(\frac{\varepsilon}{\sigma_0 a}\right)\theta = 1 + \sqrt{g_{\max}}\,\theta. \qquad (2.7)$$

3. THE THEORY OF GROWTH BY TWO DIMENSIONAL NUCLEATION

When the driving force for moving the surface is less than the critical driving force for uniform motion, the surface must advance by the motion of steps across the surface. In the absence of a screw dislocation terminating in the surface the steps are rapidly exhausted and the surface would become exactly parallel to the crystallographic plane, unless new steps can nucleate from thermal fluctuations which locally change the value of α. Classical nucleation theory considers an area of advance by one interplanar distance and surrounded by a closed step,

VOL. 8 1960

usually called a pillbox. The line tension of the step acts as force opposing the spreading of the pillbox and the pillbox will tend to disappear[10] unless

$$\frac{\varepsilon}{r} + a\Delta F_v < 0 \tag{3.1}$$

where r is the radius of the pillbox and ΔF_v is the driving force for the formation of the new phase.

The work W of forming a pillbox of critical radius r_c is

$$W = -\frac{\pi\varepsilon^2}{a\Delta F_v} \tag{3.2}$$

$$= \pi r_c \varepsilon \tag{3.3}$$

$$= -\frac{\pi}{2} r_c^2 a\Delta F_v \tag{3.4}$$

where

$$r_c = -\frac{\varepsilon}{a\Delta F_v}. \tag{3.5}$$

Because the step may be of considerable width these equations will lose their meaning if the critical radius becomes less than the width of a step. This condition gives

$$w < r_c = \frac{W}{\pi\varepsilon} \tag{3.6}$$

$$\frac{a}{\sqrt{g_{\max}}} < \frac{W}{\pi a\sigma_0\sqrt{g_{\max}}} \tag{3.6}$$

or

$$W > \pi a^2\sigma_0. \tag{3.7}$$

This condition automatically implies that

$$-\Delta F_v < \frac{\sigma_0 g_{\max}}{a} \tag{3.8}$$

or that the driving force is less, by a factor of π, than the critical driving force necessary for uniform motion (equation 1.10).

Growth by a two dimensional nucleation mechanism is expected to be measurable when W is less than 50 kT. We can therefore expect to observe growth occurring by classical two dimensional nucleation if

$$\pi a^2\sigma_0 < 50kT \tag{3.9}$$

and it will occur for a driving force less than $(\sigma_0 g_{\max})/a$. This condition for expecting a range of driving force in which observable growth by classical two dimensional nucleation is expected does not explicitly depend on the interface diffuseness.

If condition (3.8) is not met, that is, if the driving force is increased so that w is no longer less than the calculated radius of a classical nucleus then classical nucleation theory is not expected to hold. The critical nuclei are then given by particular saddle-points of the total free energy of the system as a function of $\alpha(x, y)$.

$$F = \int\left\{\alpha\Delta F_v + \sigma_0\left[1 + g(\alpha) + \tfrac{1}{2} + \left(\left(\frac{d\alpha}{dx}\right)^2 + \left(\frac{d\alpha}{dy}\right)^2\right)\right]\right\} dx\,dy.$$

This equation is the two dimensional analogue of the equation used by Cahn and Hilliard[11] for three dimensional nucleation with $(\alpha\Delta F_v + \sigma_0 g)$ the two dimensional equivalent to their quantity f, and

$$\tfrac{1}{2}\sigma_0\left[\left(\frac{d\alpha}{dx}\right)^2 + \left(\frac{d\alpha}{dy}\right)^2\right]$$

equivalent to the gradient energy. Here critical driving force is equivalent to the spinodal and it is expected that the W will go to zero continuously as $-\Delta F_v$ approaches the critical driving force. The radius of the critical nucleus is expected to decrease with increasing driving force until it equals w and then is expected to become larger again, becoming infinite at the critical driving force. The maximum required change in α is expected to remain close to a until $w = r_c$ and then with increasing driving force approach zero. Thus the critical nucleus begins to look more and more like a uniformly advancing interface.

4. THE SCREW MECHANISM IN A DIFFUSE INTERFACE

When a dislocation having a Burgers vector with a component normal to the surface intersects the surface, it gives rise to a step which must always terminate at the intersection.[1] When a driving force is applied which favours one phase over the other this step will move and because it is anchored will rotate about the dislocation. The part of the step at large distances from the dislocation will have a much greater distance to travel per revolution and so will lag behind causing the step to form a spiral. A steady state spiral will be reached after a while where the retarding forces due to the curvature of the edge and geometrical factors combine to give each part of the spiral equal angular velocity. With increasing driving force the spiral rotates more rapidly and the spiral arms are closer together. The growth velocity is given by[1]

$$G = \frac{\omega a}{2\pi}$$

and ω the angular velocity of spiral is given approximately by

$$\omega = \frac{V_\infty}{2r_c}$$

where V_∞ is the velocity of a straight step for this driving force and r_c is the radius of a two dimensional nucleus also for this driving force. The spacing between arms of the spiral is equal to $2r_c$.

This theory is independent of the assumption about the sharpness of the interface and should hold until the driving force is so large that the spacing between arms is comparable with the width of a step. This again is given by

$$w < r_c = -\frac{\varepsilon}{a\Delta F_v}$$

or

$$-\Delta F_v < \frac{\sigma_0 g_{\max}}{a}.$$

As ΔF_v becomes greater than $(\sigma_0 g_{\max})/a$ the steady state spiral arms begin to overlap giving a more or less continuous slope instead of a spiral ramp. Until the critical driving force is reached, growth must still be considered as occurring by a lateral mechanism for the advance originates at the screw dislocation.

SUMMARY AND DISCUSSION

It has been shown that the mechanism of the motion of an interface in a crystalline material depends on the driving force rather than on the nature of the interface. At sufficiently large driving forces, the interface can move uniformly without the benefit of either a nucleation or screw mechanism. What constitutes a sufficiently large driving force depends on the diffuseness of the interface, so that for very diffuse interfaces any perceptible driving force will be sufficient, whereas for sharp interfaces the necessary driving force is so large that it may be difficult to achieve.

The intuitive feeling that non-singular interfaces should be able to grow without the benefit of steps is not quite justified but in many cases the necessary driving force before this is so will be quite small. It may even be so small that the difference in driving force resulting from a nonequilibrium shape will be sufficient to let the crystal or surface approach the equilibrium shape dictated by the Wolff construction. For such a case it will never be possible to produce a crystal with flat surfaces by growing at a sufficiently low applied driving force since, if the incremental driving force due to the nonequilibrium shape is sufficiently large, it will enable the crystal surfaces to achieve the other orientations. But many non-singular surfaces will not be so extreme so that the driving force necessary to move them uniformly will be appreciable and these must rely on a nucleation or screw dislocation mechanism.

At small driving forces, the lateral growth mechanisms will be found, either the screw dislocation spiral or, in the absence of a screw dislocation, the two dimensional nucleation mechanism. The step energies and step widths for diffuse interfaces were computed. Since these steps tend to be quite wide, allowance must be made in the lateral growth mechanisms when the scale of the important features of these mechanisms becomes of the order of the step width. It was found convenient to distinguish according to the driving force $-\Delta F_v$ as follows.

(1) For $0 < -\Delta F_v < \sigma_0 g_{\max}/a$ classical lateral growth mechanisms should be observed. By this we mean that in this range the growth is governed by phenomena which can be understood in terms of a step energy ε which is independent of ΔF_v and is given by equation (2.4) or (2.5).

(2) For $\sigma_0 g_{\max}/a < -\Delta F_v < \pi\sigma_0 g_{\max}/a$ the lateral growth mechanism has to be modified to take into account that the size of the critical nucleus and the spacing of the spiral arms are comparable with the step width. In this region a gradual transition is made from classical lateral growth to uniform advance of the interface normal to itself.

(3) For $-\Delta F_v > \pi\sigma_0 g_{\max}/a$ the interface can advance normal to itself without the benefit of the lateral motion of steps.

The application of these principles to solidification kinetics will be discussed in a subsequent paper.[12]

ACKNOWLEDGMENTS

I am indebted to C. P. Bean, J. C. Fisher, G. Horvay, R. Kikuchi and D. S. Rodbell for many helpful discussions and to J. E. Hilliard and D. Turnbull for critical reviews. I am especially indebted to G. W. Sears and D. A. Vermilyea for their encouragement and continued interest.

REFERENCES

1. W. K. Burton, N. Cabrera and F. C. Frank, *Phil. Trans.* **A243,** 299 (1950).
2. K. A. Jackson in *Growth and Perfection of Crystals* (Edited by R. H. Doremus, B. W. Roberts and D. Turnbull) p. 319. Wiley, New York (1958).
3. F. C. Frank, p. 1 in Ref. (2).
4. N. Cabrera, *Disc. Faraday Soc.* **28,** 16 (1959).
5. C. P. Bean, private communication.
6. J. W. Cahn and J. E. Hilliard, *J. Chem. Phys.* **28,** 258 (1958).

VOL. 8 1960

7. F. Bloch, *Z. Phys.* **74,** 295 (1932).
8. P. M. Morse and H. Feshbach, *Methods of Theoretical Physics* Vol. 1, p. 483. McGraw-Hill, New York (1953). This method was used by F. R. N. Nabarro, *Proc. Phys. Soc.* **59,** 256 (1947) in computing the Peierls force on a dislocation.
9. J. W. Cahn and R. Kikuchi, to be published.
10. J. W. Gibbs, *Collected Works* Vol. 1, p. 325. Yale University Press, New Haven, Connecticut (1948).
11. J. W. Cahn and J. E. Hilliard, *J. Chem. Phys.* **31,** 688 (1959).
12. J. W. Cahn and G. W. Sears, to be published.

SOME ELASTIC PROPERTIES OF AN EDGE DISLOCATION WALL*

JAMES C. M. LI†

A detailed elastic theory calculation is given to reveal the stress field of a dislocation wall consisting of a finite number of uniformly spaced edge dislocations of the same slip vector. The wall is normal to the slip plane. It is found that only at distances from the wall closer than the dislocation spacing in the wall does the stress field begin to resemble that of a simple tilt boundary or of a wall containing an infinite number of dislocations. At large distances from the wall, the stress field approaches that of a single dislocation with a Burgers' vector equal to the sum of the Burgers' vectors of all dislocations in the wall. Based on the calculated stress field, the process of polygonization is illustrated and some rate laws are suggested concerning the growth of a wall and the coalescence of two walls. The interaction of solute atoms with a finite dislocation wall is discussed in terms of the dilatational strain field which is also quite different from that of an infinite wall. The strain energy of a dislocation wall is calculated and compared with that of a set of randomly distributed dislocations to confirm the energetics of polygonization. Finally, some mechanical properties are discussed in terms of the ability of a dislocation wall to resist the penetration of approaching dislocations and its contribution to the brittleness of the material.

QUELQUES PROPRIETES ELASTIQUES D'UNE PAROI DE DISLOCATION-COIN

Un calcul détaillé à partir des théories de l'élasticité permet d'établir le champ de tensions d'une paroi de dislocations-consistant en un nombre fini de dislocations-coin uniformément espacées, de même vecteur de glissement.

La paroi est normale au plan de glissement. On montre que à des distances de la paroi plus grandes que celles de l'espace entre les dislocations dans la paroi, le champ de tension ressemble à celui d'une simple frontière de rotation ou d'une paroi contenant un nombre fini de dislocations.

A des grandes distances de la paroi, le champ de tension approche celui d'une dislocation simple ayant un vecteur de Burgers égal à la somme des vacteurs de Burgers de toutes les dislocations dans la paroi. En se basant sur le champ de tensions calculées, la polygonisation est étudiée et quelques lois sont suggérées concernant la croissance d'une paroi et la connaissance de deux parois. L'interaction d'atomes en solution avec une paroi de dislocations définiés a été étudiée en partant d'un champ de dilatation qui est aussi très différent de celui d'une paroi infinie.

L'énergie de déformation d'une paroi de dislocation a été calculée et comparée avec celle d'une série de dislocations distribuées d'une manière quelconque afin de confirmer le niveau énergétique de la polygonisation.

Enfin, des propriétés mécaniques ont été discutées au point de vue de la capacité d'un mur de dislocations de résister à la pénétration ou l'approche de dislocations; sa contribution à la fragilité du matériau a été également analysée.

EINIGE ELASTISCHE EIGENSCHAFTEN EINER STUFENVERSETZUNGSWAND

Eine ausführliche elstizitätstheoretische Rechnung zur Bestimmung des Spannungsfeldes einer Versetzungswand aus einer endlichen Anzahl von Stufenversetzungen mit gleichmäßigem Abstand und gleichem Gleitvektor wird durchgeführt. Die Wand steht senkrecht auf der Gleitebene. Es ergibt sich, daß das Spannungsfeld erst bei Abständen von der Wand, die kleiner sind als der Versetzungsabstand in der Wand, anfängt einer einfachen Kleinwinkelkorngrenze oder einer Wand aus unendlich vielen Versetzungen ähnlich zu werden. Bei großen Abständen von der Wand nähert sich das Spannungsfeld der Wand demjenigen einer Einzelversetzung mit einem Burgersvektor, welcher gleich der Summe der Burgersvektoren aller Versetzungen in der Wand ist. Auf Grund des berechneten Spannungsfeldes wird der Vorgang der Polygonisation betrachtet und Geschwindigkeitsgesetze über das Wachstum einer Wand und die Vereinigung von zwei Wänden werden vorgeschlagen. Die Wechselwirkung gelöster Atome mit einer endlichen Versetzungswand wird mit Hilfe des Dilatationsfeldes diskutiert, das sich ebenfalls von demjenigen einer unendlichen Wand völlig unterscheidet. Um die energetischen Verhältnisse bei der Polygonisation zu betrachten, wird die Verzerrungsenergie einer Versetzungswand berechnet und verglichen mit derjenigen einer Anzahl statistisch verteilter Versetzungen. Schließlich werden im Zusammenhang mit der Fähigkeit einer Versetzungswand, ankommende Versetzungen aufzuhalten, einige mechanische Eigenschaften sowie der Beitrag einer Wand zur Versprödung des Materials besprochen.

INTRODUCTION

Polygonization is a very important process in the initial stages of recovery of deformed crystals. Evidence of increasing interest has been shown by repeated reviews on this and related subjects.[1–9] This recent development is mainly due to improved and new

* Received August 18, 1959; revised November 5, 1959. Presented in part before the annual meeting of the Metallurgical Society of AIME, Feb. 14–19, 1960, in New York. *J. Metals*, **12**, 72 (1960).

† Edgar C. Bain Laboratory for Fundamental Research, United States Steel Corporation Research Center, Monroeville, Pennsylvania.

VOL. 8 1960

techniques of revealing dislocations and to successful confirmation of the dislocation model of substructure boundaries. A study of polygonization will not only lead to the understanding of the recovery process but also give an opportunity to learn about other properties such as mechanical and chemical behavior of the polygonized stable boundaries. It seems desirable at this stage to supply information which can be obtained purely from the elastic theory of dislocations. This should help both the interpretation of experimental results and the design of new experiments. It is the purpose of this report to present the results of the simplest polygon boundary, namely, an edge dislocation wall. It is hoped that from the stress field of such a dislocation wall, some isothermal rate laws of polygonization can be deduced and the elastic interaction with solute atoms and some mechanical properties can be discussed.

Some previous work on the elastic properties of a dislocation wall consisting of a finite number of dislocations has been reviewed by Amelinckx and Dekeyser[10] including some of their own work. They discussed also both edge and screw dislocation walls with an infinite number of dislocations. The interaction of approaching dislocations with an infinite dislocation wall has been discussed by Li[11]. A detailed analysis of the stress field of a finite dislocation wall is not available and is the object of this communication.

THE STRESS FIELD OF A DISLOCATION WALL

The stress field of an edge dislocation wall can be obtained by adding up the stresses of individual dislocations[12]

$$\sigma_{xx} = -\frac{\mu b}{2\pi(1-\nu)} \sum_{n=1}^{N} \frac{y_n(3x^2 + y_n^2)}{(x^2 + y_n^2)^2} \tag{1}$$

$$\sigma_{yy} = \frac{\mu b}{2\pi(1-\nu)} \sum_{n=1}^{N} \frac{y_n(x^2 - y_n^2)}{(x^2 + y_n^2)^2} \tag{2}$$

$$\sigma_{xy} = \frac{\mu b x}{2\pi(1-\nu)} \sum_{n=1}^{N} \frac{x^2 - y_n^2}{(x^2 + y_n^2)^2} \tag{3}$$

where N is the total number of dislocations in the wall, μ is the shear modulus, ν is the Poisson ratio, and b is the Burgers' vector. The coordinates are such that the wall lies in the y–z plane with dislocations parallel to the z-axis. In the case when N is infinitely large, some properties of the wall have been discussed before.[11] Here we shall discuss only the case when N is finite.

At large distances from the wall, the stresses can be calculated by replacing the above summations with integrations:

$$\sigma_{xx} = \frac{\mu b}{2\pi(1-\nu)h} \left[\frac{1}{2} \ln \frac{x^2 + (y-L)^2}{x^2 + (y+L)^2} + \frac{x^2}{x^2 + (y+L)^2} - \frac{x^2}{x^2 + (y-L)^2}\right] \tag{4}$$

$$\sigma_{yy} = \frac{\mu b}{2\pi(1-\nu)h} \left[\frac{1}{2} \ln \frac{x^2 + (y-L)^2}{x^2 + (y+L)^2} + \frac{x^2}{x^2 + (y-L)^2} - \frac{x^2}{x^2 + (y+L)^2}\right] \tag{5}$$

$$\sigma_{xy} = \frac{\mu b x}{2\pi(1-\nu)h} \left[\frac{y+L}{x^2 + (y+L)^2} - \frac{y-L}{x^2 + (y-L)^2}\right] \tag{6}$$

where h is the dislocation spacing in the wall and L is one half of the height of the wall:

$$L = Nh/2. \tag{7}$$

In equations (4), (5) and (6), rectangular coordinates with the origin at the center of the wall are used.

It is seen from equation (4) that σ_{xx} is negative when $y > 0$, positive when $y < 0$ and zero when $y = 0$. The contours of σ_{xx} are shown in Fig. 1. The intercepts of these curves on the y-axis are represented by

$$y = L \tanh \frac{\pi(1-\nu)h\sigma_{xx}}{\mu b} \text{ between 0 and } L \tag{8}$$

and

$$y = L \coth \frac{\pi(1-\nu)h\sigma_{xx}}{\mu b} \text{ from } L \text{ to } \infty \quad . \tag{9}$$

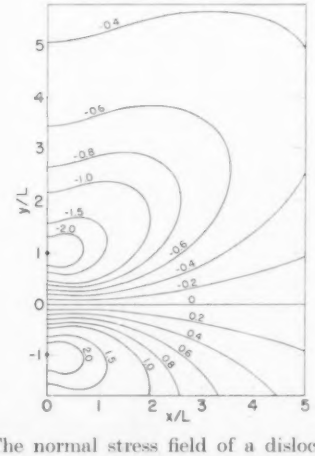


FIG. 1. The normal stress field of a dislocation wall, σ_{xx}. The wall is situated between 1 and −1 on the y-axis. Unit of stress = $\mu b/2\pi(1-\nu)h$

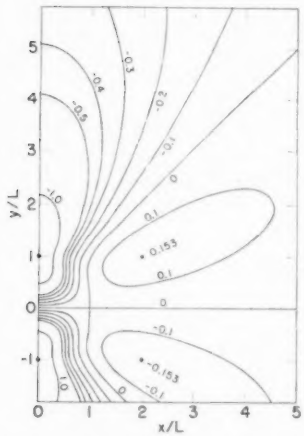


FIG. 2. The normal stress field of a dislocation wall, σ_{yy}.

It is seen that the two intercepts of each curve are reciprocals to each other as shown in Fig. 1. In fact, the y-coordinates of the two intercepts of each curve on any straight line passing through one end of the wall [(0,1) or (0, − 1)] are reciprocals to each other.

The zero stress curves for σ_{yy} are a little more complicated. The contours of σ_{yy} are shown in Fig. 2. It is seen that farther away from the zero stress curve in the x-direction, the magnitude of the stress never exceeds

$$(\tfrac{1}{2} + \tfrac{1}{2} \ln \tfrac{1}{2}) \frac{\mu b}{2\pi(1 - \nu)h}. \tag{10}$$

The arguments on the intercepts just mentioned for the case of σ_{xx} apply here also for σ_{yy}. The intercepts of these curves on the y-axis are also given by

$$y = L \tanh \frac{\pi(1 - \nu)h\sigma_{yy}}{\mu b} \text{ between 0 and } L \tag{11}$$

and

$$y = L \coth \frac{\pi(1 - \nu)h\sigma_{yy}}{\mu b} \text{ from } L \text{ to } \infty. \tag{12}$$

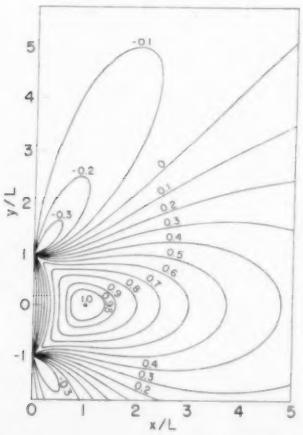


FIG. 3. The shear stress field of a dislocation wall, σ_{xy}.

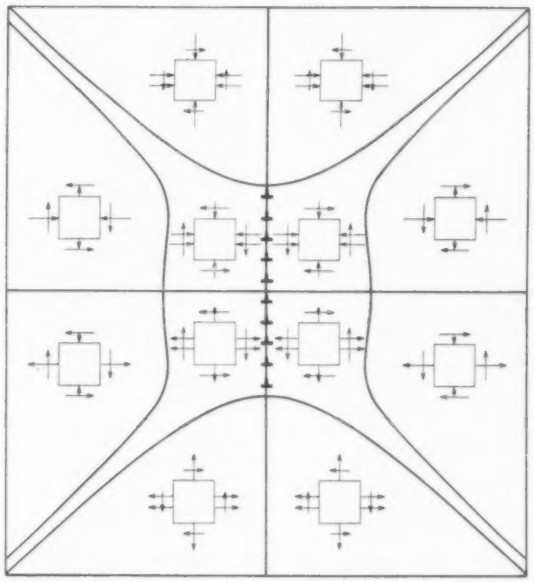


FIG. 4. The stress field of an edge dislocation wall.

The zero stress curves for σ_{xy} are represented by

$$y^2 - x^2 = L^2 \tag{13}$$

and

$$x = 0 \tag{14}$$

as shown by Nabarro[13]. The contours of σ_{xy} are shown in Fig. 3. It is seen that the shear stress never exceeds $\mu b/[2\pi(1 - \nu)h]$.

It is to be remembered that equations (4), (5) and (6) are large-distance approximations. For stresses at small distances from the wall, a combination of the infinite-wall stresses and the finite-wall stresses is necessary. We shall discuss this later. Following

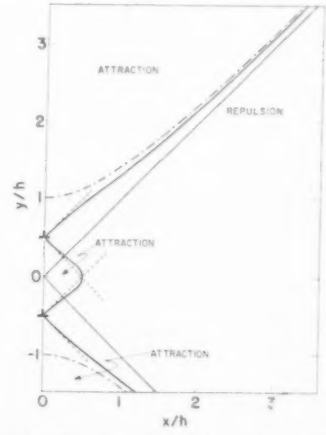


FIG. 5. The zero shear-stress curves for a two-dislocation wall.
——— Exact
— · — Nabarro approximation (equation 13)
– – – – Asymptotes for single dislocation
—— $x = \pm y$

VOL. 8 1960

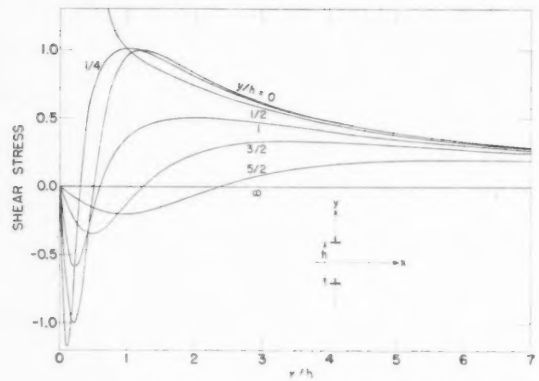


FIG. 6. The shear-stress field of a two-dislocation wall.
Unit of stress = $\mu b/2\pi(1-\nu)h$

Read[14], the stress field of a dislocation wall is summarized in Fig. 4. When $x > L$ and $y > L$, the stress field resembles that of a single dislocation. In fact, at very large distances from the wall, the stress field approaches that of a single dislocation of strength Nb situated at the center of the wall, where N is the total number of dislocations in the wall and b is the Burgers' vector of each dislocation.

To obtain some idea of the approximation of equations (4), (5) and (6), some exact calculations using equations (1), (2) and (3) are carried out for comparison. In Fig. 5 the zero shear-stress curves for a two-dislocation wall is given by, in polar coordinates (r, θ),

$$\sin^2\theta = \frac{1-\rho^2}{2} + \frac{1}{32\rho^2} \pm \sqrt{\left[\left(\frac{\rho^2}{2} - \frac{1}{2} - \frac{1}{32\rho^2}\right)^2 + \frac{1}{2}\left(1+\frac{1}{4\rho^2}\right)^2\left(\rho^2 - \frac{1}{4}\right)\right]} \tag{15}$$

where

$$\rho = r/h \tag{16}$$

or in terms of the two angles (θ_1, θ_2) between the x-axis and the lines joining each dislocation and the point of interest:

$$(\tfrac{1}{2} + \cos 2\theta_1)^2 + (\tfrac{1}{2} + \cos 2\theta_2)^2 = \tfrac{1}{2}. \tag{17}$$

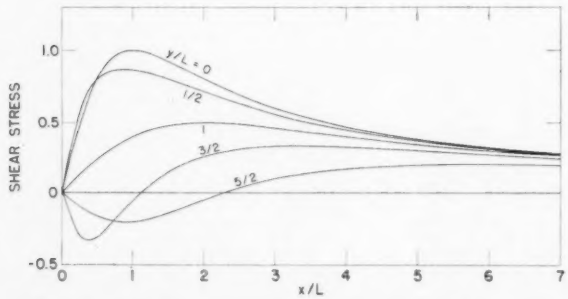


FIG. 7. The shear-stress distribution of a dislocation wall, equation (6), in the x-direction.
Unit of stress = $\mu b/2\pi(1-\nu)h$

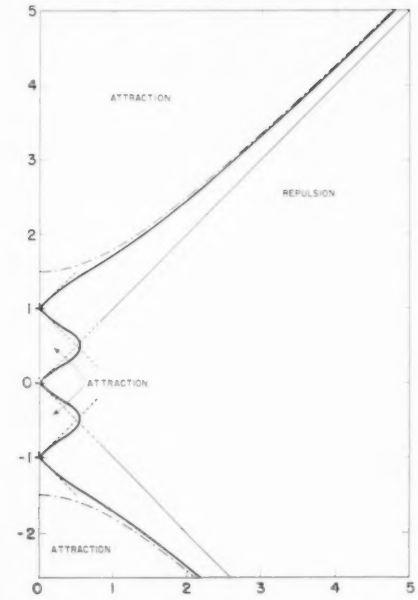


FIG. 8. The zero shear-stress curves for a three-dislocation wall.
——— Exact
— · — Nabarro approximation (equation 13)
– – – – Asymptotes for single dislocation
——— $x = \pm y$

The Nabarro approximation equation (13) is also plotted for comparison. The regions of attraction possess a negative σ_{xy} so that any edge dislocation of the same sign as those in the wall will be attracted by the wall in these regions. The repulsive regions, on the other hand, possess a positive σ_{xy}. It is seen that the Nabarro approximation does not include the small attractive region in the middle of the wall. Equation (6) gives correct stresses only after a distance of about h from the wall. This is seen from comparison of the curves in Fig. 6 and 7, in which the shear stress of a two-dislocation wall is calculated exactly and plotted in Fig. 6 and the Nabarro approximation is plotted in Fig. 7.

To see the effect of a higher wall, the zero shear-stress curves of a three-dislocation wall are plotted in Fig. 8 together with the Nabarro approximation equation (13). It is seen that the approximation is much better than in the case of the two-dislocation wall. The width of the small attractive region in the middle of the wall is now slightly more than the dislocation spacing in the wall. Since the Nabarro approximation does not include the attractive regions in the middle of the wall and since an infinite wall

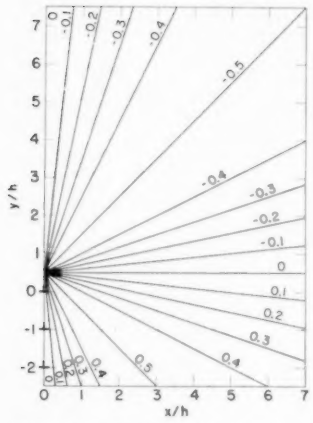


FIG. 9. The shear-stress field of a semi-infinite dislocation wall. Unit of stress $= \mu b/2\pi(1-\nu)h$

has infinitely wide attractive regions, it is important to know the size of the attractive regions of a finite wall. This will be discussed later after we discuss the stress field of a semi-infinite wall.

The stress field of a semi-infinite wall can be obtained from equations (4), (5) and (6) by letting L become infinite. Let the wall lie in the negative y-axis (y–z plane) and let the origin be the center of the first dislocation. We observe from equation (6):

$$\sigma_{xy} = -\frac{\mu b x}{2\pi(1-\nu)h} \cdot \frac{y - \frac{1}{2}h}{x^2 + (y - \frac{1}{2}h)^2}. \tag{18}$$

The contours of σ_{xy} are straight lines as shown in Fig. 9. The slopes of these straight lines are also the limiting slopes of the curves at the top of a finite wall as shown in Fig. 3. The maximum magnitude of the shear stress is $0.5\ \mu b/[2\pi(1-\nu)h]$ instead of $\mu b/[2\pi(1-\nu)h]$ of a finite dislocation wall at large distances. It is seen from equations (4) and (5) that the normal stresses of a semi-infinite wall tend to go to infinity when the height of the wall increases without limit. However, it is interesting to note that the stress field of two semi-infinite walls (made up by removing a finite number of consecutive dislocations from an infinite wall) are equivalent to a finite wall made up of the set of dislocations which were removed from the infinite wall but with a negative Burgers' vector. This is due to the fact that an infinite wall has no long-range stresses. Equations (4), (5) and (6) with a negative sign can then apply to two semi-infinite walls with the origin at the center. This is a good approximation of the stresses in the spaces between the two semi-infinite walls and enables calculation of the stress field at the middle of a finite wall.

The stress field near a finite wall can be calculated by regarding the finite wall to be constructed from removing two semi-infinite walls from an infinite wall. This leads to the following equations:

$$\sigma_{xx} = -\frac{\mu b}{2\pi(1-\nu)h} \times \left[\frac{\pi}{2} \frac{\sin\frac{2\pi y}{h}\left(\sinh^2\frac{\pi x}{h} + \sin^2\frac{\pi y}{h} + \frac{\pi x}{h}\sinh\frac{2\pi x}{h}\right)}{\left(\sinh^2\frac{\pi x}{h} + \sin^2\frac{\pi y}{h}\right)^2} + \frac{1}{2}\ln\frac{x^2 + (y + N_2 h + \frac{1}{2}h)^2}{x^2 + (y - N_1 h - \frac{1}{2}h)^2} + \frac{x^2}{x^2 + (y - N_1 h - \frac{1}{2}h)^2} - \frac{x^2}{x^2 + (y + N_2 h + \frac{1}{2}h)^2} \right] \tag{19}$$

$$\sigma_{yy} = \frac{\mu b}{2\pi(1-\nu)h} \times \left[\frac{\pi}{2} \cdot \frac{\sin\frac{2\pi y}{h}\left(\frac{\pi x}{h}\sinh\frac{2\pi x}{h} - \sinh^2\frac{\pi x}{h} - \sin^2\frac{\pi y}{h}\right)}{\left(\sinh^2\frac{\pi x}{h} + \sin^2\frac{\pi y}{h}\right)^2} + \frac{1}{2}\ln\frac{x^2 + (y - N_1 h - \frac{1}{2}h)^2}{x^2 + (y + N_2 h + \frac{1}{2}h)^2} + \frac{x^2}{x^2 + (y - N_1 h - \frac{1}{2}h)^2} - \frac{x^2}{x^2 + (y + N_2 h + \frac{1}{2}h)^2} \right] \tag{20}$$

$$\sigma_{xy} = \frac{\mu b x}{2\pi(1-\nu)h} \left[\frac{\pi^2}{2h} \cdot \frac{\cosh\frac{2\pi x}{h}\cos\frac{2\pi y}{h} - 1}{\left(\sinh^2\frac{\pi x}{h} + \sin^2\frac{\pi y}{h}\right)^2} + \frac{y + N_2 h + \frac{1}{2}h}{x^2 + (y + N_2 h + \frac{1}{2}h)^2} - \frac{y - N_1 h - \frac{1}{2}h}{x^2 + (y - N_1 h - \frac{1}{2}h)^2} \right] \tag{21}$$

The coordinates are such that one of the dislocations in the wall is taken as the z-axis and there are N_1 dislocations above it and N_2 dislocations below it.

We are now in a position to calculate the width of the attractive regions in the middle of a finite wall. For simplicity, we are only going to investigate the case where the wall consists of an even number of

VOL. 8 1960

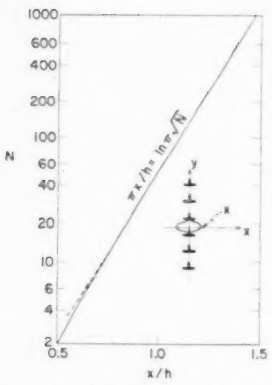


FIG. 10. The attractive region at the middle of a finite dislocation wall.

dislocations. The shear stress along the slip plane at the middle of the wall can be calculated from equation (21),

$$\sigma_{xy} = \frac{\mu b x}{2\pi(1-\nu)h}\left[-\frac{\pi^2}{h\cosh^2\dfrac{\pi x}{h}} + \frac{Nh}{x^2 + \frac{1}{4}N^2h^2}\right]. \tag{22}$$

The zero stress point can be approximated by

$$x = \frac{h}{\pi}\ln \pi\sqrt{N} \tag{23}$$

at large N. When N is small, an exact solution is possible. This can be obtained by trial and error on the following equation:

$$\left(\frac{x}{h}\right)^2 = \left(\frac{1}{2}\right)^2 + \frac{\sum_{n=0}^{\frac{1}{2}N-1} \dfrac{n(n+1)}{[(x/h)^2 + (n+\frac{1}{2})^2]^2}}{\sum_{n=0}^{\frac{1}{2}N-1} \dfrac{1}{[(x/h)^2 + (n+\frac{1}{2})^2]^2}}. \tag{24}$$

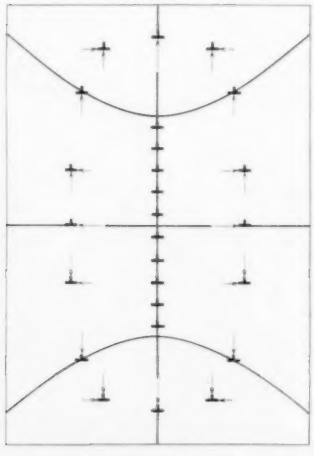


FIG. 11. The interaction of a dislocation wall with neighboring dislocations of the same slip vector. Mechanism of polygonization.

Both equations (23) and (24) are plotted in Fig. 10. It is seen that equation (23) is a very good approximation for $N > 15$. The logarithmic dependence of the width on the number of dislocations in the wall indicates that the attractive region is actually very small, only of the order of the dislocation spacing in the wall. The attractive region between any other two dislocations in the wall is even smaller than that between the two middle dislocations. This can be seen again from equation (21) at $y = \frac{1}{2}h$:

$$x = \frac{h}{\pi}\ln 2\pi\sqrt{\left[\frac{(N_1+\frac{1}{2})(N_2+\frac{1}{2})}{N}\right]} \tag{25}$$

which indicates that x is largest when $N_1 = N_2$.

POLYGONIZATION

From the stress field of a dislocation wall as shown in Fig. 4, the nature of force exerted by the wall on the neighboring dislocations can be shown in Figs. 11 and 12. The mechanism of polygonization is illustrated in Fig. 11. All the forces seem to help the important natural process of releasing the strain in the lattice through the formation of dislocation walls. Dislocations located in the attractive regions will glide to join the wall whereas those located in the repulsive regions will climb upward or downward until they reach the attractive region where they can then glide into the wall. The nature of the forces exerted by the wall on neighboring dislocations of a perpendicular Burgers' vector is shown in Fig. 12, and one can see how the dislocation wall is able to get rid of such dislocations by pushing them away through the northwest and southeast corners. Similarly, edge dislocations with the extra half plane of atoms on the right will be pushed away by the wall through the northeast and southwest corners. These

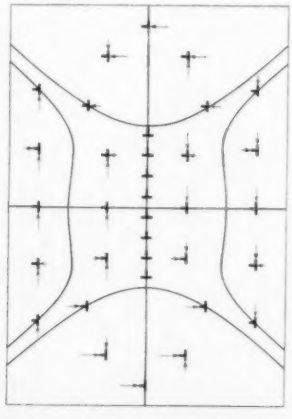


FIG. 12. The interaction of a dislocation wall with neighboring dislocations of perpendicular slip vector.

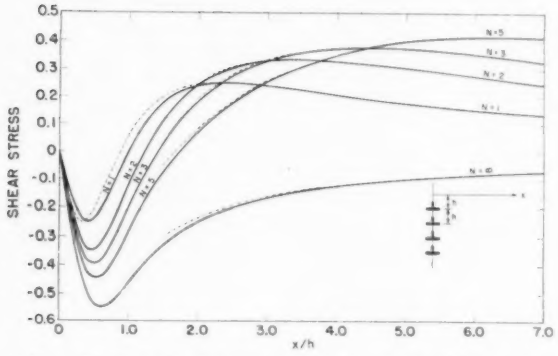


FIG. 13. The shear-stress at the top of a dislocation wall. Unit of stress $= \mu b/2\pi(1-\nu)h$.
– – – – Nabarro approximation

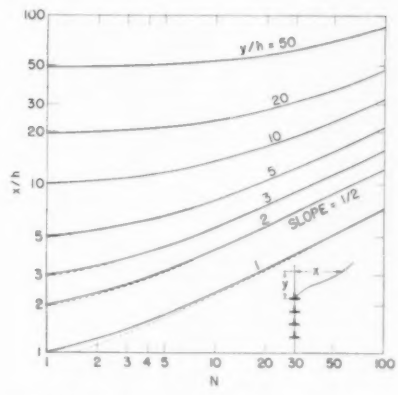


FIG. 14. The attractive region at the top of a dislocation wall.
– – – – Nabarro approximation

forces will also help the formation of other dislocation walls.

It is desirable to discuss here some possible rate laws of polygonization. Mott[15] has discussed the kinetics in terms of the climb of dislocations. At the initial stage of polygonization or when the temperature is not high enough, the dislocation walls may be formed by gliding instead of climbing of the neighboring dislocations to join the wall. In Fig. 13 is plotted the shear stress in the slip plane at one dislocation spacing above the top of the wall. This plane is most likely the one through which an additional dislocation will glide to join the wall if the angle of the wall is not going to be altered. The probability for the additional dislocations to join the wall through other planes is small because the shear stress is smaller in the other planes than it is in this plane. It is seen from Fig. 13 that the attractive region (the position where the stress is zero) increases with the number of dislocations in the wall. The solid lines are the exact stresses while the dotted lines are calculated from the Nabarro approximation, equation (6). The solid lines can be approximated within graphical error by the use of the Euler–Maclaurin summation formula:[16]

$$\sigma_{xy} = \frac{\mu b}{2\pi(1-\nu)h}\left\{\left[\frac{\xi_2}{1+\xi_2^2} + \frac{h}{2x}\frac{1-\xi_2^2}{(1+\xi_2^2)^2} - \frac{\xi_2 h^2}{6x^2}\frac{3-\xi_2^2}{(1+\xi_2^2)^3}\right] - \left[\frac{\xi_1}{1+\xi_1^2} - \frac{h}{2x}\frac{1-\xi_1^2}{(1+\xi_1^2)^2} - \frac{\xi_1 h^2}{6x^2}\frac{3-\xi_1^2}{(1+\xi_1^2)^3}\right]\right\} \tag{26}$$

where

$$\xi_1 = [y - \tfrac{1}{2}(N-1)h]/x$$

and

$$\xi_2 = [y + \tfrac{1}{2}(N-1)h]/x. \tag{27}$$

In the summation formula, only the terms involving the first derivative are included. It is interesting to note that equation (26) reduces exactly to the formula of the shear stress of a single dislocation when $N = 1$. The coordinates for equation (26) are still such that the wall is on the y-axis and the origin is at the center of the wall. Equation (26) can be used to calculate the width of the attractive region by equating the stress to zero. This is shown in Fig. 14. It is seen that the limiting slope is $\frac{1}{2}$ as indicated by the Nabarro approximation equation (6):

$$x = \sqrt{[(y-L)(y+L)]}. \tag{28}$$

If the rate of growth of the wall is proportional to the width of the attractive region at the top of the wall, we can predict a rate law of the following kind:

$$\frac{dL}{dt} = k\sqrt{L}. \tag{29}$$

This indicates that the growth of a dislocation wall is an autocatalytic process. Integration of equation (29) shows that a plot of $\sqrt{L}$ with time should be a straight line. Experimental measurement of this kind does not seem to be available in the literature.

It is interesting to note that, although the assumption that the rate of growth of the wall is proportional to the width of the attractive region may not be very realistic, other considerations lead also to the same rate law. One of them is that not all the dislocations in the attractive region can move to the wall because it requires a minimum stress (the Peierls–Nabarro stress, for example) to move a dislocation. According to Fig. 3, there exists a region of the form of a small loop within which the attractive stress exceeds some critical value. All the dislocations in the loop can therefore move into the wall. The height of such a loop is proportional to the height of the wall. The

VOL. 8 1960

average distance between the loop and the y-axis is also proportional to the height of the wall Assuming that the force acting on the moving dislocation is nearly constant during its travel to the wall (the wall is growing during its travel), we can say that the time required for a dislocation to move from a loop to the wall is proportional to the square root of the height of the wall. Such consideration leads also to the rate law equation (29). Another consideration is that the rate controlling step may not be the gliding but rather the climbing of neighboring dislocations to reach the attractive region. According to Fig. 1, the forces exerted by the wall to cause climb of neighboring dislocations are concentrated at the top and the bottom of the wall. To imagine the process, it has to be assumed that gathered at the top (or the bottom or both) are a number of dislocations within a small loop as shown in Fig. 1 but outside the attractive region of that of Fig. 3. All these dislocations will climb and if one of them gets into the attractive region it will immediately join the wall. If the angle of the wall is going to remain constant, the attractive region is pushed upward (or downward) by a distance h for each additional dislocation joining the wall. Since all the dislocations in the group will have nearly the same rate of jumping, the whole group will have to jump a distance h before any one of them can reach the attractive region and join the wall again. According to this mechanism, the rate of growth of the wall is the same as that of the climb of the group of dislocations. If the force is nearly the same during the growth of the wall, it can be expected that such a motion has a constant acceleration. This leads again to the rate law equation (29).

Since the details of the motion of a dislocation are not yet known, it should be pointed out that the above considerations can also lead to a constant speed of the growth of the wall if a constant force applied to a dislocation will produce a constant velocity of glide or climb instead of a constant acceleration. Thus, the autocatalytic growth process will have a kinetic order between 0 and $\frac{1}{2}$.

It should also be pointed out here that the climb process requires actually a constant supply or removal of vacancies. If this supply or removal of vacancies changes with the height of the wall, the deduced rate law involving the climb process will not be true. In the extreme case where there is no vacancy source or sink near a growing wall, the wall can still grow by operating its own source and sink, namely, by growing in two directions simultaneously so that the bottom will serve as a source and the top will serve as a sink of vacancies. Now the rate of growth of the wall is controlled by the rate of diffusion of vacancies. It will be apparent later in this paper that the gradient of the standard chemical potential of vacancies will be inversely proportional to the height of the wall (see Fig. 16). For simplicity, let us suppose that the concentration of vacancies is far less than the equilibrium value and that the contribution to the free energy from distribution of vacancies is not important. The gradient of the standard chemical potential of vacancies will be the driving force for diffusion. In such a case, we can predict a rate law of the following kind,

$$\frac{dL}{dt} = \frac{k'}{2L}. \tag{30}$$

Integration of equation (30) shows that a plot of L^2 with time should be a straight line. The constant k' should show a temperature dependence from which we should obtain the activation energy for diffusion of vacancies.

We shall conclude this section by discussing an important process which is the coalescence of two small angle boundaries to form a large angle boundary. This has been discussed first by Dunn and Daniels[17] and later by Gilman[18]. We shall examine first the rate of moving of the "Y" junction as shown in Fig. 15. For simplicity, let us assume that the walls are much higher than the distance $2a$ between the two low angle branches so that the stress field of the walls near the "Y" junction can be approximated by that of the semi-infinite walls as shown in Fig. 9. With this approximation, it is easily seen that if the shape

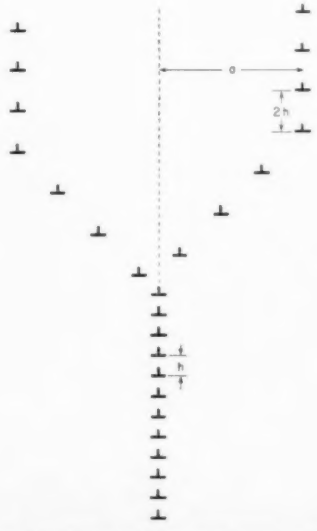


FIG. 15. The coalescence of two walls.

of the "Y" junction is to remain unchanged with time, the moving dislocations between the walls should form straight lines. According to Fig. 9, the "Y" junction will move the fastest if the line of moving dislocations makes an angle of 45° with the walls. In this manner, the force exerted on each moving dislocation, considering only the effect of two nearby walls, is $0.5\mu b/[4\pi(1-\nu)h]$ at all times. A steady state can be achieved if this force creates a constant velocity on each moving dislocation. The "Y" junction will then move with the same speed as that of the moving dislocation. This can be seen by imagining that the "Y" junction will move a distance a in the time period in which a dislocation moves from the low angle wall to the high angle wall. This consideration leads to the conclusion that the speed of the "Y" junction does not depend on the distance a. It depends only on the angle of the wall. At some specified temperature, if there exists a critical stress below which no dislocation can move, there should also exist a critical angle of the wall (or h) below which the "Y" junction can not move. Let this angle be θ_0 (or b/h_0). We can propose a possible rate law of the motion of the "Y" junction:

$$\frac{dL}{dt} = k''(\theta - \theta_0)\,. \tag{31}$$

This states that the larger the angle, the faster should be the rate. In view of the small attractive region in the middle of a wall as indicated in Fig. 10, to increase the angle of the wall by attracting dislocations into the middle of the wall is not very likely the situation. The coalescence of small-angle walls is more likely the way to increase the angle. It seems that we can discuss the kinetics of the rate of increasing the angle from the above considerations. However, the observations of Gilman[18] indicate that the rate-determining step of the coalescence of two small-angle walls is apparently the nucleation of the "Y" junction. At this stage of the understanding, since the nucleation is an unknown process, a macroscopic kinetic treatment is probably better than any microscopic hypothesis. We shall regard this nucleation as a thermally activated process. The application of the absolute reaction rate theory[19] may be appropriate. For simplicity, let us assume that at time zero, the low angle walls, having an angle θ_0, are uniformly spaced $2a_0$ apart. Therefore at any time t, the angle of the walls, θ, is related to the distance between the walls, $2a$, by

$$a = a_0\theta/\theta_0. \tag{32}$$

Suppose further that there are 2^m low-angle walls at time zero. At time t, there will be $2^m\theta_0/\theta$ walls with angle θ. To continue the coalescence at time t, $2^{m-1}\theta_0/\theta$ "Y" junctions are to be nucleated. The free energy of each "Y" junction can be roughly estimated using the semi-infinite wall approximation to be

$$\frac{2\mu a_0 b\theta^2}{2\pi(1-\nu)\theta_0} \text{ per unit length.} \tag{33}$$

The frequency factor for the process of the nucleation of the "Y" junctions from the activated state is unknown but it can be expected that it is proportional to $1/\theta$. This expectation comes from the following consideration. The activated state is assumed to be of the shape of an "X" at metastable equilibrium. To nucleate a "Y" junction, all the dislocations in "X" will have to move toward the middle. The time required for this motion is the reciprocal of the frequency factor. To start the process, several dislocations at the middle join to form a small section of a higher angle wall. The rest of the dislocations in the "X" will then move to their stable positions. This motion will probably take place in a consecutive way rather than at one time because it is more likely that the stable positions are created one by one rather than all at once. The expectation of the $1/\theta$ variation of the frequency factor will then follow from the fact that the number of dislocations in the "X" is proportional to θ^2 and that the distance which each dislocation will travel is proportional to $1/\theta$. All the above considerations lead to a rate law for the coalescence of small-angle walls of the following form:

$$\frac{d\ln\theta}{dt} = \frac{k'''}{\theta}\exp\left(-\frac{2^m\mu a_0 b\theta A}{2\pi(1-\nu)T}\right). \tag{34}$$

The constant A includes the Boltzmann constant, etc. Integration of equation (34) indicates a linear plot between the angle and log $(t + C)$ where C is the integration constant and is related to the angle of the walls at time zero. Such a rate law has been observed by Gilman[18] for zinc single crystals. The present consideration indicates that the activation energy may depend on the initial arrangement of the low angle walls. However, whether this can explain the variation of activation energy with temperature is open to question. Furthermore, in the formation or reaction of the activated complex, some climb process is probably involved. This adds an extra term into the activation energy and may be reflected in the experimental results when it is controlling. The highly idealized case just discussed is probably far from the actual situation but should serve as a

VOL. 8 1960

stimulant toward the understanding of the real problem.

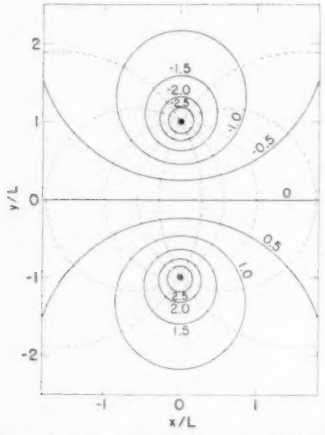


FIG. 16. The dilatational field of a dislocation wall. Unit of dilatation $= b(1-2\nu)/2\pi h(1-\nu)$

THE INTERACTION OF SOLUTE ATOMS WITH A DISLOCATION WALL

The interaction of solute atoms with an infinite edge dislocation wall has been discussed by Webb[20]. Following the same lines, we shall discuss here the case of a finite wall. The dilatational strain field of a finite wall can be obtained, as a first approximation, by integrating the dilatational strain of individual dislocations:

$$\frac{\Delta V}{V} = -\frac{b}{4\pi h}\frac{(1-2\nu)}{(1-\nu)}\ln\frac{x^2+(y+L)^2}{x^2+(y-L)^2}. \qquad (35)$$

The contours of equivalue dilatation are circles of the following type:

$$x^2+(y+L\coth\delta)^2 = (L\operatorname{cosech}\delta)^2 \qquad (36)$$

where

$$\delta = \frac{\Delta V}{V}\cdot\frac{2\pi h}{b}\cdot\frac{1-\nu}{1-2\nu}. \qquad (37)$$

This is shown in Fig. 16. The trajectories of all the circles are again circles but going through the top and bottom of the wall. These circles (or to be more exact, cylindrical surfaces) are the flow lines of solute atoms. They are also shown in Fig. 16. It is seen that the dilatational strain field of a finite dislocation wall approaches that of a single dislocation of strength Nb at large distances from the wall. At small distances from the wall, equation (35) has to be modified to reveal the dilatation of individual dislocations:

$$\frac{\Delta V}{V} = -\frac{b(1-2\nu)}{2\pi h(1-\nu)}\left[\frac{\sin(2\pi y/h)}{\sin^2(\pi y/h)+\sinh^2(\pi x/h)}\cdot\frac{\pi}{2} + \frac{1}{2}\ln\frac{x^2+(y+N_2h+\frac{1}{2}h)^2}{x^2+(y-N_1h-\frac{1}{2}h)^2}\right]. \qquad (38)$$

Equation (38) is derived in a similar way as equations (19)–(21) with the same coordinate system. Equation (38) reveals the fact that the positive dilatational regions in the upper half of the wall, or the negative dilatational regions in the lower half of the wall, are only small loops instead of long bands as in the case of the infinite wall. The width of these loops can be approximated from equation (38) in the case of large N_1 and N_2 ($N_2 > N_1$) using $y = 3h/4$,

$$x = \frac{h}{2\pi}\ln\frac{4\pi {N_1}^2}{N(\frac{3}{2}+N_2-N_1)}. \qquad (39)$$

It is seen that the width is only of the order of the dislocation spacings in the wall. The width is also largest at the middle of the wall; it becomes smaller the farther away from the middle. This indicates that only half of the dislocations in a finite wall have long-range interactions with some solute atoms. It follows also that half of the dislocations in a freshly formed finite wall may not easily be pinned by point defects. This creates a possibility of separating a wall into two half walls by external stress and thereby producing a crack as described by Stroh[21]. We shall discuss this some more later.

THE STRAIN ENERGY OF A DISLOCATION WALL

The strain energy of a finite edge dislocation wall can be estimated from equation 6, by relaxing the shear stresses along the slip planes of the dislocations so that the whole wall is removed from the crystal. Taking into account the extra stresses required to eliminate the normal stresses in the cores of the dislocations (the core has a radius r_0) and at the external surface (the specimen has a radius R) and using integration as an approximation for the summation, we obtain the strain energy of a wall relative to the perfect lattice to be:

$$\Delta F = \frac{\mu b^2}{4\pi(1-\nu)}\left\{N^2\left(\ln\sqrt{\left[\frac{R^2+4L^2}{{r_0}^2+4L^2}\right]}-\frac{1}{2}\right) + \left(\frac{R}{h}\right)^2\ln\sqrt{\left[\frac{R^2+4L^2}{R^2}\right]}\right\} \text{ per unit length of wall.} \qquad (40)$$

It is seen that this is higher than that of a set of N widely separated dislocations, which is

$$\Delta F = \frac{\mu b^2}{4\pi(1-\nu)}\left[N\left(\ln\frac{R}{r_0}-1\right)\right] \text{ per unit length of set.} \qquad (41)$$

However, consider the set of N dislocations with an

average distance r between any two of them. The strain energy of such a set is

$$\Delta F = \frac{\mu b^2}{4\pi(1-\nu)}\left[N\left(\ln\frac{R}{r_0}-1\right)+N(N-1)\times\left(\ln\frac{R}{r}-\frac{1}{2}\right)\right] \text{ per unit length of set.} \quad (42)$$

A comparison between equations (40) and (42) indicates that the strain energy of a wall is smaller than that of a set of N dislocations of the same sign distributed within a circle whose diameter is about the same as the height of the wall. This confirms the fact that polygonization is energetically feasible.

It is worth mentioning here that from equation (42) the strain energy is more likely proportional to N^2 than to N. This questions the possibility of measuring dislocation density by the amount of stored energy if there exist in the specimen local groupings of dislocations of the same sign. Special attention is required in a specimen obtained from a deformation such as bending where many dislocations of the same sign are created.

Similar calculation of the strain energy of two parallel similar walls indicates that the strain energy is generally smaller than that of a single wall resulting from coalescence of the two. A decrease of strain energy is possible only when the two walls are so close together such that the distance between them is of the order of the dislocation spacing in the wall or when the two walls are infinitely high. In the latter case, a decrease in energy per dislocation is

$$\Delta F = \frac{\mu b^2}{4\pi(1-\nu)}\ln 2 \text{ per unit length.} \quad (43)$$

This represents the maximum amount of energy per dislocation that can be reduced through the process of coalescence of two walls.

SOME MECHANICAL PROPERTIES OF A DISLOCATION WALL

The nature of the interaction of an approaching dislocation with an infinite tilt boundary has been discussed before.[11] The same characteristics should be found when the approaching dislocation reaches a distance to the wall of the order of the dislocation spacings in the wall where the stress field of an infinite wall operates. However, before this event, if the approaching dislocation comes from far away, it has to go through a stress field as shown in Fig. 3 in the case of a finite wall in order even to approach the wall. This stress field has a maximum of $\mu b/[2\pi(1-\nu)h]$ which is the external stress required to push a dislocation through in the middle slip plane of the dislocation wall. This stress is larger than that required to displace a free dislocation in an infinite wall by an approaching dislocation.[11] At this stress level, therefore, approaching dislocations will have no trouble penetrating a partially pinned finite wall.

To find out whether a finite dislocation wall is a better barrier than a set of randomly distributed dislocations before polygonization, it is interesting to compare this maximum stress with that required to push a dislocation through a square grid work of dislocations uniformly spaced $N^{1/2}h$ apart. According to the strain energy calculation in the previous section, a dislocation wall can be formed only from the dislocations within this square. The shear stress field of such a grid work of dislocations can be approximated by integration to be:

$$\sigma_{xy} = \frac{\mu b}{2\pi(1-\nu)h}\frac{1}{4L}\left\{(y-L)\ln\frac{(x-L)^2+(y-L)^2}{(x+L)^2+(y-L)^2} - (y+L)\ln\frac{(x-L)^2+(y+L)^2}{(x+L)^2+(y+L)^2}\right\}. \quad (44)$$

The coordinate system is such that the center of the square is the origin and the axes are parallel to the sides. The height of the wall, $2L$, is now also the side of the square. Equation (44) has a maximum at $y=0$ and $x=\sqrt{2}L$ with the magnitude:

$$\sigma_{xy} = \frac{\mu b}{2\pi(1-\nu)h}\tfrac{1}{2}\ln(3+2\sqrt{2}) \quad (45)$$

which is about 10 per cent smaller than that exerted by the wall. This indicates that polygonized edge dislocation walls will not significantly increase the strength of the material.

On the other hand, the presence of finite dislocation walls which terminate in the middle of a grain will contribute to the brittleness of the material. To illustrate this, the normal stress at the end of a finite wall, which is from equations (1) or (2),

$$\sigma_{xx} = \sigma_{yy} = -\frac{\mu b}{2\pi(1-\nu)}\sum_{n=1}^{N}\frac{1}{y_n} \quad (46)$$

is plotted in Fig. 17 together with the approximations obtained by integration. It is seen that the stress at $y=h$ from the last dislocation is equivalent to that of a single dislocation of strength $2b$ situated at the last dislocation when $N=5$, to that of a single dislocation of strength $3b$ when $N=10$, and to that of a single dislocation of strength $5b$ when $N=100$. The structure at the end of the wall for small h is almost like a microcrack. The propagation of such a crack may proceed at very low external stress.

VOL. 8 1960

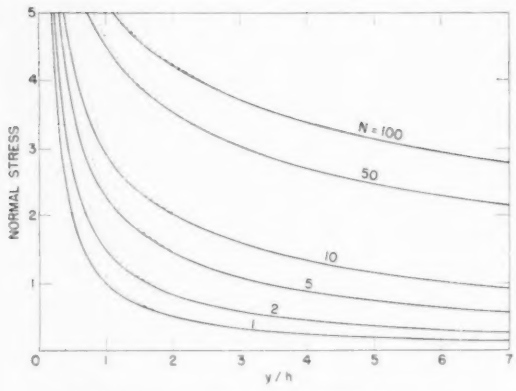


FIG. 17. The normal stress at the top of a dislocation wall.
Unit of stress $= \mu b/2\pi(1-\nu)h$

Orowan[22] has discussed ductile fracture and fatigue in terms of such a mechanism. Stroh[21] has analysed the cleavage of metal single crystals by shearing a tilt boundary.

CONCLUSIONS

(1) The stress field of a finite dislocation wall resembles that of an infinite wall at small distances (of the order of the dislocation spacing in the wall) from the wall and approaches that of a single dislocation of strength Nb (N is the total number of dislocations in the wall; each dislocation has a Burgers' vector b) at large distances from the wall.

(2) At the initial stage of polygonization when the supply of dislocations to the wall is not rate controlling, the growth process should show an autocatalytic behavior with a kinetic order between 0 and $\frac{1}{2}$.

(3) A dislocation wall can grow by operating its own source and sink of vacancies under the condition where the climb of dislocations is rate controlling. The rate of such growth process resembles that of a diffusion-controlled process, namely, the square of the height of the wall being linear with time.

(4) The rate of coalescence of two walls is probably controlled by the nucleation of a "Y" junction. The experimental rate law, namely that the angle of the wall is linear with the logarithm of time, can be explained if it is assumed in the reaction of the activated complex that a consecutive motion of the dislocations takes place during the nucleation of a "Y" junction.

(5) The dilatational strain field of a dislocation wall is such that the flow lines of point imperfections are circular arcs passing through the two ends of the wall. The fact that the positive dilatational regions in the upper half of the wall or the negative dilational regions in the lower half of the wall are only small loops near the core of the dislocations indicates that only half of the wall has long range interactions with certain solute atoms. It follows that half of the dislocations in a freshly formed wall may not be easily pinned by point defects.

(6) The strain energy of a dislocation wall of "N" dislocations is less than that of a set of the same number of dislocations distributed within a circle whose diameter is the same as the height of the wall.

(7) The ability of a dislocation wall to resist penetration of foreign dislocations from a distance larger than the height of the wall is slightly (about 10 per cent) more than that of a dislocation grid work formed by the same number of dislocations uniformly distributed in a square whose side is the same as the height of the wall. This indicates that polygonized edge dislocation walls will not significantly increase the strength of the material.

ACKNOWLEDGMENT

The author wishes to thank Dr. H. Wilsdorf of the Franklin Institute for suggesting this calculation and Drs. L. S. Darken, R. A. Oriani, Professors E. R. Parker and T. Vreeland, Jr., for some discussions and comments.

REFERENCES

1. R. KING and B. CHALMERS, *Progr. Metal Phys.* **1,** 127 (1949).
2. R. W. CAHN, *Progr. Metal Phys.* **2,** 151 (1950).
3. A. GUINIER and J. TENNEVIN, *Progr. Metal Phys.* **2,** 177 (1950).
4. C. CRUSSARD, F. AUBERTIN, B. JAOUL and G. WYON, *Progr. Metal Phys.* **2,** 193 (1950).
5. B. CHALMERS, *Progr. Metal Phys.* **3,** 293 (1952).
6. E. OROWAN, in *Dislocations in Metals* (Edited by M. COHEN) p. 176. Amer. Inst. Min. (Metall.) Engrs. (1954).
7. J. FRIEDEL, *Les Dislocations* p. 190. Gauthier-Villars, Paris (1956).
8. P. B. HIRSCH, *Progr. Metal Phys.* **6,** 236 (1956).
9. S. AMELINCKX and W. DEKEYSER, *Solid State Physics* **8,** 327 (1959).
10. Ref. (9), p. 396.
11. J. C. M. LI, to be published in *Acta Met.*
12. A. H. COTTRELL, *Dislocations and Plastic Flow in Crystals*, p. 34. Clarendon Press, Oxford (1953).
13. F. R. N. NABARRO, *Advanc. Phys.* **1,** 269 (1952).
14. W. T. READ, JR., *Dislocations in Crystals*, p. 118, McGraw-Hill, New York (1953).
15. N. F. MOTT, *Proc. Phys. Soc., Lond.* B**64,** 729 (1951).
16. J. E. MAYER and M. G. MAYER, *Statistical Mechanics*, p. 431. Wiley, New York (1940).
17. C. G. DUNN and F. W. DANIELS, *Trans. Amer. Inst. Min. (Metall.) Engrs.* **191,** 147 (1951).
18. J. J. GILMAN, *Acta Met.* **3,** 277 (1955).
19. S. GLASSTONE, K. J. LAIDLER and H. EYRING, in *The Theory of Rate Processes*. McGraw-Hill, New York (1941).
20. W. W. WEBB, *Acta Met.* **5,** 89 (1957).
21. A. N. STROH, *Phil. Mag.* **3,** 497 (1958).
22. Ref. (6), p. 188.

THE ω-PHASE IN ZIRCONIUM BASE ALLOYS*

B. A. HATT and J. A. ROBERTS†

The metastable ω-phase in zirconium base alloys has been found to be truly hexagonal with $c/a = 0.622 \pm 0.002$. The orientation relationships with respect to the parent β-phase (b.c.c.) are

$$\langle 0001 \rangle_\omega \parallel \langle 111 \rangle_\beta$$
$$\langle 2\bar{1}\bar{1}0 \rangle_\omega \parallel \langle \bar{1}01 \rangle_\beta.$$

The interpretation of X-ray data from high solute content alloys quenched from the β-phase indicates that the ω formed during quenching is heavily faulted. The ω structure in this state is designated diffuse ω. A model for the $\beta \rightarrow \omega$ transformation which satisfactorily accounts for the observed diffraction effects is developed. This is based on the gliding of $\{112\}_\beta$ planes in $\langle 111 \rangle_\beta$ directions in a distinct sequence. The magnitude of the glide component is realistically altered to account for intensity differences in the diffractions from diffuse ω and bulk ω.

LA PHASE ω DANS LES ALLIAGES DE ZIRCONIUM

On a montré que la phase métastable ω dans des alliages de zirconium était hexagonale avec un rapport $c/a = 0{,}622 \pm 0{,}002$. Les relations d'orientation avec la phase β (b.c.c.) sont

$$\langle 0001 \rangle_\omega \parallel \langle 111 \rangle_\beta$$
$$\langle 2\bar{1}\bar{1}0 \rangle_\omega \parallel \langle \bar{1}01 \rangle_\beta.$$

L'interprétation d'essais aux rayons X à partir d'alliages riches en éléments en solution trempés à partir de la phase β, indique que la phase ω formée au cours de la trempe contient de nombreuses fautes d'empilement.

La structure ω dans cet état est indiquée comme phase ω diffuse.

Un modèle pour la transformation $\beta \rightarrow \omega$ qui satisfait l'ensemble des effets de diffraction observés, a été développé. Il est basé sur le glissement des plans $\{112\}_\beta$ dans des directions $\langle 111 \rangle_\beta$ suivant une séquence définie.

La grandeur de la composante du glissement peut être altérée, ce qui explique les différences d'intensité lors de la diffraction de la phase diffuse ω ou de la phase ω massive.

DIE ω-PHASE IN LEGIERUNGEN AUF ZIRKON-BASIS

Die metastabile ω-Phase von Legierungen auf Zirkon-Basis erwies sich als echt hexagonal mit $c/a = 0{,}622 \pm 0\,002$. Die Orientierungsbeziehungen in Bezug auf die β-Phase (kubisch-raumzentriert; aus ihr entsteht die ω-Phase) sind

$$\langle 0001 \rangle_\omega \parallel \langle 111 \rangle_\beta$$
$$\langle 2\bar{1}\bar{1}0 \rangle_\omega \parallel \langle \bar{1}01 \rangle_\beta.$$

Die Deutung der Röntgenmessungen an Legierungen mit hohem Zusatzgehalt, die von der β-Phase abgeschreckt wurden, zeigt, daß die beim Abschrecken gebildete ω-Phase sehr fehlerhaft ist. Die ω-Struktur wird in diesem Zustand als diffus bezeichnet. Es wird ein Modell für die Umwandlung $\beta \rightarrow \omega$ entwickelt, das die beobachteten Beugungseffekte zur Genüge erklärt. Es basiert darauf, daß $\{112\}_\beta$-Ebenen in bestimmter Reihenfolge in $\langle 111 \rangle_\beta$-Richtungen gleiten. Die Größe der Gleitkomponente wird der Wirklichkeit so angepaßt, daß die Intensitätsdifferenzen der Interferenzen von diffuser und massiver ω-Phase erklärt werden.

INTRODUCTION

The quenched high temperature β-phase of certain titanium and zirconium alloys transforms via an intermediate phase, designated ω, on ageing to the equilibrium state. Under certain conditions the ω-phase may be obtained in a state of metastable equilibrium. The first part of this paper concerns a detailed crystallographic study of the metastable ω-phase in a Zr–7 at.% vanadium alloy. The second part of the paper is devoted to the interpretation of the diffuse ω diffractions observed in high solute content alloys in the as-quenched condition and in the early stages of ageing. This interpretation leads to the advancement of a possible mechanism for the formation of the ω-phase.

1. THE CRYSTAL STRUCTURE OF THE METASTABLE ω-PHASE

Previous workers have made crystallographic studies of the ω-phase as it occurs in titanium base alloys. Austin and Doig[1] suggest that the ω-phase is b.c.c. with side three times that of the basic β b.c.c. cell. Silcock *et al.*[2] and Bagaryatskii *et al.*[3] independently proposed a hexagonal structure based on the hexagonal (rhombohedral) unit cell, which is an alternative unit cell for a b.c.c. lattice. The crystal structure of the ω-phase in zirconium base alloys to be

* Received October 13, 1959.

† Fulmer Research Institute Limited, Stoke Poges, Bucks.

VOL. 8 1960

presented here is based on that of Silcock and Bagaryatskii and their interpretation is briefly described.

Figure 1(a) shows how the three possible unit cells for a b.c.c. lattice are related. The b.c.c. lattice is outlined by the fine lines, the heavy lines show the rhombohedral cell and the hatched lines the base of the hexagonal cell. Fig. 1(b) is a projection of the atoms on to a $\{111\}_\beta$ plane showing the hexagonal cell which is oriented with respect to the β cell with

$$\langle 0001\rangle_{\text{hex}} \,||\, \langle 111\rangle_{\text{b.c.c.}}$$
$$\langle 2\bar{1}\bar{1}0\rangle_{\text{hex}} \,||\, \langle \bar{1}01\rangle_{\text{b.c.c.}}$$

thus there are four orientations of the hexagonal cell, each with a $\langle 0001\rangle_{\text{hex}}$ parallel to a $\langle 111\rangle_{\text{b.c.c.}}$ of the β. The cell parameters are related as follows:

$$a_{\text{hex}} = \sqrt{2}\, a_{\text{b.c.c.}}$$
$$c_{\text{hex}} = \tfrac{1}{2}\sqrt{3}\, a_{\text{b.c.c.}}$$
$$\therefore \qquad c/a = \tfrac{1}{2}\sqrt{(3/2)} = 0.613.$$

The atomic positions in the hexagonal cell are (0,0,0); $\pm(\frac{2}{3},\frac{1}{3},\frac{2}{3})$.

Both Silcock and Bagaryatskii chose the above hexagonal cell with $c/a \simeq 0.613$ and proposed new atomic positions:

$$(0,0,0);\ \pm(\tfrac{2}{3},\tfrac{1}{3},\tfrac{1}{2})$$
$$(0,0,0);\ \pm(\tfrac{2}{3},\tfrac{1}{3},0.52)$$

respectively for the ω-phase. These two structures differ in that the atoms near the plane $z = \frac{1}{2}$ lie in the plane for Silcock's structure but alternately 0.02 above and below in Bagaryatskii's structure.

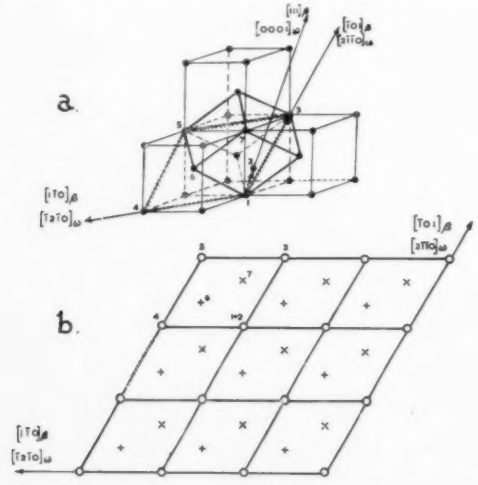


FIG. 1. (a) Three possible unit cells for a body-centred cubic structure.
——— b.c.c. lattice
——— Rhombohedral lattice
–|–|– Base of hexagonal lattice
(b) A projection of the atoms in a b.c.c. structure onto {111} plane.

		β	ω
○	Atom at	000	000
×	Atom at	$\frac{2}{3}\frac{1}{3}\frac{2}{3}$	$\frac{2}{3}\frac{1}{3}\frac{1}{2}$
+	Atom at	$\frac{1}{3}\frac{2}{3}\frac{1}{3}$	$\frac{1}{3}\frac{2}{3}\frac{1}{2}$

The atoms numbered are common to both (a) and (b).

It can be shown that provided $c/a = 0.613$ and that the four hexagonal orientations have developed to the same extent, then both the cubic and hexagonal interpretations of ω will show cubic Laue symmetry. Thus it is only possible to distinguish between the cubic and hexagonal structures by detailed intensity measurements. However if $c/a \neq 0.613$ extra diffractions will occur which provide an alternative method of discriminating between the two structures.

Preliminary work[4] on polycrystalline material by the present authors showed that the ω diffractions in Zr-base alloys could be best explained on a hexagonal cell with $c/a > 0.613$ and this interpretation has been verified in detail by the single crystal studies to be described.

Experimental results

Single crystals were oriented from Laue photographs with $\langle 001\rangle_\beta$ coincident with the oscillation axes and $\langle 100\rangle_\beta$ coincident with the incident X-ray beam. Since ω is oriented with respect to β, a specimen which is fully transformed to ω still shows cubic Laue symmetry and can thus be oriented in terms of the original β. Oscillation and Weissenberg photographs were taken with filtered Cu$K\alpha$ and monochromatic Mo$K\alpha$ radiation with the $\langle 100\rangle_\beta$ oscillating from 0° to 40° to the direct X-ray beam.

The diffractions recorded in this way did not lie on straight layer lines as would be expected if ω were cubic or hexagonal with the ideal value of $c/a = 0.613$. Since Debye–Scherrer photographs from polycrystalline material had indicated a hexagonal cell with $c/a > 0.613$ and equal to 0.622 in the metastable state, the single crystal diffractions were compared with those which would be obtained from four orientations of a hexagonal cell with $c/a = 0.622$. The diffractions were first indexed on a b.c.c. cell with lattice parameter three times the β lattice parameter. These cubic indices were then transformed to hexagonal indices corresponding to the hexagonal orientations with

$$\langle 0001\rangle_\omega \,||\, \langle 111\rangle_\beta$$
$$\langle 2\bar{1}\bar{1}0\rangle_\omega \,||\, \langle \bar{1}01\rangle_\beta$$

and

$$a_\omega = \sqrt{2}\, a_\beta, \qquad c_\omega = \tfrac{1}{2}\sqrt{3}\, a_\beta \text{ by the matrix}$$

Cubic → Hexagonal

$$\begin{vmatrix} \bar{\frac{1}{3}} & 0 & \frac{1}{3} \\ \frac{1}{3} & \frac{1}{3} & 0 \\ \frac{1}{6} & \frac{1}{6} & \frac{1}{6} \end{vmatrix}.$$

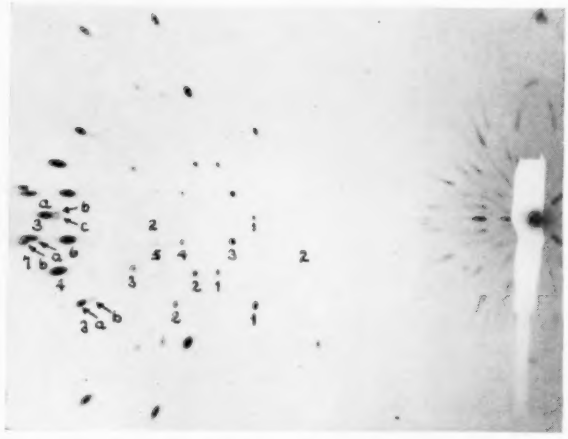


FIG. 2. Oscillation photograph of a single crystal of Zr–7 at.% V with filtered Cu$K\alpha$ radiation. The crystal oscillated about $\langle 001\rangle_\beta$ with the $\langle 100\rangle_\beta$ oscillated $0 \rightarrow 46°$ to the direct X-ray beam. The crystal was water quenched after 2 hr at 920°C and then aged 30 min at 400°C.

These hexagonal indices were then retransformed to indices corresponding to cubic axes, parallel to the β axes, but related to the hexagonal cell by

$$a_\omega = \sqrt{2}\, a'_\beta$$

$$c_\omega = 0.622\, a'_\beta \neq \tfrac{1}{2}\sqrt{3}\, a_\beta$$

where a'_β is the lattice parameter of a new cubic cell and the transformation matrix is

Hexagonal →	Cubic		
	$\bar{1}$	1	1.97
	$\bar{1}$	$\bar{2}$	1.97
	2	1	1.97

The difference between the two sets of cubic indices indicates the change in the positions of the diffractions resulting from c/a changing from 0.613 (ideal) to 0.622. On oscillation photographs about $\langle 001\rangle_\beta$, the axial ratio change shows as small deviations of the diffractions from the straight layer line positions, and the separation of superimposed diffractions. Fig. 2 is a film taken with Cu$K\alpha$ of a Zr–7.0 at.% V specimen aged ½ hr at 400°C and consisting of ~98 per cent ω. Table 1 gives the analysis of this film. Here the (hkl) cubic indices for $c/a = 0.613$ are compared with those for $c/a = 0.622$ together with the observed l-indices. The agreement between the observed values and those corresponding to $c/a = 0.622$ is considered adequate proof that β transforms to four hexagonal cells with $c/a \sim 0.622$ and oriented with respect to β with

$$\langle 0001\rangle_\omega \,||\, \langle 111\rangle_\beta$$
$$\langle 2\bar{1}\bar{1}0\rangle_\omega \,||\, \langle \bar{1}01\rangle_\beta.$$

Table 1 also gives the F^2 values for the atomic positions

$$(0,0,0);\ \pm(\tfrac{2}{3},\tfrac{1}{3},\tfrac{1}{2}).$$

Apart from angular factors these values are proportional to the intensities of the diffractions. No detailed intensity measurements have been made but visual inspection indicates that the intensities calculated from these atomic positions give satisfactory agreement with observed intensities. Some idea of the permissible movements in the c direction of the atoms in the positions $\pm(\frac{2}{3},\frac{1}{3},\frac{1}{2})$ as visualized by Bagaryatskii can be seen from Table 2, where the intensities of the zero layer diffractions have been calculated for atomic positions (0,0,0); $\pm(\frac{2}{3},\frac{1}{3},0.52)$. Hence the original $(12, 0, 0)_\omega$ (cubic indices) which consists of the following two diffractions when $c/a = 0.622$

$$\text{2(a), Table 2,} \begin{cases} (11.92,\ 0.08,\ \overline{0.08}) \\ (11.92,\ \overline{0.08},\ \overline{0.08}) \end{cases}$$

$$\text{2(b), Table 2,} \begin{cases} (11.92,\ 0.08,\ 0.08) \\ (11.92,\ \overline{0.08},\ 0.08) \end{cases}$$

will have zero intensity for atomic positions (0,0,0); $\pm(\frac{2}{3},\frac{1}{3},\frac{1}{2})$ but will have an intensity proportional to 0.44 for atomic positions (0,0,0); $\pm(\frac{2}{3},\frac{1}{3},0.52)$ This intensity is greater than half the intensity of the adjacent $(4\bar{2}\bar{2}3)$ diffraction. A very weak single diffraction is recorded near this position on some films although it has not the above intensity and is not split. It is thought that this weak diffraction corresponds to a very small amount of β. Thus there is no evidence to indicate rumpling of the atoms near the plane $z = \frac{1}{2}$.

The X-ray examination of single crystal specimens of aged Zr–Nb alloys in the range 8–20 at.% Nb revealed that the metastable ω-phase has an identical crystal structure to that described above for the Zr-7 at.% V alloy. The axial ratio was found to be 0.622 ± 0.002 but the lattice spacing values are dependent on alloy composition and ageing temperature.

Additional evidence supporting the hexagonal version of the crystal structure has been obtained from a Zr–8 at.% Nb single crystal specimen which had been strained at 400°C while in the metastable ω condition. On examination at room temperature it was found that the ω developed on only two of the four possible orientations.

VOL. 8 1960

TABLE 1

Ident. No.	*hkil*	Orient.	F^2	*hkl* cubic $c/a = 0.613$	*hkl* cubic $c/a = 0.622$ calculated *h*	*k*	*l*	observed *l*
Zero layer, left-hand side of direct beam								
1	$3\bar{1}22$	1	0	930	8.94	$\bar{2}.94$	$\bar{0}.06$	—
	$3\bar{4}11$	2	4	930	8.96	$\bar{3}.04$	$\bar{0}.04$	0*
	$1\bar{2}3\bar{2}$	3	0	930	8.94	$\bar{2}.94$	0.06	—
	$3\bar{4}11$	4	4	930	8.96	$\bar{3}.04$	0.04	0*
β		1, 2, 3, and 4	9	$3\bar{1}0$				
2	$\bar{4}042$	1	0	12,0,0	11.94	$\bar{0}.06$	$\bar{0}.06$	Weak diffractions on some films
	$\bar{4}402$	2	0	12,0,0	11.94	$\bar{0}.06$	$\bar{0}.06$	
	$0\bar{4}42$	3	0	12,0,0	11.94	$\bar{0}.06$	0.06	
	$\bar{4}402$	4	0	12,0,0	11.94	$\bar{0}.06$	0.06	
β		1, 2, 3 and 4	9	400				
3b	$\bar{4}223$	1	1	12,6,0	11.91	$\bar{5}.9\bar{1}$	$\bar{0}.09$	$\bar{0}.10$
a	$\bar{4}621$	2	4	12,6,0	11.96	$\bar{6}.04$	$\bar{0}.04$	0*
c	$2\bar{2}43$	3	1	12,6,0	11.91	$\bar{5}.9\bar{1}$	0.09	0.10
a	$\bar{4}62\bar{1}$	4	4	12,6,0	11.96	$\bar{6}.04$	0.04	0
β		1, 2, 3 and 4	9	420				
1st layer, left-hand side								
2	$2\bar{1}\bar{1}2$	1	9	7,4,1	6.94	$\bar{3}.94$	0.94	0.92
3	$3\bar{0}\bar{3}2$	1	9	10,1,1	9.94	$\bar{0}.94$	0.94	0.92
	$3\bar{3}02$	2	9	10,1,1	9.94	$\bar{0}.94$	0.94	
4	$\bar{3}52\bar{1}$	2	4	10,5,1	9.96	$\bar{5}.04$	0.96	0.93
	$1\bar{3}\bar{4}2$	3	0	11,2,1	10.94	$\bar{1}.94$	1.06	—
	$4\bar{3}\bar{1}2$	4	0	11,2,1	10.94	$\bar{1}.94$	1.06	—
5	$\bar{4}5\bar{1}1$	4	1	11,4,1	10.96	$\bar{4}.04$	1.04	1.05
6	$4\bar{1}52$	1	9	13,2,1	12.94	$\bar{2}.06$	0.94	0.93
	$\bar{4}5\bar{1}2$	2	9	13,2,1	12.94	$\bar{2}.06$	0.94	
7a	$\bar{4}313$	2	4	13,4,1	12.91	$\bar{3}.9\bar{1}$	0.91	0.87
b	$\bar{4}133$	4	4	11,8,1	10.91	$\bar{7}.9\bar{1}$	1.09	1.09
2nd layer, left-hand side								
1	$\bar{4}\bar{4}0\bar{1}$	4	4	10,2,2	9.96	$\bar{2}.04$	2.04	2.04
2	$\bar{4}\bar{2}\bar{2}2$	4	9	10,4,2	9.94	$\bar{3}.94$	2.06	2.07
3	$3\bar{1}23$	1	4	11,5,2	10.91	$\bar{4}.9\bar{1}$	1.91	1.90
4	$1\bar{4}52$	3	9	13,1,2	12.94	$\bar{0}.94$	2.06	2.02
	$5\bar{4}\bar{1}2$	4	9	13,1,2	12.94	$\bar{0}.94$	2.06	
3rd layer, left-hand side								
1	$2\bar{1}\bar{3}2$	1	0	9,0,3	8.94	$\bar{0}.06$	2.94	
	$2\bar{3}\bar{1}2$	2	0	9,0,3	8.94	$\bar{0}.06$	2.94	
	$1\bar{3}\bar{4}1$	3	4	9,0,3	8.96	$\bar{0}.06$	3.04	3.00
	$4\bar{3}\bar{1}1$	4	4	9,0,3	8.96	$\bar{0}.06$	3.04	
β		1, 2, 3 and 4	9	301				
3b	$3\bar{0}\bar{3}3$	1	1	12,3,3	11.91	$\bar{2}.9\bar{1}$	2.91	2.89
	$3\bar{5}\bar{2}2$	2	0	12,3,3	11.94	$\bar{3}.06$	2.94	—
a	$2\bar{3}\bar{5}2$	3	0	12,3,3	11.94	$\bar{2}.94$	3.06	—
	$5\bar{5}0\bar{1}$	4	4	12,3,3	11.96	$\bar{3}.04$	3.04	2.99
b	$3\bar{2}\bar{5}2$	1	0	12,3,3	11.94	$\bar{3}.06$	2.94	—
	$3\bar{3}0\bar{3}$	2	1	12,3,3	11.92	$\bar{2}.91$	2.91	2.89
a	$0\bar{5}\bar{5}1$	3	4	12,3,3	11.96	$\bar{3}.04$	3.04	2.99
b	$5\bar{3}\bar{2}2$	4	0	12,3,3	11.94	$\bar{3}.06$	2.94	—

* Mean of two overlapping diffractions with *l* indices $\pm$ 0.04 for diffractions with Identity No. 1a and similarly for diffraction 3a.

TABLE 2

Ident. No.	*hkl* cubic $c/a = 0.613$	*hkil*	Orient.	*hkl* cubic $c/a = 0.622$			F^2 $z = 0.50$	F^2 $z = 0.52$
				h	*k*	*l*		
Zero layer, left-hand side of direct beam								
1	930	3$\bar{1}$22	1	8.92	2.92	0.08	0	0.22
	930	34$\bar{1}$1	2	8.96	3.04	0.04	4	3.14
	930	1232	3	8.92	2.92	0.08	0	0.22
	930	34$\bar{1}$1	4	8.96	3.04	0.04	4	3.14
2a	12,0,0	40$\bar{4}$2	1	11.92	0.08	0.08	0	0.22 } 0.44
	12,0,0	4402	2	11.92	0.08	0.08	0	0.22 }
b	12,0,0	04$\bar{4}$2	3	11.92	0.08	0.08	0	0.22 } 0.44
	12,0,0	4402	4	11.92	0.08	0.08	0	0.22 }
3b	12,6,0	42$\bar{2}$3	1	11.88	5.88	0.12	1	0.74
a	12,6,0	4621	2	11.96	6.04	0.04	4	4.88
c	12,6,0	22$\bar{4}$3	3	11.88	5.98	0.12	1	0.74
a	12,6,0	46$\bar{2}$1	4	11.96	6.04	0.04	4	4.88
Zero layer, right-hand side of direct beam								
Ia	990	33$\bar{6}$0	1	9	9	0	9	9
b	990	3033	2	8.88	8.88	0.12	1	0.74
a	990	36$\bar{3}$0	3	9	9	0	9	9
c	990	3033	4	8.88	8.88	0.12	1	0.74
2a	12,6,0	42$\bar{6}$1	1	11.96	6.04	0.04	4	4.88
b	12,6,0	4223	2	11.88	5.88	0.12	1	0.74
a	12,6,0	26$\bar{4}$1	3	11.96	6.04	0.04	4	4.88
c	12,6,0	4223	4	11.88	5.88	0.12	1	0.74

Atomic positions (0,0,0); $\pm(\frac{2}{3},\frac{1}{3},z)$

From the above results it may be concluded that

(1) The metastable ω-phase in aged Zr base alloys has a hexagonal crystal structure with axial ratio $c/a = 0.622 \pm 0.002$ for all alloys examined. The lattice constants are approximately $a_\omega = 5.02$ and $c_\omega = 3.00$ Å, varying slightly with alloy composition and ageing temperature.

(2) The ω-phase is oriented with respect to the β-phase according to the relationships

$$\langle 0001 \rangle_\omega \,||\, \langle 111 \rangle_\beta$$

$$\langle 2\bar{1}\bar{1}0 \rangle_\omega \,||\, \langle \bar{1}01 \rangle_\beta.$$

(3) The original β transforms to the four possible orientations of hexagonal ω without showing preference for a particular orientation, except when the specimen is subjected to external strain.

(4) In the bulk (metastable) ω examined here there is no evidence for the displacement in the c direction of atoms in $\pm(\frac{2}{3},\frac{1}{3},\frac{1}{2})$ positions as suggested by Bagaryatskii for ω in titanium alloys. However in Section 2 it will be shown that some such displacements can occur in the diffuse ω which precedes the development of the metastable ω structure.

2. THE DIFFUSE ω-STRUCTURE

Section 1 of this paper has been concerned entirely with the ω-phase in its metastable state. However, when alloys of increasing solute content are rapidly quenched from the β-field a characteristic sequence of structures is observed.[5] At low solute concentrations complete transformation to the h.c.p. Zr-α phase cannot be suppressed. On increasing the solute concentration the ω-phase together with the α-phase is observed while at slightly higher concentrations it is possible to obtain almost 100 per cent ω phase. Further increase of the solute concentration results in a certain amount of Zr-β phase being retained together with ω which does not produce sharp X-ray diffractions. The ω-phase in this state is designated diffuse ω. The diffuseness of the diffractions increases with increasing solute content although the amount of diffuse ω present may still be about 70 per cent of the total volume.

In certain alloy systems where the solid solubility of

VOL. 8 1960

the β-phase is limited, it is not possible to observe the complete sequence of as-quenched structures described and for this reason diffuse ω is not observed in the Zr–Cr and Zr–V systems but is readily detected in the Zr–Nb and Zr–U systems.

The mode of formation suggests that the ω-phase occurs by a martensitic type transformation. The term "martensitic" is taken here to describe the regular movement of particular lattice planes relative to adjacent planes of the parent matrix in definite crystallographic directions, the movement resulting in a new crystallographic structure. The interpretation of the diffuse ω study presented below leads to the formulation of a mechanism, not involving diffusion, which accounts for the observed diffraction effects and will also explain the formation of bulk ω.

On ageing alloys which form diffuse ω during the quench, the diffuse diffractions or streaks coalesce and the characteristic ω diffraction pattern becomes apparent. This coalescence is accompanied by solute enrichment of the β-phase and impoverishment of the diffuse ω-phase.

Experimental results

The diffuse ω-phase has been examined by the single crystal technique using monochromatic radiation from a curved quartz monochromator.

Figure 3 shows a single crystal oscillation photograph from a water quenched Zr–20 at.% Nb alloy with the crystal oscillating about $[1\bar{1}0]_\beta$. The photograph shows sharp β diffractions together with areas of diffuse intensity, the latter being the diffuse ω diffractions;

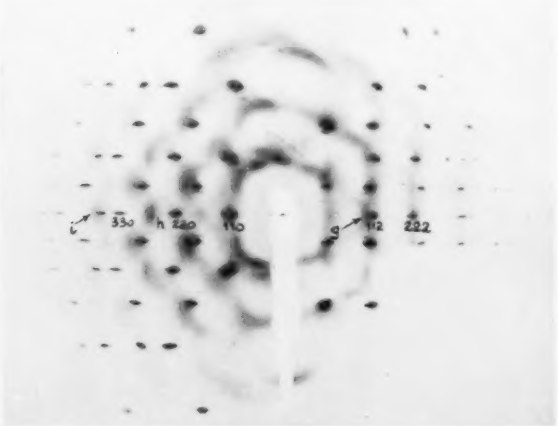


FIG. 3. Oscillation photograph of a single crystal of Zr–20 at.% Nb with monochromatic Mo$K\alpha$ radiation. The crystal oscillated about $\langle 110\rangle_\beta$ with the $\langle 001\rangle_\beta$ oscillated through $0 \rightarrow 45°$ to the direct X-ray beam. The crystal was water quenched after 2 hr at 920°C and the photograph shows diffractions from β, diffuse ω and β''.

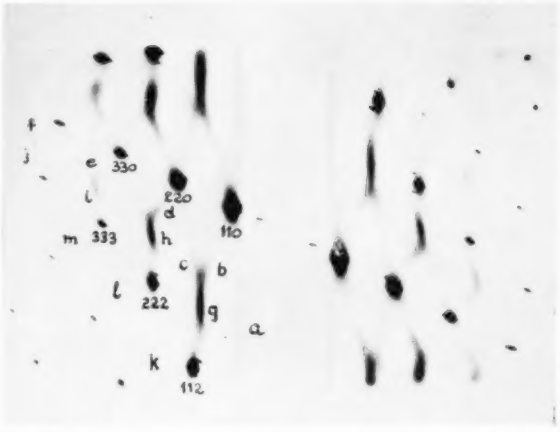


FIG. 4. Weissenberg photograph of the zero layer perpendicular to $\langle 110\rangle_\beta$ from the same crystal as used for Fig. 3.

also present are some weak diffractions from another phase designated β''.* Fig. 4 is the Weissenberg photograph of the zero layer perpendicular to $[1\bar{1}0]_\beta$, and Fig. 5 is the reciprocal lattice plot of this layer, only one quadrant being shown since the other three are symmetrical to this. The diffuse ω diffractions common to both Fig. 3 and Fig. 4 are labelled and as can be seen these are elongated both in the $(1\bar{1}0)_\beta$ plane and perpendicular to this plane. In Fig. 5 these diffractions can be divided into two groups, viz.

(A) Streaks which are elongated in $[\bar{1}\bar{1}2]_\beta$ and hence perpendicular to $[111]_\beta$

(B) Streaks which are elongated in $[112]_\beta$ and hence perpendicular to $[\bar{1}\bar{1}1]_\beta$.

Thus in reciprocal space the diffractions in group (A) can be interpreted as disks of intensity perpendicular to $[111]_\beta$ or three rods of intensity perpendicular to $[\bar{1}\bar{1}\bar{1}]_\beta$ which due to symmetry make angles of 120° with each other. Similarly diffractions in group (B) would correspond to either disks of intensity perpendicular to $[\bar{1}\bar{1}1]_\beta$ or three rods of intensity perpendicular to $[\bar{1}\bar{1}\bar{1}]_\beta$.

Table 3 gives the indices and F^2 values for those bulk ω diffractions which can occur in the reciprocal lattice section shown in Fig. 5. The table shows that apart from those diffractions which overlap β diffractions only ω orientations 2 and 4 diffract in this section; the reciprocal lattice points corresponding to these orientations are shown by crosses and dots, respectively. Thus each of the streaks belonging to

* The β''-phase has a b.c. tetragonal structure with $a = 3.52$ Å and $c/a = 1.13$ and is orientated to the β-phase having $\langle 001\rangle_{\text{b.c.t.}} \parallel \langle 001\rangle_\beta$ and $\langle 100\rangle_{\text{b.c.t.}} \parallel \langle 100\rangle_\beta$. The phase exists in small amounts (less than 5 per cent of the total volume) in high solute content niobium alloys.

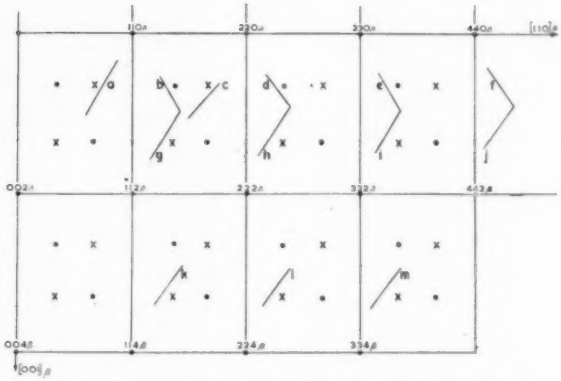


FIG. 5. A reciprocal lattice plot of the zero layer perpendicular to $\langle 110 \rangle$ reciprocal lattice direction showing the direction of the diffuse ω streaks and the position of the corresponding bulk ω diffractions.
● ω orientation 4
× ω orientation 2

group (A) above can be associated with a diffraction from bulk ω in orientation 2 and those belonging to group (B) with a diffraction from bulk ω in orientation 4. However the intensities of the streaks do not agree with the corresponding bulk ω intensities, but as will be shown later better agreement is obtained if small atomic movements are given to the atoms in bulk ω to give a structure intermediate between β and bulk ω.

The diffuseness of the diffraction streaks from diffuse ω as compared with the bulk ω diffractions results from relaxed Laue conditions caused by the diffracting region either being restricted in size or not having exact periodicity in three dimensions. Since it has not been possible to resolve whether the intensity distribution in reciprocal space is a disk of intensity perpendicular to $\langle 111 \rangle_\beta$ or three rods perpendicular to $\langle 111 \rangle_\beta$ both possible interpretations will be developed.

If the intensity distribution corresponds to disks in reciprocal lattice space those disks associated with ω in orientation 2 correspond either to rods of ω in orientation 2 in the crystal where the axes of the rods are parallel to $[111]_\beta$, as is shown in Fig. 6(c) or to ω in orientation 2 with exact periodicity only in the $[111]_\beta$ direction. A similar argument applies for the disks

TABLE 3

Ident. No.	*hkl* cubic	*hkil* hex.	Orient.	Intensity observed	Intensity $F^2_{0.50}$	Intensity $F^2_{0.58}$	*hkl* cubic	*hkil* hex.	Orient.	Intensity observed	Intensity $F^2_{0.50}$	Intensity $F^2_{0.58}$
	112	10$\bar{1}$0	4	*	0	0	$\bar{1}$12	10$\bar{1}$0	2	*	0	0
a	222	0001	2	w	1	0.6	$\bar{2}$22	0001	4	w	1	0.6
b	442	20$\bar{2}$1	4	wm	4	1.0	$\bar{4}$42	2021	2	wm	4	1.0
c	552	$\bar{1}$012	2	wm	0	1.0	552	1012	4	wm	0	1.0
d	772	3032	4	sm	9	4.3	772	3032	2	sm	9	4.3
	882	2023	2	—	4	0.4	$\bar{8}$82	2023	4	—	4	0.4
e	10,10,2	4043	4	sm	4	7.8	$\bar{1}$0,10,2	4043	2	sm	4	7.8
	11,11,2	3034	2	—	9	<0.1	$\bar{1}$1,11,2	3034	4	—	9	<0.1
f	13,13,2	5054	4	w	0	9.0	$\bar{1}$3,13,2	5054	2	w	0	9.0
	114	10$\bar{1}$1	2	*	4	1.0	$\bar{1}$14	10$\bar{1}$1	4	*	4	1.0
	224	2020	4	*	0	0	$\bar{2}$24	2020	2	*	0	0
g	444	0002	2	s	9	4.3	$\bar{4}$44	0002	4	s	9	4.3
	554	30$\bar{3}$1	4	vw	1	0.6	$\bar{5}$54	30$\bar{3}$1	2	vw	1	0.6
h	774	1013	2	s	4	7.8	$\bar{7}$74	1013	4	s	4	7.8
	884	4042	4	—	0	3.7	$\bar{8}$84	4042	2	—	0	3.7
i	10,10,4	2024	2	s	0	9.0	$\bar{1}$0,10,4	2024	4	s	0	9.0
	11,11,4	5053	4	—	4	0.4	$\bar{1}$1,11,4	5053	2	—	4	0.4
j	13,13,4	3035	2	w	4	6.9	$\bar{1}$3,13,4	3035	4	w	4	5.9
	118	30$\bar{3}$1	4	*	1	0.6	$\bar{1}$18	30$\bar{3}$1	2	*	1	0.6
	228	2022	2	*	0	1.0	$\bar{2}$28	2022	4	*	0	1.0
	448	4040	4	—	0	0	$\bar{4}$48	4040	2	—	0	0
	558	10$\bar{1}$3	2	—	4	0.4	$\bar{5}$58	10$\bar{1}$3	4	—	4	0.4
	778	50$\bar{5}$1	4	—	4	1.0	$\bar{7}$78	50$\bar{5}$1	2	—	4	1.0
	888	0004	2	—	9	<0.1	$\bar{8}$88	0004	4	—	9	<0.1
	10,10,8	6062	4	—	9	4.3	$\bar{1}$0,10,8	6062	2	—	9	4.3
	1,1,10	3032	2	*	9	4.3	1,1,$\bar{1}$0	3032	4	*	9	4.3
	2,2,10	4041	4	—	1	1.0	2,2,$\bar{1}$0	4041	2	—	1	1.0
k	4,4,10	2023	2	w	4	7.9	4,4,$\bar{1}$0	2023	4	w	4	7.9
	5,5,10	5050	4	—	0	0	5,5,$\bar{1}$0	5050	2	—	0	0
l	7,7,10	1014	2	m	0	9.0	7,7,$\bar{1}$0	1014	4	m	0	9.0
	8,8,10	6061	4	—	1	0.6	8,8,$\bar{1}$0	6061	2	—	1	0.6
m	10,10,10	0005	2	w	1	6.9	$\bar{1}$0,10,10	0005	4	w	1	6.9

— Not observed. * Oscillation range too small to include this diffraction.
There are also ω diffractions from all ω orientations superimposed on the β diffractions
$(110)_\beta$ $(220)_\beta$ $(330)_\beta$ $(440)_\beta$ $(002)_\beta$ $(112)_\beta$
$(222)_\beta$ $(332)_\beta$ $(442)_\beta$ $(114)_\beta$ $(224)_\beta$
ω Orientation (2) $[0001]_\omega \parallel [111]_\beta$ $[2\bar{1}\bar{1}0]_\omega \parallel [\bar{1}01]_\beta$
ω Orientation (4) $[0001]_\omega \parallel [\bar{1}\bar{1}1]_\beta$ $[2\bar{1}\bar{1}0]_\omega \parallel [101]_\beta$

VOL. 8 1960

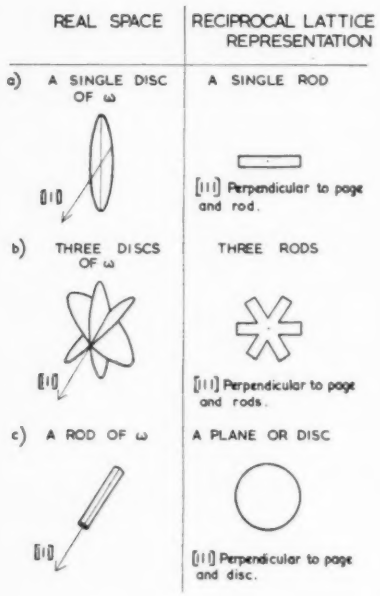


FIG. 6. Representation of ω in real and reciprocal lattice space.

associated with orientation 4 but here the axis of the rods of ω would be parallel to $[\bar{1}\bar{1}\bar{1}]_\beta$.

Alternatively if the disks of intensity in reciprocal space are in fact three rods of intensity those associated with ω in orientation 2 will correspond either to three disks (or more probably oblate spheroids) of ω in orientation 2 in the crystal, each disk being parallel to $[111]_\beta$ but making 120° with each other (Fig. 6b) or three blocks of ω with orientation 2 in the crystal, each block having periodicity in two orthogonal directions but not in the third which is perpendicular to $[111]_\beta$.

The above interpretations may not be very different since both relate to regions of ω in the crystal which are structurally perfect in only one direction, for example ω with orientation 2 is structurally perfect in only the $[111]_\beta$ direction and any direction perpendicular to this will intersect a large number of defects.

A $\beta \rightarrow \omega$ transformation model

The experimental results given above suggest that movement of $\{112\}_\beta$ planes is involved in the $\beta \rightarrow \omega$ transformation as is the case for the $\beta \rightarrow \alpha$ transformation mechanism proposed by Burgers[6].

A projection of the atoms in a b.c.c. structure onto a $(1\bar{1}0)_\beta$ plane is shown in Fig. 7. The packing sequence of the $(\bar{1}\bar{1}2)_\beta$ planes is given by 1,2,3,4,5,6,1,2,3, etc. The ω structure can be generated by the $\{112\}_\beta$ planes gliding as follows:

$\{\bar{1}\bar{1}2\}_\beta$	1	2	3	4	5	6	1	2	3	4	5	6
glide component	0	g	$\bar{g}$	0	g	$\bar{g}$	0	g	$\bar{g}$	0	g	$\bar{g}$
ω	1	ω_3^2	ω_3^2	4	ω_6^5	ω_6^5	1	ω_3^2	ω_3^2	4	ω_6^5	ω_6^5

where g is the glide component which glides a $\{\bar{1}\bar{1}2\}_\beta$ plane by $\frac{1}{6}\sqrt{3}/2 \cdot a_\beta$ in the $\langle 111 \rangle_\beta$ direction contained in that plane. A gliding sequence occurring on any particular set of $\{\bar{1}\bar{1}2\}_\beta$ planes of a particular zone necessarily implies an identical gliding sequence occurring on each of the other two sets of $\{\bar{1}\bar{1}2\}_\beta$ planes of that zone. Hence bulk ω in orientation 2 can be generated by extensive gliding on the $(\bar{1}\bar{1}2)_\beta$, $(\bar{1}2\bar{1})_\beta$ or $(2\bar{1}\bar{1})_\beta$ planes in a $[111]_\beta$ direction, i.e. g above is in the $[111]_\beta$ direction. Similarly disks of ω will be produced if glide takes place on a limited number of the above planes. The disks will be parallel to $[111]_\beta$ and perpendicular to $[\bar{1}\bar{1}2]_\beta$, $[\bar{1}2\bar{1}]_\beta$ and $[2\bar{1}\bar{1}]_\beta$. This is shown in Fig. 8 which is a projection of atoms in a b.c.c. structure onto a $(1\bar{1}0)_\beta$ plane.

The disks would degenerate into rods of ω parallel to $[111]_\beta$ if the width of disks in the $\langle 110 \rangle_\beta$ directions, which lie in the plane of the disks, is restricted to a few atoms while the glide along the $\langle 111 \rangle_\beta$ has occurred for many atoms.

The restriction of the width of the disks in the $\langle 110 \rangle_\beta$ directions can be brought about by faulting between the disks. Fig. 9 is a projection of the atoms in a b.c.c. structure onto a $(111)_\beta$ plane, that is a projection at right angles to that of Fig. 8. The three sets of $\{\bar{1}\bar{1}2\}_\beta$ planes belonging to the $[111]_\beta$ zone are

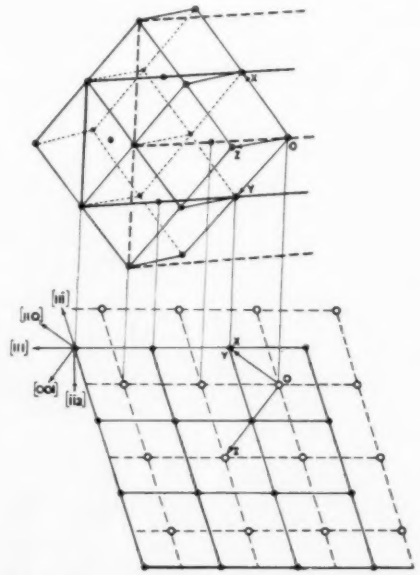


FIG. 7. Projection of the atoms in a b.c.c. structure onto a {110} plane illustrating the {112} packing sequence.

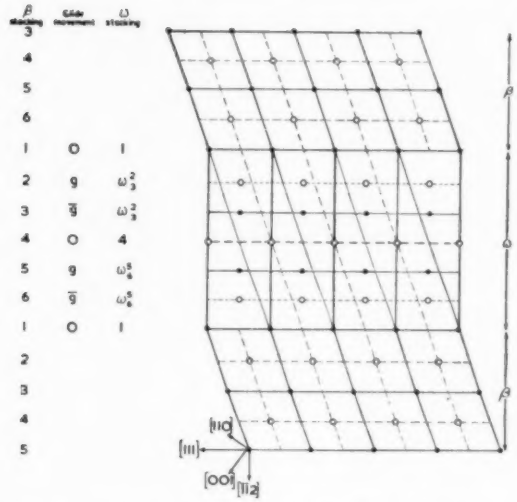


FIG. 8. Projection of the atoms in a b.c.c. structure onto a {110} plane showing the glide sequence to produce ω.

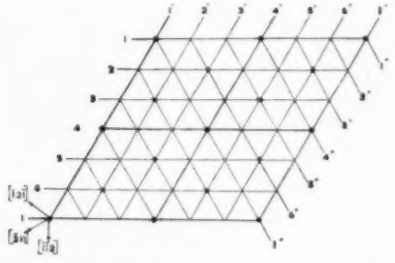


FIG. 9. Projection of the atoms in a b.c.c. structure onto a {111} plane illustrating the three {112} planes of a $\langle 111 \rangle$ zone.

● Atoms in the plane of projection

× Atoms $\frac{2\sqrt{3}a_\beta}{6}$ above the plane

+ Atoms $\frac{\sqrt{3}a_\beta}{6}$ above the plane

shown by unprimed numbers for the $(112)_\beta$, primed numbers, 1′, 2′, etc., for the $(2\bar{1}\bar{1})_\beta$ and doubly primed numbers, 1″, 2″, etc., for the $(\bar{1}2\bar{1})_\beta$ planes. Faulting will occur between disks if simultaneous nucleation occurs on non equivalent $\{112\}_\beta$ planes of the $[111]_\beta$ zone as defined by the glide sequence given above in which planes 1, 1′ and 1″ have zero glide component. If, for example, simultaneous nucleation of ω occurs on planes 3′ and 5″, where plane 3′ glides $\bar{g}$ and plane 5″ glides g, a series of faults will develop where the disks merge.

Many permutations and combinations of the above gliding sequence of $\{112\}_\beta$ planes which could result in faulting are possible when a large number of nucleation sites are present. Interaction must be considered of each of the three $\{112\}_\beta$ planes in each of the four $\langle 111 \rangle_\beta$ zones and also the interaction of the gliding of $\{112\}_\beta$ planes in different zones. If it is assumed that nucleation of gliding is purely random then the chance of faulting between any two sets of $\{112\}_\beta$ planes in the same zone is 2:1. The case of interaction of $\{112\}_\beta$ planes of different zones is complex and will not be developed in detail here but it does not alter the general conclusions concerning mechanism.

Table 3 shows that the intensities of the diffuse ω streaks do not agree with the intensities of the corresponding bulk ω diffractions. However, a better correlation is obtained if in diffuse ω the above glide sequences do not go to completion. When the glide component is $0.087(\sqrt{3}/2 \cdot a_\beta)$ instead of $0.167(\sqrt{3}/2 \cdot a_\beta)$, the ω produced has atomic positions (0,0,0); $\pm(\frac{2}{3},\frac{1}{3},0.58)$ as compared with (0,0,0); $\pm(\frac{2}{3},\frac{1}{3},0.50)$. F^2 values corresponding to these new positions are shown in Table 3 under $F^2_{0.58}$ and it will be seen that better agreement with the observed intensities is obtained. Since diffuse ω exists as disks on $\{112\}_\beta$ planes it is probable that coherency strains resulting from transformation prevent the gliding sequence from going to completion.

It is of interest to note that the new atomic positions reported for the diffuse ω structure are similar to those proposed by Bagaryatskii for bulk ω in a Ti–5% Cr alloy. However, since little is known of the heat treatment of Bagaryatskii's alloys it is not possible to relate the rumpling of the mid plane of atoms in the ω-phase in Ti–5% Cr to coherency strains.

Conclusions

The model proposed for the $\beta \rightarrow \omega$ transformation satisfactorily accounts for the diffraction effects observed from the diffuse ω-phase and implies that the gliding sequence suggested is operative during the formation of bulk ω.

The mechanism of formation of bulk ω from diffuse ω, on ageing, is considered to be in part an annealing out of faults.

ACKNOWLEDGMENTS

The authors wish to acknowledge the assistance of D. Stewart, B. Bradford and G. Hansen with the experimental programme and are also grateful to Dr. E. A. Calnan, Dr. G. I. Williams of the Fulmer Research Institute, and Dr. M. B. Waldron and Mr. B. Butcher of Atomic Energy Research Establishment, Harwell, for the many useful discussions.

This work was sponsored by the Atomic Energy Research Establishment, Harwell, and the authors are grateful to the Director for permission to publish.

VOL. 8 1960

REFERENCES

1. A. E. Austin and J. R. Doig, *J. Metals, N.Y.* **9,** 27 (1957).
2. J. M. Silcock, M. H. Davies and H. K. Hardy, in *Symposium on the Mechanism of Phase Transformations in Metals*. London, Institute of Metals (1955).
3. Yu A. Bagaryatskii, G. I. Rosova and T. W. Saganova, *Dokl. Akad. Nauk SSSR* **105,** 1225 (1955).
4. B. A. Hatt, J. A. Roberts and G. I. Williams, *Nature, Lond.* **180,** 1406 (1957).
5. B. A. Hatt and J. A. Roberts, unpublished work.
6. W. G. Burgers, *Physica, s'Grav.* **1,** 561 (1934).

VOL
8
196

Low-temperature stress-relaxation peaks in plastically deformed polycrystalline niobium*

Measurement of internal friction above room temperature has become a standard tool in the study of diffusion-controlled processes in b.c.c. metals,[1] and recently considerable attention has been directed to the study of low-temperature relaxation processes in f.c.c. metals.[2] The following is an account of some observations of stress-relaxation absorption peaks found at low temperatures in a plastically deformed b.c.c. metal.

Acoustical-energy absorption peaks for frequencies in the tens of kilocycles were observed at 10°K and 165°K in plastically deformed, commercially pure polycrystalline niobium. The measurements of internal friction were made from 4°K to 300°K by means of a resonant-bar technique in which alternating longitudinal stress in the 10–100 kc/s range was employed. The use of electromagnetic transducers permitted measurements to be performed over a wide range of strain amplitudes (10^{-8}–10^{-4}).

Niobium rod stock, $\frac{3}{4}$ in. in diameter, was swaged into 0.160 in. dia. rods. Ten 6-in. rods were annealed in a vacuum (10^{-5} mm Hg) at 1050°C for 1 hr. The annealed rods were then subjected to various amounts of tensile prestrain at a strain rate of 10^{-4}/sec. After final preparation, the niobium specimens contained the following weight percentages of impurities: 0.2 Ta, 0.1 Zr, 0.01 N, 0.01 C and 0.001 H.

Figure 1 is a typical plot of the internal friction, Q^{-1} (proportional to the fractional energy loss per half cycle), versus temperature for the prestrained specimens. The main acoustical-energy absorption peak is centered at 167°K $\pm$ 3°K, and a smaller peak lies in the vicinity of 10°K. Fig. 2 shows the dependence of the relaxation strength, or peak height, of the main peak on the amount of prestrain. In the as-annealed condition, no peaks are discernible. The relaxation strength increases rapidly with increasing prestrain until about 3 per cent deformation; thereafter, it decreases with additional increase in prestrain. The relaxation strength of the peak in the as-swaged specimens is about $\frac{1}{5}$ that in the 3 per cent prestrained specimen.

If the prestrained specimens are annealed in high vacuum at 210°C for 25 min, the peaks are eliminated. Another consequence of such an anneal is seen in Fig. 3, where the dependence of Q^{-1} on the oscillating strain amplitude, ε, used in the measurements is plotted. The amplitude dependence of Q^{-1} is greatly

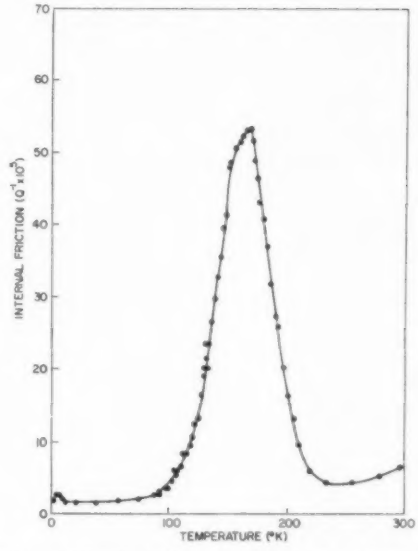


FIG. 1. Acoustical relaxation spectrum measured in the vicinity of 18,000 c/s in polycrystalline niobium prestrained 5 per cent in tension at 23°C.

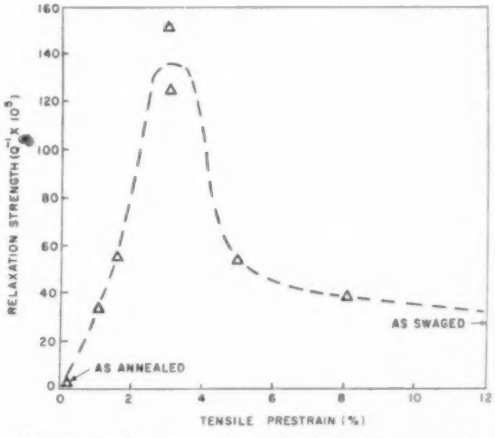


FIG. 2. Relaxation strength of 165°K peak of prestrained polycrystalline niobium as a function of tensile prestrain (per cent).

modified as a result of the anneal; the amplitude at which Q^{-1} becomes strongly dependent on amplitude is increased tenfold for measurements made at room temperature and at the temperature of the relaxation peak. However, annealing the specimens at room temperature for 5 days resulted in little observable change in the strength of the relaxation peak and caused essentially no alteration in the amplitude dependence.

The temperature at which the main peak appears rises with increased frequency. Measurements of this

VOL. 8 1960

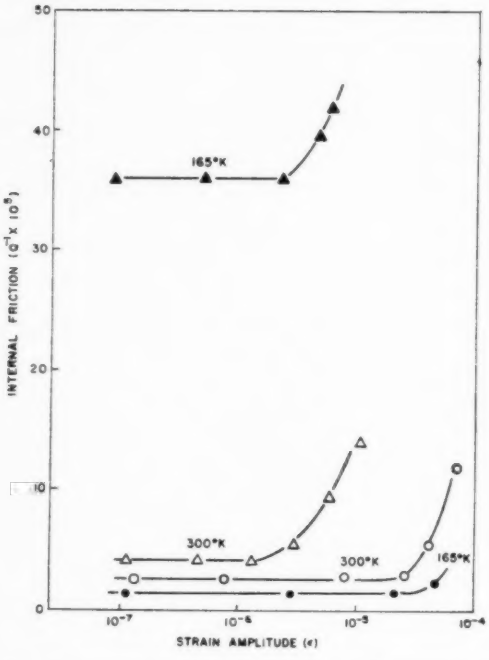


FIG. 3. Acoustical energy loss, Q^{-1}, of polycrystalline niobium prestrained 1 per cent in tension at 23°C as a function of oscillating longitudinal strain amplitude, ϵ, and annealing history.
△ 1 per cent tensile strain, measured at 300°K
▲ 1 per cent tensile strain, measured at 165°K
○ 1 per cent tensile strain, annealed at 210°C for 25 min, measured at 300°K
● 1 per cent tensile strain, annealed at 210°C for 25 min, measured at 165°K.

shift in temperature indicate that the peak is associated with a relaxation process having an activation energy not in excess of 0.3 eV. On the other hand, a lower limit of 1 eV on the activation energy for annealing was estimated from consideration of the times necessary to cause depression of the main peak at 150°C and 210°C.

If this relaxation process is considered to be associated with the stress-induced diffusive motion of a defect, as in the Snoek mechanism,[1] the defect must be able to migrate readily at room temperature, since such a low activation energy for diffusion implies that the jump frequency at 300°K is of the order of 10^7 sec^{-1}. Hence, the average migration distance should be of the order of 10^{-2} cm/hr.

From these considerations it would appear that the main peak is due to either (A) a mobile defect with a 0.3-eV migration energy, that can be trapped only by surmounting a 1-eV barrier, or (B) a mobile defect bound to a relatively immobile structure. Possibility (A) appears to be unlikely since most defect-annealing processes discussed in the current literature are thought to be diffusion controlled. Furthermore, if the defects responsible for the peak are associated with plastic deformation, as is suggested by the data in Fig. 2, the theories of Mott[3] and of van Bueren[4] and the molybdenum resistivity experiments of Peiffer[5] show that the concentration of defects resulting from plastic deformation is at least a monotonically increasing function of strain in the strain range of interest here. Thus the relaxation strength of a peak caused by such defects should also be a monotonically increasing function of strain. This does not agree with the data presented in Fig. 2.

Two models consistent with possibility (B) would consider the mobile defects as being either (1) thermally activated pairs of kinks on relatively immobile dislocation lines,[2,6] or (2) very mobile gaseous atoms, such as hydrogen or point defects produced during the deformation process (e.g. divacancies), loosely trapped near dislocation lines in a manner similar to that considered by Schoek and Seeger[7] for carbon in iron. The motion of dislocation lines so decorated by point defects is strongly coupled by a Snoek effect[1,7] to the diffusive jumps of the point defects, thus producing a point-defect-bound dislocation–relaxation oscillator.

In either case (1) or (2), the annealing on the 165°K peak could then be attributed to the migration of gaseous interstitials into dislocation lines.[8] These interstitials strongly interact with the lines, thus pinning them, which results in a lowering of the relaxation strength. A probable interstitial here is oxygen, which has an activation energy for diffusion in niobium of 1.1 eV;[9] this energy compares well with the activation energy for annealing. Another consequence of this pinning process should be to increase the oscillating strain amplitude necessary to produce a large increase in internal friction.[10] This increase, in fact, is seen in the data shown in Fig. 3. Such interstitial interaction should also produce other effects, e.g. the establishment of a definite yield point. Dyson *et al.*[11] have strained polycrystalline niobium in tension at liquid-nitrogen temperature and then annealed it at successively higher temperatures. They found that a yield point begins to appear after annealing at 160°C for 3 hr and concluded that oxygen is the interstitial responsible for the yield phenomenon.

Finally, the dependence of the relaxation strength of the main peak on the amount of total strain is qualitatively consistent with the dislocation model. In the early stages of deformation, increased stress produces large numbers of dislocations and hence large numbers of dislocation–kink oscillators or point-defect-bound dislocation–relaxation oscillators.

As the density of the dislocations increases, the average distance between intersections of the dislocation network decreases until a critical length is reached at which the line tension of the dislocation-line segments dominates the motion of the lines, so that the influence of the relaxation process is reduced.

This work was supported in part by the Atomic Energy Commission under Contract AT(04-3)-167.

R. H. Chambers
J. Schultz

John Jay Hopkins Laboratory for Pure and Applied Science, General Atomic Division of General Dynamics Corporation, San Diego, California

VOL. 8 1960

References

1. J. L. Snoek, *Physica s'Grav.* **8,** 711 (1941).
2. A. Seeger, N. Donth and F. Pfaff, *Disc. Faraday Soc.* **23,** 19 (1957).
3. N. F. Mott, *Phil. Mag.* **43,** 1151 (1952); **44,** 187, 742 (1958).
4. H. G. van Bueren, *Philips Res. Rep.* **12,** 1 (1957).
5. H. R. Peiffer, *J. Appl. Phys.* **29,** 1581 (1958).
6. P. G. Bordoni, *J. Acoust. Soc. Amer.* **26,** 495 (1954).
7. G. Schoek and A. Seeger, *Acta Met.* **7,** 469 (1959).
8. F. R. N. Nabarro, *Mechanical Effects of Carbon in Iron,* reported at a Conference on Strength of Solids. The Physical Society of London (1948).
9. C. Y. Ang, *Acta Met.* **1,** 123 (1953).
10. A. Granato and K. Lücke, *J. Appl. Phys.* **27,** 583 (1956).
11. B. F. Dyson, R. B. Jones and W. J. McG. Tegart, *J. Inst. Met.* **87,** 340 (1959).

* Received December 12, 1959.

VOL
8
196

A STUDY OF ELONGATION AND AGEING IN Al–4% Cu AND Al–4% Cu 0.05% In CRYSTALS*

J. M. SILCOCK†

The relation between deformation characteristics and θ' nucleation has been studied in Al–4% Cu and Al–4% Cu 0.05% In crystals. Preferred nucleation of θ' occurs in the orientations which do not contain the slip direction in the $(100)_{\theta'}$ plane. This is attributed to the atomic configuration at the edges of partial dislocations.

Deformation of aged crystals has shown that crystals hardened by G.P.[1] at 130°C show characteristics similar to those of "as quenched" crystals. The slip lines are fainter and fewer when G.P.[2] zones are present, and are not detected at all until heavy deformations when large quantities of θ' are present. This is attributed to different hardening mechanisms.

ETUDE DE L'ELONGATION ET DU VIEILLISSEMENT DANS DES CRISTAUX Al–4% Cu et Al–4% Cu–0,05% In

La relation entre les caractéristiques de déformation et la germination θ' a été étudiée dans des cristaux de Al–4% Cu et Al–4% Cu 0,05% In. La germination préférentielle de θ' a lieu suivant des orientations qui ne contiennent pas la direction de glissement dans le plan $(100)_{\theta'}$. Ceci est attribué à la configuration atomique aux bords des dislocations partielles.

La déformation de cristaux vieillis a montré que les cristaux durcis par zones G.P. [1] à 130°C ont des caractéristiques similaires aux cristaux trempés. Lorsque les zones de G.P. [2] sont présentes, les lignes de glissement sont plus faibles et moins nombreuses et, lorsque des quantités importantes de θ' sont présentes, elles ne sont visibles que pour des grandes déformations. Ce phénomène est attribué à des mécanismes de durcissement différents.

EINE UNTERSUCHUNG ZUR VERFORMUNG UND ZUR AUSHÄRTUNG VON KRISTALLEN AUS Al–4% Cu UND AUS Al–4% Cu–0,05% In

Die Beziehung zwischen dem Verformungsverhalten und der Keimbildung von θ' wurde bei Kristallen aus Al–4% Cu und aus Al–4% Cu 0,05% In untersucht. θ'-Keime bilden sich vorzugsweise in solchen Orientierungen, welche die Gleitrichtung nicht in der $(100)_{\theta'}$ Ebene enthalten. Dies wird mit der Konfiguration der Atome in der Umgebung einer Halbversetzung in Zusammenhang gebracht.

Die Verformung ausgelagerter Kristalle zeigte, daß Kristalle, die durch G.P. [1] bei 130°C ausgehärtet worden waren, ähnliche Züge aufweisen, wie abgeschreckte Kristalle. Bei Anwesenheit von G.P. [2]-Zonen treten schwächere und weniger zahlreiche Gleitlinien auf und sie lassen sich erst nach starker Verformung nachweisen, wenn große Mengen von θ' vorhanden sind. Dies wird auf verschiedene Verfestigungsmechanismen zurückgeführt.

VOL. 8 1960

1. INTRODUCTION

In aluminium copper alloys, the intermediate structure θ' forms after much shorter ageing times if the alloy is cold worked between solution treatment and ageing.[1] The θ' is frequently nucleated in only two of the possible three orientations. Wilsdorf and Kuhlmann-Wilsdorf[2] have shown that two orientations of θ' generally form in each slip plane. They postulated that the orientation not obtained is that with the slip direction in the $(001)_{\theta'}$ plane. In the present work this has been proved to be true. Crystals of known orientation have been elongated and the nucleated orientations compared with the slip system. When primary $[101](11\bar{1})$ or primary and cross[3] $[101](1\bar{1}\bar{1})$ slip occur, only two orientations are nucleated. When duplex slip on the primary and conjugate[3] $[110](1\bar{1}1)$ systems occurs, two slip directions operate and the resulting θ' nucleation is random on the macroscopic scale of X-ray examination.

Deformation characteristics of aged crystals have also been examined. Carlson and Honeycombe[4] have reported that no slip was visible in age hardened Al–3½% Cu crystals (aged 3 days at 190°C) except for some coarse bands in the region of necking. No evidence of slip lines was observed in copper hardened by internal oxidation[5] or in age hardened Al–7% Mg[6] alloy. Thomas and Nutting[7] have found by electron microscopy of oxide replicas that the slip characteristics change from wavy single steps of large displacement when G.P. zones [1] are present to small steps and relatively few lines when G.P. [2] and θ' are present at peak hardness. The present work, which was almost complete before Thomas and Nutting's paper was published, is on single crystals and is in fair agreement with their work, if their structures in Table 1 are corrected to that obtained by X-ray examination. It is apparent, however, that the absence of slip lines is associated with a critical dispersion of θ' and not with high hardness.

X-ray examination of the ageing products after deformation shows no change in structure.

* Received July 3, 1959.

† Fulmer Research Institute, now at Liverpool University.

VOL. 8 1960

2. EXPERIMENTAL

Crystals were prepared and examined by X-rays using the methods described previously.[8] Since no crystals covered the entire gauge length, a smaller "gauge length" was carefully prepared in many specimens by filing and polishing within a crystal. This enabled aged crystals to be elongated without accompanying grain boundary deformation. The gauge length was of the order of 0.9 cm and the width 0.2 cm. Small gauge lengths were not cut in strips 5 and 14 which consisted of several fairly large crystals. All crystals were electro-polished before solution treatment and immediately before elongation. The slip traces were examined with the light microscope and a few with the electron microscope. The orientation was determined by the transmission Laue method. Since a large beam was used, the orientation after elongation was an average of the majority of the crystal and ignored deformation bands. The fragmentation and asterism of Laue spots after deformation varied but were generally greater in aged crystals. It was found that measurements of the tension axis orientation repeated to within $\pm 1\frac{1}{2}°$ for a work free crystal, and to about $\pm 3°$ for worked crystals. The absolute accuracy is probably lower.

In Figs. 1, 7, 10 and 13, the orignial orientation of the tension axis is that nearest the (100)–(110) boundary. With the orientation given in the figures,

primary slip is on the $(11\bar{1})$ plane and the [101] direction,

cross slip is on the $(1\bar{1}\bar{1})$ plane and the [101] direction and

conjugate slip is on the $(1\bar{1}1)$ plane and the [110] direction.

3. RESULTS

(a) *Acetone quenched* Al–Cu *crystals, elongated and aged*

The orientations of the tension axes are given in Fig. 1. The change in orientation in the tension directions corresponds within experimental error to a rotation towards the primary [101] slip direction, except for crystals 5_3 and 35.

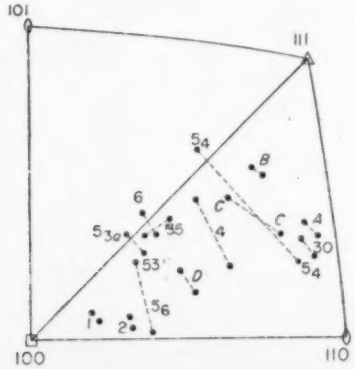


FIG. 1. Orientations of tension axes for acetone quenched and room temperature aged crystals.



FIG. 2.

In the following crystals, with the total elongation given in brackets, only one slip trace could be observed and on subsequent ageing for 16 hr at 165°C X-ray photographs showed strong θ' spots from two orientations and only weak θ' spots from the third orientation: *A* (4%), *B* ($1\frac{1}{2}$%), *C* (20%), 2 ($3\frac{1}{2}$%), 4 (20%), 30 (5%) and 42 (5%). The appearance of the slip traces varied with the surface examined; they were generally wavy, but occasionally fairly straight (Fig. 2). In all cases the average direction corresponded with the trace to be expected for the primary slip plane. Those crystals showing straight traces had the primary slip direction within about 15° from the surface and the primary slip plane almost 90° to the surface so that a change of the slip plane,[5] which is the probable cause of wavy lines, would not be detected. Electron micrographs using all-metal replicas also showed straight and wavy traces.

A number of crystals—1 (4%), 5_6 (15%), *D* (5%)—had bands of short secondary slip lines, the direction of which agreed with slip on the cross slip plane. Occasionally the continuity of the secondary cross slip

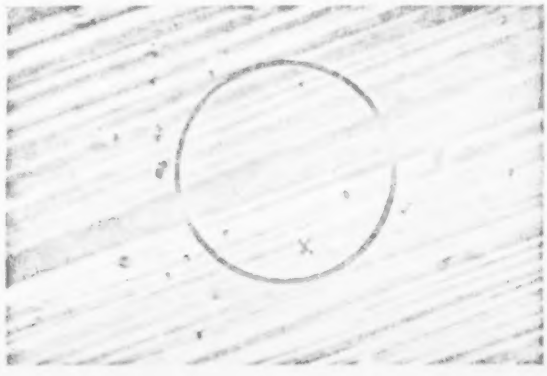


FIG. 3.

trace from one set of primary to another set of primary traces could be observed, for example Fig. 3, which was taken in an area showing relatively few cross slip markings. On subsequent ageing for 16 hr at 165°C all these crystals showed only very weak θ' spots from the orientation with the slip direction in the $(001)_{\theta'}$ plane but strong θ' spots from the other orientations, that is to say, the θ' orientations nucleated were the same as in crystals where only the trace corresponding to the primary slip system was observed.

Crystals 3 (10%), 5_3 (31%), 5_4 (100%), 6 (37%) and 35 (5%) showed two prominent slip traces which agreed with the directions of the primary and conjugate slip planes (Fig. 4). After ageing for 16 hr at

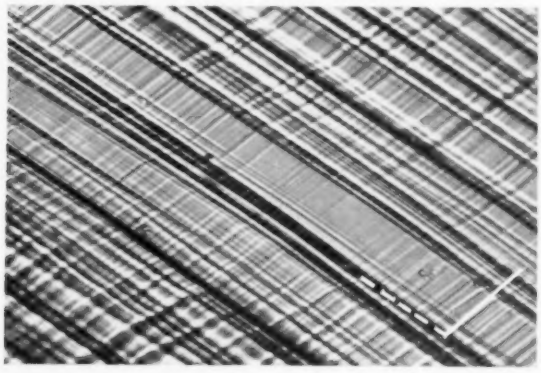


FIG. 4.

165°C these crystals, except for crystal 3, gave equally strong θ' spots for all orientations. Crystal 3 showed relatively few conjugate slip traces (see Fig. 5) and only medium intensity θ' spots from the orientation with the primary slip direction in the (001) θ' plane.

In Table 1, the quantities of θ' in the three orientations are given for crystals elongated 5 per cent before ageing 16 hr at 165°C. Orient *c* is the orientation with the primary slip direction in the (001) θ'

TABLE 1. Quantity of θ' produced by ageing for 16 hr at 165°C after 5 per cent elongation

Crystal	Slip traces observed	Quantities of θ'*	
		(Orients *a* and *b*, Fig. 15)	(Orient *c*, Fig. 15)
D	Primary and cross slip	12	0
30	Primary only—straight	20	1.4
35	Primary and conjugate	15	15
42	Primary only	15	0.9

* Per cent of the total possible quantity of θ' in each orientation for random nucleation.

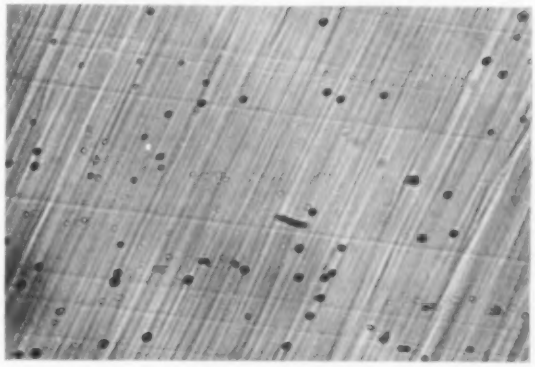


FIG. 5.

plane. In crystal 35 presumably the "primary" and "conjugate" slip systems operated together but the quantity of θ' observed was equal to that given by nucleation due to primary slip alone and the quantity of θ' in the orientation *a* containing neither primary nor conjugate slip directions in the basal plane was not doubled.

All the crystals which appear to have overshot the (100)–(111) boundary showed duplex slip well before the end of the extension. Crystals 6 and 5_4 gave the clearest indication of overshoot but in both cases the degree of overshoot is only just greater than the experimental error, so that although there is an indication, it is not proved beyond doubt that overshoot can occur.

(b) *Crystals aged before elongation*

The aged crystals display greater fragmentation and asterism of Laue spots after elongation than do the quenched crystals. The "final" orientation of the tension axis is therefore of less accuracy for the aged crystals. However, the change of orientation is in most cases within the experimental error (+3°) of the direction expected for rotation towards the primary slip direction (Fig. 6). The exceptions were crystals

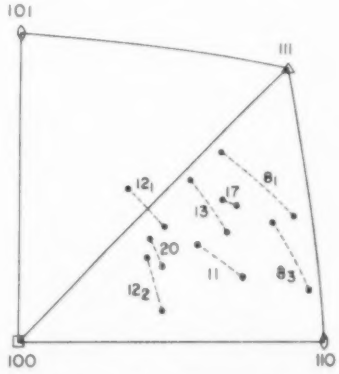


FIG. 6. Orientations of tension axes for aged crystals.

VOL. 8 1960

TABLE 2. Elongation of aged crystals

Crystal 4% Cu	Previous† ageing treatment	Precipitate‡ spots present	V.P.N.§ before elong.	Elong. %	Slip trace characteristics	Precipitates present*‡ after additional ageing of 16 hr at 165°C
14_1	10 d.R.T.	GP.[1]	80	4	Widely spaced clusters	M.GP.[2] + {MW.θ' W. θ'
14_2	10 d.R.T.	GP.[1]		6	Two fine intersecting sets of lines fairly uniform	MS. θ'. No preferred orientation
14_4	10 d.R.T.	GP.[1]		5	Primary and cross slip traces	MW.GP.[2] + {MS. θ' VM. θ'
20	1 d.130°C	GP.[1]	103	10	Very wavy traces banded and showing coarse traces attributed to cross slip,	M.GP.[2] + {S. θ' VW.θ'
8_1	16 hr 165°C	MS.GP.[2] broad spots	103	33	Wavy irregular lines,	{S. θ' VW.θ'
8_3	16 hr 165°C	MS.GP.[2] broad spots		19	Similar appearance to 8_1	VW.GP.[2] + {S. θ' VW.θ'
13	6 d.165°C	S.GP.[2] fairly sharp spots + VW.θ'	111	15	Fine irregular slip traces first observed at about 1.5 per cent elong. (Fig. 8)	{S. θ' VW.θ'
12_1	3 d.190°C	M.θ' + M.GP.[2] both sharp		13	Very fine irregular lines observed before 5 per cent elong.	
12_2	3 d.190°C	M.θ' + M.G.P.[2] both sharp		17	No slip lines for about half the elongation. Slip lines "spilled" along from one end. Second system developed at the same end	{S. θ' M. θ'
17	22 hr 220°C	S. θ'	70	6	No slip lines visible	
3% Cu 11	2 d.190°C	S. θ'	90	10	No slip traces except near fractured edge	

* Where preferred nucleation of θ' has occurred the smaller θ' concentration is always that orientation with the primary slip direction in its (001) plane.

† d; days RT: Room temperature

‡ G.P.; Guinier Preston zones. Intensity of reflections: VW; very weak W; weak MW; medium weak M; medium MS; medium strong S; strong.

§ VPN Vickers Pyramid Number.

11 and 17 which were aged to give θ' and these crystals did not show slip traces on elongation.

When G.P.[1] zones are present the slip traces are still wavy, Table 2. The slip traces become fewer and more difficult to see with increasing G.P.[2] zones (Fig. 7). When θ' is present, the traces are still more difficult to observe; and when θ' is the only structure present, slip traces could not be observed until the crystals had been elongated more than 10 per cent. Rumples could be seen in the surface (Fig. 8) after large extensions, but irregular lines also occur with an average direction near to that expected for the primary slip plane. Conjugate slip traces were generally straighter than primary traces (Figs. 8 and 9). The necked region showed prominent steps and these were parallel to the predicted direction of either primary or conjugate slip plane traces.

It can be seen that the characteristics of the slip traces vary with the precipitate type present and not with the hardness. Abundant slip lines can be seen in crystal 20 (V.P.N. = 103), but none in crystal 11 (V.P.N. = 90) which is of slightly lower hardness. The elongations of the two crystals were the same and it must be presumed that the slip in crystal 11 is finely

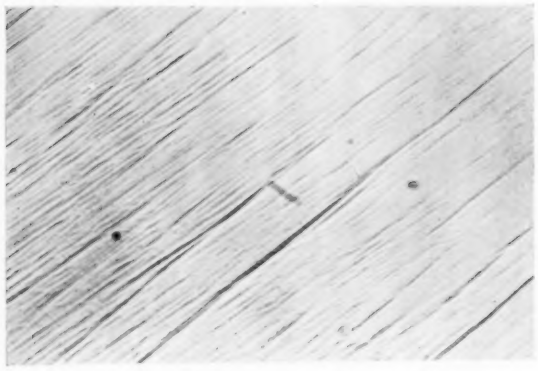


FIG. 7.

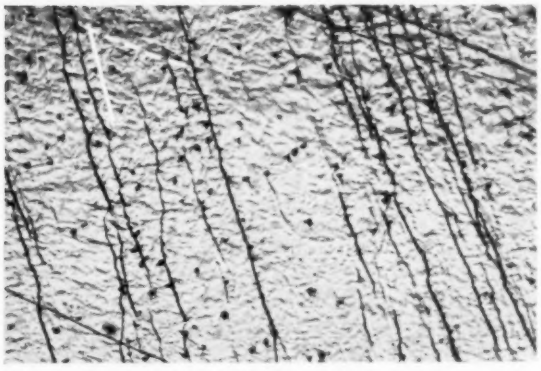


FIG. 8.

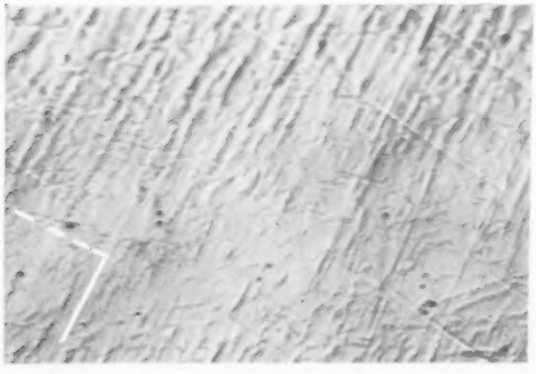


FIG. 9.

dispersed over many slip planes. Although the rotation of the tension axis for crystal 11 is not accurately towards [101] it is predominantly in this direction, and therefore it may be assumed that this is the predominant slip direction. It appears therefore that θ' platelets are more effective in stopping or deflecting dislocations than G.P.[1] or [2]. The G.P. zones being fully coherent are apparently more easily sheared, but the θ' has no close packed plane parallel to $(111)_{Al}$, and shearing is more difficult. Recently published[7,9] electron micrographs show θ' platelets which are bent rather than sheared in two.

Further ageing for 16 hr at 165°C produces θ' in preferred orientations as indicated in Table 2. The weak orientation is again that containing the slip direction in the basal plane. The results show that:

(i) G.P.[2] is rendered unstable on deformation and subsequent ageing (crystals 8_1, 8_3 and 13).

(ii) The prior presence of θ' does not prevent nucleation by slip (viz. crystal 12_2).

Therefore it is suggested that, in the deformation of material containing G.P. zones [2] initially, some dislocations remain in the vicinity of the zones, which are then the source of copper for the growth of θ' on the orientated dislocation nuclei.

(c) *Tensile curves*

Tensile curves were obtained for a number of crystals using a Hounsfield tensometer. The orientations of the tension axes for these crystals are given in Fig. 10 and the tensile curves are given in Figs. 11 and 12.

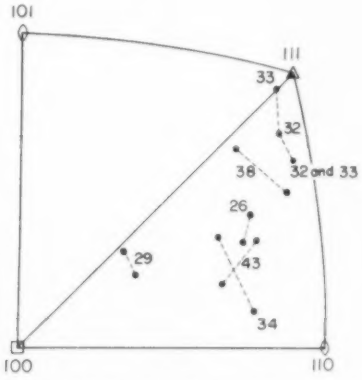


FIG. 10. Orientations of tension axis for crystals giving the tensile curves of Figs. 4 and 5.

Crystal 32 (hardened by θ') did not show readily observable slip lines until the extension corresponding to a decrease in stress. Crystal 38 (hardened by G.P. [1]) shows a low rate of work hardening, but crystal 29 does not. Crystal 29 is near the boundary and appears to have cross and conjugate slip lines, whereas crystal 38 shows primary slip traces only. The reason for the increased rate of work hardening of crystal 32 towards the end of the extension is also due to the operation of a second slip system. A low rate of work hardening may therefore be associated with crystals aged to the G.P.[1] state which are oriented to give one slip system only.

Some crystals were given a 10-min rest with no load after 5 to 10 per cent elongation. Two such

VOL. 8 1960

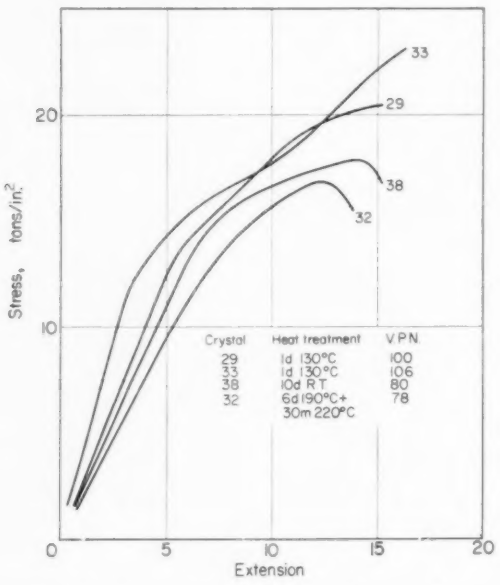


FIG. 11. Comparison between tensile curves for crystals with different preliminary ageing treatment.

curves are shown in Fig. 12. Crystals hardened by G.P. zones [1], e.g. 34, showed after the 10-min rest a definite increase in the resolved shear stress required to give deformation, but the initial slope for the "elastic" extension was the same as for the first extension. Crystals hardened by θ', e.g. 43, did not show an increase in the yield stress after the second extension but the initial slope was much steeper. This indicates that some plastic deformation does occur in the initial extension of crystals containing θ'.

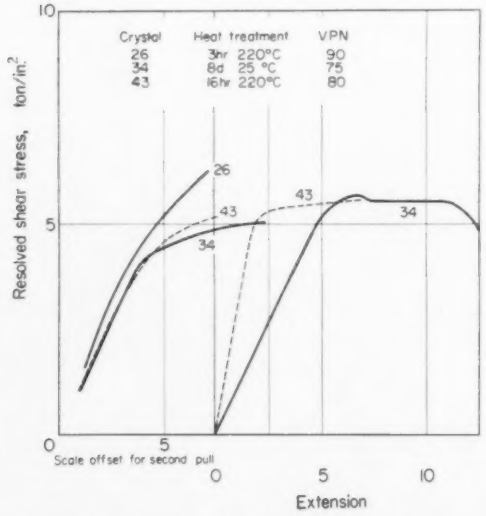


FIG. 12. Comparison of tensile curves for crystals of similar orientation given a 10-min interval with no load during extension.

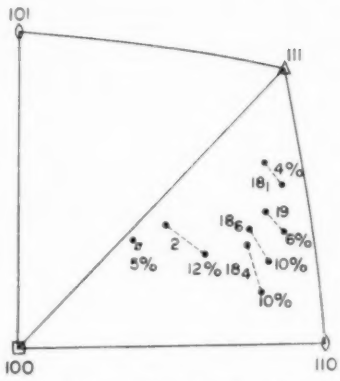


FIG. 13. Orientations of tension axes for ternary alloy crystals

The reason[4] for the increased yield stress in crystals containing G.P. zones [1] is perhaps an indication that the G.P. zones are able to rearrange themselves to give more effective locking, that is, the copper atoms probably migrate to dislocations. The total extension of crystal 43 was larger than normally obtained from crystals hardened by θ'. This may perhaps be associated with the rest at room temperature allowing a redistribution of internal stresses. In neither of the crystals containing θ' (26 and 43) did the tension axis follow the normal direction of rotation towards [101].

(d) *Ternary* Al–4% Cu 0.05% In *crystals*

The changes in the orientation of the tension axes (Fig. 13) of the quenched crystals are within the experimental error of a rotation toward the primary slip direction [101]. (The orientation of crystal *a* was only obtained after elongation.)

Both wavy and straight slip traces were observed and the difference in the appearance of slip traces was due to different surface orientations. The traces were straight in crystals where the slip direction was near (e.g. at about 10°) to the surface, but wavy (Fig. 14) for

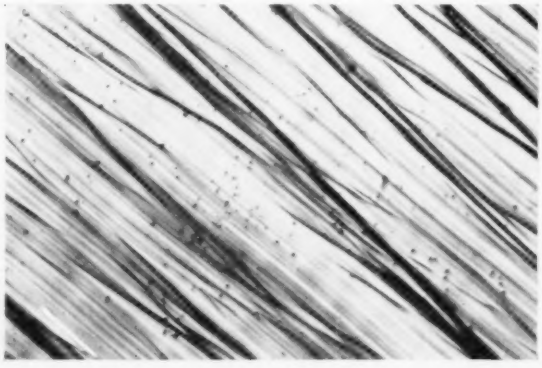


FIG. 14.

crystal 18_4 where the slip direction was at about 40° to the surface.

The effect of an ageing treatment at 165°C is somewhat erratic. Preferred nucleation of θ' can occur, but is not invariably the case. Two crystals (2 and 18_1), which it was thought had slipped on one system only, did not show preferred nucleation. Perhaps the elongation of crystal 18_1 was insufficient to destroy nucleation by cadmium, and crystal 2 may have also slipped on the conjugate system, the direction for which is also only 9° from the surface and the traces would be difficult to observe. When preferred nucleation of θ' occurs (a, 18_4 and 18_6) it is in the same orientations as in the binary Al–4% Cu crystals.

Only one aged crystal has been examined. Crystal 19 was at peak hardness after an ageing treatment of 4 hr at 190°C. The θ' platelets are smaller but more numerous than in the binary Al–4% Cu crystals. No slip lines were observed after 6 per cent elongation, but the rotation of the tension axis was towards the expected primary slip direction.

4. EFFECT OF DEFORMATION ON THE AGED STRUCTURES

There was little difference in the appearance of the diffraction patterns before and after deformation except for a slight increase in fuzziness. This could partly be explained by an increase in the range of orientations present. There was also slight broadening of the θ' reflections after high elongations which could not entirely be attributed to a range of orientations and is presumably due to a slight decrease in θ' size or to strains remaining in the θ' particles.

The G.P. zones [1] showed only a slight increase in the extent of the maxima around (002) obtained with Cu radiation. If these are due to the stress pattern around a G.P. zone [1], it might be expected that the maxima will be readily affected by stresses imposed on the matrix, but this is apparently not so. The intensity along the $000 \rightarrow 00l$ streak shows a slight increase in slope which has not been explained.

5. SUMMARY AND DISCUSSION

(a) *Slip trace characteristics*

The quenched crystals show wavy slip traces in agreement with Honeycombe[4] and Thomas and Nutting[7]. This is presumably due to the ease of cross slip owing to the short distance between the partial dislocations.[10]

Large quantities of G.P. zones [1], although raising the hardness, do not alter the slip trace characteristics appreciably. Slip lines become fewer and more difficult to observe when G.P.[2] zones are present, indicating that the slip steps are smaller. However, many slip lines are observed at peak hardness at 165°C when fairly large G.P.[2] zones are present. This is not in agreement with Thomas and Nutting who state that only a few slip lines occur when G.P. [2] is present; but in their experiments G.P. [2] was obtained by ageing at 205°C, and a mixture of G.P.[2] and θ'—and probably a majority of θ'—would be expected from single crystal X-ray work.[8]

When θ' was the only precipitate structure and present to more than about 20 per cent of the total possible, slip lines were observed only after heavy deformations and near necked regions. The traces were generally very irregular but they formed lines in the general direction expected for traces of the primary slip plane. The change of orientation of the tension axis in the specimens containing θ' was in some cases not very different from that required for primary slip. Several specimens containing θ' did, however, show considerable deviation and the direction of the deviation was variable. More fragmentation than usual was apparent in the Laue photographs of these crystals, and it is obvious that the deformation of crystals hardened by θ' is inhomogeneous. Since the conjugate slip traces are straight a high proportion of the slip must be in the primary direction but spread out over many co-operating planes. The smaller θ' platelets in ternary alloys act in the same way but larger θ' platelets formed at 240°C are not so effective.

(b) *Nucleation of θ'*

Slip on the primary system must leave behind oriented θ' nuclei. The orientations of θ' platelets nucleated are those which do not contain the slip direction in the $(001)_{\theta'}$ plane. That is, with reference to Fig. 15, if D is the slip direction, the orientations of θ' with $[001]_{\theta'}$ in directions a and b are nucleated, but the θ' with [001] in direction c is not nucleated. To form θ' from the matrix compression in the $[001]_{\theta'}$ direction is required. The deformation will leave behind an excess of edge dislocations with their Burgers vectors in the direction of slip. There is therefore the required compression for forming nuclei of θ' in orientations a and b (Fig. 15) but not in orientation c.

If we now consider that the edge dislocation is probably split into partial dislocations (but the partial dislocations will only be separated by a few atomic distances) we can see that the atomic positions at a partial dislocation, Fig. 16, give a θ' like arrangement. It is probable that copper atoms will segregate

VOL. 8 1960

to regions of compression so that a θ' nucleus may be formed. One partial will nucleate the θ' orientation a and the other the θ' orientation b. After cold work G.P.[2] frequently forms only in the same two orientations as θ' which indicates that a copper-rich layer can more easily form along the $\{100\}_{Al}$ planes containing the slip direction. No θ' would form in the work free crystal with the ageing treatment given and yet there would be a number of dislocations present, so it appears that one partial dislocation is insufficient for nucleation. It seems that either a pile up of dislocations is required, or some special grouping of dislocations such as at a Lomer–Cottrell lock. It is difficult to see how Lomer–Cottrell locks can lead to nucleation of only two orientations since to form the lock a partial on a system besides the primary system is required. The locks introduce[11] a neighbouring dislocation of Burgers vector $[0\bar{1}1]$, for primary slip on $(11\bar{1})[101]$. This lies within the basal plane of one of the nucleated θ' orientations. The basal θ' plane, however, does not require compression but requires vacancies on alternate planes. It does not appear, therefore, that this neighbouring dislocation would aid nucleation in the observed orientations.

Easy θ' nucleation can occur if there is a line of partial dislocations either in the [110] direction in the plane of Fig. 1, or in the $[1\bar{1}0]$ direction perpendicular to the plane of Fig. 1, or in fact in any direction in the $(00\bar{1})$ plane. The direction $[1\bar{1}0]$ is in the slip plane and could be the line of a dislocation. The other direction [110] is a direction of a possible Burgers vector of a Lomer–Cottrell lock, whether this could cause a line up of partial dislocations is not known. It seems probable that extension of the nucleus depicted in Fig. 1 is required in both directions. The direction in which the partials are lined up will control

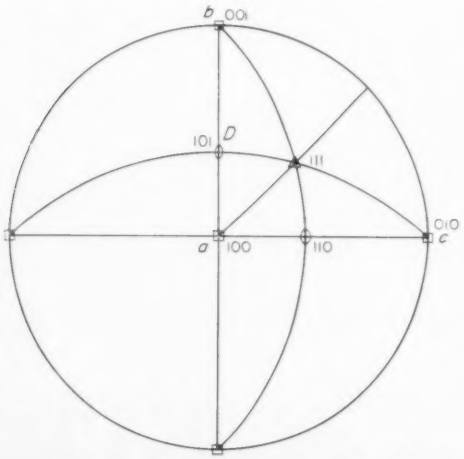


FIG. 15. Orientations of θ' platelets.

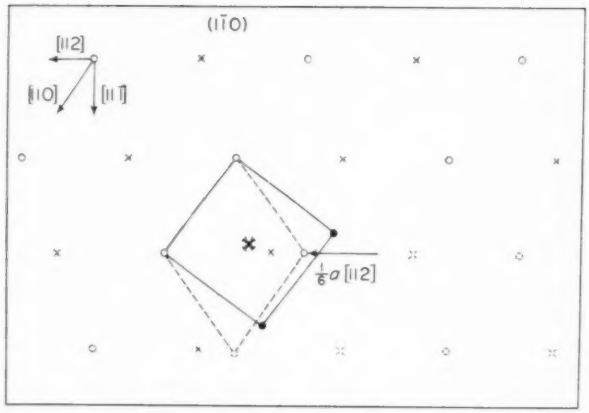


FIG. 16. Formation of a θ' nucleus at the edge of a partial dislocation.

which of the two possible orientations is favoured. In the large volume examined by X-ray methods the chances for nucleation in either direction are equal.

It is known that nucleation of θ' can occur at low angle boundaries,[2,12] and that at these polygon boundaries there is often only one of the possible two orientations nucleated. A polygon boundary is formed by an aggregate of dislocations, the majority having their Burgers vector approximately perpendicular to the boundary. The orientations that will not be nucleated are, therefore, those with $[001]_{\theta'}$ perpendicular to the boundary. In agreement with this, electron micrographs,[2,12] generally show θ' platelets almost parallel to small angle boundaries. The orientation which is nucleated will depend on the angle between the boundary plane and the edge dislocations. The nearer the polygon boundary is to a $(100)_{Al}$ plane, the more exactly will the partials be lined up in correct array for nucleation of the θ' with its [001] direction (normal to the platelet) perpendicular to that plane. Therefore it would be expected that platelets will tend to be as nearly as possible parallel to the polygon boundary, and the more parallel they are the fewer should be the nuclei in the other orientation. This does appear to be generally true.

(c) *Relation between mechanical properties and slip trace characteristics of aged crystals*

The outstanding feature in the deformation behaviour of these alloys is that the presence of well marked slip lines is not an indication of low hardness. For example, crystals 20, 8 and 13 are relatively hard

TABLE 3. Summary of the effect of precipitates in Al-Cu alloys on the propagation of dislocations

Preprecipitate or precipitate	Slip traces	Hardening	Apparent Contribution of	
			source locking	dislocation blocking
GP.[1]	Very well-defined	Moderate	Stronger the larger the particle	Very weak
GP.[2]	Well-defined	High	Very strong	Moderate
θ'	Absent	Moderate	Weak	Strong
Small θ' in ternary alloys	Absent	Very high	Weak?	Very strong

and yet form well marked slip traces, while crystal 17 of similar hardness showed no slip lines. The absence of visible slip lines is attributed to the blocking and deflection of dislocations by the precipitate particles, so that only short lengths of a dislocation line operate in any one plane. In the crystals hardened by G.P. zone [1] the dislocations, once moving, apparently continue, and there is no obstacle to a large number operating in one plane. It is apparently the locking of the dislocation sources which increases the hardness. The hardness is far greater than in the solid solution, so that the locking is not simply by solute atmospheres but by the zones themselves or their strain fields.

If dislocation sources operate easily but the dislocations are stopped or deflected by the particles so that the slip distance is small and deformation from a given source is spread on many slip planes, the yield stress should be relatively low but work hardening high. The tensile curves obtained on single crystals show that there is a tendency for the yield stress to be lower and the work hardening higher in crystals hardened by θ' than those hardened by G.P.[1] zones. In Table 3 the behaviour of precipitates occurring in the Al–Cu alloys are summarized according to the interpretation given above.

ACKNOWLEDGMENTS

The author wishes to thank her former colleagues at Fulmer Research Institute, and particularly Dr. Calnan, for many helpful discussions.

REFERENCES

1. J. M. SILCOCK, T. H. HEAL and H. K. HARDY, *J. Inst. Met.* **84,** 23 (1955–56).
2. H. WILSDORF and D. KUHLMANN-WILSDORF, *Defects in Crystalline Solids* p. 175 Physical Society, London (1955).
3. E. SCHMID and W. BOAS, *Plasticity of crystals* F. A. HUGHES, London, (1950).
4. K. M. CARLSEN and R. W. HONEYCOMBE, *J. Inst. Met.* **83,** 449 (1954–55).
5. G. C. SMITH and D. W. DEWHIRST, *Research, Lond.* **2,** 492 (1949).
6. C. EDELEANU, *J. Inst. Met.* **81,** 649 (1951–52).
7. G. THOMAS and J. NUTTING, *J. Inst. Met.* **86,** 7 (1957–58).
8. J. M. SILCOCK, H. K. HARDY and T. J. HEAL, *J. Inst. Met.* **82,** 239 (1953–54).
9. S. KODA and T. TAKEYAMA, *J. Inst. Met.* **86,** 277 (1957–58).
10. A. SEEGER, J. DIEHL, S. MADER and H. REBSTOCK, *Phil. Mag.* **2,** 323 (1957).
11. J. FRIEDAL, *Phil. Mag.* **46,** 1182 (1955).
12. E. LANGER, *J. Inst. Met.* **84,** 471 (1955–56).

VOL. 8 1960

EFFECTS OF NON-UNIFORMITIES ON THE HARDENING OF CRYSTALS*

R. L. FLEISCHER†

The ease of motion of a dislocation in a crystal is influenced by changes in lattice parameter and elastic modulus. For solid solutions where such changes are gradual the hardening is negligible, but for abrupt changes, such as occur at a precipitate, the effect is important. The changes in lattice parameter lead to the production of interface dislocations and suggest a work hardening model for one class of precipitation hardened alloys. Interface dislocations may also affect flow near a free surface.

EFFETS DES NON-UNIFORMITES SUR LE DURCISSEMENT DES CRISTAUX

La facilité du déplacement d'une dislocation dans un cristal est influencée par les modifications du paramètre réticulaire et du module élastique.

Dans le cas de solutions solides où de telles modifications sont progressives, le durcissement est négligeable. Par contre, lors de variations brusques de ces paramètres, l'effet est important: c'est le cas notamment pour un précipité.

Les modifications du paramètre réticulaire provoquent la formation de dislocations d'interfaces et on peut en déduire un modèle pour le durcissement structural d'un type déterminé d'alliages durcissant par précipitation. Les dislocations d'interfaces peuvent également affecter le glissement près de la surface libre.

EINFLÜSSE VON UNGLEICHMÄSSIGKEITEN AUF DIE VERFESTIGUNG VON KRISTALLEN

Die Beweglichkeit einer Versetzung in einem Kristall wird durch Änderungen der Gitterparameter und der elastischen Konstanten beeinflußt. Bei festen Lösungen, in denen solche Änderungen allmählich auftreten, ist die Härtesteigerung vernachlässigbar; jedoch entsteht ein großer Effekt bei plötzlichen Änderungen, wie sie bei einer Ausscheidung auftreten. Die Änderungen der Gitterparameter führen zur Erzeugung von Grenzflächenversetzungen. Daraus folgt ein Vorschlag eines Verfestigungsmodells für eine Klasse von ausgehärteten Legierungen. Grenzflächenversetzungen können sich auch auf das plastische Fließen in der Nähe einer freien Oberfläche auswirken.

A previous article[1] has indicated that solid solution hardening can be produced by at least three effects of a non-uniform solute distribution: changes in elastic constants, changes in lattice parameters and stress fields of individual solute atoms. The last of these factors was considered quantitatively. It is the purpose of this discussion to examine in some detail the effect of changes in elastic modulus and lattice parameter.

It will be shown that in the case of gradual changes, as in a solid solution, the effects considered here will be much less than the effect of the stress fields of individual atoms. For very rapid or abrupt changes, however, effects may be large. These effects represent an approach to understanding the hardening of a two phase alloy. The two effects will be evaluated separately in idealized cases for rapid and gradual changes, and then their possible relation to real systems will be discussed.

1. ESTIMATE OF EFFECTS OF CHANGE IN ELASTIC MODULUS

1.1 *Discrete change*

If an edge dislocation in a medium of shear modulus G_1 is a distance x from a region where the modulus abruptly becomes G_2 across a plane normal to the slip vector, Head[2] has shown that the dislocation is repelled by an effective stress of about

$$\frac{G_1(G_2 - G_1)b}{4\pi(1 - \nu_1)(G_1 + G_2)x} \tag{1.1}$$

where ν_1 is Poisson's ratio. If $G_2 - G_1 = \Delta G \ll G_1$ the stress becomes approximately $\Delta G b/8\pi(1 - \nu)x$.

1.2 *Gradual change*

If there exists a uniform gradient (dG/dx) of the shear modulus, then the total effect may be estimated by adding the effects of many small discrete steps each of strength $(dG/dx)b$ and placed a distance b apart. For a step at a distance nb from the dislocation the stress is

$$\tau(n) = (dG/dx)b^2/8\pi(1 - \nu)nb. \tag{1.2}$$

Hence for steps starting at a distance b and extending to r_∞,

$$\tau = (dG/dx)b/8\pi(1 - \nu)\sum_{n=1}^{r_\infty/b}(1/n)$$

$$\approx (dG/dx)b \log (r_\infty/b)/8\pi(1 - \nu).$$

If the gradient extends from $-r_\infty$ to $+r_\infty$,

$$\tau = (dG/dx)b \log (r_\infty/b)/4\pi(1 - \nu),$$

where the step at the dislocation has been neglected.

* Received July 19, 1959; revised October 6, 1959.

† Department of Metallurgy, Massachusetts Institute of Technology, Cambridge, Mass. Now at General Electric Research Laboratory, Schenectady, New York.

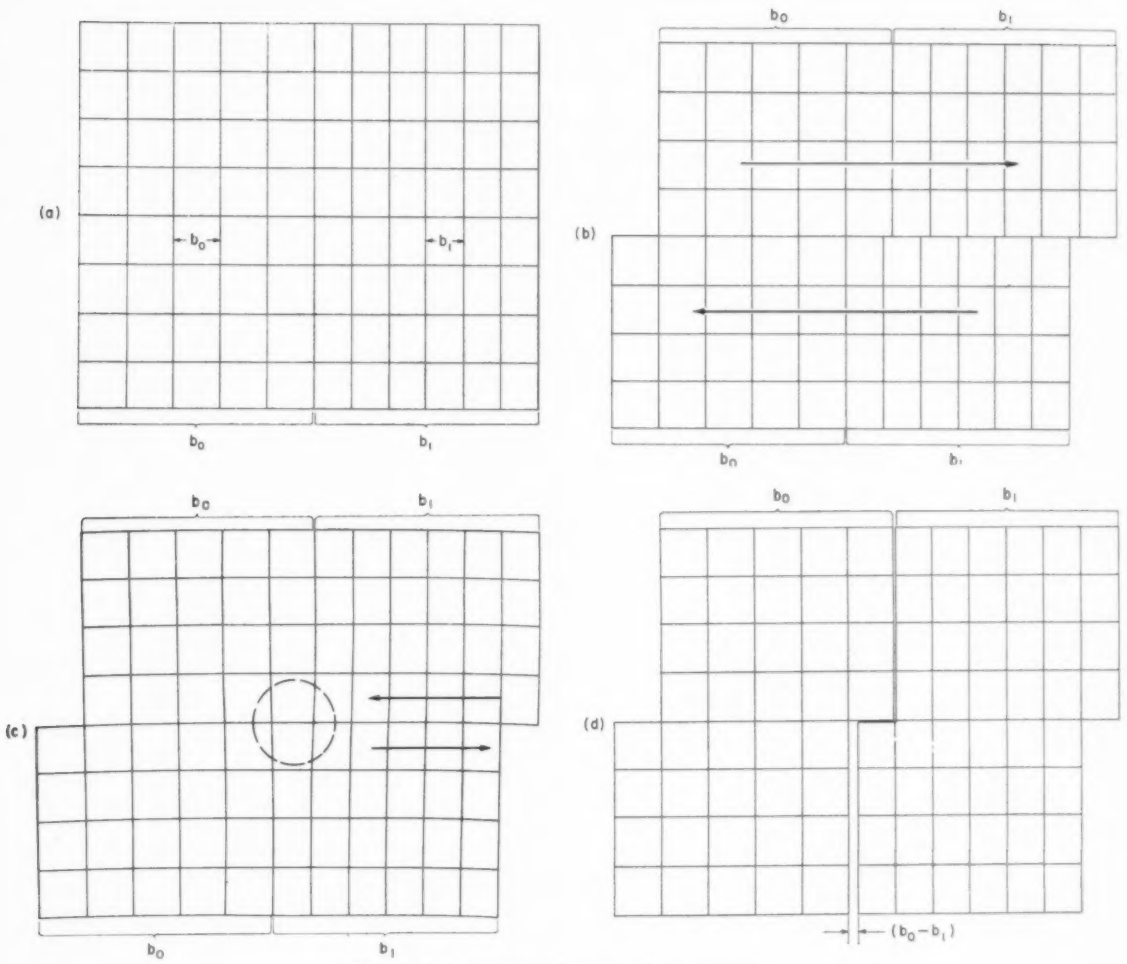


FIG. 1. Slip across a change in lattice spacing.

If the change in modulus is due to a concentration gradient, the stress may be written

$$\tau = (dG/dc)(dc/dx)b \log (r_\infty/b)/4\pi(1 - \nu), \quad (1.3)$$

where c is the concentration. This result will be discussed in more detail in Section 3.

2. EFFECTS OF CHANGING LATTICE SPACING

2.1 *Discrete change*

First a qualitative discussion will be presented, followed by some quantitative estimates.

Imagine a medium such as is described by the lattice in Fig. 1(a), where the lattice constant in the horizontal direction changes abruptly from b_0 to b_1, which is less than b_0. If an edge dislocation of slip vector b_0 moves horizontally into the region of constant b_1, it then obtains a slip vector b_1. A decrease of amount $b_0 - b_1$ has occurred, and hence a dislocation of that slip vector must be retained at the interface between the b_0 and b_1 parts of the lattice.

The above result may be visualized by the following hypothetical sequence of events: (i) A cut is made along the slip plane extending from the b_0 into the b_1 region and a relative horizontal displacement b_0 supplied. This displacement restores fit in the b_0 region, leaves a misfit surface from the boundary to the end of the slipped region and creates a dislocation of slip vector b_0, which has moved out of the field of view in Fig. 1(b). (ii) The dislocation of slip vector b_0 dissociates into one of vector b_1 and a second of vector $b_0 - b_1$, decreasing its energy in the process. (iii) The dislocation of $b_0 - b_1$ moves to the boundary between the two regions, thus erasing the surface of misfit. As before, the end result is a dislocation of vector b_1 in the region of lattice constant b_1 and a dislocation at the boundary. By the process just described it can be seen that this second dislocation will be sessile, since its motion away from the interface would create the misfit surface which was just

pictured as erased. Fig. 1(c) shows the final configuration with the glissile dislocation still out of the picture to the right. The lattice bending due to the remaining dislocation is visible.

A third and probably the most direct way of viewing the necessity for a built-in dislocation is indicated in Fig. 1(d), where two lattices with unit steps are brought together. There is a failure to match amounting to a layer of thickness $b_0 - b_1$, which therefore requires a dislocation of slip vector $b_0 - b_1$.

It is, however, worth noting that there exists no extra half plane of atoms such as is associated with the usual edge dislocation. In fact all atoms, even at the core of this dislocation, have correct nearest neighbor relations, aside from elastic distortions. The dislocations created will be referred to here as interface dislocations.

The example considered may be described by the reaction

$$b_0 \rightarrow (b_0 - b_1) + (b_1).$$

The total energy is thus decreased—i.e. the dislocation is attracted toward and through the interface. However subsequent dislocations on the same plane have the stress field of $b_0 - b_1$ to overcome and each additional full dislocation adds a new sessile interface dislocation to hinder later full dislocations.

For a dislocation moving from right to left in Fig. 1, the slip vector of the full dislocation must increase from b_1 to b_0:

$$b_1 \rightarrow b_0 - (b_0 - b_1).$$

In short a new dislocation pair $\pm(b_0 - b_1)$ must be created at the interface, $+(b_0 - b_1)$ adding to b_1 to give b_0 and $-(b_0 - b_1)$ remaining as an interface dislocation. This interface dislocation, being negative, will attract a following dislocation b_1, but will make still more difficult its continued motion past the interface, since to do so it would need to create two interface dislocations. Hence regardless of the direction of slip, dislocations encounter more and more difficulty in passing through the interface.

If there is a change in lattice parameter in a direction normal to Fig. 1(a), then a screw dislocation with slip vector in that direction must alter its slip vector as it enters the region of different lattice parameter. Hence there may be screw as well as edge interface dislocations.

2.2 *Estimate of stresses involved*

Assume an edge interface dislocation has a vector $\Delta b\ (= b_0 - b_1)$. Its shear stress on the slip plane will then be given by[3]

$$G\ \Delta b/2\pi(1 - \nu)x, \qquad (2.1)$$

where G = effective shear modulus, ν = Poisson's ratio and x = distance from the interface. Hence a second dislocation will be opposed by an effective stress given by equation (2.1). If n dislocations have crossed the interface, then there will be n interface dislocations spaced a distance $b\left(= \dfrac{b_0 + b_1}{2}\right)$ apart. If these extend from $x = 0$ to $x = -(n - 1)b$, then the shear stress is given by

$$\tau = \sum_{j=0}^{n-1} \tau_0 b/(x + jb),$$

where $\tau_0 = G\ \Delta b/2\pi(1 - \nu)b$.

Approximately $\tau = \tau_0 \int_0^n dj/(j + x/b)$

$$= \tau_0 \log (nb/x + 1), \qquad (2.2)$$

so that the stress increases with increasing n. If there is just one interface dislocation, the stress as given by equation (2.1), will cease to be meaningful when a dislocation approaches within one atomic distance; setting $x = b$ and $\Delta b/b = 1/20$, a stress of $G/80$ is obtained, indicating that it should be much easier to slip on adjacent parallel atomic planes rather than continuing slip on the given plane. A dislocation on a parallel plane a distance y from the interface dislocation must overcome a stress of approximately[3]

$$G\ \Delta b/8\pi(1 - \nu)\, y. \qquad (2.3)$$

If this motion supplies a shear strain γ equal to b/y, work hardening is given by

$$\tau = [G\ \Delta b/8\pi(1 - \nu)b]\, \gamma, \qquad (2.4)$$

a hardening rate of about $G/300$ when $\Delta b/b = 1/20$. This calculation will be discussed in greater detail in Section 4.

2.3 *Gradual change in lattice spacing*

A constant gradient of lattice spacing will be assumed and considered to be equivalent to a series of abrupt changes each b apart and of amount $(db/dx)b$. An edge dislocation moving in the x-direction will then create an interface dislocation of strength $(db/dx)b$ each atomic distance b along its path, and the nth dislocation leaves interface dislocations of strength $n(db/dx)b$. It is assumed that the gradient begins at $x = 0$ and extends to $-r_\infty$. The stress on a following dislocation at x is

$$\tau = \frac{Gb}{2\pi(1 - \nu)} \left(\frac{db}{dx}\right) \left(\frac{1}{x} + \frac{1}{x + b} + \frac{1}{x + 2b} + \cdots + \frac{1}{x + r_\infty}\right)$$

$$\approx [G/2\pi(1 - \nu)]\ (db/dx) \log (r_\infty/x), \qquad (2.5)$$

if $r_\infty/x \gg 1$.

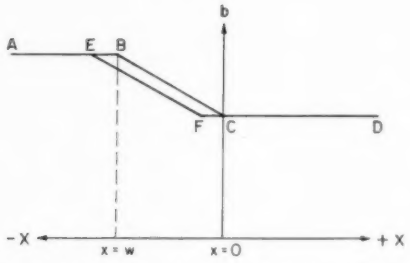


FIG. 2. Lattice parameter as a function of position. *ABCD* initial values and final values below slip plane; *AEFC* final values above slip plane.

If the changes in lattice parameter are due to a solute concentration change,

$$\tau = [(G/2\pi(1-\nu)] \log (r_\infty/x)(db/dc)(dc/dx).$$

When n dislocations have passed,

$$\tau = n[G/2\pi(1-\nu)] \log (r_\infty/x)(db/dc)(dc/dx), \tag{2.6}$$

so that the maximum value of τ will be approximately

$$\tau = n[G/2\pi(1-\nu)] \log (r_\infty/b)(db/dc)(dc/dx), \tag{2.7}$$

as long as $n \ll r_\infty/b$ so that the effects of the end of the gradient are small relative to the overall gradient itself. Fig. 2 illustrates the variation of the lattice parameter. *ABCD* represents the variation before any slip has occurred. After a slip of n-distances *ABCD* still represents the spacing in the lower half of the crystal, while *AEFD* gives the spacing in the upper half. If *BE* is small ($n \ll w/b$), this results approximately in interface dislocations of slip vector $n(db/dx)b$ from $x = 0$ to $x = -w$.

3. RELATION TO MECHANICAL PROPERTIES OF SOLID SOLUTIONS

Values derived for the possible contribution to the flow stress of elastic moduli and lattice parameter changes are indicated in equations (1.3) and (2.7). If the stress due to the change in modulus is τ_G and that due to change in lattice parameter τ_b, then

$$\tau_G/\tau_b = \frac{d \log G/dc}{2n\, d \log b/dc}.$$

The ratio $(d(\log G)/dc)/d(\log b)/dc)$ has been computed for a number of alloys using existing data.[4,5] The results are summarized in Table 1. It can be seen that values between -8 and -50 and $+3$ and $+22$ are obtained, so that the two contributions may either add or subtract. Choosing ± 18 as typical, $(\tau_G/\tau_b = (9/n)$ so that the two effects may be comparable after about nine dislocations have passed. Comparing one of these effects with the Cottrell effect due to the stress fields of individual atoms as considered previously,[1] it is found that if the Cottrell effect contributes a stress τ_c, then

$$\tau_b/\tau_c = \frac{d \log b/dc \log (r_\infty/b)}{8\pi(1-\nu)\varepsilon(r_\infty/b)},$$

where ε represents the misfit of the impurity atom. Selecting as reasonable values $d \log b/dc = \varepsilon$[6] and $r_\infty/b = 10^4$, $(\tau_b/\tau_c) < 10^{-4}$, so that the effects of lattice parameter change and elastic modulus change are negligible relative to those of the atomic stress fields.

TABLE 1. Ratio $(d \log G/dc)/(d \log b/dc)$ for various alloys

Metal	Solute (at. %)	$(d \log G/dc)/d \log b/dc)$*
Cu	Zn (4.59)	−14
	(28)	−8.2
	Al (4.81)	−12
	(9.98)	−8.0
	Ga (1.58)	−20
	(4.15)	−13
	Si (4.17)	−43
	(5.16)	−49
	(7.69)	−50
	Ge (1.03)	−23
	(1.71)	−20
Al	Cu (5)	+2.9
Ag	Mg (3.07)	−20
	(7.33)	−16
	Zn (2.4)	+22
	(3.53)	+11
	Cd (1.34)	−9.8
	(1.92)	−6.8
	In (8.36)	−9.7
	Sn (3.17)	−11
	Pd (6.22)	−11

* For G the quantity $\sqrt{[C_{44}(C_{11} - C_{12})/2]}$ has been used.

4. RELATION TO PRECIPITATION HARDENING

In contrast to the effects of gradual changes in modulus or lattice parameter, abrupt changes contribute large effects. Hence the approach developed here gives a means of understanding the hardening of a crystal containing a precipitate. Since the discussion has assumed that changes occur across a plane, the results should apply most directly to layer shaped precipitates, which are frequently obtained[7] and have been predicted theoretically.[8] The type of consideration involving interface dislocations, however, applies whenever two phases have nearly

VOL. 8 1960

matching lattices. It should also be noted that coherency between precipitate and matrix is not in general necessary, as long as the lattices have common slip plane orientations.

Section 2.2 assumed a simplified work hardening model in terms of interface dislocations. It was assumed that the flow stress was determined by the ease of moving a normal dislocation on one atomic plane past a (sessile) interface dislocation on another plane (or alternatively, moving dislocations between pairs of interface dislocations spaced $2y$ apart). Two assumptions implicit in this description deserve discussion. The first is the statement that an interface dislocation is sessile, which may be shown by the following estimate of the stress needed to move such a dislocation: Assume an applied stress moves a unit length of interface dislocation of slip vector Δb through a unit distance. The energy supplied is $\tau\,\Delta b$ and this energy is stored in a misfit surface which is a result of a shear $\Delta b/b$ on the slip plane, assumed to be spaced b from the next atomic plane. The energy stored in this layer of thickness b is

$$\int_{\text{volume}} \int G\,d\gamma\,dV = G(\Delta b^2/2b^2)b$$

so that $\tau = G\,\Delta b/2b$, which will usually be higher than observed flow stress. Relaxing the implicit assumption that the strain $\Delta b/b$ occurs according to Hooke's law will not alter the conclusion that an interface dislocation will be sessile.

The second assumption in equation (2.4) is a more critical one, since it is almost certainly wrong: For the model to be meaningful, dislocations must be available on nearly all atomic planes. At yield this is clearly unlikely, so that higher hardening is to be expected before large amounts of dislocation generation have taken place along with cross slip or climb. Later during deformation high stresses may allow by-passing of precipitates in the manner envisioned by Orowan[9], so that the hardening rate diminishes.

Therefore it is expected that equation (2.4) should apply best at intermediate strains and should be compared with some average hardening rate of a precipitation hardened alloy.

Livingston and Becker[10] have considered a copper alloy containing a precipitate of face-centered-cubic cobalt, which has the same orientation as the copper matrix. If one assumes that Δb for equation (2.4) is given by the difference in the room temperature atomic diameters for f.c.c. Co and Cu, then $\Delta b/b = 1/50$, and from equation (2.4) $d\tau/d\gamma = 7$ kg/mm^2. As the average rate of tensile strain hardening over the first 10 per cent of tensile strain, Livingston and Becker give values from 200,000 to 290,000 lb/in^2 which, using Kocks'[11] method of resolving stress and strain, corresponds to a shear hardening rate from 14.5 to 21 kg/mm^2. As suggested earlier, for early strains equation (2.4) should give a value that is too small. Since in the case quoted[10] the precipitate is in the form of spheres rather than plates and because of the simplifying assumptions in equation (2.4), its use is intended only to indicate the magnitude of the effect rather than to provide a reliable check of the theory.

An alternative view of hardening which should be examined is that of Orowan[9] and Fisher *et al.*[12]. Orowan suggested that the flow stress would be that necessary to bend dislocations around impenetrable precipitates, encircling and by-passing them. Fisher *et al.* then considered the work hardening due to the loops which remain around the precipitates. The smallest possible value of the flow stress to allow by-passing is that shown by Orowan[9] to be Gb/l, where l is the spacing of particles. If there is a volume concentration c of spheres of diameter d, the spacing can be found approximately from $c = (4\pi/3)(d/2)^3/(l + d)^3$. On this basis, calculated values of the flow stress are compared with yield stresses observed by Livingston. Two values of observed shear stresses are given in Table 2, one as an upper limit assuming a resolved shear stress factor of 0.5, the other, which is more realistic, assuming homogeneous deformation and slip on five slip systems (resolved shear factor 0.32).

Table 2 indicates that observed yield stresses are considerably less than those required to by-pass precipitates and hence that by-passing could occur, as suggested in an earlier paragraph, only in advanced stages of deformation after considerable work hardening. In the calculation a value of $d = 140$ Å was used, corresponding to maximum observed hardness; i.e. the comparison was made as favorably as possible. The fact that the effective size of the precipitate particle is probably larger than the particle itself—due to coherency stresses[13] and image

TABLE 2. Evaluation of impenetrable particle hypothesis

Concentration (vol. %)	Shear stress (kg/mm^2)		
	Calculated	Observed* (homogeneous deformation)	Observed* (maximum resolved shear stress)
0.2	9	2	3
1.0	16	5	7
2.0	22	7	11

* From data by Livingston and Becker[10].

stresses from elastic modulus changes—has been ignored, so that the true value of the stress for by-passing is likely to be well above the values calculated here.

A second and even more decisive reason for ruling out by-passing was the observation[10] that the precipitate did deform homogeneously with the matrix up to a strain of 35 per cent. This behavior is consistent with the view proposed here, which also predicts fine slip such as must have occurred in Livingston and Becker's[10] work and has been observed for other precipitation hardened alloys.[14]

It should also be remarked that the effects which have been discussed here are supplementary to the one considered by Mott and Nabarro[13], who calculated the effect on the yield stress of the elastic strain around a coherent precipitate. The effects are also supplementary to what is essentially a disordering energy effect on the yield stress,[15] which was considered by Kelly and Fine. The contribution due to the precipitate possessing elastic properties that are different from the matrix will be present regardless of the coherency of the second phase, and as has already been noted, interface dislocations may also be important regardless of coherency.

VOL. 8 1960

5. CREATION AND ANNIHILATION OF DISLOCATIONS AT FREE SURFACES

The view has often been expressed that the lattice spacing of a crystal near a free surface differs from its value well inside the sample.[16–19] There appears to be little agreement, however, on the depth of the altered zone, since there are estimates indicating from one[16] to "several hundred"[19] atomic spacings. The sign of the change has been thought to correspond to an expansion in ionic crystals[16] and a contraction[17,18] in metals. Observations of small crystals by means of electron diffraction[20] show that the lattice parameter of the ionic and metallic crystals which were examined decreases as crystal size is reduced. Though not conclusive, this result suggests that surface layers are spaced differently than interior ones. Regardless of whether the change in spacing is inherent or produced by the accidental or intentional presence of impurity atoms in the surface layers, this change may lead to surface obstacles to slip.

Figure 3(a) shows schematically a crystal having a variation of lattice constant over the first four layers from the surface. If an edge dislocation were to pass out of such a crystal (from left to right), as indicated in Fig. 3(b), not only is a surface step created but also a region of atomic misfit extending into the crystal at least five atomic distances. This misfit region would

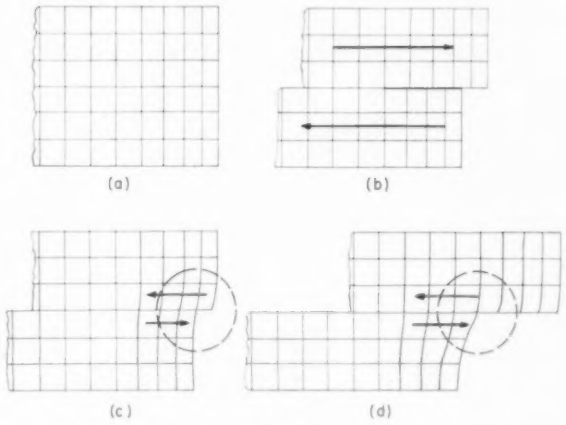


FIG. 3. Slip across changing lattice spacing near a free surface.

be expected to readjust by a slip displacement Δb into the distortion indicated in Fig. 3(c). Because energy must be supplied to create the step[21] and the distorted region, the motion of the dislocation will be opposed. Because the surface step energy alone is nearly sufficient to prevent edge dislocations from escaping a crystal,[21] this additional energy should be significant.

The same effect may arise if one considers a crystal already containing a step, as is shown in Fig. 3(c). Since crystals are not likely to be atomically flat, such steps are likely to exist without prior motion of dislocations. With each step is a region of atomic misfit which, it can be seen, is an interface dislocation at a free surface. Fig. 3(d) shows that the distortion becomes greater as the step height increases toward the thickness of the layer of non-uniform lattice parameter.

An estimate of the built-in stresses at the step can be made by the following procedure: Imagine adding to the crystal in Fig. 3(c) or (d) a crystal obtained by rotating the original crystal 180° about an axis along the step. The two parts can now be seen to match. Hence the stress from the interface dislocation at a free surface may be approximated by two interface dislocations of opposite sign in an infinite crystal. If the shelf width is w and the distance x along the slip plane is measured from the midpoint of the shelf, then the shear stress τ on the slip plane is given by

$$\tau = [G\,\Delta b/2\pi(1-\nu)]\left(\frac{1}{x-w/2}-\frac{1}{x+w/2}\right)$$
$$= G\,\Delta b w/2\pi(1-\nu)\,x^2 \text{ for } x \gg w.$$

This result is only an approximate one. Were the spacing of surface layers known as a function of x, the distribution of displacement along the slip plane

could be described more accurately by a distribution of dislocations. They would extend from $x = w/2$ to wherever the lattice parameter resumes its usual value, and the sum of their slip vectors would be Δb.

6. CONCLUSIONS

Hardening effects due to change in elastic modulus and lattice parameter have been considered. It has been shown that these effects should be important for two phase systems but not for solid solutions.

Dislocations crossing into a region of different lattice constant along the slip direction must create sessile dislocations at the interface. A work hardening calculation due to these interface dislocations was consistent with rates observed in a relevant precipitation hardening alloy.

It was also noted that interface dislocations may exist at free surfaces and hence give rise to surface hardening.

ACKNOWLEDGMENTS

The author is pleased to give thanks to his friends and associates for helpful discussions, particularly to Professor B. Chalmers, Dr. J. D. Livingston, and Professor A. N. Stroh. The financial support of the Atomic Energy Commission is gratefully acknowledged.

REFERENCES

1. R. L. Fleischer, *Acta Met.* **8,** 32 (1960).
2. A. K. Head, *Phil. Mag.* **44,** 92 (1953).
3. W. T. Read, *Dislocations in Crystals*, McGraw-Hill, New York (1953).
4. W. B. Pearson, *Handbook of Lattice Spacings and Structure of Metals and Alloys.* Pergamon Press, New York (1958).
5. R. F. S. Hearmon, *Rev. Mod. Phys.* **8,** 409 (1946); *Advanc. Phys.* **5,** 323 (1956).
6. F. R. N. Nabarro, *Proc. Phys. Soc., Lond.* **58,** 669 (1946).
7. H. K. Hardy and T. J. Heal, *Progr. Met. Phys.* **5,** 143 (1954).
8. F. R. N. Nabarro, *Proc. Phys. Soc., Lond.* **52,** 90 (1940).
9. E. Orowan, *Symposium on Internal Stresses* p. 451. Institute of Metals, London (1947).
10. J. D. Livingston and J. J. Becker, *Trans. Amer. Inst. Min. (Metall.) Engrs.* **212,** 316 (1958); J. D. Livingston *Trans. Amer. Inst. Min. (Metall.) Engrs.* **215,** 566 (1959).
11. U. F. Kocks, *Acta Met.* **6,** 85 (1958).
12. J. C. Fisher, E. W. Hart and R. H. Pry, *Acta Met.* **1,** 336 (1953).
13. N. F. Mott and F. R. N. Nabarro, *Proc. Phys. Soc., Lond.* **52,** 86 (1940).
14. K. M. Carlsen and R. W. K. Honeycombe, *J. Inst. Met.* **83,** 449 (1954-55).
15. A. Kelly and M. E. Fine, *Acta Met.* **5,** 365 (1957).
16. J. E. Lennard-Jones and B. M. Dent, *Proc. Roy. Soc.* A**121,** 247 (1928).
17. H. H. Uhlig, *Metal Interfaces*, p. 312. Amer. Soc. Metals, Cleveland (1952).
18. C. Herring, *Metal Interfaces*, p. 19. Amer. Soc. Metals, Cleveland (1952).
19. W. A. Weyl, *Structure and Properties of Solid Surfaces*, p. 156. Chicago University Press, Chicago, (1953).
20. F. W. C. Boswell, *Proc. Phys. Soc., Lond.* A**64,** 465 (1951).
21. F. R. N. Nabarro, *Advanc. Phys.* **1,** 332 (1952).

THE THERMAL DIFFUSION OF CARBON IN α AND γ IRON†

P. SHEWMON‡

The heats of transport, Q^*, for carbon in α and γ iron have been accurately measured for the first time. A radioactive tracer technique was used and the following values obtained. $Q_c^*(\alpha) = -24 \pm 1.5$ kcal at 700°C, $Q_c^*(\gamma)$ ranged from −2 kcal to zero in going from 0.02 per cent C to 0.92 per cent C at approximately 940°C. A kinetic treatment due to Wirtz explains the data for $Q_c^*(\alpha)$ if it is assumed that all of the activation energy for carbon diffusion goes into preparing the lattice around the site the atom jumps into. From this satisfactory explanation of Q^* it would appear that studying the effect of a temperature gradient on other simple diffusion systems would give information on the spacial distribution of the activation energy which is required before an atom can change position.

LA DIFFUSION THERMIQUE DU CARBONE DANS LE FER α ET γ

L'auteur a mesuré pour la première fois, avec précision, les chaleurs de transport (Q^*) du carbone dans le fer α et le fer γ. Il a utilisé une technique de traceurs radioactifs. Les valeurs suivantes ont été obtenues. $Q_c^*(\alpha) = -24 \pm 1{,}5$ kcal à 700°C, $Q_c^*(\gamma)$ varie de −2 kcal à zéro lorsque l'on passe de 0,02% à 0,92% C à 940°C environ. Une détermination de la cinétique due a Wirtz explique les résultats pour $Q_c^*(\alpha)$ si l'on fait l'hypothèse que toute l'énergie d'activation pour la diffusion du carbone est utilisée à préparer le réseau autour du site au saut d'un atome dans ce dernier.

A partir de cette interprétation satisfaisante de Q^*, il apparaît que l'étude de l'effet d'un gradient de température sur d'autres systèmes à diffusion simple devrait donner des informations sur la distribution spatiale de l'énergie d'activation requise avant qu'une atome puisse changer de position.

DIE THERMISCHE DIFFUSION VON KOHLENSTOFF IN α- UND γ-EISEN

Die Transportwärmen Q^* von Kohlenstoff in α- und γ-Eisen wurden zum erstenmal genau gemessen. Unter Benützung einer radioaktiven Spurenmethode wurden folgende Werte erhalten: $Q_c^*(\alpha) = -24 \pm 1{,}5$ kcal bei 700°C, $Q_c^*(\gamma)$ erstreckte sich von −2 kcal bis Null bei Kohlenstoffkonzentrationen von 0,02% bis 0,92% bei 940°C. Eine kinetische Behandlung nach Wirtz kann die Daten für $Q_c^*(\alpha)$ erklären unter der Annahme, daß die ganze Aktivierungsenergie für die Kohlenstoffdiffusion benützt wird, um das Gitter vorzubereiten in der Umgebung des Platzes, in welchen das Atom springt. Nach dieser befriedigenden Erklärung von Q^* erscheint es lohnend, den Einfluß eines Temperaturgradienten auf andere einfache Diffusionssysteme zu untersuchen. Man würde daraus Kenntnisse über die räumliche Verteilung der Aktivierungsenergie gewinnen, die für den Platzwechsel eines Atoms erforderlich ist.

VOL. 8 1960

When a solid, single phase alloy is placed in a temperature gradient, the concentration of one component decreases at the cold end and increases at the hot end. This phenomena is called the Ludwig–Soret effect or thermal diffusion. It has been studied extensively in gases, moderately in liquids[1] and little in solids. The theoretical understanding of the phenomena in gases is satisfactory. However in condensed phases the attempts at theoretical interpretation have been rudimentary and their agreement with experimental observation usually leaves much to be desired.

The author's interest in this problem stems from two sources. With the advent of nuclear reactor technology, metal alloys are being subjected to much higher temperatures and temperature gradients than before. This can result in thermal diffusion effects playing an important role in phase redistribution in the high temperature components.[2] There is barely a rudimentary knowledge of the driving force for this deceptively simple phenomena. And the problem of establishing a quantitative theory for thermal diffusion in solids is made impossible because of the qualitative nature of the data available and the small quantity of data which exists.[3]

The purpose of the present work was to obtain accurate data for the heat of transport of carbon, Q_c^*, in α and γ iron over a range of carbon contents.† The resulting data allows a quantitative comparison with the predictions of some of the simpler theories for Q^*.

EXPERIMENTAL PROCEDURE

In a dilute interstitial solid solution where the mobility of the solute atoms is much higher than that of the solvent atoms, one can safely assume that only the movement of the solute atoms is important in the redistribution of material. The flux for the interstitial

† Received August 28, 1959.

‡ Metals Research Laboratory, Carnegie Institute of Technology, Pittsburgh, Pa. Formerly Westinghouse Research Laboratory.

† Q^* is proportional to the force that the temperature gradient exerts on the solute atoms, see equation (1) below.

solute, J_i in the direction parallel to the temperature gradient, dT/dx, can then be written[4]

$$J = \frac{-D_i N_i}{RT}\left[\left(\frac{\partial \mu_i}{\partial x}\right)_T + \frac{Q_i^*}{T}\frac{dT}{dx}\right] \qquad (1)$$

where D_i is the diffusion coefficient, N_i the concentration of the solute, μ_i is its chemical potential, T the absolute temperature, and R the gas constant. Equation (1) can be looked upon as a mobility (D/RT), times N, times a force, in brackets. The first term in brackets is closely related to the usual Fick's First Law. The second term inserts the empirical fact that a temperature difference in a homogeneous system gives rise to a flux. It is simply assumed that this flux is linear in (dT/dx). The use of the constant of proportionality, Q_i^* arises from irreversible thermodynamics which allows a physical definition of the term. Q_i^* can be either positive or negative, thus the sign and magnitude of the temperature gradient contribution to the force will be determined by Q_i^*. It is assumed in the absence of evidence to the contrary, that Q_i^* varies only slowly with temperature and composition.

To measure Q_i^* one can use either a dynamic technique in which J_i is measured, or a steady state technique in which the anneal is continued until J_i has gone to zero, in which case equation (1) simplifies to

$$-\frac{Q_i^*}{T}\frac{dT}{dx} = \left(\frac{\partial \mu_i}{\partial x_i}\right)_T \simeq \frac{RT\, d \ln N_i}{dx}. \qquad (2)$$

The second procedure is inherently more accurate since data on D_i and the absolute value of N_i are not required. This latter procedure was used in the present work.

The alloys used were made by vacuum melting electrolytic iron and carbon. The elements other than carbon in the final alloy totaled less than 0.07 per cent.[5] The alloys as cast were 0.10, 0.40 and 0.60 per cent C. The 0.10 per cent C alloy was decarburized in wet H_2 at 800°C before charging with C^{14} and the 0.6 per cent C alloy carburized to 0.9 per cent by enclosing it in vycor with graphite, $BaCO_3$ and H_2 followed by an anneal at 900°C.

The samples used were 0.40 in. in diameter and 0.080 in. thick. They were charged with C^{14} in the form of CH_4 in an evacuated vycor tube containing the steel samples. The tube was then closed off and annealed. The major pitfalls to be avoided here stemmed from the H_2O in the vycor, and the oxide on the steel. If these sources of oxygen were not reduced to a low level, little carbon would go into solution in the steel since the amount of oxygen in these two places would have been sufficient to combine with the majority of the C^{14} during the anneal and keep it in the gaseous phase as CO and CO_2.[6] To overcome this the following procedure was carried out. The entire system shown in Fig. 1 was torched under vacuum, the cold trap was filled with liquid nitrogen and system torched again. Next valve no. 1 was closed, a partial pressure of H_2 was admitted into the system and the specimen heated to reduce the oxide formed on the steel surface during the torching. The system was then evacuated again, valves no. 1 and no. 2 closed and the CH_4 admitted into the system by breaking the glass tit. Liquid nitrogen was then placed around the specimens to condense all of the CH_4 in this region and the tube closed off from the system. This tube was then annealed for several days at 900°C to charge the samples with C^{14}.

All counting was done using a flowing methane counter with a 0.7 mg/cm gold plated mylar window. With this arrangement the charged samples counted 15–20,000 cts/min.

The temperature gradient was maintained across the sample in the apparatus shown in Fig. 2. Each thermocouple wire was actually welded to the sample face by discharging a condenser between the wire and the face. The thermocouple indicates the true temperature of the specimen face at the point. Linde B (Al_2O_3) powder was dusted on the top and bottom of the specimen to inhibit the welding of the sample to the copper face plates. The gradient in the specimen could be varied by the type of insulating material put between the copper sink and a water cooled support.

To eliminate decarburization during annealing the setup shown in Fig. 2 was placed in a vycor tube with

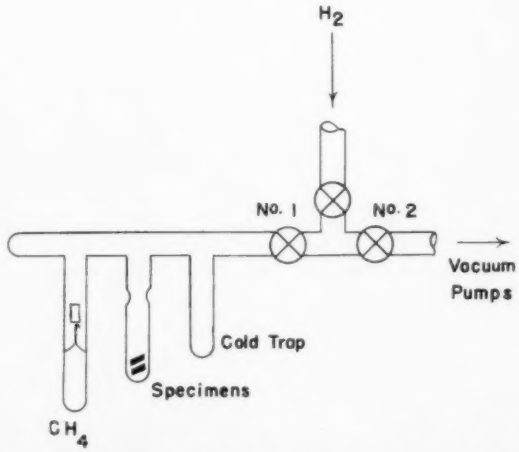


FIG. 1. Schematic drawing of apparatus used to combine C^{14} and iron specimens.

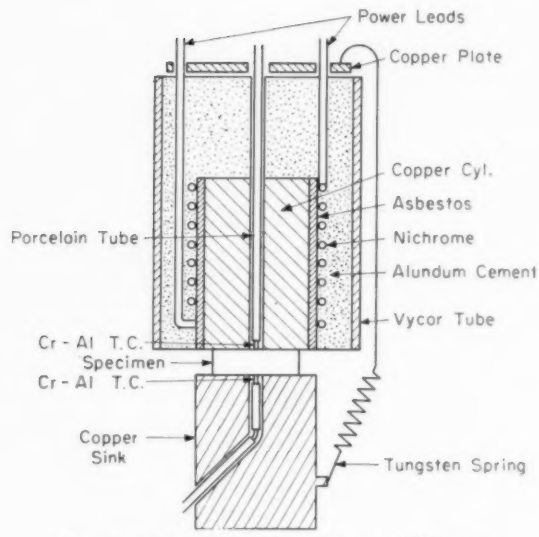


FIG. 2. Schematic section of thermal diffusion apparatus.

ball joints on the ends. The ends were then closed with water cooled copper mating joints, and the power and thermocouple leads brought out through Stupacoff glass to metal seals soldered into the copper. Through this vacuum tight system was passed Argon purified by passing it over titanium chips at 700°C and then through glass up to the system. A further piece of titanium was coiled around a power lead on top of the furnace. With this system anneals could be performed up to 950°C without a decrease in the carbon activity.

The difference between the initial and final carbon distribution decreases as $\exp(-t/\theta)$ where $\theta = h^2/\pi^2 D$,[7] and h is the specimen thickness along the gradient. All samples were annealed for at least 4θ and then rapidly cooled by turning off the power. After cooling one needs to determine the ratio of the carbon concentration at the hot face, N_h, to that at the cold face, N_c. Even with rapid cooling from the austenite field the colder face would become richer in the proeutectoid phase than the region just below the surface. Thus this transition region had to be removed to obtain a value of N_c which reflects the actual concentration which existed at the face when it was austenitic. After the initial counting of the cooled sample, uniform layers 0.001 in. thick were ground from the top and bottom using polishing paper and a jig similar to that of Birchenall and Eisen[8] which allowed the removal of thin, uniform sections. The sample was recounted and if the value of Q^* calculated with this new ratio did not agree with that of the first counting, the above grinding and counting was repeated. In only one case was the concentration gradient through the sample determined. Usually after a constant value of Q^* was obtained, the grinding was stopped so that the sample could be used again.

The samples were counted until the probable error in the ratio N_h/N_c was ± 0.5 per cent. Thus in austenitic alloys where N_h/N_c was $\simeq 1.0$ counting errors were the main source of error in Q^*. For the ferritic alloys $N_h/N_c \simeq 1.2$ and the uncertainty in ΔT was the main source of error. This error in ΔT stemmed from "aging" of the thermocouples and uneven contact between the faces and the specimen. When a run was started the temperature difference indicated by the thermocouple corresponded closely to the actual ΔT. However, in the higher temperature runs the thermocouple emf decreased with time even though a constant power input was maintained and the cooling geometry was constant. Since specimens sometimes welded one would expect the actual ΔT to increase but not to decrease. In cases where this was a problem the initial, stable ΔT was assumed to apply for the entire run. The error in ΔT of ± 1°C arose primarily from the uncertainty in this initial ΔT value. Uneven contact between the specimen and the face plates arose partially from inability to keep the face plates absolutely parallel and also from the fact that the specimen often tended to weld locally to the face plates, especially at the higher temperatures. Thus there may always have been regions in the samples which had larger and smaller values of ΔT than that indicated.

RESULTS

Ferritic alloys

Q_c^* in ferrite was measured in two samples. The results are summarized in Table 1. The carbon activity of specimen no. 10 was determined throughout the thickness. 0.001 in. was removed from the low temperature side of the specimen and then a series of sections was removed from the high temperature side using the jig mentioned above. Since the specimen support in the counter was a fixed distance from the tube, the distance between the specimen surface and the counter increased as material was removed. To avoid complicated corrections, both sides of the specimen were counted after each polishing of the one

TABLE 1. Summary of results

Spec. no.	%C	T(°C)	ΔT(°C)	N_h/N_c	Q^* kcal/mol
10	0.02	689	44	graphed	-22.8 ± 1.5
11	0.02	700	13	1.20	-26.5 ± 2.5
12	0.02	937	19	1.01	-2.2 ± 1.5
5	0.33	920	21	1.01	-2.0 ± 1.5
7	0.84	951	26	1.00	0 ± 1.0
8	0.92	965	15	1.00	0 ± 1.0

VOL. 8 1960

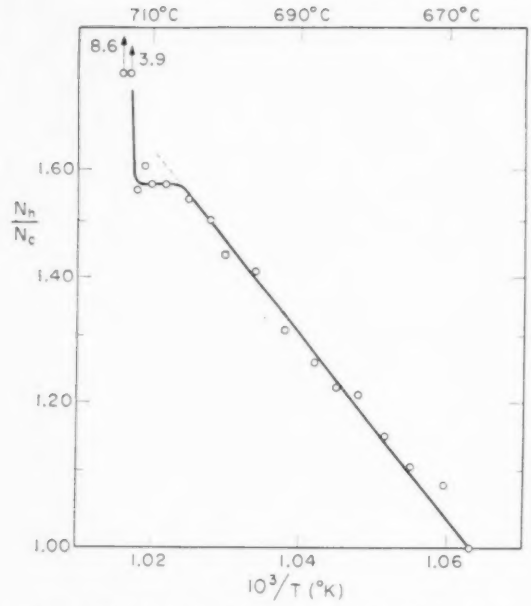


FIG. 3. Plot of carbon content (logarithmic scale) vs. $1/T$ for sectioned alpha iron specimen. (Specimen no. 10.)

side. Thus the low temperature side was used as a standard to correct for variable specimen to tube distance and the ratio of $\ln(N_h/N_c)$ vs. $1/T$ was used to determine Q_c^*. Fig. 3 shows the data. The value of Q^* obtained is 22.8 ± 1.5 kcal/mol. The uncertainty arises from the uncertainty in the temperature. Since a straight line fits the data satisfactorily the assumption of a Q^* which varies only slowly with T and N is justified.

Figure 3 shows that the final carbon content on the high temperature side was a factor of 5 higher than the extrapolation of the low temperature line. With the removal of 0.003 in. the ratio had dropped to 1.57. Integration under this curve shows that the initial, uniform, carbon content corresponded to about 1.45 N_c. Thus initially the carbon was all in solution in ferrite. However as thermal diffusion swept the carbon to the hot end, carbides formed and carbon was drained from the low temperature portion and precipitated at the hot end. This effect is discussed in detail in Ref. (2), where it is shown that the carbon content corresponding to 1.57 N_c is the solubility of Fe_3C in ferrite at 710°C or about 0.019 wt.% C.[9]

Specimen no. 11 was annealed at approximately the same temperature as no. 10 and metal was removed only until a constant Q^* was obtained. In this case Q^* was obtained from the integration of Equation (2), namely,

$$\frac{-Q^*}{RT^2} = \frac{\ln N_h/N_c}{\Delta T}.$$

The value obtained was 26.5 ± 2.5 kcal/mol. The larger probable error comes from an uncertainty of ± 1°C in the ΔT of 13°C. Because of the uncertainties in each, the two values of $Q_c^*(\alpha)$ are essentially in agreement. The best value of $Q_c^*(\alpha)$ will be taken as 24 kcal/mol since the lower number is more reliable.

Austenite alloys

As can be seen in Table 1, $Q_c^*(\gamma)$ was measured in a series of austenitic alloys ranging from 0.02 to 0.92% C. The values are still negative but they are much smaller. The probable errors in these cases arise from counting; the uncertainty coming from a lack of exact reproducibility after successive cuts rather than statistical counting errors. Due to the large effect of the counting errors, no correction was made for the nonideality of the solutions at high carbon contents. It should be noted that $Q_c^*(\gamma)$ varies little with carbon contents.

DISCUSSION

There have been a few earlier attempts to measure Q_c^* in α and γ iron. Darken and Oriani[10] have determined the thermal diffusion of carbon and nitrogen in α iron. From their work there is no doubt that $Q_c^*(\alpha)$ is negative and appreciably different from zero. However, due to decarburization during the anneal and failure to reach a steady state, it was impossible to get an accurate value. For nitrogen in α iron these authors reported a Soret coefficient, S_t, of 0.021°C^{-1} at 720°C. By definition $S_t RT^2 = Q^*$, so this correspondence to $Q^* \simeq 40$ kcal. This value was obtained from the slope of an extrapolated curve "at the highest temperature". If the value of Q^* is calculated from the two highest temperature points on their graph, and one assumes that the steady-state gradient was attained in the hot end, a value of $Q^* = 24$ kcal is obtained.† The latter value is the lower limit set by their data and seems the more reasonable, to the author.

The previous data for $Q_c^*(\gamma)$ are even more qualitative than those for $Q_c^*(\alpha)$. Lebedev[11] has shown that $Q_c^*(\gamma) < 0$ and from unpublished work by Luchok and Paxton[12] one can estimate that $Q_c^*(\gamma)$ is roughly -1 kcal/mol in a 1030 SAE steel.

The most straightforward physical interpretation for Q^* for interstitials comes from a kinetic treatment

† Since D varies markedly with temperature, a quasi-steady state value of the concentration gradient will be established at the hot end long before it is at the cold end. Using $D = 3 \times 10^{-7}$ cm^2/sec[13] and taking $\theta = 96$ hr, the time of their run, the equation $h^2 = \pi^2 D\theta$ gives $h^2 = 1$ cm. It would thus seem that the high temperature end of the sample had nearly attained the steady-state gradient though not the steady-state concentration.

of diffusion in a temperature gradient. The basic assumption to be made is how the jump frequency of the diffusing atom, f, varies with the temperature and the temperature gradient. In the most general formulation f, at a given point, can vary with the direction of the jump relative to the temperature gradient; thus it should be represented as a vector. The simplest treatment assumes that f from a given isothermal plane is a scalar and a function only of the temperature of the initial plane. At the steady-state the net flux is zero. The flux out of any plane is proportional to the concentration on the plane, c, times f, so that for the steady-state fc is the same for all planes. Since f increases exponentially with temperature, c decreases in like manner. If the formalism is followed out one obtains

$$Q^* = \Delta H \tag{3}$$

where ΔH is the heat of activation for diffusion.[13] Equation (3) indicates that Q^* for any interstitial is positive and fairly large (e.g. 20 kcal). All of the data mentioned above for α and γ iron are decisively at variance with this prediction. From this it must be concluded that the initial assumption of this analysis is incorrect and that the jump frequency depends at least on the temperature of the initial and the final planes.

A sufficiently detailed, yet simple model for calculating f has been given by Wirtz[14]. He assumes that *before* an atom can make a successful jump, rearrangements must occur simultaneously around its original site, its intermediate site, and its final site. The activation energy thus consists of three parts

$$\Delta H = E_0 + E_i + E_f \tag{4}$$

where E_0, E_i and E_f are the quantities of energy which must be absorbed at, or on the planes of, the original, intermediate and final sites. The probability of an atom making a successful jump from an initial site at temperature T to a final site at temperature $T + \Delta T$ is then taken to be proportional to the product of the probabilities of the occurrence of each fluctuation independently.

$$\exp(-E_0/RT)\exp[-E_i/R(T + \tfrac{1}{2}\Delta T)] \exp[-E_f/R(T + \Delta T)] \tag{5}$$

the probability of the reverse jump is proportional to

$$\exp[-E_0/R(T + \Delta T)] \exp[-E_i/R(T + \tfrac{1}{2}\Delta T)]\exp(-E_f/RT).$$

At the steady state the concentration will be adjusted so that the fluxes up and down the temperature gradient are equal. For this case the concentrations will be in the ratio

$$\frac{N_{T+\Delta T}}{N_T} = \frac{\exp(-E_0/RT)\exp[-E_f/R(T + \Delta T)]}{\exp(-E_f/RT)\exp(-E_0/R(T + \Delta T)}$$

If b is the jump distance and it is remembered that $\Delta T \ll T$

$$1 + \frac{1}{N}\frac{\partial N}{\partial T}\frac{\partial T}{\partial x} b \simeq \frac{N_{T+\Delta T}}{N_T} \simeq 1 + \frac{(E_f - E_0)}{RT^2}\frac{\partial T}{\partial x} b$$

or

$$Q^* = -RT^2 \frac{1}{N}\frac{\partial N}{\partial T} = E_0 - E_f. \tag{6}$$

Physically this equation states that if more of the activation energy must be adsorbed around the site receiving the atom, than around the site it leaves, the sites which absorb enough energy to receive the atom will appear more frequently on the hot side of the jumping atoms than on the cold side.

It follows from the normalization of the probabilities for the energy fluctuations that each of the E in equation (4) must be positive. As a result of this, and equations (4) and (6), it follows that for this model

$$|Q^*| < \Delta H. \tag{7}$$

Since each of the E is positive, the unsatisfactory model leading to equation (3) is seen to correspond to the case where all of ΔH is absorbed at the initial site, while if $Q^* \ll 0$ one must say that much of ΔH is absorbed at the final site to prepare it for the incoming atom.

In the case of carbon in ferrite $Q^* \ll 0$ and we might examine in more detail the plausibility of the assertion that $E_f \gg E_0$. From the existence of the Snoeck effect one can conclude that carbon in ferrite lies at the center of the cube edge ($\frac{1}{2}$, 0, 0) and that it creates a tetragonal distortion in the lattice. The relative sizes of the carbon atom, iron atoms and interstice can be inferred from X-ray work on the tetragonality of martensite[15] or from Pauling radii.[16] In either case it can be seen that the carbon atom is so large relative to the initial interstice that in addition to severely distorting the interstice tetragonally it almost "touches" the other four atoms around it. The relative sizes and positions of the atoms are shown in Fig. 4. In jumping from a ($\frac{1}{2}$, $\frac{1}{2}$, 0) position to the adjacent ($\frac{1}{2}$, 0, 0) site the carbon atom does not go through any constriction midway between the final and initial sites as is the case for substitutional atoms in a close packed lattice. Rather it crowds in between the two new iron atom neighbors until they are distorted to their new positions. The magnitude

VOL. 8 1960

of this distortion and the path of the carbon atom can be seen in Fig. 4 if one imagines the carbon atom moved out toward the viewer and between the front most atoms shown. It is thus quite reasonable to conclude that the activation process is the creation of sufficient tetragonal distortion about the new site for the carbon atom to make its jump. Using this model and elastic continuum theory Ferro[17] has calculated ΔH for a wide range of interstitial atoms in various b.c.c. metals and finds satisfactory agreement with the experimental values of ΔH.

A reasonable model of the activation process thus shows that the activation energy goes to prepare the new site for the incoming carbon atom. Using equation (4) this corresponds to $E_0 \simeq 0$, $E_f \simeq \Delta H$ or $Q^* \simeq -\Delta H$. The most reliable value of ΔH for this temperature range is 24 kcal.[18] If this value is inserted in the above equation the predicted value of Q^* is exactly equal to the measured value. Modesty and honesty demands the introduction of the word "fortuitous" at this point. However the agreement certainly lends support to both the assumptions leading to equation (6) and the model given for the activation process for carbon diffusion in ferrite.

As Ferro pointed out, the model given above for the activation process should apply to all interstitials in a b.c.c. lattice. Thus a large negative value for Q^* equal in magnitude to ΔH, would be expected for N, O, C and B in all b.c.c. metals. The only case in which this expectation can be checked experimentally is for N in α iron. In this case ΔH from room temperature internal friction data is 18.2 kcal. and Q^* appears to be approximately -24 kcal as discussed above. Since the relation $|Q^*| < \Delta H$ is a necessary consequence of Wirtz' model it would be interesting to know Q^* more accurately and whether or not ΔH would be larger for nitrogen at 700°C than at room temperature as is the case for carbon.

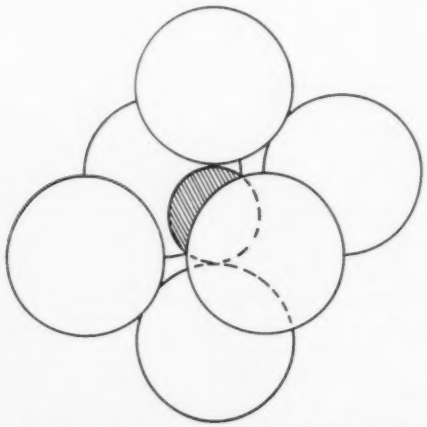


FIG. 4. Perspective drawing showing relative sizes and positions of iron atoms (clear circles) and interstitial carbon atom (hatched circle) in alpha iron.

The barrier for carbon diffusing in γ iron is quite different from that in α iron. In austenite the lattice is much more closely packed and there is a pronounced constriction midway between the final and initial sites which has to expand before the carbon atoms can pass from one site to another. Thus one would expect from Wirtz' model that most of the ΔH would show up in the term E_i and would not contribute to Q^*. This is consistent with the experimental data. As to why there is any Q^* or why it goes to zero as the per cent carbon increases, one could give several interpretations but this is too fine a detail for the present state of knowledge on the subject.

An alternative interpretation of Q^* which has been used previously by the author[3] and others,[20] uses a result of macroscopic irreversible thermodynamics. This shows that Q^* can be interpreted as the energy per unit flux which must be added to the region that atoms are leaving to keep it isothermal. In the case of $Q_c^*(\alpha\text{Fe})$ one says that the strain energy of the lattice around the site being vacated is given up when the atom leaves and is equal in magnitude to the energy that went into preparing the new site, i.e. ΔH. Thus $Q^* = -\Delta H$. To the author it is more satisfactory to use the kinetic argument of Wirtz. The main difference is that the kinetic model emphasizes how the energy must be distributed before a successful jump can occur and thus helps to elucidate the details of the activation process. In the case of Q^* for zinc in zinc,[3] the experimental work showed simply that $Q^* = H_f$(H_f = molar heat of formation of vacancies). The thermodynamic rationalization of Q^* implied that energy equal to H_f was added at some time around the site the atom left. The kinetic model is more demanding and says that a requisite for activation is the adsorption of H_f at the site the atom is leaving. The conclusion that $H_f = Q_i^*$ also appear to be valid for copper and iron.[21] It was shown above that Wirtz' model requires that $|Q^*| < H_j$ where H_j is the heat of activation for a jump. Thus one has the interesting conclusion that $H_f < H_j$ at least for these metals. Values of H_j and H_f are not available for these metals, but quenching experiments have shown that $H_f > H_j$ for Au, Al and Pt.[22] Thus either the data on Q^* or the applicability of Wirtz' model is in doubt here.

There is one other well documented case of $Q^* > 0$ for interstitials and that is hydrogen in zirconium. In this case $\Delta H = 7$ kcal[23] while $Q^* \simeq 5$ kcal.[24] This could be said to indicate that a local bonding exists between the hydrogen atoms (or proton) and

the zirconium around the initial site, and that part of the activation process must include the overcoming of this localized interaction energy.

From the above discussion it would appear that Wirtz' kinetic model of Q^* can add another dimension to the study of the activation process in solids. The emphasis it places on the preparation of the lattice around the diffusion path is one that has been suggested before but is not generally emphasized. Special attention should be drawn to the conclusion $|Q^*| < \Delta H$. This is an essential corollary of Wirtz' theory and though it may have been pointed out in the 15 years since the theory was put forward, it is not generally appreciated. Since ΔH has been measured for a wide number of interstitials, and H_j measured for self-diffusion in many cases, it would seem that this provides a straightforward and conclusive check on the range of applicability of the theory.

REFERENCES

1. J. Agar, *Rev. Pure Appl. Chem.* **8,** 1 (1958).
2. P. G. Shewmon, *Trans. Amer. Inst. Min. (Metall.) Engrs.* **212,** 642 (1958).
3. P. G. Shewmon, *J. Chem. Phys.* **29,** 1032 (1958).
4. R. O. Davies, *Rep. Progr. Phys.* **19,** 327 (1956).
5. M. L. Hill, Westinghouse Research Laboratory, private communication.
6. B. J. Todd, *J. Appl. Phys.* **26,** 1238 (1955).
7. J. A. Bierlein, *J. Chem. Phys.* **23,** 10 (1955).
8. F. H. Eisen and C. E. Birchenall, *Acta Met.* **5,** 265 (1957).
9. L. Darken and R. Gurry, *Physical Chemistry of Metals* p. 418. McGraw-Hill, New York (1953).
10. L. S. Darken and R. Oriani, *Acta Met.* **2,** 841 (1954).
11. T. A. Lebedev, *Metallurg., Leningrad* **15,** 51 (1940).
12. C. Luchok, Senior thesis with Prof. H. Paxton, Carnegie Institute of Technology, Pittsburgh, Pa. (May 1955).
13. J. A. Brinkman and A. D. LeClaire, *Phys. Rev.* **93,** 344 (1954).
14. K. Wirtz, *Phys. Z.* **44,** 221 (1943). The theory is also summarized by W. Jost in his book *Diffusion,* p. 526. Academic Press, New York (1952).
15. A. W. Cochardt, G. Schoek and H. Wiedersich, *Acta Met.* **3,** 533 (1955).
16. K. A. Moon, *J. Phys. Chem.* **59,** 71 (1955).
17. A. Ferro, *J. Appl. Phys.* **28,** 895 (1957).
18. R. Smith and L. Darken, U.S. Steel Research Laboratory, private communication. This value is 4 kcal larger than the value obtained at much lower temperature with internal friction.
19. C. Wert, *J. Appl. Phys.* **21,** 1196 (1950).
20. R. Oriani, *Symposium on Thermal Properties,* Purdue Univ., Feb. 1959. Amer. Soc. Metalg., Cleveland (1959). E. D. Eastman, *J. Amer. Chem. Soc.* **50,** 283 (1928). K. G. Denbigh, *Trans. Faraday Soc.* **48,** 1 (1952).
21. W. Brammer, *Bull. Amer. Phys. Soc.* **2,** 388 (1957).
22. (Au) J. E. Bauerle and J. S. Koehler, *Phys. Rev.* **106,** 1492 (1957). (Pt) F. J. Bradshaw and S. Pearson, *Phil. Mag.* **1,** 812 (1956). (Al) F. J. Bradshaw and S. Pearson, *Phil Mag.* **2,** 570 (1957).
23. M. Mallet and W. Albrich, *J. Electrochem. Soc.* **104,** 142 (1957).
24. J. M. Markowitz, Westinghouse Bettis Site, has obtained 3.5 kcal. A. Sawatzky, Chalk River, has obtained 6.0. Both results are unpublished.

VOL.
8
1960

CRITERIA FOR YIELDING OF DISPERSION-STRENGTHENED ALLOYS*

G. S. ANSELL and F. V. LENEL†

A dislocation model is presented in order to account for the yield behavior of alloys with a finely dispersed second-phase. The criteria for yielding used in the model, is that appreciable yielding occurs in these alloys when the shear stress due to piled-up groups of dislocations is sufficient to fracture or plastically deform the dispersed second-phase particles, relieving the back stress on the dislocation sources.

Equations derived on the basis of this model, predict that the yield stress of the alloys varies as the reciprocal square root of the mean free path between dispersed particles. Experimental data is presented for several SAP-Type alloys, precipitation-hardened alloys and steels which are in good agreement with the yield strength variation as a function of dispersion spacing predicted by this theoretical treatment.

CRITERE DE RUPTURE POUR UN ALLIAGE DURCI PAR DISPERSION

Un modèle de dislocation a été présenté pour expliquer le comportement de la rupture des alliages à phase secondaire finement dispersée. Le critère de rupture employé dans ce modèle est qu'une déformation appréciable se produit dans ces alliages quand la tension de cisaillement due à des empilements de dislocations, est suffisante pour causer une rupture ou une déformation plastique des particules de la phase secondaire dispersée relachant la tension arrière sur les sources de la dislocation.

Des équations dérivées sur la base de ce modèle prédisent que la limite élastique des alliages varie en raison inverse du carré des libres parcours moyens entre les particules dispersées. Des valeurs expérimentales sont connues pour quelques alliages du type SAP, des alliages à précipitation structurale et des aciers, qui sont en bon accord avec la variation de la limite élastique en fonction de la distance entre particules dispersées prédites par ces considérations théoriques.

FLIEßKRITERIEN FÜR DISPERSIONSGEHÄRTETE LEGIERUNGEN

Ein Versetzungsmodell, welches dem Fließverhalten von Legierungen mit einer feindispersen zweiten Phase Rechnung trägt, wird ausgearbeitet. Das in diesem Modell benützte Fließkriterium besagt, daß in solchen Legierungen ausgiebiges Fließen einsetzt, wenn die von aufgestauten Versetzungsgruppen herrührende Schubspannung ausreicht, um die dispersen Teilchen der zweiten Phase zu durchbrechen oder plastisch zu verformen; die Rückspannung auf die Versetzungsquelle wird dann verringert.

Die auf Grund dieses Modells abgeleiteten Gleichungen sagen voraus, daß sich die Fließspannung wie die reziproke Quadratwurzel aus der mittleren freien Weglänge zwischen den dispersen Teilchen verhält. Experimentelle Ergebnisse an verschiedenen SAP-Legierungen, ausscheidungsgehärteten Legierungen und Stählen werden mitgeteilt, bei welchen die Variation der Fließspannung als Funktion der Teilchenabstände gut mit den Voraussagen der theoretischen Behandlung übereinstimmt.

INTRODUCTION

Plastic deformation in crystals is due to movement of dislocations. Yielding takes place when many dislocations move large distances through the lattice. Dislocations are nucleated at sources in the lattice due to an applied stress. If the stress required to nucleate dislocations is greater than the stress necessary to move dislocations appreciable distances along a slip plane, the yield stress of the material will equal the stress necessary to propagate dislocations from a source. In alloys where a continuous three-dimensional dislocation network provides Frank–Read sources, this stress is equal to

$$\text{nucleating stress } N = \frac{\mu b}{L} \qquad (1)$$

where μ is a shear modulus, b is the Burgers vector and L is the linear distance between nodes in the network. For unresolved stresses and strains the right hand side of this equation should be multiplied by two.

In a dispersion-strengthened alloy, however, the stress necessary to move dislocations appreciable distances along a slip plane may be higher than the stress necessary to nucleate dislocations from a source. In this case, the yield stress of the alloy is determined by the stress required to move dislocations freely in a crystal lattice containing a uniformly dispersed second-phase. This paper presents a model for calculating this stress.

MODEL

Dislocation loops are considered to be formed at some source under the action of an applied stress. The

* Received August 19, 1959.

† Department of Metallurgical Engineering, Rensselaer Polytechnic Institute, Troy, New York.

nature of the source is not critical in considering the model. As the dislocation loops expand from the source, they are either blocked from further motion by the dispersed second-phase particles, or they continue to move by bowing about the dispersed particles leaving residual dislocation loops surrounding each particle. The stress required to bow dislocation loops about the dispersed particles is the yield stress in the Orowan criterion,[1,2] which predicts the yield stress of dispersion strengthened materials to be inversely proportional to the dispersed-particle spacing. Several investigators[3–5] have tried to apply this relationship to their experimental data. However, in our model, it is postulated that even when the dislocations move past the dispersed particles, leaving residual loops surrounding the particles, yielding does not result. This postulate can be supported by the following argument. The first dislocation nucleated at a source moves in the slip plane until it is blocked from further movement by its interaction with dislocations nucleated from other sources. In single phase materials this blockage of the lead dislocation is overcome by the increase of stress on the dislocation due to the pile-up of subsequently nucleated dislocations behind the lead dislocation. In a dispersion strengthened alloy, however, the lead dislocation remains blocked because (1) the stress field of the residual loops—as in the Fisher *et al.*[6] work hardening model—decreases the effective stress on the dislocation source. Therefore, fewer dislocations are nucleated at each source; (2) the stress field of the residual loops interacts with the piled-up dislocation group changing the pile-up spacing. Both of these factors decreases the stress on the lead dislocation making it easier to be blocked. Therefore, the plastic strain, ε, of the dispersion strengthened alloy is

$$\varepsilon = MN\pi R^2 b \qquad (2)$$

where M is the dislocation source density, N is the number of dislocations nucleated at each source, R is the average radius of the dislocation loops and b is the Burgers vector of the dislocation. Assuming reasonable values for these: $M = 10^9$ sources/cm^3, $N = 10$ dislocations/source, $R = 1/2$ $(M^{-1/3})$ and $b = 2 \times 10^{-8}$ cm^2, the resultant strain is about 10^{-4}. This is much less than the strain usually associated with yielding. Therefore, plastic deformation stops and yielding has not occurred when the back stress on the dislocation source, due to an array of either blocked dislocations or of residual loops around the particles, exceeds the applied stress.

Under these conditions, in alloys with fine dispersions, no apparent yielding has yet occurred. In order to cause such yielding, the shear stress due to the dislocations piled-up around or against the particles must fracture or plastically deform the dispersed second-phase particles. This relieves the back stress on the dislocation source and also increases the stress on the lead dislocation. The dislocations then can sweep out areas on the slip plane which are large with respect to the dispersion spacing.

The fineness of a second-phase dispersion necessary to make its fracture or plastic deformation the critical requirement for yielding, depends upon the density of dislocation sources in the alloy. Even at one half or more of the absolute melting temperature of the matrix metal, fracture or plastic deformation of the second-phase particles should be necessary for appreciable yielding unless recovery takes place. Recovery can occur either by climb of piled-up dislocations at a rate exceeding the applied strain rate, or by cross slip of piled-up dislocations out of the slip plane if the geometry of the dispersed second-phase particles permits. The possibility of recovery is not considered in the following calculation.

THEORY

On the basis of the preceding model, the yield strength of a dispersion strengthened alloy is now evaluated. In this evaluation the shear stress on the dispersed particles due to dislocations piled-up against or residual loops piled-up around the particles is calculated for straight dislocation segments piled-up against a straight barrier. This calculation is applicable to dispersion-strengthened alloys which contain dispersed particles of such a size and shape, e.g. flat plates and large spheres, that the piled-up dislocations have a large radius of curvature and can be considered straight. This is the case for many of these alloys, e.g. SAP-type alloys and most steels. When the radius of curvature is small this calculation of the shear stress on the particles no longer holds and the Fisher *et al.*[6] treatment becomes applicable. These two approaches are then compatible, each being the limiting case of the other. In this treatment the shear stress, τ, on a dispersed second-phase particle due to a piled-up array of dislocations can be considered to be equal to

$$\tau = n\sigma, \qquad (3)$$

where n is the number of dislocation loops piled-up against or around a dispersed particle and σ is the applied stress. The number of dislocations, n, acting on a particle depends on the space between the particles, by

$$n = \frac{2\lambda\sigma}{\mu b}, \qquad (4)$$

VOL. 8 1960

where λ is the spacing between dispersed particles and μ is a shear modulus of the matrix metal ($\mu \approx \sqrt{[\frac{1}{2}C_{44}(C_{11} - C_{12})]}$, for cubic metals, C_{ij} being the usual elastic constants). Combining equations (3) and (4), the shear stress, τ, on the particle is equal to

$$\tau = \frac{2\lambda\sigma^2}{\mu b}. \tag{5}$$

The dispersion strengthened alloy yields when the shear stress on the particle is equal to either the yield stress or fracture stress of the dispersed particle.

The limiting stress, F, that will either plastically deform or fracture the dispersed particles is proportional to a shear modulus, μ^*, of the particle. Therefore

$$F = \frac{\mu^*}{C}, \tag{6}$$

where C is a constant of proportionality dependent upon the degree of lattice perfection of the dispersed particles. One would not expect to find any dislocations within particles whose volumes are less than 10^{-15} cm^3. Even larger particles of refractory materials will not deform plastically under simple shear stresses except at very high temperatures, e.g. 1200°C for Al_2O_3.[7] For these cases, the yield stress of the dispersed particles is approximately equal to the fracture stress, and it can theoretically be shown that the constant of proportionality, C, in equation (6) is somewhere in the neighborhood of thirty.[8] For larger particle sizes and for refractory particles at high temperatures, the yield stress is much less than the fracture stress. For these cases, the constant of proportionality, C, in equation (6) is experimentally found to be equal to 10^4 for most metals.[9]

Combining equations (5) and (6) gives the maximum stress that can be applied to the alloy before yielding occurs.

The yield stress of the alloy is therefore equal to

$$\text{yield stress} = \sqrt{\frac{\mu b \mu^*}{2\lambda C}}. \tag{7}$$

If the distribution of second-phase particles is such that the stress calculated from equation (7) is less than the stress necessary to cause a dislocation source to nucleate dislocations, the equation is no longer applicable. In this case, the yield stress of the alloy should be calculated from this dislocation nucleating stress, which is the yield stress of the matrix metal without a dispersed second-phase. If a continuous three-dimensional dislocation network provides Frank–Read dislocation sources, this stress is given by equation (1).

This model is based on yielding occurring when the area swept out per dislocation loop is large as compared to the dispersed particle spacing. The particles act to hinder dislocation motion. The derivation is similar to that given by Petch[10], where grain boundaries are the blocking structure.

EXPERIMENTAL VERIFICATION AND DISCUSSION

With the model outlined, it should be possible to predict the yield strength of an alloy containing a finely dispersed second-phase. In most of these alloys it is not possible to evaluate yield strength quantitatively from equation (7) for two reasons: (i) the value of the constant of proportionality, C, in equation (6) is very approximate since it depends upon what assumptions are made in its calculation; and (ii) the value of the shear modulus of the dispersed phase may not be known, or if it is known for the phase in bulk form, it may not apply to the fine particles in the dispersion because of differences in structure and composition. The model predicts, however, the variation of the yield strength with the degree of dispersion in these alloys, and under certain circumstances, the variation of yield strength with temperature.

According to equation (7) the yield strength should vary linearly with the reciprocal of the square root of the dispersion spacing. The line should extrapolate to zero for dispersions with an infinite spacing. In order to verify this relation, data are necessary for these alloys on the spacing of the second-phase and their yield strengths. The yield strength predicted by the model is the stress required to produce apparent yielding in the alloy. In single crystals this stress can be identified with the critical resolved shear stress. In polycrystalline materials this stress corresponds most closely to the elastic limit, an experimentally difficult property to determine. In place of the elastic limit, the stress required to produce 0.2 per cent offset may be used. This stress is assumed to be a constant amount greater than the elastic limit for a given series of alloys, and therefore should also vary with the dispersion spacing as predicted by equation (7). In this case, the intercept for alloys with an infinite dispersion spacing is no longer zero, but is some positive stress. Roberts *et al.*[11] determined the lower yield strength of several hypoeutectoid, eutectoid and hypereutectoid steels, some of them with a pearlitic, others with a spheroidized structure. In a few cases the elastic limit was also measured. For this same series of steels, the authors determined the mean ferrite path, which they defined as the mean distance between carbide particles or pearlite patches.

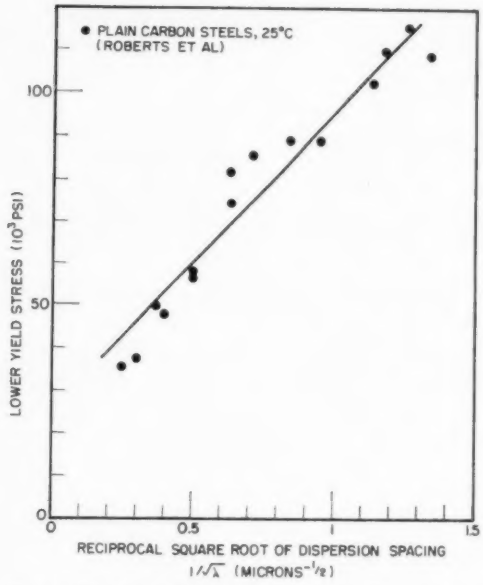


FIG. 1. The lower yield points of several hypoeutectoid, eutectoid and hypereutectoid steels are plotted versus the reciprocal square root of dispersion spacing. The line represents the least-squares fit of the data.

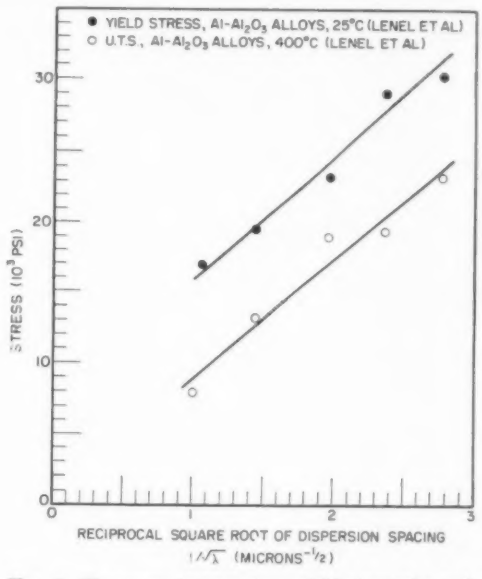


FIG. 2. The room temperature yield strengths and the ultimate tensile strengths at 400°C for several Al–Al_2O_3 SAP-type alloys are plotted versus the reciprocal square root of the dispersion spacing. Each line represents the least-squares fit of the data.

They plotted the lower yield point, and where available the elastic limit, versus the logarithm of the mean free path. This relationship, which was first proposed by Gensamer *et al.*[12] for flow stress is empirical however. The explanation Gensamer and co-workers proposed was based upon an assumed relationship between the rate at which dislocations are generated and the applied stress. This explanation no longer seems adequate in the light of modern dislocation theory. In accordance with the model postulated in this paper, the lower yield points of Roberts *et al.* were re-plotted in Fig. 1 versus the reciprocal of the square root of the spacings. A least-squares line has been drawn assuming a linear relationship. The fit is as satisfactory as that shown in the original plot of Roberts *et al.* Unfortunately, too few values were available for establishing a valid correlation between elastic limit and spacing.

Lenel *et al.*[13] determined, by quantitative electron microscopy, the average spacing between the plate-like oxide particles for a series of flake aluminum powder extrusions. For these same extrusions, Lenel and co-workers[4] determined the room temperature yield strength at 0.2 per cent offset and the ultimate tensile strength at 400°C. At 400°C, the ultimate tensile strength and the tensile yield strength are almost equal.[14] In Fig. 2, the strength values at the two temperatures are again plotted vs. the reciprocal of the average spacing, with the lines representing the least-squares fit of the data. This plot does not exhibit any more scatter than the empirical Gensamer type of plot suggested by Lenel for his data.

The critical resolved shear stress of a series of overaged high-purity aluminum–copper alloys and the spacing between the second-phase particles in these alloys was determined by Dew-Hughes and Robertson[5]. They interpreted the data as supporting Orowan's yield strength theory. A least-squares analysis of the data plotted according to Orowan's theory, however, shows neither predicted linear variation of critical resolved shear stress with the reciprocal of the dispersion spacing, nor a line intercept of zero for an infinite spacing. On the other hand, if their values for critical resolved shear stress are plotted vs. the reciprocal of the square root of the particle spacing as is shown in Fig. 3, a better fit is obtained. The line representing the least-squares fit of the data goes through the origin. This indicates that the proposed model, in which yielding takes place when the second-phase particles shear, would also apply to aluminum alloys containing a dispersion of the theta phase. Dew-Hughes and Robertson consider this possibility, but conclude from an examination of the micrograph of a fractured sample near its fracture surface that the particles do not shear during plastic deformation of the matrix. However, we do not believe that the shear of the particles can actually be detected by this type of examination.

VOL. 8 1960

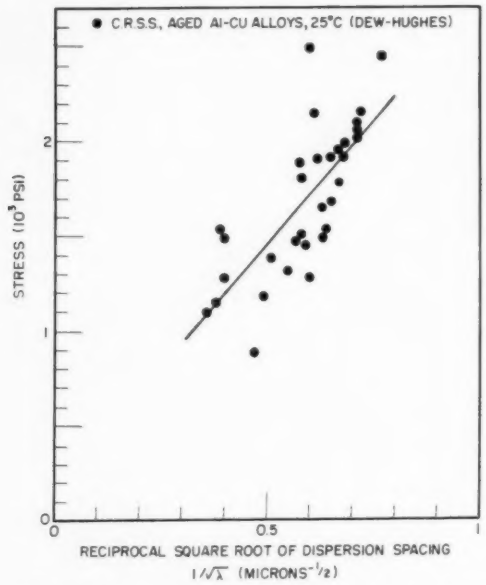


FIG. 3. The critical resolved shear stress of several overaged Al–Cu alloys are plotted versus the reciprocal square root of the dispersion spacing. The line represents the least-squares fit of the data.

Inspection of equation (7) shows that of the terms which determine yield stress, only the shear moduli have an appreciable temperature dependence. Therefore, if the temperature dependence of these shear moduli is known, or a reasonable approximation can be made, the variation of yield strength with temperature should be predictable according to the equation

$$\sigma_T = \sigma_{25}(\mu_T \mu_T^* / \mu_{25}\mu_{25}^*)^{1/2} \qquad (8)$$

in which σ is the yield stress, μ and μ^* the shear moduli of the matrix metal and dispersed phase, respectively; the subscripts T and 25, refer to the values of the properties at the test temperature and at 25°C.

This predicted temperature dependence can only be checked by determining the temperature dependence of the elastic limit, not that of the offset yield strength. Although it is reasonable to assume that the off set yield strength for a given series of alloys at any given temperature is a constant amount greater than the elastic limit, this amount is a function of temperature. Therefore, the temperature dependence of the elastic limit cannot be deduced from that of the off set yield strength. Unfortunately, no data on the variation of the elastic limit with temperature for any dispersion strengthened alloy are currently available.

CONCLUSIONS

(1) The model presented appears to explain the yielding behavior of a series of dispersion-strengthened alloys for which no other theory seems satisfactory.

(2) The strengthening effect given by equation (7), due to the dispersed second-phase will be apparent only if it is greater than the yield stress of the matrix metal. This indicates that the fineness of dispersion required for strengthening is a function of the shear moduli of the matrix metal and of the dispersed second-phase and is thus dependent upon the particular alloy system and test temperature.

(3) When treated in terms of this model, coherency effects of the dispersed second-phase particles are only important where the range of additional lattice strain is of the order of the dispersed particle spacing. Under these conditions, the effect of a coherent second-phase would be to change the dispersion spacing.

(4) Particle geometry is important in two ways: For determining the mode of particle shear which causes yielding, and preventing recovery by cross-slip and climb.

(5) Much additional work must be done in order to verify the model, such as quantitatively evaluating from fundamental constants and determining the temperature dependence of the yield strengths for several alloy systems. The difficulties involved in these areas have been mentioned previously, but these should not prove insurmountable.

ACKNOWLEDGMENTS

The authors wish to thank Dr. R. Guard for his helpful discussions concerning the proposed model, and both the International Nickel Company and the National Aeronautics and Space Administration for their financial support.

REFERENCES

1. E. OROWAN, Discussion of paper by Sir L. BRAGG: *Effects Associated with Stresses on a Microscopic Scale* in *Symposium on Internal Stresses in Metals and Alloys*. Institute of Metals, London (1948).
2. E. OROWAN, *Dislocations in Metals*. *Amer. Inst. Min. (Metall.) Engrs.*, New York (1954).
3. E. GREGORY and N. J. GRANT, *Trans. Amer. Inst. Min. (Metall.) Engrs.* **200,** 247 (1954).
4. F. V. LENEL, A. B. BACKENSTO and M. V. ROSE, *Amer. Inst. Min. (Metall.) Engrs.* **209,** 124 (1957).
5. D. DEW-HUGHES and W. D. ROBERTSON, *Acta Met.*
6. J. C. FISHER, E. W. HART and R. H. PRY, *Acta Met.* **1,** 336 (1953).
7. J. A. STAVROLAKIS and F. H. NORTON, *J. Amer. Ceram. Soc.* **33,** 263 (1950).
8. A. H. COTTRELL, *Dislocations and Plastic Flow in Crystals* p. 11. Clarendon Press, Oxford (1953).
9. A. H. COTTRELL, *Dislocation and Plastic Flow in Crystals* p. 18. Clarendon Press, Oxford (1953).
10. N. J. PETCH, *J. Iron St. Inst.* **174,** 25 (1953).
11. C. S. ROBERTS, R. C. CARRUTHERS and B. C. AVERBACH, *Trans. Amer. Soc. Metals* **44,** 1150 (1952).
12. M. GENSAMER, E. B. PEARSALL, W. S. PELLINI and J. R. LOW, Jr. *Trans. Amer. Soc. Metals* **30,** 983 (1942).
13. F. V. LENEL, G. S. ANSELL and E. C. NELSON, *Trans. Amer. Inst. Min. (Metall.) Engrs.* **209,** 117 (1957).
14. J. P. LYLE, Jr., *Metal Progr.* **62,** 109 (1952).

THE MECHANISM OF OXIDATION OF IRON IN CARBON MONOXIDE–CARBON DIOXIDE MIXTURES*

F. PETTIT,† R. YINGER‡ and J. B. WAGNER, Jr.†

The oxidation of iron in carbon monoxide–carbon dioxide mixtures has been studied in the temperature range of 925°–1075°C. For oxide thicknesses between about 4×10^{-4} and 1.8×10^{-3} cm, the oxidation rate was found to be a linear function of the mole fraction of CO_2 in the gas phase and the sum of the partial pressures of CO_2 and CO between 0.4 and 1.0 atm pressure.

These data confirm the rate-determining step for the process to be the dissociation of carbon dioxide into carbon monoxide and adsorbed oxygen atoms or ions in accordance with a mechanism proposed by C. Wagner. For the reaction, $CO_2 + x\,Fe = Fe_xO + CO$, the kinetics may be described by the equation,

$$\mathring{n}/A = k'P'(1 + K)[N'_{CO_2} - N'_{CO_2(equil.)}]$$

where $\mathring{n}$ is the number of equivalents of oxide formed per second, A is the surface area, k' is the rate constant of the phase boundary reaction, P' is the sum of the partial pressures of CO and CO_2, K is the equilibrium constant for iron, wüstite and the gas mixture, N'_{CO_2} is the mole fraction of CO_2 in the gas mixture of CO and CO_2, and $N'_{CO_2(equil.)}$ is the mole fraction of CO_2 in the mixture CO–CO_2 in equilibrium with iron and wüstite.

LE MECHANISME D'OXYDATION DU FER DANS LES MELANGES D'OXIDE ET D'ANHYDRIDE DE CARBONE

Les auteurs ont étudié l'oxydation du fer dans des mélanges d'oxyde de carbone et d'anhydride carbonique pour des températures comprises entre 925°–1075°C. Lorsque l'épaisseur de la couche d'oxyde est comprise entre 4×10^{-4} et $1{,}8 \times 10^{-3}$ cm, la vitesse d'oxydation est une fonction linéaire de la fraction molaire de CO_2 dans la phase gazeuse et de la somme des pressions partielles de CO_2 et de CO entre 0,4 et 1,0 atm.

En accord avec le mécanisme proposé par C. Wagner, ces résultats confirment que le facteur qui détermine la vitesse d'oxydation est la dissociation de l'anhydride carbonique en oxide de carbone et en atomes ou ions d'oxygène adsorbé. Pour la réaction $CO_2 + x\mathrm{Fe} = Fe_xO + CO$, la cinétique peut être décrite par l'équation:

$$\mathring{n}/A = k'P'(1 + K)[N'_{CO_2} - N'_{CO_2\,(equil.)}]$$

où $\mathring{n}$ est le nombre d'équivalents d'oxide formé par seconde. A la surface, k' la constante de vitesse de la réaction à la frontière de phase, P' la somme des pressions partielles de CO et CO_2, K la constante d'équilibre pour le fer, la wüstite et le mélange gazeux, N'_{CO_2} la fraction molaire de CO_2 dans le mélange CO–CO_2 et $N'_{CO_2(equil.)}$ est la fraction molaire de CO_2 dans le mélange CO–CO_2 en équilibre avec le fer et la wüstite.

DER OXYDATIONSMECHANISMUS VON EISEN IN KOHLENMONOXYD-KOHLENDIOXYD-GEMISCHEN

Die Oxydation von Eisen in Kohlenmonoxyd-Kohlendioxyd-Gemischen wurde im Temperaturbereich von 925° bis 1075°C untersucht. Für Oxyddicken zwischen etwa $4 \cdot 10^{-4}$ und $1{,}8 \cdot 10^{-3}$ cm ergab sich die Oxydationsgeschwindigkeit als lineare Funktion des Molenbruchs von CO_2 in der Gasphase und der Summe der Partialdrücke von CO_2 und CO zwischen 0,4 und 1,0 at Druck.

Diese Daten bestätigen, daß in Übereinstimmung mit einem von C. Wagner vorgeschlagenen Mechanismus die Dissoziation von Kohlendioxyd zu Kohlenmonoxyd und adsorbierten Sauerstoffatomen oder -Jonen der geschwindigkeitsbestimmende Schritt des Vorgangs ist. Für die Reaktion $CO_2 + x\mathrm{Fe} = Fe_xO + CO$ kann die Kinetik durch folgende Gleichung beschrieben werden:

$$\mathring{n}/A = k'P'(1 + K)[N'_{CO_2} - N'_{CO_2(Gleichgew.)}],$$

wobei $\mathring{n}$ die Zahl der pro Sekunde gebildeten Oxydäquivalente, A die Oberfläche, k' die Geschwindigkeitskonstante der Phasengrenzenreaktion, P' die Summe der Partialdrücke von CO und CO_2 und K die Gleichgewichtskonstante für Eisen, Wüstit und die Gasmischung ist. N'_{CO_2} ist der Molenbruch von CO_2 in der Gasmischung aus CO und CO_2 und $N'_{CO_2(Gleichgew.)}$ der Molenbruch von CO_2 in der CO–CO_2-Mischung im Gleichgewicht mit Eisen und Wüstit.

STATEMENT OF THE PROBLEM

When a metal such as iron or copper is oxidized at elevated temperatures, a relatively smooth, compact oxide layer is formed. The overall process involves both phase boundary reactions and the diffusion of ions and electrons in the oxide layer.

* Received November 4, 1959. This work represents part of a thesis by F. Pettit presented to the faculty of the School of Engineering of Yale University in partial fulfillment of the requirements of the Master of Engineering Degree in Metallurgy.

† Yale University, New Haven, Connecticut.

‡ Present address: Department of Metallurgy, The Pennsylvania State University.

VOL. 8 1960

Under special conditions, the rate may be controlled by the phase boundary reactions, especially that at the outer surface, and accordingly be independent of the instantaneous thickness of the oxide layer. Such a case has been found by Hauffe and Pfeiffer[1] for the oxidation of iron to wüstite in CO–CO_2 mixtures between 900 and 1000°C according to the equation,

$$CO_2 + x\,Fe = Fe_xO + CO. \tag{1}$$

At a given total pressure of one atmosphere, the rate was found to be proportional to $(p_{CO_2}/p_{CO})^{2/3}$ or proportional to the one-third power of the equilibrium oxygen partial pressure of the CO–CO_2 mixture. Such a dependence may suggest a chemisorption mechanism as has been discussed briefly by Hauffe and Pfeiffer.

The purpose of the present investigation was to test an alternative explanation suggested by C. Wagner[2]. Assume that the rate-determining step is the dissociation of CO_2 into CO and adsorbed oxygen atoms or ions,

$$CO_2(g) = CO(g) + O(ad). \tag{2}$$

Then we may write

$$\mathring{n}/A = k'p_{CO_2} - k''p_{CO} \tag{3}$$

where $\mathring{n}$ is the number of equivalents of oxide formed per unit time, A is the surface area, k' and k'' are two constants, and p_{CO_2} and p_{CO} are the partial pressures of carbon dioxide and carbon monoxide. The last term in equation (3) accounts for the reverse reaction. In view of the results obtained for the dissociation of H_2S on the surface of Ag_2S by Kobayashi and Wagner[3], the rate of dissociation of CO_2 on the surface of wustite is supposed to depend not only on the composition of the gas phase but also on the composition of the solid phase, in particular the concentration of excess electrons and electron holes. If, however, the reaction at the wüstite surface is the rate-determining step, the Fe/O ratio in the wüstite layer is that in equilibrium with metallic iron. Thereby the concentration of excess electrons and electron holes is fixed and accordingly does not appear in the rate equation, equation (3).

The equilibrium condition between iron, wüstite and the gas mixture, CO–CO_2, may be written as,

$$p_{CO_2}/p_{CO} = K. \tag{4}$$

At equilibrium, $\mathring{n}/A = 0$ and we have

$$k''/k' = p_{CO_2}/p_{CO} = K. \tag{5}$$

Therefore we may write equation (3) as,

$$\mathring{n}/A = k'(p_{CO_2} - Kp_{CO}). \tag{6}$$

Writing the partial pressures in terms of the total pressure of CO and CO_2, we have,

$$p_{CO_2} = P'N'_{CO_2} \tag{7}$$

and

$$p_{CO} = P'(1 - N'_{CO_2}) \tag{8}$$

where N'_{CO_2} denotes the mole fraction of CO_2 in the CO–CO_2 mixture. Substitution of equations (7) and (8) into equation (6) yields,

$$\mathring{n}/A = k'P'[(1 + K)N'_{CO_2} - K]. \tag{9}$$

Equation (9) may be rearranged to yield,

$$\mathring{n}/A = k'P'(1 + K)[N'_{CO_2} - N'_{CO_2(equil.)}] \tag{10}$$

where the subscript, equil., denotes the mole fraction of CO_2 in the CO–CO_2 gas mixture in equilibrium with iron and wüstite.

The dependence of the oxidation rate on the CO_2/CO ratio reported by Hauffe and Pfeiffer[1] is compatible with equation (10). In contrast to the relation suggested by Hauffe and Pfeiffer, however, the rate is supposed to depend not only on the CO_2/CO ratio of the gas mixture, but to be proportional to the sum of the partial pressures of CO_2 and CO. Thus, to test the above mechanism for iron, rate studies in the temperature range of 925°C were performed such that the dependence of rate on mole fraction of carbon dioxide and on the total pressure of carbon monoxide and carbon dioxide was tested.

EXPERIMENTAL

The oxidation chamber consisted of a McDanel tube, $\frac{3}{4}$ in. i.d. and 2 ft long, to which were fastened Pyrex glass connections. A quartz spiral spring which was capable of sustaining a 0.5 g load with a sensitivity of about 5×10^{-5} g was situated in a constant temperature (35.0 ± 0.2°C) chamber above the oxidation chamber (see Fig. 1). A magnetic-clutch device actuated a pulley system which raised and lowered the spring. In this manner the sample could be lowered into and raised from the hot zone of the furnace. The furnace was wound with Kanthal wire in a manner to eliminate temperature gradients in the hot zone. In addition, a nickel cylinder, 6 in. long, was placed around the McDanel tube at the hottest zone in the furnace. With these precautions, the temperature gradient at the highest temperature studied, 1075°C, was less than 2 deg/$\frac{1}{2}$ in. and at 925°C the gradient was less than 1 deg/$\frac{1}{2}$ in. over the region where the sample was oxidized. A Leeds and Northrup AZAR controller maintained the temperature better than ±1°C between 925 and 1075°C. The accuracy of the temperature was determined by a

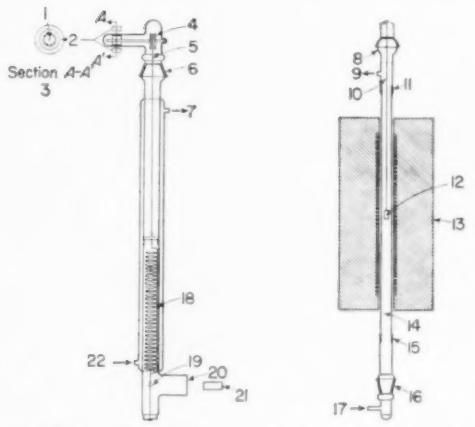


FIG. 1. Schematic diagram of oxidation apparatus. The nomenclature of parts numbered on the diagram are as follows:
(1) Iron. (2) Magnet. (3) Magnet clutch assembly. (4) Pulley. (5) Rhodium plated silver chain. (6) 34/45 Standard taper Pyrex joint. (7) Thermostated water outlet. (8) 50/30 Standard taper ball joint. (9) Gas outlet. (10) Quartz fibre. (11) McDanel to Pyrex seal. (12) Specimen. (13) Kanthal-wound furnace. (14) McDanel tube. (15) McDanel to Pyrex seal. (16) 34/45 Standard taper Pyrex joint. (17) Gas inlet. (18) Quartz spring. (19) Pointer. (20) Optically flat window. (21) Telescope. (22) Thermostated water inlet.

VOL. 8 1960

separate calibrated platinum, platinum–10% rhodium thermocouple whose accuracy was determined to be better than ± 1°C.

The procedure for a typical experiment was as follows: An iron sheet, Ferrovac *E** with an analysis of better than 99.967 per cent iron, 0.0055 in. thick, was cut into a rectangular coupon, approximately 1.2 in. long by 0.5 in. wide. A hole, 0.054 in. in diameter, was drilled in one end of the coupon in order to suspend it on a quartz fibre hook. A typical sample had an apparent surface area of about 1.2 in^2 or 7.8 cm^2.

The sample was polished with metallographic paper through number 4/0 and then lapped on a wheel covered with Buehler *AB* microcloth which was saturated with Linde Type *A* fine abrasive. Occasionally this surface treatment was followed by an electropolish, by a chemical polish, or by an etch in a nitric acid solution. No significant differences in oxidation rate resulted from these types of surface treatment. Therefore most experiments were carried out using lapped specimens.

The apparent surface area was determined using a micrometer. The sample was weighed on an analytical balance and suspended by means of a quartz fibre attached to the quartz spring in the oxidation system. The system was evacuated and flushed with hydrogen. The sample was heated in a static system of hydrogen at 500–550°C overnight in order to reduce any surface oxide and to relieve any stresses in the metal. After the hydrogen anneal, the sample was raised from the hot zone and the furnace temperature was increased to the desired oxidation temperature. The hydrogen was evacuated and a well-defined mixture of CO–CO_2 or CO–CO_2 diluted with argon was admitted to the system. The gas flowed upward through the vertical tube furnace. Commercial gases were used. The carbon dioxide was purified by passing successively through tubes containing activated alumina, reduced copper oxide at 500°C and activated alumina. The carbon monoxide passed through tubes containing magnesium perchlorate, Ascarite and magnesium perchlorate. The argon passed through tubes containing reduced copper oxide at 500°C, magnesium perchlorate, Ascarite and magnesium perchlorate.

The gases were allowed to flow through the oxidation system for 1 hr in order to flush it and to ensure that the desired gas ratio was present. The sample was then lowered into the hot zone. Measurements of the spring deflection versus time were obtained using a cathetometer whose precision was 1.7×10^{-4} cm which corresponded to a weight change of approximately 2×10^{-5} g. The time required for lowering the sample was 20–30 sec. The spring and sample oscillated for about 1 min before damping. In addition, the sample was initially at room temperature and it was subject to a heat of oxidation as it was lowered into the hot zone. For these reasons the initial portion of the rate curve was not well-defined. Therefore the procedure was adopted to take as zero time, the time when the sample was half-way down into the hot zone. Readings were obtained as soon as the spring stopped oscillating and the results were extrapolated back to zero time for the initial weight. It was found that the results were within the experimental error whether zero time was taken as that time when the sample was half-way into the hot zone or fully into the hot zone.

To terminate a run, the sample was raised to the cool zone of the furnace. The system was evacuated and the sample remained *in vacuo* until the specimen cooled to room temperature. The sample was then removed from the system and reweighed on an analytical balance. In order to check for consistency of the data, the difference in weight was expressed as $(\Delta m/A)$ for the total oxidation time and it was compared with the results using the quartz spring in the oxidation system. Results were consistent

* Ferrovac *E* is the trade designation of a vacuum-melted iron kindly furnished by the Crucible Steel Company of America.

within a few tenths of a milligram or better than $1\frac{1}{2}$ per cent in the weight change. The sample was photographed, examined under the microscope and in some instances mounted in an epoxy resin so that the cross section could be examined metallographically.

Using the above-described procedure data on the oxidation rate of iron in CO–CO_2 mixtures were obtained at various pressures and concentrations of carbon monoxide and carbon dioxide in the temperature range 925–1075°C. Typical rate curves for oxidation in a 60 vol.% mixture of CO_2 in CO at 1 atm pressure, $(P' = p_{CO_2} + p_{CO})$, between 925° and 1075°C are shown in Fig. 2. The effects of pressure and concentration of carbon dioxide on oxidation rate are shown in Figs. 3–5 for the temperatures 925°, 967° and 1075°C, respectively.

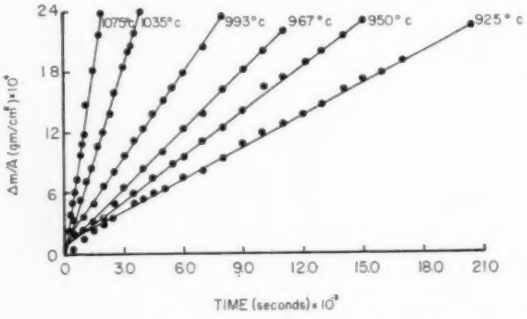


FIG. 2. Typical rate curves for oxidation of iron in a 60 vol. % mixture of CO_2 in CO at 1 atm pressure, $(P' = p_{CO_2} + p_{CO} = 1$ atm).

RESULTS AND DISCUSSION

The rate of oxidation of iron in CO–CO_2 mixtures in the temperature range of 925–1075°C has been shown to be linear for oxide thicknesses greater than 4×10^{-4} but less than 1.8×10^{-3} cm (see Figs. 2–5). Furthermore the dependence of rate on mole fraction of CO_2, N'_{CO_2} and pressure, $P' = p_{CO_2} + p_{CO}$, has been shown to agree with the mechanism expressed by equation (10). Fig. 3(b) shows a plot of the practical rate constant versus the pressure, $P' = p_{CO} + p_{CO_2}$ at 925°C. This data shows more explicitly that the mechanism suggested by Wagner involves not only the mole fraction of CO_2 in the CO–CO_2 mixture but also the sum of the partial pressures, $p_{CO} + p_{CO_2}$. Similar relations, of course, may be obtained from Figs. 4 and 5 corresponding to 967° and 1075°C, respectively. The practical rate constant k_L(g/cm²-sec) divided by the equivalent weight of oxygen gives $\mathring{n}/A$(eq./cm²-sec). Substitution into equation (10) of the values for $\mathring{n}/A$, K, $N'_{CO_2(equil.)}$, and P', as defined previously for the temperature at which the value k_L was obtained, permits evaluation of the rate constant of the phase boundary reaction

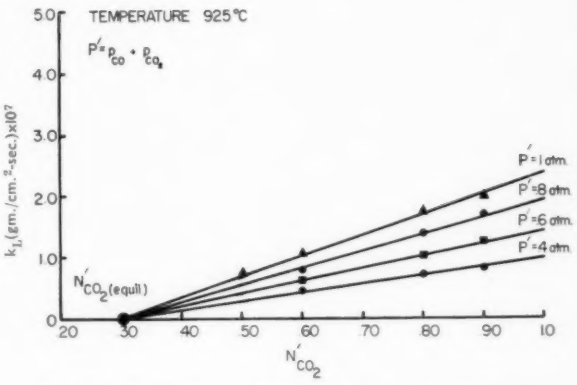


FIG. 3(a) Dependence of the oxidation rate of iron on the mole fraction of CO_2 and the sum of the partial pressures of CO_2 and CO in the gas mixture for the temperature 925°C.

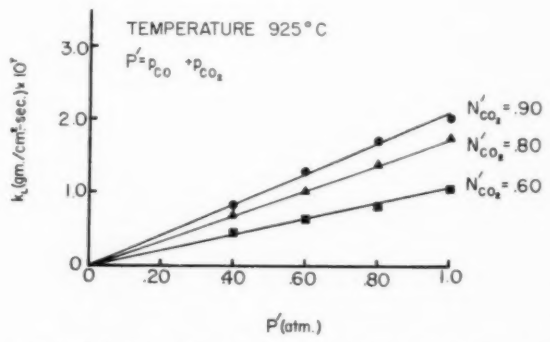


FIG. 3(b) Dependence of the oxidation rate of iron on the sum of the partial pressures of CO_2 and CO and the mole fraction of CO_2 in the gas mixture for the temperature 925°C. The data used in this graph are the same as those in Fig. 3(a). This type graph has been made in order to emphasize the dependence of the oxidation rate on the sum of the partial pressures of CO_2 and CO.

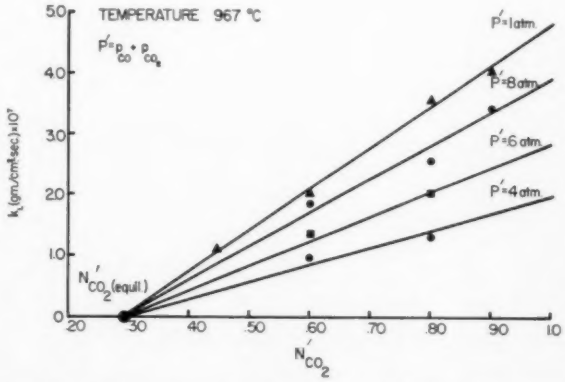


FIG. 4. Dependence of the oxidation rate of iron on the mole fraction of CO_2 and the sum of the partial pressures of CO_2 and CO in the gas mixture for the temperature 967°C.

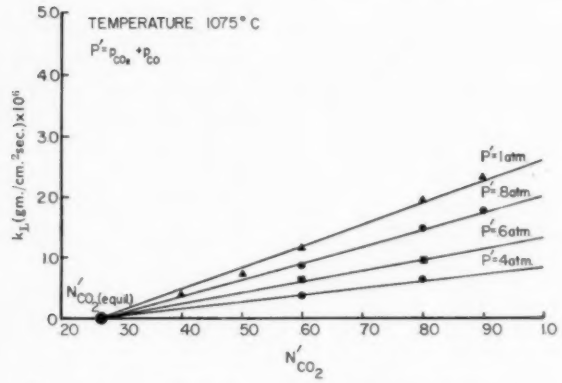


FIG. 5. Dependence of the oxidation rate of iron on the mole fraction of CO_2 and the sum of the partial pressures of CO_2 and CO in the gas mixture for the temperature 1075°C.

k'(eq./cm²-sec-atm). The plot of log k' versus the reciprocal of the absolute temperature (see Fig. 6) expresses this rate constant as a function of temperature. From these data in conjunction with equation (10), the oxidation rate of iron can be calculated for any CO–CO_2 mixture within the pressure range 0.4–1 atm and for the specified temperature and thickness limits. The activation energy as obtained from the slope of the curve in Fig. 6 was found to be 50.5 kcal/mole. This value may be compared to 30 kcal/mole required for vacancy diffusion in wüstite.[4]

The data presented in Fig. 2 are applicable for oxide films between 4×10^{-4} cm and 1.8×10^{-3} cm. Oxidation curves typical of those obtained for oxidation of all the iron to wüstite are shown in Fig. 7 for the temperatures, 925°, 1000° and 1075°C. This type curve can be divided into four parts. While the initial portion of the curve is not well-

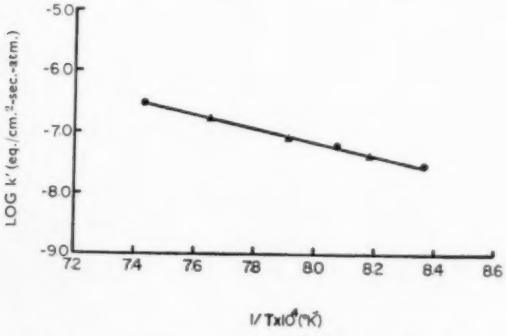


FIG. 6. The rate constant of phase boundary reaction, k', as a function of the reciprocal of the absolute temperature. The activation energy calculated from the slope of this curve is 50.5 kcal/mole. The circles represent the average values of rate constant obtained from the family of curves for temperatures 924°, 967° and 1074°C. The solid triangles represent single values of rate constant calculated from oxidation rates obtained for 60 vol. % CO_2 and $p_{CO_2} + p_{CO} = 1$ atm.

defined for the higher temperatures, results at 950°, 925°, 900° and 850°C indicate that the initial rate obeys a logarithmic equation for thicknesses up to about 4×10^{-4} cm. Since equation (10) is valid for thick films, this observation does not conflict with the proposed mechanism. Thin film oxidation under the above described experimental conditions will be the subject of another study.

The next part which is linear has been discussed previously and forms the basis of this paper. This region has been found to obey the mechanism proposed by Wagner for the temperature range 925°–1075°C. Tests were initially performed at 900°C. However results obtained at 900°C were sometimes inconsistent in that abrupt changes in oxidation rate were sometimes observed. This phenomenon may

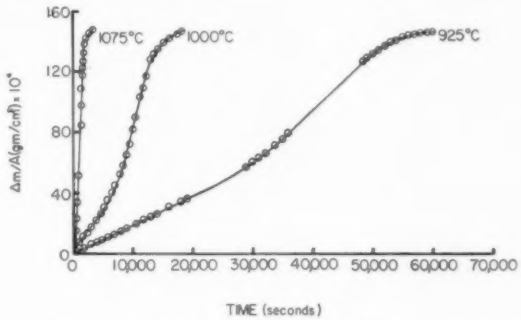


FIG. 7. Typical oxidation curves for complete oxidation of all iron to wüstite for iron samples about 0.005 in. thick.

possibly have been the result of the alpha–gamma phase transition in iron. Therefore it was decided to perform tests at 925°C and above in order to ensure the presence of only gamma iron.

The third part of the curve corresponds to the rapid acceleration of oxidation rate followed by a virtually linear rate. This phenomenon occurred at a minimum oxide thickness of 1.8×10^{-3} cm. Higher temperatures and greater CO_2 concentrations appeared to favor the onset of the rapid acceleration at this minimum oxide thickness. Microscopic examination of the oxidized specimens which yielded rate curves with an accelerated rate were found to have a non-uniform oxide surface topography. For example, there were spiral growths, filamentary growths and non-uniform oxide grain size. Figs. 8 and 9 show cross sections of samples which were obtained by oxidizing the iron to thicknesses corresponding, respectively, to the first linear region and second, virtually linear region of the rate curve. No cracking or fissures were present in either case, but the gas-oxide interface of the latter specimen showed a very rugged surface topography. Wagner's mechanism

VOL. 8 1960



FIG. 8. Cross-sectional view of an iron specimen oxidized in a mixture of 60 per cent CO_2 in CO at a temperature of 925°C for 500 min with $p_{CO} + p_{CO_2} = 0.8$ atm. The relatively smooth, crack-free, oxide–atmosphere interface is typical of specimens yielding rate curves in the first linear region. × 200

appears to be valid in this second, virtually linear region but the lack of measurements on the change of surface area has so far prevented a rigorous test. Studies are in progress to elucidate the structural features of the film and the observed oxidation rate.

The fourth part of the rate curve is characterized by a decelerated rate. A decrease in rate is to be expected when the oxide layer becomes sufficiently thick for diffusion of ions and electrons to become the rate-determining step. The thickness at which the rate changes from a linear behavior to a parabolic behavior is determined by the relative energies for the diffusion process and the dissociation process. Available data indicates that for iron specimens, 0.005 in. thick, the rate becomes parabolic for temperatures exceeding 925°C before all of the iron is converted to wüstite. Below this temperature, the present specimens were completely converted to wüstite before the onset of parabolic oxidation. For the latter case, the decelerated rate corresponded to the oxidation of wüstite. Fig. 10 shows the cross section of a specimen which was oxidized completely to wüstite. A coffin-type structure is apparent, indicating the migration of iron ions via cation vacancies through the oxide layer to react with oxygen.

The present results differ from those of Hauffe and Pfeiffer[1] in two respects. The linear rates obtained for region two are about a factor of ten lower than those reported by Hauffe. Secondly the rate curves reported by Hauffe do not show an accelerated region. In the present work an effort was made to ascertain the magnitude of possible experimental errors. These included: (1) gas flow and regulation,

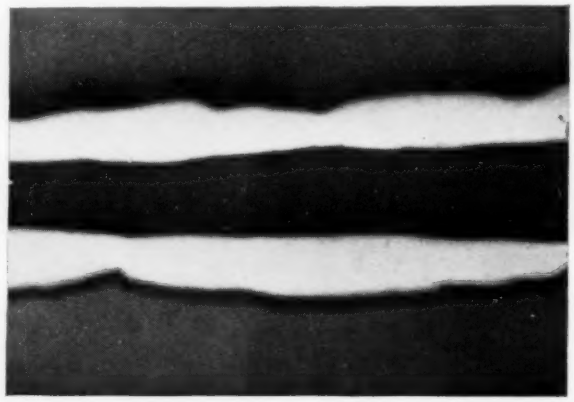


FIG. 10. Cross sectional view of a specimen oxidized completely to wüstite. The center (dark region) is a void which is bounded on both sides by a layer of wüstite. × 50

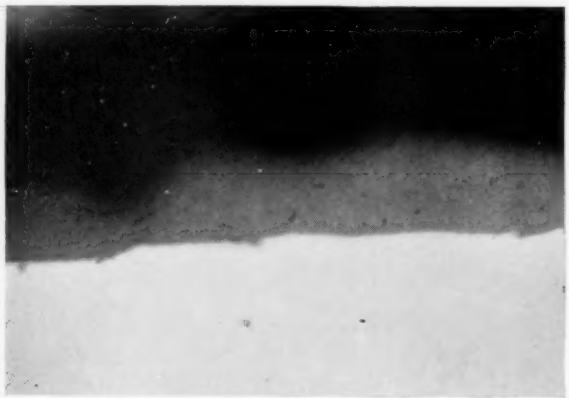


FIG. 9. Cross-sectional view of an iron specimen oxidized in a mixture of 80% CO_2 in CO at a temperature of 1075°C for 25 min with $p_{CO} + p_{CO_2} = 0.8$ atm. The rugged, crack-free, oxide-atmosphere interface is characteristic of specimens yielding rate curves in the second linear region. × 200

(2) thermal diffusion of the gases in the oxidation system, (3) temperature control and (4) prior history of the metal specimen. Each of the above is discussed in what follows:

(1) *Gas flow and regulation.* Conventional manometric flow-meters using a capillary construction and containing di-butyl phthalate in the two arms were used to meter the carbon monoxide, carbon dioxide and argon. These flowmeters were calibrated using a Precision Wet-Test Meter. These results were checked by displacing a soap bubble up a glass tube of known volume. The results were in good agreement. It is estimated that the maximum error in the gas ratio as a result of the flowmeter technique was less than 1 per cent.

(2) *Thermal diffusion of gases.* It has been shown by Darken and Gurry[5] that thermal diffusion in a CO–CO_2 mixture may change the ratio of these gases in

a heated, vertical tube. From tests at 1100°C, these authors found that flow velocity greater than 0.6 cm/sec would ensure an error of less than 0.25 per cent in the CO–CO_2 ratio as a result of thermal diffusion. On the other hand it was found that a flow rate of 1.2 cm/sec introduced an error of over 1°C in temperature measurement. Consequently a flow rate of 0.9 cm/sec was recommended in order to ensure the absence of an appreciable contribution of thermal diffusion. In the present work the gas flow was varied from one to about 9 l/hr. This corresponds to a calculated linear flow of 0.098–0.90 cm/sec measured at room temperature. These changes in gas flow rate did not change the observed oxidation rates nor was there any correlation between gas flow rate and oxide surface topography. To confirm further these observations, experiments were performed in which the gases flowed downward through the vertical tube furnace and also tests were made using a horizontal furnace. Results obtained were consistent with data obtained in the vertical tube furnace using the procedure described previously.

(3) *Temperature control.* Because of the relatively large activation energy for the oxidation process, small differences in temperature could cause large differences in the observed oxidation rate. As mentioned previously fluctuations in temperature were held better than ± 1°C, and the nickel cylinder surrounding the hot zone of the oxidation chamber ensured a maximum temperature gradient at 1075°C of 6°C over a 1.5-in. vertical distance. This was the maximum distance occupied by the specimen during the oxidation test. Therefore the maximum temperature fluctuation over the entire specimen at 1075°C was the reported temperature ± 4°C. The maximum temperature fluctuation over the specimen at temperatures below 975°C was the reported temperature ± 2°C. The internal consistency of the data also appears to obviate the possibility of large temperature errors as well as errors resulting from thermal diffusion of the gases.

(4) *Prior history of the metal sample.* Hauffe and co-workers[1] used a helium-anneal prior to oxidation. A similar anneal was carried out in the present studies and the only difference in behavior from samples annealed in hydrogen was the presence of a thin oxide layer prior to oxidation in the CO–CO_2 mixture. Hauffe and co-workers used Armco iron, apparently in the "as-received" condition. Several types of iron of varying purity, including decarburized Armco iron, were studied in the present work. Results were consistent with data obtained using Ferrovac *E* Iron.

All reasonable precautions have been taken to ensure a clean, stress-free metal sample and the present data were reproducible and self-consistent. It was therefore concluded that the present data represented valid results for the conditions reported herein. The apparent discrepancy between the rates obtained in the present study and those of Hauffe[1] can be explained as follows. The measurements reported by Hauffe corresponded to a minimum oxide thickness of about 1.1×10^{-3} cm. The measurements of the present study corresponded to a minimum oxide thickness of less than 7.7×10^{-5} cm. Consequently the first linear region of oxidation (4×10^{-4}–1.8×10^{-3} cm oxide thickness) which was observed in the present study was missed by Hauffe. Furthermore, rates obtained for the second, virtually linear region of the present work are in agreement with the data of Hauffe. However, the present authors have been unable to use the data from this virtually linear second region for the confirmation of Wagner's mechanism since, as mentioned previously, measurements on the change in surface area, which from these data appear to be responsible for the increase in oxidation rate of the region, have not as yet been performed.

SUMMARY AND CONCLUDING REMARKS

In the temperature range of 925°–1075°C and for oxide films between 4×10^{-4}–1.8×10^{-3} cm, the rate of oxidation in CO–CO_2 mixtures has been shown to be a linear function of the mole fraction of CO_2 and the sum of the partial pressures of CO_2 and CO. These data substantiate the proposed rate-determining step to be the dissociation of carbon dioxide into carbon monoxide and adsorbed oxygen atoms or ions. Furthermore, preliminary tests indicate that this process also holds for the other transition metals, cobalt and nickel. Studies on these metals are in progress.

ACKNOWLEDGMENTS

This research was supported by a grant from the Union Carbide Metals Company. The authors also gratefully acknowledge advice from Professor Carl Wagner. One of the writers (F. P.) was the holder of the Dwight N. and Noyes D. Clark Fellowship.

REFERENCES

1. K. Hauffe and P. Pfeiffer, *Z. Elektrochem.* **56,** 390 (1952); *Z. Metallk.* **44,** 27 (1953).
2. C. Wagner, Mimeographed notes, Course 3.23 *Kinetics in Metallurgy*, Massachusetts Institute of Technology (Spring 1955).
3. H. Kobayashi and C. Wagner, *J. Chem. Phys.* **26,** 1609 (1957).
4. L. Himmel, R. F. Mehl and C. E. Birchenall, *J. Metals, N.Y.* **5,** 827 (1953).
5. L. S. Darken and R. W. Gurry, *J. Amer. Chem. Soc.* **67,** 1398 (1945).

VOL. 8 1960

INITIAL STAGES OF PLASTIC DEFORMATION IN COPPER AND ALUMINUM*

A. R. ROSENFIELD and B. L. AVERBACH†

The early stages of plastic flow and microcreep have been studied in single crystals and in polycrystalline copper and aluminum using a method with a strain sensitivity of 2×10^{-6} in the temperature range −196 to 25°C. The temperature dependence of the 10^{-6} yield stress is interpreted as arising from a thermal activation of stacking faults under stress. This model results in a value of 25 ergs/cm² for the stacking fault energy of copper and 100 ergs/cm² for aluminum.

STADES INITIAUX DE LA DEFORMATION PLASTIQUE DANS LE CUIVRE ET L'ALUMINIUM

Les auteurs ont étudié les premiers stafles de la déformation plastique et du microfluage de monocristaux et de polycristaux de cuivre et d'aluminium. Ils ont utilisé une méthode dont la sensibilité à la déformation est de 2×10^{-6} dans la zone de température comprise entre −196 et 25°C.

La relation entre la température et la limite élastique à 10^{-6} est interprétée comme provenant d'une activation thermique des fautes d'empilement sous l'effet de la tension. A l'aide de ce modèle, on peut estimer que l'énergie des fautes d'empilement du cuivre et de l'aluminium a une valeur respective de 25 ergs/cm² et 100 ergs/cm².

ANFANGSSTADIUM DER PLASTISCHEN DEFORMATION VON KUPFER UND ALUMINIUM

Die Anfangsstadien von plastischem Fließen und Mikrokriechen wurden an Einkristallen und polykristallinen Proben von Kupfer und Aluminium untersucht. Die verwendete Methode hatte im Temperaturgebiet von −196° bis 25°C eine Empfindlichkeit von 2×10^{-6} bei der Messung der Verzerrung. Die Temperaturabhängigkeit der 10^{-6} -Fließspannung wird so gedeutet, daß sie von einer thermischen Aktivierung von Stapelfehlern unter Spannung herrührt. Aus diesem Modell ergibt sich für die Stapelfehlerenergie von Kupfer 25 erg/cm² und für Aluminium 100 erg/cm².

1. INTRODUCTION

The factors which control the initiation of plastic flow are not well understood and current theories usually select one of the following for the critical step: (1) the friction in the lattice, i.e. the Peierls–Nabarro force, (2) the resistance to activation of a dislocation generator, such as a Frank–Read source, or (3) the resistance to the motion of glide dislocations provided by a forest of intersecting dislocations. These mechanisms should be distinguishable in part from the temperature dependence of the stress required to initiate plastic flow. This initial yield stress should have the same temperature dependence as the elastic constants for the friction[1] and the source activation[2] mechanisms. In the case of the forest mechanism the initiation stress should depend on a thermal activation energy which is a function of the applied stress[3] and should depend on the number of dislocations present at the onset of flow.

The temperature dependence of the stress to initiate flow was studied in single crystals and in polycrystalline copper and aluminum with a view toward separating these mechanisms. The stress required to produce a plastic strain of 2×10^{-6} (hereafter called the 10^{-6} yield) was measured from room temperature down to the boiling point of liquid nitrogen. In order to obtain additional insight into the interaction of glide dislocations with barriers, the influence of prior plastic deformation on the 10^{-6} yield was studied.

The results of these observations are presented in the following sections. Comparisons with theory are presented in the discussion and it is shown that the mechanism for flow initiation must be reconsidered.

2. PROCEDURE

The materials were received in the form of $\frac{3}{4}$ in. rod and the compositions are listed in Table I. Unthreaded tensile bars 0.252 in. in diameter with a 2.5 in. gauge length were machined, etched to remove cold work, and annealed according to the schedules in Table I. The 10^{-6} yield was measured by unloading from successively higher stresses and observing the residual strain using electrical resistance strain gauges mounted on the specimens.[4,5] The first detectable permanent strain on unloading (2×10^{-6}) was defined as the 10^{-6} yield and stress–plastic strain curves were determined for each specimen. Considerable care was taken to achieve axiality and readings on strain gauges mounted on opposite sides of the specimen showed that each gauge recorded within 5 per cent of the average strain.

Single crystals of high purity copper were grown in the form of tensile bars using the method of Blewitt[6]. These specimens were also annealed at 300°C for

* Based on a thesis submitted by A. R. Rosenfield in partial fulfillment for the Sc.D. degree in June, 1959. This work was sponsored by the Office of Naval Research. Received July 23, 1959; revised version February 10, 1960.

† Department of Metallurgy, Massachusetts Institute of Technology, Cambridge, Massachusetts.

TABLE 1. Materials and treatments

Alloy	Cu	Al	Fe	Si	Pb	Ni	S	Ag	Annealing treatment	Intercept grain size (mm)
High purity copper	99.999	—	—	—	—	—	—	—	300°C for 24 hr in vacuum	0.27
OFHC	99.97	—	0.005	—	0.001	0.005	0.004	0.010	500°C for 24 hr in vacuum	0.045
High purity aluminum	0.002	99.995	0.001	0.002					260°C for 1 hr in air	0.25
2S (1100) aluminum	0.15	99.15	0.59	0.11					370°C for 1 hr in air	0.045*

* Etchants did not clearly reveal grain boundaries in this material and this value is an approximation.

24 hr in a vacuum. Plastic flow occurred at such low stresses for the single crystal specimens that these were tested by the application of dead loads.

3. RESULTS

Figure 1 shows the initial yield stress for the polycrystalline specimens. The 10^{-6} yield stress of copper increases by about 150 p.s.i. as the temperature is lowered from 25 to −196°C. On the other hand, the impurities present in OFHC copper raise the 10^{-6} yield by about a factor of 3 but do not affect the temperature dependence. Adjusting the results to compensate for the difference in grain size[4] accounts for about one-third of the difference between the high purity copper and the OFHC curves. The 10^{-6} yield of aluminum increases by about a factor of 3 as the temperature is lowered, but the impurities present in the 2S (1100) material do not seem to affect either the value of the yield stress or its temperature dependence.

The resolved 10^{-6} yield stresses were determined for single crystals of high purity aluminum and copper by resolving the tensile stress to produce a strain of 2×10^{-6} on the most favorably oriented slip plane and direction. The tensile axes of the copper crystals were clustered around [111] and around [110] for the aluminum crystals. The single crystal data are compared with the data for polycrystals in Fig. 2. The numbers next to the single crystal points refer to the specimen identity, and in two cases for aluminum, one crystal was used to determine the 10^{-6} yield at more than one temperature. Care was taken in these instances not to introduce a plastic strain of more than 50×10^{-6}, and the crystal was then annealed according to the procedure listed in Table 1 before a second determination of the yield initiation was made. The 10^{-6} yield observed for copper and aluminum single crystals at room temperature was very low, of the order of 30 p.s.i. (0.021 kg/mm²) and it was about one-third of the generally reported values of the critical resolved shear stress. The single crystal yields are much lower than those predicted from an extrapolation of the grain size dependence of similar

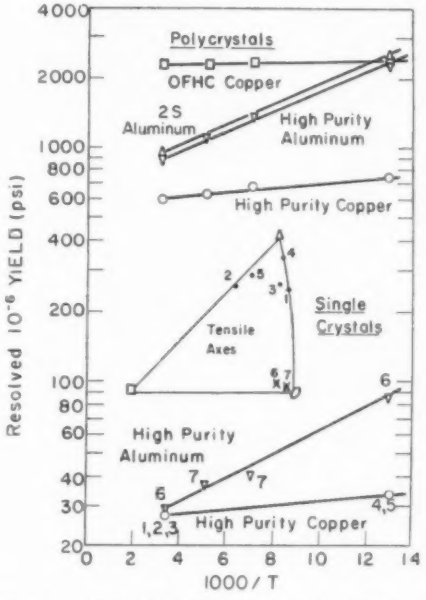


FIG. 2. 10^{-6} yield of copper and aluminum single crystals and polycrystalline materials.

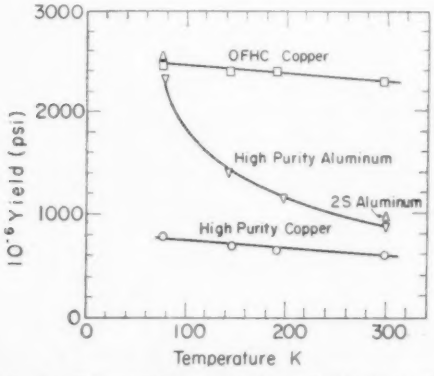


FIG. 1. Temperature variation of the 10^{-6} yield of polycrystalline copper and aluminum.

VOL. 8 1960

TABLE 2. Effect of temperature on 10^{-6} yield stress and elastic modulus

Material	10^{-6} yield, Y (p.s.i.)		Young's Modulus, E (10^6 p.s.i.)		$\frac{Y(-196)}{Y(25)}$	$\frac{E(-196)}{E(25)}$
	25°C	−196°C	25°C	−196°C		
Copper, high purity polycrystalline	600	750	18.5	19.4	1.3	1.05
Copper, single crystal	27	32	25.6	27.0	1.2	1.06
Aluminum, high purity polycrystalline	900	2320	10.2	11.1	2.6	1.09
Aluminum, single crystal	30	85	9.8	10.7	2.8	1.09

material.[4] The temperature dependence of Young's modulus was also measured at 25 and −196°C and the values for the polycrystalline material agree well with those of Köster[7]. In the case of the single crystals the Young's moduli are affected in the expected fashion with direction, but the temperature dependence is the same as in the polycrystals. It is evident from the data in Table 2 that the 10^{-6} yield stresses have a somewhat greater temperature dependence than the elastic constants in the case of copper and that the yields have a very much greater temperature dependence in the case of aluminum.

The influence of repeated loading on the resolved shear stress of a single crystal of copper is shown in Fig. 3. The 10^{-6} yield increases from 30 p.s.i. to about 60 p.s.i. after a prior plastic strain of 160×10^{-6}. Continued plastic prestrain beyond this did not further increase the initial yield. One of the interesting features of the curves is the kink in the early portion of the flow curve, and similar kinks were observed in all of the single crystal samples tested. These kinks may be an experimental confirmation of the hypothesis that the number of dislocation loops produced is not a smooth function of the stress, and the loops may be produced in bursts.[8] The easy glide region is observed at values of about 100 p.s.i.

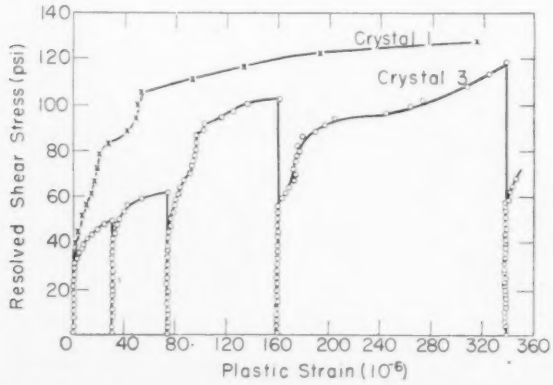


FIG. 3. Repeated load experiments on copper single crystals at 25°C.

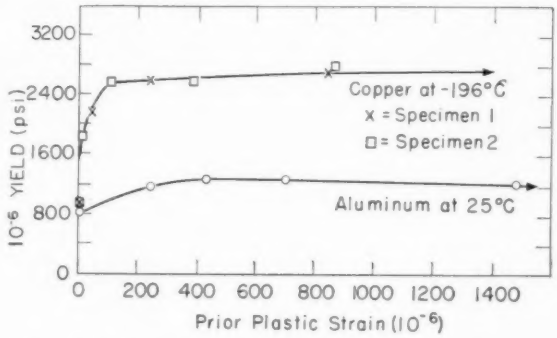


FIG. 4. Effect of prestrain on the 10^{-6} yield of polycrystalline materials.

(0.070 kg/mm²) and this corresponds to the value usually given as the critical resolved shear stress.

The influence of prior plastic strain followed by an immediate determination of the 10^{-6} yield stress is shown in Fig. 4 for polycrystalline high purity copper at −196°C and for polycrystalline high purity aluminum at room temperature. The plastic prestrain was carried out to at least 1200×10^{-6} for the polycrystalline specimens and these showed the same trend as the single crystals. The 10^{-6} yield showed an increase after small prestrains of the order of 200–400 $\times 10^{-6}$, but additional prestrain did not produce any further increase in the yield.

A further feature of the initial stages of deformation was the discontinuous microcreep observed in both aluminum and copper polycrystalline samples at stresses somewhat above the 10^{-6} yield. Typical microcreep behavior is shown in Fig. 5 for high purity copper at −196°C, and this type delayed creep has also been observed by Kayako Hirano[9] in high purity copper involving many successive discontinuous strain increments over prolonged periods of time. These discontinuous creep steps appear to be related to the delayed yielding recently observed in copper,[10] and may be interpreted in terms of piled-up dislocations breaking through barriers on the discontinuous generation of dislocations.

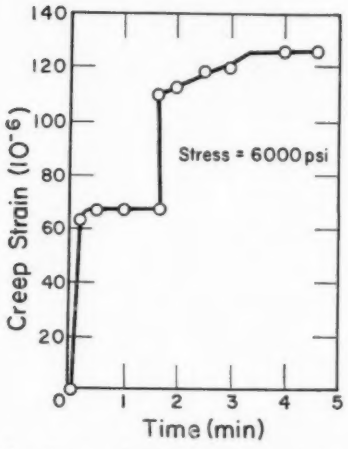


FIG. 5. Creep of high purity copper at −196°C showing delayed yielding.

4. DISCUSSION

The principal feature exhibited by the data obtained in this investigation is the strong temperature dependence of the stress required to produce a plastic strain of 10^{-6}. The temperature dependence of the 10^{-6} yield is too large, even for copper, to be explained by current theories of friction forces on dislocations or in terms of the resistance to activation of a dislocation generator. Furthermore, if the resistance to initiation was caused by the presence of intersecting dislocations, the 10^{-6} yield should increase greatly with prior plastic flow; only a small increase was noted after a small plastic flow, and the yield did not continue to increase even with large deformations. In addition, the activation energy for the forest mechanism should involve the energy for the formation of a jog, and copper, which has the higher jog formation energy,[11] should exhibit a greater temperature dependence than aluminum. It is evident that some other effect must determine the temperature dependence for the initial yield, and it is proposed that the ease of dissociation of glide dislocations in the materials controls the initiation of plastic flow.

Let us consider the stress required to initiate slip in an unworked crystal. The passage of about 100 dislocations through the crystal is sufficient to provide a strain of 10^{-6}, and the 10^{-6} yield stress of about 30 p.s.i. (2×10^6 dyn/cm^2) observed for copper and aluminum single crystals at room temperature thus approaches the stress to start the slip process. We shall assume that the dislocation length is not increased at the very onset of slip and that none of the initially applied strain energy is expended in increasing the length of the dislocation loops already present. If we consider that the initial obstacle is the creation of a source by overcoming the line tension of a dislocation, the initial stress is given by $\sigma = \mu \mathbf{b}/l$ where μ is the shear modulus, $\mathbf{b}$ is the Burgers vector, and l is the length of the unpinned dislocation line. For copper, taking $\sigma = 2 \times 10^6$ dyn/cm^2, $\mu = 4.8 \times 10^{11}$ dyn/cm^2 (see Table 2) and $\mathbf{b} = 2.5 \times 10^{-8}$, this requires a value of $l = 6 \times 10^{-3}$ cm. The density of dislocations in the annealed crystals, measured by etch pit and X-ray rocking curve methods* is about 10^7/cm^2 and it seems unlikely that loops of this size would exist. Furthermore, the only temperature dependence arises from that of the elastic constants and this is clearly insufficient.

The frictional force on a dislocation arising from the lattice forces is not easily calculated, and the stress required to overcome this has been approximated as:

$$\sigma_0 = \frac{2\,\mu}{(1-\nu)} \exp\left(-2\pi \frac{w}{\mathbf{b}}\right), \qquad (1)$$

where ν is Poisson's ratio, and w is the width of the dislocation. If the width of the dislocation is taken as the distance between partials for an extended dislocation, e.g. w is about 10^{-7} cm in copper, the initial stress is close to the observed value, but the temperature dependence is still insufficient.

Extended dislocations are generally assumed to move together as a unit on the application of a force. It is now suggested that one of the partials moves forward first by a distance equal to its Burgers vector, extending or shrinking the stacking fault and that the other then moves to restore the equilibrium separation. Thus, for slip to start, a non-equilibrium amount of stacking fault must be formed, and it is suggested that this process is thermally activated. A schematic representation of this mechanism is shown in Fig. 6.

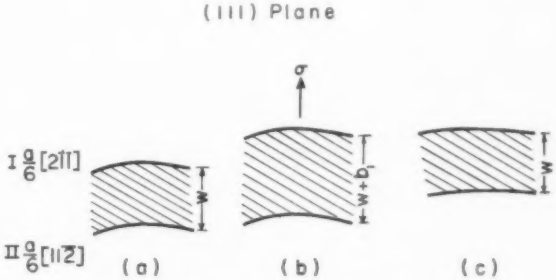


FIG. 6. Motion of partial dislocations on application of stress:
(a) Initial position of partials.
(b) One partial has moved forward, resulting in an extension of the stacking fault.
(c) Other partial moves forward under influence of applied stress and elastic attraction.

* These measurements are described in another paper.

VOL. 8 1960

The partial dislocation I forms the outer part of a dislocation loop of unit length and the partial II forms the inner. The equilibrium width of the stacking fault, w, is increased to the non-equilibrium width $(w + \mathbf{b}_1)$ as the outer partial moves forward under the influence of the applied stress σ and then returns to w as the second partial follows along.

The additional area of stacking fault is $\mathbf{b}_1$, where $\mathbf{b}_1$ is the Burgers vector of the partial and its energy of formation is given by:

$$U_s = \mathbf{b}_1\gamma, \tag{2}$$

where γ is the unit stacking fault energy. The energy supplied to the partial by the applied stress is:

$$U_m = \sigma\mathbf{b}_1^2, \tag{3}$$

where σ is the resolved initial shear stress. Since the energy required for the fault formation is much greater than that supplied by the applied stress, the additional energy for the dislocation motion must be supplied by thermal activation.

Consider that n layers of slip planes are associated with the stacking fault, and the number of atoms per unit length of dislocation involved in the first motion of the partial is thus $n/\mathbf{b}$. Assuming an average thermal energy per atom of kT, the thermal energy of these atoms is thus:

$$U_t = (n/\mathbf{b})kT. \tag{4}$$

Under thermal activation the probability of forming a new stacking fault is:

$$P = C \exp(U_s/U_t) = C \exp(\mathbf{b}\mathbf{b}_1\gamma/nkT). \tag{5}$$

In the case of f.c.c. lattices it is reasonable to assume that the stacking fault will extend over three layers on each side of the slip plane, since it would require three planes to re-establish the original stacking sequence. Thus, taking $n = 6$, $\mathbf{b} = a/\sqrt{3}$, and $\mathbf{b}_1 = a/\sqrt{6}$, where a is the lattice parameter and considering the stress to initiate plastic flow σ_0 as proportional to the activation probability:

$$\sigma_0 = A \exp[a^2\gamma/(35.1)T], \tag{5a}$$

where a is given in Angstrom units and γ in ergs/cm^2.

The resultant values of the stacking fault energies calculated from the slopes in Fig. 2 are listed in Table 3. The value of 30 ergs/cm^2 for copper is close to the calculated value of 40 ergs/cm^2, and the value of 100 ergs/cm^2 for aluminum is reasonably close to the calculated value of 200 ergs/cm^2 [11] in view of assumptions involved in this model and in the calculations. It is evident that this approach leads to reasonable values of stacking fault energies and provides a basis for understanding the large temperature dependence

TABLE 3. Stacking fault energy

Material	γ (ergs/cm^2)
High purity copper—polycrystal	27
High purity copper—single crystal	24
average	25
OFHC copper—polycrystal	6
High purity aluminum—polycrystal	94
High purity aluminum—single crystal	106
average	100
28 (1100) aluminum	94

of the yield. Thermally activated extensions of stacking faults may be considered as a chemical contribution to the Peierls–Nabarro frictional force. In accordance with the model presented here this effect is more important than the physical displacement of a dislocation from its equilibrium position. The argument here has been applied to f.c.c. metals but it should hold for h.c.p. metals also.

It is interesting to note that the impurities in OFHC copper appear to lower the stacking fault energy (Table 3) but they increase the value of the 10^{-6} yield stress in comparison with high purity copper. These effects may result from the presence of the impurities in solution. On the other hand, the impurities in aluminum do not appear to affect either the stacking fault energy or the 10^{-6} yield and the metallographic evidence suggests that the impurities may be present principally in the form of precipitates.

Body-centered cubic metals offer an interesting situation since it is well known that the 10^{-6} yield of these metals increases by a factor of 5 or 6 between 25 and -196°C. Fig. 7 shows values of the 10^{-6} yield of low carbon ferrite.[12] The data at high temperature, where the initial yield is due to slip, do not fall on a straight line as required by this model. On this basis it does not appear likely that the glide dislocations dissociate. However, at low temperatures, where the yield initiation is caused by twinning the data do seem to satisfy the model. It is probable that mechanical twinning requires a dissociation of dislocations and a stacking fault energy would thus be involved.

Assuming the twinning plane to be (112), a stacking of six planes on each side of the dissociation plane would be required to restore the original sequence and thus $n = 12$. Taking $\mathbf{b}_1$ as $a/2\sqrt{3}$ and the spacing of planes in the [110] as $a/(\sqrt{2})$ the value of the stacking fault energy γ is determined to be 112 ergs/cm^2.

The situation in iron is anomalous in comparison to that in copper and aluminum. Copper has a low stacking fault energy and has been observed to

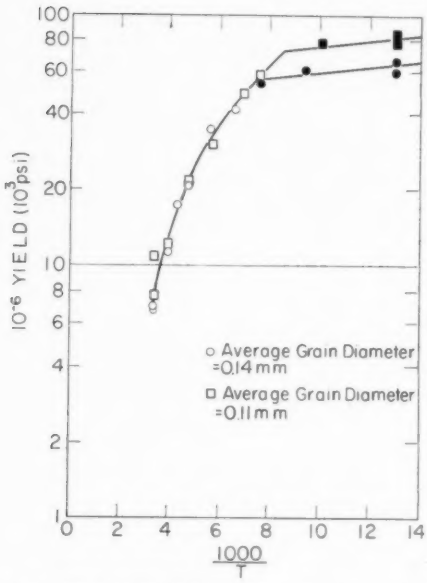


FIG. 7. 10^{-6} yield of low-carbon ferrite according to Hahn *et al.*[12].

deform by twinning at low temperatures. Aluminum has a stacking fault energy close to that of iron, but mechanical twinning has not been observed in aluminum whereas it occurs readily in iron. It is possible that the probability of initiating a twin in iron is greater since it is easier for glide dislocations to dissociate out of the plane of slip to form twins whereas glide dislocations in aluminum cannot do this without a much greater expenditure of energy. The large temperature dependence of the initial yield at high temperatures may result from carbon locking or from the necessity of initiating cross slip in order to accommodate the multiple slip systems which are active.

ACKNOWLEDGMENTS

The authors would like to acknowledge the assistance of Rupert Whittemore in the experimental phases of the program and the sponsorship of the Office of Naval Research.

REFERENCES

1. A. J. FOREMAN, M. A. JASWON and J. K. WOOD, *Proc. Phys. Soc.* A**64,** 156 (1951).
2. F. C. FRANK and W. T. READ, JR., *Phys. Rev.* **79,** 722 (1950).
3. A. SEEGER, *Dislocations and Mechanical Properties of Crystals* p. 243 Wiley, New York (1957).
4. D. A. THOMAS and B. L. AVERBACH, *Acta Met.* **7,** 69 (1959).
5. W. S. OWEN, M. COHEN and B. L. AVERBACH, *Trans. Amer. Soc. Metals* **50,** 517 (1958).
6. T. H. BLEWITT, *Phys. Rev.* **91,** 1115 (1953).
7. W. KÖSTER, *Z. Metallk.* **39,** 1 (1948).
8. N. F. MOTT, *Dislocations and Mechanical Properties of Crystals*, p. 458 Wiley, New York (1957).
9. KAYAKO HIRANO, Private communication.
10. I. R. KRAMER, *Trans. Amer. Inst. Min. (Metall.) Engrs.* **215,** 226 (1959).
11. A. SEEGER, *Phil. Mag.* **46,** 1194 (1955).
12. G. T. HAHN, B. L. AVERBACH, W. S. OWEN and M. COHEN, *Fracture*, p. 91 Cambridge (1959).

VOL. 8 1960

SELF-DIFFUSION OF ALPHA-IRON IN A LARGE TEMPERATURE GRADIENT*

W. G. BRAMMER†

Experimental results of an attempt to measure the thermal gradient self-diffusion in iron are given. A temperature gradient of 2500°C/cm was placed on each of three iron samples for 550 hr. Platinum wire markers were placed 0.01 in. apart, normal to the sample length; the marker spacings were measured before and after the diffusion anneal. No marker shift greater than the 0.0001-in. probable error was observed; whereas marker shifts of the order of 0.001 in. were anticipated from theoretical calculations. Each of several alternative possible conclusions which may be drawn from these results are discussed: (1) self-diffusion in α-iron is not via a vacancy mechanism, or (2) if the vacancy mechanism predominates in α-iron, then either (a) the activation energies for formation, E_f, and migration of vacancies, E_m, are nearly equal, or (b) the role of the barrier atoms must be explicitly considered in the process of thermal activation for an atom jump in a temperature gradient, in which case the mass flow is not proportional to the difference in E_f and E_m. The model of thermal gradient self-diffusion is discussed and several experiments are suggested. In addition, a calculation is given for the dependence of thermal gradient self-diffusion on the separation of vacancy sources and sinks, using parallel grain boundaries normal to the temperature gradient as the only sources and sinks which are important.

AUTODIFFUSION DU FER ALPHA DANS UN GRADIENT IMPORTANT DE TEMPERATURE

L'auteur expose les résultats expérimentaux obtenus au cours d'un essai de mesure de gradient thermique d'autodiffusion dans le fer. Trois échantillons de fer ont été soumis pendant 550 heures à un gradient de température de 2500°C/cm. Des repères en platine ont été placés à des distances de 0,01 inch normalement à la longueur de l'échantillon. Les écartements des repères ont été mesurés avant et après le recuit de diffusion. L'auteur n'a pas observé des variations de l'écartement des repères supérieures à l'erreur probable de la mesure (0,0001 inch) bien qu'un calcul théorique ait permis de prévoir des variations de l'ordre de 0,001 inch.

L'auteur discute ensuite les différentes conclusions qu'il est possible de tirer de ces résultats:

(1) l'autodiffusion dans le fer α n'est pas un mécanisme qui fait intervenir des lacunes.

(2) si l'effet des lacunes prédomine dans le fer α alors les énergies d'activation pour la formation (E_f) et la migration (E_m) des lacunes sont quasi égales ou bien le rôle des atomes formant les barrières intervient explicitement dans le mécanisme d'activation thermique permettant un saut atomique lorsqu'il existe un gradient de températures; dans ce cas, la masse en mouvement n'est pas proportionnelle à la variation E_f et E_m. L'auteur discute encore du modèle d'autodiffusion dans un gradient thermique et il suggère de nombreuses expériences.

En outre, il expose un calcul permettant de déterminer l'effet de l'autodiffusion dans un gradient sur la séparation des sources de lacunes et des puits.

Pour ce faire, il considère comme seules sources et puits importants, les frontières de grains parallèles qui sont normales au gradient de température.

SELBSTDIFFUSION VON α-EISEN BEI GROßEM TEMPERATURGRADIENT

Die experimentellen Ergebnisse eines Versuchs, die Selbstdiffusion von Eisen in einem Temperaturgradienten zu messen, werden mitgeteilt. An drei Eisenproben wurde 550 Stunden lang ein Temperaturgradient von 2500°C/cm angelegt. Senkrecht zur Längsrichtung der Proben wurden Marken aus Platindraht in Abständen von 0.01 in. angebracht; der Abstand der Marken wurde vor und nach dem Diffusions-Glühen gemessen. Es wurde keine Verschiebung einer Marke beobachtet, die über den wahrscheinlichen Fehler von 0.0001 in. hinausging; auf Grund theoretischer Überlegungen dagegen erwartet man Verschiebungen der Größenordnung 0.001 in. Die Schlüsse, die sich aus diesen Experimenten als Alternativen ziehen lassen, werden diskutiert: (1) Die Selbstdiffusion in α-Eisen beruht nicht auf einem Leerstellenmechanismus, oder (2), wenn der Leerstellenmechanismus in α-Eisen vorherrscht, sind entweder (a) die Aktivierungsenergien für Bildung, E_f, und für Wanderung von Leerstellen, E_m, nahezu gleich, oder (b) die Rolle der Atome, die beim Sprung eines Atoms im Temperaturgradienten die zu überwindende Schwelle bilden, muß beim Prozeß der thermischen Aktivierung explizit berücksichtigt werden; in diesem Fall ist der Massenstrom nicht der Differenz von E_f und E_m proportional. Das Modell für die Selbstdiffusion im Temperaturgradienten wird diskutiert und mehrere Experimente werden vorgeschlagen. Zusätzlich werden Rechnungen darüber angestellt, wie die Selbstdiffusion im Temperaturgradienten vom Abstand der Versetzungsquellen und -senken abhängt; dabei werden als einzige Quellen und Senken von Bedeutung parallele Korngrenzen senkrecht zum Temperaturgradienten angesehen.

1. INTRODUCTION

The Kirkendall effect, which has been observed in a large number of metal systems,[1–3] strongly implies that the interdiffusion of atoms in these systems takes place by a defect mechanism. Based on the calculations of the energies of the formation of vacancies and interstitials,[4] diffusion by vacancy flow appears to be the predominating mechanism. The formation of voids, apparently by precipitation of vacancies on the side of the faster diffusing species of the Kirkendall

* Received December 8, 1959. This research was supported by the U.S. Atomic Energy Commission.

† Atomics International, A Division of North American Aviation, Inc.

diffusion couple, tends to confirm this viewpoint. Sintering experiments involving mass transport also frequently require a defect mechanism of diffusion in many pure metals systems.[5,6]

If the vacancy mechanism of diffusion is assumed to operate ,the elementary atomic jump frequency may be calculated by considering the product of the probability, P_v, that an atom site adjacent to the jumping atom is vacant and the probability, P_j, that this atom has the required energy to jump over the potential barrier to exchange places with the adjacent vacancy. Since both probabilities are governed by Boltzmann statistics, the resulting diffusion coefficient is

$$D = D_0 \exp\left[-(E_f + E_m)/kT\right],$$

in agreement with empirical observations. Here E_f and E_m are the activation energies for formation and migration of vacancies, respectively, k is Boltzmann's constant, and T is the absolute temperature.

A simple extension of this theory has been made by Shockley[7], Brinkman[8] and LeClaire[9] for self-diffusion of the metal placed in a temperature gradient. A slightly expanded version will be given here. The expression for the rate of net mass transport in the temperature gradient case is similar to the expression governing ordinary Kirkendall diffusion[10–13] except that the concentration gradient is here replaced by the temperature gradient and the direction of marker flow is dependent upon the difference in activation energies for formation and migration of vacancies rather than the difference in the two atomic diffusion coefficients. A discussion will be given of the limitations of the diffusion model, the extent of the expected net mass transfer (and corresponding marker movement) and of the failure to observe an effect in iron outside the limits of experimental error.

VOL. 8 1960

2. MODEL

The following assumptions are made for our model of diffusion in a close-packed metal lattice placed in a temperature gradient: (1) the only defect important in the diffusion process is the vacancy, (2) the temperature difference, ΔT, between adjacent lattice planes normal to the temperature gradient, $(dT)/(dx)$, is given by $\Delta T = (dT)/(dx)\lambda$, where λ is the lattice spacing, and (3) the concentration of vacancies at any point in the lattice at a temperature, T, is the same as that which would exist in a lattice isothermally at this temperature (see Fig. 1). This last assumption is examined in detail in the Appendix. It is there shown that only a slight error is involved if the separation of sources and sinks is relatively large compared to atomic dimensions but small compared to the usual sample size.

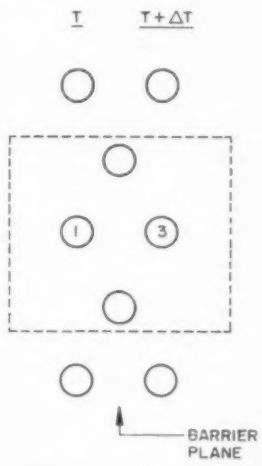


FIG. 1. Lattice configuration in temperature gradient. Lattice sites (1) and (3) in two adjacent equivalent planes, which are normal to the temperature gradient, are separated by a barrier plane of atoms.

The flux, J_{13}, of atoms in plane (1) at temperature, T, jumping to an equivalent site in plane (3) at temperature, $T + \Delta T$, occupied by a vacancy is given, using Boltzmann statistics, by the product of the probability that an adjacent lattice site is vacant and the probability that the atom has the energy required to jump:

$$J_{13} = P_v(3) \cdot P_j(1) = A\left\{\exp\left[\frac{-E_f}{k(T+\Delta T)}\right]\right\} B\left\{\exp\left[\frac{-E_m}{kT}\right]\right\}. \quad (1)$$

The probability of an atom jump in the opposite direction is similarly given by

$$J_{31} = P_v(1)P_j(3) = A\left\{\exp\left[\frac{-E_f}{kT}\right]\right\} B\left\{\exp\left[\frac{-E_m}{k(T+\Delta T)}\right]\right\}. \quad (2)$$

The net flux of atoms flowing toward higher temperatures is given by the difference

$$J = J_{13} - J_{31}.$$

Since ΔT is small, the exponentials can be expanded as

$$\exp\left[\frac{-E_m}{k(T+\Delta T)}\right] = \exp\left[\frac{-E_m\left(1-\frac{\Delta T}{T}\right)}{kT}\right] = \left\{\exp\left[\frac{-E_m}{kT}\right]\right\}\left\{1-\left(\frac{E_m}{kT^2}\right)\Delta T\right\}.$$

The net current now becomes

$$J = AB\left\{\exp\left[-\frac{E_f+E_m}{kT}\right]\right\}\left[\frac{E_f-E_m}{kT}\right]\left(\frac{\Delta T}{T}\right). \quad (3)$$

Using the second assumption, the resulting net atom flow is

$$J = AB\left\{\exp\left[-\frac{E_f + E_m}{kT}\right]\right\} \times \left(\frac{1}{T}\right)\left(\frac{dT}{dx}\right)\lambda\left[\frac{E_f - E_m}{kT}\right]. \quad (4)$$

The constants A and B are related to the usual diffusion theory frequency factor, D_0, i.e. $D_0/\lambda^2 = AB$. Furthermore, $E_f + E_m = E_D$, is the activation energy for self diffusion. Thus,

$$J = \frac{D_0}{\lambda}\left\{\exp\left[\frac{-E_D}{kT}\right]\right\}\left[\frac{E_f - E_m}{kT}\right]\left(\frac{1}{T}\right)\left(\frac{dT}{dx}\right). \quad (5)$$

The net flow of atoms calculated above gives rise to a redistribution of atoms which results in the accumulation and loss of lattice sites in different parts of the crystal. Inert markers placed in the crystal provide a convenient means of measuring the number of lattice sites between fixed points since any accumulation or loss of lattice sites between such inert markers is reflected in a change in the marker spacings. Just as in the normal Kirkendall effect, the marker spacings are measured before and after a diffusion anneal, which in the present case occurs in a temperature gradient. Since all other quantities in the flow equation are known for the experimental conditions imposed, the change in marker spacing should provide a good measure of the relative values of E_m and E_f.

The marker spacings increase at the high temperature end if the net atom flow is up the temperature gradient, a case which arises if E_f is greater than E_m. Conversely, a decrease in the high temperature marker spacings results if E_f is less than E_m. No change in the marker spacings occur if $E_m = E_f$. The change in spacing, ΔM_{ij}, between any two markers i and j at any time t is given by

$$\Delta M_{ij} = -\lambda t(J_j - J_i), \quad (6)$$

where λ is the lattice spacing and J_i and J_j are the net atom flow rates past the ith and jth markers as determined from equation (5).

In f.c.c. metals, theory indicates that E_d should be divided nearly equally between E_m and E_f.[4,14] For instance, Buffington and Cohen[14] have predicted that E_m should be approximately 0.6 of E_d. A large number of experiments have been performed to determine these energies, but some uncertainty about the relative magnitudes of E_m and E_f still persists.[15] The measured values of E_m range from $0.4E_D$ to $0.6E_D$.

Buffington and Cohen[14] also predict that vacancies are formed relatively easier in b.c.c. than in f.c.c. metals. A more asymmetric division of the self-diffusion energy has been predicted[14] in which $E_m \approx 0.85E_d$. Sodium is the only b.c.c. metal in which a division of E_d into two parts has been experimentally determined.[16] The migration energy of vacancies in Na is believed to be about $0.15E_d$,[16,17] in direct contrast to these predictions.

The possibility of a very asymmetric division of E_d makes any b.c.c. metal with a reasonably large diffusion coefficient a logical material for the temperature-gradient self-diffusion experiment. However, the possibility still exists that the self-diffusion process in b.c.c. metals is ring diffusion,[18] in which case no marker movement is to be expected. Observations of the Kirkendall effect in the b.c.c. phase in two diffusion couples, a titanium–molybdenum couple[19] and a couple consisting of two different β-phase brass alloys,[20] indicate that a defect mechanism of interdiffusion is involved in these systems. Thus, the model developed above is expected to apply to b.c.c. metals.

3. EXPERIMENTAL PROCEDURE AND RESULTS

Iron and copper were chosen as typical b.c.c. and f.c.c. metals in which the temperature-gradient influence on self-diffusion was to be studied. Only work on iron has been completed. Copper presents more imposing experimental difficulties due to its high thermal conductivity.

The b.c.c. α-phase of iron extends to 910°C. In order that the diffusion coefficient be as large as possible, a top temperature of 900°C was desired. Platinum wires, 0.001 in.–0.0015 in. diameter, were chosen as the smallest practical wires to be used as markers. It was then necessary to select the cross-sectional area of the sample to be large relative to the marker in order that the marker should not interfere with the diffusion process. However, it was also necessary to restrict the cross-sectional area of the sample so as to obtain a large enough temperature gradient to allow measurable marker migration in reasonable times. With these considerations in mind, samples of 0.040-in. diameter and 0.125 in. long were fabricated. The platinum wires could be placed in the sample, in a manner described below, such that the probable error of forty measurements of the marker spacing change was 0.10×10^{-3} in.

Platinum wires, 0.0015 in. diameter, were imbedded in a $\frac{1}{4}$-in. diameter, $\frac{3}{8}$-in. long iron rod. The wires which passed through the center of the cylinder normal to the cylinder axis were 0.010 in. apart.

The positioning of these wires was accomplished by placing them in 0.0015-in. square parallel grooves in

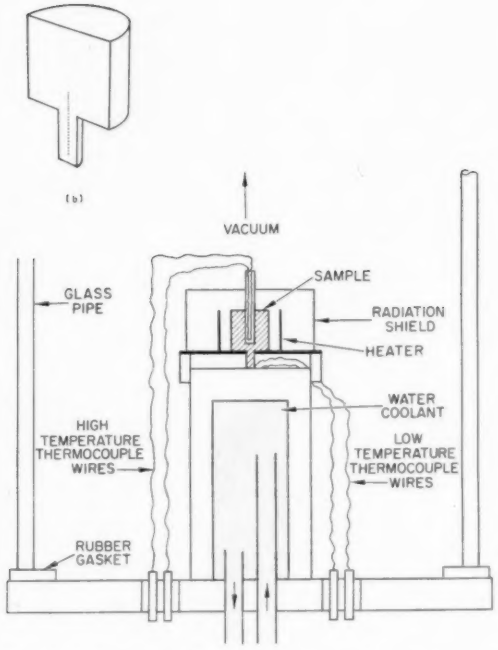


FIG. 2. Schematic of the experimental arrangement. Insert (b) is a lengthwise section of a typical sample, the dots corresponding to wire markers.

VOL. 8 1960

the half cylinder, covering with a complementing half cylinder, and sintering the assembly in an argon atmosphere. To determine the wire spacing at the center of the cylinder, the cylinder was sectioned lengthwise at right angles to the sintered interface. The wire ends were exposed on this surface. The center of the cylinder was approached by carefully polishing 0.005 inch from the surface between each set of measurements of marker separation. These "before" measurements were obtained using the vernier eyepiece of the microscope on a Tukon hardness tester with a total magnification of 230. Again a complementing half cylinder was sintered to the half cylinder containing the wires. The final sample shape was fabricated by making a single lathe cut to 0.040 in. for a distance of $\frac{1}{8}$ in. along the sample. This reduced section housed the marker wires and was the section across which the temperature gradient was applied. A $\frac{1}{4}$-in. diameter, $\frac{1}{4}$ in. long top section was preserved and used as the heat source for the gradient section of the sample. The sample and experimental arrangement are shown schematically in Fig. 2. Wires were placed at the hot end where there was no temperature gradient and in the colder part of the temperature gradient where the diffusion coefficient was very small, to establish stable reference points for the expected marker shift in the high temperature part of the gradient.

The thermocouple which provided the signal to the magnetic amplifier continuous controller was placed deep within this top to a point about 0.050 in. from the top end of the gradient section of the sample. Heat was supplied to the top end of the sample by a tantalum ribbon-filament which was wrapped around the top in close proximity. The Joule-heated filament (30 to 40 A) radiated to the top section of the sample; the gradient section of the sample conducted heat from the top section to a water-cooled base, thereby establishing a temperature gradient in the sample. A radiation shield and a Lavite insulation spacer were placed between the hot filament and sample top and the water-cooled base. To reduce heat losses a tantalum radiation shield in the form of an open-bottom box was placed over the sample top and filament. The Pt–Pt,10% Rh thermocouple was encased in a molybdenum sheath, within the sample top and led out of the radiation shield through Morganite thermocouple tubing. The bottom of the sample was fitted friction-tight into the water-cooled base which remained around 80°C, as measured by a chromel–alumel thermocouple also imbedded in the base. The temperature gradient in the sample of 2500°C/cm was maintained for the 550-hr duration of the run. The vacuum pressure around the sample was maintained at less than 10^{-6} mm of Hg.

After a run each sample was cast in Lucite and sectioned perpendicular to the wire markers. Each sample was polished and etched before every set of measurements of the marker spacing. 0.005 in. was removed from the surface between each set of readings. The average of three sets of reading composed the after-run marker spacings, which were compared with the before-run measurements on the same sample.

The comparisons between "before" and "after" measurements on each of the samples revealed no change in the marker spacings greater than the probable error of these measurements. The expected marker movement at 900°C relative to a marker in the cold end or in the isothermal part of the hot end was 0.001 in. obtained by evaluating equation (6), using the known self-diffusion coefficient[14] and assuming that $E_m = 0.85E_d$.

4. DISCUSSION

Shewmon[21] and Cahn[22] have both found similar negative results in other systems. Shewmon failed to detect any changes in spacing between surface indentations in a zinc bar heated for 480 hr in a 310°C/cm temperature gradient. Cahn also failed to detect any marker shift in silver heated in a 1000°C/cm temperature gradient.

The negative results in each case may result from

the use of inappropriate markers, although there is much evidence to the contrary. Howard and Lidiard[23] have suggested that if each face of a surface indentation marker can act as a source and sink for vacancies, then during a vacancy flow under a temperature gradient one face of the indentation absorbs vacancies while the other face emits vacancies. The indentations would then move in such a manner as to exactly compensate for the addition of lattice planes between each pair of indentations, i.e. the indentations would be carried with the atom flow and no relative changes in their spacing would occur. They also suggest that a hole, which contains a marker wire, and also the wire may be carried along in a similar manner, which requires that the surface of the hole be a source and sink for vacancies.

There is experimental evidence which is in disagreement with the latter argument. Barnes *et al.*[24] have found in alpha-particle irradiated copper that inclusions do not act as sources for vacancies. Small pores were observed to act as vacancy sources, but they rapidly close and lose this capability. Grain boundaries and external surfaces appear to supply all of the vacancies that are required for the formation of helium gas bubbles which were formed.

Additional confidence in the propriety of wires as markers in temperature gradient self-diffusion is gained from results of the extensive experimental study of a large variety of markers by da Silva and Mehl which has shown that the Kirkendall effect is not dependent upon the form or kind of marker material used. Any explanation of the negative results in b.c.c. iron appears more likely to be found in one of the following reasons:

(1) Insufficient sources and sinks for vacancies exist in the iron sample.
(2) The vacancy mechanism of diffusion is not important in α-iron.
(3) The division of E_d is $E_m = E_f$ in α-iron.
(4) E_m and E_f are not the appropriate quantities to be used in the theory of thermal gradient self-diffusion, but instead two other closely related energies should be used.

Each of these possibilities will now be considered in turn.

(1) The possibility that a quasi-equilibrium situation might be established within single crystals (or large grains) such that the predicted flow of vacancies ceases must be considered before it is reasonable to consider the other possibilities. LeClaire[9] has pointed out that a low rate of production and annihilation of vacancies compared to the diffusion flux, as might be expected in large crystals, would lead to this condition. A calculation is included in the Appendix which indicates that even if grain boundaries are the only sources and sinks of vacancies, the deviation from the predictions of equation (5) is very slight, even though the third assumption in the derivation of the expression is equivalent to the assumption of atomically dispersed sources and sinks. The contribution from isolated dislocations, which would further assist thermal gradient diffusion, is ignored in this calculation, although there is evidence that such isolated dislocations may provide all of the vacancies required in the normal Kirkendall effect, since the effect has been observed between two metals composed of large crystals.[25,26]

(2) The possibility exists that the vacancy mechanism is not the important mechanism of self-diffusion in b.c.c. iron. In this case the temperature-gradient Kirkendall theory does not apply and the marker movement would not be expected. There is no direct evidence to support the vacancy mechanism of self-diffusion in α-iron; thus the failure to observe marker movement could be evidence for another mechanism of self-diffusion in α-iron. It should be noted that the discontinuous drop by a factor of 300 in the diffusion coefficient[27] at the phase change from b.c.c. iron to f.c.c. iron could be explained by a different diffusion mechanism in the two phases.

(3) The uncertainties in the calculations of Buffington and Cohen[14] leave the possibility open that the activation energies E_f and E_m are nearly equal.

(4) The activation energy which is supplied during the atom jump can logically be split into various parts.[28] For an atom jumping toward higher temperature, these parts are:

(a) The extra kinetic energy E_m', supplied to the jumping atom at a temperature, T.
(b) The energy, E_b, supplied to the barrier atoms at a temperature, $T + (\Delta T)/2$, which are midway between the initial and final position of the jumping atom, in order that the jumping atom may pass.
(c) The energy E_n required to open up the relaxed vacancy, at a temperature, $T + T\Delta T$, so that it can accommodate the jumping atom.

The activation energy of vacancy migration under these considerations might be expressed as:

$$E_m = E_m' + E_b + E_n.$$

If the model is redeveloped using this division of E_m, the term $(E_f - E_m)$ in equation (5) is replaced by $(E_f' - E_m')$, where $E_f' = E_f + E_n$ is the formation energy of an unrelaxed vacancy. It should be noted that E_b does not appear in this expression because it

enters symmetrically for atom jumps up or down the temperature gradient. Although E_m may be somewhat larger than E_f for isothermal self-diffusion in α-iron, it is quite possible that E_f' and E_m' may be nearly equal, in agreement with the present experimental results. It is not known how large the terms are which may make up E_m, but it appears that some corrections to the theory should be made along these lines. It should be noted that any arbitrary separation of E_m into parts as done above cannot be observed in isothermal self-diffusion.

5. CONCLUSIONS

The results of this experiment permit one to draw at least one of the following conclusions:

(1) The mechanism of self-diffusion in α-iron is not a vacancy mechanism.

(2) If this vacancy mechanism of self-diffusion predominates in α-iron then either,

(a) The activation energies for formation and migration of vacancies are equal to within 0.1 eV.

(b) The quantities similar to E_m and E_f are nearly equal.

If the interpretation of this experiment is to be made more definitive, additional information about the various energies, and the process of self-diffusion in α-iron is needed. Sintering type diffusion data would be useful for comparison with available tracer diffusion data in α- and γ-iron to determine the diffusion process in each phase. If self-diffusion can be established to occur by a vacancy mechanism in α-iron, then attempts should be made to determine E_f and E_m in α-iron. Studies of recovery of property changes brought about by excess vacancies which have been introduced by irradiation, cold-work or quenching could help to determine E_f and E_m. The latter two alternative conclusions may then be resolved on the basis of these determinations.

VOL. 8 1960

ACKNOWLEDGMENTS

The author would like to thank D. R. Warner for his help in the experimental setup and during the many experimental runs. Numerous helpful discussions are acknowledged with J. A. Brinkman who suggested this experiment and with A. Sosin concerning the calculations in the Appendix.

REFERENCES

1. E. O. Kirkendall, *Trans. Amer. Inst. Min. (Metall.) Engrs.* **147,** 104 (1942).
2. A. O. Smigelskas, and E. O. Kirkendall, *Trans. Amer. Inst. Min. (Metall.) Engrs.* **171,** 130 (1957).
3. L. C. Correa Da Silva and R. F. Mehl, *Trans. Amer. Inst. Min. (Metall.) Engrs.* **191,** 155 (1951).
4. H. B. Huntington, *Phys. Rev.* **61,** 315 (1942); *Phys. Rev.* **61,** 325 (1942).
5. C. Herring, *J. Appl. Phys.* **21,** 301 (1950).
6. G. C. Kuczynski, *J. Appl. Phys.* **21,** 632 (1950).
7. W. Shockley, *Phys. Rev.* **91,** 1563 (1953); *Phys. Rev.* **93,** 345 (1954).
8. J. A. Brinkman, *Phys. Rev.* **93,** 345 (1954).
9. A. D. LeClaire, *Phys. Rev.* **93,** 344 (1954).
10. L. S. Darken, *Trans. Amer. Inst. Min. (Metall.) Engrs.* **175,** 184 (1948).
11. F. Seitz, *Phys. Rev.* **74,** 1513 (1948); *Acta Cryst., Camb.* **3,** 355 (1950).
12. J. Bardeen, *Phys. Rev.* **76,** 1403 (1949).
13. A. D. LeClaire, *Progr. Metal Phys.* **1,** 265 (1949).
14. F. S. Buffington and M. Cohen, *Acta Met.* **2,** 660 (1954).
15. A. H. Cottrell in *Vacancies and Other Point Defects in Metals and Alloys;* Institute of Metals, London (1958); A. S. Nowick, *Phys. Rev.* **103,** 296 (1956).
16. D. K. C. McDonald, *J. Chem. Phys.* **21,** 177, 2097 (1953).
17. S. Machlup, *J. Chem. Phys.* **24,** 169 (1956).
18. C. Zener, *J. Appl. Phys.* **22,** 372 (1951); A. D. LeClaire, *Acta Met.* **1,** 438 (1953).
19. P. G. Shewmon and J. H. Bechtold, *Acta Met.* **3,** 452 (1955).
20. U. S. Landergren and R. F. Mehl, *J. Metals, N.Y.* **5,** 153 (1953).
21. P. G. Shewmon, *J. Chem. Phys.* **29,** 1032 (1958).
22. J. W. Cahn, private communication.
23. R. E. Howard and A. B. Lidiard, to be published.
24. R. S. Barnes, G. B. Redding and A. H. Cottrell, *Phil. Mag.* **3,** 97 (1958).
25. W. Seith and A. Kottmann, *Naturwissenschaften* **39,** 40 (1952).
26. W. Seith and A. Kottman, *Angew. Chem.* **64,** 376 (1952).
27. F. S. Buffington, T. D. Bakelar and M. Cohen, *Trans. Amer. Inst. Min. (Metall.) Engrs.* **108,** 1374 (1950).
28. K. Wirtz, *Z. Phys.* **118,** 510 (1941); W. Jost, *Diffusion in Solids, Liquids, Gases,* p. 526. Academic Press, New York (1952).

APPENDIX

Grain boundaries as sources and sinks for vacancies

It is generally believed that external surfaces, grain boundaries and isolated dislocations act as sources and sinks for maintaining the thermal equilibrium concentration of vacancies in crystals. Where a large flux of vacancies is expected, as in thermal gradient self-diffusion, LeClaire[9] has pointed out that, if grain boundaries are too widely separated, a quasi-equilibrium condition may become established and the diffusional flux of vacancies would cease. LeClaire ignored the source-sink contributions of isolated dislocations in such large, well-annealed single crystals. In the model adopted here for the calculation of vacancy flow for a specific distribution of sources and sinks the additional contribution by isolated vacancies is disregarded; only the contribution from a very simple grain boundary configuration is considered. The grain boundaries are considered as a series of parallel internal surfaces normal to the temperature gradient and separated by a distance, Δ. Grain boundary diffusion along the temperature gradient is also ignored. The essential difference between this model and the one used implicitly in Section 2 is that, rather than every lattice plane acting as a source or sink, only those planes separated by a distance Δ have such capabilities. It is necessary to consider only the flux of vacancies between two of this series of parallel grain boundaries in our calculation. This boundary-value problem is one-dimensional under these assumptions. The grain size, Δ, is a parameter which may be varied in order that the effects of finite grains may be determined.

The grain boundaries are located at $x = l_0$ and $x = l_1$ which corresponds to the absolute temperatures, T_0 and T_1 respectively, such that the temperature gradient is

$\alpha = (T_1 - T_0)/(l_1 - l_0) = (T_1 - T_0)/\Delta$. A temperature $T = 0$ is taken at the position $x = 0$. It is assumed that the thermal equilibrium concentrations of vacancies are maintained at the grain boundaries. The concentration, which is a function of x, remains constant for all time. The boundary conditions are

$$C(l_1) = A \exp\left(-\frac{E_f}{kT_1}\right) \equiv A \exp\left(\frac{-P}{l_1}\right) \quad \text{(A 1)}$$

$$C(l_0) = A \exp\left(-\frac{E_f}{kT_0}\right) \equiv A \exp\left(\frac{-P}{l_0}\right) \quad \text{(A 2)}$$

$$\frac{\partial C}{\partial t} = 0 \quad \text{(A 3)}$$

where $$P \equiv \frac{E_f}{k\alpha}.$$

The equation for the vacancy flux at an arbitrary point, x, located between the grain boundaries, is

$$J_v = C(x)\left\{B \exp\left[-\frac{E_m}{k\alpha(x + \lambda)}\right]\right\} - C(x + \lambda)\left\{B \exp\left[-\frac{E_m}{k\alpha x}\right]\right\} \quad \text{(A 4)}$$

$$= B\lambda \exp\left(\frac{-Q}{x}\right)\left[C(x)\frac{Q}{x^2} - \frac{\partial C}{\partial x}\right]. \quad \text{(A 5)}$$

The interplanar distance is λ and $E_m/(k\alpha) \equiv Q$, since $\nabla \cdot \mathbf{J}_v = (\partial C)/(\partial t) = 0$, J_v = constant. This is obviously required since the current must be the same throughout the grain due to the absence of sources and sinks in the grain interior.

We can integrate equation (A 5) by writing it as

$$\exp\left(\frac{-2Q}{x}\right)\frac{d}{dx}\left[C \exp\frac{Q}{x}\right] = K_0, \quad \text{(A 6)}$$

where $$K_0 \equiv \frac{J_v}{B\lambda}.$$

Integrating expression (A 6),

$$C \exp\frac{Q}{x} = K_0\left[\int_{l_0}^{x} dx' \exp\frac{2Q}{x'}\right] + A \exp\frac{Q - P}{l_0}. \quad \text{(A 7)}$$

The constant of integration has been evaluated using boundary condition, equation (A 2). Using the boundary conditions (A 1), equation (A 7) becomes

$$K = \frac{A\left[\exp\dfrac{(Q - P)}{l_1} - \exp\dfrac{(Q - P)}{l_0}\right]}{\displaystyle\int_{l_0}^{x_1} dx' \exp\left(\frac{2Q}{x'}\right)}. \quad \text{(A 8)}$$

The integral in equation (A 8) may be integrated in the following manner:

Put $l_0 = l_1 - \Delta$, and

$$F(\Delta) = \int_{l_1 - \Delta}^{l_1} dx' \exp\frac{(2Q)}{(x')}. \quad \text{(A 9)}$$

Let $x' = l_1 - \Delta Z$, then

$$F(\Delta) = \Delta \int_0^1 dZ \exp\left[\frac{2Q}{l_1}\left(1 - \frac{Z\Delta}{l_1}\right)^{-1}\right] \quad \text{(A 10)}$$

or, by algebraic manipulations,

$$F(\Delta) = \Delta \exp\frac{2Q}{l_1}\int_0^1 dZ \exp\left\{\frac{2Q}{l_1^2}\left[Z\Delta\left(1 - \frac{Z\Delta}{l_1}\right)^{-1}\right]\right\} \quad \text{(A 11)}$$

Now, put $y = Z\left[1 - \dfrac{Z\Delta}{l_1}\right]^{-1}$ or $Z = y\left[1 + \dfrac{y\Delta}{l_1}\right]^{-1}$,

so that $$dZ = \left[1 + \frac{y\Delta}{l_1}\right]^{-2} dy.$$

Therefore,

$$F(\Delta) = \Delta \exp\frac{2Q}{l_1}\int_0^{[1 - (\Delta/l_1)]^{-1}} \frac{\exp\left[\left(\dfrac{2Q}{l_1^2}\right)\Delta y\right]}{\left[1 + \left(\dfrac{\Delta}{l_1}\right)y\right]^2} dy. \quad \text{(A 12)}$$

In the present experiment Δ/l_1 is small, so that terms in the denominator in equation (A 12) may be set equal to one and the approximate form of expression (A 12) can be immediately integrated,

$$F(\Delta) = \Delta \exp\frac{2Q}{l_1}\int_0^1 dy \exp\left[\left(\frac{2Q}{l_1^2}\right)\Delta y\right] = \frac{l_1^2}{2Q}\exp\left(\frac{2Q}{l_1}\right)\left[\exp\left(\frac{2Q}{l_1^2}\Delta\right) - 1\right]. \quad \text{(A 13)}$$

The numerator of equation (A 8) can be expressed similarly in

$$\exp\left(\frac{Q - P}{l_1}\right) - \exp\left(\frac{Q - P}{l_0}\right) = \exp\frac{Q - P}{l_1}\left[1 - \exp\left(\frac{Q - P}{l_1^2}\Delta\right)\right]. \quad \text{(A 14)}$$

The vacancy current is then given by

$$J_v = \frac{2AB\,Q}{l_1^2}\exp - \frac{(P + Q)}{l_1}\frac{\left[\exp\left(\dfrac{Q - P}{l_1^2}\Delta\right) - 1\right]}{\left[\exp\left(\dfrac{2Q}{l_1^2}\Delta\right) - 1\right]}. \quad \text{(A 15)}$$

In the limit as $\Delta \to 0$, the part in brackets becomes $\dfrac{Q - P}{2Q}$, and equation (A 15) reduces to the negative of the expression for the current for atomically dispersed sources and sinks as given by equation (5) of Section 2. That is, $J_v = -J$.

By expanding the exponentials in the brackets, the equation (A 14) can be put into the form of equation (5) except multiplied by a correction factor, C.F., which is a function of Δ:

$$\text{C.F.} = \frac{1 + \dfrac{a\Delta}{2!} + \dfrac{a^2\Delta^2}{3!} + \cdots}{1 + \dfrac{b\Delta}{2!} + \dfrac{b^2\Delta^2}{3!} + \cdots} \quad \text{(A 16)}$$

where $$a = \frac{Q - P}{l_1^2} = \frac{E_m - E_f}{kT_1^2}; \quad b = \frac{2Q}{l_1^2} = \frac{2E_m}{kT_1^2}.$$

Values of the C.F. are given in the following table for grain sizes which bracket the average grain sizes of 0.005 cm found in an α-iron in the present experiment. The activation energies used were $E_m = 2.15$ eV and $E_f = 0.45$ eV.

Δ	C.F.
0.01 cm	0.75
0.005 cm	0.87
0.002 cm	0.94

PHASE TRANSFORMATIONS IN CERIUM*

C. J. McHARGUE and H. L. YAKEL, Jr.†

The room temperature crystal structure of cerium which has not been cooled to lower temperatures is face-centered cubic. The face-centered cubic structure transforms upon cooling to a hexagonal close-packed structure ($c/a = 3.239$) with a $ABAC$ stacking sequence of close-packed planes. This transformation has many of the typical martensitic characteristics. The transformation starts at 263° ± 10°K. At 100°K, that portion of the face-centered cubic phase which has not transformed to hexagonal close-packed begins to transform to a second face-centered cubic phase with a volume decrease of 16.5 per cent. The kinetics of this transformation also resemble that of the martensite reaction. Below a temperature between 77° and 43°K the hexagonal structure appears to also transform to the collapsed cubic form. Plastic deformation at any temperature suppresses the transformation to the hexagonal form and may even cause it to revert to the normal cubic form. Deformation below 100°K favors the collapsed cubic form. Thermal cycling produces more of the hexagonal phase than can be obtained on one cooling. After a large number of cycles, neither the hexagonal nor normal cubic phase will transform to the collapsed cubic phase upon cooling. Plastic deformation at 4.2°K removes the thermal cycling effects.

TRANSFORMATION DE PHASES DANS LE CERIUM

La structure cristalline à température ambiante du cérium qui n'a pas été refroidi à des températures inférieures est cubique à faces centrées. En refroidissant, la structure cubique à faces centrées se transforme en une structure hexagonale compacte ($c/a = 3{,}239$) avec une séquence d'empilement $ABAC$ des plans les plus habités. Cette transformation a plusieurs caractéristiques de la transformation martensitique typique. La transformation commence à 263° ± 10°K. A 100°K, la portion de la phase cubique à faces centrées qui n'a pas été transformée en phase hexagonale compacte commence à se transformer en une seconde phase cubique à faces centrées avec une diminution de volume de 16,5%. La cinétique de cette transformation ressemble également à celle de la réaction martensitique. En dessous d'une température entre 77° et 43°K il apparaît que la structure hexagonale se transforme également en phase cubique dense. La déformation plastique à haute température supprime la transformation qui donne la forme normale. La déformation en dessous de 100°K favorise la forme cubique dense. Le cyclage thermique produit une quantité de phase hexagonale supérieure à celle qui se forme en un cycle. Après un grand nombre de cycles ni la phase hexagonale, ni la phase cubique normale ne se transforment en refroidissant en la phase cubique dense. Une déformation plastique à 4,2°K supprime les effets du cyclage thermique.

PHASEN-UMWANDLUNGEN BEI ZERIUM

Bei Raumtemperatur ist die Kristallstruktur von Zerium, das nicht auf tiefere Temperaturen abgekühlt wurde, kubisch-flächenzentriert. Bei Abkühlung verwandelt sich die kubisch-flächenzentrierte Struktur in eine hexagonal-dichtgepackte ($c/a = 3.239$) mit einer $ABAC$-Folge von dichtgepackten Ebenen. Diese Umwandlung hat viele typisch martensitische Eigenschaften, sie beginnt bei 263° ± 10°K. Bei 100°K wandelt sich der Teil der kubisch-flächenzentrierten Phase, der sich nicht in die hexagonale struktur verwandelt hat, in eine zweite kubisch-flächenzentrierte Phase um, wobei die Volumabnahme 16.5% beträgt. Auch bei dieser Reaktion ähnelt die Kinetik der der Martensitreaktion. Unterhalb einer Temperatur, die zwischen 77° und 43°K liegt, scheint sich auch die hexagonale Form in die kollabierte kubische umzuwandeln. Plastische Deformation bei beliebiger Temperatur unterdrückt die Umwandlung zur hexagonalen Form und kann sogar eine Rückbildung der kubischen bewirken. Deformation unterhalb 100°K begünstigt die kollabierte kubische Form. Bei zyklischem Erwärmen und Abkühlen erhält man eine größere Menge an hexagonaler Phase als beim einfachen Abkühlen. Nach einer größeren Anzahl von Zyklen wandelt sich weder die hexagonale noch die normale kubische Phase bei Abkühlung in die kollabierte kubische um. Plastische Verformung bei 4.2°K beseitigt die Wirkungen der zyklischen Temperaturbehandlung.

INTRODUCTION

There is a great deal of interest in systematic investigations of the rare earth elements in order to study relationships between the physical and chemical properties of metals and their electronic structures. In general, the metals of this group have three valence or conduction electrons and differ in the degree to which the incomplete $4f$ level is filled.

There has always been some question as to the crystal structure of cerium present under various conditions of temperature, pressure, and purity. Hull[1] in 1921 reported cerium powder to contain

* Received October 21, 1959; revised version December 18, 1959.

† Metallurgy Division, Oak Ridge National Laboratory, operated for the U.S. Atomic Energy Commission by Union Carbide Corporation.

VOL. 8 1960

both a face-centered cubic* and a hexagonal close-packed ($c/a = 1.62$) phase at room temperature. Klemm and Bommer[2] noted that the intensities of the lines indexed on the basis of a simple hexagonal close-packed structure were not in agreement with calculated intensities but apparently did not consider their evidence to be sufficiently conclusive to justify reporting a different structure. Later workers have often reported both the face-centered cubic and hexagonal close-packed phases to be present at room temperature.[3,4] The best crystallographic work appears to be that of Spedding *et al.*[5] who give the room temperature form of 99.9 per cent pure cerium as face-centered cubic with $a_0 = 5.1612$ Å.

Studies of physical properties by Trombe and Föex[3,6–9] established that three phases appear in the temperature range between 77°K and room temperature. In 1949, Lawson and Tang[10] showed by means of a high-pressure X-ray camera that two face-centered cubic phases were present in cerium at room temperature at a pressure of 15,000 atm. They noted a volume difference of 16.5 per cent in the two phases, confirming earlier estimates of Bridgman who deduced a transformation from compressibility measurements.[11–13] Schuch and Sturdivant[14] showed two face-centered cubic phases to exist at 77°K and 1 atm in a limited X-ray study. Recently, pressure–temperature diagrams have shown the low temperature–low pressure "collapsed" cubic phase to be the same as the room temperature–high pressure denser cubic phase.[15–17] The explanation given for the existence of a second face-centered cubic structure with a smaller volume has been in terms of the movement of the one $4f$ electron to the conduction band.[18,19] Such a view has also been used to explain anomalies in specific heat,[20–22] magnetic susceptibilities,[22–26] and resistivity[4] measurements.

In none of the studies has the nature of the transformations been examined and in many cases interpretation of the results has been hindered by the lack of knowledge concerning the crystal structure of the phase or phases present. The object of the present study was to establish the conditions under which the various phases appear, and to study the nature and kinetics of the transformations.

PROCEDURE

The cerium used was of the highest purity available and was loaned by the Institute for Atomic Research, Iowa State College. The as-received metal was melted in a dynamic vacuum of 10^{-7} mm Hg to reduce further volatile impurities and to outgas. Tantalum crucibles were used, and specimens subsequently heat treated were wrapped in tantalum foil. A typical analysis† of a specimen after being melted and annealed gave 0.006 Mg, 0.012 Si, <0.006 Ca, <0.025 Fe, 0.018 O, 0.001 N, and 0.005 H (per cent). All other elements were below limits of detection.

X-ray observations were made on polycrystalline sheet specimens in the temperature range 4.2–475°K using copper K-alpha radiation. The cryostat used in the temperature range 77–475° allowed observations to be made on both heating and cooling.[27] A modified version of Barrett's cryostat[28] was used for temperatures below 77°K. The surface of the specimen in each cryostat could be plastically deformed by scratching at any temperature.

RESULTS

Transformations in an annealed specimen. Since the behavior of a given specimen was found to be influenced by its thermal and mechanical history, the results for an annealed sample will be discussed first. Most of the results were obtained on specimens annealed for one hour at 625°K in a vacuum of 10^{-6} mm Hg or better.

The room temperature crystal structure of all annealed specimens which had never been cooled to a lower temperature was face-centered cubic with lattice parameter $a_0 = 5.15$ Å. As the specimen was cooled a second phase was found to appear at 263 $\pm$ 10°K.

The pattern of the second phase was found to index to a hexagonal unit cell with dimensions of $a_0 = 3.68$ Å, $c_0 = 11.92$ Å and $c/a = 3.239$ at 298°K. The diffraction data for the first 19 lines are listed in Table 1. The structure is a double hexagonal-close-packed unit cell, with four atoms in the positions (0,0,0), (0,0,1/2), (1/3,2/3,1/4) and (2/3,1/3,3/4) of space group $P6_3/mmc$. The relative intensities of the reflections were calculated from the expression $I\alpha|F|^2mLp$ where F is the structure factor, m is the multiplicity factor, L is the Lorentz factor and p is the polarization factor. Typical X-ray diffractometer traces for copper K_α radiation showing the lines for the face-centered cubic and the hexagonal phase at 195°K are given in Fig. 1.

Thus the observations of Klemm and Bommer[2a] that perhaps the c-axis ought to be doubled are confirmed and the hexagonal phase in cerium is

* The adjective "face-centered cubic" (f.c.c.) will be used throughout this paper to denote a cubic close-packed (A-1) crystal structure.

† Mg, Si, Ca and Fe were determined by spectrographic analysis, O, N and H were determined by the vacuum fusion method.

TABLE 1. X-ray diffraction data for cerium hexagonal phase

{*hkil*}	Observed		Calculated intensity
	d(Å)	Rel. intensity	
0002	—	0	0
1010	3.186	6	7.8
1011	3.078	40	43.3
0004	2.980	35	34.7
1012	2.810	100	100.0
1013	2.486	26	23.7
1014	2.177	4	5.3
0006	—	0	0
1015	1.910	11	10.7
1120	1.840	24	25.0
1122	—	0	0
1016	1.686	18	21.1
2020	—	0	1.0
2021	1.579	10	5.7
1124	1.566	30	29.4
2022	1.539	7	15.6
1017	1.502	3	4.8
0008	1.490	3	4.1
2023	1.479	3	4.5

Copper K-alpha radiation
$\lambda = 1.5418$ Å

isomorphous to the hexagonal forms of lanthanum, praseodymium, and neodymium.[5,29]

The amount of f.c.c. cerium which transformed to the h.c.p. form is shown as a function of temperature by the cooling portion of the curve of Fig. 2. The amount of each phase was calculated from integrated X-ray intensities with an estimated accuracy of about 5 per cent. No isothermal transformation was ever observed for periods of time greater than 10 min and less than 24 hrs. (Ten minutes represents the time required to change the temperature and obtain the X-ray data.) In all cases, the amount of h.c.p. appeared to depend only on the degree of cooling below T_s* (263 ± 10°K).

There is a pronounced and reproducible break in the f.c.c. → h.c.p. curve in the vicinity of 240°K. The rate of transformation for a given temperature interval changes markedly at this point. For example, Fig. 2 shows that in the 25° interval between T_s and this "knee," 65 per cent of the f.c.c. phase in the 625°K annealed specimen transformed to h.c.p. but only an additional 15 per cent transformed in a 145° interval below 235°K.

The effect of annealing temperature on the f.c.c. →

* T_s will be used to denote the temperature at which the first amount of transformed product was observed.

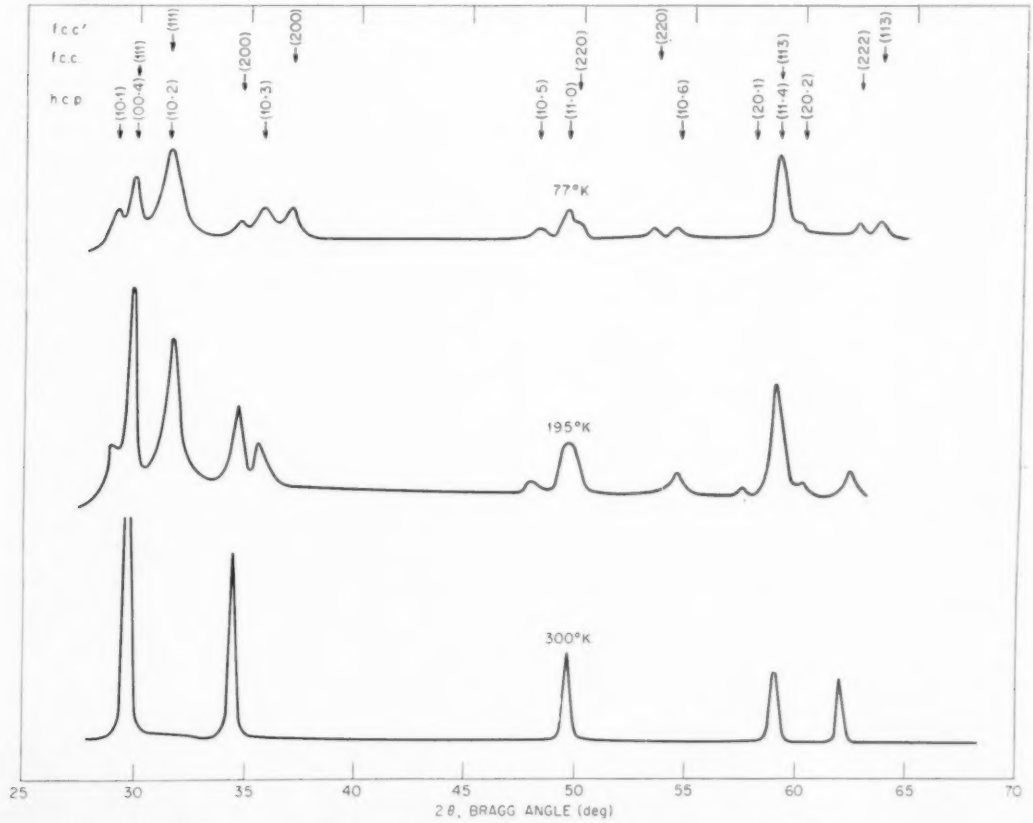


FIG. 1. Typical X-ray diffractometer traces of cerium. Copper K_α radiation.

VOL. 8 1960

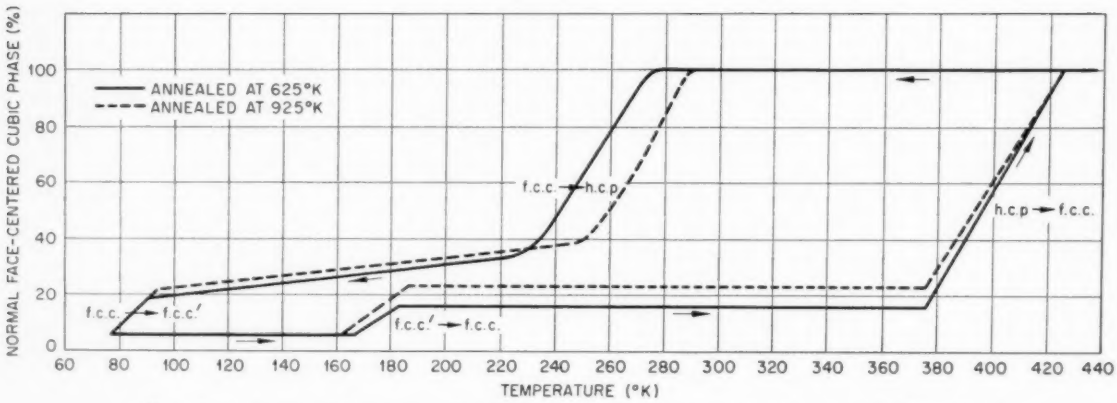


FIG. 2. Amount of face-centered cubic phase versus temperature in an annealed specimen.

h.c.p. transformation is also shown in Fig. 2. The dotted curve represents results for a specimen annealed at 925°K and the solid line for a specimen annealed at 625°K. The higher annealing temperature resulted in the initial portion of the curve being shifted to higher temperatures. This is probably a grain size effect, the larger grain size favoring a higher T_s, as in the case of cobalt.[30]

The phenomenon of stabilization due to holding for some period within the transformation range was not observed. On the contrary it was found that interrupted cooling between T_s and 77°K resulted in more f.c.c. being converted to h.c.p. than was observed after direct quenches to 77°K.

At $95° \pm 5°$K, the f.c.c. cerium which had not transformed to h.c.p., began to transform to a second face-centered cubic phase (f.c.c.′) with a 16.5 per cent volume decrease. The positions of the diffraction lines for this phase are shown in Fig. 1 on the 77°K trace. The measured lattice parameter of this phase was 4.85 Å at 77°K. Again there was no isothermal transformation and the amount of f.c.c.′ appeared to be a function of the degree of cooling below the T_s for this reaction. It was established that only the f.c.c. phase transformed to f.c.c.′ in the range 95–77°K. However, at lower temperatures both the f.c.c. and h.c.p. phases appeared to transform to the more dense cubic form. In annealed specimens, the h.c.p. → f.c.c.′ transformation began between 77° and 43°K. Fig. 3 shows that a specimen which contained 60 per cent f.c.c.′, 32 per cent h.c.p. and 8 per cent f.c.c. after being quenched to 77°K, entirely transformed to f.c.c.′ after being further cooled to 4.2°K.

The heating curve of Fig. 3 shows that the f.c.c.′ phase reverts to both the normal cubic and hexagonal phases. In many of the experiments, the collapsed cubic form transformed into about the same relative amounts of the two phases that had existed at 77°K just prior to cooling to 4.2°K. This observation might be interpreted as showing a memory effect whereby each f.c.c.′ grain reverts to its original structure. However, as will be discussed later there are other reasons to believe that this may not be so.

Figure 2 shows the reversion of the low temperature phases h.c.p. and f.c.c.′ to f.c.c. For both phases, there is a large hysteresis, and the h.c.p. to f.c.c. transformation occurs only above room temperature. There is no break in the h.c.p. → f.c.c. transformation curve corresponding to that noted for the reverse process upon cooling. These data were obtained by

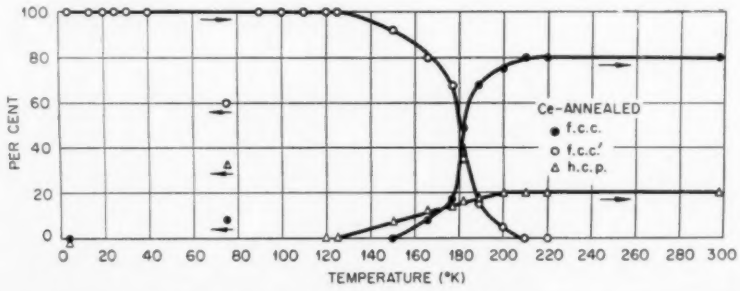


FIG. 3. Phase composition of annealed specimen as function of temperature upon heating. The points with arrows pointing to the left show the amount of each phase present at 77°K during the cooling portion of the experiment.

TABLE 2. Transformation temperatures in cerium

Transformation	Start (°K)	Finish (°K)
f.c.c. → h.c.p.*	263 ± 10	†
h.c.p. → f.c.c.	373 ± 5	420 ± 5
f.c.c. → f.c.c.′	96 ± 5	near 4.2
f.c.c.′ → f.c.c.	160 ± 10	195 ± 15
h.c.p. → f.c.c.′	between 40 and 77	†
f.c.c.′ → h.c.p.	125 ± 5	200 ± 10

* Specimens annealed at 625°K.
† Reaction never observed to go to completion.

changing the temperature in 5–10° steps and the time at each temperature was 10-15 min.

The temperatures for the start and finish of transformation for the various phase changes are summarized in Table 2.

It was found that although the transformation from f.c.c. to h.c.p. had no isothermal component, reversion to the cubic phase did have a small isothermal component. This was shown in a specimen which contained only the f.c.c. phase at room temperature after a 625°K anneal. The specimen was cooled to 77°K where it contained 12 per cent f.c.c., 30 per cent h.c.p. and 58 per cent f.c.c.′. At 388°K the specimen was held for a total of 360 min while the {10.2} h.c.p. and {200} f.c.c. X-ray reflections were recorded. At a two-*theta* scanning speed of 2° per min it took 2 min to record these two lines. As is illustrated in Fig. 4, the specimen contained 50 per cent f.c.c. and 50 per cent h.c.p. during the time interval 2-4 min. The amount of cubic phase increased to 60 per cent at the end of 28-30 min and remained constant during the next 330 min. The temperature was then raised by 6°, and it was found that an additional 8 per cent had transformed during the first 5 min.

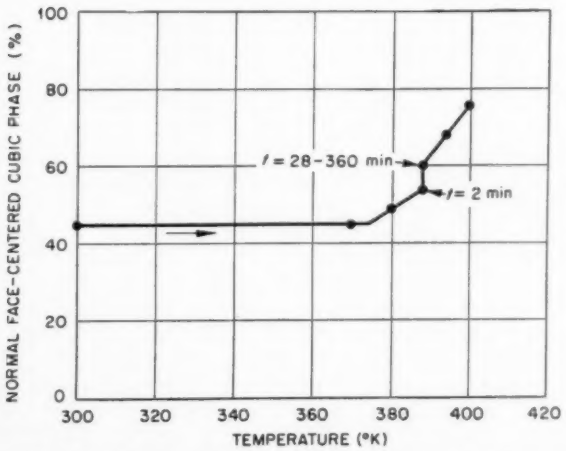


FIG. 4. Transformation of h.c.p. to f.c.c. as function of temperature and time.

The fact that the isothermal transformation ceased after a relatively short time indicates that it is due to relief of the transformation stresses produced by the first grains to transform. One of the possible self-stopping mechanisms for the growth of transformation products is the distortion of the matrix near the interface. Relaxation of the stresses or recovery of the matrix would be expected to allow further growth of the plates of the new phase. Apparently such recovery cannot occur at temperatures below about 250°K and no isothermal transformation occurs upon cooling.

Effects of plastic deformation. Plastic deformation was found to have a marked effect on the transformation from f.c.c. to both h.c.p. and f.c.c.′. Deformation of the f.c.c. phase always inhibited the transformation to h.c.p. Fig. 5 shows the course of transformation to f.c.c.′ in a specimen where the h.c.p. phase has been completely suppressed by deformation above T_s. The specimen was annealed and then given a reduction in thickness of 50 per cent by rolling at room temperature. Comparison of this figure with Fig. 2 shows that this deformation had little effect on either the amount of f.c.c.′ phase subsequently formed or on the transformation temperatures.

Plastic deformation of the hexagonal phase appears to cause it to revert to the high-temperature cubic form. Annealed specimens were (a) deformed at 199°K, (b) deformed at 77°K, and (c) deformed at room-temperature after being cooled to 77°K. The deformation in these experiments was performed by peening the specimen surfaces with an electric vibrating tool. The results are summarized in Table 3 and in each case show a marked decrease in the amount of hexagonal phase present. The appearance of the lines in the X-ray pattern is shown in Fig. 6. Note that marked decrease in the intensities of (10.2), (10.3), (10.5) and (10.6) and the obvious increase in (111) and (222). Deformation at 77°K decreased the

TABLE 3. Effect of deformation on cerium phases

Phase	Deformation temperature					
	77°K		199°K		298°K*	
	Before	After	Before	After	Before	After
f.c.c. (%)	16	8	52	77	22	46
h.c.p. (%)	74	43	48	23	78	54
f.c.c.′ (%)	10	49	—	—	—	—

* Specimen cooled to 77°K then brought to 298°K before being deformed.

VOL. 8 1960

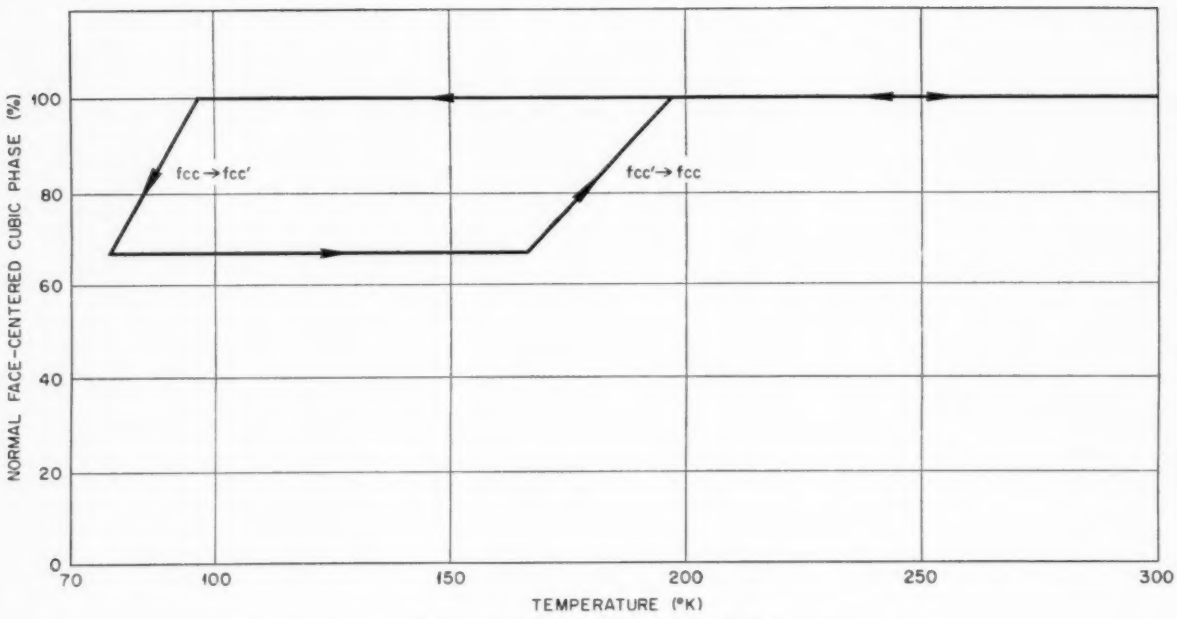


FIG. 5. Amount of f.c.c. phase versus temperature in deformed specimen.

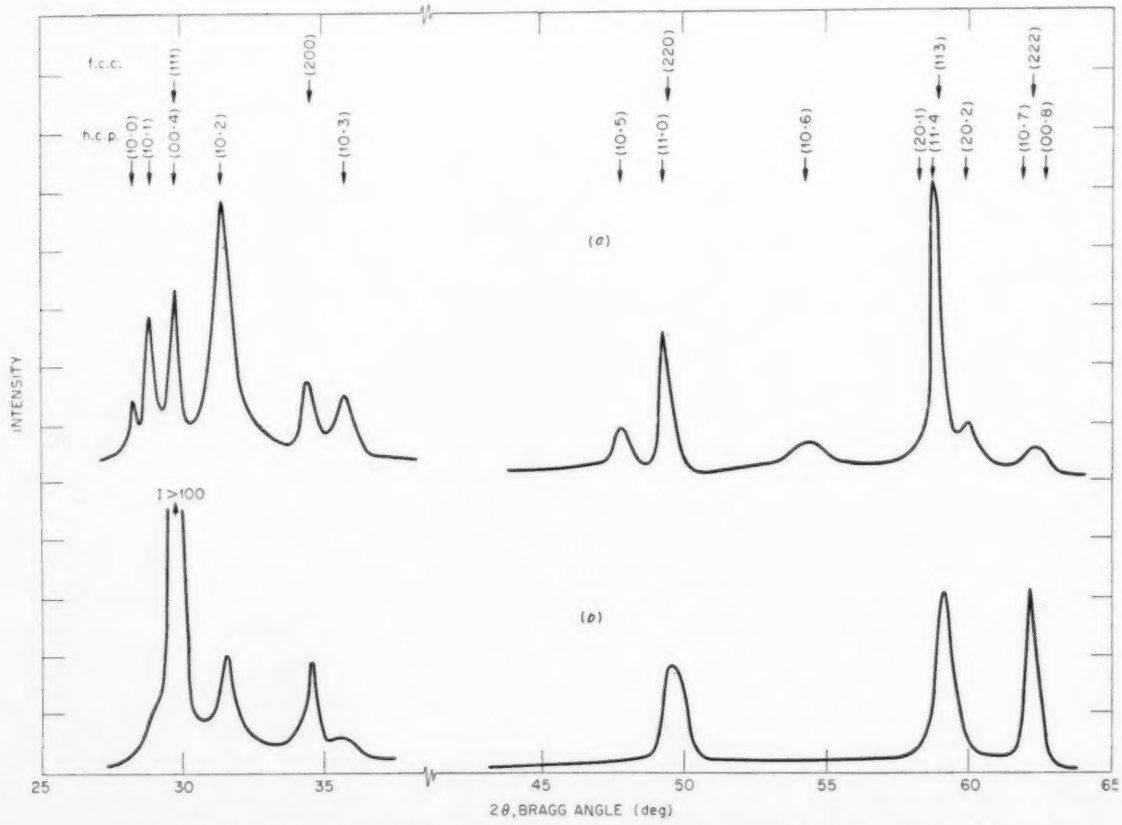


FIG. 6. Effect of deformation at 199°K on the X-ray pattern of cerium. (a) Before and (b) after deformation.

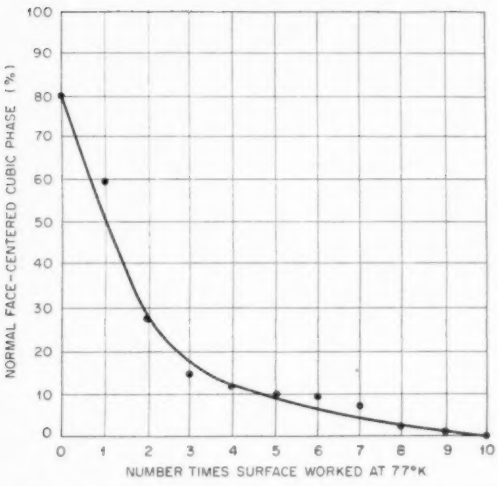


FIG. 7. Effect of deformation at 77°K on amount of f.c.c. present.

amount of each of the h.c.p. and f.c.c. phase and increased the amount of f.c.c.′.

It was possible to convert the entire specimen to the low temperature cubic form, f.c.c.′, by plastic deformation at 77°K or lower. Fig. 7 shows that this required relatively large amounts of work at 77°K, e.g. a total of 5 min of peening. On the other hand, a few scratches with a tool built into the helium cryostat was sufficient to cause complete conversion at 4.2°K. Fig. 8 shows the behavior of a specimen initially containing only f.c.c. which was stabilized against h.c.p. formation on cooling by room temperature deformation. Upon being cooled to 77°K, 20 per cent of the volume transformed to f.c.c.′, and further cooling to 4.2°K caused a total of 80 per cent to transform to f.c.c.′. Deformation at 4.2°K caused the remaining 20 per cent of f.c.c. to transform to f.c.c.′. The heating curve shows complete reversion to f.c.c.

Effect of thermal cycling. In a study of the magnetic susceptibility of cerium at low temperatures, Lock noted that the large thermal hysteresis loop in the temperature range 50-200°K gradually disappeared in the course of experiments.[23] The next cooling of a specimen which had been previously cycled 100 times between a liquid hydrogen bath and room temperature resulted in very little hysteresis. At the same time the height of a maximum in the magnetic susceptibility curve at 12.5°K varied with the thermal history, being the largest for the specimen thermally cycled. These data were interpreted as showing less transformation to the f.c.c.′ upon each cooling cycle and the magnetic effects were ascribed to antiferromagnetism in the normal face-centered cubic phase.

Similar cycling experiments were conducted during this study. Specimens were cycled 100 times between 77°K and room temperature and between 4.2°K and room temperature. In each case the specimen contained more (75–90 per cent) of the hexagonal close-packed phase at room temperature than had been produced by any other treatment. No changes were noted upon cooling again to the lowest temperature reached during cycling. As is shown by the data in Table 4, no f.c.c.′ phase appeared at 77°K in specimen 1 during the 106th cooling and none appeared in specimen 3 during the 101st cooling to 4.2°K. Thus the effect of thermal cycling was to stabilize the h.c.p. phase in the temperature range where the cycling occurred and to suppress the f.c.c. → f.c.c.′ transformation. However, cooling below the cycling range again resulted in a decrease in the amount of h.c.p. and f.c.c. phases. Specimen 2 which contained only the h.c.p. and f.c.c. phases at room temperature and 77°K after 100 cycles to 77°K transformed to 64 per cent f.c.c.′ upon being cooled to 4.2°K.

Since the present thermal cycling experiments to 4.2°K resulted in most of the specimen being converted into the hexagonal form which did not transform upon subsequent cooling, it was thought that the magnetic effects noted by Lock at 12.5°K occurred in the hexagonal phase. A neutron diffraction study carried out in cooperation with members of the ORNL Physics Division showed this to be the case.[31] These results will be published in detail elsewhere.

In each of these experiments, plastic deformation at 4.2 or 77°K caused a large amount of both the f.c.c. and h.c.p. phases to transform to f.c.c.′. Furthermore,

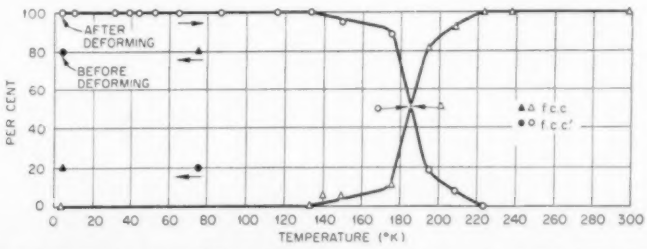


FIG. 8. Effect of deformation at 4.2°K on transformation of a specimen previously deformed at 298°K.

TABLE 4. Results of thermal cycling experiments

Observation temp. (°K)	Condition	Per cent f.c.c.	h.c.p.	f.c.c.′
	Specimen 1			
298	Annealed	100	—	—
298	1 cycle to 77°	80	20	—
77	2nd cooling	10	40	50
298	106 cycles to 77°	15	85	—
77	107th cooling	15	85	—
77	Above deformed at 77°	10	50	40
298	Heated	50	50	—
77	Cooled	9	55	36
	Specimen 2			
298	Annealed	100	—	—
298	100 cycles to 77°	36	64	—
77	101st cooling	27	73	—
4.2	Above cooled	10	26	64
298		60	40	—
77	102nd cooling	50	50	—
4.2		5	15	80
4.2	Above deformed	—	5	95
	Specimen 3			
298	Annealed	100	—	—
298	100 cycles to 4.2°	10	90	—
77	101st cooling	10	90	—
4.2	101st cooling	10	90	—
4.2	Above deformed	5	15	80
298	Above heated	85	15	—

after having been deformed, specimen 1 behaved on subsequent heating and cooling as if it had never been cycled. When specimen 3 was heated from 4.2°K, the f.c.c.′ phase produced by plastic deformation transformed only to f.c.c., contrary to the usual case where it transformed to both h.c.p. and f.c.c. phases (Fig. 3).

DISCUSSION OF RESULTS

The transformation from the face-centered structure to the four-layer repeat hexagonal form in cerium has many similarities to the face-centered cubic—hexagonal transformation in cobalt. It therefore seems reasonable to examine the mechanisms proposed for the latter transformation for clues to the behavior of cerium.

It is convenient to use the notation of stacking operators introduced by Frank for the description of lattices made up of close-packed planes. The symbol $\bigtriangledown$ is used to represent the transition between two adjacent planes in the ABC direction and $\bigtriangleup$ is used to represent the opposite sequence, e.g. CBA. Thus a face-centered cubic lattice is $\ldots \bigtriangledown\bigtriangledown\bigtriangledown\bigtriangledown \ldots$, the hexagonal close-packed structure is $\ldots \bigtriangledown\bigtriangleup\bigtriangledown\bigtriangleup \ldots$, and the four layer hexagonal close-packed structure of cerium is $\ldots \bigtriangledown\bigtriangledown\bigtriangleup\bigtriangleup\bigtriangledown\bigtriangledown\bigtriangleup\bigtriangleup \ldots$. The transition from one lattice to another can occur by glide on parallel planes in the $\langle 10\bar{1}0 \rangle$ hexagonal or $\langle 211 \rangle$ cubic directions. If the glide displacement is represented by the vector $\mathbf{v}$, then $\bigtriangledown + \mathbf{v} \rightarrow \bigtriangleup$.

A model for the transformation is shown in Fig. 9. As illustrated by Sebilleau and Bibring[30], the cobalt transformation consists of a succession of identical glide motions on every other plane while the cerium transformation requires successive glide on two adjacent planes and no glide on the next two planes in the stacking sequence.

Since the above formal description of the structures involves glide movements, Christian[32] proposed a mechanism for cobalt based on the movement of Shockley partial dislocations In order for the layer of transformed material to grow into the face-centered cubic matrix, he suggested that moving half-dislocations would be reflected into the second next plane at boundaries It seems unlikely that such reflections can occur, and Basinski and Christian[33] have proposed a dislocation mechanism similar to that of Cottrell and Bilby[34] for mechanical twinning. This dislocation node theory, which has been further developed by Seeger[35,36], suggests the transformation begins from individual extended dislocations (Shockley partials) which are anchored at a screw dislocation extending into the hexagonal region along the c-axis. Rotation of the half dislocation about the point of emergence of the screw advances the hexagonal region by two planes for each turn Although this theory explains many features of the cobalt transformation, there are reservations about its completeness.[30,37] Sebilleau and Bibring prefer the concept of the



FIG. 9. Model showing glide movements for transforming face-centered cubic lattice to hexagonal close-packed.

displacement of Shockley half-dislocations spontaneously created at the interphase boundary during the transformation.

It can be seen from Fig. 9 that the conversion of the face-centered cubic stacking sequence ABC into the double-hexagonal $ABAC$ sequence is equivalent to the introduction of a positive Frank partial dislocation. According to Read[37] such a dislocation possibly could be formed by the combination of a Shockley partial with a total dislocation on an intersecting slip plane. If the resulting 1/6 ⟨411⟩ partial splits and the Shockley partial glides away from the sessile positive Frank partial, it leaves behind a two-layer fault connecting it with the Frank partial in which the stacking sequence is $ABAC$. On the other side of the Shockley partial is a one-layer fault.

The above picture provides a means for nucleating and growing a thin layer of the hexagonal phase but does not explain the growth normal to this layer. It appears that this normal growth might occur by the continuous formation of layers by dislocation interactions—a procedure somewhat similar to the view of Sebilleau and Bibring cited above.

The dislocation node theory is also geometrically possible for the growth of the hexagonal phase. The transformation dislocation in this case is equivalent to a Shockley partial on each of two neighboring planes. Each revolution of this dislocation about a screw existing in the hexagonal phase converts the face-centered cubic ABC stacking into one unit of $ABAC$.

The effect of deformation on the stability of the h.c.p. phase is unusual. Plastic deformation which is carried out at temperatures as much as 200°K below T_s (f.c.c. → h.c.p.) appear to cause the h.c.p. phase to revert to the high temperature form. Further studies of this phenomenon are planned.

The cubic-cubic′ transformation is unique in that there is a large (16.5 per cent) volume change but no change in crystal structure. When it first became known that two such phases existed, Zachariasen[18] and Pauling[19] suggested that the transformation was a consequence of a transition of the one $4f$ electron to the conduction band. Varley[38] concluded from a study of the factors controlling coefficients of volume expansion in pure metals that there are two isomorphous states possible differing only in volume.

From an analysis of the paramagnetic scattering in the neutron diffraction study cited earlier, it was concluded that there is one magnetic electron in the $4f^1$ ($^2F_{5/2}$) electronic state in both the room temperature cubic and hexagonal close-packed phases and no electrons in this state in the collapsed cubic phase. Thus both the f.c.c. → f.c.c.′ and h.c.p. → f.c.c.′ transformations are directly related to an electron transition from the bound state to the conduction band. Since the transformation from f.c.c. to f.c.c.′ involves a change in the effective ion size, a simple mechanism might be envisioned which requires only a hydrostatic shrinkage of the lattice. A low temperature metallographic study is planned for determining what type of interface exists between the two cubic structures.

ACKNOWLEDGMENTS

This work could not have been accomplished without the aid of J. C. Ogle who prepared the specimens and obtained much of the data. Frequent discussions with Dr. E. E. Stansbury have been instrumental in determining the course of this study. The authors wish to thank M. K. Wilkinson, W. C. Koehler, H. R. Child and E. O. Wollan of the ORNL Physics Division for their cooperation on the neutron diffraction studies. Finally, the authors wish to thank Dr. F. H. Spedding of the Institute for Atomic Research, Iowa State College who made available the material used.

REFERENCES

1. A. W. Hull, *Phys. Rev.* **18,** 88 (1921).
2. W. Klemm and H. Bommer, *Z. Anorg. Chem.* **231,** 144 (1937); W. Klemm and H. Bommer, *Z. Anorg. Chem.* **241,** 264 (1939).
3. F. Trombe and M. Föex, *C.R. Acad. Sci., Paris,* **223,** 949 (1946).
4. N. R. James, S. Legvold and F. H. Spedding, *Phys. Rev.* **88,** 1092 (1952).
5. F. H. Spedding, A. H. Daane and K. W. Hermann, *Acta Cryst., Camb.* **9,** 559 (1956).
6. F. Trombe, *C.R. Acad. Sci., Paris,* **198,** 1951 (1934).
7. F. Trombe and M. Föex, *Ann. Chim.* **19,** 416 (1944).
8. F. Trombe, *C.R. Acad. Sci., Paris* **219,** 90 (1944).
9. M. Föex, *C.R. Acad. Sci., Paris,* **219,** 117 (1944).
10. A. W. Lawson and L. Y. Tang, *Phys. Rev.* **76,** 301 (1949).
11. P. W. Bridgman, *Phys. Rev.* **48,** 825 (1935).
12. P. W. Bridgman, *Proc. Amer. Acad. Arts Sci.* **76,** 55 (1948).
13. P. W. Bridgman, *Proc. Amer. Acad. Arts Sci.* **76,** 71 (1948).
14. A. F. Schuch and J. H. Sturdivant, *J. Chem. Phys.* **18,** 145 (1950).
15. M. G. Gonigberg, G. P. Shakhovskoi and V. P. Vutuzov, *Zh. Fiz. Khim.* **31,** 350 (1957).
16. E. G. Ponyatovski, *Dokl. Akad. Nauk. SSSR,* **120,** 102 (1958).
17. R. Herman and C. A. Swenson, *J. Chem. Phys.* **29,** 398 (1958).
18. W. H. Zachariasen, quoted in Reference 10.
19. L. Pauling, quoted in Reference 14.
20. D. H. Parkinson, F. E. Simon and F. H. Spedding, *Proc. Roy. Soc.* A**207,** 137 (1951).
21. L. M. Roberts and J. M. Lock, *Phil. Mag.* **2,** 811 (1957).
22. J. M. Lock, *Conf. de Phys. des Basses Temp. Paris* 155, (1955).
23. J. M. Lock, *Proc. Phys. Soc., Lond.* **70,** 566 (1957).
24. L. F. Bates, S. J. Leach and R. G. Loosby, *Proc. Phys. Soc., Lond.* **68,** 859 (1955).
25. H. Leipfinger, *Z. Phys.* **150,** 415 (1958).
26. L. F. Bates and M. M. Newmann, *Proc. Phys. Soc., Lond.* **72,** 345 (1958).
27. L. K. Jetter, C. J. McHargue, R. O. Williams and H. L. Yakel, *Rev. Sci. Instrum.* **28,** 1087 (1957).

VOL. 8 1960

28. C. S. Barrett, *Acta Cryst., Camb.* **9,** 671 (1956).
29. F. H. Ellinger, *Trans. Amer. Inst. Min. (Metall.) Engrs.*, **203,** 411 (1955).
30. F. Sebilleau and H. Bibring, *Mechanism of Phase Transformation in Metals*, p. 209. Institute of Metals, London (1955).
31. M. K. Wilkinson, H. R. Child, W. C. Koehler and E. O. Wollan, *Bull. Amer. Phys. Soc.* **4,** 183 (1959).
32. J. W. Christian, *Proc. Roy. Soc.* A**206,** 51 (1951).
33. Z. S. Basinski and J. W. Christian, *Phil. Mag.* **44,** 791 (1953).
34. A. H. Cottrell and B. A. Bilby, *Phil Mag.* **42,** 573 (1951).
35. A. Seeger, *Z. Metallk.* **44,** 247 (1953).
36. A. Seeger, *Z. Metallk.* **47,** 653 (1956).
37. W. T. Read, Jr., *Dislocations in Crystals* pp. 92–113. McGraw-Hill, New York (1953).
38. J. H. O. Varley, *Phil. Mag.* **2,** 384 (1957).

EVAPORATION AND THERMAL ETCHING*

E. D. HONDROS and A. J. W. MOORE†

Measurements of the loss of weight during thermal etching of silver have been compared with estimates of the mass of silver which would have to be removed to produce the etched structure (valley capacity). Up to about 5 hr etching time at 900°C the two figures correspond. After this there is little change in the valley capacity of the surface, although silver continues to be removed at a constant rate.

If net evaporation is prevented by heating the silver in air in a silver container, a polished surface will not become etched and an etched surface will become smooth. Thus, it is concluded that net evaporation is necessary to produce and to maintain the thermally etched structure and that the tendency to establish a minimum of surface energy is not the driving force of the process.

EVAPORATION ET ATTAQUE THERMIQUE

Des mesures de pertes en poids lors d'une attaque thermique de l'argent ont été comparées avec les pertes estimées en argent qui a dû être enlevé pour produire la structure attaquée (volume des vallées). Pour un temps d'attaque jusqu'à 5 heures à 900°C, les deux valeurs correspondent. Après ce temps, il y a un petit changement de volume des vallées de la surface, quoique la vitesse de l'enlèvement de l'argent reste constante.

Si l'on évite l'évaporation en chauffant l'argent à l'air dans un récipient en argent, une surface polie ne sera pas attaquée et une surface attaquée sera lisse. Ainsi on a conclu qu'une évaporation est nécessaire pour produire et maintenir la structure attaquée à chaud et que la tendance pour établir un minimum d'énergie de surface, n'est pas la cause du processus.

VERDAMPFUNG UND THERMISCHES ÄTZEN

Messungen des Gewichtsverlustes während thermischen Ätzens von Silber wurden verglichen mit Abschätzungen der Menge an Silber, die man zur Erzeugung der Ätzstruktur entfernen müßte (Voluminhalt der Täler). Bei bis zu fünfstündigem Ätzen bei 900°C entsprechen beide Zahlen einander. Danach ändert sich das Volumen der Täler wenig, obwohl weiter Silber mit konstanter Geschwindigkeit entfernt wird.

Verhindert man Verluste durch Verdampfen, indem man das Silber in einem Silberbehälter in Luft erhitzt, so wird eine polierte Oberfläche nicht geätzt und eine geätzte wird glatt. Es wird daher geschlossen, daß ein Masseverlust durch Verdampfen nötig ist, um die thermische Ätzstruktur zu erzeugen und aufrecht zu erhalten, und daß die Tendenz, ein Minimum der Oberflächenenergie zu erreichen, nicht die treibende Kraft des Prozesses ist.

VOL. 8 1960

1. INTRODUCTION

When a metal is heated in oxygen at a partial pressure below that at which an oxide film visible in the microscope is formed, then the surface may show a characteristic striated structure. Thermal etching has been studied most extensively on silver, although it has also been observed with many other metals such as copper, platinum, cadmium, a nickel-chromium alloy etc.[1] It occurs when silver is heated in air for some hours at temperatures near its melting point. Moore[2] has shown that the system of striations consists of parallel ridges with a "saw-tooth" section. In the case of silver the plane exposed on one side of the ridges is either {111} or {100} depending on the orientation of the original surface, while the plane exposed on the other side of the ridges is, in general, one of high indices (complex plane). Further, the angle between the complex plane and {111} or {100} respectively was found to be independent of the orientation.

Leroux and Raub in 1930[3] observed that a loss in weight accompanied the formation of striations when silver was heated in a stream of oxygen. However, in hydrogen no surface change occurred and no weight loss was recorded. It was concluded that oxygen attacked certain crystallographic planes preferentially and that the oxide immediately volatilized, thereby exposing the more heavily attacked planes. Similarly, Elam in 1936[4] showed that copper, thermally etched by heating in air at a pressure of 0.5 mm Hg, revealed facets of {100} and {110} planes. Other experiments showed that the presence of cuprous oxide was necessary, either in the body of the metal or as a surface layer, before etching would occur. Here also a mechanism of preferential oxidation of certain planes followed by evaporation of the oxide was proposed. However, if certain planes of low indices are preferentially oxidized, all equivalent planes should be exposed on etching, thus giving a pitted structure, as

* Received September 17, 1959; revised version November 30, 1959.

† C.S.I.R.O. Division of Tribophysics, University of Melbourne, Carlton, Victoria, Australia.

in solution etching, rather than a system of parallel ridges.

In 1948 Chalmers *et al.*[5] in a systematic study of the part played by oxygen in the thermal etching of facets in silver, proposed that the amount of silver lost by evaporation is so small that the etched structure remains in equilibrium with the gaseous phase. Thus, the etched surface is one of minimum total surface free energy. The idea was further developed by Moore[2], who deduced the energy relationships which would therefore exist between the exposed planes and also between the etched surface and the original surface. The observed angles between the exposed planes were found to be consistent with these relationships.

If equilibrium conditions prevail, the substantial weight losses reported by Leroux and Raub are surprising. To check this fact the losses of weight of single crystals of silver during thermal etching have been measured and it is shown in this paper that the weight losses are closely related to the form of the etched contour. It is also shown that the tendency to establish a minimum of surface energy is not the driving force of the process.

2. EVAPORATION LOSS AND THERMAL ETCHING

(a) *Experimental procedure*

The measurements of the loss of weight were carried out on single crystals in order to avoid anomalies occurring at grain boundaries. The flat crystals of total surface area of about 20 cm² were grown in graphite moulds from silver of 99.995 per cent purity by the method described by Sosnovsky[6]. They were electropolished in a complex silver cyanide solution[7] before being heated in an atmosphere containing oxygen.

The crystal used in these experiments has an orientation such as to reveal {111} facets on etching. Since the angle between the {111} and the complex plane was found to be 33°,[2] the pole of the complex plane lies on the arc shown in the stereographic projection of Fig. 1. The particular crystal whose orientation is marked in this figure has the advantage that the angles of tilt which the two planes make to the surface are approximately equal and hence greater accuracy is achieved in the estimate of the volume contained in the valleys between the ridges.

The crystal was heated for a given time in a closed horizontal tube furnace in a slow current of air which was passed through a saturated solution of potassium permanganate in sulphuric acid, then over soda asbestos and then through a liquid air trap. Before

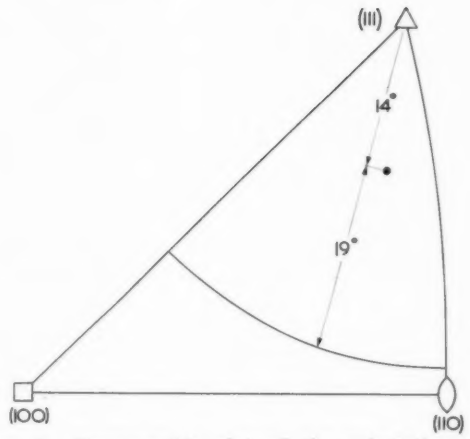


FIG. 1. Stereographic plot of the orientation of specimen selected for evaporation studies.

and after heating, the specimen was weighed to ±0.05 mg and the formation of facets was observed microscopically. After representative fields had been selected and photographed it was replaced in the furnace for further etching.

(b) *Valley capacity*

The mass of silver originally contained in the valleys of the etched surface (this will be termed the "valley capacity" of the etched surface) can be estimated from a micro-examination and a knowledge of the angles of tilt of the exposed planes. Fig. 2 shows a typical area of the crystal whose surface is oriented 14° to the {111} plane. It was etched at 900°C for 287 hr. The curving of the striations indicates those parts of the surface containing local depressions or elevations, but these introduce only a small error in determining the average distance between the ridges. On an enlarged print of this field a line was drawn perpendicular to

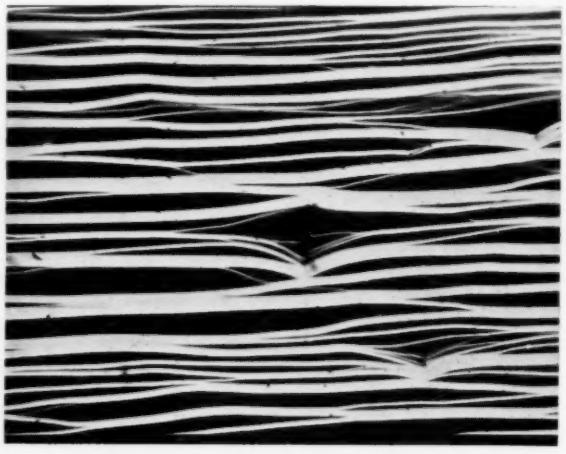


FIG. 2. A typical area on the single crystal after thermal etching for 287 hr at 900°C in air. The black bands are the {111} facets. ×800

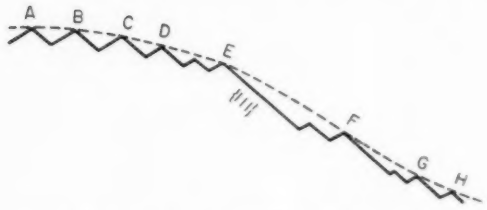


FIG. 3. The profile of an etched surface.

the striations and the intercepts of the boundaries between the two types of exposed planes were measured with a travelling microscope. The valley capacity was then estimated by two methods as follows:

(i) From the measurements of the distances between valleys and ridges taken from the photomicrograph of the field shown in Fig. 2 and from a knowledge of the angles of the two sides of the ridges, a scale profile of a sample field was drawn on graph paper. This chart of approximately 30 ft length was laid out and the peaks were joined as for the line A to H of Fig. 3 so as to preserve the major undulations of the surface. The area between this line and the profile of the surface was measured by "counting squares". From this measure, the valley capacity of such a surface for the whole area of the crystal of 21.5 cm² was estimated to be 5.6×10^{-3} g.

(ii) An approximation to the above surface can be made by joining the points AB, BD, DE, etc. of Fig. 3 by straight lines as shown in detail in Fig. 4. The area of the triangle ABC is

$$(xy/2)(\tan \alpha + \tan \beta)$$

where x and y are the projected widths of the {111} plane and complex plane facets respectively and α and β are the angles between the crystal surface and the {111} plane and the complex plane respectively. For a representative part of length $\sum_{i=1}^{i=n} (x_i + y_i)$ of a typical cross-section the total area Δ of n such triangles is

$$\Delta = (\tan \alpha + \tan \beta) \sum_{1}^{n} \frac{x_i y_i}{2}$$

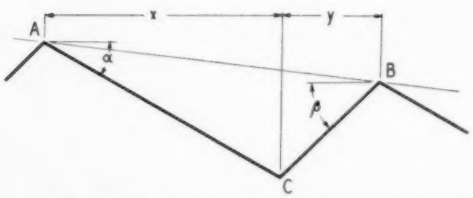


FIG. 4. Geometrical approximation to a profile of an etched surface.

and hence the valley capacity (W) of a specimen of area A

$$W = \frac{\rho \Delta A}{\sum_{i}^{n} x_i + y_i}$$

where ρ = density of silver.

For the example shown in Fig. 2, $W = 5.3 \times 10^{-3}$ g. This compares well with the tedious graphical measurement and the method was used for subsequent measurements of valley capacities.

(c) *Results*

The valley capacities so determined after various periods of heating and the observed weight losses are plotted in Fig. 5 (a and b). The two curves are very

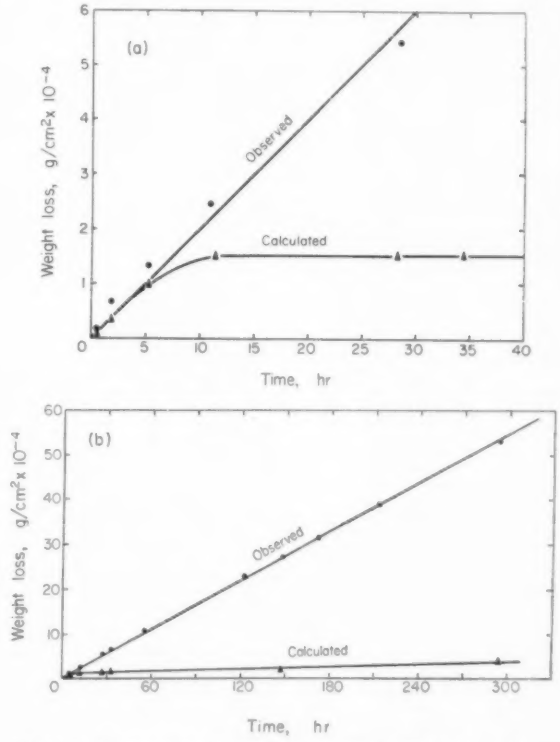


FIG. 5. Comparison between observed losses of weight and the calculated valley capacity of the etched structures, after various periods of heating at 900°C in air. Specimen orientations as in Fig. 1.

similar up to about 5 hr etching time. After this there is little further change in the valley capacity of the surface, although silver continues to be evaporated at a constant rate.

Measurements of loss of weight and microscopical examinations of crystals of other orientations which had undergone prolonged etching, qualitatively confirmed the conclusion that the loss in weight was much greater than that required to form the valleys.

VOL. 8 1960

It was also found that crystals heated in a vacuum showed a loss in weight about 100 times greater than those heated in air at the same temperature and that the surface became covered with rounded pits. In nitrogen the evaporation rate was approximately double that in air and the surface remained smooth.

In view of the extensive evaporation accompanying the thermal etching, further experiments were designed to show how silver behaves when heated in air under conditions in which no net evaporation from the surface occurs.

3. EQUILIBRIUM CONDITIONS AND THERMAL ETCHING

If silver is heated in air, in a sealed isothermal enclosure at atmospheric pressure, the weight loss should be only that necessary to establish the equilibrium vapour pressure for silver. The first attempts to obtain this condition were carried out on electropolished single crystals heated in silica tubes sealed at an air pressure which would correspond to 760 mm Hg at 900°C. The silver became etched and showed a considerable loss of weight and the silica became yellow indicating that chemical reaction between silica and silver in the presence of oxygen took place and prevented the equilibrium vapour pressure being established.

A suitable enclosure was therefore made of silver. A silver block which was cast *in vacuo* was bored to give a cavity about 15 mm dia. The crystal was hung freely from a hook set on the inside of a silver lid. As the enclosure was heated, air was expelled at the junction between the lid and block and when the working temperature was reached, the lid and block welded together, thus giving a tight enclosure containing air at atmospheric pressure at the working temperature.

Experiments on crystals of various orientations showed that no losses of weight could be detected and in most cases thermal etching could not be detected even at high magnifications. The results of the measurements on a crystal with a surface oriented 18° from the [111] pole and heated in air in the enclosure for 308 hr are given in Table 1 as an example. After

TABLE 1. Weight losses with and without an enclosure (surface area 5 cm²), temperature 900°C, time 308 hr

	Experiment in silver enclosure	Experiment in open air
Weight before heating (g)	0.3424 ± 0.0001	0.1787 ± 0.0001
Weight after heating for 308 hr (g)	0.3426 ± 0.0001	0.1597 ± 0.0001

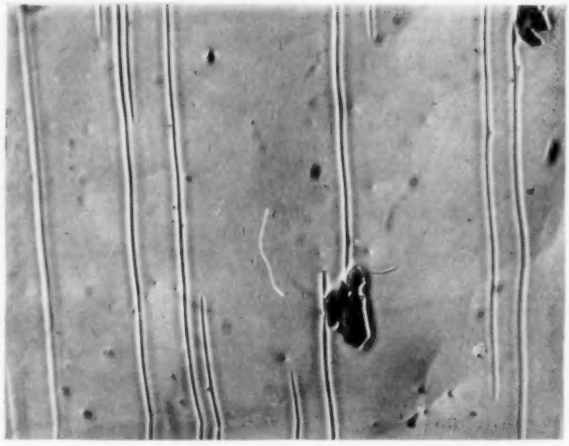


FIG. 6. Most advanced etching observed on specimen heated in the isothermal silver enclosure. This was observed only on small area of surface. ×800

being heated, most of the specimen appeared bright and smooth under the microscope. One small area showed slight etching and Fig. 6 is a photomicrograph showing the heaviest etching on this small area. For comparison, the specimen was electropolished and suspended in open air in the same position in the furnace. After 308 hr the specimen was heavily etched (Fig. 7) and had lost 19 mg in weight.

Experiments were also conducted on specimens which had been previously thermally etched in air. Fig. 8 shows a field on a polycrystalline specimen which was etched for 100 hr in air, and Fig. 9 shows the same field after the etched specimen was heated in a silver enclosure at 900°C for 100 hr. The ridged surface became smooth when net evaporation from the surface was prevented; however, the grain boundary grooves were retained.



FIG. 7. Typical field on the same specimen as for Fig. 6 after heating in open air. ×800



FIG. 8. Field on polycrystalline specimen after heating for 100 hr at 900°C in open air. ×250

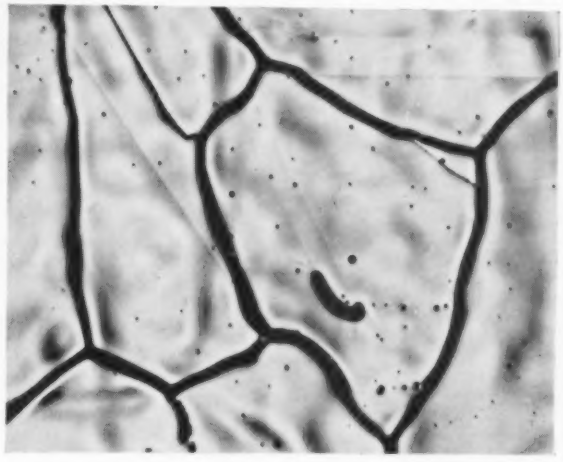


FIG. 9. The same field as for Fig. 8 after the etched specimen had been heated 100 hr in air at 900°C in the isothermal silver enclosure. ×250

In order to be sure that the oxygen in the cavity in the enclosure was not dissolved in the silver of the enclosure so that the concentration was reduced below that necessary to cause thermal etching, these experiments were repeated with silver enclosures which had been heated in air to 900°C for some hours so that the silver was saturated with oxygen. Again it was found that no etching would occur within the enclosure and an etched surface became smooth.

VOL. 8 1960

4. DISCUSSION

It is clear from Fig. 5 that in the initial stages of etching, the loss of silver is approximately equal to the silver which would have to be removed to produce the etched structure. In addition, when this loss is prevented, etching does not occur. Thus, net evaporation (either of silver or of oxide) appears to be the dominating mechanism for the formation of the etched structure.

In Fig. 10 the original polished surface and the positions of the etched ridges below that surface after etching for various times are drawn to scale at depths deduced from the weight loss. After 287 hr of etching, the depth of the new etched profile below the original surface is approximately ten times the height of the etched ridges. Thus, during the later stages of etching, a new metal-vapour interface is continuously formed but the general shape of the etched surface remains unchanged. Moreover, when an etched surface is heated under conditions where there is no net evaporation, the surface becomes smooth. Thus, net evaporation from the surface is also apparently necessary to maintain the etched structure. The results indicate that in any thermal etching operation there is a transport of metal through the vapour phase to a point where it is removed from the system. The sink for the vapour can be a part of the furnace at a lower temperature or can be a substance which will combine with the metal in the vapour, e.g. silica.

The view was taken in an earlier paper[2] that the shape of a thermally etched surface is determined by the relative surface energy of different crystal planes. However, in this case an etched surface should remain etched when heated in air in an isothermal enclosure. Thus this theory does not now appear to be justified in

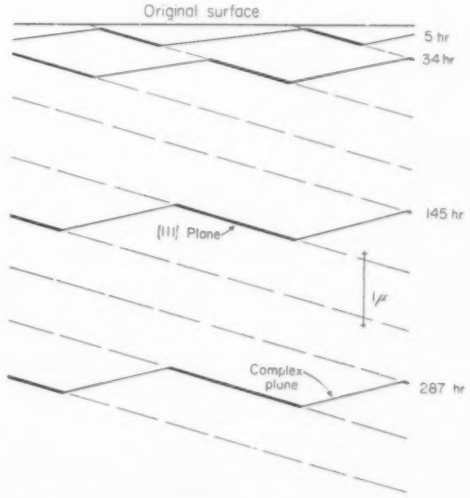


FIG. 10. Relation between the depth of material removed and the relative widths of the facets exposed during each stage of thermal etching.

spite of the fact that it provided an explanation for the constancy of angle between the sides of the ridges.

The grain boundary grooves which are formed when the silver is heated in air under conditions of no net loss by evaporation appear very similar to those produced after heating in an inert atmosphere under conditions where evaporation can occur. In the present experiments true thermal equilibrium was set up and the assumption which has been made by many previous workers, e.g. Bailey and Watkins[8], Greenough and King[9], that the groove shapes are determined by surface forces, appears justified. However, the groove angles produced under these conditions of true equilibrium have not been compared with the angles produced when evaporation can occur.

It has been confirmed by the present authors that oxygen must be present before thermal etching to produce facets will take place. In vacuum, pits are formed in the surface and in an inert atmosphere (nitrogen) the surface becomes smooth. It would appear, therefore, that oxygen modifies the kinetics of the evaporation from different planes. Although bulk silver oxide decomposes at about 200°C in air, evidence for the interaction between oxygen and silver at much higher temperatures is available. Buttner *et al.*[10] showed the effects of an oxygen atmosphere on the surface tension of silver at 900–960°C and deduced that a {111} plane adsorbs 1.4 atoms of oxygen per silver atom. Davies[11] deduced from electrometric experiments and from the wetting characteristics of silver by mercury that silver heated to high temperatures is covered by an oxide film 5 Å thick. An intermediate view is given by Watanabe[12], who concluded from electron diffraction evidence that silver had an oriented oxygen film of complex structure and not that of an oxide or of a close-packed monolayer.

For those surface orientations of silver which have been shown to thermally etch[2] the ideal crystal surface will consist of relatively widely spaced monatomic steps. A large proportion of the surface will already consist of the plane of low indices which will be revealed when thermal etching takes place.

The following mechanism can explain many of the experimental facts. On evaporation atoms will be removed from the step edges, thus causing a continual drift of the monatomic steps across the surface. With statistical fluctuations of the distance between steps, certain adjacent steps would group together but in the presence of an inert gas they separate again, whereas in oxygen it appears that these groups continue to grow. For this growth it is therefore necessary that their rate of drift should be either increased so that they could overtake and adsorb the smaller steps or the rate should be decreased so that the smaller steps should overtake them. The latter case is shown diagrammatically in Fig. 11. A possible role of the adsorbed oxygen would be in modifying the rate of evaporation from any group of steps which have come together so that one of the above alternatives could occur. A further requirement for the grouping of the steps is that they should be continually moving in the same direction. When evaporation and recondensation are equal, as when an etched silver surface is in equilibrium with its vapour, the steps move randomly, the groups break up, and the surface becomes smooth. This general idea has been developed by Cabrera and Vermilyea[13] and Frank[14] for solution etching where the time-dependent adsorption of impurities on the step faces (plane of low indices) can cause the grouping of monatomic steps as they move in the same direction. The sharp angles found at both the bottom of the valley and the top of the ridge in thermal etching are not, however, entirely consistent with their theory.

The progression of steps has been observed by Newkirk[15] in a study of the growth of mercuric iodide crystals. He observed curved growth lamellae of variable thickness (the order of thousands of Ångström units) moving across the surface and proposed that the visible lamellae were the accumulation of many much thinner layers. We have observed similar lamellae produced by evaporation from thermally etched silver. Fig. 12 shows portion of {111} facet of a crystal with surface orientation only 2° from the [111] pole.

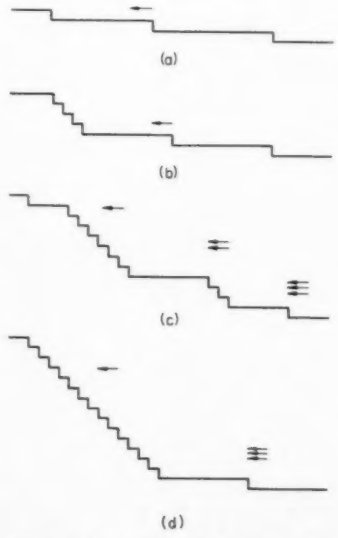


FIG. 11. Growth of a complex plane by absorption of rapidly moving monatomic steps.

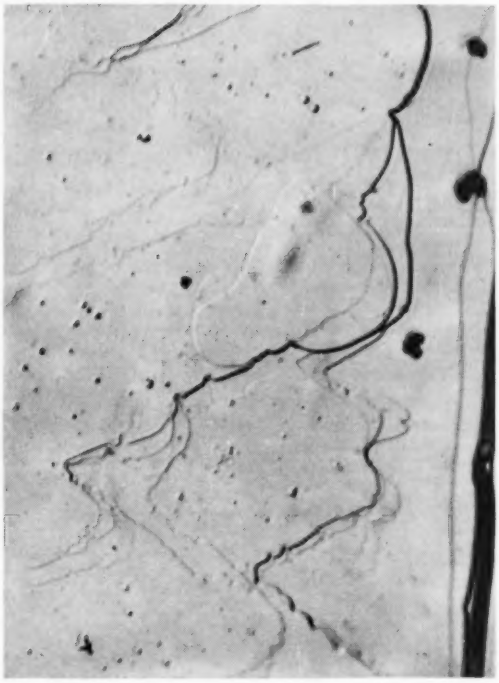


FIG. 12. Field on a "decorated" {111} plane of a thermally etched single crystal showing the presence of steps. The black band on the right represents the complex plane for a thermally etched crystal of this orientation. ×2000

After etching for 80 hr, the specimen was left near a piece of plasticine and "decoration" has apparently improved the contrast.[16] Many fine lamellae are shown and they are kinked at points where it appears that their movement towards the black complex plane has been arrested by crystal imperfections. Further supporting evidence for the coalescence of steps is our observation that at the initial stages of thermal etching the facets are seen to grow by a coarsening of facets.

The "treads" of the monatomic steps which constitute an ideal crystal surface consist of the particular plane of low indices which makes the smallest angle with the surface. As the steps coalesce, the "treads" widen out and this plane becomes the only one of its family which is revealed by the etching. Thus the coalescence of steps explains how thermal etching takes the form of parallel ridges and how, in general, only one plane of simple indices is revealed. However, as was shown by Moore[2], the angle between the plane of simple indices and the complex plane remains constant over a wide range of initial surface orientation and the problem still remains to explain this in terms of an evaporation mechanism. This work is being continued.

REFERENCES

1. B. D. CUMING and A. J. W. MOORE, *J. Aust. Inst. Met.* **3,** 124 (1958).
2. A. J. W. MOORE, *Acta Met.* **6,** 293 (1958).
3. J. A. A. LEROUX and E. RAUB, *Z. Anorg. Chem.* **188,** 205 (1930).
4. C. F. ELAM, *Trans. Faraday Soc.* **32,** 1604 (1936).
5. B. CHALMERS, R. KING and R. SHUTTLEWORTH, *Proc. Roy. Soc.* A**193,** 465 (1948).
6. H. M. C. SOSNOVSKY, *J. Phys. Chem. Solids* **10,** 304 (1959).
7. L. GILBERTSON and O. M. FORTNER, *Trans. Electrochem. Soc.* **81,** 199 (1942).
8. G. BAILEY and H. WATKINS, *Proc. Phys. Soc.* B**63,** 350 (1950).
9. A. P. GREENOUGH and R. KING, *J. Inst. Met.* **79,** 415 (1951).
10. F. H. BUTTNER, E. R. FUNK and H. J. UDIN, *J. Phys. Chem.* **56,** 657 (1952).
11. D. E. DAVIES, *Nature Lond.* **179,** 1293 (1957).
12. Y. WATANABE, *X Sen* (X-rays) **8,** 31 (1954).
13. N. CABRERA and D. A. VERMILYEA, *Growth and Perfection of Crystals*, p. 393. John Wiley, New York (1958).
14. F. C. FRANK, *Growth and Perfection of Crystals*, p. 411. John Wiley, New York (1958).
15. J. P. NEWKIRK, *Acta Met.* **4,** 316 (1956).
16. A. J. FORTY and F. C. FRANK, *Proc. Roy. Soc.* A**217,** 262 (1953).

VOL. 8 1960

DISLOCATIONS AND BRITTLE FRACTURE IN ELEMENTAL AND COMPOUND SEMICONDUCTORS*

M. S. ABRAHAMS and L. EKSTROM†

The predominant {110} cleavage plane of the IIIb–Vb compounds has been explained by employing a dislocation model. This model postulates the formation and coalescence of Lomer dislocations to form (nucleate) a microcrack; cleavage results from the propagation of the microcrack. Unlike previous models, the one herein proposed is able to account for the unique three-fold symmetry of the crack pattern which results from indenting a (111) surface with a pointed, conical diamond. The fact that Ge only exhibits {110} cleavage under special conditions is attributed to a difference in structure of the Lomer dislocation between the IVb elements and IIIb–Vb compounds. The occurrence of octahedral cleavage in the IVb elements is thought to be due to the growth of a microcrack resulting from the piling-up and coalescence of glissile dislocations on {111} planes. A combination of this mechanism with the one yielding dodecahedral cleavage accounts for cleavage on planes other than those of the {110} type in the IIIb–Vb compounds.

DISLOCATIONS ET RUPTURE FRAGILE DANS LES SEMI-CONDUCTEURS ELEMENTAIRES ET COMPOSES

Le plan prédominant de clivage {110} de composés des groupes IIIb–Vb est expliqué au moyen d'un modèle de dislocations. Ce modèle postule la formation et la coalescence de dislocations de Lomer pour former (initier) une microfissure; le clivage est la conséquence de la propagation de la microfissure. Contrairement aux modèles antérieurs, celui proposé ici est en mesure de tenir compte de la symétrie ternaire unique du réseau de fissures, obtenues en pénétrant une surface (111) avec un diamant cônique pointu. Le fait que le Ge seul présente le clivage {110} dans des conditions particulières est attribué à la différence de structure de la dislocation Lomer entre les éléments du groupe IVb et les composés IIIb–Vb. On pense que la présence d'un clivage octaédrique dans les éléments IVb est due à la croissance d'une microfissure provenant de l'empilement et la croissance de dislocations glissantes sur les plans {111}. Une combinaison de ce mécanisme avec celui produisant un clivage dodécaédrique tient compte du clivage sur les plans autres que {110} dans les composés IIIb–Vb.

VERSETZUNGEN UND SPRÖDBRUCH BEI HALBLEITERN AUS ELEMENTEN UND VERBINDUNGEN

Das Vorherrschen der Spaltebene{110}bei IIIb-Vb-Verbindungen ist mit Hilfe eines Versetzungsmodells erklärt worden. Dies Modell postuliert, daß Lomer-Versetzungen gebildet werden, sich vereinigen und so einen Mikrobruch bilden (Keimbildung); die Weiterentwicklung des Mikrobruchs führt zur Spaltung. Im Gegensatz zu früheren Modellen trägt das hier vorgeschlagene der einzigartigen dreizähligen Symmetrie Rechnung, die das Spaltmuster beim Eindrücken eines spitzen konischen Diamanten in eine (111)-Fläche zeigt. Die Tatsache, daß Ge {110}-Spaltung nur unter speziellen Bedingungen zeigt, wird auf eine unterschiedliche Struktur der Lomer-Versetzungen in IVb-Elementen und IIIb-Vb-Verbindungen zurückgeführt. Das Auftreten von Oktaeder-Spaltung bei den IVb-Elementen beruht vermutlich auf dem Wachstum eines Mikrobruchs, der durch das Aufstauen und die Vereinigung von gleitfähigen Versetzungen in {111}-Ebenen entsteht. Kombiniert man diesen Mechanismus mit dem, der zur Dodekaeder-Spaltung führt, so hat man die Begründung für das Auftreten von anderen Spaltebenen als {110} bei IIIb-Vb-Verbindungen.

I. INTRODUCTION

The occurrence of dodecahedral cleavage in zinc blende has been known for many years.[1] More recently, the same cleavage planes were observed in the Group IIIb–Group Vb compounds, which crystallize with the zinc blende structure.[2,3] In contrast to these findings, diamond, Ge, and Si usually exhibit cleavage parallel to octahedral planes.[3] It has been postulated[4,2,3] that the difference in the choice of cleavage plane between the diamond-type lattice and the zinc blende-type is due to the partial ionic character of the bonding in the zinc blende structure. The nature of the atomic structure on {110} planes in the zinc blende structure is such that a displacement of the planes will cause atoms with like charges on adjacent planes to approach. A coulomb repulsion results which is believed to initiate fracture by cleavage parallel to {110} planes. Since the atoms in the elemental structures are uncharged, this same displacement does not develop a repulsive force and hence, this mechanism of cleavage is inoperative.

In the course of the present investigation into the cleavage habits of IIIb–Vb compounds in general, certain results were obtained which could not be explained by the above repulsion mechanism. In order to account for these observations as well as the cleavage plane in both the IIIb–Vb compounds and IVb elements, a dislocation mechanism is employed.

* Received June 24, 1959; revised version October 7, 1959.

† RCA Laboratories, Princeton, N.J.

2. EXPERIMENTAL PROCEDURE AND RESULTS

In the present experiments, the cleavage habit of seven Group IIIb–Group Vb compounds was investigated. Cleavage of the various specimens was initiated by several different methods. The compounds studied and the methods of obtaining the cleavage faces are shown in Table 1.

TABLE 1

Material	Method of cleavage
GaAs	Compression; bending; impact
InAs	Compression; thermal quenching; impact
GaSb	Impact
InSb	Tension; bending; impact
AlSb	Impact
GaP	Impact
InP	Bending; impact

The experiments were all performed at room temperature except in the case of thermal quenching. In this instance fracture was obtained by cooling the specimen rapidly from just below the melting point to room temperature in vacuum.

In every case cleavage occurred on a {110} plane, which was identified by the Laue back reflection X-ray technique. It is noteworthy that the Laue spots in every case were sharp and free from asterism, indicating that the fracture is brittle and involves little or no plastic deformation. This was corroborated by failure to observe slip lines on metallographic examination.

Figure 1 shows a cleaved surface of InAs obtained by thermal quenching. The mirror-like quality of the surface is apparent from the reflection of the grid paper upon which the specimen rests. Macroscopically,

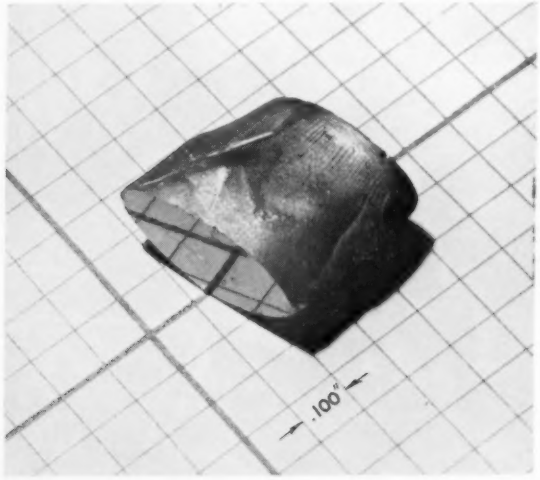


FIG. 1. A {110} cleavage plane in InAs obtained by thermal quenching.

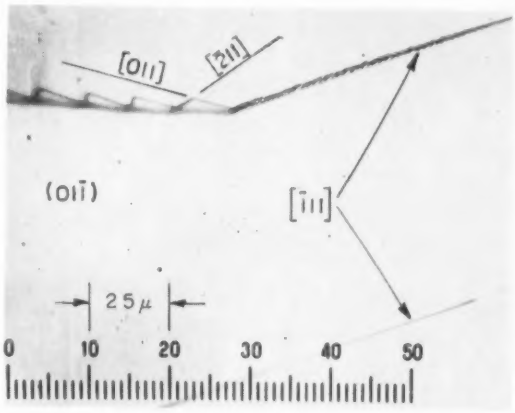


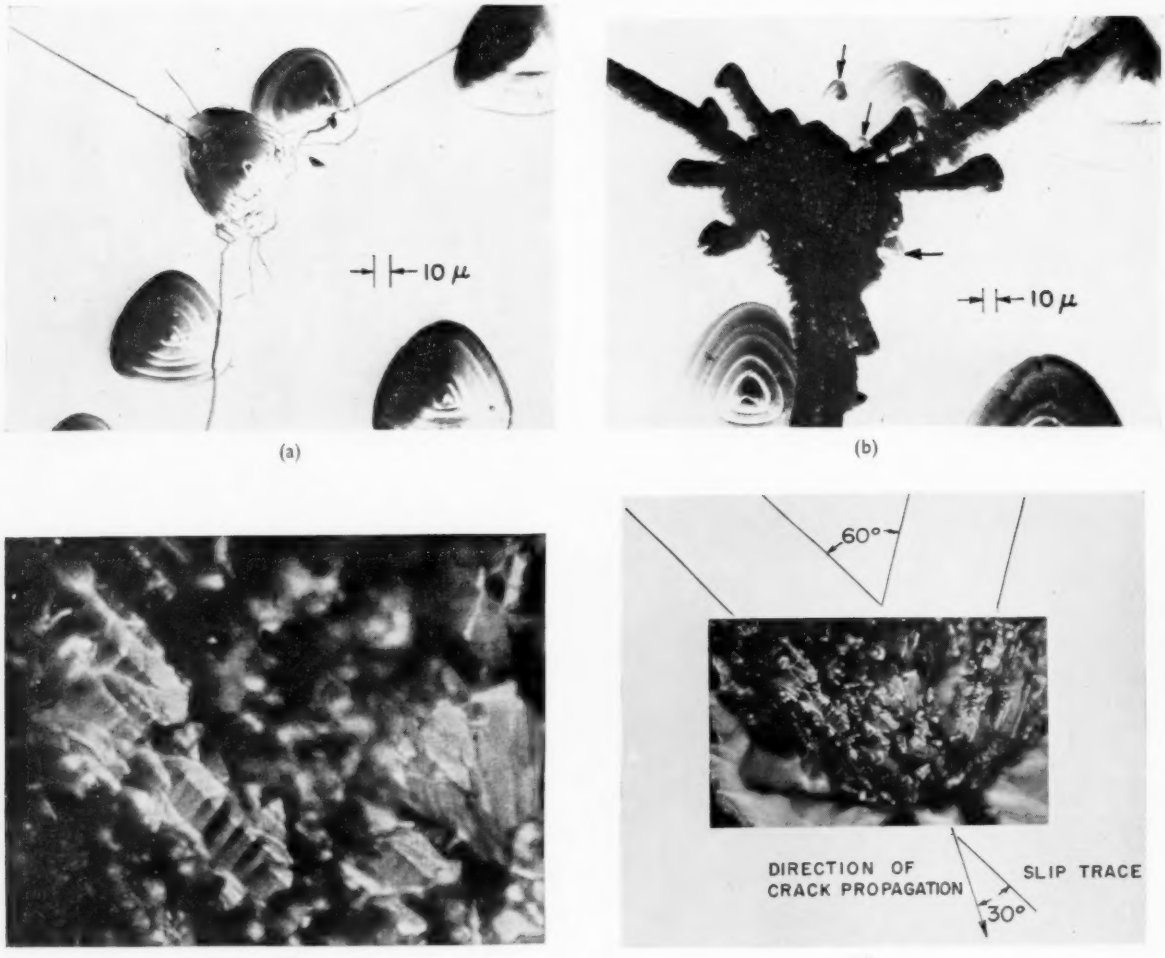
FIG. 2. Cleavage steps on the (011) cleavage plane in InSb.

all the cleavages tended to occur on one plane of the form {110} rather than on many such planes. This was true regardless of the specimen orientation. Microscopically, however, the perfection of all the cleaved surfaces was marred by numerous cleavage steps. A typical example of these steps is shown in Fig. 2, occurring here on a specimen of InSb cleaved in tension. The tensile axis of the rectangular specimen was [14$\bar{5}$] and the bounding faces were (111) and (3$\bar{2}$1). The cleavage occurred on the (01$\bar{1}$) plane, that member of the {110} family on which the maximum normal stress is developed for the given orientation.

Crystallographic analysis showed that the edges of the longest cleavage steps lay in ⟨111⟩ directions. These directions can correspond to the line of intersection of the (01$\bar{1}$) cleavage plane with another {110} plane associated with the step. In addition to the ⟨111⟩ directions, edges were also found lying in ⟨110⟩ and ⟨211⟩ directions (e.g. as in Fig. 2). The appearance of edges lying in ⟨110⟩ directions on cleaved surfaces of InSb has also been reported by Pfister[2]. It can be shown by geometrical considerations that two {110} planes can only intersect along ⟨100⟩ or ⟨111⟩ directions. Therefore, both of the planes comprising a step cannot be of the type {110}, if their line of intersection is other than cubic or octahedral. On this basis, the planes forming cleavage steps with the (01$\bar{1}$) gross cleavage plane and having lines of intersection parallel to ⟨110⟩ and ⟨211⟩ are not {110} planes. Thus, it is believed that a limited amount of cleavage can occur on non-dodecahedral planes in zinc blende-type structures.

In addition to the results presented above, it was also ascertained that a limited amount of plastic flow can occur in GaAs deformed at room temperature. This conclusion was reached through the following experiments. A polished (111) face of GaAs was

VOL. 8 1960



(a) (b) (c) (d)

FIG. 3. Indentation of a (111) face of GaAs at room temperature by a pointed conical diamond: (a) the effect of indenting the etched surface showing the typical three-fold symmetry; (b) the surface re-etched without prior polishing with new etch pits visible near the arrows; (c) the central area of (b) showing parallel rows of etch pits suggestive of slip lines, ×1600; (d) the central area of (b) showing non-parallel rows of etch pits suggestive of {111} slip traces and their relation to the crack direction. ×500

etched using a solution of 1 part HNO_3 (70%)–2 parts H_2O described by Schell[5]. He found the pits produced by this etch to be reproducible, and on this basis concluded that the etch pits represented the intersection of dislocation lines with the specimen surface.* Following the etching, the specimen was indented with a conical diamond to a depth of about 10^{-3} in. at room temperature. The specimen surface then appeared as in Fig. 3a. The indentation is at the center of the field of view and emanating from it are three major cracks which are traces of $\{1\bar{1}0\}$ planes and which lie in the $[1\bar{2}1]$, $[\bar{2}11]$ and $[11\bar{2}]$ directions. The specimen was then re-etched without prior polishing so as to preserve the original markings. The same area of the specimen then appeared as in Fig. 3b. It is apparent that the etchant has attacked both the cracks and the original etch pits and enlarged them. In addition, new and smaller etch pits can be seen in the area surrounding the indentation. Besides the new pits visible in Fig. 3b, examination at high magnification (×2000) showed that most of the central area also contained new dislocations. Such an area is shown in Fig. 3c. The limited depth of field at this magnification permits only a small number of these pits which are located on an irregular surface to be in focus at one time. It is noted that the pits are

* The present authors have demonstrated more fully that these etch pits do correspond to dislocation sites. See M. S. ABRAHAMS and L. EKSTROM, *Properties of Elemental and Compound Semi-conductors*, p. 225, Interscience, New York (1960). In addition, the orientation of the pits is unique. The projection on the (111) plane of the three vectors drawn from the pit center to the three vertices lie in the [121], [211] and [112] directions.

arranged in rows suggestive of slip lines. In Fig. 3d, rows of etch pits can be seen aligned along two directions which intersect at about 60°. This is the angle formed by the traces of two {111} slip planes on the (111) observation face. It was further observed that the extension of the bisector of this angle beyond the apex points in the direction of one of the three cracks. These observations were a consistent feature of twenty-one specimens. On this basis, it is believed that limited dislocation motion or plastic flow can occur in GaAs at room temperature. The phenomenon of room temperature dislocation motion has also been reported in InSb subjected to impact.[6]

It is further noteworthy that while the crack patterns in Fig. 3a might be expected to exhibit six-fold symmetry, the observed pattern in a total of twenty-one observations showed only three-fold symmetry. Also, if the center of the indentation were translated without rotation to the center of one of the surrounding triangular etch pits, whose sides are parallel to $\langle 1\bar{1}0 \rangle$ directions, the cracks would always appear to emanate from the mid-points of the sides of the etch pit rather than from the vertices.

VOL. 8 1960

3. DISCUSSION

(a) *Cleavage mechanism*

It is thought that cleavage in the IIIb–Vb compounds occurs by a mechanism proposed by Cottrell[7]. The basic requirement of this model is that slip occurs on each of two intersecting slip planes. Cottrell has shown how, in a b.c.c. lattice, two dislocations having Burgers vectors of the form $(a/2)\langle 111 \rangle$ and gliding in {110} planes may react to form a new dislocation lying in a (100) cleavage plane and having a Burgers vector of the form $a[100]$. That the resulting dislocation is stable is apparent from a consideration of the change in the elastic energy of the reaction. The missing half plane is visualized as a "cleavage knife" lying in the cleavage plane; this cleavage knife can grow by the repeated occurrence of such a reaction under the action of a sufficient shear stress and by the coalescence of the resultant dislocations; with further coalescence, the cleavage knife becomes a microcrack in the cleavage plane and increases in length. As the microcrack becomes comparable in length to the slip bands from which it originated, the normal stress acting directly on the microcrack becomes the predominant factor in determining further growth of the crack. Cottrell[7] has given the conditions for which the crack either reaches a stable length or grows indefinitely. The implication is that a crack *once nucleated* on any plane would continue to propagate on that plane provided that the energetics of the growth process are satisfied. In what follows, we will be concerned primarily with the nucleation of microcracks, since certain of the observations can be explained on the basis of selective nucleation, but not on the basis of growth criteria.

On the basis of the experimental evidence for limited slip in InSb and GaAs, it is reasonable to assume that dislocation motion can occur in all the IIIb–Vb compounds at room temperature. Since InSb has the smallest band gap and largest Burgers vector of the compounds under consideration and GaAs has one of the largest band gaps and one of the smallest Burgers vectors, these compounds effectively cover the range of bond strengths and Burgers vectors. Thus, it is expected that the other members of this series will exhibit a similar mechanical behavior.

The cleavage of IIIb–Vb compounds is thought to be controlled by the interaction of dislocations on intersecting {111} glide planes to form Lomer dislocations[8] by a reaction of the type

$$\frac{a}{2}[\bar{1}10] + \frac{a}{2}[0\bar{1}1] \rightarrow \frac{a}{2}[\bar{1}01]. \qquad (1)$$

In this example, the first of the reactant dislocations glides in $(\bar{1}11)$, while the second glides in $(\bar{1}11)$; the glide plane of the product Lomer dislocation is (010). The missing half-plane of the Lomer will act as a "cleavage knife" which can lead to dodecahedral cleavage. It is thus possible to think of cleavage as a nucleation and growth process. Nucleation is associated with the formation and coalescence of Lomer dislocations under a shear stress; growth of the resulting microcrack is due to a normal stress on the plane of the microcrack.

Since experimental evidence has been found for the existence of Lomer dislocations in silicon[9] and dislocation motion at room temperature in germanium,[10,11] it is reasonable to ask why Si and Ge do not cleave by this mechanism. The authors propose that the difference in the cleavage habits of, for example, Ge and GaAs is due to the nature of the bonding around Lomer dislocations in these materials. A consideration of both reactant and Lomer dislocations in both the IVb elements and the IIIb–Vb compounds follows.

(b) *Structure of dislocations**

Both the diamond and the zinc blende structures consist of two interpenetrating f.c.c. lattices, and for

* In the following discussion, the dislocations are considered to be undissociated. This view is taken because X-ray analysis of deformed elemental and compound semiconductors has indicated the probable absence of stacking faults. See C. KOLM, E. D. WARekois and S. A. KULIN, *Trans. Amer. Inst. Min. (Metall.) Engrs.* **212,** 827 (1958).

convenience we shall refer to the atoms on one lattice as α-atoms and to those on the other as β-atoms. In the diamond structure both the α- and β- atoms are chemically identical while in the zinc blende structure, one element supplies all the α-atoms and the other all the β-atoms.

(i) *Reactant dislocations.* The dislocations which can react to form a Lomer dislocation in both the IVb elements and the IIIb–Vb compounds are similar. In particular, they are the mixed dislocations first discussed by Shockley[12] and Read[13]. The axis of the dislocation, which lies along a $\langle 110 \rangle$ direction, and the Burgers vector, $(a/2)\langle 110 \rangle$, form an angle of 60°; the plane determined by the dislocation line and its Burgers vector is $a\{111\}$. The extra half-plane is visualized as a $\{111\}$ double layer of atoms oblique to the slip plane and is believed to terminate between the wide spaced $\{111\}$ layers parallel to the slip plane. Since the half-plane terminates with a row of incompletely bonded atoms lying parallel to $\langle 110 \rangle$, the atoms in this row are either all α- or all β-type. Further, the reactant dislocations in equation (1) are so oriented that their half-planes both terminate with the same type of atom. Each terminating atom lacks one nearest neighbor, and so it is left with a "dangling" bond.

(ii) *Lomer dislocations.** The Lomer dislocation formed by the reaction in equation (1) is a pure edge dislocation whose Burgers vector is $(a/2)[\bar{1}01]$ and whose axis is $[101]$. The glide plane of this Lomer dislocation is (010) and, as glide on this plane is rare in f.c.c. materials, it is reasonable to suppose that the dislocation will be "sessile". The "extra half-plane" is a pair of two $(\bar{1}01)$ half-planes which are separated by $(a/4)[\bar{1}01]$. We shall refer to one half-plane as the a-plane and to the other as the b-plane. Viewed along the $[\bar{1}01]$ direction, the projection of the b-plane on the a-plane has α-atoms displaced $(a/4)[121]$ from α-atoms in the a-plane. This difference exists for all adjacent pairs of $\{101\}$ planes in f.c.c. structures. The a-half-plane of the Lomer will terminate with either all α- or all β-atoms as the terminating row lies along the $[101]$ direction. The b-half-plane will also terminate with the same type of atoms as is in the terminating row of the a-half-plane. Fig. 4 is a schematic representation of the Lomer dislocation formed in reaction (1) and viewed along its axis. The incompletely bonded atoms are shown as open circles with short lines drawn from them in the direction of their missing nearest neighbors or "dangling" bonds. As indicated, the atoms at the edge of the b-half-plane have the correct number and type of nearest neighbors. The incompletely bonded atoms, which are either all α- or all β-type atoms, are situated on the a-planes enclosing the b-half-plane.

We are now able to discuss the possibilities for bonding at a Lomer dislocation and its effect on the choice of the cleavage plane. The "dangling" bonds shown in Fig. 4 lie in the same plane, so that the distortion of the $(\bar{1}01)$ planes around the dislocation will tend to make these dangling bonds colinear. In Ge or Si, where the α- and β-atoms are not chemically different, it is reasonable to expect that a distorted covalent bond can form between each pair of otherwise incompletely bonded atoms. The attractive force of this bond will be directly opposed to any normal force tending to cause cleavage on $(\bar{1}01)$ planes. The addition of this force to those in the surrounding crystal which resist cleavage is sufficient to make cleavage on $\{110\}$ planes more difficult than that on $\{111\}$ planes. However, this bond will be weaker than a normal covalent bond of the element, so that it can be disrupted by properly oriented applied forces at room temperature or by thermal vibrations. Thus, one can expect cleavage in Ge and Si to be both temperature and orientation dependent.

In the compounds, such bond formation between

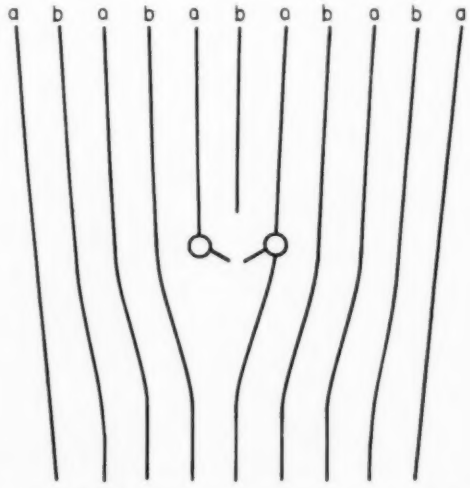


FIG. 4. The postulated structure of a Lomer dislocation in IVb elements and IIIb–Vb compounds. The $[101]$ axis is normal to the plane of the figure and the alternating a- and b- $(\bar{1}01)$ planes are viewed on edge. The positions of the incompletely bonded atoms are shown as open circles. It should be noted that because of symmetry either of the two incompletely bonded a-planes can be considered to be non-terminating.

* Although an alternative configuration for the Lomer dislocation is possible, the configuration described is the one formed by the Lomer reaction in equation (1). Conversion to the other configuration requires mass transport which is unlikely to occur under the experimental conditions. See Figs. 5a and 5b in J. HORNSTRA, *J. Phys. Chem. Solids*, **5**, 129 (1958), for both the alternative configurations and also for another way of picturing these dislocations.

pairs of incompletely bonded atoms will not be favored because bonding would have to occur between two IIIb atoms or between two Vb atoms. Without this bond, the force which opposes {110} cleavage in the elements does not exist in the compounds; and the Cottrell mechanism can operate more easily here.

(c) *Model for cleavage of elemental semiconductors*

In view of the preceding discussion, it can be expected that elemental semiconductors with the diamond structure will exhibit dodecahedral cleavage under certain conditions of stress orientation and temperature. This type of cleavage would proceed as already described by the formation and coalescence of Lomer dislocations and the propagation of the resulting microcrack. Several experimental results support this belief. The occurrence of dodecahedral microcleavage in diamond, Si, and Ge is known.[3] In addition, Kolm[14] has shown that samples of Ge subjected to a uniform shear stress in bending about a ⟨211⟩ axis always cleave on a {110} plane. The tensile and compressive faces were parallel to {111} and the normal to the cleavage plane was normal to both a ⟨111⟩ and the bend axis. Near the tensile face, the observed cleavage plane is that plane across which the maximum tensile stress is developed. In the present work two instances of {110} cleavage were observed in Ge. First, Ge was subjected to bending under four-point loading about the [111] axis, with the tensile and compressive faces parallel to (3$\bar{2}$1). While at room temperature the cleavage plane was invariably of the {111} type, at elevated temperatures (~600°C) cleavage occurred parallel to the (01$\bar{1}$) plane. The (01$\bar{1}$) plane is that {110} plane on which the maximum normal stress exists, near the tensile faces. It is noteworthy that the normal stress to a latent cleavage plane acts in that direction in which the proposed bond at the edge of a Lomer dislocation is already distorted, and would be the stress most effective in breaking it. In the second instance, when the indentation procedure employed on GaAs was applied to {111} faces of Ge, the resulting crack pattern exhibited the same three-fold symmetry and orientation as GaAs.

Until recently Ge was believed to exhibit only octahedral cleavage. The exceptions discussed above are the only reported instances of {110} cleavage. A possible model which predicts the predominant {111} cleavage in Ge as well as in diamond and Si is presented here. It is believed that cleavage will occur by this mechanism at room temperature where the applied stress does not favor the Lomer mechanism. In this model a Lomer dislocation is formed by the interaction of dislocations moving in intersecting {111} planes just as in the model for dodecahedral cleavage. The formation of additional Lomer dislocations and their coalescence is not required, but many occur.* Instead, the Lomer acts as a barrier to the motion of dislocations in one of the glide planes, which leads to a dislocation pile-up. The missing half-planes of these 60° dislocations are {111} double layers oblique to the slip plane, so upon coalescence a microcrack having the same orientation as the half-planes is formed. Stroh[15] has shown that the maximum normal stress resulting from the stress field of the pile-up occurs on a plane passing through the head of the pile-up, and making an angle of 70.5° with the slip plane. As the microcrack in question has precisely this orientation, cleavage is thus favored on the {111} plane occupied by the microcrack.

Although it may be thought that a Lomer dislocation will not be able to withstand the stress field of the piled-up group, an estimate shows that the size of the pile-up required for crack formation is not excessive. Stroh[16] has shown that crack initiation is possible if,

$$n\sigma\mathbf{b} > \tfrac{3}{8}\pi^2\gamma, \qquad (2)$$

where n is the number of dislocations in the pile-up, σ is the resolved shear stress acting on the pile-up, $\mathbf{b}$ is the Burgers vector, and γ is the energy per unit area of the crack surface. For $|\mathbf{b}| = 4 \times 10^{-8}$ cm, $\gamma = 10^3$ ergs/cm^2 and $\sigma = 10^9$ dyn/cm^2, which is reasonable for a well prepared sample, a value of $n = 100$ is obtained. By analogy with Stroh's[17] calculation of the strength of a Lomer–Cottrell dislocation in metals, it is believed that a Lomer dislocation in diamond-type structures can support a pile-up of this size.

(d) *Cleavage step formation in* IIIb–Vb *compounds*

It was seen earlier that cleavage steps involving planes not of the {110} type can occur in InSb. A model which can explain their occurrence will now be proposed. Cleavage is initiated on a {110} plane by the formation of Lomer dislocations, their coalescence, and the growth of the resulting microcrack. Following Cottrell[7], these processes are shown in Figs. 5a, b and c. It is believed that the resulting crack will propagate completely across the crystal if there are no obstacles to its growth. However, a cleavage step may form if an obstacle exists in the path of the propagating crack. In Fig. 5d the advancing crack

* Coalescence is expected to be more difficult in the elements than in the compounds because of the bonding at the Lomer dislocation discussed above.

VOL. 8 1960

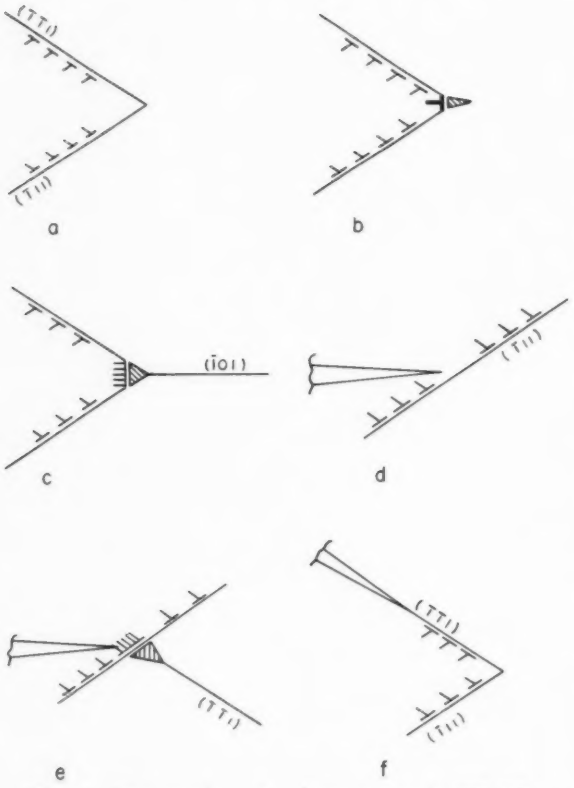


FIG. 5. The creation of a cleavage step in IIIb–Vb compounds: (a) glissile dislocations on intersecting {111} planes; (b) the formation of a Lomer dislocation and cleavage knife due to the interaction of the dislocations in (a) near the line of intersection of the {111} planes; (c) the formation of additional Lomer dislocations and their coalescence to produce a microcrack leading to cleavage on the (10$\bar{1}$) plane; (d) the advancing crack in (c) approaching a {111} slip plane containing 60° dislocations; (e) the initiation of a cleavage step by the motion and coalescence of the dislocations in (d); (f) the termination of the step when the crack in (e) reaches the vicinity of dislocations lying on intersecting {111} planes, followed by the reoccurrence of the processes in (a), (b) and (c).

from Fig. 5c is shown intersecting the trace of a {111} slip plane containing 60° dislocations. Under the influence of the stress field of the advancing crack, motion and coalescence of some of these dislocations may occur, forming a microcrack on a {111} plane (i.e. the half-plane structure of a 60° dislocation lies parallel to {111}). The crack follows this octahedral plane until it reaches the vicinity of dislocations lying on intersecting {111} slip planes. Under the combined action of the applied stress and the stress field of the crack, the situation shown in Fig. 5a, b and c reoccurs, and the cleavage reverts to the dodecahedral pattern.

In Fig. 2, cleavage step edges were observed lying in ⟨110⟩ and ⟨211⟩ directions. Although positive identification of the planes associated with the steps is not possible, these directions can correspond to the intersection of {111} planes with {110} planes. By properly choosing the {111} orientation of the half-planes associated with the dislocations lying on the intersected slip plane of Fig. 5d, the above model accounts for the appearance of these directions, if it is assumed that the planes associated with both types of steps are {111}. Cleavage on this plane has been observed in InSb, InAs, InP and GaSb.[3]

The model can also account for the appearance of the observed ⟨111⟩ directions. Since the line of intersection of two {110} planes can lie in this direction, it is assumed that the plane associated with the step is of this type. In this case the obstacle is not a single plane, but two intersecting {111} planes containing slip dislocations, and the cleavage step results from a Lomer reaction, just as in the initiation of the principal crack.

(e) *On the cracks produced by indentation*

It will be shown now that the ideas presented so far are able to explain both the orientation and symmetry of the crack pattern recorded in Fig. 3a.

In the first place, the idea that dodecahedral cleavage results from the growth of a microcrack produced by the formation and coalescence of Lomer dislocations is consistent with the observation that the cracks lie parallel to {110} planes. In the second place, the idea that the microcracks grow first, if at all, on those {110} planes on which the normal stress is greatest explains the fact that the cracks are parallel to ($\bar{1}$10), (0$\bar{1}$1) and ($\bar{1}$01). This follows from a consideration of the triaxial stress system produced by the conical indenter. The compressive and tangential components are most effective at opening a crack when they act on planes normal to the plane of indentation, while the radial component is indifferent to orientation in this case. The {110} planes normal to the (111) plane of indentation are the observed ($\bar{1}$10), (0$\bar{1}$1) and ($\bar{1}$01) planes.

Finally, we must consider why the crack pattern exhibits only three-fold symmetry when the intersection of the three aforementioned planes at a point on the (111) surface exhibits six-fold symmetry. Presumably, Lomer formation is not confined to any particular set of intersecting {111} planes provided that the operative shear stress on these planes is sufficient to cause dislocation motion; however, it is believed that the resulting microcracks will grow only on those planes where the normal stress is of sufficient magnitude. For the orientation under consideration, the Lomer axes have the form ⟨110⟩, where the indices are all of the same sign and lie in

those planes on which the maximum normal stresses are developed.

If we consider, for example, the $(\bar{1}11)$ plane containing a reactant dislocation parallel to $[101]$, this 60° dislocation can have either $[110]$, $[\bar{1}\bar{1}0]$, $[0\bar{1}1]$ or $[01\bar{1}]$ as its Burgers vector direction. Reference to Fig. 6 will show that each of these dislocations can combine with a specific dislocation lying in $(11\bar{1})$ to form a Lomer dislocation having a $[101]$ or $[\bar{1}0\bar{1}]$ axis. There are thus four reactions possible between dislocations lying in this pair of reactant planes. These reactions are,

$$\frac{a}{2}[0\bar{1}1] + \frac{a}{2}[\bar{1}10] \rightarrow \frac{a}{2}[\bar{1}01] \tag{3}$$

$$\frac{a}{2}[\bar{1}\bar{1}0] + \frac{a}{2}[011] \rightarrow \frac{a}{2}[\bar{1}01] \tag{4}$$

$$\frac{a}{2}[01\bar{1}] + \frac{a}{2}[1\bar{1}0] \rightarrow \frac{a}{2}[10\bar{1}] \tag{5}$$

$$\frac{a}{2}[110] + \frac{a}{2}[0\bar{1}\bar{1}] \rightarrow \frac{a}{2}[10\bar{1}]. \tag{6}$$

Reactions (3) and (4) produce the same Lomer dislocation while reactions (5) and (6) produce the Lomer of opposite sign. It will now be indicated why either of the first two reactions proceeds more readily than the last two. Choosing $[101]$ as the direction of positive advance* along the axes of all the dislocations in equations (3)–(6), we can determine the directions of their extra half-planes. Under this convention, the extra half-planes of all the dislocations in either equation (3) or (4) will be directed toward the interior of the tetrahedron shown in Fig. 6. The dislocations in equations (5) and (6) are the negatives of those on the corresponding glide planes in equations (3) and (4). Since the stress field decreases rapidly with distance away from the indenter, and because glide is difficult at room temperature in these materials, dislocation motion on the plane segments making up the tetrahedron will predominate over dislocation motion on the extension of these planes beyond their line of intersection. Also, the shear stress component which moves dislocations toward the Lomer axes under consideration will be greater on the planes drawn, than on the parallel planes lying on the opposite side of the indenter. Therefore, we can confine our attention to dislocations gliding on the plane segments bounding the tetrahedron. It will be noted that the reactant dislocations appearing in equations (3) and (4), and lying close to the $[101]$ Lomer axis will move toward this line where the Lomer reaction can take place. On the other hand, the reactants in equations (5) and (6) will move away from the position at which they could combine. In addition, it is apparent that any reactant dislocations produced by the operative stress system will be of the type in equations (3) and (4), rather than in equations (5) and (6). Thus, since a majority of the Lomer reactions are of the type given in equations (3) and (4), the "cleavage knives" of the resulting Lomer dislocations will point in a preferred direction. The microcrack resulting from coalescence of the Lomers also will point in this direction of preferred orientation. Therefore, under the action of a sufficient normal stress, the development of a crack from this microcrack will apparently proceed in only one direction from the origin.

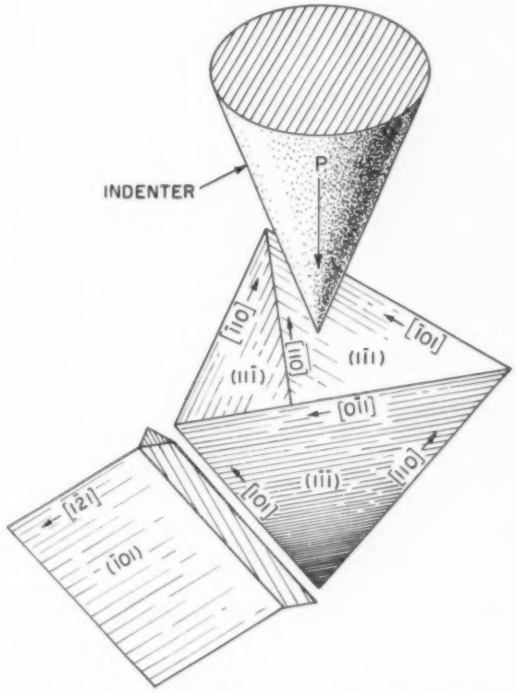


FIG. 6. Indentation of a (111) plane. The operative glide planes are shown along with their intersections which represent the three favorable Lomer dislocation axes. The crack along $(\bar{1}01)$ is indicated.

Due to the three-fold symmetry of the [111] axis, two additional cracks must form, resulting in an overall pattern consisting of three cracks oriented 120° from one another. Viewed normal to the (111) surface of indentation, the intersections of the cracks with this surface lie in the $[1\bar{2}1]$, $[\bar{2}11]$ and $[11\bar{2}]$ directions. If these directions are considered to originate at a point centered on an etch pit, they will appear to emanate from the midpoints of the sides of

* The definition of this sign convention will be found in W. T. READ, *Dislocations in Crystals*, p. 33 McGraw-Hill, New York, (1953).

VOL. 8 1960

the etch pits, in agreement with the cleavage geometry in Fig. 3a.

It is apparent that any theory attempting to establish the (*hkl*) plane as the cleavage plane of a crystal, which is based solely on the properties (e.g. interplanar spacing, atom density, surface energy, etc.) of the (*hkl*) plane relative to those of other planes, cannot explain the occurrence of the three-fold symmetry of the crack pattern.

ACKNOWLEDGMENTS

The authors would like to express their appreciation to G. W. Neighbor for performing the X-ray analyses and to S. G. Ellis and F. D. Rosi for constructive criticism of the manuscript.

REFERENCES

1. R. Scharizer, *Z. Kristallogr.* **55,** 440 (1920).
2. H. Pfister, *Z. Naturf.* **10a,** 79 (1955).
3. G. A. Wolff, *Acta Cryst. Camb.* **12,** 313 (1959).
4. H. F. G. Winkler, *Heidelberg. Beitr. Min.* **2,** 255 (1950).
5. H. A. Schell, *Z. Metallk.* **48,** 158 (1957).
6. J. W. Allen, *Phil. Mag.* **2,** 1475 (1957).
7. A. H. Cottrell, *Trans. Amer. Inst. Min. (Metall.) Engrs.* **212,** 192 (1958).
8. W. M. Lomer, *Phil. Mag.* **42,** 1327 (1951).
9. F. L. Vogel, Jr., *Acta Met.* **6,** 532 (1958).
10. T. L. Johnston, R. L. Stokes and C. H. Li, *Acta Met.* **6,** 713 (1958).
11. G. C. Kuczynski and R. F. Hochman, *J. Appl. Phys.* **30,** 267 (1957).
12. W. Shockley, *Phys. Rev.* **91,** 228 (1953).
13. W. T. Read, Jr., *Phil. Mag.* **45,** 775 (1954).
14. C. Kolm. Private communication.
15. A. N. Stroh, *Proc. Roy. Soc.* A**223,** 409 (1954).
16. A. N. Stroh, *Advanc. Phys.* **6,** 418 (1957).
17. A. N. Stroh, *Phil. Mag.* **1,** 489 (1956).

Knight shifts in potassium, indium and yttrium metals*

Information about the conduction electron wavefunction in a metal or alloy may be obtained from measurements of the Knight shifts of the nuclear magnetic resonance of the constituent nuclei Although the Knight shifts of many metals have been measured, several shifts have not been reported because of inconveniently low resonance frequencies or nuclear quadrupole effects. We report here the shifts in potassium, indium, yttrium metals. These Knight shifts were measured with a Varian Associates Model V-4200B wide-line nuclear magnetic resonance spectrometer. The interval between the centers of the nuclear resonances in the metal and in a diamagnetic reference sample were measured using the dispersion mode of the nuclear magnetic resonance signal. In the dispersion mode, the location of the resonance center is insensitive to the position of the noise baseline of the recorded trace.

The potassium sample of reagent grade was dispersed in sodium-dried xylene. Particle size averaged less than 40 μ, significantly smaller than the skin depth of 90 μ. The reference used for the Knight shift was a saturated aqueous solution of potassium formate (HCOOK). The results of the measurement are summarized in Table 1. Sufficient data on potassium are present in the literature to permit calculating the probability density at the nucleus in the atom, $|\psi_A(0)|^2$, and in the metal, $\langle|\psi_F(0)|^2\rangle_{\text{av}}$, and their ratio from the following equations.[1]

$$|\psi_A(0)|^2 = P_A = (3/16\pi)\,(I/\mu_I)\,(a(s)/\mu_B)$$

$$\langle|\psi_F(0)|^2\rangle_{\text{av}} = P_F = (3/8\pi)\,(\Delta H/\chi_p \Omega H)$$

$$\xi = P_F/P_A.$$

Calculation gives $P_A = 1.1086$ Bohr units,

$P_F = 1.035$ Bohr units,

$\xi = 0.934$.

The values $\chi_P = 0.6 \times 10^{-6}$ e.g.s. volume units[2] and $a(s) = 7.7011 \times 10^{-3}$ cm^{-1}[3] were used. The above value of ξ agrees well with the corresponding values of this quantity given for the other alkali metals by Benedek and Kushida[1].

Indium in the solid state does not yield a nuclear magnetic resonance because of the large nuclear quadrupole interaction.[4] Thus, indium of high purity, supplied by the Consolidated Mining and Smelting Co. of Canada, was dispersed in silicone oil (particle size less than 20 μ, skin depth 46 μ) and the nuclear magnetic resonance recorded in the molten state. It was possible, after melting the sample at 155°C, to observe the resonance at temperatures as low as 130°C because of supercooling. The resonance shift measured with respect to a saturated aqueous solution of indium tribromide ($InBr_3$) was found to be independent of temperature within experimental error. The results are summarized in Table 1.

Yttrium of better than 99.9 per cent purity was filed to give an average particle size much less than the skin depth of 280 μ. The shift relative to a saturated hydrochloric acid solution of yttrium trichloride (YCl_3) is reported in Table 1. For some of the measurements, a small amount of ferric chloride was added to the yttrium trichloride reference solution to decrease its value of T_1 and hence permit the use of higher r.f. power levels. The addition of the paramagnetic ion caused no apparent shift in the resonance frequency of the standard. Because of its hexagonal crystal structure, yttrium would be expected to give an anisotropic Knight shift.[5] However, the signal-to-noise ratio of the absorption mode was too small to determine the magnitude of the anisotropy.

The authors wish to thank Dr. A. H. Daane of this laboratory for supplying the yttrium sample. They also thank Mr. R. A. Hultsch for some of the preliminary work on indium.

Institute for Atomic Research and Department of Physics
Iowa State University
Ames, Iowa

W. H. Jones, Jr.
T. P. Graham
R. G. Barnes

* Contribution No. 837. This work was performed in the Ames Laboratory of the U.S. Atomic Energy Commission. Received January 11, 1960.

Table 1. Summary of relevant Knight shift data for potassium, indium and yttrium

Nucleus	Reference	Temperature (°C)	Magnetic field (oe)	$\Delta H/H$ (%)
K^{39}	HCOOK (aq)	25	12,400	0.265 ± 0.002
In^{115}	$InBr_3$ (aq)	130–200	10,300	0.794 ± 0.002
Y^{89}	YCl_3 (in HCl)	25	10,200	0.337 ± 0.005

VOL. 8 1960

References

1. G. B. Benedek and T. Kushida, *J. Phys. Chem. Solids* **5**, 241 (1958).
2. D. Pines, *Solid State Physics* Vol. 1, p. 419. Academic Press, New York (1953).
3. H. Kopfermann, *Nuclear Moments*, p. 316. Academic Press, New York (1958).
4. W. D. Knight, *Phys. Rev. Letters* **3**, 18 (1959).
5. N. Bloembergen, *Canad. J. Phys.* **34**, 1299 (1956).

Residual resistance of copper annealed in an O_2 atmosphere*

Measurements have been made of the residual resistivity at 4.2°K ($\rho_{4.2°K}$) of high purity copper polycrystalline specimens. Upon annealing in vacuum ($\sim 10^{-5}$ mm Hg) at different temperatures >400°C, which should be sufficient to anneal out most physical defects,[1] $\rho_{4.2°K}$ was found to vary with the annealing temperature. Recently it has been shown[2] that the presence of oxygen or chlorine in the annealing atmosphere will enhance the electrical annealing of copper and improve the resistance ratio $\rho_{273°K}/\rho_{4.2°K}$. Since a trace of oxygen may be present in most vacuum annealing, a determination was made of the optimum conditions for the annealing of copper in an oxygen atmosphere.

Presumably the oxygen diffuses into the copper during annealing and in some manner neutralizes the effectiveness of certain existing impurities which act as scattering centers.[3] Thus the increase in number of neutralized scattering centers caused by the oxygen could be expected to depend upon the time and temperature of the anneal, as well as the concentration of the oxygen in the ambient atmosphere. Using a constant anneal time of 4 hr, measurements were made of the influence of annealing temperature and oxygen concentration on the residual low temperature resistivity of specimens prepared from successive lengths of the same high purity wire.† Typical results are given in Fig. 1.

Optimum annealing for these specimens is seen to yield a maximum resistance ratio of about 1000. The data suggest that oxygen absorbed into the copper is not only effective in neutralizing certain scattering centers, but when present in excess contributes new scattering centers. For a given oxygen concentration an increase of the annealing temperature permits more rapid diffusion of the oxygen into the copper with consequent improvement (increase) in resistance ratio up to a maximum value representing optimum balance of neutralization of existing centers and the contribution of new scattering centers introduced by excess absorbed oxygen. Further diffusion of oxygen into the metal results in a net increase in scattering centers with resulting degradation of the resistance ratio. The peak is broadened and the degradation seems to be less pronounced (if present) at very low oxygen concentrations.

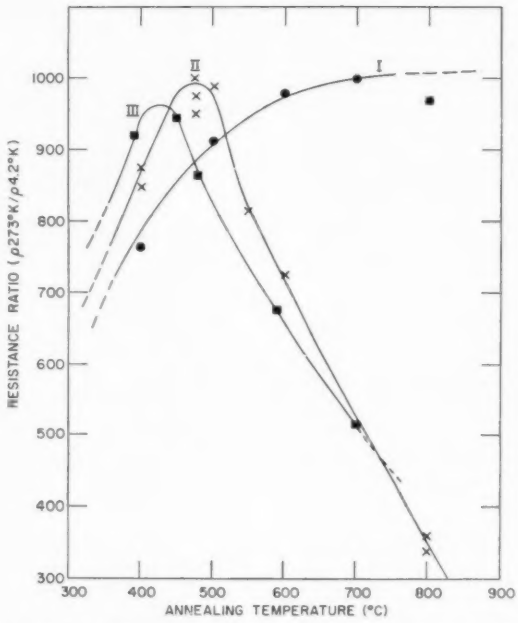


Fig. 1. Influence of temperature and oxygen concentration during annealing on the residual low temperature resistivity of copper. The resistance ratio $\rho_{273°K}/\rho_{4.2°K}$ is plotted as ordinate and the temperature of annealing as abscissae. Curve I (circles) is for high vacuum annealing ($<10^{-5}$ mm Hg), Curve II (crosses) for an ambient atmosphere (air) of 20 μ and Curve III (squares) for 50 μ.

The relatively high peak resistance ratio obtained would have been thought to indicate a well-annealed, high purity copper specimen. The even higher ratios reported by others[4] and for natural copper crystals may be due to higher over-all purity, to the presence of less effective impurities or a combination of both. However, since enhancement of the resistance ratio can apparently result from the neutralization of impurities, larger resistance ratios do not necessarily mean chemically purer samples as it could be the result of more, other or different types of compensations. Also, the nature of the neutralized centers is unknown and their properties may differ considerably from the normal scattering centers of pure copper.[5] The existence of neutralization of electron scattering

† 99.999 per cent pure copper (American Smelting and Refining) drawn into 0.039 cm diameter wires and furnished to us through the courtesy of Dr. H. Sherman of the Los Alamos Scientific Laboratory.

centers lends direct support to the conclusion of van den Berg[6] that "an absolute purity scale of metals cannot be based on the measurements of residual resistance of single crystals or polycrystalline wires".

U.S. Naval Research Laboratory R. L. Dolecek
Washington, D.C. D. J. Schultz

References

1. H. G. van Bueren, *Philips Res. Rep.* **12,** 190–239 (1957).
2. J. K. Redman, R. R. Coltman, T. H. Blewitt and C. F. Klanbunde, *Bull. Amer. Phys. Soc.* **4,** 150 (1959).
3. J. S. Smart and A. A. Smith, *Trans. Amer. Inst. Min. (Metall.) Engrs.* **147,** 48 (1942).
4. J. E. Kunzler and J. H. Wernick, *Trans. Amer. Inst. Min. (Metall.) Engrs.* **212,** 856 (1958).
5. S. T. Sekula, *Phys. Rev. Ltrs.* **3,** 416 (1959).
6. G. J. van den Berg, *Supplement au Bulletin de l'Institute International du Froid, annexes* 2, 31 (1956).

* Received February 8, 1960.

Effect of grain size on crack propagation*

Currently there is much interest in increasing the fracture resistance of materials by decreasing their grain sizes. This interest is based upon the fact that the fracture stresses of some materials (notably steels) vary as $S^{-1/2}$ where S is the average grain diameter. Although this behavior is observed for a fairly wide range of grain sizes, it is obvious that it cannot hold for very small grain sizes. If it did, very small grain size would give infinite fracture strength. The factors that determine the fracture resistance as the grain size approaches zero will be discussed.

By resistance to fracture we mean the resistance that the material offers to the motion of a crack that is large compared to the grain size of the material. A measure of this resistance is the fracture-surface energy, γ_F (ergs/cm^2). This is an *effective* surface energy which includes the energy dissipated at cleavage steps, by plastic flow, etc.

We assume that the grain boundaries of the material are clean so that premature fracture does not occur at them. Three cases must be considered: ductile, brittle, and ductile–brittle materials.

Case I (*ductile*). High fracture resistance, no grain size effect because once the material begins to deform the grain boundaries are obliterated.

Case II (*brittle*). The grains cleave and many steps are formed at the boundaries where the cleavage planes are misaligned. However, since the steps are not localized to the grain boundaries but tend to run straight across the grains, the concentration of steps will not vary much with grain size although it will depend on the relative orientations of the grains. Also, the effect of the steps on the fracture resistance will be relatively small. Since the fracture is completely brittle, the total specific surface area of the steps, and their risers, times the true surface energy (γ) of the material will give the fracture surface energy, γ_F. γ is typically about 10^3 ergs/cm^2 and the total surface area will seldom exceed 5 times the projected surface area. Therefore γ_F will not exceed about $5\gamma = 5 \times 10^3$ ergs/cm^2. Thus grain size is not expected to have large effects in this case, provided our assumption of clean boundaries is fulfilled.

Case III (*ductile–brittle*). In this case the crack propagation will tend to be discontinuous; that is, grains ahead of an advancing crack will tend to cleave before the main crack reaches them. Then, since the plane of the main crack and the planes of the premature cracks will not be co-planar, ductile tearing will occur at the grain boundaries when the cracks join up. The ductile tearing will be localized to regions along the grain boundaries that have a thickness, d. The disturbed regions will extend beneath the surface to a depth $\simeq d$, so the volumes of these regions per unit length will be $\simeq d^2$. The number of boundary regions per cm^2 of surface area will be $\simeq 2/S$; so the volume of material that is involved in ductile tearing is $\simeq 2d^2/S$ per cm^2 of surface.

It seems reasonable that d will tend to be a constant, d_0, for large grain sizes where the properties of the grain boundaries will determine its value. However, when the grain size becomes equal to d_0, then d must become equal to the grain size. This results because the concentrated stresses due to a given cracked grain do not extend more than a distance $\simeq S$ from the cracked grain.

The energy that is absorbed during plastic flow is $\sigma_y \varepsilon_P$ where σ_y is the flow stress, and ε_P is the plastic strain. Most materials fail by ductile fracture when the plastic work is less than $\sigma_y \varepsilon_P \simeq 5 \times 10^8$ ergs/cm^3. Therefore, it is proposed that the fracture surface energy for ductile–brittle fracture is:

$$\gamma_F = \gamma + \gamma_P \simeq \frac{2d^2}{S}(\sigma_y \varepsilon_P) \simeq 10^9 \frac{d^2}{S} \text{ (ergs/cm}^2\text{)}$$

where

$$d = d_0 \quad \text{for} \quad S \geqslant d_0 \quad \text{and} \quad d = S \quad \text{for} \quad S \leqslant d.$$

Thus the fracture-surface energy increases with decreasing grain size up to a maximum value (Fig. 1) and then decreases to γ with further decrease in the grain size. At the maximum (when $S = d_0$):

$(\gamma_F)_{\max} \simeq 10^9 S =$	if $d_0 =$
10^4 ergs/cm^2	1 μ
10^5 ergs/cm^2	10 μ
10^6 ergs/cm^2	100 μ.

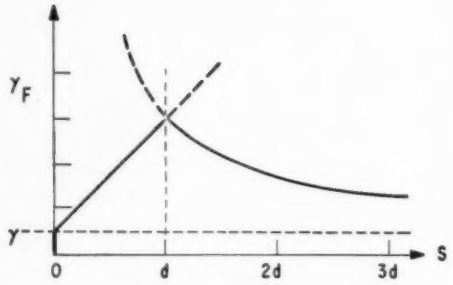


FIG. 1. Variation of fracture-surface energy with grain size for ductile–brittle fractures.

These values have approximately the right order of magnitude for the particular case of iron.

This analysis indicates that one cannot improve the fracture resistance of materials indefinitely by simply decreasing their grain sizes. A point of diminishing returns exists; probably at a grain size of about 1 μ for typical materials. In completely brittle substances, grain size should have little effect on fracture resistance. In the cases where such effects have been reported, the effects have probably been caused by impurities that have been segregated at the grain boundaries.

J. J. GILMAN

General Electric Research Laboratory
Schenectady, New York

* Received January 25, 1960.

Athermal stabilization of austenite*

In a recent note[1] on the stability of retained austenite on ageing, the authors have examined the role of martensite in setting up an adequate concentration gradient for carbon, to permit its interstitial diffusion towards and neutralization of the strain embryos in the retained austenite, rendering it correspondingly stable. It has been indicated that for diffusion to take place, a concentration gradient must be set up, but as the probability of such a gradient being set up by microsegregation of the carbon atoms in austenite is vanishingly small, it could arise only from the carbon-rich regions formed near the associated martensite phase. From rather different considerations, Cohen and others[2] have recently arrived at a similar conclusion, that the stabilization of austenite should be understood with particular reference to the associated martensite phase.

In this note, the above concepts regarding the stabilization of retained austenite have been extended to its athermal stabilization, when directly cooled.

Although microscopically detectable martensite will not be found in austenite unless cooled to the M_s temperature or lower, the possibility of martensite nuclei or of sub-microscopic martensite existing above the M_s temperature cannot be ruled out. The concept of martensitic embryos put forward by Fisher, Hollomon and Turnbull[3] may be mentioned in this connexion. In the face-centred cubic austenitic lattice could be visualized small groups of iron atoms, taking up configurations corresponding to a body-centred structure and initially possessing a size, insufficient to enable them to be microscopically recognized as martensite but capable of subsequent growth to recognizable martensitic regions. These groups of atoms may be considered to constitute "pre-martensite zones" similar to the G–P zones arising in Al–Cu and other age-hardening systems and to retain carbon atoms interstitially in a state of considerable supersaturation and activity. Regions near these zones could conceivably become carbon-rich, setting up a concentration gradient for carbon, resulting in its diffusion towards strain embryos of the austenite, as with retained austenite and its associated martensite phase.

The diffusion would be at speeds determined by temperature and concentration gradients and the stabilization of austenite would take place at times determined by these speeds, as the distances which carbon atoms are to migrate to reach strain embryos can be calculated. Comparison of these diffusion times with the times taken by austenite to cool through any range of temperature when quenched in various media, will determine whether athermal stabilization can take place and can also be observed to take place.

Migration speeds for interstitial diffusion of carbon atoms in austenite, for a concentration gradient of about 1 per cent calculated from the data of Harris[4], over the ranges of temperature, 350–500°C, 200–350°C and 100–200°C are approximately 10^{-4} cm/hr, 10^{-6} cm/hr and 10^{-7} to 10^{-8} cm/hr respectively, giving times required for stabilization to take place, over these ranges of temperature, of the order of 1 sec, 100 sec and a few hours respectively. (The average distance separating two carbon atoms in a 1 per cent carbon, homogenized austenite is approximately 6×10^{-8} cm and the distance which a carbon atom, has, on the average, to diffuse to reach a strain embryo is hence approximately 3×10^{-8} cm.) When actual cooling times of austenite over these ranges of temperature when quenched in different media are either too small or too large compared to the times required for stabilization, differences in austenite stability and final austenite content, when quenched

in these media, will not be detected. Differences in austenite content and stability, when quenched in different media, will be detectable only if the migration times (times required for stabilization) are intermediate in value to the times taken by austenite to cool over these temperature ranges during quenching.

Thus, when quenched in a salt bath and in an air furnace, austenite requires times much longer than about 1 sec to cool from 500 to 350°C and hence, would be stabilized to practically the same extent in both the quenches and no difference in the final austenite content can therefore be observed. Over the range 200–350°C, however, austenite cools in most salt or oil baths in a few seconds, but over considerably longer times (several hundred seconds) when cooled in an air furnace. As the time required for stabilization is of the order of 100 sec, austenite, when cooled in an air furnace would be stabilized but not when quenched in a salt bath. Differences in austenite content would, therefore, be observed between the two quenches. Again, over the range 100–200°C, both liquid and air quenching will cool austenite, in times very much shorter than the time required for carbon atoms to migrate 3×10^{-8} cm and stabilize the austenite and hence, once again no difference in stability and the final austenite content would be observed.

Athermal stabilization of austenite would, therefore, be normally observed to take place over a particular range of temperature, depending upon the quenching media used. With generally used quenching media, like salt and oil baths and air, this range will normally be about 200–350°C. With special quenching media, other ranges will become operative. It will be appreciated that these temperature ranges and the demarcation temperatures between them are approximate, but it would appear that the range of temperature over which athermal stabilization of austenite is most clearly observed, is not particularly related to the M_s temperature of the steel.

Experimental proof of the above conclusions is available from the authors' investigation[5] on the athermal stabilization behaviour when quenched at different rates, in aqueous, salt, oil and air baths over a temperature range of approximately 18–600°C, of the austenite of both a high-carbon, high-chromium die steel and a low-carbon, low-chromium tool steel as well as from the experimental observations of Morgan and Ko[6] on a nickel steel. The athermal stabilization range in the two chromium steels has been found to be approximately 180–350°C. For the nickel steel, investigated by Morgan and Ko, the range is somewhat higher, approximately 300–400°C, even though the M_s temperature is actually lower. The lower range in the chromium steels can well be attributed to the higher affinity for carbon of chromium as compared to nickel and the greater tendency for the pre-martensite zones to be formed in austenite containing chromium as compared to austenite containing nickel, because of the less perfect lattice registry between austenite and chromium as compared to austenite and nickel.

We thank Dr. B. R. Nijhawan, Director, National Metallurgical Laboratory for discussion and permission to publish this note.

E. G. Ramachandran
C. Dasarathy

Physical Metallurgy Division
National Metallurgical Laboratory
Jamshedpur-7, India

VOL. 8 1960

References

1. E. G. Ramachandran and C. Dasarathy, *Acta Met.* **8,** 274 (1960).
2. J. Woodila, P. G. Winchell and M. Cohen, *Trans. Amer. Inst. Min. (Metall.) Engrs.* **215,** 849 (1959).
3. J. C. Fisher, J. H. Hollomon and D. Turnbull, *J. Appl. Phys.* **19,** 775 (1948).
4. W. J. Harris, *Metal Progr.* **2,** 44 (1943).
5. E. G. Ramachandran and C. Dasarathy, to be published.
6. E. R. Morgan and T. Ko, *Acta Met.* **1,** 36 (1953).

* Received January 21, 1960.

VOL
8
196

DISCONTINUOUS MODE OF DISSOLUTION OF A β PHASE PRECIPITATE INTO α Cu–Cd SOLID SOLUTIONS*

M. S. SULONEN†

A discontinuous mode of process apparently occurs, under certain circumstances, at dissolution of a solid phase into another. It has been found at dissolution of β precipitate into α Cu–Cd solid solutions and studied by metallographic and X-ray methods.

The process occurs by formation of dissolved regions, nearly simultaneously, at all the matrix grain boundaries and growth of regions, at time-independent rate, into the grain interiors. The dependence of isothermally dissolved volume fraction x on solution time t agrees with a kinetic law of form $x = 1 - \exp(-Bt^{1.1})$, B being a parameter.

The activation energy, Q, for growth resulting in complete dissolution is 21 kcal/g at., which, together with some other data, suggests that the process is controlled by grain boundary diffusion along the transformation front. For growth in the $\alpha + \beta$ range Q is as high as 100–160 kcal/g at. which is explicable on the basis of the retarding effect of undissolved β on growth. The free energy relations and the origin of the driving force are also discussed.

DISSOLUTION DISCONTINUE D'UN PRECIPITE DE PHASE DANS UNE SOLUTION SOLIDE DE CuCd–α

Sous certaines conditions, la dissolution de deux phases l'une dans l'autre peut s'opérer de façon discontinue.

L'auteur a observé ce phénomène lors de la dissolution d'un précipité de phase β dans une solution solide d'αCuCd.

Il a étudié ce phénomène au moyen de diverses techniques: observation métallographique et rayons X.

Le processus a lieu par formation de régions de dissolution simultanément aux frontières des grains et par croissance de ces régions à une vitesse indépendante du temps vers l'intérieur des grains. La fraction x du volume en dissolution isotherme dépend du temps de mise en solution t suivant une loi cinétique de la forme:

$$x = 1 - \exp(-Bt^{1.1})$$ B étant une constante.

L'auteur a montré que l'énergie d'activation Q, pour une dissolution totale est de 21 kcal/g. at. De ceci, il formule l'hypothèse que la dissolution a lieu sous l'action du phénomène de diffusion entre les grains. Pour la solubilisation d'une phase $\alpha + \beta$ l'énergie d'activation Q est de l'ordre de 100 à 160 kcal/g. at. ce qui s'explique par le fait que la phase β non dissoute retarde la propagation de la dissolution à l'intérieur des grains. L'auteur examine aussi la relation entre l'énergie libre et la force occasionnant le déplacement des régions dissoutes.

UNSTETIGER VERLAUF DER AUFLÖSUNG VON AUSGESCHIEDENER β-PHASE ZUR FESTEN LÖSUNG α-CuCd

Offenbar tritt unter gewissen Umständen bei der Auflösung einer festen Phase in einer anderen eine unstetige Art von Prozess auf. Ein solcher wurde gefunden bei der Auflösung von β-Ausscheidung in die feste Lösung-α-CuCd und mittels metallographischer und röntgenographischer Methoden studiert.

Der Prozeß verläuft so, daß sich nahezu gleizeitig an allen Korngrenzen der Matrix Lösung enthaltende Bezirke bilden und mit zeitunabhängiger Geschwindigkeit in das Innere der Körner hineinwachsen. Die Zeitabhängigkeit des Volumbruchteils x, der von der Lösung eingenommen wird, stimmt bei konstanter Temperatur mit einem kinetischen Gesetz der Form $x = 1 - \exp(-Bt^{1.1})$ überein, wo B ein Parameter ist.

Für solches Wachstum, das zur vollständigen Auflösung führt, beträgt die Aktivierungsenergie Q 21 kcal/g-At.; zusammen mit anderen Gründen spricht das dafür, daß die Geschwindigkeit durch Korngrenzendiffusion entlang der Umwandlungsfront bestimmt wird. Für Wachstum im Bereich $\alpha + \beta$ hat Q den hohen Wert 100 bis 160 kcal/g-At.; das läßt sich erklären, wenn man einen verzögernden Einfluß von noch nicht aufgelöster β-Phase auf das Wachstum annimmt. Die Beziehungen zwischen den Freien Energien und der Ursprung der treibenden Kraft werden diskutiert.

INTRODUCTION

Dissolution of a solid phase into another has been generally considered to be a process essentially occurring by volume diffusion, whereas grain boundary diffusion would take part only in the very small volume fraction consisting of the grain boundaries and their nearest neighborhood. The role played by grain boundary diffusion in dissolution may, however, become even a predominating one. This may happen when the rate of grain boundary diffusion considerably exceeds that of volume diffusion, and when, in addition, grain boundaries move through the heterogeneous structure dissolution taking place simultaneously. Since the boundaries in such a case act as sweeping diffusion short-circuits, dissolution

* Received January 7, 1960.

† Laboratory of Physical Metallurgy, Institute of Technology, Helsinki, Finland.

VOL. 8 1960

would be accomplished more rapidly than by action of volume diffusion.

Grain boundary motion is expected to originate, at least under certain circumstances, in the boundary dissolution process itself. This can provide a driving force for boundary motion analogically with discontinuous precipitation. Hence, in that case, the process could be assumed to have characteristics in some respects related to that of the discontinuous mode of precipitation. In fact, some single observations reported by Ageew *et al.*[1] and Margolin and Hibbard[2] seem to be in accordance with this assumption.

The present work was done to obtain more information about the discontinuous mode of dissolution. After some preliminary investigations had indicated the existence of the process in Cu–Cd alloys, these were chosen for the purpose. Later experiments with Cu–Ag,[3] Ag–Cu and Pb–Sn alloys have ascertained the process in these alloys, too.

The copper–cadmium system

The maximum limit of solid solubility of Cd in α Cu–Cd solid solutions, 4.5 wt.% Cd, is reached at 650°C which is about 100°C above the peritectic temperature, 549°C, at which the next intermediate phase, β or Cu_2Cd phase, forms on solidification.[4] The solidus line is thus of the retrograde type. The β phase has an extremely narrow range of solid solubility. The position of the $\alpha/\alpha+\beta$ solvus line can be expressed as[5]

$$\log_{(10)} X_e = -\left(\frac{1750}{T}\right) + 0.40$$

where X_e is the atomic fraction of Cd in α Cu–Cd solid solution at the solubility limit at T°K.

Precipitation of β out of supersaturated α occurs almost exclusively by the discontinuous mode.[5] Here two alternative mechanisms exist. At high supersaturations, $X_0/X_e > 1.5$ (X_0 = atomic fraction of Cd in supersaturated α), the "ordinary" mechanism appears. The result is a needle formed β precipitate embedded with rigid orientation relationship in depleted α which in the immediate vicinity of the transformation front contains an excess amount of about 0.5 wt.% Cd of solute. An "extraordinary" mechanism appears at lower supersaturations resulting in rounded, randomly oriented β in depleted α with practically no supersaturation.

Scope of the present work

As a first approach to the new mode of dissolution, the following points seemed especially worth studying:

(i) Morphology.

(ii) The critical temperature, T_{cr}, at which, in up-cycling, regions which have undergone discontinuous precipitation (these are called "nodules", "cells" or "colonies") at a lower temperature will have a tendency to grow by further advance of discontinuous precipitation equal to the tendency to dissolve by advance of colony boundary in the opposite direction.

(iii) Time dependence in isothermal process:

—the kinetic law of dissolution, $x = f(t)$, correlating the dissolved volume fraction, x, with the time of solution anneal, t.

—the growth rate of dissolved regions, G.

EXPERIMENTAL METHODS AND PROCEDURES

Materials

Three Cu–Cd alloys were used. These were processed[5] into cold rolled sheet materials of 1 mm thickness, out of which the actual specimens were cut into a size of about 8 × 12 mm. Analysis, made in the Chemical laboratory of the Outokumpu Metal Works, (Pori, Finland), showed the following contents of Cd and impurities in the sheet materials:

Alloy no.	Cd (wt. %)	Impurities (p.p.m.) Ag	Bi	Fe	Mn	Ni	Pb	Zn
1	1.82	10	1.5	20	7	30	50	50
2	2.75	10	—	30	2	30	50	50
3	4.21	10	3.5	42	1	45	15	—

The reduction given in the last cold rolling was chosen for each alloy appropriately to permit achieving of an equal grain size, about 0.1 mm, by recrystallization during the homogenization anneal.

Heat treatment

The procedure used in heat treatment is schematically shown in Fig. 1.

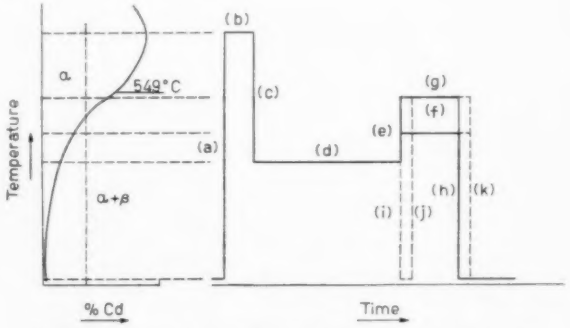


FIG. 1. Schematic representation of the heat treatment procedures (for alloy 1): (b) homogenization anneal; (d) precipitation anneal; (f,g) solution anneals (at two alternative temperature ranges); (a,c,e,h,i,j,k) up- or down-quenches.

After the homogenization anneal, which always consisted of soaking for 1 hr at 650°C, the procedure was as follows:

For the determination of T_{cr}, discontinuous precipitation was allowed to proceed to $x_{pr} = 0.2$. A number of precipitation temperatures T_{pr}, the extremes being 250 and 470°C, were used. The actual determination of T_{cr} was made by finding experimentally the value of up-cycling or dissolution temperature T_s resulting in a situation corresponding to the definition of T_{cr}. Customarily 5–7 anneals, spaced with 2–3°C intervals, were needed for a determination of T_{cr} with a reproducibility of ± 1–2°C.

For the determination of $x = f(t)$ and G, the precipitation anneal was continued to transformation of the whole volume by discontinuous precipitation, i.e. up to $x_{pr} = 1$, $T_{pr} = 350$°C being used most frequently. For T_s, temperatures with 20–30°C intervals from about T_{cr} up to 560°C were selected. The upper limit is above the melting point, 549°C, of β. At each temperature a series of different durations was needed, of course.

Occasionally, a few series of specimens were quenched after the precipitation anneal to room-temperature, instead of being up-cycled for dissolution, then cold-rolled 10 per cent in thickness and finally up-cycled for dissolution.

For the homogenization anneal a $BaCl_2 + KCl + NaCl$ bath was used, whereas for the precipitation and solution anneals $KNO_3 + NaNO_2$ baths were used. The accuracy of temperature control of the baths was respectively about ± 5, ± 2 and ± 1°C.

Microscopic and X-ray techniques

The methods of specimen preparation for microscopic and X-ray examination, as well as the method for the determination of G, were the same as those previously described.[5]

The transformed volume fractions x or x_{pr} were measured microscopically using the point counting method.

Powder X-ray photograms were made with 57.3 and 114.6 mm dia. Debye–Scherrer cameras and using K radiation from a Co anode target.

EXPERIMENTAL RESULTS

Morphology

Microscopical examination showed the appearance of the discontinuous mode of dissolution within a certain range of temperatures. The lower limit of this range apparently varies with X_0 and T_{pr} in about the same way as T_{cr} (see below). The upper limit is placed at about 600–650°C. The discontinuous dissolution plays a predominant role from about T_{cr} up to about 600°C.

The process begins at the matrix (α) grain boundaries and spreads from there on, under motion of boundaries, into the grain interiors, Figs. 2–4. The start seems to happen nearly simultaneously and uniformly along the boundaries, except the small angle grain boundaries, at which the process is evidently delayed. The resulting new α solid solution has an identical orientation with the α grain adjacent to the original grain boundary position at which the process started. However, it has no orientation relationship with the grain to be consumed, i.e. Smith's orientation law for discontinuous precipitation applies even to discontinuous dissolution. In addition, the cyclic precipitation–dissolution process results in considerable grain refinement of matrix, from the grain size of 0.1 mm to that of 0.03 mm, Fig. 4.

Lattice parameter determinations showed that solute concentration in the new α at dissolution in the $\alpha + \beta$ range is equal to X_e in alloys 1 and 2 (for $T_{pr} = 350$°C), whereas in alloy 3 it exceeds X_e by an amount which increases with increasing T_s. These supersaturations, for alloy 3, in dissolution at $T_s = 520$, 530 and 540°C were found to be 0.2, 0.4 and 0.6 wt.% Cd, respectively. Hence, in these cases, a discontinuous retrogression or reversion phenomenon is involved. Complete retrogression would apparently be expected to occur at about 550°C.

Whenever complete discontinuous dissolution occurred, microscopic examination revealed peculiar ghosts, which evidently show the former positions of the dissolution front, Fig. 5, or, less frequently, those of β particles, Fig. 6. Prolonged anneal makes the phenomenon disappear.

Critical temperature

A micrograph showing a situation characteristic for T_{cr} is seen in Fig. 7.

The experimental values of T_{cr} are given in Table 1. For alloy 3 with $T_{pr} = 250$°C, two values of T_{cr} were found, probably because of the circumstance that precipitation can occur by the ordinary as well as extraordinary mechanism at this range of T_{cr}. Apart from the lower value of T_{cr} for alloy 3 with $T_{pr} = 250$°C, T_{cr} seems to correspond to the temperature for which X_e is an average of X_0 and solute concentration of depleted matrix formed at T_{pr}.

The lattice parameter determinations made in the present work and earlier[5] allowed some calculations

VOL. 8 1960

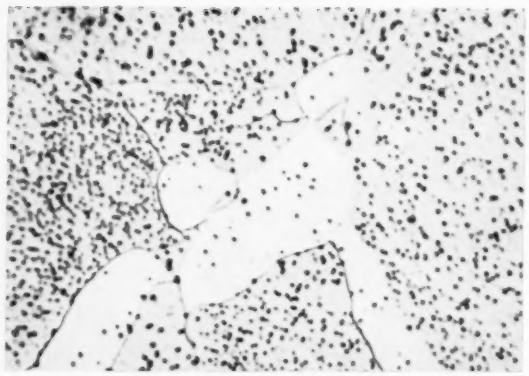


FIG. 2. A slightly advanced stage of the discontinuous dissolution process in the $\alpha + \beta$ range. The 2.75 wt. % Cd alloy solution annealed 2 min at 500°C after complete discontinuous precipitation at 350°C. ×2500

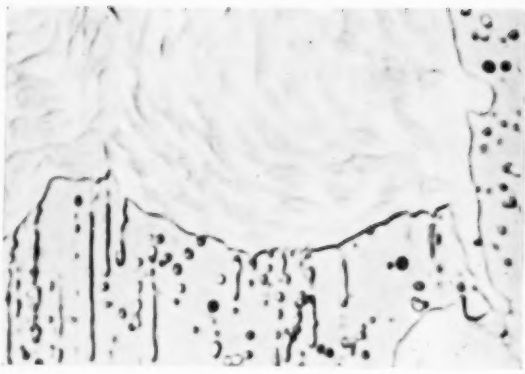


FIG. 5. Ghosted structure in the dissolved regions. The 1.82 wt. % Cd alloy solution annealed 10 min at 540°C after complete discontinuous precipitation at 350°C. ×2500

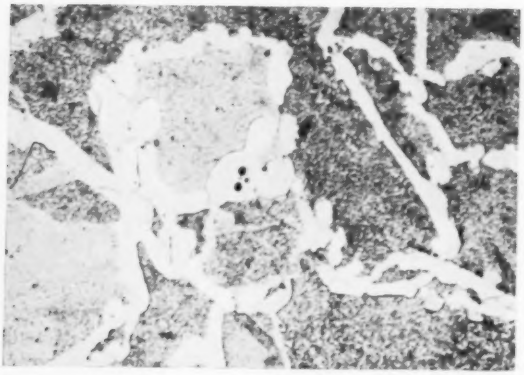


FIG. 3. A slightly advanced stage of the process in the α range. The same alloy as in Fig. 2 solution annealed 0.6 min at 540°C. ×300

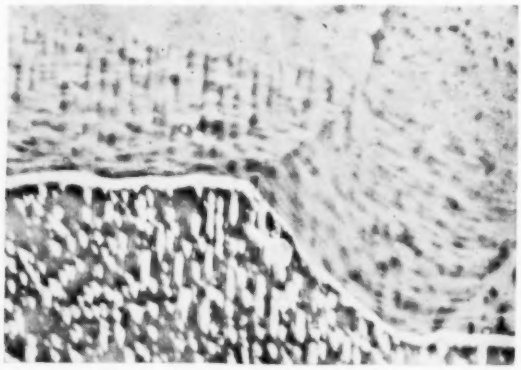


FIG. 6. A special case of ghosted structure showing the former positions of β particles. The same alloy as in Fig. 2 solution annealed, after partial discontinuous precipitation at 350°C, 1 min at 540°C. A phase contrast micrograph. ×2000

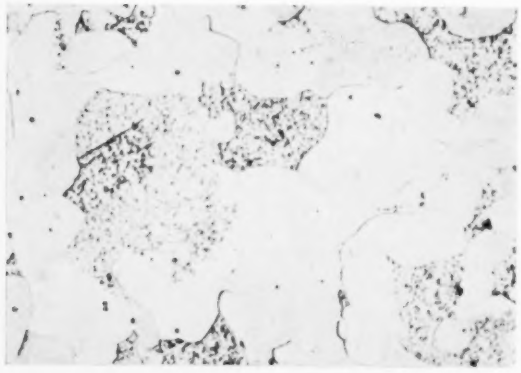


FIG. 4. A rather advanced stage of the process in the α range. The same alloy as in the above figures solution annealed 2 min at 540°C. ×300



FIG. 7. Alternating regions of discontinuous precipitation and dissolution started at $T_{cr} = 520$°C in front of a colony previously formed at $T_{pr} = 350$°C. ×1500

TABLE 1. Values of T_{cr}, ΔX_{pr} and ΔX_s

Alloy, (wt. % Cd)	T_{pr}, (°C)	T_{cr}, (°C)	ΔX_{pr}, (wt. % Cd)	ΔX_s, (wt. % Cd)
1.82	350	432	—	—
2.75	280	459	—	—
	350	478	−0.7	0.9
	400	488	−0.55	0.6
	470	499	−0.4	0.4
		494	—	—
4.21	250	504	—	—
	280	507	—	—
	350	520	−1.5	1.7
	400	531	−1.3	1.4
	450	544	−1.0	1.1

of the changes in solute concentration of α due to discontinuous precipitation and dissolution at T_{cr}, ΔX_{pr} and ΔX_s, respectively. The results are also given in Table 1. Apparently $|\Delta X_{pr}|$ and $|\Delta X_s|$ are of nearly the same magnitude, at least when T_{pr} is comparatively high.

Kinetic law

According to Fig. 8, a linear relationship generally exists, for constant X_0 and T_s, between $\log \ln(1/1-x)$ and $\log t$. Exceptions occur when T_s is near the temperature range of continuous process. Apart from these exceptions, the kinetic law of discontinuous dissolution is expressible in the form

$$x = 1 - \exp\{-(t/\tau)^n\}$$

where n equals the slope of the $\log \ln\{1/(1-x)\}$ vs. $\log t$ plot corresponding to a particular solution isotherm and τ is the duration of the solution anneal required for $x = (e-1)/e = 0.632$. The average of the values of n for isotherms in Fig. 8 is 1.1, which is just one half of the value of n obtained for precipitation isotherms.[5]

Growth rate

Since n obtains values near 1 and the process starts almost simultaneously along all boundaries, the dissolved regions evidently grow, in slab form, at a time independent rate, G, into the grains. This is shown also by the results in Fig. 9. Moreover, because extrapolation to $d = 0$ gives zero intercept at the time axis in Fig. 9, no incubation period for growth apparently exists. The retardation sometimes appearing in growth, with longer durations, is evidently caused by a simultaneous continuous process, and is also manifested in deviations from the kinetic law.

As can be seen from Table 2, G varies strongly not only with X_0 and T_s, but also, for constant X_0 and T_s, with T_{pr}.

Comparisons between the rate of colony growth in discontinuous precipitation and the rate G of dissolution, both at T_{cr}, showed these to be nearly equal.

Temperature dependence of growth rate

The graph in Fig. 10 shows that a sharp change occurs at the solvus temperature T_S (corresponding to the constitutional or metastable α/β equilibrium) in the temperature dependence of G with the change of T_s from α region into the $\alpha + \beta$ region.

Above T_S, up to the peritectic temperature, $\log G$ varies linearly with the reciprocal of the absolute solution temperature, if X_0 and T_{pr} are held constant. On the basis of this relationship an activation energy Q of 21 kcal/g at. is obtained. Below T_S, the linearity apparently is not valid and activation energies of 100–160 kcal/g at. can be derived.

It is further notable that, below T_S, for constant

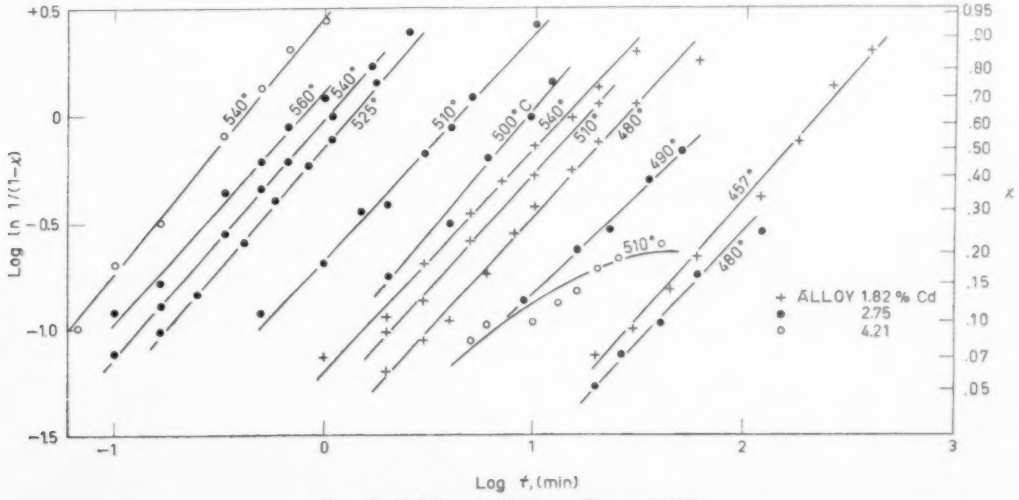


FIG. 8. Solution isotherms. $T_{pr} = 350°C$.

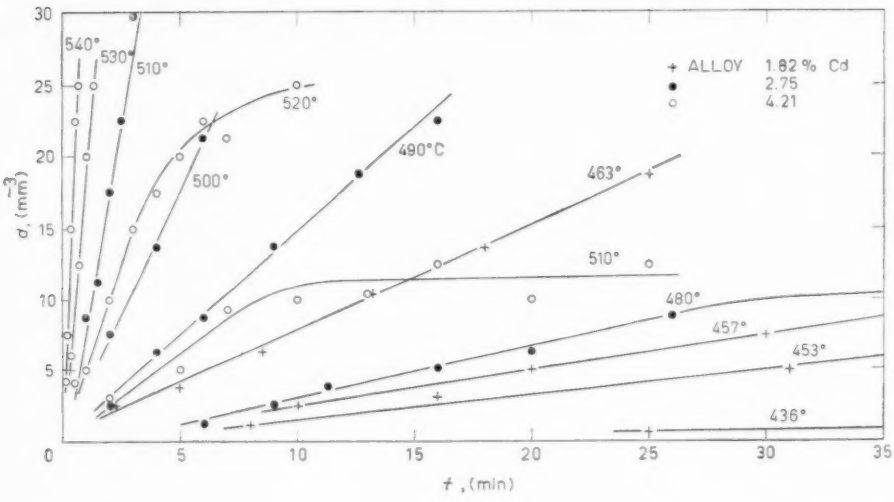


FIG. 9(a).

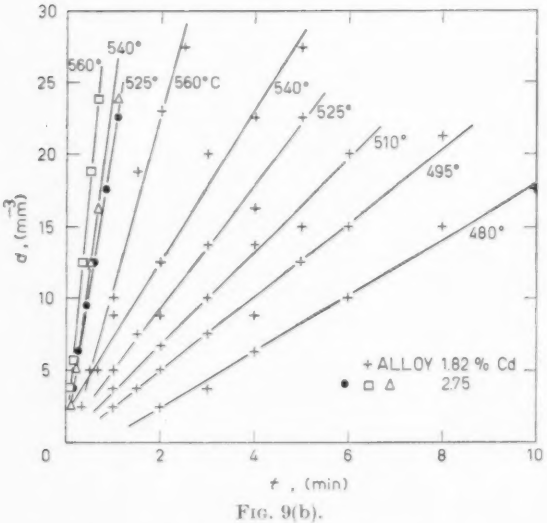


FIG. 9(b).

FIG. 9a-b. Thickness d of slab-formed dissolved regions as a function of solution time t. $T_{pr} = 350°C$.

T_{pr} and T_s, G is the higher, the smaller X_0, whereas above T_s the opposite holds.

Effects of cold working

Cold rolling of 10 per cent in thickness before the solution anneal caused, a.o. the following effects in dissolution process:

(1) Discontinuous dissolution can start even within the grains.

(2) T_{cr} is lowered, though very inconsistently.

(3) G increases, and, relatively speaking, the more, the smaller $|\Delta X_s|$. E.g. for alloy 1 with $T_{pr} = 350°C$, G at $T_s = 436$, 480 and 540°C was 75, 3.3 and 3.0 times higher, respectively, than in unstrained specimens. The corresponding numbers for alloy 2 at $T_s = 490$, 510, 525 and 540°C were 3.5, 1.9, 1.9 and 1.7 times, respectively.

(4) The continuous dissolution process becomes also accelerated.

DISCUSSION

The transport of material in discontinuous dissolution occurs, without doubt, by diffusion along the

TABLE 2. Values of G

Alloy, (wt. % Cd)	T_{pr}, (°C)	T_s, (°C)	G, (mm^{-3}/min)	Alloy, (wt. % Cd)	T_{pr}, (°C)	T_s, (°C)	G, (mm^{-3}/min)
1.82	350	436	0.02	2.75	350	500	3.4
		453	0.19			510	8.8
		457	0.25			525	21
		463	0.75			540	25
		480	1.9			560	36
		495	2.5		400	525	10.7
		510	3.2		450	525	5.0
		525	4.1	4.21	350	510	1.1
		540	5.3			520	5.0
		560	12.0			530	19
2.75	350	480	0.37			540	37
		490	1.5		400	520	2.1

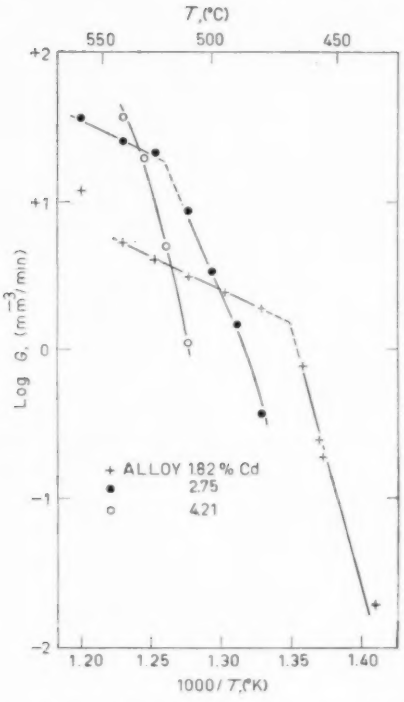


FIG. 10. Dependence of log G on the reciprocal of absolute solution temperature, $1/T$. $T_{pr} = 350$°C.

moving boundaries. Turnbull's method[6] for estimating the diffusion coefficient D_b in such boundaries gives, e.g. for alloy 2 at 540°C ($G = 4 \times 10^{-5}$ cm sec^{-1}, $T_{pr} = 350$°C, diffusion distance = precipitate spacing[5] $= 0.6 \times 10^{-4}$ cm) a D_b of the order 10^{-7} cm^2 sec^{-1}. This D_b is only 3 orders of magnitude higher than the volume diffusion coefficient D_v calculable according to Kubaschewski's data for diffusion in 1 at.% (1.78 wt.%) Cd alloy:[7]

$$D_v = 3.5 \times 10^{-3} \exp(-29200/RT) \text{ cm}^2 \text{ sec}^{-1}.$$

The comparatively small difference between D_b and D_v and the fact that Q_v (29.2 kcal/g at.) is higher than Q for dissolution in the α range (21 kcal/g at.) are compatible with the observation that the continuous dissolution process predominates at temperatures above 600°C.

There are certain reasons to suppose that the diffusion along the moving boundaries controls the growth rate at complete dissolution, i.e. in the α range. This assumption agrees well with the relatively low value of Q in comparison with Q_v. Furthermore, this control mechanism would require that, for constant T_s (and X_0), the growth rate would vary inversely with the square of the diffusion distance, l^2. In fact, the ratio of the values of G (Table 2) for alloy 1, $T_{pr} = 350$°C, and for alloy 2, $T_{pr} = 450$, 400 and 350°C, all with $T_s = 525$°C, is 0.8:1:2.1:4.2 which is well compatible with 1:1:2.3:4.2, derivable, on the basis of the author's previous experimental results, for the ratio of reciprocals of squares of the precipitate spacings (Ref. 5, Fig. 30). In addition, cold working increases G by a small amount only at complete dissolution.

The occurrence of dissolution by grain boundary diffusion gives a reasonable explanation for the ghosted structures observed when complete dissolution occurs. At that temperature range, the solute concentration of α in equilibrium with β is higher than X_0. As a result, the solute concentration tends to be higher than X_0 in those parts of α which are easily accessible for diffusion from and to β. Such are regions swept over by boundary simultaneously in contact with a neighboring β. Consequently, the concentration must be smaller in other parts. Thus, concentration differences of certain configuration are created and appear as ghosts. Occasionally these can visualize the extent of grain boundary diffusion from a single β particle.

The driving force of boundary motion in discontinuous precipitation has generally been attributed to the net free energy decrease ΔF in the process. Obviously the same may apply to discontinuous dissolution. Due to complete or partial disappearence of the α/β surfaces in dissolution, ΔF is higher than the chemical free energy decrease ΔF_c, Fig. 11, by an amount ΔF_s corresponding to the energy of the disappearing surfaces. In this connection one must take into account, that the specific α/β surface energy probably increases because undissolved β loses its low energy orientation in matrix reorientation.

The idea of a chemical driving force for boundary

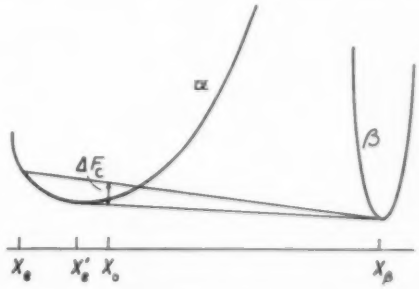


FIG. 11. Chemical free energy relations in dissolution (schematically). The phase mixture $\alpha + \beta$, with compositions X_α and X_β, respectively, resulting from precipitation in alloy X_0 at T_{pr} is converted in dissolution to the mixture $\alpha + \beta$, with compositions X_α' and X_β, or to α, with composition X_α', depending on whether X_0 is greater or smaller than X_α'. ΔF_c apparently reaches its maximum, for constant T_{pr} and T_s, for the alloy with or near the composition X_α'.

VOL. 8 1960

motion, in discontinuous precipitation and dissolution, may, however, be suspected. It can namely be expected that a coherent matrix zone, of (nearly) equilibrium composition, would be developed at the boundary on the side of grain to be consumed. This zone would be created by rapid grain boundary diffusion, and thermal fluctuations of boundary position, and its development would also be enhanced by volume diffusion. Once developed, it would probably tend to grow and thus to check further action of the chemical driving force.

Instead of that, one may suppose that if the matrix lattice parameters vary with composition, coherency strain energy is created, it concentrates in the zone, and causes the atoms in this zone to order on the other side of boundary. In fact, it thus provides the driving force for boundary motion. If the lattice parameters vary linearly with composition, the driving force would be some function of $(\Delta X)^2$, i.e. it would vary approximately as ΔF_c. This explanation applies equally well to discontinuous precipitation as to discontinuous dissolution.

From the approximate equality of $|\Delta X_{pr}|$ and $|\Delta X_s|$ at T_{cr} follows that the driving forces for discontinuous precipitation and dissolution at this temperature can be considered approximately equal. The fact that also the growth rates of the transformed regions in these two processes are equal, at T_{cr}, although the diffusion distances differ strongly, indicates that the growth rate in the temperature range of $\alpha + \beta$ is not controlled by diffusion along the transformation front, at least not for one of the processes. Moreover, in the same temperature range, G decreases strongly when X_0 increases, for constant T_{pr} and T_s. This can only mean that the more the amount of undissolved β increases with increasing X_0, the more strongly it retards the growth, just like inclusions behave in recrystallization. On the other hand, its amount decreases, for constant X_0 and T_{pr}, with increasing T_s. This explains the alarming high values of Q, 100–160 kcal/g at., for the process in the $\alpha + \beta$ range.

The absence of an incubation period for growth is well in accordance with the fact that no nucleation is needed for the process. The mechanisms of discontinuous dissolution and precipitation differ fundamentally in this respect.

It is immaterial, as far as the dissolution process is concerned, what the driving force is for grain boundary motions. When these are not created by the process itself, they can be caused, e.g. by normal recrystallization. For such an effect speaks, partly at least, the metallurgical practice of speeding up dissolution and homogenization by inducing recrystallization through cold or hot working of the material.

ACKNOWLEDGMENTS

The author wishes to express his gratitude to Professor H. M. Miekk-oja for his encouragement and providing of the laboratory facilities. The cooperation of Lieut. Col. K. Miettinen in the preliminary phase of the work is also gratefully acknowledged. For the financial support thanks are due to the representatives of the Finnish Cultural Foundation (Suomen Kulttuurirahasto).

REFERENCES

1. N. Ageew, M. Hansen and G. Sachs, *Z. Phys.* **66,** 350 (1930).
2. H. Margolin and W. R. Hibbard, *J. Metals, N.Y.* **3,** 247 (1951).
3. P. Ylijoki, M.Sc. Thesis, Institute of Technology, Helsinki (1959).
4. M. Hansen and K. Anderko, *Constitution of Binary Alloys* (2nd Ed.) McGraw-Hill, New York (1958).
5. M. Sulonen, *Ann. Acad. Sci. Fenn.* **AVI,** No. 4 (1957).
6. D. Turnbull, *Acta Met.* **3,** 55 (1955).
7. O. Kubaschewski, *Trans. Faraday Soc.* **46,** 713 (1950).

THE LATTICE SPACING RELATIONSHIPS IN CLOSE-PACKED α AND ζ PHASES BASED ON GOLD*

T. B. MASSALSKI† and H. W. KING†

The lattice spacings of eight close-packed hexagonal ζ Au–Sn alloys and one Au–Hg alloy are reported and discussed as a function of composition and electron : atom ratio, using quenched alloys and X-ray powder methods. The results show that in the Au–Sn system the axial ratio and the a and c spacings change with increasing electron concentration in a similar manner to that observed earlier in Au–In alloys.[1] Previously reported lattice spacing values in the α and ζ phase ranges for the four gold-based systems Au–Hg, Au–Cd, Au–In and Au–Sn are compared with the present work and discussed in terms of systematic deviations $\Delta a'$, $\Delta c'$ and Δa observed in all these alloys.

RELATIONS DU PARAMETRE DU RESEAU DES PHASES COMPACTES α ET ζ DES ALLIAGES A BASE D'OR

Les auteurs ont étudié l'influence de la composition et du rapport: nombre d'électrons de valance—nombre d'atomes sur les dimensions de la maille de huit alliages ζ Au–Sn cristallisant dans le sytème hexagonal compact et d'un alliage Au–Hg. Pour ce faire, ils ont utilisé des alliages trempés et déterminé le rapport électrons-atomes au moyen de méthodes de poudres en rayons X.

Les résultats montrent que pour les alliages Au–Sn le rapport des axes et les paramètres a et c varient lorsque le nombre d'électrons croit d'une manière semblable à celle observée dans les alliages Au–In.[1]

Les valeurs des paramètres déterminées précédemment pour les phases α et ζ de quatre alliages à base d'or : Au–Hg, Au–Cd, Au–In, et Au–Sn, ont été comparées avec les résultats obtenus dans ce travail et ont été examinées en fonction des déviations systématiques $\Delta a'$, $\Delta c'$ et Δa observées dans ces alliages.

BEZIEHUNGEN ZWISCHEN DEN GITTERKONSTANTEN DICHT GEPACKTER α UND ζ PHASEN VON GOLDLEGIERUNGEN

Die Gitterkonstanten von acht hexagonal dicht gepackten ζ Au–Sn Legierungen und einer Au–Hg Legierung werden mitgeteilt und als Funktion der Zusammensetzung und der Elektronenkonzentration diskutiert. Zur Untersuchung wurden abgeschreckte Legierungen und röntgenographische Pulvermethoden verwendet. Die Ergebnisse zeigen, daß im Au–Sn System das Achsenverhältnis und die a und c Abstände mit zunehmender Elektronenkonzentration sich in ähnlicher Weise ändern, wie es früher bei Au–In Legierungen beobachtet worden war.[1] Frühere Ergebnisse von Gitterkonstantenmessungen an α und ζ Phasen der vier Goldlegierungssysteme Au–Hg, Au–Cd, Au–In und Au–Sn werden mit der vorliegenden Arbeit verglichen und diskutiert mit Hilfe von systematischen Abweichungen $\Delta a'$, $\Delta c'$ und Δa, die in allen diesen Legierungen auftreten.

VOL. 8 1960

1. INTRODUCTION

In recent publications[1–4] the lattice spacings of a number of binary close-packed hexagonal (c.p.hex.) intermediate phases based on noble metals have been reported and discussed. If the range of homogeneity of such phases occurs in the broad region of electron concentration (e/a) values between 1.2 and 1.6, they are usually described as ζ phases, and if their range occurs in the vicinity of $e/a = 1.75$, they are described as ε phases. In both cases they are frequently referred to as electron compounds,[5,6] and the term electron concentration (e/a) is used to denote the ratio of all valency electrons to the number of atoms. It has been shown[3,4,6] that e/a is an important factor which influences the systematic changes of lattice spacings and axial ratio of c.p.hex. based on noble metals. The lattice spacing relationships between the α (f.c.c.) and ζ(c.p.hex.) phases have been discussed recently for the systems Cu–Ga, Cu–Ge and Ag–Al.[2] Following this work it became of interest to examine similar relationships in gold-based systems for the cases where the primary solid solution is followed by an intermediate phase which is close-packed hexagonal.

In gold-based alloys, ζ phases are known to occur in four binary systems: Au–Cd, Au–Hg, Au–In and Au–Sn. The lattice spacings for the first three systems have been reported earlier,[1] and in the present investigation the lattice spacings of eight Au–Sn alloys and one Au–Hg alloy are presented and discussed.

As a result of the present study it became clear that certain trends in the changes of lattice spacings with e/a already established for c.p.hex. phases based on copper and silver also occur in gold-based alloys. This suggested that the values of lattice spacing reported in the literature which fall outside these trends may be inaccurate. A re-examination of one Au–Hg alloy confirmed this possibility. Other differences between various values reported for Au–Cd and Au–In alloys are discussed below.

The interpretation of the present and previous data provides information about various possible types of interactions between the Fermi surface and the Brillouin zone of the c.p.hex. structure in alloys based upon

* Received December 23, 1959.

† Mellon Institute, Pittsburgh 13, Pennsylvania.

TABLE 1. Composition, heat-treatment and lattice spacings at 30°C of c.p.hex. alloys in systems Au–Sn and Au–Hg

Alloy No.	Composition of alloy (At.%)			Homogenizing temperature (°C)	Homogenizing time (days)	Structure	a, c.p.hex. (Å)	c, c.p.hex. (Å)	c/a	e/a
	Au	Sn	Hg							
1*	88.93	11.07	—	275	68	ζ	2.9084	4.7864	1.6457	1.332
2	88.00	12.00	—	275	68	ζ	2.9117	4.7874	1.6442	1.360
3	87.00	13.00	—	275	68	ζ	2.9170	4.7856	1.6406	1.390
4	86.00	14.00	—	275	68	ζ	2.9228	4.7823	1.6362	1.420
5*	84.74	15.26	—	275	68	ζ	2.9305	4.7761	1.6298	1.458
6	84.00	16.00	—	275	68	ζ	2.9350	4.7717	1.6258	1.480
7	83.83	16.17	—	275	68	ζ	2.9362	4.7707	1.6248	1.485
8*	83.69	16.31	—	275	68	ζ	2.9368	4.7694	1.6240	1.489
9*	71.45	—	28.55	275	53	ζ + 2nd phase	2.9217	4.8150	1.6480	1.263†

* Analysed chemically.
† e/a value estimated for ζ phase from the vol/atom curve (see Fig. 3).

copper, silver and gold. This is the subject of a separate paper.[7]

2. MATERIALS AND EXPERIMENTAL METHODS

Alloys were prepared from spectroscopically standardized materials.* Weighed quantities of the pure metals were melted under reduced pressure of helium in small, sealed thin-walled tubes of fused quartz or "Vycor" with vigorous shaking; details of this technique have been published earlier.[1-8]

A few alloys were analysed chemically, the values obtained being in agreement with the intended compositions within the errors of chemical analysis.

Details of homogenization, heat-treatment, metallographic examination and preparation of X-ray samples were the same as in earlier investigations.[1-8]

In order to obtain accurate values of the lattice spacings, the last ten high-angle X-ray lines, resolved into doublets, were plotted against the Nelson and Riley function,[9] and the lattice spacings were then evaluated by extrapolation to $\theta = 90°$. To obtain a straight-line plot, the axial ratio was first adjusted by a trial and error method. The c lattice spacings were then calculated from the evaluated a and c/a values. All values are reported in Ångstrom units, based upon the following values assumed for the Cu Kα radiation:

$$\text{Cu } K_{\alpha 1} = 1.5405006 \text{ Å}$$
$$\text{Cu } K_{\alpha 2} = 1.5443412 \text{ Å}.$$

The temperature at which measurements were recorded was 30 ± 1°C. The accuracy of the reported results is ± 0.0002 Å for the a spacings, and ± 0.0004 Å for the c spacings. These limits were determined by the best possible fit into a straight-line Nelson and Riley extrapolation.

* Supplied by Messrs. Johnson, Matthey and Co., Ltd.

3. EXPERIMENTAL RESULTS

The values of the a and c lattice spacings and of axial ratio, together with composition and other pertinent data, for the eight Au–Sn alloys and one Au-Hg alloy are given in Table 1. The X-ray films for the Au–Sn alloys showed only the lines of the c.p.hex. diffraction pattern and no indication of distortion or ordering of the structure could be detected. For the Au–Hg alloy very weak diffraction lines of a second phase, in addition to the c.p.hex. pattern, were observed.

In the Au-Sn system the axial ratio decreases throughout the entire range of the c.p.hex. phase in agreement with earlier work by Stenbeck and Westgren[10]. This decrease in c/a is from 1.6457 at the gold-rich end of the phase to 1.6240 at the tin-rich boundary, passing through the ideal value of axial ratio (1.633) between 14.01 and 15.3 at.% Sn. Au–Sn is thus the only one of the gold-based alloy systems in which the axial ratio becomes less than the ideal value at high solute contents. While the a spacing shows an increase with increasing tin content, the c spacing first increases, passes through a maximum and then decreases. This maximum occurs in the region of 12 at.% Sn. These results for the Au–Sn system are strikingly similar to those obtained earlier[1] for Au–In alloys.

In the Au–Hg system only one alloy was cast to fall in the mercury-rich end of the somewhat uncertain composition range of the c.p.hex. phase. After homogenizing at 395°C this alloy was found to contain a liquid phase, but after re-casting and annealing for 53 days at 275°C it consisted almost entirely of a c.p.hex.

phase together with a trace of a second phase. The axial ratio obtained for this alloy, which may be taken to represent the mercury-rich end of the phase at 275°C is in good agreement with previous work.[1] Further, the present results confirm the earlier findings that there is only a very small change in axial ratio throughout this c.p.hex. phase.[1,11] The a and c spacings of the alloy, however, are somewhat higher than those reported previously.*

4. DISCUSSION

The present results for the c.p.hex. Au–Sn alloys are shown in Fig. 1. The extent of the α and ζ phases in terms of atomic composition is shown in the upper portion of the figure. In the lower portion the a and c spacings of the c.p.hex. phase, and the volume of the unit cell per atom, are plotted as functions of e/a. The results for the α phase, based on the work by Owen and Roberts[13], are included to complete the comparison.

As in an earlier treatment by Massalski and Cockayne[2] the a spacings of the cubic α phase have been divided by $\sqrt{2}$ to provide a direct comparison between the lattice spacings of the α and ζ structures in their closest packed planes {111} and {0001}, respectively. These values are plotted as a'. In addition to the observed c spacings in the ζ range, hypothetical c' spacings have been calculated and included in the α range as shown in Fig. 1. These values correspond to c spacings of an ideally close-packed c.p.hex. structure extending throughout the α phase region and possessing a closest distance of approach of atoms in the {0001} planes, which is equal to the closest distance of approach of atoms in the {111} planes of the cubic α alloys.†

It can be seen that for Au–Sn alloys the a' spacings of the α phase do not extend linearly, and smoothly, into the ζ range as was the case reported earlier[2] for the Cu–Ge and Cu–Ga alloys. Instead a definite contraction, $\Delta a'$, is observed on passing from the α to the ζ alloys. Fig. 1 shows that subsequently the initial portion of the a spacing curve in the ζ range for e/a values between 1.33 and 1.35 appears to lie parallel to the a' spacing curve. Above $e/a \simeq 1.35$ the curve exhibits a gradual change of slope marked Δa in Fig. 1, the rise in the a spacing being accelerated with further increases in e/a.

At the gold-rich end of the ζ phase the c spacings deviate to higher values, by the amount $\Delta c'$, from the values indicated by the extrapolation of the hypothetical c' spacings from the α phase. This is consistent with the fact that these particular alloys have higher-than-ideal axial ratios, as may be seen from Fig. 3. The c spacing curve shows a slight maximum near $e/a \simeq 1.36$ and then falls to values below the extrapolation of c' as e/a is further increased: it intersects the extrapolation of c' at $e/a \simeq 1.44$, which is the same value at which the a spacing curve cuts the extrapolation of a' and the axial ratio passes through the ideal value (Fig. 3).

The values of volume per atom shown in Fig. 1 fall almost exactly upon the curve extrapolated from the primary solid solution. This extrapolated curve was obtained by calculating the volume per atom at various points in the ζ phase region using the linear extrapolation of the a' values.

The only previous work on ζ Au–Sn alloys is that of Stenbeck and Westgren[10] whose results for two alloys are included in Figs. 1 and 3. These results are in general agreement with the present work, although the a spacing of the gold-rich alloy falls slightly lower than the present values and hence leads to a low value of volume per atom and a high axial ratio. The tin-rich alloy, on the other hand, agrees closely with the present data.

Similar behavior to that discussed above of lattice spacings, volume per atom and axial ratio, when plotted against e/a, is evident in other systems based on gold as shown in Figs. 2 and 3.† In the Au–In system, for example, the results of Massalski[1] together with those of Wegst and Schubert[14] clearly demonstrate that the a lattice spacing curve is parallel to the a' curve, after the initial contraction $\Delta a'$, for e/a values between 1.23 and 1.36. Above that latter value the a spacings deviate to higher values by an amount shown as Δa in Fig. 2. In the systems Au–Hg and Au–Cd, in which the ζ phases terminate before $e/a = 1.36$, after the initial shrinkage $\Delta a'$, the a spacing curves possess slopes similar to their respective

* In an earlier investigation[1] the lattice spacings of four c.p.hex. Au–Hg alloys were reported. These alloys were analysed chemically after a long homogenizing treatment at 379°C. The X-ray films showed only the diffraction lines from the c.p.hex. structure. Re-measurement and re-calculation of the original films during the present work confirmed the earlier published data. However, the present results and a detailed comparison of the data for other gold-based systems (Figs. 2 and 3) indicate that the values obtained earlier for the two mercury-rich alloys are not consistent with their analysed compositions. Similar inconsistencies between lattice spacings and expected chemical composition have been reported for the f.c.c. (α) Au–Hg alloys,[12] and the discrepancies may be attributed to volatilization of mercury from the X-ray powders during annealing. To avoid this in the present study the filings for X-ray study were annealed for 10 min at 150°C, instead of at the homogenizing temperature of 275°C.

† Hence, the a' and c' spacings are related to the cubic a spacings in the following way: $a' = a/\sqrt{2}$; $c' = a' \times$ (ideal axial ratio) $= a/\sqrt{2} \times \sqrt{8}/\sqrt{3} = 2a/\sqrt{3}$.

† The data for the α alloys (solid black symbols) is based on the work of Owen and Roberts[13] for Au–In and Au–Cd, and Rayson and Calvert[12] for Au–Hg alloys.

VOL. 8 1960

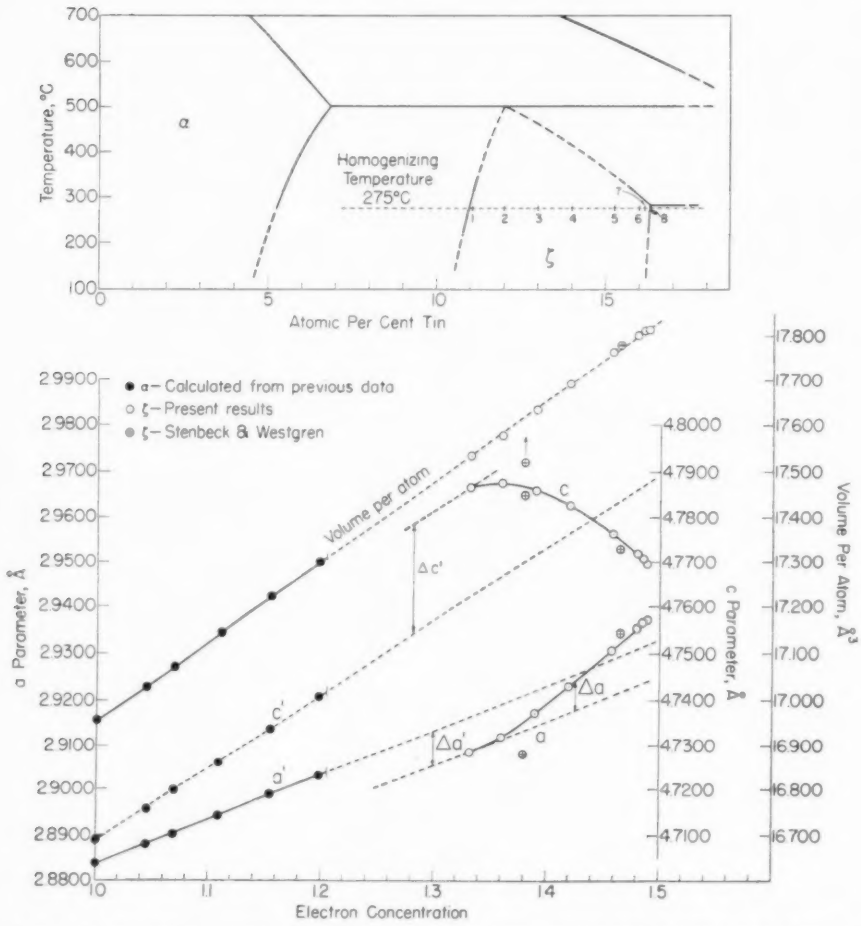


FIG. 1. Portion of the Au–Sn equilibrium diagram showing composition of the alloys and changes of the lattice spacings and volume per atom with electron concentration in both α and ζ ranges.

a' spacing plots, but no accelerated rise (Δa) is observed. The $\Delta a'$ displacement is demonstrated most clearly in the system Au–Cd since the a' and a curves actually overlap over a wide range of electron concentration (Fig. 2). The c lattice spacings for the Au–In system are higher initially, by an amount $\Delta c'$, than those values predicted by the extrapolation of the c' curve from the α phase to the ζ phase range, but nevertheless they lie parallel to the c' curve over the same values of e/a for which the a spacings curve is parallel to the a' curve. The c spacings tend to fall off at e/a about 1.36 (i.e. at the same electron concentration at which the a spacings rise more steeply) and pass through a maximum at e/a about 1.38. The limit of the phase is reached before the decreasing c spacing curve intersects the extrapolation of c', and the axial ratio never falls to the ideal value. The results of Massalski[1] for Au–Cd, and for two gold-rich Au–Hg alloys combined with the present Au–Hg alloy, also show that for e/a values below about 1.36 the c spacing curves lie parallel to the respective c' curves, being displaced from them by a positive increment $\Delta c'$. The similarity between the variation of lattice spacings with e/a in the systems Au–Sn and Au–In indicates that the c curve for the Au–Sn alloys very probably also lies parallel to the c' curve over a narrow range of e/a just above 1.33 (Fig. 1).

The values of volume per atom calculated from the data for the Au–In system, and from lattice spacings quoted above for the Au–Cd and Au–Hg systems, all fall close to the extrapolated curves from the α alloys as was found for Au–Sn alloys. This is shown in Fig. 3. Also indicated in this figure are the results for the axial ratios for the above alloys. These results together with those for the Au–Sn system fit into a general pattern for the variation of axial ratio with electron concentration in which there is very little change in c/a up to a value of e/a about 1.36, and beyond this a steep fall towards, and below, the ideal value. This steep fall in c/a is caused by the combined effects of rising a

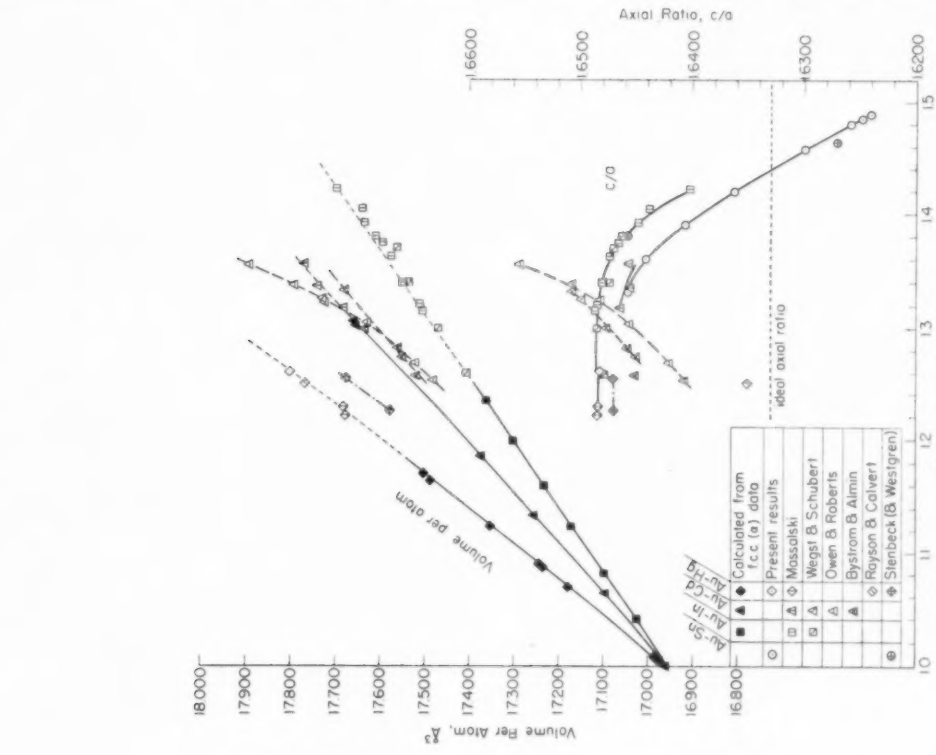


FIG. 3. Variation of the volume per atom and the axial ratio with electron concentration in systems Au–Sn, Au–In, Au–Cd and Au–Hg.

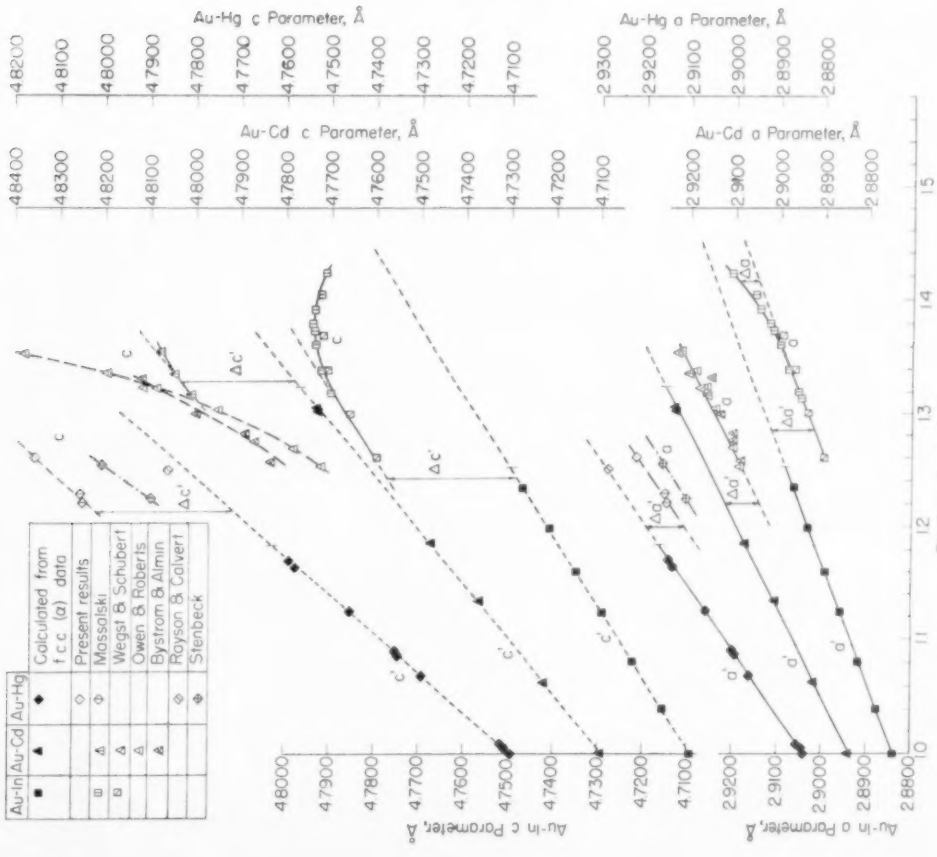


FIG. 2. Variation of the lattice spacings with electron concentration in systems Au–In, Au–Cd and Au–Hg.

VOL. 8 1960

spacing and falling c spacing, which occur in this region of electron concentration.*

The above detailed results can now be compared with other data in the literature which show poor agreement with the present general conclusions. Particularly marked differences occur in the systems Au–Hg and Au–Cd.

The lattice spacings of two alloys in the Au–Hg system studied in earlier work by Stenbeck[11] are slightly lower than the other data for this system shown in Figs. 2 and 3 but exhibit the same general trends as a function of electron concentration. The results of two mercury-rich alloys reported by Massalski[1], and not included in Figs. 2 and 3, do not conform to the established trends, but are considered to be unreliable for reasons discussed above (p. 679). Rayson and Calvert[12] report data for one Au–Hg alloy, of assumed composition 25 at.% Hg, which does not show any $\Delta a'$ or $\Delta c'$ displacement with respect to the extrapolation of the a' and c' curves from the α phase region. Further, since the axial ratio of this alloy (reported to be almost ideal) is at variance with all other data for gold-based systems (Fig. 3), it must be considered that the lattice spacings reported by Rayson and Calvert are unreliable.

Even though the a spacings of all the data for the Au–Cd system in Fig. 2 show a displacement $\Delta a'$ and lie parallel to a', the data for the c spacings, and hence also for the c/a and volume per atom, reported by Owen and Roberts[13] and by Bystrom and Almin[16], differ considerably from the trends in all other gold-based c.p.hex. alloys and in particular from the results of Massalski[1] for this system. The rate of increase in c reported by these investigators indicates no tendency to fall off or pass through a maximum at electron concentration values in the region of 1.36, and the corresponding increase in c/a is directly opposite to that expected at these values of e/a (Fig. 3). This behavior is significant, especially as the discrepancies are only observed in the c spacings. The answer is most likely in the temperature difference from which the alloys were quenched. Wegst and Schubert[15] have reported recently that a Au–Cd alloy of composition corresponding to $e/a = 1.325$, quenched from 350°C, contained a c.p.hex. phase which was ordered. The a lattice spacing of this alloy conforms to other data in Fig. 2, but the c spacing and axial ratio agree very closely with those of Owen and Roberts[13] and Bystrom and Almin[16] for the same composition, and are thus at variance with the data of Massalski[1]. No such tendency for ordering or distortion was observed by Massalski in the X-ray films of the alloys quenched from 439°C. The annealing temperature used by Bystrom and Almin[16] was the same as that of Wegst and Schubert (350°C), and Owen and Roberts[13] have not quoted their temperature. However, if it was below about 350°C, the results of Schubert indicate that these alloys would very likely be ordered or distorted, which might account for the abnormal behavior of the c spacings as a function of e/a.

In conclusion the following evaluation of the available data is possible:

(a) On passing from the α primary solid solutions to the ζ c.p.hex. phases a contraction, $\Delta a'$, occurs in the closest packed planes.

(b) The a spacing curves in the ζ phases initially lie parallel to the a' spacings extrapolated from the α phases; the a spacings deviate to higher values by an amount Δa in the systems Au–Sn and Au–In in the region of e/a above approximately 1.35–1.36.

(c) The c spacings of the ζ phases are initially higher, by an amount $\Delta c'$, than the hypothetical c' values extrapolated from the primary solid solutions.

(d) With increasing e/a the c spacings increase with slopes parallel to the c' spacings extrapolated from this phase; in the systems Au–Sn and Au–In the c spacings pass through a maximum and begin to decrease when e/a exceeds values of about 1.36–1.38.

(e) The initial value of axial ratio in the ζ phases is distorted from the ideal value to about 1.648 and remains fairly constant with increases of e/a until the value $e/a = 1.36$ is reached; at higher values of e/a the axial ratio decreases.

(f) The values of volume per atom fall very nearly upon the same curve in both the α and ζ ranges.

(g) Alloys for which the c spacings, axial ratios and volumes per atom show a positive deviation from the trends summarized above appear to be ordered.

ACKNOWLEDGMENTS

We are indebted to Messrs. R. Carbonara and R. Fager for their help in producing X-ray films of very high quality and great care in computation of the lattice spacings. Miss M. Bachelder of the University of Chicago has kindly performed chemical analyses on three Au–Sn alloys and one Au–Hg alloy. Thanks are due to Drs. H. P. Klug and L. R. Alexander for the use of their precision film-measuring instrument. We are grateful to Dr. L. F. Vassamillet for many stimulating discussions.

* Wegst and Schubert[14,15] state that the steep fall in the axial ratios of Au–In alloys quenched from 350°C, in the region of e/a values above 1.36, may be a result of ordering and orthorhombic distortion. However, no order X-Ray reflections were observed by Massalski[1] in powders quenched from between 398 and 500°C. Present results for Au–Sn alloys show similarly that a steep fall in c/a also occurs in this system without the presence of order.

REFERENCES

1. T. B. MASSALSKI, *Acta Met.* **5,** 541 (1957).
2. T. B. MASSALSKI and B. COCKAYNE, *Acta. Met.* **7,** 762 (1959).
3. G. V. RAYNOR and T. B. MASSALSKI, *Acta Met.* **3,** 480 (1955).
4. T. B. MASSALSKI, *Metallurg. Rev.* **3,** 45 (1958).
5. W. HUME-ROTHERY and G. V. RAYNOR, *The Structure of Metals and Alloys. Monogr. Ser. Inst. Metals.* No. 1 (1954).
6. T. B. MASSALSKI, presented at *Symposium on the Theory of Alloy Phases,* 1955. American Society for Metals, Cleveland (1956).
7. T. B. MASSALSKI and H. W. KING, *Acta. Met.* **8,** 684 (1960).
8. T. B. MASSALSKI and G. V. RAYNOR, *J. Inst. Met.* **82,** 539 (1954).
9. J. B. NELSON and D. P. RILEY, *Proc. Phys. Soc., Lond.* **A57,** 160 (1945).
10. S. STENBECK and A. WESTGREN, *Z. Phys. Chem.*, B**14,** 95 (1931).
11. S. STENBECK, *Z. Anorg. Chem.* **214,** 16 (1933).
12. H. W. RAYSON and L. D. CALVERT, *J. Inst. Met.* **87,** 88 (1958).
13. E. A. OWEN and E. A. O'D. ROBERTS, *J. Inst. Met.* **66,** 389 (1940); **71,** 213 (1945).
14. J. WEGST and K. SCHUBERT, *Z. Metallk.* **49,** 533 (1958).
15. J. WEGST and K. SCHUBERT, *Acta. Met.* **6,** 721 (1958).
16. A. BYSTROM and K. E. ALMIN, *Acta. Chem. Scand.* **1,** 76 (1947).

VOL.
8
1960

LATTICE SPACING RELATIONSHIPS AND THE ELECTRONIC BAND STRUCTURE OF CLOSE-PACKED α AND ζ PHASES OF GOLD-BASED ALLOYS*

T. B. MASSALSKI† and H. W. KING†

The lattice spacing relationships in the α and ζ alloys based on gold are discussed in the light of previous similar studies. It is shown that the systematic deviations $\Delta a'$, $\Delta c'$, and Δa, observed in the lattice spacings of the ζ alloys, can be interpreted in terms of the interactions of the Fermi surface with the faces of the Brillouin zone of the c.p.hex. structure. When the present results are viewed in the light of the band structure theory they indicate that, similarly to the interpretation of Cohen and Heine[10], the Fermi surface must be considerably more distorted in the gold-based alloys than in alloys of copper or silver.

PARAMETRE DE RESEAU ET STRUCTURE ELECTRONIQUE DE PHASES COMPACTES α ET ζ DANS LES ALLIAGES A BASE D'OR

Les auteurs examinent les paramètres du réseau des phases α et ζ des alliages à base d'or, en fonction de résultats obtenus préalablement.

Ils montrent que les déviations systématiques $\Delta a'$, $\Delta c'$ et Δa des paramètres de la maille de la phase ζ peuvent être interprétées comme une interaction entre les surfaces de Fermi et les faces de la zone de Brillouin de la structure à réseau hexagonal compact. Ils examinent ces résultats en fonction de la structure électronique et montrent tout comme Cohen et Heine[10] que les surfaces de Fermi sont plus déformées dans les alliages à base d'or que dans les alliages de cuivre et d'argent.

BEZIEHUNGEN ZWISCHEN DEN GITTERKONSTANTEN UND DER ELEKTRONISCHEN BANDSTRUKTUR DICHT GEPACKTER α UND ζ PHASEN VON GOLDLEGIERUNGEN

Die Beziehungen zwischen den Gitterkonstanten der α und ζ Phasen von Goldlegierungen werden angesichts der Ergebnisse vorhergehender ähnlicher Untersuchungen diskutiert. Es wird gezeigt, daß die systematischen Abweichungen $\Delta a'$, $\Delta c'$ und Δa, die bei den Gitterkonstanten der ζ Legierungen beobachtet werden, als Folge der Wechselwirkung der Fermioberfläche mit der Brillouinzone der hexagonal dicht gepackten Struktur gedeutet werden können. Betrachtet man die vorliegenden Resultate im der Theorie der Bandstruktur, so zeigen sie, daß die Fermioberfläche bei Goldlegierungen erheblich mehr verzerrt sein muß, als bei Kupfer—oder Silberlegierungen, wie es einer Interpretation von Cohen und Heine[10] entspricht.

1. INTRODUCTION

The relationship between changes in lattice spacings of close-packed hexagonal (c.p.hex.) intermediate phases in alloys of the noble metals with the B-subgroup elements has been the subject of a number of experimental and theoretical papers.[1–7] In many of these papers attention has been focused on the interpretation of particular experimental observations such as the stability of the ζ[2,8] and ε[1] phases at values of electron concentration (e/a)‡ near 3/2 and 7/4, respectively, the higher-than-ideal axial ratios in certain gold alloys[9] and variations in the rate of change of the a and c spacings at particular values of e/a.[7] Recently a detailed comparison has been made by the present authors[9] between the lattice spacings of the α and ζ phases of the four gold systems in which the ζ phase is known to occur. The lattice spacings, axial ratios and volumes of the unit cell per atom of these phases were found to follow distinctive trends when plotted as functions of electron concentration. The significance of these general trends in the changes of lattice spacings in the close-packed hexagonal phases of gold alloys will be discussed in relation to known distortion mechanisms associated with the interactions of the Fermi surface with the faces of the Brillouin zone. Special reference will be made to similar relationships reported earlier for the systems Cu–Ge and Cu–Ga.[7] The data available at the present time[7] for ζ phases in silver alloys is considered to be insufficient for detailed comparison with the gold systems.

Finally the present interpretation of the lattice spacings data for the α and ζ phases of gold-based alloys will be considered in the light of the new approach to the theory of the band structure of noble metals and their α phase alloys recently proposed by Cohen and Heine[10].

2. PREVIOUS CORRELATIONS BETWEEN LATTICE SPACINGS AND ELECTRON CONCENTRATION IN C.P.HEX. INTERMEDIATE PHASES

The earlier interpretations of the significance of lattice spacing changes in c.p.hex. phases of the noble metals can be conveniently discussed in terms of the

* Received December 23, 1959.

† Mellon Institute, Pittsburgh 13, Pennsylvania.

‡ It is assumed that the ratio e/a denotes the total number of valency electrons over the number of atoms in the alloy.

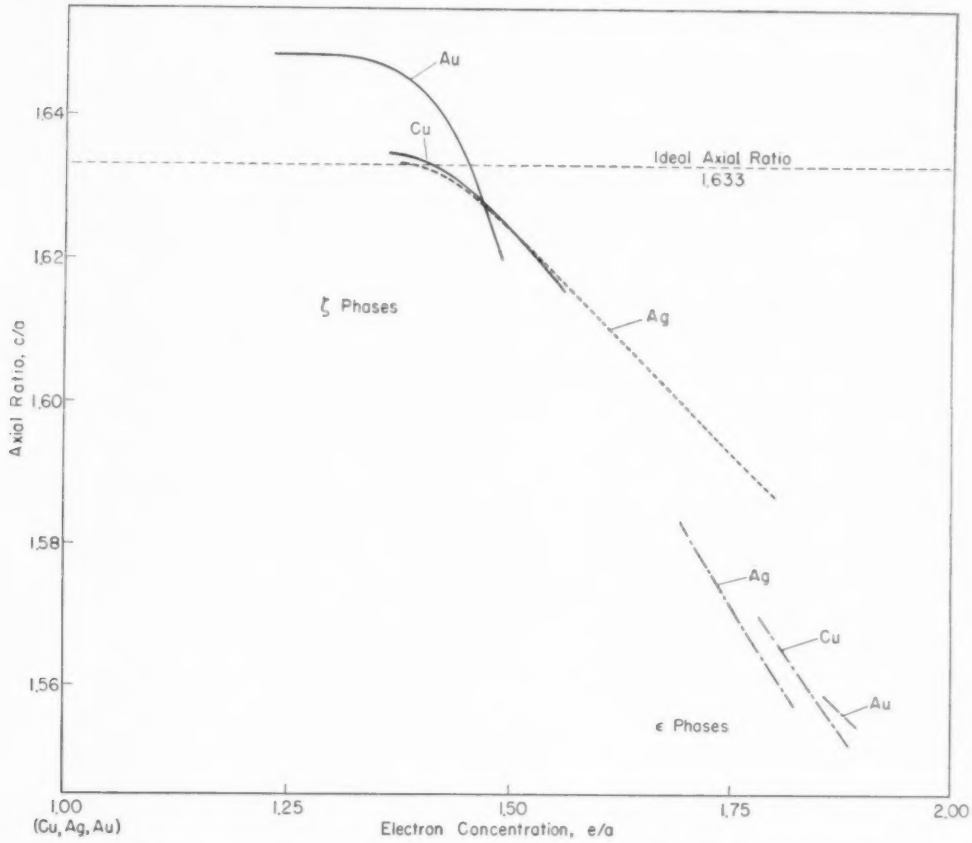


FIG. 1. Diagramatic representation of the changes of axial ratio with electron concentration in c.p.hex. ζ and ε phases of the noble metals.

variation in axial ratio as a function of electron concentration. This is shown schematically in Fig. 1,[5-7] for copper and gold alloys; the probable variation of c/a in silver-based alloys appears to be similar to that of copper as indicated by the dotted line. The c.p.hex. phases are usually described as ζ if they are stable in the region of e/a near 1.5, and as ε if they are stable near e/a about 7/4.

A vertical section through the Brillouin zone of the c.p.hex. structure proposed by Jones[1] is shown in Fig. 2. Theoretical considerations indicate[1,3,4] that interactions between the Fermi surface and the faces of the Brillouin zone can result in two possible general distortions of the c.p.hex. lattice: the zone overlap distortion suggested by Jones[1] and the zone-approach distortion suggested by Goodenough[3]. Both of these types of interaction tend to distort the Brillouin zone in such a way that the zone faces involved are brought closer to the origin of the k-space; hence, they produce an expansion of the corresponding lattice spacings in real space. Jones[1] proposed that the lower-than-ideal values of axial ratio in the ε phases (Fig. 1) result from an overlap of Fermi electrons across the $\{10\bar{1}0\}$ faces of the Brillouin zone, which would in turn cause an expansion of the a spacings in the real lattice. This suggestion was later adopted by Raynor and Massalski[2] to account for the stability of the ζ phases in copper-based alloys.

As illustrated in Fig. 1, within the range of e/a from about 1.23–1.36, the axial ratios of gold-based alloys remain approximately constant and are greater than the ideal value of 1.633. At higher values of electron concentration the axial ratios fall steeply and eventually become less than ideal. The corresponding fall in axial ratios in copper alloys, on the other hand, is much less steep and appears at relatively higher values of e/a. The higher-than-ideal values of axial ratio at the onset of the ζ phase in gold alloys were discussed by Massalski[5,6] and attributed to the Goodenough zone-approach distortion with respect to the {0002} faces of the Brillouin zone, shown in Fig. 2. This mechanism was also thought to be responsible for the continued increase in the c spacings which occurs in these alloys up to electron concentrations of about

VOL. 8 1960

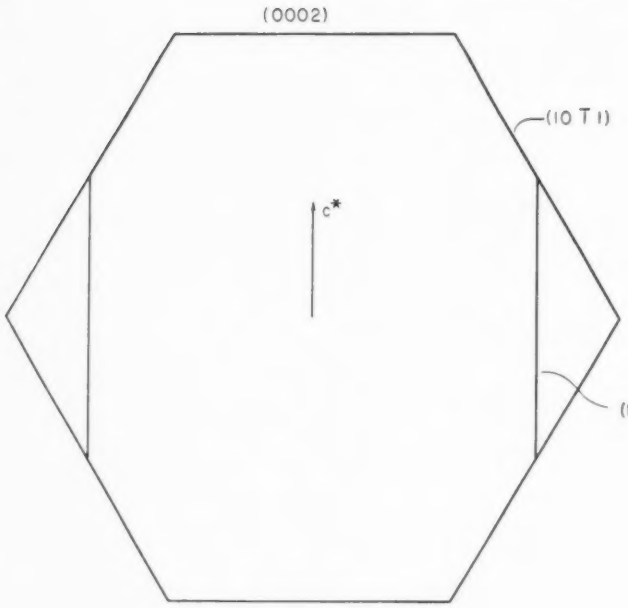


FIG. 2. Vertical section through the Brillouin zone of the c.p.hex. structure suggested by Jones[1].

1.38. The steep fall in the axial ratio was attributed to an overlap of Fermi electrons across the $\{10\bar{1}0\}$ faces of the Brillouin zone when the electron concentration exceeded about 1.36; which by the Jones mechanism would result in an expansion of the a spacings. This latter suggestion, however, was not substantiated by a detailed study of the gold-based alloys.

Massalski and Cockayne[7] later investigated the decrease in axial ratios of the ζ phases in the systems Cu–Ge, Cu–Ga and Ag–Al by studying changes in the lattice spacings and comparing them with the lattice spacing of the primary solid solutions (α). A schematic representation of their results for Cu–Ge and Cu–Ga is shown in Fig. 3. It can be seen that for these systems the spacings a' of the closest packed planes of the cubic α solid solutions* extended almost without a change into the c.p.hex. ζ phases up to a value of e/a near 1.4, above which they show a deviation (Δa) towards higher values. This acceleration in the rate of change of the a spacings at e/a near 1.4 was again associated with the onset of overlap across the $\{10\bar{1}0\}$ faces of the Brillouin zone. Massalski and Cockayne[7] proposed that a measure of the distortion due to overlap could be obtained from the rate of the expansion of the a spacings $[\Delta a/(a - \Delta a)]$ when plotted as a function of e/a. It was found that the rates of distortion were very nearly the same for the copper-based and silver-based alloys which were examined.

* For the purpose of comparison the cubic a spacings are divided by $\sqrt{2}$.

3. LATTICE SPACINGS OF α AND ζ PHASES IN GOLD-BASED ALLOYS

The general pattern of lattice spacing changes when plotted as functions of e/a for α and ζ phases of the systems Au–Sn, Au–In, Au–Cd and Au–Hg is summarized diagrammatically in Fig. 4. For a detailed

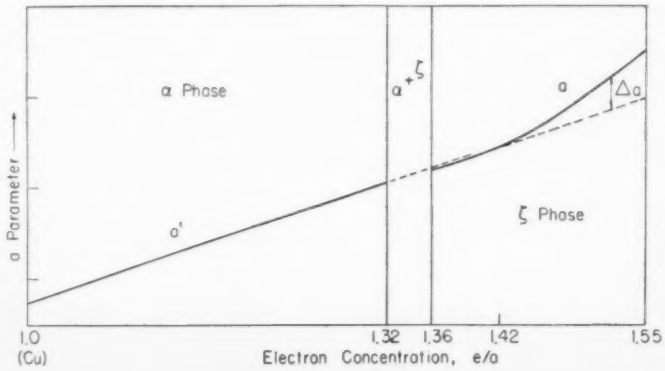


FIG. 3. Typical variations of the a lattice spacings with electron concentration in α and ζ phases in Cu–Ge and Cu–Ga.

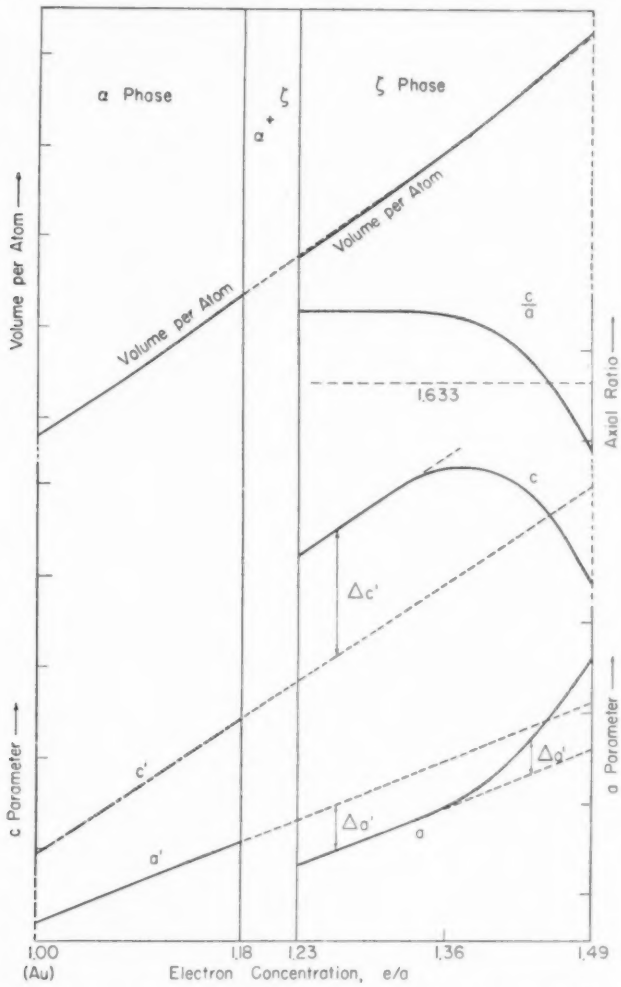


FIG. 4. Typical variations of lattice spacings, axial ratio and volume per atom with electron concentration in α and ζ phases in gold-based alloys.

description reference should be made to the authors' earlier paper.[9] The general behavior of the a spacings of the ζ phases and the occurrence of the Δa deviations is similar to that reported for Cu–Ge and Cu–Ga;[7] however, the Δa deviations in the gold systems occur at a lower value of electron concentration, i.e. at e/a 1.35–1.36. In addition, Fig. 4 also shows an initial deviation $\Delta a'$ which occurs in the a spacings at the onset of the c.p.hex. ζ phases in all four gold-based systems. This deviation was not apparent* in the Cu–Ge and Cu–Ga systems.[7] A complementary deviation $\Delta c'$ may also be observed in the c spacings if a suitable comparison is made with hypothetical c' spacings† calculated for the α primary solid solutions.[9]

In the systems Au–In and Au–Sn, for which the ζ phases are stable at values of e/a exceeding 1.36–1.38, the c spacings pass through a maximum and begin to decrease. However, in all four alloy systems, values of volume of the unit cell per atom in the ζ phases fall almost exactly on the curve of volume per atom extrapolated from the primary solid solutions, as indicated in Fig. 4. The trend in the axial ratio changes with e/a is also shown. It is of interest to notice that for e/a values at which the axial ratios begin to decrease the a lattice spacings show the Δa deviation.

4. INTERPRETATION OF THE LATTICE SPACING DATA FOR α AND ζ PHASES OF GOLD-BASED ALLOYS

In this section an attempt will be made to interpret the consistent trends in lattice spacings of the α and ζ

* A close examination of the data of Massalski and Cockayne[7], in the light of the results for gold-based ζ alloys, reveals the possibility of a very small deviation $\Delta a'$ in the copper-based systems, as indicated in Fig. 3.

† c' spacings correspond to c spacings of a hypothetical c.p.hex. structure with an ideal axial ratio having a spacings equal to the spacings in the closest packed planes of the cubic (α) structure. Hence, $c' = a' \times$ ideal axial ratio $= a_{\text{cubic}}/\sqrt{2} \times \sqrt{8}/\sqrt{3}$.

VOL. 8 1960

phases of gold-based alloys in terms of the known zone distortion mechanisms referred to above. The $\Delta c'$ deviation can be interpreted in the following way: If the Fermi surface possessed a perfectly spherical shape, then for an ideally close-packed hexagonal structure the three principal faces of the Brillouin zone shown in Fig. 2, $\{10\bar{1}0\}$, $\{0002\}$ and $\{10\bar{1}1\}$, would be touched at e/a values of 1.14, 1.36‡ and 1.68, respectively.[8] Now the Goodenough type of interaction occurs between the Fermi surface and the Brillouin zone before the zone faces are touched. Such an interaction with respect to the $\{0002\}$ faces of the zone would cause an expansion of the c spacings in real space, and hence could account for both the $\Delta c'$ deviation and the higher-than-ideal axial ratios found in ζ phases. However, as is illustrated in Fig. 4, the results for gold-based alloys show that the $\Delta c'$ deviation is actually observed at much lower values of e/a than 1.36, i.e. at the onset of the c.p.hex. phases.[9] It must be concluded, therefore, that the Goodenough type of interaction with respect to the $\{0002\}$ faces of the zone occurs in gold-based alloys at lower values of e/a than would be consistent with an approaching *spherical* Fermi surface. Hence, according to this interpretation, it follows that the Fermi surface must be considerably distorted from the spherical shape.

Considering the origin of the $\Delta a'$ deviation it must be remembered that there seems to be no known zone distortion mechanism which can result in a *decrease* of the lattice spacings with increasing electron concentration. Hence, it seems reasonable to assume that the $\Delta a'$ deviation is a contraction in the a spacings which merely compensates for the expansion $\Delta c'$ in the c spacings in such a manner that the volume per atom of the structure remains virtually unchanged. This suggestion is in accordance with the observation that the volume of the unit cell per atom of the ζ phases, when plotted as a function of e/a, falls almost exactly on the extrapolation of the volume per atom of the α primary solid solution (Fig. 4).

Immediately after the onset of the ζ phases the a and c lattice spacing curves lie parallel to the a' and c' curves extrapolated from the α solid solutions and hence follow the normal course dictated by the size and valency relationships between solvent and solute atoms as discussed by Raynor[11] for the primary solid solutions. Therefore, the axial ratios of the ζ phases change very little in the range of e/a from the onset of the ζ phase up to about 1.35–1.36; remaining at $c/a \simeq 1.648$.

At e/a near 1.35–1.36 the Δa deviation is observed. Following the earlier work on gold-based alloys[6] and the more recent results in copper- and silver-based alloys[7] it may be concluded that in the Au–Sn and Au–In systems, for which the ζ phases show the Δa deviation, an overlap of Fermi electrons takes place across the $\{10\bar{1}0\}$ faces of the Brillouin zone. This overlap is responsible for the accelerated increase in the a spacings at electron concentration values greater than 1.35–1.36. The magnitude of the distortion due to overlap can be conveniently compared for different systems when the values of $\Delta a/(a - \Delta a)$ are plotted against e/a. Comparison of the data for the Au–Sn and Au–In alloys with similar data obtained by Massalski and Cockayne[7] for Cu–Ge, Cu–Ga and Ag–Al alloys is shown in Fig. 5. It can be seen that the rate of the a lattice spacings distortion at higher values of e/a is greater in the gold-based alloys than in these copper-based or silver-based alloys. It amounts to a change of 4.2×10^{-3} per 0.1 change in e/a, compared with 3.5×10^{-3} per 0.1 change in e/a for the copper and silver alloys. Fig. 5 also shows that the rate of the distortions, immediately following overlap, is at first very low and then accelerates smoothly to some steady value, indicating that the overlap of Fermi electrons across the zone face is a gradual and continuous process. The extrapolation of the $\Delta a/(a - \Delta a)$ curves to

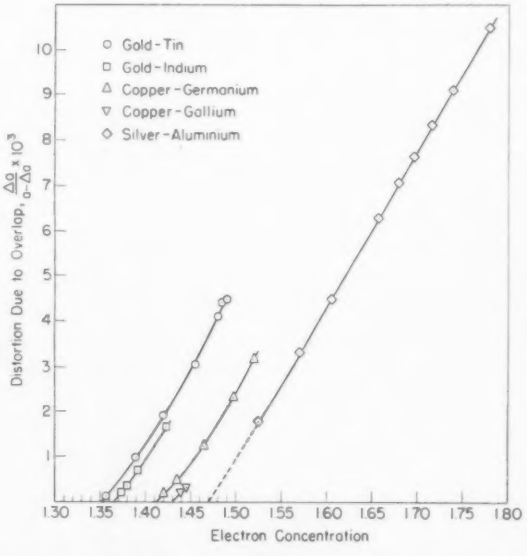


FIG. 5. Plot of the distortion due to overlap $[\Delta a/(a - \Delta a)]$ against electron concentration for the systems, Au–Sn, Au–In, Cu–Ge, Cu–Ga and Ag–Al.

‡ The value of e/a at which the $\{0002\}$ faces of the Brillouin zone would just be *touched* by an expanding spherical Fermi surface should not be confused with similar values of e/a (1.35–1.36) at which it is proposed that the distorted Fermi surface in gold-based ζ phases *overlaps* the $\{10\bar{1}0\}$ faces of the zone. For a more nearly spherical Fermi surface this overlap would occur in the region of e/a nearer 1.4 as was suggested for Cu-based and Ag-based alloys.[7]

the values at which $\Delta a/(a - \Delta a) = 0$ suggests that overlap across the $\{10\bar{1}0\}$ faces in Au–Sn and Au–In occurs near the e/a values of 1.352 and 1.365, respectively. These results are much lower than the corresponding values of 1.415 and 1.43 in Cu–Ge and Cu–Ga, respectively. It is possible that the extrapolation for Ag–Al alloys should not be linear, as plotted by Massalski and Cockayne[7] and as reproduced in Fig. 5, but in fact should turn to lower values of e/a, nearer to those for Cu–Ge and Cu–Ga.

Simultaneously with the accelerated increase in the a lattice spacings at e/a values near 1.35–1.36, the c spacing curves for the Au–Sn and Au–In alloys show a deviation to lower values and thus no longer remain parallel to the respective c' curves. Since once again there seems to be no known zone distortion mechanism which can cause a decrease in lattice spacings with increasing electron concentration, this deviation in the c spacings to lower values must be considered as a compensating effect for the increase, Δa, in a spacings due to overlap of Fermi electrons across the $\{10\bar{1}0\}$ faces of the Brillouin zone. Both the occurrence and position of the maxima in the c spacings are thus a result of the superposition of this compensating effect upon the increase in the c spacings dictated by the normal size and valency relationships. Had the normal trends in the lattice spacings been to decrease with increasing e/a, as for example in Ag–Al[7] no maximum would have been observed in the c spacing curve due to the compensating effect, but merely a change in slope to a more negative value. In accordance with the fact that the size of the indium atom is larger than that of the tin atom[12] the lattice spacings of Au–In alloys increase more rapidly than those of Au–Sn alloys,[9] when plotted as functions of e/a. The superposition of the compensating effect on these trends in lattice spacings should thus cause the maximum in the c spacings to occur at higher values of e/a in the Au–In system than in the case of Au–Sn, which is in agreement with the observed values of $e/a \simeq 1.38$ and 1.36 for the position of the maxima in these systems, respectively.

Following the lattice spacing work in Au–In ζ alloys,[6] Massalski *et al.*[13] studied the magnetic susceptibility of three ζ alloys as a function of composition and temperature. They observed a low diamagnetic susceptibility in the e/a region below 1.36 and an increased susceptibility above that value. They interpreted their results by suggesting that low diamagnetic susceptibility reflects a decrease in the density of states $N(E)$ immediately preceding the touching of the $\{0002\}$ faces of the Brillouin zone. The lattice spacings trends discussed above now indicate that the low density of states at e/a values lower than 1.36 must be associated with the shape of the Fermi surface in the Brillouin zone immediately preceding an overlap across the $\{10\bar{1}0\}$ faces.

5. THE DISTORTION OF THE FERMI SURFACE IN α AND ζ PHASES OF GOLD-BASED ALLOYS

Attention to the theory of the band structure of the noble metals and their α alloys has been given recently by Cohen and Heine[10]. They suggest that for monovalent metals the energy states at the center of Brillouin zone faces are either pure s-like or pure p-like in character. According to their model the magnitude of the band gap at a zone face may be expressed as a difference between the energies of the s and p states, i.e. $E_s - E_p$; this difference is then estimated in terms of the s–p excitation energy Δ_{sp} of the free atom. Cohen and Heine[10] conclude that for copper $E_p < E_s$, and for gold $E_p > E_s$.

Further it is suggested that the magnitude of the band gap, $E_s - E_p$, influences the shape of the Fermi surface and causes a distortion

$$d = \frac{1/2(E_s - E_p)}{1/2(E_s + E_p) - E_F} \tag{1}$$

where E_F is the energy at the Fermi level. In contrast with the rigid-band theory put forward by Jones[1], they propose that the band gap $E_s - E_p$ is changed upon alloying. Since for alloys based on the noble metals with additions of the B-subgroup elements, the solute always has a larger value of Δ_{sp} than the solvent, the energy of E_p will be raised relative to E_s by alloying. Hence, the addition of solute atoms to copper, where $E_p < E_s$, should lower the band gap and cause the Fermi surface to become more spherical. On the other hand, for gold where $E_p > E_s$ the addition of solute atoms should cause the band gap to be increased still further, and the Fermi surface to become grossly distorted from the spherical shape. Thus in gold-based α alloys the Fermi surface should touch the zone faces at relatively low values of e/a. In agreement with this conclusion the α phases based on gold are known to terminate at lower values of e/a than in the case of copper and silver alloys.

The present interpretation of the lattice spacings data for ζ alloys based on gold agrees well with the model of Cohen and Heine. Both the magnitude of the $\Delta a'$ and $\Delta c'$ deviations, and the low e/a values at which the ζ phases occur, point to a considerably distorted Fermi surface. Conversely, for the Cu–Ge and Cu–Ga systems, the seeming lack of the $\Delta a'$ and $\Delta c'$ distortion and the onset of the ζ phases at higher values of e/a are consistent with low energy gaps in the

VOL. 8 1960

Brillouin zone and a more nearly spherical Fermi surface in the c.p.hex. ζ alloys.

Now the larger the band gap the greater will be the difference between the value of e/a at which the Fermi surface first touches a zone face and the value at which overlap eventually takes place across it. Presuming that the band gaps in gold-based ζ phases are large, and that overlap across the $\{10\bar{1}0\}$ faces occurs at $e/a \simeq 1.35$–1.36 (from the extrapolation of $\Delta a/(a - \Delta a)$ to zero, as shown in Fig. 5), there must be considerable contact between the Fermi surface and these faces even at the onset of ζ phases near $e/a = 1.23$.

The relative distorting effect of a particular solute on the band gap of a solvent may be assessed, to a first approximation, by using the parameter η defined by Cohen and Heine[10] as follows:

$$\eta_{sp} = \left(1 + \frac{1}{(z-1)}\right)[(\Delta_{sp})_{\text{solute}} - (\Delta_{sp})_{\text{solvent}}] \quad (2)$$

where Δ_{sp} again refers to the s–p excitation energy of the free atom, and the inclusion of the solute valency, z, scales the parameter in terms of electron concentration. For alloys of gold with In, Hg, Sn and Cd the values of η are approximately 4.2, 4.0, 1.2 and 1.0, respectively.[10] Thus at any given electron concentration the magnitude of the band gaps should be greater, and hence the Fermi surface more distorted (equation 1), in alloys with In or Hg as solutes compared to alloys containing Sn or Cd. According to the present argument, therefore, this should result in more pronounced deviations towards higher initial axial ratios in the former alloys (Au–In and Au–Hg) than in the latter (Au–Sn and Au–Cd). This prediction is confirmed by the lattice spacings data.[9] At the onset of the ζ phases in Au–Hg and Au–In, at $e/a \simeq 1.22$ and 1.26, respectively, the axial ratios of the alloys are both of the order of 1.6485 and remain at this value till $e/a \simeq 1.33$. In Au–Cd and Au–Sn, however, not only do ζ phases occur at higher values of e/a, but the axial ratios are relatively lower, being equal to 1.6464 and 1.6457 at the onset of the ζ phases at $e/a \simeq 1.32$ and 1.33, respectively.

Knowledge of both lattice spacing relationships and the nature of the band gap in silver-based alloys is less detailed. The distortion due to overlap across the $10\bar{1}0$ faces of the Brillouin zone for Ag–Al (Fig. 5) is very similar to that for the Cu–Ga and Cu–Ge systems.[7] It therefore points to small band gaps and a nearly spherical Fermi surface. The ζ phase alloys based on silver are more numerous than those based on copper and gold, and many of them extend over a wide range of e/a as indicated schematically in Fig. 1. It is probable, therefore, that the conditions for stability of these phases are even more favorable in the silver-based systems than in those based on copper and gold. In order to clarify this possibility, the lattice spacings relationships of several such phases are being investigated at the authors' laboratory

It is very likely that the situation at the onset of the c.p.hex. ζ phase is indicative of the shape of the Fermi surface at the termination of the preceding α phases. Hence, the present conclusions regarding the large distortion of the Fermi surface in ζ phases based on gold add support to the interpretation by Cohen and Heine as to why the α phases based on gold terminate at relatively low values of e/a. Further, it may be noted that the previous interpretations of this latter fact were in terms of a greater-than unity valency for gold,[12,15] relative sizes of the atoms and ions of copper, silver and gold[14] or the differences in electrochemical factors.[12] All such effects cannot account for the strong $\Delta a'$ deviation in the a spacings on passing from the α to the ζ phases. Hence, it seems very probable that the major difference between the α and ζ alloys of gold and those of copper and silver can be attributed to the difference in the distortion of the Fermi surface.

ACKNOWLEDGMENT

We are indebted to Professor M. H. Cohen for many stimulating and informative discussions.

REFERENCES

1. H. Jones, *Proc. Roy. Soc.* A**147,** 396 (1934).
2. G. V. Raynor and T. B. Massalski, *Acta Met.* **3,** 480 (1955).
3. J. Goodenough, *Phys. Rev.* **89,** 282 (1953).
4. J. W. McClure, *Phys. Rev.* **98,** 449 (1955).
5. T. B. Massalaki, presented at *Symposium on the Theory of Alloy Phases*, 1955. American Society for Metals, Cleveland (1956).
6. T. B. Massalski, *Acta Met.* **5,** 541 (1957).
7. T. B. Massalski and B. Cockayne *Acta Met.* **7,** 762 (1959).
8. T. B. Massalski, *Metallurg. Rev.* **3,** 45 (1958).
9. T. B. Massalski and H. W. King, *Acta Met.* **8,** 677 (1960).
10. M. H. Cohen and V. Heine, *Advanc. Phys.* **7,** 395 (1958).
11. G. V. Raynor, *Trans. Faraday Soc.* **45,** 698 (1949).
12. G. V. Raynor, *Prog. Met. Phys.* **1,** 1 (1949).
13. T. B. Massalski, L. Meyer and D. Weiner, *Phys. Rev.* **115,** 301 (1959).
14. E. A. Owen and E. A. O'Donnel Roberts, *J. Inst. Met.* **73,** 471 (1947).
15. K. Schubert, *Naturwissenschaften* **39,** 159 (1952).

IRRADIATION HARDENING IN COPPER AND NICKEL*

M. J. MAKIN† and F. J. MINTER†

The lattice and dislocation components of irradiation hardening have been measured in polycrystalline copper and nickel as a function of (a) testing temperature and (b) neutron dose. The results are compared with Seeger's theory of lattice hardening, which is based on dislocations cutting through a forest of obstacles under the action of both stress and thermal activation. The observed temperature dependence of the lattice hardening in both metals is in excellent agreement with the theory in the as-irradiated condition. Mild annealing treatments greatly reduce the temperature sensitivity however and the theory is no longer obeyed. From the results it is concluded that the obstacles do not have a constant activation energy as assumed by Seeger and theories of the temperature dependence should include this factor. It is shown that the dose dependence of lattice hardening may be described by the new formula

$$\sigma_i = A(1 - e^{-B\phi})^{1/2}$$

which is derived by combining the theoretically predicted dependence on $\phi^{1/2}$ with a saturation effect. The existence of obstacles of various sizes is also indicated from measurements of the temperature dependence of the constants in this equation. No definite conclusions as to the mechanism of formation of the obstacles can be made at present. The dislocation hardening component is shown to be independent of testing temperature in copper but not in nickel.

DURCISSEMENT PAR IRRADIATION DU CUIVRE ET DU NICKEL

Les auteurs mesurent pour différentes températures et divers flux de neutrons, les deux composantes de durcissement de polycristaux de cuivre et de nickel. Ils comparent les résultats obtenus avec la théorie de Seeger. Selon celui-ci, le durcissement du réseau (première composante de durcissement) est causé par la présence d'obstacles entravant la propagation des dislocations sous l'action des contraintes et de l'activation thermique. Si, pour les deux métaux irradiés, on observe un accord parfait avec la théorie de la variation du durcissement en fonction de la température, un léger recuit diminue cependant la sensibilité à la température. Les auteurs en concluent que les obstacles ne présentent pas une énergie d'activation constante comme le suppose Seeger. D'autre part, afin de tenir compte de la saturation, ils proposent une nouvelle formule de la variation du durcissement du réseau en fonction du flux de neutrons:

$$\sigma_i = A(1 - e^{-B\phi})^{1/2}$$

Enfin, puisque les constantes de cette équation dépendent de la température, il existe donc des obstacles de dimensions variées.

On ne peut formuler de conclusions définitives, par exemple, quant au mécanisme de formation des obstacles.

Les auteurs terminent en montrant que la seconde composate de durcissement (Accroissement de la résistance à la formation de dislocations) est indépendante de la température pour le cuivre, mais pas pour le nickel.

BESTRAHLUNGSVERFESTIGUNG VON KUPFER UND NICKEL

Die Bestrahlungsverfestigung läßt sich in eine vom Kristallgitter und in eine von den Versetzungen herrührende Komponente aufteilen; beide wurden an polykristallinem Kupfer und Nickel als Funktion (a) der Versuchstemperatur und (b) der Neutronendosis gemessen. Die Ergebnisse werden mit Seegers Theorie der Gitterverfestigung verglichen. Dieser liegt ein Modell zugrunde, bei dem die Versetzungen unter der Wirkung von Spannung und thermischer Aktivierung einen Wald von Hindernissen durchschneiden. Die beobachtete Temperaturabhängigkeit stimmt bei beiden Metallen im Zustand nach der Bestrahlung ausgezeichnet mit der Theorie überein. Die Temperaturempfindlichkeit wird jedoch durch leichtes Erwärmen zum großen Teil abgebaut und stimmt dann nicht mehr mit der Theorie überein. Aus den Resultaten ergibt sich die Folgerung, daß den Hindernissen keine konstante Aktivierungsenergie zuzuschreiben ist, wie Seeger angenommen hatte, und die Theorien der Temperaturabhängigkeit sollten diesen Faktor berücksichtigen. Es wird gezeigt, daß die Dosisabhängigkeit der Gitterverfestigung durch die neue Formel

$$\sigma_i = A(1 - e^{-B\phi})^{1/2}$$

beschrieben werden kann, die sich aus der theoretisch vorhergesagten Abhängigkeit von $\phi^{1/2}$ zusammen mit einem Sättigungseffekt ableiten läßt. Die Messungen der Temperaturabhängigkeit der Konstanten in dieser Gleichung zeigen ebenfalls, daß Hindernisse verschiedener Größe existieren. Über den Bildungsmechanismus der Hindernisse können zur Zeit keine bestimmten Aussagen gemacht werden. Es wird gezeigt, daß die von den Versetzungen herrührende Verfestigungskomponente bei Kupfer von der Verformungstemperatur unabhängig ist, jedoch bei Nickel von der Temperaut abhängt.

INTRODUCTION

It is theoretically possible for radiation to harden a metal in two basically different ways: either (a) by making the nucleation of slip difficult (source hardening) or (b) by making the propagation of slip difficult (lattice hardening), and there is now considerable evidence that in well annealed metals such as copper and nickel both types of hardening occur on

* Received October 16, 1959.

† Metallurgy Division, A.E.R.E., Harwell.

VOL. 8 1960

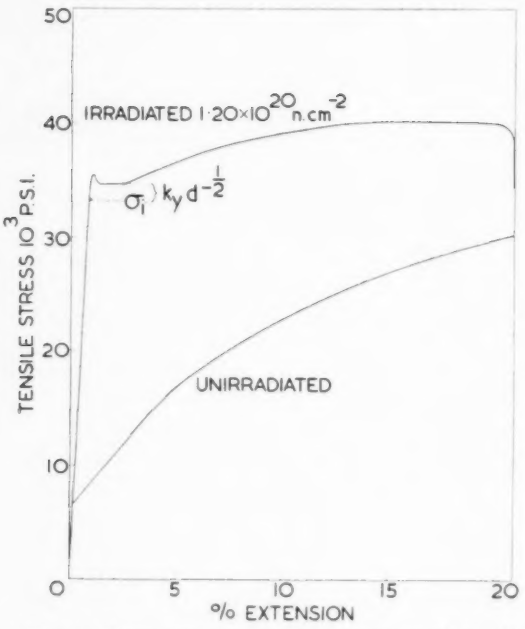


FIG. 1. Stress–strain curves for copper tested at 20°C showing the analysis into lattice σ_i and dislocation hardening σ_d.

irradiation. This conclusion is based upon the shape of the stress–strain curve of the polycrystalline metal after irradiation, Fig. 1, which shows a sharp yield point followed by a region of Luders strain. This type of yield occurs in mild steel and it has been shown both theoretically[1,2] and experimentally[1,3,4] that in such cases there is a relationship between the lower yield stress and the grain size:

$$\sigma_y = \sigma_i + k_y d^{-1/2} \tag{1}$$

where σ_y is the lower yield stress, σ_i is the lattice friction stress, $2d$ is the grain diameter and k_y is a measure of the stress required to operate dislocation sources. This relationship has also been shown to hold for irradiated copper.[5] The values of σ_i and k_y can therefore be determined from equation (1) when the yield stress is known as a function of the grain size. Alternatively σ_i and $\sigma_d\,(=k_y d^{-1/2})$ can be determined from the Luders strain by projecting back the stress–strain curve after the yield point as shown in Fig. 1. This is so because the Luders strain occurs while the metal is recovering by strain hardening the reduction in yield strength σ_d which occurs when it yields.

Seeger[6] has proposed a theory for lattice hardening based upon the cutting of dislocations through a forest of obstacles under the action of both stress and thermal activation. The theory is similar to that of the temperatue dependent part of the critical shear stress of unirradiated single crystals and is general in that the exact nature of the obstacles need not be specified. The theory states that the strain rate is given by the equation

$$\dot{\varepsilon} = \frac{Nb}{N_z} \cdot \nu_0 \cdot e^{-U(\sigma)/KT} \tag{2}$$

where $\dot{\varepsilon}$ = strain rate, N is the number of dislocations per unit volume held up against obstacles, N_z is the number of obstacles per unit area of glide plane, b is the Burgers vector, ν_0 is the frequency of oscillation of a dislocation $\sim 10^{10}$/sec, $U(\sigma)$ is the activation energy for cutting through the obstacles at a stress σ and T is the absolute temperature. Assuming an energy profile for $U(\sigma)$ and taking into account the probability that the larger the stress the smaller the average spacing between obstacles due to dislocations bowing out and so meeting another obstacle,[7] an equation is derived for σ of the form

$$\sigma^{2/3} = A - BT^{2/3}$$

where

$$A = \left[\frac{N_z}{Gb}\right]^{1/3} \frac{U_0}{4x_0 b}$$

and

$$B = A\left[\frac{k}{U_0} \ln \frac{Nb\nu_0}{N_z \dot{\varepsilon}}\right]^{2/3}.$$

The predicted temperature dependence has been shown by Seeger to be in excellent agreement with experimental results obtained by Blewitt[8] on irradiated copper single crystals.

In the present experiments the lattice and source hardening components, σ_i and σ_d have been measured by the Luders strain method on polycrystalline copper and nickel as a function of neutron dose and temperature of testing. The experimental results are compared with Seeger's theory of lattice hardening outlined above.

EXPERIMENTAL DETAILS

The results of spectrographic analyses on the materials used are given in Table 1.

TABLE 1

Impurity	Copper % impurity	Nickel % impurity
Iron	0.0003	0.05
Copper		0.01
Silver	0.005	Not detected
Lead	0.002	0.005
Tin	0.0002	Not detected
Nickel	0.005	
Cobalt	Not detected	0.05
Aluminium	Not detected	0.0002
Calcium	0.0005	0.0001
Magnesium	0.0001	~0.1
Bismuth	0.0005	Not detected
Zinc	0.001	0.002
Cadmium	0.0001	Not detected
Silicon	0.0001	0.04
Manganese	Not detected	0.0008
Chromium	Not detected	0.001

The copper was an "oxygen free high conductivity" grade and the nickel was designated "pure". Both materials were initially in the form of annealed wire, the copper 0.080 in. dia. and the nickel 0.048 in. dia. Wire specimens (3 in. long × 0.048 in. dia.) were used throughout to minimize the induced radioactivity and to enable a large number of specimens to be irradiated at one time under similar conditions. The copper specimens were prepared by drawing the 0.080 in. dia. wire down to 0.048 in. dia. and then annealing at 450° for 60 min. The nickel wire as supplied was straightened by applying slight tension and then annealing at 615°C for 60 min. Metallographic examination was carried out before irradiation, the average grain diameter of the copper specimens was 0.010–0.015 mm and of the nickel 0.015–0.020 mm. The specimens were mounted in robust aluminium jigs and sealed in a helium atmosphere to prevent contamination. The irradiations were carried out for various times in three different reactors, BEPO, Windscale and NRX in Canada. Cobalt monitors were included in each specimen batch to measure the total thermal neutron flux. The quoted figures are epithermal flux which has been calculated from the slow neutron dose (as measured by the cobalt monitors) by using either the experimentally determined ratio of epithermal/slow flux where available, or the caculated value of this ratio. The irradiation temperature did not exceed 100°C.

Tensile tests were carried out at a variety of temperatures in a conventional hard beam tensile testing machine fitted with motor drive. The copper specimens were gripped in pin vices which were attached in a special jig to ensure good alignment of the specimen during mounting. The nickel specimens were gripped in clamp type grips. All tests were carried out at a strain rate of 7.0×10^{-5} sec^{-1}. The stress was measured to 0.25 per cent of the maximum value and the strain to 0.01 per cent. Tests at various temperatures were made by enclosing the specimen in liquid baths; details of the baths used are given in Table 2.

TABLE 2

Temperature (°C)	Bath	Fixed point
−195	Liquid N_2	Boiling point
−183	Liquid O_2	Boiling point
−158.5	Iso-pentane	Melting point
−115	Ethyl alcohol	Melting point
−78	Solid CO_2 and acetone	Sublimation point
−50–−5	Aqueous $CaCl_2$	Freezing point
0	Ice	Melting point
20	Water	Room temperature
50–200	Silicone oil	Controlled to ±1°C

EXPERIMENTAL RESULTS

A typical curve for unirradiated and irradiated copper is shown in Fig. 1 and the method whereby the total hardening is analysed into lattice and dislocation components by projecting back the stress–strain curve after the yield is illustrated in this figure. The accuracy of this method of determining the lattice hardening is good in the present experiments because the early part of the stress–strain curve after the yield is almost linear for a considerable extension beyond the Luders strain, for example in irradiated copper the curve is practically linear up to about 4 per cent extension of which only the first 0.9 per cent is occupied by the Luders strain.

Careful measurements in this linear region therefore enable the slope of the line to be accurately determined. In addition the dislocation hardening is found to amount to only a few per cent of the lattice hardening in the specimens used so that errors in the dislocation hardening have very little effect on the determination of the lattice hardening. Whilst this enables the lattice hardening to be accurately measured (±1,000 lb/in^2) it has, of course, the converse effect of making the dislocation hardening difficult to determine and the scatter of results is ±15 per cent of the mean value.

To determine the detailed temperature dependence of irradiation hardening, a large batch of copper specimens was irradiated with 7.9×10^{19} neutrons cm^{-2} and a batch of nickel specimens with 7.0×10^{19} neutrons cm^{-2}.

The effect of testing temperature on the shape of the stress–strain curve is shown in Fig. 2 where results are given on nickel. The curves are very nearly parallel and the extent of the Luders strain is constant at about 2.5 per cent. The slope of the linear hardening part of the curve following the Luders strain is almost constant between −160°C and 239°C and increases only at −195°C. The results on copper are very similar.

The variation in lower yield stress with temperature for irradiated copper and nickel is given in Fig. 3. The lower yield stress of copper is almost linear with testing temperature between −195°C and +80°C but this is not significant since the division into lattice and dislocation components has not yet been made. Analysing the results into these two components by the method described in the introduction enables the temperature dependence of the lattice and dislocation hardening to be determined, Figs. 3 and 4. The lattice hardening term σ_i is very temperature dependent in both irradiated copper and nickel and is not a linear function with temperature in either metal.

VOL. 8 1960

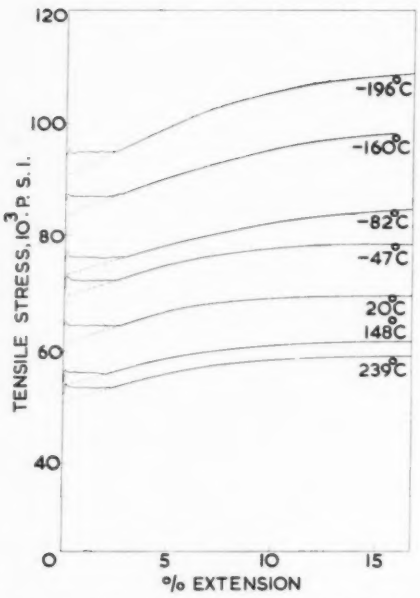


FIG. 2. The effect of testing temperature on the stress–strain curve of irradiated (7.0×10^{19} neutrons cm^{-2}) nickel.

The dislocation hardening term σ_d is almost independent of testing temperature in copper but in nickel σ_d decreases from 4500 lb/in^2 at -195°C to $\sim$3000 lb/in^2 at $+200$°C. In copper, however, although σ_d was substantially constant at about 1300 lb/in^2 between -160°C and $+200$°C persistently low values

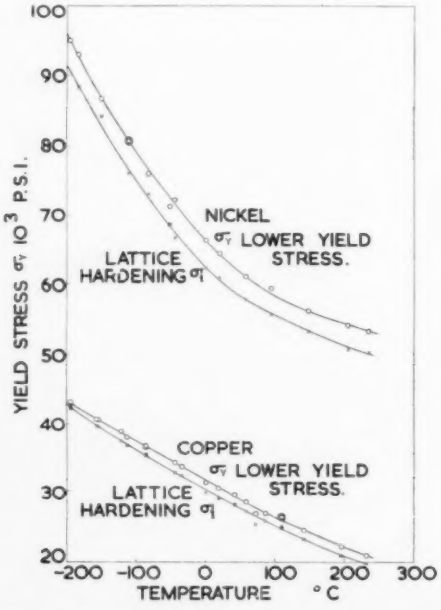


FIG. 3. The temperature dependence of σ_y and σ_i in irradiated copper ($\phi = 7.9 \times 10^{19}$ neutrons cm^{-2}) and nickel ($\phi = 7.0 \times 10^{19}$ neutrons cm^{-2}).

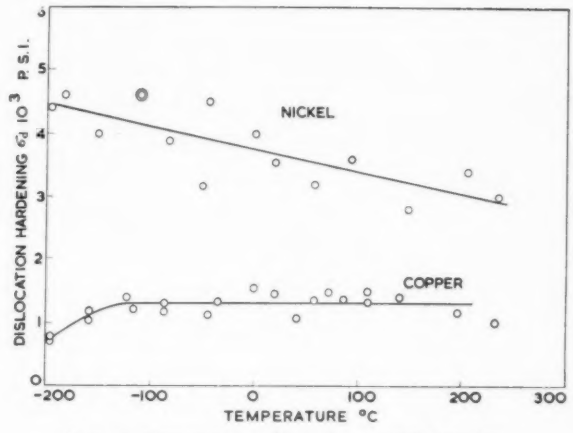


FIG. 4. Temperature dependence of dislocation hardening σ_d in irradiated copper and nickel.

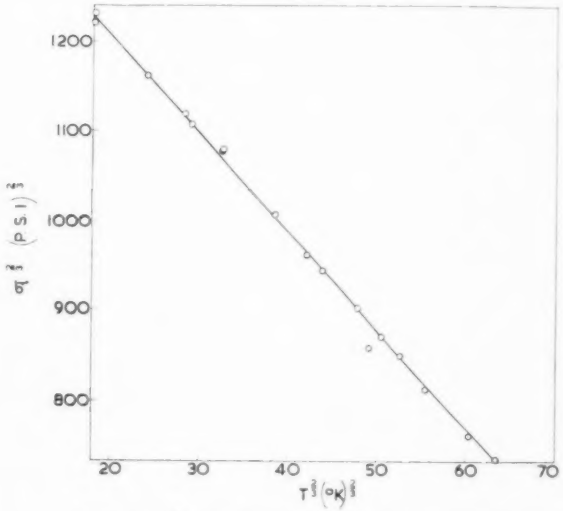


FIG. 5. $\sigma_i^{2/3}$ as a function of $T^{2/3}$ for copper. The equation of the line is $\sigma_i^{2/3} = 1426 - 11{\cdot}0T^{2/3}$.

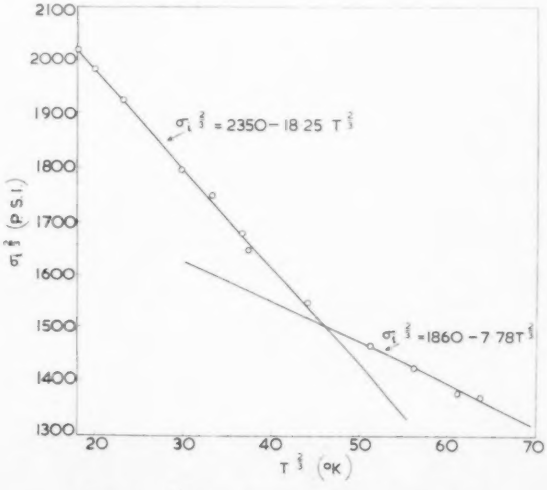


FIG. 6. $\sigma_i^{2/3}$ as a function of $T^{2/3}$ for nickel.

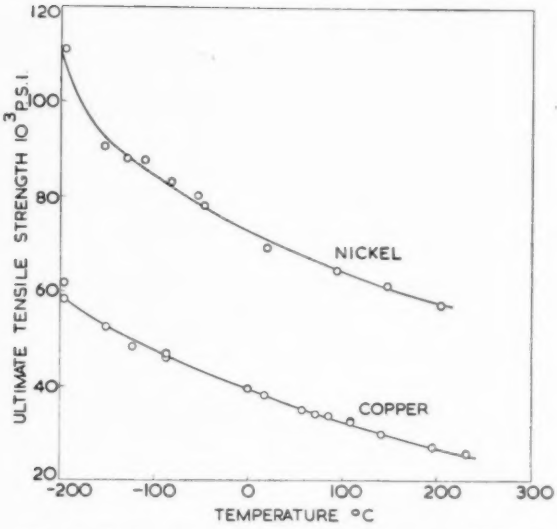


FIG. 7. Temperature dependence of the ultimate tensile strength of irradiated copper and nickel. (copper $\phi = 7.9 \times 10^{19}$ neutrons cm^{-2}) (nickel $\phi = 7.0 \times 10^{19}$ neutrons cm^{-2}).

were obtained at −195°C. In nickel this was not observed.

Seeger's[6] theory of lattice hardening, described in the introduction, predicts a linear relationship between $\sigma_i^{2/3}$ and $T^{2/3}$ and the results are plotted in this way for copper and nickel in Figs. 5 and 6. A very good straight line relationship is obtained for copper and in nickel the results fall on two straight lines intersecting at $T = 39$°C.

The variation in ultimate tensile strength with temperature is shown in Fig. 7 for both irradiated metals. In each case the curve follows the general shape of the yield stress–temperature curve except for the high results obtained at −195°C. Although the

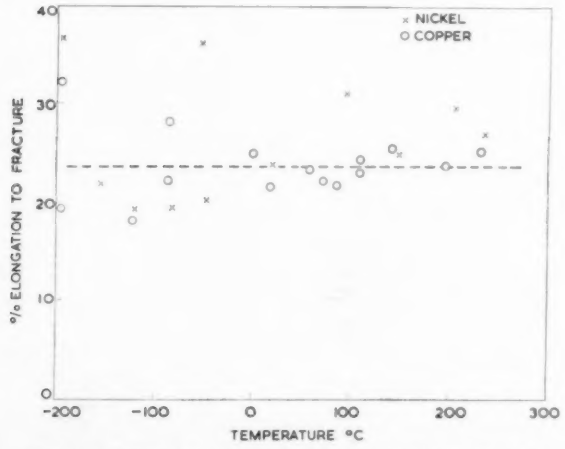


FIG. 8. Elongation to fracture of irradiated copper and nickel.

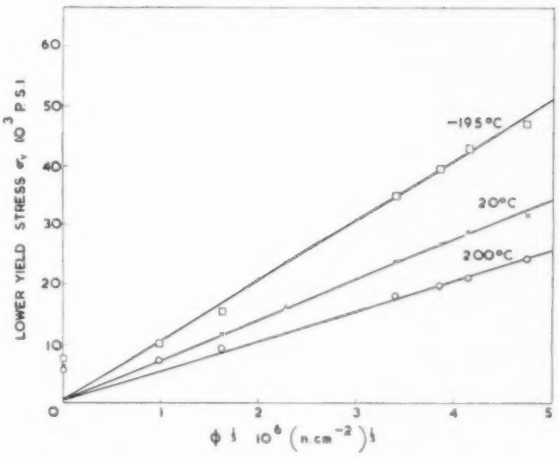


FIG. 9. The dose dependence of σ_y in copper. The rates of increase of σ_y with $\phi^{1/3}$ are:
−195°C, 10,020 lb/in^2/10^6 (neutrons cm^{-2})$^{1/3}$
20°C, 6850 lb/in^2/10^6 (neutrons cm^{-2})$^{1/3}$
200°C, 5020 lb/in^2/10^6 (neutrons cm^{-2})$^{1/3}$.

elongation before fracture values for the two irradiated metals are very scattered, Fig. 8, there does not appear to be any systematic variation in this quantity with testing temperature for either metal.

The dose dependence of the mechanical properties of both metals has been measured at three testing temperatures (−195°, 20° and +200°C) for doses between 9.5×10^{17} neutrons cm^{-2} and 1.07×10^{20} neutrons cm^{-2}. The variation in yield stress plotted against $\phi^{1/3}$ at three testing temperatures is given in Figs. 9 and 10 for copper and nickel, respectively. At each testing temperature the results fall on a straight

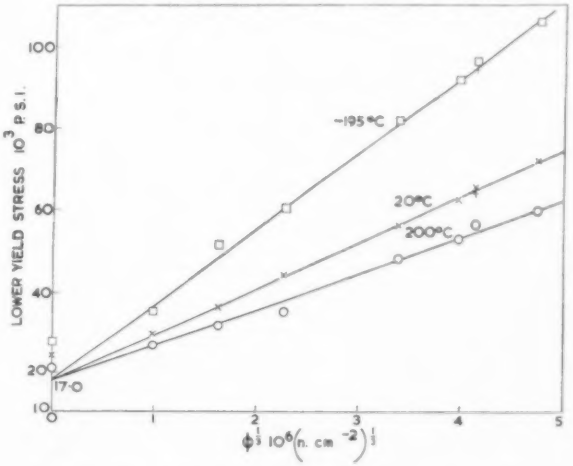


FIG. 10. The dose dependence of σ_y in nickel. The rates of increase of σ_y with $\phi^{1/3}$ are:
−195°C, 18,710 lb/in^2/10^6 (neutrons cm^{-2})$^{1/3}$
20°C, 11,380 lb/in^2/10^6 (neutrons cm^{-2})$^{1/3}$
200°C, 8940 lb/in^2/10^6 (neutrons cm^{-2})$^{1/3}$.

VOL. 8 1960

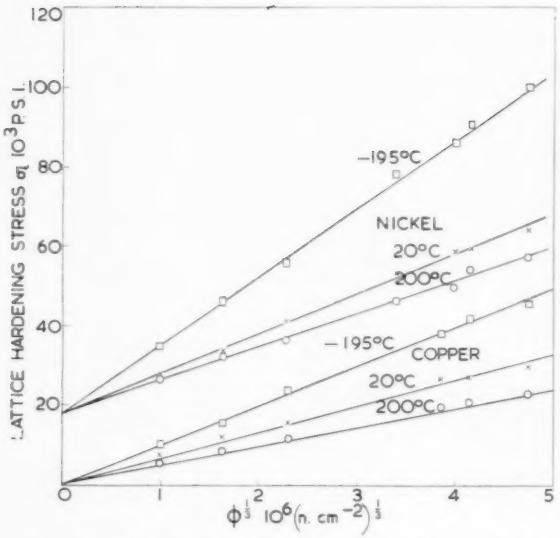


FIG. 11. The lattice hardening stress σ_i as a function of $\phi^{1/3}$ for copper and nickel at various temperatures. The rates of increase of σ_i with $\phi^{1/3}$ in lb/in^2/10^6 (neutrons cm^{-2})$^{1/3}$ are:

Temp.	Nickel	Copper
−195°C	17,000	9880
20	10,060	6580
200	8400	4800.

line, indicating that over the range of doses investigated there is a linear dependence of σ_y with $\phi^{1/3}$ and the lines obtained at various testing temperatures intersect at a point when $\phi^{1/3} = 0$. The stress at this intersection is less than the yield stress of the unirradiated material at any of the three testing temperatures and an "incubation" period at the start of the irradiation is observed. Similar behaviour has been observed in copper single crystals[9] where a series of tests at

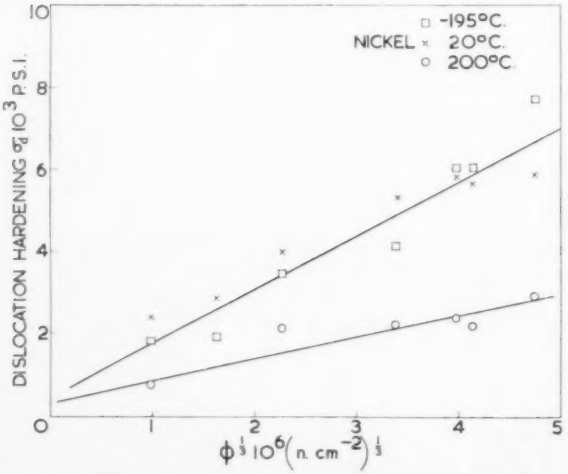


FIG. 12. The dislocation hardening stress σ_d of nickel as a function of $\phi^{1/3}$.

very low doses has shown that the critical shear stress rises very slowly with $\phi^{1/3}$ until the line appropriate to the testing temperature is reached.

Analysis of the stress–strain curves into the lattice and dislocation hardening components σ_i and σ_d has been carried out and are shown in Figs. 11 and 12. It is found that σ_i is proportional to $\phi^{1/3}$ for both metals at all testing temperatures. The linearity of σ_i with $\phi^{1/3}$ agrees with the experimental observations on copper single crystals, where the critical shear stress (which is effectively σ_i, since the grain size $2d$ is theoretically infinite) is approximately proportional to $\phi^{1/3}$.[9,10] The straight line relationships observed between σ_i and $\phi^{1/3}$ at different testing temperatures intersect at the same point on the stress axis when

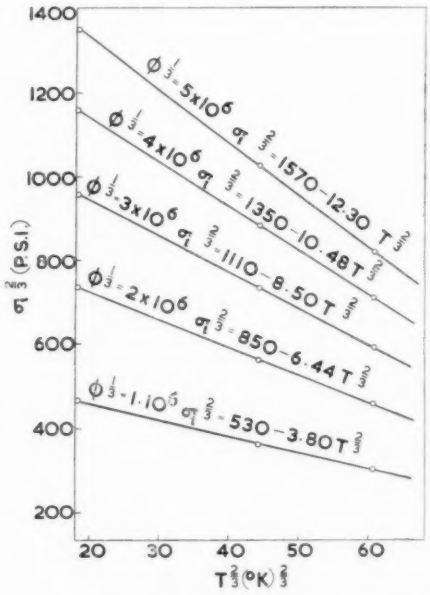


FIG. 13. $\sigma_i^{2/3}$ as a function of $T^{2/3}$ in copper at various dose levels.

$\phi^{1/3} = 0$ as the yield stress $\sigma_y/\phi^{1/3}$ relationships. The results enable the temperature dependence of σ_i to be investigated at various neutron doses. In Fig. 13, $\sigma_i^{2/3}$ is plotted as a function of $T^{2/3}$ for copper at various neutron doses from 1×10^{18} to 1.25×10^{20} neutrons/cm^2. Linear relationships are obtained for all the neutron doses in excellent agreement with Seeger's theory. The values of the constants in the equation

$$\sigma_i^{2/3} = A - BT^{2/3}$$

are given as a function of neutron dose for copper in Fig. 14. In the case of nickel sufficient specimens were not available to determine accurately at each dose the slope of both of the linear relationships

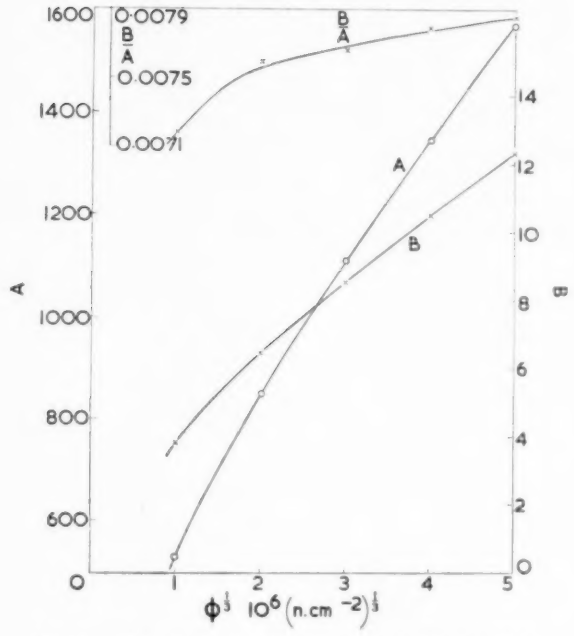


FIG. 14. The variation of the constants in the equation $\sigma_i^{2/3} = A - BT^{2/3}$ as a function of $\phi^{1/3}$.

between $\sigma_i^{2/3}$ and $T^{2/3}$. In copper both A and B increase with dose but are not linear with $\phi^{1/3}$ and the ratio B/A increases with dose.

The variation in ultimate tensile strength with neutron dose at various testing temperatures is shown in Figs. 15 and 16 for copper and nickel, respectively. There is a long incubation period at low doses during which the UTS is very little affected by the irradiation. Following this region it increases linearly with $\phi^{1/3}$ in a similar manner to the yield strength. This behaviour is observed at −195°C, 20° and 200°C in both metals. The UTS/$\phi^{1/3}$ relationships obtained at various testing temperatures do not intersect at $\phi = 0$ as the $\sigma_y/\phi^{1/3}$ relationships do. The rate of increase of the UTS with $\phi^{1/3}$ is much less rapid than that of the yield stress σ_y; in copper the UTS increases at about 50 per cent of the rate of increase of σ_y with $\phi^{1/3}$ and in nickel the corresponding figure is ~70 per cent.

The elongation to fracture is reduced at all testing temperatures (below the annealing temperature) by irradiation, and in Fig. 17 the results are plotted as a function of $\phi^{1/3}$. There is considerable scatter but the general reduction with increasing dose can be clearly seen.

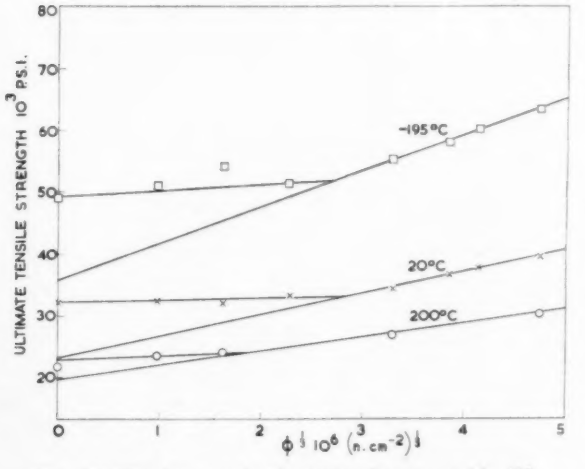


FIG. 15. The increase in the UTS of copper with $\phi^{1/3}$.
The rates of increase are:
−195°C, 5860 lb/in^2/10^6 (neutrons cm^{-2})$^{1/3}$
20°C, 3480 lb/in^2/10^6 (neutrons cm^{-2})$^{1/3}$
200°C, 2260 lb/in^2/10^6 (neutrons cm^{-2})$^{1/3}$.

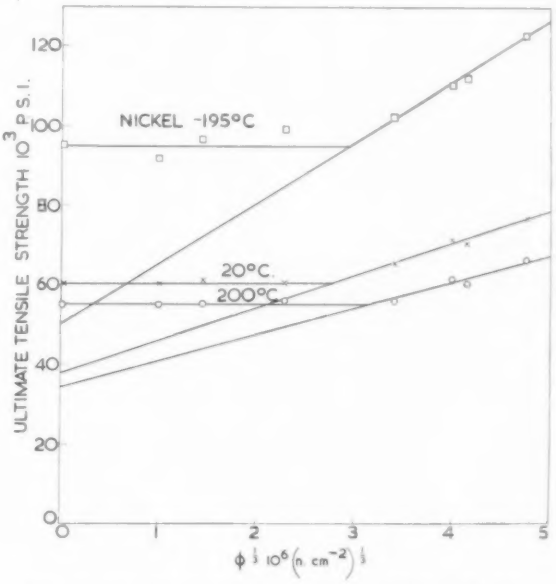


FIG. 16. The increase in the UTS of nickel with $\phi^{1/3}$.
The rates of increase are:
−195°C, 15,240 lb/in^2/10^6 (neutrons cm^{-2})$^{1/3}$
20°C, 8200 lb/in^2/10^6 (neutrons cm^{-2})$^{1/3}$
200°C, 6600 lb/in^2/10^6 (neutrons cm^{-2})$^{1/3}$.

DISCUSSION

The division of irradiation hardening into two components, lattice and dislocation hardening, is now well established and the results will be discussed in terms of these two components.

Lattice hardening must be caused by "obstacles" of some kind distributed throughout the crystal structure which oppose the motion of dislocations across the glide plane. In Seeger's theory of this hardening it is assumed that (a) the activation energy U_0 required by a dislocation to cut through an obstacle is a constant and (b) that N_z, the number of obstacles per unit area of glide plane, is directly proportional to the dose ϕ.

VOL. 8 1960

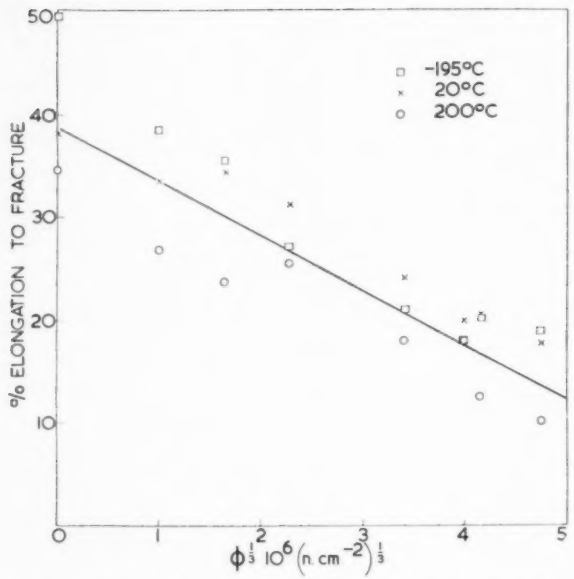


FIG. 17. The elongation to fracture of irradiated nickel. The rate of decrease is ~5.3 per cent/10^6 (neutrons cm^{-2})$^{1/3}$.

The observed temperature dependence of lattice hardening in copper and nickel is in excellent agreement with Seeger's theory, Figs. 5 and 6, there being a linear relationship between $\sigma_i^{2/3}$ and $T^{2/3}$ as predicted by equation (3).

In nickel two linear relationships are observed indicating that in this metal there are two types of defect contributing to the temperature dependence. The results obtained after various neutron doses can be used to throw further light on the theory, which predicts that

$$\frac{B}{A} = \left[\frac{k}{U_0} \ln \frac{Nbv_0}{N_z \dot{\varepsilon}}\right]^{2/3}.$$

In this relationship N,b, v_0, k and $\dot{\varepsilon}$ are independent of neutron dose, which can affect only U_0 and N_z. Experimentally it is observed that the ratio B/A increases with increasing dose, Fig. 14. This can occur only by a decrease in U_0 with increasing dose $\left[\ln \frac{Nbv_0}{N_z \dot{\varepsilon}}\right.$ will decrease with increasing $\left.N_z\right]$. This is contrary to Seeger's assumption that U_0 is a constant.

Further insight into the validity of the theory is given by the observation that the excellent agreement between theory and experiment holds only in the "as-irradiated" condition, and after mild annealing treatments the lattice hardening does not obey equation (3). The effect of mild annealing (306°C for 10 min) on irradiated copper is to reduce the temperature sensitivity of the lattice hardening by reducing

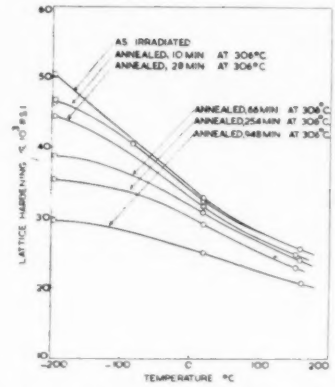


FIG. 18. The effect of annealing treatments on the temperature dependence of copper irradiated with 1.20×10^{20} neutrons cm^{-2}.

σ_i at low testing temperatures while having little effect on the hardening at higher testing temperatures, Fig. 18. Mild annealing also completely removes the work softening phenomena[11] in irradiated copper. These results strongly suggest that obstacles with a range of activation energies are present in irradiated copper. Obstacles with small activation energies offer resistance to dislocation motion at low temperatures but are transparent at high temperatures. On annealing, the obstacles with a low activation energy and also consequently a small size, will disappear first resulting in a rapid reduction in the temperature sensitivity of the lattice hardening, as is observed.

These observations indicate that Seeger's assumption of a constant U_0 is an over-simplication, and that the expression he uses for the energy for a dislocation to cut an obstacle $U(\sigma)$ in equation (2), is unnecessarily complicated. Probably a better model at this stage is to adopt a simple expression for $U(\sigma)$, namely that

$$U(\sigma) = U_0\left(1 - \frac{\sigma}{\sigma_0}\right).$$

Inserting in equation (2) this gives a temperature dependence of the form

$$\sigma = A - BT. \qquad (4)$$

Both A and B will depend upon the characteristics of the obstacle and will be larger for small obstacles. With a range of obstacle sizes a family of straight lines of the form of equation (4) will be formed and the upper curved surface of their intersections represents the variation of σ_i with temperature.

The linear relationship between the lattice hardening stress σ_i and the cube root of the neutron dose, $\phi^{1/3}$, is purely an empirical one which has no firm basis in

theory. The theory of the cutting of an obstacle by a dislocation line[12] suggests that σ_i should be proportional to $N_z^{1/2}$. Initially N_z is expected to be proportional to the neutron dose ϕ, but as the dose increases a saturation effect may occur which limits the number of new obstacles which can be formed. In general it is possible to associate a volume v with each obstacle within which a new obstacle cannot form. The number of new obstacles dN_z can then be written

$$dN_z = a\dot{\phi} - vN_z a\dot{\phi}$$

where $a\dot{\phi}$ = rate of production of obstacles per neutron.

Integrating

$$N_z = \frac{1}{v}[1 - e^{-av\phi}]$$

and hence if $\sigma_i \propto N_z^{1/2}$

then $$\sigma_i = A'[1 - e^{-B'\phi}]^{1/2} \qquad (5)$$

where $$A' \propto \frac{1}{v^{1/2}} \quad \text{and} \quad B' = av.$$

This equation has been fitted to the experimental results at each temperatue by selecting the initial slope ($A'B'^{1/2}$) and the value of σ_i at 10^{19} neutron cm^{-2}. The results for nickel are shown in Fig. 19, where the curve is the theory and the points experimental values. The fit is as good as that of $\sigma_i \propto \phi^{1/3}$ and the relation avoids the awkward incubation period at the start of the irradiation. An unequivocal decision between the two relations is not possible with the present data which does not extend to sufficiently high doses, where the divergence between the two relations becomes large, and further work is in progress to determine the point. Experiments on the critical shear stress of electron irradiated lithium fluoride,[12] however, indicate that in this material equation (5) is obeyed very accurately and saturation is actually observed. The relationship $\sigma \propto \phi^{1/3}$ is capable of describing the results only up to electron doses of $\sim 3 \times 10^{15}$ electrons/cm^2 beyond which it predicts a greater hardening than is measured.

The saturation theory predicts that after a considerable irradiation obstacles with a range of sizes will be present which is the conclusion derived from the effect of mild annealing treatments on the temperature dependence of σ_i and the work softening phenomenon. Further evidence of the variation in the size of

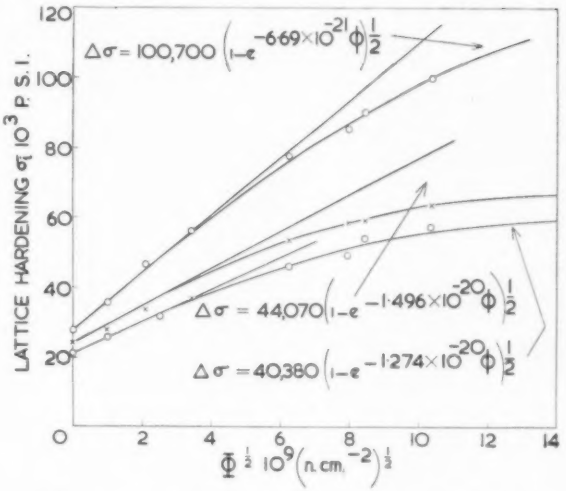


FIG. 19. σ_i as a function of $\phi^{1/2}$. The points are experimental and the curves theoretical relationships of the type $\sigma_i = A(1 - e^{-B\phi})^{1/2}$.

the obstacles is given by the variation in the quantity B' ($= av$) with testing temperature. In Fig. 19 (av) at -195°C is 0.669×10^{-20} cm^{-3} whereas at higher temperatures it is approximately 1.3×10^{-20} cm^{-3}. This decrease in v (a, the initial production rate of obstacles, is a constant) implies that more obstacles are effective at -195°C than at 20°C. Since the distribution of obstacles is obviously the same in specimens tested at 20° and -195°C (all have been irradiated together) there must be a large number of obstacles which are effective in resisting dislocation motion at -195°C but are completely transparent at 20°C.

REFERENCES

1. N. J. PETCH, *J. Iron St. Inst.* **174,** 25 (1953).
2. A. H. COTTRELL, *Trans. Amer. Inst. (Metall.) Engrs.* **212,** 192 (1958).
3. E. O. HALL, *Proc. Phys. Soc., Lond.* B**64,** 747, (1951).
4. D. HULL and I. L. MOGFORD, *Phil. Mag.* **3,** 1213, (1958).
5. M. A. ADAMS and P. R. B. HIGGINS, *Phil. Mag.* **4,** 777 (1959).
6. A. K. SEEGER, reported at *Proc. 2nd Int. Conf. Peaceful Uses Atomic Energy, Geneva*, 1958. United Nations, New York (1958).
7. J. FRIEDEL *Les Dislocations*. Gauthiers-Villars, Paris (1956).
8. T. H. BLEWITT, see Ref. (6).
9. M. J. MAKIN, unpublished work.
10. T. H. BLEWITT, see G. H. KINCHIN and R. S. PEASE, *Rep. Prog. Phys.* **18,** (1955).
11. M. J. MAKIN, *Acta Met.* **7,** 233 (1959).
12. A. D. WHAPHAM and M. J. MAKIN, *Phil. Mag.* **5,** 237 (1960).
13. J. SILCOX and P. B. HIRSCH, *Phil. Mag.* **4,** 1356 (1959).

VOL. 8 1960

DIFFUSION DANS LE SYSTÈME URANIUM–TITANE*

Y. ADDA† et J. PHILIBERT‡

Les auteurs ont étudié la diffusion intermétallique dans le système uranium–titane entre 650 et 1050°C au moyen de diverses techniques: micrographie, microdureté et microsonde de Castaing. Les coefficients de diffusion, les facteurs de fréquence et les énergies d'activation ont été déterminées, pour des concentrations atomiques en uranium comprises entre 0,05 et 0,9, dans la phase γ (cubique centrée).

Après avoir mis en évidence un effet Kirkendall très important dans ce système, les auteurs ont calculé d'après les relations de Darken, les coefficients de diffusion intrinsèques de l'uranium et du titane. Ces résultats, comparés à ceux qui avaient été obtenus lors d'une étude antérieure sur le système uranium–zirconium, montrent que la mobilité des atomes de titane est plus élevée que celle des atomes de zirconium. De plus, dans le but d'interpréter les différences de porosité observées dans les couples U–Zr et U–Ti, les auteurs ont évalué les sursaturations en lacunes dues à l'effet Kirkendall, et trouvé des valeurs très voisines ($\sim 10^{-3}$) pour ces deux couples. On est donc conduit à supposer que les différences de porosité sont dues à des conditions de germination différentes.

DIFFUSION IN THE SYSTEM URANIUM–TITANIUM

The intermetallic diffusion in the system U–Ti is studied between 650 and 1050 °C with various techniques: metallography, microhardness and the Castaing microanalyser. The diffusion coefficient the frequency factors and the activation energies were determined in the γ phase (centered cubic) for uranium concentrations between 0.05 and 0.9.

An important Kirkendall effect was in evidence and the intrinsic diffusion coefficients of U and Ti were calculated on the basis of Darken's relations. These results compared to those previously obtained on the system U–Zr, show that the mobility of Ti atoms is higher than that of Zr atoms. Furthermore, the vacancies supersaturation due to the Kirkendall effect was evaluated in order to explain the difference in porosity observed in the couples U–Zr and U–Ti. Values very near 10^{-3} were found for these two couples. It is concluded that the difference in porosity is due to different conditions of nucleation.

DIE DIFFUSION IM SYSTEM URAN–TITAN

Die intermetallische Diffusion im System Uran–Titan wurde zwischen 650° und 1050°C mit verschiedenen Methoden untersucht: metallographisch, durch Messung der Mikrohärte und durch Messungen mit der Mikrosonde nach Castaing. Die Diffusionskoeffizienten, die Frequenzfaktoren und die Aktivierungsenergien wurden im Bereich der Atomkonzentrationen des Urans von 0,05 bis 0,9 in der kubisch raumzentrierten γ-Phase untersucht.

Nachdem in diesem System ein beträchtlicher Kirkendall-Effekt aufgezeigt worden war, wurden nach den Beziehungen von Darken die inneren Diffusionskoeffizienten zwischen Uran und Titan berechnet. Die Ergebnisse werden verglichen mit denjenigen einer vorhergehenden Arbeit über das System Uran–Zirkon. Sie zeigen, daß die Bewaglichkeit der Titanatome größer ist, als die der Zirkon Atome. Weiterhin wurde die Leerstellenübersättigung, die vom Kirkendall–Effekt herrührt, abgeschätzt um die bei den U–Zr- und U–Ti-Paaren beobachteten Unterschiede der Porosität zu erklären; dabei wurden für beide Paare sehr ähnliche Werte ($\sim 10^{-3}$) gefunden. Es ist also anzunehmen, daß die Unterschiede in der Porosität von verschiedenen Bedingungen bei der Keimbildung herrühren.

Au cours de recherches sur la diffusion chimique de l'uranium avec les métaux de transition, nous avons entrepris l'étude du système uranium–titane. Celui-ci présente beaucoup de points communs avec le système uranium–zirconium qui avait fait l'objet d'une étude antérieure.[1] En effet, si le titane diffère quelque peu du zirconium par son rayon atomique, il en est par contre très voisin par sa structure électronique et son point de fusion. De plus, comme le zirconium, le titane forme avec l'uranium, à haute température et à toutes concentrations, une solution solide homogène cubique centrée. Ainsi, en raison de ces analogies, l'étude des processus de diffusion dans les systèmes U–Ti et U–Zr peut faire apparaître une corrélation entre la mobilité atomique et certaines propriétés physiques.

Dans le présent travail, nous exposons nos résultats expérimentaux relatifs à la diffusion dans le couple U–Ti, et, dans les cas qui nous ont paru les plus intéressants, nous les comparons à ceux que nous avions obtenus précédemment avec le couple U–Zr.

TECHNIQUE OPÉRATOIRE

Les couples de diffusion sont préparés par soudage sous vide à 600°C, sous forte pression, durant 2 h, de

* Reçu le 10 Août, 1959.
† Centre d'Études Nucléaires de Saclay.
‡ I.R.S.I.D., St. Germain en Laye.

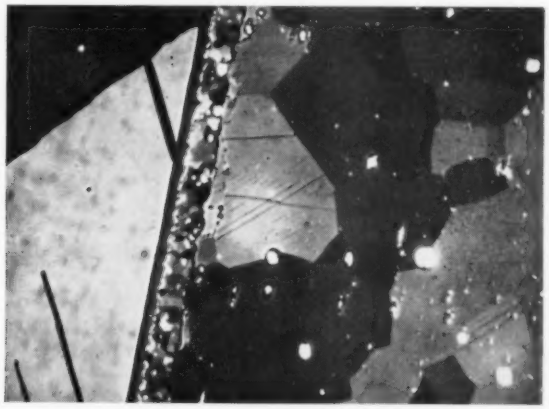


FIG. 1. 96 h à 650°C (trempe à l'air) Lumière polarisée. ×187·5.

plaquettes d'uranium et de titane polies électrolytiquement (il s'agit d'uranium du Commissariat à l'Energie Atomique et de titane obtenu par le procédé Kroll).[1]

Ces échantillons sont traités sous un vide inférieur à $5 \cdot 10^{-6}$ mm de Hg, à des températures comprises entre 600 et 1075°C, pendant des durées variant de 5–300 h. Ils sont refroidis lentement ou bien trempés suivant la technique d'étude envisagée, comme on le verra plus loin. Les couples de diffusion sont ensuite sectionnés perpendiculairement à l'interface de soudure et polis métallographiquement.

ÉTUDE MICROGRAPHIQUE

Après polissage mécanique à la poudre de diamant (1–5 μ) les échantillons sont polis 10 sec sous 50 V, à une température inférieure à 5°C (agitation énergique) dans le bain suivant:

acide perchlorique	60 cm³
butyl-cellosolve	350 cm³
alcool méthylique	590 cm³.

L'aspect micrographique des couples U–Ti présente une grande analogie avec celui des couples U–Zr; en effet, on observe au-dessous de 650°C une diffusion du titane suivant les joints de grains de l'uranium superposée à une diffusion en volume (Fig. 1). Au-dessus de cette température, la diffusion se produit exclusivement en volume et les limites de phases révélées par attaque au cours du polissage délimitent une zone de diffusion très régulière, d'une épaisseur rigoureusement constante dans tout l'échantillon. Les Figs. 2–10 montrent l'aspect de la zone de diffusion après un traitement thermique de 24 h à des températures variant de 650 à 1050°C et trempe à l'air.

On observe sur les micrographies une zone nettement différenciée de l'uranium et du titane. Pour une température de diffusion donnée, la largeur x de cette zone varie linéairement avec la racine carrée de la durée de diffusion t. Les micrographies des Figs. 11–14 montrent l'évolution de la zone de diffusion à 750°C pour des durées variant de 16–64 h. Les

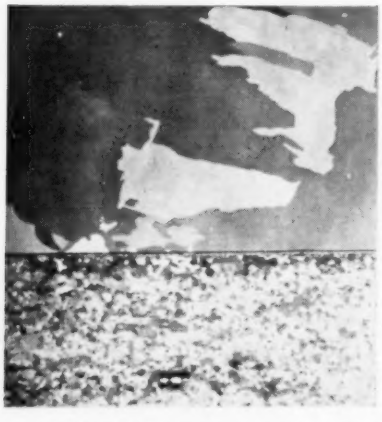


FIG. 2. 24 h à 650°C (trempe à l'air). ×37·5.



FIG. 3. 24 h à 700°C (trempe à l'air). ×37·5.

VOL. 8 1960

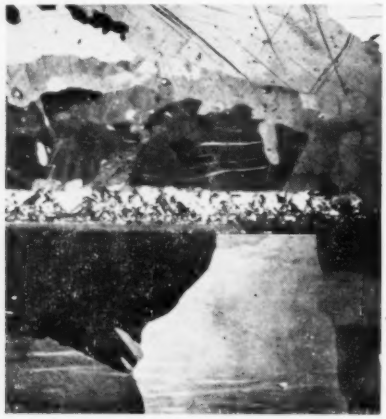


FIG. 4. 24 h à 750°C (trempe à l'air).

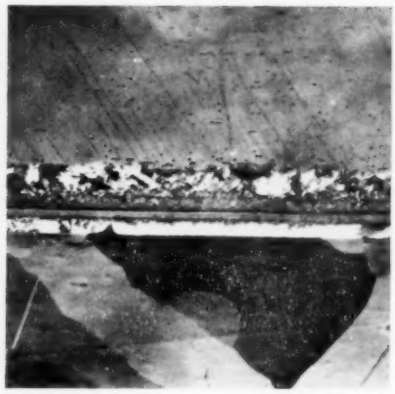


FIG. 5. 24 h à 800°C (trempe à l'air).



FIG. 6. 24 h à 859°C (trempe à l'air). ×37·5



FIG. 7. 24 h à 900°C (trempe à l'air). ×37·5



FIG. 8. 24 h à 950°C (trempe à l'air).

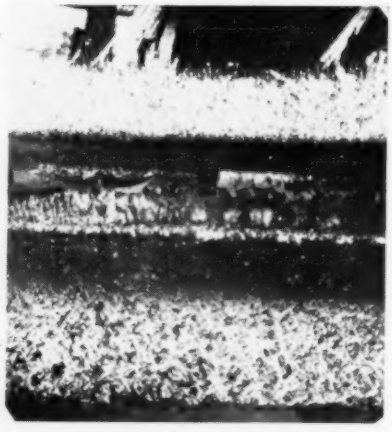


FIG. 9. 24 h á 1000°C (trempe à l'air).



FIG. 10. 24 h à 1050°C (trempe à l'air). ×37·5



FIG. 11. 16 h à 750°C (trempe à l'air). ×75



FIG. 12. 24 h à 750°C (trempe à l'air).

courbes donnant x en fonction de $\sqrt{t}$ sont portées sur la Fig. 15 pour des températures comprises entre 650° et 950°C. On peut alors définir à chaque température un "coefficient de pénétration" P tel que:

$$x = P\sqrt{t}.$$

Portant log P en fonction de l'inverse $1/T$ de la température absolue, on obtient une série de segments de droite (Fig. 16). Chaque segment devrait correspondre à un domaine de températures du diagramme d'équilibre caractérisé par le nombre et al nature des phases qui peuvent se former.

DÉTERMINATION DES COEFFICIENTS DE DIFFUSION

Les courbes concentration-pénétration, correspondant à la diffusion en phase homogène à des températures supérieures au point de transformation du titane, ont été établies par analyse ponctuelle au moyen du microanalyseur à sonde électronique[2,3] en utilisant les raies $K\alpha_1$ du titane et $L\alpha_1$ de l'uranium (Fig. 17).

Ces courbes nous ont permis de calculer le coefficient de diffusion chimique $\tilde{D}$ au moyen de la méthode de Matano[4]. Les valeurs du coefficient $\tilde{D}$ pour les températures de 950°, 1000°, 1050° et 1075°C,

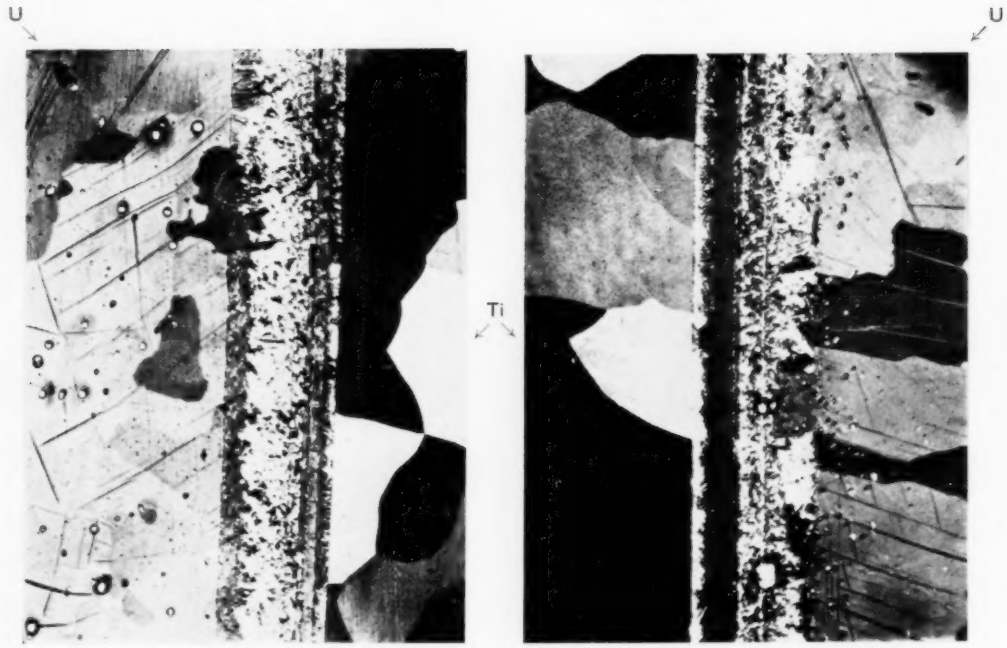


FIG. 13. 48 h à 750°C (trempe à l'air).

FIG. 14. 64 h à 750°C (trempe à l'air).

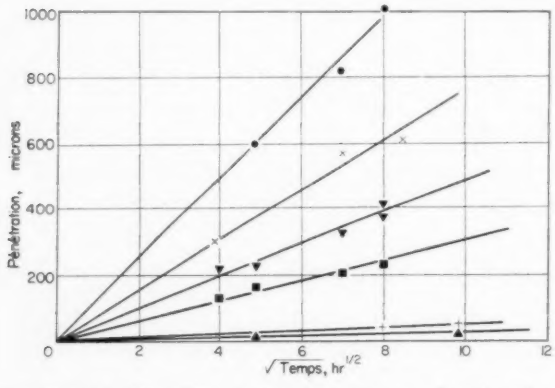


FIG. 15. Variation de la pénétration en fonction du (temps)$^{1/2}$.
● 950°C × 850°C ▼ 800°C
■ 750°C + 700°C ▲ 650°C

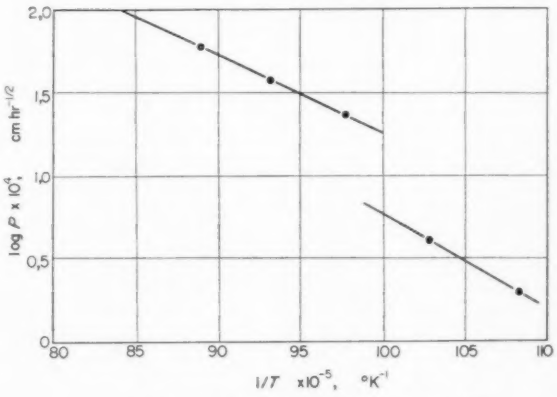


FIG. 16. Courbe log $P = f(1/T)$. T en °K.

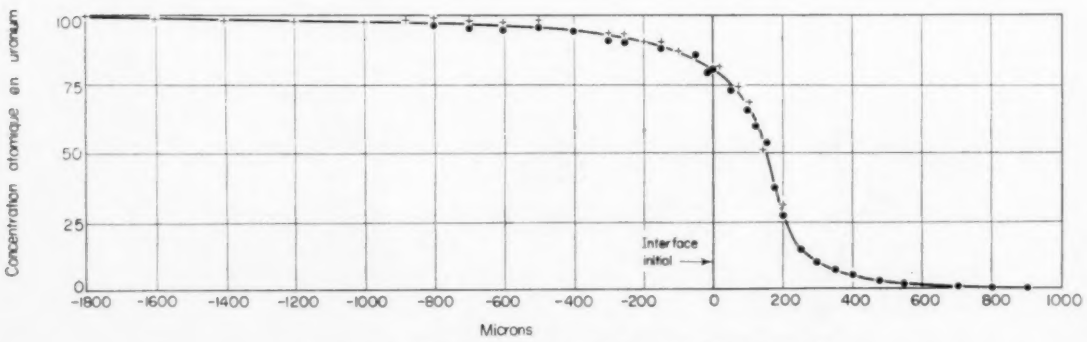


FIG. 17. Diffusion uranium–titane à 1050°C pendant 24 h.
● Concentration déterminée au moyen de la raie $L\alpha$- de l'uranium
+ Concentration déduite des mesures effectuées avec la raie $K\alpha$ du titane

TABLEAU I

Conc. at. N_U	$\tilde{D}$ cm² sec.$^{-1}$				Q kcal/ at. g	$\tilde{D}_0$ cm² sec^{-1}
	950°	1000°	1050°	1075°		
0,05	$1,7 \cdot 10^{-9}$	$2,6 \cdot 10^{-9}$	$4,5 \cdot 10^{-9}$	$5,7 \cdot 10^{-9}$	30,2	$4,6 \cdot 10^{-4}$
0,1	$1,0 \cdot 10^{-9}$	$1,6 \cdot 10^{-9}$	$3,1 \cdot 10^{-9}$	$3,4 \cdot 10^{-9}$	33,8	$1,1 \cdot 10^{-3}$
0,2	$4,6 \cdot 10^{-10}$	$7,1 \cdot 10^{-10}$	$1,3 \cdot 10^{-9}$	$1,9 \cdot 10^{-9}$	37,5	$2,2 \cdot 10^{-3}$
0,3	$2,3 \cdot 10^{-10}$	$5,7 \cdot 10^{-10}$	$8,9 \cdot 10^{-10}$	$1,1 \cdot 10^{-9}$	39,4	$2,6 \cdot 10^{-3}$
0,4	$2,7 \cdot 10^{-10}$	$4,2 \cdot 10^{-10}$	$8,6 \cdot 10^{-10}$	$1,2 \cdot 10^{-9}$	39,4	$2,6 \cdot 10^{-3}$
0,5	$2,9 \cdot 10^{-10}$	$4,6 \cdot 10^{-10}$	$1,1 \cdot 10^{-9}$	$1,5 \cdot 10^{-9}$	42	$9,5 \cdot 10^{-3}$
0,6	$6,2 \cdot 10^{-10}$	$8,6 \cdot 10^{-10}$	$1,7 \cdot 10^{-9}$	$2,6 \cdot 10^{-9}$	38,4	$4 \cdot 10^{-3}$
0,7	$1,1 \cdot 10^{-9}$	$1,5 \cdot 10^{-9}$	$3,1 \cdot 10^{-9}$	$4,1 \cdot 10^{-9}$	34,8	$1,6 \cdot 10^{-3}$
0,8	$1,9 \cdot 10^{-9}$	$2,8 \cdot 10^{-9}$	$5,5 \cdot 10^{-9}$	$6,5 \cdot 10^{-9}$	33	$1,4 \cdot 10^{-3}$
0,9	$3,4 \cdot 10^{-9}$	$5,4 \cdot 10^{-9}$	$1,2 \cdot 10^{-8}$	$1,25 \cdot 10^{-8}$	36,6	$1,1 \cdot 10^{-2}$

sont portées dans le Tableau 1 ainsi que sur la Fig. 18, pour des concentrations atomiques en uranium comprises entre 0,05 et 0,9.

On constate que, à toutes les températures, $\tilde{D}$ passe par un minimum en fonction de la concentration N_U. La forme des courbes $\tilde{D}(N_U)$ est entièrement analogue à celles que nous avions déterminées dans le couple U–Zr;[1] mais généralement, pour une même température et une même concentration, le coefficient $\tilde{D}$ est plus faible dans le cas du couple U–Zr.

De plus, nous avons déterminé l'énergie d'activation Q pour la diffusion chimique. Le Tableau 1 et la Fig. 19 montrent qu'en fonction de la concentration Q varie en passant par un maximum voisin de 40 kcal/at. g pour $N_U = 0,5$.

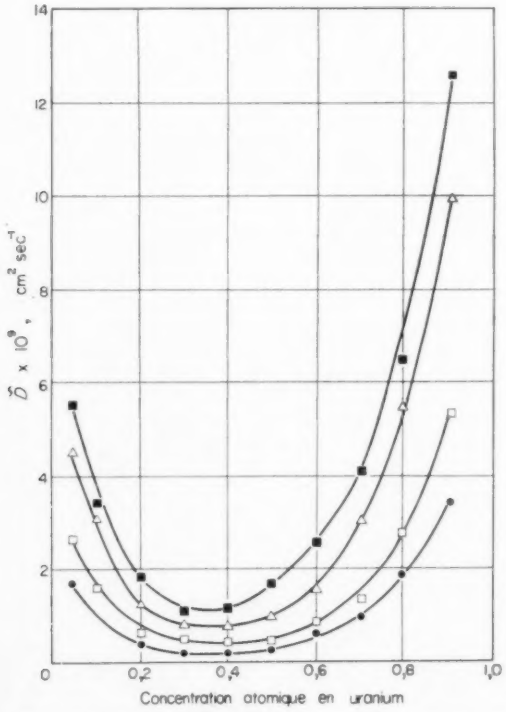


FIG. 18. Variation du coefficient de diffusion chimique en fonction de la concentration.
● 950°C □ 1000°C
△ 1050°C ■ 1075°C

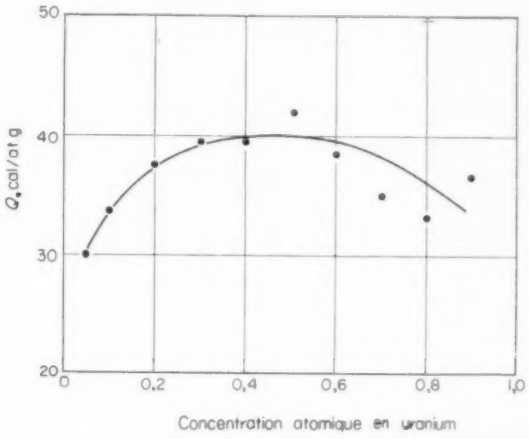


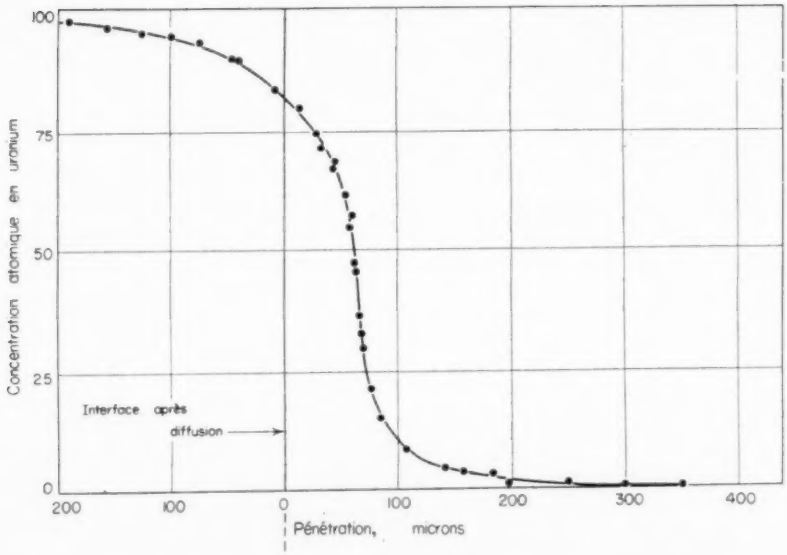
FIG. 19. Variation de l'énergie d'activation pour la diffusion chimique en fonction de la concentration.

VARIATION DE L'ASPECT MICROGRAPHIQUE AVEC LA CONCENTRATION: ESSAI D'ÉTALONNAGE

On peut se demander si les limites entre les zones qui présentent un aspect micrographique déterminé, après des traitements de diffusion effectués à des températures différentes, correspondent à des valeurs bien définies de la concentration. C'est ce que nous avons vérifié en comparant les courbes concentration-pénétration obtenues au moyen du microanalyseur avec les abscisses des limites mesurées sur les micrographies. Une telle comparaison est faite sur la Fig. 20, où courbe et micrographie sont à la même échelle, l'origine a été choisie dans les deux cas à l'ancien interface de soudure. Les résultats de ces comparaisons effectuées sur des échantillons refroidis lentement après diffusion sont groupés dans le Tableau 2.

On vérifie bien sur ce tableau qu'à un aspect micrographique donné correspond une concentration constante, quelle que soit la température de diffusion entre 950° et 1050°C. De plus, il apparaît que le

VOL. 8 1960



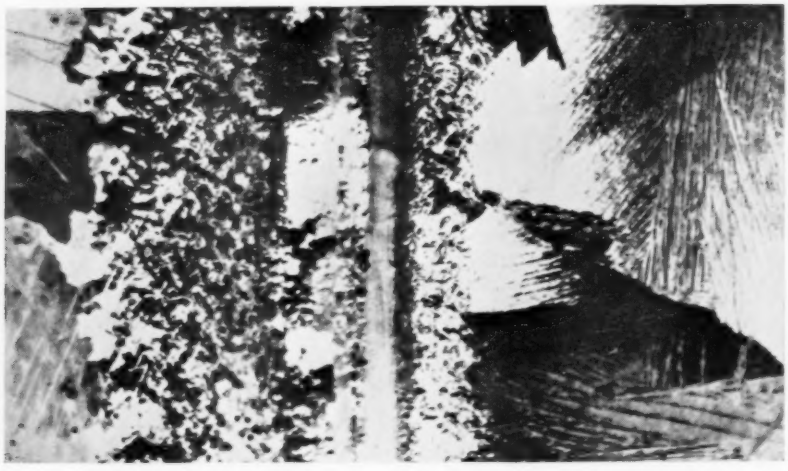


FIG. 20. Diffusion uranium–titane à 950°C pendant 24 h. Courbe établie au moyen du microanalyseur à sonde électronique.

TABLEAU 2

Température (°C)	950	1000	1050
Limite des précipités fins, côté Ti	0,025	0,01	0,005
Première limite γ'	0,10	0,06	0,06
Deuxième limite γ'	0,275	0,275	0,275
Première limite U_2Ti	0,57	0,58	0,60
Deuxième limite U_2Ti	0,69	0,69	0,70
Ancien interface de soudure	0,82	0,82	0,82
Première limite du précipité aciculaire	0,92	0,94	0,94
Deuxième limite du précipité aciculaire, côté U	0,97	0,98	0,975

domaine de stabilité de la phase U_2Ti est d'environ 10% at. Ce resultat, en accord avec les diagrammes de Buzzard *et al.*[5] et de Udy et Boulger[6] est en contradiction avec les déterminations récentes de Knapton[7]. Des études ultérieures au microanalyseur Castaing nous permettront probablement de préciser les limites du domaine de stabilité de U_2Ti.*

Enfin, à l'aide de cet étalonnage, et d'après la micrographie d'un couple de diffusion traité entre 950 et 1050°C, il est possible d'établir en quelques minutes la courbe concentration-pénétration correspondante, avec une erreur moyenne de 3–4 pour-cent (Fig. 21).

* Des résultats récents confirment les déterminations de Knapton.

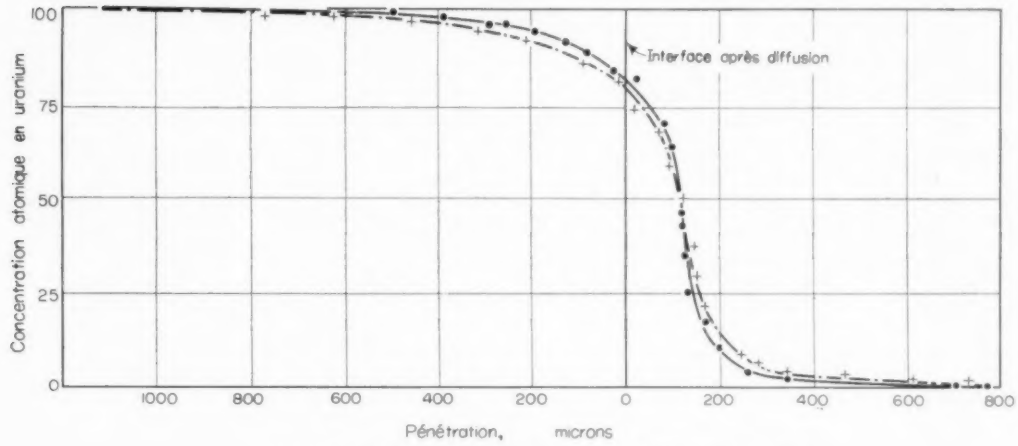


FIG. 21. Diffusion uranium–titane à 950°C pendant 24 h.
+ — · — + Courbe établie par micrographie ● — ● Courbe déterminée au moyen du microanalyseur à sonde électronique

ÉTUDE MICROSCLÉROMÉTRIQUE

On a mesuré la microdureté Vickers suivant des directions perpendiculaires au front de diffusion. Celle-ci présente des variations très importantes, et la courbe microdureté-pénétration est encore plus complexe que celle qui avait été obtenue sur les couples U–Zr.[1] On note en particulier une chute appréciable de la dureté au voisinage de l'ancien interface de soudure (Fig. 22).

De la même façon que dans des études précédentes,[1,8,9] on peut établir un étalonnage microdureté–pénétration, et ainsi déduire des courbes de microdureté, les courbes concentration-pénétration, avec une bonne approximation (Tableau 3 et Fig. 23).

ÉTUDE DE L'EFFET KIRKENDALL

L'observation micrographique de la zone de diffusion ne montre que très rarement la présence d'une porosité. Ayant noté une chute de la microdureté au voisinage de l'ancien interface de soudure (zone correspondant approximativement au maximum de sursaturation en lacunes), nous avions pensé qu'une microporosité, trop faible pour être visible au microscope optique, en était responsable. Des micrographies électroniques de la zone de diffusion ne nous ont pas permis jusqu'à présent de vérifier cette hypothèse.

En dépit de l'absence de porosité dans la zone de diffusion, nous avons observé un effet Kirkendall[10] très net. Il est cependant légèrement plus faible que dans le couple U–Zr, comme le montrent les valeurs des déplacements x_i de l'interface repéré au moyen de fils de tungstène;[11] ainsi, par exemple, après 48 h de diffusion à 1000°C, on note des déplacements x_i de 200 μ dans le couple U–Zr et de 180 μ dans le couple U–Ti.

Ces déplacements x_i varient comme la racine carrée de la durée de diffusion t (Fig. 24): ils peuvent

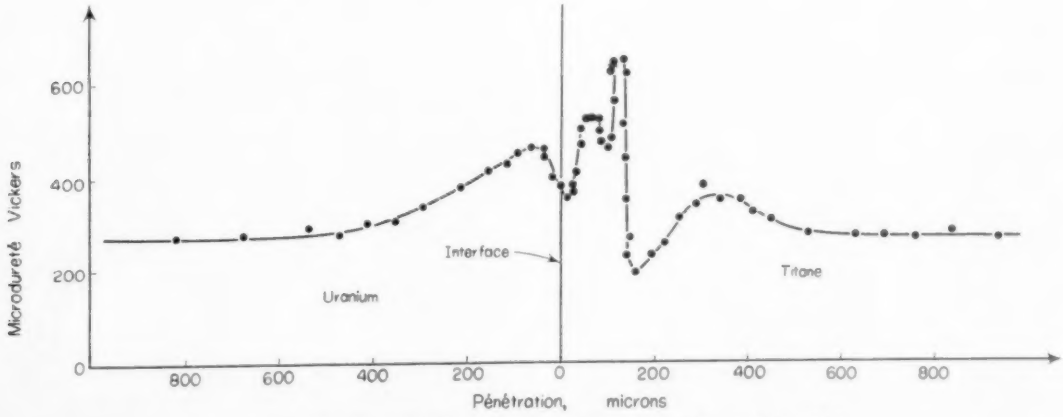


FIG. 22. Diffusion uranium–titane à 950°C pendant 24 h.

TABLEAU 3

Conc. at. U%	Dureté Vickers	Conc. at. U%	Dureté Vickers	Conc. at. U%	Dureté Vickers	Conc. at. U%	Dureté Vickers
0	⩽300	22	240	50	699	78	505
1	342	24	280	52	685	80	430
2	382	26	350	54	675	82	397
3	⩾388	28	459	56	657	84	416
4	355	30	526	58	622	86	422
5	318	32	583	60	588	88	⩽398
6	304	34	653	62	570	90	417
8	265	36	713	64	559	92	⩾417
10	253	38	719	66	⩽544	94	389
12	223	40	⩾722	68	547	96	360
14	212	42	722	70	554	98	295
16	⩽203	44	719	72	566	100	⩽283
18	203	46	715	74	⩾578		
20	216	48	707	76	556		

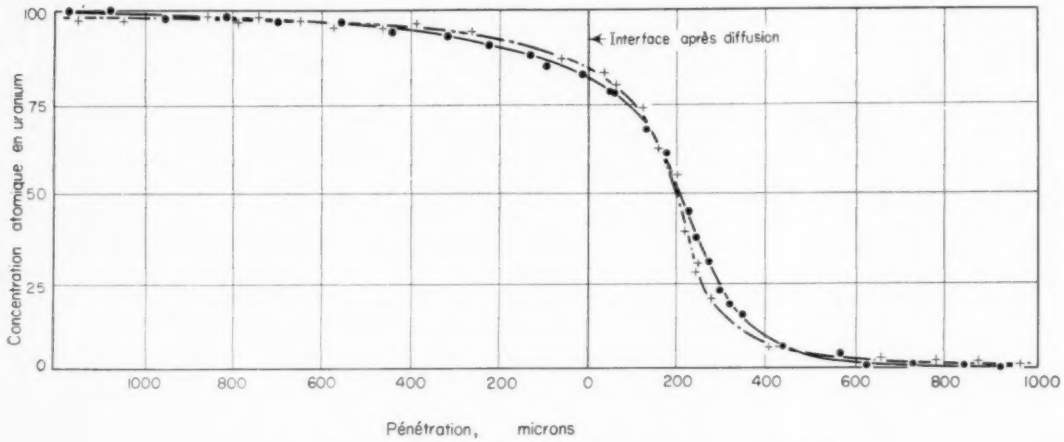


FIG. 23. Diffusion uranium–titane à 1050°C pendant 24 h.
+ — · — + Courbe déterminée au moyen du microanalyseur à sonde électronique
● ——— ● Mesures effectuées par microdureté

s'exprimer en fonction de t et de la température absolue T par la relation (Fig. 25)

$$x_i = 0{,}9\, t^{1/2} \exp -\left(\frac{14\,600}{RT}\right). \qquad (1)$$

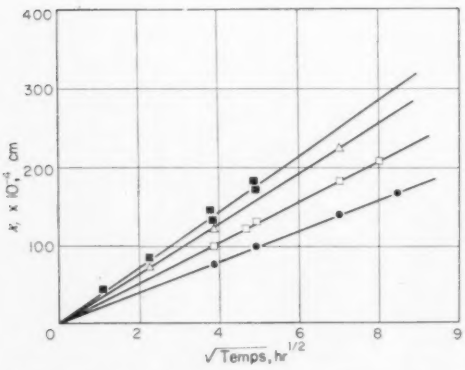


FIG. 24. Déplacement de l'interface en fonction du (temps)$^{1/2}$.
■ 1075°C △ 1050°C
□ 1000°C ● 950°C

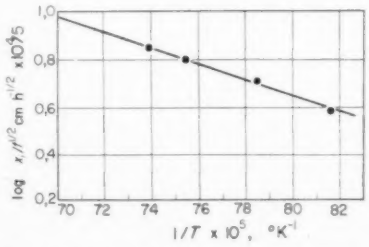


FIG. 25. Courbe log $(X_i/t) = f(1/T)$. T en °K.
$X_i = 0{,}9\, t^{1/2} \exp -(14\,600/RT)$ t en h.

Enfin, nous avons pu calculer les coefficients de diffusion intrinsèques D_U et D_{Ti} au moyen des deux équations de Darken[12]

$$v = \left(D_U - D_{Ti}\right)\frac{dN}{dx} \qquad (2)$$

$$\tilde{D} = N_U D_{Ti} + N_{Ti} D_U$$

où v est la vitesse de déplacement de l'interface repéré, déterminée d'après la relation (1) et dN/dx le gradient de concentration à l'interface repéré. Les

TABLEAU 4

Température (°C)	950°	1000°	1050°	1075°
N_U	0,82	0,82	0,82	0,835
N_{Ti}	0,18	0,18	0,18	0,165
D_U	$4,7 \cdot 10^{-9}$	$9,5 \cdot 10^{-9}$	$1,6 \cdot 10^{-8}$	$2,2 \cdot 10^{-8}$
D_{Ti}	$1,2 \cdot 10^{-9}$	$2,9 \cdot 10^{-9}$	$4,1 \cdot 10^{-9}$	$5,8 \cdot 10^{-9}$
D_U/D_{Ti}	3,9	3,3	3,9	3,8

résultats de ce calcul sont présentés dans le Tableau 4.

On constate d'après ce tableau que la concentration à l'interface parait indépendante de la température; on peut donc calculer les énergies d'activation Q_U et Q_{Ti} pour les coefficients intrinsèques D_U et D_{Ti}, comme le montre la Fig. 26; on trouve alors:

$$Q_U = 38{,}5 \text{ kcal/at. g} \quad \text{et} \quad Q_{Ti} = 40 \text{ kcal/at. g}.$$

On voit, de plus, d'après le Tableau 4, que le rapport D_U/D_{Ti} ne varie pratiquement pas avec la température; sa valeur moyenne est de 3,7 environ.

DISCUSSION ET CONCLUSION

Il nous semble intéressant de comparer ces résultats à ceux que nous avions obtenus dans une étude antérieure sur le couple U–Zr.[1,11] Nous avions déterminé pour le déplacement des repères une relation analogue à l'équation (1):

$$x_i = 1{,}78 t^{1/2} \exp(-16\,000/RT). \qquad (1 \text{ bis})$$

Nous avions également calculé les coefficients de diffusion intrinsèques au moyen des relations (2). Les résultats de ce calcul sont portés dans le Tableau 5.

TABLEAU 5

Température (°C)	950°	1000°	1040°	1075°
N_U	0,875	0,885	0,89	0,905
N_{Zr}	0,125	0,115	0,11	0,095
D_U	$7,7 \cdot 10^{-9}$	$1,6 \cdot 10^{-8}$	$2,1 \cdot 10^{-8}$	$3,7 \cdot 10^{-8}$
D_{Zr}	$6,5 \cdot 10^{-10}$	$1,0 \cdot 10^{-9}$	$2,3 \cdot 10^{-9}$	$2,9 \cdot 10^{-9}$
D_U/D_{Zr}	11,8	16	9,2	12,8

En outre, les énergies d'activation que nous avions trouvées pour les coefficients intrinsèques D_U et D_{Zr} étaient respectivement égales à

$$Q_U = 36 \text{ kcal/at. g} \quad \text{et} \quad Q_{Zr} = 40 \text{ kcal/at. g}.$$

Ces valeurs sont très voisines de celles que nous avons calculées plus haut dans le cas du couple U–Ti.

Les rapports D_U/D_{Zr} et D_U/D_{Ti} ne semblent pas varier d'une façon significative avec la température. Comme ils sont de plus très différents, la mobilité des atomes de titane est donc plus élevée que celle des atomes de zirconium. Ces résultats s'expliqueraient peut-être par la différence entre les rayons atomiques

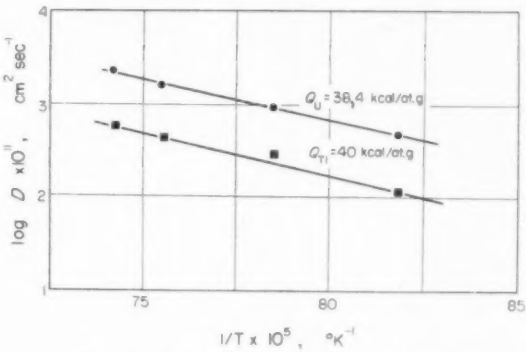


FIG. 26. Coefficient de diffusion intrinsèque.
● Uranium ■ Titane

r_{Ti} et r_{Zr} du titane et du zirconium: En effet, d'après les mesures du paramètre réticulaire à 900°C de Kaufmann et Magel[13], on calcule pour rayon r de la sphère atomique:

$$r_{Ti} = 1{,}66 \text{ Å} \quad \text{et} \quad r_{Zr} = 1{,}81 \text{ Å}.$$

On peut se demander si cette différence des mobilités du titane et du zirconium dans l'uranium conduit à des valeurs différentes de la sursaturation en lacunes dans les couples U–Ti et U–Zr. Cette sursaturation ρ peut être évaluée, dans la zone de diffusion voisine des repères, au moyen d'une méthode de calcul due à Baluffi[14]:

$$\frac{N_{v0}}{N}\frac{\rho}{\tau} \cong -\left[\frac{1-K}{N_X + KN_U}\right]\left\{ D\frac{\delta^2 N_U}{\delta x^2} + \left[\frac{\delta D}{\delta N_U} + \frac{\tilde{D}(1-K)}{N_X + KN_U}\right]\left(\frac{\delta N_U}{\delta x}\right)^2\right\} \qquad (3)$$

la sursaturation ρ étant mesurée par le rapport:

$$\rho = (N_v - N_{v0})/N_{v0}$$

N_v et N_{v0} désignant les concentrations de lacunes par unité de volume dans les conditions de l'expérience et à l'équilibre, N le nombre total d'atomes par unité de volume, τ la durée de vie d'une lacune, K le rapport D_X/D_U, X l'élément Zr ou Ti, $\tilde{D}$ le coefficient de diffusion chimique et x la distance mesurée perpendiculairement au front de diffusion.

Le second membre de l'équation (3) peut se calculer à partir des résultats expérimentaux. Un calcul simple (1) permet d'évaluer N_{v0}/N (de l'ordre de 10^{-4} à 10^{-3}) et τ (compris entre 0,1 et 1 s). On trouve ainsi pour la sursaturation ρ des valeurs de l'ordre de 10^{-3} dans le couple U–Zr et de $0{,}5 \cdot 10^{-3}$ dans le couple U–Ti. Ces valeurs ne semblent pas très différentes, bien que l'observation micrographique montre l'existence d'une forte porosité dans le système

VOL. 8 1960

U–Zr, tandis que la présence de pores demeure exceptionnelle dans le système U–Ti.

Or, on sait que lorsqu'elles sont en sursaturation, les lacunes peuvent s'éliminer suivant plusieurs processus dont les plus probables sont: la précipitation sous forme de pores ou l'élimination sur les crans de dislocations. Comme il n'y a pas de raison théorique pour que les lacunes s'éliminent exclusivement suivant le second processus, dans le couple U–Ti, on est donc conduit à penser que les différences de porosité observées doivent s'expliquer par des différences dans la germination des pores.

La nature de ces germes est encore sujette à discussion.[15] Ils peuvent être constitués soit par certaines configurations de dislocations, soit par des microfissures ou de petites inclusions (Seitz[16], Barnes et Mazey[17], Resnick et Seigle[18].) En considérant les conditions d'équilibre d'un pore sphérique, on a montré que le rayon critique du germe R est inversement proportionnel à la sursaturation en lacunes

$$\frac{2\gamma}{R} = kTN \log \frac{N_v}{N_0} \simeq kTN\rho \qquad (4)$$

puisque $\log (N_v/N_{v0}) = \log (1 + \rho)$, $\sim\rho$. γ désigne la tension superficielle à la température absolue T.

Dans le cas d'une germination hétérogène, par exemple pour une inclusion sphérique de rayon R', on peut écrire une relation analogue à (4), en supposant que, en première approximation, l'énergie interfaciale est la même que dans le cas précédent:

$$\frac{2\gamma}{R'} \sim kTN\,\rho'. \qquad (4')$$

Pour une sursaturation en lacunes ρ', les pores ne pourront se développer que si les inclusions ont un diamètre supérieur à R'.

Nous avons montré plus haut que la sursaturation était sensiblement la même dans les deux couples U–Zr et U–Ti. Les différences importantes de porosité constatées expérimentalement pourraient donc être attribuées à des valeurs différentes du rayon des inclusions qui jouent le rôle de germes. Ces inclusions peuvent être préexistantes dans un des métaux de départ, ou au contraire se former au cours de la diffusion par suite d'un processus faisant appel à la diffusion des impuretés elles-mêmes.

Etant donné que la pureté de l'uranium utilisé est toujours la même dans les couples U–Zr et U–Ti, et que d'autre part la porosité apparaît toujours dans une zone du couple riche en uranium ($N_U \simeq 0{,}85$), on peut supposer que les impuretés présentes dans le

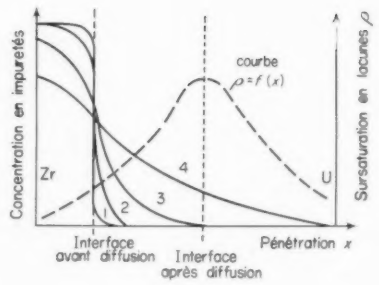


FIG. 27.

zirconium et dans le titane diffusent dans l'uranium à des vitesses différentes. Sur la Fig. 27 nous avons porté la courbe de sursaturation en lacunes et quelques courbes schématisant la diffusion de diverses impuretés. Si une impureté donnée diffuse assez vite (courbe 4, par exemple), sa concentration dans la zone de sursaturation en lacunes peut être suffisamment élevée pour dépasser la limite de solubilité dans l'uranium et précipiter.

D'autre part, si le rôle des impuretés dans la formation des germes semble important, ces impuretés pourraient encore agir en augmentant la concentration moyenne en lacunes, par suite d'un accroissement de la vitesse de diffusion de celles-ci. Cet accroissement peut être dû, soit à un mécanisme analogue à celui qu'a proposé Accary[19] pour expliquer l'action des impuretés sur la diffusion dans les laitons, soit à un effet de couplage entre les lacunes et les atomes d'impuretés.

BIBLIOGRAPHIE

1. Y. Adda, J. Philibert et Mme H. Farraggi, *Rev. Métall.* **54,** 597 (1957).
2. R. Castaing, Thèse (1951); *Publ. Off. Nat. Étud. Rech. Aéro.* no. 55 (1952).
3. R. Castaing et J. Descamps, *Rech. Aéronaut.* no. 53, 47 (1958).
4. C. Matano, *Jap. J. Phys.* **8,** 109 (1933).
5. R. W. Buzzard, R. B. Liss et D. P. Fickle, *J. Res. Nat. Bur. Stand.* **50,** 209 (1953).
6. M. C. Udy et F. W. Boulger, *Trans. Amer. Inst. Min. (Metall.) Engrs.* **200,** 207 (1954).
7. A. G. Knapton, *J. Inst. Metals* **83,** 497 (1955).
8. Y. Adda, J. Philibert, C. Mairy et Mme P. Bouchet, *Rapp. Comm. Énergie Atom.* no. 880 (1958).
9. H. Buckle et J. Descamps, *C.R. Acad Sci., Paris* **230,** 752 (1950).
10. A. D. Smigelskas et E. O. Kirkendall, *Trans. Amer. Inst. Min. (Metall.) Engrs.* **171,** 130 (1947).
11. Y. Adda, J. Philibert et C. Mairy, *C.R. Acad. Sci., Paris* **243,** 1115 (1956).
12. R. S. Darken, *Trans. Amer. Inst. Min. (Metall.) Engrs.* **175,** 184 (1948).
13. A. R. Kaufmann et T. T. Magel, *Metallurgy of Zirconium* (Lustman et Kerze, eds.) p. 349. McGraw-Hill, New York (1955).
14. R. W. Ballufi, *Acta Met.* **2,** 294 (1954).
15. F. Seitz, *Advanc. Phys.* **1,** 43 (1952).
16. F. Seitz, *Acta Met.* **1,** 355 (1953).
17. R. S. Barnes et D. J. Mazey, *Acta Met.* **6,** 1 (1958).
18. R. Resnick et L. Seigle, *J. Met. N.Y.* **9,** 87 (1957).
19. A. Accary, *Rapp. Comm. Énergie Atom.* no. 759 (1958).

PRECIPITATION IN GOLD–PLATINUM ALLOYS—I

THERMODYNAMICS*

L. J. VAN DER TOORN† and T. J. TIEDEMA†

An expression is derived for the increase in the Gibbs' free energy which arises from the mixing of a total amount of 1 mole of the components of a binary system. The six constants of this expression are calculated for the gold–platinum system from experimental data.

A comparison of this expression with those of other investigators is made.

PRECIPITATION DANS LES ALLIAGES OR-PLATINE—I. THERMODYNAMIQUE

Les auteurs présentent une expression de l'accroissement d'énergie libre des constituants d'un système binaire lors du mélange d'une quantité globale égale à une môle. A partir de données expérimentales, ils calculent les six constantes de cette expression dans le cas du système Or–Platine. Enfin, ils la comparent avec celles d'autres chercheurs.

ÜBER AUSSCHEIDUNGEN IN GOLD-PLATINLEGIERUNGEN—I. THERMODYNAMIK

Für die Zunahme der Gibbsschen freien Energie, die durch die Mischung des Gesamtbetrags 1 Mol von Komponenten eines binären Systems entsteht, wird ein Ausdruck abgeleitet. Die sechs Konstanten dieses Ausdrucks werden für das Gold-Platinsystem aus experimentellen Daten berechnet.

Dieser Ausdruck wird verglichen mit denjenigen anderer Forscher.

VOL. 8 1960

1. INTRODUCTION

A few years ago Tichelaar[1] suggested that the mechanism of precipitation in supersaturated solid solutions might be different if decomposition takes place above or beneath the spinodal curve.‡ As for the gold–platinum system this curve has been determined already by Wictorin[2], it seemed worth while to test Tichelaars suggestion upon this system. Moreover experiments in this direction would give the possibility to study the influence of the spinodal curve on the rate of precipitation (cf. part II[3]) and also Wictorin[2].

Unfortunately we have found that the expression for the free energy, as given in Wictorins paper, does not hold for temperatures below 900°C. Consequently for these temperatures the spinodal curve is also uncertain. For this reason we have calculated another formula for the free energy, which enables a more precise determination of the spinodal curve, especially for the temperature range where the experiments were carried out (500–750°C). The way in which this formula has been obtained from the experimental data and the calculation of the spinodal curve will be given in the following paragraphs.

2. DERIVATION OF AN EXPRESSION FOR ΔG

The general condition for equilibrium of an isothermal system at constant pressure is given by a minimum value for

$$G = H - TS \tag{1}$$

G being the Gibbs' free energy, H the enthalpy and S the entropy. If a total amount of 1 mole of components A and B is mixed, the increase in free energy of the system is given by

$$\Delta G = \Delta H - T\Delta S \tag{2}$$

where ΔH is the molar enthalpy of mixing and ΔS is the molar entropy of mixing. For the case of ideal mixing $\Delta H = 0$ and ΔS is given by the term of Gibbs so that

$$\Delta G^{id} = RT\{(1-x)\ln(1-x) + x\ln x\} \tag{3}$$

x being the atomic fraction of component B. In practically all cases there is, however, a non zero heat of mixing and an entropy of mixing not equalling the Gibbs term. This can be taken into account by putting $\Delta G = \Delta G^{id} + \Delta G^{ex}$ and $\Delta S = \Delta S^{id} + \Delta S^{ex}$. With (2) and (3) it is easily seen that

$$\Delta G^{ex} = \Delta H - T\Delta S^{ex}. \tag{4}$$

This expression has to be zero for $x = 0$ and $x = 1$, whereas on the base of thermodynamics for these same values the first derivative of ΔG^{ex} with respect to

* Received May 21, 1959.

† Dutch Foundation for Fundamental Research (F.O.M.).

‡ The spinodal curve is the locus of the inflexion points of the free energy/compositional curves by changing temperature.

composition must have a finite value. These conditions are fulfilled if ΔG^{ex} is taken as a power series of x which is divisible by $x(1-x)$, thus

$$\Delta G^{ex} = x(1-x)\,f(x). \tag{5}$$

From calculations concerning binary mixtures of liquids it turns out that generally experimental values for ΔG^{ex} can be represented with reasonable precision if three terms of the power series are taken into account. Supposing that this might also be the case for the gold–platinum system, $f(x)$ must be written as

$$f(x) = f_0 + f_1 x + f_2 x^2. \tag{6}$$

Moreover, as we are considering a certain temperature range it is advisable to take a temperature influence into account. Therefore (cf. equation 4) in supposing h_i and s_i to be constants ($\Delta c_p = 0$*)

$$f_i = R(h_i - Ts_i). \tag{7}$$

With the aid of the above equations the following expression for ΔG can be derived

$$\begin{aligned}\frac{\Delta G}{R} = {} & x(1-x)\{h_0 - Ts_0 \\ & + (h_1 - Ts_1)x + (h_2 - Ts_2)x^2\} \\ & + T\{(1-x)\ln(1-x) + x\ln x\}.\end{aligned} \tag{8}$$

In order to determine the constants of equation (8) six independent equations are necessary. Using the properties of the top of the solid solubility-gap, namely that the second and the third derivative of the free energy with respect to composition must be zero for this point, two equations result, namely:

$$\begin{aligned}\frac{\partial^2(\Delta G/R)}{\partial x^2} = 0 = {} & -2(h_0 - Ts_0) \\ & + (2-6x)(h_1 - Ts_1) \\ & + (6x - 12x^2)(h_2 - Ts_2) + \frac{T}{x(1-x)}\end{aligned} \tag{9}$$

and

$$\begin{aligned}\frac{\partial^3(\Delta G/R)}{\partial x^3} = 0 = {} & -6(h_1 - Ts_1) + (6-24x) \\ & \times (h_2 - Ts_2) + \frac{(2x-1)\,T}{x^2(1-x)^2}.\end{aligned} \tag{10}$$

Furthermore, keeping in mind that

$$\Delta\mu_i = \mu_i - \mu_i^0 \tag{11}$$

(where μ_i = partial molar Gibbs' free energy of component i in the mixture and μ_i^0 = molar Gibbs' free energy of the pure component i) and that

$$\Delta\mu_{Au} = \Delta G - x\,\frac{\partial\Delta G}{\partial x} \tag{12a}$$

$$\Delta\mu_{Pt} = \Delta G + (1-x)\,\frac{\partial\Delta G}{\partial x}\,. \tag{12b}$$

The equilibrium conditions for the two equilibrium phases viz. $\Delta\mu_{Au_{x_1}} = \Delta\mu_{Au_{x_2}}$ and $\Delta\mu_{Pt_{x_1}} = \Delta\mu_{Pt_{x_2}}$ provide two other equations, namely:

$$\begin{aligned}T\ln(1-x_1) + {} & x_1^2\{h_0 - Ts_0 \\ & + (2x_1 - 1)(h_1 - Ts_1) \\ & + x_1(3x_1 - 2)(h_2 - Ts_2)\} \\ = {} & T\ln(1-x_2) + x_2^2\{h_0 - Ts_0 \\ & + (2x_2 - 1)(h_1 - Ts_1) \\ & + x_2(3x_2 - 2)(h_2 - Ts_2)\}\end{aligned} \tag{13}$$

and

$$\begin{aligned}T\ln x_1 + {} & (1-x_1)^2\{h_0 - Ts_0 \\ & + 2x_1(h_1 - Ts_1) + 3x_1^2(h_2 - Ts_2)\} \\ = {} & T\ln x_2 + (1-x_2)^2\{h_0 - Ts_0 \\ & + 2x_2(h_1 - Ts_1) + 3x_2^2(h_2 - Ts_2)\}.\end{aligned} \tag{14}$$

By introducing the values of T and x for the top of the solubility gap—namely $T = 1531$°K and $x = 0.592$ (cf. Darling *et al.*[4] and Raub and Wörwag[5])—into equations (9) and (10) and moreover two sets of values obtained from the two phase-boundary—namely $T = 892$°K, $x_1 = 0.214$, $x_2 = 0.973$ and $T = 1156$°K, $x_1 = 0.286$, $x_2 = 0.931$ as given by Tiedema *et al.*[6] —into equations (13) and (14), the following six values for the constants are derived:

$$\begin{aligned} h_0 &= -1997.6 & s_0 &= -1.5322 \\ h_1 &= +11822.9 & s_1 &= +4.5256 \\ h_2 &= -4726.5 & s_2 &= -1.1346. \end{aligned}$$

This gives for equation (8):

$$\begin{aligned}\frac{\Delta G}{R} = {} & x(1-x)\{-1997.6 + 1.5322T \\ & + x(11822.9 - 4.5256T) + x^2(-4726.5 \\ & + 1.1346T)\} + T\{(1-x)\ln(1-x) + x\ln x\}.\end{aligned}$$

From this equation follows the variation of $\dfrac{\Delta H/R}{x(1-x)}$ and $\dfrac{\Delta S^{ex}/R}{x(1-x)}$ with composition. They are represented in Fig. 1 ($T = 1000$°K) together with $\dfrac{\Delta G^{ex}/R}{x(1-x)}$. Fig. 2 shows $\Delta G/R$ as a function of composition for a number of temperatures.

* If Δc_p is not zero, $\Delta G(T)$ may be expanded in a series to $T - T_m$, T_m being a mean value in the range considered. The first order terms with Δc_p then cancel out, so that even with a finite Δc_p equation (7) is often a fair approximation.

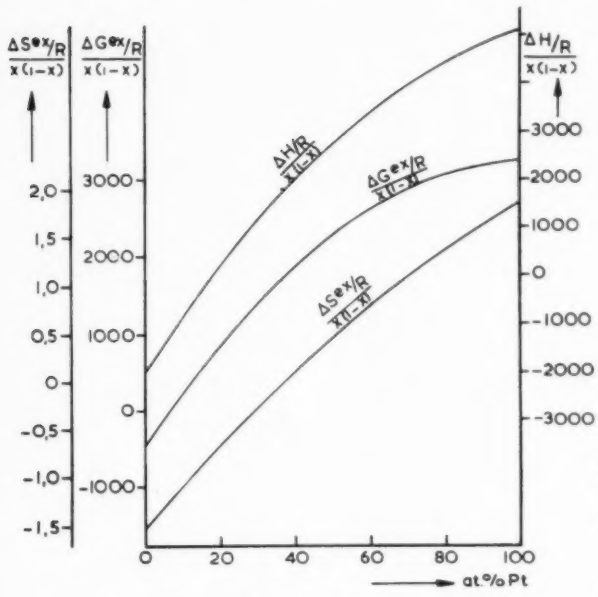


FIG. 1. Variation of $\frac{\Delta H/R}{x(1-x)}$; $\frac{\Delta S^{ex}/R}{x(1-x)}$ and $\frac{\Delta G^{ex}/R}{x(1-x)}$ with composition ($T = 1000°K$).

3. DETERMINATION OF THE SPINODAL CURVE

The locus of the inflexion points of the free energy/compositional curve as a function of temperature has been determined by finding the roots of equation (9) between $x = 0$ and $x = 1$ after the approximation method of Newton. The values so obtained for the inflexion points x_{s_1} and x_{s_2} are listed in Table 1, whereas the complete spinodal curve is plotted in Fig. 3.

TABLE 1

T°K	T°C	x_{s_1}	x_{s_2}
1500	1227	0.537	0.655
1400	1127	0.488	0.726
1300	1027	0.461	0.774
1200	927	0.441	0.811
1100	827	0.426	0.842
1023	750	0.416	0.862
973	700	0.411	0.874
923	650	0.405	0.885
873	600	0.400	0.896
823	550	0.396	0.905[5]
773	500	0.392	0.915[5]

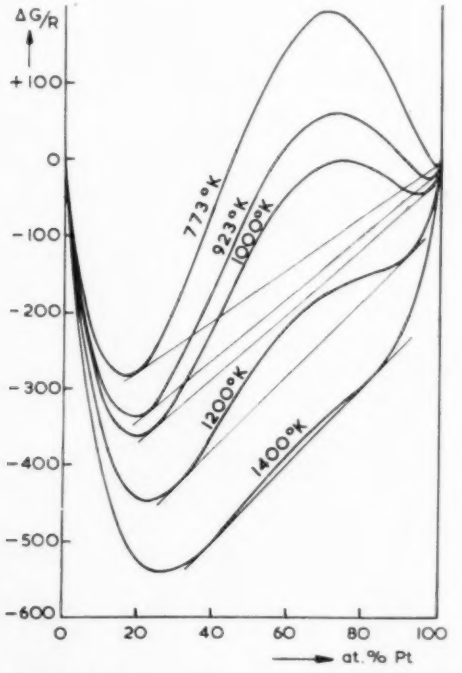


FIG. 2. $\Delta G/R$ as a function of composition at 773, 923, 1000, 1200 and 1400°K. The common tangents to the curves determine the equilibrium phases.

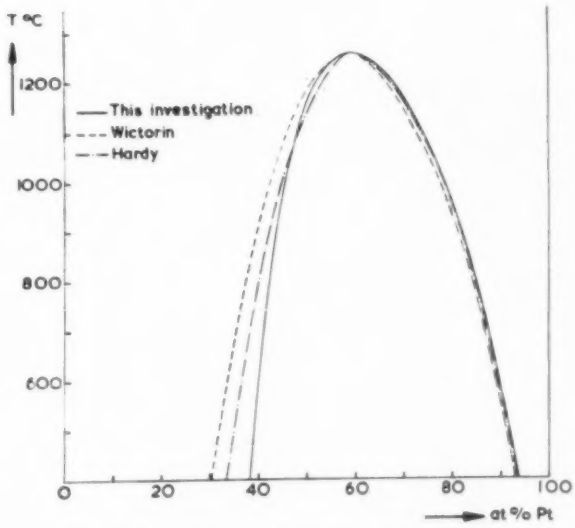


FIG. 3. Spinodal curve as calculated by Wictorin, Hardy and the authors of this paper.

4. DISCUSSION

If the common tangents to the free energy/compositional curves of Fig. 2 are drawn, it turns out that the contact points, giving the equilibrium phases at a certain temperature, are in very good agreement with the experimentally determined points (cf. Ref. 6). However if we do the same with Wictorins ΔG-equation at temperatures between 500°C and 750°C, the agreement with the experimental points is very poor. Wictorin started also with the equation (2)

$$\Delta G = \Delta H - T\Delta S,$$

assuming, however, $\Delta S = \Delta S^{id}$ and the heat of

VOL. 8 1960

mixing to be represented by a four constant exponential function of x, namely

$$\frac{\Delta H}{R} = x(1-x)\{a_1(1-x)^3 + a_2x(1-x)^2 + a_3x^2(1-x) + a_4x^3\}.$$

(If we compare this equation with equations (5) and (6) of this paper we could take $a_1 = f_0$; $-3a_1 + a_2 = f_1$; $3a_1 - 2a_2 + a_3 = f_2$ and $-a_1 + a_2 - a_3 + a_4 = f_3$.) The four constants of this relation were determined by the method of the least squares from ten equations, obtained by introducing the experimentally determined equilibrium compositions at 971, 1082, 1136, 1184 and 1215°C. In plotting the obtained G-values, the points of contact of the common tangents differed appreciably from the experimental points. By a slight modification of the constants Wictorin obtained a fairly good agreement for temperatures above 900°C.

Hardy[7,8] introduced Wictorins experimental data into his expression for sub-regular solutions

$$\frac{\Delta G^{ex}}{R} = x(1-x)(A_0 + A_1x)$$

with the constants A_0 and A_1 temperature dependent. The spinodal curve calculated with the aid of this formula lies in between that calculated after Wictorin and that calculated after the method described in this paper (cf. Fig. 3). Obviously it is doubtful if the simple equation of Hardy may be supposed to represent the case of the gold–platinum system, this again with a view to mixtures of fluids.

Finally we mention a calculation of Weiss and Tauer[9]. Although their theoretical approach to the problem seems in principal a good one, they did not take into account that the third derivative of free energy with respect to composition must be zero, for the upper critical demixing point. If we apply this criterium to their formula it turns out that the top of the solubility-gap is found at a composition of about 50 at.% Pt. This is far apart from the experimental value, so that their basic assumptions have to be modified. It seems that as long as sufficiently precise experimental values for the constants used in their paper are lacking, calculations of this type do not provide more reliable data than those obtained with the classical thermodynamical approach.

ACKNOWLEDGMENT

The authors wish to express their sincerest thanks to Professors A. E. Korvezee and W. G. Burgers for many valuable discussions.

This work is part of the research programme of the research group Metals F.O.M.—T.N.O. of the Stichting voor Fundamenteel Onderzoek der Materie (Foundation for Fundamental Research of Matter, F.O.M.) and was also made possible by financial support from the Nederlandse Organisatie voor Zuiver-Wetenschappelijk Onderzoek (Netherlands Organization for Pure Research, Z.W.O.).

REFERENCES

1. G. W. Tichelaar, Thesis, Delft (1956).
2. C. G. Wictorin, Thesis, Stockholm (1947).
3. L. J. van der Toorn, *Acta Met.* **8,** 715 (1960).
4. A. S. Darling, R. A. Mintern and J. C. Chaston, *J. Inst. Met.* **81,** 125 (1952).
5. E. Raub and G. Wörwag, *Z. Metallk.* **46,** 513 (1955).
6. T. J. Tiedema, J. Bouman and W. G. Burgers, *Acta Met.* **5,** 310 (1957).
7. H. K. Hardy, *Acta Met.* **1,** 202 (1953).
8. H. K. Hardy and T. J. Heal, *Progr. Met. Phys.* **5,** 143 (1954).
9. R. J. Weiss and K. J. Tauer, *J. Phys. Chem. Solids* **7,** 249 (1958).

PRECIPITATION IN GOLD–PLATINUM ALLOYS—II

INFLUENCE OF THE SPINODAL CURVE ON THE RATE AND THE MECHANISM OF THE PRECIPITATION PROCESS*

L. J. VAN DER TOORN†

The influence of the spinodal curve on the rate and the mechanism of the precipitation process in gold–platinum alloys has been studied by means of X-rays. An exposition is given of the theories of Borelius and Tichelaar and of the considerations put forward by Dehlinger *et al.* and Cohen. The experimental conditions of the present investigation are outlined, after which a description of the results is given with the aid of a large number of X-ray photographs. In the last part of the paper it is shown that although the theories of Borelius and Tichelaar roughly predict the observed phenomena, they probably require a modification because it may be expected that lattice imperfections play an important role in the precipitation process.

PRECIPITATION DANS LES ALLIAGES OR-PLATINE—II

INFLUENCE DE LA COURBE SPINODALE SUR LA VITESSE ET LE MÉCANISME DU PROCESSUS DE PRÉCIPITATION

Les auteurs étudient à l'aide de rayons X l'influence de la courbe spinodale sur la vitesse et le mécanisme du processus de précipitation dans les alliages Au–Pt. Ils exposent les théories de Borelius et Tichelaar ainsi que les suggestions de Dehlinger et Cohen. Après avoir décrit les conditions expérimentales, ils rapportent les résultats obtenus. Enfin, ils montrent que les phénomènes observés, quoique grossièrement prévus par les théories de Bohr et et Tichelaar demandent qu'elles soient modifiées, étant donné le rôle important joué par les imperfections du réseau.

ÜBER AUSSCHEIDUNGEN IN GOLD–PLATINLEGIERUNGEN—II

EINFLUß DER SPINODALEN AUF DIE GESCHWINDIGKEIT UND DEN MECHANISMUS DES AUSSCHEIDUNGSVORGANGS

Der Einfluß der Spinodalen auf die Geschwindigkeit und den Mechanismus des Ausscheidungsvorgangs in Gold–Platinlegierungen ist röntgenographisch untersucht worden. Die Theorie von Borelius und Tichelaar und die von Dehlinger *et al.* und von Cohen eingeführten Betrachtungen werden dargestellt. Die experimentellen Bedingungen der vorliegenden Untersuchung werden umrissen; danach folgt eine Beschreibung der Ergebnisse mit Hilfe einer großen Anzahl von Röntgenaufnahmen. Im letzten Teil der Arbeit wird gezeigt, daß die Theorien von Borelius und Tichelaar zwar die Beobachtungen ungefähr vorhersagen, aber wahrscheinlich doch einer Änderung bedürfen, weil man erwarten kann, daß Gitterfehler beim Ausscheidungsvorgang eine wichtige Rolle spielen.

VOL. 8 1960

1. INTRODUCTION

From the fact that a solubility-gap exists in the solid state of the gold–platinum system (cf. Fig. 1a),[1,2] it follows that precipitation occurs from homogeneous alloys if annealed at temperatures within this region. In part I of this paper[3] an expression was derived for the free energy of mixing of a binary system AB, namely:

$$\Delta G = Rx(1-x)\{h_0 - Ts_0 + (h_1 - Ts_1) \times x + (h_2 - Ts_2)x^2\} + RT\{(1-x) \times \ln(1-x) + x \ln x\}$$

where x is the atomic fraction of component B. For the system under consideration (A being gold and B being platinum) the following values for the constants were found:

$$h_0 = -1997.6 \qquad s_0 = -1.5322$$

$$h_1 = +11822.9 \qquad s_1 = +4.5256$$

$$h_2 = -4726.5 \qquad s_2 = -1.1246.$$

Fig. 1(b) shows the free energy/compositional curve $\Delta G(x)$, at a temperature of 650°C, obtained with the above equation. The curve can be divided into three regions, namely a central region for alloys with a free energy given by the concave-downwards part of the free energy/compositional curve, corresponding to a negative value of the second differential ($\partial^2 \Delta G/\partial x^2$)

* Received May 21, 1959.
A preliminary communication of the results described in this paper was made in Paris at the *Journées d'Automne* 1958 of the Société Française de Métallurgie.

† Dutch Foundation for Fundamental Research (F.O.M.).

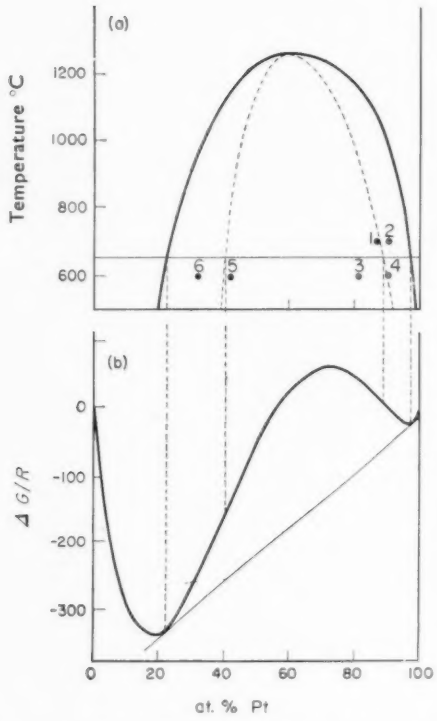


FIG. 1a. The solid solubility-gap and the calculated spinodal curve of the gold-platinum system. (After Tiedema, Bouman and Burgers[2] and van der Toorn and Tiedema[3].)
FIG. 1b. The free energy/compositional curve at 650°C.

and two side regions for alloys given by the concave-upwards parts of the curve, where the supersaturation is such that $(\partial^2 \Delta G/\partial x^2)$ is positive. A dashed curve has been inserted in Fig. 1(a), corresponding to $(\partial^2 \Delta G/\partial x^2)$ equal to zero for all temperatures, this curve being the spinodal curve.

2. THEORY OF PRECIPITATION

According to a theory of Borelius[4] the rate of precipitation in a supersaturated solid solution is influenced by the sign of the second differential of the free energy with respect to composition. Borelius assumes precipitation to be preceded by a local accumulation of one of the atomic components. This accumulation arises from accidental fluctuations in the matrix, the decrease in free energy of the system being the final driving force for the precipitation process. As a measure for this force, the difference in the free energy of mixing ΔG, given by the distance between the free energy/compositional curve and the common tangent to this curve (cf. Fig. 1b) may be used. A qualitative explanation of this theory can be given with the aid of Fig. 2. In an alloy with composition $x_1(\partial^2 \Delta G/\partial x^2 < 0)$ even small fluctuations of composition cause a decrease of free energy $(M_1 \rightarrow A_1 + B_1)$ and so tend to be increased, which can lead to the formation of stable nuclei. On the contrary small fluctuations in an alloy with composition $x_2(\partial^2 \Delta G/\partial x^2 > 0)$ will cause an increase in free energy $(M_2 \rightarrow A_2 + B_2)$ and thus have a greater tendency to redissolve than to grow. In this case only fluctuations resulting in a large difference in composition (B_2) can increase with a reduction in free energy of the system. As the probability for small fluctuations is higher than that for large fluctuations, it is reasonable to expect that at a given annealing temperature alloys for which $\partial^2 \Delta G/\partial x^2 < 0$ will have a higher rate of nucleation and consequently of precipitation than alloys for which $\partial^2 \Delta G/\partial x^2 > 0$.

Electrical resistance measurements in the Pb–Sn-[5] and the Au–Pt-[6] system and for the first one also the X-ray investigations[7] appear to be in accordance with this theory.*

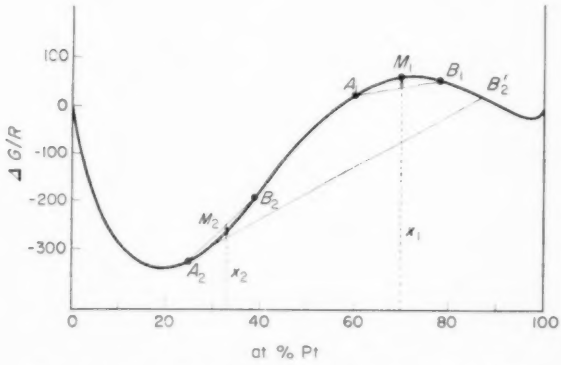


FIG. 2. Free energy/compositional curve at 650°C. Fluctuations below (x_1) and above the spinodal curve (x_2).

* Unpublished investigations in this laboratory by J. W. Geus and P. H. van Lent have made it highly probable that similar conclusions hold for the decomposition of metastable supersaturated mixed crystals of NaCl and KCl of suitable composition. For this system the position of the spinodal curve with regard to the curve of complete solubility is known in particular from calculations by Tichelaar[11].

Geus investigated mixed crystals with 35 and 40 at.% NaCl, respectively, for which the difference between the critical temperature of complete miscibility and the spinodal temperature amounts to about 50°C. It was found that crystals quenched from temperatures above the solubility curve to temperatures just below the spinodal curve decomposed within a certain time, whereas crystals of the same composition remained completely homogeneous when held for equal or even much longer times at temperatures just above the spinodal curve.

Van Lent investigated crystals containing 90 at.% NaCl; here the difference in critical and spinodal temperature is about 100°C. Again it was found that the decomposition was much slower at temperatures above than at temperatures below the spinodal curve.

The X-ray photographs also made it probable that the mechanism of decomposition in these two temperature/composition regions was different. In particular above the spinodal curve the matrix changed gradually in composition during the precipitation process (cf. later in this paper).

The attention is drawn to the fact, however, that in this theory the strain and interfacial energies of the nuclei are neglected. Moreover, the free energy/compositional curve as considered by Borelius and also in this paper is based on experimental data (such as composition of equilibrium phases and heats of mixing) relating to macroscopic quantities of matter, containing a large number of atoms and supposed to be in equilibrium. The influence of regions of locally increased free energy (e.g. due to the presence of grain-boundaries or dislocations) is not explicitly taken into consideration. But, as was already pointed out—in particular in papers by Dehlinger and Knapp[8] and Dehlinger and Franz[9]—it must be kept in mind that these factors will influence the precipitation process (cf. also Hardy and Heal[10]).

The thermodynamic considerations mentioned above were elaborated by Tichelaar[11] into different precipitation mechanisms for both groups of alloys, as can be elucidated with the aid of Fig. 3. If in an alloy with composition $x_1(\partial^2 \Delta G/\partial x^2 < 0)$ the precipitation process starts, leading to the formation of an A-rich and a B-rich area (cf. Fig. 3a) the concentration differences will be accentuated by uphill-diffusion from the surrounding matrix, accompanied by a decrease in free energy of the system. As a result this nucleation process causes a sequence of alternative A-rich and B-rich segregates, which finally results in the formation of both equilibrium phases directly from the homogeneous solid solution. By considering Fig. 3(b), for an alloy with $\partial^2 \Delta G/\partial x^2 > 0$, one sees that once there has been formed a stable B-rich area (B_2), this area can likewise become richer in B-atoms by uphill-diffusion, again accompanied by a reduction in free energy. On the contrary the concentration difference between the A-rich area (A_2) and the matrix can disappear by downhill-diffusion as only this process decreases the free energy of the system.

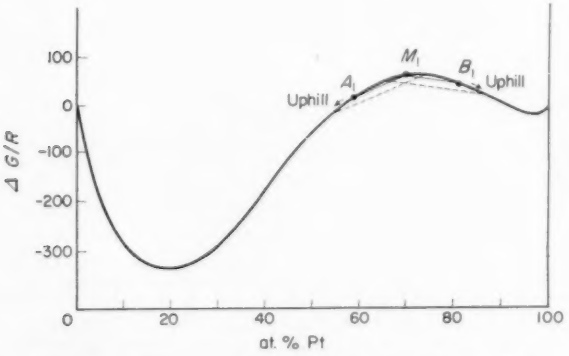


FIG. 3a. Free energy/compositional curve at 650°C. Mechanism of precipitation in an alloy with $\partial^2 \Delta G/\partial x^2 < 0$ (below the spinodal curve).

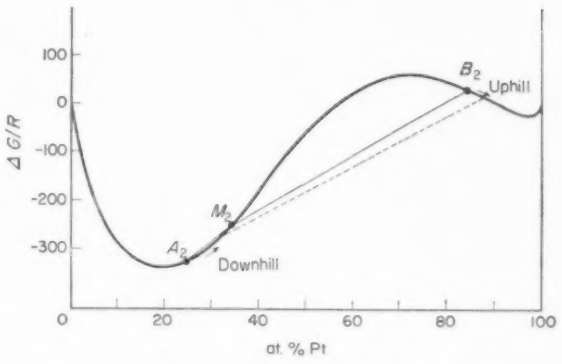


FIG. 3b. Free energy/compositional curve at 650°C. Mechanism of precipitation in an alloy with $\partial^2 \Delta G/\partial x^2 > 0$ (above the spinodal curve).

So for these alloys it is obvious to expect the segregation of one phase—namely in the composition of the most deviating equilibrium phase—in a continuously depleting matrix. This latter passes by normal downhill-diffusion into the other equilibrium phase.

Dehlinger *et al.* propose a slightly different model for the precipitation at temperatures and compositions above the spinodal curve. A metastable equilibrium of local order type regions ("Komplexe") might be formed by uphill-diffusion above the spinodal curve, because the random distribution of these regions provides an extra entropy term, which will lead to an overall decrease of the free energy if their size does not surpass a critical value. With a view to the limited size of the "Komplexe" however, only pre-precipitation phenomena are in the scope of this model and, as already pointed out by Dehlinger and co-workers a completion of the precipitation is only conceivable with the aid of pre-existing lattice faults (e.g. dislocations).

Moreover, Cohen[12] has recently drawn attention to the discrepancy between calculated and measured activation energies of precipitation. This discrepancy is an indication that nucleation requires the co-operation of pre-existing dislocations for the precipitation above as well as below the spinodal curve. If this point of view is correct, nucleation would occur in lattice regions with a suitable arrangement of dislocations and consequently these regions would have a higher free energy than indicated in Fig. 1(b). Due to the fact that this condition should be required for nucleation above as well as below the spinodal curve, the calculated spinodal curve is not necessarily the exact boundary between the two temperature-composition areas, with different precipitation processes.

In order to promote the evolution of these theories,

VOL. 8 1960

precipitation experiments were performed on gold–platinum alloys, below and above the spinodal curve at both sides of the phase diagram. The results of the experiments will be described in this paper.

3. EXPERIMENTAL PART

We first performed experiments with single crystals, prepared after a method analogous to that described by Tiedema *et al.*[2]. A piece of polycrystalline platinum wire with a length of about 100 mm and a diameter of 0.5 mm was annealed for 2 min by electrical heating at 780–800°C. Then the wire was stressed 3 per cent and recrystallized by pulling it through a small furnace, centre temperature 1050°C, with a velocity of 48 mm/hr. The so obtained single crystal was cut into pieces of about 20 mm, which were electrolytically coated with a thin layer of gold (thickness 50 μ) in an electrolytic cell containing a solution of $AuCl_3$ with excess KCN, using a current density of 1/3 amp/cm^2. By means of heating at a well-defined temperature the gold was made to diffuse into the crystal under formation of the equilibrium composition of the platinum-rich phase corresponding to that temperature. The simultaneously formed gold-rich layer was removed by etching in boiling aqua regia. It is not to be expected that the composition of the single crystal is the same throughout the whole specimen. However, as the copper-radiation, used in the X-ray investigation, penetrates only for a distance of about 10 μ into the specimen, this does not matter as long as a surface layer of this thickness is homogeneous. This turned out to be actually the case.

In order to get information about the precipitation process, a so obtained specimen was annealed for several periods at a well-defined temperature, naturally below the temperature used in the preparation of the mix-crystal. The treatment was as follows: After annealing for a short time the specimen was quenched in water, after which a rotation photograph was made with filtered CuK_α-radiation. Then the same test-piece was again annealed for some time, quenched in water etc. In this way single crystals, containing 87–91 at.% Pt, obtained by diffusion at 1000–1100°C, were annealed at temperatures between 500 and 750°C; they were chosen so that for some specimens the second differential ($\partial^2 \Delta G/\partial x^2$) was positive, whereas for others it was negative.

In addition experiments were carried out with polycrystalline alloys, prepared by Firma Drijfhout, Amsterdam, in the shape of wires with a diameter of 0.5 mm. These alloys contained 31.7; 37.9; 41.8; 62.3; 81.2 and 89.6 at.% Pt, as determined by means of X-rays after they were homogenized by heating 1½ hr at a temperature of 1200°C (except for the wires containing 62.3 at.% Pt which were homogenized at 1300°C). Test-pieces with a length of about 20 mm were brought to a well-defined temperature directly after homogenizing. The treatment was then the same as described for the single crystals, with the only difference that this time a new test-piece was used for every annealing. In this way a large number of specimens was annealed at temperatures between 500 and 650°C.

Finally with the aid of a Leitz Durimet the Vickers' micro-hardness of the polycrystalline test-pieces was determined.

4. DESCRIPTION OF THE RESULTS

(a) *X-ray photographs*

Figures 4 and 5 show two series of rotation photographs, taken after annealing two different single crystals at 700°C for various annealing times, one (Fig. 4) containing 86.6 at.% Pt ($\partial^2 \Delta G/\partial x^2 < 0$) (no. 1 in Fig. 1a) and the other (Fig. 5) containing 90.1 at.% Pt ($\partial^2 \Delta G/\partial x^2 > 0$) (no. 2 in Fig. 1a). From these photographs it follows, first of all, that the rate of decomposition of the single crystal no. 1 is at least 10 times as large as that with which crystal no. 2 decomposes (cf. Fig. 5f with Fig. 4d, e). Secondly, the series of Fig. 4 shows clearly for the shorter annealing times (photographs a and b) the occurrence of "sidebands" ("ghosts") accompanying the main reflections (see also Fig. 11a). Similar side-bands have been often observed during pre-precipitation in alloys: see particularly Daniel and Lipson[13], Hargreaves[14] and Guinier[15] for iron–nickel–copper alloys and Manenc for nickel-base alloys [16] and nickel–chromium-base alloys.[17] The side-bands are absent in the series of photographs shown in Fig. 5; in this latter series, the mechanism of precipitation, consisting of the formation of the gold-rich equilibrium phase in a continuously depleting matrix can be derived from the continuous decrease in diameter of the high-order reflections. The gold-rich equilibrium phase is directly segregated (cf. Table 1). The photographs also show that for both crystals the finally gold- and platinum-rich phases have the same orientation as the original homogeneous alloy. Uphill-diffusion is apparently the governing process for crystal 1, giving rise (according to Fig. 2) to a sequence of alternating gold- and platinum-rich layers. As the difference in atom sizes of the two components is small, it is to be expected that especially in the beginning of the process the arising strains are so small that a coherency of the alternating gold- and

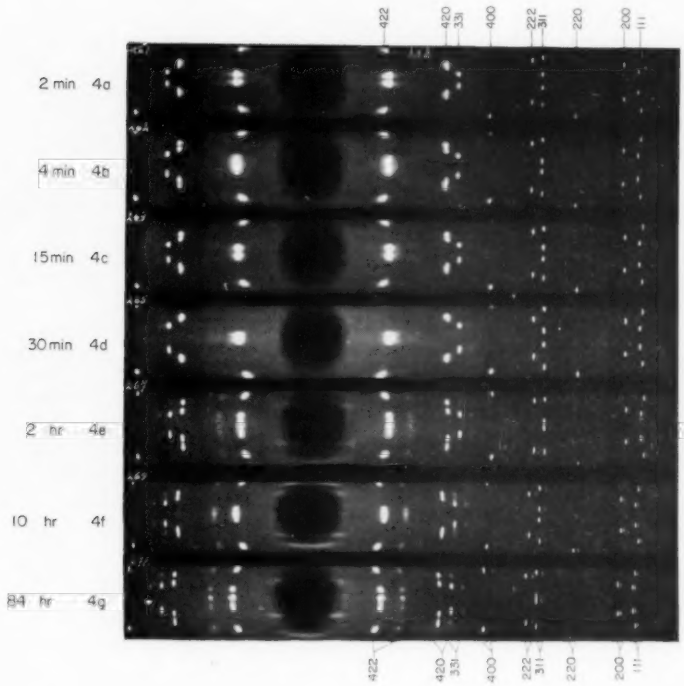


FIG. 4. Rotation photographs of single crystal no. 1 containing 86.6 at.% Pt ($\partial^2 \Delta G/\partial x^2 < 0$), annealed at 700°C for 2, 4, 15, 30 min and 2, 10, 84 hr respectively. Taken with filtered CuK_α- radiation.

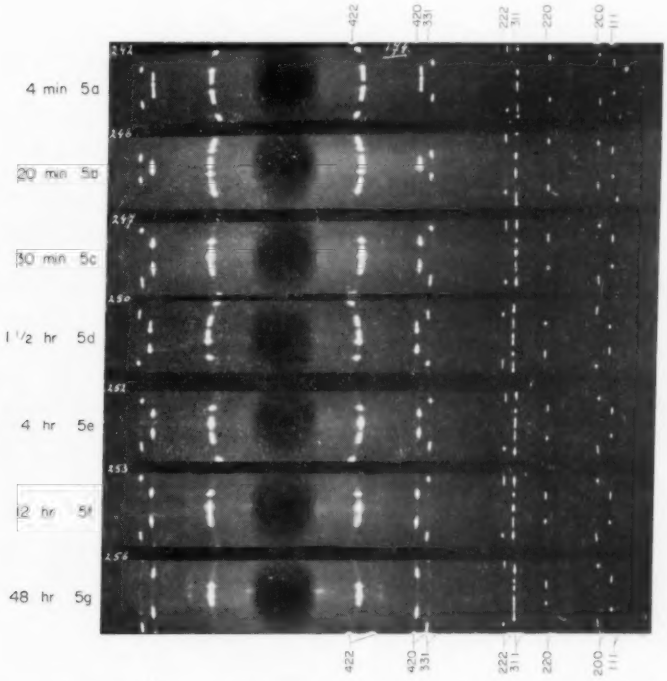


FIG. 5. Rotation photographs of single crystal no. 2, containing 90.1 at.% Pt ($\partial^2 \Delta G/\partial x^2 > 0$), annealed at 700°C for 4, 20, 30 min and 1½, 4, 12, 48 hr, respectively. Taken with filtered CuK_α- radiation.

VOL. 8 1960

TABLE 1

Crystal 1, containing 86.6 at.% Pt, annealed at 700°C. $\partial^2 \Delta G/\partial x^2 < 0$

annealing time		diameter of 422 reflection		diameter of 331 reflection	
		Pt-rich phase	Au-rich phase	Pt-rich phase	Au-rich phase
2 min	Fig. 4(a)	67.9 mm + SB*		126.6 mm + SB*	
4 min	Fig. 4(b)	67.9 mm + SB		126.6 mm + SB	
7 min		67.9 mm + SB		126.6 mm + SB	
15 min	Fig. 4(c)	DS + Str†		DS + Str†	
30 min	Fig. 4(d)	DS + Str		DS + Str	
1 hr		DS + Str	82.5 mm	DS + Str	134.5 mm
2 hr	Fig. 4(e)	64.8 mm	82.5 mm	124.9 mm	134.4 mm
4½ hr		64.8 mm	82.6 mm	124.9 mm	134.4 mm
10 hr	Fig. 4(f)	64.9 mm	82.5 mm	124.9 mm	134.4 mm
33 hr		64.8 mm	82.5 mm	125.0 mm	134.5 mm
84 hr	Fig. 4(g)	64.8 mm	82.6 mm	124.9 mm	134.4 mm

Crystal 2, containing 90.1 at.% Pt, annealed at 700°C. $\partial^2 \Delta G/\partial x^2 > 0$

annealing time		diameter of 422 reflection		diameter of 420 reflection	
		Pt-rich phase	Au-rich phase	Pt-rich phase	Au-rich phase
2 min		66.1 mm		115.8 mm	
4 min	Fig. 5(a)	66.1 mm		115.8 mm	
7 min		66.2 mm		115.8 mm	
10 min		66.2 mm		115.8 mm	
15 min		66.1 mm		115.7 mm	
20 min	Fig. 5(b)	66.2 mm		115.8 mm	
30 min	Fig. 5(c)	66.1 mm		115.7 mm	
1 hr		66.0 mm		115.6 mm	
1½ hr	Fig. 5(d)	66.0 mm		115.5 mm	
2½ hr		65.9 mm		115.3 mm	
4 hr	Fig. 5(e)	65.8 mm	82.4 mm	115.3 mm	124.9 mm
7 hr		65.6 mm	82.4 mm	115.1 mm	125.0 mm
12 hr	Fig. 5(f)	65.4 mm	82.4 mm	115.1 mm	124.9 mm
30 hr		65.0 mm	82.3 mm	114.9 mm	125.0 mm
48 hr	Fig. 5(g)	64.9 mm	82.4 mm	114.9 mm	125.0 mm

* SB = side-bands
† DS + Str = diffuse spots + streaks

platinum-rich segregates with the surrounding matrix is possible, thus giving rise to the appearance of side-bands at both sides of the original reflections of the homogeneous alloy. A remarkable point is that the side-bands differ in intensity; in Fig. 4 they have the greatest intensity on the higher θ side. An explanation of this fact with regard to this system is given by Tiedema *et al.*[2]. In a somewhat later stage of the precipitation process the side-bands approach the reflections of the homogeneous alloy, which themselves still lie at the same value of θ as for the quenched alloy. This fact shows that the alternating periods grow in period lengths as function of annealing time, a point that is in agreement with the pre-precipitation phenomena as described by Manenc[16]. Finally the reflections of the gold- and platinum-rich equilibrium phases existing at 700°C appear on the photographs, with the same orientation as the parent crystal (see also Table 1).*

To get data about the precipitation in polycrystalline alloys a number of Straumanis photographs were made after annealing at some well-defined temperatures. Figs. 6–9 show four series of photographs, taken after annealing a number of different polycrystalline alloys for different times at 600°C.

Fig. 6: Pt-rich alloy, containing 81.2 at.% Pt. $\partial^2 \Delta G/\partial x^2 < 0$

Fig. 7: Pt-rich alloy, containing 89.6 at.% Pt. $\partial^2 \Delta G/\partial x^2 > 0$

Fig. 8: Au-rich alloy, containing 41.8 at.% Pt. $\partial^2 \Delta G/\partial x^2 < 0$

Fig. 9: Au-rich alloy, containing 31.7 at.% Pt. $\partial^2 \Delta G/\partial x^2 > 0$

(see phase-diagram Fig. 1a, nos. 3, 4, 5 and 6, respectively). The photographs show that the "overall" precipitation takes place in the same way as described for the corresponding single crystals. A difference in precipitation mechanism is unquestionably visible on the photographs, due to the appearance of side-bands

* For the streaks visible on Fig. 4(d) and (e) see later, p. 724.

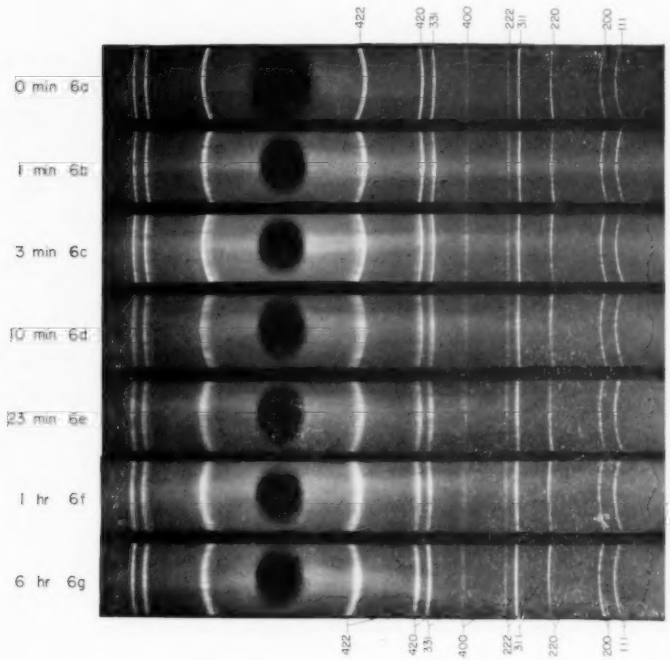


FIG. 6. Straumanis photographs of polycrystalline alloy no. 3, containing 81.2 at.% Pt ($\partial^2 \Delta G/\partial x^2 < 0$), annealed at 600°C for 0, 1, 3, 10, 23 min and 1 and 6 hr, respectively. Taken with filtered CuK_α radiation.

VOL. 8 1960

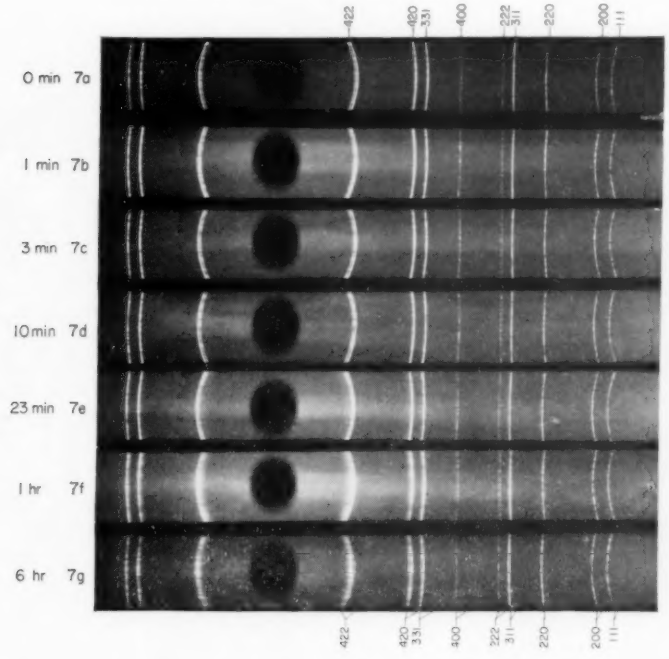


FIG. 7. Straumanis photographs of polycrystalline alloy no. 4, containing 89.6 at.% Pt ($\partial^2 \Delta G/\partial x^2 > 0$), annealed at 600°C for 0, 1, 3, 10, 23 min and 1 and 6 hr, respectively. Taken with filtered CuK_α radiation.

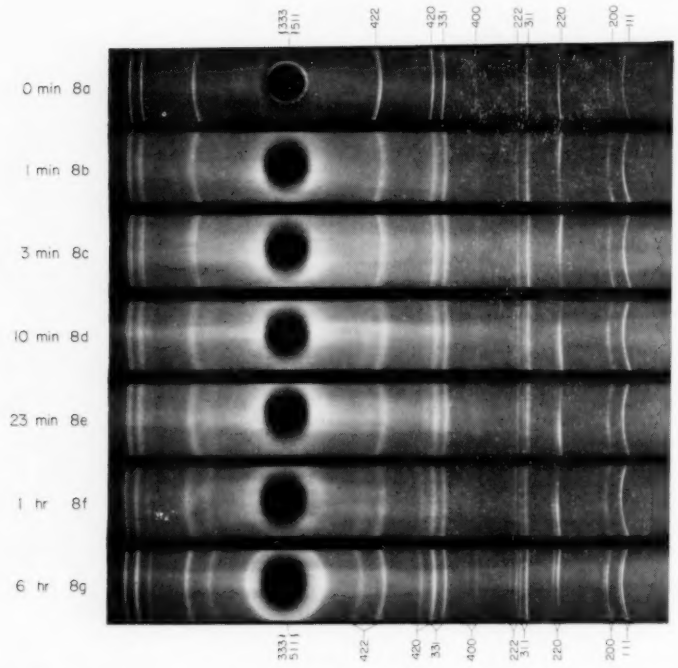


FIG. 8. Straumanis photographs of polycrystalline alloy no. 5, containing 41.8 at.% Pt ($\partial^2 \Delta G/\partial x^2 < 0$), annealed at 600°C for 0, 1, 3, 10, 23 min and 1 and 6 hr, respectively. Taken with filtered CuK_α- radiation.

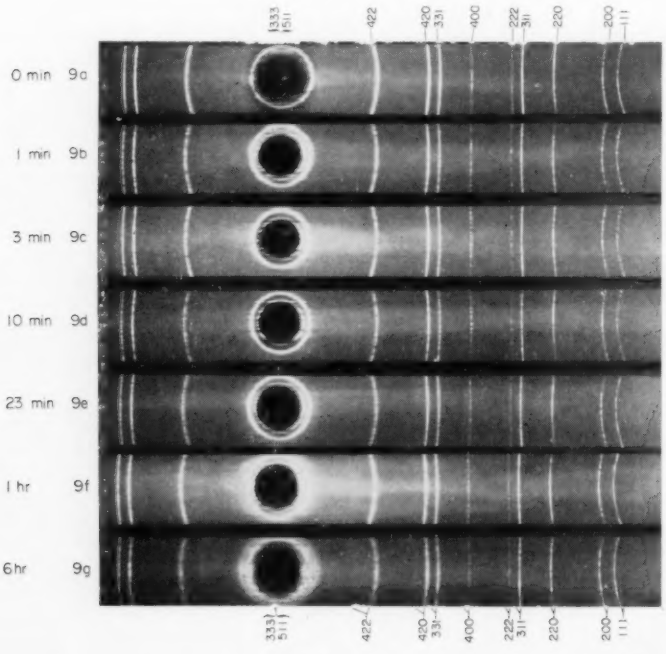


FIG. 9. Straumanis photographs of polycrystalline alloy no. 6, containing 31.7 at.% Pt ($\partial^2 \Delta G/\partial x^2 > 0$), annealed at 600°C for 0, 1, 3, 10, 23 min and 1 and 6 hr, respectively. Taken with filtered CuK_α- radiation.

TABLE 2

Alloy 3, containing 81.2 at.% Pt, annealed at 600° C. $\partial^2 \Delta G/\partial x^2 < 0$

annealing time		diameter of 422 reflection		diameter of 420 reflection	
		Pt-rich phase	Au-rich phase	Pt-rich phase	Au-rich phase
0 min	Fig. 6(a)	69.0 mm		117.3 mm	
1 min	Fig. 6(b)	69.0 mm + SB*		117.2 mm + SB	
3 min	Fig. 6(c)	68.9 mm + SB		117.3 mm + SB	
10 min	Fig. 6(d)	69.0 mm + SB		117.3 mm + SB	
23 min	Fig. 6(e)	69.0 mm DS†		117.3 mm DS	
1 hr	Fig. 6(f)	DS		DS	
6 hr	Fig. 6(g)	DS	84.2 mm	DS	

Alloy 4, containing 89.6 at.% Pt, annealed at 600°C. $\partial^2 \Delta G/\partial x^2 > 0$

annealing time		diameter of 422 reflection		diameter of 420 reflection	
		Pt-rich phase	Au-rich phase	Pt-rich phase	Au-rich phase
0 min	Fig. 7(a)	66.7 mm		116.0 mm	
1 min	Fig. 7(b)	66.6 mm		116.0 mm	
3 min	Fig. 7(c)	66.6 mm		116.1 mm	
10 min	Fig. 7(d)	66.6 mm		116.0 mm	
23 min	Fig. 7(e)	66.6 mm		116.1 mm	
1 hr	Fig. 7(f)	66.7 mm		116.0 mm	
6 hr	Fig. 7(g)	not measurable		not measurable	

Alloy 5, containing 41.8 at.% Pt, annealed at 600°C. $\partial^2 \Delta G/\partial x^2 < 0$

annealing time		diameter of 422 reflection		diameter of 420 reflection	
		Pt-rich phase	Au-rich phase	Pt-rich phase	Au-rich phase
0 min	Fig. 8(a)		79.3 mm		123.4 mm
1 min	Fig. 8(b)		79.3 mm + SB		123.4 mm + SB
3 min	Fig. 8(c)		79.3 mm + SB		123.4 mm + SB
10 min	Fig. 8(d)		79.3 mm + SB		123.4 mm + SB
23 min	Fig. 8(e)		DS		DS
1 hr	Fig. 8(f)		DS		DS
6 hr	Fig. 8(g)	64.4 mm	84.2 mm	114.7 mm	126.2 mm
675 hr		64.3 mm	84.2 mm	114.6 mm	126.2 mm

Alloy 6, containing 31.7 at.% Pt, annealed at 600°C. $\partial^2 \Delta G/\partial x^2 > 0$

annealing time		diameter of 422 reflection		diameter of 420 reflection	
		Pt-rich phase	Au-rich phase	Pt-rich phase	Au-rich phase
0 min	Fig. 9(a)		81.6 mm		124.6 mm
1 min	Fig. 9(b)		81.6 mm		124.6 mm
3 min	Fig. 9(c)		81.4 mm		124.5 mm
10 min	Fig. 9(d)		81.5 mm		124.5 mm
23 min	Fig. 9(e)		81.7 mm		124.7 mm
1 hr	Fig. 9(f)		82.0 mm		124.9 mm
6 hr	Fig. 9(g)		82.1 mm		125.1 mm

* SB = side-bands
† DS = diffuse spots

in Figs. 6 and 8, whereas they are not visible in Figs. 7 and 9 (cf. also Table 2). As the test-pieces were annealed not longer than 6 hr at the temperature of 600°C, the continuously depleting matrix-concentration by annealing above the spinodal curve can not be derived from the values of Table 2. Therefore Table 3 shows the diameter of some reflections by annealing the gold- and platinum-rich alloys 4 and 6 at 650°C. In this table low-order reflections are given instead of high-order reflections because they could be measured with more accuracy (cf. also Fig. 7f, g and Fig. 9f, g). It follows from the photographs of the specimens annealed at 600°C that the rate of decomposition of the alloys, annealed below the spinodal curve, is at least 10 times as large as that of the crystals annealed above the spinodal curve. This turned out to be also the case for annealing at 650°C. Due to lack of grain-boundaries in single crystals, precipitation in this case is much slower than in polycrystalline material. For the latter case, even

VOL. 8 1960

TABLE 3

Alloy 4, containing 89.6 at.% Pt, annealed at 650°C. $\partial^2 \Delta G/\partial x^2 > 0$

annealing time	diameter of 220 reflection		diameter of 222 reflection	
	Pt-rich phase	Au-rich phase	Pt-rich phase	Au-rich phase
0 min	134.7 mm		170.7 mm	
3 min	134.9 mm		171.0 mm	
6 min	135.0 mm		171.1 mm	
20 min	135.1 mm		171.2 mm	
1 hr	135.2 mm		171.4 mm	
3 hr	135.4 mm	131.3 mm	171.7 mm	
6 hr	135.5 mm	131.3 mm	171.8 mm	
18 hr	135.7 mm	131.5 mm	172.0 mm	166.2 mm
41 hr	135.8 mm	131.4 mm	172.0 mm	166.1 mm
72 hr	135.7 mm	131.3 mm	172.1 mm	166.1 mm
120 hr	135.6 mm	131.4 mm	172.0 mm	166.2 mm

Alloy 6, containing 31.7 at.% Pt, annealed at 650°C. $\partial^2 \Delta G/\partial x^2 > 0$

annealing time	diameter of 220 reflection		diameter of 222 reflection	
	Pt-rich phase	Au-rich phase	Pt-rich phase	Au-rich phase
0 min		132.0 mm		166.9 mm
3 min		131.8 mm		166.7 mm
6 min		131.8 mm		166.8 mm
10 min		131.9 mm		166.7 mm
20 min		131.8 mm		166.7 mm
1 hr	135.4 mm	131.7 mm		166.6 mm
3 hr	135.4 mm	131.6 mm	171.8 mm	166.5 mm
6 hr	135.5 mm	131.5 mm	172.0 mm	166.3 mm
18 hr	135.4 mm	131.3 mm	171.9 mm	166.1 mm
42 hr	135.5 mm	131.3 mm	171.9 mm	166.0 mm
72 hr	135.5 mm	131.3 mm	171.9 mm	166.0 mm

at 650°C, the side-bands have disappeared already after an annealing period of 1 min whereas they are still visible after annealing the corresponding single crystal for 4 min at 700°C (Fig. 4b).

In order to find a correction for the influence on the rate of precipitation caused by the difference in composition, the two platinum-rich alloys (3 and 4) were also annealed at 510°C, thus both below the spinodal curve. The mechanism of the precipitation process was exactly the same for both test pieces, showing the appearance of side-bands in the beginning of the process, whereas alloy 3 decomposed with a rate about 2 times as large as that with which alloy 4 decomposed, which is in accordance with the higher solute concentration of crystal 3.

In addition a polycrystalline specimen, containing 37.9 at.% Pt, was annealed at 600 and 650°C in order to get information about the behaviour in the region between the spinodal curve calculated by Wictorin and the curve calculated in part I of this paper (cf. Fig. 3 in part I). These experiments were not very conclusive because the observed phenomena were not unambiguously in accordance with precipitation either below or above the spinodal curve.

Another important phenomenon in the final stage of side-bands is the appearance of non-Laue streaks on the photographs. This is most clearly visible on photographs taken with monochromatized CuK_α-radiation. Fig. 10 is due to a single crystal containing 86.8 at.% Pt annealed at 550°C during 8 hr, Fig. 11(b) to a polycrystalline specimen with 62.3 at.% Pt annealed 4 hr at 510°C. (Fig. 11a shows the side-bands after annealing this specimen 2 hr at 510°C.) In order to get more information about this phenomenon, a partly decomposed single crystal was made to rotate around an ⟨100⟩ axis with the X-ray beam perpendicular to this axis. From the photographs so obtained (Fig. 12a) it can be deduced that the streaks

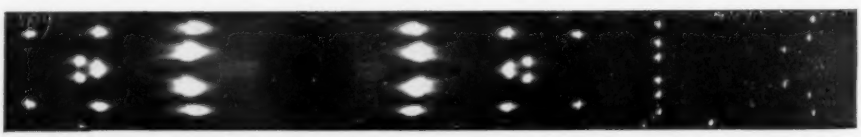


FIG. 10. Rotation photograph of a single crystal, containing 86.8 at.% Pt, annealed at 550°C for 8 hr, showing non-Laue streaks. Taken with monochromatized CuK_α- radiation.

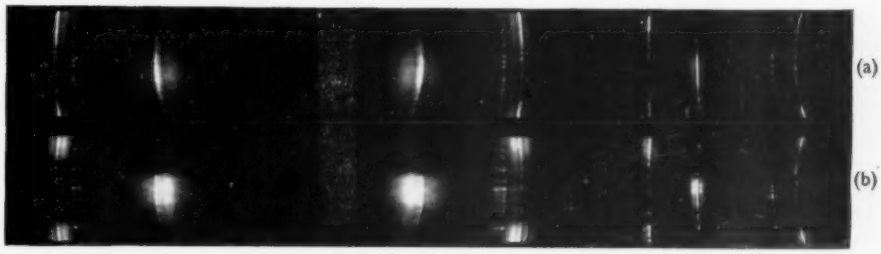


FIG. 11. Straumanis photographs of a polycrystalline alloy, containing 62.3 at.% Pt, annealed at 510°C. Taken with monochromatized CuK_α-radiation. (a) annealed for 2 hr; showing side-bands. (b) annealed for 4 hr; showing non-Laue streaks.

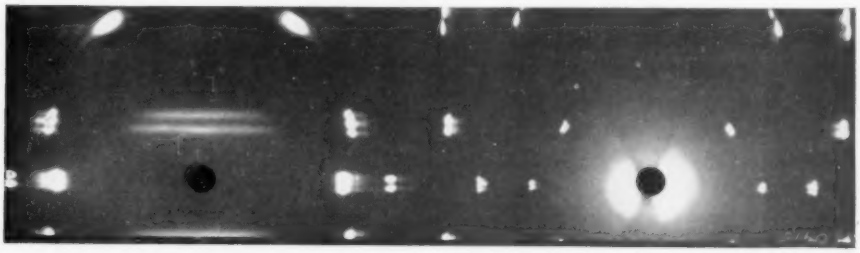


FIG. 12a. Rotation photograph of a single crystal, containing 87.2 at.% Pt, annealed at 550°C for 6 hr, showing non-Laue streaks. Taken with monochromatized CuK_α- radiation. The crystal was made to rotate around a ⟨100⟩ axis.

VOL. 8 1960

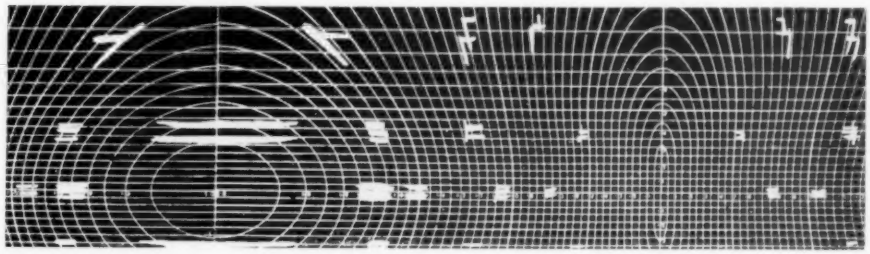


FIG. 12b. Part of Bernal chart with the non-Laue streaks of Fig. 12(a).

occur from plate-like precipitates parallel to the {100} planes of the original crystal. This can be made clear by treating this problem with the method of the reciprocal lattice. Fig. 12(b) shows part of a Bernal chart[18] adapted to the experimental conditions. The non-Laue streaks of Fig. 12(a) are also drawn on this chart and they follow exactly the same directions as the layer and row lines. As the single crystal was made to rotate around an ⟨100⟩ axis, it is obvious that the streaks can only arise from thin plates parallel to the {100} planes of the real lattice, represented by rods in the ⟨100⟩ directions of the reciprocal lattice.

(b) *Hardness measurements*

The course of the Vickers' micro-hardness was measured for the polycrystalline alloys 3, 4, 5 and 6. The measurements did not show an important difference for alloys annealed below and above the spinodal temperature. All specimens show about the same course of this quantity as a function of annealing time, being a rapid increase in the beginning of the precipitation process followed by an at first rapid and then gradual decrease till the hardness reaches a value which is about the same as that of the homogeneous alloy after quenching (cf. Figs. 13 and 14).

5. DISCUSSION

It is obvious from the experiments with single crystals as well as with polycrystalline specimens of the platinum-rich alloys that in this region of the phase diagram the spinodal curve coincides with the transition of one precipitation process into another. The type of precipitation mechanism as well as the rate of decomposition on either side of the spinodal curve is in agreement with the theories of Tichelaar and Borelius. Below the spinodal curve precipitation

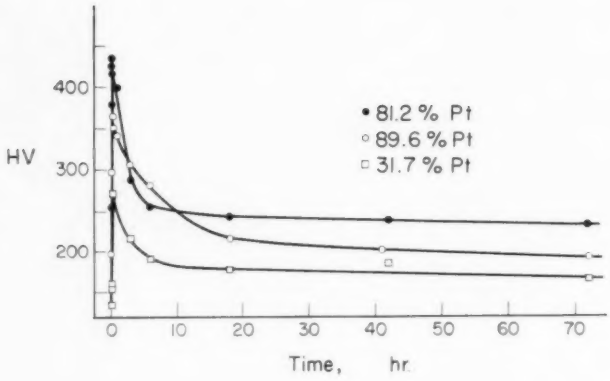


FIG. 13. Vickers' micro-hardness as function of annealing time at 650°C.

follows qualitatively the path indicated in Fig. 3a, as can be derived from Figs. 4 and 6 and Tables 1 and 2, whereas above the spinodal curve precipitation follows the path indicated in Fig. 3b, cf. Figs. 5 and 7 and Tables 1, 2 and 3. Moreover the rate of precipitation below the spinodal curve is markedly higher than that above the spinodal curve.

At the gold-rich-side of the diagram roughly the same phenomena were observed, cf. Figs. 8 and 9 and Tables 2 and 3. However, as indicated by the behaviour of the 37.9 at.% Pt alloy, at this side of the diagram the calculated spinodal curve does not constitute a sharp boundary between two regions with different precipitation processes. Attention is also drawn to the fact that resistance measurements of Wictorin showed already a marked difference in the course of the resistance as a function of annealing temperature (plotted as $\log\left(\frac{1}{\Delta}\frac{\Delta R}{10}\right)$ versus $1/T$) for the 36 at.% Pt alloy in comparison with the other curves. Besides his experimentally determined points of the spinodal curve at the platinum-rich side are in much better agreement with the calculated line than those at the gold-rich side of the diagram, although it is perhaps more exact to say that the points are in better agreement at lower concentrations of the solute component.

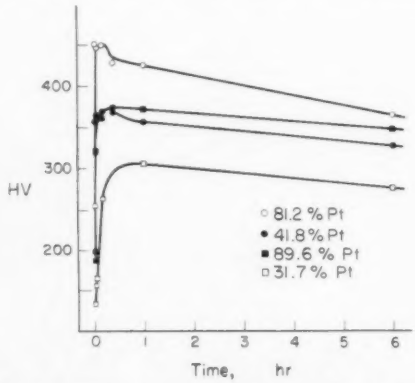


FIG. 14. Vickers' micro-hardness as function of annealing time at 600°C.

A tentative explanation of the different behaviour between alloys at the platinum-rich-side and at the gold-rich-side of the diagram may be formulated as follows. The gold-rich alloys being higher in solute concentration are probably more strained than the platinum-rich alloys. These strains were not taken into consideration in the theories of Borelius and Tichelaar. Although these theories roughly predict the observed precipitation phenomena in the gold–platinum system, the above mentioned quantitative deviations require probably a modification according to the suggestions of Dehlinger *et al.* and Cohen. The original B_2-rich area (cf. Fig. 3b) may be initiated by the formation of the "Komplexe" as proposed by Dehlinger and co-workers.

The anomalous behaviour at the gold-rich side of the diagram may be attributed to a higher concentration of lattice imperfections (e.g. dislocations) due to the strains arising from the high concentration of the solute component as already mentioned in section 2. These lattice imperfections may play an important role during the nucleation as predicted in particular by Cohen.

There are as yet no experiments available for alloys in the composition range 50 : 50, annealed at high temperatures. Together with the experiments of Wictorin they could perhaps enable a choice between Borelius' and Becker's conceptions on the origin of a maximum rate of the precipitation process as a function of the temperature of annealing, as put forward recently by Stadelmaier and Hütter[19] for the NaCl–KCl system. Unfortunately also in this latter paper a fundamental difficulty remains, namely the fact that an observed nucleation frequency need not be equal to the rate at which the nuclei are formed. It is only a measure of the rate at which these

centers become visible and thus it can not be separated from the growth kinetics.

ACKNOWLEDGMENT

The author would like to thank Professor W. G. Burgers, the originator of this work, for continued interest and encouragement. Further thanks are due to Dr. T. J. Tiedema for many helpful discussions and other assistance during the course of the investigation.

This work is part of the research programme of the research group Metals F.O.M.—T.N.O. of the Stichting voor Fundamenteel Onderzoek der Materie (Foundation for Fundamental Research of Matter, F.O.M.) and was also made possible by financial support from the Nederlandse Organisatie voor Zuiver-Wetenschappelijk Onderzoek (Netherlands Organization for Pure Research, Z.W.O.).

REFERENCES

1. A. S. Darling, R. A. Mintern and J. C. Chaston, *J. Inst. Met.* **81,** 125 (1952).
2. T. J. Tiedema, J. Bouman and W. G. Burgers, *Acta Met.* **5,** 310 (1957).
3. L. J. van der Toorn and T. J. Tiedema, *Acta Met.* **8,** 711 (1960).
4. G. Borelius, *Ann. Phys. Lpz.* **20,** 57 (1934); *Ann Phys., Lpz.* **24,** 489 (1935); *Ann. Phys., Lpz.* **28,** 507 (1937); *Ann. Phys., Lpz.* **33,** 517 (1938); *Ark. Mat. Astr. Fys.* **32A** no. 1 (1945).
5. G. Borelius, F. Larris and E. Ohlson, *Ark. Mat. Astr. Fys.* **31A,** no. 10 (1944).
6. C. G. Wictorin, Thesis, Stockholm (1947).
7. T. J. Tiedema and W. G. Burgers, *Appl. Sci. Res.* **A4,** 243 (1953).
8. U. Dehlinger and H. Knapp, *Z. Metallk.* **43,** 223 (1952).
9. U. Dehlinger and H. Franz, *Z. Metallk.* **48,** 176 (1957).
10. H. K. Hardy and T. J. Heal, *Progr. Met. Phys.* **5,** 143 (1954).
11. G. W. Tichelaar, Thesis, Delft (1956); see also W. G. Burgers and G. W. Tichelaar, *Proc. Acad. Sci. Amst.* **B57,** 73 (1954).
12. M. Cohen, *Trans. Amer. Inst. Min. (Metall.) Engrs.* **212,** 171 (1958).
13. V. Daniel and H. Lipson, *Proc. Roy. Soc.* **A181,** 368 (1943); **A182,** 378 (1944).
14. M. E. Hargreaves, *Acta Cryst., Camb.* **4,** 301 (1951).
15. A. Guinier, *Acta Met.* **3,** 510 (1955); *J. Metals, N.Y.* **8,** 673 (1956).
16. J. Manenc, *Acta Met.* **7,** 124 (1959).
17. J. Manenc, *Rev. Métall.* **54,** 867 (1957).
18. J. D. Bernal, *Proc. Roy. Soc.* **A113,** 117 (1926).
19. H. H. Stadelmaier and L. J. Hütter, *Z. Metallk.* **50,** 41 (1959).

VOL. 8 1960

Note on the interaction of interstitially dissolved carbon atoms in α-iron*

Previously,[1] measuring the time decrease of initial permeability caused by interstitially dissolved nitrogen in α-iron, we observed a relaxation phenomenon at times very long compared with the relaxation time due to single jumps of the interstitial atoms. Such an effect might be explained in several ways; the mean time of stay of an interstitial situated near an impurity atom (e.g. silicon) may differ widely from that of an interstitial atom situated in the pure iron lattice; diffusion over large distances may occur, due to migration of the interstitials into a Bloch-wall,[2] or to the fact that the interstitial atoms follow dislocations moving under the influence of magnetostrictive stress-fields; finally, interaction between the interstitial atoms may cause long relaxation times as shown by Powers and Doyle[3] in the case of oxygen in tantalum. It will be shown that in the case of interstitially dissolved carbon in α-iron the relaxation phenomenon at long times is mainly due to interaction of the interstitials.

Using a method described previously[1] we measured the time decrease of permeability due to the redistribution of carbon atoms in α-iron at 273°K. In Fig. 1 we have plotted as approximation to $[r_\infty - r(t)]/[r_\infty - r_0]$ the ratio

$$\frac{r(180\text{ min}) - r(t)}{r(180\text{ min}) - r(0)} = \frac{\Delta r_p(t)}{\Delta r}$$

versus Δr, for $t = 2$ min, $t = 3$ min and $t = 4$ min, where $r(t)$ is the reluctivity at time t after demagnetization. The total effect, Δr, is mainly due to a redistribution of isolated carbon atoms and is proportional to the carbon concentration. $\Delta r_p(t)$ represents the relaxation phenomenon at long times. $\Delta r_p(t)/\Delta r$ is seen to be proportional to Δr, which means that $\Delta r_p(t)$ is proportional to the square of the carbon concentration.

Our conclusion is that $\Delta r_p(t)$ is mainly due to a redistribution of pairs of carbon atoms, even though we do not know exactly the diffusion mechanisms leading to this redistribution.

By roughly extrapolating the values for $\Delta r_p(t)$ at a concentration of 0.024 at.% (i.e. 0.005 wt.%, $\Delta r = 4 \times 10^{-3}$ Oe/G) up to $t = 0$ assuming an exponential decay (relaxation time about 4 min), we estimate that the effect due to the redistribution of pairs is about 7 per cent of the total effect. At times longer than 2 min after demagnetization the main relaxation effect—with a relaxation time at this temperature of about 15 sec— is almost terminated; its contribution, less than 1 per mille of the total effect, is neglected.

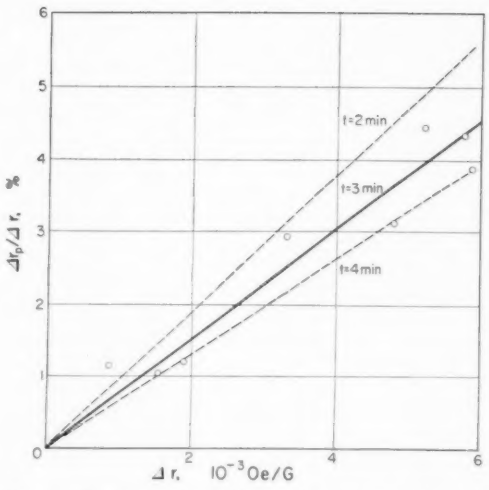


FIG. 1. The ratio $\Delta r_p(t)/\Delta r$ as a function of Δr. $t = 3$ min for the solid line and the measuring points as indicated. The broken lines represent the experimental results for $t = 2$ min and $t = 4$ min, respectively.

From the binding energies for the carbon pairs, as calculated by Fisher[4], it may be estimated that at the concentration and temperature mentioned above about 15 per cent of the carbon atoms is bound in pairs. If it is assumed that the interaction between interstitial and direction of the magnetization vector is the same irrespective of whether the interstitial is isolated or one partner of a pair, the relaxation effect due to the redistribution of pairs is expected to be 9 per cent of the total effect. The measured effect therefore agrees in order of magnitude with the calculated value.

A. J. BOSMAN
P. E. BROMMER
L. C. H. EYKELENBOOM
C. J. SCHINKEL
G. W. RATHENAU

Natuurkundig Laboratorium der Universiteit van Amsterdam, Amsterdam Holland

* This work has been supported by the General Electric Research Laboratory, Schenectady, N.Y.

References

1. A. J. BOSMAN, P. E. BROMMER, H. J. VAN DAAL and W. G. RATHENAU, *Physica, s'Grav.* **23,** 989 (1957).
2. G. DE VRIES, *Physica, s'Grav.* **25,** 1211 (1959).

3. R. W. Powers, M. V. Doyle, *Trans. Amer. Inst. Min. (Metall.) Engrs.* **215,** 655 (1959).
4. J. C. Fisher, *Acta Met.* **6,** 13 (1958).

Received April 25, 1960.

Hydrogen and austenite stabilization*

Cohen *et al.*[1] first suggested in 1949 that the extent to which the "strain embryos" of austenite were neutralized or deactivated, determined its stability and the extent to which it was retained during heat treatment. The strain embryos were considered to be centred round dislocations and/or other defects in the lattice and the deactivation to take place when carbon atoms, present interstitially in the austenite, migrated towards and were captured by the strain embryos. In an attempt to explain on the basis of this concept, the thermal stabilization of austenite, when held at constant temperature as well as when directly cooled, the authors have been led to propose[2,3] that migration of carbon atoms towards the strain embryos requires the setting up of an adequate concentration gradient for carbon, which may be due either to the martensitic regions, contiguous to the retained austenite at temperatures below the M_s or to "premartensite zones", supposed to be formed spontaneously in the austenite, above the M_s value.

As, *a priori*, the strain embryos of austenite may be deactivated by the capture of any interstitial solute atom, hydrogen—present in interstitial solid solution in steel—may also be expected to stabilize austenite. The possible role of hydrogen in stabilizing austenite is briefly examined in this note.

As with carbon, there must be a build-up of hydrogen to permit its diffusion towards the austenitic strain embryos. However, unlike carbon, there is, with hydrogen, no particularly strong tendency for the atoms to come out of the lattice of iron, when it changes from the face-centred to the body-centred configuration. The solid solubilities[4] of hydrogen in the α and γ phases of iron do not differ as much as in the case of carbon. A build-up of hydrogen, at the interface between the austenite and the associated martensite (or even the premartensite zone) with solid solubilities differing by no more than a factor of two or three, to set up an adequate concentration gradient is thus much less probable than with carbon, where the factor is very much greater. Any tendency for the hydrogen to come out of martensite would further be matched by the nearly equal tendency for it to come out of austenite and hence migration towards the austenitic strain embryos becomes more unlikely. Furthermore, the extent to which the steel, after normal austenitizing, is supersaturated with respect to hydrogen, is considerably smaller than with respect to carbon (about 3 or 4 : 1 as compared to 40 or 50 : 1) and hence the tendency for the hydrogen to come out of the body-centred iron lattice is itself quite small.

Because of the improbability, therefore, of the required build-up of hydrogen, the possibility of any stabilization of austenite being caused by hydrogen atoms may perhaps be discounted.

A comparison can also be made of the times required for stabilization of austenite to take place at any specified temperature, if hydrogen is indeed the responsible factor and observed experimentally for such stabilization to take place. Edmondson[5], Glover and Smith[6], Imai and Izumiyama[7] and Otte and Ko[8], amongst others, have observed that at temperatures of the order of 20°C and 100°C, a few hundred hours and a few minutes respectively are required for stabilization (maximum) to take place. An approximate idea of the times required for such stabilization to take place can be obtained from the average speeds of migration of hydrogen atoms in austenite at these temperatures and the average separation between a hydrogen atom in austenite and an austenitic strain embryo. With 5 cm^3 of hydrogen per 100 g of austenite—an amount which is well on the high side—the required times are calculated to be of the order of 1 sec and 10^{-3} sec, respectively, for the above mentioned temperatures. The calculated and experimentally observed times differ so greatly, that the deactivation of the embryos by hydrogen can be taken as quite unlikely.

There is, unfortunately, not much information available on the stabilization of austenite containing hydrogen. In a high carbon high chromium die steel, containing quite small amounts of hydrogen (of the order of only 0.2 cm^3 per 100 g) considerable athermal stabilization over the temperature range 200°–350°C has been observed and adequately accounted for[3] on the basis of the formation of premartensite zones and carbon diffusion. On the other hand, Ko and Edmondson[9] could not detect any stabilization effects above M_s in a steel cathodically impregnated with hydrogen, although a year earlier, Morgan and Ko had reported considerable stabilization in the same steel. As, however, the hydrogen introduced in steel by cathodic impregnation at room temperature and at pressures estimated to reach fantastically high values[4] (of the order of 10^{10} atmospheres or even higher) will virtually completely come out of the steel

VOL. 8 1960

when it is austenitized at high temperatures in vacuum (or even at atmospheric pressure) it is not quite certain that after the high temperature soaking carried out by Ko and Edmondson, hydrogen was indeed retained by the austenite to an extent appreciably greater than before cathodic impregnation, to enable its effect on austenite stability to be determined.

While, therefore, more experimental data on the effect of hydrogen on the stabilization of austenite would be undoubtedly interesting, it would appear that the deactivation of the strain embryos in austenite, resulting in its stabilization, is unlikely by hydrogen, at least in the amounts present in normally heat-treated steels.

Grateful thanks are due to Dr. B. R. Nijhawan, Director, National Metallurgical Laboratory, for discussion and permission to publish this note and to Mr. N. G. Banerjee, Junior Scientific Officer, for the hydrogen analyses.

E. G. Ramachandran
C. Dasarathy

Physical Metallurgy Division, National Metallurgical Laboratory Jamshedpur, India

References

1. M. Cohen, E. S. Machlin and V. G. Paranjpe, *Thermodynamics in Physical Metallurgy* p. 162. American Society for Metals, Cleveland (1949).
2. E. G. Ramachandran and C. Dasarathy, *Acta. Met.*, **8,** 274 (1960).
3. E. G. Ramachandran and C. Dasarathy, *Acta. Met.*, to be published.
4. D. P. Smith, *Hydrogen in Metals.* University of Chicago Press, Chicago (1948).
5. B. Edmondson, *Acta. Met.* **5,** 208 (1957).
6. S. G. Glover and T. B. Smith, *Mechanism of Phase Transformations in Metals* p. 265. Institute of Metals, London (1956).
7. Y. Imai and M. Izumiyama, *Sci. Rep. Res. Inst. Tohuku Univ.* **11,** 393 (1959).
8. H. M. Otte and T. Ko, *J. Iron. St. Inst.* **173,** 31 (1953).
9. T. Ko and B. Edmondson, *Acta. Met.* **1,** 466 (1953).

* Received April 20, 1960.

On the temperature dependence of flow stress in quenched aluminum crystals*

The temperature dependence of flow stress for single and polycrystalline aluminum has been investigated by Cottrell and Stokes[1] and, more recently, by Basinski[2]. These investigators found a difference in flow stress when specimens, in the well annealed state, were deformed to the same strain at different temperatures. They suggested that the difference arose from two contributions: (a) one which is reversible and due to the thermal assistance given dislocations to overcome obstacles and (b) an irreversible effect resulting from variations of dislocation configurations with temperature. In the case of the former, the ratio of flow stresses at the end of pre-straining at a high temperature and subsequent reloading at a lower one was found to be a constant with increasing strain and a unique value for given combinations of temperatures. This ratio was adjusted for the temperature variation of elastic modulus and plotted against temperature. The resulting curve indicated the ratio remained relatively unchanged down to about 200°K, followed by a distinct increase with further decrease in temperature. The temperature independent portion was interpreted as evidence that glide dislocations can easily cut through "forest" dislocations with the aid of thermal fluctuations. Below 200°K, such assistance becomes less available and the deformation process becomes increasingly difficult. The irreversible difference was manifested by a drop in flow stress after yielding at a high temperature following pre-straining at a lower one. This "work softening" was said to be stress initiated instability of dislocation configurations formed at the low temperature.

With the above in mind, it was considered of interest to look into the possible effects of quenching on the temperature dependence of flow stress of aluminum crystals. The effect of quenching on mechanical behavior at room temperature has been documented.[3,4] Also, the recent direct observations of small dislocation loops in quenched foils of aluminum by Hirsch and his co-workers[5–7] has led to speculations concerning the mechanism of hardening. These results were in good agreement with the predictions on the origin of dislocations by Kuhlmann-Wilsdorf[8], who proposed that quenched-in vacancies agglomerate in discs that subsequently collapse to form dislocation loops. The loops (of average size 200 Å)

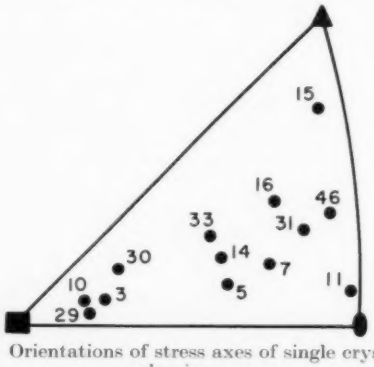


Fig. 1. Orientations of stress axes of single crystals of aluminum.

* Based on work carried out at Armour Research Foundation, Chicago, Ill., sponsored by the ARF Research and Invention Committee.

TABLE 1. Flow stress at T relative to that at 293°K

Temperature (°K)	273	200	78	Condition
Specimen No. 3b			1.340	quenched
5a			1.333	furnace cooled
7b		1.069		quenched
7c			1.334	quenched
14c			1.339	quenched
16c	1.017			quenched

TABLE 2. Flow stress at T relative to that at 78°K

Temperature (°K)	293	273	200	Condition
Specimen No. 3b	0.746			quenched
5a	0.750			furnace cooled
7c	0.744			quenched
14b		0.767		quenched
14c	0.747			quenched
16b			0.795	quenched

appear too small to be activated in the manner of a Frank–Read source at the flow stresses observed in quenched crystals. However, as dislocations, they would be expected to contribute additional stress fields, as well as increase the population of "trees" on the "forest" planes. Thus, the number of obstacles to glide would be increased, which in turn, could account for quench hardening.[5]

In the present investigation a series of experiments, patterned after those of Cottrell and Stokes[1], were carried out with quenched crystals. The techniques for preparation and testing of high purity crystals (99.999+%)* were similar to those reported in an earlier publication.[4] Crystal orientations are shown in Fig. 1. The samples were strained in an Instron machine, utilizing a specially designed tensile fixture and cryostat, at combinations of the following temperatures: 78, 200, 273 and 293°K. Temperatures were maintained to ±1°K. In addition to the cycling tests, uninterrupted tensile tests on crystals with widely different orientations were performed at both 78 and 293°K.

The results of cycling tests indicated that quenched crystals not only behave in a manner similar to fully annealed ones (i.e. the flow stress ratio for any two temperatures being a constant, independent of strain) but also, the numerical values for this relationship are quite nearly identical. This is seen clearly when the ratios: $\frac{\sigma_T}{\sigma_{78°K}}$ and $\frac{\sigma_T/\mu_T}{\sigma_{78°K}/\mu_{78°K}}$ †, taken from the data in Tables 1 and 2, are plotted against temperature in conjunction with the data of Cottrell and Stokes[1] normalized to 78°K (see Fig. 2). The above is not too surprising if, indeed, the "forest" effect is operative. It was seen that the flow stress ratio is independent of the increase of dislocation density produced by plastic deformation. Therefore, it is unlikely that it would be affected by an increase in density resulting from quenching.

Additional identical behavior was seen in the presence of "work softening" in the load–extension curves (see example in Fig. 3). The stress–strain curves of uninterrupted tensile tests at 78 and 293°K are presented in Fig. 4. When comparing these with curves for well annealed crystals of comparable orientations,‡ it is seen that orientation dependence is also quite similar while yield stresses are higher and work hardening rates are lower for the quenched crystals at both temperatures.

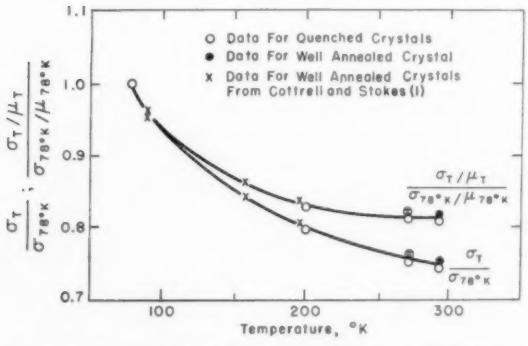


FIG. 2. Reversible changes of flow stress with temperature before and after correction for the variation of shear modulus with temperature.

* Supplied by ALCOA Research Laboratories.

† The term μ is the shear modulus determined by the method suggested by Basinski[2].

‡ From the work of Stawbwasser[3].

VOL. 8 1960

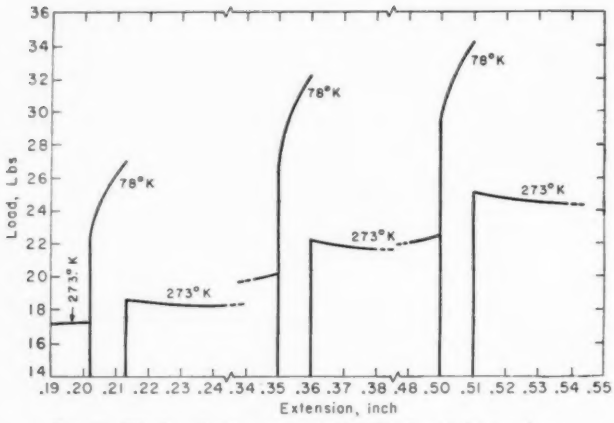


FIG. 3. Work softening seen at 273°K after deformation at 78°K in crystal No. 14b.

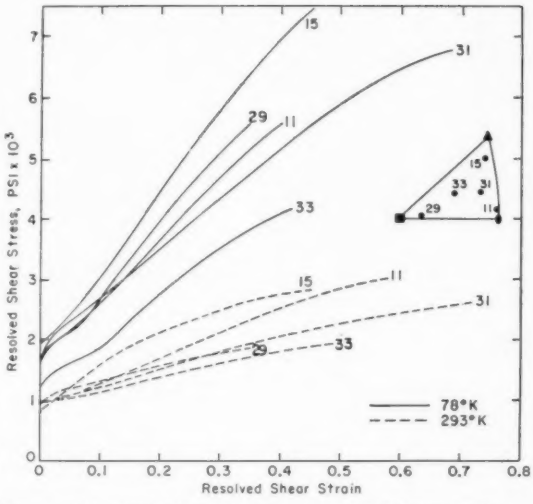


FIG. 4. Resolved shear stress vs. resolved shear strain at 78° and 293°K for single crystals of various orientations.

The evidence presented seems to indicate that, despite the apparent extreme changes in the deformation process due to quenching, there are certain areas that remain unaffected. This leads to the suggestion that the "forest" effect is important in explaining the mechanical behavior of aluminum crystals independent of prior thermal history.

L. E. TANNER

Research Division
Manufacturing Laboratories, Inc.
Cambridge, Mass.

References

1. A. H. COTTRELL and R. J. STOKES, *Proc. Roy. Soc.* A**233**, 17 (1955).
2. Z. S. BASINSKI, *Phil. Mag.* **4**, 393 (1959).
3. R. MADDIN and A. H. COTTRELL, *Phil. Mag.* **46**, 1021 (1955).
4. L. E. TANNER and R. MADDIN, *Acta Met.* **7**, 76 (1959).
5. P. B. HIRSCH and J. SILCOX, *Growth and Perfection of Crystals* p. 262. Wiley, New York (1958).
6. P. B. HIRSCH, J. SILCOX, R. E. SMALLMAN and K. E. WESTMACOTT, *Phil. Mag.* **4**, 897 (1959).
7. P. B. HIRSCH, *J. Inst. Met.* **4**, 406 (1959).
8. D. KUHLMANN-WILSDORF, *Phil. Mag.* **3**, 125 (1958).
9. W. STAWBWASSER, *Acta Met.* **7**, 43 (1959).

Received March 14, 1960.

Method for measuring the free energy of a solid surface*

In recent years, several novel methods have been devised to measure free energies of solid surfaces.[1–3] The present note proposes a method which is applicable to solids that evaporate by a lamellar mechanism.[4–10]

During lamellar evaporation, a crystal loses atoms from the edge surfaces of lamellae whose flat surfaces are low-index, crystallographic planes. The lamellae originate from sources such as crystal edges and screw dislocations. Fig. 1(a) shows a lamella defined by an edge surface at A (hereafter called a "riser") and plane surfaces at B and C (hereafter called "lamellar planes"). If a lamellar plane is nearly coincident with the crystal surface, the lamellae may traverse the entire surface during evaporation. The individuality of a lamella from a given source depends on interactions with other lamellae and with obstacles such as inclusions.

Fraser *et al.*[11] noted that refractory inclusions (Al_2O_3 and MgO), lying in the lamellar planes of chromium ({001} and {011})[12] are able to impede the recession of the lamellae during evaporation. It is easy to demonstrate that this will occur when

$$\gamma_{i/r} < \gamma_{r/v} + \gamma_{i/v},$$

where r, i and v represent riser, inclusion and vapor, respectively. The above inequality is probably

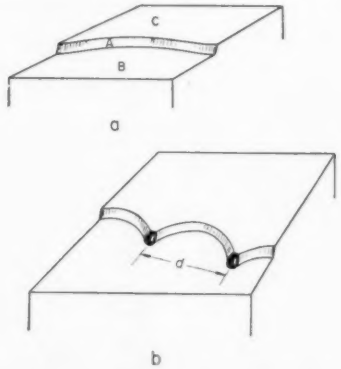


FIG. 1.

satisfied for oxide inclusions in a metal.[13] In addition to simple point retardation, two inclusions, coplanar with the lamellar plane, can cooperate to prevent migration of the portion of the riser which lies between them (Fig. 1(b)). This cooperative locking will occur when the distance between the inclusions, d, is less than the critical diameter for the nucleation of a two dimensional hole in the close-packed lamellar plane.

The portion of the riser locked between the two inclusions will form an equilibrium shape which is a function of the surface free energy of the riser, the temperature and the partial pressure of the vapor above the surface. At equilibrium the riser will neither advance or retreat, and it is under these conditions only that the following analysis can be applied. If the equilibrium shape and the partial pressure or undersaturation of vapor are known, it is possible to determine the surface energy of the riser assuming

(1) the anisotropy of surface free energy in the lamellar plane is negligible,
(2) the surface free energy of the riser is independent of curvature and
(3) the riser has only one principal radius of curvature.

The chemical potential of an atom in the curved riser surface and in the vapor (referred to a plane riser surface) are $\gamma_r\Omega/_r$ and $kT \ln P_r/P_0$, respectively, where

γ_r = surface free energy of the riser
Ω = molecular volume
r = radius of curvature of the riser
P_r = partial pressure of the crystal vapor in equilibrium with the riser
P_0 = partial pressure of the crystal vapor in equilibrium with a flat riser surface $\equiv$ vapor pressure.

At equilibrium the chemical potentials of atoms in the vapor and riser surface must be equal. Thus,

$$\gamma_r = \frac{-rkT}{\Omega} \ln P_r/P_0.$$

It is apparent that the model chosen is somewhat restrictive. It requires that the solid undergo lamellar evaporation, which implies an anisotropy of surface free energy. Further, the anisotropy must be limited to the extent that it is negligible in the lamellar plane. These constraints imply an equilibrium shape which is composed of plane sections, corresponding to principal low-index orientations, connected by smoothly curved surfaces, i.e. not a polyhedron. In the absence of anisotropy, a lamella higher than some few unit spacings would be unstable due to the curvatures necessarily developed at the top and bottom of its riser. On the other hand, strong anisotropy in the lamellar plane would destroy the circular symmetry required by this method. Recent experiments by Moore[14,15] indicate that silver may exhibit the necessary type of equilibrium shape in air at about 900°C.

The expression for γ_r is independent of the height of the lamella, which, while influencing the rate of riser motion, does not enter into the equilibrium considerations. Physically, this illustrates the fact that a unit riser and a riser of arbitrary height are retained equally well by the inclusion pair.

It is a common observation that the riser of a given lamella is not smooth but composed of a series of small steps.[12,16] Although the occurrence of such small steps (presumably the scale extends to unit steps) does alter the surface free energy of the riser, the effect is not expected to be large. However, with suitably-refined observations, it may be possible to define the specific edge energy of a unit lamella.

Since cooperative locking of a riser requires that the precipitate spacing be less than the critical diameter for two dimensional nucleation of a hole in the lamellar plane, it is evident that the proposed method generally will require refined techniques. Electron microscopy will be needed to measure curvatures and the production of controlled under-saturations necessitate good thermal control coupled with hot-finger or possible Knudsen-cell techniques. The possibility of relaxation of the riser curvature during cooling of the specimen implies the need for a rapid quench from the evaporation temperature. The specimen geometry is particularly simple. All that is required is that the crystal evaporate by a lamellar mechanism, according to the limitations noted above, and that a suitable inclusion dispersion can be produced. The surface to be evaporated should be nearly coincident with a lamellar plane. With respect to the inclusions, it should be noted that their presence generally implies a two or more component matrix, and therefore the method is not applicable to strictly pure materials.

Westinghouse Research Laboratories M. J. FRASER
Pittsburgh, Pennsylvania

VOL. 8 1960

References

1. A. SKAPSKI, R. BILLUPS and A. ROONEY, *J. Chem. Phys.* **26,** 1350 (1957).
2. R. C. SILL and A. SKAPSKI, *J. Chem. Phys.* **24,** 644 (1956).
3. H. UDIN, A. J. SHALER and J. WULFF, *Trans. Amer. Inst. Min. (Metall.) Engrs.* **185,** 186 (1949).
4. N. CABRERA and M. M. LEVINE, *Phil. Mag.* **1,** 450 (1956).
5. G. W. SEARS, *J. Chem. Phys.* **24,** 868 (1956); **27,** 1308 (1957).
6. S. AMELINCKX and E. VOTAVA, *Naturwissenschaften* **41,** 422 (1954).

7. J. P. Hirth and G. M. Pound, *J. Chem. Phys.* **26,** 1216 (1957); *Acta Met.* **5,** 649 (1957).
8. E. Votava and A. Berghezan, *Acta Met.* **7,** 392 (1959).
9. J. B. Newkirk, *Acta Met.* **4,** 316 (1956).
10. H. Suzuki, *J. Phys. Soc. Japan* **10,** 981 (1955).
11. M. J. Fraser, D. Caplan and A. A. Burr, *Acta Met.* **4,** 186 (1956).
12. M. J. Fraser, D. Caplan and A. A. Burr, to be published.
13. A. Bondi, *Chem. Rev.* **52,** 417 (1953).
14. A. J. W. Moore, *Acta Met.* **6,** 293 (1958).
15. E. D. Hondros and A. J. W. Moore, *Acta Met.* **7,** 521 (1959).
16. T. Taoka and S. Sakata, *J. Electronmicr.* **4,** 41 (1956).

* Received October 15, 1959; revised March 21, 1960.



Fig. 1. Electron micrograph showing stacking faults and dislocations in a typical evaporated [001] gold film. ×60,000

Mechanical twinning in thin evaporated gold films*

In a recent series of investigations, thin single-crystal gold films have been grown and subjected to mechanical stress. These experiments seem to indicate that mechanical twinning can occur in thin evaporated gold films between 1000 and 5000 Å in thickness, at temperatures up to 200°C. Such twinning has been reported by other investigators for copper at low temperatures,[1] and for silver–gold alloys at temperatures up to 0°C.[2]

The thin gold films with a (001) orientation were prepared by vacuum deposition on a substrate of sodium chloride. The substrate blanks were cleaved along the (100) plane and then heated in an induction furnace in the vacuum system. When the pressure had been reduced below 0.005 mm and the sodium chloride blanks raised to a temperature of 375°C a thin film of gold was evaporated on the blanks from a molybdenum filament. Single-crystal films of gold were obtained in this manner which were continuous (free of holes) and varied in thickness from 1000 to 5000 Å. The films were separated from the sodium chloride substrate and examined with an RCA EMU-3B electron microscope operated at 100 kV. Transmission photographs and diffraction patterns indicated that the films were single crystals, with a high density of stacking faults and dislocations. An electron micrograph of a typical film is shown in Fig. 1.

The gold films were tested in two different ways. One method involved the drilling of a small hole through the sodium chloride substrate with a water jet, perpendicular to the plane of the film. This gave a circular area of the gold film, approximately 0.5 mm in diameter, that was no longer supported by the substrate. The film in this area was then tested by slowly reducing the pressure on the bottom of the gold film, bulging the film down through the hole in the substrate. In this method, the pressure differential between the two sides of the film, and thus the stress applied to the film, was controlled. The films were observed continuously during the stress application by means of an optical microscope.

The other method of testing consisted of mechanically stretching a narrow sample of the film about 0.5 mm wide and 5 mm long which had been removed from the substrate. The stress was applied in the direction of the long dimension of the film sample, which was the [110] crystallographic direction. A linear stretching device was used in which the strain applied to the film was controlled.

In both cases, apparent mechanical twinning was observed at resolved shear stresses of approximately 5×10^8 dyn/cm^2 (resolved shear strain of 0.3 per cent). As the stress was increased, the appearance was noted of many small bands oriented with their long dimension in a ⟨110⟩ direction. These bands would appear suddenly and usually grow slightly in length and width with increasing stress. Upon application of further stress, these small or minor bands would group together into one or more large or major bands, these latter appearing to have a laminated fine structure and consisting of bundles of the minor bands. The minor bands had a length of 25 to 50 μ, while the major bands had lengths of up to 1000 μ. In the bulged samples, two major bands would usually appear at right angles to each other, extending almost all the way across the bulged area. The optical micrograph in Fig. 2 shows such an example.

These observations were normally made at room temperature of 20°C, but a series of experiments was performed using the bulge technique at a temperature of 200°C. In these samples the minor bands were observed, but they first appeared at a higher value of stress than in the samples tested at room temperature. The major bands were not observed in any of these heated films.

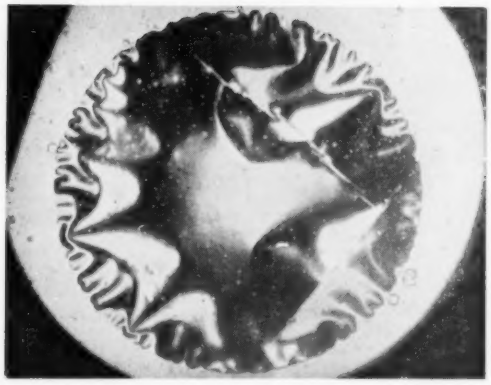


FIG. 2. Optical micrograph of bulged area of gold film showing twin bands. ×54

X-ray diffraction studies were made to determine the crystallographic orientation in these bands. Transmission Laue photographs were taken using a highly collimated X-ray beam. The gold films were oriented so that the beam was along the [111] direction of the film, with the beam incident on the deformed area. The diffraction patterns were plotted on a stereographic projection and showed octahedral poles, apparently due to the bands, rotated 180° about the [111] pole from their position in the original orientation. These X-ray studies thus indicated that the bands were twin bands and that the twinning had occurred on the [111] planes.

Electron microscope studies were made of the stressed gold films after removal from the sodium chloride substrate. The contrast of the bands and the appearance of the extinction contours indicated a distinct change in orientation within both the minor and major bands. Fig. 3 is a low magnification



FIG. 3. Electron micrograph showing small twin bands in gold films. The small dark spots are stacking faults. ×3150

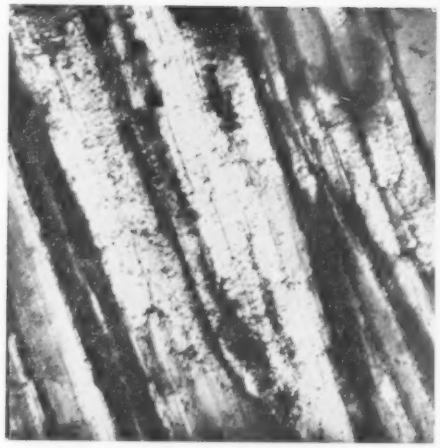


FIG. 4. Electron micrograph of twin band showing many dislocations and the laminar structure of the band. ×14,000

electron micrograph which shows the typical appearance of some of the smaller bands. The characteristic laminated appearance of the bands and the manner in which the width of a band decreases at its end to approximately the projected width of a stacking fault can be seen. The small black points in the area between the bands are stacking faults such as those in Fig. 1.

The general appearance of the bands at higher magnification is shown in Fig. 4. Many dislocations, but few stacking faults, were visible within the bands. Dislocation movement within the bands was frequently observed during electron microscope examination, but this was not observed in other areas of the film. The bands in general showed a lenticular shape, similar to mechanical twins observed optically in other metals.

The appearance of these bands formed during stressing, and the X-ray diffraction results, both indicate that mechanical twinning has taken place in thin single-crystal gold films.

Grateful acknowledgment is due to Dr. J. W. Beams, Dr. N. Cabrera and Dr. J. W. Mitchell for their assistance and guidance in interpreting the results of these investigations.

Departments of Engineering and Physics, University of Virginia — A. CATLIN, W. P. WALKER

Department of Chemistry, University of Virginia, Charlottesville, Virginia — K. R. LAWLESS

References

1. T. H. BLEWITT, R. R. COLTMAN and J. K. REDMAN, *J. App. Phys.* **28**, 651 (1957).
2. H. SUZUKI and C. S. BARRETT, *Acta Met.* **6**, 156 (1958).

* Received March 17, 1960.
Supported by the Office of Ordnance Research, U.S. Army.

VOL. 8 1960

Discussion of Williams' comments on "The influence of grain size on the stored energy and mechanical properties of copper"* —Part I

In a recent communication, Williams[1] commented on the results we obtained for the influence of grain size on the energy stored in plastically deformed copper.[2] He replotted our results and to explain the deviation of the points from a straight line favoured the conclusion that the results are less accurate than claimed by us, and that there is no dependence of stored energy on grain size, rather than the conclusion that the stored energy, at low strains, is a complex function of strain and is also a sensitive function of grain size.

We would like to make two important points in connexion with Williams' comments.

(1) He has incorrectly plotted our results apparently using the formula involving tensile elongation in calculating the true strain, whereas our specimens were deformed in compression. The abscissa of his Fig. 1 is, however, labelled for compression. The correct plot of our results, together with those obtained by Gordon[3], is shown in Fig. 1. It can be seen that neither our results nor Gordon's can be fitted by a straight line. In fact, a curve rather than a straight line is generally observed when stored energy is plotted as a function of true strain.[4]

(2) Since Williams questions the accuracy of the results, for low strains, quoted in our original paper, the actual values of stored energy for the lowest strain, 10 per cent compression, are listed in Table 1. It can be seen that, for each grain size, the reproducibility is ± 5 per cent as claimed, even for this low strain, whereas the energy stored for the fine-grained material is nearly twice that for the coarse-grained material. The reproducibility is at least as good for the other strains. Thus we consider that the influence of grain size on the energy stored in plastically deformed copper is amply substantiated.

TABLE 1. Influence of grain size on the energy stored in copper after 10 per cent compression

Energy stored (cal/g)	
Grain size 0.030 mm	Grain size 0.150 mm
0.041	0.022
0.040	0.021
0.037	0.022

Since the main object of the initial investigation was to examine the influence of grain size, the specimens of different grain size for each particular deformation were always taken from adjacent positions in the bar of commercial copper used. It is well known that the total stored energy is influenced by the purity of the material[5] and it is very likely that in a 12 ft bar of commercial copper 2 in. square there would be sufficient variation in composition along the length to effect the results. Of necessity, the specimens for the different deformations came from different positions along the bar so that no particular significance was, or should be, attached to the exact relationship between stored energy and strain. In order to determine exactly the relation between stored energy and strain, it would be essential to use specimens known to be of identical composition for the different strains.

L. M. CLAREBROUGH
M. E. HARGREAVES
M. H. LORETTO

Division of Tribophysics
Commonwealth Scientific and Industrial Research Organization
University of Melbourne
Australia

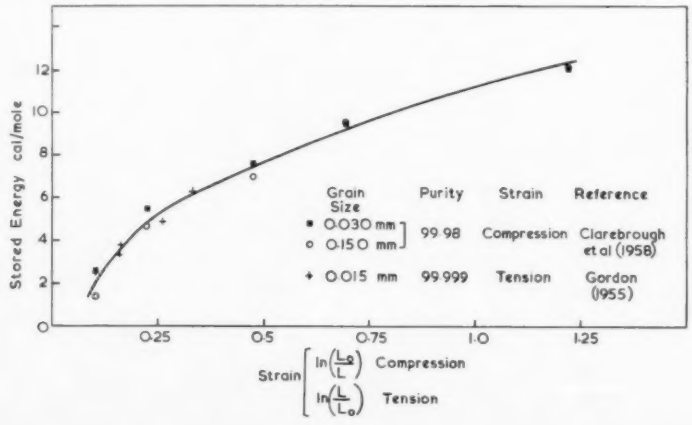


FIG. 1.

VOL. 8 1960

—Part II

It should also be noted that the equation quoted by Williams[1] can be applied only to isothermal work since the introduction of an activation energy implies that the equation has been derived by integrating a rate equation and this integration must have been carried out on the assumption that T is constant. Various workers (e.g. Johnson and Mehl[6], Avrami[7], Cook and Richards[8]) have developed different rate equations for recrystallization. However, provided the activation energies of all processes involved are assumed to be equal, each equation integrates under isothermal conditions to give the relation quoted by Williams, with k somewhere in the range 1–4.

If any of these rate equations is now integrated on the assumption that

$$T = T_0 + vt$$

and T is sufficiently greater than T_0, we find

$$X = 1 - \exp\left[-Y(T/v)^k\{Ei_2(Q/RT)\}^k\right], \qquad (1)$$

where $Ei_2(x) = x\int_x^\infty (e^{-\xi}/\xi^2)\,d\xi$

$$\sim \frac{e^{-x}}{x}\left(1 - \frac{2!}{x} + \frac{3!}{x^2} - \ldots\right)$$

and the symbols are defined in Williams[1]. For reasonably large x, $Ei_2(x) \simeq e^{-x}/x$, so that for $Q \gg RT$, we can rewrite equation (1) as

$$X \simeq 1 - \exp\left[-Y_0(T/v)^{2k}\exp(-kQ/RT)\right] \qquad (2)$$

where $Y_0 = Y(vR/Q)^k = \text{constant}$.

In order to plot curves comparable to the ΔP curves of Clarebrough *et al.*[2], we need to differentiate equation (1) to give

$$\begin{aligned}\Delta P \propto^{\text{al}} dX/dT &= (kY/v)(T/v)^{k-1}\{Ei_2(Q/RT)\}^{k-1} \\ &\quad \times \exp\left[-Q/RT - Y(T/v)^k\{Ei_2(Q/RT)\}^k\right] \\ &\simeq (kY_0Q/RT^2)(T/v)^{2k}\exp\left[-kQ/RT \right. \\ &\quad \left. - Y_0(T/v)^{2k}\exp(-kQ/RT)\right] \qquad (3)\end{aligned}$$

and this should be compared with the result of differentiating Williams'[1] equation, viz.

$$\begin{aligned}dX/dT &= (kYQ/RT^2)(T/v)^k\exp\left[-kQ/RT \right. \\ &\quad \left. - Y(T/v)^k\exp(-kQ/RT)\right] \qquad (4)\end{aligned}$$

where again it has been assumed that $Q \gg RT$. A detailed consideration of equation (3) shows that it yields ΔP curves similar to those found experimentally.[2] In fact, equations (3) and (4) yield very similar curves since dX/dT is only significantly different from zero over a small range of T for reasonable values of k, Y, Q.

From equation (3) it can be shown that, very approximately, the width at half-height is $2RT_p^2/kQ$ where T_p is the temperature of the peak of the ΔP curve. We might, therefore, ascribe some of the variation in width of the experimental curves to a variation in k. However, a far more probable explanation is that in all specimens there is a range of activation energies operating during recrystallization. Even a small range of Q-values can increase the width of a ΔP curve significantly. Furthermore, the isothermal results from a specimen in which recrystallization involves a narrow spectrum of activation energies, all processes having a given value of k, will be almost indistinguishable from those of a specimen in which recrystallization occurs with a unique activation energy and a rather lower value of k. On this basis, the variation in k_{exptal} found by Gordon[3] may in reality be due to a variation in the distribution of activation energies.

J. F. NICHOLAS

Division of Tribophysics
Commonwealth Scientific and
Industrial Research Organization
University of Melbourne
Australia

References

1. R. O. WILLIAMS, *Acta Met.* **7,** 676 (1959).
2. L. M. CLAREBROUGH, M. E. HARGREAVES and M. H. LORETTO, *Acta Met.* **6,** 725 (1958).
3. P. GORDON, *Trans. Amer. Inst. Min. (Metall.) Engrs.* **203,** 1043 (1955).
4. A. L. TITCHENER and M. B. BEVER, *Progress in Metal Physics* Vol. 7. Pergamon Press, London (1958).
5. L. M. CLAREBROUGH, M. E. HARGREAVES and G. W. WEST, *Proc. Roy. Soc.* A**232,** 252 (1955).
6. W. A. JOHNSON and R. F. MEHL, *Trans. Amer. Inst. Min. (Metall.) Engrs.* **135,** 416 (1939).
7. M. AVRAMI, *J. Chem. Phys.* **7,** 1103 (1939); **8,** 212 (1940) **9,** 177 (1941).
8. M. COOK and T. L. RICHARDS, *J. Inst. Met.* **73,** 1 (1946).

* Received January 28, 1960.

The low temperature tensile properties of niobium*

The tensile yield stress, σ_y, of body-centred cubic metals has been shown to vary with grain diameter, $2d$, according to the relation[1,2,3]

$$\sigma_y = \sigma_i + k_y d^{-1/2}. \qquad (1)$$

Both the lattice friction stress, σ_i, and k_y, which is a measure of the dislocation unlocking stress, increase with decreasing temperature and are important factors in determining the temperature of the ductile–brittle transition. According to one recent theory[4] the transition occurs when the condition

$$(\sigma_i d^{1/2} + k_y)k_y \geq \beta\mu\gamma \qquad (2)$$

is satisfied, where β is a constant which is nearly unity, μ the rigidity modulus, and γ the effective surface energy for fracture.

In the experiments described in this letter the grain size dependence of the tensile properties of niobium was studied at a series of low temperatures, with the intention of obtaining the temperature dependence of σ_i and k_y. The results show that, within the limits of experimental error, k_y was zero at all the temperatures studied, but that σ_i increased with decreasing temperature, as expected. Complete brittleness was not observed even at the lowest temperature used, which was 20°K.

A 0.25 in. diameter swaged rod was prepared from a block of Murex sintered niobium of commercial purity. The rod was divided into six parts, each of which was annealed in a vacuum furnace at a different temperature in the range 1100–2300°C. Metallographic examination showed that these annealing treatments had produced grain sizes, as measured by the linear intercept method, ranging from 0.037 to 0.138 mm. Each of the rods was machined into Hounsfield type tensile specimens of 0.75 in. gauge length and 0.10 or 0.05 in. gauge diameter. The 0.10 in. diameter specimens were tested at 76, 195 or 293°K in a modified Hounsfield tensometer at a strain rate of 0.88×10^{-4} sec^{-1}. Liquid nitrogen, and a mixture of solid CO_2 and acetone were used as coolants to obtain the temperature 76° and 195°K respectively. The specimens of 0.05 gauge diameter were tested at 20°K in a hard beam tensometer, at a strain rate of 2.82×10^{-4} sec^{-1}, using liquid hydrogen as a coolant.

The nominal non-gaseous inpurity content of the rod, as stated by the manufacturers, is given in Table 1. Analyses for nitrogen, oxygen, and hydrogen,

TABLE 1. Non-gaseous impurity content of niobium rod

Impurity	Amount present (wt. %)
Tantalum	<0.3
Titanium	<0.05
Iron	0.03
Carbon	0.01
Silicon	0.01
Tin	<0.005
Lead	<0.005
Potassium	<0.002
Sodium	<0.002

were carried out on one specimen of each grain size after it had been tested to fracture. The oxygen and hydrogen were determined by vacuum fusion and the nitrogen by a chemical method. All of the results were within the limits: oxygen 340 ± 50 p.p.m., nitrogen 140 ± 30 p.p.m., and hydrogen 14 ± 9 p.p.m.

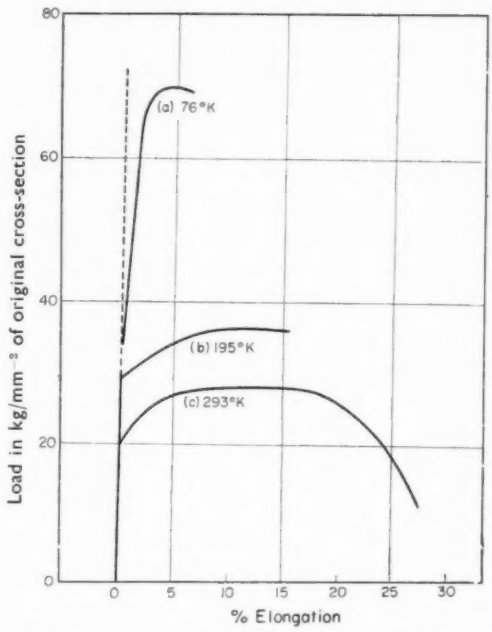


FIG. 1. Typical load–elongation curves for niobium tested at 76°, 195° and 293°K.

Specimens covering the complete range of grain sizes were tested at 76, 195 and 293°K and load–elongation curves typical of those obtained at each of these temperatures are shown in Fig. 1.

Yield points were not observed at any temperature, but the yield stress increased rapidly with decreasing temperature. The strain to fracture increased with increasing temperature, and pronounced necking was observed at 293°K. All the fracture surfaces were fibrous except for two specimens tested at 76°K which showed a few cleavage facets. At 76°K large pre-yield plastic strains were observed. This effect did not occur when a molybdenum specimen was tested under the same conditions and is therefore not a property of the testing machine.

At 195° and 293°K the shape of the load–elongation curves was completely independent of grain size. This was also practically true at 76°K, but the results suggest an increase in pre-yield plastic strain with increasing grain size (Fig. 2). Further experiments will be required to confirm this point. It should be particularly noted that the yield stress was independent of grain size at all three temperatures (Fig. 3).

The results obtained at 20°K are shown in Fig. 4. The discontinuities in the Hooke's law part of the load–elongation curves were accompanied by audible clicks and were assumed to be due to mechanical twinning, adiabatic slip, or a combination of the two.

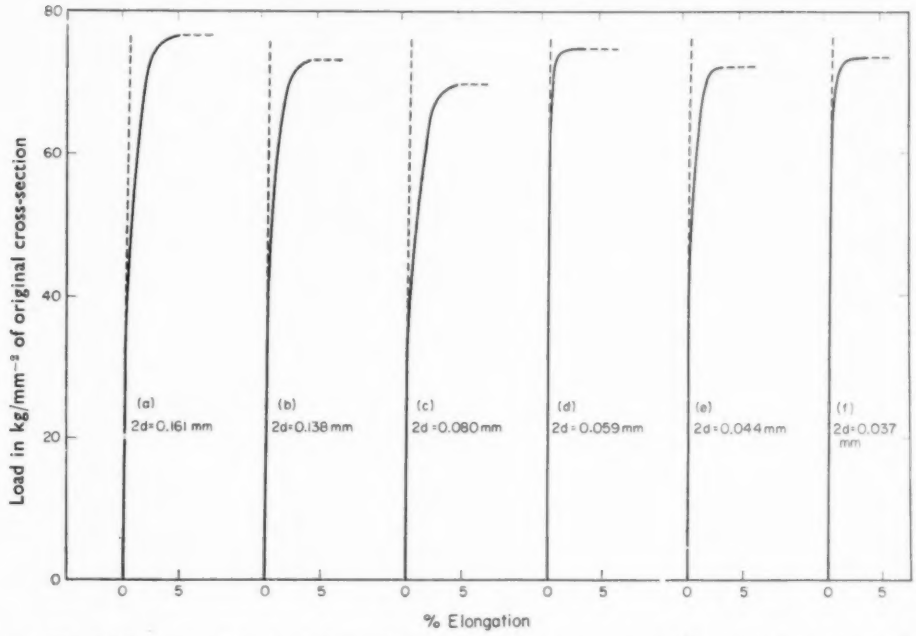


FIG. 2. The initial parts of the load–elongation curves of six specimens of different grain sizes tested at 76°K.

A metallographic examination of longitudinal polished and etched sections through two of the fracture surfaces showed that fracture had occurred by transcrystalline cleavage. The yield and fracture stress results showed more scatter than those at higher temperatures but there was no evidence for systematic grain size effects.

Similar experiments to these have recently been reported by Adams *et al.*[3]. In their work niobium behaved more like other body-centred cubic metals in so far as it showed a yield point and a finite value of k_y. The value of k_y was smaller than for either molybdenum or iron but was reflected in a strong dependence of the strain to fracture on grain size. It is in this last respect that the results of Adams *et al.* differ most strikingly from those reported here.

The value of k_y is usually regarded as a measure of the stress, σ_d, required to free a dislocation from its Cottrell atmosphere of impurity atoms and, according to one theory,[4] is equal to $\sigma_d l^{1/2}$, where l is the average distance from a grain boundary to the nearest dislocation source. It therefore depends on the type and concentration of impurity atoms present in the metal. The material used by Adams *et al.* was also of commercial quality but was considerably less pure than that used in the present investigation, particularly in respect of the iron (0.3 per cent), silicon (0.15 per cent), carbon (0.07 per cent), nitrogen (0.05 per cent), and hydrogen (0.02 per cent), contents. It therefore seems reasonable to conclude that in the experiments reported here the dislocations were not appreciably locked by impurity atoms whereas in those of Adams *et al.* locking was provided by some of the additional impurity atoms present in their material.

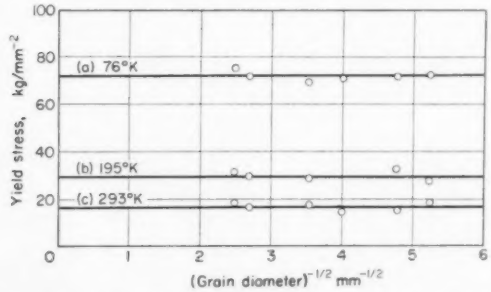


FIG. 3. The effect of grain size on the yield stress of niobium at 76°, 195° and 293°K.

Pre-yield plastic strains rather smaller than those shown in Fig. 2 have been observed by Wessel[5] in both niobium and molybdenum specimens tested at low temperatures. Wessel attributed the effect to the formation of large groups of dislocations piled-up against grain boundaries but, since large pile-ups can only be sustained in a material with strongly locked dislocations, i.e. with a high k_y, this cannot be the correct explanation, at least for the niobium used in this investigation.

The author is indebted to Drs. G. L. Miller and F. J. Cox of Murex Ltd., for supplying the niobium rod and for carrying out the heat treatments on it, to Mr. A. Parker of the U.K.A.E.A. Outstation, Woolwich, for

VOL. 8 1960

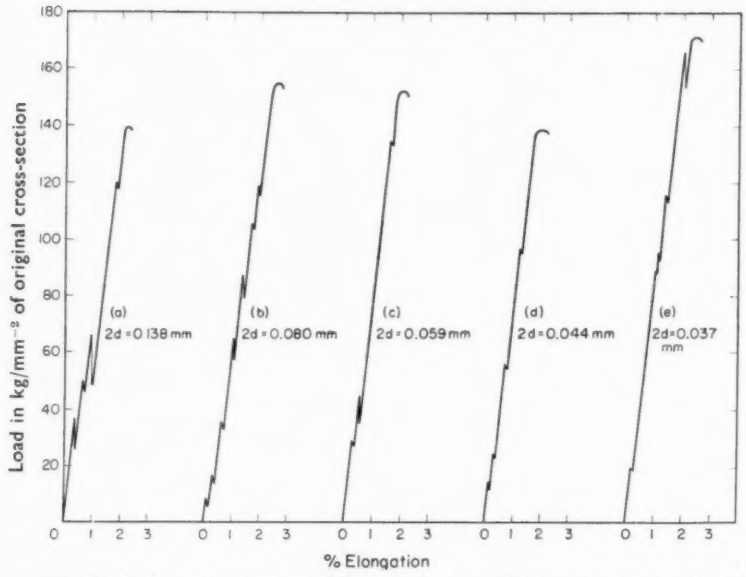


FIG. 4. The load–elongation curves of five specimens of different grain sizes tested at 20°K.

performing the gas analyses, and to Dr. H. M. Rosenberg for the use of the low-temperature hard-beam tensometer. The work was carried out during the tenure of an I.C.I. Research Fellowship awarded by the University of London, and was financially supported by the U.K. Atomic Energy Authority and Central Electricity Generating Board.

A. A. JOHNSON

Physical Metallurgy Dept.
Imperial College
London, S.W.7

REFERENCES

1. N. J. PETCH, *Progress in Metal Physics* Vol. 5, p. 1. Pergamon Press, London (1954).
2. A. A. JOHNSON, *Phil. Mag.* **4**, 194 (1959).
3. M. A. ADAMS, A. C. ROBERTS and R. E. SMALLMAN, A.E.R.E. Report M/R 2530 (1959); *Acta Met.* **8**, 328 (1960).
4. A. H. COTTRELL, *Trans. Amer. Inst. Min. (Metall.) Engrs.* **212**, 192 (1958).
5. E. T. WESSEL, *Trans. Amer. Inst. Min. (Metall.) Engrs.* **209**, 930 (1957).

* Received February 5, 1960.

Observations on the work-hardening of zinc crystals in alternating tension and compression*

The hardening behaviour of single crystals of zinc in which only one set of slip planes is usually operative, has been briefly investigated at two amplitudes of alternating straining and in tension, in order to provide a comparison with similar work on copper single crystals.[1,2] The specimen material was zinc of 99.998 per cent purity, from which single crystals about 1.5 mm diameter and 8 cm long were grown by the Bridgman method at a rate of 1.5 cm/hr, in spectrographically pure graphite moulds.

The four orientations studied were determined by the back-reflection Laue X-ray method to within about $\pm 1°$, and did not vary by more than this amount along a crystal. There was no metallographic evidence for mosaic structure. Each crystal provided five specimens which were electropolished in a solution containing 200 g chromium trioxide and 15 g sodium sulphate per litre. The same testing machine and technique were used as in the previous work on copper,[1–3] except that the lower end of each crystal was set in a bath of lead–tin eutectic (melting point 183°C).

Tests were carried out at room temperature both in reversed straining at amplitudes of 0.02 and 0.0001 glide per half-cycle (equal to the maximum and minimum values used for copper[1]), and in tension. Two series of tests were performed at the larger amplitude, at 0.06 and at 0.003 glide per min respectively. The tensile tests were done at the larger of these strain rates, and the reversed strain tests at amplitude 0.0001 at the smaller rate.

The work-hardening curves obtained in *tension* are presented in Fig. 1. The only unusual feature noted was that the hardening rate for orientation 2 was greater than that for orientation 1; no new metallographic features were observed.

In all tests under *reversed strain*, the curves obtained from duplicate tests agreed to within about 10 per

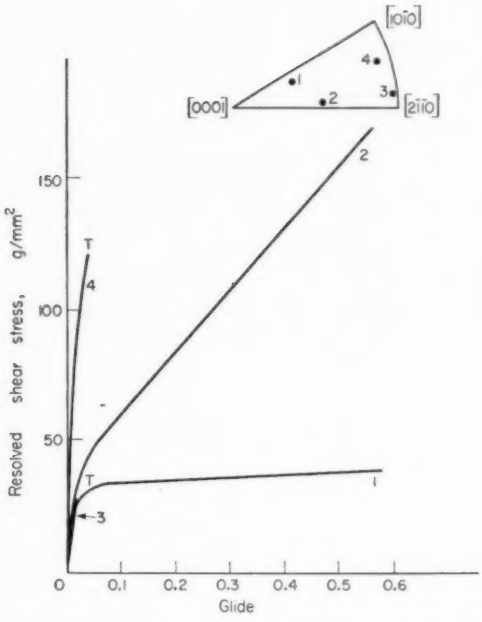


FIG. 1. Tensile straining. T = occurrence of twinning. Work-hardening curves. The numbers on the curves refer to the orientations.

VOL. 8 1960

cent and only the lower curve is plotted in the figures.

The hardening behaviour at amplitude 0.0001 is shown in Fig. 2: there is some variation in stress level, but the rate of hardening is very low and is similar for each orientation. The curves from tests at amplitude 0.02 at the same rate of straining as at amplitude 0.0001 are given in Fig. 3; they show a linear hardening rate similar to that obtained at the low amplitude, but preceded by greater initial hardening. The curves from further tests at amplitude 0.02 but at the rate of straining employed in the

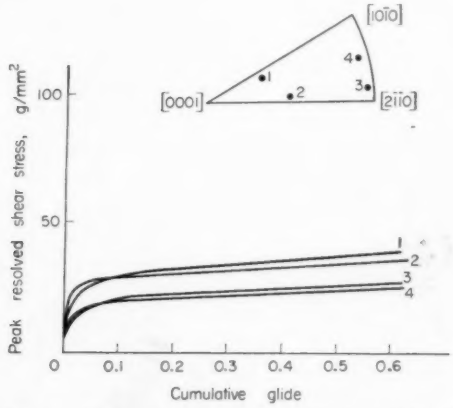


FIG. 2. Reversed straining, amplitude 0.0001. Work-hardening curves. The numbers on the curves refer to the orientations.

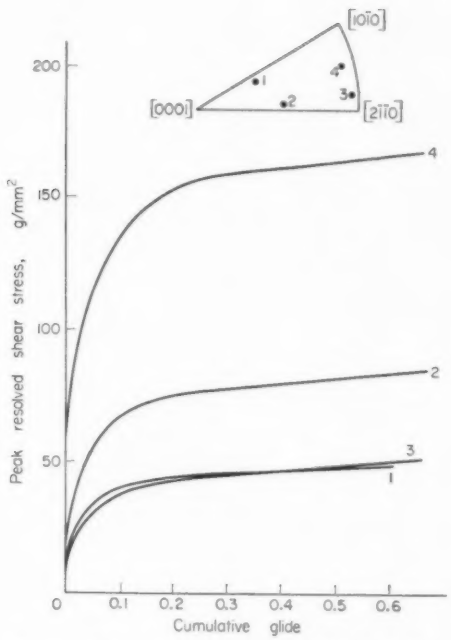


FIG. 3. Reversed straining, amplitude 0.02; rate of straining 0.003 glide per min. Work-hardening curves. The numbers on the curves refer to the orientations.

tensile tests are given in Fig. 4. Comparison of Figs. 3 and 4 indicates that recovery has a strong influence on the form of the curves, since the hardening

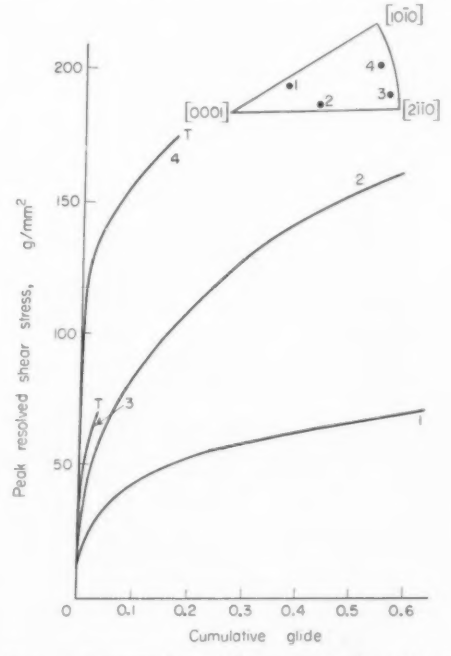


FIG. 4. Reversed straining, amplitude 0.02; rate of straining, 0.06 glide per min. T = occurrence of twinning. Work-hardening curves. The numbers on the curves refer to the orientations.

rate is greater when the test is carried out at a higher strain rate.

The average value of *critical resolved shear stress*, measured as the first departure from elastic strain, was approximately 9 g/mm^2. No yield phenomenon was observed in any test.

In *reversed deformation*, there was no apparent difference in the slip patterns of specimens of orientations 1 and 2 tested at the two rates of straining at amplitude 0.02. The slip patterns were similar to those produced by tension, except that no kink bands were apparent. Specimens of orientations 3 and 4 tested under *fast* conditions at amplitude 0.02 twinned after a few cycles in a tensile half-cycle; no slip lines were observed prior to twinning. Attempts to produce "untwinning" by stress reversal were not successful. In specimens of orientations 3 and 4 strained *slowly* at amplitude 0.02, no twinning occurred, but slip lines were observed on two systems (Fig. 5.); neither of the operative slip planes could have been (0001) planes, since these were almost parallel to the specimen axis. At amplitude 0.0001, a single set of faint evenly distributed lines was observed for *all* orientations; however, the lines on specimens of orientations 3 and 4 were again obviously not traces of (0001) planes. A stereographic analysis was made of the operative slip systems in each specimen after reversed deformation, and showed that the slip plane for orientations 1 and 2 at both amplitudes was the basal plane; however, the operative planes at both amplitudes in orientations 3 and 4 were found to be all of $\{10\bar{1}1\}$ type and the operative directions $\langle\bar{2}113\rangle$.

Although the recovery which occurs during deformation of zinc at room temperature is a complicating factor, both hardening and slip appear to be more reversible at lower amplitude, and at this amplitude, presumably involve the movement of dislocations in only one of the possible directions in the operative slip plane (cf. the "basic hardening process" in the reversed deformation of copper).[1] At amplitude 0.02 the hardening increases and slip lines become more prominent, i.e. the reversibility of hardening and of slip decreases. This may be due to dislocation interaction between the primary slip direction and a secondary direction in the slip plane, or to the participation of a second plane of non-basal type.

Neither the plane nor the direction of the non-basal slip in orientations 3 and 4 is close-packed. In a hexagonal crystal, there are six $\{10\bar{1}1\}$ planes, each containing two $\langle\bar{2}113\rangle$ directions, one of which will be common to two planes. Comparison of the values of the factor $\cos\chi\,\cos\lambda$ for each of these twelve slip systems with that for basal slip shows that non-basal slip of this type would be geometrically favoured for each orientation except 2. However, microscopically visible non-basal slip was not present in orientation 1, which may indicate that the critical resolved shear stress for this slip is greater than for basal slip (cf. Ref. 4).

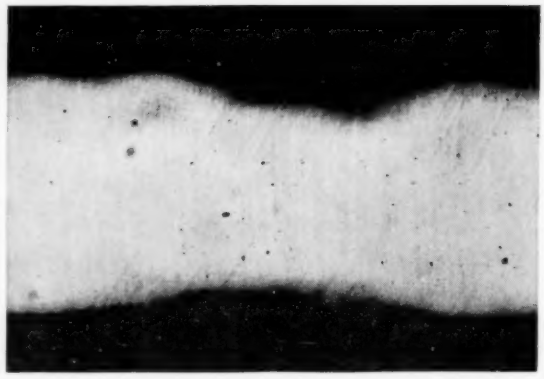


FIG. 5. Photomicrograph of the surface of a specimen of orientation 3 after reversed straining at amplitude 0.02 and 0.003 glide per min, illustrating non-basal slip on two sets of planes. ×160

Slip on the $\{10\bar{1}1\}$ planes was only observed after reversed deformation, which at least at amplitude 0.0001 involved stresses considerably lower than those in tension. A possible explanation of this is that the critical resolved shear stress for $\{10\bar{1}1\}$ slip is lower in compression than in tension (cf. Gilman[5]). Slip in a $\langle\bar{2}113\rangle$ direction on planes other than $\{10\bar{1}1\}$ has been observed by Bell and Cahn[4] and Gilman[5].

The occurrence of non-basal slip after reversed straining may be related to the suggestion made by Feltham[6] that some form of non-basal slip probably occurs in hexagonal metals during fatigue.

The author is grateful to the Department of Supply and the Aeronautical Research Laboratories, Melbourne, and to Professor J. C. Jaeger and Dr. M. S. Paterson of the Australian National University, for making this work possible. He also thanks the Chief Scientist, Department of Supply, for permission to publish this letter.

D. S. KEMSLEY

The Queen's College, Oxford
(*Formerly Department of Geophysics*
The Australian National University
Canberra, Australia)

REFERENCES

1. D. S. KEMSLEY and M. S. PATERSON, *Acta Met.* **8,** 453 (1960).
2. M. S. PATERSON, *Acta Met.* **3,** 491 (1955).
3. M. S. PATERSON, *J. Sci. Instrum.* **32,** 356 (1955).

4. R. L. Bell and C. W. Cahn, *Proc. Roy. Soc.* A**239**, 494 (1957).
5. J. J. Gilman, *Trans. Amer. Inst. Min. (Metall.) Engrs.* **206**, 998 (1956).
6. R. Feltham, *Phil. Mag.* **3**, 806 (1958).

* Received November 24, 1959; revised version March 8, 1960.

Identification of the diffusion of iron ions in magnetite employing markers*

Recently, several publications have appeared[1–4] describing the use of markers to identify whether the controlling process, during oxidation of iron at high temperatures, is the diffusion of iron ions or oxygen ions, or whether both diffuse simultaneously.

When impure iron, such as the ARMCO used in this case, is oxidized, the impurities tend to concentrate around the metal–oxide interface.[5] These impurities probably Ni, Cu and Co oxides, seem to be insoluble in iron and its oxides. If we separate the oxide from the metal, part of these impurities remain held to the inner part of the layer of oxides. On reoxidation of the layer of oxides in any atmosphere, a clear rectilinear line appears at a definite distance from the oxide–atmosphere interface. This line must indicate the original oxide–atmosphere interface.[6]

After observing quite a large number of specimens (layers of FeO oxidized in pure steam between 600° and 1200°C) we have been able to establish that the line is found in the layer of Fe_3O_4 formed through the oxidation of FeO, and that after a sufficient length of time the ratio between the thickness of magnetite (e) and the distance (M) from the line to the external surface tends to the value 4. This fact can be appreciated in the micrograph of Fig. 1, which shows a layer of FeO oxidized in steam at 800°C for 12 hr. The line can be seen only on one side, where it corresponds to the original metal–oxide interface. Fig. 2 shows the same phenomenon, at a greater magnification, in the layer of magnetite.

This phenomenon is not only seen in the oxidation

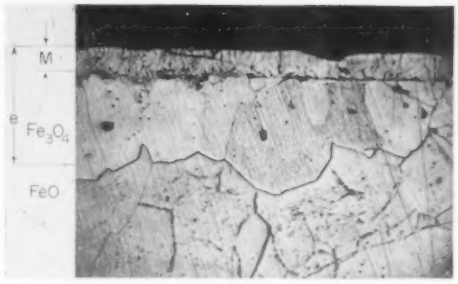


Fig. 2. Sectional view of a FeO specimen oxidized in steam at 800°C for 12 hr. ×200

of FeO in steam. Figs. 3 and 4 indicate that it is also present when FeO is oxidized in air, the first corresponding to oxidation at 700°C for 6 hr and the second

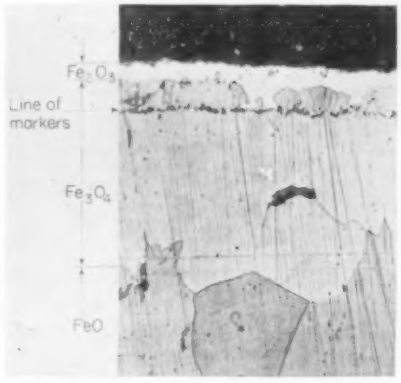


Fig. 3. Sectional view of a FeO specimen oxidized in air at 700°C for 6 hr. ×625

at 750°C for 1 hr. In this case also the ratio e/M is approximately 4.

The fact that e/M should tend to 4 has led us to the following interpretation.

After the layer of FeO is saturated with oxygen at the temperature of the experiment, there comes a decomposition of FeO at the magnetite–protoxide interface, according to the following equation:

$$4FeO \rightarrow Fe + Fe_3O_4. \qquad (1)$$

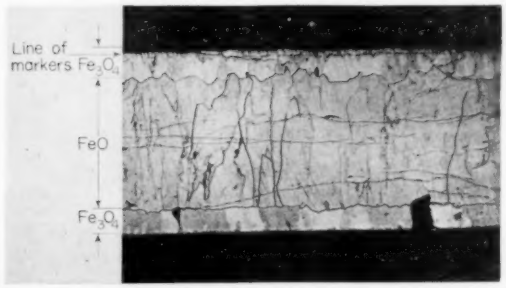


Fig. 1. Sectional view of a FeO specimen oxidized in steam at 800°C for 12 hr. ×50

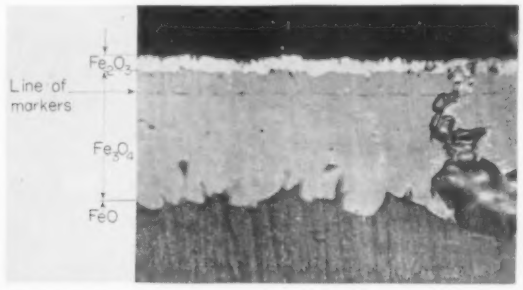


Fig. 4. Sectional view of a FeO specimen oxidized in air at 750°C for 1 hr. ×625

VOL. 8 1960

The Fe_3O_4 formed becomes a film of magnetite below the line of impurities which we have mentioned above. The iron ion formed by reaction (1) diffuses through the layer of Fe_3O_4 and reacts with oxygen on reaching the surface:

$$Fe + \tfrac{2}{3}O_2 \rightarrow \tfrac{1}{3}Fe_3O_4. \qquad (2)$$

This magnetite formed by reaction (2) becomes the layer of Fe_3O_4 between the line of markers and the oxidizing atmosphere.

As both magnetites are formed at the same temperature and under the same controlling conditions, their molecular volumes are equal. Therefore, according to our hypothesis the ratio between the magnetite formed by precipitation (1) and that formed by oxidation (2) is 1 : 1/3, and e/M would be 4.

This would be the ideal condition in the case where only iron diffuses. Reasoning in a similar way, if one supposed that only oxygen diffuses, the ratio e/M would be ∞; in other words the line would remain in the magnetite–atmosphere interface.

Summing up what we have said:

$e/M = 4$ means diffusion only of iron

$e/M = \infty$ means diffusion only of oxygen.

In Fig. 5 we have indicated the ratio e/M for specimens oxidized at 1000°C during increasing periods of time. It can be seen that for short periods of oxidation the ratio e/M increases with time of oxidation, and tends towards the value 4.27 for long periods of time.

Figure 5 shows that for short periods of oxidation, ratio e/M increases with time of oxidation. This is due to the fact that the layer of FeO which was in contact with the metal is not initially saturated with oxygen; on the contrary it is saturated with iron, and this iron must be oxidized first until it is saturated with oxygen. From this moment on, the ratio e/M should be 4.

This first phase of the phenomenon can be appreciated in the micrograph of Fig. 6, corresponding to a specimen oxidized at 800°C for 30 min.

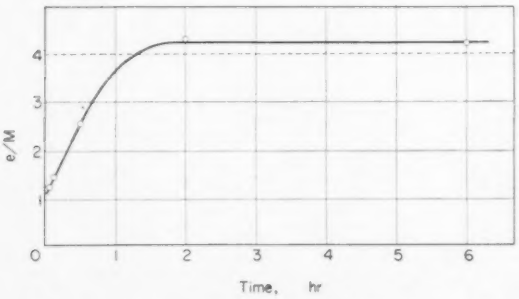


FIG. 5. Variation of the e/M value with time of oxidation at 1000°C.

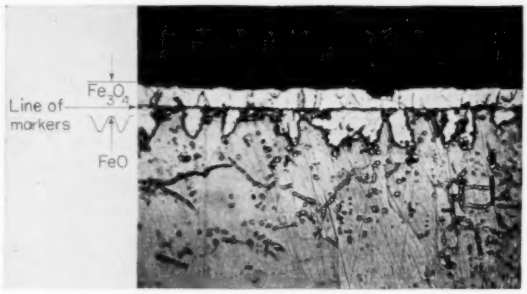


FIG. 6. Sectional view of a FeO specimen oxidized in steam at 800°C for 30 min. ×425

We have reproduced, in Fig. 5, the graph for all the temperatures studied and have determined the maximum values corresponding to each temperature. These results can be found in Fig. 7.

From Fig. 7 it can be appreciated that the ratio e/M is practically 4; the points with large deviations can be considered as experimental errors. In any case these points are nowhere near ∞. The value found for the ratio e/M clearly demonstrated that, in the range of temperature studied, the oxidation of FeO to Fe_3O_4 in steam is controlled by the diffusion of iron ions from the FeO–Fe_3O_4 interface to the oxide–atmosphere interface.

The kinetics of oxidation of FeO to Fe_3O_4 would correspond, according to our results, to the kinetics of diffusion of iron ions through the layer of magnetite.

Laboratory of Metallurgy D. FULLER
University of Concepción, Chile

References

1. M. H. DAVIES, M. T. SIMNAD and C. E. BIRCHENALL, *J. Metals* **3,** 889 (1951).
2. H. ENGELL and F. WEVER, *Acta Met.* **5,** 695 (1957).
3. M. CAGNET and J. MOREAU, *Acta Met.* **7,** 427 (1959).
4. F. WEVER and H. J. ENGELL, *Acta Met.* **7,** 429 (1959).
5. J. PAIDASSI, *Bol. Soc. Chilena Quim. VII,* 20 (1955).
6. A. D. SMIGELSKAS and E. O. KIRKENDALL, *Trans. Amer. Inst. Min. (Metall.) Engrs.* **171,** 130 (1947).

* Received November 3, 1959.

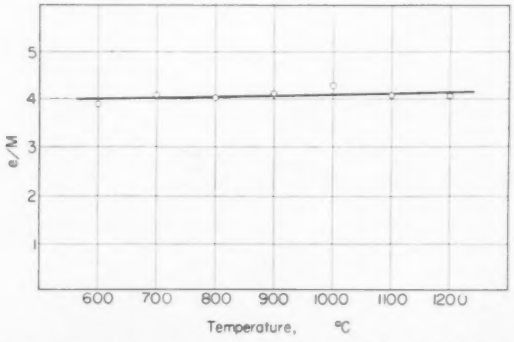


FIG. 7. Variation of the e/M equilibrium value with temperature of oxidation.

ERRATUM

G. SAADA, *Acta Met.* **8,** 200–208 (1960)

Une erreur s'est glissée dans notre article à la page 202, paragraphe 2.3.1

Au lieu de:

"Si ρ est le rayon de courbure de L_0' . . . . jusqu'à la fin du paragraphe

Lire:

"Il est nécessaire d'effectuer une correction d'antiprojection. L'équation (1a) devient alors:

$$\frac{A}{\tau}\frac{G(\theta')}{r'} - \frac{1}{\rho} = 0. \tag{1b}$$

Ici θ' et r' sont les coordonnées polaires de M' dans le plan x_1Oy. Le calcul de $\frac{G(\theta')}{r'}$ en fonction de $\frac{G_c(\theta)}{r}$ est un simple calcul géométrique.

On montre aisément que:

$$\frac{G(\theta')}{r'} = \frac{1}{r'}\frac{1}{(1-\sin^2\alpha\cos^2\theta')^2}\{(1-2\nu)\cos^3\alpha\sin^3\theta' - e\cos^2\alpha$$
$$\sin^2\theta'\cos\theta' - (1-2\nu)\cos\alpha\sin\theta\cos^2\theta' + e\cos^3\theta'\}$$

L'équation (1b) donne alors la forme d'équilibre de la boucle L'.

Dans cet article la valeur de cos α est voisine de l'unité et cos $\alpha\,\frac{G_c(\theta)}{r}$ est très peu différent de $\frac{G(\theta')}{r'}$. Les conclusions énoncées ici restent donc valables.

Nous avons de plus effectué les calculs dans le cas le plus général; ce travail est exposé dans notre thèse et permet de compléter les résultats obtenus ici.

VOL. 8 1960

KINETICS OF LATER STAGES OF CLUSTERING IN Al–Cu ALLOY*

D. TURNBULL and R. L. CORMIA†

Clustering in Al–Ag and Al–Cu alloys may occur in two stages. The first stage proceeds rapidly at temperatures as low as −30 to −60°C and is governed by an activation energy of 0.5 eV. It is sometimes followed by a slow reaction which requires several weeks at room temperature or a few hours at 80°C for its virtual completion. We have investigated this second stage in Al–Cu alloy resistometrically. The apparent activation energy was found to be 1.02 ± 0.03 eV which is near the value found for the corresponding process in Al–Ag alloy. The extent of the reaction in Al–Cu is diminished greatly if the quench from the homogenization temperature is interrupted by a few seconds hold at 200°C. It appears that the reaction may be effected by vacancies which were trapped during the first stage of clustering by highly curved dislocation loops or as Hart has suggested, by solute clusters.

CINETIQUE DES DERNIERS STADES DE SEGREGATION DANS LES ALLIAGES Al–Cu

La ségrégation dans des alliages Al–Cu et Al–Ag peut se produire en 2 étapes.

La première s'effectue rapidement à une température comprise entre −30 et −60°C. Elle est régie par une énergie d'activation de 0,5 eV. Parfois, elles est suivie d'une réaction lente dont l'achèvement virtuel nécessite plusieurs semaines à température ambiante ou quelques heures à 80°C.

C'est à l'étude, par des mesures de résistance de cette seconde étape dans un alliage Al–Cu que les auteurs se sont attachés.

Ils ont trouvé que l'énergie apparente d'activation était de 1,02 ± 0,03 eV, valeur proche de celles trouvées pour le processus analogue dans les alliages Al–Ag.

La progression de la réaction dans un alliage Al–Cu, diminue lors de l'interruption, pendant quelques secondes à 200°C, de la trempe effectuée à partir de la température d'homogénéisation.

Il semble que la réaction puisse s'effectuer par l'intermédiaire de lacunes bloquées lors de la première étape, par des boucles de dislocation à forte courbure ou, comme Hart l'a suggéré, par les zones enrichies en soluté.

KINETIK DER SPÄTEREN ENTMISCHUNGSSTADIEN DER LEGIERUNG Al–Cu

Die Entmischung kann bei den Legierungen Al–Ag und Al–Cu in zwei Stufen erfolgen. Die erste Stufe verläuft schnell bei so niedrigen Temperaturen wie −30° bis −60°C und wird durch eine Aktivierungsenergie von 0,5 eV bestimmt. Manchmal folgt darauf eine langsame Reaktion, die bei Raumtemperatur einige Wochen, bei 80°C einige Stunden braucht, um praktisch abgelaufen zu sein. Wir haben diese zweite Stufe bei der Legierung Al–Cu durch Widerstandsmessungen verfolgt. Dabei tritt eine Aktivierungsenergie von 1,02 ± 0,03 eV auf, nahezu der Wert für den entsprechenden Prozeß bei Al–Ag. Das Ausmaß der Reaktion wird bei Al–Cu erheblich vermindert, wenn man das Abschrecken von der Homogenisierungs-Temperatur einige Sekunden bei 200°C unterbricht. Es sieht so aus, als würde die Reaktion durch Leerstellen bewirkt, die im ersten Entmischungsstadium durch stark gekrümmte Versetzungslinien oder, wie Hart vorschlug, durch Zusammenlagerungen der Zusatzatome festgehalten wurden.

In some supersaturated aluminum rich alloys, which have been quenched from high temperatures, a large number of solute rich regions known as "clusters" or "zones" form quite rapidly at room temperature and below. The kinetics of the early stages of this process in Al–Ag,[1,4,5] Al–Cu[2,5] and Al–Zn[3,5,6] alloys now have been investigated quite extensively.[1–6] The process proceeds at rates many orders of magnitude greater than it should if it were governed by the diffusion constants obtained by extrapolation of the high temperature diffusion data. This disparity is reflected in the activation energies for clustering, Q_1, and solute diffusion, Q_D, which are:

	Q_1 (eV)	Q_D (eV)
Al–Zn[3,5,6]	0.4	1.2
Al–Cu[2,5]	0.5	1.4
Al–Ag[1,5]	0.5	1.5

Federighi[7] and DeSorbo *et al.*[2] have shown independently that the kinetics of the early stage of clustering are explained most simply and adequately on the hypothesis that the solute transport is effected by point defects which are retained in the specimen during the quench from high temperature. Thus the concentration of point defects initially present at the low temperature will greatly exceed the equilibrium value and the solute diffusion coefficient will be correspondingly larger than that characteristic of defect equilibrium. The point defect supersaturation will, of course, decay with time and in pure aluminum this decay process should be virtually complete after several hours to 1 day at room temperature.[8]

If point defect decay in the alloys occurred at the same rate as in pure aluminum, the clustering reaction should virtually stop after a few hours at room temperature. Actually the mechanical[9] and electrical properties of Al–Cu alloys often continue to change appreciably over periods of many weeks at room

* Received March 10, 1960.

† General Electric Research Laboratory, Schenectady, N.Y.

VOL. 8 1960

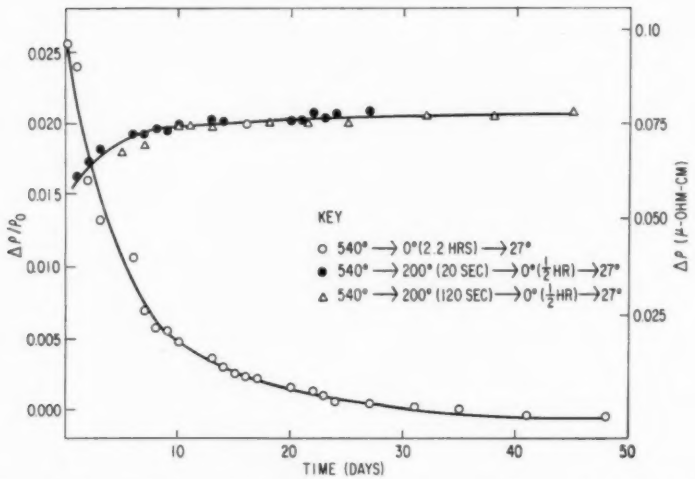


FIG. 1. Change of resistivity ($\Delta\rho$) of Al–Cu alloy with time at 27° following the indicated thermal treatments. ρ_0 is the resistivity at 0°C.

temperature. It seems likely that these changes are due to the continued growth of clusters. An apparently analogous reaction in Al–Ag alloys was reported by Turnbull *et al.*[5]. They inferred from a kinetic analysis that this reaction is governed by a diffusive process requiring an energy (assuming normal values for the pre-exponential term) of 1.0–1.2 eV for activation which is still well below that (1.5 eV) for the high temperature diffusion of silver in aluminum.

In this paper a resistometric investigation of the slow reaction in Al–Cu is described.

EXPERIMENTAL

The reaction was studied by the resistometric procedures described in earlier papers.[2,5] Also the alloy Al–1.75 at.% Cu was prepared as before and fabricated into strip specimens 0.01 cm in thickness, 0.25 cm in width and 3.5 cm in length.

RESULTS

We first investigated the course of the reaction at room temperature. In these experiments the specimens were homogenized at 540°C and then quenched either directly into an ice bath at 0° or into the ice bath after an intermediate quench and a few seconds hold in an oil bath at 200°C. After a period of $\frac{1}{2}$–2 hr the specimens were taken out of the ice bath and kept in the room, whose temperature averaged 27°C. The specimen resistance was measured from time to time over a period of 2 months. Some typical results of these measurements are displayed in Fig. 1. It is seen that the rate and direction of resistance change are strongly dependent upon the thermal history of the specimen. The resistance of specimens quenched directly to 0° decreased with time at 27°C at rates which remained significantly different from zero for a period of at least 30 days. The resistance of specimens, whose quench from 540° had been interrupted at 200°, increased slightly during the first 10 days at 27° and then remained constant, within the scatter of the measurements, thereafter. It is likely that the resistance changes in the directly quenched specimens are associated with the movement of solute atoms through distances of at least several atom diameters. Thus the results provide further confirmation that the room-temperature clustering reaction may continue for an extraordinarily long period.

This slow reaction also was manifested in continuous heating experiments. In these experiments a specimen was quenched directly into an ice bath at 0°, held there for 2 hr and heated to 150° at an approximate rate of 0.8°/min. The specimen resistance was measured at close intervals throughout this process. Some results typical of these experiments are shown in Fig. 2. The total isothermal increase in resistivity, indicated by the vertical arrow in the figure, at 0° after the quench was about 0.10 μ-Ω-cm. The resistivity temperature relation obtained on heating from 0° is linear to about 70–80°. Then it falls away from the line and above 120° merges into a second straight line which lies about 0.10 μ-Ω-cm below the first. After the continuous heating experiment the resistivity of the specimen at 0°C was constant and just below that after the quench from 540°. It is likely that the reaction responsible for the 0.1 μ-Ω-cm loss in resistivity in the continuous heating experiments is the same as the long time reaction at room temperature.

In the temperature range 75–100° about 3–4 hr are required for the virtual completion of the reaction.

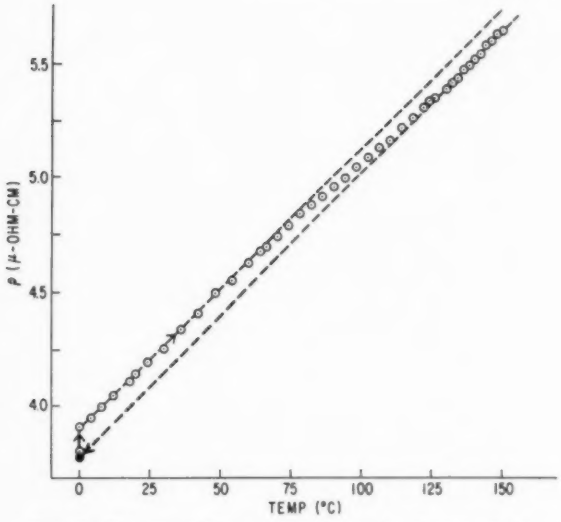


FIG. 2. The vertical arrow indicates the change of the resistivity of an Al–Cu specimen in 2 hr at 0° after a quench from 540°. The curve represents the resistivity of the specimen during continuous heating at a rate of 0.8°/min from 0°. After reaching 150°C the specimen was quenched again to 0°C following which its resistivity had the value corresponding to the lowest point at 0°.

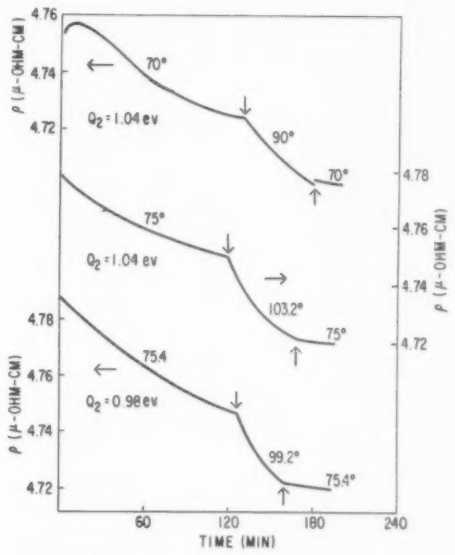


FIG. 3. Resistivity–time relation for Al–Cu alloy during the "slow" reaction. At the time indicated by the first vertical arrow the specimen was quenched to the higher temperature. At the time indicated by the second vertical arrow it was quenched back to the lower temperature. In plotting the curves the resistivities at the higher temperature were shifted by a constant amount so as to bring the resistivity–time relations for the upper and lower temperatures into coincidence at the time of the upquench. The horizontal arrows indicate the appropriate resistivity scale.

VOL. 8 1960

This period is about 100 times smaller than the 20–30 day period required at room temperature. The activation energy, Q_2, was determined (see Kauffman and Koehler[10]) from the ratio, f, between the rates of resistivity change just before and after an abrupt change in temperature from a value T_1 to a value T_2. Then:

$$Q_2 = \frac{T_1 T_2}{T_2 - T_1} R \ln f . \qquad (1)$$

Fig. 3 shows the data used for three such determinations of activation energy. In this figure the resistivity scale is in all cases that appropriate for the lower temperature. The plotted resistivities for the higher temperature were shifted by a constant amount so that the resistivity–time curves for the two temperatures intersect at the upquench point. It is seen that with this displacement the resistivities just before and after the last temperature shift also coincide within the experimental error.

The activation energies were evaluated from the slopes taken from the derivative curves (i.e. $\dot{\rho}$ vs. t). The average activation energy is $Q_2 = 1.02$ eV which is in close agreement with that, 1.0–1.2 eV, for the corresponding reaction in Al–Ag alloys.[5]

We found that an interruption of the quench from 540° to 0° by a 2-min intermediate hold at 200° had the effect of reducing the rate of resistivity change at 75° to zero within the experimental uncertainty. The outline of the thermal treatment in this case is as follows:

$$540° \rightarrow 200° \text{ (2 min)} \rightarrow 0° \text{ (2–3 hr)} \rightarrow 75°.$$

Also if, after the reaction at 100° was virtually completed in a directly quenched specimen, the specimen was heated to 200° in order to redissolve the zones there was no measurable resistivity change with time when it was returned to the 100° bath.

INTERPRETATION OF RESULTS

Several possible mechanisms for the second reaction were considered in the earlier paper.[5] In view of the present results we believe that a mechanism based on the hypothesis of some type of vacancy trapping is likely to be the operative one. If we suppose that the activation energy for the first reaction (0.5 eV for Al–Cu) is just that for moving vacancies it follows that the vacancies which effect the second reaction are bound with an energy of about 0.5 eV. This energy level would be about 0.3 eV above the vacuum if we took 0.8 eV for the total energy of creating a vacancy in the alloy.

There are two hypotheses about the nature of the vacancy traps. One, due to Hart[11], is that the

solute clusters themselves are the traps.* In this case the binding energy of the trapped vacancy would be the energy of interaction between the vacancy and the cluster atoms. The other hypothesis, proposed in our earlier paper, is that dislocation loops formed by vacancy condensation at high vacancy supersaturation levels are the traps. Such loops have been observed in pure aluminum by Hirsch *et al.*[12] and in dilute aluminum alloys by Thomas and Whelan[13] and by Thomas[14]. The density of resolvable loops in the alloys decreased with increasing solute concentration. The binding energy E_l of vacancies to dislocation loops should be given by

$$E_l = E_f - \frac{\sigma v}{\bar{s}} \tag{2}$$

where E_f is the total energy for creating a vacancy, σ is the line tension of the dislocation loop and $\bar{s}$ is the mean radius of the loops. We estimated before that a loop radius of the order of 2×10^{-7} cm could account for the observed binding energy. Panseri and Federighi[15] have already proposed a vacancy-cluster trapping mechanism to account for the "second stage" sometimes observed in the annealing of vacancies out of pure aluminum. They attribute this process, which occurs only if the initial vacancy supersaturation is very great, to the annihilation of vacancies freed by vacancy clusters possibly having the form of dislocation loops.

A critical test of the dislocation loop mechanism is whether or not the occurrence of the second reaction correlates with the presence of small loops. Some of our experimental evidence suggests, though it does not prove, that the second reaction occurs only if small loops are present. Thus in the earlier investigation there was indirect evidence that the short quench interruption at 200°C had the effect of preventing copious loop formation at lower temperature. As we have seen this treatment also has the effect of virtually eliminating the manifestation of the second reaction by resistivity change. However this result does not rule out the Hart mechanism. Thus the quench interruption also would have the effect of lowering the vacancy concentration and the subsequent extent of clustering at low temperatures. The binding energy of vacancies to clusters might well be smaller the smaller are the clusters.

* Hart suggests further that the clusters move and join upon mutual encounter as a result of the motion of the trapped vacancy when in their surface.

REFERENCES

1. D. Turnbull and H. N. Treaftis, *Acta Met.* **5,** 534 (1957).
2. W. DeSorbo, H. N. Treaftis and D. Turnbull, *Acta Met.* **6,** 401 (1958).
3. A. Guinier in *Solid State Physics* (Edited by F. Seitz and D. Turnbull) Vol. 9, pp. 294–400. Academic Press, New York (1959).
4. T. Federighi and L. Passari, *Acta Met.* **7,** 422 (1959).
5. D. Turnbull, H. S. Rosenbaum and H. N. Treaftis, *Acta Met.*, **8,** 277 (1960).
6. C. Panseri and T. Federighi, *Acta Met.* **8,** 217 (1960).
7. T. Federighi, *Acta Met.* **6,** 379 (1958).
8. W. DeSorbo and D. Turnbull, *Phys. Rev.* **115,** 560 (1959).
9. L. F. Mondolfo, *Trans. Amer. Inst. Min. (Metall.) Engrs.* **215,** 289 (1959).
10. J. W. Kauffman and J. S. Koehler, *Phys. Rev.* **97,** 555 (1955).
11. E. W. Hart, *Acta Met.* **6,** 553 (1958).
12. P. B. Hirsch, J. Silcox, R. E. Smallman and K. H. Westmacott, *Phil. Mag.* **3,** 897 (1958).
13. G. Thomas and M. J. Whelan, *Phil. Mag.* **4,** 511 (1959).
14. G. Thomas, *Phil. Mag.* **4,** 1213 (1959).
15. C. Panseri and T. Federighi, *Phil. Mag.* **3,** 1223 (1958).

THE INFLUENCE OF AN ELECTRIC POTENTIAL GRADIENT ON THE THERMAL ETCHING OF SILVER*

E. D. HONDROS† and A. J. W. MOORE‡

The size of the etched facets produced on a single crystal of silver when heated to 720°C for 150 hr in air while a direct current is passing through it, is shown to vary by a factor of about 10 depending on the polarity of the field relative to the crystal orientation. The effect does not occur in nitrogen or *in vacuo* with a direct current or in air with an alternating current.

It is suggested that, due to the electric field, silver ions on the surface migrate away from the edges of steps and therefore are more likely to evaporate. This promotes a drift of the steps across the surface in the opposite direction to the migrating ions. The presence of oxygen is assumed to cause the monatomic steps on the surface to aggregate and leads to the development of facets.

INFLUENCE D'UN CHAMP ELECTRIQUE SUR L'ATTAQUE A CHAUD DE L'ARGENT

Les dimensions des facettes produites par l'attaque à l'air d'un cristal d'argent à une température de 720°C pendant 150 heures et sous l'action d'un courant continu qui le traverse, varient d'un facteur 10 qui dépend de la polarité du champ par rapport à l'orientation cristalline.

Cet effet n'apparaît pas sous atmosphère d'azote ou sous vide avec action d'un courant continu, ni à l'air avec action d'un courant alternatif.

Les auteurs supposent que sous l'action du champ électrique, les ions argent migrent à partir des bords de la structure étagée et ont de ce fait, plus facilement tendance à s'évaporer.

Ceci occasionne un déplacement de la structure étagée sur la surface du cristal dans une direction opposée à la migration des ions. Les auteurs supposent que la présence d'oxygène provoque l'agrégation des structures étagées monoatomiques et conduit à la formation des facettes.

EINFLUSS EINES ELEKTRISCHEN POTENTIALGRADIENTEN AUF DAS THERMISCHE ÄTZEN VON SILBER

Die Größe der Ätzfacetten auf einem Silbereinkristall, der 150 Stunden lang auf 720°C in Luft erhitzt wurde und dabei von Gleichstrom durchflossen war, ändert sich etwa um den Faktor 10, je nach der Richtung des Feldes relativ zur Kristallorientierung. In Stickstoff oder Vakuum bei Gleichstrom oder in Luft bei Wechselstrom tritt der Effekt nicht auf.

Es wird vorgeschlagen, daß infolge des elektrischen Feldes Silberionen auf der Oberfläche von den Stufenkanten wegwandern und daher eine höhere Verdampfungswahrscheinlichkeit haben. Daher wandern die Stufen über die Oberfläche in umgekehrter Richtung wie die wandernden Ionen. Es wird angenommen, daß die Anwesenheit von Sauerstoff zur Zusammenlagerung der monoatomaren Stufen und damit zur Entstehung von Facetten führt.

VOL. 8 1960

1. INTRODUCTION

It has been shown[1] that when silver is thermally etched in an atmosphere containing oxygen, a stepped surface develops consisting partly of facets of {100} or {111} planes, and partly of planes of high indices ("complex" planes). This paper describes the effects of electric and thermal gradients on the etching behaviour.

The influence of an electric field in developing surface facets was apparently first reported by Johnson[2] in 1938 for tungsten lamp filaments, which when heated by direct current *in vacuo* showed a step-like surface. This was attributed to a preferential migration of positive metal ions on the surface as a result of the longitudinal electric field. Large temperature gradients produced a similar effect. Mrowca[3] and later Langmuir[4] showed that for tantalum ribbons with surfaces nearly parallel to {211} planes, two distinct types of surface contour were developed on opposite faces after the passage of direct current *in vacuo*. These were explained by considering a perferred migration of positive metal ions in conjunction with a high rate of diffusion on {211} planes.

In the present work with silver no effects of thermal gradients could be detected, but a small electrical field had a marked effect on the etching in the presence of oxygen.

2. EXPERIMENTAL PROCEDURE

The apparatus shown in Fig. 1 was used for heating the specimens in air. The silica base supports two silver rods (E), each 0.5 cm diameter, which act as electrical conductors to the ribbon-shaped specimen

* Received February 19, 1960.

† Present address: Lab. de Chimie Minérale B, 11 Rue Pierre Curie, Paris 5e.

‡ C.S.I.R.O. Division of Tribophysics, University of Melbourne, Australia.

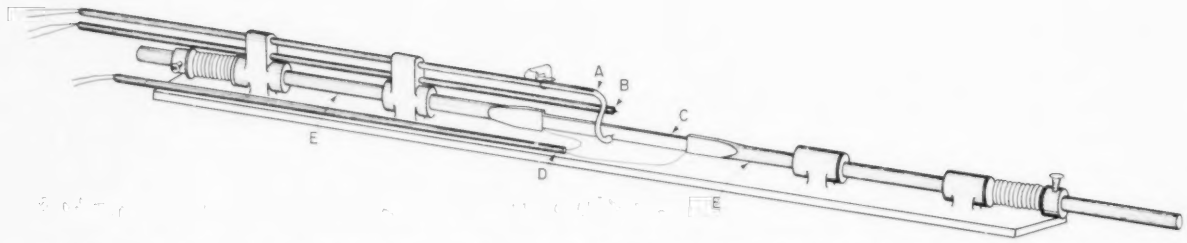


FIG. 1. Device for passing an electric current through a single crystal ribbon while it is being heated in a tube furnace.

(*C*) clamped between them, the broad faces of the specimen being vertical. The temperature along one face of the specimen was measured with a sliding thermocouple (*A*), which was in contact with the specimen surface only during temperature measurement. Another thermocouple (*B*) above the centre of the specimen controlled the temperature of the tube furnace into which the whole assembly was fitted. The potential drop across the specimen was measured by means of the leads (*D*). The weak springs at each end of the apparatus ensure that the specimen does not buckle due to the thermal expansion of the metal parts. The mean temperature and the temperature gradient in the specimen can be controlled by adjusting the furnace temperature and the current in the specimen. The most convenient conditions which gave a central region of approximately constant temperature were those in which the furnace was maintained at about 700°C and the current through the specimen was adjusted to maintain the central region at about 720°C. This current varied between 14 and 31 A depending on the cross sectional area of the specimen. The central region about 1 cm long had a temperature gradient less than 6°C/cm. Towards the ends where the heat was conducted away by the heavy silver rods the temperature was 640°C and the gradient was about 25°C/cm.

The modification to the apparatus when specimens were heated in nitrogen or *in vacuo* are described in the relevant sections.

The specimens were single crystals (99.995 per cent Ag) measuring approximately 5 × 0.4 × 0.05 cm cut from larger single crystals by a chemical dissolution technique which kept distortion to a minimum. Each specimen was electropolished, mounted in the apparatus and heated for up to 150 hr. A single specimen used in the experiments described in Section 3(a)(i–iv), had a surface whose normal was 20° from ⟨111⟩ and it was cut in such a way that the facets of the (111) planes and complex planes produced by thermal etching would intersect on lines perpendicular to the direction of the applied electric field. A second specimen was used for experiments described in Section 3(a)(v), (b) and (c), and had a surface whose normal was 15° from ⟨100⟩ and was cut in such a way that the boundaries of the facets of the (100) planes developed at an angle of about 40° to the direction of the applied field. Confirmatory experiments were carried out with additional specimens cut from the same parent crystals.

3. RESULTS

(a) *Etching in air*

(i) {111} *orientation—d.c. potential applied.* The centre of the specimen was maintained at 730°C, the current being 31 A, the applied voltage 0.19 V and the potential gradient 0.04 V cm^{-1}. After heating for 150 hr, the specimen was examined under the microscope.

Where the facets of the developed (111) plane sloped into the specimen towards the *positive* end (i.e. as in face *A* of Fig. 10) the etching was as shown in Fig. 2(a), where the black areas represent the well developed facets of {111} planes. This etching was less pronounced the greater the distance from the centre of length of the specimen, and it was barely noticeable close to the specimen supports. The effect was symmetrical about the centre of length.

On the other face of the specimen, the facets of the same plane sloped into the specimen towards the *negative* end (face *B*, Fig. 10). Here, the exposed facets were up to 10 times smaller (Fig. 2b) than those of the opposite face (Fig. 2a). As before, the extent of this etching decreased symmetrically as the distance from the centre of length increased.

(ii) {111} *orientation—polarity reversed.* The specimen was electropolished and remounted in the apparatus in an identical manner, special precautions being taken to ensure correct positioning. The polarity of the d.c. with respect to that of paragraph (i) was reversed and the experiment repeated for the same temperature and potential gradient.

The results are shown in Fig. 3. The nature of the etching on the faces is completely reversed. The face which gave the coarse etching, Fig. 2(a), is now finely etched, Fig. 3(a), while the face shown in Fig. 2(b)

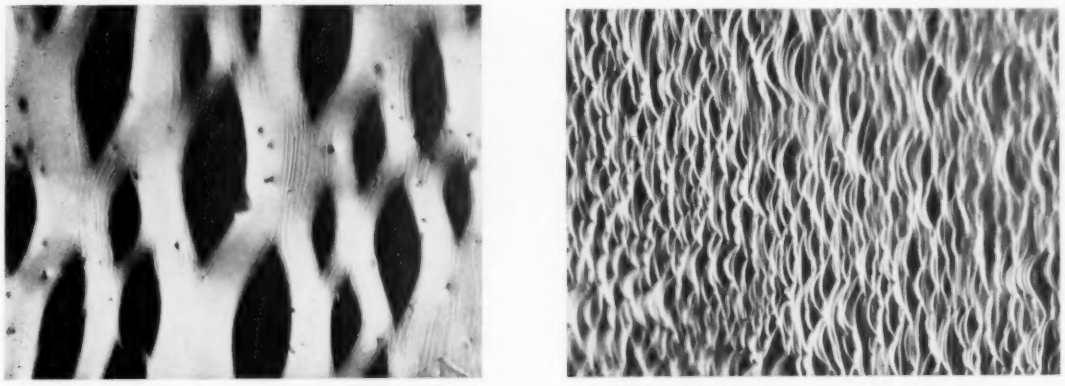


FIG. 2. Etch patterns produced on opposite faces of a single crystal oriented at 20° to a (111) plane after heating in air for 150 hr at 730°C in an electric potential gradient 0.04 V cm^{-1}. × 700

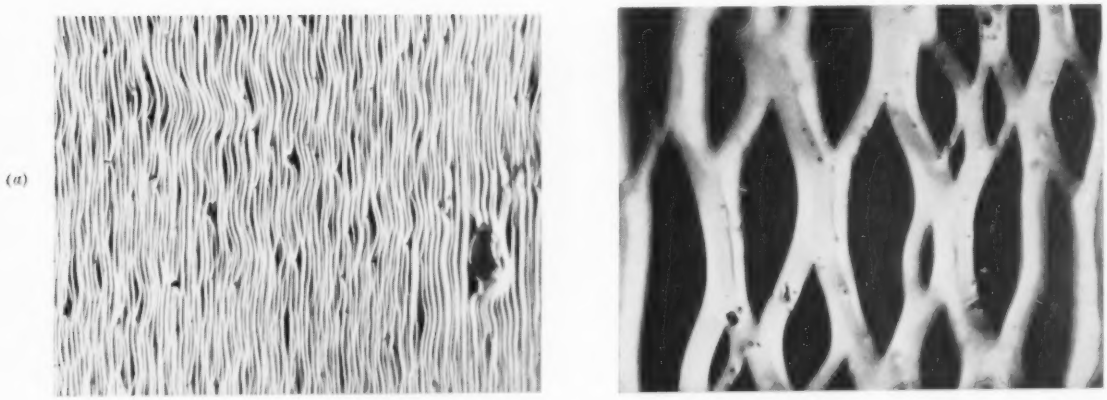


FIG. 3. Etch patterns produced on the same specimen as Fig. 2 with the polarity of the field reversed. Same time, temperature and potential gradient. The pairs of Figs. 2(a)–3(a) and 2(b)–3(b) show the same faces. × 700

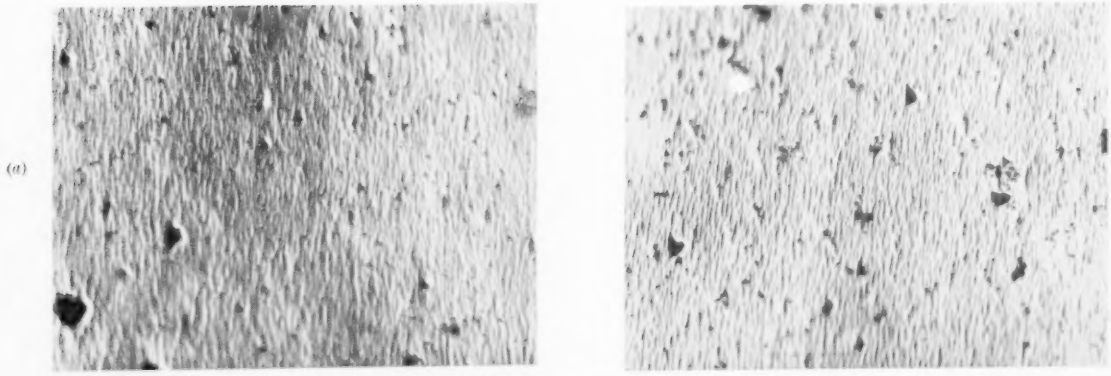


FIG. 4. Etch patterns on opposite faces of the single crystal after heating in air for 150 hr at 720°C. ×700

VOL. 8 1960

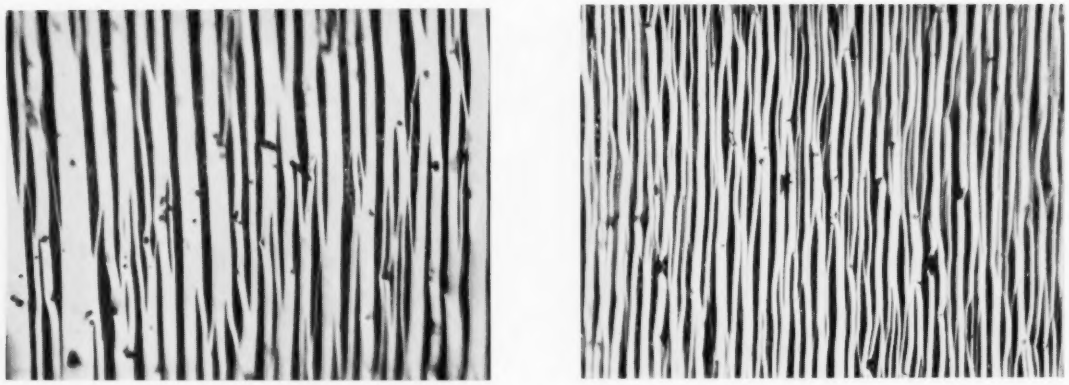


FIG. 5. Etch patterns on opposite faces of the single crystal after heating in air for 150 hr at 720°C in an alternating potential gradient of 0.034 V cm^{-1}. × 700

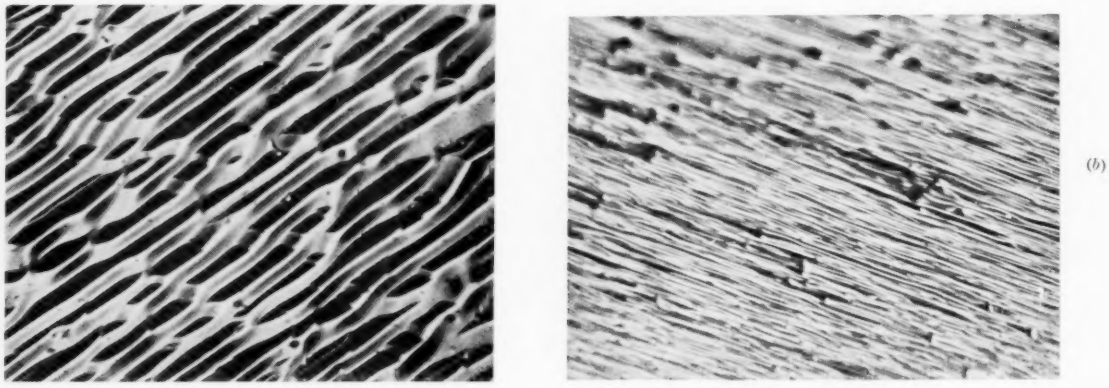


FIG. 6. The etch patterns produced on opposite faces of a single crystal oriented at 15° to a (100) plane after heating in air for 50 hr at 750°C in a potential gradient of 0.04 V cm^{-1}. × 262

is now etched as in Fig. 3(b) and shows facets more than 10 times larger than those shown in Fig. 3(a). The etching again became less pronounced as the distance from the centre of length of the specimen increased.

(iii) {111} *orientation—no applied potential.* In a control experiment the specimen was electropolished and heated in the apparatus by means of the tube furnace only. The temperature of the specimen ranged from 720°C in the centre to 710°C at the ends, and in a central region about 3 cm long, the temperature gradient was less than 10°C/cm.

After 150 hr of heating, a fine etching was observed (Fig. 4). The facets developed were the same as those observed after etching with a potential gradient applied. There were no discernible differences between the etching on the two faces of the specimen. As usual, the extent of the etching diminished symmetrically as the distance from the centre of length increased.

(iv) {111} *orientation—alternating potential applied.* After being electropolished the specimen was mounted in the apparatus and heated in the furnace and an alternating current of 19.5 A was passed through it. The central region of the specimen was at 720°C and the potential gradient was 0.034 V/cm.

Figure 5 illustrates the type of etching observed after 150 hr of heating. The facets of {111} and the complex planes are well developed and the two faces show no essential differences in etching behaviour. Again, the etching was less well pronounced as the distance from the centre of length increased.

(v) {100} *orientation—d.c. potential applied.* A specimen in which a {100} plane lies within 26° of the surface will normally etch in air to expose {100} facets and complex planes.[1] In order to study the effects of an applied field for such a crystal, a specimen with faces oriented 15° to {100} was heated for 50 hr. The central part of the specimen was at 730°C and the potential gradient was 0.032 V/cm. Fig. 6 shows the types of etching on the two opposite faces.

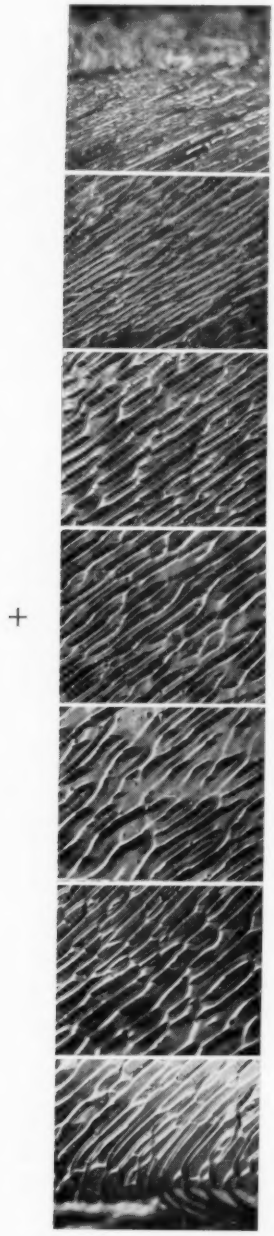


FIG. 7. Traverse across the face of the same specimen as in Fig. 6(a). The top of the figure corresponds with the top of the specimen as placed in the apparatus. The traces of the etched planes lie at an angle of 40° to the direction of the field. The etching is more pronounced at the bottom of the specimen. × 75

It is clear that the applied potential affects the etching of crystals with surfaces near a {100} plane, as well as for crystals with surfaces near a {111} plane. The etching is coarse on one face and much finer on the opposite side. After electropolishing and reheating with the polarity of the field reversed the nature of the etching on the surfaces was reversed.

Figure 7 is a series of photomicrographs taken in the centre of length of the specimen along a line perpendicular to the field and the top of the figure corresponds to the upper edge of the specimen as it is placed in the apparatus. It is seen that the etching becomes noticeably heavier from the top edge to the bottom edge. This effect was only observed on specimens where the facets run at an oblique angle to the direction of the applied field.

(b) *Etching in nitrogen—d.c. potential applied*

The specimen from Section 3(a)(v) was electropolished and mounted between two adjacent long conductors of silver together with a fixed thermocouple at the centre. The entire assembly was fitted into a silica tube one metre long with both current conductors protruding through the same end of the tube. This was then evacuated and filled with nitrogen containing less than 20 p.p.m. oxygen. The tube was inserted in the furnace held at 700°C and as before a potential was applied sufficient to maintain the middle part of the specimen at 730°C.

The results are shown in Fig. 8. Both faces of the specimen showed pitting but virtually no etching after 150 hr heating.

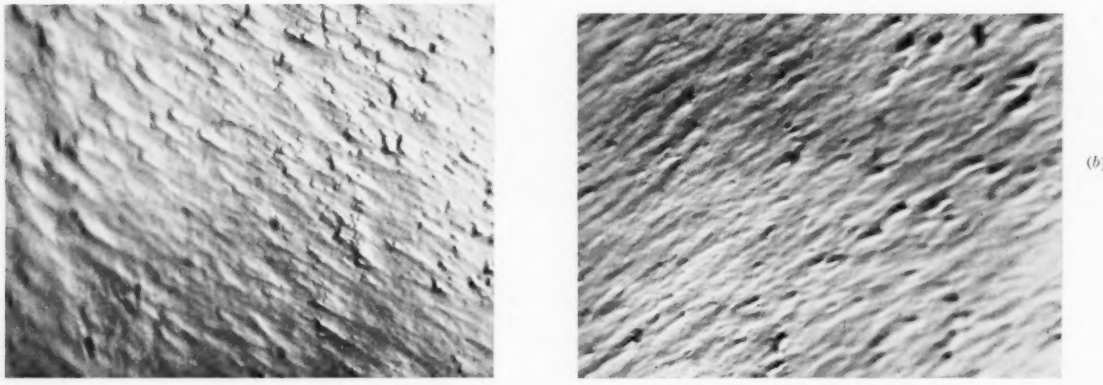
(c) *Etching* in vacuo—*d.c. potential applied*

An experiment was carried out, heating the specimen from Section 3(b) with d.c. alone *in vacuo*. The specimen was held between two silver conductors inserted in a glass bulb approximately 15 cm in diameter and this was sealed off at a steady pressure of 10^{-5} mm of Hg, and the specimen was then heated by direct current for about 5 hr. A brown film formed on the walls of the glass bulb indicating that considerable evaporation was taking place. The hottest region of the specimen at its centre of length reached a temperature of approximately 700–750°C and typical results from this central region are shown in Fig. 9. Both faces of the specimen showed large pits or craters. The size of the pits diminished as the distance from the centre of length of the specimen increased.

4. DISCUSSION

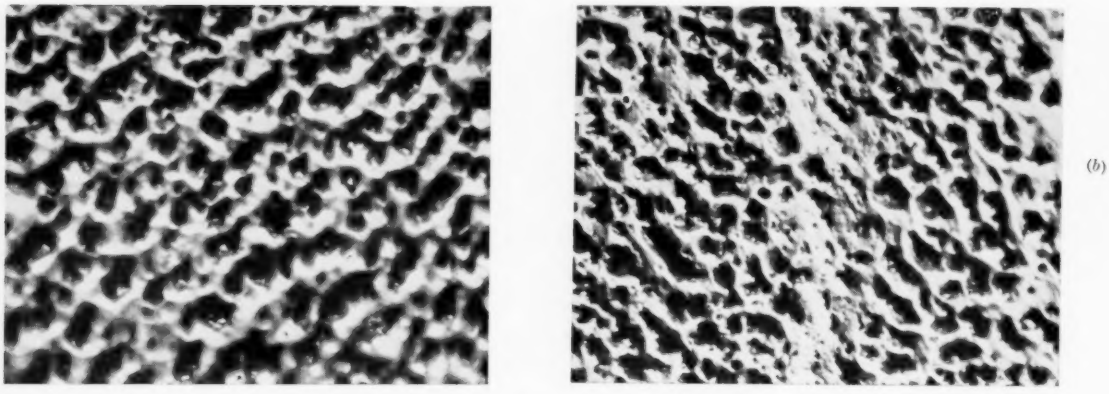
Hondros and Moore[5] have shown recently that metal must be continuously evaporated from the surface in the presence of oxygen in order to produce and maintain a thermally etched structure on silver. In general a surface before etching would consist of a series of steps with the "risers" of the steps one atom high and the "treads" parallel to either {100} or {111} depending on the surface orientation. It was

VOL. 8 1960



(a) (b)

FIG. 8. Opposite faces of the single crystal after heating in nitrogen for 150 hr at 730°C in a potential gradient. × 700



(a) (b)

FIG. 9. Pitting of opposite faces of the single crystal after heating *in vacuo* for 5 hr at 700–750°C in a potential gradient. × 700

suggested that the monatomic steps drifted across the surface, as atoms first migrated from the step edges, and then evaporated from the "tread" of the step. The presence of oxygen caused the drifting steps to aggregate together thus forming the facets of complex planes. In a horizontal tube furnace evaporation at 900°C is sufficient to cause etching in a few hours,[5] but in the experiment carried out here at 720°C with no potential gradient, the evaporation is reduced and the etching is very slight after 150 hr (Fig. 4).

When a potential gradient is applied the same facets are developed, but there is a wide variation in the width of the facets, depending on the polarity relative to the crystallographic orientation of the crystal surface. The condition least favourable to etching is that when the facets of the (111) or (100) plane which is developed slope into the specimen in the direction of the negative end. The etching in this case is comparable to that produced by heating without current. When the facets developed slope into the specimen in the direction of the positive end, they are large. With alternating current, smaller facets are formed giving an etched structure intermediate between the two extremes.

Previous authors[2–4] have explained the effects of a potential gradient on etching in terms of ionic migration in an electric field. In the present case the evaporation which is known to accompany thermal etching, and the necessity for the presence of oxygen, must also be considered. It is assumed here that the less strongly bound silver atoms on the surface of silver have some positive charge and may have a small drift in the direction of the field imposed upon their thermal motion. With no electric field, a silver atom could be detached from a step edge and in this weakly bound condition wander around the face of the step until it is either evaporated, or recaptured by the step edge. An electric field of the appropriate polarity will tend to cause the atom to

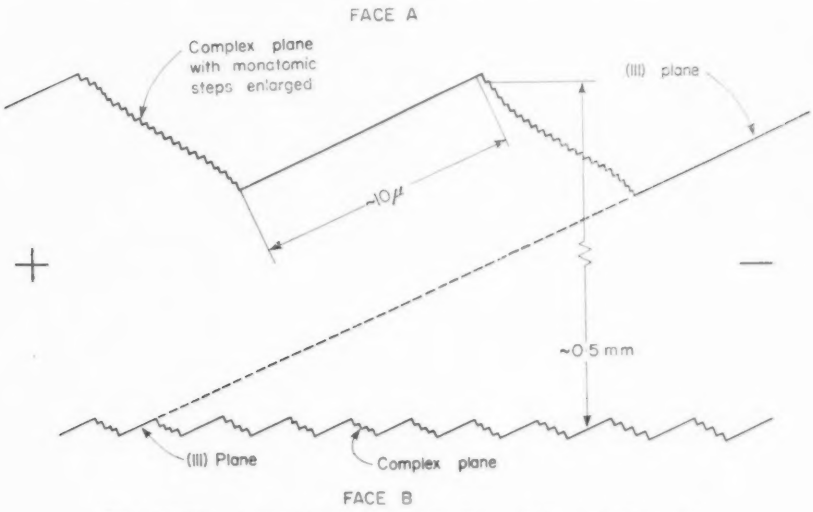


FIG. 10. The step pattern on opposite faces of the etched crystal.

drift away from the step edge and it will be less likely to return and hence more likely to evaporate. Thus the electric field increases the evaporation rate and hence increases the movement of steps across the surface. The presence of oxygen would have the same effect of stabilizing aggregations of monatomic steps as in normal thermal etching.[5] Fig. 10 shows diagrammatically the effect of polarity on types of steps on each side of the specimen.

With an alternating field, it appears that there is an increase in the probability of etching during the appropriate cycle which is greater than the decrease during the unfavourable cycle, since the etching is enhanced on each side. A possible explanation is that when the field is favourable atoms will drift right across the tread of the step to sites on the "brink" of the next step, and at these positions there would be an increased probability of evaporation.

The etching has not been noticeably influenced by thermal gradients. From the centre to either end of the specimen the maximum temperature gradient for the a.c. and d.c. experiments was 25°C/cm. However with the crystal oriented so that the etched ridges were perpendicular to the electric field, there was no asymmetry of the etching about the mid-point of the specimen where the temperature was highest. Thus a temperature gradient of 25°C/cm has little effect on the etching compared with an electrical gradient of 0.04 V/cm.

When the direction of the traces of {111} or {100} planes is oblique to the long axis of the specimen, then the striations do not appear uniformly across the specimen (Fig. 7), but tend to be reduced at one edge. It may be suggested that the electric field causes migration along the step edge after an atom has left a kink site. This is analogous to the field promoting migration across the face of the step after the atom has been detached from the step edge. These more complex effects are being investigated.

ACKNOWLEDGMENTS

The authors would like to thank their colleagues at the Division of Tribophysics, C.S.I.R.O., for many helpful discussions, particularly Dr. J. V. Sanders, Mr. J. F. Nicholas and Dr. M. E. Hargreaves.

REFERENCES

1. A. J. W. MOORE, *Acta Met.* **6**, 293 (1958).
2. R. F. JOHNSON, *Phys. Rev.* **54**, 459 (1938).
3. A. D. MROWCA, *J. Appl. Phys.* **14**, 684 (1943).
4. D. LANGMUIR, *Acta Met.* **5**, 13 (1957).
5. E. D. HONDROS and A. J. W. MOORE, *Acta Met.* **8**, 647 (1960).

VOL. 8 1960

THE OXIDATION OF TITANIUM IN OXYGEN AT HIGH TEMPERATURES*

J. STRINGER†

The oxidation of titanium has been studied in the range 850°–1000°C and the results compared with those of earlier investigations. The oxidation rate is initially parabolic, the parabolic rate constant being the sum of two terms; one representing the formation of a rutile scale by the migration of anion defects with an activation energy of 25,400 ± 1000 cal/mole, and one representing the formation of an oxygen solid solution by the diffusion of interstitial oxygen atoms in alpha titanium with an activation energy of 61,800 ± 2000 cal/mole. Eventually the scale detaches by blistering away from the metal surface and reacts with oxygen to become stoichiometric. When this is repeated, a white laminar porous film forms and the rate law becomes linear.

Finally it appears that gaseous diffusion of oxygen through the porous scale becomes the controlling step, and a new rate law is established, initially parabolic, but tending to linear at very long times. A model is suggested for this step and a rate law of the right form derived. When the pores are identified with screw dislocation cores, quantitative agreement is obtained between calculated and observed rates.

L'OXYDATION DU TITANE DANS L'OXYGENE A HAUTES TEMPERATURES

L'oxydation de titane a été étudiée dans le domaine de température de 850–1000°C et les résultats ont été comparés avec ceux qu' l'on a obtenus lors des essais antérieurs. Au début, la vitesse d'oxydation suit une courbe parabolique et la constante parabolique est la somme de deux termes: l'un représente la formation d'une couche de rutile par migration de lacunes d'anion avec une énergie d'activation de 25.400 ± 1000 cal/mole et l'autre représente une solution solide d'oxygène par diffusion d'atomes interstitiels d'oxygène dans du titane alpha avec une énergie d'activation de 61.800 ± 2000 cal/mole. Eventuellement la couche d'oxyde se détache du métal par formation de soufflures et réagit avec l'oxygène jusqu'à avoir une composition stoechiométrique. Ce phénomène étant répété, il se forme un film lamellaire poreux et la vitesse d'oxydation devient linéaire.

Finalement, il apparaît que la diffusion gazeuse d'oxygène à travers la couche poreuse deveint le facteur déterminant et une nouvelle loi de vitesse est établie dont la courbe est parabolique au début et linéaire pour des temps très longs.

L'auteur suggère un modèle pour cette étape et établit une loi de vitesse. Lorsqu'on identifie les pores avec les sources de dislocation, on obtient un accord quantittatif entre les vitesses calculées et observées.

DIE OXYDATION VON TITAN IN SAUERSTOFF BEI HOHEN TEMPERATUREN

Die Oxydation von Titan wurde im Bereich 850° bis 1000°C untersucht und die Ergebnisse mit denen früherer Untersuchungen verglichen. Die Oxydationsgeschwindigkeit verläuft zu Beginn parabolisch, die parabolische Geschwindigkeitskonstante ist die Summe von zwei Termen; der eine entspricht der Bildung einer Rutilschicht durch Wanderung von Anionen-Defekten mit einer Aktivierungsenergie von 25,400 ± 1000 cal/Mol, der andere der Bildung einer festen Lösung von Sauerstoff durch Zwischengitter-Diffusion von Sauerstoff in α-Titan mit einer Aktivierungsenergie von 61,800 ± 2000 cal/Mol. Schließlich löst sich die Schicht durch Blasenbildung von der Metalloberfläche ab und reagiert mit dem Sauerstoff bis zur stöchiometrischen Zusammensetzung. Wenn sich dies wiederholt, bildet sich ein weißer poröser Film und das Zeitgesetz ist linear.

Schließlich wird offenbar die Diffusion von gasförmigem Sauerstoff durch die poröse Schicht der geschwindigkeitsbestimmende Schritt, so daß sich ein neues Zeitgesetz herausbildet, das zunächst parabolisch ist, sich aber bei sehr langen Zeiten einem linearen nähert. Für diese Stufe wird ein Modell vorgeschlagen und ein Zeitgesetz der richtigen Form abgeleitet. Wenn man die Poren mit Schraubenversetzungskernen identifiziert, erhält man quantitative Übereinstimmung zwischen berechneten und beobachteten Reaktionsgeschwindigkeiten.

INTRODUCTION

Although a number of compounds of titanium with oxygen are stable, only one oxide, the rutile modification of TiO_2, has been found on titanium heated in oxygen. In addition, a considerable amount of oxygen dissolves in the metal, which in the alpha modification can dissolve 14 wt. % (35 at. %) of oxygen, the oxygen atoms being accommodated interstitially.

Previous investigations of the kinetics of the oxidation suggest that above 250°C the oxidation is parabolic,[1] but that at higher temperatures the rate may deviate from the initial parabola after about 100 min, becoming linear.[2] The time at which this deviation occurs appears to be variable. In two investigations[3,4] it is reported that a second faster parabolic rate supersedes the linear stage. During the initial stages of the reaction oxygen is dissolved in the metal as well as absorbed by the scale forming reaction. The proportion of the total absorbed oxygen entering the

* Received October 2, 1959; revised November 18, 1959.
† University of Liverpool, Liverpool.

metal initially increases from 22 per cent at 800°C to 40 per cent at 900°C.[4] The proportion falls off with time. Simnad *et al.*[5] attempted to separate the scale-forming part of the oxidation reaction from the oxygen-solution part by oxidizing specimens previously saturated with oxygen. The oxidation rate was still parabolic, and there was little difference in the rates, but the activation energy was smaller.

The scale formed during the initial parabolic stage is dark grey-blue in colour,[4] but later in the reaction this changes to white. The grey scale has a high conductivity, while that of the white scale is very small.[3] The grey scale when detached from the specimen and heated in oxygen turns white. Conversely, the white scale turns grey when heated *in vacuo*. The weight change associated with either of these reactions is very small, less than 4 parts in 10,000, and there is no detectable change in lattice parameter. Both scales have the structure of rutile.[3,4] These results suggest that the grey scale is very slightly oxygen deficient and it seems probable that the deficiency is accommodated by anion defects.[6] This idea is supported by the observation that oxygen is the mobile species in the scale.[2,4]

The white scale formed in the later stages of oxidation contains lenticular fissures parallel to the surface of the metal giving the scale a laminar structure.[3,4] Each lamination is composed of columnar crystals with the major axis normal to the plane of the lamination. The grain diameter in the plane of the lamination is shown by X-ray measurements to be less than 10^{-4} cm.[3,4]

It is likely that the presence of significant amounts of nitrogen in the atmosphere alters the details of the oxidation considerably.[7]

EXPERIMENTAL PROCEDURE

The major discrepancies in the published data relate to oxidation above about 850°C. Consequently, the experimental part of the present work was confined to reactions in the range 850°–1000°C. Sievert's method was used. The oxygen absorbed by the specimen was measured as a pressure drop in a fixed reaction volume. This method is only useful for oxidations which are known to be independent of pressure.

The specimen material was magnesium reduced titanium in the form of arc-melted buttons* which were hot-forged in air at 750°C and hot-rolled to 0.020 in. The thin surface film of oxide was removed by abrasion with 100 through 500 silicon carbide papers followed by 15 sec immersion in an aqueous solution containing 2 per cent HF and 5 per cent HNO_3. The edges of the specimens were prepared by filing and abrasion while clamped in a hardened steel jig. The final specimen size was $5 \times 0.6 \times 0.05$ cm, the weight of each specimen being approximately 0.7 g and the surface area about 7 cm^2. A standard surface was prepared by annealing under a pressure of less than 5×10^{-5} mm Hg for 30 min at 950°C. During vacuum annealing the specimens lost weight by evaporation at the rate of about 0.05 mg/hr. A bright thermally etched surface was produced. The beta grain size of the specimens was large, about 2 mm diameter. The thermally etched beta grain structure was visible on the oxide surface after oxidation, although the grain structure of the oxide was in no way related to the metal grain structure. Oxidation was carried out in oxygen of commercial purity at pressures slightly less than atmospheric. The pressure drop during the reaction did not exceed 20 cm of mercury.

Calculations of the accuracy of the method indicate that the oxygen reacting with the metal can be measured to ± 0.02 mg/cm^2, and this figure is confirmed by the scatter of experimental points about the best smooth curve.

The structure of the scale was checked by X-ray methods using the Debye-Scherrer technique with filtered CuKα radiation. As expected[4,8] these measurements showed only rutile to be present.

RESULTS

Throughout the temperature range studied (850°–1000°C) the oxidation was initially parabolic after a very short period of about 1 min, probably associated with the attainment of steady state conditions. Eventually the rate deviated from this parabola, approaching a straight line. The straight line is parallel to a tangent to the parabola at a point rather earlier than the break-away. Eventually the linear rate was superseded by a second parabolic rate, considerably more rapid than the first. In general, the lower the temperature, the longer before the first parabolic rate law broke down. Some typical oxidation curves plotted according to a parabolic rate law are shown in Fig. 1.

To determine the effect of varying the surface preparation two series of runs were performed, the first with a 15-min and the second with a 2-hr vacuum anneal at reaction temperature before oxidation. With the shorter anneal the parabolic rate was considerably slower and the break-away occurred at longer times. The parabolic rate constants for both

* The titanium as supplied by ICI Metals Division had the following analysis: 0.040% O_2; 0.012% N_2; 0.04% C and 0.1% W. Fe not given: prob. 0.05%. Hardness was in the range 120–130 VPN.

VOL. 8 1960

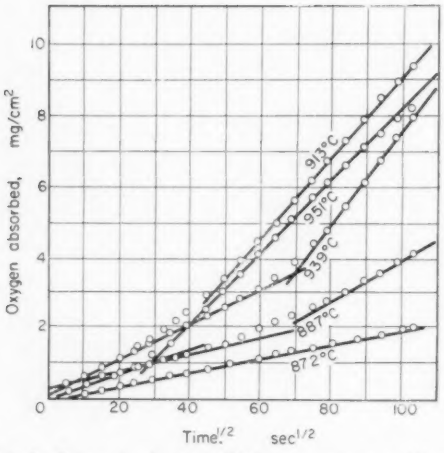


FIG. 1. Some typical oxidation curves for titanium plotted according to a parabolic law.

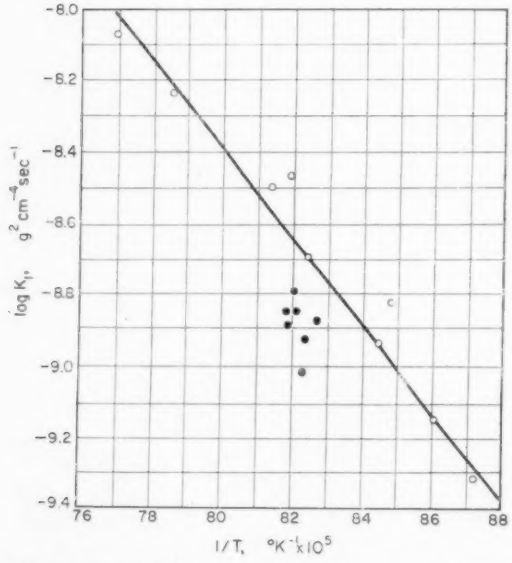


FIG. 2. An Arrhenius plot of first stage parabolic rate constants showing effect of vacuum anneal. Closed points, short anneal; open circles, long anneal.

series are plotted on an Arrhenius graph in Fig. 2, which clearly shows the drop in rate associated with the shorter anneal.

The scale was grey-black during the period of the first parabola. Deviation from the parabolic rate was accompanied by the appearance of white blisters on the scale. These blisters were locations where the scale had detached from the metal surface and reacted with oxygen to become stoichiometric. The blisters spread until the entire scale was white and detached from the metal. The white stoichiometric scale so formed was apparently porous to gaseous oxygen because new coherent oxide formed beneath the detached layer. This blistered in turn and the cycle was repeated. As each layer blistered it pressed against the already detached scale from underneath. The sequence is represented diagrammatically in Fig. 3. This mechanism explains the scale structure found in earlier investigations[2,4] and the surface markings on the stripped metal core noted by Jenkins[4]. Fig. 4 shows two blisters on a coherent scale. Fig. 5 shows a

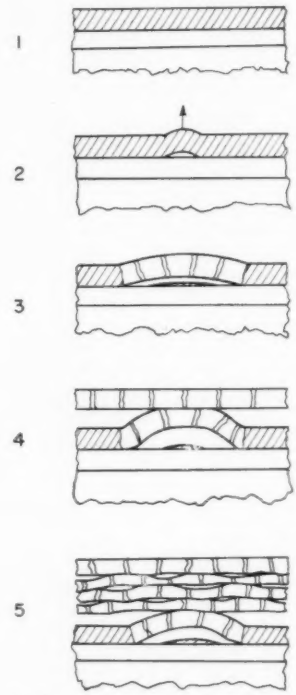


FIG. 3. A diagrammatic representation of the formation of a laminated porous scale by the repeated blistering of coherent layers.

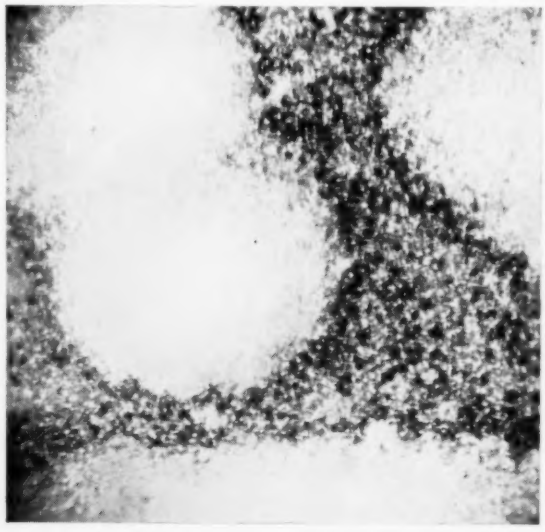


FIG. 4. White stoichiometric blisters on grey coherent scale. ×30

blister cracked to reveal a second blister formed underneath; this is also cracked to reveal the metal surface.

The white scale structure formed during both the linear and the second parabolic stages. The second rate change was not accompanied by any change in the structure of the oxide layer.

the total oxygen absorbed since the start of the reaction present in solution drops sharply after the break-away, very little oxygen must be entering the metal during the later stages. Again, there was no discontinuity in behaviour associated with the second rate change.

For the series of runs at 950°C the metal was

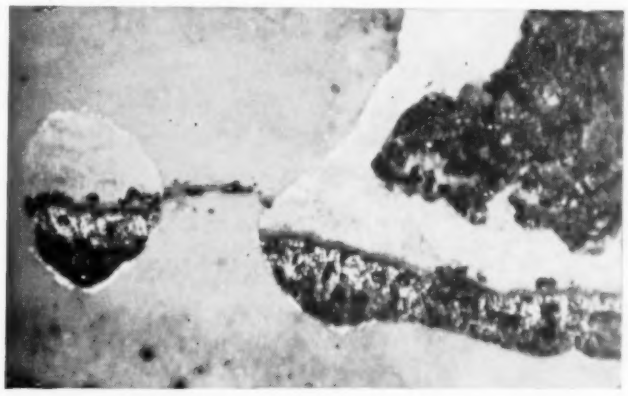


FIG. 5. Outer blister (grey) cracked to reveal a second blister (white). This also is cracked to reveal the black metal surface.

VOL. 8 1960

A number of oxidations of different duration at 950°C were performed to determine the partition of oxygen between the scale-forming and oxygen-solution reactions. This was done by quenching the oxidized specimens in water, when most of the scale spalled from the surface. The remainder was removed by careful abrasion. The weight of scale was found by taking the difference between the total weight as indicated by the Sievert's apparatus and the weight of the stripped specimen. Assuming the scale to be 100 per cent stoichiometric rutile the relative proportions of the oxygen entering the metal and the scale were calculated. This method produced quite reproducible results. As long as the scale was adherent, that is, during the first parabolic section, the proportion of oxygen entering the metal remained constant at about 45 per cent. After the break-away the proportion dropped until by the time the second parabola was established only about 5 per cent of the total oxygen absorbed was present in the metal. This is in agreement with earlier investigations.[4] Since the proportion of the total oxygen involved in each reaction during the first parabolic stage remains constant, both the formation of scale and the solution of oxygen separately must be parabolic. This is in agreement with the results of Simnad *et al.*[5] on oxygen saturated specimens. As the proportion of initially in the beta condition. However a small amount of oxygen dissolved in the metal is sufficient to stabilize alpha. It is therefore to be expected that during oxidation a layer of alpha will form on the surface of the specimen. Microscopic examination of the sectioned specimens revealed such a layer and measurements of its thickness coupled with the knowledge of the total weight of oxygen dissolved in the metal showed the average oxygen content to be constant at about 5 wt. %. The hardness of alpha increases considerably with increasing oxygen content.[4] Microhardness measurements across the alpha layer showed a gradient suggesting an oxygen concentration gradient across the layer, in agreement with earlier investigations.[4,7] Thus it is reasonable to assume that the rate of increase in thickness of this layer is determined by the diffusion of oxygen across it.

The second parabolic stage appeared to be pressure dependent, since when the pressure was allowed to drop markedly during oxidation the rate decreased, as shown in Fig. 6. The pressure dependence was not investigated further at this time.

Jenkins has reported[4] that the second parabolic stage tends to become linear at long times. One oxidation in the present study, in which the second parabolic stage was followed for 3 hr, appeared to confirm this observation.

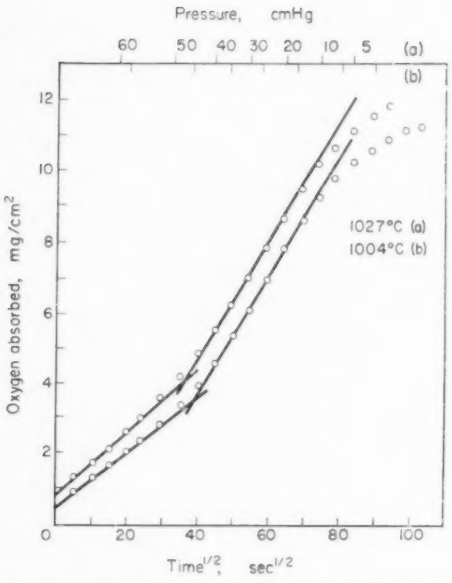


FIG. 6. Oxidation of titanium, parabolic plot. The effect of pressure on the second stage parabolic rate.

DISCUSSION

First parabolic stage

In this stage there is the simultaneous formation of rutile scale, by the migration of anion vacancies created at the scale/metal interface, and of an oxygen solid solution layer by the migration of interstitial oxygen introduced at the scale/metal interface. These two diffusion processes are independent of each other. At any temperature the growth of each layer is parabolic, and the overall reaction rate, which is a simple sum of the reaction rates of the two processes, will also be parabolic. This conclusion is confirmed experimentally.[5] Thus

$$k_1 = k_s + k_m \tag{1}$$

where k_1 is the overall parabolic rate constant for the first parabolic stage, k_s is the parabolic rate constant for the growth of the scale layer, and k_m is the parabolic rate constant for the growth of the oxygen solid solution layer. The temperature dependence of these rates will depend on the temperature dependence of the diffusion processes and of the various interface concentrations. In the titanium–oxygen system the stability ranges of the phases are affected only slightly by temperature, and thus variation of the interface concentrations can be neglected in comparison with the Arrhenius terms; thus

$$k_s = k_{0,s} \exp(-Q_s/RT) \tag{2}$$

$$k_m = k_{0,m} \exp(-Q_m/RT) \tag{3}$$

where $k_{0,s}$ and $k_{0,m}$ are the frequency factors for the scale forming and solid solution forming reactions respectively; Q_s is the activation energy for the diffusion of anion vacancies in rutile, and Q_m is the activation energy for the interstitial diffusion of oxygen in alpha titanium. The approximation made above is that the temperature dependence of the frequency factors can be neglected. Inserting these values in equation (1),

$$k_1 = k_{0,s} \exp(-Q_s/RT) + k_{0,m} \exp(-Q_m/RT). \tag{4}$$

Equation (4) suggests that a plot of the logarithm of the overall first stage parabolic rate constant for the oxidation of titanium versus the inverse of the absolute temperature will be curvilinear and the experimental data collected from the literature and plotted in Fig. 7 show that this is so. The full line drawn through the experimental points in Fig. 7 satisfies the equation

$$k_1 = 1.007 \times 10^{-6} \exp(-25{,}400/RT) + 320 \exp(-61{,}800/RT). \tag{5}$$

It is to be concluded therefore that the activation energy for the diffusion of anion vacancies in rutile is 25,400 cal/mole and for the diffusion of interstitial oxygen in alpha titanium 61,800 cal/mole. These results seem reasonable compared with analogous results from other systems.

After the forming operations there was a small concentration of oxygen near the surface of the specimen, which diffused into the main body of the specimen during vacuum annealing. The oxidation rate should properly be expressed as a parabolic increase in thickness of the oxide layer, and this rate can be expected to be sensibly independent of small variations in the oxygen content of the metal. The average composition of the solid solution layer is 5 wt. % oxygen, and if 1 wt. % is already present in the metal a given rate of increase in thickness of the layer will require only 4/5 of the oxygen required by a pure specimen. The rate constant as measured by the Sievert's technique will accordingly be less in the case of the specimen containing a small amount of dissolved oxygen, and also the proportion of the oxygen entering the metal will be less. Prolonged vacuum annealing before oxidation, by permitting the high surface concentration of oxygen to diffuse into the bulk of the metal will therefore produce an increase in the measured first stage rate constant, and in the proportion of oxygen absorbed by the metal. These conclusions agree with observation.

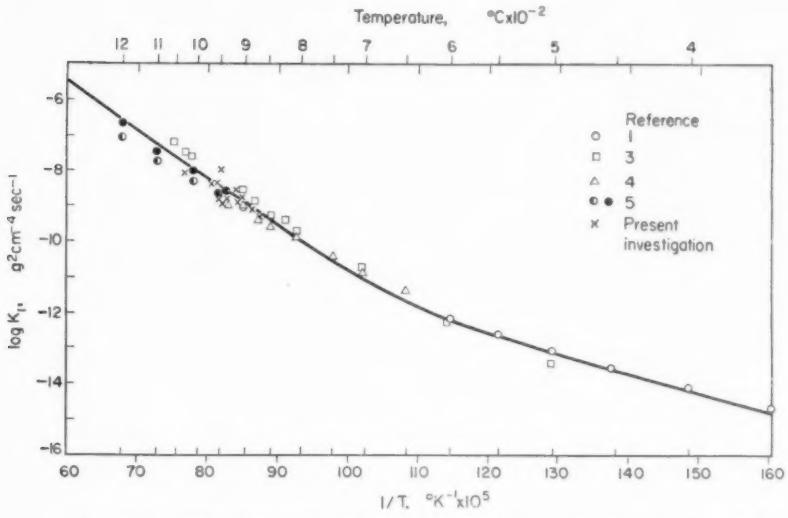


FIG. 7. An Arrhenius plot of first stage parabolic rate constants collected from the literature.

Blistering stage

Because blistering occurs without loss of continuity in the scale layer, the initial formation of blisters will be a process requiring activation. Blistering releases the stored elastic energy in the strained coherent film, but introduces two new energy terms; the surface energy of the detached region and the elastic energy stored in bending the oxide at the edges of the blister to maintain continuity with the still-coherent film. When the blister is very small, the last term will clearly predominate. The driving force is provided by the film maintaining coherency after the critical thickness has been reached. Accordingly, the oxidation rate first deviates from the first stage parabola at some time after the scale has exceeded the critical thickness. The blisters then spread rapidly over the surface. Since blistering will not in general proceed at exactly the same rate over the whole metal surface, the scale layer will cease to be composed of uniformly detaching envelopes. This means that a number of blistered scale/coherent scale fronts will always be present. Consequently, the blistering will not require activation but will occur as soon as the scale reaches critical thickness.

The removal of metal to form scale will be faster on a newly-blistered surface than the movement of the alpha/beta interface inwards. The solution layer will thus decrease in thickness until it reaches a value which will be constant when averaged over the whole metal surface. This thickness will be that corresponding to the mean thickness of coherent scale according to the first stage mechanism.

On each element of surface at steady state the oxide grows to the critical thickness w_c in t_c seconds, where

$$w_c^2 = k_1 t_c \tag{6}$$

k_1 is the first stage parabolic rate constant. At the end of this time, the scale is removed by blistering, and oxidation starts again. Thus a linear oxidation rate is established:

$$dw/dt = w_c/t_c = k_1/w_c. \tag{7}$$

During this linear rate the thickness of the alpha layer remains constant, and only sufficient oxygen enters the metal to compensate for that removed by the scale forming reaction. It would be expected therefore that the proportion of oxygen entering the metal decreases sharply at the start of blistering, and then approaches zero asymptotically. This is in fact the behaviour found in the present investigation and in that of Jenkins[4]. In addition, if the small temperature dependence of w_c is neglected the Arrhenius plot of the linear rate constant should be curved in the same way as that for the first stage rate constant. Fig. 8 shows the linear rate constants for the present investigation and for that of Davies and Birchenall[2] on an Arrhenius graph, and it can be seen that the prediction is correct. Calculation of the critical thickness of the scale from the parabolic and linear rate constants gives reasonable values; generally about 3/4 of the break-away thickness.

Second parabolic stage

There is no detectable change in the scale or the specimen at the change-over from linear to the second

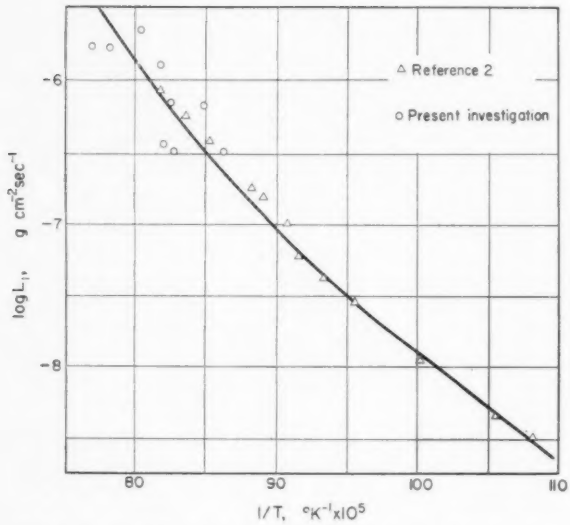


FIG. 8. An Arrhenius plot of intermediate stage linear rate constants.

parabolic rate, and the rate curve is continuous, that is, the straight line is tangential to the start of the second parabola. This means that the rate law alters discontinuously at the change over. Therefore it appears that the second change in rate is not due to an alteration in mechanism. This behaviour suggests that some step in the oxidation becomes slower than the reaction in the neighbourhood of the metal surface, and so becomes controlling. The most probable step is the gaseous diffusion of oxygen through the porous scale.

The scale is observed to contain large fissures parallel to the metal surface, but these are merely due to irregularities in the laminations of the scale. The pores through which the oxygen gains access to the metal surface must pass through the laminations. Microscopic examination at a magnification of 2000 diameters reveals no such pores. However, if ink is dropped on one side of a detached scale, it eventually penetrates through to the other side. Under the microscope it can be seen that the flow of ink between scale laminations is very rapid, but the flow through laminations is slow. The ink penetrates the laminations at a number of discrete points. Again at 2000× no pore is visible at any of these points. Thus it is concluded that the rate of gas flow through the scale is determined by the flow through very small pores through the laminations of oxide.

Under steady state conditions, every layer that detaches from the metal will be identical. It is assumed that in each square centimetre of scale layer there are n circular pores of radius r_0 normal to the surface. Then, using Knudsen's expression for the steady-streaming of a gas through fine pores the following rate law is obtained:

$$X^2 = \frac{16}{3}\left(\frac{\rho_1}{2}\right)^{1/2}\frac{\pi}{M\rho_x}pn^{3/2}r_0{}^4t \qquad (8)^*$$

where X is the scale thickness; ρ_x is the density of the oxide; ρ_1 is the density of the gas at the temperature of the experiment and a pressure of 1 dyn/cm^2; p is the pressure difference across the scale; and M is the weight fraction of oxygen in the oxide.

Thus the rate constant should be linearly dependent on the pressure. There are insufficient experimental data to check this point.

Equation (8) is only valid for the growth of an oxide on an infinite flat surface. When a finite specimen is oxidised, an envelope of oxide detaches and achieves a strain-free position at some distance from the metal. A second layer forms and in time becomes detached, but because the density per metal atom in the scale is lower than that in the metal, the strain-free equilibrium position of the second envelope overlaps the first. Since the tensile strength of an oxide layer is small compared to its compressive strength, the first-formed layer will be expanded. It is assumed that this expansion is accommodated by an enlargement of the pores in the first envelope. Thus the total pore area available for gas to diffuse through will increase as the layer is forced further and further away from its equilibrium position by successive layers blistering beneath. Using this more general model, the following rate law is obtained for the growth of an oxide on a cube of side Q:

$$\frac{dX}{dt} = \frac{n}{M\rho_x}\frac{8}{3\sqrt{2}}\pi^{1/2}\rho^{1/2}p\frac{4r_0{}^2}{(n\pi Q^2)^{1/2}} \times\left(\frac{n\pi Q^2 r_0{}^2}{4QX+4X^2}+1\right). \qquad (9)^*$$

In deriving this equation it has been assumed that the enlargement of the pore area is accommodated by an increase in the radius of the pores, their number remaining constant.

At very short times as $X \to 0$ equation (9) reduces to equation (8), but at long times, large X, equation (9) gives a linear rate law:

$$X = \frac{32}{3\sqrt{2}}\frac{\rho_1{}^{1/2}p}{M\rho_x}\frac{n^{1/2}r_0{}^2}{Q}t. \qquad (10)$$

Equation (9) thus represents a rate law which is initially parabolic, but tends at long times to become linear. This is qualitatively in agreement with the form reported for second stage oxidation.[4]

* See Appendix.

In order to calculate rate constants from equations (8) and (10) it is necessary to assume values for n and r_0. In the present experiments microscopic examination showed that the grain size of the oxide was approximately 2500 Å, in agreement with the observations of Jenkins[4] and of Morton and Baldwin[3]. If it is assumed that there is one pore per grain $n \sim 1.6 \times 10^9$ cm^2. Since there is no sign of any pores, it can be assumed that $r_0 < 1000$ Å and probably of the order of 100 Å.

Keller *et al.*[8] and Booker *et al*[9] have found that oxide formed anodically on aluminium consists of small columnar grains normal to the surface with a pore of diameter 120–330 Å down the centre of each grain. The grain density was $\sim 100 \times 10^9$ cm^2. Dragsdorf and Webb[10] examined whiskers of delta Al_2O_3 formed on aluminium, and found each had a screw dislocation down the centre, with a step height of about four repeat distances. Down the centre of each whisker was a pore of a diameter of the same magnitude as is given by Frank's equation:[11]

$$r = 10\frac{b}{\pi} - 200\frac{\gamma}{\mu} \qquad (11)$$

where r is the radius of the pore; b is the step height of the dislocation; γ is the specific surface free energy of the material; and μ is the rigidity modulus. γ/μ has the dimensions of a length, and for most materials is in the range $0.05–0.56 \times 10^{-8}$ cm. Using these data for rutile, a weighted mean step height of five repeat distances (= 23 Å) gives for the maximum possible pore radius

$$r_0 = 60 \text{ Å}$$

the actual value depending on the magnitude chosen for γ/μ. Using this value of r_0 together with the value of n given above and numerical values for the density terms for a temperature of 950°C equation (8) gives

$$k_{2\,\text{calc}} = 2 \times 10^{-8} \text{ g}^2 \text{ cm}^{-4} \text{ sec}^{-1}$$

and observed values for k_2 at 950°C are

$$k_{2\,\text{obs}} = 1.66 \times 10^{-8}$$

and $$1.06 \times 10^{-8} \text{ g}^2 \text{ cm}^{-4} \text{ sec}^{-1}.$$

Equation (10) gives for L, the linear rate constant,

$$L_{\text{calc}} = 5 \times 10^{-6} \text{ g cm}^{-2} \text{ sec}^{-1}$$

and the one observed value of a long time linear rate is

$$L_{\text{obs}} = 0.8 \times 10^{-6} \text{ g cm}^{-2} \text{ sec}^{-1}.$$

These results show that a gaseous diffusion model can result in rates of the right magnitude.

Finally, the stresses in the scale are such that failure in tension of the outer layers can be expected eventually. This would lead to irregular breaks in the rate of exactly the type found at long time.[4]

The second parabolic rate constant appears to be strongly dependent on the material. Up to the limits of their experiments Davies and Birchenall found no second parabola superseding the straight line. Morton and Baldwin[3] found a second parabola only in the purest grade of commercial titanium then available, and the rate they found is approximately 10^2 greater than that found in the present investigation. Jenkin's[4] second stage appears to have been little different from the first stage. On the basis of the model proposed here these variations are easily explained in terms of the variation in pore density and size to be expected with changes in the purity of the metal.

ACKNOWLEDGMENTS

Thanks are due to the Department of Scientific and Industrial Research for the award of a maintenance grant, and to ICI Metals Division for supplying the material. Thanks are also due to Dr. R. J. Wasilewski for help and advice during the early part of the research. Finally, the author is indebted to Professor W. S. Owen for much helpful criticism.

REFERENCES

1. E. A. Gulbransen and K. F. Andrew, *Trans. Amer. Inst. Min. (Metall.) Engrs.* **185,** 741 (1949) and *Trans. Electrochem. Soc.* **96,** 364 (1949).
2. M. H. Davies and C. E. Birchenall, *J. Metals, N.Y.* **3,** 877 (1951).
3. P. H. Morton and W. M. Baldwin, *Trans. Amer. Soc. Met.* **44,** 1004 (1952).
4. A. E. Jenkins, *J. Inst. Met.* **82,** 213 (1954); **84,** 84 (1955).
5. M. Simnad, A. Spilners and O. Katz, *J. Metals, N.Y.* **7,** 645 (1955).
6. P. Ehrlich, *Z. Elektrochem.* **45,** 362 (1939).
7. O. Kinna and W. Knorr, *Z. Metallk.* **47,** 594 (1956).
8. F. Keller, M. S. Hunter and D. L. Robinson, *J. Electrochem. Soc.* **100,** 411 (1953).
9. C. J. L. Booker, J. L. Wood and A. Walsh, *Brit. J. Appl. Phys.* **8,** 347 (1957).
10. R. D. Dragsdorf and W. W. Webb, *J. Appl. Phys.* **29,** 817 (1958).
11. F. C. Frank, *Acta Cryst., Camb.* **4,** 497 (1951).

APPENDIX

Rate of growth of the oxide film

Consider gas flowing down a tube the cross sectional area A and circumference C of which are both functions of the length measured from one end:

$$A = f(x); \quad C = g(x).$$

The momentum communicated to an element of the tube length dx in time dt by the streaming gas is

$$\frac{3\pi}{32} vm\bar{c}vg(x)\,dx\,dt$$

where v is the number of molecules per unit volume; m the mass of a single molecule; $\bar{c}$ is the arithmetic mean velocity of the molecules and v the velocity of the mass of gas. This expression can be rewritten:

$$\frac{3}{8}\left(\frac{\pi}{2}\right)^{1/2}\left(\frac{P}{\rho}\right)^{1/2}\rho vg(x)\,dx\,dt$$

VOL. 8 1960

where P is the pressure difference between the ends of the pore and ρ is the density of the gas at experimental temperature and pressure. This momentum must be equal to the loss of momentum by the streaming gas which is, in the same element:

$$-f(x)\frac{dp}{dx}\,dx\,dt.$$

The mass of gas flowing through the tube in unit time is G where

$$G=\int_0^X f(x)v\rho\,dx=\frac{8}{3}\left(\frac{2}{\pi}\right)^{1/2}\rho_1^{1/2}P\left(\int_0^X\frac{g(x)}{\{f(x)\}^2}\,dx\right)^{-1}$$

where ρ_1 is the density of the gas at unit pressure. It is now required to find the time dependence of X, the thickness of the film. If the density of the forming oxide extending the pore is ρ_x and M is the weight fraction of oxygen in the oxide, a flow G corresponds to the formation of $G/M\rho_X$ volumes of oxide. If there are n pores per unit area then $nG/M\rho_X$ volumes per unit area are formed.

That is,

$$\frac{dX}{dt}=\frac{nG}{M\rho_X}.$$

Substituting for G, the general growth law becomes

$$\frac{dX}{dt}=\frac{n}{M\rho_X}\left(\frac{8}{3}\right)\left(\frac{2}{\pi}\right)^{1/2}\rho_1^{1/2}P\left(\int_0^X\frac{g(x)}{[f(x)]^2}\,dx\right)^{-1}. \qquad \text{(A1)}$$

Now consider the oxidation of a cube side Q. After a scale layer thickness X has formed by repeated blistering, the outer layer has to cover an area of $6(Q^2+4QX+4X^2)$ representing an increase in area of $(4QX+4X^2)/Q^2$ per unit area. This assumes that the volume per metal ion of the oxide is large compared to that of the metal, so that the movement of the metal surface can be ignored. If the increase is entirely accommodated by a dilation of existing pores, each pore increases in area by $(4QX+4X^2)/nQ^2$.

Now suppose the pores are circular, so $f(x)=\pi r^2$, $g(x)=2\pi r$; $r=h(x)$ where r, the radius of the pore, is a new function of x. Let the original pore radius of the just-blistered film be r_0. This is the radius of the pore close to the metal, and we regard it as independent of time.

Then

$$\pi r^2=\pi r_0{}^2+\frac{4Qx+4x^2}{nQ^2}.$$

So

$$r=h(x)=\left(r_0{}^2+\frac{4Qx+4x^2}{n\pi Q^2}\right)^{1/2}.$$

Putting this value in equation (A1) and evaluating the integral gives equation (9), the limits of which for small and large values of X, respectively, are given by equations (8) and (10) in the text.

CONTRIBUTION OF DISLOCATION LINE TENSION AND THE DENSITY OF THE SOLUTE ATMOSPHERE TO THE YIELD POINT IN STRAIN AGED INGOT IRON*†

T. MURA‡ and J. O. BRITTAIN‡

An investigation was made of the 77°K yielding behavior of ingot iron specimens that had been prestrained and aged while under stress at 303°K. It was observed that the presence of a yield point at 303°K after a strain aging treatment does not result in a yield point at 77°K until the strain aging treatment is prolonged so as to result in an increase in the 303°K yield point of about 20 per cent. The sharpness and magnitude of the yield point at both 303°K and 77°K increased with an increase in the aging time and or an increase in the stress which was maintained upon the specimen during the aging treatment. The observations of the effect of the aging time and aging stress are discussed in terms of the contribution of the dislocation line tension and solute atmosphere density along the dislocation.

CONTRIBUTION DE LA TENSION DES LIGNES DE DISLOCATIONS ET DE LA DENSITE DES ATMOSPHERES DES ATOMES DISSOUS AU DECROCHEMENT DANS UN LIQUIDE DE FER VIEILLI APRES DEFORMATION

Une étude a été entreprise sur le comportement du décrochement à 77°K d'échantillons de lingots de fer qui ont été prédéformés et vieillis sous tension à 303°K. On a observé que la présence du décrochement à 303°K après un traitement de vieillissement de déformation ne donne pas un décrochement à 77°K tant que le traitement de vieillissement de deformation n'est pas prolongé et que le décrochement à 303°K n'augmente d'environ 20%.

La forme et la grandeur du décrochement tant à 303°K qu'à 77°K s'accroissent avec une augmentation du temps de vieillissement et/ou un accroissement de la tension à laquelle se trouve l'échantillon au cours du traitement de vieillissement.

Les observations de l'effet du temps et de la tension de vieillissement ont été discutées en fonction de la contribution de la tension des lignes de dislocations et de la densité dés atmosphères le long de celles-ci.

BEITRAG DER VERSETZUNGS-LINIENSPANNUNG UND DER DICHTE DER VERUNREINIGUNGS-ATMOSPHÄRE ZUR STRECKGRENZE VON VERFORMUNGSGEALTERTEM ROHSTAHL

Von Kokillenguß-Rohstahl-Proben, die vorverformt und bei 303°K unter Spannung gealtert worden waren, wurde das Verhalten der Streckgrenze bei 77°K untersucht. Es wurde beobachtet, daß das Vorhandensein einer Streckgrenze bei 303°K nach einer Verformungs-Alterungs-Behandlung nur dann zu einer Streckgrenze bei 77°K führt, wenn man die Alterung solange fortsetzt, daß die Erhöhung der Streckgrenze bei 303°K etwa 20% betragt. Schärfe und Größe der Streckgrenze bei 303°K wie bei 77°K nahmen zu mit Zunahme der Alterungszeit und (bzw. oder) der Zunahme der Spannung, der die Probe während der Alterung unterworfen war. Die Beobachtungen über den Einfluß von Alterungszeit und Alterungsspannung werden diskutiert, wobei die Beiträge der Linienspannung der Versetzung und der Dichte der Atmosphäre gelöster Atome entlang der Versetzung in Betracht gezogen werden.

VOL. 8 1960

1. INTRODUCTION

In a previous study[1] it has been demonstrated that the application of a tensile stress during strain aging has a pronounced effect on the rate of strain aging. In a subsequent series of strain aging experiments it has been observed that contrary to an implication of Cottrell and Bilby[2], the presence of a yield point in ingot iron at an elevated temperature does not result in a more pronounced yield point at a lower temperature. The current paper is concerned with the interrelation of the low temperature yielding phenomena and strain aging under an applied stress.

2. EXPERIMENTAL PROCEDURE

Ingot iron (0.013 C, 0.025 Mn, 0.023 Si, 0.005 P, 0.023 Si, 0.11 Cu, 0.004 N) tensile specimens which had a reduced gage section of 1.25 in. and a diameter of 0.1 in. were annealed at 973°K for ½ hr in a dry hydrogen atmosphere and furnace cooled. The heat treatment resulted in a grain size of 0.042 mm. The specimens were deformed in tension at 303°K at a head speed of 0.01 in/min to a plastic strain of 0.04. Following the plastic deformation the load was reduced to a predetermined stress level and the specimens were aged while under load. The stress maintained on the specimens during aging is designated the aging stress. The aging times were varied so as to produce an increase in the yield point* of about 2–20 per cent on a set of specimens tested at 303°K. A second set of specimens that had been given a similar strain aging treatment at 303°K were immersed and held in liquid nitrogen for 15–20 min. The tension tests were then continued at 77°K. During the temperature change sequence care was taken to hold the load on the specimens constant so that the specimens were not overloaded during cooling operation.

* Received December 10, 1959.

† This research was supported by the U.S. Air Force through the Air Force Office of Scientific Research of the Air Research and Development Command.

‡ Department of Metallurgy and Materials Science, Northwestern University, Evanston, Illinois.

* Here defined as $\Delta\sigma/\sigma_f$ where $\Delta\sigma = \sigma_y - \sigma_f$, σ_y is the stress at the upper yield point after aging and σ_f is the flow stress at a plastic strain of 0.04.

3. EXPERIMENTAL RESULTS

The stress–strain curves are shown in Fig. 1 where the solid curves are the results of tests carried out at 303°K after the strain aging treatment at a constant aging stress at 303°K while the dash curves refer to the tensile data obtained at 77°K after the strain aging treatment at 303°K.

It is quite apparent that specimens aged for 90–860 sec have pronounced yield point when tested at 303°K, but the yield point does not appear in tests at 77°K until the strain aging treatment is extended to about 2000–2800 sec. The stress for initiation of plastic deformation at 77°K, here defined as the departure from linearity of stress–strain in the absence of a yield point, increased with aging time at a constant aging stress, and finally approached the yield point of the material at the critical aging time, Fig. 1(d). The stress strain curve at 77°K of a specimen which was not strain aged at 303°K is also shown in Fig. 1(f). The yield point of the unstrained specimen is quite sharp, but the lower yield point is appreciably less than that in the strain age condition where at least part of the increase must be attributed to the prior plastic flow.

In order to investigate the relationship between the yield stress at the critical point (upper yield point equal to lower yield point) and the aging stress σ_0, specimens which had been plastically strained 0.04 and aged for 2800 sec at 303°K at various aging stresses 0–30,000 lb/in² were subsequently deformed in tension at 77°K. The stress–strain curves in Fig. 2 show that both the magnitude and sharpness of the yield point varied with the aging stress. Thus, the stress for the initiation of plastic flow increased with aging

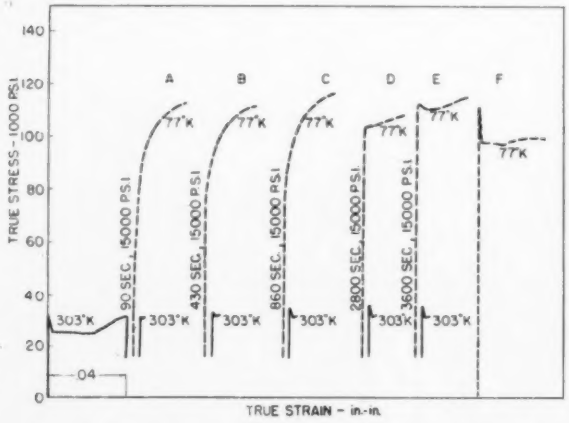


FIG. 1. Stress–strain curves; the solid curves are the results of tests carried out at 303°K after the strain aging treatment at a constant aging stress 15,000 lb/in² at 303°K while the dash curves refer to the tensile data obtained at 77°K after the same strain aging treatment at 303°K.

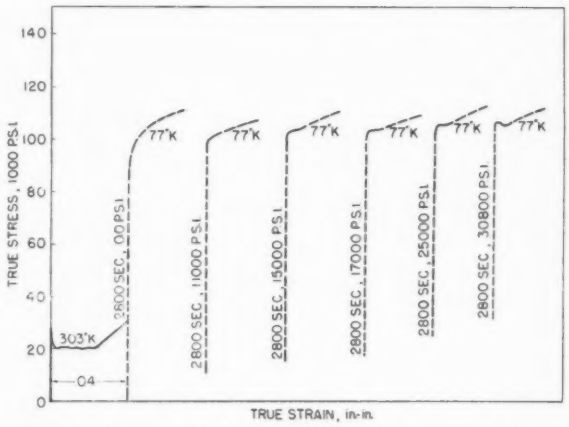


FIG. 2. Stress–strain curves obtained at 77°K after strain aging for 2800 sec at 303°K at various aging stresses 0–30,000 lb/in².

stress at a constant aging time and finally approached the yield point of the material at the critical aging stress.

4. DISCUSSION

According to Cottrell and Bilby[2] carbon and nitrogen atoms form an atmosphere around dislocations and increase the resistance to motion of the dislocations. The dimensionless applied stress, $\bar{X}$ versus the dimensionless displacement of the dislocation $\bar{Y}$ in their theory is shown by the curve denoted by $C = \infty$ in Fig. 3. The consequence of the maximum in the $\bar{X} \sim \bar{Y}$ curve is the attainment of a yield point at $\bar{X} = 0.66$. Thermal energy can assist yielding, in that a part of an infinitely long dislocation can move under a thermal fluctuation and exceed the maximum point even though $\bar{X} \leq 0.66$. The Cottrell–Bilby theory requires some modification in order to be applicable to the present observations that a yield point is observed under conditions of high thermal energy fluctuation but is not observed when the contribution of thermal energy to yielding is quite small.

Utilizing the model proposed by Cottrell and Bilby, Fig. 4, assume that the dislocations are pinned by obstacles at A and B and that the average distance AB of the dislocation is subsequently maintained at the state ADB, (Fig. 4) by the aging stress σ_0. During the aging treatment at 303°K carbon atoms diffused to ADB and pinned the dislocation at this position. When the applied stress is increased, the dislocation moves, leaving the carbon atmosphere. Since the dislocation is bent, the line tension affects the interaction between the dislocation and carbon atoms. When the strength of the line tension is large or the aging time is short, the interaction between the solute atoms and the dislocation will be minimized

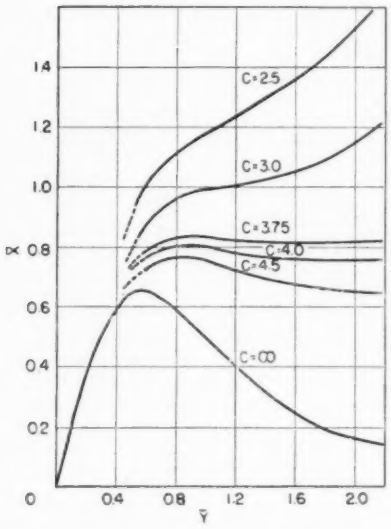


FIG. 3. The family of curves for the dimensionless applied stress $\bar{X}$ versus the dimensionless displacement of the dislocation $\bar{Y}$ with a parameter $C = (2L^2AK/T\rho^3)^{1/2}$, where $2L$ is the distance between pinning points, K number of solute atoms per unit length of the dislocation, T the line tension, A the interaction coefficient between solute atoms and the dislocation and ρ the initial distance between the solute atom and the dislocation.

and the maximum of the stress-displacement curves will disappear. The calculations presented in the next section lead to the family of curves shown in Fig. 3 as the relation between the dimensionless applied stress $\bar{X}$ and the displacement $\bar{Y}$ of the midpoint D of the dislocation.

The portion of the dislocation ACB, Fig. 4, is assumed to be straight in the unloaded state after the plastic strain of 0.04. The origin of coordinates is taken to be A with the x,y coordinate axis parallel and normal to ACB, respectively. Under the action of the aging stress, σ_0, the dislocation is bowed into the form ADB with the new position of the dislocation described by $y_0(x)$. The solute atoms migrate to the

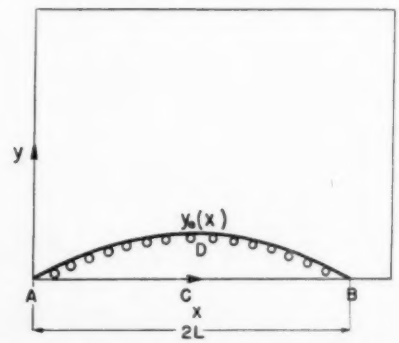


FIG. 4. Configuration of the movable part of a pinned dislocation.

curve $y_0(x)$ of the dislocation during aging, and it is assumed that the density of solute along the dislocation is not uniform. When the stress is increased, the "break away" of the dislocation from the solute atmosphere will occur in that region with the lowest density of carbon atoms, i.e. ADB.[3] The displacement of the dislocation is described in terms of $y(x)$. The increase in potential energy of the dislocation due to the displacement y is

$$E_0 = \int_0^{2L} \tfrac{1}{2}(y')^2 T\, dx,$$

where T is the line tension of the dislocation and y' the first derivative of y with respect to x. T is assumed to be independent of x and $y' \ll 1$.

The work done by the applied stress σ is

$$W = \int_0^{2L} \sigma b y\, dx$$

where b is the Burgers vector.

The interaction energy between the dislocation and the array of solute atoms along ADB is approximately

$$E_{CD} = AK \int_0^{2L} \frac{\rho}{(y - y_0)^2 + \rho^2}\, dx$$

where A is the constant for the interaction between dislocation and the solute atoms, K is the number of solute atoms per unit length along the dislocation, and ρ is the distance between the dislocation ADB in the initial state and the solute atoms. The displacement y of the dislocation by the stress σ is determined by the principle of virtual work of the total energy:

$$\delta(W - E_0 - E_{CD}) = 0. \tag{1}$$

The Euler equation of (1) is

$$\sigma b + y''T - AK\rho \frac{2(y - y_0)}{\{(y - y_0)^2 + \rho^2\}^2} = 0. \tag{2}$$

This equation for equilibrium of the dislocation can be integrated by multiplying each term by $(y' - y_0')$ and noting that

$$-y_0'' = 1/R = \sigma_0 b/T \tag{3}$$

is independent of x, where R is the radius of curvature. Thus,

$$(y - y_0)(\sigma b - \sigma_0 b) + \tfrac{1}{2}T(y' - y_0')^2 + AK\rho/\{(y - y_0)^2 + \rho^2\} = C_1. \tag{4}$$

The integral constant, C_1, is determined from the condition $y'(L) = y_0'(L) = 0$ because of symmetry of y and y_0 with respect to x at the point $y = L$, thus,

$$C_1 = \{y(L) - y_0(L)\}(\sigma b - \sigma_0 b) + AK\rho/[\{y(L) - y_0(L)\}^2 + \rho^2].$$

VOL. 8 1960

The integration of equation (4) gives:

$$x = \sqrt{\frac{T}{2}}\int_0^{Y(x)} \left\{(Y_L - Y)(\sigma b - \sigma_0 b) + AK\rho\left(\frac{1}{Y_L^2 + \rho^2} - \frac{1}{Y^2 + \rho^2}\right)\right\}^{-1/2} dY, \quad (5)$$

where $Y = Y(x) = y(x) - y_0(x)$, $Y_L = Y(L)$, and the integral constant is taken to be zero from the condition $Y(0) = 0$.

In order to obtain a relation between the stress $\sigma - \sigma_0$ and the displacement $y(L) - y_0(L)$ of the midpoint D of the dislocation, let $x = L$ in equation (5), then.

$$C\sqrt{\bar{X}} = \int_0^{\bar{Y}} \left\{(\bar{Y} - r) + \frac{1}{\bar{X}}\left(\frac{1}{\bar{Y}^2 + 1} - \frac{1}{r^2 + 1}\right)\right\}^{-1/2} dr, \quad (6)$$

where

$$C = \{2L^2AK/T\rho^3\}^{1/2},$$
$$\bar{Y} = \{y(L) - y_0(L)\}/\rho = Y_L/\rho$$
$$\bar{X} = (\sigma - \sigma_0)b\rho^2/AK,$$
$$r = \{y(x) - y_0(x)\}/\rho = Y/\rho.$$

The curves $\bar{X}$ versus $\bar{Y}$ have been plotted in Fig. 3 from the results obtained by using an IBM 650 computer to numerically integrate equation (6). The integral has been approximated by the Simpson rule and values of C were taken as 2.5, 3.0, 3.75, 4.0 and 4.5.

In the Cottrell and Bilby theory, ADB is an infinitely long straight dislocation. This is a special case of $C = \infty$ in this paper. In this special case, r in equation (6) approaches $\bar{Y}$ and the denominator of the integral of equation (6) approaches zero, thus,

$$\bar{X} = -\lim_{r \to \bar{Y}} \left(\frac{1}{\bar{Y}^2 + 1} - \frac{1}{r^2 + 1}\right)/(\bar{Y} - r),$$
$$= 2\bar{Y}/(\bar{Y}^2 + 1)^2. \quad (7)$$

This special case can be obtained also directly by taking y'' and y_0 as zero in equation (2). The Cottrel and Bilby formula (7) is shown in Fig. 3 as a curve for $C = \infty$.

It should be noted that the contribution of thermal energy to yielding has been neglected in this formulation, but the introduction of this effect can be carried out in the same way as in the Cottrell and Bilby theory. In this paper the magnitude of T is assumed to depend also on the temperature, though the quantitative relation is not known except that T increases as the temperature decreases.

The shape of the curves is dependent upon the constant

$$C = (2L^2AK/T\rho^3)^{1/2}. \quad (8)$$

The curves with $C < 4$ do not show maximum points. This is interpreted as meaning that dislocation solute interaction for which C is less than 4 will not show a yield point. The curves with $C > 4$ have a maximum point similar to that found in the Cottrell and Bilby theory and the larger the value of C the more pronounced the maximum of the curve, and thus the material can be expected to show a sharp yield point. The proposed modification of the Cottrell–Bilby theory predicts that the critical yield point, i.e. the upper yield equal the lower yield point, should occur when C equals 4.

It is interesting to check the critical value $C = 4$ by the following physical constants used by Cottrell and Bilby[2]

$$A = 3 \times 10^{-21} \text{ dyn/cm}^2,$$

the saturated value of $K = 1/b = (1/3) \times 10^8$ cm^{-1},

$$\rho = 2 \times 10^{-8} \text{ cm},$$
$$T = 3 \text{ eV per atomic plane.}$$

We find $L^2 = 100b^2$ in order to obtain $C = 4$.

Thomas and Leak[4] reported the saturated number of solute atoms (carbon or nitrogen) is 9.4 ~ 15.6 per atomic plane, Dahl and Lücke[5] 45 ~ 118 per atomic plane and Harper[6] 6 ~ 13 per atomic plane. These values of K result in rather small values of $L(L^2 = 10b^2)$.

The low values of L are at least an order of magnitude less than the accepted value of the length of a Frank–Read source. It would appear that the discrepancy in the length of the source could result from either the influence of the prior plastic deformation on the source length or the interpretation placed upon the solute atmosphere density parameter, K. Plastic deformation could influence the active source length in that the multiple slip process in iron could lead to an increase in the density of the forest dislocations as well as those on the initially active system. The idea that the yielding phenomenon in iron is not due entirely to a solute atmosphere is not a new one.[7–9] There is substantial evidence that can be interpreted as indicating the presence of a precipitate along the dislocation as well as the presence of a solute atmosphere.[7–9] The observation of the effect of the aging time on the 77°K yielding can be rationalized in terms of a precipitation process that first involves the formation of a solute atmosphere around the dislocations, the solute atmosphere in turn gives way to a precipitate that forms at the longer aging times. In either case, the increase in forest dislocations or the formation of a precipitate along the dislocation, the initially active

length of the dislocation would be reduced. The initially active length of the dislocation is of course only a part of a Frank–Read source.[3]

The experimental observation depicted in Fig. 1 can be explained as follows. As the temperature in the tension tests is decreased, the strength of the line tension T is increased, partly because the width of the dislocation is smaller at low temperatures than at the higher temperatures. The line tension of the dislocation increases with a decrease of the width of the dislocation, according to Nabarro[10] or Fig. 6. Thus, since C decreases with an increase in T, in equation (8) and the $\bar{X} \sim \bar{Y}$ curve does not have a maximum for values of C less than 4, the specimen should not show a sharp yield point at the low temperatures. However, since C is also a function of K, the density of solute atoms per unit length along the dislocation, a yield point will be realized at the low temperatures provided K is increased. Since the solute atoms arrive at the dislocation by a diffusion process, the density of solute atoms at the dislocation K is time dependent[2–6] of the form:

$$K \propto t^{2/3}. \tag{9}$$

At a constant aging temperature the density of solute atoms at the dislocations increases with aging time and for sufficiently large aging times C is greater than 4 and thus a sharp yield point occurs at the larger aging time.

The experimental observations shown in Fig. 2—that under a constant aging time, the elastic limit of the material increased with the aging stress and finally approached the yield point of the material at the critical aging stress, and the yield point became sharper with increasing aging stress—can be explained as follows: Schoeck and Seeger's[11] calculation of the increase of elastic energy, ΔE, of a dislocation of width θ which was displaced from a straight line to a semi-circle of radius R is shown in Fig. 5. The line tension, T, is obtained from Fig. 5 by taking the slope of the curve, i.e. $T = d(\Delta E)/d(\pi R)$, and as shown in Fig. 6, T increases with R. The curvature of the dislocation during aging is proportional to the aging stress, thus,

$$1/R \propto \sigma_0, \tag{10}$$

and as σ_0 increases, R decreases and therefore T also decreases. Thus an increase in σ_0 results in a larger value of C and consequently a sharper yield point as experimentally observed in Fig. 2. Since the width of the dislocation, θ, decreases with decreasing temperature, the value of T increases with decreasing temperature as previously mentioned in the discussion.

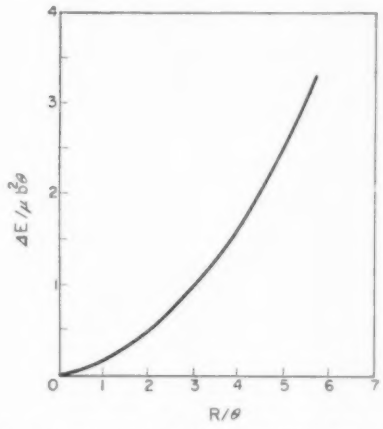


FIG. 5. The increase of elastic energy ΔE, of a dislocation with a width θ, which was displaced to a semi-circle of radius R from a straight line, where μ is the shear modulus of the material.

If the critical yielding occurs at a constant value of C, there should be a relation between the aging time and the aging stress for the occurrence of a yield point at 77°K. We cannot obtain the exact form of this relation since the dependency of the line tension on the aging stress and temperature has no explicit form. However, it is possible to obtain an approximate relation which can be used to summarize the qualitative check of the theory with the experimental observation. It should be noted that the technique used to obtain the relation is based upon the assumptions that were discussed with reference to equations (9) and (10) and Fig. 6.

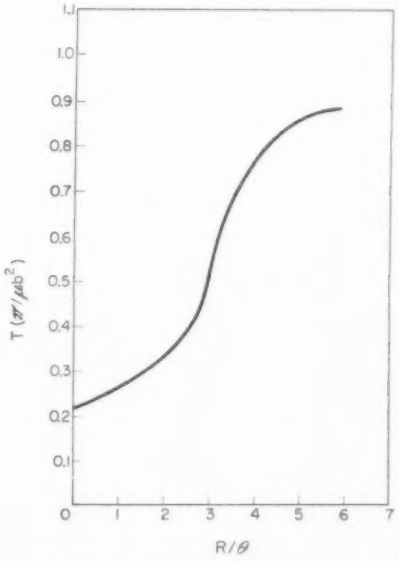


FIG. 6. The line tension T of a semi-circle dislocation of a radius R.

VOL. 8 1960

The yielding parameter C is taken as a function of t and σ_0 by means of equations (8), (9), (10) and Fig. 6 for a given testing temperature. The assumptions that the experimental observation of Fig. 1(d) represents the critical yield point, $t = 2800$ sec and $\sigma_0 = 15000$ lb/in^2, and that the density of solute atoms at the dislocation $K = 1/b$ resulted in a proportionality constant of 1.7×10^5 cm^{-1} sec$^{-2/3}$ in equation (9). Thus, the expression for the yielding criteria $C = 4$ becomes

$$t^{2/3}/T = 1.4 \times 10^6 \text{ sec}^{2/3}/\text{dyn}. \qquad (11)$$

The values of L, A, b and ρ are the same as previously used. By taking $T = 3$ eV per atomic plane under the aging stress of $\sigma_0 = 15000$ lb/in^2, the corresponding value of $R/\theta = 3.5$ is obtained from Fig. 6 and equation (10) becomes

$$\sigma_0 = 52500 \text{ lb/in}^2/R/\theta. \qquad (12)$$

Fig. 6 used in conjunction with equation (12) enables us to evaluate T as a function of σ_0 in equation (11), and the relation between t and σ_0 under the condition $C = 4$ is shown in Fig. 7 by a solid line.

There is of course some uncertainty in the selection of a critical yield point as defined in this paper. Thus if the aging parameter of $t = 2000$ sec and $\sigma_0 = 15000$ lb/in^2 are used as the critical yield point in the determination of the proportionality constant of equation (9), the lower dashed curve is obtained. The results shown in Fig. 7 are supported by the experimental data. In agreement with the theory those specimens which had aging stress and aging time coordinates above the band had a yield point, while the loci of aging times and stresses below the band did not have a yield point. The intensity of the yield point increased as the aging stress–aging time coordinates for a specimen lie further from the band on the yield point region of the graph.

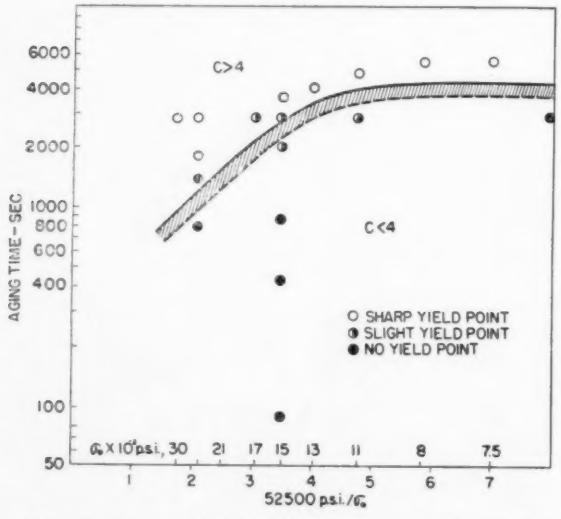


FIG. 7. The cross-hatched band shows the aging times and stresses which resulted in critical yielding.

In the approximations used to obtain the curves shown in Fig. 7 it should be noted that the evaluation of the line tension is uncertain. However, a variation in the value of the line tension results in a change of the curve with respect to the abscissa thus leaving the form of the curve unchanged. We conclude then that the qualitative aspects of the mathematical treatment are in reasonable agreement with the experimental observations.

5. CONCLUSION

The dislocation theory of the yield point phenomena in iron and steel is based upon the concept of the presence of an atmosphere along the dislocations. It has been found that under certain conditions a yield point is not found even though an atmosphere exists. Thus, we conclude that while the presence of an atmosphere for a yield point may be a necessary condition for the existence of a yield point it is not a sufficient condition. The dislocation line tension and solute atmosphere density along the dislocation are factors that also influence the yielding of ingot iron.

REFERENCES

1. S. BRONISZ and J. O. BRITTAIN, *Trans. Amer. Inst. Min. (Metall.) Engrs.*, **218,** 289 (1960).
2. A. H. COTTRELL and B. A. BILBY, *Proc. Phys. Soc., Lond.* **A62,** 49 (1949).
3. P. GIBBS, U.S. Armed Services Technical Information Agency No. 137462.
4. W. R. THOMAS and G. M. LEAK, *J. Iron St. Inst.*, **180,** 155 (1955).
5. W. DAHL and K. LÜCKE, *Arch. Eisenhüttenw.* **25,** 241 (1954).
6. S. HARPER, *Phys. Rev.* **83,** 709 (1951).
7. B. B. HUNDY, *Metallurgia Manchr.* **53,** 203 (1956).
8. *Discussion on Strain Aging, J. Iron St. Inst.*, **184,** 64 (1957).
9. R. H. DOREMUS, *Acta Met.* **6,** 674 (1958).
10. F. R. N. NABARRO, *Proc. Phys. Soc., Lond.* **59,** 256 (1947).
11. G. SCHOECK and A. SEEGER, *Rep. Bristol Conf. on Defects in Crystalline Solids*, p. 340. Physical Society, London (1955).

DISPERSION HARDENING*

W. H. MEIKLEJOHN† and R. E. SKODA†

The increase in yield strength of solid mercury due to dispersed iron particles is experimentally determined to be proportional to $d/(\Lambda - d)$[1] and therefore a function only of d/Λ, where d is the particle diameter and Λ is the spacing between centers of the particles. Since d/Λ is proportional to $f^{1/2}$, where f is the volume fraction of precipitate, these results show that the yield strength is a function only of the volume fraction of precipitate. In the case of coherent particles, the stressed region through which dislocations will not pass must be included. An investigation of the temperature dependence of the yield strength shows that the increase in yield strength at any absolute temperature T is proportional to $d(T_m - T)/(\Lambda - d)$, where T_m is the melting point of the mercury matrix.

The decrease in yield strength of overaged precipitation hardened systems is attributed to a loss in coherency between the matrix and precipitate and not to an increase in spacing between particles.

DURCISSEMENT DE DISPERSION

L'accroissement de la résistance à la rupture du mercure solide dû à la présence de particules de fer dispersées, a été déterminée expérimentalement. Il est proportionnel à : $d/(\Lambda - d)$[1] et il est uniquement fonction de d/Λ, où d est le diamètre de la particule et Λ la distance entre centres de particules. Puisque d/Λ est proportionnel à $f^{1/2}$ où f est la fraction de précipité exprimée en volume, ces résultats montrent que la résistance est fonction uniquement de la fraction volumétrique de précipités.

Dans le cas de particules cohérentes, la région sous tension, qui ne peut pas être traversée par les dislocations, doit être inclue. Une étude de l'effet de la température sur la résistance à la rupture montre que l'accroissement de celui-ci est proportionnel à $d(T_m - T)/(\Lambda - d)$, où T_m est la température de fusion du mercure et T une temperature absolue quelconque.

Les auteurs attribuent la diminution de résistance des systèmes survieillis, à une diminution de cohérence entre la matrice et le précipité, et non à un accroissement de la distance entre particules.

DISPERSIONSAUSHÄRTUNG

Die Zunahme der Fließspannung von festem Quecksilber, die von feinverteilten Eisenteilchen herrührt, ergibt sich experimentell als proportional zu $d/(\Lambda - d)$[1] und ist deshalb nur eine Funktion von d/Λ, wobei d der Teilchendurchmesser und Λ der Abstand zweier Teilchen ist. Da d/Λ proportional zu $f^{1/3}$ ist, wobei f den Volumanteil der Ausscheidung bedeutet, zeigen die Resultate, daß die Fließgrenze nur eine Funktion des Volumanteils der Ausscheidung ist. Im Fall kohärenter Ausscheidungen muß das verspannte Gebiet, durch welches die Versetzung nicht dringt, mit eingeschlossen werden. Eine Untersuchung der Temperaturabhängigkeit der Fließspannung zeigt, daß der Fließspannungszuwachs bei der absoluten Temperatur T proportional zu $d(T_m - T)/(\Lambda - d)$ ist, wobei T_m die Schmelztemperatur der Quecksilbermatrix bedeutet.

Die Abnahme der Fließspannung in überalterten Aushärtungssystemen wird dem Verschwinden der Kohärenz zwischen Matrix und Ausscheidungsteilchen zugeordnet und nicht einer Zunahme des Abstands zwischen den einzelnen Teilchen.

VOL. 8 1960

INTRODUCTION

The theories of dispersion hardening which deal with the yield strength are due to Mott[2,3,5,6], Nabarro[2,4,5,] and Orowan[7]. The theories of Mott and Nabarro deal with a flexible dislocation line moving through a stress field caused by the precipitate particles. They calculate that the yield strength is a function of the volume fraction of solute atoms and the state of dispersion. This prediction is in disagreement with the results of this investigation which show that the yield strength is a function only of the volume fraction of the dispersed phase through which dislocations will not pass.

The theory of Orowan was put forward to explain over-aging in dispersion hardened systems and predicts that the yield strength is proportional to $1/\Lambda$ when $\Lambda > Gb/\sigma_i$ and $\Lambda \gg d$, where Λ is distance between the center of the particles, G is the rigidity modulus, b is the Burgers vector, σ_i is the internal shear stress and d is the diameter of the particles. The prediction is in disagreement with the result of this investigation which shows that $\sigma \simeq d/\Lambda$ for the case of $\Lambda \gg d$ and $\Lambda > Gb/\sigma_i$.

In spite of this disagreement, we wish to emphasize even more strongly that the concept of the flexible dislocation line put forth by Mott and Nabarro and the concept of the "by-passing" of obstacles by dislocation lines with the prediction of $\sigma \alpha 1/\Lambda$ put forth by Orowan were the starting points of this investigation.

* Received December 28, 1959; revised January 29, 1960.

† General Electric Research Laboratory, Schenectady, New York.

The iron mercury system was chosen for this investigation because iron particles can easily be created in mercury by electrodeposition. Iron particles are created in the mercury after the solubility (1 part in 10^6) is reached. The particles can be made as small as 50 Å diameter. These iron particles are very uniform in size and are wet by the mercury. The particles are essentially ellipsoids of axial ratio 1.5–1. They can be grown by heat treatment (100–200°C) to any size up to 1000 Å, and even larger, still maintaining the same shape. Having iron particles of a given diameter in mercury, the spacing between the particles can be varied by merely adding mercury, or removing mercury.

The tensile tests were performed at liquid nitrogen temperature on extruded wire specimens.

PREPARATION OF TENSILE SPECIMENS

As a result of previous work[8] on the magnetic properties of iron amalgams we could prepare mercury containing iron particles of uniform diameter in the size range of 50 Å–1000 Å. The procedure consisted of placing 80 cm³ of pure mercury in a 600 ml beaker with a 0.35 molar ferrous ammonium sulfate solution above the mercury.

An iron anode was suspended in the electrolyte above the mercury and electrical contact was made to the mercury cathode. A current of 3 A (5.6 A/cm²) was passed through the solution while the mercury was being stirred. The plating time was varied to obtain the desired concentration. The cathode efficiency of plating was about 90 per cent. The iron particles obtained from this procedure are about 50 Å diameter and are uniformly dispersed in the mercury.

Let us concern ourselves right now with the preparation of tensile specimens containing these 50 Å diameter particles with various spacings between particles. The mercury obtained from the plating procedure has 50 Å particles of a given spacing between particles that is determined by the amount of iron electrodeposited in the mercury. This 80 cm³ of mercury was then divided into eight batches of 10 cm³ each. Different amounts of mercury were added to four of the batches to increase the spacing between the particles to a predetermined value. The spacing between the particles in the remaining four batches was decreased by holding a beaker containing a 10 cm³ batch in a 20,000 Oe magnetic field and pouring off a predetermined amount of mercury. The magnetic field holds the iron particles while some of the mercury is free to be poured off. Because the iron particles wet the mercury, there is a lot of mercury that cannot be poured off. To decrease further the spacing between the particles it is necessary to force the mercury through a chamois, which will hold back the iron particles.

In order to ensure that the particles are uniformly distributed in the tensile specimen it is necessary to chill cast the mercury containing the iron particles. If this is not done the particles will be pushed ahead of the solid–liquid interface as the mercury solidifies. Moreover, in order to insure a small grain size, compared to the diameter of the test specimen, the chill cast mercury was extruded, as suggested by Guttman[9].

The extrusion die was immersed in liquid nitrogen. This cooled the die to liquid nitrogen temperature and also excluded moisture from the die. One of the batches of mercury containing iron particles was then poured into the die and it solidified very rapidly. The die was then placed in a press and a 0.064-in. diameter wire of mercury containing iron particles was extruded into liquid nitrogen bath. The wire was cut with a pair of wire cutters to the proper length for tensile test as it was being extruded.

HEAT TREATMENT

The particles of iron were grown to a larger diameter than that obtained in the plating procedure by placing the beaker of iron amalgam in an air oven. The oven was constructed to condense the mercury vapor formed during the heat treatment.

The time and temperature of heat treatment to obtain a given particle diameter was determined from the previous work of Meiklejohn[8] and Luborsky[10] on the magnetic properties of iron amalgams. Using the curves of particle diameter vs. time of heat treatment, Fig. 1, Ref. (7), it was possible to select a heat treatment that would give approximately the desired particle diameter. The actual particle diameter was determined in a manner to be described later.

Tensile specimens of the heat treated iron amalgams with various spacings between particles were prepared in the same manner as described for the 50 Å particles.

PARTICLE SIZE AND SPACING

The diameter of the iron particles was determined by magnetic coercive force measurements and by electron microscopy. The coercive force was measured in a manner described in Ref. (7). Using the coercive force and the curve of coercive force vs. particle diameter shown in Fig. 3. Ref. (10), it was possible to determine the iron particle diameter. This method was used to obtain the particle diameters shown in Fig. 7 of this paper.

The particle diameters shown in Figs. 3 and 4 of this

paper were determined by electron microscopy. The mercury containing the iron particles was placed in a "mercury oxifier" which allows oxygen to diffuse to the iron particles and oxidize the surface of the particles. The particles are no longer wet by the mercury and they float to the surface to form a black powder. This powder is collected and prepared in the usual manner for electron microscopy. An electron micrograph of 115 Å particles is shown in Fig. 5 of Ref. (8). It should be emphasized that this dispersion of particles is not that of the particles in the mercury. Work is in progress to replicate the surface of the solid mercury to determine the dispersion of the particles, as well as the grain size.

The dispersion of the iron particles in the solid mercury was assumed to be uniform. The spacing between particles was determined by the formula $\Lambda = n^{-1/3}$ where Λ is the spacing between centers of the particles and n is the number of particles per cubic centimeter.

The number of particles per cubic centimeter was determined by the formula $n = 6V_f/\pi d^3 V_t$ where V_f is the volume of iron in the mercury, d is the diameter of the iron particles and V_t is the total volume of iron and mercury.

From these formulae it is found that

$$\Lambda = 0.82d/f^{1/3} \tag{1}$$

where f is the volume fraction of iron in mercury.

TENSILE TESTING PROCEDURE

The tensile testing equipment is quite similar to that described by Andrade[11]. The horizontal arrangement of the test specimen as shown in Fig. 1 lends itself better to loading the equipment than does a vertical arrangement. The specimen can be easily manipulated while it is under liquid nitrogen. The liquid nitrogen container is styrofoam and an Instron head is mounted on rollers to measure the load. The Instron chart is not shown in Fig. 1. A synchronous motor turns a pulley to apply the load at a constant strain rate of 0.1 in/in/min.

The horizontal guide consists of a rod that has been milled flat along its length on three sides with 120° between flats. Ball bearings push against these flat surfaces to provide a minimum of friction, and yet guide the slide. Resistors are attached near these rollers and are used as heaters to prevent ice from forming on the slide.

The major problem that had to be solved in the testing equipment was the breaking of the specimens at the chucks. The chucks are standard pin vices that are mounted in ball bearings so that the specimen could be rotated. A mesh screen wire was used inside the chucks and this reduced the breaks at the chuck to a small percentage of the total breaks.

YIELD STRENGTH AS A FUNCTION OF Λ AND d

We decided to plot the yield strength against the reciprocal of the particle spacing to determine if the Orowan relation for the yield strength (σ_y), $\sigma_y \alpha 1/\Lambda$ was true for this iron mercury system. We found that we did not get straight lines and shifted to the modified Orowan relation

$$\sigma_y \alpha 1/(\Lambda - d) \tag{2}$$

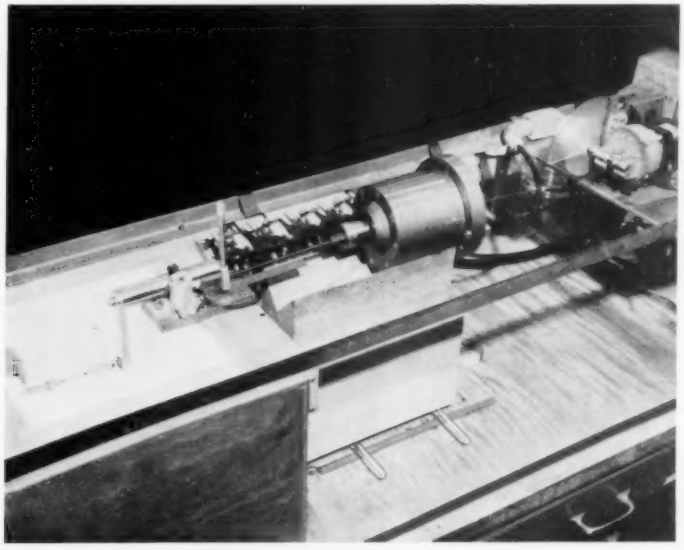


FIG. 1. Apparatus for measuring the yield strength of mercury wires at liquid nitrogen temperature.

VOL. 8 1960

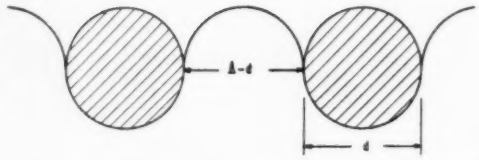


FIG. 2. A dislocation loop passing between particles of diameter d and spacing between centers Λ.

and found that this did hold for a given particle diameter. Fig. 2 shows a dislocation line pinned in the modified Orowan fashion.

The yield strength was taken as the strength at 1/4 per cent strain, and the stress–strain curves were measured at 0.1 in/in/min strain rate. Essentially the same results are obtained if the yield strength is determined at ± 50 per cent of this strain. The effect of strain rate was not investigated.

A plot of the yield strength as a function of $(\Lambda - d)^{-1}$ is shown in Fig. 3 for different particle diameters. It is observed that the results do obey equation (2) for a given particle diameter. The data has also been plotted against $(\Lambda)^{-1}$ and $\overline{(\Lambda - d)}^{-1}$ without obtaining a linear relationship. $\overline{(\Lambda - d)}$ is the mean free path between particles, and is given by $\overline{\Lambda - d} = d(\pi f/6)^{-\frac{1}{2}} - 2/3d$ where Λ is the spacing between centers of particles, d is the particle diameter and f is the volume fraction of precipitate.

The result shown in Fig. 3 is described by the equation

$$\sigma_y - \sigma_0 = f(d)/(\Lambda - d) \tag{3}$$

where σ_y is the yield strength with particles of diameter d and spacing Λ, σ_0 is the yield strength of the mercury matrix, $f(d)$ is the slope of the lines and is a function of the particle diameter.

It was necessary to determine $f(d)$, so the slopes were plotted as a function of the particle diameter as shown

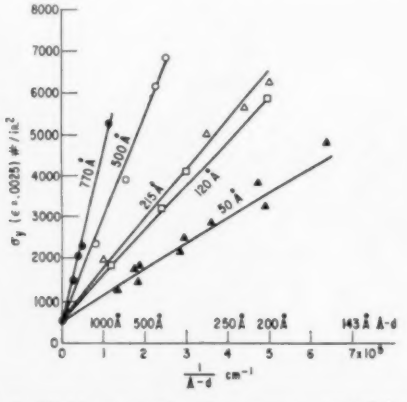


FIG. 3. Yield strength of mercury containing iron particles of the diameter shown plotted against $(\Lambda - d)^{-1}$. Measurements at 77°K.

in Fig. 4. Since this result is described by the relation

$$f(d) = ad \tag{4}$$

where a is a constant we can substitute equation (4) into equation (3) and obtain

$$\sigma_y - \sigma_0 = ad/(\Lambda - d) = \frac{a(d/\Lambda)}{1 - (d/\Lambda)}. \tag{5}$$

Equation (4) tells us that the increase in yield strength due to a dispersed second phase is a function only of d/Λ. The particles can be of any diameter and any spacing and as long as d/Λ is the same value, the yield strength will have the same value.

If we substitute equation (1) into equation (5) we obtain

$$\sigma_y - \sigma_0 = af^{1/3}/(0.82 - f^{1/3}). \tag{6}$$

Now we see that the increase in yield strength due

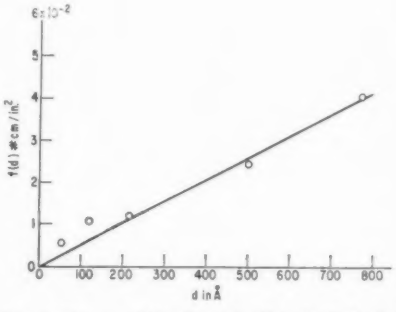


FIG. 4. Slopes of the lines in Fig. 3 plotted as a function of particle diameter.

to a dispersed second phase is a function only of the volume fraction of dispersed phase. Obviously the dispersion must be uniform on a macroscopic scale, i.e. a tensile specimen containing one steel ball would not obey equation (6).

INFLUENCE OF EXTRUSION

The extrusion of the mercury containing iron particles probably results in some work hardening of the material which should be eliminated by an anneal in order to measure only the particle hardening.

We measured the yield strength of material containing 50 Å iron particles in various concentrations, both as extruded and after annealing for 3 hr at 190°K (80 per cent of the melting point) and found a very small difference. The results are shown in Table 1. Only the pure mercury specimen showed an appreciable change due to the anneal. One explanation of these results is that the increase in yield strength due to the extrusion process is very small compared to the effect of the particles.

TABLE 1. The ratio of the yield strength of annealed (80 per cent of melting point) specimens to extruded specimens is shown for various per cent volume fractions of iron particles (50 Å diameter)

f (%)	σ_y annealed / σ_y extruded
0.7	0.95
0.54	1.02
0.10	0.98
0.03	0.98
0.013	0.92
0	0.72

YIELD STRENGTH AND COHERENCY

If a "best fit" straight line had been drawn through the data of Fig. 4, it would not go through the origin. The line was drawn through the origin because we believe that the yield strength of the 50 Å and 120 Å particles are high because of coherency with the matrix.

The lattice spacing of the (100) face of iron is 2.861 and the lattice spacing of the (100) face of the mercury is 2.999. This is a 5 per cent difference which is a little greater than one would like in order to predict coherency. The rhombohedral cell of the mercury has an angle of 98°15′. Although the lattice parameters are not as close as one would like in order to predict coherency, they certainly are not so different as to preclude coherency.

X-ray diffraction experiments have not elucidated the problem. An indirect approach was taken to investigate the idea of coherency in the 50 Å and 120 Å particle sizes. The reasoning proceeds as follows. If the yield strength is a function only of the volume fraction of precipitate, then a batch of material of a given volume fraction of iron should have a yield strength vs. particle diameter curve as shown in Fig. 5. An important point to be established is that, as coherent particles grow in diameter, the coherent region increases in such a manner that if the volume fraction of iron remains constant the volume fraction of coherent region plus iron remains constant, although greater in value.

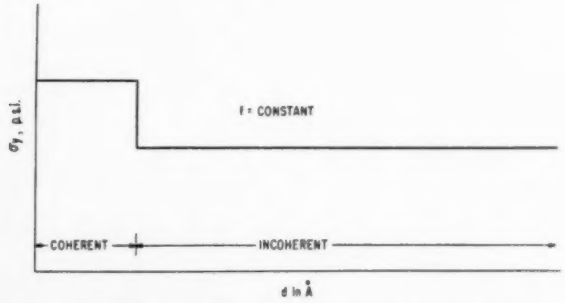


FIG. 5. Predicted behavior of the yield strength as a function of particle diameter for a constant volume fraction of particles.

Consider a particle of radius r_0 as shown in Fig. 6. From elasticity theory $\varepsilon = \varepsilon_0(r_0/r)^3$ where ε is the strain, ε_0 is the strain at the surface and r_0 is the radius vector. This relationship is shown in Fig. 6 and for convenience the curve is shown in relation to the particle. Also we may write $\sigma = G\varepsilon = G\varepsilon_0(r_0/r)^3$ where G is the shear modulus. Now if the dislocation moves toward the particle until it reaches a stress region σ_0 which it cannot pass through, then the effective particle diameter is r_1. So we have $\sigma_0 = G\varepsilon_0(r_0/r_1)^3$. Now we wish to show that the ratio of the volume of the iron particle to the volume of region

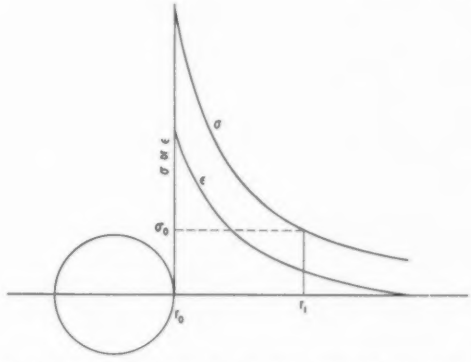


FIG. 6. Stress and strain in the matrix around a coherent particle of radius r_0.

through which the dislocation will not pass is independent of the particle diameter.

$$\frac{4/3\ \pi r_0^3}{4/3\ \pi r_1^3} = \frac{\sigma_0}{G\varepsilon_0} = \frac{f'}{f}$$

where f' is the volume fraction of coherent volume plus particle volume and f is the volume fraction of particles. Since σ_0, G and ε_0 are constants then f'/f remains constant as the particles grow.

Such an experiment was performed on a given volume of iron and mercury prepared by T. O. Paine to have a very uniform particle diameter. The material was tested, heat treated to a larger particle diameter and tested, re-heat treated and tested many times.

The results of this experiment are shown in Fig. 7. Although we established the behavior predicted in Fig. 5, we also found a peculiar behavior below 50 Å diameter (25 Å particle radius). The loss of coherency appears over a very narrow region of 100–125 Å particle diameter. The fact that it is not an abrupt drop may be due to a slight spread in particle diameters or a statistical distribution of coherent and incoherent particles for a given particle diameter.

VOL. 8 1960

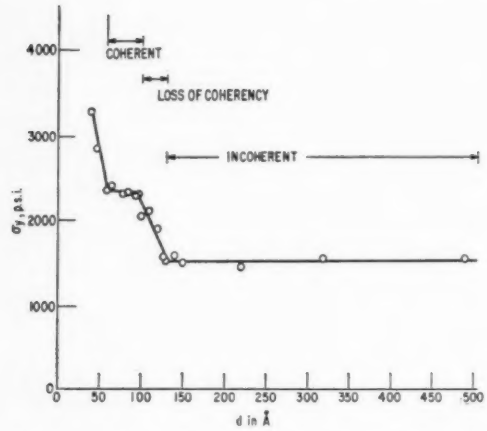


FIG. 7. Yield strength of mercury containing iron particles as a function of particle diameter with a constant volume fraction of particles. Measurements at 77°K.

Although these results do not establish coherency in the range of 50–125 Å particle diameters, the results are certainly consistent with this point of view. In fact one can determine that the effective particle diameter has a reasonable value. Assuming an effective volume fraction f' in the coherent region and a volume fraction f in the incoherent region we have $\frac{\sigma'}{\sigma} = \frac{(0.82 - f^{1/3})}{(0.82 - f'^{1/3})}\left(\frac{f'}{f}\right)^{1/3}$ where σ' and σ are the yield strengths in the coherent region and incoherent regions, respectively. Using equation (6) and the data of Fig. 7 one obtains $d' = 1.5d$ where d' is the effective diameter in the coherent region and d is the actual particle diameter. Hence, the thickness of the highly stressed shell around the 50 Å particle is 12 Å and around the 100 Å particle is 25 Å. These are reasonable values.

The reason for the increase in yield strength below the 50 Å particle diameter is still being investigated.

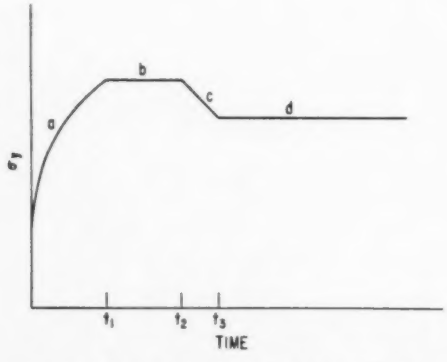


FIG. 8. Predicted behavior of yield strength as a function of time of heat treatment for a precipitation hardened alloy.

PRECIPITATION HARDENING

Equation (6) describes the yield strength as a function of the volume fraction of dispersed phase through which dislocations will not pass.

The application of this equation to a precipitation hardened system predicts a curve for the yield strength as a function of time as shown in Fig. 8. Section a of the curve represents precipitation of a coherent second phase at a constant rate until it is all precipitated at time t_1, then the yield strength remains constant as in section b until time t_2. Section c represents loss of strength due to loss of coherency which occurs over a period of time due to a particle size distribution. At time t_3 all the second phase is incoherent and the yield strength remains constant as in section d. The curve will tend to be smoothed out if there is a large particle size distribution or if the precipitation does not occur at a constant rate.

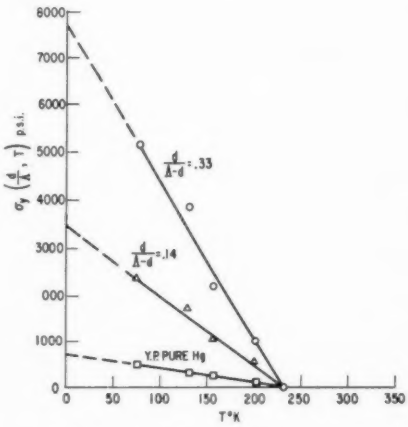


FIG. 9. Yield strength of mercury containing iron particles as a function of temperature for specific values of $d/(\Lambda - d)$. Measurements at 77°K.

TEMPERATURE DEPENDENCE OF THE YIELD STRENGTH

The temperature dependence of the yield strength for a given value of d/Λ was investigated with the result shown in Fig. 9. These results are expressed by the equation

$$\sigma_y(d/\Lambda, T) = F(d/\Lambda)(T_M - T) \qquad (7)$$

where $\sigma_y(d/\Lambda, T)$ is the yield strength of iron particles in mercury of diameter d and spacing Λ measured at a temperature T. $F(d/\Lambda)$ is the slope of the lines in Fig. 9 which is a function of d/Λ. T_M is the melting point of the mercury matrix.

To determine $F(d/\Lambda)$ the slopes were plotted as a

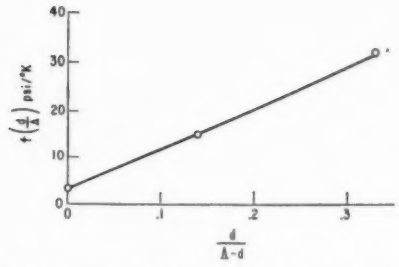


FIG. 10. Slopes of the lines of Fig. 9 plotted against $d/(\Lambda - d)$.

function of $d/(\Lambda - d)$ as shown in Fig. 10. This data is expressed by

$$F(d/\Lambda) = F(0) + bd/(\Lambda - d) \tag{8}$$

where $F(0)$ is the slope of line for pure mercury.

Combining equations (7) and (8)

$$\sigma_y(d/\Lambda, T) = F(0)(T_M - T) + \frac{bd}{\Lambda - d}(T_M - T) \tag{9}$$

but it is obvious from equation (7) that

$$F(0)(T_M - T) = \sigma_y(0, T) \tag{10}$$

so we may write

$$\frac{\sigma_y(d/\Lambda, T) - \sigma_y(0, T)}{T_M - T} = \frac{bd}{\Lambda - d}. \tag{11}$$

Substituting equation (1) into this equation we obtain

$$\frac{\sigma_y(f, T) - \sigma_y(0, T)}{T_M - T} = \frac{b f^{1/3}}{0.82 - f^{1/3}}. \tag{12}$$

Equation (12) describes the dispersion strengthening of the iron mercury system as a function of temperature and the volume fraction of precipitate. This equation was used to describe the data shown in Fig. 11. The data on the "coherent" 50 Å and 120 Å particles has been omitted because the volume fraction of particle plus coherent region cannot be determined. The data agree with equation (12).

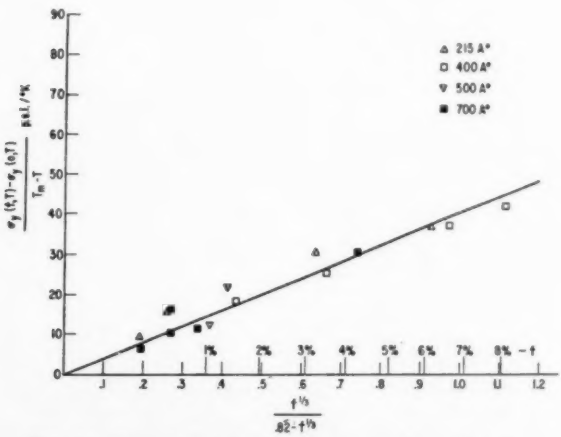


FIG. 11. Experimental data compared with the predictions of equation (12).

BEHAVIOR AT HIGHER VOLUME FRACTIONS

The data shown in Fig. 11 were extended to higher volume fractions of iron and the results are plotted in Fig. 12. The yield strength becomes independent of the volume fraction at a stress of 7000 lb/in^2 and 8 per cent volume fraction. This break in the curve is believed to be due to reaching a stress at which other slip planes become active. At this stress, cross-slip occurs and the dislocation loops climb over the particle.

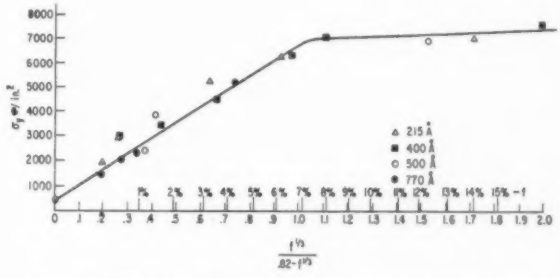


FIG. 12. Yield strength of mercury containing iron particles.

LIMITING YIELD STRESS

The yield stress for iron particles in mercury reaches a maximum value as shown in Fig. 12 and remains constant as the spacing between particles is decreased. There are two possible reasons for this behavior. One is that at this maximum stress of 7000 lb/in^2 cross-slip takes place, and the dislocation loops climb over the particles instead of leaving a dislocation loop around the particles as in the Orowan mechanism.

Another explanation of the behavior would be that the dislocations pass through the particles at this stress level. A rough calculation of the stress due to a pile-up of the dislocations gives a value of 10^5 lb/in^2 which is greater than the yield strength of iron of usual dislocation content. However, since these particles are small, there is the chance that they are free of dislocations and this stress would not be sufficient to shear the particles.

Which process is operative in this mercury iron system has not been determined.

EXTENSION OF RESULTS TO USEFUL MATERIALS

We believe that the results of our investigation of the iron mercury system are directly applicable to

VOL. 8 1960

other materials that derive their properties, or change in properties with heat treatment, solely from a dispersed phase. An additional requirement is that the dispersed phase must be infinitely strong compared to the matrix so that the dislocations will not shear the particles.

Equations (5) and (6) are directly applicable to these materials and even equation (12) may apply in many cases. Since it is extremely difficult to measure the particle diameter and spacing in useful materials, equation (6) is better to use for a comparison. Even here there is some difficulty, because one must determine the actual volume fraction of dispersed phase and know that it is incoherent with the lattice, or know the volume fraction of particles plus coherent region. We believe that in most cases, the iron mercury system being an exception, the amount of dispersed phase cannot be determined from chemistry and a phase diagram. We believe that the determination of the volume fraction of dispersed phase by electron microscopy is much more reliable.

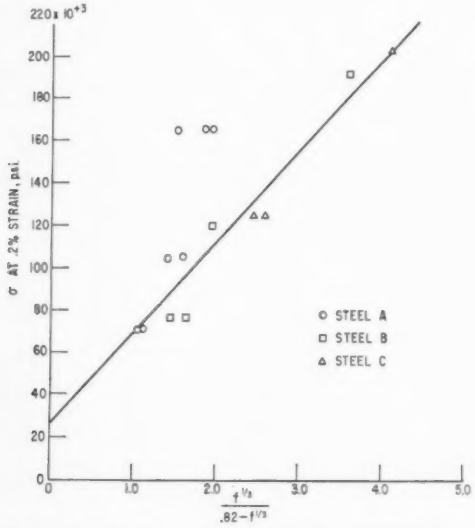


FIG. 13. Data of Turkalo and Low compared with the predictions of equation (12).

Figure 13 shows a comparison of equation (16) and the room temperature data of Turkalo and Low[12] on the yield strength of steels. The volume fraction of precipitate was determined by electron microscopy and therefore should compare favorably with equation (6). The data on one steel departs considerably from the curve and we have no explanation for this behavior. The extrapolated value of the yield strength for pure iron is in good agreement with actual data.

ACKNOWLEDGMENTS

We would like to thank L. Guttman for suggesting the extrusion of the test samples and T. O. Paine for the preparation of a uniform dispersion of 20 Å iron particles in mercury. Very helpful discussions were held with J. R. Low, Jr.

REFERENCES

1. W. H. MEIKLEJOHN and R. E. SKODA, *Acta Met.* **7,** 675 (1959).
2. N. F. MOTT and F. R. N. NABARRO, *Proc. Phys. Soc., Lond.* **52,** 86 (1940).
3. N. F. MOTT, *J. Inst. Met.* **62,** 367 (1946).
4. F. R. N. NABARRO, *Proc. Phys. Soc. Lond.* **58,** 669 (1946).
5. N. F. MOTT and F. R. N. NABARRO, *Rep. Conf. on Strength of Solids* p. 1. Physical Society, London (1948).
6. N. F. MOTT in *Imperfections in nearly Perfect Crystals* (Edited by SHOCKLEY *et al.*) p. 173. Wiley, New York (1952).
7. E. OROWAN, *Symposium on Internal Stresses in Metals and Alloys*, p. 451. Institute of Metals, London (1948).
8. W. H. MEIKLEJOHN, *Rev. Mod. Phys.* **25,** 302 (1953).
9. Private communication.
10. F. E. LUBORSKY, *J. Phys. Chem.* **61,** 1936 (1957).
11. E. N. DA C. ANDRADE, *Proc. Roy. Soc.* A**148,** 120 (1935).
12. A. TURKALO and J. R. LOW, JR., *Trans. Amer. Inst. Min. (Metall.) Engrs.* **212,** 750 (1958).

A THEORY OF DIFFUSION OF IMPURITIES IN PURE SILVER*

J. M. TOBIN†

A new ionic model for the determination of H and D by the method used by Lazarus has been used to obtain values for period V elements in silver with an improved agreement between calculated and observed values.

With the same model, the difference in ion core size and effective nuclear charge in periods IV and VI was used to calculate values of H and D. The agreement for the activation energy values is within 3 per cent except for the element gold. The observed lower values of activation energies for periods IV and VI than for corresponding elements in period V is explained to be a result of their effects on the repulsive potentials.

THEORIE DE LA DIFFUSION DES IMPURETES DANS L'ARGENT PUR

L'auteur utilise un nouveau modèle ionique pourla détermination de H et de D par la méthode de Lazarus. Il obtient des valeurs pour les éléments de la période V qui conduisent à un meilleur accord entre les valeurs calculées et expérimentales. En utilisant le même modèle, l'auteur a calculé également les valeurs de H et D en utilisant la différence de dimensions du noyau ionique et la charge nucléaire effective des éléments des périodes IV et VI. Sauf pour l'or, l'erreur dans la détermination des valeurs de l'énergie d'activation, est inférieure à 3%.

On explique que les faibles valeurs observées pour les énergies d'activation des éléments des périodes IV et VI par rapport aux éléments correspondant de la période V, résultent d'effets sur les potentiels répulsifs.

THEORIE DER DIFFUSION VON VERUNREINIGUNGEN IN REINEM SILBER

Für die Bestimmung von H und D nach der Methode von Lazarus wurde ein neues Ionenmodell benutzt. Damit wurden Werte für Elemente der Periode V in Silber bestimmt, es ergab sich verbesserte Übereinstimmung zwischen berechneten und beobachteten Werten.

Mit demselben Modell wurden Werte von H und D für Elemente der Perioden IV und VI auf Grund der Unterschiede der Größe der Ionenschalen und der effektiven Kernladung berechnet. Abgesehen von Gold stimmen die Werte der Aktivierungsenergie innerhalb 3% überein. Daß man für Elemente der Perioden IV und VI geringere Werte der Aktivierungsenergie beobachtet als für die entsprechenden Elemente der Periode V, wird als Ergebnis ihrer Wirkung auf die Abstoßungspotentiale erklärt.

VOL. 8 1960

INTRODUCTION

The recent use of radioisotopes in the study of diffusion has made it possible to obtain more accurate diffusion coefficient measurements. Much of this gain in accuracy is attributed to the high specific activity of the isotopes and the improved sensitivity of analysis of the concentration of the impurity atoms diffusing in pure solvent metals. It is now possible to interpret the data to find regular relationships indicating the mechanisms involved in impurity diffusion.

An important step towards an understanding of the diffusion of impurities in metals was made by Lazarus[1]. He showed a correlation between the frequency factor, D_0, and the activation energy, H, in the equation

$$D = D_0 \exp -(H/RT) \qquad (1)$$

which expresses the usual temperature dependence of a diffusion coefficient, D, when T is the absolute temperature and R is the gas constant. He also developed equations for calculation of the activation energy and frequency factor by comparison with the corresponding values for silver self-diffusion. The theory is successful in explaining the measured values of D_0 and H for cadmium, indium, and tin[2] and antimony[3] as impurities in pure silver. The calculation is based on the electrostatic repulsion between silver and impurity ions, and the effect of this repulsion on the microscopic elastic moduli.

The success of the theory is limited thus far to a few impurity elements in period V because it deals primarily with the screened nuclear charge and does not account for the chemical nature of the impurities, the periodic variation in their chemical nature, nor the difference in effective nuclear charge between chemical periods. Improvements in the theory, as suggested by Lazarus, deal with the interaction energy between the screened solute atom and a vacancy, as shown by Alfred and March[4], or with the size of the impurity ion.

A new model of the impurity ion in silver has been found which accounts for variations in the electronic configuration of the impurity ions, their effect on the electrostatic repulsion potential and the size of the ion

* Received December 30, 1959.
† General Atomic, San Diego, California.

cores. Using this model, the Lazarus theory has been extended successfully to elements in periods IV and VI, including the recent data on diffusion of krypton[5] and xenon[6] in silver.

THEORY AND RESULTS

(1) *Model of impurity ion in silver*

For many years, the mobility of impurity atoms diffusing through a metal was compared with the size of the atom. In particular, the activation energy, H, was thought to be proportional to the Goldschmidt *atomic* radius, where the atoms larger than solvent metal atoms are more mobile than atoms which are smaller. The large atom was said to be easily rejected from a lattice site because of its misfit, or its elastic strain energy. The available data for the diffusion of thirteen impurity elements in silver do not follow this relationship, as indicated in Fig. 1. In fact, both large and small atoms diffuse in silver with low activation energies.

One model of an impurity atom present in a monovalent metal was suggested by Jones[7]. He assumed that the impurity atom releases its valence electrons to the monovalent metal lattice upon solution. Then the dissolved ion has extra positive charges, Q, equal to the difference in valence. This model was used by Lazarus, and he called Q the *excess valence*. The impurity ion in this model is *isoelectronic* with the silver ion, Ag^{+1}: that is, it is considered to have the same number of electrons as the pseudo-inert gas ion, Ag^{+1}. The excess valence in this series of isoelectronic ions is the difference in nuclear charge, and therefore

$$Q = Z_{\text{imp}} - Z_{\text{Ag}}. \tag{2}$$

Lazarus used examples of $Q = +4$ for antimony ($Z = 51$) in silver ($Z = 47$), and $Q = -3$ for ruthenium ($Z = 44$). These values of Q are determined by the number of the element in the periodic table.

The application of equation (2) is limited to those elements which can form ions which have the electronic configuration of $1s^2$, $2s^22p^6$, $3s^23p^63d^{10}$, $4s^24p^64d^{10}$ in silver. Elemental palladium (Pd^0), monovalent silver (Ag^{+1}) and divalent cadmium ions (Cd^{+2}) have this electronic configuration. However, a considerable amount of energy is required to form In^{+3}, Sn^{+4} or Sb^{+5}. The chlorides of these elements are primarily *covalent*, rather than ionic, which indicates that the valence electrons are not removed from the atom, but are shared with the chlorine atoms. $InCl_3$, for example, has physical properties similar to $AlCl_3$. The possibility of forming the multivalent ion Xe^{+8} is even more remote.

Therefore, the present model assumes that there is not sufficient energy available by solution in silver to form multivalent ions. Silver, copper and gold will be monovalent in the metal lattice. The rest of the metallic elements will appear to be divalent. The nonmetallic elements will be assumed to be monovalent so that they will be small enough not to strain the lattice.

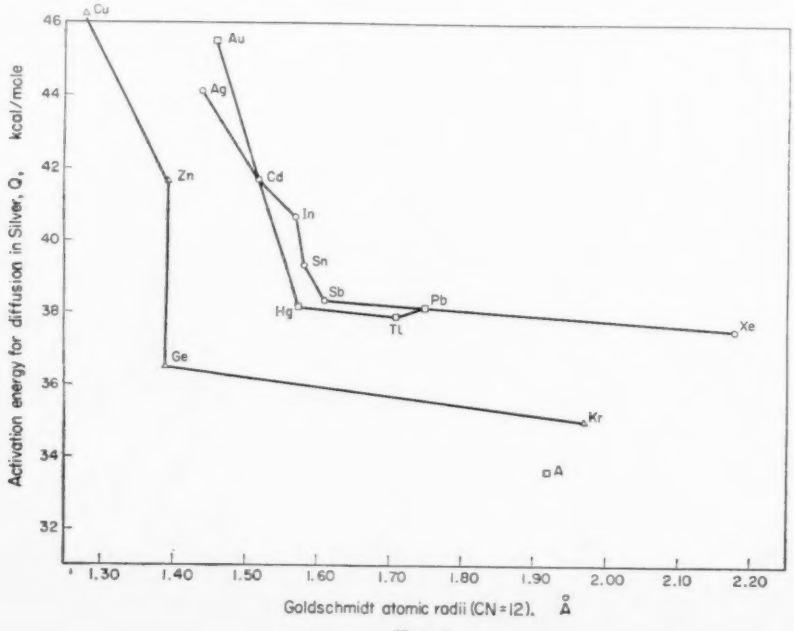


FIG. 1.

Thus, all the elements from copper to krypton, silver to xenon, and gold to radon will be either monovalent or divalent positive ions in silver. The electrostatic repulsion potential for the multivalent ions can be simply related to that for the monovalent or divalent ion models, as shown in the following section.

It is also assumed that there is a simple periodic relationship between the diffusion mobilities of ions having the same electronic configuration, but different principal quantum numbers. The electron density around the $Cu^+(3d^{10})$, $Ag^+(4d^{10})$, and $Au^+(5d^{10})$ ions is spherically symmetrical, according to Unsöld[8]. Using these three ions as basic structures, it is possible to make approximate quantum-mechanical calculation of the forces operating between silver and impurity ions by the methods described by Pauling[9].

(2) *Electrostatic potential around the ions*

According to the laws of electrostatics, the potential, ϕ, around the positively charged nucleus of an atom decreases inversely with distance, r, and directly with the charge, Ze, thus

$$\phi(r) = (Ze)/r \tag{3}$$

where Z is the nuclear charge of the element, and e is the unit of charge. However, the decrease of potential is more rapid than indicated in equation (3) because of the electrons circulating around the nucleus. The charge on the nucleus is said to be screened by the electrons. A part of the nuclear charge is neutralized by the electrons. A screened potential has been given for metals by Mott[7]; thus,

$$\phi = (ze)/r \exp(-qr) \tag{4}$$

where q is a *screening constant*. The value of q was calculated for the silver metal solvent by Mott using a linearized Thomas–Fermi equation, and is numerically equal to $1/0.58$ Å.

The charge z is the ionic charge and is equal to the positive charge on the nucleus minus the number of orbital electrons, ε, or

$$z = Z_{\text{imp}} - \varepsilon. \tag{5}$$

In the Lazarus theory, z was set equal to the excess valence, Q, since the ionic charge is equal to the valence for the multivalent ion model. For the monovalent model, $z = 1$, and for the divalent model, $z = 2$.

The potential energy of a crystal changes with the separation distance between ions. This change can be used to determine the effect of ionic charge and ion core size on the mobility of impurity ions. The potential energy, V, can be written as the sum of the Coulombic and Born repulsive energies and the electronic attractive energy, I.

$$V = Az^2e^2/r + Be^2/r^n - I \tag{6}$$

where A and B are constants and r is the separation distance. The exponent n is the *Born exponent* and can be obtained from compressibility data. A table of values for n is given in Table 1.

The first differential of the potential energy with respect to r, if I is uniform throughout the metal crystal, can be used to determine the effect of ion core size on the diffusion mobility. Thus,

TABLE 1. Values of the Born exponent

Ion type	n
A and Cu^+	9
Kr and Ag^+	10
Xe and Au^+	12

$$\frac{dV}{dr} = -\frac{Az^2e^2}{r^2} - \frac{nBe^2}{r^{n+1}}. \tag{7}$$

At the equilibrium separation distance, the potential is at a minimum, and $dV/dr = 0$, thus

$$r = \frac{-nB^{1/(n-1)}}{Az^2}. \tag{8}$$

The equilibrium separation distance depends upon the ionic charge, z, so that the apparent size of the ion in the metal, if the ion is multivalent ($z = a$) is

$$r = \left(\frac{-nB}{AQ^2}\right)^{1/(n-1)}. \tag{9}$$

And if the ion is monovalent, ($z = 1$),

$$r = \left(\frac{-nB}{A}\right)^{1/(n-1)}. \tag{10}$$

The monovalent ion is larger by the factor $Q^{2/(n-1)}$. When this is applied to the potential function for the multivalent ion model, a new potential is obtained which accounts for the effect of a decrease in size of the monovalent ions on the potential with increasing atomic number in a periodic series of elements:

$$\phi(r) = \frac{Qe}{r} Q^{-2/(n-1)} \exp -(qr) \tag{11}$$

or

$$\phi(r) = \frac{Q^{n-3/n-1}e}{r} \exp -(qr). \tag{12}$$

(3) *Activation energy, H*

(a) *Period V (Non-transition elements).* The activation energy, H, for diffusion of an atom is the sum

VOL. 8 1960

of the energy, E_f, for formation of a vacancy next to the atom and the energy, E_m, for motion of the atom into the vacancy,

$$H = N_0(E_f + E_m) \tag{13}$$

N_0 is Avogadro's number. Since these energy barriers will be temperature dependent, the sum in equation (13) can be written as a Taylor's expansion

$$E_f + E_m = (E_f + E_m)_{T=0} + T\, d(E_f + E_m)/dT + \ldots . \tag{14}$$

where second and higher order terms are neglected, since the observed temperature dependence of D is given by equation (1), and may be written as

$$D = [r_0^2 \nu \exp -\{dN_0(E_f + E_m)/R\, dT\}] \exp -[N_0(E_f + E_m)_{T=0}/RT] \tag{15}$$

where r_0 is the jump distance and ν is the atomic vibration frequency. Thus, D_0 is given by

$$D_0 = r_0^2 \nu \exp -\{dN_0(E_f + E_m)/R\, dT\} \tag{16}$$

and H is given by

$$H = N_0(E_f + E_m)_{T=0}. \tag{17}$$

The increase in the energy of formation of a vacancy near the impurity atom depends upon its repulsive potential as

$$\Delta E_f = -e\phi(r). \tag{18}$$

The increase in the energy for motion of the impurity into the vacancy was determined by Lazarus[1] from microscopic shear moduli in the face-centered cubic lattice to be

$$\Delta E_m = \tfrac{1}{4} e\phi(r)\,[q^2r^2 - 5qr - 5]. \tag{19}$$

So that the activation energy for the impurity atom is given by

$$H(\text{imp}) = -N_0 e\phi(r)[1 - \tfrac{1}{4}(q^2r^2 - 5qr - 5)] + H(\text{solv.}) \tag{20}$$

where r is 2.88 Å. The activation energy for self-diffusion was measured as 44.09 kcal/mole by Tomizuka and Sonder[10] and as 45.5 kcal/mole by Sawatsky and Jaumot[11]. The mean value is

$$H(\text{solv.}) = 44.8 \text{ kcal/mole.}$$

The activation energies for the elements to the right of silver in the periodic table are found from equation (20) using the potential function of equation (12). The calculated values for the monovalent and divalent models are compared to the observed values in Table 2. A comparison is made between the calculated and measured values of activation energy by plotting each against $Q^{n-3/n-1}$, for the assumed monovalent ions, and against $(Q+1)^{n-3/n-1}$ for the divalent in Fig. 2. The straight line gives the calculated values of activation energy and has the slope

$$\Delta H/\Delta(Q^{n-3/n-1}) = 1.84 \text{ kcal/mole}$$

and passes through the observed mean value for silver self-diffusion. The agreement with the observed values is good, for the assumed ionic charges.

(b) *Periods* IV *and* VI (*Non-transition elements*). The activation energies for many period IV and VI elements have been determined experimentally. In a previous article[6] it was pointed out that a periodic relationship exists among the measured values of H(imp). Another observation of theoretical interest is that elements in both period IV and VI diffuse with lower activation energies than the corresponding elements in period V, when present as impurities in silver. It is apparent that an independent consideration of size without allowance for nuclear and ionic charge effects is not sufficient to explain this effect. A combination of the effects is required for the explanation, since the repulsive force is directly proportional to the positive ionic and nuclear charges and inversely proportional to the distance separating the charges.

A simple relationship of the sizes of an isoelectronic

TABLE 2. Activation energies for period V non-transition elements

Element	Z	Monovalent		Divalent		Observed	Ref.
		$Q^{n-3/n-1}$	H(imp)	$(Q+1)^{n-3/n-1}$	H(imp)	H(obs) (kcal/mole)	
Ag	47	0	44.8	1.00	—	44.8	(10, 11)
Cd	48	1.00	(43.0)	1.72	41.6	41.7	(2)
In	49	1.72	(41.6)	2.35	40.5	40.63	(2)
Sn	50	2.35	(40.5)	2.94	39.4	39.3	(2)
Sb	51	2.94	(39.4)	3.50	38.4	38.32	(3)
Te	52	3.50	38.4	4.04	(37.4)	—	
I	53	4.04	37.4	4.54	(36.3)	—	
Xe	54	4.54	36.3	5.04	—	37.5	(6)

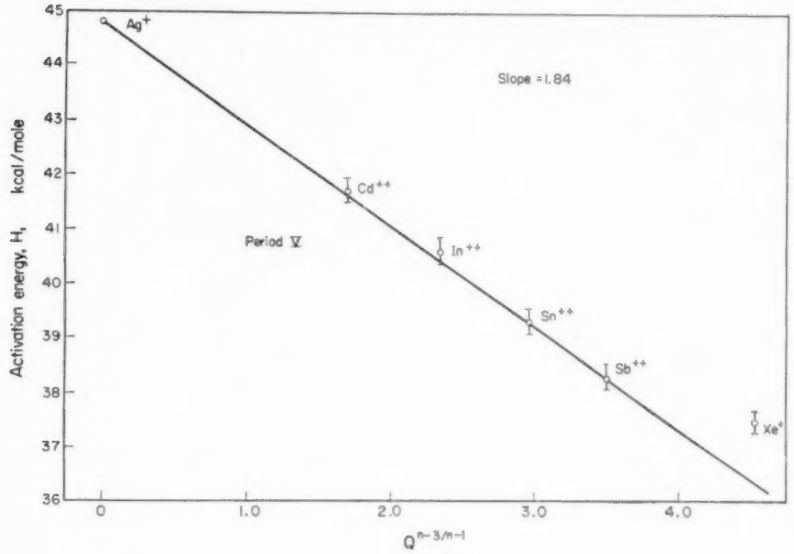


FIG. 2.

series of ions which have a unit ionic charge but increasing effective nuclear charge was given by Pauling[9] as

$$r = \frac{C_n}{Z - S} = \frac{C_n}{Z_{\text{eff}}} \tag{21}$$

where C_n is a constant, and $Z - S$ is the effective nuclear charge ($\equiv Z_{\text{eff}}$). The screening constant, S, was determined by Pauling from mole refraction[12] and X-ray term values.[13] The values for C_n and Z_{eff} are given in Table 3.

TABLE 3. Values for C_n and Z_{eff}

Series	C_n	S	Z_{eff}
Cu^+	10.81	17.4	11.6^+
Ag^+	15.05	35.1	11.9^+
Au^+	22.31	62.7	16.3^+

The size of the ions is directly propotional to C_n. The period IV impurities have lower activation energies because of the relatively smaller size, and period VI impurities have lower activation energies because of the greater effective nuclear charge, Z_{eff}.

If the difference in effective nuclear charge is given as

$$\Delta Z_{\text{eff}} \equiv Z_{\text{eff}}(\text{imp}) - Z_{\text{eff}}(\text{solv.}) \tag{22}$$

then the potential function for periods IV, V and VI is

$$\phi(r) = (\Delta Z_{\text{eff}} + Q)^{n-3/n-1} \frac{C_n(\text{solv.})}{C_n(\text{imp})} \frac{1}{r} \exp - (qr). \tag{23}$$

The calculated and observed values of period IV and VI impurities are compared in Table 4. The predicted values of activation energy are also compared in

TABLE 4

Element	Z	Monovalent			Divalent			Observed	Ref.
		$\Delta Z_{\text{eff}} + Q$	$[\Delta Z_{\text{eff}} + Q]^{n-3/n-1}$	H(imp)	$\Delta Z_{\text{eff}} + Q + 1$	$[\Delta Z_{\text{eff}} + Q + 1]^{n-3/n-1}$	H(imp)	H(obs) (kcal/mole)	
Cu	29	−0.3	−0.405	46.2	0.7	0.846	—	46.1	(14)
Zn	30	0.7	0.846	(41.8)	1.7	1.49	41.0	41.7	(11)
Ga	31	1.7	1.49	(41.0)	2.7	2.11	39.4	—	
Ge	32	2.7	2.11	(29.4)	3.7	2.67	38.0	36.5	(15)
As	33	3.7	2.67	(38.0)	4.7	3.19	36.6	—	
S	34	4.7	3.19	26.6	5.7	3.69	(35.4)	—	
Br	35	5.7	3.69	35.4	6.7	4.16	(34.2)	—	
Kr	36	6.7	4.16	34.2	7.7	4.62	—	35.0	(5)
Au	79	4.4	3.07	41.0	5.4	3.98	—	45.5	(16)
Hg	80	5.4	3.98	(39.9)	6.4	4.57	39.1	38.1	(14)
Tl	81	6.4	4.57	(39.1)	7.4	5.14	38.4	37.9	(17)
Pb	82	7.4	5.14	(38.4)	8.4	5.70	37.7	38.1	(18)
Bi	83	8.4	5.70	(37.7)	9.4	6.26	37.0	—	
Po	84	9.4	6.26	(37.0)	10.4	6.79	36.4	—	
At	85	10.4	6.79	36.4	11.4	7.33	(35.7)	—	
Rn	86	11.4	7.33	35.7	12.4	7.85	—	—	

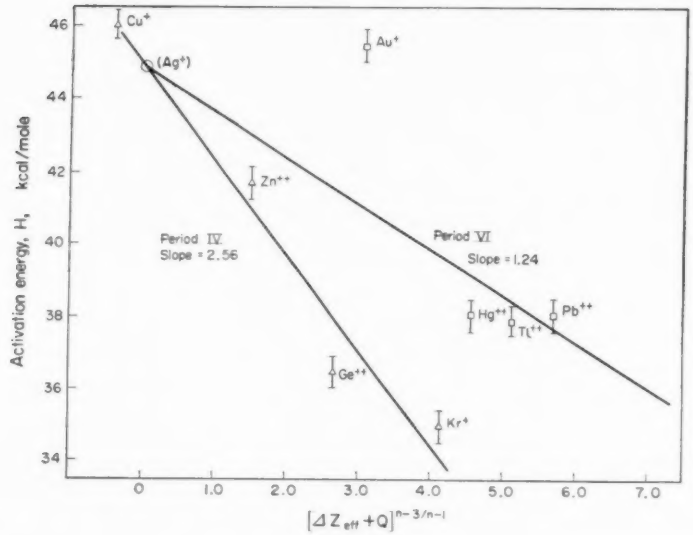


FIG. 3.

Fig. 3 by plotting both predicted and observed values against $(\Delta Z_{\text{eff}} + Q)^{n-3/n-1}$ for assumed monovalent ions and $(\Delta Z_{\text{eff}} + Q + 1)^{n-3/n-1}$ for divalent ions. The calculated slope for the period IV line is 2.56 kcal/mole and the slope for period VI is 1.24 kcal/mole. Both lines pass through the observed value for silver self-diffusion.

The calculated values are within 3 per cent of the observed values for the elements considered, with the exception of gold.

(4) *Frequency factor* D_0

An estimation of the derivative of equation (16) was made by Lazarus:

$$d(E_f + E_m)/dT = r_0\alpha[(\delta E_f/\delta r)_T + C(\delta E_m/\delta r)_T] \quad (24)$$

where α is the linear thermal expansion coefficient (1.9×10^{-5} deg.$^{-1}$). The value of the constant C is obtained from the self-diffusion measurements, and $C = 3$.

The ratio of frequency factors for impurity and solvent can be found from equation (16), using equation (24), and

$$D_0(\text{imp})/D_0(\text{solv}) = \exp\{-\alpha e\phi(r)/k[(qr + 1) + C/4(-q^3r^3 + 6q^2r^2 + 5qr + 5)]\}. \quad (25)$$

The general potential function of equation (23) may be used with equation (25) to obtain a set of calculated values for the frequency factors of periods IV, V and VI non-transition elements. These values are given in Table 5, along with the experimentally measured values. The agreement is not good. The calculated values are about one-half of the measured values. The value for krypton is off by a factor of 10.

Although the agreement of experimental and calculated values of the frequency factor is not as close as for the activation energies, the diffusion coefficient is less sensitive to error in the frequency factor (see equation 1).

SUMMARY AND CONCLUSIONS

A new ionic model for the elements to the right of silver in period V has been used in the determination of H and D_0 by the method used by Lazarus[1]. The result has been an improved agreement between calculated and observed values.

With the same model, the difference in ion core size and effective nuclear charge in periods IV, V and VI was used to calculate values of H and D_0 for the three periods. The agreement of experimental and calculated values of H is within 3 per cent except for the element gold. The fact that observed values of activation energies are less for period IV and VI elements in silver than the corresponding elements in period V is explained to be a result of their effects on the repulsive potential. The mobility of the impurity elements is found to be inversely proportional to the calculated ion core size and directly proportional to the effective nuclear charge. The agreement of experimental and calculated values of D_0 is not as good; however, the diffusion equation is not as sensitive to errors in D_0.

The diffusion coefficients of the elements considered

TABLE 5. Values of the frequency factor, D_0, for period IV, V and VI non-transition elements (Mean obs. D_0 for silver = 0.560 cm²/sec)

Element	Monovalent		Divalent		Observed	Ref.
	$(\Delta Z_{eff} + Q)^{n-3/n-1}$	D_0(imp) (cm²/sec)	$(\Delta Z_{eff} + Q + 1)^{n-3/n-1}$	D_0(imp) (cm²/sec)	D_0(obs) (cm²/sec)	
Cu	−0.405	0.63	0.846	—	1.23	(14)
Zn	0.846	(0.39)	1.49	0.31	0.54	(11)
Ga	1.49	(0.31)	2.11	0.25	—	
Ge	2.11	(0.25)	2.67	0.20	0.084	(15)
As	2.67	(0.20)	3.19	0.16	—	
S	3.19	0.16	3.69	(0.14)	—	
Br	3.69	0.14	4.16	(0.11)	—	
Kr	4.16	0.11	4.62	—	1.05	(16)
Ag	0	0.560	1.00	—	0.560	(10, 11)
Cd	1.00	(0.37)	1.72	0.29	0.44	(2)
In	1.72	(0.29)	2.35	0.22	0.41	(2)
Sn	2.35	(0.22)	3.94	0.18	0.25	(2)
Sb	2.94	(0.18)	3.50	0.15	0.169	(3)
Te	3.50	0.15	4.04	(0.12)	—	
I	4.04	0.12	4.54	(0.10)	—	
Xe	4.54	0.10	5.04	—	0.036	(6)
Au	3.07	0.17	3.98	—	0.26	(17)
Hg	3.98	(0.12)	4.57	0.10	0.079	(18)
Tl	4.57	(0.10)	5.14	0.08	0.15	(19)
Pb	5.14	(0.08)	5.70	0.06	0.22	(20)
B	5.70	(0.06)	6.26	0.05	—	
Po	6.26	(0.05)	6.79	0.04	—	
At	6.79	0.04	7.33	(0.03)	—	
Rn	7.33	0.03	7.85	—	—	

in periods IV, V and VI are obtained by substitution of H and D_0 into equation (1)

$$D = D_0 \exp -(H/RT) \qquad (1)$$

and reasonable values can be obtained for twelve of the thirteen impurity elements which have been measured. The exception is the element gold.

This agreement is used to support the basic assumption made in the present ionic model, that the so-called multivalent elements need not be multi-ionic when dissolved in silver. The agreement is best if silver, copper and gold are considered to be singly ionized and the other metals doubly ionized.

Non-integral ionic charges will be a reasonable extension of the present model. If the decrease in activation energy per unit ionic charge is essentially correct, the ionic charge of zinc in silver would be interpreted to be somewhat less than doubly ionized ($\sim 1.7^+$) and germanium greater than doubly ionized ($\sim 2.8^+$). Furthermore, the inert gases, krypton and xenon, appear to be less than singly ionized (~ 0.5–0.7^+).

REFERENCES

1. D. LAZARUS, *Impurities and Imperfection* p. 107. American Society for Metals, Cleveland (1955).
2. C. T. TOMIZUKA and L. SLIFKIN, *Phys. Rev.* **96,** 610 (1954).
3. E. SONDER, L. SLIFKIN and C. T. TOMIZUKA, *Phys. Rev.* **93,** 970 (1954).
4. L. C. R. ALFRED and N. H. MARCH, *Phil. Mag.* **2,** 985 (1957).
5. J. M. TOBIN, *Acta Met.* **5,** 398 (1957).
6. J. M. TOBIN, *Acta Met.* **7.** 701 (1959).
7. N. F. MOTT, *Proc. Camb. Phil. Soc.* **32,** 281 (1936). Contains Ref. to JONES.
8. A. UNSÖLD, *Ann. Phys. Lpz.* **82,** 355 (1927).
9. L. PAULING, *The Nature of the Chemical Bond* p. 335 Cornell Press, Ithaca (1948).
10. C. T. TOMIZUKA and E. SONDER, *Phys. Rev.* **103,** 1182 (1956).
11. A. SAWATSKY and F. E. JAUMOT, JR. *Phys. Rev.* **100,** 1627 (1955).
12. L. PAULING, *Proc. Roy. Soc.* A**114,** 181 (1927).
13. L. PAULING and J. SHERMAN, *Z. Kristallogr.* **81,** 1 (1932).
14. A. SAWATSKY and F. E. JAUMONT, JR., *J. Metals, N.Y.* **9,** 1207 (1957).
15. R. E. HOFFMAN, *Self-Diffusion in Dilute Binary Solid Solutions,* General Electric, Schenectady N.Y. (1957).
16. F. E. JAUMONT, JR. and A. SAWATSKY, *J. Appl. Phys.* **27,** 1186 (1956).
17. R. E. HOFFMAN, *Acta Met.* **6,** 95 (1958).
18. R. E. HOFFMAN, D. TURNBULL and E. W. HART, *Acta Met.* **3,** 417 (1955).

VOL. 8 1960

ON THE EFFECTIVE SURFACE ENERGY INVOLVED IN THE BRITTLE FRACTURE OF 70/30 BRASS*

H. NICHOLS and W. ROSTOKER†

A 70/30 brass wetted with mercury fails at about the engineering yield stress in a brittle manner. The degree of embrittlement is temperature dependent, showing an abrupt reversion to the fully ductile state in the manner of the transition displayed by body-centered cubic metals. The effective surface energy associated with this brittle fracture has been analysed from experimental measurement of σ_F vs. $d^{-1/2}$ and σ_F vs. C (crack length). In both cases, the evidence is that the effective surface energy is less than 10^3 ergs/cm^2.

ENERGIE EFFECTIVE DE SURFACE MISE EN OEUVRE LORS DE LA RUPTURE FRAGILE D'UN LAITON 70/30

Un laiton 70/30 imbibé de mercure se rompt d'une manière fragile aux environs de sa limite d'élasticité pratique. Le degré de fragilité dépend de la température et on peut montrer qu'il y a transition brusque et retour à l'état ductile.

Cette transition s'effectue de manière semblable à celle observée dans les métaux à réseau cubique. La relation entre l'énergie effective de surface et la rupture fragile a été étudiée à partir de mesures expérimentales de σ_F en fonction de $d^{-1/2}$ et σ_F en fonction de C (longueur des fissures).

Dans les deux cas, il apparaît que l'énergie effective de surface est inférieure à 10^3 ergs/cm^2.

ZUR EFFEKTIVEN OBERFLÄCHENENERGIE BEIM SPRÖDBRUCH VON 70/30-MESSING

70/30-Messing, das mit Quecksilber angefeuchtet ist, bricht in spröder Weise bei ungefähr der normalen Fließspannung. Der Grad der Versprödung hängt von der Temperatur ab und zeigt einen abrupten Übergang zum vollduktilen Zustand, ähnlich dem Übergang, den kubisch-raumzentrierte Metalle aufweisen. Die effektive Oberflächenenergie, die mit diesem Sprödbruch verknüpft ist, wurde aus den Versuchsergebnissen von σ_F gegen $d^{-1/2}$ und σ_F gegen C (Rißlänge) abgeleitet. In beiden Fällen stellt sich heraus, daß die effektive Oberflächenenergie kleiner als 10^3 erg/cm^2 ist.

Recrystallized alpha brass containing 30 per cent Zn when wetted with liquid mercury or mercury amalgams will fracture in simple tension at room temperature at or near its normal engineering yield point; with increasing temperature of testing, ductility is progressively restored. A graphic plot of tensile ductility against test temperature takes the form of the transition from brittle to ductile behavior found with most body-centered cubic metals. The transition temperature, which is quite sharp, is governed by the recrystallized grain size in the same fashion as predicted for body-centered cubic metals.[1] It is the intent of this paper to demonstrate further that fracture originating at the wetted interface is basically the same as encountered in brittle body-centered cubic metals and that true surface energy is a dominant factor in the process.

The structure of 70/30 brass provides a good opportunity to demonstrate the magnitude of liquid metal embrittlement on a micro-scale. The recrystallized structure is populated by twin bands. In cross-section the twin interfaces are straight lines which terminate abruptly and without change of direction at grain boundaries. Since the brittle fracture produced by wetting with mercury is exclusively intergranular in recrystallized metals, bending of the twin band interfaces provides an observable measure of plastic distortion. The microstructure at 250 × magnification of the cracked zone in a coarse-grained brass specimen is illustrated in Fig. 1. Clearly any plastic distortion is beyond the resolution used, which means that if a plastically deformed zone exists at the fracture surface it is less than about 1×10^{-3} mm in thickness. This is considerably less than the 3×10^{-1} mm thickness of plastically worked metal discovered by Orowan[2] on



FIG. 1. Intersection of twin interfaces with an intergranular crack in 70/30 brass embrittled by wetting with mercury. × 250

* Received February 5, 1960.

† Metals Division, Armour Research Foundation, Chicago, Illinois.

the fracture surface of low carbon steel broken below the transition temperature. This point is of considerable importance since, according to Orowan, the effective surface energy associated with common brittle fracture must be of the order of 10^6 ergs/cm^2 rather than the 1–2 $\times$ 10^3 ergs/cm^2 characteristic of true surface energies.

Assuming for the moment that the brittle fracture of 70/30 brass wetted with mercury does not involve a plastic energy dissipation term, the effective surface energy can be estimated from the Cottrell–Petch criterion for a ductile–brittle transition. Rearranging the terms of their equation of parameters, the surface energy, γ, becomes

$$\gamma = \frac{\sigma_y K_y d^{1/2}}{\beta G}$$

where σ_y = flow stress;
K_y = slope of the flow stress vs. $d^{-1/2}$ function;
d = mean grain diameter;
β = numerical factor;
G = modulus of rigidity.

For a mean grain diameter of 0.062 mm, the flow stress of 70/30 brass was determined as 15.8 $\times$ 10^3 lb/in^2; values of K_y and G were determined as 13.5 $\times$ 10^3 and 6.03 $\times$ 10^6 lb/in^2, respectively. Using Petch's[3] estimate of β as equal to 4, γ is calculated to be 2.4 $\times$ 10^3 ergs/cm^2. This signifies that in the truly brittle fracture of 70/30 brass, the associated surface energy should be less than this value.

The surface energy associated with brittle fracture can be estimated from the relationship

$$\sigma_F = \sigma_0 + Kd^{-1/2}$$

where σ_F = fracture stress;
σ_0 = an intercept value;
K = the function $\sqrt{\left(\frac{6\pi G\gamma}{1-\nu}\right)}$;
ν = Poisson's ratio.

Stroh[4] has shown that the measured values of K permit the derivation of reasonably correct values of γ for Fe, Zn, Mg and Mo. In these cases γ refers to the surface energy of the metal with respect to its own vapor. Petch[5] has shown that hydrogen embrittlement of iron can be interpreted on a model of reduced surface energy (reduced value of K) brought about by adsorption of hydrogen to crack nuclei surfaces.

The fracture stresses of recrystallized 70/30 brass wetted with mercury for a range of grain sizes have been measured at room temperature and are plotted in Fig. 2. It will be noted that a linear relationship exists between σ_F and $d^{-1/2}$. From the measured

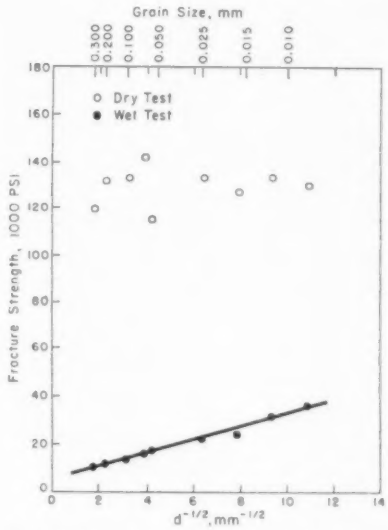


FIG. 2. Fracture stress at room temperature of 70/30 brass as a function of grain size, d, when unwetted and when wetted with mercury.

value of K, the magnitude of γ* is computed to be 280 ergs/cm^2. This is well below the maximum value set by the Cottrell–Petch criterion and supports the assumption that brittle fracture is obtained without significant plastic strain energy absorption.

The effective surface energy associated with brittle fracture can be estimated from the Griffith condition for the propagation of an existing crack:

$$\sigma_i = \sqrt{(E\gamma/C)}$$

where σ_i = stress to re-initiate propagation in an existing crack of length, C;
E = Young's modulus.

If the crack propagation follows the Griffith relationship, the slope of the plot of σ_i against $C^{-1/2}$ yields a term which is equal to $(E\gamma)^{1/2}$. This analysis applied to ship plate steel below its transition temperature led Felbeck and Orowan[6] to estimate the apparent surface energy to be of the order of 10^6 ergs/cm^2, which was in good agreement with the plastic energy associated with the plastically worked zone revealed by X-ray diffraction.[2]

Crack propagation studies have been made on annealed brass sheets (0.020 in. thick $\times$ 12 in. wide $\times$ 16 in. long) under uniaxial tensile loading. Susceptibility to brittle fracture was produced by wetting the sheet specimens with mercury in a broad band across the 12 in. width of the test specimen. A 5/64 in. slot was located in the wetted zone at a point equidistant from both edges: It is characteristic

* This should signify the surface energy of 70/30 brass with an adsorbed film of mercury.

VOL. 8 1960

of brittle fracture in brass that velocities of propagation are not high. One can initiate a crack and stop its propagation by rapid unloading of the tensile machine. On re-loading, two observers watched and measured the crack length on demand, and another recorded the applied load. The crack could be essentially "walked" across the width of the specimen and a series of crack lengths and their associated propagation loads measured. In all cases, the cracks remained in the wetted zone and propagated transversely to the axis of tension.

Two types of curves were obtained. When the specimen was wetted with mercury only on one side, the crack propagated across the width of the specimen faster than through the thickness direction, with the result that there was brittle fracture on one side and superficial ductile fracture apparent on the other. The plot of σ_i against $C^{-1/2}$ for this test is shown in Fig. 3. From the slope of the linear plot obtained, the value of apparent surface energy was computed to be about 10^6 ergs/cm^2 in good agreement with the work of Felbeck and Orowan.

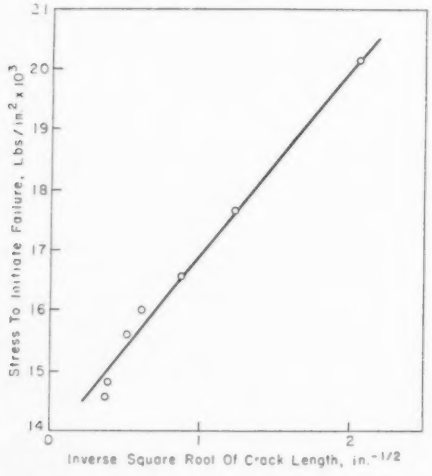


FIG. 3. Stress to propagate a crack as a function of crack length. 70/30 brass sheet wetted on one side with mercury.

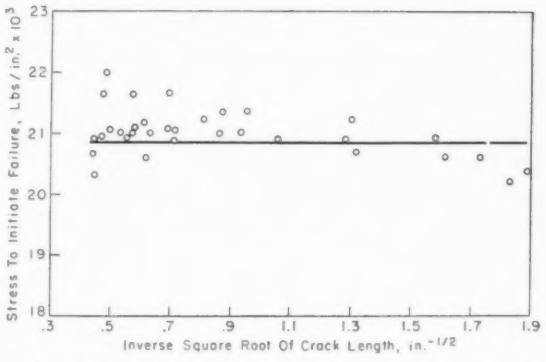


FIG. 4. Stress to propagate a crack as a function of crack length. 70/30 brass sheet wetted on both sides with mercury.

By wetting both sides of the thin brass sheet, the ductile portion of fracture, by all appearances, was eliminated. The results of several specimens are plotted together in Fig. 4. This was necessary because the slope is obviously approaching zero as is to be expected if the surface energy is to decrease from 10^6 to 10^3 ergs/cm^2 or less. Within the scatter band of the data, one cannot do other than estimate the surface energy as between zero and about 10^3 ergs/cm^2.

By all methods of evaluation, the fracture of 70/30 brass wetted with mercury appears to be nearly ideally brittle.

ACKNOWLEDGMENT

This work was performed under research contract with the Pitman-Dunn Laboratory of Frankford Arsenal, whose sponsorship and permission to publish are gratefully acknowledged.

REFERENCES

1. H. NICHOLS and W. ROSTOKER, paper submitted for publication in *Acta Met.*
2. E. OROWAN, *Weld. J.* **34,** 157*S* (1955).
3. N. J. PETCH, *Proc. Conf. on Fracture* Shampscott 1959. Wiley, New York (1959).
4. A. N. STROH, *Advanc. Phys.* **6,** 428 (1957).
5. N. J. PETCH, *Phil. Mag.* **1,** 331 (1956).
6. D. K. FELBECK and E. OROWAN, *Weld. J.* **34,** 570*S* (1955).

COTTRELL LOCKING AND THE FLOW STRESS IN IRON*

H. CONRAD† and G. SCHOECK‡

The effect of temperature and grain size on the yield and flow stress of electrolytic iron at a constant structure was investigated. It was found that the flow stress σ_{fl} for a strain beyond the Lüders strain obeyed the equation

$$\sigma_{fl} = \sigma_{fl_1}(T) + \sigma_{fl_2}'(st) + kd^{-1/2}$$

where st represents the structure due to strain, solute atoms, precipitates, etc., and d is the grain diameter. The thermal component of the flow stress $\sigma_{fl_1}(T)$ exhibited the same temperature dependence as the lattice friction stress σ_i obtained from plots of the lower yield stress versus $d^{-1/2}$. The value of k was equal to that for the lower yield stress from 300° to 110°K. In this temperature range k was relatively independent of temperature. Below 110°K, k increased with decrease in temperature for the lower yield stress but not for the flow stress. It is suggested that this increase may be due to the occurrence of twinning.

The equivalence of the temperature and grain size dependence of the lower yield and the flow stress suggests that the lower yield represents the movement of dislocation and does not include a thermally-activated locking term. Since the upper yield stress exhibited a stronger temperature dependence than the lower yield, it is suggested that this stress represents the tearing of dislocations from their Cottrell atmosphere.

BLOCAGES DES "COTTRELL" ET LA TENSION D'ECOULEMENT DANS LE FER

Les auteurs envisagent l'effet de la température et de la dimension du grain sur la tension de décrochement et d'écoulement dans du fer électrolytique de structure constante.

Ils montrent que la tension d'écoulement σ_{fl} pour une déformation au delà de la déformation de Lüders obéit à l'équation

$$\sigma_{fl} = \sigma_{fl_1}(T) + \sigma_{fl_2}'(st) + kd^{-1/2}$$

ou st représente la structure due à la déformation, aux atomes en solution, aux précipités, etc. . . et d est le diamètre du grain.

La composante thermique de la tension d'écoulement $\sigma_{fl_1}(T)$ dépend de la température comme la tension de friction du réseau cette tension étant obtenue en portant la tension élastique inférieure en fonction de $d^{-1/2}$.

La valeur de k est la même que celle de la limite élastique inférieure entre 300 et 110°K. Dans cette gamme de température, k est relativement indépendante de celle-ci.

En dessous de 110°K, k s'accroît avec diminution en température pour la limite élastique inférieure, mais non pour la tension d'écoulement. Il est suggéré que cet accroissement est dû au maclage qui peut apparaître à ces températures. L'équivalence de la dépendance de la température et de la dimension du grain sur la limite élastique inférieure et la tension d'écoulement suggère que la première représente le mouvement des dislocations et n'inclut pas un terme de blocage activé thermiquement.

Comme la limite élastique supérieure dépend plus fortement de la température que de la limite inférieure, il est suggéré que cette tension représente l'arrachement des dislocations de leur atmosphère de Cottrell.

COTTRELL-VERANKERUNG UND DIE FLIESSSPANNUNG IN EISEN

Der Einfluß von Temperatur und Korngröße auf die Streckgrenze und Fließspannung von Elektrolyt-Eisen (mit konstanter Struktur) wurde untersucht. Für eine Verformung, die größer ist als die Lüders-Verformung, gehorcht die Fließspannung der Gleichung

$$\sigma_{fl} = \sigma_{fl_1}(T) + \sigma_{fl_2}'(st) + kd^{-1/2}$$

wo st die Struktur infolge Verformung, gelöster Atome, Ausscheidungen usw. bedeutet, und d der Korndurchmesser ist. Die temperaturabhängige Komponente der Fließspannung zeigte dieselbe Temperaturabhängigkeit wie die Gitterreibungsspannung, die sich bei Auftragung der unteren Streckgrenze gegen $d^{-1/2}$ ergibt. Der Wert von k war zwischen 300° und 110°K gleich dem für die untere Streckgrenze. In diesem Temperaturbereich war k relativ temperaturunabhängig. Unterhalb 110°K nahm k für die untere Streckgrenze mit abnehmender Temperatur zu, aber nicht für die Fließspannung. Es wird vorgeschlagen, daß diese Zunahme auf dem Auftreten von Zwillingsbildung beruhen kann.

Die gleichartige Abhängigkeit der unteren Streckgrenze und der Fließspannung von Temperatur und Korngröße legt die Vermutung nahe, daß die untere Streckgrenze der Bewegung von Versetzungen entspricht und keinen Verankerungsterm enthält. Da die obere Streckgrenze eine stärkere Temperaturabhängigkeit zeigt als die untere, wird vorgeschlagen, daß diese Spannung dem Wegziehen der Versetzungen von ihrer Cottrell-Atmosphäre entspricht.

* Received January 28, 1960.

† Formerly with Westinghouse Research Laboratories; now with Atomics International, Box 309, Canoga Park, California.
‡ Metallurgy Department, Westinghouse Research Laboratories, Pittsburgh 35, Pa.

VOL. 8 1960

INTRODUCTION

The lower yield stress σ_{LY} of polycrystalline iron obeys an equation of the form[1-3]

$$\sigma_{LY} = \sigma_i + kd^{-1/2} \tag{1}$$

where d is the grain diameter. A theoretical interpretation of this equation has been given by Petch[2,4] and Cottrell[5]. They suggest that yielding is caused by the stress concentration of dislocation pile-ups at grain boundaries. σ_i then represents a frictional stress impeding the individual dislocations in the pile-up. The constant k is given by $k = (2l)^{1/2}\sigma_l(T)$ where $\sigma_l(T)$ is the stress required to unlock the dislocation of a Frank–Read source a distance l ahead of the pile-up. Heslop and Petch[6] have shown that the frictional stress σ_i depends on the temperature, and therefore the temperature dependence of the yield stress does not represent the temperature dependence of the locking stress.

To obtain the magnitude of σ_i and its temperature dependence one has to measure the dependence of the lower yield stress on the grain size d at various temperatures. This usually involves a large number of tests with samples of different grain sizes. In order to obtain the different grain sizes, different heat treatments are required. This may well produce different dislocation structures in the different samples and hence, by influencing l, change the value of k in equation (1).

There is some uncertainty about the nature of the frictional stress σ_i. According to Heslop and Petch[6], it is the sum of a part $\sigma_{i_1}(T)$ which is only dependent on temperature and a part $\sigma_{i_2}(st)$ which is only dependent on the structure and which results from lattice imperfections such as solute atoms and precipitates. Thus

$$\sigma_i = \sigma_{i_1}(T) + \sigma_{i_2}(st). \tag{2}$$

It has been suggested[6] that $\sigma_{i_1}(T)$ is due to a large Peierls force. Since this would only act on dislocations lying in certain crystallographic directions, it is hard to see why the arbitrary pile-up should all have such an orientation. $\sigma_{i_2}(st)$ depends on the structure of the crystal and has been found to increase linearly with the concentration of C and N in solid solution. It can be shown that such an effect is expected.[7] However, $\sigma_{i_2}(st)$ is also increased by the presence of precipitates. It is hard to see how the periodic stress-field of precipitates should act like a frictional force on each single dislocation in the pile-up.

If we assume the interpretation of equation (1) to be correct, then σ_i is a frictional force which acts on free dislocations.[6] Hence, σ_i should also give a contribution to the flow stress under conditions where the dislocations have been freed from their atmosphere by preceding deformation. Especially the temperature dependence of σ_i should show up in the temperature dependence of the flow stress σ_{fl}. By measuring the difference between σ_{LY} and σ_{fl}, in principle it should then be possible to obtain a direct determination of the constant k and in turn an evaluation of σ_i. This was the object of the present investigation.

EXPERIMENTAL PROCEDURE

The material employed was vacuum melted electrolytic iron of the following composition (Wt.%):

C	N	O	Si	P	S	Mn
0.014	0.003	0.005	0.06	0.003	0.011	0.002

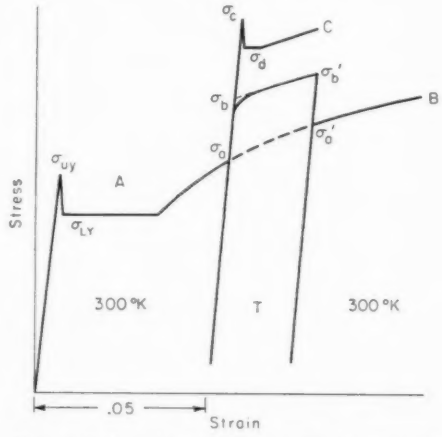


FIG. 1. Schematic of test procedure in present investigation.

Wire of 1.6 mm dia. was prepared by cold swaging, without intermediate annealing, a previously hot-rolled 12.5 mm dia. rod. Test specimens 10 cm long were cut from the wire and chemically etched to give a reduced section of 1.3 mm dia. and 6 cm length. To obtain a variation in grain size, the etched specimens were sealed in evacuated quartz tubes and heated for various times at 720°–920°C. Specimens annealed above 720°C were first furnace cooled to 720°C. All specimens were air cooled from 720°C. Following cooling to room temperature the specimens were aged for 24 hr at 150°C to obtain a stable precipitated structure.

The essential objective of the experiments was to make a direct comparison between the yield stress and the flow stress for the same dislocation structure. In order to accomplish this, the testing procedure

given in Fig. 1 was employed. The annealed and stabilized specimens were initially strained approximately 5 per cent at room temperature to σ_a and then unloaded, except for a small load to maintain axial alignment. One group of specimens was then immediately cooled to a lower temperature (3–5 min were required for the cooling) and the straining continued at this lower temperature, giving the value of the flow stress σ_b at the new temperature T. This established the effect of temperature on the flow stress associated with the movement of unlocked dislocations.

A second group of the strained specimens was aged for 1 hr at 150°C under a small load required to maintain specimen alignment. These were then tested at various temperatures to establish the effect of temperature on the strain-aged upper yield stress σ_c and lower yield stress σ_d. It is believed that this additional aging treatment did not change the distribution of the original precipitate because the samples had been previously aged for 24 hr at the same temperature. Also, 150°C is below the temperature where recovery might change the dislocation structure formed during the initial straining. The only change one expects from the aging treatment is that a cloud of C and N atoms forms around the dislocations. We may therefore assume that the freshly deformed and the strain-aged crystals have the same dislocation structure, but the dislocations are free in the first group of specimens and locked by a Cottrell atmosphere in the second.

The tensile tests were conducted with an Instron tensile-testing machine operating at a constant crosshead speed of 0.25 cm min^{-1}. The strain was taken from the time axis of the speedomax load-recorder. The stress and strain sensitivity were estimated to be 0.1 kg/mm^2 and 2×10^{-4}, respectively.

Temperatures below room temperature were obtained by the method described by Wessel and Olleman[8], which employs a nitrogen vapor spray on the specimen. The temperature was controlled by an on-off magnetic valve which regulated the flow of nitrogen vapor from a large dewar. Temperatures above room temperature were obtained by controlling the current passing through nichrome heating elements which had been inserted in the low-temperature test chamber. In all cases the temperature was maintained within ± 1°C.

DISCUSSION OF EXPERIMENTAL RESULTS

1. *Effect of grain size*

Since Petch and others[1–3] had already established the validity of equation (1) in regard to the effect of grain size on the initial lower yield stress in iron, it was decided that only a limited number of grain sizes need be investigated to evaluate the parameters σ_i and k for the electrolytic iron used in the present study. The effect of grain size on the initial lower yield stress observed for the present material is given in Fig. 2. The value of k at 300°K is 2.2 kg/mm^2–mm$^{-1/2}$, in good agreement with that of Petch and co-workers[2,3,6,9,10] for various irons and mild steel.

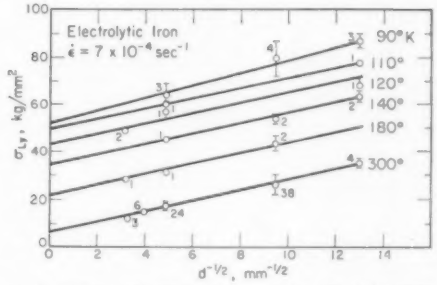


FIG. 2. Effect of grain size on the initial lower yield stress of electrolytic iron. (Numbers refer to number of specimens.)

It is seen from Fig. 2 that k is relatively independent of temperature between 300°K and 110°K; only at 90°K is the slope greater than that at 300°K, being 2.6 kg/mm^2–mm$^{-1/2}$. Data by Petch[9] and Heslop and Petch[10] indicate that k is relatively independent of temperature between 300° and 194°K. At 78°K they found k about $2\frac{1}{2}$ times that at 300°K. Since they did not give data between 194° and 78°K, comparisons cannot be made in this temperature range.

Figure 3 gives the effect of grain size on the flow stress at 300°K for a strain of 5 per cent (i.e. on the stress σ_a in Fig. 1). It is seen from Fig. 3 that the data points for the flow stress lie on a straight line parallel to that for the initial yield stress. Thus, the effect of grain size on the flow stress is given by

$$\sigma_{fl} = \sigma_{fl}^{\,0} + kd^{-1/2} \tag{3}$$

where k has the same value as for the initial lower yield stress.

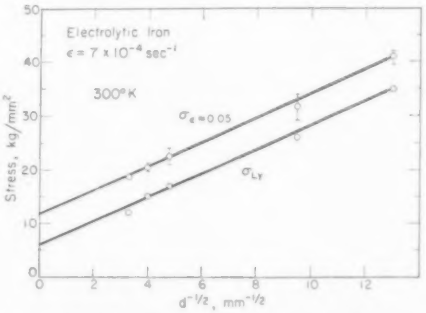


FIG. 3. Effect of grain size on the initial lower yield stress σ_{LY} and on the flow stress after a strain of 0.05 $\sigma_{\epsilon \approx 0.05}$ at 300°K.

VOL. 8 1960

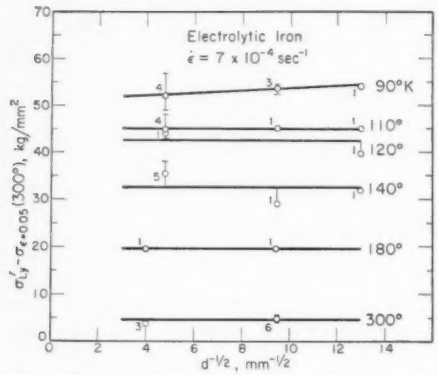


FIG. 4. Effect of grain size on the difference between the lower yield stress after strain aging σ_{LY}' and the flow stress $\sigma_{\varepsilon \approx 0.05}$ at 300°K previous to aging. (Numbers refer to number of specimens.)

Subtracting equation (3) from equation (1) one obtains

$$\sigma_{LY} - \sigma_{fl} = (\sigma_i - \sigma_{fl}^0) + (k_{LY} - k_{fl})d^{-1/2}. \quad (4)$$

If $\sigma_{LY}'(T)$ is defined as the strain-aged lower yield stress at a given temperature T and $\sigma_{fl}(T_0)$ is the flow stress ($\sigma_\varepsilon = 0.05$) at 300°K previous to aging, then one expects from equation (4) that $\sigma_{LY}'(T) - \sigma_{fl}(T_0)$ will be independent of grain size in the temperature range where $k_{LY} = k_{fl}$ and k_{LY} is independent of temperature, i.e. from 300° to 110°K. At 90°K a plot of $\sigma_{LY}'(T) - \sigma_{fl}(T_0)$ versus $d^{-1/2}$ should have a slope given by the difference in k_{LY} between 90°K and 300°K. Fig. 4 shows that these predictions are realized for the strain-aged lower yield stress, while Fig. 5 shows similar behavior for the upper yield stress. Figs. 3–5 thus indicate that the flow stress in iron obeys the same grain size dependence as the upper and lower yield stress in the range 300° to 110°K.

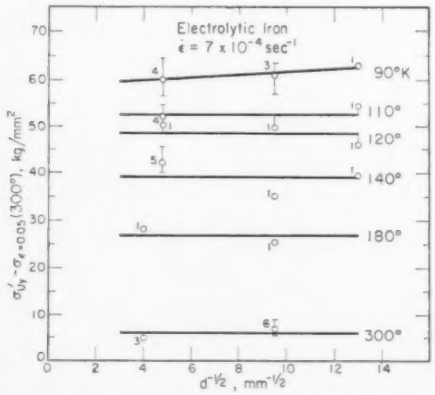


FIG. 5. Effect of grain size on the difference between the upper yield stress after strain aging σ_{UY}' and the flow stress $\sigma_{\varepsilon \approx 0.05}$ at 300°K previous to aging. (Numbers refer to number of specimens.)

The slope observed in Figs. 4 and 5 at 90°K and data on the effect of grain size on the temperature dependence of σ_{fl} (to be discussed below) indicate that k_{UY} and k_{LY} are larger than k_{fl} at 90°K.

Of significance in regard to the effect of grain size on the flow stress are the results obtained for metals with close-packed crystal structures (f.c.c. and c.p.h.). The flow stress at small strains, "yield stress", for these metals also obeys a $d^{-1/2}$ grain size dependence,[11] indicating that the $d^{-1/2}$ relationship is not restricted to materials which exhibit a pronounced yield point.*

2. *Effect of temperature*

The temperature dependence of the flow stress (i.e. the applied stress required for further deformation after the lower yield elongation) cannot be determined by comparing the flow stress of different samples at different temperatures. This is because the flow stress depends on the structure of the material, and

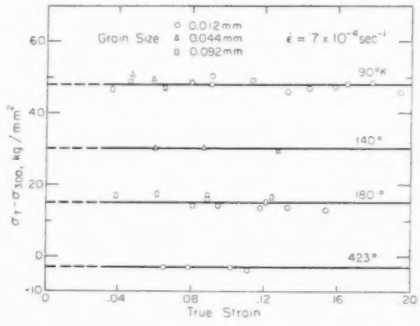


FIG. 6. Effect of grain size and strain on the change in flow stress associated with a change in temperature.

even if the measurements are taken at the same elongation, the preceding yield process may produce different dislocation structures at different temperatures. Therefore, in the present investigation the temperature dependence of the flow stress was measured by changing the temperature during deformation,[13,14] in this way ensuring that comparisons are made at the same structure.

Typical results for the temperature change tests are shown in Fig. 6. Here the change in flow stress $\Delta\sigma_{fl} = \sigma_T - \sigma_{300}$ (i.e. $\sigma_b - \sigma_a$ of Fig. 1) for a temperature change between 300°K and the indicated temperature is plotted versus the strain ε for several

* The value of k is, however, smaller for the close-packed metals than that observed for the electrolytic iron used in the present investigation. However, Petch[12] has indicated that k for iron with very low C + N contents is approximately that for close-packed metals.

grain sizes. It is seen from Fig. 6 that $\Delta\sigma_{fl}$ is independent of grain size and total previous strain.* The results of Fig. 6 thus indicate that although the flow stress σ_{fl} depends on the structure *st* (i.e. on the grain size, strain, precipitates, solute atoms, etc.), the change in flow stress with temperature $\Delta\sigma_{fl}$ is independent of structure. We can, therefore, express the results of Fig. 6 by the differential equation

$$\left(\frac{\delta\sigma_{fl}(T, st)}{\delta T}\right) = f(T) \tag{5}$$

which gives upon integration

$$\sigma_{fl} = \sigma_{fl_1}(T) + \sigma_{fl_2}(st). \tag{6}$$

Further, combining equations (3) and (6) one obtains

$$\sigma_{fl} = \sigma_{fl_1}(T) + \sigma_{fl_2}'(st) + kd^{-1/2}. \tag{7}$$

Equation (6) indicates that the temperature dependence of the flow stress is due to an intrinsic frictional force, which is not influenced by preceding deformation. The behavior of iron is thus different than that of f.c.c. metals where at higher deformations the change in flow stress with temperature increases in proportion to the applied stress.[13–16] An increase is expected if the temperature dependent part of the flow stress is due to the intersection of the dislocation forest and the density of the forest increases with strain.

A behavior similar to that indicated by equation (6) has been observed in the easy-glide of f.c.c. single crystals[15,16] and in Mg single crystals[17,18] (which has a c.p.h. structure), where the density of the forest does not increase during deformation, because only one glide plane is operating. This, however, cannot explain the behavior of polycrystalline iron, for at the stresses which were employed, many glide planes are expected to be operating.

In view of equations (2) and (6) it appears reasonable to obtain the temperature dependence of the flow parameters σ_{LY}, σ_i and σ_{fl} by plotting the difference between the stress at a temperature T and at a fixed reference temperature T_0 (which was chosen to be 300°K) versus the temperature. In such a plot any athermal component of the flow stress due to the structure is eliminated. σ_i and σ_{fl} obtained in the present tests are plotted in this manner in Fig. 7. Also included are data on mild steel: σ_i by Heslop and Petch[6] and σ_{LY} for a grain size of 0.065 mm by Wessel[19,20].

From Fig. 7 it is seen that σ_i and σ_{fl} for the

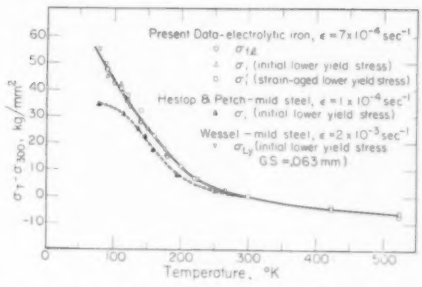


FIG. 7. Effect of temperature on the flow stress σ_{fl} and the friction stress σ_i.

electrolytic iron of the present investigation exhibit the same temperature dependence. Between 300° and 110°K the curve for σ_i for mild steel by Heslop and Petch[6] falls only slightly below that for σ_i and σ_{fl} of the present investigation; however, below 110°K the difference between the two curves becomes greater. This difference in the temperature dependence of σ_i between the two sets of data is probably for the most part due to the difference in strain rate employed.† Support for this is provided by Wessel's data[19,20] on σ_{LY}, which were obtained at a strain rate of 2×10^{-3} sec^{-1}, and which are in good agreement with the present results.

The data of Fig. 7 indicate that the flow parameters σ_{LY}, σ_i and σ_{fl} all exhibit the same temperature dependence. However, the upper yield stress σ_{UY} was found to exhibit a temperature dependence greater than that observed for these flow parameters. This is shown in Fig. 8, where the difference between the upper and lower yield stress is plotted versus the temperature for the electrolytic iron of the present investigation and for the mild steel by Wessel[19,20].

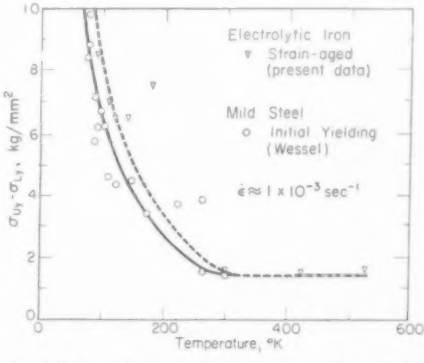


FIG. 8. Effect of temperature on the difference between the upper yield stress and the lower yield stress.

* In these tests the specimen temperature was alternated between room temperature and the indicated temperature until fracture occurred.

† Although Heslop and Petch do not give the strain rate, it is estimated to be 10^{-4} sec^{-1} on the basis of other data by these investigators.[3,9,10] The present tests were conducted at a strain rate of 7×10^{-4} sec^{-1}.

VOL. 8 1960

It is here seen that the difference between the upper and lower yield stress in both cases increases with decrease in temperature.

CONCLUSIONS

The identity of k for σ_{LY} and σ_{fl} between 300°K and 110°K and the fact that σ_{LY}, σ_i and σ_{fl} show the same temperature dependence indicates that σ_{LY}, σ_i and σ_{fl} all represent the same deformation mechanism in the range 300° to 110°K. It seems reasonable to assume that this mechanism is the motion of free dislocations through the lattice.

If the flow parameters σ_{LY}, σ_i and σ_{fl} represent the motion of free dislocations, it is desirable to know the mechanism which controls this motion, because it is responsible for the strong temperature dependence that is observed for these parameters. Heslop and Petch[6] have suggested that the motion is controlled by the Peierls stress. However, as indicated in the introduction this idea needs further evaluation before it can be accepted without reservation.

The stronger temperature dependence of the upper yield as compared to the other flow parameters suggests that another mechanism is controlling here. This may be the thermally-activated tearing of dislocations from their Cottrell atmosphere.

Finally, there is the question of the significance of k. Since k is independent of temperature in the range of 300° to 110°K, it must represent some athermal mechanism rather than the thermally activated unpinning of dislocations as suggested by Cottrell[5]. One such mechanism in iron is the athermal tearing of dislocations from a Snock-type atmosphere.[7] However, since k is independent of the interstitial content[3] and since k also occurs in the expression for the flow stress of f.c.c. metals as well as b.c.c. metals, it may represent the athermal generation of dislocations from sources in or near the grain boundary. Inserting the value of k obtained in the present experiments in the equations given by Cottrell[21] for the stress concentration due to a pile-up of dislocations at a grain boundary, one obtains for the stress σ_s to operate a source at distances of b to 10^{-4} cm ahead of the piled-up group values of $10^{-3}\ \mu - 10^{-2}\ \mu$ (where μ is the shear modulus). These are of the order of magnitude one might expect for the generation of dislocations at sources other than the Frank–Read type. A third possibility is that k may represent the relationship between the dislocation substructure in the grains and the grain size. A variation of substructure with grain size may result from the different annealing treatments which are employed to obtain the different grain sizes. In this latter case the quantity $kd^{-1/2}$ would merely represent a contribution to the long range internal stress and would be proportional to the shear modulus. From this it is evident that additional investigations are needed to establish the significance of k.

The increase in k at temperatures of 90°K and below may be due to twinning, which is known to occur at low temperatures.[22–24]

ACKNOWLEDGMENT

The authors wish to acknowledge helpful discussions with Dr. H. Wiedersich. They would also like to thank R. Leseck and L. Hays for carrying out the experimental part of this investigation.

REFERENCES

1. E. O. Hall, *Proc. Phys. Soc., Lond.* B **64,** 747 (1951).
2. N. J. Petch, *J. Iron St. Inst.* **174,** 25 (1953).
3. A. Cracknell and N. J. Petch, *Acta Met.* **3,** 186 (1955).
4. N. J. Petch, *Progr. Met. Phys.* **5,** 1 (1954).
5. A. H. Cottrell, *Trans. Amer. Inst. Min. (Metall.) Engrs.* **212,** 192 (1958).
6. J. Heslop and N. J. Petch, *Phil. Mag.* **1,** 866 (1956).
7. G. Schoeck and A. Seeger, *Acta Met.* **7,** 469 (1959).
8. E. T. Wessel and R. Olleman, *Bull. Amer. Soc. Test. Mat.* **187,** 56 (1953).
9. N. J. Petch, *Phil. Mag.* **3,** 1089 (1958).
10. J. Heslop and N. J. Petch, *Phil. Mag.* **3,** 1128 (1958).
11. W. M. Baldwin, *Acta. Met.* **6,** 139 (1958).
12. N. J. Petch, private communication.
13. A. C. Cottrell and R. T. Stokes, *Proc. Roy. Soc.* **233,** 17 (1955).
14. M. A. Adams and A. H. Cottrell, *Phil. Mag.* **46,** 1187 (1955).
15. H. Conrad, *Acta. Met.* **6,** 339 (1958).
16. P. Hassen, *Phil. Mag.* **3,** 384 (1958).
17. H. Conrad and W. D. Robertson, *Trans. Amer. Inst. Min. (Metall.) Engrs.* **209,** 503 (1957).
18. H. Conrad, R. Armstrong, H. Wiedersich and G. Schoeck, submitted to *Phil. Mag.*
19. E. T. Wessel, *Proc. Amer. Soc. Test. Mat.* **56,** 540 (1956).
20. E. T. Wessel, *Trans. Amer. Inst. Min. (Metall.) Engrs.* **207,** 903 (1957).
21. A. H. Cottrell, *Dislocations and Plastic Flow in Crystals* p. 107. Clarendon Press, Oxford (1953).
22. N. S. Owen, M. Cohen and B. L. Overbach, *Trans. Amer. Soc. Metals* **50,** 517 (1958).
23. F. S. Deronja and M. Gensamer, *Trans. Amer. Soc. Metals* **51,** 667 (1959).
24. G. T. Hahn, B. L. Averbach, W. S. Owen and M. Cohen, *Swampscott Conf. on Fracture, N.A.S.* 1959. Wiley, New York (1959).

THE INFLUENCE OF IMPURITIES ON THE ANNEALING OF NICKEL AFTER COLD WORK*

L. M. CLAREBROUGH, M. E. HARGREAVES, M. H. LORETTO AND G. W. WEST†

Measurements of stored energy and of changes in electrical resistivity and density accompanying annealing have been made on nickel of 99.85 per cent purity deformed in torsion and compression. There are notable differences from the behaviour found previously for nickel 99.6 per cent purity. The results suggest that, in the purer nickel, little or no recovery involving dislocations occurs between room temperature and the recrystallization temperature, in contrast to previous results for 99.6 per cent pure nickel. There appear to be two stages of annealing prior to recrystallization in the 99.85 per cent material although they are not clearly resolved. These are centred at 120°C and 260°C and are tentatively ascribed to the annealing of interstitials and vacancies respectively. On this basis the observed changes in resistivity and density can be explained.

Stored energy measurements on still purer nickel specimens, 99.96 per cent, deformed in compression indicate that in this material these first two stages are clearly resolved, provided the deformation is low enough to ensure that recrystallization does not interfere with their observation.

INFLUENCE DES IMPURETES SUR LE RECUIT DU NICKEL APRES DEFORMATION A FROID

Les auteurs ont déformé en torsion et compression des échantillons de nickel de pureté 99,85%. Ils ont mesuré l'énergie retenue et les variations de la résistivité électrique et de la densité qui se produisent au cours du recuit.

Ils ont observé de notables différences vis-à-vis du comportement du nickel de pureté 99,6%.

Ces résultats suggèrent que dans le nickel le plus pur, il ne se produit que peu ou pas de restauration faisant intervenir des dislocations lors du chauffage depuis la température ambiante jusqu'à la température de recristallisation.

Bien qu'ils n'aient pas été clairement reconnus, il semble qu'il existe deux stades de recuit précédent la recristallisation du nickel à 99,85%. Ils se produisent aux environs des températures 120°C et 260°C. Les auteurs pensent pouvoir les attribuer respectivement au recuit des interstitiels et des lacunes. Ils expliquent alors sur cette base les variations qu'ils ont observée dans les valeurs de la résistivité et de la densité. Les mesures de l'énergie retenue dans le cas d'échantillons de nickel très pur (99,96%) déformé par compression indiquent que pour ce métal les deux premiers stades sont nettement distincts lorsque la déformation est suffisamment faible pour éviter une interférence de la recristallisation.

DER EINFLUSS VON VERUNREINIGUNGEN AUF DIE ERHOLUNG VON NICKEL NACH KALTVERFORMUNG

An 99,85% reinem Nickel wurden Erholungsversuche nach Torsions- und Kompressionsverformung durchgeführt. Dabei wurden die gespeicherte Energie und die Änderungen des elektrischen Widerstands und der Dichte gemessen. Es bestehen bemerkenswerte Unterschiede zu dem Verhalten, das früher bei 99,6% reinem Nickel gefunden worden war. Die Ergebnisse deuten darauf hin, daß in reinem Nickel zwischen Raumtemperatur und der Rekristallisationstemperatur wenig oder keine Erholung auftritt, die mit Versetzungen verknüpft ist, im Gegensatz zu früheren Ergebnissen an 99,6% reinem Nickel. Es scheinen im 99,85% reinem Material vor der Rekristallisation zwei Erholungsstufen aufzutreten, sie lassen sich allerdings nicht klar auflösen. Ihre Schwerpunkte liegen bei 120°C und bei 260°C; sie werden versuchsweise dem Ausheilen von Zwischengitteratomen bzw. von Leerstellen zugeschrieben. Auf diese Weise lassen sich die beobachteten Änderungen des Widerstands und der Dichte erklären.

Messungen der gespeicherten Energie an noch reineren Nickelproben von 99,96% nach Kompressionsversuchen zeigen, daß diese beiden ersten Stufen in diesem Material klar aufgelöst sind, wenn die Verformung genügend gering ist, so daß die Rekristallisation die Beobachtung dieser Stufen nicht stört.

1. INTRODUCTION

Previous papers have described investigations of the annealing of deformed nickel of commercial purity (99.6 per cent nickel) by means of measurements of stored energy, electrical resistivity, density and hardness.[1,2] Two definite stages were found for this material, one of which was attributed to the disappearance of vacancies at temperatures up to 350°C, and the second to recrystallization at temperatures in the neighbourhood of 600°C.

Recently Sosin and Brinkman[3] have published the results of an investigation of the recovery of electrical resistivity in nickel of purity 99.98 per cent after cold-work and after electron irradiation. In interpreting their results they make considerable use of the

* Received December 21, 1959.

† Division of Tribophysics, C.S.I.R.O., University of Melbourne, Australia.

VOL. 8 1960

measurements referred to above. They discern three stages in the recovery of resistivity in the range of temperature from room temperature to the recrystallization temperature. The first of these stages, centred near 100°C, was not observed for nickel of 99.4 per cent purity nor was it found in our investigations of nickel of 99.6 per cent purity.

This paper describes measurements of stored energy, density and electrical resistivity on two grades of nickel purer than that used in our previous experiments. These experiments have evidently been proceeding concurrently with those of Sosin and Brinkman.

2. EXPERIMENTAL

2.1 *Specimens*

The specimens were of two grades of nickel kindly supplied to us by The Mond Nickel Company Ltd.: one was of purity 99.85 per cent, batch *M*, and the other of purity 99.96 per cent, batch *N*. Specimens for deformation in torsion were prepared from batch *M*, and these were of the type used previously, having a gauge length of 8 in. and a diameter of $\frac{3}{4}$ in. After machining they were annealed for 30 min at 700°C *in vacuo*, prior to deformation. To obtain specimens of this material of suitable dimensions for deformation in compression it was necessary to hot-upset the bar available. During this process grain growth took place at the forging temperature and thus the compression specimens were of larger grain size than the torsion specimens. From the forged pieces specimens $1\frac{1}{2}$ in. in diameter were machined, the initial length depending on the degree of deformation required. After machining these were annealed at 700°C *in vacuo*, prior to deformation.

For the high purity specimens of batch *N* only deformation by compression was used. The specimens were of the same form as those of batch *M* and were annealed at 600°C *in vacuo*, after machining and prior to deformation.

From the deformed bars, specimens for the determination of stored energy, density and electrical resistivity were machined, care being taken to use slow speeds of machining and a copious flow of coolant.

2.2 *Stored energy measurements*

The form of the specimens used and the technique of measuring the stored energy have been fully described previously.[4] Briefly the power required to heat the deformed specimen through a particular range of temperature is compared continuously with that required to heat a similar annealed specimen. The comparison is made under conditions which ensure that the specimens are virtually isolated thermally. The rate of heating in these experiments was 6°C/min. The result obtained is a curve of power difference (ΔP) as a function of temperature (or time) which shows the instantaneous rate of release of stored energy at any temperature, and which may be integrated to obtain the amount of energy released in any interval of temperature.

2.3 *Measurements of density*

The differential method used for determining the change in density associated with the annealing of the deformed specimens was similar to that described previously.[2,5] The density of the deformed specimens is compared to that of a fully annealed standard, of almost identical mass, taken from the same deformed bar as the specimen itself. The weights of the two specimens are compared in air and when immersed in a dense liquid (1,1,2,2-tetrabromoethane).

The only change in the apparatus previously described was the use of an air-damped, semi-micro balance of capacity 100 g fitted with a projection scale which could be read to 0.01 mg. The measurements were made at ambient temperature as it had been established that the variations in room temperature encountered were too small to affect the results of the differential method for the small differences in density observed.

The specimens were cylinders ground to a fine surface finish under coolant and were approximately $1\frac{1}{2}$ in. in length, $\frac{3}{4}$ in. in diameter and 80 g in weight.

After determination of the difference in density between an annealed specimen and the corresponding specimen in the deformed state, the deformed specimen was annealed in stages and the difference in density determined at each stage. The annealing was done in a stainless steel tube under pure nitrogen at atmospheric pressure, a thermocouple being attached to the specimen. The tube was placed in a furnace and heated at 6°C/min until the specimen reached the first temperature selected. The tube was removed and cooled in water and the density of the specimen determined. The specimen was returned to the tube and heated rapidly to the temperature reached previously, in a second furnace maintained at a high temperature. Then the tube was transferred to the first furnace to continue heating at 6°C/min to the next temperature selected. This procedure was repeated as required. It was designed to make the annealing of the density specimens as similar as possible to the continuous heating used in the measurements of stored energy, by minimizing the time the specimen was at elevated

temperatures during heating to, or cooling from, a particular annealing temperature.

2.4 *Measurements of electrical resistivity*

These measurements were made with a Kelvin double bridge on specimens $2\frac{1}{2}$ in. $\times \frac{1}{4}$ in. $\times \frac{1}{8}$ in. maintained at 0°C. During measurement the specimens were held in a jig in which current leads could be screwed to the ends and potential contacts made by pressing the specimen against a pair of gramophone needles fixed in the jig. The specimen could be removed from the jig and replaced in the same position so that the needles fitted exactly into the small indentations made in the previous insertion.

The procedure for annealing these specimens in stages was exactly the same as for the density specimens.

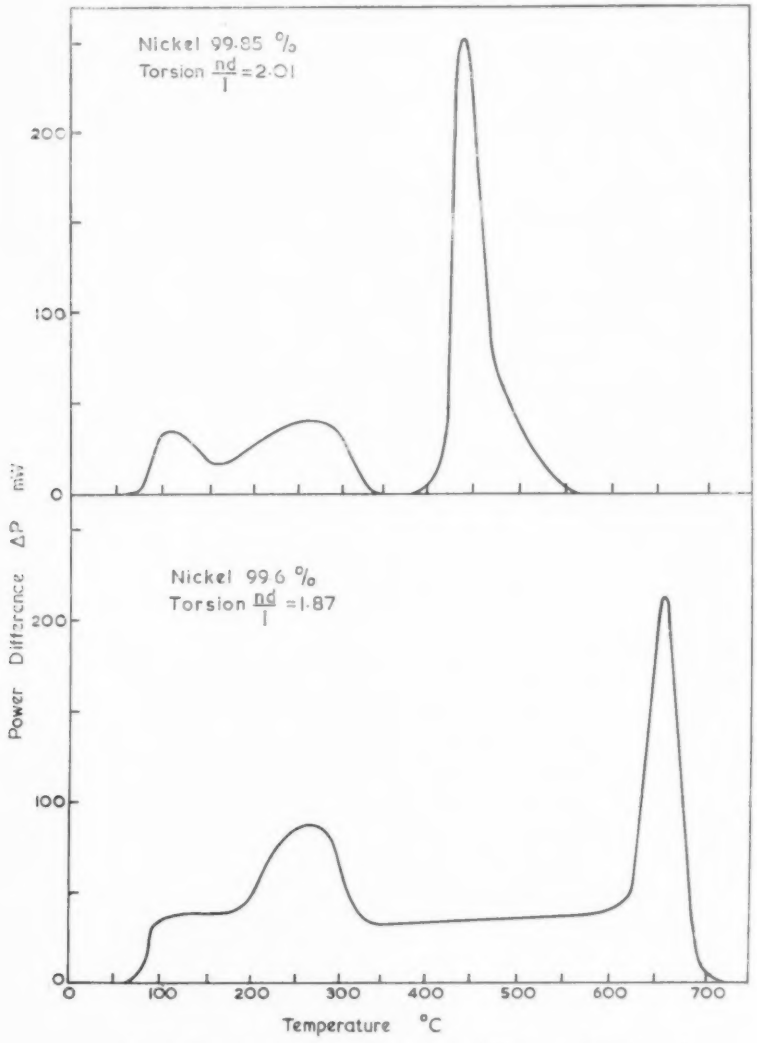


FIG. 1. Curves of power difference (ΔP) as a function of temperature for samples of nickel of two purities deformed in torsion. Above, *M* nickel, 99.85 per cent purity, deformed to $nd/l = 2.01$. Below, nickel of 99.6 per cent purity deformed to $nd/l = 1.87$, where n = number of turns, d = diameter of gauge length and l = gauge length. Heating rate 6°C/min.

3. RESULTS

3.1 *Stored energy*

In Fig. 1 the stored energy (ΔP) curve for specimens of nickel of batch *M* (99.85 per cent purity) is compared with that for the specimens of nickel of 99.6 per

VOL. 8 1960

cent purity used in previous experiments,[1,2] the specimens having been given similar deformations in torsion. It is evident that the purity of the specimen has a considerable effect on the manner in which the energy is released. For the less pure material, the peak at low temperatures, previously identified with the tures, for M nickel, these being centred at approximately 120 and 260°C.

In Fig. 2 the ΔP curve for M nickel deformed 70 per cent in compression is shown together with the results of electrical resistivity and density measurements. The ΔP curve shows the same general features

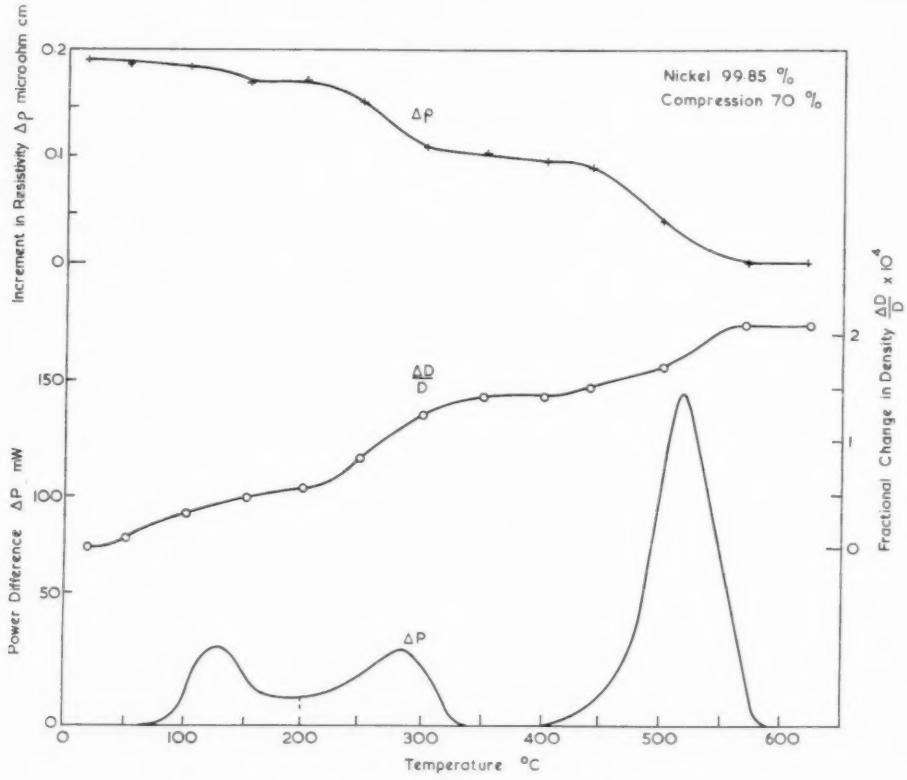


FIG. 2. Curves of power difference (ΔP), as a function of temperature, and of the increment in electrical resistivity ($\Delta\rho$) and fractional change in density ($\Delta D/D$) after annealing to various temperatures, for M nickel, 99.85 per cent purity, deformed 70 per cent in compression. Heating rate in the stored energy determination and the annealing treatments 6°C/min.

disappearance of vacancies, is superimposed on a plateau-like area which extends up to the second peak, which corresponds to recrystallization. This plateau-like area has been attributed to recovery involving the rearrangement and annihilation of dislocations.[1] However, for the M nickel this plateau-like area is not apparent and the ΔP curve descends to zero at approximately 340°C and does not rise again until recrystallization commences. The recrystallization temperature is considerably lower for the M nickel than for the specimen of lower purity as would be expected. In addition to these changes in the ΔP curve it is apparent that there are two peaks at lower temperas that for deformation in torsion, but the recrystallization peak is broader because of the larger grain size of the specimens before deformation.[6] This curve may be compared to those for the high purity, N, nickel shown in Fig. 3.

For N nickel (99.96 per cent purity) after the heavier deformation of 70 per cent compression, only two separate peaks can be distinguished because the recrystallization temperature decreases to 325°C for this material. However, at the lower deformation of 10 per cent compression three stages are clearly resolved. The first two stages correspond approximately in temperature with the first two stages

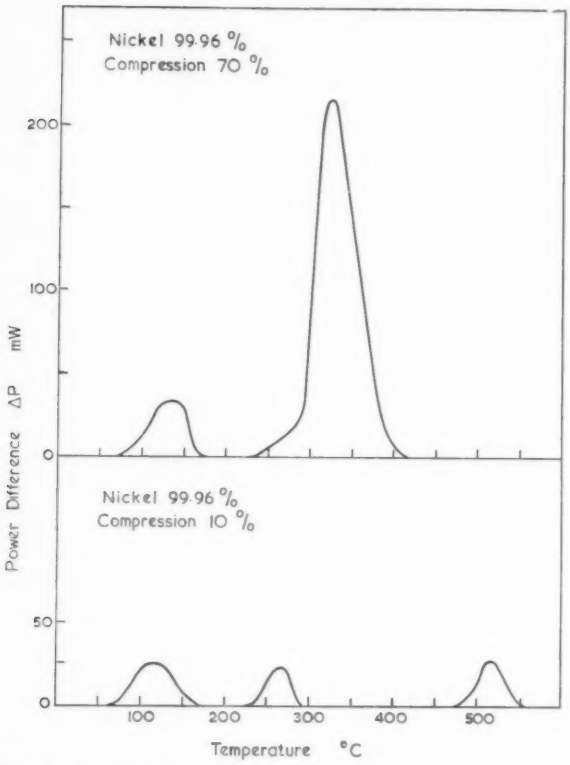


FIG. 3. Curves of power difference (ΔP) as a function of temperature for specimens of *N* nickel, 99.96 per cent purity, deformed in compression. Heating rate 6°C/min. Above 70 per cent compression; below, 10 per cent compression.

observed for the M nickel. It appears that the tail on the low-temperature side of the recrystallization peak for 70 per cent deformation is due to the second of these stages.

3.2 *Density and electrical resistivity*

The curves showing the changes in density and resistivity which occur during the stage by stage annealing treatment are shown in Fig. 2, for the *M* nickel deformed 70 per cent in compression. It is clear that changes in these properties accompany each of the stages of release of energy which are observed in the ΔP curve. For recrystallization the changes in resistivity and density are clearly resolved: the density curve shows distinct evidence of resolution of the first two stages and there is some indication of this resolution in the curve for resistivity. The changes in density, resistivity and the corresponding values of stored energy for each of the stages are collected in Table 1.

4. DISCUSSION

4.1 *Dislocations*

The discussion in this section is so intimately connected with that in a previous paper,[1] that it will be assumed that the reader is familar with that paper, in order to avoid considerable repetition.

The most marked effect of increasing the purity on the ΔP curves for nickel is the virtual disappearance of the plateau-like area preceding recrystallization. The behaviour of nickel is therefore similar to that of copper in this respect as only a single peak corresponding to recrystallization is observed for the purest copper examined, whereas the plateau occurs for arsenical copper.[1]

The release of energy corresponding to this plateau has been attributed to recovery involving the rearrangement and annihilation of dislocations. It appears that the effect of impurities is to inhibit the movement of dislocations during recovery. In the relatively pure metals, recovery involving movement of dislocations is virtually complete at room temperature, and so no release of energy due to this process is observed. In the impure materials this recovery is delayed until higher temperatures, and the plateau-like areas in the ΔP curves are observed. For the intermediate case in copper of 99.96 per cent purity a tail appears on the low temperature side of the recrystallization peak[1] and this has been attributed

TABLE 1. Changes in properties in *M* nickel (99.85 per cent Ni) during annealing following deformation in compression (70 per cent)

Stage	Defect assumed	Stored energy (cal/g)	$\Delta D/D$ exptl.	$\Delta\rho$ exptl. ($\mu\Omega$ cm)	Concentration* calc.	$\Delta D/D$ calc.†	$\Delta\rho$ calc.‡ ($\mu\Omega$ cm)
→ 200°C	Interstitials	0.044	5.5×10^{-5}	0.02	2.2×10^{-3} at. %	4.5×10^{-5}	0.017
200–350°C	Vacancies	0.056	8.7×10^{-5}	0.07	9.5×10^{-3} at. %	7.6×10^{-5}	0.038
Recrystallization	Dislocations	0.201	6.6×10^{-5}	0.10	1.06×10^{11} cm/cm³	7.0×10^{-5}	0.0019

$\Delta D/D$ = Fractional change in density. $\Delta\rho$ = Increment in electrical resistivity.

* Calculated from stored energy assuming the following energies:
Interstitial 5 eV, Vacancy 1.5 eV, Dislocation 4.4×10^8 eV cm^{-1}.

† Calculated from concentration assuming the following dilatations: Interstitial 2 at. vol., Vacancy 0.8 at. vol., Dislocation 1.5 at. vol. per length $a/\sqrt{2}$,[8] a = lattice parameter.

‡ Calculated from concentration assuming the following changes in resistivity:
Interstitial 8 $\mu\Omega$ cm/at. %, Vacancy 4 $\mu\Omega$ cm/at. %, Dislocation 1.8×10^{-14} N, $\mu\Omega$ cm.[9]

VOL. 8 1960

to the completion of recovery.* It is important to decide whether recovery involving dislocations contributes to the release of energy prior to recrystallization in the intermediate case of *M* nickel (99.85 per cent purity). This appears to be unlikely in view of the results obtained for copper, where any residual recovery immediately precedes recrystallization, even though in fine-grained material it may appear as a small discrete release of energy.[6] Therefore most, if not all, the energy released in the two stages observed below 350°C in *M* nickel must be attributed to causes other than dislocations.

With respect to measurements of resistivity, there is an indication in the present results of two stages in the decrease of resistivity on annealing below 350°C for the *M* nickel (99.85 per cent). Definite resolution into two stages was observed by Sosin and Brinkman for nickel of 99.98 per cent purity.[3] Measurements on nickel of 99.6 per cent purity[1] showed only a decrease in resistivity corresponding to the second stage of annealing centred at approximately 260°C. Similarly, for nickel of 99.4 per cent purity, Sosin and Brinkman found no decrease, but in fact a slight increase, in resistivity in the temperature range in which the first decrease in resistivity is observed for the purer materials. Both sets of experiments indicate that the first stage is not observed in the presence of substantial concentrations of impurities.

It was shown previously that for arsenical copper the initial stages of recovery were accompanied by an increase in resistivity and this was attributed to the dispersal of atmospheres of impurity atoms when the dislocations moved away under thermal activation during recovery.[1] Subsequent experiments on single crystals by Schröder[7] have shown that strain ageing does occur in this material. Clearly the operation of a similar mechanism in impure nickel could mask the first stage observed for the purer materials. This agrees with the conclusion reached by Sosin and Brinkman.

The relations between the values of stored energy and the changes in resistivity and density for *M* nickel during recrystallization, shown in Table 1, are similar to those found previously for copper[5] and nickel.[2] The value of the change in density calculated from the dislocation density agrees with the observed value. For resistivity there is the usual large discrepancy by a factor of about 50. Seeger[10] has suggested that this discrepancy can be removed by taking into account the contribution of the stacking faults to the resistivity, which he considers increases the resistivity due to the dislocation by a factor of 40.

4.2 *Point defects*

For all samples of nickel investigated, a peak in the ΔP curve centred at 260–270°C is observed, the temperature at which this peak occurs being almost independent of the purity of the specimen and the degree and nature of the deformation. Evidence that this peak is due to the disappearance of vacancies has been presented previously,[1] for the impure nickel (99.6 per cent), and presumably this interpretation is valid for the purer materials. This view has been adopted by Sosin and Brinkman[3].

These authors suggest that the stage in the annealing of resistivity centred near 100°C is due to the disappearance of interstitials. If this interpretation is adopted for the releases of energy centred at approximately 120°C, observed for the purer samples of nickel in the present experiments, it is then possible to compare the values of stored energy and the changes in density and resistivity with those to be expected from theoretical estimates. The results of such a comparison for the *M* nickel are shown in Table 1, the separation between experimental observations for interstitials and vacancies being made somewhat arbitrarily at 200°C. The possible contribution of dislocations to the stored energy or changes in properties below 350°C has been ignored in compiling the table. There are wide discrepancies between various estimates of the effects of point defects on the properties of metals in general and few estimates for nickel.[11] The values selected have been chosen, in some cases by analogy with values for copper, as intermediate between the extremes of the estimates available.

There is quite good agreement between the measured and calculated values for the changes in properties. This indicates only that the values taken for the changes produced by particular defects are in approximately the right ratios to one another, as the calculated values of the changes in properties depend directly on the value for the energy assumed for the defects. However, the value assumed for the dilatation due to a vacancy, i.e. 0.8 atomic volume, should not be in error by a large factor, so that, if the assignment of the processes responsible for the changes in properties is correct, the comparison suggests that the other values are not greatly in error.

ACKNOWLEDGMENT

We are greatful to The Mond Nickel Co. Ltd. who kindly prepared and supplied the samples of nickel.

* In this connection it should be noted that Sosin and Brinkman[3], in their Fig. 1, have reproduced one of these curves for copper of 99.96 per cent purity and labelled it incorrectly as being for copper of 99.98 per cent purity. For the purer material the tail is virtually absent.

REFERENCES

1. L. M. Clarebrough, M. E. Hargreaves and G. W. West, *Proc. Roy. Soc.* A**232,** 252 (1955).
2. L. M. Clarebrough, M. E. Hargreaves and G. W. West, *Phil. Mag.* **1,** 528 (1956).
3. A. Sosin and J. A. Brinkman, *Acta Met.* **7,** 478 (1959).
4. L. M. Clarebrough, M. E. Hargreaves, D. Michell and G. W. West, *Proc. Roy. Soc.* A**215,** 507 (1952).
5. L. M. Clarebrough, M. E. Hargreaves and G. W. West, *Acta Met.* **5,** 738 (1957).
6. L. M. Clarebrough, M. E. Hargreaves and M. H. Loretto, *Acta Met.* **6,** 725 (1958).
7. K. Schröder, *Proc. Phys. Soc., Lond.* **72,** 33 (1958).
8. H. Stehle and A. Seeger, *Z. Phys.* **146,** 217 (1956).
9. W. Boas in *Dislocations and Mechanical Properties of Crystals* p. 340. Wiley, New York (1958).
10. A. Seeger in *Dislocations and Mechanical Properties of Crystals* p. 348. Wiley, New York (1958).
11. T. Broom and R. K. Ham, *Vacancies and other Point Defects in Metals and Alloys*, p. 41. Institute of Metals, London (1958).

VOL.
8
1960

NOTE ON THE THERMODYNAMICS OF THE LIQUIDUS AND SOLIDUS CURVES IN SYSTEMS WITH COMPLETE SOLID SOLUBILITY; THE SYSTEM SILVER–GOLD*

O. J. KLEPPA†

A simple, general expression is derived which permits the calculation of $\Delta F^s - \Delta F^l$ from the phase diagrams for binary systems with complete solid solubility. In systems with a narrow liquidus–solidus gap good values of $\Delta(\Delta F)$ may be obtained without any use of detailed information on the free energy of formation of the equilibrium phases. For silver–gold the use of this method gives the expression

$$\Delta(\Delta F) = -187 X_{Au} X_{Ag} \text{ cal/mole.}$$

NOTE SUR LA THERMODYNAMIQUE DES COURBES DE LIQUIDUS ET DE SOLIDUS DANS LES SYSTEMES A SOLUBILITE SOLIDE COMPLETE; LE SYSTEME ARGENT–OR

L'auteur établit une expression générale et simple qui permet de calculer $\Delta F^s - \Delta F^l$ à partir des diagrammes de phases de systèmes binaires, à solubilité solide complète. Dans le cas de systèmes qui présentent une lacune liquidus–solidus étroite, on peut obtenir de bonnes valeurs de $\Delta(\Delta F)$ sans utiliser d'indications complémentaires sur l'énergie libre de formation des phases d'équilibre. Pour le système argent–or, l'emploi de cette méthode conduit à l'expression: $\Delta(\Delta F) = -187 X_{Au} X_{Ag}$ cal/mole.

BEMERKUNGEN ÜBER DIE THERMODYNAMIK DER LIQUIDUS- UND SOLIDUS-LINIEN BEI SYSTEMEN MIT VOLLSTÄNDIGER GEGENSEITIGER LÖSLICHKEIT; DAS SYSTEM SILBER–GOLD

Es wird ein einfacher, allgemeiner Ausdruck hergeleitet, der die Differenz $\Delta F^s - \Delta F^l$ für binäre Systeme mit vollständiger gegenseitiger Löslichkeit aus dem Phasendiagramm zu berechnen gestattet. Bei Systemen mit geringem Abstand zwischen Liquidus- und Solidus-Linien bekommt man gute Werte von $\Delta(\Delta F)$, ohne daß genaue Kenntnis der freien Bildungsenergie der Gleichgewichtsphasen nötig wäre. Für Silber–Gold ergibt die Methode den Ausdruck

$$\Delta(\Delta F) = -187 X_{Au} X_{Ag} \text{ cal/Mol.}$$

A few years ago it was pointed out by Wagner[1], that the accepted phase diagram for silver–gold, which is based on thermal analysis information only, shows a much wider liquidus–solidus "gap" than should be expected from the reported thermodynamic properties of the solid and liquid alloys formed by these two metals. Wagner calculated that if this system were ideal both in the solid and in the liquid state, the gap ($X_{Au}^s - X_{Au}^l$) should be about 2.3 at.% near the equiatomic composition. In fact both the solid and the liquid phase show pronounced negative deviations from ideality. Therefore an even smaller gap must be expected. On the basis of approximate values for the excess free energy of mixing Wagner estimated that the gap should be 1.3 at.% near the 50–50 composition. More recently White *et al*[2] have made an extensive survey of the available thermodynamic data for silver–gold. From these data they calculate a "theoretical" phase diagram for this system. Their diagram exhibits the narrow liquidus–solidus gap predicted by Wagner with both phase boundaries reasonably close to the "old" liquidus. Only last year White confirmed this narrow gap experimentally.[3] However, his new liquidus–solidus values show a slight systematic difference from the old data and from the "theoretical" curves of White *et al*. This led us to reconsider the thermodynamic consequences of White's work. We are interested in particular in the possibility of deriving from his data improved values of the interesting quantity

$$\Delta(\Delta F) = \Delta F^s - \Delta F^l,$$

i.e. the free energy of formation of the solid alloy referred to the pure solids, less the free energy of formation of the liquid alloy of the same composition referred to the pure liquids.

On the basis of certain reasonable and simplifying assumptions regarding the free energy of mixing of the liquid alloys, White *et al*. arrived at the following expression for this quantity:

$$\Delta(\Delta F) = -(194 \pm 80) X_{Ag} X_{Au} \text{ cal/mole.}$$

White made an attempt to derive improved values of $\Delta(\Delta F)$ from his own data. However, his method relates $\Delta(\Delta F)$ to the gap width. For small gaps this

* This work was supported by the O.N.R. under Contract No. Nori-2121 with the University of Chicago. Received February 1, 1960.

† Institute for the Study of Metals, University of Chicago.

will necessarily introduce a large uncertainty in the calculated values of $\Delta(\Delta F)$.

It is the purpose of the present note to show that quite reliable values of $\Delta(\Delta F)$ can be readily derived from White's phase diagram data. In our derivation the gap width and the free energy of mixing for the alloy solution enter only in the form of a small correction term. Therefore our computation provides an independent check of the internal consistency of the White *et al.* data. Our method may also be used for other systems with a known and larger gap width, in cases where free energy data are available for the solid or for the liquid solution system.

Let $\bar{F}_1(X_1)$ be the relative partial free energy of component 1 at composition X_1 referred to the pure component in the same state of aggregation. If we make the usual assumption that the entropy of fusion of the pure metal ΔS_1 is independent of temperature between the melting point T_1 and the considered temperature T, we may write the following equilibrium condition for component 1:

$$\bar{F}_1^{\,s}(X_1) = \bar{F}_1^{\,l}(X_1') + \Delta S_1(T_1 - T). \qquad (1a)$$

Similarly for component 2:

$$\bar{F}_2^{\,s}(X_1) = \bar{F}_2^{\,l}(X_1') + \Delta S_2(T_2 - T). \qquad (1b)$$

Here $X_1\,(= 1 - X_2)$ is the mole fraction of component 1 in the solid solution, while X_1' is the mole fraction of the same component in the co-existing liquid.

Let us now denote the width of the liquidus–solidus gap by

$$\delta = X_1 - X_1' = X_2' - X_2.$$

If we multiply equation (1a) by $X_1 = X_1' + \delta$ and equation (1b) by $X_2 = X_2' - \delta$ and add, we obtain

$$\begin{aligned} X_1\bar{F}_1^{\,s}(X_1) + X_2\bar{F}_2^{\,s}(X_1) &= X_1\Delta S_1(T_1 - T) \\ &\quad + X_2\Delta S_2(T_2 - T) \\ &\quad + (X_1' + \delta)\bar{F}_1^{\,l}(X_1') \\ &\quad + (X_2' - \delta)\bar{F}_2^{\,l}(X_1') \end{aligned} \qquad (2a)$$

or more simply

$$\begin{aligned} \Delta F^s(X_1) &= X_1\Delta S_1(T_1 - T) \\ &\quad + X_2\Delta S_2(T_2 - T) + \Delta F^l(X_1') \\ &\quad + \delta\{\bar{F}_1^{\,l}(X_1') - \bar{F}_2^{\,l}(X_1')\}. \end{aligned} \qquad (2b)$$

Since, at constant pressure and temperature

$$\Delta F^l(X_1) = \Delta F^l(X_1') + (X_1 - X_1')\frac{d\Delta F^l}{dX_1'} + \frac{1}{2}(X_1 - X_1')^2\frac{d^2\Delta F^l}{dX_1'^2} + \text{h.o.t.} \qquad (3)$$

and

$$\frac{d\Delta F^l}{dX_1'} = \bar{F}_1^{\,l}(X_1') - \bar{F}_2^{\,l}(X_1') \qquad (4)$$

we finally obtain

$$\begin{aligned} \Delta\{\Delta F(X_1)\} &= X_1\Delta S_1(T_1 - T) \\ &\quad + X_2\Delta S_2(T_2 - T) \\ &\quad - \frac{\delta^2}{2}\frac{d^2\Delta F^l}{dX_1'^2} + \text{h.o.t.} \end{aligned} \qquad (5a)$$

A completely analogous expression is

$$\begin{aligned} \Delta\{\Delta F(X_1')\} &= X_1'\Delta S_1(T_1 - T) \\ &\quad + X_2'\Delta S_2(T_2 - T) \\ &\quad + \frac{\delta^2}{2}\frac{d^2\Delta F^s}{dX_1^2} + \text{h.o.t.} \end{aligned} \qquad (5b)$$

These expressions may be used to make a precise calculation of $\Delta(\Delta F)$ from the phase diagram if we have thermodynamic data which permit an evaluation of $(d^2\Delta F/dX^2)$ i.e. of the curvature of ΔF, for either the solid or the liquid phase. Note that

$$\frac{d^2\Delta F}{dX^2} = \frac{RT}{X(1 - X)} + \frac{d^2F^E}{dX^2} \qquad (6)$$

where F^E is the excess free energy. Thus for an ideal system at 50–50 composition this term is $4\,RT$. It should also be recognized that for systems with a negative deviation from ideality the curvature is larger, while for systems with a positive deviation it is smaller than the ideal. It is this very fact which gives rise to *small* liquidus–solidus gaps in systems with negative deviations from ideality (e.g. Ag–Au) and *wide* gaps in systems with positive deviations (e.g. Au–Pt).

A particularly simple situation exists where $\delta = 0$, i.e. when the liquidus–solidus gap vanishes. This occurs in the two trivial cases when $X = 0$ and $X = 1$, and at phase diagram maxima and minima. Then we have simply

$$\Delta(\Delta F) = X_1\Delta S_1(T_1 - T) + X_2\Delta S_2(T_2 - T). \qquad (7)$$

This equation was previously derived by Wagner[1], and was used by him to evaluate $\Delta(\Delta F)$ for a few systems with phase diagram minima. However, we

VOL. 8 1960

TABLE 1. Values of $\Delta(\Delta F) = \Delta F^s - \Delta F^l$ for the silver–gold system as calculated from the liquidus data of White[3]. The entropies of fusion of silver and gold were taken from Kubaschewski and Evans[4]

Liquidus composition X_{Au}	Liquidus temperature (°K)	$\Delta(\Delta F)$ equation (7) (cal/mole)	$\Delta(\Delta F)/X_{Au}X_{Ag}$ (cal/mole)
0.251	1279	−40	−213
0.262	1282	−44	−228
0.501	1308	−48	−192
0.503	1309	−50	−200
0.522	1308	−44	−176
0.760	1327	−33	−181
0.761	1327	−33	−181
0.768	1329	−35	−198

will show that the same expression may be used with nearly equal confidence for solid solution systems with a narrow liquidus–solidus gap.

In Table 1 we give the values of $\Delta(\Delta F)$ for silver–gold as derived from equation (7) by the use of White's liquidus data. This calculation, which makes no specific use of information on the liquidus–solidus gap, yields the following expression

$$\Delta(\Delta F) = -196 X_{Au} X_{Ag} \text{ cal/mole}$$

with a mean deviation of about 7 per cent.

It remains to estimate the error arising from our omission of the last term in equation (5b). At the 50–50 composition $(d^2\Delta F^s/dX^2) \sim 15{,}000$ calories, while $(\delta^2/2) \sim 10^{-4}$. This gives a correction term of the order of +1.5 cal/mole (or 3 per cent). At the 25–75 composition the corresponding corrections are about +2 cal/mole (or 5–6 per cent).

With these corrections our expression for $\Delta(\Delta F)$ becomes

$$\Delta(\Delta F) = -187 X_{Ag} X_{Au} \text{ cal/mole.}$$

This differs by less than 4 per cent from the one recommended by White *et al.*

In order to estimate the absolute error in our calculation we must consider the uncertainty arising from the adopted values of the entropies of fusion (probably less than 3 per cent), and in particular the possible error in the liquidus. We believe that White's estimate of an absolute uncertainty of ±4° in his liquidus values probably is too conservative. The corresponding errors in the values of $\Delta(\Delta F)$ would be ±15 to ±20 cal/mole.

REFERENCES

1. C. WAGNER, *Acta Met.* **2,** 292 (1954).
2. J. L. WHITE, R. L. ORR and R. HULTGREN, *Acta Met.* **5,** 747 (1957).
3. J. L. WHITE, *Trans Amer. Inst. Min. (Metall.) Engrs.* **215,** 178 (1959).
4. O. KUBASCHEWSKI and E. L. EVANS, *Metallurgical Thermochemistry.* Butterworths–Springer, London (1951).

Porosity in plastically deformed single crystals*

The concept of vacancy generation at jogs in moving screw dislocations is well known.[1–3] As part of an inquiry into this matter, single crystals of Ag, Cu and a Cu–0.1% Al alloy were extended to fracture at room temperature and at a uniform strain rate (0.003 min^{-1}). The specimens were prepared by the Bridgman technique in a vacuum of 10^{-5} mm Hg. Chemical analyses of the Ag and Cu specimens are given in Table 1. The following elements were looked for but were not found in either specimen and are not included in the Table: Al, As, Au, Be, Bi, Cd, Co, Cr, Cs, Ga, Ge, H, Hg, K, Li, Mo, Na, P, Pt, Pb, Sr, Ta, Te, Ti, V, W, Zn, Zr. The tensile axis of the specimens was a ⟨100⟩. The gross features of the fractures in Ag and Cu are shown in Fig. 1. Both crystals failed at about 45° to the tensile axis (Fig. 1 a,c). The Ag specimen displayed *V*-type fracture surfaces while the Cu specimen exhibited knife-edge fracture surfaces (Fig. 1 b, d). It is apparent that considerable necking occurred prior to fracture, the reduction in area at the fracture surface being almost 100 per cent.

Under the experimental conditions, the necking phenomenon is dynamically unstable and could be related to the occurrence of local, intense multiple glide and the subsequent production and coalescence of vacancies. In fact, the ⟨100⟩ crystal orientation was selected to produce large amounts of slip on intersecting planes. If this is so, it might be expected that metallographic sections near the fracture surface would exhibit observable porosity. The photomicrographs in Fig. 2(*a–c*) show the porosity existing in sections about 1 mm from and parallel to the fracture surface in Ag, Cu and the Cu–0.1% Al alloy. The holes associated with the porosity in Cu (Fig. 2a) are round while those in Ag (Fig. 2b) are lenticular, and are oriented in the *A–B* direction shown in Fig. 1(a). It is noteworthy that the large axis of the cavities is perpendicular to the stress axis. Close examination of the cavities indicate that the lenticularity is due to a coalescence of several spherical pores. Such a phenomenon is indicated by the cavity above the arrow in Fig. 2(b). The sections in Fig. 2(a) and (b) were prepared by metallographic polishing and are unetched. The effect of etching such a section is shown in Fig. 2(c) for the Cu–0.1% Al alloy. This procedure was used for enlarging the pores by preferential attack, and serves to emphasize that most of the porosity occurs parallel and very close to the plane which bisects the crystal along its largest dimension.

If the observed porosity is due to vacancy condensation as a result of extensive multiple glide, then it is thought that some significance can be given to the empirical concept of an equicohesive temperature.[4] The equicohesive temperature is that temperature above which the fracture of polycrystalline metals changes from a transgranular to an intercrystalline nature. Transgranular fractures are favored by (1) low temperatures, (2) fast rates of deformation, (3) large grain size and (4) high impurity contents. It is noteworthy that all the factors favoring transgranular fracture would also inhibit vacancy migration and condensation at grain boundaries, which could lead to intercrystalline failure. The low temperature would lower the diffusion rate of vacancies; the fast deformation rate would provide less time for the migration of vacancies to the boundaries; the larger grain size would increase the average distance for the vacancies to reach the boundaries; and the high impurity content could provide sinks for vacancies within the grain.

As a final observation, it would seem from the data in Table 1 that the porosity observed in these crystals on fracture cannot be attributed directly or indirectly to the presence of dissolved gases or a second phase.

RCA Laboratories F. D. Rosi
Princeton, New Jersey M. S. Abrahams

References

1. W. T. Read, *Dislocation in Crystals* p. 85. McGraw–Hill, New York (1953).
2. N. F. Mott, *Proc. Phys. Soc., Lond.* B**64**, 729 (1951).
3. F. Seitz, *Advanc. Phys.* **1**, 43 (1952).
4. Z. Jeffries, *J. Amer. Inst. Metals* **11**, 300 (1917).

* Received May 19, 1960.

Table 1. Chemical analyses of the Ag and Cu tensile specimens

Specimen	Impurities (p.p.m.)												
	Cu	Ag	Fe	Ni	Mg	Si	Sn	Ca	Sb	Mn	B	N	O
Ag	1000	—	100	—	10	0.1	30	—	—	—	—	1.4	2.6
Cu	—	100	30	10	3	10	—	10	30	3	1	0.3	2.3

VOL. 8 1960

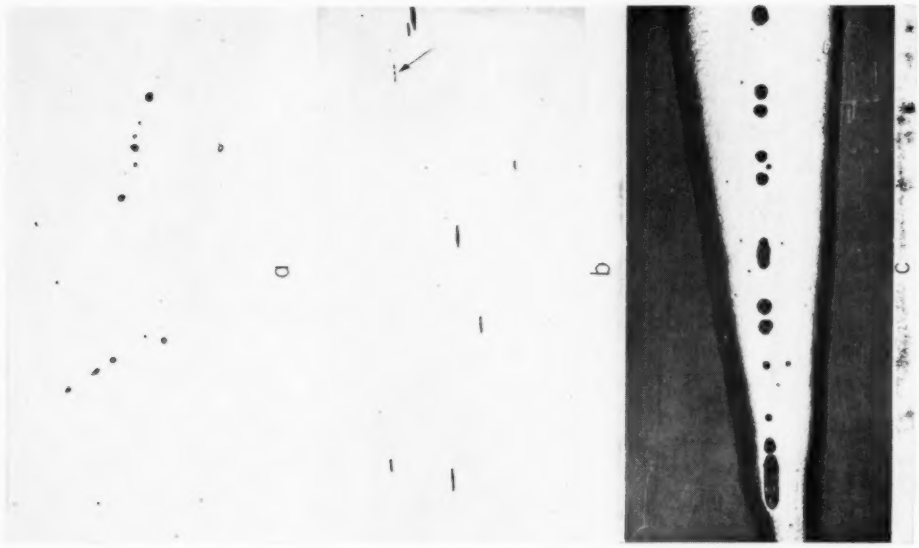


FIG. 2. Appearance of porosity in sections near and parallel to the fracture surface in: (a) Cu, unetched, ×250; (b) Ag, unetched, ×250; (c) Cu–0.1% Al alloy, etched, ×30.

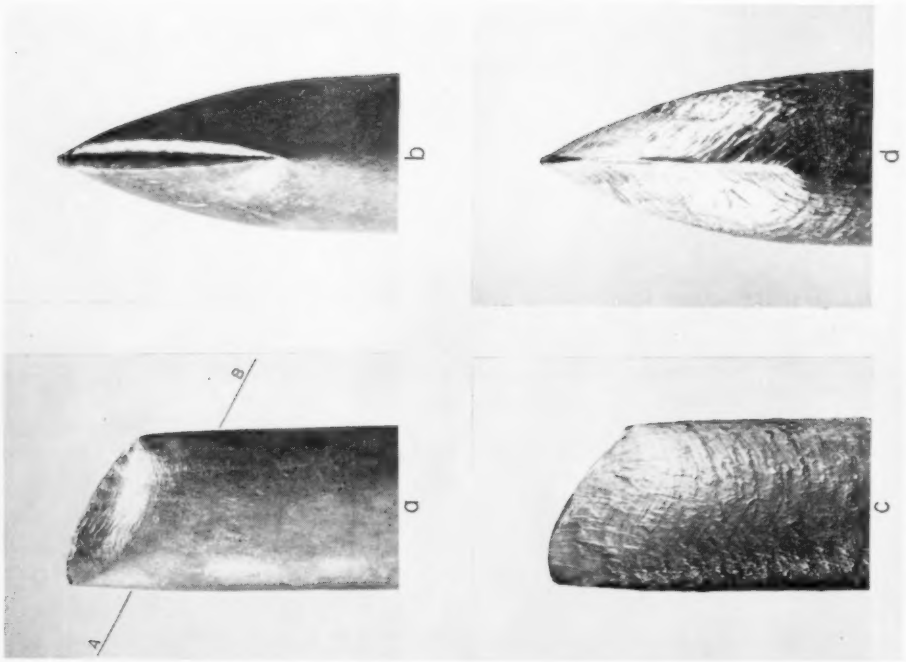


FIG. 1. Appearance of ductile fractures in f.c.c. single crystals: (a) ×2.65 and (b) ×3.85, side and front view of Ag; (c) ×2.65 and (d) ×3.85, side and front view of Cu.

VOL. 8 1960

Twinning in iron*

In 1953 Paxton[1] could state that "Alpha-iron and its dilute alloys appear to be the only body-centered cubic metals in which mechanical twinning has been definitely demonstrated". Generally deformation at very low temperature or deformation by impact is needed to produce mechanical twins (Neumann bands or lamellae), and less pure iron seemed to show a greater ease of twinning than the purer.[2,3]

An indication that in contradiction to this the ease of twinning may increase with increase of purity was obtained in this laboratory when during rolling of a zone melted iron bar to 20 per cent reduction of thickness at *room temperature* mechanical twins were found in the areas near to the edges of the rolled strip. Similar twins, but now heavily deformed due to deformation after their formation, were found after rolling of other specimens to 60 per cent reduction of thickness. In another as-melted bar in one area mechanical twins had been formed due to an accidental deformation. Slow bending of a neighboring area at room temperature produced no twins in the bent region, but a new twin appeared close to the already twinned area. An interesting detail found in this specimen is the easy crossing of subgrain boundaries by twins as shown in Fig. 1. The subgrain boundaries by remaining visible in the twin nicely illustrate the displacement of the parts of the crossed subgrains and the twin nature of the Neumann bands.

Further support for a hypothesis that increased purity increases the ease of twinning has been found in the frequent formation of *annealing twins* in zone melted iron observed in this laboratory. Thus annealing twins were repeatedly observed in specimens used in experiments for production of single crystals. Lately annealing twins were also observed on the as-zone-melted surface of iron bars. One of these annealing twins which particularly well illustrates the twin nature is shown in Fig. 2.

A more frequent occurrence of annealing twins in purer metals has been suggested by Berghezan[4] when working on face-centered cubic metals. Generally annealing twins have not been considered to occur in body-centered cubic metals, although among others McKeehan[5] produced some annealing twins in iron by a very special heat treatment, and Lacombe and Berghezan[6] reported on the appearance of many insular crystals in twin position to the matrix grains after a special heat treatment of Armco iron in

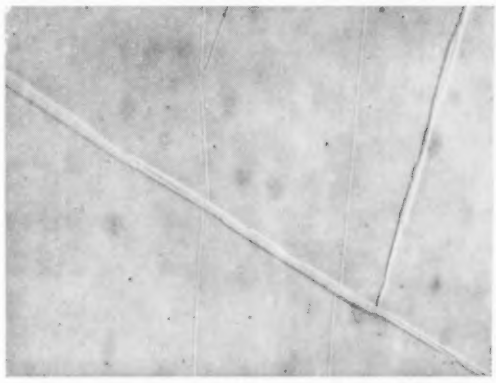


FIG. 1. Crossing of two subgrain boundaries by a mechanical twin.

hydrogen. At least McKeehan's annealing twins might be explained as the result of a purification considering the very high temperature (1400°C), the hydrogen atmosphere and the slow zone heating method applied to his 1 mm dia. wire made from Armco iron welding rod. The removal of e.g. oxygen and sulphur from iron—which results in a considerable increase of the surface tension of liquid iron—most probably will also, by increasing the mean grain boundary energy more than the coherent twin boundary energy, increase the ratio of these two energies and thus favour the growth of annealing twins in iron. As to the mechanical twins, among others Smith and Rutherford[7] found the most extensive mechanical twinning during slow deformation at low temperatures in their purest iron.

Recent data on other body-centered cubic metals also support the hypothesis that increasing the purity increases the ease of twinning, as pointed out by Anderson and Bronisz[8] when they produced twinning in pure electron beam melted tantalum by hammering

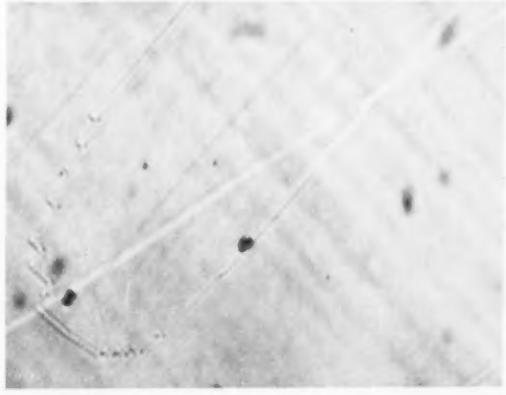


FIG. 2. Annealing twin on as-zone-melted surface of iron bar. Block spots are due to lengthy handling, and are not inclusions.

* The project of which this work is a part was sponsored by the Union Carbide Corporation, New York, N.Y. Received May 19, 1960.

at room temperature, while less pure tantalum only twins at liquid nitrogen temperature. Thus Adams *et al.*[9] report that electron bombardment melted niobium can be made to twin, while Fourdeux and Berghezan by transmission electron microscopy[10] find stacking faults in zone melted niobium rolled at room temperature and annealed.

It may prove fruitful to examine what relation there is to another phenomenon which is definitely favoured by increase of purity, namely the formation of subgrains.

E. Bull Simonsen

European Research Associates, s.a.
Brussels, Belgium

References

1. H. W. Paxton, *Acta Met.* **1,** 141 (1953).
2. C. F. Tipper and E. O. Hall, *J. Iron St. Inst.* **175,** 9 (1953).
3. J. R. Low and R. G. Feustel, *Acta Met.* **1,** 185 (1953).
4. A. Berghezan, Thesis, Université de Paris, p. 30 (1952).
5. L. W. McKeehan, *Trans. Amer. Inst. Min. (Metall.) Engrs.* **78,** 453 (1928).
6. P. Lacombe and A. Berghezan, *Métaux et Corros.* **24,** 1 (1949).
7. R. L. Smith and J. L. Rutherford, *J. Metals, N.Y.* **9,** 857 (1957).
8. R. W. Anderson and S. E. Bronisz, *Acta Met.* **7,** 645 (1959).
9. M. A. Adams, A. C. Roberts and R. E. Smallman, *Acta Met.*, **8,** 328 (1960).
10. A. Fourdeux and A. Berghezan, to be published in *J. Inst. Metals.*

The effect of pressure on the second stage parabolic rate in the oxidation of titanium*

The oxidation of titanium at high temperatures is initially parabolic, a coherent rutile scale forming and growing by anion vacancy migration.[1] The scale is under compressive stresses and eventually blisters from the metal surface, absorbing oxygen to become stoichiometric. The detached stoichiometric envelope is evidently porous, for oxidation restarts underneath it, and the cycle is repeated. During this process, the rate becomes linear, a laminar scale forming from the repeated blistering envelopes. Eventually the linear rate is superseded by a second parabolic rate, which is considerably more rapid than the first stage parabola. The scaling behaviour is the same for this second parabolic stage as for the intermediate linear stage, and at the point where the linear rate gives way to the second parabola the two curves have the same slope. Because of this, it has been concluded[1] that the appearance of a second parabolic rate indicates that a step in the oxidation process, hitherto more rapid than the reaction near the metal surface, becomes slower than this reaction, and thus determines the rate. The only step

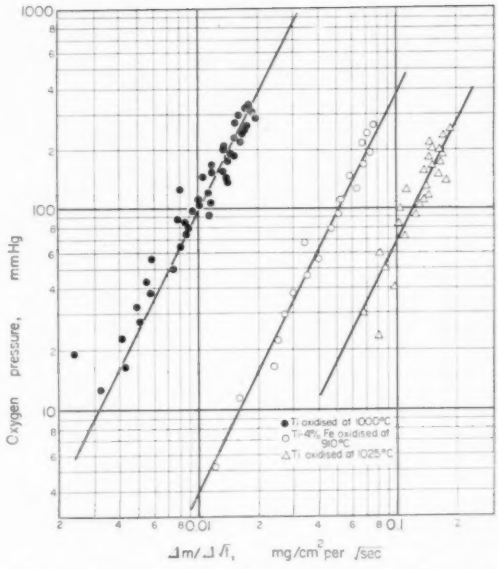


Fig. 1. Pressure dependence of the second parabolic stage in the oxidation of titanium. The lines drawn through the experimental points correspond to a linear dependence of the parabolic rate constant on oxygen pressure. The points representing the oxidation of titanium at 1000°C have been displaced to the left for clarity.

in the oxidation which could produce a parabolic rate without altering the scale appearance is the gaseous diffusion of oxygen through the scale. On the basis of this model a parabolic rate law has been calculated[1] which, when reasonable values for the size and density of the pores in the scale are inserted, gives oxidation rates close to those observed.

The calculated rate law predicted a linear dependence of the parabolic rate constant on oxygen pressure. The experimental evidence of this point was inconclusive. Jenkins[2] attempted to measure the pressure dependence of the oxygen rate when a porous scale was formed by abruptly lowering the oxygen pressure, but found that the results obtained suggested a slow evolution of oxygen from the porous scale.

In this investigation the pressure dependence was studied by oxidizing separately two samples of titanium and one titanium-4% iron in a Sieverts apparatus of the type described earlier.[1] The pressure was allowed to fall to low values during the oxidation. Then the difference ΔM between two consecutive readings of the weight of oxygen absorbed per unit area by the scale was divided by the difference $\Delta(t^{1/2})$ in the square roots of the times of the two readings and plotted on a logarithmic scale versus the logarithm of the mean pressure p between the two readings. The results are shown in Fig. 1.

This method overcomes the difficulty encountered by Jenkins[2], but it has some disadvantages. The

difference between adjacent readings is only about 10 times the estimated error of the Sieverts method at the most,[1] and becomes even less as the rate becomes slow at low pressures. There is a small error possible in the time readings as well, since the experimental method requires simultaneous reading of two manometer arms. For this reason $\Delta m/\Delta\sqrt{t}$ versus p is plotted rather than the more natural $(\Delta m)^2/\Delta t$ versus p since squaring the term containing both the possible errors would magnify the scatter. The possible error increases as the pressure falls.

The theory for the oxidation process requires that

$$m^2 = k'pt$$

where k' is a constant independent of pressure. Thus $\Delta m/\Delta\sqrt{t}$ should vary as $p^{1/2}$. This relation is shown as the full lines in Fig. 1. It can be seen that the agreement is extremely good.

The effect of sharply varying the pressure was studied by adding further amounts of oxygen and measuring the change in rate. A rate curve plotted as mg/cm^2 of oxygen absorbed versus time is shown in Fig. 2. The oxidation was allowed to proceed until the atmosphere was nearly exhausted, and a small amount of oxygen added, sufficient to alter the pressure to 550 mm Hg. The rate immediately increased, falling off as the atmosphere was again exhausted, retracing the last part of the original oxidation curve. At this point a large addition of oxygen was made, sufficient to raise the pressure nearly to atmospheric. In this case the rate rose sharply for a very short while, then fell off until the reaction almost stopped. The rate then slowly increased, eventually reaching a normal rate.

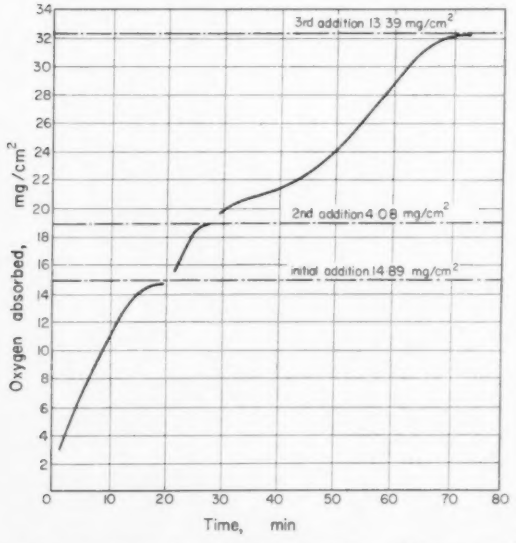


FIG. 2. The effect of abrupt pressure changes on the oxidation rate of Ti–4% Fe at 910°C.

This is the inverse of the effect noted by Jenkins[2] on dropping the pressure.

This effect can be accounted for in terms of the gaseous diffusion model. The gas diffuses through small pores through the laminations. Large fissures between the laminations connect the ends of the pores in adjacent layers without introducing any resistance to flow.[1] This is the situation under normal conditions, when the pressure difference across any single lamination is small. However, if the pressure is suddenly raised on the outside of the scale, the outer laminations will be compressed, thus reducing or removing the parallel fissures between the laminations which connect the pores. The number of diffusion paths to the metal surface will therefore be much reduced, until the slow flow of gas through the remaining paths has equalised the pressure distribution through the scale. The rate will then increase to the steady state value.

The results obtained in this series of experiments confirm that the controlling step in the second parabolic stage in the oxidation of titanium is the diffusion of gaseous oxygen through the porous scale, and in particular they show that the parabolic rate constant is linearly dependent on oxygen pressure, as required by theory.

The materials for this investigation were supplied by I.C.I. Metals Division.

J. STRINGER

Department of Metallurgy
University of Liverpool

References

1. J. STRINGER, *Acta Met.*, **8**, 758 (1960).
2. A. E. JENKINS, *J. Inst. Met.* **82**, 213 (1953–54).

* Received February 26; revised April 1, 1960.

The structure of slip band extrusion revealed by transmission electron microscopy*

Earlier observations[1] on various materials have shown that fatigue stress caused the extrusion of thin scrolls of debris from slip bands. This phenomenon was very marked in solution treated aluminium–4% copper alloy fatigued at room temperature, where it was observed to occur suddenly within a few stress cycles.[2] The maximum height of the extrusions observed in this alloy was approximately 10 μ, and interferometric measurements suggested that they were not thicker than 0.1 μ. A light micrograph of a typical slip band extrusion is shown in Fig. 1. In an earlier study[2] the extrusions stripped from a specimen on a "Perspex" replica were examined both by reflected

VOL. 8 1960

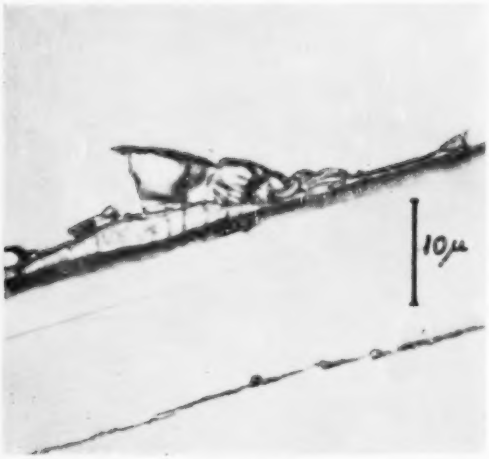


FIG. 1. Optical micrograph of a typical slip band extrusion. ×1500

and transmitted light. Their high reflectivity and their opacity suggested that they were metallic.

In order to understand the extrusion mechanism it is important to know if the extrusion has been enriched with or depleted of solute atoms, but at the time of writing no satisfactory method of analysis has been evolved. We have, however, been able to study the structure of the slip band extrusion by transmission electron microscopy.

Specimens of aluminium–4% copper alloy were solution heat treated at 520°C, cold water quenched and fatigued at room temperature. The slip band extruded material was stripped from the specimen surface embedded in either carbon or formvar replicas. Judging from the appearance of extrusions when viewed in the electron microscope, they must all be remarkably similar in thickness, and the 0.1 μ upper thickness limit originally estimated by interferometry is consistent with their transparency to electrons. The back ends of the extrusions were serrated in a manner similar to fractures we have produced by straining thin aluminium foils in the electron microscope.[3] These torn edges must have occurred during the stripping operation, and this suggests that the extrusions were still coherent with the crystal material when stripped. This continuity between extrusion and crystal has been confirmed by "fractographic" examination of the edges of the fatigue fracture where extrusions still adhere. Figs. 2 and 3 are transmission electron micrographs of extrusion stripped on a formvar replica showing a striated or elongated substructure typical of all extrusions examined.

This structure seemed to be composed of elongated crystallites lying in a direction parallel to the slip band from which the extrusion came. No discrete dislocations could be detected in these long parallel boundaries (indicated by arrow *A*, Fig. 3) although cross linking boundaries (indicated by arrow *B*) were sometimes resolved as small angle dislocation arrays. The



FIG. 2. Transmission electron micrograph of slip band extrusion showing elongated substructure. ×12,000

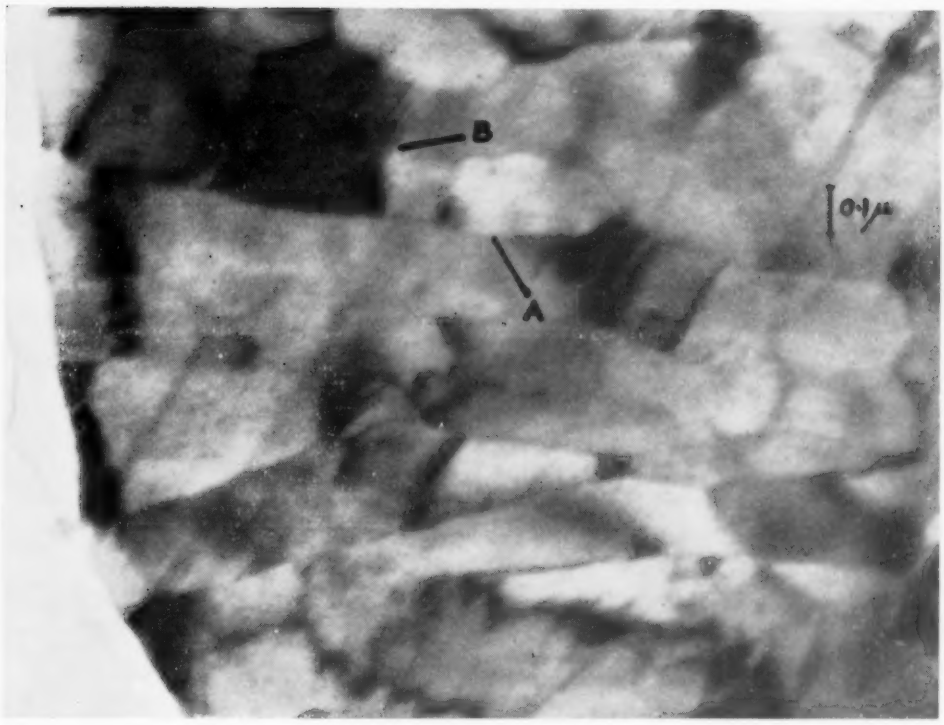


FIG. 3. Transmission electron micrograph of slip band extrusion showing elongated substructure. ×62,000

VOL. 8 1960

electron diffraction pattern shown in Fig. 4 confirms the presence of this substructure. The long boundaries were unusually straight and were not jogged by the cross linking boundaries. They were in all respects similar in appearance to large angle grain boundaries, but prolonged heating in the electron microscope caused complete polygonization to an equiaxed form.

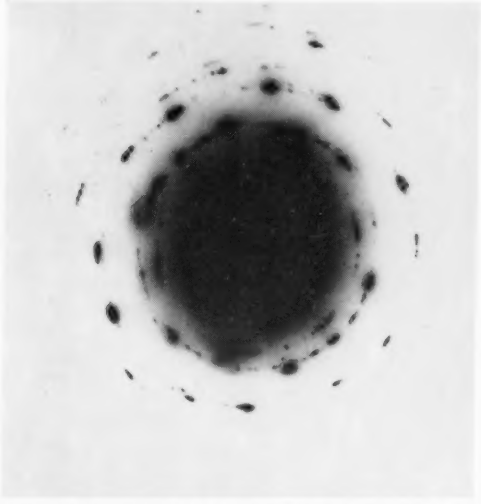


FIG. 4. Electron diffraction pattern from slip band extrusion (III).

It is known from observation that extrusion occurs in a few stress cycles (~10 cycles) and as there are about the same number of striations in the extrusions it is reasonable to suppose that each striation corresponds to, and is the result of, one cycle of stress. It is, however, difficult to ascertain the true nature of the boundaries between the elongated crystallites. They may be arrays of edge dislocations lying parallel to the extrusion surface with their Burger's vector in the extrusion direction. These could result from the polygonization of buckles formed in the extrusion process, or directly from sharply kinked bands as illustrated in Fig. 5. It can be seen that a kink band would naturally form where the extrusion emerged from the crystal surface, during that part of the cycle

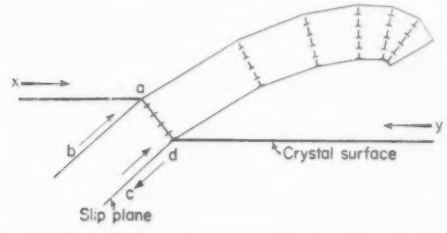


FIG. 5. Diagrammatic representation of extrusion process.

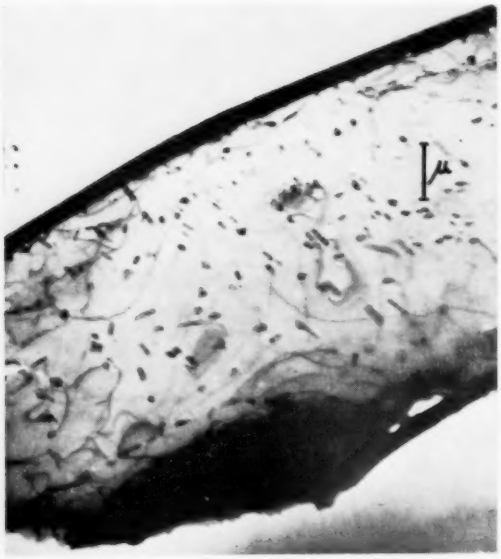


FIG. 6. Transmission electron micrograph of slip band extrusion showing precipitation produced by heating in the electron beam. ×8,000

when two parts of the crystal on each side of the extrusion were moving together in the directions x and y. We visualize that during this part of the cycle sliding will occur along c–d as indicated by the arrows, but a–b will be stuck.

When the cycle reverses sliding will occur along a–b, and c–d will be stuck. If a kink band forms during this half of the cycle, i.e. when the crystal surface is extended, it must be less heavily bent than its predecessor because a rolling up of the extrusion is always observed as indicated in Fig. 5. This suggests that edge dislocations of one sign predominate in the extrusion. This predomination of one sign becomes greater near the tip because the sub-boundaries that exist there are more closely spaced, and this results in the curling observed at the tips.

It has been stated that the thickness of these extrusions was remarkably constant, and in this respect they are dissimilar to those observed in silver chloride[4] and in many metals. It seems that in aluminium–4% copper—and we suspect in other aluminium alloys—the sliding involved in the extrusion process occurs on a relatively small number of slip planes. In many other cases slip is occurring on a more widely distributed series of planes. It is clear that reverse glide is the mechanism of extrusion, but it is difficult to ascribe a particular dislocation mechanism. It is certain that a gyrating screw dislocation mechanism[5] is untenable in this case, nor can the mechanism of interfering slip on different planes be applicable.[6]

Any mechanism would have to take into account the new observation that dislocation arrays, most probably edge dislocations predominantly of one sign, exist in the extrusion. This is most likely to be the result of changing frictional forces under extension and closure of the surrounding crystal. It may be that reverse sliding occurs on the plane a–b and only in one direction on the plane c–d. Slip cannot occur in the reverse direction d–c because the kink band across a–d acts as an obstacle. It is likely that true cohesion is soon lost along a–b, but the friction between the two faces will be greater under the closure half of the cycle than on the extending half.

There is evidence that, as with silver chloride, extrusion in aluminium–4% copper alloy does not leave behind a void. It is likely that the extrusion–crystal interface a–b nearest the specimen surface, i.e. the interface that forms an acute angle with the surface, loses cohesion and becomes a crack. This loss of cohesion could occur before the extrusion and be the cause rather than the effect.

Prolonged heating in the electron beam caused precipitation of θ' in about the same quantity and form as appeared in thin foils of the homogeneous aluminium–4% copper alloy heated in a similar manner.[7] This is shown in Fig. 6. If any change in the distribution of solute had occurred with fatigue stress it does not seem to have affected the material extruded. It may be that the important structural changes occur on the extrusion–crystal interface rather than in the material that is eventually extruded. If this is so it will make detection very much more difficult, and illustrates in a striking manner how sharply confined to a few crystal planes the true fatigue damage may be.

P. J. E. FORSYTH
C. A. STUBBINGTON

Ministry of Aviation
Farnborough, Hants.

References

1. P. J. E. FORSYTH and C. A. STUBBINGTON, *Nature, Lond.* **175,** 767 (1955).
2. P. J. E. FORSYTH and C. A. STUBBINGTON, *J. Inst. Met.* **83,** 395 (1954–55).
3. R. N. WILSON and P. J. E. FORSYTH, *J. Sci. Instrum.*, in press.
4. P. J. E. FORSYTH, *Bull. Amer. Soc. Test. Mat.* No. 237 (June 1958).
5. N. F. MOTT, *Acta Met.* **6** (1958).
6. A. H. COTTRELL and D. HULL, *Proc. Roy. Soc.* A**242,** 211 (1957).
7. C. BEAUVAIS, *Métaux et Corros.* **406,** 247 (1959).

* Received February 26, 1960.

This letter is published by permission of The Controller, H.M. Stationery Office. Crown copyright is reserved.

Migration energies in quenched and deformed gold*

Activation energies as determined by slope intersection method were measured for the recovery of residual resistivity in gold which had been quenched and then subsequently plastically deformed at −195.8°C. The purpose of this investigation was the study of the physical nature of the interactions between point defects and dislocations. These results indicate that other processes must be considered in addition to that previously considered, which was the factor of increased sink density due to the increase in dislocation density resulting from plastic deformation.

The experimental procedure was as follows: Gold samples of specified purity 99.999 per cent, and with a ratio of room temperature resistivity to that of liquid helium of 2000 or higher were quenched from 1000°C down to 0°C with a quenching speed of 30,000°C/sec. The wires were immediately transferred from the 0°C bath into a liquid nitrogen bath. Plastic deformation was introduced by bending while the specimen was still in the liquid nitrogen bath following the quench. The residual resistivity was then measured at 4.2°K. The specimen was then placed in various constant temperature baths and the resistivity again measured at 4.2°K following each annealing period. For one of the annealing runs an unquenched sample was used and was deformed at −195.8°C and subsequently annealed as for the quenched and deformed samples.

The recovery of residual resistivity at raised temperatures is shown in Fig. 1. In Fig. 2 the activation energies obtained from Fig. 1 are plotted against the fractional residual resistivity $(\rho - \rho_0)/(\rho_i - \rho_0)$ where ρ_i is the resistivity after quenching and deformation, and ρ_0 is the resistivity at the completion of aging at 100°C. The effect of the plastic deformation is the very low activation energies observed in the early part of the recovery process. These activation energies are considerably below those for quenched and undeformed samples. The activation energy increases monotonically with aging back to that for the quenched and undeformed specimens. About 80 per cent of the resistivity recovers with close to the same activation energy as the quenched but undeformed samples. The unquenched sample which was subjected to the same deformation and subsequent annealing as the quenched and deformed samples exhibited a recovery similar to that of the early part of the recovery process for the quenched and deformed samples, except that the magnitude of the recovered resistivity was much less than when quenched-in defects were present.

The striking feature of the present results is the very low activation energies. These cannot be accounted for merely by the additional sinks of vacancies due to

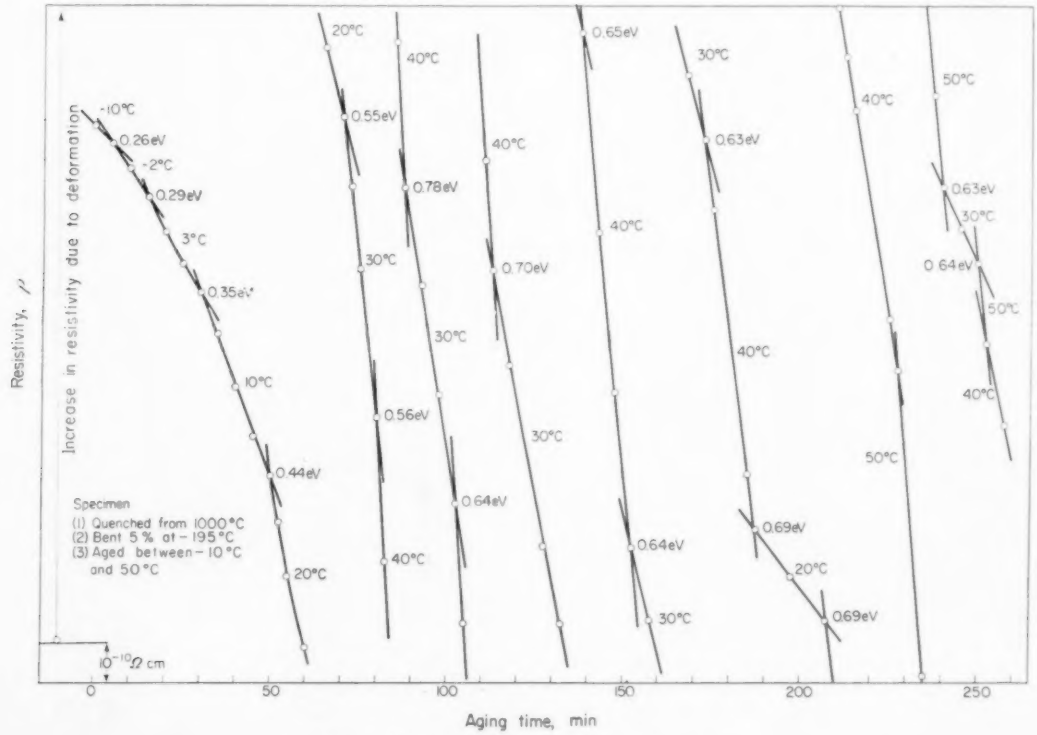


FIG. 1. Determination of activation energies.

VOL. 8 1960

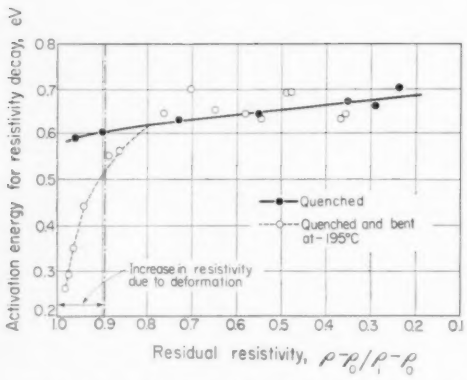


FIG. 2. Activation energies obtained in Fig. 1 plotted against the fraction of residual resistivity.

the increase in dislocation density. The possibility that elastic interaction between vacancies and dislocations may account for the low activation energy observed seems unlikely, because the interaction is not great enough to account for the low values observed.

The possibility that the low energy processes are due to the motion of vacancy clusters can be excluded because vacancy clusters are present even in quenched and undeformed material, and for this case such low activation energies have never been observed. We also note that this rejects the possibility that first recovery step in gold deformed at −195.8°C is due to migration of vacancy aggregates.[1]

Two possible solutions which can account for the observed results are the following: (1) Plastic deformation may produce clustered interstitials, probably in the form of rows or platelets. During annealing the interstitials may break away from the clusters and recombine with the lattice vacancies present as a result of quenching. (2) If, following the quenching and deformation processes there is a significant concentration of vacancies near dislocation lines, a possible mechanism for the rate controlling process would be the migration of vacancies along the dislocation lines. However, this seems the less likely process, because such a process should occur more rapidly than that which is observed experimentally. It is concluded that the first mechanism is the one which corresponds to the experimental data obtained.

We may further note that the difference in the recovery characteristics of resistivity between cold worked copper and irradiated copper may be explained by the difference in the production of interstitial atoms, that is, local regions containing interstitial atoms are expected for the case of cold work, whereas a random distribution of interstitial atoms is likely to be created for the case of electron irradiation. Therefore one may conclude that the apparent lack of any recovery process in cold worked copper below about 120°K does not eliminate the possibility of interstitial atoms produced as a result of cold work.

Department of Materials Science M. MESHII
Northwestern University J. W. KAUFFMAN
Evanston, Illinois

References

1. J. A. MANINTVELD, *Nature, Lond.* **169,** 623 (1952).

* This investigation was performed with the support of the Office of Naval Research of the United States Government.
Received May 26, 1960.

On Meiklejohn and Skoda's letter "Dispersion Hardening"*

Meiklejohn and Skoda[1] have shown that the yield strength, σ_y, of mercury hardened by electrodeposited iron particles, tested at 77°K, is given by:

$$\sigma_y = \frac{Ad}{\lambda - d} + \sigma_0 \qquad (1)$$

where d is the particle diameter, λ is the distance between centers of the particles, σ_0 is the yield strength of the matrix, and A is a constant. Later tests,[2] as a function of temperature, gave

$$\frac{\sigma_y(T) - \sigma_0(T)}{(T_M - T)} = \frac{\alpha d}{\lambda - d} \qquad (2)$$

where T is the test temperature, T_M is the melting point of mercury, and α is another constant.

The following explanation of the observed dependence of yield strength on particle size, spacing and temperature of test, is proposed. As the mercury is cooled from its melting point to the testing temperature, strains will develop due to differential contraction between the mercury and the iron particles. It is supposed that these strains can be relieved by the creation of dislocation loops, as has been observed in silver chloride.[3] The volume change per particle due to differential contraction is:

$$\frac{1}{6}\pi\,\varepsilon(T_M - T)\,d^3$$

where ε is the difference in volume thermal expansion coefficients of iron and mercury ($\varepsilon \simeq 9 \times 10^{-5}$/°C).[4] The volume change accommodated by each dislocation loop is:

$$\pi R^2 b$$

where b is the Burger's vector, and R the radius of the loop. This radius is approximately equal to $1/\sqrt{2}$ times the particle radius.[3] Each particle must give off N loops to accommodate all the strain, such that

$$N\pi\frac{d^2}{8}\,b = \frac{1}{6}\,\pi\varepsilon(T_M - T)\,d^3 \qquad (3)$$

whence:

$$N = \frac{4\varepsilon}{3b}(T_M - T)\,d. \tag{4}$$

The enhanced strength of the material, due to the presence of the precipitate particles, arises from the necessity for deformation dislocations to cut through these dislocations loops. The yield strength is then given by:

$$\sigma_y(T) = \mu b \rho(T) + \sigma_0(T) \tag{5}$$

where μ is the shear modulus of the matrix ($\mu \simeq 5 \times 10^{10}$ dyn/cm^2 for mercury),[4] and ρ is the number of loops per unit length through which a dislocation must cut.

$$\rho = \frac{N}{3(\lambda - d)} \tag{6}$$

since $(\lambda - d)$ is the distance between particles, and the loops may be given off in three directions.

Substituting equations (4) and (6) in equation (5)

$$\sigma_y(T) = \frac{4\mu\varepsilon}{9}\frac{(T_M - T)\,d}{(\lambda - d)} + \sigma_0(T) \tag{7}$$

or

$$\sigma_y(T) - \sigma_0(T) = \frac{4\mu\varepsilon}{9}\frac{d}{\lambda - d}. \tag{8}$$

This is the same as Meiklejohn and Skoda's result (equation 2) with $\alpha = 4\mu\varepsilon/9$. This ignores any change with temperature in μ or ε, but such changes are expected to be small. Using the above values of μ and ε, the calculated value of α is 28.4 lb/in^2/°C. Meiklejohn and Skoda give an experimental value for this constant of approximately 30 lb/in^2/°C. The excellent agreement between these values needs no comment.

D. Dew-Hughes

IBM Research Center
Poughkeepsie, New York
Now at
Department of Metallurgy
Cambridge University

References

1. W. H. Meiklejohn and R. E. Skoda, *Acta Met* **7**, 675 (1959).
2. W. H. Meiklejohn and R. E. Skoda, presented at AIME meeting, New York, February 1960.
3. D. A. Jones and J. W. Mitchell, *Phil. Mag.* **3**, 1 (1958).
4. E. Grüneisen and O. Sckell, *Ann. Phys., Lpz.* (5) **19**, 387 (1934).

* Received March 28, 1960.

Thermal cycling creep of α-uranium*

When a polycrystalline material contains intergranular stresses that bring its grains to the point of yielding, it is unable to support even small applied loads without giving way plastically. In many cases such intergranular stresses are smoothed away by differential plastic deformation during the early stages of loading and because of this "shakedown" of the stresses the material quickly becomes able to oppose its full yield strength to the applied load. However, under certain circumstances the intergranular stresses can be continually regenerated and the inability of the material to support small applied loads then persists as a permanent feature. The material then responds to such loads as if it were a viscous fluid and obeys Newton's law of viscosity in the limit of small applied stresses, even though its grains fully retain their original crystal structure and mechanical properties.

Table 1. Coefficients of thermal expansion ($\times 10^{-6}$) along crystal axes in alpha uranium

Axis	25–125°C	25–325°C	25–650°C
100	21.7	26.5	36.7
010	−1.5	−2.4	−9.3
001	23.2	23.9	34.2

A good example of the effect is the "irradiation creep" that occurs when alpha uranium is irradiated with neutrons.[1] The intergranular stresses in this case are produced by the anisotropic "irradiation growth" that occurs in the temperature range 0–450°C. The effect is also expected to appear when alpha uranium is subjected to thermal cycling, since the coefficient of thermal expansion is very anisotropic, as shown in Table 1.[2]

The experiments described below were made to test this point.

Four uranium rods 6 mm diameter were cut from a cast bar of calcium reduced uranium. The rods were swaged to 1 mm diameter wire and to minimize texturing were vacuum annealed at 600°C after every 50 per cent reduction. The wires were coiled into springs of 1 cm diameter and after a heat treatment to produce a small grain size were mounted vertically in a glass furnace in a helium atmosphere. The specimens were then cycled between two given temperatures controlled to ±4°C. At intervals the furnace was cooled to room temperature and the length of the springs measured without removing the specimens from the apparatus by using a cathetometer.

As a control, some springs were held at a constant temperature of 350°C under the maximum applied load for 200 hr; they showed no observable creep.

The full lines in Fig. 1 show the results of cycling between the limits 100°C and 300°C on specimens loaded to 186, 1048 and 1697 lb/in^2. The initial elastic deflections produced by these loads were 0.06,

VOL. 8 1960

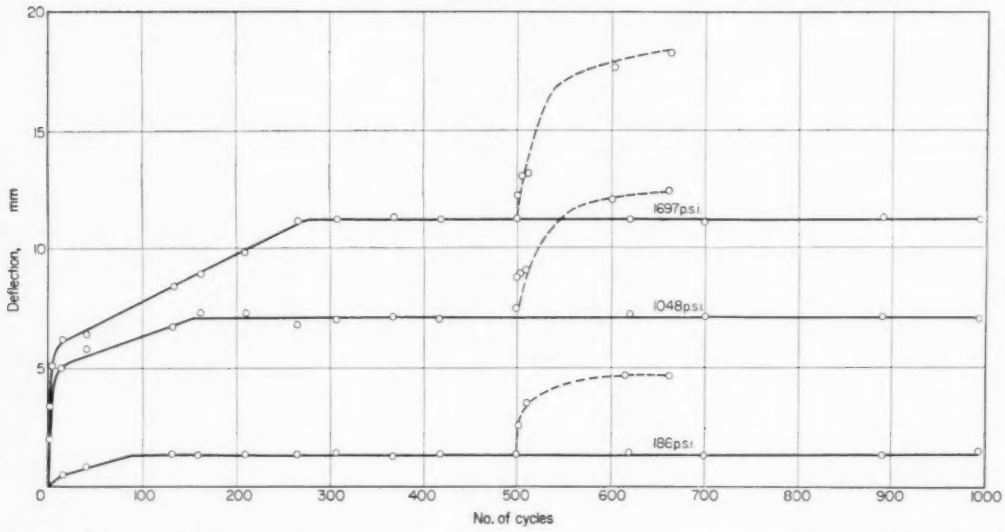


FIG. 1. Spring deflection versus number of cycles for Ca-reduced uranium cycled between 100°C and 300°C and also between 50°C and 300°C. The broken line shows the effect of recommencing cycling after disturbing the internal stresses.

0.32, and 0.46 mm, respectively. It will be seen that deflections of about 10 times these amounts occurred during the first few cycles. Thereafter the deflections increased gradually until they reached 20–25 initial elastic deflections and then stopped.

The initial yield strength was determined from experiments on uncycled springs to be 27,500 lb/in^2 which corresponds to an elastic strain at the yield point of 10^{-3}. From the values of thermal expansion in Table 1 we expect a change of 200°C to create a maximum thermal strain between neighbouring grains of about 5×10^{-3}. This is much greater than the elastic yield strain so that the experimental conditions were suitable for producing the observed effect of cycling.

Two effects may contribute to the decrease in creep rate as the number of cycles increases. First is the "shakedown" of the intergranular stresses. If, at a given temperature and stress, one grain happens to be straining plastically at a faster rate than its neighbours, the stress in that grain relaxes and the rate of straining there falls towards the average value. The intergranular stresses thus shake down into a pattern which subsequently minimizes the individual plastic strains of the grains. In effect, after the first few cycles each grain becomes able to use its whole elastic range, from compression to tension, to accommodate the intergranular thermal strains. Thus the effective total elastic yield strain increases from 10^{-3} to about 2×10^{-3}. If the latter was enough to accommodate the thermal strains completely, we would expect from the shakedown argument that after the first few cycles the specimen would stop deforming plastically.

However, the thermal strains are much larger than 2×10^{-3} and to account for the observed decrease of creep rate to zero, we must suppose that the elastic range is widened by work hardening from the alternating thermally induced plastic strain. In fact, the yield strength at room temperature after 400 cycles from 100 to 300°C was found to be 79,000 lb/in^2, which corresponds to an initial elastic yield strain of 3×10^{-3} and a total elastic range of 6×10^{-3}. Since the yield strength of uranium decreases by 10,000–15,000 lb/in^2 on heating from room temperature to 300°C[3] the total elastic range at the temperature of the experiment is about equal to the thermal strain. This is to be expected, for once the elastic range has grown sufficiently to accommodate the thermal strain, plastic deformation and work hardening should cease provided the state of intergranular stress is not disturbed in any way.

Experiments were made to test these deductions and specimens were first cycled between the limits 50°C and 300°C. It was found that they followed the curves for the 100°C to 300°C cycling range. One set, at 500 cycles, was cooled to room temperature, removed from the apparatus, pulled to their yield points and reassembled in the apparatus to continue the cycling experiment. The reason for pulling the specimens was to disturb the shakedown state of intergranular stresses so that the material would no longer be able to offer its total elastic range to resist the thermal strains until the shakedown state had been

established again. As a result, the thermal cycling treatment then becomes capable once more of producing plastic strains, shown by the broken lines in Fig. 1.

The shakedown state of the intergranular stresses may also be disturbed by raising the upper temperature of the thermal cycle. Specimens were first cycled between 50°C and 300°C for 350 cycles at which point they had stopped elongating, and were then cycled between 50°C and 400°C. Creep recommenced and gave no indication of stopping, probably because the thermal strain always exceeds the elastic range.

The experiments show that when alpha uranium is subjected to large thermal cycles in the range up to 300°C it initially cannot support even small applied loads without deforming plastically. After a few cycles, provided the amplitude of thermal cycle is not too large, the material becomes able to support small loads elastically partly due to a redistribution of the intergranular stresses and partly to work hardening which increases the elastic range.

I would like to thank Professor A. H. Cottrell, F.R.S., for suggesting the experiment and for many useful discussions, and the Director, A.E.R.E. Harwell, for the facilities made available during my attachment to his Establishment when the above work was carried out.

A. C. Roberts

Research Laboratories of
The General Electric Company Ltd.
Wembley, Middlesex, England

VOL. 8 1960

References

1. A. C. Roberts and A. H. Cottrell, *Phil. Mag.* **1**, 711 (1956).
2. F. G. Foote, presented at *Int. Conf. Peaceful Uses of Atomic Energy, Geneva*, 1955, Paper No. 555.
3. A. N. Holden, *Physical Metallurgy of Uranium*. Addison Wesley, Reading, Mass. (1958).

* Received December 15, 1959; revised March 23, 1960.

Use of the marker method in studying the mechanism of oxidation of metals*

In recent years the application of the marker method in investigating the mechanism of scale formation on metals and alloys has become more and more common. In many cases, however, the results of these investigations (when interpreted conventionally) do not agree with theoretical considerations and with self-diffusion data.[1–4] Cagnet and Moreau[5] rightly suggest that the results obtained by marker method should be interpreted very cautiously because of the possibility of secondary processes which can disturb the location of the marker in the scale layer.

The authors mentioned emphasize that the successful use of this method is conditioned chiefly by the exact contact between the marker and the original metal surface. Therefore, Cagnet and Moreau fastened their wire-marker on the metal surface by welding. The contact between the wire and the metal surface can, however, in this case be only fragmentary. Moreover the alloy formed during the welding process covers a considerable part of the specimen surface, which can lead to further errors.[5] Czerski has earlier[6] proposed another method consisting in "clinging" the wire-marker to the surface of metal by means of an electrolytically deposited layer of the same metal. The thickness of this layer should amount to about 1/10 of the diameter of the used wire-marker. In the discussion of the results obtained, the presence of this electrolytically deposited layer should be taken into account. This method seems to be better than the method proposed by Cagnet and Moreau because it gives the guaranty of a very tight contact between the marker and the surface of the specimen.

According to Cagnet and Moreau[5] the location of the marker in the scale layer formed on iron at 1000°C is not determined by the inward diffusion of the oxidant (as it was assumed by Engell and Wever[7]); the location of the marker is believed to be influenced by the "flow" of the scale around the marker owing to the plasticity of the wüstite phase. We agree with the opinion of the authors mentioned, according to which the location of the marker in the scale layer can not be treated as sufficient evidence of the inward diffusion of the oxidant, but in our opinion this location does not depend on the plasticity only. In Fig. 1 a photomicrograph of a transverse section of a sulphide layer formed on silver at 444°C is shown. The location of the platinum marker at the metal–scale interface is clearly observable on this micrograph. As can be seen, the Pt-marker flowed, during the growth of the sulphide layer, with the scale towards the metal in spite of the fact that—before starting the reaction—the platinum wire was stretched on the silver surface similarly as in the experiments of Engell and Wever[7]. The location of the marker at the metal–scale interface indicates that during the growth of the scale its location relative to the marker does not change, although at 444°C the plasticity of α-Ag_2S is almost the same as the plasticity of wüstite in high temperatures.

After longer times of oxidation the scale thickness passes a certain critical value depending on the

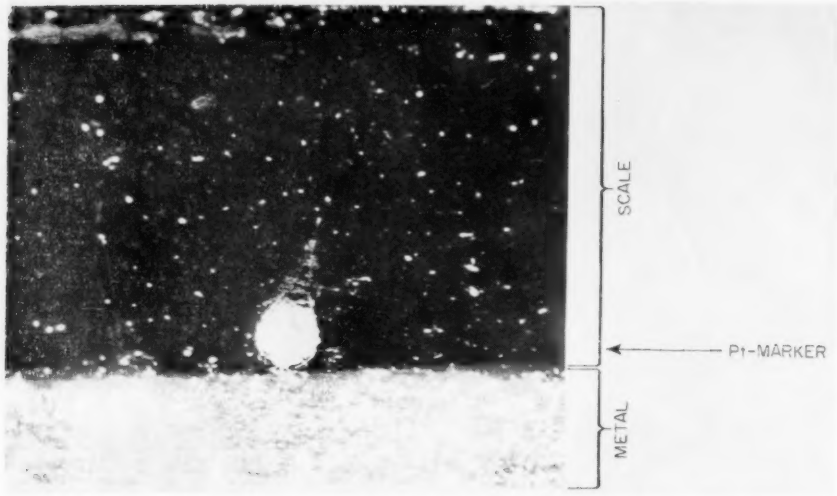


FIG. 1. Photomicrograph of a transverse section of sulphide scale formed on silver in liquid sulphur at 444 C. ×105

temperature of the reaction and on the geometry of the specimen. At this stage, however, the loss of metal can not be compensated by shrinking of the scale layer due to its plasticity: between the metal and the scale layer a longitudinal crack is formed, the contact between the metal and the scale becomes interrupted and the chemical potential of the metal contained in the scale layer decreases. Therefore, vapour pressure of the oxidant in the longitudinal crack becomes greater than the dissociation pressure of the scale remaining in equilibrium with the metal. On the metal surface starts a secondary process consisting in formation of compounds from metal and oxidant. This reaction is accompanied by the decomposition of the scale on the scale–crack interface and results in formation of an inner scale layer according to the mechanism proposed by the authors in the case of sulphurization of copper[8] and of silver.[9] The growth of the inner layer results in formation of "bridges" connecting the metal surface with the outer scale layer. This leads to a partial re-establishment of contact between the scale and the metal. The oxidation can thus proceed in spite of the longitudinal cracks formation. Basing on results of their experiments, Rickert[10] and Birchenhall and Meussner[11] have drawn analogous conclusions in the case of sulphurization of silver and iron. A similar mechanism of the inner scale layer formation was first suggested by Dravnieks and McDonald[12].

In the case discussed the two-layer scale is formed exclusively due to the outward diffusion of metal. Until the moment of crack formation the marker is to be found at the metal–scale interface (Fig. 1). At this stage the conventional interpretation of results obtained by the marker method is correct. When the longitudinal cracks are formed, the marker is carried off from the metal surface together with the scale and is to be found on the scale–crack interface. Between the metal and the marker, the inner scale layer begins to be formed according to the mechanism discussed above. After the reaction has been finished the marker can be found imbedded in the scale at the interface of both its layers in spite of the fact that the inward diffusion of the oxidant did not take part in the oxidation process. This was definitely proved by our investigations carried out on systems $Cu–S^{(liquid)}$ and $Ag–S^{(liquid)}$ using both the marker and the radioactive indicators method.[9,13]

It is very probable that, in the case of oxidation of iron and other metals at high temperatures, the location of the marker in the scale layer is also determined by the formation of an inner scale layer, analogous to the mentioned sulphurization processes. The probability of such a mechanism of scale formation on iron is confirmed by the fact that this scale consists of two layers (the inner one being porous). If the scale is moving with reference to the marker and this motion is due to plasticity, there ought to be no structural differences between the scales on both sides of the marker (one-layer scale).

Recent investigations of Wallwork and Jenkins[14] have demonstrated that the inner scale layer can also be formed as a result of dissolution of the oxidant in the metal. As the metal-core thickness decreases, an oversaturated solution of oxidant in the metal is formed and a corresponding compound is deposited on the metal–scale interface. In this case it can be expected that the marker shall be found also in the

interior of the scale, although the inward diffusion of the oxidant did not take part in the oxidation process.

From these considerations it will be evident that the conventional interpretation of results obtained by the marker method is insufficient and should take into consideration the following:

(a) The location of the marker at the metal–scale interface indicates that the scale is formed exclusively due to the outward diffusion of metal;

(b) the location of the marker at the scale–oxidant interface indicates that the scale is formed due to the inward diffusion of the oxidant;

(c) location of the marker in the interior of the scale indicates only that the outer layer—between the marker and the oxidant—is formed due to the outward diffusion of metal. The inner layer—between the marker and the metal—can be formed as a result of (i) inward diffusion of the oxidant, (ii) formation of cracks and then of the inner porous scale layer by the mechanism discussed above, (iii) formation of oversaturated solutions of oxidant in the metal, (iv) simultaneous occurrence of all mentioned processes.

From the location of the marker in the interior of the scale formed on relatively small specimens no conclusions about the mechanism of the inner scale layer formation can be derived. Neither is it possible to decide which of the mentioned partial processes are the most important in a given case.

S. Mrowec
T. Werber

Department of General and Coal Chemistry
School of Mining and Metallurgy
Krakow, Poland

References

1. B. Ilschner and H. Pfeiffer, *Naturwissenschaften* **40**, 603 (1953).
2. L. Czerski, S. Mrowec and T. Werber *Arch. Hutn. Pol. Akad. Nauk* **3**, 37 (1958).
3. I. Pfeiffer, *Z. Metallk.* **49**, 267 (1958).
4. C. Wagner, private communication.
5. M. Cagnet and J. Moreau, *Acta Met.* **7**, 427 (1959).
6. L. Czerski, *Arch. Hutn. Pol. Akad. Nauk* **2**, 3 (1954).
7. H. Engell and F. Wever, *Acta Met.* **5**, 695 (1957).
8. S. Mrowec and T. Werber, *Acta Met.* **7**, 696 (1959).
9. J. Mikulski, S. Mrowec and T. Werber, *Bull. Acad. Polon. Sci. Cl. III* **7**, 737 (1959).
10. H. Rickert, *Z. Phys. Chem. N.F.*, in press. (1960).
11. C. Birchenall and R. Meussner, *Corrosion* **13**, 677 (1957).
12. A. Dravnieks and H. McDonald, *J. Electrochem. Soc.* **94**, 139 (1948).
13. J. Mikulski, S. Mrowec, I. Stroński and T. Werber *Z. Phys. Chem. N.F.*, **22**, 20 (1959).
14. G. Wallwork and A. Jenkins, *J. Electrochem. Soc.* **106**, 10 (1959).

* Received November 9, 1959.

VOL. 8 1960

MAGNETIC ANALYSIS OF THE PRECIPITATION OF IRON FROM BETA BRASS*

A. E. BERKOWITZ‡ and P. J. FLANDERS†

Single crystals of beta brass containing 0.07 wt. % iron were annealed at 300°C and 400°C to precipitate the iron. At various stages in the anneals, magnetization curves, hysteresis loops and torque curves were measured. These magnetic data were analysed in terms of the concepts of fine particle ferromagnetism to derive size and shape distributions of the iron precipitate particles and the orientations of their crystallographic and shape symmetry axes.

In the superparamagnetic size range average diameters were determined up to 140 Å. These particles showed no shape anisotropy, and had the same saturation magnetization and magnetocrystalline anisotropy symmetry as bulk iron. The crystal habit of the particles coincided with that of the beta brass matrix. With further annealing single domain properties appeared, and the particles showed increasing elongation in the ⟨100⟩ directions as determined by analysis of the torque data. Distributions of shapes and sizes of the single domain particles were calculated from remanent torque data. These calculations were consistent with the conclusions from remanence measurements. The shapes of the hysteresis loops and the spread in annealing time between maximum coercive force and maximum remanence could be simply interpreted on the basis of mixtures of superparamagnetic, single and multidomain particles. When the particles were principally in the multidomain (>300 Å diameter) range, little information about size distributions could be derived, although the data indicated that the particles become progressively elongated in the ⟨100⟩ directions. Electron micrographs of replicas gave qualitative confirmation of the conclusions from the magnetic analysis.

ANALYSE MAGNETIQUE DE LA PRECIPITATION DU FER DANS LE LAITON β

Les auteurs ont recuit à 300 et 400°C des monocristaux de laiton β contenant 0,07% en poids de fer afin de précipiter ce dernier. A divers stades des recuits, ils ont tracé les courbes d'aimantation, d'hystérésis et de torsion. Ils ont analysé résultats de ces mesures magnétiques en fonction des concepts de ferromagnétisme des fines particules et en ont déduit les distributions en forme et en dimension des particules de fer précipitées ainsi que les orientations de leurs axes cristallographiques et de leurs axes de symétrie.

Ils ont relevé que, jusqu'à 140 Å de diamètre moyen, les particules sont superparamagnétiques. Elles ne présentent pas d'anisotropie de forme et possèdent les mêmes aimantation à saturation et anisotropie magnétocristalline que le fer massif. Leur structure coïncide avec celle de la matrice de laiton β. Lors d'un recuit ultérieur, les propriétés des domaines simples apparaissent et les particules montrent, par l'analyse des résultats de torsion, un allongement croissant dans les directions ⟨100⟩.

Les auteurs ont également calculé, à partir des valeurs du couple rémanent, les distributions en forme et en dimension des particules ne comportant qu'un seul domaine. Les résultats se sont avérés compatibles avec les conclusions des mesures de rémanence. Ils ont pu interpréter simplement les formes des courbes d'hystérésis et la dispersion des temps de recuit entre les maximum de force coercitive et de rémanence, sur la base de mélanges de particules superparamagnétiques, à simple et à multiples domaines.

Quant aux particules à domaines multiples (de diamètre supérieur à 300 Å), les auteurs n'ont pu déduire des mesures que peu d'informations sur leur distribution dimensionnelle, si ce n'est un allongement progressif dans les directions ⟨100⟩.

Enfin, des micrographies électroniques de répliques ont donné une confirmation qualitative des conclusions de l'analyse magnétique.

MAGNETISCHE UNTERSUCHUNG DER AUSSCHEIDUNG VON EISEN AUS β-MESSING

Einkristalle von ß-Messing mit 0.07 Gewichtsprozent Eisen wurden bei 300°C und 400°C ausgelagert, um das Eisen auszuscheiden. In verschiedenen Stadien der Auslagerung wurden Magnetisierungskurven, Hystereseschleifen und Drehmomentkurven gemesse. Diese magnetischen Ergebnisse wurden mit Hilfe der Vorstellung eines Ferromagnetismus kleiner Teilchen analysiert und daraus die Verteilung von Größe und Gestalt der ausgeschiedenen Eisenpartikeln und die Orientierung ihrer kristallographischen und Gestalt-Symmetrie-Achsen bestimmt.

Im Größenbereich des Superparamagnetismus wurden Durchmesser bis zu 140 Å gemessen. Diese Partikeln zeigten keine Gestalt-Anisotropie, und ihre Sättigungsmagnetisierung und Symmetrie der kristallographischen Anisotropie war dieselbe wie bei massivem Eisen. Der Kristallhabitus der Partikeln stimmte mit dem der ß-Messing-Matrix überein. Bei weiterem Anlassen traten Eigenschaften von einzelnen Bezirken auf, und die Partikeln zeigten eine wachsende Verlängerung in den ⟨100⟩-Richtungen wie sich aus einer Analyse der Drehmomentmessungen ergab. Verteilungsfunktionen für Größe und Gestalt der Ein-Bezirks-Partikeln wurden aus den Angaben über das remanente Drehmoment berechnet, es ergab sich Übereinstimmung mit den Schlußfolgerungen aus den Remanenzmessungen. Die Formen der Hystereseschleifen und die unterschiedlichen Auslagerungszeiten für maximale Koerzitivkraft bzw. maximale Remanenz ließen sich einfach erklären durch die Vorstellung einer Mischung von superparamagnetischen, Ein- und Mehr-Bezirkspartikeln. Wenn die Partikeln hauptsächlich im Bereich mehrerer Bezirke (Durchmesser > 300 Å) liegen, ist über die Größenverteilung wenig Auskunft zu bekommen; die Messungen deuten jedoch darauf hin, daß die Teilchen zunehmend in den ⟨100⟩-Richtungen verlängert sind. Elektronenmikroskopische Abdruckaufnahmen ergaben qualitative Bestätigung der Schlüsse aus den magnetischen Untersuchungen.

* This research was supported by the United States Air Force through the Air Force Office of Scientific Research of the Air Research and Development Command under Contract AF 49(638)-159. Received August 28, 1959; revised April 11, 1960.

† The Franklin Institute, Philadelphia 3, Pennsylvania.

‡ IBM Research Center, Yorktown Heights, New York.

VOL. 8 1960

INTRODUCTION

The theory of fine particle ferromagnetism can be usefully applied in the investigation of ferromagnetic precipitate particles in a non-magnetic matrix. The magnetic behavior of these systems can be analysed to infer various structural properties of the precipitate particles such as total volume, size and shape distributions, crystallographic and shape orientation, and strain. Conversely, these precipitating systems often simplify the study of the magnetic properties of fine particles since the particles are generally well separated and oriented with respect to crystallographic and shape symmetry axes. Much of the previous research in this area has been concerned with the Alnicos.[1–5] More recently, simpler alloys have been investigated in this manner.[6–19] The work of Smith[20] indicated that α-Fe precipitated quite readily from beta brass. Presumably this occurs because of the similarity in lattice spacing and crystal structure, and because of the limited solubility of copper and zinc in iron at moderate temperatures.

The interpretation of the magnetic data is made on the assumption that three classes of ferromagnetic fine particles can be distinguished; namely, superparamagnetic, single domain and multidomain. The properties of these three classes have been discussed elsewhere,[21–28] and will be noted only briefly here.

(a) Superparamagnetic (generally <150 Å diameter). These particles are always spontaneously magnetized to saturation. However, they are so small that their magnetic anisotropy energy, which would tend to stabilize their direction of magnetization, is less than, or of the same magnitude as thermal fluctuation energy at the measuring temperature. Therefore, their magnetization rotates randomly under thermal activation. Assemblies of these particles show a paramagnetic behavior although the moment of each particle may be quite large since

$$\mu = VI_s \tag{1}$$

where μ is the particle moment, V its volume, and I_s the spontaneous magnetization per cm^3 of the particle material. At low enough temperatures, the particles have single domain properties.

(b) Single domain (generally 150 Å to 500 Å diameter). These particles are also uniformly magnetized, but are large enough so that, in zero applied field, they are magnetized in an "easy" direction determined by a minimum in their magnetic anisotropy energy, K. K can represent shape, magnetocrystalline or magnetostatic anisotropy. These particles have a magnetic hysteresis determined by K and I_s.

(c) Multidomain (generally >500 Å diameter). These particles are so large that their magnetization is non-uniform. Thus, changes of magnetization can be accomplished by the relatively easy process of domain wall motion, and magnetic hysteresis is low.

EXPERIMENTAL PROCEDURE

Cylindrical and disc shaped samples were cut from a high purity single crystal rod of beta brass containing 0.07 wt.% iron. The axis of the rod was 12° from the nearest ⟨111⟩ direction. The disc samples had (100) or (110) faces and weighed about 300 mg. The cylindrical samples were sections of the crystal 7/8 in. long × 1/4 in. diameter.

The samples were coated with magnesium oxide and enclosed in brass foil during annealing. The rod was initially given a solution anneal for 2 weeks at 850°C. After cutting off the samples, and electropolishing off deformed layers, the samples were given an additional solution anneal for 15 min before quenching into water. Sample surfaces were electropolished when occasional minor evidence of oxidation or dezincification were noted. X-ray diffraction patterns of the quenched samples indicated that only the b.c.c. beta phase of brass was present.

The total aging times for different samples were approximately 30,000 min at 300 and 400°C. The magnetic data, obtained after quenching at intervals during the anneals, included magnetization curves, hysteresis loops and torque curves.

RESULTS AND DISCUSSION

(a) *Magnetization data*

For short annealing times, magnetization data obtained at three temperatures (77, 200 and 300°K) superimposed when plotted against H/T. Fig. 1 is an example of this superposition for a sample annealed 40 min at 300°C. This superparamagnetic behavior is described by the Langevin relation

$$\frac{\sigma}{\sigma_s} = \coth\frac{\mu H}{kT} - \frac{kT}{\mu H} \tag{2}$$

where σ_s is the saturation magnetization per gram, μ the moment of each particle (defined in equation 1), H the applied field, k is Boltzmann's constant, and T the absolute temperature. The low and high field approximations give

$$\frac{\sigma}{H} = \frac{\mu\sigma_s}{3kT} \tag{3}$$

for the initial susceptibility and

$$\frac{\sigma}{\sigma_s} = 1 - \frac{kT}{\mu H} \tag{4}$$

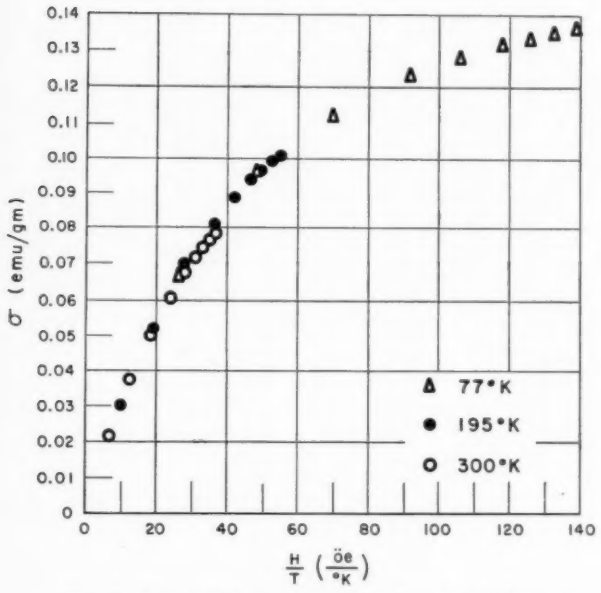


FIG. 1. Superposition of magnetization data taken at three temperatures when the precipitate particles are in the superparamagnetic size range. Sample annealed 40 min at 300°C.

for the approach to saturation. Equations (3) and (4), in combination with equation (1) can be used to estimate the average particles size of the superparamagnetic assembly. Average particle sizes from equation (3) will be weighted toward the larger particles since they are most easily magnetized; whereas equation (4) will weight the average size toward the smaller ones since they are the most difficult to magnetize. Becker[7] has pointed out that if the data indicate that the distribution includes very small particles, then the mean volume determined from equation (3) is not very sensitive to the actual shape of the distribution.

σ_s must be known to apply equations (3) and (4). Fig. 2 shows σ_s as a function of annealing time at 300°C. An extremely large temperature dependence is noted for short annealing times. These data were obtained by extrapolating on a $1/H$ plot from a maximum field of 11,000 Oe. If these data are valid, they imply that σ_s of small iron particles has a much greater temperature dependence than does bulk iron (about 2 per cent between 77°K and 300°K). Bean and Livingston[24] have discussed the available data relating to this problem and have concluded that both iron and cobalt particles with diameters greater than 20 Å apparently have no anomalous temperature dependence. In support of this conclusion are the following:

Equation (3) for the initial susceptibility can be transposed to

$$\frac{\sigma T}{H} = \frac{\mu \sigma_s}{3k} \propto I_s^2 \propto \sigma_s^2. \tag{5}$$

Thus, if an anomalous temperature dependence exists, the ratio

$$\frac{\left(\frac{\sigma T}{H}\right)300°\text{K}}{\left(\frac{\sigma T}{H}\right)77°\text{K}} = \frac{(\sigma_s)^2\ 300°\text{K}}{(\sigma_s)^2\ 77°\text{K}} \tag{6}$$

should show a corresponding trend. A plot of $(\sigma T/H)\ 300°\text{K}/(\sigma T/H)\ 77°\text{K}$ versus annealing time showed random scatter about an average value of $\sigma_s(300°\text{K})/\sigma_s(77°\text{K}) = 0.96$ as compared to 0.98 for bulk iron.

The temperature dependence indicated in Fig. 2 for the shorter annealing times probably results from the fact that our highest measuring field was too small. Consideration of the Langevin relation[23] indicates that for the fields available, reliable $1/H$ extrapolations should be obtained for iron particles with diameters greater than 30 Å. The discussion below shows that during the initial annealing stages, there were appreciable volumes of particles with diameters <30 Å.

When equations (3), (4) and (1) were used to compute particle diameters it was assumed that, (a) the particles were spherical and (b) σ_s was the equilibrium value after long anneal. Assumption (a) is confirmed by torque data discussed below; (b) follows from the discussion above. Even if the values of σ_s in Fig. 2 were used, they would have yielded a difference of only 5 per cent in the values computed for the particle diameters. Fig. 3 shows the computed particle diameters for the 300°C and 400°C anneals as functions of aging time. Data are shown for measurements at 300°K and 77°K. The diameters for

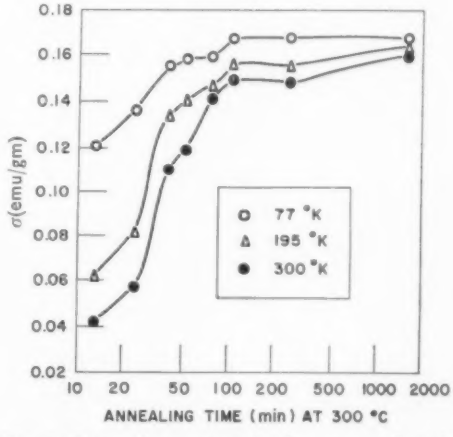


FIG. 2. Saturation magnetization as a function of annealing time at 300°C.

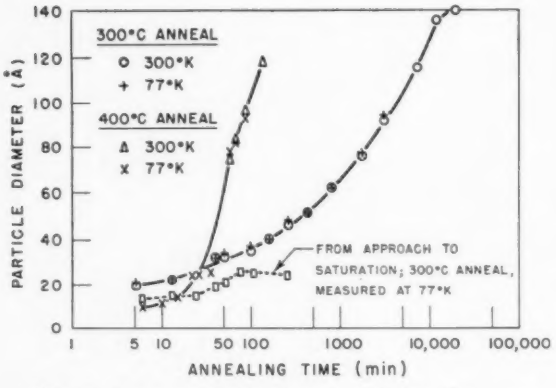


FIG. 3. Average particle diameters during the superparamagnetic stage of the 300°C and 400°C anneals. Upper two curves calculated from initial susceptibility data; lower curve calculated from approach to saturation during 300°C anneal.

the 300°C anneal were computed from both initial susceptibility and approach to saturation data and showed the expected larger and smaller average values, respectively. The diameters computed from the approach to saturation data clearly demonstrate the presence of very small particles, in agreement with the discussion above concerning the difficulty in saturating the small particles during the early annealing stages. From Fig. 2, it is noted that single domain properties are first observed for average particle diameters of ~100 Å at 77°K and 140 Å at 300°K. Since a distribution of sizes is evident, and the larger particles in the distribution first show single domain properties, these diameters represent minimum values for the critical single domain size. As such, they are in good agreement with various theoretical estimates of the critical single domain size in iron (200–300 Å).

Neel's theory of superparamagnetism defines a relaxation time, τ, for the magnetization. Assuming that a superparamagnetic particle becomes stable (i.e. single domain) when $\tau \approx 100$ sec, Neel's expression gives[24]

$$\frac{KV}{4} = 25\,kT \qquad (7)$$

when a particle is spherical with positive magnetocrystalline anisotropy. For iron, equation (7) gives diameters of 160 Å and 250 Å for the single domain transition at 77°K and 300°K, respectively. The transition diameters from Fig. 2 are in reasonable agreement with these values since the former are averages of a distribution.

Further annealing produced more evidence of single domain characteristics. Fig. 4 shows coercive force ($_IH_c$) and remanence/saturation (I_R/I_S) as functions of annealing time at 300°C and 400°C. The data were obtained at 77°K and 300°K. At the top of Fig. 4 are traces of hysteresis loops obtained after the indicated aging times; in each case, the upper loop was taken at 77°K, the lower one at 300°K. The interpretation of the data in Fig. 4 can be made on the assumptions that the average particle size increases with aging time and that there always exists a distribution of particle sizes. Thus, for shorter annealing times, a mixture of superparamagnetic and single domain particles are present; as aging progresses, the particles become principally single domain and multidomain. Furthermore, the initial susceptibility of the superparamagnetic particles is much higher than that of multidomain particles. Thus the superparamagnetic particles reduce the coercive force of the single domain particles to a much greater extent than do the multidomain particles. The first set of hysteresis loops were taken at the time of maximum I_R/I_S at 77°K for the 400°C anneal. The very large temperature dependence of both $_IH_c$ and I_R/I_S shows that as the temperature is lowered, many superparamagnetic particles become stable single domains. The high initial susceptibility of the superparamagnetic particles combined with the rather square loop of oriented single domain particles produced the "wasp-waisted" loop at 300°K. The same behavior is noted in the third set of loops taken at an equivalent time during the 300°C anneal. The second set of hysteresis loops was obtained at a much later time during the 300°C anneal, corresponding to maximum $_IH_c$. The particles have grown to

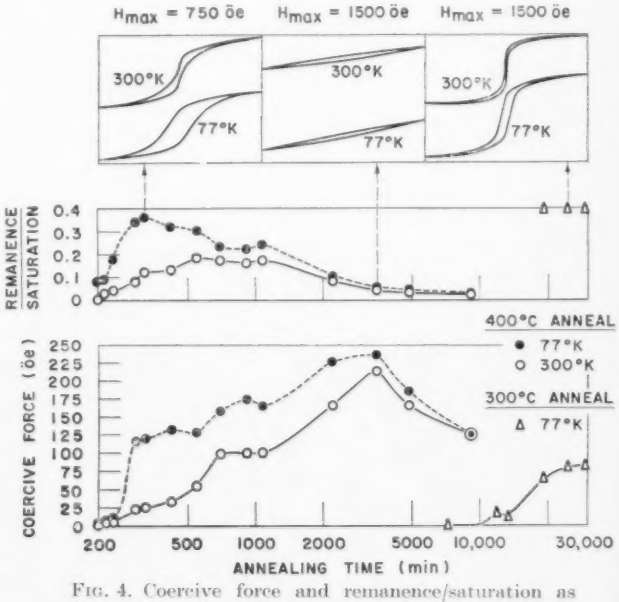


FIG. 4. Coercive force and remanence/saturation as functions of annealing time at 300°C and 400°C. Data obtained at 300°K and 77°K; top curves show hysteresis loops taken at 300°K and 77°K at the indicated annealing times.

the point where they are principally single and multidomain. The very flat loops are due to the small initial susceptibility of the multidomain particles. Thus, even though there is a much smaller volume of single domain particles at this time than at the time corresponding to maximum I_R/I_S, the coercive force is higher because the multidomain particles have a much smaller susceptibility than do the single domain particles. Therefore, the long spread in aging time between the I_R/I_S maximum and the ${}_IH_c$ maximum is quite reasonable. It should be noted from Fig. 4 that up to 30,000 min aging time at 300°C, no hysteresis was observed at 300°K.

(b) *Torque measurements on demagnetized samples*

Torque curves were measured in the (100) and (110) planes of samples annealed for various times at 300° and 400°C. The torque was measured as a function of field at 77°K and 300°K. For the 300°C anneal, anisotropy was apparent at both measuring temperatures after 40 min, at which time the magnetic particle diameter was 30 Å. The symmetry of the torque curves in both planes was the same as that for materials with positive, cubic magnetocrystalline anisotropy (e.g., Fe). During the early anneals, the torque amplitudes showed large temperature dependence, and could not be sufficiently saturated to determine accurately the anisotropy coefficient K. Torque curves were measured at intervals during the 300°C anneal up to a total annealing time of 1600 min. No hysteresis was observed in the samples during this time (see Fig. 4). As the annealing progressed, the torque maintained the same symmetry and could be very nearly saturated in fields ~10,000 G. After 1600 min, when the particle diameter was 80 Å, the calculated magnetocrystalline anisotropy constants were 4.2×10^5 and 5.6×10^5 ergs/cm³ at 300°K and 77°K, respectively. These values are in fair agreement with the recent determination of the anisotropy constants of iron by Graham[29], namely: 4.8×10^5 and 5.2×10^5 at the same temperatures. Livingston and Bean[30] have discussed torque measurements on systems of aligned superparamagnetic particles. Their analysis involves the approximation $KV \ll kT$, which is not valid for these data. However, it appears that the symmetry and amplitude of the torque curves measured during the superparamagnetic stage of the 300°C anneal are compatible with iron particles precipitated with the same crystal habit as the beta brass matrix.

Torque curves were measured during the 400°C anneal up to a total aging time of 9000 min. During the initial, superparamagnetic stage, the conclusions

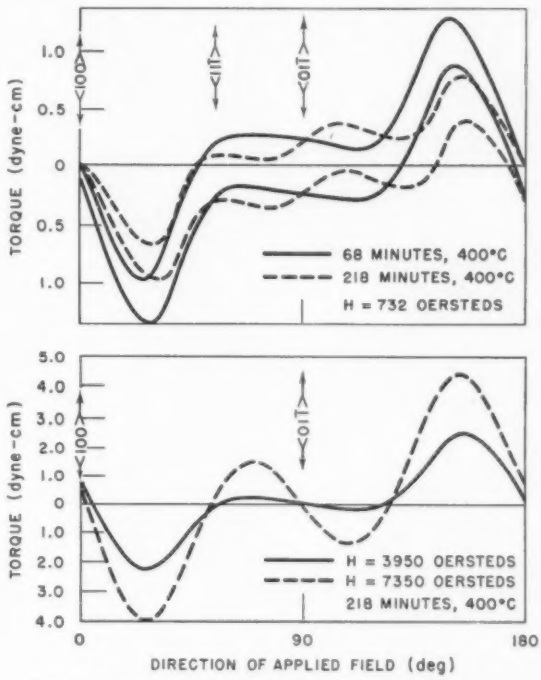


FIG. 5. Torque curves in (110) plane on demagnetized samples during the 400°C anneal.
Upper curves: Torque in low field after 68 and 218 min at 400°C showing increased shape anisotropy with annealing time. Lower curves: Torque in increased fields after 218 min anneal showing disappearance of shape anisotropy component.

were the same as for the 300°C anneal. After 68 min at 400°C, when the average particle diameter was about 90 Å, the symmetry of the torque curves indicated a component due to shape anisotropy superimposed on the magnetocrystalline anisotropy. At high fields, the shape component was reduced to zero, as was previously observed in Alnico.[3] At this stage, the measured magnetocrystalline anisotropy constants were 5.4×10^5 and 6.6×10^5 ergs/cm³ at 300°K and 77°K, respectively. Rotational hysteresis also appeared at this annealing time. As the 400°C anneal progressed to the point at which single domain behavior was noted (see Fig. 4), increased evidence of shape anisotropy and rotational hysteresis were observed. Fig. 5 shows some typical torque curves after 68 and 218 min at 400°C measured in the (110) plane at 300°K. The upper curves were taken in the same field after the two annealing times. It is noted that after the longer annealing time, much greater evidence of shape anisotropy is present, producing an extra peak in the torque curve. The lower curves were taken at higher fields after the 218 min anneal. As the field is increased the component due to shape anisotropy disappears, and the torque symmetry is that of a single crystal with positive, cubic

VOL. 8 1960

magnetocrystalline anisotropy. Furthermore, the rotational hysteresis apparent at the lower fields is not present at the higher fields. As the 400°C anneal was extended beyond the times at which single domain behavior was dominant, the shape component became increasingly difficult to reduce to zero in the available fields. Evidence for increasing shape anisotropy with annealing time is discussed in the next section. This increasing shape anisotropy could account for part of the difficulty in saturating the shape component. However, it is likely that the general difficulty in saturating a particle with only a few domains (as discussed by Amar[28]) is mostly responsible for this behavior.

The measured values for the magnetocrystalline anisotropy quoted above for the 400°C anneal are typical for all stages of that anneal for which such data could be obtained. We have no satisfactory explanation for the fact that the values for the 400°C anneal were about 25 per cent higher than the bulk values, whereas substantially better agreement was noted for the one annealing time at 300°C for which these data were obtained. It seems unlikely that this behavior could arise from the increasing solubility with temperature of copper and zinc in iron, since most observations[31] indicate a decrease in the magnetocrystalline anisotropy of iron when other elements are dissolved in it. A strain induced anisotropy also seems unlikely since no decrease in anisotropy was noted with longer annealing times. There remains the possibility that the volume of precipitated iron (necessary for the calculation of K) was incorrectly determined from the measured saturation magnetization of the sample. However, this latter possibility seems to be ruled out by the relatively constant saturation magnetization with annealing time.

In principle, it should be possible to decompose the torque curves into the shape and magnetocrystalline components and thereby determine the directions of elongation of the particles. Sometimes this is quite difficult in practice. In the first place, the net torque curves from equal volumes of particles elongated in each of a family of directions are always skewed and vary in a complex manner with field strength and degree of elongation. Furthermore, the peak amplitudes of the shape component usually occur at fields in which the magnetocrystalline component is not saturated. Therefore, it is difficult to determine the amplitude of either component which is to be subtracted from the net experimental curve. Also, if the elongation of the particles is not extreme (as in the present case), it is sometimes uncertain as to which of two families of elongation better fits the data. In the present case, torque curves in the (100) and (110) planes were synthesized by adding magnetocrystalline anisotropy torque to that resulting from particles elongated in the ⟨100⟩, ⟨110⟩ or ⟨111⟩ families. The most extensive deviation from magnetocrystalline symmetry was noted in the experimential curves taken in the (100) plane in moderate fields (~4000 Oe). This symmetry was matched only by the (100) curves synthesized from magnetocrystalline anisotropy torque added to the torque from ⟨100⟩ particles in corresponding fields. The experimental data taken in the other planes were also consistent with the assumption of ⟨100⟩ particles. However in these planes, it was more difficult to make a unique choice from among the three possibilities. Therefore, it was concluded that the shape anisotropy that appeared in the torque curves at the same annealing times at which hysteresis was first noted, originated from particles elongated in the ⟨100⟩ family.

In the discussion above of shape anisotropy, and in those to follow, the term "elongation" is always used. Actually, the symmetries of the torque curves on demagnetized samples, discussed above, are as consistent with the assumption of (100) platelets as with ⟨100⟩ elongations. Further, if the platelets are elongated in their planes, then all of the data discussed below is equally consistent with elongated platelets as with elongated particles. Thus the term "elongated particles" shall be understood to include "elongated platelets". Platelets whose planes are magnetically isotropic can probably be ruled out because rotational hysteresis was observed in fields up to 2000 Oe which would be inconsistent with such platelets.

(c) *Remanent torque curves*

Two types of torque measurements were made on samples in the remanent state. These data were obtained in order to clarify the problems of the distributions of anisotropies (elongations) of the single domain particles, and the orientations of the elongated axes of the particles. It is assumed that in the remanent state all single domain particles are magnetized in the "easy" direction closest to the saturating field direction. The easy directions for spherical single domain particles would be the ⟨100⟩ directions. For sufficiently elongated single domain particles, the "easy" direction would be along the longitudinal axis. Thus, the torque curve of a sample in the remanent state will have a sin θ symmetry when measured at sufficiently low fields. The net "easy" direction of such a sample is defined as the direction in which the torque goes through zero with a negative slope.

The first type of remanent torque measurement was

to determine the dependence of the resulting "easy" direction on the saturation direction. These measurements were made in the (100) and (110) planes. In the (100) plane, the results were as follows: When saturated in any member of the ⟨100⟩ or ⟨110⟩ families of directions the resulting easy direction was in the saturation direction. When saturated in any other direction, the "easy" direction was between the saturation direction and the nearest ⟨100⟩ type direction. This behavior may be interpreted by assuming that the single domain particles are classified into two groups: (a) spherical single domain particles with "easy" axes along the ⟨100⟩ directions, (b) elongated single domain particles with "easy" axes along the elongation direction. The elongated particles are divided into three equal groups, each of which is elongated in one of the ⟨100⟩ directions. When saturated in any direction other than a ⟨110⟩, the spherical particles in the remanent state are magnetized in the ⟨100⟩ direction nearest the saturation direction. When saturated in a ⟨110⟩ direction equal volumes of the spherical single domain particles are magnetized, at remanence, in the two ⟨100⟩ directions nearest the ⟨110⟩ saturation direction. This gives a net ⟨110⟩ "easy" direction. When the elongated single domain particles are saturated in any direction other than a ⟨100⟩, the particles are magnetized at remanence in their elongation direction closest to the saturation direction. This produces a net ⟨110⟩ "easy" direction. When the elongated particles are saturated in a ⟨110⟩ direction, those particles elongated normal to the saturation direction are randomly magnetized at remanence, and do not contribute to the torque. Therefore, the easy direction is in the saturation direction. Thus, considering both spherical and elongated particles, the following net easy directions result: (a) When saturated in either a ⟨100⟩ or ⟨110⟩ direction both types of particles have a net "easy" direction in the saturation direction; (b) when saturated in any other direction, the spherical particles are magnetized at remanence in the ⟨100⟩ nearest the saturation direction; the elongated particles have a net ⟨110⟩ easy direction. Therefore, the resultant easy axes lie between the ⟨100⟩ and ⟨110⟩ nearest the saturation direction. These various situations are shown schematically in Fig. 6. The results in the (110) plane produced the same conclusions. The data were not consistent with elongation in any of the other low index families of directions.

The second type of remanent torque data provided information about the shape distributions of the single domain particles after various annealing times. The sample was saturated in the ⟨001⟩ direction in the (100) plane. Sin θ torque curves were then measured in increasing fields and the peak torque amplitude (occurring in the ⟨010⟩ direction) was plotted as a function of measuring field. According to the above discussion concerning the orientations of the longitudinal axes of the elongated particles, we would expect the following to be the distribution of magnetizations among the single domain particles in the remanent state: All particles with nominal elongations <1.1 (i.e. length to width ratios approximately <1.1) would be magnetized in the ⟨001⟩ direction. Of the particles with greater elongations, 1/3 would be magnetized in the ⟨001⟩ direction. The rest would be equally distributed among the ⟨010⟩, ⟨0$\bar{1}$0⟩, ⟨100⟩ and ⟨$\bar{1}$00⟩ and would contribute no net torque with the measuring field in the ⟨010⟩ direction. With these assumptions about the distributions of magnetization, the experimental curves of peak torque vs. measuring field can be synthesized by weighted curves of the same quantities calculated for particles of different anisotropy values K. These curves are calculated from the relation

$$L = HI_s\left[1 - \frac{H^2 I_s^2}{4K^2}\right]^{1/2}$$

where L is the torque amplitude in the measuring field H; $K = 1/2(N_b - N_a)I_s^2$ where N_a and N_b are the demagnetizing coefficients in the transverse and longitudinal directions, respectively; and I_s is the magnetization of the particles. The weighting of the calculated curves for different K-values required to fit

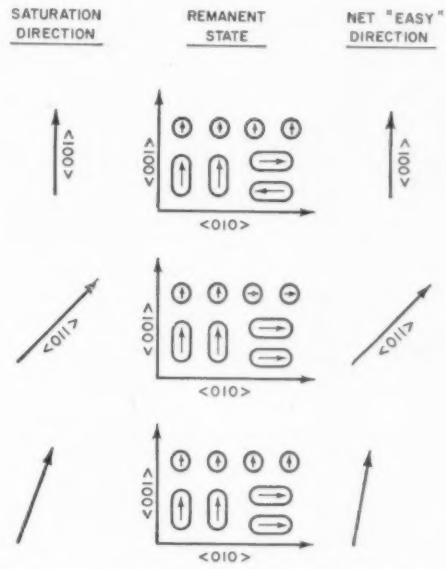


Fig. 6. Dependence on saturation direction in the (100) plane of the net "easy" direction of spherical and elongated single domain particles in the remanent state.

VOL. 8 1960

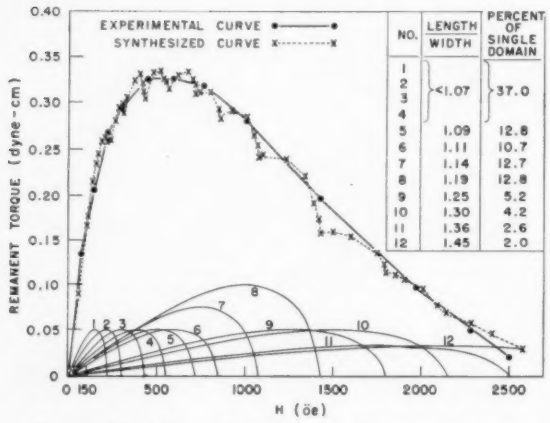


FIG. 7. Synthesis of experimental remanent torque curve by weighted, calculated torque curves for particles of various elongations.
Sample saturated in ⟨001⟩ direction in (100) plane; peak torque measured ⟨010⟩ direction. Sample annealed 1619 min at 400°C.

the experimental curve gives the distribution of single domain particle shapes.

An example of the fitting of the experimental curve is shown in Fig. 7. The data were obtained on a sample annealed for 1619 min at 400°C. The properly weighted calculated curves for various K (or $N_b - N_a$) values are shown in the lower part of Fig. 7. When these curves are summed, it is seen that a good fit with the experimental curve is obtained.

The resulting distribution does not include the 2/3 of the elongated particles which contributed no net torque. The correction is made by tripling the volume of particles with $(N_b - N_a) > 0.33$ which is the value for which the resulting K is equal to the magnetocrystalline anisotropy. The resulting distributions of single domain particles for three annealing times are shown in Table 1. The data in Table 1 show a progressive elongation of the single domain particles with annealing time. However, the average elongations of the particles are not very great. Although these distributions refer only to the single domain particles, the moderate elongations would suggest that the difficulty in saturating the shape component in the torque curves on demagnetized samples was indeed due to the general difficulty in saturating particles having only a few domains.

When the magnetocrystalline anisotropy was explicitly introduced into the analysis of the sample described in Fig. 7, the resulting distribution did not differ significantly from that obtained by the procedure discussed above.

A check on the validity of these distributions can be made as follows. The distributions in Table 1 give the volume of single domain iron present. This can be expressed as a fraction of the total iron in the sample. The same fraction can be determined from the remanence data (Fig. 4) for the same annealing time. The remanence values were measured on a cylindrical sample in which the orientation of the axis was known. It is assumed that in the remanent state, the spherical single domain particles are magnetized in the ⟨100⟩ direction nearest the cylinder axes; the elongated single domain particles are magnetized along their longitudinal axis nearest the saturation direction. The comparison of the results from these two methods of computing the volume of single domain particles is shown in Table 2. The agreement is quite good and suggests that the distributions in Table 1 are probably valid.

The distributions in Table 1 were also used to calculate the torque curves of demagnetized samples for various applied fields. The calculated curves were subtracted from the experimental curves for the corresponding fields. The resulting net curves always had the symmetry corresponding to a magnetocrystalline anisotropy with $K > 0$. This served as a confirmation both of the validity of the distributions and the assumption of elongation in the ⟨100⟩ family of directions.

TABLE 1. Distribution of elongations of single domain particles as calculated from remanent torque data obtained after various annealing times (400°C)

$N_b - N_a$	Length/width	Diameter (A)*	Per cent of single domain volume		
			364 min	1619 min	32,893 min
0.33	1.07	315	60.7	37.0	
0.40	1.08	314	9.0		
0.42	1.09	314	8.5	12.8	
0.50	1.11	314	7.3	10.7	
0.63	1.14	312	2.9	12.7	20.6
0.73	1.16	310	2.5		
0.84	1.19	308	4.3	12.8	
1.06	1.25	305	3.4	5.2	
1.26	1.30	304	1.4	4.2	46.4
1.47	1.36	302		2.6	
1.76	1.45	300		2.0	33.0

* Using the criterion discussed by W. F. BROWN[27].

TABLE 2. Volume per cent of single domain iron precipitated after various annealing times at 400°C as determined from remanence saturation and remanent torque data

Annealing time (min)	Volume per cent single domain iron	
	Rem./sat.	Rem. torque
364	56	58
1619	21	20
10,000	7*	
32,893		12

* Using the fractions of elongated and spherical particles determined from the 32,893 min remanent torque data.

(d) *Electron micrographs*

A number of electron micrographs were made of replicas taken from the surfaces of various samples. The object was to obtain size and shape distributions of the iron precipitate particles and to compare these distributions with those determined from the magnetic data. Great difficulty was encountered in obtaining replicas showing clearly defined iron particles which could be readily distinguished from the beta brass background. This problem prevented the determination of a reliable size-shape distribution. Fig. 8 shows one of the best of the micrographs. The sample was mechanically polished and then electropolished at ice temperature in the solution:

50% orthophosphoric acid

25% ethyl alcohol

25% water.

The current density was approximately 500 mA/cm². The silicon monoxide replica was shadowed with tungsten oxide. The sample was the end of a single crystal cylinder which had been annealed for 9215 min at 400°C. The cylinder axis was 12° from the nearest ⟨111⟩. In this micrograph, the background shows considerably less structure than was apparent in the majority of cases. The large (~2500 Å) particles are assumed to be the iron precipitate. At this annealing time, the remanence indicated that less than 5 per cent of the particles were single domains. This is in agreement with the particle sizes in the micrograph; they are mostly in the multi-domain size range. Only moderate shape anisotropy is noted; this was the case for particles observed at all annealing stages.

CONCLUSIONS

The investigation demonstrated that the significant structural features of the iron precipitate particles can be determined for sizes up to the single domain

VOL. 8 1960



FIG. 8. Electron micrograph of replica of sample annealed 9215 min at 400°C.

limit (~300 Å). These properties included size and shape distributions and the orientations of the crystallographic and shape symmetry axes. For larger particle sizes, the shape symmetry axes could be distinguished, but particle sizes could not be inferred due to the inadequacy of fine particle theory in this size range.

The magnetic data indicated that the saturation magnetization of superparamagnetic iron particles is the same as that of bulk iron, confirming previous data.[24] The symmetry of the magnetocrystalline anisotropy of superparamagnetic iron particles is also the same as that of bulk iron, although the torque of the small particles could not be saturated sufficiently to determine the magnitude of K. The variation in shapes of hysteresis loops and the wide separation in annealing time between maximum ${}_IH_c$ and I_R/I_S could be simply interpreted in terms of the properties of the three classes of ferromagnetic fine particles. The data suggests that a relatively hard process of magnetization exists for particle sizes just above the single domain size limit. The superposition of shape and magnetocrystalline anisotropy could be successfully analysed. Torque data are extremely useful in this type of investigation. In particular, the remanent torque data provide a technique for analysing the distribution of properties of any set of single domain particles.

ACKNOWLEDGMENTS

We are grateful to R. Campbell for taking the electron micrographs and to H. Wilsdorf for advice concerning the interpretation of the micrographs. Discussions with H. Amar were very useful.

REFERENCES

1. R. D. Heidenreich and E. A. Nesbitt, *J. Appl. Phys.* **23,** 352 (1952).
2. E. A. Nesbitt and R. D. Heidenreich, *J. Appl. Phys.* **23,** 366 (1952).
3. E. A. Nesbitt, H. J. Williams, and R. M. Bozorth, *J. Appl. Phys.* **25,** 1014 (1954).
4. K. Hoselitz and M. McCaig, *Proc. Phys. Soc., Lond.* B**64,** 549 (1951).
5. H. Fahlenbrach, *Tech. Mitt. Krupp* **12,** 177 (1954).
6. A. H. Geisler, *Trans. Amer. Soc. Metals* **43,** 70 (1951).
7. J. J. Becker, *Trans. Amer. Inst. Min. (Metall.) Engrs.* **209,** 59 (1957).
8. D. S. Rodbell, *J. Appl. Phys.* **29,** 311 (1958).
9. J. D. Livingston and J. J. Becker, *Trans. Amer. Inst. Min. (Metall.) Engrs.* **212,** 316 (1958).
10. J. W. Cahn, *Trans. Amer. Inst. Min. (Metall.) Engrs.* **209,** 1309 (1957).
11. L. Weil and L. Gruner, *C.R. Acad. Sci., Paris* **243,** 1692 (1956).
12. G. Bate, D. Schofield and W. Sucksmith, *Phil. Mag.* **46,** 621 (1955).
13. W. Sucksmith, *J. Phys. et Rad.* **20,** 290 (1959).
14. C. P. Bean, J. D. Livingston, and D. S. Rodbell, *J. Phys. et Rad.* **20,** 298 (1959).
15. L. Weil, L. Gruner and A. Dechamps, *C.R. Acad. Sci., Paris* **244,** 2143 (1957).
16. C. P. Bean, J. Livingston, D. Rodbell, *Acta Met.* **5,** 682 (1957).
17. A. E. Berkowitz and P. J. Flanders, *AIEE Publ.* T-19, p. 275 (1957).
18. A. E. Berkowitz and P. J. Flanders, *J. Appl. Phys.* **29,** 314 (1958).
19. A. E. Berkowitz and P. J. Flanders, *J. Appl. Phys.* **30,** 111*s* (1959).
20. C. S. Smith, *Trans. Amer. Inst. Min. (Metall.) Engrs.* **147,** 111 (1942).
21. L. Neel, *C.R. Acad. Sci., Paris* **228,** 664 (1949).
22. L. Neel, *Ann. Geophys.* **5,** 99 (1949).
23. C. P. Bean and I. S. Jacobs, *J. Appl. Phys.* **27,** 1448 (1956).
24. C. P. Bean and J. D. Livingston, *J. Appl. Phys.* **30,** 120*s* (1959).
25. L. Neel, *C.R. Acad. Sci., Paris* **224,** 1488, 1550 (1947).
26. E. C. Stoner and E. P. Wohlfarth, *Trans. Roy. Soc.* A**240,** 599 (1948).
27. W. F. Brown, *Phys. Rev.* **105,** 1479 (1957): contains pertinent references.
28. H. Amar, *Phys. Rev.* **111,** 149 (1958): contains pertinent references.
29. C. D. Graham, *J. Appl. Phys.* **30,** 317*s* (1959).
30. J. D. Livingston and C. P. Bean, *J. Appl. Phys.* **30,** 318*s* (1959).
31. R. M. Bozorth, *Ferromagnetism* p. 574. Van Nostrand, Princeton, N.J. (1951).

THERMODYNAMICS OF THE SOLID SOLUTIONS OF MERCURY IN SILVER AND GOLD*

H. W. RAYSON† and W. A. ALEXANDER‡

Thermodynamic properties of the silver–mercury and gold–mercury f.c.c. solid solutions have been determined using an isopiestic technique, the equilibrium compositions of the alloys being mainly obtained by X-ray analysis. Dilute solutions in the two systems have similar entropies and may be "regular". Excess entropies occur in the mercury-rich gold–mercury solutions. Integral heats of solution for the gold–mercury system are parabolically related to composition throughout the solid solution range, but for silver–mercury alloys the relationship is more complicated, as shown by the partial heat curves.

Partial heats of solution of liquid mercury in solid silver and gold at infinite dilution are −4.05 and −2.19 kcal/g atom, respectively. The magnitudes of the heats of solution for silver–mercury and gold–mercury are discussed and compared with those in closely related systems. The present data are used to evaluate conflicting results regarding the position of the solidus in the silver–mercury equilibrium diagram.

THERMODYNAMIQUE DES SOLUTIONS SOLIDES DU MERCURE DANS L'ARGENT ET L'OR

Les auteurs ont déterminé à l'aide d'une technique isopiestique les propriétés thermodynamiques des solutions solides c.f.c. Argent–Mercure et Or–Mercure. Les compositions à l'équilibre ont été principalement déterminées par rayons X.

Dans les deux systèmes, les solutions diluées ont des entropies semblables et peuvent être considérées comme idéales. Les solutions Or–Mercure, riches en mercure, possèdent des entropies en excès. Pour le systeme or–mercure, les chaleurs totales de dissolution varient paraboliquement avec la composition dans tout le domaine de la solution solide. Pour les alliages argent–mercure, la relation est plus complexe, ainsi que le montrent les courbes de chaleur partielle.

Les chaleurs partielles de dissolution du mercure liquide dans l'argent et dans l'or sont respectivement de −4,05 et −2,19 Kcal/at.gr.

Les auteurs discutent et comparent les valeurs des chaleurs de dissolution des systèmes argent–mercure et or–mercure avec celles de systèmes analogues.

Enfin, les résultats de cette étude permettent la critique des différentes positions du solidus du diagramme argent–mercure fournies par la littérature.

DIE THERMODYNAMIK DER FESTEN LÖSUNG VON QUECKSILBER IN SILBER UND GOLD

Die thermodynamischen Eigenschaften fester kubisch-flächenzentrierter Lösungen von Quecksilber in Silber und Gold wurden gemessen, dabei wurden die Gleichgewichtszusammensetzungen hauptsächlich röntgenographisch ermittelt. Die verdünnten Lösungen beider Systeme haben ähnliche Entropien und können "regulär" sein. Überschußentropien treten bei quecksilberreichen Gold–Quecksilber-Legierungen auf. Die integralen Lösungswärmen im Gold–Quecksilber-System hängen im ganzen Löslichkeitsbereich parabolisch von der Zusammensetzung ab, während bei Silber–Quecksilber-Legierungen der Zusammenhang komplizierter ist, wie die Kurven der partiellen Lösungswärmen zeigen.

Die partiellen Lösungswärmen von flüssigem Quecksilber in festem Silber und Gold betragen bei unendlicher Verdünnung −4,05 bzw. −2,19 Kcal/gAtom. Die Größenordnungen der Lösungswärmen bei Silber–Quecksilber und Gold–Quecksilber werden diskutiert und mit denen in verwandten Systemen verglichen. Die vorliegenden Daten werden verwendet, um zwischen widersprüchlichen Ergebnissen über die Lage der Soliduslinie im Silber–Quecksilber-Gleichgewichtsdiagramm zu entscheiden.

VOL. 8 1960

INTRODUCTION

The present work on silver–mercury was undertaken to fill a gap in thermodynamic knowledge of what appeared to be a particularly simple solid solution, having small size and electrochemical effects. Gold–mercury was included as it had only once been previously examined in any detail[1] and the reported constancy of heat of formation with composition called for further investigation.

EXPERIMENTAL DETAILS

The metals used were: mint grade, 0.25 mm silver wire (99.99 % Ag) containing traces of copper, cadmium and lead; triply distilled mercury containing less than 1 p.p.m. each of copper, silver and silicon; 0.25 mm gold wire, drawn from doubly electrolysed gold and equivalent in purity to the best available spectrographic standard.

The experimental method was similar to that described by Herasymenko[2]. The silica reaction vessel (Fig. 1) contained a concentric central tube which supported a series of specimen wire rings. The wires fitted in narrow grooves in a silica specimen carrier, reproducibly located relative to the bottom of

* Received November 28, 1959; revised April 26, 1960.

† Institute of Technology, Bradford, Yorks; formerly at N.R.C., Ottawa.

‡ Applied Chemistry Division, National Research Council, Ottawa, Canada.

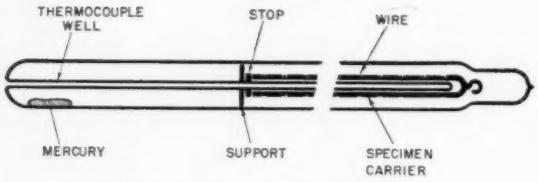


FIG. 1. Quartz reaction vessel.

the central tube, in which the measuring thermocouple was inserted. After charging with a series of specimens of silver or gold wire and an excess of mercury, the vessel was evacuated to 0.2 μ and sealed. It was placed in a gently sloping tubular gradient furnace so that the mercury remained at one end of the vessel. The furnace had three independently controlled, tapped windings separated by narrow cooling coils, enabling a variety of temperature gradients to be attained. Temperatures were controlled with commercial proportioning controllers, one of which was fitted with a "failsafe" device. Each controller was actuated by two chromel–alumel thermocouples in series, placed near the furnace windings. During an initial period of 2 days, adjustments were made to place the excess mercury in a position corresponding to a shallow temperature minimum, the temperatures of the specimens increasing to a suitable maximum at the opposite end of the tube. Temperature control was then established to within ± 1.5°C at the hotter end, and ± 0.5°C elsewhere for the duration of the experiment—normally about 3 weeks. Radial temperature gradients between the measuring thermocouple and the specimens were found to be negligible.

At the end of the heating period, the temperatures of the specimens and of the mercury were measured with a platinum–platinum 10% rhodium thermocouple calibrated before and after the experiments. The vessel was rapidly cooled in oil, the specimens taken out as soon as possible and stored at -5°C until required.

Times necessary to reach equilibrium throughout the wires were found to be excessive below 550°C. High temperature experiments were undesirable because of the deviation of mercury vapour from ideal gas behaviour at pressures much above atmospheric.[3] In a few long-term experiments of about 6 weeks duration, at moderate temperatures, equilibrium compositions were obtained from the increases in weight of the specimens. In other cases, the permissible temperature range was increased by using X-ray analysis of the wire surfaces, allowing shorter times of heating at lower temperatures. An equilibrium surface layer only 10^{-3} cm deep was sufficient to give reliable results because of the small penetration of the CuK radiation used—calculation showed that the intensity of the incident beam was reduced to 1/600 of its original value, i.e. became too weak to give visible reflections, after passing through 2.7×10^{-3} cm of a silver specimen. The absorption was similar in the presence of mercury or gold atoms.

RESULTS

The first experiments were carried out on silver alone, but in runs 9, 10 and 11, gold wires were also included. Sufficient specimens were analysed—generally with X-rays, using the lattice-parameter relationships previously determined[4]—to define the isobars, which are plotted against reciprocal alloy temperature in Figs. 2 and 3. These reciprocal plots were linear at higher mercury contents, permitting accurate short extrapolations. The smoothed curves only are given for runs 4 and 5. Experimental points fitted these curves as closely as in the other runs. The

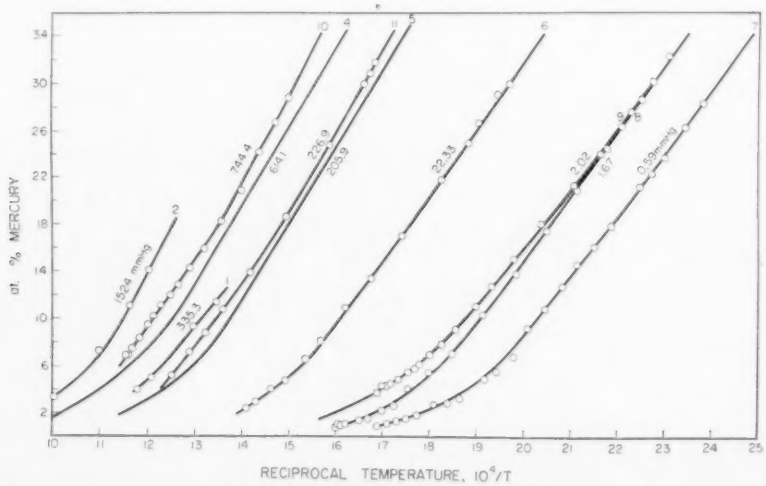


FIG. 2. Isobars for silver–mercury alloys.

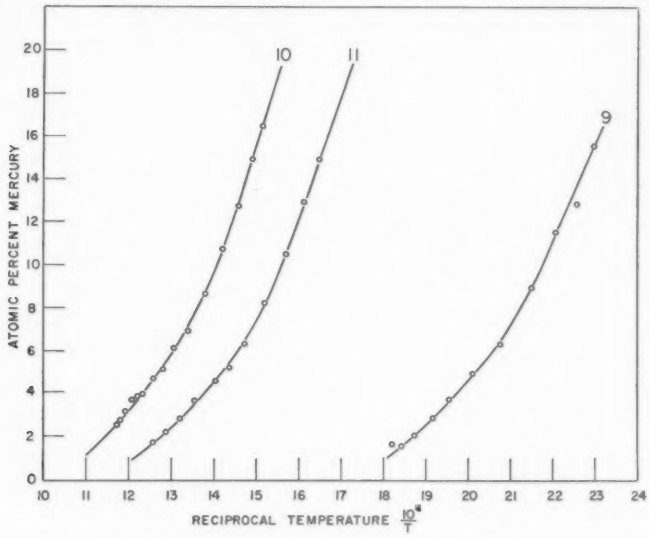


FIG. 3. Isobars for gold–mercury alloys.

third experiment was not satisfactorily completed. Compositions obtained by weighing were consistent with X-ray analysis and no inconsistency was found between the runs composed of silver alone and those combined with gold. Spectrographic analysis showed that the residual mercury maintained its original purity, with one exception, when 40 p.p.m. of silver were found. In the combined runs, contamination of silver was negligible, as might be anticipated since the vapour pressures of Ag and Au at 800°C (the highest temperature used) are only 4.6×10^{-5} mm and 1.7×10^{-9} mm.

It is readily shown from the Clausius–Clapeyron equation that

$$\frac{1}{T_0} = \frac{\Delta H_1}{\Delta H_0} \cdot \frac{1}{T_1} + (C_0 - C_1)\frac{R}{\Delta H_0}$$

where T_0, T_1 are the temperatures of a solute and a solution in equilibrium, ΔH_0 and ΔH_1 are the respective heats of vaporization, C_0 and C_1 are integration constants, and R is the gas constant. $1/T_0$ is proportional to $1/T_1$ if the heats of vaporization are independent of temperature. Birchenall and Cheng[5] have used this method for checking the consistency of results obtained by the dew-point technique. Although ΔH_0 for mercury is not constant,[3] straight lines were obtained, within experimental error, by plotting reciprocal alloy temperatures for integral compositions, obtained from Figs. 2 and 3, against the known reciprocal mercury temperatures corresponding to the isobars (see Figs. 4 and 5). The linearity—perhaps due, n the present case, to compensating changes in ΔH_1 with temperature—allowed the results to be summarized by equations (Table 1) of the form

$$1/T_0 = a/T_1 + b \qquad (1)$$

for any particular alloy. The lines were generally obtained from the experimental data by the "least squares" method. Mean deviations corresponded to an error of 1.5°C.

Knowing the coefficients a and b, and using the mercury vapour pressure equation given by Kubaschewski and Evans[6]

$$\log_{10} p_0 = \frac{-3305}{T} - 0.795 \log_{10} T + 10.355 \qquad (2)$$

the appropriate activities and partial molar free energies of mixing were calculated. The latter appear in Table 1 with other important thermodynamic properties. Values of $\Delta\bar{G}_{Hg}$ were first calculated at 500°K and 600°K, well within the experimental range. Partial entropies were obtained from the relationship

$$\Delta\bar{S} = \frac{\Delta\bar{G}(T_2) - \Delta\bar{G}(T_1)}{T_2 - T_1}. \qquad (3)$$

As a check on the validity of equation (3), part ia entropies were also calculated by an alternative method for selected compositions at a specific temperature of 550°K. It is readily shown, using equations (1) and (2) that

$$\Delta\bar{G} = 4.574\,[-3305(a + bT_1 - 1) + 0.795T_1 \log_{10}(a + bT_1)] \qquad (4)$$

VOL. 8 1960

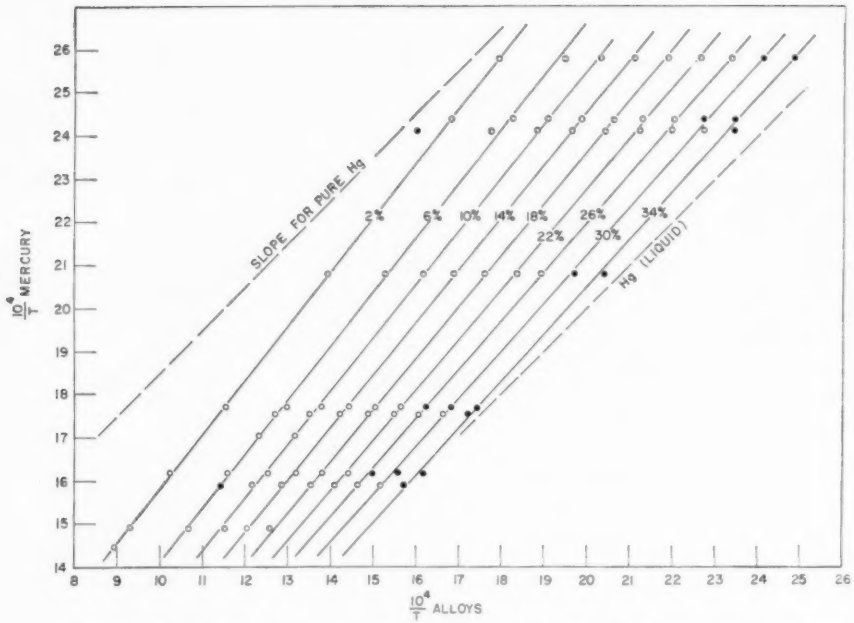


FIG. 4. Relationships between reciprocal temperatures of the silver–mercury alloys and pure mercury. ● Extrapolated beyond the experimental range

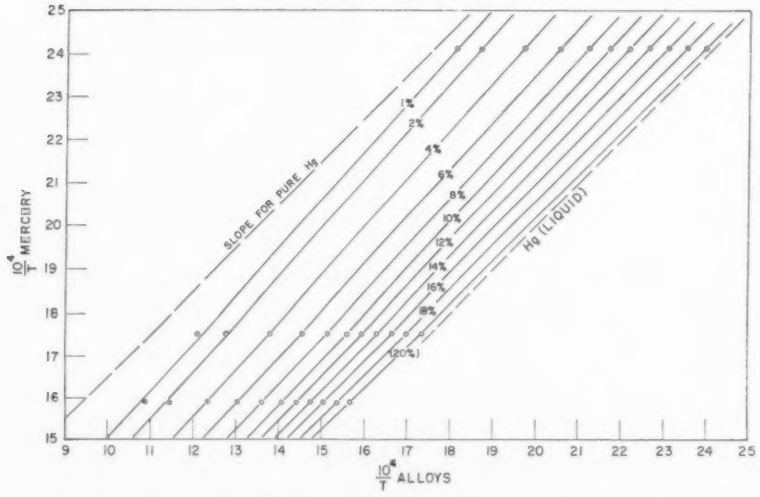


FIG. 5. Relationships between reciprocal temperatures of the gold–mercury alloys and pure mercury.

and

$$\Delta\bar{S} = -15117b + \frac{1.579bT_1}{a + bT_1} + 3.6363 \log_{10}(a + bT_1) \qquad (5)$$

at temperature T_1 for an alloy with coefficients a and b. The two methods of obtaining $\Delta\bar{S}$ agreed closely.

The average partial entropies (500–600°K) for both systems are plotted in Fig. 6 together with the "regular" partial entropy relation $\Delta\bar{S} = -R \ln c$. The difference between the "ideal" and actual values of $\Delta\bar{S}$ is constant, within experimental error, over the whole range of the Ag–Hg solid solution. $\Delta\bar{S}_{Hg}$ may thus be expressed in terms of the ideal expression, as $\Delta\bar{S}_{Hg} = \Delta\bar{S}_{id} - 3.83$ (± 0.08) cal/g atom.

The entropies of the gold–mercury alloys are slightly higher, except in dilute alloys, where the entropies in both systems are seen to be equal.

Partial heats of solution for 500–600°K are plotted in Fig. 7. Heats of solution at infinite dilution in solid Ag and Au are −4050 and −2190 cal, respectively, relative to liquid mercury. Integral ΔH values

TABLE I. (Thermodynamic functions are relative to liquid mercury)

Hg (at.%)	a	b ($\times 10^6$)	$-\Delta\bar{G}_{Hg}$ 500°K (cal/g atom)	$-\Delta\bar{G}_{Hg}$ 600°K (cal/g atom)	$\Delta\bar{S}_{Hg}$ (cal/deg)	$-\Delta\bar{H}_{Hg}$ smoothed (cal/g atom)	$-\Delta H$ (cal/g atom)
Silver alloys							
2	1.259	322.4	6080	6494	4.14	4010	81
4	1.257	214.5	5260	5523	2.63	3946	160
6	1.251	163.4	4807	4995	1.88	3865	238
8	1.243	119.0	4364	4494	1.30	3743	314
10	1.238	76.3	3981	4053	0.72	3620	386
12	1.231	43.0	3639	3665	0.26	3450	456
14	1.213	28.0	3270	3278	0.07	3262	522
16	1.210	−8.0	2966	2925	−0.41	3061	583
18	1.191	−19.1	2607	2555	−0.51	2860	641
20	1.180	−39.0	2309	2229	−0.79	2642	692
22	1.162	−46.6	1994	1904	−0.89	2441	741
24	1.147	−57.0	1703	1604	−0.99	2230	776
26	1.135	−73.4	1417	1296	−1.21	2020	814
28	1.120	−78.0	1163	1040	−1.23	1820	844
30	1.107	−89.7	889.2	752.8	−1.36	1616	868
32	1.096	−103.6	630.1	476.4	−1.54	1407	887
34	1.085	−116.8	377.8	212.7	−1.65	1203	899
Gold alloys							
1	1.114	391	4465	4987	5.21	2072	21.3
2	1.119	318	4009	4425	4.16	1960	41.5
4	1.111	220	3190	3476	2.86	1723	78.5
6	1.093	164	2525	2736	2.11	1500	112
8	1.079	122	2013	2169	1.56	1270	137
10	1.070	87	1623	1732	1.09	1041	159
12	1.058	65	1300	1382	0.82	814	177
14	1.039	60	997.6	1074	0.76	591	188
16	1.021	55	688.6	766.2	0.78	361	195
18	1.005	48	415.5	476.5	0.61	112	197
20	0.989	41	143.2	195.4	0.52	−118	192

VOL. 8 1960

(Table 1 and Fig. 8) were obtained by graphical integration of the Duhem–Margules equation in the form

$$\Delta H = N_A \int_0^x \Delta\bar{H}_{Hg}\, dx$$

where N_A = mol. fraction of Ag or Au, $x = N_B/N_A$ and N_B = mol. fraction of Hg. Values of $\Delta\bar{H}$ were first smoothed as in the Table, and have in effect undergone a "double smoothing" process, the first stage occurring when data were transferred from Figs. 2 and 3, to Figs. 4 and 5. The point at 1 per cent Hg in Au was ignored, since it was based on extrapolated evidence and appears inconsistent with the other results.

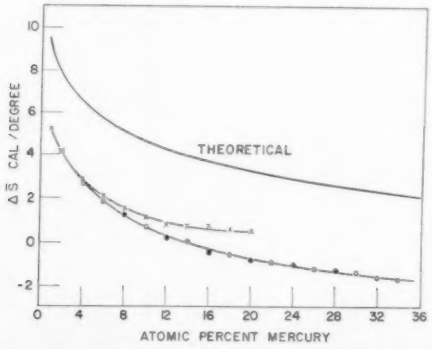


FIG. 6. Partial molar entropies of solution of liquid mercury in its alloys with silver and gold.

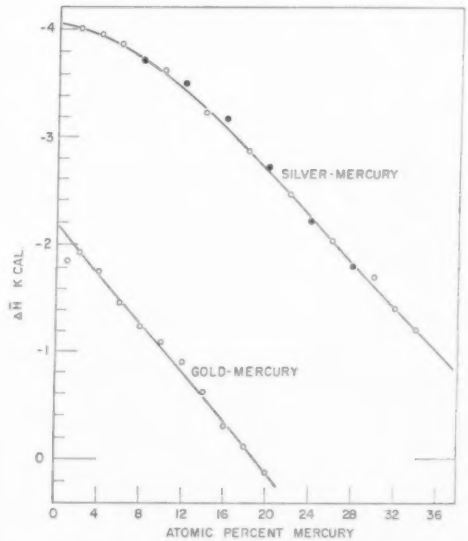


FIG. 7. Partial heats of solution of liquid mercury in silver and gold alloys.
● Obtained by visual estimation
○ Obtained by "mean square" method

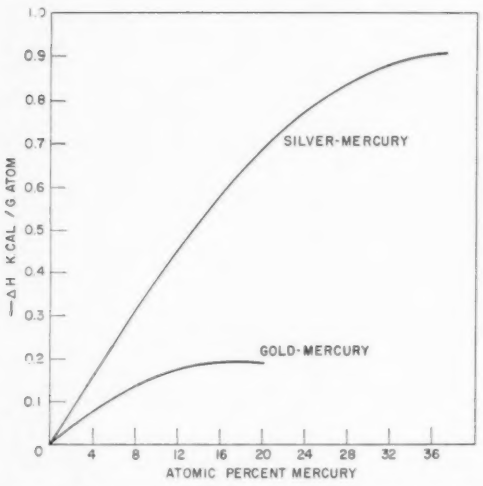


FIG. 8. Integral molar heats of solution relative to liquid mercury, solid silver and gold.

DISCUSSION

(1) *Comparison with previous work*

(a) *Silver–mercury.* The authors are not aware of any other detailed investigation of the thermodynamics of the Ag–Hg solid solution. A liquid alloy containing 92 per cent Hg was found by Eastman and Hildebrand[7] to have an activity of 0.98 at 590°K. In the present work on solid alloys, the activity near the limit of the solid solution (i.e. at 34 per cent Hg) was 0.84 at a similar temperature (600°K).

(b) *Gold–mercury.* Results obtained by Biltz and Meyer[1] indicated that an alloy containing 24 per cent Hg had the same vapour pressure as pure mercury. As observed by Kubaschewski and Catterall[8], this is extremely unlikely, since there is a 20 per cent solubility of gold in liquid mercury at the temperature of their investigation. In the present work, the vapor pressures observed were generally about 30 per cent lower than those of Biltz and Meyer. In addition, $\Delta\bar{H}_{Hg}$ varied between −2072 (1 per cent Hg) and −112 cal/g atom (18 per cent Hg), although previously reported as constant at +1400 cal across the α solid solution at 573°K. Eastman and Hildebrand[7] investigated liquid Au–Hg alloys at 590°K obtaining activities of 0.93 in the region of the liquidus compared with the present value of 0.67 for a composition (18 per cent) near the solidus at 600°K.

(2) *Entropies of solution*

The partial entropies of the dilute solutions of mercury in silver and in gold are about 3.8 cal/deg less than than those for regular liquid solutions. This discrepancy, which remains remarkably constant across the whole range, i.e. 36 per cent, of the silver–mercury solid solution but is gradually reduced with increasing mercury content in the gold–mercury system, can be explained in the following ways:

(i) If the silver–mercury and gold–mercury solid solutions were in fact "regular", their partial entropy curves would coincide and would be displaced from the plot of $-R \ln c$ (Fig. 6) by a constant amount, equivalent to the entropy of melting of the hypothetical f.c.c. modification of pure mercury. Since constant displacement is observed for silver–mercury and coincidence with the gold–mercury curve occurs in dilute solutions, it is possible to assume that 3.8 cal/deg is the entropy of melting of f.c.c. mercury at 550°K. This conclusion is dependent on extrapolation across the major portion of the silver–mercury system, but is worthy of consideration because of the accuracy with which the data follow the fundamental logarithmic relationship to the limit of the solid solution.

The above argument then suggests that the silver–mercury and the dilute gold–mercury solid solutions are "regular".

(ii) It may be assumed that the entropy of melting of f.c.c. mercury, like that of other f.c.c. metals, is of the order of 2.2. cal/deg. It must be emphasized that since mercury never adopts this structure, it cannot necessarily be assumed that its hypothetical entropy of melting must be similar to that of real transformations. If this hypothetical melting entropy were 2.2 cal/deg, then the dilute solutions of the gold and mercury systems have an entropy deficit of 1.6 cal/deg compared with regular solutions.

(iii) Intermediate possibilities cannot be completely ruled out, in which the melting entropies of f.c.c. Hg lie between 2.2. and 3.8 cal/deg. As in (ii), the entropies of mixing would be smaller than the ideal values. The similarities observed between entropy behaviour in the silver-rich and gold-rich alloys are remarkable if both systems are showing appreciable negative entropy deviations.

(iv) It can be deduced in any case that the partial entropy of silver in silver–mercury solid solution is "regular".

If the dilute solutions are regular, as justified in the first argument, the mercury-rich gold mercury alloys display excess entropy. Such excess entropies of mixing have been reported in a number of other gold systems, e.g. Au–Fe[9] Au–Sn, Au–Pb, Au–Bi[10] Au–Ni[11] and have occasionally been observed in systems containing silver e.g. Ag–Zn.[12] Although an excess of unlike neighbours may be anticipated in solutions formed exothermally, randomness is largely preserved by thermal agitation unless the heat of solution much exceeds RT cal. A large degree of randomness could thus be anticipated in Ag–Hg

and Au–Hg solutions. For Ag–Cd[2] and Cu–Zn[13] solutions, to which similar arguments apply, kinks in the entropy curves, attributed to local ordering at specific compositions, have been reported. No sharp irregularities were observed for Ag–Hg and Au–Hg, although it is believed that alloys were examined at sufficiently frequent intervals of composition to observe such effects if they had occurred.

(3) *Heats of solution*

Heats of solution depend on size effects, generally believed to give only endothermic contributions and on electronic effects due to differences in valency and electron affinity of the components.

An important possibility in studying heats of solution at infinite dilution is to obtain information on the solvent Fermi level, in simple cases of negligible strain energy effect. The ideal gas reference state is fundamentally the most suitable for the solute, since the type of bonding in its condensed state is eliminated as a variable. Even this approach is limited, since many metals do not form ideal gases. Certain qualitative conclusions which are independent of the solute reference state can, however, be drawn from the present data. The difference in heats of solution of mercury in silver and gold may be compared with similar paired observations for other solutes. The Au–Hg and Ag–Hg size factors are small and their valency effects are identical, therefore some criterion of electron affinity must explain the more negative heat of solution with silver, e.g. the bigger difference of the first ionization energies of Ag and Hg than of the Au–Hg pair (2.85 eV and 1.21 eV respectively). Conversely, the standard electrode potential series indicates a stronger electronegativity difference between gold and mercury. Kleppa has investigated the solutions of cadmium, indium and antimony in silver and gold[15] obtaining a more negative heat effect with gold for every solute. This is explicable in terms of the electrode potential series, since gold is the most electropositive of the metals, and silver is more electropositive than Cd, In and Sb. It must be observed that the alloying behaviour of gold can be rather complex. The theory of heats of solution developed by Varley[14] is much less acurate for gold than for other metals, a fact which he explains by the strong Van der Waals interaction of the well screened outer electrons of the gold atom.

Regarding the general form of the observed heats of solution curve, it can be shown by plotting $\Delta H/c$ against $(1-c)$ that their usual linear relationship applies over wide ranges of composition; $\partial^2 H/\partial c^2$ is positive in both systems at the mercury deficient end, in agreement with Friedel's theory[16] for solutions in which the solute valency exceeds that of the solvent.

The lattice spacing curve shows negative deviations for Ag–Hg,[4] (Au–Hg is linear), indicating that the system finds some means of lowering its internal energy below the value possible by simple geometric close packing. Thus both the lattice parameter and ΔH curves are consistent in indicating an exothermic heat of formation for Ag–Hg in excess of that derivable from elementary theories of atomic interaction.

Estimation of maximum solid solubilities

Conflicting data on the position of the solidus in the Ag–Hg system can be evaluated from the present work, since maximum solubilities are obtainable by extrapolating the composition/reciprocal temperature

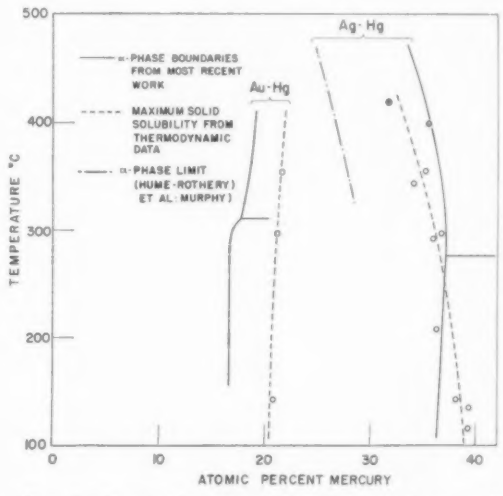


FIG. 9. Comparison of solubility limits from various sources with thermodynamic data.

curves of Figs. 4 and 5 to the reciprocal temperature of the mercury for each experiment. (The solidus composition obtained by combination of the present activity data with data on liquid alloys is more accurate, but the error in neglecting change of activity in the liquid is only about 1 per cent mercury.)

It is seen from Fig. 9 that the solidus obtained by Day and Mathewson[17] (full-line) is above the maximum permissible mercury content and that of Murphy[18] and Hume-Rothery[19], must be preferred. Fig. 9 also shows that the solid solubility in the Au–Hg system, based on recent work,[4] is compatible with the thermodynamic data.

ACKNOWLEDGMENTS

The authors are indebted to Drs. L. D. Calvert, W. G. Henry and E. Whalley for helpful discussion. Miss T. Clarke kindly made the X-ray measurements, Dr.

VOL. 8 1960

T. Dauphinee supervised the thermocouple calibration and Mr. D. S. Russell the chemical analyses.

REFERENCES

1. W. Biltz and F. Meyer, *Z. Anorg. Chem.* **176,** 23 (1928).
2. P. Herasymenko, *Acta Met.* **4,** 1 (1956).
3. R. H. Busey and W. F. Giauque, *J. Amer. Chem. Soc.* **75,** 806 (1953).
4. H. W. Rayson and L. D. Calvert, *J. Inst. Metals.* **87,** 88 (1958).
5. C. E. Birchenall and C. H. Cheng, *J. Metal, N.Y.* **1,** 428 (1949).
6. O. Kubaschewski and E. Ll. Evans, *Metallurgical Thermochemistry.* Pergamon, London (1956).
7. E. D. Eastman and J. H. Hildebrand, *J. Amer. Chem. Soc.* **36,** 2020 (1914).
8. O. Kubaschewski and J. A. Catterall *Thermochemical Data of Alloys.* Pergamon, London (1956).
9. L. L. Seigle, *J. Metal, N.Y.* **8,** 91 (1956).
10. O. J. Kleppa, *J. Amer. Chem. Soc.* **71,** 3275 (1949); **72,** 3346 (1950); **73,** 385 (1951).
11. L. L. Seigle, M. Cohen and B. L. Averbach, *J. Metal, N.Y.* **4,** 1320 (1952).
12. G. Scatchard and R. A. Westlund, *J. Amer. Chem. Soc.* **75,** 4189 (1953).
13. B. B. Argent and D. W. Wakeman, *Trans. Faraday Soc.* **54,** 799 (1958).
14. J. H. O. Varley, *Phil. Mag.* **45,** 887 (1954).
15. O. J. Kleppa, *J. Phys. Chem.* **60,** 846 and 858 (1956).
16. J. Friedel, *Advanc. Phys.* **3,** 446 (1954).
17. H. M. Day and C. H. Mathewson, *Trans. Amer. Inst. Min. (Metall.) Engrs.* **128,** 273 (1938).
18. A. J. Murphy *J. Inst. Metals* **46,** 507 (1931).
19. W. Hume-Rothery, G. W. Mabbott and K. M. Channel-Evans, *Phil. Trans. Roy. Soc.* A**233,** 1 (1934).

SUR LE DURCISSEMENT DÛ À LA RECOMBINAISON DES DISLOCATIONS*

G. SAADA†

Nous étudions deux modèles simplifiés qui montrent comment la recombinaison des dislocations influe sur le durcissement. Nous établissons ainsi que, dans une forêt, le franchissement des arbres "attractifs" conduit à des contraintes nettement plus fortes que le franchissement des arbres "répulsifs." Le mécanisme de recombinaison est responsable de la formation de lacunes et d'interstitiels, et le rôle joué par l'activation thermique est négligeable.

Nous supposons les dislocations non dissociées.

ON HARDENING DUE TO THE RECOMBINATION OF DISLOCATIONS

Two simplified models have been studied which show how the recombination of dislocations influence hardening. It has also been established that, in a dislocation "forest", the piercing of attracting "trees" results in stresses which are decidedly greater than those accompanying the penetration of repulsing "trees".

The recombination mechanism is responsible for the formation of vacancies and interstitials; the role played by thermal activation being negligible. It is supposed that the dislocations are not dissociated.

ÜBER DIE VERFESTIGUNG INFOLGE REKOMBINATION VON VERSETZUNGEN

An zwei vereinfachten Modellen wird der Einfluß der Rekombination von Verestzungen auf die Verfestigung gezeigt. Es wird festgestellt, daß in einem Versetzungswald das Schneiden von "anziehenden" Bäumen zu etwas stärkeren Spannungen führt als das Schneiden von "abstoßenden" Bäumen. Für die Bildung von Leerstellen und Zwischengitteratomen ist der Mechanismus der Rekombination verantwortlich, die Rolle der thermischen Aktivierung ist zu vernachlässigen.

Die Versetzungen werden als nicht dissoziiert vorausgesetzt.

VOL. 8 1960

1. INTRODUCTION

Lorsqu'une dislocation L de vecteur de Burgers $\mathbf{b}_2$ glisse dans son plan de glissement P et rencontre une dislocation L_1 de vecteur de Burgers $\mathbf{b}_1$, elle se combine partiellement avec L_1 pour donner une dislocation L' de vecteur de Burgers $\mathbf{b}'$ si:[1]

$$|\mathbf{b}_1 + \mathbf{b}_2| \leq |\mathbf{b}_1| + |\mathbf{b}_2|$$

Alors:

$$\mathbf{b}' + \mathbf{b}_1 + \mathbf{b}_2 = 0.$$

La dislocation L' se situe à l'intersection de P et P_1 (Fig. 1).

La cission σ qui provoquait le glissement de L doit alors être suffisante pour courber L et détruire tout

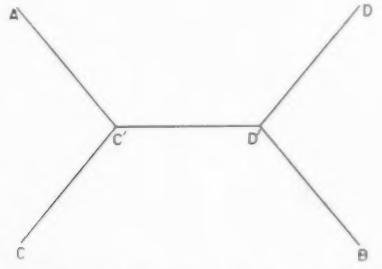


FIG. 1. Décomposition d'un point quadruple en deux points triples.

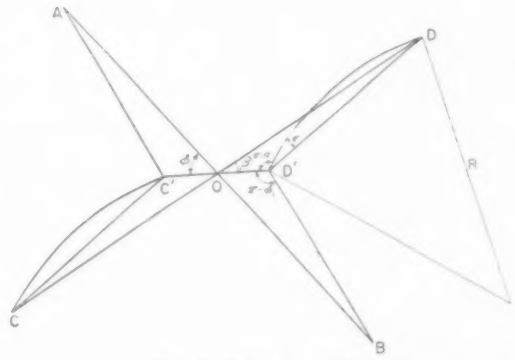


FIG. 2. Premier modèle.

au moins partiellement la dislocation recombinée L'; Hirsch *et al.*[2] ont fait remarquer que cette interaction contribue au durcissement des solides au cours de la déformation.

Dans cet article, nous étudions ce mécanisme de durcissement sur deux modèles simples.

Dans le premier (Fig. 2), la dislocation fixe est inclinée d'un angle φ sur le plan P; la dislocation mobile est ancrée à ses deux extrémités C et D, symétriquement, par rapport à la dislocation fixe, mais suivant une orientation quelconque.

La Fig. 3 représente un cas particulier de ce modèle dans lequel les points C et D sont situés sur l'intersection des plans P et P_1. Dans le deuxième modèle (Fig. 4), nous considérons une rangée de dislocations

* Reçu le 3 Decembre, 1959.

† Source de Physique, IRSID, Saint Germain en Laye (S.O.).

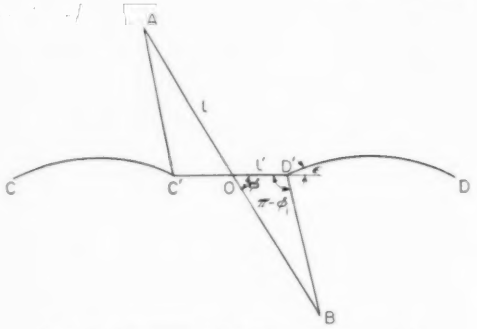


FIG. 3. Cas particulier du premier modèle.

fixes, parallèles, équidistantes situées dans le même plan P_1, inclinées d'un angle φ variable sur le plan P; la dislocation mobile est infinie.

Pour ces deux modèles, nous négligeons les interactions élastiques à grandes distances entre dislocations et supposons que les dislocations ne sont pas dissociées. Nous supposons par ailleurs que la dislocation recombinée ne peut se déplacer; nous justifierons cette approximation. Nous étudions l'équilibre de la dislocation mobile sous l'action d'une contrainte σ; et nous allons montrer que cet équilibre n'est possible que pour $\sigma \leqslant \sigma_0$: σ_0 est une contrainte dépendant des paramètres du problème. La cission σ_0 est atteinte avant que la recombinaison ne soit entièrement détruite. Nous évaluons la valeur moyenne de σ_0 dans tous les cas et indiquons comment ce mécanisme peut être cause de la formation de lacunes et interstitiels.

Dans un dernier paragraphe, nous précisons le rôle joué par l'activation thermique.

2. PREMIER MODÈLE

2.1. *Généralités. Équations du problème*

La dislocation L_1 de longueur $2l$ est fixée en A et B; la dislocation mobile, de longueur $4l$, est fixée en C et D. Les deux dislocations se coupent en leur milieu O (Fig. 2).

Nous supposerons de plus $|\mathbf{b}_1 + \mathbf{b}_2| = |\mathbf{b}_1| = |\mathbf{b}_2|$; nous négligerons les contraintes élastiques exercées par les dislocations les unes sur les autres et nous supposerons que $C'D'$ est une barrière de Lomer–Cottrell. Ces conditions correspondent aux cas les plus fréquemment rencontrés dans les structures cubiques à faces centrées. Ecrivons l'équilibre du point triple D' sous l'action d'une contrainte. Avec les notations de la figure et pour α et φ différents de O, nous pouvons écrire:

$$OD = AB = 2l$$

$$OD' = \sin(\varphi_1 - \varphi)/\sin \varphi_1$$

$$OD' + AB \cos \beta = 2l \cos \alpha$$

$$AB \sin \beta = 2l \sin \alpha/\sin \beta = 2R \sin \varepsilon.$$

Si nous avons un écrouissage assez fort, la tension de ligne[1] τ des dislocations est donnée par

$$\tau \simeq \mu b^2/2.$$

L'équilibre du point triple D' exige que

$$\cos \varphi_1 + \cos (\beta + \varepsilon) = 1. \qquad (1)$$

L'équilibre de l'arc CD exige que

$$\sigma = \tau/R.$$

Nous poserons $\sigma = \gamma \mu b/2l$; en tenant compte des relations précédentes, nous pouvons écrire-les relations

$$\sin (\varphi_1 - \varphi)/\sin \varphi_1 = 2 \sin (\beta - \alpha)/\sin \beta \qquad (2)$$

$$\gamma = \sin \beta \sin \varepsilon/\sin \alpha. \qquad (3)$$

Pour α et φ donnés, les équations 1, 2 et 3 permettent de déterminer la contrainte réduite $\gamma = 2l\sigma/\mu b$ en fonction de l'angle φ_1. Nous avons effectué numériquement les calculs pour $\varphi = 20°, 40°, 60°, 80°$, et pour chaque valeur de φ, nous avons tracé les courbes $\gamma(\varphi_1)$

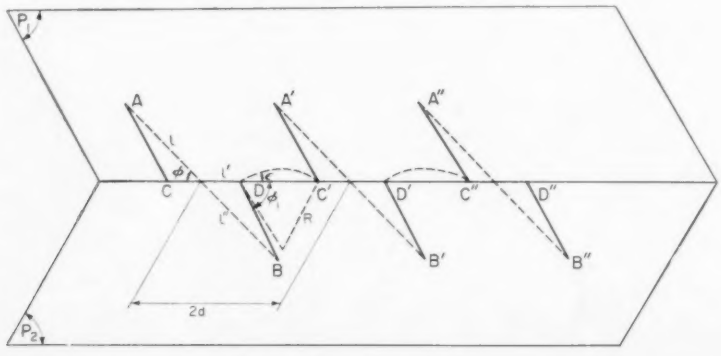


FIG. 4. Deuxième modèle.

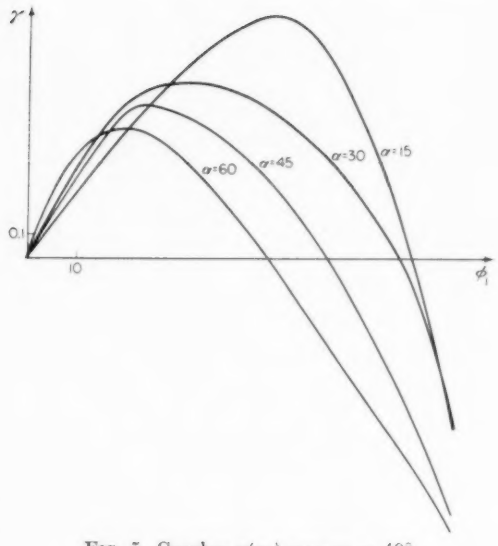


FIG. 5. Courbes $\gamma(\varphi_1)$ pour $\varphi = 40°$.

pour $\alpha = 15°, 30°, 45°, 60°$; nous avons représenté Fig. 5 les courbes $\gamma(\varphi_1)$ pour $\varphi = 40°$.

2.2. *Interprétation des résultats*

Les courbes $\gamma(\varphi_1)$ présentent un maximum, s'annulent et deviennent négatives:

(a) Les parties négatives correspondent à une cission sur DD' dirigée en sens inverse de celle qui est représentée sur la figure. Nous pouvons encore dire que ceci correspond à l'action de la cission telle que nous l'avons représentée, mais s'exerçant sur l'arc CC'. Autrement dit, la contrainte représentée sur la figure a tendance à déplacer le point C' vers la gauche.

(b) Les parties positives présentent un maximum.

(i) Pour une contrainte supérieure à celle du maximum, la portion DD' va se développer en spirale tandis que D' se déplace vers C'. Autrement dit, le système cesse d'être stable avant que la dislocation recombinée ne soit complètement détruite.

(ii) Ce maximum correspond parfois à une valeur de φ_1 inférieure à φ. Dans ce cas, la configuration d'équilibre est représentée Fig. 6. Il arrive même que le point D' rattrape le point C' avant que la contrainte maximum ne soit atteinte. Dans ce cas, le système cesse d'être stable avant que la contrainte correspondant au maximum ne soit atteinte. Dans les moyennes que nous calculons plus loin, nous ne tenons pas compte des corrections trés légères dues à cet effet.

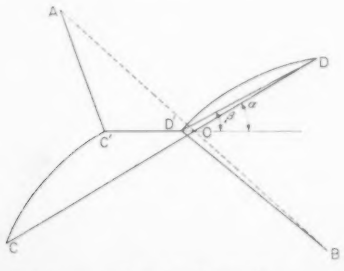


FIG. 6. Déplacement de la dislocation recombinée.

De toutes façons, nous pouvons dire que, au moment où la dislocation mobile est arrachée de la barrière, la dislocation fixe voit son centre fortement déplacé.

Afin de pouvoir effectuer la moyenne des contraintes obtenues, il est nécessaire de faire les mêmes calculs pour $\alpha = 0$.

2.3. *Cas particulier* $\beta = \alpha = 0$

2.3.1. *Généralités. Equations du problème.* Avec les notations de la Fig. 3, nous avons alors:

$$\cos \varepsilon + \cos \varphi_1 = 1 \tag{4}$$

$$\gamma = \frac{2 \sin \varepsilon}{2 - \cos \varphi - \sin \varphi \cot g \varphi_1}. \tag{5}$$

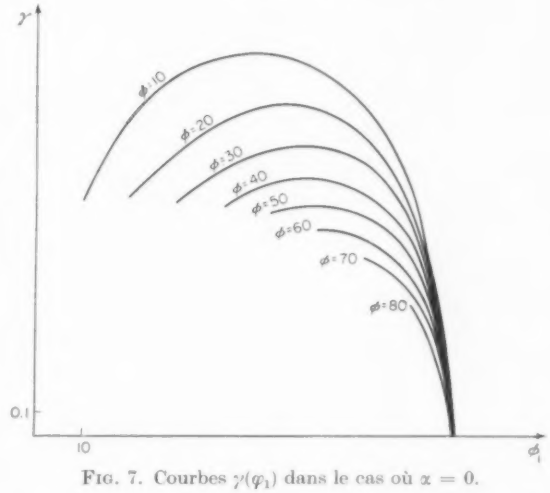


FIG. 7. Courbes $\gamma(\varphi_1)$ dans le cas où $\alpha = 0$.

Le problème est sensiblement plus facile à résoudre. Nous avons représenté Fig. 7 les courbes $\gamma(\varphi_1)$ pour φ variant de 10° en 10° de 10° à 80°.

Pour $\varphi = 0, \gamma = 2$; pour $\varphi = \pi/2, \gamma = 0$.

Soit $2l'$ la longueur de la dislocation recombinée au moment de l'arrachement.

Si l'on pose $\rho = l'/l$, on peut dresser le Tableau 1.

TABLEAU 1

ϕ	10	20	30	40	50	60	70	80
γ_m	1,6	1,4	1,23	1,08	0,97	0,87	0,75	0,56
ρ	0,88	0,69	0,55	0,38	0,2	0	0	0

VOL. 8 1960

2.3.2. *Interprétation des résultats.* Les courbes $\gamma(\varphi_1)$ présentent encore un maximum; mais elles n'ont pas cette fois, de portions négatives, en raison de la symétrie existant entre CC' et DD'. Les arcs CC' et DD' se développent simultanément en spirale. Le milieu de la dislocation fixe n'est donc pas déplacé par l'arrachement.

Nous pouvons maintenant, à l'aide des résultats obtenus au paragraphe 2 étudier la variation de γ_m avec α pour $\varphi = 20°, 40°, 60°, 80°$. Les résultats sont représentés sur Fig. 8. On peut remarquer que ces courbes sont même allure sauf pour φ voisin de 90°, et qu'elles sont toutes pratiquement confondues pour $\alpha \geqslant 70°$. A partir de ces courbes, nous pouvons

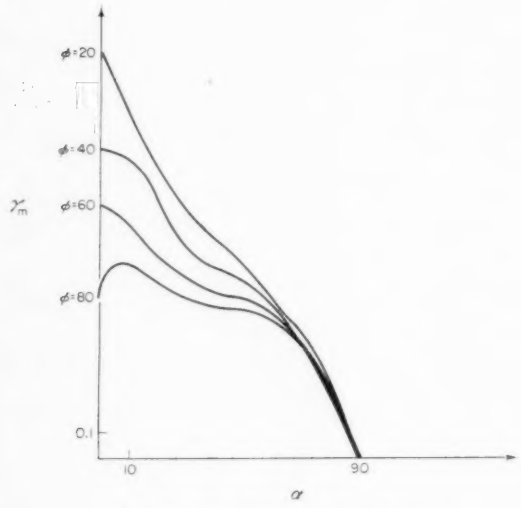


Fig. 8. Variation de $\gamma_m(\varphi,\varphi_1)$ avec α.

pour chaque valeur de φ indiquée, faire une moyenne de $\gamma_m(\varphi,\alpha)$ sur les angles α. On peut dresser le tableau suivant:

ϕ	20	40	60	80
$\gamma_m(\phi)$	0,72	0,63	0,505	0,455

Nous pouvons alors évaluer la moyenne de $\bar{\gamma}_m(\varphi)$ lorsque φ varie de 0 à $\pi/2$. Pour cela, nous pondérons $\bar{\gamma}_m(\varphi)$ par $\sin\varphi$, probabilité pour qu'une dislocation AB coupe le plan de glissement. Nous évaluons donc

$$\bar{\gamma}_m = \frac{\int_0^{\pi/2} \gamma_m(\varphi) \sin\varphi \, d\varphi}{\int_0^{\pi/2} \sin\varphi \, d\varphi} . \qquad (6)$$

Nous avons tracé Fig. 9 la courbe $\bar{\gamma}_m(\varphi)\sin\varphi$. On trouve $\bar{\gamma}_m \simeq 0{,}40$. Si nous nous étions contentés

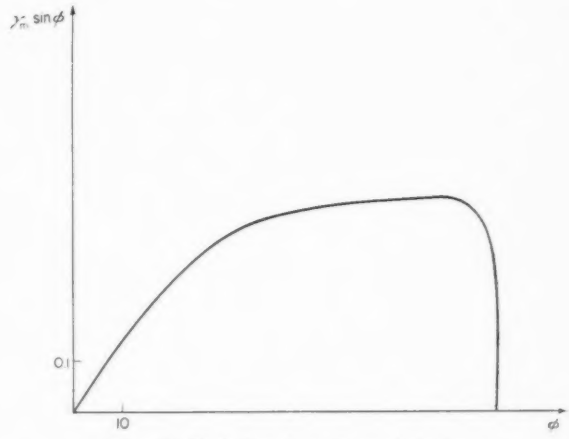


Fig. 9. Variation de $\gamma_m(\varphi,\varphi_1,\alpha)\sin\varphi$.

d'étudier de cas particulier $\alpha = 0$, nous aurions obtenu des contraintes environ 50 pour-cent trop fortes.

Nous avons également calculé le rapport $\rho = C'D'/AB$ à l'équilibre et nous avons fait des moyennes comme précédemment. Le résultat est

$$\bar{\rho} = 0{,}05.$$

3. DEUXIÈME MODÈLE

3.1. *Introduction. Équations du problème*

Avec les mêmes hypothèses que précédemment, nous considérons cette fois une rangée de dislocations $AB, A'B' \ldots$ identiques et parallèles, de longueur $2l$, coupant le plan de glissement de la dislocation fixe sous l'angle φ (Fig. 4). Si les vecteurs de Burgers des dislocations de la barrière et de la dislocation mobile satisfont aux mêmes conditions que précédemment, la recombinaison se produit et nous pouvons écrire avec les notations de la figure:

$$\frac{l'}{\sin(\varphi_1 - \varphi)} = \frac{l''}{\sin\varphi} = \frac{l}{\sin\varphi_1}$$

$$R = \frac{d - l'}{\sin\varepsilon} = \frac{\tau}{\sigma b}$$

d'ou

$$\sin\varepsilon = \frac{\sigma l b}{\tau}\left[\lambda - \frac{\sin(\varphi_1 - \varphi)}{\sin\varphi_1}\right]. \qquad (7)$$

L'équilibre aux points triples entraîne que:

$$\cos\varphi_1 + \cos\varepsilon = 1. \qquad (8)$$

En posant $\sigma = \gamma\mu b/2l$, $\lambda = 1$, $\tau = \mu b^2/2$, l'équation (7) devient:

$$\gamma = \frac{\sin\varepsilon}{1 - \cos\varphi + \sin\varphi \cot g\, \varphi_1}. \qquad (9)$$

Nous avons résolu numériquement le système (8,9) par diverses valeurs de φ.

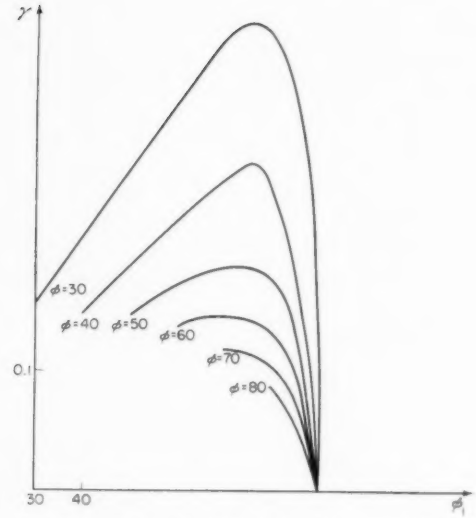


FIG. 10. Courbes $\gamma(\varphi_1)$, deuxième modèle.

3.2. *Résultats*

3.2.1. *Valeurs de* γ. Nous avons tracé les courbes $\gamma(\varphi_1)$ lorsque φ varie de 2° à 85° et représenté Fig. 10 les courbes $\gamma(\varphi_1)$ pour $\varphi \geqslant 30°$. Nous pouvons remarquer que les résultats du paragraphe précédent restent qualitativement valables; les courbes $\gamma(\varphi_1)$ présentent un maximum pour une valeur de $\varphi_1 - \varphi$ non négligeable: la partie recombinée $C'D'$ a encore une longueur notable au moment de l'arrachement. Nous pouvons dresser le Tableau 2.

3.2.2. *Étude de* $\gamma_m(\varphi)$. Pour que $\varphi = \pi/2$ on voit physiquement que $\gamma_m(\varphi) = 0$. Lorsque φ tend vers 0 on remarque que φ_{1m} tend vers $\pi/2$. Précisons cette remarque par un calcul.
Posons:

$$\pi/2 - \varphi_1 = \theta.$$

Les équations 8 et 9 deviennent:

$$\cos\ \varepsilon = 1 - \sin\theta \tag{10}$$

$$\gamma = \frac{\sin\varepsilon}{1 - \cos\varphi + \sin\varphi\,\mathrm{tg}\theta}. \tag{11}$$

Dérivons les équations (10) et (11) par rapport à θ, il vient:

$$\frac{d\varepsilon}{d\theta} = \frac{\cos\theta}{\sin\ \varepsilon} \tag{12}$$

$$\frac{d\gamma}{d\theta} = \frac{(1 - \cos\varphi + \sin\varphi\,\mathrm{tg}\theta)\cos\varepsilon\dfrac{d\varepsilon}{d\theta} - \dfrac{\sin\varepsilon\sin\varphi}{\cos^2\theta}}{(1 - \cos\varphi + \sin\varphi\,\mathrm{tg}\theta)^2}$$

En utilisant les équations (10) et (12), on peut écrire:

$$\frac{d\gamma}{d\theta} = \frac{(1 - \cos\ \varphi + \sin\varphi\,\mathrm{tg}\theta)(1 - \sin\theta)\cos^2\theta + [(1 - \sin\theta)^2 - 1]\sin\varphi}{\cos^2\theta\sin\varepsilon(1 - \cos\varphi + \sin\varphi\,\mathrm{tg}\theta)^2}.$$

Si nous faisons l'hypothèse que θ et φ sont du même ordre de grandeur lorsque φ tend vers 0, on peut voir en développant au second ordre que

$$\frac{d\gamma}{d\theta} \simeq \left(\theta - \frac{\varphi}{2}\right)\frac{F_1(\theta,\varphi)}{F_2(\theta,\varphi)}$$

F_1 et F_2 étant tels que, pour $\theta = \varphi/2$, F_1/F_2 tend vers 0 avec φ. La valeur maximum γ_m est donc obtenue pour $\theta = \varphi/2$ lorsque φ tend vers 0. On a alors:

$$\lim_{\varphi\to 0}\frac{\gamma_m(\varphi)}{\varphi^{-3/2}} \simeq \varphi^{-3/2}. \tag{13}$$

3.2.3. *Valeurs moyennes.* Nous calculons suivant les mêmes méthodes que précédemment la moyenne de ρ et de $\gamma_m(\varphi)$ lorsque φ varie de 0 à 90°.
Il vient $\bar{\rho} = 0{,}2$.
La courbe $\gamma_m(\varphi)$ présente une branche infinie lorsque $\varphi \to 0$, mais $\gamma_m(\varphi)\sin\varphi \simeq \varphi^{-1/2}$ lorsque $\varphi \to 0$ et l'intégrale de la formule (6) est finie. Nous avons évalué numériquement:

$$\int_{\varphi=2°}^{\varphi=30°}\gamma_m(\varphi)\sin\varphi\,d\varphi \quad \text{et calculé} \int_{0°}^{2°}\varphi^{-1/2}\,d\varphi.$$

Le deuxième terme est de l'ordre de l'ordre de 0,03 et nous pouvons le négliger.

Nous avons représenté Fig. 11 la courbe $\gamma_m(\varphi)\sin\varphi$. Nous avons

$$\bar{\gamma}_m = 1{,}9.$$

4. APPLICATION AU DURCISSEMENT

4.1. *Généralités*

Les modèles précédents correspondent au cas où $|\mathbf{b}_1| = |\mathbf{b}_2| = |\mathbf{b}_1 + \mathbf{b}_2|$ et s'appliquent aux métaux cubiques à faces centrées ou aux solides ioniques de structure NaCl. Cependant les résultats que nous établissons ici restent qualitativement valables pour d'autres systèmes.

Nous avons supposé d'autre part que la dislocation recombinée était une barrière de Lomer. Si $\mathbf{b}_1 + \mathbf{b}_2$ est parallèle à l'intersection des plans de glissement, ce n'est pas le cas et en toute rigueur les calculs précédents ne sont pas valables. Cependant la contrainte est en général telle que la dislocation mobile est la plus favorisée, ce qui minimise l'effet des contraintes extérieures sur la dislocation recombinée aussi bien que sur la ou les dislocations fixes. D'autre part, le mouvenent des éléments que nous avons supposés fixes va se produire alternativement dans un sens ou dans l'autre pour une contrainte donnée. Les valeurs moyennes calculées plus haut peuvent donc être considérées comme satisfaisantes.

VOL. 8 1960

TABLEAU 2

ϕ	2	5	10	20	30	40	50	60	70	80	85
γ_m	116	34	13,5	4,1	2,45	1,75	1,2	0,94	0,75	0,56	0,43
ϕ_{1m}	88	84	86	80	75	75	73	69	70	80	85
ρ	0,999	0,987	0,972	0,88	0,74	0,6	0,4	0,17	0	0	0

γ_m et ρ sont évalués avec une meillieure précision que ϕ_{1m}.

4.2. *Durcissement dû à la traversée d'un forêt de dislocations*

Le premier modèle représente assez bien une forêt de de dislocations de longeur moyenne $l_F = 2l$, perçant le plan de glissement en des points distants en moyenne de l_F: l'hypothèse consistant à fixer C et D est en effet à peu près équivalente à celle de dislocations fixes placées en C et D et empêchant la dislocation mobile de progresser.

La contrainte $\bar{\sigma}$ calculée est de la forme

$$\bar{\sigma} = \frac{\mu b}{k l_F} \qquad \text{avec } k \simeq 2{,}5.$$

Le résultat est nettement supérieur à celui que nous avions obtenu dans le cas répulsif[3] ou nous avions trouvé $k \simeq 5$.[5,6]

Le terme de durcissement dû aux dislocations attractives est donc supérieur à celui dû aux dislocations répulsives. Ceci ne contrarie pas l'hypothèse que la dislocation peut être arrêtée en A et B par d'autres dislocations.

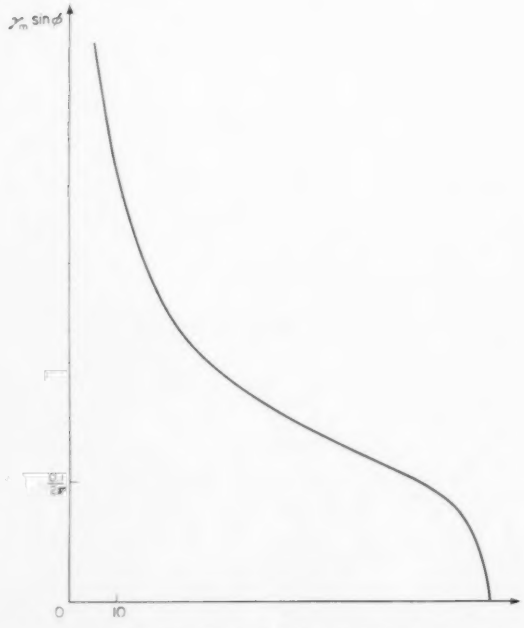


FIG. 11. Variation de $\gamma_m(\varphi,\varphi_1)\sin\varphi$.

4.3. *Déviation d'une dislocation au cours de la traversée d'une forêt*

Lorsqu'une dislocation traverse une forêt, elle se recombine partiellement avec un certain nombre d'arbres ce qui lui donne une forme de zig-zag. On peut refaire ici avec la valeur de ρ calculée plus haut le calcul de Friedel[4] (Fig. 12).

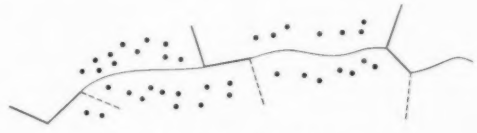


FIG. 12. Dislocation zig-zag.

Si W est la tension de ligne, l' la portion recombinée, l'énergie gagnée par la recombinaison est en moyenne $E_1 = \frac{1}{2}Wl' = \frac{1}{2}W\bar{\rho}l$, $\bar{\rho}$ étant le rapport calculé au paragraphe 2.

En déviant de sa course, la dislocation dépense une énergie:

$$E_2 = \frac{W}{D}\left[(D^2 + x^2)^{1/2} - D\right] \simeq \frac{Wx^2}{2D^2}.$$

Les recombinaisons interviennent à peu près 1 fois sur 3 dans le système C.F.C., d'où:

$$xD \simeq 3l^2.$$

En remplaçant x par cette valeur et en minimisant $E = E_1 - E_2$ par rapport à D, il vient avec $\bar{\rho} = 0{,}05$:

$$D \simeq 9l$$
$$x \simeq 0{,}33l.$$

Ces valeurs sont un peu différentes de celles données par Friedel mais elles confirment le fait qu'une dislocation est trés peu déviée lorsqu'elle traverse une forêt.

4.4. *Intersection de deux systèmes de glissements*

Le deuxième modèle sert à décrire exactement ce qui se passe à l'intersection de deux systèmes de glissement Il indique que les contraintes exercées peuvent être considérables, en moyenne de l'ordre de $2\mu b/d$ si d est la distance entre dislocations. Ce résultat ne doit pas surprendre: en effet lorsque les dislocations de la

barrière sont suffisamment rapprochées et inclinées (angle φ faible), la recombinaison est telle que les arcs CD de la Fig. 4 sont très petits et la cission nécessaire à leur déformation devient de ce fait considérable.

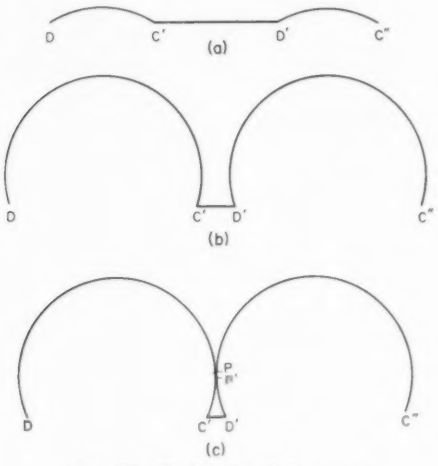


FIG. 13. Production de lacunes.

4.5. *Production de lacunes et d'interstitiels*

Les deux modèles conduisent à affirmer que la dislocation mobile commence à se développer en spirale avant que la dislocation recombinée ne soit détruite.

On peut voir sur les Fig. 13 (a–c) que le cran formé en P sur la dislocation après passage aura de la peine à glisser pour deux raisons: tout d'abord l'angle formé en P par les deux branches de la dislocation est aigu; il faut remarquer ensuite que la dislocation n'est pas en équilibre au moment où le cran se forme et que le déplacement dynamique de la dislocation fait monter le cran. Ceci a pour conséquence d'amener la formation d'un certain nombre de lacunes et d'interstitiels par montée de P et par montée de P' lorsque la boucle laissée autour de l'arbre se referme.[5,7]

4.6. *Activation thermique*[5,7]

Pour arracher la dislocation mobile de la dislocation recombinée il faut obtenir des angles $\varepsilon \simeq 40°$. Si donc

$$\sigma < \sigma_m$$

la dislocation ne peut franchir l'arbre même avec l'aide de l'agitation thermique en raison de l'importance des déplacements à effectuer.

Lorsque $\sigma > \sigma_m$ au contraire, le franchissement a lieu et le déplacement ultérieur de la dislocation est tel que l'énergie nécessaire à la formation du cran peut être prélevée sur l'énergie cinétique de la dislocation mobile. L'activation thermique joue donc un rôle faible même pour la formation du cran.

REMERCIEMENTS

Je tiens à exprimer mes remerciements à Monsieur le Professeur J. Friedel qui m'a proposé cette étude et qui a bien voulu me guider tout au long de mon travail.

BIBLIOGRAPHIE

1. J. FRIEDEL, *Les Dislocations*. Gauthiers Villars, Paris (1956).
2. P. B. HIRSCH, *Aachen Colloquium*, 1958; P. R. THORNTON and P. B. HIRSCH, *Phil. Mag.* **3**, 738 (1958).
3. G. SAADA, *Acta Mét.* **8**, (1960).
4. J. FRIEDEL, *Dislocation, Interactions and Internal Strains*, Detroit Symposium, Warren (1958).
5. G. SAADA, Thèse. Faculté des Sciences Paris (1960).
6. G. SAADA, *Métaux et Corrosions*, Juillet Août (1960).
7. G. SAADA, *Métaux et Corrosions*, Septembre (1960).

VOL. 8 1960

DUCTILE–BRITTLE TRANSITION IN ALPHA BRASS*

H. NICHOLS and W. ROSTOKER†

It is demonstrated that embrittlement of alpha brass by liquid mercury is temperature dependent and that the functional relationship is a transition from ductile to brittle behavior in the same manner as experienced by iron and other body-centered cubic metals tested in their normal recrystallized state. The transition temperature is governed by the recrystallized grain size. The significance of this dependency is discussed in terms of current dislocation theory of the transition effect.

TRANSITION DE RUPTURE DUCTILE–FRAGILE DANS LES LAITONS ALPHA

Les auteurs démontrent que la fragilité d'un laiton α sous l'action du mercure est fonction de la température. Ils indiquent ensuite que la relation fondamentale montre une transition de l'état ductile à l'état fragile, semblable à celle observée dans le cas du fer et d'autres métaux à structure cubique centrée étudiés dans leur état normal de cristallisation.

La température à laquelle s'opère cette transition et fonction de la dimension des grains cristallisés. Ils discutent cette relation en fonction dela théorie courante des dislocations sur l'effet de transition.

DER ÜBERGANG VOM DUKTILEN ZUM SPRÖDEN BRUCH IN ALPHA-MESSING

Es wird gezeigt, daß die Versprödung von Alpha-Messing durch flüssiges Quecksilber von der Temperatur abhängt und daß der funktionale Zusammenhang einen Übergang vom duktilen zum spröden Verhalten in derselben Art darstellt, wie er bei Eisen und anderen kubisch raumzentrierten Metallen in ihrem normalen rekristallisierten Zustand auftritt. Die Übergangstemperatur wird bestimmt durch die Korngröße des rekristallisierten Materials. Die Bedeutung dieser Abhängigkeit wird an Hand der neueren versetzungstheoretischen Deutung des Übergangseffektes diskutiert.

It has been known for many years that residual stresses in 70/30 brass cause cracking on immersion in aqueous mercurous nitrate solution. The cracking can occur instantaneously or after a lapse of time, but is always associated with the deposition of metallic liquid mercury on the surface of the brass. The aqueous solution is only a convenience for removal of oxide films and for supply of metallic mercury by chemical displacement. Identical cracking effects can be brought about by any other means by which liquid mercury or its amalgams can be made to wet the surface of brass sustaining residual or applied tensile stresses.

The correlations of fracture with stress and wetting by a liquid metal are more conveniently studied in the simple uniaxial, continuous-loading tensile test. Under these circumstances, annealed 70/30 brass wetted by liquid mercury or mercury amalgams over a small area in the gauge section will break at or slightly above the engineering yield point. The fracture always occurs in the wetted zone. In recrystallized metal the fracture is invariably intergranular. Microstructural examination reveals no plastic distortion of grains on either side of the crack. Time of prior exposure to liquid mercury is not a factor in cracking under continuous loading. Except at elevated temperatures, as will be pointed out later, mercury does not visibly diffuse or penetrate into brass before the initiation of fracture.

With increasing temperature of testing, the brittleness engendered by wetting with liquid mercury undergoes a sharp reversion to the ductile state. The transition from ductile to brittle behavior of structural materials wetted by liquid metals is a characteristic behavior of many systems. By way of examples, high-strength aluminum alloys wetted by molten mercury, indium and tin exhibit this.[1] Rozhanski *et al.*[2] have shown that single crystals of zinc wetted with mercury also experience temperature-dependent

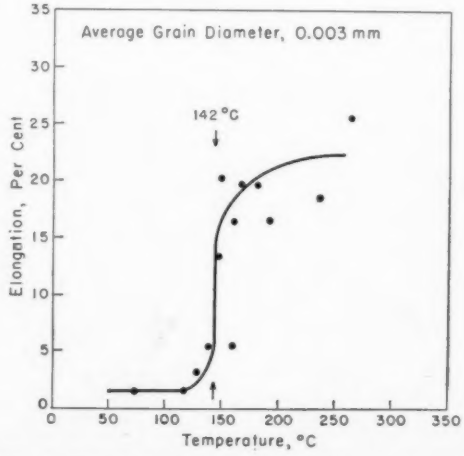


FIG. 1. Tensile elongation as a function of temperature for 70/30 brass wetted with mercury, at one grain size.

* Received January 6, 1960; revised April 14, 1960.

† Metals Division, Armour Research Foundation, Chicago, Illinois.

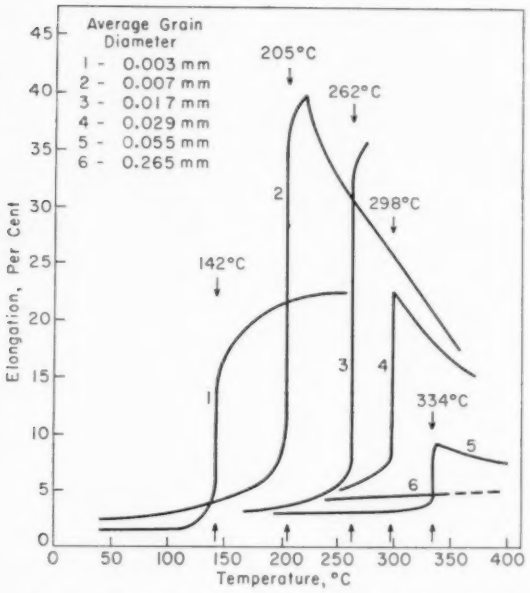


FIG. 2. Curves of transition from brittle to ductile behaviour of 70/30 brass wetted with mercury at various grain sizes.

transition from brittle to ductile behavior. An example of the transition from brittle to ductile behavior of 70/30 brass wetted with liquid mercury is shown in Fig. 1. The present work has undertaken to provide evidence that the transition in 70/30 brass is governed by the same model and mechanisms currently proposed for body-centered cubic metals.

According to various models proposed by Stroh[3], Petch[4] and Cottrell[5], a stable crack nucleus can result from the shear stress operative on a line of dislocations in a slip plane piled up against a barrier. This barrier can be either a grain boundary or the intersection with another slip band. From this, the grain size is deduced to be a primary factor governing the temperature at which a transition from ductile to brittle behavior occurs. Experimental work on mild steel,[4] molybdenum[6] and niobium[7] amply verify this. Recently, Petch[3] in analysing the dislocation model for initiation of a brittle crack has postulated that the interrelation between transition temperature, T_c, and average grain diameter, d, should be of the form:

$$T_c \propto \ln d.$$

The transitions from brittle to ductile behavior of 70/30 brass of various annealed grain sizes, all wetted with liquid mercury, are shown in Fig. 2. The transitions are all quite sharp and so the transition temperature can be estimated with good accuracy. In Fig. 3, the transition temperatures for five grain sizes are plotted against the logarithm of the mean grain diameter, demonstrating an excellent linear correlation.

This is taken as evidence that brittle fracture produced by the establishment of a liquid metal–solid metal interface is governed by the same processes as occur in body-centered cubic metals at low temperatures. One must wonder about the nature of the obstacle to dislocation pile-up which can exist at the liquid–solid interface and, of course, one can only speculate at this point. The simple picture wherein a slip band emerges to the free surface or interface cannot provide the proper conditions. In their study of dislocation distribution by etch pit patterns in coarse grained silicon ferrite, Low and Guard[8] showed that these assumed the appearance of the pile-ups against grain boundaries postulated by Stroh[3]. Micrographs showed etch-pit identified slip bands held up by grain boundaries and slip bands which had forced continued propagation into adjacent grains. From this one can deduce that slip directions can develop not only at various inclinations with respect to the surface but also in the surface plane itself. When the free surface becomes a liquid–solid interface, it must be those slip systems with slip directions in the

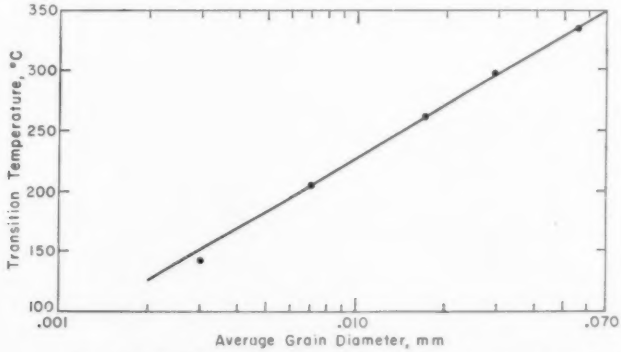


FIG. 3. Correlation between transition temperature and average grain diameter for 70/30 brass wetted with mercury.

VOL. 8 1960

plane of the interface which generate the crack nuclei.

The dislocation models for the transition in ductility[4,5] construct a balance between yield stress and effective surface energy associated with crack formation such that a high surface energy and a low flow stress are conductive to ductile behavior and a low surface energy and a high flow stress are conductive to brittle behavior. In a forthcoming paper it will be shown that the creation of a liquid–solid interface can significantly reduce the effective surface energy. It remains therefore to apply the temperature dependence of the flow stress of 70/30 brass to the model to produce the condition where a critically low surface energy and a critically high flow stress combine to produce brittle fracture. The brass represented in Fig. 1 showed an almost linear yield point dependence rising from 38,000 lb/in^2 at 250°C to 56,000 lb/in^2 at 100°C.

It will be noted in Fig. 2 that the resurgence of ductility in the coarser grain sized brasses is progressively more restricted with increasing temperature. Metallographic examination shows that this is related to the visible occurrence of mercury diffusion into the brass. This clearly demonstrates that two species of liquid metal embrittlement can occur—one which is accentuated by decreasing temperature and one which is accentuated by increasing temperature.

ACKNOWLEDGMENT

This work was made possible by the financial support of the Pitman-Dunn Laboratory of Frankford Arsenal of the Army Ordnance Corps.

REFERENCES

1. W. Rostoker, to be published.
2. V. N. Rozhanski, N. N. Pertsov, E. D. Shchukin and P. A. Rebinder, *Dokl. Akad. Nauk* SSSR **116,** 769, (1954).
3. A. N. Stroh, *Proc. Roy. Soc.* A**223,** 404, (1954).
4. N. J. Petch in *Proc. Conf. on Fracture, Swampscott, Mass., April* 1959. Technology Press of Massachusetts Institute of Technology and Wiley, New York. Also, Chapman and Hall, London.
5. A. H. Cottrell, *Trans. Amer. Inst. Min. (Metall.) Engrs.* **212,** 192, (1958).
6. J. H. Bechtold, *Trans. Amer. Inst. Min. (Metall.) Engrs.* **197,** 1469, (1958).
7. E. T. Wessell and D. D. Lawther, *Technology of Columbium* p. 66. Wiley, New York (1958).
8. J. R. Low and R. Guard, *Acta Met.* **7,** 171, (1959).

THE GROWTH OF TWINS IN TIN SINGLE CRYSTALS AS OBSERVED BY TRANSMISSION ELECTRON MICROSCOPY*

J. T. FOURIE†, F. WEINBERG‡ and F. W. C. BOSWELL‡

The nucleation and growth of twins in melt-grown tin single crystals has been examined by transmission electron microscopy. The fact that the structures observed were twins was established by selective area electron diffraction. Twins were observed to nucleate after the crystal had been exposed for several minutes in the electron beam. They formed primarily at the edge of the foil, as well as at etch pits, other twin boundaries, and in several cases at defects in the foil. In general, nucleation occurred in areas relatively free from dislocations.

Twins were observed to grow at rates in the order of 10^{-6} cm/sec. A cine film was made by photographing the screen of the electron microscope. From the film, measurements of the growth rates of individual twins and groups of twins were made.

LA CROISSANCE DE MACLES DANS DES MONOCRISTAUX D'ETAIN, OBSERVEE PAR MICROSCOPIE ELECTRONIQUE DE TRANSMISSION

Les auteurs examinent par transmission au microscope électronique, la formation et la croissance de macles sur un monocristal d'étain préparé par cristallisation et croissance a partir bain fondu.

En choisissant différents plans de diffraction, ils ont pu établir que la structure observée était celle de macles. Celles-ci se forment après quelques minutes d'exposition au faisceau d'électron.

Elles apparaissent d'abord aux bords de la lame, aux endroits attaqués, au voisinage d'autres macles et dans plusiers cas aux imperfections de la lame. En général, la naissance de macles a lieu sur une surface relativement exempte de dislocations.

Les auteurs obserbent que la vitesse de croissance des macles est de l'ordre de 10^{-6} cm/sec. Ils ont réalisé un film en photographiant l'écran du microscope électronique.

A partir de ce film, ils ont effectué des mesures de vitesse de croissance de macles seules ou groupes de macles.

UNTERSUCHUNG DES WACHSTUMS VON ZWILLLINGEN IN EINKRISTALLEN AUS ZINN MITTELS ELEKTRONENMIKROSKOPISCHER DURCHSTRAHLUNG

Keimbildung und Wachstum von Zwillingen in Schmelzfluß-Einkristallen aus Zinn wurde mittels elektronenmikroskopischer Durchstrahlung untersucht. Durch Feinbereichsbeugung wurde sichergestellt, daß die beobachteten Strukturen Zwillinge sind. Die Keimbildung der Zwillinge setzte ein, nachdem der Kristall mehrere Minuten dem Elektronenstrahl ausgesetzt worden war. Die Zwillinge bildeten sich hauptsächlich an den Kanten der Folie und an Ätzgrübchen, an anderen Zwillingsgrenzen und in einigen Fällen an Defekten in der Folie. Im allgemeinen erfolgte die Keimbildung in relativ versetzungsfreien Gebieten.

Die Zwillinge wuchsen mit Geschwindigkeiten der Größenordnung 10^{-6} cm/sec. Vom Leuchtschirm des Mikroskops wurden kinematographische Aufnahmen gemacht. Auf dem Film wurde die Wachstumsgeschwindigkeit von einzelnen Zwillingen und von Zwillingsgruppen ausgemessen.

VOL. 8 1960

1. INTRODUCTION

Although increasing attention has been directed towards the study of plastic deformation in metals in recent years, relatively little has been reported concerning mechanical twinning. The reason for this, at least in part, is the difficulty in obtaining significant observations of the twinning process since twins are initially small, nucleate under relatively complex deformation conditions and grow at very rapid rates. As a result, there is appreciable disparity in the results reported in the literature, with at least two distinct mechanisms being proposed for the nucleation and growth of twins.

In examining thinned single crystals of tin by transmission electron microscopy, it was observed by the present authors that twins were sometimes nucleated by stresses arising from the action of the electron beam, and that they often grew at rates sufficiently slow to allow observation of their growth characteristics. The present report deals with these observations and the conclusions derived from them regarding the twinning process. Comparisons are made between the present conclusions and those reported in the literature.

The general characteristics of the twinning process in bulk materials has been described in a number of articles[1–5] along with a summary of existing observations and proposed mechanisms. The pertinent points concerning the nucleation and growth of twins are summarized below:

(1) The resolved shear stress required to initiate twins is considerably greater than that required to initiate slip ($\times 100$ for basal slip in zinc[5]).
(2) No unique critical resolved shear stress exists for twinning.[5]
(3) The stress required to propagate twins is less than that required to nucleate twins (by a factor of 10 in zinc[5]).
(4) Twinning in metals is always preceded by slip.[5]

* Published by permission of the Director, Mines Branch, Department of Mines and Technical Surveys, Ottawa, Canada. Received January 26, 1960.

† Present address C.S.I.R., Pretoria, South Africa.

‡ Metal Physics Section, Physical Metallurgy Division, Mines Branch, Department of Mines and Technical Surveys, Ottawa, Canada.

(5) Twins are initiated in bursts and grow in a spasmodic manner. The rate of propagation is very rapid (2×10^3 cm/sec in cadmium[4]). Twins widen at slower rates (10^{-2} cm/sec in zinc[6]).

(6) Two different basic mechanisms are proposed for the nucleation of twins.

(a) A dislocation mechanism described by Thompson and Millard[4] and Cottrell and Bilby[7]. Essentially, the mechanism consists of the rotation of a twinning dislocation about a sessile screw dislocation whose Burgers vector equals the spacing of the twinning planes. As the twinning dislocation rotates and climbs, loops are generated on successive twinning planes. The loops expand to produce a macroscopic twin.

(b) Homogeneous nucleation as described by Bell and Cahn[5] and by Orowan[8]. Stresses applied to the specimen are locally enhanced by the presence of dislocation pile-ups against sessile dislocations. When local stresses reach the theoretical twinning stress, twin nuclei form homogeneously. The nuclei, if greater than a critical size ($\approx$250 Å in zinc[5]), will generally grow rapidly into macroscopic twins since the stress required to propagate twins is less than that required to nucleate them.

2. EXPERIMENTAL

Controlled orientation single crystals were grown from the melt in a horizontal graphite boat according to the method described by Chalmers[9]. The crystals were normally grown in slabs of rectangular cross-section of 1 mm $\times$ 20 mm. The purity of the tin used was 99.997 per cent Sn with Fe as the major impurity.

All of the crystals investigated were grown with the $\langle 110 \rangle$ direction parallel to the growth direction. The faces of the crystal used for the major part of the investigation were parallel to (001) planes and in the other cases to (110) planes.

The crystals were thinned down by electrolytic polishing methods which are described in detail elsewhere.[10] The polishing was performed in two stages, the first giving rapid dissolution of the specimen down to a thickness of 0.2 mm. The second stage produced a high quality mirror-like polish and was continued until holes appeared in the foil. Relatively large regions near the edges of the holes were found sufficiently thin for transmission electron microscopy. With reasonable care, the thinning and mounting procedure could be carried out without deforming the crystal in the regions to be investigated.

In order to make a quantitative study of the rates of propagation of twins under conditions existing in the electron microscope, a cine film of growing twins was produced.

A Kodak-special 16 mm cine-camera was used to record (at 16 ft/sec) the images appearing on the fluorescent screen of a Siemens Elmiskop I, operated at 80 or 100 kV. Two lenses were employed, namely, a 25 mm $f/1.4$ lens and a 50 mm $f/1.6$ lens, of which the latter was found more suitable because of its greater magnification. To measure the rates of twin propagation, the image of the cine film was projected onto a ruled screen at a total magnification of $\times$200,000. Successive positions of the tips of the twins were measured at 5-sec intervals.

3. OBSERVATIONS

When a tin single crystal with a (001) face was placed in the microscope, and one area exposed to the electron beam for a period of 2–5 min, bands occasionally appeared near the edge of the foil. On further exposure the bands became larger, appearing as shown in Fig. 1. They were observed to grow parallel to the edge of etch pits in the foil, which corresponds to growth along traces of the (301) plane, suggesting that they might be twins. To determine whether they were, in fact, twins, selected area diffraction measurements were made in regions of the foil where these structures were present.

3.1 *Diffraction evidence for twins*

β-tin has a body-centred tetragonal structure, with a c/a ratio of 0.541. The twinning plane is $\{301\}$ and the twinning shear direction is $\langle 103 \rangle$.

The diffraction pattern from an untwinned crystal with [001] parallel to the beam direction consists of spots having indices of the form $(2h, 2k, 0)$, where h and k are integers $\geqslant 0$. These are the intense spots arranged on a square grid in Fig. 2. Twinning consists of a rotation of the lattice about a [100] axis. In general, such a rotation will give rise to a diffraction pattern with spots of indices $(2h, mk, nl)$ where h, k and l are integers $\geqslant 0$ and m, n are integers > 0. For twinning in tin, the angle of rotation is 63° 10′ which brings the $\{011\}$ planes within 2° of the beam direction and hence in this case $n = m = 1$. Thus in a pattern from material containing both untwinned and twinned material, there will be two sets of spots with indices $(2h, 2k, 0)$ and $(2h, k, l)$. Such a spot pattern was obtained from regions containing the bands and is shown in Fig. 2. Normal to the [100] direction in the pattern, the spacing of the main spots corresponds to $1/d_{020} = 0.3430$ Å^{-1} while that of the secondary (twin) spots corresponds to $1/d_{011} = 0.3580$ Å^{-1}.

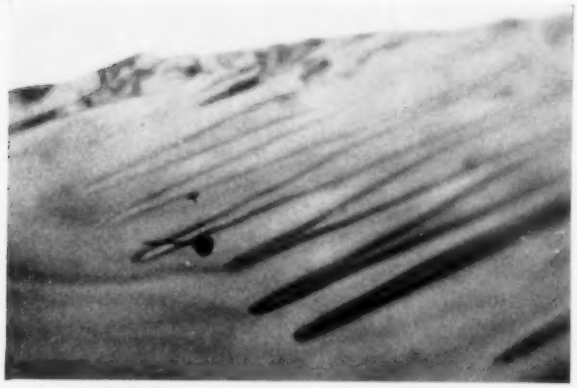
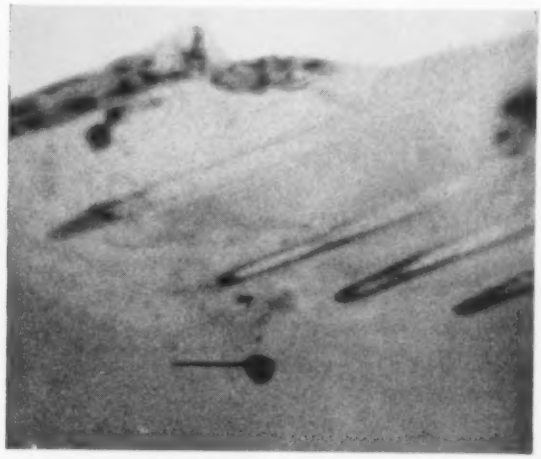


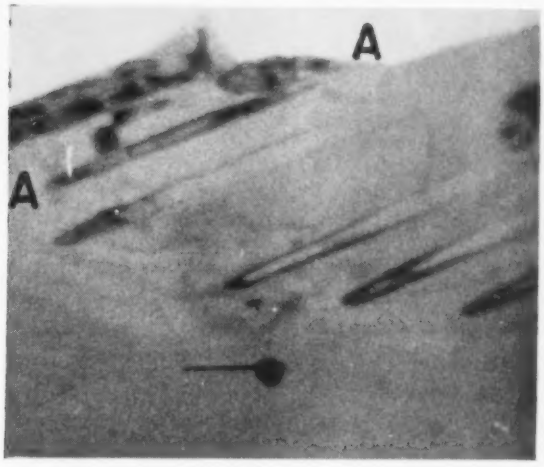
FIG. 1. Regular sequence of twins growing from the edge of a foil. (From cine film.) ×17,500



FIG. 2. Part of the electron diffraction pattern of a (001) tin foil containing a twin.



(a)



(b)

FIG. 3. Nucleation of twin *A*–*A* near the edge of the foil. Adjacent frames from the cine film (1/16 sec interval). ×25,000

3.2 *Nucleation of twins*

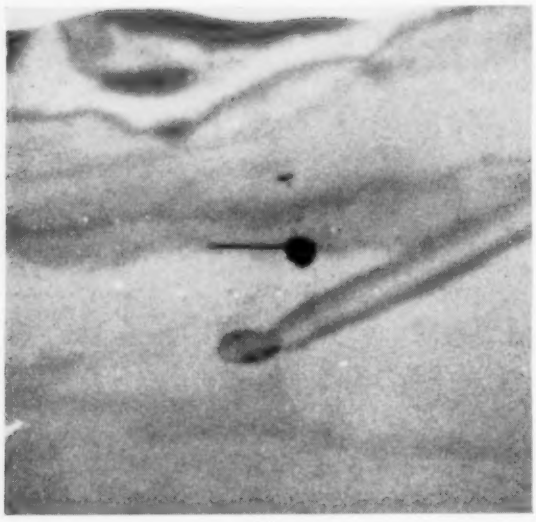
The stress required to nucleate twins in the foils examined was produced by allowing the electron beam to pass through a local area of the foil for several minutes. Estimates of the value of the stress will be discussed later.

It was observed that twins generally nucleated near the edge of the foil or at etch pits near the edge. The regions of the foil in which they nucleated appeared to be relatively perfect; they did not nucleate in regions where a high density of dislocations was observed. An example of the nucleation of a twin is shown in Fig. 3(a) and (b), which are adjacent frames taken from the cine film. It can be seen that twin *A*–*A* has nucleated and grown to the size shown within a period of less than 1/16 of a second. Measurements of the initial dimensions of twins which appeared in this manner were made from the film. The minimum size measured was 400 Å thick by 20,000 Å long. The dimensions of a critical twin nucleus must therefore be equal to or less than these values.

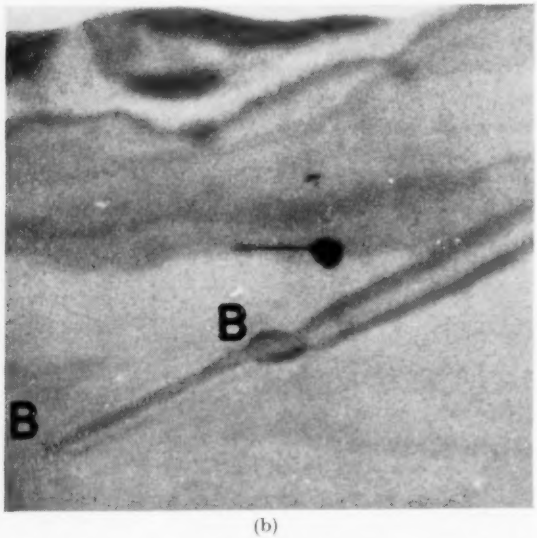
It was generally observed that once one twin had nucleated others nucleated in the same vicinity, often with remarkably uniform spacing between nucleating sites. This is shown by the regularity of the spacings of the twins in Fig. 1.

In several cases twins were observed to nucleate at loop-like discontinuities of unknown origin in the foil. An example is shown in Fig. 4(a) and (b), which shows adjacent frames in the cine film. In Fig. 4(a) a twin has nucleated from the discontinuity and grown out of the field of view. In Fig. 4(b) a second twin, *B*–*B*, has nucleated from the same source and grown in the opposite direction. Fig. 5 shows another example of

VOL. 8 1960



(a)



(b)

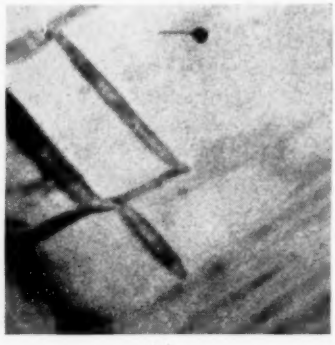
FIG. 4. Nucleation of twin *B–B* from discontinuity in foil. Adjacent frames from cine film. ×25,000

nucleation from a loop discontinuity. Here, however, one twin has nucleated on the (301) planes and the other on the (031) planes.

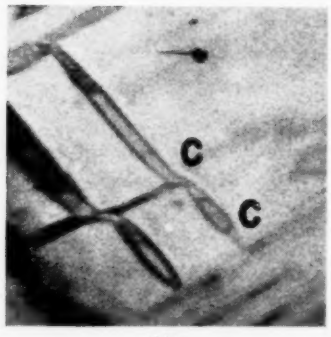
Twins which belong to an alternate system of twinning planes are often nucleated at the boundaries of existing twins. An example is shown in Fig. 6, where adjacent frames of the cine film show the nucleation and growth of a twin *C–C* from an existing twin. It can be observed in Fig. 6(b) that the freshly nucleated twin can be associated with a twin which had previously impinged on the other side of the parent twin. This was found to be the case, generally, in the thin foil observations.



FIG. 5. Nucleation of twins on (301) and (031) planes from the same discontinuity in the foil. ×9000



(a)



(b)

FIG. 6. Nucleation of twin *C–C* at the boundary of an existing twin. Adjacent frames from cine film. ×25,000

3.3 *Propagation of twins*

Measurements were made of the positions of an advancing twin interface as a function of time, from the cine film. Some of the results are shown in Fig. 7,

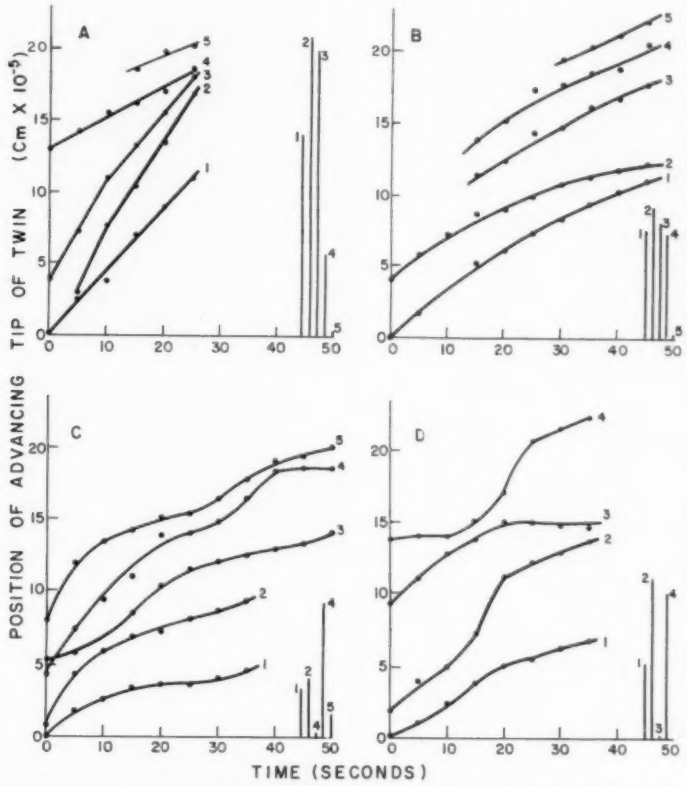


FIG. 7. Curves showing the position of the tips of advancing twins as a function of time in four fields of view. Zero time is an arbitrarily selected point. The final relative positions of the tips of the twins are indicated by the height of the vertical lines.

where the position of the tip of an advancing twin is plotted as a function of time, starting at an arbitrary stage in its growth. Four sets of curves are shown. Each curve corresponds to an individual twin; each set of curves pertains to a number of parallel adjacent twins which were observed and measured at the same time. In order to prevent the curves from overlapping, they have been shifted along the vertical axis by arbitrary amounts. However, the relative positions of the twins are indicated by the vertical lines to the right of the curves, the height of each line indicating the final relative positions of the corresponding twin interfaces.

Starting with the series of curves in Fig. 7(a), it is seen that, in this case, the rates of propagation of the twins were relatively constant over the distances measured. Two of the curves, 2 and 3, had a higher rate of propagation than the others; they were also ahead of the other twins, as shown by the vertical lines. In the case of series *B*, all of the curves are similar, and show a gradual decrease in the rate of propagation as growth continued; twin interfaces here were close together. In series *C* the leading twins again have the highest rate of propagation; however, in this case the rate cycled as the twins advanced. In the series *D* the two leading twins, 2 and 4, were arrested temporarily in the region of $t = 20$ sec, then propagated at a more rapid rate while the lagging two twins progressively slowed down.

In general, therefore, the leading twins have the highest rate of propagation. Rates of propagation can be constant, gradually decreasing or cyclic, depending on the particular twin being measured. Similar variations in the rate often occur simultaneously in neighbouring twins. All of the rates shown are in the order of 10^{-6} cm/sec. The maximum rate observed, based on movements between adjacent frames in the cine film, was 5×10^{-3} cm/sec.

In two instances measurements were made of the twin interface as it approached the edge of the foil. The results are shown in Fig. 8, where the distance from the tip of the twin to the edge of the foil is plotted as a function of time. In both cases the rate of propagation progressively decreased with time, and the twins stopped before reaching the edge of the foil.

When twins are formed in thin foils they are usually observed to grow transversely as well as in the forward direction. The rate of transverse growth is

VOL. 8 1960

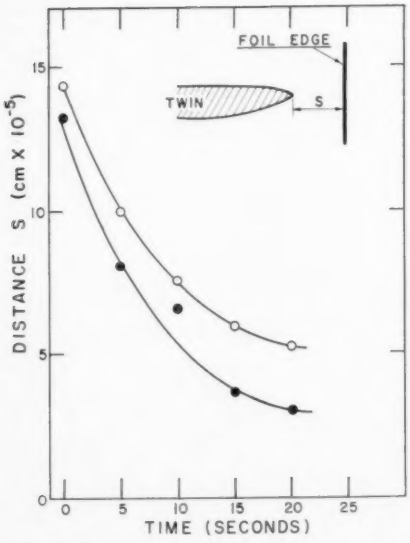


FIG. 8. Position of the tips of twins approaching the edge of the foil as a function of time.

usually a number of orders smaller than the rate of forward propagation. It is further a general observation that fast propagating twins grow relatively slowly in width.

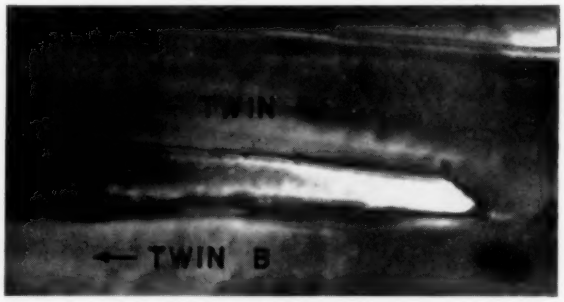
A twin is usually wider at its origin than in the vicinity of the tip, as shown for example in Figs. 1 and 3. On occasion, however, it has been observed that the leading part of the twin is a number of times wider than its width nearer to the origin. An example of this is found in Fig. 9.

3.4 *Coalescence of twin boundaries*

When a number of twins are nucleated side by side, their boundaries will generally move transversely until they touch one another. At the point of contact a coalescence of the boundaries will appear to take place, and this point will begin to move in the forward direction of twin propagation. The movement of this point of contact between the boundaries can take place either slowly or at a rate comparable to the fastest twin propagation observed. In this manner the boundaries between "elementary" twins eliminated and very wide twinned regions have been observed to form as a result of the coalescence of a number of twins.



FIG. 9. Twins which widen close to the tip. (From cine film.) ×25,000



(a)



(b)

FIG. 10. Same area of foil at different times, showing coalescence of twins *A* and *B*. ×28,000

In Fig. 10(a) and (b) an example is shown of two twins coalescing. Here a relatively narrow twin is coalescing with a wider one of which only the one boundary is shown. The configuration which can be seen at the tip of the coalescing point is typical of many others that were observed. The micrograph for Fig. 10(a) was taken after reducing the beam current to a minimum, which caused the coalescence to be halted temporarily. The beam current was then increased for a short period, during which the coalescence point moved to the new position shown in Fig. 10(b). It is interesting to note that a dislocation has been left in the wake of the coalescing point. From the tracks in Fig. 10 it is likely that this dislocation moved through twin *B* to the boundary and

was stopped there. When the twins coalesced, the dislocation was left behind in the same position.

3.5 *Deviating twins*

As a group of twins grew in the normal [100] direction, it was occasionally observed that one or more of the twins deviated from this direction. Examples of this phenomenon can be observed in Fig. 11(a) and (b). It will be noted in Fig. 11(a) that there are two twins which deviate in opposite directions.

The possibility that a different twinning system might be operative in the case of deviating twins was rejected for two reasons. First, the angle of deviation was found to differ in six cases examined, with the maximum angle of deviation equal to 13°. Secondly, the diffraction pattern obtained for deviating twins was identical to that obtained for normal twins.

A special case of deviation is shown in Fig. 12 where



(a)



(b)

FIG. 11. Twins deviating from normal [100] growth direction. (From cine film.) ×25,000



(a)



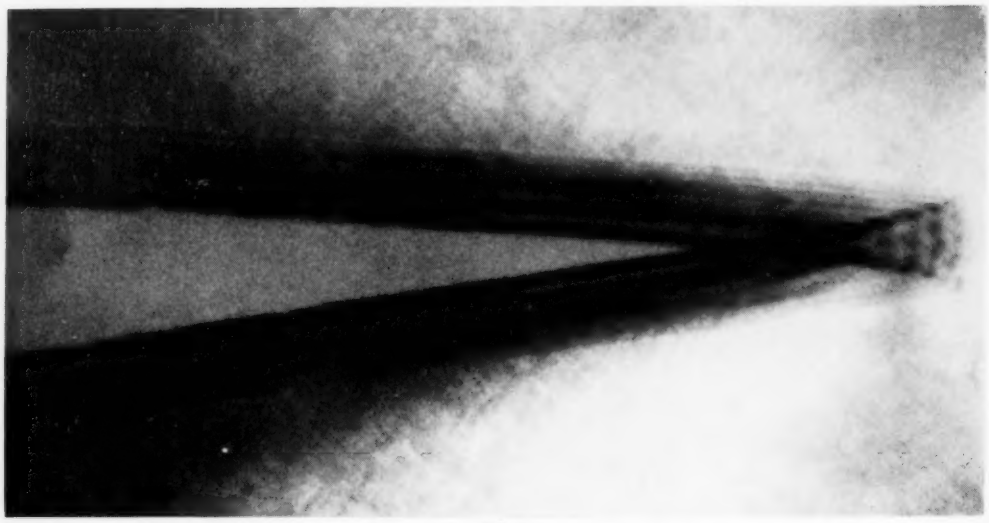
(b)



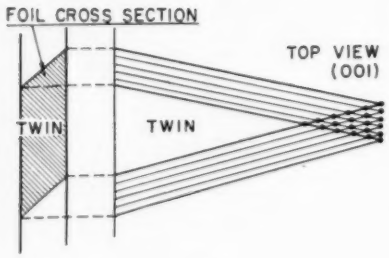
(c)

FIG. 12. Twin growing around an obstacle in its path. (From cine film—not consecutive frames.) ×22,000

VOL. 8 1960



(a)



(b)

FIG. 13. (a) Tip of twin. ×190,000
(b) Sketch showing features of (a) related to the cross section of the foil.

a twin deviated to escape an obstacle, and then proceeded in the normal direction.

3.6 *The configuration of the tips of growing twins*

It is generally difficult to obtain high resolution micrographs of the tips of twins. This is largely due to the fact that the tips are usually in motion, and also to the fact that twins do not form before a certain amount of contamination has built up on the foil.

However, several reasonable photographs of twin tips at high resolution have been obtained. An example is shown in Fig. 13(a); in Fig. 13(b) the geometry of the twin in relation to the foil is shown diagrammatically. The fringes parallel to the sides of the twin are due to interference effects resulting from the presence of overlapping wedge shaped crystals as described by Whelan *et al.*[11]. The system of dots at the tip apparently arises from the overlapping of the two fringe systems in that region.

The boundaries of the twin shown in Fig. 13(a) can only converge as a result of the presence of twinning dislocations. By assuming a twinning dislocation to be present on every twinning plane one can estimate the density of dislocations in the boundaries from the degree of convergence observed. For the twin shown in Fig. 13(a) a twinning dislocation should be situated about every 15 Å along the boundary to account for the convergence. Thus, even if it were possible to see an isolated single twinning dislocation (which is open to question because of the small Burgers vector involved), they would not be resolved in the present case.

It is evident from the uniform spacing of the dots in the tip shown in Fig. 13(a), that the convergence and hence the dislocation density in the boundaries remains approximately constant to the very tip. However, in Fig. 14 an example is shown where the spacing between the row of dots decreases markedly towards the tip. This can be explained by assuming an increasing convergence and hence an increasing dislocation density towards the front of the twin.

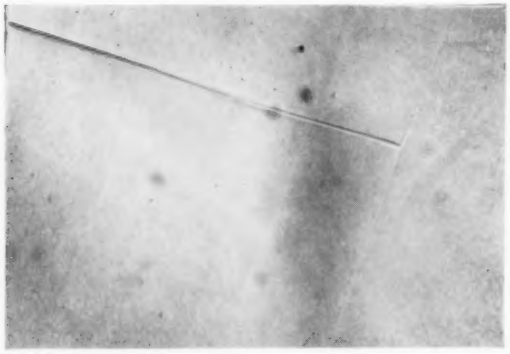


FIG. 14. Tip of twin with curved twin boundaries. ×69,000

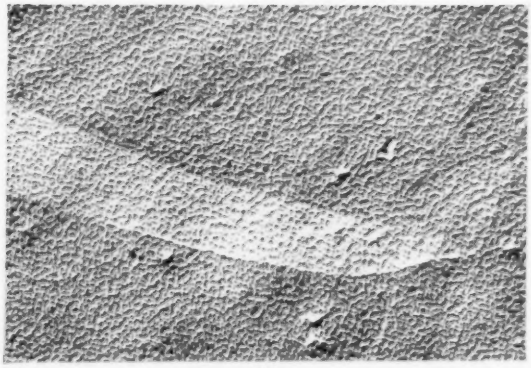
Some photographs of the tips of twins produced by impact in a bulk specimen were also obtained. An example is shown in Fig. 15(a) and (b). Fig. 15(a) is a light micrograph of a twin which ended in the matrix and which at this magnification appeared to have a rounded tip. An electron micrograph obtained from a replica of the same area by the method of Fourie[12] is shown in Fig. 15(b), from which it is evident that the configuration at the tip is generally similar to that of twins observed in the foils.

3.7 *Substructure in non-coherent twin boundaries*

In general, individual dislocations could not be observed in twin boundaries, even at the highest magnification used. However, in some cases, a substructure could be observed in segments of non-coherent boundaries. Examples are shown in Figs. 16 and 17. In the former photograph one segment of a twin is joined by non-coherent boundaries to a displaced segment. The substructure can be seen as a series of alternately dark and light regions in the non-coherent boundaries. The "wedge" fringes can be observed in the relatively coherent as well as in the non-coherent boundaries. Fig. 17 shows a twin formed in a (110) foil. In this particular case the substructure can be observed in the non-coherent boundary on one side of the twin, and not on the other side which appears straight and coherent.



(a)



(b)

FIG. 15. (a) Specimen surface showing twin produced by impact in bulk specimen. ×150
(b) Electron micrograph from surface replica of (a). ×15,700

Measurements of the spacing between the dark bands in the substructure were made and the average number of twinning planes $N_{(301)}$ between each band determined from the relation

$$N_{301} = \frac{x}{dn}$$

where x is the lateral displacement of a section of incoherent boundary,
d is the distance between the intercepts of adjacent (301) planes with the plane of the foil,
n is the number of bands measured in the region x.

The results for six specimens are given in Table 1.

TABLE 1

Sample	Foil orientation	d(Å)	n	x(Å)	$N_{(301)}$
*M*27	(001)	1.945	16	760	24
*M*27	(001)	1.945	9	560	32
*H*2	(001)	1.945	22	1420	33
*N*5	(001)	1.945	10	500	26
*K*3	(110)	2.08	17	1000	28
*K*4	(110)	2.08	12	650	26

Average $N_{301} = 28$ planes

3.8 *Pre-twinned foils*

Twins which had previously been produced by impact in a bulk specimen gave a similar diffraction pattern to those produced in thinned tin crystals by the electron beam.

Although some of the existing twins produced by impact could be made to move slowly under the influence of the electron beam, the majority remained stationary. The rate of propagation of those which did move was much less than the average rate of those which had nucleated in undeformed foils. In no instance were any new twins observed to nucleate in pre-twinned foils.

A number of cases were observed where twins in a pre-twinned foil would shrink in the foil during observation in the electron microscope. This is illustrated in Fig. 18(a) and (b), which represents electron micrographs taken in that order.

3.9 *Movement of individual dislocations*

In many cases, individual dislocations were observed to move in the foil, and produce tracks similar to those

VOL. 8 1960

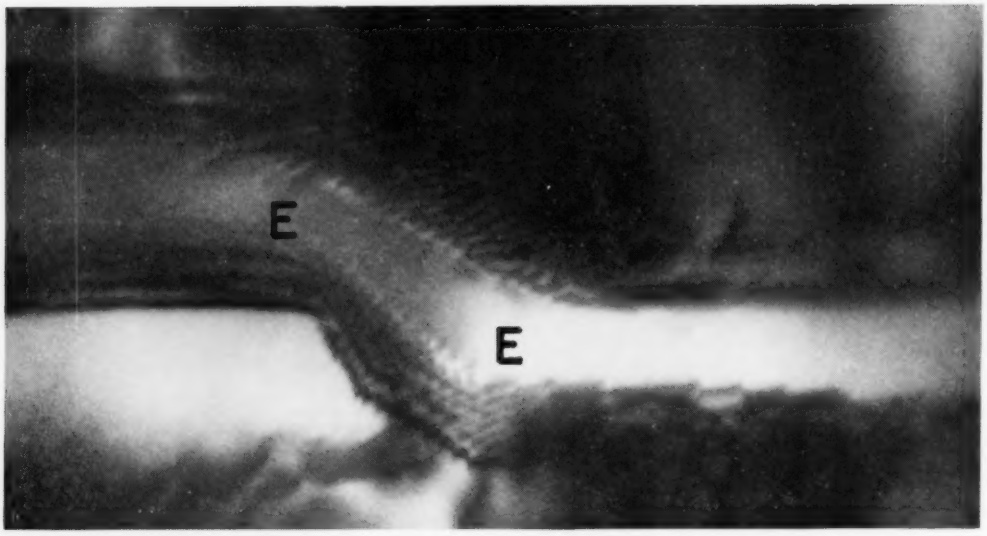


FIG. 16. Substructure in non-coherent twin boundary (001) foil. ×200,000

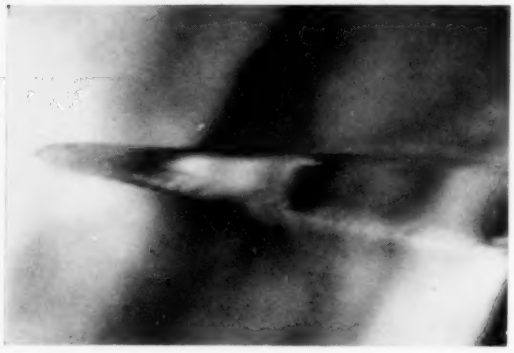


FIG. 17. Substructure along one twin boundary (110) foil. ×66,000

observed in other metals. An example is shown in Fig. 19, where the track left by a dislocation which had cross-slipped can be clearly noticed. The track appeared suddenly—within 1/16 of a sec—and subsequent to its formation slowly disappeared. In other cases dislocations were observed which had irregular curved paths. This implies that only the slip direction is fixed and that slip can occur on any plane containing this direction. In this respect, the slip process in tin resembles that in iron.

In a number of cases, individual dislocations were clearly observed to slow down, temporarily, the propagation of a twin. No clear case was observed where the twins were entirely stopped by dislocations.

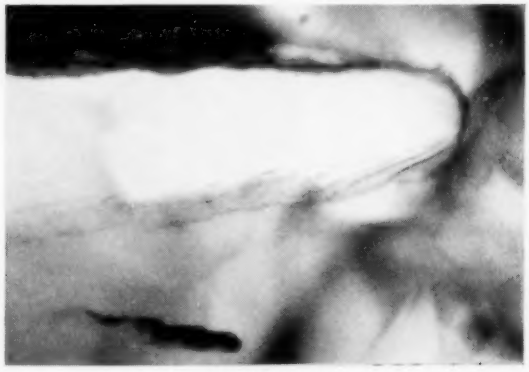
4. DISCUSSION

4.1 *Nucleation of twins*

The present observations pertaining to the nucleation of twins in foils are summarized below:

(a) A time interval of 2–5 min elapses after the foil is placed in the electron beam before twins nucleate.

(b) On nucleating, the twins initially grow very rapidly, then continue at a slower, comparatively uniform rate.



(a)



(b)

FIG. 18. Shrinking of a twin which had been produced by impact in a bulk specimen. ×85,000



FIG. 19. Dislocation trace in (001) faced specimens. (From cine film.) ×20,000

(c) Twins nucleate near the edge of the foil, at etch pits close to the edge, at the boundaries of other twins; and in isolated cases at crystal imperfections in the body of the foil

(d) No appreciable buckling of the foil precedes nucleation. Dislocations or dislocation pile-ups are not generally observed in the nucleating region.

(e) The nucleation of a twin is often followed by the nucleation of an adjacent twin. This can result in the formation of a regular sequence of twins, nucleated progressively along the edge of the foil.

VOL. 8 1960

The observation that a time interval elapses before twins nucleate suggests that progressively increasing local stresses are introduced in the foil by the action of the electron beam. This is in keeping with the observations of Hirsch *et al.*[14] who found that a time period elapsed before dislocations were observed to move in foils examined under similar conditions.

The detailed mechanism by which local stresses are introduced in the foil by the electron beam is not clearly understood. Hirsch[13] suggests that the stresses are produced by the growth of a contaminating carbon layer on the surface of the specimen. The local stresses would then increase as the contaminating layer thickened. In the present investigation it was observed that a contaminating layer always formed and progressively thickened on the specimen surface, as indicated by the progressive darkening of the image in the microscope. Further, a contaminating layer was clearly observed in some cases projecting from the edge of the foil.

A value for the stress produced in aluminum foils by the action of the electron beam has been estimated by Whelan *et al.*[11], on the basis of the curvature of the dislocation lines moving under stress, to be approximately 4×10^8 dyn/cm^2. Since the shear modulus for tin is within 10 per cent of that of aluminum, this value will be assumed to be applicable to the tin foils examined in the present investigation.

It is interesting to compare this stress with the estimated stress required to nucleate twins. This latter stress is given approximately[5] by the expression $(G/2\pi)\gamma$, where G is the appropriate shear stress and γ is the twinning shear. In the case of tin this is 3.5×10^9 dyn/cm^2, which is an order of magnitude higher than the stress in the foil. However, it is reasonable to suppose that twins would be nucleated more readily near the edge of the foil, as is observed with dislocations,[11] in which case the stress in the foil could be of the order required to nucleate twins.

The above considerations and the observation that dislocations were not observed in the immediate vicinity of twin nuclei, suggest that the Cottrell–Bilby mechanism for the nucleation of twins is not applicable in the present case. It is possible that some dislocations in the foil were not observed in the microscope. However, the Cottrell–Bilby mechanism requires a specific configuration of dislocations for each of the twins nucleated, and had these been present, some of the dislocations would have been favourably oriented for observation in the electron image. In addition, to account for the regular sequence of twins which were often observed (Fig. 1), a regular series of twin sources would be required near the edge of the foil, which is improbable.

The present observations thus support the nucleating mechanism proposed by Bell and Cahn[5] and Orowan[8] in which homogeneous twinning takes place at the theoretical shear stress required for twinning. The manner in which homogeneous twinning occurs is not clearly understood. Bell and Cahn suggest that a twin nucleus is created *as a whole* by local homogeneous shear of the lattice and not by the progressive motion of a dislocation. For zinc they estimate the critical nucleus diameter to be 250 Å. In the present observations, twins of widely varying dimensions were observed to form in the interval between adjacent frames of the cine film. However, it is not clear whether small nuclei form and expand rapidly, or whether the observed twins are near the critical size when formed.

Bell and Cahn proposed, on the basis of their investigation, that dislocation pile-ups resulting from plastic deformation were a necessary condition for the nucleation of twins in bulk material. They estimated that the applied stresses had to be increased by a factor of 35 in order to reach the theoretical shear stress for twinning. The present observations clearly indicate that twinning can occur without the presence of dislocation pile-ups in thin foils.

Twins were observed to nucleate at the boundaries of existing twins. This occurred in the body of the foil where the local stresses were estimated to be less than that required for the nucleation of twins. In general, each of the twins nucleated in this manner could be associated with another twin which had impinged on the other side of the parent twin. It is possible (see Fig. 6) that the impinging twin can cause slip to occur in the parent twin. This would result in the formation of a dislocation pile-up on the other side of the parent twin which would enhance the local stress sufficiently to cause twins to nucleate. In this particular case the mechanism is very similar to that proposed by Bell and Cahn.

Twins were also observed to nucleate, in isolated cases, at lattice imperfections which had an appearance suggestive of loops. The nature of the imperfections is not clear. Presumably their presence in the lattice results in sufficient local enhancement of the stress to cause the formation of a twin.

Regular sequences of twins were observed to nucleate and grow at the edge of the foil, as shown in Fig. 1. This could be accounted for if the stress relaxation resulting from the formation of a twin causes a local stress concentration near the edge of the foil, a distance S away. Since the overall stress is steadily increasing during observation, a second twin will eventually be nucleated at S and so on to produce a regular series.

4.2 *Propagation of twins*

In general, the manner in which twins were observed to propagate is consistent with the assumption that the advancing non-coherent twin interface consists of an array of twinning dislocations. For the (001) tin crystals, they would be screw dislocations terminating at the surfaces of the foil, and having a Burgers vector equal to the twinning shear dislacement.

The above assumption would account for the observation that twins propagate in the body of the foil where the stress level is below that required to nucleate twins. Also that the rate of twin propagation is roughly comparable to the rate of movement of slip dislocations in the foil under similar stresses. The observation that twins often propagate in jumps, can be attributed to both the presence of obstacles, such as dislocations, in the path of the twin, and the interaction of the twinning dislocations with the contaminated surface of the foil. The latter factor is similar to the interaction of slip dislocations with the surface as discussed by Whelan *et al.*[11].

The twinning dislocations at the incoherent twin interface would be produced in the nucleating process and would be confined to the twinning plane on which they initially formed. The present observations indicate that twin dislocations can also form as the twins propagate, since twins were observed to widen appreciably during growth (Fig. 9) and deviate appreciably from the normal [100] growth direction (Fig. 11). The mechanism by which twins widen is not clear. However, if twins can nucleate homogeneously, it appears reasonable that additional twinning dislocations should be formed on the interface during growth. The most notable examples of local widening in the present observations generally occurred when an advancing twin was slowed down or stopped by an obstacle in its path (Fig. 12).

In many cases, the appearance of neither the deviating twins nor the matrix in which they grew gave any indication as to why these twins deviated and others did not. The deviation could be a result of higher local stresses on one side of a twin, leading to an enhanced rate of nucleation on that side as the twin widened, due to inhomogeneities in the contaminating layer in the foil producing the local stresses. Or, a partial blocking of one side of a twin by a dislocation or dislocation array, which was not favourably oriented to be observed in the microscope, could result in enhanced growth on one side of the twin.

The rate of propagation of the twins observed in the present investigation was found to be of the order of 10^{-6} cm/sec. This is very much slower than the growth rate of twins in bulk specimens, estimated to be 1/10 the velocity of sound[1] (2.5×10^5 cm/sec). This difference in growth rate can be attributed primarily to the different conditions existing during the growth of twins in the thin foils as compared to the bulk specimens. In the case of thin foils, it is probable that the contaminating layer produced a high localized stress in the foil. This stress is relieved almost entirely in the immediate vicinity of the nucleated twin, and the rate of further propagation of the twin is a measure of the rate of contamination build up, which takes place in a slow and controlled manner. In the case of bulk specimens, the stresses are not localized and thus twins can propagate at high rates over large distances.

4.3 *Substructure in non-coherent twin boundaries*

In Fig. 16 the fringes due to overlapping wedge shaped crystals appear to be stepped in the region E–E. A tentative explanation can be advanced as follows:

When a narrow twin terminates in the matrix, an elastic shear displacement parallel to the twinning plane is required for coherency at the twin boundaries,

the extent of the displacement depending on the width of the twin. It can be seen, by comparing atom positions across the coherent twin boundaries, that this shear displacement is an almost periodic function of the twin width, passing through a minimum at every thirty-four (301) plane spacings. As a result, for narrow twins, the elastic strain energy will similarly pass through minima. Hence twins will widen in increment of thirty-four (301) planes. Further, an incoherent boundary such as E–E will tend to be stepped, with the step heights corresponding to about thirty-four (301) plane spacings which compares reasonably with the measured step heights of twenty-eight (301) plane spacings in Fig. 16.

ACKNOWLEDGMENTS

We wish to thank K. S. Milliken for helpful discussions.

REFERENCES

1. E. O. Hall, *Twinning and Diffusionless Transformations in Metals*. Butterworths, London (1954).
2. R. W. Cahn, *Advanc. Phys.* **3,** 363 (1954).
3. R. Clark and G. B. Craig, *Prog. Met. Phys.* **3,** 115 (1953).
4. N. Thompson and D. J. Millard, *Phil. Mag.* **43,** 422, (1952).
5. R. L. Bell and R. W. Cahn, *Proc. Roy. Soc.* A**239,** 494 (1957).
6. R. Siems and P. Haasen, *Z. Metallk.* **49,** 312 (1958).
7. A. H. Cottrell and B. A. Bilby, *Phil. Mag.* **42,** 573 (1951).
8. E. Orowan, *Dislocations in Metals*. p. 116. A.I.M.E. (1954).
9. B. Chalmers, *Canad. J. Phys.* **31,** 136 (1953).
10. J. T. Fourie, F. Weinberg and F. W. C. Boswell, *J. Appl. Phys.* **31,** 1136 (1960).
11. M. J. Whelan, P. B. Hirsch, and R. W. Horne, *Proc. Roy. Soc.* A**240,** 524 (1957).
12. J. T. Fourie, *J. Appl. Phys.* **29,** 608 (1958).
13. P. B. Hirsch, *J. Inst. Met.* **87,** 406 (1959).
14. P. B. Hirsch, R. W. Horne and M. J. Whelan *Phil. Mag.* **1,** 677 (1956).

VOL.
8
1960

GASEOUS DECARBURIZATION OF WHITE CAST IRONS*

J. BURKE†, J. BELL‡ and D. R. BOURNE§

Decarburization of two white cast irons, differing only in microstructure, has been studied using a 20% carbon dioxide–80% carbon monoxide atmosphere. Carbon loss and depth of decarburization at 1000°C and 1050°C were measured as a function of time. A mathematical analysis of decarburization is developed and from a comparison of this with the experimental results it is concluded that the diffusion of carbon in austenite is the rate controlling process.

DECARBURATION GAZEUSE DE FONTES BLANCHES

Les auteurs étudient la décarburation de deux fontes blanches se différencient uniquement par leur microstructure. Ils utilisent un mélange gazeux contenant 20% d'anhydride carbonique et 80% d'oxyde de carbone. Ils déterminent la perte en carbone et la profondeur de décarburation en fonction du temps. Ils font ensuite l'analyse mathématique de ce phénomène et en comparant avec les résultats expérimentaux déduisent que la diffusion du carbone dans l'austénite détermine la vitesse de décarburation.

ENTKOHLUNG VON WEIßEM GUßEISEN IN GASATMOSPHÄRE

Die Entkohlung von zwei Sorten weißen Gußeisens, die sich nur in der Mikrostruktur unterschieden, wurde in einer Atmosphäre von 20% Kohlendioxyd und 80% Kohlenmonoxyd untersucht. Kohlenstoffverlust und Tiefe der Entkohlung wurden bei 1000°C und 1050°C als Funktion der Zeit gemessen. Eine mathematische Beschreibung der Entkohlung wird entwickelt; aus einem Vergleich mit den experimentellen Ergebnissen läßt sich dann schließen, daß die Diffusion von Kohlenstoff in Austenit der geschwindigkeitsbestimmende Prozeß ist.

1. INTRODUCTION

The gaseous decarburization of cast irons involves the following basic steps: (a) removal of carbon in solution in austenite by reaction at the surface with the gas, (b) diffusion of carbon through the austenite from the core to the surface and (c) dissolution of the carbon-rich phase to maintain the supply of carbon to the surface. If the starting material is a white iron graphitization proceeds concurrently with decarburization. It was commonly assumed following the work of Baukloh *et al.*[1] that the rate of carbon removal is governed by the diffusion of carbon in austenite. However some recent experimental results[2] cannot be reconciled with this theory. Moore[2] showed that during the decarburization of commercial white irons the onset of graphitization retards decarburization. Since there is only a slight change in the austenite composition as a result of graphitization diffusion rates should not be affected. Furthermore, the rate of decarburization of pre-graphitized malleable irons was shown to be dependent on the form of the graphite, being greatest when the graphite was finely dispersed. It was concluded that the rate of solution of the graphite was the rate determining step. Moore[3] later studied decarburization of white irons prior to graphitization. Again it was found that the finer the structure the more rapid the rate of loss of carbon. Since the finer structure is associated with the greater carbide–austenite interfacial area, the conclusion was that the rate of solution of cementite was the rate controlling step. Evidently, more work is required, preferably using different experimental methods before the range of applicability of the two theories can be defined. The present work consists of a study of decarburization of two white cast irons whose purity is higher than those alloys examined previously using a new experimental approach.

2. THEORETICAL BASIS OF EXPERIMENTS

Consider a cylindrical sample of white cast iron maintained in a decarburizing atmosphere at a constant temperature in the austenite range. Let

R_1 be the radius of the sample,

c_1 be the carbon content of the alloy,

c_2 be the carbon content of austenite in "equilibrium" with cementite at that temperature,

c_3 be the carbon content at the surface in equilibrium with the gaseous atmosphere.

It is assumed that the temperature and composition are such that no graphitization occurs during the experiment and that decarburization takes place by the inward growth of a zone, of thickness x, free from cementite. This assumption is justified experimentally—see, for example Fig. 5 and Moore's work.[3]

Neglecting losses from the ends, the weight loss per

* Received January 27, 1960.

† Department of Metallurgy, The University, Liverpool 3.
‡ Now at William Park and Co., Forgemasters Ltd., Wigan Lancs.
§ Now at United Kingdom Atomic Energy Authority, Dounreay, Scotland.

unit length of sample is dw in time dt; this equals the weight of carbon dissolved from the cementite whilst the interface between the decarburized zone and the original structure moves dx plus the carbon loss due to the concentration gradient in the zone extending a distance dx.
Then

$$\begin{aligned} dw &= 2\pi(R_1 - x)(c_1 - c_2)\,dx \\ &\quad + X\pi\,(R_1 - x)\,(c_2 - c_3)\,dx \\ &= 2\pi(R_1 - x)[c_1 - \tfrac{1}{2}(c_2 + c_3)]\,dx. \end{aligned} \tag{1}$$

Equation (1) applies irrespective of the controlling mechanism. In any step-wise process the rate of reaction is equal to that of the slowest step. Below, the rate of decarburization is calculated for each of the possible controlling steps.

(a) *Decarburization when the rate of solution of cementite is the controlling process*

The rate of solution of cementite, S, is defined as the mass of carbon dissolving in austenite per unit time per unit area of cementite surface. The amount of carbon entering the austenite depends upon the surface area. This is difficult to estimate since particles other than those contiguous with the decarburized zone may dissolve if the austenite is continuous throughout the specimen. The effective surface is related to the area of the inner surface of the decarburized zone, $2\pi(R_1 - x)$, by some factor A which can be greater or less than unity.

Amount of carbon dissolving in time dt is

$$2\pi(R_1 - x)AS\,dt$$

$$\therefore 2\pi(R_1 - x)\,dx\,[c_1 - \tfrac{1}{2}(c_2 + c_3)] = 2\pi(R_1 - x)AS\,dt \tag{2}$$

i.e.
$$\frac{dx}{dt} = \frac{AS}{[c_1 - \tfrac{1}{2}(c_2 + c_3)]} = \alpha \text{ (say)}. \tag{3}$$

From equation (3) and (1)

$$dw/dt = 2\pi(R - \alpha t)\,\alpha[c_1 - \tfrac{1}{2}(c_2 + c_3)]. \tag{4}$$

Integrating

$$W = \pi\alpha(2Rt - \alpha t^2)[c_1 - \tfrac{1}{2}(c_2 + c_3)]. \tag{5}$$

The constant of integration is zero in this equation. Thus if the rate of solution of the cementite is rate controlling, x, the depth of decarburization, is a linear function of time, and the weight loss per unit length is a quadratic function. If solution is the controlling factor the rate of decarburization will depend on the microstructure since the parameter A will increase as the cementite–austenite eutectic is refined.

(b) *Decarburization when the rate of diffusion of carbon in austenite is the slowest step*

In this case the flux of carbon atoms is given by Fick's law

$$\text{Flux} = -2\pi(R_1 - x)D\,\partial c/\partial R_{(R_1 - x)}. \tag{6}$$

where D is the diffusion coefficient assumed independent of composition. The steady state solution of Fick's law for cylindrical symmetry is[4]

$$\frac{\partial c}{\partial R} = \frac{c_2 - c_3}{\log \dfrac{R_1 - x}{R_1}} \cdot \frac{1}{R}. \tag{7}$$

Combining equations (1), (6) and (7) gives

$$\begin{aligned} &2\pi(R_1 - x)D\,\frac{c_2 - c_3}{\log\left(\dfrac{R_1}{R_1 - x}\right)} \cdot \frac{1}{(R_1 - x)} \\ &\qquad = 2\pi(R_1 - x)[c_1 - \tfrac{1}{2}(c_2 + c_3)]\,\frac{dx}{dt} \end{aligned} \tag{8}$$

and rearranging

$$D\,\frac{c_2 - c_3}{[c_1 - \tfrac{1}{2}(c_2 + c_3)]}\,.\,dt = \left\{\log\left(\frac{R_1}{R_1 - x}\right)\right\}(R_1 - x)\,dx. \tag{9}$$

Integration of equation (9) gives

$$\begin{aligned} &D\,\frac{c_2 - c_3}{[c_1 - \tfrac{1}{2}(c_2 + c_3)]}\,.\,t = \\ &\qquad \frac{(R_1 - x)^2}{4}\left[2\log\left(\frac{R_1 - x}{R_1}\right) - 1\right] + \frac{{R_1}^2}{4}. \end{aligned} \tag{10}$$

The second term on the right hand side is the integration constant. Equation (10) can be simplified by means of the expansion

$$\log\,(1 - y) = -y - \tfrac{1}{2}y^2 - \tfrac{1}{3}y^3. \tag{11}$$

Taking the first two terms of this series gives

$$\begin{aligned} &D\,\frac{c_2 - c_3}{[c_1 - \tfrac{1}{2}(c_2 + c_3)]}\,.\,t \simeq \\ &\qquad -\frac{(R_1 - x)^2}{4}\cdot\left\{\frac{2x}{R_1} + \frac{x^2}{{R_1}^2} + 1\right\} + \frac{{R_1}^2}{4} \end{aligned} \tag{12}$$

$$= \tfrac{1}{2}x^2 - \frac{x^4}{4{R_1}^2}. \tag{13}$$

The second term in equation (13) is small compared to the first and thus

$$x^2 \simeq 2D\,\frac{c_2 - c_3}{[c_1 - \tfrac{1}{2}(c_2 + c_3)]}\,t = \beta t. \tag{14}$$

Thus if decarburization is controlled by the rate of diffusion x^2 is approximately a linear function of time.

VOL. 8 1960

For the initial stages of decarburization equation (14) can be combined with equation (1)

$$\frac{dw}{dt} = \pi (R_1\sqrt{\beta/t} - \beta)[c_1 - \tfrac{1}{2}(c_2 + c_3)]. \quad (15)$$

Thus

$$w = \pi [2R_1\sqrt{(\beta t)} - \beta t][c_1 - \tfrac{1}{2}(c_2 + c_3)]. \quad (16)$$

Equation (16) should be obeyed initially, the divergence increasing with time.

(c) *Decarburization controlled by the surface reaction*

In this case the rate of weight loss is constant

$$w = \text{const. } t. \quad (17)$$

(d) *Multiple control*

Since the rate of reaction for the cases of solution and diffusion control decreases with time it is possible for the controlling mechanism to change during the course of decarburization. The possibilities are (1) the surface reaction controls initially followed by solution and then diffusion or (2) the surface reaction is followed by diffusion. Which of these is applicable depends upon the actual values of the parameters in the equations. The sequence can vary from alloy to alloy, and maybe, from temperature to temperature.

3. EXPERIMENTAL DETAILS

The present experimental method consisted of studying the time dependence of the weight loss and depth of decarburization in two white irons of nearly identical composition but of different microstructure. The data were compared with equations (3), (5), (7), (10), (14), (16) and (17). The analysis of the weight loss results demands that the decarburization via the ends of the specimens is negligible. Since this was not achieved experimentally greater importance was placed upon measurement of the depth of decarburization.

The two white cast irons studied had the following composition:

	C	Si	Mn	S	P
Alloy 1	3.86	0.15	<0.02	0.016	0.027
Alloy 2	3.73	0.15	<0.01	0.018	0.024

Alloy 1 had a relatively coarse structure (Fig. 1), having been cast into a refractory mould, whilst alloy 2 possessed a fine structure (Fig. 2). Both alloys were made by the British Cast Iron Research Association and had been melted in vacuum and cast in argon.

Cylindrical specimens, 1 cm diameter and 1 cm long, were suspended by nichrome wires in a vertical tube furnace the temperature of which was controlled to $\pm 3°C$. The decarburizing gas was led into the bottom of the furnace and out of the top. Specimens were inserted into the furnace, previously equilibrated at the required temperature, with the gas

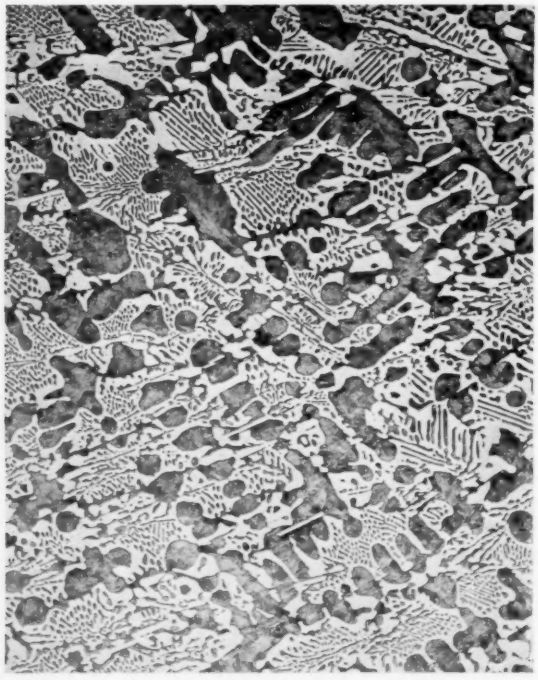


FIG. 1. Microstructure of alloy 1. Etched in 4% picral. ×60

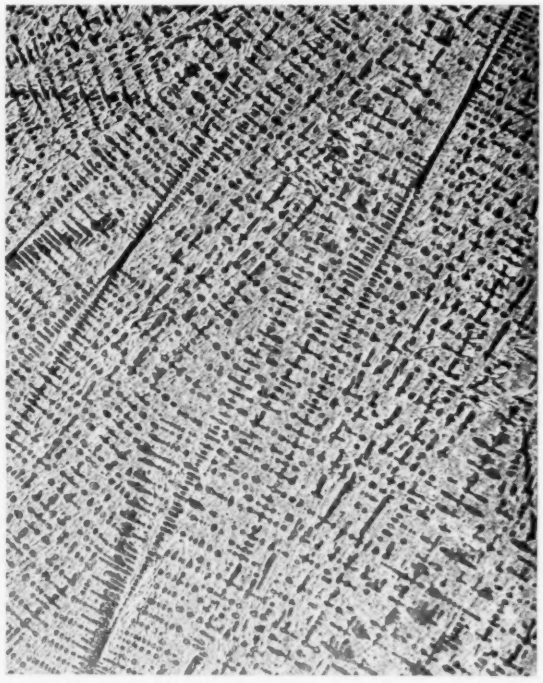


FIG. 2. Microstructure of alloy 2. Etched in 4% picral. ×60

flowing. The time required for the specimen to attain the furnace temperature was approximately 1 min which is small compared to the time of decarburization. At the end of a run the specimen was raised into a cooler zone of the furnace, allowed to cool to about 500°C and then quenched. This slow cool permitted the pro-eutectoid and eutectoid reactions to proceed normally and the resultant microstructure was a valuable guide to the composition gradient existing in the decarburized zone at the experimental temperature.

Decarburization was effected in a mixture consisting of 20 per cent carbon dioxide and 80 per cent carbon monoxide (volume composition). The relevant equilibria are

$$Fe + CO_2 \rightleftharpoons FeO + CO \qquad (18)$$

$$k = p_{CO}/p_{CO_2}$$

and

$$C(\text{in } \gamma \text{ Fe}) + CO_2 \rightleftharpoons 2\,CO \qquad (19)$$

$$k = p^2_{CO_2}/p_{CO_2} \cdot a_c.$$

In writing equation (18) it is permissible to ignore the carbon in solution since the surface concentration is maintained at a low value throughout the experiment. The values of k for this reaction have been tabulated by Darken and Gurry[5]. Mixtures with less than 26 per cent CO_2 are reducing at all temperatures below 1090°C. Smith's[6] data for reaction (19) indicates that at 1000°C 20 per cent CO_2 is capable of reducing the surface to 0.05 wt. % carbon. Thus the mixture used was both decarburizing and reducing.

The gases were mixed in a suitable gas holder and, before entering the furnace, they were dried by passing over calcium chloride, magnesium perchlorate and phosphorous pentoxide. The flow rate was 200 cm³/min, equivalent to a linear velocity past the specimen of 8 cm/min which is considerably greater than the value of 1 cm/min which, from Baukloh's results,[1] is the minimum velocity that will ensure that the surface reaction does not limit the rate of decarburization.

The progress of decarburization was followed by noting the loss in weight of specimens heated for successively longer times. After decarburization each specimen was sectioned transversely through its midpoint, care being taken to ensure that the section was normal to the cylindrical axis. The depth of decarburization x, defined as the difference in the radii of the specimen and of the cylinder circumscribing the undissolved cementite, was measured microscopically after suitable polishing and etching. The results quoted are the average of not less than ten readings taken around the circumference.

4. RESULTS AND DISCUSSION OF RESULTS

Decarburization at 1000 and 1050°C

The weight loss curves for both alloys are shown in Fig. 3 (1050°C) and Fig. 4 (1000°C). The important features are: (1) the rate of weight loss decreases with time indicating that the surface reaction is not the rate limiting process over the major portion of the time. The accuracy of the data is not sufficient to establish the period for which the control must be exercised by the surface reaction (c.f. Section 2d) but

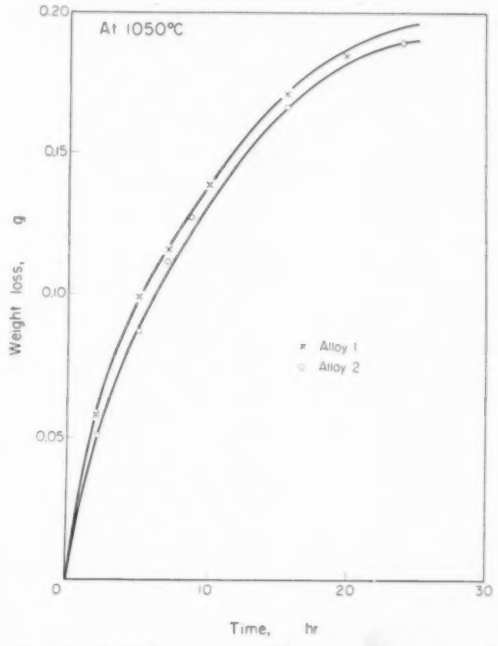


FIG. 3. Weight loss versus time for alloys 1 and 2 at 1050°C.

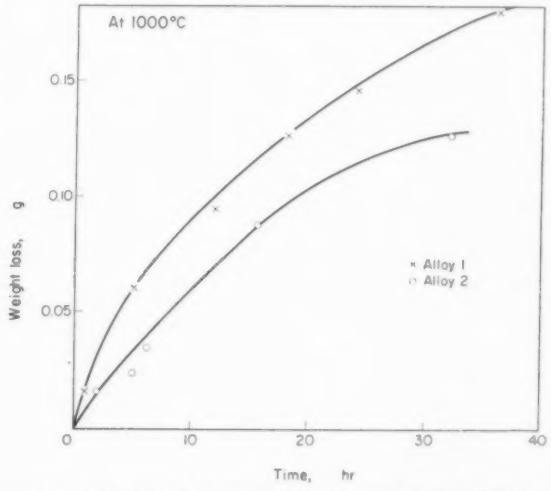


FIG. 4. Weight loss versus time for alloys 1 and 2 at 1000°C.

VOL. 8 1960

it must be very short. (2) The loss of carbon is greater in the alloy having the coarse structure (alloy 1). This observation is contrary to the results of Moore[3]; it implies that the rate of solution of cementite is not the rate limiting process (c.f. Section 2a). (3) The difference between the weight losses of the two alloys is greater at 1000 than 1050°C.

The microstructure of the decarburized zone in a typical specimen is shown in Fig. 5. It is to be noted that there is a sharply defined boundary between the decarburized zone and the residual cementite. The

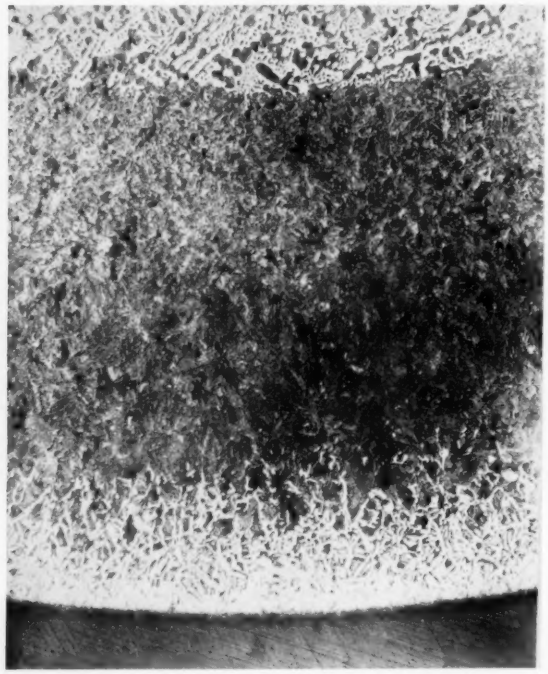


FIG. 5. Microstructure of a typical decarburized zone. Alloy 1 at 1000°C. ×80

only exceptions were specimens heated for more than 15 hr at 1050°C in which extensive decarburization and graphitization had combined to produce an ill-defined boundary. Thus the assumption made in Section 2 is justified. The surface of the specimens was ferritic which demonstrates that the surface reaction did not limit the rate of decarburization, in accordance with the form of the weight loss curves.

The depth of decarburization x is plotted against time in Fig. 6. Decarburization is more extensive in alloy 1 than alloy 2, confirming the weight loss results. The rate of increase of x decreases with time. Thus in view of equation (3) it can be concluded that, in these alloys, decarburization is not governed by the rate of solution of cementite.

Figure 7 shows x^2 as a function of time. The graphs

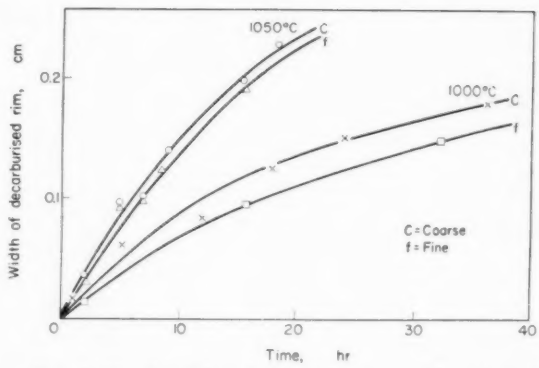


FIG. 6. Depth of decarburization, x, as a function of time.

are approximately linear in all four cases, in conformity with equation (14) based upon diffusion controlled decarburization. Extrapolation of the graphs does not pass through the origin but intercepts the time axis at some positive value. This implies the existence of a delay period prior to the onset of decarburization, being greater for alloy 2 than alloy 1. The production of a white iron requires a fast solidification rate resulting in there being less austenite and of a lower carbon content than indicated by the iron-cementite-silicon constitutional diagram. The delay periods are probably associated with the time required to restore internal equilibrium. This phenomenon will be more pronounced in the more rapidly cooled alloy 2, and this, in fact, has the longer delay period (Fig. 8.). The differences in the decarburization of the two alloys is much less at 1050 than at 1000°C. This can be explained on the basis of a more rapid restoration of equilibrium at the higher temperature.

Thus the results suggest that decarburization of these alloys at 1000 and 1050°C is diffusion controlled.

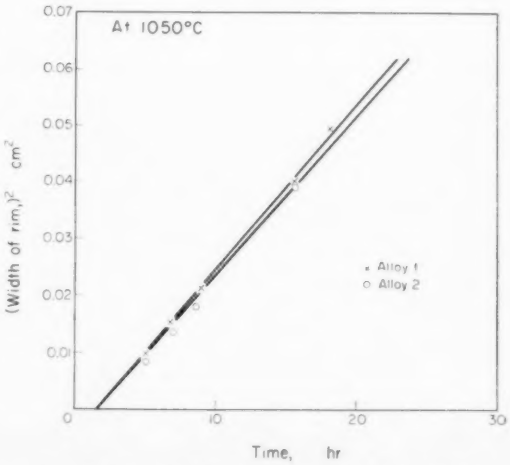


FIG. 7. Graphs of x^2 versus time at 1050°C.

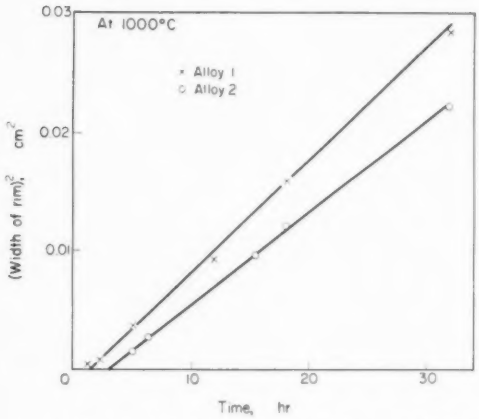


FIG. 8. Graphs of x^2 versus time at 1000°C.

5. ANALYSIS OF RESULTS

It was shown in the previous section that the results at 1050 and 1000°C are qualitatively in agreement with the theory that the diffusion of carbon is the slowest step in the decarburization reaction. Complete proof demands that the experimental results be in agreement with those predicted by the analysis in Section 2(b).

Equation (14) gives the slope of the x^2 versus t graph as β where

$$\beta = 2D\frac{c_2 - c_3}{[c_1 - \frac{1}{2}(c_2 + c_3)]}.$$

The value of the diffusion coefficient for carbon in austenite was determined by Wells *et al.*[7]. D varies appreciably over the range of carbon contents existing in the decarburized rim, and thus it is necessary to select some mean value. It can be shown from the solution of Fick's law that during diffusion out of a cylinder the concentration decreases logarithmically as the radius increases. Thus the value of D selected must be weighted in favour of lower carbon concentrations. The value of D at 0.2 per cent carbon has been arbitrarily selected for the calculations.

The value of c_2 was obtained from the cementite solubility line calculated thermodynamically by Darken and Gurry[8]; c_3 was evaluated by interpolation of Smith's data.[6] The density values used to convert the concentrations into units of weight per unit volume were obtained from the densities and thermal expansion data given in Ref. (9). The accuracy of these calculated densities is difficult to assess but it is of little importance because the value of β is insensitive to the actual values used. In fact, using the concentrations in weight per cent (implying that the density is independent of carbon content) has no appreciable effect on β.

The results of the calculations are given in Table 1 for alloy 1 at 1000 and 1050°C. Alloy 2 was not considered because the departure from equilibrium is more severe, as discussed previously. Satisfactory agreement is obtained between the calculated and experimental values of β.

In making the estimate of β the effect of the small silicon content was ignored. Since silicon increases the activity of carbon in austenite c_1, c_2 and c_3 will be reduced. Since this affects both the numerator and the denominator of the expression in a similar manner the net effect is very small, and it is considered justifiable to ignore it.

Equation (10) in Section 2 gives x as a function of t throughout the process, and it is of interest to compare the calculated and the experimental curves. Equation (10) is plotted in Fig. 9 for alloy 1 at 1000 and 1050°C. In order to compare the experimental results with

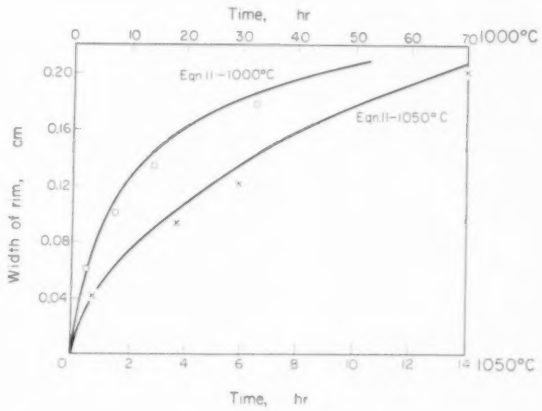


FIG. 9. Comparison between the calculated and measured values of depth of decarburization for alloy 1 at 1000 and 1050°C. Full curves were calculated from equation (10); the points are experimental measurements.

TABLE 1. Values of quantities used in the calculation of β for alloy 1

Temperature (°C)	c_1		c_2		c_3		D (cm²/sec)	β (cm²/sec)	
	(wt.%)	(g/cm³)	(wt.%)	(g/cm³)	(wt.%)	(g/cm³)		Calculated	Experimental
1050	3.86	0.2786	1.70	0.1269	0.038	0.0028	5×10^{-7}	5.52×10^{-7}	8.33×10^{-7}
1000	3.86	0.2886	1.53	0.1142	0.060	0.0045	2.87×10^{-7}	2.60×10^{-7}	2.50×10^{-7}

VOL. 8 1960

these curves it is necessary to make allowance for the "delay period" because this is not allowed for in equation (10). This can be done by taking zero time as the end of the delay period. Experimental points thus modified are seen to fit reasonably well to the calculated curves.

The final point of correlation between theory and experiment is between the weight loss and equations (16) and (17). A difficulty is to make allowance for the carbon extracted from the end of the specimens. In one series of tests (alloy 1 at 1000°C) end losses were reduced (but by no means eliminated) by mechanical clamps. Thus, this is the only one for which even approximate agreement is to be expected. Table 2

TABLE 2. Values of weight loss in alloy 1 at 1000°C

Time (hr)	Weight loss (g)	
	Calculated	Measured
1	0.0227	0.012
2	0.0307	0.030
4	0.0430	0.050
5	0.0485	0.060
12	0.0650	0.098

gives measured and calculated values; up to 5 hr the agreement is fair but becomes progressively worse at longer times. The disparity at long times is due to (a) equation (16) being less accurate at longer times and (b) the influence of the end losses.

6. GENERAL DISCUSSION

The agreement between the experimental results and those calculated on the basis of diffusion controlled decarburization leads to the conclusion that the process is governed by the rate of diffusion of carbon in austenite. The qualitative observations are also consistent with this conclusion. Thus the present alloys must differ from the commercial alloys studied by Moore[3]. It would appear that slight changes in composition or microstructure or some other more subtle factor can cause an alteration of the controlling process due, presumably, to its effects on the rates of diffusion or solution of carbide. It is of interest to note that recent work on the analogous process of graphitization shows that different controls are also possible for that reaction in alloys which differ little in composition.[10] However, for graphitization the available data indicate that solution of cementite is the slowest step in high purity alloys and diffusion the slowest step in commercial alloys,[10] the reverse of the situation during decarburization. At the moment there is no obvious explanation of these effects and it is clear that much more work is required before the reactions will be fully understood.

ACKNOWLEDGMENT

The authors are pleased to acknowledge the help given by Mr. C. T. Moore of the British Cast Iron Research Association, who provided the alloys and offered many critical comments and suggestions during the course of the work.

REFERENCES

1. W. BAUKLOH, F. SCHULTE and H. FRIEDRICHS, *Arch. Eisenhüttenw.* **16**, 341 (1943).
2. C. T. MOORE, *J. Res. Brit. Cast Iron Res. Assoc.* **7**, 82 (1957).
3. C. T. MOORE, *J. Res. Brit. Cast Iron Res. Assoc.* **7**, 258 (1958).
4. R. M. BARRER, *Diffusion in and through Solids*, p. 15. Cambridge University Press (1941).
5. L. S. DARKEN and R. W. GURRY, *Physical Chemistry of Metals*, p. 219. McGraw-Hill, New York (1954).
6. R. P. SMITH, *J. Amer. Chem. Soc* **68**, 1163 (1946).
7. C. WELLS, W. BATZ and R. F. MEHL, *Trans. Amer. Inst. Min. (Metall.) Engrs.* **188**, 553 (1950).
8. L. S. DARKEN and R. W. GURRY, *Trans. Amer. Inst. Min. (Metall.) Engrs.* **1015** (1951).
9. *Metals Handbook* pp. 309 and 508. American Society for Metals, Cleveland (1948).
10. J. BURKE, *J. Iron St. Inst.*, **194**, 443 (1960).

ON THE DETERMINATION OF DIFFUSION COEFFICIENTS IN CHEMICAL DIFFUSION*

R. W. BALLUFFI†

The equations describing chemical diffusion in the general case where the partial molal volumes of the diffusing components may differ and may vary with composition are reviewed and discussed. Exact and easily applied relations for obtaining chemical and intrinsic diffusivities are derived. The results should replace the standard Darken equations and Boltzmann–Matano analysis whenever there is any possibility that differences and variations of the partial molal volumes are of significance.

SUR LA DETERMINATION DES COEFFICIENTS DE DIFFUSION DANS LA DIFFUSION CHIMIQUE

L'auteur examine et discute les équations relatives au coefficient de diffusion chimique dans le cas général où les volumes partiels molaires des constituants peuvent différer ou varier suivant la composition. Il déduit des relations exactes et facilement applicables qui donnent le coefficient de diffusion chimique et le coefficient de diffusion intrinsèque. Ces relations pourraient les équations de Darken et de Boltzmann–Matano chaque fois qu'il y a possibilité de différences et de variations du volume partiel molaire.

ÜBER DIE BESTIMMUNG VON DIFFUSIONSKOEFFIZIENTEN BEI CHEMISCHER DIFFUSION

Die Gleichungen, die die chemische Diffusion im allgemeinen Fall beschreiben, wo die partiellen molaren Volumina der diffundierenden Komponenten verschieden und von der Zusammensetzung abhängig sein können, werden zusammengestellt und diskutiert. Zur Bestimmung chemischer und innerer Diffusionskonstanten werden exakte und leicht anwendbare Beziehungen hergeleitet. Wenn die Möglichkeit besteht, daß Unterschiede und mangelnde Konstanz der partiellen molaren Volumina von Bedeutung sein können, sollten die Ergebnisse an die Stelle der Gleichungen von Darken und der Durchrechung nach Boltzmann–Matano treten.

VOL. 8 1960

1. INTRODUCTION

Most analyses of chemical diffusion have ignored possible effects due to differences in the partial molal volumes of the diffusing components and variations of these partial molal volumes with composition. For example, the standard Darken[1] equations assume that the partial molal volumes of the diffusing components are constant and equal. In the general case, this condition does not hold and the analysis of diffusion then becomes more complicated. An excellent discussion of this problem has been given by Crank[2]. These complicating effects generally have been ignored by workers in the field since they are usually small (at least in metallic systems). However, with the development of more accurate techniques for measuring diffusion coefficients, these effects should be of significance in a number of systems. The purpose of the present paper is to present a set of exact and easily applied relations for obtaining chemical diffusivities from experimental data. It turns out that the labor involved in the application of the general equations is not much greater than in the case where constant and equal partial molal volumes are assumed. It is strongly recommended that the general relations be used whenever there is any possibility that effects due to differences and variations of the partial molal volumes are significant.

2. GENERAL EQUATIONS

We shall limit our discussion to unidimensional diffusion in a binary sandwich-type couple of constant cross section. Measurements on actual diffusion couples have shown that the cross section of such a diffusion couple remains essentially constant when the couple is sufficiently massive in the x directions.[3–5] The initial condition is

$$\left.\begin{aligned} C_1 &= C_1(-\infty) \quad x < 0 \quad t = 0 \\ C_1 &= C_1(+\infty) \quad x > 0 \quad t = 0 \end{aligned}\right\}. \tag{1}$$

The $x = 0$ plane is fixed with respect to the non-diffused end of the couple at $x = -\infty$ for all t. Also, $\partial C_1/\partial x = 0$ at $x = \pm\infty$.

The fluxes across any section fixed with respect to the origin are

$$J_i = -D_i \frac{\partial C_i}{\partial x} + C_i v \tag{2}$$

where $i = 1$ or 2. The D_i are the intrinsic diffusivities of Darken[1] and Hartley and Crank[6] and measure the fluxes relative to the crystal which is mechanically flowing with a velocity, v, relative to $x = 0$. As Bardeen and Herring[7] point out, equation (2) holds for a vacancy diffusion model as long as vacancy supersaturation effects are negligible. This condition should be met in most diffusion couples at diffusion

* This research was supported by the United States Air Force through the Air Force Office of Scientific Research. Received February 15, 1960.

† Department of Mining and Metallurgical Engineering, University of Illinois, Urbana, Illinois.

times of interest.[8] The C_i are measured in moles per unit volume and obey the standard equations

$$\left.\begin{aligned} C_1\bar{V}_1 + C_2\bar{V}_2 &= 1 \\ C_1\,d\bar{V}_1 + C_2\,d\bar{V}_2 &= 0 \\ \bar{V}_1\,dC_1 + \bar{V}_2\,dC_2 &= 0 \end{aligned}\right\} \tag{3}$$

where the $\bar{V}_i$ are partial molal volumes. Following Prager[9] and Crank[2] the accumulation equations are

$$\frac{\partial C_i}{\partial t} = \frac{\partial}{\partial x}\left[D\frac{\partial C_i}{\partial x} - C_i\int_{-\infty}^{x}\frac{D}{\bar{V}_2 C_1}\left(\frac{\partial \bar{V}_2}{\partial C_1}\right)\left(\frac{\partial C_1}{\partial x}\right)^2 dx\right] \tag{4}$$

where D is the chemical diffusion coefficient which is given by

$$D = D_1\bar{V}_2C_2 + D_2\bar{V}_1C_1. \tag{5}$$

The velocity of flow is

$$v = \bar{V}_1(D_1 - D_2)\frac{\partial C_1}{\partial x} + \int_{-\infty}^{x}\frac{D}{\bar{V}_2 C_1}\left(\frac{\partial \bar{V}_2}{\partial C_1}\right)\left(\frac{\partial C_1}{\partial x}\right)^2 dx. \tag{6}$$

We note that the macroscopic diffusion is described in terms of a single chemical diffusion coefficient. However, the usual simple forms of Fick's laws do not pertain. The integral term in equation (6) is a small velocity term arising from variations of the partial molal volumes with composition. Such variations will generally cause the couple, as a whole, to swell or shrink.

3. THE DETERMINATION OF THE CHEMICAL AND INTRINSIC DIFFUSIVITIES

The determination of the chemical diffusivity, D, is somewhat complicated by the fact that it appears behind the integral in equation (4). Crank[2] reviews two approximate methods for its determination. In the following we solve for D exactly. The solution is expedited by introduction of the functions

$$\theta_i = D_i - vC_i\left(\frac{\partial x}{\partial C_i}\right). \tag{7}$$

Then

$$j_i = -\theta_i\frac{\partial C_i}{\partial x}, \tag{8}$$

$$\frac{\partial C_i}{\partial t} = \frac{\partial}{\partial x}\left(\theta_i\frac{\partial C_i}{\partial x}\right), \tag{9}$$

and

$$D = C_1\bar{V}_1\theta_2 + C_2\bar{V}_2\theta_1. \tag{10}$$

For the present boundary conditions, the θ_i may be determined by the usual Boltzmann–Matano method where the variable $\lambda \equiv xt^{-\frac{1}{2}}$ is introduced and the solution $C_1 = C_1(\lambda)$ is assumed. We first note that the θ_i are functions of λ of the form

$$\theta_i = D - C_i\frac{d\lambda}{dC_i}\int_{-\infty}^{\lambda}\frac{D}{\bar{V}_2C_1(\lambda)}\left(\frac{d\bar{V}_2}{d\lambda}\right)\left(\frac{dC_1}{d\lambda}\right)d\lambda. \tag{11}$$

Since the θ_i are functions of λ, they are also functions of the composition since $\lambda = \lambda(C_1)$. However, the θ_i are not functions of composition in the general sense since the relation $\lambda = \lambda(C_1)$ depends upon the particular boundary conditions of the diffusion couple under investigation. The Matano integration of equation (9) yields

$$\theta_i = -\frac{1}{2t}\left(\frac{\partial x}{\partial C_i}\right)\int_{C_i(-\infty)}^{C_i(x)} x\,dC_i. \tag{12}$$

Using equations (12), (10) and (3) we solve for D in the convenient form

$$D = -\frac{1}{2t}\left(\frac{\partial x}{\partial C_1}\right)\left\{[1 - C_1(\bar{V}_1 - \bar{V}_2)]\int_{C_1(-\infty)}^{C_1(x)} x\,dC_1 + \bar{V}_2C_1\int_{C_1(-\infty)}^{C_1(x)}\left(\frac{\bar{V}_1 - \bar{V}_2}{\bar{V}_2}\right)x\,dC_1\right\}. \tag{13}$$

Equation (13) may be solved graphically by the usual means. The second integral will generally be quite small compared to the first and is readily evaluated by scaling down the x coordinate of the penetration curve by the factor $(\bar{V}_1 - \bar{V}_2)/\bar{V}_2$. It is stressed that the origin is located at the $x = 0$ plane under all circumstances. The plane defined by

$$\int_{C_1(-\infty)}^{C_1(+\infty)} x\,dC_1 = 0$$

will not generally coincide with the $x = 0$ plane. Inspection of equations (7) and (12) shows that coincidence is only obtained in the special case when the couple as a whole does not expand or shrink. This result may also be demonstrated by integrating under the diffusion curve to find the amount of either component which has crossed the $x = 0$ plane during the diffusion.

When marker movement data are available, the intrinsic diffusivities may be obtained from the relations

$$D_1 = \frac{1}{2t}\left(\frac{\partial x}{\partial C_1}\right)\left[2tv_mC_1 - \int_{C_1(-\infty)}^{C_1(x)} x\,dC_1\right], \tag{14}$$

$$D_2 = -\frac{1}{2t}\left(\frac{\partial x}{\partial C_1}\right)\left[2tv_mC_2 + \int_{C_1(-\infty)}^{C_1(x)} x\,dC_1 + \int_{C_1(-\infty)}^{C_1(x)}\left(\frac{\bar{V}_1 - \bar{V}_2}{\bar{V}_2}\right)x\,dC_1\right]\frac{\bar{V}_2}{\bar{V}_1}. \tag{15}$$

The slopes and integrals in equations (14) and (15) are the same as in equation (13); and, therefore, the

D_i are readily determined if the marker velocity, v_m, is known.

We conclude by showing that an inert marker initially placed at $x = 0$ will move parabolically with time. For this marker then, the term $2tv_m$ in equations (14) and (15) is simply represented by the marker displacement: i.e.

$$2tv_m = x_m. \tag{16}$$

The instantaneous velocity of any marker is given by equation (6). Making the λ substitution we have

$$v = \left[\bar{V}_1(D_1 - D_2)\frac{\partial C_1}{\partial \lambda} + \int_{-\infty}^{\lambda} \frac{D}{\bar{V}_2 C_1(\lambda)} \left(\frac{d\bar{V}_2}{d\lambda}\right)\left(\frac{dC_1}{d\lambda}\right) d\lambda \right] \frac{1}{t^{\frac{1}{2}}}. \tag{17}$$

This equation is satisfied by a particular marker traveling at constant composition at a constant value of λ, say λ_m, whose motion is given by

$$x_m = \lambda_m t^{\frac{1}{2}}. \tag{18}$$

In this case $v_m = dx_m/dt = \lambda_m/2t^{\frac{1}{2}}$ where

$$\lambda_m = 2\left[\bar{V}_1(D_1 - D_2)C_1'(\lambda_m) + \int_{-\infty}^{\lambda_m} \frac{D}{\bar{V}_2 C_1(\lambda)} \left(\frac{d\bar{V}_2}{d\lambda}\right)\left(\frac{dC_1}{d\lambda}\right) d\lambda \right] = \text{constant}.$$

4. CONCLUDING REMARKS

The previous equations may be readily applied when $\bar{V}_1$ and $\bar{V}_2$ are known as functions of composition. In such a case, the labor in determining diffusion coefficients is not markedly greater than when the standard Darken equations[1] are employed as an approximation. In many cases, an excellent first order approximation is obtained when it is assumed that $\bar{V}_1$ and $\bar{V}_2$ are each constant. The equations then become quite simple. The integral term in equation (4) and (6) vanishes, $\theta_i = D_i$, and the usual forms of Fick's laws pertain. When the detailed behavior of $\bar{V}_1$ and $\bar{V}_2$ is unknown, it is suggested that the investigator measure the density of the two terminal alloys employed in the couple and use the approximation of constant $\bar{V}_1$ and $\bar{V}_2$.

Another method of coping with volume changes during diffusion is to employ a non-laboratory coordinate system where equal increments of the coordinate in the direction of diffusion contain equal numbers of atoms.[2,6,10] In this type of space, the simple form of Fick's laws always pertain. However, in order to determine D by this method, $\bar{V}_1$ and $\bar{V}_2$ must be known; a Boltzmann–Matano type integration must be carried out; and further manipulations are required. The advantages of this method, therefore, appear open to question.

REFERENCES

1. L. S. Darken, *Trans. Amer. Inst. Min. (Metall.) Engrs.* **175,** 184 (1948).
2. J. Crank, *The Mathematics of Diffusion* p. 219. Oxford University Press (1956).
3. L. C. C. da Silva and R. F. Mehl, *Trans. Amer. Inst. Min. (Metall.) Engrs.* **191,** 155 (1951).
4. R. W. Balluffi and L. L. Seigle, *J. Appl. Phys.* **25,** 607 (1954).
5. R. Resnick and R. W. Balluffi, *Trans. Amer. Inst. Min. (Metall.) Engrs.* **203,** 1004 (1955).
6. G. S. Hartley and J. Crank, *Trans. Faraday Soc.* B**42,** 12 (1946).
7. J. Bardeen and C. Herring, *Atom Movements* p. 87. American Society for Metals, Cleveland (1951).
8. H. Fara and R. W. Balluffi, *J. Appl. Phys.* **30,** 325 (1959).
9. S. Prager, *J. Chem. Phys.* **21,** 1344 (1953).
10. M. Cohen, C. Wagner and J. E. Reynolds, *Trans. Amer. Inst. Min. (Metall.) Engrs.* **197,** 1534 (1953); **200,** 702 (1954).

VOL. 8 1960

ELECTRON-MICROSCOPIC STUDY OF RECRYSTALLIZATION TWINS IN COPPER*

E. VOTAVA and H. HATWELL†

By the use of transmission electron microscopy of thin copper foils, direct evidence has been found of twinning dislocations and of their association with recrystallization twins. Although several properties of recrystallization twins can be explained on the basis of these dislocations, the origin of the twins is still a matter of speculation.

ETUDE PAR MICROSCOPIE ELECTRONIQUE DES MACLES DE RECRISTALLISATION DANS LE CUIVRE

Par observation directe au microscope électronique, de feuilles minces de cuivre, les auteurs mettent en évidence les dislocations de macles et montrent leur association avec les macles de recristallisation. Bien que la plupart des propriétés de ces dernières puissent être expliquées sur la base des dislocations observées, l'origine des macles n'est pas encore bien déterminée.

ELEKTRONENMIKROSKOPISCHE UNTERSUCHUNG VON REKRISTALLISATIONS-ZWILLINGEN IN KUPFER

Dünne Kupferfolien wurden im Elektronenmikroskop durchstrahlt. Dabei wurden direkte Beweise für die Existenz von Zwillingsversetzungen und ihren Zusammenhang mit Rekristallisationszwillingen gefunden. Obwohl sich verschiedene Eigenschaften der Rekristallisationszwillinge mit Hilfe dieser Versetzungen erklären lassen, ist doch der Ursprung der Zwillinge noch nicht ganz aufgeklärt.

In preceding papers[1,2] it has been shown that non-coherent recrystallization-twin boundaries are the emergence points of a certain kind of imperfect dislocation, called a twinning dislocation. This has been shown by the formation of evaporation spirals at these points by the reversed spiral-growth mechanism of Frank.

In continuation of this work, efforts have been made to get direct evidence of these dislocations, by the use of transmission electron microscopy, in order to arrive at a better understanding of recrystallization twins.

EXPERIMENTAL TECHNIQUE

By 70–80 per cent cold-rolling, copper foils of about 0.025 mm thickness were produced and then electrolytically thinned until they were suitable for transmission electron microscopic work. Zone-refined copper with a purity of 99.995 per cent was used in most cases, but occasionally also 99.999 per cent copper from the American Smelting and Refining Company. Some of the copper foils were recrystallized in high-vacuo after cold-rolling and then thinned; the rest were thinned in the deformed state and after mounting on the grids were heated in high-vacuo in a metal boat, directly heated by current, between 600–1000°C for some seconds (flash heating). This method permits the production of small recrystallization nuclei in the thin foils in a controlled way. For both sets care was taken that only primary recrystallization take place, because only then can one obtain sufficiently small recrystallization twins.

The electrolytic thinning was usually carried out with the Jacquet electrolyte[3] but occasionally the Knuth–Winterfeld electrolyte *D2* was used with success. It was observed that the copper foils were attacked more strongly on the electrolyte–air interface than in the electrolyte itself, so that the foils became detached; the foils were therefore gradually pulled up during polishing. Only the last, pointed part of the foils was allowed to detach itself by continued polishing, and the fragments were attached to copper grids without adhesives.

EXPERIMENTAL RESULTS

In general a twin boundary shows up in the electron microscope as a set of fringes parallel to the direction of the boundary. These fringes have been explained in terms of the dynamic theory of electron diffraction.[4] As mentioned by Hirsch *et al.*[5] these fringes are not related to the structure of the twin boundaries because the spacing of the fringes changes on tilting the sample. However, at certain angles of the twin boundary with respect to the electron beam one can reach a stage where, superposed on these fringes, one can see the twinning dislocations, as is clearly shown in Fig. 1(a). In this micrograph a part of a recrystallization nucleus is seen to be surrounded by a strongly deformed matrix. Inside the nucleus a series of recrystallization twins are evident and the non-coherent boundaries of these twins are clearly visible as short black lines, representing the imperfect dislocations. That one is really dealing in this case with recrystallization twins becomes evident from

* Received March 14, 1960.

† European Research Association, s.a., Bruxelles 18, Belgium.



(a)



(b)

FIG. 1.

VOL.
8
1960



FIG. 2.

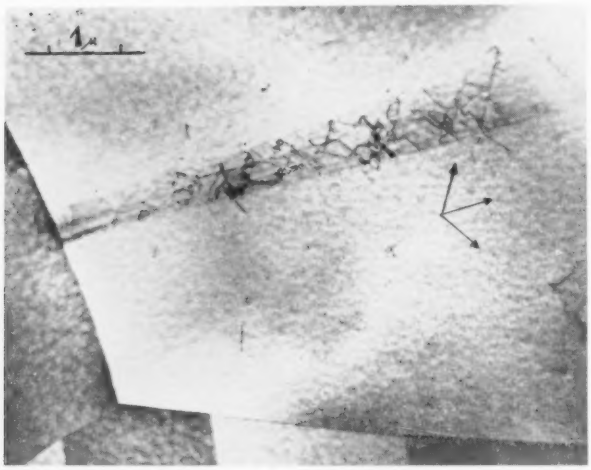


FIG. 3.

Fig. 1(b), which shows the same part of the sample at another tilting angle. The twin relation is demonstrated here by the difference in diffraction.

An additional noteworthy detail in Fig. 1(a) is the arrangement of the twinning dislocations in the two crossed twins in the left upper part of the micrograph. In this case the disolcations are bent from one twin plane to the other and thus build up corresponding non-coherent boundaries on the two different twin interfaces.

In general the dislocation structure is more complex than in this simple case where the twins have just formed. This can be seen on Fig. 2. At the place marked with an arrow a twinning dislocation is found partly surrounding the area of misfit. Other twinning dislocations on the interface are arranged at angles of 60° to one another. This angular relation is still more evident in Fig. 3, which shows a twin boundary in a completely recrystallized foil.

Up to now only cases have been discussed where the upper and lower part of the twinned crystal terminates on the surface. The most general case would be a twin completely embedded in the untwinned matrix, as seen in Fig. 4. In the left and right parts of this micrograph two twins have formed and these twins are separated from the untwinned matrix by twinning dislocations which are partly surrounding them. However, the left twin shows also dislocation networks at places where the twin changes its direction. This twin is probably composed

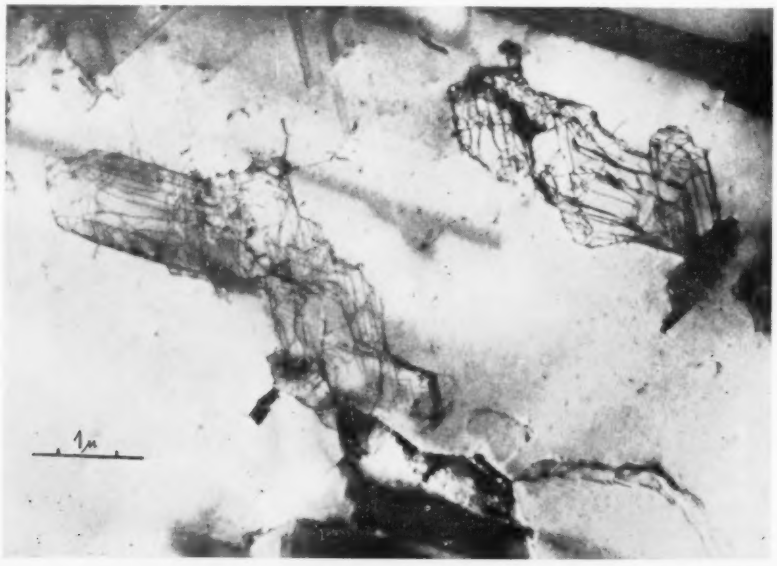


FIG. 4.

of two crystals with different orientation and the network is produced by the interaction of the twinning dislocations of the two twins. The pronounced cross-slip taking place in the vicinity of the different twins is also noteworthy (see Fig. 4).

CONCLUSION

These experimental results clearly demonstrate the association of twinning dislocations with recrystallization twins and also verify in a direct way our earlier observations.[1,2] Therefore the properties of recrystallization twins depend on the properties of the twinning dislocations. Thus, phenomena like the growth and disappearance of twins parallel to the (111)-twin plane, preferential etching of non-coherent twin boundaries in contrast to coherent boundaries,[6–8] or preferential precipitation on such places[9,10] are now explicable. Some other problems such as the origin of recrystallization twins still remain a matter of speculation,[11] and it cannot be decided on the basis of these results whether the mechanical nucleation hypothesis is more or less valid than the growth fault hypothesis.

VOL. 8 1960

ACKNOWLEDGMENTS

This work is part of a program sponsored by Union Carbide Corporation, New York, N.Y. The authors wish to thank Dr. R. H. Gillette, Director of E.R.A., for his constant interest in this work and Mr. Reynders for his valuable assistance.

REFERENCES

1. E. Votava, A. Berghezan and R. H. Gillette *Naturwissenschaften* **44,** 372 (1957).
2. E. Votava and A. Berghezan, *Acta Met.* **7,** 292 (1959).
3. P. A. Jacquet, *Rev. Mét.* **42,** 133 (1945).
4. M. J. Whelan and P. B. Hirsch, *Phil. Mag.* **2,** 1303 (1957).
5. M. J. Whelan, P. B. Hirsch, R. W. Horne and W.Bollmann, *Proc. Roy. Soc.* A**240,** 524 (1957).
6. P. Lacombe and N.Yannaquis, *C. R. Acad. Sci., Paris* **224,** 921 (1947).
7. N. Yannaquis and P. Lacombe, *C. R. Acad. Sci., Paris* **226,** 498 (1948).
8. G. Chaudron, P. Lacombe, N. Yannaquis, *C. R. Acad. Sci., Paris* **226,** 1372 (1948).
9. A. Berghezan, Doctoral Thesis, University of Paris (1952); *Publ. sci. Ministr. Air* No. 283, p. 29 (1953).
10. H. Hatwell and A. Berghezan, reported at *Conf. on Precipitation in Steel, Sheffield, July* 1958. *J. Iron Steel Inst. Spec. Rep.* No. 64 (1958).
11. J. E. Burke, *Trans. Amer. Inst. Min. (Metall.) Engrs.* **188,** 1324 (1950).

INFLUENCE OF PLASTIC DEFORMATION ON THE ANNEALING OF QUENCHED GOLD*

S. YOSHIDA† and J. S. KOEHLER‡

It is found that small amounts of plastic deformation greatly enhance the rate of annealing in gold quenched from 700°C. It is found that the activation energy of motion before deformation is 0.82 eV, whereas after deformation it is 0.64 ± 0.03 eV. Using the theory of Cochardt *et al.*[2] it is shown that this change can be understood by supposing that near a dislocation lattice vacancies prefer to exist as divacancies, since as divacancies there is a larger attractive interaction. The possibility of trapping defects of low symmetry near dislocations is discussed.

INFLUENCE DE LA DEFORMATION PLASTIQUE SUR LE RECUIT DE L'OR APRES TREMPE

De faibles pourcentages de déformation plastique ralentissent fortement la vitessee de recuit de l'or trempé à partir de 700°C. L'énergie d'activation qui, avant la déformation est de 0.82 eV, est devenue après 0.64 ± 0.03 eV. En utilisant la théorie de Cochardt *et al.*,[2] les auteurs montrent que cette modification peut s'interpréter en admettant qu'au voisinage d'une dislocation du réseau, les lacunes existent préférentiellement par paire: en effet, dans cette disposition il existe une interaction attractive plus élevée. Enfin, l'attraction des défauts de faible symétrie par les dislocations, est envisagée.

EINFLUß PLASTISCHER VERFORMUNG AUF DIE ERHOLUNG VON ABGESCHRECKTEM GOLD

Schon geringe plastische Verformungen beschleunigen die Erholung von Gold, das von 700°C abgeschreckt wurde, sehr. Vor der Verformung ist die Wanderungsenergie 0.82 eV, nach der Verformung 0.64 ± 0.03 eV. Mit Hilfe der Theorie von Cochardt u.a.[2] wird gezeigt, daß dieser Wandel auf Grund der Annahme verstanden werden kann, daß in der Nähe einer Versetzung die Leerstellen vorzugweise als Doppelleerstellen existieren; für Doppelleerstellen ist nämlich die anziehende Wechselwirkung größer. Die Möglichkeit, daß Defekte mit niedriger Symmetrie in der Nähe von Versetzungen eingefangen werden, wird diskutiert.

1. INTRODUCTION

Quenching experiments are among the simplest experiments in which non equilibrium defect concentrations are observed during annealing. In spite of this, unexpected features are observed; for example, in gold the annealing behavior of specimens quenched from 800°C and above differs markedly from that seen in specimens quenched from 700°C.[1] The present observations were also unexpected. However, we would like to suggest a possible way in which the observations can be understood.

2. EXPERIMENTS AND RESULTS

The experiments were designed to study the influence of plastic deformation on the annealing behavior of lattice vacancies. The 99.999% pure polycrystalline gold specimens were therefore quenched from 700°C. The specimens were of 0.40 mm diameter and were quenched into water (cooling rate 3×10^4 °C sec). All resistance measurements were made at liquid nitrogen temperature.

The annealing of an undeformed specimen was similar to that observed by Bauerle and Koehler[1]. In particular the quenched-in resistance decayed exponentially with time. The time τ required for the resistance to decay to one ith the original value was 150 hr on annealing at 40°C and 25 hr on annealing at 60°C. This gives an energy of motion of 0.82 ± 0.05 eV which is just Bauerle and Koehler's value.

In the deformation experiments after quenching the specimen wire was chucked at two positions each about 1 cm outside one of the potential leads and the specimen was pulled in tension at room temperature. Extensions ranged from 0.1 to 0.5 per cent. In a separate test experiment a well annealed specimen was deformed. An increase in the liquid nitrogen resistance was observed of an amount consistent with the change in specimen geometry. No annealing of this specimen was observed on holding at 40°C.

During the annealing after deformation the initial rate of decay was often found to be rapid, but after the initial transient the decay was exponential. The decay time τ was 30–35 hr on annealing at 40°C and 7–8.5 hr on annealing at 60°C. The activation energy for the motion of this defect was determined from the ratio of the decay rates at 40°C and 60°C. One finds $E_M = 0.64 \pm 0.03$ eV. Typical data are shown in Figs. 1 and 2. In plotting this data the resistance increase produced by deformation was subtracted from the values observed after deformation and during subsequent annealing.

* Research partially supported by the U.S. Office of Ordnance Research. Received March 18, 1960.

† National Research Institute for Metals, Tokyo, Japan.
‡ Department of Physics, University of Illinois.

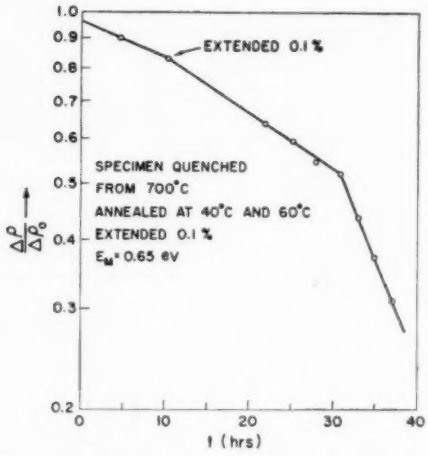


FIG. 1. Influence of deformation on the activation energy for motion of the defect. Specimen quenched from 700°C, annealed first at 40°C, extended 0.1 per cent, annealed at 40°C, then at 60°C.

3. SUGGESTED INTERPRETATION

The fact that the observed activation energy is less than that observed before deformation suggests that for some reason more divancies and perhaps more higher vacancy clusters exist in the deformed specimens than in the annealed specimens.

It is of interest to inquire why a deformed specimen should have a higher divacancy–vacancy ratio than an annealed specimen. This can be understood as follows: Divacancies have on the average a larger attractive interaction with dislocations than vacancies for two reasons: First, the relaxation around a divacancy is probably larger than that around a single vacancy. This results from the fact that the twelve atoms around a lattice vacancy support one another somewhat so that only limited inward relaxation occurs. In the case of the divacancy the four atoms which neighbor both vacancies have added freedom. This results in more relaxation of the entire structure. Secondly, the divacancy has axial rather than cubic symmetry. Now Cochardt *et al.*[2] in an excellent paper have shown that a defect having axial symmetry will have an elastic interaction with both edge and screw dislocations whereas a defect of cubic symmetry will only interact with edge dislocations. Their detailed calculation refers to interstitial carbon in body-centered cubic iron but one can use exactly the same methods to establish the above result for a divacancy in a face-centered cubic metal. The detailed calculation yields the following form for the intersection energy:

$$\varepsilon(r\theta) = \frac{A}{r} f(\theta)$$

where r is the distance to the dislocation and $f(\theta)$ is the other cylindrical coordinate which gives the position of the defect relative to the dislocation. One finds that:

$$\int_0^{2\pi} f(\theta) d\theta = 0.$$

In addition, the positions around the dislocation at which $f(\theta)$ has its maxima and minima differ for various orientations of the divacancy.

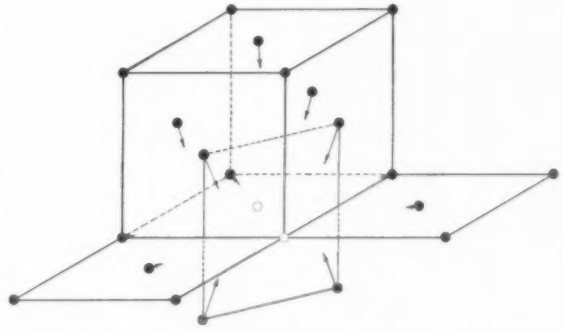


FIG. 3. The atomic relaxations near a divacancy in a face-centered cubic metal.

To make the discussion quantitative, it is first necessary to estimate the relaxations which occur in various directions near the divacancy. Two points stand out. First, the contraction of the four atoms which are nearest neighbors of both vacancies is very large. Secondly, the amount of relaxation is very anisotropic. Fig. 3 shows the atomic displacements in the vicinity of the divacancy. Note that even if the atoms were rigid spheres one would find that

$$a\varepsilon_1 = a\left(\frac{1}{2} - \frac{1}{2\sqrt{2}}\right) = 0.1464\, a$$

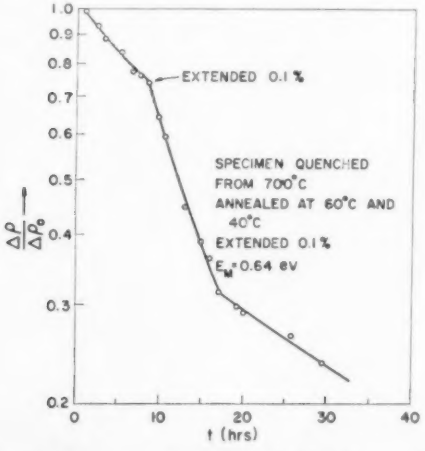


FIG. 2. Specimen quenched from 700°C, annealed first at 60°C, extended 0.1 per cent, annealed at 60°C, then at 40°C.

VOL. 8 1960

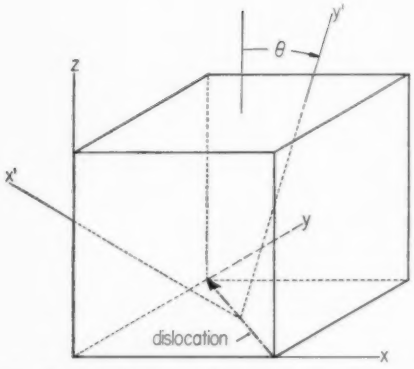


FIG. 4. Coordinates of a divacancy near a screw dislocation in a face-centered cubic metal. (The divacancy is on the y' axis.)

where a is the lattice parameter. Actually, one expects a slightly larger value. The contractions in the other directions should be small and they will be taken to be both equal to $\varepsilon_2 a$.

Consider the interactions of various divacancies with a screw dislocation along the $[\bar{1}10]$ direction (see Fig. 4). The interaction energies of the six different kinds of divacancies with this dislocation are:

$$U^S[101] = U^S[\bar{1}01] = -\frac{A(\varepsilon_1 - \varepsilon_2)\cos\theta}{r} \tag{1}$$

$$U^S[110] = U^S[\bar{1}10] = 0 \tag{2}$$

$$U^S[011] = U^S[0\bar{1}1] = +\frac{A(\varepsilon_1 - \varepsilon_2)\cos\theta}{r} \tag{3}$$

where θ is the angle the radius vector r makes with the [001] direction. One finds that:

$$A = \frac{Gba^3}{2\pi} \tag{4}$$

where G is the modulus of rigidity, b is the magnitude of the Burgers vector and a is the lattice parameter. The $[ijk]$ above refer to the direction of the divacancy axis. The material has been assumed to be elastically isotropic in this calculation, an assumption which is certainly not very good for gold. Since the relaxation around a divacancy is not very well known for gold, it is rather difficult to estimate the strength of the interaction. However, we will use $\varepsilon_1 = 0.170$ and $\varepsilon_2 = 0.020$. For a full screw dislocation one finds $A = 0.862 \times 10^{-19}$ erg cm (where we have taken $G = 2.78 \times 10^{11}$ dyn/cm^2). If a divacancy is three interatomic distances away from the center of the dislocation, the resulting attractive interaction using the above figures is 0.094 eV which is measureable.

If we consider an edge dislocation along a $[11\bar{2}]$ direction which has its Burgers vector along $[\bar{1}10]$,

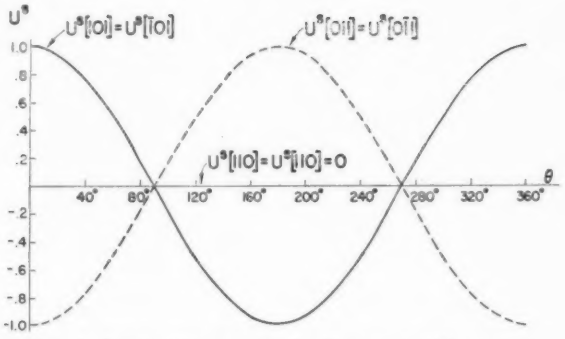


FIG. 5. Interaction energy of a divacancy with a screw dislocation as a function of the angle θ.

one finds that

$$U^E[101] = U^E[10\bar{1}] = -\frac{D\sin\phi}{6r} \times$$
$$[(5+2\nu)\varepsilon_1 + (7+10\nu)\varepsilon_2 + 2(\varepsilon_1 - \varepsilon_2)\cos^2\phi] + \frac{2D\cos\phi\cos 2\phi}{3r}(\varepsilon_1 - \varepsilon_2) \tag{5}$$

$$U^E[011] = U^E[0\bar{1}1] = -\frac{D\sin\phi}{6r} \times$$
$$[(5+2\nu)\varepsilon_1 + (7+10\nu)\varepsilon_2 + 2(\varepsilon_1 - \varepsilon_2)\cos^2\phi] - \frac{2D\cos\phi\cos 2\phi}{3r}(\varepsilon_1 - \varepsilon_2) \tag{6}$$

$$U^E[\bar{1}10] = U^E[110] = -\frac{D\sin\phi}{3r} \times$$
$$[(1+4\nu)\varepsilon_1 + (5+2\nu)\varepsilon_2 - 2(\varepsilon_1 - \varepsilon_2)\cos^2\phi] \tag{7}$$

where ϕ is the angle that the radius vector makes with the Burgers vector. For an isotropic elastic solid one finds:

$$D = \frac{Gba^3}{2\pi(1-\nu)}. \tag{8}$$

The largest attractive interaction (using Poissons's ratio, i.e. ν to be 0.42) occurs in equation (5) when $\phi \cong 70°$. The value is 0.246 eV when r is three interatomic distances. Hence, the binding energy to edge dislocations is more than twice that to screw dislocations. Moreover, the binding energy is large enough so that it will probably play a role in the annealing phenomena.

4. DISCUSSION

It should be noted that the interaction imposes certain restrictions on divacancy diffusion since changes from one type of divacancy to another may be associated with increases in the energy of the specimen. In Figs. 5 and 6 the interaction energy has been plotted against θ and ϕ respectively for given r.

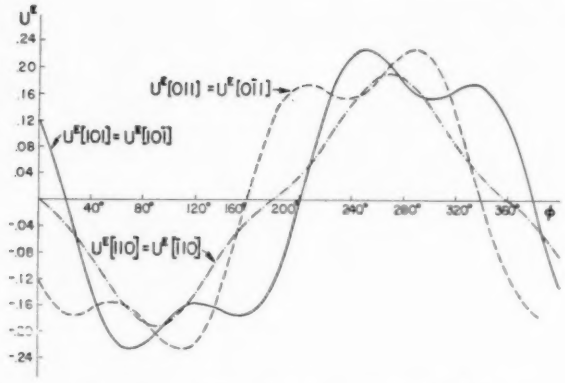


FIG. 6. Interaction energy of a divacancy with an edge dislocation as a function of the angle ϕ.

Note that a [101] divacancy, which is in the [001] direction from a screw dislocation running along [$\bar{1}$10], is associated with lowest energy for the given r. Since this divacancy must move by having one of its vacancies jump to an atomic site which is a nearest neighbor to both vacancies of the divacancy it can change to an [011], [0$\bar{1}$1], [110] or [$\bar{1}$10] divacancy. Note that any of these jumps will be discriminated against because they all involve an increase in the interaction energy of the system.

In the case of edge dislocations, a [101] type divacancy having ϕ in the region between 80° and 45° has lowest energy. It can, however, jump changing into a [$\bar{1}$10] or a [110] type without too large an increase in energy. Even when r is only three interatomic distances the increase is only 0.053 eV.

This restriction is much more serious in the case of carbon in iron where more than half of the angular positions around a screw dislocation give rise to trapped carbon atoms which cannot move without very materially raising their interaction energy (see Cochardt *et al.*[2]). Such interactions should be capable of very severely anchoring the dislocations in iron because a very large number of carbon atoms can take part. In fact, carbon atoms out to a distance such that the difference in energy between two orientations is an appreciable fraction of E_M (the activation energy required to move a carbon atom) are all involved in anchoring the dislocation. It should also be pointed out that carbon can also be trapped near an edge dislocation in iron (see Fig. 4 of Cochardt *et al.* where an [010] carbon atom is trapped if ψ is in the vicinity of 0°).

In any specimen there will be a region sufficiently near the dislocations so that $U(r,\phi)$ is large compared with the thermal fluctuations. In this region the energy of the system dislocation plus two vacancies will be lowered by $B^* = B - U(r,\phi)$ where B is the divacancy binding energy in a stress free region. Hence, if the divacancy is attracted to the dislocation, i.e. if $U(r,\phi)$ is negative the effective binding energy B^* is increased. Note also that the divacancies which are attracted toward the dislocation will be especially effective for annealing since the force field sweeps them in.

Let us now return to the experiments. In a well annealed specimen the fraction of the vacancies which are close enough to a dislocation to have B^* differ from B by more than kT is so small that the annealing is controlled by the energy of motion of a single vacancy. In the deformed specimens the average vacancy is closer to a dislocation and hence the interaction energy becomes more important.

It should of course be mentioned that in the deformed specimen the divacancy diffusion should be treated taking into account the influence of the interaction.

Detailed calculations aimed at giving the strength of the interaction are in progress. The influence of partial dislocations and the diffusion of divacancies in the force field of the dislocations should be investigated.

REFERENCES

1. J. E. BAUERLE and J. S. KOEHLER, *Phys. Rev.* **107**, 1493 (1957).
2. A. W. COCHARDT, G. SCHOEK and H. WIEDERSICH, *Acta Met.* **3**, 533 (1955).

VOL. 8 1960

DILUTE SOLUTIONS IN ALLOYS*

C. B. ALCOCK and F. D. RICHARDSON†

By a quasi-chemical approach an equation has been derived for the activity coefficient of a dilute solute in a mixture of two metals. This is simply related to the activity coefficients of the solute in each metal separately, and the separate activity coefficients of the metals in the mixture. The equation is an advance on that derived earlier for a random solution and in cases where the energies of interaction of the solute with the two metals differ widely, e.g. Fe + Al + O, it removes a significant source of error.

Application of the equation to data on sulphur and oxygen in various liquid alloys leads to the conclusion that the pairwise interaction energies of a solute atom with each of the surrounding metal atoms, may vary considerably with alloy composition. In the cases considered variations up to 50 per cent are necessary to account for the changes which occur in the activity coefficient of the solute when the atom fractions of the two components of the alloy vary from zero to unity.

LES SOLUTIONS DILUEES DES ALLIAGES

Par une méthode de calcul quasi-chimique, les auteurs établissent une équation donnant le coefficient d'activité d'un élément dissous à très faible teneur dans un mélange de deux métaux. Cette équation fait simplement intervenir les coefficients d'activité du soluté dans chacun des métaux et les coefficients d'activité de ces métaux dans le mélange. Elle présente un progrès sur celle établie précédemment pour une solution quelconque. Dans les cas où les énergies d'interaction du soluté avec les deux métaux diffèrent fortement, par exemple Fe + Al + O, elle élimine une source importante d'erreurs. L'emploi de cette relation aux données concernant le soufre et l'oxygène dans différents alliages liquides conduit à la conclusion que les énergies d'interaction de l'atome dissous avec chacun des atomes métalliques environnant peut varier considérablement avec la composition de l'alliage. Dans les cas étudiés, des variations jusque 50% sont nécessaires pour tenir compte des modifications du coefficient d'activité du soluté lorsque les fractions atomiques des deux compositions de l'alliage varient de 0 à l'unité.

VERDÜNNTE LÖSUNGEN IN LEGIERUNGEN

Eine quasichemische Näherung führt zu einer Gleichung für den Aktivitätskoeffizienten eines in einer Mischung zweier Metalle verdünnt gelösten Stoffes. Dieser wird einfach mit den Aktivitätskoeffizienten des gelösten Stoffes in jedem einzelnen Metall und mit den einzelnen Aktivitätskoeffizienten der Metalle in der Mischung verknüpft. Die Gleichung ist ein Fortschritt gegenüber der früher für eine statistische Lösung abgeleiteten Gleichung und sie beseitigt bedeutende Fehlerquellen in Fällen, bei denen die Wechselwirkungsenergien des gelösten Stoffes mit den beiden Metallen sehr verschieden sind, zum Beispiel Fe + Al + O.

Die Anwendung der Gleichung auf Daten von Schwefel und Sauerstoff in verschiedenen flüssigen Legierungen führt zur Folgerung, daß die paarweisen Wechselwirkungsenergien eines gelösten Atoms mit jedam der umgebenden Metallatome sich beträchtlich mit der Legierungszusammensetzung ändern kann. In den betrachteten Fällen sind Variationen bis zu 50% notwendig, um die Änderungen zu erklären, die bei den Aktivitätskoeffizienten des gelösten Stoffes auftreten, wenn die Molenbrüche der beiden Legierungskomponenten zwisch null und eins variieren.

In a recent paper[1] an equation was derived for the activity coefficient of a dilute solute, S, in an alloy of two metals, X and Y. This equation, which is given below, was based on the assumption that the distribution of atoms in the solution is random, that the co-ordination number of all three types of atoms is equal and that the energy of interaction between atom pairs is independent of concentration.

$$\ln \gamma_{S(X+Y)} = N_X \ln \gamma_{S(X)} + N_Y \ln \gamma_{S(Y)} - N_X \ln \gamma_{X(X+Y)} - N_Y \ln \gamma_{Y(X+Y)}. \quad (1)$$

For the same model the following equation was also derived,

$$\left[\frac{\partial \ln \gamma_{S(X+Y)}}{\delta N_Y}\right]_{N_Y \to 0} = \ln \gamma_{S(Y)} - \ln \gamma_{S(X)} - \ln \gamma_{Y(X)} \quad (2)$$

It was shown that with these equations, it was possible to predict with useful accuracy, the behaviour of dilute solutes in ternary solutions from data for the three binary systems concerned. The first equation was reasonably accurate in cases where the differences between $\ln [\gamma_{S(X)}/\gamma_{X(X+Y)}]$ and $\ln [\gamma_{S(Y)}/\gamma_{Y(X+Y)}]$ were less than unity. The second gave values of the interaction parameter ε, (defined by the first term in equation (2)) which were correct in sign, but between two and three times smaller than the measured values. It was suggested that these differences might be partly or entirely caused by clustering about the solute atoms, of that component of the alloy which interacted more strongly with the solute. It has subsequently been pointed out that an extreme example of clustering may occur in mixtures of iron and aluminium when oxygen is the solute. Gokcen and Chipman[2] have derived a value of -780 for ε from their measurements at 1760°C, whereas an estimate based on the likely thermodynamics of oxygen in

* Received January 28, 1960.

† Department of Metallurgy, Royal School of Mines, London, S.W.7.

aluminium, and the known properties of solutions of oxygen in iron and of aluminium in iron leads (*vide infra*) to values of the order of -10.

In an attempt to account for this behaviour, equations based on a quasi-chemical model have been derived. Oriani[3] has already indicated that the application of this model to binary *metal* mixtures* is not very helpful, for it leads to free energies of mixing which are little different from those calculated with the regular solution model. The major source of error in the regular model is probably the assumption that the energies of interaction between atom pairs are independent of the composition of the solution. This error remains in the quasi-chemical model and in most cases is likely to be greater than any error arising from the neglect of clustering. Nevertheless in certain ternary mixtures, particularly non-metals in metals, (such as Fe + Al + O mentioned above) the main error might conceivably arise from neglect of clustering, when there are great differences between the pairwise energies of interaction.

DERIVATION OF EQUATION

Let us consider the case of a dilute solute S in a mixture of X and Y, and assume that each atom interacts with the same number of nearest neighbours z, which would normally be taken equal to the co-ordination number. Thus in the melt there are $z(n_S + n_X + n_Y)/2$ atom–atom interactions or contacts. It will be assumed that the molar fraction of S is so small that the number of S–S contacts is negligible, and that the distribution of X and Y atoms is random except in the co-ordination shell around each S atom. If the number of Y–S contacts is represented by the symbol $n(Y\text{–}S)$ etc. it follows that

$$\frac{n(Y\text{–}S)}{n(X\text{–}S)} = \frac{N_Y}{N_X} \exp\,(w/zkT) \qquad (3)$$

where w/z is the energy change which occurs when a Y–S contact is changed to an X–S contact, by exchange of a Y atom in the co-ordination shell of the S atom with an X atom in the body of the melt.

From the equations given immediately below, it is clear that

$$w/zk = W/zR$$

where

$$W = \Delta\bar{H}_{S(X)} - \Delta\bar{H}_{S(Y)} - \Delta\bar{H}_{X(X+Y)} + \Delta\bar{H}_{Y(X+Y)}$$

$$\tfrac{1}{2}S_2 + \frac{z}{2}(X\text{–}X) = z(X\text{–}S) \qquad \Delta H = \Delta\bar{H}_{S(X)}$$

$$z(Y\text{–}S) = \tfrac{1}{2}S_2 + \frac{z}{2}(Y\text{–}Y) \qquad \Delta H = -\Delta\bar{H}_{S(Y)}$$

$$\frac{z}{2}(Y\text{–}Y) + \text{soln.} = Y \text{ in soln.} \qquad \Delta H = \Delta\bar{H}_{Y(X+Y)}$$

$$X \text{ in soln.} = \frac{z}{2}(X\text{–}X) \qquad \Delta H = -\Delta\bar{H}_{X(X+Y)}$$

and $(X\text{–}X)$, $(X\text{–}S)$ etc. represent atom–atom contacts. To a first approximation $RT \ln \gamma_{S(X)}$ etc. may be put equal to $\Delta\bar{H}_{S(X)}$ etc.

$$\frac{n(Y\text{–}S)}{n(X\text{–}S)} = \frac{N_Y}{N_X} \cdot \left[\frac{\gamma_{S(X)}\,\gamma_{Y(X+Y)}}{\gamma_{S(Y)}\,\gamma_{X(X+Y)}}\right]^{\frac{1}{z}} \qquad (4)$$

where N_X and N_Y obtain in the bulk of the solution. If the last term is put equal to K, we have for the mole fractions (N^0) of X and Y in the co-ordination shells around the solute atoms

$$N_X{}^0 = \frac{N_X}{KN_Y + N_X}, \quad N_Y{}^0 = \frac{KN_Y}{KN_Y + N_X}.$$

The heat change associated with the addition of n_S atoms of S to a large volume of $X + Y$ is then given by the equation

$$\begin{aligned}\Delta H = {} & \tfrac{1}{2}D \cdot n_S + n_S z \cdot N_X{}^0 E_{XS} + n_S z \cdot N_Y{}^0 \cdot E_{YS} \\ & - n_S \frac{z}{2}[N_X{}^0 N_X E_{XX} + (N_X{}^0 N_Y + N_Y{}^0 N_X)E_{XY} \\ & + N_Y{}^0 N_Y E_{YY}]\end{aligned}$$

where D is the dissociation energy of the solute such as O_2 or S_2, and E_{XX} etc. are the pairwise energies of interaction. When allowance is made for the fact, that $\Delta\bar{H}_{S(X)} = \tfrac{1}{2}D + zE_{XS} - \frac{z}{2}E_{XX}$, $\Delta\bar{H}_{S(Y)} =$ etc., it follows that

$$\begin{aligned}\Delta H = {} & n_S[N_X{}^0\Delta\bar{H}_{S(X)} + N_Y{}^0\Delta\bar{H}_{S(Y)} \\ & - N_X{}^0\Delta\bar{H}_{X(X+Y)} - N_Y{}^0\Delta\bar{H}_{Y(X+Y)}]\end{aligned}$$

where $\Delta\bar{H}_{X(X+Y)}$ and $\Delta\bar{H}_{Y(X+Y)}$ hold for the composition N_X and N_Y, and

$$\begin{aligned}\Delta\bar{H}_{S(X+Y)} = {} & N_X{}^0[\Delta\bar{H}_{S(X)} - \Delta\bar{H}_{X(X+Y)}] \\ & + N_Y{}^0[\Delta\bar{H}_{S(Y)} - \Delta\bar{H}_{Y(X+Y)}].\end{aligned}$$

$\Delta\bar{G}_{S(X+Y)}$ can be obtained by integration of this equation, according to the general relationship,

$$\frac{\partial\left(\frac{(\Delta\bar{G})}{T}\right)}{\partial T} = -\frac{\Delta\bar{H}}{T^2}.$$

* In which the heats of mixing do not normally exceed a few kcal.

VOL. 8 1960

One then obtains, after converting partial heats to activity coefficients,

$$\frac{\Delta\bar{G}_{S(X+Y)}}{RT} = N_X^0 \ln\frac{\gamma_{S(X)}}{\gamma_{X(X+Y)}} + N_Y^0 \ln\frac{\gamma_{S(Y)}}{\gamma_{Y(X+Y)}} + zN_X^0 \ln\frac{N_X^0}{N_X} + zN_Y^0 \ln\frac{N_Y^0}{N_Y} + \ln N_S$$

where N_S the atom fraction of solute in the solution is much less than 1. The first two terms represent $\Delta\bar{H}_{S(X+Y)}/RT$ and the last three $\Delta S_{S(X+Y)}/R$. The last term is the ideal partial entropy of solution and the third and fourth terms are the excess entropy of solution arising from the fact that N_X^0 is not equal to N_X.

It follows that,

$$\ln\gamma_{S(X+Y)} = \frac{N_X}{KN_Y+N_X}\ln\frac{\gamma_{S(X)}}{\gamma_{X(X+Y)}} + \frac{KN_Y}{KN_Y+N_X}\ln\frac{\gamma_{S(Y)}}{\gamma_{Y(X+Y)}} + z\frac{N_X}{KN_Y+N_X}\ln\frac{1}{KN_Y+N_X} + z\frac{KN_Y}{KN_Y+N_X}\ln\frac{K}{KN_Y+N_X}. \quad (5)$$

With the substitution $\alpha = 1/(KN_Y+N_X)$, $\beta = K/(KN_Y+N_X)$, equation (5) can be simplified to

$$\ln\gamma_{S(X+Y)} = \ln\frac{\gamma_{S(X)}}{\gamma_{X(X+Y)}} + z\ln\alpha = \ln\frac{\gamma_{S(X)}}{\gamma_{X(X+Y)}} - z\ln(KN_Y+N_X) \quad (6),*$$

whence

$$\frac{\partial\ln\gamma_{S(X+Y)}}{\partial N_Y} = \frac{\partial\ln\gamma_{S(X)}}{\partial N_Y} - \frac{\partial\ln\gamma_{X(X+Y)}}{\partial N_Y} - \frac{z\left(K-1+N_Y\dfrac{\partial K}{\partial N_Y}\right)}{KN_Y+N_X}.$$

The activity coefficents of solute in X and Y are constant and the activity coefficients of X and Y are independent of N_Y, as N_Y tends to 0 or unity. Thus

$$\frac{\partial\ln\gamma_{S(X)}}{\partial N_Y} = \frac{\partial\ln\gamma_{X(X+Y)}}{\partial N_Y} = \frac{\partial K}{\partial N_Y} = 0$$

and

$$\left[\frac{\partial\ln\gamma_{S(X+Y)}}{\partial N_Y}\right]_{N_Y \text{ or } N_X\to 0} = \varepsilon = \frac{-z(K-1)}{N_X+KN_Y}. \quad (7)*$$

By rewriting equation (6) and simplifying the resulting expression, it can be shown that

$$N_X\left[\frac{\gamma_{X(X+Y)}}{\gamma_{S(X)}}\right]^{1/z} + N_Y\left[\frac{\gamma_{Y(X+Y)}}{\gamma_{S(Y)}}\right]^{1/z} = \left[\frac{1}{\gamma_{S(X+Y)}}\right]^{1/z} \quad (8)$$

when $N_X \pm N_Y \sim 1$.

The following equation, which was obtained by Wagner[4] for the solubility, M, of a dilute solute at constant activity in a Raoultian binary solvent, is a particular solution of this equation.

$$[M_{S(X+Y)}]^{1/z} = N_X[M_{S(X)}]^{1/z} + N_Y[M_{S(Y)}]^{1/z}. \quad (9)$$

Because the activity coefficients in equation (8) may be related to partial molar heats, e.g.

$$\gamma_{S(X+Y)} = \exp\left[\frac{\Delta\bar{H}_{S(X+Y)}}{RT}\right],$$

the equation can be expressed in the form

$$\exp-\left[\frac{\Delta\bar{H}_{S(X+Y)}}{zRT}\right] = N_X\exp-\left[\frac{\Delta\bar{H}_{S(X)}-\Delta\bar{H}_{X(X+Y)}}{zRT}\right] + N_Y\exp-\left[\frac{\Delta\bar{H}_{S(Y)}-\Delta\bar{H}_{Y(X+Y)}}{zRT}\right].$$

If the exponentials are expanded and all except the first terms are ignored, i.e. it is assumed that $\Delta\bar{H}_{S(X+Y)}$, $\Delta\bar{H}_{S(X)}-\Delta\bar{H}_{X(X+Y)}$ and $\Delta\bar{H}_{S(Y)}-\Delta\bar{H}_{Y(X+Y)}$ are all small compared with zRT, the equation reduces, as one would expect, to the form,

$$\ln\gamma_{S(X+Y)} = N_X\ln\frac{\gamma_{S(X)}}{\gamma_{X(X+Y)}} + N_Y\frac{\ln\gamma_{S(Y)}}{\gamma_{X(X+Y)}}$$

which is identical with equation (1).

DISCUSSION

It is interesting to compare the values of ε calculated from equations (2) and (7) for a case where the energies of interaction between the dilute solute and the two metals differ greatly. The only extreme case for which any relevant data exist is the system Fe + Al + O. As mentioned above, Chipman has derived a value of −780 for ε at 1760°C from experiment and this is probably correct to ±50 per cent. From measurements of the activity coefficient of

* N_Y, the concentration of Y outside the co-ordination shells of S, is effectively equal to the atom fraction of Y over the entire solution if

$$-N_S\varepsilon \ll 1 \quad \text{or} \quad N_Y \gg zN_S$$

and this is so for the solutions considered in this paper.

* See footnote on previous column.

TABLE 1

System*	Temp. (°C)	Values of ε			Interchange energy (cal)	
		Exptl.	Quasi-chemical	Random	Exptl.	Quasi-chemical
Cu[S + Fe]	1500	−4.6	−3.5	−3.0	−1,620	−1,290
Fe[S + Cu]	1500	−0.8	−2.5	−1.6	−360	−1,300
Fe[O + Al]	1760	−780	−17	−9	−18,600	−4,600
Fe[O + Ni]	1600	+0.5 to 0.9	+3.1	+4.6	+240	+2,440
NI[O + Fe]	1600	−7.4	−3.7	−2.8	−2,420	−1,400
Fe[O + Co]	1600	+1.7	+2.4	+2.9	+870	−1,350
Co[O + Fe]	1600	−3.5	−3.5	−2.9	−1,350	+1,350

* The element outside the square brackets corresponds to element "X" in equation (7).

aluminium in iron[5] it is evident that $\Delta\bar{H}_{Al(Fe)}$ is not likely to be much more negative than −13 kcal. The value of $\Delta\bar{H}_{O(Al)} - \Delta\bar{H}_{O(Fe)}$ is not likely to differ greatly from −50 kcal, which is the difference between the chemical potentials of oxygen, per gram atom, in equilibrium with Fe + FeO and of Al + Al_2O_3. If z is taken as 8, equation (7) gives a value of 3.2 for K at 1600°C, and a value of −17 for ε. The latter is nearly twice the value which would be obtained for ε from equation (2). The quasi-chemical value of ε is markedly influenced by the choice of co-ordination number: it would, for example, become −36 if z were taken as 4, with the same values for the partial molar heats. It is evident that although equation (7) looks a better proposition than equation (2), it falls far short of accounting for the experimental value of ε.

The values of ε which can be derived from equations (2) and (7) for the system Cu + Fe + S, may be compared with the experimental values that are available.[1] The results for $z = 8$ are given in Table 1. The values of log γ_S which can be calculated by the application of equation (6) assuming $z = 8$ are indicated by the broken curve in Fig. 1. The full line represents the experimental results. The values calculated from equation (1) lie slightly above the broken line but never more than 0.015 from it.

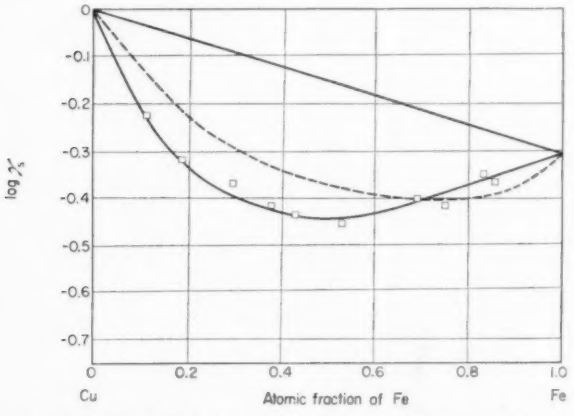


FIG. 1. The activity coefficients of sulphur at high dilution in alloys of iron and copper. Full line: experimental values at 1500°C; broken line: values derived from equation (6).

Attention has been drawn elsewhere[1] to the fact that the behaviour of oxygen in iron–nickel alloys is different from that given by equation (1). According to this equation ln γ_O should deviate from the full straight line shown in Fig. 2 by an amount equal to $\Delta G^{XS}/RT$ for the Fe + Ni system. This function, the negative of which is plotted at the base of the figure, can be derived from the activity measurements of Zellars *et al.*[6]. The oxygen activity coefficients obtained experimentally by Chipman and Wriedt[7] are represented by the full curve A. The two broken curves show the values calculated from equation (8) for different values of z, 8 (curve C) and 2 (curve D).

From the data so far considered, one is forced to the conclusion that although the quasi-chemical

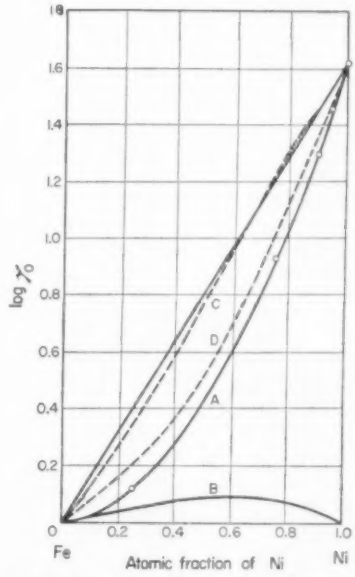


FIG. 2. The activity coefficient of oxygen at high dilution in alloys of iron and nickel at 1600°C. Full lines: A, experimental values of Chipman and Wriedt[7] B, $-\Delta G^{XS}/RT$ for Fe + Ni from Zellars *et al.*[6]; broken lines: C, values from equation (6) with $z = 8$, D, values with $z = 2$, to show effect of changing z by an extreme amount.

VOL. 8 1960

equation (8) with z equal to the co-ordination number (i.e. about 8) appears to be a slight improvement on equation (1), it often falls far short of accounting for the measured values of ε. One or all of the following would seem to be possible reasons for the discrepancies.

(a) The energies associated with the pairwise interactions between the atoms of the ternary may differ from those for the three separate binaries.

(i) The solute–solvent interactions may vary with the proportions of each solvent atom about the solute.

(ii) The interactions between unlike neighbouring solvent atoms in the co-ordination shell around each solute atom may be different from those between unlike solvent atoms in the remainder of the solution.

Experimentally, (i) and (ii) are not likely to be distinguishable.

(b) The co-ordination number for the solute z_S may be different from those for the other atoms of the solution: in that event the third and fourth terms on the right hand side of equation (1) would have to be increased or decreased according to whether z_S is greater or less than z. In equation (4) the two solute activity coefficients would have to be raised to the power z/z_S.

(c) The number of strong pairwise interactions about any solute atom may be much less than the co-ordination number.

The most reasonable explanations seem to lie in (a,i) and (a,ii). The values of ε found experimentally in the case of Fe + Ni + O are about +0.5 in nearly pure iron and −7.4 in nearly pure nickel. One thus concludes that the value of W/z, the energy change (per gram mole) associated with altering a nickel + oxygen contact in the alloy to an iron + oxygen contact, varies from −240 cal in nearly pure iron to −2420 cal in nearly pure nickel, when $z = 8$. The values calculated from the equation

$$W/z = -\frac{RT}{z} \ln \frac{\gamma_{O(Ni)}}{\gamma_{O(Fe)}} \frac{\gamma_{Fe(Ni)}}{\gamma_{Ni(Fe)}} = -RT \ln K \quad (10)$$

are −2440 cal at the iron limit and −1400 cal at the nickel limit. In order to account for the difference in the iron rich alloys one can suppose–possibility (a,i) for example—that the introduction of a nickel atom into the co-ordination shell of the oxygen results in the strengthening of the remaining seven iron + oxygen contacts by 310 cal apiece: alternatively the nickel + oxygen contact may be strengthened by 2200 cal in the presence of seven iron atoms or both contact energies in the alloy may differ from their values in the separate metals. Correspondingly in nearly pure nickel, each nickel + oxygen contact may be strengthened by some 150 cal when a single iron atom enters the co-ordination shell of the oxygen; alternatively the single iron may be bonded to the oxygen 1020 cal more strongly than when it is in company with seven other iron atoms, or again both contact energies may be altered together.

Of these possibilities the simplest appear to be the second in each case. In any event the changes which have to be assumed in the metal + oxygen interaction energies—or metal + metal interaction energies, if the differences are attributed to (a,ii) instead of (a,i)—are not unreasonable in comparison with the total energies: these are −20,000 ± 2000 cal for each O + Fe or O + Ni contact. These may be calculated from the heats of solution of oxygen in iron and nickel,* if z is taken as 8 and allowance is made for the dissociation energy of oxygen, and the energies of the metal + metal contacts which can be derived from the heats of vaporisation. It is of interest to note that a linear relationship between the Fe + O and Ni + O contact energies, and the atom fractions of Fe and Ni is not compatible with the experimental results. One possible relationship, but not the only one, can be derived by taking tangents and intercepts in Fig. 2.

This requires that,

$$N_{Ni}\left(\frac{\partial E_{Ni\text{–}O}}{\partial N_{Ni}}\right) = -N_{Fe}\left(\frac{\partial E_{Fe\text{–}O}}{\partial N_{Ni}}\right)$$

where $E_{Ni\text{–}O}$ etc. are the contact energies.

Variation of the pairwise interaction energies between solute and metal atoms could also reasonably account for the great difference between the calculated and experimental values of the system, Fe + Al + O. If z is again taken as 8, the pairwise Al–O interaction energy when only one aluminium atom (and seven iron atoms) are associated with the oxygen would have to be 14,000 cal more negative than when the oxygen is surrounded entirely by aluminium.† This increase may be compared with an estimated value of −26,000 cal for the Al–O pairwise interaction energy in pure aluminium. On the other hand possibility (c) might apply in this case and in other cases where there is a very great difference between the affinities of the two solvent metals for the dilute solute.

---

* −27,900 and −14,310 cal, respectively.

† It is interesting to note that this value leads to nearly the same variation of ε with temperature as reported by Gokcen and Chipman. Because in their experiments N_O was about 10^{-4}, N_{Al} about 3×10^{-4} and ε about −800, N_{Al} for the entire solution would be rather more than N_{Al} outside the co-ordination shells of the oxygen atoms. It can be shown that this would make the measured value for ε smaller than the theoretical value by only some 10 per cent.

The assumption that the energies associated with the interactions vary with composition does not affect the validity of the calculation of limiting values for K and W/z from ε. When the concentration of one component of the alloy tends to zero, the values of the energies for the two pairwise solute–metal interactions must become constant, because the only possible co-ordination shells about the solute atoms are those containing z of one component only or $z - 1$ of one component and 1 of the other. Thus the conditions for passing from equation (6) to equation (7) are still maintained.

Possibility (a) is an acceptable explanation for the data for the solutions Cu + Fe + S shown in Fig. 1. In this case, however, a co-ordination number for sulphur which is equal to that of the metal atoms in the iron rich solutions and is 1.5 × as great in the copper rich solutions, is an alternative conceivable explanation. Values of W/z are also given for some of the other solutions in Table 1.

The activity coefficients of oxygen in cobalt and two iron + cobalt alloys have been measured by Floridis and Chipman[8] at 1600°C. These agree more closely with values derived from the quasi-chemical equation (the activity coefficients of Co and Fe being taken as unity) than do those for oxygen in iron + nickel mixtures. The extent to which the pairwise interaction energies change with composition is therefore variable, depending presumably on the chemical properties of the components of the solution. The next task would seem to be to relate these changes in interaction energy with the positions of the components in the periodic table.

REFERENCES

1. C. B. Alcock and F. D. Richardson, *Acta Met.* **6,** 385 (1958).
2. N. Gokcen and J. Chipman, *Trans. Amer. Inst. Min. (Metall.) Engrs.* **197,** 173 (1953).
3. R. A. Oriani, *National Physical Laboratory Symposium No.* 9, Paper 2A H.M. Stationery Office, London (1959).
4. C. Wagner, *Thermodynamics of Alloys.* Addison-Wesley, Reading, Mass. (1952).
5. J. Chipman and T. P. Floridis, *Acta Met.* **3,** 456 (1955).
6. G. R. Zellars, S. L. Payne, J. P. Morris and K. L. Kipp, *Trans. Amer. Inst. Min. (Metall.) Engrs.* **215,** 181 (1959).
7. J. Chipman and H. A. Wriedt, *Trans. Amer. Inst. Min. (Metall.) Engrs.* **206,** 1195 (1956).
8. T. P. Floridis and J. Chipman *Trans. Amer. Inst. Min. (Metall.) Engrs.* **212,** 549 (1958).

VOL. 8 1960

ACTIVITIES OF MANGANESE IN SOLID PLATINUM*

K. P. ABRAHAM, M. W. DAVIES, J. L. BARTON and F. D. RICHARDSON†

The activities of manganese in solid alloys of manganese and platinum have been measured at 1500° and 1650°C. The activity coefficients range from 1.3×10^{-5} and 3.2×10^{-5} at extreme dilution to 6.0×10^{-4} and 1.4×10^{-3} at 25 at.% manganese. $\Delta\bar{H}_{Mn}$ is about −40 kcal.

ACTIVITIES DU MANGANESE DANS LE PLATINE SOLIDE

Les activités du manganèse dans les alliages solides de manganèse et de platine sont mesurées à 1500° et 1650°C. Les coefficients d'activité s'étalent de $1,3 \times 10^{-5}$ et $3,2 \times 10^{-5}$ pour une dilution maximum jusque $6,0 \times 10^{-4}$ et $1,4 \times 10^{-3}$ pour une concentration atomique de 25% en manganèse. ΔH_{Mn} est voisin de −40 Kcal.

AKTIVITÄT VON MANGAN IN FESTEM PLATIN

Die Aktivität von Mangan in festen Mangan-Platin-Legierungen wurde bei 1500°C und 1650°C gemessen. Die Aktivitätskoeffizienten reichen von 1.3×10^{-5} und 3.2×10^{-5} bei extremer Verdünnung bis zu 6.0×10^{-4} und 1.4×10^{-3} bei 25 Atom% Mangan. ΔH_{Mn} hat etwa den Wert −40 kcal.

In the course of measurements of the activities of manganese oxide in silicate melts at high temperatures, it became necessary to determine the activities of manganese in its solid alloys with platinum at 1500° and 1650°C and at concentrations up to about 25 at.%. The only information at present available on the Mn + Pt system is the phase diagram which has been investigated by Nemilov *et al.*[1] and Raub and Mahler[2].

The technique adopted was to measure the manganese taken up by solid platinum, when brought into equilibrium with pure manganese oxide at controlled partial pressures of oxygen, ranging from 10^{-7} to 10^{-3} atm. Account has to be taken of the non-stoichiometry of manganous oxide which has already been established.[3]

EXPERIMENTAL

Materials

Manganous oxide. The oxide was prepared by dissolving electrolytic manganese (99.99 per cent) in concentrated nitric acid and evaporating the solution to dryness. The residue of pure manganese dioxide was baked at 200°C for 1 hr, crushed and then reduced to green manganous oxide by heating in a stream of hydrogen at 1100°C for 2 hr. Analysis showed the oxide to be virtually stoichiometric.

Platinum strips. Foil 0.002 in. thick (99.98 per cent) was used.

Containers. Platinum cups 1 cm in diameter and 3 mm deep were made from foil 0.005 in. thick. They held about 0.5 g of oxide, and were supported in trays made from alumina cement.

Gas mixtures. Mixtures of H_2, CO_2 and oxygen-free N_2 were used, the proportions being adjusted to give the oxygen potentials required at the temperature of the experiments. The gases were taken from cylinders and dried by passage through magnesium perchlorate. Mixing was controlled by capillary flow meters containing *n*-dibutylphthalate.

Equilibrium apparatus. This was similar to that used by Fincham and Richardson[4] except for slight modifications. The molybdenum winding of the furnace was supported on a separate alumina tube, within which the reaction tube was held. The control thermocouple was inserted between the furnace tube and the reaction tube, the hot junction being at a point about 120°C cooler than the hottest zone, so as to lengthen its useful life. The flowing gases (about 600 ml/STP/min) were made to leave from both ends of the reaction tube so as to eliminate any possible lack of control in the gas composition which might arise from the dead space between the end of the gas inlet tube and the end of the reaction tube.

Procedure. Strips of platinum 1.25 in. long and 0.1 in. wide were wound into open spirals. One was placed in each of four platinum cups, which were then filled with pure manganous oxide. The four cups were mounted in the alumina tray.

The furnace was brought to the required temperature and the reaction tube flushed with a stream of nitrogen. With the nitrogen still flowing, the tray of cups was put into the reaction tube and pushed slowly into the central even-temperature zone. The nitrogen was passed for a further 15 min before the controlled gas mixture ($CO_2 + H_2 + N_2$) was allowed to enter. Nine hours were required to bring the platinum to equilibrium with the solid oxide at both

* Received February 12, 1960.

† Nuffield Research Group in Extraction Metallurgy, Imperial College, London.

TABLE 1

Temp. (°C)	pO_2	Wt. % Mn (mean)	No. of samples	No. of separate expts.	N_{Mn} (mean)	log γ_{Mn}
1500	10^{-4}	2.28	4	2	0.077	−4.384
1500	10^{-5}	3.77	3	2	0.123	−4.079
1500	10^{-6}	5.58	3	2	0.174	−3.721
1500	10^{-7}	7.92	3	2	0.234	−3.347
1650	10^{-3}	2.30	4	2	0.077	−3.994
1650	10^{-4}	3.87	3	2	0.125	−3.695
1650	10^{-5}	5.87	3	2	0.182	−3.343
1650	10^{-6}	7.97	4	2	0.236	−2.949

Errors:
Temperature, reading and calibration of optical pyrometer: ±6° C.
Ingoing gas composition, calibration and reading of flowmeters: ±1 per cent.
Analysis. Mn in the alloy: ±1 per cent.

temperatures, so the experiments were normally run for periods of 9–12 hr.

At the end of each experiment, the mixed gases were turned off and the reaction tube again flushed with nitrogen. The oxide samples were pulled rapidly into the water cooled end of the reaction tube and allowed to cool. The platinum spiral was separated from the oxide and cleaned by rubbing on 00 emery paper. It was then examined under a binocular microscope and any remaining traces of the oxide scraped off.

Analysis

The platinum manganese alloy was dissolved in *aqua regia* and evaporated to dryness. The residue was treated with concentrated sulphuric acid and heated until fuming started, in order to drive off HCl. The product was dissolved in water. The manganese was oxidized to permanganate by KIO_4 and finally measured colorimetrically with a Unicam spectrophotometer.

RESULTS

The results obtained are listed in Table 1.

DISCUSSION

The values of the activity coefficient of manganese listed in Table 1, have been calculated by application of the equation

$$\log \gamma_{Mn} = \log \frac{a_{MnO}}{p^{1/2}O_2 . N_{Mn}} + \frac{\Delta G^\circ_T}{2.303\, RT}.$$

Here pO_2 and N_{Mn} are measured values, and a_{MnO} is the activity of stoichiometric MnO in the oxide, which is non-stoichiometric when pO_2 exceeds 10^{-9} atm: this activity has already been measured by Davies and Richardson[3]. ΔG°_T is the free energy of formation of one mole of stoichiometric MnO from solid manganese and oxygen, the values being derived by extrapolation above 1244°C of the ΔG° values calculated by Coughlin[5] from heat of formation and heat capacity data.

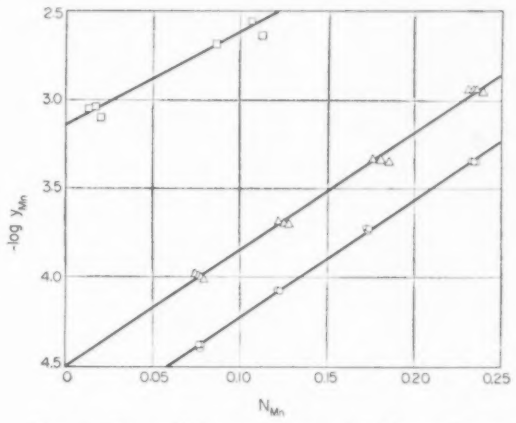


FIG. 1. The activity coefficient of solid manganese in solid Mn + Pt alloys at 1500° ○ and 1650°C △. The top line ⊡ shows on the same scale, values for the activity coefficient of liquid iron in solid Fe + Pt alloys at 1550°C as measured by Larson and Chipman[6].

Log γ_{Mn} is shown as a function of composition in Fig. 1. The points represent the individual values for the different samples and not the mean values given in Table 1; the reproducibility of the results can thus be clearly seen. Any error in ΔG°_T for MnO would influence the calculated activity coefficients. Coughlin estimates this error to be ±150 cal at 298°K: at about 1600°C, ±250 cal is more likely, and this would give rise to an error of ±0.031 in log γ. The sources of error listed earlier would contribute a further error of ±0.022 to log γ, and the possibility of 0.01 per cent O_2 in the CO_2 might bring in an additional error of 0.05 on log $p^{1/2}O_2$ at the highest oxygen pressures, and a far smaller one at the lowest. The error in the logarithms of the activity of manganese oxide in the non-stoichiometric oxide might reasonably amount to 0.02. It would thus appear that the values of log γ are correct to about 0.05 and γ is correct to about ±10 per cent.

Also shown in Fig. 1 are some of the results obtained by Larson and Chipman[6] for iron in solid platinum at 1550°C. Liquid is the standard state but because 1550°C is so near its melting point, the activity coefficients of solid iron are indistinguishable from the values shown. The linear relation between log γ and atom fraction which Larson and Chipman found to hold from 0 to 0.2 atom fraction of iron appears to hold for manganese also.

Extrapolation to infinite dilution gives an activity coefficient for manganese of 1.26×10^{-5} at 1500°C and 3.16×10^{-5} at 1650°C. These values are some 10 times smaller than those for iron in platinum. The heat of solution of solid manganese in solid platinum can be calculated from the variation of log γ_{Mn} with temperature. In view of the fact that the lines for

VOL. 8 1960

TABLE 2

Atom fraction of Mn	Activities			
	1500°C		1650°C	
	a_{Mn}	a_{Pt}	a_{Mn}	a_{Pt}
0.05	1.38×10^{-6}	0.93	3.34×10^{-6}	0.93
0.10	5.89×10^{-6}	0.83	1.43×10^{-5}	0.83
0.15	1.91×10^{-5}	0.70	4.59×10^{-5}	0.70
0.20	5.52×10^{-5}	0.56	1.29×10^{-4}	0.57
0.25	1.49×10^{-4}	0.42	3.45×10^{-4}	0.42

manganese are almost parallel, $\Delta\bar{H}_{Mn}$ is approximately constant and equal to -39 ± 7 kcal g-atom^{-1} over the range of compositions, which all lie within the α region.[2] The value of $\Delta\bar{G}^{xs}{}_{Mn}$ at 0.08 Mn and 1500°C, is -35.4 ± 0.3 kcal. The agreement between these two values indicates that the values of $\Delta\bar{S}_{Mn}$ may not be far from ideal at this composition. In so far, however, as $\Delta\bar{G}^{xs}{}_{Mn}$ becomes less negative as the concentration of Mn increases (-27.2 ± 0.03 kcal at a Mn of 0.23) whilst $\Delta\bar{H}_{Mn}$ remains about the same, $\Delta\bar{S}_{Mn}$ may become greater than ideal at higher concentrations and less than ideal at lower. The precision of the measurements does not justify further calculations of partial properties. Activities for platinum can be derived by extrapolating the values of log γ_{Mn} linearly to zero manganese and then making a Gibbs–Duhem integration. The values obtained are given in Table 2.

ACKNOWLEDGMENT

The authors wish to thank the British Iron and Steel Research Association for financial support of this and related work and for bursaries for K. P. A. and M. W. D.

REFERENCES

1. V. A. NEMILOV, T. A. VIDUSOVA and M. N. PIVOVAROVA, *Izv. Akad. Nauk. SSSR Ser. Khim.* p. 743 (1937).
2. E. RAUB and W. MAHLER, *Z. Metallk.* **46,** 282 (1955).
3. M. W. DAVIES and F. D. RICHARDSON, *Trans. Faraday Soc.* **55,** 604 (1959).
4. C. J. B. FINCHAM and F. D. RICHARDSON, *Proc. Roy. Soc.* A**223,** 40 (1954).
5. J. P. COUGHLIN, *Bull. U.S. Bur. Min.* No. 542 (1954).
6. H. R. LARSON and J. CHIPMAN, *Acta Met.* **2,** 1 (1954).

Stress induced ordering in gold–silver alloys*

The preliminary work described here was undertaken to determine if stress induced ordering could be observed in a system whose components have the same valence and essentially the same size. The purpose of this letter is to report the unexpected existence of stress induced ordering in several concentrations of the AuAg system. Internal friction studies have been made on a number of systems which exhibit a Zener peak (attributed to stress induced ordering). Lulay and Wert[1] point out, however that even with all the data so far available it is difficult to establish criteria for the existence and magnitude of the effect in terms of the other facts known about a given alloy system. The first explanation, presented by Zener[2], interpreted the effect as being due to a preferential orientation of atom pairs under the applied stress, to relieve partially the strain resulting from the different sizes of solute and solvent atoms. LeClaire and Lomer[3] have developed a theory which takes the solution to be ideal and considers only interactions with nearest neighbors. The work of Seraphim and Nowick[4] indicates that this theory must be modified. Nevertheless it satisfactorily accounts for the differences in the effect determined by the relaxation strength of the CuZn, CuAl, and AgZn systems.

The theory of LeClaire and Lomer states that the relaxation time is proportional to the rate of change of lattice spacing with concentration. For a system whose components have essentially the same size there will be a negligible change in lattice spacing with concentration. Consequently, on the basis of current theory one does not expect to see a Zener peak in such a system.

The selection of the AuAg system to test this conclusion was at the suggestion of Professor Lawrence Slifkin. The positive result of this test is even more significant because the availability of internal friction data, coupled with diffusion data can lead to a better understanding of small scale atomic movements. To this end the AuAg system is indeed ideal and not subject to the limitations pointed out by Childs and LeClaire[5]. For the solid solution exists over the entire range of concentrations, and reliable thermodynamic and physical data are available for each pure component and various alloy concentrations.

The data presented were obtained employing an inverted torsion pendulum for relaxation measurements of the order of one second and an elastic-after-effect apparatus for measurements of the order of 1000 sec. This equipment is similar to the conventional type described by Wert[6]. The 0.030 in. samples were maintained in a vacuum of approximately 10^{-5} mm of Hg, and the temperature difference over their 9 in. length was 1 C° or less.

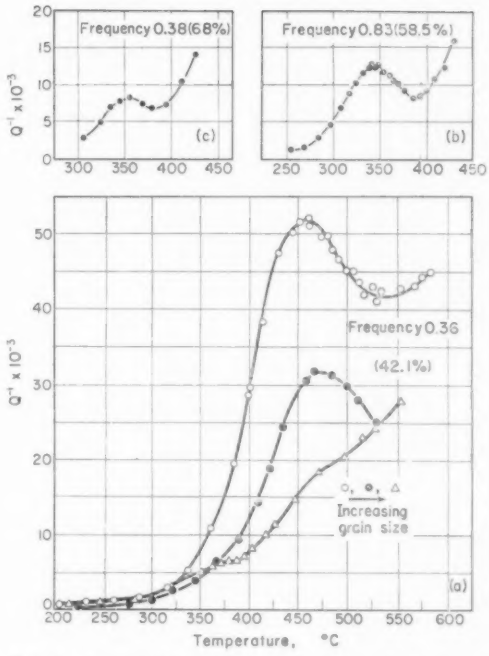


FIG. 1. Internal friction as a function of temperature for a series of silver–gold solid solutions.

In part (a) of Fig. 1 are plotted three torsion pendulum runs for 42 per cent gold in silver. The same specimen was used but the grains were coarsened prior to each run by the strain anneal technique in a vacuum better than 10^{-5} mm of Hg. The peak which occurs at approximately 450°C is due to grain boundary relaxation since as the grains are coarsened this peak is suppressed. With sufficient suppression one can see a peak which appears at approximately 320°C. Parts (b) and (c) of Fig. 1 show the occurrence of this peak in samples of 58.5 and 68 per cent gold, respectively.

Figure 2 is a plot of relaxation time as a function of inverse temperature. Assuming an Arrhenius type equation the slope of this line yields an activation energy of 43.8 kcal/mole.

From the appearance and behavior of the peaks

VOL. 8 1960

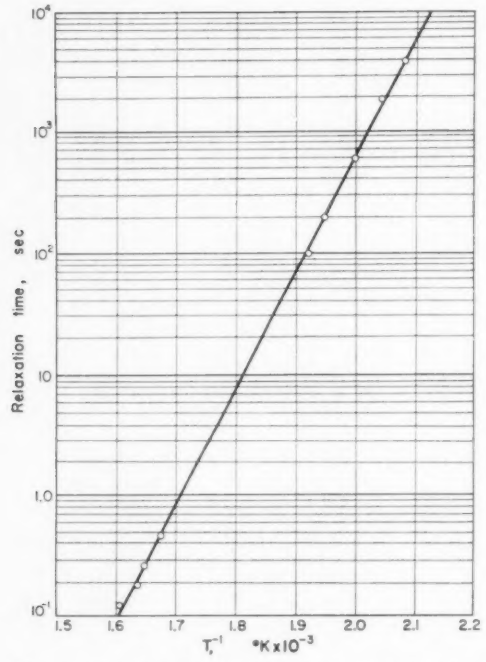


FIG. 2. The time of relaxation for stress induced ordering as a function of inverse temperature for a 58 per cent gold in silver solid solution.

illustrated in Fig. 1 it is concluded that they are Zener peaks attributed to stress induced ordering. It is significant that the peak exists in an alloy whose components differ in atomic size by only 0.01 Å. This is strong evidence that an "effective size" resulting from compressibility difference may be the most important criterion for stress induced ordering.

The theory of LeClaire and Lomer predicts a relaxation strength which is symmetrical in that it makes no distinction between solute and solvent atoms. Consequently they no longer consider the movement of one type of atom alone as being responsible for the relaxation. The peak heights shown in Fig. 5 of Ref. (3) illustrate that the effect is not symmetrical about the 50 per cent concentration. Preliminary data indicated that the effect is a maximum on the gold-rich side.

Hino *et al.*[7] have performed a careful study of internal friction and diffusion in alpha-brass. The overall objective of their work was to see if the internal friction which gives rise to the ordering peak is closely related to diffusion. They found the activation energy for the Zener effect to be less than that for tracer diffusion of copper or zinc into alpha-brass. This result correlates with incomplete relaxation data obtained in this laboratory on AgCd and AgIn. However the activation energy of 43.8 kcal/mole for the Zener effect in the 58 per cent AuAg alloy lies between the values obtained by Mallard *et al*[8]. These are approximately 42 and 44.3 kcal/mole for silver and gold into AuAg, respectively.

A more complete report to be published later will include the results of work now in progress on other concentrations and using much shorter relaxation times obtained with high frequency apparatus.

Department of Physics T. J. TURNER
Wake Forest College G. P. WILLIAMS JR.
Winston-Salem, North Carolina

References

1. J. LULAY and C. WERT, *Acta Met.* **4**, 627 (1956).
2. C. ZENER, *Phys. Rev.* **71**, 34 (1947).
3. A. D. LECLAIRE and W. M. LOMER, *Acta Met.* **2**, 731 (1954).
4. D. P. SERAPHIM and A. S. NOWICK, *Bull. Amer. Phys. Soc.* **2**, 123 (1957); **3**, 122 (1958).
5. B. G. CHILDS and A. D. LECLAIRE, *Acta Met.* **2**, 718 (1954).
6. C. WERT, *Modern Research Techniques in Physical Metallurgy* p. 225. American Society for Metals, Cleveland (1953).
7. J. HINO, C. TOMIZUKA and C. WERT, *Acta Met.* **5**, 41 (1957).
8. W. MALLARD, L. SLIFKIN and R. BASS, private communication.

* This work is supported in part by the U.S. Atomic Energy Commission. Received March 7, 1960.

The orientation of martensite in austenite†

New measurements have been made of the orientation of single martensite plates in an austenite matrix using the back reflection Laue method and an X-ray microbeam technique with pinholes 10–50 μ in diameter.[1] The accuracy of the results, briefly reported here, is considerably greater than can be achieved with the pole figure method or variations of it.[2,3] Also any arbitrarily polished surface of the specimen could be examined thus avoiding laborious and delicate sectioning of the specimen to obtain a pre-selected martensite plate and yet retaining and possibly even surpassing under favorable conditions, the precision attainable by that method.[4] A small number of martensite plates in the specimen is desirable, otherwise the distortion of the retained austenite becomes too great to give Laue photographs suitable for accurate orientation determination.

Figure 1 shows a martensite plate in an Fe–32% Ni alloy cooled to liquid nitrogen temperature. Table 1 gives the angles between certain prominent zones of the austenite and the martensite as measured from the Laue photographs. The habit plane (given in Table 2) and the surface of polish were estimated as being parallel to within better than 3°. In such a case no further

† RIAS (Research Institute for Advanced Study), Baltimore, Md., U.S.A.

TABLE 1. Angles between the $(111)_A$ and $(011)_M$ spots and between prominent zones of the austenite (A) and martensite (M) as determined from Laue photographs (column headed "Observed") and by calculation for the orientation relationship (Table 2) which gives the best fit with the observed angles

	Fe–32% Ni		28 Cr 150	
	Observed ($\pm\frac{1}{2}°$)	Calculated* ($c/a = 1$)	Observed ($\pm 1°$)	Calculated* ($c/a = 1.068$)†
$(111)_A \wedge (011)_M$	1°	0.7°	~1°	1.0°
$[0\bar{1}1]_A \wedge [1\bar{1}1]_M$	6°	5.9°	~7°	7.0°
$[10\bar{1}]_A \wedge [11\bar{1}]_M$	$4\frac{1}{2}°$	4.6°	~3°	2.0°
$[1\bar{1}0]_A \wedge [100]_M$	1°	0.9°	~$2\frac{1}{2}°$	2.5°
$[11\bar{2}]_A \wedge [0\bar{1}1]_M$	—	0.7°	—	2.7°

* For orientation relationship given in Table 2.
† From Ref. (13) for 1.5 per cent C.

TABLE 2. Summary of orientation relationships and habit planes for iron alloys

Present investigation	c/a (or % C)	Orientation relationship		Habit plane
		Axis of rotation*	Angle of rotation	
Fe–32% Ni	1.00 (0% C)	(+) 0.043 (−) 0.007_5 (+) 0.949_5	$45.1° \pm 0.15°$	0.77 0.17 0.61_5
28 Cr 150	~1.068 (~1.5% C)	(+) 0.029 (−) 0.014 (+) 0.957	$44.2° \pm 0.15°$	0.30 0.86 0.41 (see text)
Earlier investigations				
Kurdjumov and Sachs (1930): 1.4% C $(111)_A \| (011)_M$ $[01\bar{1}]_A \| [11\bar{1}]_M$ (approximate)	1.000 (0% C)	(+) 0.031_5 (−) 0.031_5 (+) 0.937	$42.8_5°$	—
	1.045 (1% C)	(+) 0.024_5 (−) 0.023_5 (+) 0.952	43.0°	(252) or (252) (see text)
	1.063 (1.4% C)	(+) 0.022 (−) 0.021 (+) 0.957	43.0°	
	1.090 (2% C)	(+) 0.018 (−) 0.017 (+) 0.965	$43.1_5°$	—
	1.414 ($\sqrt{2}$) (~9.2% C)	0 0 (+) 1	45.0°	—
Nishiyama (1934): Fe–29.90% Ni $(111)_A \| (011)_M$ $[11\bar{2}]_A \| [01\bar{1}]_M$ (approximate)	1.00 (0% C)	(+) 0.040 (−) 0.007 (+) 0.953	46.0°	{295} (see text)
Greninger and Troiano (1941, 1949): 0.8% C, 22% Ni	1.045 (≡1% C)	(+) 0.027 (−) 0.009_5 (+) 0.963_5	$43.9_5°$	0.18_5 0.82 0.54

* Squares of the direction cosines of axis of rotation given. Sign in brackets to be applied after extraction of square root.

VOL. 8 1960

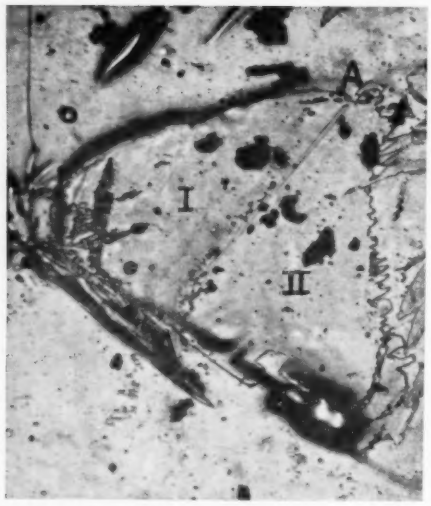


FIG. 1. Martensite plate (untempered) in Fe–32% Ni alloy; electrolytically polished. ×200

information is obtained by exposing a second face at right angles (two-surface analysis) because of practical limitations on the sharpness of the edge that can be retained after polishing and etching. Removing a determined amount from the same surface by re-polishing is more informative.

The experimental error for the normal to the habit plane (Table 2) of the Fe–32% Ni alloy is defined by a cone with semi-angle approximately 1° and with the normal as its axis.

The martensite plate appeared to be divided into two parts, I and II, Fig. 1: the direction AA was found to be nearly parallel to $[7\bar{1}5]_M$* (a few degrees from $[111]_A$), and the orientation of both parts was essentially identical. AA could conceivably be a fine twin in the martensite since $[7\bar{1}5]_M$ lies in $(12\bar{1})_M$ which is a possible twin plane for b.c.c. structures.



FIG. 2. Martensite plate (untempered) in 28 Cr 150 alloy; electrolytically polished. ×400

* The subscripts A and M denote that the indices are referred to the austenite and martensite axes, respectively.

Also listed in Table 1 is the orientation of a martensite plate shown in Fig. 2. The iron alloy in this case contained 2.8 per cent Cr, 1.5 per cent C, and was cooled to −52°C after austenitizing 50 hr at 1200°C.[5] The directions of the martensite plate and of the mid-rib as observed in the surface of polish (Fig. 2) are given in Table 3. The two directions are approximately 5° apart. The value for the direction of the martensite plate was used in applying the phenomenological theories[6] to calculate the habit plane given in Table 2. This habit plane falls within the range of those determined in an earlier investigation[5] of the same alloy.

The Laue photographs were carefully inspected for any evidence that might suggest the presence of twins in the martensite, but none that could be conclusive was found.

The orientation relationships have been worked out in terms of an axis and an angle of rotation, which, when applied to the austenite axes would bring them into coincidence with the martensite axes.[7,8] The axes and angles of rotation are given in Table 2. Since the sum of the squares of the direction cosines is unity, a triangular co-ordinate net can be used to plot quite rapidly the axes of rotation. In Fig. 3 the axes of rotation have been plotted into one stereographic triangle to indicate clearly the amount by which the new observations differ from earlier ones.[2,3,4] (Note that the unit stereographic triangle has, in such a plot, straight lines for all three of its sides.) The inhomogeneous distortion has also been calculated for the present data, using the current phenomenological theories.[6] Table 4 gives the results and compares them with similar calculations for data gathered from the literature (orientation relationships,[2–4] habit planes,[4,9] lattice parameters[10–13]). In all cases, except one, $[111]_M$ is a shear direction. This is consistent with the concept[14] that the shear elements of the inhomogeneous distortion in the formation of martensite correspond to those characteristic of slip or twinning in b.c.c. metals.

TABLE 3. Directions of the martensite plate and of the mid-rib for alloy 28 Cr 150, in the plane of polish, Fig. 2

	As measured on stereographic net with respect to austenite axes	After normalizing
Direction of martensite plate in surface of polish (Fig. 2)	$-60.8° \pm 0.3°$ $-76.5 \pm 0.3°$ $32.5 \pm 0.3°$	-0.48_7 -0.23_3 0.84_2
Direction of mid-rib in surface of polish (Fig. 2)	$-63.5° \pm 0.3°$ $-72.1 \pm 0.3°$ $32.8 \pm 0.3°$	-0.44_6 -0.30_7 0.84_0

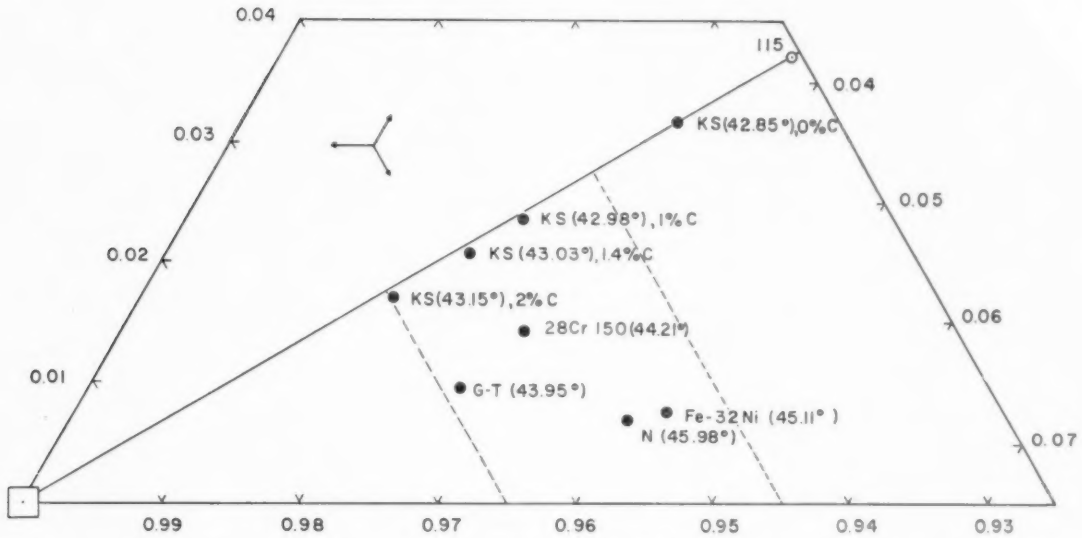


FIG. 3. Various orientation relationships plotted in terms of the axis and angle of rotation. Values in brackets represent angular rotation about the relevant axis to bring the austenite axes into coincidence with martensite axes. The axis $\hat{n} = [n_1 n_2 n_3]$ is plotted on a triangular co-ordinate net in terms of $n_1^2 n_2^2 n_3^2$.

TABLE 4. Theoretically calculated slip systems (assuming $\delta = 1$) of the inhomogeneous deformation in the formation of martensite for the known orientation relationships and habit planes listed in Table 2

Present investigation	(Possible variants of) habit plane for variant of orientation relationship given in Table 2	Slip system (with respect to austenite axes)		Slip system (with respect to martensite axes)
		Shear plane	Shear direction	
Fe–32% Ni $c/a = 1.00$, $V = 1.0136$	0.77 5 0.17 1° from 1 0.61_5 4	-0.08 0 0.73 5° from 1 0.67 1	0.07 0 -0.67 5° from $\bar{1}$ 0.74 1	$(\bar{1}12)[1\bar{1}1]$
28 Cr 150 $c/a = 1.068$, $V = 1.0383$	0.30 2 0.86 4½° from 5 0.41 2	0.30 1 -0.92_5 4½° from 3 0.23 1	-0.69_5 $\bar{1}$ -0.03 2° from 0 0.72 1	$(2\bar{1}1)[\bar{1}\bar{1}1]$
Data from the literature				
Kurdjumov and Sachs $c/a = 1.063$ (1.4% C), $V = 1.04$	0.34 2 0.87 1° from 2 0.36 5	0.49 1 0.69 9° from 1 0.53 1	-0.70 $\bar{1}$ -0.05 3° from 0 0.71_5 1	$(01\bar{1})[\bar{1}\bar{1}1]$
	0.32 2 0.87 2° from 5 0.37_5 2	0.51_5 1 0.65 5½° from 1 0.56 1	-0.36_5 $\bar{1}$ -0.42_5 2½° from $\bar{1}$ 0.83 2	$(01\bar{1})[0\bar{1}1]$
Nishiyama $c/a = 1.00$, $V = 1.028$ ($V = 1.04$ actually used)	-0.20 2 0.84_5 1½° from 9 0.49_5 5	0.79_5 1 -0.01 8° from 0 0.60_5 1	-0.60 $\bar{1}$ -0.10_5 10° from 0 0.79 1	$(\bar{1}12)[1\bar{1}1]$
	0.84_5 9 -0.20 1½° from 2 0.49_5 5	-0.01 0 0.79_5 8° from 1 0.60_5 1	-0.10_5 0 -0.60 10° from $\bar{1}$ 0.79 1	$(\bar{1}12)[1\bar{1}1]$
Greninger and Troiano $c/a = 1.045$, $V = 1.0384$	0.18_5 2 0.82 4° from 9 0.54 5	0.71 1 -0.05_5 3° from 0 0.70 1	-0.70_5 $\bar{1}$ -0.02 1½° from 0 0.71 1	$(\bar{1}12)[\bar{1}\bar{1}1]$

VOL. 8 1960

This was done employing one or more of the following methods: (1) Stereographic manipulation combined with matrix algebra; (2) Vector algebra using the stereographic projection and Rodrigue's formula;[7] (3) Mackenzie's method.[8]

If the condition $\delta = 1$ is relaxed, the analysis to determine the elements of the inhomogeneous distortion can be carried through without knowing the lattice parameter ratios. The resulting values are however too sensitive to the number in the third decimal place of the input data, and are therefore not included here.

Numerous valuable comments by Dr. M. S. Wechsler are gratefully acknowledged.

H. M. Otte

Research Institute for Advanced Study
Baltimore, Maryland, U.S.A.

References

1. H. M. Otte and R. W. Cahn, *J. Sci. Instrum.* **36,** 463 (1959).
2. G. Kurdjumov and G. Sachs, *Z. Phys.* **64,** 325 (1930).
3. Z. Nishiyama, *Sci. Rep. Tohoku Univ.* **23,** 637 (1934).
4. A. B. Greninger and A. R. Troiano, *Trans. Amer. Inst. Min. (Metall.) Engrs.* **145,** 289 (1941); **185,** 590 (1949).
5. H. M. Otte and T. A. Read, *Trans. Amer. Inst. Min. (Metall.) Engrs.* **209,** 412 (1957).
6. B. A. Bilby and J. W. Christian, *The Mechanism of Phase Transformations in Metals*, p. 121. The Institute of Metals, London (1956).
7. H. M. Otte, *Acta Cryst., Camb.* (in press).
8. J. K. MacKenzie, *Acta Cryst., Camb.* **10,** 61 (1957).
9. A. B. Greninger and A. R. Troiano, *Trans. Amer. Inst. Min. (Metall.) Engrs.* **140,** 307 (1940).
10. E. R. Jette and F. Foote, *Trans. Amer. Inst. Min. (Metall.) Engrs.* **120,** (1936) (Technical Publication 670, Jan. 1956).
11. A. J. Bradley, A. H. Jay and A. Taylor, *Phil. Mag.* **23,** 545 (1937).
12. E. A. Owen and A. H. Sully, *Phil. Mag.* **31,** 314 (1941).
13. C. S. Roberts, *Trans. Amer. Inst. Min. (Metall.) Engrs.* **197,** 203 (1953).
14. H. M. Otte, *Trans. Amer. Inst. Min. (Metall.) Engrs.* **218,** 342 (1960).

Received August 18, 1959; revised March 14, 1960.

Effect of zone-refining and orientation on the hardness of high purity rhenium*

A single crystal of rhenium (close packed hexagonal, $c/a = 1.615$) 0.23 cm dia. × 15 cm long was grown from sintered round bar using the electron bombardment floating zone technique. The single crystal occupied the central portion of the 25 cm long bar, with a recrystallized matrix adjacent to the first and last zones to freeze. The orientation, and longitudinal and circumferential Knoop hardness were determined after two, four and six zone passes along the original 15-cm long single crystal.

From Fig. 1, it is seen that crystals grow with the basal plane approximately parallel to the rod axis.

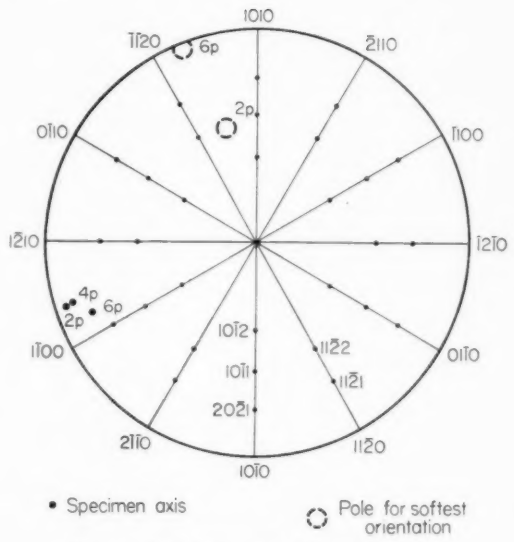


FIG. 1. Orientation of rhenium crystals.

Circumferential hardness, taken at the mid-point of the crystal, is plotted in Fig. 2. With the orientation given in Fig. 1, these curves give the hardness variation for planes with a common [1$\bar{1}$00] zone axis.

The material is extremely anisotropic, with a variation in Knoop hardness from ~250 down to ~50 (5:1) and has a minimum in hardness for impressions made on planes making angles of $> \sim 60°$ with the basal plane (Fig. 2). Similar measurements for zinc give an anisotropy factor of only 3:1 i.e. from 18 Knoop up to ~60 Knoop hardness, with a minimum in hardness on the basal plane. This is consistent with the c/a ratios of 1.615 for rhenium and 1.856 for zinc since for $c/a < 1.633$ compression parallel to the basal plane leads to twinning with a shortening of the axis of compression. For zinc, compression perpendicular to (0001) leads to twinning and shortening of the compression axis.

Longitudinal hardness for the softest and hardest

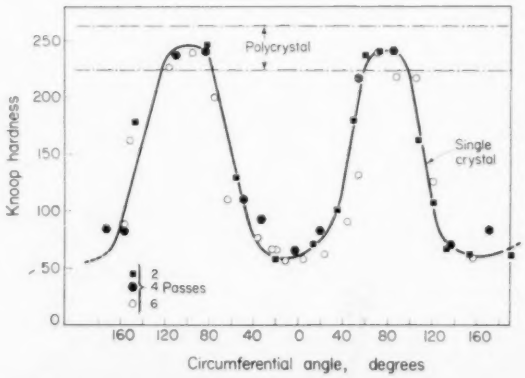


FIG. 2. Circumferential hardness variation for rhenium single crystals.

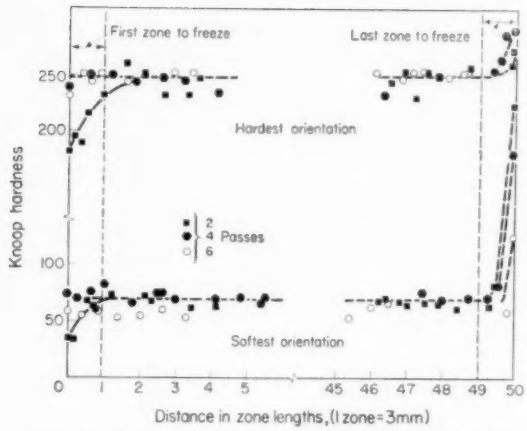


FIG. 3. Longitudinal hardness as a function of zone passes.

orientations, after two, four and six zone passes, is plotted in Fig. 3. For two zone passes (the zone length is 3 mm) the Knoop hardness of material in the first zone to freeze rises from 34 up to ~68 Knoop and from 180 up to ~240 Knoop for the soft and hard orientations, respectively. After four and six zone passes, hardness is constant along the crystal except in the last zone to freeze where the material is considerably harder.

The shape of the hardness curves for two passes indicates that purification by zone refining is occurring, after which the ultimate hardness appears to be relatively unaffected by further zoning. Hardness of recrystallized material adjacent to the end zones is in the range 220–265 Knoop depending upon grain size. This Knoop figure, identical to that at the maxima of the cyclic curves in Fig. 2 again indicates that the zoning reduces the impurity content; otherwise, the polycrystalline hardness figure would be expected to lie near to the average for the anisotropic single crystal. There is certainly a reduction in gas content during electron beam zone refining.

Back reflection Laue spots from the impure last zone gave no evidence of lineage substructure. For a refractory close packed hexagonal material of melting point 3167°C, the extremely low Knoop figure of 50 in the softest orientation indicates low resistance to dislocation movement on the close packed planes.

This work is part of a programme sponsored by the Office of Naval Research on contract NONR 551 (19). The rhenium used was loaned by the Chase Brass and Copper Co., Waterbury, Connecticut.

A. LAWLEY
R. MADDIN

School of Metallurgical Engineering
University of Pennsylvania
Philadelphia, Pa.

* Received March 14, 1960.

VOL. 8 1960

Entstehung und Orientierung von Wolfram-Whiskern*

Wie Cech[1] an Nickel zeigen konnte, ist die Bildung von Whiskern durch Reduktion der Oxydphase möglich. Während er aber von der von Brenner[2] beschriebenen Reduktion von Halogeniden ausging, soll im folgenden ein Verfahren beschrieben werden, bei dem Wolfram-Whisker nur durch Reduktion des Oxyds erzeugt wurden.

Die Whisker entstehen, wenn 0,2 mm starke Drähte aus handelsüblichem "Nonsag-Wolfram" in feuchtem Wasserstoff im direkten Stromdurchgang auf Temperaturen über 2800°C erhitzt werden. Dabei kommt es zu einer Verdampfung des flüchtigen Wolframoxyds. Glühungen in getrocknetem Wasserstoff führten nicht zu Whiskerbildung.

Während der Glühung wachsen am Draht viele kleine, aber auch einzelne längere Whisker auf, wie es Abb. 1 zeigt. Sie sind bis zu 1 mm lang und einige μ dick. Von einer punktförmigen Aufwachsstelle am Draht verdicken sie sich kegelförmig und sind an der Spitze von deutlich erkennbaren Kristallflächen begrenzt. Abgesehen von dem hierdurch gebildeten Kubus haben die Whisker kreisförmigen oder polygonalen Querschnitt. Die Seiten erscheinen durch stufenförmig hervortretende Kristallflächen häufig schuppig.

Entgegen den bisher bei den meisten Whiskern gefundenen, niedrig indizierten Wachstumsrichtungen,[3] haben die Wolfram-Whisker höher indizierte Richtungen als Längsachse. Drehkristall-Aufnahmen zeigten, daß die Orientierung der Whiskerachse innerhalb einer Fehlergrenze von $\pm 4°$ mit der Längsachse (Drahtachse) des Aufwachskristalles übereinstimmt. In Abb. 2 sind die Orientierungen von 20 Whiskern und den zugehörigen sehr großen, bei der Sekundär-Rekristallisation entstandenen Drahtkristallen, an denen sie aufwuchsen, dargestellt.

Die Bildung der Whisker wird durch die beim Glühen stattfindende Rekristallisation weder herbeigeführt noch beeinflußt, da auch an bereits sekundär rekristallisierten Drähten Whisker mit derselben Orientierungsbeziehung aufwuchsen.

Laue-Aufnahmen der Mutterkristalle zusammen



ABB. 1. Wolframdraht mit aufgewachsenen Whiskern. ×14

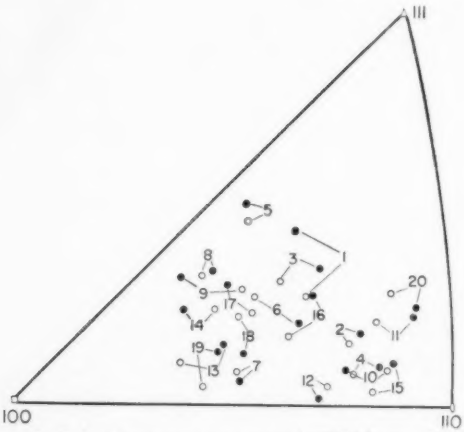


ABB. 2. Orientierungen von zwanzig Whiskern. Whiskerachse (●), Drahtachse des Aufwachskristalls (○).

mit den aufgewachsenen Whiskern zeigten in vierundzwanzig von fünfundzwanzig Fällen eine Übereinstimmung eines {110}-Flächenpoles vom Whisker mit einem {110}-Flächenpol vom Drahtkristall. Whisker und Draht hatten also eine gemeinsame ⟨110⟩-Richtung und somit eine {110}-Fläche parallel zueinander. In dem einen Ausnahmefall lag eine {100}-Fläche des Whiskers einer {110}-Fläche im Drahtkristall parallel. Bei sieben der untersuchten fünfundzwanzig Whisker stimmte die Orientierung völlig mit der des Drahtkristalles überein, d.h. der Whisker war eine Fortsetzung des Mutterkristallgitters. In den anderen Fällen war der Whiskerkristall gegen den Drahtkristall um die gemeinsame ⟨110⟩-Richtung gedreht. Abgesehen von der {211} ⟨111⟩-Zwillingslage, die in drei Fällen gefunden wurde, ließen die Verdrehwinkel keine bevorzugte Lage erkennen.

Offensichtlich erfolgt der Aufwachsvorgang über die gemeinsame {110}-Fläche, also die dichtest belegte Netzebene. Bemerkenswert ist, daß die Indizes der Längsachse des Whiskers durch die des Drahtkristalls bestimmt sind, nicht jedoch durch eine niedrig indizierte eigene Wachstumsrichtung.

Rieck[4] nimmt als Ursache der höher indizierten Faserachse sekundär rekristallisierter Wolfram-Drahtkristalle eine orientierte Keimbildung im Zusammenhang mit der vorhergegangenen Verformung an. Bei der Bildung der Whisker handelt es sich um einen reinen Wachstumsvorgang. Es ist daher zu vermuten, daß auch das Kornwachstum bei der sekundären Rekristallisation des gedopten Wolframs einen Wachstumsvorgang darstellt, der nicht mehr in ursächlichem Zusammenhang mit der vorherigen Verformung steht. Die Versuche werden fortgesetzt.

Institut für Metallkunde H. AHLBORN
Bergakademie Clausthal G. WASSERMANN

Literatur

1. R. E. CECH, *Acta Met.* **7**, 787 (1959).
2. S. S. BRENNER, *Acta Met.* **4**, 62 (1956).
3. F. R. N. NABARRO und P. J. JACKSON in *Growth and Perfection of Crystals* (hrsg. von R. H. DOREMUS, B. W. ROBERTS und D. TURNBULL) S. 13. Wiley, New York (1958).
4. G. D. RIECK, *Acta Met.* **6**, 360 (1958).

* Eingegangen 24 Mai, 1960.

Growth substructures in weld metal*

Recent investigations have revealed the presence of growth substructures in both mild and stainless steel weld pools, after melting and rapid cooling, using an argon tungsten arc spot welding torch. Following the original work on solidification substructures by Rutter and Chalmers[1], Winegard and Chalmers[2] used the concept of constitutional supercooling to explain the solidification of castings. Since then a number of investigators have described the formation of substructures in low melting point alloys solidified under controlled laboratory conditions; but to the authors' knowledge ranges of substructures of a similar type have not previously been reported in welds. Previous work and present theoretical ideas on the formation of substructures have recently been reviewed by Elbaum[3]. The formation of substructures in systems with a positive liquid temperature gradient results from the build-up of a concentration of solute in the liquid ahead of the solid–liquid interface. The distribution of the solute in this region after steady state conditions are attained is given by:

$$C_L = C_0\left[1 + \frac{1-k}{k}\exp\left(-\frac{R}{D}x\right)\right]$$

where

C_L = concentration of solute in the liquid at a distance x from the solid–liquid interface
C_0 = initial concentration of solute in liquid
k = equilibrium partition coefficient of solute between solid and liquid
R = rate of advance of interface
D = diffusibility of solute in the liquid.

A typical curve of C_L against x is shown in Fig. 1(a) and the corresponding liquidus temperatures are shown in Fig. 1(b). If the real temperature gradient is now superimposed upon this latter curve, e.g. a line $0G$, it is clear that if the gradient is less than that of $0G'$ (the tangent to the curve) constitutional supercooling will occur. The type of substructure developed will depend upon the degree of this constitutional supercooling. During welding a very high

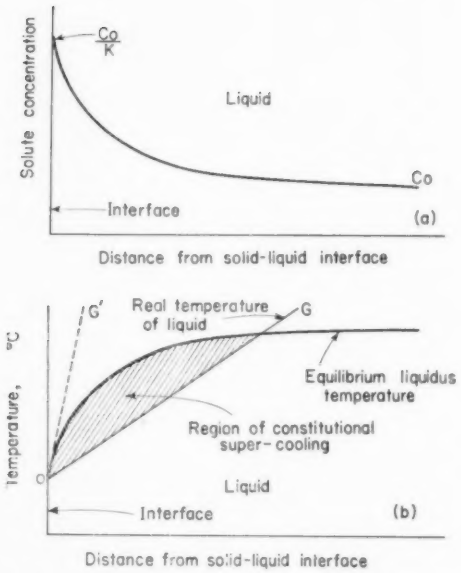


FIG. 1. (a) Variation of solute concentration in the liquid, with increasing distance from the solid–liquid interface. (b) Equilibrium liquidus temperature curve, corresponding to the variation of solute concentration ahead of the solid–liquid interface shown in Fig. 1(a). The actual temperature gradient existing in the liquid has been superimposed.

temperature gradient exists initially in the liquid of a weld pool, but the gradient will decrease progressively during solidification. Thus one might expect a range of solidification structures between the edge and centre of the weld pool.

Figure 2 shows the surface of a weld pool in a low carbon steel. Cell or corrugation structures have developed along the direction of solidification. These growth structures were formed in the original delta ferrite and are independent of the subsequent phase changes.



FIG. 2. Surface corrugations on the surface of a weld pool in a low carbon steel, due to cellular growth substructures developed during solidification.
×87.5

The grain boundaries and varying contrast on the surface have been revealed by the thermal etching and slight oxidation taking place during cooling in impure argon. The cell diameter appears to vary between 3 and 10 μ whilst the diameters of individual cells in any one group are approximately constant and do not vary significantly along their length. Measurements have also been made on the cell structures revealed after grinding off the surface to a depth of about 250 μ, polishing and heavily etching. The cells were revealed less distinctly but were not significantly different in appearance from those on the original surface. Fig. 3 shows a region where a group of cells have grown in a direction normal to the surface, revealing their essentially hexagonal shape.

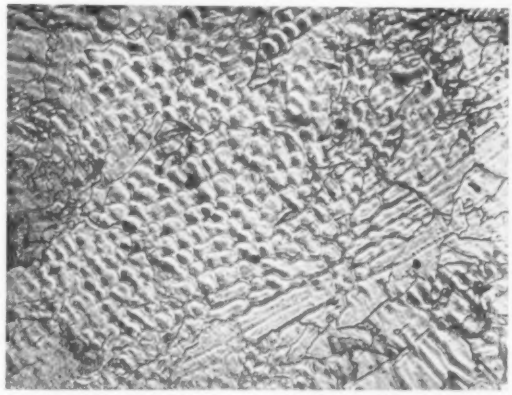


FIG. 3. Same specimen as in Fig. 2, ground, repolished and heavily etched. Shows cells growing normally to the surface near the centre of the molten pool.
×210

Stainless steel is of course more heavily alloyed than mild steel and consequently the degree of constitutional supercooling is greater. Thus the cells rapidly begin to assume a dendritic form as the centre of the weld is approached. Fig. 4 shows a region transitional from cells to columnar dendrites. The transition is orientation dependent so that neighbouring grains do not necessarily show the transition simultaneously even though they previously experienced similar thermal histories. Nearer the centre of the pool where the thermal gradient in the liquid was smaller, there was a further transition from columnar dendrites to dendrites of various orientations nucleated ahead of the advancing interface. It is thus possible to rationalise the formation of substructures in welds in terms of constitutional supercooling as had previously been done for castings.[2] Further work is in progress to try to control the formation of growth structures by varying the welding conditions. In

VOL. 8 1960

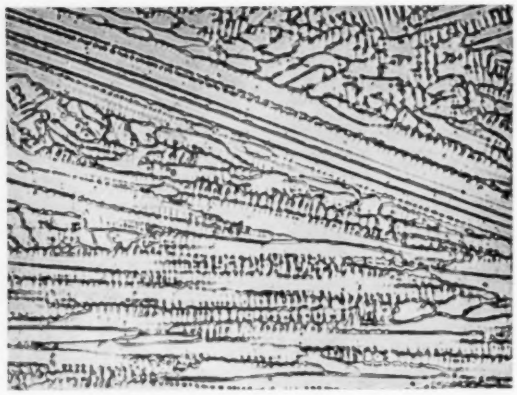


FIG. 4. Substructures produced in austenitic 18 Cr–12 Ni–Nb steel weld metal, showing a region of transition from cell to columnar dendritic structure. ×280

such a way it might be possible to control the mechanical properties of weld metal more precisely.

The authors are grateful to Professor W. C. Winegard for helpful discussions and advice and to Mr. G. Regelous for his assistance with the experimental work. They are also grateful to Dr. R. Weck for his interest and encouragement.

F. A. C. CALVO
British Welding Research Association K. P. BENTLEY
Abington Hall, Cambridge, England R. G. BAKER

References

1. J. W. RUTTER and B. CHALMERS, *Canad. J. Phys.* **31,** 15 (1953).
2. W. C. WINEGARD and B. CHALMERS, *Trans. Amer. Soc. Metals* **46,** 1214 (1954).
3. C. ELBAUM, *Progr. Met. Phys.* **8,** 203 (1959).

* Received June 6, 1960.

Twinning in vanadium*

Recent studies have shown that niobium[1] and tantalum[2,3] deform by formation of mechanical twins with relative ease. Both metals were reported to form twins under impact loading even at room temperature if the purity was high. On the other hand, data reported by Clough and Pavlovic[4] show commercially pure vandium to form deformation twins only for impact loading below −78°C and only within one or two grains of a cleaved surface.

At this laboratory, twins have been observed in electron-beam melted vanadium after deformation by slow compression at liquid nitrogen temperature. Single crystals were cut from an ingot having the following interstitials content: 0.033 per cent C, 0.0047 per cent O_2, 0.0005 per cent N_2, and 0.0012 per cent H_2. The oxygen and nitrogen contents of this material were an order of magnitude lower than in that studied by Clough and Pavlovic[4] while the carbon and hydrogen contents were only slightly lower.

The twins were quite similar in appearance to those found in the other body-centered cubic metals—thin with serrated boundaries. A two-surface analysis of the twin traces established the twin plane as {112}, as expected.

Thus, it appears that all of the Group Va body-centered cubic metals twin with relative ease below room temperature if they are very pure and have a large grain size.

C. J. MCHARGUE
Metallurgy Division
Oak Ridge National Laboratory†
Oak Ridge, Tennessee

References

1. C. J. MCHARGUE, to be published.
2. C. S. BARRETT and R. BAKISH, *Trans. Amer. Inst. Min. (Metall.) Engrs.* **212,** 122 (1958).
3. R. W. ANDERSON and S. E. BRONISZ, *Acta Met.* **7,** 645 (1959).
4. W. R. CLOUGH and A. S. PAVLOVIC, *Trans. Amer. Soc. Metals* **52,** 948 (1960).

* Received June 27, 1960.
† Operated for the U.S. Atomic Energy Commission by Union Carbide Corporation.

The use of lattice spacings data to evaluate the effective valency of transition metals in Ag-based h.c.p. phases*

Studies of certain ternary h.c.p. phases based on copper and silver have shown that the axial ratio is affected very little in a ternary system if one solute is substituted for another along a line of constant electron-to-atom ratio.[1,2] On the basis of this observation it has been suggested by one of the present authors (T. B. M.)[3] that lattice spacing measurements could be employed to study the electronic contributions to the binary copper- or silver-based h.c.p. phases caused by the addition of second solute elements, the valency of which is not certain. This suggestion is of some interest since it provides a new approach to the study of the effective valencies and also possible changes of valency of the transition elements when dissolved in alloys based on noble metals.

It is an implicit assumption of this method that all the plots of axial ratio versus electron-to-atom ratio

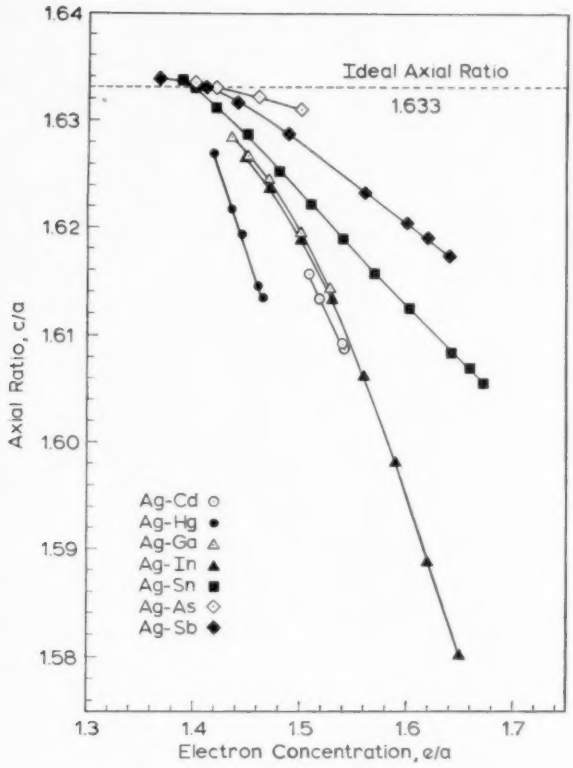


FIG. 1. Variation of axial ratio as a function of electron concentration for silver-based h.c.p. phases.

for binary alloys based on copper or silver should very nearly superimpose to give a master curve. However, a recent study[4] of several binary h.c.p. phases based on silver has shown that the assumption of a master curve is valid only in a limited range of electron concentration near 1.4, where the plots converge towards a value near the ideal axial ratio as shown in Fig. 1. At higher values of electron concentration the rate of change of axial ratio varies with differing solutes, and hence variable valencies of an additional solute would be obtained depending on which binary plot is selected as the master curve. For example, the valency of indium when referred to silver–tin as a standard (Ag valency = 1, Sn valency = 4) would vary from 3.08 to 3.39 for the alloys shown in Fig. 1. Conversely, using silver–indium as a standard (In valency = 3), the calculated value for tin would vary from 3.9 to 3.5. Similar apparent changes of valency may be obtained also for other combinations of solute elements. Thus, the application of a method relating valency to axial ratio in silver-based alloys may prove fruitful only for the case of alloys which possess nearly ideal axial ratios as indicated in Fig. 1. The use of a similar approach at values of axial ratio for which the plots do not superimpose will lead to estimated valencies, or to apparent changes in valency, the meaning of which may be uncertain.

T. B. MASSALSKI
H. W. KING
Mellon Institute
Pittsburgh 13, *Pennsylvania*

References

1. G. V. RAYNOR and T. B. MASSALSKI, *Acta Met.* **3**, 480 (1955).
2. T. B. MASSALSKI, *J. Inst. Metals* **88**, 232 (1960).
3. T. B. MASSALSKI, *Metallurg. Rev.* **3**, 45 (1958).
4. H. W. KING and T. B. MASSALSKI, to be published.

* Received June 27, 1960.

Electron microscopic investigation of the phase transformation of thin cobalt samples*

Cobalt in bulk form shows at 417°C[1] a reversible phase transformation from the hexagonal to the face-centred cubic form. This transformation has been observed directly in the electron microscope by heating and cooling recrystallized and electrolytically thinned cobalt samples (some 1500 Å thick) in a special sample holder.[2] The following results have been obtained:

(a) At room temperature in the hexagonal form the samples are covered extensively with stacking faults, as can be seen in Figs. 1 and 2. Total dislocations, also present in the lattice, are evident as black lines.

(b) On heating the stacking faults start to disappear at about 450°C with formation of total dislocations by the coalescence of the partials. This is demonstrated by comparing Fig. 2 with Fig. 3. Further heating to 800°C almost completely eliminates stacking faults from the samples. Some total dislocations remain, but most have moved and are pinned on grain boundaries or other obstacles.

(c) On cooling (cooling rate: around 30°C/min) from above the transformation temperature, the total dislocations start to split individually between 200°C and room temperature with formation of long stacking faults. This is demonstrated by comparing Fig. 4 with Figs. 2 and 3. During this period some stacking faults can be moved to and fro by displacing the electron beam from the sample. This can be due either to small stresses, produced by the local variation of heat flux in the sample, or to the change of the magnetic field, produced by the traversing electron beam. Some total dislocations still remain at room temperature, as can also be seen from Fig. 4.

VOL. 8 1960

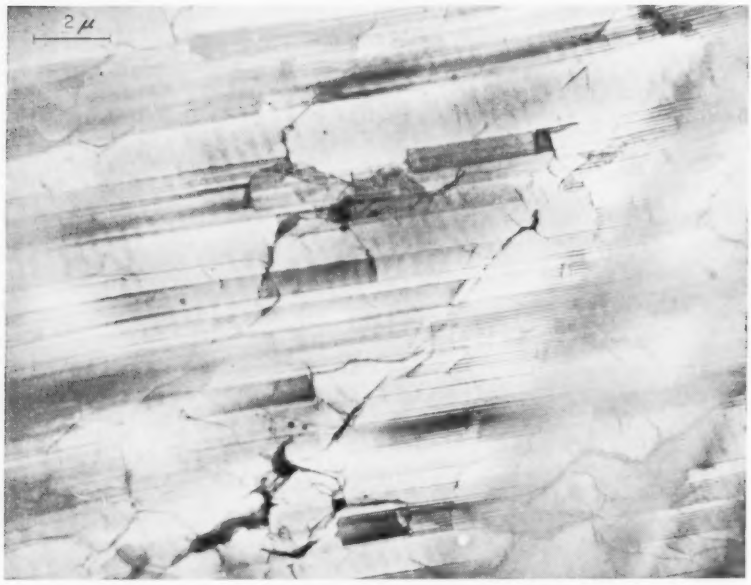


FIG. 1. Aspect of cobalt at room temperature after thinning. One observes many stacking faults and also total dislocations, which are evident as black lines.

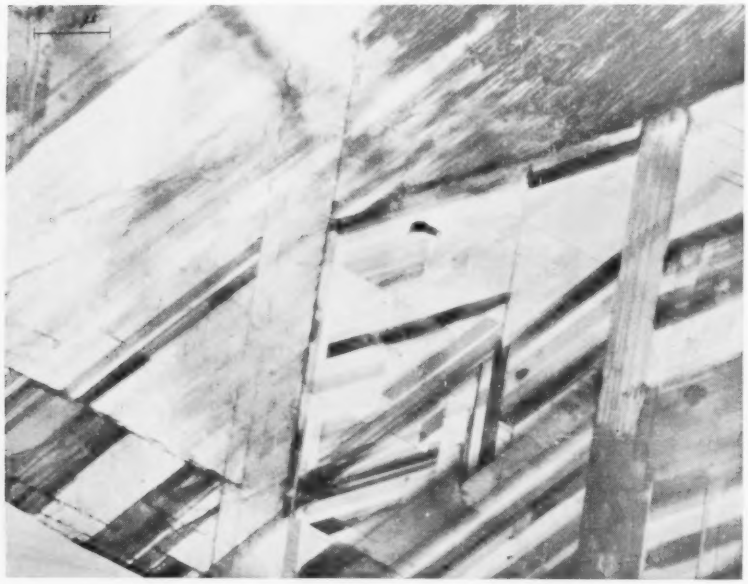


FIG. 2. Recrystallized cobalt after thinning.

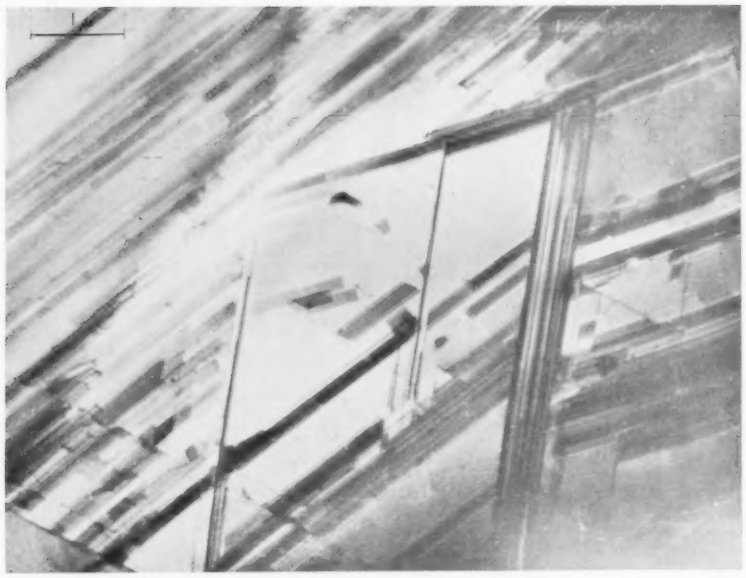


FIG. 3. Same field as Fig. 2, but heated to 470°C and photographed at this temperature. As compared with Fig. 2 it shows that many stacking faults have disappeared, thus transforming the hexagonal into the f.c.c. lattice.

VOL.
8
1960

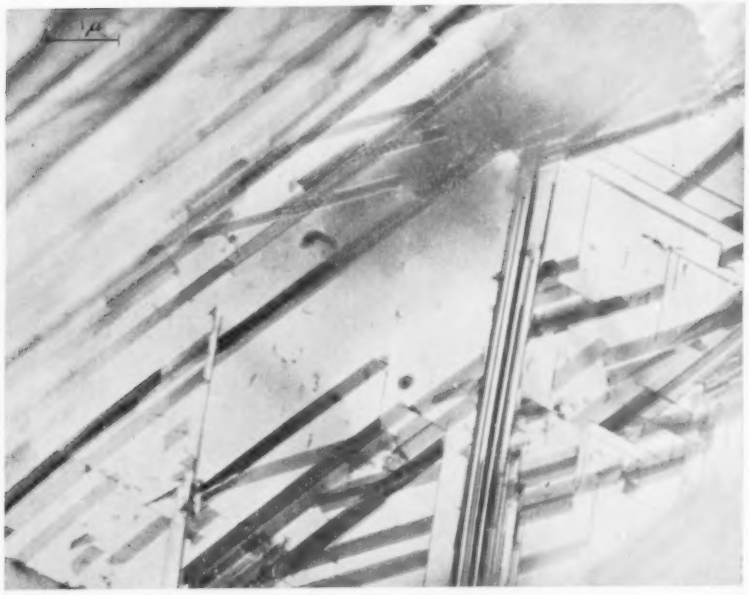


FIG. 4. Same field as Figs. 2 and 3, but further heated to 550°C and then cooled down to room temperature. The total dislocations have split into long stacking faults, some remaining unchanged. Compared with Fig. 2 the number of stacking faults has decreased considerably after the heating cycle.

These results show clearly that the phase transformation of cobalt proceeds by the help of partial dislocations, but it shows also that the properties of thin cobalt samples of some 1500 Å thickness are somewhat different from that of the bulk material. This is demonstrated in the first place by the extensive supercooling as shown by the lowering of the transformation temperature. Secondly, a comparison of the quantity of stacking faults present in Figs. 2 and 4 shows that the number has been greatly diminished after one heating cycle. Because the stacking faults are responsible for the phase transformation f.c.c. → hexagonal on cooling, this means that in thin foils the f.c.c. structure can be preserved in much greater quantity than in a bulk material. This has also been confirmed by electron diffraction work, carried out by Dr. N. Terao of our laboratory.

These differences can be interpreted by assuming that the dislocation nodes of two partials and one pole dislocation, proposed by Bilby[3] and Seeger[4] for the phase transformation of cobalt, are drastically hampered from development by the thinness of the foil. After thinning most of the stacking faults no longer have common pole dislocations and on heating disappear mostly as total dislocations on grain boundaries and other obstacles, where they are pinned. The few remaining total dislocations in the matrix will split up on cooling, but at a much lower temperature because they are pinned on both surfaces of the sample. This also explains why the f.c.c. structure is preserved after one heating cycle.

It is planned to publish these results in greater detail elsewhere. This work is part of a research program, sponsored by Union Carbide Corporation, New York, N.Y., for whose assistance the author is grateful.

E. Votava

European Research Association, s.a.
Bruxelles 18, *Belgium*

References

1. J. B. Hess and C. S. Barrett, *J. Metals N.Y.* **4,** 645 (1952).
2. A. Berghezan and A. Fourdeux, *C.R. Acad. Sci., Paris* **274,** 1194 (1958); *4th Int. Conf. on Electron Microscopy, Berlin* **1,** 567 (1958).
3. B. A. Bilby, *Phil. Mag.* **44,** 782 (1953).
4. A. Seeger, *Z. Metallk.* **44,** 247 (1953); *Z. Metallk.* **47,** 653 (1956).

* Received June 24, 1960.

VOL.
8
1960

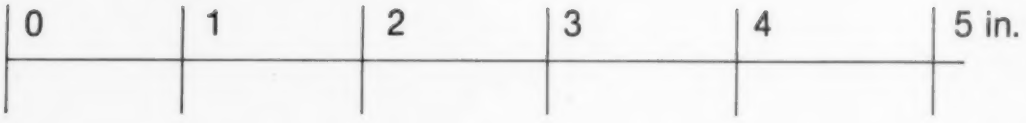
Vol. 9
1961

PERGAMON PRESS INC.



MICROFORMS INTERNATIONAL
MARKETING CORPORATION
FAIRVIEW PARK, ELMSFORD, NEW YORK 10523





PRODUCED AT

MIMC MICROFORMS LABORATORY
ELMSFORD, NEW YORK